CODEN: JASMAN

The Journal of the Acoustical Society of America

ISSN: 0001-4966

Vol. 121, No. 6 June 2007

(Continued)

CONTENTS—*Continued from preceding page*

(Continued)

CONTENTS—*Continued from preceding page*

(Continued)

CONTENTS—*Continued from preceding page*

Talker intelligibility differences in cochlear implant listeners

Tim Green, Sotira Katiri, Andrew Faulkner, and Stuart Rosen
Department of Phonetics and Linguistics, University College London, 4 Stephenson Way, London NW1 2HE, United Kingdom
tim@phon.ucl.ac.uk, katiri@gmail.com, andy@phon.ucl.ac.uk, stuart@phon.ucl.ac.uk

Abstract: People vary in the intelligibility of their speech. This study investigated whether across-talker intelligibility differences observed in normally-hearing listeners are also found in cochlear implant (CI) users. Speech perception for male, female, and child pairs of talkers differing in intelligibility was assessed with actual and simulated CI processing and in normal hearing. While overall speech recognition was, as expected, poorer for CI users, differences in intelligibility across talkers were consistent across all listener groups. This suggests that the primary determinants of intelligibility differences are preserved in the CI-processed signal, though no single critical acoustic property could be identified.

© 2007 Acoustical Society of America
PACS numbers: 43.66.Ts, 43.71.Gv [QJF]
Date Received: October 9, 2006 **Date Accepted:** March 8, 2007

1. Introduction

While it is well established that individual talkers can make their speech more intelligible by using a "clear" rather than a "conversational" speaking style (e.g., Ferguson and Kewley-Port, 2002; Krause and Braida, 2002, 2004; Picheny *et al.*, 1985, 1986; Uchanski *et al.*, 1996), comparatively little research has investigated the acoustic-phonetic properties related to differences in intelligibility *across* talkers. Initial studies with relatively few talkers implicated factors such as word and vowel duration, size of vowel space, and fundamental frequency (F0) range (Bond and Moore, 1994; Bradlow *et al.*, 1996). Hazan and Markham (2004) conducted a more extensive study using single word materials from 45 talkers. Two measures, the total energy in the 1–3 kHz region, and word duration, together accounted for about half the variability in intelligibility. Interestingly, profiles of individual high and low intelligibility talkers revealed considerable differences in the patterning of various acoustic-phonetic measures for talkers of similar intelligibility. Thus, it appears that while, at least for normally-hearing listeners, talker intelligibility is very consistent across listeners, high intelligibility can result from various combinations of characteristics.

A further important issue concerns the extent to which intelligibility will be similarly affected across different listening populations. As might be expected, hearing-impaired listeners benefit from talkers using a clear, as opposed to a conversational, speaking style (e.g., Payton *et al.*, 1994; Picheny *et al.*, 1985; Uchanski *et al.*, 1996). Cochlear implant (CI) users might also be expected to benefit from clear speech. However, while modern CI systems typically allow good speech perception, at least in quiet, the auditory information provided by an implant differs markedly from that available in normal hearing. For example, CI processing provides only weak cues to F0 (Green *et al.*, 2002, 2004); allows very limited spectral resolution (Friesen *et al.*, 2001); and typically involves distortion of normal frequency-place mappings (Faulkner *et al.*, 2006; Shannon *et al.*, 1998). These differences raise the possibility that factors that have been suggested to contribute to intelligibility differences for normally-hearing listeners, such as F0 range and the size of the vowel space, may not operate in the same way for CI listeners.

Despite this Liu *et al.*, (2004) found that the advantage for clear over conversational speech produced by a single female talker was similar for normally-hearing listeners, CI users, and normally-hearing listeners presented with acoustic simulations of implant processing.

Since implant processing eliminates much spectral detail and temporal fine structure, this suggests that the primary cues contributing to the clear speech advantage were carried by variations in duration, temporal envelope, or relatively gross spectral differences. However, the properties that distinguish between clear and conversational speech may vary between different talkers and may not map straightforwardly onto the properties that determine across-talker differences in intelligibility. The present study focuses on such across-talker differences, examining whether differences in intelligibility observed in normally-hearing listeners are maintained in cochlear implant listeners and acoustic simulations of implant processing.

2. Methods

2.1 Stimuli

Stimuli were taken from the UCL Talker database (Markham and Hazan, 2002). Two male adults, two female adults, and two female schoolchildren were selected. One in each pair had high intelligibility and one low, based on mean single word error rates calculated by Markham and Hazan (2002).

Recordings of 108 individual words were assigned to six lists of 18 words each, based on mean error rates across the six talkers. To confirm equivalence of intelligibility across lists, error rates were submitted to a two-way ANOVA with talker and list as factors. As expected, this analysis showed a significant effect of talker [$F(5,612)=16.67$, $p<0.001$], but importantly neither the main effect of list nor the interaction were significant [Fs <1]. In order to allow an adequate speech sample for perceptual attunement all single words were concatenated to the carrier phrase "And now please say" recorded from the appropriate talker.

Intelligibility in connected speech was evaluated using 20 semantically unpredictable sentences (SUS) (Benoit *et al.*, 1996). These sentences, each containing four key words, provide no semantic contextual cues so that each word of the sentence is unpredictable, e.g., "The front press scores the saint." Sentence material was available only for the two male talkers.

2.2 Speech processing

Noise-excited vocoding (Shannon *et al.*, 1995) was implemented in Matlab and comprised the following steps: analysis bandpass filtering (sixth-order Butterworth IIR, three orders per upper and lower side) to divide the spectrum into four or eight bands; half-wave rectification and low-pass filtering (fourth-order Butterworth, 400 Hz) to extract the amplitude envelope for each band; modulation of a noise carrier by each envelope; output filtering matching the initial analysis filtering; adjustment of rms level at filter outputs to match the original analysis outputs; summation across channels. Analysis filters covered the range 100 Hz–5 kHz with spacing based on equal basilar membrane distance (Greenwood, 1990). Frequency responses crossed 3 dB down from the pass-band peak.

In an attempt to avoid ceiling effects, unprocessed stimuli for normally hearing listeners were presented in twenty-talker babble at a signal-to-noise ratio (SNR) of +6 dB, as in Hazan and Markham (2004). For each utterance, a section of noise of equivalent duration was selected at random from the 15 s available. Calculations of signal and noise power were performed over the entire length of the speech utterance and the noise. After summation, all stimuli were normalized to the same rms level. No noise was added to vocoded stimuli, or those presented to CI listeners.

2.3 Participants

Six users of Clarion cochlear implants took part. Three had C2 implants and used the Hi-Res processing strategy. The remaining three had C1 implants and included one user each of the continuous interleaved sampling (CIS), paired pulsatile sampler (PPS), and simultaneous analog stimulation (SAS) processing strategies. Their ages ranged from 32–77 (mean 61) and all had at least four years experience of implant use. Eighteen female adults with normal hearing also participated. Their ages ranged from 21–46 (mean 25). None had any history of hearing deficit.

2.4 Design and procedure

Testing was carried out under computer control. Cochlear implant users were tested using their normal speech processor settings in a sound-proofed room. Unprocessed words and sentences were presented via loudspeaker (QUAD PRO-63) at an individually-determined comfortable level.

Normally-hearing listeners were randomly assigned to one of three groups tested with different types of stimuli: vocoded speech with either four or eight channels, or speech-in-babble. Stimuli were presented via Sennheiser HD 540 headphones in a quiet room at a comfortable listening level fixed for all listeners.

In single word tests, each of the six word lists for each talker was presented to a different participant. Each participant heard one list from each talker, a total of 108 words, presented in random order. Participants heard six practice stimuli, one for each talker. Practice stimuli were processed in the same way as those about to be presented but consisted of words not contained in the main test. In sentence tests each participant heard ten sentences spoken by each of the two male talkers. With this constraint, the choice of talker for each sentence and the order of presentation were random. Because no other SUS sentences were available from these two talkers, the six practice sentences were similar sentences spoken by a female talker.

3. Results

3.1 Single words

Due to the binomial nature of the outcome measure (proportion correct), a logistic regression was used to determine the dependence of word identification performance upon talker type (male, female, or child), intelligibility (high or low), and processing condition (CI, four channel vocoding, eight channel vocoding or babble). Logistic regression also has the advantage of minimizing floor and ceiling effects. Model fitting proceeded from a fully saturated model ($3 \times 2 \times 4$) with methods appropriate for overdispersion applied (Collett, 2003, pp. 206–210). Terms that were not significant at the $p < 0.05$ level were excised sequentially using changes in deviance. There were no significant interactions, but all three main effects were significant ($p < 0.05$).

The significant effect of talker type reflected poorer performance with the child talkers. Averaged across the different processing conditions mean performance with the male talkers was 62.7% and 47.5% for the high intelligibility and low intelligibility talkers, respectively, while the corresponding figures were 62.7% and 47.7% for the female talkers and 56.3% and 42.1% for the child talkers. Although the interaction between talker type and processing condition was not significant, the tendency for poorer performance with the child talkers was more pronounced in the two vocoded conditions.

Figure 1(a) plots performance (averaged across talker type) with high intelligibility talkers against that with low intelligibility talkers for each individual listener. Nearly all listeners showed better performance with the high intelligibility talkers (most points lie above and to the left of the diagonal). For normally-hearing listeners, overall performance levels are clearly highest in the babble condition, lowest with four channel vocoding and intermediate with eight channel vocoding. Individual CI users' performance was quite widely spread within the range covered by the two vocoded conditions. The advantage for high over low intelligibility talkers appears broadly similar in all four processing conditions, reflecting the absence of any interaction between the two factors.

In order to assess the influence of the two major determinants of intelligibility differences identified by Hazan and Markham (2004), single word recognition scores were first averaged across listeners for each combination of talker and processing condition and then normalized by processing condition to the overall mean (Fig. 2). Both mean word duration and mean energy in the 1–3 kHz region were significantly correlated with normalized word recognition (r=0.419, p=0.021 and r=0.592, p=0.001, respectively). Linear regressions showed that in each case the proportion of the variance accounted for was not significantly increased by allowing

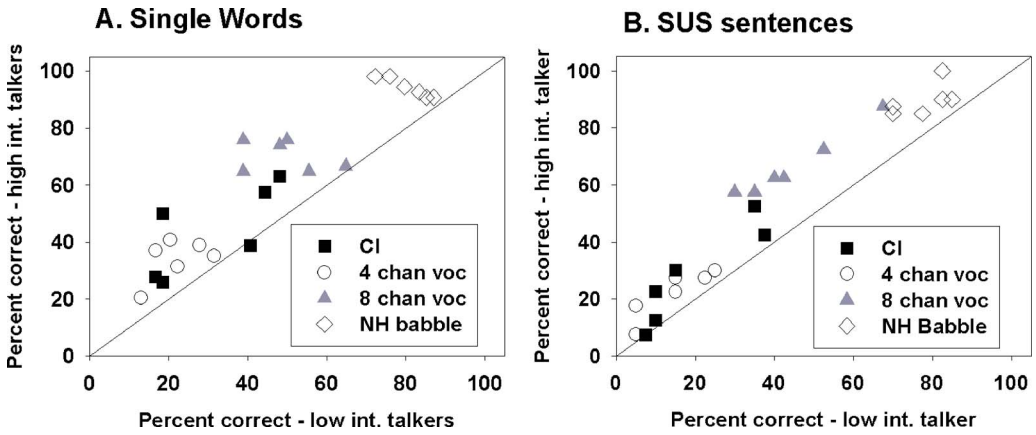

Fig. 1. Speech perception performance with high intelligibility talkers plotted against that with low intelligibility talkers for each individual listener. (A) Single word recognition averaged across talker type; (B) performance on key words in SUS sentences (male talkers only). Diagonal lines represent identical performance for high and low intelligibility talkers.

separate slopes for each processing condition, compared to a single slope. Thus, there was no evidence that the dependence of word recognition on either duration or energy differed across processing conditions.

The 1–3 kHz energy measure accounted for 35.1% of the variance in normalized word recognition. The addition of word duration did not significantly increase the proportion of variance accounted for as the two predictors were strongly correlated for the six talkers used here ($r=0.865$, $p<0.001$). Note, though, that these two properties were uncorrelated across Hazan and Markham's (2004) complete set of talkers.

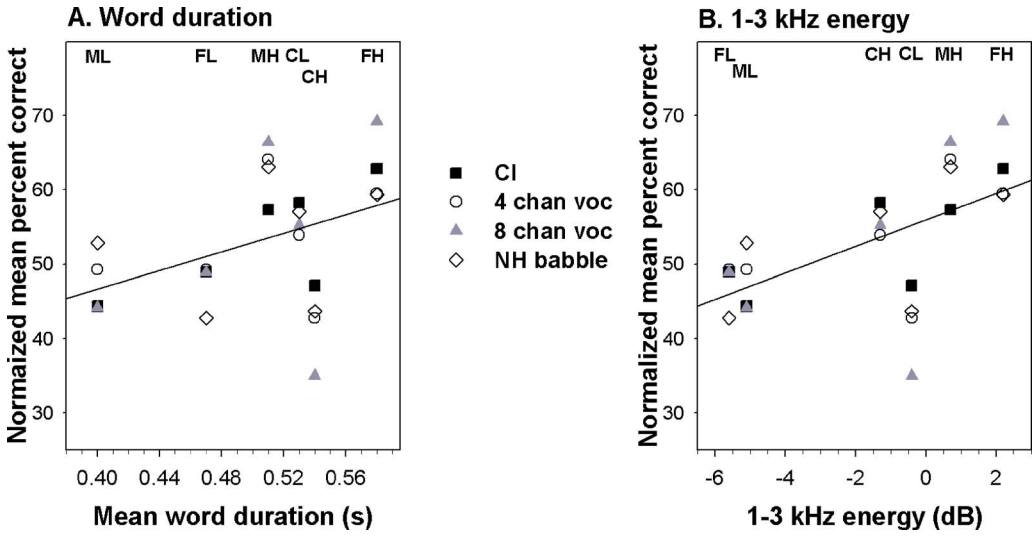

Fig. 2. Normalized mean single word recognition for each processing condition plotted against (A) word duration and (B) amount of energy in the 1–3 kHz range. Talkers are identified by the text symbols at the top of each plot (e.g., MH=high intelligibility male talker). Mean duration and energy values are taken from the data of Hazan and Markham (2004). Best fitting regression lines are shown in each case.

3.2 Semantically unpredictable sentences

A similar logistic regression analysis was applied to scores on correct key words [Fig. 1(b)], to assess the effects of intelligibility and processing condition. The interaction between the two factors was not significant, but both main effects were ($p < 0.001$). Overall performance varied across processing condition in a similar fashion to that seen with single word recognition.

4. Discussion

The key finding was that, while speech recognition performance varied substantially with processing condition, differences in intelligibility across talkers were apparent for all the different listening groups. Consistent with the findings of Liu *et al.* (2004) for a single talker employing either clear or conversational speaking styles, the present results suggest that intelligibility differences across different talkers are largely preserved despite the degradation of the speech signal associated with CI processing.

Although Markham and Hazan (2002) reported that the mean intelligibility scores for the talkers that we selected varied little across the different types of talker (male, female, and child), in the present study there was a significant effect of talker type. While there were no significant interactions with other factors, this effect appears to be primarily attributable to poorer performance with vocoded speech from the two girl talkers. Poorer vowel recognition for girl talkers compared to men, women, and boys has previously been observed in CI users (Loizou *et al.*, 1998) but we found word recognition performance for CI listeners to be unaffected by talker type. Most importantly, in the present context, the differences between the high and low intelligibility talkers within each pair were unaffected by whether the talkers were male adults, female adults, or children.

Unsurprisingly, overall speech perception was highest for the normally-hearing listeners presented with unprocessed stimuli in babble. The better performance in noise-excited vocoder conditions with eight channels than with four can be attributed to the greater degree of spectral resolution in the former case. In the majority of cases the performance of CI users was similar to that in the four channel condition. It should be noted, though, that because there are many aspects of electrical hearing that cannot be emulated in acoustic simulations, this cannot be taken as a measure of the degree of spectral resolution available to the implant users in this study.

The present data set is too limited to allow definitive conclusions regarding the impact of the various processing conditions on possible factors underlying across-talker intelligibility differences. However, the fact that broadly comparable differences between high and low intelligibility talkers were observed in all processing conditions and for all talker types suggests that, for this talker set, the primary factors determining intelligibility differences were largely unaffected by the manipulations involved in simulated and actual implant processing. In addition to properties dependent on a high level of spectral resolution or fine structure temporal information, this would appear to rule out a major role for F0-related factors.

The main factor identified by Hazan and Markham (2004), mean energy in the 1–3 kHz region, accounted for 35.1% of the variance in normalized single word recognition in the present study. Word recognition was also quite strongly correlated with mean word duration, but inclusion of this factor in the regression did not significantly increase the proportion of the variance accounted for. It might, perhaps, have been expected that the much reduced spectral resolution associated with CI processing would have resulted in an increase in the contribution to intelligibility differences of temporal properties, such as word duration, relative to spectral properties. However, in the present limited data set there was no evidence of any difference in the role of either 1–3 kHz energy or word duration across the different processing conditions.

One aspect of the speech signal that would be expected to be well preserved by implant processing is low-frequency modulation of the amplitude envelope and it has been suggested that this temporal information plays an important role in determining within-talker intelligibility differences between clear and conversational speech. Using techniques developed in prior speech intelligibility research (Payton and Braida, 1999; Steeneken and Houtgast, 1980), Liu *et*

al. (2004) calculated envelope modulation spectra from concatenated sentence material in octave bands with center frequencies ranging from 125–4000 Hz. For their female talker, in all octave bands, modulation index values were larger and peaked at lower modulation frequencies (1–3 Hz) for clear compared to conversational speech. For the male talker, a similar pattern was present above 2000 Hz, but there was little difference between clear and conversational speech in the lower octave bands.

Using the methods of Liu *et al.* (2004) envelope modulation spectra were derived from recordings of a read passage (around 2 min) for the adult talkers in the present study (the required material was not available for the children). Separate spectra were obtained for speech in quiet and in the conditions in which speech was presented to listeners in the present study (i.e., in babble or noise-vocoded to four or eight channels).[11] In general, there was little difference in modulation spectra between the high and low intelligibility talkers in most octave bands. Only in the 2 kHz band for the female talkers was there consistent evidence of greater low frequency modulation for the high intelligibility talker. On this evidence, it does not appear that the modulation spectra capture an essential feature responsible for across-talker differences in intelligibility. However, as noted by Hazan and Markham (2004), there is much heterogeneity in the patterning of acoustic-phonetic features for talkers of similar intelligibility. Similarly, it is noteworthy that the child talkers in the present study had very similar measures of both word duration and 1–3 kHz energy, despite the large difference in intelligibility between them. Thus, it is possible that low frequency amplitude modulation is a contributing factor in the intelligibility of some talkers, but not all.

On the basis of the present results it would appear that, while across-talker intelligibility differences are similar in normal hearing and actual and simulated electric hearing, there is no single property that is critical in determining intelligibility differences in implant users. Instead, it seems likely that implant processing may adequately preserve a number of different properties that contribute to intelligibility differences. However, this conclusion needs to be tested further with research employing a larger talker set and incorporating a more detailed investigation of variation in the contribution of possible determinants of talker intelligibility, both across different CI users and between CI users and normally-hearing listeners.

Acknowledgments

The authors thank all participants and are grateful to the cochlear implant team at the Royal National Throat Nose and Ear Hospital for help in recruiting implant users. Thanks also to Paul Iverson and Valerie Hazan for assistance in setting up and running the experiment. Our implant work, and Tim Green in particular, is supported by the RNID. Some of the work reported here was performed as part of the UCL Speech Sciences BSc thesis of Sotira Katiri.

References and links

[1]See EPAPS Document No. E-JASMAN-121-502705 for Fig. 3 which shows envelope modulation spectra calculated in quiet for modulation frequencies in the range 0.5–20 Hz in octave bands from 125–4000 Hz. This document can be reached via a direct link in the online article's HTML reference section or via the EPAPS homepage (http://www.aip.org/pubservs/epaps.html).

Benoit, C., Grice, M., and Hazan, V. (**1996**). "The SUS test: A method for the assessment of text-to-speech synthesis intelligibility using semantically unpredictable sentences," Speech Commun. **18**, 381–392.
Bond, Z. S., and Moore, T. J. (**1994**). "A note on the acoustic-phonetic characteristics of inadvertently clear speech," Speech Commun. **14**, 325–337.
Bradlow, A. R., Torretta, G. M., and Pisoni, D. B. (**1996**). "Intelligibility of normal speech: 1. Global and fine-grained acoustic-phonetic talker characteristics," Speech Commun. **20**, 255–272.
Collett, D. (**2003**). *Modelling binary data*, 2nd ed. (CRC Press, Boca Raton, FL), pp. 206–210.
Faulkner, A., Rosen, S., and Norman, C. (**2006**). "The right information can matter more than frequency-place alignment: Simulations of frequency-aligned and upward shifting cochlear implant processors for an electrode array insertion depth of 17 mm," Ear Hear. **27**, 139–152.
Ferguson, S. H., and Kewley-Port, D. (**2002**). "Vowel intelligibility in clear and conversational speech for normal-hearing and hearing-impaired listeners," J. Acoust. Soc. Am. **112**, 259–271.

Friesen, L. M., Shannon, R. V., Baskent, D., and Wang, X. (**2001**). "Speech recognition in noise as a function of the number of spectral channels: Comparison of acoustic hearing and cochlear implants," J. Acoust. Soc. Am. **110**, 1150–1163.
Green, T., Faulkner, A., and Rosen, S. (**2002**). "Spectral and temporal cues to pitch in noise-excited vocoder simulations of continuous-interleaved-sampling cochlear implants," J. Acoust. Soc. Am. **112**, 2155–2164.
Green, T., Faulkner, A., and Rosen, S. (**2004**). "Enhancing temporal cues to voice pitch in continuous interleaved sampling cochlear implants," J. Acoust. Soc. Am. **116**, 2298–2310.
Greenwood, D. D. (**1990**). "A cochlear frequency-position function for several species—29 years later," J. Acoust. Soc. Am. **87**, 2592–2605.
Hazan, V., and Markham, D. (**2004**). "Acoustic-phonetic correlates of talker intelligibility for adults and children," J. Acoust. Soc. Am. **116**, 3108–3118.
Krause, J. C., and Braida, L. D. (**2002**). "Investigating alternative forms of clear speech: The effects of speaking rate and speaking mode on intelligibility," J. Acoust. Soc. Am. **112**, 2165–2172.
Krause, J. C., and Braida, L. D. (**2004**). "Acoustic properties of naturally produced clear speech at normal speaking rates," J. Acoust. Soc. Am. **115**, 362–378.
Liu, S., Del Rio, E., Bradlow, A. R., and Zeng, F.-G. (**2004**). "Clear speech perception in acoustic and electric hearing," J. Acoust. Soc. Am. **116**, 2374–2383.
Loizou, P. C., Dorman, M. F., and Powell, V. (**1998**). "The recognition of vowels produced by men, women, boys, and girls by cochlear implant patients using a six-channel CIS processor," J. Acoust. Soc. Am. **103**, 1141–1149.
Markham, D., and Hazan, V. (**2002**). "UCL Speaker Database," Speech, Hearing and Language: UCL work in progress **14**, 1–17 (available at http://www.phon.ucl.ac.uk/home/shl14/pdffiles/markhamH.pdf). Viewed 4/1/07.
Payton, K. L., and Braida, L. D. (**1999**). "A method to determine the speech transmission index from speech waveforms," J. Acoust. Soc. Am. **106**, 3637–3648.
Payton, K. L., Uchanski, R. M., and Braida, L. D. (**1994**). "Intelligibility of conversational and clear speech in noise and reverberation for listeners with normal and impaired hearing," J. Acoust. Soc. Am. **95**, 1581–1592.
Picheny, M. A., Durlach, N. I., and Braida, L. D. (**1985**). "Speaking clearly for the hard of hearing. I. Intelligibility differences between clear and conversational speech," J. Speech Hear. Res. **28**, 96–103.
Picheny, M. A., Durlach, N. I., and Braida, L. D. (**1986**). "Speaking clearly for the hard of hearing. II. Acoustic characteristics of clear and conversational speech," J. Speech Hear. Res. **29**, 434–446.
Shannon, R. V., Zeng, F.-G., Kamath, V., Wygonski, J., and Ekelid, M. (**1995**). "Speech recognition with primarily temporal cues," Science **270**, 303–304.
Shannon, R. V., Zeng, F.-G., and Wygonski, J. (**1998**). "Speech recognition with altered spectral distribution of envelope cues," J. Acoust. Soc. Am. **104**, 2467–2476.
Steeneken, H. J. M., and Houtgast, T. (**1980**). "A physical method for measuring speech-transmission quality," J. Acoust. Soc. Am. **67**, 318–326.
Uchanski, R. M., Choi, S. S., Braida, L. D., Reed, C. M., and Durlach, N. I. (**1996**). "Speaking clearly for the hard of hearing. 4. Further studies of the role of speaking rate," J. Speech Hear. Res. **39**, 494–509.

Classifying multi-frequency fisheries acoustic data using a robust probabilistic classification technique

C. I. H. Anderson and J. K. Horne
School of Aquatic and Fishery Sciences,University of Washington, Box 355020, Seattle, Washington 98195
ciha@u.washington.edu, jhorne@u.washington.edu

J. Boyle
Institute for Systems Biology, 1441 North 34th Street, Seattle, Washington 98103
jboyle@systemsbiology.org

Abstract: A robust probabilistic classification technique, using expectation maximization of finite mixture models, is used to analyze multi-frequency fisheries acoustic data. The number of clusters is chosen using the Bayesian Information Criterion. Probabilities of membership to clusters are used to classify each sample. The utility of the technique is demonstrated using two examples: the Gulf of Alaska representing a low-diversity, well-known system; and the Mid-Atlantic Ridge, a species-rich, relatively unknown system.

© 2007 Acoustical Society of America
PACS numbers: 43.30.Sf, 43.60.Bf, 43.60.Lq [NX]
Date Received: January 23, 2007 **Date Accepted:** March 21, 2007

1. Introduction

Acoustic classifications, discriminations, and identifications of fish and zooplankton species have traditionally integrated prior knowledge, pattern recognition, and direct sampling methods (Horne, 2000). Species identifications have been limited to subjective classification by operators (i.e., scrutinizing; e.g., Dalen *et al.*, 2003) or artificial intelligence (e.g., Haralabous and Georgakarakos, 1996). The use of mean volume backscatter (MVBS) (Kang *et al.*, 2002) and target strength differencing (Gauthier and Horne, 2004) provide objective separations but still assign each target or pixel to a single classification category. The use of multiple frequencies and long-term deployments (e.g., ocean observatories) has increased the need for automated, or semi-automated, data processing techniques, capable of efficient, robust discrimination of ecosystem components and explicit quantification of uncertainty.

Despite the widespread use of probabilistic techniques for prediction and classification in other disciplines [e.g., since the 18th century in weather forecasting (Murphy, 1998)], the certainty of classification has not been included in the analysis of fisheries acoustic data. The increased availability of multi-frequency acoustic data, coupled with ever increasing computing power, facilitates incorporation of probabilistic classification techniques from other fields [e.g., analysis of gene expression data (Boyle, 2005)]. We demonstrate advantages of using unsupervised probabilistic clustering over subjective categorization to classify fish and invertebrates in contrasting ecosystems—low diversity, well-known, and high diversity, relatively unknown.

2. Methodology

2.1 Approach

Probabilistic clustering techniques, such as mixture modeling, differ from partition-based clustering in that each sample is assigned a probability of membership to each cluster rather than an absolute assignment to a single cluster. Partition-based clusters can be described by their centroids (MacQueen, 1967)—the mean position in sample space of all data points assigned to the cluster. In our finite mixture modeling a set of vector models (equivalent to cluster centroids) is

 © 2007 Acoustical Society of America

defined, using frequency-specific S_v values, which provide the "best" description of the data. Analytic steps are optimized to allow robust analysis of large data volumes typical of fisheries acoustic data sets (e.g., five frequencies over 250 m depth range for 1 h generate over 23.8 million data values). As samples are assigned probabilities of membership to all clusters, rules must be defined to assign samples to specific clusters.

Applying probabilistic clustering techniques to acoustic data requires three steps: acoustic data processing; generation of clusters and membership probabilities; and analysis of membership probabilities, which includes defining the optimum number of clusters.

2.2 Acoustic data processing

Acoustic data were collected using Simrad EK60 echosounders operating at multiple frequencies between 18 and 200 kHz. Power data were converted to volume backscattering strength (S_v, dB re 1 m^{-1}; cf. Simmonds and MacLennan, 2005), including a range offset of half a pulse length and a transmission loss correction of $20*\log(r)+2\alpha r$ (where r=range from the transducer face and α=frequency-dependent absorption coefficient). Maximum data resolution (i.e., 0.19 m vertical, 1 "ping" horizontal) was retained to maintain the spatial structure of the scattering components. For this analysis, each sample (i.e., image pixel) was assumed to be spatially coincident across frequencies, and no attempt was made to align samples from different transducers. The transducers used to collect the data for both examples were arranged to maximize beam overlap within the physical constraints of transducer placement and beam angles (cf., Korneliussen and Ona, 2002).

2.3 Generation of clusters

Generation of clusters requires the initial selection of the number of clusters, generation of initial vector model values, and then iterative refinement of models. Initial values for vector models were estimated using K-means by median clustering, based on the Euclidean distance measure between S_v values at each frequency, for each sample. Expectation maximization (EM) for finite mixture models (Dempster *et al.*, 1977), where model residuals are based on direct linear distance, was used to refine the models. The expectation step is given by

$$P(x|\mu) = \frac{e^{-\sum_{d\in D}(\mu_d - x_d)^2}}{\sum_{\mu'} e^{-\sum_{d\in D}(\mu'_d - x_d)^2}}, \tag{1}$$

and the maximization step is given by

$$\mu_d = \frac{\sum_{x\in X} x_d P(x|\mu)}{\sum_{x\in X} P(x|\mu)}, \tag{2}$$

where $P(x|\mu)$ is the probability of sample x belonging to model μ, for the set of X samples and D frequencies. The log likelihood (LL) values were approximated using

$$LL = \sum_{x\in X} \log\max(P(x|\mu)). \tag{3}$$

Vector models were iteratively refined until a level of convergence was reached. Convergence was said to occur when the sum of the lowest residuals (i.e., those from the best fitted vector model for each sample) stopped decreasing or a maximum of 15 iterations were completed. Fifteen iterations was chosen as a trade-off between achieving convergence and efficiency in processing large data sets. The posterior probabilities of cluster membership for each sample were then reported. The sum of the probabilities of membership to all clusters is one for each sample.

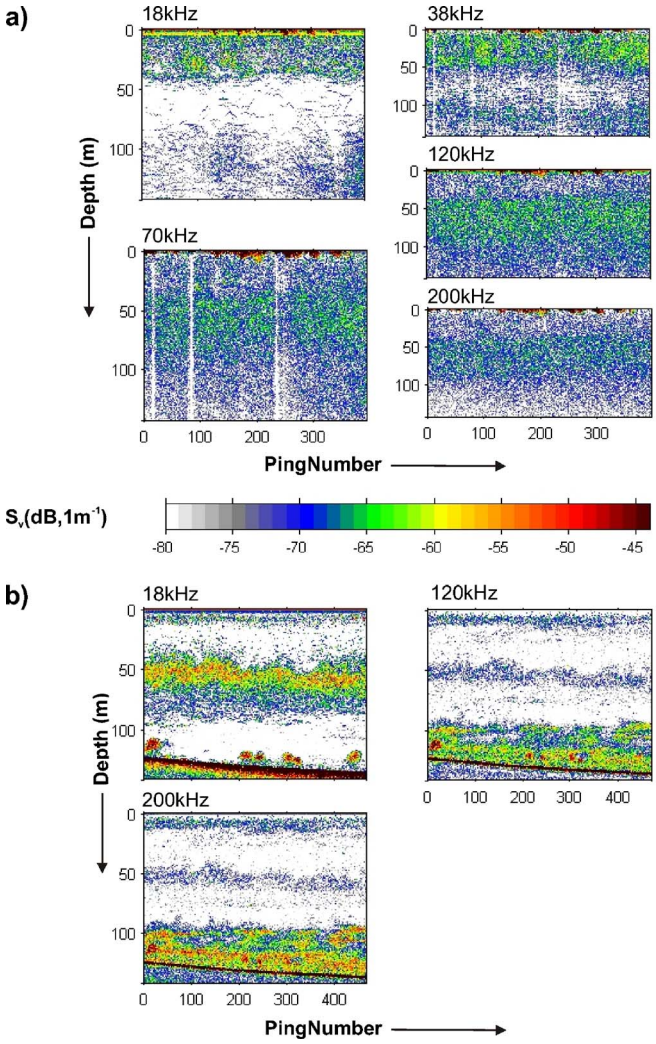

Fig. 1. (Color online) Echograms showing mean volume backscatter (S_v, dB re 1 m^{-1}) data at multiple frequencies from (a) the open ocean above the Mid-Atlantic Ridge (MAR) and (b) the Gulf of Alaska (GoA).

2.4 Analysis of membership probabilities

Probabilities of cluster membership were used to generate synthetic echograms (i.e., probability "maps") to display spatial properties of membership probabilities. Probabilities were also used to assign samples to clusters and as input to cluster metrics. Cluster metrics, including one derived from the Bayesian Information Criterion (BIC) (Schwarz, 1978), were used to determine the optimum number of clusters. Mixture modeling violates the requirements for using the BIC in statistical tests, but versions of the metric are widely acknowledged as useful in assessing the fit of a set of clusters to data (e.g., Fraley and Raftery, 1998). The BIC used here is defined as

$$BIC = -2 * LL + ((M-1) * D) * \log(X * D), \tag{4}$$

where M is the number of models, D is the number of frequencies, and X is the number of samples. BIC values will always be greater than 0, and a higher score represents a poorer description of the data by the vector models. A gradual increase in the score with an increasing

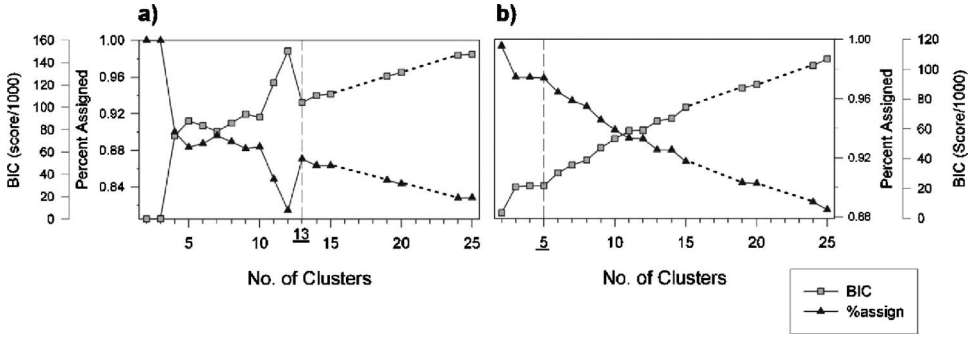

Fig. 2. The Bayesian Information Criterion (BIC) and percentage of clearly assigned samples (%assign) plotted against number of clusters for data from (a) the Mid-Atlantic Ridge (MAR) and (b) the Gulf of Alaska (GoA).

number of clusters is expected as membership probabilities are dissipated among clusters. Large deviations from this upward trend are informative as they represent transitions to another "state." An alternative cluster metric is the percentage of samples clearly assigned to clusters (%assign), where sample x is clearly assigned if $\max(P(x|\mu)) \geqslant 2 * \max - 1(P(x|\mu))$. A higher %assign value represents a better description of the data. The trajectory of the %assign values closely mirrors that of the BIC scores as it is based on the same underlying probabilities.

Selecting the optimum number of clusters is a challenge as the strongest "natural" clusters in acoustic data typically discriminate high S_v values, associated with surface noise and bottom returns where present, from weak returns associated with most biological backscatter. By generating cluster metrics (i.e., BIC or %assign) over a range of numbers of clusters, transitions within the data description can be identified. Interpreting transition points using biological knowledge allows the optimum number of clusters to be identified for each application. An additional benefit of sequentially clustering at an increasing number of clusters is that fidelity of samples to clusters and relationships between clusters can be examined.

3. Examples

3.1 Data

Data for the first example were collected at 18, 38, 70, 120, and 200 kHz during a cruise over the Mid-Atlantic Ridge (MAR) in the North Atlantic [Fig. 1(a)]. This area represents a mid-latitude pelagic ecosystem with a diverse but poorly known epi- and mesopelagic fauna. Echograms are dominated by amorphous horizontal layers and a variety of noise artifacts. The shallowest samples of each ping contain high S_v values due to transducer saturation and intermittent bubbles passing under the transducers. At 38 and 70 kHz vertical white stripes represent "dropped pings" in the data record.

Data were also collected at three frequencies (18, 120, and 200 kHz) in the Gulf of Alaska (GoA) in the northeast Pacific [Fig. 1(b)]. These data are from a continental shelf, high latitude ecosystem with a well-known but limited pelagic fauna. The echograms contain the same transducer saturation feature as seen in the MAR data as well as strong initial returns from the bottom and weaker sub-bottom returns. Biological features include high intensity backscatter from fish schools near the bottom and a series of horizontal layers comprised mainly of forage fish and zooplankton (Stienessen and Wilson, 2002).

3.2 Determining the optimum number of groups

Examination of cluster metrics for the MAR data shows strong transitions at 3 and 13 clusters [Fig. 2(a)]. As expected, 2–3 clusters separate high S_v features (i.e., bubbles and transducer saturation) from low S_v features including biological backscatter (Table 1). This clear discrimination of noise features may be used to remove noise from data sets but does not provide bio-

Table 1. Vector model parameter values (S_v, dB re 1 m^{-1}) defining sets of clusters generated from the Mid-Atlantic Ridge (MAR) and Gulf of Alaska (GoA) data.

Data	Group no.	18 kHz	38 kHz	70 kHz	120 kHz	200 kHz	Comment
MAR- 2	1	−80.81	−74.30	−74.25	−72.12	−75.30	Non-noise features
clusters	2	−37.77	−34.31	−30.28	−28.67	−30.77	Intense noise features
MAR- 3	1	−80.82	−74.32	−74.24	−72.12	−75.29	Non-noise features
clusters	2	−52.49	−48.80	−45.30	−45.14	−49.45	Near-surface bubbles
	3	9.62	12.63	15.78	22.08	24.83	Transducer saturation
MAR- 13	1	−75.34	−72.90	−74.70	−72.66	−87.24	
clusters	2	−91.40	−74.60	−76.20	−73.30	−79.06	
	3	−67.90	−66.20	−70.24	−71.03	−73.76	Includes "fish tracks"
	4	−76.34	−79.87	−72.94	−70.57	−74.14	
	5	−76.54	−72.23	−74.52	−83.90	−76.28	
	6	−61.16	−57.83	−54.80	−53.66	−58.69	Bubble margin+"biota"
	7	−91.29	−87.65	−74.98	−71.01	−73.48	
	8	−71.67	−70.55	−81.48	−72.90	−75.66	
	9	−82.78	−69.58	−70.17	−68.99	−71.61	
	10	−47.33	−43.71	−39.54	−39.93	−43.41	Near-surface bubbles
	11	9.62	12.63	15.78	22.08	24.83	Transducer saturation
	12	−81.96	−81.01	−87.32	−75.56	−78.18	Includes dropped pings
	13	−94.53	−76.06	−69.88	−68.09	−70.49	
GoA- 2	1	−77.44	–	–	−80.95	−79.21	"Low S_v"
clusters	2	−51.70	–	–	−44.83	−42.98	"High S_v"
GoA- 5	1	−27.31	–	–	−38.18	−39.68	1st bottom echo+intense schools
clusters	2	7.33	–	–	21.63	27.32	Transducer saturation
	3	−63.11	–	–	−78.58	−78.16	"Fish"
	4	−85.16	–	–	−90.21	−87.97	"Background"
	5	−86.97	–	–	−68.19	−64.96	"Zooplankton"
GoA- 6	1	−57.63	–	–	−73.47	−72.68	"Large fish"
clusters	2	−22.04	–	–	−32.00	−34.15	1st bottom echo+ intense schools
	3	−87.54	–	–	−68.24	−64.97	"Zooplankton"
	4	−90.99	–	–	−91.53	−88.84	"Background"
	5	−71.70	–	–	−84.76	−84.06	"Small fish"
	6	7.33	–	–	21.64	27.34	Transducer saturation

logically useful resolution of species or species groups. The marked degradation of metric values from 10–12 clusters followed by the strong improvement at 13 clusters suggests a transition in the intrinsic acoustic features described by the clusters. A 13-cluster classification was used to extract the features described beyond the transition point.

Consistent with the MAR data, the "best" description of the GoA data was obtained using two clusters that separated high S_v features, including transducer saturation, bottom echoes, and dense schools, from low S_v values [Fig. 2(b), Table 1]. After a transition in metric values, 3–5 clusters were equivalent in their ability to describe the data, and there was very little structure apparent in metric values above five clusters. A five-cluster classification was chosen for the GoA data to maximize the number of well described biological categories.

3.3 Probabilities of group membership

The 13-cluster classification of the MAR data captures the transducer saturation (cluster 11), intense bubble noise at the surface (cluster 10), and the margins of the bubble features (cluster

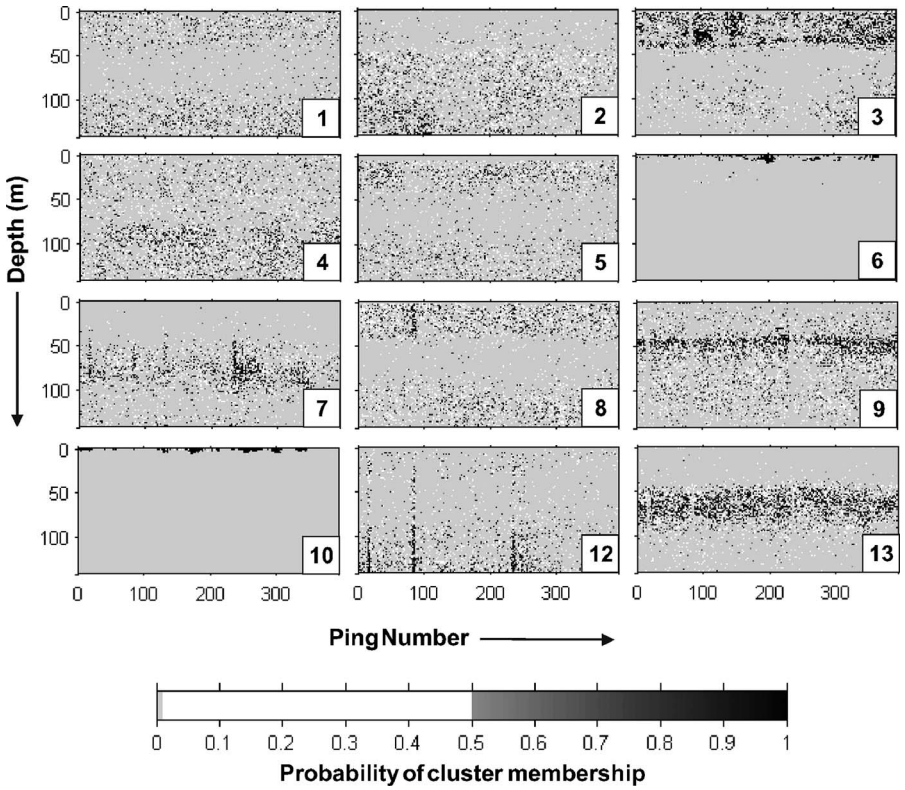

Fig. 3. Probability maps of cluster membership for the 13-cluster classification of Mid-Atlantic Ridge (MAR) data. Notes: Cluster 11 is not shown but is equivalent to cluster 2 shown in Fig. 4. The palest gray tone indicates a membership probability of zero.

6; Table 1, Fig. 3). Dropped pings, along with other samples that have low to moderate S_v values across all frequencies, are found in cluster 12. Similar patterns are evident in clusters 7 and 8. Samples assigned to biological clusters are arranged in horizontal layers, with the three largest clusters (3, 9, and 13) showing contiguous features comprised of high probabilities. Cluster 3 contains individual fish tracks at the same depths as the high probability layer in cluster 13. Vector model parameter values for clusters 3 and 13 show opposite trends in backscatter intensities across frequencies, with cluster 3 containing higher S_v values than cluster 13 at 18 and 38 kHz, and lower values at 120 and 200 kHz, suggesting different types of scattering components (e.g., fish and zooplankton; Table 1). This example demonstrates the ability of objective clustering techniques to extract biological and non-biological features within regions of interest that could not be separated using subjective assignment of contiguous areas within echograms to categories.

GoA probability maps contain a larger percentage of high $\max(P(x|\mu))$ values, which are more spatially contiguous than those in the MAR clusters (compare Fig. 3 and 4). This concentration of high probability values is attributed to both statistical and biological factors. The GoA data are partitioned into 5 rather than 13 clusters resulting in a higher mean $\max(P(x|\mu))$ value (all samples: GoA 5 clusters=0.974, GoA 13 clusters=0.924). However, spatially consistent backscatter intensity patterns, attributed to single species aggregations, also resulted in higher mean $\max(P(x|\mu))$ for clearly assigned samples in the GoA clusters compared to those in the MAR data (clearly assigned samples: GoA 5 clusters=0.989, GoA 13 clusters=0.963, MAR 5 clusters=0.936, MAR 13 clusters=0.927). The presence of spatially

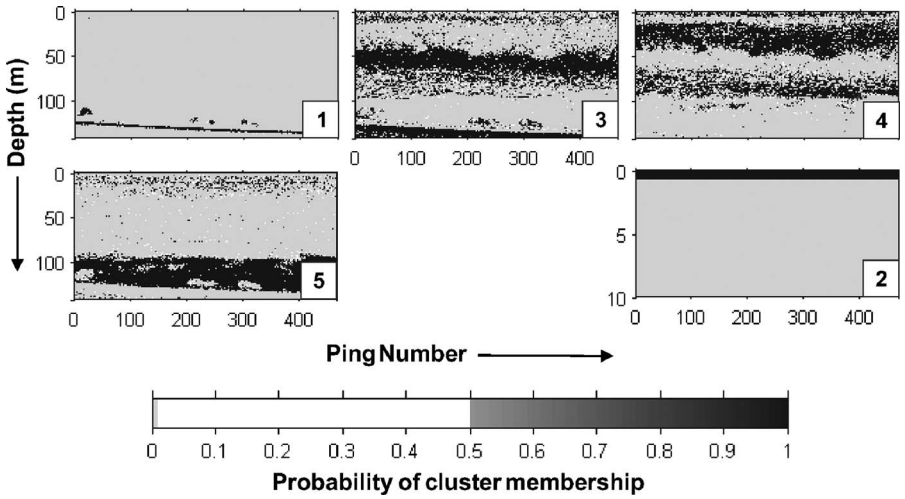

Fig. 4. Probability maps of cluster membership for the five-cluster classification of Gulf of Alaska (GoA) data. Notes: Cluster 2 is drawn on a different depth scale. The palest gray tone indicates a membership probability of zero.

coherent patterns in probability maps from both examples, when no spatial information was used in the clustering process, supports this approach to multi-frequency data classification.

The use of five clusters for the GoA data captures transducer saturation (cluster 2), high intensity backscatter from fish schools and the bottom (cluster 1), and two clusters of horizontally layered biological backscatter with sub-bottom returns (clusters 3 and 5; Fig. 4). The relative magnitudes of vector model S_v values from cluster 3 (higher at 18 kHz and equally low at 120 and 200 kHz) match those from cluster 1 but at lower intensities (Table 1). Frequency-dependent S_v values from cluster 5 are different, lower at 18 kHz and then higher at 120 and 200 kHz. Cluster 4 has relatively low S_v values at all three frequencies, which is interpreted as "empty water" or background backscatter. Results from acoustic and trawl surveys in the GoA (Stienessen and Wilson, 2002) support the biological interpretation of cluster 1 as dense schools of adult walleye pollock, cluster 3 as a mixture of fish at lower densities/sizes (adult and age 0 walleye pollock plus capelin), and cluster 5 as zooplankton (mainly euphausiids). Increasing the number of clusters to six primarily divides cluster 3 into two clusters (1 and 5), with similar relative vector S_v values but at different intensities (Table 1). Inspection of probability maps in conjunction with echograms suggests that this division potentially separates samples containing small from large fish. The use of six clusters to categorize GoA data provides a poorer mathematical description of the data, but may be more appropriate when the objective is to estimate adult walleye pollock biomass independent of other ecosystem components.

4. Future work

The classification of backscatter from contrasting ecosystems demonstrates the potential of probabilistic clustering to analyze multi-frequency fisheries acoustic data. Future work will address: the type of mathematical model used in the EM process, the choice of distance measures to distinguish clusters (including the incorporation of depth and spatial location), and the choice of metrics used to select the optimum number of clusters. Specific issues include the spatial coincidence of samples within transducer beams (Korneliussen and Ona, 2002), and the frequency-dependent loss of signal with depth, which affects choice of EM model. Investigations of spatial and temporal cluster dynamics, including their stability in contrasting ecosystems, will follow refinement of the methodology, with the ultimate goal of automated, robust discrimination of ecosystem components in a wide variety of environments.

Acknowledgments

We thank the MARECO program (www.mareco.no) for providing an opportunity to participate in the MAR cruise and Dr. Alex de Robertis from the NOAA Alaska Fisheries Science Center for providing the GoA data. Two of the authors (C.I.H.A. and J.K.H.) were supported by the Office of Naval Research (NOO14-00-1-0180) and the Alaska Fisheries Science Center (NA17RJ1232-AM01).

References and links

Boyle, J. (**2005**). "Gene-expression omnibus integration and clustering tools in SeqExpress," Bioinformatics **21**, 2550–2551.

Dalen, J., Nedreaas, K., and Pedersen, R. (**2003**). "A comparative acoustic-abundance estimation of pelagic redfish (*Sebastes mentella*) from hull-mounted and deep-towed acoustic systems," ICES J. Mar. Sci. **60**, 472–479.

Dempster, A. P., Laird, N. M., and Rubin, D. B. (**1977**). "Maximum likelihood from incomplete data via EM algorithm," J. R. Stat. Soc. Ser. B (Methodol.) **39**, 1–38.

Fraley, C., and Raftery, A. E. (**1998**). "How many clusters? Which clustering method? Answers via model-based cluster analysis," Comput. J. **41**, 578–588.

Gauthier, S., and Horne, J. K. (**2004**). "Potential acoustic discrimination within boreal fish assemblages," ICES J. Mar. Sci. **61**, 836–845.

Haralabous, J., and Georgakarakos, S. (**1996**). "Artificial neural networks as a tool for species identification of fish schools," ICES J. Mar. Sci. **53**, 173–180.

Horne, J. K. (**2000**). "Acoustic approaches to remote species identification: a review," Oceanogr. **9**, 356–371.

Kang, M., Furusawa, M., and Miyashita, K. (**2002**). "Effective and accurate use of difference in mean volume backscattering strength to identify fish and plankton," ICES J. Mar. Sci. **59**, 794–804.

Korneliussen, R. J., and Ona, E. (**2002**). "An operational system for processing and visualizing multi-frequency acoustic data," ICES J. Mar. Sci. **159**, 293–313.

MacQueen, J. (**1967**). "Some methods for classification and analysis of multivariate observations," in *Proceedings of the Fifth Berkeley Symposium in Mathematical Statistics and Probability*, edited by L. LeCam and J. Neyman (University of California Press, Berkeley), pp. 281–297.

Murphy, A. H. (**1998**). "The early history of probability forecasts: Some extensions and clarifications," Weather Forecast. **13**, 5–15.

Schwarz, G. (**1978**). "Estimating dimension of a model," Ann. Stat. **6**, 461–464.

Simmonds, J., and MacLennan, D. (**2005**). *Fisheries acoustics: theory and practice* (Blackwell Science, Oxford), pp. 437.

Stienessen, S., and Wilson, C. (**2002**). "Preliminary results of an interaction study between commercial fishing and walleye pollock (*Theragra chalcogramma*) off East Kodiak, August–September 2002." Cruise number MF2002-009. (Available from RACE Division, Alaska Fish Sci. Cent., NOAA, Natl. Mar. Fish. Serv., 7600 Sand Point Way NE, Seattle, WA 98115.)

Simulating listener errors in using genetic algorithms for perceptual optimization

Deniz Başkent and Brent Edwards
Starkey Hearing Research Center, 2150 Shattuck Ave., Ste. 408, Berkeley, California 94704
deniz_baskent@starkey.com, brent_edwards@starkey.com

Abstract: The genetic algorithm (GA) was previously suggested for fitting hearing aid or cochlear implant features by using listener's subjective judgment. In the present study, two human factors that might affect the outcome of the GA when used for perceptual optimization were explored with simulations. Listeners with varying sensitivity in discriminating sentences of different intelligibility and with varying error rates in entering their judgment to the GA were simulated. A comparison of the simulation results with the results from human subjects reported by Başkent *et al.* Ear Hear. **28**(3) 277–289 (2007) showed that these factors could reduce the performance of the GA considerably.

© 2007 Acoustical Society of America
PACS numbers: 43.66.Yw, 43.71.An, 43.66.Ts [QJF]
Date Received: January 4, 2007 **Date Accepted:** March 22, 2007

1. Introduction

Most modem hearing aids and cochlear implants offer many features in addition to providing basic audibility. As individual users might have different pathologies and listening preferences (Preminger and Van Tasell, 1995), the numerous device features need to be customized for each patient to maximize benefit. This adjustment can be a complicated and time-consuming process, especially if some of the device features also interact with each other.

Optimization algorithms can be used as a tool to achieve the individual customization in a reasonable time. The modified simplex algorithm was proposed for fitting gain in hearing aids (Kuk and Pape, 1992; Neuman *et al.*, 1987; Preminger *et al.*, 2000; Stelmachowicz *et al.*, 1994). Genetic algorithms (GAs) were suggested for fitting features related to hearing aids (Durant *et al.*, 2004) or cochlear implants (Bourgeois-République *et al.*, 2005; Wakefield *et al.*, 2005). In such perceptual optimization, candidate parameter sets are first evaluated by a listener and then modified according to listener's preferences following the rules of the particular method used. The steps of evaluation and modification continue iteratively, until a satisfactory set of parameters is found. The main advantages that optimization algorithms offer are speed, because the final optimal solution is typically reached by evaluating only a fraction of all possible solutions, and flexibility, because they can be implemented to optimize any device feature.

In perceptual optimization, the input to the program is the subjective human response and the appropriateness of the final solution is, again, judged by the listener. Therefore, there is often no metric available to quantitatively analyze how well the program works (Takayagi, 2001). Başkent *et al.* (2007b) systematically distorted speech using three parameters of the noiseband vocoder processing (Shannon *et al.*, 1995), to generate a listening problem with a metric. The acute effects of these manipulations on intelligibility of speech by normal-hearing subjects were known from previous studies (Fu and Shannon, 1999; Başkent and Shannon, 2003; 2007a; Başkent, 2006), so the final solutions produced by the GA could similarly be evaluated. Speech intelligibility scores measured with the settings produced by the GA were, on average, very high, indicating that the subjects must have been able to provide sufficiently reliable subjective input. Analysis of data from individual subjects showed that there was generally a good agreement between the subjective and objective measures of intelligibility, and only a small number of inconsistencies were observed.

 © 2007 Acoustical Society of America

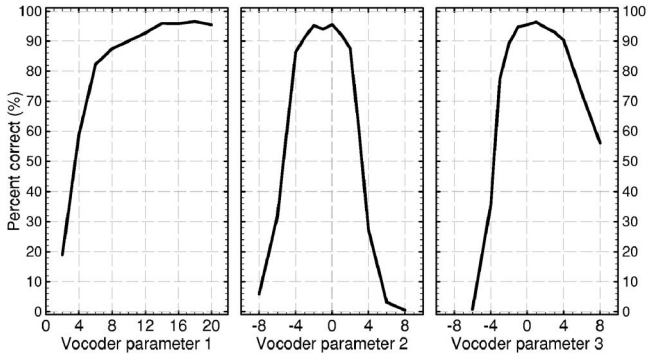

Fig. 1. Speech recognition performance, averaged across nine normal-hearing subjects, shown for each vocoder parameter separately. Reproduced from Başkent *et al.* (2007b).

The subjects who participated in the study by Başkent *et al.* (2007b) were young, with no auditory or cognitive deficits. Therefore, the results can be interpreted as how well the GA would work with ideal listeners. In real applications, some hearing aid and cochlear implant users might have difficulty in making a reliable judgment due to varying peripheral or central auditory deficits or diminished cognitive skills, for example, as a result of aging. In the present study, the effects of such human factors on perceptual optimization with the GA are explored with simulations. One factor that was simulated was the sensitivity in distinguishing sentences of varying intelligibility. The second factor was the errors a subject might make in entering the subjective input into the GA. The same GA program was used as Başkent *et al.* (2007b) study, and the results from the simulations were compared to the results with real listeners, reported in the same study.

2. Methods

2.1 Noiseband vocoder processing

Noiseband vocoder has been widely used to systematically explore the effects of temporal and spectral degradations on speech perception, or to simulate cochlear implant processing with normal-hearing subjects. Narrow bands of noise (carrier bands) are modulated with envelopes extracted from individual bands of speech (analysis bands). The processed speech, a synthesis of these modulated noise bands, has only the crude spectral and temporal elements of the input speech (Shannon *et al.*, 1995).

Başkent *et al.* (2007b) had selected three vocoder parameters to optimize with the GA: (1) the number of the spectral channels of the vocoder, (2) a shift between the analysis and carrier band frequency ranges, and (3) a widening/narrowing of analysis band frequency range over the carrier band frequency range. The percent correct scores with IEEE sentences (IEEE, 1969), averaged across nine normal-hearing subjects, are reproduced from Başkent *et al.* (2007b) in Fig. 1 for each of the three parameters.

The intelligibility of a solution produced by the GA with a simulated subject was evaluated with predicted percent correct (PPC), a measure estimated from a multiplicative combination of the average scores, shown in Fig. 1 for each vocoder parameter. Hence, the effects of the three vocoder parameters were assumed to be independent, even though Başkent and Shannon (2007a) had shown that there was interaction between vocoder parameters 2 and 3 for a small number of conditions.

2.2 Genetic algorithm

For consistency, the same GA that was used by Başkent *et al.* (2007b) was implemented in the present study. The GA is an inherently stochastic optimization method that is based on concepts related to the evolution theory (Mitchell, 1997). For example, one set of parameters that will be

optimized is called a gene. In the present study, every gene was a combination of the three vocoder parameters mentioned in the previous section. The levels of the parameters 1 to 3 were selected as 19, 17, and 15, respectively, producing a search space of 4845 possible solutions. Unlike the conventional bitstring coding, actual parameter values were used in the genes. GAs work on a population of genes (six was used in the present study) rather than an individual set of parameters, and the genes in the initial population are generated randomly. In the present study, a uniform distribution was used for all random processors, except for the mutation operator. In each iteration, all genes in the population are evaluated for fitness and genes with better fitness have a higher probability to pass to the next generation. In applications that involve human subjects, the fitness is determined by the listener's preferences. Başkent *et al.* (2007b) presented vocoder-processed IEEE sentences in paired comparisons, 15 to compare all six genes to each other, to the subjects. The subjects were asked to enter a preference for the sentence with higher subjective intelligibility (A better than B, or vice versa), with an additional option for equal intelligibility (A B same). The genes that were preferred more often had higher fitness value, and all six genes of the population were then rank-ordered such that the genes with the highest and lowest fitness were ranked as the top and the bottom genes, respectively. The next generation of genes was produced from the rank-ordered genes of the old population using one of these methods: (1) Elitism: the top two genes with highest fitness values passed onto the next generation with no alterations. The top third gene was also passed onto the next generation, but with a probability of being mutated. (2) Cross-over: two non-identical parent genes were randomly selected from the old population, and two new child genes were produced by averaging the parameters from the parent genes. The offspring genes replaced the fourth and fifth genes of the old population. (3) Mutation: two of the three genes (third, fourth, and fifth genes of the new population) were randomly selected. One randomly selected parameter of each of the two genes was changed to a randomly selected value, using a normal distribution with the mean at the parameter's old value and the standard deviation of one third of the number of levels used for the parameter to be mutated. The sixth gene in the old population was not used in producing the next generation of genes; the old one was discarded and the sixth gene of the new population was produced randomly. These steps were repeated iteratively, until a convergence criterion was satisfied: if the same two genes were ranked as the best genes of the population in three consecutive iterations, convergence was assumed. If the GA failed to converge in 15 iterations, then the program was stopped manually. The gene that was ranked as the top gene in the final iteration was accepted as the final optimal solution.

2.3 Simulations

Başkent *et al.* (2007b) compared objective and subjective measures of intelligibility and in a small number of occasions subjects were not accurate in judging the intelligibility of a sentence. If this happens during the comparison of a pair of sentences, the subject might enter a higher preference for the sentence with lower intelligibility that might lead the GA toward poorer solutions. This factor was modeled by the probability of error (P_{err}), the probability of making an incorrect decision in a paired comparison. For small values of P_{err}, the simulated listener makes fewer mistakes in selecting the sentence with higher intelligibility in the paired comparisons. For very high values of P_{err}, the simulated subject frequently enters incorrect choices, leading the GA to produce poorer solutions.

A second factor that could affect the outcome of the GA would be the just noticeable difference (JND) between the intelligibility levels of the sentences presented in a pair. The subject has to be able to hear the difference between the sentences to make a judgment, and how much of a difference a subject needs for a reasonable judgment most likely varies from subject to subject. This factor was modeled with the parameter JND_{PC}. In the simulations, the intelligibility related to a set of vocoder parameters was directly estimated by the PPC. The simulated subject entered a preference for one of the sentences in the pair only if the absolute difference in the intelligibility of the sentences, expressed in PPC scores, was larger than JND_{PC}. Otherwise, there was no preference and "A B same" option was selected. A small JND_{PC} models a subject

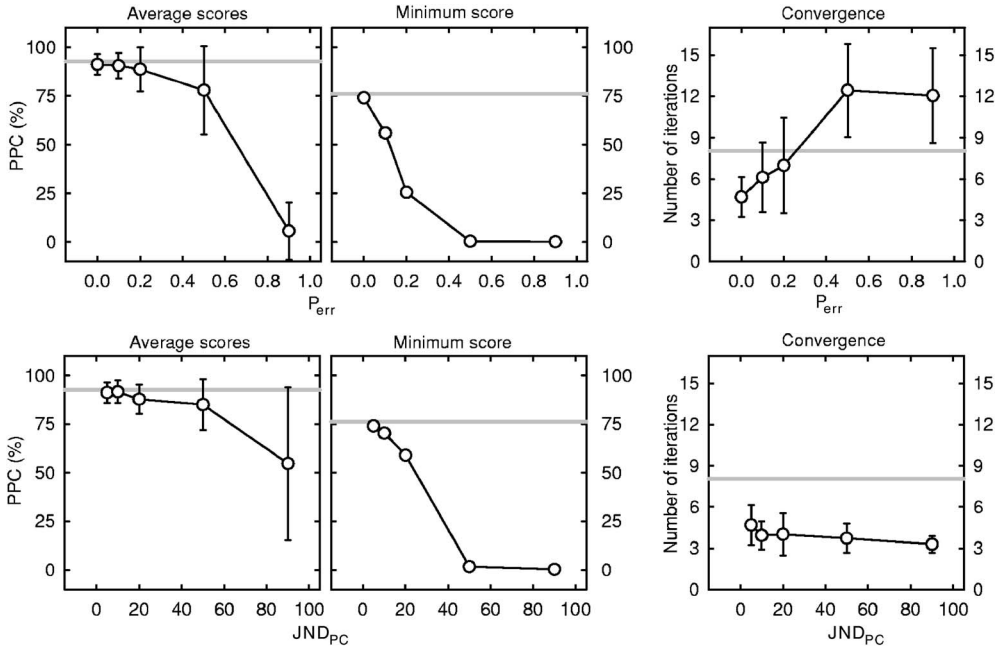

Fig. 2. Simulation results, averaged from 50 GA runs. The upper row shows the simulated performance as a function of P_{err}, probability of error in paired comparisons, and the lower row shows the performance as a function of the JND_{PC}, the smallest difference in percent correct scores that the simulated subject can perceive between the intelligibility levels of two sentences. In each row, the panels from left to right show the average predicted percent correct (PPC) scores, the lowest PPC score observed in 50 GA runs, and the average number of iterations. The gray lines show the data by real listeners, adapted from Başkent *et al.* (2007b). The error bars show one standard deviation.

that can hear a small difference and can correctly judge which sentence is more intelligible. For higher values of JND_{PC}, the simulated subject registers more of the "A B same" option. Therefore, this factor does not produce an error *per se*; rather it decreases the amount of useful information entered into the GA.

3. Results

The effects of the simulated factors were explored by running multiple simulations of the GA and observing the changes in the overall performance. Figure 2 presents the results for the factors of P_{err} and JND_{PC} in the upper and lower panels, respectively. The figure shows the effects of each factor individually; when P_{err} was varied, JND_{PC} was equal to 5%, and when JND_{PC} was varied, P_{err} was equal to 0. The panels from left to right show the average PPC scores averaged across 50 runs, the minimum PPC score of the 50 runs, and the number of iterations at convergence averaged across 50 runs. The gray lines show the corresponding data with real subjects, adapted from Başkent *et al.* (2007b). In each panel, the smallest values of P_{err} and JND_{PC}, 0 and 5%, respectively, simulated the ideal listener. The performance remained high for $P_{err} \leqslant 0.10$ and $JND_{PC} \leqslant 10\%$. As the value of P_{err} increased, the simulated listener made more errors in the paired comparisons, and the overall performance, shown by average PPC, and the probability of the GA producing a poor result in an individual run, shown by the minimum PPC score, decreased, both reaching 0% for very large P_{err}. For high P_{err} values, the number of iterations needed for convergence also increased as the user preferences were not consistent from one iteration to the next. For $P_{err} \geqslant 0.50$, the GA failed to converge for most of the runs and was manually stopped by 15 iterations. JND_{PC} had similar effect on the average and minimum PPC scores. For large JND_{PC} values, the average PPC approached 50% as there was almost no useful information entered by the simulated subject into the GA and the GA would produce

random results that are dominated by the initial random gene population. Similar convergence was observed for all JND_{PC} values. For large JND_{PC} values, this situation indicated a premature convergence, as the GA produced poor solutions despite the fast convergence.

Simulations showed that both factors could affect the outcome of the GA negatively. Further simulations, not included in the present manuscript to ensure brevity, showed that combined effects of these factors could lead to poorer solutions and/or convergence. The experimental data from human subjects, as shown by the gray lines, was most similar to the ideal listener, implying that the input by real subjects into the GA program was sufficiently reliable.

4. Conclusion

Başkent *et al.* (2007b) showed that the GA can produce reasonable solutions with young normal-hearing listeners under controlled laboratory settings. When the data with human listeners was compared to the data with simulated listeners of the present study, it was observed that the performance by real listeners was similar to the ideal user, who was able to distinguish sentences with a small difference in intelligibility and who was also fairly accurate with paired comparisons. Simulations also showed that the particular GA implementation by Başkent *et al.* (2007b) could handle these factors for small values, most probably because all genes were compared to each other in every iteration, which provided plenty of information and many chances for the GA to correct itself. However, for larger values, simulating a situation more likely to occur with elderly and/or hearing-impaired listeners, performance dropped considerably.

Previous studies had proposed optimization algorithms for customizing hearing aids (Durant *et al.*, 2004; Kuk and Pape, 1992; Neuman *et al.*, 1987; Preminger *et al.*, 2000; Stelmachowicz *et al.*, 1994) or cochlear implants (Bourgeois-République *et al.*, 2005; Wakefield *et al.*, 2005) with real patients. Even though the simulation results of the present study would be applicable specifically to the GA implementation reported by Başkent *et al.* (2007b), similar simulations could be used to characterize the effects of differing user skills on how well any perceptual optimization method might work for general population. For example, Başkent *et al.* (2007b) suggested that a smaller number of paired comparisons are made, with the rest being inferred from previous comparisons, to shorten the running time. However, if the listener makes many errors, these errors might carry over to following iterations, and might cause the GA to produce poorer solutions. Using the present study as a guideline, similar simulations can be developed to use as a tool for assessment of such potential modifications. A customized simulation method could be useful in evaluating the potential success of a specific optimization program and also in deciding which operators would result in best performance, in a faster manner before the actual testing with human listeners.

References and links

Başkent, D. (**2006**). "Speech recognition in normal hearing and sensorineural hearing loss as a function of the number of spectral channels," J. Acoust. Soc. Am. **120**, 2908–2925.

Başkent, D., and Shannon, R. V. (**2003**). "Speech recognition under conditions of frequency-place compression and expansion," J. Acoust. Soc. Am. **113**, 2064–2076.

Başkent, D., and Shannon, R. V. (**2007a**). "Combined effects of frequency-place compression-expansion and shift on speech recognition," Ear Hear. **28**, 277–289.

Başkent, D., Eiler, C. N., and Edwards, B. (**2007b**). "Using genetic algorithms with subjective input from human subjects: Implications for fitting hearing aids and cochlear implants," Ear Hear. **28**, 370–380.

Bourgeois-République, C., Chabrier, J. J., and Collet, P. (**2005**). "An interactive evolutionary algorithm for cochlear implant fitting: First results," *Proceedings of the 2004 ACM Symposium on Applied Computings*, pp. 231–235, Santa Fe, New Mexico.

Durant, E. A., Wakefield, G. H., Van Tasell, D., and Rickert, M. E. (**2004**). "Efficient perceptual tuning of hearing aids with genetic algorithms," IEEE Trans. Speech Audio Process., **12**, 144–155.

Fu, Q.-J., and Shannon, R. V. (**1999**). "Recognition of spectrally degraded and frequency-shifted vowels in acoustic and electric hearing," J. Acoust. Soc. Am. **105**, 1889–1900.

Institute of Electrical and Electronics Engineers (**1969**). IEEE recommended practice for speech quality measurements.

Kuk, F. K., and Pape, N. M.C. (**1992**). "The reliability of a modified simplex procedure in hearing aid frequency-response selection," J. Speech Hear. Res. **35**, 418–429.

Mitchell, T. M. (**1997**). *Machine learning* (McGraw-Hill International Ed., Singapore).

Neuman, A. C., Levitt, H., Mills, R., and Schwander, T. (**1987**). "An evaluation of three adaptive hearing aid selection strategies," J. Acoust. Soc. Am. **82**, 1967–1976.
Preminger, J. E., and Van Tasell, D. J. (**1995**). "Measurement of speech quality as a tool to optimize the fitting of a hearing aid," J. Speech Hear. Res. **38**, 726–736.
Preminger, J. E., Neuman, A. C., Bakke, M. H., Walters, D., and Levitt, H. (**2000**). "An examination of the practicality of the simplex procedure," Ear Hear. **21**, 177–193.
Shannon, R. V., Zeng, F-G., Kamath, V., Wygonski, J., and Ekelid, M. (**1995**). "Speech recognition with primarily temporal cues," Science **270**, 303–304.
Stelmachowicz, P. G., Lewis, D. E., and Carney, E. (**1994**). "Preferred hearing aid frequency responses in simulated listening environments," J. Speech Hear. Res. **37**, 712–719.
Takayagi, H. (**2001**). "Interactive evolutionary computation: Fusion of the capabilities of EC optimization and human evaluation," Proc. IEEE **89**, 1275–1296.
Wakefield, G. H., van den Honert, C., Parkinson, W., and Lineaweaver, S. (**2005**). "Genetic algorithms for adaptive psychophysical procedures: Recipient-directed design of speech-processor MAPs," Ear Hear. **26**, 57S–72S.

Resonant frequency shifts induced by a large spherical object in an air-filled acoustic cavity

María Luisa Cordero[a] and Nicolás Mujica
Departamento de Física, Facultad de Ciencias Físicas y Matemáticas, Universidad de Chile, Avenida Blanco Encalada 2008, Santiago, Chile
cordero@ladhyx.polytechnique.fr, nmujica@dfi.uchile.cl

Abstract: Acoustic resonances are modified when objects are introduced into a chamber. The magnitude of these changes depends on the object position, size, and shape, as well as on its acoustic properties. Here, an experimental study concerning the resonant frequency shifts induced by a solid spherical object in a quasi-one-dimensional air-filled acoustic cavity is reported. It is shown that Leung's theory does not account quantitatively for the observations. A novel and simple approach is proposed, based on the wave equation in a cavity of variable cross section. The results fit more accurately the measured frequency shifts.

© 2007 Acoustical Society of America
PACS numbers: 43.20.Ks, 43.20.Mv [AN]
Date Received: March 11, 2007 **Date Accepted:** April 9, 2007

1. Introduction

The acoustic resonances of a cavity are modified when objects are introduced into the chamber. It is well understood that these changes are more pronounced when either the object size increases or the object itself is a very efficient scatterer. Thus, large solid spheres in air-filled cavities, as in this study, or gas bubbles in a liquid, can have considerable effects on the acoustic properties of resonance chambers. These observations indicate that both volumetric and scattering effects are important.

The inclusion of an object in a resonant chamber is analogous to the one-dimensional problem of a mass attached to a string studied a long time ago by Rayleigh.[1] More recently, the two-dimensional version has also been studied by Laura *et al.*[2] The interest in the use of acoustic levitation for space applications, the detection of blockage in nuclear reactors, and the measurements of properties and volumes of objects, in particular rocks, has drawn attention to the effect of introducing an object in acoustic resonant cavities.[3–9] Most of these studies are theoretical, dealing with more or less elaborate techniques to predict the frequency resonance shifts for various object shapes and sizes, as well for different boundary conditions. Experimental results are scant, exceptions being the rather complete studies performed by Barmatz *et al.*[5] and Chen *et al.*[9]

In this letter, we present an experimental study of longitudinal mode resonant frequency shifts induced by a solid spherical object in a quasi-one-dimensional air-filled acoustic cavity. We compare our results with Leung's theory, which does not account quantitatively for the observations. We propose a novel and simple approach based on the wave equation in a cavity of variable cross section. The results fit more accurately the measured frequency shifts.

2. Experimental setup

The experimental setup is composed of a square section quasi-one-dimensional cavity, of dimensions $L_x \equiv L = 100$ mm and $L_y = L_z = 6.8$ mm. Two duraluminum walls allow rigidity and hold two other static dissipative acrylic walls which in turn allow visualization (see Fig. 1). Another two duraluminum end walls close the cavity on each side. One of them is attached to an

[a]Present address: Laboratoire d'Hydrodynamique, Ecole Polytechnique, 91128 Palaiseau Cedex, France.

 © 2007 Acoustical Society of America

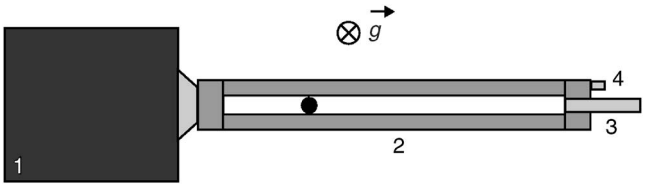

Fig. 1. Experimental setup. (1) Electromechanical vibrator, (2) quasi-one-dimensional square section cavity, (3) microphone, and (4) accelerometer. A metallic magnetic sphere is placed inside and held fixed by another magnetic sphere from outside. The origin is chosen at the wall close to the vibrator.

electromechanical vibrator (Bruel & Kjaer mini-shaker 4810), which provides a maximum force of 10 N in a large frequency range, typically between 100 Hz and 18 kHz, but provides a constant acceleration amplitude in the 100–5000 Hz range. The cavity is placed such that both acrylic walls are normal to gravity, hence the system is visualized from above. It oscillates entirely in the direction of the vibrator's axis, which has been shown to be an efficient way to amplify resonant acoustic modes.[10]

A microphone and an accelerometer (PCB 130D20 and 340A65, respectively) allow measurements of the cavity's end side acoustic pressure and acceleration of the whole system. The microphone is placed inside the cavity, flush with the end wall, and it has a 6.35-mm-diam active surface. The accelerometer is placed at the external end side with its axis parallel to the cavity's axis. The electromechanical shaker is powered by an amplifier with a signal generated by a spectrum analyzer (SR780). Experiments are performed in the analyzer's swept sine mode. The analyzer measures both the pressure and acceleration amplitude values.

At low frequencies, where the cavity is considered as quasi-one-dimensional, the empty cavity resonant frequencies differ very little from those predicted theoretically. The predicted fundamental frequency is given by $\hat{f}_0 = c/2L$, where c is the sound speed in air. c depends on temperature,[11]

$$c = 331.5\sqrt{1 + \frac{T_C}{273}}\ \text{m/s}, \tag{1}$$

where T_C is in degrees Celsius. Hence, $\hat{f}_0$ also has a temperature dependence. However, a temperature variation of $\pm 1\ ^\circ\text{C}$ only induces a $\pm 0.2\%$ change in $\hat{f}_0$. Care was taken in order to avoid larger temperature variations.

At the operating temperature $T_C = 20.75 \pm 0.5\ ^\circ\text{C}$, we have $c = 343.9 \pm 0.3$ m/s, and thus the predicted resonant frequency is $\hat{f}_0 = 1719.3$ Hz. However, the measured value is $f_0 = 1702.7$ Hz, 1% lower than $\hat{f}_0$. We assume this difference is due to a slightly larger effective length $L_{\text{eff}} = 0.101$ m, which is only 1 mm longer. Considering that the pressure sensor front—active—surface is rather soft, it is reasonable to consider the real stiff element to be slightly behind it.

In order to study the resonant frequency shifts induced by a spherical object, a 6.35-mm-diam metallic, magnetic sphere is placed inside and held fixed by means of a similar magnetic sphere placed outside the cavity. Once the intruder is fixed and its position determined, a pressure spectrum is obtained between 1 and 10 kHz, with a roughly constant dimensionless peak acceleration (≈ 0.5 g), resulting in a maximum pressure of ≈ 10 Pa. This was performed for 90 different positions, separated by 1 mm, from $X_0 = 4$ mm to $X_0 = 94$ mm. Because of the magnetic nature of the spheres, no measurements were possible for $X_0 < 4$ mm or $X_0 > 94$ mm.

3. Experimental results and comparison with Leung's theory

The measured resonant frequencies as functions of X_0 are presented in Fig. 2. Results are shown from the first to the fifth longitudinal resonant mode. As previously observed by Leung *et al.*,[3]

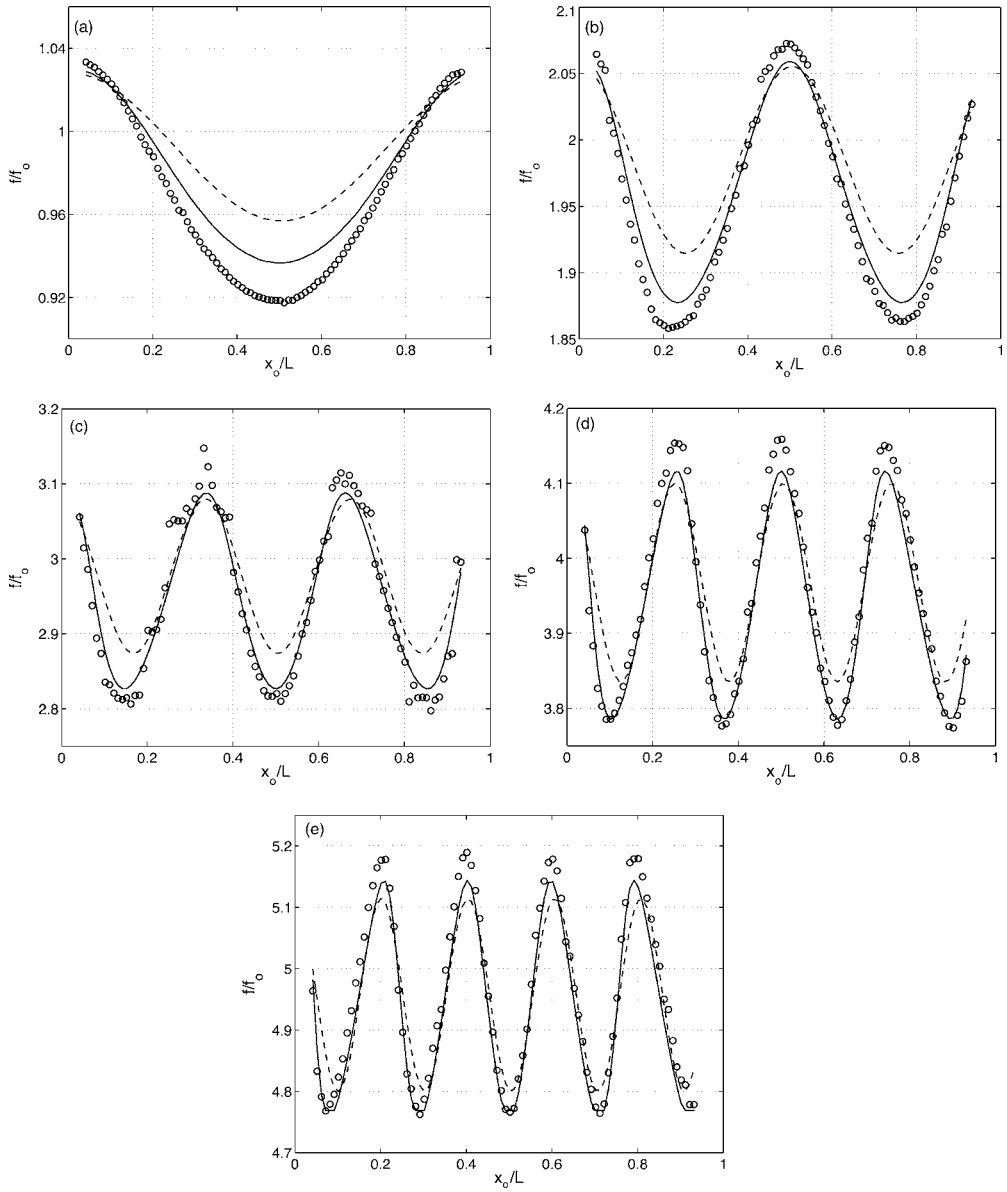

Fig. 2. Normalized resonant frequencies f/f_0 vs X_0 for the first five longitudinal modes (a) $n=1$, (b) $n=2$, (c) $n=3$, (d) $n=4$, and (e) $n=5$: Experiments (○), Leung's prediction (dashed line), and solution of the variable cross-section model (continuous line). Both theoretical predictions are computed using $L_{\text{eff}}=0.101$ m.

the resonant frequencies depend on the sphere's position, varying in an oscillatory way as a function of X_0, such that the number of oscillations is equal to the mode number, $n=1,\ldots,5$. In our case, however, variations are stronger, of the order of 10% peak-to-peak, due to the larger sphere-to-cavity volume ratio. Notice that all except one mode show relatively smooth variations; the third mode indeed presents some noise due to the difficulty in measuring the resonant frequencies from pressure spectra in this case as it was of particularly low amplitude, i.e., with a small signal-to-noise ratio.

We can qualitatively understand the fact that the resonant frequencies vary roughly periodically with X_0 with a very simple argument: By integrating the Helmholtz equation, the wave number is given by[3]

$$k^2 = \frac{\frac{1}{2}\int |\nabla p|^2 dV}{\frac{1}{2}\int p^2 dV} \propto \frac{K}{V}, \tag{2}$$

where integration is performed in the available volume. K and V stand for the kinetic and potential energy, respectively. Thus, when the sphere is located near a pressure maximum, for example at a cavity end wall, which in turn is a velocity node ($\nabla p \approx 0$), the kinetic energy does not change much but the potential energy is reduced. The final result is an increase in the corresponding wave number, hence an increase in the resonant frequency is expected. The inverse argument can be made when the intruder is near a velocity maximum, for example, at $X_0/L \approx 1/2$ for the first mode. In this case k, and thus f, is expected to decrease.

An analytical expression was obtained by Leung *et al.*[3] From a Green's function scattering calculation they obtained the resonant wave number as a function of three parameters: the sphere to cavity volume ratio V_s/V, the sphere to cavity length ratio R/L, and the sphere's relative position X_0/L. Assuming small spherical scatters, such that $kR \ll 1$ where R is the sphere radius and k is the wave number, they performed their calculation for longitudinal modes in a rectangular cavity of length L. The predicted wave number shift is

$$\frac{\delta k}{k_n} = \frac{V_s}{V}\left[-\left(\frac{1}{4} + \frac{67}{360}(k_n R)^2\right)\right] + \frac{V_s}{V}\left[\left(\frac{5}{4} - \frac{229}{360}(k_n R)^2\right)\cos(2k_n X_0)\right], \tag{3}$$

where $\delta k = k - k_n$. The calculation is done up to order $(k_n R)^2$, $k_n = n\pi/L$ being the nth longitudinal mode wave number for the empty cavity. $V_s(V)$ is the sphere (cavity) volume, and X_0 is the sphere's position. From Eq. (3) we obtain the resonant frequencies

$$f = \frac{ck_n}{2\pi}\left(1 + \frac{\delta k}{k_n}\right).$$

The comparison made in Fig. 2 shows that this expression does follow qualitatively the measured resonant frequencies for all modes although important differences are present. In fact, Eq. (3) considers both volumetric and scattering effects [$\sim(k_n R)^2$], being the volumetric effects dominant. The discrepancies between Leung's prediction and our measurements are probably due to the breakdown of the single spherical scattering approximation (no wall contributions). It is also important to note that Leung *et al.* did not observe differences in resonant frequencies for scatterers made of different solid materials, as expected when both the density and compressibility differences are so large between solids and air. We also verified this in our setup with plastic spheres.

In order to compare quantitatively the predicted resonant frequencies and the measured ones, we define the difference parameter, or error estimator, for the nth mode as

$$\chi_n^2 = \sum_{i=1}^{N} \frac{(f_t^n(i) - f_m^n(i))^2}{N f_0^2}, \tag{4}$$

where $f_t^n(i)$ and $f_m^n(i)$ are the theoretical and measured resonant frequencies, respectively, for the sphere at the ith position, and $N=90$ is the number of positions (i.e., measured resonant frequencies). The χ_n^2 parameters calculated for $n=1,\ldots,5$ are presented in Table 1.

Table 1. Error estimator χ_n^2 for the first five modes, using Leung's formula and the results obtained considering a variable section cavity. All values are $\times 10^{-3}$. The ratio between both parameters is given in the third row.

	$n=1$	$n=2$	$n=3$	$n=4$	$n=5$
Leung	0.68	1.57	2.49	2.21	2.50
Wave Eq. (8)	0.14	0.21	0.62	0.64	1.03
Ratio	5.0	7.6	4.0	3.5	2.4

4. Resonant frequecy shifts obtained from the wave equation in a cavity of variable cross section

We assume that we have an acoustic cavity of cross section $S(x)$, in which a homogeneous fluid sustains acoustic waves. In this case the wave equation is modified. Using the usual linear approximation $\rho=\rho_0+\rho'$ and $P=P_0+p$, in the quasi-one-dimensional limit of interest, one obtains[12]

$$\frac{1}{c^2}\frac{\partial^2 p}{\partial t^2}=\frac{1}{S}\frac{\partial}{\partial x}\left(S\frac{\partial p}{\partial x}\right). \tag{5}$$

We can identify three regions in the cavity: Regions I, II and III, for $x<X_0-R$, $X_0-R<x<X_0+R$, and $x>X_0+R$, respectively. The transverse section then is written

$$S=\begin{cases} S_0 & \text{if } x<X_0-R \\ S_0-\pi(R^2-(x-X_0)^2) & \text{if } X_0-R<x<X_0+R \\ S_0 & \text{if } x>X_0+R, \end{cases} \tag{6}$$

where $S_0=L_y\times L_z$. Notice that the exact sphere position in the (y,z) plane does not matter in this framework.

Now, let us impose wave solutions of the form $p(x,t)=p(x)e^{-i\omega t}$. We obtain two equations that must be solved. First, the Helmholtz equation

$$k^2 p+\frac{d^2 p}{dx^2}=0, \tag{7}$$

which must be solved in regions I and III. The second equation, valid for region II, is

$$k^2 p+\frac{1}{\hat{S}(x)}\frac{d}{dx}\left[\hat{S}(x)\frac{dp}{dx}\right]=0, \tag{8}$$

where $\hat{S}(x)=S_0-\pi[R^2-(x-X_0)^2]$. In addition to the rigid termination conditions ($dp/dx=0$) at $x=0$ and $x=L$, the solutions of these equations have to satisfy pressure and acoustic velocity continuity conditions at $x=X_0-R$ and $x=X_0+R$.

The solutions in regions I and III are the usual plane wave solutions

$$p(x)=\begin{cases} P_0\cos kx & \text{(Region I)} \\ P_1\cos k(L-x) & \text{(Region III)}, \end{cases} \tag{9}$$

which satisfy the rigid conditions in the ends of the cavity. Here we put P_0 and P_1 as the (unknown) pressure amplitudes at the left and right sides of the sphere.

In order to solve Eq. (8), we make the change of variable $z=(x-X_0)/R$, obtaining

$$\frac{d^2p}{dz^2} + \frac{2z}{\sigma - 1 + z^2}\frac{dp}{dz} + (kR)^2 p = 0 \tag{10}$$

with $-1 < z < 1$ and $\sigma = s_0/\pi R^2$. The solution of this equation can be expressed in terms of the confluent Heun function[13] $\mathrm{HC}(\alpha, \beta, \gamma, \delta, \eta; x)$:

$$p(z) = A\mathrm{HC}\left(0, -\frac{1}{2}, 0, -\frac{1}{4}(kR)^2(\sigma - 1), \frac{1}{4} + \frac{1}{4}(kR)^2(\sigma - 1); -\frac{z^2}{\sigma - 1}\right) + B\mathrm{HC}\left(0, \frac{1}{2}, 0, -\frac{1}{4}(kR)^2(\sigma - 1), \frac{1}{4} + \frac{1}{4}(kR)^2(\sigma - 1); -\frac{z^2}{\sigma - 1}\right) z. \tag{11}$$

The boundary conditions (continuity of both pressure and acoustic velocity) can then be written as an homogeneous linear system with four unknowns, P_0, P_1, A, and B. Imposing the determinant of the system to be equal to zero it is possible to find a trascendental equation for k. The results obtained with this procedure are also presented in Fig. 2. We observe that for all modes the comparison is better than the results obtained with Leung's calculation. As before, the parameter χ_n^2 is computed for each mode. Table 1 shows that overall, despite its simplicity, our model performs much better that Leung's calculation.

5. Conclusions

In summary, we have performed an experimental study of the resonance frequency shifts of longitudinal modes in a quasi-one-dimensional air-filled acoustical cavity of rectangular cross section induced by the inclusion of a spherical solid object of diameter comparable to the cross-section length. Measurements were performed for the first five longitudinal modes. Depending on the object position, the measured resonant frequencies vary in an oscillatory way.

Leung's theory, which is valid in the small sphere limit, does account qualitatively for the observations, although important differences are observed. Surprisingly these predictions are not so bad quantitatively, even when the single sphere—no wall—approximation does not hold in our setup. This is probably due to the fact that for a solid sphere in air and for long wavelengths, single scattering effects are small. The question about how the sphere wall interaction (multiple scattering) modifies this remains an open question.

We have developed a simple quasi-one-dimensional model where we consider the cavity with the intruder as a chamber of variable cross section. Hence, this model solely considers volumetric effects. For the well-known wave equation (5) we impose a given form of $S(x)$ from which we can compute the resonant wave numbers, and therefore the resonant frequencies. The global performance of each model is quantified through a difference parameter χ_n^2 for each longitudinal mode. The new predictions agree much better with measurements than Leung's theory.

Acknowledgments

The authors acknowledge support from CONICYT Fondecyt Grant No. 1050331 and *Fundación Andes* Grant No. C-13960/9. N.M. also acknowledges support from ACT Grant No. 15 (*Anillo en Ciencia y Tecnología*), and Fondap Grant No. 11980002.

References and links

[1] J. W. S. Rayleigh, *The Theory of Sound*, 2nd ed. (MacMillan, London, 1894).
[2] P. A. A. Laura, R. H. Gutierrez, and G. S. Sarmiento, "Comparison of variational and finite element solutions of Helmholtz equation," J. Acoust. Soc. Am. **68**, 1160 (1980).
[3] E. Leung, C. P. Lee, N. Jacobi, and T. G. Wang, "Resonance frequency shift of an acoustic chamber containing a rigid sphere," J. Acoust. Soc. Am. **72**, 615–620 (1982).
[4] M. El-Raheb and P. Wagner, "Acoustic propagation in rigid ducts with blockage," J. Acoust. Soc. Am. **72**, 1046–1055 (1982).
[5] M. Barmatz, J. L. Allen, and M. Gaspar, "Experimental investigation of the scattering effects of a sphere in a cylindrical resonant chamber," J. Acoust. Soc. Am. **73**, 725–732 (1983).
[6] J. B. Mehl and R. N. Hill, "Acoustic eigenfrequencies of cavities with an internal obstacle: A modified

perturbation theory," J. Acoust. Soc. Am. **85**, 1841–1851 (1989).
[7]J. A. Roumeliotis, "Eigenfrequencies of an acoustic rectangular cavity containing a rigid small sphere," J. Acoust. Soc. Am. **93**, 1710–1715 (1993).
[8]J. M. Harris, D.-L. Xu, X.-M. Wang, Y.-J. Song, J.-S. Cong, and D.-H. Chen, "Resonance frequency shift in a cylindrical cavity with an inner small coaxial cylinder," Chinese J. of Geophysics **48**, 493–500 (2005).
[9]D.-H. Chen, X.-M. Wang, J.-S. Cong, D.-L. Xu, Y.-J. Song, and S.-L. Ma, "Experimental studies on perturbed acoustic resonant spectroscopy by a small rock sample in a cylindrical cavity," Sci. China, Ser. G **49**, 683–701 (2006).
[10]C. C. Lawrenson, B. Lipkens, T. S. Lucas, D. Perkins, and T. W. van Doren, "Measurements of macrosonic standing waves in oscillating closed cavities," J. Acoust. Soc. Am. **104**, 623–636 (1998).
[11]M. F. Hamilton and D. T. Blackstock, *Nonlinear Acoustics* (Academic, New York, 1998).
[12]L. D. Landau and E. M. Lifshtz, *Fluid Mechanics* (Pergamon, London, 1959).
[13]A. Ronveaux, *Heun's Differential Equations* (Oxford University Press, New York, 1995).

Hybrid passive-active absorption of a microperforated panel in free field conditions

Pedro Cobo and María Cuesta
Instituto de Acústica, CSIC, Serrano 144, 28006 Madrid, Spain
pcobo@ia.cetef.csic.es, mcuesta@ia.cetef.csic.es

Abstract: Although hybrid passive-active absorption in impedance tubes has been widely analyzed, its study in more realistic conditions remains to be accomplished. This letter describes the practical measurement of the passive-active absorption coefficient in a free field. The passive absorber consists of a microperforated panel backed by an air cavity and a wooden panel. A multichannel active system controls the sound pressure in a reduced cell behind the absorber. Measured absorption coefficients between 200 and 400 Hz account for 0.2–0.4 and 0.72–0.75, in the passive and active cases, respectively, and above 500 Hz both are comparable.

© 2007 Acoustical Society of America
PACS numbers: 43.55.Ev, 43.50.Ki, 43.50.Gf [MS]
Date Received: March 8, 2007 **Date Accepted:** April 20, 2007

1. Introduction

Many results have proven the reliability of combining passive and active absorbers to control broadband standing-wave fields (Furtoss *et al.*, 1997; Beyene and Burdisso, 1997; Cobo *et al.*, 2003, 2004; Sellen *et al.*, 2006). Traditional absorbers are realized with a porous material backed by an air cavity and a rigid ending. According to the acoustic properties of the material as well as the size of each layer, the absorption spectrum of such a two-layer liner is tuned in a specific medium and high frequency bandwidth. Guiking and Lorentz (1984) proposed an equivalent low frequency absorber, by replacing the rigid termination with a loudspeaker driven so as to minimize the pressure in a microphone just behind the material (*pressure-release condition*). This first active absorber provided an absorption coefficient of 0.6–0.7 between 200 and 500 Hz, using an analogue electronic device. Furtoss *et al.* (1997) proposed a low frequency absorber that actively controlled the impedance at the input of the liner. This methodology was recently applied to flow duct applications (Sellen *et al.*, 2006). Another strategy for designing active absorbers was the *impedance matching condition* (Beyene and Burdisso, 1997) which attempted to cancel the reflected sound field inside the air gap at the rear face of the material. Cobo *et al.* (2003) demonstrated that the performance of both approaches (*pressure release and matching impedance*) depended on the properties of the material, the pressure-release condition affording higher absorption when the flow resistance of the porous layer was matched to the acoustic impedance of the air. Since the final prototype must be lightweight and thin for practical implementations, the porous material can be substituted by a microperforated panel (MPP). Cobo *et al.* (2004) designed a hybrid passive-active absorber with a MPP properly perforated and 5 cm of air gap, reporting 82% of absorption in the frequency range from 100 to 1600 Hz. In general, good agreement is found between theoretical and experimental hybrid passive-active absorption coefficients in standing wave tubes.

To the knowledge of the authors, the performance of such absorbers has still not been proven in more realistic conditions. When trying to extrapolate the results obtained in the impedance tube to the free field, some difficulties are encountered. The first one regards the measurement technique. In free field measurements, reflection techniques are more suitable to afford the absorption coefficient of the sample (Garai, 1993; Cobo, 2007). The main complexity of such a technique is to separate the reflected from the diffracted events at the measured reflec-

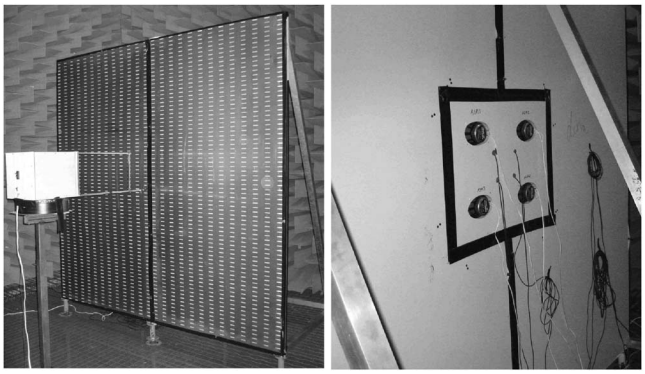

Fig. 1. Front (left) and rear (right) views of the hybrid passive-active microperforated absorber in anechoic room.

tion trace. This is carried out by time windowing the reflected event. Cobo *et al.* (2007) have demonstrated that this procedure can be improved by shaping the frequency response of the loudspeaker-microphone in order to radiate shorter pulses.

The second limitation is that the sound field in an extended absorber is much more complex than in an impedance tube. Only plane waves are propagated at frequencies below the first radial mode in an impedance tube. Consequently, when the sound pressure just behind the material is released, the input impedance of the system matches that of the air at low frequencies, and high active absorption is guaranteed. However, it has not yet been confirmed that this reduction of the pressure field at the rear face of the material furnishes active absorption in an extended panel.

The aim of this letter is to assess the practical capability of an extended microperforated liner to provide hybrid passive-active absorption in free field conditions. Such a hybrid passive-active absorber is described in Sec. 2. Results on passive and active absorption in an anechoic room are reported in Sec. 3.

2. Hybrid passive-active absorber in anechoic room

The passive absorber consists of a (2.44 m $\times$ 2.44 m $\times$ 1 mm) perforated sheet in front of a rigid panel, with a 5-cm-deep air cavity in between. According to Maa (1998), an optimally tuned MPP absorber has a thickness of the same order as its perforation diameter. Since for optimal absorption the perforation diameter should be less than 1 mm, the resulting low thickness of the panel would constrain its mechanical implementation in such a two-layer absorber configuration. Pfretzschner *et al.* (2006) proposed an alternative methodology to construct more structurally robust MPPs, combining a thick panel with large perforations with a thinner one highly perforated. The passive absorption of such an extended absorber has already been measured, at normal incidence (Pfretzschner *et al.*, 2006), at low angles of incidence in a free field (Cobo *et al.*, 2006a), and in a reverberation room (Cobo *et al.*, 2006b). The current research is concerned with the design of the active absorber as well as the hybrid passive-active absorption measurements.

Figure 1 shows front and rear views of such an extended hybrid passive-active absorber in an anechoic room. The MPP layer is made with a 1-mm-thick steel panel whose perforation diameter and perforation ratio are 8 mm and 10%, respectively. This sheet is backed by a mesh 39 μm thick, with a perforation ratio of 14% and holes with a diameter of 39 μm. In order to experimentally check the reliability of the pressure release condition in such an extended absorber, an active cell has been implemented in a reduced size (62 cm $\times$ 54 cm $\times$ 5 cm) centered panel at the wooden back of the prototype. As can be seen in Fig. 1, this active cell is divided into four separated equal units. Each one is acting as a local feedforward control system. The loudspeaker in each cavity is driven according to the FXLMS algorithm so as to minimize a broadband field picked up by a microphone centered just behind the MPP. The

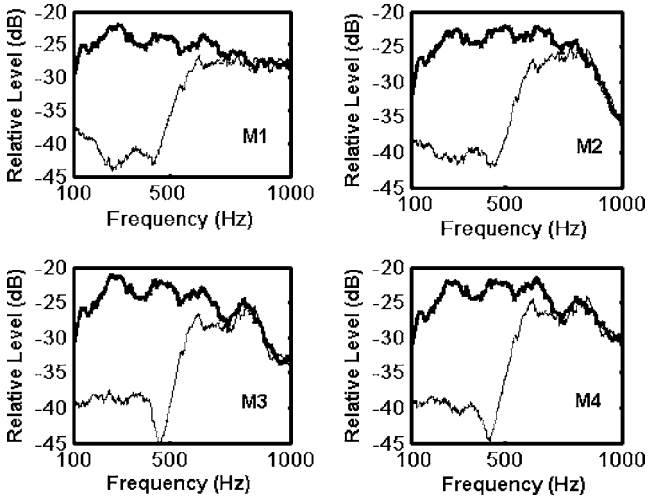

Fig. 2. Spectral levels of the error microphones inside the active cell with the active controller switched off (thick line) and on (thin line).

electrical signal driving the primary loudspeaker placed in front of the absorber (see Fig. 1) is also used as reference signal for the active controller. The control and error path identification filters operate concurrently. Both the number of taps and the algorithm convergence parameter of the control and error path identification filters can be modified to optimize the cancellation at the microphones.

Both passive and active absorption coefficients of such a prototype have been measured with the method outlined by Cobo *et al.* (2006a, 2007). This MLS (maximum length sequences) impulsive technique requires a loudspeaker-microphone system optimally positioned according to their relative distances to the sample (see Fig. 1). First, the electroacoustic system should record the direct event (without absorber). Then, it is turned toward the absorber and the reflection trace is measured. Since this latter trace also contains diffractions from the edges, the reflected event is picked up by windowing. Direct and reflected events, both filtered with the same window, are use to obtain the passive absorption coefficient of the prototype (Cobo, 2007). First, the passive absorption (active cells off) is measured. Then, the multichannel controller is configured to reduce the MLS primary field radiated by the measuring loudspeaker, at the error sensor locations. Once this cancellation is optimal, the filter coefficients are locked and the active absorption is measured.

3. Results

Results reported in this section concern normal incidence. Figure 2 shows the spectra of the four error microphones inside each local active cell with the active controller switched off (thick line) and on (thin line). The primary MLS noise is sampled at 2500 Hz. The active controller cancels this primary noise between 15 and 20 dB below 500 Hz. Both the adaptive control and error path filters have been optimally set up to 70 taps and a convergence parameter of 0.1.

Figure 3 shows the direct trace (above) and both reflected traces in front of the extended absorber, for the passive (center) and active (below) configuration. These traces have been measured at normal incidence, with the loudspeaker and the microphone 90 and 5 cm away from the center of the panel, respectively. This is the optimal loudspeaker-microphone configuration for the size of the tested panel (Cobo *et al.*, 2006a). Time windowing removes low frequencies from the measured signals, so that this method has a lowest reliable frequency inversely related with the window length (Cobo, 2007). For the time window illustrated in Fig. 3, the lowest reliable frequency was 217 Hz.

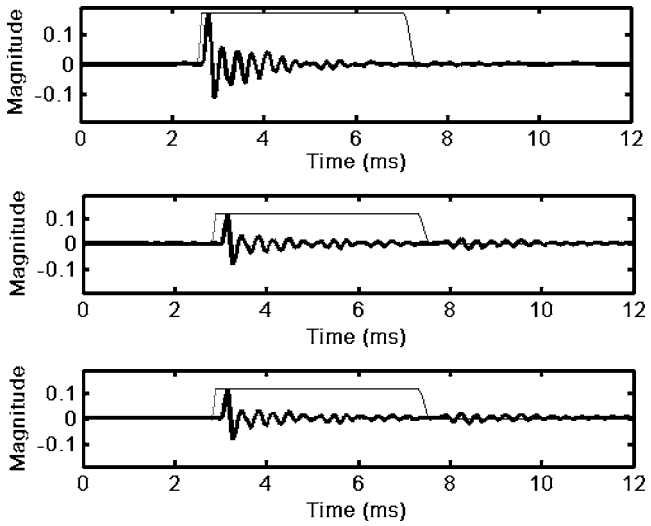

Fig. 3. Direct (above), passive reflected (center), and active reflected (below) traces, with the selecting windows overlapped (thin lines).

Figure 4 shows the passive and active reflection coefficients obtained from the traces of Fig. 3. Both passive and active theoretical absorption coefficients at normal incidence (Cobo *et al.*, 2004) are also included for the sake of comparison. The experimental passive curve presents a slight notch around 600 Hz. It is believed to be due to the aperture made to the back wooden panel in order to place the active cell. The active absorption coefficient, as expected theoretically, improves the absorption curve in the low frequency range. The cut-off frequency between the passive and active configuration appears around 470 Hz. The absorption coefficient from 200 to 400 Hz ranges from 0.2 to 0.4 for the passive absorber and from 0.72 to 0.75 for the active-passive absorber, demonstrating the low frequency enhancement expected for the active component of the system. Above 500 Hz the passive and the active-passive systems provided comparable performance, as expected. The absorption coefficient averaged from

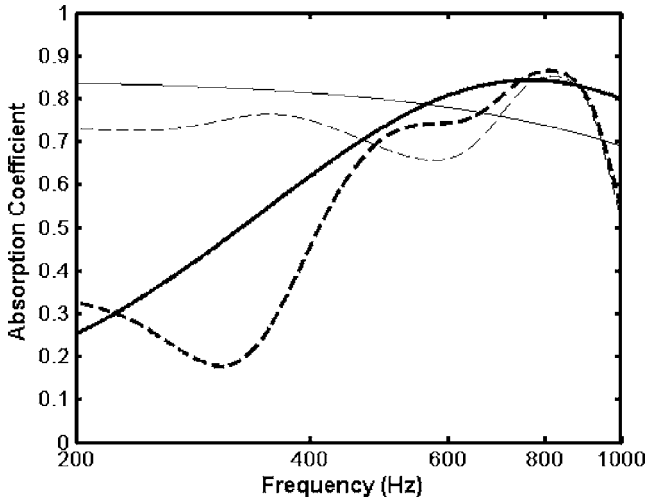

Fig. 4. Passive theoretical (thick solid line), passive experimental (thick dashed line), active theoretical (thin solid line), and active experimental (thin dashed line) absorption coefficients of the MPP.

217 to 1000 Hz is 0.6 for the passive absorber and 0.75 for the active one.

4. Summary and conclusions

Authors have demonstrated in previous papers that hybrid passive-active systems are able to provide broadband noise absorption in an impedance tube. A passive-active microperforated absorber of only 5 cm thickness afforded 82% of absorption in the frequency band from 100 to 1600 Hz. Although such a high hybrid absorption can be hopefully foreseen with extended samples, experimental results supporting this presumption have not been reported yet. This letter is pioneering in accounting for such results.

Measurements of passive-active absorption of an extended microperforated absorber of (2.44 m $\times$ 2.44 m $\times$ 5 cm) in an anechoic room are reported. Absorption coefficients have been measured according to a MLS impulsive technique which allows separating by windowing the reflected event at the sample from diffractions at its edges. Since this time windowing removes low frequencies from the traces, this method has a lowest reliable frequency inversely related to the window length. The lowest reliable frequency of measurements was 217 Hz.

A multichannel active control system has been set up in a reduced size cell (62 cm $\times$ 54 cm $\times$ 5 cm) at the back of the absorber. It was implemented with four loudspeaker-microphone units, each one acting as a local active cell. The loudspeaker in each local cell was driven according to the FXLMS algorithm so as to minimize the MLS primary field picked up by a microphone just behind the microperforated panel. These error signal spectra were attenuated between 15 and 20 dB in the frequency band up to 500 Hz. Results have proven that active reduction of the sound pressure behind the extended liner can provide improved absorption at low frequency. The absorption coefficient from 200 to 400 Hz ranges from 0.2 to 0.4 for the passive absorber and from 0.72 to 0.75 for the active-passive absorber, demonstrating the low frequency enhancement expected for the active component of the system. Above 500 Hz the passive and the active-passive systems provided comparable performance, as expected.

Acknowledgment

This work has been supported by the Spanish Ministry of Education and Science through Grant No. DPI2004-05504-C02-01.

References and links

Beyene, S., and Burdisso, R. A. (**1997**). "A new hybrid passive/active noise absorption system," J. Acoust. Soc. Am. **101**, 1512–1515.

Cobo, P. (**2007**). "A model comparison of the absorption coefficient of a Microperforated Insertion Unit in the frequency and time domains," Appl. Acoust. (in press).

Cobo, P., Cuesta, M., Pfretzschner, J., Fernández, A., and Siguero, M. (**2006a**). "Measuring the absorption coefficient of panels at oblique incidence by using inverse filtered MLS signals," Noise Control Eng. J. **54**, 414–419.

Cobo, P., de la Colina, C., Pfretzschner, J., Cuesta, M., and Fernández, A. (**2006b**). "Characterisation of a Microperforated Insertion Unit (MIU) in a reverberant room," Acta. Acust. Acust. **92** (Supp. 1), S108.

Cobo, P., Fernández, A., and Cuesta, M. (**2007**). "Measuring short impulse responses with inverse filtered maximum length sequences," Appl. Acoust. **68**, 820–830.

Cobo, P., Fernández, A., and Doutres, O. (**2003**). "Low frequency absorption using a two-layer system with active control of input impedance," J. Acoust. Soc. Am. **114**, 3211–3216.

Cobo, P., Pfretzschner, J., Cuesta, M., and Anthony, D. K. (**2004**). "Hybrid passive-active absorption using microperforated panels," J. Acoust. Soc. Am. **116**, 2118–2125.

Furstoss, M., Thenail, D., and Galland, M. A. (**1997**). "Surface impedance control for sound absorption: Direct and hybrid passive/active strategies," J. Sound Vib. **203**, 219–236.

Garai, M. (**1993**). "Measurement of the sound absorption coefficient in situ: The reflection method using periodic pseudo-random sequences of maximum length," Appl. Acoust. **39**, 119–139.

Guicking, D., and Lorentz, E. (**1984**). "An active sound absorber with porous plate," Trans. ASME, J. Vib., Acoust., Stress, Reliab. Des. **106**, 389–392.

Maa, D. Y. (**1998**). "Potential of microperforated panel absorber," J. Acoust. Soc. Am. **104**, 2861–2866.

Pfretzschner, J., Cobo, P., Simón, F., Cuesta, M., and Fernández, A. (**2006**). "Microperforated insertion units: An alternative strategy to design microperforated panels," Appl. Acoust. **67**, 62–73.

Sellen, N., Cuesta, M., and Galland, M. A. (**2006**). "Noise reduction in a flow duct: Implementation of a hybrid passive/active solution," J. Sound Vib. **297**, 492–511.

Directive sources in acoustic discrete-time domain simulations based on directivity diagrams

José Escolano[a] **and José J. López**
Audio and Communication Research Group, iTEAM, Technical University of Valencia, E-46021 Valencia, Spain
escolano@ujaen.es, jjlopez@dcom.upv.es

Basilio Pueo
Signals, Systems and Telecommunication Research Group, University of Alicante, E-03690 Alicante, Spain
basilio@ua.es

Abstract: Discrete-time domain methods provide a simple and flexible way to solve initial boundary value problems. With regard to the sources in such methods, only monopoles or dipoles can be considered. However, in many problems such as room acoustics, the radiation of realistic sources is directional-dependent and their directivity patterns have a clear influence on the total sound field. In this letter, a method to synthesize the directivity of sources is proposed, especially in cases where the knowledge is only based on discrete values of the directivity diagram. Some examples have been carried out in order to show the behavior and accuracy of the proposed method.

© 2007 Acoustical Society of America
PACS numbers: 43.55.Ka, 43.58.Ta, 43.28.Js [NX]
Date Received: March 28, 2007 **Date Accepted:** April 22, 2007

1. Introduction

The limitations involved in the analytical solving of initial boundary value problems in different research fields, such as acoustics, is a familiar problem. Numerical methods have been proposed as accurate and efficient models to determine the sound field distribution in *N*-dimensional problems. In room acoustics, sound field distribution can be predicted in this way and the use of numerical approaches, among other proposed methods, which are based on discrete-time domain methods, has gained popularity.[1,2]

Discrete-time domain methods are based on the spatial-temporal discretization of the wave equation. According to this, a mesh of discretized spatial points represents the sound field for a given time step. Among different paradigms in the discrete-time domain applied to the room acoustic problems, the most frequently used methods are the finite-difference time-domain[3] (FDTD), digital waveguide mesh[4] (DWM), transmission line matrix[5] (TLM), and the recently proposed functional transformation method[6] (FTM).

The initial conditions for these methods are uniquely expressed as a distribution of monopoles (pressure sources), and dipoles (particle velocity sources) particularly in the case of the FDTD method; but in practical and more general problems, sources are too far to be represented as monopole or dipole sources and more complex source modeling is required. Sound source modeling aims to achieve realistic sound inside a virtual environment with characteristics resembling those of a real source. One of these characteristics is the directivity,[7] whose effects over the sound perception of the virtual room becomes highly significant.[8] Although this topic has been addressed in other auralization methods, such as image-source methods[9] or ray-tracing,[10] complex directive sources have only been proposed, very recently, in a particular discrete-time domain method—the DWM method.[11] However, this is not a generalized method

[a]Also at Telecommunication Engineering Department, University of Jaen, E-23700, Linares, Spain.

 © 2007 Acoustical Society of America

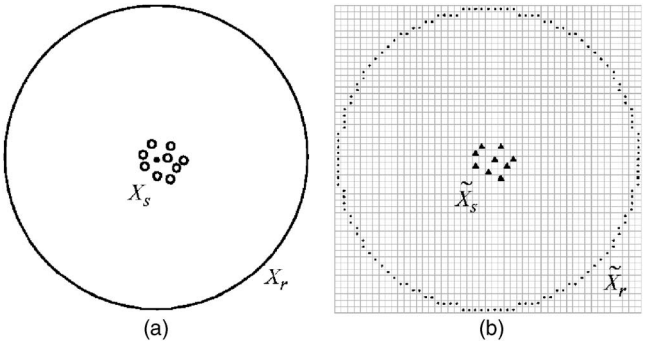

Fig. 1. (a) Source-receiver points distribution. (b) Space sampled distribution of source-receiver points.

that can be used in the rest of the methods and it only allows non-frequency-dependent implementations. A method able to solve more general problems (frequency-dependent directivities) and other more efficient discrete-time domain methods, such as FDTD and FTM, is necessary.[12]

Furthermore, in order to obtain information regarding the directivity of real sources as a function of the angles in a three-dimensional (3D) space and also as a function of the frequency in the bandwidth of interest, complex facilities are required, e.g., anechoic chambers. Unfortunately though, available public databases on this topic are not widespread. However, directivity diagrams of sources for discrete frequencies are more common and they are available in technical literature.[13]

This letter proposes a method of incorporating directive sources for discrete-time domain methods, based on the information obtained in the directivity diagrams for discrete frequencies. It can be applied to other more general problems in acoustics, but in this letter its use in room acoustics is emphasized.

2. Method

As mentioned in Sec. I, the proposed method tries to simulate the behavior of a directive source when it is used in discrete-time simulations. To accomplish this task its uses an array of basic sources (monopoles) placed around the position of the directive source to be synthesized [see Fig. 1(a)]. The method is based on the combination of an array of monopoles with different amplitudes and phases in order to reproduce a desired sound field at given points.[14] If such points are selected for spherical distribution in far field, the resulting pressure pattern is directly the directivity diagram of the source.

Therefore, the objective is to obtain the proper combination of signals that excite the source distribution in order to obtain the desired angle-dependent behavior. However, the space sampling process forces the source and receiver points to be located at discrete positions [see Fig. 1(b)], but as will be shown in Sec. III this will not cause any problems. Next, the algorithm is mathematically formulated in terms of the wave propagation.

Let us consider a harmonic 3D time-varying sound field $p(\mathbf{x},t)=P(\mathbf{x},\omega)e^{j\omega t}$, where $P(\mathbf{x},\omega)=\|P(\mathbf{x},\omega)\|e^{j\measuredangle P(\mathbf{x},\omega)}$ is defined as the complex pressure amplitude of the sound field in a position $\mathbf{x}$ for the angular frequency ω. Also, let us define source matrix position $\mathbf{X}_s=[\mathbf{x}_{s_1},\ldots,\mathbf{x}_{s_n},\ldots,\mathbf{x}_{s_N}]^T$ and receiver matrix position $\mathbf{X}_r=[\mathbf{x}_{r_1},\ldots,\mathbf{x}_{r_m},\ldots,\mathbf{x}_{r_M}]^T$, where the superscript T indicates transposed vector. Note that for this purpose, $\mathbf{X}_r$ must correspond to a circular distribution as shown in Fig. 1(a). The pressure at a point $\mathbf{x}_{r_m}$ is calculated as a weighted sum of the pressure sources as

$$P(\mathbf{x}_{r_m},\omega)e^{j\omega t}=\frac{1}{4\pi}\sum_{n=1}^{N}P(\mathbf{x}_{s_n},\omega)e^{j\omega t}\frac{e^{-j(\omega/c)|\mathbf{x}_{s_n}-\mathbf{x}_{r_m}|}}{|\mathbf{x}_{s_n}-\mathbf{x}_{r_m}|}, \tag{1}$$

where c represents the speed of sound.

The weights that relate the pressure distribution of the sound field to the sound sources are known as three-dimensional Green's functions. In Eq. (1), the Green's function for point sources is employed. Assuming a far field approximation ($(\omega/c)|\mathbf{x}_{s_n}-\mathbf{x}_{r_m}| \gg 1$), or equivalently a plane wave approach, the Green's function can be simplified. This simplification is made assuming that in far field $|\mathbf{x}_{s_n}-\mathbf{x}_{r_m}|$ is a constant K, and Eq. (1) is expressed as

$$P(\mathbf{x}_{r_m},\omega) \simeq \frac{1}{K_{3\mathrm{D}}}\sum_{n=1}^{N} P(\mathbf{x}_{s_n},\omega)e^{-j(\omega/c)|\mathbf{x}_{s_n}-\mathbf{x}_{r_m}|}, \tag{2}$$

where $K_{3\mathrm{D}}=4\pi K$. However, this constant can be avoided in the equations taking into account that the directivity is expressed in relative terms. This simplification has the advantage of the formulation remaining the same in the two-dimensional (2D) case, in far field,[15] where the constant changes to $K_{2\mathrm{D}}=4e^{-j(\pi/4)}/j\sqrt{\pi\omega K/(2c)}$.

The summation of Eq. (2) can be expressed in matrix form as

$$\mathbf{p}_r = \mathbf{C}\mathbf{p}_s, \tag{3}$$

where $\mathbf{p}_s=[P(\mathbf{x}_{s_1},\omega),\ldots,P(\mathbf{x}_{s_N},\omega)]^T$ and $\mathbf{p}_r=[P(\mathbf{x}_{r_1},\omega),\ldots,P(\mathbf{x}_{r_M},\omega)]^T$, and then the matrix $\mathbf{C}$ of Green's functions is defined as

$$\mathbf{C}=\begin{pmatrix} e^{-j(\omega/c)|\mathbf{x}_{s_1}-\mathbf{x}_{r_1}|} & \cdots & e^{-j(\omega/c)|\mathbf{x}_{s_N}-\mathbf{x}_{r_1}|} \\ \vdots & \ddots & \vdots \\ e^{-j(\omega/c)|\mathbf{x}_{s_1}-\mathbf{x}_{r_M}|} & \cdots & e^{-j(\omega/c)|\mathbf{x}_{c_N}-\mathbf{x}_{r_M}|} \end{pmatrix}. \tag{4}$$

In that problem, $\mathbf{p}_r$ are known data, representing the angular pressure distribution around the sources, according to the directivity diagram. Despite directivity diagrams being expressed in terms of absolute values and $\mathbf{p}_r$ being a complex number, this is not a handicap, as will be shown later in the results.

In general, Eq. (3) cannot be solved as $\mathbf{p}_s=\mathbf{C}^{-1}\mathbf{p}_r$, because it normally corresponds to an under- or overdetermined system (the number of sources and the angular resolution, i.e., the number of receivers—they are not usually the same). In these cases, an approximate solution is usually obtained in a least-squares sense. This can be carried out by means of minimum least-squares method, i.e., by means of the pseudoinverse.[16] Equation (5) shows the solution expression where matrix $\mathbf{C}^T\mathbf{C}$ is always square:

$$\mathbf{p}_s = (\mathbf{C}^T\mathbf{C})^{-1}\mathbf{C}^T\mathbf{p}_r. \tag{5}$$

It must be taken into account that the point source distribution affects the sound field resolution. For a proper solution, the distribution of point sources must comply with a relation between distances to properly synthesize the field. This relation depends on the frequency. In this way, it is possible to correctly synthesize a sound field between a maximum $f_{\max}$ and a minimum frequency $f_{\min}$ in a given distribution of sources[17]

$$f_{\max} = \frac{c}{2\|\mathbf{x}_{s_i}-\mathbf{x}_{s_j}\|_{\min}}, \quad \forall\, i \neq j, \tag{6}$$

$$f_{\min} = \frac{c}{2\|\mathbf{x}_{s_i}-\mathbf{x}_{s_j}\|_{\max}}, \quad \forall\, i \neq j, \tag{7}$$

where $\|\cdot\|$ represents the norm of the vector.

The application of the proposed algorithm to the different paradigms (FDTD, DWM, TLM, etc.) is straightforward: pressure values $p(\mathbf{x},t)$ are given into discretized spatial points ($\mathbf{x}=[x,y,z]=[i\Delta x, j\Delta y, k\Delta z]$) in a particular time step $t=n\Delta t$; in the sequel, $\tilde{\mathbf{X}}_s$ and $\tilde{\mathbf{X}}_r$ must be considered as the discrete point position of sources and receivers [see Fig. 1(b)].

It is important to note than the calculations are made in the frequency domain. Once the pressure values $\mathbf{p}_s$ are calculated at the point sources, the discrete-time domain excitation signals must be achieved. For each point source of the array, when a sinusoidal signal with a given frequency ω_0 is employed, it is done by

$$p(\tilde{\mathbf{x}}_{r_m}, n)\big|_{\omega=\omega_0} = \mathrm{Re}\{\|P(\tilde{\mathbf{x}}_{r_m}, \boldsymbol{\omega}_0)\| e^{j(\omega_0 n\Delta t + \angle P(\tilde{\mathbf{x}}_{r_m}, \omega_0))}\}. \quad (8)$$

3. Examples and results

In this section, some examples of synthesis of directive sources are presented in order to validate the proposed algorithm. As mentioned previously, the application of the method is valid for all these paradigms and also produces equivalent results among the different methods.[18]

3.1 Simulation setup

To carry out the following experiments, the FDTD method has been selected because it is one of the most efficient methods and its theory for implementing absorbing boundary conditions is well known. More precisely, the perfect matched layer[19] method has been selected and implemented into the mesh boundaries in order to minimize the effects of the associated reflections.

In these examples, a 2D mesh has been used (a 3D application is straightforward). Searching for an efficient implementation, the FDTD method has been carried out in a one-step approach (only pressure has been considered).[20] Simulations have been developed for two frequencies, 500 and 2000 Hz. Due to the effects of the inherent dispersion in FDTD, the sampling frequency f_s has been selected as 20 times the maximum frequency to be simulated, $f_s = 40$ kHz. According to the Courant formula[3] ($\Delta x = \sqrt{2} c \Delta t$), each cell represents 0.012 m^2.

The source points are distributed in a staircase circle, taking space sampling into account. The setup is composed of 12 sources forming a circle with a radius of 0.096 m (around 8 cells of distance over the center point) for the frequency of 500 Hz and 12 sources for the frequency of 2000 Hz (around 30 cells of radius); this setup is accomplished with Eqs. (6) and (7). This selection implies that the first distribution allows the synthesis of frequencies between approximately 450–900 Hz and the second distribution around 1700–3300 Hz.

The receiver points have been placed in a circle with a $10\lambda_{\max}$ radius around the central point in order to guarantee far field conditions, where $\lambda_{\max}$ is the maximum wavelength of the synthesized field. A mesh of 500×500 cells has been used to accommodate the receiving points and leave some free space.

3.2 Results

According to the mathematical development presented in the previous section, the complex amplitude of the sources is calculated. Since the directivity diagram does not give any information about phase, a zero phase or random phase at receiver can be assumed, giving nearly the same results in absolute value terms. In all of the following experiments, a zero phase has been considered for $\mathbf{p}_r$.

In the first example, let us consider a distribution of pressure for a given frequency $\omega_1 = 2\pi 500$ rad/s with an angular resolution of $\Delta\theta = \pi/4$. The directivity data are defined in an counterclockwise manner as $\mathbf{p}_{r1_{(\mathrm{dB})}} = [0, -3, -7, -4, -5, -10, -4, -1]$.

Figure 2(a) shows, in the form of a continuous line, the expected directivity diagram and, in the form of a dotted line, the one obtained. A high level of agreement exists between the expected and the obtained results, and it is even difficult to differentiate the two. However, note that in the radiated sound field [Fig. 2(b)], sharp variations in the directivity between the eight data angles occur. When input information has a low angular resolution, this effect is more noticeable. When representing these results with a higher angular resolution, as shown in Fig. 2(c), some nonexpected irregularities arise.

In cases with low angle resolution information, a possible solution could be to interpolate the original directivity in the unknown angles of the diagram, obtaining more angular resolution and then applying the algorithm. Figure 3 shows the results obtained by increasing

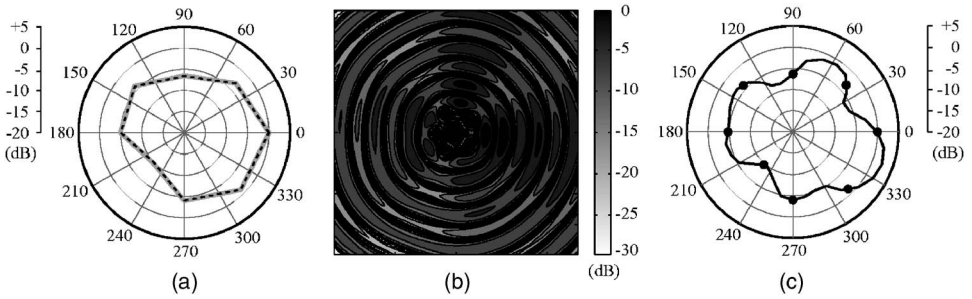

Fig. 2. (a) Comparison between the expected (gray-continuous line) and the obtained (black-dotted line) diagram directivity in a discrete-time domain method. (b) Obtained radiated sound field simulated in a FDTD mesh. (c) Obtained directivity diagram measured with a higher angular precision (dots indicate points used in the calculations).

the angular resolution (5°) and interpolating data with spline functions.[21] It shows how the results follow a much smoother change and in a more natural way, as with real sources. However, as expected, some differences exist between the results obtained with a low and a higher directivity angular resolution, due to the characteristics of the minimum least-squares method. This is manifested as a directivity curve that does not pass exactly through the expected points of the original directivity diagram. There is a tradeoff between the curve smoothness and the precision at the reference points when the number of receivers increases.

It is also possible to find in the literature examples of directivity diagrams with a higher angular resolution. For instance, in the next example, a directivity diagram of a baffled kettledrum is used,[22] with a selected frequency of 500 Hz, corresponding to the mode (31) [see Fig. 4(a)]. The number of sources is the same as the previous example (12 sources), but the angular resolution of the directivity diagram is 10° (36 receivers). In Fig. 4(a) the high similarity between the theoretical and the obtained directivity diagram can be observed and Fig. 4(b) shows the sound field produced for the configuration of sources calculated by means of a FDTD simulation.

One of the main advantages of discrete-time domain methods is their capacity to deal with broadband results, allowing several discrete frequency directivities to be carried out in a unique simulation. In order to show this, let us consider a directivity at two frequencies, one is $\mathbf{p}_{r1}$ at $\omega_1 = 2\pi 500$ rad/s, and the new one, for $\omega_2 = 2\pi 2000$ rad/s, is $\mathbf{p}_{r2_{(\mathrm{dB})}} = [0, -10, -12, -4, 0, -6, -5, -2]$. The results in Fig. 5 show the sound field produced as the combination of both signals. This property allows the creation of complex directive sources as a result of the combination of the single directivity diagram for different frequencies in a unique simulation.

Finally, the results obtained with FDTD have been compared to other discrete-time methods and it can be concluded that directivity diagrams are the same for the DWM and

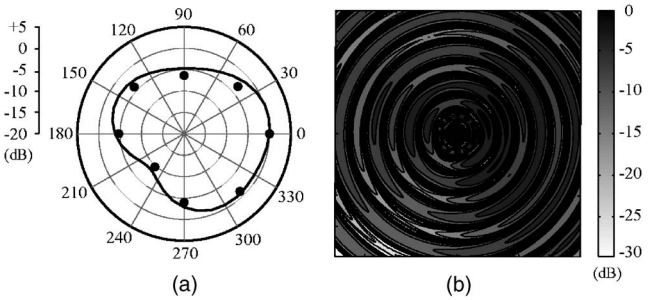

Fig. 3. (a) Directivity diagram obtained increasing the angular resolution by interpolation of the data of Fig. 2. (b) Obtained radiated sound field simulated in a FDTD mesh.

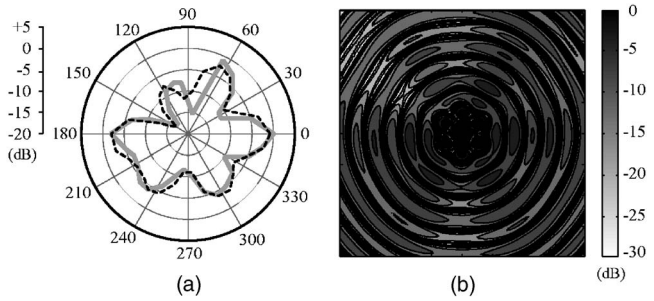

Fig. 4. (a) Comparison between the expected (gray-continuous line) and the obtained (black-dotted line) directivity diagram of baffled kettledrum in a discrete-time domain method. (b) Obtained radiated sound field simulated in a FDTD mesh.

TLM.[18] Compared to the FTM, very few, almost negligible, differences have been found. It must be taken into account that FTM is free of dispersion,[6] and for the presented examples, the FDTD mesh has been selected for a low level of dispersion because oversampling has been used. In summary, efficacy of the proposed algorithm is independent of the discrete-time method used.

It should be noted that the pressure sources mentioned in this work correspond to hard sources (the sources are not affected by the surrounding points). The influence in cases of transparent sources and realistic boundary conditions (partial reflections and frequency-dependent boundary conditions) should be analyzed.

4. Conclusions

In this letter, an approach to the synthesis of directive sources for discrete-time methods has been presented. The information relative to the directivity of the source is based on a set of points of the directivity diagrams. A combination of an array of monopole sources is used to create a particular sound field according to a directivity diagram, that demonstrates real source behavior. To obtain the weights for each source the least-squares method has been employed, allowing the creation of several directivities for different frequencies in a unique simulation for discrete-time domain methods. By means of different examples, the method has been tested and validated. Moreover, it has been implemented in several discrete-time methods and the results are independent of the method selected.

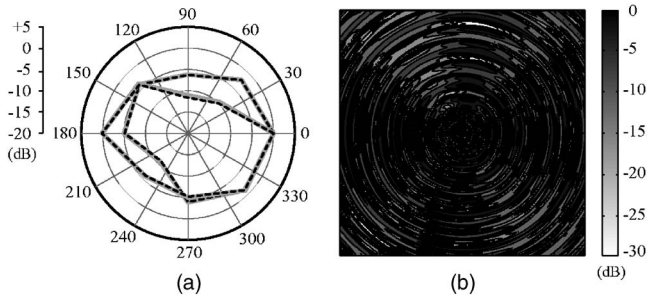

Fig. 5. (a) Comparison between the expected (gray-continuous line) and the obtained (black-dotted line) diagram directivity for two different frequencies in a discrete-time domain method. (b) Obtained radiated sound field simulated in a FDTD mesh.

Acknowledgments

This work has been supported by Spanish Ministry of Science and Technology (MCYT) under Project ref. TEC2006-13883-C04-01 and FEDER funds.

References and links

[1]M. Kleiner, B. I. Dalenback, and U. P. Svensson, "Auralization—An overview," J. Audio Eng. Soc. **41**, 861–874 (1993).
[2]U. P. Svensson and U. R. Kristiansen, "Computational modelling and simulation of acoustic spaces," Proceedings of the 22nd International AES Conference, Helsinki, Finland, June 2002.
[3]D. Botteldooren, "Finite-difference time-domain simulation of low-frequency room acoustic problems," J. Acoust. Soc. Am. **98**, 3302–3308 (1995).
[4]M. J. Beeson and D. T. Murphy,"Roomweaver: A digital waveguide mesh based room acoustics research tool," Proceedings of the Seventh International Conference on Digital Audio Effects (DAFX-04), Naples, Italy, October 2004, pp. 268–273.
[5]P. Johns and R. Beurle, "Numerical solution of 2-dimensional scattering problems using a transmission-line matrix," Proc. IEEE **118**, 1203–1208 (1971).
[6]S. Petrausch and R. Rabenstein, "Wave field simulation with the functional transformation method," IEEE Proceedings of the International Conference on Acoustics, Speech & Signal Processing (ICASSP'06), Toulouse, France, May 2006.
[7]L. Savioja, J. Huopaniemi, T. Lokki, and R. Väänänen, "Creating interactive virtual acoustic environments," J. Audio Eng. Soc. **47**, 675–705 (1999).
[8]F. Otondo and J. H. Rindel, "The influence of the directivity of musical instruments in a room," Acta. Acust. Acust. **90**, 1178–1184 (2004).
[9]J. Huopaniemi, M. Karjalainen, V. Välimki, and T. Huotilainen, "Virtual instruments in virtual rooms—A real-time binaural room simulation environment for physical models of musical instruments," Proceedings of the International Comp. Music Conference, Aarhus, Denmark, September 1994, pp. 455–462.
[10]M. C. Vigeant, L. M. Wang, and J. H. Rindel, "Differences in directional sound source behavior and perception between assorted computer room models," J. Acoust. Soc. Am. **116**, 2485 (2004).
[11]H. Hacihabiboğlu, B. Günel, and A. M. Kondoz, "Source directivity simulation in digital waveguide mesh based room acoustics models," Proceedings of the AES 30th International Conference on Intelligent Audio Environments, Saariselkä, Finland, March 2007.
[12]U. P. Svensson, "Modeling room acoustics," Proceedings of the Baltic-Nordic Acoustical Meeting, Mariehamn, Finland, June, 2004.
[13]N. H. Fletcher and T. D. Rossing, *The Physics of the Musical Instruments* (Springer, New York, 2005).
[14]Z. Wang and S. F. Wu, "Helmholtz equation least-squares method for reconstructing the acoustic pressure field," J. Acoust. Soc. Am. **102**, 2020–2032 (1997).
[15]M. Abramowitz and I. A. Stegun, *Handbook of Mathematical Functions* (Dover, New York, 1972).
[16]C. R. Rao and S. K. Mitra, *Generalized Inverse of Matrices and Its Applications* (Wiley, New York, 1971).
[17]E. G. Williams, *Fourier Acoustics* (Academic, London, 1999).
[18]M. Karjalainen and C. Erkut, "Digital waveguides vs. finite difference schemes: Equivalance and mixed modeling," Eurasip J. Applied Sig. Proc. **7**, 978–989 (2004).
[19]X. Yuan, D. Borup, J. W. Wiskin, M. Berggren, R. Eidens, and S. A. Johnson, "Formulation and validation of Berenger's PML absorbing boundary for the FDTD simulation of acoustic scattering," IEEE Trans. Ultrason. Ferroelectr. Freq. Control **44**, 816–822 (1997).
[20]L. Savioja, T. Rinne, and T. Takala, "Simulation of room acoustics with a 3-D finite difference mesh," Proceedings of the International Computer Music Conference (ICMC'94), Aarhus, Denmark, 12–17 September 1994, pp. 413–466.
[21]H. Ahlberg, E. Nielson, and J. Walsh, *Theory of Splines and Their Applications* (Academic, London, 1967).
[22]H. Fleischer, *Die Pauke: Mechanismer Schwinger und akustiche Strahler (The Kettledrum: Mechanic Transducers and Acoustic Emitters)* (University der Bundeswehr, Munich, 1998).

Phase velocity and normalized broadband ultrasonic attenuation in Polyacetal cuboid bone-mimicking phantoms

Kang Il Lee
Department of Physics, Kangwon National University, Chuncheon 200-701, Republic of Korea
acustica@kangwon.ac.kr

Min Joo Choi
Department of Medicine, Cheju National University, Jeju 690-756, Republic of Korea and
Medical Physics Department, Guy's & St Thomas' NHS Foundation Trust, London SE1 7EH, United Kingdom
mjchoi@cheju.ac.kr

Abstract: The variations of phase velocity and normalized broadband ultrasonic attenuation (nBUA) with porosity were investigated in Polyacetal cuboid bone-mimicking phantoms with circular cylindrical pores running normal to the surface along the three orthogonal axes. The frequency-dependent phase velocity and attenuation coefficient in the phantoms with porosities from 0% to 65.9% were measured from 0.65 to 1.10 MHz. The results showed that the phase velocity at 880 kHz decreased linearly with porosity, whereas the nBUA increased linearly with porosity. This study provides a useful insight into the relationships between ultrasonic properties and porosity in bone at porosities lower than 70%.

© 2007 Acoustical Society of America
PACS numbers: 43.80.Qf [CCC]
Date Received: December 12, 2006 **Date Accepted:** March 2, 2007

1. Introduction

It is now widely accepted that quantitative ultrasound (QUS) technologies have the potential for the assessment of osteoporosis and bone status (Laugier, 2004). Most of the current clinical QUS devices measure the speed of sound (SOS) and the broadband ultrasonic attenuation (BUA) at easily accessible peripheral sites such as the calcaneus and finger phalanges (Njeh *et al.*, 1999). SOS and BUA are sometimes combined linearly into a single index, which compensates for the temperature variation and offers better stability than either parameter taken alone (Njeh *et al.*, 1999; Wear and Armstrong, 2001). However, the underlying physics for the variations of QUS parameters in trabecular bone is not well understood yet.

Clarke *et al.* (1994) and Strelitzki *et al.* (1997) showed that a trabecular bone phantom material consisting of small cubic gelatin granules randomly distributed in epoxy (the Leeds Bone Phantom) is useful for the prediction of the variations of ultrasonic properties, such as phase velocity, dispersion, and attenuation, with porosity and pore size of trabecular bone. Recently, Wear (2005) reported the dependencies of phase velocity and dispersion on trabecular thickness, spacing, and volume fraction, using a trabecular-bone-mimicking phantom consisting of two-dimensional arrays of parallel nylon wires. Although the phantoms used in those studies are substantially different in materials and shapes of inclusions and ranges of porosities spanned, those phantom studies enable us to understand the relationships between ultrasonic properties and trabecular microarchitecture.

The present study aims to provide an insight into the variations of phase velocity and normalized broadband ultrasonic attenuation (nBUA) with porosity in bone, using Polyacetal cuboid bone-mimicking phantoms with circular cylindrical pores running normal to the surface along the three orthogonal axes. The frequency-dependent phase velocity and attenuation coefficient in the phantoms with porosities from 0% to 65.9% were measured from 0.65 to

Table 1. Properties of four phantoms.

Phantom	Pore diameter (a)	Pore spacing (s)	Porosity (β)
1	Pure Polyacetal without pores		0.0%
2	0.8 mm	3.0 mm	14.9%
3	0.8 mm	2.0 mm	31.3%
4	0.8 mm	1.3 mm	65.9%

1.10 MHz, using a matched pair of transducers with a diameter of 0.5 in. and a center frequency of 1.0 MHz.

2. Materials and methods

2.1 Bone-mimicking phantoms

Four Polyacetal cuboid phantoms with a square cross section of 20×20 mm^2 and a thickness of 10 mm (custom built by Nam Il Optical Components Corp., Incheon, Republic of Korea) were interrogated. Their dimensions were measured using a micrometer with a precision of 0.5 mm. The porosity of the phantoms was altered by changing the pore spacing only, since the pore size was fixed. One phantom consisted of pure Polyacetal without pores and three phantoms had circular cylindrical pores, running normal to the surface along the three orthogonal axes, with a diameter (a) of 0.8 mm and three different spacing (s) of 3.0, 2.0, and 1.3 mm, respectively (see Table 1). A phantom with $a=0.8$ and $s=1.3$ mm is shown in Fig. 1. The porosity, β, occupied by pores is given by

$$\beta = \frac{a^2}{s^2}\left(\frac{3\pi}{4} - \frac{a}{s}\right). \tag{1}$$

As seen in Table 1, the values for the porosity of four phantoms were 0%, 14.9%, 31.3%, and 65.9%, which resulted in porosities lower than the range reported for human calcaneus, 86% – 98% (Wear *et al.*, 2005). The porosities investigated here are relatively lower than values seen in human cancellous bone but cover ranges of cortical bone (0% – 30%) and dense cancellous bone (30% – 70%).

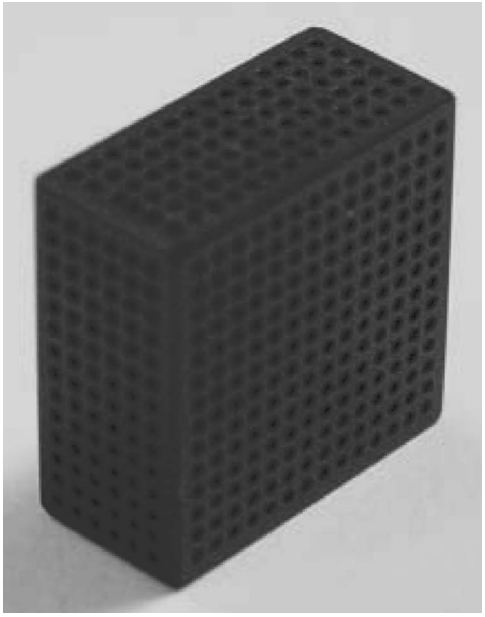

Fig. 1. Photograph of the phantom with $a=0.8$ mm and $s=1.3$ mm.

Table 2. Acoustic properties of Polyacetal measured in the present study and mineralized bone (or cortical bone) material in the literature. The longitudinal velocity and attenuation coefficient in the Polyacetal were measured at 880 kHz.

Material	Density	Longitudinal velocity	Attenuation coefficient
Polyacetal	1406±26 kg/m^3	2434±5 m/s	6.6±0.3 dB/cm
Mineralized bone material[a]	2040–2150 kg/m^3	2520–4290 m/s	6–52 dB/cm

[a]Njeh *et al.*, 1999.

The phantom design simplifies the complex architecture of trabecular bone filled with fatty marrow as a cuboid structure of Polyacetal with circular cylindrical pores, running normal to the surface along the three orthogonal axes, filled with water. Polyacetal comprising the skeletal frame of the phantoms corresponds to mineralized bone and water inside the pores to marrow. The pore diameter of 0.8 mm is comparable with typical values for trabecular separation in human calcaneus (Hans *et al.*, 1995; Ulrich *et al.*, 1999). Table 2 shows the acoustic properties of Polyacetal measured in the present study and mineralized bone (or cortical bone) material in the literature (Njeh *et al.*, 1999). As seen in Table 2, the longitudinal velocity and attenuation coefficient at 880 kHz in the Polyacetal were 2434±5 m/s and 6.6±0.3 dB/cm, respectively. This indicates that the Polyacetal used here is similar in acoustic properties to typical mineralized bone material. The substitution of water for bone marrow may be justified by the fact that many *in vitro* measurements performed with water instead of marrow result in consistency with *in vivo* measurements (Wear, 2005).

2.2 Ultrasonic measurements

Ultrasonic measurements were performed in a water bath filled with distilled water at room temperature (18 °C), using the through-transmission method. A matched pair of broadband, plane (unfocused) transducers with a diameter of 0.5 in. and a center frequency of 1.0 MHz (Panametrics V303) was used in order to cover the wide range of frequencies of interest. The two transducers were coaxially aligned, facing each other. Their opposing faces were separated by a distance of 50 mm, greater than the near-field distance of 26.5 mm stated by the manufacturer. The phantom was coaxially aligned with the transducers and placed in a soundproof mount to prevent diffraction around the edges of the phantom. A 200 MHz pulser/receiver (Panametrics 5900PR) was used to generate ultrasonic pulses through a transducer (transmitter) and to receive signals transmitted through the phantom at the other transducer (receiver). Received signals were averaged over 100 pulses in time domain using a 500 MHz digital storage oscilloscope (LeCroy LT342) and stored on a computer for offline analysis.

In order to measure the phase velocity, the received signals were recorded with and without the phantom in the acoustic path. The frequency-dependent phase velocity, $c_p(\omega)$, was determined by

$$c_p(\omega) = \frac{c_w}{1 - [c_w \Delta\phi(\omega)/\omega d]}, \tag{2}$$

where ω is the angular frequency of the wave, d is the thickness of the phantom, and $\Delta\phi(\omega)$ is the difference in unwrapped phases of the received signals with and without the phantom. The unwrapped phase difference, $\Delta\phi(\omega)$, was calculated by taking the fast Fourier transform of the digitized received signals (Wear, 2005). The temperature-dependent speed of sound in distilled water, c_w, is given by (Kaye and Laby, 1995)

$$c_w = 1402.9 + 4.835 \times T - 0.047016 \times T^2 + 0.00012725 \times T^3, \tag{3}$$

where T is the temperature in °C. It was verified that the estimates of Eq. (3) were consistent with the measurements performed in the water bath given the precision of the digital thermometer used.

The attenuation coefficient was determined using the same signal acquired for phase

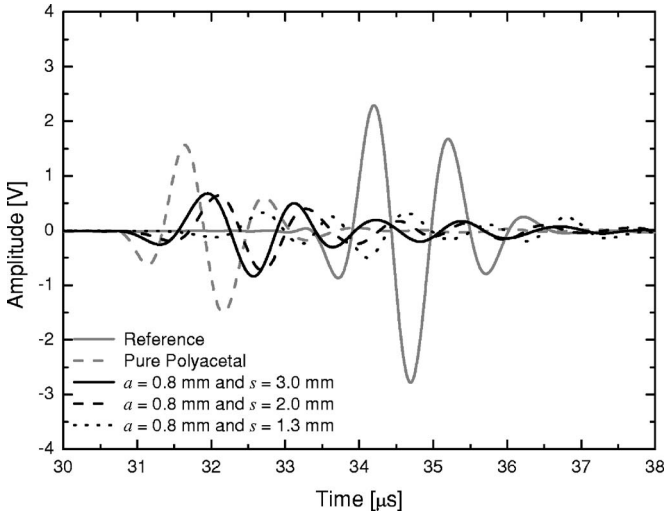

Fig. 2. Temporal reference signal transmitted through water only and phantom signals transmitted through four phantoms.

velocity measurements. The frequency-dependent attenuation coefficient, $\alpha(\omega)$, in unit of dB/cm was calculated by

$$\alpha(\omega) = \frac{20\log(e)}{d}\left[\ln\frac{|A_0(\omega)|}{|A_s(\omega)|} + \ln|\tau(\omega)|\right], \tag{4}$$

where $A_0(\omega)$ is the amplitude spectrum of the signal through water only, $A_s(\omega)$ is the amplitude spectrum of the signal through the phantom, d is the thickness of the phantom in cm, and $\tau(\omega)$ is the power transmission coefficient at the interface between water and the phantom. The first term on the right hand side of Eq. (4) is the apparent attenuation (i.e., signal loss) and the second term is the transmission losses at each interface, water/phantom and phantom/water. The transmission losses were determined from separate measurements of density and phase velocity of the phantom. Meanwhile, they are generally assumed to be negligible in human trabecular bone (Njeh *et al.*, 1999).

A total of ten measurements were performed on each phantom, repositioning the phantom after each measurement. The experimental data of phase velocity, attenuation coefficient, and nBUA presented here represent the average of the ten measurements. Their standard deviations (the random uncertainty of their measurements) were observed within 5% and are not indicated in the figures.

3. Results and discussion

Figure 2 shows the temporal reference signal transmitted through water only and phantom signals transmitted through four phantoms. As seen in Fig. 2, each phantom signal exhibits an earlier arrival time than that observed in water. This is because the sound speed in the phantoms is greater than that in water. It is notable that the signals through the phantoms with pores exhibit pulse elongation with the higher frequencies arriving later, characteristic of negative dispersion. This may be due to the interference between fast and slow waves, resulting in the negative dispersion (Marutyan *et al.*, 2006). The amplitude spectrum level of the reference signal transmitted through water only reached a maximum at the frequency of 880 kHz. As expected, the center frequencies of the signals transmitted through the phantoms were shifted to lower frequencies, resulting from increasing attenuation with frequency. The usable (−6 dB) frequency bandwidth was found between 0.65 and 1.10 MHz.

Figure 3 (left) shows the phase velocity as a function of frequency measured for four phantoms. The solid lines are linear fits to the measured data. As seen in Fig. 3 (left), the phase velocity in the phantom with a porosity of 65.9% has an apparent negative slope with frequency

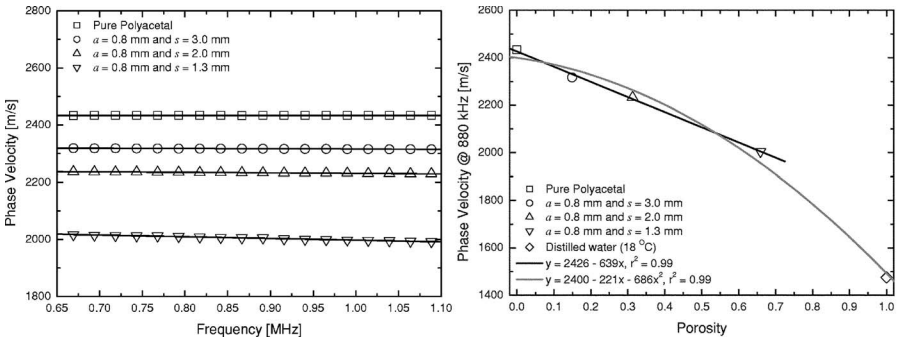

Fig. 3. (left) Phase velocity as a function of frequency measured for four phantoms. The solid lines are linear fits to the measured data. (right) Phase velocity at 880 kHz as a function of porosity measured for four phantoms. The black line is a linear fit to the measured data on the phantoms and the gray curve is a polynomial fit of second order to all data including the measurement at 100%.

over the range from 0.65 to 1.10 MHz (-60 ± 15 m/sMHz). This negative dispersion has been observed in several *in vitro* measurements in trabecular bone (Nicholson *et al.*, 1996; Strelitzki and Evans, 1996; Droin *et al.*, 1998; Wear, 2000, 2001; Waters and Hoffmeister, 2005) and also measured in bone-mimicking phantoms (Strelitzki *et al.*, 1997; Wear, 2001, 2005). Wear (2001) successfully applied the stratified model to predict the negative dispersion in human trabecular bone, modeling it as a simple layered structure of periodically alternating bone-marrow plates. Recently, Marutyan *et al.* (2006) proposed that the apparent negative dispersion in trabecular bone can result from the interference between fast and slow waves, based on computer simulations of the Biot-Johnson and stratified models. It should be noted that, in the present study, significant negative dispersion was observed only in the phantom with the highest porosity of 65.9%. As can be observed in Fig. 3 (left), the phantoms with the lower porosities of 14.9% and 31.3% exhibited a slightly negative dispersion over the frequency range available. Although the slope of phase velocity as a function of frequency may have clinical significance, the physical mechanism responsible for the variation of dispersion with porosity in trabecular bone is not well understood yet.

Figure 3 (right) shows the phase velocity at 880 kHz (the frequency at which the amplitude spectrum level reaches a maximum) as a function of porosity measured for four phantoms. The value of about 1475 m/s at a porosity of 100% represents the phase velocity measured in distilled water at 18 °C. The black line is a linear fit to the measured data on the phantoms and the gray curve is a polynomial fit of second order to all data including the measurement at 100%. It can be found that the phase velocity in the Polyacetal cuboid bone-mimicking phantoms decreases linearly with porosity over the range from 0% to 65.9%. This is attributed to the increase in porosity (i.e., the decrease in volume fraction of Polyacetal) resulting from decreases in pore spacing of the phantoms. These findings underpin the fact that SOS in trabecular bone is highly correlated with bone mineral density over a wide range of densities (Nicholson *et al.*, 1994; Han *et al.*, 1996; Serpe and Rho, 1996). It may be worthwhile to note previous phantom studies on the relationship between phase velocity and porosity, even if their porosity ranges are relatively high compared to that considered in the present study. For example, Wear (2005) observed that the phase velocity in a trabecular-bone-mimicking phantom, consisting of two-dimensional arrays of parallel nylon wires, is a linearly decreasing function of porosity from 88% to 98%. Meanwhile, Strelitzki *et al.* (1997) reported that a quadratic model provides a more appropriate fit for a different bone phantom, consisting of small cubic gelatin granules randomly distributed in epoxy, over a wide range of porosities from 46% to 83%. The polynomial fit in Fig. 3 (right) also shows that the phase velocity tends to decrease nonlinearly, but still monotonically with porosity over the entire range from 0% to 100%. Indeed, there is some indication of nonlinearity in human trabecular bone with very high porosities (Wear *et al.*, 2005). This nonlinear variation of phase velocity with porosity in trabecular bone has been predicted using the Biot model (Williams, 1992; Hosokawa and Otani, 1997, 1998;Wear *et al.*,

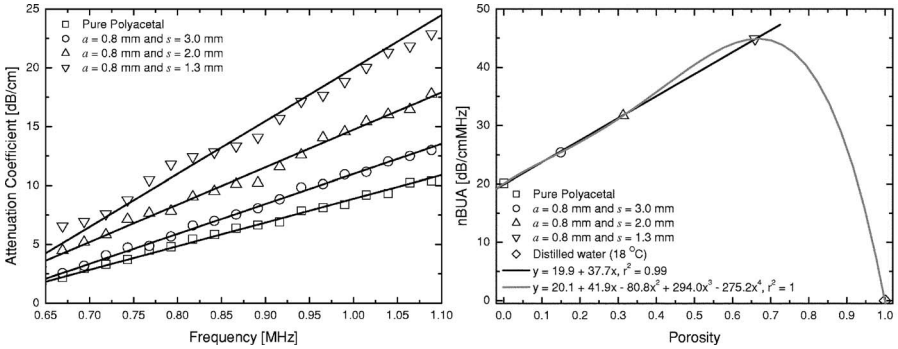

Fig. 4. (left) Attenuation coefficient as a function of frequency measured for four phantoms. The solid lines are linear fits to the measured data. (right) nBUA as a function of porosity measured for four phantoms. The black line is a linear fit to the measured data on the phantoms and the gray curve is a polynomial fit of fourth order to all data including the mearuement at 100%.

2005; Lee and Yoon, 2006) and the modified Biot-Attenborough (MBA) model (Lee *et al.*, 2003). Lin *et al.* (2001) also demonstrated that the theoretical relationship between velocity and porosity is not strictly linear, using the stratified model.

Figure 4 (left) shows the attenuation coefficient as a function of frequency measured for four phantoms. The solid lines are linear fits to the measured data. As seen in Fig. 4 (left), the attenuation coefficients in all the phantoms increase linearly with frequency over the range from 0.65 to 1.10 MHz. These results are consistent with the fact that the attenuation is a linear function of frequency over the chosen range in trabecular bone. The slope of the linear fit to the frequency-dependent attenuation over the bandwidth of interest, typically from 200 to 600 kHz, which is referred to as nBUA, has been shown to be useful to indicate bone health (Langton *et al.*, 1984). Nevertheless, the nBUA approach, implying a simple linear relationship between attenuation coefficient and frequency, does not rely upon any physical bases.

Figure 4 (right) shows the nBUA as a function of porosity measured for four phantoms. The value of about 0 dB/cm at a porosity of 100% represents the nBUA measured in distilled water at 18 °C. The nBUA was determined by the linear regression of attenuation coefficient over the frequency bandwidth from 0.65 to 1.10 MHz. The black line is a linear fit to the measured data on the phantoms and the gray curve is a polynomial fit of fourth order to all data including the measurement at 100%. It can be found that the nBUA in the Polyacetal cuboid bone-mimicking phantoms increases linearly with porosity over the range from 0% to 65.9%. The increasing nBUA with porosity at porosities lower than 70% seems to be consistent with those previously observed in trabecular bone by several authors (Han *et al.*, 1996; Hodgkinson *et al.*, 1996; Serpe and Rho, 1996). They found that the nBUA increased slowly with porosity, showing a peak at the porosity of roughly 70%, and decreased rapidly thereafter. Similar nonlinear relationships between nBUA and porosity have been reported in a trabecular bone phantom material (the Leeds Bone Phantom), with a peak at the porosity of about 50% (Clarke *et al.*, 1994; Strelitzki *et al.*, 1997). Some theoretical models, such as the scattering model (Nicholson *et al.*, 2000) and the stratified model (Lin *et al.*, 2001), successfully predicted such nonlinear trends experimentally observed in trabecular bone and bone-mimicking phantoms. One of our previous works employing the MBA model also predicted the nonlinear dependence of nBUA on porosity in bovine trabecular bone (Lee *et al.*, 2003).

In summary, the variations of phase velocity and nBUA with porosity were investigated in Polyacetal cuboid bone-mimicking phantoms with circular cylindrical pores running normal to the surface along the three orthogonal axes. The results showed that the phase velocity at 880 kHz decreased linearly with porosity over the range from 0% to 65.9%, whereas the nBUA increased linearly with porosity. The dependencies of phase velocity and nBUA on porosity in the phantoms were consistent with those previously observed in trabecular bone and bone-mimicking phantoms. This study provides a useful insight into the relationships between ultrasonic properties and porosity in bone at porosities lower than 70%.

Acknowledgment

The research was supported in part by the industrial technology innovation program of the Ministry of Commerce, Industry and Energy, Republic of Korea.

References and links

Clark, A. J., Evans, J. A., Truscott, J. G., Milner, R., and Smith, M. A. (**1994**). "A phantom for quantitative ultrasound of trabecular bone," Phys. Med. Biol. **39**, 1677–1687.
Droin, P., Berger, G., and Laugier, P. (**1998**). "Velocity dispersion of acoustic waves in cancellous bone," IEEE Trans. Ultrason. Ferroelectr. Freq. Control **45**, 581–592.
Han, S., Rho, J., Medige, J., and Ziv, I. (**1996**). "Ultrasound velocity and broadband attenuation over a wide range of bone mineral density," Osteoporosis Int. **6**, 291–296.
Hans, D., Arlot, M. E., Schott, A. M., Roux, J. P., Kotzki, P. O., and Meunier, P. J. (**1995**). "Do ultrasound measurements on the os calcis reflect more the bone microarchitecture than the bone mass? A two-dimensional histomorphometric study," Bone (N.Y.) **16**, 295–300.
Hodgkinson, R., Njeh, C. F., Whitehead, M. A., and Langton, C. M. (**1996**). "The non-linear relationship between BUA and porosity in cancellous bone," Phys. Med. Biol. **41**, 2411–2420.
Hosokawa, A., and Otani, T. (**1997**). "Ultrasonic wave propagation in bovine cancellous bone," J. Acoust. Soc. Am. **101**, 558–562.
Hosokawa, A., and Otani, T. (**1998**). "Acoustic anisotropy in bovine cancellous bone," J. Acoust. Soc. Am. **103**, 2718–2722.
Kaye, G. W. C., and Laby, T. H. (**1995**). *Tables of Physical and Chemical Constants and Some Mathematical Functions* (Longman, London, UK).
Langton, C. M., Palmer, S. B., and Porter, R. W. (**1984**). "The measurement of broadband ultrasonic attenuation in cancellous bone," Eng. Med. **13**, 89–91.
Laugier, P. (**2004**). "An overview of bone sonometry," International Congress Series **1274**, 23–32.
Lee, K. I., Roh, H. S., and Yoon, S. W. (**2003**). "Acoustic wave propagation in bovine cancellous bone: Application of the modified Biot-Attenborough model," J. Acoust. Soc. Am. **114**, 2284–2293.
Lee, K. I., and Yoon, S. W. (**2006**). "Comparison of acoustic characteristics predicted by Biot's theory and the modified Biot-Attenborough model in cancellous bone," J. Biomech. **39**, 364–368.
Lin, W., Qin, Y. X., and Rubin, C. (**2001**). "Ultrasonic wave propagation in trabecular bone predicted by the stratified model," Ann. Biomed. Eng. **29**, 781–790.
Marutyan, K. R., Holland, M. R., and Miller, J. G. (**2006**). "Anomalous negative dispersion in bone can result from the interference of fast and slow waves," J. Acoust. Soc. Am. **120**, EL55–EL61.
Nicholson, P. H. F., Haddaway, M. J., and Davie, M. W. J. (**1994**). "The dependence of ultrasonic properties on orientation in human vertebral bone," Phys. Med. Biol. **39**, 1013–1024.
Nicholson, P. H. F., Lowet, G., Langton, C. M., Dequeker, J., and Van der Perre, G. (**1996**). "A comparison of time-domain and frequency-domain approaches to ultrasonic velocity measurement in trabecular bone," Phys. Med. Biol. **41**, 2421–2435.
Nicholson, P. H. F., Strelitzki, R., Cleveland, R. O., and Bouxsein, M. L. (**2000**). "Scattering of ultrasound in cancellous bone: Predictions from a theoretical model," J. Biomech. **33**, 503–506.
Njeh, C. F., Hans, D., Fuerst, T., Gluer, C. C., and Genant, H. K. (**1999**). *Quantitative Ultrasound: Assessment of Osteoporosis and Bone Status* (Martin Dunitz, London, UK).
Serpe, L., and Rho, J. Y. (**1996**). "The nonlinear transition period of broadband ultrasound attenuation as bone density varies," J. Biomech. **29**, 963–966.
Strelitzki, R., and Evans, J. A. (**1996**). "On the measurement of the velocity of ultrasound in the os calcis using short pulses," Eur. J. Ultrasound **4**, 205–213.
Strelitzki, R., Evans, J. A., and Clarke, A. J. (**1997**). "The influence of porosity and pore size on the ultrasonic properties of bone investigated using a phantom material," Osteoporosis Int. **7**, 370–375.
Ulrich, D., Van Rietbergen, B., Laib, A., and Ruegsegger, P. (**1999**). "The ability of three-dimensional structural indices to reflect mechanical aspects of trabecular bone," Bone (N.Y.) **25**, 55–60.
Waters, K. R., and Hoffmeister, B. K. (**2005**). "Kramers-Kronig analysis of attenuation and dispersion in trabecular bone," J. Acoust. Soc. Am. **118**, 3912–3920.
Wear, K. A. (**2000**). "Measurements of phase velocity and group velocity in human calcaneus," Ultrasound Med. Biol. **26**, 641–646.
Wear, K. A. (**2001**). "A stratified model to predict dispersion in trabecular bone," IEEE Trans. Ultrason. Ferroelectr. Freq. Control **48**, 1079–1083.
Wear, K. A. (**2005**). "The dependencies of phase velocity and dispersion on trabecular thickness and spacing in trabecular bone-mimicking phantoms," J. Acoust. Soc. Am. **118**, 1186–1192.
Wear, K. A., and Armstrong, D. W. (**2001**). "Relationships among calcaneal backscatter, attenuation, sound speed, hip bone mineral density, and age in normal adult women," J. Acoust. Soc. Am. **110**, 573–578.
Wear, K. A., Laib, A., Stuber, A. P., and Reynolds, J. C. (**2005**). "Comparison of measurements of phase velocity in human calcaneus to Biot theory," J. Acoust. Soc. Am. **117**, 3319–3324.
Williams, J. L. (**1992**). "Ultrasonic wave propagation in cancellous and cortical bone: Prediction of some experimental results by Biot's theory," J. Acoust. Soc. Am. **91**, 1106–1112.

ACOUSTICAL NEWS—USA

Elaine Moran
Acoustical Society of America, Suite 1NO1, 2 Huntington Quadrangle, Melville, NY 11747-4502

***Editor's Note**: Readers of the journal are encouraged to submit news items on awards, appointments, and other activities about themselves or their colleagues. Deadline dates for news items and notices are 2 months prior to publication.*

2007 Medwin Prize in Acoustical Oceanography Awarded to Brian Dushaw

Brian D. Dushaw was named the recipient of the 2007 Medwin Prize in Acoustical Oceanography. "For contributions to the acoustic measurement of climate change." Dr. Dushaw is Senior Oceanographer, Applied Physics Laboratory, University of Washington, Seattle. He received an A.B. degree in Physics from Occidental College, an M.A. in Physics from the University of California, Davis, and a Ph.D. from the University of Callifornia, San Diego, in Physical Oceanography.

The prize was awarded to Dr. Dushaw at the meeting of the Acoustical Society of America held in Salt Lake City, UT, 4–8 June 2007. During the meeting he presented the Acoustical Oceanography Prize Lecture titled "The recent history of our understanding of low-mode internal tides in the ocean."

The Medwin Prize in Acoustical Oceanography was established in 2000 through a grant made to the Acoustical Society Foundation by Herman and Eileen Medwin to recognize a person for the effective use of sound in the discovery and understanding of physical and biological parameters and processes in the sea. Previous recipients have been Timothy G. Leighton, Bruce D. Cornuelle, Jeffrey A. Nystuen, Stan E. Dosso, Svein Vagle, and John K. Horne.

Applications and/or nominations for the award are due in September each year. For further information about the award, please contact the Acoustical Society of America, Suite 1NO1, 2 Huntington Quadrangle, Melville, NY 11747-4502, Tel: 516-576-2360; Fax: 516-576-2377; E-mail: asa@aip.org. Application information can also be found on the ASA Home Page at http:// asa.aip.org/fellowships.html.

USA Meetings Calendar

Listed below is a summary of meetings related to acoustics to be held in the U.S. in the near future. The month/year notation refers to the issue in which a complete meeting announcement appeared.

2007

24–26 July	Revolutionary Aircraft for Quiet Communities, Hampton, VA [A NASA workshop hosted by the National Institute of Aerospace and co-sponsored by the Joint Planning and Development Office and the Council of European Aerospace Societies; Web: www.nianet.net].
5–8 Oct.	123rd Audio Engineering Society Convention, New York, NY [Audio Engineering Society, 60 E. 42 St., Rm. 2520, New York, NY 10165-2520, Tel: 212-661-8528; Fax: 212-682-0477; Web: www.aes.org].
22–24 Oct.	NOISE-CON 2007, Reno, NV [Institute of Noise Control Engineering, INCE Business Office, 210 Marston Hall, Ames, IA 50011-2153, Tel.: 515-294-6142; Fax: 515-294-3528; E-mail: ibo@inceusa.org]
27 Nov.–2 Dec.	154th Meeting of the Acoustical Society of America, New Orleans, LA (note Tuesday through Saturday) [Acoustical Society of America, Suite 1NO1, 2 Huntington Quadrangle, Melville, NY 11747-4502; Tel.: 516-576-2360; Fax: 516-576-2377; E-mail: asa@aip.org; Web: http://asa.aip.org].

2008

29 June–4 July	Acoustics08, Joint Meeting of the Acoustical Society of America (ASA), European Acoustics Association (EAA), and the Acoustical Society of France (SFA), Paris, France [Acoustical Society of America, Suite 1NO1, 2 Huntington Quadrangle, Melville, NY 11747-4502; Tel.: 516-576-2360; Fax: 516-576-2377; E-mail: asa@aip.org; Web: http://asa.aip.org/meetings.html].
27–30 Jul	NOISE-CON 2008, Dearborn, MI [Institute of Noise Control Engineering, INCE Business Office, 210 Marston Hall, Ames, IA 50011-2153, Tel.: 515-294-6142; Fax: 515-294-3528; E-mail: ibo@inceusa.org].
28 Jul–1 Aug	9th International Congress on Noise as a Public Health Problem, Quintennial Meeting of ICBEN (the International Commission on Biological Effects of Noise), Foxwoods Resort, Mashantucket, CT [Jerry V. Tobias, ICBEN 9, P.O. Box 1609, Groton CT 06340-1609; Tel.: 860-572-0680; Web: www.icben.org; E-mail: icben2008@att.net].

Cumulative Indexes to the Journal of the Acoustical Society of America

Ordering information: Orders must be paid by check or money order in U.S. funds drawn on a U.S. bank or by Mastercard, Visa, or American Express credit cards. Send orders to Circulation and Fulfillment Division, American Institute of Physics, Suite 1NO1, 2 Huntington Quadrangle, Melville, NY 11747-4502; Tel.: 516-576-2270. Non-U.S. orders add $11 per index.

Some indexes are out of print as noted below.

Volumes 1–10, 1929–1938: JASA and Contemporary Literature, 1937–1939. Classified by subject and indexed by author. Pp. 131. Price: ASA members $5; Nonmembers $10.

Volumes 11–20, 1939–1948: JASA, Contemporary Literature, and Patents. Classified by subject and indexed by author and inventor. Pp. 395. Out of Print.

Volumes 21–30, 1949–1958: JASA, Contemporary Literature, and Patents. Classified by subject and indexed by author and inventor. Pp. 952. Price: ASA members $20; Nonmembers $75.

Volumes 31–35, 1959–1963: JASA, Contemporary Literature, and Patents. Classified by subject and indexed by author and inventor. Pp. 1140. Price: ASA members $20; Nonmembers $90.

Volumes 36–44, 1964–1968: JASA and Patents. Classified by subject and indexed by author and inventor. Pp. 485. Out of Print.

Volumes 36–44, 1964–1968: Contemporary Literature. Classified by subject and indexed by author. Pp. 1060. Out of Print.

Volumes 45–54, 1969–1973: JASA and Patents. Classified by subject and indexed by author and inventor. Pp. 540. Price: $20 (paperbound); ASA members $25 (clothbound); Nonmembers $60 (clothbound).

Volumes 55–64, 1974–1978: JASA and Patents. Classified by subject and indexed by author and inventor. Pp. 816. Price: $20 (paperbound); ASA members $25 (clothbound); Nonmembers $60 (clothbound).

 0001-4966/2007/121(6)/3249/4/$23.00 © 2007 Acoustical Society of America

Volumes 65–74, 1979–1983: JASA and Patents. Classified by subject and indexed by author and inventor. Pp. 624. Price: ASA members $25 (paperbound); Nonmembers $75 (clothbound).
Volumes 75–84, 1984–1988: JASA and Patents. Classified by subject and indexed by author and inventor. Pp. 625. Price: ASA members $30 (paperbound); Nonmembers $80 (clothbound).
Volumes 85–94, 1989–1993: JASA and Patents. Classified by subject and indexed by author and inventor. Pp. 736. Price: ASA members $30 (paperbound); Nonmembers $80 (clothbound).
Volumes 95–104, 1994–1998: JASA and Patents. Classified by subject and indexed by author and inventor. Pp. 632. Price: ASA members $40 (paperbound); Nonmembers $90 (clothbound).
Volumes 105–114, 1999–2003: JASA and Patents. Classified by subject and indexed by author and inventor. Pp. 616. Price: ASA members $50; Nonmembers $90 (paperbound).

REVISION LIST

New Associates

Adams, Keith, 69 Kooyong Rd., Caulfield North,VIC 3161, Australia
Anagnos, Daniel P., 36 Peach Highlands, Marblehead, MA 01945
Ashton, Ray E., 14260 W. Newberry Rd., Newberry, FL 32669
Bataille, Donald W., HBMA, PLLC Architects, 524 Mt. Hope Ave., Ste. 100, Rochester, NY 14620
Beach, Kirk W., Ty Gywn Kiln Rd., Abergavenny NP7 9NE, UK
Belshaw, Richard J., 155 Main St. S., Halton Hills, ON L7G 3E7, Canada
Bemman, Ya-Yuan, Eberspaecher NA, 29101 Haggerty, Novi, MI 48377
Biswas, Mita, DTS, Inc., 5171 Clareton Dr., Agoura Hills, CA 91301
Brewe, Ian R., Eilar Associates, Inc., 539 Encinitas Blvd., Ste. 206, Encinitas, CA 92024
Burns, Peter N., Medical Biophysics, Univ. of Toronto, Sunnybrook HSC, 2075 Bayview Ave., S660, Toronto, ON M4N 3M5, Canada
Burrill, Michael, Eilar Associates, Inc., 539 Encinitas Blvd., Ste. 206, Encinitas, CA 92024
Cardoso, Isabel, Rua da Regueira, 44-2 Dto, 4400-278 Vila Nova De Gaia, Portugal
Chi, Ruidong, Sensus Metering Systems, Electronic Engineering, 450 N. Gallatin Ave., Uniontown, PA 15401
Clark, Mike G., 675 46th St., Des Moines, IA 50312
Clarke, Mark P., Donaghmoyne Rd., Carrickmacross, Co. Monaghan, Ireland
Cudney, Harley H., 72 Lyme Rd., Hanover, NH 03755
Daniel, John, Rm. No. 407, New Shahera Palaca, 18/641 Mannady St., Chennai 1, India
de Kerckhove, Diane N., Physics Dept., Univ. of Guelph, 50 Stone Rd. East, Guelph, ON N1G 2W1, Canada
Dennis, Bobby D., 3 Yorkshire Court, Richardson, TX 75082
Deuchars, Angus M., Arup Acoustics, 901 Market St., Ste. 260, San Francisco, CA 94103
Ebrahim, Assad E. K., BioSonics, Inc., 4027 Leary Way, NW, Seattle, WA 98107
Edwards, Joseph R., VASA Associates, Inc., 1 Charles St. S., Unit 6F, Boston, MA 02116
Evers, Laeslo G., KNMI, Seismology Division, P.O. Box 201, De Bilt, 3730 AE, The Netherlands
Eidsvik, Paul, 733 Coolidge, Westfield, NJ 07090
Farina, Angelo, Viale Duca Alessandro 8, Parma 43100, Italy
Fernandez, Andres, The ARcane Paradigm, Parque Arturo Leon D-2 11-f, Valladolid 47008, Spain
Fiebig, Andre, Schildstr. 20, 52062 Aachen, Germany
Field, Chris D., Arup Acoustics, 901 Market St., Ste. 260, San Francisco, CA 94103
Fine, Michael L., Biology, Virginia Commonwealth Univ., 1000 W. Cary St., Richmond, VA 23129
Foulk, Aaron M., 2738 Denise St., Newbury Park, CA 91320
Guzman, Sandra J., Motorola, CXD Design Research, 600 N. US Hwy. 45, MD S1-46M, Libertyville, IL 60048
Hall, Deborah A., MRC Inst. of Hearing Research, University Park, Nottingham NG7 2RD, UK
Hargrove, James V., Manufacturing Dept., Sabian Cymbal Makers, 219 Main St., Meductic, NB E6H 2L5, Canada
Hayes, Donald, Unitron Hearing Ltd., 20 Beasley Dr., Kitchener, ON N2G 4X1, Canada
Hedlin, Michael A. H., Scripps Inst. of Oceanography, Univ. of California, San Diego, 9500 Gilman Dr., La Jolla, CA 92093-0225
Hickey, Rich, Sente Software, LLC, 2172 White Birch Dr., Yorktown Heights, NY 10598
Hill, Bernard R., Collins & Aikman, Product Development, 1506 E. Main St., P.O. Box 669, Old Fort, NC 28762
Hopkins, Jonathan K., 10974 Rose Ave., #2, Los Angeles, CA 90034
Jaramillo, Ana M., calle 41 # 63 C-49, Medellin, Colombia
Jeng, Fuh-Cherng, School of Hearing, Speech and Lang. Sci., Ohio Univ., Grover Center W218, Athens, OH 45701
Kalapinski, Erik J., 17 Lyman St., Southborough, MA 01772
Kantti, Timo-Pekka, Sepantie 12A, Uotila, Satakunta 26510, Finland
Katz, J. Lawrence, 22100 Shaker Blvd., Shaker Heights, OH 44122-2646
Kawashima, Takayuki, Dept. of Cognitive and Behavioral Sciences, Univ. of Tokyo, 3-8-1 Komaba, Meguro-ku, Tokyo 153-8901, Japan
Kennedy, E. Dale, Albion College, Biology, 611 E. Porter St., Albion, MI 49224
Khosla, Sid M., 3158 Willis, Cincinnati, OH 45208
King, Charles B., 2913 W. Walnut, Chicago, IL 60612
Krahe, Detlef, Univ. of Wuppertal, FB E, Rainer-Gruenter-Str. 21, Wuppertal 42119, Germany
Kuchukhidze, Giorgi, 12591 Shelley Dr., #8, Garden Grove, CA 92840
Langenberg, Lawrence A., Stoddard Silencers, Inc., Engineering, 1017 Progress Dr., Grayslake, IL 60030
Lepper, David, Optimal Engineering, 7185 Liberty Centre Dr., Ste. D, West Chester, OH 45069
Litobarski, Stuart L. H., Flat 2, 1 Beach Rd., Southsea, PO5 2JH, UK
Lorenzi, Christian, CNRS, Ecole Normale Superieure, 29 Rue D'Ulm, Paris 75005, France
Maddux, William A., AECOM/EDAW, Inc., Environmental, 1420 Kettner Blvd., Ste. 620, San Diego, CA 92101
Manning, Angelina V., Naval Undersea Warfare Center Div., Keyport, Engineering and Planning, 610 Dowell St., Keyport, WA 98345
Matchett, Noel, Information Security Incorporated, 10776 State Route 108, Ellicott City, MD 21042-6104
Memoli, Gianluca, Chemical Engineering, Imperial College London, South Kensington Campus, London SW7 2AZ, UK
Mercado, Miriam, Retorno Rada Edif. 86 Depto. 18, U. Patera Vallejo, Gustavo A. Madero 07710 Mexico
Meyer, Glen E., Physical Facilities Dept., The Church of Jesus Christ of Latter-Day Saints, 50 E. North Temple St., Rm. 1000, Salt Lake City, UT 84150-6310
Minasyan, George, 851 Hamilton Dr., Lafayette Hill, PA 19444
Morris, Adam, Piezotech LLC, 8431 Georgetown Rd., Indianapolis, IN 46268
Nilesh, Bhattad, H305, Rohan Vashantha, near Marthahalli Railway Bridge, Bangalore, India
Norcross, Scott G., Communication Research Centre, VPBT Advanced Audio Systems, 3701 Carling Ave., P.O. Box 11490, Stn. H, Ottawa, ON K2H 8S2, Canada
Nordquist, Peter R., Southern Oregon Univ., Computer Science, 1250 Siskiyou Blvd., Ashland, OR 97520
Pantea, Cristian, 2060A 41st, Los Alamos, NM 87544
Psaras, Marios, Flat 52, Stonebridge House, 5 Cobourg St., Manchester M1 3GB, UK
Rajaram, Shankar, 11849 Goshen Ave., Apt. 8, Los Angeles, CA 90049
Reiley, Evan S., Performance Media Industries, 9 Mono Ave., Unit A, Fairfax, CA 94930
Roney, Alfred B., 317 N. Broad St., Apt. 311, Philadelphia, PA 19107
Sakamoto, Shinichi, Inst. of Industrial Science, Univ. of Tokyo, 5th Dept., 4-6-1 Komaba, Meguro-ku, Tokyo 153-8505, Japan
Sachau, Delf, Helmut-Schmidt-Univ., Mechanical Engineering, Holstenhofweg 85, Hamburg 22043 Germany
Scofield, William C., Kyocera Wireless Corp., Advanced Development and Production Def., 10300 Campus Point Dr., San Diego, CA 92121
Scott, Anthony A., 25 Manchester Rd., Eastchester, NY 10709
Sieber, Arne, Austrian Research Centers GmbH, 2444 Seibersdorf, Austria
Slater, Michael, P.O. Box 364, Bremerton, WA 98337

Smith, Justin D., Eilar Associates, Inc., 539 Encinitas Blvd., Ste. 206, Encinitas, CA 92024
Spulber, Tiberiu, BKL Consultants Ltd., 308-1200 Lynn Valley Rd., North Vancouver, BC V7J 2A2, Canada
Solberg, Stephen E., Coffeen Fricke & Associates, Inc., 14827 W. 95th St., Lenexa, KS 66215
Terrell, Virgil E., GRAS Sound & Vibration, 23621 Lorain Rd., North Olmsted, OH 44070
Terry, Charles C., Eilar Associates, Inc., 539 Encinitas Blvd., Ste. 206, Encinitas, CA 92024
Tikriti, Walid M., 3027 Renaissance Court, Dallas, TX 75287
Wagenaars, Wil, Philips Consumer Electronics Lab, Interleuvenlaan 74-82, Leuven B-3001, Belgium
Walker, Ian T., Audio Communications Solutions Ltd., 4 Brompton Rd., York YO306 NJ, UK
Wang, Tongan, 4035 Kessler Ave., Apt. 1002, Garden City, GA 31408
Webster, Jeremy, Natl. Center for Physical Acoustics, 1 Coliseum Dr., University, MS 38677
Wong, Galen S. W., 5-3409 Centre St., NW, Calgary, AB T2E 2X7, Canada
Xiong, Blong, Colin Gordon and Associates, 883 Sneath Ln., Ste. 150, San Bruno, CA 94066
Yamakami, Ken, Foster Electric Co., Ltd., HP Div., Eng. Dept. 6, Design Gr. 2, Miyazawa-cho 512, Akishima, Tokyo, 196-8550 Japan
Yamamoto, Kohei, Kobayasi Inst. of Physical Research, 3-20-41 Higashi-Motomachi Kokubunji, Tokyo 185-0022, Japan
Yasin, Ifat, Experimental Psychology, Univ. of Oxford, South Parks Rd., Oxford OX1 3UD, U.K.

New Students

Abbott, John Paul R., 580 N. 100 East, Apt. 17, Provo, UT 84606
Al-Wohaibi, Abdulrahman A., Badaya P.O. Box No. 502, Gassim 51951, Saudi Arabia
Anderson, Seth, Bethel Univ., 3900 Bethel Univ., #243, St. Paul, MN 55112
Ballard, John R., Electrical and Computer Engineering, Univ. of Minnesota, Rm. 4-174, 200 Union St., SE, Minneapolis, MN 55455
Bavu, Eric, Faculte de Genie Mecanique, Groupe d'Acoustique, Univ. de Sherbrooke, 2500 Blvd. de l'Universite, Sherbrooke, QC J1K 2R1, Canada
Bok, Tae-Hoon, Oceanic Info. and Syst. Eng., Cheju National Univ., 66 Jejudaehakno, Jeju 690-756, South Korea
Boughan, C. Chaya, Rensselaer Polytechnic Inst., Applied Mathematics, Amos Eaton Hall, 110 8th St., Troy, NY 12180
Briggs, Heather, 012 Smyth Hall, Newark, DE 19717
Brothers, Jonathan S., 2100 W. Berwyn Ave., Chicago, IL 60625
Butler, Lynnika, 215 E. Pommel St., Safford, AZ 85546
Cassidy, Matthew, 5 Ascot House, Windsor Ave. N., Belgast, Antrim, BT9 6EL, Ireland
Chevillote, Fabien, Mechanical Engineering, Univ. de Sherbrooke, 2500 Boulevard de l'Universite, Sherbrooke, QC J1K 2R1, Canada
Choiniere, Marc, 1601 S. 64th St, Omaha, NE 68106
Crimmins, Katherine A., 1364 Geddes Ave., Apt. 4, Ann Arbor, MI 48104
Desjardins, Jamie L., Audiology, Syracuse Univ., 805 S. Crouse Ave., Syracuse, NY 13244
Field, Jim P. Field, 1405 Sigur Ave., Metairie, LA 70005
Freedman, Joseph S., 458 Calhoun St., Atlanta, GA 30318
Friedman, Sarah A., 627 Muriel St., Rockville, MD 20852
Giardiello, Bradley E., 221 Massachusetts Ave., Apt. 917, Boston, MA 02115
Good, Erin, 3661 N. Campbell Ave., #352, Tucson, AZ 85719
Henry, Ryan A., 334 N 450 E, Valparaiso, IN 46383
Hickman, Tracy, 1830 W. Wilson Ave., #5, Chicago, IL 60640
Hwang, HaDong, 525 W. Brompton, #112, Chicago, IL 60657
Johann, Stefan, Ruptisch, Johannes Kepler Univ., Inst. for Measurement Technology, Altenbergerstrasse 69, Linz 4040, Austria
John, Andrew B., Dept. of Communication Sci. & Disorders, Univ. of Florida, P.O. Box 117420, Gainesville, FL 32611
John, Thomas K., 296 Wood St., Preston, Melbourne, VIC 3072, Australia
Johner, Stacy L., 4138 Warwick Blvd., Apt. 35, Kansas City, MO 64111
Johnsen, Eric, Mechanical Engineering, California Inst. of Tech., 1200 E. California Blvd., Pasadena, CA 91125
Katsika, Argyro, Linguistics, Yale Univ., 370 Temple St., Rm. 204, New Haven, CT 06520-8366
Khalaf, Daniel G., Karen S. Khalaf, AIA, 86 Summit Ave., Summit, NJ 07901
Khoklova, Tatiana D., Vorob'yovy gory L-14, Moscow 119234, Russia
Kiel, Andrew H., 525 S. State. St., Chicago, IL 60605
Kopechek, Jonathan A., 2921 Scioto Ln., Apt. 501, Cincinnati, OH 45219
Kosherick, Barry M., 8 Boynton St., Worcester, MA 01609
Krueger, Todd M., Washington Univ., Lab. for Ultrasonics, 1 Brookings Dr., University City, MO 63130
Lee, Kyogu, 65 Abrams Court, #102, Stanford, CA 94305
Lefebvre, Antoine, 4595 Boul. Rosemont, App. 9, Montreal, QC H1T 2E3, Canada
Levitte, Emmanuel E. L., 320 Rue Chartier, Sherbrooke, QC J1J 3B2, Canada
Loughran, Roisin B., 37 Headford, Mount Ave., Dundalk, Louth, Ireland
Majdak, Piotr, Vs. Akademie d. Wissenschaften, Institut fur Schallforschung, Reichsratsstrasse 17, 1010 Wien, Austria
Malik, Mashkoor A., Univ. of New Hampshire, NRESS, 24 Colovos Rd., Durham, NH 03824
Manning, John, Bauer Industries, 445 Dutton Dr., Waterloo, ON N2L 4C7, Canada
Marek, Kenneth, 219 Maple St., Hapeville, GA 30354
Markel, Deborah, 7309 Diagonal Rd., Kent, OH 44240
Mazur, Ruth Anne, 343 S. Dearborn St., Apt. 1803, Chicago, IL 60604
McCartney, Nicholas P., 4205 N. Ozanam, Norridge, IL 60706
McGovern, Megan E., 3154 Forestview Trail, Crete, IL 60417
McNeill, Nathan, Engineering Education, Purdue Univ., 400 Centennial Dr., West Lafayette, IN 47907
Mendis, Joseph J., 28 Swarkestone Dr., Littleover, Derby, Derbyshire, DE2 32PA, UK
Meyer, Justin E., 342 Dearborn St., Apt. 1604, Chicago, IL 60604
Millhouse, Thomas J., 29/215 Aspinall St., Watson, ACT 2602, Australia
Ongel, Aybike, 3800 Solano Park Circle, Apt #2124, Davis, CA 95616
Oldham, Justin J., Univ. of Alaska Southeast, 11120 Glacier Highway, Juneau, AK 99801
Rasmus, Luke N., 2615 21st, Lubbock, TX 79410
Ravindran, Apoorv, 1716 N. Vassar St., Apt. 5, Wichita, KS 67208
Ringer, Ashley, 325 SE Williamsburg Dr., Lees Summit, MO 64063
Roberts, Jordan L., 1527 W. Chicago Ave., #2, Chicago, IL 60622
Roberts, Philip, 8875-1 Kephart Ln., Berrien Springs, MI 49103
Schattner, William L., 1436 W. Addison St., Apt. 3, Chicago, IL 60613
Scherrer, Nicole M., 512 E. Fairmont Dr., Tempe, AZ 85282
Sebastian, Daniel M., Columbia College Chicago, Acoustics, 600 S. Michigan Ave., Chicago, IL 60605
Sirny, Dustin, 6744 15th Ave. S., Richfield, MN 55423
Smith, Jason K., CEAT, Univ. of Hartford, Box 2663, 200 Bloomfield Ave., West Hartford, CT 06117
Sturgis, Joe M., 1227 S. Roanoke, Springfield, MO 65807
Tanaka, Ryota, 3950 N. Lake Shore Dr., #1002, Chicago, IL 60613
Thompson, Christopher L., 301 N. 6th St., Hamilton, MT 59840
Thomson, Clint D., ATK Launch Systems, Health Management, P.O. Box 707, MS 245C, Bldg. 519-C, Brigham City, UT 84602-0707
Thornock, Brian T., Brigham Young Univ., Physics, 273 ESC, Provo, UT 84606
Walsh, Kyle P., Dept. of Psychology, Univ. of Texas at Austin, 1 University Station A8000, Austin, TX 78712
Weinberg, Samuel N., 2442 Brentwood Rd., Bexley, OH 43209
Weirathmueller, Michelle, Ocean Engineering/CCOM, Univ. of New Hampshire, 24 Colovos Rd., Durham, NH 03824-3515
Wilson, Lindsay J., Scottish Assoc. Marine Sci., Ecology Dept., Dunstaffnage Marine Lab, Oban, PA37 1QA, United Kingdom
Wodzinski, Sylvie M., 1809 1st St., Unit A, Indian Rocks Beach, FL 33785
Xu, Jinshan, 550 Memorial Dr., Apt. 15B4, Cambridge, MA 02139
Ying, Li, Oceanic Info. and Syst. Eng., Cheju National Univ., 66 Jejudaehakno, Jeju, 690-756, South Korea
Zaba, Aleksandra, Linguistics, Univ. of Utah, 255 S. Central Campus Dr., Rm. 2330, Salt Lake City, UT 84112
Zhang, Peng, Boston Univ., AME, 110 Cummington St., Boston, MA 02215
Zhao, Yixin, Tsinghua Univ., Inst. of Microelectronics, Rm. #913, Main Bldg., Beijing, 100084, P.R. China

New Electronic Associates

Adachi, Jingo, 3-12-22 Shibuya Shibuya-ku, Tokyo, 150-0002, Japan
Aston, Kelly A., Artec Acoustics, 114 W. 26th St., 12th Floor, New York, NY 10001
Atkins, Philip R., Dept. of Electronic, Electrical & Computer Eng., Univ. of Birmingham, Birmingham B15 2TT, UK
Backer, Steven L., 6 Godeus St., San Francisco, CA 94110
Bishop, Martin J. D., 22 Herringston Rd., Dorchester DT1 2BSA, UK
Bjelica, Rajko, DaimlerChrysler Corp., Audio and Telematics Group, 800 Chrysler Dr., CIMS #482-10-08, Auburn Hills, MI 48326
Cahill, Thomas P., 215 Adams St., 15J, Brooklyn, NY 11201
Carson, Timothy M., Collins & Aikman, 47785 W. Anchor Ct., Plymouth, MI 48170
Drioli, Carlo, Univ. of Verona, Computer Science, Ca Vignal 2, strada le Grazie 15, Verona 37134, Italy
Gainer, Dean, Sound Progression LLC, 9728 Dayton Ave., North, Seattle, WA 98103
Guillaume, Patrick, Vrije Universiteit Brussel, Mechanical Engineering, VUB-MECH-AVRG, Pleinlaan 2, B-1050 Brussel, Belgium
Hakkinen, Markku, 45 Lawrencia Dr., Lawrenceville, NJ 08648
Have, Helmut, Landuse Planning & Environment, Phoenixstraat 49c, 2611 AL Delft, The Netherlands
Hopper, Clare, British Geological Survey, Kingsley Durham Centre, Keyworth, Nottingham, NG12 5GG, UK
Hult, Vern A., Oil Lift Technology Inc., 1820 30 Ave. NE, #3, Calgary, AB T2E 7M5, Canada
Israelsson, Hans G., 2716 27th St. NW, Washington, DC 20008
Johnsrude, Ingrid S., Queen's Univ., Psychology, 63 Arch St., Kingston, ON K7L 3N6, Canada
Lerin Borao, Maria Eva, Apartado de correos 2025, 29600 Marbella, Spain
Mancuso, Antonio, via Fratelli Gruppi 18, Bologna 40129, Italy
Moilanen, Petro, Makelantie 3 and 4, Saynatsalo KS 40900, Finland
Nokes, Jim R., ABOG LLC, Thumper Project, 1380 Gardner St., Stayton, OR 97383
Norli, Petter, Det Norske Veritas AS, MTPNO366, Veritasveien 1, Hovik, Akershus 1322 Norway
Orbelo, Diana, Mayo Clinic, Otorhinolaryngology, 200 1st St., SW, Mayo W5, Rochester, MN 55905
Perea, James D., 1527 E. Falkland Ln., #243, Silver Spring, MD 20910
Raake, Alexander, Ernst-Reuter-Platz 7, 10587 Berlin, Germany
Rankin, David B., Ambit Research, Development, 1834 Wake Forest Rd., Ste. 6116, Winston-Salem, NC 27109
Rok, Vladimir E., Tarusskaja 4-344, Moscow 117588, Russia
Stephenson, Catriona M., CREEM, Univ. of St. Andrews, The Observatory, Buchanan Gardens, St. Andrews, Fikfe, KY16 9LZ, UK
Young, Tim, 681 Linville Falls Dr., West Melbourne, FL 32904
Yuen, Ivan, Royal Holloway, Univ. of London, Psychology, Surrey TW20 0EX, UK

New Corresponding Electronic Associate

Alwi, Hasan A., Univ. Kebangsaan Malaysia, Pusat Fizik, Bangi, Selangor, 43600 Malaysia
Ben Jebara, Sofia, MASC, Ecole Superieure des Communications de Tunis, MASC, Route Raoued Km. 3-5, El Ghgazala, Ariana 2088, Tunisia
Fulgencio, Leon, Calle 37 #192 col. Ampliacion Las Aguilas, Nezahualcoyotl 57900, Mexico
Gopinathan, Sudheer, G. V. P. College of Engineering, Madhurawada, Visakhapatnam, Andhra Pradesh 530041, India
Karuppiah, Jayaraj, ASA Acoustics Pvt. Ltd., 80 4th Trust Cross St., Mandavelipakkam, Chennai, Tamilnadu 600028, India
Lopez, Samuel, Vinedos Sta Teresa 159, Aguascalientes, SN Fco de los Romos 20364, Mexico
Mohammadi, Nader, 4th Floor, No. 2, Ghoodarzi Al, Shenasa St., Emamzedeh Ghasem, Tehran 19749, Iran
Ng, Yatming, 1B, Hoover Towers 2, Sau Wa Fong, Wanchai, Hong Kong, Hong Kong
Yoon, Taeseok, Renaultsamsung Motor Company, NVH Team, 447-4 Gongse-ri, KiHueng, Kyunggido 446-796, Korea

Reinstated

R. Duraiswami—Member
D. M. Lfrederick, K. A. Legleiter, J. M. Opie—Associates

Members Elected Fellows

M. R. Bailey, D. J. Doria, J. M. Eargle, S. J. Elliott, H. E. Gockel, K. M. Li, A. Migliori

Associates Elected Fellows

P. E. Barbone, S. I. Finette, T. D. Mast, C. Prada

Electronic Associate Elected Fellow

K. G. Sabra

Associates Elected Members

S. E. Bard, M. M. Buret, F. P. Curra, W. P. Ko, S. M. Mukdadi, B. C. Poteet, S. C. Renaud, D. R. Smith, K. Shanker, D. S. Woolworth, E. M. Zwerling

Students to Associates

C. Barroso, N. R. Blum, A. J. Boone, E. E. Bowden, S. Brown, M. Cappiello, R. C. Diaz, G. R. Dix, A. Farnetani, A. C. Faszer, M. J. Green, M. M. Holt, K. Hoyt, J. R. Hurd, Y. Kwon, N. W. Larsen, B. Li, A. Loubeau, J. E. Lyons, A. O. MacGillivray, J. Mahn, E. T. Miller-Klein, G. S. Morrison, J. A. Mossbridge, P. G. Muzzy, S. Ortallono, C. A. Sanford, H.V. Savitala, T. Schultz, K. R. Shank, D. E. Shub, A. Sirovic, P. Smitthakorn, J. Songer, Y. Sun, D. F. Winker, M. S. Wochner, Y. S. Yunusova

Associate to Electronic Associate

H. R. Graf, J. Gramtorp

Resigned

T. G. Bouliane, W. E. Cooper, H. Endo, C. E. Hanson, T. F. Johnston, W. Kinney, M. Podiesak, J. S. Ryder, G. B. Smith, M. Tohyama, D. Wellsted, T. Yokoyama, Members
B. C. Baddorf, L. A. Challis, B. E. McClure, A. N. Hadjicostic, J. F. Holzrichter, K. Konishi, V. Tarnow, R. L. Tubbs, G. Wittek, Associates
Z. Nagy, Z. Vavva, Students
P. Stickar, Corresponding Electronic Associate

Deceased

B. A. Becken, M. Lawrence, G. Moushegian, L. H. Sibul, W. Thompson, Jr., H. E. von Gierke—*Fellows*
A. E. Galef, G. Herman, D. K. Lewis, N. Niwa, I. C. Simpson, H. M.Walkinshaw—*Members*
E. Zelnick—*Associate*

Fellows	891
Members	2152
Associates	2535
Students	968
Electronic Associates	628
	7174

ACOUSTICAL NEWS—INTERNATIONAL

Walter G. Mayer
Physics Department, Georgetown University, Washington, DC 20057

International Meetings Calendar

Below are announcements of meetings and conferences to be held abroad. Entries preceded by an * are new or updated listings.

June 2007

1–3 **Second International Symposium on Advanced Technology of Vibration and Sound**, Lanzhou, China (Web: www.jsme.or.jp/dmc/Meeting/VSTech2007.pdf).

3–6 **14th International Conference on Noise Control (noise control '07)**, Elblag, Poland (Web:www.ciop.pl/noise-07).

3–7 **11th International Conference on Hand-Arm Vibration**, Bologna, Italy (Web:associazioneitalianadiacustica.it/HAV2007/index.htm).

4–6 **Japan-China Joint Conference on Acoustics**, Sendai, Japan (Fax: +81 3 5256 1022; Web: www.asj.gr.jp/eng/imdex.html).

18–21 **Oceans07 Conference**, Aberdeen, Scotland, UK (Web: www.oceans07ieeeaberdeen.org).

25–27 **31st International AES Conference—New Directions in High Resolution Audio**, London, UK (Web: www.aes.org/events/31/).

25–29 **2nd International Conference on Underwater Acoustic Measurements: Technologies and Results**, Heraklion, Crete, Greece (Web: www.uam2007.gr).

July 2007

2–6 **8th International Conference on Theoretical and Computational Acoustics**, Heraklion, Crete, Greece (Web: www.iacm.forth.gr/~ictca07).

3–5 **First European Forum on Effective Solutions for Managing Occupational Noise Risks**, Lille, France (Web: www.noiseatwork.eu).

4–7 **International Clarinet Association Clarinetfest**, Vancouver, British Columbia, Canada (e-mail: john.cipolla@wku.edu; Phone: 1 270 745 7093).

9–12 **14th International Congress on Sound and Vibration (ICSV14)**, Cairns, Australia (Web: www.icsv14.com).

16–21 **12th International Conference on Phonon Scattering in Condensed Matter**, Paris, France (Web: www.isen.fr/phonons2007).

August 2007

6–10 **16th International Congress of Phonetic Sciences (ICPhS2007)**, Saarbrücken, Germany (Web: www.icphs2007.de).

27–31 **Interspeech 2007**, Antwerp, Belgium (Web: www.interspeech2007.org).

28–31 **inter-noise 2007**, İstanbul, Turkey (Web: www.internoise2007.org.tr).

September 2007

2–7 **19th International Congress on Acoustics (ICA2007)**, Madrid, Spain (SEA, Serrano 144, 28006 Madrid Spain; Web: www.ica2007madrid.org).

9–12 **ICA Satellite Symposium on Musical Acoustics (ISMA2007)**, Barcelona, Spain (SEA, Serano 144, 28006 Madrid, Spain; Web: www.ica2007madrid.org).

9–12 **ICA Satellite Symposium on Room Acoustics (ISRA2007)**, Sevilla, Spain (Web: www.ica2007madrid.org).

10–13 **54th Open Seminar on Acoustics (OSA2007)**, Przemysl, Poland (Web: www.univ.rzeszow.pl/osa2007/).

17–19 **3rd International Symposium on Fan Noise**, Lyon, France (Web: www.fannoise.org).

18–19 **International Conference on Detection and Classification of Underwater Targets**, Edinburgh, UK (Web: ioa.org.uk).

19–21 **Autumn Meeting of the Acoustical Society of Japan**, Kofu, Japan (Acoustical Society of Japan, Nakaura 5th-Bldg., 2-18-20 Sotokanda, Chiyoda-ku, Tokyo 101-0021, Japan; Fax: +81 3 5256 1022; Web: www.asj.gr.jp/index-en.html).

20–22 **Wind Turbine Noise 2007**, Lyon, France (Web: www.windturbinenoise2007.org).

24–28 **XIX Session of the Russian Acoustical Society**, Nizhny Novgorod, Russia (Web: www.akin.ru).

27–29 ***3rd Congress of the Alps Adria Acoustical Association**, Graz, Austria (Web: www.alpsadriaacoustics.org)

October 2007

3–5 **Pacific Rim Underwater Acoustics Conference 2007**, Vancouver, BC, Canada (Web: PRUAC.apl.washington-.edu).

9–12 **2007 Canadian Acoustic Conference**, Montréal, Québec, Canada (Web: caa-aca.ca).

17–18 ***Institute of Acoustics Autumn Conference 2007**, Oxford, UK (Web:www.ioa.org.uk/viewupcoming.asp).

25–26 **Autumn Meeting of the Swiss Acoustical Society**, Bern, Switzerland (Web: www.sga-ssa.ch).

December 2007

6–9 ***International Symposium on Sonochemistry and Sonoprocessing (ISSS2007)**, Kyoto, Japan (Web: www.j-sonochem.org/ISSS2007).

June 2008

30–4 **Acoustics'08 Paris: 155th ASA Meeting + 5th Forum Acusticum (EAA) + 9th Congrès Français d'Acoustique (SFA)**, Paris, France (Web: www.acoustics08-paris.org).

July 2008

7–10 **18th International Symposium on Nonlinear Acoustics (ISNA18)**, Stockholm, Sweden (Web: www.congrex.com/18th-isna).

28–1 **9th International Congress on Noise as a Public Health Problem**, Mashantucket, Pequot Tribal Nation (ICBEN 9, P.O. Box 1609, Groton, CT 06340-1609, USA; Web: www.icben.org).

August 2008

25–29 **10th International Conference on Music Perception and Cognition (ICMPC 10)**, Sapporo, Japan (Web: icmpc10.typepad.jp).

September 2008

22–26 **INTERSPEECH 2008—10th ICSLP**, Brisbane, Australia (Web: www.interspeech2008.org).

October 2008

26–29 **inter-noise 2008**, Shanghai, China (Web: www.internoise2008.org).

November 2008

2–5 **IEEE International Ultrasonics Symposium**, Beijing, China (Web: www.ieee-uffc.org/ulmain.asp?page=symposia).

September 2009

6–10 **InterSpeech 2009**, Brighton, UK (Web:www.interspeech2009.org).

August 2010

23–27 **20th International Congress on Acoustics (ICA2010)**, Sydney, Australia (Web: www.ica2010sydney.org/).

 0001-4966/2007/121(6)/3253/1/$23.00 © 2007 Acoustical Society of America

REVIEWS OF ACOUSTICAL PATENTS

Lloyd Rice
11222 Flatiron Drive, Lafayette, Colorado 80026

The purpose of these acoustical patent reviews is to provide enough information for a Journal reader to decide whether to seek more information from the patent itself. Any opinions expressed here are those of reviewers as individuals and are not legal opinions. Printed copies of United States Patents may be ordered at $3.00 each from the Commissioner of Patents and Trademarks, Washington, DC 20231. Patents are available via the Internet at http://www.uspto.gov.

Reviewers for this issue:

GEORGE L. AUGSPURGER, *Perception, Incorporated, Box 39536, Los Angeles, California 90039*
ANGELO CAMPANELLA, *3201 Ridgewood Drive, Hilliard, Ohio 43026-2453*
JOHN M. EARGLE, *JME Consulting Corporation, 7034 Macapa Drive, Los Angeles, California 90068*
JOHN ERDREICH, *Ostergaard Acoustical Associates, 200 Executive Drive, West Orange, New Jersey 07052*
SEAN A. FULOP, *California State University, Fresno, 5245 N. Backer Avenue M/S PB92, Fresno, California 93740-8001*
JEROME A. HELFFRICH, *Southwest Research Institute, San Antonio, Texas 78228*
DAVID PREVES, *Starkey Laboratories, 6600 Washington Ave. S., Eden Prarie, Minnesota 55344*
CARL J. ROSENBERG, *Acentech Incorporated, 33 Moulton Street, Cambridge, Massachusetts 02138*
NEIL A. SHAW, *Menlo Scientific Acoustics, Inc., Post Office Box 1610, Topanga, California 90290*
ERIC E. UNGAR, *Acentech, Incorporated, 33 Moulton Street, Cambridge, Massachusetts 02138*
ROBERT C. WAAG, *Department of Electrical and Computer Engineering, University of Rochester, Rochester, New York 14627*

7,122,801

43.20.Ye SYSTEM AND METHOD FOR GENERATING CHAOTIC SOUND FOR SONIC INFRARED IMAGING OF DEFECTS IN MATERIALS

Lawrence D. Favro *et al.*, assignors to Wayne State University
17 October 2006 (Class 250/341.6); filed 14 September 2004

The pulsed output of ultrasonic transducer **14** is coupled via horn **18** and gasket **16** into a component **12**, which may be a metal, ceramic, composite, or another material. The pulse propagates into the material, the depth of which is a function of the pulse frequency. Gasket **16** may be soft metal, leather, cork, duct tape, Teflon, paper, etc., as appropriate for component **12**.

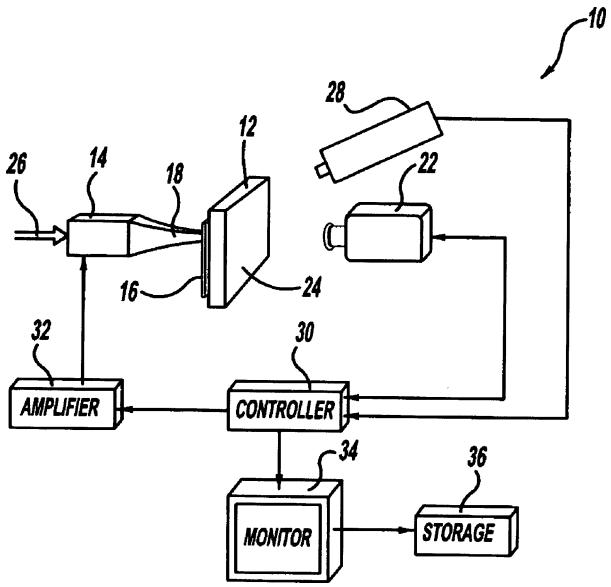

The pulses cause ''acoustic chaos'' in the material under test. A detection system consists of a thermal imaging camera **22**, vibrometer **28**, and controller **30**, which capture images and process them to show defects uncovered by the heat produced by the acoustic pulses.—NAS

7,123,725

43.20.Ye HIGH INTENSITY INFRASONIC TUNABLE RESONANT ACOUSTIC TEST CELL

Harold E. Boesch, Jr. *et al.*, assignors to The United States of America as represented by the Secretary of the Army
17 October 2006 (Class 381/58); filed 29 December 2000

By varying the cross section and/or length of port **50**, limiting the dimensions of volume **20** to less than one-half the longest wavelength of interest (1–30 Hz) to prevent standing waves, the Helmholtz resonator formed by **20** and **50** can be tuned to match the output of source **40** so that

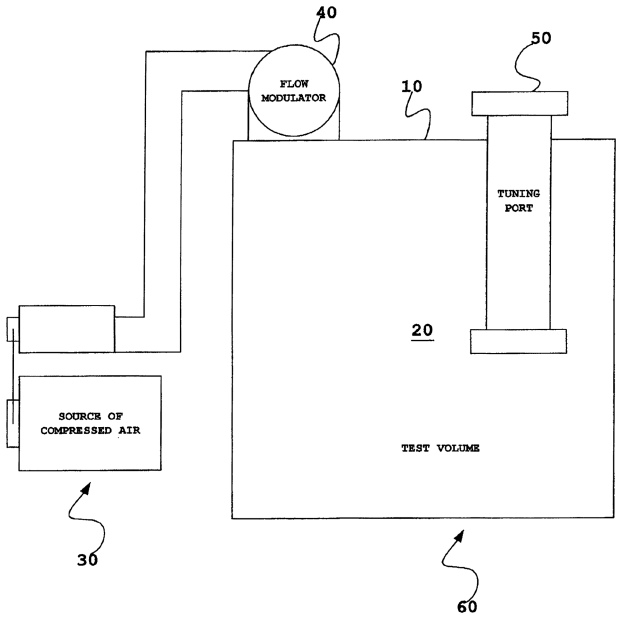

the intensity and spectral purity of the sound in **20** are amplified. Another embodiment uses two volumes with the duct connecting one to another, with small diameter long pipe(s), connected to at least the driving chamber, to exhaust the dc component of the air modulator source.—NAS

 0001-4966/2007/121(6)/3255/21/$23.00 © 2007 Acoustical Society of America

7,151,424

43.35.Pt BOUNDARY ACOUSTIC WAVE DEVICE

Hajime Kando, assignor to Murata Manufacturing Company, Limited
19 December 2006 (Class 333/193); filed in Japan 8 November 2002

As cellular phones with multiple functions become smaller, flatter, and lighter, further miniaturization of electronic components is required. A miniature (2×2 mm) laminated SAW device for gigahertz frequencies is claimed where Stonley waves propagate at the interfaces of two dielectric materials having different density or SAW velocities and whose package accordingly does not require voids. SAW device interdigital electrodes **2b** are laid on lithium niobate monocrystal substrate **2a** and covered with a

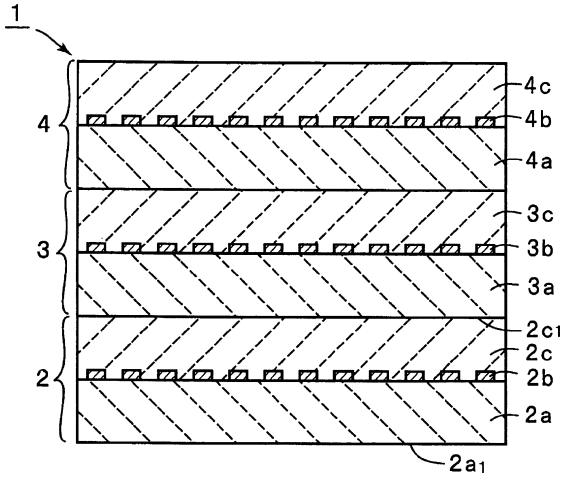

material **2c** that is both piezoelectric and insulating, e.g., silicon dioxide. The resulting Stonley wave has a propagation speed between 2000 and 10 000 m/s, resulting in a GHz SAW wavelength of about 2–10 μm. Most SAW energy is confined in a region that is one to three wavelengths thick. Both substrates may be about 100 wavelengths thick, so stacking Stonley wave elements **2abc**, **3abc**, **4abc**, etc., will not result in a significant overall SAW system thickness.—AJC

7,154,360

43.35.Pt FILTER USING PIEZOELECTRIC MATERIAL

Koichi Wada *et al.*, assignors to Fujitsu Media Devices Limited
26 December 2006 (Class 333/194); filed in Japan 29 September 2003

This patent discloses a novel concept for cancelling the negative effects of electric field leakage from the tips of SAW resonator electrodes. The

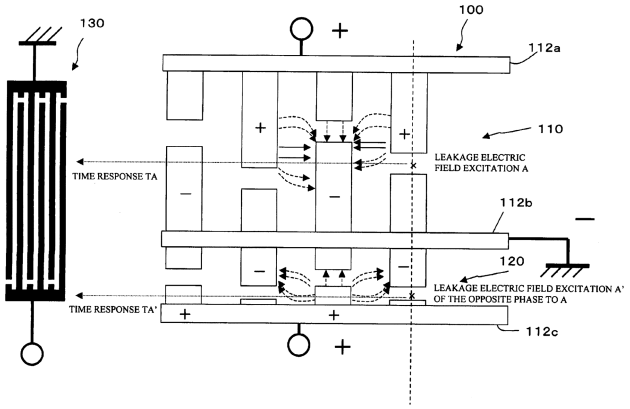

authors describe the problem very well and go over in detail the compensation technique given in the figure. Basically, a parallel electrode arrangement is set up so that the emissions from the tip of each pair in the main field can be canceled by the emission from its neighboring compensation pair. It is a neat and clean solution to a significant problem with SAW filters.—JAH

7,145,286

43.35.Zc WEDGE SHAPED UNIFORM ENERGY MEGASONIC TRANSDUCER

Mark J. Beck *et al.*, assignors to Product Systems Incorporated
5 December 2006 (Class 310/367); filed 16 September 2005

In an effort to increase the throughput of chip fabrication processes, semiconductor equipment manufacturers are looking at all sorts of process improvements, including the cleaning of silicon wafers. This patent applies primarily to the cleaning of wafers and disk drive platters, whose surfaces are planar and circular. The authors describe a technique for fabricating a high-intentsity ultrasonic transducer in a wedge shape so that the disc to be cleaned can be rotated underneath the transducer and cleaned in the shortest time possible by equalizing the ultrasonic energy across a radius. The ideas involved here are quite simple and it is an implementation of the usual techniques for matching a stiff transducer (PZT) to a compliant liquid.—JAH

7,148,611

43.35.Zc MULTIPLE FUNCTION BULK ACOUSTIC WAVE LIQUID PROPERTY SENSOR

James Z. T. Liu, assignor to Honeywell International Incorporated
12 December 2006 (Class 310/366); filed 11 October 2005

The author of this patent describes the various uses of electrodes within a liquid bath. He concludes that you can attach another electrode to a bulk acoustic wave device and measure conductivity within the liquid. This is neither novel nor surprising. The patent then goes on to include measurement of the corrosive effects of the liquid by measurement of the rate of frequency change due to what is supposed to be the etching of the metal electrodes in the solution. Overall there is nothing new here; these sensors have been made and demonstrated individually before.—JAH

7,150,779

43.35.Zc MODULATED ACOUSTIC AGGLOMERATION SYSTEM AND METHOD

George Douglas Meegan, Jr., assignor to Board of Regents, The University of Texas System
19 December 2006 (Class 95/29); filed 27 February 2004

An airborne particle agglomerating system is claimed having multiple sound sources **20** facing the flow in duct **12** of fluid or gas **14** to be cleaned. The gas stream contains solids, lignite fly ash, for instance, having particle sizes from about 1–5 μm. When a 150 dB re 20 μPa sound field **22** is induced into the flow at a frequency of about 600 Hz, the smallest particles will readily move with the acoustic wave displacements while the larger particles may not, resulting in collisions and, as often as not, subsequent

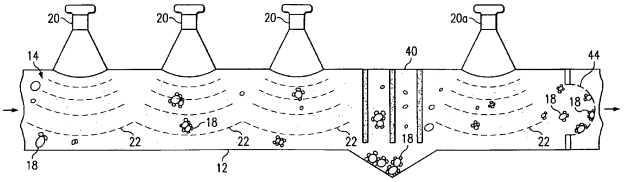

cohesion and agglomeration. It was found empirically that, when either the sound frequency in range or the sound amplitude is varied at rate of about 150 Hz, agglomerated particles up to 20 μm in size will result. The gas flow is passed through the fields of several sound sources **20**, through an electrostatic precipitator **40**, where some particles **18** are captured, through the sound field of another sound source **20a**, and then into a bag house **44**,

where more agglomerated particles **18** are captured before the gas flow is released into the atmosphere. Other liquids, gasses, and operating frequencies are claimed.—AJC

7,157,649

43.38.Ar CONTACT SENSITIVE DEVICE

Nicholas P. R. Hill, assignor to New Transducers Limited
2 January 2007 (Class 178/18.04); filed in the United Kingdom 23 December 1999

A passive contact-sensitive screen **32** is claimed, where bending waves produced by the impact of a tapping stylus or pen **30** propagate to three perimeter transducers **26**, whose signals are processed to determine the contact point coordinates. An active version is also claimed, where the right

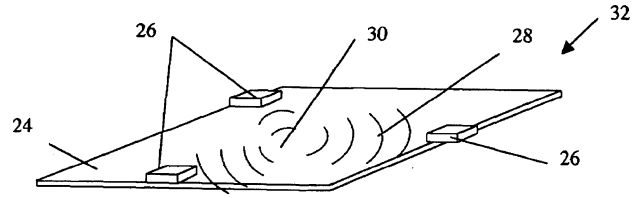

transducer emits bending waves while the contact at **30** perturbs the propagation of those waves to the left two transducers. The signal processing algorithms are also claimed.—AJC

7,123,738

43.38.Dv LOUDSPEAKER

Shinya Mizone *et al.*, assignors to Matsushita Electric Industrial Company, Limited
17 October 2006 (Class 381/406); filed in Japan 4 October 1999

Electrodynamic transducers with a single cone **5** or a single cone and an inductively driven LED assembly **81**, **82**, **83** (claims 2 to 4) is made more moisture resistant, is said to have better environmental characteristics, to be more resistant to UV radiation, and to sound better (due to the high speed of

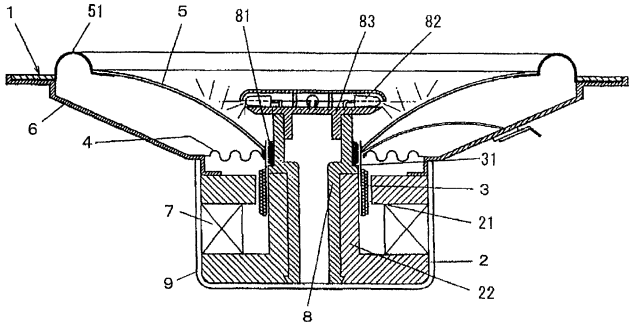

sound and higher internal damping of the cone material) by using a polyethylene naphthalate resin (PEN) or polyethylene terephthalate resin (PET) with an ultramicro foam of 30 μm or less in average cell size. It takes one page of text, five figures, and four claims.—NAS

7,146,014

43.38.Fx MEMS DIRECTIONAL SENSOR SYSTEM

Eric C. Hannah, assignor to Intel Corporation
5 December 2006 (Class 381/92); filed 11 June 2002

This patent discloses a MEMS device that utilizes a discrete mechanical delay line to sense direction of arrival of sound waves. Two sensors, **104A** and **104B**, are mechanically coupled to the set of discrete mechanical filters represented by elements **112**. It is not specified how this coupling is achieved without destroying the sensitivity of the diaphragms **104**, nor how the mechanical filters are made to fit over the two or three orders of magnitude in frequency that the device is supposed to work over. Nevertheless,

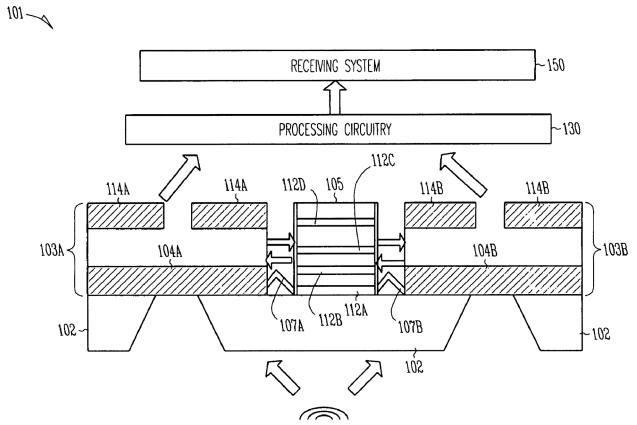

the authors maintain that the signals from the two sensors **104** can be processed to derive direction of arrival information from the outputs. This is based on the research that has been done on the directivity of the Ormia fly's ears, but the device appears to be so general in its description that there is no way to judge how it would really work.—JAH

7,148,608

43.38.Fx MULTI-LAYER CERAMIC ACOUSTIC TRANSDUCER

Charles E. Baumgartner *et al.*, assignors to General Electric Company
12 December 2006 (Class 310/334); filed 26 January 2006

In medical ultrasound imaging at high frequencies, low-capacitance array-element transducers are needed to match that of the signal cable (typically 50–72 Ω) to the signal processing system. A laminate is made comprising N thin slices of typically lead zirconate titanate (PZT) piezoelectric material, paired as 2–4 layers with metal contact interfaces **6** in between and bonded **8** to form a stack. With alternate contacts connected to form parallel electrical connection and the acoustical output from face **4** in series, a low impedance transducer of high output is achieved. Outer electrodes **4** are

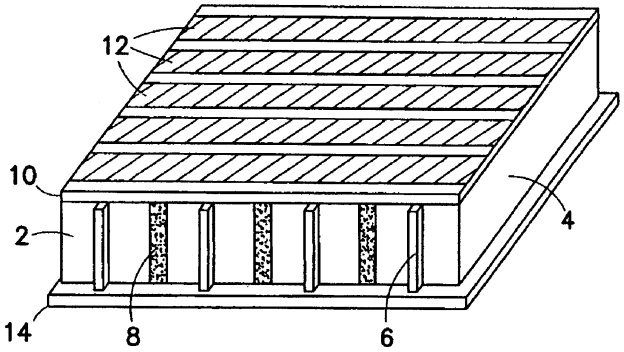

separately connected by straps **12**, also acting as a wrap-around shield and as the acoustic output face. Inner electrodes **6** (not shown) are connected in parallel to be the signal electrode when polarization is proper. The electrical impedance of this laminated stack element is diminished by a factor of N^2 as compared to a solid block of PZT of the same overall dimensions. Spacer material **14** provides acoustical isolation from adjacent array elements and is ground to a thickness that achieves the desired array spacing of such elements.—AJC

7,154,358

43.38.Fx FILM BULK ACOUSTIC RESONATOR STRUCTURE AND METHOD OF MAKING

Qing Ma *et al.*, assignors to Intel Corporation
26 December 2006 (Class 333/187); filed 16 September 2004

This patent discloses a method of fabricating thin-film bulk acoustic wave transducers (FBARs) that are acoustically isolated from their substrate and, so, have high Qs. The technique involves simply turning the resonators on their sides so that the electrodes are vertical plates **1610**, **1612**, bracketing the piezoelectric element that sticks up vertically. This process uses

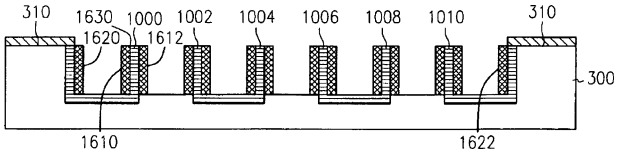

standard semiconductor fabrication techniques and could be relatively easily adapted to an existing process. It does not really involve any new ideas, since the mounting of an FBAR on edge has been done and patented before.—JAH

7,146,019

43.38.Ja PLANAR RIBBON ELECTRO-ACOUSTIC TRANSDUCER WITH HIGH SPL CAPABILITY AND ADJUSTABLE DIPOLE/MONOPOLE LOW FREQUENCY RADIATION

Igor Levitsky, Richmond Hill, Ontario, Canada
5 December 2006 (Class 381/399); filed 5 September 2002

Flat-diaphragm loudspeakers using what used to be called printed circuit voice coils are now labeled planar ribbon loudspeakers. In this variant, the array of bar magnets on one side of the diaphragm is shallower than that on the other. Moreover, the depth of the shallow assembly is less than a

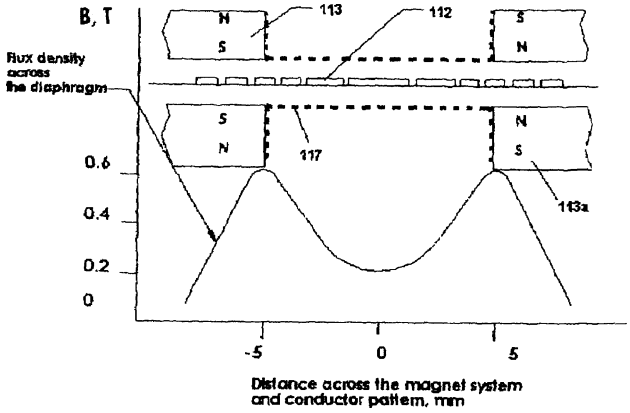

quarter-wavelength at 10 kHz. Other refinements include heat-conducting mesh **117**, a voice coil of varying width, and an optional sealed back chamber.—GLA

7,118,649

43.38.Ja DEVICE AND METHOD FOR MANUFACTURING SPEAKER DIAPHRAGM, THE DIAPHRAGM, AND SPEAKER

Yukinori Morohoshi *et al.*, assignors to Matsushita Electric Industrial Company, Limited
10 October 2006 (Class 162/228); filed in Japan 1 February 2002

Although loudspeakers are only about 150 years old, the material commonly used for the mechanical interaction with the medium, air, is more than two thousand years old. The invention relates to a method of better controlling the manufacture of paper cones on an industrial scale. Plunger **21b** is drawn down syringe **21a** to hasten the removal of water from the tank

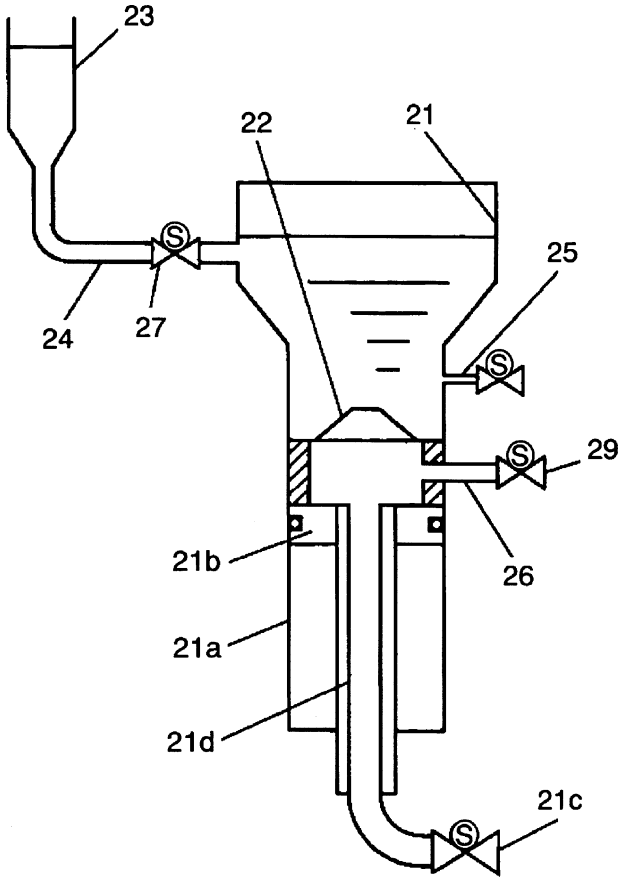

21. This is said to reduce turbulence at the mesh paper mold **22**. Two of the figures in the patent are identical, although they purport to describe a loudspeaker according to a preferred embodiment of the invention and a conventional loudspeaker.—NAS

7,146,021

43.38.Ja WHIZZER CONE FOR LOUDSPEAKER FOR PRODUCING UNIFORM FREQUENCY RESPONSE

Benny L. Danovi, assignor to Pioneer Speakers, Incorporated
5 December 2006 (Class 381/432); filed 29 December 2003

Inexpensive full-range loudspeakers often include a small whizzer cone to reproduce high frequencies. In some designs, the outer edge of this auxiliary cone is damped or contoured to minimize edge reflections. This

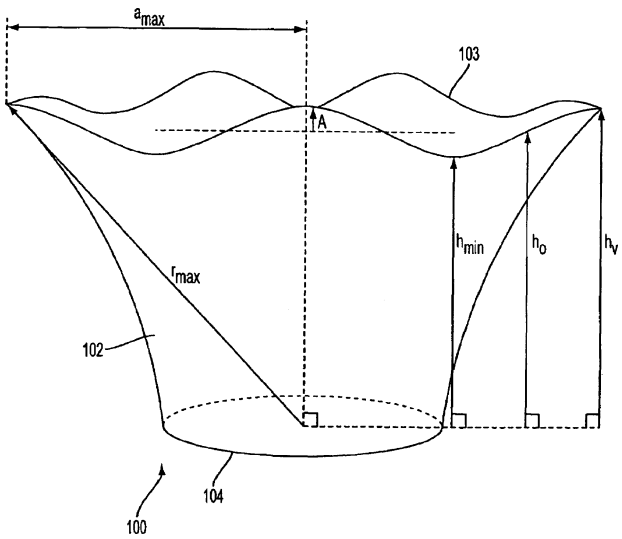

patent asserts that scalloping the edge in a kind of sine wave pattern significantly reduces high-frequency peaks and dips.—GLA

7,149,322

43.38.Ja MAGNETIC CIRCUIT FOR LOUDSPEAKER AND LOUDSPEAKER COMPRISING IT

Ryo Kuribayashi *et al.*, assignors to Matsushita Electric Industrial Company, Limited
12 December 2006 (Class 381/412); filed in Japan 16 January 2002

If loudspeaker magnet **2** is very thin, as shown, then a conventional magnetic pot structure may not allow sufficient clearance for long voice-coil

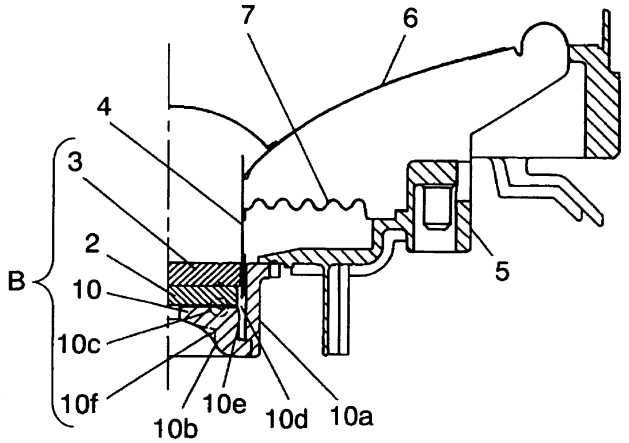

excursions. Rather than add a spacer, this design saves weight and cost by casting the back plate **10** in the form of an inverted pot.—GLA

7,151,836

43.38.Ja SPEAKER APPARATUS AND SOUND REPRODUCTION APPARATUS

Osamu Funahashi *et al.*, assignors to Matsushita Electric Industrial Company, Limited
19 December 2006 (Class 381/150); filed in Japan 31 March 1999

A single-ended bandpass woofer consists of a box divided into two chambers with a loudspeaker mounted on the dividing panel. One chamber is sealed and the other is vented to the exterior, forming a Helmholtz resonator. To save space, a passive radiator can take the place of the vent tunnel. Moreover, if the passive radiator is larger than the speaker, then it can

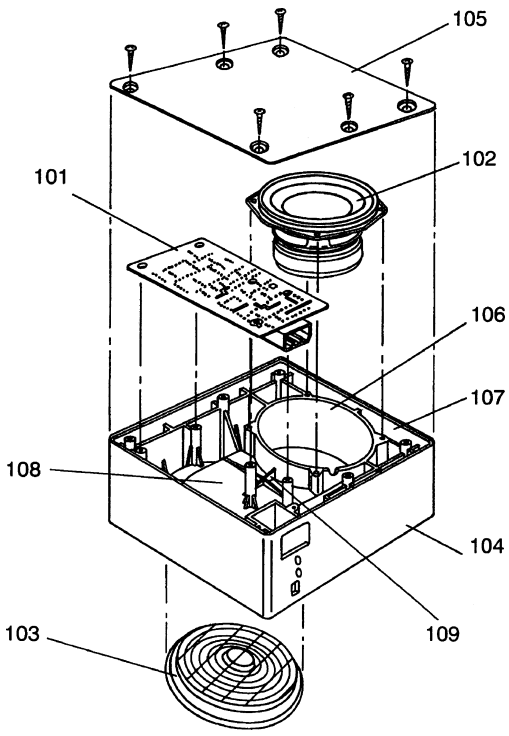

provide access to the speaker, eliminating the need for any removable cabinet panels. This patent argues that mounting the speaker and the passive radiator side-by-side somehow eliminates the divider panel and simplifies construction. Skeptical readers may observe that the geometry includes a front chamber, a rear chamber, and a removable panel, no matter how the arrangement is described.—GLA

7,158,647

43.38.Ja ACOUSTIC DEVICE

Henry Azima *et al.*, assignors to New Transducers Limited
2 January 2007 (Class 381/152); filed in United Kingdom 2 September 1995

This is a long and unusual patent. It contains more than 70 illustrations and a ten-page summary of planar loudspeaker design, including the exten-

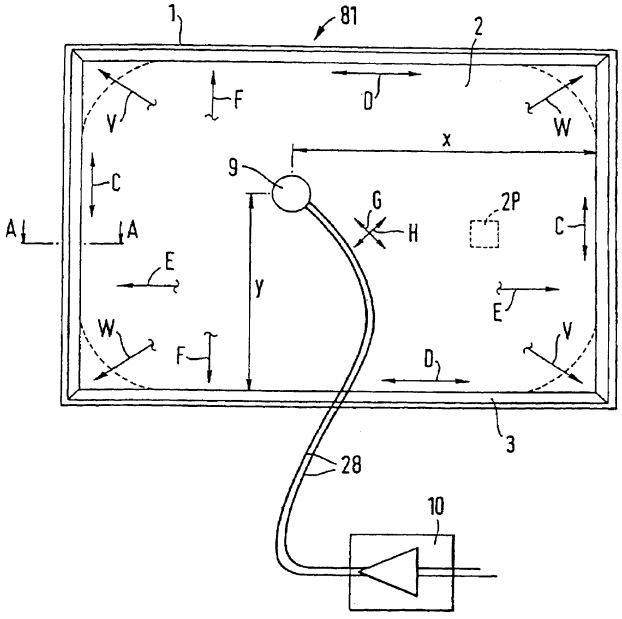

sive prior work patented by New Transducers Limited. In effect, the patent can serve as a handbook of the state of the art in this field. Anyone interested in planar loudspeakers is advised to order a copy.—GLA

7,158,651

43.38.Ja ELECTROMAGNETIC DRIVER FOR A PLANAR DIAPHRAGM LOUDSPEAKER

Wolfgang Bachmann *et al.*, assignors to Harman/Becker Automotive Systems GmbH
2 January 2007 (Class 381/412); filed in Germany 23 November 2000

This patent describes a contemporary version of the long-obsolete vibrating reed magnetic loudspeaker. In this case, a rocking armature rests on

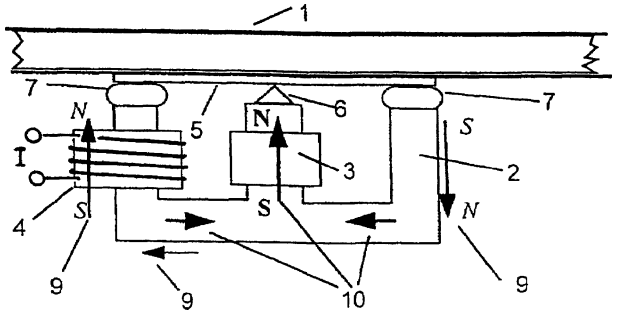

pivot **6** and is maintained in its rest position by non-magnetic springs **7**. Its seesaw motion generates bending waves in planar diaphragm **1**.—GLA

7,155,019

43.38.Kb ADAPTIVE MICROPHONE MATCHING IN MULTI-MICROPHONE DIRECTIONAL SYSTEM

Zezhang Hou, assignor to Apherma Corporation
26 December 2006 (Class 381/92); filed 14 March 2001

Directional microphones are often synthesized by using two closely-spaced omnidirectional elements combined anti-phase and with a slight delay in one element. Under conditions of normal usage, the sensitivities of the

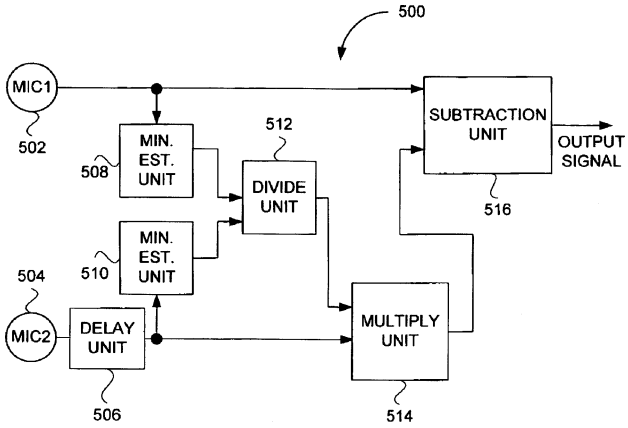

elements may vary, causing shifts in pickup pattern and perceived noise levels. The patent describes a means of tracking and compensating for these shifts.—JME

7,149,315

43.38.Md MICROPHONE ARRAY FOR PRESERVING SOUNDFIELD PERCEPTUAL CUES

James David Johnston and Eric R. Wagner, assignors to AT&T Corporation
12 December 2006 (Class 381/92); filed 15 July 2004

This patent is listed as a continuation of United States Patent 6,845,163, reviewed in J. Acoust. Soc. Am. **117**, 3354 (2005). Curiously, the present document appears to use exactly the same body text as the previous patent. Only the claims have been slightly changed, ostensibly to broaden them somewhat.—JME

7,157,991

43.38.Rh SURFACE ACOUSTIC WAVE DEVICE HAVING REFLECTORS WITH BOTH OPEN AND SHORTED ELECTRODES

Osamu Kawachi *et al.*, assignors to Fujitsu Media Devices Limited
2 January 2007 (Class 333/195); filed 29 December 2003

In constructing SAW rf bandpass filters, the out-of-band attenuation

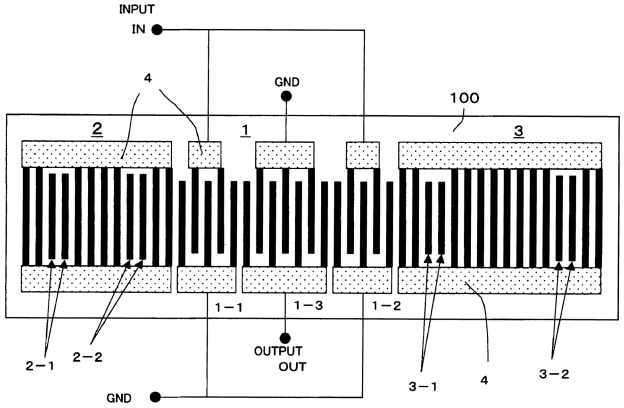

can be improved by disconnecting certain guard reflector fingers from terminal pads **4**, e.g., fingers **2-1**, **2-2**, **3-1**, and **3-2**.—AJC

7,148,769

43.38.Rh SURFACE ACOUSTIC WAVE DEVICE AND PROCESS FOR FABRICATING THE SAME

Atsushi Takano, assignor to Matsushita Electric Industrial Company, Limited
12 December 2006 (Class 333/193); filed in Japan 15 March 2004

To quell undesirable transmission modes **4** of a SAW rf filter, grooves **5** are cut into the back side of the lithium tantalate or niobate piezoelectric substrate **1** in which all SAW waves propagate. The frequencies considered are around 1843 MHz, where SAW wavelengths are about 2 μm. A thick, partly crystallized region **17** is formed on the substrate back side in fabrication to randomize wave propagation there. Grooves **5** are cut on that

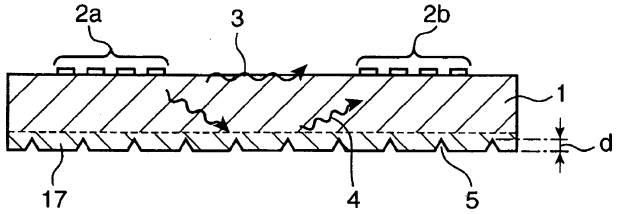

surface of depth **d** from 0.1 to five wavelengths. Such grooves further deflect and diminish waves **4** of undesirable transmission frequencies and modes. Groove paths are somewhat parallel to one another, but the spacings

are curved from one side of the substrate to the other so as not to be frequency selective. The author claims these grooves, their spiral path configuration, the fabrication and grinding processes to create them, and the disturbed region **17**.—AJC

7,155,025

43.38.Si SURROUND SOUND HEADPHONE SYSTEM

Sergio W. Weffer, Salt Lake City, Utah
26 December 2006 (Class 381/370); filed 30 August 2002

In an earlier patent the inventor proposed mounting several tiny transducers in a large ear muff. A listener wearing a pair of these multisource muffs presumably could enjoy portable surround sound. We now have a new patent: "It is, therefore, an object of the present invention to provide a new surround sound headphone system apparatus and method which has many of the advantages of the headphones mentioned heretofore and many novel

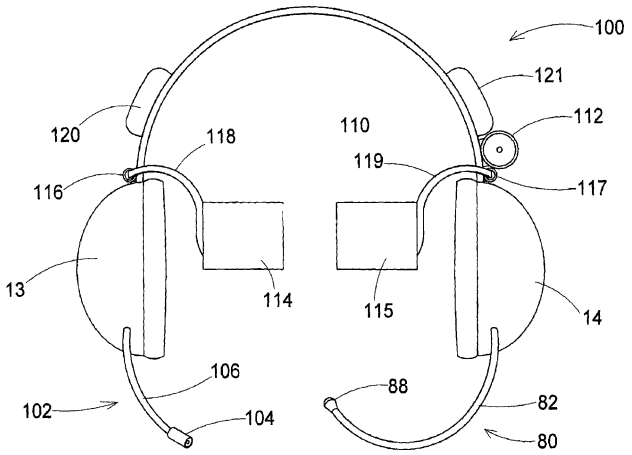

features that result in a new surround sound headphone system which is not anticipated, rendered obvious, suggested, or even implied by any of the prior art headphones, either alone or in any combination thereof." These revolutionary improvements include a volume control, a plug-in connection cord, and clip-on video screens.—GLA

7,146,010

43.38.Vk TWO METHODS AND TWO DEVICES FOR PROCESSING AN INPUT AUDIO STEREO SIGNAL, AND AN AUDIO STEREO SIGNAL REPRODUCTION SYSTEM

Christer Heed and Fredrik Gunnarsson, assignors to Embracing Sound Experience AB
5 December 2006 (Class 381/1); filed in the World Intellectual Property Organization 25 November 1999

Over the past ten years or so a number of technical papers and patents have described techniques for reproducing full Surround sound from two closely-spaced loudspeakers. The processing circuitry shown here is about

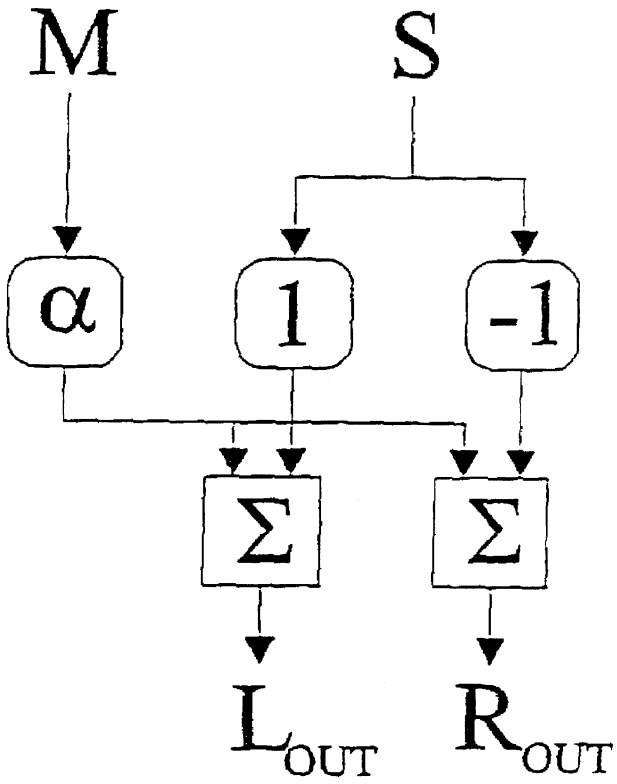

as simple as you can get. The attenuation factor alpha can range from −3 to −10 dB.—GLA

7,155,017

43.38.Vk SYSTEM AND METHOD FOR CONTROLLING AUDIO SIGNALS FOR PLAYBACK

Jong-Ho Kim *et al.*, assignors to Samsung Electronics Company, Limited
26 December 2006 (Class 381/59); filed in Republic of Korea 22 July 2003

Some 5.1 surround-sound systems provide adjustable signal delay for each channel. This is intended to compensate for unequal distances from the preferred listening location to individual loudspeakers. The distances can simply be measured or a test signal can be used to determine actual transit times. But suppose that the room temperature or humidity changes while the

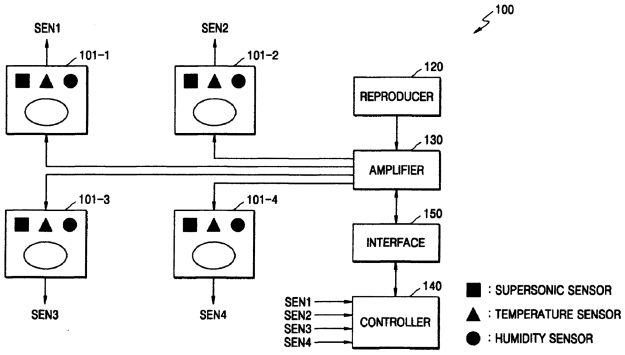

listener is engrossed in Wagner's Ring Cycle. The timing might then be off by a fraction of a millisecond! Not to worry—this Samsung system senses temperature and humidity at each speaker and automatically makes the necessary adjustments.—GLA

7,158,844

43.38.Vk CONFIGURABLE SURROUND SOUND SYSTEM

Paul Cancilla, Brampton, Ontario, Canada
2 January 2007 (Class 700/94); filed 21 July 2003

The invention is described as an improved spatial acoustic sequencer. It allows the user to select from a number of motion paths and other parameters, after which it generates appropriate DSP algorithms ''based upon the locations and orientations of the sound outputs in the playback environment relative to the source object.''—GLA

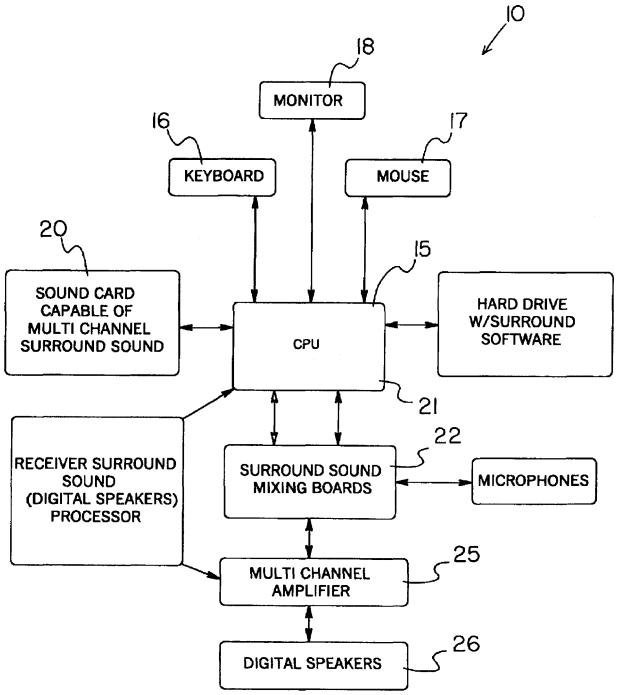

7,158,643

43.38.Vk AUTO-CALIBRATING SURROUND SYSTEM

Bruce S. Lavoie and William R. Michalson, assignors to Keyhold Engineering, Incorporated
2 January 2007 (Class 381/58); filed 20 April 2001

In this digital age, any audio-frequency transfer function can theoretically be corrected perfectly, yielding flat frequency response and zero phase distortion. This would seem to be an ideal approach to loudspeaker/room equalization. All that is needed in a typical listening room is an accurate impulse response measurement covering two or three seconds. In practice, however, the technique is fraught with unintended consequences and numerous schemes have been proposed for truncating, smoothing, averaging, or otherwise processing the data. This patent describes an automated equalization system that preferably generates a maximum length sequence (MLS) test signal to derive the impulse response—a commonly used procedure.

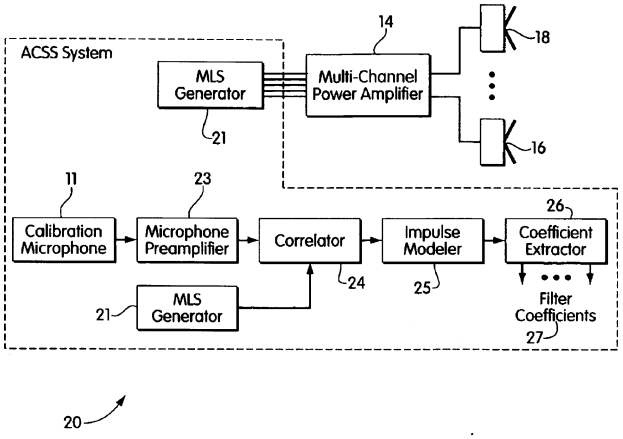

From this it determines the filter coefficients needed to produce a whitened version of the transfer function, using procedures described at some length in the patent text.—GLA

7,118,493

43.40.Kd MULTIPLE MATERIAL GOLF CLUB HEAD

J. Andrew Galloway, assignor to Callaway Golf Company
10 October 2006 (Class 473/329); filed 2 July 2004

Sound modifying component **59**, which can be a ring, washer, a cup as shown, or may be composed of ''any suitable shape,'' is located in the interior of club face component **60**. Titanium is the preferred material. The patent discusses club design, center of gravity, coefficient of restitution, energy transfer from club to ball, and the losses inherent in same. Oh, and the sound of the ''thwack'' is modified—NAS

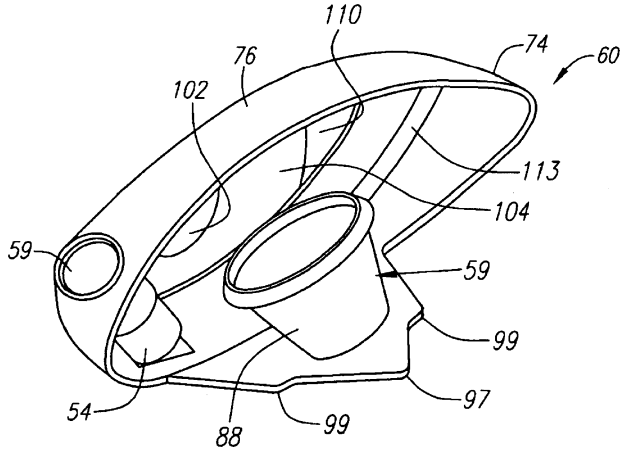

7,152,481

43.40.Qi CAPACITIVE MICROMACHINED ACOUSTIC TRANSDUCER

Yunlong Wang, Fremont, California
26 December 2006 (Class 73/718); filed 13 April 2005

A micromachined miniature acoustic condenser microphone is claimed where a conducting diaphragm **11** has low tension stress to maximize sensitivity. Stress relief is claimed to result from shallow corrugation **20**. Diaphragm **11** is anchored at one end to substrate **12**, but free at the other end **22**. Perforated plate **13** has holes **14** of diameter and spacing **15** that forms an acoustic filter to optimize a certain frequency or to be a low-pass acoustic filter. Electrode **13** in conjunction with diaphragm **11** forms a variable capacitor which, in turn, will produce a variable voltage from acoustical pressure variations on **11** when a bias voltage is applied. When bias voltage is increased, the resulting attraction causes bending of diaphragm **11** from its

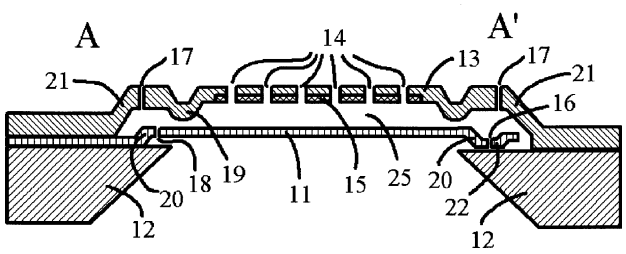

slack flat shape, increasing its tension, thus becoming less sensitive on that count, and thereby maintaining a more constant acoustic pressure sensitivity.—AJC

7,150,152

43.40.Tm VIBRATION LIMITER FOR COAXIAL SHAFTS AND COMPOUND TURBOCHARGER USING SAME

Jonathan P. Kilkenny *et al.*, assignors to Caterpillar Incorporated
19 December 2006 (Class 60/612); filed 21 October 2004

The vibration limiters described here consist of bearings that fit around one of the shafts with some clearance and that make contact if the shaft's lateral excursions exceed this clearance.—EEU

7,155,951

43.40.Tm MILL VARIATION CONTROL APPARATUS AND METHOD

Thomas William Dashwood Farley, assignor to Novelis, Incorporated
2 January 2007 (Class 72/205); filed in the European Patent Office 20 December 2000

In cold rolling of metal, a continuous strip of metal is passed through a series of rolls so as to reduce its thickness or ''gauge.'' Gauge chatter, a self-excited phenomenon that limits the speed at which rolling can be done acceptably in practice, results because the entry speed of the strip into a roll differs from its exit speed, in view of the strip's change in thickness. In order to overcome this chatter, the strip is made to pass over a roller that is provided with a torsional dynamic absorber consisting of a flexible shaft element and a flywheel.—EEU

7,157,822

43.40.Tm SMALL VIBRATION MOTOR AND METHOD OF MANUFACTURING THE SAME

Koji Yoshida *et al.*, assignors to Sony Corporation
2 January 2007 (Class 310/81); filed in Japan 30 July 2002.

This vibrator, intended for use in cell phones and the like, consists of a small motor with an unbalanced weight. The motor is driven by a three-phase voltage, converted from a dc source by means of an integrated circuit chip.—EEU

7,157,831

43.40.Tm ENERGY EFFICIENT VIBRATION DRIVEN MOTOR

Daryoush Allaei, assignor to Quality Research, Development & Consulting, Incorporated
2 January 2007 (Class 310/323.02); filed 30 September 2004

A vibration source, potentially consisting of piezoelectric elements, is arranged to drive a mechanical structure at resonance. The vibrations of this structure are converted to rotational motion of a shaft via a mechanical linkage. The patent gives no indication of suitable practical linkages.—EEU

7,143,682

43.40.Vn LARGE MANIPULATOR HAVING A VIBRATION DAMPING CAPACITY

Dirk Nissing *et al.*, assignors to Schwing GmbH
5 December 2006 (Class 91/358 R); filed in Germany 15 January 2001

Large manipulators, such as are used with truck-mounted concrete pumps, consist of a number of hinged segments and hydraulic units that adjust the relative positions of adjacent segments. A desired manipulator configuration, set by an operator, is maintained in the presence of disturbances by means of a system that senses the unsteady pressures in the hydraulic units and adjusts these via a controller.—EEU

7,150,257

43.40.Vn VIBRATION DAMPING ENGINE MOUNT FOR INTERNAL COMBUSTION ENGINE

Kouji Yamada and Nobukazu Takahashi, assignors to Nissan Motor Company, Limited
19 December 2006 (Class 123/192.1); filed in Japan 22 October 2002

An engine mount according to this patent includes two gas chambers in which the pressures are controlled so as to oppose the motion of the engine that the mount supports. Control of these pressures is accomplished by means of compressors and valves that are actuated as directed by a controller on the basis of signals corresponding to the crank angle, the fuel injection, and the exhaust pressure.—EEU

7,158,840

43.40.Vn TUNING CONTROL PARAMETERS OF VIBRATION REDUCTION AND MOTION CONTROL SYSTEMS FOR FABRICATION EQUIPMENT AND ROBOTIC SYSTEMS

Robert Jacques, assignor to Cymer, Incorporated
2 January 2007 (Class 700/28); filed 29 June 2001

This patent describes adaptive control systems in which plant identification is accomplished from measurements made when the physical system to be controlled is not operating. Alternatively, the plant initially is modeled and then the model is updated on the basis of its observed behavior, which updating may be determined by means of inducing a motion in the physical system and measuring its frequency response. A method for deriving optimal controllers is provided.—EEU

7,146,858

43.40.Yq VIBRATION SENSING DEVICE

Uwe L. Beckmann, assignor to Search Systems, Incorporated
12 December 2006 (Class 73/649); filed 9 July 2004

A vibration sensing transducer **22** (details not given) is aligned on the diagonal to the x, y,and z axes of a cubical box **20**. It is said that this orientation makes the transducer sensitive to vibrations in all directions when placed on rubble **10** in which persons may be buried after a catastrophic event. Signals of vibration and sound (as vibration) so sensed are

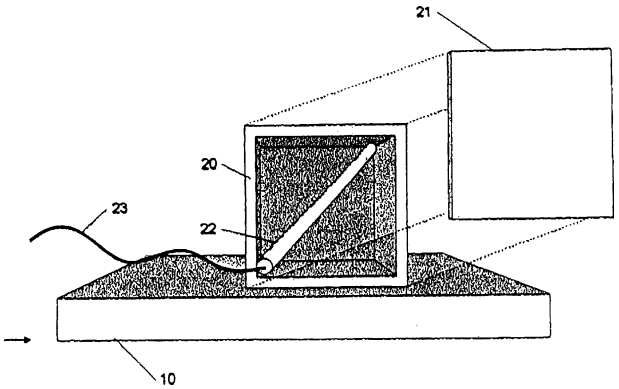

fed over wire **23** to be amplified and fed to headphones or a speaker. The author does not address the problem that a single axis transducer can have at least one direction of insensitivity.—AJC

7,143,736

43.50.Gf FILTER BOX WITH RESONATOR AND RESERVOIR

Thomas Jessberger *et al.*, assignors to Mann & Hummel GmbH
5 December 2006 (Class 123/198 E); filed 14 June 2005

A composite engine air-intake filter-box resonator **16**, second resonator **14**–**34**, windshield washer fluid reservoir **12**, and engine coolant expansion tank is claimed. Combustion air enters inlet **18** and exits manifold **21** to the engine. The washer fluid pump is internal, fed via electric connection **40**. An

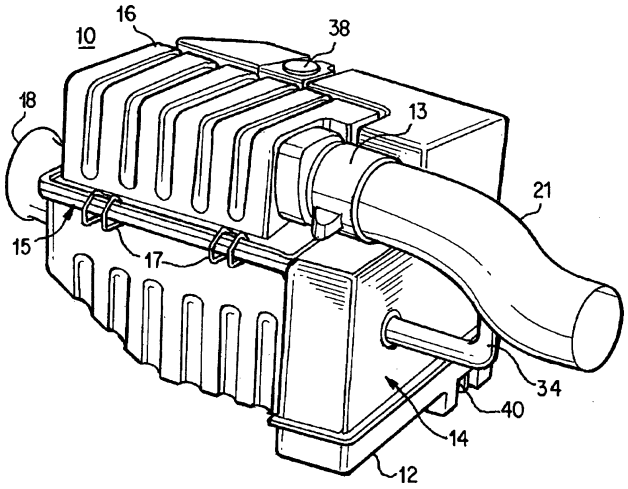

engine-coolant expansion tank (not shown) may be integrated as a second wall inside surface **16**, where the vacant volume above the fluid is vented to the first resonator volume. The second resonator **14** communicates via tube **34** to the engine air manifold **21** where most of the intake noise exists.—AJC

7,155,333

43.50.Gf METHOD AND APPARATUS FOR CONTROLLING SOUND OF AN ENGINE BY SOUND FREQUENCY ANALYSIS

Kwin Abram *et al.*, assignors to Arvin Technologies, Incorporated
26 December 2006 (Class 701/111); filed 2 September 2005

Controller **14** comprises a processor **24** and a memory **26** that contains information of undesired sound frequencies according to the number of cylinders that are firing in the engine, as determined by cylinder deactivation unit **44**. Processor **24** is provided with acoustic signals from sensor **16** to determine when the peak sound level at an undesirable frequency occurs in

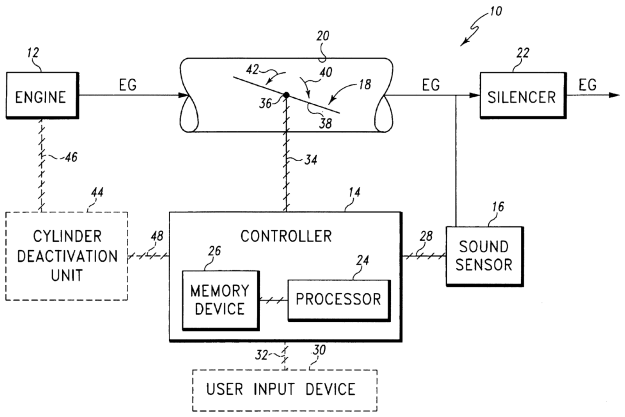

exhaust gas **EG**. The position of valve **18** is controlled to remove or reduce that sound by restricting the **EG** flow. Cylinder deactivation is determined by other driving parameters. A user can "customize" the predetermined sound levels by input **30**–**32** to enter into the memory **26** a sound level different from the default value.—AJC

7,151,835

43.50.Rq PERSONAL NOISE MONITORING APPARATUS AND METHOD

Al Yonovitz and Leslie Yonovitz, both of Marrara NT, Australia
19 December 2006 (Class 381/56); filed 28 March 2003

This dosimeter is to be permanently assigned to a worker. It incorporates a database of hearing protector ratings for devices used by the worker who selects a device currently in use. The worker dose is calculated based on the performance of the protector and the noise exposure. Feedback is given when a criterion dose is exceeded, which the worker must acknowledge. One wonders how the actual performance of the protector used in the dose calculation is determined.—JE

7,144,925

43.55.Ev FIRE RESISTANCE ACOUSTIC FOAM

Sandrine Burgun *et al.*, assignors to Dow Global Technologies Incorporated
5 December 2006 (Class 521/79); filed 9 May 2002

The patent asserts that by using a flame retardant adjuvant with particle size less than 1 μm, it is possible to increase the amount of retardant used for a given foam cell size or to increase the foam cell size for a given amount of fire retardant. These macrocellular foams with large, well-defined cells have improved acoustic performance.—CJR

7,146,296

43.55.Mc ACOUSTIC MODELING APPARATUS AND METHOD USING ACCELERATED BEAM TRACING TECHNIQUES

Ingrid B. Carlbom and Thomas A. Funkhouser, assignors to Agere Systems Incorporated
5 December 2006 (Class 703/5); filed 7 August 2000

While acousticians may debate the relative merits of physical architectural modeling and computer-based ray tracing and image modeling, there is little doubt that in the long run—and in the modern world of gaming and interaction on the Internet—computer techniques are the only choice. Early programs were rudimentary and assumed only specular reflections; the results were often useless and in some cases misleading. A useful program must consider effects of diffraction as well as the variation of absorption

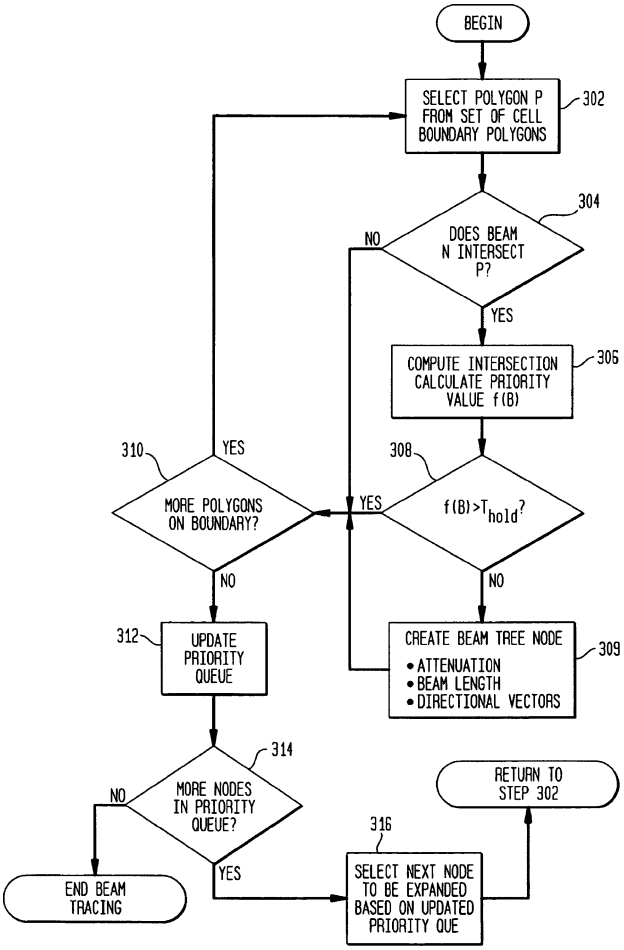

coefficient as a function of angle of incidence. Above all, the program must be capable of intelligently prioritizing the copious amounts of data generated. The authors speak with considerable authority in these areas and the patent is essential reading for anyone involved in this specialized field.—JME

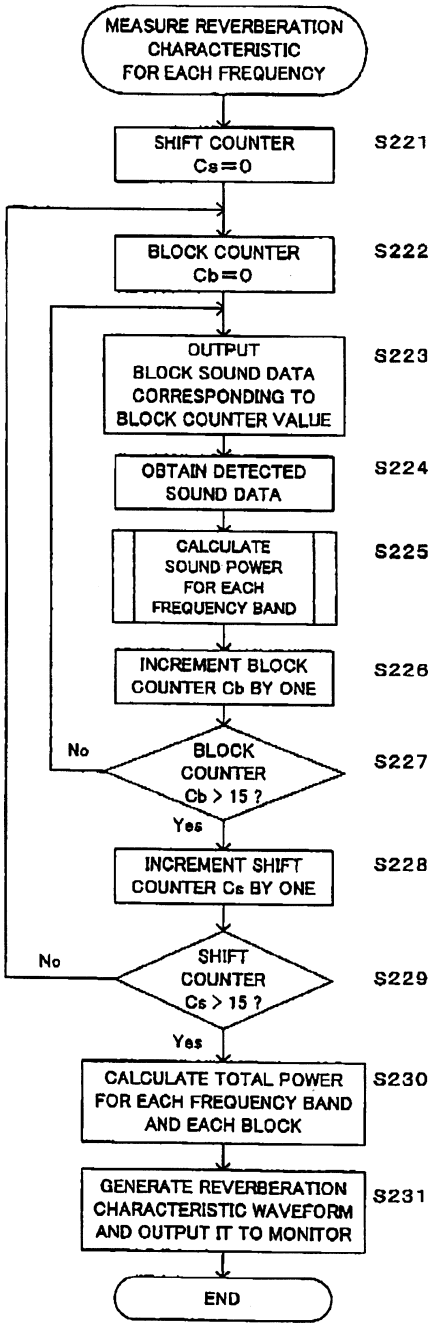

7,143,649

43.60.Mn SOUND CHARACTERISTIC MEASURING DEVICE, AUTOMATIC SOUND FIELD CORRECTING DEVICE, SOUND CHARACTERISTIC MEASURING METHOD AND AUTOMATIC SOUND FIELD CORRECTING METHOD

Hajime Yoshino, assignor to Pioneer Corporation
5 December 2006 (Class 73/579); filed in Japan 19 November 2003

This patent is one of many that deal with adaptive equalization of loudspeakers *in situ* to achieve uniform response at a given listening position. Typically, the adaptation cycle is determined by the lowest frequency desired to adjust and multiple periods of that frequency may be required to achieve a given accuracy. The patent proposes a method by which sequential short-term analyses are carried out step-wise. These short-term differences ultimately converge, enabling the system to make an estimate of the reverberant signal level in a shorter analysis time than the traditional measuring method.—JME

7,158,645

43.60.Mn ORTHOGONAL CIRCULAR MICROPHONE ARRAY SYSTEM AND METHOD FOR DETECTING THREE-DIMENSIONAL DIRECTION OF SOUND SOURCE USING THE SAME

Sun-do June *et al.*, assignors to Samsung Electronics Company, Limited
2 January 2007 (Class 381/92); filed in Republic of Korea 27 March 2002

The patent describes a pair of circular microphone arrays mounted orthogonally—one horizontal, the other vertical. The horizontal array iden-

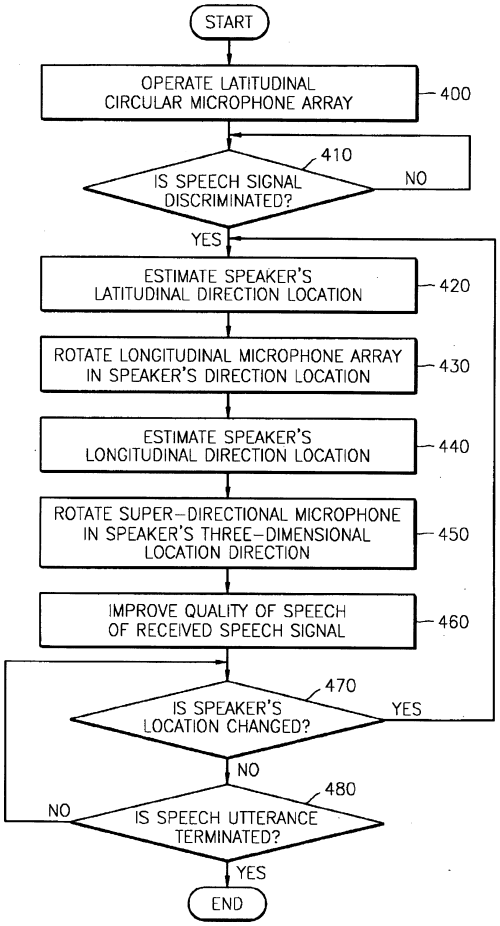

tifies the direction of a sound source in the azimuthal plane, and the entire array rotates so that the source then lies on the plane of the vertical array. The vertical array then takes over, identifying the elevation angle of the source. Further rotation of the vertical array about its axis allows the sound source to be identified and picked up with considerable acuity. It seems to this reviewer that equivalent performance could be attained by a stationary sphere with its surface densely covered by microphones. Which would be more economical: relatively few microphones with considerable mechanical complexity or more microphones with zero mechanical complexity?—JME

7,146,013

43.60.Mn MICROPHONE SYSTEM

Nozomu Saito *et al.*, assignors to Alpine Electronics, Incorporated
5 December 2006 (Class 381/92); filed in Japan 28 April 1999

This well-written patent describes a noise-canceling system for automotive communications applications. Visualize a pair of directional microphones placed on a sun visor within a few centimeters of each other. Further, splay one of these microphones so that its primary pickup axis is pointing away from the talker. It is then clear that the on-axis microphone will have a higher *S*/*N* ratio than the off-axis microphone, while the low- and mid-frequency noise pickup will be roughly the same for both microphones. Through the adaptive network, the two noise levels are adjusted so that they

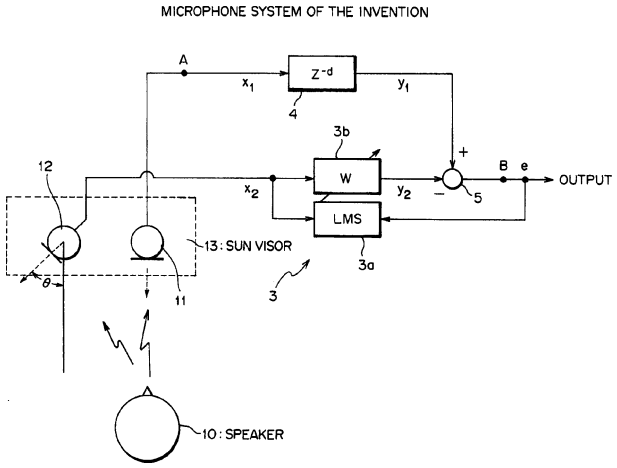

are effectively equal and can be subtracted. However, the two voice signals will be different in level and will not cancel. The authors show measured data indicating an average increase in useful *S*/*N* ratio of about 6 dB.—JME

7,158,446

43.60.Qv DIRECTIONAL ACOUSTIC TELEMETRY RECEIVER

Wallace R. Gardner *et al.*, assignors to Halliburton Energy Services, Incorporated
2 January 2007 (Class 367/81); filed 23 July 2004

Measurement while drilling (MWD) systems collect down-hole information from well loggers while drilling oil and gas wells. Information from down-hole sensors **26** is telemetered via acoustic transmitter **28**. A piezo-

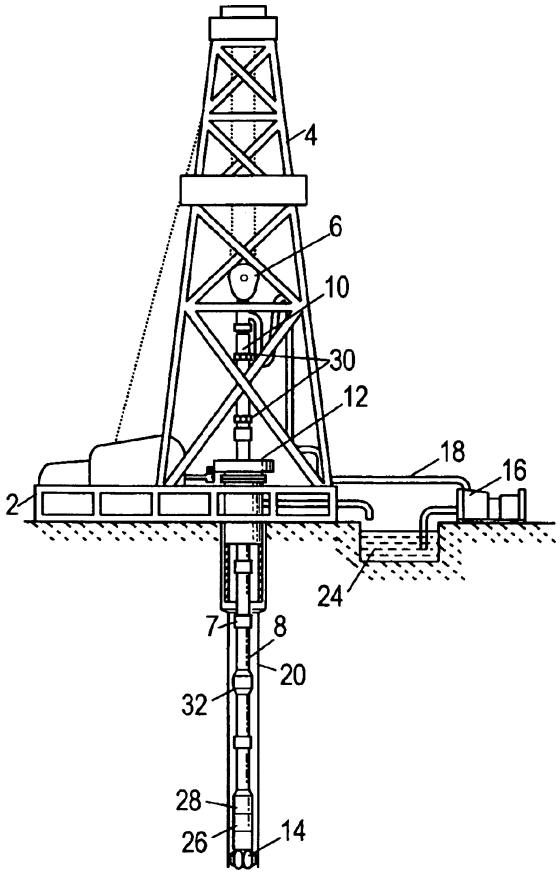

electric stack produces axial and circumferential pipe vibrations that propagate up the pipe string **8** up to receiver pack **30**.—AJC

7,137,946

43.66.Ts ELECTROPHYSIOLOGICAL MEASUREMENT METHOD AND SYSTEM FOR POSITIONING AN IMPLANTABLE, HEARING INSTRUMENT TRANSDUCER

Bernd Waldmann, assignor to Otologics LLC
21 November 2006 (Class 600/25); filed 11 December 2004

This is a signal source that generates test signals to elicit an electrocochleographic response for positioning an implantable transducer in the middle or inner ear of a patient. The electric potential response is measured

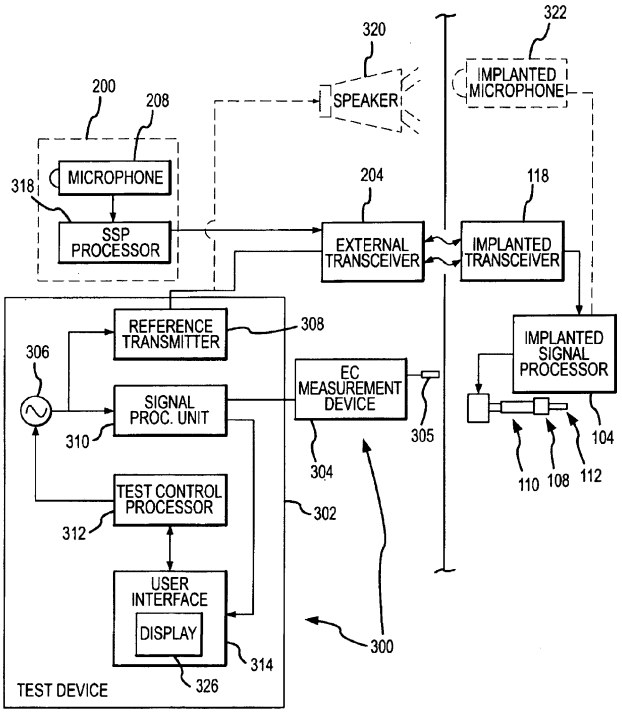

in timed relation to the test signals and processed to determine the relative desirability of possible transducer locations.—DAP

7,149,319

43.66.Ts TELECOMMUNICATION SYSTEM, SPEECH RECOGNIZER, AND TERMINAL, AND METHOD FOR ADJUSTING CAPACITY FOR VOCAL COMMANDING

Hans-Ueli Roeck, assignor to Phonak AG
12 December 2006 (Class 381/314); filed 23 January 2001

The status of a hearing device is communicated to users with several menu-selectable audio notification signals having a predetermined duration. The notification signals selected by the user may be stored in an external storage unit and retrieved via wireless means. Applications include acknowledgment of wireless control signals produced by a remote device such as an MP3 player.—DAP

7,149,320

43.66.Ts BINAURAL ADAPTIVE HEARING AID

Simon Haykin *et al.*, assignors to McMaster University
12 December 2006 (Class 381/320); filed 12 December 2003

Each channel of a two-channel hearing aid has a directional system whose output drives a correlator for reducing noise by identifying and tracking a speech signal. Signals from the correlator are preprocessed through

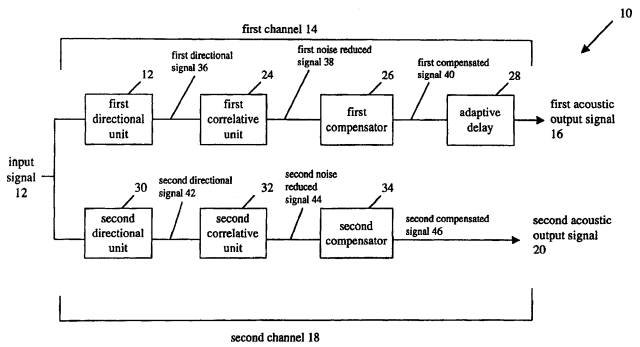

models of normal and impaired hearing, whose outputs are compared to derive and minimize an error signal. Processing in the two hearing aid channels is similar except that one of the channels has an adaptive delay following the correlator. The two channels are adjusted to process synchronous neural signals in the auditory cortex.—DAP

7,151,838

43.66.Ts DIGITAL HEARING AID BATTERY CONSERVATION METHOD AND APPARATUS

Bernard A. Galler and John Sayler, both of Ann Arbor, Michigan
19 December 2006 (Class 381/312); filed 21 August 2003

A digital hearing aid system compares the magnitude of audio input signals to a predetermined threshold and uses the result to multiplex between a power-saving mode and a high-power mode. If the audio signal

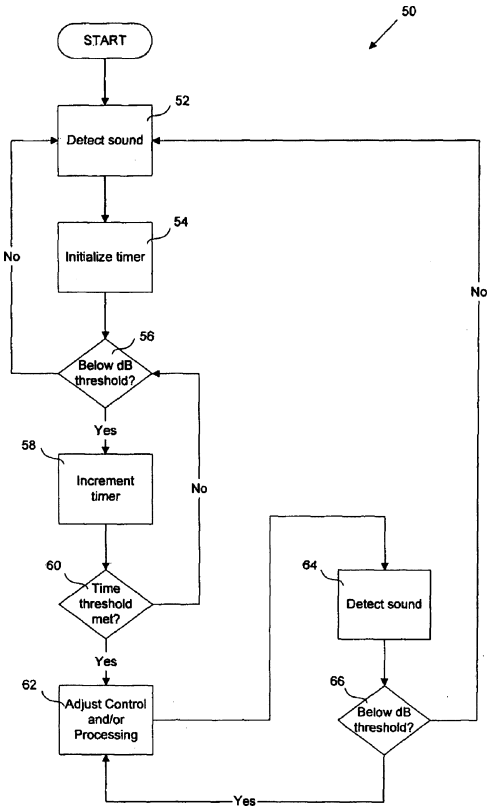

magnitude is determined to be less than the predetermined threshold for a period of time, the system switches at least the digital processing module or audio amplification circuit to a power-saving mode.—DAP

7,151,839

43.66.Ts MODULAR HEARING AID DEVICE

Torsten Niederdränk, assignor to Siemens Audiologische Technik GmbH
19 December 2006 (Class 381/324); filed in Germany 27 June 2002

A detachable module containing at least one microphone forms a uniform and complete housing with a behind-the-ear or in-the-ear hearing aid module housing. The external surface of the microphone module housing

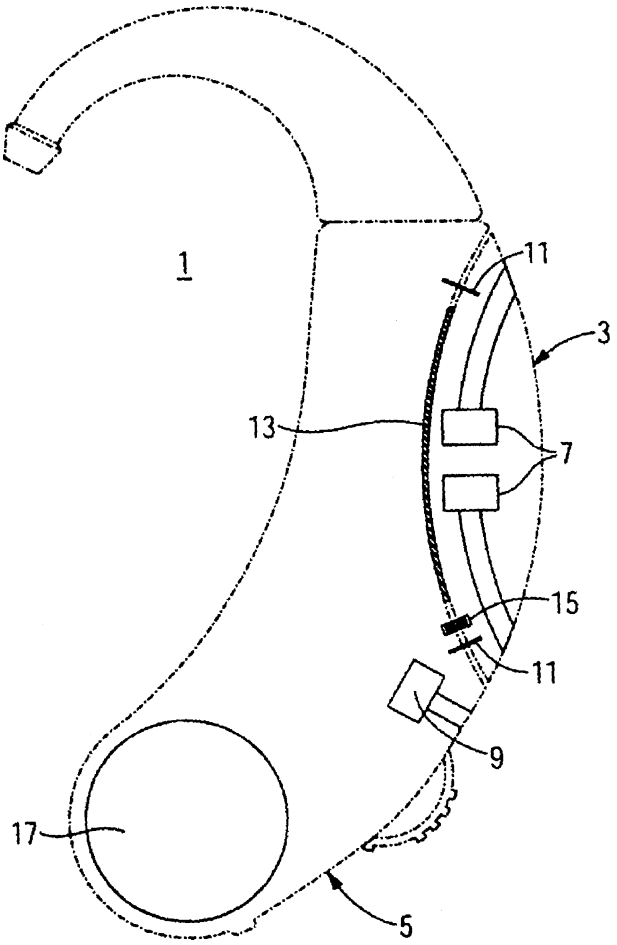

has a curvature identical to an external surface of the hearing aid module housing. Damping is placed at appropriate locations between the two housings to suppress mechanical oscillations.—DAP

7,155,023

43.66.Ts SWITCH FOR A BODY-WORN ELECTRONIC DEVICE

Erich Dittli, assignor to Phonak AG
26 December 2006 (Class 381/330); filed in the World Intellectual Property Organization 16 June 1999

Although the title, abstract, and a portion of the text describe a single element that operates in two different directions and can perform two different switching functions, there are no claims to support such a switch. Rather, the claims are mostly about a one-piece housing embodiment for a

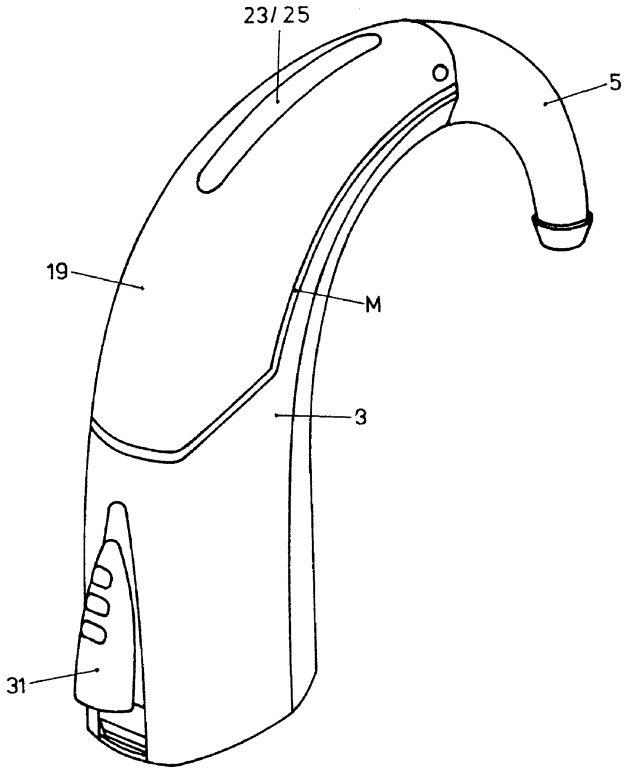

behind-the-ear hearing aid. A module mounted on a removable cover may also be incorporated.—DAP

7,155,289

43.66.Ts AUTO-REFERENCING MIXED MODE PHASE LOCKED LOOP FOR AUDIO PLAYBACK APPLICATIONS

Lee F. Hartley, assignor to Advanced Bionics Corporation
26 December 2006 (Class 607/57); filed 13 August 2002

As a diagnostic tool, asynchronous audio streaming is available at several address locations within the processing chain of the digital signal

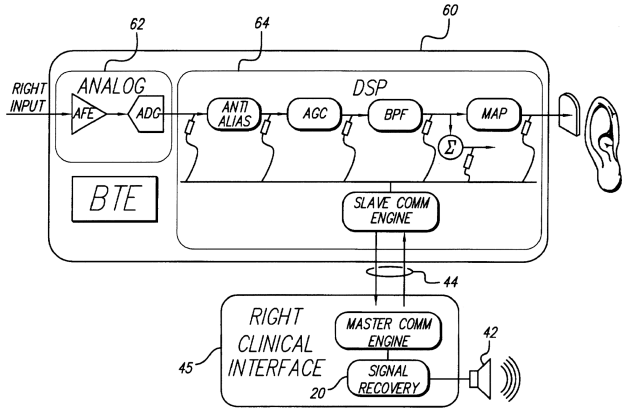

processor in a cochlear implant. The average rate of the audio samples is extracted and a local clock is generated to resynchronize the audio samples to allow phase-locked playback.—DAP

7,021,314

43.70.Dn STOMA STENT WITH INTEGRATED SPEECH FLAP VALVE

Charles J. Lane, Duxbury, Massachusetts
4 April 2006 (Class 128/207.29); filed 19 July 2004

The word ''stent'' has popularly been associated with a device to hold a blood vessel open. Here, it refers to a device to hold a throat incision open. In cases where a patient cannot breathe normally, it is sometimes necessary to open a breathing hole directly into the trachea. This device would be

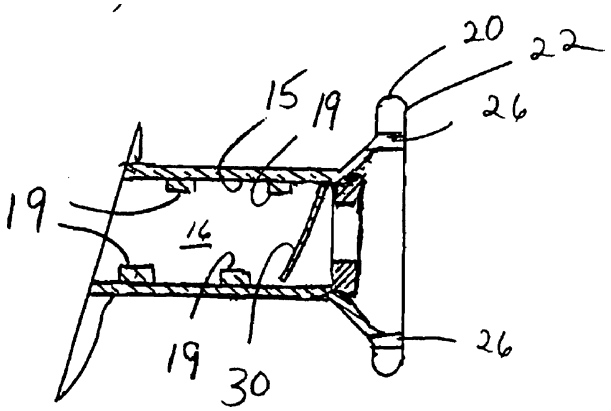

inserted into such an opening, primarily to hold open a passage for breathing. But a one-way valve would close during exhalation, directing the air flow through the larynx, thus permitting speech. Other such devices have been patented. It is not clear what is new here.—DLR

7,149,682

43.70.Fq VOICE CONVERTER WITH EXTRACTION AND MODIFICATION OF ATTRIBUTE DATA

Yasuo Yoshioka *et al.*, assignors to Yamaha Corporation
12 December 2006 (Class 704/205); filed in Japan 15 June 1998

This thick document addresses the desideratum that ''it would be amusing to have a karaoke apparatus provide a capability of simulating not only the voice quality but also the singing mannerism of a particular singer.'' In the pursuit of this interesting goal, methods are described for generating a synthesized waveform from a speaker's input voice by using what seems to be standard additive sinusoidal synthesis. The parameters for the sine waves are obtained from the attributes of a target voice that is supposed to be imitated, including pitch and spectral shape. There is also an attempt at vibrato production in the synthesized waveform.—SAF

7,128,651

43.72.Ar CARD GAME FOR DISPLAYING IMAGES BASED ON SOUND RECOGNITION

Tomoji Miyamoto *et al.*, assignors to Kabushiki Kaisha Sega Enterprises
31 October 2006 (Class 463/35); filed in Japan 12 November 1997

This patent envisions a computerized card game in which the computer plays the part of the dealer. The game's actions, visuals, etc., can be changed in response to certain acoustic and visible features detected from the human participants. To mention the acoustic features, references are made to determining the pitch of the voice and its intensity in the hopes of detecting features of elation or dejection in the participants. Beyond these vagaries, we are left to wonder about the precise acoustic correlates of emotions that will be employed.—SAF

7,133,824

43.72.Dv NOISE REDUCTION METHOD

Kuo-Guan Wu and Po-Cheung Chen, assignors to Industrial Technology Research Institute
7 November 2006 (Class 704/226); filed in Taiwan 28 September 2001

Another in a constant barrage of patents relating to speech noise reduction by spectral subtraction, a method is here outlined which promises to (what else?) provide better performance than the prior art. The idea implemented here involves partitioning the noisy speech signal into frequency subbands and, in essence, performing the noise spectrum subtraction differently for each subband depending on the signal-to-noise ratio in that subband. Test results are briefly reported which show that ''the present method has the potential of achieving 40% improvement over the conventional method.''—SAF

7,146,316

43.72.Dv NOISE REDUCTION IN SUBBANDED SPEECH SIGNALS

Rogerio G. Alves, assignor to Clarity Technologies, Incorporated
5 December 2006 (Class 704/233); filed 17 October 2002

One of seemingly hundreds of new ways of reducing noise in a speech signal is described here, this one focusing on two key procedures. The first is a scheme for detecting speech so that noise floor estimation can be suspended during periods of speech in the signal. The second is a subbanding scheme that divides the frequency spectrum of the signal into a number of bands, each of which is processed separately. Each subband has its own noise floor estimate and variable gain function, and the subbands are then combined, with the result being like a complicated sort of filtering.—SAF

7,149,685

43.72.Dv AUDIO SIGNAL PROCESSING FOR SPEECH COMMUNICATION

Adoram Erell and Avi Kleinstein, assignors to Intel Corporation
12 December 2006 (Class 704/233); filed 3 September 2004

This patent looks like it will put forth a method for noise reduction in a speech signal which can specifically cope with ''intermittent'' and periodic noise like background music. In fact, only a means of detecting the presence of such signal contamination is presented, relying on autocorrelation computations to search for recurrent aspects of the signal, while the means of dealing with it is left open-ended and is not really addressed beyond a brief remark.—SAF

7,151,924

43.72.Ew COMMUNICATION SYSTEM, HOLD CONTROL METHOD THEREFOR, TELEPHONE SET, CONTROL METHOD THEREFOR AND RECORDING MEDIUM

Keiichi Hayashi, assignor to NEC Corporation
19 December 2006 (Class 455/414.1); filed in Japan 14 August 2002

Here is a simple idea to facilitate multitasking with a mobile phone. It is recognized that the sounds emitted by nonspeech oriented functions of a phone can intrude on speech-sensitive modes of operation. The patent de-

scribes a ''hold control'' which senses the user's operation of the phone's functions and turns off the microphone as needed to prevent sound intrusions. During the hold period, the phone sends a signal to the network side to ''hold'' the voice communication. One must surmise that a means for recording and then replaying a signal is involved, perhaps on the network side.—SAF

7,152,032

43.72.Ew VOICE ENHANCEMENT DEVICE BY SEPARATE VOCAL TRACT EMPHASIS AND SOURCE EMPHASIS

Masanao Suzuki *et al.*, assignors to Fujitsu Limited
19 December 2006 (Class 704/262); filed 17 February 2005

Prior art techniques for voice enhancement have frequently involved the principle of increasing the amplitude of formants higher than the first. The authors point out that this has conventionally been implemented by the approach of simple band-splitting followed by high-band emphasis. This is not really an adequate way of accomplishing the goal, and this patent describes a way of enhancing higher formants by actually separating the vocal tract filter using linear predictive analysis and then directly acting on the LPC spectrum as, for example, by increasing the amplitude of the peaks which presumably correspond to formants in the speech signal. Methods are also described for enhancing the LPC residual (voice source), such as by increasing the pitch periodicity to improve perceived clarity.—SAF

7,158,933

43.72.Ew MULTI-CHANNEL SPEECH ENHANCEMENT SYSTEM AND METHOD BASED ON PSYCHOACOUSTIC MASKING EFFEJCTS

Radu Victor Balan and Justinian Rosca, assignors to Siemens Corporate Research, Incorporated
2 January 2007 (Class 704/226); filed 10 May 2002

This patent involves many of the usual techniques for speech-signal noise reduction, using a voice activity detector to aid in the measurement of the noise spectrum. A novel twist is provided by developing a model of the noise filtering that, first, can be constructed from any number of different transmission channels and, second, is optimized using psychoacoustic masking thresholds to avoid cleansing the signal of more noise than necessary. A considerably detailed presentation is provided, along with some brief results of testing that support the advantages of a two-channel implementation over a single-channel version.—SAF

7,136,811

43.72.Gy LOW BANDWIDTH SPEECH COMMUNICATION USING DEFAULT AND PERSONAL PHONEME TABLES

Thomas Michael Tirpak and Weimin Xiao, assignors to Motorola, Incorporated
14 November 2006 (Class 704/221); filed 24 April 2002

This patent refers to prior art ''phoneme-based speech communication techniques'' that have been used to accomplish extremely low bit-rate speech transmission. Without explaining any such method, the patent proposes to improve the mechanical, impersonal voice sound resulting from such methods by the use of a ''personal phoneme table.'' There is no indication of why a slight tweaking of the phoneme parameters should be expected to dramatically improve upon the mechanical and impersonal sound, which logic dictates is largely a result of discarding the voice source information to achieve the low bit rate.—SAF

7,146,008

43.72.Gy CONDITIONAL ACCESS TELEVISION SOUND

Eric C. Hannah and Benjamin M. CahillIII, assignors to Intel California
5 December 2006 (Class 380/236); filed 16 June 2000

To control the access to certain programs, the audio signal in a video broadcast program is encrypted with orthogonal frequency-division multiplexing and is then used to modulate a carrier. The resulting overlapping

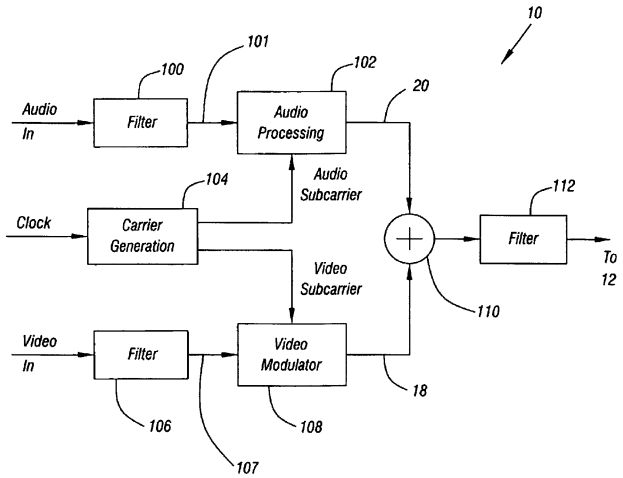

subcarriers are broadcast along with an obscured modulated video signal. A pattern identifier enables the receiver to decode the encrypted audio signal.—DAP

7,146,324

43.72.Gy AUDIO CODING BASED ON FREQUENCY VARIATIONS OF SINUSOIDAL COMPONENTS

Albertus Cornelis Den Brinker *et al.*, assignors to Koninklijke Philips Electronics N.V.
5 December 2006 (Class 704/500); filed in the European Patent Office 26 October 2001

In a basic sinusoidal coder, the frequencies of signal components are estimated as an average within each analysis frame. That approach was later improved using a time-warping method. In this patent, the frequencies of signal components are tracked and accounted for by coding the linear rate of frequency change or by generating polynomials that estimate the next values of frequency. The polynomial fitting approach can track several different frequency variations that go in opposite directions within a frame.—DAP

7,149,594

43.72.Gy DIGITAL AUDIO SIGNAL FILTERING MECHANISM AND METHOD

Philip R. Wiser *et al.*, assignors to Microsoft Corporation
12 December 2006 (Class 700/94); filed 29 June 2005

As a response to a received signal that specifies which transmission medium to use, stored processing parameter data associated with one of several mediums are used in two or more selected cascaded processing

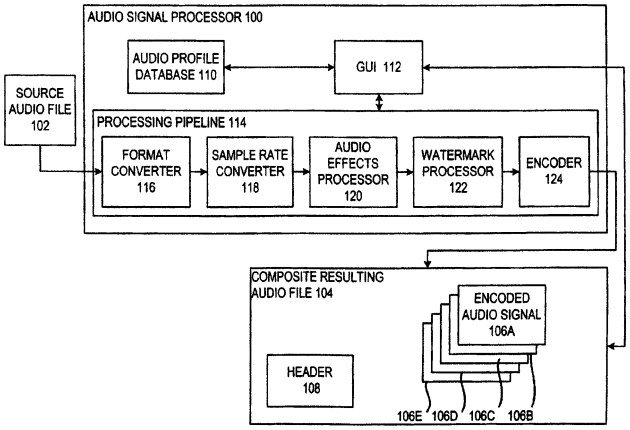

stages to encode audio signals to meet sound quality and delivery bandwidth requirements. Processing stages available for selection include a format converter, sample rate converter, filtering, and watermarking.—DAP

7,130,799

43.72.Ja SPEECH SYNTHESIS METHOD

Katsumi Amano *et al.*, assignors to Pioneer Corporation
31 October 2006 (Class 704/262); filed in Japan 15 October 1999

A simple plan for a phoneme-based concatenative speech synthesizer is outlined. Since there is nothing novel about that, it appears that the patent claims are built upon a linear predictive frame-based method for equalizing the sound power at the boundaries between concatenated segments.—SAF

7,139,712

43.72.Ja SPEECH SYNTHESIS APPARATUS, CONTROL METHOD THEREFOR AND COMPUTER-READABLE MEMORY

Masayuki Yamada, assignor to Canon Kabushiki Kaisha
21 November 2006 (Class 704/266); filed in Japan 9 March 1998

This patent proposes three different embodiments which all purport to decrease processing time of the phoneme search process in a concatenative speech synthesizer. The document is difficult and short on details, but the general ideas revolve around determining suitable phoneme substitutions in a given context where the perfect matching phoneme (with matching prosody as well) that would be desired is not present in the recorded database.—SAF

7,143,029

43.72.Ja APPARATUS AND METHOD FOR CHANGING THE PLAYBACK RATE OF RECORDED SPEECH

Moustafa Elshafei, assignor to Mitel Networks Corporation
28 November 2006 (Class 704/211); filed in the United Kingdom 4 December 2002

A novel method is described for changing the playback rate of a digital speech signal. The method is embodied in an arcane scheme of *ad hoc* decision rules that promise to take the best possible actions to achieve a user-entered playback speed. The decision rules somehow depend upon extracting, for each speech frame, the periodicity jitter, energy jitter, and periodicity strength jitter, and then making the right decisions accordingly. It is not possible to determine at a glance why the given rules should work.—SAF

7,143,038

43.72.Ja SPEECH SYNTHESIS SYSTEM

Nobuyuki Katae, assignor to Fujitsu Limited
28 November 2006 (Class 704/258); filed 3 March 2005

A method is described (using the term charitably) which employs an arcane scheme to augment a typical concatenative speech synthesizer with an ability to select recorded segments which are longer than those usually employed. The use of longer segments (such as pairs of syllables or entire words) drawn from the prerecorded speech corpus is intended to complement the usual short segment concatenation, with the aim of improving naturalness insofar as is possible given the corpus at hand.—SAF

7,155,390

43.72.Ja SPEECH INFORMATION PROCESSING METHOD AND APPARATUS AND STORAGE MEDIUM USING A SEGMENT PITCH PATTERN MODEL

Toshiaki Fukada, assignor to Canon Kabushiki Kaisha
26 December 2006 (Class 704/254); filed in Japan 31 March 2000

This patent presents a technique for generating a pitch pattern for speech synthesis, given a segment sequence. The method involves a ''polynomial segment model'' which is described in some detail. It is a statistical time series model for aligning a pitch contour with the segment sequence.—SAF

7,020,607

43.72.Ne DIALOGUE PROCESSING SYSTEM AND METHOD

Akira Adachi, assignor to Fujitsu Limited
28 March 2006 (Class 704/257); filed in Japan 13 July 2000

The grammar used in this human-computer dialog system is somewhat similar to the simple ''item in position''-type of grammar, sometimes referred to as a slot grammar. What is called a ''slot'' **11** in this patent, however, is more abstract in that it represents items of information needing to be satisfied as the dialog proceeds, but which need not be ''filled in'' by the user in any particular sequence or grammatical structure. Details of the application, such as plane schedules, prices, etc., are provided by a database **9**, which plugs into the dialog system much as does the slot package. As a dialog proceeds, the user may follow a relatively free-form style, while the

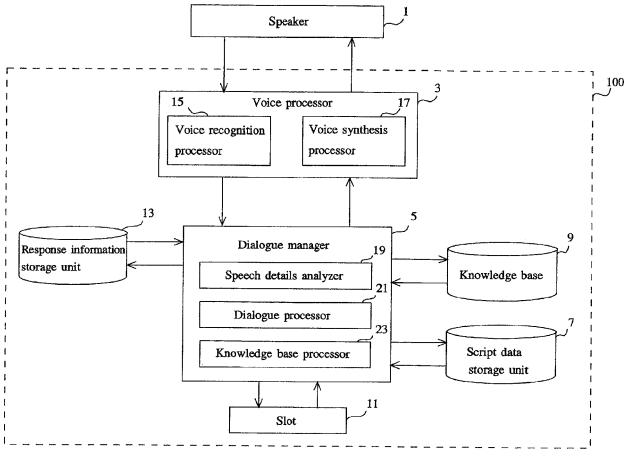

dialog manager tracks progress by filling in slot information as it is provided. Finally, the dialog manager may request items of information needed to complete the slot and finalize the transaction.—DLR

7,020,608

43.72.Ne SPEECH RECOGNITION HANDLING WITH SYNTHESIZED MANUAL INPUT EVENTS

Sagarika A. Chavan, assignor to Delphi Technologies, Incorporated
28 March 2006 (Class 704/270); filed 21 June 2001

This speech recognition system receives inputs from a mechanical subsystem as well as from the speech input. Mechanical functions may then be performed either by voice inputs or by mechanical operations. The way the functions are performed when using voice inputs is described as a system of simulated mechanical operations, which are then transformed into the actual mechanical functions, thus allowing the same mechanical control system to be used for either voice or physical commands. It all seems like a rather elaborate way to implement a dual control system.—DLR

7,024,363

43.72.Ne METHODS AND APPARATUS FOR CONTINGENT TRANSFER AND EXECUTION OF SPOKEN LANGUAGE INTERFACES

Liam David Comerford and David Carl Frank, assignors to International Business Machines Corporation
4 April 2006 (Class 704/270); filed 14 December 1999

This speech recognition system and dialog manager would centralize the voice interface functions in a hand-held device, isolating such functions from the various applications that would use the speech interface. It thus moves in the direction that operating systems have been moving inexorably, toward centralization of commonly needed capabilities and simplification of the application software. The key issues are the same as what recognition system builders have struggled with for many years, how to manage application-specific speaker data, grammars, vocabulary, etc. As has always been the case, such a move was not possible until the application builders could agree on the details of the needed functions. To what extent those thorny issues have yet been settled remains to be seen. Furthermore, it seems clear that the process of reaching compromises on the corresponding issues in dialog design has hardly begun.—DLR

7,027,565

43.72.Ne VOICE CONTROL SYSTEM NOTIFYING EXECUTION RESULT INCLUDING UTTERED SPEECH CONTENT

Masahiko Tateishi and Kunio Yokoi, assignors to Denso Corporation
11 April 2006 (Class 379/88.01); filed in Japan 25 June 2002

The essence of this patent on speech recognition system design is simply that, as a word is recognized, it is associated with both a word code and a command code. The word code can be sent to a synthesizer to request confirmation of the impending action and the command code can be sent to a control mechanism to implement the desired function.—DLR

7,027,985

43.72.Ne SPEECH RECOGNITION METHOD WITH A REPLACE COMMAND

Heribert Wutte, assignor to Koninklijke Philips Electronics, N.V.
11 April 2006 (Class 704/235); filed in the European Patent Office 8 September 2000

This patent, concerned with the use of a speech recognition system for dictation and editing of the resulting text, deals entirely with some low-level details concerning how the editing operations would be performed by voice commands and how the commanded operations are carried out in the process of modifying the text. The author charges that previous voice editing systems did this in a clumsy way.—DLR

7,027,991

43.72.Ne VOICE-RESPONSIVE COMMAND AND CONTROL SYSTEM AND METHODOLOGY FOR USE IN A SIGNAL MEASUREMENT SYSTEM

Jay A. Alexander and Michael J. Karin, assignors to Agilent Technologies, Incorporated
11 April 2006 (Class 704/275); filed 26 March 2002

The implementation of a speech recognizer set up to operate electronic test equipment in a circuit design or repair shop or lab is described. Text line **610** shows a sample of text which has just been entered via the voice input and recognized. The patent includes extensive tables and flowcharts of the

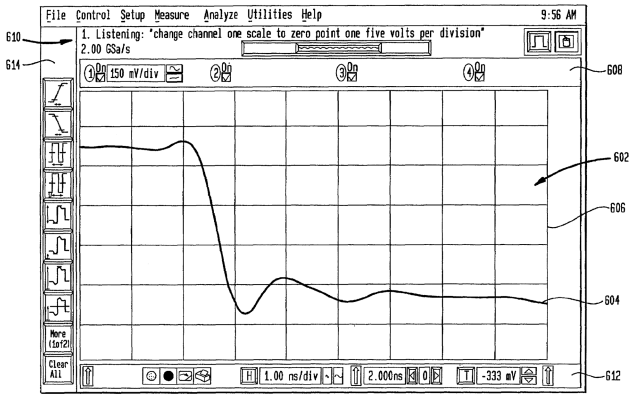

special vocabulary for this application and how such vocabulary items are translated into control operations. In this oscilloscope example, the intent is that no manual actions would be required. Everything can be done using speech.—DLR

7,031,917

43.72.Ne SPEECH RECOGNITION APPARATUS USING DISTANCE BASED ACOUSTIC MODELS

Yasuharu Asano, assignor to Sony Corporation
18 April 2006 (Class 704/238); filed in Japan 22 October 2001

Apparently, when you build a speech recognizer into a toy robotic animal, you have to deal with a severe case of a lack of control over the speaker's distance from the microphone. The patent describes several studies done to determine the spectral and amplitude effects of very close and very far mic distances. CCD visual sensors **22L** and **22R** are located in the

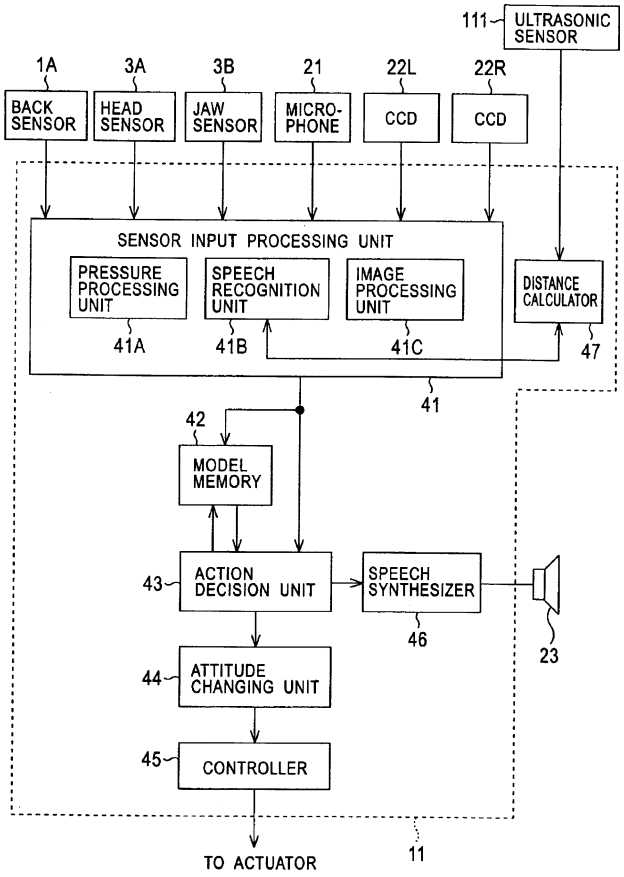

robot pet's eyes. A simple stereo image analyzer performs triangulation to measure the distance to an object in the robot's view. An optional ultrasound sensor **111** may be located in the pet's nose or mouth and provides an additional distance calculation. The recognizer includes multiple acoustic models, each trained for best results at a particular speaking distance.—DLR

7,031,918

43.72.Ne GENERATING A TASK-ADAPTED ACOUSTIC MODEL FROM ONE OR MORE SUPERVISED AND/OR UNSUPERVISED CORPORA

Mei Yuh Hwang, assignor to Microsoft Corporation
18 April 2006 (Class 704/243); filed 20 March 2002

It is well known that a speech recognizer trained by a single speaker using utterances pertaining to a specific task will perform with significantly lower error rates than if the training situation is less well controlled. However, such training can be tedious and expensive. Vast amounts of recorded speech data are available, but by various speakers with wide-ranging vocabulary, and often with no available transcription of the content. This patent describes methods by which the recognizer can be used in various "bootstrap" modes to make use of such unstructured speech data. One technique is to obtain confidence measures on one pass, then to use that information during the model-building stage of a second recognition pass. Many of the techniques covered here have been in use by recognition system builders for many years and some have been described in other patents.—DLR

7,146,319

43.72.Ne PHONETICALLY BASED SPEECH RECOGNITION SYSTEM AND METHOD

Melvyn J. Hunt, assignor to Novauris Technologies Limited
5 December 2006 (Class 704/254); filed 31 March 2003

A method is presented for modifying the standard sort of matching algorithm that takes the (errorful) output phone sequence from a speech acoustic-phonetic decoder and finds the best matching reference pronunciation. Three different modifications are presented separately here, all having the common signature of using some kind of "extra information" to augment the reference pronunciations and the match cost matrix, in the pursuit of closer matches and fewer errors. One embodiment suggests adding stress information, a second suggests adding syllable structure information, while a third suggests using "combined" (disjunctive) phonetic units and freely deletable phonetic units.—SAF

7,146,320

43.72.Ne ELECTRONIC MAIL REPLIES WITH SPEECH RECOGNITION

Yun-cheng Ju and Peter K. L. Mau, assignors to Microsoft Corporation
5 December 2006 (Class 704/257); filed 29 May 2002

This speech recognition system would allow the user to reply verbally to email messages that are read to the user via a text-to-speech converter. However, the method would be applicable only for the special case where

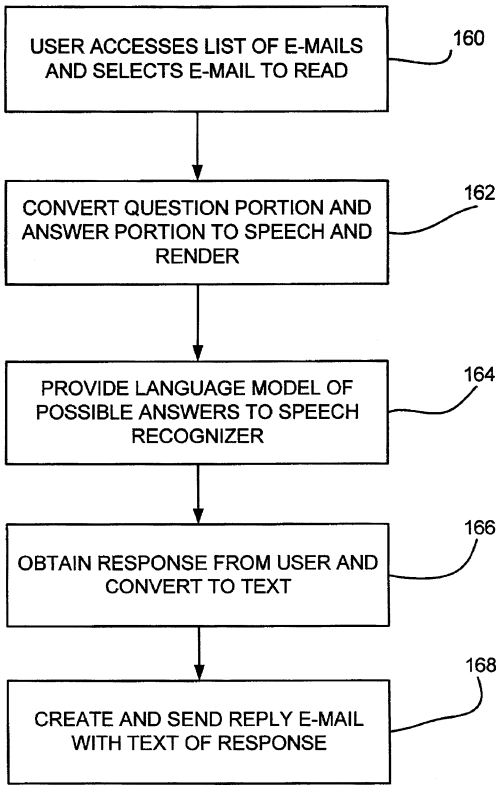

the original email poses a question and, ideally, also includes a list of possible answers. The question and any proposed answers are converted to speech and sent to the user. A response from the user is associated with a

proposed answer via the speech recognizer and is converted from speech to text and transmitted via email back to the sender.—DAP

7,155,391

43.72.Ne SYSTEMS AND METHODS FOR SPEECH RECOGNITION AND SEPARATE DIALECT IDENTIFICATION

George W. Taylor, assignor to Micron Technology, Incorporated
26 December 2006 (Class 704/257); filed 24 May 2004

To reduce the time taken to reliably transcribe speech into text, a processor queries users in an attempt to determine their dialect. The queries include at least one of the following: user's age, gender, educational level,

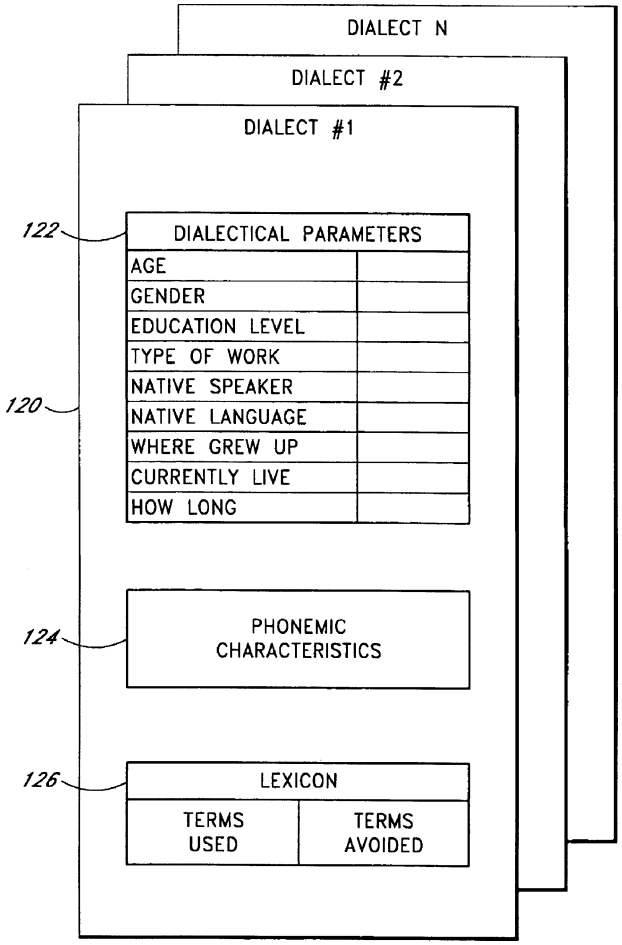

native language, geographic origin, and current geographic residence. The user provides non-verbal answers to the queries and the system then compares the dialect parameters obtained from the user to the stored dialect parameter data to determine the likely dialect.—DAP

7,146,321

43.72.Ne DISTRIBUTED SPEECH RECOGNITION SYSTEM

James Cyr *et al.*, assignors to Dictaphone Corporation
5 December 2006 (Class 704/270.1); filed 31 October 2001

Speech files from several users are stored until they can be forwarded to a selected speech recognition engine for processing. Selection of the speech recognition engine is based on comparing availability and turnaround time.—DAP

7,149,689

43.72.Ne TWO-ENGINE SPEECH RECOGNITION

Sherif Yacoub, assignor to Hewlett-Packard Development Company, L.P.
12 December 2006 (Class 704/255); filed 30 January 2003

In voice-enabled telephony and interactive voice response applications, two speech recognition engines produce separate recognition output hypotheses after receiving the same speech inputs. For each speech recognition engine, a confusion matrix is generated and converted into an alternatives matrix in which every column is ordered by highest-to-lowest priority. The speech recognition engine outputs are cross-compared with the alternatives matrices to find matches.—DAP

7,158,764

43.72.Ne SYSTEM AND METHOD FOR SENDING HIGH FIDELITY SOUND BETWEEN WIRELESS UNITS

Peter A. Thayer *et al.*, assignors to Electronic Data Systems Corporation
2 January 2007 (Class 455/90.1); filed 13 December 2001

Wireless techniques, such as Bluetooth™, typically transmit analog audio signals using a telephone standard of 8 K samples/s. In order to transmit a higher fidelity audio signal, the signal is sampled twice and encoded into two separate signals which are individually transmitted over a

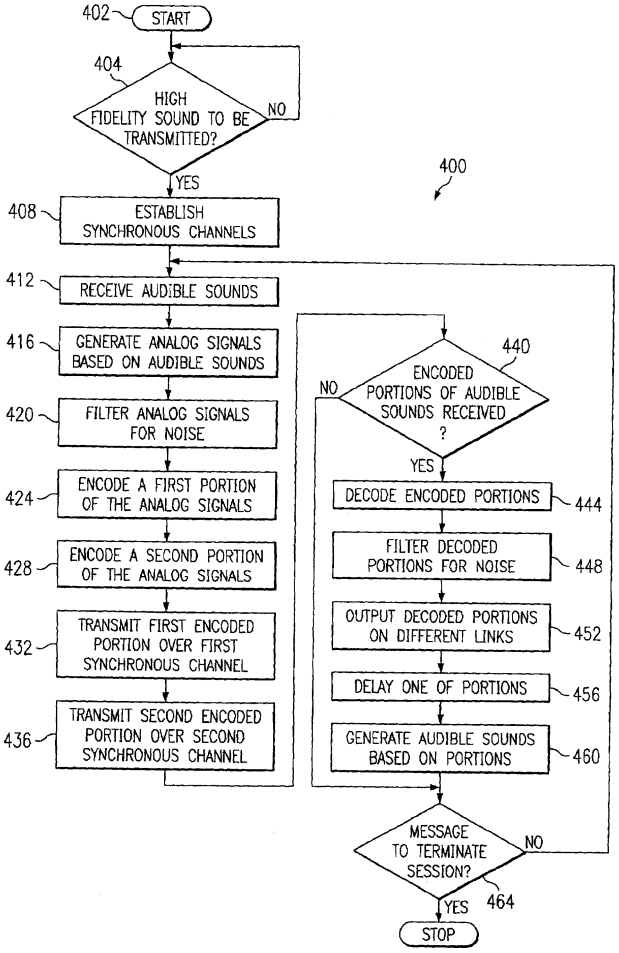

wireless synchronous channel. At the receiver, at least two samples each of the two transmitted signals are grouped and then combined, resulting in a sampling rate greater than eight kHz.—DAP

7,144,370

43.80.Vj METHOD AND APPARATUS FOR IMAGING OF TISSUE USING MULTI-WAVELENGTH ULTRASONIC TAGGING OF LIGHT

Pavel Alexeyevich Fomitchov, assignor to General Electric Company
5 December 2006 (Class 600/438); filed 30 November 2004

Electromagnetic radiation is emitted at two or more wavelengths and propagates through a volume of tissue to be imaged. Ultrasonic waves are also directed through the imaging volume and modulate the electromagnetic radiation at the ultrasonic frequency. The modulated electromagnetic radiation is detected by electromagnetic radiation detectors.—RCW

7,144,371

43.80.Vj TRANSESOPHAGEAL ULTRASOUND PROBE HAVING A ROTATING ENDOSCOPE SHAFT

Stephen Dodge Edwardsen and Dag Jordfald, assignors to GE Medical Systems Global Technology Company, LLC
5 December 2006 (Class 600/459); filed 22 March 2004

This probe includes an endoscope with an imaging element mounted on the distal end of a rotating shaft. The probe also includes a mechanism in the handle to control the imaging element and a rotatable tube that extends through the rotating endoscope shaft into the control handle. The motion of the shaft is relative to the rotatable tube and independent of the tube rotation.—RCW

7,149,566

43.80.Vj SOFT TISSUE ORIENTATION AND IMAGING GUIDE SYSTEMS AND METHODS

Roberta Lee, assignor to Manoa Medical, Incorporated
12 December 2006 (Class 600/429); filed 31 October 2002

A frame defines an opening into which tissue fits, immobilizes the tissue, and includes means to secure the frame to the tissue.—RCW

7,150,716

43.80.Vj MEASURING TRANSDUCER MOVEMENT METHODS AND SYSTEMS FOR MULTI-DIMENSIONAL ULTRASOUND IMAGING

Paul H. Jones *et al.*, assignors to Siemens Medical Solutions USA, Incorporated
19 December 2006 (Class 600/446); filed 20 February 2003

An optical sensor in the transducer of an ultrasound imaging system measures motion along the skin surface in a way similar to the measurement of motion by a personal computer mouse. The motion information is used to position *b*-scan images accurately relative to one another. The image positions are angle corrected when the transducer is scanned at an angle that is not perpendicular to the skin surface.—RCW

7,153,268

43.80.Vj MOTION ADAPTIVE FRAME AVERAGING FOR ULTRASOUND DOPPLER COLOR FLOW IMAGING

Yadong Li *et al.*, assignors to General Electric Company
26 December 2006 (Class 600/455); filed 9 September 2004

Motion is determined by comparison of *b*-scan image frames and the number of frames averaged is changed according to a motion factor that is computed from the frame comparisons.—RCW

7,156,811

43.80.Vj ULTRASONIC IMAGING METHOD AND APPARATUS

Franco Bertora, assignor to Esaote, S.p.A.
2 January 2007 (Class 600/447); filed in Italy 16 October 2002

Backpropagation is used to obtain signals that reduce the number of channels needed to beamform received signals.—RCW

7,156,812

43.80.Vj VOLUMETRIC IMAGE ULTRASOUND TRANSDUCER UNDERFLUID CATHETER SYSTEM

James Bernard Seward and Abdul Jamil Tajik, assignors to Mayo Foundation for Medical Education & Research
2 January 2007 (Class 600/466); filed 27 March 2003

This catheter system contains an ultrasonic transducer array mounted near the distal end of the catheter. A lens mounted on the array spreads the ultrasound beam in a direction perpendicular to the axis of the array to illuminate a volume of fluid. Alternatively, multiple rows of transducer elements are used to illuminate the volume. Features in the volumetric field of view can be imaged, measured, or treated therapeutically.—RCW

LETTERS TO THE EDITOR

This Letters section is for publishing (a) brief acoustical research or applied acoustical reports, (b) comments on articles or letters previously published in this Journal, and (c) a reply by the article author to criticism by the Letter author in (b). Extensive reports should be submitted as articles, not in a letter series. Letters are peer-reviewed on the same basis as articles, but usually require less review time before acceptance. Letters cannot exceed four printed pages (approximately 3000–4000 words) including figures, tables, references, and a required abstract of about 100 words.

Retrofocusing techniques in a waveguide for acoustic communications (L)

H. C. Song[a] and S. M. Kim[b]
Marine Physical Laboratory, Scripps Institution of Oceanography, La Jolla, California 92093-0238

(Received 8 November 2006; revised 29 January 2007; accepted 2 March 2007)

In the paper "Retrofocusing technique for high rate acoustic communications" [M. Stojanovic, J. Acoust. Soc. Am. **117**, 1173–1185 (2005)], it is suggested that the time reversal approach requires a large number of array elements to compete with other approaches. Here the analysis of that paper is extended with a modified example to compare the performance of various approaches in three respects: (1) array element distribution across the water column, (2) channel normalization, and (3) phase delay across the array. In contrast, our results show that the time reversal approach combined with channel equalization can offer nearly optimal performance with a very small four element array. © *2007 Acoustical Society of America.* [DOI: 10.1121/1.2721877]

PACS number(s): 43.60.Dh, 43.60.Gk, 43.60.Fg [ADP] Pages: 3277–3279

A recent paper by Stojanovic[1] explored various possible approaches to the acoustic communication between a single element and a multi-element array including time reversal[2,3] and channel equalization,[4] under the assumption that the channel transfer function is available to the transmitter and/or the receiver. Motivated by the limitations of the time reversal approach (SNR_0) due to residual intersymbol interference (ISI),[5,6] optimization techniques (SNR_1 and SNR_2) were developed which simultaneously eliminate ISI and maximize the output signal-to-noise ratio (SNR), while maintaining maximal data rate in a given bandwidth subject to a constraint on the transmitted symbol energy. In addition, an optimal solution involving channel equalization (SNR_4) was proposed to offer the best performance at the expense of the complexity of the overall system. The paper[1] provides theoretical bounds on the performance of various approaches in terms of the output SNR and examines the performance using a simple model channel.

However, the simple channel model chosen for the analysis in Ref. 1 did not include important propagation physics that, if included, potentially alter some of the conclusions in Ref. 1. In this letter, the analysis of the paper is extended to arrays that are capable of utilizing the spatial diversity of the model channel to compare the performance of the various approaches. It is found that the various approaches collapse to basically four different approaches: (1) time reversal alone, (2) time reversal with equalization, (3) equalization with a fixed transmit array, and (4) optimal approach. Approach (3) does not use the channel information and generally performs poorly as compared to the other approaches except approach (1). In this letter, we address the following three components in the model channel used for performance analysis: (i) array element spacing, (ii) channel normalization, and (iii) phase delay across the array.

(i) The major issue is the inter-element spacing employed in the channel model. The typical requirement of the element spacing being equal to or less than half the wavelength ($d \leqslant \lambda/2$) to avoid spatial aliasing can be relaxed for a vertical array in an underwater waveguide since the propagation angles are almost horizontal (broadside to the array) as extensively studied in matched field processing.[7] Thus, the important question is how to distribute array elements across the water column given the number of elements (M) where the element spacing (d) constrains the aperture of the array [i.e., $L=d(M-1)$]. Specifically, the example in the paper using $M=4$ elements with $d=\lambda/2$ spacing has an aperture of $L=3\lambda/2$ which is not large enough to resolve the three multipaths propagating at low grazing angles (e.g., $\theta=0°, 2.7°, 5.4°$). Then a four-element array with this small inter-element spacing behaves effectively as a clustered single element. As a result, there needed to be an increase in the number of elements until the time reversal array reached an aperture sufficient to resolve the three multipaths, requiring a large number of array elements (e.g., $M=32$) to compete with the other approaches.

Here we use the same number of array elements, $M=4$, but with an element spacing of $d=4\lambda$ which provides a suf-

[a]Author to whom correspondence should be addressed. Electronic mail: hcsong@mpl.ucsd.edu
[b]Dr. Sea-Moon Kim is now with Korea Ocean Research and Development Institute, Daejeon, Korea. Work done while at MPL.

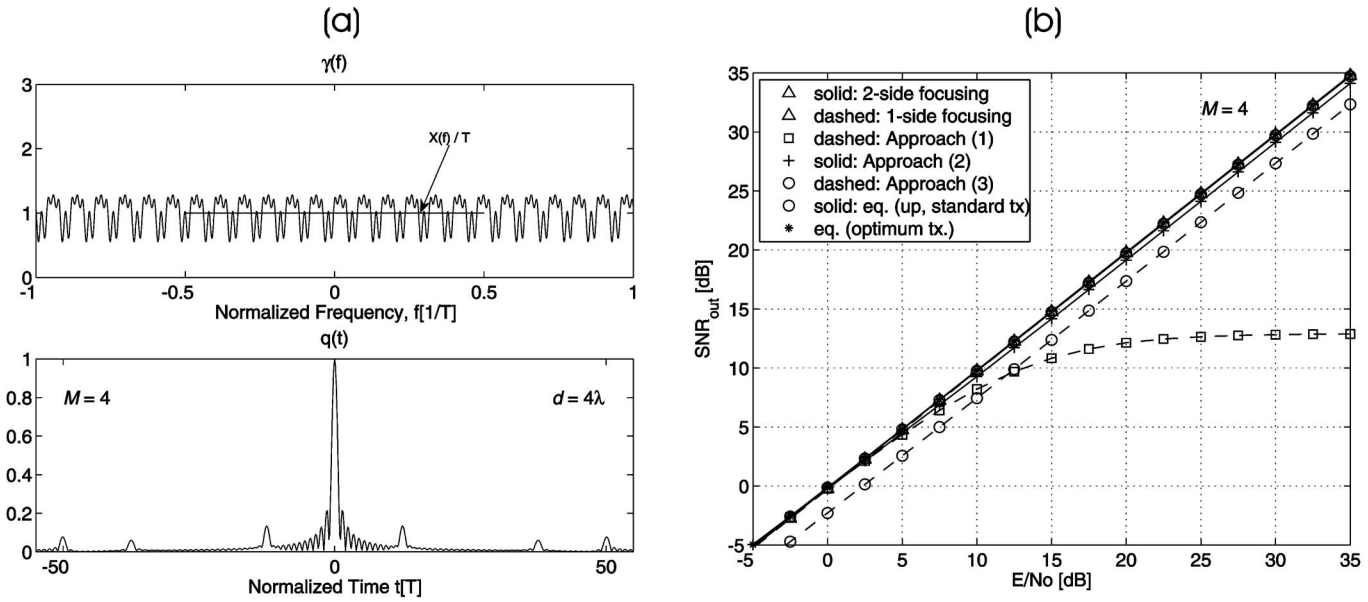

FIG. 1. (a) Composite channel power spectral density $\gamma(f)$ when $M=4$ and $d=4\lambda$, and the corresponding impulse response of time-reversal $q(t)$ which is the inverse Fourier transform of $\gamma(f)$. (b) Performance of various techniques on the example channel: output SNR vs E/N_0. The array aperture is $L=1.2$ m. Note that the four curves (marked with two $\triangle$s, solid $\bigcirc$, and $*$) collapse to each other and can be grouped simply as optimal approach (4).

ficient aperture to benefit from the spatial diversity[3] of the field as illustrated in Fig. 1. The difference between $\lambda/2$ and 4λ element spacing results in as many as eight times the number of elements. The composite channel function $\gamma(f)$ is shown in Fig. 1(a) (top) while the impulse response of the overall system with time reversal $q(t)$[3] is shown in Fig. 1(a) (bottom). The performance of time reversal communications depends on the behavior of q-function[2] whose Fourier transform is $\gamma(f)$ defined in Eq. 12 of Ref. 1 as the summation of autocorrelation functions of each channel impulse responses $C_i(f)$. To minimize the ISI, it would be desirable to have a q-function that approaches a Dirac delta function. Even with $M=4$ elements, however, the $\gamma(f)$ flattens out and the overall system obtained with time reversal $q(t)$ shows much smaller sidelobes as compared to those in Fig. 3 of Ref. 1 with $d=\lambda/2=0.05$ m. In fact, the aperture of $M=4$ elements with 4λ spacing is still modest with $L=1.2$ m in 75-m deep water.

Figure 1(b) summarizes the corresponding performance results using $M=4$, $L=1.2$ m array. Several observations can be made. First, Fig. 1(b) looks very similar to Fig. 4 of Ref. 1 where $L\approx 1.6$ m with $M=32$ and $d=\lambda/2$, clearly indicating the redundancy of the array elements with smaller element spacing. Second, note that there are only four distinct curves shown in Fig. 1(b) while there are seven different legends. Apparently, all the optimal techniques (SNR_1, SNR_2, SNR_4) as well as passive time reversal with equalization ($SNR_{3,up}$) collapse onto one another, which can be grouped as an optimal approach (4). The other three curves represent: time reversal alone [SNR_0, dashed with squares, approach (1)], active time reversal with equalization [$SNR_{3,tr}$, cross, approach (2)], and equalization with a fixed transmit array [$SNR_{3,down}$, circle/dashed, approach (3)]. Third, approach (2) also offers performance very close to the optimal approach (4), suggesting that time reversal alone (either active or passive) can be optimized in conjunction with channel equalization by removing the residual ISI.[2] Approach (4) shows a linear curve proportional to the input SNR, E/N_0, which provides an upper bound to the other approaches. Fourth, it is noticeable that time reversal approach (1) saturates eventually due to residual ISI at a value $1/\rho$ (defined in Eq. 34 of Ref. 1) which is determined by the channel function $\gamma(f)$. On the other hand, approach (1) is almost identical to the optimal approach (4) at low SNR below $E/N_0\approx 7$ dB. This is because the impact of ISI through ρ will be either comparable to or negligible with respect to the noise level at low SNR and as $E/N_0\to 0$, the output SNR_0 reduces to $SNR_{0L}=(E/N_0)\int_{-\infty}^{\infty}X(f)\gamma(f)df$, linearly proportional to E/N_0. The characteristics of the q-function affect the point of separation from the optimal curves. Finally, approach (3), which does not use the channel knowledge consistently, is outperformed (about 2 dB) by the optimal approach (4).

(ii) For convenience, the q-function is normalized such that $q(0)=1$ in Fig. 1 where $q(0)$ represents the total energy of the channel impulse responses (three multipaths in our example). However, this normalization should not be imposed when calculating the performance bounds since we have a constraint on the transmitted symbol energy E independent of M. This allows us to distinguish the impact of varying the number of array elements from the impact of varying the total transmitted power.[8] For uplink scenarios, one should pick up more energy by increasing the number of receivers for a fixed transmitted power.

Performance sensitivity with respect to the number of array elements (or, equivalently, array size) is shown in Fig. 2(a) illustrating the output SNR as a function of M for a given symbol SNR of $E/N_0=20$ dB. The performance characteristics are quite different from Fig. 5 of Ref. 1 where $d=\lambda/2$ with the normalization imposed. Three observations can be made. As in Fig. 1(b), the performance of all of the optimal focusing techniques collapse onto each other as well as approach (2) forming a single curve, while the perfor-

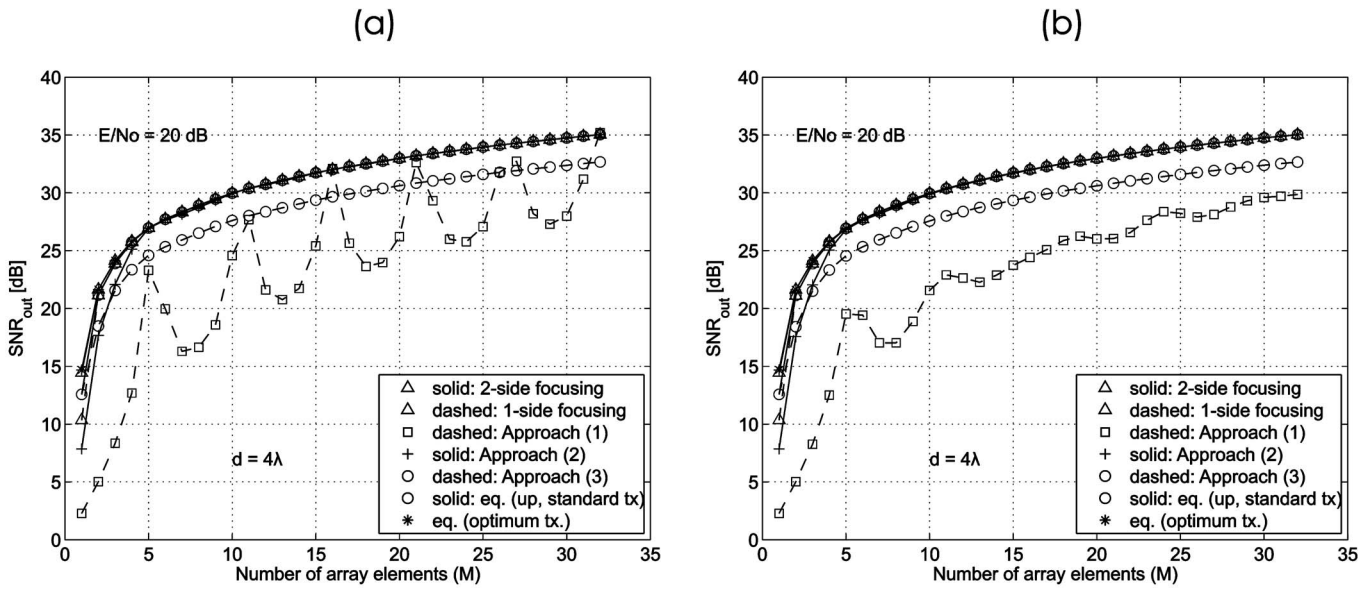

FIG. 2. Performance of various techniques on the example channel: output SNR vs M for fixed symbol SNR$=E/N_0=20$ dB. (a) $d=4\lambda$ without the channel normalization $q(0)=1$ imposed. Note the aperture of $M=35$ elements array is 17 m in 75-m deep water. (b) Reproduction of plot (a) when the phase delay is frequency-dependent such that $\phi(f)=2\pi(d/\lambda)\sin\theta$.

mance improves quite rapidly with the first few elements where the spatial diversity is exploited maximally.[3] Second, approach (3) is outperformed by the optimal approach (4) as in Fig. 1(b). In addition, approach (3) initially shows better performance than approach (1) up to $M=4$, but is saturated and eventually outperformed by approach (1) due to an inefficient use of energy without exploiting the channel knowledge. Finally, the oscillatory behavior of time reversal approach is quite peculiar with a period of $\Delta M=5$, corresponding to about 2 m in the array aperture. The period of 2 m turns out consistent with the period shown in Fig. 6 of Ref. 1, which is explained below.

(iii) The vertical wave number interference between two multipaths denoted by Δ_{ij} is

$$\Delta_{ij}=\frac{2\pi}{|(k_z)_i-(k_z)_j|}=\frac{\lambda}{|\sin\theta_i-\sin\theta j|}, \tag{1}$$

where k_z is a vertical wave number. For the three multipaths shown in Fig. 1 of Ref. 1, the interference distances at 15 kHz are $\Delta_{13}\approx 1.06$ m, $\Delta_{23}\approx 2.13$ m, and $\Delta_{12}\approx 2.12$ m, respectively. The least common denominator (LCD) is then $\Delta=2.12$ m, which is approximately the period of the oscillatory characteristics.

Since we are dealing with a broadband signal of 5 kHz bandwidth centered at 15 kHz in the example, the oscillatory phenomenon normally would not occur if the phase delay was frequency-dependent such that $\phi(f)=2\pi(d/\lambda)\sin\theta$ where $\lambda=c/f$. This is because the interference varies with frequency [or λ in Eq. (1)] and smears out over the band of frequency. It should be mentioned that the frequency dependent phase across the array is a direct result of the simple time delay relationship between the array elements. Figure 2(b) re-evaluates Fig. 2(a) using the frequency-dependent phase $\phi(f)$. As expected, the oscillatory behavior of time reversal approach (1) clearly has diminished.

[1]M. Stojanovic, "Retrofocusing techniques for high rate acoustic communications," J. Acoust. Soc. Am. **117**, 1173–1185 (2005).
[2]H. Song, W. Hodgkiss, W. Kuperman, M. Stevenson, and T. Akal, "Improvement of time reversal communications using adaptive channel equalizers," IEEE J. Ocean. Eng. **31**, 487–496 (2006).
[3]H. Song, W. Hodgkiss, W. Kuperman, W. Higley, K. Raghukumar, T. Akal, and M. Stevenson, "Spatial diversity in passive time reversal communications," J. Acoust. Soc. Am. **120**, 2067–2076 (2006).
[4]M. Stojanovic, J. A. Capitovic, and J. G. Proakis, "Adaptive multi-channel combining and equalization for underwater acoustic communications," J. Acoust. Soc. Am. **94**, 1621–1631 (1993).
[5]G. Edelmann, T. Akal, W. Hodgkiss, S. Kim, W. Kuperman, and H. Song, "An initial demonstration of underwater acoustic communication using time reversal," IEEE J. Ocean. Eng. **27**, 602–609 (2002).
[6]D. Rouseff, D. Jackson, W. Fox, C. Jones, J. Ritcey, and D. Dowling, "Underwater acoustic communications by passive-phase conjugation: Theory and experimental results," IEEE J. Ocean. Eng. **26**, 821–831 (2001).
[7]A. B. Baggeroer, W. A. Kuperman, and P. N. Mikhalevsky, "An overview of matched field methods in ocean acoustics," IEEE J. Ocean. Eng. **18**, 401–424 (1993).
[8]A. Narula, M. Trott, and W. Wornell, "Performance limits of coded diversity methods for transmitter antenna arrays," IEEE Trans. Inf. Theory **4**, 2418–2433 (1999).

On the relation between the phonation threshold lung pressure and the oscillation frequency of the vocal folds (L)

Jorge C. Lucero[a)]
Department of Mathematics, University of Brasilia, Brasilia DF 70910-900, Brazil

Laura L. Koenig[b)]
Haskins Laboratories, 300 George Street, New Haven, Connecticut 06511
and Long Island University, Brooklyn, New York 11201-8423

(Received 21 December 2006; revised 12 March 2007; accepted 12 March 2007)

This Letter presents an extension of a previous equation for the phonation threshold pressure by Titze [I. R. Titze, J. Acoust. Soc. Am. **83**, 1536–1552 (1988)]. The extended equation contains the vocal-fold oscillation frequency as an explicit factor. It is derived from the mucosal wave model of the vocal folds by considering the general case of an arbitrary time delay for the mucosal wave to travel the glottal height. The results are illustrated with a numerical example, which shows good qualitative agreement with experimental measures. © *2007 Acoustical Society of America.*
[DOI: 10.1121/1.2722210]

PACS number(s): 43.70.Aj, 43.70.Bk [BHS] Pages: 3280–3283

I. INTRODUCTION

Almost two decades ago, Titze (1988) set forth the dynamical principles of the vocal-fold oscillation. He proposed a mucosal wave model in which motion of the vocal-fold tissues is represented as a surface wave propagating in the direction of the airflow. His model demonstrated the aeroelastic nature of the oscillation, born from the interaction between the airflow blowing through the glottis and the elastic structure of the tissues. Since then, the original model and its several variations have been used in further studies of phonation dynamics (e.g., Chan and Titze, 2006; Drioli, 2005; Laje *et al.*, 2001; Lucero, 1999), and have even been applied to the production of sound in the avian syrinx (Laje and Mindlin, 2005).

An important result of Titze's work was an equation for the phonation threshold value of lung pressure, defined as the minimum value required to initiate the vocal-fold oscillation. At this threshold value, the energy transferred from the airflow to the vocal folds is large enough to overcome the energy dissipated in the tissues, so that an oscillatory movement of growing amplitude may take place. Titze's equation related the threshold pressure to biomechanical parameters, namely, glottal geometry, tissue damping coefficient, and mucosal wave velocity. It has found important applications in studies of glottal aerodynamics (Titze, 1992), and its validity has been tested in various experimental setups (e.g., Chan *et al.*, 1997; Chan and Titze, 2006; Titze *et al.*, 1995). The threshold pressure value has also been interpreted as a measure of ease of phonation, and proposed as a diagnostic tool for vocal health (Titze *et al.*, 1995). Its clinical significance has been explored in several studies (e.g., Fisher and Swank, 1997; Fisher *et al.*, 2001; Milbrath and Solomon, 2003; Roy *et al.*, 2003; Sivasankar and Fisher, 2002; Verdolini *et al.*, 2002).

Naturally, the mucosal wave model included several simplifying assumptions, necessary to permit the analytical treatment. One of those assumptions was a small time delay for the mucosal wave to travel along the vertical dimension of the vocal folds. This is equivalent to a small phase delay of the oscillatory motion of the upper edge of the vocal folds in relation to the lower edge.[1] As will be shown later, a consequence of that assumption is that the equation for the phonation threshold pressure lacks the oscillation frequency as a parameter. It is well-known that phonation threshold pressure increases with frequency, as demonstrated by experimental measures (e.g., Titze, 1992). This result is consistent with data suggesting that phonation onset is delayed when speakers use higher frequencies (e.g., Koenig *et al.*, 2005). The data on how frequency affects phonation are somewhat conflicting, however (cf. McCrea and Morris, 2005). Titze (1988, 1992) pointed out the lack of a frequency factor and offered a possible solution by relating other parameters in the phonation threshold pressure expression, such as vocal-fold thickness and mucosal wave velocity, to the oscillation frequency.

This Letter will show that a more general analysis of the model allowing for arbitrary time delay results in an extended equation for the phonation threshold pressure which includes the oscillation frequency explicitly.

II. MUCOSAL WAVE MODEL

For details on the derivation of the model's equations, we refer the reader to Titze's (1988) original work. Figure 1 shows a schematic of the mucosal wave model. Complete right-left symmetry of the folds is assumed, and motion of tissues is allowed only in the horizontal direction. A surface wave propagates through the superficial tissues, in the direction of the airflow (upward).

[a)]Electronic mail: lucero@unb.br
[b)]Electronic mail: koenig@haskins.yale.edu

 0001-4966/2007/121(6)/3280/4/$23.00 © 2007 Acoustical Society of America

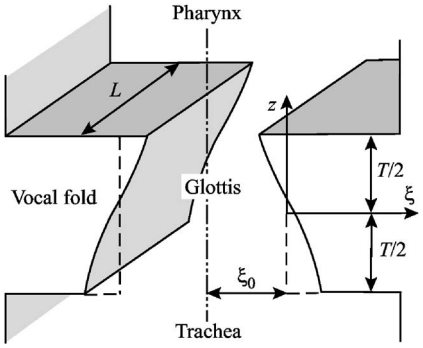

FIG. 1. Vocal-fold model (after Titze, 1988).

The equation of motion of the vocal-fold tissues is obtained by lumping their biomechanical properties at the midpoint of the glottis, and assuming that they are forced by the mean glottal pressure P_g, which yields

$$M\ddot{\xi} + B\dot{\xi} + K\xi = P_g, \tag{1}$$

where ξ is the tissue displacement at the midpoint, and M, B, K are the mass, damping, and stiffness, respectively, per unit area of the medial surface of the vocal folds.

The glottal aerodynamics is modeled by assuming that the flow is frictionless, stationary, and incompressible. Under such conditions, the mean glottal air pressure P_g may be expressed by

$$P_g = P_i + (P_s - P_i)(1 - a_2/a_1 - k_e)/k_t, \tag{2}$$

where P_s is the subglottal pressure, P_i is the supraglottal pressure (at the entry of the vocal tract), k_e is a pressure recovery coefficient for the turbulent region at the glottal exit ($0 \leqslant k_e \leqslant 0.2$, depending on the relation of the vocal-tract input area to the glottal area), k_t is a transglottal pressure coefficient ($k_t = k_c - k_e$, where k_c is a pressure loss coefficient for the region upstream the glottal exit, with values $1.0 \leqslant k_c \leqslant 1.4$ depending on the glottal channel shape), and a_1, a_2 are the glottal areas at the lower and upper edges of the glottal channel, respectively. The time-varying glottal areas are given by

$$a_1(t) = 2L(\xi_{01} + \xi(t+\tau)), \tag{3}$$

$$a_2(t) = 2L(\xi_{02} + \xi(t-\tau)), \tag{4}$$

where ξ_{01} and ξ_{02} are the lower and upper prephonatory glottal half-widths, respectively, τ is the time delay for the mucosal wave to travel half the glottal height ($T/2$ in Fig. 1), and L is the vocal-fold length. The delay τ depends on the velocity of the mucosal wave, which is related to the compliance of superficial tissues (Titze, 1992).

Following Titze, we assume that the subglottal pressure P_s is equal to a constant lung pressure P_L, the vocal-tract pressure is atmospheric ($P_i = 0$), and the vocal-tract input area is much larger than the glottal area so that $k_e \approx 0$. Further, and for simplicity of the present analysis, we consider only the case in which the prephonatory glottal channel is rectangular, i.e., the glottal half-width has a constant value $\xi_0 = \xi_{01} = \xi_{02}$ along the glottal height. Under such conditions, the mean glottal pressure simplifies to

$$P_g = \frac{P_L}{k_t}\left(1 - \frac{a_2}{a_1}\right). \tag{5}$$

Substituting into Eq. (1), we obtain the final equation for the vocal-fold oscillation

$$M\ddot{\xi} + B\dot{\xi} + K\xi = \left(\frac{P_L}{k_t}\right)\frac{\xi(t+\tau) - \xi(t-\tau)}{\xi_0 + \xi(t+\tau)}. \tag{6}$$

III. STABILITY ANALYSIS

A. Small τ approximation

Equation (6) is a functional differential equation with advance and delay arguments ($t+\tau$ and $t-\tau$, respectively). First, let us assume that the time delay τ is small enough so that the advanced-delay terms may be approximated by the linearization

$$\xi(t \pm \tau) \approx \xi(t) \pm \tau\dot{\xi}(t), \tag{7}$$

which reduces Eq. (6) to an ordinary differential equation

$$M\ddot{\xi} + B\dot{\xi} + K\xi = \left(\frac{P_L}{k_t}\right)\frac{2\tau\dot{\xi}}{\xi_0 + \xi + \tau\dot{\xi}}. \tag{8}$$

The above equation may now be analyzed by standard qualitative methods for dynamical systems. It has a unique fixed point at $\xi = 0$ (the prephonatory position). This position is stable for low values of P_L, and becomes unstable when P_L reaches the threshold value

$$P_{\text{th}} = \frac{k_t\xi_0 B}{2\tau}. \tag{9}$$

At this threshold value, the vocal-fold oscillation is generated. The oscillation threshold constitutes a Hopf bifurcation of the subcritical type, where the prephonatory position becomes unstable and at the same time absorbs an unstable limit cycle (Lucero, 1999).

B. General case for arbitrary τ

Let us consider now the general case, given by Eq. (6). The stability of the prephonatory position at $\xi = 0$ is determined by the roots of the characteristic equation associated with the linearization (variational equation) around that position (see, e.g., Hale, 1977). The linearization may be obtained by replacing the right side of Eq. (6) by the linear terms of a Taylor expansion around $\xi = 0$, which produces

$$M\ddot{\xi} + B\dot{\xi} + K\xi = \left(\frac{P_L}{k_t\xi_0}\right)[\xi(t+\tau) - \xi(t-\tau)]. \tag{10}$$

The characteristic equation may be obtained by the standard technique of proposing a solution $\xi(t) = Ce^{\lambda t}$, where C and λ are constants, and seeking nonzero solutions, which yields

$$M\lambda^2 + B\lambda + K - \frac{2P_L}{k_t\xi_0}\sinh(\lambda\tau) = 0. \tag{11}$$

For $P_L = 0$, Eq. (11) has the roots

$$\lambda = -\frac{B}{2M} \pm \sqrt{\left(\frac{B}{2M}\right)^2 - \frac{K}{M}}, \tag{12}$$

which have negative real parts. For $P_L > 0$, Eq. (11) may have an indefinite number of roots. Let us assume a pair of imaginary roots $\lambda = i\omega$. Substituting into Eq. (11), using the identity $\sinh(ix) = i\sin(x)$, and separating real and imaginary parts, we obtain

$$-\omega^2 M + K = 0, \tag{13}$$

$$\omega B - \frac{2P_L}{k_t \xi_0} \sin(\omega\tau) = 0. \tag{14}$$

The first equation produces the oscillation angular frequency $\omega = \sqrt{K/M}$. The value of P_L given by the second equation is the oscillation threshold pressure

$$P_{\text{th}} = \frac{k_t \xi_0 B \omega}{2\sin(\omega\tau)}, \tag{15}$$

with $0 < (\omega\tau) < \pi$.

According to Rouché's theorem (Dieudonné, 1960), the roots of the characteristic equation depend continuously on the parameter P_L. Hence, for $0 \leqslant P_L < P_{\text{th}}$, all roots have negative real parts, and at $P_L = P_{\text{th}}$, a pair of roots becomes imaginary. We verify next that those roots cross the imaginary axis from left to right. Implicit differentiation of Eq. (11) produces

$$\left[2M\lambda + B - \frac{2\tau P_L}{k_t \xi_0} \cosh(\lambda\tau)\right] \frac{d\lambda}{dP_L} = \frac{2}{k_t \xi_0} \sinh(\lambda\tau). \tag{16}$$

Substituting $\lambda = i\omega$, $P_L = P_{\text{th}}$, given by Eq. (15), and separating the real part, we obtain finally

$$\left.\frac{d\,\text{Re}(\lambda)}{dP_L}\right|_{P_L = P_{\text{th}}} = \frac{4\omega M \sin(\omega\tau)}{k_t \xi_0 \{B^2[1 - \omega\tau\cot(\omega\tau)]^2 + 4\omega^2 M^2\}} > 0, \tag{17}$$

for $0 < (\omega\tau) < \pi$. This is the transversatility condition, which proves that the roots cross the imaginary axis and therefore their real parts become positive.

The above results imply that the equilibrium position at $\xi = 0$ is stable for $P_L < P_{\text{th}}$, and unstable for $P_L > P_{\text{th}}$. Further, by the Hopf bifurcation theorem for functional differential equations (Hale, 1977), a limit cycle is generated at $P_L = P_{\text{th}}$.

IV. PHONATION THRESHOLD PRESSURE

The phonation threshold pressure is then given by Eq. (15). Note that it now contains the oscillation frequency ω as an explicit factor. Rewriting it in the form

$$P_{\text{th}} = \frac{k_t \xi_0 B}{2\tau} \frac{\omega\tau}{\sin(\omega\tau)}, \quad 0 < (\omega\tau) < \pi, \tag{18}$$

and considering that $\sin(x)/x$ is a monotonically decreasing function in $(0, \pi)$, then we have that P_{th} increases with the oscillation frequency ω, if all other factors are fixed. Note also that, for $\tau \to 0$, $\sin(\omega\tau) \to \omega\tau$, it simplifies to Titze's result [Eq. (9)].

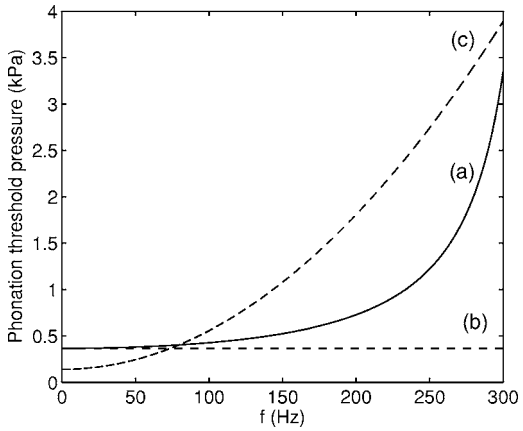

FIG. 2. Phonation threshold pressure vs oscillation frequency. (a) Value given by our extended expression Eq. (15); (b) Titze's (1988) theoretical expression, (c) Titze's (1992) empirical model.

Let us consider a numerical example, with $k_t = 1.1$, $\xi_0 = 1$ mm, $B = 1000$ Pa s/m, $c = 1$ m/s, $K = 2 \times 10^6$ Pa/m, $T = 3$ mm, $\tau = T/(2c) = 1.5$ ms (Titze, 1988). Figure 2 shows the phonation threshold pressure computed from Eq. (15), as a function of the frequency $f = \omega/(2\pi)$. For comparison, the figure also shows values from Titze's (1988) Eq. (9). That equation produces a horizontal line, since it is independent of the frequency f, and coincides with Eq. (15) at $f = 0$. Finally, it also shows results from an empirical model by Titze (1992), expressed by $P_{th} = 0.14 + 0.60(f/120)^2$. This equation was obtained by fitting a quadratic polynomial to experimental measures of phonation pressures. As the example illustrates, Eq. (15) provides a good qualitative prediction of the relation of phonation threshold pressure with oscillation frequency.

V. CONCLUSION

We have presented an equation for the phonation threshold pressure as a function of vocal-fold biomechanical parameters, which extends a previous result by Titze (1988). It contains the vocal-fold oscillation frequency as an explicit factor, and provides a good prediction for the observed increase of the threshold pressure with oscillation frequency.

The analysis was based on Titze's mucosal wave model, and considering the general case of an arbitrary time delay for the the mucosal wave to travel the glottal height. Several interesting questions appear now for further research, such as: (1) In the case of small time delay, the Hopf bifurcation at threshold is of the subcritical type (Lucero, 1999). Is it still subcritical at large time delays? (2) Titze (1992) built an empirical model of the relation between phonation threshold pressure vs frequency by fitting a quadratic polynomial to empirical data. Could a better model be obtained by fitting a function with the factor $x/\sin(x)$? (3) Our analysis assumed a rectangular prephonatory glottis, but it may be extended to a convergent-divergent shaped glottis, as in Titze's (1988) work. (4) The mucosal wave model has been used to study many aspects of phonation, including the following: the balance between the energy transferred from the airflow to the tissues and the energy dissipated (Lucero, 1999); the optimal glottal geometry for ease of phonation (Lucero, 1998); the

influence of vocal-tract acoustics on phonation threshold pressure (Chan and Titze, 2006); and characteristics of labial oscillation in the avian syrinx (Laje and Mindlin, 2005). Those and other similar studies could be improved by extending them to the general case of arbitrary time delay.

Finally, let us note that the two-mass model of the vocal folds predicts a linear increase of phonation threshold pressure when the natural frequencies of the model are increased (e.g., Lucero and Koenig, 2005; Mergell *et al.*, 1999), instead of the above nonlinear relation. The consequences of that difference, and a possible way to reconcile both models is also a good subject for further analysis.

ACKNOWLEDGMENTS

This work was supported by Grant No. DC-00865 from the National Institute on Deafness and Other Communication Disorders of the National Institutes of Health, and MCT/CNPq (Brazil).

[1]This assumption was incorporated through a small angle phase approximation; see Titze (1988), p. 1540, 2nd column.

Chan, R. W., and Titze, I. R. (**2006**). "Dependence of phonation threshold pressure on vocal tract acoustics and vocal fold tissue mechanics," J. Acoust. Soc. Am. **119**, 2351–2362.

Chan, R. W., Titze, I. R., and Titze, M. R. (**1997**). "Further studies of phonation threshold pressure in a physical model of the vocal fold mucosa," J. Acoust. Soc. Am. **101**, 3722–3727.

Dieudonné, J. (**1960**). *Foundations of Modern Analysis* (Academic, New York).

Drioli, C. (**2005**). "A flow waveform-matched low-dimensional glottal model based on physical knowledge," J. Acoust. Soc. Am. **117**, 3184–3195.

Fisher, K. V., and Swank, P. R. (**1997**). "Estimating phonation threshold pressure," J. Speech Lang. Hear. Res. **40**, 1122–1129.

Fisher, K. V., Ligon, J., Sobecks, J. L., and Roxe, D. M. (**2001**). "Phonatory effects of body fluid removal," J. Speech Lang. Hear. Res. **44**, 354–367.

Hale, J. (**1977**). *Theory of Functional Differential Equations* (Springer, New York).

Koenig, L. L., Mencl, W. E., and Lucero, J. C. (**2005**). "Multidimensional analyses of voicing offsets and onsets in female speakers," J. Acoust. Soc. Am. **118**, 2535–2550.

Laje, R., and Mindlin, G. B. (**2005**). "Modeling source-source and source-filter acoustic interaction in birdsong," Phys. Rev. E **72**, 036218.

Laje, R., Gardner, T., and Mindlin, G. B. (**2001**). "Continuous model for vocal fold oscillations to study the effect of feedback," Phys. Rev. E **64**, 056201.

Lucero, J. C. (**1998**). "Optimal glottal configuration for ease of phonation," J. Voice **12**, 151–158.

Lucero, J. C. (**1999**). "Theoretical study of the hysteresis phenomenon at vocal fold oscillation onset-offset," J. Acoust. Soc. Am. **105**, 423–431.

Lucero, J. C., and Koenig, L. L. (**2005**). "Phonation thresholds as a function of laryngeal size in a two-mass model of the vocal folds," J. Acoust. Soc. Am. **118**, 2798–2801.

McCrea, C. R., and Morris, R. J. (**2005**). "The effect of fundamental frequency level on voice onset time in normal adult speakers," J. Speech Lang. Hear. Res. **48**, 1013–1024.

Mergell, P., Fitch, W. T., and Herzel, H. (**1999**). "Modeling the role of nonhuman vocal membranes in phonation," J. Acoust. Soc. Am. **105**, 2020–2028.

Milbrath, R. L., and Solomon, N. P. (**2003**). "Do vocal warm-up exercises alleviate vocal fatigue?" J. Speech Lang. Hear. Res. **46**, 422–436.

Roy, N., Tanner, K., Gray, S. D., Blomgren, M., and Fisher, K. V. (**2003**). "An evaluation of the effects of three laryngeal lubricants on phonation threshold pressure," J. Voice **17**, 331–342.

Sivasankar, M., and Fisher, K. V. (**2002**). "Oral breathing increases P_{th} and vocal effort by superficial drying of vocal fold mucosa," J. Voice **16**, 172–181.

Titze, I. R. (**1988**). "The physics of small-amplitude oscillation of the vocal folds," J. Acoust. Soc. Am. **83**, 1536–1552.

Titze, I. R. (**1992**). "Phonation threshold pressure: a missing link in glottal aerodynamics," J. Acoust. Soc. Am. **91**, 2926–2935.

Titze, I. R., Schmidt, S. S., and Titze, M. R. (**1995**). "Phonation threshold pressure in a physical model of the vocal fold mucosa," J. Acoust. Soc. Am. **97**, 3080–3084.

Verdolini, K., Min, Y., Titze, I. R., Lemke, J., Brown, K., van Mersbergen, M., Jiang, J., and Fisher, K. (**2002**). "Biological mechanisms underlying voice changes due to dehydration," J. Speech Lang. Hear. Res. **45**, 268–281.

A modified diffusion equation for room-acoustic predication (L)

Yun Jing and Ning Xiang[a)]
Graduate Program in Architectural Acoustics, School of Architecture, Rensselaer Polytechnic Institute, Troy, New York 12180

(Received 20 December 2006; revised 20 March 2007; accepted 20 March 2007)

This letter presents a modified diffusion model using an Eyring absorption coefficient to predict the reverberation time and sound pressure distributions in enclosures. While the original diffusion model [Ollendorff, Acustica **21**, 236–245 (1969); J. Picaut *et al.*, Acustica **83**, 614–621 (1997); Valeau *et al.*, J. Acoust. Soc. Am. **119**, 1504–1513 (2006)] usually has good performance for low absorption, the modified diffusion model yields more satisfactory results for both low and high absorption. Comparisons among the modified model, the original model, a geometrical-acoustics model, and several well-established theories in terms of reverberation times and sound pressure level distributions, indicate significantly improved prediction accuracy by the modification. © *2007 Acoustical Society of America.* [DOI: 10.1121/1.2727331]

PACS number(s): 43.55.Br, 43.55.Ka [EJS] Pages: 3284–3287

I. INTRODUCTION

Recently, a diffusion equation has drawn attention in room-acoustic predictions. Ollendorff[1] first proposed the diffusion equation to describe diffuse sound fields in enclosures. More recently, Picaut[2] and his co-workers[3–5] have extended the application of the diffusion equation model based on the concept of acoustic particles[6,7] to a variety of space types, including elongated space, such as street canyons,[3] single-space enclosures,[4] and coupled-volume spaces.[5] The previous work, however, shows that the diffusion model is only suitable for low absorption coefficients.[3,4] The subject of this work is to present a modification to the diffusion model, as already applied in room acoustics,[3–5] using an improved absorption coefficient from Eyring's equation,[8] which suggests a better prediction of the sound fields in enclosures with both low and high absorption coefficients.

Predicted reverberation times and sound pressure levels (SPLs) are compared among the modified diffusion model, the original diffusion model, and other classical theories for cubic rooms with both uniformly and nonuniformly distributed absorbing surfaces of varied absorption coefficients. For flat and long rooms, a geometrical-acoustics model is used for comparisons of the SPL distributions. The results show that the modified diffusion model improves the room acoustic prediction. Experimental work of SPL distributions for various room types to verify the modified diffusion model is being undertaken.

In Sec. II, the modified diffusion equations are formulated based on the original diffusion equations. Section III briefly discusses simulation results for different kinds of spaces in terms of comparisons among the modified, the original diffusion model, and other approaches. Section IV concludes the paper.

II. DIFFUSION EQUATION MODIFICATION

The energy balance for a room of volume V containing a sound source of power output $F(\mathbf{r},t)$ can be written by a diffusion equation,[2–4]

$$\frac{\partial w(\mathbf{r},t)}{\partial t} - D\nabla^2 w(\mathbf{r},t) + \frac{cS\bar{\alpha}}{4V} w(\mathbf{r},t) = F(\mathbf{r},t), \tag{1}$$

where $F(r,t)$ is an acoustic source term and D is termed diffusion coefficient for introducing a term of Laplace operator ∇^2 on sound energy density $w(\mathbf{r},t)$ for a nonuniform distribution of the sound energy.[1,2] $\bar{\alpha}$ is the average absorption coefficient of the room, and S is the surface area of the room.

The original diffusion equation is only valid when the absorption is very weak since it is the first-order approximation of an integral equation.[9] In fact, the absorption term $(cS\bar{\alpha}/4V)$ in Eq. (1) is the probability rate of a particle to be absorbed during 1 s when the average absorption coefficient is small.[2,8] However, in room acoustics, the absorption coefficient can be very large, for instance, the audience in a concert hall. In the statistical theory of room acoustics, a similar case is that Sabine equation is usually only valid for low absorption because it essentially represents the first-order approximation of Eyring equation. The later is valid for both low and high absorptions. Reducing Eq. (1) to the classical statistical model[4] by dropping the term with the diffusion coefficient D, a sound energy decay equation is written as

$$\frac{\partial w(t)}{\partial t} + \frac{c\bar{\alpha}S}{4V} w(t) = 0, \tag{2}$$

the solution of this equation is

$$w(t) = w_0 e^{-(c\bar{\alpha}S/4V)t}, \tag{3}$$

where w_0 is the initial sound energy density of the sound source. The solution leads to the well-know Sabine's formula. Changing Eq. (2) to

[a)]Author to whom correspondence should be addressed; electronic mail: xiangn@rpi.edu

 0001-4966/2007/121(6)/3284/4/$23.00 © 2007 Acoustical Society of America

$$\frac{\partial w(t)}{\partial t} - \frac{c\ln(1-\bar{\alpha})S}{4V} w(t) = 0, \tag{4}$$

its solution leads to the Erying's formula.

In similar fashion, a substitution of $\bar{\alpha}$ by $-\ln(1-\bar{\alpha})$ according to Eyring's formula modifies the original diffusion equation in Eq. (1) to

$$\frac{\partial w(\mathbf{r},t)}{\partial t} - D\nabla^2 w(\mathbf{r},t) - \frac{\ln(1-\bar{\alpha})cS}{4V} w(\mathbf{r},t) = F(\mathbf{r},t). \tag{5}$$

Solutions of this equation require certain boundary conditions. For rooms with uniformly absorbing surfaces, a homogenous Neumann boundary condition[4]

$$\frac{\partial w}{\partial n} = 0 \quad \text{on } \partial V, \tag{6}$$

can be used with ∂V being the surface of the room. For nonuniformly distributed surface properties, a mixed boundary condition can be derived using an exchange coefficient h.[4] The term h is chosen so that the energy flux through the room boundaries equals the absorption over the whole room due to the absorption term from Eq. (5),

$$\int_V - \frac{\ln(1-\bar{\alpha})cS}{4V} w(\mathbf{r},t)dV = \int_{\partial V} h(S)w(\mathbf{r},t)dS, \tag{7}$$

while the sound field is diffusive, which means the sound energy density is quite uniform in the room, $w(\mathbf{r},t)$ can be treated as a constant and taken out of the integral, thus

$$-\frac{\ln(1-\bar{\alpha})cS}{4} = \int_{\partial V} h(S)dS. \tag{8}$$

For a room with N walls, an h_i can be attributed to each wall S_i with different absorption coefficient α_i in terms of

$$h_i \approx -\frac{\ln(1-\alpha_i)c}{4}, \quad i = 1, \ldots, N, \tag{9}$$

since

$$\ln(1-\bar{\alpha}) = \ln\left(1 - \sum_{i=1}^{N} \frac{\alpha_i S_i}{S}\right) \approx \sum_{i=1}^{N} \ln(1-\alpha_i)\frac{S_i}{S}. \tag{10}$$

The equation to describe the energy exchanges at boundaries is written as

$$-D\frac{\partial w}{\partial n} = hw(\mathbf{r},t) \quad \text{on } \partial V, \tag{11}$$

where $\partial w/\partial n$ is the gradient of $w(\mathbf{r},t)$ along the boundary normal.

Overall, the local diffusion equation and the mixed boundary condition can be written as

$$\frac{\partial w(\mathbf{r},t)}{\partial t} - D\nabla^2 w(\mathbf{r},t) = F(\mathbf{r},t) \quad \text{in V}, \tag{12}$$

$$D\frac{\partial w(\mathbf{r},t)}{\partial n} - \frac{c\ln(1-\alpha)}{4} w(\mathbf{r},t) = 0 \quad \text{on } \partial V, \tag{13}$$

which is more practical than Eq. (5) along with Eq. (6) because it defines the boundary condition to each specific surface with specific absorption coefficients. Moreover, this boundary condition is also an appropriate approximation when applied to flat rooms or long rooms.[3,4] To solve the diffusion equations, a volume sound source is used.[4]

The difference between the modified diffusion equation and the original form lies in a substitution of the logarithmic absorption term to the absorption term. Section III discusses simulation results indicating that this modified model improves predictions of SPL distributions and sound energy decays in rooms with varied shapes not only for low, but also for high absorption coefficients.

III. SIMULATION RESULTS

This section investigates three basic room shape variations with varying absorption coefficients on interior wall surfaces. For cubic rooms with uniformly distributed absorption properties of wall surfaces, several classic theories are used, since the sound energy density is assumed uniform for totally diffusive sound field. For flat or long rooms, the geometrical-acoustics model is considered because the sound energy density is known to be not uniform.

The original and modified diffusion model are implemented by a finite element modeling software with 1500 mesh elements for cubic rooms and 3000 mesh elements for flat and long rooms. The size of the elements is chosen to be on order of or smaller than one mean free path $4V/S$.[4] Equation (5) along with Eq. (6) and Eq. (12) along with Eq. (13) are solved for different initial conditions,

$$w(\mathbf{r},0) = 0 \quad \text{in } V, \tag{14}$$

$$w(\mathbf{r},0) = w_0 \quad \text{in } V_s \tag{15}$$

in the room under acoustic excitations by the volume sound source to obtain the reverberation time (RT), V_s is the volume occupied by the sound source.

With a time dependent solution $w(\mathbf{r},t)$, the SPL can be expressed as[10]

$$L_p(\mathbf{r},t) = 10\log\left(\frac{w(\mathbf{r},t)\rho c^2}{P_{\text{ref}}^2}\right), \tag{16}$$

where P_{ref} is equal to 2×10^{-5} Pa. The sound energy decay functions can then be obtained.

To calculate the steady state sound field, Eq. (5) along with Eq. (6) and Eq. (12) along with Eq. (13) are solved for a given sound power W_s of the source, and then $F(\mathbf{r},t)$ is set to be equal to W_s/V_s. With a stationary solution $w(\mathbf{r})$, the total SPL can be expressed as[4]

$$L_p^{\text{tot}}(\mathbf{r}) = 10\log\{\rho c[W_s/(4\pi r^2) + w(\mathbf{r})c]/P_{\text{ref}}^2\}, \tag{17}$$

where the time variable t is omitted here.

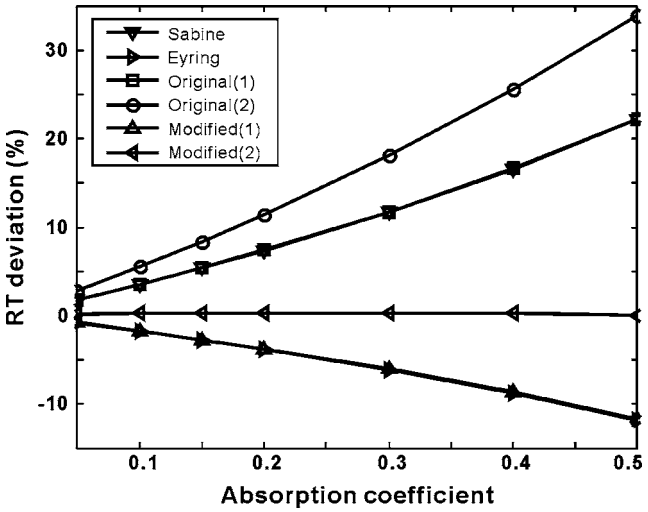

FIG. 1. Deviations of the reverberation times calculated by Kuttruff's formula and other classical methods, along with the original and the modified diffusion models. (1) Homogeneous Neumann boundary condition, and (2) the mixed boundary condition.

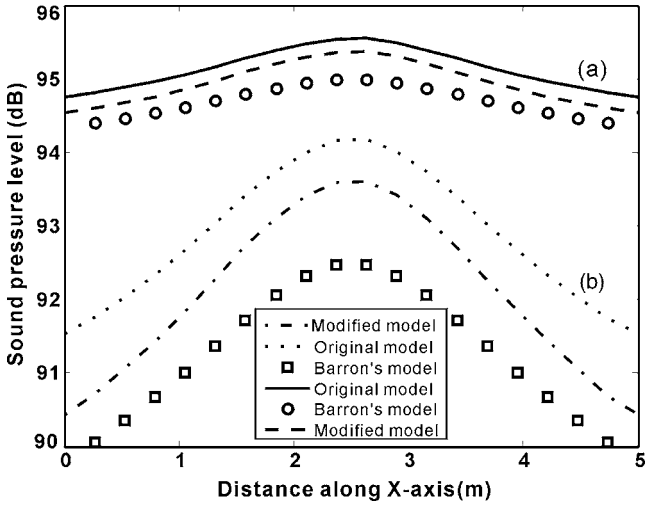

FIG. 2. Comparison of sound pressure level distributions along $y=1$ m ($x=-2.5-2.5$ m, $z=1$ m), by three different models in a cubic room with two configurations of absorption coefficients: 0.1 for each wall (a) and 0.5 for each wall (b).

A. Cubic rooms with uniformly distributed absorption coefficients

A cubic room ($-2.5\ \text{m} \leqslant x \leqslant 2.5\ \text{m}$, $-2.5\ \text{m} \leqslant y \leqslant 2.5\ \text{m}$, $-2.5\ \text{m} \leqslant z \leqslant 2.5\ \text{m}$) is modeled. The source is in the middle of the room with coordinate (0, 0, 0) m. The absorption coefficient is assigned uniformly for all room surfaces. RT is estimated over sound energy level range from -5 to -35 dB.[11] RTs are determined from results of both diffusion models with two kinds of boundary conditions, Sabine's formula, Eyring's formula, and Kuttruff's formula.[8] To compare these different methods in terms of predicted RTs, Fig. 1 illustrates the difference between the results from Kuttruff's formula and other methods. In Fig. 1, the original model with homogeneous Neumann boundary condition agrees more with Sabine's formula, the modified model with this boundary condition agrees more with Eyring's formula. The modified model with mixed boundary condition is very close to the prediction of Kuttruff's formula even when the absorption coefficient is relatively high, and thus has the best performance.

The SPLs are calculated using Eq. (17) along a line having a distance $\sqrt{2}$ m to the source ($y=1$ m, x is from -2.5 to 2.5 m, z is 1 m) by two diffusion models with the mixed boundary condition, and are compared to the results of Barron-Lee's equation which has been verified by the measurements of "reasonably diffusive hall."[12] Figure 2 illustrates comparison results for two different cases. For case (a), the power of the source is 0.01 W and the absorption coefficient of each wall is 0.1. In case (b), the power of the source is 0.02 W and the absorption coefficient of each wall is 0.5. As shown in Fig. 2 the modified diffusion model shows predicted values closer to those determined by Ref. 12.

B. Cubic rooms with nonuniformly distributed absorption coefficients

Again, a cubic room with dimension $5\ \text{m} \times 5\ \text{m} \times 5\ \text{m}$, but interior surfaces are featured with two different absorption coefficients. The source is in the middle of the room. In this case, only the mixed boundary condition is used because each wall can be assigned to a specific absorption coefficient. Results of RTs are compared to Kuttruff's formula and Kuttruff-Embleton's formula,[13,14] the latter one deals with a room having only two distinct types of surfaces. The results listed in Table I indicate that the modified diffusion model agrees more with Kuttruff-Embleton's formula.

C. Flat rooms

The modified diffusion model and the original diffusion model are compared with a geometrical-acoustics model (CATT Acoustics®). For a flat room with dimension $15\ \text{m} \times 15\ \text{m} \times 2\ \text{m}$, the source is at $(2,5,1)$ m, the sound power level W_s is 100 dB. The total SPL is obtained using Eq. (17). Figure 3(a) illustrates SPL distributions along the line $x=2.5$ (y is from 0 to 15 m) and at the height 1 m. Figure 3(b) illustrates a sketch of the configuration. The absorption co-

TABLE I. Reverberation times [s] for nonuniformly distributed absorptions in a room predicted by Kuttruff's formula, Kuttruff-Embleton formula, the original diffusion model and the modified one.

Distribution of absorption	Kuttruff	Kuttruff-Embleton	Original	Modified
One wall with 0.9, others with 0	0.8491	0.7148	1.2134	0.6826
One wall with 0.5, others with 0	1.5652	1.4311	1.9232	1.4774
One wall with 0.5, others with 0.1	0.7596	0.7346	0.8716	0.7441
One wall with 0.5, others with 0.2	0.4905	0.4835	0.5723	0.4869

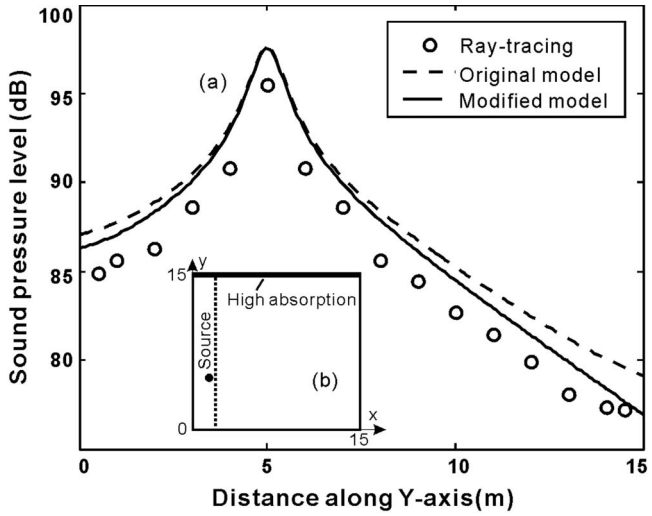

FIG. 3. (a) Comparison of sound pressure level distribution along $x=2.5$ m line in a flat room by the original, modified diffusion model and the geometrical-acoustics (ray tracing) model in a flat room. One wall surface is featured with absorption coefficient 0.8 while the other wall surfaces with absorption coefficient 0.3. (b) Top view of the flat room with dimension 15 m $\times$15 m $\times$2 m, the sound source is at (2,5,1).

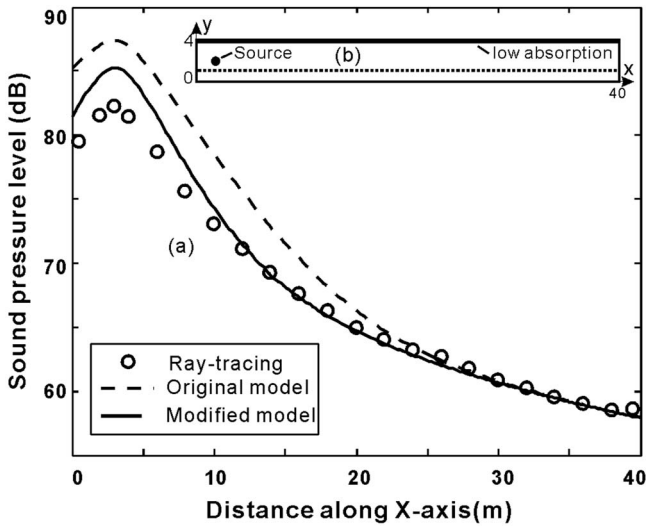

FIG. 4. (a) Comparison of sound pressure level distribution along $y=0.5$ m in a long room by the original, modified diffusion model and the geometrical-acoustics (ray-tracing) model in a long room. One wall surface is featured with absorption coefficient 0.9 while the other wall surfaces with absorption coefficient 0.4. (b) Top view for the long room with dimension 4 m$\times$4 m$\times$40 m, the sound source is at (3,2,3) m, the sound pressure level is calculated along $y=0.5$ m line.

efficient of one wall is 0.8, other walls are 0.3. CATT Acoustics software is used, the number of rays and the ray truncation time are chosen as 5×10^4 and 1000 ms, respectively. These numbers are assumed to be big enough to achieve well-converged results. The reflections are set to be completely diffusive. The modified model agrees better with the geometrical-acoustics model.

D. Long rooms

For a long room with dimension 4 m$\times$4 m$\times$40 m, the source is at (3,2,3) m, the sound power level is 100 dB. Figure 4(b) illustrates a sketch of the room configuration. The SPL distribution is calculated in the same way as the flat room and is plotted in Fig. 4(a) along the line $y=0.5$ m (x is from 0 to 40 m) and at the height 1 m. The absorption coefficient of one wall is 0.4, other walls are 0.9. CATT Acoustics software is again used. The modified model still agrees more with the geometrical-acoustics model.

IV. CONCLUSIONS

This work introduces a modification into a diffusion equation recently applied in room-acoustic predictions, the substitution of Eyring coefficient for Sabine coefficient in the diffusion equation results in more accurate results, especially for high absorption coefficients. Examples of cubic rooms are first given and compared with several well-established classical room-acoustic theories. For uniformly distributed absorption coefficients, the modified diffusion model shows a good agreement with Kuttruff's formula[8] and Barron-Lee's equation,[12] for nonuniformly distributed absorption coefficients, the results of the modified diffusion model are more close to Kuttruff-Embleton's formula.[13,14] At last, the sound pressure distributions of a flat and a long room are simulated. The modified diffusion model yields more similar results to those estimated by the geometrical-acoustics method. Comparisons carried out in this work among the modified model, the original model, the geometrical-acoustics model, and several classical theories indicate that a slight modification of the diffusion equation, as already applied in room acoustics, results in significant improvement in the prediction accuracy.

ACKNOWLEDGMENTS

The authors would like to thank Dr. Jason Summers, Dr. Vincent Valeau, and Dr. Edward Larsen.

[1]F. Ollendorff, "Statistical room-acoustics as a problem of diffusion (a proposal)," Acustica **21**, 236–245 (1969).
[2]J. Picaut, L. Simon, and J. D. Ploack, "A mathematical model of diffuse sound field based on a diffusion equation," Acust. Acta Acust. **83**, 614–621 (1997).
[3]J. Picaut, L. Simon, and J. Hardy, "Sound field modeling in streets with a diffusion equation," J. Acoust. Soc. Am. **106**, 2638–2645 (1999).
[4]V. Valeau, J. Picaut, and M. Hodgson, "On the use of a diffusion equation for room-acoustic prediction," J. Acoust. Soc. Am. **119**, 1504–1513 (2006).
[5]A. Billon, V. Valeau, A. Sakout, and J. Picaut, "On the use of a diffusion model for acoustically coupled rooms," J. Acoust. Soc. Am. **120**, 2043–2054 (2006).
[6]W. B. Joyce, "Sabine's reverberation time and ergodic auditoriums," J. Acoust. Soc. Am. **58**, 643–655 (1975).
[7]W. B. Joyce, "Classical-particle description of photons and phonons," Phys. Rev. D **9**, 3234–3256 (1974).
[8]H. Kuttruff, *Room Acoustics*, 4th ed. (Spon, New York, 2000).
[9]P. M. Morse and H. Feshbach, *Methods of Theoretical Physics* (McGraw Hill Book Company, New York, 1953).
[10]A. D. Pierce, *Acoustics: An Introduction to Its Physical Principles and Applications* (Acoustical Society of America, New York, 1981).
[11]ISO 3822, "Acoustics—Measurement of the reverberation time of rooms with reference to other acoustical parameters," (International Organisation for Standardization, Geneva, 1997).
[12]M. Barron and L.-J. Lee, "Energy relations in concert auditoriums. I," J. Acoust. Soc. Am. **84**, 618–628 (1988).
[13]T. M. W. Embleton, "Absorption coefficients of surfaces calculated from decaying sound fields," J. Acoust. Soc. Am. **50**, 801–811 (1971).
[14]J. E. Summers, R. R. Torres, and Y. Shimizu, "Statistical-acoustics models of energy decay in systems of coupled rooms and their relation to geometrical acoustics," J. Acoust. Soc. Am. **116**, 958–969 (2005).

Complete transmission through a periodically perforated rigid slab

Lin Zhou[a)]
Department of Mathematical Sciences, University of Delaware, Newark, Delaware 19711

Gregory A. Kriegsmann
Department of Mathematical Sciences, New Jersey Institute of Technology, University Heights, Newark, New Jersey 07029

(Received 2 October 2006; revised 1 March 2007; accepted 5 March 2007)

The propagation of a normally incident plane acoustic wave through a three-dimensional rigid slab with periodically placed holes is modeled and analyzed. The spacing of the holes A and B, the wavelength λ, and the thickness of the slab L are order one parameters compared to the characteristic size D of the holes, which is a small quantity. Scattering matrix techniques are used to derive expressions for the transmission and reflection coefficients of the lowest mode. These expressions depend only on the transmission coefficient, τ_0, of an infinitely long slab with the same configuration. The determination of τ_0 requires the solution of an infinite set of algebraic equations. These equations are approximately solved by exploiting the small parameter $D/\sqrt{AB}$. Remarkably, this structure is transparent at certain frequencies and opaque for all others. Such a structure may be useful in constructing narrow-band filters and resonators. © *2007 Acoustical Society of America.* [DOI: 10.1121/1.2721878]

PACS number(s): 43.20.El, 43.20.Mv, 43.20.Bi [RMW] Pages: 3288–3299

I. INTRODUCTION

The propagation of acoustic and elastic waves through periodic structures with different mechanical properties has received considerable study.[1–9] These phenomena are similar to the propagation of electromagnetic waves in photonic crystals. The existence of pass and stop bands is a common feature shared by all. These are observed both theoretically[1,3,7] and experimentally.[5,6,8,9] In electromagnetic applications these photonic structures are used to construct frequency selective filters. Similarly, their acoustic counterparts are used in constructing vibrationless environments,[4] building ultrasonic transducers and filters, and designing new acousto-optical devices.[9]

In this paper, the propagation of acoustic waves is investigated for a particular periodic structure. It is a rigid slab with periodically perforated holes. The motivation for this research partly comes from the analogy between the periodic elastic composites and periodic dielectrics. Recently considerable attention has been focused on the propagation of electromagnetic waves through a particular two-dimensional, metallic grating.[10–12] This grating is a perfectly conducting metallic slab of finite thickness in which slits are periodically cut through it. It was found that at certain frequencies there is complete electromagnetic transmission through the structure although the width of the slits is much smaller than the incident wavelength and the spatial period of the structure. Several explanations of this phenomenon are given.[13,14] The acoustic analog of this problem consists of a rigid material, which plays the role of the metal slab, and an incident plane, acoustic wave, which takes the role of a properly polarized electromagnetic wave. Since the two-dimensional electromagnetic and acoustic problems are mathematically equivalent, the phenomenon will be the same. This is true when the grating is composed of a periodic array of closely space hard cylinders.[15] The purpose of this paper is to show that our three-dimensional structure has the same feature of complete transmission at certain discrete frequencies.

Our structure has been studied[16] for a slab of infinite length, with circular holes; it was used as a model of a simple porous medium. Reflection coefficients over a wide range of frequencies were investigated in detail to the first cutoff frequency by using perturbation analyses.

In this paper, we apply a scattering matrix technique to theoretically find the acoustic transmission properties of a rigid slab with periodically arranged air holes. Specifically, the scattering matrix of the structure is derived for arbitrarily shaped holes. It is found that this matrix depends on only one parameter. Under the assumption that the incident wavelength is of the same order as the spacing of the holes and is much bigger than the hole size, the total transmission and total reflection properties of the structure at certain frequencies are obtained for circular holes. In constructing the scattering matrices to show this interesting phenomena we revisit the problem considered in Ref. 16 and re-derive some of the results contained therein. However, the derivations in this paper are more straightforward and the results are obtained for general hole shapes. In this paper we show that our periodic structure possesses very sharp pass bands and very broad stop bands. That is, only certain discrete frequencies pass through the slab. This feature may be exploited to build filters and Fabry Perot resonators, the latter being constructed by placing two parallel slabs a few wavelengths apart.

[a)]Electronic mail: zhoulin@math.udel.edu

 0001-4966/2007/121(6)/3288/12/$23.00 © 2007 Acoustical Society of America

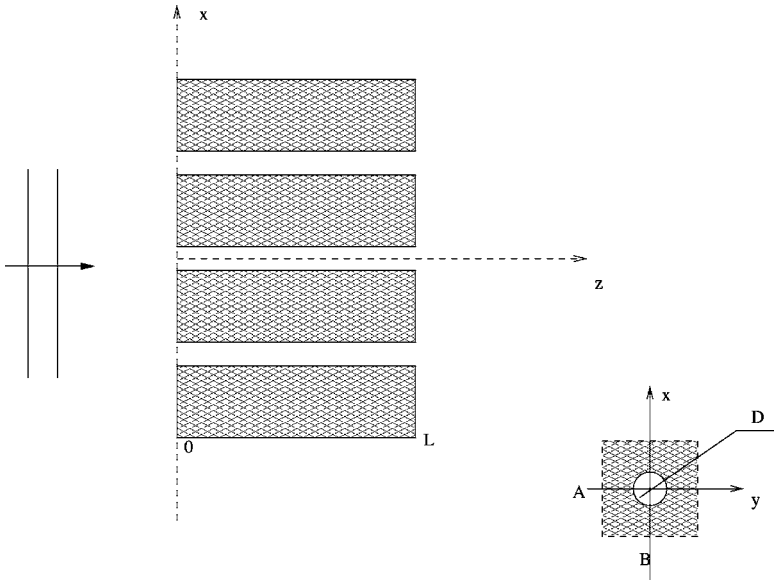

FIG. 1. Schematic diagram of the periodic structure considered in this problem.

The remainder of this paper is organized as follows. In Sec. II we present the mathematical formulation of the problem and our assumptions. This is followed by presenting modal solutions for each part of the structure. The form of the solution outside the slab is explicit. The solution inside the holes depends on their shape. However, the lowest eigenvalue and the eigenfunction for different shapes are found to be the same. In Sec. III we present and discuss two auxiliary problems, which are to construct the scattering matrix S for the structure. This allows both the transmission and the reflection coefficients to be obtained using S. We find remarkably that the transmission and reflection coefficients of our structure only depend upon one parameter, τ_0. This parameter is the transmission coefficient of the first auxiliary problem. In Sec. IV we present a Green's function argument in conjunction with a modal analysis to derive an infinite system of algebraic equations whose solution gives τ_0. In Sec. V, we exploit the small parameter D/S to obtain an approximation of τ_0 for the circular holes. In Sec. VI, we show that our structure possesses the complete transmission property described above. Finally, we present our conclusions in Sec. VII.

II. MATHEMATICAL FORMULATION

A schematic diagram of the structure is shown in Fig. 1. It is a rigid slab, infinitely long in both X and Y directions. In the Z direction the thickness of the slab is L. Holes are arranged periodically in the XY plane, and the cross section of the hole is uniform along the Z direction. All the holes are of the same shape. Since the structure is periodic, we consider a fundamental cell, which is also shown in Fig. 1. The length and the width of the fundamental cell are A and B, respectively. For an arbitrarily shaped hole, we define D, the square root of the hole's area, as the characteristic size of the hole.

A plane acoustic wave with frequency ω is normally incident on the perforated slab. The incident wavelength λ is of the same order as A and B. We assume that the viscosity of air is small enough so that the boundary layer on the surface of the hole channel can be neglected. Then the acoustic pressure U satisfies Helmholtz equation, $\nabla^2 U + K^2 U = 0$ both inside the pores and outside the slab. The constant K in the Helmholtz equation is the wave number defined by $K = 2\pi/\lambda$. The boundary condition is $\partial U/\partial n = 0$ on the rigid portions of the slab, where n denotes the normal direction to the rigid surfaces.

We assume that the hole is small compared to the size of the fundamental cell, that is, $D \ll \sqrt{AB}$. Under this assumption, it is intuitive that most of the incident wave will be reflected from the slab and only a small remnant of the wave will be able to reach the region $Z > L$. However, as mentioned above, we shall show that complete transmission is achieved at certain frequencies and slab thicknesses.

All upper case letters used so far represent dimensional parameters and variables. We will use lower case letters to denote the corresponding dimensionless quantities. We scale all lengths by $\sqrt{AB}$. Therefore, the fundamental cell has length a and width b, and $ab = 1$. The slab thickness $l = L/\sqrt{AB}$ and the dimensionless wave number $k = K\sqrt{AB}$ are both order one parameters in our problem. The dimensionless size of the hole is $d = D/\sqrt{AB} \ll 1$ by our assumption that $D \ll \sqrt{AB}$. The pressure U is scaled by the amplitude of the incident wave. After nondimensionalization, the governing equation and the boundary conditions become

$$\nabla^2 u + k^2 u = 0, \qquad \frac{\partial u}{\partial n} = 0. \tag{1}$$

Since the structure is periodic and the incident wave strikes it normally, it is expected that in regions $z < 0$ and $z > l$, both u and its normal derivative are periodic functions of x and y with period a and b, respectively. By applying the boundary conditions, the solutions in regions $z < 0$ and $z > l$ can be written as eigenfunction expansions,

$$u(x,y,z) = e^{ikz}\psi_{00} + \sum_{m=0}^{\infty}\sum_{n=0}^{\infty} R_{mn}\psi_{mn}(x,y)e^{-i\beta_{mn}z}, \quad z < 0, \tag{2a}$$

$$u(x,y,z) = \sum_{m=0}^{\infty}\sum_{n=0}^{\infty} T_{mn}\psi_{mn}(x,y)e^{i\beta_{mn}z}, \quad z > l, \tag{2b}$$

where we have suppressed a time dependence of $e^{-i\omega t}$. In the region $z<0$, the solution consists of the incident wave $u_i = e^{ikz}$ and reflected waves. The unknowns R_{mn} are the amplitudes of the mnth reflected modes and β_{mn} are the corresponding propagation constants. In the region $z>l$, the mnth mode of the transmitted wave has an unknown amplitude T_{mn}. In (2a) and (2b) ψ_{mn} are normalized eigenfunctions of the periodic structure. If we choose the origin of the coordinate system to be at the center of the fundamental cell, these eigenfunctions can be written explicitly as

$$\psi_{00} = 1, \tag{3a}$$

$$\psi_{0n} = \sqrt{2}\cos\frac{2n\pi y}{b}, \quad \psi_{m0} = \sqrt{2}\cos\frac{2m\pi x}{a}, \tag{3b}$$

$$\psi_{mn} = 2\cos\frac{2m\pi x}{a}\cos\frac{2n\pi y}{b}, \quad m,n = 1,2,3,\ldots, \tag{3c}$$

and the propagation constants are

$$\beta_{mn} = \sqrt{k^2 - \frac{4m^2\pi^2}{a^2} - \frac{4n^2\pi^2}{b^2}}, \quad m,n = 0,1,2,\ldots. \tag{4}$$

In the channel where $0<z<l$, there are waves in both z and $-z$ directions. If we can find the eigenvalues and eigenfunctions corresponding to a particular hole shape, we can write down the solution of the Helmholtz equation in terms of the eigenvalues and eigenfunctions in this region, just as we did for the regions outside the slab. We know that for the Laplace operator with a Neumann boundary condition, all the eigenvalues are real and positive, therefore the eigenvalues can be ordered. Let λ_p denote the eigenvalues and φ_p denote the corresponding eigenfunctions, where $p = 0,1,2,\ldots$. Then the solution in the channel can be expressed as

$$u(x,y,z) = \sum_{p=0}^{\infty}(A_p e^{-ik_p z} + B_p e^{ik_p z})\varphi_p(x,y), \quad 0 < z < l. \tag{5}$$

In Eq. (5) the propagation constants k_p are defined as $k_p = \sqrt{k^2-\lambda_p^2}$, and the amplitudes A_p and B_p of each mode are unknown. Although the eigenvalues and eigenfunctions depend on the shape of the hole, the smallest eigenvalue and its corresponding normalized eigenfunction are the same for all shapes. The smallest eigenvalue is $\lambda_0 = 0$ and its corresponding eigenfunction is $\varphi_0 = 1/d$. Therefore, we have

$$k_0 = k, \tag{6a}$$

$$\varphi_0 = \frac{l}{d}. \tag{6b}$$

All the eigenvalues λ_p for $p \geq 1$ are greater than 0 and of order $1/d$. (The proof is given in Appendix A.) Since $\lambda_p \gg 1$, $k_p = i\sqrt{\lambda_p^2 - k^2}$ for any fixed k as $d \to 0$. Therefore, the propagation constants k_p can be approximated by

FIG. 2. A typical component of microwave circuits.

$$k_p \approx i\tilde{\lambda}_p/d, \quad p = 1,2,\ldots, \tag{7}$$

with $\tilde{\lambda}_p$ being order one quantities. This means that all the higher modes in the hole channel are highly damped.

III. THE METHOD

A. Scattering matrix method

In Sec. II, we derived solutions of the slab problem in terms of eigenfunction expansions. By finding the unknown coefficients of each mode, the problem will be solved completely. One way to find the unknown coefficients is by using the boundary conditions that connect the three regions, $z<0$, $0<z<l$, and $z>l$. This can be attained by using Green's function arguments to derive two integral equations, one at $z=0$ and the other at $z=l$, and substituting these modal solutions in the integral equations. Then, by exploiting the orthonormal properties of eigenfunctions, two coupled infinite systems of algebraic equations can be derived and solved numerically to obtain the transmission coefficients T_{mn} and the reflection coefficients R_{mn}.

The other approach to solve the problem is by the application of scattering matrix theory. In microwave circuit analysis and design, the scattering matrix is widely used to characterize a component, such as an amplifier or other circuit elements.[17] As shown in Fig. 2, a two-port circuit has two input voltages, a_0 and b_0, and two output voltages, c_0 and d_0. These are proportional to the strengths of the incident and reflected modes, respectively. They are connected through the scattering matrix S, which is often obtained experimentally, that is, the inputs and the outputs are related by the following equation,

$$\begin{bmatrix} c_0 \\ d_0 \end{bmatrix} = \begin{bmatrix} S_{11} & S_{12} \\ S_{21} & S_{22} \end{bmatrix}\begin{bmatrix} a_0 \\ b_0 \end{bmatrix} = S\begin{bmatrix} a_0 \\ b_0 \end{bmatrix}. \tag{8}$$

Once the scattering matrix S of the device is known and a_0 and b_0 are prescribed, the scattered amplitudes c_0 and d_0 are found from (8).

We are going to construct a scattering matrix for the slab problem, which connects the lowest mode of transmitted and reflected waves to the amplitudes of the incident waves. In order to do so, we will divide the slab into two parts at $z = l/2$. A scattering matrix for each part will be constructed individually. Then, neglecting the evanescent modes at $z = l/2$, a very good approximation by Eq. (7), we can combine these two matrices to construct S for our slab structure.

As a consequence of neglecting the exponentially small evanescent modes the acoustic field in the channel near $z = l/2$ is given by

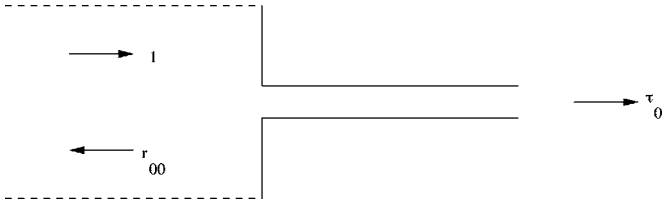

FIG. 3. Schematic diagram illustrating the structure and the incident, reflected, and transmitted waves considered in the first auxiliary problem.

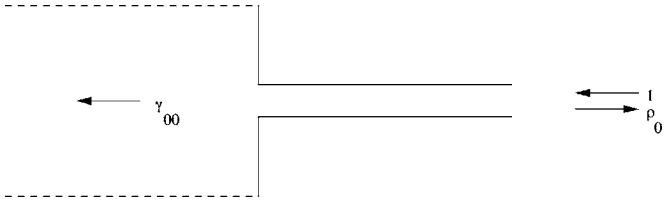

FIG. 4. Schematic diagram illustrating the structure and the incident, reflected, and transmitted waves considered in the second auxiliary problem.

$$u = (A_0 e^{-ikz} + B_0 e^{ikz})\varphi_0. \tag{9}$$

We now assume that $k<2\pi/a$ if $a>b$, otherwise $k<2\pi/b$. Then from Eq. (4) it follows that all the β_{mn} are purely imaginary except for β_{00}, which is equal to k. Thus, at a distance several wavelengths to the left of the aperture $z=0$, the field is

$$u = (e^{ikz} + R_{00}e^{-ikz})\psi_{00}. \tag{10}$$

Similarly, the transmitted acoustic field in the region $z>l$ is given by

$$u = T_{00}e^{ikz}\psi_{00}. \tag{11}$$

As we shall soon demonstrate, there exists a scattering matrix S_1 that connects the amplitudes of the outgoing waves R_{00} and. B_0 with the amplitudes of the incident waves 1 and A_0. The scattering matrix S_1 can be considered to characterize the first half of the structure $(-\infty<z<l/2)$.

We shall also show that there exists another scattering matrix S_2 that characterizes the second half of the structure $(l/2<z<\infty)$ and connects A_0, B_0, and T_{00}. A combination of the two scattering matrices S_1 and S_2 yields the scattering matrix S of the slab.

B. Two auxiliary problems

In order to determine matrices S_1 and S_2, we consider two auxiliary problems. The structure of these two auxiliary problems is the same as that of the fundamental cell, except that the channel is infinitely long $(l=\infty)$. This is the structure studied in Ref. 16.

In the first auxiliary problem, the wave is incident upon the periodic structure and is transmitted into the channel, as shown in Fig. 3. As before, we can write a modal solution of the problem as follows,

$$u(x,y,z) = e^{ikz}\psi_{00} + \sum_{m=0}^{\infty}\sum_{n=0}^{\infty} r_{mn}\psi_{mn}(x,y)e^{-i\beta_{mn}z}, \quad z<0, \tag{12a}$$

$$u(x,y,z) = \sum_{p=0}^{\infty} \tau_p\varphi_p(x,y)e^{ik_p z}, \quad z>0, \tag{12b}$$

in which u_1 denotes the acoustic pressure in the first auxiliary problem. The first transmission coefficient τ_0 and the first reflection coefficient r_{00} in Eqs. (12) are related by the simple equation

$$1 - r_{00} = d\tau_0. \tag{13}$$

Equation (13) is derived in the following way. To the left of $z=0$ (at $z=-\delta$), we differentiate u_1 with respect to z, then multiply $\partial u_1/\partial z$ by ψ_{00}. After integrating it over the area of the fundamental cell and using the orthonormality of the eigenfunctions, we obtain

$$\int_{-a/2}^{a/2}\int_{-b/2}^{b/2}\left(\left.\frac{\partial u_1}{\partial z}\right|_{z=-\delta}\right)\psi_{00}\,dx\,dy = ike^{-ik\delta} - ikr_{00}e^{ik\delta}. \tag{14}$$

Similarly, to the right of $z=0$ (at $z=\delta$) we have

$$\int\int_H\left(\left.\frac{\partial u_1}{\partial z}\right|_{z=\delta}\right)\varphi_0\,dx\,dy = ik\tau_0 e^{ik\delta}, \tag{15}$$

in which the double integral $\int\int_H$ is over the area of the hole. Letting $\delta\to 0$, the region of integration in (14) will coincide with H because $\partial u_1/\partial z=0$ outside the hole. Equation (13) now follows from the facts that $\partial u_1/\partial z$ is continuous in the hole at $z=0$ and $\varphi_0 d=\psi_{00}$.

The second auxiliary problem has the same structure as the first one. However, the wave is incident from the channel and is transmitted into the air region, as shown in Fig. 4. Therefore, the modal solution to this problem is

$$u_2(x,y,z) = \sum_{m=0}^{\infty}\sum_{n=0}^{\infty}\gamma_{mn}\psi_{mn}(x,y)e^{-i\beta_{mn}z}, \quad z<0, \tag{16a}$$

$$u_2(x,y,z) = e^{-ikz}\varphi_0 + \sum_{p=0}^{\infty}\rho_p\varphi_p(x,y)e^{ik_p z}, \quad z>0. \tag{16b}$$

Using the same argument as in the derivation of Eq. (13), it follows that the first transmission coefficient γ_{00} and the first reflection coefficient ρ_0 in the second auxiliary problem are related by

$$\gamma_{00} = d(1-\rho_0). \tag{17}$$

The two auxiliary problems are not independent. In Appendix B we prove that

$$\gamma_{00} = \tau_0. \tag{18}$$

Equations (13), (17), and (18) form a system of three equations in four unknowns. Thereby, we are able to express any three parameters in terms of the fourth. We choose to express γ_{00}, r_{00}, and ρ_0 in.terms of τ_0. Explicitly we have

$$r_{00} = 1 - d\tau_0, \tag{19a}$$

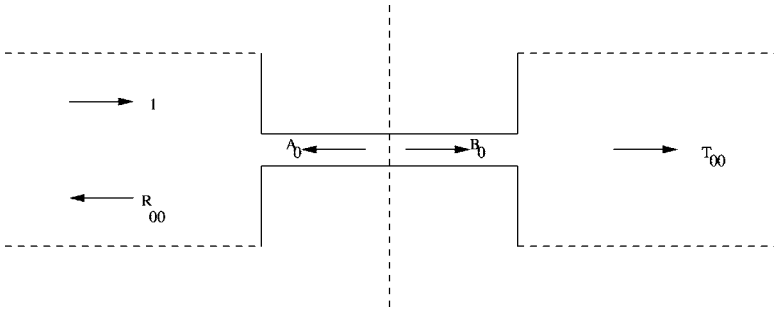

FIG. 5. Schematic diagram illustrating the structure and the incident, reflected, and transmitted waves considered in the slab structure.

$$\rho_0 = 1 - \frac{\tau_0}{d}, \tag{19b}$$

$$\gamma_{00} = \tau_0. \tag{19c}$$

The above result that any three of the four fundamental reflection and transmission coefficients can be written in terms of the fourth coefficient is also derived in Ref. 16, in which, a more complicated integral representation method is involved with the results holding only for circular holes.

These two auxiliary problems and their simple results enable us to find the scattering matrix of the slab, which depends on only one parameter.

C. Scattering matrix of the slab structure

Now we consider the slab problem. The scattering matrix for the first half ($-\infty < z < l/2$) is derived by linearly combining the two auxiliary problems, since both the Helmholtz equation and the boundary conditions are linear. From Fig. 5 we observe that the first half of the structure can be viewed as having incident modes with amplitudes 1 and A_0, and reflected modes with amplitudes R_{00} and B_0. Hence, the results of the two auxiliary problems imply that

$$R_{00} = r_{00} \cdot 1 + \gamma_{00} A_0, \tag{20a}$$

$$B_0 = \tau_0 \cdot 1 + \rho_0 A_0. \tag{20b}$$

Rewriting Eq. (20) in matrix notation and using the relations given in Eq. (19) gives

$$\begin{bmatrix} R_{00} \\ B_0 \end{bmatrix} = S_1 \begin{bmatrix} 1 \\ A_0 \end{bmatrix}, \tag{21}$$

where the scattering matrix S_1 is

$$S_1 = \begin{bmatrix} 1 - d\tau_0 & \tau_0 \\ \tau_0 & 1 - \tau_0/d \end{bmatrix}. \tag{22}$$

The scattering matrix S_1 represents the first half of the slab structure. In Appendix C we prove that S_1 is unitary, i.e., $S_1 \bar{S}_1^T = I$, where T denotes the transpose of the matrix, the bar denotes the complex conjugate, and I is the 2×2 identity matrix. From this relationship it follows that

$$\left| \tau_0 - \frac{d}{1 + d^2} \right|^2 = \left(\frac{d}{1 + d^2} \right)^2. \tag{23}$$

The locus of Eq. (23) is a circle in the complex τ_0 plane. This circle can be equivalently expressed by

$$\tau_0 = \frac{2d}{1 + d^2 + i\eta}, \tag{24}$$

where $-\infty < \eta < \infty$, which is just a conformal mapping of the real line onto the circle.

We now derive the scattering matrix S_2, which relates the amplitudes of incident and reflected modes at the channel opening $z = l$. We introduce a new independent variable $\bar{z} = l - z$, which maps the second half of the structure into the first half. Using the result of S_1, we deduce that

$$S_2 = \begin{bmatrix} (1 - d\tau_0) e^{-2ikl} & \tau_0 \\ \tau_0 & (1 - \tau_0/d) e^{2ikl} \end{bmatrix}, \tag{25}$$

where e^{2ikl} and e^{-2ikl} take into account the physical location of the channel at $z = l$. Therefore, the amplitudes of outgoing waves T_{00} and A_0 are related to the amplitudes of the incoming waves B_0 by S_2, as follows,

$$\begin{bmatrix} T_{00} \\ A_0 \end{bmatrix} = S_2 \begin{bmatrix} 0 \\ B_0 \end{bmatrix} \tag{26}$$

One of the input wave amplitudes is 0 because there is no incident wave in the region $z > l$.

To determine a scattering matrix of our perforated slab structure, we first solve for A_0 in terms of B_0 from Eq. (21). Then we substitute A_0 in Eq. (26) and find B_0. The transmission coefficient T_{00} and the reflection coefficient R_{00} are determined from (21) and (26), respectively. These results are summarized as

$$\begin{bmatrix} R_{00} \\ T_{00} \end{bmatrix} = S \begin{bmatrix} 1 \\ 0 \end{bmatrix}, \tag{27}$$

where

$$S = \begin{bmatrix} (1 - d\tau_0) + \dfrac{\tau_0^2 (1 - \tau_0/d) e^{2ikl}}{M} & \dfrac{\tau_0^2}{M} \\ \dfrac{\tau_0^2}{M} & (1 - d\tau_0) e^{2ikl} + \dfrac{\tau_0^2 (1 - \tau_0/d)}{M} \end{bmatrix}, \tag{28}$$

and $M = 1 - (1 - \tau_0/d)^2 e^{2ikl}$. The scattering matrix S connects the reflected and transmitted waves of the lowest mode to the incident wave, as long as k is restricted to ensure single mode propagation in the regions $z < 0$ and $z > l$. It is important to note that S only depends on τ_0, which, from (24), is completely specified by η. Therefore, the reflection and transmission coefficients, R_{00} and T_{00}, only depend upon this one real parameter. This feature arises in the two-dimensional grating analyzed in Ref. 14. In the following

sections, we will approximate η numerically and find the transmission properties of the slab structure.

IV. THE DETERMINATION OF τ_0

The diagram of the first auxiliary problem is shown in Fig. 3. A part of the normally incident wave is reflected from this structure and the rest is transmitted into the channel. The modal solution, Eq. (12), of this problem was presented in Sec. III B, where the reflection and transmission coefficients are unknown. We shall now derive an expression for the field u_1 in the region $z<0$ using a standard Green's function representation. From this result we will deduce an infinite system of algebraic equations for the τ_n from which τ_0 will be determined.

The Green's function we employ satisfies

$$\nabla^2 G + k^2 G = \delta(\boldsymbol{x}-\boldsymbol{x}'), \quad z' < 0, \tag{29a}$$

$$\frac{\partial G}{\partial z} = 0, \quad z = 0, \tag{29b}$$

which is periodic in both x and y directions and represents outgoing, or evanescent, modes as $z \to \pm\infty$. It is explicitly given by

$$G(\vec{x}|\vec{x}') = \begin{cases} \displaystyle\sum_{-\infty}^{\infty}\sum_{-\infty}^{\infty} \frac{\cos\beta_{mn} z'}{i\beta_{mn}} e^{2m\pi i(x-x')/a} e^{2n\pi i(y-y')/b} e^{-ikz}, & -\infty < z < z', \\ \displaystyle\sum_{-\infty}^{\infty}\sum_{-\infty}^{\infty} \frac{\cos\beta_{mn} z}{i\beta_{mn}} e^{2m\pi i(x-x')/a} e^{2n\pi i(y-y')/b} e^{-ikz'}, & z' < z < 0. \end{cases} \tag{30}$$

Applying standard Green's function arguments, using the periodicity of both u_1 and G, their behaviors at infinity, and boundary conditions at $z=0$, we find that

$$u_1(x,y,z) = (2\cos kz)\psi_{00} - \int\int_H G(x',y',0^-|x,y,z) \frac{\partial u_1}{\partial z}(x',y',0^-)\, ds'. \tag{31}$$

Equation (31) is our integral representation of u_1 in the region $z<0$. The first term in Eq. (31) is the sum of the normally incident wave e^{ikz} and its rigid reflection e^{-ikz}. It is the field that would occur if no holes were present. In the second term, the integration is over the surface of the hole. Since the hole is small, the second term can be considered as a perturbation to the field in the region $z<0$ due to the existence of small holes in the structure.

Setting $z=0^-$ in Eq. (31), we obtain the field at the interface $z=0$,

$$u_1(x,y,0^-) = 2\psi_{00} - \int\int_H G(x',y',0^-|x,y,0^-) \times \frac{\partial u_1}{\partial z}(x',y',0^-)\, dx'\, dy'. \tag{32}$$

Since both u_1 and $\partial u_1/\partial z$ are continuous across $z=0$ on the surface of the hole, we let $z=0^+$ and substitute the modal expansion (12b) to obtain

$$\sum_{p=0}^{\infty} \tau_p \varphi_p(x,y) = 2\psi_{00} - \int\int_H G(x',y',0|x,y,0) \times \sum_{p=0}^{\infty} ik_p \tau_p \varphi_p(x',y')\, dx'\, dy'. \tag{33}$$

Multiplying both sides of this equation by φ_q, integrating the resulting equation over the surface of the hole, and using the othonormality of the eigenfunctions yields

$$\tau_q = 2d\delta_{q0} - i\sum_{p=0}^{\infty} k_p \tau_p Z_{qp}, \quad q = 0,1,2,\ldots, \tag{34}$$

where

$$Z_{qp} = \int\int_H \int\int_H G(x',y',0|x,y,0)\varphi_p(x',y') \times \varphi_q(x,y)\, dx'\, dx\, dy'\, dy \tag{35}$$

and δ_{q0} is the Kronecker delta function. We recall from Eq. (7) and our limit $d\to 0$ that $k_p = i|k_p|$ for $p \geq 1$. Using this observation we rewrite Eq. (34) as

$$\tau_0 = 2d - ik\tau_0 Z_{00} + \sum_{p=1}^{\infty} |k_p| Z_{0p}\tau_p, \tag{36a}$$

$$\tau_q = ik\tau_0 Z_{q0} + \sum_{p=1}^{\infty} |k_p| Z_{qp}\tau_p, \quad q = 1,2,\ldots. \tag{36b}$$

The equations in (36) form an infinite system of algebraic equations with unknowns τ_p. The quantities Z_{qp} are defined in (35). If the eigenfunctions φ_p are known, Z_{qp} can be found either analytically or numerically for each p and q. There-

fore, each τ_p can be solved for approximately by truncating the infinite system.

Before truncating the algebraic system (36), we simplify it further, so as to find an explicit representation for τ_0 that is comparable to (24). Setting $\alpha_q=\tau_q/(-ik\tau_0)$ for $q\geq 1$ and substituting α_q in (36b) gives

$$\alpha_q = Z_{q0} + \sum_{p=1}^{\infty} |k_p| Z_{qp}\alpha_p, \quad q = 1,2, \ldots . \tag{37}$$

The same change of variable applied to (36a) yields

$$\tau_0 = \frac{2d}{1 + ikZ_{00} + ik\sum_{p=1}^{\infty} |k_p| Z_{0p}\alpha_p}. \tag{38}$$

Thus, τ_0 can be found explicitly provided that Eq. (37) can be solved for the α_q.

The quantities Z_{qp} depend upon the shape of the hole. However, the first eigenfunction $\varphi_0=1/d$ is the same for all shapes. Therefore, we deduce from Eq. (35) that Z_{00} is given by

$$Z_{00} = \int \int_H \int \int_H G(x',y',0|x,y,0)\frac{1}{d^2}\, dx'\, dx\, dy'\, dy. \tag{39}$$

Now, G in Eq. (30) can be rewritten for $z=z'=0$ as

$$\begin{aligned} G(x',y',0|x,y,0) = \frac{1}{ik} &- \sum_{n=1}^{\infty} \frac{2}{|\beta_{0n}|} \cos\frac{2n\pi(y-y')}{b} \\ &- \sum_{m=1}^{\infty} \frac{2}{|\beta_{m0}|} \cos\frac{2m\pi(x-x')}{a} \\ &- \sum_{m=1}^{\infty}\sum_{n=1}^{\infty} \frac{4}{|\beta_{mn}|} \cos\frac{2m\pi(x-x')}{a} \\ &\times \cos\frac{2n\pi(y-y')}{b}, \end{aligned} \tag{40}$$

where we have used that fact that $\beta_{nm}=i|\beta_{nm}|$ for our restricted values of k. Substituting this into the expression for Z_{00} and integrating the first term implies that the first term is d^2/ik for any shape of the hole. Hence, Z_{00} can be rewritten as

$$Z_{00} = \frac{d^2}{ik} + \tilde{Z}_{00}, \tag{41}$$

where $\tilde{Z}_{00}$ is real. Finally, substituting this result into Eq. (38) gives

$$\tau_0 = \frac{2d}{1 + d^2 + ik(\tilde{Z}_{00} + \sum_{p=1}^{\infty} |k_p| Z_{0p}\alpha_p)}. \tag{42}$$

Equations (42) and (24) are identical with

$$\eta = k\left(\tilde{Z}_{00} + \sum_{p=1}^{\infty} |k_p| Z_{0p}\alpha_p\right). \tag{43}$$

Thus, τ_0 lies on the circle given by Eq. (23) regardless of the shape of the hole. We observe that the system (37) must be truncated in order to obtain an approximate solution for the α_q. Once these are determined, then Eqs. (42) and (43) can be truncated to yield an approximation to τ_0, and this in turn will be used to approximate T_{00}. It is interesting to note in closing this section that our truncated approximation of τ_0 satisfies (24) regardless of either the truncation level or the accuracy used in computing the Z_{qp}. However, the accurate location of τ_0 on this circle requires careful approximations and truncations.

V. AN APPROXIMATION TO τ_0 FOR CIRCULAR HOLES

In the expression for τ_0 in Eq. (42), the real number η needs to be computed. Since η is a function of Z_{qp} and α_q [Eq. (43)], we shall first evaluate the parameters Z_{qp} and α_q in order to determine η and hence determine τ_0. In this section, τ_0 is determined for circular holes.

If the dimensional radius of the hole is R, then the characteristic size of the hole is $D=\sqrt{\pi}R$. After nondimensionalization, we obtain that $d=\sqrt{\pi}r$. Therefore, the eigenfunctions corresponding to the circular hole can be easily obtained as follows,

$$\varphi_0 = \frac{1}{d}, \tag{44}$$

$$\varphi_p(r) = \frac{1}{d}\frac{J_0(\lambda_p r)}{J_0(\lambda_p d/\sqrt{\pi})}, \quad p = 1,2, \ldots , \tag{45}$$

where J_0 is the zeroth order Bessel function. The corresponding eigenvalues are found to be $\lambda_p=j_{1p}\sqrt{\pi}/d$, where j_{1p} is the pth root of the first order Bessel function. Note that only the radial eigenfunctions are employed since the incident wave impinges normally upon the slab. As mentioned before, for $d\ll 1$, the propagation constants

$$k_p = \sqrt{k^2 - \lambda_p^2} \tag{46}$$

in the channel can be approximated by

$$k_p \approx ij_{1p}\sqrt{\pi}/d, \quad p \geq 1. \tag{47}$$

Now, the quantities Z_{qp} can be found explicitly using the explicit expressions of the Green's functions and the eigenfunctions. The integral in Eq. (35) is computed by interchanging the order of integration and the summation. The results of these calculations yield

$$\begin{aligned} Z_{00} = \frac{d^2}{ik} + d^2\Bigg(&\sum_{m=1}^{\infty} \frac{-8}{|\beta_{m0}|}\frac{J_1^2(\mu_1)}{\mu_1^2} + \sum_{n=1}^{\infty} \frac{-8}{|\beta_{0n}|}\frac{J_1^2(\mu_2)}{\mu_2^2} \\ &+ \sum_{m=1}^{\infty}\sum_{n=1}^{\infty} \frac{-16}{|\beta_{mn}|}\frac{J_1^2(\mu_3)}{\mu_3^2}\Bigg) \equiv \frac{d^2}{ik} + d^2 S_{00}, \end{aligned} \tag{48}$$

$$Z_{qp} = d^2 \sum_{m=1}^{\infty} \frac{-8}{|\beta_{m0}|} \frac{\mu_1^2 J_1^2(\mu_1)}{(\mu_1^2 - j_{1p}^2)(\mu_1^2 - j_{1q}^2)} + d^2 \sum_{n=1}^{\infty} \frac{-8}{|\beta_{0n}|} \frac{\mu_2^2 J_1^2(\mu_2)}{(\mu_2^2 - j_{1p}^2)(\mu_2^2 - j_{1q}^2)} + d^2 \sum_{m=1}^{\infty} \sum_{n=1}^{\infty} \frac{-16}{|\beta_{mn}|} \frac{\mu_3^2 J_1^2(\mu_3)}{(\mu_3^2 - j_{1p}^2)(\mu_3^2 - j_{1q}^2)} \equiv d^2 S_{qp},$$

$$p^2 + q^2 \geq 1, \tag{49}$$

where μ_1, μ_2, and μ_3 are defined as

$$\mu_1 = 2m\sqrt{\pi}d/a, \tag{50a}$$

$$\mu_2 = 2n\sqrt{\pi}d/b, \tag{50b}$$

$$\mu_3 = \sqrt{(2m\sqrt{\pi}d/a)^2 + (2n\sqrt{\pi}d/b)^2}. \tag{50c}$$

We observe that in Eq. (49), the quantities Z_{qp} are symmetric and hence $S_{pq}=S_{qp}$. Substituting the new notation in Eqs. (37) and (42), respectively, gives

$$\alpha_q = d^2 S_{q0} + d^2 \sum_{p=1}^{\infty} |k_p| S_{qp} \alpha_p, \quad q = 1,2, \ldots, \tag{51}$$

and

$$\tau_0 = \frac{2d}{1 + d^2 + id^2(kS_{00} + k\sum_{p=1}^{\infty} |k_p| S_{0p}\alpha_p)}. \tag{52}$$

The infinite system of equations (51) cannot be solved exactly; it must be truncated to obtain approximations to the α_q. For a fixed N we denote by $\hat{\alpha}_q$ the approximate solution of (51), which satisfies

$$\hat{\alpha}_q = d^2 S_{q0} + d \sum_{p=1}^{N} j_{1p}\sqrt{\pi} S_{qp} \hat{\alpha}_p, \tag{53}$$

where (47) has been used for simplification. The corresponding approximation to τ_0 is denoted by $\hat{\tau}_0$, which is obtained from (52) by truncating the series at $p=N$. We have solved (53) for values of d ranging from 0.01 to 0.1, for several values of N. We have found for these values of d that the corresponding values of $\hat{\tau}_0$ are accurate to four decimal places when $N=3$, i.e., increasing N does not significantly alter their values. These results are similar to the trends seen in the related problem of Ref. 14.

We will now derive an approximate solution of (53) and the corresponding approximation of $\hat{\tau}_0$ by exploting the smallness of d. Before doing this, we first check the order of S_{qp} as d approaches 0. Figures 6, 7, and 8 show this behavior for S_{00}, S_{0p}, and S_{qp}, respectively. In Fig. 6 we observe that, as d approaches 0, S_{00} increases and behaves like $1/2d$. In Figs. 7 and 8 we observe that the S_{0p} and S_{qp} are very small compared to S_{00}, and both the S_{0p} and S_{qp} are order one quantities as d approaches 0.

Using the fact that both the S_{0p} and S_{qp} are of $O(1)$ for small values of d and the fact that $d \ll 1$, a simple approximation to Eq. (53) yields

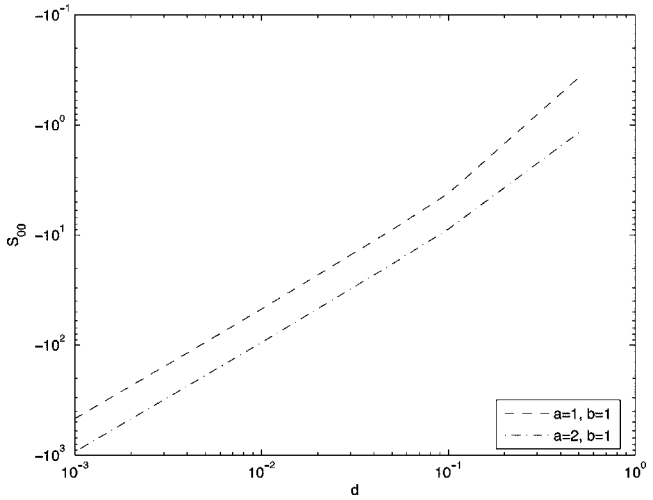

FIG. 6. The behavior of S_{00} for small values of d.

$$\hat{\alpha}_q = d^2 S_{q0} + O(d^3), \quad 1 \leq q \leq N. \tag{54}$$

Substituting this expression into the truncated version of Eq. (52) we obtain the approximation to $\hat{\tau}_0$:

$$\hat{\tau}_0 = \frac{2d}{1 + d^2 + ikd^2\{S_{00} + d^2 \sum_{p=1}^{N} j_{1p}\sqrt{\pi} S_{0p}^2\}}. \tag{55}$$

As d approaches 0, the second term in curly brackets is much smaller than the first term. This is because the S_{0p} are of $O(1)$ and S_{00} is of $O(1/d)$ for $d \ll 1$. Therefore, neglecting the second term in (55) we obtain

$$\hat{\tau}_0 = \frac{2d}{1 + d^2 + id^2 k S_{00}}. \tag{56}$$

This approximation satisfies the constraint (24) and, more importantly, is remarkably accurate. It agrees to within three decimal places of the numerical results obtained from solving (53) and the truncated version of (52).

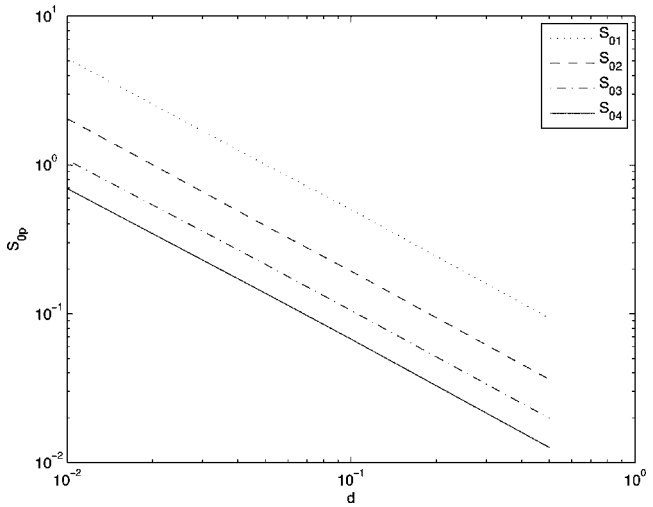

FIG. 7. The behavior of S_{0p} for small values of d.

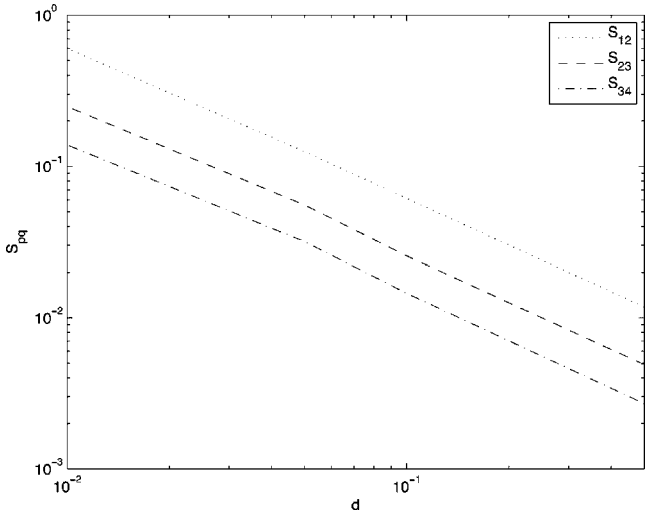

FIG. 8. The behavior of S_{qp} for small values of d.

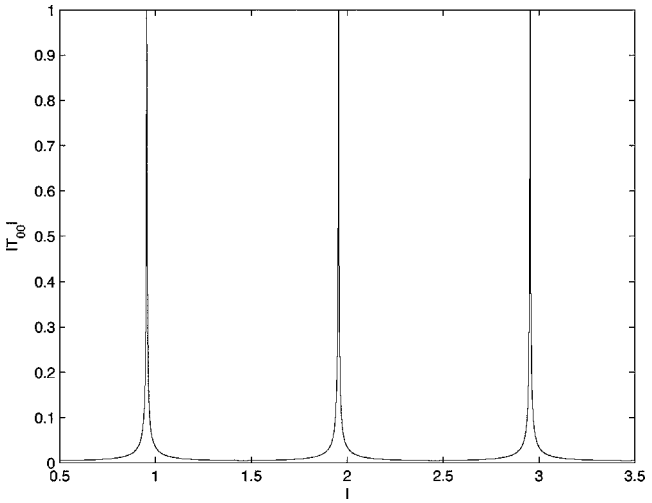

FIG. 9. Transmission coefficient T_{00} versus the thickness of the slab l for $d=0.05$, $k=\pi$, and $a=b=1$.

VI. TRANSMISSION PROPERTIES

Through the analysis in Sec. V, we obtained an approximation of τ_0 for small values of d. We are now ready to numerically approximate T_{00}. From Eqs. (27) and (28) we readily solve for T_{00} and find

$$T_{00} = \frac{\tau_0^2}{1-(1-\tau_0/d)^2 e^{2ikl}}. \tag{57}$$

Substituting the approximation $\hat{\tau}_0$ from Eq. (56), we find that

$$|\hat{T}_{00}| = \frac{2d^2}{\sqrt{(2d^2\nu_1)^2+\nu_2^2}},$$

$$\nu_1 = d^2 k S_{00} \sin kl + \cos kl, \tag{58}$$

$$\nu_2 = (1+d^4-d^4k^2S_{00}^2)\sin kl - 2d^2kS_{00}\cos kl.$$

We note here that the formula (58) for T_{00} can be obtained by carefully summing up the internal reflections within the slit using the reflection and transmission coefficients from the two auxiliary problems and their relationships to τ_0.

From this expression of the transmission coefficient, we observe that if kl is such that ν_2 is an order one quantity, then T_{00} is $O(d^2)$, which is very small and there is very little transmission into the region $z>l$. This agrees with our intuition, because when the holes are small, most of the acoustic wave reflects back into $z<0$. However, there exist values of kl such that $\nu_2=0$, that is,

$$\tan kl = \frac{2d^2kS_{00}}{1+d^4(1-k^2S_{00})}; \tag{59}$$

then, in this case,

$$|\hat{T}_{00}| = 1/\nu_1 = \frac{1/\cos kl}{1+d^2kS_{00}\tan kl}. \tag{60}$$

Using the fact that $d \ll 1$, the values of kl that approximately satisfy (59) are

$$kl \approx M\pi + 2d^2kS_{00} + O((d^2S_{00})^2), \tag{61}$$

where M is any positive integer. Using the these values of kl in Eq. (60), we deduce

$$|\hat{T}_{00}| \approx 1 - O((d^2S_{00})^4). \tag{62}$$

Therefore, for these values of kl, the slab is almost transparent. This transparency is caused by a resonance phenomenon in the small channels. Although only a small amount of the wave propagates into a channel, $\tau_0=O(1)$, it constructively reflects back and forth within. This reflection is almost perfect within the channel because $\rho_0=1-\tau_0/d\sim-1$. The leading order approximation of kl from (61), $kl\sim M\pi$, would occur if the channel openings were replaced by sound soft surfaces. Thus, the result given by (61) shows the channels behave as leaky resonators. The numerical results presented in the next two paragraphs support this interpretation.

The transmission coefficient given Eq. (58) is plotted in Fig. 9 as a function of l for $k=\pi$ and $d=0.05$. It shows that T_{00} is almost 0 for all thicknesses l of the slab except at $l \approx 1,2,3,\ldots$, where $T_{00}\approx 1$. Actually, the peaks occur just to the left of these integers. The difference agrees with our approximation for l. This agreement is also seen in Fig. 10, where $k=\pi$, $S_{00}=-4.33$, and $d=0.1$. In this figure, the peaks appear some distance to the left of $l=1,2,3,\ldots$, and the difference is 0.086, which equals $2d^2S_{00}$. Also, Figs. 9 and 10 verify that, away from the peaks, the values of T_{00} are $O(d^2)$. The resonances shown in these figures are very sharp due to the fact that there are no losses in our model. We can relax this idealization in a phenomenological way by making the wave number k slightly complex. The result is shown in Fig. 11 where the dashed curve corresponds to $\mathrm{Im}(k)=0.05$ and the solid to $\mathrm{Im}(k)=0.01$. In both cases $\mathrm{Re}(k)=\pi$ and $d=0.1$. It is clear that increasing the imaginary part of k diminishes the resonant peaks and effectively spreads out the response as a function of l.

Similarly, we can fix the thickness of the slab and solve Eq. (59) for k to find the frequency at which the structure is transparent. Since S_{00} is also a function of k, it is not easy to find an explicit expression. However, it is easy to check nu-

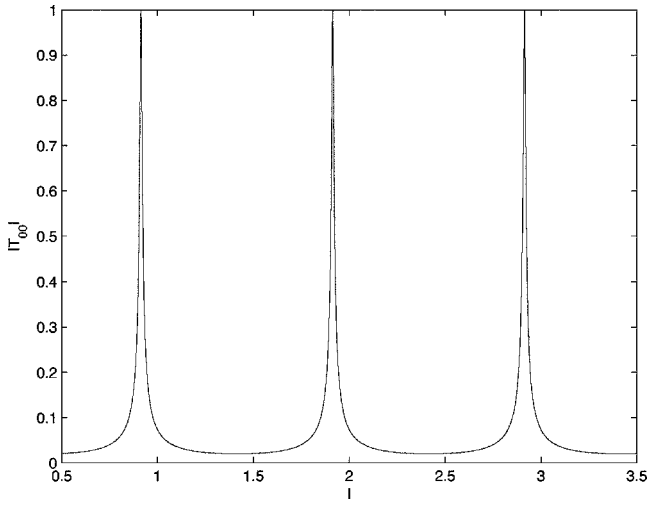

FIG. 10. Transmission coefficient T_{00} versus the thickness of the slab l for $d=0.1$, $k=\pi$, and $a=b=1$.

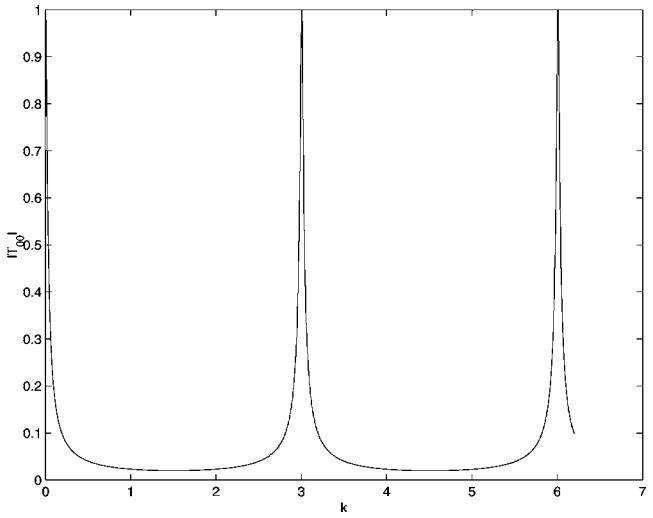

FIG. 12. Transmission coefficient T_{00} versus wave number k for $d=0.1$, $l=1$, and $a=b=1$.

merically that, when $k<2\pi/a$, S_{00} is not a sensitive function of k. Thus from Eq. (61), k can be approximated as

$$k \approx \frac{M\pi}{l - 2d^2 S_{00}}. \tag{63}$$

For these values of k, $T_{00} \approx 1$. The behaviors of $|T_{00}|$ as a function of k are illustrated in Figs. 12 and 13, where $l=1$ and 2, respectively. The peaks occur just at the position estimated by Eq. (63). The number of peaks increases as l increases when the upper limit of k is fixed. Again, the resonance shown in these figures is very sharp. These can be smoothed somewhat by taking into account a small amount of viscosity in the acoustic fluid. This amounts to letting the imaginary part of the wave number depend quadratically on frequency, or equivalently replacing k by $k+ik^2\epsilon$, where ϵ is a small number depending upon viscosity. The results for this case are shown in Fig. 14. The resonances become less pronounced as ϵ and the frequency are increased.

It is clear from these figures that the perforated rigid slab behaves like a narrow-band filter, in the absence of losses. For certain frequencies, energy is transmitted almost 100%; for other frequency bands, almost all the energy is reflected. Also, the widths of the pass bands depend on the dimensionless radius of the holes. If dimensions are reintroduced, then these widths would depend upon the porosity of the rigid slab. However, it is also clear from our figures that the practical use of this structure, as a filter, will be limited by the losses present in a real application.

Finally, we note that our results can be extended to noncircular channels. The calculations become complex, even in the case of square crossections. The reader is referred to Ref. 18 for the details of this case.

VII. CONCLUSION

In this paper, we have analyzed the transmission properties of a periodically perforated rigid slab under normal, plane wave incidence. We have assumed that the characteristic size of a hole is much smaller than the spacing of the holes, while the incident wave length is of the same order as

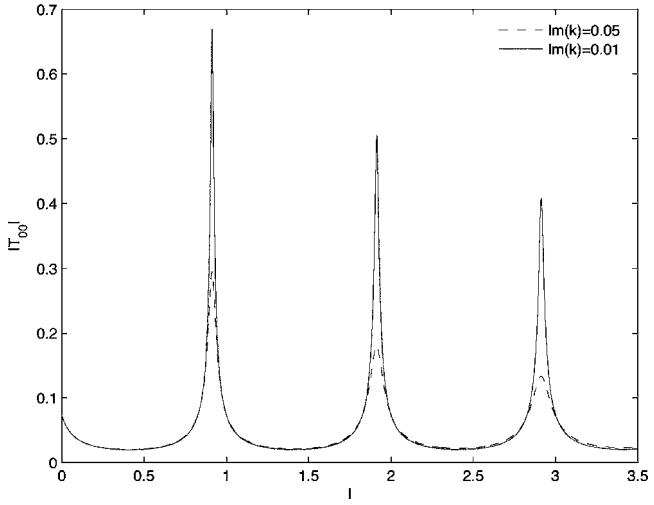

FIG. 11. Transmission coefficient T_{00} versus the thickness of the slab l for $d=0.1$, $\mathrm{Re}(k)=\pi$, and $a=b=1$.

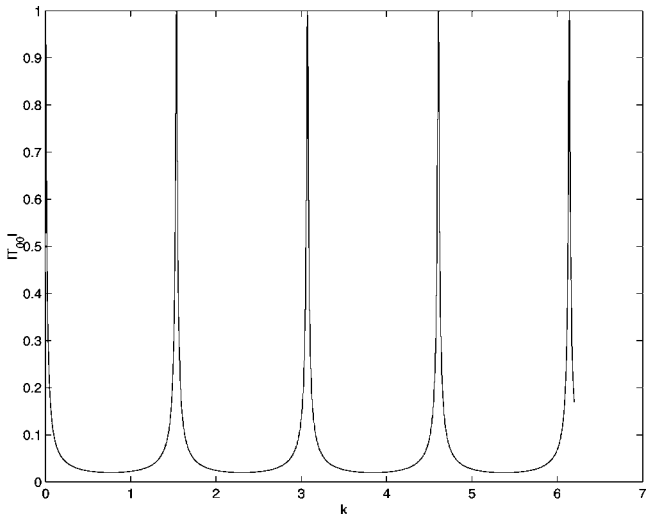

FIG. 13. Transmission coefficient T_{00} versus wavenumber k for $d=0.1$, $l=2$, and $a=b=1$.

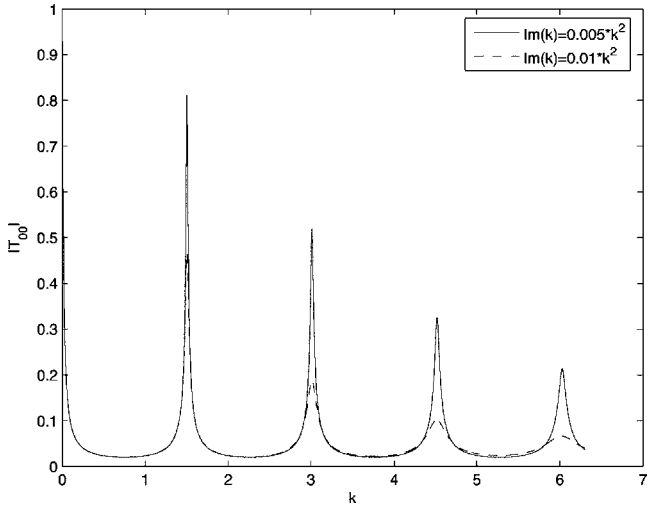

FIG. 14. Transmission coefficient T_{00} versus $Re(k)$ for $d=0.1$, $l=2$, and $a=b=1$.

the hole spacing. We have also restricted the range of the incident wave frequency such that only one mode propagates outside the slab and inside the holes. The length of the slab in our problem is long enough so that all the evanescent modes are negligible in the middle of the hole channel. Under these assumptions, we have considered two auxiliary problems. Both of the auxiliary problems have the same structure as the slab except that they are infinitely long. In the first auxiliary problem, the wave is incident from the air; in the second auxiliary problem, the wave is incident from the hole. The relationship of the transmission and the reflection coefficients of the two problems were discussed in detail. The linear combination of the two auxiliary problems gave a scattering matrix S for the original structure. Through this matrix, the transmission coefficient T_{00} and the reflection coefficient R_{00} of the slab were found explicitly. We have found that, for arbitrary shaped holes, the coefficients T_{00} and R_{00} depend only on one parameter τ_0, which is the transmission coefficient of the first auxiliary problem. This coefficient was found to lie on a circle in the complex plane.

Numerical values of τ_0 were found for circular holes. Specifically, an infinite system of algebraic equations was derived from the integral representation of the solution of the first auxiliary problem. The coefficient τ_0 was explicitly obtained from these algebraic equations. By using the fact that the hole size is very small compared to the spacing of the holes, τ_0 was obtained numerically. The plots of $|T_{00}|$ were given for circular holes. The plots showed that for fixed thickness of the slab, the function $|T_{00}|$ is $O(d^2)$ quantities except at certain frequencies, at which the wave can transmit almost completely. On the other hand, if the frequency of the incident wave is fixed, by adjusting the thickness of the slab, we can have either completely transmitted or a completely reflected wave. We have also considered the effects of losses on the resonant behavior of our structure. If these are not too large, then our structure may be potentially useful in constructing filters and resonators.

APPENDIX A

In this appendix we will find the order of eigenvalues of a general hole shape. The characteristic size of the hole is d, which is defined as the square root of the area of the hole. We assume that the eigenvalues and the eigenfunctions are λ_p and φ_p, respectively, with $p=0,1,2,\ldots$. They satisfy the following equation:

$$\nabla^2\varphi_p(x,y) = -\lambda_p^2\varphi_p(x,y). \tag{A1}$$

Let $x'=x/d$ and $y'=y/d$. Then x' and y' are $O(1)$ variables. After changing of variables, the eigenvalue problem becomes

$$\frac{\partial^2\varphi_p}{\partial x'^2} + \frac{\partial^2\varphi_p}{\partial y'^2} = -d^2\lambda_p^2\varphi_p, \tag{A2}$$

where the domain is independent of d and is thus $O(1)$. The eigenvalues for this problem are $\Lambda_p=d^2\lambda_p^2$ and these are $O(1)$ quantities, which depend upon the geometry of this scaled domain. Hence the $\lambda_p=O(1/d)$ as $d\to 0$.

APPENDIX B

To prove $\gamma_{00}=\tau_0$, we consider the equation

$$\nabla\cdot\{u_2\nabla u_1 - u_1\nabla u_2\} = 0. \tag{B1}$$

Integrating it over the cube $|z|<z_\infty$, $|x|<a/2$, $|y|<b/2$ and applying the divergence theorem, we obtain

$$\int\int\left(u_2\frac{\partial u_1}{\partial n} - u_1\frac{\partial u_2}{\partial n}\right)ds = 0, \tag{B2}$$

where the double integral is over the six surfaces of the cube and n is the normal direction of each surface. The integrals over four surfaces cancel off with each other because of the periodic boundary conditions. Therefore, only the surface integrals over the top and the bottom remain, which gives

$$\int_{-a/2}^{a/2}\int_{-b/2}^{b/2}\left(u_2\frac{\partial u_1}{\partial z} - u_1\frac{\partial u_2}{\partial z}\right)\Bigg|_{z=-\infty} dx\,dy = \int\int_H\left(u_2\frac{\partial u_1}{\partial z} - u_1\frac{\partial u_2}{\partial z}\right)\Bigg|_{z=\infty} dx\,dy. \tag{B3}$$

After substituting infinite series expansions for u_1 and u_1 in this equation, most terms cancel off. We obtain

$$2ik\gamma_{00} = 2ik\tau_0, \tag{B4}$$

which yields the result $\gamma_{00}=\tau_0$.

APPENDIX C

Suppose we chose k properly such that all the higher order modes are evanescent. Then, generally, we have $u_1=a_0e^{-ikz}+b_0e^{ikz}$ at $z=-\infty$ and $u_1=c_0e^{ikz}+d_0e^{-ikz}$ at $z=\infty$. Considering $\nabla\cdot\{\bar{u}_1\nabla u_1 - u_1\nabla\bar{u}_1\}=0$, which is equivalent to $\nabla\cdot\{\Im(\bar{u}_1\nabla u_1)\}=0$, by using the same procedure as was done in Appendix A, we obtain

$$\int_{-a/2}^{a/2}\int_{-b/2}^{b/2}\Im\left(\bar{u}_1\frac{\partial u_1}{\partial z}\right)\Bigg|_{z=-\infty} dx\,dy = \int\int_H\Im\left(\bar{u}_1\frac{\partial u_1}{\partial z}\right)\Bigg|_{z=\infty} dx\,dy. \tag{C1}$$

Substituting the expression of u_1 at $z=\pm\infty$ in Eq. (C1) yields

$$|a_0|^2 + |c_0|^2 = |b_0|^2 + |d_0|^2. \tag{C2}$$

We know that a_0, b_0, c_0, and d_0 are related by matrix S_1, that is,

$$b_0 = (1 - d\tau_0)a_0 + \tau_0 c_0, \tag{C3a}$$

$$d_0 = \tau_0 a_0 + (1 - \tau_0/d)c_0. \tag{C3b}$$

Inserting them into Eq. (C2) gives

$$\{|1 - d\tau_0|^2 + |\tau_0|^2 - 1\}|a_0|^2 + \{|1 - \tau_0/d|^2 + |\tau_0|^2 - 1\}|c_0|^2 + 2\Re\{(1 - d\bar{\tau}_0)\tau_0\bar{a}_0 c_0 + (1 - \tau_0/d)\bar{\tau}_0\bar{a}_0 c_0\} = 0. \tag{C4}$$

Setting $a_0=1$, $c_0=0$ and $a_0=0, c_0=1$, respectively, we have three equations

$$|1 - d\tau_0|^2 + |\tau_0|^2 = 1, \tag{C5a}$$

$$|1 - \tau_0/d|^2 + |\tau_0|^2 = 1, \tag{C5b}$$

$$\tau_0 + \bar{\tau}_0 - d|\tau_0|^2 - |\tau_0|^2/d = 0, \tag{C5c}$$

which proves that $S_1 \cdot \bar{S}_1^T = I$.

[1] M. Sigalas and E. Economou, "Band structure of elastic wave in two dimensional systems," Solid State Commun. **86**, 141–143 (1993).
[2] M. Kushwaha, P. Halevi, L. Dobrzynski, and B. Djafari-Rouhani, "Acoustic band structure of periodic elastic composites," Phys. Rev. Lett. **71**, 2022–2025 (1993).
[3] M. Kushwaha, P. Halevi, G. Martinez, L. Dobrzynski, and B. Djafari-Rouhani, "Theory of acoustic band structure of periodic elastic composite," Phys. Rev. B **49**, 2313–2322 (1994).
[4] M. Kushwaha, "Stop-band for periodic metallic rods: Sculptures that can filter the noise," Appl. Phys. Lett. **70**, 3218–3220 (1997).
[5] Z. Liu, X. Zhang, Y. Mao, Y. Zhu, Z. Yang, C. Chan, and P. Sheng, "Locally resonant sonic materials," Science **289**, 1734–1736 (2000).
[6] S. Yang, J. Page, Z. Liu, M. Cowan, C. Chan, and P. Sheng, "Ultrasound tunneling through 3D photonic crystals," Phys. Rev. Lett. **88**, 104301-1–104301-4 (2002).
[7] C. Goffaux and J. Sanchez-Dehesa, "Two-dimensional photonic crystals studies using a variational method: Application to lattices of locally resonant materials," Phys. Rev. B **67**, 144301 (2003).
[8] S. Zhang and J. Cheng, "Existence of broad acoustic band gaps in three-component composite," Phys. Rev. B **68**, 245101 (2003).
[9] T. Gorishnyy, C. Ullal, M. Maldovan, G. Fytas, and E. Thomas, "Hypersonic photonic crystals," Phys. Rev. Lett. **94**, 115501 (2005).
[10] T. W. Ebbesen, H. J. Lezek, H. F. Ghaemi, T. Thio, and P. A. Wolff, "Extraordinary optical transmission through sub-wavelength hole arrays," Nature (London) **391**, 667–669 (1998).
[11] A. P. Hibbins and J. R. Sambles, "Remarkable transmission of microwaves through a long wall of metallic bricks," Appl. Phys. Lett. **79**, 2844–2846 (2001).
[12] J. A. Porto, F. J. Garcia-Vidal, and J. B. Pendry, "Transmission resonances on metallic gratings with very narrow slits," Phys. Rev. Lett. **83**, 2845–2848 (1999).
[13] I. Anderson, "Comment on Remarkable transmission of microwaves through a wall of long metallic bricks," Appl. Phys. Lett. **82**, 308–309 (2003).
[14] G. A. Kriegsmann, "Complete transmission through a two-dimensional diffraction grating," **65**, 24–42 (2004).
[15] X. Zhang, "Acoustic resonant transmission through acoustic gratings with very narrow slits: Multiple-scattering numerical simulation," Phys. Rev. B **71**, 241102 (2005).
[16] A. N. Norris and H. A. Luo, "Acoustic radiation and reflection from a periodically perforated rigid solid," J. Acoust. Soc. Am. **82**, 2113–2122 (1987).
[17] G. Gonzalez, *Microwave Transistor Amplifiers: Analysis and Design*, 2nd ed. (Prentice-Hall, Englewood Cliffs, 1997).
[18] L. Zhou, Electromagnetic and Acoustic Propagation in Strip Lines and Porous Media Ph.D. thesis, New Jersy Inst. of Technology (2005).

Acoustic scattering by a rigid elliptic cylinder in a slightly viscous medium

Robert W. Scharstein[a)]
Electrical Engineering Department, University of Alabama, Tuscaloosa, Alabama 35487-0286

Anthony M. J. Davis
Mathematics Department, University of Alabama, Tuscaloosa, Alabama 35487-0350

(Received 16 November 2006; revised 21 March 2007; accepted 21 March 2007)

A complete solution is obtained for the two-dimensional diffraction of a time-harmonic acoustic plane wave by an impenetrable elliptic cylinder in a viscous fluid. Arbitrary size, ellipticity, and angle of incidence are considered. The linearized equations of viscous flow are used to write down expressions for the dilatation and vorticity in terms of products of radially and angular dependent Mathieu functions. The no-slip condition on the rigid boundary then determines the coefficients. The resulting computations are facilitated by recently developed library routines for complex input parameters. The solution for the circular cylinder serves as a guide and a differently constructed solution for the strip is also given. Typical results in the "resonant" range of dimensionless wave number, displaying the surface vorticity and the far-field scattering pattern are included, with the latter allowing comparison with the inviscid case. © *2007 Acoustical Society of America.*
[DOI: 10.1121/1.2727332]

PACS number(s): 43.20.Fn, 43.28.Ra [TDM] Pages: 3300–3310

I. INTRODUCTION

The elliptic cylinder is an interesting and important two-dimensional scatterer of finite cross section because it is simple enough to conform to coordinate surfaces where the wave equation is separable, and it naturally includes a degree of geometric flexibility, i.e., the ellipticity. The two limiting cases of the ellipse, namely the strip and the circle, are important canonical scatterers. Although a fundamental study, the physical insight gained from this paper has important implications for engineering systems that exploit the acoustic signatures of elongated bodies in real fluid media: One obvious application is antisubmarine warfare. The effect of a small kinematic viscosity upon the scattered acoustic field is analyzed, with particular attention to the vorticity of the velocity field that exists in a boundary layer close to the surface of the hard elliptic cylinder. The appropriate no-slip boundary condition was first applied by Alblas[1] to include the effect of a small viscosity in the classic Sommerfeld half-plane problem. A sequence of studies of viscosity effects on sound scattering by Davis and Nagem considered the half plane,[2] the circular aperture,[3] and the circular disk,[4] avoiding possible ambiguities associated with the Helmholtz representation by writing down the solution form of the pressure and deducing expressions for the velocity components before applying the boundary conditions. This method tended to merge the distinct contributions from the dilatation (div) and vorticity (curl) but, in a further paper, Davis and Nagem[5] constructed the scattered field due to a solid or elastic sphere by deducing the velocity components directly from the dilatation and vorticity.

Very few previous authors have included viscous effects and very few have given complete solutions in terms of elliptic coordinates. The most notable predecessor of this paper is by Barakat,[6] who used the notation of Morse and Feshbach[7] to construct far field approximations to plane wave inviscid diffraction by an elliptic cylinder. Without modern computational power, the far field was necessarily the focus of attention, yielding tables of results.[8] This paper fills that computational gap and shows how to work from the dilatation and vorticity whose governing equations, but not boundary conditions, are independent.

Murga[9] used an ad hoc combination of potential and boundary layer theory to study the two-dimensional (2D) half plane problem but this method did not display the Stokes wave feature. Tsoi[10] used the Helmholtz representation and a Watson transformation to consider the high frequency far field approximation. Zhuk[11] retained inertia terms to predict the time averaged force on a solid circular cylinder. Hinders[12] studied the scattering by liquid or elastic spheres but with rather lengthy algebra, despite his neglect of the small damping factor in the acoustic component of the external field. Homentkovschi *et al.*[13] introduced the unnecessary complications of singular integral equations for 2D scattering by a planar array of strips.

Elliptic geometry appears in the inviscid literature but no serious use is made of elliptic coordinates which are often unmentioned. Chinnery and Humphrey,[14] with an impedance boundary condition, give a solution in terms of Mathieu functions but add only experimental results. Leon *et al.*[15] prefer to handle the multiple interactions in a Fourier modal method and give an extensive reference list.

The basic theory to accommodate a small viscosity is summarized in Sec. II and the technique of simultaneously considering the vorticity and divergence of the acoustic ve-

[a)]Electronic mail: rscharst@bama.ua.edu

 0001-4966/2007/121(6)/3300/11/$23.00 © 2007 Acoustical Society of America

locity is first explained in context of the simpler circle geometry. The full treatment of the elliptic cylinder is presented in Sec. III. Separation of variables of the relevant Helmholtz equations in elliptic cylinder coordinates introduces the celebrated Mathieu functions. A library of Mathieu function routines developed by Wilson and Scharstein[16] facilitates the calculations which require complex input parameters. Mathieu functions of both the angular and radial type depend upon a parameter that derives from the wave number in the appropriate Helmholtz equation, as well as the physical dimensions of the ellipse. This parameter is complex-valued because of the presence of viscosity, and in fact the divergence (dilatation) and curl (vorticity) expansions require two different parameters. This feature complicates the analysis and calculations are performed that exploit the structure and make efficient use of the Mathieu function numerics.[16] Interpretation of the boundary layer nature of the vorticity is aided by a WKB(J) or LG asymptotic expansion of the radial Mathieu functions having a large imaginary parameter.

Expressions for the far scattered field are summarized in Sec. IV. An independent analysis of the limiting case of the strip is the subject of Sec. V, where expansions of the normal and tangential surface stress explicitly include the proper edge-condition singularity dictated by viscous flow. Graphical results of the surface vorticity and far scattered field pattern are discussed in Sec. VI, with due attention to the relationship between the ellipse and its degenerate (circle and strip) forms.

II. THEORY AND CIRCULAR CYLINDER

The standard acoustic equations for linearized flow in a homogeneous viscous fluid medium are the equation of continuity

$$\frac{\partial \rho}{\partial t} + \rho_0 \nabla \cdot \mathbf{v} = 0, \tag{1}$$

the momentum equation

$$\frac{\partial \mathbf{v}}{\partial t} = -\frac{1}{\rho_0} \nabla p + \nu \nabla^2 \mathbf{v} + \frac{\nu}{3} \nabla (\nabla \cdot \mathbf{v}), \tag{2}$$

and the equation of state

$$\frac{dp}{d\rho} = c_0^2, \tag{3}$$

in which $\mathbf{v}$ is the fluid velocity vector, ρ_0 is the ambient fluid density, ρ is the density perturbation, p is the fluid pressure, c_0 is the sound speed, and ν is the kinematic viscosity. Equation (2) assumes a Stokesian fluid for which the convective part of the acceleration is neglected. It may be deduced from Eqs. (1)–(3) that the vorticity $\mathbf{\Omega} = \nabla \times \mathbf{v}$ satisfies

$$\frac{\partial \mathbf{\Omega}}{\partial t} = \nu \nabla^2 \mathbf{\Omega}, \tag{4}$$

as in unsteady creeping flow, while p and $E = \nabla \cdot \mathbf{v}$ satisfy an acoustic wave equation with viscous damping, namely

$$\frac{\partial^2}{\partial t^2}[p,E] = \left(c_0^2 + \frac{4}{3}\nu \frac{\partial}{\partial t}\right) \nabla^2 [p,E]. \tag{5}$$

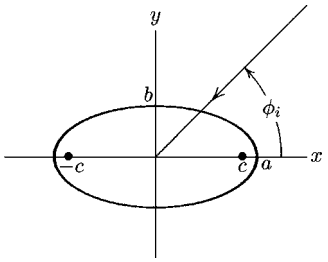

FIG. 1. Plane wave incident upon elliptic cylinder.

In the 2D disturbance of period $2\pi/\omega$ considered here, $E = E(x,y)$, $\mathbf{\Omega} = \hat{z}\Omega(x,y)$ and the time-harmonic dependence $\exp(-i\omega t)$ is suppressed. Then Eqs. (4) and (5) reduce to

$$(\nabla^2 + k^2)[p,E] = 0, \tag{6}$$

$$\left(\nabla^2 + \frac{i\omega}{\nu}\right)\Omega = 0, \tag{7}$$

where the complex acoustic wave number is

$$k = \frac{k_0}{\sqrt{1 - 4i\epsilon^2/3}}, \tag{8}$$

with

$$k_0 = \omega/c_0, \quad \epsilon^2 = \omega\nu/c_0^2 \ll 1. \tag{9}$$

The pressure p and dilatation E are related, according to Eqs. (1) and (3), by

$$\frac{p}{\rho_0 c_0^2} = \frac{E}{i\omega}. \tag{10}$$

The geometric configuration for the elliptic cylinder diffraction is illustrated in Fig. 1. The exciting plane wave (irrotational) propagates in the $\phi_i + \pi$ direction, that is, incident from the azimuthal angle ϕ_i, and is given by

$$\mathbf{v}^i = \frac{v_0}{k} \nabla [e^{-ik(x \cos \phi_i + y \sin \phi_i)}]. \tag{11}$$

The scattered field $\mathbf{v}$ is determined by application of the no-slip condition $\mathbf{v} + \mathbf{v}^i = 0$ at the ellipse. Two direct methods of solution, avoiding the introduction of potentials, are available for the ellipse scattering. One involves writing down a solution form for the pressure and using the momentum equation to establish associated forms for the velocity components. Alternatively, the latter can be deduced from solution forms for the dilatation E and vorticity Ω. The second method is adopted here except for the limiting case of the strip. To facilitate understanding of the ellipse analysis; the simpler circle case is presented first.

If $b \to a$ the resulting symmetrical scatterer does not require any incidence angles other than $\phi_i = 0$. The incident plane wave (irrotational) propagating in the $-x$ direction is

$$\mathbf{v}_i = \frac{v_0}{k} \nabla [e^{-ikx}], \tag{12}$$

in which

$$e^{-ikx} = e^{-ikr\cos\phi} = J_0(kr) + 2\sum_{n=1}^{\infty} i^{-n} J_n(kr)\cos n\phi. \tag{13}$$

On setting

$$\mathbf{v} = \hat{r}v_r + \hat{\phi}v_\phi,$$

the incident wave components are given by

$$v_r^i = v_0\left[J_0'(kr) + 2\sum_{n=1}^{\infty} i^{-n} J_n'(kr)\cos n\phi\right],$$

$$v_\phi^i = -\frac{2v_0}{kr}\sum_{n=1}^{\infty} n i^{-n} J_n(kr)\sin n\phi. \tag{14}$$

In the inviscid case, only the normal component of the total velocity must vanish at the circle. The vanishing of the $n=0$ term in Eq. (14) shows that scattering of the axisymmetric component is unaffected by the presence of viscosity. The $n\neq 0$ Fourier components in Eq. (14) generate viscosity-driven vorticity analogous to the Stokes wave in a viscous fluid bounded by a tangentially vibrating plane.[17] However, dependence of the vorticity on both r and ϕ means that the acoustic diffraction has to be modified, as in reflection at a plane. Suitable solutions of Eq. (6), constructed to display the above-described physics, are

$$E(r,\phi) = v_0 k\left\{J_0'(ka)\frac{H_0^{(1)}(kr)}{H_0^{(1)\prime}(ka)} + 2\sum_{n=1}^{\infty} i^{-n}[J_n'(ka) + A_n]\frac{H_n^{(1)}(kr)}{H_n^{(1)\prime}(ka)}\cos n\phi\right\}, \tag{15}$$

$$\Omega(r,\phi) = 2v_0\kappa^2 a\sum_{n=1}^{\infty} i^{-n}\frac{B_n}{n}\frac{H_n^{(1)}(\kappa r)}{H_n^{(1)}(\kappa a)}\sin n\phi, \tag{16}$$

where

$$\kappa = \sqrt{\frac{i\omega}{\nu}} = \frac{k_0}{\epsilon}\frac{1+i}{\sqrt{2}}. \tag{17}$$

The equations

$$\frac{\partial}{\partial r}(rv_r) + \frac{\partial}{\partial\phi}v_\phi = Er$$

$$\frac{\partial}{\partial r}(rv_\phi) - \frac{\partial}{\partial\phi}v_r = \Omega r$$

are then solved by observing that Bessel's Equation implies that

$$rH_n^{(1)}(kr)e^{in\phi} = \frac{\partial}{\partial r}\left[-\frac{r}{k}H_n^{(1)\prime}(kr)e^{in\phi}\right] + \frac{\partial}{\partial\phi}\left[-\frac{in}{k^2 r}H_n^{(1)}(kr)e^{in\phi}\right]. \tag{18}$$

Thus the lamellar and solenoidal components are given by

$$v_r^E = -v_0\left\{J_0'(ka)\frac{H_0^{(1)\prime}(kr)}{H_0^{(1)\prime}(ka)} + 2\sum_{n=1}^{\infty} i^{-n}[J_n'(ka) + A_n]\frac{H_n^{(1)\prime}(kr)}{H_n^{(1)\prime}(ka)}\cos n\phi\right\},$$

$$v_\phi^E = \frac{2v_0}{kr}\sum_{n=1}^{\infty} n i^{-n}[J_n'(ka) + A_n]\frac{H_n^{(1)}(kr)}{H_n^{(1)\prime}(ka)}\sin n\phi,$$

$$v_r^\Omega = \frac{2v_0 a}{r}\sum_{n=1}^{\infty} i^{-n} B_n\frac{H_n^{(1)}(\kappa r)}{H_n^{(1)}(\kappa a)}\cos n\phi,$$

$$v_\phi^\Omega = -2v_0\kappa a\sum_{n=1}^{\infty} i^{-n}\frac{B_n}{n}\frac{H_n^{(1)\prime}(\kappa r)}{H_n^{(1)}(\kappa a)}\sin n\phi. \tag{19}$$

Evidently, $A_n = B_n$ $(n\geqslant 1)$ ensures that the additional normal velocities cancel. Then

$$v_\phi^E(a,\phi) + v_\phi^\Omega(a,\phi) + v_\phi^i(a,\phi) = 0 \quad (-\pi < \phi \leqslant \pi)$$

implies the coefficients are given by

$$A_n = B_n = \frac{2i}{\pi ka H_n^{(1)}(ka)}\left[1 - \frac{ka}{n}\frac{H_n^{(1)\prime}(ka)}{H_n^{(1)}(ka)}\frac{\kappa a}{n}\frac{H_n^{(1)\prime}(\kappa a)}{H_n^{(1)}(\kappa a)}\right]^{-1} \quad (n\geqslant 1).$$

III. THE ELLIPTIC CYLINDER

Elliptic coordinates (ξ,η) are related to the Cartesian coordinates (x,y) through $x+iy = c\cosh(\xi+i\eta)$. Separation of variables in the Helmholtz equation (6) allows the solution to be written in terms of the Mathieu functions, with the parameter

$$q = \frac{1}{4}(kc)^2, \tag{20}$$

in the notation of Jones,[18] except for $\exp(-i\omega t)$ time behavior instead of his $\exp(i\omega t)$. The expansion of Eq. (11) corresponding to Eq. (13) is

$$\begin{aligned}\exp[-ik(x\cos\phi_i + y\sin\phi_i)] &= \exp[-i2q^{1/2}(\cosh\xi\cos\eta\cos\phi_i + \sinh\xi\sin\eta\sin\phi_i)]\\ &= 2\sum_{m=0}^{\infty}(-i)^m ce_m(\phi_i,q)ce_m(\eta,q)Mc_m^{(1)}(\xi,q)\\ &\quad + 2\sum_{m=1}^{\infty}(-i)^m se_m(\phi_i,q)se_m(\eta,q)Ms_m^{(1)}(\xi,q),\end{aligned} \tag{21}$$

in which it is noted that the functions of η also depend on q. The elliptical scatterer boundary of Fig. 1 is the surface $\xi = \xi_0$ where

$$\tanh\xi_0 = b/a, \quad c^2 = a^2 - b^2.$$

The deduction of a vector field

$$\mathbf{F}(\xi,\eta)=\hat{\xi}F_{\xi}(\xi,\eta)+\hat{\eta}F_{\eta}(\xi,\eta)$$

defined by

$$\nabla\cdot\mathbf{F}(\xi,\eta)=\Xi(\xi)H(\eta), \tag{22}$$

with

$$\frac{d^2\Xi(\xi)}{d\xi^2}+\left[-\alpha+\frac{1}{2}(kc)^2\cosh 2\xi\right]\Xi(\xi)=0,$$

$$\frac{d^2H(\eta)}{d\eta^2}+\left[\alpha-\frac{1}{2}(kc)^2\cos 2\eta\right]H(\eta)=0 \tag{23}$$

is achieved by noting that

$$\frac{\partial}{\partial\xi}[\Xi'(\xi)H(\eta)]+\frac{\partial}{\partial\eta}[\Xi(\xi)H'(\eta)]$$
$$=\Xi''(\xi)H(\eta)+\Xi(\xi)H''(\eta)=-k^2h^2\Xi(\xi)H(\eta) \tag{24}$$

where the metric $h(\xi,\eta)$ is given by

$$h=c(\cosh^2\xi-\cos^2\eta)^{1/2}=c\left[\frac{1}{2}(\cosh 2\xi-\cos 2\eta)\right]^{1/2}.$$

Comparison of Eq. (24) with the component form of Eq. (22), namely

$$\frac{\partial}{\partial\xi}(hF_{\xi})+\frac{\partial}{\partial\eta}(hF_{\eta})=h^2\Xi H, \tag{25}$$

then indicates

$$\mathbf{F}(\xi,\eta)=-\frac{1}{k^2h(\xi,\eta)}[\hat{\xi}\Xi'(\xi)H(\eta)+\hat{\eta}\Xi(\xi)H'(\eta)] \tag{26}$$

which is irrotational. Similarly,

$$(\nabla\times\mathbf{F}(\xi,\eta))_z=\Xi(\xi)H(\eta),$$

that is

$$\frac{\partial}{\partial\xi}(hF_{\eta})-\frac{\partial}{\partial\eta}(hF_{\xi})=h^2\Xi H, \tag{27}$$

has the solenoidal solution

$$\mathbf{F}(\xi,\eta)=\frac{1}{k^2h(\xi,\eta)}[\hat{\xi}\Xi(\xi)H'(\eta)-\hat{\eta}\Xi'(\xi)H(\eta)]. \tag{28}$$

The incident plane wave (11) has, by substitution of Eq. (21), the components

$$v^i_{\xi}(\xi,\eta)=\frac{2v_0}{kh(\xi,\eta)}\left\{\sum_{m=0}^{\infty}(-i)^m ce_m(\phi_i,q)ce_m(\eta,q)Mc_m^{(1)\prime}(\xi,q)\right.$$
$$\left.+\sum_{m=1}^{\infty}(-i)^m se_m(\phi_i,q)se_m(\eta,q)Ms_m^{(1)\prime}(\xi,q)\right\}, \tag{29}$$

$$v^i_{\eta}(\xi,\eta)=\frac{2v_0}{kh(\xi,\eta)}\left\{\sum_{m=0}^{\infty}(-i)^m ce_m(\phi_i,q)ce'_m(\eta,q)Mc_m^{(1)}(\xi,q)\right.$$
$$\left.+\sum_{m=1}^{\infty}(-i)^m se_m(\phi_i,q)se'_m(\eta,q)Ms_m^{(1)}(\xi,q)\right\}. \tag{30}$$

Equations (6) and (7) show that E and Ω depend on the parameters

$$q=\frac{1}{4}(kc)^2=\frac{1}{4}(ka)^2[1-(b/a)^2],$$

$$s=\frac{i\omega}{4\nu}c^2=\frac{i}{4\epsilon^2}(k_0a)^2[1-(b/a)^2], \tag{31}$$

respectively. Their solutions in terms of separated functions may be written as

$$E(\xi,\eta)=2v_0k\sum_{m=0}^{\infty}[A_m+Mc_m^{(1)\prime}(\xi_0,q)ce_m(\phi_i,q)]$$
$$\times(-i)^m ce_m(\eta,q)\frac{Mc_m^{(3)}(\xi,q)}{Mc_m^{(3)\prime}(\xi_0,q)}$$
$$+2v_0k\sum_{m=1}^{\infty}[B_m+Ms_m^{(1)\prime}(\xi_0,q)se_m(\phi_i,q)]$$
$$\times(-i)^m se_m(\eta,q)\frac{Ms_m^{(3)}(\xi,q)}{Ms_m^{(3)\prime}(\xi_0,q)} \tag{32}$$

$$\Omega(\xi,\eta)=2v_0\kappa\sum_{m=0}^{\infty}C_m ce_m(\eta,s)\frac{Mc_m^{(3)}(\xi,s)}{Mc_m^{(3)}(\xi_0,s)}$$
$$+2v_0\kappa\sum_{m=1}^{\infty}D_m se_m(\eta,s)\frac{Ms_m^{(3)}(\xi,s)}{Ms_m^{(3)}(\xi_0,s)}. \tag{33}$$

Use of Eq. (26) shows that the irrotational (lamellar) part of the scattered velocity has components

$$v^E_{\xi}(\xi,\eta)=-\frac{2v_0}{kh(\xi,\eta)}\left\{\sum_{m=0}^{\infty}[A_m+Mc_m^{(1)\prime}(\xi_0,q)ce_m(\phi_i,q)]\right.$$
$$\times(-i)^m ce_m(\eta,q)\frac{Mc_m^{(3)\prime}(\xi,q)}{Mc_m^{(3)\prime}(\xi_0,q)}$$
$$+\sum_{m=1}^{\infty}[B_m+Ms_m^{(1)\prime}(\xi_0,q)se_m(\phi_i,q)]$$
$$\left.\times(-i)^m se_m(\eta,q)\frac{Ms_m^{(3)\prime}(\xi,q)}{Ms_m^{(3)\prime}(\xi_0,q)}\right\},$$

$$v^E_{\eta}(\xi,\eta)=-\frac{2v_0}{kh(\xi,\eta)}\left\{\sum_{m=0}^{\infty}[A_m+Mc_m^{(1)\prime}(\xi_0,q)ce_m(\phi_i,q)]\right.$$
$$\times(-i)^m ce'_m(\eta,q)\frac{Mc_m^{(3)}(\xi,q)}{Mc_m^{(3)\prime}(\xi_0,q)}$$
$$+\sum_{m=1}^{\infty}[B_m+Ms_m^{(1)\prime}(\xi_0,q)se_m(\phi_i,q)]$$

$$\times(-i)^m se'_m(\eta,q)\frac{Ms_m^{(3)}(\xi,q)}{Ms_m^{(3)\prime}(\xi_0,q)}\Bigg\}, \tag{34}$$

in which the terms with inviscid structure are identified. Similarly, use of Eq. (28) shows that the solenoidal part of the scattered velocity has components

$$v_\xi^\Omega(\xi,\eta)=\frac{2v_0}{\kappa h(\xi,\eta)}\Bigg\{\sum_{m=0}^{\infty}C_m ce'_m(\eta,s)\frac{Mc_m^{(3)}(\xi,s)}{Mc_m^{(3)}(\xi_0,s)}+\sum_{m=1}^{\infty}D_m se'_m(\eta,s)\frac{Ms_m^{(3)}(\xi,s)}{Ms_m^{(3)}(\xi_0,s)}\Bigg\},$$

$$v_\eta^\Omega(\xi,\eta)=-\frac{2v_0}{\kappa h(\xi,\eta)}\Bigg\{\sum_{m=0}^{\infty}C_m ce_m(\eta,s)\frac{Mc_m^{(3)\prime}(\xi,s)}{Mc_m^{(3)}(\xi_0,s)}+\sum_{m=1}^{\infty}D_m se_m(\eta,s)\frac{Ms_m^{(3)\prime}(\xi,s)}{Ms_m^{(3)}(\xi_0,s)}\Bigg\}. \tag{35}$$

The no-slip boundary is now enforced by setting

$$v_\xi^E(\xi_0,\eta)+v_\xi^\Omega(\xi_0,\eta)+v_\xi^i(\xi_0,\eta)=0,$$

$$v_\eta^E(\xi_0,\eta)+v_\eta^\Omega(\xi_0,\eta)+v_\eta^i(\xi_0,\eta)=0, \tag{36}$$

over the entire elliptical surface where $-\pi\leqslant\eta\leqslant\pi$. The even (in η) part of the ξ component of this boundary condition is

$$\sum_{m=0}^{\infty}[A_m+Mc_m^{(1)\prime}(\xi_0,q)ce_m(\phi_i,q)](-i)^m ce_m(\eta,q)-\frac{k}{\kappa}\sum_{m=1}^{\infty}D_m se'_m(\eta,s)=\sum_{m=0}^{\infty}(-i)^m ce_m(\phi_i,q)ce_m(\eta,q)Mc_m^{(1)\prime}(\xi_0,q). \tag{37}$$

The odd (in η) part of the ξ component of Eq. (36) is

$$\sum_{m=1}^{\infty}[B_m+Ms_m^{(1)\prime}(\xi_0,q)se_m(\phi_i,q)](-i)^m se_m(\eta,q)-\frac{k}{\kappa}\sum_{m=0}^{\infty}C_m ce'_m(\eta,s)=\sum_{m=1}^{\infty}(-i)^m se_m(\phi_i,q)se_m(\eta,q)Ms_m^{(1)\prime}(\xi_0,q). \tag{38}$$

The odd (in η) part of the η component of Eq. (36) is

$$\sum_{m=0}^{\infty}[A_m+Mc_m^{(1)\prime}(\xi_0,q)ce_m(\phi_i,q)]\times(-i)^m ce'_m(\eta,q)\frac{Mc_m^{(3)}(\xi_0,q)}{Mc_m^{(3)\prime}(\xi_0,q)}+\frac{k}{\kappa}\sum_{m=1}^{\infty}D_m se_m(\eta,s)\frac{Ms_m^{(3)\prime}(\xi_0,s)}{Ms_m^{(3)}(\xi_0,s)}=\sum_{m=0}^{\infty}(-i)^m ce_m(\phi_i,q)ce'_m(\eta,q)Mc_m^{(1)}(\xi_0,q). \tag{39}$$

The even (in η) part of the η component of Eq. (36) is

$$\sum_{m=1}^{\infty}[B_m+Ms_m^{(1)\prime}(\xi_0,q)se_m(\phi_i,q)]\times(-i)^m se'_m(\eta,q)\frac{Ms_m^{(3)}(\xi_0,q)}{Ms_m^{(3)\prime}(\xi_0,q)}+\frac{k}{\kappa}\sum_{m=0}^{\infty}C_m ce_m(\eta,s)\frac{Mc_m^{(3)\prime}(\xi_0,s)}{Mc_m^{(3)}(\xi_0,s)}=\sum_{m=1}^{\infty}(-i)^m se_m(\phi_i,q)se'_m(\eta,q)Ms_m^{(1)}(\xi_0,q). \tag{40}$$

At this stage, major difficulties associated with the elliptic coordinates are encountered. The periodic functions have the expansions[19]

$$ce_{2m+p}(\eta,q)=\sum_{j=0}^{\infty}A_{2j+p}^{2m+p}(q)\cos[(2j+p)\eta]$$

$$(m=0,1,2,\ldots,\ p=0,1),$$

$$se_{2m+p}(\eta,q)=\sum_{j=0}^{\infty}B_{2j+p}^{2m+p}(q)\sin[(2j+p)\eta] \tag{41}$$

$$(m=0,1,2,\ldots,\ p=0,1),$$

and have the orthogonality properties

$$\int_{-\pi}^{\pi}ce_m(\eta,q)ce_n(\eta,q)d\eta=\pi\delta_{mn}\quad(m,n\geqslant 0),$$

$$\int_{-\pi}^{\pi}se_m(\eta,q)se_n(\eta,q)d\eta=\pi\delta_{mn}\quad(m,n\geqslant 1), \tag{42}$$

but, in contrast to $\cos n\eta$ and $\sin n\eta$, the derivative of one is not a multiple of the other, the derivatives are not orthogonal and they depend on the parameter q, giving different sets of periodic functions in E and Ω. Inspection of Eqs. (37)–(40) shows that the introduction of the inner products

$$\Lambda_{m,n}(q,s)=\langle ce_m(q),se'_n(s)\rangle=\int_{-\pi}^{\pi}ce_m(\eta,q)se'_n(\eta,s)d\eta\quad(m\geqslant 0,n\geqslant 1) \tag{43}$$

suffices to exploit the orthogonality (42) because integration by parts and the periodicity of the angular Mathieu functions yields

$$-\Lambda_{m,n}(q,s)=\langle ce'_m(q),se_n(s)\rangle = \int_{-\pi}^{\pi} ce'_m(\eta,q)se_n(\eta,s)d\eta \quad (m\geqslant 0,n\geqslant 1). \tag{44}$$

This inner product is zero if m and n are of different parity and, although the functions are complex-valued, does not involve any complex conjugation. In terms of the coefficients in Eq. (41),

$$\int_{-\pi}^{\pi} ce_{2m+p}(\eta,q)se'_{2n+r}(\eta,s)d\eta = \pi\delta_{pr}\sum_{j=0}^{\infty} A_{2j+p}^{2m+p}(q)B_{2j+r}^{2n+r}(s)(2j+p)$$

$$(m,n\geqslant 0,p,r=0 \text{ or } 1,n+r\neq 0). \tag{45}$$

Multiplication of Eqs. (37)–(40) by $ce_n(\eta,q)$, $se_n(\eta,q)$, $se_n(\eta,s)$, $ce_n(\eta,s)$, respectively, and subsequent integration of each from $\eta=-\pi$ to $\eta=\pi$ yields the sets of linear equations

$$A_n=\frac{1}{\pi(-i)^n}\frac{k}{\kappa}\sum_{m=1}^{\infty} D_m\Lambda_{nm}(q,s) \quad (n\geqslant 0), \tag{46}$$

$$B_n=-\frac{1}{\pi(-i)^n}\frac{k}{\kappa}\sum_{m=0}^{\infty} C_m\Lambda_{mn}(s,q) \quad (n\geqslant 1), \tag{47}$$

$$\frac{k}{\kappa}D_n=\frac{Ms_n^{(3)}(\xi_0,s)}{\pi Ms_n^{(3)\prime}(\xi_0,s)}\sum_{m=0}^{\infty}\Lambda_{mn}(q,s)(-i)^m \times\left[A_m\frac{Mc_m^{(3)}(\xi_0,q)}{Mc_m^{(3)\prime}(\xi_0,q)}+\frac{2ce_m(\phi_i,q)}{i\pi Mc_m^{(3)\prime}(\xi_0,q)}\right] \times(n\geqslant 1), \tag{48}$$

$$\frac{k}{\kappa}C_n=\frac{-Mc_n^{(3)}(\xi_0,s)}{\pi Mc_n^{(3)\prime}(\xi_0,s)}\sum_{m=1}^{\infty}\Lambda_{nm}(s,q)(-i)^m \times\left[B_m\frac{Ms_m^{(3)}(\xi_0,q)}{Ms_m^{(3)\prime}(\xi_0,q)}+\frac{2se_m(\phi_i,q)}{i\pi Ms_m^{(3)\prime}(\xi_0,q)}\right] \quad (n\geqslant 0), \tag{49}$$

after use of the Wronskians

$$Mc_m^{(1)\prime}(\xi_0,q)Mc_m^{(3)}(\xi_0,q)-Mc_m^{(1)}(\xi_0,q)Mc_m^{(3)\prime}(\xi_0,q)=\frac{2}{\pi i},$$

$$Ms_m^{(1)\prime}(\xi_0,q)Ms_m^{(3)}(\xi_0,q)-Ms_m^{(1)}(\xi_0,q)Ms_m^{(3)\prime}(\xi_0,q)=\frac{2}{\pi i}. \tag{50}$$

The two disjoint pairs of linear systems may be written symbolically as

$$\begin{bmatrix}[I] & -[P]\\ -[R] & [I]\end{bmatrix}\begin{bmatrix}[A]\\ [D]\end{bmatrix}=\begin{bmatrix}[0]\\ [F]\end{bmatrix}, \tag{51}$$

$$\begin{bmatrix}[I] & -[Q]\\ -[S] & [I]\end{bmatrix}\begin{bmatrix}[B]\\ [C]\end{bmatrix}=\begin{bmatrix}[0]\\ [G]\end{bmatrix},$$

or, if elimination of one set of coefficients from each is preferred,

$$\{[I]-[R][P]\}[D]=[F], \tag{52}$$

$$\{[I]-[S][Q]\}[C]=[G]. \tag{53}$$

The infinite series are truncated at suitably large indices, such that the results exhibit satisfactory numerical or "self" convergence.

The definition (31) indicates the need for an approximation to the modified Mathiéu function of large imaginary parameter $q=i|q|$ with $|q|\to\infty$. The first equation of Eq. (23) has the form

$$\frac{d^2f(\xi)}{d\xi^2}+(2q\cosh 2\xi-\alpha)f(\xi)=0, \tag{54}$$

whose solutions are of four types, even/odd functions of even/odd orders. McLachlan[19] gives asymptotic forms for α as $|q|\to\infty$. For example, with $q=i|q|$,

$$q^{1/2}=|q|^{1/2}e^{i\pi/4}, \tag{55}$$

$$\alpha_{2n}\sim -2i|q|+(8n+2)|q|^{1/2}e^{i\pi/4}, \tag{56}$$

and application of the WKB(J) or LG method to Eq. (54) eventually yields

$$f(\xi)\sim\frac{1}{\sqrt{\cosh\xi}}\exp\{-[(1-i)|2q|^{1/2}\sinh\xi + (2n+1/2)i\tan^{-1}(\sinh\xi)]\}, \tag{57}$$

which is a decaying solution, with $f(0)=1$. Evidently $f'(\xi)$ has a dominant term of $\mathcal{O}(|q|^{1/2})$.

According to p. 240 of McLachlan,[19] the even order modified Mathieu functions of the cosine type and the odd order functions of the sine type have the same asymptotic eigenvalues, and thus, as $|q|\to\infty$,

$$Mc_{2n}^{(3)}(\xi,i|q|)\sim Ms_{2n+1}^{(3)}(\xi,i|q|) \sim\frac{1}{\sqrt{\cosh\xi}}\exp\{-[(1-i)|2q|^{1/2}\sinh\xi + (2n+1/2)i\tan^{-1}(\sinh\xi)]\}, \tag{58}$$

and similarly,

$$Mc_{2n+1}^{(3)}(\xi,i|q|)\sim Ms_{2n}^{(3)}(\xi,i|q|) \sim\frac{1}{\sqrt{\cosh\xi}}\exp\{-[(1-i)|2q|^{1/2}\sinh\xi + (2n+3/2)i\tan^{-1}(\sinh\xi)]\}. \tag{59}$$

The system of linear equations (51) requires the ratios

$$\frac{Mc_n^{(3)}(\xi,i|q|)}{Mc_n^{(3)\prime}(\xi,i|q|)}\sim\frac{Ms_n^{(3)}(\xi,i|q|)}{Ms_n^{(3)\prime}(\xi,i|q|)}\sim\frac{\operatorname{sech}\xi}{(i-1)|2q|^{1/2}} \tag{60}$$

without regard for either the type or the parity of the order. By calling the eigenvalue solver once only for a given q, the

Mathieu function calculations are fast.[16]

IV. FAR SCATTERED FIELD

For the circle, substitution of the asymptotic form

$$H_n^{(1)}(kr) \underset{kr\to\infty}{\to} \sqrt{\frac{2}{i\pi kr}} i^{-n} e^{ikr}$$

in Eq. (16) demonstrates that the vorticity Ω is limited to a thin boundary layer on the surface of the scatterer. Since $\mathbf{v}$ and p are related by Eq. (10), the single scalar function of interest in the far field is the divergence E, which is simply proportional to the acoustic pressure field and given by Eq. (15). In the far field,

$$E(r\to\infty,\phi) = v_0 k \sqrt{\frac{2}{i\pi kr}} e^{ikr} F(\phi), \tag{61}$$

where

$$F(\phi) = \sum_{n=-\infty}^{\infty} i^{-n}\left[i^{-n}\frac{J_n'(ka)}{H_n^{(1)\prime}(ka)} + \frac{A_n}{H_n^{(1)}(ka)}\right] e^{in\phi}. \tag{62}$$

This separation of the radial and angular factors facilitates the graphical display of the scattering pattern $F(\phi)$.

For the ellipse, $ce^{\xi}/2 \sim r\to\infty$, $\eta\to\phi$ in the far field and the required asymptotic forms, deduced from the first equation of Eq. (23), are[18]

$$\left.\begin{matrix} Mc_m^{(3)}(\xi,q) \\ Ms_m^{(3)}(\xi,q) \end{matrix}\right\} \underset{\xi\to\infty}{\to} \sqrt{\frac{2}{i\pi kr}} e^{ikr}(-i)^m. \tag{63}$$

The asymptotic forms (58) and (59) verify the exponential decay of the vorticity. From Eq. (32), the scattering pattern is given by

$$\begin{aligned} F(\phi) = {} & 2\sum_{m=0}^{\infty} [A_m + Mc_m^{(1)\prime}(\xi_0,q) ce_m(\phi_i,q)](-i)^m \frac{ce_m(\phi,q)}{Mc_m^{(3)\prime}(\xi_0,q)} \\ & + 2\sum_{m=1}^{\infty} [B_m + Ms_m^{(1)\prime}(\xi_0,q) se_m(\phi_i,q)] \\ & \times (-i)^m \frac{se_m(\phi,q)}{Ms_m^{(3)\prime}(\xi_0,q)}. \end{aligned} \tag{64}$$

V. THE STRIP

The incident plane wave defined by Eq. (11) requires the scattered field on the surface of the strip ($b\to 0$ in Fig. 1) to satisfy

$$\mathbf{v}(x,0) = iv_0(\hat{x}\cos\phi_i + \hat{y}\sin\phi_i) e^{-ikx\cos\phi_i} \quad (|x|<a). \tag{65}$$

The solution structure follows the Wiener-Hopf analysis of Davis and Nagem[2] as far as the imposition of the boundary conditions at $y=0$. As in these authors' subsequent aperture[3] and disk[4] studies in 3D, a method suited to creeping flow is then adopted and therefore passage to the inviscid limit is precluded. Functional forms displaying the square root edge singularity are posed for the pressure and tangential stress discontinuities across the strip and their coefficients determined by application of Eq. (65).

On defining dimensionless Fourier transforms

$$[\mathbf{V}(\alpha,y), P(\alpha,y)] = \int_{-\infty}^{\infty} k_0 \left[\frac{\mathbf{v}(x,y)}{v_0}, \frac{p(x,y)}{\rho_0 c_0 v_0}\right] e^{-i\alpha x} dx, \tag{66}$$

the continuity equation gives

$$i\alpha V_x(\alpha,y) + \frac{\partial}{\partial y} V_y(\alpha,y) = \frac{i\omega}{c_0} P(\alpha,y) \tag{67}$$

and the momentum equation yields

$$\left(\frac{d^2}{dy^2} + \frac{i\omega}{\nu} - \alpha^2\right)\begin{bmatrix} V_x(\alpha,y) \\ V_y(\alpha,y)\end{bmatrix} = \frac{c_0}{\nu}\left(1 - \frac{i\epsilon^2}{3}\right)\begin{bmatrix} i\alpha P(\alpha,y) \\ \dfrac{d}{dy}P(\alpha,y)\end{bmatrix}. \tag{68}$$

The Helmholtz equation (6) implies

$$\left(\frac{d^2}{dy^2} + k^2 - \alpha^2\right) P(\alpha,y) = 0, \tag{69}$$

whose solution is

$$P(\alpha,y) = [A(\alpha) + B(\alpha)\operatorname{sgn} y]\exp\{-(\alpha^2-k^2)^{1/2}|y|\}. \tag{70}$$

Hence the scaled Fourier transform of the velocity field is

$$\begin{aligned} \mathbf{V}(\alpha,y) = {} & \begin{bmatrix} C(\alpha) + D(\alpha)\operatorname{sgn} y \\ \dfrac{i\alpha}{(\alpha^2 - i\omega/\nu)^{1/2}}[C(\alpha)\operatorname{sgn} y + D(\alpha)] \end{bmatrix} \\ & \times \exp\{-(\alpha^2 - i\omega/\nu)^{1/2}|y|\} \\ & + \frac{k_0}{k^2}\begin{bmatrix} \alpha[A(\alpha) + B(\alpha)\operatorname{sgn} y] \\ i(\alpha^2-k^2)^{1/2}[A(\alpha)\operatorname{sgn} y + B(\alpha)] \end{bmatrix} \\ & \times \exp\{-(\alpha^2-k^2)^{1/2}|y|\}. \end{aligned} \tag{71}$$

The continuity of $\mathbf{V}$ gives

$$D(\alpha) + \frac{k_0\alpha}{k^2} B(\alpha) = 0, \tag{72}$$

$$\frac{\alpha}{(\alpha^2 - i\omega/\nu)^{1/2}} C(\alpha) + \frac{k_0}{k^2}(\alpha^2-k^2)^{1/2} A(\alpha) = 0, \tag{73}$$

whence

$$\begin{aligned} \mathbf{V}(\alpha,0)] &= \begin{bmatrix} \left\{1 - \dfrac{\alpha^2}{(\alpha^2 - i\omega/\nu)^{1/2}(\alpha^2-k^2)^{1/2}}\right\} C(\alpha) \\ \left\{\dfrac{i\alpha}{(\alpha^2 - i\omega/\nu)^{1/2}} - \dfrac{i(\alpha^2-k^2)^{1/2}}{\alpha}\right\} D(\alpha) \end{bmatrix} \\ &= K(\alpha)\begin{bmatrix} (\alpha^2-k^2)^{-1/2} C(\alpha) \\ -\dfrac{i}{\alpha} D(\alpha) \end{bmatrix}, \end{aligned} \tag{74}$$

where

$$K(\alpha) = (\alpha^2 - k^2)^{1/2} - \frac{\alpha^2}{(\alpha^2 - i\omega/\nu)^{1/2}} \tag{75}$$

is the Wiener-Hopf kernel of Davis and Nagem.[2] Also, the jump in the normal derivative of $\mathbf{V}$ is given by

$$\frac{1}{2}\left[\frac{d\mathbf{V}(\alpha,y)}{dy}\right]_{y=0^-}^{0^+} = \begin{bmatrix} \dfrac{i\omega/\nu}{(\alpha^2 - i\omega/\nu)^{1/2}} C(\alpha) \\ -\dfrac{ik^2}{\alpha} D(\alpha) \end{bmatrix}, \tag{76}$$

after substitution of Eqs. (72) and (73).

The discontinuity in normal stress across the strip has square root edge singularities and is conveniently represented as

$$\begin{aligned} [\text{normal stress}]_{y=0^-}^{0^+} &= \rho_0 c_0 v_0 \left[-\frac{p(x,y)}{\rho_0 c_0 v_0}\left(1 + \frac{2i}{3}\epsilon^2\right) \right. \\ &\quad \left. + \frac{2\nu}{\omega}\frac{k_0}{v_0}\frac{\partial}{\partial y} v_y(x,y) \right]_{y=0^-}^{0^+} \\ &= 2\rho_0 c_0 v_0 \sum_{n=0}^{\infty} \epsilon_n i^n a_n \frac{T_n(x/a)}{\sqrt{1-(x/a)^2}} \\ &\quad (|x| < a). \end{aligned} \tag{77}$$

Then the Fourier coefficient

$$\int_{-a}^{a} \frac{T_n(x/a)}{\sqrt{1-(x/a)^2}} e^{-i\alpha x} dx = \pi a (-i)^n J_n(\alpha a) \tag{78}$$

enables the Fourier transform of Eq. (77) to be written as

$$\pi a \sum_{n=0}^{\infty} \epsilon_n a_n J_n(\alpha a) = \frac{D(\alpha)}{\alpha}, \tag{79}$$

after substitution of Eqs. (8), (9), and (72). Similarly, the representation

$$\begin{aligned} &[\text{tangential stress}]_{y=0^-}^{0^+} \\ &\quad = \rho_0 c_0 k_0 \frac{\nu}{\omega}\left[\frac{\partial}{\partial y} v_x(x,y) + \frac{\partial}{\partial x} v_y(x,y)\right]_{y=0^-}^{0^+} \\ &\quad = 2\rho_0 c_0 v_0 \sum_{n=0}^{\infty} \epsilon_n i^n b_n \frac{T_n(x/a)}{\sqrt{1-(x/a)^2}} \quad (|x| < a) \end{aligned} \tag{80}$$

has the Fourier transform

$$\begin{aligned} \pi a \sum_{n=0}^{\infty} \epsilon_n b_n J_n(\alpha a) &= \frac{\nu}{2\omega}\left[\frac{d}{dy} V_x(\alpha,y)\right]_{y=0^-}^{0^+} \\ &= \frac{i}{(\alpha^2 - i\omega/\nu)^{1/2}} C(\alpha), \end{aligned} \tag{81}$$

after substitution of Eqs. (76) and (78).

Equations for the coefficients $\{a_n, b_n; n \geq 0\}$ are now established by enforcing the no-slip condition (65). For $|x| < a$, Eqs. (66) and (74) yield

$$\begin{aligned} i\begin{bmatrix} \cos\phi_i \\ \sin\phi_i \end{bmatrix} e^{-ikx\cos\phi_i} &= \frac{\mathbf{v}(x,0)}{v_0} \\ &= \frac{1}{2\pi k_0}\int_{-\infty}^{\infty} [\mathbf{V}(\alpha,0)] e^{i\alpha x} d\alpha \\ &= \frac{1}{2\pi k_0}\int_{-\infty}^{\infty} K(\alpha) \\ &\quad \times \begin{bmatrix} (\alpha^2 - k^2)^{-1/2} C(\alpha) \\ -\dfrac{i}{\alpha} D(\alpha) \end{bmatrix} e^{i\alpha x} d\alpha, \end{aligned} \tag{82}$$

whose Chebyshev coefficients are determined by applying the operator

$$\frac{i^m}{\pi a}\int_{-a}^{a} \frac{T_m(x/a)}{\sqrt{1-(x/a)^2}} dx \quad (m \geq 0).$$

Thus, by using Eq. (78) and substituting Eqs. (79) and (81),

$$\begin{aligned} &-\begin{bmatrix} \cos\phi_i \\ \sin\phi_i \end{bmatrix} J_m(ka\cos\phi_i) \\ &\quad = \frac{(-1)^m}{2\pi k_0}\int_{-\infty}^{\infty} K(\alpha) \begin{bmatrix} i(\alpha^2 - k^2)^{-1/2} C(\alpha) \\ \dfrac{D(\alpha)}{\alpha} \end{bmatrix} J_m(\alpha a) d\alpha \\ &\quad = \frac{a}{2k_0}(-1)^m \int_{-\infty}^{\infty} K(\alpha) \sum_{n=0}^{\infty} \epsilon_n J_n(\alpha a) \\ &\quad \times \begin{bmatrix} b_n\left(\dfrac{\alpha^2 - i\omega/\nu}{\alpha^2 - k^2}\right)^{1/2} \\ a_n \end{bmatrix} J_m(\alpha a) d\alpha \\ &\quad = \frac{a}{2k_0}\sum_{n=0}^{\infty} \epsilon_n [(-1)^m + (-1)^n] \int_0^{\infty} K(\alpha) \\ &\quad \times \begin{bmatrix} b_n\left(\dfrac{\alpha^2 - i\omega/\nu}{\alpha^2 - k^2}\right)^{1/2} \\ a_n \end{bmatrix} J_m(\alpha a) J_n(\alpha a) d\alpha, \end{aligned} \tag{83}$$

since $K(\alpha)$ and the factor $(\,)^{1/2}$ are even functions of α.

From Eq. (80), the vorticity discontinuity across the plate is

$$\begin{aligned} [\Omega(x,y)]_{y=0^-}^{0^+} &= \left[-\frac{\partial}{\partial y} v_x(x,y)\right]_{y=0^-}^{0^+} \\ &= -\frac{k_0 v_0}{\epsilon^2}\sum_{n=0}^{\infty} \epsilon_n b_n i^n \frac{T_n(x/a)}{\sqrt{1-(x/a)^2}} \end{aligned} \tag{84}$$

while the continuous vorticity at the strip is the continuous part of

$$\frac{v_0}{2\pi k_0}\int_{-\infty}^{\infty} \left(i\alpha V_y(\alpha,0) - \frac{dV_x}{dy}(\alpha,0)\right) e^{i\alpha x} d\alpha$$

at the strip ($|x| < a$), which is

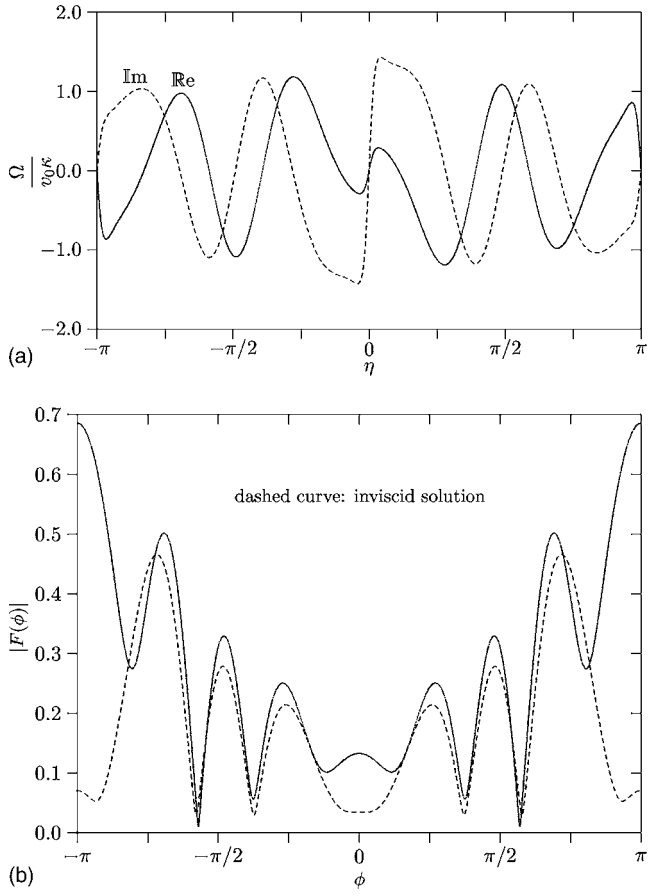

FIG. 2. Plane wave excitation of elliptic cylinder. Case: $k_0a=5$, $b/a=0.1$, $\epsilon=0.1$, and $\phi_i=0$. (a) Surface vorticity $\Omega(\xi_0,\eta)$ and (b) scattering pattern.

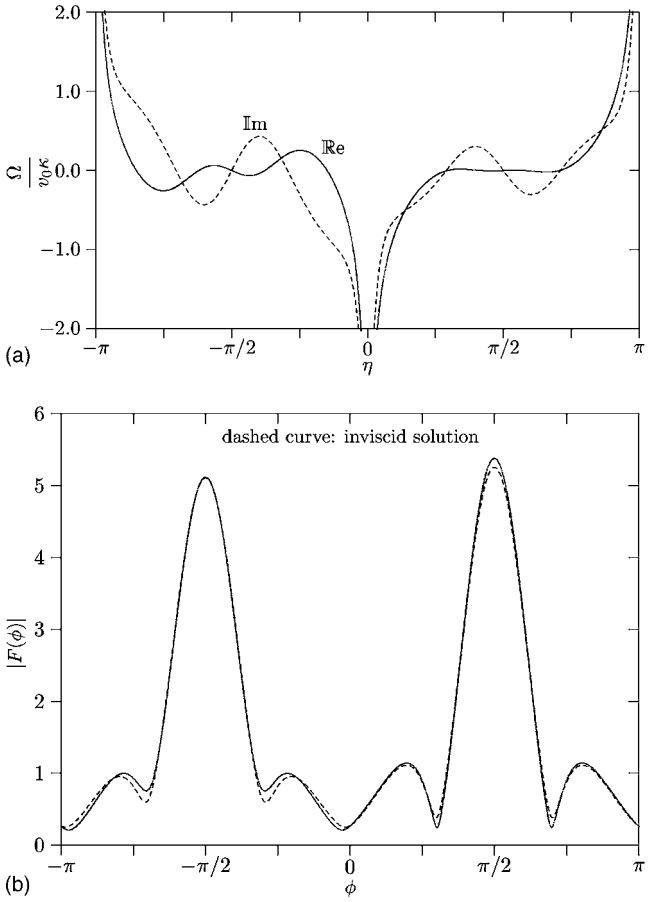

FIG. 3. Plane wave excitation of elliptic cylinder. Case: $k_0a=5$, $b/a=0.1$, $\epsilon=0.1$, and $\phi_i=\pi/2$. (a) Surface vorticity $\Omega(\xi_0,\eta)$ and (b) scattering pattern.

$$\frac{v_0}{2\pi k_0}\int_{-\infty}^{\infty}\left[K(\alpha)D(\alpha)+(\alpha^2-i\omega/\nu)^{1/2}D(\alpha)+\frac{k_0\alpha}{k^2}(\alpha^2-k^2)^{1/2}B(\alpha)\right]e^{i\alpha x}d\alpha=\frac{v_0}{2\pi k_0}\left(\frac{-i\omega}{\nu}\right)\pi a\times\int_{-\infty}^{\infty}\frac{e^{i\alpha x}\alpha}{(\alpha^2-i\omega/\nu)^{1/2}}\sum_{n=0}^{\infty}\epsilon_n a_n J_n(\alpha a)d\alpha$$

$$=\frac{\omega a v_0}{k_0\nu}\int_0^{\infty}\frac{\alpha d\alpha}{(\alpha^2-i\omega/\nu)^{1/2}}\sum_{n=0}^{\infty}\epsilon_n a_n J_n(\alpha a)\times\begin{cases}\sin\alpha x & (n\text{ even})\\ -i\cos\alpha x & (n\text{ odd})\end{cases}\tag{85}$$

after substitution of Eqs. (71), (72), (75), and (79). For comparison with the ellipse and circle, the vorticity on either side of the strip is deduced from Eqs. (84) and (85). The normalization $\Omega/v_0\kappa$ is used in the graphs.

VI. RESULTS

The acoustical size of the cylinder characterized by $k_0a=5$ is neither small (quasistatic regime) nor large (ray acoustics regime) in terms of the wavelength of the exciting plane wave, and therefore this scatterer is truly in the "resonant" frequency range. The dimensionless viscosity parameter of Eq. (9) is fixed at $\epsilon=0.1$. An extremely flattened elliptic cylinder having $b/a=0.1$ (ellipticity $e=[1-(b/a)^2]^{1/2}=0.995$) is selected, in Figs. 2 and 3, to demonstrate the variations in the scattering with plane-wave incidence angle. Figure 2 is for incidence from the $+x$ axis, that is, from the azimuthal angle $\phi_i=0$, which is the "endfire" direction. Figure 3 is for incidence from the $+y$ axis, that is, from the azimuthal angle $\phi_i=\pi/2$, which is the "broadside" direction. Figures 2(a) and 3(a) depict the complex-valued surface vorticity $\Omega(\xi_0,\eta)$, whose driving mechanism is the tangential component of the incident field. This is analogous to the unidirectional viscous flow known as a Stokes wave. As expected, endfire incidence generates vorticity along the narrow ellipse but broadside incidence yields vorticity confined near the ends. Viscosity effects on the far field are displayed in Figs. 2(b) and 3(b), which graph, for the two cases, the scattering pattern $|F(\phi)|$ of Eq. (64). Viscosity is clearly more influential far from the scatterer when the incident acoustic wave is essentially grazing to the elongated obstacle. Note that in the limiting case of the hard strip ($b/a\rightarrow 0$) in an inviscid medium, no scattered field is produced when $\phi_i=0$. The elongated ellipse still presents some disturbance to the field generated by the endfire source, but the scattering pattern curve of Fig. 2(b) is an order-of-magnitude less than the curve of Fig. 3(b).

As $b/a\rightarrow 1$ the ellipse degenerates to the circle, and Figs. 4(a) and 4(b) present the companion curves for this case. The numerical values from the analysis of Sec. III in

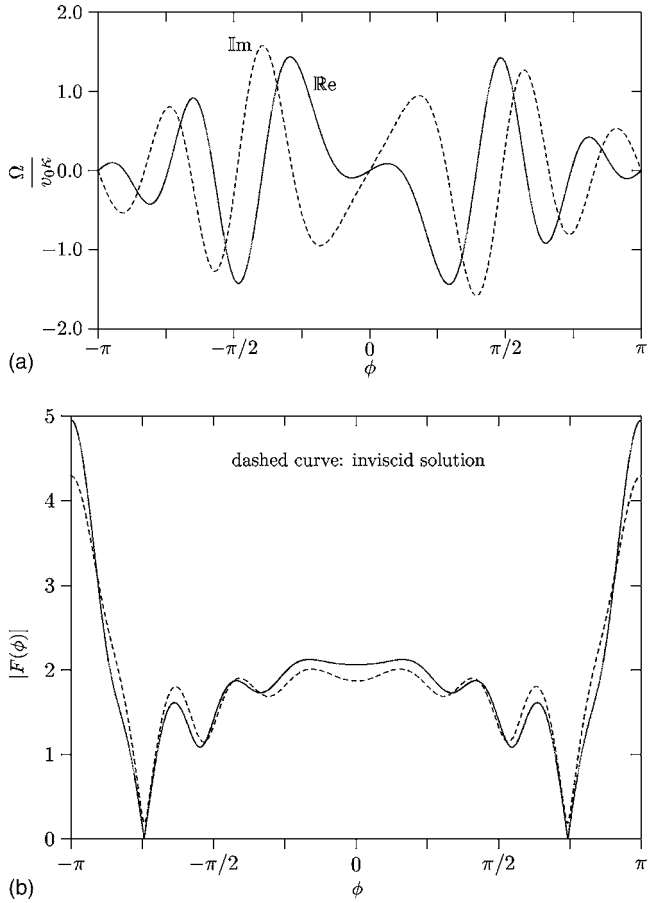

FIG. 4. Plane wave excitation of circular cylinder. Case: $k_0a=5$, $\epsilon=0.1$. (a) Surface vorticity $\Omega(a,\phi)$ and (b) scattering pattern.

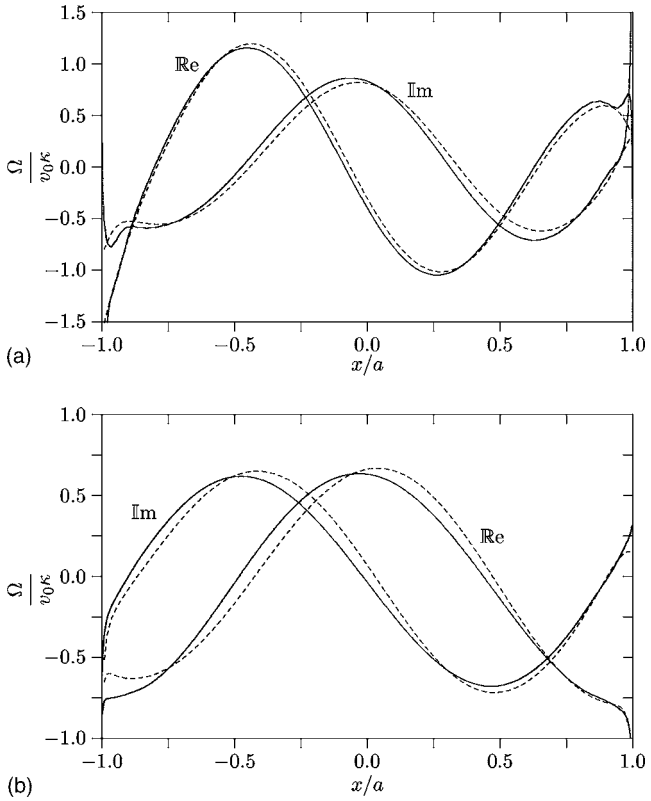

FIG. 5. Continuous and discontinuous components of vorticity across strip surface. Case: $k_0a=5$, $\epsilon=0.1$, and $\phi_i=\pi/4$. Solid curve: Ellipse with $b/a=0.05$ using 100 Mathieu functions. Dashed curve: Strip using six Chebyshev polynomials. (a) Continuous component $\frac{1}{2}[\Omega(x,0^+)+\Omega(x,0^-)]$ and (b) discontinuous component $\frac{1}{2}[\Omega(x,0^+)-\Omega(x,0^-)]$.

terms of Mathieu functions approach the values obtained from the circle analysis of Sec. II. When $b/a=0.99$, the resulting curves for the ellipse are visually indistinguishable from the given results for the circular scatterer. In contrast, the convergence of the series of Mathieu functions is not so robust as $b/a\to 0$, and for $k_0a=5$, the numerical integrity of the ellipse solution degrades if b/a gets as small as 0.01. This is because viscosity plays a dominant role in the construction of the field in the $b/a\to 0$ limit, whereas the field for $0<b/a<1$ is constructed as a viscous perturbation of an inviscid-type field. In the inviscid limit, the pressure reverts from a normal stress to a velocity potential. The contrast is most evident in the endfire case in which the inviscid scattered field vanishes. Resultant graphs of the continuous and discontinuous components of the surface vorticity appear in Figs. 5(a) and 5(b), respectively, for the case when $b/a=0.05$, which lies safely within the range where the solution is numerically convergent. Dashed curves from the strip solution of Sec. V are reasonably close to the solid curves for the ellipse having $b/a=0.05$ and where the representative angle of incidence is $\phi_i=\pi/4$.

VII. CONCLUSIONS

The presence of a slight medium viscosity can have a substantial effect on the scattering pattern of an impenetrable elliptic cylinder, even though the viscosity-induced vorticity is confined to a narrow boundary layer on the ellipse. Unlike the inviscid case, the forward scatter in a viscous medium can be significant when a plane wave strikes an elongated ellipse from the mostly grazing direction. The analysis and its implementation are validated via the agreement between the Mathieu function calculations for the elliptic cylinder and the independent calculations for the limiting cases of the circle and the strip. Though presented as a fundamental study, the results provide an obvious warning that endfire sonar detection of slender bodies can be unreliable.

[1] J. B. Alblas, "On the diffraction of sound waves in a viscous medium," Appl. Sci. Res., Sect. A **6**, 237–262 (1957).
[2] A. M. J. Davis and R. J. Nagem, "Acoustic diffraction by a half-plane in a viscous fluid medium," J. Acoust. Soc. Am. **112**, 1288–1296 (2002).
[3] A. M. J. Davis and R. J. Nagem, "Influence of viscosity on the diffraction of sound by a circular aperture in a plane screen," J. Acoust. Soc. Am. **113**, 3080–3090 (2003).
[4] A. M. J. Davis and R. J. Nagem, "Effect of viscosity on acoustic diffraction by a circular disk," J. Acoust. Soc. Am. **115**, 2738–2748 (2004).
[5] A. M. J. Davis and R. J. Nagem, "Curle's equation and acoustic diffraction by a sphere," J. Acoust. Soc. Am. **119**, 2018–2026 (2006).
[6] R. Barakat, "Diffraction of plane waves by an elliptic cylinder," J. Acoust. Soc. Am. **35**, 1990–1996 (1963).
[7] P. M. Morse and H. Feshbach, *Methods of Theoretical Physics* (McGraw-Hill, New York, 1953), Part II, pp. 1407–1422.
[8] R. Barakat, A. Houston, and E. Levin, "Power series expansions of Mathieu functions with tables of numerical results," Journal of Mathematics and Physics **42**, 200–247 (1964).
[9] V. A. Murga, "Sound diffraction by a plane barrier in a viscous fluid," Sov. Phys. Acoust. **37**, 378–381 (1991).
[10] P. I. Tsoi, "Diffraction of plane sound waves by a sphere in a viscous medium," Sov. Phys. Acoust. **16**, 381–386 (1971).
[11] A. P. Zhuk, "Interaction of a solid cylinder with a sound wave in a viscous

fluid," Sov. Appl. Mech. **24**, 94–99 (1988).
[12]M. K. Hinders, "Extinction of sound by spherical scatterers in a viscous fluid," Phys. Rev. A **43**, 5628–5637 (1991).
[13]D. Homentcovschi, R. N. Miles, and L. Tan, "Influence of viscosity on the diffraction of sound by a periodic array of screens," J. Acoust. Soc. Am. **117**, 2761–2771 (2005).
[14]P. A. Chinnery and V. F. Humphrey, "Fluid column resonances of water-filled cylindrical shells of elliptic cross section," J. Acoust. Soc. Am. **103**, 1296–1305 (1998).
[15]F. Léon, F. Chati, and J. M. Conoir, "Modal theory applied to the acoustic scattering by elastic cylinders of arbitrary cross section," J. Acoust. Soc. Am. **116**, 686–692 (2004).
[16]H. B. Wilson and R. W. Scharstein, "Computing elliptic membrane high frequencies by Mathieu and Galerkin methods," J. Eng. Math. **57**, 41–55 (2007).
[17]G. K. Batchelor, *An Introduction to Fluid Dynamics* (Cambridge University Press, Cambridge, 1967), pp. 186–193.
[18]D. S. Jones, *Acoustic and Electromagnetic Waves* (Clarendon, Oxford, 1986), Appendix C, pp. 689–692.
[19]N. W. McLachlan, *Theory and Application of Mathieu Functions* (Clarendon, Oxford, 1947), pp. 21, 240.

Fresnel approximations for acoustic fields of rectangularly symmetric sources

T. Douglas Mast[a)]
Department of Biomedical Engineering, University of Cincinnati, Cincinnati, Ohio 45267-0586

(Received 8 December 2006; revised 19 March 2007; accepted 20 March 2007)

A general approach is presented for determining the acoustic fields of rectangularly symmetric, baffled, time-harmonic sources under the Fresnel approximation. This approach is applicable to a variety of separable source configurations, including uniform, exponential, Gaussian, sinusoidal, and error function surface velocity distributions, with and without focusing in either surface dimension. In each case, the radiated field is given by a formula similar to that for a uniform rectangular source, except for additional scaling of wave number and azimuthal distance parameters. The expressions presented are generalized to three different Fresnel approximations that correspond, respectively, to diffracted plane waves, diffracted spherical waves, or diffracted cylindrical waves. Numerical results, for several source geometries relevant to ultrasonic applications, show that these expressions accurately depict the radiated pressure fields, except for points very near the radiating aperture. Highest accuracy near the source is obtained by choice of the Fresnel approximation most suited to the source geometry, while the highest accuracy far from the source is obtained by the approximation corresponding to diffracted spherical waves. The methods are suitable for volumetric computations of acoustic fields including focusing, apodization, and attenuation effects. © *2007 Acoustical Society of America.* [DOI: 10.1121/1.2726252]

PACS number(s): 43.20.Rz, 43.20.El [JJM] Pages: 3311–3322

I. INTRODUCTION

Radiated fields from rectangularly symmetric apertures, and from arrays of rectangularly symmetric elements, are important to many acoustic applications. In particular, certain ultrasound applications require computation of diffracted pressure fields over a large number of spatial points in two or three dimensions. These include modeling of ultrasound-induced heating for simulation of ultrasound therapy,[1–3] simulation of ultrasound imaging systems,[4–7] and compensation for diffraction effects in quantitative scattering measurements.[8–10] In such problems, individual elements of ultrasonic linear arrays, phased arrays, or two-dimensional arrays can be modeled as baffled rectangular sources, each of which may be unfocused, or focused in one or both dimensions, with possibly different focal lengths in each direction. The position-dependent surface velocity of such an array element may be approximately uniform over the entire rectangular aperture, or may be spatially varying (e.g., apodized to reduce beam sidelobes).[11]

A number of numerical methods are available for computation of ultrasonic fields from rectangular sources. Fields can be computed accurately using the angular spectrum method,[12,13] in which the Rayleigh integral is numerically evaluated by fast Fourier transform operations. Several numerically exact methods have been based on numerical integration of the aperture's space-time impulse response[14] for uniform, flat[15–18] or spherically focused[19] rectangular sources. A more general and computationally intensive method employs numerical evaluation of the two-dimensional Rayleigh integral[20] or the impulse response integral[6,21] by dividing a radiating surface into many small canonical elements. Recent work using the impulse-response method has included a method for rapid computation of the exact time-harmonic field for flat rectangular sources[18] and an approximate method for cylindrically focused sources.[22]

Approximate methods for computation of ultrasonic fields include several based on the Fresnel approximation, in which the phase of a wave front emanating from the radiating surface is replaced within the Rayleigh integral by a binomial-series expansion, truncated at second (quadratic) order.[23] In contrast to available numerical methods, the Fresnel approximation allows simple, analytic solutions for diffracted pressure fields to be obtained for rectangularly symmetric sources,[24] including apodized radiators for which "exact" numerical methods such as the impulse response approach may not be tractable.[25] In addition, the Fresnel approximation forms the basis for efficient numerical methods such as Gaussian beam expansions.[26–28] Analytic solutions obtained from the Fresnel approximation are desirable because they are amenable to further analysis, and can provide physical insight.

Analytic solutions for rectangularly symmetric apertures, under the Fresnel approximation, have previously been presented for a uniform, flat rectangular aperture[24] as well as for unfocused rectangularly symmetric apertures with several apodization patterns.[25] Szabo has pointed out that under the Fresnel approximation, the effect of focusing is similar to a scaling of the field of unfocused transducers.[11] Still, several investigators have implied that simple analytic solutions for Fresnel diffraction from focused rectangular transducers are not tractable outside the focal plane.[4,8,29,30]

[a)]Electronic mail: doug.mast@uc.edu

In this paper, analytic solutions are derived for the acoustic fields of a large class of rectangularly symmetric apertures under the Fresnel approximation. The general approach derived here for solution of the Rayleigh integral is valid for separable surface velocity distributions under three variations of the Fresnel approximation, respectively representing diffracted plane, spherical, and cylindrical waves. The result of this approach is a single, compact analytic formula for the fields of several focused and unfocused rectangularly symmetric apertures with various apodizations, all of which take a similar functional form except for shifting and scaling of wave number and azimuthal coordinates. Numerical results obtained from this simple approach indicate that each of the Fresnel approximations considered provides different numerical accuracy, dependent on the region of interest. An appropriate choice of Fresnel approximation, based on the aperture geometry, allows accurate field computations to be made over a wide region including the geometric near field. In addition, the simple form of the derived solutions, written in terms of the complex error function or Fresnel integral, facilitates further mathematical analysis of radiated acoustic fields. Thus, the methods introduced here should be useful for a wide variety of ultrasound applications that require detailed knowledge of the ultrasound field structure.

II. THEORY

In the following, an analytic approach is given that provides closed-form solutions of the Rayleigh integral for a variety of rectangularly symmetric apertures, under the Fresnel approximation. Four related variants of the Fresnel approximation are presented, which represent the radiated acoustic field respectively as a diffracted plane wave, a diffracted spherical wave, or diffracted cylindrical waves centered on either axis of symmetry. These four Fresnel approximations are generalized into a common form. Compact analytic solutions for this generalized Fresnel approximation are then derived for rectangularly symmetric apertures with uniform, exponential, sinusoidal, Gaussian, or error-function apodization, both for unfocused and focused apertures. In all cases, the pressure field is specified by a formula similar to that for a uniform, unfocused rectangular aperture,[24] but with complex, position-dependent shifting and scaling of the acoustic wave number and azimuthal distance coordinates.

A. General solution

The problem geometry considered here is the classic baffled piston, sketched in Fig. 1. A planar source at $z=0$, placed within an infinite rigid baffle, oscillates with time-harmonic surface velocity $u(x_0,y_0)=u_0A(x_0,y_0)e^{-i\omega t}$. For such a source, the resulting linear acoustic field pressure at any point in a homogeneous medium is given exactly by the Rayleigh integral:[31]

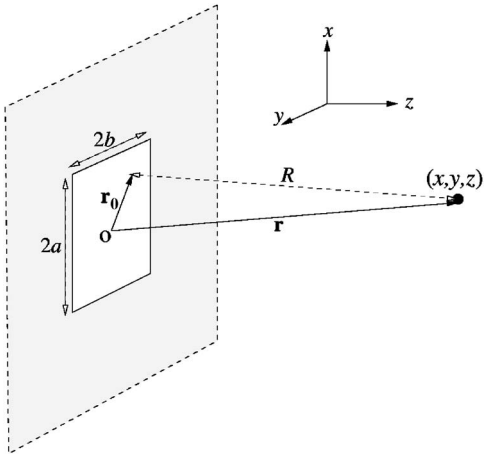

FIG. 1. Problem geometry. A rectangularly symmetric source with dimensions $2a$ in the x direction and $2b$ in the y direction oscillates within an infinite rigid baffle. The origin $\mathbf{o}$ of the coordinate system is at the aperture center. The pressure field at a field point $\mathbf{r}=(x,y,z)$ is given by the Rayleigh integral over the surface coordinate $\mathbf{r}_0=(x_0,y_0)$, with an integrand dependent on the distance $R=|\mathbf{r}-\mathbf{r}_0|$.

$$p(\mathbf{r},t)=-\frac{ik}{2\pi}\rho c u_0 e^{-i\omega t}\int_{-\infty}^{\infty}\int_{-\infty}^{\infty}A(x_0,y_0)\frac{e^{ik|\mathbf{r}-\mathbf{r}_0|}}{|\mathbf{r}-\mathbf{r}_0|}dx_0dy_0, \tag{1}$$

where ρ is the medium mass density, c is the speed of sound, k is the wave number ω/c, and the distance between a field point (x,y,z) and a surface point (x_0,y_0) is

$$|\mathbf{r}-\mathbf{r}_0|=\sqrt{(x-x_0)^2+(y-y_0)^2+z^2}. \tag{2}$$

This expression for the pressure field is also valid for attenuating media, in which case k is complex with $\mathrm{Im}[k]>0$. In the derivations given here, the time-dependent factor $e^{-i\omega t}$ will be suppressed and the nominal surface pressure $p_0=\rho c u_0$ will be assumed equal to unity.

The usual Fresnel approximation[23,24] starts with the assumption that

$$(x-x_0)^2+(y-y_0)^2 \ll z^2$$

for the surface points that contribute significantly to the pressure at a field point. This assumption, which is not required to hold for all points on the radiating surface, is consistent with the principle of stationary phase.[23] In this case, the distance $|\mathbf{r}-\mathbf{r}_0|$ can be approximated by the leading terms of its binomial expansion,

$$|\mathbf{r}-\mathbf{r}_0|\approx z+[(x-x_0)^2+(y-y_0)^2]/(2z), \tag{3}$$

so that the exponential term of Eq. (1) can be approximated as

$$\frac{e^{ik|\mathbf{r}-\mathbf{r}_0|}}{|\mathbf{r}-\mathbf{r}_0|}\approx\frac{e^{ikz}}{z}e^{ik[(x-x_0)^2+(y-y_0)^2]/(2z)}. \tag{4}$$

The pressure field given by the Rayleigh integral (1) is thus approximated as a plane wave multiplied by an integral diffraction term. For this reason, the Fresnel approximation of Eq. (4) is particularly useful for large sources in their acoustic near field and within the paraxial region.

Other implementations of the Fresnel approximation result from alternate binomial expansions of the distance $|\mathbf{r}-\mathbf{r}_0|$ into a position-independent distance plus a quadratic, position-dependent perturbation term, similar to Eq. (3). The result in each case is an expression of the radiated field as a simple geometric wave field (e.g., a plane, spherical, or cylindrical wave) multiplied by an integral diffraction term. In a given problem, optimal choice for the form of this expansion depends on the source geometry as well as the field position, as demonstrated by the numerical results presented later in this paper.

One alternate Fresnel approximation is more appropriate for small acoustic sources, such as rectangular elements of a two-dimensional ultrasonic array. For such sources, an appropriate scaling is based on the assumption

$$x_0^2 + y_0^2 - 2xx_0 - 2yy_0 \ll r^2,$$

where $r=\sqrt{x^2+y^2+z^2}$. This assumption is valid wherever the distance from the source center to the field point is much larger than any source dimension, so that it also applies in the geometric far field of any acoustic source. The most appropriate Fresnel approximation for this case represents a diffracted spherically spreading wave, so that the integrand of the Rayleigh integral (1) is approximated as

$$\frac{e^{ik|\mathbf{r}-\mathbf{r}_0|}}{|\mathbf{r}-\mathbf{r}_0|} \approx \frac{e^{ikr}}{r} e^{ik(x_0^2+y_0^2-2xx_0-2yy_0)/(2r)}. \tag{5}$$

A third approximation is useful for the common source configuration where an acoustic source is small in one dimension and large in the other dimension, such as an element of a typical linear or phased ultrasonic array. In the acoustic near field of such a transducer, one may assume that

$$(x-x_0)^2 + y_0^2 - 2yy_0 \ll y^2 + z^2$$

for source points that significantly contribute to the pressure field, where x is the direction of the longer element dimension (elevation or height) and y is the direction of the shorter element dimension (azimuth or pitch). In this case, an approximation analogous to Eqs. (4) and (5) is

$$\frac{e^{ik|\mathbf{r}-\mathbf{r}_0|}}{|\mathbf{r}-\mathbf{r}_0|} \approx \frac{e^{ikw_y}}{w_y} e^{ik[(x-x_0)^2+y_0^2-2yy_0]/(2w_y)}, \tag{6}$$

where $w_y \equiv \sqrt{y^2+z^2}$. This represents a diffracted yz-plane cylindrically spreading wave, centered on the long axis of the source.

Similarly, for a source that is much larger in the y dimension than the x dimension, one may make the approximation

$$\frac{e^{ik|\mathbf{r}-\mathbf{r}_0|}}{|\mathbf{r}-\mathbf{r}_0|} \approx \frac{e^{ikw_x}}{w_x} e^{ik[(y-y_0)^2+x_0^2-2xx_0]/(2w_x)}, \tag{7}$$

where $w_x \equiv \sqrt{x^2+z^2}$. This represents a diffracted wave cylindrically spreading in the xz plane, centered on the long axis of the radiating aperture.

The Rayleigh integral can be solved in a similar manner for any of these Fresnel approximations. For convenience, the four approximations are generalized here so that analytic expressions derived for the pressure field are valid under any of these approximations. To achieve this, a distance ζ is defined as the position-independent portion of any binomial expansion for $|\mathbf{r}-\mathbf{r}_0|$, e.g., $\zeta=z$ for Eq. (4). Given this definition, Eqs. (4)–(7) can be summarized by the compact expression

$$\frac{e^{ik|\mathbf{r}-\mathbf{r}_0|}}{|\mathbf{r}-\mathbf{r}_0|} \approx \frac{e^{ik(r^2+\zeta^2)/(2\zeta)}}{\zeta} e^{ik(x_0^2+y_0^2-2xx_0-2yy_0)/(2\zeta)}, \tag{8}$$

where one may choose $\zeta=z$ to represent the field as a diffracted plane wave (4), $\zeta=r$ for a spherically spreading wave (5), or $\zeta=w_y$ (6) or $\zeta=w_x$ (7) for cylindrically spreading waves. In each case, the coordinate ζ can be regarded as the nominal propagation distance from the source to a field point.

For sources with a separable surface velocity distribution such that $A(x_0,y_0)=A_x(x_0)A_y(y_0)$, the Rayleigh integral (1) can be written for any of the Fresnel approximations represented by Eq. (8) as

$$p(\mathbf{r}) = -\frac{ike^{ik(r^2+\zeta^2)/(2\zeta)}}{2\pi\zeta} \int_{-\infty}^{\infty} A_x(x_0) e^{ik(x_0^2-2xx_0)/(2\zeta)} dx_0 \times \int_{-\infty}^{\infty} A_y(y_0) e^{ik(y_0^2-2yy_0)/(2\zeta)} dy_0, \tag{9}$$

where the harmonic time dependence has been suppressed and the surface pressure $\rho c u_0$ is taken without loss of generality to be unity. Thus, the Fresnel approximation can allow the pressure field to be represented by two multiplicative integral terms, one depending on each of the azimuthal coordinates x and y.

Many surface velocity distributions of practical interest can be represented by simple exponential functions that are conveniently expressed in the form

$$A_x(x_0) = e^{\xi_2 x_0^2 + \xi_1 x_0}, \quad |x| < a,$$

$$A_y(y_0) = e^{\eta_2 y_0^2 + \eta_1 y_0}, \quad |y| < b, \tag{10}$$

where ξ_1, ξ_2, η_1, and η_2 may have both real parts, representing amplitude weightings such as apodization, and imaginary parts, representing phase weightings such as used for focusing. Source velocity distributions that can be represented in this form include focused and unfocused uniform, exponentially apodized, Gaussian, and sinusoidally varying apertures, all of which are specifically considered in the following section.

For surface velocity profiles of the form described by Eq. (10), the pressure field defined by Eq. (9) can be then written as

$$p(\mathbf{r}) = -\frac{ike^{ik(r^2+\zeta^2)/(2\zeta)}}{2\pi\zeta} \int_{-a}^{a} e^{i(\tilde{k}_x x_0^2 - 2k\tilde{x}x_0)/(2\zeta)} dx_0 \times \int_{-b}^{b} e^{i(\tilde{k}_y y_0^2 - 2k\tilde{y}y_0)/(2\zeta)} dy_0, \tag{11}$$

where

$$\tilde{k}_x \equiv k - 2i\xi_2\zeta, \quad \tilde{k}_y \equiv k - 2i\eta_2\zeta,$$

TABLE I. Summary of the four instances of the Fresnel approximation considered here, including the defining coordinates ζ, regions of greatest applicability, and forms of the multiplicative term $\Phi(\mathbf{r},\zeta)$.

Approximation	Most useful region	$\Phi(\mathbf{r},\zeta)$
$\zeta=z$ (diffracted plane wave)	$\lvert x\rvert\leqslant a$, $\lvert y\rvert\leqslant b$	$e^{ikz}e^{ik[x^2+y^2-k(\tilde{x}^2/\tilde{k}_x+\tilde{y}^2/\tilde{k}_y)]/(2z)}$
$\zeta=r$ (diffracted spherical wave)	$r\geqslant\sqrt{a^2+b^2}$	$e^{ikr}e^{-ik^2(\tilde{x}^2/\tilde{k}_x+\tilde{y}^2/\tilde{k}_y)/(2r)}$
$\zeta=w_y=\sqrt{y^2+z^2}$ (diffracted yz-plane cylindrical wave)	$\lvert x\rvert\leqslant a$	$e^{ikw_y}e^{ik[x^2-k(\tilde{x}^2/\tilde{k}_x+\tilde{y}^2/\tilde{k}_y)]/(2w_y)}$
$\zeta=w_x=\sqrt{x^2+z^2}$ (diffracted xz-plane cylindrical wave)	$\lvert y\rvert\leqslant b$	$e^{ikw_x}e^{ik[y^2-k(\tilde{x}^2/\tilde{k}_x+\tilde{y}^2/\tilde{k}_y)]/(2w_x)}$

$$\tilde{x}\equiv x+i\frac{\xi_1\zeta}{k},\quad \tilde{y}\equiv y+i\frac{\eta_1\zeta}{k}. \tag{12}$$

Comparison with Eq. (9) indicates that Eq. (11) represents the pressure fields for a wide variety of rectangularly symmetric sources in terms of the field of an unfocused, unapodized rectangular source, with the introduction of scaled and shifted wave numbers $\tilde{k}_x$, $\tilde{k}_y$ and distances $\tilde{x}$, $\tilde{y}$. In general, these scaled and shifted parameters are complex and position-dependent.

For any source velocity distribution represented by Eq. (10), the resulting pressure field under any of the approximations (4)–(7) is given by Eq. (11). Solutions to the integrals appearing in Eq. (11) are obtained by completing the square in each exponent and applying definitions of the complex error function or the complex Fresnel integral. This results in closed-form expressions for the pressure field under the Fresnel approximation:

$$\begin{aligned}p(\mathbf{r}) &= \frac{k\Phi(\mathbf{r},\zeta)}{4\sqrt{\tilde{k}_x}\sqrt{\tilde{k}_y}}\left(\operatorname{erf}\left[\frac{k\tilde{x}+\tilde{k}_x a}{\sqrt{2i}\sqrt{\tilde{k}_x\zeta}}\right]-\operatorname{erf}\left[\frac{k\tilde{x}-\tilde{k}_x a}{\sqrt{2i}\sqrt{\tilde{k}_x\zeta}}\right]\right)\\ &\quad\times\left(\operatorname{erf}\left[\frac{k\tilde{y}+\tilde{k}_y b}{\sqrt{2i}\sqrt{\tilde{k}_y\zeta}}\right]-\operatorname{erf}\left[\frac{k\tilde{y}-\tilde{k}_y b}{\sqrt{2i}\sqrt{\tilde{k}_y\zeta}}\right]\right)\\ &= -\frac{ik\Phi(\mathbf{r},\zeta)}{2\sqrt{\tilde{k}_x}\sqrt{\tilde{k}_y}}\left(\mathbf{F}\left[\frac{k\tilde{x}+\tilde{k}_x a}{\sqrt{\pi}\sqrt{\tilde{k}_x\zeta}}\right]-\mathbf{F}\left[\frac{k\tilde{x}-\tilde{k}_x a}{\sqrt{\pi}\sqrt{\tilde{k}_x\zeta}}\right]\right)\\ &\quad\times\left(\mathbf{F}\left[\frac{k\tilde{y}+\tilde{k}_y b}{\sqrt{\pi}\sqrt{\tilde{k}_y\zeta}}\right]-\mathbf{F}\left[\frac{k\tilde{y}-\tilde{k}_y b}{\sqrt{\pi}\sqrt{\tilde{k}_y\zeta}}\right]\right),\end{aligned} \tag{13}$$

where the multiplicative term $\Phi(\mathbf{r},\zeta)$ is defined as

$$\Phi(\mathbf{r},\zeta)=e^{i[k(r^2+\zeta^2)-k^2(\tilde{x}^2/\tilde{k}_x+\tilde{y}^2/\tilde{k}_y)]/(2\zeta)}. \tag{14}$$

In Eq. (13), erf denotes the error function[32] and $\mathbf{F}$ denotes the complex Fresnel integral

$$\mathbf{F}(\zeta)=C(\zeta)+iS(\zeta)\equiv\int_0^\zeta e^{i\pi u^2/2}du. \tag{15}$$

These two functions are related by the identity[32]

$$\mathbf{F}(\zeta)=\sqrt{\frac{i}{2}}\operatorname{erf}\left(\sqrt{\frac{\pi}{2i}}\zeta\right). \tag{16}$$

Both of these functions have been analyzed in depth[32] and can be computed efficiently using series expansions, rational approximations, or other available numerical methods, similar to other tabulated special functions.[33,34]

Specific expressions for the factor $\Phi(\mathbf{r},\zeta)$ are given in Table I for the cases $\zeta=z$, $\zeta=r$, $\zeta=w_x$, and $\zeta=w_y$ corresponding to the four Fresnel approximations described earlier. Table I also lists the regions where each approximation is most likely to be valid, based on simple geometric considerations borne out by the numerical results presented in Sec. III. Notable is that, although $\Phi(\mathbf{r},\zeta)$ takes the form of a complex exponential function, this factor does not have unity magnitude except in special cases (e.g., an unapodized rectangular aperture in a lossless medium).

The general expressions given by Eq. (13) for the pressure field have functional form equivalent to previous results for the field of uniform rectangular sources under the Fresnel approximation,[24,25] but with scaled and shifted variables according to Eq. (12). Thus, the same computational and analytic formulas can be applied, with modification only to the independent variables, to any unfocused or focused radiator described by Eq. (10). Solutions for specific apertures are detailed in the following section.

B. Pressure fields for specific apertures

Pressure fields for a number of practically important amplitude distributions can be obtained directly from the general result of Eq. (13), using scaled wave numbers $\tilde{k}_x$, $\tilde{k}_y$ and scaled coordinates $\tilde{x}$, $\tilde{y}$ defined by Eq. (12). Table II lists values of the scaled wave number $\tilde{k}_x$ and the scaled distance $\tilde{x}$ for several apertures of the form given by Eq. (10), including unfocused and focused rectangular, sinusoidal, and Gaussian distributions, as well as the general quadratic exponential function that encompasses all these cases.

The scaled wave number and distance parameters listed in Table II are in general complex. In the case of a Gaussian aperture, the scaled wave number $\tilde{k}_x$ has a positive imaginary part, similar to the positive imaginary part of the physical

TABLE II. Complex apodization functions $A_x(x_0)$, scaled wave numbers $\tilde{k}_x$; and scaled azimuthal distances $\tilde{x}$ for four unfocused and focused apertures.

Aperture type	$A_x(x_0)$	$\tilde{k}_x$	$\tilde{x}$
Quadratic exponential	$e^{\beta_2 x_0^2+\beta_1 x_0}$	$k-2i\beta_2\zeta$	$x+i\frac{\beta_1\zeta}{k}$
Rectangular	1	k	x
Sinusoidal	$e^{i\kappa x_0}$	k	$x-\frac{\kappa\zeta}{k}$
Gaussian	$e^{-x_0^2/(2\sigma_x^2)}$	$k+i\frac{\zeta}{\sigma_x^2}$	x
Focused quadratic exponential	$e^{\beta_2 x_0^2+\beta_1 x_0 e^{-ikx_0^2/(2F_x)}}$	$k\left(1-\frac{\zeta}{F_x}\right)-2i\beta_2\zeta$	$x+i\frac{\beta_1\zeta}{k}$
Focused rectangular	$e^{-ikx_0^2/(2F_x)}$	$k\left(1-\frac{\zeta}{F_x}\right)$	x
Focused sinusoidal	$e^{i\kappa x_0}e^{-ikx_0^2/(2F_x)}$	$k\left(1-\frac{\zeta}{F_x}\right)$	$x-\frac{\kappa\zeta}{k}$
Focused Gaussian	$e^{-x_0^2/(2\sigma_x^2)}e^{-ikx_0^2/(2F_x)}$	$k\left(1-\frac{\zeta}{F_x}\right)+\frac{i\zeta}{\sigma_x^2}$	x

wave number k in an attenuating medium. This is consistent with the spatial smoothing of the diffraction pattern caused by amplitude apodization, which is qualitatively similar to the smoothing observed for uniform apertures in an attenuating medium.[35] Similarly, an exponential amplitude term of the form $A_x(x_0)=e^{\beta_1 x_0}$ results in a positive imaginary part for the scaled azimuthal coordinate $\tilde{x}$, suggesting a corollary with inhomogeneous plane waves, in which the pressure amplitude varies exponentially with the azimuthal position.[36] However, the general solution of Eq. (13) also depends on the unscaled wave number k and unscaled azimuthal coordinates x and y, so that precise physical interpretation of the scaled wave numbers $\tilde{k}_x$, $\tilde{k}_y$ and coordinates $\tilde{x}$, $\tilde{y}$ is not straightforward.

Focusing at a distance F_x is represented in Table II by phase factors of the form

$$A_x(x_0)=e^{-ikF_x\left(1-\sqrt{1-x_0^2/F_x^2}\right)}\approx e^{-ikx_0^2/(2F_x)},$$

$$A_y(y_0)=e^{-ikF_y\left(1-\sqrt{1-y_0^2/F_y^2}\right)}\approx e^{-iky_0^2/(2F_y)}, \tag{17}$$

where F_x and F_y are focal lengths for the elevation and azimuth directions, respectively. Thus, the phasing associated with geometric focusing at radii F_x or F_y is approximated quadratically, consistent with the quadratic truncation of the binomial series that results in the Fresnel approximations (4)–(7).

To obtain the time-harmonic pressure field for any focused or unfocused aperture of a form listed in Table II, the coordinates ζ, $\tilde{k}_x$, $\tilde{k}_y$, $\tilde{x}$, and $\tilde{y}$ are specified based on Tables I and II, and the pressure field is then given in terms of the complex error function or the complex Fresnel integral by Eq. (13). For the special case of unfocused rectangular apertures, pressure fields obtained by this method are analogous to results previously reported in the literature,[24,25] but are more general because they are applicable to any of the Fresnel approximations (4)–(7). In Sec. III, it is shown that an appropriate choice of ζ can substantially improve the accuracy of pressure computations in the nearfield.

The definitions given in Table II for the sinusoidal aperture can be employed with Eq. (13) to compute pressure fields for a number of apodizations of interest. For example, fields due to truncated-cosine, Hanning, or Hamming-apodized sources can be obtained by appropriately superposing the fields from sinusoidal apertures with spatial frequencies κ, $-\kappa$, and 0. As a specific example, the radiated field can be computed for a velocity distribution

$$A(x_0,y_0)=A_x(x_0)A_y(y_0)$$

with

$$A_x(x_0)=\cos\left(\frac{\pi}{2a}x_0\right),\quad |x|<a,$$

$$A_y(y_0)=\cos\left(\frac{\pi}{2b}y_0\right),\quad |y|<b, \tag{18}$$

which corresponds to the lowest-order vibration mode of a rectangular membrane and is similar to the "simply-supported piston" distribution used by Greenspan.[37] Using the complex representation of the cosine, the radiated pressure for this velocity distribution under the Fresnel approximation is found to be

$$p(\mathbf{r})=\frac{1}{4}\left[p_s\left(\mathbf{r},\frac{\pi}{2a},\frac{\pi}{2b}\right)+p_s\left(\mathbf{r},\frac{\pi}{2a},-\frac{\pi}{2b}\right)+p_s\left(\mathbf{r},-\frac{\pi}{2a},\frac{\pi}{2b}\right)+p_s\left(\mathbf{r},-\frac{\pi}{2a},-\frac{\pi}{2b}\right)\right], \tag{19}$$

where $p_s(\mathbf{r},\kappa_x,\kappa_y)$ is the pressure field defined by Eq. (13) and Table II for a sinusoidal velocity distribution with spatial frequencies κ_x and κ_y.

Similarly, fields of more complex, general asymmetric apertures can be obtained by representing their surface velocity distribution as a spatial-frequency Fourier series and superposing the fields computed for each Fourier component. In the resulting summation, the superposed field for each spatial-frequency component would be weighted by the complex Fourier coefficient of the surface velocity distribution for that spatial frequency.

For the source velocity distributions listed in Table II, the pressure field defined by Eq. (11) simplifies further in several limiting cases. One such case occurs when the quadratic terms in the exponential arguments of Eq. (11) can be neglected. This requires either that $\zeta \gg \tilde{k}_x x_0^2$ and $\zeta \gg \tilde{k}_y y_0^2$ (the far field or Fraunhofer approximation), or $\tilde{k}_x=\tilde{k}_y=0$, as for

certain focused apertures when the coordinate ζ is equal to the focal distance. For the Fresnel approximation obtained by setting $\zeta=z$, the latter case results in a pressure distribution in the focal plane that is equivalent to a scaled far-field pattern of the same source distribution.[11,23] For either of these conditions, the pressure field resulting from Eq. (9) becomes

$$p(\mathbf{r}) \to -\frac{2ikab}{\pi}\frac{e^{ik(r^2+\zeta^2)/(2\zeta)}}{\zeta}\mathrm{sinc}\left(\frac{ka\tilde{x}}{\zeta}\right)\mathrm{sinc}\left(\frac{kb\tilde{y}}{\zeta}\right), \quad (20)$$

where $\mathrm{sinc}(\mu)\equiv\sin(\mu)/\mu$. Thus, the far-field pressure (or similarly, the focal-plane pressure) obtained for any rectangularly symmetric aperture of the form given by Eq. (10) can be written in terms of the far-field pattern of a uniform, unfocused rectangular aperture, given appropriate scaling and shifting of wave number and azimuthal coordinates according to Eq. (12).

In a second limiting case, the pressure field due to an unfocused or focused Gaussian amplitude distribution takes the form of a Gaussian beam in the limit of an infinite aperture, so that $a\to\infty$ and $b\to\infty$. In this limit, the pressure field becomes the Gaussian beam

$$\begin{aligned} p(\mathbf{r}) &\to \frac{k}{\sqrt{\tilde{k}_x}\sqrt{\tilde{k}_y}}\Phi(\mathbf{r},\zeta) \\ &= -\frac{i\zeta}{k\tilde{\sigma}_x\tilde{\sigma}_y}e^{ik(r^2+\zeta^2)/(2\zeta)}e^{-x^2/(2\tilde{\sigma}_x^2)}e^{-y^2/(2\tilde{\sigma}_y^2)}, \end{aligned} \quad (21)$$

where

$$\begin{aligned} \tilde{\sigma}_x &\equiv \frac{\zeta\sqrt{1-ik\sigma_x^2(1/\zeta-1/F_x)}}{k\sigma_x}, \\ \tilde{\sigma}_y &\equiv \frac{\zeta\sqrt{1-ik\sigma_y^2(1/\zeta-1/F_y)}}{k\sigma_y}, \end{aligned} \quad (22)$$

and the scaled parameters $\tilde{k}_x$, $\tilde{k}_y$, $\tilde{x}$, and $\tilde{y}$ are those defined in Table II for the truncated Gaussian aperture. This is consistent with previous results showing that beams from Gaussian sources remain Gaussian in shape at all ranges.[25,38]

C. Error function aperture

One potential apodization design uses an essentially rectangular amplitude distribution, with tapered edges to reduce sidelobes.[11] A simple mathematical representation for such apertures is a Gaussian function convolved with a rectangle, resulting in an error function amplitude distribution. This representation has been successfully employed in modeling the nonuniform amplitude distribution of conventional, nominally nonapodized transducers, and can provide better agreement with experiment than uniform amplitude distributions.[39] The resulting apodization has an effect similar to the piecewise-continuous "step function with 'smooth' edge" introduced by Tjøtta and Tjøtta.[40] For the general case including focusing, the error-function velocity distribution can be written for the approximations considered here as

$$\begin{aligned} A_x(x_0) &= \frac{e^{-ikx_0^2/(2F_x)}}{\sqrt{2\pi}\sigma_x}\int_{-a}^{a}e^{-(x_1-x_0)^2/(2\sigma_x^2)}dx_1 \\ &= \frac{e^{-ikx_0^2/(2F_x)}}{2}\left(\mathrm{erf}\left[\frac{x_0+a}{\sqrt{2}\sigma_x}\right]-\mathrm{erf}\left[\frac{x_0-a}{\sqrt{2}\sigma_x}\right]\right) \end{aligned} \quad (23)$$

for the x direction, and similarly for the y direction in terms of F_y and σ_y, where σ_x and σ_y are nonzero real parameters that determine the sharpness of the aperture taper.

The pressure field defined by Eq. (9) can thus be written for the error function aperture as a product of double integrals,

$$\begin{aligned} p(\mathbf{r}) = -\frac{ike^{ik(r^2+\zeta^2)/(2\zeta)}}{4\pi^2\sigma_x\sigma_y\zeta}&\int_{-\infty}^{\infty}\int_{-a}^{a}e^{-(x_1-x_0)^2/(2\sigma_x^2)} \\ &\times e^{-ikx_0^2/(2F_x)}e^{ik(x_0^2-2xx_0)/(2\zeta)}dx_1dx_0 \\ &\times\int_{-\infty}^{\infty}\int_{-b}^{b}e^{-(y_1-y_0)^2/(2\sigma_y^2)} \\ &\times e^{-iky_0^2/(2F_y)}e^{ik(y_0^2-2yy_0)/(2\zeta)}dy_1dy_0. \end{aligned} \quad (24)$$

After some algebraic manipulation and exchanging the order of integration, this can be rewritten as

$$\begin{aligned} p(\mathbf{r}) = -\frac{ike^{ik(r^2+\zeta^2)/(2\zeta)}e^{-k^2(\sigma_x^2\tilde{x}x+\sigma_y^2\tilde{y}y)/(2\zeta^2)}}{4\pi^2\sigma_x\sigma_y\zeta} \\ \times\int_{-a}^{a}\left[\int_{-\infty}^{\infty}e^{-(x_0-\chi_x)^2/(2\sigma_x^2\tilde{x}/x)}dx_0\right]e^{i(\tilde{k}_xx_1^2-2k\tilde{x}x_1)/(2\zeta)}dx_1 \\ \times\int_{-b}^{b}\left[\int_{-\infty}^{\infty}e^{-(y_0-\chi_y)^2/(2\sigma_y^2\tilde{y}/y)}dy_0\right]e^{i(\tilde{k}_yy_1^2-2k\tilde{y}y_1)/(2\zeta)}dy_1, \end{aligned} \quad (25)$$

where

$$\begin{aligned} \tilde{k}_x &\equiv \frac{k(1-\zeta/F_x)}{1+ik\sigma_x^2(1/F_x-1/\zeta)}, \\ \tilde{x} &\equiv \frac{x}{1+ik\sigma_x^2(1/F_x-1/\zeta)}, \\ \chi_x &\equiv \frac{x+ix_1\zeta/(k\sigma_x^2)}{1-\zeta/F_x+i\zeta/(k\sigma_x^2)}, \end{aligned} \quad (26)$$

and $\tilde{k}_y$, $\tilde{y}$, and $\tilde{\chi}_y$ are similarly defined in terms of y, y_1, F_y, and σ_y.

The integral over x_0 from Eq. (25) has the value $\sqrt{2\pi}\sigma_x/\sqrt{x/\tilde{x}}$, while the integral over y_0 similarly has the value $\sqrt{2\pi}\sigma_y/\sqrt{y/\tilde{y}}$. Equation (25) thus takes a form that is similar, except for multiplicative terms outside the integrals, to the integral pressure field expression of Eq. (9). Thus, the field pressure for the focused error-function aperture is given, in analogy to Eq. (13), by

$$p(\mathbf{r}) = \frac{k\Phi_e(\mathbf{r},\zeta)}{4\sqrt{\tilde{k}_x}\sqrt{\tilde{k}_y}}\left(\operatorname{erf}\left[\frac{k\tilde{x}+\tilde{k}_x a}{\sqrt{2i}\sqrt{\tilde{k}_x\zeta}}\right]-\operatorname{erf}\left[\frac{k\tilde{x}-\tilde{k}_x a}{\sqrt{2i}\sqrt{\tilde{k}_x\zeta}}\right]\right)$$
$$\times\left(\operatorname{erf}\left[\frac{k\tilde{y}+\tilde{k}_y b}{\sqrt{2i}\sqrt{\tilde{k}_y\zeta}}\right]-\operatorname{erf}\left[\frac{k\tilde{y}-\tilde{k}_y b}{\sqrt{2i}\sqrt{\tilde{k}_y\zeta}}\right]\right)$$
$$=-\frac{ik\Phi_e(\mathbf{r},\zeta)}{2\sqrt{\tilde{k}_x}\sqrt{\tilde{k}_y}}\left(\mathbf{F}\left[\frac{k\tilde{x}+\tilde{k}_x a}{\sqrt{\pi}\sqrt{\tilde{k}_x\zeta}}\right]-\mathbf{F}\left[\frac{k\tilde{x}-\tilde{k}_x a}{\sqrt{\pi}\sqrt{\tilde{k}_x\zeta}}\right]\right)$$
$$\times\left(\mathbf{F}\left[\frac{k\tilde{y}+\tilde{k}_y b}{\sqrt{\pi}\sqrt{\tilde{k}_y\zeta}}\right]-\mathbf{F}\left[\frac{k\tilde{y}-\tilde{k}_y b}{\sqrt{\pi}\sqrt{\tilde{k}_y\zeta}}\right]\right), \quad (27)$$

where the multiplicative term $\Phi_e(\mathbf{r},\zeta)$ is defined as

$$\Phi_e(\mathbf{r},\zeta) = \frac{e^{i[k(r^2+\zeta^2)-k^2(\tilde{x}^2/\tilde{k}_x+\tilde{y}^2/\tilde{k}_y)+ik^2(\sigma_x^2\tilde{x}x+\sigma_y^2\tilde{y}y)/\zeta]/(2\zeta)}}{\sqrt{x/\tilde{x}}\sqrt{y/\tilde{y}}} \quad (28)$$

and $\tilde{k}_x$, $\tilde{k}_y$, $\tilde{x}$, and $\tilde{y}$ are defined by Eq. (26). For an error function aperture that is unfocused in one or both dimensions, the field pressure under the Fresnel approximation is given by Eqs. (27) and (28) with either or both of the focal lengths set to infinity, so that $F_x\to\infty$ or $F_y\to\infty$ in the definitions from Eq. (26).

Thus, the pressure field of a focused or unfocused error-function aperture is functionally similar to that for other rectangularly symmetric sources, except for different scaled wave number and azimuthal distance parameters and a position-dependent multiplicative term. In the limit $\sigma_x\to 0$, $\sigma_y\to 0$, Eq. (27) reduces to the pressure field of a similarly focused or unfocused, uniform rectangular source.

III. NUMERICAL RESULTS

Since the general field expressions described earlier are exact, closed-form solutions of the Rayleigh integral under the Fresnel approximation, their accuracy depends mainly on the validity of the Fresnel approximations employed. To characterize the accuracy of the Fresnel approximations derived here, the field expressions derived earlier were compared with the impulse response method for three unfocused, uniform rectangular sources with dimensions relevant to ultrasonic applications. Accuracy of these field expressions, as a function of the source geometry and field position, should be comparable in the case of more complicated, apodized and focused apertures, for which the impulse response method is not applicable in general.

The computations reported here employed a wave number $k=20$ rad/mm, corresponding to a wavelength of 0.31 mm and a frequency of 5 MHz for radiation into water. The three sources examined included a small element with half-widths $a=0.5$ mm and $b=0.25$ mm (surface area $3.2\lambda\times 1.6\lambda$), a linear array element with $a=5.0$ mm and $b=0.15$ mm (area $32\lambda\times 1\lambda$), and a rectangular source with $a=5.0$ mm and $b=2.5$ mm (area $32\lambda\times 16\lambda$). In each case, fields for unfocused rectangular apertures were computed using Eq. (13) with $\tilde{x}=x$, $\tilde{y}=y$, and $\tilde{k}_x=\tilde{k}_y=k$ for each for the four Fresnel approximations (4)–(7).

For comparison, fields were computed at the same points using direct numerical evaluation of the impulse-response integral for time-harmonic excitation. The form used was the pressure impulse response derived by McGough, in which numerical conditioning is improved by subtraction of singularities that appear in the usual impulse-response integral, resulting in greater accuracy at lower computational cost.[18] The resulting field can be written for any point in space as

$$p(\mathbf{r}) = I(|x+a|,|y+b|) + \operatorname{sgn}(|a|-|x|)I(|x-a|,|y+b|)$$
$$+\operatorname{sgn}(|b|-|y|)I(|x+a|,|y-b|)$$
$$+\operatorname{sgn}(|a|-|x|)\operatorname{sgn}(|b|-|y|)I(|x-a|,|y-b|), \quad (29)$$

where sign is the signum function and I is an integral term computed numerically, defined as

$$I(s,l) = -\frac{1}{2\pi}\left(s\int_0^l \frac{e^{ik\sqrt{z^2+\sigma^2+s^2}}-e^{ikx}}{\sigma^2+s^2}d\sigma\right.$$
$$\left.+l\int_0^s \frac{e^{ik\sqrt{z^2+\sigma^2+l^2}}-e^{ikx}}{\sigma^2+l^2}d\sigma\right). \quad (30)$$

Both the Fresnel approximation of Eq. (13) and the numerical solution of Eqs. (29) and (30) were implemented directly on a commercial software package (MATHEMATICA 5.2, Wolfram Research), using complex error function and numerical integration routines provided in that package. The computation time required, for MATHEMATICA 5.2 under Linux on an AMD Athlon 64 3000+ processor running at 1.8 GHz, averaged 1.7×10^{-3} s per point for the Fresnel approximations and 1.2×10^{-2} s per point for direct numerical evaluation of the impulse response integral. Since these computation times were obtained using direct implementation of the respective formulas in a high-level, interpreted software language designed for high numerical precision, either method can achieve significantly greater performance when optimized for speed. With the Fresnel approximations derived here, comparable computational efficiency will also be obtained for any aperture with apodization and focusing characteristics described by Eq. (10), including cases for which the impulse response method may not be tractable.

Validity of the Fresnel approximations considered here can be qualitatively depicted, as a function of spatial position and transducer geometry, by representative computed fields. Figure 2 shows fields computed with the impulse-response integral and the four Fresnel approximations over a plane spanning 30×30 mm^2 at a range of 10 mm, displayed with a 40 dB dynamic range. These field plots illustrate the nature of each Fresnel approximation, with patterns corresponding to diffracted spherically spreading waves ($\zeta=r$), diffracted plane waves ($\zeta=z$), or diffracted cylindrically spreading waves ($\zeta=w_x$ and $\zeta=w_y$).

In Fig. 2(a), illustrating the field of a small element, the Fresnel approximation based on diffracted spherical waves ($\zeta=r$) captures the detailed field features accurately, while the other Fresnel approximations poorly represent the field in this case. In Fig. 2(b), showing the field of a linear array element, the field is accurately depicted by the Fresnel approximations associated with diffracted spherically spreading

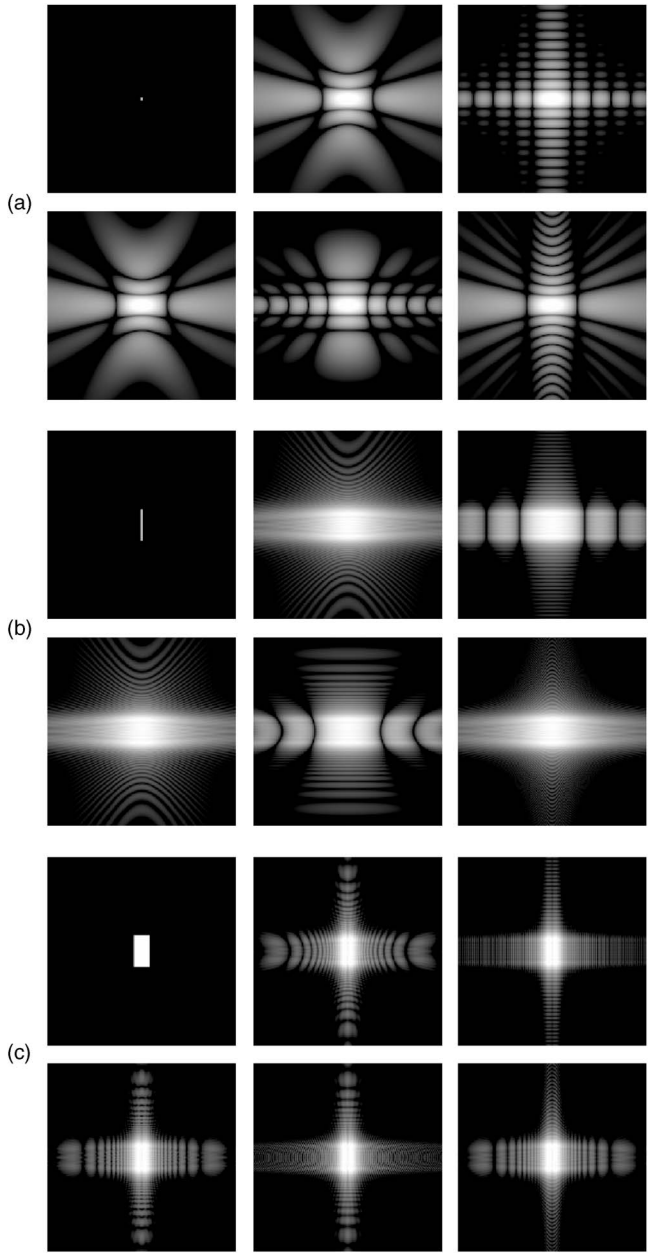

FIG. 2. Aperture velocity distributions and computed pressure fields at a range of 10 mm for three apertures with wave number $k=20$ rad/mm. Computed pressure magnitudes are shown on a logarithmic grayscale with 40 dB dynamic range. Each plot shows a region of size 30×30 mm^2. Top left: Aperture velocity distribution. Bottom left: Reference field from numerical solution of the impulse-response integral. Computed fields from the four Fresnel approximations considered are arranged with $\zeta=r$ (diffracted spherical wave) at top middle, $\zeta=z$ (diffracted plane wave) at top right, $\zeta=w_x$ (diffracted yz-plane cylindrical wave) at bottom middle, and $\zeta=w_y$ (diffracted xz-plane cylindrical wave) at bottom right. (a) $a=0.5$ mm, $b=0.25$ mm. (b) $a=5.0$ mm, $b=0.15$ mm. (c) $a=5.0$ mm, $b=2.5$ mm.

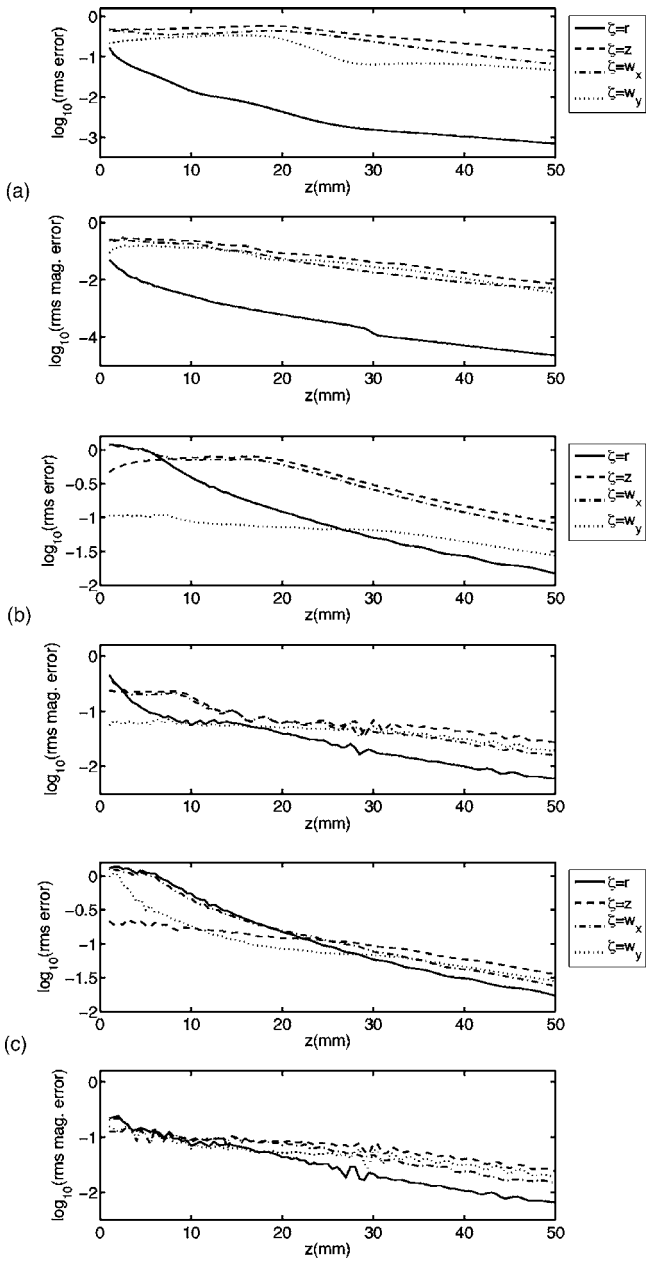

FIG. 3. Computed rms error for four Fresnel approximations and three aperture configurations, plotted as a function of range z for a wave number $k=20$ rad/mm. In each panel, logarithmic plots are shown for both the rms complex pressure error, $\langle|p-p_{\mathrm{refl}}|\rangle/\langle|p_{\mathrm{refl}}|\rangle$, and the rms pressure magnitude error, $\langle|p|-|p_{\mathrm{refl}}|\rangle\langle|p_{\mathrm{refl}}|\rangle$, as defined in Eqs. (31) and (32). (a) $a=0.5$ mm, $b=0.25$ mm. (b) $a=5.0$ mm, $b=0.15$ mm. (c) $a=5.0$ mm, $b=2.5$ mm.

waves ($\zeta=r$) and with diffracted cylindrically spreading waves around the element's long axis ($\zeta=w_x$), while the other Fresnel approximations are inaccurate for this source geometry. It may be noted that at this range, the $\zeta=r$ approximation more closely resembles the low-level detail of the linear-array element field, even though the $\zeta=w_x$ approximation achieves better overall quantitative accuracy, as shown in Fig. 3. Figure 2(c), which shows fields computed for a large rectangular element, shows that all four Fresnel approximations properly depict the collimated main beam. The low-level field details in this case are captured partially by each of the four Fresnel approximations. In all cases, the regions of greatest computational accuracy are consistent with those listed in Table I for each Fresnel approximation.

The quantitative accuracy achieved by each of the four Fresnel approximations is illustrated in Fig. 3 for the three source configurations shown in Fig. 2. In each case, fields were computed using the four Fresnel approximations over a three-dimensional region spanning from 0.2 to 50 mm in range (z) and 0–10 mm in the elevation and azimuthal di-

rections (x and y), with a spatial step size of 0.2 mm in each direction. The rms error for the complex pressure field in each z plane was defined as

$$\frac{\langle |p - p_{\text{ref}}| \rangle}{\langle |p_{\text{ref}}| \rangle} = \sqrt{\frac{\sum_x \sum_y |p(\mathbf{r}) - p_{\text{ref}}(\mathbf{r})|^2}{\sum_x \sum_y |p_{\text{ref}}(\mathbf{r})|^2}}, \tag{31}$$

where $p(\mathbf{r})$ is the complex pressure wave field computed using a Fresnel approximation and $p_{\text{ref}}(\mathbf{r})$ is the complex pressure wave field computed using direct numerical solution of the impulse-response integral. Similarly, the rms error for the pressure magnitude was defined as

$$\frac{\langle |p| - |p_{\text{ref}}| \rangle}{\langle |p_{\text{ref}}| \rangle} = \sqrt{\frac{\sum_x \sum_y (|p(\mathbf{r})| - |p_{\text{ref}}(\mathbf{r})|)^2}{\sum_x \sum_y |p_{\text{ref}}(\mathbf{r})|^2}}. \tag{32}$$

The error results shown in Fig. 3 illustrate how the applicability of each approximation varies depending on the source configuration as well as the range of interest. For the small source (a), the Fresnel approximation based on spherical spreading ($\zeta = r$) is the most accurate at all ranges. For the linear array element (b) and the larger rectangular source (c), the $\zeta = r$ approximation provides the most accurate results at larger ranges, but near the source more accurate results are obtained by the Fresnel approximation corresponding to the source geometry. For the linear array element (b), the diffracted cylindrical-wave approximation ($\zeta = w_x$) is the most accurate near the source, while for the rectangular source (c) the diffracted plane-wave approximation ($\zeta = z$) is the most accurate near the source.

In all cases, choice of the most appropriate approximation yields pressure fields with complex pressure errors on the order of 10% or less and magnitude errors of several percent, except for points very near the transducer surface. This performance is consistent with previous results demonstrating amplitude and phase errors of 1% to 2% for the Fresnel approximation applied to collimated beam propagation within the near field.[41] This level of accuracy is sufficient for many practical ultrasound applications. Comparable accuracy can be expected for other, more general source distributions of the form given by Eq. (10).

The Fresnel approximation methods described here provide simple analytic expressions for pressure fields from many aperture configurations, including various amplitude distributions and independent azimuthal and elevation focusing. These features are illustrated in Figs. 4–6, which illustrate the fields of 10×10 mm^2 rectangular apertures with uniform and error-function apodizations, focused at a distance of 20 mm in an attenuating medium. The wave number employed was $k = 20 + 0.0288i$ rad/mm, corresponding to a 5 MHz frequency for radiation into a water-like medium with a tissue-mimicking attenuation of 2.5 dB/cm. Figure 4 shows the on-axis pressure magnitude for the uniform, focused rectangular aperture case ($\sigma = 0$), computed both by the Fresnel approximation ($\zeta = r$) and by direct numerical evaluation of the Rayleigh integral [Eq. (1)], both with the quadratic focusing phase specified by Eq. (17). In the software package employed (MATHEMATICA 5.2, with the above-described computer configuration), the required computation time for this plot was 0.63 s for the Fresnel approximation and 3.7×10^3 s for direct evaluation of the Rayleigh integral. The Fresnel approximation predicts the peak position in this case with less than 3% error and the peak pressure magnitude with less than 2% error. Positions of local, diffraction-induced peaks and nulls are less accurate for small axial distances where the Fresnel approximation is less valid.

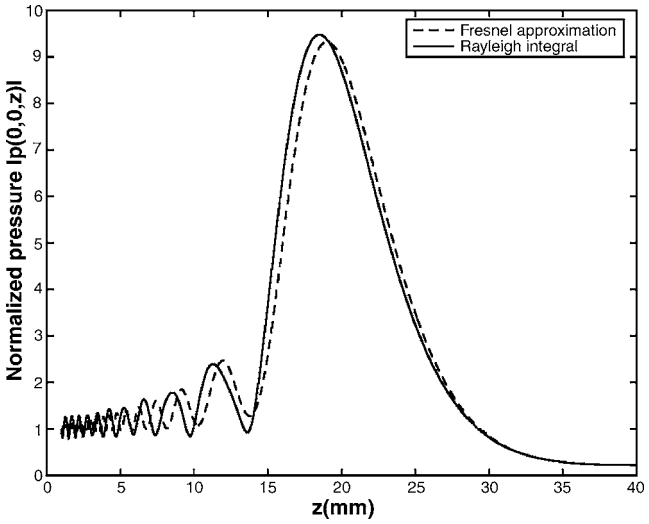

FIG. 4. On-axis pressure magnitudes, computed using the Fresnel approximation and numerical evaluation of the Rayleigh integral, for a 10×10 mm^2 aperture with a focal length of 20 mm in both the x and y directions and a wave number of $20 + 0.0288i$ rad/mm.

To illustrate use of the solutions presented here for computation of source apodization effects, the focused aperture configuration used for Fig. 4 can be compared to error-function apodized sources of the same dimensions. The four error function apodizations employed, ranging from no apodization ($\sigma = 0$ mm) to significant smoothing

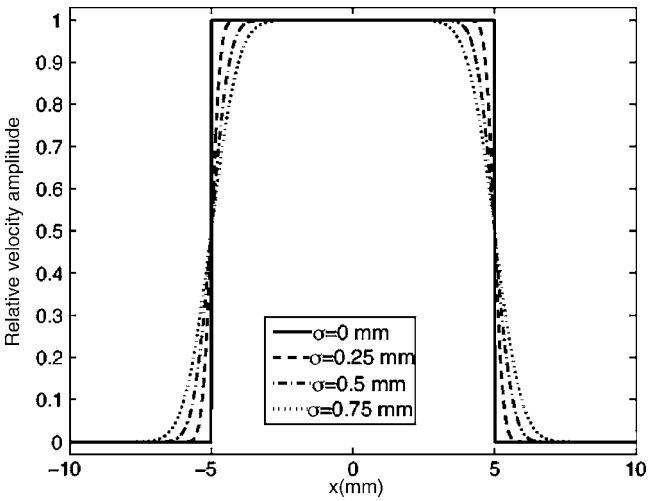

FIG. 5. Error function apodizations used in the test computation for a focused aperture. The parameter $\sigma = 0$ mm corresponds to a rectangular aperture while increasing σ results in greater smoothing of the source amplitude distribution.

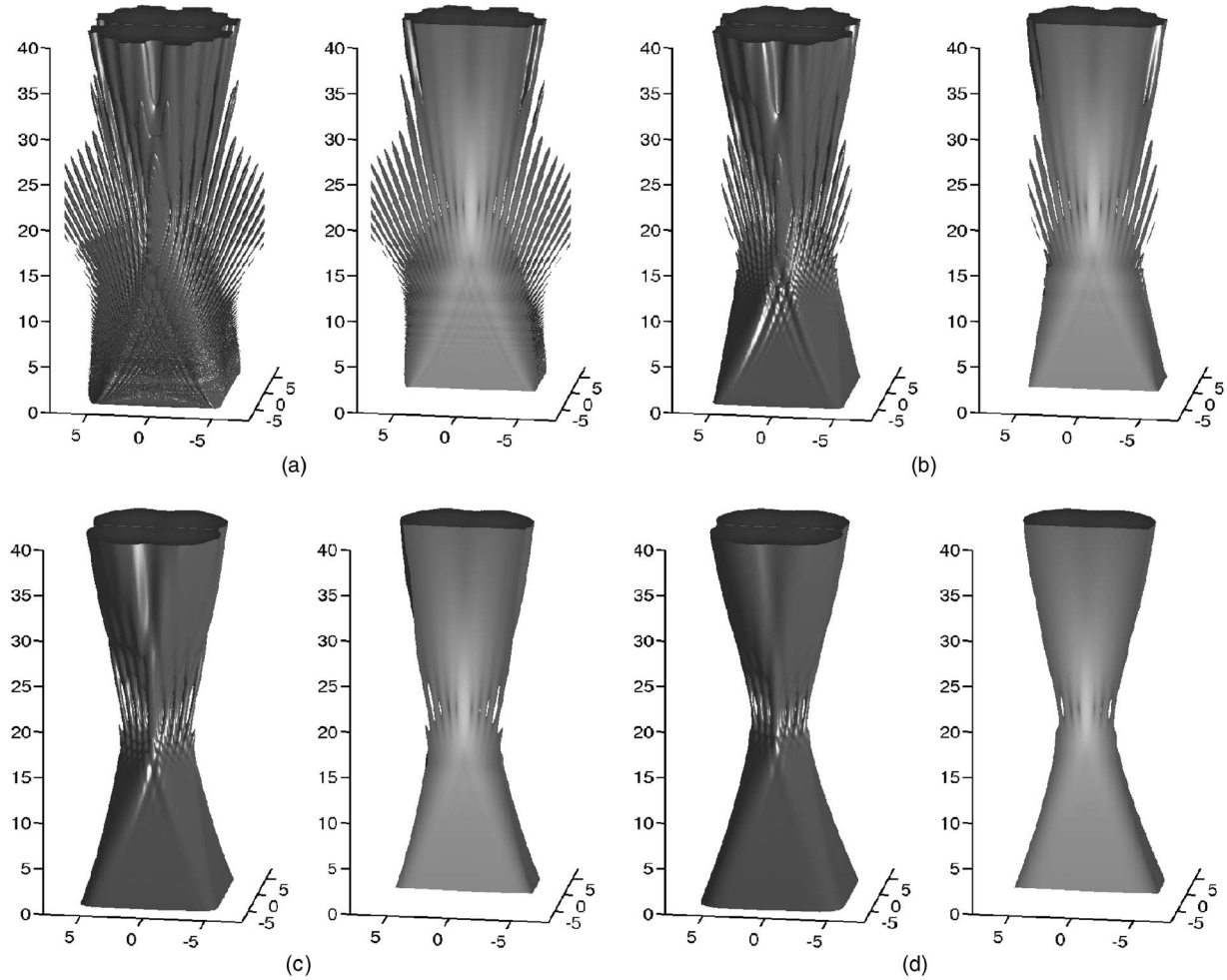

FIG. 6. Three-dimensional pressure fields for the four error function apodizations of Fig. 5, applied to a 10×10 mm^2 aperture with a focal length of 20 mm in both the x and y directions and a wave number of $20+0.0288i$ rad/mm. Each panel shows a rendering of the pressure magnitude isosurface at a level 36 dB below the peak (left) as well as the xz-plane pressure magnitude, logarithmically scaled and superimposed on a half-space −36 dB isosurface rendering (right).

($\sigma=0.75$ mm), are plotted in Fig. 5. Isosurface renderings and xz-plane cross sections of pressure magnitudes for the four apodization conditions, computed using Eq. (27) with $\zeta=z$, are displayed in Fig. 6. As the parameter σ increases, the rectangular aperture is increasingly smoothed, causing the sidelobes to fall markedly while the width of the main lobe remains essentially constant.

IV. DISCUSSION

The approximations described here should be useful for large-scale computations of radiated acoustic fields, as well as for further analytic studies. Several aspects concerning the practical application of these methods are discussed here.

A. Accuracy and efficiency of computations

As illustrated by Figs. 2 and 3, accuracy of computations can be affected by the choice of Fresnel approximation employed. The numerical results reported here suggest that the Fresnel approximation based on diffracted spherically spreading waves ($\zeta=r$) provides the most accurate results for a variety of source configurations, if the distance of interest is more than several source diameters from the center of the aperture. For distances less than several source diameters, the appropriate choice of approximation depends on the source configuration. For sources that are much longer in one dimension, the most appropriate Fresnel approximation near the source is based on diffracted cylindrical waves centered on the long axis of the source, e.g., $\zeta=w_x$ for the source configuration shown in Fig. 2(b). For sources that are large compared to the wavelength in two dimensions, the most appropriate Fresnel approximation near the source represents the field as a diffracted plane wave ($\zeta=z$).

The absolute accuracy achievable using the Fresnel approximations is good, with relative errors on the order of 10% near the source, and errors of less than 1% at distances large compared to the source dimensions. Thus, these approximations should be suitable for many ultrasound applications, including characterization of beam patterns for diffraction correction in scattering and attenuation measurements and simulation of ultrasound imaging methods. For simulation of ultrasound imaging methods,[4–7] accurate depiction of low-level detail in ultrasound beams may be particularly important, in which case the Fresnel approximation describing diffracted spherical waves ($\zeta=r$) may be most appropriate throughout the region of interest. The methods provide increased accuracy when only the pressure mag-

nitude is of interest, as is the case for many applications such as simulation of heating caused by therapeutic ultrasound arrays.[1–3]

The numerical efficiency of the Fresnel approximations shown here is excellent, although definitive optimization of computation speed is beyond the scope of the present paper. Since pressure fields for all the apertures considered have been expressed in closed form in terms of the error function and Fresnel integral, available methods for optimizing computation of these special functions[42,43] would further improve the efficiency of the pressure computations. For example, both the Fresnel integral and the complex error function can be evaluated accurately using rational approximations,[32,43] which can be used to compute these special functions using only a few arithmetic operations at each point.

B. Extension to other configurations

The methods described here provide explicit analytic formulas for the time-harmonic fields of rectangularly symmetric, unfocused or focused apertures with a variety of surface velocity distributions. These formulas can be employed to compute fields for more complex configurations including radiation from arrays of rectangularly symmetric elements and from pulsed sources.

Radiation from transducer arrays composed of rectangularly symmetric elements can be simulated by computing the field from each individual element in a coordinate system originating from the element center, and superposing the fields with the desired amplitude and phase weighting. This process has been described elsewhere[3,10] and has been shown to result in good agreement between computed and measured array fields.[44]

The Fresnel approximations described here are based on the frequency-domain Rayleigh integral, so that they are directly applicable to continuous-wave sources. Many ultrasound applications, such as modeling of ultrasound ablation,[1–3] continuous-wave imaging systems,[5] and analysis of scattering measurements,[8–10] require only computation of continuous-wave radiated fields. Fields of narrow-band (e.g., tone burst) sources can also be closely approximated by these single-frequency fields, using amplitude envelopes specified by the source wave form and the acoustic travel time to the field point.[45] Thus, for a source wave form

$$u(t) = w(t)e^{-i\omega t},$$

the time-domain pressure field is given approximately by

$$p(\mathbf{r},t) = \mathrm{Re}[p(\mathbf{r})w(t-\zeta/c)e^{-i\omega t}], \tag{33}$$

where $p(\mathbf{r})$ is a single-frequency pressure field as given by Eqs. (9), (13), or Eq. (27), and ζ is the nominal propagation distance for the Fresnel approximation employed (e.g., $\zeta=z$ for a diffracted plane wave, $\zeta=r$ for a diffracted spherical wave, and $\zeta=w_y$ or $\zeta=w_x$ for a diffracted cylindrical wave).

For wideband sources such as ultrasonic array elements excited by short pulses, time-domain pressure fields can be obtained from the approximations derived here by computing separate frequency components and performing an inverse temporal Fourier transform of the field at each spatial point. This process is most efficient for relatively narrow-band signals, for which the field can be accurately characterized using a small number of temporal frequency components.

V. CONCLUSION

This work has provided analytic expressions for the acoustic fields of a wide variety of baffled, rectangularly symmetric sources, including focused and unfocused apertures with various forms of amplitude apodization. All of these analytic expressions can be expressed in a form similar to the previously derived field of an unfocused rectangular piston, and are valid for several different instances of the Fresnel approximation. Given the choice of the Fresnel approximation most suited to the source geometry and field region of interest, the analytically determined fields accurately approximate the true radiated fields, allowing both field computations and further analytic study of radiation from rectangularly symmetric sources.

[1] C. Lafon, F. Prat, J. Y. Chapelon, F. Gorry, J. Margonari, Y. Theillere, and D. Cathignol, "Cylindrical thermal coagulation necrosis using an interstitial applicator with a plane ultrasonic transducer: *in vitro* and *in vivo* experiments versus computer simulations," Int. J. Hyperthermia **16**, 508–522 (2000).

[2] R. Chopra, M. J. Bronskill, and F. S. Foster, "Feasibility of linear arrays for interstitial ultrasound thermal therapy," Med. Phys. **27**, 1281–1286 (2000).

[3] T. D. Mast, I. R. S. Makin, W. Faidi, M. M. Runk, P. G. Barthe, and M. H. Slayton, "Bulk ablation of soft tissue with intense ultrasound: Modeling and experiments," J. Acoust. Soc. Am. **118**, 2715–2724 (2005).

[4] Y. Li and J. A. Zagzebski, "A frequency domain model for generating B-mode images with array transducers," IEEE Trans. Ultrason. Ferroelectr. Freq. Control **46**, 690–699 (1999).

[5] T. Jansson, T. D. Mast, H. W. Persson, and K. Lindström, "Frequency dependence of speckle in continuous-wave ultrasound with implications for blood perfusion measurements," IEEE Trans. Ultrason. Ferroelectr. Freq. Control **49**, 715–725 (2002).

[6] J. A. Jensen, "Simulation of advanced ultrasound systems using Field II," Proceedings of the 2004 IEEE International Symposium on Biomedical Imaging, Arlington, VA, April 2004, pp. 636–639.

[7] Y.-T. Shen and J. C. Lacefield, "First-order speckle statistics of ultrasound breast images synthesized from a computational anatomy model," Can. Acoust. **33**, 86–87 (2005).

[8] M. F. Insana, T. J. Hall, and L. T. Cook, "Backscatter coefficient estimation using array transducers," IEEE Trans. Ultrason. Ferroelectr. Freq. Control **41**, 714–723 (1994).

[9] X. Chen, D. Phillips, K. Q. Schwarz, J. G. Mottley, and K. J. Parker, "The measurement of backscatter coefficient from a broadband pulse-echo system: A new formulation," IEEE Trans. Ultrason. Ferroelectr. Freq. Control **44**, 515–525 (1997).

[10] T. T. Jansson, T. D. Mast, and R. C. Waag, "Measurements of differential scattering cross-section using a ring transducer," J. Acoust. Soc. Am. **103**, 3169–3179 (1998).

[11] T. L. Szabo, *Diagnostic Ultrasound Imaging: Inside Out* (Elsevier, Burlington, MA, 2004), Chap. 6.

[12] P. R. Stepanishen and K. C. Benjamin, "Forward and backward projection of acoustic fields using FFT methods," J. Acoust. Soc. Am. **71**, 803–812 (1982).

[13] E. G. Williams and J. D. Maynard, "Numerical evaluation of the Rayleigh integral for planar radiators using the FFT," J. Acoust. Soc. Am. **72**, 2020–2030 (1982).

[14] P. R. Stepanishen, "The time-dependent force and radiation impedance on a piston in a rigid infinite planar baffle," J. Acoust. Soc. Am. **49**, 841–849 (1971).

[15] J. C. Lockwood and J. G. Willette, "High-speed method for computing the exact solution for the pressure variations in the nearfield of a baffled piston," J. Acoust. Soc. Am. **53**, 735–741 (1973).

[16] J. L. San Emeterio and L. G. Ullate, "Diffraction impulse-response of rectangular transducers," J. Acoust. Soc. Am. **92**, 651–662 (1992).

[17]A. Neild and D. A. Hutchins, "A theoretical model for a finite-size acoustic receiver," J. Acoust. Soc. Am. **155**, 1546–1556 (2004).
[18]R. J. McGough, "Rapid calculations of time-harmonic nearfield pressures produced by rectangular pistons," J. Acoust. Soc. Am. **115**, 1934–1941 (2004).
[19]P. Faure, D. Cathignol, and J. Y. Chapelon, "On the pressure field of a transducer in the form of a curved strip," J. Acoust. Soc. Am. **95**, 628–637 (1994).
[20]K. B. Ocheltree and L. A. Frizzell, "Sound field calculation for rectangular sources," IEEE Trans. Ultrason. Ferroelectr. Freq. Control **46**, 242–248 (1989).
[21]C. Lee and P. J. Benkeser, "A computationally efficient method for the calculation of the transient field of acoustic radiators," J. Acoust. Soc. Am. **96**, 545–551 (1994).
[22]B. Ü. Karbeyaz, E. L. Miller, and R. O. Cleveland, "Semi-analytical computation of the acoustic field of a segment of a cylindrically concave transducer in lossless and attenuating media," J. Acoust. Soc. Am. **121**, 1226–1237 (2007).
[23]J. W. Goodman, *Introduction to Fourier Optics*, 3rd ed. (Roberts & Co., Greenwood Village, CO, 2005), Chap. 4.
[24]A. Freedman, "Sound field of a rectangular piston," J. Acoust. Soc. Am. **32**, 197–209 (1960).
[25]T. L. Szabo, "Generalized Fourier transform diffraction theory for parabolically anisotropic media," J. Acoust. Soc. Am. **63**, 28–34 (1978).
[26]D. Ding,Y. Zhang, and J. Liu, "Some extensions of the Gaussian beam expansion: Radiation fields of the rectangular and the elliptical transducer," J. Acoust. Soc. Am. **113**, 3043–3048 (2003).
[27]B. D. Cook and W. J. Arnoult III, "Gaussian-Laguerre/Hermite formula for the nearfield of an ultrasonic transducer," J. Acoust. Soc. Am. **59**, 9–11 (1976).
[28]J. J. Wen and M. A. Breazeale, "A diffraction beam field expressed as the superposition of Gaussian beams," J. Acoust. Soc. Am. **83**, 1752–1756 (1988).
[29]A. Sahin and A. C. Baker, "Ultrasonic pressure fields due to rectangular apertures," J. Acoust. Soc. Am. **96**, 552–556 (1994).
[30]K. Sha, J. Yang, and W.-S. Gan, "A complex virtual source approach for calculating the diffraction beam field generated by a rectangular planar source," IEEE Trans. Ultrason. Ferroelectr. Freq. Control **50**, 890–897 (2003).
[31]A. D. Pierce, *Acoustics: An Introduction to its Physical Principles and Applications*, 2nd ed. (Acoustical Society of America, Melville, NY, 1989), Chap. 5.
[32]M. Abramowitz and I. A. Stegun, *Handbook of Mathematical Functions* (National Bureau of Standards, Washington, DC, 1972), Chap. 7.
[33]S. Zhang and J. Jin, *Computation of Special Functions* (Wiley, New York, 1996), Chap. 16.
[34]S. Wolfram, *The Mathematica Book*, 4th ed. (Cambridge University Press, New York, 1999), pp. 766, 1125, 1143.
[35]T. D. Mast and F. Yu, "Simplified expansions for radiation from a baffled circular piston," J. Acoust. Soc. Am. **118**, 3457–3464 (2005).
[36]N. F. Declercq and J. Degneck, "The Laplace transform to describe bounded inhomogeneous waves," J. Acoust. Soc. Am. **116**, 51–60 (2004).
[37]M. Greenspan, "Piston radiator: Some extensions of the theory," J. Acoust. Soc. Am. **65**, 608–621 (1979).
[38]I. M. Mason, "Anisotropy, diffraction scaling, surface wave lenses, and focusing," J. Acoust. Soc. Am. **53**, 1123–1128 (1973).
[39]T. Lawu, M. Tabei, and M. Ueda, "Near-field ultrasonic scattering from a cavity in steel considering the velocity amplitude on the transducer face using an error function model," J. Acoust. Soc. Am. **104**, 1242–1245 (1998).
[40]J. Naze Tjøtta and S. Tjøtta, "Nearfield and farfield of pulsed acoustic radiators," J. Acoust. Soc. Am. **118**, 3457–3464 (2005).
[41]W. H. Southwell, "Validity of the Fresnel approximation in the near field," J. Opt. Soc. Am. **71**, 7–14 (1998).
[42]G. Poppe and C. Wijers, "More efficient computation of the complex error function," ACM Trans. Math. Softw. **16**, 38–46 (1990).
[43]J. A. C. Weideman, "Computation of the complex error function," SIAM (Soc. Ind. Appl. Math.) J. Numer. Anal. **31**, 1497–1518 (1994).
[44]I. R. S. Makin, T. D. Mast, W. Faidi, M. M. Runk, P. G. Barthe, and M. H. Slayton, "Miniaturized ultrasound arrays for interstitial ablation and imaging," Ultrasound Med. Biol. **31**, 1539–1550 (2005).
[45]J. A. Campbell and R. C. Waag, "Normalization of ultrasonic scattering measurements to obtain average differential scattering cross sections for tissues," J. Acoust. Soc. Am. **74**, 393–399 (1983).

Liquid jet response to internal modulated ultrasonic radiation pressure and stimulated drop production

Joel B. Lonzaga, Curtis F. Osterhoudt, David B. Thiessen, and Philip L. Marston[a)]
Department of Physics and Astronomy, Washington State University, Pullman, Washington 99164-2814

(Received 15 June 2006; revised 8 January 2007; accepted 30 March 2007)

Experimental evidence shows that a liquid jet in air is an acoustic waveguide having a cutoff frequency inversely proportional to the jet diameter. Ultrasound applied to the jet supply liquid can propagate within the jet when the acoustic frequency is near to or above the cutoff frequency. Modulated radiation pressure is used to stimulate large amplitude deformations and the breakup of the jet into drops. The jet response to the modulated internal ultrasonic radiation pressure was monitored along the jet using (a) an optical extinction method and (b) images captured by a video camera. The jet profile oscillates at the frequency of the radiation pressure modulation and where the response is small, the amplitude was found to increase in proportion to the square of the acoustic pressure amplitude as previously demonstrated for oscillating drops [P.L. Marston and R.E. Apfel, J. Acoust. Soc. Am. **67**, 27–37 (1980)]. Small amplitude deformations initially grow approximately exponentially with axial distance along the jet. Though aspects of the perturbation growth can be approximated from Rayleigh's analysis of the capillary instability, some detailed features of the observed jet response to modulated ultrasound are unexplained neglecting the effects of gravity.
© *2007 Acoustical Society of America.* [DOI: 10.1121/1.2734493]

PACS number(s): 43.25.Qp, 43.35.Ty, 43.25.Uv, 43.20.Mv [MFH] Pages: 3323–3330

I. INTRODUCTION

The coupling of modulated ultrasonic radiation pressure with the capillary modes of a liquid jet described in the present paper extends earlier research on modulated radiation pressure. Marston and Apfel[1,2] drove shape oscillations of liquid drops surrounded by an immiscible host liquid using modulated ultrasonic radiation pressure. Marston[3] analyzed the coupling for the case where the ultrasonic wave has two sidebands (with a suppressed carrier) so that the radiation pressure oscillates at a single frequency. Modulated radiation pressure was later used by Trinh *et al.*[4] to study the decay of oscillations following the removal of the modulated radiation pressure and the steady-state oscillation mode spectrum of drops. Other studies of radiation pressure induced shape oscillations of drops surrounded by an immiscible host liquid include Marston and Goosby[5] and Hsu and Apfel.[6] Holt *et al.*[7] discuss observation of radiation pressure induced oscillations of drops in air. Modulated radiation pressure also provides a method for controlled excitation of the capillary modes of bubbles in water.[3] This was experimentally demonstrated by Asaki *et al.*[8] A refined method of detecting the free decay of shape oscillations was used by Asaki and Marston[9] to compare with a theory for boundary layer damping based on a generalization of the approach in Marston.[3] Modulated radiation pressure has also been shown an effective way of selectively exciting the hydrodynamic capillary modes of liquid bridges suspended between two fixed supports.[10] Acoustic radiation stresses have also been used to suppress the capillary break up of slender liquid bridges in situations where it was not previously possible to suppress break up by other hydrodynamic means.[11]

The instability of a liquid jet issuing from a nozzle as a cylinder is one of the classic problems in physics and currently has great practical and industrial importance in atomization, ink jet printing, fuel injection, particle sorting, and polymer fiber spinning. The phenomenon of jet break up was studied experimentally by Savart[12] and studied theoretically by Plateau,[13] Maxwell,[14] and Rayleigh[15] and extended by Chandrasekhar[16] and others for a viscous fluid. From the consideration of surface energy, Plateau derived the minimum capillary wavelength for a disturbance to be unstable on an infinitely long liquid cylinder as $\Lambda_{\min}=\pi D$, where $D=2a$ is the liquid jet cylinder diameter. For an inviscid, incompressible, cylindrical liquid jet sprayed into a vacuum, Rayleigh derived the optimum wave number for a disturbance to be most unstable as $k_{\mathrm{opt}}=0.697/a$. Donnelly *et al.*[17] presented elaborate experiments on the instability of a liquid jet supporting Rayleigh's calculation. Lin[18] and Pan and Suga[19] review a wide range of jet breakup processes. Unlike the jets considered here, in high velocity jets the interaction with the surrounding gas influences drop production.

Acoustically stimulated break up of liquid jets has been used experimentally by various investigators to produce droplet streams.[20,21] For instance, Berglund and Liu[20] devised a system now commonly known as the Berglund-Liu aerosol generator that produces droplets at a frequency approximately equal to the vibration frequency of a piezoelectric ceramic coupled to the jet. While there are several articles in the literature about the growth rate of the instability, none of those actually made use of *modulated ultrasonic radiation pressure* as the source of the perturbation of the jet. In our experiment, we devise a quite different system to be described in Sec. III that employs modulated ultrasonic radiation pressure. In this system, the high frequency ultrasonic wave is applied and is modulated at a frequency suit-

a)Electronic mail: marston@wsu.edu

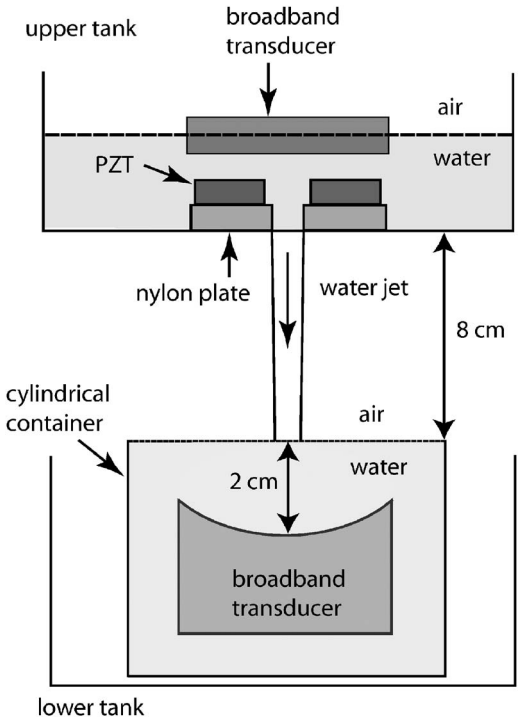

FIG. 1. Experimental setup for studying the instability of a water jet and detecting the ultrasonic signal transmitted through the water jet. In studying the jet instability, the cylindrical container is removed so that the jet is directly impinging on the bottom tank.

able for coupling to relatively low-frequency drop production rates.

Another relevant property of a liquid jet is its ability to act as an acoustic waveguide. Jacobi[22] analyzed the uniform liquid cylinder waveguide with various nondissipative boundary conditions. He calculated the field patterns, phase velocities, and cut-off frequencies for the natural modes of propagation in the cases of a liquid cylinder with rigid walls and of a liquid cylinder with pressure-release boundary walls, to mention a few. While he presented experimental measurements of phase velocities, he did not report any direct experimental verification of an acoustic cut-off frequency in the liquid cylinder. Recent investigations of ultrasonic radiation forces within cylindrical waveguides have emphasized the case where the waveguide had a solid elastic wall.[23]

The purpose of this paper is to: (a) describe a technique of generating drops that exploits modulation of ultrasonic radiation pressure, (b) provide direct experimental evidence of the acoustic cut-off frequency in a liquid jet waveguide, (c) demonstrate the second-order effect of the drive voltage on the amplitude of jet oscillation analogous to the case of bubble and drop oscillation previously studied, and (d) report other aspects of the jet response revealed using a light extinction method. A related analysis of modulated radiation stress in Refs. 1 and 2 is generalized to the case of a liquid cylinder in the Appendix.

II. EXPERIMENTAL SETUP

Two plastic tanks are used in this project where one is placed directly above the other as depicted in Fig. 1. A hole is made at the bottom of the upper tank where a nylon plate of 25.4 mm diameter is glued. A 3.57-mm-diam orifice is drilled through the nylon plate. A piezoelectric PZT ring transducer slightly smaller in diameter than the nylon plate is glued concentrically at the top of this plate. The PZT ring had a thickness of 0.6 cm, and outside and inside diameters of 3.5 and 1.4 cm, respectively. The flat sides of the ring were plated with electrodes. For most experiments, the water jet empties from the upper tank through the orifice and impinges on the lower tank. Ultrasound from the piezoelectric ring transducer is coupled to the liquid jet through the orifice. The volumetric flow rate is 5.1 cm^3/s. The water is pumped back up to the upper tank by way of a separate reservoir which removes pump related fluctuations. A diagnostic broadband transducer placed a few millimeters above the ring transducer is used to reflect the sound beam back to the latter creating acoustic resonance. It is also used for the purpose of monitoring the signal. Additional information on the use of these transducers and on the method of driving the source transducer will be described subsequently.

For the purpose of demonstrating the cutoff frequency through the jet, a 15.2-cm tall cylindrical container with 6.4-cm radius is temporarily placed inside the lower tank. The jet impinges at the center of the filled container. A curved broadband transducer is situated at the center of the cylindrical container about 2 cm below the water surface. It is facing upward to detect the transmitted signal through the jet.

Without any applied perturbation or special preparation, a liquid jet tapers as it falls and eventually breaks up into drops. We achieve a longer jet by: (a) placing 6-mm-diam glass beads in the upper tank to dampen disturbances within the flow, (b) mounting the entire experimental setup on a table that mechanically isolates the setup from building vibration, and (c) putting a rubber sheet underneath the bottom tank that isolates the mechanical vibration caused by the impinging water jet.

The principal electronic components used to excite the PZT transducer will now be summarized. The voltage from an SRS DS345 function generator was attenuated and then amplified by an EIN model A150 linear power amplifier. The output was applied directly to the PZT transducer. Because of the broad bandwidth of the transducers, in some of the experiments the applied voltage was as large as 90 V peak. The function generator was operated either in a CW mode (as in Sec. IV) or in a double-sideband-suppressed carrier (DSSC) mode (as in Secs. III and V). As reviewed in the Appendix, DSSC signals consist of two sidebands. They may be expressed as the product $\cos(2\pi f_c t)\cos(2\pi f_o t)$ where the signal at frequency f_o is supplied by a separate modulation oscillator.

III. STIMULATED DROP PRODUCTION

A modulated radiation pressure with the ultrasonic carrier frequency near to or above the cutoff frequency was found to excite varicose modes of the liquid jet. Large drive amplitudes trigger the break up (see Fig. 2) into droplets at the radiation pressure oscillation frequency rather than at (or

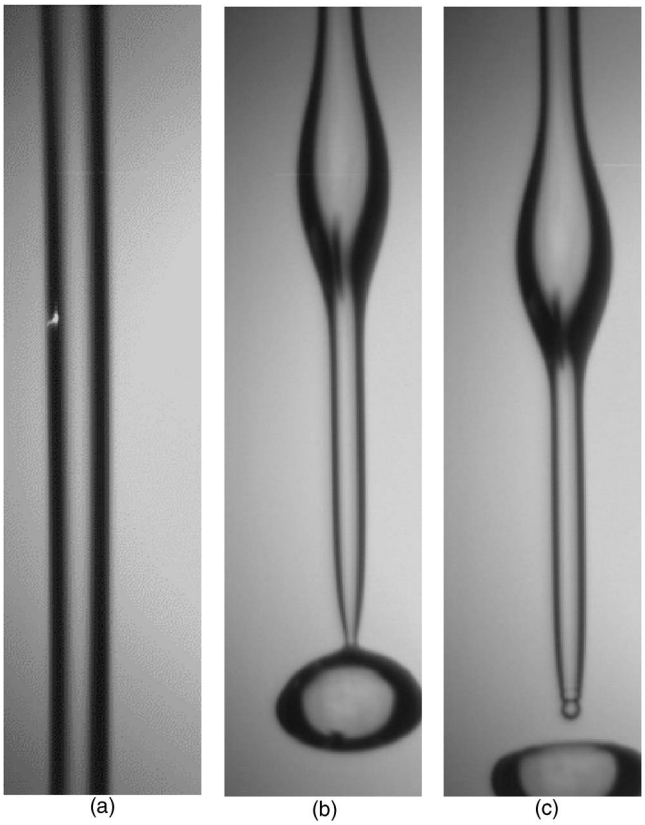

FIG. 2. Display of jet images showing the quiescent jet (a) when no ultrasound is applied and the onset of break up shown in (b) when an oscillating radiation pressure is applied and the break up 1.67 ms later shown in (c). The frequency of the radiation pressure oscillation is 94 Hz and the carrier frequency is 680 kHz. The distance of both image midsections from the nozzle is 8.3 cm and the nozzle velocity is 51.2 cm/s.

near) the ultrasonic carrier frequency as in the case of Berglund-Liu aerosol generator that produces drops through the vibration of a piezoelectric ceramic at the orifice. This is a significant finding because it applies to relatively low-frequency drop production. Furthermore, by using modulated radiation pressure it is relatively easy to alter the drop production rate by shifting the modulation frequency. An advantage of using modulated radiation pressure to drive the jet has to do with the ability to maintain a constant forcing amplitude as the modulation frequency is changed. For DSSC modulation with orders of magnitude difference between the carrier and modulation frequency, the frequency at which the electromechanical system is driven is nearly constant over a broad range of modulation frequencies. This would allow a resonant mechanical drive to be kept on resonance as the drop production rate is changed. In the example shown in Fig. 2 DSSC modulation is used with peak applied transducer voltage of 90 V.

IV. ACOUSTIC WAVEGUIDE MODES AND CUTOFF

The treatment of a liquid cylinder as an acoustic waveguide has been theoretically explored.[22] In the present application, the jet radius decreases as the jet accelerates vertically downward due to gravity. Nevertheless, a similar treatment can be used to calculate the cutoff frequency f_{co} below which the ultrasonic transmission down the jet is greatly reduced. The predicted f_{co} will be compared with the experimental value.

The acoustic pressure amplitude of a single mode within a liquid cylinder can be expressed as the real part of

$$P_{nj} = A_{nj} J_n(k_{nj} r) e^{i(n\theta + \beta_j z)} e^{-i\omega t}, \tag{1}$$

where A_{nj} is a constant to be found from the boundary conditions, θ is the azimuthal angle, J_n is the nth order cylindrical Bessel function of the first kind, k_{nj} is the radial wave number associated with J_n, r is the radial coordinate, β_j is the axial wave number of the (n,j) mode, j is the radial index, z is the axial coordinate, and ω is the angular frequency. The radial and axial wave numbers are related to each other as shown by

$$\left(\frac{\omega}{c}\right)^2 = (k_{nj})^2 + \beta_j^2, \tag{2}$$

where c is the acoustic velocity in the waveguide. If the liquid cylinder is in the air, the pressure release boundary condition applies approximately.[22] For an axisymmetric mode $n=0$, this condition requires that $J_0(k_{0j}a)=0$ or $k_{0j}=\alpha_j/a$, where α_j and a are the jth root of J_0 and the cylinder radius, respectively. At cutoff, this axisymmetric mode has $\beta_j=0$, and Eq. (2) is reduced to $\omega_{co}/c=\alpha_j/a$. Taking the first root of J_0, the lowest cutoff frequency for the axisymmetric mode is thus given by

$$f_{co} = \frac{c}{2\pi}\frac{2.4048}{a}. \tag{3}$$

The preceding equation shows that the cutoff frequency is inversely proportional to the radius of a cylindrical liquid jet in air. Liquid jets in normal gravity are tapered. When applied to such a liquid jet, for the purpose of finding the cutoff frequency for transmission down the jet a becomes the *minimum* jet radius.

The validity of Eq. (3) was verified by sending an acoustic signal from the upper liquid reservoir down through the jet whose minimum radius close to the water surface in the lower reservoir was about 1.0 mm so that Eq. (3) predicts $f_{co}=566$ kHz. This radius is measured at the first trough from the liquid surface formed by standing capillary waves captured by a video camera shown in Fig. 3(a). (Localized low amplitude standing capillary waves are known to occur when a jet enters a reservoir.[24]) The frequency of the signal is increased from 300 to 800 kHz in increments of 0.5 kHz. The amplitude of the transmitted signal as a function of frequency is shown in Fig. 4. This was extracted with a two-phase lock-in amplifier (PAR model 5202). The observed transition at 554 kHz is consistent with Eq. (3) considering the uncertainty of 0.1 mm in the minimum diameter.

V. OPTICAL DETECTION OF THE JET RESPONSE

A. Light-extinction method

A laser beam is employed to illuminate the water jet. A horizontal slit is used to block part of the circular beam to produce a horizontally planar beam shown in Fig. 5. This rectangular beam impinges on the jet and is partially scat-

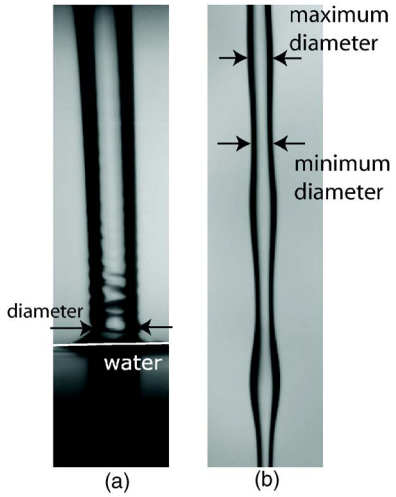

FIG. 3. (Color online) (a) An image of the jet impinging on the surface of the bottom reservoir showing the measured local diameter used to calculate the cutoff frequency. (b) The first of a series of 39 images of the jet showing the selected maximum and minimum diameters. Since these diameters change position with time as a surface wave propagates, these images are used to calculate the wave velocity and temporal growth rate of the perturbation.

tered. The unscattered light makes its way through a convex lens and then to a photodetector. The signal collected by the photodetector is analyzed with the aid of a two-phase lock-in amplifier (SRS model SR530). The reduction in the power of the detected light is approximately proportional to the instantaneous local radius of the jet where it is assumed that the planar laser beam has uniform intensity. Hence, the amplitude of the oscillation of the jet is proportional to the oscillation in the detected optical power. This pseudoextinction scheme was previously employed by Stroud and Marston[25] to detect transient bubble oscillations. Additional discussion of the optical principles can be found in that paper.

The ultrasound employed in this experiment is modulated. The modulation is achieved by multiplying a high-

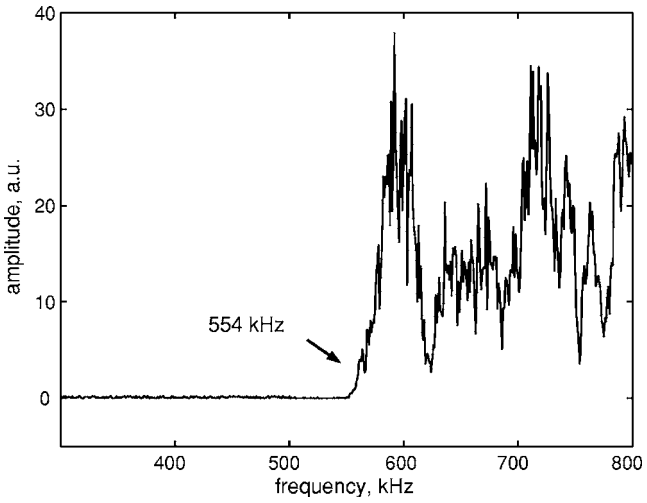

FIG. 4. Plot of the amplitude of the transmitted acoustic signal through the water jet as a function of the frequency. No significant acoustic signal is picked up by the detector transducer for carrier frequencies below 554 kHz. The jet radius at the water surface in the bottom tank is approximately 1.0 mm. "a.u." denotes arbitrary unit.

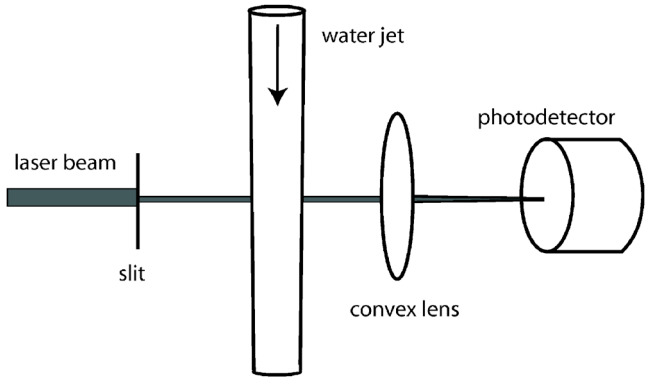

FIG. 5. (Color online) Schematic diagram of a light-scattering method used to detect the jet response. The photodetector is connected to a lock-in amplifier that is not shown.

frequency signal (0.30–1.0 MHz, subsequently referred to as the carrier) and a low-frequency signal f_o (10–100 Hz) referred to as the modulation. When such a signal is amplified and applied to a linear ultrasonic transducer it has been shown[1,2] that the resulting radiation pressure oscillates at a frequency $2f_o$, called the radiation pressure oscillation frequency, and that the oscillation of radiation pressure amplitude is proportional to the square of the drive amplitude. (See also the Appendix.) Consequently, the lock-in amplifier reference signal is set to $f=2f_o$ where f_o is the oscillator frequency.

B. Jet response to varying drive voltage

The carrier and modulation frequencies are maintained at 680 kHz and 47 Hz, respectively. The carrier frequency chosen is a characteristic resonance frequency of the ring transducer while the significance of the modulation frequency selected is noted in the succeeding section. The drive voltage V_g of the SRS generator is increased by 0.1 V from 0.1 to 2.0 V while the laser beam is illuminating the water jet at a fixed distance from the orifice. The jet response is measured as a function of the drive voltage. This enables us to determine the dependence of the amplitude of jet oscillation on the acoustic drive. Figure 6 shows that the amplitude of oscillation as a function of the square of the drive voltage has the predicted linear relationship.

C. Axial growth of the oscillation amplitude

To study the growth rate of the amplitude of jet oscillation, the laser beam is used to illuminate the jet at a distance 7.0 cm below the orifice. The nozzle velocity of the jet determined from the volumetric flow rate is 51.2 cm/s. The response of the jet is measured as a function of the modulation frequency while the drive voltage V_g and the carrier frequency are kept constant at 1.5 V and 680 kHz, respectively. This measurement of the jet response to the modulation frequency is repeated a few times as the axial distance is increased by 0.76 cm each time farther down the jet. The results plotted and shown in Fig. 7 show that the response is maximum at the same modulation frequency of 47 Hz for all of the distances observed. This corresponds to 94 Hz radiation pressure oscillations. Figure 7 also shows that the per-

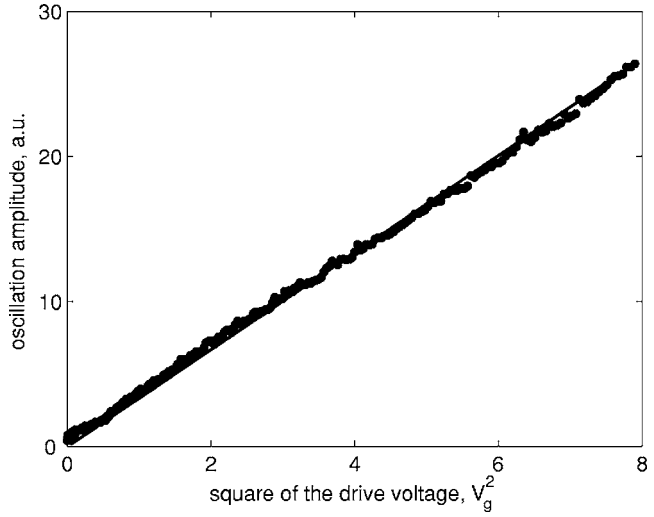

FIG. 6. Plot of the amplitude of jet oscillation as a function of the square of the SRS generator drive voltage.

turbation grows with increasing distance from the nozzle. Further analysis shows that this perturbation grows exponentially as depicted in the semilog plot in Fig. 8 for the data taken at 47 Hz.

D. Photography method

Another method employed to investigate the response of the water jet is by the use of a high speed digital video camera (Phantom v4.2, Vision Research Inc.) capable of processing 3000 frames/s for a 512×128-pixel viewing screen. The water jet is subjected to the same condition as in Sec. V C, namely: orifice velocity 51.2 cm/s, a carrier frequency of 680 kHz, and voltage V_g of 1.5 V. In addition, the modulation frequency is kept at 47 Hz. Movies with a frame rate of 1076 frames/s taken at almost the same segment of the jet as before are converted into a series of still images and analyzed. The top and the bottom of each frame are 6.0 and 10.5 cm from the orifice, respectively. Adjacent local maximum and minimum radii of the jet are chosen from the video records and then measured to determine the amplitude of oscillation.

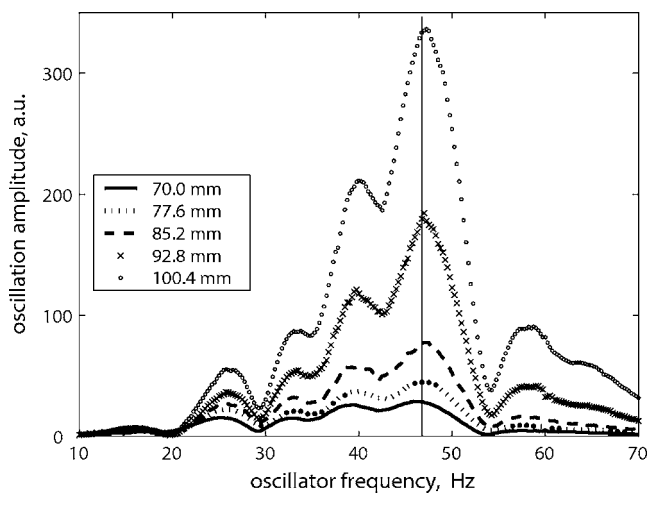

FIG. 7. The dependence of the amplitude of jet oscillation on the oscillator frequency. Frequency scans are shown for five different axial distances from the orifice beginning at 70.0 mm and incremented by 7.6 mm. The symbols used for different axial distances are identified in the box. The vertical line is at an oscillator frequency of 47 Hz, which is the frequency used in Fig. 8.

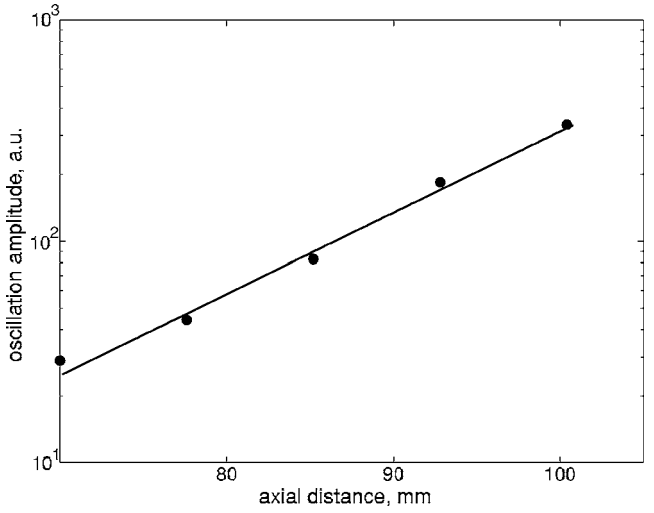

FIG. 8. The dependence of the local amplitude of jet oscillation on the axial distance from the nozzle. The data are taken from the plot in Fig. 7 at an oscillator frequency of 47 Hz (corresponding to a radiation pressure frequency of 94 Hz). The slope of this semilog plot yields the spatial growth rate of the amplitude of oscillation.

The amplitude of jet oscillation is calculated from the difference between the maximum and minimum radii shown in Fig. 3(b). The growth of the amplitude is monitored by tracking these local extrema as time progresses from a series of 39 images. The amplitude is plotted in a semilog plot as a function of time displayed in Fig. 9. This plot is similar to one obtained by Donnelly and Glaberson[17] using direct low frequency excitation of a jet. Measurement of the wave velocity with respect to the laboratory frame is also performed from this series of images by measuring the position of the chosen local maximum radius as a function of time and results are plotted as shown in Fig. 10.

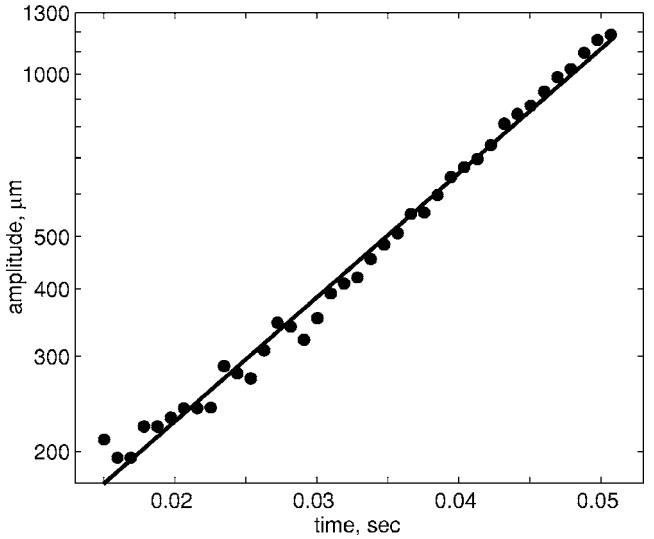

FIG. 9. Plot of the amplitude of the jet perturbation in a convected frame vs elapsed time determined from 39 frames of a video record of the jet similar to the frame shown in Fig. 3(b). The camera used is adjusted to give a resolution of 9.5 pixels/mm and a frame rate of 1076/s.

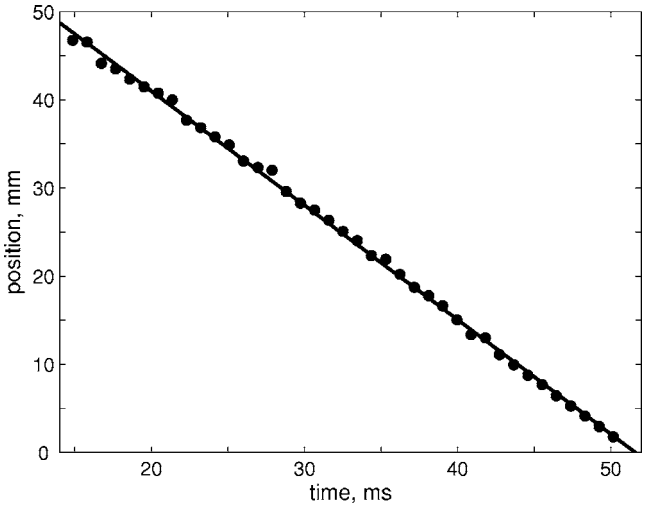

FIG. 10. Plot of the position of a chosen local maximum radius of the jet from 39 frames of a video record as a function of time. The reference position is taken to be the bottom of each frame. The slope yields the velocity of the capillary wave.

VI. DISCUSSION

Figure 2 shows the effect of the applied modulated radiation pressure on the liquid jet. In both frames, the nozzle velocity is 51.2 cm/s and the distance of the image midsection from the nozzle is 8.3 cm. The jet assumes an approximately cylindrical shape without applied ultrasound as shown in Fig. 2(a). When modulated sound with an oscillator frequency of 47 Hz is applied, the jet perturbation oscillates [Fig. 2(b)] at the frequency of 94 Hz, twice the oscillator frequency. The resulting jet break up shown in Fig. 2(c) can be enhanced by increasing the drive voltage. Shown in Fig. 6, the oscillation amplitude increases linearly with the square of the drive voltage. This agrees with prior results for levitated drops[2] and with the generalization to a liquid cylinder in air given in the Appendix.

Without modulation and with low enough acoustic amplitude, the jet can act as an acoustic waveguide. Figure 4 shows that there is no significant signal transmitted below a carrier frequency of 554 kHz. The fine peaks in the amplitude of the transmitted signal are caused by the acoustic resonances of the water-filled cylindrical glass container in the lower tank. The amplitude of these peaks is modulated (approximate spacing of 70 kHz) by a resonance between the face of the detector transducer situated inside the container and the water surface. While the pair of ring and diagnostic transducers in the upper tank also have resonances, the width of the resonance frequencies are so wide (about 170 kHz) that they can hardly be noticed in the plot. The radius of the jet close to the surface of the water in the bottom tank is approximately 1.0 mm. Equation (3) predicts the cutoff frequency to be 566 kHz at this radius. Thus, the experimental cutoff frequency agrees well with the predicted value. The discrepancy could be attributed to the uncertainty of measurement of the jet radius. This confirms that the jet acts like a cylindrical waveguide having a cutoff frequency that is inversely proportional to the jet diameter.

The curves displayed in Fig. 7 show the amplitude of jet oscillation as a function of oscillator frequency for five different axial distances. This family of plots has the highest peaks at $f_o=47$ Hz with the corresponding radiation pressure oscillation frequency of 94 Hz. The amplitude of oscillation at f_o is shown in a semilog plot as a function of axial distance in Fig. 8. The amplitude of jet oscillation is seen to be approximately an exponential function of the axial distance. The slope of this graph yields a spatial growth rate of 0.417 cm^{-1}.

Figure 9 shows the measured amplitude following a specific wave peak plotted versus time. According to this plot, the amplitude grows exponentially as a function of time. The slope of this plot gives the temporal growth rate of 52.84 s^{-1}. The ratio of the temporal to the spatial growth rates is 129.6 cm/s.

Figure 10 is the plot of position of a selected maximum radius of the jet (see Fig. 3) as a function of time where the top and bottom of each frame used are about 6.0 and 10.5 cm below the orifice. The average wave velocity u in this jet region can be calculated from the slope of this plot and is approximately 127.0 cm/s. This is very close to the propagating wave velocity determined from the temporal-to-spatial-growth-rate ratio.

As for the local jet velocity, using Bernoulli's principle and neglecting the effect of surface tension on the jet gives the following approximation for the velocity: $v=v_0\sqrt{1+Gz/a_0}$ where v_0 is the orifice velocity, a_0 the orifice radius, z the distance from the orifice, and G the inverse Froude number defined as $G\equiv 2ga_0/v_0^2$ where g is the acceleration due to gravity. With $G=0.133$, $v_0=51.2$ cm/s and $a_0=0.179$ cm as used in this experiment, the jet velocity at distances 6.0, 8.3, and 10.5 cm below the orifice are 119.8, 136.9, and 152.1 cm/s, respectively. The wave velocity averaged over the jet segment studied is not only well within the local velocities of the jet at the top and at the bottom of this segment, it is also close to the jet velocity at the middle of this segment. This suggests that the surface wave (perturbation) is approximately stationary in the jet frame.

The significance of the optimum response of the jet at the radiation pressure frequency of 94 Hz is related to $k_{\mathrm{opt}}a=0.697$, Rayleigh's wave number of maximum instability of a liquid cylinder. Following the finding in the preceding paragraph, the wave number corresponding to this optimum response can be expressed as $ka\simeq 2\pi fa/u$, where f is the modulation frequency of the radiation pressure, u the wave velocity just determined, and a the jet radius at the region of interest measured with a video camera. Substitution of $f=94$ Hz, $u=127.0$ cm/s, and $a=0.13$ cm (the measured local jet radius) yields $ka=0.60$. Considering the simplifying assumption that the wave is stationary in the jet frame and some experimental error, it is suggestive that Rayleigh's linear stability analysis, as far as maximum instability is concerned, is relevant to local properties of the freely falling jet.

The ratio of inertia to surface tension in the jet is commonly expressed as the Weber number We where $\mathrm{We}=\rho av^2/\sigma$ where σ is the surface tension and ρ the liquid density. The local Weber number for the jet at the axial position of the above-noted measurement is approximately 29.

The maximum spatial growth rate for a constant velocity jet issuing from a nozzle for this Weber number is predicted by Keller *et al.*[26] to occur at a ka very close to that predicted by Rayleigh[15] for the maximum temporal growth rate of an infinite stationary liquid cylinder, namely $ka=0.697$.

Because the quiescent jet is slightly tapered, ultrasound can propagate close to the nozzle at frequencies significantly below the cutoff frequency f_{co} of 554 kHz demonstrated in Fig. 4. Using the nozzle radius of 1.78 mm in Eq. (3) gives a local f_{co} of 320 kHz near the nozzle. It was verified by measuring the optical response of the jet to modulated ultrasound that the jet responded with f_{co} as low as 370 kHz, though in some cases the response was quite weak.

A noteworthy feature of the laser-based measurements of the jet response shown in Fig. 7 is the superposed modulation of the response. This modulation corresponds to an increment of 9 Hz in the modulation oscillator frequency (18 Hz in the radiation pressure frequency). The cause of these is unknown. They appear to be outside the scope of prior investigations because similar measurements of the response of low velocity jets are not available.[17–19]

Inspection of Fig. 2 and other video records of the breaking jet reveal a swelling between the crests of the primary perturbations. The primary perturbation grows into the large drop visible in Fig. 2(b). The large drops are produced at the frequency $2f_o$. Just above the drop in Fig. 2(b) is a secondary swelling which evolves to produce a smaller drop. The characterization of the smaller "satellite" drops is outside the scope of the present study since Rutland and Jameson[27] have previously studied them by direct application of low-frequency sound in the vicinity of the jet. They note that the secondary drops are a consequence of a nonlinear hydrodynamic response not considered by Rayleigh.[15]

Prior disclosure of some of these results was given at the 148th meeting of the Acoustical Society of America.[28]

ACKNOWLEDGMENT

This research was supported by NASA.

APPENDIX: MODULATED RADIATION STRESS ON JETS

The purpose of this Appendix is to demonstrate the form of the radial component of radiation stress on a stationary circular cylindrical liquid column resulting from an internal axisymmetric guided acoustic wave. The notation is similar to Sec. II B of Ref. 29. The analysis uses the Brillouin acoustic radiation stress tensor $\mathbf{S_T}$ based on an Eulerian description of the fluid motion. Angular brackets $\langle\ \rangle$ are used for time averages over a period comparable to the period of the carrier frequency of the ultrasonic wave. Imposing DSSC ultrasound having a difference in the sideband frequencies $(\omega_2-\omega_1)$ small in comparison to the frequency of the suppressed carrier, $\omega_c=(\omega_2+\omega_1)/2$, gives time averages containing a term which oscillates at $(\omega_2-\omega_1)$ and no other oscillating terms as shown in the following in Eq. (A4). A linear analysis of the acoustic fields is used in which the acoustic particle velocity is denoted by $\mathbf{u}$ and the acoustic particle pressure by p. The Brillouin stress tensor may be written (Ref. 29 and papers cited therein):

$$\mathbf{S_T}=(\langle K\rangle-\langle V\rangle)\mathbf{I}-\rho\langle\mathbf{uu}\rangle, \tag{A1}$$

where $\mathbf{I}$ is the unit tensor, $\langle K\rangle=(\rho/2)\langle u^2\rangle$ is the local average of the acoustic kinetic energy density, $\langle V\rangle=\langle p^2\rangle/(2\rho c^2)$ is the local average of the potential energy density, and ρ and c are the density and sound speed in the liquid cylinder, respectively. The radiation stress produces a radial force per area

$$\Gamma=-\hat{\mathbf{r}}\cdot\mathbf{S_T}\cdot\hat{\mathbf{r}}=-(\langle K\rangle-\langle V\rangle)+\rho\langle u_r^2\rangle. \tag{A2}$$

Here and in the following, subscripts r and z are used to denote radial and axial components of $\mathbf{u}$. The external fluid has negligible density compared with the liquid so the acoustic boundary condition is approximated as $p=0$ so that $\langle V\rangle=0$ and Eq. (A2) gives

$$\Gamma=\frac{\rho}{2}(\langle u_r^2\rangle-\langle u_z^2\rangle). \tag{A3}$$

Note that evaluation of the analogous expression for sound internally reflected from a water surface recovers the result for Γ given by Elrod *et al.*[30] For the special case of steady ultrasound in the absence of gravity, the surface of the liquid deforms so that Γ is balanced by capillary stress. In the case of a modulated ultrasonic wave considered here, low-frequency wave motion is executed on the liquid interface. When this wave motion is small in amplitude, the effect of the surface motions is neglected in the approximation of the first-order acoustic quantities u and p. A similar approach is commonly used for approximating radiation stresses on weakly deformed drops and bubbles. For a DSSC-modulated wave, radial and axial components of $\mathbf{u}$ are the superposition $u_r=u_{r1}+u_{r2}$ and $u_z=u_{z1}+u_{z2}$, respectively. These are expressed at the jet's surface as

$$u_{r\ell}=\Re e[U_{r\ell}(z)e^{-i\omega_\ell t}],\quad u_{z\ell}=\Re e[U_{z\ell}(z)e^{-i\omega_\ell t}],\quad \ell=1,2.$$

Let the index q denote r or z. The required time averages are

$$\langle u_q^2\rangle=\frac{1}{2}\{|U_{q1}|^2+|U_{q2}|^2+[U_{q1}^*U_{q2}e^{-i(\omega_2-\omega_1)t}+U_{q1}U_{q2}^*e^{i(\omega_2-\omega_1)t}]\}, \tag{A4}$$

where the final terms are a conjugate pair. It follows that Γ is modulated at the difference frequency $(\omega_2-\omega_1)$ of the applied ultrasonic waves and that Γ depends on the axial coordinate z because of the z dependence of u_{r1}, u_{r2}, u_{z1}, and u_{z2}. Since the quantities are each linear in the oscillator source voltage V_g, it follows that Γ is predicted to increase in proportion to V_g^2.

The aforementioned z dependence may be found for the ideal case of z directed axisymmetric waveguide modes.[22] In the case for a cylinder of radius a,

$$U_{r\ell}=\alpha A_\ell J_1(\alpha)e^{i\beta_\ell z},\quad U_{z\ell}=-i\beta_\ell a A_\ell J_0(\alpha)e^{i\beta_\ell z} \tag{A5}$$

$$\left(\frac{\omega_\ell}{c}\right)^2 = \left(\frac{\alpha}{a}\right)^2 + \beta_\ell^2, \quad \ell = 1,2, \tag{A6}$$

where A_ℓ specifies the amplitude, α is a root of $J_0(\alpha)=0$, and $J_0(\alpha)$ is the zeroth-order Bessel function of the first kind. The lowest mode has $\alpha=2.4048$. Since $U_{z\ell}$ vanishes Γ is non-negative, and the radiation pressure is radially outward. Inspection of Eqs. (A4) and (A5) shows that the axial dependence of Γ is influenced by the proximity of the ω_ℓ to the cutoff frequency $\omega_{co}=c\alpha/a$. For an actual liquid jet in normal gravity, however the axial dependence of Γ is complicated by the taper of the walls of the falling jet. The effect of the superposed flow velocities of the jet on the ultrasonic field is anticipated to be small when the flow velocities are small compared with the sound speed c.

There has been significant recent interest in medical ultrasonic imaging based on the response of tissue to DSSC modulated ultrasound or to other types of modulation.[31–33] Some authors have noted that low frequency oscillations of objects can be induced because of the absorption of a modulated ultrasonic beam.[31,32] Such absorption related processes are neglected in our analysis because the stresses resulting from absorption should be weaker than radiation stresses for the conditions of the experiment described here involving pure water. The coupling described here is more closely analogous to the radiation pressure induced responses of tissue.[33] It is plausible, however, that for a sufficiently viscous liquid jet, momentum transfer to the jet resulting from the absorption of ultrasound could become similar in magnitude as the radiation pressure approximated by Eq. (A3). It is known, however, that increasing the viscosity of the liquid lowers the growth rate of the capillary instability.[16–18]

[1] P. L. Marston and R. E. Apfel, "Acoustically forced shape oscillations of hydrocarbon drops levitated in water," J. Colloid Interface Sci. **68**, 280–286 (1979).

[2] P. L. Marston and R. E. Apfel, "Quadrupole resonance of drops driven by modulated acoustic radiation pressure—Experimental properties," J. Acoust. Soc. Am. **67**, 127–137 (1980).

[3] P. L. Marston, "Shape oscillation and static deformation of drops and bubbles driven by modulated radiation stresses—Theory," J. Acoust. Soc. Am. **67**, 15–26 (1980); erratum **71**, 511 (1982).

[4] E. Trinh, A. Zwern, and T. G. Wang, "An experimental study of small-amplitude drop oscillations in immiscible liquid systems," J. Fluid Mech. **115**, 453–474 (1982).

[5] P. L. Marston and S. G. Goosby, "Ultrasonically stimulated low-frequency oscillation and breakup of immiscible liquid drops: Photographs," Phys. Fluids **28**, 1233–1242 (1985).

[6] C. J. Hsu and R. E. Apfel, "Model for the quadrupole oscillations of drops for determining interfacial tension," J. Acoust. Soc. Am. **82**, 2135–2144 (1987).

[7] R. G. Holt, Y. Tian, J. Jankovsky, and R. E. Apfel, "Surface-controlled drop oscillations in space," J. Acoust. Soc. Am. **102**, 3802–3805 (1997).

[8] T. J. Asaki, P. L. Marston, and E. H. Trinh, "Shape oscillations of bubbles in water driven by modulated ultrasonic radiation pressure: Observations and detection with scattered laser light," J. Acoust. Soc. Am. **93**, 706–713 (1993).

[9] T. J. Asaki and P. L. Marston, "Free decay of shape oscillations of bubbles acoustically trapped in water and sea water," J. Fluid Mech. **300**, 149–167 (1995).

[10] S. F. Morse, D. B. Thiessen, and P. L. Marston, "Capillary bridge modes driven with modulated ultrasonic radiation pressure," Phys. Fluids **8**, 3–5 (1996).

[11] M. J. Marr-Lyon, D. B. Thiessen, and P. L. Marston, "Stabilization of a cylindrical capillary bridge far beyond the Rayleigh-Plateau limit using acoustic radiation pressure and active feedback," J. Fluid Mech. **351**, 345–357 (1997).

[12] F. Savart, "Memoire sur la constitution des veines liquides lancees par des orifices circulaires en mince paroi" ("Report on the constitution of liquid veins launched by circular openings in a thin wall"), Ann. Chim. Phys. **53**, 337–386 (1833).

[13] J. Plateau, *Statique Experimentale et Theoretique des Liquides Soumis aux Seules Forces Moleculaires (Experimental and Theoretical Statics of Liquids Subject to Molecular Forces Only)* (Gauthier-Villars, Paris, 1873).

[14] J. C. Maxwell to W. Thomson, Letter dated August 24, 1857 reproduced in S. G. Brush, C. W. F. Everitt, and E. Garber, *Maxwell on Saturn's Rings* (MIT, Cambridge, MA, 1983), pp. 44–48. See also *The Scientific Letters and Papers of James Clerk Maxwell: Volume 1, 1846–1862*, edited by P. M. Harman (Cambridge University Press, Cambridge, 1990), pp. 533–537.

[15] Lord Rayleigh, "On the instability of jets," Proc. London Math. Soc. **10**, 4–13 (1879).

[16] S. Chandrasekhar, *Hydrodynamic and Hydromagnetic Stability* (Clarendon, Oxford, 1961).

[17] R. J. Donnelly and W. Glaberson, "Experiments on the capillary instability of a liquid jet," Proc. R. Soc. London, Ser. A **290**, 547–556 (1966).

[18] S. P. Lin, *Breakup of Liquid Sheets and Jets* (Cambridge University Press, Cambridge, 2003).

[19] Y. Pan and K. Suga, "A numerical study on the breakup process of laminar liquid jets into a gas," Phys. Fluids **18**, 052101 (2006).

[20] R. N. Berglund and B. Y. H. Liu, "Generation of monodisperse aerosol standards," Environ. Sci. Technol. **7**, 147–153 (1973).

[21] K. C. Chaudhary and T. Maxworthy, "The nonlinear capillary instability of a liquid jet. 2. Experiments on jet behaviour before droplet formation," J. Fluid Mech. **96**, 275–286 (1980).

[22] W. J. Jacobi, "Propagation of sound waves along liquid cylinders," J. Acoust. Soc. Am. **21**, 120–127 (1949).

[23] G. Goddard and G. Kaduchak, "Ultrasonic particle concentration in a line-driven cylindrical tube," J. Acoust. Soc. Am. **117**, 3440–3447 (2005).

[24] K. M. Awati and T. Howes, "Stationary waves on cylindrical fluid jets," Am. J. Phys. **64**, 808–811 (1996).

[25] J. S. Stroud and P. L. Marston, "Optical detection of transient bubble oscillations associated with the underwater noise of rain," J. Acoust. Soc. Am. **94**, 2788–2792 (1993).

[26] J. B. Keller, S. I. Rubinow, and Y. O. Tu, "Spatial instability of a jet," Phys. Fluids **16**, 2052–2055 (1973).

[27] D. F. Rutland and G. J. Jameson, "A non-linear effect in the capillary instability of liquid jets," J. Fluid Mech. **46**, 267–271 (1971).

[28] J. B. Lonzaga, C. F. Osterhoudt, D. B. Thiessen, and P. L. Marston, "Optical detection of the response of liquid jets to internal modulated ultrasonic radiation pressure," J. Acoust. Soc. Am. **116**, 2598(A) (2004).

[29] W. Wei, D. B. Theissen, and P. L. Marston, "Acoustic radiation force on a compressible cylinder in a standing wave," J. Acoust. Soc. Am. **116**, 201–208 (2004).

[30] S. A. Elrod, B. Hadimioglu, B. T. Khuri-Yakub, E. G. Rawson, E. Richley, C. F. Quate, N. N. Mansour, and T. S. Lundgren, "Nozzleless droplet formation with focused acoustic beams," J. Appl. Phys. **65**, 3441–3447 (1989).

[31] K. Nightingale, M. L. Palmeri, R. W. Nightingale, and G. E. Trahey, "On the feasibility of remote palpation using acoustic radiation force," J. Acoust. Soc. Am. **110**, 625–634 (2001).

[32] S. Callé, J. P. Remenieras, O. B. Matar, M. E. Hachemi, and F. Patat, "Temporal analysis of tissue displacement induced by a transient ultrasound radiation force," J. Acoust. Soc. Am. **118**, 2829–2840 (2005).

[33] M. W. Urban, R. R. Kinnick, and J. F. Greenleaf, "Measuring the phase of vibration of spheres in a viscoelastic medium as an image contrast modality," J. Acoust. Soc. Am. **118**, 3465–3472 (2005).

Maxwell rheological model for lipid-shelled ultrasound microbubble contrast agents

Alexander A. Doinikov[a)]
Institute of Nuclear Problems, Belarus State University, 11 Bobruiskaya Street, Minsk 220050, Belarus

Paul A. Dayton
Department of Biomedical Engineering, University of California, 451 East Health Sciences Dr., Davis, California 95616

(Received 20 June 2006; revised 13 March 2007; accepted 13 March 2007)

The present paper proposes a model that describes the encapsulation of microbubble contrast agents by the linear Maxwell constitutive equation. The model also incorporates the translational motion of contrast agent microbubbles and takes into account radiation losses due to the compressibility of the surrounding liquid. To establish physical features of the proposed model, comparative analysis is performed between this model and two existing models, one of which treats the encapsulation as a viscoelastic solid following the Kelvin-Voigt constitutive equation and the other assumes that the encapsulating layer behaves as a viscous Newtonian fluid. Resonance frequencies, damping coefficients, and scattering cross sections for the three shell models are compared in the regime of linear oscillation. Translational displacements predicted by the three shell models are examined by numerically calculating the genera1, nonlinearized equations of motion for weakly nonlinear excitation. Analogous results for free bubbles are also presented as a basis to which calculations made for encapsulated bubbles can be related. It is shown that the Maxwell shell model possesses specific physical features that are unavailable in the two other models. © *2007 Acoustical Society of America.* [DOI: 10.1121/1.2722233]

PACS number(s): 43.25.Yw, 43.35.Ei, 43.80.Qf, 43.80.Ev [CCC] Pages: 3331–3340

I. INTRODUCTION

Encapsulated microbubbles, known as ultrasound contrast agents, are effectively used in ultrasound medical diagnostics for increasing blood-tissue contrast during an ultrasonic examination. They are also employed in therapy as a vehicle for targeted drug delivery. Ultrasound contrast agents typically consist of a gas core surrounded by a shell of albumin, lipid, or a polymer material. A number of theoretical models have been proposed for different types of contrast agents.[1–16] Most of them assume that the encapsulating layer behaves as a viscoelastic solid following the Kelvin-Voigt constitutive equation. There are also models that treat the encapsulation as a viscous Newtonian fluid.[1,10,13,14] A viscoelastic solid appears to be an adequate model for polymer and albumin microbubble shells. For lipid shells, however, analysis of experimental data available in the literature suggests that a better approximation may be achieved by treating a lipid coating as a viscoelastic fluid. To substantiate this observation, let us analyze some experimental results obtained for lipid-shelled contrast agents.

An interesting observation as to resonance frequencies of lipid-shelled bubbles can be made from a paper by Dayton, Allen, and Ferrara.[11] The paper presents experimental measurements of translational displacement for the contrast agent MP1950. MP1950 is a phospholipid-shelled microbubble with a decafluorobutane core. Figure 4 of this paper shows that at the excitation frequency 2.25 MHz the maximum displacement is observed for a bubble with a resting radius of about 1.5 μm. It is reasonable to assume that the maximum displacement is reached by a resonant bubble. Hence it turns out that a 1.5 μm radius lipid-shelled bubble has a resonance frequency of 2.25 MHz. For comparison, the linear damped resonance frequency of a free bubble of the same size is about 2.45 MHz. It is well known that a viscoelastic solid shell increases considerably the resonance frequency as compared with a free bubble.[5] Therefore the fact that such a low resonance frequency is observed experimentally for lipid-shelled bubbles appears strange if the lipid shell is treated as a viscoelastic solid.

Another demonstrative work bringing to light the difference between lipid- and polymer-shelled contrast agents is that by Bloch *et al.*[17] Figures 1(a) and 1(b) of their paper show the behavior of two contrast agents, BR14 and BG1135, in response to increasing acoustic forcing. BR14 is a perfluorobutane-filled microbubble, stabilized by a phospholipid shell a few nanometers thick. BG1135 is an air-filled microsphere with a 100-nm-thick polymer shell. Figure 1(b) shows that up to very high acoustic pressures, as long as the shell of the polymer-shelled agent BG1135 remains intact, its oscillation is very insignificant. This is a typical behavior of an elastic solid in response to a destructive action. The response of the lipid-shelled agent BR14 to increasing acoustic forcing, shown in Fig. 1(a), is much smoother, as if its shell were much more yielding. The destruction mechanisms of the two agents are also different. The polymer-shelled agent BG1135 appears to acquire a shell defect, al-

[a)]Author to whom correspondence should be addressed. Electronic mail: doinikov@bsu.by

lowing gas to stream out and form a new gas bubble, but leaving the original shell intact. Whereas the formation of a shell defect has never been observed for the lipid-shelled agent BR14. Instead, its shell fragmented along with its gas contents, forming a set of smaller bubbles. The impression arises that the breakdown of the lipid shell occurs as if its volume were insufficient to cover the entire bubble surface when the expansion of the bubble becomes large, in contrast to the polymer shell which breaks up in the traditional manner for elastic solid materials. Similar distinctions in destruction mechanisms were also observed between albumin-shelled agents and the lipid-shelled agent MP1950.[18] They become explainable if we assume that the lipid shell has some fluid properties similar to the properties of Maxwell media. Indeed, a discontinuity in a solid shell, if once appeared, never vanishes completely, resulting in gas escape, while a discontinuity in a Maxwell material can close.

It is well known that the Maxwell constitutive equation has been proposed to describe complex materials that at fast effects behave as a solid, that is, they can deform, buckle, fold, etc., while at slow effects, they behave as a fluid. In particular, stresses in such media can relax in time, which is behavior impossible in traditional elastic solids. Among materials which are modeled by the Maxwell constitutive equation are such different substances as rosin, asphalt, glass, etc.[19] In experimental papers on lipid shells,[20–23] it is reported that these consist of condensed phase (polycrystalline or gel-like) domains surrounded by regions which are observed to have glassy or in some cases fluid-like properties. It is reasonable to assume that, when considered as a single whole, such a structure can have some properties of a Maxwell material. Note also that in biomedical ultrasound applications we deal with fast, MHz effects. Therefore, the buckling of lipid shells in response to compression at such high frequencies is not contradictory to the Maxwell model.

It should be noted that good agreement between experimental and simulated radius-time curves for lipid-shelled contrast agents has been reported recently by Marmottant *et al.*,[15] even though they treated a lipid coating as a viscoelastic solid. A possible explanation for this result is as follows. The elastic regime is only a part of a compound model applied by Marmottant *et al.* This part appears not to be of decisive importance. The entire model of Marmottant *et al.* assumes that, when the bubble oscillates, the elastic regime holds only in a narrow range of radii. Outside this range, the dynamics of the bubble is governed by an *ad hoc* law for surface tension that is introduced by Marmottant *et al.* According to their law, if in the course of expansion the radius of the bubble exceeds a threshold value, the shell breaks up, the surface tension becomes equal to that for free bubbles, and the elastic term becomes zero. A second threshold value is set for compression and if the radius of the bubble goes below it, both the surface tension term and the elastic term vanish. As a result, the effect of the shell in these two cases reduces to the shell viscosity term alone. We suppose that bubbles in the simulation carried out by Marmottant *et al.* were mostly in this regime of lacking elasticity. Thus their results do not necessarily refute the arguments presented above.

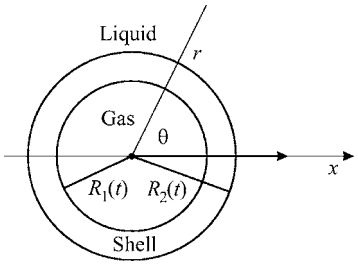

FIG. 1. Schematic sketch of an encapsulated bubble.

The present paper proposes a model that approximates the rheological behavior of the lipid shell by the linear Maxwell constitutive equation. The model also takes into account the effect of translation on the radial motion of an encapsulated microbubble and acoustic radiation losses due to the compressibility of the surrounding liquid. For comparison, parallel with the Maxwell shell model, two existing models are considered. One of them treats the encapsulation as a viscoelastic solid following the Kelvin-Voigt constitutive equation and the other assumes that the encapsulating layer behaves as a viscous Newtonian fluid. To demonstrate physical differences between the three models, they are examined in the regime of linear oscillation.

II. THEORY

Let us consider a spherical encapsulated gas bubble surrounded by a liquid and undergoing radial oscillations in response to an imposed acoustic field. The geometry of the system is shown in Fig. 1. Assuming the surrounding liquid and the encapsulating layer to be incompressible, from the continuity equation it follows that both the velocity of the surrounding liquid and the velocity inside the bubble shell are subject to the equation

$$\nabla \cdot \boldsymbol{v} = 0, \tag{1}$$

where $\boldsymbol{v}$ stands for both of the above velocities. From this it follows further that

$$v(r,t) = \frac{R_1^2(t)\dot{R}_1(t)}{r^2}, \tag{2}$$

where $v(r,t)$ is the radial component of $\boldsymbol{v}$, $R_1(t)$ is the inner radius of the bubble shell, and the over-dot denotes the time derivative. If $R_1 \leqslant r \leqslant R_2$, where $R_2(t)$ denotes the outer radius of the bubble, v is the velocity inside the encapsulating layer; if $r > R_2$, v is the velocity of the surrounding liquid. Note also that the assumption of incompressible shell gives the following equations:

$$R_2^3 - R_1^3 = R_{20}^3 - R_{10}^3, \quad R_1^2\dot{R}_1 = R_2^2\dot{R}_2, \tag{3}$$

where R_{10} and R_{20} are, respectively, the inner and the outer radii of the bubble shell at rest. These equations will be used in further calculations.

Conservation of radial momentum yields[24]

$$\rho\left(\frac{\partial v}{\partial t}+v\frac{\partial v}{\partial r}\right)=-\frac{\partial p}{\partial r}+\frac{\partial \tau_{rr}}{\partial r}+\frac{3\tau_{rr}}{r}, \tag{4}$$

where ρ is equal to ρ_S or ρ_L, ρ_S and ρ_L, are respectively, the equilibrium densities of the shell and the liquid, p is the pressure, and τ_{rr} is the stress deviator in the shell or the liquid.

The boundary conditions at the two interfaces are given by

$$P_g(R_1,t)=p_S(R_1,t)-\tau_{rr}^{(S)}(R_1,t)+\frac{2\sigma_1}{R_1}, \tag{5a}$$

$$p_S(R_2,t)-\tau_{rr}^{(S)}(R_2,t)=p_L(R_2,t)-\tau_{rr}^{(L)}(R_2,t)+\frac{2\sigma_2}{R_2}+P_{\mathrm{ac}}(t), \tag{5b}$$

where $P_g(R_1,t)$ is the pressure of the gas inside the bubble, σ_1 and σ_2 are the surface tension coefficients for the corresponding interfaces, and $P_{\mathrm{ac}}(t)$ is the driving acoustic pressure at the location of the bubble. Integrating Eq. (4) over r from R_1 to R_2 using the parameters appropriate for the encapsulating layer and from R_2 to ∞ using those appropriate for the surrounding liquid, assuming that the liquid pressure at infinity is equal to the hydrostatic pressure P_0, and combining the resulting equation with Eqs. (5), one obtains

$$R_1\ddot{R}_1\left[1+\left(\frac{\rho_L-\rho_S}{\rho_S}\right)\frac{R_1}{R_2}\right]+\dot{R}_1^2\left[\frac{3}{2}+\left(\frac{\rho_L-\rho_S}{\rho_S}\right)\times\left(\frac{4R_2^3-R_1^3}{2R_2^3}\right)\frac{R_1}{R_2}\right]=\frac{1}{\rho_S}\left[P_g(R_1,t)-\frac{2\sigma_1}{R_1}-\frac{2\sigma_2}{R_2}-P_0-P_{\mathrm{ac}}(t)+3\int_{R_1}^{R_2}\frac{\tau_{rr}^{(S)}(r,t)}{r}dr+3\int_{R_2}^{\infty}\frac{\tau_{rr}^{(L)}(r,t)}{r}dr\right]. \tag{6}$$

This equation is very convenient to test various rheological models for the shell material and the surrounding liquid. Testing can be done by just substituting respective rheological laws for $\tau_{rr}^{(S)}(r,t)$ and $\tau_{rr}^{(L)}(r,t)$. Equation (6) was used previously by Roy, Church, and Calabrese[1] who treated the encapsulating shell as a viscous Newtonian fluid, and by Church[5] who treated the encapsulating shell as a viscoelastic solid. In the present study, we will apply it to model a lipid coating by a viscoelastic fluid following the Maxwell constitutive equation.

Pursuing our calculation further and assuming that the behavior of the gas core is adiabatic, one has

$$P_g(R_1,t)=P_{g0}\left(\frac{R_{10}}{R_1}\right)^{3\gamma}, \tag{7}$$

where P_{g0} is the equilibrium gas pressure in the bubble and γ is the ratio of specific heats. Assuming that the surrounding liquid is a viscous Newtonian fluid, $\tau_{rr}^{(L)}(r,t)$ is written as[16]

$$\tau_{rr}^{(L)}=2\eta_L\frac{\partial v}{\partial r}, \tag{8}$$

where η_L is the shear viscosity of the liquid. By using Eqs. (2) and (8), the second integral term in Eq. (6) is found to be

$$3\int_{R_2}^{\infty}\frac{\tau_{rr}^{(L)}(r,t)}{r}dr=-4\eta_L\frac{R_1^2\dot{R}_1}{R_2^3}. \tag{9}$$

The behavior of the shell will be approximated by the linear Maxwell constitutive equation which can be expressed as[19]

$$\tau_{rr}^{(S)}+\lambda\frac{\partial\tau_{rr}^{(S)}}{\partial t}=2\eta_S\frac{\partial v}{\partial r}, \tag{10}$$

where λ is the relaxation time and η_S is the shear viscosity of the shell. Equation (10) deserves further comment. The Maxwell model is known to be an interpolation equation for intermediate cases between an elastic solid and a viscous fluid. To demonstrate this, let us assume that $\tau_{rr}^{(S)}(r,t)$ and $v(r,t)$ depend on time as $\exp(i\omega t)$, where ω is the angular frequency of the driving field. Then Eq. (10) gives

$$\tau_{rr}^{(S)}=\frac{2\eta_S/\lambda}{(1-i/\omega\lambda)}\frac{\partial u}{\partial r},$$

where u is the radial displacement, $du/dt=v$. For $\omega\lambda\gg 1$ (fast effects), this equation reduces to Hooke's law for solids, $\tau_{rr}^{(S)}=2\mu_S\partial u/\partial r$, with the shear modulus $\mu_S=\eta_S/\lambda$. While for $\omega\lambda\ll 1$ (slow effects), one obtains $\tau_{rr}^{(S)}=2i\omega\eta_S\partial u/\partial r=2\eta_S\partial v/\partial r$, which is Newton's viscous law for fluids. These properties of the Maxwell model allow us to suppose that Eq. (10) may be an appropriate approximation for the specific structure of lipid shells as described in the Introduction.

By using Eq. (10), the first integral term in Eq. (6) can be worked out in the following way. Substituting Eq. (2) into Eq. (10), one has

$$\tau_{rr}^{(S)}+\lambda\frac{\partial\tau_{rr}^{(S)}}{\partial t}=-4\eta_S\frac{R_1^2\dot{R}_1}{r^3}. \tag{11}$$

Equation (11) suggests that $\tau_{rr}^{(S)}(r,t)$ can be written as

$$\tau_{rr}^{(S)}(r,t)=-4\eta_S\frac{D(t)}{r^3}. \tag{12}$$

Substituting Eq. (12) into Eq. (11) shows that the function $D(t)$ obeys the equation

$$D(t)+\lambda\dot{D}(t)=R_1^2\dot{R}_1. \tag{13}$$

Using Eqs. (12) and (3), the first integral term in Eq. (6) is calculated as

$$3\int_{R_1}^{R_2}\frac{\tau_{rr}^{(S)}(r,t)}{r}dr=-4\eta_S\frac{D(t)(R_{20}^3-R_{10}^3)}{R_1^3R_2^3}. \tag{14}$$

Substitution of Eqs. (7), (9), and (14) into Eq. (6) yields

$$R_1\ddot{R}_1\left[1+\left(\frac{\rho_L-\rho_S}{\rho_S}\right)\frac{R_1}{R_2}\right]+\dot{R}_1^2\left[\frac{3}{2}+\left(\frac{\rho_L-\rho_S}{\rho_S}\right)\times\left(\frac{4R_2^3-R_1^3}{2R_2^3}\right)\frac{R_1}{R_2}\right]=\frac{1}{\rho_S}\left[P_{g0}\left(\frac{R_{10}}{R_1}\right)^{3\gamma}-\frac{2\sigma_1}{R_1}-\frac{2\sigma_2}{R_2}-4\eta_L\frac{R_1^2\dot{R}_1}{R_2^3}-4\eta_S\frac{D(t)(R_{20}^3-R_{10}^3)}{R_1^3R_2^3}-P_0-P_{\mathrm{ac}}(t)\right], \tag{15}$$

where the function $D(t)$ is calculated from Eq. (13).

Equation (15) can be modified to take account of the translation motion of the bubble and radiation losses due to the compressibility of the surrounding liquid. The modification can be performed by directly adopting necessary corrections from the equations of motion obtained in Ref. 16. The result is

$$R_1\ddot{R}_1\left[1+\left(\frac{\rho_L-\rho_S}{\rho_S}\right)\frac{R_1}{R_2}\right]+\dot{R}_1^2\left[\frac{3}{2}+\left(\frac{\rho_L-\rho_S}{\rho_S}\right)\times\left(\frac{4R_2^3-R_1^3}{2R_2^3}\right)\frac{R_1}{R_2}\right]-\frac{1}{c}\frac{\rho_L}{\rho_S}H=\frac{\rho_L}{\rho_S}\frac{\dot{x}^2}{4}+\frac{1}{\rho_S}\left[P_{g0}\left(\frac{R_{10}}{R_1}\right)^{3\gamma}-\frac{2\sigma_1}{R_1}-\frac{2\sigma_2}{R_2}-4\eta_L\frac{R_1^2\dot{R}_1}{R_2^3}-4\eta_S\frac{D(t)(R_{20}^3-R_{10}^3)}{R_1^3R_2^3}-P_0-P_{\mathrm{ac}}(x,t)\right],\tag{16}$$

where c is the speed of sound in the surrounding liquid, the function H is defined by

$$H=\left[1+\left(\frac{\rho_L-\rho_S}{\rho_S}\right)\frac{R_1}{R_2}\right]^{-1}\left\{R_1\frac{dG}{dt}+2R_1\dot{R}_1\ddot{R}_1\times\left[1+\left(\frac{\rho_L-\rho_S}{\rho_S}\right)\frac{R_1^4}{R_2^4}\right]+2\dot{R}_1^3\left[1+\left(\frac{\rho_L-\rho_S}{\rho_S}\right)\frac{R_1^4(2R_2^3-R_1^3)}{R_2^7}\right]\right\},\tag{17}$$

$x(t)$ is the position of the center of the bubble in an inertial frame, and G denotes the right-hand side of Eq. (16). Note also that the acoustic pressure is now written as $P_{\mathrm{ac}}(x,t)$, where the spatial argument x explicitly indicates that $P_{\mathrm{ac}}(x,t)$ is the value of the driving pressure at the location of the bubble. The compressibility correction is given by the last term on the left-hand side of Eq. (16), while the first term on the right-hand side of Eq. (16) provides the coupling with the translational equation. This latter is given by

$$m_b\ddot{x}+\frac{2\pi}{3}\rho_L\frac{d}{dt}(R_2^3\dot{x})=-\frac{4\pi}{3}R_2^3\frac{\partial}{\partial x}P_{\mathrm{ac}}(x,t)+F_d,\tag{18}$$

where m_b is the mass of the bubble, the second term on the left-hand side of Eq. (18) is the added mass force, the first term on the right-hand side is the acoustic radiation force, and F_d is the viscous drag force which can be taken, for example, in the form of Oseen's law[24]

$$F_d=-\frac{1}{4}\pi\eta_L R_2\dot{x}(24+9\rho_L R_2|\dot{x}|/\eta_L).\tag{19}$$

Oseen's formula is known to be more relevant than the Stokes law when the Reynolds number is close to unity. The Reynolds numbers in experiments on contrast agents are just on this order.

For $D(0)=0$, from Eq. (16) it follows that

$$P_{g0}=P_0+\frac{2\sigma_1}{R_{10}}+\frac{2\sigma_2}{R_{20}}.\tag{20}$$

It is also worth noting that in the general case $\dot{x}$ in Eqs. (16) and (18) should be considered as the velocity of the bubble with respect to the velocity of the surrounding liquid. That is, if there is a stream in the bulk liquid, due to the propagation of the acoustic wave, acoustic streaming and so forth, $\dot{x}$ should be replaced with $\dot{x}-v_{\mathrm{ex}}$, where v_{ex} denotes the liquid velocity unrelated to the presence of the bubble.

Thus, we have the set of three ordinary differential equations: radial Eq. (16), translational Eq. (18), and Eq. (13) for $D(t)$. The set is supplemented with the first of Eqs. (3) and Eqs. (17), (19), and (20). The initial conditions can be specified by $R_1(0)=R_{10}$, $R_2(0)=R_{20}$, $\dot{R}_1(0)=\dot{R}_2(0)=0$, $x(0)=x_0$, $\dot{x}(0)=0$, and $D(0)=0$. Simultaneous numerical solution of all these equations yields the time-varying radius of the bubble and its translational displacement.

For comparison, parallel with the Maxwell shell model, we will examine two other existing models that treat the encapsulation as a viscoelastic solid or a viscous Newtonian fluid. For the first of them, which assumes that the shell material follows the Kelvin-Voigt constitutive equation,

$$\tau_{rr}^{(S)}=2\mu_S\frac{\partial u}{\partial r}+2\eta_S\frac{\partial v}{\partial r},\tag{21}$$

with u the radial displacement in the shell and μ_S the shear modulus of the shell, the radial equation takes the form[5,16]

$$R_1\ddot{R}_1\left[1+\left(\frac{\rho_L-\rho_S}{\rho_S}\right)\frac{R_1}{R_2}\right]+\dot{R}_1^2\left[\frac{3}{2}+\left(\frac{\rho_L-\rho_S}{\rho_S}\right)\times\left(\frac{4R_2^3-R_1^3}{2R_2^3}\right)\frac{R_1}{R_2}\right]-\frac{1}{c}\frac{\rho_L}{\rho_S}H=\frac{\rho_L}{\rho_S}\frac{\dot{x}^2}{4}+\frac{1}{\rho_S}\left[P_{g0}^{\mathrm{KV}}\left(\frac{R_{10}}{R_1}\right)^{3\gamma}-\frac{2\sigma_1}{R_1}-\frac{2\sigma_2}{R_2}-P_0-P_{\mathrm{ac}}(x,t)\right]-\frac{4\dot{R}_1}{\rho_S R_1R_2^3}[\eta_L R_1^3+\eta_S(R_{20}^3-R_{10}^3)]-\frac{4\mu_S(R_{20}^3-R_{10}^3)}{\rho_S R_2^3}\left(1-\frac{R_{1e}}{R_1}\right)\times\left[1+\frac{1}{2}\left(1-\frac{R_{1e}}{R_1}\right)\left(1-\frac{3R_1^3}{R_2^3}\right)\right],\tag{22}$$

where the equilibrium gas pressure in the bubble, ρ_{g0}^{KV}, is now given by

$$P_{g0}^{\mathrm{KV}}=P_0+\frac{2\sigma_1}{R_{10}}+\frac{2\sigma_2}{R_{20}}+4\mu_S\left(1-\frac{R_{10}^3}{R_{20}^3}\right)\left(1-\frac{R_{1e}}{R_{10}}\right)\times\left[1+\frac{1}{2}\left(1-\frac{R_{1e}}{R_{10}}\right)\left(1-\frac{3R_{10}^3}{R_{20}^3}\right)\right].\tag{23}$$

The function H in Eq. (22) is defined by Eq. (17) as before but G in Eq. (17) is now the right-hand side of Eq. (22), not Eq. (16). R_{1e} denotes the unstrained equilibrium position of the gas-shell interface and is given by[16]

$$R_{1e} = R_{10}\left[1 - \frac{1}{4\mu_s}\left(P_0 + \frac{2\sigma_2}{R_{20}}\right)\frac{R_{20}^3}{R_{10}^3}\right]. \tag{24}$$

For the viscous shell model, which assumes that the shell behaves as a viscous Newtonian fluid, one has[1]

$$R_1\ddot{R}_1\left[1 + \left(\frac{\rho_L - \rho_S}{\rho_S}\right)\frac{R_1}{R_2}\right] + \dot{R}_1^2\left[\frac{3}{2} + \left(\frac{\rho_L - \rho_S}{\rho_S}\right)\times\left(\frac{4R_2^3 - R_1^3}{2R_2^3}\right)\frac{R_1}{R_2}\right] - \frac{1}{c}\frac{\rho_L}{\rho_S}H = \frac{\rho_L}{\rho_S}\frac{\dot{x}^2}{4} + \frac{1}{\rho_S}\left[P_{g0}\left(\frac{R_{10}}{R_1}\right)^{3\gamma} - \frac{2\sigma_1}{R_1} - \frac{2\sigma_2}{R_2} - 4\eta_L\frac{R_1^2\dot{R}_1}{R_2^3} - 4\eta_S\frac{\dot{R}_1(R_{20}^3 - R_{10}^3)}{R_1R_2^3} - P_0 - P_{\mathrm{ac}}(x,t)\right], \tag{25}$$

where H is calculated from Eq. (17) with G being the right-hand side of Eq. (25).

The translational equation for the Kelvin-Voigt and viscous models remains the same as defined by Eq. (18).

III. LINEAR ANALYSIS

In this section, we will compare predictions of the three shell models in the regime of linear oscillation. The purpose of this analysis is to reveal physical differences between the models which result from the fact that the models are based on different rheological laws.

Let us assume that the incident field is weak so the amplitude of the radial oscillation is small. Then one can write

$$R_1 = R_{10} + \xi(t), \quad R_2 = R_{20} + \frac{R_{10}^2}{R_{20}^2}\xi(t), \tag{26}$$

where it is assumed that $|\xi| \ll R_{10}$. Linearizing Eq. (13) with respect to ξ, one has

$$\dot{D} + \frac{1}{\lambda}D = \frac{R_{10}^2}{\lambda}\dot{\xi}. \tag{27}$$

Assuming that the acoustic pressure can be expressed as $P_{\mathrm{ac}}(t) = P_a \exp(i\omega t)$, where P_a is the pressure amplitude and ω is the angular driving frequency, solution to Eq. (27) can be represented as

$$D(t) = a\xi + b\dot{\xi}. \tag{28}$$

Substituting Eq. (28) into Eq. (27), one finds

$$a = \frac{\lambda\omega^2 R_{10}^2}{1 + (\lambda\omega)^2}, \quad b = \frac{R_{10}^2}{1 + (\lambda\omega)^2}. \tag{29}$$

For the Maxwell shell model, linearizing Eq. (16) by means of Eqs. (26) and using Eqs. (28) and (29) one obtains

$$\ddot{\xi} + \delta_M\dot{\xi} + \omega_{0M}^2\xi = -\frac{P_{\mathrm{ac}}(t)}{\alpha\rho_S R_{10}}, \tag{30}$$

where

$$\alpha = 1 - (1 - \rho_L/\rho_S)R_{10}/R_{20}, \tag{31}$$

$$\delta_M = \delta_r + \delta_{\eta L} + \delta_{\eta S}^M, \tag{32}$$

$$\delta_r = \frac{\rho_L R_{10}\omega^2}{\alpha c\rho_S}, \tag{33}$$

$$\delta_{\eta L} = \frac{4\eta_L R_{10}}{\alpha\rho_S R_{20}^3}, \tag{34}$$

$$\delta_{\eta S}^M = \frac{4\eta_S(R_{20}^3 - R_{10}^3)}{\alpha\rho_S R_{10}^2 R_{20}^3[1 + (\lambda\omega)^2]}, \tag{35}$$

$$\omega_{0M}^2 = \omega_0^2 + \lambda\omega^2\delta_{\eta S}^M, \tag{36}$$

$$\omega_0^2 = \frac{1}{\alpha\rho_S R_{10}^2}\left(3\gamma P_{g0} - \frac{2\sigma_1}{R_{10}} - \frac{2\sigma_2 R_{10}^3}{R_{20}^4}\right). \tag{37}$$

It is somewhat unusual that in Eq. (30) the resonance frequency ω_{0M} is a function of the driving frequency ω. Of prime interest is, however, not ω_{0M} because it is common knowledge that the real resonance frequency of a system with damping differs from the undamped resonance frequency ω_{0M}.[25] To evaluate the damped (real) resonance frequency of Eq. (30), let us consider a solution to this equation,

$$\xi(t) = A\exp(i\omega t + i\phi), \tag{38}$$

where

$$\phi = \arctan[\omega\delta_M/(\omega^2 - \omega_{0M}^2)], \tag{39}$$

$$A = P_a Q(\omega)/(\alpha\rho_S R_{10}\omega_0^2), \tag{40}$$

$$Q(\omega) = \omega_0^2/[(\omega^2 - \omega_{0M}^2)^2 + \omega^2\delta_M^2]^{1/2}. \tag{41}$$

The resonance response of the bubble corresponds to a maximum of the function $Q(\omega)$. One can see that $Q(\omega)$ is a fairly complicated function of ω. Therefore it will be examined numerically below. The damped resonance frequency of the Maxwell shell model will be denoted by ω_{dM} below.

For the Kelvin-Voigt shell model, expressions for the undamped and damped resonance frequencies as well as damping terms were obtained in Ref. 16:

$$\delta_{\mathrm{KV}} = \delta_r + \delta_{\eta L} + \delta_{\eta S}^{\mathrm{KV}}, \tag{42}$$

$$\delta_{\eta S}^{\mathrm{KV}} = \frac{4\eta_S(R_{20}^3 - R_{10}^3)}{\alpha\rho_S R_{10}^2 R_{20}^3}, \tag{43}$$

$$\omega_{0\mathrm{KV}}^2 = \frac{1}{\alpha\rho_S R_{10}^2}\left\{3\gamma P_{g0}^{\mathrm{KV}} - \frac{2\sigma_1}{R_{10}} - \frac{2\sigma_2 R_{10}^3}{R_{20}^4} + \frac{4\mu_S(R_{20}^3 - R_{10}^3)}{R_{20}^3}\left[1 - \frac{1}{4\mu_S}\left(P_0 + \frac{2\sigma_2}{R_{20}}\right)\times\left(3 + \frac{R_{20}^3}{R_{10}^3}\right)\right]\right\}. \tag{44}$$

Note that the equations for α, δ_r, and $\delta_{\eta L}$ remain the same. The quantity $\omega_{0\mathrm{KV}}$ denotes the undamped resonance frequency. The damped resonance frequency is given by

$$\omega_{d\mathrm{KV}} = \frac{1}{\beta\sqrt{3}}\{[\beta^2(\delta_{\eta L}+\delta_{\eta S}^{\mathrm{KV}})^2 + 4\beta(\delta_{\eta L}+\delta_{\eta S}^{\mathrm{KV}}) + 6\beta^2\omega_{0\mathrm{KV}}^2 + 1]^{1/2} - 2\beta(\delta_{\eta L}+\delta_{\eta S}^{\mathrm{KV}}) - 1\}^{1/2}, \quad (45)$$

where $\beta=\delta_r/\omega^2=\rho_L R_{10}/(\alpha c\rho_S)$.

The undamped resonance frequency, ω_{0V}, and damping constants for the viscous shell model can be obtained from Eqs. (32)–(37) by setting $\lambda=0$. The result is

$$\delta_{\eta S}^{V}=\delta_{\eta S}^{\mathrm{KV}}, \quad \delta_V=\delta_r+\delta_{\eta L}+\delta_{\eta S}^{V}=\delta_{\mathrm{KV}}, \quad \omega_{0V}^2=\omega_0^2. \quad (46)$$

To obtain the damped resonance frequency of the viscous shell model, one needs only to replace $\omega_{0\mathrm{KV}}$ in Eq. (45) with $\omega_{0V}=\omega_0$ since $\delta_{\eta S}^{V}=\delta_{\eta S}^{\mathrm{KV}}$,

$$\omega_{dV} = \frac{1}{\beta\sqrt{3}}\{[\beta^2(\delta_{\eta L}+\delta_{\eta S}^{\mathrm{KV}})^2 + 4\beta(\delta_{\eta L}+\delta_{\eta S}^{\mathrm{KV}}) + 6\beta^2\omega_0^2 + 1]^{1/2} - 2\beta(\delta_{\eta L}+\delta_{\eta S}^{\mathrm{KV}}) - 1\}^{1/2}. \quad (47)$$

In the process of comparing the shell models we will also refer to a free bubble. The undamped resonance frequency, ω_{0f}, and damping constants for a free bubble can be immediately obtained from Eqs. (31)–(37) by setting $R_{10}=R_{20}$. This yields

$$\delta_f=\delta_r^f+\delta_{\eta L}^f, \quad \delta_r^f=R_0\omega^2/c, \quad \delta_{\eta L}^f=4\eta_L/(\rho_L R_0^2), \quad (48)$$

$$\omega_{0f}^2=\frac{1}{\rho_L R_0^2}\left(3\gamma P_0+\frac{2(3\gamma-1)\sigma_f}{R_0}\right), \quad (49)$$

where R_0 is the equilibrium radius of a free bubble and σ_f is the surface tension at the gas-liquid interface. It is easy to verify that these equations are identical to those obtained by Prosperetti.[26] Setting $R_{10}=R_{20}$ in Eq. (45) gives the damped resonance frequency of a free bubble as

$$\omega_{df} = \frac{1}{\beta_f\sqrt{3}}\{[(\beta_f\delta_{\eta L}^f)^2 + 4\beta_f\delta_{\eta L}^f + 6(\beta_f\omega_{0f})^2 + 1]^{1/2} - 2\beta_f\delta_{\eta L}^f - 1\}^{1/2}, \quad (50)$$

with $\beta_f=R_0/c$.

Finally, we need to estimate the order of the shell parameters which will be used in further calculations. The dynamics of lipid-shelled bubbles was modeled previously by Marmottant *et al.*[15] Neglecting the liquid compressibility correction, their model takes the form

$$\rho_L\left(R\ddot{R}+\frac{3}{2}\dot{R}^2\right)=\left[P_0+\frac{2\sigma(R_0)}{R_0}\right]\left(\frac{R_0}{R}\right)^{3\gamma}-\frac{2\sigma(R_0)}{R}-P_0 - P_{\mathrm{ac}}-4\eta_L\frac{\dot{R}}{R}-4\kappa_s\frac{\dot{R}}{R^2}-4\chi\left(\frac{1}{R_0}-\frac{1}{R}\right), \quad (51)$$

where R denotes the instantaneous outer radius of an encapsulated bubble, R_0 is the radius of the bubble at rest, κ_s is the dilatational viscosity, and χ is the elastic compression modulus. Equation (51) belongs to the type of the so-called zero-thickness encapsulation models. It is reported by Marmottant *et al.* that good agreement with experimental data is reached for $\kappa_s=7.2\times10^{-9}$ N s/m and $\chi=1$ N/m. Now, if we neglect the compressibility correction and the translational term in Eq. (22) and assume that the shell thickness $R_S=R_2-R_1$ is much smaller than R_1 and R_2, Eq. (22) reduces to an equation of the above-named type as well:

$$\rho_L\left(R\ddot{R}+\frac{3}{2}\dot{R}^2\right)=\left[P_0+\frac{2\sigma}{R_0}\right]\left(\frac{R_0}{R}\right)^{3\gamma}-\frac{2\sigma}{R}-P_0-P_{\mathrm{ac}} - 4\eta_L\frac{\dot{R}}{R}-12\eta_S R_S\frac{\dot{R}}{R^2}-12\mu_S R_S\frac{R_0^2}{R^2} \times\left(\frac{1}{R_0}-\frac{1}{R}\right), \quad (52)$$

where $\sigma=\sigma_1+\sigma_2$. One can see that Eqs. (51) and (52) are in agreement provided that

$$\kappa_s=3R_S\eta_S \quad \text{and} \quad \chi=3R_S\mu_S. \quad (53)$$

Using these relations, one finds that for $R_S=2$ nm, $\eta_S=1.2$ Pa s and $\mu_S=166.7$ MPa. From what is said after Eq. (10) it follows that the order of the relaxation time λ corresponding to these values of η_S and μ_S can be estimated as $\lambda=\eta_S/\mu_S\approx0.007$ μs. These values will be used as a guide in further calculations.

The values of the other physical parameters used in our calculations are $p_0=101.3$ kPa, $\rho_L=1000$ kg/m^3, $\eta_L=0.001$ Pa s, $c=1500$ m/s, $\gamma=1.07$, $\sigma_f=0.072$ N/m, $\rho_S=1100$ kg/m^3, and $\sigma_2=0.051$ N/m. The parameters for the surrounding liquid correspond to water. The value of σ_2 was chosen following Morgan *et al.*[9] For simplicity, we set $\sigma_1=0$. We believe this point is not principal in the case of lipid encapsulation and cannot noticeably distort results. It is apparent that for a very thin coating, as with lipid shells, the net effect of the two terms $2\sigma_1/R_1$ and $2\sigma_2/R_2$ can be approximated with a good accuracy by the single term $2\sigma/R_2$ with $\sigma=\sigma_1+\sigma_2$, i.e., as if σ_1 were equal to zero while σ_2 were equal to the sum $\sigma_1+\sigma_2$. Note that Marmottant *et al.*[15] also offer considerations from which it follows that the surface tension at the gas-lipid interface can be taken to be zero.

A. Resonance frequencies

Figure 2 shows the damped resonance frequency of an encapsulated bubble as a function of equilibrium radius for the three shell models at three values of the shell viscosity, $\eta_S=0.5$, 1.0, and 1.5 Pa s. The values of the other shell parameters used in these calculations are $R_S=2$ nm, $\mu_S=166.7$ MPa, and $\lambda=0.02$ μs. The range of bubble radii was chosen to correspond to the size of contrast agent microbubbles used in ultrasound medical applications. The dashed line represents the damped resonance frequency of a free bubble, $f_{df}=\omega_{df}/2\pi$, calculated from Eq. (50). Figure 2(a) demonstrates a well-known fact that a viscous shell decreases the resonance frequency with respect to that of a free bubble and leads to the utter extinction of resonance response for small bubbles. On the contrary, a viscoelastic solid shell increases the resonance frequency relative to a free bubble, see Fig. 2(b). For small bubbles, however, the viscous damping inside the shell again results in the absence of resonance. The Maxwell model, Fig. 2(c), shows a specific behavior that is not observed in the two previous cases,

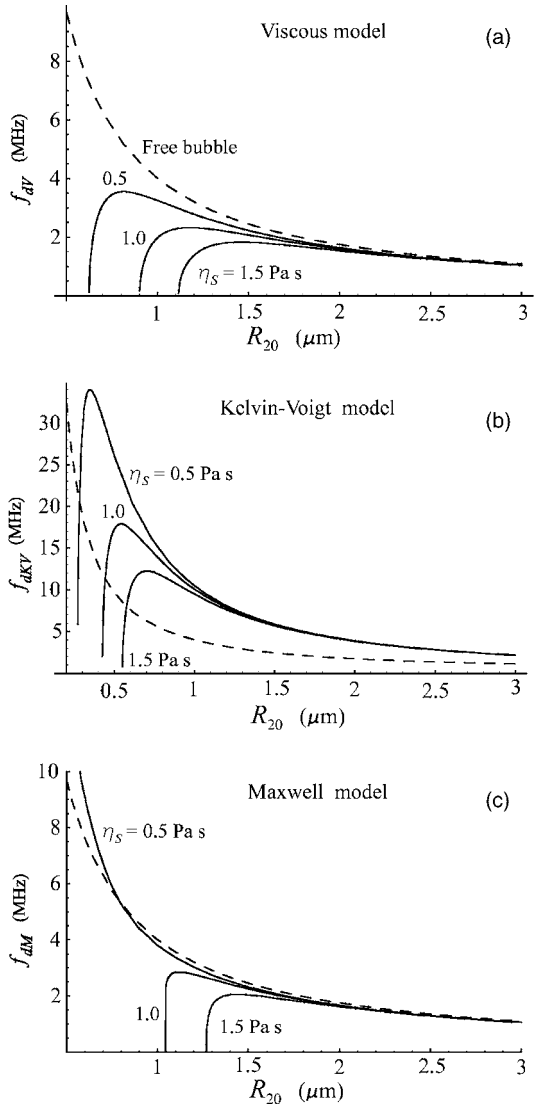

FIG. 2. Damped resonance frequency as a function of equilibrium bubble radius for three values of the shell viscosity η_S. (a) Viscous model, $f_{dV}=\omega_{dV}/2\pi$; (b) Kelvin-Voigt model, $f_{dKV}=\omega_{dKV}/2\pi$, $\mu_S=166.7$ MPa; (c) Maxwell model, $f_{dM}=\omega_{dM}/2\pi$, $\lambda=0.02$ μs. The shell thickness $R_S=2$ nm. The dashed line shows the damped resonance frequency of a free bubble.

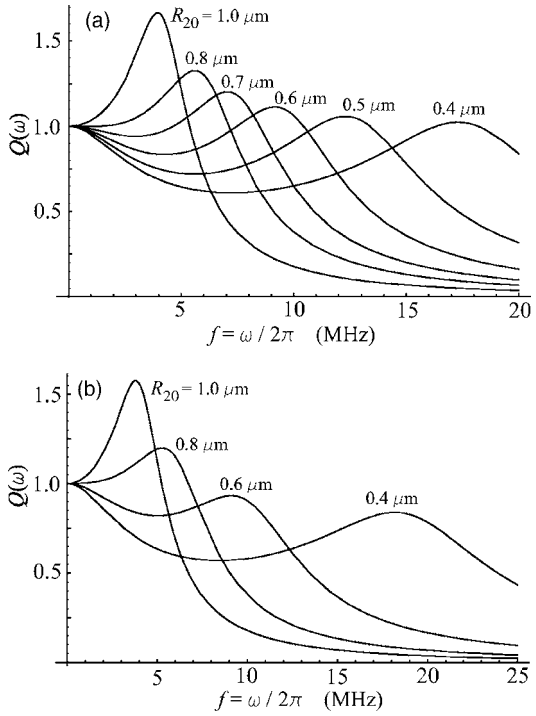

FIG. 3. The resonance function $Q(\omega)$ of the Maxwell shell model for various values of the equilibrium radius R_{20}. (a) $\lambda=0.025$ μs; (b) $\lambda=0.02$ μs. The shell viscosity $\eta_S=0.5$ Pa s and the shell thickness $R_S=2$ nm.

namely, if the shell viscosity is not too high, the resonance frequency of a bubble with a viscoelastic fluid shell can be both lower and higher than that of a free bubble. In other words, as could be expected from what was said following Eq. (10), the Maxwell shell can behave in both the viscous and elastic manner. The damped resonance frequency of a bubble with a Maxwell shell, $f_{dM}=\omega_{dM}/2\pi$, becomes higher than that of a free bubble, f_{df}, when the elastic properties of the shell begin to predominate over its viscous properties. This takes place when $\omega_{dM}\lambda$ is large enough. It is found that it is not necessary for this quantity to be large compared to unity. For example, from Fig. 2(c) it follows that f_{dM} becomes higher than f_{df} at $\omega_{dM}\lambda\approx 0.68$, which corresponds to the resonant radius $R_{20}=0.79$ μm at $\lambda=0.02$ μs and $\eta_S=0.5$ Pa s. With increasing λ, which means increasing elasticity of the shell, the critical value of R_{20} increases as well. For example, for $\lambda=0.025$ μs and the same shell viscosity, the critical radius $R_{20}=0.95$ μm. Note also that if $f_{dM}>f_{df}$ and the Maxwell model goes into the elastic regime, the resonance response persists for arbitrarily small bubbles as the Maxwell model reduces to Hooke's law which ignores viscous damping. In regard to the $\eta_S=0.5$ Pa s curve in Fig. 2(c), it is also interesting to note that, despite the presence of the encapsulating shell, this curve remains very close to the resonance curve for free bubbles within a wide enough range of radii.

The form of the resonance function $Q(\omega)$ of the Maxwell shell model, Eq. (41), in the elastic regime is specific as well. The resonance functions of the two other models can be only of two types, either with a global resonance peak or, if the resonance response is suppressed by the shell viscosity, monotonically decreasing as the driving frequency increases. Figure 3 shows that the resonance function of the Maxwell model in the range of bubble sizes corresponding to the elastic regime can take the form of a curve with a local maximum. This effect gives rise to the resonance response for indefinitely small bubbles. However, the strength of the resonance oscillation of such bubbles can be smaller than the strength of their nonresonance oscillation at a lower driving frequency, see the $R_{20}=0.4$ μm curve in Fig. 3(b).

B. Damping coefficients

For the Kelvin-Voigt and viscous models, the damping coefficients are identical, see Eq. (46). The difference with the Maxwell model is only in the shell viscosity term $\delta^M_{\eta S}$, cf. Eqs. (35) and (43). Due to the factor $[1+(\lambda\omega)^2]^{-1}$, $\delta^M_{\eta S}$ is always smaller than $\delta^{\mathrm{KV}}_{\eta S}=\delta^V_{\eta S}$, the divergence increasing as frequency increases. This means that the total damping for a Maxwell shell is always smaller than that for the two other types of encapsulation. The totals of the damping constants

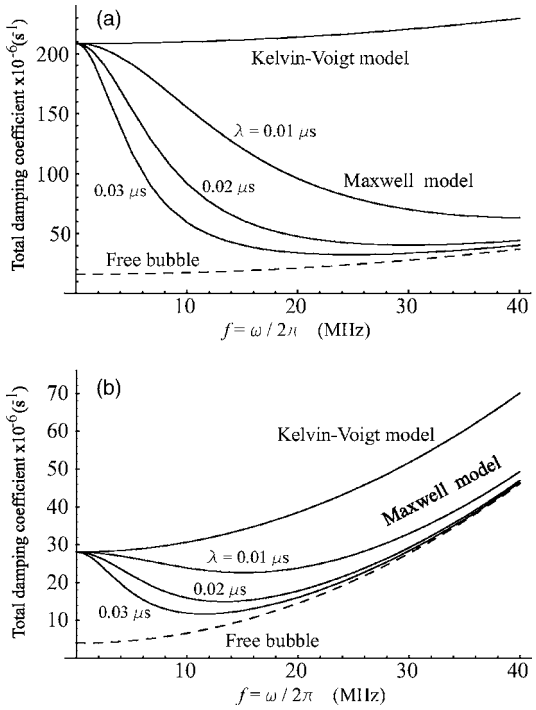

FIG. 4. Total damping coefficients as a function of frequency. (a) R_{20} =0.5 μm; (b) R_{20}=1.0 μm. The shell viscosity η_S=1.0 Pa s and the shell thickness R_S=2 nm.

of the shell models are shown in Fig. 4 as functions of frequency for equilibrium bubble radii of 0.5 μm, Fig. 4(a), and 1 μm, Fig. 4(b), assuming η_S=1.0 Pa s and R_S=2 nm. The upper curve in both the parts of Fig. 4 corresponds to the Kelvin-Voigt and viscous models. The bottom (dashed) curve gives the total damping coefficient for a free bubble, δ_f, calculated from Eq. (48). The three intervening curves were obtained for the Maxwell model at three values of the relaxation time, λ=0.01, 0.02, and 0.03 μs. It is seen that the larger the relaxation time, the closer the Maxwell curve is to that for a free bubble. As with resonance frequencies, we again observe an interesting effect inherent in the Maxwell model, namely the damping of a bubble with a Maxwell shell can be fairly close to that for a free bubble.

Comparison of Figs. 4(a) and 4(b) shows that increasing the bubble size makes all the curves approach each other. This is an expected result since the relative contribution of the viscous damping decreases with increasing bubble size as follows from Eqs. (34), (35), (43), and (48). On the contrary, the relative contribution of the acoustic damping increases as is seen from Eq. (33). But the acoustic damping coefficient is the same for all the three shell models. Moreover, if the shell thickness is small as in our case, the result of Eq. (33) does not differ much from the acoustic damping for a free bubble, Eq. (48). As a consequence, the damping-frequency curves for all the shell models and the free bubble come closer together as the equilibrium bubble radius increases.

Both $\delta_{\eta S}^{M}$ and $\delta_{\eta S}^{KV}$ are linearly dependent on the shell viscosity η_S. Therefore variations in η_S cannot lead to qualitative changes in Fig. 4 and are not exemplified here. Note also that our analysis ignores the thermal damping. This neglect is justified for MHz frequencies and micron-sized

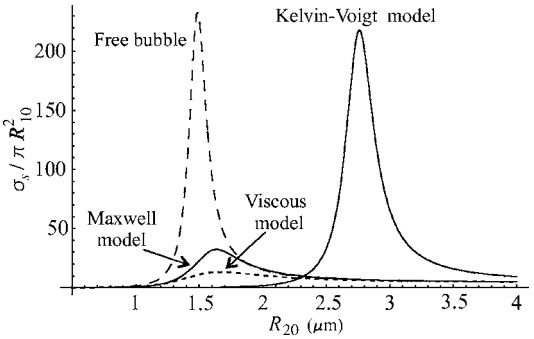

FIG. 5. Scattering cross sections as a function of equilibrium radius for the three shell models and free bubbles (long-dashed line) at a driving frequency of 2.5 MHz. The shell parameters are R_S=2 nm, η_S=1.0 Pa s, μ_S =166.7 MPa, and λ=0.05 μs.

bubbles which are used in ultrasound medical applications since the relative contribution of the thermal damping is negligible under such conditions.[5,26]

C. Scattering cross sections

The scattering cross section of a bubble is defined as

$$\sigma_s = 4\pi r^2 |P_s^2|/P_a^2, \tag{54}$$

where P_a is the pressure amplitude of the incident acoustic wave and P_s is the pressure wave scattered by the bubble. In the case of linear oscillation, P_s can be written as

$$P_s = \rho_L R_{10}^2 \ddot{\xi}/r, \tag{55}$$

where ξ is defined by Eqs. (38)–(41), provided the expressions for the resonance frequency and the damping constant are changed to those needed for the shell model considered. Substituting Eq. (55) into Eq. (54), one finds

$$\sigma_s = \frac{4\pi\rho_L^2 R_{10}^2 \omega^4}{\alpha^2 \rho_S^2 [(\omega^2 - \omega_m^2)^2 + \omega^2 \delta^2]}, \tag{56}$$

where, according to the model required, δ is δ_M, δ_{KV}, or δ_V, and ω_m is ω_{0M}, $\omega_{0\mathrm{KV}}$, or ω_{0V}, respectively. For a free bubble, one has

$$\sigma_{sf} = \frac{4\pi R_0^2 \omega^4}{(\omega^2 - \omega_{0f}^2)^2 + \omega^2 \delta_f^2}, \tag{57}$$

where R_0=R_{20} in our calculations.

Calculated values for the linear scattering cross sections of the three shell models, normalized to the respective geometrical cross sections of bubbles, are given in Fig. 5 as a function of equilibrium bubble radius for a driving frequency of 2.5 MHz. The values of the shell parameters used in these calculations are R_S=2 nm, η_S=1.0 Pa s, μ_S=166.7 MPa, and λ=0.05 μs. The scattering cross section for free bubbles is presented by the long-dashed line. It is seen that the Kelvin-Voigt model gives the vastly greater amplitude of the scattering cross section than the two other models. This occurs as the Kelvin-Voigt shell increases considerably the resonance radius of encapsulated bubbles, while the resonant scattering of larger bubbles is known to be of greater intensity. The resonance radii of bubbles with the Maxwell and viscous shells remain close to those for free bubbles, but unlike free

bubbles, bubbles with the Maxwell and viscous shells undergo the additional damping due to the shell viscosity. As a result, the amplitudes of their scattering cross sections are much less than for free bubbles resonant at the same frequencies.

Figure 6 shows that increasing the relaxation time in the Maxwell model increases the amplitude of the scattering cross section, not giving rise, however, to an increase in the resonance radius of the encapsulated bubble. As one would expect, increasing the shell viscosity in the Maxwell model results in decreasing amplitude of the scattering cross section, see Fig. 7.

IV. TRANSLATIONAL MOTION

To compare predictions of the three shell models regarding the translational displacement of encapsulated bubbles, the values of the shell parameters were chosen as follows. The shell thickness and the shell viscosity were set equal to $R_S=2$ nm and $\eta_S=1.0$ Pa s, respectively. The shear modulus μ_S responsible for the elastic properties of the Kelvin-Voigt model was set equal to $\mu_S=100$ MPa. The relaxation time λ specifying the elastic properties of the Maxwell model was taken to be equal to $\lambda=\eta_S/\mu_S=0.01$ μs. This choice allows one to reckon that the shell parameters of all the models are commensurable so that differences in the predictions of the models are due to qualitative rather than quantitative differences in their behavior. The values of the other physical parameters used in these calculations were the same as indicated after Eq. (53). It was assumed that bubbles were set in motion by a single 20-cycle acoustic pulse with a pressure amplitude of 100 kPa and a center frequency of 2.5 MHz. The translational displacement was fixed after the termination of the pulse. Simulations were carried out by numerically calculating Eqs. (16) and (18) for the Maxwell model, Eqs. (22) and (18) for the Kelvin-Voigt model, and Eqs. (25) and (18) for the viscous model. The translational displacement for free bubbles was calculated using the equations of motion presented in Ref. 27. The results obtained are given in Fig. 8. One can see that the peak displacement given by the Kelvin-Voigt model exceeds those predicted by the other two shell models. Since the Kelvin-Voigt shell increases the resonance frequency of an encapsulated bubble with respect to that of a free bubble of the same size, the bubble radius

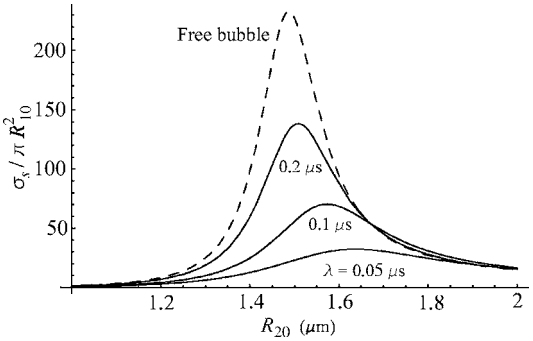

FIG. 6. Scattering cross sections as a function of equilibrium radius for the Maxwell shell model with $\lambda=0.05$, 0.1, and 0.2 μs, at a driving frequency of 2.5 MHz. The shell viscosity $\eta_S=1.0$ Pa s and the shell thickness $R_S=2$ nm. The dashed line corresponds to free bubbles.

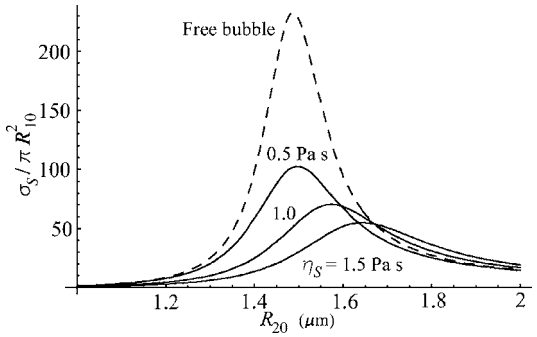

FIG. 7. Scattering cross sections as a function of equilibrium radius for the Maxwell shell model with $\eta_S=0.5$, 1.0, and 1.5 Pa s, at a driving frequency of 2.5 MHz. The relaxation time $\lambda=0.1$ μs and the shell thickness $R_S=2$ nm. The dashed line corresponds to free bubbles.

corresponding to the Kelvin-Voigt peak displacement is considerably larger than those for the other two shell models and free bubbles. It is interesting to note that the Maxwell model allows one to increase the value of the peak displacement by increasing the relaxation time, not changing the value of the shell viscosity and not increasing the value of the bubble radius corresponding to the peak displacement. This effect is illustrated in Fig. 8 by the upper Maxwell curve obtained at $\lambda=0.03$ μs, all the other parameters being the same.

V. CONCLUSIONS

Experimental data show that lipid-shelled contrast agents have properties that distinguish them from albumin- and polymer-shelled agents. Among such properties are low resonance frequencies of lipid-shelled bubbles, different destruction mechanisms, and the specific structure of lipid monolayer coatings being a combination of condensed phase domains surrounded by fluid-like regions. These experimental observations suggest that a viscoelastic fluid may be a better approximation for lipid shells than a viscoelastic solid or a simple viscous fluid. Based on this hypothesis, a new theoretical model for a lipid-shelled bubble has been proposed. The model assumes that the rheological behavior of the lipid shell follows the linear Maxwell constitutive equation. The model also incorporates the translational motion of the bubble and radiation losses due to the compressibility of

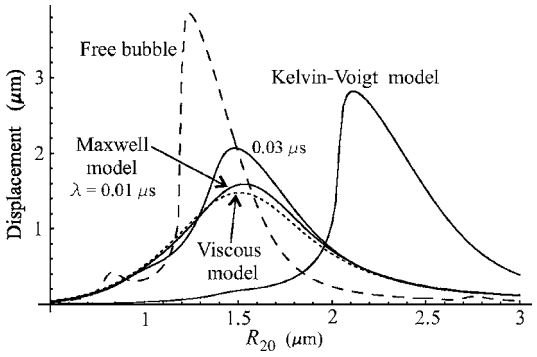

FIG. 8. Translational displacement as a function of equilibrium bubble radius. Bubbles are insonified with a 20 cycle, 2.5 MHz, 100 kPa acoustic pulse. The displacement is fixed after the termination of the pulse. The shell parameters are $R_S=2$ nm, $\eta_S=1.0$ Pa s, and $\mu_S=100$ MPa. The curves for the Maxwell model are calculated at $\lambda=0.01$ and 0.03 μs.

the surrounding liquid. To reveal physical features of the new model, comparative analysis has been performed between this model and two existing models. One of them treats the encapsulation as a viscoelastic solid following the Kelvin-Voigt constitutive equation, and the other assumes that the encapsulating layer behaves as a viscous Newtonian fluid. Comparison between the three shell models was carried out for resonance frequencies, damping coefficients, and scattering cross sections in the regime of linear oscillation. Numerical simulations on the translational dynamics were made for weakly nonlinear excitation by using the general, nonlinearized equations of motion. Analogous results for free bubbles were used as a common basis to which calculations made for encapsulated bubbles can be related. It has been shown that the new model possesses specific physical features that are unavailable in the two other models.

ACKNOWLEDGMENTS

A. A. D. wishes to acknowledge the financial support of the International Science and Technology Center (ISTC) under Contract No. B-1213. P. A. D. acknowledges support from NIH R21EB005325. The authors wish to thank Mark Borden and Katherine Ferrara for helpful discussions regarding lipid-coated microbubbles.

[1]R. A. Roy, C. C. Church, and A. Calabrese, "Cavitation produced by short pulses of ultrasound," in *Frontiers of Nonlinear Acoustics: Proceedings of 12th ISNA*, edited by M. F. Hamilton and D. A. Blackstock (Elsevier, London, 1990), pp. 476–481.
[2]N. de Jong, L. Hoff, T. Skotland, and N. Bom, "Absorption and scatter of encapsulated gas filled microspheres: Theoretical consideration and some measurements," Ultrasonics **30**, 95–103 (1992).
[3]N. de Jong and L. Hoff, "Ultrasound scattering of Albunex microspheres," Ultrasonics **31**, 175–181 (1993).
[4]N. de Jong, R. Cornet, and C. T. Lancee, "Higher harmonics of vibrating gas-filled microspheres. Part one: Simulations," Ultrasonics **32**, 447–453 (1994).
[5]C. C. Church, "The effect of an elastic solid surface layer on the radial pulsations of gas bubbles," J. Acoust. Soc. Am. **97**, 1510–1521 (1995).
[6]Z. Ye, "On sound scattering and attenuation of Albunex bubbles," J. Acoust. Soc. Am. **100**, 2011–2028 (1996).
[7]P. J. A. Frinking and N. de Jong, "Acoustic modeling of shell-encapsulated gas bubbles," Ultrasound Med. Biol. **24**, 523–533 (1998).
[8]L. Hoff, P. C. Sontum, and J. M. Hovem, "Oscillations of polymeric microbubbles: Effect of the encapsulating shell," J. Acoust. Soc. Am. **107**, 2272–2280 (2000).
[9]K. E. Morgan, J. S. Allen, P. A. Dayton, J. E. Chomas, A. L. Klibanov, and K. W. Ferrara, "Experimental and theoretical evaluation of microbubble behavior: Effect of transmitted phase and bubble size," IEEE Trans. Ultrason. Ferroelectr. Freq. Control **47**, 1494–1509 (2000).
[10]J. S. Allen, D. J. May, and K. W. Ferrara, "Dynamics of therapeutic ultrasound contrast agents," Ultrasound Med. Biol. **28**, 805–816 (2002).
[11]P. A. Dayton, J. S. Allen, and K. W. Ferrara, "The magnitude of radiation force on ultrasound contrast agents," J. Acoust. Soc. Am. **112**, 2183–2192 (2002).
[12]D. B. Khismatullin and A. Nadim, "Radial oscillations of encapsulated microbubbles in viscoelastic liquids," Phys. Fluids **14**, 3534–3557 (2002).
[13]D. Chatterjee and K. Sarkar, "A Newtonian rheological model for the interface of microbubble contrast agents," Ultrasound Med. Biol. **29**, 1749–1757 (2003).
[14]K. Sarkar, W. T. Shi, D. Chatterjee, and F. Forsberg, "Characterization of ultrasound contrast microbubbles using in vitro experiments and viscous and viscoelastic interface models for encapsulation," J. Acoust. Soc. Am. **118**, 539–550 (2005).
[15]P. Marmottant, S. van der Meer, M. Emmer, M. Versluis, N. de Jong, S. Hilgenfeldt, and D. Lohse, "A model for large amplitude oscillations of coated bubbles accounting for buckling and rupture," J. Acoust. Soc. Am. **118**, 3499–3505 (2005).
[16]A. A. Doinikov and P. A. Dayton, "Spatio-temporal dynamics of an encapsulated gas bubble in an ultrasound field," J. Acoust. Soc. Am. **120**, 661–669 (2006).
[17]S. H. Bloch, M. Wan, P. A. Dayton, and K. W. Ferrara, "Optical observation of lipid- and polymer-shelled ultrasound microbubble contrast agents," Appl. Phys. Lett. **84**, 631–633 (2004).
[18]P. A. Dayton, K. E. Morgan, A. L. Klibanov, G. H. Brandenburger, and K. W. Ferrara, "Optical and acoustical observations of the effects of ultrasound on contrast agents," IEEE Trans. Ultrason. Ferroelectr. Freq. Control **46**, 220–232 (1999).
[19]L. D. Landau and E. M. Lifshitz, *Theory of Elasticity* (Pergamon, Oxford, 1986).
[20]M. A. Borden and M. L. Longo, "Dissolution behavior of lipid monolayer-coated, air-filled microbubbles: Effect of lipid hydrophobic chain length," Langmuir **18**, 9225–9233 (2002).
[21]D. H. Kim, M. J. Costello, P. B. Duncan, and D. Needham, "Mechanical properties and microstructure of polycrystalline phospholipid monolayer shells: Novel solid microparticles," Langmuir **19**, 8455–8466 (2003).
[22]M. A. Borden, G. Pu, G. J. Runner, and M. L. Longo, "Surface phase behavior and microstructure of lipid/PEG-emulsifier monolayer-coated microbubbles," Colloids Surf., B **35**, 209–223 (2004).
[23]M. A. Borden, G. V. Martinez, J. Ricker, N. Tsvetkova, M. Longo, R. J. Gillies, P. A. Dayton, and K. W. Ferrara, "Lateral phase separation in lipid-coated microbubbles," Langmuir **22**, 4291–4297 (2006).
[24]L. D. Landau and E. M. Lifshitz, *Fluid Mechanics* (Pergamon, Oxford, 1987).
[25]L. D. Landau and E. M. Lifshitz, *Mechanics* (Pergamon, Oxford, 1976).
[26]A. Prosperetti, "Thermal effects and damping mechanisms in the forced radial oscillations of gas bubbles in liquids," J. Acoust. Soc. Am. **61**, 17–27 (1977).
[27]A. A. Doinikov, "Equations of coupled radial and translational motions of a bubble in a weakly compressible liquid," Phys. Fluids **17**, 128101 (2005).

Optical measurements of the self-demodulated displacement and its interpretation in terms of radiation pressure

Mathieu Rénier,[a] Christophe Barrière, and Daniel Royer
Laboratoire Ondes et Acoustique, Université Paris 7, CNRS, ESPCI, 10 rue Vauquelin 75231Paris, France

(Received 3 October 2006; revised 8 March 2007; accepted 25 March 2007)

Using a sensitive optical interferometer, the low frequency displacement nonlinearly generated by an ultrasonic tone burst propagating in a liquid is studied. Close to the source, the low frequency displacement contains a quasi-static component, which is affected by diffraction effects farther from the transducer. The experimental setup provides quantitative results, which allow the determination of the nonlinearity parameter of the liquid with a good accuracy. Such measurements are carried out in water and ethanol. Finally, the pressure associated with the low frequency displacement is discussed. Introducing the temporal mean value of the displacement, as already done in lossless solids, the noncumulative part of this second order pressure is associated with the static part of the low frequency displacement. This interpretation leads to extend the definition of the Rayleigh radiation pressure usually introduced for a continuous plane wave radiated in a confined fluid.
© *2007 Acoustical Society of America.* [DOI: 10.1121/1.2730624]

PACS number(s): 43.25.Zx, 43.25.Ba, 43.25.Qp [MFH] Pages: 3341–3348

I. INTRODUCTION

Due to their complexity, optical sensors are rarely used to measure acoustic quantities. Nevertheless, they offer several advantages compared with standard piezoelectric hydrophones, like a better spatial resolution (typically 50 μm), a good sensitivity and a larger bandwidth (especially in the low frequency domain). Indeed, optical probes are able to measure transient displacements smaller than 0.1 nm, in a frequency range running from a few kHz to 50 MHz.[1] They constitute a reference method for the characterization of ultrasonic transducers[2] and for the absolute calibration of piezoelectric hydrophones.[3,4] In this paper, the ability of optical interferometers to measure accurately weak amplitude displacements of relatively low frequencies is used to study the nonlinear self-demodulation of an ultrasonic tone burst in the MHz range.

"Self-demodulation" refers to the low frequency signal, which is nonlinearly generated by the propagation of a higher frequency tone burst. It results from the nonlinear interaction of the harmonic components contained in the tone burst spectrum. Berktay derived an asymptotic far field axial solution for the demodulated wave, proportional to the second time derivative of the amplitude modulation.[5] This demodulated wave form expression has been experimentally confirmed by far field axial measurements.[6,7] Gurbatov, Demin, and Malakhov[8] have also studied the effect of an additional frequency modulation. Averkiou, Lee, and Hamilton have experimentally and theoretically studied the case of strongly thermo-viscous fluid.[9] They found that the KZK (Khokhlov-Zabolotskaya-Kuznetsov) nonlinear parabolic wave equation[10] accurately describes the entire process, from near field to far field areas. Recently, Tournat, Gusev, and Castagnède have investigated the self-demodulation process in granular materials.[11]

Using Lagrangian coordinates (a,t), let us consider the nonlinear propagation equation for a plane wave, in a semi-infinite $(a>0)$ lossless fluid[12]

$$\frac{1}{c_0}\frac{\partial U}{\partial t}+\frac{\partial U}{\partial a}=\frac{\beta}{2}\left(\frac{\partial U}{\partial a}\right)^2. \tag{1}$$

U is the displacement of the fluid particle referenced by its position a at rest, c_0 is the sound speed of the fluid at rest, and β is the acoustic nonlinearity parameter.

Since we focus on the nonlinear propagation of a tone burst, the transient source condition is:

$$U(a=0,t)=U_0(t)\sin(\omega_0 t), \tag{2}$$

where $U_0(t)$ is the amplitude modulation, which slowly varies versus time in comparison with the term of angular frequency ω_0. In order to establish an approximate solution of Eq. (1), we use the method of successive approximations: $U=U_1+U_2+\ldots$, where $U_2 \ll U_1$. In this "quasi-linear" approach (or weak nonlinearity approximation), U_1 denotes the displacement in linear regime (first order in acoustic Mach number $M=\omega_0 U_0/c_0$) and U_2 represents the waves induced by the nonlinear propagation (second order in M). Introducing the retarded time $\tau=t-a/c_0$, assuming that the primary wave U_1 propagates without any change of its wave form (so that $\partial U_0(\tau)/\partial a=0$) and omitting the nonlinear term corresponding to the second harmonic, Eq. (1) becomes at second order in M

[a]Author to whom correspondence should be addressed; electronic mail: mathieu.renier@espci.fr

$$\left(\frac{\partial U_2}{\partial a}\right)_\tau = \frac{\beta\omega_0^2}{4c_0^2}U_0^2(\tau). \tag{3}$$

The low frequency (LF) displacement of the fluid particle located at a distance z from the source is deduced from Eq. (3)

$$U_{\mathrm{LF}}(a=z,t) = \frac{\beta}{4}k_0^2 z U_0^2\left(t-\frac{z}{c_0}\right), \tag{4}$$

where $k_0=\omega_0/c_0$ is the wave number. Increasing linearly with the acoustic intensity and with the propagation distance z, as the amplitude of the second harmonic component simultaneously generated, this LF displacement results clearly from a nonlinear and cumulative process. For a high frequency continuous wave, the displacement U_{LF} is static and it is proportional to the square of the amplitude U_0 of the emitted displacement.

In a real fluid, where thermoviscous phenomena have to be taken into account, the LF displacement U_{LF} and the absorption coefficient α_0 of the primary wave both increase as the square of the frequency. So this frequency must be appropriately chosen in order to lead to a sufficiently large LF displacement, without any prohibitive absorption dramatically limiting the nonlinear process. For example, in water ($c_0=1500$ m/s, $\beta=3.5$) and for a primary wave amplitude $U_0=5$ nm at a frequency $f_0=10$ MHz ($\alpha_0=2.4$ Np/m), a 1 nm LF displacement would be expected at a distance $z=25$ mm from the transducer. At this distance, the primary wave attenuation is only 0.5 dB.

In this paper, we show that such small LF displacements can be measured with a sensitive optical interferometer. Measurements are carried out in a large water tank at different distances from the transducer and for various amplitudes of a tone burst whose temporal shape is rectangular. We verify experimentally that, close to the source, the LF displacement contains a quasistatic component, which is affected by diffraction effects farther from the transducer. If diffraction effects do not invalidate Eq. (4), the acoustic nonlinearity parameter of the fluid can be measured. Finally, we discuss the LF pressure p_{LF} associated with U_{LF}. This pressure contains both a standard cumulative contribution and a noncumulative one. Studying the latter, we suggest that close to the source, a quasi-static pressure is associated with the quasi-static part of the LF displacement. Using a plane wave analysis, we show that this quasi-static pressure is a consequence of a constant (with respect to the spatial coordinate) mean displacement gradient. It may be identified as an extension of the Rayleigh radiation pressure usually introduced for plane continuous waves radiated in a confined fluid. Because of the diffraction of the LF displacement, this quasi-static pressure is cancelled when the propagation distance increases.

II. EXPERIMENTS

An optical interferometer is used to measure the LF displacement nonlinearly induced by an ultrasonic tone burst having a rectangular shape. Measurements at various distances from the transducer and for different amplitudes of emission are carried out with planar and focused transducers. From these results, the nonlinearity parameters of both water and ethanol are deduced.

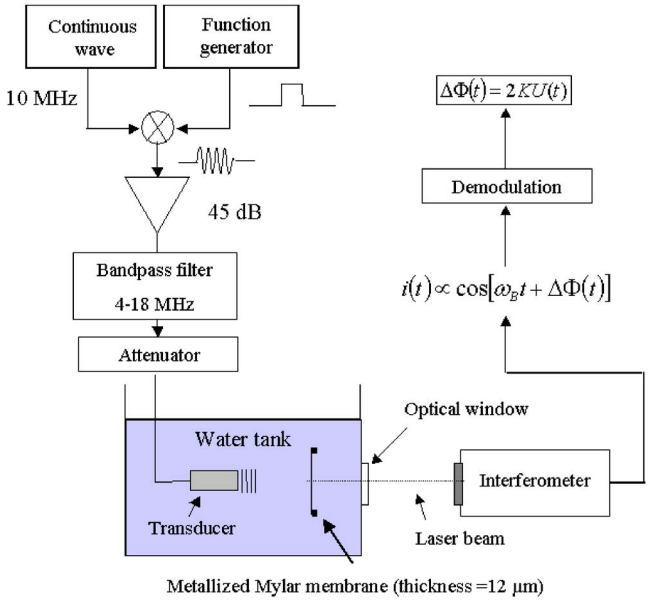

FIG. 1. (Color online) Experimental setup.

A. Experimental setup

The experimental setup is represented in Fig. 1. A piezoelectic transducer (central frequency $f_0=10$ MHz, diameter $d=10$ mm) is immersed in a water tank whose size is very much larger than the acoustic beam. This transducer is mounted on a micrometric stage allowing displacements along the three perpendicular axes. It radiates a tone burst, which is obtained by multiplying a harmonic signal with an adjustable duration rectangular envelope. The duration is chosen short enough to lead to a quasi-transient diffraction regime, allowing the assumption of a plane wave in the near field area. Furthermore, as shown in Sec. II E, short durations avoid important acoustic streaming effects. The amplitude of the transmitted ultrasonic wave is controlled via an attenuator. Before its application to the transducer, the electric signal is bandpass filtered, in order to eliminate the possible components nonlinearly generated by the emission device.

Wave induced displacements are measured by a high sensitive optical heterodyne interferometer, whose probe beam is reflected by a thin metallized membrane of Mylar (thickness 12 μm) immersed in front of the transducer.[3] As already described elsewhere[13] the modulation of the path of the probe beam is transposed into a phase modulation $\Delta\Phi$ of the photodiode current in the radio frequency domain by a change of the optical frequency with an acousto-optic modulator (Bragg cell operating at the frequency $f_B=70$ MHz). Then, the normal displacement U of the membrane modulates the optical beam phase, according to the relation

$$\Delta\Phi(t) = 2K_{\mathrm{eff}}U(t), \tag{5}$$

where $K_{\mathrm{eff}}=2\pi n_{\mathrm{eff}}/\Lambda$ is the effective optical wave number, taking into account the modification of the optical refraction

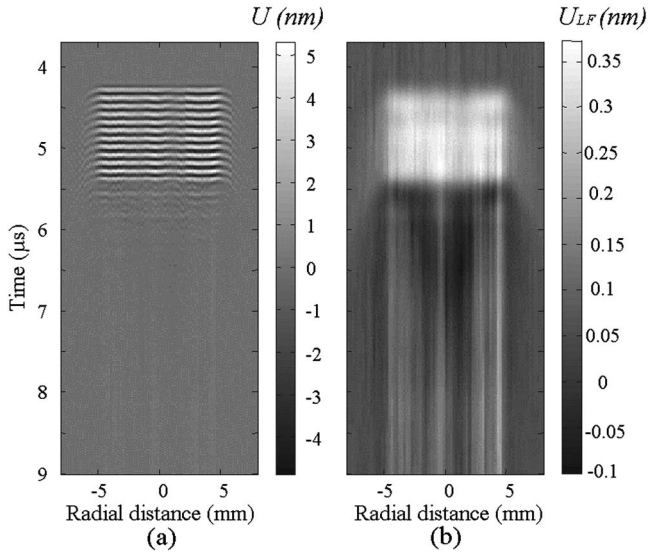

FIG. 2. Space-time representations of the tone burst displacement U (a) and associated low frequency component U_{LF} (b), at a distance $z=3$ mm.

index of water induced by the acousto-optic interaction. For a plane wave propagating in water, it can be shown[3,14] that $n_{\mathrm{eff}} \approx 1$.

This phase modulation can be numerically or analogically extracted from the photodiode current. In order to reduce electronic noise, the photocurrent is bandpass filtered between $f_B \pm 25$ MHz. The low frequency displacement U_{LF}, corresponding to the low frequency components of the phase modulation, is selected by using a narrower bandpass filter ($f_B \pm 3$ MHz).

This experimental setup leads to the displacement measurement of a fixed fluid particle. Moreover, taking into account the thickness of the membrane (12 μm) and the impedance of Mylar (2.9 MRayl.), the membrane can be considered as transparent to ultrasounds in this frequency range. This transparency ensures the absence of a reflected wave. Then, the measured displacements are Lagrangian quantities.

B. Experimental results

First experiments were carried out at 10 MHz with a planar transducer having a 10 mm diameter. In Fig. 2, space-time representations of both tone burst and LF displacements are reported for a distance from the transducer to the membrane equal to $z=3$ mm. The LF displacement component has a rectangular temporal shape similar to the tone burst envelope and an amplitude smaller than 1 nm. When placing the membrane as close as possible to the transmitter, no LF component is detected. Thus, this component is not directly radiated by the transducer. The spatial extension of the LF frequency displacement corresponds to the transducer diameter.

In Figs. 3 and 4, displacements are represented as a function of time, for $z=3$ mm, for various amplitudes of emission and for two tone burst durations (1 and 2 μs). We find a rectangular LF displacement shape. Neither its amplitude nor its shape vary when the tone burst duration changes,

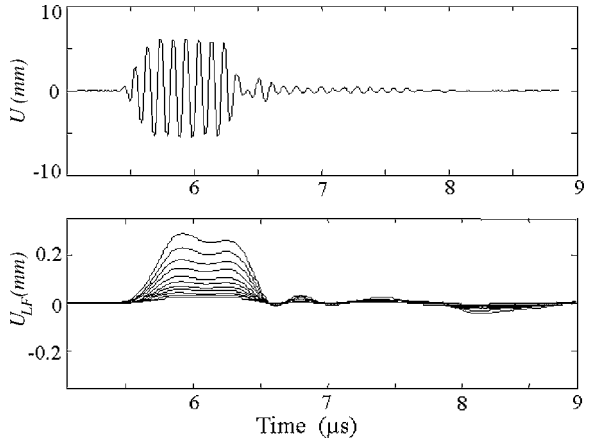

FIG. 3. Displacements (tone burst U and low frequency component U_{LF}) at a distance $z=3$ mm from the source, measured for various excitation amplitudes. The tone burst duration is 1 μs. The tone burst displacement corresponds to the highest level amplitude.

in opposition to what was mentioned by Yost and Cantrell in similar measurements performed in solids.[15] The LF displacement amplitude varies quadratically with the tone burst amplitude (see also Fig. 9). These results are similar to those recently published in the case of a solid.[16] A discussion about the pressure associated to the quasi-static part of the LF displacement is presented in Sec. III.

At a distance $z=22$ mm, the temporal shape of the low frequency displacement changes (Fig. 5). It tends towards the time derivative of the wave form observed close to the source. In linear acoustics, this is a characteristic of a transient diffraction regime: in the far field, the temporal wave form tends towards two short pulses with opposite signs.[17]

To specify the study of the LF displacement diffraction regime, a measurement was implemented at the 70 mm focal point of a focused transducer in water (diameter $d=10$ mm and central frequency $f_0=10$ MHz). Despite the filtering consequence, the obtained signal is closed to the time derivative of the tone burst envelope (Fig. 6). On the space-time representation (Fig. 7), we distinguish a contribution to the LF displacement whose lateral extension corresponds to that

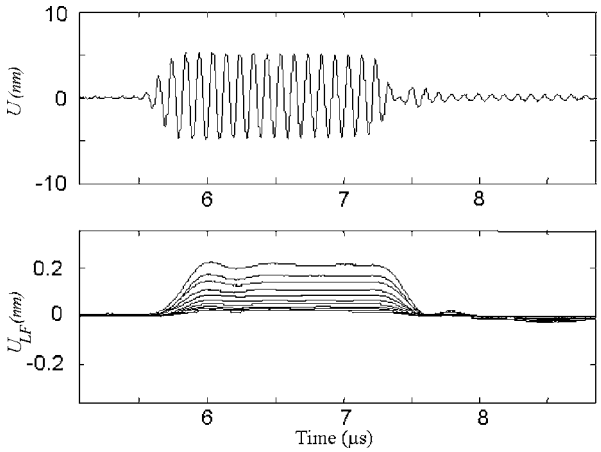

FIG. 4. Displacements (tone burst U and low frequency component U_{LF}) at a distance $z=3$ mm from the source, measured for various excitation amplitudes. The tone burst duration is 2 μs. The tone burst displacement corresponds to the highest level amplitude.

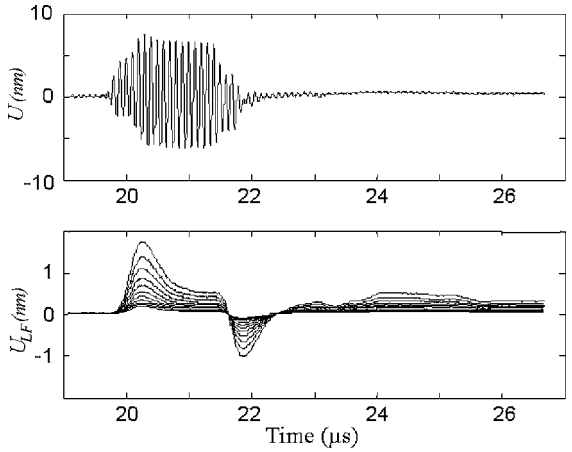

FIG. 5. Displacements (tone burst U and low frequency component U_{LF}) at a distance $z=22$ mm from the source, measured for various excitation amplitudes. The tone burst duration is 2 μs. The tone burst displacement corresponds to the highest level amplitude.

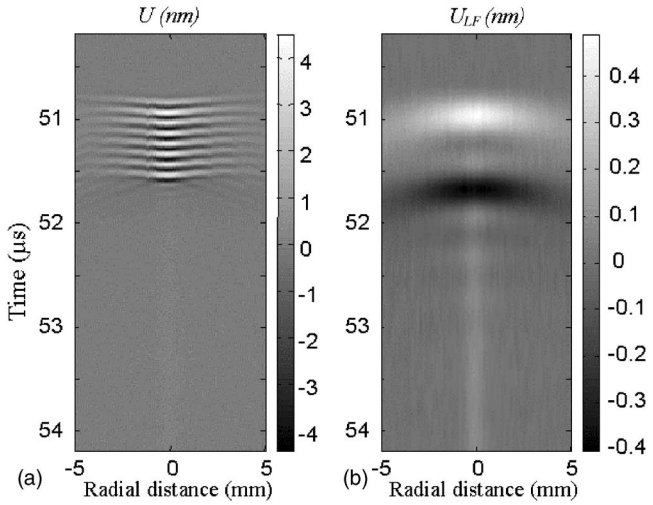

FIG. 7. Space-time representations of tone burst and low frequency displacements, measured at the focal distance of a focused transducer.

of the focal spot but which is temporally more extended than the tone burst. This membrane displacement corresponds to a momentum transfer to the membrane induced by acoustic streaming. Thought this is not the subject of the paper, we briefly discuss this effect in Sec. II E.

Figure 8 shows the LF displacement amplitude versus the distance z between the planar transducer and the membrane. The amplitude increases linearly until a distance $z=25$ mm, from which the cumulative process is limited by the diffraction of the LF component. These measurements have been performed using a $\Theta=1$ μs duration envelope. So the Fresnel diffraction distance $d^2/(8c_0\Theta)$, calculated as if U_{LF} was emitted in linear regime by the transducer, is about 8 mm. Increasing Θ, we have checked experimentally that the diffraction distance of U_{LF} decreases. However, in this experiment, the interference of the main and edge LF waves occurs at a larger distance ($z\approx 20$ mm). Thus, in spite of the linear diffraction effect, the LF displacement component remains collimated farther, thanks to the nonlinear cumulative antenna effect. The attenuation and Fresnel distances of the high frequency tone burst are, respectively: $L_a=1/\alpha_0=42$ cm and $d^2f_0/(4c_0)=16.7$ cm. So neither the attenuation nor the diffraction of the primary beam limits the cumulative process.

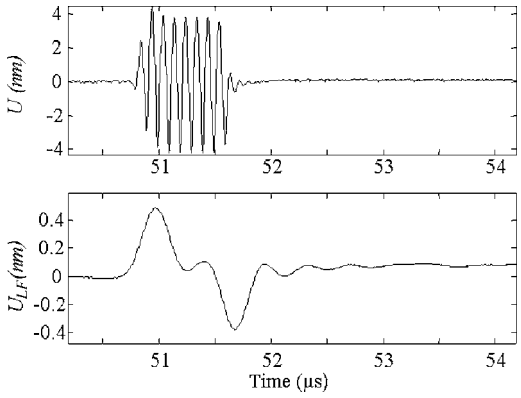

FIG. 6. Displacements (tone burst U and low frequency component U_{LF}) measured at the focal distance of a focused transducer.

C. Nonlinearity parameter measurement

The nonlinearity parameter of the fluid can be determined from Eq. (4). For this purpose, we use again a tone burst with a relatively short duration (1 μs). This choice is the result of a trade-off between the need for a quasi-transient diffraction mode of the tone burst (allowing us to measure U_0) and an emitted spectrum which is sufficiently narrow to clearly identify the LF component. Then, the LF displacement amplitude is measured for various emission amplitudes U_0, at a distance z where it is not perturbed by diffraction effects.

The LF displacement amplitude is represented in Fig. 9, as a function of the quantity $x=zk^2U_0^2/4$ (in nanometer). A linear dependence is clearly observed, which confirms the quadratic behaviour of U_{LF} versus U_0. According to Eq. (4), the slope value, deduced from a least mean squared linear regression, is equal to the fluid nonlinearity parameter β. Values obtained for water ($\beta=3.57$), and ethanol ($\beta=6.42$) are in good agreement with those found in the literature

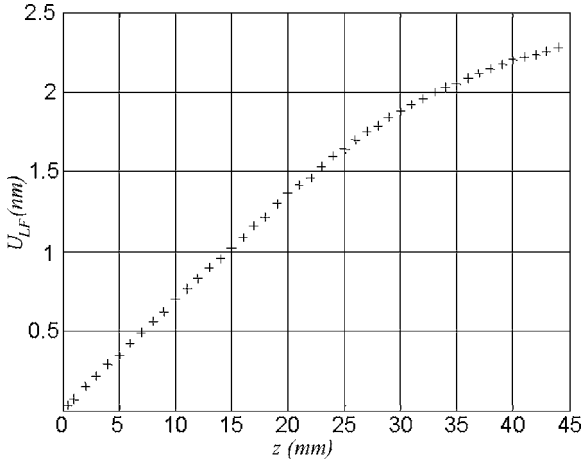

FIG. 8. Low frequency displacement amplitude U_{LF} versus the propagation distance z.

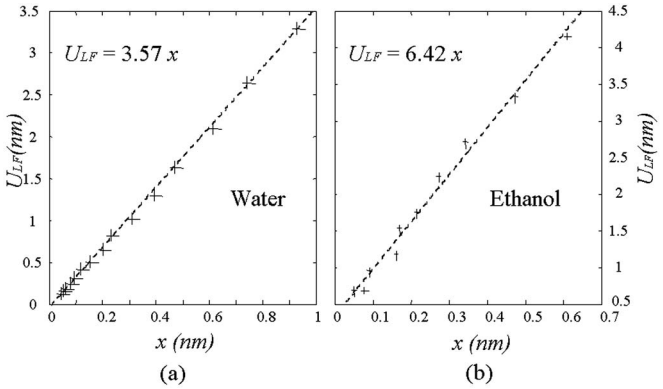

FIG. 9. Nonlinearity parameter β measurement: (a) in water (z=20 mm), (b) in ethanol (z=15.5 mm). Crosses mark measurement points. Straight lines are obtained by a least squared linear regression. The slope gives the value of the nonlinearity parameter β.

(β_{water}=3.5 and $\beta_{ethanol}$=6.15).[18] Thus, the self-demodulated signal can provide another method to measure nonlinearity parameters, alternative to usual ones.[19–21]

D. Far field measurements

Using the same planar transducer, as in previous sections, we have measured in water, without any filtering, the total displacement at a longer distance from the source z =34 cm. The obtained signal for an initial 6 MHz frequency tone burst is represented in Fig. 10(a). A remaining nonzero high frequency component can be observed. At 6 MHz, the attenuation distance is L_a=1.16 m. The signal obtained with a tone burst of initial frequency 15 MHz (L_a=0.19 m) is represented in Fig. 10(b). The 15 MHz spectral component has completely disappeared. The remaining signal is only composed of two short pulses, corresponding to the diffracted low frequency displacement. This axial far field displacement corresponds to the asymptotic expression formulated by Berktay, where the LF pressure is proportional to the second time derivative of the envelope.[5]

E. Acoustic streaming

In this section, we discuss the influence of the acoustic streaming in our experiments. The propagation of powerful sound waves in liquids and gases frequently leads to the appearance of nonperiodic motions of the medium (flows)

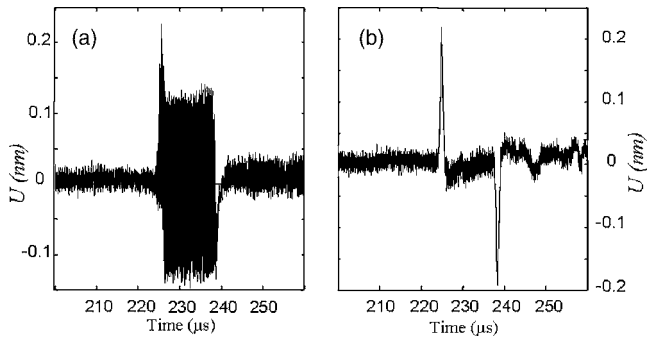

FIG. 10. Total displacement U, measured (without narrowband filtering) at a distance z=34 cm from the source. (a) Tone burst of initial frequency 6 MHz. (b) Tone burst of initial frequency 15 MHz.

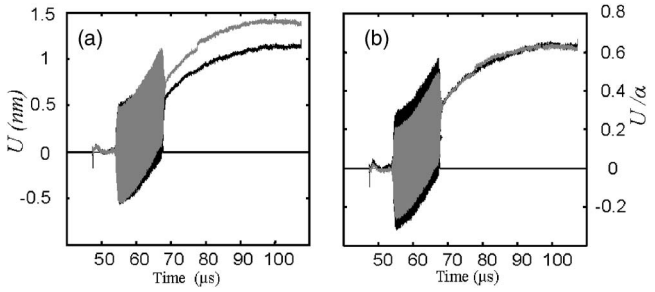

FIG. 11. (a) Total displacement U, measured (without narrowband filtering) at the focal point of a focused transducer, for a 15 μs tone burst duration, and for two frequencies: black curve (f=9 MHz), gray curve (f=10 MHz). (b) The amplitude is divided by the absorption coefficient α_0.

called acoustic streaming. Due to its tensile strength, the Mylar membrane is no longer transparent for a very low frequency signal. Thus, such flows are able to transfer a momentum quantity and then to move the membrane. The force F exerted by the streaming depends on the viscosity of the fluid[22,23]

$$F = \frac{\alpha_0}{(\rho_0 c_0)^2} p^2, \tag{6}$$

where p is the acoustic pressure and ρ_0 is the fluid density at rest.

In Sec. II B, we have assumed that the temporally extended displacement observed in Figs. 6 and 7 at the focus of the concave transducer was induced by a streaming effect. In order to check this assumption, we have studied the influence of the central frequency f_0 of the tone burst. Figure 11 represents total displacements at the focal point of the transducer for 9 and 10 MHz tone bursts having a Θ=15 μs time duration. We have checked that at these two frequencies the same amplitude was transmitted by the transducer. We observed that such long tone bursts induce large "nonperiodic" displacements increasing with the frequency like the attenuation coefficient α_0. If we compare the nonperiodic displacement induced by the 15 μs tone burst [Fig. 11(a)] with that induced by the 1 μs tone burst (Fig. 6), we notice that the amplitude of this effect is a function of the tone burst duration. This nonperiodic displacement seems to result from an accumulation of the momentum transfer from the wave to the medium.[22] Then, a tone burst short enough, as chosen in our experiments (1 μs), avoids strong disturbances due to the acoustic streaming effect.

III. DISCUSSION ABOUT THE ASSOCIATED PRESSURE

In this section, we discuss the pressure associated with the LF displacement experimentally studied. Let us first consider the second order state equation in a lossless fluid

$$P - P_0 = A\left(\frac{\rho - \rho_0}{\rho_0}\right) + \frac{B}{2}\left(\frac{\rho - \rho_0}{\rho_0}\right)^2, \tag{7}$$

where P and ρ are the fluid pressure and density, P_0 and ρ_0 are their values at rest and $A=\rho_0 c_0^2$ and $B=\rho_0^2(\partial^2 P/\partial\rho^2)_{\rho_0}$ are, respectively, the first and second order coefficients of the

Taylor expansion. Using the one-dimensional continuity equation $(\rho_0/\rho)=1+\partial U/\partial a$, Eq. (7) becomes

$$P - P_0 = -A\frac{\partial U}{\partial a} + \beta A\left(\frac{\partial U}{\partial a}\right)^2. \tag{8}$$

Following the perturbation method described in the introduction, the second order acoustic pressure in M is: $p_2 = -A(\partial U_2/\partial a) + \beta A(\partial U_1/\partial a)^2$. Since we focus only on the LF components of p_2, Eq. (4) is used to calculate the second order displacement U_2. The LF pressure is then

$$p_{\mathrm{LF}}(a=z,\tau) = \frac{A\beta k_0^2}{4}\left(\frac{z}{c_0}\frac{\partial U_0^2(\tau)}{\partial \tau} + U_0^2(\tau)\right), \tag{9}$$

where p_{LF} contains both a cumulative contribution (proportional to the propagation distance z) and a noncumulative one. Following the weak nonlinearity approximation, the superposition principle still holds for nonlinearly induced waves and these two contributions to the pressure add.

A. Cumulative contribution to the LF pressure

Since for a plane wave, the nonlinear local term of the propagation equation is cancelled,[24,25] the cumulative contribution to p_{LF} can also be derived from Eq. (4) using the relation $P_{\mathrm{LF}}^C(z,\tau)=\rho_0 c_0(\partial U_{\mathrm{LF}}/\partial\tau)$. This pressure results from the nonlinear interaction of the different frequency components contained in the spectrum of the emitted tone burst. It has been fully studied in literature, where measurements have been realized using hydrophones.[7–9] Taking into account diffraction and attenuation effects, Averkiou, Lee, and Hamilton have derived an analytical expression of this LF pressure on the axis of a piston-like transducer.[9] Assuming far field conditions, where the emitted tone burst is totally attenuated, the axial LF pressure is shown to be inversely proportional to the propagation distance a and proportional to the second time derivative of the squared envelope $U_0^2(\tau)$. In Eq. (9), the cumulative contribution to p_{LF}, derived for a plane wave in a lossless fluid, is consistent with their expression: if the initial tone burst is fully attenuated, the linear dependence with z no longer stands and diffraction acts in far field as the operator $1/z\,\partial/\partial\tau$. In our experiments, close to the source, this contribution to the LF pressure would be zero between the edges of the rectangular envelope of the tone burst.

B. Noncumulative contribution to the LF pressure

Instead of using a perturbation method, we propose now, as already done in the case of lossless solids,[12] to consider the constant part of the LF displacement in the near field of the transducer, as a nonzero temporal mean value of the corresponding part of the total displacement. So we derive the mean excess pressure generated by the part of our rectangular tone burst that is in steady state regime, assuming also that it is a plane wave. In other words, the following calculus is valid for a plane continuous wave, so it is not applied to the transient parts of the rectangular envelope.

Since, in steady state regime, the mean particle velocity $\langle\partial U/\partial t\rangle_{T_0}$ vanishes in Lagrangian coordinates,[26] time averaging Eq. (1) over a cycle (i.e., averaging over the period $T_0=1/f_0$, that corresponds in practice to a low-pass filtering in experiments) leads to the mean value of the displacement gradient

$$\left\langle\frac{\partial U}{\partial a}\right\rangle_{T_0} = \frac{\beta}{2}\left\langle\left(\frac{\partial U}{\partial a}\right)^2\right\rangle_{T_0}. \tag{10}$$

Besides, in linear regime, kinetic and potential energy densities are equal for a plane wave, so that the total energy density is

$$E = A\left(\frac{\partial U}{\partial a}\right)^2. \tag{11}$$

By time averaging Eq. (8) and using Eqs. (10) and (11), the Lagrangian mean excess pressure expresses as

$$\langle P - P_0\rangle_{T_0} = -A\left\langle\frac{\partial U}{\partial a}\right\rangle_{T_0} + A\beta\left\langle\left(\frac{\partial U}{\partial a}\right)^2\right\rangle_{T_0} = \frac{\beta}{2}\langle E\rangle_{T_0}. \tag{12}$$

The common expression of the Rayleigh radiation pressure exerted on a perfectly absorbing target, usually derived for a continuous wave in a confined fluid, is retrieved here.[26–28] $\langle P-P_0\rangle_{T_0}$ is a second order quantity, which is noncumulative and which is both proportional to the nonlinearity parameter and to the linear energy density.

Introducing the static displacement $U_s=\langle U(a,t)\rangle_{T_0}$ and integrating Eq. (10) from the source ($a=0$) to the observation point ($a=z$), we obtain

$$U_S(a=z,t) = \frac{\langle P - P_0\rangle_{T_0}}{A}z. \tag{13}$$

Since in linear regime the energy density is $E = Ak_0^2U_0^2\cos^2(\omega\tau)$, Eq. (13) leads to the same result as Eq. (4) in harmonic regime. Moreover, the LF pressure defined by Eq. (9) is retrieved with Eq. (12) in the particular case of a continuous wave (where U_0 remains constant). We notice that in harmonic regime, there is no cumulative component of the pressure. The only "LF" pressure component has a frequency equal to zero: it is the static Rayleigh radiation pressure.

C. Experiment interpretation

Thus, the quasi-static part of the LF displacement measured in the near filed of our transducer can be related to a quasi-static pressure. This interpretation leads to extend the definition of the Rayleigh radiation pressure, which usually concerns continuous plane waves in confined fluids. In our experiment, the transducer is sufficiently directive to confine the nonlinearly induced quasi-static pressure in its near field. Farther from the source, the diffraction effect affecting U_{LF} can be regarded as the equalization of this quasi-static pressure with the ambient pressure P_0 in the surrounding fluid. The self-demodulated displacement can also be linked to this quasi-static pressure, but it requires the tone burst to reach a steady state regime (i.e., to have a sufficiently large rectangular envelope, compared with T_0).

The order of magnitude of the quasi-static pressure can be deduced from Fig. 8: in the linear zone, the slope of the curve (7×10^{-8}) corresponds to the mean displacement gradient. In water ($A=2.25$ GPa), the mean excess pressure, deduced from Eqs. (10) and (12), is then found to be of the order of 150 Pa. Such a small pressure would be difficult to measure with piezoelectric hydrophones.

Since the total LF pressure generated by the tone burst is the sum of the noncumulative quasi-static component with a cumulative pressure [Eq. (9)], the order of magnitude of this latter also has to be examined. In our experiments, for a propagation distance $z=3$ mm, its amplitude (calculated by time differentiating the LF displacement represented in Fig. 3) is ten times greater than the quasi-static pressure one. Moreover, as it is cumulative, it increases with the propagation distance, whereas diffraction cancels the quasi-static pressure. However, even if the cumulative part of the acoustic pressure dominates, the two contributions do not appear at the same time in the signal.

IV. CONCLUSION

This experimental study deals about the self-demodulation of a high frequency tone burst, having a rectangular envelope with a relatively short time duration. These conditions ensure several advantages. First, the central frequency chosen for the tone burst provides measurable nonlinear effects. Second, in the near field domain, diffraction effects can be neglected in transient regime, allowing a plane wave analysis. Furthermore, the short duration of the tone burst avoids strong acoustic streaming effects.

Using a sensitive optical interferometer coupled with a metallized Mylar membrane immersed in the fluid, measurements have been carried out for various emission amplitudes, at different distances from the source. In the near field, the self-demodulation corresponds to a low frequency displacement having a rectangular shape like the tone burst envelope. For water and ethanol, the acoustic nonlinearity parameters deduced from the LF displacement measurements are in good agreement with previous results. Farther from the source, the increase of the LF displacement amplitude with the propagation distance is limited by the effect of diffraction.

The pressure associated with the LF displacement was discussed under a plane wave assumption. The first contribution, well known, is cumulative and results from the nonlinear interaction of the different frequency components of the tone burst. A second one, noncumulative, results from a constant mean displacement gradient. This quasi-static pressure associated with the static part of the LF displacement has been formally identified as the Rayleigh radiation pressure, which is here extended to the case of a tone burst in an unconfined fluid. Indeed, near the transducer, the beam directivity confines the sound field sufficiently to create a quasi-static pressure in a volume, without balancing immediately with the surrounding fluid equilibrium pressure. However, since this quasi-static pressure is not cumulative: as the distance from the transducer increases, it becomes small in comparison with the cumulative LF pressure. Furthermore, as a consequence of the diffraction effects affecting the LF component, the quasi-static pressure is cancelled.

ACKNOWLEDGMENT

The authors thank Dr. Jean-Louis Thomas at I.N.S.P, Paris, France, for helpful discussions.

[1] D. Royer, N. Dubois, and M. Fink, "Optical probing for pulsed, focused ultrasonic fields using a heterodyne interferometer," Appl. Phys. Lett. **61**, 153–155 (1992).
[2] D. Certon, O. Casula, F. Patat, and D. Royer, "Theoretical and experimental investigation of lateral modes in 1-3 piezocomposites," IEEE Trans. Ultrason. Ferroelectr. Freq. Control **44**, 643–651 (1996).
[3] D. R. Bacon, "Characteristics of a PVDF membrane hydrophone for use in the range 1–100 MHz," IEEE Trans. Sonics Ultrason. **SU-29**, 18–25 (1982).
[4] R. C. Preston, S. P. Robinson, B. Zeqiri, T. J. Esward, P. N. Gelat, and N. D. Lee, "Primary calibration of membrane hydrophones in the frequency range 0.5 MHz to 60 MHz," Metrologia **36**, 331–343 (1999).
[5] H. O. Berktay, "Possible exploitation of non-linear acoustics in underwater transmitting applications," J. Sound Vib. **2**, 435–461 (1965).
[6] M. B. Moffett, P. J. Westervelt, and R. T. Beyer, "Large-amplitude pulse propagation—a transient effect," J. Acoust. Soc. Am. **47**, 1473–1474 (1970).
[7] M. B. Moffett, P. J. Westervelt, and R. T. Beyer, "Large-amplitude pulse propagation—a transient effect. II," J. Acoust. Soc. Am. **49**, 339–343 (1971).
[8] S. N. Gurbatov, I. Yu. Demin, and A. N. Malakhov, "Influence of phase fluctuations on the characteristics of parametric arrays," Sov. Phys. Acoust. **26**, 217–220 (1980).
[9] M. A. Averkiou, Y.-S. Lee, and M. F. Hamilton, "Self-demodulation of amplitude-and frequency-modulated pulses in a thermo viscous fluid," J. Acoust. Soc. Am., **94** 2876–2883, (1993).
[10] N. S. Bakhvalov, Ya. M. Zhileikin, and E. A. Zabolotskaya, *Nonlinear Theory of Sound Beams* (American Institute of Physics, New York, 1987).
[11] V. Tournat, V. E. Gusev, and B. Castagnède, "Self-demodulation of elastic-waves in one-dimensional chains," Phys. Rev. E **70**, 056603 (2004).
[12] J. H. Cantrell, W. T. Yost, and P. Li, "Acoustic radiation induced static strains in solids," Phys. Rev. B **35**, 9780–9782 (1987).
[13] D. Royer and O. Casula, "Quantitative imaging of transient acoustic fields by optical heterodyne interferometry," 1994 IEEE Ultrasonics Symp. Proc., 1153–1162 (1994).
[14] C. B. Scruby and L. E. Drain, *Laser Ultrasonics Techniques and Applications* (Hilger, London, 1990).
[15] W. T. Yost and J. H. Cantrell, Jr., "Acoustic radiation stress in solids. II. Experiments," Phys. Rev. B **30**, 3221–3229 (1984).
[16] X. Jacob, R. Takatsu, C. Barrière, and D. Royer, "Experimental study of acoustic radiation strain in solids," Appl. Phys. Lett. **88**, 134111 (2006).
[17] P. R. Stephanishen, "Transient radiation from pistons in an infinite planar baffle," J. Acoust. Soc. Am. **42**, 1629–1638 (1971).
[18] R. T. Beyer, "The Parameter B/A," in *Nonlinear Acoustics*, edited by M. F. Hamilton and D. T. Blackstock (Academic, New York, 1998), Chap. 2, p. 25–39.
[19] A. B. Coppens, R. T. Beyer, M. B. Seiden, J. Donohue, F. Guepin, R. H. Hodson, and C. Townsend, "Parameter of nonlinearity in fluids II," J. Acoust. Soc. Am. **38**, 797–804 (1965).
[20] M. A. Breazeale and J. Philip, *Physical Acoustics* (Academic, New York, 1984), Vol. **17**, pp. 1–60.
[21] C. Barrière and D. Royer, "Diffraction effects in the parametric interaction of acoustic waves: Application to measurements of the nonlinearity parameter B/A in liquids," IEEE Trans. Ultrason. Ferroelectr. Freq. Control **48**, 1706–1715 (2001).
[22] T. Kamakura, T. Sudo, K. Matsuda, and Y. Kumamoto, "Time evolution of acoustic streaming from planar ultrasound source," J. Acoust. Soc. Am. **100**, 132–138 (1996).
[23] O. V. Rudenko, A. P. Sarvazyan, and S. Y. Emelianov, "Acoustic radiation force and streaming induced by focused nonlinear ultrasound in a dissipative medium," J. Acoust. Soc. Am. **99**, 2791–2798 (1993).

[24]S. I. Aanonsen, T. Barkve, J. Naze Tjøtta, and S. Tjøtta, "Distortion and harmonic generation in the near field of a finite amplitude sound beam," J. Acoust. Soc. Am. **75**, 749–768 (1984).
[25]M. F. Hamilton and C. L. Morfey, "Model equations," in *Nonlinear Acoustics*, edited by M. F. Hamilton and D. T. Blackstock (Academic, New York, 1998), Chap. 3, p. 41–64.
[26]B. T. Chu and R. E. Apfel, "Acoustic radiation pressure produced by a beam of sound," J. Acoust. Soc. Am. **72**, 1673–1687 (1982).
[27]R. T. Beyer, "Radiation pressure–the history of a mislabeled tensor," J. Acoust. Soc. Am. **63**, 1025–1030 (1978).
[28]T. G. Wang and C. P. Lee, "Radiation pressure and acoustic levitation,", *Nonlinear Acoustics*, edited by M. F. Hamilton and D. T. Blackstock (Academic, New York, 1998).

Causality and the velocity of acoustic signals in bubbly liquids

Gregory J. Orris,[a] Dalcio K. Dacol, and Michael Nicholas
U.S. Naval Research Laboratory, Washington, DC 20375

(Received 25 January 2006; revised 7 March 2007; accepted 19 March 2007)

Several versions of the dispersion formula governing the acoustic propagation in bubbly liquids are shown to exhibit acausal behavior. The cause of this behavior is due to the inappropriate application of a low frequency approximation in the determination of the extinction of the signal from radiative scattering. Using a corrected causal formula, several principles of wave propagation in bubbly media consistent with the general theory of wave propagation in dispersive media are demonstrated: There exist two precursors to any finite signal. Both propagate without regard to the source characteristics at velocities, frequencies, and amplitudes dependent wholly upon the characteristics of the medium supporting the wave motion. The first travels at the infinite frequency phase velocity that is coincident with the infinite frequency limit of the group velocity. That part of a propagating wave oscillating at the source frequency arrives at a time determined by the signal velocity. Analogous to the well known signal velocity of electromagnetic wave propagation in conducting media, the value of the signal velocity depends on the detailed structure of the dispersion formula in the complex frequency plane. [DOI: 10.1121/1.2724242]

PACS number(s): 43.30.Es, 43.20.Bi, 43.20.Hq, 43.25.Yw [TDM] Pages: 3349–3362

I. INTRODUCTION

In this work we present a correction that makes the dispersion formula for acoustic wave propagation in bubbly liquids based on the material contained within the work of Devin[1] analytic in the upper-half complex frequency plane.[2,3] The main physical consequence of analyticity in this domain is causality. The velocity of any signal will be seen to be limited by the infinite frequency limit of the phase velocity of the medium. A further consequence is the existence of a frequency dependent signal velocity distinct from both the group and phase velocities. This is the true velocity of the broadcast signal. The group velocity is, in fact, only a close approximation to the signal velocity at the infinite frequency limit. The causal form of the dispersion formula provides a correction to the attenuation of the wave predominantly at frequencies far above bubble resonance, providing an asymptotic floor of the attenuation of an acoustic wave in a bubbly liquid and explains an apparent discrepancy between the theory and experimental values reported in Ref. 2.

The acausal behavior of the linearized effective medium theory of signal propagation in bubbly media should not be surprising given that the paragraph following Ref. 2, Eq. (30) explicitly states that errors of order c_0^{-2} of Keller's bubble radius equation can be neglected.[4–6] Thus justifying using the bubble radius as the small amplitude bubble oscillation expansion parameter. The proper expansion factor should have been the unitless scattering parameter $\delta=ka=\omega a/c_0 \ll 1$, where ω is the incident wave's angular frequency, a the bubble radius, and c_0 the infinite frequency phase speed equivalent to the quiescent phase speed of a liquid without bubbles. While the uncorrected dispersion formulas and our correction are nonetheless valid over a wide range of bubble sizes and environmental parameters, typical oceanic environments where the bubble size distribution is peaked for bubble radii on the order of a few tens of microns, $\delta \approx \omega \times 10^{-8}$ s, the signal frequencies would need to be of the order of 10 MHz before $\delta \approx 1$. This high frequency behavior relative to the bubble size is a regime that may very well lie outside the realm of validity for the theory. However, we will demonstrate that a self-consistent theory is necessary at lower frequencies as well.

Theoretically one calculates a signal's space-time dependence for times, such that the dimensionless time $\tau=tc_0/x > 1$, for x and t the signal propagation distance and time of flight, respectively, via the Fourier integral describing wave propagation. Due to the physically complex nature of the dispersion relations, the behavior of the integrand is best understood by using an analytical method, specifically the method of steepest descent.[7,8] Application of this method leads to the result that a receiver of any signal propagating in a dispersive medium could expect to detect three separate arrivals spread out in time. See, for example, Ref. 8 pp. 296–325 for an especially lucid discussion of waves traveling in a mildly dispersive medium. The first arrival, called the Sommerfeld precursor, always travels at the phase speed of the asymptotic high frequency limit for the medium but with an amplitude dependent only upon the physical characteristics of the dispersive medium and not on the source characteristics (i.e., frequency, amplitude, etc.). In this limit the precursor's velocity is also coincident with the infinite frequency limit of the group velocity for which the identification of the velocity of the carrier frequency portion of the wave is exact. A second arrival, called the Brillouin precursor, arrives some time later with larger amplitude, but prior to the arrival of the signal oscillating with the carrier frequency. Again the characteristics of the Brillouin precursor are dependent only upon the physical characteristics of the medium.

[a]Author to whom correspondence should be addressed Electronic mail: gregory.orris@nrl.navy.mil

That part of the signal driven at the carrier frequency arrives some time later yet, leading to the definition of a velocity called the signal velocity.[9,10] The velocity of a signal is heuristically defined as the time for which the path of integration of the steepest descent method passes through the real ω axis at the broadcast carrier frequency.[10] As it turns out its value for most frequencies with weak dispersion coincides very nearly with Stokes' original definition of the group velocity. However, at frequencies within the anomalous absorption region, corresponding to the maximum of the absorption peak, the time of arrival of the signal is clearly differentiated from what one would expect if the wave front traveled at the group velocity, defined via the derivative of the angular frequency with respect to the wave vector.

The subject of causality and acoustic signal propagation in bubbly media has relatively recently been revisited in a series of articles by Leander and Ye.[11–14] One of the conclusions of these articles is that a dispersion formula based on linearized low frequency solutions of the bubble radius pulsations are acausal. While providing a proof of the infinite frequency limit of the velocity of a signal, the treatment in these articles was incomplete since it did not explicitly contain the necessary correction to bring the bubbly liquid acoustic dispersion formula into compliance with causality. This is despite the fact that there appears to be an unpublished correction to the formulation attributable to Leander.[6] Nor did these treatments calculate a wave front's velocity save for the infinite frequency limit. The velocity in this infinite frequency limit was therein identified with the propagation of the energy of a wave front.[7] We shall demonstrate that this definition of the wave front velocity is incorrect. This is, in fact, the velocity of the first precursor to the forced oscillations with its behavior being wholly dependent upon the specific parameters of the bubbly liquid, not the source characteristics. Even more recently a series of articles has appeared investigating the propagation of extremely short pulses in a bubbly liquid. This work is encouraging since it predicts and presents experimental evidence of these wave phenomena. However, the systems considered were of very low void fraction.[15,16]

Our aim in this paper is to present modifications to the dispersion formulas that are valid for void fractions more appropriately found, but not limited to ocean acoustic experiments. Thus we start the next section by briefly revisiting the definitions of group velocity and phase velocity for a one-dimensional scalar wave in a dispersive medium. The remainder of this paper will explore the concepts of signal velocity for the highly dispersive medium of bubbly liquids. As it turns out this system parallels aspects of the theory of Somerfeld[9] and Brillouin[10] precisely because the systems can be cast in very similar form due to their origins. In the electromagnetic case this form is the Lorentz conduction electron theory where the harmonic motion of the electrons is damped. In the bubbly liquid theory it is the damped harmonic oscillation of the gas bubble in the liquid. We will offer an analysis for the bubbly media case based upon the lucid description found in the textbooks of Jackson, Stratton, and Brillouin.[7,8,17] This method will be used to calculate arrival times for a monodispersed bubble size population from frequencies of a few hundred Hertz to well above resonance, around 100 kHz. Generalization to the full model with a continuum of bubble sizes is straightforward, however much more computationally intensive and not any more enlightening for the present purposes since the basic physics and analysis remain the same.

II. CAUSALITY AND THE BUBBLY LIQUID DISPERSION FORMULAS

In this section we briefly review the bubbly liquid dispersion formula and discuss the relationship between dispersion formulas and causality in bubbly liquids by introducing the concepts of Sommerfeld and Brillouin that were used to prove the causality of electromagnetic signals in the presence of dispersive metallic compounds.

A. Causality for general dispersive media

We will address the case of a finite length pulse composed of plane waves propagating in a general dispersive acoustic medium. This medium is assumed to be homogeneous and isotropic. Specifically, we will consider a pulse centered on the angular frequency ω_c originating from a point source located at position $x=0$ at time $t=0$, and propagating through an infinite dispersive acoustic medium created by the introduction of many small scatterers (i.e., bubbles) into a quiescent base medium. In one dimension the disturbance is described at the point x at time t by the Fourier integral

$$f(x,t) = \frac{1}{2\pi}\int_{-\infty}^{\infty} d\omega \tilde{f}(\omega)\exp[-i\omega t + ik(\omega)x], \tag{1}$$

where $\tilde{f}(\omega)$ is the distribution of frequencies of the initial disturbance at the origin. If $f(0,t)$ is real, as is true for real signals, then so should $f(x,t)$, therefore one can show via analyticity arguments that

$$\tilde{f}(-\omega) = \tilde{f}^*(\omega), \tag{2a}$$

$$k(-\omega) = -k^*(\omega), \tag{2b}$$

for real frequencies ω. (See Ref. 18, pp. 17 and 18, for a much fuller discussion on the analyticity requirements of the dispersion formula of real signals.)

Because the signal is of finite duration, it is not simply a monochromatic wave which has no beginning nor end. Thus every realizable signal must contain a continuous spectrum of frequencies. In following Refs. 13 and 14 we specifically consider a doubly terminated sinewave of N cycles at angular frequency ω, thus the Fourier transform is

$$\tilde{f}(\omega) = \frac{\omega_c}{\omega_c^2 - \omega^2}(1 - \exp[i\omega T]), \tag{3}$$

where $T=2\pi N/\omega_c$ is the total time the initial disturbance is broadcast. Using Eq. (3), Eq. (1) can be made equivalent to[9]

$$f(x,t) = \frac{1}{2\pi}\,\mathrm{Re}\left[\int_{-\infty}^{\infty} d\omega \frac{e^{-i\omega[t-T]} - e^{-i\omega t}}{\omega - \omega_c} e^{ik(\omega)x}\right]. \tag{4}$$

Since the portion of the integrand of Eq. (4) containing the term $t-T$ in the exponential is clearly a delayed portion of the signal needed to terminate the signal, we need only consider the analytic behavior of the second term.

We follow Sommerfeld and investigate the solution to Eq. (1) via complex integration techniques for the two separate cases[9]

$$\text{Case 1: } \mathrm{Re}[\psi(\omega)/\omega] > 0 \tag{5a}$$

$$\text{Case 2: } \mathrm{Re}[\psi(\omega)/\omega] < 0, \tag{5b}$$

where the phase of the integral in Eq. (1) is defined as $\psi(\omega) \equiv k(\omega)x - \omega t$. It can be shown that, if the integrand $\tilde{f}(\omega)$ and thus $k(\omega)$ of Eq. (1) are analytic in the upper half complex ω plane and $\lim_{\omega\to\infty} n(\omega) = 1$, where n is the index of refraction defined as $n(\omega) \equiv k(\omega)c_0/\omega$, then the system is causal.[18]

Provided these two conditions are met and that Eq. (5a) is satisfied, the proof that the system is causal proceeds by integrating each factor of Eq. (4) along the contour $\Gamma = \Gamma_+ \cup \Gamma_R$ of Fig. 1(a) separately. The path Γ does not contain any poles or branch cuts within it (as per constraints on the index of refraction), and lies above the $\mathrm{Re}(\omega)$ axis. Analyticity and Cauchy's theorem are sufficient to cause the integral along Γ to be identically zero. However, the integrand contributes nothing along top contour, Γ_R, due to the argument of the exponential having real and negative contribution in the upper half ω plane if this contour is taken to infinity. Thus the integral must be identically zero along the remaining portion of the path, Γ_+, proving that no signal can exist at position x at any time t such that ψ satisfies Eq. (5a).[7]

B. Bubbly liquid dispersion formulas

First, let us review the considerations required to adequately describe the interaction of a single bubble with an ensonifying signal. The physical relationship between the relevant measurable physical quantities relating the pressure and radius of a single bubble undergoing forced oscillations from a pressure wave at angular frequency ω were summarized in the work of Devin.[1] These relationships were refined and their realm of validity expanded in a series of publications culminating in the linearized dispersion formula of Commander and Prosperetti.[2,6,19–23] The relevant physical quantities are the ambient quiescent static pressure (p_∞), the water density (ρ), the surface tension (σ), the water viscosity (μ_0), the thermal conductivity of the bubble gas (κ_g), quiescent sound speed (c_0), gas temperature (T_g), and the ratio of specific heats of the gas (γ_g).

While the general oscillations of an individual bubble membrane can assume complex multimodal forms under either high intensity ensonification or physical perturbations due to hydrodynamic effects including collisions, coalescence, or dissipation, the oscillation of a bubble is dominated by the breathing mode, i.e., a purely radial oscillation.[24] For the typical acoustic wave we will be considering herein the incident pressure field intensity is small enough that this is still a valid assumption. Thus the total volume of an individual bubble may be calculated as a sphere with a time dependent radius equal to its unperturbed state plus some small perturbation, $aX(t)$ where a is the unperturbed bubble radius and $X(t)$ is a small dimensionless oscillating function. The pressure can then be related to the instantaneous bubble radius by the function $\Phi p_0 X(t)$, where the phase factor Φ takes into account the effects of thermal heating of the internal gas and its dissipation into the surrounding liquid.[21]

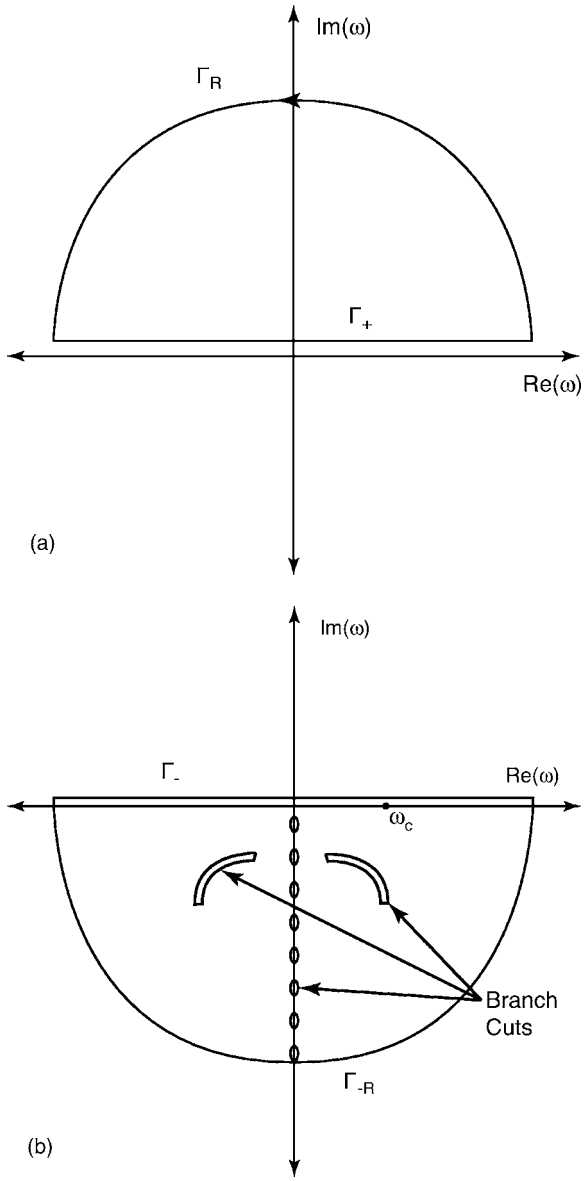

FIG. 1. Complex integration of Eq. (1) follows paths $\Gamma = \Gamma_+ \cup \Gamma_R$ for $\mathrm{Re}(k(\omega)/\omega x - t) < 0$ and $\Gamma = \Gamma_- \cup \Gamma_{-R}$ for $\mathrm{Re}(k(\omega)/\omega x - t) < 0$.

$$\Phi(\omega,a) = \frac{3\gamma_g}{1 + 3(\gamma_g - 1)i\chi(\omega,a)[\sqrt{1/i\chi(\omega,a)}\coth(\sqrt{1/i\chi(\omega,a)}) - 1]}, \tag{6}$$

where $\chi(\omega,a) = D_g/\omega a^2$ and $D_g = (\gamma_g - 1)\kappa_g T_g/\gamma_g p_\infty$.

The limiting behavior of Φ for the cases of $\omega \to 0$ and $\omega \to \infty$ will prove important in our analysis. In the former case, the oscillations behave approximately isothermally, as changes are made on such long time scales that the temperature of the system is not significantly affected having the necessary time to diffuse into the surrounding liquid. Thus the thermodynamic equation of state implies a direct relationship between the bubble's volume and internal pressure, thus $\lim_{\omega \to 0} \Phi(\omega, a) \to 3$. Conversely, in the latter case the system behaves adiabatically and $\lim_{\omega \to \infty} \Phi(\omega, a) = 3\gamma_g$.

We will use Keller's bubble radius equation relating the bubble radius to the internal pressure,[2,5]

$$\left(1 - \frac{1}{c_0}\frac{dR}{dt}\right) R\frac{d^2R}{dt^2} + \frac{3}{2}\left(1 - \frac{1}{3c_0}\frac{dR}{dt}\right)\left(\frac{dR}{dt}\right)^2 = \frac{1}{\rho}\left(1 + \frac{1}{c_0}\frac{dR}{dt} + \frac{R}{c_0}\frac{d}{dt}\right)(p_B - P), \tag{7}$$

where p_B is the internal bubble pressure and P is the external pressure field including both static and oscillating components. Upon linearization Eq. (7) is put into the small amplitude harmonic form from Ref. 2's Eq. (30) as

$$-\omega^2 a^2 X = \frac{1}{\rho}\left(1 - i\frac{\omega a}{c_0}\right) \times \left[\left(-p_0\Phi + \frac{2\sigma}{a} + 4\mu_0 i\omega\right)X - Q\right], \tag{8}$$

where the factor of $(1 - i\omega a/c_0)$ taken as approximately equal to 1 in the solution leading to the apparent bubble resonance frequency and damping factor of Eqs. (9a) and (9b). This is valid provided $\omega a/c_0 \ll 1$.

In Eq. (8) one can define the quantities $\omega_0^2(\omega, a)$ and $b(\omega, a)$ identified as the effective bubble resonance frequency and damping constant, respectively[2]

$$\omega_0^2(\omega, a) = \frac{p_0}{\rho a}\left(\mathrm{Re}[\Phi(\omega, a)] - \frac{2\sigma}{a p_0}\right) \tag{9a}$$

$$b(\omega, a) = \frac{2\mu_0}{\rho a^2} + \frac{p_0}{2\rho\omega a^2}\,\mathrm{Im}[\Phi(\omega, a)] + \frac{\omega^2 a}{2c_0}. \tag{9b}$$

In this theoretical context the physical mechanisms responsible for energy loss in the incident wave associated with each term in Eq. (9b) are viscosity, mechanical heating, and scattering, respectively. In Eqs. (9a) and (9b) the Laplace pressure and internal resting bubble pressure are defined as $p_L = \frac{2\sigma}{a}$, and $p_0 = p_\infty + p_L$, respectively. We conclude from the limiting behavior of Φ and Eq. (9b) that in the high frequency limit where optical approximations are valid, radiation scattering becomes the dominant damping mechanism over thermal and viscous energy loss mechanisms. Physically this is because at this high frequency limit the driving field is oscillating too fast for the bubble to efficiently transport its thermal energy to the surrounding liquid, or for much energy to be lost to viscous stretching of the fluid near the bubble.

Extending the single bubble theory to a volume containing a distribution of bubbles in both size and space is still a topic of interest, with several methods having been employed.[25–28] The Commander and Properetti's formula, linearized for small radial oscillations, results in an effective wave number in the bubbly medium given by

$$k_{\mathrm{eff}}^2(\omega) = \frac{\omega^2}{c_0^2} + 4\pi\omega^2 \int_0^\infty da \frac{a\rho_{\mathrm{BSD}}(a)}{\omega_0^2(a, \omega) - \omega^2 - 2i\omega b(a, \omega)}, \tag{10}$$

where the bubble size distribution function, $\rho_{\mathrm{BSD}}(a)$, is normalized such that the bulk volume ratio of gas to total (the void fraction) is

$$\beta = \frac{V_g}{V_l + V_g} = \frac{4\pi}{3}\int_0^\infty \mathrm{d}a a^3 \rho_{\mathrm{BSD}}(a), \tag{11}$$

where V_g is the volume of the gas and V_l is the volume of the liquid. From Eq. (10) the phase speed v_p is defined in the usual manner, $v_p = \omega/\mathrm{Re}[k_{\mathrm{eff}}]$, and the index of refraction is

$$n^2 = 1 + 4\pi c_0^2 \int_0^\infty \mathrm{d}a \frac{a\rho_{\mathrm{BSD}}(a)}{\omega_0^2(a, \omega) - \omega^2 - 2i\omega b(a, \omega)}. \tag{12}$$

We note here that Eqs. (6), (10), and (12) differ from that given by Ref. 2's Eqs. (35) and (36) by a change in sign of the damping factor in the denominator. This is due to the choice of the dependence of $\psi(\omega)$ on frequency to maintain consistency with Sommerfeld's, Brillouin's, and Jackson's standardized choice of time dependence (i.e., $e^{-i\omega t}$ instead of $e^{i\omega t}$).[7–10]

For the remainder of this work we will assume that the bubble size distribution can be well approximated by a monodispersed bubble population, i.e., $\rho_{\mathrm{BSD}} = N\delta(a - a_0)$, where N is a normalization constant for Eq. (11) to be satisfied, and $\delta(a - a_0)$ is a Dirac delta function. In this case we find the effective wave number for the bubbly liquid to be

$$k_{\mathrm{eff}}^2(\omega) = \frac{\omega^2}{a_0^2 c_0^2} \times \left(a_0^2 + \frac{3\beta c_0^2}{\omega_0^2(a_0, \omega) - \omega^2 - 2i\omega b(a_0, \omega)}\right). \tag{13}$$

Applying Cauchy's theorem to the integral of Eq. (4) for times and positions satisfying Eq. (5a), we find that Eq. (13) is no longer analytic in the upper-half ω plane. In fact, it must have a branch cut along the positive imaginary ω axis owing to the ω^2 dependence of the radiation damping factor in Eq. (9b), causing the high frequency behavior of the denominator of Eq. (13) to behave approximately as a cubic polynomial for $\omega \gg 1$. In the region away from the origin there will be three roots and poles in the complex ω plane. These two points together will form a branch cut in the upper-half ω plane. Having violated the necessary requirements that the dispersion formula be analytic in this region, there is no way to enforce causality, since any infinite integration of Eq. (4) must contend with integrating around this branch cut. For arbitrary values of x and t satisfying Eq. (5a), the contribution from the integration path around the branch will be nonzero. We are thus left to conclude that the dispersion formulas using Eq. (9) are acausal.

To correct this theory we notice that the factor of $(1 - i\omega a/c_0)$ was taken as approximately equal to 1 in the solution leading to the apparent bubble resonance frequency and

damping factor of Eqs. (9a) and (9b). This is valid provided $\omega a/c_0 \ll 1$. However, this assumption is violated in the infinite frequency limit of $k_{\text{eff}}(\omega)$ and thus the short time limit of $f(x,t)$ that defines the arrival of pulsed signals. Removing this approximation and solving the equation leads to a new radiative damping factor and apparent bubble resonance so that Eq. (12) becomes

$$n_{\text{cm}}^2 = 1 + 4\pi c_0^2 \int_0^\infty \mathrm{d}a \frac{a\rho_{\text{BSD}}(a)}{\dfrac{p_0\Phi(\omega,a)}{\rho a^2} - \dfrac{2\sigma}{\rho a^3} - \dfrac{\omega^2}{1 - i\dfrac{\omega a}{c_0}} - i\dfrac{4\omega\mu_0}{\rho a^2}}, \tag{14}$$

where we have written the denominator out in terms of its individual components instead of in terms of $\omega_0^2(\omega,a)$ and $b(\omega,a)$.

Application of Eq. (14) to calculate the phase velocity and attenuation for a bubble population representative of the environmental parameters for experiments reported on in Ref. 29 are shown in Figs. 2(a) and 2(b). The physical parameters used to calculate the curves in Fig. 2 and throughout this work are $\beta=0.00018$, $\gamma_g=1.4$, $\kappa_0=0.0241$ W/meter°K, $\rho=1000$ kg/m^3, $T_g=292$ K, $p_\infty=117{,}268$ Pa, $\mu_0=0.001{,}307$ Ns/m^2, $\sigma=0.050$ kg/s^2, and $c_0=1482$ m/s. The bubble size distribution (BSD) reported on in Ref. 29 was fit to the function

$$\rho_{\text{BSD}}(a) = d_1 e^{-\left(d_2 \log \frac{a}{d_3}\right)^2},$$

where the constant parameters are $d_1=0.16$, $d_2=6.48$, and $d_3=4.6\times10^{-4}$ m. This is a distribution sharply peaked at an effective bubble radius of 0.46 mm. It is this value for the radius that we use whenever a calculation with a monodispersed bubble size distribution is made.

As can be seen in Fig. 2 there is almost no deviation in the peaks of the phase velocity and attenuation from those that result from using Eqs. (9a) and (9b) in Eq. (10). However, for frequencies far beyond resonance, the correct theoretical attenuation plateaus and remains constant. The behavior of this curve at these frequencies is commensurate not only with data taken recently,[29] but also with these plotted in the original work of Commander and Prosperetti (Ref. 2 Figs. 16 and 17).

Having now corrected the high frequency behavior we are left to show that the new dispersion formula is analytic in the upper half ω plane. To simplify the proof we work with a monodispersed bubble size distribution. A full proof with a multi-valued bubble size distribution is not any more enlightening, while at the same time significantly more involved. Equation (14) collapses to the corrected effective wave vector for our monodispersed bubbly liquid

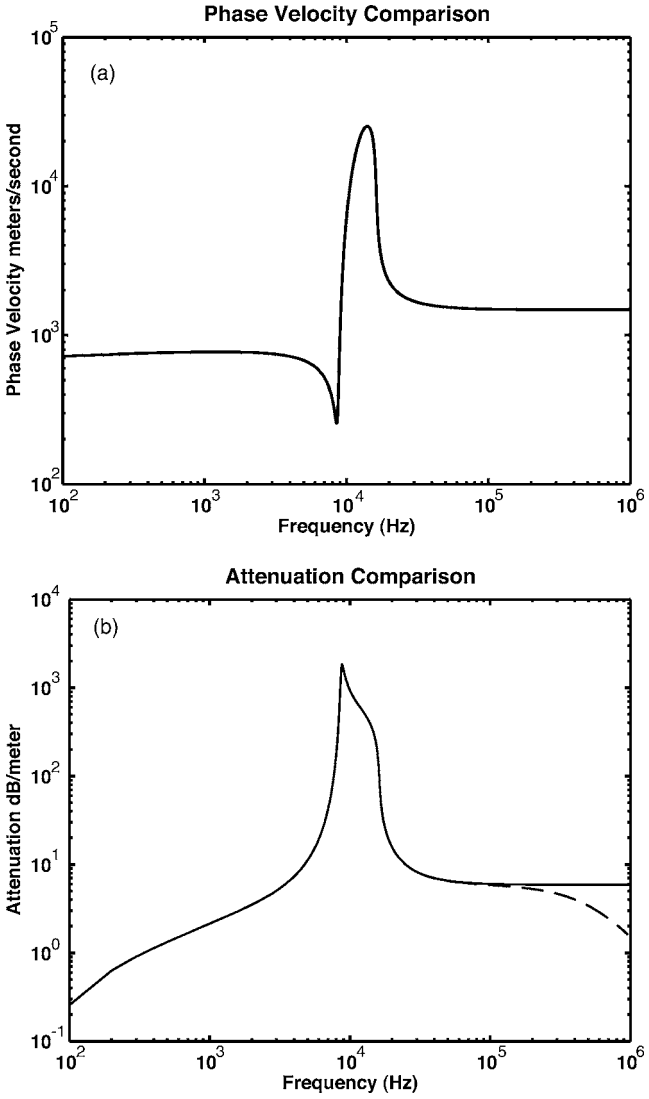

FIG. 2. Phase velocity comparison (a) between corrected (solid) and uncorrected (dashed) dispersion formulas shows no differences in phase velocity. However, the attenuation (b) at high frequency shows a marked difference for the causal dispersion formula.

$$k_{\text{cm}}^2 = \frac{\omega^2}{c_0^2} n_{\text{cm}}^2(\omega) = \frac{\omega^2}{c_0^2}\left(1 + \frac{3\beta c_0^2\rho}{p_0\Phi(\omega,a) - \dfrac{2\sigma}{a_0} - \dfrac{\omega^2 a_0^2\rho}{1 - i\dfrac{\omega a_0}{c_0}} - 4i\omega\mu_0}\right). \tag{15}$$

Analyticity is proved by showing that the equations

$$p_0\Phi(\omega,a_0) = \frac{2\sigma}{a_0} + \frac{\omega^2 a_0^2\rho}{1 - i\dfrac{\omega a_0}{c_0}} + 4i\mu_0\omega, \tag{16a}$$

$$p_0\Phi(\omega,a_0)=\frac{2\sigma}{a_0}+\frac{\omega^2a_0^2\rho}{1-i\dfrac{\omega a_0}{c_0}}+4i\mu_0\omega-3\beta c_0^2\rho, \qquad (16b)$$

have no solutions in the upper half ω plane. This can be proven in a straightforward manner by noting that the imaginary parts of Eqs. (16a) and (16b) are satisfied only on the imaginary ω axis in the upper half ω plane. Then one can show that the only negative contribution to the real part of the right hand size of Eqs. (16a) and (16b) comes from the surface tension term. Thus as long as the condition

$$p_0\,\mathrm{Re}[\Phi(\omega,a_0)]>\frac{2\sigma}{a_0},\ \forall\ \mathrm{Im}[\omega]>0,\quad \text{and}\quad \mathrm{Re}[\omega]=0 \qquad (17)$$

is satisfied, neither Eq. (16a) nor Eq. (16b) have zeros in the upper half ω plane. While this condition could, in principle, be violated by the smallest of bubbles, i.e., $a_0<10$ nm for water, bubbles of these sizes are exceedingly short lived being quickly dissolved.

III. SIGNAL PRECURSORS IN BUBBLY LIQUIDS

A. Sommerfeld signal precursor

We have seen that a propagating wave obeying the dispersion formula of Eq. (15) is a causal wave, and that the minimum time any signal could be recorded at a receiver a distance x from a source initiating a signal at time $t=0$ is given by $t_0=x/c_0$. The value of the Fourier integral of Eq. (1) for subsequent times is determined by application of the integral equation definition of the Bessel functions and the Method of Steepest Descent.[8–10] This method requires detailed knowledge of the saddle points of the phase function $\psi(\omega)$ in the complex ω plane for the dispersion formula governing the system

$$\frac{c_0}{x}\frac{\partial\psi}{\partial\omega}=n(\omega)+\frac{\omega}{2n(\omega)}\frac{dn^2}{d\omega}-\tau=0, \qquad (18)$$

where we have introduced the dimensionless time $\tau=tc_0/x$. One can show that $\partial\psi/\partial\omega$ satisfies a symmetry similar to Eq. (2) for $\omega\in\mathbb{C}$

$$\left(\frac{\partial\psi}{\partial\omega}(\omega)\right)^*=\frac{\partial\psi}{\partial\omega}(-\omega^*). \qquad (19)$$

Equation (19) states simply that the complex conjugate of the saddle point equation is equivalent to a reflection through the imaginary axis. Thus, if a solution to Eq. (18) exists for $\mathrm{Re}[\omega]>0$, then there must be a corresponding solution for $\omega\to-\omega^*$, i.e., solutions are either along the negative imaginary axis, or occur in pairs on opposite sides of the imaginary axis. Saddle points for $\mathrm{Re}[\omega]<0$ control the negative frequencies and those for which $\mathrm{Re}[\omega]>0$ control the positive frequencies. We shall only need to concern our investigation with either the negative or positive frequencies to determine when a real signal arrives at a given location, since both must arrive simultaneously.

We observe that in Eq. (1) the time dependence of the source function is exactly the function $f(0,t)$. It is the behavior of this function for $t\to0^+$ that we are interested in investigating. We may assume that for some small time $0<t\ll1$ that we may expand the source function in terms of a power series, such that the largest nonzero term is[8]

$$f(0,t)\propto\frac{t^m}{m!}, \qquad (20)$$

for some possibly large integer m. The Fourier transform of this series expansion would then be dominated by the high frequency limit and is given by

$$\tilde{f}(\omega)\propto\left(\frac{i}{\omega}\right)^{m+1}. \qquad (21)$$

For example, in the case of a doubly ended sine wave, $m=1$.

Asymptotically expanding the monodispersed form of n_{cm} in powers of $1/\omega$ as $\omega\to\infty$, we find to order $1/\omega^2$

$$n_{\mathrm{cm}}(\omega)\approx1+\frac{A_0}{\omega}+\frac{B_0}{2\omega^2}, \qquad (22)$$

where the coefficients A_0 and B_0 are given by

$$A_0=\frac{3i\beta\rho c_0^2}{2(a_0\rho c_0+4\mu_0)}, \qquad (23a)$$

$$B_0=\frac{3\beta\rho c_0^2(a_0\rho c_0^2(3\beta-4)+8(3\gamma_g-1)\sigma+12a_0\gamma_g p_\infty)}{4a_0(a_0\rho c_0+4\mu_0)^2}. \qquad (23b)$$

The fact that the point at infinity plays an important contribution to the integrand of Eq. (1) for small times after $\tau=1$ could have been expected since $dn^2/d\omega\to0$ as $\omega\to\infty$, however $n(\omega)\to1$.

Because the integrand of Eq. (1) is analytic in the upper half ω plane, the integral can then be calculated by first deforming the path of integration in the upper half ω plane to a semicircle of radius $R\to\infty$, as shown in Fig. 3. We may add another semicircle in the lower half ω plane further deforming the contour of integration into a whole circle. The contribution to the integral from the semicircle in the lower half ω plane is zero due to the fact that $t-t_0>0$ and thus the exponential $\exp[-i(t-t_0)\omega]\to0$ as $\mathrm{Im}[\omega]\to-\infty$. The resulting integral can be identified as a version of the integral definition of the Bessel function of the first kind.

$$f(x,t)\propto\oint_{\Gamma_R}\mathrm{d}\omega\frac{\exp[-i(t-t_0)\omega+\xi/\omega-\eta]}{\omega^{m+1}}$$
$$\propto e^{-\eta}\left(\frac{t-t_0}{\xi}\right)^{m/2}J_m[2\sqrt{\xi(t-t_0)}], \qquad (24)$$

where we have defined the parameters η and ξ using Eqs. (23a) and (23b), respectively,

$$\eta=|A_0|t_0, \qquad (25a)$$

$$\xi=\frac{B_0t_0}{2}. \qquad (25b)$$

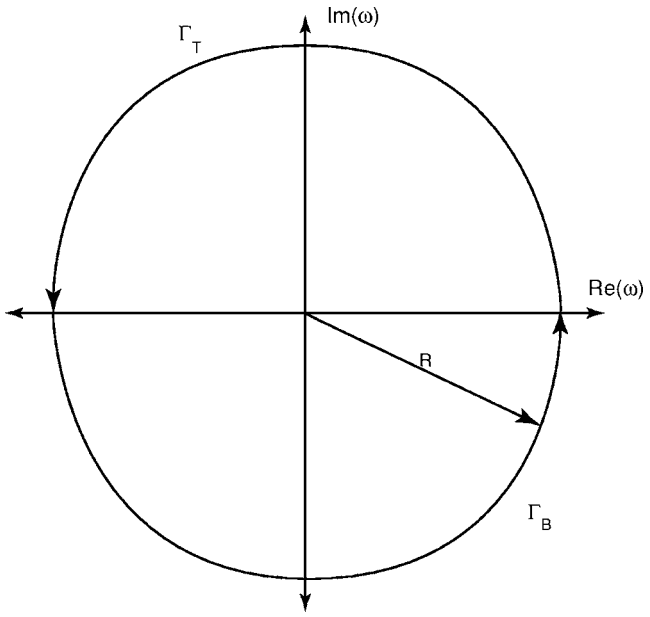

FIG. 3. Integration in the upper half plane can be extended first to Γ_T. The contribution to the integral from adding the piece Γ_B can be seen to be exponentially decaying as a function of radius and thus zero in the limit $R \to \infty$.

There are three important points to be made by Eqs. (24), (25a), and (25b): One is that all of the values involved in this calculation are independent of the broadcast frequency. In fact, all of the parameters are physical parameters of the medium in which the signal propagates. The second, is that this is the part of the signal that travels nearest to the quiescent medium's phase velocity, arriving at time $t_0 = x/c_0$. Lastly, the amplitude of the received precursor is an exponential function of η and hence an exponential function of the void fraction. This fact has been previously reported in both theoretical and experimental settings under extremely low void fractions, β.[15,16]

B. Brillouin signal precursor

The specifics concerning the arrival of the second, or Brillouin, precursor to the signal is determined by the behavior of the dispersion formula near the origin of the complex ω plane. As we shall presently demonstrate there is a small and exponentially increasing amplitude up to the time τ_1 defined by the solution to the saddle point equation in the zero frequency limit.[7]

$$\tau_1 = c_0 \left.\frac{dk}{d\omega}\right|_{-\omega=0} = n_{\mathrm{cm}}(0) = \sqrt{1 + \frac{3\beta\rho c_0^2}{3p_0 - \frac{2\sigma}{a_0}}}. \tag{26}$$

For example, using the physical parameters cited above, Eq. (26) gives the numerical result $\tau_1 \approx 2.09$. After this time, there is an exponentially decaying sinusoidal field of instantaneous frequency proportional to $\sqrt{\tau - n_{\mathrm{cm}}(0)}$.

To determine the behavior of the saddle points near $\omega = 0$ we expand the index of refraction in a power series at $\omega = 0$

$$n_{\mathrm{cm}}(\omega) \approx n_{\mathrm{cm}}(0) + \omega n'_{\mathrm{cm}}(0) + \frac{\omega^2}{2} n''_{\mathrm{cm}}(0) + \mathcal{O}(\omega^3)$$

$$= c_0 \left(\left(\frac{1}{c_0^2} + \frac{3\beta\rho}{3p_0 - \frac{2\sigma}{a_0}} \right)^{\frac{1}{2}} + \left(\frac{3\beta i\rho \left(\frac{a_0^2 p_0^2}{5T\kappa_0} + 4\mu_0 \right)}{2\left(3p_0 - \frac{2\sigma}{a_0}\right)^2 \left(\frac{1}{c_0^2} + \frac{3\beta\rho}{3p_0 - \frac{2\sigma}{a_0}} \right)^{\frac{1}{2}}} \right) \omega \right.$$

$$\left. + \left(\frac{9\beta^2\rho^2 \left(\frac{a_0^2 p_0^2}{5T\kappa_0} + 4\mu_0 \right)^2}{8\left(3p_0 - \frac{2\sigma}{a_0}\right)^4 \left(\frac{1}{c_0^2} + \frac{3\beta\rho}{3p_0 - \frac{2\sigma}{a_0}} \right)^{\frac{3}{2}}} - \frac{3\beta\rho \left(\frac{\left(\frac{a_0^2 p_0^2}{5T\kappa_0} + 4\mu_0 \right)^2}{\left(3p_0 - \frac{2\sigma}{a_0}\right)} + \frac{2a_0^4(3\gamma+7)p_0^3}{525T^2(\gamma-1)\kappa_0^2} + a_0^2\rho \right)}{2\left(3p_0 - \frac{2\sigma}{a_0}\right)^2 \left(\frac{1}{c_0^2} + \frac{3\beta\rho}{3p_0 - \frac{2\sigma}{a_0}} \right)^{\frac{1}{2}}} \right) \omega^2 + \mathcal{O}(\omega^3) \right), \tag{27}$$

where the prime denotes differentiation with respect to ω prior to evaluation at $\omega = 0$. As seen in Fig. 4 the actual values of the derivatives of the index of refraction are likely to be small near the origin. However, unlike the electromag-

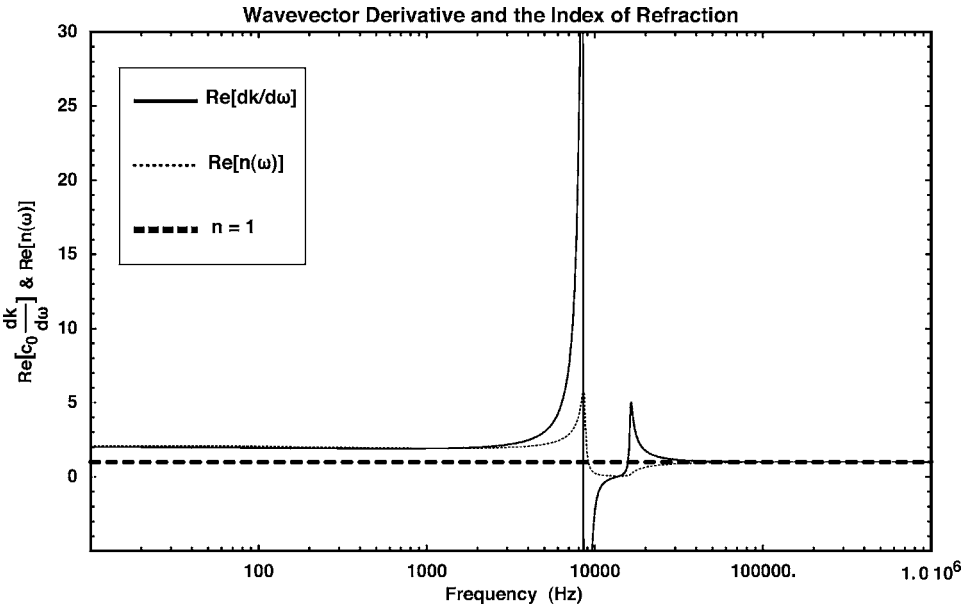

FIG. 4. The real part of the normalized group velocity and the index of refraction both show near zero slope in the zero frequency limit.

netic case, we may not neglect the damping and assume that $|n'_{\mathrm{cm}}(0)| \ll |n''_{\mathrm{cm}}(0)|$.[8] So we must consider in detail the behavior the saddle points of the complex phase function $i\psi(\omega) = (x/c_0)\phi(\omega)$,

$$\phi(\omega) = -i\omega(\tau - n_{\mathrm{cm}}(\omega)) \approx -i\omega\left(\tau - n_{\mathrm{cm}}(0) - \omega n'_{\mathrm{cm}}(0) - \frac{1}{2}\omega^2 n''_{\mathrm{cm}}(0)\right). \quad (28)$$

Taking the derivative of Eq. (28) with respect to ω and setting it to zero we arrive at the quadratic saddle point equation in the neighborhood of $\omega=0$,

$$\frac{d\phi}{d\omega} = 0 = \tau - n_{\mathrm{cm}}(0) - \frac{n''_{\mathrm{cm}}(0)}{2}(3\omega + 4n'_{\mathrm{cm}}(0)) = B_1 - A_1\omega(3\omega + 4i\delta), \quad (29)$$

where $B_1 = \tau - n_{\mathrm{cm}}(0)$, $A_1 = n''_{\mathrm{cm}}(0)/2$, and $\delta = -in'_{\mathrm{cm}}(0)/n''_{\mathrm{cm}}(0)$.[7] In this notation δ can be directly identified with the total damping constant in the harmonic oscillator model at zero frequency. In solving Eq. (29) we see that the behavior of the saddle points in the complex plane near $\omega=0$ can be separated into two distinct classes. Both are independent of the broadcast carrier frequency, yet dependent on the time τ and the physical parameters of the supporting medium:

$$\text{Case 1: } B_1 < \tfrac{4}{3}A_1\delta^2, \quad (30a)$$

$$\text{Case 2: } B_1 > \tfrac{4}{3}A_1\delta^2. \quad (30b)$$

If Eq. (30a) is satisfied, then the solution to Eq. (29) is purely imaginary and the saddle points are given by

$$\omega^{\pm}_{p<} = -\frac{2}{3}i\delta \pm \frac{i}{3}\sqrt{4\delta^2 - 3\frac{B_1}{A_1}} = i\eta^{\pm}_{p<}, \text{ where } \eta^{\pm}_{p<} \in \mathbb{R}. \quad (31)$$

Since along the integration path $\mathrm{Im}(\phi)$ is constant, this path proceeds through the saddle point parallel to the abscissa passing through $\omega^{+}_{p<}$. The integration path for the saddle point $\omega^{-}_{p<}$ is similar to that shown for the top saddle point in Fig. 7, where the integration path is seen to proceed initially along the ordinate. The absolute value of $\omega^{-}_{p<}$ is significantly larger than that of $\omega^{+}_{p<}$, the contribution to the integral of Eq. (1) from $\omega^{-}_{p<}$ will be insignificant in comparison to $\omega^{+}_{p<}$.

The complex phase can be approximated near $\omega^{+}_{p<}$ as

$$\phi(\omega) \approx \phi(\omega^{+}_{p<}) + \frac{1}{2}(\omega - \omega^{+}_{p<})^2\phi(\omega_{p<}) = \phi(\omega^{+}_{p<}) + \frac{1}{2}\xi^2\phi''(\omega^{+}_{p<}), \quad (32)$$

where $\phi''(\omega^{+}_{p<})$ can be expanded in terms of the zero frequency expansion from Eq. (29) as

$$\phi''(\omega^{+}_{p<}) \approx -2A_1(3\eta^{+}_{p<} + 2\delta). \quad (33)$$

Notice that both $\phi''(\omega^{+}_{p<}) \in \mathbb{R}$ and $\xi \in \mathbb{R}$. Now the evaluation of Eq. (4) by the saddle point method integration formula is approximately[30]

$$f(x,t) = \frac{1}{2\pi}\mathrm{Re}\left[\int d\omega \frac{e^{\frac{x}{c_0}\phi}}{\omega - \omega_c}\right] \approx \frac{e^{\frac{x}{c_0}\phi(\omega^{+}_{p<})}}{2\pi}\left(\frac{\omega_c}{\omega_c^2 + \eta^{+2}_{p<}}\right)\int_{-\epsilon}^{c} d\xi e^{-\frac{x}{2c_0}|\phi''(\omega^{+}_{p<})|\xi^2}, \quad (34)$$

where the last integral can be approximated as a Gaussian integral over the entire real line (i.e., $\epsilon \to \infty$), so that the final result is

$$f(x,t) = \frac{\omega_c}{(\omega_c^2 + \eta^{+2}_{p<})}\sqrt{\frac{c_0}{2\pi\phi''(\omega^{+}_{p<})x}}e^{\frac{x}{c_0}|\phi(\omega^{+}_{p<})|}. \quad (35)$$

For times such that, $1 < \tau < \tau_1$, $\phi(\omega^{+}_{p<}) < 0$, and thus $f(x,t)$ grows exponentially reaching a maximum value at τ_1.

If on the other hand, Eq. (30b) is satisfied then the solution for the saddle point is given by

$$\omega_{p>}^{\pm} = -\frac{2}{3} i\delta \pm \eta_{p>}, \tag{36}$$

where $\eta_{p>} = 1/3\sqrt{3B_1/A_1 - 4\delta^2}$. The saddle points have now moved off the ordinate and are now mirrored on each side, since now $\eta_{p>} \in \mathbb{R}$. The lines of constant phase are such that the integration path must then proceed at approximately an angle of $\pm\pi/4$ from the abscissa causing an additional complex exponential factor to be applied to the integral.[30] The expansion of ϕ near the points $\omega_{p>}^{\pm}$ proceeds as in Eq. (32),

$$\begin{aligned}\phi(\omega) &\approx \phi(\omega_{p>}^{\pm}) + \frac{1}{2}(1 \pm i)^2 \xi^2 \phi''(\omega_{p>}^{\pm}) \\ &= \phi(\omega_{p>}^{\pm}) - \frac{1}{2}\xi^2 |\phi''(\omega_{p>}^{\pm})| = \phi(\omega_{p>}^{\pm}) - (6A_1\eta_{p>})\xi^2,\end{aligned} \tag{37}$$

where again $\xi \in \mathbb{R}$. Using the substitutions

$$\begin{aligned}\omega - \omega_{p>}^{\pm} &\to (1 \pm i)\xi \\ d\omega &\to \sqrt{2}\exp[\pm i\pi/4]d\xi,\end{aligned} \tag{38}$$

and dividing $\phi(\omega_{p>}^{\pm})$ into its real and imaginary parts, such that

$$\begin{aligned}\phi(\omega_{p>}^{\pm}) &= \phi^*(\omega_{p>}^{\mp}) \\ &= \mathrm{Re}[\phi(\omega_{p>}^{+})] \pm \mathrm{Im}[\phi(\omega_{p>}^{+})] \\ &= \frac{2}{3}\delta\left(-B_1 + \frac{8}{9}A_1\delta^2\right) \\ &\quad \pm i\eta_{p>}\left(-B_1 + A_1\eta_{p>}^2 + \frac{4}{3}\delta^2 A_1\right)\end{aligned} \tag{39}$$

we obtain

$$\begin{aligned}f(x,t) \approx &\sqrt{\frac{c_0}{2\pi|\phi''(\omega_{p>}^{+})|x}} \\ &\times \mathrm{Re}\left[\frac{e^{\frac{x}{c_0}\phi(\omega_{p>}^{+}) + i\frac{\pi}{4}}}{\omega_{p>}^{+} - \omega_c} + \frac{e^{\frac{x}{c_0}\phi(\omega_{p>}^{-}) - i\frac{\pi}{4}}}{\omega_{p>}^{-} - \omega_c}\right].\end{aligned} \tag{40}$$

Formal substitution of Eq. (39) into Eq. (40) will produce an exponentially decaying sinusoidal function, since $\mathrm{Re}[\phi(\omega_{p>}^{\pm})] < 0$ given Eq. (30b). Furthermore, the instantaneous frequency of oscillation is given by the differential $d(\mathrm{Im}[\phi(\omega_{p>}^{\pm})])/dt$, and is independent of the carrier frequency, ω_c, and proportional to $B_1^{1/2}$.

IV. SIGNAL ARRIVAL AND SIGNAL VELOCITY

We next consider the problem of determining the arrival of the wave oscillating at the carrier frequency, since up to now while wave motion is present, its frequency and amplitude are independent of the source characteristics. One could proceed by asking, "At what time will a signal be received at position x, if the signal's carrier frequency is ω_c?" However this "forward" problem is somewhat hard to answer precisely for carrier frequencies near the anomalous absorption regime, where signals do not travel with a simply derived group velocity.

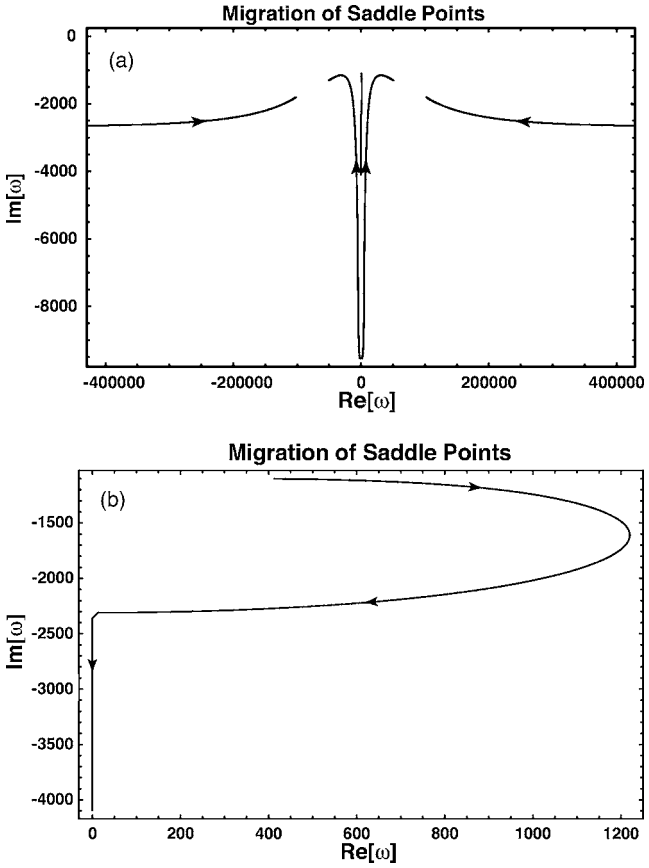

FIG. 5. Due to the time dependence of ψ, the saddle points move in the complex plane. In (a) we show the time evolution of the most important saddle points that are found numerically but roughly correspond to the four valid solutions of the adiabatic or $|\omega| \gg 1$ limit of the dispersion formulas. In (b) we show the time evolution of the saddle point nearest the origin, seen as the vertical line near the imaginary axis in (a). Its evolution is seen to quickly converge toward the imaginary ω axis where the total contribution to the integral is vanishingly small. In each the saddle points move from close to the branch cuts at $\tau=1$ to far from the branch cuts, with the final time $\tau=30$.

For times following τ_0 and τ_1 signifying the arrivals of the Sommerfeld and Brillouin precursors, respectively, the path of integration of the method of steepest descent follows one along which $\mathrm{Re}[\psi]$ is constant passing through saddle points determined by the solutions to Eq. (18). The phase function ψ is not only a function of the frequency, but also of the time. Thus the solutions to Eq. (18) move in the complex ω plane as a function of the time. We demonstrate this evolution graphically for four saddle points (two on each side of the imaginary ω axis) in Fig. 5(a), where starting at $\tau=1$ the saddle points are the furthest from the branch cuts. The branch cuts are seen as the break in the lines in Fig. 5(a). The saddle points migrate in the direction of the arrows toward the positions closest to the branch cut, with the final plotted saddle point corresponding to th time $\tau=30$. We additionally show the migration of the saddle point along the imaginary axis closest to the branch cut (and real axis) in 5(b). Its path is in the opposite direction from the main saddle points, i.e., from near the saddle points toward $\mathrm{Im}[\omega] = -\infty$. Despite the

proximity of the imaginary axis saddle points to the real axis, their corresponding imaginary values of the phase function are such that the integration path via the saddle point method through these points crosses the real axis, the importance of which we shall demonstrate.

Since the integration path Γ is a function of τ, for some combination of distance x_2 and time t_2 the integration path will intersect the real ω axis. If this intersection is at the point ω_c, then $\Gamma(\tau_2)$ will need to be modified to exclude the pole at this frequency, such that the interior of the integration region contains no poles. This is done by modifying the path of integration around the point ω_c including a semicircular arc around the pole. This adds a contribution to Eq. (4) equal to $\pm 1/2$ its residue at the carrier frequency. As previously seen, the value of the real part of the exponential in the integrand of Eq. (4) is large and negative, thus the contribution from the saddle points will be small and the residue contribution will dominate the value of the integral. If there is no pole intersected on the real ω axis there is no added contribution and the value of the integral is still dominated by precursors. The time at which the integration path intersects the pole defines the arrival of the signal of forced oscillations at the carrier frequency, and the signal velocity is determined by the equation (see Ref. 11 pp. 74–79)

$$V_{\text{signal}} = (\omega_c) \equiv \frac{x_2}{t_2} = \frac{c_0}{\tau_2}. \tag{41}$$

We have implemented a numerical method to solve Eq. (18). For most times and positions the solution to the full problem can be approximated by using the adiabatic, or high frequency approximation of the index of refraction, thus avoiding difficulties that may arise from including the rather cumbersome thermal phase-lag function $\Phi(\omega, a_0)$. Solutions using the adiabatic limit are readily available because Eq. (18) can be put into polynomial form and can thus be solved using algebraic methods. These points once determined, are used as a seed for a numerical method to determine the solution to the full set of nonlinear equations. After the set of saddle points $\{\omega_s\}$ are determined in the complex ω plane, the value of $\mathrm{Re}[\psi(\omega_s)]$ is readily calculated. Finally we use a bisection numerical search along the real ω axis to determine those values of ω that are solutions to the equation

$$\mathrm{Re}[\psi(\omega_s)] = \mathrm{Re}[\psi(\omega)],\ \omega \in \mathbb{R}. \tag{42}$$

Figures 6 and 7 show an example for $\tau = 2$. We have calculated the phase function and determined the value of the saddle points on either side of the branch cut. The branch cut is seen as the distinct demarcation between large positive and negative values of $\mathrm{Im}[\psi(\omega)]$ for $\omega < 0$. The contour plot in Fig. 6(a) is the imaginary part of the phase $\psi(\omega)$ and Fig. 6(b) is the real part. Lines of constant $\mathrm{Re}[\psi(\omega)]$ for three saddle points are also plotted as black lines. The intersection of the lines denotes the location of a saddle point solution of Eq. (18). The direction of integration through each saddle point is toward or away from the branch cut along the lines that pass through the large negative values of $\mathrm{Im}[\psi(\omega)]$.[7] These are marked with arrows showing the corresponding direction of integration. The lines of steepest ascent are plotted as the locally perpendicular set of lines of constant

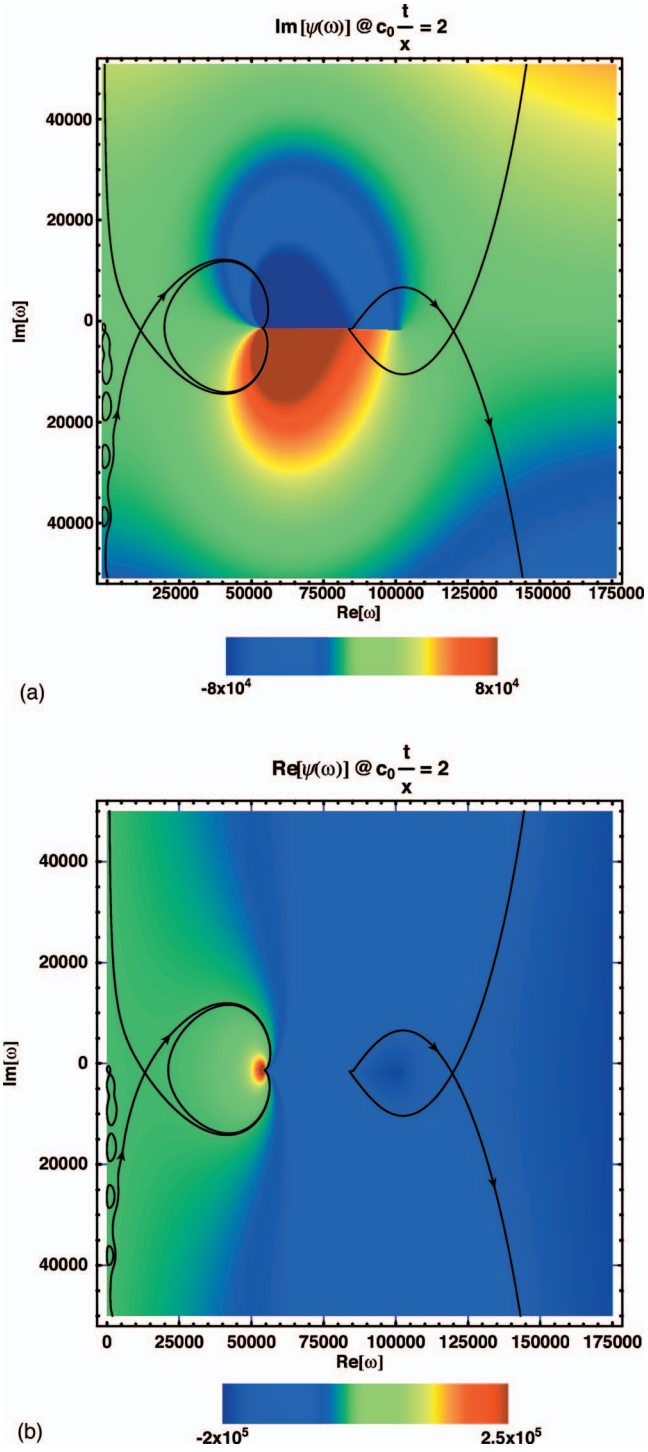

FIG. 6. The real portion of the complex phase ψ in the complex ω plane for all points such that $c_0 t/x = 2$. The saddle points are those points for which $d\phi/d\omega = 0$ and are marked by the intersection of the paths. Integration proceeds along the line through each saddle point toward the branch cut, for which the saddle point is a maximum along the trajectory. The trajectories are calculated as the equipotential lines of the imaginary portion of ψ as seen in Fig. 6(b).

$\mathrm{Re}[\psi(\omega)]$ passing through the large positive values of $\mathrm{Im}[\psi(\omega)]$. These paths are not used to calculate the value of the integral via the saddle point method. In Fig. 7 we have expanded the view of the saddle point near the imaginary ω axis. Despite the proximity of the saddle point to the real ω axis, the path of integration derived from $\mathrm{Re}[\psi(\omega)] =$ Con-

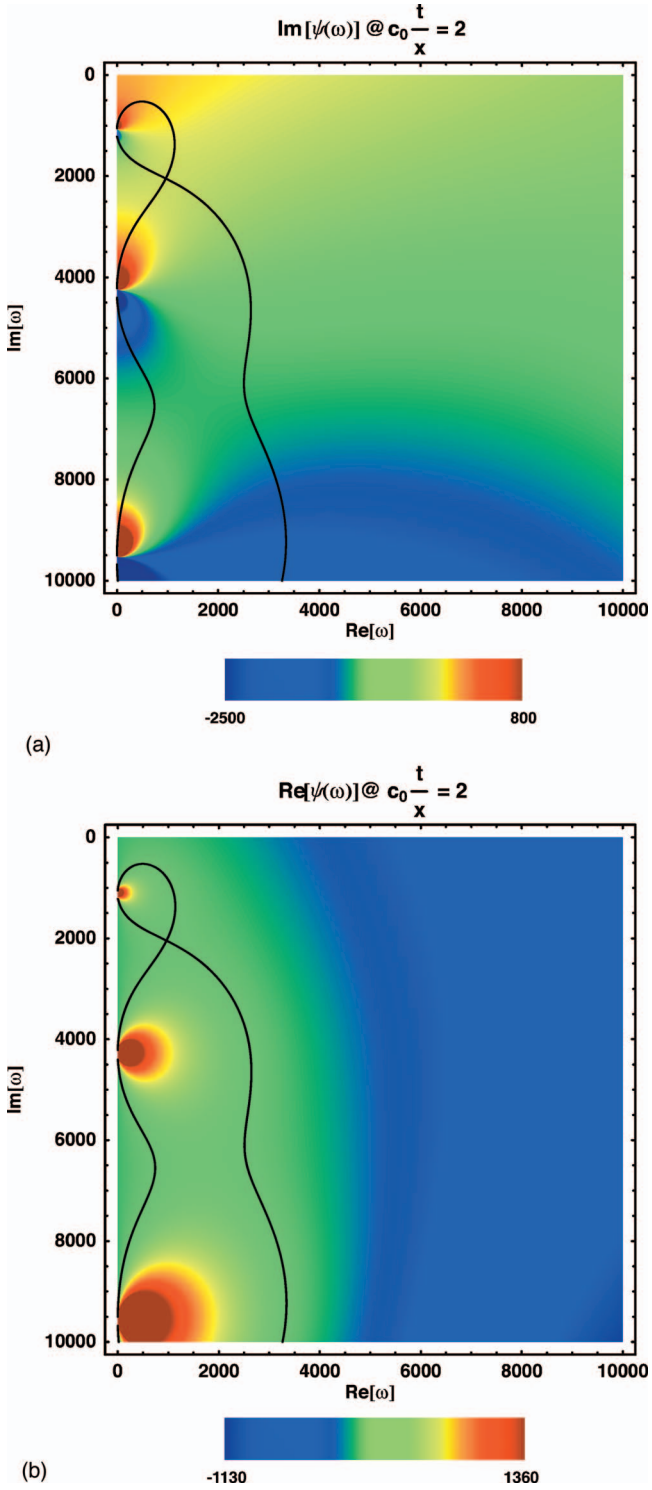

FIG. 7. These two figures show the imaginary (a) and real (b) part of the complex phase ψ near the imaginary axis for times and distances such that $c_0t/x=2$. While there are an infinite number of saddle points near, or on the imaginary ω axis, their contribution to the integral as shown previously is exponentially small and the paths are disconnected from the real ω axis. Thus, they are inconsequential in determining the signal velocity.

stant does not intersect the real axis, and thus the contribution from these saddle points is relatively weak, because the path of integration cannot include a residue or path deformation around one.

In Figs. 8(a) through 8(c) we show the progression of the integration path through the complex ω plane for a pulse with carrier frequency $\omega_c=15{,}000$ rads/s. The point $\omega_c=15{,}000$ is marked by the intersection of the two white lines at the center of the contour plot. Prior to the time $\tau=2.004$ the integration path safely excludes the carrier frequency from any contribution to the integral of Eq. (4), as seen in Fig. 8(a). At time $\tau=2.004$ the path of integration goes directly through the point $\omega=15{,}000$. Thus the integration path must include a semicircular arc around the pole created by the factor of $\omega-\omega_c$ in the denominator of the integrand of Eq. (1) (Fig. 8(b)). The signal velocity as per Eq. (41) is $V_{\text{signal}}=c_0/2.004$. Finally, as seen in Fig. 8(c) the pole at ω_c is entirely encircled by the integration path and thus contributes a factor of $-2\pi i$ times the residue at ω_c. (This contribution is negative because of the integration path being clockwise about the pole.)

For three different times we have plotted the graphical solution in Fig. 9 as the crossing of each curve with its associated constant phase value of a saddle point for three different times $\tau=1.91$ (dotted), 1.92 (dashed), and 1.93 (solid). The corresponding horizontal lines intersection with each curve represents the frequency(ies) that may arrive at that time. As can be seen, one or several frequencies can arrive simultaneously. Each saddle point was tabulated for the range of times $1.0001<\tau<30$ in 0.0001 time-step increments. Using the numerical method outlined, the real positive frequencies satisfying Eq. (42) were determined for each time. Thus a table of frequencies as a function of arrival times could be determined and a signal velocity calculated for each frequency. We have plotted the numerically determined signal velocity results with the phase velocity and a calculated group velocity in Fig. 10. There it is seen that the group velocity and signal velocity are in agreement for frequencies large compared to the resonance frequency of the bubbles. However, there are clear deviations in the region of highest absorption, where the group velocity is not well defined as well as a significant deviation at low frequencies.

V. CONCLUSIONS

The importance that all acoustic signals be causal, even those in bubbly media, cannot be understated. This requirement has led us to consider a modification of a wide class of dispersion formulas. Specifically we have modified the dispersion formula of Commander and Prosperetti.[2] However, this modification is necessary for all of the theories of acoustic dispersion for bubbly liquids based upon the work of Devin as well.[1] In Sec. II B we demonstrated that the acausal nature of the original formulation was due to the use of a low frequency approximation to the solution of Keller's oscillating bubble radial equation. This resulted in an ω^3 dependence in the denominator of the dispersion formula that caused it to be nonanalytic in the upper-half ω plane. Similar types of dispersion formulas for electromagnetic cases had been previously investigated and determined to be essentially nonphysical.[18] This behavior with respect to acoustic signal propagation in bubbly media has indeed been known for some time, as alluded to in the work of Leander.[13] While there has been recent work in this field including a theoretical model with relaxation,[16] there has been no explicit equa-

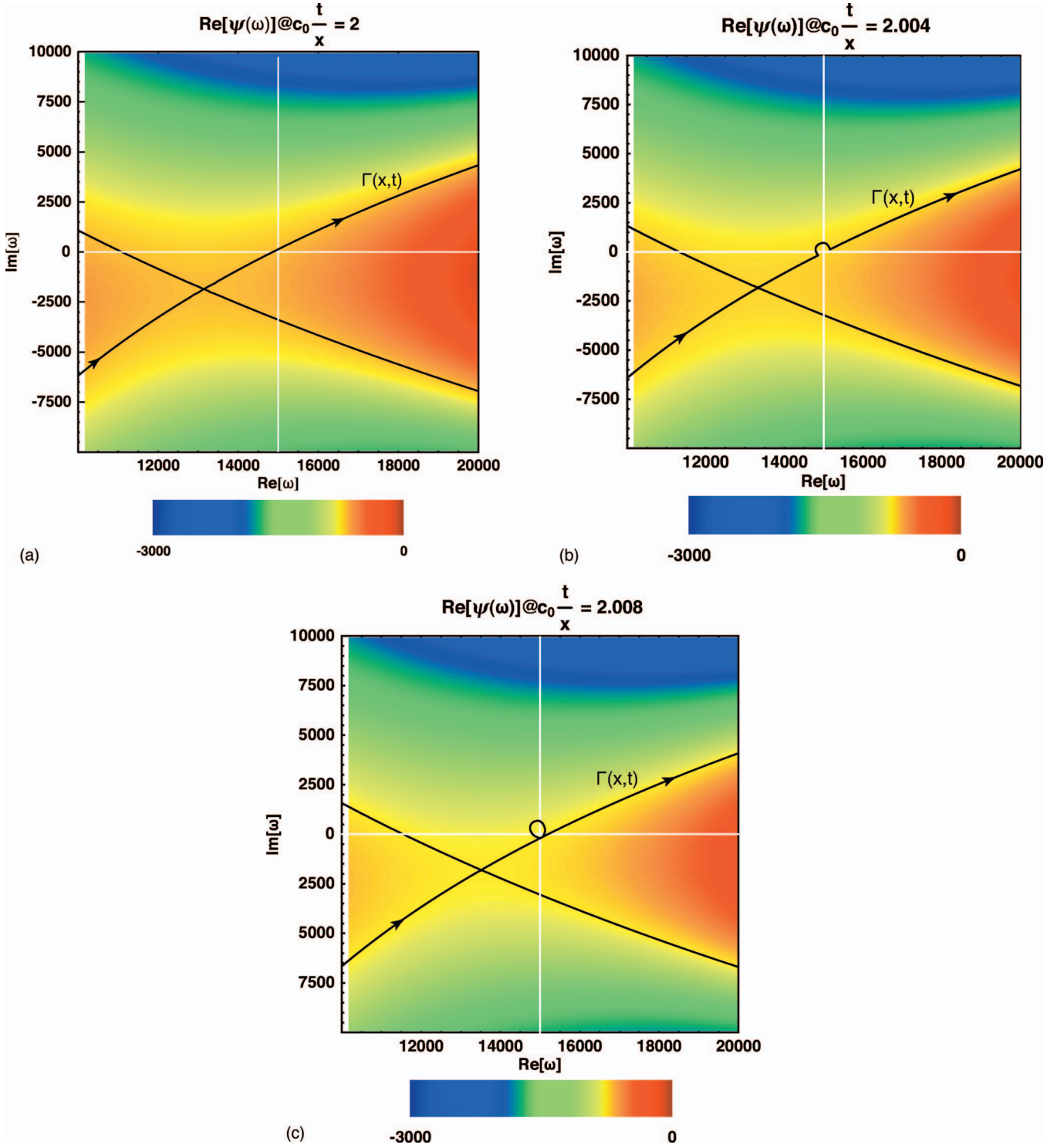

FIG. 8. These three figures show the migration of the integration path as a function of time near $c_0t/x=2$. The carrier frequency is $\omega=15{,}000$ rad/s, and is represented by the intersection of the two white lines. For $\tau=2$ in (a) the integration path is above the line and there is only the contribution from the saddle point. As τ becomes larger the integration path must first arc around it (b) and then completely encircle it (c) giving the contribution of residue at $\omega=15{,}000$ rad/s to the integral.

tion for the correction necessary to make the dispersion formula of the work based upon Devin representative of an internally self-consistent and causal theory in the literature; a fact noted in Ref. 6.

Our correction is valid to all orders of the dimensionless expansion factor $\omega a/c_0$. The effect on the phase velocity and attenuation is seen to be negligible at frequencies for which $|\omega a/c_0| \lesssim 1$. The real part of the wave vector controlling the phase and group velocities is essentially unaffected. For $|\omega a/c_0| \gg 1$ the magnitude and phase of the wave vector deviate significantly from its uncorrected value and cause the contribution from this correction to asymptote to effectively a linear behavior. This manifests itself in several ways, of which one is plotted in Fig. 2(b), where a clear deviation in

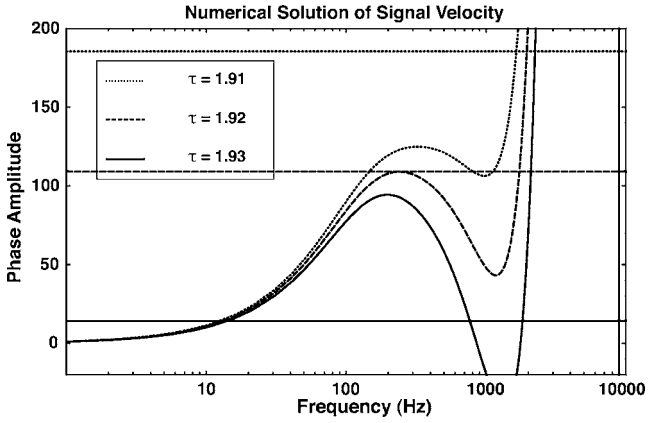

FIG. 9. The phase function is seen here as a function of both time and frequency. The different times are $\tau=1.91$ (dotted), 1.92 (dashed), and 1.93 (solid). The solution to the numeric problem is the intersection of the corresponding horizontal line with the curve. It is clear that for times x/c_0 near 1 that the high frequency components have phase values near zero.

the attenuation occurs between the corrected and uncorrected values at high frequency. We stress that it would be incorrect to assume from Figs. 2(a) and 2(b) that this correction only affects the high frequency behavior of the signals. The signal is intrinsically an integral of a complex quantity and is required to be analytic in the upper-half ω plane to enforce causality at the possible expense of incurring nonanalytic behavior in the lower-half ω plane, e.g., branch cuts, poles, and saddle points. As such, any evaluation of the Fourier integral of Eq. (4) for any real signal will require a detailed knowledge of the behavior of the dispersion formula throughout the entire complex plane, and not just the curves of phase speed and attenuation calculated only for values of $\mathrm{Im}(\omega)=0$, as in Fig. 2.

The speed of acoustic signal propagation in bubbly media has been determined via the application of the theory of Sommerfeld and Brillouin originally developed for the propagation of electromagnetic waves in dispersive media.[9,10] In their case, metals with bound electrons that were modeled as damped harmonic oscillators served as the physical mechanism of the dispersion of electromagnetic

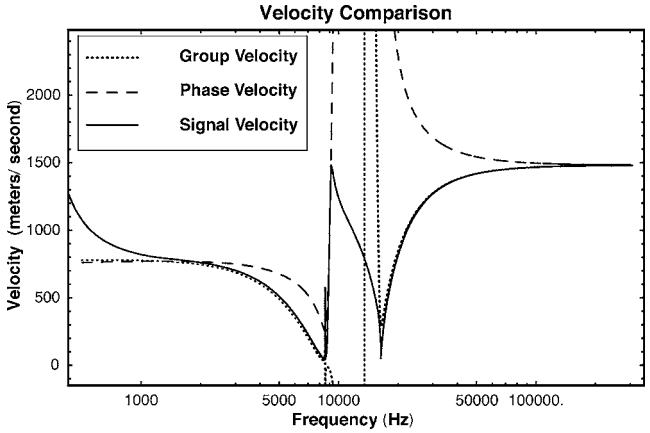

FIG. 10. The numerically calculated signal velocity (black) as a function of frequency is plotted against the phase velocity (dashed) and group velocity (dotted). Both the low and high frequency behavior asymptote to the quiescent value of the group velocity for the medium without bubbles.

waves. By application of their theoretical methods that require the dispersion formula of wave theories to be analytic in the upper-half complex ω plane, we have shown that acoustic signals propagating in media governed by the aforementioned corrected dispersion formula cannot travel faster than the infinite frequency limit of the speed of sound in a quiescent medium absent bubbles. As in the electromagnetic case the physical manifestations of these requirements are causality, the existence of two types of motion prior to arrival of the wave oscillating at the carrier frequency called signal precursors, and the existence of a signal velocity distinct from both the phase and group velocities.

One is left with the following picture of the nature of the acoustic wave motion in bubbly media. Until $\tau=1$ there is no motion. At $\tau=1$ all of the constituent particles of the underlying medium are disturbed ever so slightly by the passage of the first, or Sommerfeld precursor. This part of the signal oscillates approximately as the Bessel function of order one for a doubly ended sine wave source function, as per Eq. (24). The argument to this Bessel function is independent of the carrier frequency, but dependent on the high frequency asymptotic expansion of the index of refraction. For the physical parameters considered here the amplitude of the first precursor is in general small, being approximately proportional to $\sqrt{a_0^2(t-t_0)/(t_0c_0^2)}\exp[-\beta\tau_0 x/a_0]$. In the time between τ_0 and τ_1 the second precursor is exponentially increasing in amplitude. At τ_1 the second precursor reaches its maximum value and begins an oscillatory motion of very low frequency. The instantaneous frequency of this precursor is approximately proportional to $\sqrt{\tau-n_{\mathrm{cm}}(0)}$, and is again independent of the carrier frequency. The second precursor is quickly damped exponentially. The physics of wave propagation in bubbly media up this point is completely derived from the asymptotic analysis of the effective index of refraction in both the high and low frequency limits via the method of steepest descent.

That portion of the wave propagating at the signal's carrier frequency ω_c arrives at a time that is differentiated from both of the precursors. The signal velocity, denoted by V_{signal}, is determined by numerically solving a set of equations: First the saddle point equation, Eq. (18), followed by the phase crossing equation, Eq. (42). As expected, this velocity asymptotically approaches the group velocity in the high frequency limit. This is because in this limit the wave vector becomes asymptotically linear as a function of frequency. Near the anomalous absorption region the group velocity ceases to be well defined. This is in contrast to the signal velocity, which shows a continuous connection between the frequencies above and below the anomalous absorption band.

ACKNOWLEDGMENTS

This work is supported by the Naval Research Laboratory and the Office of Naval Research.

[1]J. C. Devin, "Survey of therma radiation and viscous damping of pulsating air bubbles in water," J. Acoust. Soc. Am. **31**, 1654–1667 (1959).
[2]K. W. Commander and A. Prosperetti, "Linear pressure waves in bubbly liquids: Comparison between theory and experiments," J. Acoust. Soc.

Am. **85**, 732–746 (1989).
[3]C. S. Clay and H. Medwin, *Acoustical Oceanography: Principles and Applications* (Wiley, New York, 1977).
[4]J. B. Keller and I. I. Kolodner, "Damping of underwater explosion bubble oscillations," J. Appl. Phys. **27**, 1152–1161 (1956).
[5]J. B. Keller and M. Miksis, "Bubble oscillations of large amplitude," J. Acoust. Soc. Am. **68**, 628–633 (1980).
[6]A. Prosperetti and A. Lezzi, "Bubble dynamics in a compressible liquid. Part 1. First-order theory," J. Fluid Mech. **168**, 457–478 (1986).
[7]L. Brillouin, *Wave Propagation and Group Velocity* (Academic, New York, 1960).
[8]J. D. Jackson, *Classical Electrodynamics*, 2nd ed. (Wiley, New York, 1975).
[9]A. Sommerfeld, "About the propagation of light in dispersive media," Ann. Phys. **44**, 177 (1914).
[10]L. Brillouin, "About the propagation of light in dispersive media," Ann. Phys. **44**, 203 (1914).
[11]J. L. Leander, "On the relation between the wavefront speed and the group velocity concept," J. Acoust. Soc. Am. **100**, 3503–3507 (1996).
[12]Z. Ye, "Acoustics dispersion and attenuation in many spherical scatter systems and the Kramers-Kronig relations," J. Acoust. Soc. Am. **101**, 3299–3305 (1997).
[13]J. L. Leander, "A note on transient underwater bubble sound," J. Acoust. Soc. Am. **103**, 1205–1208 (1998).
[14]J. L. Leander, "Wavefront and group velocity in relaxing and bubbly fluids," J. Acoust. Soc. Am. **105**, 3044–3048 (1999).
[15]G. A. Maksimov and V. A. Larichev, "Propagation of a short pulse in a medium with resonance relaxation: The exact solution," Acoust. Phys. **49**, 555–564 (2003).
[16]A. A. Karabutov, V. A. Larichev, G. A. Maksimov, I. M. Pelivanov, and N. B. Podymova, "Relaxation dynamics of a broadband nanosecond acoustic pulse in a bubbly medium," Acoust. Phys. **52**, 582–588 (2006).
[17]J. A. Stratton, *Electromagnetic Theory* (McGraw–Hill, New York, 1941).
[18]H. M. Nussenzveig, *Causality and Dispersion Relations* (Academic, New York, 1972).
[19]A. Lezzi and A. Prosperetti, "Bubble dynamics in a compressible liquid, Part 2. Second-order theory," J. Fluid Mech. **185**, 289–321 (1987).
[20]A. Prosperetti, "Application of the subharmonic threshold to the measurement of damping of oscillating gas bubbles," J. Acoust. Soc. Am. **61**, 11–16 (1977).
[21]A. Prosperetti, "Thermal effects and damping mechanisms in the forced radial oscillations of gas bubbles in liquids," J. Acoust. Soc. Am. **61**, 17–27 (1977).
[22]A. Prosperetti, "The equation of bubble dynamics in a compressible liquid," Phys. Fluids **30**, 3626–3628 (1987).
[23]A. Prosperetti, L. A. Crum, and K. W. Commander, "Nonlinear bubble dynamics," J. Acoust. Soc. Am. **83**, 502–514 (1988).
[24]S. H. Lamb, *Hydrodynamics* (Dover, New York, 1932).
[25]F. S. Henyey, "Corrections to Foldy's effective medium theory for propagation in bubble clouds and other collections of very small scatters," J. Acoust. Soc. Am. **105**, 2149–2154 (1999).
[26]S. G. Kargl, "Effective medium approach to linear acoustics in bubbly liquids," J. Acoust. Soc. Am. **111**, 168–173 (2002).
[27]S. Temkin, "Attenuation and dispersion of sound in dilute suspensions of spherical particles," J. Acoust. Soc. Am. **108**, 126–146 (2000).
[28]A. S. Sangani, "A pairwise interaction theory for determining the linear acoustic properties of dilute bubbly liquids," J. Fluid Mech. **232**, 221–284 (1991).
[29]M. Nicholas and G. J. Orris, "Measurements of the attenuation and sound speed in bubbly fresh and salt water," in *Boundary Influences in High Frequency, Shallow Water Acoustics*, edited by N. G. Pace and P. Blondel (University of Bath, Bath, UK, 2005), pp. 457–462.
[30]G. Arfken, *Mathematical Methods for Physicists*, 2nd ed. (Academic, New York, 1970).

Observable parameters from multipath bottom reverberation in shallow water

Michael A. Ainslie
Underwater Technology Department, TNO, Oude Waalsdorperweg 63, P.O. Box 96864, 2509 JG The Hague, The Netherlands

(Received 16 November 2006; revised 28 February 2007; accepted 1 March 2007)

Multipath ocean reverberation originating from the seabed in shallow isovelocity water, with particular attention to its information content in the cylindrical spreading and mode stripping regions, is considered. The reverberation is evaluated using Weston's flux integral method, both analytically with various simplifying approximations and numerically with all but one of these approximations rescinded. The functional form of the analytical solution is used to infer which physical seabed parameters can be extracted from measurements of reverberation. Coarse- and fine-grained sediments (sand and clay) are both considered. The main purpose of the numerical solutions is to check the accuracy of the analytical approximations; they also serve as a convenient surrogate for measured reverberation. © *2007 Acoustical Society of America.*
[DOI: 10.1121/1.2722044]

PACS number(s): 43.30.Pc, 43.30.Gv, 43.30.Hw, 43.30.Ma, 43.30.Ft [RCG] Pages: 3363–3376

I. INTRODUCTION

The reverberation produced by scattering of sound from the seabed is sensitive to the sediment properties. If the scattering process can be modeled well enough, it follows that a measurement of reverberation can be used to infer those seabed parameters to which the reverberation is sensitive.[1–4] A trivial example is the determination of Lambert's parameter from the sound scattered from the seabed (after having traveled along a straight line path directly to the seabed and back), but what other parameters can be measured from the bottom reverberation? The purpose of this article is to answer this question for the long range situation involving multiple reflections in shallow isovelocity water. This knowledge has consequences for the design of effective inversion experiments.

Weston's flux approach for propagation[5,6] was used by Lurton and Marchal[7] to derive a simple closed form expression for the reverberation at long range in shallow water (Weston's "mode stripping" region, henceforth abbreviated "MS") with an arbitrary power law for the angle dependence of the scattering coefficient. The same result was derived independently by Ainslie[8] and by Harrison and Nielsen[9] and extended to a range-dependent bathymetry for selected scattering rules by Harrison,[10] including one that is not separable in angle. Holland[11] derived an approximation for power laws that are intermediate between the Lambert and angle-independent scattering rules. Some of the derivations[8,10,11] are valid at short range in the "cylindrical spreading" region (abbreviated "CS") as well as at long range and in the intermediate transition region. This last point is important in the context of reverberation inversion, as the measurement may include data from both CS and MS regions, and these provide qualitatively different information about the seabed.

Harrison[10] points out that the Lambert parameter μ and reflection properties are not easily measured separately from MS reverberation. Ainslie *et al.*[4] noticed a similar ambiguity in their inversion using synthetic short range (CS) reverberation between inverted values of μ and the exponent q of the scattering coefficient power law. Harrison and Nielsen[9] show that scattering and reflection properties can be separated in the presence of refraction in the water if the sound speed gradient is known, and not otherwise.

The purpose of the present article is

(i) to make available to a wider audience the findings of Ref. 8 for arbitrary power laws of scattering coefficient versus angle,
(ii) to extend those results to *combinations* of power laws, and
(iii) to test the suitability of such power laws and combinations for specific cases involving uniform sand and uniform clay sediments.

The main assumptions are listed in Sec. II. Section III follows Weston[12] and describes the CS and MS regions for one-way multipath (MP) propagation in terms of energy flux theory. This sets the scene for the two-way problem and introduces (together with Sec. II) the present notation. The theoretical functional form for MP reverberation is derived in Sec. IV for arbitrary power laws and combinations of these, followed by a discussion of the implied observability of the parameters describing the scattering strength (μ and q) and others controlling the seabed reflection coefficient (such as the critical angle θ_c). Section V provides some specific examples for two different sediment types, sand and clay. This is followed by a discussion of the likely effects of frequency dependence (Sec. VI) and refraction in water (Sec. VII). Conclusions are drawn in Sec. VIII.

II. ASSUMPTIONS

Consider a ray incident on the seabed at grazing angle θ_{in}. Restricting attention to scattering in the vertical plane of

the incoming ray, a separable but otherwise completely general form for the scattering coefficient is considered,

$$S(\theta_{\text{in}}, \theta_{\text{out}}) = \sqrt{S_{\text{B}}(\theta_{\text{in}})}\sqrt{S_{\text{B}}(\theta_{\text{out}})}, \tag{1}$$

where θ_{in} is the grazing angle of the ray path incident on the seabed, θ_{out} is the grazing angle of the scattered ray, and $S_{\text{B}}(\theta)$ is the back-scattering coefficient, defined as

$$S_{\text{B}}(\theta) \equiv S(\theta, \theta). \tag{2}$$

The reverberation envelope is calculated for the special case with S_{B} of the form

$$S_{\text{B}}(\theta) = \mu \sin^{2q} \theta \quad (q \geqslant 0), \tag{3}$$

and simple combinations or variants thereof, where μ and q are constants. The functional form of the predicted reverberation is then used to infer what can and cannot be measured. For the particular case $q=1$, the parameter μ is the Lambert parameter ($10 \log_{10} \mu$ in decibels). It is referred to as "Lambert's parameter" in this article for all values of q.

The following assumptions are made about the reverberation:

(i) The reverberation is due entirely to scattering from the seabed (surface and volume reverberation are neglected).
(ii) It is loud enough to neglect noise.
(iii) The time dependence of the reverberation envelope is known, but not its angle dependence.
(iv) The reverberation envelope is featureless (or, rather, the information in any fluctuations is discarded, regardless of their cause).

The following further assumptions are made about the environment and acoustic scenario:

(i) The acoustic frequency and distance to the scatterers are large enough to ensure a continuum of modes or ray paths, consistent with the flux integral approach.
(ii) Near surface cancellation effects (known as "surface decoupling") are assumed negligible, requiring the sonar transmitter and receiver to be at least several acoustic wavelengths from the sea surface.
(iii) Variations of sound speed in water with depth and range are neglected.
(iv) Variations of water depth and seabed properties with range are neglected.
(v) Effects of sea surface scattering, near surface bubbles, and volume attenuation on bottom reverberation are neglected.

Some of these assumptions can be relaxed, but this would be at the expense of complicating the mathematics and hence obscuring the main message concerning the information content of bottom reverberation. The effect of sea surface scattering on geoacoustic inversion is investigated by Zhou *et al.*[13] Harrison and Nielsen[9] describe the effect of refraction on parameter observability and simulate the effect of surface decoupling by means of a dipole receiver.

III. MULTIPATH PROPAGATION REGIMES

Weston[12] identifies two waveguide propagation regimes in shallow water, known as "cylindrical spreading" (CS), in which boundary reflection losses are negligible, and "mode stripping" (MS), in which the cumulative effect of multiple reflections takes its toll in the form of a $15 \log_{10} r$ decay in decibels instead of $10 \log_{10} r$ for CS. The multipath situation results in CS behavior if reflection losses are small and MS if not. Additional regimes described by Weston, such as the single mode region, are not considered here. The equations for the propagation factors in the two regimes for a receiver at range r from the source in water of depth h are

$$F_{\text{CS}} = \frac{2\theta_{\text{c}}}{h} r^{-1}, \tag{4}$$

and, assuming small grazing angles for MS,

$$F_{\text{MS}} = \left(\frac{\pi}{\eta h}\right)^{1/2} r^{-3/2}. \tag{5}$$

In these equations, the seabed is characterized by means of a critical angle θ_{c} and a parameter η defined as the reflection loss gradient at grazing incidence (in units of nepers per radian). Thus, if $V(\theta)$ is the seabed reflection coefficient, its magnitude can be approximated by

$$|V(\theta)| \approx \text{H}(\theta_{\text{c}} - \theta) \exp(-\eta \sin \theta), \tag{6}$$

where $\text{H}(x)$ is the Heaviside step function. Rays traveling at angles steeper than θ_{c} are assumed to be heavily attenuated, with effectively infinite reflection loss.

The range at which the curves for F_{CS} and F_{MS} cross can be thought of as a transition range between the two regimes, given by

$$r_0 = \frac{\pi h}{4 \eta \theta_{\text{c}}^2}. \tag{7}$$

A more general expression for the multipath (MP) propagation factor, encompassing CS and MS behavior as limiting cases for small and large r, is[6]

$$F_{\text{MP}}(r) = \int_0^{\pi/2} G(r, \theta)\, \text{d}\theta, \tag{8}$$

where

$$G(r, \theta) = \frac{2}{hr} |V(\theta)|^{[(\tan \theta)/h]r}. \tag{9}$$

In order to evaluate the integral of Eq. (8), the following simplification strategy is adopted. For the CS region, losses due to reflection from the seabed are assumed negligible. In other words, for short range calculations, $\eta \approx 0$ is assumed in Eq. (6), and Eq. (4) then follows from Eq. (8). For longer ranges, reflection losses are included using Eq. (6) for $V(\theta)$, which, assuming small θ, results in[7,10]

$$F_{\text{MP}} = \left(\frac{\pi}{\eta h}\right)^{1/2} r^{-3/2} \text{erf}\left[\left(\frac{\eta r}{h}\right)^{1/2} \theta_{\text{c}}\right]. \tag{10}$$

Equations (4) and (5) follow as special cases in the limits of small and large values of the ratio r/r_0, respectively.

IV. MULTIPATH REVERBERATION REGIMES

A. General separable scattering coefficient

Let us define a "reverberation factor" $R(t)$ as the mean square reverberation pressure due to an omnidirectional unit source for a pulse of unit duration. Before examining the multipath reverberation it is convenient to consider what happens before the onset of CS propagation, i.e., in the immediate vicinity of the source—the spherical spreading (SS) region. The SS reverberation factor can be written (including the direct path and a surface reflected one, but without bottom reflections)

$$R_{\mathrm{SS}}(t) = \frac{64}{c^4} S_{\mathrm{B}}(\theta) A_0(t) t^{-4}, \tag{11}$$

where A_0 is the monostatic scattering area per unit of pulse duration

$$A_0(t) = \frac{\pi c^2 t}{2}. \tag{12}$$

In reality, the surface reflected path must be slightly steeper than the direct one if it is to arrive at the same time. The difference in angle is not necessarily small, but a more precise formulation is not needed here because Eq. (11) is used only as an order of magnitude indicator for comparison with other reverberation components.

In the multipath regions the flux integral for reverberation can be written (adding all possible paths to and from the scatterer)

$$R_{\mathrm{MP}}(t) = \frac{1}{4} \int_0^{\pi/2} G(r, \theta_{\mathrm{out}}) \int_0^{\pi/2} \times G(r, \theta) S(\theta_{\mathrm{in}}, \theta_{\mathrm{out}}) A(t; \theta_{\mathrm{in}}, \theta_{\mathrm{out}}) \, \mathrm{d}\theta_{\mathrm{in}} \, \mathrm{d}\theta_{\mathrm{out}}, \tag{13}$$

where

$$r = \frac{ct}{\sec \theta_{\mathrm{in}} + \sec \theta_{\mathrm{out}}}. \tag{14}$$

The scattering area at range r is $2\pi r \, \delta r$, where the width of the annulus δr is determined by the projection of the sonar pulse at grazing angle θ onto the horizontal plane and hence proportional to $c/(\cos \theta_{\mathrm{in}} + \cos \theta_{\mathrm{out}})$. It follows that[14]

$$A(t; \theta_{\mathrm{in}}, \theta_{\mathrm{out}}) = \frac{4 \sec \theta_{\mathrm{in}} \sec \theta_{\mathrm{out}}}{(\sec \theta_{\mathrm{in}} + \sec \theta_{\mathrm{out}})^2} A_0(t). \tag{15}$$

The factor $\frac{1}{4}$ in front of the integral in Eq. (13) is needed to ensure that only downward traveling rays are included in the incident field, and upward traveling ones in the scattered field.

The objective of the following derivation is first to express Eq. (13) in terms of scattering and reflection coefficients without approximation. The resulting formula [Eq. (17)] is then simplified to a more manageable form for further analysis [Eq. (21)]. Unlike for propagation [see Eqs. (8) and (9)], for reverberation the $1/r$ terms cannot be factored out of the integral because (for fixed t) they vary with θ_{in} and θ_{out} according to Eq. (14). Instead, Eqs. (14) and (15) can be combined to give

$$\frac{A(t; \theta_{\mathrm{in}}, \theta_{\mathrm{out}})}{r^2} = \frac{4 A_0(t)}{(ct)^2} \sec \theta_{\mathrm{in}} \sec \theta_{\mathrm{out}}. \tag{16}$$

Substituting Eq. (16) into Eq. (13) gives

$$R_{\mathrm{MP}}(t) = \frac{4 A_0}{(cth)^2} \int_0^{\pi/2} \sec \theta_{\mathrm{in}} \times \left[\int_0^{\pi/2} \sec \theta_{\mathrm{out}} \left| V(\theta_{\mathrm{out}}) \right|^{(ct/h) \tan \theta_{\mathrm{out}} / (\sec \theta_{\mathrm{in}} + \sec \theta_{\mathrm{out}})} \times \left| V(\theta_{\mathrm{in}}) \right|^{(ct/h) \tan \theta_{\mathrm{in}} / (\sec \theta_{\mathrm{in}} + \sec \theta_{\mathrm{out}})} S(\theta_{\mathrm{in}}, \theta_{\mathrm{out}}) \right] \mathrm{d}\theta_{\mathrm{in}}. \tag{17}$$

Equation (17) can be used as it stands to evaluate reverberation as a function of time t, with A_0 given by Eq. (12). However, the double integration is cumbersome, so it is worth investing some effort in simplifying it by separating the θ_{in} and θ_{out} integrals. To achieve this it is necessary to make the approximation

$$\left| V(\theta_{\mathrm{out}}) \right|^{(ct/h) \tan \theta_{\mathrm{out}} / (\sec \theta_{\mathrm{in}} + \sec \theta_{\mathrm{out}})} \times \left| V(\theta_{\mathrm{in}}) \right|^{(ct/h) \tan \theta_{\mathrm{in}} / (\sec \theta_{\mathrm{in}} + \sec \theta_{\mathrm{out}})} \approx \left| V(\theta_{\mathrm{out}}) \right|^{(ct/2h) \sin \theta_{\mathrm{out}}} \left| V(\theta_{\mathrm{in}}) \right|^{(ct/2h) \sin \theta_{\mathrm{in}}}. \tag{18}$$

It is convenient at this point to introduce the dimensionless variable

$$X(t) \equiv \sqrt{\frac{h^2 t}{2\pi} R(t)}, \tag{19}$$

referred to hereafter as the reverberation coefficient. With this definition the reverberation level RL for a pulse of source level SL and duration T (assumed short) is

$$\mathrm{RL}(t) = 20 \log_{10} X(t) - 10 \log_{10} \frac{ct}{2h} + 10 \log_{10} \frac{\pi c T}{h^3} + \mathrm{SL}. \tag{20}$$

Using Eq. (18), and assuming also that $S(\theta_{\mathrm{in}}, \theta_{\mathrm{out}})$ is a separable function of its arguments [Eq. (1)], Eq. (19) can then be written

$$X_{\mathrm{MP}}(t) = \int_0^{\pi/2} \sec \theta \left| V(\theta) \right|^{(c \sin \theta / 2h) t} \sqrt{S_{\mathrm{B}}(\theta)} \, \mathrm{d}\theta. \tag{21}$$

From Eq. (21), it is reasonable to expect reverberation to be sensitive to Lambert's parameter μ and scattering exponent q (through S_{B}) as well as to the critical angle θ_{c} and reflection loss gradient η (through V). Consequently, these four parameters, or at least some combination of them, are expected to be observable from reverberation measurements.

In order to evaluate X_{MP}, the same strategy is adopted here as for F_{MP} in Sec. III. The formula for X_{CS} is obtained by neglecting η in Eq. (6), so that

$$X_{\mathrm{CS}} \approx \int_0^{\theta_{\mathrm{c}}} \sec \theta \sqrt{S_{\mathrm{B}}(\theta)} \, \mathrm{d}\theta. \tag{22}$$

The MS reverberation factor is found by substituting Eq. (6) in Eq. (21) and assuming small θ and large $\eta ct/h$, so that

TABLE I. Integrals needed for CS reverberation coefficient, with integer power law scattering coefficient ($q=N$). The function $L(x)$ is defined by $L(x)=\log_e \tan(\pi/4+x/2)$.

N	$\int \sec x \sin^N x \, dx$
0	$L(x)$
1	$\log_e \sec x$

$$X_{\mathrm{MS}}(t) \approx \int_0^{\infty} \exp\left(-\frac{\eta c t}{2h}\theta^2\right)\sqrt{S_\varepsilon(\theta)}\, d\theta. \tag{23}$$

Here, the function $S_\varepsilon(\theta)$ is equal to the lowest order term in a Maclaurin expansion for $S_B(\theta)$. For example, if $S_B(\theta)$ were of the form $\sin^x \theta$, then $S_\varepsilon(\theta)$ would be θ^x. Notice that the upper limit of the integral is extended to $+\infty$ in the MS region. This is justified because, if $\eta c t/h$ is sufficiently large, the integrand vanishes for $\theta > \theta_c$.

Consider now the approximation involved in using Eq. (18). In the CS regime it is bound to hold because in this region the cumulative boundary losses are (by definition) negligible, and hence the left- and right-hand sides are both equal to 1. In the MS region, angles are assumed small and in this situation both left- and right-hand sides approximate to $|V(\theta_{\mathrm{out}})|^{(ct/2h)\theta_{\mathrm{out}}}|V(\theta_{\mathrm{in}})|^{(ct/2h)\theta_{\mathrm{in}}}$, so the equality again holds. The only question is in the transition region between CS and MS, after the losses begin to bite but before the steep angles have been stripped away.

B. Power law(s)

Substituting Eq. (3) into Eq. (22) gives for the CS reverberation coefficient

$$X_{\mathrm{CS}} \approx \mu^{1/2}\int_0^{\theta_c} \sec\theta \sin^q\theta \, d\theta. \tag{24}$$

If q is an integer (say N), this integral can be expressed in terms of simple functions, the first two examples of which, for $N=0$ and 1, are included in Table I. For larger N the following recurrence equation can be used

$$I_N(x) = I_{N-2}(x) - \frac{1}{N-1}\sin^{N-1} x \quad (N \geqslant 2), \tag{25}$$

where $I_q(\theta_c)$ is the integral of Eq. (24).

For all q satisfying $q > -1$ (including nonintegers), the integral can be simplified by assuming small angles to obtain[8]

$$X_{\mathrm{CS}} \approx \mu^{1/2}\frac{\theta_c^{q+1}}{q+1}. \tag{26}$$

In order to derive a corresponding expression for X_{MS}, Eq. (21) can be simplified in the same manner, so that

$$X_{\mathrm{MP}}(t) \approx \mu^{1/2}\int_0^{\theta_c} \theta^q \exp(-\eta u \theta^2)\, d\theta, \tag{27}$$

where

TABLE II. Reverberation coefficients and observable parameters for CS and MS regimes, with power law scattering coefficient. The parameter u is equal to $ct/2h$.

	Cylindrical spreading (CS, $\eta u \theta_c^2 \ll 1$)	Mode stripping (MS, $\eta u \theta_c^2 \gg 1$)
Reverberation coefficient $X(t)$	$\mu^{1/2}\theta_c^{q+1}/(q+1)$	$\mu^{1/2}\Gamma[(q+1)/2]/2(\eta u)^{(q+1)/2}$
Observable parameters (if h/c known)	$\mu\theta_c^{2q+2}/(q+1)^2$	q, μ/η^{q+1}

$$u = u(t) = \frac{ct}{2h} \tag{28}$$

and hence[8]

$$X_{\mathrm{MP}}(t) \approx \frac{\mu^{1/2}}{2}\frac{\gamma(a, \eta u \theta_c^2)}{(\eta u)^a}, \tag{29}$$

where

$$a = \frac{q+1}{2}. \tag{30}$$

Here γ is the lower incomplete gamma function, defined for $\alpha > 0$ as[15,16]

$$\gamma(\alpha, x) \equiv \int_0^x e^{-t} t^{\alpha-1}\, dt. \tag{31}$$

Equation (29) is the main result of this section. It is analogous to the erf expression for F_{MP} [Eq. (10)] except for the additional small θ_c assumption in the CS region (in the MS region the requirement is a weaker one, requiring only that $\eta\theta_c^2$ be small compared with the dimensionless reciprocal time u^{-1}). Limiting cases for small and large values of the product $\eta\theta_c^2 u$ (and for arbitrary q satisfying $a > 0$) lead to the expressions for X_{MS} and X_{CS} in Table II. Also tabulated are the associated observable parameters. The table assumes that the ratio h/c is known and that θ_c is small in the sense that θ and $\sin\theta$ are approximately equal for angles less than θ_c.

The CS result sheds some light on the observation in Ref. 4 of a linear correlation between inverted values of $\log\mu$ and q from modeled CS reverberation. The observation can be explained by writing the CS result in the form

$$\log\mu = [\mathrm{const} - 2\log\theta_c + 2\log(q+1)] - (2\log\theta_c)q. \tag{32}$$

If the critical angle is fixed, this equation approximates to a straight line with gradient $-(2\log\theta_c)$, consistent with Ref. 4, because the expression in square brackets is independent of μ and only weakly dependent on q.

For all non-negative integer values of q, the incomplete gamma function of Eq. (29) can be expressed in terms of exponential and error functions as follows. The equations for $q=0$ and $q=1$ [which lead, respectively, to Eqs. (25) and (28) from Ref. 10 for the reverberation factor] are

TABLE III. Integrals needed for CS reverberation coefficient, with integer power law scattering coefficients added in parallel. The function $L(x)$ is defined in the same way as in Table I.

N	$\int \sec x \frac{\sin^N x}{\sin x + B}\,\mathrm{d}x$ (integral for $n=1$)	$\int \sec x \frac{\sin^N x}{\sin^2 x + B}\,\mathrm{d}x$ (integral for $n=2$)
1	$\{L(x)+B\log_e[\cos x/(B+\sin x)]\}/(1-B^2)$	$[1/2(B+1)]\log_e[(B+\sin^2 x)/\cos^2 x]$
2	$\{BL(x)+\log_e[\cos x/(B+\sin x)^{B^2}]\}/(B^2-1)$	$[L(x)-B^{1/2}\tan^{-1}(B^{-1/2}\sin x)]/(B+1)$

$$\gamma\left(\tfrac{1}{2},x\right) = \sqrt{\pi}\,\mathrm{erf}(\sqrt{x}) \tag{33}$$

and

$$\gamma(1,x) = 1 - \mathrm{e}^{-x}. \tag{34}$$

Then, for $q=N$, where N is any integer greater than 0, integration by parts of Eq. (31) gives the following recurrence equation

$$\gamma(1+N/2,x) = \frac{N}{2}\gamma(N/2,x) - x^{N/2}\mathrm{e}^{-x} \quad (N \geqslant 1), \tag{35}$$

with Eq. (33) as a seed for odd integers and Eq. (34) for even ones.

Holland[11] proposes a nonlinear interpolation for $0 \leqslant q \leqslant 1$. His Eq. (7) (with n and m equal) implies use of the approximation

$$\gamma\left(\frac{q+1}{2},x\right) \approx \pi^{(1-q)/2}\exp\left[-\frac{1}{12}(1-|1-2q|)\right] \times (1-\mathrm{e}^{-x})^q[\mathrm{erf}(\sqrt{x})]^{1-q}. \tag{36}$$

C. Combinations of power law(s)

There may be cases for which two or more different power laws can be combined to describe a complete scattering coefficient curve that is otherwise not well characterized by either power law on its own. Examples of situations for which such a combination may be necessary or useful include

(i) transition through the critical angle from a regime dominated by rough boundary scattering ($q=2$, say) to one dominated by volume scattering at steeper angles ($q=0$);
(ii) transition through a limiting angle from a regime dominated by volume scattering ($q=0$) to one dominated by diffuse scattering at steeper angles ($q=1$).

These numerical values of q are indicative only. What matters is that the variation of the scattering coefficient with angle is usually more complicated than can be represented by a single power law, whereas *combinations* of these are able to emulate more realistic behavior. With this objective in mind, two possible ways of combining the individual power laws are considered below.

1. Addition of $S_B^{1/2}$ (in "series")

Power laws can be added in the form

$$\sqrt{S_B(\theta)} = A_1\sin^{q_1}\theta + A_2\sin^{q_2}\theta, \tag{37}$$

so that $S_B(\theta)$ then follows the larger of the two terms, like adding resistors in series. Assuming small θ_c, the MP reverberation coefficient is

$$X_{MP}(t) \approx \int_0^{\theta_c} \exp[-\eta u(t)\theta^2]\sqrt{S_B(\theta)}\,\mathrm{d}\theta, \tag{38}$$

where $u(t)$ is given by Eq. (28). The main results follow trivially by evaluating the integral for each of the two terms of Eq. (37) separately before adding, so that

$$X_{MP}(t) = \frac{A_1}{2}(\eta u)^{-a_1}\gamma(a_1,\eta u\theta_c^2) + \frac{A_2}{2}(\eta u)^{-a_2}\gamma(a_2,\eta u\theta_c^2), \tag{39}$$

where

$$a_i = \frac{q_i+1}{2}. \tag{40}$$

These results can be generalized by the addition of multiple terms in the obvious way.

2. Addition of $S_B^{-1/2}$ (in "parallel")

As an alternative to adding individual power law terms in series, consider addition in parallel as follows:

$$\frac{1}{\sqrt{S_B(\theta)}} = \frac{1}{A_1\sin^{q_1}\theta} + \frac{1}{A_2\sin^{q_2}\theta} \quad (q_1 > q_2 \geqslant 0), \tag{41}$$

such that the combined scattering coefficient $S_B(\theta)$ follows the smaller of the two individual terms. It is convenient to put $q_1=q$ and $q_2=q-n$ and write Eq. (41) in the form

$$\sqrt{S_B(\theta)} = A_2\frac{\sin^q\theta}{B+\sin^n\theta} \quad (n>0, \quad q \geqslant n), \tag{42}$$

where

$$B = \frac{A_2}{A_1}. \tag{43}$$

The CS reverberation coefficient for this case is

$$X_{CS} \approx A_2\int_0^{\theta_c}\sec\theta\frac{\sin^q\theta}{B+\sin^n\theta}\,\mathrm{d}\theta. \tag{44}$$

This integral is evaluated in Table III for four combinations involving two integer values of q (1 and 2) and the same two values of n. For larger values of q, the following recurrence equation can be used:

$$J_{N,n}(x,B) \equiv \int_0^x \sec y \sin^{N-n} y \, dy - BJ_{N-n,n}(x,B), \quad (45)$$

where $J_{q,n}(\theta_c,B)$ is the integral of Eq. (44) and the remaining term can be written $I_{N-n}(x)$ and evaluated using Eq. (25) and Table I.

The MP integral is

$$X_{MP}(t) \approx A_2 \int_0^{\theta_c} \frac{\theta^q}{B+\theta^n} \exp\left[-\eta u(t)\theta^2\right] d\theta. \quad (46)$$

The MS integral is the same except with the upper limit extended to ∞. For $n=2$, this integral can be written in terms of the *upper* incomplete gamma function $\Gamma(\alpha,x)$, as follows:

$$X_{MS}(t) \approx \frac{A_2}{2} B^{a-1} \exp(B\eta u)\Gamma(a)\Gamma(1-a,B\eta u), \quad (47)$$

where a is given by Eq. (30), and $\Gamma(\alpha,x)$ is defined as[16,17]

$$\Gamma(\alpha,x) \equiv \int_x^\infty e^{-t} t^{\alpha-1} dt, \quad (48)$$

valid for negative as well as positive α.

For MP it is convenient to define the following function:

$$D_q(x,\alpha) \equiv \frac{2}{\sqrt{\pi}} \int_0^{\sqrt{x\alpha}} \frac{v^q}{x+v^2} \exp(-v^2)\, dv, \quad (49)$$

so that for the special case $q=2$, Eq. (46) becomes (still for $n=2$)

$$X_{MP}(t) \approx \frac{A_2}{2} \sqrt{\frac{\pi}{\eta u}} D_2\left(B\eta u, \frac{\theta_c^2}{B}\right). \quad (50)$$

For odd integer values of q, Eq. (49) can be expressed in terms of the exponential integral.[15] For example, putting $q=3$, the required integral is

$$\int \frac{v^3}{a+v^2} \exp(-v^2)\, dv = -\frac{1}{2} a e^a \, \mathrm{Ei}(-v^2-a) - \frac{e^{-v^2}}{2}. \quad (51)$$

The integrals for larger values of q follow from the recurrence equation

$$K_N(v,a) = \frac{1}{2}\gamma\left(\frac{N-1}{2}, v^2\right) - a\exp(a) K_{N-2}(v,a), \quad (52)$$

where $K_N(v,a)$ is the integral of Eq. (51), except with the v^3 term in the integrand replaced by v^N.

V. EXAMPLES

Two examples are considered, one for a seabed comprising a uniform sand sediment with a rough water-sediment boundary, and the other for a clay sediment with a smooth boundary. In the latter case the scattering originates from heterogeneities in the sediment itself. The objective is to test the assumptions of linear reflection loss and power law scattering coefficient.

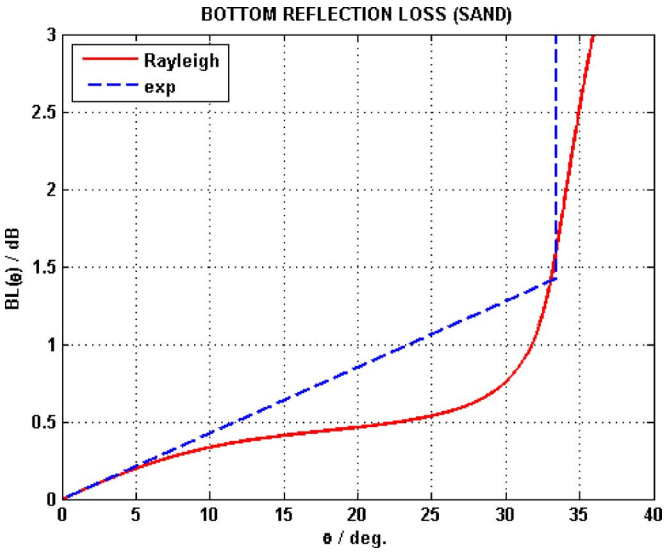

FIG. 1. (Color online) Reflection loss versus grazing angle for sand sediment ($M_z=1.5$).

A. Sand

1. Reflection and scattering coefficients

Consider a sand sediment with a high sound speed so that little energy is transmitted into the sediment at low grazing angles. (The sound speed in sand sediments typically exceeds 1650 m/s.) Bottom reflection loss $\mathrm{BL}(\theta)$ is plotted in Fig. 1 for the sand parameters of Table IV, with a grain diameter of 0.35 mm (i.e., $M_z=1.5$), corresponding to medium sand according to the Udden-Wentworth sediment classification scheme.[18] The reflection loss is defined as

$$\mathrm{BL}(\theta) \equiv -10 \lg |V(\theta)|^2, \quad (53)$$

where V is the plane wave reflection coefficient, previously approximated by Eq. (6). Assuming a uniform fluid sediment, it is given by

$$V(\theta) = \frac{\rho v \sin\theta - \sin\theta_{sed}}{\rho v \sin\theta + \sin\theta_{sed}}, \quad (54)$$

where θ_{sed} is the ray grazing angle in the sediment, and ρ and v are the sediment density and its (complex) sound speed, relative to those of water, such that

TABLE IV. Geoacoustic parameters for medium sand ($M_z=1.5$) and coarse clay ($M_z=8.5$). The grain size M_z is defined as minus the base 2 logarithm of the grain diameter d in millimeters.

Parameter	Symbol	Medium sand	Coarse clay
Sound speed ratio	v	1.1978	0.9923
Density ratio	ρ	2.086	1.378
Attenuation parameter	β	0.88 dB/λ	0.08 dB/λ
Spectral coefficient, defined by Eq. (61)	b	44 mm^4	⋯
Spectral exponent, defined by Eq. (61)	ξ	3.0	⋯
Scattering attenuation ratio, defined by Eq. (91)	ε	⋯	0.008 69

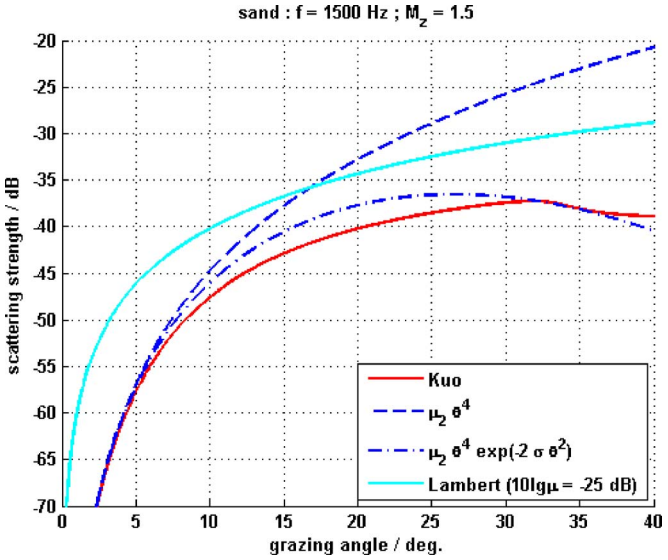

FIG. 2. (Color online) Scattering strength versus grazing angle for sand sediment (M_z=1.5).

$$\theta_c = \cos^{-1}\left(\mathrm{Re}\,\frac{1}{v}\right) \tag{55}$$

and

$$\sin\theta_{sed} = \sqrt{1 - v^2\cos^2\theta}. \tag{56}$$

Also plotted, for comparison, is the approximation of Eq. (6) with[12]

$$\eta \approx \frac{\rho\beta}{20\pi\log_{10}\mathrm{e}}\frac{\cos\theta}{\sin^3\theta_c} = 0.32, \tag{57}$$

where β is the attenuation in the sediment, in units of decibels per wavelength. This parameter is related to the sediment attenuation coefficient α, in nepers per meter, through the relation

$$\alpha = \frac{k\beta}{40\pi\log_{10}\mathrm{e}}\,\mathrm{Re}\,\frac{1}{v}, \tag{58}$$

where k is the acoustic wave number in water. In order to distinguish unambiguously between α and β, these are referred to henceforth as the attenuation coefficient and attenuation parameter, respectively.

It is assumed that in the situation described the scattering is dominated by contributions from the rough boundary, whose wavenumber roughness spectrum is denoted $W(\chi)$. Kuo[19] applies perturbation theory to derive the following expression for the back-scattering coefficient

$$S_B(\theta) = 4k^4\sin^4\theta|Y(\theta)|^2 W(2k\cos\theta), \tag{59}$$

where

$$Y(\theta) = V(\theta) + \frac{2\rho(\rho-1)}{(\rho\tan\theta + i\sqrt{1 - v^{-2}\sec^2\theta})^2}. \tag{60}$$

The solid black line in Fig. 2 shows $S_B(\theta)$ evaluated using Eq. (59) for a sand sediment and a frequency of 1500 Hz. The calculation assumes a power law roughness spectrum of the form

$$W(\chi) = b\left(\frac{1\ \mathrm{cm}^{-1}}{\chi}\right)^{\xi}. \tag{61}$$

The values used for b and ξ are listed in Table IV, together with other geoacoustic parameters required by Kuo's scattering model. Parameter values in this table are based on Refs. 20 and 21. Also plotted in Fig. 2 (solid gray line) is a reference curve showing Lambert's rule with $10\log_{10}\mu = -25$ dB. The dashed line is a power law approximation to Eq. (59), namely $S_B(\theta) = \mu_2\theta^4$, where the subscript indicates the implied value of the exponent q, equal to 2 for this example. The dash-dot line is introduced later (see Sec. V A 3).

The assumptions that the linear reflection loss and power law scattering coefficient are adequate representations for a sand sediment are now evaluated. From Figs. 1 and 2 it is apparent that these assumptions are well satisfied at small grazing angles and not at steeper ones. Long range propagation (and to some extent also reverberation) is dominated by near-horizontal paths, so it is not obvious whether the departures lead to significant errors in the analysis. Two attempts, or "passes," are made at estimating the values of the observable parameters. In the first pass the two assumptions are tested, and shortcomings are then addressed in the second pass.

2. Observable parameters (first pass)

Of interest to long range reverberation is the behavior of Eq. (59) at small angles, for which it can be approximated by

$$S_B(\theta) \approx \mu\theta^{2q}, \tag{62}$$

with q=2, and

$$\mu = 4k^4|Y(0)|^2 W(2k), \tag{63}$$

equal to 0.0356 for the parameters of Table IV. For small θ, $Y(\theta)$ approaches the constant asymptotic value:

$$Y(0) = -1 - \frac{2\rho(\rho-1)}{\sin^2\theta_c}. \tag{64}$$

The accuracy of this small angle approximation can be assessed by comparing Eq. (62) (dashed line in Fig. 2) with Kuo's formula (solid line). Up to a grazing angle of 5 deg the errors are seen to be small, after which they increase steadily to about 13 dB at the critical angle of 33 deg. The discrepancy at these relatively steep angles is addressed in Sec. V A 3, but for the first pass it is disregarded.

Assuming that the correct value of q can be inferred from the MS data, the remaining MS observable would be

$$Q_{sand} = \frac{\mu}{\eta^3}. \tag{65}$$

The CS observable, relying on information from steeper angles, is

$$P = \mu\theta_c^6. \tag{66}$$

In principle the variables P and Q contain all the information there is to know, so one could stop here. In practice, however, it is useful to relate this information to geoacoustic parameters like the sediment density and critical angle, as

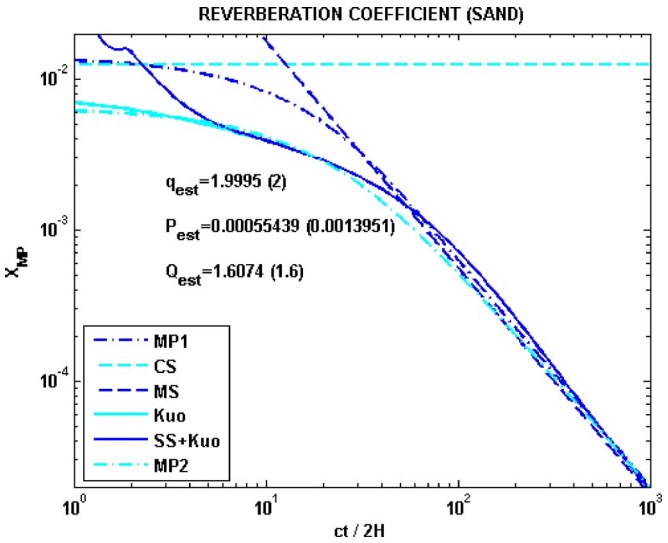

FIG. 3. (Color online) Reverberation coefficient versus dimensionless time u ($=ct/2H$) for sand sediment ($M_z=1.5$). MP1=Eq. (29), CS and MS =Table II, Kuo=Eq. (21) [+ Eq. (59)], SS+Kuo=Eq. (11) [+ Eq. (59)], and MP2=Eq. (82).

follows. Using Eq. (63) for μ and keeping only lowest order terms in θ_c, Eq. (65) can be written

$$Q_{\text{sand}} \approx \frac{2k^4}{\rho(\alpha/k)^3}(\rho-1)^2 W(2k)\theta_c{}^5, \tag{67}$$

where the attenuation coefficient is introduced through the relationship[12]

$$\eta \approx 2\rho(\alpha/k)\theta_c{}^{-3}. \tag{68}$$

Similarly, from Eq. (66),

$$P \approx 16k^4\rho^2(\rho-1)^2 W(2k)\theta_c{}^2. \tag{69}$$

Figure 3 shows $X(t)$ plotted versus dimensionless time. This parameter is related to the reverberation level through Eq. (20).

The curve marked "Kuo" is evaluated by numerical integration of Eq. (21) with the Rayleigh reflection coefficient for sand, and Kuo's scattering model. In the following text, this result is denoted $X_{\text{Kuo}}(t)$. On a practical note, an upper limit of $\pi/4$ is chosen for the integral instead of $\pi/2$, in order to avoid a logarithmic singularity that arises at normal incidence.

Also shown, labeled "SS+Kuo," is an estimate of the total reverberation coefficient, calculated as

$$X_{\text{tot}} = \sqrt{X_{\text{SS}}{}^2 + X_{\text{Kuo}}{}^2}, \tag{70}$$

where X_{SS} is evaluated using Eq. (11) for the reverberation factor and Eq. (59) for the scattering coefficient. The grazing angle is calculated with the assumption that the sonar is close to the sea surface, so that

$$\theta = \arcsin\frac{2h}{ct}. \tag{71}$$

To assess the potential information content of reverberation, $X_{\text{Kuo}}(t)$ is treated as a synthetic measurement and estimates of the observables q, Q, and P are extracted from it. One way to do this might be to search for a combination of these three parameters that minimizes the difference between predicted and measured reverberation. Such a search is beyond the present scope. Instead, the values of q, Q are deduced from the long range asymptotic behavior of $X_{\text{Kuo}}(t)$. Specifically, if for $t\to\infty$,

$$\log_e X_{\text{Kuo}}(t) \to m \log_e \frac{ct}{2h} + g, \tag{72}$$

then, by comparing Eq. (72) with X_{MS} from Table II, the following estimates of q and Q are obtained:

$$q_{\text{est}} = -2m - 1 \tag{73}$$

and

$$Q_{\text{est}} = \frac{4e^{2g}}{\left[\Gamma\left(\frac{q_{\text{est}}+1}{2}\right)\right]^2}. \tag{74}$$

Similarly, the short range (i.e., $t\to 0$) asymptotic behavior provides an estimate of P as follows:

$$P_{\text{est}} = (q_{\text{est}}+1)^2\left[\lim_{t\to 0} X_{\text{Kuo}}(t)\right]^2. \tag{75}$$

The results for q, P, and Q are shown in Table V. Recall that P is the CS observable sensitive to the critical angle (proportional to $\theta_c{}^{2q+2}$) and Q is the MS observable sensitive to the reflection loss (inversely proportional to η^{q+1}). Reasonable estimates of q and Q are obtained from the MS behavior, but the estimated value of P, from CS, is in error by a factor of 2.5. This problem is addressed in pass 2.

TABLE V. Inferred parameters for sand sediment (first pass), using Eqs. (73)–(75).

Parameter	True value	Estimated value
q	2	2.00
P	0.001 40	0.000 55
Q	1.60	1.61

3. Observable parameters (second pass)

The departure of S_{Kuo} from $\mu\theta^4$ close to the critical angle leads to errors in the short range reverberation prediction of the first pass; in turn this leads to errors in the inferred value of P (or θ_c). The error in using the power law approximation is attributed to the approximation of $|Y(\theta)|$ as a constant, whereas Fig. 4 (solid line) shows that this parameter varies by about 15 dB in the angle interval $[0\ \theta_c]$.

Errors associated with the other approximations are small by comparison, so improved results are expected if $Y(0)$ is replaced by a suitable function of angle. Specifically, the following approximation (a Gaussian fit, matching at $\theta=0$ and θ_c) is proposed and shown as the dashed line in Fig. 4, given by

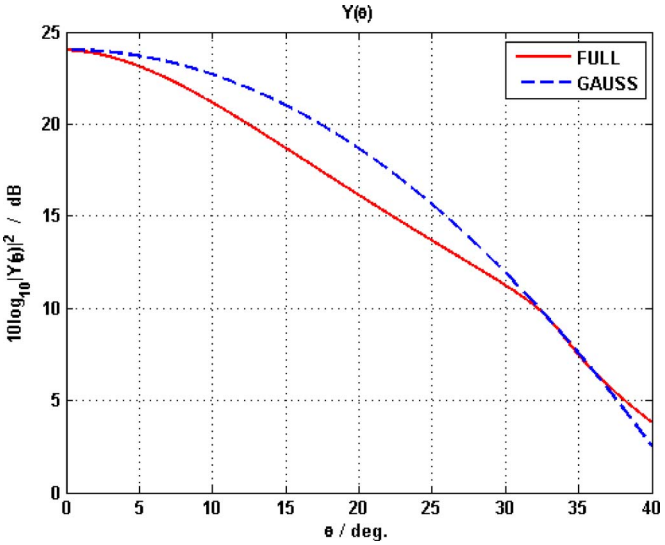

FIG. 4. (Color online) Variation of $Y(\theta)$ with angle for sand sediment (M_z =1.5): FULL=Eq. (60), GAUSS=Eq. (76).

$$|Y(\theta)| \approx Y_0 \left(\frac{Y_c}{Y_0} \right)^{\theta^2/\theta_c^2}, \tag{76}$$

where

$$Y_0 \equiv |Y(0)| \tag{77}$$

and

$$Y_c \equiv |Y(\theta_c)|. \tag{78}$$

The reason for choosing a Gaussian form to approximate $Y(\theta)$ is that it enables an improved approximation to the back-scattering coefficient to be written as a product of a power of θ with a Gaussian:

$$S_B(\theta) = \mu \theta^{2q} \exp\left(-\frac{\theta^2}{\psi^2} \right), \tag{79}$$

where

$$\frac{1}{\psi^2} = \frac{2}{\theta_c^2} \log_e \frac{Y_0}{Y_c} + \frac{q}{3} - \frac{\xi}{2}. \tag{80}$$

The angular width ψ is equal to 0.33 rad (19 deg) for the case in hand (with q=2 and Table IV parameters). The resulting back-scattering coefficient, shown as a dash-dotted line in Fig. 2, is clearly a better fit to Kuo up to the critical angle.

In order to use the improved approximation, Eq. (21) can be written in the form

$$X_{MP}(t) \approx \int_0^{\pi/2} \exp\left(\frac{1}{2}\theta^2 \right) \exp\left(-\eta \frac{ct}{2h} \theta^2 \right) \sqrt{S_B(\theta)}\, d\theta, \tag{81}$$

where the sec θ and $|V(\theta)|^{(ct/2h)\sin\theta}$ terms are both replaced by approximations of the form $\exp(K\theta^2)$, where K is independent of angle. Substitution of Eq. (79) in Eq. (81) gives Eq. (29), with u replaced by $u+\tau$,

$$X_{MP}(t) \approx \frac{Q^{1/2}}{2} \frac{\gamma\left[\frac{3}{2}, (u+\tau)\eta\theta_c^2 \right]}{(u+\tau)^{3/2}}, \tag{82}$$

where Q is given by Eq. (65) and

$$\tau = \frac{\psi^{-2} - 1}{2\eta}. \tag{83}$$

Equation (82) is plotted in Fig. 3 as MP2. For large $t(u \gg \tau)$, this result is identical to that of the first pass, so the long range observables (q, Q) are unchanged.

Disregarding the time variable and with Q assumed known, Eq. (82) is a function of $\eta\theta_c^2$ and τ only, implying that these are the two short range observables. The parameter $\eta\theta_c^2$ can be written as $(P/Q)^{1/3}$ and hence provides an improved value of P compared with the first pass. (Recall that P is the CS observable determined by the critical angle [Eq. (66)] and Q is the MS observable related to the reflection loss [Eq. (65)].) The parameter τ [see Eq. (83)] is a time offset caused by the departure of $S_B(\theta)$ from a perfect power law according to Eq. (79). It contains information about θ_c, ρ, α, and (to a lesser extent) the roughness exponent ξ through ψ and η. In particular, ψ can be written (assuming small θ_c)

$$\psi^{-2} = \frac{4}{\theta_c^2} \log_e \rho + O(\theta_c^0) \tag{84}$$

and hence [substituting this result into Eq. (83), with Eq. (68) for η]

$$\tau \approx \frac{\theta_c}{\rho(\alpha/k)} \log_e \rho + O(\theta_c^3). \tag{85}$$

Thus, the three observables (in addition to the exponent q, which is assumed at this point to be equal to 2 and known exactly) can be expressed in terms of combinations of the more common geoacoustic parameters θ_c, μ, ρ, and α as follows:

$$Q_{\text{sand}} = \frac{\mu}{\eta^3} \approx \frac{\mu\theta_c^6}{8\rho^3(\alpha/k)^3}, \tag{86}$$

$$\tau = \frac{\theta_c}{\alpha/k} \frac{\ln \rho}{\rho}. \tag{87}$$

and

$$P = \mu\theta_c^6. \tag{88}$$

If any one of the four geoacoustic parameters is known through prior knowledge (or if some correlation between them is known to exist[20]), the remaining three can then be inferred.

A practical experiment to infer these parameters from reverberation measurements would involve the use of a reverberation model in combination with a global or local search algorithm to minimize the mismatch between measurement and prediction. The useful time window is limited by the presence of SS paths at early times and by background noise at late times.

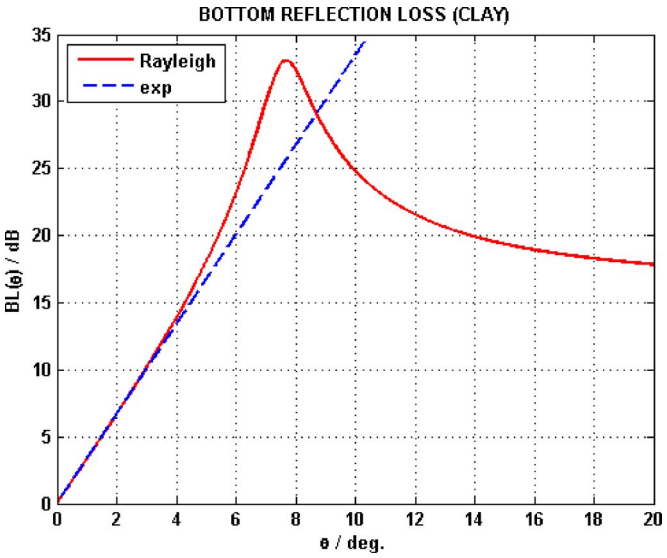

FIG. 5. (Color online) Reflection loss versus grazing angle for clay sediment (M_z=8.5).

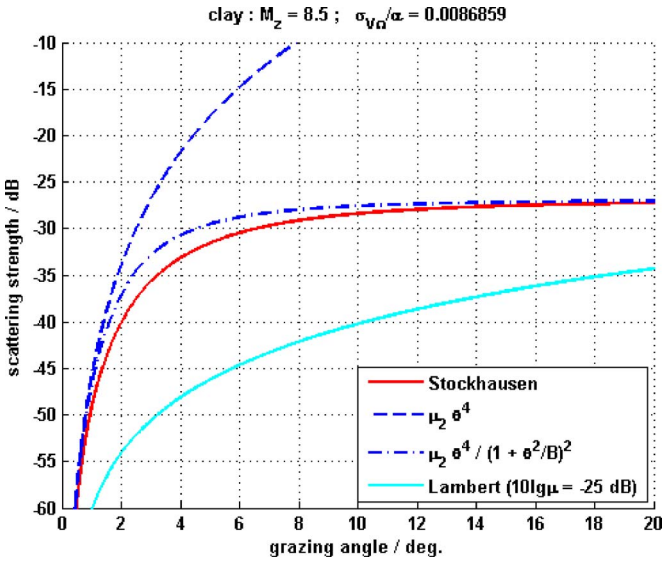

FIG. 6. (Color online) Scattering strength versus grazing angle for clay sediment (M_z=8.5).

B. Clay

1. Reflection and scattering coefficients

A fine-grained sediment like clay is characterized by a low sound speed, approximately equal to, and often slightly less than, that in seawater. In this situation there is no critical angle (and hence no CS region) and consequently sound is easily transmitted across the interface and into the sediment. The parameter η is then given by [22]

$$\eta = \frac{2\rho v}{(1-v^2)^{1/2}} \tag{89}$$

and equal to 22.0 for the clay parameters of Table IV. Even though there is no critical angle for this case, Eq. (6) can still be used with a nominal value of $\theta_c = \pi/2$. The result is plotted in Fig. 5, which also shows the Rayleigh reflection coefficient for comparison. The grain diameter for the clay sediment is 2.8 μm (i.e., M_z=8.5).

It is apparent that the reflection loss for clay is huge by comparison with that for sand (cf. Fig. 1). Steep angles are stripped away immediately, leaving a narrow horizontal beam whose subsequent behavior relies crucially on the isovelocity water assumption. There is also a requirement for the frequency to be high enough to populate the narrow beam with enough modes to justify the continuum treatment.

The scattering is deemed to originate from irregularities within the bulk of the clay sediment. According to the theory of Stockhausen[23] (as described by Jackson and Briggs[24]), the back-scattering coefficient is given by

$$S_B(\theta) = \frac{|1 - V(\theta)^2|^2}{4} \frac{\sin^2\theta}{|\sin^2\theta_{sed}|}\varepsilon, \tag{90}$$

where ε is a dimensionless ratio, defined as the volumic differential scattering cross section of these irregularities (denoted σ) divided by the attenuation coefficient α:

$$\varepsilon \equiv \frac{\sigma}{\alpha}. \tag{91}$$

In Eq. (90), θ_{sed} is the (complex) grazing angle in the sediment given by Snell's law. Notice that ε (hereafter referred to as the scattering attenuation ratio) is closely related to the parameter σ_2 of Ref. 24 according to

$$\varepsilon = (20 \log_{10} e)\sigma_2. \tag{92}$$

Using $V(\theta)$ from Eq. (54) it follows that

$$S_B(\theta) = \frac{4(\rho v)^2}{\left|1 + \rho v \dfrac{\sin\theta}{\sin\theta_{sed}}\right|^4} \frac{\sin^4\theta}{\sin^4\theta_{sed}}\varepsilon. \tag{93}$$

This function is plotted in Fig. 6 (solid black curve, labeled "Stockhausen"). The gray curve is the reference curve from Fig. 2.

C. Observable parameters (first pass)

In the limit of small θ, Eq. (93) reduces to a power law [i.e., Eq. (3)] with q=2 and

$$\mu_2 = 4\frac{(\rho v)^2}{(1-v^2)^2}\varepsilon, \tag{94}$$

equal to 274 for the clay parameters of Table IV.

The MS reverberation coefficient is calculated in the same way as for sand and plotted in Fig. 7 alongside the full integral ($X_{Stockhausen}$). For clay there is no CS region.

The values of q and Q can be estimated in the same way as for sand [see Eqs. (73) and (74)]. The parameter Q is then related to the geoacoustic parameters for clay according to

$$Q_{clay} = \frac{\mu_2}{\eta^3} \approx \frac{\varepsilon}{2\rho v(1-v^2)^{1/2}}. \tag{95}$$

The outcome for q and Q is shown in Table VI. The estimated value of q is close to its true value, while Q is underestimated by about 25%.

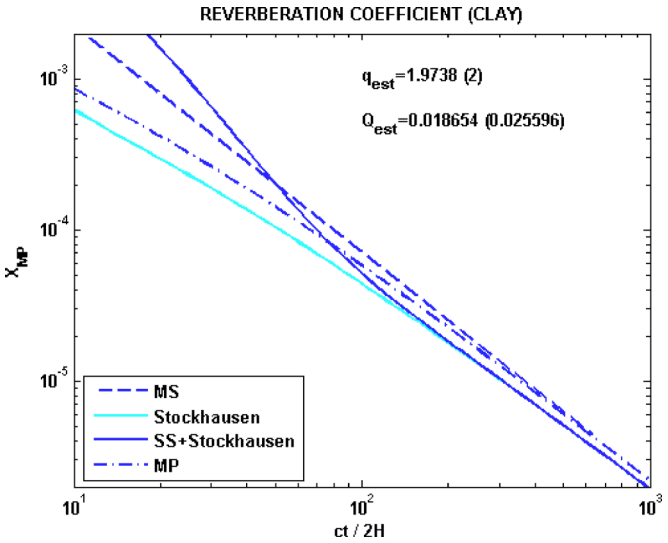

FIG. 7. (Color online) Reverberation coefficient versus dimensionless time u ($=ct/2h$) for clay sediment ($M_z=8.5$). MS=Table II, Stockhausen=Eq. (21), SS+Stockhausen=Eq. (11) + Eq. (93), and MP=Eq. (100).

1. Observable parameters (second pass)

As was the case for sand, the power law S_B is only valid for small grazing angles. The difference in back-scattering strength between the Stockhausen model and the simple power law reaches 15 dB at 6 deg and 5 dB at only 1 deg. Thus, even though the beam is a narrow one, it is nevertheless wide enough for these errors to manifest themselves in the reverberation. It is apparent from Fig. 6 that the scattering strength approaches a constant value at moderate angles. This shape suggests an improved result by use of parallel addition with $q=2$ and $n=2$, i.e.,

$$\frac{1}{\sqrt{S_B(\theta)}} = \frac{1}{\sqrt{\mu_2}\theta^2} + \frac{1}{\sqrt{\mu_0}}, \tag{96}$$

with $\mu_2=274$ as before, and [equating θ and θ_{sed} in Eq. (93)]

$$\mu_0 = \frac{(2\rho v)^2 \varepsilon}{(1+\rho v)^4}, \tag{97}$$

which for the clay parameters is equal to 0.0021.

The reverberation coefficient for parallel addition is given by Eq. (50), with

$$B = \sqrt{\mu_0/\mu_2} \tag{98}$$

and

$$A_2 = \sqrt{\mu_0}. \tag{99}$$

As there is no critical angle it makes sense to extend the integration of Eq. (46) to ∞. Hence

TABLE VI. Inferred parameters for clay sediment (first pass), using Eqs. (73) and (74).

Parameter	True value	Estimated value
q	2	1.97
Q	0.0256	0.0187

$$X_{MP}(t) \to X_{MS}(t) = \sqrt{\frac{\pi Q_0}{4u}} \lim_{\alpha\to\infty} D_2\left(\sqrt{\frac{Q_0}{Q_2}}u, \alpha\right), \tag{100}$$

where the function $D_q(x,\alpha)$ is defined by Eq. (49) and Q_2 and Q_0 are the observables that would be expected for simple power laws with $q=2$ and $q=0$, respectively. Specifically, Q_2 is Q_{clay} from Eq. (95) and

$$Q_0 = \frac{\mu_0}{\eta} \approx \frac{2\rho v}{(1+\rho v)^4}(1-v^2)^{1/2}\varepsilon. \tag{101}$$

Notice that Eq. (100) is a function of Q_0 and Q_2 only. For large u it becomes

$$X_{MS}(t) \to \frac{1}{4}\sqrt{\frac{\pi Q_2}{u^3}}. \tag{102}$$

As would be expected from Table II, the long range observable is Q_2, consistent with the first pass. The short range observable is Q_0. Both can be inferred in principle from the measured reverberation using an optimization algorithm as described for sand. The lossy seabed means that long range reverberation is expected to be weak compared with the sand case, although for the same reason the background noise is also expected to be weaker.

VI. FREQUENCY DEPENDENCE

Thus far, reverberation is considered for a single frequency only. In principle, the frequency dependence of reverberation contains additional information that is not available in measurements at a single frequency. In this section, four different causes of frequency dependence of reverberation are considered, with a brief discussion for each on the impact on the observable parameters.

A. Geoacoustic parameters

For seabed effects it is useful to consider the sand and clay cases separately. Starting with sand, if the physical model involving a uniform fluid sediment provides a good description of the seabed, it follows that the sediment density ρ and scattering exponent q are both constants (independent of frequency f). The critical angle θ_c is also independent of frequency if dispersion is neglected. On the other hand, both $\mu(f)$ and $\alpha(f)$ are expected to vary with f, and any such dependence would be apparent through variations in the observables $P(f)$ and $Q(f)$. This geoacoustic model is considered appropriate for frequencies between a few hundred hertz and a few tens of kilohertz, although above 1 kHz it may become necessary to consider attenuation due to sea surface scattering and absorption.

For the clay case, with the chosen uniform fluid model there is only one frequency dependent parameter, namely the scattering attenuation ratio $\varepsilon(f)$. Both $Q_2(f)$ and $Q_0(f)$ are proportional to $\varepsilon(f)$, so a measurement of either one would suffice. The other, if also measured, would provide a consistency check.

A convincing case can be made that the clay model is *not* a realistic one. Because most of the sound is not reflected, but transmitted, the likely presence of a positive

sound speed gradient in the sediment[25] results in a correction that is especially important for low frequency reverberation (a few hundred hertz). The loss (η) would be inversely proportional to the sound speed gradient in the sediment and, assuming a constant attenuation in decibels per wavelength, proportional to frequency. Despite these complications, the MS observable is still μ/η^{q+1}.

The increasing attenuation at high frequency suggests an alternative application for the clay model above about 10 kHz. For example, Jackson and Briggs[24] successfully apply the Stockhausen model to backscattering from a clay sediment (Arafura Sea) at 20 kHz, although the effects of a density gradient should be considered.[26,27] Further, multipath propagation at high frequency is inevitably sensitive to scattering at the sea surface, and the effects of refraction may also be important.

B. Water attenuation

Irrespective of the bottom type, there will be some frequency dependence arising from frequency-dependent attenuation arising from chemical relaxations in water.[28,29] This effect can be quantified without difficulty and is not considered to affect the observability of seabed parameters.

C. Surface scattering and absorption

At frequencies around 1 kHz and higher the assumption of perfect acoustic reflection at the sea surface must be questioned, except in very calm conditions. A $\frac{3}{2}$ power law dependence on frequency is anticipated due mainly to sea surface scattering but with an important role played by near-surface bubbles.[30–32] The influence of surface scattering (neglecting bubbles) on reverberation inversion is investigated in Ref. 13. These effects are mitigated in the presence of a downward refracting sound speed profile, in which case it is necessary instead to model the refraction.

D. Surface decoupling

The reverberation model developed in Sec. IV assumes that the frequency is high enough to neglect the cancellation that occurs between similar ray paths when they are in antiphase due to one of them having suffered one more surface reflection than the other. This assumption translates to a requirement that the product of sonar depth z and vertical wave number $k \sin\theta$ must exceed approximately $\pi/4$:

$$kz \sin\theta > \pi/4. \tag{103}$$

A marked variation of the reverberation field with depth is expected close to the sea surface when this requirement is not satisfied (and to a lesser extent if the sonar is close to the seabed). The depth at which this happens depends on the maximum grazing angle of interest, which in turn depends on how far the sound has traveled in the horizontal direction. This maximum grazing angle, referred to henceforth as the "effective angle," can be very small, making the inequality difficult to satisfy at long range. This statement can be quantified by defining the effective angle θ_{eff} as the value of the critical angle θ_c that would be necessary for F_{CS} and F_{MS} from Sec. III to be equal, i.e.,

$$\theta_{\text{eff}} = \theta_{\text{eff}}(r) = \frac{1}{2}\left(\frac{\eta}{\pi h} r\right)^{-1/2}. \tag{104}$$

Because F_{MS} is a function of range, so too is θ_{eff}. Notice in particular that $\theta_{\text{eff}}(r)$ tends to zero for $\eta r \gg h$.

In the context of reverberation it makes sense to define θ_{eff} instead by equating X_{CS} and X_{MS} from Sec. IV, so that

$$\theta_{\text{eff}} = \theta_{\text{eff}}(t) = \left[\Gamma\left(\frac{q+3}{2}\right)\right]^{1/(q+1)}\left(\frac{c\eta}{2h} t\right)^{-1/2}. \tag{105}$$

If the inequality [Eq. (103)] is not satisfied, a near-surface correction is needed, resulting in an additional dependence on depth that affects the relationships described in Sec. IV. This depth dependence (the details of which depend also on frequency) contains further information about the seabed because it depends on the angular distribution of reverberation energy. The effect of the pressure release surface is to scale the propagation factor by a term of the form $2\sin^2(kz\sin\theta)$ for each of source and receiver.[9] Assuming that both source and receiver are close to the surface, the result is that q is replaced with $q+2$ wherever it appears in the analysis, so that the new MS and CS observables (ignoring factors of k^4 and z^2) are μ/η^{q+3} and $\mu\ \theta_c^{2q+6}/(q+3)^2$. Armed with this information plus the existing observables at greater depth [i.e., P and Q from Eqs. (86) and (88)], it would then become possible to separate the three unknowns η, μ, and θ_c. Although the above discussion risks oversimplifying the necessary analysis, it conveys the general principle. The feasibility of the approach for separating the MS observables is demonstrated by Harrison and Nielsen.[9]

VII. EFFECT OF REFRACTION

Of the assumptions listed in Sec. I, one of the most restrictive in the context of long range propagation is that of isovelocity water. For the clay seabed in particular there is a conflict between the requirement for straight ray paths and hence steep angles (the isovelocity assumption) on the one hand, and the inexorable stripping of energy from steep ray paths due to multiple seabed reflections on the other. While a full treatment of the effects of refraction on reverberation[33] is outside the present scope, some general remarks are made below. Other relevant publications include Refs. 7 and 9.

The effect of a slightly nonuniform sound speed profile would be to curve the ray paths, placing an upper limit on the ray cycle distance. This upper limit, or a distance close to the upper limit, typically defines a characteristic cycle distance Δ, and a characteristic angle associated with it. If the reflection loss at this angle is denoted L, the result is cylindrical spreading with—assuming downward refraction for the sake of argument—an exponential decay whose time constant is Δ/Lc. Turning this reasoning on its head, a measurement of this time constant provides an estimate of L. (The sound speed profile, and hence also the cycle distance, are assumed known.) Once L is found, measurement of the scattering strength from absolute reverberation level is straightforward. Thus, in contrast to the isovelocity case, the effects of the scattering coefficient S and reflection coefficient $|V|$ can be separated for this case, albeit only within a narrow range of

angles around the characteristic angle. If multiple measurements are made, and if the sound speed profile changes between them (if one measurement is made in the early morning, say, and the other after a warm afternoon), each new measurement of S and $|V|$ will be at a slightly different angle, thus providing new information.

VIII. CONCLUSIONS

Assuming a power law dependence of the backscattering coefficient S_B on grazing angle θ, of the form $S_B(\theta) \approx \mu\theta^{2q}$ for small θ, it is shown that the associated exponent q can be inferred from the decay rate of long range reverberation in isovelocity water (in the mode stripping region). Given q, the intercept of Eq. (72) then provides μ/η^{q+1} (see Table II), where η is the loss per unit grazing angle.

If the power law behavior extends to the seabed critical angle θ_c, and if mode stripping and cylindrical spreading measurements are both available, it is found that there is one more independent piece of information available from the reverberation, proportional to $\mu\theta_c{}^{2q+2}$ (see Table II). Specific examples considered are seabeds made, respectively, of uniform sand (dominated by rough boundary scattering) and uniform clay (volume scattering).

Theory predicts an exponent $q=2$ as $\theta \to 0$ for both sand and clay. Thus, for both sediment types the long range observable is μ/η^3, although significant departures from a perfect power law are predicted at steeper angles. Despite this, for sand it turns out that $\mu\theta_c{}^6$ is still measurable, while the departure from a perfect power law results in a time offset, denoted τ, that provides further information about the geoacoustic parameters via Eq. (83). For clay, although there is no critical angle, there is nevertheless a transition between short and long range power laws (from $q=0$ to $q=2$). This transition provides information about the impedance of the sediment as well as the ratio ε of volumic scattering cross section to the attenuation coefficient.

The effects of frequency dependence and refraction, though outside the main scope, are considered in the discussion in Sec. VI and VII. It is argued that additional information, with the potential to break some of the ambiguity, is available if multiple measurements are made at different depths or frequencies, or for different sound speed profiles.

ACKNOWLEDGMENTS

The author thanks Gerrit Blacquière and two anonymous reviewers for their considered comments on an earlier version of this article. Extensive use of the on-line integrator at http://integrals.wolfram.com made light work of the integrals, especially for Table III. This work was sponsored by the Defence Research and Development Department of the Netherlands Ministry of Defence.

[1] J. Zhou, D. Guan, E. Shang, and E. Luo, "Long-range reverberation and bottom scattering strength in shallow water," Chin. J. Acoust. **1**, 54–63 (1982).

[2] J. D. Bishop, M. T. Sundvik, and D. W. Grande, "Inverting sea bed parameters from reverberation data," in *Full Field Inversion Methods in Ocean and Seismo-Acoustics*, edited by O. Diachok, A. Carini, P. Gerstoft, and H. Schmidt (Kluwer, Dordrecht, 1995), pp. 401–406.

[3] D. D. Ellis and P. Gerstoft, "Using inversion techniques to extract bottom scattering strengths and sound speeds from shallow-water reverberation data," *3rd European Conference on Underwater Acoustics*, edited by J. S. Papadakis, Heraklion, Crete, 24–28 June 1996, pp. 557–562.

[4] M. A. Ainslie, W. Boek, D. G. Simons, and S. H. E. Lentze-Muller, "Technical Report on Inversion of the First RUMBLE Sea Trial Data," TNO Report FEL-03-A042 (2003).

[5] D. E. Weston, "Guided propagation in a slowly varying medium," Proc. Phys. Soc. London, **73**, 365–384 (1959).

[6] D. E. Weston, "Acoustic flux methods for oceanic guided waves," J. Acoust. Soc. Am. **68**, 287–296 (1980).

[7] X. Lurton and J. Marchal, "Long range propagation losses and reverberation levels in shallow water using an average intensity model," *3rd European Conference on Underwater Acoustics*, edited by J. S. Papadakis, Heraklion, Crete, 24–28 June 1996, pp. 569–574.

[8] M. A. Ainslie, "Derivation of reverberation equations," Appendix A of Ref. 4.

[9] C. H. Harrison and P. L. Nielsen, "Separability of seabed reflection and scattering properties in reverberation inversion," J. Acoust. Soc. Am. **121**, 108–119 (2007).

[10] C. H. Harrison, "Closed-form expressions for ocean reverberation and signal excess with mode stripping and Lambert's law," J. Acoust. Soc. Am. **114**, 2744–2756 (2003).

[11] C. W. Holland, "Constrained comparison of ocean waveguide reverberation theory and observations," J. Acoust. Soc. Am. **120**, 1922–1931 (2006).

[12] D. E. Weston, "Intensity-range relations in oceanographic acoustics," J. Sound Vib. **18**, 271–287 (1971).

[13] J. Zhou, X. Zhang, Z. Peng, and J. S. Martin, "Sea surface effect on shallow-water reverberation," J. Acoust. Soc. Am. **121**, 98–107 (2007).

[14] M. A. Ainslie, C. H. Harrison, and P. W. Burns, "Signal and reverberation prediction for active sonar by adding acoustic components," IEE Proc., Radar Sonar Navig. **143**(3), 190–195 (1996).

[15] *Handbook of Mathematical Functions*, edited by M. Abramowitz and I. Stegun (Dover, New York, 1965).

[16] E. W. Weisstein, Incomplete Gamma Function, Math World, http://mathworld.wolfram.com/IncompleteGammaFunction.html, last viewed 1 November 2006.

[17] *Tables of Integrals, Series and Products*, edited by I. S. Gradshteyn and I. M. Ryzhik (Academic, New York, 1980).

[18] W. C. Krombein and L. L. Sloss, *Stratigraphy and Sedimentation*, 2nd ed. (Freeman, San Francisco, 1963).

[19] E. Y. T. Kuo, "Wave scattering and transmission at irregular surfaces," J. Acoust. Soc. Am. **36**, 2135–2142 (1964).

[20] R. T. Bachman, "Acoustic and physical property relationships in marine sediment," J. Acoust. Soc. Am. **78**, 616–621 (1985).

[21] D. D. Sternlicht and C. P. de Moustier, "Time-dependent seafloor acoustic backscatter (10–100 kHz)," J. Acoust. Soc. Am. **114**, 2709–2725 (2003).

[22] M. A. Ainslie, "The sound pressure field in the ocean due to bottom interacting paths," Ph.D. thesis, University of Southampton, 1992.

[23] J. H. Stockhausen, "Scattering from the volume of an inhomogeneous half-space," Report No. 63/9, Naval Research Establishment, Canada (1963).

[24] D. R. Jackson and K. B. Briggs, "High-frequency bottom backscattering: Roughness versus sediment volume scattering," J. Acoust. Soc. Am. **92**, 962–977 (1992).

[25] E. L. Hamilton, "Geoacoustic modeling of the sea floor," J. Acoust. Soc. Am. **68**, 1313–1340 (1980).

[26] P. D. Mourad and D. R. Jackson, "High frequency sonar equation models for bottom backscatter and forward loss," in *Proc. Oceans 89*, Seattle, WA, 18–21 September 1989 (Marine Technology Society and IEEE, 1989), pp. 1168–1175.

[27]P. A. van Walree, M. A. Ainslie, and D. G. Simons, "Mean grain size mapping with single-beam echo sounders," J. Acoust. Soc. Am. **120**, 2555–2566 (2006).
[28]R. E. Francois and G. R. Garrison, "Sound absorption based on ocean measurements. Part II: Boric acid contribution and equation for total absorption," J. Acoust. Soc. Am. **72**, 1879–1890 (1982).
[29]M. A. Ainslie and J. G. McColm, "A simplified formula for viscous and chemical absorption in sea water," J. Acoust. Soc. Am. **103**, 1671–1672 (1998).
[30]D. E. Weston and P. A. Ching, "Wind effects in shallow-water transmission," J. Acoust. Soc. Am. **86**, 1530–1545 (1989).
[31]G. V. Norton and J. C. Novarini, "On the relative role of sea-surface roughness and bubble plumes in shallow-water propagation in the low-kilohertz region," J. Acoust. Soc. Am. **110**, 2946–2955 (2001).
[32]M. A. Ainslie, "Effect of wind-generated bubbles on fixed range acoustic attenuation in shallow water at 1–4 kHz," J. Acoust. Soc. Am. **118**, 3513–3523 (2005).
[33]C. H. Harrison, "Closed form bistatic reverberation and target echoes with variable bathymetry and sound speed," IEEE J. Ocean. Eng. **30**, 660–675 (2005).

Ocean acoustic interferometry

Laura A. Brooks[a] and Peter Gerstoft
Marine Physical Laboratory, Scripps Institution of Oceanography, La Jolla, California 92093

(Received 12 January 2007; revised 13 March 2007; accepted 16 March 2007)

Ocean acoustic interferometry refers to an approach whereby signals recorded from a line of sources are used to infer the Green's function between two receivers. An approximation of the time domain Green's function is obtained by summing, over all source positions (stacking), the cross-correlations between the receivers. Within this paper a stationary phase argument is used to describe the relationship between the stacked cross-correlations from a line of vertical sources, located in the same vertical plane as two receivers, and the Green's function between the receivers. Theory and simulations demonstrate the approach and are in agreement with those of a modal based approach presented by others. Results indicate that the stacked cross-correlations can be directly related to the shaded Green's function, so long as the modal continuum of any sediment layers is negligible.
© *2007 Acoustical Society of America.* [DOI: 10.1121/1.2723650]

PACS number(s): 43.30.Yj, 43.30.Gv, 43.60.Ac [AIT] Pages: 3377–3385

I. INTRODUCTION

Approximation of the Green's function between two points in both open and closed environments has been a subject of interest over the last few years. Lobkis and Weaver[1] showed, both theoretically and experimentally, that the Green's function between two points can be determined from their temporal cross-correlation within a diffuse ultrasonic field. This concept was extended by Derode *et al.*[2] who showed that the Green's function can be conditionally recovered in an open scattering medium. They concluded that although the Green's function can be determined from cross-correlations from a single source within a lossless closed cavity in which it is assumed that the eigenmodes do not degenerate, the Green's function will only emerge from cross-correlations within an open scattering medium if the cross-correlations are summed over a perfect time-reversal mirror. Wapenaar[3] and Van Manen *et al.*[4] demonstrated that retrieval of the Green's function through summed cross-correlations can also be achieved in an inhomogeneous medium. Sánchez-Sesma *et al.* presented the canonical problem of elastodynamic Green's function retrieval in a homogeneous medium[5] and in an infinite space with a cylinder inclusion.[6] They showed that the Fourier transform of the mean cross-correlation of motion between two points is proportional to the imaginary part of the corresponding exact Green's tensor, provided that there is equipartitioning of energy.

Extraction of the Green's function by cross-correlation from ultrasonic noise,[7–9] ambient noise in a homogeneous medium,[10] ambient ocean acoustic noise,[11–14] seismic noise,[15–20] helioseismic noise,[21] and even moon-seismic noise[22] has been undertaken, and the governing concepts are now quite well understood.

Three papers are of particular relevance to this work. Using a modal approach, Roux and Fink[23] showed theoretically in the frequency domain and through simulation that the Green's function between two points in a waveguide can be determined by summing the cross-correlations from a vertical line of sources that are located in the same plane as the two receivers, external to the two receivers. Sabra *et al.*[12] used a stationary phase argument to formulate the time domain Green's function for time-averaged surface generated ambient noise cross-correlation, where the sources were modeled as a horizontal plane of point sources at a constant depth. Also using the method of stationary phase, Snieder *et al.*[24] presented a formulation that suggests that seismic interferometry using sources equally spaced along the surface of a homogeneous medium, with a horizontal reflector and no free surface, in the same vertical plane as two receivers located within said medium, can be used to determine the Green's function between the two receivers. They showed that when multiple bottom reflectors are included, spurious multiples may occur due to the region of interest not being completely enclosed by sources, and concluded that, theoretically, these spurious multiples could be removed by including an additional set of sources below the reflectors.

Within this paper, the relationship between cross-correlations from a vertical line of active sources to two receivers within a waveguide, and the shaded time domain Green's function between said receivers, is explored. We call this approach ocean acoustic interferometry (OAI), as it is related to classical and seismic interferometry,[25] where interferometry refers to the determination of information from the interference phenomena between pairs of signals. The method of stationary phase is applied to simple reflective environments, providing an alternative theoretical means of describing and understanding the physics governing the cross-correlation of such a source configuration, and how this can be used to extract an amplitude shaded time domain Green's function. This work is distinct from work presented by Roux and Fink,[23] Sabra *et al.*,[12] and Snieder *et al.*,[24] in that a stationary phase derivation is applied to a column of sources in a waveguide. A detailed physical and mathematical discussion of spurious arrivals obtained in connection with OAI is presented. Numerical simulations of these envi-

[a]Also at the School of Mechanical Engineering, University of Adelaide, Australia; electronic mail: lbrooks@mecheng.adelaide.edu.au

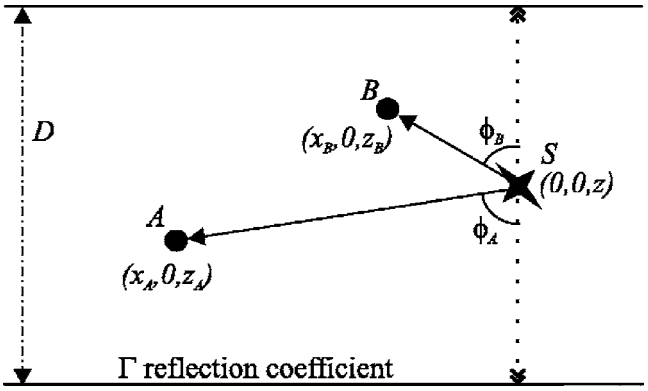

FIG. 1. Source-receiver geometry and notation: the source S is located at $(0,0,z)$, and receivers A and B are located at $(x_A,0,z_A)$ and $(x_B,0,z_B)$, respectively, within a waveguide of depth D.

ronments support the theory. A refractive environment with more realistic water column, sediment, and bottom parameters is also analyzed through numerical simulations. These geometrically simple scenarios are chosen as they allow for understanding of the results, but the underlying concepts are applicable to complex environments. Both the unstacked cross-correlations as a function of depth and the stacked cross-correlations are analyzed. The effect of limiting the sources to the water column is discussed and it is shown that the accuracy of OAI increases if the source column is extended through the sediment. The spurious arrivals obtained here are compared with those obtained by Sabra *et al.*[12] and Snieder *et al.*[24] The manifestations of these aberrations are distinct in each case and these differences are explained by considering the different environments and geometrical setup used.

II. THEORY

Consider the waveguide depicted in Fig. 1. The x, y, and z directions are defined as the horizontal axis, the axis in-and-out of the page, and the vertical axis, respectively. A vertical plane of sources spanning the water column (i.e., the z direction) and extended in the y direction would form a perfect time-reversal mirror, meeting the requirements for determination of the Green's function between two points via cross-correlation methods.[2] However, it has previously been shown that only sources in the same vertical plane as the two receivers will contribute significantly to the correlation integral.[12,24] A vertical line of sources is therefore uniformly and densely distributed within the vertical plane containing receivers A and B, external to the two receivers, and closer to B. The sum of the cross-correlations of the signals received at A and B (adapted from Ref. 24) in the frequency domain is

$$C_{AB}(\omega) = |\rho_s S(\omega)|^2 n \int_0^D G(\mathbf{r}_A,\mathbf{r}_S) G^*(\mathbf{r}_B,\mathbf{r}_S)\, dz, \tag{1}$$

where ρ_s is the density at the source, $S(\omega)$ is the source spectrum, n is the number of sources per unit length, $G(\mathbf{r}_\psi,\mathbf{r}_S)$ is the Green's function between the source S and receiver ψ, and * denotes complex conjugation. The lower bound of the integral is 0 since the waveguide has a free surface at $z=0$ and the upper bound is the waveguide depth D since there are no reflective surfaces below this depth. This summed cross-correlation can, in the time domain, be determined from real or simulated data by calculating the cross-correlation for each source depth and then summing (also known as "stacking") the result. The sum of the cross-correlations is related to the Green's function between A and B. This relationship is derived here for reflective environments using the method of stationary phase.

The 3D Green's function within a homogeneous medium is

$$G_f(R) = \frac{e^{ikR}}{4\pi R}, \tag{2}$$

where k is the wave number and R is the distance from the source. The full Green's function at each receiver can be written as the superposition of the direct and reflected waves. If the medium is an isovelocity waveguide, bounded above by a free surface and below by a reflective bottom with reflection coefficient Γ, the Green's function between the source S and receiver ψ is written in terms of the waveguide and source-receiver geometry[26] as

$$G(\mathbf{r}_\psi,\mathbf{r}_S) = \sum_{b_\psi=0}^{\infty} \Gamma^{b_\psi} G_f\left(\sqrt{x_\psi^2 + (2b_\psi D + z \pm z_\psi)^2}\right) + \sum_{b_\psi=1}^{\infty} \Gamma^{b_\psi} G_f\left(\sqrt{x_\psi^2 + (2b_\psi D - z \pm z_\psi)^2}\right), \tag{3}$$

where b_ψ is the number of bottom bounces for a given path and D is the depth of the waveguide. The first term on the rhs includes all upgoing waves and the second term includes all downgoing waves as measured from the source.

Inserting Eq. (3) into Eq. (1) yields an expression for the correlation that consists of the sum of the integrals of all possible combinations of the interaction between any path to the first receiver and any path to the second. Although the cross-correlation includes the sum of all path interactions, each path interaction can be analyzed separately and summed together at the end to yield the complete solution. Hence, only one of these individual interactions is considered here. Substitution of Eq. (2) into Eq. (1) (i.e., cross-correlation between two arbitrary paths) yields

$$I = \frac{\Gamma^{b_A+b_B}}{(4\pi)^2} \int \frac{e^{ik(L_A-L_B)}}{L_A L_B}\, dz, \tag{4}$$

where b_ψ is the number of bottom bounces for the path to receiver ψ, and $L_\psi = \sqrt{x_\psi^2 + (2b_\psi D \pm z \pm z_\psi)^2}$ is the length of the given path between the source S and receiver ψ. The sign in front of z is positive when the wave departing the source is upgoing and negative when it is downgoing. Similarly, the sign in front of z_ψ is positive when the wave arriving at the receiver is downcoming and negative when it is upcoming.

A. Stationary phase evaluation

Since $1/(L_A L_B)$ varies slowly and the phase $k(L_A - L_B)$ varies quickly within the region of interest, rapid oscillations of $e^{ik(L_A-L_B)}$ over the integrand allow for the integral, Eq. (4), to be solved via the method of stationary phase.[27] Similar

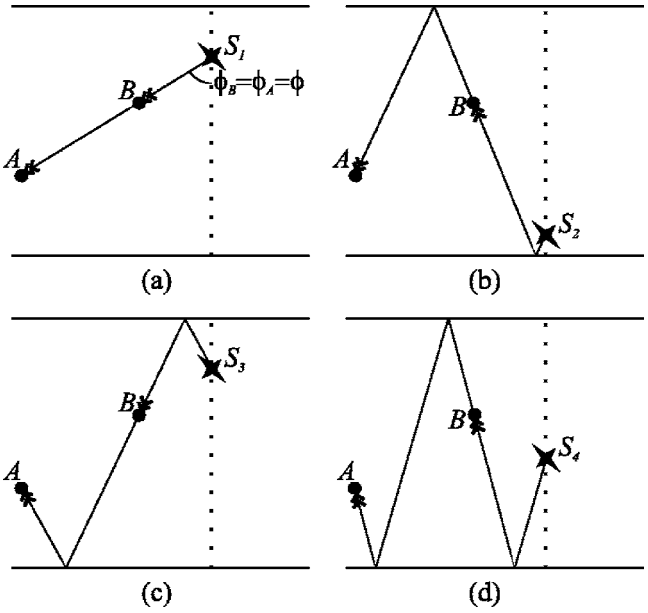

FIG. 2. Examples of wave paths that correspond to stationary points ($\phi_A = \phi_B = \phi$): (a) direct wave, (b) surface reflected wave, (c) bottom reflected wave, and (d) surface and bottom reflected wave, between the receivers.

interferometric integrals have been solved by others.[12,16,24] We follow the idea of Snieder *et al.*, but assume a vertical rather than horizontal line of sources, and also extend the theory to a waveguide.

The stationary points of the integrand are found by evaluating the partial z derivative of the phase term and setting this to equal zero. The phase term is

$$L = L_A - L_B = \sqrt{x_A^2 + (2b_A D + \alpha_A z \pm z_A)^2} - \sqrt{x_B^2 + (2b_B D + \alpha_B z \pm z_B)^2}, \tag{5}$$

where $\alpha_\psi = 1$ denotes an upgoing wave and $\alpha_\psi = -1$ denotes a downgoing wave, as measured from the source. The partial differential with respect to z is

$$\frac{\partial L}{\partial z} = \alpha_A \left(\frac{2b_A D + \alpha_A z \pm z_A}{L_A} \right) - \alpha_B \left(\frac{2b_B D + \alpha_B z \pm z_B}{L_B} \right). \tag{6}$$

Writing Eq. (6) in terms of the acute angle ϕ_ψ between the path and the vertical, at the point of departure from the source (see Fig. 1), yields

$$\frac{\partial L}{\partial z} = \alpha_A \cos \phi_A - \alpha_B \cos \phi_B. \tag{7}$$

Setting the partial z derivative to zero yields $\phi_A = \phi_B$ when $\alpha_A = \alpha_B$ (i.e., both waves depart as either upgoing or downgoing), and $\phi_A = \pi - \phi_B$ when $\alpha_A = -\alpha_B$ (i.e., one wave departs as upgoing and the other as downgoing). Since both ϕ_A and ϕ_B are less than $\pi/2$, the latter equation has no solutions. Thus a stationary point will only occur when both signals depart the source at the same angle. Therefore, the path to the farther receiver passes through the closer receiver, as shown in Fig. 2 for four different paths (remember that the above derivation holds for any individual path interaction and that the overall cross-correlation includes the sum of all path interactions). Not all path combinations will exhibit a stationary point; for example, the direct path to A and any boundary interacting path to B will never satisfy $\phi_A = \phi_B$.

The integral, Eq. (4), is rewritten within the region of a given stationary point z_s as

$$I(z_s) \approx \frac{\Gamma^{b_A + b_B}}{(4\pi)^2} \frac{1}{L_A(z_s) L_B(z_s)} \int_{-\infty}^{\infty} e^{ik(L_A(z) - L_B(z))}\, dz. \tag{8}$$

Realistically, the sources exist over the finite limit $(0, D)$; however, extension of these limits to infinity is valid as virtual sources exist over an infinite limit. The phase term can be approximated as a truncated Taylor series within the neighborhood of any stationary point:

$$L(z) \approx L(z_s) + \frac{(z - z_s)^2}{2} \left(\left. \frac{\partial^2 L}{\partial z^2} \right|_{z = z_s} \right), \tag{9}$$

$$\left. \frac{\partial^2 L}{\partial z^2} \right|_{z = z_s} = \sin^2 \phi_s \left(\frac{1}{L_A(z_s)} - \frac{1}{L_B(z_s)} \right). \tag{10}$$

Substituting the phase term and its second derivative, at the stationary point, into the truncated Taylor series, Eq. (9), and rewriting the integral, Eq. (8), assuming that $L_A(z_s) > L_B(z_s)$ (which is valid since the source is closer to B than to A), yields

$$I(z_s) = \frac{\Gamma^{b_A + b_B}}{(4\pi)^2} \frac{e^{ik(L_A(z_s) - L_B(z_s))}}{L_A(z_s) L_B(z_s)} \times \int_{-\infty}^{\infty} \exp\left(-ik \frac{(z - z_s)^2}{2} \xi \sin^2 \phi_s \right) d(z - z_s), \tag{11}$$

where $\xi = (1/L_B(z_s) - 1/L_A(z_s))$. Equation (11) is a Fresnel integral and can therefore be solved by making the substitution $k[(z - z_s)^2/2] \xi \sin^2 \phi_s = (\pi/2)\tau^2$:

$$I(z_s) = \frac{\Gamma^{b_A + b_B}}{(4\pi)^2} \frac{e^{ik(L_A(z_s) - L_B(z_s))}}{L_A(z_s) L_B(z_s)} \times 2 \sqrt{\frac{\pi}{k\xi \sin^2 \phi_s}} \int_0^{\infty} \exp\left(-i \frac{\pi}{2} \tau^2 \right) d\tau = e^{i(3\pi/4)} \frac{\Gamma^{b_A + b_B}}{\sin \phi_s} \sqrt{\frac{\xi}{8k\pi}}\, G_f(R(z_s)), \tag{12}$$

where $R(z_s) = L_A(z_s) - L_B(z_s)$ is the path length between A and B. Inclusion of the source factor, $n|\rho_s S(\omega)|^2$, and the relationship $k = \omega/c$, yields

$$C_{AB}(\omega) = \sum_{z_s} n|\rho_s S(\omega)|^2 I(z_s) = e^{i(3\pi/4)} n|S(\omega)|^2 \times \sum_{z_s} \left(\frac{\Gamma^{b_A + b_B} \rho_s^2 G_f(R(z_s))}{\sin \phi_s} \sqrt{\frac{\xi c}{8\pi\omega}} \right), \tag{13}$$

where the summation is over all stationary points.

Cross-correlation of the signals received from a vertical column of sources located in the same vertical plane as the receivers can therefore be seen to produce an amplitude and phase shaded Green's function. The amplitude shading consists of constant, path dependent, and frequency dependent components, while the phase shading is simply a $3\pi/4$ phase

shift. If the summed cross-correlations are multiplied by $e^{-i(3\pi/4)}$, phase information, and hence travel times, of the $|S(\omega)|^2/\sqrt{\omega}$ shaded Green's function can be determined. It will, however, be difficult to obtain the correct amplitudes since $\Gamma^{b_A+b_B}$, ϕ_s, and $\xi=\sqrt{1/L_B(z_s)-1/L_A(z_s)}$ are all path dependent.

The cross-correlation equation, Eq. (13), is in this particular form due to the mismatch between a 3D Green's function and a 1D source distribution (as commented by Snieder *et al.*[24]). If a 2D plane instead of the 1D column of sources were used, Eq. (1) would be a double integral spanning both the z and y directions, which could be solved as a product of two stationary phase integrals. If either a 2D plane of sources or the far-field approximation of the 2D Green's function, $G(R)=e^{ikr}/\sqrt{r}$, were incorporated, there would not be a dimensionality mismatch, and the sum of the cross-correlations, Eq. (13), would be

$$\tilde{C}_{AB}(\omega)=-in|S(\omega)|^2\sum_{z_s}\left(\frac{\Gamma^{b_A+b_B}\rho_s^2 G_f(R(z_s))}{\sin\phi_s}\times\frac{c}{2\omega}\right), \tag{14}$$

where n is the number of sources per unit surface area for the plane of sources or the number of sources per unit length for the column of sources. Note that there is now no term (apart from the Green's function) containing $L_A(z_s)$ and $L_B(z_s)$ and therefore the amplitude shading is only dependent on the travel path through the $\Gamma^{b_A+b_B}$ and $\sin\phi_s$ terms.

The $1/\omega$ factor in Eq. (14) means that the time domain Green's function is proportional to the derivative of the summed cross-correlations.[10,12,16] Due to a mismatch between the source dimensions and the Green's function, there is only a factor of $1/\sqrt{\omega}$ in Eq. (13). The time domain Green's function is therefore proportional to a fractional derivative of the summed cross-correlation.[24]

B. Incorporation of sediment layers

When the water column is bounded by fully reflective boundaries, as assumed for the preceding derivation, all of the energy is contained within the water column and truncation of the cross-correlation integral in Eq. (1) is avoided. The addition of sediment layers can cause truncation errors since the true integral will then extend to infinity (or at least to the basement) to account for sound that interacts with the sediment:

$$C_{AB}(\omega)=|\rho_s S(\omega)|^2 n\int_0^\infty G(\mathbf{r}_A,\mathbf{r}_S)G^*(\mathbf{r}_B,\mathbf{r}_S)\,dz. \tag{15}$$

If the source column is restricted to the water, the calculated integral still ceases at D and the stacked cross-correlations may vary from the frequency and phase shaded Green's function. As an example, consider a (purely theoretical) reflective environment, with constant sound speed, consisting of a water column and M sediment layers. The length of any path between the source S and receiver ψ becomes

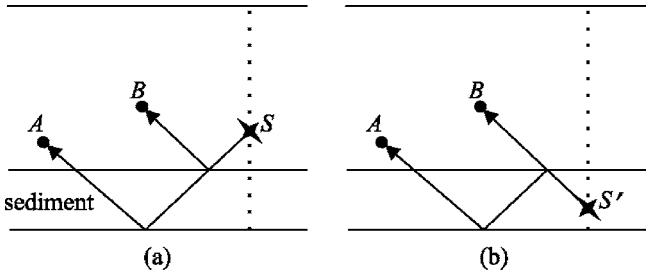

FIG. 3. Example of (a) water source and (b) sediment source stationary points that cancel with one another and do not contribute to the Green's function.

$$L_\psi=\sqrt{x_\psi^2+\left(2pD+\sum_{m=1}^{M}(2q_m D_{sm})\pm z\pm z_\psi\right)^2}, \tag{16}$$

where p and q_m are the multiple order in the water and each sediment layer m, and D_{sm} is the depth of the mth sediment layer. The stationary phase condition is still $\phi_A=\phi_B$; however, there exist paths satisfying this condition whose path length differences are not identical to any component lengths of the Green's function between the two receivers. For example, in Fig. 3(a) the path to receiver B is a reflection from the sediment-water interface. The path to receiver A is a transmission through this interface, a reflection from the basement, and a transmission back into the water. The stationary phase condition of $\phi_A=\phi_B$ is satisfied; however, the path length difference is

$$L=\sqrt{x_A^2+(2D+2D_s-z-z_A)^2}-\sqrt{x_B^2+(2D-z-z_B)^2}, \tag{17}$$

which, in general, differs from the path length of any wave that travels between the two receivers, and therefore should not contribute to the Green's function. Note that the path length difference and hence the time at which these spurious arrivals occur is dependent on the horizontal distance separating the source column from the receivers. If the column of sources were extended into the sediment, a second stationary point of equal amplitude and opposite phase would exist [see Fig. 3(b)], canceling the contribution of the water-source stationary point.

Note that Eq. (13) contains a ρ_s^2 term, but pressure is proportional to $\rho_s G_f$, and hence the individual cross-correlations need to be normalized by the density at the source location before summing. More complex paths may exhibit multiple stationary points, located in both the water column and the sediment, corresponding to a particular path length difference; however, they will sum to zero so long as the source column spans all paths that have a stationary point.

Introduction of a varying sound speed profile will further complicate the problem; however, OAI is still applicable. Snieder *et al.* (Appendix A)[24] present work that generalizes their arguments for the direct wave in a homogeneous medium to a direct wave in a heterogeneous medium with variations in velocity that are sufficiently smooth for ray theory to remain applicable. The environment and geometry used here are different from that of Snieder *et*

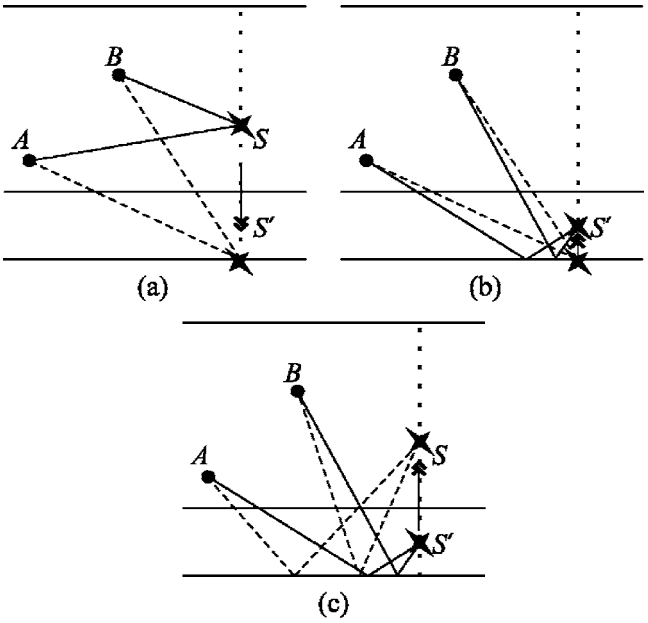

FIG. 4. The direct path (a) and bottom bounce path [dashed line in (c)] are linked via a continuous transition through sediment source configurations (a)–(c); a truncation of the integral results in a discontinuity in the arrival structure of the paths if sediment sources are not considered.

al.; however, the idea of generalizing from a homogeneous to a heterogeneous medium is the same. The inclusion of attenuation will also add complications since it will generally result in the paths not canceling exactly; the degree to which they will cancel one another is environment dependent.

Truncations in the integral of Eq. (15) may also be apparent as peaks in the summed cross-correlation at time intervals corresponding to correlations between paths from sources located at the water-sediment interface. Consider, as an example, the paths depicted in Figs. 4(a)–4(c). As the source is moved towards the water-sediment interface, the direct paths [solid line in Fig. 4(a)] converge to the direct paths from a source in the sediment [dashed line in Fig. 4(a)]. At the bottom of the sediment these paths converge with the bottom bounce paths [solid line in Fig. 4(b)], which in turn converge to the dashed path shown in Fig. 4(c) at the water-sediment interface. If the sources in the sediment are not included in the summation, discontinuities in the integral will exist at the water-sediment interface for the water source paths in both Figs. 4(a) and 4(c). The path length difference for this discontinuity is

$$\Delta L = \sqrt{(D - z_A)^2 + x_A^2} - \sqrt{(D - z_B)^2 + x_B^2} - \left(\sqrt{(D - z_A + 2D_s)^2 + x_A^2} - \sqrt{(D - z_B + 2D_s)^2 + x_B^2}\right), \tag{18}$$

where D_s is the depth of the sediment. If the sediment is shallow ($D_s \ll D$), these discontinuities may not be observable in the summed cross-correlations since the path length differences for a source at the sediment-water interface will be small; however, if the sediment is deep, the discontinuity may be observed as two distinct spurious peaks separated temporally by $\Delta L/c$.

Restricting the sources to the water column can therefore lead to spurious peaks in the cross-correlation function. If the sources are extended through the sediment and the cross-correlation function is normalized by the density at the source, these spurious peaks may be avoided.

In a generalized environment, the mathematics becomes more complex; however, the fundamental ideas hold. An amplitude and $3\pi/4$ phase shaded Green's function will still be obtained by summing the density normalized source cross-correlations, so long as the source column spans the water column and all underlying sediments. The effect of limiting the sources to the water column, upon the similarity between the summed cross-correlations and the shaded Green's function, is environment dependent.

C. Spurious arrivals

Snieder *et al.*[24] and Sabra *et al.*[12] determined that spurious arrivals also exist for their particular geometries and environments. The spurious arrivals that they discuss and the ones described here are all due to the volume of interest not being fully enclosed by sources; however, each of these aberrations is distinct.

The spurious arrivals described in Sec. II B occur when the sources are limited to the water column. The integral does not extend to infinity, resulting in two causes of spurious arrivals. As the source approaches the upper and lower boundaries (surface and basement), different paths will converge. Hence, when the sources are contained to the water column, paths that would converge at the sediment bottom do not converge. Spurious peaks therefore occur at these path discontinuities. The second mechanism of spurious arrivals is a stationary-phase contribution from a source in the water column that does not actually contribute to the full Green's function. This contribution occurs from correlations between waves that are reflected at the water-sediment interface and waves that pass into the sediment. It should cancel with a stationary-phase contribution of equal amplitude and opposite phase from the sediment and therefore a false peak is recorded when sediment sources are not included.

Sabra *et al.*[12] modeled time-averaged surface generated ambient noise using a horizontal plane of point sources at a constant depth in a waveguide. The spurious arrivals they described are caused by stationary-phase contributions from correlations between a wave that initially undergoes a surface reflection and one that does not (for an isovelocity water column, one wave departs at an angle of ϕ from the horizontal, and the other departs at an angle of $-\phi$). These stationary points are intrinsic to the horizontal source configuration. If the depth of the plane of sources is reduced, the spurious peaks converge to the same time delay as the true Green's function paths; however, they are π out of phase and will still result in shading of the Green's function.

Snieder *et al.*[24] used a horizontal line of evenly spaced sources in a homogeneous medium, with one or more horizontal reflectors below and no free surface above. Snieder's assumption of there being no free surface means that the spurious paths described by Sabra *et al.* did not exist in their analysis. The spurious arrivals described by Snieder *et al.* are

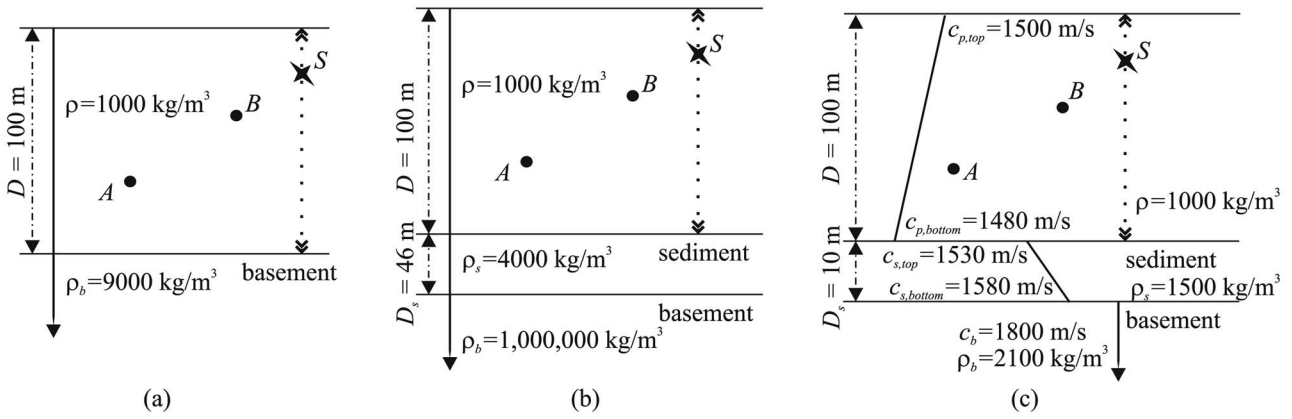

FIG. 5. Simulated waveguide environments: (a) isovelocity waveguide with a purely reflective bottom (constant $c=1500$ m/s), (b) isovelocity purely reflective waveguide with a sediment layer (constant $c=1500$ m/s), and (c) more realistic refractive environment with a sediment layer.

due to false stationary-phase contributions caused by correlation of waves reflected from distinct reflectors, which occur due to the sources only being in the upper layer. To eliminate these spurious multiples, a second surface of sources would have to be included below the bottom reflector.

III. SIMULATIONS

Three simulation environments were selected to clearly demonstrate application of OAI from a physical perspective. The Green's function between two receivers is approximated using the OAI approach for a vertical line of sources. Oases[28] was used for both the OAI approach and to compute the true Green's function between the receivers. The theory derived via the method of stationary phase in Sec. II is used only for discussion purposes.

The environments, depicted in Fig. 5, comprise (a) an isovelocity waveguide with a purely reflective bottom, (b) a completely reflective environment comprising an isovelocity waveguide and an isovelocity sediment layer, and (c) a more realistic environment with a downward refractive sound speed profile (SSP) waveguide, and an upward refractive SSP sediment layer. Receivers A and B are located at depths of 80 and 50 m, respectively. The two receivers are separated 100 m horizontally. A column of sources, spaced at 0.5-m increments, spans the water column in the same vertical plane as the two receivers, 40 m to the right of receiver B. The source is a Ricker wavelet with a center frequency of 350 Hz.

The sum of the cross-correlations, Eq. (1), is evaluated by treating the integral as a sum over the source column. For each source location, the acoustic pressure at A and B is evaluated assuming a constant source spectrum of $S(\omega)$. The pressures are cross-correlated, normalized by the density at the source, and then summed over the source locations and compared to the frequency and phase shaded Green's function between the two receivers:

$$\frac{\rho|S(\omega)^2|}{\omega} e^{i(3\pi/4)} G(R). \tag{19}$$

A. Isovelocity waveguide

The unstacked cross-correlations and the stacked response, C, are depicted in Fig. 6(a). The true [$3\pi/4$ phase and $|S(\omega)|^2$ amplitude] shaded simulated Green's function, G, is also included for comparative purposes.

The direct path stationary point is the temporal maxima of the direct wave cross-correlation arrival structure to each receiver. It occurs at 38-m depth at a time of 0.070 s. The direct path time difference converges to 0.065 s as the source is moved towards the surface, and to 0.052 s as it is moved towards the bottom. These endpoints do not, however, result in spurious peaks in the stacked response as they converge with other paths as the source approaches the given boundary. Stationary points corresponding to arrivals of the reflected paths are more difficult to see as they occur at locations very close to the waveguide boundaries; however, they can still be seen in the stacked response. For example, the peak in the stacked correlations at 0.109 s corresponds to the stationary point of the bottom bounce path to receiver B and the bottom-surface bounce path to receiver A, which occurs at a depth of 98 m and is therefore difficult to distinguish.

Overall, the phase of the stacked cross-correlation shows good agreement with the frequency and phase shaded Green's function, with only minor deviations. The amplitude is not accurate, but this can be explained by the difference in amplitude between the stacked cross-correlations and the Green's function having path dependent components ($\Gamma^{b_A+b_B}$, ϕ_s, and ξ) as derived in Eq. (13).

B. Waveguide with single sediment layer

This particular waveguide environment was chosen in order to understand a means by which the stacked cross-correlations may show some differences from the shaded simulated Green's function. In order to emphasize what is happening, the receivers are separated only 30 m horizontally, the Ricker wavelet centre frequency has been doubled to 700 Hz, and the source column spacing halved to 0.25 m. The remainder of the source/receiver configuration is identical to that of the isovelocity waveguide example.

The unstacked cross-correlations and the stacked responses are depicted in Fig. 6(b). The stacked response ΣC

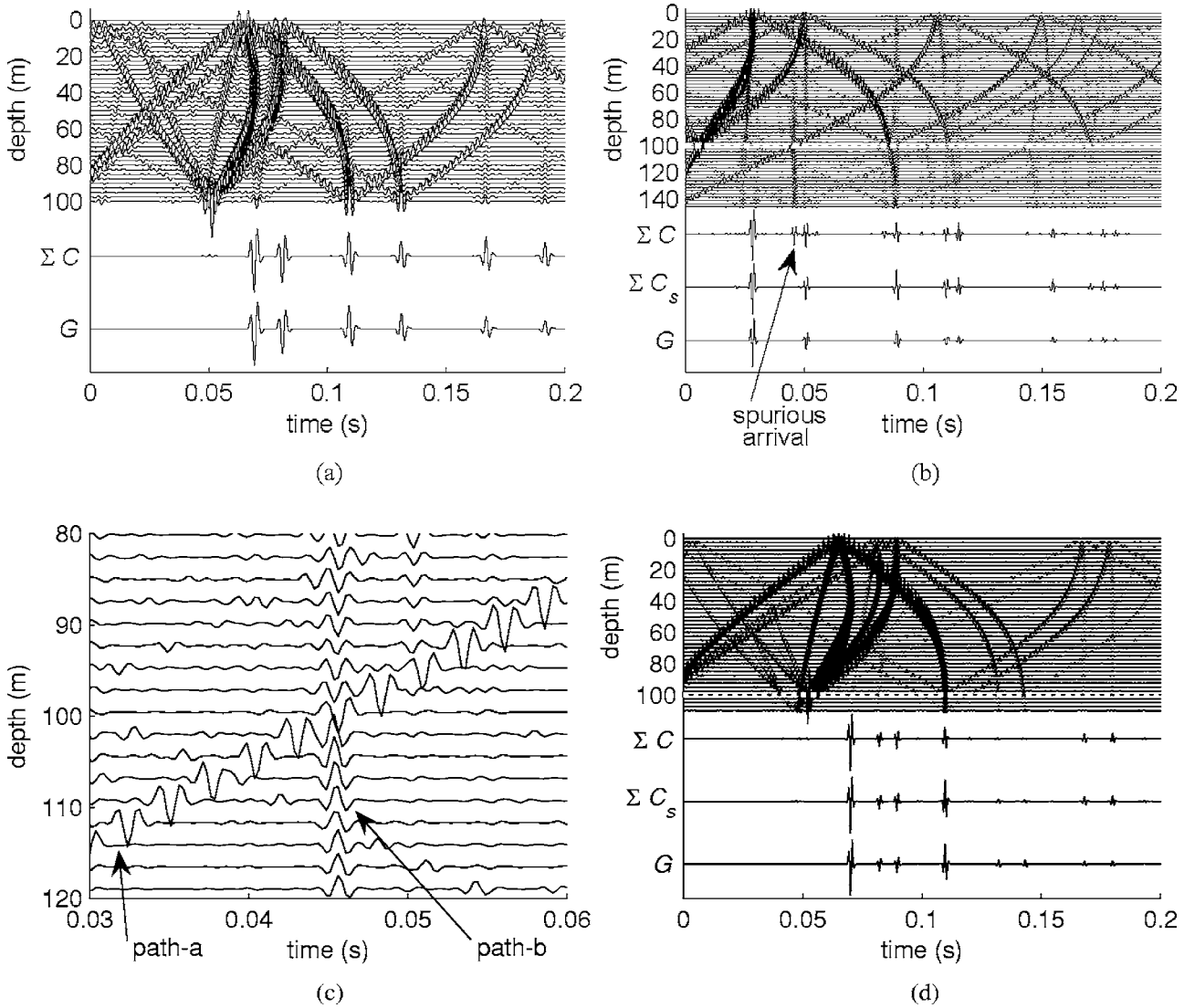

FIG. 6. The cross-correlations for (a) the isovelocity waveguide, (b) the reflective environment with a sediment, (c) a magnified portion of (b), and (d) the refractive environment, are plotted as a function of depth. The water-sediment interfaces in (b) and (d) are marked by a dashed white line. The stacked cross-correlation from a column of sources in the water, ΣC, the stacked trace with sediment sources included [(b) and (d) only], ΣC_s, and the shaded Green's function, G, are also plotted. The two paths indicated in (c) are the arrivals for the ray paths depicted in Fig. 7.

for the case when the source column terminates at the water-sediment interface contains the arrival paths observable in the shaded Green's function G; however, it also contains several spurious arrivals, the most noticeable of which occurs within the time interval 0.044–0.047 s. The stacked response ΣC_s does not contain these spurious arrivals. The spurious arrivals observable in ΣC are due to the source column not continuing through the sediment and therefore not producing a perfect time-reversal mirror.

One contribution to this spurious arrival is due to the discontinuities in the arrival structure caused by truncation of the $C_{AB}(\omega)$ integral at the bottom of the water column. The two paths affected are shown in Figs. 7(a) and 7(b) and their cross-correlations, depicted in Fig. 6(c), are denoted path-a and path-b, respectively. Paths-a and -b are cross-correlation peaks and, as such, should not be confused with real arrivals. As the source approaches the water-sediment interface the arrival time for path-a, the solid line in Fig. 7(a), transitions smoothly with the solid line, path-b, of Fig. 7(b). This can be seen by examining the arrival structure in Fig. 6(c). The two arrivals do not, however, cancel each other. For both paths-a and -b the path length difference between the source and

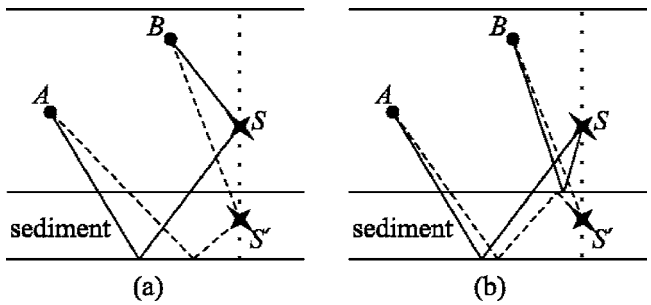

FIG. 7. Two possible sets of ray paths: (a) direct path to B and the bottom bounce path to A, and (b) a path to B with one water-sediment bounce and a path to A that has two transmissions through the interface. In both cases the solid lines represent paths from sources in the water (denoted S) and the dashed lines represent paths from sources in the sediment (denoted S').

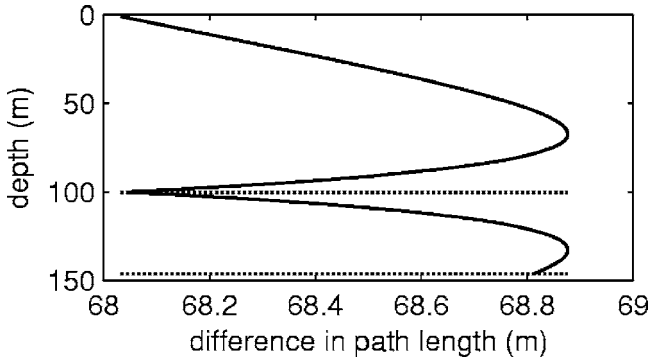

FIG. 8. The difference between the path lengths from the source to receiver *A* and the source to receiver *B* as a function of source depth for the ray path geometry of Fig. 7(b). The horizontal dotted lines represent the water-sediment interface and the sediment bottom.

each receiver decreases as the source approaches the sediment [see Figs. 6(c) and 8]. The two sets of ray paths are also in phase [see Fig. 6(c)]. The two arrivals will therefore sum together to contribute to the largest spurious arrival in trace ΣC of Fig. 6(b).

If the sources are extended through the sediment to the basement, then the summation over the arrival structure corresponding to Fig. 7 cancels completely at the water-sediment interface. At the interface the cross-correlation of the solid line representation of path-a [see Fig. 7(a)] will transition smoothly into the dashed line representation of path-a both in terms of arrival time and amplitude (for path $A+B$ the number of transmissions through the sediment remains constant). The difference in path length has a local minima here (see Fig. 8); however, the phase of the cross-correlation is inverted at the interface [see Fig. 6(c)], resulting in direct cancellation. Path-b also transitions smoothly; however, this time the difference in path length continues to decrease and there is no phase change [see Fig. 6(c)]. Cancellation at the interface therefore occurs. As the source approaches the basement, the arrival structure and amplitude will transition smoothly into that of other paths. For example, path-a will converge to the same arrival time as all other combinations of direct and single basement bounce paths to *A* and *B*, and, since the amplitudes of each set of paths will be the same, a smooth transition between the paths will occur.

A second contribution to the largest spurious arrival is a stationary-phase contribution from a source in the water column, which does not actually contribute to the full Green's function, as explained in Fig. 3. The solid line of path-b should not contribute to the Green's function as the signal received by *A* never passes through *B*, regardless of the source depth; however, a stationary point exists when the two paths depart the source at the same angle (i.e., 67.3 m source depth). This stationary point is difficult to see in the stacked response since the difference in path length of Fig. 7(b) varies by less than a meter ($\sim\lambda/5$) over the entire depth (see Fig. 8). As seen in Fig. 8, a second stationary point exists within the sediment at a depth of 133 m. If the sources are extended through the sediment, then this stationary point annuls the contribution from the stationary point in the water column.

As expected, the largest spurious peak from the water source column cross-correlation is not observable in the stacked cross-correlation of the column of sources that extends through the sediment [see trace ΣC_s of Fig. 6(b)]. Other deviations from the expected shaded Green's function are also reduced or removed.

C. Refractive environment with sediment

The source and receiver geometry and source type are identical to that of the (original) isovelocity waveguide example. The stacked responses, ΣC (sources in water column only) and ΣC_s (sources extended through sediment), and the shaded Green's function G are shown in Fig. 6(d). The phase of the water column stacked response is in reasonable agreement with the shaded simulated Green's function. The path time differences have converged almost completely to their sediment-bottom interface value at the water-sediment interface and hence the spurious arrivals, which were easily observed in the previous example, are not apparent here. Even if the source column could be extended into the sediment, only a minor increase in accuracy would be obtained. These results agree with the simulations of Roux and Fink,[23] who concluded that the effect of limiting sources to the water column is negligible when the modal continuum of the sediment is small relative to that of the water.

IV. CONCLUSION

Ocean acoustic interferometry (OAI) refers to the process of recording the signals from a line of sources on two receivers and using this to infer the Green's function between the receivers. The time domain Green's function is approximated by summing or integrating, over all source positions, the cross-correlations between the receivers. The source used in this work was a vertical (drop) source spanning the water column; however, the source could also have been a horizontal (tow) source.

Analytical stationary phase based OAI was used to solve the summation of cross-correlations for a line of vertical sources, located external to, and in the same plane as, two receivers, and to relate this to the Green's function between said receivers. It was shown that in an isovelocity waveguide, the stacked cross-correlations show very good agreement with the $|S(\omega)|^2/\omega$ amplitude, and $3\pi/4$ phase, shaded Green's function.

Numerical simulations of OAI were used to confirm the theoretical findings and also to show what can happen in a more complex environment. A concern is that the introduction of a sediment can produce, in addition to arrivals pertaining to the true time domain shaded Green's function, spurious arrivals due to the sources ceasing at the water-sediment interface. The origin of these spurious arrivals was discussed in detail. These aberrations can, theoretically, be removed by extending the line of sources into the sediment.

In the refractive environment presented here the phase of the water column stacked response ΣC was shown to be in reasonable agreement with the shaded simulated Green's function G; however, the extent to which ΣC and G agree is environmentally dependent. If the modal continuum of the

sediment were higher relative to that of the water, differences between ΣC and G would be more prevalent.

In an experimental setting the vertical source column source/receiver geometry could be achieved using a source that is slowly lowered through the water by a ship-operated winch, and by recording data on either two vertical arrays or an L-shaped array. One application for this could be monitoring changes in the ocean environment between two arrays.

ACKNOWLEDGMENTS

This work was supported by the Office of Naval Research under Grant No. N00014-05-1-0264. The first author is also appreciative of support from a Fulbright Postgraduate Award in Science and Engineering, sponsored by Clough Engineering, as well as support from the Defence Science and Technology Organisation, Australia.

[1]O. I. Lobkis and R. L. Weaver, "On the emergence of the Green's function in the correlations of a diffuse field," J. Acoust. Soc. Am. **110**, 3011–3017 (2001).
[2]A. Derode, E. Larose, M. Tanter, J. de Rosny, A. Tourin, M. Campillo, and M. Fink, "Recovering the Green's function from field-field correlations in an open scattering medium," J. Acoust. Soc. Am. **113**, 2973–2976 (2003).
[3]K. Wapenaar, "Retrieving the elastodynamic Green's function of an arbitrary inhomogeneous medium by cross correlation," Phys. Rev. Lett. **93**, 254301 (2004).
[4]D-J. van Manen, J. O. A. Robertsson, and A. Curtis, "Modeling of wave propagation in inhomogeneous media," Phys. Rev. Lett. **94**, 164301 (2005).
[5]F. J. Sánchez-Sesma and M. Campillo, "Retrieval of the Green function from cross correlation: The canonical elastic problem," Bull. Seismol. Soc. Am. **96**, 1182–1191 (2006).
[6]F. J. Sánchez-Sesma, J. A. Pérez-Ruiz, M. Campillo, and F. Luzón, "Elastodynamic 2D Green function retrieval from cross-correlation: Canonical inclusion problem," Geophys. Res. Lett. **33**, L13305 (2006).
[7]R. L. Weaver and O. I. Lobkis, "Ultrasonics without a source: Thermal fluctuation correlations at MHz frequencies," Phys. Rev. Lett. **87**, 134301 (2001).
[8]A. E. Malcolm, J. A. Scales, and B. A. van Tiggelen, "Extracting the Green function from diffuse, equipartitioned waves," Phys. Rev. E **70**, 015601 (2004).
[9]K. van Wijk, "On estimating the impulse response between receivers in a controlled ultrasonic experiment," Geophysics **71**, SI79–SI84 (2006).
[10]P. Roux, K. G. Sabra, W. A. Kuperman, and A. Roux, "Ambient noise cross correlation in free space: Theoretical approach," J. Acoust. Soc. Am. **117**, 79–84 (2005).
[11]P. Roux, W. A. Kuperman, and the NPAL Group, "Extracting coherent wave fronts from acoustic ambient noise in the ocean," J. Acoust. Soc. Am. **116**, 1995–2003 (2004).
[12]K. G. Sabra, P. Roux, and W. A. Kuperman, "Arrival-time structure of the time-averaged ambient noise cross-correlation function in an oceanic waveguide," J. Acoust. Soc. Am. **117**, 164–174 (2005).
[13]K. G. Sabra, P. Roux, A. M. Thode, G. L. D'Spain, W. S. Hodgkiss, and W. A. Kuperman, "Using ocean ambient noise for array self-localization and self-synchronization," IEEE J. Ocean. Eng. **30**, 338–347 (2005).
[14]M. Siderius, C. H. Harrison, and M. B. Porter, "A passive fathometer technique for imaging seabed layering using ambient noise," J. Acoust. Soc. Am. **120**, 1315–l323 (2006).
[15]M. Campillo and A. Paul, "Long-range correlations in the diffuse seismic coda," Science **299**, 547–549 (2003).
[16]R. Snieder, "Extracting the Green's function from the correlation of coda waves: A derivation based on stationary phase," Phys. Rev. E **69**, 046610 (2004).
[17]N. M. Shapiro, M. Campillo, L. Stehly, and M. H. Ritzwoller, "High-resolution surface-wave tomography from ambient seismic noise," Science **307**, 1615–1618 (2005).
[18]K. G. Sabra, P. Gerstoft, P. Roux, W. A. Kuperman, and M. C. Fehler, "Extracting time-domain Green's function estimates from ambient seismic noise," Geophys. Res. Lett. **32**, L03310 (2005).
[19]P. Gerstoft, K. G. Sabra, P. Roux, W. A. Kuperman, and M. C. Fehler, "Green's functions extraction and surface-wave tomography from microseisms in southern California," Geophysics **71**, S123–S131 (2006).
[20]K. Wapenaar and J. Fokkema, "Green's function representations for seismic interferometry," Geophysics **71**, SI33–SI46 (2006).
[21]J. Rickett and J. Claerbout, "Acoustic daylight imaging via spectral factorization; helio-seismology and reservoir monitoring," The Leading Edge **18**, 957–960 (1999).
[22]E. Larose, A. Khan, Y. Nakamura, and M. Campillo, "Lunar subsurface investigated from correlation of seismic noise," Geophys. Res. Lett. **32**, L16201 (2005).
[23]P. Roux and M. Fink, "Green's function estimation using secondary sources in a shallow water environment," J. Acoust. Soc. Am. **113**, 1406–1416 (2003).
[24]R. Snieder, K. Wapenaar, and K. Larner, "Spurious multiples in seismic interferometry of primaries," Geophysics **71**, SI111–S1124 (2006).
[25]A. Curtis, P. Gerstoft, H. Sato, R. Snieder, and K. Wapenaar, "Seismic interferometry—turning noise into signal," The Leading Edge **25**, 1082–1092 (2006).
[26]L. M. Brekhovskikh, *Waves in Layered Media* (Academic, New York, 1960).
[27]C. M. Bender and S. A. Orszag, *Advanced Mathematical Methods for Scientists and Engineers* (McGraw-Hill, New York, 1978).
[28]H. Schmidt, *OASES Version 3.1 User Guide and Reference Manual*, Department of Ocean Engineering, Massachusetts Institute of Technology (2004).

An extended coupled phase theory for the sound propagation in polydisperse concentrated suspensions of rigid particles

Michael Baudoin[a)]
Institut Jean Le Rond D'Alembert (IJLRDA), UMR CNRS 7190 and Institut des NanoSciences de Paris (INSP), UMR CNRS 7588, Université Pierre et Marie Curie - Paris 6, 4 place Jussieu, 75252 Paris Cedex 05, France

Jean-Louis Thomas
INSP, CNRS and Université Pierre et Marie Curie - Paris 6, 75252 Paris Cedex 05, France

François Coulouvrat and Daniel Lhuillier
IJLRDA, CNRS and Université Pierre et Marie Curie - Paris 6, 75252 Paris Cedex 05, France

(Received 15 November 2006; revised 7 March 2007; accepted 15 March 2007)

An extension of the classical coupled phase theory is proposed to account for hydrodynamic interactions between neighboring rigid particles, which are essential to describe properly the sound propagation in concentrated suspensions. Rigorous ensemble-averaged equations are derived for each phase and simplified in the case of acoustical wave propagation. Then, closure is achieved by introducing a self-consistent scheme originally developed by Buyevich and Shchelchkova [Prog. Aerosp. Sci. **18**, 121–151 (1978)] for incompressible flows, to model the transfer terms between the two phases. This provides an alternative to the effective medium self-consistent theory developed by Spelt *et al.* [J. Fluid Mech. **430**, 51–86 (2001)] in which the suspension is considered as a whole. Here, a significantly simpler formulation is obtained in the long wavelength regime. Predictions of this self-consistent theory are compared with the classical coupled phase theory and with experimental data measuring the attenuation in concentrated suspensions of silica in water. Our calculation is shown to give a good description of the attenuation variation with volume fraction. This theory is also extended to the case of polydisperse suspensions. Finally, the link between the self-consistent theory and the different orders of the multiple scattering theory is clarified. © *2007 Acoustical Society of America.* [DOI: 10.1121/1.2723648]

PACS number(s): 43.35.Bf [AJS] Pages: 3386–3397

I. INTRODUCTION

The propagation of sound waves through dilute suspensions of different natures has been the subject of many studies since the pioneering article of Sewell[1] in 1910 who considered immovable rigid particles suspended in a gas. Several phenomena can be involved in the attenuation and dispersion of sound, depending on the particles nature and the wave frequency. In hydrosols, the acoustic damping is mainly induced by the visco-inertial terms (Lamb[2]).

To study the influence of particles on the sound propagation in suspensions, two methods have been principally developed. First, the scattering theory, also called ECAH theory based on the work of Epstein and Carhart[3] and Allegra and Hawley.[4] In this model, a spherical particle is considered and the waves propagating inside and outside the particle are decomposed into three modes: compressional, shear, and thermal ones. Potentials are expressed in terms of Bessel functions series satisfying the boundary conditions at the particle surface. Second, there is the coupled phase theory[5,6] based on the two-phase hydrodynamic equations. The primary advantage of the scattering theory is to be valid over the whole frequency range, although some difficulties arise with the series truncation due to the nonuniform convergence of the Bessel series.[7] The coupled phase theory gives a good framework to incorporate phenomena that would be difficult to include in the scattering theory such as mass transfers or chemical reactions. Moreover, it also leads to an explicit dispersion equation that is simpler to interpret physically and calculate, which can be useful when dealing with the inverse problem.

These theories agree well with experimental data in dilute suspensions, but they both neglect some parts, of the "multiple scattering" whose importance increases with concentration. The coupled phase theory inherently integrates "multiple scattering" but only at first order (cf. Sec. II C). Thus, it neglects interactions that occur when the viscous or/and thermal boundary layer of neighboring particles overlap one another. The ECAH theory was originally considering a simple superposition of each particle contribution and was therefore not considering "multiple scattering."

To incorporate the "reverberant multiple scattering" (in the sense of geometrical redirection of energy), the multiple scattering theory[8–13] has been introduced into the ECAH theory.[14]

To account for "dissipative multiple scattering," that is to say overlapping of thermal waves in the case of emulsions, Hemar *et al.*[15] have introduced a so-called "core-shell model:" the particle is surrounded by a cell of pure fluid,

a)Electronic mail: baudoin@lmm.jussieu.fr

where the presence of the particle is rather unlikely, which is itself embedded in an effective medium. Such models show a good agreement with experiments, but they require the introduction of several unknown parameters. The first one is the radius of the pure medium cell b. Many investigators choose $b=a/\alpha_d^{1/3}$ (where a is the particle radius and α_d is the volume fraction occupied by the particles), although this value is not appropriate for randomly distributed spheres. It would be more adequate for systems in which the distance between particles is almost uniform (cf. Refs. 16 and 17). Then, the effective properties of the medium must also be introduced. In the work by Hemar *et al.* and in the article by Hipp *et al.*,[18] the volume averaged parameters are introduced, but one could also choose a different set of effective parameters. The primary advantage of the present study is that the effective properties are introduced in a consistent way. One can note that the multiple scattering theory and the "core-shell model" have been merged in the article by McClements and Hermann.[19] The results of this model have then been compared in detail with the classical coupled phase theory by Evans and Attenborough.[6]

Finally, and to the authors' knowledge, the only articles dealing with the overlapping of visco-inertial potentials are the articles by Dukhin and Goetz[20] and by Spelt *et al.*[17] The first one is the so-called cell model,[21,22] which is based on empirical grounds. Although it provides a relatively good estimation of viscous interactions between neighboring particles, there is no rigorous justification of this procedure. Moreover, it does not integrate the intrinsic (bulk) losses in the formulation. The second one, as the present work, uses the self-consistent approximation, but the suspension is considered as a whole. Its advantage is to give a theory that is valid whatever the frequency of the incident wave and the nature of the particle. The present work is limited to the long wavelength regime (LWR) but provides a simpler expression to describe the attenuation and dispersion in suspensions of rigid particles. This work also differs in the expression of the closure relations that are not limited to plane waves. These considerations will be developed in Sec. II D 4.

In this paper, we will first derive the ensemble averaged conservation equations and simplify them in the case of acoustical wave propagation. Then we will introduce the self-consistent scheme originally developed by Buyevich[23,24] for an incompressible flow and we will discuss the link between the closure assumptions introduced here in the effective medium theory (EMT), and the one introduced in the multiple scattering theory (MST). Once the semi-analytical dispersion equation is established, the results are compared to the experimental data of Hipp *et al.*[25] Finally, the equations will be extended to the case of polydisperse solutions.

II. THEORY

In the coupled phase theory, averaged conservation equations are written down separately for each phase. These equations are coupled by the transfer terms between the two phases. In the case of rigid particles in a liquid matrix, the thermal transfer and intrinsic absorption can be neglected as they are both proportional to γ_c-1, where γ_c is the specific heat ratio of the continuous phase that is almost equal to one in liquids. Thus, only the mass and momentum conservation equations are required. In this section, we will consider a monodisperse suspension of spherical rigid particles isotropically distributed.

A. Ensemble-averaged equations

The ensemble-averaged equations are calculated from the local constitutive equations of the continuous and dispersed phases by using a configurational average.[24]

If the interfaces between the two phases have no mass, one can introduce the generalized functions for density and momentum based on the "fine-grained" definition in each phase under the form

$$\begin{bmatrix} \rho' \\ \rho' \boldsymbol{v}' \end{bmatrix} = \sum_{k=c,d} \chi_k \begin{bmatrix} \rho_k' \\ \rho_k' \boldsymbol{v}_k' \end{bmatrix},$$

where c,d denote respectively the continuous and dispersed phase, ρ_k' and $\boldsymbol{v}_k'$ are the "fine grained" density and velocity, and χ_k is the phase function defined by

$$\chi_k(\boldsymbol{x},t) = \begin{cases} 1 & \text{if } \boldsymbol{x} \text{ is in phase } k \text{ at time } t, \\ 0 & \text{otherwise,} \end{cases} \tag{1}$$

with of course $\chi_c=1-\chi_d$.

If interface forces due to the surface tension are neglected and no external force field is considered, the generalized mass and momentum conservation equations can be written under the form

$$\frac{\partial \rho'}{\partial t} + \operatorname{div}(\rho' \boldsymbol{v}') = 0, \tag{2}$$

$$\frac{\partial}{\partial t}(\rho' \boldsymbol{v}') + \operatorname{div}(\rho' \boldsymbol{v}' \otimes \boldsymbol{v}') = \operatorname{div}(\boldsymbol{\Pi}'), \tag{3}$$

where $\boldsymbol{\Pi}'$ is the generalized stress tensor:

$$\boldsymbol{\Pi}' = \sum_{k=c,d} \chi_k \boldsymbol{\Pi}_k',$$

Π_k' being the stress tensor in the kth phase.

To obtain separate averaged equations for each phase, Eqs. (2) and (3) are multiplied by the phase function and then averaged via the configurational average:

$$\langle G'(\boldsymbol{x},t) \rangle = \int G'(\boldsymbol{x},t|\boldsymbol{x}_1,\ldots,\boldsymbol{x}_N) p(t,\boldsymbol{x}_1,\ldots,\boldsymbol{x}_N) d\boldsymbol{x}_1 \cdots d\boldsymbol{x}_N;$$

where $p(t,\boldsymbol{x}_1,\cdots,\boldsymbol{x}_N)dx_1 \cdots dx_N$ is the probability of finding the first particle center in the vicinity of $\boldsymbol{x}_1$ at t, while at the same time the second particle is in the vicinity of $\boldsymbol{x}_2$ and so forth. Considering indistinguishable particles, this expression can be rewritten as the probability $p(t,C_N)dC_N$ of finding the N particles in the vicinity of $C_N=(\boldsymbol{x}_1,\ldots,\boldsymbol{x}_N)$, regardless of their order.

The left hand side of Eqs. (2) and (3) are of the form

$$\frac{\partial G'}{\partial t} + \mathrm{div}(G'\boldsymbol{v}').$$

Providing that the fluctuations $G''=G'-\langle G'\rangle$ of the local field G' relative to the mean field $\langle G'\rangle$ are neglected and as long as no phase change occurs, the previously described average yields[26]

$$\left\langle \chi_k \left[\frac{\partial G'}{\partial t} + \mathrm{div}(G'\boldsymbol{v}') \right] \right\rangle = \frac{\partial}{\partial t}(\alpha_k G_k) + \mathrm{div}(\alpha_k G_k v_k), \tag{4}$$

with $\alpha_k=\langle\chi_k\rangle$ the mean volume fraction occupied by phase k, and G_k the phasic average of the variable G':

$$G_k = \langle \chi_k G'\rangle/\alpha_k. \tag{5}$$

The next fundamental step is to express $\langle\chi_c\mathrm{div}(\boldsymbol{\Pi}')\rangle$ and $\langle\chi_d\mathrm{div}(\boldsymbol{\Pi}')\rangle$ in terms of quantities that we will be able to calculate for a test particle in order to achieve closure. Our derivation is based on the theory developed by Buyevich,[24,27] here modified to account for the compressibility of the continuous phase as required for sound propagation. From $\chi_c = 1-\chi_d$, we easily obtain

$$\langle\chi_c\mathrm{div}(\boldsymbol{\Pi}')\rangle = \mathrm{div}\langle\boldsymbol{\Pi}'\rangle - \langle\chi_d\mathrm{div}(\boldsymbol{\Pi}')\rangle \quad \text{with } \langle\boldsymbol{\Pi}'\rangle = \langle\chi_c\boldsymbol{\Pi}'\rangle + \langle\chi_d\boldsymbol{\Pi}'\rangle. \tag{6}$$

In the continuous phase, the "fine-grained" stress tensor expression is the one of a Newtonian fluid, and thus

$$\langle\chi_c\boldsymbol{\Pi}'\rangle = -\alpha_c p_c \boldsymbol{I} + 2\mu_c\langle\chi_c\boldsymbol{D}'\rangle + \lambda_c\langle\chi_c\mathrm{div}(\boldsymbol{v}')\rangle\boldsymbol{I}, \tag{7}$$

where p_c is the phasic average of the local pressure, $\boldsymbol{D}'$ is the strain rate tensor, $\boldsymbol{I}$ is the unit tensor, and μ_c and $\zeta_c=\lambda_c+2\mu_c/3$ are respectively the shear and bulk viscosities of the continuous phase.

Owing to the rigidity of the particles, the strain rates $\boldsymbol{D}'$ and the volume variation $\mathrm{div}(\boldsymbol{v}')$ vanish inside the particle, and thus we obtain

$$\langle\chi_c\boldsymbol{D}'\rangle = \langle\boldsymbol{D}'\rangle - \langle\chi_d\boldsymbol{D}'\rangle = \langle\boldsymbol{D}'\rangle \equiv \boldsymbol{D}, \tag{8}$$

$$\langle\chi_c\mathrm{div}(\boldsymbol{v}')\rangle = \mathrm{div}\langle\boldsymbol{v}'\rangle - \langle\chi_d\mathrm{div}(\boldsymbol{v}')\rangle = \mathrm{div}\langle\boldsymbol{v}'\rangle = \mathrm{div}(\boldsymbol{v}), \tag{9}$$

with $\boldsymbol{v}=\alpha_c\boldsymbol{v_c}+\alpha_d\boldsymbol{v_d}$ and $\boldsymbol{D}=1/2(\nabla\boldsymbol{v}+\nabla^t\boldsymbol{v})$.

From Eqs. (7)–(9), we get

$$\langle\boldsymbol{\Pi}'\rangle = -\alpha_c p_c\boldsymbol{I} + 2\mu_c\boldsymbol{D} + \lambda_c\mathrm{div}(\boldsymbol{v})\boldsymbol{I} + \langle\chi_d\boldsymbol{\Pi}'\rangle. \tag{10}$$

Finally, by taking into acount (4), (6), and (10) in Eqs. (2) and (3), the following system of mass and momentum conservation stands:

$$\frac{\partial}{\partial t}(\alpha_c\rho_c) + \mathrm{div}(\alpha_c\rho_c\boldsymbol{v_c}) = 0, \tag{11}$$

$$\frac{\partial}{\partial t}(\alpha_d\rho_d) + \mathrm{div}(\alpha_d\rho_d\boldsymbol{v_d}) = 0, \tag{12}$$

$$\frac{\partial}{\partial t}(\alpha_c\rho_c\boldsymbol{v_c}) + \mathrm{div}(\alpha_c\rho_c\boldsymbol{v_c}\otimes\boldsymbol{v_c}) = \mathrm{div}(\boldsymbol{\Pi}) - \boldsymbol{F}, \tag{13}$$

$$\frac{\partial}{\partial t}(\alpha_d\rho_d\boldsymbol{v_d}) + \mathrm{div}(\alpha_d\rho_d\boldsymbol{v_d}\otimes\boldsymbol{v_d}) = \boldsymbol{F}, \tag{14}$$

with the expressions of the effective stress tensor $\boldsymbol{\Pi}=\langle\boldsymbol{\Pi}'\rangle$ given by Eq. (10) and the effective force $\boldsymbol{F}$ given by

$$\boldsymbol{F} = \langle\chi_d\mathrm{div}(\boldsymbol{\Pi}')\rangle. \tag{15}$$

B. The test particle problem

Thus, only the quantities $\langle\chi_d\boldsymbol{\Pi}'\rangle$ and $\langle\chi_d\mathrm{div}(\boldsymbol{\Pi}')\rangle$ remain to be expressed in terms of the averaged fields to achieve closure. To address this issue, the link between these expressions and the so-called test particle problem must be established. Let us introduce some notations that will be useful in this problem.

First, the conditional averages with one or two (or more) particles positions being known are defined by

$$\langle G'\rangle_{\boldsymbol{x}'}(\boldsymbol{x},t) = \int G'(\boldsymbol{x},t|C_N)p(t,C_{N-1}|\boldsymbol{x}')\,dC_{N-1},$$

$$\langle G'\rangle_{\boldsymbol{x}',\boldsymbol{x}''}(\boldsymbol{x},t) = \int G'p(t,C_{N-2}|\boldsymbol{x}',\boldsymbol{x}'')\,dC_{N-2}.$$

Then, we can introduce the unconditional probability density $p(t,\boldsymbol{x}')$ of finding one of the N sphere centers in $\boldsymbol{x}'$ at t, and $p(t,\boldsymbol{x}';\boldsymbol{x}'')$ the same probability but conditioned by the presence of another sphere center in $\boldsymbol{x}''$:

$$p(t,\boldsymbol{x}') = \sum_{j=1}^{N}\int\cdots\int p(t,C_N)_{x^j=\boldsymbol{x}'}\prod_{i\neq j}d\boldsymbol{x}^i,$$

$$p(t,\boldsymbol{x}';\boldsymbol{x}'') = \sum_{j\neq k}\int\cdots\int p(t,C_N)_{x^j=\boldsymbol{x}',x^k=\boldsymbol{x}''}\prod_{i\neq j,k}d\boldsymbol{x}^i.$$

We can note that $p(t,\boldsymbol{x}')$ is nothing but the mean concentration number of particles by volume, which will be noted $n(t,\boldsymbol{x}')$ in the rest of this paper.

From the above definitions, Buyevich and Shchelchkova[24] establish the link between quantities averaged over the dispersed phase and integrals over a test particle surface or volume:

$$\langle\chi_d G'\rangle(\boldsymbol{x},t) = \int_{|\boldsymbol{x}-\boldsymbol{x}'|\leq a} n(t,\boldsymbol{x}')\langle G'\rangle_{\boldsymbol{x}'}(\boldsymbol{x},t)\,d\boldsymbol{x}'. \tag{16}$$

With this equation and providing that the macroscopic scale L (that is to say, the wavelength λ in acoustics) is much larger than the radius a of the particle, they obtain the following formula:

$$\alpha_d(t,\boldsymbol{x}) = \langle\chi_d\rangle(t,\boldsymbol{x}) \approx 4/3\,\pi a^3 n(t,\boldsymbol{x}), \tag{17}$$

$$\boldsymbol{F} = \langle\chi_d\mathrm{div}(\boldsymbol{\Pi}')\rangle \approx \frac{3\alpha_d}{4\pi a^3}\oint\langle\boldsymbol{\Pi}'\rangle_x\cdot\mathbf{n}\,dS, \tag{18}$$

where $\mathbf{n}$ is the normal vector. Equation (18) clearly shows that $\boldsymbol{F}$ is nothing but the force applied on a test sphere by a fictitious medium, whose properties significantly differ from

the pure ambient fluid, as they include the influence of the other distributed spheres.

Finally, with a complex reasoning that we will not reproduce here, they prove that if no external torque acts on the particle, and the inertial terms due to the particle rotation can be neglected (assumptions well satisfied for acoustical waves), $\langle \chi_d \mathbf{\Pi}' \rangle$ can be expressed by the following surface integral over the test sphere surface:

$$\langle \chi_d \mathbf{\Pi}' \rangle \approx \frac{3\alpha_d}{4\pi a^3} \oint^{(s)} \boldsymbol{a} \otimes (\boldsymbol{n} \cdot \langle \mathbf{\Pi}' \rangle_{\boldsymbol{x}}) \, dS, \tag{19}$$

where the superscript (s) means that only the symmetric part of the tensor appearing in the integrand is considered.

C. The self-consistent closure scheme

The link between constitutive equations and the test particle problem is now established via (18) and (19). To compute these expressions, one should first determine the boundary conditions and secondly derive a set of equations for the conditionally averaged fields. The first issue can be solved by the following considerations:

- As no phase changes occur, the conditionally averaged velocity is equal to the velocity of the test sphere on the particle surface ($r=a$).
- Far from the test particle (when $r \to \infty$), the perturbation of the fields induced by the presence of the heterogeneity vanishes so that the conditionally averaged fields asymptotically coincide with the unconditionally averaged fields:

$$\langle G' \rangle_{\boldsymbol{x}'} \to \langle G' \rangle \quad \text{when } r \to \infty . \tag{20}$$

To address the second issue, the same equations can be derived for the conditionally averaged field as for the averaged field, but, this time, constitutive equations are expressed in terms of the averaged field with two particle positions being known:

$$\boldsymbol{F}_{\boldsymbol{x}'} = \int_{\boldsymbol{x}''} \int_{|\boldsymbol{x}-\boldsymbol{x}'| \le a} n(t,\boldsymbol{x}',\boldsymbol{x}'') \langle \mathrm{div}(\mathbf{\Pi}') \rangle_{\boldsymbol{x}',\boldsymbol{x}''} \, d\boldsymbol{x}' \, d\boldsymbol{x}'',$$

$$\langle \chi_d \mathbf{\Pi}' \rangle_{\boldsymbol{x}'} = \int_{\boldsymbol{x}''} \int_{|\boldsymbol{x}-\boldsymbol{x}'| \le a} n(t,\boldsymbol{x}',\boldsymbol{x}'') \langle (\mathbf{\Pi}') \rangle_{\boldsymbol{x}',\boldsymbol{x}''} \, d\boldsymbol{x}' \, d\boldsymbol{x}''.$$

Of course, one could also calculate the averaged equations with the position of two particles being known and so on. In such a way, one would obtain an infinite hierarchy of mutually dependent equations conditioned by the position of an increasing number of particles. So the problem arises of an efficient truncation or closure of this hierarchy. A truncation at the first level would result in the calculation of the constitutive equations when the particles are embedded in the pure ambient fluid. Here, mutual interactions of two or more spheres are completely left out. This approximation is usually used in dilute mixtures and corresponds to the classical version of the coupled phase theory. However, even at this level, a part of the multiple scattering is included because the particles are excited by the mean field (cf. Fig. 1).

At the next level, binary interactions of pairs of spheres are accounted for, while ternary, quadruple, and higher order loops are neglected. To achieve closure at this level, one should calculate the constitutive equations when two particles positions are known, which is not an easy matter.

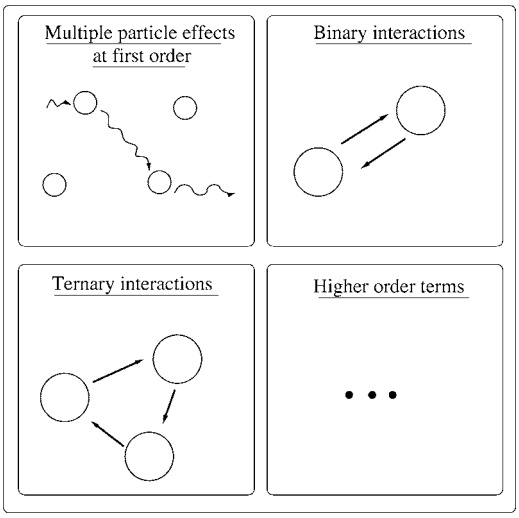

FIG. 1. Different orders of multiple scattering.

Of course, one could theoretically truncate this hierarchy at any order to integrate higher order loops, but the complexity of the calculation would greatly increase with the order. Anyway, this procedure would result in a polynomial expansion with respect to the particle concentration α_d and will thus be limited to relatively dilute mixtures. Moreover, nothing ensures that mutual interaction between n particles are dominant over interactions between $n+1$ particles when the concentration increases.

To overcome these limitations, Buyevich proposed a self-consistent scheme.[16,24] The starting point of this procedure is that, anyway, the resolution of the previous mutually dependent equations would result in an infinite polynomial series for the effective mixture properties. Instead of truncating the hierarchy at a certain level, the particles are supposed to be embedded in this *final* effective medium. Thanks to this procedure and by introducing a plausible form for integrals (18) and (19), the effective properties will be computed with an iterative scheme. All orders of interaction will thus be included in this formulation. Moreover, the correlations of particles in position can also be incorporated according to the choice of the expression of the conditional volume fraction.

D. Application to the propagation of an acoustic wave

1. Linearized equations

We will now adapt the previous system to the propagation of an acoustic wave. In this case, Eqs. (11)–(15) can be linearized. If we denote the equilibrium state with a subscript "*o*", the following equations stand:

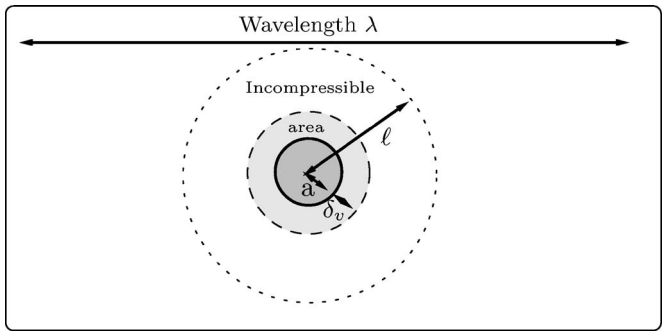

FIG. 2. The mesoscopic scale.

mass conservation:

$$\rho_{co}\left(\boxed{\frac{\partial \alpha_c}{\partial t}} + \alpha_{co}\mathrm{div}(\boldsymbol{v_c})\right) + \boxed{\alpha_{co}\frac{\partial \rho_c}{\partial t}} = 0, \tag{21}$$

$$\boxed{\frac{\partial \alpha_d}{\partial t}} + \alpha_{do}\mathrm{div}(\boldsymbol{v_d}) = 0, \tag{22}$$

$$\alpha_d = 1 - \alpha_c; \tag{23}$$

momentum conservation:

$$\alpha_{co}\rho_{co}\frac{\partial \boldsymbol{v_c}}{\partial t} = -\nabla(\alpha_c p_c) + \mu_c \Delta \mathbf{v} + \boxed{(\lambda_c + \mu_c)\boldsymbol{\nabla}\mathrm{div}(\boldsymbol{v})} + \mathrm{div}\langle \chi_d \boldsymbol{\Pi}' \rangle - \boldsymbol{F}, \tag{24}$$

$$\alpha_{do}\rho_{do}\frac{\partial \boldsymbol{v_d}}{\partial t} = \boldsymbol{F}. \tag{25}$$

In these expressions, all terms linked to the compressibility of the continuous phase have been outlined.

2. The long wavelength regime (LWR)

To perform the explicit calculation of constitutive equations, we will consider the LWR. In this case, we can introduce a mesoscopic scale l around the test particle where the compressibility of the continuous phase can be neglected and such as, when $r \to l$, the perturbation induced by the test particle vanishes (cf. Fig. 2):

$$a + \delta_v \ll l \ll \lambda,$$

where λ is the acoustic wavelength and $\delta_v = \sqrt{2\mu_c / \omega\rho_c}$ is the thickness of the viscous boundary layer. This inequality is always satisfied in the cases treated in this paper. At distances smaller than l (cf. Fig. 2), all (outlined) compressible terms can be neglected and, after Fourier transform, we obtain

$$\mathrm{div}(\boldsymbol{v_c}) = \mathrm{div}(\boldsymbol{v_d}) = 0, \tag{26}$$

$$-\alpha_{co}\rho_{co}(i\omega)\boldsymbol{v_c} = -\nabla(\alpha_c p_c) + \mu_c \Delta \boldsymbol{v} + \mathrm{div}\langle \chi_d \boldsymbol{\Pi}' \rangle - \boldsymbol{F}, \tag{27}$$

$$-\alpha_{do}\rho_{do}(i\omega)\boldsymbol{v_d} = \boldsymbol{F}. \tag{28}$$

The same equations can be derived for the conditionally averaged field, but, this time, the conditional volume fraction at equilibrium $\alpha_{do,\boldsymbol{x}'}$ replaces the unconditional one:

$$\mathrm{div}(\alpha_{co,\boldsymbol{x}'}\boldsymbol{v_{c,x}}') = \mathrm{div}(\alpha_{do,\boldsymbol{x}'}\boldsymbol{v_{d,x}}') = 0, \tag{29}$$

$$-\alpha_{co,\boldsymbol{x}'}\rho_{co}(i\omega)\boldsymbol{v_{c,x}}' = -\nabla(\alpha_{c,\boldsymbol{x}'}p_{c,\boldsymbol{x}'}) + \mu_c \Delta \boldsymbol{v}_{\boldsymbol{x}'} + div\langle \chi_d \boldsymbol{\Pi}' \rangle_{\boldsymbol{x}'} - \boldsymbol{F}_{\boldsymbol{x}'}, \tag{30}$$

$$-\alpha_{do,\boldsymbol{x}'}\rho_{do}(i\omega)\boldsymbol{v_{d,x}}' = \boldsymbol{F}_{\boldsymbol{x}'}. \tag{31}$$

3. Correlations of particles in position

The difference between $\alpha_{do,\boldsymbol{x}'}$ and α_{do} stems from the correlations of particles in position, that is to say, the perturbation of the particle repartition induced by the presence of a test sphere in $\boldsymbol{x}'$. The simplest approximation consists in neglecting this difference:

$$\alpha_{do,\boldsymbol{x}'} = \alpha_{do}, \tag{32}$$

and thus ignoring the non-overlapping property of the spheres. For the sake of simplicity, we will adopt this hypothesis and we will precisely discuss its validity in Sec. III. Of course, more elaborate expressions[16] can be derived to describe properly the repartition of particles within groups of several spheres (cf. the Kirkwood and Percus-Yevick models as reviewed in the book by Croxton[28]) and therefore include the correlations of position.

4. The self-consistent condition

Even if the equations have been simplified in the incompressible region, we still have to deal with the entire hierarchy of equations, and we therefore need to close the system. For that purpose, we will use the condition expressed in the Sec. II C: the particles will be supposed to be embedded in the *final* effective medium (made of the whole series expansion). Let us apply this condition to our case.

First, Eqs. (29)–(31) can be rewritten in a convective reference frame related to the velocity of the test particle center, that is to say $\boldsymbol{v_d}|_{r=0}$:

$$\mathrm{div}(\boldsymbol{V_{c,x}}') = \mathrm{div}(\boldsymbol{V_{d,x}}') = 0, \tag{33}$$

$$-\alpha_{co}\rho_{co}(i\omega)\boldsymbol{V}_{\boldsymbol{c,x}'} = -\nabla(\alpha_{c,\boldsymbol{x}'}p_{c,\boldsymbol{x}'}) + \mu_c \Delta \boldsymbol{V}_{\boldsymbol{x}'} + \mathrm{div}\langle \chi_d \boldsymbol{\Pi}' \rangle_{\boldsymbol{x}'} - \boldsymbol{F}_{\boldsymbol{x}'} - \alpha_{co}\rho_{co}\nabla\Psi, \tag{34}$$

$$-\alpha_{do}\rho_{do}(i\omega)\boldsymbol{V}_{\boldsymbol{d,x}'} = \boldsymbol{F}_{\boldsymbol{x}'} - \alpha_{do}\rho_{do}\nabla\Psi, \tag{35}$$

with

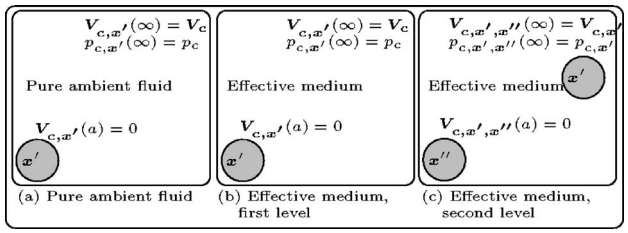

FIG. 3. Calculation of closure terms at different levels of the hierarchy.

$$\{\boldsymbol{V}_{\boldsymbol{d},\boldsymbol{x}'}, \boldsymbol{V}_{\boldsymbol{c},\boldsymbol{x}'}\} = \{\boldsymbol{v}_{\boldsymbol{d},\boldsymbol{x}'}, \boldsymbol{v}_{\boldsymbol{c},\boldsymbol{x}'}\} - \boldsymbol{v}_{\boldsymbol{d}}|_{r=0},$$

$$\Psi = -i\omega \boldsymbol{r} \cdot \boldsymbol{v}_{\boldsymbol{d}}|_{r=0}. \tag{36}$$

The terms proportional to $\nabla\Psi$ appearing in these equations are due to the change of reference frame. The boundary conditions can also be rewritten:

$$\boldsymbol{V}_{\boldsymbol{c},\boldsymbol{x}'} \to 0 \quad \text{when } r \to a, \tag{37}$$

$$\boldsymbol{V}_{\boldsymbol{c},\boldsymbol{x}'} \to \boldsymbol{V}_{\boldsymbol{c}} \quad \text{and} \quad p_{c,\boldsymbol{x}'} \to p_c \quad \text{when } r \to \infty. \tag{38}$$

Then, integrands (18) and (19) can be calculated for a particle embedded in a pure incompressible fluid, with boundary conditions (37) and (38) [cf. Fig. 3(a)]. The first integrand (18) corresponds to the classical calculation of the force applied on a moving sphere embedded in an unsteady nonuniform velocity field, sometimes called the Basset-Boussinesq-Oseen force.[29] The calculation of the second integrand (19) is less usual and can be found in some papers by Buyevich:[29,23]

$$\boldsymbol{F} = m_1(\boldsymbol{V}_{\boldsymbol{c}} - \boldsymbol{V}_{\boldsymbol{d}}) + m_2 \Delta \boldsymbol{V}_{\boldsymbol{c}} + m_3 \nabla \Psi, \tag{39}$$

$$\mathrm{div}\langle \chi_d \boldsymbol{\Pi}' \rangle = -\nabla(\alpha_d p_c) + m_0 \Delta \boldsymbol{V}_{\boldsymbol{c}}, \tag{40}$$

where m_0, m_1, m_2, and m_3 depend on the properties of the pure ambient fluid (μ_c, ρ_{co}) and on frequency ω. In these expressions, $m_1(\boldsymbol{V}_{\boldsymbol{c}} - \boldsymbol{V}_{\boldsymbol{d}})$ corresponds to the sum of the Stokes drag, the Basset hereditary, and the total inertial forces; $m_2 \Delta \boldsymbol{V}_{\boldsymbol{c}}$ is the Oseen correction due to the nonuniformity of the ambient fluid velocity; and $m_3 \nabla \Psi$ comes from the change of reference frame.

In the effective medium, the same relations stand:

$$\boldsymbol{F} = m_1^*(\boldsymbol{V}_{\boldsymbol{c}} - \boldsymbol{V}_{\boldsymbol{d}}) + m_2^* \Delta \boldsymbol{V}_{\boldsymbol{c}} + m_3^* \nabla \Psi, \tag{41}$$

$$\mathrm{div}\langle \chi_d \boldsymbol{\Pi}' \rangle = -\nabla(\alpha_d p_c) + m_0^* \Delta \boldsymbol{V}_{\boldsymbol{c}}, \tag{42}$$

but m_0^*, m_1^*, m_2^*, and m_3^* depend on the effective properties of the surrounding fluid (μ_{eff}, ρ_{eff1}, ρ_{eff2}), where ρ_{eff1} and ρ_{eff2} are some effective volume fractions, respectively linked to the inertial phenomena and the change of frame of reference, and μ_{eff} is the effective viscosity of the suspension.

Here arises the problem of determining these effective properties and this is the fundamental point in which our theory differs from the so-called "core shell model." These effective densities and viscosity will be calculated in a consistent way instead of being empirically introduced.

The expressions of $\boldsymbol{F}$ and $\mathrm{div}\langle \chi_d \boldsymbol{\Pi}' \rangle$ come from the calculation of integrands (18) and (19) in the *final* effective medium with boundary conditions (37) and (38) as illustrated by Fig. 3(b). At the next level of the hierarchy, the particles are also embedded in the *final* effective medium and the boundary conditions become [cf. Fig. 3(c)]

$$\boldsymbol{V}_{\boldsymbol{c},\boldsymbol{x}',\boldsymbol{x}''} \to 0 \quad \text{when } r \to a, \tag{43}$$

$$\boldsymbol{V}_{\boldsymbol{c},\boldsymbol{x}',\boldsymbol{x}''} \to \boldsymbol{V}_{\boldsymbol{c},\boldsymbol{x}'} \quad \text{and } p_{c,\boldsymbol{x}',\boldsymbol{x}''} \to p_{c,\boldsymbol{x}'} \quad \text{when } r \to \infty. \tag{44}$$

This is exactly the same problem, but the boundary conditions are expressed in terms of the conditionally averaged fields instead of the averaged fields. So $\boldsymbol{F}_{\boldsymbol{x}'}$ and $\mathrm{div}\langle \chi_d \boldsymbol{\Pi}' \rangle$ will be related to $\boldsymbol{V}_{\boldsymbol{c},\boldsymbol{x}'}, \boldsymbol{V}_{\boldsymbol{d},\boldsymbol{x}'}$, and $\nabla\Psi$ with *exactly the same coefficients* m_0^*, m_1^*, m_2^*, and m_3^*:

$$\boldsymbol{F}_{\boldsymbol{x}'} = m_1^*(\boldsymbol{V}_{\boldsymbol{c},\boldsymbol{x}'} - \boldsymbol{V}_{\boldsymbol{d},\boldsymbol{x}'}) + m_2^* \Delta \boldsymbol{V}_{\boldsymbol{c},\boldsymbol{x}'} + m_3^* \nabla \Psi, \tag{45}$$

$$\mathrm{div}\langle \chi_d \boldsymbol{\Pi}' \rangle_{\boldsymbol{x}'} = -\nabla(\alpha_{d,\boldsymbol{x}'} p_{c,\boldsymbol{x}'}) + m_0^* \Delta \boldsymbol{V}_{\boldsymbol{c},\boldsymbol{x}'}. \tag{46}$$

It is the equality of these coefficients at every order of the hierarchy that expresses the self-consistent condition. With this condition, there is no need to truncate the hierarchy at a finite order because the system is already closed as we will see.

To determine the expressions of the effective parameters in a consistent way, previous equations must be combined properly to obtain a final system of equations in the effective medium similar to the equations that would stand in the pure medium, that is to say,

$$\mathrm{div}(\boldsymbol{V}_{\boldsymbol{c},\boldsymbol{x}'}) = 0, \tag{47}$$

$$-\rho_{\mathrm{eff1}}(i\omega)\boldsymbol{V}_{\boldsymbol{c},\boldsymbol{x}'} = -\nabla p_{c,\boldsymbol{x}'} + \mu_{\mathrm{eff}} \Delta \boldsymbol{V}_{\boldsymbol{c},\boldsymbol{x}'} - \rho_{\mathrm{eff2}} \nabla \Psi. \tag{48}$$

If we replace relations (45) and (46) in Eqs. (33)–(35), we obtain together with Eq. (48) a set of 11 equations. On the other hand, we have 11 unknown parameters: the six components of velocities $\boldsymbol{V}_{\boldsymbol{d},\boldsymbol{x}'}$ and $\boldsymbol{V}_{\boldsymbol{c},\boldsymbol{x}'}$, the three effective parameters ρ_{eff1}, ρ_{eff2}, and μ_{eff}, the volume fraction $\alpha_{d,\boldsymbol{x}'}$, and the pressure $p_{c,\boldsymbol{x}'}$. Therefore, the effective properties can be expressed in terms of the coefficients m_k^* (for more details, cf. the original derivation by Buyevich[23]):

$$\rho_{\mathrm{eff1}} = \alpha_{co}\rho_{co} + \frac{\alpha_{do}\rho_{do} m_1^*}{m_1^* - i\omega\alpha_{do}\rho_{do}}, \tag{49}$$

$$\mu_{\mathrm{eff}} = \alpha_{co}\mu_c + m_0^* + \frac{\alpha_{do}\rho_{do} i\omega m_2^* + \alpha_{do}\mu_c(m_1^* - i\omega m_2^* \rho_{\mathrm{eff1}}/\mu_{\mathrm{eff}})}{m_1^* - i\omega\alpha_{do}\rho_{do}}, \tag{50}$$

$$\rho_{\mathrm{eff2}} = \alpha_{co}\rho_{co} + \alpha_{do}\rho_{do}\frac{m_1^* - m_3^* i\omega}{m_1^* - i\omega\alpha_{do}\rho_{do}}. \tag{51}$$

Now Eqs. (47) and (48) can be solved[29,23] with boundary conditions (37) and (38) to calculate integrands (18) and (19). We will obtain the same expressions as in the case of the pure fluid, but the effective properties (μ_{eff}, ρ_{eff1}, ρ_{eff2}) will stand instead of the pure fluid properties (μ_c, ρ_{co}):

$$m_0^* = \frac{5\alpha_{do}\mu_{\text{eff}}\exp(\beta)}{2(1+\beta)}, \tag{52}$$

$$m_1^* = \frac{9\alpha_{do}}{2a^2}(1+\beta+\beta^2/3)\mu_{\text{eff}}, \tag{53}$$

$$m_2^* = \frac{9\alpha_{do}}{2\beta^2}(\exp(\beta)-(1+\beta+\beta^2/3))\mu_{\text{eff}}, \tag{54}$$

$$m_3^* = \alpha_{do}\rho_{\text{eff2}}, \tag{55}$$

with

$$\beta^2 = -(i\omega)\rho_{\text{eff1}}a^2/\mu_{\text{eff}}. \tag{56}$$

Thus, coefficients m_k^* are expressed in terms of the effective properties and the system is closed. There only remains to solve numerically the self-consistent system formed by Eqs. (49)–(55) in the complex plane. This can be achieved by a simple iterative procedure, but some more elaborate schemes such as the so-called "Globally Convergent Newton's Method" can also be used.

We can notice that in the steady regime, we simply obtain

$$\rho_{\text{eff1}} = \rho_{\text{eff2}} = \alpha_{co}\rho_{co} + \alpha_{do}\rho_{do} \equiv \rho, \quad \mu_{\text{eff}} = \mu_c/(1-5/2\alpha_{do}).$$

This simple case illustrates the strength of the self-consistent scheme. A truncation of the hierarchy at the first order would have given the well-known Einstein formula:

$$\mu_{\text{eff}} = \mu_c(1+5/2\alpha_{do}) + O(\alpha_{do}^2).$$

It can be simply obtained from the expression (50) of μ_{eff} by replacing the coefficients m_k^* by their expression in the pure fluid m_k and by taking the asymptotic limit when $\omega=0$.

A truncation at order n would have given a formula of the form

$$\mu_{\text{eff}} = 1+5/2\alpha_{do} + \sum_{i=2}^{n} K_i\alpha_{do}^i + O(\alpha_{do}^{n+1}).$$

Thus all these formulas are limited to $\alpha_{do} \ll 1$. With the self-consistent theory, we directly obtain the whole series expression.

To conclude this part we would like to point out some differences with other models. First, we can note that the above steady effective properties are commonly used in the "core shell" model. Thus, the evolution of these parameters with frequency is neglected, contrary to the present study. Then, one of the differences with the model proposed by Spelt *et al.*[17] is that, in our theory, the relation between the closure terms and the averaged fields (expressed by coefficients m_k^*) is deduced from the pure fluid expressions. In the article by Spelt *et al.*, the authors say that each closure relation can be expressed in terms of any of the averaged fields as these field are also related to each other through algebraic equations that depend on the frequency and the effective wave number. This is a correct argument but only for plane waves because more complicated relations stand between averaged fields when dealing with spherical or more complicated wavefronts.

E. Dispersion equation for a plane acoustic wave

Now, we will derive the dispersion equation for a plane wave such as $G=G_o+\tilde{G}e^{i(k_* x-\omega t)}$, where $\tilde{G}$ is the amplitude of the wave, G_o is the equilibrium state, and k_* is the complex effective wave number. In this case, from Eqs. (21)–(25) and the expression of closure relations (41) and (42) we get the final system:

mass conservation:

$$-i\omega(\rho_{co}\tilde{\alpha}_c + \alpha_{co}\tilde{\rho}_c) + ik_*\alpha_{co}\rho_{co}\tilde{v}_c = 0, \tag{57}$$

$$i\omega\tilde{\alpha}_c + ik_*\alpha_{do}\tilde{v}_d = 0; \tag{58}$$

momentum conservation:

$$i\omega\alpha_{co}\rho_{co}\tilde{v}_c - ik_*\tilde{p}_c = k_*^2(\lambda_c+2\mu_c)(\alpha_{co}\tilde{v}_c + \alpha_{do}\tilde{v}_d) + k_*^2 m_0^*\tilde{v}_c + [m_1^*(\tilde{v}_c-\tilde{v}_d) - k_*^2 m_2^*\tilde{v}_c - i\omega m_3^*\tilde{v}_d], \tag{59}$$

$$-i\alpha_{do}\rho_{do}\omega\tilde{v}_d = m_1^*(\tilde{v}_c-\tilde{v}_d) - k_*^2 m_2^*\tilde{v}_c - i\omega m_3^*\tilde{v}_d; \tag{60}$$

state equation:

$$\tilde{p}c = c_{co}^2\tilde{\rho}_c, \tag{61}$$

where c_{co} is the sound velocity at rest in the continuous phase and parameters m_k^* can be numerically calculated from expressions (49)–(55) as mentioned earlier. This system is therefore a linear system of five equations, with five unknowns, $\tilde{\alpha}_c$, $\tilde{\rho}_c$, $\tilde{v}_c$, $\tilde{v}_d$, and $\tilde{p}_c$, and is consequently well posed. If we introduce the following parameters,

$$M_k^* = \frac{m_k^*}{\alpha_{do}\rho_{do}}, \quad d_r = \frac{\alpha_{do}\rho_{do}}{\alpha_{co}\rho_{co}}, \quad \text{and} \quad r = \frac{\rho_{co}}{\rho_{do}},$$

we get from (60)

$$\tilde{v}_d = [h_v - k_*^2 h_c]\tilde{v}_c \tag{62}$$

with

$$h_v = \frac{M_1^*}{M_1^* + i\omega(M_3^*-1)} \quad \text{and} \quad h_c = \frac{M_2^*}{M_1^* + i\omega(M_3^*-1)}.$$

Finally, by combining the conservation equations, we obtain the following bicubic equation, which can easily be solved to calculate the effective wave number:

$$Ak_*^4 + Bk_*^2 + C = 0, \tag{63}$$

$$A = d_r h_c\left[\frac{(\lambda_c+2\mu_c)}{\rho_{do}i\omega} + \frac{rc_{co}^2}{\alpha_{co}\omega^2}\right], \tag{64}$$

$$B = -d_r\left[h_c + \frac{M_0^* + (\lambda_c+2\mu_c)(\alpha_{co}+\alpha_{do}h_v)}{i\omega}\right] - \frac{c_{co}^2}{\alpha_{co}\omega^2}[1+d_r r h_v], \tag{65}$$

$$C = 1 + d_r h_v. \tag{66}$$

This calculation can be simplified because $h_v/k_*^2 h_c \gg 1$. This can be proved either by calculating it numerically or by noticing that this ratio is of the form of an effective acoustic Reynolds number, which is therefore large compared to unity. Thus, all terms proportional to h_c in the preceding equations can be neglected and we finally obtain

$$\left(\frac{k_*}{\omega} c_{co}\right)^2 = I(\omega) V(\omega),$$

$$I(\omega) = \left[1 - \frac{\alpha_{co} d_r i\omega}{c_{co}^2 (1 + d_r r h_v)} \times \left[M_0^* + \frac{(\lambda_c + 2\mu_c)(\alpha_{co} + \alpha_{do} h_v)}{\alpha_{do} \rho_{do}}\right]\right]^{-1},$$

$$V(\omega) = \left[1 + d_r \frac{(\alpha_{co} - r) h_v - \alpha_{co} r}{1 + d_r r h_v}\right].$$

In this expression $I(w)$ corresponds to the intrinsic (bulk) losses in the medium and $V(\omega)$ to the visco-inertial interactions between the two phases.

III. COMPARISON WITH EXPERIMENTS AND OTHER THEORIES

In this section, we will first compare the effective medium theory (EMT) with the multiple scattering theory (MST) from a theoretical point of view. Then, we will compare the predictions of our theory with the experimental data of Hipp *et al.*[25] and also with the "classical coupled phase theory" in which the calculation of the closure terms is based on the pure ambient fluid parameters instead of the effective ones.

A. Theoretical comparison with the multiple scattering theory

The hierarchy appearing in the EMT is similar to the hierarchy that also appears in the MST [see Ref. 11, Eq. (2.13)]. However, in the EMT the hierarchy is a succession of mutually dependent equations governing the conditionally averaged fields, whereas in the MST the hierarchy concerns the exciting field. This is one of the fundamental points in which these two theories differ.

Before delving into this crucial problem, let us clarify the terminology used here. The exciting field ($G_j'^E$) acting on the jth particle is the sum of the original field that would exist in the absence of particles (G'^0), and the wave scattered by every particle ($G_k'^S$) except the jth:

$$G_j'^E(\boldsymbol{x}, t|\boldsymbol{x_1}, \ldots, \boldsymbol{x_N}) = G'^0(\boldsymbol{x}, t) + \sum_{k \neq j} G_k'^S(\boldsymbol{x}, t|\boldsymbol{x_1}, \ldots, \boldsymbol{x_N}). \tag{67}$$

Note that this deterministic formulation is exact and that only the last scattering event of the particle j is omitted. Thus $G_k'^S$ may involve previous scattering by the jth particle. Otherwise, resonant scattering between a cluster of particles, i.e., loops, would be neglected.

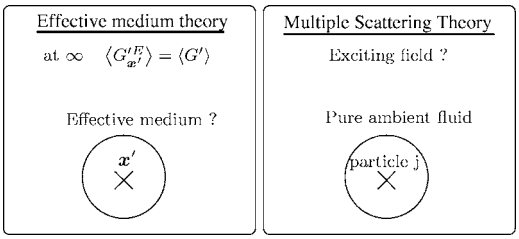

FIG. 4. Comparison between the self-consistent theory and the multiple scattering theory.

In the linear regime, the wave scattered by the jth particle can be related to the exciting field acting on it by the introduction of a linear operator T_j so that

$$G_j'^E(\boldsymbol{x}, t|\boldsymbol{x_1}, \ldots, \boldsymbol{x_N}) = G'^0(\boldsymbol{x}, t) + \sum_{k \neq j} T_k G_k'^E(\boldsymbol{x}, t|\boldsymbol{x_1}, \ldots, \boldsymbol{x_N}). \tag{68}$$

The introduction of this operator is a crucial step in the MST and it means that this theory is limited to the linear regime whereas the EMT is not. We can also note that the operator T_j is computed by using the properties of the pure ambient fluid.

The following relation stands between the total field (G'), the exciting field acting on the jth particle ($G_j'^E$), and the wave scattered by the same particle ($G_j'^S$):

$$G'(\boldsymbol{x}, t|\boldsymbol{x}_1, \ldots, \boldsymbol{x}_N) = G_j'^E(\boldsymbol{x}, t|\boldsymbol{x}_1, \ldots, \boldsymbol{x}_N) + G_j'^S(\boldsymbol{x}, t|\boldsymbol{x_1}, \ldots, \boldsymbol{x_N}). \tag{69}$$

Now we can clarify the previous assertion. In the EMT, a test particle is considered in $\boldsymbol{x}'$, and the value of the averaged exciting field acting on it is known far from the particle as the influence of the test particle vanishes:

$$\langle G_{\boldsymbol{x}'}'^E \rangle_{\boldsymbol{x}'} \to \langle G' \rangle \quad \text{when } r \to \infty \quad \text{as } \langle G_{\boldsymbol{x}'}'^S \rangle_{\boldsymbol{x}'} \to 0, \tag{70}$$

where $G_{\boldsymbol{x}'}'^E$ and $G_{\boldsymbol{x}'}'^S$ are respectively the exciting field acting on the particle located in $\boldsymbol{x}'$ and the wave scattered by this particle. This relation corresponds to the boundary condition (20). The fundamental problem here is thus to determine the expression of the effective medium surrounding the particle to perform integrands (18) and (19).

In the multiple scattering theory, we suppose that all particles are embedded in the pure ambient fluid (by introducing the operator T) and the problem, in this case, is to determine the form of the exciting field. These two approaches can be summarized by Fig. 4. We will now show that, at the lowest level, these two theories are equivalent. For that purpose, let us recall the assumptions implicitly made by Foldy[8] (and listed by Waterman and Truell[11]), when he identifies the average of the exciting field with the average of the total field to achieve closure. The starting point of his derivation is Eq. (68).

(1) Its first assumption is that the exciting field acting on the jth particle is the total field that would exist if this particle was not there:

$$G_j'^E(\boldsymbol{x},t|\boldsymbol{x}_1,\ldots,\boldsymbol{x}_N) = G'(\boldsymbol{x},t|\boldsymbol{x}_1,\ldots,\boldsymbol{x}_{j-1},\boldsymbol{x}_{j+1},\ldots\boldsymbol{x}_N),$$

Here, Foldy neglects all mutual interactions of the particles (loops) as the jth particle cannot influence the other particles that produce the exciting field.

(2) Then he assumes that the probability density conditioned by the position of one particle $p(t,\boldsymbol{x}_1,\ldots,\boldsymbol{x}_{j-1},\boldsymbol{x}_{j+1},\ldots,\boldsymbol{x}_N|\boldsymbol{x}_j)$ is equal to the unconditional probability: $p(t,\boldsymbol{x}_1,\ldots,\boldsymbol{x}_{j-1},\boldsymbol{x}_{j+1},\ldots,\boldsymbol{x}_N)$. This assumption leads to the statistical independence so that the correlations of particles in position are neglected and thus the particles can overlap one another.
(3) His third hypothesis is not restrictive; he assumes that the contributions of a single particle on the mean field can be neglected. This will be valid whenever the number N of particles appearing in the statistical average process is large enough, as the contribution of a single particle is of the order $1/N$.

Of course the first and second hypotheses are linked: to account properly for interactions of two or more particles, one should determine the correlations in position. But they are also undoubtedly distinct. One could, for example, estimate the interactions of pairs with an inaccurate distribution of the particles, for example by supposing that they can overlap one another. This would lead to an expression that would not be valid for too concentrated solutions but that would nevertheless incorporate pair interactions.

Assumptions 1–3 lead to the simple relation:

$$\langle G_j'^E(\boldsymbol{x},t)\rangle_j = \langle G'(\boldsymbol{x},t)\rangle. \tag{71}$$

So, the average of the exciting field acting on the jth particle is equal to the mean field, and the particle is embedded in the pure ambient fluid. This situation is therefore equivalent to the first level of the EMT hierarchy. However, even at this level, there is still a fundamental difference between these two theories. In the coupled phase theory, averaged equations are derived with respect to the volume fraction occupied by each phase. In the derivation of Foldy, however, the particles are supposed to be pointlike. Thus the decrease of the volume fraction occupied by the continuous phase due to the increase of the number of particles is not accounted for. The difference between these two theories can be neglected when the number of particles is large but the corresponding volume fraction is small. However, this difference becomes important when the particles occupy a large volume fraction: in the coupled phase theory when $\alpha_{do}\to 1$, only the intrinsic absorption in the dispersed phase remains whereas in the theory of Foldy the effects are maximum.

To account for interactions of pairs of particles, Lax introduced the so-called "quasi-crystalline approximation"[10] according to which the averaged exciting field acting on the jth particle when the position of two particles is known (j,k) is approximately equal to the averaged exciting field acting on the jth particle when only the position of the latter is known

$$\langle G_j'^E(\boldsymbol{x},t)\rangle_{jk} \approx \langle G_j'^E\rangle_j. \tag{72}$$

This approximation comes within the scope of a more general frame in which the averaged exciting field with n positions of particles being known is supposed to be approximately equal to the averaged exciting field with $n-1$ known positions.

To conclude this part, we can underline the fact that such a procedure will always result in a polynomial development with respect to the particle concentration and will thus be limited to relatively dilute mixtures whereas the EMT is not.

B. Comparison with the classical coupled phase theory and experimental data

Figure 5 compares the results obtained with our theory with the experimental data of Hipp *et al.*[14] and also with the "classical coupled phase theory." In this figure, we can see how much the predictions are improved by the introduction of the effective parameters instead of the pure fluid values, for low frequencies, when the interactions between the particles are strong because of the overlapping of boundary layers. However, when the frequency increases, some differences between the predictions and the experiments appear. They may be explained by the following considerations.

When the correlations of particles in position are considered, the more we approach the test particle, the more unlikely is the presence of another particle because they cannot overlap one another. So, it means that the conditional volume fraction $\alpha_{do,\boldsymbol{x}'}\to 0$ when $r\to a$. On the opposite, far from the test particle, the modification of the particle distribution induced by the presence of the test sphere vanishes so that $\alpha_{do,\boldsymbol{x}'}\to\alpha_{do}$ when $r\to\infty$. The transition between these two regimes appears approximately when $r\approx 2a$, which is the characteristic length that can be introduced because of the non-overlapping property of the particles. On the other hand, we can notice that the boundary layer thickness δ_v is inversely proportional to the square root of the frequency, so that when the frequency increases, this thickness decreases.

In our model, the correlations of particles in position are not considered and thus the effective properties do not depend on the distance from the particle surface. As long as $\delta_v \gg a$, approximating the effective medium surrounding the particle by homogeneous parameters based on the approximation $\alpha_{do,\boldsymbol{x}'}(r)=\alpha_{do}$ is accurate. But when $\delta v\approx a$, the variations of the conditional volume fraction with the distance r from the particle center cannot be neglected anymore. When $\delta_v \ll a$, the parameters of the effective medium in the boundary layer are even very close to the pure fluid values as almost no particles are present in this region. Consequently, the approximation that consists in taking the pure fluid parameters (ρ_{co},μ_c) to calculate the closure terms should give better results in this frequency range. To verify the validity of this hypothesis, we have plotted the attenuation curves for larger particles (cf. Fig. 6). In this case the characteristic frequency coresponding to $\delta_v=a$ is equal to $f_c=11$ MHz, whereas for Fig. 5 it was equal to 101 MHz.

On the above curves, we can observe the transition between the two asymptotic limits, around the characteristic frequency f_c, therefore corroborating our hypothesis. Our

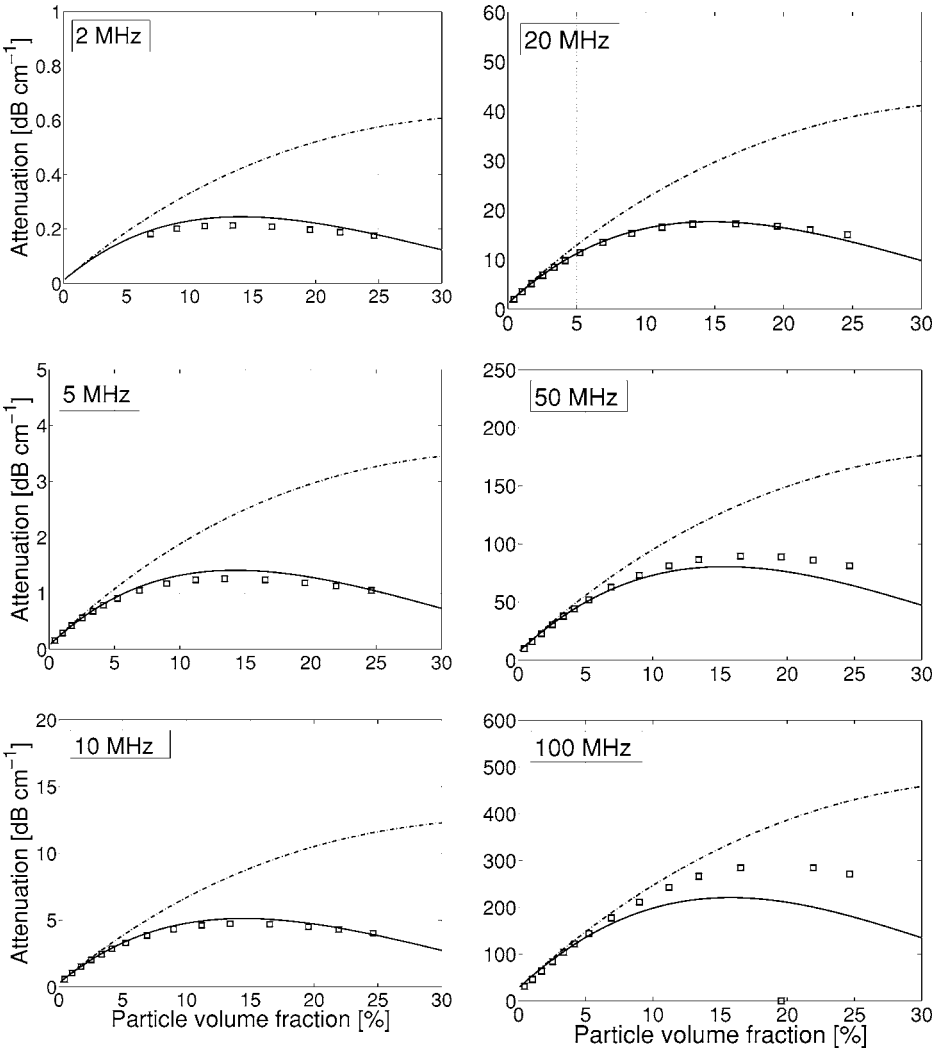

FIG. 5. Attenuation as a function of the volume fraction at various frequencies for silica particles of 56-nm radius in water. The solid lines correspond to our theory (—), the broken line to the classical coupled phase theory (- · -), and the symbols to the experimental data.

analysis shows how important the correlations in position are in the calculation of the effective parameters in acoustics. Thus, their integration in the calculation of coefficients m_k^* should give the smooth transition between these two limiting cases.

To conclude this section, we also plotted the curves with and without the intrinsic (bulk) losses, which are often neglected in the coupled phase models (cf. Fig. 7). These effects prove to be important for volume fraction up to 6% and must therefore be included correctly in formulation.

IV. EXTENSION TO THE POLYDISPERSE CASE

In this section, we will extend previous equations to polydisperse suspensions by using the same procedure as the one introduced by Gubaidullin and Nigmatulin[30] in their treatment of polydisperse aerosols. When a polydisperse suspension is considered, the probability $p(t,\boldsymbol{x})$ of finding any particle in x at t is replaced by the probability $p(t,\boldsymbol{x},a)$ of finding a particle of radius a in x at t. In this case, the properties of the dispersed phase also depend on the particule radius. So instead of introducing directly the phasic average over the whole dispersed phase $\langle \chi_d G' \rangle / \alpha_d$, we will split it into two steps:

- first, an average over all particles with the same radius $G_p(a) = \langle \chi_a G' \rangle / \alpha_p(a)$, where

$$\chi_a(\boldsymbol{x},t) = \begin{cases} 1 & \text{if } \boldsymbol{x} \text{ is in a particle of size } a \text{ at time } t, \\ 0 & \text{otherwise,} \end{cases}$$

  and $\alpha_p(a) = \langle \chi_a(\boldsymbol{x},t) \rangle$ is the volume fraction occupied by particles of radius a,
- and second, an average $\langle \rangle_a$ over all the particles sizes:

$$G_d = \frac{1}{\alpha_d} \langle G_p(a) \rangle_a = \frac{1}{\alpha_d} \int_{a_{\min}}^{a_{\max}} \alpha_p(a) G_p(a)\, da.$$

We can now derive the equations in the polydisperse case. The equations of the continuous phase will remain the same, but the momentum conservation equation of the dispersed phase will be derived for each particle size so that the set of Eqs. (57)–(61) becomes

mass conservation:

$$-i\omega(\rho_{co}\tilde{\alpha}_c + \alpha_{co}\tilde{\rho}_c) + ik_*\alpha_{co}\rho_{co}\tilde{v}_c = 0,$$

$$i\omega\tilde{\alpha}_c + ik_*\alpha_{do}\langle \tilde{v}_p \rangle_a = 0;$$

momentum conservation:

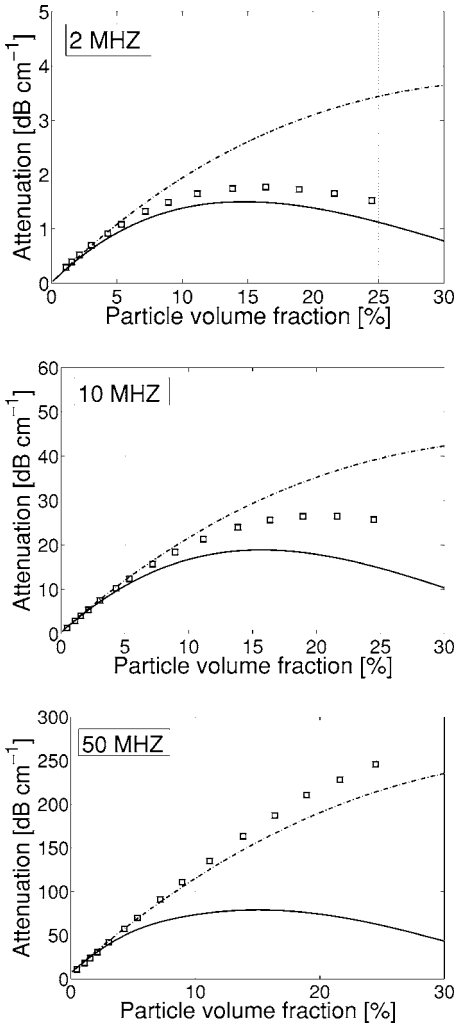

FIG. 6. Attenuation as a function of the volume fraction at various frequencies for silica particles of 164.5-nm radius in water. The solid lines correspond to our theory (—), the broken line to the classical coupled phase theory (- · -), and the symbols to the experimental data.

$$i\omega\alpha_{co}\rho_{co}\tilde{v}_c - ik_*\tilde{p}_c$$
$$= k_*^2(\lambda_c + 2\mu_c)(\alpha_{co}\tilde{v}_c + \alpha_{do}\langle\tilde{v}_p\rangle_a) + k_*^2\langle m_0^*\rangle_a\tilde{v}_c$$
$$+ \langle m_1^*(\tilde{v}_c - \tilde{v}_p)\rangle_a - k_*^2\langle m_2^*\rangle_a\tilde{v}_c - i\omega\langle m_3^*\tilde{v}_p\rangle_a,$$
$$- i\alpha_{do}\rho_{do}\omega\tilde{v}_p = m_1^*(\tilde{v}_c - \tilde{v}_p) - k_*^2 m_2^*\tilde{v}_c - i\omega m_3^*\tilde{v}_p;$$

state equation:

$$\tilde{p}_c = c_{co}^2\tilde{\rho}_c.$$

In these equations, the coefficients m_k^* depend on the particle size and must therefore be calculated for each radius a.

Then we can express the velocity of the dispersed phase $\tilde{v}_p$ in terms of the velocity of the continuous $\tilde{v}_c$ phase, which is independent of the particle radius:

$$\tilde{v}_p = [h_v(a) - k_*^2 h_c(a)]\tilde{v}_c.$$

In this way, we can extract the continuous phase properties from the average $\langle\rangle_a$. If we now combine the conservation equations, we finally obtain the same dispersion equation as in the monodisperse case but with respectively $\langle h_v\rangle_a$, $\langle h_c\rangle_a$, and $\langle M_0^*\rangle_a$ instead of h_v, h_c, and M_0^*. Thus, only the average

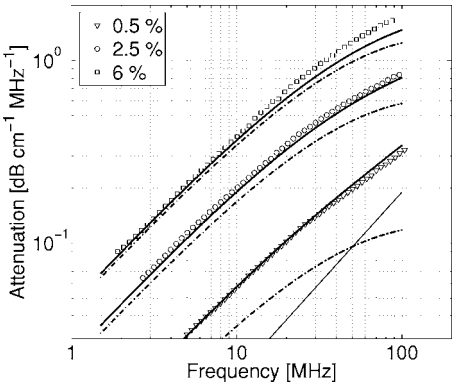

FIG. 7. Attenuation as a function of the frequency at different volume fractions for silica particles of 56-nm radius in water. The solid lines correspond to the complete theory (—), the broken line to the theory without intrinsic losses (- · -), the symbols to the experimental data, and the thin straight line to the intrinsic losses in water.

of these three parameters must be calculated to extend the validity of our dispersion relation to the polydisperse case.

V. CONCLUSION

The coupled phase theory has been improved to consider polydisperse suspensions and viscous interactions with the use of an effective medium, self-consistent theory. Our derivation is based on Buyevich's incompressible hydrodynamic model extended here to acoustical waves propagation. This theory turns out in practice to be very effective, as it amounts finally to a dispersion relation, which can be used directly for measurements or simulations. When compared with experiments, this model provides an accurate description of the attenuation at low frequencies, for concentrated suspensions for which interactions between particles are strong. In particular, the self-consistent approach has the ability to take properly into account interactions at all orders, such as the overlapping of viscous boundaries layers and the loops in the sense of the multiple scattering theory (MST) of waves. The link between the MST and the effective medium theory (EMT) has also been clarified.

Finally, our derivation could be extended to higher frequencies (or equivalently larger particles) and higher volume fractions by taking into account the correlations of particles in position, which would affect the effective properties of the medium. Its validity could even be enlarged to the high frequency regime by including the compressibility of the liquid when calculating the closure terms.[31,32]

ACKNOWLEDGMENTS

The authors would like to thank A. K. Hipp, G. Storti, and M. Morbidelli (Department of Chemical Engineering, ETH Zürich) for kindly providing us with the results of their experiments.

[1]C. J. T. Sewell, "On the extinction of sound in a viscous atmosphere by small obstacles of cylindrical and spherical form," Philos. Trans. R. Soc. London **210**, 239–270 (1910).
[2]H. Lamb, *Hydrodynamics* (Dover, New York, 1945).
[3]P. S. Epstein and R. R. Carhart, "The absorption of sound in suspensions and emulsions. I. Waterfog in air," J. Acoust. Soc. Am. **25**(3), 553–565

(l953).
[4]J. R. Allegra and S. A. Hawley, "Attenuation of sound in suspensions and emulsions: Theory and experiments," J. Acoust. Soc. Am. **51**, 1545–1564 (1972).
[5]A. H. Harker and J. A. G. Temple, "Velocity and attenuation of ultrasound in suspensions of particles in fluids," J. Phys. D **21**, 1576–l588 (1988).
[6]J. M. Evans and K. Attenborough, "Coupled phase theory for sound propagation in emulsions," J. Acoust. Soc. Am. **102**(1), 278–282, (1997).
[7]O. G. Harlen, M. J. Holmes, M. J. W. Povey, Y. Qiu, and B. D. Sleeman, "A low frequency potential scattering description of acoustic propagation in dispersions," SIAM J. Appl. Math. **61**(6), 1906–1931 (2001).
[8]L. L. Foldy, "The multiple scattering of waves. I. General theory of isotropic scattering by randomly distributed scatterers," Phys. Rev. **67**, 107–119 (1945).
[9]M. Lax, "Multiple scattering of waves," Rev. Mod. Phys. **23**, 287–310 (l951).
[10]M. Lax, "Multiple scattering of waves. II. The effective field in dense systems," Phys. Rev. **85**, 621–629 (1952).
[11]P. C. Waterman and R. Truell, "Multiple scattering of waves," J. Math. Phys. **2**, 512–537 (1961).
[12]V. Twersky, "On scattering of waves by random distributions. I. Free-space scatterer formalism," J. Math. Phys. **3**, 700–715 (1962).
[13]P. Lloyd and M. V. Berry, "Wave propagation through an assembly of spheres. IV. Relations between different multiple scattering theories," Proc. Phys. Soc. London **91**, 678–688 (1967).
[14]A. K. Hipp, G. Storti, and M. Morbidelli, "On multiple-particle effects in the acoustic characterization of colloidal dispersions," J. Phys. D **32**, 568–576 (1999).
[15]Y. Hemar N. Herrmann, P. Lemaréchal, R. Hocquart, and F. Lequeux, "Effective medium model for ultrasonic attenution due to the thermo-elastic effect in concentrated emulsions," J. Phys. II **7**, 637–647 (1997).
[16]Yu. A. Buyevich, "Heat and mass transfer in disperse media. II. Constitutive equations," Int. J. Heat Mass Transfer **35**(10), 2453–2463 (1992).
[17]P. D. M. Spelt, M. A. Norato, A. S. Sangani, M. S. Greenwood, and L. L. Tavlarides, "Attenuation of sound in concentrated suspensions: theory and experiments," J. Fluid Mech. **430**, 51–86. (2001).
[18]A. K. Hipp, G. Storti, and M. Morbidelli, "Acoustic characterization of concentrated suspensions and emulsions. 1. model analysis," Langmuir **18**, 391–404 (2002).
[19]D. J. McClements, Y. Hemar, and N. Herrmann, "Incorporation of thermal overlap effects into multiple scattering theory," J. Acoust. Soc. Am. **2**, 915–918 (1999).
[20]A. S. Dukhin and P. J. Goetz, "Acoustic spectroscopy for concentrated polydisperse colloids with high density contrast," Langmuir **12**, 4987–4997 (1996).
[21]J. Happel and H. Brenner, *Low Reynolds Number Hydrodynamics* (Martinus Nijhoff, Dordrecht, 1973).
[22]T. A. Strout, "Attenuation of sound in high-concentration suspensions: development and application of an oscillatory cell model," Ph.D. thesis, The University of Maine, 1991.
[23]Yu. A. Buyevich, "Interphase interaction in fine suspension flow," Chem. Eng. Sci. **50**(4), 641–650 (1995).
[24]Yu. A. Buyevich and I. N. Shchelchkova, "Flow of dense suspensions," Prog. Aerosp. Sci. **18**, 121–151 (1978).
[25]A. K. Hipp, G. Storti, and M. Morbidelli, "Acoustic characterization of concentrated suspensions and emulsions. 2. experimental validation," Langmuir, **18**, 391–404 (2002).
[26]D. A. Drew "Mathematical modelling of two-phase flow," Annu. Rev. Fluid Mech. **15**, 261–292 (1983).
[27]Yu. A. Buyevich and T. G. Theofanous, "Ensemble averaging in the mechanics of suspensions," FED (Am. Soc. Mech. Eng.) **243**, 41–60 (1997).
[28]C. A. Croxton, *Liquid State Physics. A Statistical Mechanical Introduction* (Cambridge U. P. Cambridge, 1974).
[29]Yu. A. Buyevich and V. G. Markov, "Rheology of concentrated mixtures of fluids with small particles," J. Appl. Math. Mech. **36**(3), 452–464 (1972).
[30]D. A. Gubaidullin and R. I. Nigmatulin, "On the theory of acoustic waves in polydispersed gaz-vapor-droplet suspensions," Int. J. Multiphase Flow **26**, 207–228 (2000).
[31]S. Temkin, "Viscous attenuation of sound in dilute suspensions of rigid particles," J. Acoust. Soc. Am. **100**(2), 825–831 (1996).
[32]S. Temkin and C.-M. Leung, "On the velocity of a rigid sphere in a sound wave," J. Sound Vib. **49**(1), 75–92 (1976).

Numerical investigation of elastic modes of propagation in helical waveguides

Fabien Treyssède[a)]
Laboratoire Central des Ponts et Chaussées, Division for Metrology and Instrumentation, Route de Pornic, BP 4129, 44341 Bouguenais Cedex, France

(Received 11 December 2006; revised 19 February 2007; accepted 20 February 2007)

Steel multi-wire cables are widely employed in civil engineering. They are usually made of a straight core and one layer of helical wires. In order to detect material degradation, nondestructive evaluation methods based on ultrasonics are one of the most promising techniques. However, their use is complicated by the lack of accurate cable models. As a first step, the goal of this paper is to propose a numerical method for the study of elastic guided waves inside a single helical wire. A finite element (FE) technique is used based on the theory of wave propagation inside periodic structures. This method avoids the tedious writing of equilibrium equations in a curvilinear coordinate system yielding translational invariance along the helix centerline. Besides, no specific programming is needed inside a conventional FE code because it can be implemented as a postprocessing step of stiffness, mass and damping matrices. The convergence and accuracy of the proposed method are assessed by comparing FE results with Pochhammer-Chree solutions for the infinite isotropic cylinder. Dispersion curves for a typical helical waveguide are then obtained. In the low-frequency range, results are validated with a helical Timoshenko beam model. Some significant differences with the cylinder are observed. © *2007 Acoustical Society of America.*
[DOI: 10.1121/1.2730741]

PACS number(s): 43.35.Cg, 43.20.Bi, 43.20.Mv [YHB] Pages: 3398–3408

I. INTRODUCTION

In civil engineering, steel multi-wire cables are widely employed as load-carrying members for many applications such as prestressed structures and bridges. The basic element of these cables, which can be exposed or embedded in concrete, is usually a simple straight strand made of a straight core and one layer of helical wires. The work presented in this paper is limited to exposed cables.

Mainly because of corrosion, material degradation of steel may result in fractures of wires,[1,2] which can lead to the collapse of the overall civil structure. Therefore, a structural health monitoring approach based on nondestructive evaluation methods is strongly needed in order to prevent or detect such failures or for determining the extent of degradation. Ultrasonics is one of the most popular techniques. It consists of analyzing the propagation of elastic guided waves, which are known to be multimodal and dispersive: many propagation modes can propagate simultaneously with propagation velocities depending on frequency. For a better physical understanding of these complex effects—and thus for improving the efficiency of ultrasonic methods—some theoretical models are often required.

The simplest approximating geometry of a multi-wire cable is that of an infinite cylinder. Since the early works of Pochhammer in 1876 and Chree in 1889, wave propagation inside cylindrical elastic waveguides has been widely investigated, theoretically, numerically and experimentally. Papers on this subject are numerous. For instance, we can cite the paper of Zemanek,[3] who was one of the first authors to present a complete analytical and experimental investigation.

However, some recent experimental studies of multi-wire strands have been realized pointing out the fact that the Pochhammer-Chree dispersion curves cannot accurately predict propagation inside multi-wire strands.[2,4–7] In fact, the theoretical understanding of guided ultrasonic waves in multi-wire strands is complicated by the helical geometry of peripheral wires, the inter-wire coupling and contact effects, and the presence of applied loads.[4–8]

As a first step toward an increasing complexity, the goal of this paper is to address the first above complicating effect, by proposing a numerical method allowing the study of elastic guided waves inside a single helical wire. To the author's knowledge, no such model is yet available in the literature.

In order to deal with complex geometry, some of the most popular and efficient numerical techniques are based on finite element (FE) methods. The so-called semi-analytical finite element (SAFE) method is a first approach that has been used to study uniform waveguides of arbitrary cross section—see, for instance, Refs. 9–14. Assuming an exponential dependence of the form $e^{i(kz-\omega t)}$ (where k is the wave number, z the axis waveguide, and ω is the frequency), SAFE methods are interesting from a computational point of view because only the cross section has to be meshed, hence drastically reducing the number of degrees of freedom (dofs). A drawback of these methods is that they require some specific programming inside a FE code. This can be circumvented by an interesting alternative proposed by Wilcox *et al.*[15] based on the use of an axisymmetric harmonic approach, which allows the study of straight waveguides (of arbitrarily large radius) as well as toroidal structures.[16] How-

a)Electronic mail: fabien.treyssede@lcpc.fr

 0001-4966/2007/121(6)/3398/11/$23.00 © 2007 Acoustical Society of America

ever, only a limited number of real wave numbers can be considered with this procedure (in particular, modes with imaginary or complex wave numbers cannot be dealt with).

A second approach is based on the theory of wave propagation in periodic structures. From Floquet's principle, this theory allows to study the single repetitive substructure alone, thanks to the application of a set of periodic boundary conditions involving a propagation constant corresponding to the eigenvalue. A review on the topic can be found in Ref. 17. Based on a general theory presented by Mead,[18] some periodic FE approaches and procedures have then been developed—see, for instance, Refs. 19–22. These methods are more general than SAFE's because nonuniform waveguides can be analyzed (propagation constants can be considered as the nonuniform waveguides generalization of axial wave numbers in uniform waveguides). Similarly to SAFE methods, periodic FE approaches only need the mesh of one repetitive cell, which tremendously reduces the computational cost. Besides, they can be implemented as a post-process step of a standard FE code providing stiffness, mass and damping matrices.

For modeling a single helical wire, which is a uniform waveguide, both SAFE and periodic FE approaches can be applied. However, the use of SAFE methods would a priori raise some calculation and programming difficulties. First, the elasticity equilibrium equations should be written in a helical curvilinear coordinate system, usually nonorthogonal, yielding a translational invariance along the helix centerline. Second, solving the obtained equations would require a complete reprogramming inside a standard FE code (that typically uses a Cartesian or a cylindrical coordinate system).

In this paper, the numerical technique developed is based on a periodic FE approach. It uses the outputs of a conventional FE code, that are the stiffness, mass and damping matrices. In Sec. II, the equilibrium equations and some FE procedures are first recalled. Unlike Refs. 21 and 22, the considered final eigensystem involves interior dofs, which may avoid some costly matrix inversion. A three-dimensional mapping yielding a translational invariance is then proposed in Sec. III. Based on this mapping, a peculiar mesh is generated, and the left and right dofs are transformed into their curvilinear counterparts. Numerical results are given in Sec. IV. The method is first validated with the Pochhammer-Chree solution. The numerical accuracy and convergence of the proposed numerical method is also briefly studied. Computations for a single helical wire are then realized with characteristics typically encountered in civil engineering. In the low-frequency range, the results are validated by comparing those obtained from a one-dimensional Timoshenko helical beam. Section V finally gives some general conclusions.

II. FINITE ELEMENT MODELING OF PERIODIC ELASTIC WAVEGUIDES

Waveguides can be considered as periodic systems. Because we are only interested in one-dimensional waveguides in this paper, the unit periodic cells are only connected end to end (but with multiple dofs coupling between them). This section describes the FE approach for one-dimensional periodic systems.

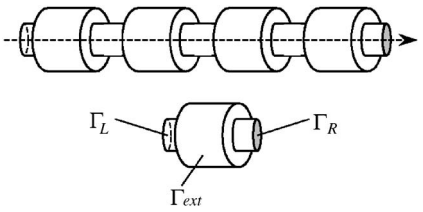

FIG. 1. Example of a nonuniform periodic waveguide with its unit periodic cell and boundaries notations.

A. Equilibrium equations

Assuming a linearly elastic material, small strains and displacements and a time harmonic $e^{-i\omega t}$ dependence, the governing equilibrium equations are given by

$$\nabla \cdot \boldsymbol{\sigma} + \rho\omega^2 \mathbf{u} = \mathbf{0} \quad \text{in } \Omega, \tag{1}$$

where $\mathbf{u}$ and $\boldsymbol{\sigma}$ respectively denote the displacement vector field and the Cauchy stress tensor, ρ is the material density and Ω represents the domain occupied by one periodic cell (or an integer multiple) constituting the overall infinite periodic structure. Let us denote by L the axial length of this cell. Of course, there is no external body force for the purpose of studying propagation modes. The stress-strain and strain-displacement relations are respectively given by $\boldsymbol{\sigma}=\mathbf{C}:\boldsymbol{\varepsilon}$ and $\boldsymbol{\varepsilon}=1/2(\nabla\mathbf{u}+\nabla\mathbf{u}^T)$.

Γ_{ext}, Γ_L and Γ_R are, respectively, the external boundary, the left cross-section boundary and the right cross-section boundary of the waveguide periodic cell ($\partial\Omega = \Gamma_{\text{ext}} \cup \Gamma_L \cup \Gamma_R$), as shown in Fig. 1. A typical waveguide may be subjected to some traction-free or zero-displacement boundary conditions on its external boundary

$$\boldsymbol{\sigma} \cdot \mathbf{n} = \mathbf{0} \quad \text{or } \mathbf{u} = \mathbf{0} \quad \text{on } \Gamma_{\text{ext}}. \tag{2}$$

From Floquet's theorem and as defined by Mead,[18] free wave motion through an infinite periodic system occurs when there is no external force and is characterized by the displacements in one element being equal to the corresponding displacements in the adjacent element times a factor denoted λ (to be found). Hence from displacement and stress continuities, the following periodic boundary conditions hold (see, for instance, Ref. 23):

$$\boldsymbol{\sigma} \cdot \mathbf{n}\big|_{\Gamma_R} = -\lambda\, \boldsymbol{\sigma} \cdot \mathbf{n}\big|_{\Gamma_L} \quad \text{and } \mathbf{u}\big|_{\Gamma_R} = \lambda\, \mathbf{u}\big|_{\Gamma_L}, \tag{3}$$

where $\mathbf{n}$ is the outer unit normal from the subsystem Ω. Setting $\lambda = e^{ikL}$, ikL is often called the axial propagation constant; k then corresponds to the axial wave number. The real and imaginary parts of kL, respectively, govern the phase change and the attenuation (or growth) over a periodic cell. Re kL can only be determined up to $2m\pi$, and as noticed in Ref. 19, only the principal value of the phase constant is calculated (i.e., $-\pi < \text{Re}\, kL < \pi$). It should be noted that some more general periodic boundary conditions than Eqs. (3) may be found in Ref. 23, taking into account the presence

of some additional connecting structures (periodic supports or stiffeners, for instance).

Without loss of generality in this paper, we will only consider waveguides having free external boundaries and no additional connecting structures.

B. Finite element method

Applying a conventional FE analysis, the discretized equations of motion (1) become after applying boundary conditions (2):

$$(\mathbf{K} - i\omega\mathbf{C} + \omega^2\mathbf{M})\mathbf{u} = \mathbf{f}, \tag{4}$$

where $\mathbf{K}$, $\mathbf{M}$ and $\mathbf{C}$ are the stiffness, mass and damping symmetric matrices; $\mathbf{u}$ and $\mathbf{f}$ are, respectively, the vector of nodal dofs (usually the nodal displacements) and the vector of nodal forces. It should be outlined that the stiffness matrix $\mathbf{K}$ might be complex when the presence of viscoelastic damping, if any, is modeled through the use of complex material properties. Depending on the damping model used, such properties can also be frequency dependent. Besides, the matrix $\mathbf{C}$ corresponding to viscous damping should be zero here because this kind of damping model has been implicitly neglected in Eq. (1) (without loss of generality for the proposed FE method); $\mathbf{u}$ may be partitioned into dofs associated with the left (L) and right (R) cross-section nodes, and with the interior (I) nodes, yielding the following system:

$$\begin{bmatrix} \mathbf{D}_{LI} & \mathbf{D}_{LL} & \mathbf{D}_{LR} \\ \mathbf{D}_{II} & \mathbf{D}_{IL} & \mathbf{D}_{IR} \\ \mathbf{D}_{RI} & \mathbf{D}_{RL} & \mathbf{D}_{RR} \end{bmatrix} \begin{Bmatrix} \mathbf{u}_L \\ \mathbf{u}_I \\ \mathbf{u}_R \end{Bmatrix} = \begin{Bmatrix} \mathbf{f}_L \\ \mathbf{0} \\ \mathbf{f}_R \end{Bmatrix}, \tag{5}$$

where we have introduced the dynamic stiffness matrix $\mathbf{D} = \mathbf{K} - i\omega\mathbf{C} + \omega^2\mathbf{M}$ from Eq. (4).

In addition, the discretized periodic condition (3) becomes

$$\mathbf{u}_R = \lambda\mathbf{u}_L \quad \text{and } \mathbf{f}_R = -\lambda\mathbf{f}_L. \tag{6}$$

Applying Eq. (6) into Eq. (5) and solving for $\mathbf{f}_R$, Eq. (5) becomes

$$\left(\mathbf{D}_1 + \lambda\mathbf{D}_2 + \frac{1}{\lambda}\mathbf{D}_3\right)\mathbf{q} = \mathbf{0} \tag{7}$$

with the notations

$$\mathbf{D}_1 = \begin{bmatrix} \mathbf{D}_{LL} + \mathbf{D}_{RR} & \mathbf{D}_{LI} \\ \mathbf{D}_{IL} & \mathbf{D}_{II} \end{bmatrix},$$
$$\mathbf{D}_2 = \begin{bmatrix} \mathbf{D}_{LR} & \mathbf{0} \\ \mathbf{D}_{IR} & \mathbf{0} \end{bmatrix}, \quad \mathbf{D}_3 = \begin{bmatrix} \mathbf{D}_{RL} & \mathbf{D}_{RI} \\ \mathbf{0} & \mathbf{0} \end{bmatrix}, \quad \mathbf{q} = \begin{Bmatrix} \mathbf{u}_L \\ \mathbf{u}_I \end{Bmatrix}. \tag{8}$$

The above system is a quadratic eigenvalue problem to be solved for λ.

Because of the symmetry of $\mathbf{D}$ (yielding $\mathbf{D}_1^T = \mathbf{D}_1$ and $\mathbf{D}_2^T = \mathbf{D}_3$) and using the property $\det \mathbf{A}^T = \det \mathbf{A}$ ($\mathbf{A}$ is any matrix), it can easily be checked that if λ is an eigenvalue of Eq. (7), then $1/\lambda$ is also an eigenvalue. Hence, the eigenproblem has two sets of eigensolutions $(\lambda_j, \boldsymbol{\varphi}_j^+)$ and $(1/\lambda_j, \boldsymbol{\varphi}_j^-)(j = 1, \ldots, n)$, representing n positive-going and n negative-going wave types. As proved by Mead,[18] n is the minimum number of coupling dofs obtainable by appropriate choice of the junction between cells. In the absence of damping, eigenvalues for which $|\lambda_j| = 1$ (i.e., k real) represent freely propagating waves and those for which λ_j is real (i.e., k imaginary) represent evanescent waves. The other eigenvalues (for which k is complex) represent decaying but oscillatory waves.

The eigenproblem (7) may be first recast into a generalized linear eigensystem (see Eqs. (9) or (10), for instance) and then solved using some standard numerical solvers. However, it may lead to ill conditioning due to the fact that it has both very large and small eigenvalues λ and $1/\lambda$ (such eigenvalues represent some rapidly decaying waves). This typically happens when the number of dofs is not small anymore, as for two-dimensional sections (even if interior dofs are eliminated[21]). In order to overcome these difficulties, a reformulation of the eigensystem in terms of $(\lambda + 1/\lambda)$ has been proposed by some authors.[20,21,24]

Then, following the same procedure as in Ref. 21, the system (7) is first recast into both following equivalent forms of linear eigenproblem:

$$\left(\begin{bmatrix} -\mathbf{D}_3 & -\mathbf{D}_1 \\ \mathbf{0} & -\mathbf{D}_3 \end{bmatrix} - \lambda\begin{bmatrix} \mathbf{0} & \mathbf{D}_2 \\ -\mathbf{D}_3 & \mathbf{0} \end{bmatrix}\right)\begin{Bmatrix} \mathbf{q} \\ \lambda\mathbf{q} \end{Bmatrix} = \begin{Bmatrix} \mathbf{0} \\ \mathbf{0} \end{Bmatrix} \tag{9}$$

and

$$\left(\begin{bmatrix} \mathbf{D}_2 & \mathbf{0} \\ \mathbf{D}_1 & \mathbf{D}_2 \end{bmatrix} - \frac{1}{\lambda}\begin{bmatrix} \mathbf{0} & \mathbf{D}_2 \\ -\mathbf{D}_3 & \mathbf{0} \end{bmatrix}\right)\begin{Bmatrix} \mathbf{q} \\ \lambda\mathbf{q} \end{Bmatrix} = \begin{Bmatrix} \mathbf{0} \\ \mathbf{0} \end{Bmatrix}. \tag{10}$$

The sum of Eqs. (9) and (10) yields, after some rearrangements, an eigenproblem written in terms of $(\lambda + 1/\lambda)$ only

$$\left(\begin{bmatrix} -\mathbf{D}_1 & \mathbf{D}_3 - \mathbf{D}_2 \\ \mathbf{D}_2 - \mathbf{D}_3 & -\mathbf{D}_1 \end{bmatrix} - \left(\lambda + \frac{1}{\lambda}\right)\begin{bmatrix} \mathbf{D}_3 & \mathbf{0} \\ \mathbf{0} & \mathbf{D}_2 \end{bmatrix}\right)\begin{Bmatrix} \mathbf{q} \\ \lambda\mathbf{q} \end{Bmatrix} = \begin{Bmatrix} \mathbf{0} \\ \mathbf{0} \end{Bmatrix}. \tag{11}$$

Note that the eigensystems (9)–(11) are all unsymmetric. Now, the eigenvalues of Eq. (11) occur in pairs of equal values $(\lambda_j + 1/\lambda_j)$. The associated eigenvectors, denoted as $\boldsymbol{\Phi}_j'$ and $\boldsymbol{\Phi}_j''$, correspond with a linear combination of the original eigenvectors, denoted as $\boldsymbol{\Phi}_j^+$ and $\boldsymbol{\Phi}_j^-$, associated with λ_j and $1/\lambda_j$ and obtained from Eq. (9) (or Eq. (10)). This linear combination is arbitrarily obtained in a computer code. For restoring the original eigenvectors, we proceed as in Ref. 20. First, we expand the original eigenvectors as $\boldsymbol{\Phi}_j = \alpha_1\boldsymbol{\Phi}_j' + \alpha_2\boldsymbol{\Phi}_j''$ (the superscripts + and − have been dropped for simplicity). Introducing this expansion into Eq. (9) (for instance), and left multiplying by $\boldsymbol{\Phi}_j'^T$, we get the following relation between α_1 and α_2:

$$\alpha_2 = -\frac{\boldsymbol{\Phi}_j'^T\mathbf{A}_\lambda\boldsymbol{\Phi}_j'}{\boldsymbol{\Phi}_j'^T\mathbf{A}_\lambda\boldsymbol{\Phi}_j''}\alpha_1 \quad \text{with } \mathbf{A}_\lambda \triangleq \begin{bmatrix} -\mathbf{D}_3 & -\mathbf{D}_1 \\ \mathbf{0} & -\mathbf{D}_3 \end{bmatrix} - \lambda\begin{bmatrix} \mathbf{0} & \mathbf{D}_2 \\ -\mathbf{D}_3 & \mathbf{0} \end{bmatrix}. \tag{12}$$

The constant α_1 is finally obtained by normalizing eigenvec-

tors. From the computed eigenvalues, the axial wave numbers are given up to $2m\pi$ by

$$k_j^{\pm}L = \pm\cos^{-1}\left\{\frac{1}{2}(\lambda_j + 1/\lambda_j)\right\} + 2m\pi. \quad (13)$$

It has to be noted that the interior dofs $\mathbf{u}_I$ could have been condensed out in Eqs. (7)–(11), as is usually done in the literature when using a transfer matrix approach.[20–22,24] However, it would have required the computation of the inverse of $\mathbf{D}_{II}$. This can be costly from a numerical point of view when the number of interior dofs becomes large, which may indeed be the case in this paper.

III. REQUIREMENTS FOR HELICAL WAVEGUIDES

The three-dimensional cell domain is meshed using standard FE. Nevertheless, the mesh must satisfy a compatibility constraint between the left section and the right section: each dof of the right section must be related to a corresponding dof of the left section chosen in such a way that the periodic conditions (6) hold. This implies that the two-dimensional meshing of the right section must be compatible with that of the left section and that the ordering of left and right dofs must be carefully considered.

For instance, for an infinite isotropic cylindrical straight waveguide, the mesh of the right section must simply be a translation of the left section mesh along the cylinder axis. Because of the obvious geometrical translational invariance along that axis, the axial length of a periodic cell can be arbitrarily small (typically one element length).

At first sight, the unit periodic cell of a helical waveguide should have a length that equals the helix step, denoted as L_0 below. Nevertheless, such a length would require a three-dimensional mesh involving a large number of dofs in practice. Fortunately, as shown in the following, the length of this unit periodic cell can be arbitrarily reduced by considering a specific mapping yielding a translational invariance along the helix centerline.

The helix centerline curve can be described by the following position vector:

$$\mathbf{R}(s) = R_0\cos\left(\frac{2\pi}{l_0}s\right)\mathbf{e_x} + R_0\sin\left(\frac{2\pi}{l_0}s\right)\mathbf{e_y} + \frac{L_0}{l_0}s\mathbf{e_z}, \quad (14)$$

where $l_0=(L_0^2+4\pi^2R_0^2)^{1/2}$. $(\mathbf{e_x},\mathbf{e_y},\mathbf{e_z})$ denotes the Cartesian orthonormal basis. R_0 and L_0 are, respectively, the radius of the centerline in the (x,y) plane and the helix step along the z axis. A complete period can thus be described by the parameter s varying from 0 to l_0. It should be noted that the parameter s has been chosen so that it corresponds to the arc length (hence, l_0 is the curvilinear length of one helix step). The unit tangent vector to the centerline is then directly given by $\mathbf{T}=d\mathbf{R}/ds$. The unit normal can be defined from the Serret-Frenet formulas $d\mathbf{T}/ds=\kappa_0\mathbf{N}$, and the unit binormal vector is $\mathbf{B}=\mathbf{T}\wedge\mathbf{N}$ (the following Serret-Frenet formulas also hold: $d\mathbf{N}/ds=\tau_0\mathbf{B}-\kappa_0\mathbf{T}$, $d\mathbf{B}/ds=-\tau_0\mathbf{N}$). For the curve defined by Eq. (14), both the curvature κ_0 and the tortuosity τ_0 are constant: $\kappa_0=4\pi^2R_0/l_0^2$ and $\tau_0=2\pi L_0/l_0^2$.

Now, a new coordinate system is constructed from the orthonormal basis $(\mathbf{T},\mathbf{N},\mathbf{B})$, for which any Cartesian vector $\mathbf{x}$ can be expressed as

$$\mathbf{x}(\alpha,\beta,s) = \mathbf{R}(s) + \alpha\mathbf{N}(s) + \beta\mathbf{B}(s). \quad (15)$$

The so defined coordinates (α,β,s) are single valued only if α and β are small enough on the cross section (this restriction will be implied in the remaining). Using the above Serret-Frenet formulas, it can be shown that this kind of mapping yields a nonorthogonal covariant basis $(\partial\mathbf{x}/\partial\alpha,\partial\mathbf{x}/\partial\beta,\partial\mathbf{x}/\partial s)$, denoted by $(\mathbf{g}_1,\mathbf{g}_2,\mathbf{g}_3)$. The metric tensor of such a mapping, defined by $g_{mn}=\mathbf{g}_m\cdot\mathbf{g}_n$, is given by

$$\mathbf{g} = \begin{bmatrix} 1 & 0 & -\tau_0\beta \\ 0 & 1 & \tau_0\alpha \\ -\tau_0\beta & \tau_0\alpha & \tau_0^2(\alpha^2+\beta^2)+(1-\kappa_0\alpha)^2 \end{bmatrix}. \quad (16)$$

Consequently, $\mathbf{g}$ does not depend on the third curvilinear coordinate s (for a helix, κ_0 and τ_0 are constant). Provided that the cross section of the waveguide does not vary along s (nor the material properties), this means that this curvilinear coordinate system yields a translational invariance along s.

To be more precise, this transformation allows the investigation of the propagation modes because s would not appear explicitly in the equilibrium equations written in the curvilinear system, except for derivatives with respect to s. Hence, an exponential e^{iks} might be separated from all field components, and $\partial/\partial s$ replaced by ik. In other terms, a Fourier transform in the s direction can be performed so that we can still speak of propagation modes. It has to be pointed out that similar kinds of the above helical mapping had already been considered in electromagnetics to study helical waveguides, analytically[25] or numerically.[26]

In this paper, we are interested in solving the equilibrium equations through a periodic FE modeling. This avoids the writing of equilibrium equations in the above curvilinear coordinates, which would be very tedious and would also require some specific programming inside a FE code.

With the proposed method instead, what must be done is relating the right section nodes of the three-dimensional mesh to the left section nodes through the mapping defined by Eq. (15). And as a consequence of the translational invariance along s, the length of one unit periodic cell may be arbitrarily small as for the cylinder case. Besides, in order for the translational invariance along s to hold, the left and right dofs involved in Eqs. (6) must be the components in the curvilinear basis. However, the outputs of a conventional FE code are usually the Cartesian (x,y,z) components of the nodal displacement and force, and thus need to be transformed into the curvilinear (α,β,s) components through the Jacobian matrix, as follows:

$$\begin{Bmatrix} u_k^x \\ u_k^y \\ u_k^z \end{Bmatrix} = \mathbf{J}(\alpha_k,\beta_k,s_k)\begin{Bmatrix} u_k^1 \\ u_k^2 \\ u_k^3 \end{Bmatrix}, \quad \begin{Bmatrix} f_k^x \\ f_k^y \\ f_k^z \end{Bmatrix} = \mathbf{J}^{-T}(\alpha_k,\beta_k,s_k)\begin{Bmatrix} f_{1k} \\ f_{2k} \\ f_{3k} \end{Bmatrix}, \quad (17)$$

where k denotes the node number, u_k^i is the contravariant displacement component with respect to the covariant basis vector $\mathbf{g}_i$ $(i=1,2,3)$. $\mathbf{J}(\alpha_k,\beta_k,s_k)$ is the covariant Jacobian matrix, whose column i corresponds to the Cartesian components of $\mathbf{g}_i$ evaluated at node k. From Eq. (15), it can be shown that

$$\mathbf{J}(\alpha_k,\beta_k,s_k)=\begin{bmatrix} -\cos\frac{2\pi}{l_0}s_k & \frac{L_0}{l_0}\sin\frac{2\pi}{l_0}s_k & \frac{2\pi}{l_0}(\alpha_k-R_0)\sin\frac{2\pi}{l_0}s_k+\tau_0\beta_k\cos\frac{2\pi}{l_0}s_k \\ -\sin\frac{2\pi}{l_0}s_k & -\frac{L_0}{l_0}\cos\frac{2\pi}{l_0}s_k & -\frac{2\pi}{l_0}(\alpha_k-R_0)\cos\frac{2\pi}{l_0}s_k+\tau_0\beta_k\sin\frac{2\pi}{l_0}s_k \\ 0 & \frac{2\pi R_0}{l_0} & \frac{L_0}{l_0} \end{bmatrix}. \tag{18}$$

From the previous notations, $\mathbf{J}^{-T}(\alpha_k,\beta_k,s_k)$ corresponds to the contravariant Jacobian matrix and f_{ik} $(i=1,2,3)$ denote the covariant force components with respect to the contravariant basis $(\mathbf{g}^1,\mathbf{g}^2,\mathbf{g}^3)$, defined by $\mathbf{g}^i\cdot\mathbf{g}_j=\delta_j^i$.

The above matrix (18) may be assembled on the left (resp. right) dofs, yielding a matrix denoted by $\mathbf{J}_L$ (resp. $\mathbf{J}_R$). The initial Cartesian components, denoted by a superscript c, can be transformed using a global transformation matrix $\mathbf{Q}$ into $\mathbf{u}^c=\mathbf{Q}\mathbf{u}$, $\mathbf{f}^c=\mathbf{Q}^{-T}\mathbf{f}$ with the notations

$$\mathbf{u}^c=\begin{Bmatrix}\mathbf{u}_L^c\\ \mathbf{u}_I^c\\ \mathbf{u}_R^c\end{Bmatrix},\quad \mathbf{u}=\begin{Bmatrix}\mathbf{u}_L\\ \mathbf{u}_I\\ \mathbf{u}_R\end{Bmatrix},\quad \mathbf{f}^c=\begin{Bmatrix}\mathbf{f}_L^c\\ \mathbf{f}_I^c\\ \mathbf{f}_R^c\end{Bmatrix},\quad \mathbf{f}=\begin{Bmatrix}\mathbf{f}_L\\ \mathbf{f}_I\\ \mathbf{f}_R\end{Bmatrix},$$

$$\mathbf{Q}=\begin{bmatrix}\mathbf{J}_L & 0 & 0\\ 0 & \mathbf{I} & 0\\ 0 & 0 & \mathbf{J}_R\end{bmatrix}. \tag{19}$$

Then, before applying the procedures detailed in Sec. II B, the initial Cartesian dynamic system obtained from a standard FE code, denoted $\mathbf{D}^c\mathbf{u}^c=\mathbf{f}^c$, must be first transformed into $\mathbf{D}\mathbf{u}=\mathbf{f}$ where $\mathbf{D}$ is given by

$$\mathbf{D}=\mathbf{Q}^T\mathbf{D}^c\mathbf{Q}. \tag{20}$$

$\mathbf{D}$ is still symmetric thanks to the transformation choice (17). Note that if contravariant components had also been chosen for forces, unsymmetric dynamic stiffness matrices might result.

IV. NUMERICAL RESULTS

In this section, the material is assumed to be isotropic. No structural damping will be considered for simplicity. E and ν will denote the Young's modulus and the Poisson coefficient, respectively. For a steel wire, a typical value of $\nu=0.30$ will be chosen. We consider waveguides with a circular cross section of radius a.

A. Preliminary numerical considerations

In order to obtain the adequate meshing between the left and right cross section, the technique used in this paper consists in generating a two-dimensional mesh in the (α,β) plane of the left section (at $s=s_L$ constant). This mesh is then extruded into a three-dimensional mesh by simply translating each node – with (α,β) held constant—along the centerline s. The two-dimensional elements used are three-node triangles, extruded into six-node prisms.

The eigenproblem (11) is solved using an algorithm based on the generalized Jacobi method. Variables are first adimensionalized with some characteristic length and time, chosen as a and ω/c_s, respectively ($c_s=\sqrt{E/2\rho(1+\nu)}$ is the shear velocity). Hence, the dimensionless frequency is given by $\Omega=\omega a/c_s$. In order to reduce the computational time, some upper and lower bounds can be set for the eigenvalue searching interval. The real value of the computed eigenvalues is given by $\mathrm{Re}(\lambda+1/\lambda)=2\cos(\mathrm{Re}\,kL)\cosh(\mathrm{Im}\,kL)$. Then, it can be noticed that propagating (resp. evanescent) waves satisfy the inequality $|\mathrm{Re}(\lambda+1/\lambda)|<2$ (resp. ≥ 2). One is usually interested in the propagating and less attenuated waves, so that the upper and lower bounds can be set to $\pm 2\cosh\gamma$ (where γ is a user-defined parameter).

The accuracy of numerical results is independent of the axial number of elements (but it may be dependent on the axial element length as shown further). Hence, only one layer of elements would be enough. This is interesting because in practice, the cell length L is thus sufficiently small in order to have $-\pi<\mathrm{Re}\,k_j^{\pm}L<\pi$ in Eq. (13), which avoids the undetermination up to $2m\pi$. In this paper, two layers have generally been used because a faster convergence was observed with the Arnoldi algorithm used.

B. Validation for an infinite isotropic cylinder and accuracy

The numerical model is first validated with the Pochhammer-Chree semianalytical model,[3,27] describing elastic propagation in an infinite isotropic cylinder (i.e., $L_0\rightarrow\infty$). FE and analytical axial wavelengths are compared for a given dimensionless frequency $\Omega=1$, for the three lowest real solutions, the first imaginary and the first complex solutions, which, respectively, correspond to: the $L(0,1)$ longitudinal mode, the torsional mode, the $F(1,1)$ flexural mode, the $F(1,2)$ flexural mode (evanescent), and the F(2,1 and 2) mode (inhomogeneous).

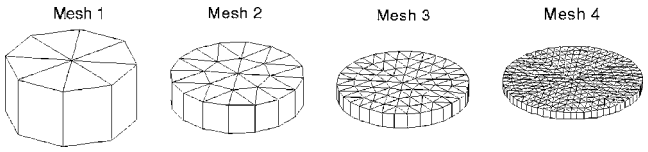

FIG. 2. Meshes 1–4, with successive refinements.

In order to assess the convergence and accuracy of the numerical method, FE results have been computed with a sequence of four refined meshes, shown in Fig. 2 with characteristics given in Table I. The successive refinements have been made by dividing each triangle of the previous cross-section mesh into four triangles. Plots of the dispersion error vs. the mesh fineness parameter $1/h$ are then obtained (h is chosen as the dimensionless maximum element length). The dispersion error is chosen as the ratio $|ka-k_{\mathrm{ref}}a|/k_{\mathrm{ref}}a|$, where ka and $k_{\mathrm{ref}}a$ are, respectively, the adimensional FE and Pochhammer-Chree axial wave numbers. Note that only one layer of element has been used, with an axial length of elements equal to h (as a first choice). Also shown in Table I is the rough criterion given by the ratio λ_s/h (where $\lambda_s=2\pi/\Omega$ is the dimensionless shear wavelength), often used in FE methods to characterize the fineness of a mesh at a given frequency. The Pochhammer-Chree solutions for the $L(0,1)$, torsional, $F(1,1)$, $F(1,2)$ and $F(2,1$ and $2)$ modes are, respectively, $k_{\mathrm{ref}}a=0.626$, 1.000, 1.421, $0.740i$, $0.953+1.905i$.

Figure 3 gives the convergence curve for each mode. It can be observed that the rate of convergence approaches a quadratic behavior for every type of mode. The accuracy for the propagating bending mode is somewhat lower, as well as for the imaginary and complex solutions (corresponding to upper bending modes). As intuitively expected, a general trend for the accuracy of a given mode is to decrease as its order increases (i.e., as its mode shapes becomes more and more complex). The same behavior has been reported with a SAFE method by Damljanovic and Weaver.[13]

With mesh 3, a dispersion error less than 1% is reached for all modes, except for the inhomogeneous one (2%). It can be concluded that a rough criterion of $\lambda_s/h=25$ is thus quite acceptable, which may be not the case for $\lambda_s/h=10$. Note that it coincides well with the criterion proposed for SAFE methods by Galan and Abascal[28,29] when using 3-node triangles.

In the above results, the axial length of elements, denoted by h_{axis}, was set to h. This is the worst element size. By reducing h_{axis}, dispersion results may be further improved for a given cross-section mesh, as shown in Fig. 4. The mesh used for the cross section is that of mesh 2, with a criterion

TABLE I. Characteristics of meshes (in parenthesis: λ_s/h criterion for $\Omega=1$).

No.	h (λ_s/h)	No. of elements	No. of dofs
1	1 (6)	32	54
2	0.5 (12)	112	150
3	0.25 (25)	416	486
4	0.125 (50)	1600	1734

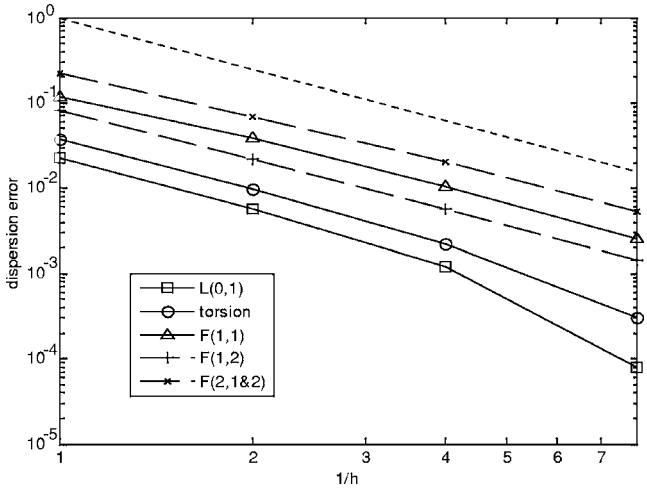

FIG. 3. Dispersion error with respect to the Pochhammer-Chree solution vs. $1/h$ at $\Omega=1$ for the first propagating, evanescent and inhomogeneous modes. As a reference, the dotted line is the quadratic rate $(1/h)^2$.

$\lambda_s/h=10$. By reducing h_{axis} to $0.3h$, the dispersion error becomes less than 1% for all propagating modes, whereas the improvement is weaker for the imaginary and complex solutions. Of course, the element axial length cannot be infinitely reduced due to machine rounding errors ($0.3h$ was found to be a limit, under which the algorithm used hardly converges).

C. Dispersion analysis of a typical helical wire

The wave modes propagating inside a peripheral wire constituting a typical seven-wire strand are now numerically studied. The helix radius of such a peripheral wire is $R_0=2a$. The helix step is given by $L_0=2\pi R_0/\tan\phi$, where ϕ denotes the lay angle of the helix.

In order to make a consistent comparison of wave numbers with those of a cylindrical wire, L is not chosen as the axial length along the z axis, but as the arc length along the helix centerline of the FE cell.

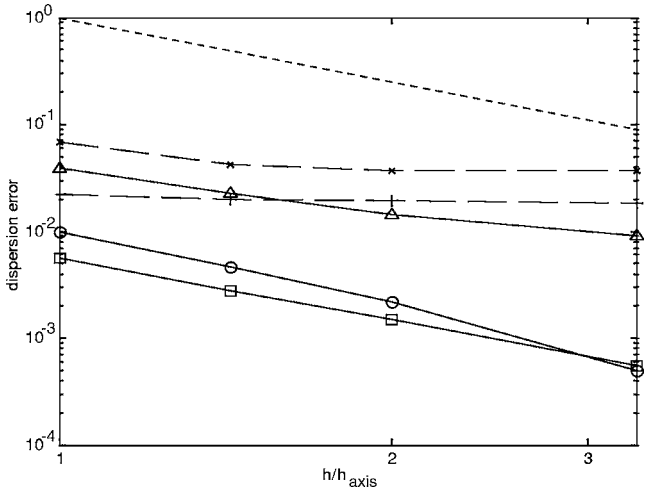

FIG. 4. Dispersion error at $\Omega=1$ vs. h/h_{axis}, obtained by reducing the axial element length (same legend as in Fig. 1). The cross-section mesh of mesh 2 is taken ($\lambda_s/h=10$).

TABLE II. FE adimensional wave numbers computed with the same cross-sectional mesh ($\lambda_s/h=20$) but a varying number of layers of elements ($\phi=45°$ and $\Omega=0.75$).

	1 layer	10 layers	30 layers	Whole step
$L(0,1)$	0.4057	0.4057	0.4058	0.4058
Torsion	0.6305	0.6305	0.6305	0.6305
$F(1,1)^-$	1.0135	1.0135	1.0135	1.0136
$F(1,1)^+$	1.4476	1.4476	1.4476	1.4476

As a first example, some FE wave numbers are computed for a helical waveguide having a significant lay angle $\phi=45°$ and for a given adimensional frequency $\Omega=0.75$. In order to demonstrate the validity of the approach, a varying number of layers of elements has been used while keeping the same cross-sectional mesh ($\lambda_s/h=20, h_{\text{axis}}=0.7h$). Figure 5 exhibits two examples of meshes, used for only one layer and for 60 layers. The 60 layer mesh exactly represents the whole helix step (6771 dofs). Hence, FE results obtained with this mesh should be understood as reference solutions because this mesh is the obvious periodic unit cell, so that the specific mapping described in Sec. III is not needed. These reference solutions are given by the last column of Table II for the propagating modes denoted as $L(0,1)$, torsional, $F(1,1)^-$ and $F(1,1)^+$ (the notation ± is explained further below). For a cylinder, these values are found to be $ka=0.4669$, 0.7485, 1.1550 and 1.1550 (with an error less than 1% compared with the Pochhammer-Chree solutions), thus yielding a strong difference with the helical behavior. The important conclusion that can be drawn from Table II is that, as expected, results are not dependent upon the axial number of layers and are identical to those obtained with a whole step mesh. This would not have been the case if the mapping proposed in Sec. III were not translationally invariant. As a side remark, results given by Table II have been corrected when necessary, because of the $2m\pi$ undetermination of Eq. (13) occuring when L is large enough.

The remaining of this paper is now devoted to dispersion analysis of helical waveguides having smaller lay angles, more realistic in civil engineering. In the following, two layers of elements have been used. Dispersion curves have been obtained by computing wave numbers for discrete frequencies. In order to reduce computation time, frequency steps have been only refined near cutoffs, where wave numbers may be scarce. Note that the method only returns discrete points and does not provide continuous lines representing dispersion curves. The task of joining points together that lie on the same mode has been done by comparing mode shapes between two successive frequencies. Because purely real or imaginary (resp. fully complex) solutions occur in pairs of opposite signs (resp. in quadruples of complex conjugates and opposite signs), only the absolute values of real and imaginary parts are plotted, on the same axis (which is more readable than a three-dimensional plot).

In order to validate the numerical model, the FE results are first compared in the low-frequency range with results obtained from a helical Timoshenko beam model. Such a model was initially proposed by Wittrick[30] in 1966 in order to study analytically the validity of simplified spring models.

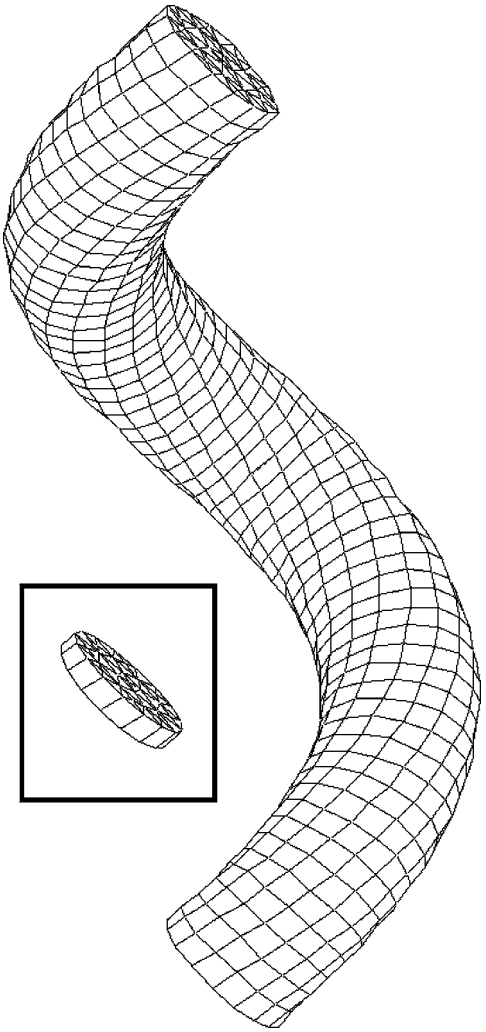

FIG. 5. Meshes of the helical waveguide ($\phi=45°$) with only one layer of elements and for the whole helix step (60 layers).

Wittrick's model is briefly recalled in the Appendix, as well as the numerical method used in this paper to solve it. This mono-dimensional model has 12 eigenvalues, corresponding to six positive and six negative traveling modes.

The lay angle of the helix is set to a common value of 7.5° (for a typical radius $a=2.5$ mm, it corresponds to a step $L_0=23.9$ cm). Figure 6 shows the dispersion curves obtained from both models with the adimensional frequency Ω varying from 0.02 to 2, and for both the cylindrical and helical geometry. Following the conclusions drawn previously, a rough criterion of $\lambda_s/h=25$ (at $\Omega=2$) has been chosen for the mesh, shown in Fig. 7, with h_{axis} set to $0.7h$; 3048 elements and 3564 dofs have been generated.

A very good agreement between both models is obtained in the low-frequency range. In the cylinder case, it has been verified that FE results yield an error less than 0.5% for all modes (except for wave numbers near cutoff because of their high sensitivity to a small frequency variation) compared with the Pochhammer-Chree solution. In order to further asses the convergence of FE results in the helical case, Fig. 8 plots the convergence and accuracy curves for every propagation mode at $\Omega=2$, obtained by using four refined meshes (as done in the previous subheading). Because no analytical

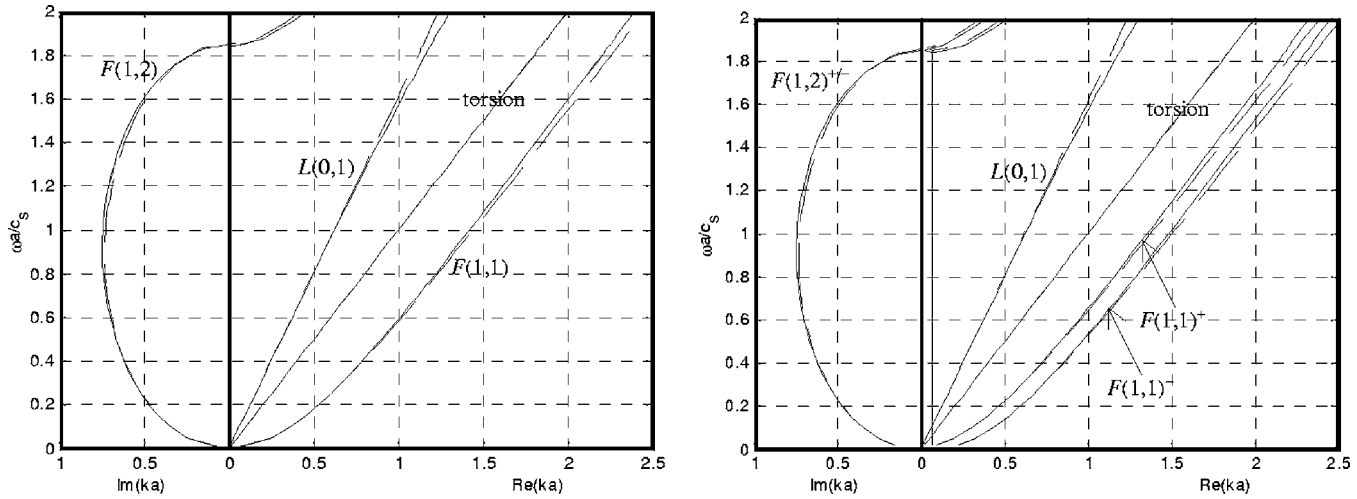

FIG. 6. Dispersion curves for the first six propagating modes for Ω ranging from 0.02 to 2 (ϕ=7.5°). Left: cylinder, right: helical. Solid lines: FE model, dashed lines: Timoshenko beam model.

solution is available for the helical geometry, the reference value has been chosen as the one obtained with the most refined mesh (h=0.06, corresponding to approximately λ_s/h=50). The reference adimensional wave numbers computed for the propagating modes, denoted as $L(0,1)$, torsion, $F(1,1)^-$, $F(1,1)^+$, $F(1,2)^-$ and $F(1,2)^+$, are, respectively, 1.306, 1.999, 2.335, 2.464, 0.394 and 0.523. As observed previously in the cylinder case, the curves exhibit a nearly quadratic rate of convergence, and an error less than 1% for the λ_s/h=25 mesh (h=0.12).

All the above results tend to demonstrate that a good accuracy is achieved by the helical FE model. Now, from a physical point of view, an interesting feature can be observed by comparing the cylindrical and helical cases. The wave numbers of the compressional $L(0,1)$ and the torsional modes are unchanged by the helical geometry (provided that the helix arc length is considered, as stated earlier). This is not the case for flexural modes, which occur in distinct roots instead of double roots because of the lack of symmetry of the helical geometry. A similar phenomenon was observed by Demma, Cawley, and Lowe[16] for toroidal waveguides when studying bends in pipelines. For simplicity, and though this notation may be somewhat abusive, the pairs of helical flexural modes identified from their cylindrical counterparts have been denoted with superscripts + and − in this paper. It should also be noted that the flexural modes $F(1,2)^{\pm}$ are not strictly evanescent anymore but inhomogeneous, unlike their cylindrical counterparts. Figure 7 gives some FE mode shapes obtained at Ω=1.

As a side but interesting remark, Fig. 6 also allows to evaluate the high-frequency limit of a Timoshenko model. For Ω=2.0, the wave number differences between FE and Timoshenko models are approximately 3, 0, 5 and 9%, respectively, for the $F(1,1)$, torsional mode, $L(0,1)$ and $F(1,2)$ modes (for both the cylindrical and helical cases). For instance, if a maximum dispersion error of about 2% is sought, this limit is Ω_{lim}=1.4 (for a typical cross-sectional radius a=2.5 mm, it corresponds to f_{lim}=280 kHz). As expected, significant differences increase above the $F(1,2)$ cut-on frequency and as the next upper mode (not taken into account by a Timoshenko model) is reaching its cut-on frequency.

Figure 9 gives dispersion curves for the helical case of both FE and Timoshenko models with Ω varying from near 0 to 0.02. The agreement between both models is still perfect, as expected for this very low-frequency range. However,

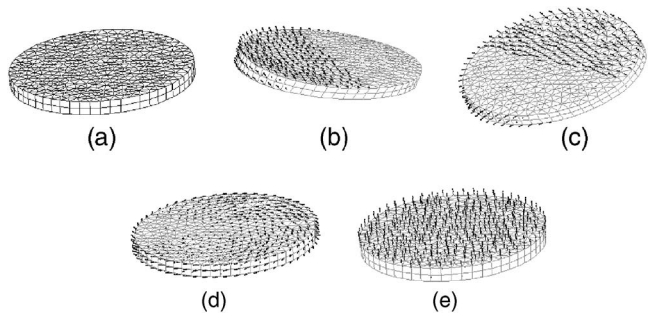

FIG. 7. (a) Undeformed FE mesh used for the helical waveguide for computations between Ω=0 and 2, (b) $F(1,1)^+$, (c) $F(1,1)^-$, (d) torsional and (e) $L(0,1)$ mode shapes (displacement real part, with deformed mesh) computed for Ω=1.

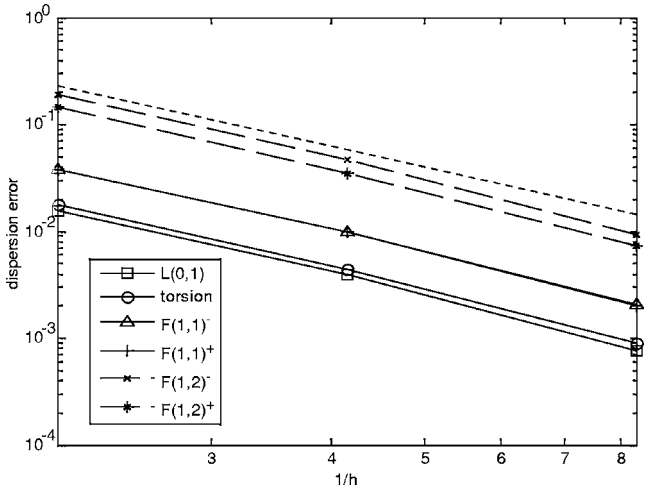

FIG. 8. Dispersion error with respect to the reference solution (λ_s/50 mesh) vs. $1/h$ at Ω=2 for the six modes (dotted line: quadratic rate).

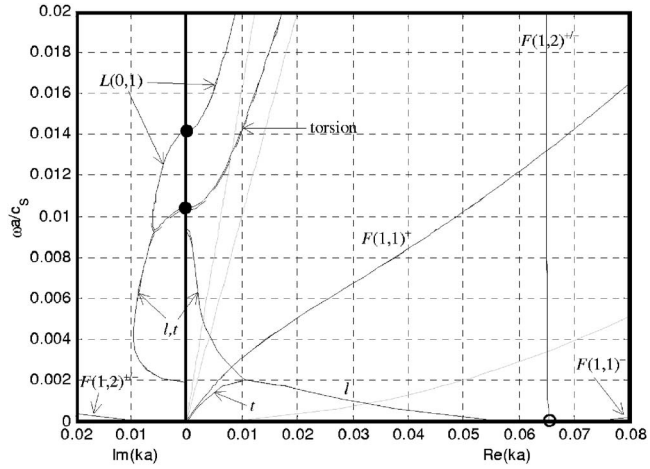

FIG. 9. Dispersion curves of the helical waveguide ($\phi=7.5°$) with Ω varying from 0 to 0.02. Solid lines: FE model, dashed lines: Timoshenko beam model (gray lines: cylinder). •: cutoff frequencies, ◦: rigid-body modes.

what physically happens must be outlined. Strong differences occur in the helical case so that a direct analogy with the cylinder becomes difficult. The torsional and $L(0,1)$ modes are respectively cut off near $\Omega=0.010$ and 0.014 (for the cylinder, these modes are always propagative). Between $\Omega=0.009$ and 0.002, both modes have the same wave numbers and are strongly coupled. It is then difficult to distinguish which mode shapes correspond to a compressional or torsional behavior. Thus, l and t notations have been replaced to denote, respectively, compression and torsion dominant modes (but this choice may be somewhat subjective). Besides, it should be noted that these modes are still attenuated but become inhomogeneous (nonzero real and imaginary parts) for this frequency range. Under 0.002, both modes propagate again, with different phase velocities. The l mode has a decreasing slope indicating a negative group velocity (while its phase velocity is positive). For the helical waveguide considered, it can be concluded that bandcut attenuation zones exist for the torsional and $L(0,1)$ modes, which are, respectively, about [0.002; 0.010] and [0.002; 0.0014] (with $a=2.5$ mm, [400; 2000] Hz and [400; 2800] Hz).

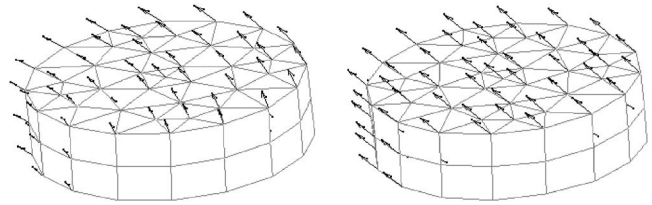

FIG. 10. Real part of displacement for mode shapes t (left) and l (right) computed for $\Omega=0.0011$.

Figure 10 gives l and t mode shapes computed for $\Omega=0.0011$. They look like each other but the mode t exhibits a slight torsional behavior, unlike the mode l.

In order to briefly examine the influence of the helix step, some computations have also been made for the lay angles 6° and 9°. As shown in Fig. 10, all the abovementioned differences between helical and cylinder geometry increase as the lay angle increases. Pairs of flexural modes become more and more distinct and the bandcut zone grows.

Then, it is also observed that there exists some rigid-body modes ($\omega=0$) for wave numbers coinciding with $2\pi/l_0$ (see Figs. 9 and 11), i.e., an axial wavelength equal to the arc length of one helix step (this wave number value is also the real part of the inhomogeneous $F(1,2)^{\pm}$ modes). This result was already reported by Tso[31] in 1972 when studying lower propagation modes of a helical Euler-Bernoulli beam.

Finally, in order to show the capabilities of the FE method proposed in this paper, Fig. 12 exhibits the dispersion curves of the cylinder and the helical waveguides ($\phi=7.5°$) for a higher-frequency range, varying from 0 to 5 (which is far above the limit of Timoshenko-type approximation). A rough criterion of $\lambda_s/h=20$ at $\Omega=5$ has been chosen for the mesh with $h_{\text{axis}}=0.7h$, yielding 10,456 elements and 11,997 dofs (deformed mesh depicted in Fig. 13). Only modes that propagate at $\Omega=5$ have been plotted on the dispersion curves. At this frequency, there are three propagating compressional modes: $L(0,1)$, $L(0,2)$ and $L(0,3)$, represented in bold solid lines for clarity. In the cylinder case, the FE dispersion error remains less than 1% compared with the Pochhammer-Chree solutions, so that a good accuracy can be

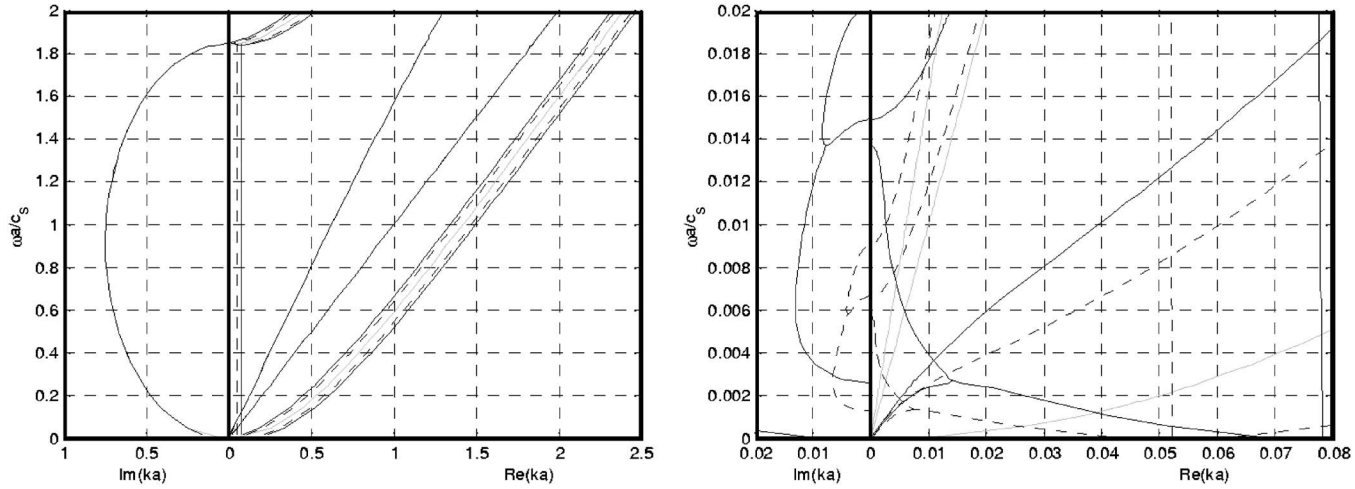

FIG. 11. Dispersion curves of the helical waveguide (FE model only) with Ω varying: from 0.02 to 2 (left) and from 0 to 0.02 (right). Solid lines: $\phi=9.0°$, dashed lines: $\phi=6.0°$, gray lines: cylinder $\phi=0°$.

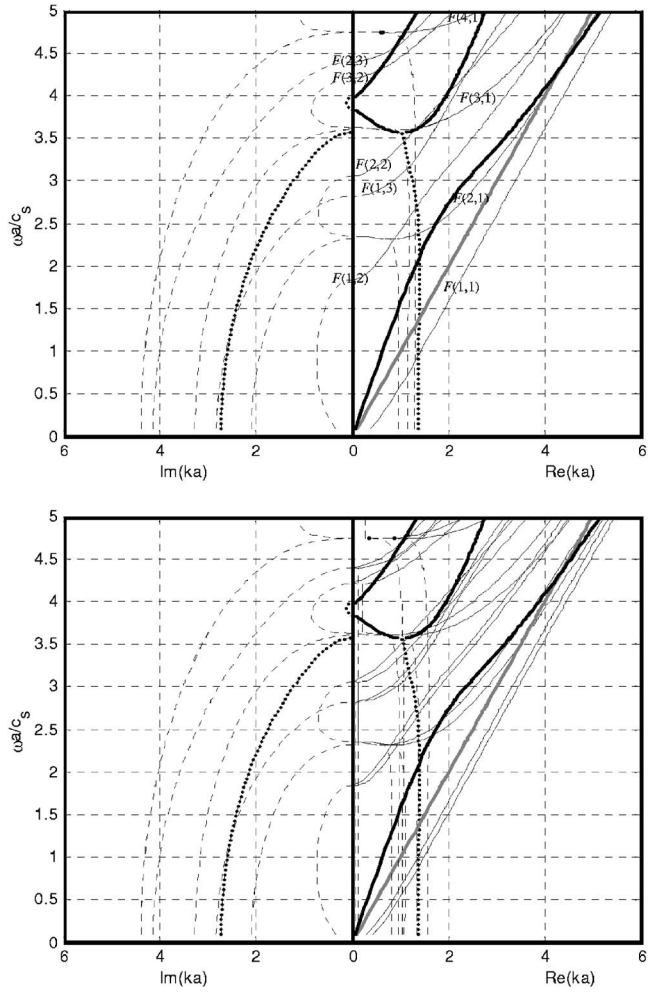

FIG. 12. FE Dispersion curves of cylindrical (up) and helical $\phi=7.5°$ (bottom) waveguides. Bold lines: compressional modes ($L(0,1)$, $L(0,2)$ and $L(0,3)$), gray line: torsional mode, thin lines: flexural modes. Lines are dotted when modes are nonpropagating (evanescent or inhomogeneous).

expected for the helical FE model. The comparison of results obtained with the cylindrical and helical waveguides clearly shows that the wave numbers of compressional and torsional modes are unchanged, while those of flexural modes are different and do not occur in double roots in the helical case (though their imaginary parts seem to remain unchanged). As an illustrative example, Fig. 13 exhibits the $L(0,2)$ mode shapes at $\Omega=5$.

V. CONCLUSION

Elastic wave propagation inside a helical waveguide has been analyzed through a three-dimensional FE method based on periodic boundary conditions and a translationally invariant mapping. This method can be implemented as a postprocessing step of a conventional FE code providing stiffness, mass and damping matrices. As opposed to SAFE methods, it avoids writing equilibrium equations in a helical curvilinear coordinate system, somewhat difficult to use, as well as a complete re-programming inside a FE code. The convergence and accuracy of the proposed method have been studied, and were shown to be similar to a SAFE method. With linear prisms (triangles in a section), a criterion of about $\lambda_s/20$ can be applied to generate the FE mesh.

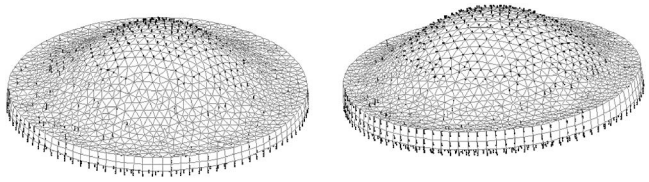

FIG. 13. Real part of displacement for the $L(0,2)$ mode shapes computed for $\Omega=5$ for the cylinder (left) and the helical waveguide (right).

From a physical point of view, the dispersion curves of a helical waveguide exhibit several differences compared with the cylinder. Wave numbers for compression modes remain identical—provided that the arc length of the helix centerline is considered—but flexural modes do not occur in pairs of equal wave numbers due to the lack of symmetry of the helical geometry. This difference is stronger as the lay angle increases. Besides, there exists some low-frequency bandcut zones where both the compressional and torsional modes become nonpropagating. These bands grow with an increasing helix lay angle. In the low-frequency range, FE results have been verified with a helical Timoshenko beam model, which has also allowed evaluating the high-frequency limit of such a model. Further studies should deal with the use of higher order finite elements and a comparison with experimental results.

APPENDIX: HELICAL TIMOSHENKO BEAM MODEL

Assuming a $e^{i(ks-\omega t)}$ dependence, it can be shown that the equilibrium equations for a helical Timoshenko beam are written as follows:[30]

$$(\mathbf{A}_1 - \omega^2\mathbf{A}_2 - ik\mathbf{B} - k^2\mathbf{C})\mathbf{u} = \mathbf{0} \tag{A1}$$

with notations

$$\mathbf{A}_1 = \begin{bmatrix} \tau_0^2\sigma_2 + \kappa_0^2\sigma_p & 0 & 0 & 0 & \tau_0\sigma_2 & 0 \\ 0 & \tau_0^2\sigma_1 & -\kappa_0\tau_0\sigma_1 & \tau_0\sigma_1 & 0 & 0 \\ 0 & -\kappa_0\tau_0\sigma_1 & \kappa_0^2\sigma_1 & -\kappa_0\sigma_1 & 0 & 0 \\ 0 & \tau_0\sigma_1 & -\kappa_0\sigma_1 & \sigma_1 + \tau_0^2\beta_2 & 0 & -\tau_0\kappa_0\beta_2 \\ \tau_0\sigma_2 & 0 & 0 & 0 & \sigma_2 + \tau_0^2\beta_1 + \kappa_0^2\beta_T & 0 \\ 0 & 0 & 0 & -\tau_0\kappa_0\beta_2 & 0 & \kappa_0^2\beta_2 \end{bmatrix}, \quad \mathbf{u} = \begin{Bmatrix} u \\ v \\ w \\ \theta_1 \\ \theta_2 \\ \theta_T \end{Bmatrix}$$

$$\mathbf{B} = \begin{bmatrix} 0 & -\tau_0(\sigma_1+\sigma_2) & \kappa_0(\sigma_1+\sigma_p) & -\sigma_1 & 0 & 0 \\ \tau_0(\sigma_1+\sigma_2) & 0 & 0 & 0 & \sigma_2 & 0 \\ -\kappa_0(\sigma_1+\sigma_p) & 0 & 0 & 0 & 0 & 0 \\ \sigma_1 & 0 & 0 & 0 & \tau_0(\beta_1+\beta_2) & 0 \\ 0 & -\sigma_2 & 0 & -\tau_0(\beta_1+\beta_2) & 0 & \kappa_0(\beta_2+\beta_T) \\ 0 & 0 & 0 & 0 & -\kappa_0(\beta_2+\beta_T) & 0 \end{bmatrix},$$

$$\mathbf{A}_2 = \mathrm{diag}(m,m,m,mk_1^2,mk_2^2,mk_T^2), \quad \mathbf{C} = -\mathrm{diag}(\sigma_1,\sigma_2,\sigma_p,\beta_1,\beta_2,\beta_T) \tag{A2}$$

where u, v, w denote the components of displacements of the centroid of the cross section in the Frenet basis $(\mathbf{N},\mathbf{B},\mathbf{T})$, θ_1, θ_2, θ_T are the components of rotation of the cross section, m is the mass per unit length and σ_1, σ_2 are the shear rigidities and σ_p the extensional rigidity. β_1, β_2 are the flexural rigidities and β_T the torsional rigidity, k_1, k_2 are the radii of gyration and k_T is the polar radii of gyration of the cross section. It is assumed that the condition $(\kappa_0 k_T)^2 \ll 1$ is satisfied, which implies that the wire curvature has a negligible effect on the various rigidities (and that the cross-sectional dimensions of the wire are small compared with the radius of curvature of the helix). For further theoretical details, the reader is referred to the paper of Wittrick.[30] For a circular cross section of radius a, the properties are given by

$$m = \rho\pi a^2, \quad \sigma_1 = \sigma_2 = \eta E\pi a^2/2(1+\nu),$$
$$\sigma_p = E\pi a^2, \quad \eta = 6/7,$$
$$\beta_1 = \beta_2 = E\pi a^4/4, \quad \beta_T = E\pi a^4/4(1+\nu), \quad k_1 = k_2 = a/2, \quad k_T = a\sqrt{2}/2. \tag{A3}$$

Equation (A1) is a quadratic eigenvalue problem. Its characteristic equation, which is a polynomial of degree 12, was not solved by Wittrick. In this paper, the eigensystem (A1) is solved using a standard numerical eigensolver instead.

[1] B. N. Pavlakovic, M. J. S. Lowe, and P. Cawley, "High-frequency low-loss ultrasonic modes in imbedded bars," J. Appl. Mech. **68**, 67–75 (2001).
[2] P. Rizzo and F. Lanza di Scalea, "Load measurement and health monitoring in cable stays via guided wave magnetostrictive ultrasonics," Mater. Eval. **62**, 1057–1065 (2004).
[3] J. Zemanek, "An experimental and theoretical investigation of elastic wave propagation in a cylinder," J. Acoust. Soc. Am. **51**, 265–283 (1972).
[4] H. Kwun, K. A. Bartels, and J. J. Hanley, "Effects of tensile loading on the properties of elastic-wave propagation in a strand," J. Acoust. Soc. Am. **103**, 3370–3375 (1998).
[5] M. D. Beard, M. J. S. Lowe, and P. Cawley, "Ultrasonic guided waves for inspection of grouted tendons and bolts," J. Mater. Civ. Eng. **212**, 212–218 (2003).
[6] P. Rizzo and F. Lanza di Scalea, "Wave propagation in multi-wire strands by wavelet-based laser ultrasound," Exp. Mech. **44**, 407–415 (2004).
[7] P. Rizzo, "Ultrasonic wave propagation in progressively loaded multi-wire strands," Exp. Mech. **46**, 297–306 (2006).
[8] L. Laguerre, J.-C. Aime, and M. Brissaud, "Magnetostrictive pulse-echo device for non-destructive evaluation of cylindrical steel materials using longitudinal guided waves," Ultrasonics **39**, 503–514 (2002).
[9] L. Gavric, "Computation of propagative waves in free rail using a finite element technique," J. Sound Vib. **185**, 531–543 (1995).
[10] N. Rattanawangcharoen, W. Zhuang, A. H. Shah, and S. K. Datta, "Axisymmetric guided waves in jointed laminated cylinders," J. Eng. Mech. **123**, 1020–1026 (1997).
[11] W. Zhuang, A. H. Shah, and S. B. Dong, "Elastodynamic Green's function for laminated anisotropic circular cylinders," J. Appl. Mech. **66**, 665–674 (1999).
[12] T. Hayashi, W.-J. Song, and J. L. Rose, "Guided wave dispersion curves for a bar with an arbitrary cross section, a rod and rail example," Ultrasonics **41**, 175–183 (2003).
[13] V. Damljanovic and R. L. Weaver, "Propagating and evanescent elastic waves in cylindrical waveguides of arbitrary cross section," J. Acoust. Soc. Am. **115**, 1572–1581 (2004).
[14] T. Hayashi, C. Tamayama, and M. Murase, "Wave structure of guided waves in a bar with an arbitrary cross section," Ultrasonics **44**, 17–24 (2006).
[15] P. Wilcox, M. Evans, O. Diligent, M. Lowe, and P. Cawley, "Dispersion and excitability of guided acoustic waves in isotropic beams with arbitrary cross section," Rev. Prog. Quant. Nondestr. Eval. **21**, 203–210 (2002).
[16] A. Demma, P. Cawley, and M. Lowe, "The effect of bends on the propagation of guided waves in pipes," J. Pressure Vessel Technol. **127**, 328–335 (2005).
[17] D. J. Mead, "Wave propagation in continuous periodic structures: Research contributions from Southampton, 1964–1995," J. Sound Vib. **190**, 495–524 (1996).
[18] D. J. Mead, "A general theory of harmonic wave propagation inlinear periodic systems with multiple coupling," J. Sound Vib. **27**, 235–260 (1973).
[19] A. Ghoshal, M. L. Accorsi, and M. S. Bennett, "Wave propagation in circular cylindrical shells with periodic axial curvature," Wave Motion **23**, 339–352 (1996).
[20] L. Gry and C. Gontier, "Dynamic modeling of railway track: A periodic model based on a generalized beam formulation," J. Sound Vib. **199**, 531–558 (1997).
[21] B. R. Mace, D. Duhamel, and M. J. Brennan, "Finite element prediction of wave motion in structural wave guides," J. Acoust. Soc. Am. **117**, 2835–2843 (2005).
[22] D. Duhamel, B. R. Mace, and M. J. Brennan, "Finite element analysis of the vibrations of wave guides and periodic structures," J. Sound Vib. **294**, 205–220 (2006).
[23] R. S. Langley, "A variational principle for periodic structures," J. Sound Vib. **135**, 135–142 (1989).
[24] W. X. Zhong and F. W. Williams, "On the direct solution of wave propagation for repetitive structures," J. Sound Vib. **181**, 485–501 (1995).
[25] W. Sollfrey, "Wave propagation on helical wires," J. Appl. Phys. **22**, 905–910 (1951).
[26] A. Nicolet, F. Zola, and S. Guenneau, "Modeling of twisted optical waveguides with edge elements," Eur. Phys. J.: Appl. Phys. **28**, 153–157 (2004).
[27] T. R. Meeker and A. H. Meitzler, *Guided wave propagation inelongated cylinders and plates, Physical Acoustics* (Academic, New York, 1964), Vol. **1**, Sec. A2.
[28] J. M. Galan and R. Abascal, "Elastodynamic guided wave scattering in infinite plates," Int. J. Numer. Methods Eng. **58**, 1091–1118 (2003).
[29] J. M. Galan and R. Abascal, "Lamb mode conversion at edges. A hybrid boundary-element–finite-element solution," J. Acoust. Soc. Am. **117**, 1777–1784 (2005).
[30] W. H. Wittrick, "On elastic wave propagation in helical springs," Int. J. Mech. Sci. **8**, 25–47 (1966).
[31] W. K. Tso, "On the motion of a curved and twisted rod," Acta Mech. **13**, 163–178 (1972).

Reflection and transmission coefficients for guided waves reflected by defects in viscoelastic material plates

Bernard Hosten,[a] Ludovic Moreau, and Michel Castaings
Laboratoire de Mécanique Physique, Université Bordeaux 1, UMR C.N.R.S. 5469 351 cours de la Libération, 33405 Talence Cedex, France

(Received 11 September 2006; revised 18 January 2007; accepted 16 March 2007)

The paper presents a Fourier transform-based signal processing procedure for quantifying the reflection and transmission coefficients and mode conversion of guided waves diffracted by defects in plates made of viscoelastic materials. The case of the S_0 Lamb wave mode incident on a notch in a Perspex plate is considered. The procedure is applied to numerical data produced by a finite element code that simulates the propagation of attenuated guided modes and their diffraction by the notch, including mode conversion. Its validity and precision are checked by the way of the energy balance computation and by comparison with results obtained using an orthogonality relation-based processing method. © *2007 Acoustical Society of America.* [DOI: 10.1121/1.2723652]

PACS number(s): 43.35.Cg, 43.20.El, 43.20.Fn, 43.20.Gp, 43.35.Mr [PEB] Pages: 3409–3417

I. INTRODUCTION

Using ultrasonic guided waves for the integrity control of materials and structures is very efficient in nonabsorbing materials since these waves can travel long distances. For absorbing materials, the necessity of using low frequencies limits the resolution for detecting the defects.[1,2] In modern materials, such as composites, the inspected area is drastically reduced because of the strong attenuation of the ultrasonic waves, and the very low amplitudes of the measured signals can prevent the detection of defects. Even when a signal is measured at a given position remote from a defect, its amplitude depends on the reflection by the defect or the transmission past the defect and also on the attenuation along the distance of propagation between the defect and the measuring location. Considering the well-known mode conversion phenomenon (production of several modes when an incident mode hits a defect), it becomes then quite difficult to evaluate the reflection and transmission coefficients that represent the ratios between the amplitudes of each reflected or transmitted wave to that of the incident wave at the defect location.

This paper presents a signal processing procedure to quantify such reflection and transmission coefficients in plates made of viscoelastic materials. This procedure is based on a double Fourier transformation from the temporal/spatial domains to the frequency/wave number domains. Alleyne and Cawley[3] presented this procedure for separating the various guided modes that can propagate together along nonabsorbing plates. As already mentioned,[4] the viscoelasticity causes some difficulties for evaluating the effects of a defect on the diffraction of guided waves, since the results of the Fourier transforms strongly depend on the position and the length of the monitoring zone, and also on the shape of the spatial window used for reducing the amplitudes of unwanted side lobes in the wave-number domain. Here, this problem is solved with the hypothesis that the viscoelastic properties of the material are known, as well as the position of the defect inside the plate.

Since it is experimentally difficult to generate a pure mode incident on a defect,[5] the procedure is checked here by processing numerical data produced by a finite element (FE) code.[6] Indeed a defect by itself can generate various modes and the identification of the defect diffraction is more complex in the presence of many incident modes. The FE model is chosen for its ability to simulate the generation of a pure mode and to supply accurate data.[7]

The scattering phenomenon in a medium may be simulated either by considering this medium as a viscoelastic material modeled by using complex stiffness moduli, or by considering the medium as an elastic material modeled by using real stiffness moduli. The reflection and transmission coefficients of guided modes scattered by a notch are compared when considering the material as elastic or viscoelastic, and it is shown that the results are similar or different depending on the frequency domain. The processing procedure used for quantifying the amplitudes of the various incident or diffracted modes is validated by computing the energy balance and by comparing its results to those obtained using an orthogonality relation-based processing method.[8,9]

II. THEORY

The normal displacement field of guided waves is decomposed in plane waves such as

$$u(x_2,t)|_{x_1=h/2} = \left(\sum_m A_m \exp\left(-i2\pi\mu_m x_2\right) \right) f(t), \tag{1}$$

where x_2 is the direction of propagation and x_1 is the direction perpendicular to the plate (Fig. 1). Here

$$A_m = a_m U_m\big|_{x_1=h/2} \tag{2}$$

represents the intrinsic amplitude a_m of the mode m multiplied by the value of the normal displacement $U_m|_{x_1=h/2}$ at the

[a]Author to whom correspondence should be addressed. Electronic mail: b.hosten@lmp.u-bordeaux1.fr

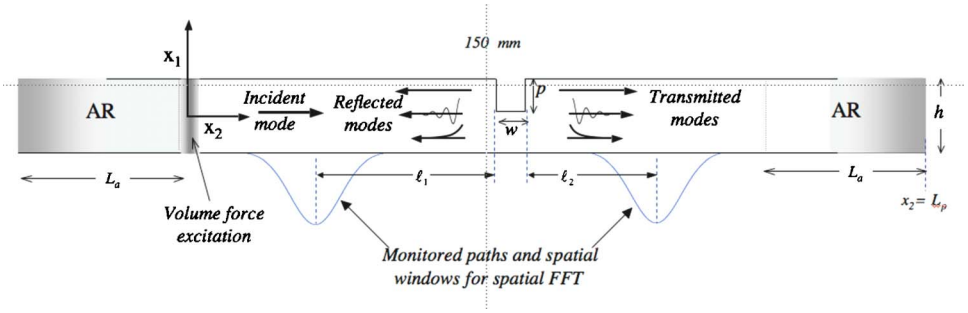

FIG. 1. (Color online) Schematic of the incident and diffracted wave modes along a plate with notch.

surface of the plate ($x_1=h/2$) and for the spatial origin $x_2=0$.

Here $\mu_m=\mu'_m-i\mu''_m$ is the complex spatial frequency of the wave, the real part being the inverse of the wavelength λ_m ($\mu'_m=1/\lambda_m$). This complex spatial frequency is linked to the complex wave number by $2\pi\mu_m=k'_m-ik''_m$, where k''_m is the wave attenuation.

A first direct Fourier transform gives a representation of the field in the temporal frequency domain ν:

$$S(\nu,x_2)=\left(\sum_m A_m \exp(-i2\pi\mu_m x_2)\right)F^{+t}(f(t)). \quad (3)$$

In the following, harmonic displacements are considered, i.e., for single temporal frequency components ($\nu=\nu_i$):

$$S(\nu,x_2)|_{\nu=\nu_i}=S(x_2)|_{\nu=\nu_i}=\sum_m A_{mi}\exp(-i2\pi\mu_m x_2), \quad (4)$$

and the subscript i is omitted for simplification.

In this paper, the direct and inverse Fourier transforms are defined by

$$F^{+t}(f(t))=\int_{-\infty}^{+\infty} f(t)\exp(-i2\pi\nu t)\,dt \quad \text{and}$$

$$F^{-\nu}(g(\nu))=\int_{-\infty}^{+\infty} g(\nu)\exp(+i2\pi\nu t)\,d\nu,$$

respectively.

If needed, an inverse Fourier transform can be used later on to reconstruct temporal waveforms. Due to experimental or numerical limitations, the displacement field is known in limited temporal and spatial windows only. Working with narrow temporal pulses or bursts permits us to define the temporal Fourier transform. However, the spatial window corresponds to a monitoring zone that cuts off parts of the spatial field and this is likely to affect the wave-number diagram that is to be processed. Therefore, it is required to take into account these unavoidable effects when the amplitudes of modes are sought.

For any central position $x_2=x_0$ of the spatial window, the monitored field is filtered by the function $h_L(x_2-x_0)$, which describes the shape of the window (Hamming, Gaussian,…). L is the length of the monitoring zone. Because of the minus sign in Eq. (1), an inverse Fourier is used to give a representation of the field in the spatial frequency domain μ:

$$\tilde{U}(\mu)=\sum_m A_m\int_{-\infty}^{+\infty} h_L(x_2-x_0)\exp(-k''_m x_2)\times\exp(+i2\pi(\mu-\mu'_m)x_2)\,dx_2. \quad (5)$$

By changing the variable x_2 into x_2+x_0, this representation for each mode m becomes

$$\tilde{U}(\mu)=\delta(\mu-\mu'_m)\otimes A_m\exp(-k''_m x_0)\times\exp(+i2\pi\mu x_0)F^{-x_2}(h_L(x_2)\exp(-k''_m x_2)) \quad (6)$$

where $\delta(\mu)$ represents the Dirac delta function and $\otimes$ is the convolution product.

The inverse Fourier transform of the positive and real function $h_L(x_2)\exp(-k''_m x_2)$ takes the shape of a lobe centered on $\mu=0$.

For each mode m (Fig. 2), the amplitude of this lobe, centered on $\mu=\mu_m$, is given by the modulus of the amplitude $|A_m|$ multiplied by $G_L(k''_m)$, which is the inverse Fourier transform of $h_L(x_2)\exp(-k''_m x_2)$ at $\mu=0$:

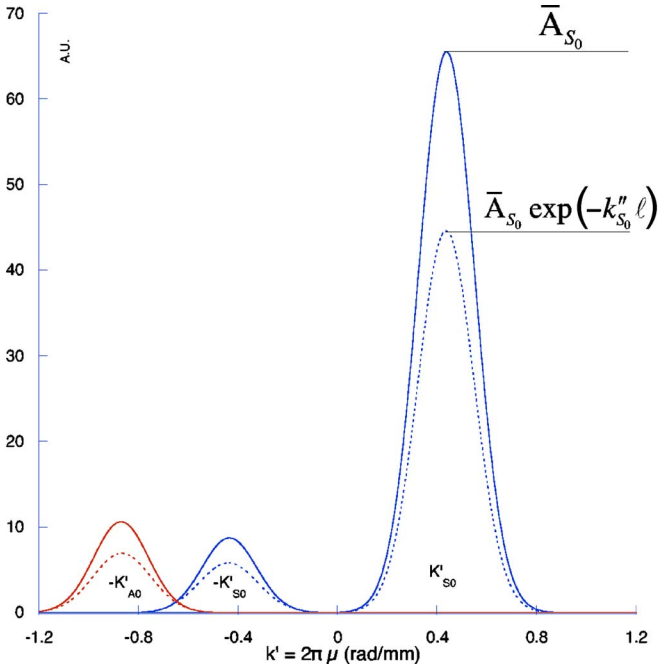

FIG. 2. (Color online) Amplitudes of the spatial Fourier transform for an incident mode S0 and two reflected modes S0 and A0 at two monitoring zones distant of $\ell=50$ mm−Frequency=0.15 MHZ−Monitoring zones: 40–100 mm and 90–150 mm.

$$|\bar{A}_m| = |A_m| \exp(-k''_{mr}x_0)\left|F^{-x_2}(h_L(x_2)\exp(-k''_{mr}x_2))\right|_{\mu=0}$$
$$= |A_m| \exp(-k''_{mr}x_0) G_L(k''_m). \quad (7)$$

$G_L(k''_m)$ is simply the integral of the spatial window multiplied by the attenuation function $\exp(-k''_m x)$, relative to the mode m:

$$G_L(k''_m) = \int_{-\infty}^{+\infty} h_L(x) \exp(-k''_{mr}x)\, dx. \quad (8)$$

$G_L(k''_m)$ is independent of the position of the monitoring window, but it depends on both its length L and its shape, and also on the attenuation of the mode. The computation of $G_L(k''_m)$ allows the amplitude of any mode to be known at any frequency and at the central position of the window.

Two applications connected to this analysis are presented in the following: (1) the evaluation of modes attenuation when the properties of the material are unknown and (2) the estimation of the transmission past, reflection by, or conversion of a mode by a notch. In the second application, the mode's materials properties and therefore the attenuation are supposed to be known.

III. EVALUATION OF THE ATTENUATION

The monitoring zone is shifted by a distance ℓ. Then for each mode m, the amplitude of the lobe (Fig. 2) at $\mu=\mu_m$ is

$$|\bar{A}_m|_\ell| = |A_m| \exp(-k''_{mr}x_0) \exp(-k''_m \ell) G_L(k''_m)$$
$$= |\bar{A}_m|_{x_0} \exp(-k''_m \ell). \quad (9)$$

The variation of the amplitude of the lobe for any mode m in two zones of the same length and remote from each other at a distance ℓ permits its attenuation to be computed at any temporal frequency:

$$k''_m = -\frac{1}{\ell} \ln\left(\frac{\bar{A}_m|_\ell}{|\bar{A}_m|_{x_0}}\right). \quad (10)$$

IV. REFLECTION BY/TRANSMISSION PAST A DEFECT

For an incident mode i of amplitude A_i, a defect in the plate can generate many reflected modes and transmitted modes the amplitudes of which can be written $A_{rm}={}_iR_m A_i$ and $A_{tm}={}_iT_m A_i$, respectively. ${}_iR_m$ and ${}_iT_m$ define the reflection and transmission coefficients of mode i to mode m, respectively. This definition is based on the ratio between the amplitudes of normal displacements at the surface of the structure. This corresponds to an experimenter point of view, since these coefficients can be deduced easily from the spatial Fourier transform of measurements or here from FE data. As shown by Eq. (2), these amplitudes of normal displacements are related to the intrinsic amplitude a_m of the mode and to the power-normalized normal displacement it produces at the surface of the guide. Then the procedure furnishes also the intrinsic amplitudes of the modes if one computes the displacements fields at any frequencies for each mode.

The original monitoring zone is located at the distance ℓ_1 before the defect and the second monitoring zone is located at the distance ℓ_2 past the defect (Fig. 1). Here the same spatial window $h_L(x_2)$ is used for these two monitoring zones, so that only the attenuations of the modes affect the values of the Fourier transform $G_L(k''_{i\ or\ m})$.

A. Reflection/transmission of the incident mode

If $\bar{A}_i$ is the amplitude of the lobe for the incident mode at the original monitoring zone, i.e., before the defect, then the amplitude of the incident mode i at this position is given by $A_i=\bar{A}_i/G_L(k''_i)$. At the defect position it is

$$A_i \exp(-k''_i \ell_1) = \frac{\bar{A}_i}{G_L(k''_i)} \exp(-k''_i \ell_1)$$

and

$$\bar{A}_{it} = {}_iT_i A_i \exp(-k''_i \ell_1) G_L(k''_i) \exp(-k''_i \ell_2)$$

is the amplitude of the lobe for the incident mode at the monitoring position past the defect, where

$${}_iT_i = \frac{\bar{A}_{it} \exp(+k''_i(\ell_2))}{\bar{A}_i \exp(-k''_i(\ell_1))} \quad (11)$$

defines the transmission coefficient for the incident mode.

A similar approach gives the reflection coefficient for the incident mode:

$${}_iR_i = \frac{\bar{A}_{ir} \exp(+k''_i(\ell_1))}{\bar{A}_i \exp(-k''_i(\ell_1))}. \quad (12)$$

B. Reflection and transmission of the converted modes

The amplitude of any reflected converted mode m at the original monitoring zone is given by $A_{mr}=\bar{A}_{mr}/G_L(k''_m)$.

Since the direction of propagation of reflected modes is opposed to that of the incident mode, the amplitude at the defect position becomes

$$A_{mr} \exp(+k''_m \ell_1) = \frac{\bar{A}_{mr} \exp(+k''_m \ell_1)}{G_L(k''_m)}$$
$$= {}_iR_m \frac{\bar{A}_i}{G_L(k''_i)} \exp(-k''_i \ell_1). \quad (13)$$

Then, the reflection coefficient ${}_iR_m$ of the mode m is

$${}_iR_m = \frac{G_L(k''_i)}{G_L(k''_m)} \frac{\exp(+k''_m \ell_1)}{\exp(-k''_i \ell_1)} \frac{\bar{A}_{mr}}{\bar{A}_i}. \quad (14)$$

A similar computation leads to the definition of the transmission coefficient of a converted mode m:

$${}_iT_m = \frac{G_L(k''_i)}{G_L(k''_m)} \frac{\exp(+k''_m \ell_2)}{\exp(-k''_i \ell_1)} \frac{\bar{A}_{mt}}{\bar{A}_i}. \quad (15)$$

V. ENERGY BALANCE

The computation of the energy balance and the knowledge of the intrinsic amplitudes are not mandatory to compute the previous coefficients. However, it is computed here in order to check the procedure. The real part of the in-plane component of the Poynting vector, integrated across the thickness h and averaged over a temporal period, gives the average power flow defined by[8]

$$P_{x_2} = \frac{1}{2}\,\mathrm{Re}\int_h (-\mathbf{v}_m^* \bar{\bar{\sigma}}_m)\mathbf{x}_2\, dx_1. \tag{16}$$

If the displacement and stress fields of each mode are normalized by the square root of the average power flow, i.e., by $\sqrt{P_{x2}}$

$$u_{m\ \mathrm{norm}} = \frac{u_m}{\sqrt{P_{x_2}}} \quad \text{and} \quad \bar{\bar{\sigma}}_{m\ \mathrm{norm}} = \frac{\bar{\bar{\sigma}}_m}{\sqrt{P_{x_2}}}, \tag{17}$$

then the energy P_m carried by a normalized mode m is given by the square of the intrinsic amplitude:

$$\begin{aligned} P_m &= \frac{1}{2}\,\mathrm{Re}\int_h (-(a_m \mathbf{v}_{m\ \mathrm{norm}})^* a_m \bar{\bar{\sigma}}_{m\ \mathrm{norm}})\mathbf{x}_2\, dx_1 \\ &= |a_m|^2 = \left(\frac{A_m}{U_m}\right)^2. \end{aligned} \tag{18}$$

The energy balance is satisfied, if the energy carried by the incident mode is equal to the sum of the reflected and transmitted energies:

$$P_i \sum_m P_m = \left(\frac{A_i}{U_i}\right)^2 = \sum_m \left(\frac{A_{mr}}{U_m}\right)^2 + \sum_m \left(\frac{A_{mt}}{U_m}\right)^2. \tag{19}$$

This is true everywhere in the plate if there is no leakage and no viscoelastic damping (elastic case). It is also true at the defect position if the defect does not consume energy. Of course, this may happen in a viscoelastic material.

Then, the energy balance can be checked in terms of reflected and transmitted coefficients and is satisfied if Δ_E is close to 1:

$$\Delta_E = \sum_m \left(\frac{U_i}{U_m}{}_i R_m\right)^2 + \left(\frac{U_i}{U_m}{}_i T_m\right)^2. \tag{20}$$

VI. VALIDATION WITH THE FINITE ELEMENTS METHOD

In previous references,[4,7] it was verified that the use of the FE method for solving the equation of dynamic equilibrium in the frequency domain permits us to simulate properly the propagation of attenuated guided waves in viscoelastic plates. This model is used here to produce numerical data used in turn for validating the signal processing procedure previously described.

A. Material sample

The procedure is tested for several guided modes propagating along a Perspex plate, the thickness of which is 3.9 mm. Its viscoelastic properties, given in Table I, have been measured using a standard ultrasonic technique.[10] The C_{ij}^* represent the viscoelastic moduli with the usual contracted notation[8] in a coordinate system such that directions 1 and 2 are normal to the plate and lying in the plate, respectively. In the general case of an orthotropic material, these axes correspond to the principal axes of symmetry of the material. Here, the slight anisotropy of the plate is due to the fabrication process.

TABLE I. Complex viscoelasticity moduli (in GPa) of the Perspex plate.

Thickness (mm)=3.90		Density ρ (g/cm^3)=1.19	
C_{11}^*	8.5+I 0.3	C_{66}^*	2.3+I 0.06
C_{22}^*	8.3+I 0.4	C_{12}^*	4.4+I 0.2

The Rayleigh-Lamb equations[8] permit the complex wave numbers of Lamb modes in the Perspex plate to be computed using the stiffness moduli (Table I) as input data. The corresponding dispersion curves are plotted in the frequency domain chosen for this study (Fig. 3).

B. Finite elements model and postprocessing

The use of the FE model for generating and propagating guided modes in viscoelastic plates was already described in details in Refs. 4 and 7. Here only the main aspects are reminded. Also presented is a way for generating a perfectly pure mode that is mandatory for the verification of the proposed procedure.

The propagation of plane waves in a plate made of an orthotropic viscoelastic material of density ρ is considered, the plane of propagation being a plane of symmetry. The problem is solved in two dimensions for which one component of the displacement vector is null ($u_3=0$), thus leading to the following equations in the frequency domain:

$$\begin{aligned} &C_{11}^* \frac{\partial^2 \tilde{u}_1}{\partial x_1^2} + C_{66}^* \frac{\partial^2 \tilde{u}_1}{\partial x_2^2} + (C_{12}^* + C_{66}^*)\frac{\partial^2 \tilde{u}_2}{\partial x_1\, \partial x_2} + \rho\omega^2 \tilde{u}_1 \\ &\quad = f_1(x_1, x_2), \\ &C_{22}^* \frac{\partial^2 \tilde{u}_2}{\partial x_2^2} + C_{66}^* \frac{\partial^2 \tilde{u}_2}{\partial x_1^2} + (C_{12}^* + C_{66}^*)\frac{\partial^2 \tilde{u}_1}{\partial x_1\, \partial x_2} + \rho\omega^2 \tilde{u}_2 \\ &\quad = f_2(x_1, x_2), \end{aligned} \tag{21}$$

where $(\tilde{u}_1, \tilde{u}_2)$ is the Fourier transform of the displacement vector. The above differential equations must be written in the following FE code form:[6]

$$\nabla(c\,\nabla\,\mathbf{U}) - a\mathbf{U} = \mathbf{f}(x_1, x_2), \tag{22}$$

where c is a 2×2 matrix composed of four submatrices such that

$$\begin{aligned} c_{11} &= \begin{pmatrix} C_{11}^* & 0 \\ 0 & C_{66}^* \end{pmatrix}, \quad c_{12} = \begin{pmatrix} 0 & C_{12}^* \\ C_{66}^* & 0 \end{pmatrix}, \\ c_{21} &= \begin{pmatrix} 0 & C_{66}^* \\ C_{12}^* & 0 \end{pmatrix}, \quad c_{22} = \begin{pmatrix} C_{66}^* & 0 \\ 0 & C_{22}^* \end{pmatrix}, \end{aligned} \tag{23}$$

and a is a 2×2 matrix given by

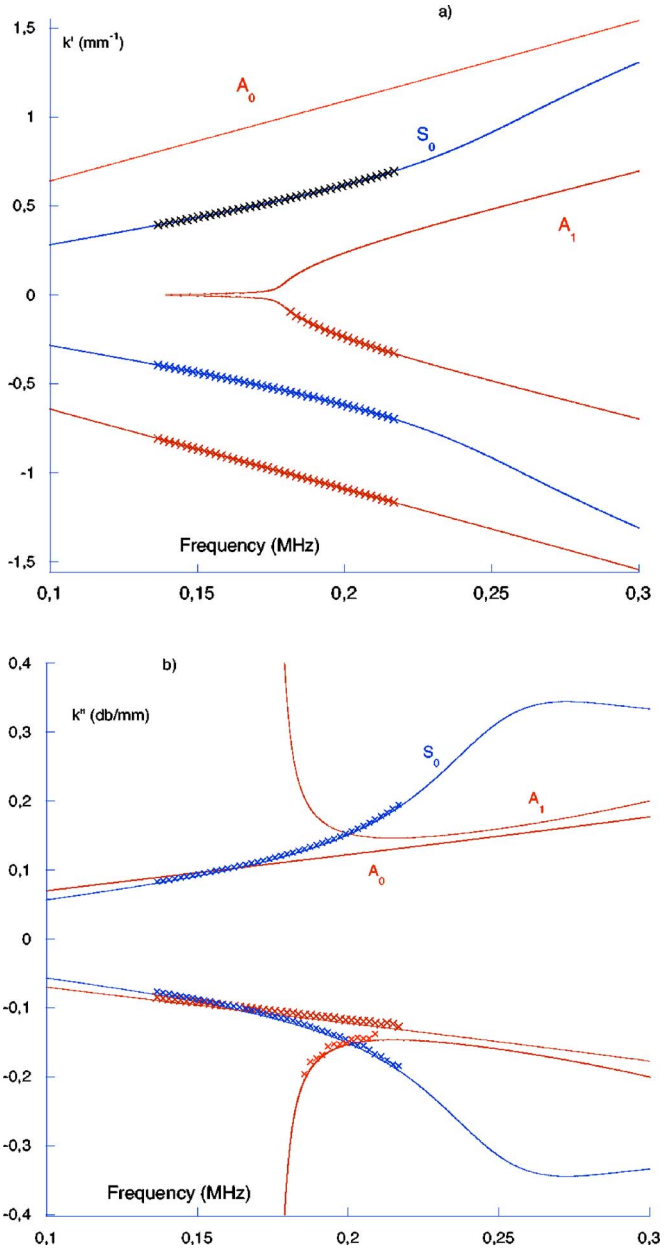

FIG. 3. (Color online) Lamb wave dispersion curves for a 3.9-mm-thick plate made of Perspex. (a) Real and (b) imaginary parts of the wave numbers. Rayleigh-Lamb solution (—) and FE predictions+spatial processing FFT (xxxx). Monitoring zone is from 1 to 140 mm.

$$a = \begin{pmatrix} -\rho\omega^2 & 0 \\ 0 & -\rho\omega^2 \end{pmatrix}. \tag{24}$$

There are many ways to numerically simulate the generation of a guided mode. One can apply the through-thickness displacement or stress field at one edge of the plate. When modeling the propagation in stationary mode (frequency domain), this approach is not satisfying for an elastic plate, for which it is necessary to include absorbing regions (AR on Fig. 1) at both ends of the plate to suppress unwanted infinite reflections between these ends and a defect in the plate. It is also possible to apply a sinusoidal stress field distribution to a portion of the surface of the plate to simulate the excitation of a wedge-transducer. This increases the size of the plate and consequently increases the number of mesh elements. The second problem with this technique is that it is not suitable for launching any pure mode. For instance, if the excitation is optimized for generating the S_0 mode close to the "plateau" in the dispersion curves (below 0.25 MHz in Fig. 3), then the unwanted A_0 is systematically produced with an amplitude of about 10% to 20% that of S_0.

It is then proposed to simulate an adapted volume force source inside the plate. In this purpose, the function $\mathbf{f}(x_1,x_2)$ in Eq. (22) is given the following shape:

$$\begin{aligned} &f_1(x_1,x_2) = \sigma_6(x_1) \\ &f_2(x_1,x_2) = \sigma_2(x_1) \end{aligned} \quad \text{for } x_{2\,\min} \le x_2 \le x_{2\,\max}$$
$$f_1(x_1,x_2) = f_2(x_1,x_2) = 0 \quad \text{elsewhere} \tag{25}$$

where $\sigma_2(x_1)$ and $\sigma_6(x_1)$ are the through-thickness shapes of the in-plane and shear stress components, respectively, produced by the mode that is to be generated. $x_{2\,\min}$ and $x_{2\,\max}$ define the length along the direction x_2 of the excitation zone, which is in fact limited to a couple of mesh elements. In this paper, the through-thickness stress field of the mode S_0 is computed for 42 frequencies between 0.13 and 0.22 MHz and used as input data for setting $\mathbf{f}$ as a function of the variable x_1. In this case, the volume force is imposed at the position $x_2=0$, along 2 mm in the x_2 direction. As shown in Fig. 2, a spatial Fourier analysis of normal displacements monitored at the plate surface, from $x_2=40$ to 100 mm, every 2 mm, and for the frequency 0.15 MHz, shows that the mode S_0 propagating in the direction $+x_2$ is pure. In fact, the A_0 mode can be identified in this wave-number diagram, but its amplitude is less than 0.1% that of S_0. The same figure shows that two modes, S_0 and A_0, are propagating in the direction $-x_2$, at 0.15 MHz. They are reflected by a 0.6-mm-wide, 1.8-mm-deep notch, located at $x_2=150$ mm (see Fig. 1).

Figure 3 presents the comparison between the Rayleigh-Lamb dispersion curves and the real and imaginary parts of the wave numbers obtained by postprocessing the FE normal displacement data monitored along a large zone extending from $x_2=1$ to 140 mm, at the plate surface. The attenuation can be derived using the formula (10), the monitoring zone being divided into two zones of equal lengths. For better accuracy, it is also possible to divide the large zone into several zones of equal lengths, to apply the spatial FFT for establishing the amplitudes of each lobe, and to optimize a decreasing exponential curve fitting these values. The only restriction is that the width of each window should be large enough to separate the modes in the wave-number domain. Figure 4(a) presents such a realization with seven windows; Fig. 4(b) shows the results of the Fourier transforms applied to this series of data ($\bar{A}_m$ for each position) and the three curves $\exp(\pm k''_m x_2)$ plotted for the three modes, at the frequency 0.15 MHz, the value of k''_m being optimized for each mode m. This procedure was applied for each frequency to obtain the results shown in Fig. 3(b).

1. Elastic/viscoelastic models

The width of the notch (0.6 mm) is very small in comparison with the smallest wavelength (>6 mm) in these

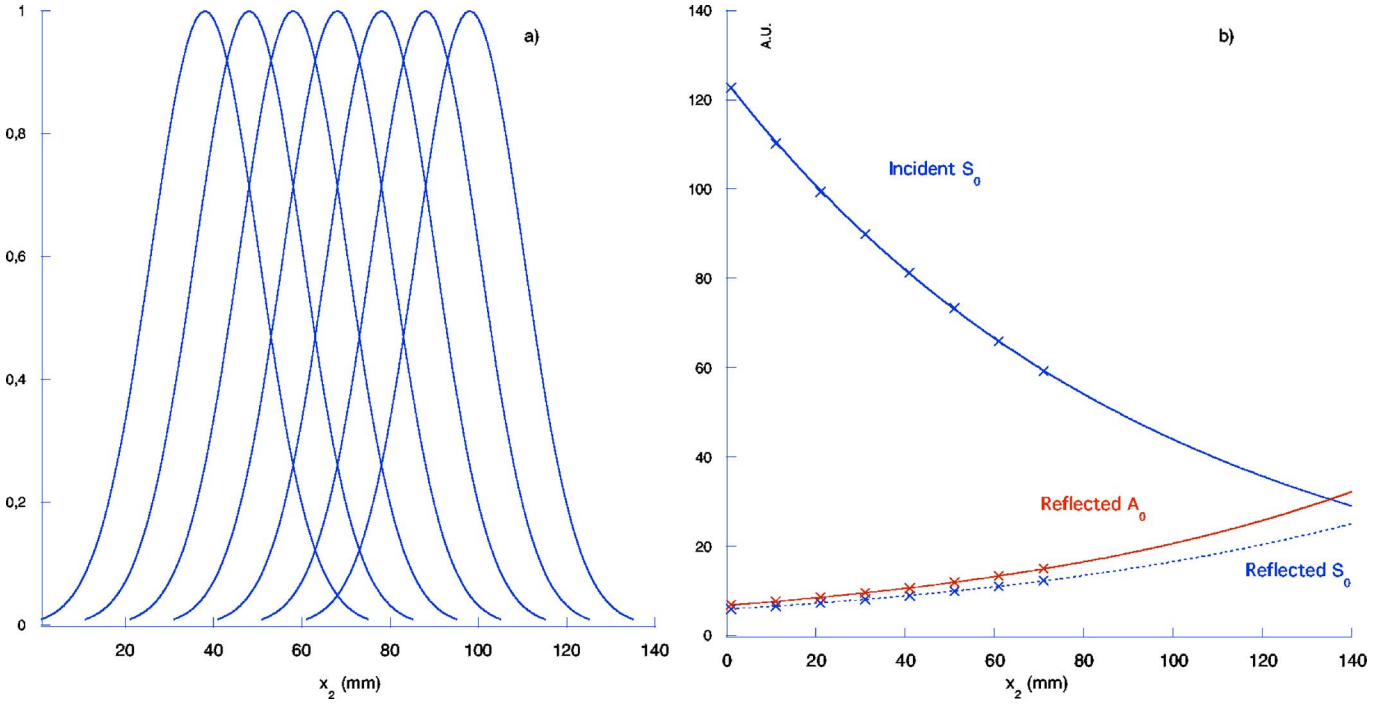

FIG. 4. (Color online) (a) Sequence of windows applied to several monitoring zones to compute the amplitudes $\bar{A}_m$. (b) Variation with position x_2 of the amplitudes $\bar{A}_m$ estimated for each zone and the optimized amplitude curves (frequency: 0.15 MHz).

tests. The reflection and transmission coefficients associated to the notch are computed by considering the plate as an elastic or viscoelastic material. One could expect very similar results in both cases, since the attenuation over a distance equivalent to the width of the notch is negligible. The spatial FFT-based procedure proposed in this paper is used to verify whether considering the material viscoelasticity in the FE model affects or not the response of the thin notch, i.e., the values of the reflection and transmission coefficients (at the notch location).

To realize the switch between elastic and viscoelastic, the viscoelastic moduli given in Table I are considered as real or complex data, i.e., V is set equal to 0 or 1 in the following formula:

$$C_{ij}^{*} = C_{ij}'(1 + i(a_l + a_r)) + iVC_{ij}''. \tag{26}$$

Note that a_l and a_r are used to define the absorbing regions in the model:

$$a_l = (-x_2/L_a)^3 \quad \text{if } (x_2 < 0), \quad \text{else } a_l = 0;$$

$$a_r = ((x_2 - (L_p - L_a))/L_a)^3 \quad \text{if } x_2 > L_p - L_a, \quad \text{else } a_r = 0; \tag{27}$$

where L_p(500 mm) is the position of the right edge of the plate and L_a (150 mm) is the length of the absorbing zones (Fig. 1). Figure 5 shows the meshing details around the notch and the efficiency of the absorbing zones for the elastic case.

2. Comparison between elastic and viscoelastic model

The transmission and reflection coefficients were computed according to the formulas (14) and (15) and using results of the Fourier transform. For the elastic case ($k_m''=0$), if the same spatial window is used for all the modes, the function $G_L(0)$ is divided out and the coefficients are simplified by ${}_iR_m=\bar{A}_{mr}/\bar{A}_i$ and ${}_iT_m=\bar{A}_{mt}/\bar{A}_i$. They are given in a frequency domain (Fig. 6) where two (S_0,A_0) or three (S_0,A_0,A_1) propagating modes are present. The monitoring zones were defined by a Gaussian window situated before the notch, starting at 40 mm and finishing at 120 mm, for the

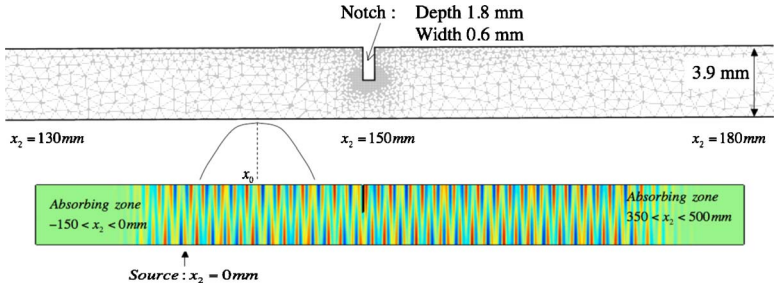

FIG. 5. (Color online) Elements repartition around the notch and snapshot of normal displacements (mode S0 incident) at the frequency 0.15 MHz.

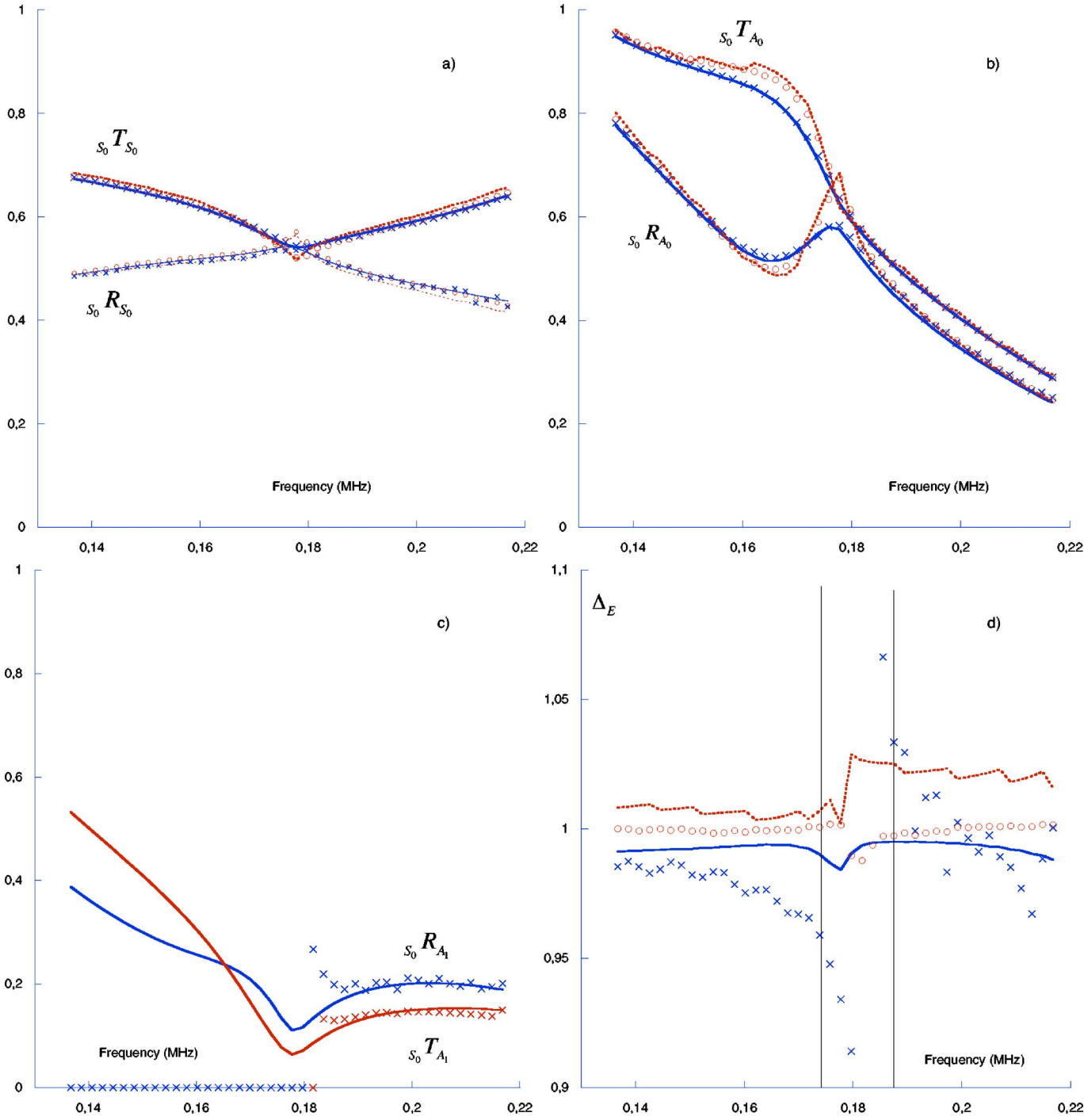

FIG. 6. (Color online) Reflection and transmission coefficients from normal displacement fields at the notch location, for the incident mode S0. (a) Mode S0. (b) Mode A0. (c) Mode A1. (d) Energy balance. Solid line: viscoelastic case. Dashed line: elastic case from orthogonality relations x: viscoelastic case. ∘: elastic case from spatial processing FFT.

incident and reflected modes. The Gaussian window for the transmitted modes was defined from 180 to 260 mm, past the notch.

For the viscoelastic case, the reflection and transmission coefficients (Fig. 6) are still obtained with Eqs. (14) and (15), but this time the attenuating or growing terms are included and computed using the k_m'' wave-number imaginary parts for each mode. Figure 6 shows that the coefficients are very similar, whether the viscoelasticity of the material is taken into account or not for computing the scattering phenomenon, except in the zone near the frequency cutoff of the A_1 mode (≈0.178 MHz). In Fig. 6(b), the transmission coefficient $_{s_0}T_{A_0}$ is slightly different for the two cases in the largest frequency zone. That means there is a significant effect of the viscoelasticity on this coefficient even for this narrow notch.

As an example for which the viscoelasticity has no effect on the diffraction coefficients, a comparison between the elastic and viscoelastic cases is given in Table II for the frequency 0.201 MHz, which is sufficiently far from the A_1

TABLE II. Reflection and transmission coefficients at 0.201 MHz. Elastic and viscoelastic cases.

Elastic	$_{S_0}R_{S_0}$	0.467	$_{S_0}R_{A_0}$	0.346	$_{S_0}R_{A_1}$	0.203
	$_{S_0}T_{S_0}$	0.595	$_{S_0}T_{A_0}$	0.395	$_{S_0}T_{A_1}$	0.150
	Δ_E	1.007				
Viscoelastic	$_{S_0}R_{S_0}$	0.467	$_{S_0}R_{A_0}$	0.342	$_{S_0}R_{A_1}$	0.207
	$_{S_0}T_{S_0}$	0.592	$_{S_0}T_{A_0}$	0.396	$_{S_0}T_{A_1}$	0.146
	Δ_E	0.996				

cutoff. The reflection and transmission coefficients values are very similar and the computation of the energy balance gives a number Δ_E very close to 1.

To calculate the energy balance, the power-normalized surface normal displacements of the three modes are computed for each frequency. For instance, Fig. 7 displays the whole through-thickness displacement fields for the frequency 0.201 MHz.

It is established that in an elastic plate, the nonpropagating modes do not carry energy.[8] At the opposite, the nonpropagating modes carry and absorb energy in a viscoelastic plate, since in fact they are quasi-non-propagating.[11] In the frequency range where the mode A_1 is passing from the quasi-non-propagating state to the attenuated propagating state, the differences between the two computations (elastic and viscoelastic materials) are more important. The energy balance Δ_E is comprised between 0.99 and 1 in the elastic case and between 0.90 and 1.10 in the viscoelastic case [Fig. 6(d)]. This is due to the fact that the spatial Fourier transform is applied to data monitored far away from the defect, thus making the quasi-non-propagating modes too greatly attenuated to be detected. In an experiment, their level would be under the noise level and, in a FE simulation, they are under the numerical precision.

The transition frequency zone is not well defined, as it is shown at Fig. 8, where the complex wave number of the mode A_1 is plotted versus the frequency. In fact, what is called cutoff in the elastic case does not happen in the viscoelastic case. The mode becomes progressively quasi-non-propagating when the frequency decreases. The width of the zone would depend on the numerical precision (FE method) or on the measurement precision (experiment). Here it is seen on Fig. 6(d) that the zone lies down from 0.170 to 0.180 MHz for an error in the energy balance lower than 5%.

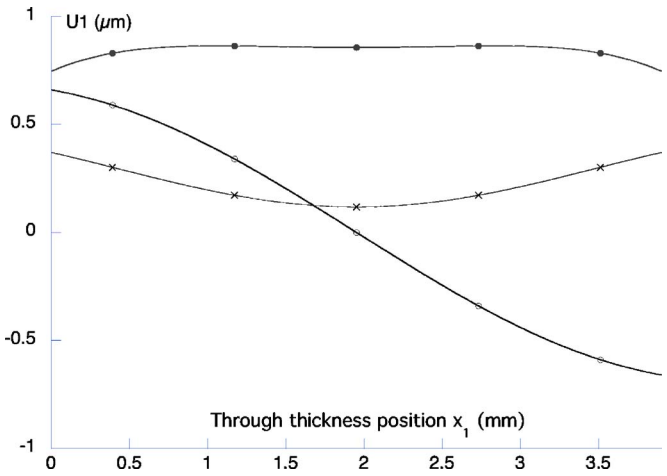

FIG. 7. (Color online) Power-normalized normal displacement fields of S0, A0, and A1 modes at 0.201 MHz versus the through-thickness position in the plate.

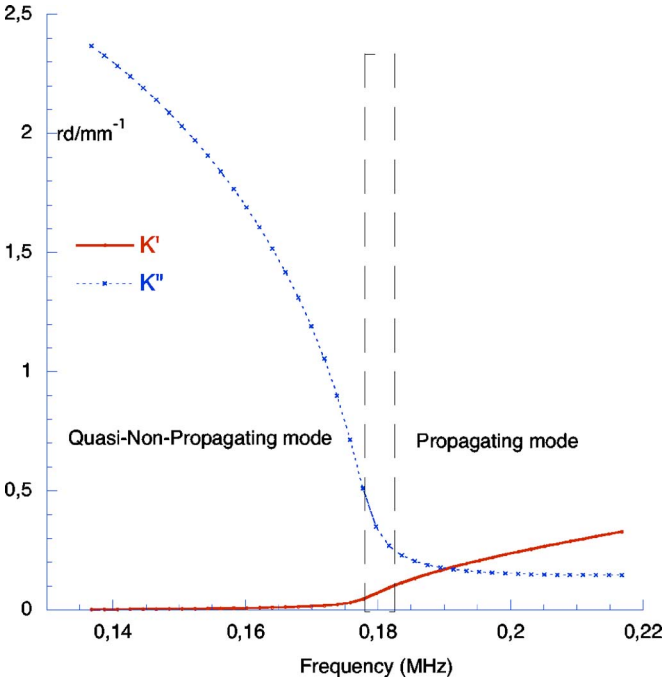

FIG. 8. (Color online) Complex wave number of mode A1 (—: real part; --- imaginary part).

3. Comparison with the orthogonality relation-based method

In a recent paper,[9] another method for postprocessing data furnished by the FE model was presented. Since this method, which is based on the orthogonality between two modes, analyzes the through-thickness fields as close as possible to the defect, the amplitudes of all the modes can be evaluated and the error in the energy balance is therefore smaller than 3%, in the whole frequency range. Of course, this method cannot be used for postprocessing experimental data since the fields inside the structures cannot be measured. But, it is an accurate and fast method to compute the reflection and transmission coefficients for a defect.

This method was first applied to the elastic plate with the notch investigated in this paper and the results presented by Fig. 6 (dashed lines and markers o) are perfectly similar.

The comparison for the viscoelastic plate is also given in Fig. 6 (solid lines and markers x). In that case also, there is a very good fitting between the results relative to modes A_0 and S_0. This validates the signal processing based on the Fourier transform presented in this paper. Figure 6(c) proves that the reflection and transmission of mode A_1, defined in terms of normal displacements close to the defect, are important before the transition zone, separating the quasi-non-propagating to the propagating behavior of the mode A_1. But the mode is so attenuated that it cannot be detected when the monitoring zone needed for the spatial FFT is far away from the defect.

This comparison establishes that the reflection and transmission coefficients for the modes that have enough energy in the monitoring zone can be well estimated with the spatial Fourier, even if the energy balance is not satisfied. From the experimenter point of view, this is satisfactory.

VII. CONCLUSIONS

A signal processing procedure for evaluating the amplitudes of guided modes propagating along an absorbing structure at different frequencies was presented. This procedure is based on a spatial Fourier transform applied to normal surface displacements picked up along monitoring zones and weighted by a spatial window in order to remove unwanted side lobes in the wave-number domain. It has been shown that dividing the resulting spectrum amplitudes by the amplitude of the spatial window spectrum removes the effects of the shape, the length, and the position of the spatial window. In this way, the amplitudes of any forwards or backwards traveling mode can be estimated.

The procedure was tested to estimate the transmission and reflection coefficients of guided waves propagating in a viscoelastic plate incorporating a notch, the positions of the windows and of the defect, and also the attenuation of the guided modes being initially known.

For a narrow notch (in comparison with the wavelength), perpendicular to the direction of propagation, the procedure gave similar coefficients when the plate was considered either elastic or viscoelastic, except in narrow frequency ranges close to the transition of the modes from the quasi-non-propagating behavior to the attenuated propagating behavior. But, even for this very narrow notch, there is a small effect of the viscoelasticity on some coefficients. The complete study of this influence is out of the scope of this paper and will be investigated later on.

These results were corroborated with the energy balance computations in both cases and compared with results obtained from the orthogonality relation-based processing method. The good fitting between the results of both methods relative to modes that have enough energy far from the defect validates the signal processing based on the Fourier transform presented in this paper.

[1]P. Cawley, "The rapid non-destructive inspection of large composite structures," Composites **25**(5), 351–357 (1994).

[2]R. Ruzek, R. Lohonka, and J. Jironc, "Ultrasonic C-Scan and shearography NDI techniques evaluation of impact defects identification," NDT & E Int. **39**(2), 132–142 (2006).

[3]D. Alleyne and P. Cawley, "A two-dimensional Fourier transform method for the measurement of propagating multimode signals," J. Acoust. Soc. Am. **89**(3), 1159–1168 (1991).

[4]B. Hosten and M. Castaings, "FE modeling of Lamb mode diffraction by defects in anisotropic viscoelastic plates," NDT & E Int. **39**, 195–204 (2006).

[5]S. Zhongqing, Y. Lin, and L. Ye, "Guided Lamb waves for identification of damage in composite structures: A review," J. Sound Vib. **295**, 753–780 (2006).

[6]FEMLAB, User's Guide and Introduction, version 3.0 by COMSOL AB 2004. http://www.comsol.com/, viewed 4/22/2007.

[7]M. Castaings, C. Bacon, B. Hosten, and M. V. Predoi, "Finite element predictions for the dynamic response of thermo-viscoelastic material structures," J. Acoust. Soc. Am. **115**(3), 1125–1133 (2004).

[8]B. A. Auld, *Acoustic Fields and Waves in Solids* (Wiley-Interscience, New York, 1973), Vol. **2**.

[9]L. Moreau, M. Castaings, B. Hosten, and M. V. Predoi, "An orthogonality relation-based technique for post-processing finite element predictions of waves scattering in solid guides," J. Acoust. Soc. Am. **120**(2), 611–620 (2006).

[10]M. Castaings, B. Hosten, and T. Kundu, "Inversion of ultrasonic, plane-wave transmission data in composite plates to infer viscoelastic material properties," NDT & E Int. **33**(6), 377–392 (2000).

[11]F. Simonetti and M. J. S. Lowe, "On the meaning of Lamb mode non propagating branches," J. Acoust. Soc. Am. **118**(1), 186–192 (2005).

Multiple scattering from assemblies of dislocation walls in three dimensions. Application to propagation in polycrystals

Agnès Maurel[a)]
Laboratoire Ondes et Acoustique, UMR CNRS 7587, Ecole Supérieure de Physique et de Chimie Industrielles, 10 rue Vauquelin, 75005 Paris, France

Vincent Pagneux
Laboratoire d'Acoustique de l'Université du Maine, UMR CNRS 6613 Av. Olivier Messiaen, 72085 Le Mans Cedex 9, France.

Felipe Barra and Fernando Lund
Departamento de Física, Facultad de Ciencias Físicas y Matemáticas, Universidad de Chile, Casilla 487–3, Santiago, Chile and Centro para la Investigación Interdisciplinaria Avanzada en Ciencias de los Materiales (CIMAT), Universidad de Chile, Santiago, Chile

(Received 20 June 2006; revised 21 March 2007; accepted 30 March 2007)

The attenuation of ultrasound in polycrystalline materials is modeled with grain boundaries considered as arrays of dislocation segments, a model valid for low angle mismatches. The polycrystal is thus studied as a continuous medium containing many dislocation "walls" of finite size randomly placed and oriented. Wave attenuation is blamed on the scattering by such objects, an effect that is studied using a multiple scattering formalism. This scattering also renormalizes the speed of sound, an effect that is also calculated. At low frequencies, meaning wavelengths that are long compared to grain boundary size, then attenuation is found to scale with frequency following a law that is a linear combination of quadratic and quartic terms, in agreement with the results of recent experiments performed in copper [Zhang *et al.*, J. Acoust. Soc. Am. **116**(1), 109–116 (2004)]. The prefactor of the quartic term can be obtained with reasonable values for the material under study, without adjustable parameters. The prefactor of the quadratic term can be fit assuming that the drag on the dynamics of the dislocations making up the wall is one to two orders of magnitude smaller than the value usually accepted for isolated dislocations. The quartic contribution is compared with the effect of the changes in the elastic constants from grain to grain that is usually considered as the source of attenuation in polycrystals. A complete model should include this scattering as well. © *2007 Acoustical Society of America.* [DOI: 10.1121/1.2734488]

PACS number(s): 43.35.Cg, 43.20.Hq, 43.20.Fn [RLW] Pages: 3418–3431

I. INTRODUCTION

Ultrasonic materials characterization and nondestructive evaluation need the scattering of elastic waves in polycrystalline materials to be precisely understood since ultrasonic attenuation and backscatter measurements are used widely to extract the microstructural parameters such as grain size and also to detect flaws in materials.

Most of the current understanding of the acoustic attenuation in polycrystals is due to models that consider the wave scattering caused by the variations of the elastic properties from one grain to the other that result from the different orientations of the single crystals. Grain boundaries are, at least implicitly, treated as structureless, as well as passive, surfaces. Pioneer works from the 1940s to the 1960s[1–4] predicted a quartic dependence of the attenuation on the frequency (Rayleigh scattering) in the low frequency regime. Further refinements have been considered, mainly to include the texture or anisotropy of materials[5–10] (see also the review in Ref. 11) all producing the Rayleigh scattering solution at low frequencies.

Recent improvements in sample preparation and in measurement methods have allowed the comparison, on a quantitative basis, of experimental results with theoretical models. Zhang *et al.*[12] performed accurate measurements of ultrasound attenuation in copper and copper-aluminum samples; they were able to establish a frequency dependence of the attenuation as a combination of quadratic and quartic terms, a behavior that is not explained by current theoretical models. Let us also mention the recent work of Hurley *et al.*[13] where the refraction of surface acoustic waves across a single grain boundary has been visualized and measured using optical techniques.

In a previous paper,[14] we have proposed a model that focuses on the grain boundaries as the source of scattering. This was done by modeling grain boundaries as dislocation arrays in two dimensions. In the present study, we generalize the study to three-dimensional configurations: the grains are assumed to be limited by "walls" formed of arrays of dislocations, as pictured in Fig. 1. We expect that scattering by such dislocation walls can produce the combination of quadratic and quartic frequency terms for the attenuation in the low frequency regime, as we have observed this behavior for randomly distributed dislocation segments.[15]

[a)]Electronic mail: agnes.maurel@ espci.fr

 0001-4966/2007/121(6)/3418/14/$23.00 © 2007 Acoustical Society of America

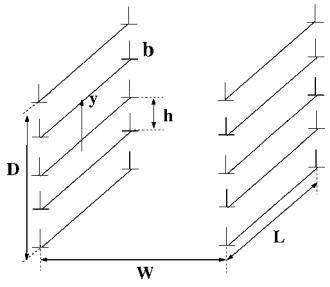

FIG. 1. Schematic representation of two low-angle grain boundaries of size $L \times D$ separated by a distance w. The dislocation segment holds edge dislocations, with Burgers vector b, separated by a distance h.

Since Burgers[16] and Bragg[17] in 1940, low angle grain boundaries are known to be described by arrays of edge dislocations. In the 1950s, the works of Shockley and Read[18,19] showed that the grain boundary energy can be expressed as the energy of a suitable periodic array of dislocations with dislocation spacing h expressed as a function of Burgers vector b and of the misorientation θ between two grains in the so-called Frank formula $b=2h \sin \theta/2$.[20] The validity of this model appears to be well established for typical dislocation spacings larger than about four interatomic distances.[21,22]

There does not appear the same degree of consensus concerning the structure of high angle grain boundaries, for whose modeling different approaches have been proposed. Most of them belong to, or are derived from, the coincident site lattice model, from the O-lattice model or from dislocation theories[23–26] (see also the review in Ref. 27, and references herein) and they are based on a geometrical analysis of the crystallography of the boundary. The experimental works on grain boundary structure[28–33] contribute to that kind of analysis. Let us also mention the work of Kobayashi *et al.*[34] that analyzes the energy of a grain boundary in a continuum model and the work of Meilikhov,[35] who recovered superconductive features of grain boundaries using a model of edge dislocations randomly distributed on the boundary, instead of regularly spaced.

The main simplification of this paper is to consider a polycrystal endowed only with low angle grain boundaries, pictured as walls holding dislocations distributed in both directions of the walls. The distribution law of the dislocation lines on the grain boundaries is discussed in the paper, either periodic or random, discrete or continuous. Otherwise, the elastic properties of the grains are isotropic and homogeneous. Thus, the only source of scattering is the presence of dislocation lines.

The paper is organized as follows: In Sec. II, we present the basic relations that allow one to treat the problem of scattering by a dislocation wall of finite size $L \times D$ that is the picture of a grain boundary. This is accomplished using a wave equation with a source term that encapsulates the wave-grain boundary interaction. The formalism of multiple scattering using the Dyson equation is applied to this differential equation and calculations, for low scattering strength, up to second order are given. This leads to a derivation of the velocity change and attenuation of both longitudinal and transverse waves, the results of which are presented in Sec. III. One important aspect of the present study is that we find a frequency dependence of acoustic attenuation that is a linear combination of quadratic and quartic terms, in agreement with the results of Zhang *et al.*[12] A more detailed comparison with those experiments is presented and discussed in Sec. IV. The quartic contribution found in our model is also compared with the quartic contribution usually found when considering the changes in elastic constants from grain to grain. Including this effect in a complete model is easy since both effects simply superimpose, as shown in Appendix C. Concluding remarks are given in Sec. VI, and technical details are given in the appendices.

II. PROPAGATION OF WAVE THROUGH A RANDOM DISTRIBUTION OF GRAIN BOUNDARIES

In this section, we present the derivation of the wave numbers for coherent waves propagating in an effective medium that is an elastic medium filled with a random distribution of dislocation walls of finite size. This is our picture of the grain boundaries. It does not consider their actual topology, an effect that should not be important at long wavelengths. These wave numbers have a real part, which differs from the real wave numbers $\omega/c_{L,T}$ in the absence of grain boundaries, and an imaginary part, corresponding to the attenuation of the propagating waves.

The derivation is performed using a usual multiple scattering theory, solving the Dyson equation assuming low scattering strength. This approach has been previously developed for isolated dislocation segments in Ref. 15.

In the paper, we denote (λ, μ) the Lame's coefficients and ρ the density of the elastic medium that composes the grains. With an isotropic medium, we use $c_{ijkl}=\lambda \delta_{ij}\delta_{kl} + \mu(\delta_{ik}\delta_{jl}+\delta_{il}\delta_{jk})$. With ω the angular frequency of the incident wave, the velocities of the transverse and longitudinal waves are $c_L=\sqrt{(\lambda+2\mu)/\rho}$ and $c_T=\sqrt{\mu/\rho}(\gamma \equiv c_L/c_T)$.

A. Derivation of a wave equation with a source ("potential") term

It has been shown in previous paper[36,37] that the interaction of a single moving edge dislocation with elastic waves is described by a wave equation with a source term. To do that, we described the two step scattering mechanism as pictured in Fig 2.

First, the wave incident on the dislocation segment (pinned at both extremities) induces it to oscillate. Low accelerations are also assumed, so that the backreaction of the radiation on the dislocation dynamics can be neglected. Following Ref. 38 and under these hypotheses, the equation of motion of an edge dislocation takes the form of the equation of motion for a string endowed with mass and line tension, forced by the usual Peach-Koehler force[39,40]

$$m\ddot{X}_k(s,t) + B\dot{X}_k(s,t) - \Gamma X_k''(s,t) = F_k(t), \tag{2.1}$$

and the associated boundary conditions at pinned ends $X_k(\pm L/2,t)=0$. In Eq. (2.1), $m \simeq \rho b^2$ defines a mass per unit length, $\Gamma \simeq \rho b^2 c_T^2$ a line tension, B is the drag coefficient, and $F_k=\epsilon_{kjm}\tau_m b_i \sigma_{ij}$ the Peach–Koehler force (ϵ_{ijk} denotes the usual completely antisymmetric tensor). The dislocation is assumed to be a gliding edge dislocation, so that the motion

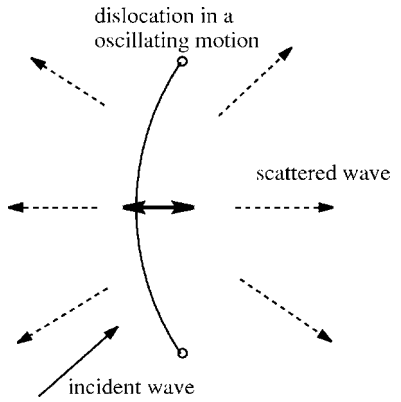

FIG. 2. Two step scattering mechanism of an elastic wave by a dislocation segment. The incident wave hits the dislocation, causing it to oscillate in response; the oscillation motion generates an outgoing scattered wave.

X occurs along the direction of the Burgers vector. We denote **t** this direction, with $\mathbf{b}=b\mathbf{t}$, $\boldsymbol{\tau}$ the direction along the dislocation line, and $\mathbf{n}\equiv\boldsymbol{\tau}\times\mathbf{t}$.

In previous papers[15,37] where interest was in the low frequency regime, this equation was solved in the limit $kL \ll 1$, so that all the points of the segment received a wave with the same phase. Here, we choose to treat the general case and the solution is

$$\dot{X}(\sigma,y,\omega) = -\frac{2}{L}\frac{\mu b}{m}\mathsf{M}_{lk}\sum_n \left\langle \frac{\partial}{\partial x_l} v_k[\mathbf{X}(\sigma',y),\omega] \middle| \chi_n(\sigma') \right\rangle \times p_n(\omega)\chi_n(\sigma) \tag{2.2}$$

with $p_n(\omega)\equiv 1/(\omega^2-n^2\omega_1^2+i\omega B/m)$, $\omega_1\equiv\pi c_T/L$, $\mathsf{M}_{lk}\equiv t_l n_k + t_k n_l$, $\chi_n(\sigma)\equiv\sin[(n\pi/L)(\sigma+L/2)]$ and where $\langle a|b\rangle \equiv \int_{-L/2}^{L/2} ab$ denotes an inner product.

In the second step, the moving dislocation emits a scattered wave whose form can be derived using the wave equation and the discontinuity relation $[\mathbf{u}]=\mathbf{b}$, first given in Ref. 41, see also Ref. 14,

$$v_m^s(\mathbf{x},t) = \epsilon_{jnh}c_{ijkl}\int_{-D/2}^{D/2} dy\, p(y)\int_{-L/2}^{L/2} d\sigma dt'\, b_i\dot{X}_n(\sigma,y,t') \times \tau_h\frac{\partial}{\partial x_l}G_{km}^0[\mathbf{x}-\mathbf{X}(\sigma,y),t-t'], \tag{2.3}$$

where the Green tensor of free space G^0 verifies

$$\rho\frac{\partial^2}{\partial t^2}G_{im}^0(\mathbf{x},t) - c_{ijkl}\frac{\partial^2}{\partial x_j\,\partial x_l}G_{km}^0(\mathbf{x},t) = \delta(\mathbf{x})\,\delta(t)\,\delta_{im}. \tag{2.4}$$

In Eq. (2.4), $p(y)$ describes the distribution of the dislocation lines along the grain boundary of length D (along the y axis), with $\int dy\, p(y)=N$ the number of elementary dislocation lines held by the grain boundary.

A number of possibilities are open for $p(y)$. To wit,

(1) Discrete distribution of dislocation lines, in which case $p(y)=\Sigma_{n=1}^N \delta(y-y_n)$. This can be a periodic distribution, with $y_n=nh$ ($Nh=D$) or a random distribution with the $N-y_n$ values randomly distributed in $[-D/2,D/2]$.

(2) Continuous distributions, among which $p(y)=1/h$ is the continuous extension of the periodic discrete distribution.

The choice of a particular distribution is expected to influence significantly the expression of the field scattered by one/several grain boundary/ies in Eq. (2.3) only when the wavelength is comparable to the distance among dislocations within the grain boundary. However, when the interest is in the characterization of the effective medium (namely the attenuation and the velocity change), many grain boundaries are considered and an ensemble average is performed over all the parameters describing the grain boundaries. It will be seen that this average smoothes the differences between the different distributions $p(y)$: The result at first order is independent of the choice of $p(y)$ and at second order, the limit $kD<1$ is found to be roughly independent of $p(y)$.

Combining Eqs. (2.2) and (2.3) leads to a wave equation with a source ("potential") term

$$\rho\frac{\partial^2}{\partial t^2}v_i(\mathbf{x},t) - c_{ijkl}\frac{\partial^2}{\partial x_j\,\partial x_l}v_k(\mathbf{x},t) = V_{ik}v_k, \tag{2.5}$$

where

$$V_{ik}(\mathbf{x},\omega) = \frac{2}{L}\frac{(\mu b)^2}{m}\mathsf{M}_{ip}\mathsf{M}_{jk}\int dy\, p(y) d\sigma d\sigma' \frac{\partial}{\partial x_p}\delta[\mathbf{x}-\mathbf{X}(\sigma,y)] \times\sum_n p_n(\omega)\chi_n(\sigma)\chi_n(\sigma')\left.\frac{\partial}{\partial x_k}\right|_{\mathbf{x}=\mathbf{X}(\sigma',y)}. \tag{2.6}$$

B. Derivation of the modified wave numbers

The derivation of the potential in Eq. (2.6) allows one to treat the problem of the propagation of elastic waves through a polycrystal following a usual multiple scattering theory. Let us consider a configuration with an ensemble of grain boundaries described by a set of parameters (the position and the orientation of the boundaries for instance). This realization is described by a potential $V^T=\Sigma_i V^i$ in the wave equation as in Eq. (2.5), with V^i the potential of the ith grain boundary, as given in Eq. (2.6).

The problem can be formulated in terms of the modified Green tensor $\langle G\rangle$, that gives the impulse response of the medium averaged over all realizations of disorder, the average being taken over the set of parameters that describe a given configuration. The multiple scattering theory gives the modified Green tensor in the Dyson equation:[42–44]

$$\langle G\rangle = [(G^0)^{-1}-\Sigma]^{-1},$$

where Σ is the so-called mass operator related to the potential. The main difficulty in solving the Dyson equation is to find Σ but a closed form can be written if an approximation of Σ is performed for weak scattering. In that case, Σ can be expanded and, up to second order in a small parameter that measures the scattering strength, we have

$$\Sigma^{(1)} = \langle V^T \rangle,$$
$$\Sigma^{(2)} = \langle V^T G^0 V^T \rangle - \langle V^T \rangle G^0 \langle V^T \rangle. \tag{2.7}$$

In the case where V^T is a sum of individual potentials and assuming no correlations between the scatterers (that is no correlation between the parameters that define the disorder), the mass operator takes a simpler form as a function of the potential for a single scatterer. In Fourier space, this is written as

$$\Sigma_{ij}^{(1)}(\mathbf{k}) = n \int d\mathbf{x} d\mathbf{C}\, e^{-i\mathbf{kx}} V_{ij}(\mathbf{x}) e^{i\mathbf{kx}},$$
$$\Sigma_{ij}^{(2)}(\mathbf{k}) = n \int d\mathbf{x} d\mathbf{x}' d\mathbf{C}\, e^{-i\mathbf{kx}} V_{in}(\mathbf{x}) \times G_{nl}^0(\mathbf{x}-\mathbf{x}') V_{lj}(\mathbf{x}') e^{i\mathbf{kx}'}, \tag{2.8}$$

where n is the density of scatterers and where the integral over $d\mathbf{C}$ corresponds to the average over all the parameters of disorder.

In our calculation, (1) all elementary dislocation lines have the same Burgers vector b and the same mass per unit length m and (2) all grains have the same dimension $L \times D$. What differs from one grain boundary to the other is (3) the grain boundaries have different line spacing h, or equivalently different N values. This allows one to account for different misorientations between adjacent grains since a growing misorientation angle is expected to produce a decreasing line spacing and (4) the grain boundaries have random position and random orientations. To simplify the calculations, assumptions (3) is reduced to its simplest form where h can take any value in the interval $[\bar{h}-\Delta h, \bar{h}+\Delta h]$, with $\Delta h \ll \bar{h}$ [implying, for all f functions, $\langle f(h) \rangle \simeq f(\bar{h})$]. In summary, a realization of disorder corresponds to many grain boundaries of same size (dislocation walls), with density n, randomly distributed and orientated in an elastic medium (otherwise homogeneous and isotropic) with different (low) misorientation angles.

The whole task is now to derive the wave numbers $K_{L,T}$ of the modified Green function $\langle G \rangle$. The details of the calculations are reported in Appendix A and we find, for $\mathbf{k} = k\mathbf{e}_3$

$$\langle G \rangle^{-1}(\mathbf{k}) = G_0^{-1}(\mathbf{k}) - \Sigma(\mathbf{k}) = \rho c_T^2 \begin{pmatrix} (k^2 - k_T^2) & 0 & 0 \\ 0 & (k^2 - k_T^2) & 0 \\ 0 & 0 & \gamma^2 (k^2 - k_L^2) \end{pmatrix} - \rho c_T^2 k^2 \begin{pmatrix} F_{1T}(k,\omega) + F_{2T}(k,\omega) & 0 & 0 \\ 0 & F_{1T}(k,\omega) + F_{2T}(k,\omega) & 0 \\ 0 & 0 & F_{1L}(k,\omega) + F_{2L}(k,\omega) \end{pmatrix}. \tag{2.9}$$

With the notations

$$x \equiv \frac{\omega}{\omega_1}, \quad v \equiv kL/\pi, \tag{2.10}$$

$B_c \equiv 2m\omega_1$, and $\beta \equiv B/B_c$, the first-order terms are

$$F_{1T} \equiv \frac{2}{\pi^4} \frac{D}{\bar{h}} nL^3 \int_0^1 du (1-u^4) S(uv,x),$$
$$F_{1L} \equiv \frac{4}{\pi^4} \frac{D}{\bar{h}} nL^3 \int_0^1 du (1-u^2)^2 S(uv,x), \tag{2.11}$$
$$S(uv,x) \equiv \sum_j \frac{f_j(\pi uv/2)}{j^2(j^2 - x^2 - 2ix\beta)[(uv/j)^2 - 1]^2},$$

where $f_j \equiv \sin^2$ for j even and $f_j = \cos^2$ for j odd. This result at first order is independent of the distribution law $p(y)$ for the dislocation lines along the grain boundaries. This is because the first-order calculation corresponds to single scattering process averaged over all possible positions and orientations of the grain boundaries. The average causes the particular organization encapsulated in $p(y)$ to disappear. The calculation at second order, however, does depend on the choice on $p(y)$ since it involves a self-irradiation term: it is the contribution of the waves hitting twice the same scatterer. This contribution depends on the structure of the scatterer [here on $p(y)$], and the sum of waves hitting successively two dislocation lines of the same grain boundary will be different when, say, the line spacing is constant or random, since interferences are expected. The second-order terms are

$$F_{2T} \equiv \frac{i}{2\pi^7} \left(\frac{D}{\bar{h}} \right)^2 nL^3 x^3 \int_{-1}^1 du [\cos^2 \xi u^2 + \sin^2 \xi (1-2u^2)^2] \times \int_{-1}^1 da\, h_x(a,u) \int_0^{2\pi} d\xi\, g_x(\xi,u),$$
$$F_{2L} \equiv \frac{4i}{\pi^7} \left(\frac{D}{\bar{h}} \right)^2 nL^3 x^3 \int_{-1}^1 du\, u^2 (1-u^2) \times \int_{-1}^1 da\, h_x(a,u) \int_0^{2\pi} d\xi \sin^2 \xi\, g_x(\xi,u), \tag{2.12}$$

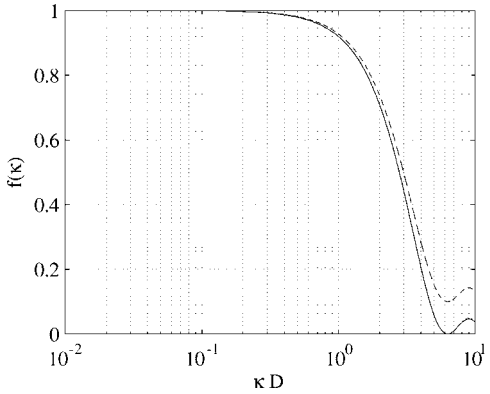

FIG. 3. Plots of the function $f(\kappa D)$ appearing at the second-order calculation in h_x in Eq. (2.12) for different distribution laws of the dislocation lines along the grain boundary. Full line; continuous distribution; dotted line (almost indistinguishable from the full line); discrete periodic distribution; dashed line; discrete random distribution. This plot considers for $D/\bar{h}=10$.

$$h_x(a,u) \equiv (1-3a^2+4a^4) f[(k_T a - ku)D] + \frac{4}{\gamma^5} a^2(1-a^2) f[(k_L a - ku)D],$$

$$g_x(\xi,u) \equiv R[S(\sqrt{1-u^2}\cos\xi v, x)]^2.$$

The function f appearing in h_x in Eq. (2.12) depends on $p(y)$ and we found

(1) $f(\kappa D)=\mathrm{sinc}^2(\kappa D/2)$ for a continuous distribution [with $\mathrm{sinc}(x)\equiv \sin x/x$].
(2) $f(\kappa D)=[\sin(\kappa D/2)/(D/\bar{h})\sin(\kappa\bar{h}/2)]^2$, characteristic of interference pattern produced by periodic arrays, for a discrete periodic distribution.
(3) $f(\kappa D)=[1-\mathrm{sinc}^2(\kappa D/2)]\bar{h}/D+\mathrm{sinc}^2(\kappa D/2)$ for a discrete random distribution.

Note that $f(\kappa D)$ tends to unity for $\kappa D \ll 1$ whatever the form of $p(y)$. The function f are quite the same for the continuous distribution and for the discrete periodic one, as it can be seen in Fig. 3.

Since the effective wave numbers $K_a, a=L,T$, are expected to be close to the undisturbed wave numbers k_a, we easily find, using $v(k_T)=x$ and $v(k_L)=x/\gamma$,

$$K_T \simeq k_T\left[1+\frac{1}{\pi^4}\frac{D}{\bar{h}} nL^3\left(f_{1T}(x)+\frac{i}{4\pi^3}\frac{D}{\bar{h}} f_{2T}(x)\right)\right],$$
$$K_L \simeq k_L\left[1+\frac{2}{\gamma^2\pi^4}\frac{D}{\bar{h}} nL^3\left(f_{1L}(x)+\frac{i}{\pi^3}\frac{D}{\bar{h}} f_{2L}(x)\right)\right], \tag{2.13}$$

with

$$f_{1T}(x) \equiv \int_0^1 du(1-u^4)S(ux,x),$$

$$f_{1L}(x) \equiv \int_0^1 du(1-u^2)^2 S(ux/\gamma,x),$$

$$f_{2T} \equiv x^3 \int_{-1}^{1} du[\cos^2\xi u^2 + \sin^2\xi(1-2u^2)^2] \times \int_{-1}^{1} da\, h_{xT}(a,u) \int_0^{2\pi} d\xi\, g_{xT}(\xi,u),$$

$$f_{2L} \equiv x^3 \int_{-1}^{1} du\, u^2(1-u^2) \int_{-1}^{1} da\, h_{xL}(a,u) \times \int_0^{2\pi} d\xi\, g_{xL}(\xi,u), \tag{2.14}$$

$$h_{xT}(a,u) \equiv (1-3a^2+4a^4) f[\pi x r(a-u)] + \frac{4}{\gamma^5} a^2(1-a^2) f[\pi x r(a/\gamma - u)],$$

$$h_{xL}(a,u) \equiv (1-3a^2+4a^4) f[\pi x r(a-u/\gamma)] + \frac{4}{\gamma^5} a^2(1-a^2) f[\pi x r(a-u)/\gamma],$$

$$g_{xT}(\xi,u) \equiv R[S(\sqrt{1-u^2}\cos\xi x, x)]^2,$$

$$g_{xL}(\xi,u) \equiv \sin^2\xi R[S(\sqrt{1-u^2}\cos\xi x/\gamma, x)]^2,$$

where $r\equiv D/L$. The previous expressions simplify considerably in the limit $x \ll 1$ of low frequencies, as will be seen in Sec. III B. Also, in that limit, it is easy to see that the case of isolated dislocation segments studied in Ref. 15 is recovered for $D/h=1, kD \ll 1$, in agreement with the fact that, for long wavelengths, the wave will see the grain boundary as a single, fat, dislocation segment.

III. VELOCITY CHANGES AND ATTENUATIONS

A. General expression of the velocity changes and attenuations

The attenuations $\alpha_a \equiv \mathrm{Im}[K_a]$ and modified velocity $v_a = \omega/R[K_a] (a=L,T)$ can be simply deduced from Eq. (2.13)

$$v_T \simeq c_T\left[1-\frac{1}{\pi^4}\frac{D}{\bar{h}} nL^3 R[f_{1T}(x)]\right],$$
$$v_L \simeq c_L\left[1-\frac{2}{\gamma^2\pi^4}\frac{D}{\bar{h}} nL^3 R[f_{1L}(x)]\right]. \tag{3.1}$$

and the attenuation

$$\alpha_T \simeq \frac{1}{\pi^3}\frac{D}{\bar{h}} nL^2 x\left[\mathrm{Im}[f_{1T}(x)] + \frac{1}{4\pi^3}\frac{D}{\bar{h}} f_{2T}(x)\right],$$
$$\alpha_L \simeq \frac{2}{\gamma^3\pi^3}\frac{D}{\bar{h}} nL^2 x\left[\mathrm{Im}[f_{1L}(x)] + \frac{1}{\pi^3}\frac{D}{\bar{h}} f_{2L}(x)\right]. \tag{3.2}$$

Typical behaviors of the attenuation and velocity change $\Delta v_a \equiv c_a - v_a$ are shown on Fig. 4 (technical details about the numerical calculations are given in Appendix B). We found two regimes, depending on the value of the drag B compared

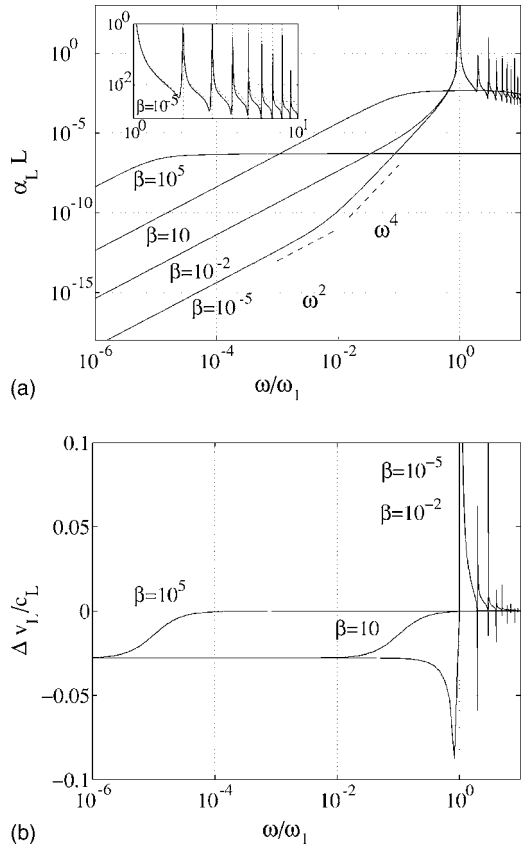

FIG. 4. Typical behaviors of (a) the attenuation $\alpha_L L$ and of (b) the velocity change $\Delta v_L/c_L$ as a function of the frequency, in the underdamped regime ($\beta=B/B_c=10^{-5},10^{-2}$) and in the overdamped regime ($B/B_c=10,10^{-5}$). Calculations have been performed using $nL^3=1$, $D/\bar{h}=10$ and $\gamma=2$ in Eqs. (3.1) and (3.2). (a) Calculations of the attenuation have been performed considering a continuous distribution of dislocation lines $p(y)$ along the grain boundaries. For $\beta=10^{-5}$ and 10^5, calculations have been performed for the discrete distributions $p(y)$ (periodic and random). The curves are superimposed but indiscernible. The inset shows a zoom for $\omega>\omega_1, \beta=10^{-5}$: the cases that are continuous (in plain line) and periodic (in dashed line) are still indiscernible. The case of discrete random distribution is represented in dotted line and here has the maximum difference 50% (otherwise lower than 0.15%). The ω^2 and ω^4 frequency laws are given for a guide to the eye.

with the critical value $B_c \equiv m\omega_1$ that fixes the limit of the over- and underdamped regimes for the dislocation motion. In the underdamped regime ($\beta \equiv B/B_c < 1$), the frequency law for the attenuation is a combination of a quadratic and quartic terms at low frequencies $\omega/\omega_1 < 1$. Above ω_1, resonances appear for incident wavelengths that are a submultiple of the grain size $L(\omega=n\omega_1)$. These resonances are smoothed because of the damping (encapsulated in B) and increasing $\beta \propto B$ causes them to disappear in the overdamped regime $\beta > 1$. A more detailed discussion on these regimes can be found in Ref. 15. The attenuation involves the second-order calculation. Calculations have been performed with the different distribution laws $p(y)$: continuous, periodic, and random. The difference between the three $p(y)$ laws decreases increasing β. This is because the second-order contribution is independent of β and increasing β makes the first-order contribution dominant [otherwise independent of $p(y)$]. For $\beta=10^{-5}$, the difference between the α values is lower than 0.15% for $\omega<\omega_1$. It reaches 50% for $\omega>\omega_1$, as shown in the inset of Fig. 4(a). For $\beta=10^5$, the differences between the α values is lower than 10^{-3}% in the whole frequency range $[10^{-6}-10]\omega_1$.

From these figures, the limit of validity of the present calculations can be commented upon. Our approach assumes that the multiple scattering medium behaves as an effective dissipative medium in which a coherent wave propagates, and a perturbative development is performed. This implies $\Delta v/c \ll 1$ and $\alpha/k \ll 1$, both conditions being a consequence of the perturbative method. It can be seen that, in the underdamped regime, frequencies $\omega > \omega_1$ give high attenuation and velocity change because of the resonances. In that regime, the weak scattering approximation will cease to be valid.

B. Velocity change and attenuation in the low frequency regime

In the low frequency regime ($\omega \ll \omega_1$ or $x \ll 1$), the expressions for velocity change simplify to

$$\frac{\Delta v_a}{c_a} \simeq \mathcal{C}_a \frac{D}{\bar{h}} nL^3 \frac{1}{1+x^2\beta^2}, \tag{3.3}$$

with $C_T=4/(5\pi^4), C_L=16/(15\gamma^2\pi^4)$, and for attenuation to

$$\alpha_a \simeq \mathcal{D}_a \frac{D}{\bar{h}} nL^2 x^2 \left[\frac{\beta}{1+x^2\beta^2} + \frac{4}{15\pi^2} \frac{3\gamma^5+2}{\gamma^5} \frac{D}{\bar{h}} \frac{x^2(1-x^2\beta^2)}{(1+x^2\beta^2)^2} \right], \tag{3.4}$$

with $\mathcal{D}_T=4/(5\pi^3)$, $\mathcal{D}_L=16/(15\gamma^3\pi^3)$, and $\beta=B/B_c$. These results agree with those obtained for isolated dislocation segments in Ref. 15 with the replacements $b \to \bar{N}b$ and $m \to \bar{N}m$ with $\bar{N} \equiv D/\bar{h}$ the number of dislocation segments held in a grain boundary [or equivalently $D/\bar{h}=1$]. This reasonably means that a grain boundary behaves as a single (fat) dislocation segment with total Burgers vector $\bar{N}b$ and total mass $\bar{N}m$ in the low frequency regime. The behaviors in the under- or overdamped regimes are illustrated in Fig. 4 and a discussion can be found in Ref. 15. In the underdamped regime, the terms $x\beta \ll 1$ vanish and the attenuation has simply a contribution in x^2 due to the drag $B \propto \beta$ and a contribution in x^4 due to multiple scattering process. This behavior is compared with experimental results in Sec. IV.

IV. COMPARISON WITH ZHANG *et al.* EXPERIMENTS

In a recent publication, Zhang *et al.*[12] have reported the experimental measurement of the attenuation of longitudinal waves with frequencies in the 10 MHz range (meaning wavelengths of the order of millimeter) in polycrystalline copper. The care taken by these authors to prepare the samples allowed them to characterize very accurately the frequency dependence, and the data clearly exhibit, in addition to the usual quartic law, a quadratic term. The data fits reported in that paper are discussed in this section.

Following Zhang's notation, we write $\alpha=\alpha_L(c=c_L)$ and

TABLE I. Coefficients of the fits for the attenuation in $\alpha=\alpha_2 f^2+\alpha_4 f^4$, from Zhang *et al.* (Ref. 12) for different grain sizes d in different prepared samples (PM and CW). Two sets of values for h and B/b^2 are reported, The first ($V1$) correspond to the values deduced from Eq. (4.2) in the polynomial approximation and the second [($V2$) in parentheses] are the values that give the best fits between our complete expression α^{th} [Eq. (3.2)] and the polynomial expansion given by Zhang.

Sample reference (in Ref. 12)	PM3		PM5		CW2		CW4	
d (μm)	9.77		26.9		10.3		33.9	
α_2 (10^{-15} m^{-1} Hz^{-2})	12		32		71		240	
α_4 (10^{-30} m^{-1} Hz^{-4})	9		180		7		280	
$\bar{h}$ (μm)	1.25	(0.79)	3.52	(2.41)	1.62	(1.98)	5.03	(11.24)
B/b^2 (10^{13} Pa s m^{-2})	0.039	(0.025)	0.0140	(0.0110)	0.254	(0.309)	0.075	(0.168)

$$\alpha = P(f) = \alpha_2 f^2 + \alpha_4 f^4. \tag{4.1}$$

Now, our expression (3.4) in the limit $x \ll 1$ and in the underdamped regime gives the same polynomial expansion as Eq. (4.1) with the identifications

$$\alpha_2 = \frac{64}{15\pi^4}\frac{BnL^5}{\rho b^2 c^3}\frac{D}{\bar{h}},$$
$$\alpha_4 = \frac{1024}{225\pi^5}\frac{3\gamma^5+2}{\gamma^4}\frac{nL^6}{c^4}\left(\frac{D}{\bar{h}}\right)^2. \tag{4.2}$$

Note the proportionality of α_2 with D. The latter is a linear dimension associated with grain boundary size, which it is not unreasonable to suppose proportional to grain size. In this case this formula provides a rationale for the linear scaling between α_2 and grain size found by Zhang *et al.*[12]

We have to introduce simplifying assumptions concerning grain shape that should not affect measurements performed at length scales much larger than grain size:

(1) Following Zhang *et al.*, we shall call d the grain size, and we shall assume it is of the same order of magnitude as all dimensions of the grain boundaries, or, in the language of the present model, the dislocation walls: $d \approx L \approx D \approx w$.
(2) With the previous assumption, we assume $nd^3 \sim 1$, which means that the grains are "cubes" uniformly distributed throughout space.

With these assumptions it is possible to find simplified expressions with only two undetermined parameters: $\bar{h}$, the mean distance between two dislocations within a grain boundary, and B/b^2, a ratio that depends on the characteristics of the dislocation in the grain boundary:

$$\alpha_2 = \frac{64}{15\pi^4}\frac{d^3}{\rho c^3}\frac{B}{b^2}\frac{1}{\bar{h}}, \quad \alpha_4 = \frac{1024}{225\pi^5}\frac{3\gamma^5+2}{\gamma^4}\frac{d^5}{c^4}\frac{1}{\bar{h}^2}. \tag{4.3}$$

Equation (4.3) does not contradict the linear scaling with D predicted by our model. It is a consequence of the assumption $L \sim D \sim w$, which is used for the numerical estimations of Table I.

For two sets of samples denoted PM (prepared by the power metallurgy method) and CW (cast-and-wrought), Zhang *et al.* give the coefficients of the polynomial fits of the experimental data [α_2 and α_4 defined in $P(f)$, Eq. (4.1)]. These results are reported in Table I, together with the values of $\bar{h}$ and of (B/b^2) they imply in our model when the polynomial simplification is considered [Eq. (4.1)]. To do that, it is sufficient to use the above-presented expression of α_4 in Eq. (4.3) to determine $\bar{h}$ without any adjustable parameters

$$\bar{h} = \frac{1024}{225\pi^5}\frac{3\gamma^5+2}{\gamma^4}\frac{d^5}{c^4}\frac{1}{\alpha_4}. \tag{4.4}$$

This value of $\bar{h}$ can then be used in the expression of α_2 to extract the ratio B/b^2,

$$\left(\frac{B}{b^2}\right) = \frac{15\pi^4}{64}\frac{\rho c^3}{d^3}\alpha_2 \bar{h}^g. \tag{4.5}$$

Results are presented in Table I (values $V1$), for $\rho=9\times10^{-3}$ kg m^{-3}, $c=4900$ m s^{-1}, and $\gamma=2$.

The results for $\bar{h}$ seem eminently reasonable: The few micrometers found for the distance between dislocation corresponds to the value, first observed by Lacombe[45] and reported by Read and Shockley in 1950.[19] It corresponds to a low angle grain boundary with a disorientation angle of about 10^{-3} rad for b around 1 nm.

The results implied for B/b^2 however, differ from the values of B commonly accepted for an isolated dislocation. Indeed, in this case b is typically below the nanometer and B is around 10^{-5} Pa s at room temperature,[46–48] giving a value for the ratio B/b^2 around 10^{13} Pa s m^{-2} if the dislocation segments within a grain boundary behave as isolated dislocation segments. This is at least one order of magnitude above the results reported in Table I, reasonably suggesting that the presence of neighboring dislocation segments strongly affects their damping dynamics. In other words, keeping the usual value of b, the drag B of the dislocation segment in the grain boundary is found around 10^{-6} Pa s, a value significantly smaller than the value for an isolated dislocation. Finally, note that we can check the assumption made that the dislocations move in an underdamped regime since the ratio B/B_c is found to typically lie between 0.02 and 0.2.

Comment on the polynomial approximation. The validity of the polynomial approximation is measured by the difference with the exact theoretical expression α^{th} given in Eq. (3.2), whose approximated form is the polynomial approxi-

mation only for $x \ll 1$. Since the experimental configurations for PM3, PM4, CW4, and CW5 cover x between 0.08 and 0.5, the approximation may be questioned. We denote $\alpha^{\exp}$ the polynomial approximation [indeed, remember that the polynomial approximation with $\bar{h}$ and (B/b^2) in Eqs. (4.4) and (4.5) gives exactly the experimental results, by construction] and $E=|\alpha^{\text{th}}-\alpha^{\exp}|/|\alpha^{\exp}|$ the difference with the exact expression.

The difference E on the attenuation is as follows (a mean value is taken in the frequency range [10–18] MHz): For PM3 ($x<0.14, B/B_c=0.03$), we get $E=7\%$. For PM5 ($x<0.4, B/B_c=0.03$), $E=25\%$. For CW2 ($x<0.15, B/B_c=0.19$), $E=1.3\%$ and for CW4 ($x<0.5, B/B_c=0.18$), $E=16\%$. As expected, E increases as x increases. Figure 6 illustrates this behavior: We have represented the experimental attenuation (identical to the polynomial approximation) and α^{th} calculated with the values of $\bar{h}$ and B/b^2 in Eqs. (4.4) and (4.5) ($V1$ values). The maximum difference is observed for the PM5 sample.

We have performed a second calculation in which the $V1$ values $(\bar{h}, B/b^2)$ are taken as initial guess values. Then, these values have been adjusted to obtain the best agreement with the polynomial fits. To do that, we have searched a minimum of $E=|\alpha^{\text{th}}-\alpha^{\exp}|/|\alpha^{\exp}|$, where α^{th} is numerically calculated with two adjustable parameters B/b^2 and $\bar{h}$: The minimum of $E(B/b^2, \bar{h})$ is found in a two-dimensional space where B/b^2 and $\bar{h}$ have been centered on the initial guess value with 100% variation. Figure 5 illustrates the procedure.

The resulting values ($V2$) are also presented in Table I and in Fig. 6. The resulting error E is decreased, around 1% for all samples.

Note that the difference between values ($V1$) and ($V2$) is significant but, as expected for relatively small x values, it does not change the order of magnitude of $\bar{h}$ and B/b^2.

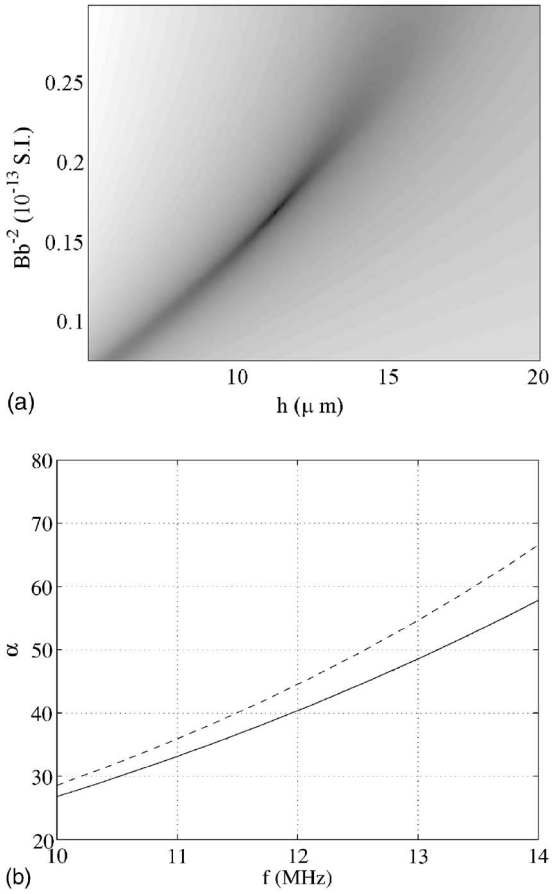

FIG. 5. (a) Example of the function error $E=|\alpha^{\text{th}}-\alpha^{\exp}|/|\alpha^{\exp}|$ [log(E) in gray scale] as a function of the two adjustable parameters B/b^2 and $\bar{h}$ (here for the case CW4 in Table I). White is the higher value (here 200%) and black the lowest value (0.08%). (b) The attenuation: in full line, the experimental fit given by Zhang *et al.* for CW4, in dotted line the attenuation calculated from Eq. (3.2) with the initial guess values $V1((B/b^2)=7.49\times10^{11}$ S.I. and $\bar{h}=5.0265$ μm and in dotted line, the best fit of the attenuation calculated from Eq. (3.2), obtained with the values $V2: B/b^2=16.81\times10^{11}$ S.I. and $\bar{h}=11.24$ μm.

V. COMMENT ON THE EFFECT OF GRAIN ANISOTROPY

The attenuation measured in polycrystals has been widely studied as originating from the variation in the elastic constants relevant for the propagation of waves from grain to grain due to the change in the grain orientation.[1–11] This effect can be encapsulated in a potential in the wave equation

$$\rho\frac{\partial^2}{\partial t^2}v_i(\mathbf{x},t)-\langle c_{ijkl}\rangle\frac{\partial^2}{\partial x_j\,\partial x_l}v_k(\mathbf{x},t)=V_{ik}^T(\mathbf{x})v_k(\mathbf{x},t),$$
$$V_{ik}^T(\mathbf{x})\equiv-\frac{\partial}{\partial x_j}\left(\delta c_{ijkl}(\mathbf{x})\frac{\partial}{\partial x_l}\,.\,\right), \tag{5.1}$$

where $\langle c_{ijkl}\rangle$ are the mean elastic constants, averaged over all possible orientations of the crystal axis, and $\delta c_{ijkl}(\mathbf{x})$ are the variations in the elastic constants from grain to grain, with respect to their mean value. In that case, the attenuation is found to be of the form

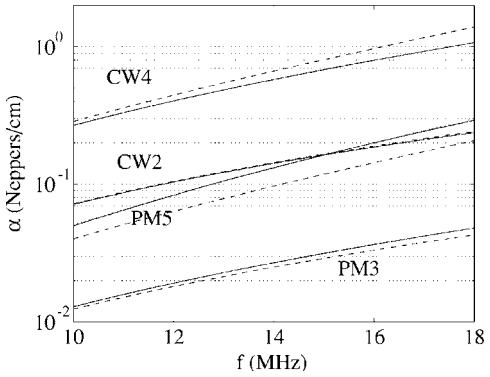

FIG. 6. Comparison with experiments reported in Zhang *et al.* for the four samples whose fits are given (see Table I): solid lines correspond to the experimental fitted curves. The correction of the simple power law in $\alpha_2 f^2+\alpha_4 f^4$ using the whole expression in Eq. (3.2) is given using $(B/b^2, \bar{h})$ coming from: in dashed line, the $V1$ values deduced from the polynomial approximation and in dotted line (almost superposed to the experimental curves) the $V2$ values minimizing the difference with the experimental configuration.

$$\alpha d \sim \mathcal{C}\left(\frac{\eta}{c_{11}}\right)^2\left(\frac{\omega d}{c_L}\right)^4, \tag{5.2}$$

where c_{11} is the first term of the stiffness matrix, equal to $\lambda+2\mu$ for isotropic media and $\eta=c_{11}-c_{12}-2c_{44}$ is a measure of the anisotropy of the single crystal. $\mathcal{C}$ is a numerical constant, of the order than $10^{-2}-10^{-3}$ (a simplified presentation of the calculation is given in Appendix C, for a more complete derivation of the Dyson equation, see Ref. 10). The contribution of the anisotropy of the crystal grain corresponds to a second-order contribution in the perturbative expansion, the first order vanishing because it is proportional to $\langle \delta c_{ijkl} \rangle$ that is zero, by definition.

It is shown in Appendix C that the attenuations due to the dislocations in the grain boundaries and due to the grain anisotropy simply superpose when both effects are considered. The attenuation could be thus written, with both effects,

$$\alpha d = \mathcal{A}\frac{B}{B_c}\frac{d}{\bar{h}}\left(\frac{\omega d}{c_L}\right)^2 + \left[\mathcal{B}\left(\frac{d}{\bar{h}}\right)^2 + \mathcal{C}\left(\frac{\eta}{c_{11}}\right)^2\right]\left(\frac{\omega d}{c_L}\right)^4, \tag{5.3}$$

where we have used the simplified expression in Eqs. (4.1)–(4.3): $\mathcal{A}=16/(15\gamma\pi^5)\simeq 2\times 10^{-3}$ and $\mathcal{B}=64(3\gamma^5+2)/(225\pi^9\gamma^4)\simeq 5\times 10^{-5}$. A comparison between the two quartic terms will depend on the characteristics of the material at hand. For copper, studied in Refs. 1 and 49, η is of the same order than the stiffness coefficients c_{ij}. With $d/\bar{h}\sim 10$ dislocations per grain boundary (as we have found in Table I), the two contributions are of the same order of magnitude. This means that including both effects in our study would not change significantly the results on the values of B and $\bar{h}$. Of course, this balance can change depending on the polycrystal.

VI. CONCLUDING REMARKS

Recent measurements of ultrasound attenuation can be understood in terms of a model that blames the attenuation on scattering by grain boundaries that are made of dislocation arrays. For low frequencies, that is, wavelengths long compared to grain size, the grain boundaries mainly behave as an ensemble of isolated dislocations, with an effective mass and an effective Burgers vector equal to the total mass and the total Burgers vector "held" by the grain boundary. A frequency law that is a linear combination of quadratic and quartic terms naturally appears. The quadratic term is due to the drag experienced by the dislocations as they respond to the externally generated acoustic wave. The quartic term is due to the damping experienced by the coherent wave as energy is taken from it by the randomly placed grain boundaries; it is an effect of disorder.

The quadratic scaling of the attenuation due to (individual) dislocation damping has been known since the 1950s[50–54] and the extra quartic contribution that appears when many, randomly located, dislocations are present, has been identified more recently.[15] In the low frequency regime, the quadratic contribution of the dislocations (say of length l) to the attenuation typically behaves as $\alpha\sim 10^{-3}\Lambda l\beta(\omega/\omega_1)^2$ with $\omega_1=\pi c/l$ the first resonance frequency and $\Lambda=nl$ the surface density of dislocations. This law has successfully explained the attenuation due to dislocations experimentally measured in the range of $10^{-2}-1$ m^{-1} (typical temporal attenuation, αc, being in the range $10^{-4}-10^{-2}$ μs^{-1} for ring-down curves).[55–61] The attenuations measured in the experiments of Zhang *et al.* are two orders of magnitude larger than in experiments that refer to dislocation damping, meaning that the contribution to the attenuation of the (individual) dislocations in the bulk of the grains can be neglected.

However, grain boundaries pictured as arrays of dislocations, a good approximation in the low-angle case, are good candidates to explain the quadratic term of the measured attenuation, with the dislocation drag significantly diminished by the presence of neighboring dislocations nearby. The quartic term can quite reasonably be understood as arising from the presence of many, randomly placed and oriented, grain boundaries, a quartic contribution that has to be compared with the usual contribution of the change in grain anisotropy.

Zhang *et al.*[12] found a difference in attenuation for samples prepared via powder metallurgy and equal channel angular extrusion, presumably linked to the difference in grain size distribution. In our work, while we can fit the data with appropriate values for the dynamic attenuation of dislocation motion B, we have taken an approximation in which grain boundaries, while randomly distributed, have identical sizes. Our formalism allows for a more general treatment with a more realistic distribution, and remains a possible direction for future work.

Finally, the dislocation walls that form grain boundaries appear to be good candidate as source of damping in polycrystals. Further measurements of the attenuation in a larger range of frequencies would be helpful (1) to confirm the results of Zhang *et al.* concerning the quadratic contribution in the low frequency regime, (2) to discriminate between the contribution due to the dislocation walls and due to the anisotropy in the transition (near ω_1) regime, and (3) to investigate the high frequency regime where resonances should be observed. Also, the low value of the drag coefficient that we obtain using the data of Zhang *et al.* needs to be further investigated if this result is confirmed.

ACKNOWLEDGMENTS

This work has been supported by ECOS Contract No. C04E01 and by FONDAP Grant No. 11980002. F.B. thanks Fondecyt Project No. 1060820. We are pleased to thank Erik Bitzek for fruitful discussions.

APPENDIX A: DERIVATION OF THE MASS OPERATOR

The task is here to derive the so-called mass operator Σ that links the modified Green tensor $\langle G \rangle$ of the effective medium (corresponding to an average of all realizations of the medium filled with random distributions of scatterers) and the Green tensor G^0 of the elastic medium free of scatterers. In the limit of weak scattering, the mass operator can be developed as in Eq. (2.8). In our case, the calculation is

performed up to second order. The first order gives the velocity change and a term of the attenuation due to internal viscosity (via the drag term B in the equation of motion for the dislocation) and the second order gives a term in the attenuation due to the energy that is taken away from the direction of propagation. This latter term exists even in the absence of any viscous effect.

To do the calculations, we restrict ourselves to the following assumptions:

(1) All the elementary dislocation lines along the grain boundary are identical, meaning they have the same Burger vector b and the same mass per unit length m.
(2) All grains have the same dimension $L \times D$.

The randomness has two sources:

(1) The grain boundaries hold different number N of dislocation lines, or equivalently different spacing h. This allows one to account for different misorientations between adjacent grains since a growing misorientation angle is expected to produce an increasing N value. We choose the simplest case where h can take any values in the interval $[\bar{h}-\Delta h, \bar{h}+\Delta h]$ with $\Delta h \ll \bar{h}$, thus we use $\langle f(h)\rangle \simeq f(\bar{h})$.
(2) The grain boundaries can have any orientation, the orientation of a grain being given by the orientation of the two vector $(\boldsymbol{\tau}, \mathbf{t})$. The two vector is described by the Euler angles (θ, φ, ξ). We denote R the rotation matrix $\mathsf{R}=\mathsf{R}(\mathbf{e}_3, \theta)\mathsf{R}(\mathbf{e}_2, \varphi)\mathsf{R}(\mathbf{e}_1, \xi)$,

$$\mathsf{R} = \begin{pmatrix} \cos\varphi\cos\theta & -\sin\theta\cos\xi - \sin\varphi\cos\theta\sin\xi & \sin\theta\sin\xi - \sin\varphi\cos\theta\cos\xi \\ \cos\varphi\sin\theta & \cos\theta\cos\xi - \sin\varphi\sin\theta\sin\xi & -\cos\theta\sin\xi - \sin\varphi\sin\theta\cos\xi \\ \sin\varphi & \cos\varphi\sin\xi & \cos\varphi\cos\xi \end{pmatrix} \tag{A1}$$

Also, when a discrete random distribution of dislocation lines is considered: $p(y)=\Sigma\delta(y-y_n)$, with y_n randomly distributed in $[-D/2, D/2]$, an additional average has to be performed to account for all possible positions of y_n. This is done through $\int dy_1 dy_2 \ldots dy_N / D^N$., indicating that each y_n has the D length as accessible space. Finally, the average over the orientations of the grain boundaries is encapsulated in the notation $\int d\mathbf{C}$.

1. First-order calculation

The first-order calculation is straightforward. We have, denoting $\chi_n(\sigma) \equiv \sin[(n\pi/L)(\sigma+L/2)]$ and $p_n(\omega) \equiv 1/(\omega^2 - \omega_n^2 + i\omega B/m)$,

$$\begin{aligned}\Sigma_{ij}^{(1)}(\mathbf{k}) &= n \int d\mathbf{x} d\mathbf{C} e^{-i\mathbf{kx}} V_{ik}(\mathbf{x}) e^{i\mathbf{kx}} \\ &= \frac{2n}{L}\frac{(\mu b)^2}{m} \int d\mathbf{x} d\mathbf{C} dy p(y) d\sigma d\sigma' e^{-i\mathbf{kx}} \mathsf{M}_{ip}\mathsf{M}_{jq} \\ &\quad \times \frac{\partial}{\partial x_p}\delta[\mathbf{x} - \mathbf{X}(\sigma, y)] \sum_n p_n(\omega)\chi_n(\sigma)\chi_n(\sigma') \frac{\partial e^{i\mathbf{kx}}}{\partial x_{q|\mathbf{x}}} \\ &= -\frac{2n}{L}\frac{(\mu b)^2}{m} \int dy p(y) \int d\mathbf{C} \mathsf{M}_{ip}\mathsf{M}_{jq}k_p k_q \\ &\quad \times \sum_n p_n(\omega) \left| \int d\sigma \chi_n(\sigma) e^{i\mathbf{k}\cdot\boldsymbol{\tau}\sigma} \right|^2 \\ &= -\frac{4L^2}{\pi^2}\frac{2n}{L}\frac{D}{\bar{h}}\frac{(\mu b)^2}{m} \int d\mathbf{C} \mathsf{M}_{ip}\mathsf{M}_{jq}k_p k_q \sum_n a_n(\omega, \mathbf{k}\cdot\boldsymbol{\tau})\end{aligned}$$

where we have used $\int dy p(y) = N = D/h$ for any distribution of dislocation lines and where

$$\begin{aligned} a_n(\omega, k) &\equiv \frac{\sin^2(kL/2)}{[(kL/n\pi)^2 - 1]^2}\frac{p_n(\omega)}{n^n} \quad \text{for } n \text{ even} \\ &\equiv \frac{\cos^2(kL/2)}{[(kL/n\pi)^2 - 1]^2}\frac{p_n(\omega)}{n^n} \quad \text{for } n \text{ odd.} \end{aligned} \tag{A2}$$

The integration over $\mathbf{C}$ has to be performed over the Euler angles (θ, φ, ξ) since we have to account for all orientations of the two vectors $(\boldsymbol{\tau}, \mathbf{b})$. We denote R the rotation matrix $\mathsf{R} \equiv \mathsf{R}(\mathbf{e}_3, \theta)\mathsf{R}(\mathbf{e}_2, \varphi)\mathsf{R}(\mathbf{e}_1, \xi)$,

$$\mathsf{R} = \begin{pmatrix} \cos\varphi\cos\theta & -\sin\theta\cos\xi - \sin\varphi\cos\theta\sin\xi & \sin\theta\sin\xi - \sin\varphi\cos\theta\cos\xi \\ \cos\varphi\sin\theta & \cos\theta\cos\xi - \sin\varphi\sin\theta\sin\xi & -\cos\theta\sin\xi - \sin\varphi\sin\theta\cos\xi \\ \sin\varphi & \cos\varphi\sin\xi & \cos\varphi\cos\xi \end{pmatrix} \tag{A3}$$

Without loss of generality, we choose $\boldsymbol{\tau}=\mathsf{R}\mathbf{e}_1, \mathbf{t}=\mathsf{R}\mathbf{e}_2, \mathbf{n}=\mathsf{R}\mathbf{e}_3$ and we choose arbitrarily $\mathbf{k}=k\mathbf{e}_3$ (the general form of the modified Green function can be obtained through rotations afterwards if desired). We obtain

$$\Sigma^{(1)}(\mathbf{k}) = -k^2 \frac{4L^2}{\pi^2} \frac{2nD}{L\bar{h}} \frac{(\mu b)^2}{m} \int d\mathbf{C}\mathbf{V}^t\mathbf{V} \sum_n a_n(\omega, k\mathsf{R}_{31}),$$

with $V_i \equiv \mathsf{R}_{i3}\mathsf{R}_{32}+\mathsf{R}_{i2}\mathsf{R}_{33}$. Since $\mathsf{R}_{31}=\sin\varphi$ is independent of θ and ξ in f_n, it is easy to integrate over θ and ξ. This allows one to show that $\Sigma^{(1)}$ is diagonal with $\Sigma^{(1)}_{11}=\Sigma^{(1)}_{22}$. We denote $\Sigma^{(1)}_T \equiv \Sigma^{(1)}_{11}$ and $\Sigma^{(1)}_L \equiv \Sigma^{(1)}_{33}$,

$$\Sigma^{(1)}_T(k) = -\rho c_T^2 k^2 \frac{D}{\bar{h}} \frac{nLc_T^2}{2} \int_0^1 du(1-u^4) \sum_n a_n(\omega, ku),$$

$$\Sigma^{(1)}_L(k) = -\rho c_T^2 k^2 \frac{D}{\bar{h}} nLc_T^2 \int_0^1 du(1-u^2)^2 \sum_n a_n(\omega, ku),$$

where we have used $\mu=\rho c_T^2$.

2. Second-order calculation

Calculations at second order are quite long but similar to the first-order ones. We report here the main steps of these calculations,

$$\begin{aligned}
\Sigma^{(2)}_{ij}(\mathbf{k}) &= n \int d\mathbf{x} d\mathbf{x}' d\mathbf{C} e^{-i\mathbf{k}\mathbf{x}} V_{in}(\mathbf{x}) G^0_{nl}(\mathbf{x}-\mathbf{x}') V_{lj}(\mathbf{x}') e^{i\mathbf{k}\mathbf{x}'} \\
&= \frac{4n}{L^2} \frac{(\mu b)^4}{m^2} \int d\mathbf{x} d\mathbf{x}' d\mathbf{C} \mathsf{M}_{ip} \mathsf{M}_{nq} \mathsf{M}_{lr} \mathsf{M}_{jt} \\
&\quad \times \int dy p(y) d\sigma d\sigma' dy' p(y') ds ds' e^{i\mathbf{k}\mathbf{x}} \frac{\partial}{\partial x_p} \\
&\quad \times \delta[\mathbf{x}-\mathbf{X}(\sigma,y)] \sum_n pn \chi_n(\sigma) \chi_n(\sigma') \\
&\quad \times \frac{\partial}{\partial x_{k|\mathbf{x}=\mathbf{X}(\sigma',y)}} G^0_{nl}(\mathbf{x}-\mathbf{x}') \frac{\partial}{\partial x'_r} \delta[\mathbf{x}'-\mathbf{X}(s,y')] \\
&\quad \times \sum_m p_m \chi_m(s) \chi_m(s') \frac{\partial e^{i\mathbf{k}\mathbf{x}'}}{\partial x'_{t|\mathbf{x}'=\mathbf{X}(s',y')}}.
\end{aligned}$$

We use $G^0(\mathbf{x}) = 1/(2\pi)^3 \int d\mathbf{q} G^0(\mathbf{q}) e^{i\mathbf{q}\mathbf{x}}$ and $\mathbf{X}(\sigma,y)=\sigma\boldsymbol{\tau}+y\mathbf{n}$ to get

$$\begin{aligned}
\Sigma^{(2)}_{ij}(\mathbf{k}) &= \frac{4n}{(2\pi)^3 L^2} \frac{(\mu b)^4}{m^2} \left(\frac{4L^2}{\pi^2}\right)^2 \\
&\quad \times \int d\mathbf{q} d\mathbf{C} \mathsf{M}_{ip} \mathsf{M}_{nq} \mathsf{M}_{lr} \mathsf{M}_{jt} q_q k_t k_q q_r G^0_{nl}(\mathbf{q}) \\
&\quad \times \left| \int dy p(y) e^{i(\mathbf{k}-\mathbf{q})\mathbf{n}y} \right|^2 \\
&\quad \times \sum_n a_n(\omega, \mathbf{k}\boldsymbol{\tau}) \sum_m a_m(\omega, \mathbf{k}\boldsymbol{\tau}),
\end{aligned}$$

which can be written without indices in a more tractable form

$$\begin{aligned}
\Sigma^{(2)}(\mathbf{k}) &= \frac{4n}{(2\pi)^3 L^2} \frac{(\mu b)^4}{m^2} \left(\frac{4L^2}{\pi^2}\right)^2 \left(\frac{D}{\bar{h}}\right)^2 k^2 \\
&\quad \times \int d\mathbf{q} d\mathbf{C} \mathcal{A} \mathbf{V}^t\mathbf{V} f[(\mathbf{k}-\mathbf{q})\cdot\mathbf{n}D] g(\mathbf{k}\cdot\boldsymbol{\tau}),
\end{aligned}$$

where $\mathcal{A} \equiv {}^t\mathbf{q}\mathsf{M}G^0(\mathbf{q})\mathsf{M}\mathbf{q}$ is a scalar term, $\mathbf{V} \equiv \mathsf{M}\hat{\mathbf{k}}$ is a vector and with $g(x) \equiv |\Sigma_n a_n(x)|^2$.

The function f depends on the distribution law considered for the dislocation lines. With

$$f(\kappa D) \equiv \left(\frac{\bar{h}}{D}\right)^2 \left\langle \left| \int_{-D/2}^{D/2} dy p(y) e^{i\kappa x} \right|^2 \right\rangle, \tag{A4}$$

where $\langle\cdot\rangle$ denotes the average over h and for the discrete random distribution, the average over the positions of the dislocation on a single grain boundary.

Let us give the expression of the function f for the continuous or discrete distributions $p(y)$:

(1) For a continuous distribution $p(y)=1/h$, it is easily found, with $\mathrm{sinc}\, X \equiv \sin X/X$,

$$f(\kappa D) = \mathrm{sinc}^2(\kappa D/2). \tag{A5}$$

(2) For a discrete periodic distribution $p(y)=\sum_{n=1}^N \delta(y-nh)$, with $D=Nh$, the integral is easily obtained

$$f(\kappa D) = \left[\frac{\sin(\kappa D/2)}{(D/\bar{h})\sin(\kappa\bar{h}/2)} \right]^2. \tag{A6}$$

(3) For a discrete random distribution $p(y)=\sum_{n=1}^N \delta(y-y_n)$ with y_n randomly distributed in $[-D/2, D/2]$, an additional average has to be performed. Denoting $\bar{N}=D/\bar{h}$, we get

$$\begin{aligned}
f(\kappa D) &= \frac{1}{\bar{N}^2} \int dh \int dy dy' \int \frac{dy_1 \cdots dy_N}{D^N} \\
&\quad \times \sum_{n=1}^N \delta(y-y_n) \sum_{m=1}^N \delta(y'-y_m) e^{i\kappa(y-y')} \\
&= \frac{1}{\bar{N}^2} \int dh \int \frac{dy_1 \cdots dy_N}{D^N} \sum_{n,m=1}^N e^{i\kappa(y_n-y_m)} \\
&= \frac{1}{\bar{N}^2} \int dh \left[N \int \frac{dy_1}{D} + N(N-1) \right. \\
&\quad \left. \times \int \frac{dy_1 dy_2}{D^2} e^{i\kappa(y_1-y_2)} \right] \\
&= \frac{\bar{h}}{D}[1-\mathrm{sinc}^2(\kappa D/2)] + \mathrm{sinc}^2(\kappa D/2).
\end{aligned} \tag{A7}$$

The typical behavior of these functions is illustrated in Fig. 3.

We choose now $\boldsymbol{\tau}=\mathsf{R}\mathbf{e}_3, \mathbf{t}=\mathsf{R}\mathbf{e}_2, \mathbf{n}=\mathsf{R}\mathbf{e}_1$, and still $\mathbf{k}=k\mathbf{e}_3$. The above-mentioned integrals can be rewritten (with a change of variable $\mathbf{q} \to {}^t\mathsf{R}\mathbf{q}$)

$$\Sigma^{(2)}(\mathbf{k}) = \frac{4n}{(2\pi)^3 L^2}\frac{(\mu b)^4}{m^2}\left(\frac{4L^2}{\pi^2}\right)^2 k^2 \times \int d\mathbf{q} d\mathbf{C} \mathcal{A}\mathbf{V}^t\mathbf{V} f[k\mathsf{R}_{31} - q\hat{\mathbf{q}}_1] g(k\mathsf{R}_{33}).$$

with $\mathcal{A} \equiv {}^t\mathbf{q}\mathsf{M}_{12}G^0(\mathbf{q})\mathsf{M}_{12}\mathbf{q}(\mathsf{M}_{12} \equiv \mathbf{e}_1{}^t\mathbf{e}_2 + \mathbf{e}_2{}^t\mathbf{e}_1)$ and $\mathbf{V} \equiv \mathsf{M}\mathbf{e}_3$.

In the absence of the functions f and g, the integrals over $\mathbf{C}$ and $\mathbf{q}$ would be separable since $\mathcal{A}$ depends only on $\mathbf{q}$ and $\mathbf{V}$ only on the Euler angles described by $\mathbf{C}$. As in the calculation of the mass operator at first order, the choice of $\mathbf{k}$ along $\mathbf{e_3}$ and $\mathbf{n}$ is motivated by the fact that $\mathsf{R}_{31} = \sin\varphi$ (appearing in the coupling function f) allows the direct integration over the two other Euler angles (θ, ξ). Here, because we have to deal with $\mathbf{k}\cdot\boldsymbol{\tau}$ and $\mathbf{k}\cdot\mathbf{n}$, we have to let in the coupling functions at least one other Euler angle: it appears in g through $\mathsf{R}_{33} = \cos\varphi\cos\xi$. It is thus possible to integrate freely the operator $\mathbf{V^t V}$ only over θ.

In a similar way, the integration of $\mathcal{A}$ over $\mathbf{q}$ can be performed singly $(\hat{\mathbf{q}}_2, \hat{\mathbf{q}}_3)$ since the coupling function f involves only $\hat{\mathbf{q}}_1$ and we choose the angles (α, β), such $\hat{\mathbf{q}}_1 = \sin\alpha$, $\hat{\mathbf{q}}_2 = \cos\alpha\cos\beta$, $\hat{\mathbf{q}}_3 = \cos\alpha\sin\beta$ so that integration of the scalar term $\mathcal{A}$ over β can be performed directly.

In addition, we are only concerned by the imaginary part of $\Sigma^{(2)}$. This appears through the calculation of $\int d\mathbf{q}\mathcal{A} f[k\mathsf{R}_{31} - q\hat{\mathbf{q}}_1]$ and (with $a \equiv \sin\alpha$ and integrating over β)

$$\mathrm{Im}\left[\int d\mathbf{q}\mathcal{A} f(k\mathsf{R}_{31} - q\hat{\mathbf{q}}_1)\right] = \frac{\pi\omega^3}{2\rho c_T^5}\int_{-1}^{1} da\left\{(1 - 3a^2 + 4a^4) f(k_T a - k\mathsf{R}_{31}) + \frac{4}{\gamma^5}a^2(1 - a^2) f(k_L a - k\mathsf{R}_{31})\right\}. \tag{A8}$$

The remaining integral over the Euler angle θ is performed over $\mathbf{V}^t\mathbf{V}$ with $V_1 = -\sin\theta\cos\xi\sin\varphi + \cos 2\varphi\cos\theta\sin\xi$, $V_2 = \cos\theta\cos\xi\sin\varphi + \cos 2\varphi\sin\theta\sin\xi$, $V_3 = \sin 2\varphi\sin\xi$. This integration is sufficient to show that $\Sigma^{(2)}$ is diagonal with $\Sigma_T^{(2)} = \Sigma_{11}^{(2)} = \Sigma_{22}^{(2)}, \Sigma_L^{(2)} = \Sigma_{33}^{(2)}$ and we get (with $u \equiv \sin\varphi$)

$$\Sigma_T^{(2)} = \rho c_T^2 k^2 F_{2T}(k,\omega), \qquad \Sigma_L^{(2)} = \rho c_T^2 k^2 F_{2L}(k,\omega), \tag{A9}$$

$$F_{2T} \equiv \frac{i}{2\pi^7}\left(\frac{D}{\bar{h}}\right)^2 nL^3x^3\int_{-1}^{1} du[\cos^2\xi u^2 + \sin^2\xi(1 - 2u^2)^2] \times \int_{-1}^{1} da\, h_x(a,u)\int_0^{2\pi} d\xi g_x(\xi,u),$$

$$F_{2L} \equiv \frac{4i}{\pi^7}\left(\frac{D}{\bar{h}}\right)^2 nL^3x^3\int_{-1}^{1} duu^2(1 - u^2) \times \int_{-1}^{1} dah_x(a,u)\int_0^{2\pi} d\xi \sin^2\xi g_x(\xi,u), \tag{A10}$$

$$h_x(a,u) \equiv (1 - 3a^2 + 4a^4) f[(k_T a - ku)D] + \frac{4}{\gamma^5}a^2(1 - a^2) f[(k_L a - ku)D],$$

$$g_x(\xi,u) \equiv \underline{R}[S(\sqrt{1 - u^2}\cos\xi v, x)]^2.$$

APPENDIX B: REMARK ON THE NUMERICAL INTEGRATION OF THE ATTENUATION

The numerical integration of the attenuations in Eq. (2.14) is fairly simple. Functions $f_{1T,1L}$ involve a single integral easy to perform with a Runge-Kutta scheme with adaptative step size. For f_{2L} (respectively, f_{2T}), the integral is of the form

$$\int_{-1}^{1} duu^2(1 - u^2)\int_{-1}^{1} dah(a,u)\int_0^{2\pi} d\xi g(\xi,u), \tag{B1}$$

and to compute it, we first choose a discretization for the u variable, and then, for each u value, we solve independently

$$\text{find } G_u(2\pi) = \int_0^{2\pi} d\xi g(\xi,u) \text{ by solving the ODE } \frac{dG_u(\xi)}{d\xi} = g(\xi,u), \text{ with } G_u(0) = 0,$$

$$\text{find } H_u(1) = \int_{-1}^{1} dah(a,u) \text{ by solving the ODE } \frac{dH_u(a)}{da} = h(\xi,u), \text{ with } H_u(-1) = 0. \tag{B2}$$

These ordinary differential equation (ODEs) are solved using a classical Runge-Kutta scheme with adaptative step size. The final integral over u is finally performed using the trapezoidal rule.

APPENDIX C: ATTENUATION DUE TO THE FLUCTUATIONS OF THE ELASTIC CONSTANTS

We give here very briefly the main steps in the derivation of the attenuation due to the fluctuations of the elastic constants $c_{ijkl}(\mathbf{x})$ from grain to grain. This is just in order to get the order of magnitude of this effect. A wave propagating in a medium with elastic constants that are space dependent is a solution of

$$\rho\frac{\partial^2}{\partial t^2}v_i(\mathbf{x},t) - \frac{\partial}{\partial x_j}\left(c_{ijkl}(\mathbf{x})\frac{\partial}{\partial x_l}\right)v_k(\mathbf{x},t) = 0. \tag{C1}$$

Writing $c_{ijkl}(\mathbf{x}) = \langle c_{ijkl}\rangle + \delta c_{ijkl}(\mathbf{x})$, where the mean has to be defined, the effect due to this spatial dependence can be encapsulated in a potential $V^T(\mathbf{x})$,

$$\rho\frac{\partial^2}{\partial t^2}v_i(\mathbf{x},t) - \frac{\partial^2}{\partial x_j\,\partial x_l}\langle c_{ijkl}\rangle v_k(\mathbf{x},t) = V_{ik}^T(\mathbf{x})v_k(\mathbf{x},t), \qquad V_{ik}^T(\mathbf{x}) \equiv -\frac{\partial}{\partial x_j}\left(\delta c_{ijkl}(\mathbf{x})\frac{\partial}{\partial x_l}\,.\right). \tag{C2}$$

Writing Eq. (C2) in terms of a potential V^T allows the application of the multiple scattering formalism to solve the Dyson equation.

Most of the literature considers that the difference in elasticity occurs because the grains are not uniformly oriented. Thus the mean $\langle c_{ijkl}\rangle$ is taken over all possible orientations. The elastic constants of a grain with arbitrary orientation can be expressed in terms of the single crystal constants c^0_{ijkl} through $c_{ijkl}=R_{ai}R_{bj}R_{ck}R_{dl}c^0_{ijkl}$. This allows one to derive $\langle c_{ijkl}\rangle$, related to c^0_{ijkl} and to a coefficient η that measures the anisotropy of the single crystal. For example, for cubic symmetry, one has $c^0_{iiii}=c_{11}, c^0_{iijj}=c_{12}$, $c^0_{ijij}=c_{44}$ (and zero otherwise) and one gets for an untextured polycrystal (that is, all possible orientations have equal probability), $\langle c_{iiii}\rangle=c_{11}-2\eta/5$, $\langle c_{ijij}\rangle=c_{44}-\eta/5$, with $\eta=c_{11}-c_{12}-2c_{44}$. Within a single grain, the elastic constants c_{ijkl} are indeed constants, and the spatial dependence in $c_{ijkl}(\mathbf{x})$ indicates that the wave travels through different grains.

Assuming small scattering strength, the mass operator can be expanded as in Eq. (2.7). The first-order expansion being proportional to $\langle \delta c_{ijkl}\rangle$, that is zero by definition. The second order is the lowest nonvanishing contribution and it takes the form $\Sigma_2=\langle V^T G^0 V^T\rangle$. In Fourier space, $\Sigma^{(2)}$ can be calculated as follows:

$$\begin{aligned}\Sigma^{(2)}_{ij}(\mathbf{k}) &= \frac{1}{\mathcal{V}}\int d\mathbf{C}d\mathbf{x}d\mathbf{x}'\, e^{-i\mathbf{k}\mathbf{x}}V^T_{ik}(\mathbf{x})G^0_{km}(\mathbf{x}-\mathbf{x}')V^T_{mj}(\mathbf{x}')e^{i\mathbf{k}\mathbf{x}'}\\ &= \frac{1}{\mathcal{V}}\int d\mathbf{C}d\mathbf{x}d\mathbf{x}'\, e^{-i\mathbf{k}\mathbf{x}}\frac{\partial}{\partial x_n}\left(\delta c_{inkl}(\mathbf{x})\frac{\partial}{\partial x_l}G^0_{km}(\mathbf{x}-\mathbf{x}')\right)\\ &\quad\times\frac{\partial}{\partial x'_p}\left(\delta c_{mpjq}(\mathbf{x}')\frac{\partial}{\partial x'_q}e^{i\mathbf{k}\mathbf{x}'}\right). \qquad \text{(C3)}\end{aligned}$$

To illustrate the calculation, consider the following term (others involve similar calculations):

$$\begin{aligned}\Sigma^{(2)}_{ij}(\mathbf{k}) &= \frac{1}{\mathcal{V}}\int d\mathbf{C}d\mathbf{x}d\mathbf{x}'\, e^{-i\mathbf{k}\mathbf{x}}\delta c_{inkl}(\mathbf{x})\delta c_{mpjq}(\mathbf{x}')\\ &\quad\times\frac{\partial^2}{\partial x_l\,\partial x_n}G^0_{km}(\mathbf{x}-\mathbf{x}')\frac{\partial}{\partial x'_q\,\partial x'_p}e^{i\mathbf{k}\mathbf{x}'}. \qquad \text{(C4)}\end{aligned}$$

We use $G^0(\mathbf{x})=\int d\mathbf{q}G^0(\mathbf{q})e^{i\mathbf{q}\mathbf{x}}/(2\pi)^3$ to get

$$\begin{aligned}\Sigma^{(2)}(\mathbf{k}) &= \frac{1}{\mathcal{V}(2\pi)^3}k^2\int d\mathbf{q}\; q^2G^0(q)\int d\mathbf{x}d\mathbf{x}'\, e^{-i(\mathbf{k}-\mathbf{q})(\mathbf{x}-\mathbf{x}')}\\ &\quad\times\int d\mathbf{C}\,\delta c_{ijkl}(\mathbf{x})\delta c_{mnpq}(\mathbf{x}'), \qquad \text{(C5)}\end{aligned}$$

where we have omitted the indices for simplicity. To evaluate the integral, we now need the geometric correlation function $W(r)$ in the two point average [$W(r)$ is implicitly included in $d\mathbf{C}$]: $W(r)$ represents the probability that two points separated by r are in the same grain. Usually, it is taken as $W(r)=e^{-r/d}$, with d the grain size. For simplicity again, we use instead $W(r)=d^3\delta(r)$. In this way we get

$$\begin{aligned}\Sigma^{(2)}(\mathbf{k}) &\sim \frac{d^3}{(2\pi)^3}k^2\int d\mathbf{q}q^2G^0(q)\langle\delta c_{inkl}\delta c_{mpjq}\rangle\\ &\sim \frac{id^3}{4\pi\mu}k^2k_L^3\langle\delta c_{inkl}\delta c_{mpjq}\rangle, \qquad \text{(C6)}\end{aligned}$$

where the angular brackets denote an average over possible orientations. We have considered the longitudinal wave using $G^0(q)=1/(\mu(q^2-k_L^2))$ and focused on the imaginary part of $\Sigma^{(2)}$ only to get the attenuation. With $\langle\delta c_{inkl}\delta c_{mpjq}\rangle=\langle c_{inkl}c_{mpjq}\rangle-\langle c_{inkl}\rangle\langle c_{mpjq}\rangle$, it is possible to end the calculation. Again, the result depends on the symmetry of the single crystal and on the presence or absence of texture. In the simple case of polycrystals of cubic symmetry, one gets $\langle c_{inkl}c_{mpjq}\rangle-\langle c_{inkl}\rangle\langle c_{mpjq}\rangle\propto\eta^2$ so that, for the longitudinal wave,

$$\Sigma^{(2)}(k_L)=\frac{id^3}{4\pi}k_L^5\frac{\eta^2}{\mu}. \qquad \text{(C7)}$$

The modified Green function $\langle G\rangle^{-1}=\mu(k^2-K_L^2)$, where K_L is the modified wave number whose imaginary part gives the attenuation coefficient. From $\langle G\rangle^{-1}=G^{0-1}-\Sigma$ with K_L expected to be close to k_L, we get, using $K_L\simeq k_L+\Sigma/(2\mu kL)$,

$$\alpha d\sim\frac{1}{8\pi}\left(\frac{\omega d}{c}\right)^4\left(\frac{\eta}{\mu}\right)^2. \qquad \text{(C8)}$$

What happens if both effects, the effect of the change of elastic constants because of the anisotropy and the effect of the dislocations, are considered together?

It is sufficient to sum the potentials $V^T=V^{\text{disloc}}+V^{\text{anisot}}$ to answer. At first order, the linearity implies $\Sigma^{(1)}$ is simply the sum of both effects, and we recover the effect of the dislocation only. At second order, cross terms appear because the nonlinearity in the potential. However, we have in that case

$$\begin{aligned}\Sigma^{(2)} &= \langle V^TG^0V^T\rangle-\langle V^T\rangle G^0\langle V^T\rangle=\Sigma^{(2),\text{disloc}}+\Sigma^{(2),\text{anisot}}\\ &\quad+\langle V^{\text{disloc}}G^0V^{\text{anisot}}\rangle+\langle V^{\text{anisot}}G^0V^{\text{disloc}}\rangle\\ &\quad-\langle V^{\text{disloc}}\rangle G^0\langle V^{\text{anisot}}\rangle-\langle V^{\text{anisot}}\rangle. \qquad \text{(C9)}\end{aligned}$$

The cross terms involving coupled effects of the dislocations and of the change in elastic effects vanish: this is because the parameters for the average for the anisotropy, typically the orientation of the crystal axis in a grain, are different from the parameters describing the parameters for the average for the grain boundaries: typically the number of dislocations per grain boundary. Thus, we get $\langle V^{\text{disloc}}G^0V^{\text{anisot}}\rangle=\langle V^{\text{disloc}}\rangle G^0\langle V^{\text{anisot}}\rangle$ and simply

$$\Sigma^{(2)}=\Sigma^{(2),\text{disloc}}+\Sigma^{(2),\text{anisot}}. \qquad \text{(C10)}$$

[1] W. P. Mason and H. J. McSkimin, "Attenuation and scattering of high frequency sound waves in metals and glasses," J. Acoust. Soc. Am. **19**, 464–473 (1947).

[2] A. B. Bathia, "Scattering of high-frequency sound waves in polycrystalline materials," J. Acoust. Soc. Am. **31**, 16–23 (1959).

[3] E. P. Papadakis, "Grain-size distribution in metals and its influence on ultrasonic attenuation measurements," J. Acoust. Soc. Am. **33**, 1616–1621 (1961).

[4] E. P. Papadakis, "Ultrasonic attenuation caused by scattering in polycrystalline metals," J. Acoust. Soc. Am. **37**, 703–710 (1965).

[5] F. E. Stanke and G. S. Kino, "A unified theory for elastic wave propagation in polycrystalline materials," J. Acoust. Soc. Am. **75**, 665–681 (1984).

[6] S. Hirsekorn, "The scattering of ultrasonic waves by polycrystals," J. Acoust. Soc. Am. **72**, 1021–1031 (1982).

[7] S. Hirsekorn, "The scattering of ultrasonic waves in polycrystalline materials with texture," J. Acoust. Soc. Am. **77**, 832–843 (1985).

[8] S. I. Rokhlin, T. K. Bolland, and L. Adler, "High-frequency ultrasonic wave propagation in polycrystalline materials," J. Acoust. Soc. Am. **91**, 151–165 (1992).

[9]S. Ahmed and R. B. Thompson, "Propagation of elastic waves in equiaxed stainless-steel polycrystal with alignes [001] axes," J. Acoust. Soc. Am. **99**, 2086–2096 (1995).
[10]J. A. Turner, "Elastic wave propagation and scattering in heterogeneous media: Textured polycrystalline materials," J. Acoust. Soc. Am. **106**, 541–552 (1999).
[11]B. R. Thompson, "Elastic-wave propagation in random polycrystals: Fundamentals and application to nondestructive evaluation," in Imaging of Complex Media with Acoustic and Seismic Waves, edited by M. Fink *et al.* [Top. Appl. Phys. **84**, 233–256 (2002)].
[12]X.-G. Zhang, W. A. Simpson, Jr., and J. M. Vitek, "Ultrasonic attenuation due to grain boundary scattering in copper and copper-aluminum," J. Acoust. Soc. Am. **116**, 109–116 (2004).
[13]D. H. Hurley, O. B. Wright, O. Matsuda, T. Suzuki, S. Tamura, and Y. Sugawara, "Time-resolved surface acoustic wave propagation across a single grain boundary," Phys. Rev. B **73**, 125403 (2006).
[14]A. Maurel, V. Pagneux, D. Boyer, and F. Lund, "Propagation of elastic waves through polycrystals: The effects of scattering from dislocation arrays," Proc. R. Soc. London, Ser. A **462**, 2607–2623 (2006).
[15]A. Maurel, V. Pagneux, F. Barra, and F. Lund, "Wave propagation through a random array of pinned dislocations: Velocity change and attenuation in a generalized Granato and Lücke theory," Phys. Rev. B **72**, 174111 (2005).
[16]J. M. Burgers, "Geometrical considerations concerning the structural irregularities to be assumed in a crystal," Proc. Phys. Soc. London **52**, 23–33 (1940).
[17]W. L. Bragg, "The structure of a cold-worked metal," Proc. Phys. Soc. London **52**, 105–109 (1940).
[18]W. Shockley and W. T. Read, "Quantitative predictions from dislocation models of crystal grain boundaries," Phys. Rev. **75**, 692 (1949).
[19]W. T. Read and W. Shockley, "Dislocation models of crystal grain boundaries," Phys. Rev. **78**, 275–289 (1950).
[20]F. C. Frank, in *Proceedings of the Symposium on the Plastic Deformation of Crystalline Solids* (Office of Naval Research, Pittsburgh, PA, 1950), p. 150 [as cited by W. T. Read in *Dislocations in Crystals* (McGraw-Hill, New York, 1953)].
[21]R. S. Wagner and B. Chalmers, "Grain boundaries in germanium," J. Appl. Phys. **31**, 581–587 (1960).
[22]A. R. Patel and C. C. Desai, "Low angle tilt boundaries in synthetic calcium fluoride," Br. J. Appl. Phys. **16**, 1297–1301 (1965).
[23]W. Bollman, *Crystal Defects and Crystalline Interfaces* (Springer, Berlin, 1970).
[24]W. Bollmann, "Basic concepts of O-lattice theory," Surf. Sci. **31**, 1–31 (1972).
[25]K. Sadanada and M. J. Marcinkowski, "Extension of the unified theory of grain boundaries. I. Structure of the boundaries," J. Appl. Phys. **45**, 1521–1532 (1974).
[26]D. Romeu, L. Bertrán del Rio, J. L. Aragón, and A. Gómez, "Detailed atomistic structure of arbitrary fcc [100] twist grain boundaries," Phys. Rev. B **59**, 5134–5141 (1999).
[27]D. M. Duffy, "Grain boundaries in ionic crystals," J. Phys. C **19**, 4393–4412 (1986).
[28]H. Jang and D. Farkas, "Determination of grain boundary geometry using TEM," J. Mater. Res. **7**, 1707–1717 (1992).
[29]L. Sagalowicz and W. A. T. Clark, "A theoretical and experimental study of non perfect grain boundary dislocations," Interface Sci. **4**, 29–45 (1996).
[30]L. Fionova, T. Watanabe, and Yulii Lisovski, "A prospect of grain boundary engineering for electronic properties in polycrystalline materials," ISIJ Int. **36**, 613–623 (1996).
[31]D. A. Hugues, Q. Liu, D. C. Chrzan, and N. Hansen, "Scaling of microstructural paramaters: Misorientations of deformation induced boundaries," Acta Mater. **45**, 105–112 (1997).
[32]X. Pan and J. G. Zheng, "Microstructural of crystal defects in the nanocrystalline tin dioxide thin film," Mater. Res. Soc. Symp. Proc. **472**, 87–92 (1997).
[33]J. Gubicza, G. Ribárik, G. R. Goren-Muginstein, A. R. Rosen, and T. Ungár, "The density and the character of dislocations in cubic and hexagonal polycrystals determined by X-ray diffraction," Mater. Sci. Eng., A **309–310**, 60–63 (2001).
[34]R. Kobayashi, J. A. Warren, and W. C. Carter, "A continuum model of grain boundaries," Physica D **140**, 141–150 (2000).
[35]E. Z. Meilikhov, "Modified dislocation model of intergrain tilt boundaries in HTSC," Physica C **271**, 277–285 (1996).
[36]A. Maurel, J.-F. Mercier, and F. Lund, "Scattering of an elastic wave by a single dislocation," J. Acoust. Soc. Am. **115**, 2773–2780 (2004).
[37]A. Maurel, V. Pagneux, F. Barra, and F. Lund, "Interaction between an elastic wave and a single pinned dislocation," Phys. Rev. B **72**, 174110 (2005).
[38]F. Lund, "Response of a stringlike dislocation loop to an external stress," J. Mater. Res. **3**, 280–297 (1988).
[39]M. O. Peach and J. S. Koehler, "The force exerted on dislocations and the stress fields produced by them," Phys. Rev. **80**, 436–439 (1950).
[40]J. S. Koehler, in *Imperfections in Nearly Perfect Crystals*, edited by W. Schockley *et al.* (Wiley, New York, 1952).
[41]T. Mura, "Continuous distribution of moving dislocations," Philos. Mag. **8**, 843–857 (1963).
[42]P. Sheng, *Scattering and Localization of Classical Waves in Random Media* (World Scientific, Singapore, 1990).
[43]P. Sheng, *Introduction to Wave Scattering, Localization, and Mesoscopic Phenomena* (Academic, New York, 1995).
[44]B. Velicky, "Sound in granular matter," lecture notes, http://cel.archives-ouvertes.fr/docs/00/09/29/42/PDF/velicky.pdf, last accessed 5 December 2006.
[45]P. Lacombe, *Report of Conference on Strength Solids* (The Physical Society of London, London, 1948).
[46]T. Suzuki, M. Aoki, and A. Ikushima, "Acoustic attenuation studies of frictional force on fast moving dislocation," Acta Metall. **12**, 1231–1240 (1964).
[47]W. P. Mason and A. Rosenberg, "Phonon and electron drag coefficients in single-crystal aluminum," Phys. Rev. **151**, 434–441 (1966).
[48]T. Ninomiya, "Frictional force acting on a dislocation-fluttering mechanism," J. Phys. Soc. Jpn. **36**, 399–405 (1974).
[49]D. W. Krautkopf, "Ultrasonic scattering and attenuation in polycrystalline copper and α-Brass," J. Acoust. Soc. Am. **32**, 824–835 (1960).
[50]A. V. Granato and K. Lücke, in *Physical Acoustics*, edited by W. P. Mason (Academic, New York, 1966), Vol. **4A**.
[51]A. V. Granato and K. Lücke, "Theory of mechanical damping due to dislocations," J. Appl. Phys. **27**, 583–593 (1956).
[52]A. V. Granato and K. Lücke, "Application of dislocation theory to internal friction phenomena at high frequencies," J. Appl. Phys. **27**, 789–805 (1956).
[53]K. Lücke and A. V. Granato, "Simplified theory of dislocation damping including point-defect drag. I. Theory of drag by equidistant point defects," Phys. Rev. B **24**, 6991–7006 (1981).
[54]A. V. Granato and K. Lücke, "Simplified theory of dislocation damping including point-defect drag. II. Superposition of continuous and pinning-point-drag effects," Phys. Rev. B **24**, 7007–7017 (1981).
[55]A. Hikata, R. Truel, A. Granato, B. Chick, and K. Lücke, "Sensitivity of ultrasonic attenuation and velocity changes to plastic deformation and recovery in aluminum," J. Appl. Phys. **27**, 396–404 (1956).
[56]H. Ogi, M. Hirao, and K. Minoura, "Noncontact measurement of ultrasonic attenuation during rotating fatigue test of steel," J. Appl. Phys. **81**, 3677–3684 (1997).
[57]H. Ogi, H. M. Ledbetter, S. Kim, and M. Hirao, "Contactless mode-selective resonance ultrasound spectroscopy: Electromagnetic acoustic resonance," J. Acoust. Soc. Am. **106**, 660–665 (1999).
[58]H. Ogi, A. Tsujimoto, M. Hirao, and H. Ledbetter, "Stress-dependent recovery of point defects in deformed aluminum: An acoustic damping study," Acta Mater. **47**, 3745–3751 (1999).
[59]M. Hirao, H. Ogi, N. Suzuki, and T. Ohtani, "Ultrasonic attenuation peak during fatigue of polycrystalline copper," Acta Mater. **48**, 517–524 (2000).
[60]T. Ohtani, H. Ogi, and M. Hirao, "Acoustic damping characterization and microstucture evolution in nickel-based superalloy during creep," Int. J. Solids Struct. **42**, 2911–2928 (2005).
[61]M. W. Barsoum, M. Radovic, T. Zhen, P. Finkel, and S. R. Kalidindi, "Dynamic elastic hysteretic solids and dislocations," Phys. Rev. Lett. **94**, 085501 (2005).

Effect of nuclei concentration on cavitation cluster dynamics

M. Arora,[a] C. D. Ohl, and D. Lohse
Physics of Fluids, Department of Applied Physics and Impact Institute, Faculty of Science and Technology, University of Twente, Postbus 217, 7500 AE Enschede, The Netherlands

(Received 5 December 2005; revised 24 January 2007; accepted 4 March 2007)

Cavitation cluster dynamics after the passage of a single pressure wave is studied for different concentrations of artificial cavitation nuclei (30 to 3×10^5 nuclei/ml). With increasing concentration of cavitation nuclei the lifetime of the cavitation cluster is prolonged. Additionally, it is found that the spatial extent of the cluster decreases with higher nuclei concentration. The experimental data for concentrations less than 400 nuclei/ml are compared to simulations with a Rayleigh-Plesset-type equation, taking into account bubble-bubble interaction. For higher concentrations (more than 1000 nuclei/ml) the observed radial cluster dynamics is compared with calculations from an axisymmetric cavity-collapse model. © *2007 Acoustical Society of America.* [DOI: 10.1121/1.2722045]

PACS number(s): 43.35.Ei, 43.25.Yw [AJS] Pages: 3432–3436

I. INTRODUCTION

Cavitation bubbles often occur in ensembles or clusters. One of the methods to generate clusters of bubbles is to apply a single, intense, pulsed pressure wave. In its tensile phase gaseous nuclei present in the liquid explode and form a cavitation cluster. When the ambient pressure is restored, these cavitation bubbles undergo violent collapse. The destructive nature of cavitation clusters is widely reported in scientific literature, for example in hydrodynamic cavitation[1–3] and in shock wave lithotripsy.[4,5]

The interaction between the bubbles in a cavitation cluster is very complex.[6–10] In this article we want to address the applicability of simple models to predict the dynamics of the individual cavitation bubbles and/or the cavitation cluster over a wide range of the nuclei concentration (i.e., 30 to 3×10^5 per ml). The work has been stimulated by the findings that the lifetime of cavitation bubbles increases with higher bubble densities.[11–13] The analysis presented in this paper might be relevant to the field of shock wave lithotripsy where recent numerical works[11,14,15] emphasize the effect of nuclei concentration on the cluster dynamics. Additionally, clusters of cavitation bubbles are also of importance in sonochemistry.[16,17]

II. CAVITATION CLUSTER EXPERIMENTS

A single pressure pulse is generated with a piezoelectric shock wave generator. It is a modified source from the commercial lithotripter Piezolith 3000 (Richard Wolf GmbH, Knittlingen, Germany). Details on the experimental setup and the acoustic source are available in Refs. 12 and 18, respectively.

In this study we use the ultrasound contrast agent SonoVue (Bracco, Geneva, Switzerland) as the cavitation nuclei. These consist of phospholipid shelled microbubbles with a mean diameter of 2.5 μm. A stock suspension of contrast agent bubbles is prepared by mixing 5 ml water per vial contrast agent bottle (≈20 mg of solids) as prescribed for medical usage. The number density of bubbles is measured with a Neubauer cell-counting chamber under a microscope. Even though the naturally present nuclei (e.g., dirt particles) may have larger variations in size (and thus corresponding nucleation threshold), the usage of artificial nuclei allows us to have control of number density independent of tensile strength used. The desired concentrations of cavitation nuclei are obtained by preparing successive intermediate dilutions. Care is taken to ensure that the suspension is well mixed at each dilution step. For all the experiments, partially degassed (~3 mg/l O_2 content, corresponding to 30% of saturation concentration) and deionized water is used.

The finally desired concentration of artificial cavitation nuclei is obtained by adding an appropriate amount of intermediate dilution to a nonseeded liquid in a bag around the acoustic focus of the shock wave generator. The bag is made from an acoustically and optically transparent plastic material (low density polyethylene). It contains approximately 10 l of liquid with the desired concentration of cavitation nuclei.

Before the cavitation nuclei are added the pressure signal at the acoustic focus of the lithotripter is recorded with a fiber optic hydrophone (FOPH-500, RP Acoustics, Germany). Pressure measurements near to cavitation bubble clusters are hampered because the fragile fiber tip is easily damaged, especially at higher nuclei concentrations.

Figure 1 shows a typical pressure recording in the absence of artificial nuclei. The pressure pulse consists of two phases: first, a fast-rising compressive phase with a peak amplitude of 35 MPa lasting for 1.5 μs. It is followed by a tensile phase with a peak amplitude of about −10 MPa lasting for ~3.5 μs. This magnitude and duration of the tensile phase is sufficient to cause cavitation without artificial cavitation nuclei (see top left frame of Fig. 2). The cavitation bubbles around the focal region are well separated and they have a typical lifetime of 150±10 μs. The lifetime of a bubble is defined as the time period between cavitation in-

[a]Electronic mail: manish.arora@eng.ox.ac.uk

 0001-4966/2007/121(6)/3432/5/$23.00 © 2007 Acoustical Society of America

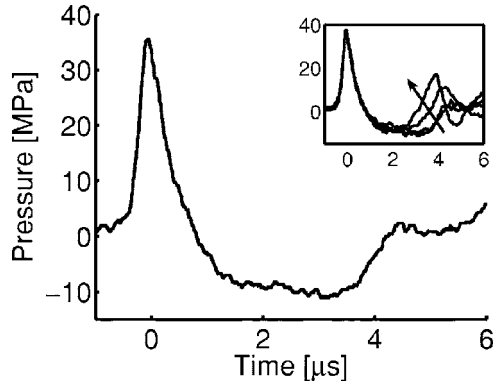

FIG. 1. A typical pressure recording at the focus of the lithotripter in the absence of artificial cavitation nuclei. The inset demonstrates the effect of addition of cavitation nuclei on the pressure wave at the focus. With increasing numbers of cavitation nuclei (indicated by the direction of the arrow) the duration of the tensile phase decreases and a secondary positive pressure pulse emerges. The primary pressure peak remains almost unaffected.

ception and the first collapse of the bubble. In the absence of artificial cavitation nuclei about 20 cavitation bubbles per ml are expanded in the focal region.

After adding artificial cavitation nuclei, the shape of the second part of the pressure wave gets strongly modified, whereas the first part remains practically the same (see inset Fig. 1). These effects are enhanced with increased concentration of cavitation bubbles. A similar finding has been reported recently by Liebler *et al.*[15]

The dynamics of the cavitation cluster is recorded with a high speed CMOS-camera (ultima APX-RS Fastcam, Photron) at a framing rate of 50 000 fps. The size of the images is 384×112 pixel^2, which corresponds to a field of view of 79×23 mm^2. The high-speed camera is triggered simultaneously with the shock wave generator and the scene is illuminated with diffuse back-illumination. The lifetime of the cavitation clusters is determined by visual inspection of the recordings. Additionally, the width of sufficiently dense cavitation clusters are determined by digital image processing.

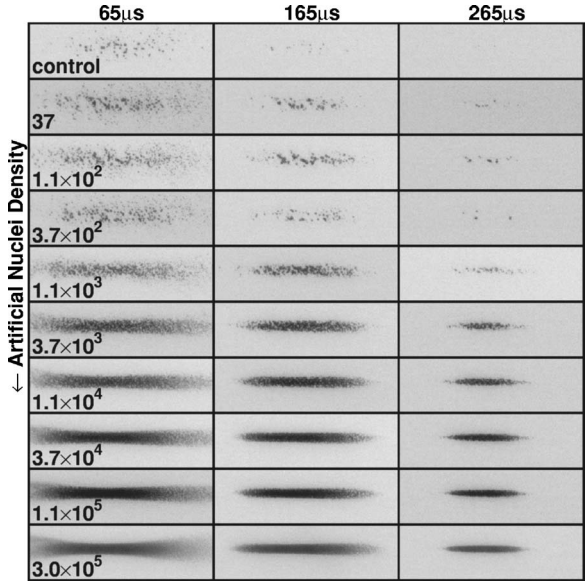

FIG. 2. Cavitation bubble clusters at three different times after the passage of the shock wave as obtained with various initial cavitation nuclei concentration, as stated at each row. The top row (control) corresponds to the case of plain water. The size of each frame is 79×23 mm^2.

Figure 2 depicts the shape of the cavitation cluster at various concentrations of cavitation nuclei, 65, 165, and 265 μs after the shock-front has passed the acoustic focus. At low to moderate concentrations of the cavitation nuclei (37 to 370 nuclei/ml) individual bubbles larger than the optical resolution of the system ($\approx$400 μm corresponding to group of 4 pixels) can be identified. Beyond 1000 nuclei/ml it becomes increasingly difficult to separate individual bubbles from each other.

Interestingly, the lifetime of the cavitation cluster increases from 150 μs for the plain water case to 350 μs for the highest concentration (see Fig. 4). In an attempt to model the cavitation cluster dynamics we distinguish between the case of sparsely populated bubble clusters, defined as a cluster of bubbles that do not grow to come close to each other, and the case of densly populated bubble cluster, in which the bubbles do come fairly close during the growth. For the first case (nuclei concentrations below 400 nuclei/ml) a modified spherical Rayleigh-Plesset equation is applied at the level of the individual bubble (Sec. III), whereas in the second case an axisymmetric model for the volume dynamics of the dense cluster is employed (Sec. IV).

III. DYNAMICS OF SPARSELY POPULATED CLUSTERS

The Rayleigh-Plesset (RP) model describes the dynamics of single spherical bubbles. It is derived by integrating the momentum balance equation in the radial direction assuming spherical symmetry:[19,20]

$$R\ddot{R}+\frac{3}{2}\dot{R}^2 = \frac{1}{\rho}\left(P_g+P_v-P(t)-P_0-\frac{2\sigma}{R}-\frac{4\eta\dot{R}}{R}-\frac{R\dot{P}_g}{c_l}\right). \quad (1)$$

Here, R is the radius of the single cavity, $P_0=1.013\times10^5$ Pa is the constant atmospheric pressure, $P(t)$ is the far-field driving sound pressure (shown in Fig. 1), and P_g is the pressure inside the cavitation bubble, calculated assuming an adiabatic gas law:

$$P_g=\left(P_0+\frac{2\sigma}{R_0}-P_v\right)\left(\frac{R_0}{R}\right)^{3\gamma}. \quad (2)$$

The remaining physical parameters are density $\rho=1000$ kg$\cdot$m^{-3}, coefficient of surface tension $\sigma=0.073$ N m^{-1}, water viscosity $\eta=1.00\times10^{-3}$ Pa$\cdot$s, and sound velocity in water $c_l=1485$ m/s. The last three terms in the parentheses of Eq. (1) refer to the effect of surface tension, viscosity, and sound emission from the bubble. Although we include these terms in the present analysis for completeness, they hardly effect the dynamics of the bubble. So far the model does not include the effect of neighboring bubbles.

To modify this equation to include bubble-bubble interaction an additional pressure term needs to be added. It can be derived from the summed velocity potential of neighboring bubbles:[10,21]

$$\phi = \sum_i \frac{1}{r_i} \dot{R}_i R_i^2, \tag{3}$$

where r_i is the distance to its ith neighbor bubble with radii R_i. The higher order interaction terms, as often derived in the case of two bubbles,[22] can also be computed for multibubble systems,[9] but are neglected in this analysis. Further, we assume that locally all bubbles show the same radial dynamics, thus subscript i can be dropped from R_i. With the assumption of a uniform number density of cavitation nuclei per unit volume, N, Eq. (3) can be rewritten as an integral in space:

$$\phi = R^2 \dot{R} \sum_i \frac{1}{r_i} \approx R^2 \dot{R} N \int_0^{\delta r} \frac{1}{r'} 4\pi r'^2 \, dr'. \tag{4}$$

Here, δr is the distance up to which bubble-bubble interactions are considered. We note that the integral, Eq. (4), grows unbounded for $\delta r \to \infty$. In reality the finite speed of sound and the acoustic shielding by bubbles prevent their mutual interaction at larger distances. Thus δr should be restricted to a finite distance. Here, we choose as a first approximation a concentration dependent cutoff distance of one average interbubble distance D_{mean}:

$$\delta r \equiv D_{\text{mean}} = \frac{1}{N^{1/3}}. \tag{5}$$

After adding the time derivative of Eq. (4) as an additional pressure term into the RP Eq. (1) we obtain

$$\alpha R \ddot{R} + \beta \dot{R}^2 = \frac{1}{\rho}\left(P_b - P(t) - P_0 - \frac{2\sigma}{R} - \frac{4\eta \dot{R}}{R} - \frac{R \dot{P}_g}{c_l} \right), \tag{6}$$

where $\alpha = (1 + 2\pi R N^{1/3})$ and $\beta = (\frac{3}{2} + 4\pi R N^{1/3})$.

Please note that, when $N \to 0$, the original RP equation is obtained. With the modified RP Eq. (6) we calculate the change in the radial dynamics of the bubbles and their collapse time for various nuclei concentrations. Figure 3 compares the radial dynamics of a single bubble with an initial size of 1 μm being driven by a single pressure pulse for $N = 0$, 1, and 100 nuclei/ml. The driving pressure pulse used in all the above cases is the measured pressure pulse (with no artificial nuclei) as shown in Fig. 1. The graph shows that the bubble lifetime is increased and its maximum size is reduced at increasing densities of cavitation nuclei. In Fig. 4 the collapse time as a function of nucleus concentration is plotted as a dashed line and it is compared with experimental measurements (vertical error bars).

In agreement with the observation, the model predicts an increase in the bubble lifetime of 50 μs when the concentration is increased from 40 nuclei/ml to $\approx$400 nuclei/ml. Although the predictions are within the measured error limits, it should be noted that the recorded pressure pulse used for the driving far-field pressure, $P(t)$, in Eq. (6) is already affected by the presence of nearby bubbles. Therefore, the agreement

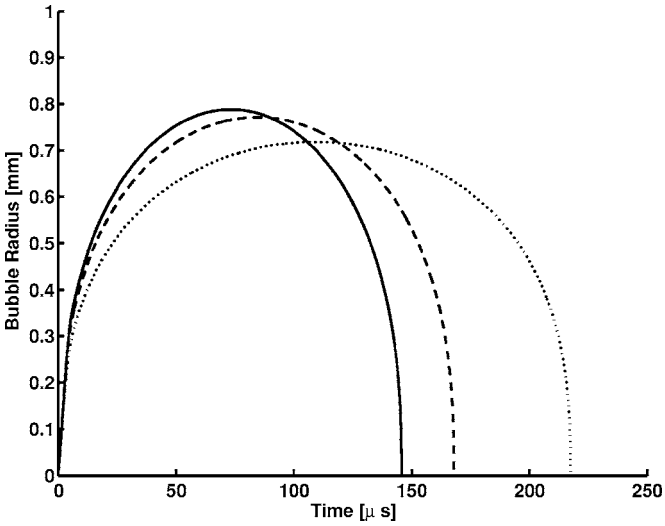

FIG. 3. Radius-time curve for individual bubbles at different nucleus concentrations when driven at the pressure pulse in Fig. 1. The solid line corresponds to the case of very low nucleus density, $N \to 0$, whereas the dashed and dotted lines correspond to 1 and 100 bubbles/ml, respectively.

of the absolute collapse time should be taken with some caution. It has been found that the peaks following the tensile phase as depicted in Fig. 1 do alter the absolute collapse time.

At higher concentrations the bubbles become very close to each other and the model becomes inapplicable. Therefore, in order to capture the cloud dynamics at higher number densities, we make use of a different model that describes the cluster as a single cylindrical void.

IV. DYNAMICS OF DENSELY POPULATED CLUSTERS

For number densities above 1000 bubbles/ml the cluster looks quite different (see Fig. 2). The shape of the cluster becomes more homogeneous and it is separated from the surrounding liquid by a sharp boundary. The collapse of the cluster proceeds progressively from the cluster boundary to-

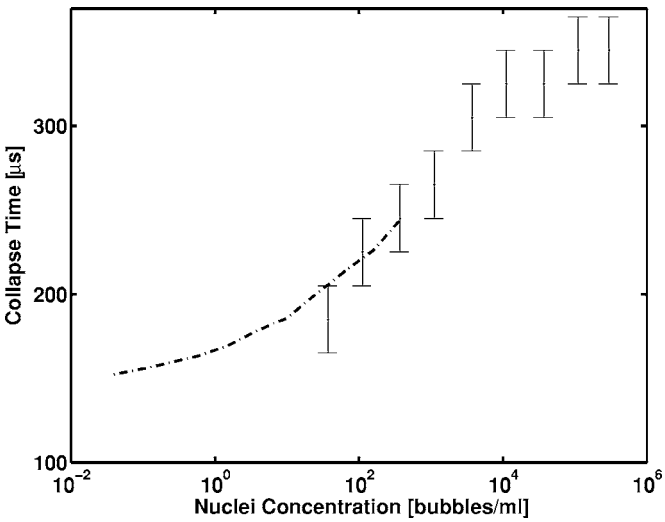

FIG. 4. The collapse times of the cavitation cluster at varying nucleus concentrations driven by the pressure pulse in Fig. 1. The dashed line shows the result of numerical model taking into account bubble-bubble interactions from neighboring bubbles in the case of sparsely populated clusters.

ward its center. These observations suggest to model the shrinkage of the cluster boundary as a shock front. The speed at which the cluster collapses, $\dot{X}$, is identified with the propagation speed of the shock front,[23,24] which is given by

$$\dot{X} = \left(\frac{P_1}{\rho\beta(1-\beta)} \right)^{1/2}. \quad (7)$$

Here, P_1 is the pressure just outside the cavitation cluster driving the collapse, and β is the void fraction within the cluster. In the case of a cavitation cluster with well separated spherical bubbles, β is given by $N\frac{4}{3}\pi R^3$, which in general is a time varying quantity. However, when the bubbles grow, those inside the cluster become increasingly shielded from the outside pressure field and for large N we can assume that inside the cluster β reaches a constant value. Note that, for large enough void fractions, $\beta > 0.1$, the time required to collapse individual bubbles is of the same order of magnitude as that for the passage of the shock front over the bubble $\sim R\sqrt{\rho/P_1}$, further justifying identification of the speed of the cluster collapse with the speed of the shock front.

The pressure P_1 just outside the cylindrical cluster is coupled with the far field pressure P_0 far away by a momentum balance in cylindrical coordinates. As derived by Hansson and Mørch,[23] the motion of the cluster boundary X can be modeled with a second order ODE

$$(X\ddot{X} + \dot{X}^2) \ln \frac{x_c}{X} - \dot{X}^2 + \frac{\beta}{2}\dot{X}^2 \left[\left(\frac{X}{x_c} \right)^2 + 1 \right] = -\frac{1}{\rho\beta} P_0. \quad (8)$$

Here x_c is the typical size scale of the experimental setup; in our case $x_c = 0.2$ m is approximately the radius of the liquid compartment. For the limiting case of $\beta = 1$, the above equation becomes the void collapse equation in cylindrical geometry[25,26] (2D-Rayleigh equation).

Figure 5 compares the experimentally measured diameter of the cavitation cluster with Eq. (8) for a cavitation nuclei density of (a) 3×10^5 bubbles/ml and (b) 3.7×10^3 bubbles/ml. As there is no simple experimental means for measuring the void fraction β, the model calculations have been fitted to the experimental collapse time by choosing $\beta = 0.34$ and 0.22. Thus, we find that the increase of the number of cavitation nuclei leads to an increase of the maximum value of β, but eventually shielding limits the growth of the bubbles, and thus the effect of increasing number density, N.

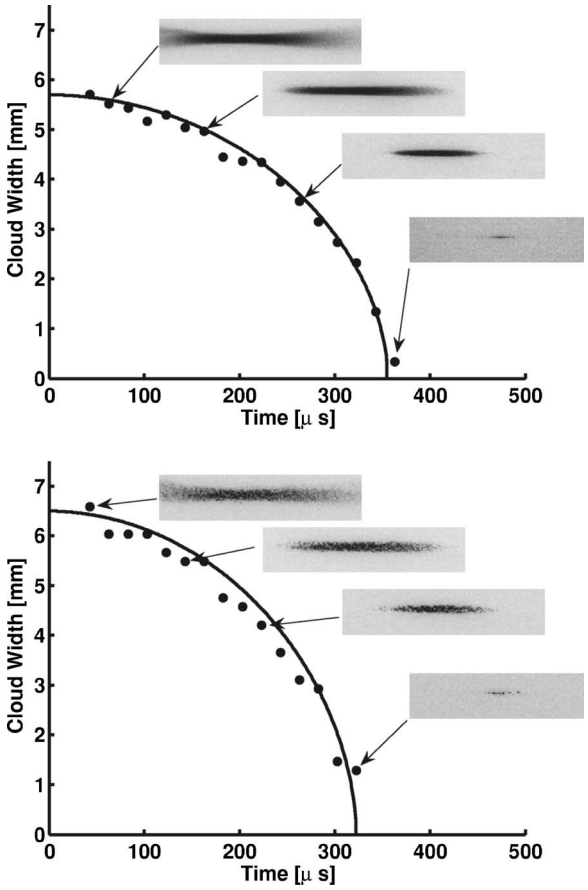

FIG. 5. Evolution of the width of the cavitation cluster at two nucleus concentrations: (a) 3.0×10^5 ml−1 and (b) 3.7×10^3 ml^{-1}. These are compared with the model for densely populated clusters [see Eq. (8)] (solid line) by choosing appropriate values of β. Selected frames at the indicated time are presented to demonstrate the cylindrical shape in both cases.

V. CONCLUSION

The dynamics of cavitation clusters is strongly modified when artificial cavitation nuclei are added. With increasing concentration of nuclei we find a prolongation of the lifetime and a decrease in the maximum bubble size. Two regimes of cluster dynamics are considered: With nuclei number densities below 400 bubbles/ml sparsely populated clusters with fuzzy boundaries are developed. For these, the presented modified RP equation including nearest neighbor interaction terms seems to give a sufficient description of the bubble dynamics at the center of the cluster. Tanguay and Colonius[11] in their numerical simulations also find an increase in the lifetime of bubbles but also an increase in the maximum size of the bubbles with increasing void fraction. They consider interactions between individual bubbles only through the pressure of an average bubbly mixture, whereas, in our approach, the effect felt by neighboring bubbles is more direct, i.e., through induced motion and pressure field. Even though the model for sparse cluster presented in this paper explains the observed experimental results, they are subject to further verification in future experiments specially designed to obtain bubble sizes and void fraction as a function of time. So far, a distinction whether the observed prolongation of bubble lifetime is a result of pressure in "average bubbly mixture" or a more direct bubble-bubble interaction cannot be made.

In the second regime, i.e., for bubble densities of 1000 nuclei/ml and above, it becomes more appropriate to model the cluster as a single entity having a constant void fraction. Here, void fractions values in the range 20%–35% best explain the result. Yet, to increase confidence in this model it will be helpful to be able to devise an experiment where void fractions can be measured independently and compared with the best fit results.

The range of cavitation nucleus densities examined in this study extends much beyond the range in which single bubble models are applicable. Real life nucleation conditions are likely to generate sparsely populated as well as densely

populated bubble clusters. For example, in lithotripsy sparsely populated clusters may arise from natural nuclei present *in vivo* or *in vitro*, while densely populated clusters require accumulation of extra nuclei. Such extra nuclei may come from fragmentation of stone pieces or may be gaseous remains of cavitation bubbles from previous shots.[12] Similarly, cavity clusters are likely to be created in high intensity ultrasonic equipment such as ultrasonic cleaners, sonochemical reactors, etc., depending only on the number of cavitation nuclei being present in the active region of the device.

The absolute values of the nucleus densities characteristic of the two regimes defined in this paper will vary depending upon the parameters of tensile phase, such as its pulse strength and duration, properties of the liquid in which cavitation is taking place, etc.

ACKNOWLEDGMENTS

The funding of the work by FOM and NWO (both The Netherlands) is acknowledged. We are very thankful to Knud Aage Mørch and Andrea Prosperetti for various insightful discussions and refining the manuscript. We are also grateful to Marko Liebler (University of Karlsruhe) for illuminating us on wave propagation at higher nuclei densities.

[1]G. E. Reisman, Y. C. Wang, and C. E. Brennen, "Observations of shock waves in cloud cavitation," J. Fluid Mech. **355**, 255–283 (1998).
[2]G. Kuiper, "Cavitation research and ship propeller design," Appl. Sci. Res. **58**, 33–50 (1998).
[3]C. E. Brennen, *Cavitation and Bubble Dynamics* (Oxford U. P., Oxford, 1995).
[4]O. A. Sapozhnikov, V. A. Khokhlova, M. R. Bailey, and L. A. Crum, "Effect of overpressure and pulse repetition frequency on cavitation in shock wave lithotripsy," J. Acoust. Soc. Am. **112**, 1183–1195 (2002).
[5]Y. Matsumoto, J. S. Allen, S. Yoshizawa, T. Ikeda, and Y. Kaneko, "Medical ultrasound with microbubbles," Exp. Therm. Fluid Sci. **29**, 225–265 (2005).
[6]L. van Wijngaarden, "On equations of motion for mixtures of liquid and gas bubbles," J. Fluid Mech. **33**, 465–474 (1968).
[7]D. Z. Zhang and A. Prosperetti, "Averaged equations for inviscid disperse two-phase flow," J. Fluid Mech. **267**, 185–219 (1994).
[8]Y. C. Wang and C. E. Brennen, "Numerical computation of shock waves in a spherical cloud of cavitation bubbles," J. Fluids Eng. **121**, 872–880 (1999).
[9]G. L. Chahine, "Pressure generated by a bubble cloud collapse," Chem. Eng. Commun. **28**, 355–367 (1983).
[10]G. L. Chahine and H. L. Liu, "A Singular Perturbation Theory of the Growth of a Bubble Cluster in a Superheated Liquid," J. Fluid Mech. **156**, 257–279 (1985).
[11]M. Tanguay and T. Colonius, "Progress in Modeling and Simulation of Shockwave Lithotripsy (SWL)," in *Fifth International Symposium on Cavitation (CAV2003)*, November 2003, Osaka, Japan, pp. 1–4.
[12]M. Arora, L. Junge, and C. D. Ohl, "Cavitation cluster dynamics in shock-wave lithotripsy: Part 1. Free field," Ultrasound Med. Biol. **31**, 827–839 (2005).
[13]N. Bremond, M. Arora, S. Dammer, C. D. Ohl, and D. Lohse, "Bubble nucleation on surfaces," J. Phys.: Condens. Matter **17**, S3603–S3608 (2005).
[14]Y. C. Wang, "Effects of nuclei size distribution on the dynamics of a spherical cloud of cavitation bubbles," J. Fluids Eng. **121**, 881–886 (1999).
[15]M. Liebler, T. Dreyer, and R. E. Riedlinger, "Nonlinear Modeling of Interactions between Ultrasound and Cavitation Bubbles," Acta Acust. **92**, 165–167 (2006).
[16]K. S. Suslick, "Sonochemistry," Science **247**, 1439–1445 (1990).
[17]P. M. Kanthale, P. R. Gogate, A. B. Pandit, and A. M. Wilhelm, "Dynamics of cavitational bubbles and design of a hydrodynamic cavitational reactor: cluster approach," Ultrason. Sonochem. **12**, 441–452 (2005).
[18]R. Riedlinger, T. Dreyer, and W. Krauss, "Small aperture piezo sources for lithotripsy," in *Proc. 17th Int. Congress on Acoustics*, Vol. **4**, edited by A. Bettucci, Rome, Italy, 2001.
[19]Lord Rayleigh, "On the pressure developed in a liquid during the collapse of a spherical cavity," Philos. Mag. **34**, 94–98 (1917).
[20]M. S. Plesset and A. Prosperetti, "Bubble dynamics and cavitation," Annu. Rev. Fluid Mech. **9**, 145–185 (1977).
[21]A. Kubota, H. Kota, and H. Yamaguchi, "A New Modeling of Cavitating Flows—A Numerical Study of Unsteady Cavitation on a Hydrofoil Section," J. Fluid Mech. **240**, 59–96 (2002).
[22]A. Harkin, T. J. Kaper, and A. Nadim, "Coupled pulsation and translation of two gas bubbles in a liquid," J. Fluid Mech. **445**, 377–411 (2001).
[23]I. Hansson and K. A. Mørch, "The Dynamics of Cavity Clusters in Ultrasonic (Vibratory) Cavitation Erosion," J. Appl. Phys. **51**, 4651–4658 (1980).
[24]K. A. Mørch, "On Cavity Cluster Formation in a Focused Acoustic Field," J. Fluid Mech. **201**, 57–76 (1989).
[25]H. N. Oguz and A. Prosperetti, "Dynamics of Bubble-Growth and Detachment from a Needle," J. Fluid Mech. **257**, 111–145 (1993).
[26]D. Lohse, R. Bergmann, R. Mikkelsen, C. Zeilstra, D. van der Meer, M. Versluis, K. van der Weele, M. van der Hoef, and H. Kuipers, "Impact on soft sand: Void collapse and jet formation," Phys. Rev. Lett. **93**, 198003 (2004).

A Green's function method for surface acoustic waves in functionally graded materials

Osamu Matsuda[a)]
Division of Applied Physics, Graduate School of Engineering, Hokkaido University, Sapporo 060–8628, Japan

Christ Glorieux
Laboratorium voor Akoestiek en Thermische Fysica, Katholieke Universiteit Leuven, Celestijnenlaan 200D, B-3001 Heverlee, Belgium

(Received 19 September 2006; revised 5 March 2007; accepted 6 March 2007)

Acoustic wave propagation in anisotropic media with one-dimensional inhomogeneity is discussed. Using a Green's function approach, the wave equation with inhomogeneous variation of elastic property and mass density is transformed into an integral equation, which is then solved numerically. The method is applied to find the dispersion relation of surface acoustic waves for a medium with continuously or discontinuously varying elastic property and mass density profiles. © *2007 Acoustical Society of America.* [DOI: 10.1121/1.2722049]

PACS number(s): 43.35.Pt, 43.20.Bi, 43.35.Cg, 43.35.Zc, 43.20.Fn [TDM] Pages: 3437–3445

I. INTRODUCTION

Acoustic waves are widely used to investigate subsurface properties over a wide range of length scales. Examples range from nondestructive testing of nanodevices to geological investigations of the earth crust. In particular, surface and interface acoustic waves (SAWs and IAWs) can probe the subsurface structure of a medium, and these methods have recently gained importance in electronic device fabrication. SAWs propagate along the surface of a medium, their elastic energy being more or less localized within a depth range comparable to their wavelength. By observing the frequency dependence of their sound velocity (dispersion relation) for a certain frequency range, one can derive the depth profile of the elastic properties. Wide bandwidth measurements have been achieved with laser ultrasonic techniques, in which a laser was used for the generation and detection of SAWS.[1–3]

It is not straightforward to solve this inverse problem. In fact, the depth profiling procedure usually involves an iterative refinement of a provisional elastic profile while comparing the experimentally obtained dispersion relation and the theoretically calculated dispersion relation for an assumed structure. The calculation of the dispersion relation for a given elastic profile forms a major part of such analysis.

In general, the calculation of the dispersion relation requires us to solve the acoustic wave equation with inhomogeneously varying elastic property and mass density. Even for a medium that varies along the depth direction, which is important for various applications, it is not an easy task. The dispersion relation of a locally isotropic medium with continuously varying elastic properties and mass density along the depth direction may be calculated by regarding the medium as a stack of many thin homogeneous layers.[2,4]

A more general treatment is developed in the state-vector method, in which the acoustic wave equation for piecewise homogeneous media or for media with continuously varying inhomogeneity is transformed into a set of six first-order ordinary differential equations for the state-vector, which consists of, e.g., the components of the acoustic displacement and stress field.[5–7] The differential equation for general inhomogeneity is solved analytically via an infinite series of multiple integrals (the Peano expansion).

Another approach using a Green's function was proposed to solve the acoustic wave equation for an isotropic medium with inhomogeneously varying elastic property and mass density profiles.[8–10] The solution is expressed in an integral form, which may be solved using expansions with some basis functions. For the case of small perturbations, the iterated Born approximation is also possible.

In this article, we extend the Green's function approach to propose a method to solve the acoustic wave equation for an anisotropic inhomogeneous medium. It handles a medium with continuously or discontinuously varying depth dependent elastic properties and mass density. In Sec. II, the anisotropic wave equation is first reduced to a one-dimensional expression. Then the inhomogeneous structure is subdivided into homogeneous and inhomogeneous parts. The Green's function obtained for the homogeneous medium is used to describe the solution for the inhomogeneous medium in an integral form of the equation. Then the integral equation is numerically solved by discretizing it. The advantage of the method is that the Green's function is relatively easily obtainable in a semi-analytical form because of the assumed homogeneity of the medium, and that a single Green's function can be used for arbitrary anisotropic inhomogeneity as long as the homogeneous part is common. In Sec. III, we illustrate the proposed method to obtain the dispersion relation for the example of a piecewise homogeneous isotropic medium and for an isotropic inhomogeneous medium with continuously varying elastic property and mass density.

[a)]Electronic mail: omatsuda@eng.hokudai.ac.jp

II. THEORY

A. Wave equation

In a continuous medium approximation, the acoustic field can be completely described by considering Newton's laws of motion in an infinitesimally small volume:

$$\rho\frac{\partial^2 u_i}{\partial t^2}=\frac{\partial \sigma_{ij}}{\partial x_j}, \tag{1}$$

where $\rho(\boldsymbol{r})$ is a position dependent mass density, $u_i(\boldsymbol{r},t)$, is the elastic displacement field with $i=x,y,z$ (or $i=1,2,3$), and $\sigma_{ij}(\boldsymbol{r},t)$ is the stress tensor field. For Eq. (1) and following, we use the summation convention for repeated indices. In the absence of any externally applied stress, the stress field in the linear response regime is related to the strain field $\eta_{ij}(\boldsymbol{r},t)$ as $\sigma_{ij}=c_{ijkl}\eta_{kl}$, where $c_{ijkl}(\boldsymbol{r})$ is the position dependent elastic stiffness tensor. Then the acoustic wave equation (1) can be transformed into

$$\rho\frac{\partial^2 u_i}{\partial t^2}=\frac{1}{2}\frac{\partial}{\partial x_j}\left\{c_{ijkl}\left(\frac{\partial u_k}{\partial x_l}+\frac{\partial u_l}{\partial x_k}\right)\right\} \tag{2}$$

Although Eq. (2), together with an appropriate boundary condition and initial condition, is sufficient to describe acoustic fields in an inhomogeneous medium, it is somehow inconvenient to use since the right hand side contains spatial derivatives of all elastic stiffness tensor components.

To relieve this difficulty to some extent, the elastic compliance tensor $s_{ijkl}(\boldsymbol{r})$, which relates the strain and stress field as $\eta_{ij}=s_{ijkl}\sigma_{kl}$, can be used instead of the stiffness. By taking the spatial derivative of Eq. (1), we get the wave equation in terms of the stress field as

$$\begin{aligned}\rho\frac{\partial^2 \eta_{ij}}{\partial t^2}&=\frac{1}{2}\left(\frac{\partial^2\sigma_{ik}}{\partial x_j\,\partial x_k}+\frac{\partial^2\sigma_{jk}}{\partial x_i\,\partial x_k}\right)\\&\quad-\frac{1}{2}\left(\frac{\partial\rho}{\partial x_j}\frac{1}{\rho}\frac{\partial\sigma_{ik}}{\partial x_k}+\frac{\partial\rho}{\partial x_i}\frac{1}{\rho}\frac{\partial\sigma_{jk}}{\partial x_k}\right)\\&=\rho s_{ijkl}\frac{\partial^2\sigma_{kl}}{\partial t^2}.\end{aligned} \tag{3}$$

This expression has the favorable property that the inhomogeneity-related position derivative only appears as $\partial\rho/\partial x_j$.[11]

We now solve Eq. (3) to find a monochromatic solution with angular frequency ω in a medium with lateral homogeneity along the $x-y$ plane. The elastic compliance tensor $s_{ijkl}(z)$ and the mass density $\rho(z)$ both depend only on z. Due to the lateral homogeneity or translational symmetry of the system, the solution takes the form of a lateral plane wave with lateral wave number q:

$$\sigma_{ij}(\boldsymbol{r},t)=\sigma_{ij}(z)\exp\{i(qx-\omega t)\}, \tag{4}$$

where the lateral direction of propagation is taken along the x axis. Note that the stress σ_{ij} appearing on the left hand side depends on the spatial coordinates through $\boldsymbol{r}$ and on time t, whereas σ_{ij} on the right hand side depends only on z. Hereafter we use the symbol σ_{ij} to denote $\sigma_{ij}(z)$.

Using the abbreviated suffix notation to express the stress and stiffness,[12] the wave equation can be expressed in a matrix form as

$$\left[\boldsymbol{L}+\boldsymbol{V}-\frac{d\rho}{dz}\boldsymbol{U}\right]\boldsymbol{\sigma}(z)=0, \tag{5}$$

where

$$\begin{aligned}\boldsymbol{L}&\equiv\begin{pmatrix}-q^2&0&0&0&iq\frac{\partial}{\partial z}&0\\0&0&0&0&0&0\\0&0&\frac{\partial^2}{\partial z^2}&0&iq\frac{\partial}{\partial z}&0\\0&0&0&\frac{\partial^2}{\partial z^2}&0&iq\frac{\partial}{\partial z}\\iq\frac{\partial}{\partial z}&0&iq\frac{\partial}{\partial z}&0&-q^2+\frac{\partial^2}{\partial z^2}&0\\0&0&0&iq\frac{\partial}{\partial z}&0&-q^2\end{pmatrix},\\\boldsymbol{V}(z)&\equiv\rho(z)\omega^2\boldsymbol{s}(z),\\\boldsymbol{U}(z)&\equiv\frac{1}{\rho(z)}\begin{pmatrix}0&0&0&0&0&0\\0&0&0&0&0&0\\0&0&\frac{\partial}{\partial z}&0&iq&0\\0&0&0&\frac{\partial}{\partial z}&0&iq\\iq&0&0&0&\frac{\partial}{\partial z}&0\\0&0&0&0&0&0\end{pmatrix},\\\boldsymbol{\sigma}(z)&\equiv\begin{pmatrix}\sigma_1(z)\\\sigma_2(z)\\\sigma_3(z)\\\sigma_4(z)\\\sigma_5(z)\\\sigma_6(z)\end{pmatrix}.\end{aligned} \tag{6}$$

The anisotropy of the medium enters Eq. (5) via $\boldsymbol{s}$ or $\boldsymbol{V}$.

B. Continuity

In the absence of delaminations or cracks, the displacement field u_i is continuous throughout the medium. By substitution of the monochromatic solution of Eq. (4) in Eq. (1), we obtain

$$-\omega^2 u_j=\frac{1}{\rho}\left(iq\sigma_{jx}+\frac{d\sigma_{jz}}{dz}\right)\quad(j=x,y,z). \tag{7}$$

As a result, besides u_x, u_y, u_z, also σ_3, σ_4, and σ_5 are continuous throughout the medium, regardless of any continuous or discontinuous inhomogeneity.

The right hand side of Eq. (7) is equivalent to the third, fourth, and fifth rows of $\boldsymbol{U\sigma}$. The first, second, and sixth rows of $\boldsymbol{U\sigma}$ are always zero. Thus $\boldsymbol{U\sigma}$ is continuous

throughout the medium. This continuity turns out to be important for the numerical solution of the wave equation in Sec. II F.

It is convenient to define the continuous quantity $\boldsymbol{b}(z)$ as

$$\boldsymbol{b}(z)=\begin{pmatrix}\sigma_3(z)\\ \sigma_4(z)\\ \sigma_5(z)\\ -\omega^2 u_x(z)\\ -\omega^2 u_y(z)\\ -\omega^2 u_z(z)\end{pmatrix}=\begin{pmatrix}\sigma_3(z)\\ \sigma_4(z)\\ \sigma_5(z)\\ \frac{1}{\rho(z)}\left\{iq\sigma_1(z)+\frac{d\sigma_5(z)}{dz}\right\}\\ \frac{1}{\rho(z)}\left\{iq\sigma_6(z)+\frac{d\sigma_4(z)}{dz}\right\}\\ \frac{1}{\rho(z)}\left\{iq\sigma_5(z)+\frac{d\sigma_3(z)}{dz}\right\}\end{pmatrix}. \tag{8}$$

The continuity of $\boldsymbol{b}$ can be expressed as

$$\boldsymbol{b}(z'+0)=\boldsymbol{b}(z'-0)=\boldsymbol{b}(z'),$$

where $\boldsymbol{b}(z'+0)$ and $\boldsymbol{b}(z'-0)$ denote the right and left side limit of $\boldsymbol{b}(z)$ at $z\to z'$, respectively. It encompasses the boundary conditions at interfaces between different materials (see Secs. II C and II E).

C. Transfer matrix method for multiple anisotropic homogeneous layers

Though the theory of acoustic waves in multiple anisotropic homogeneous layers is well established,[13] we describe the procedure in a rather detailed way, since it is also important to construct the Green's function in Sec. II E.

Within a homogeneous layer with constant ρ and s, the third term in Eq. (5) disappears. The solution is then given as a simple plane wave

$$\boldsymbol{\sigma}(z)=\boldsymbol{\sigma}_0\exp(ipz). \tag{9}$$

where $\boldsymbol{\sigma}_0$ takes a constant value. The z component of the wave vector (p) can be obtained for a given set of q and ω by solving the secular equation

$$\det(\boldsymbol{L}_h+\boldsymbol{V}_h)=0. \tag{10}$$

where

$$\boldsymbol{L}_h=\begin{pmatrix}-q^2 & 0 & 0 & 0 & -pq & 0\\ 0 & 0 & 0 & 0 & 0 & 0\\ 0 & 0 & -p^2 & 0 & -pq & 0\\ 0 & 0 & 0 & -p^2 & 0 & -pq\\ -pq & 0 & -pq & 0 & -q^2-p^2 & 0\\ 0 & 0 & 0 & -pq & 0 & -q^2\end{pmatrix}. \tag{11}$$

This is a sixth order equation in p and has six roots p_i $(i=1,\ldots,6)$. The wave numbers p_i can be either real or imaginary, corresponding to propagating bulk waves or to surface (or interface) waves, respectively. Three modes out of six are propagating or vanishing in the positive z direction ($\Re[p_i]\geq 0$ or $\Im[p_i]\geq 0$ for $i=1,2,3$), while the other three modes are propagating or vanishing in the negative z direction ($\Re[p_i]\leq 0$ or $\Im[p_i]\leq 0$ for $i=4,5,6$). For each p_i, the corresponding eigenvector $\boldsymbol{\sigma}_0^{(i)}$ can be obtained through

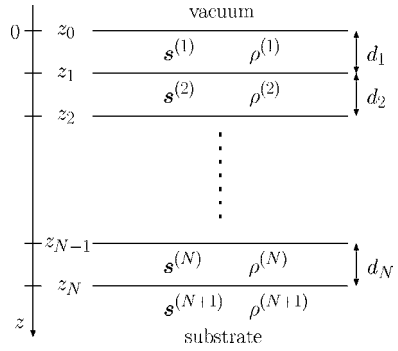

FIG. 1. Notations used to define a multilayered medium.

$$[\boldsymbol{L}_h+\boldsymbol{V}_h]\boldsymbol{\sigma}_0=0. \tag{12}$$

Because of the linearity of Eq. (5), all of the linear combinations of Eq. (9) are also solutions. The general solution for this homogenous region is thus given by

$$\boldsymbol{\sigma}(z)=\sum_{j=1}^{6}a_j\boldsymbol{\sigma}_0^{(j)}\exp(ip_j z), \tag{13}$$

where a_j is an arbitrary amplitude factor for the jth mode.

Based on the above results, we first consider acoustic waves in a medium with multiple homogeneous anisotropic layers stacked along the z direction and handle the problem using the transfer matrix method. In multilayers, the nth layer has mass density $\rho^{(n)}$, compliance $\mathbf{s}^{(n)}$, and thickness d_n as shown in Fig. 1. The outermost surface of the medium is at $z=z_0=0$, and the region $z<0$ corresponds to a vacuum.

By using Eqs. (10) and (12), the wave numbers $p_i^{(n)}$ and the corresponding eigenvectors $\boldsymbol{\sigma}_0^{(n,i)}$ are obtained for the nth layer. The general solution for the nth layer is given by

$$\boldsymbol{\sigma}^{(n)}(\zeta_n)=\sum_{j=1}^{6}a_j^{(n)}\boldsymbol{\sigma}_0^{(n,j)}\exp(ip_j^{(n)}\zeta_n), \tag{14}$$

where

$$\zeta_n\equiv z-z_{n-1}\quad\text{for } n\geq 1. \tag{15}$$

There are $6N+6$ unknowns of mode amplitude $a_j^{(n)}$ for the whole medium. However, they are not independent, but subject to the boundary conditions at the interfaces. At the interface between every nth and $(n+1)$th layer, the required boundary condition can be expressed in matrix form (see Sec. II B) as

$$\boldsymbol{b}(z_n+0)=\boldsymbol{M}^{(n+1)}\boldsymbol{a}^{(n+1)}=\boldsymbol{M}^{(n)}\boldsymbol{Q}^{(n)}\boldsymbol{a}^{(n)}=\boldsymbol{b}(z_n-0), \tag{16}$$

for $n\geq 1$ where $\boldsymbol{a}^{(n)}$ is a six-element column vector made up of $\{a_j^{(n)}\}$, and $\boldsymbol{M}$ and $\boldsymbol{Q}$ are 6 by 6 matrices whose components are defined as follows:

$$M_{1j}^{(n)} = \sigma_3^{(n,j)},$$

$$M_{2j}^{(n)} = \sigma_4^{(n,j)},$$

$$M_{3j}^{(n)} = \sigma_5^{(n,j)},$$

$$M_{4j}^{(n)} = \frac{i}{\rho^{(n)}}(q\sigma_1^{(n,j)} + p_j^{(n)}\sigma_5^{(n,j)}), \tag{17}$$

$$M_{5j}^{(n)} = \frac{i}{\rho^{(n)}}(q\sigma_6^{(n,j)} + p_j^{(n)}\sigma_4^{(n,j)}),$$

$$M_{6j}^{(n)} = \frac{i}{\rho^{(n)}}(q\sigma_5^{(n,j)} + p_j^{(n)}\sigma_3^{(n,j)}),$$

$$Q_{jk}^{(n)} = \delta_{jk} \exp(ip_j^{(n)}d_n).$$

Here $\sigma_k^{(n,j)}$ is the kth component of $\boldsymbol{\sigma}_0^{(n,j)}$, and δ_{jk} is the Kronecker delta.

The N boundary conditions lead to $6N$ equations for $\boldsymbol{a}^{(n)}$. If we arbitrarily specify six components out of $6N+6$ components of $\boldsymbol{a}^{(n)}$, the remaining $6N$ components of $\boldsymbol{a}^{(n)}$ are uniquely determined.

In the case of SAWs, there are three additional conditions for vanishing stress at $z \to +\infty$:

$$a_4^{(N+1)} = a_5^{(N+1)} = a_6^{(N+1)} = 0. \tag{18}$$

The whole stress field is further specified with three constants $a_j^{(N+1)}$ $(j=1,2,3)$ that are determined by the stress free condition at the surface:

$$\sigma_3(0) = \sigma_4(0) = \sigma_5(0) = 0. \tag{19}$$

They also correspond to the first three components of $\boldsymbol{b}(0)$. With the iterative use of Eq. (16), we obtain

$$\boldsymbol{b}(0) = \boldsymbol{M}^{(1)}\boldsymbol{a}^{(1)} = \boldsymbol{M}_f\boldsymbol{a}^{(N+1)}, \tag{20}$$

where

$$\boldsymbol{M}_f = \left(\prod_{j=1}^{N} \boldsymbol{M}^{(j)}(\boldsymbol{Q}^{(j)})^{-1}(\boldsymbol{M}^{(j)})^{-1}\right)\boldsymbol{M}^{(N+1)}. \tag{21}$$

To satisfy Eq. (19) with nonzero components of $a_j^{(N+1)}$ for $j=1,2,3$, the secular equation for the submatrix of $\boldsymbol{M}_f$ must be satisfied:

$$\det\begin{pmatrix} M_{f11} & M_{f12} & M_{f13} \\ M_{f21} & M_{f22} & M_{f23} \\ M_{f31} & M_{f32} & M_{f33} \end{pmatrix} = 0. \tag{22}$$

Since the left hand side of this equation is a function of ω and q, Eq. (22) gives the SAW dispersion relation $\omega(q)$.

D. Green's function method for dealing with inhomogeneities

Based on Eq. (5) and the definitions in Sec. II C, we now treat the stress field in a medium with one-dimensional arbitrary inhomogeneity using a Green's function. We assume that the medium is homogeneous beyond a certain value of z. The wave equation (5) can be rewritten as

$$\left[\boldsymbol{L} + \boldsymbol{V}_h + \boldsymbol{\Delta V}(z) - \frac{d\rho(z)}{dz}\boldsymbol{U}\right]\boldsymbol{\sigma} = 0, \tag{23}$$

where

$$\boldsymbol{V}_h + \boldsymbol{\Delta V}(z) = \rho(z)\omega^2\boldsymbol{s}(z), \tag{24}$$

$$\boldsymbol{V}_h = \rho_h\omega^2\boldsymbol{s}_h. \tag{25}$$

The quantities ρ_h and $\boldsymbol{s}_h$ are constants representing the homogeneous part of the medium far away from the surface.

Using the solution $\boldsymbol{\sigma}_h$ satisfying

$$[\boldsymbol{L} + \boldsymbol{V}_h]\boldsymbol{\sigma}_h = 0, \tag{26}$$

and Green's function $\boldsymbol{G}(z,z')$ satisfying

$$[\boldsymbol{L} + \boldsymbol{V}_h]\boldsymbol{G}(z,z') = -\delta(z-z')\boldsymbol{I}, \tag{27}$$

where $\boldsymbol{I}$ is the 6 by 6 identity matrix, the solution $\boldsymbol{\sigma}(z)$ satisfying Eq. (23) can be written in the following form:

$$\boldsymbol{\sigma}(z) = \boldsymbol{\sigma}_h(z) + \int_0^{+\infty} \boldsymbol{G}(z,z')\left\{\boldsymbol{\Delta V}(z') - \frac{d\rho(z')}{dz'}\boldsymbol{U}(z')\right\}\boldsymbol{\sigma}(z')\,dz'. \tag{28}$$

The expression in curly brackets in Eq. (28) can be interpreted as a scattering potential that scatters the stress wave reaching z' to the observation point z.

When $\boldsymbol{\Delta V}$ (in fact, the whole expression in curly brackets) is small, it is possible to solve Eq. (28) by iterative substitution of the right hand side of this equation to $\boldsymbol{\sigma}$ in the integral (Born approximation). However, for arbitrary $\boldsymbol{\Delta V}$, this iterative substitution may lead to divergence. So, in the general case, the integral equation, Eq. (28), has to be solved directly. To do this, it is useful to regard $\boldsymbol{\sigma}$ and $\boldsymbol{\sigma}_h$ as vectors of infinite dimension with index z, the integral term as the product between a matrix with infinite dimension indices z and z', and the vector $\boldsymbol{\sigma}(z')$ with respect to the common index z'. Obviously $\boldsymbol{\sigma}$ depends linearly on $\boldsymbol{\sigma}_h$, and $\boldsymbol{\sigma}_h$ has to be chosen so that $\boldsymbol{\sigma}$ satisfies the required boundary condition as described in Sec. II C. We will see how this can be done numerically in Sec. II F.

E. Derivation of the Green's function

In the previous section, we did not give the concrete form of the Green's function. Here we describe how to solve Eq. (27) to obtain the Green's function $\boldsymbol{G}(z,z')$, which is given as a 6×6 matrix. The jth column of the matrix is denoted as $\boldsymbol{G}_j(z,z')$ $(j=1,\ldots,6)$. Since Eq. (27) is equivalent to Eq. (26) at $z \neq z'$, $\boldsymbol{G}_j$ in this region can be expressed as a linear combination of the eigenmodes of Eq. (26):

$$\boldsymbol{\sigma}_0^{(m)} \exp(ip_m z). \tag{29}$$

According to the discussion in Sec. II D concerning the scattering nature of the Green's function, $\boldsymbol{G}_j$ in the region $z > z'$ can be assumed to contain only modes propagating in the $+z$ direction or vanishing at $z=+\infty$, whereas $\boldsymbol{G}_j$ in the region $z < z'$ can be assumed to contain only modes propagating in the $-z$ direction or vanishing at $z=-\infty$.

TABLE I. First and second derivatives of $f(z)$ containing several types of singularities.

Type of singularity	First derivative	Second derivative
$\delta(z-z')$	$\frac{\partial\delta(z-z')}{\partial z}$	$\frac{\partial^2\delta(z-z')}{\partial z^2}$
discontinuity at $z=z'$	$(f(z'+0)-f(z'-0))\delta(z-z')$	$(f(z'+0)-f(z'-0))\frac{\partial\delta(z-z')}{\partial z}$
discontinuity in the first derivative at $z=z'$	discontinuity at $z=z'$	$\left(\frac{df}{dz}(z'+0)-\frac{df}{dz}(z'-0)\right)\delta(z-z')$

The delta function on the right hand side of Eq. (27) can emerge in three ways. The first possibility is that $\boldsymbol{G}_j$ itself contains $\delta(z-z')$. The second possibility is that $\boldsymbol{G}_j$ has a discontinuity at $z=z'$, and the first z derivative gives a delta function. Finally, it is possible that the first z derivative of $\boldsymbol{G}_j$ has a discontinuity, and the second z derivative gives a delta function.

The above consideration leads to the following possible forms of the Green's function:

$$\boldsymbol{G}_j(z,z') = \boldsymbol{G}'_j(z,z') + \boldsymbol{D}_j\delta(z-z'),$$
$$\boldsymbol{G}'_j(z,z') = \begin{cases} \sum_{m=1}^{3} g_m^{(j)}(z')\boldsymbol{\sigma}_0^{(m)} \exp(ip_m z) & \text{for } z > z', \\ \sum_{m=4}^{6} g_m^{(j)}(z')\boldsymbol{\sigma}_0^{(m)} \exp(ip_m z) & \text{for } z < z', \end{cases} \tag{30}$$

where $g_m^{(j)}(z')$ is a function only of z', and $\boldsymbol{D}_j$ is a constant column vector. For later use, the 6×6 matrices $\boldsymbol{D}$ and $\boldsymbol{G}'$ are defined as having their jth column as $\boldsymbol{D}_j$ and $\boldsymbol{G}'_j$, respectively.

Now it is clear how to determine $g_m^{(j)}(z')$ and $\boldsymbol{D}_j$. To do this, it is worth keeping in mind some general features of singularities in a function. In Table I, the first and second derivatives of a general function $f(z)$ with several types of singularity at $z=z'$, such as a δ function, a discontinuity, and a discontinuity in the first derivative, are summarized. Since, on the left hand side of Eq. (27), the first and second derivative operators as well as numbers are involved, substitution of Eq. (30) to Eq. (27) may involve the δ function itself, the first derivative of the δ function, and the second derivative of the δ function. We need to cancel the first and second derivatives of the δ function and leave only the required δ function by means of an appropriate choice of $g_m^{(j)}$ and $\boldsymbol{D}_j$.

It is convenient to define the following matrices:

$$\boldsymbol{L} \equiv \boldsymbol{L}_0 + \boldsymbol{L}_1\frac{\partial}{\partial z} + \boldsymbol{L}_2\frac{\partial^2}{\partial z^2}, \tag{31}$$

where

$$\boldsymbol{L}_0 \equiv \begin{pmatrix} -q^2 & 0 & 0 & 0 & 0 & 0 \\ 0 & 0 & 0 & 0 & 0 & 0 \\ 0 & 0 & 0 & 0 & 0 & 0 \\ 0 & 0 & 0 & 0 & 0 & 0 \\ 0 & 0 & 0 & 0 & -q^2 & 0 \\ 0 & 0 & 0 & 0 & 0 & -q^2 \end{pmatrix},$$

$$\boldsymbol{L}_1 \equiv \begin{pmatrix} 0 & 0 & 0 & 0 & iq & 0 \\ 0 & 0 & 0 & 0 & 0 & 0 \\ 0 & 0 & 0 & 0 & iq & 0 \\ 0 & 0 & 0 & 0 & 0 & iq \\ iq & 0 & iq & 0 & 0 & 0 \\ 0 & 0 & 0 & iq & 0 & 0 \end{pmatrix}, \tag{32}$$

$$\boldsymbol{L}_2 \equiv \begin{pmatrix} 0 & 0 & 0 & 0 & 0 & 0 \\ 0 & 0 & 0 & 0 & 0 & 0 \\ 0 & 0 & 1 & 0 & 0 & 0 \\ 0 & 0 & 0 & 1 & 0 & 0 \\ 0 & 0 & 0 & 0 & 1 & 0 \\ 0 & 0 & 0 & 0 & 0 & 0 \end{pmatrix}$$

With these notations, Eq. (27) can be rewritten as

$$\begin{aligned}[\boldsymbol{L}+\boldsymbol{V}_h]\boldsymbol{G}_j &= \left[\boldsymbol{L}_0 + \boldsymbol{L}_1\frac{\partial}{\partial z} + \boldsymbol{L}_2\frac{\partial^2}{\partial z^2} + \boldsymbol{V}_h\right]\boldsymbol{G}_j \\ &= \Bigg\{(\boldsymbol{L}_0+\boldsymbol{V}_h)\boldsymbol{D}_j + \boldsymbol{L}_1(\boldsymbol{G}'_j(z'+0,z') \\ &\quad - \boldsymbol{G}'_j(z'-0,z')) + \boldsymbol{L}_2\left(\frac{\partial\boldsymbol{G}'_j}{\partial z}(z'+0,z')\right. \\ &\quad \left. - \frac{\partial\boldsymbol{G}'_j}{\partial z}(z'-0,z')\right)\Bigg\}\delta(z-z') \\ &\quad + \{\boldsymbol{L}_1\boldsymbol{D}_j + \boldsymbol{L}_2(\boldsymbol{G}'_j(z'+0,z') - \boldsymbol{G}'_j(z'-0,z'))\} \\ &\quad \times\frac{\partial\delta(z-z')}{\partial z} + \boldsymbol{L}_2\boldsymbol{D}_j\frac{\partial^2\delta(z-z')}{\partial z^2} \\ &= -\boldsymbol{I}_j\delta(z-z'), \end{aligned} \tag{33}$$

where $\boldsymbol{I}_j$ is the jth column of $\boldsymbol{I}$. Comparing the coefficients for the δ function and its derivatives on both sides of Eq. (33), and using the definition of $\boldsymbol{G}'_j$ in Eq. (30), we obtain

$$(\boldsymbol{L}_0+\boldsymbol{V}_h)\boldsymbol{D}_j + \sum_{m=1}^{3} g_m^{(j)}(\boldsymbol{L}_1 + ip_m\boldsymbol{L}_2)\boldsymbol{\sigma}_0^{(m)}\exp(ip_m z') - \sum_{m=4}^{6} g_m^{(j)}(\boldsymbol{L}_1 + ip_m\boldsymbol{L}_2)\boldsymbol{\sigma}_0^{(m)}\exp(ip_m z') = -\boldsymbol{I}_j, \tag{34a}$$

$$\boldsymbol{L}_1\boldsymbol{D}_j + \sum_{m=1}^{3} g_m^{(j)}\boldsymbol{L}_2\boldsymbol{\sigma}_0^{(m)} \exp(ip_m z') - \sum_{m=4}^{6} g_m^{(j)}\boldsymbol{L}_2\boldsymbol{\sigma}_0^{(m)} \exp(ip_m z') = 0, \tag{34b}$$

$$\boldsymbol{L}_2\boldsymbol{D}_j = 0. \tag{34c}$$

Equation (34c) simply gives $D_{j,k}=0$ for $k=3,4,5$ ($D_{j,k}$ is the kth component of $\boldsymbol{D}_j$). With this knowledge, it turns out that the first, second, and sixth rows of the left hand side of Eq. (34b) are zero. The remaining three nontrivial equations in Eq. (34b) and six equations in Eq. (34a) form a set of nine linear equations, which allows the determination of the nine unknowns, $g_m^{(j)}(z')$ $(m=1,\ldots,6)$ and $D_{j,k}$ $(k=1,2,6)$. In this way, we can find a unique formulation for the Green's function $\boldsymbol{G}(z,z')$.

It is informative to take a look at the role of the δ-function term in $\boldsymbol{G}(z,z')$. As a simple example, we consider a medium with one homogeneous layer with thickness $d_1=z_1$ formed on a homogeneous substrate. We find a Green's function for the substrate with parameter,

$$\boldsymbol{V}_h = \omega^2\rho^{(2)}\boldsymbol{s}^{(2)}, \tag{35}$$

where the notations follow the ones of Fig. 1. The deviation in $\boldsymbol{V}$ is given by

$$\Delta\boldsymbol{V}(z) = \begin{cases} \omega^2(\rho^{(1)}\boldsymbol{s}^{(1)} - \rho^{(2)}\boldsymbol{s}^{(2)}) & \text{for } 0 \le z \le z_1, \\ 0 & \text{else,} \end{cases} \equiv \Delta\boldsymbol{V}_0\theta(z_1 - z), \tag{36}$$

where $\theta(z)$ is the Heaviside function and $\Delta\boldsymbol{V}_0$ is a constant matrix. The z derivative of ρ involves a δ function as follows:

$$\frac{d\rho}{dz} = (\rho^{(2)} - \rho^{(1)})\delta(z - z_1). \tag{37}$$

By putting these into Eq. (28), we obtain

$$\boldsymbol{\sigma}(z) = \boldsymbol{\sigma}_h(z) + \int_0^{z_1} \boldsymbol{G}'(z,z')\Delta\boldsymbol{V}_0\boldsymbol{\sigma}(z')\,dz' + \boldsymbol{D}\Delta\boldsymbol{V}_0\boldsymbol{\sigma}(z) - (\rho^{(2)} - \rho^{(1)})\boldsymbol{G}'(z,z_1)\boldsymbol{U}(z_1)\boldsymbol{\sigma}(z_1), \tag{38}$$

for $0<z<z_1$, and

$$\boldsymbol{\sigma}(z) = \boldsymbol{\sigma}_h(z) + \int_0^{z_1} \boldsymbol{G}'(z,z')\Delta\boldsymbol{V}_0\boldsymbol{\sigma}(z')\,dz' - (\rho^{(2)} - \rho^{(1)})\boldsymbol{G}'(z,z_1)\boldsymbol{U}(z_1)\boldsymbol{\sigma}(z_1), \tag{39}$$

for $z>z_1$. Though it is hard to properly determine $\boldsymbol{U}$ and $\boldsymbol{\sigma}$ separately at $z=z_1$ because of the discontinuity there, due to the continuity of $\boldsymbol{U}\boldsymbol{\sigma}$, this quantity at $z=z_1$ can be obtained as the right or left hand side limit at $z\to z_1\pm 0$. In the limit $z\to z_1\pm 0$, Eqs. (38) and (39) become

$$\boldsymbol{\sigma}(z_1 - 0) = \boldsymbol{\sigma}_h(z_1) + \int_0^{z_1} \boldsymbol{G}'(z_1,z')\Delta\boldsymbol{V}_0\boldsymbol{\sigma}(z')\,dz' + \boldsymbol{D}\Delta\boldsymbol{V}_0\boldsymbol{\sigma}(z_1 - 0) - (\rho^{(2)} - \rho^{(1)})\boldsymbol{G}'(z_1 - 0,z_1)\boldsymbol{U}(z_1)\boldsymbol{\sigma}(z_1), \tag{40}$$

$$\boldsymbol{\sigma}(z_1 + 0) = \boldsymbol{\sigma}_h(z_1) + \int_0^{z_1} \boldsymbol{G}'(z_1,z')\Delta\boldsymbol{V}_0\boldsymbol{\sigma}(z')\,dz' - (\rho^{(2)} - \rho^{(1)})\boldsymbol{G}'(z_1 + 0,z_1)\boldsymbol{U}(z_1)\boldsymbol{\sigma}(z_1), \tag{41}$$

This gives

$$\boldsymbol{\sigma}(z_1 + 0) - \boldsymbol{\sigma}(z_1 - 0) = \boldsymbol{D}\Delta\boldsymbol{V}_0\boldsymbol{\sigma}(z_1 - 0) - (\rho^{(2)} - \rho^{(1)}) \times (\boldsymbol{G}'(z_1 + 0,z_1) - \boldsymbol{G}'(z_1 - 0,z_1))\boldsymbol{U}(z_1)\boldsymbol{\sigma}(z_1), \tag{42}$$

The discontinuity in $\boldsymbol{\sigma}$ at the interface comes partially from the δ-function term in $\boldsymbol{G}$, and partially from the discontinuity in $\boldsymbol{G}'$. It can be shown that the third, fourth, and fifth rows of the right hand side of Eq. (42) are zero, corresponding to the required continuity in σ_j for $j=3,4,5$.

F. Numerical solution of the integral equation

Now that we have the explicit form of $\boldsymbol{G}(z,z')$, we can numerically solve the integral equation, Eq. (28).

It is convenient to introduce the following definitions:

$$\frac{d\rho}{dz}\boldsymbol{U} \equiv \frac{1}{\rho}\frac{d\rho}{dz}\left(\boldsymbol{U}_0 + \boldsymbol{U}_1\frac{\partial}{\partial z}\right), \tag{43}$$

where

$$\boldsymbol{U}_0 \equiv \begin{pmatrix} 0 & 0 & 0 & 0 & 0 & 0 \\ 0 & 0 & 0 & 0 & 0 & 0 \\ 0 & 0 & 0 & 0 & iq & 0 \\ 0 & 0 & 0 & 0 & 0 & iq \\ iq & 0 & 0 & 0 & 0 & 0 \\ 0 & 0 & 0 & 0 & 0 & 0 \end{pmatrix}, \quad \boldsymbol{U}_1 \equiv \boldsymbol{L}_2. \tag{44}$$

Suppose that the deviation in ρ and $\boldsymbol{s}$ vanishes beyond a certain point $z=h$. We divide the region $0<z<h$ into m partitions with thickness $\Delta z=h/m$ each. First we consider the case in which ρ varies smoothly without any singularity in dp/dz. Then the integral in Eq. (28) can be approximated by a discrete sum:

$$\boldsymbol{\sigma}(Z_j) = \boldsymbol{\sigma}_h(Z_j) + \sum_{k=0}^{m-1} \boldsymbol{G}'(Z_j, Z_k) \left[\boldsymbol{\Delta V}(Z_k)\boldsymbol{\sigma}(Z_k) - \frac{d\rho}{dz}(Z_k)\frac{1}{\rho(Z_k)} \left\{ \boldsymbol{U}_0\boldsymbol{\sigma}(Z_k) + \boldsymbol{U}_1 \frac{d\boldsymbol{\sigma}}{dz}(Z_k) \right\} \right] \Delta z + \boldsymbol{D} \left[\boldsymbol{\Delta V}(Z_j)\boldsymbol{\sigma}(Z_j) - \frac{d\rho}{dz}(Z_j)\frac{1}{\rho(Z_j)} \times \left\{ \boldsymbol{U}_0\boldsymbol{\sigma}(Z_j) + \boldsymbol{U}_1 \frac{d\boldsymbol{\sigma}}{dz}(Z_j) \right\} \right] \tag{45}$$

where $Z_j = (j+0.5)\Delta z$ for $j = 0, \ldots, m-1$ and

$$\frac{d\boldsymbol{\sigma}}{dz}(Z_j) = \begin{cases} \dfrac{\boldsymbol{\sigma}(Z_j) - \boldsymbol{\sigma}(Z_{j-1})}{\Delta z} & \text{for } j = m-1, \\ \dfrac{\boldsymbol{\sigma}(Z_{j+1}) - \boldsymbol{\sigma}(Z_j)}{\Delta z} & \text{for } j = 0, \\ \dfrac{\boldsymbol{\sigma}(Z_{j+1}) - \boldsymbol{\sigma}(Z_{j-1})}{2\Delta z} & \text{else.} \end{cases} \tag{46}$$

Equation (45) can be regarded as a set of simultaneous linear equations with $6m$ unknowns, i.e., $\boldsymbol{\sigma}(Z_j)$, and can be solved with standard methods.

If the medium contains an interface of different materials, i.e., if it involves δ-function behavior in $d\rho/dz$, we have to go back to Eq. (28) again. It is also convenient to choose h or m such that the interface position does not exactly agree with one of the Z_j's in order to avoid the unnecessary explicit involvement of singularities in the solution process. We consider the two-layer medium described by Eqs. (36) and (37) as an example. By taking h as z_1, Eq. (28) is discretized to

$$\boldsymbol{\sigma}(Z_j) = \boldsymbol{\sigma}_h(Z_j) + \sum_{k=0}^{m-1} \boldsymbol{G}'(Z_j, Z_k)\boldsymbol{\Delta V}(Z_k)\boldsymbol{\sigma}(Z_k)\Delta z + \boldsymbol{D}\boldsymbol{\Delta V}(Z_j)\boldsymbol{\sigma}(Z_j) - \frac{\rho^{(2)} - \rho^{(1)}}{\rho^{(1)}} \times \boldsymbol{G}(Z_j, z_1) \left\{ \boldsymbol{U}_0\boldsymbol{\sigma}(Z_{m-1}) + \boldsymbol{U}_1 \frac{d\boldsymbol{\sigma}}{dz}(Z_{m-1}) \right\}. \tag{47}$$

In the last term, the continuity of $\boldsymbol{U\sigma}$ is used to approximate the value at the interface with a value nearby.

In either case, $\boldsymbol{\sigma}$ is uniquely determined with respect to a given $\boldsymbol{\sigma}_h$, which is specified by six mode amplitudes as in Eq. (13). In fact, these six amplitudes act as the arbitrary constants in the general solution for the second order differential equation (5).

In the case of SAWs, $\boldsymbol{\sigma}_h$ should contain only the three modes vanishing at $z = +\infty$ and is specified by the three amplitudes a_i $(i = 1, 2, 3)$ for these modes. We introduce the notation $\boldsymbol{\sigma}(z; a_1, a_2, a_3)$ to express a particular solution for a given set of a_i. Because of the linearity of the problem, the following relation holds:

$$\boldsymbol{\sigma}(z; a_1, a_2, a_3) = a_1\boldsymbol{\sigma}(z; 1, 0, 0) + a_2\boldsymbol{\sigma}(z; 0, 1, 0) + a_3\boldsymbol{\sigma}(z; 0, 0, 1). \tag{48}$$

To satisfy the stress-free condition of Eq. (19) at the surface, the following secular equation must be satisfied:

TABLE II. Parameters of the piecewise homogeneous medium.

	c_{11} (GPa)	c_{44} (GPa)	ρ (g/cm^3)	Thickness (μm)
Top layer	25.96	10.08	3.421	1.944
Substrate	36.80	13.72	3.801	⋯

$$\det \begin{pmatrix} \sigma_3(0;1,0,0) & \sigma_3(0;0,1,0) & \sigma_3(0;0,0,1) \\ \sigma_4(0;1,0,0) & \sigma_4(0;0,1,0) & \sigma_4(0;0,0,1) \\ \sigma_5(0;1,0,0) & \sigma_5(0;0,1,0) & \sigma_5(0;0,0,1) \end{pmatrix} = 0. \tag{49}$$

The left hand side of the equation is a function of ω and q, and the equation itself gives an implicit expression of the function $\omega(q)$ [or $q(\omega)$], the dispersion relation for the SAW.

The proposed Green's function method can be combined with the transfer matrix method in Sec. II C to handle a medium with a few inhomogeneous layers embedded in homogeneous layers. In this way, the computation load can be reduced. Another way of reducing the number of calculations is using nonequal steps for discretization: using larger steps for regions with slower variation of elastic property or mass density.

III. EXAMPLES

In this section, we show some simple examples of calculating the dispersion relation of SAWs using the Green's function method.

A. Piecewise homogenous medium

We first calculate the dispersion relation of a Rayleigh-type surface mode in a medium consisting of a homogeneous isotropic layer on a homogeneous isotropic substrate. A stress-free surface is located at $z = 0$ and the medium extends to $z \to +\infty$. The parameters used are shown in Table II. The necessary Green's function is calculated for the substrate material according to the procedure in Sec. II E. Since the assumed medium contains a discontinuous change in elastic properties and in mass density, Eq. (47) is used to calculate the acoustic field. The top layer thickness is discretized into $m = 20$ and $m = 100$ equally spaced partitions. Then the dispersion relation for the Rayleigh-type mode is calculated using Eq. (49).

Figure 2 shows the frequency dependence of the phase velocity for the Rayleigh-type mode calculated by the Green's function method as well as by the transfer matrix method in Sec. II C. Since the accuracy of the latter method is only limited by the precision of the computation, the plot gives a rough estimate of the accuracy of the Green's function method.

While the $m = 20$ calculation shows a deviation from the transfer matrix result beyond several hundred MHz, the $m = 100$ calculation sustains good accuracy ($< 0.2\%$) up to 4 GHz. At 10 GHz, the $m = 20$ calculation is far away from the exact one, while the $m = 100$ calculation still gives a good approximated value to within $\sim 0.7\%$. For $m = 100$, the step width is about 0.02 μm, which should be compared with the wavelength 0.5 μm at 10 GHz. Apparently, to have enough

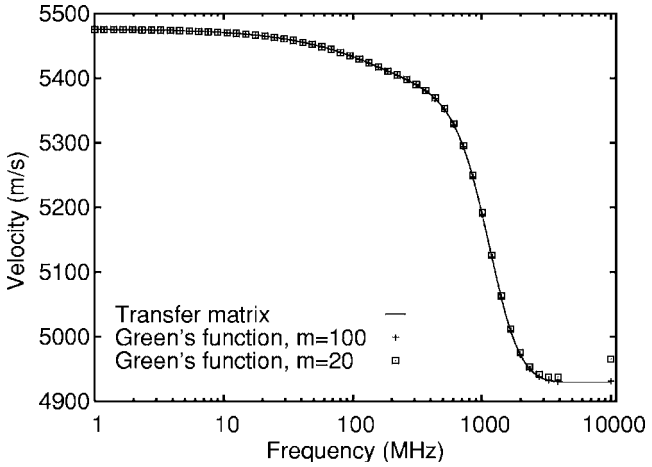

FIG. 2. Dispersion relations of a Rayleigh-type surface mode calculated for a piecewise homogeneous medium using the transfer matrix method and Green's function method with m partitions.

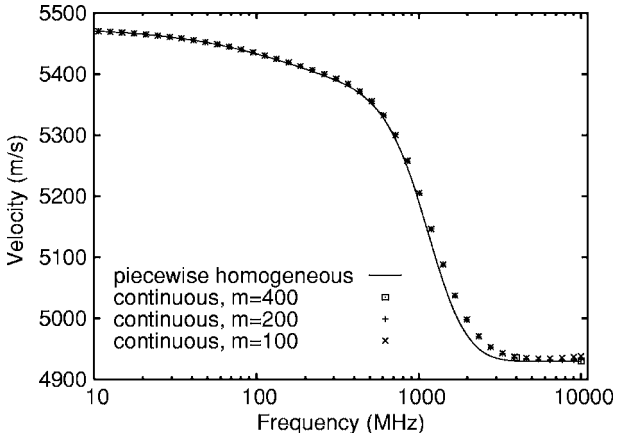

FIG. 3. Dispersion relation of a Rayleigh-type surface mode calculated for a medium with continuously varying inhomogeneity using Green's function methods with m partitions. The dispersion curve for the piecewise homogeneous medium is also shown as a solid line.

accuracy, the step width should be chosen less than a couple of tenths of a wavelength at the required frequency.

B. Medium with continuously varying inhomogeneity

In this example, the dispersion relation of a Rayleigh-type surface mode is calculated in a medium with continuously varying elastic constants and mass density along the depth direction. The medium consists of an inhomogeneous layer on a homogeneous substrate. The free surface is located at $z=0$ and the medium extends to $z\rightarrow+\infty$. The substrate has an isotropic stiffness tensor $\boldsymbol{c}_2$ and mass density ρ_2, the same as those of the substrate material in Table II. Within the inhomogeneous layer of thickness 4 μm, the elastic tensor and mass density are assumed *ad hoc* to vary as

$$\boldsymbol{c}(z)=\frac{1}{2}(\boldsymbol{c}_1+\boldsymbol{c}_2)+\frac{1}{2}(\boldsymbol{c}_2-\boldsymbol{c}_1)\tanh\left(\frac{z-\alpha}{\beta}\right),$$
$$\rho(z)=\frac{1}{2}(\rho_1+\rho_2)+\frac{1}{2}(\rho_2-\rho_1)\tanh\left(\frac{z-\alpha}{\beta}\right), \tag{50}$$

where $\boldsymbol{c}_1$ and ρ_1 are the stiffness and mass density given in Table II for the top layer. For the calculation, the parameters $\alpha=1.94$ μm and $\beta=0.5$ μm are used.

The Green's function is the same as the one obtained in Sec. III A. Since the elastic properties and mass density vary continuously, Eq. (45) is used to calculate the acoustic field. Then the dispersion relation for the Rayleigh-type mode is calculated using Eq. (49). We ignore the small discontinuity in the elastic properties and in the mass density at the interface between the homogeneous substrate and the inhomogeneous layer, at $z=4$ μm.

Figure 3 shows the dispersion relation calculated with various numbers of partitions for a 4-μm inhomogeneous layer ($m=100,200,400$). The $m=100$ calculation deviates from the $m=200$ calculation above 5 GHz. At 10 GHz, the $m=200$ calculation almost agrees with the $m=400$ calculation, which indicates that the calculation has almost converged at $m=200$ up to 10 GHz. The deviation from the $m=400$ calculation at 10 GHz is about 0.03% for $m=200$ and 0.16% for $m=100$. Roughly speaking, the width of the partition should be less than 5% of the relevant acoustic wavelength in order to have an accuracy better than 0.1%. The effect of a continuous variation in elastic properties and mass density is seen in the frequency range from 1 to 4 GHz as an increasing velocity compared to the value for the piecewise homogeneous medium.

The proposed method requires the solution of a linear equation with $6m$ unknowns, which takes most of the computation time. Though it might not be the most efficient method, it gives a good unified physical and mathematical insight for the wave propagation in an inhomogeneous and anisotropic medium as a scattering problem. It should be noted that no matter how complex the inhomogeneous part is, the same Green's function can be used as long as the elastic properties in the homogeneous substrate part remain the same.

IV. SUMMARY

The acoustic wave propagation in a medium with one-dimensional inhomogeneity was considered using a Green's function method. The proposed method was demonstrated by analyzing the dispersion relation for an isotropic piecewise homogeneous medium and for an isotropic medium with continuously varying elastic properties and mass density. Though we have only given relatively simple examples, the method is capable of handling arbitrary anisotropy. Because of the essential similarity of the problem, the method is also applicable in the field of picosecond acoustics and physical acoustics to find the reflection and transmission of bulk acoustic waves in a similar inhomogeneous medium. Like other generalized methods, the method is also applicable to other types of waves, such as electromagnetic waves and electron waves in media with one-dimensional inhomogeneity.

ACKNOWLEDGMENTS

This work has been partially supported by Japan-Belgium Research Cooperative Program ran by JSPS (Japan

Society for the Promotion of Science) and FWO-V (Fonds Wetenschappelijk Onderzoek-Vlaanderen), GOA Project No. 2002/04KU Leuven, and FWO research Project No. G.0125.03.

[1]A. Neubrand and P. Hess, "Laser generation and detection of surface acoustic waves: Elastic properties of surface layers," J. Appl. Phys. **71**, 227–238 (1992).
[2]C. Glorieux, W. Gao, S. E. Kruger, K. V. de Rostyne, W. Lauriks, and J. Thoen, "Surface acoustic wave depth profiling of elastically inhomogeneous materials," J. Appl. Phys. **88**, 4394–4400 (2000).
[3]D. C. Hurley, V. K. Tewary, and A. J. Richards, "Thin-film elastic-property measurements with laser-ultrasonic SAW spectrometry," Thin Solid Films **398-399**, 326–330 (2001).
[4]J. B. Berryman and R. R. Greene, "Discrete inverse methods for elastic waves in layered media," Geophysics **45**, 213–233 (1980).
[5]A. L. Shuvalov, O. Poncelet, and M. Deschamps, "General formalism for plane guided waves in transversely inhomogeneous anisotropic plates," Wave Motion **40**, 413–426 (2004).
[6]V. I. Alshits and G. A. Maugin, "Dynamics of multilayers: elastic waves in an anisotropic graded or stratified plate," Wave Motion **41**, 357–394 (2005).
[7]C. Baron, A. L. Shuvalov, and O. Poncelet, "Impact of localized inhomogeneity on the surface-wave velocity and bulk-wave reflection in solids," Ultrasonics **46**, 1–12 (2007).
[8]A. Wirgin, "Some quasi-analytic and numerical methods for acoustical imaging of complex media," in *Wavefield Inversion*, edited by A. Wirgin, no. 398 in CISM courses and lectures (Springer, New York, 1999), pp. 241–304.
[9]J.-P. Groby, L. D. Ryck, P. Leclaire, A. Wirgin, W. Lauriks, R. P. Gilbert, and Y. S. Xu, "Use of specific Green's functions for solving direct problems involving a heterogeneous rigid frame porous medium slab solicited by acoustic waves," Math. Methods Appl. Sci. **30**, 91–122 (2007).
[10]Green's functions have been widely used to analyze acoustic wave propagation in a different way. In Refs. 14–16, the dynamic response function (elastodynamic Green's function) for the acoustic wave equation with point excitation is used to describe SAW propagation in a homogeneous anisotropic semi-infinite medium. In Ref. 17, the poles of the elastodynamic Green's function for layered anisotropic medium are used to analyze the dispersion relation.
[11]It is also possible to construct the theory based on Eq. (2) instead of Eq. (3). In this case, Eq. (5) would be expressed using 3×3 matrices (the standard Christoffel equation). There, however, we have avoided this approach since it may bring an extra complication as follows. At an interface between two different materials, $\partial c_{ijkl}/\partial x_j$ may contain a singularity like a δ function and $\partial u_k/\partial x_l$ may have a discontinuity. These two elements appear on the right-hand side of Eq. (2) as products. In the following step of the theory, we would integrate the product with respect to x, but it is cumbersome to estimate the product of the delta function singularity and the discontinuity occurring at the same location. The approach based on Eq. (3) does not involve this sort of difficulty for the sake of the continuity of $\boldsymbol{U\sigma}$ shown in Sec. II B.
[12]B. A. Auld, *Acoustic Fields and Waves in Solids*, 2nd ed. (Krieger, Malabar, FL, 1990).
[13]T. C. T. Ting, *Anisotropic Elasticity* (Oxford U. P., New York, 1996).
[14]C. Y. Wang and J. D. Achenbach, "A new method to obtain 3-D Green's functions for anisotropic solids," Wave Motion **18**, 273–289 (1993).
[15]A. G. Every and K. Y. Kim, "Time domain dynamic response functions of elastically anisotropic solids," J. Acoust. Soc. Am. **95**, 2505–2516 (1994).
[16]A. G. Every, K. Y. Kim, and A. A. Maznev, "The elastodynamic response of a semi-infinite anisotropic solid to sudden surface loading," J. Acoust. Soc. Am. **102**, 1346–1355 (1997).
[17]V. K. Tewary, "Theory of elastic wave propagation in anisotropic film on anisotropic substrate: TiN film on single-crystal Si," J. Acoust. Soc. Am. **112**, 925–935 (2002).

Simulation of ultrasonic-driven gas separations

David R. Rector, Margaret S. Greenwood, Salahuddin Ahmed, Steven R. Doctor, Gerry J. Posakony, and V. Susan Stenkamp
Pacific Northwest National Laboratory, P.O. Box 999, Richland, Washington 99354

(Received 22 August 2006; revised 16 January 2007; accepted 24 January 2007)

The separation of components in a gas mixture is important for a wide range of applications. One method for achieving this separation is by passing a traveling acoustic wave through the gas mixture, which creates a flux of the lighter components away from the transducer. A series of simulations was performed to assess the effectiveness of this method for separating a binary mixture of argon and helium using the lattice kinetics method. The energy transport equation was modified to account for adiabatic expansion and compression. The species transport equation was modified to include a barodiffusion term. Simulations were performed on two different scales; detailed acoustic wave simulations to determine the net component flux as a function of local concentration, pressure, etc. and device scale simulations to predict the gas composition as a function of time inside a gas separation cylinder. The method is first validated using data from literature and then applied to mixtures of argon and helium. Results are presented and discussed. © *2007 Acoustical Society of America.* [DOI: 10.1121/1.2709406]

PACS number(s): 43.35.Ty [RR] Pages: 3446–3452

I. INTRODUCTION

The separation of components in gas mixtures is important for a wide range of applications, such as the large scale separation of gas or isotopic components for industrial use or the separation and concentration of gases for better detection in homeland security or environmental applications. Current separation methods include gas centrifuges, selective adsorption, and cryogenic liquifaction or distillation. Acoustic separations can afford separation of gas mixtures and offers the advantage of solid state components without the requirement of heat to effect the separation.

Two known mechanisms exist that allow molecular level separations in ultrasonic fields: barodiffusion and a combination of thermal diffusion and acoustic motion. The latter has been investigated recently both experimentally and theoretically by Swift, Spoor, and Geller,[1–3] and been shown to be an effective means of separating even isotopes by coupling the diffusion due to thermal gradients created by acoustic waves at boundaries and transport by the acoustic waves. In contrast, barodiffusion, although in existence for several decades, has not been evaluated since the advent of more efficient and powerful transducers, such as those developed for machining, welding, surgery, and various other medical applications. Furthermore, no comprehensive model has been developed to characterize the complex behavior within the system. Thus the purpose of this paper is to elucidate the possible efficacy of separation through development and evaluation of a model.

II. BACKGROUND

In barodiffusion separation, a traveling acoustic wave is passed through the gas mixture, creating a flux of the lighter components away from the transducer. This separation was first systematically investigated by Passau[4] in 1948, who was able to effect a separation between 51% and 56.5% of hydrogen and carbon dioxide after 3 h in a 3.5 cm diameter $\times 7$ cm long tube using a quartz ultrasonic Langevin transducer consuming 2 kW of power. Passau[4] noted the following: "In a traveling wave a separation should be produced: in this case, in fact, in any location under the influence of the pressure gradient that is increasing to its maximum value, the gas molecules are pulled in the direction of propagation of the wave, but the lighter molecules are pulled farther and, as it were, are pushed ahead of the wavefront, leaving behind them a mixture enriched with the heavier gas. At the next half period, the pressure gradient is reversed, and there is a suction of molecules toward the rear, which however does not compensate the result of the first diffusion, for the initial composition in this location is no longer the same." Thus, with repeated cycles of the traveling wave, there will be a progressive enrichment of the light gas at the wave front.

For the next two decades, there was relatively little activity in barodiffusion separations. In 1956, Eyraud performed experiments on the separation of a mixture of hydrogen and nitrogen and noted a partial separation of the components, but no quantitative estimate of the effect was given.[5] In 1964, Noble *et al.* were measuring the velocity of sound in a binary gas mixture by measuring the change of phase of the ultrasound. A deviation from the expected theoretical value was attributed to a partial separation of the gas mixture and Passau was cited.[6] In 1967, Streel was studying the influence of ultrasound on the nitriding and denitriding of steel. Differences were observed in the effects of ultrasound on hydrogen and ammonia and the article cited Passau research as a possible explanation.[7]

In 1967, Tikhomirov *et al.*[8] used a equimolar mixture of nitrogen and hydrogen in a chamber 30 mm in diameter and 200 mm in length. The transducer frequency was 670 kHz. After 3 h a steady-state distribution of concentration was established. There was a difference of 20% between the hydrogen concentrations at the two ends of the chamber.

 0001-4966/2007/121(6)/3446/7/$23.00 © 2007 Acoustical Society of America

In the 1980s, Dykhne *et al.*[9,10] investigated the possibility of separating gas mixtures by using a pressure gradient along an acoustic resonator. The first set of experiments was carried out using a section of cylindrical pipe having a length of 42 or 86 cm.[9] A transducer at one end of the pipe produced a standing wave. The resonant frequency ranged from 500 to 550 Hz for the 86 cm resonator. Gas mixtures consisted of helium mixed with argon, carbon dioxide, or xenon. A mass spectrometer was used to observe the separation at various sections of the pipe. The results showed that the heavy component of the mixture is reduced in the region of minimum pressure. The relative change of the heavy component of the mixture was about 10%. The experiments with an acoustic resonator continued with a similar experimental setup for mixtures of CO, CO_2, CF_2HCl, SF_6, and CF_3I.[10] They measured the degree of separation as a function of pressure. The experimental values were approximately ten times larger than the theoretical calculations. The researchers considered the role of thermodiffusive separation due to the radial temperature gradient between the wall and the center of the pipe. The experimental values were compared with the theoretical values, but the experimental values were still larger by a factor of approximately 5.

Bozhdankevich *et al.*[11] carried out experiments to study the effect of thermodiffusion using the same experimental apparatus as described above. An electrically heated wire was installed along the 86-cm resonator axis along the whole length to create a temperature difference between the wire and resonator wall of about 10 °C. The resonator radial temperature difference was measured. The heavy component concentration changes were constantly monitored through KBr windows with an infrared spectrophotometer using IR absorption spectra. The results showed that barodiffusion and thermodiffusion have opposite effects for this experimental setup.

Recently Spoor and Swift have investigated the thermoacoustic separation of a helium-argon mixture.[1–3] At the tube wall, the velocity of the gas is nearly zero and the maximum velocity occurs at the center of the tube. Compression and rarefaction causes the gas to heat up or cool down and this produces a temperature gradient relative to the isothermal wall. Light and heavier gas molecules diffuse differently in the temperature gradient. Motion in the center of the tube causes separation.

Very little work has been done to extend the original work of Passau. There are many questions to be answered about barodiffusion and the effect of attenuation and temperature gradients. In the decades since Passau's work, great strides have been made in high power ultrasonics. The review article by Gallego-Juarez[12] describes various types of ultrasonic transducers, including the stepped-plate transducer developed for generating ultrasonic energy in gases.[13] In addition, commercially available high power transducers have been developed for machining, welding, surgery, and various other medical applications. Therefore, the objective of this paper is to develop a theoretical basis for planning experiments using barodiffusion.

III. SIMULATION METHODOLOGY

A major difficulty of simulating acoustic systems is the large separation in time and length scales. In this case, the driving forces for gas species separation occurs within each individual acoustic wave. However, the net effect in a gas separation cylinder occurs over a span of hours and several centimeters. The approach we use is to perform simulations at both scales. Detailed acoustic wave simulations are performed to determine the net gas component flux as a function of local conditions, such as concentration, acoustic amplitude, frequency, etc. These results are then used to develop an expression for species flux, which is incorporated into a device scale simulation model to predict gas species concentration profiles as a function of time. The gas separation process at both scales is simulated using the lattice kinetics method, which is a derivative of the lattice Boltzmann method.

A. Lattice Boltzmann and kinetics methods

The lattice Boltzmann and lattice kinetics simulation methods solve the Boltzmann equation to predict the hydrodynamic and acoustic behavior of compressible fluids. The detailed density, pressure, velocity, temperature, and species concentration distributions are calculated as a function of time. These methods have been used to model both linear and nonlinear wave propagation,[14,15] Rayleigh and Eckart acoustic streaming,[16,17] and the acoustic force on suspended particles.[18,19]

The single particle distribution function $f(\mathbf{x},\mathbf{v},t)$ is the probability of finding particles at position $\mathbf{x}$ with velocity $\mathbf{u}$ at time t. The Boltzmann equation describes the evolution of the distribution function

$$\frac{\partial f}{\partial t} + u \cdot \nabla f = -\frac{f - f^{\mathrm{eq}}}{\tau}, \tag{1}$$

where τ is the relaxation time and f^{eq} is the equilibrium Maxwell distribution. To solve this equation on a computer, the spatial domain is discretized into a finite number of lattice sites, where each lattice site has values for density, pressure, flow, etc. The single-particle distribution function, which describes the probability of a particle traveling along a particular direction and speed, is discretized to form a finite set of displacement vectors connecting each lattice site to adjacent sites.

The lattice Boltzmann equation[20] describes the evolution of the discretized particle distribution function, $f_i(\mathbf{x},t)$, along direction i as a function of time. The new time distribution function is given by the equation

$$f_i(x + \Delta t e_i, t + \Delta t) - f_i(x,t) = -\frac{1}{\tau}[f_i(x,t) - f_i^{\mathrm{eq}}(x,t)], \tag{2}$$

where τ is a linear relaxation parameter and f^{eq} is the local equilibrium distribution. The direction vectors for two dimensions are $e_0=0$, $e_{1\text{-}4}=\{\cos[(i-1)\pi/2], \sin[(i-1)\pi/2]\}c$ and $e_{5\text{-}8}=\sqrt{2}\{\cos[(i-5)\pi/2+\pi/4], \sin[(i-5)\pi/2+\pi/4]\}c$.

The local equilibrium is expressed in the form of a quadratic expansion of the Maxwellian distribution

$$f_i^{\mathrm{eq}} = w_i \rho \left[1 + \frac{3e_i \cdot u}{c^2} + \frac{9(e_i \cdot u)^2}{2c^4} - \frac{3u^2}{2c^2} \right], \tag{3}$$

where c is the reference lattice speed, $c=\Delta x/\Delta t$, and the weight coefficients, w_i, for a two-dimensional system are $w_0=\frac{4}{9}$, $w_{1\text{-}4}=\frac{1}{9}$, and $w_{5\text{-}8}=\frac{1}{36}$.

The lattice Boltzmann equation may be rewritten to take the form

$$f_i(x+\Delta t e_i, t+\Delta t) = f_i^{\mathrm{eq}}(x,t) + \left(1 - \frac{1}{\tau}\right)[f_i(x,t) - f_i^{\mathrm{eq}}(x,t)]. \tag{4}$$

The first term on the right-hand side represents the distribution function for the special case of $\tau=1$, which corresponds to the kinetic viscosity

$$\nu = \frac{1}{6}\left(\tau - \frac{1}{2}\right)\frac{\Delta x^2}{\Delta t}. \tag{5}$$

The second term is the additional shear term resulting from a kinematic viscosity that is different from the reference case. The lattice kinetics method[21] replaces this second term with an explicit calculation of the local stress based on velocity gradients

$$f_i(x+\Delta t e_i, t+\Delta t) = f_i^{\mathrm{eq}}(x,t), \tag{6}$$

where

$$f_i^{\mathrm{eq}} = w_i \rho \left[1 + \frac{3e_i \cdot u}{c^2} + \frac{9(e_i \cdot u)^2}{2c^4} - \frac{3u^2}{2c^2} + A\Delta t \left(\frac{\partial u_\alpha}{\partial x_\beta} + \frac{\partial u_\beta}{\partial x_\alpha} \right) e_{i\alpha} e_{i\beta} \right] \tag{7}$$

and the coefficient A is related to the kinematic viscosity by the expression

$$A = 0.75 - 4.5\nu \frac{\Delta t}{\Delta x^2}. \tag{8}$$

The new time density and velocity values are determined using the expressions

$$\rho(x+\Delta t e_i, t+\Delta t) = \sum_i f_i^{eq}(x,t), \tag{9}$$

$$\rho u(x+\Delta t e_i, t+\Delta t) = \sum_i f_i^{eq}(x,t) e_i. \tag{10}$$

This procedure is repeated for the specified number of time steps until a steady-state solution is obtained. The result is a second-order solution to the Navier-Stokes and continuity equations.

A scalar transport equation is used to model both gas species concentrations and energy. The convective transport is described using an advection transport distribution function, $f_{\mathrm{adv},i}$, which is calculated using the equilibrium distribution functions from the lattice kinetics solution. The transport equation for any scalar, ϕ, has the form

$$\phi(r,t+\Delta t) = \phi(r,t) - \frac{1}{\rho}\sum_i f_{\mathrm{adv},i}\phi^* - \Delta t \sum_i D_i[\psi(r,t) - \psi(r+\Delta t e_i, t)] + R\Delta t, \tag{11}$$

where D is the diffusivity coefficient, ψ is the diffusion potential, and R is the volumetric generation rate. The star indicates the upwind scalar value, depending on the sign for $f_{\mathrm{adv},i}$. The typical diffusion potential for gas species is concentration and the potential for energy is temperature.

B. Acoustic wave simulation model

The detailed acoustic wave model is used to determine the net gas species flux as a function of local conditions, such as frequency, amplitude, gas composition, etc. Simulations were performed for both N_2-H_2 and Ar-He gas mixtures. The model consists of a 1600×3 strip with specified value boundary on one end and an absorbing boundary on the other. The system is initialized with uniform values for density, pressure, temperature, and concentration. The specified value boundary begins to oscillate at the specified frequency and amplitude, and the transient continues until the traveling wave becomes fully developed.

The internal energy (U) transport equation, as it is currently formulated, results in a constant temperature solution for the traveling wave. However, we know that the gas undergoes an adiabatic expansion and compression. A term is added to the internal energy equation to reflect the work done as the gas moves from low to high pressure regions:

$$\Delta U(r,t+\Delta t) = (\gamma - 1)\frac{1}{\rho}\sum_i f_{\mathrm{adv},i} u^*. \tag{12}$$

The parameter $\gamma=c_p/c_v$ is related to the capacity of the system to do work upon expansion. Adding this term, the energy equation becomes

$$U(r,t+\Delta t) = U(r,t) - \gamma\frac{1}{\rho}\sum_i f_{\mathrm{adv},i} u^* - \Delta t \sum_i \alpha_i [T(r,t) - T(r+\Delta t e_i, t)], \tag{13}$$

where α is the thermal diffusivity and T is temperature.

The diffusion of chemical species is usually associated with concentration gradients. However, barodiffusion is defined as species diffusion driven by pressure gradients. The mass flux is given by the expression from Bird *et al.*[22]

$$j_i^P = \frac{n^2}{\rho RT}\sum_{j=1}^{n} M_i M_j D_{ij}\left[x_j M_j\left(\frac{\bar{V}_j}{M_j} - \frac{1}{\rho}\right)\right]\nabla p, \tag{14}$$

where V_j is the specific volume of component j, x is the mole fraction, and n is the total mole concentration. The expression may be rewritten for a binary mixture as

$$j_A^P = \left(\frac{n^2}{\rho^2 RT}\right) M_A M_B D_{AB} x_A (1 - x_A)(M_A - M_B)\nabla p \tag{15}$$

and added to the species transport equation.

The acoustic wave model was tested by simulating a high frequency traveling wave through pure argon gas. The

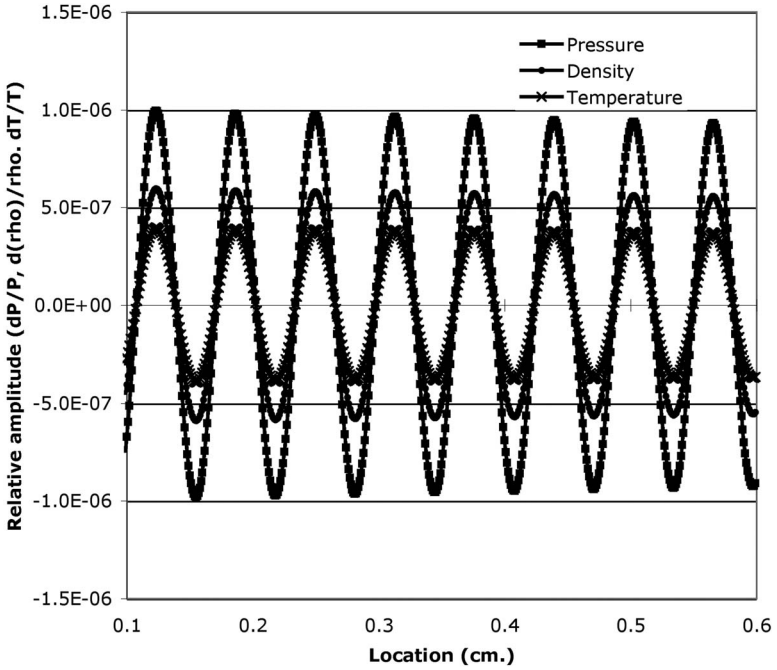

FIG. 1. Relative amplitude profiles of density, pressure, and temperature for pure argon.

frequency is 500 kHz and the amplitude of the density is 0.6×10^{-6} of the average value. A value of 1.666 was used for gamma. A snapshot of the relative amplitude profiles for density, pressure, and temperature are shown in Fig. 1. The thermodynamic relationships for adiabatic expansion and compression are

$$\frac{\rho_2}{\rho_1}=\left(\frac{P_2}{P_1}\right)^{1/\gamma},\quad \frac{T_2}{T_1}=\left(\frac{P_2}{P_1}\right)^{(\gamma-1)/\gamma}. \tag{16}$$

The ratio of peak density to pressure values is approximately 0.6 and the ratio of peak relative temperature to relative pressure values is approximately 0.4, which correspond to the theoretical values for small amplitudes.

The acoustic wavelength in Fig. 1 is approximately 0.0632 cm, resulting in a speed of sound (c) of 316 m/s. This value corresponds well to the experimental value of 319 m/s and the theoretical value of 319 m/s, obtained using the expression

$$c=\sqrt{\frac{\gamma p}{\rho}}=\sqrt{\frac{\gamma RT}{M}}. \tag{17}$$

The effect of barodiffusion on the gas composition is shown is Fig. 2. The pressure gradients during each cycle drive the lighter component, in this case helium, toward the lower pressure region. The result is a nonuniform concentration profile that is out of phase with the density, pressure, and

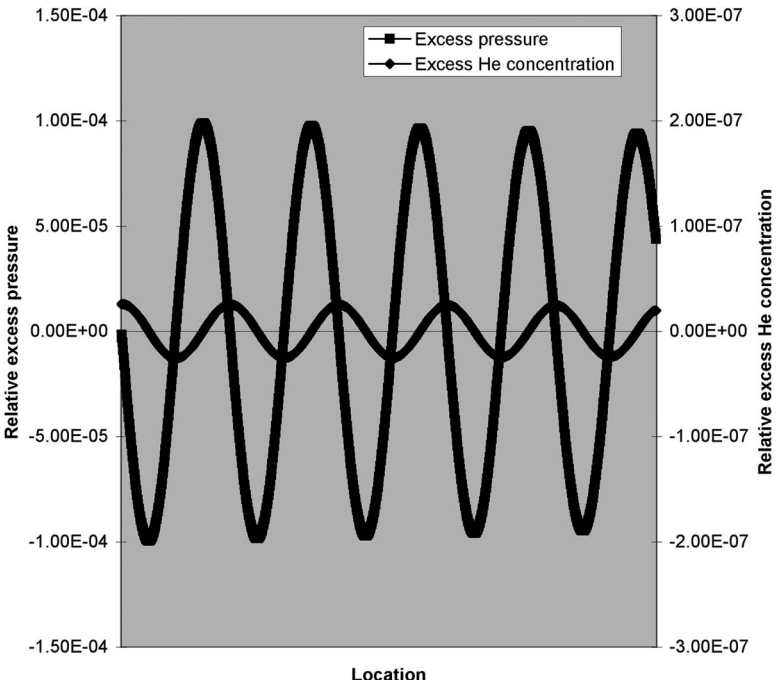

FIG. 2. Relative excess pressure and excess helium concentration as a function of location.

velocity profiles. The net helium mole flux is calculated by integrating the flux contributions over a cycle period, T,

$$\dot{n}_{\mathrm{He}} = \frac{1}{T}\int_0^T \{V(t)n_{He}(t) - D_p(t)\,\nabla\, p(t) - D_{12}\,\nabla\, x_{He}(t)\}\,dt, \tag{18}$$

where D_p is the barodiffusion coefficient and D_{12} is the binary diffusion coefficient based on mole fraction.

C. Gas separations device model

The acoustic wave simulation model can be used to characterize the relative motion of gas species for a limited number of acoustic wavelengths, but it is not practical to apply this level of detail in modeling a separation device. The approach we are using is to develop an expression describing the net transport of a gas species as a function of several variables including local composition, frequency, pressure amplitude, etc. This expression is then implemented in a device scale model.

The separation chamber is represented by a two-dimensional simulation model with zero flux boundaries on both ends. The gas species flux is applied using a positive and a negative source term for each pair of adjacent lattice sites. The model is initialized to a constant gas concentration and a transient is performed until the system reaches a steady-state solution.

IV. RESULTS AND DISCUSSION

The simulation methodology described in Sec. III was applied to two systems. The approach was validated by comparing simulation results for the Tikhomirov[8] system with the concentration data. The method was then applied to a theoretical gas separation device for argon-helium mixtures. The results were used to design a separations device that has been constructed and is currently being tested.

A. Tikhomirov system

The two scale simulation approach was tested using the data from Tikhomirov *et al.*,[8] who introduced an equimolar mixture of nitrogen and hydrogen into a cylindrical chamber 30 mm in diameter and 200 mm in length. Both gas components were assumed to have a gamma value of 1.4. The transducer operated at a frequency of 670 kHz and the gas was at atmospheric pressure.

A series of simulations as performed at different operating conditions. The results were then used to create expression for average hydrogen flux in the Tikhomirov system

$$\dot{n}_{H_2} = CAe^{-\alpha x}\omega^2 x_{\mathrm{H}_2}(1 - x_{H_2})\frac{(M_{N_2} - M_{H_2})}{\bar{M}}, \tag{19}$$

where ω is the frequency, x_{H_2} is the local hydrogen mole fraction, α is the amplitude attenuation factor, and M is the local average molecular weight. The amplitude at the transducer face, A, is related to the applied power and a conversion factor. The constant C is a function of the binary gas system being evaluated.

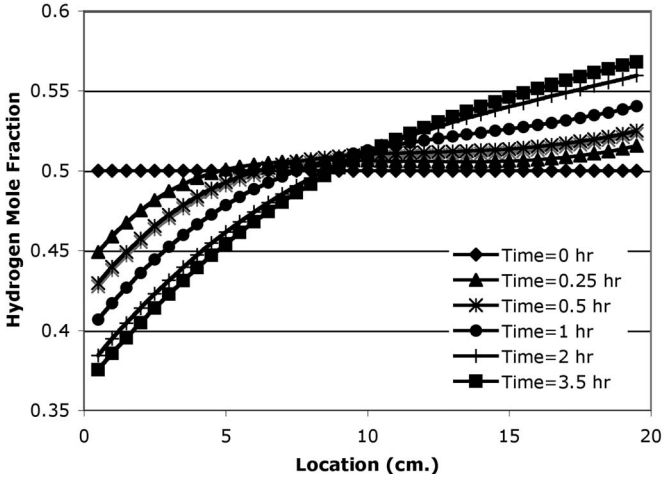

FIG. 3. Hydrogen concentration profiles as a function of time (simulation of Tikhomirov experiment).

This flux expression is implemented into the device scale simulation model and a transient simulation was performed to steady-state conditions. The results are shown in Figs. 3 and 4. Figure 3 shows the hydrogen concentration profiles as a function of time. At time equal zero, the hydrogen flux is constant throughout the device, so the only changes occur at the two ends. Note that the change is larger at the transducer end ($x=0$) due to attenuation of the traveling wave. A steady-state profile is reached when the induced flux due to barodiffusion is balanced by the molecular diffusion in the opposite direction. The time to steady-state concentration profile is predicted to be approximately 3.5 h.

The change in hydrogen concentration at the end opposite the transducer is shown as a function of time in Fig. 4. The simulation results are compared to data taken from Tikhomirov *et al.*[8] The simulation results compare well to the data, in most cases within the 7% measurement error, indicating that the methodology we have developed is capable of predicting the performance of gas separation devices based on barodiffusion.

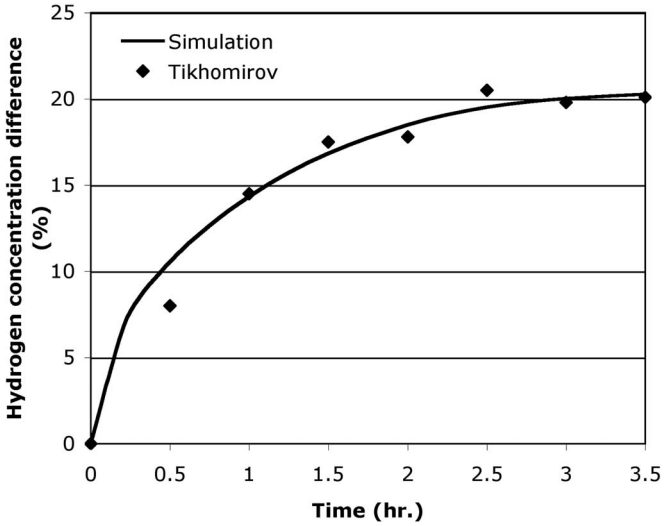

FIG. 4. Change in the hydrogen concentration as a function of time at the end opposite the transducer (data from Tikhomirov *et al.*[8]).

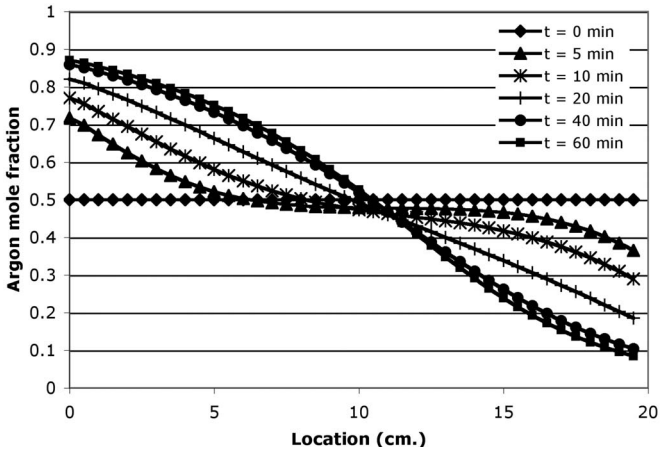

FIG. 5. Argon concentration profile as a function of time for a 50/50 argon-helium mixture.

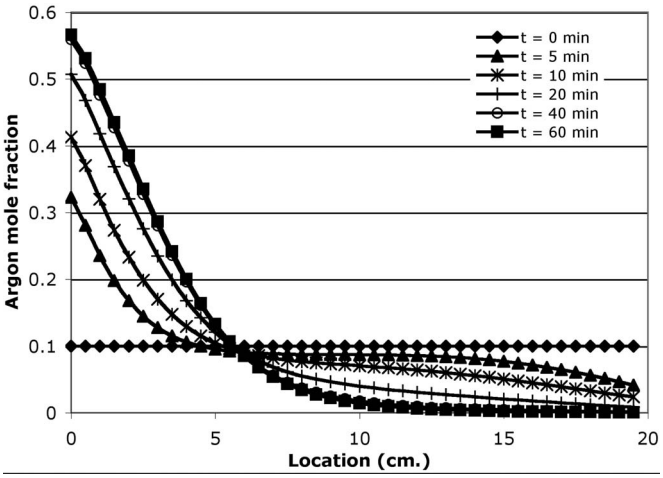

FIG. 7. Argon concentration profile as a function of time for a 10/90 argon-helium mixture.

B. Argon-helium separation simulations

The simulation methodology described above was applied to a separation device based on a transducer operating at 500 kHz with 5 kW input power and a cylinder length of 20 cm. The device was assumed to contain either 50/50 or 10/90 argon and helium gas mixtures. A series of acoustic wave simulations was performed to obtain an expression for net helium flux as a function of local composition, amplitude, etc., similar to that developed for the Tikhomirov system [Eq. (20)]. The flux expression was incorporated into the device scale model and transient simulations were performed for both gas mixtures.

The simulation results for the 50-50 argon/helium mixture are presented in Figs. 5 and 6. The argon concentration profile as a function of time is shown in Fig. 5. The profile reached steady state in less than an hour as compared to 3.5 h in the validation case. In addition, a higher separation ratio, or ratio of the mole fractions at the two ends, was achieved (greater than 10) than the validation case (2.16). The argon concentrations at the two ends of the separation cylinder are presented in Fig. 6. Over half of the separation takes place in the first 10 min of the transient. The improvement in separation performance is primarily due to the increased power of the transducer. The change in binary gas pair has only a modest impact on the performance.

The simulation results for the 10-90 argon/helium mixture are presented in Figs. 7 and 8. The argon concentration profile as a function of time is shown in Fig. 7. Note the high degree of nonlinearity in the shape of the concentration profile. This is due in part to the $x(1-x)$ terms in the flux expression. The argon concentrations at the two ends of the separation cylinder are presented in Fig. 8. The separation ratio increased to greater than 1000 in this case.

These results demonstrate the potential of using traveling acoustic waves to separate gas components. We are currently testing a device similar to the one described and we intend to investigate the advantages and limitations of this method.

V. CONCLUSIONS

A simulation methodology has been developed that accurately predicts the performance of gas component separation devices based on traveling wave barodiffusion. The method involves two types of lattice kinetics simulations,

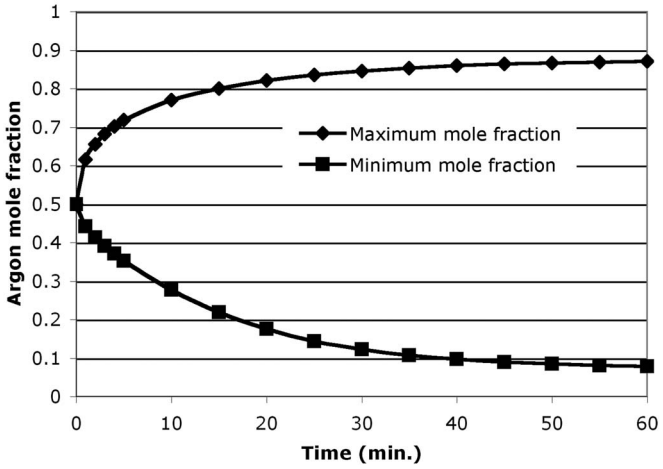

FIG. 6. Maximum and minimum argon concentrations as a function of time for a 50/50 argon-helium mixture.

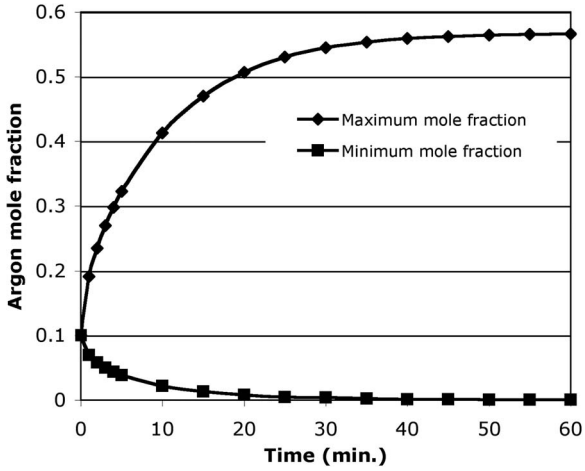

FIG. 8. Maximum and minimum helium concentrations as a function of time for a 10/90 argon-helium mixture.

detailed acoustic wave simulations to develop a net flux expression based on local conditions, and a device scale model to predict the transient evolution of the gas composition profile. The model was validated using data from literature and then applied to mixtures of argon and helium.

ACKNOWLEDGMENTS

This research was supported by the Laboratory Directed Research and Development Program at the Pacific Northwest National Laboratory, a multiprogram national laboratory operated by Battelle for the U.S. Department of Energy under Contract No. DE-AC05-76RL01830.

[1]P. S. Spoor and G. W. Swift, "Thermoacoustic separation of a He-Ar mixture," Phys. Rev. Lett. **85**, 1646–1649 (2000).
[2]G. W. Swift and P. S. Spoor, "Thermal diffusion and mixture separation in the acoustic boundary layer," J. Acoust. Soc. Am. **106**, 1794–1800 (1999).
[3]D. A. Geller and G. W. Swift, "Saturation of thermoacoustic mixture separation," J. Acoust. Soc. Am. **111**, 1675–1684 (2002).
[4]P. Passau, "Separation of the constituents of a gas mixture of different masses by means of a sound wave," Ann. Soc. Sci. Bruxelles, Ser. 1 **62**, 40 (1948).
[5]M. Charles Eyraud, "Effet separatif des ultrasons sur en mélange de constituants grazeux," ("Ultrasonic separation of components in a mixture of gases"), Compt. Rend. **242**, 474–475 (1956).
[6]F. W. Noble, K. Abel, and P. W. Cook, "Performance and characteristics of an ultrasonic gas chromatograph effluent detector," Anal. Chem. **36**, 1421 (1964).
[7]D. Streel, M. Warzee, J. Heanaut-Diltour, E. Votava, F. Montbrun, and L. Delcour, "Influence of Ultrasound on Nitriding and Denitriding of Steel," J. Iron Steel Inst., London **205**, 551–552 (1967).
[8]I. A. Tikhomirov, Yu. G. Yur'ev, and V. V. Marusin, "Separation of binary gaseous mixtures in an ultrasonic field," Russ. J. Phys. Chem. **41**, 976 (1967).
[9]A. M. Dykhne, A. F. Pal', V. D. Pis'mennyi, V. V. Pichugin, and A. N. Starostin, "Separation of gas mixtures in the field of a sound wave," Sov. Phys. Dokl. **27**, 65–67 (1982).
[10]A. M. Dykhne, A. F. Pal', V. D. Pis'mennyi, V. V. Pichugin, and A. N. Starostin, "Dynamics of gas-mixture separation in the field of a sound wave," Sov. Phys. JETP **61**, 1171–1175 (1985).
[11]V. B. Bozhdankevich *et al.*, "Thermodiffusion separation of a gas mixture in a sound wave field," Dokl. Akad. Nauk SSSR **288**(3), 605–608 (1986).
[12]J. A. Gallego-Juarez, "Piezoelectric ceramics and ultrasonic transducers," J. Phys. E **22**, 804–816 (1989).
[13]J. A. Gallego-Juarez, G. Rodriguez-Corral, and L. Gaete-Garreton, "An ultrasonic transducer for high power applications in gases," Ultrasonics **16**, 267–271 (1978).
[14]J. M. Buick, C. A. Greated, and D. L. Campbell, "Lattice BGK simulation of sound waves," Europhys. Lett. **43**, 235–240 (1998).
[15]J. M. Buick, C. L. Buckley, C. A. Greated, and J. Gilbert, "Lattice Boltzmann BGK simulation of nonlinear sound waves: The development of a shock front," J. Phys. A **33**, 3917–3928 (2000).
[16]D. Haydock and J. M. Yeomans, "Lattice Boltzmann simulations of acoustic streaming," J. Phys. A **34**, 5201–5213 (2001).
[17]D. Haydock and J. M. Yeomans, "Lattice Boltzmann simulations of attenuation-driven acoustic streaming," J. Phys. A **36**, 5683–5694 (2003).
[18]J. A. Cosgrove, J. V. Buick, D. V. Campbell, and C. A. Greated, "Numerical simulation of particle motion in an ultrasound field using the lattice Boltzmann model," Ultrasonics **43**, 21–25 (2004).
[19]D. Haydock, "Lattice Boltzmann simulations of the time-averaged forces on a cylinder in a sound field," J. Phys. A **38**, 3265–3277 (2005).
[20]M. C. Sukop and D. T. Thorne, *Lattice Boltzmann Modeling: An Introduction for Geoscientists and Engineers* (Springer, New York, 2006).
[21]T. Inamuro, "A lattice kinetic scheme for incompressible viscous flows with heat transfer," Philos. Trans. R. Soc. London, Ser. A **360**, 477–484 (2002).
[22]R. B. Bird, W. E. Stewart, and E. N. Lightfoot, *Transport Phenomena* (Wiley, New York, 1960).

k-space propagation models for acoustically heterogeneous media: Application to biomedical photoacoustics

B. T. Cox[a] and S. Kara
Department of Medical Physics and Bioengineering, University College London, Gower Street, London WC1E 6BT, United Kingdom

S. R. Arridge
Department of Computer Science, University College London, Gower Street, London WC1E 6BT, United Kingdom

P. C. Beard
Department of Medical Physics and Bioengineering, University College London, Gower Street, London WC1E 6BT, United Kingdom

(Received 29 September 2006; revised 22 February 2007; accepted 22 February 2007)

Biomedical applications of photoacoustics, in particular photoacoustic tomography, require efficient models of photoacoustic propagation that can incorporate realistic properties of soft tissue, such as acoustic inhomogeneities both for purposes of simulation and for use in model-based image reconstruction methods. *k*-space methods are well suited to modeling high-frequency acoustics applications as they require fewer mesh points per wavelength than conventional finite element and finite difference models, and larger time steps can be taken without a loss of stability or accuracy. They are also straighforward to encode numerically, making them appealing as a general tool. The rationale behind *k*-space methods and the *k*-space approach to the numerical modeling of photoacoustic waves in fluids are covered in this paper. Three existing *k*-space models are applied to photoacoustics and demonstrated with examples: an exact model for homogeneous media, a second-order model that can take into account heterogeneous media, and a first-order model that can incorporate absorbing boundary conditions.
© *2007 Acoustical Society of America.* [DOI: 10.1121/1.2717409]

PACS number(s): 43.35.Ud, 43.20.Px [TDM] Pages: 3453–3464

I. INTRODUCTION

The photoacoustic (PA) effect, in which the absorption of light leads to the generation of an acoustic wave via the thermoelastic expansion of the absorbing region, has found application in many fields,[1] some of the most important being spectroscopy,[2,3] microscopy,[4–6] and biomedicine.[7] Biomedical photoacoustic tomography (PAT), in particular, has received increasing attention in recent years.[8,9] Both clinical and life sciences applications have been proposed, including imaging of the breast,[10] vasculature,[11] and small animals.[12,13] As soft tissue is usually highly optically scattering, imaging to high resolution using purely optical means is difficult. However, for acoustic waves, even up to tens of megahertz, the scattering is considerably lower. PAT can therefore combine the good resolution of ultrasound (<100 μm) with the high contrast and spectroscopic advantages offered by images related to optical absorption.

Most PAT reconstruction algorithms assume that both the sound speed and density in the sample are uniform.[7,14–22] which is not true of soft tissue in general, particularly at high frequencies. The extent to which the naturally occurring acoustic heterogeneities distort the PAT images remains largely an open question. One way to answer such questions without undertaking extensive experimental studies is to simulate the experimental measurements using a numerical forward model, so that the effect of heterogeneities on image resolution and artifact generation can be studied systematically. A further application of a photoacoustic forward model is in model-based image reconstruction algorithms for PAT.[23,24] Model-based image reconstructions make no assumptions of acoustic homogeneity, and form an image by iteratively updating a forward model. For iterative reconstruction algorithms such as this to be practical, it is imperative that the forward model is computationally efficient.

A numerical, time domain, model based on Poisson's solution to the wave equation has been widely used for calculating the pressure time history at a point from a photoacoustically generated source in homogeneous media.[25,26] This model has also been adapted to accommodate small sound speed heterogeneities.[23] More recently, finite difference[27] and (frequency domain) finite element methods[28] have been presented as techniques for modeling photoacoustics in heterogeneous media. This paper is concerned with wave number domain or *k*-space methods, which can achieve the same accuracy as the above-mentioned methods despite using a much coarser spatial grid, and can take much larger time steps without causing instabilities. *k*-space methods are therefore computationally efficient, and are ideal as forward models in model-based image reconstruction algorithms for PAT. In addition to being efficient and

[a]Electronic mail: bencox@mpb.ucl.ac.uk

accurate, numerical *k*-space models in both two and three dimensions are straightforward to encode. In view of these advantages, it is surprising that *k*-space methods are not more widely used for studying photoacoustic propagation. To date, photoacoustic propagation has been calculated using *k*-space methods only for homogeneous media.[29–31] Here we review two further *k*-space models,[32,33] originally derived to describe ultrasonic scattering due to heterogeneous media, and by adding a photoacoustic source term to each, demonstrate their use in photoacoustics with several examples.

II. FORWARD MODELS IN PHOTOACOUSTICS

A. Photoacoustic wave equation

The forward or direct problem in photoacoustics is to predict the acoustic field as a function of time following the absorption of an optical pulse. If a region of a fluid is heated by the absorption of a pulse of light, then a sound wave is generated. In a stationary fluid, under conditions whereby the sound generation mechanism is thermoelastic and terms containing the viscosity and thermal conductivity are negligible—a regime called thermal confinement—the acoustic pressure, $p(\mathbf{x},t)$, in the linear acoustic approximation and in the absence of absorption, obeys

$$\frac{\partial^2 p}{\partial t^2} - c^2 \rho \nabla \cdot \left(\frac{1}{\rho} \nabla p \right) = \Gamma \frac{\partial \mathcal{H}}{\partial t}, \tag{1}$$

where the sound speed $c(\mathbf{x})$ and density $\rho(\mathbf{x})$ vary with position $\mathbf{x}$. Γ is a dimensionless constant called the Grüneisen parameter, which indicates the efficiency of conversion of absorbed optical energy (heat) to pressure, and is defined as $\Gamma = c^2\beta / C_p$, where β is the volume thermal expansivity and C_p is the specific heat capacity. $\mathcal{H}(\mathbf{x},t)$ is the heat energy per unit volume and per unit time deposited in the fluid and, like the pressure p, will depend, in general, on both position $\mathbf{x}$ and time t. When the sound speed and density are uniform, so $c(\mathbf{x}) = c_0$ and $\rho(\mathbf{x}) = \rho_0$, then Eq. (1) becomes

$$(\partial^2/\partial t^2 - c_0^2 \nabla^2) p = \Gamma \, \partial \mathcal{H} / \partial t. \tag{2}$$

If the photoacoustic source term $\mathcal{H}(\mathbf{x},t)$ is stationary, then it may be separated into spatial and temporal components $\mathcal{H}(\mathbf{x},t) = H_x(\mathbf{x}) H_t(t)$, where $H_x(\mathbf{x})$ is the heat deposited in the fluid per unit volume, and $H_t(t)$ describes the temporal shape of the pulse, normalized so that the integral of H_t is unity. For instance, if the heating pulse is assumed Gaussian then

$$H_t(t) = \frac{e^{-(t/\tau)^2}}{\tau \sqrt{\pi}}. \tag{3}$$

As $\tau \to 0$ this pulse $H_t(t) \to \delta(t)$ so if $c\tau$ is much shorter than a typical distance across the heated region, a regime known as "stress confinement," then the PA source term may be considered to be instantaneous and well-represented by the time-derivative of a δ function. In this case, the forward problem reduces to the initial value problem (IVP) for the homogeneous wave equation

$$(\partial^2/\partial t^2 - c_0^2 \nabla^2) p = 0 \tag{4}$$

with initial conditions

$$p|_{t=0} = \Gamma H_x, \quad \partial p / \partial t|_{t=0} = 0. \tag{5}$$

In the examples below we assume $\mathbf{x} \in \mathbb{R}^2$, as it is more straightforward to display images of a two-dimensional (2D) wave field, but all the algorithms may be easily extended to three spatial dimensions.

B. Models based on Poisson's solution

Under conditions of thermal confinement, i.e., instantaneous heating, Poisson's solution to the IVP in Eqs. (4) and (5) may be used to calculate the acoustic field

$$p(\mathbf{x},t) = \frac{\Gamma}{4\pi c_0} \frac{\partial}{\partial t} \int_{A(t)} \frac{H_x(\mathbf{x}')}{R} dA, \tag{6}$$

where $R = |\mathbf{x} - \mathbf{x}'|$, and $A(t)$ is the surface on which $R = c_0 t$ and is thus a function of time. The optical excitation pulse is taken to occur at $t = 0$. This equation has been implemented numerically by a number of authors[25,26] by defining $H_x(\mathbf{x})/R$ on a mesh and summing the contributions that lie within the two circles $A(t)$ and $A(t+\Delta t)$ for $t = 0, \Delta t, \ldots$. The resulting time series is numerically differentiated to give the acoustic pressure. This model was extended to take into account the spatial averaging effect of a finite-sized detector by Köstli and Beard,[34] by convolving the detector volume $D(\mathbf{x})$ with $H_x(\mathbf{x})$ prior to carrying out the integration over A. Xu and Wang[23] investigated the effects of sound speed heterogeneities on breast thermoacoustic tomography by developing analytical expressions for the effect on the amplitude and delay of a pulse. They concluded that the effect of a time delay is more important in imaging, and so adapted Poisson's model to incorporate a first-order correction for different times-of-flight through the heterogeneous medium, by warping the surface A.

The advantage of this model is that it is intuitive, and can be an aid to visualizing the forward problem. It is, however, computationally inefficient, and limited in the degree to which it can model boundaries or heterogeneous acoustic properties. For more complex situations, one approach is to turn to two well-established tools of numerical modeling: finite element and finite difference methods.

C. Finite element and finite difference methods

The finite element (FE) method is a popular and powerful method for calculating numerical solutions to partial differential equations because of its flexibility, accuracy, and rigorous mathematical foundations. In this method, the solution is represented by a linear combination of N-dimensional basis functions defined on the computational domain, and the unknown amplitudes of these functions are calculated to give a solution, exact at N nodes and approximate in between. The flexibility in the choice of basis functions allows domains and heterogeneities of any shape to be well-approximated, and, more important, the basis functions can be chosen to have support over only a small part of the domain, so calculation of the unknown amplitudes can be reduced to a sparse matrix equation for which there are efficient solvers available. Heterogeneous material properties can be straightforwardly included, and the well-developed

mathematical fundamentals of the technique allow thorough analyses of errors and sensitivities. Encoding the FE method, however, is not as straightforward as the finite difference (FD) or *k*-space methods discussed in the following, although many commercial packages are now available to ease this burden. Another disadvantage is that, when solving wave problems with the FE method, about 10 nodes per wavelength are required to represent the field accurately, so high-frequency, large-scale, applications soon become intractable. Jiang *et al.*[28] have used the FE method to find low frequency solutions of a PA Helmholtz-like equation which includes terms for sound speed heterogeneity and acoustic absorption.

Another group of techniques that is in widespread use for finding numerical solutions to partial differential equations is that of finite differences, in which derivatives in the partial differential equation are approximated by differences, thus converting the PDE into a difference equation which can be solved numerically. FD models are less flexible than FE models because, usually, a regular computational mesh must be used. The high-frequency sampling requirement, which is disadvantageous to FE methods, is a problem here too. Nevertheless, the popularity of FD methods endures, perhaps because of their conceptual simplicity. Huang *et al.*[27] describe a FD time-domain simulation of PA propagation, which includes nonlinear terms and dissipative effects, and is therefore more general than any of the other models described in this paper, although the underlying equations are correspondingly more complex. For biomedical applications, the assumptions of linearity and thermal confinement—which are required for all the models in this paper—seem to be valid, and allow considerable simplification of the governing equations, and therefore of the model.

For time domain problems, it is common practice to use a FD approximation to the time derivative, whether the spatial part of the solution is solved using FD or FE methods. Approximating the time derivative in this way can introduce numerical dispersion, in which the speed of the wave depends, erroneously, on its frequency, thus distorting the shape of pulses. To avoid this, small time steps must be taken, further reducing the efficiency of both FE and FD time domain models.

D. Pseudospectral and *k*-space models

The FE and FD methods, although excellent for many applications, become cumbersome and slow when modeling large scale, high-frequency acoustics applications, due to the requirements for many mesh points for wavelength, and small time steps required to minimize unwanted dispersion. In this section we briefly describe the pseudospectral (PS) method, which can help reduce the first of these problems, and *k*-space propagators, to overcome the second.

In a simple FD scheme, the gradient of the field is estimated by fitting a straight line between its values at two mesh points. A better estimate of the gradient could be obtained by fitting a higher-order polynomial to a greater number of points, and calculating the derivative of the polynomial. The more points used, the higher the degree of polynomial required, and the more accurate the estimate of the derivative. The PS method takes this idea further and fits a Fourier series to all the data on each line of the mesh. This choice of interpolating function assumes that the solution is periodic (the values and the derivatives at both ends of each line of the mesh are the same) which will rarely be the case. The "wrapping" effects of this assumption are common to PS and *k*-space methods and are seen in the example in Sec. IV A. Such effects can often be ameliorated using absorbing boundary conditions (see Sec. V and references therein). There are two significant advantages to using Fourier series. The first is that the amplitudes of the Fourier components can be calculated efficiently using the Fast Fourier transform (FFT), and the gradient calculated simply as $\mathcal{F}^{-1}\{ik_x\mathcal{F}\{p(x)\}\}$, where $\mathcal{F}\{\cdot\}$ is a Fourier transform and $\mathcal{F}^{-1}\{\cdot\}$ its inverse. The second advantage is that the basis functions assumed by the FT are sinusoidal, so only two nodes per wavelength are required in order to describe a wave, rather than 10+ in the FE and FD methods.

Now, both PS time-domain (PSTD) and *k*-space methods calculate the spatial gradients using FFTs, as just described. However, whereas the PSTD method approximates the temporal gradient with a finite difference, in *k*-space methods the field is propagated forward in time according to a *k*-space propagator, which is exact for homogeneous media, and, for heterogeneous media, allows much larger time steps for similar accuracy and stability to FD methods.[32,33,35–39] In Ref. 39 the *k*-space method is shown to give more accurate results than a second-order FD method for elastic wave propagation even when the time step is larger. References 32 and 33 describe benchmark studies of the accuracy of the *k*-space method in comparison with a leapfrog PSTD method and a time domain FD method. Examples of propagation through samples realistic of soft tissue were calculated using each model for a range of values of the Courant-Friedrichs-Lewy number, $\mathrm{CFL} \equiv c_0\Delta t/\Delta x$, and it is shown that the error norm increases much more slowly with CFL for the *k*-space method than for either of the other two methods. It was also shown that the number of mesh points per wavelength required for a given accuracy is much less (≈ 3 as opposed to ≈ 10) for the *k*-space method than for the FD method.

As well as being efficient by virtue of the reduced point-per-wavelength requirement, the use of the FFT to calculate the gradients in *k* space, and larger time steps made possible by the *k*-space time propagator, another attraction of *k*-space models is that they are straightforward to encode. In this paper, three efficient, *k*-space forward models of photoacoustic wave generation and propagation are described. All three calculate the acoustic field as a function of time, given an arbitrary distribution of absorbed optical energy. This first model applies only to homogeneous media,[29] whereas the second[32] and third[33] include the effects of acoustic heterogeneities, i.e., spatial variations in the sound speed and density. The differences between the second and third are that the latter can incorporate absorbing boundary conditions and bulk acoustic absorption.

III. *k*-SPACE MODEL FOR A HOMOGENEOUS MEDIUM

When the sound speed and density are constant everywhere, then the photoacoustic waves propagate according to Eq. (2). Following spatial Fourier transformation, Eq. (2) becomes an ODE in time, describing the motion of plane waves with wave vector $\mathbf{k}=(k_x,k_y)$,

$$\left(\frac{d^2}{dt^2}+(c_0k)^2\right)\hat{p}=\hat{S}(t), \tag{7}$$

where the caret indicates a function in $\mathbf{k}$ space, and k is the modulus of $\mathbf{k}$. The source term $\hat{S}(t)$ is given by

$$\hat{S}(t)=\Gamma\hat{H}_x\frac{\partial H_t}{\partial t}. \tag{8}$$

The Green's function solution to Eq. (7) is

$$\hat{p}(\mathbf{k},t)=\int_0^t \hat{g}(t-t')S(t')dt' \tag{9}$$

$$=\Gamma\hat{H}_x\int \hat{g}(t-t')\frac{dH_t}{dt'}(t')dt', \tag{10}$$

where the Green's function $\hat{g}$ is a solution to $d^2\hat{g}/dt^2+(c_0k)^2\hat{g}=\delta(t)$ and is given by

$$\hat{g}(\mathbf{k},t)=\begin{cases}0, & t<0\\ \sin(c_0kt)/(c_0k), & t\geqslant 0.\end{cases} \tag{11}$$

When $H_t(t)=\delta(t)$, an instantaneous pulse at $t=0$, the solution for the pressure becomes

$$\hat{p}(\mathbf{k},t)=\Gamma\hat{H}_x\int\left(\frac{\sin(c_0k(t-t'))}{c_0k}\right)\delta'(t')dt'$$

$$=\Gamma\hat{H}_x\cos(c_0kt) \tag{12}$$

so the acoustic field at time t following an optical pulse at $t=0$ can be calculated using

$$p(\mathbf{x},t)=\Gamma\mathcal{F}^{-1}\{\hat{H}_x(\mathbf{k})\cos(c_0kt)\}. \tag{13}$$

This is an exact solution, so the acoustic field can be calculated directly for any time t without having to step through the previous times from $t=0$. In this sense, the $\cos(ckt)$ term in Eq. (13) can be considered as an exact time propagator. (To calculate pressure time histories on just a single plane perpendicular to the axis of symmetry in a radially symmetric field, the vertical wave-number-frequency mapping technique described in Cox and Beard[29] is considerably more efficient.)

It is instructive to see that the solution in Eq. (13) can be written as an explicitly time-stepping, finite-difference-style solution, in which the field at $t+\Delta t$ is calculated from the field at times t and $t-\Delta t$. Consider the transformed field, $\hat{p}(\mathbf{k})$, at the two times $t+\Delta t$ and $t-\Delta t$:

$$\hat{p}(t+\Delta t)=\Gamma\hat{H}_x\cos(c_0k(t+\Delta t))$$

$$=\Gamma\hat{H}_x(\cos(c_0kt)\cos(c_0k\Delta t)$$

$$-\sin(c_0kt)\sin(c_0k\Delta t)), \tag{14}$$

$$\hat{p}(t-\Delta t)=\Gamma\hat{H}_x\cos(c_0k(t-\Delta t))$$

$$=\Gamma\hat{H}_x(\cos(c_0kt)\cos(c_0k\Delta t)$$

$$+\sin(c_0kt)\sin(c_0k\Delta t)). \tag{15}$$

So,

$$\hat{p}(t+\Delta t)+\hat{p}(t-\Delta t)=2\Gamma\hat{H}_x\cos(c_0kt)\cos(c_0k\Delta t)$$

$$=2\hat{p}(t)\cos(c_0k\Delta t)$$

$$=2\hat{p}(t)(1-2\sin^2(c_0k\Delta t/2)) \tag{16}$$

and rearranging gives

$$\hat{p}(t+\Delta t)-2\hat{p}(t)+\hat{p}(t-\Delta t)=-4\sin^2(c_0k\Delta t/2)\hat{p}(t). \tag{17}$$

This is a time-stepping solution for which steps Δt of any size may be used without introducing error. This is an exact rearrangement of Eq. (13), so by using the initial conditions $\hat{p}(-\Delta t)=\Gamma\hat{H}_x\cos(c_0k\Delta t)$ and $\hat{p}(0)=\Gamma\hat{H}_x$, exactly the same solutions for any $t>0$ will be calculated. By comparing Eq. (17) to a pseudospectral, leapfrog FD scheme, based on Eq. (7) in the absence of the source term,

$$\frac{\hat{p}(t+\Delta t)-2\hat{p}(t)+\hat{p}(t-\Delta t)}{\Delta t^2}=-(c_0k)^2\hat{p}(t) \tag{18}$$

we can see that the $4\sin^2(c_0k\Delta t/2)$ term in Eq. (17) has replaced the term $(c_0k\Delta t)^2$ in Eq. (18). For small time steps these are equal, but for larger time steps the latter leads to numerical dispersion whereas the former provides an exact, dispersion-free, solution. Of course, with δ-function heating, there is no need for such a time stepping scheme as we have an exact propagator for arbitrarily large time steps, Eq. (13). Indeed, the solution for a finite-duration Gaussian excitation pulse could be obtained by multiplying the Fourier transform of Eq. (3) to the other k-space terms in Eq. (13). However, when considering a source with an arbitrary temporal pulse shape, or propagation through heterogeneous media, a time-stepping scheme may be required. We can extend the time-stepping scheme in Eq. (17) to include a source with an arbitrary pulse shape:

$$\hat{p}(t+\Delta t)-2\hat{p}(t)+\hat{p}(t-\Delta t)=-4\sin^2(c_0k\Delta t/2)\left(\hat{p}(t)-\frac{\hat{S}(t)}{(c_0k)^2}\right). \tag{19}$$

A. Example: Laser beam incident on an absorbing half-space

A two-dimensional (2D) example of a tophat laser beam incident on a pure (nonscattering) absorber is used to dem-

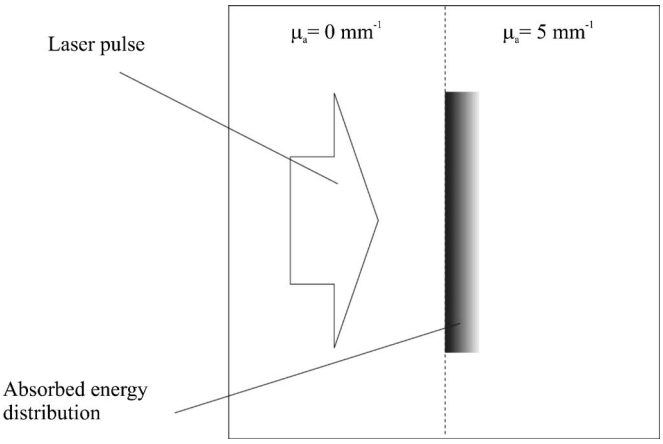

FIG. 1. A collimated laser beam with a 6-mm-diam tophat profile, indicated with an arrow, is incident on an optically absorbing half-space, the surface of which is marked by a dotted line. The optical absorption coefficient $\mu_a = 5$ mm^{-1}. The absorbed energy distribution decays exponentially from the boundary according to the Beer-Lambert law. The laser fluence at the surface was 10 mJ/cm^2 (i.e., 10 mJ/cm per cm into the plane of the paper). The sound speed and density were 1500 m/s and 1000 kg/m^3, respectively, and the Grüneisen parameter $\Gamma = 0.11$. The evolution of this acoustic field is shown in Fig. 2.

onstrate the homogeneous model in Eq. (19). Figure 1 shows the arrangement: A collimated laser beam with a 6 mm diameter tophat profile, indicated by an arrow, is incident on an optically absorbing half-space, the surface of which is marked by a dotted line. The optical absorption coefficient $\mu_a = 5$ mm^{-1}. The absorbed optical energy results in a spatially varying heating function, $\mathcal{H}_x(\mathbf{x})$, which decays exponentially from the boundary according to the Beer-Lambert law, and is shown in Figs. 1 and 2 (top left) as a dark region. As this example has 2D symmetry, with no variation into or out of the plane of the paper, the tophat beam effectively models a three-dimensional (3D) line source. The laser fluence at the surface of the absorber was set to 10 mJ/cm^2 (i.e., 10 mJ/cm per cm into the plane of the paper). The sound speed and density were 1500 m/s and 1000 kg/m^3, respectively, and the Grüneisen parameter $\Gamma = 0.11$, their values in water (the major constituent of soft tissue). The 2D computational grid of 10 mm $\times$ 10 mm, was divided into 600×600 squares, which limited the maximum frequency to about 60 MHz. The absorbed energy distribution was smoothed to ensure there were no wave number components higher than about $0.8\pi/\Delta x$ where Δx is the grid spacing. The time $t = 0$ was defined as the midway point of the temporal heating pulse, Eq. (3), whose pulse width was $\tau = 8.33$ ns, and so the program was set to begin at a time well before this so as to include all of the first half of the pulse. The validity of the use of a Gaussian function to approximate the instantaneous, δ-function, heat deposition is examined in the following. All the models in this paper were written in MATLAB (Release 13, The Mathworks, Inc.).

Figure 2 shows the pressure field as it evolves, at times 0, 0.33, 0.66, and 1 μs following the laser pulse. This acoustic pressure field can be described as a combination of two compressive plane waves and two circular, edge waves which have a tensile component. The pressure as a function of time for a point located at the point $(-1, 0)$ is shown in Fig. 6.

B. Example: Line source with a Gaussian profile

The use of a Gaussian temporal function to approximate a δ function (instantaneous heating) is valid for a pulse whose duration is much shorter than the acoustic travel time across the region of support of the source $\mathcal{H}_x$. (The "stress confinement" condition.) With the above example, this becomes the requirement that the pulse width $\tau \ll 1/(\mu_0 c_0) = 133$ ns, so the condition was met. An implication is that the less stringent assumption of "thermal confinement," required for Eq. (1) to hold, is also valid. To check this assumption, a comparison has been made with an analytical solution.

Diebold and Sun[40] provide an analytical solution for an infinitely long, cylindrical source distribution with a Gaussian radial profile that is instantaneously deposited at $t = 0$. This can be modeled in 2D by assuming the axis of the cylinder is directed perpendicular to the 2D plane. A comparison between Diebold's solution and the homogeneous k-space model shows that it is reasonable to model the temporal dependence of the photoacoustic source term with a Gaussian when the stress confinement condition applies. For a source profile with a radial width $\sigma = 1$ mm, the stress confinement condition is $\tau \ll \sigma/c_0 = 0.67$ μs. To calculate Fig. 3 τ was set to 0.01 μs, well within this criterion. Figure 3 shows how the acoustic pressure varies with time at a point 3 mm off axis. The time series were calculated using Diebold's solution (solid line) and the homogeneous k-space model (circles), and they show good agreement. Additional

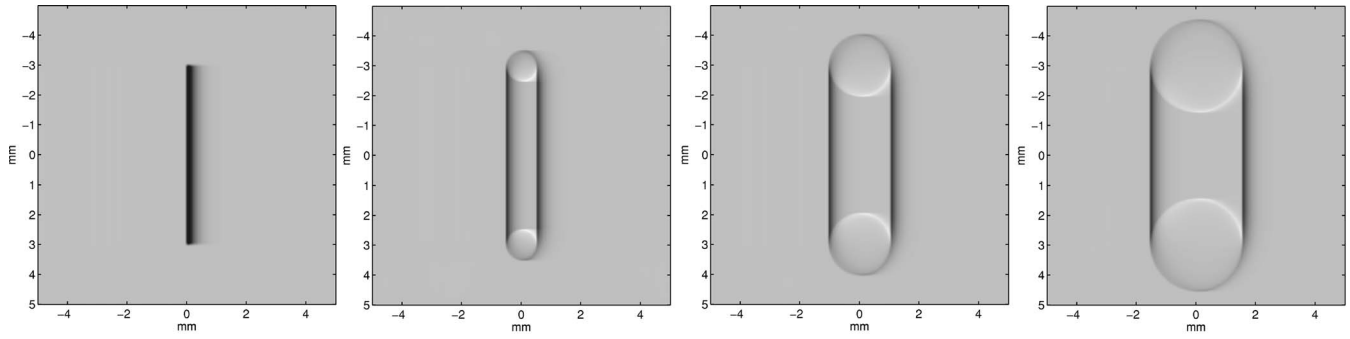

FIG. 2. The evolution of the photoacoustic pressure field for the arrangement shown in Fig. 1. The acoustic pressure is shown at times $t = 0$, 0.33, 0.66, and 1 μs following the laser pulse, calculated using the homogeneous model of Sec. III. The linear grey scale is from -10 kPa (white) to 40 kPa (black).

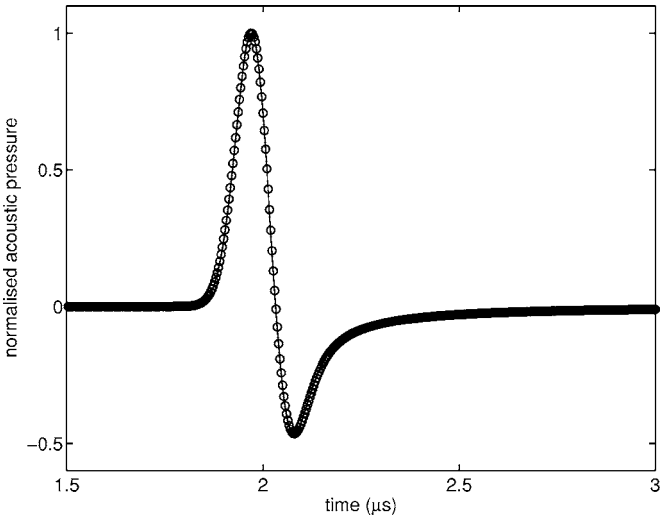

FIG. 3. Acoustic pressure 3 mm off axis for an infinitely long impulsive heating source with a Gaussian radial profile. Analytic solution (solid line) which assumes instantaneous (δ function) heat deposition, and k-space model for a homogeneous medium (circles), which uses a Gaussian approximation to the temporal δ function. When the stress confinement condition holds, as in this case, this approximation gives good agreement. The Gaussian radial width $\sigma=1$ mm.

examples, comparing a model of photoacoustic propagation based on Poisson's solution, Eq. (6), to the k-space model of Eq. (13) can be found in Cox and Beard.[29]

IV. HETEROGENEOUS MEDIUM: SECOND-ORDER *k*-SPACE MODEL

An accurate model of the propagation of PA waves in tissue must include the effects of the sound speed and density heterogeneities. We follow the approach taken by Mast *et al.*[32] By defining a new variable $f(\mathbf{x},t)\equiv p(\mathbf{x},t)\rho(\mathbf{x})^{-1/2}$, sometimes called a Liouville transform, the wave equation for inhomogeneous media, Eq. (1), may be rearranged into the homogeneous form of the wave equation with effective source terms due to sound speed and density heterogeneities on the right-hand side:

$$\nabla^2 f - \frac{1}{c_0^2}\frac{\partial^2 f}{\partial t^2} = \frac{1}{c_0^2}\left(q + \frac{\partial h}{\partial t} + \frac{\partial^2 v}{\partial t^2}\right), \tag{20}$$

where c_0 is a fixed sound speed, usually chosen as the maximum of $c(\mathbf{x})$ for reasons of stability. There are three terms on the right-hand side corresponding to waves generated in three different ways: at changes in density, Eq. (21), photoacoustically, Eq. (22), and at changes in sound speed, Eq. (23):

$$q(\mathbf{x},t) = c_0^2\sqrt{\rho(\mathbf{x})}\nabla^2(\rho(\mathbf{x})^{-1/2})f(\mathbf{x},t), \tag{21}$$

$$h(\mathbf{x},t) = -\rho(\mathbf{x})^{-1/2}\Gamma\mathcal{H}(\mathbf{x},t), \tag{22}$$

$$v(\mathbf{x},t) = (c_0^2/c(\mathbf{x})^2 - 1)f(\mathbf{x},t). \tag{23}$$

As the heating pulse is assumed to be Gaussian, Eq. (3), the photoacoustic source term becomes

$$\frac{\partial h(\mathbf{x},t)}{\partial t} = \rho^{-1/2}\Gamma H_x(\mathbf{x})\left(\frac{2te^{-(t/\tau)^2}}{\tau^3\sqrt{\pi}}\right). \tag{24}$$

Now, by introducing the auxiliary field, $w=f+v$, and transforming from $\mathbf{x}$ space to $\mathbf{k}$ space, Eq. (20) may be rearranged into the form

$$\frac{\partial \hat{w}^2}{\partial t^2} = (c_0 k)^2(\hat{v} - \hat{w}) - \hat{q} - \frac{\partial \hat{h}}{\partial t}, \tag{25}$$

where ∇^2 has been replaced by $-k^2$. Eliminating f from Eqs. (21) and (23) gives

$$\hat{q}(\mathbf{k},t) = c_0^2\mathcal{F}\{\tilde{\rho}(\mathbf{x})(w(\mathbf{x},t) - v(\mathbf{x},t))\}, \tag{26}$$

$$\hat{v}(\mathbf{k},t) = \mathcal{F}\{(1 - (c(\mathbf{x})/c_0)^2)w(\mathbf{x},t)\}, \tag{27}$$

where we have used the shorthand $\hat{\rho}\equiv\rho^{1/2}\nabla^2(\rho^{-1/2})$. By comparing Eq. (25) with Eqs. (7) and (19) we see that it may be approximated by

$$\hat{w}(\mathbf{k},t+\Delta t) - 2\hat{w}(\mathbf{k},t) + \hat{w}(\mathbf{k},t-\Delta t) \approx 4\sin^2\left(\frac{c_0 k\Delta t}{2}\right)\left[\hat{v} - \hat{w}\frac{(\hat{q} + \partial\hat{h}/\partial t)}{(c_0 k)^2}\right]. \tag{28}$$

Given two initial conditions, $\hat{w}(\mathbf{k},-\Delta t)$ and $\hat{w}(\mathbf{k},0)$, this difference equation may be used to step the field $\hat{w}$ forward in time. Here, both initial conditions are set to zero. In the homogeneous limit, this gives exact solutions, and is equivalent to Eq. (19).

So, with $w(-\Delta t)=w(0)=0$ and $\partial h/\partial t$ known for all t from Eq. (24), the procedure for calculating the pressure field as function of time using this model is as follows: For every t calculate, in this order, $\hat{v}(\mathbf{k},t)$ using Eq. (27), $v(\mathbf{x},t)$ by transforming $\hat{v}$, $\hat{q}(\mathbf{k},t)$ using Eq. (26), and $\hat{w}(\mathbf{k},t+\Delta t)$ using Eq. (28). The acoustic pressure may then be obtained from $p(\mathbf{x},t)=\rho^{1/2}(w(\mathbf{x},t)-v(\mathbf{x},t))$.

Examples including acoustic heterogeneities. The example of a light pulse with a tophat profile, used in Sec. III A to demonstrate the homogeneous model of Eq. (19), is adapted to show the effect of an acoustic homogeneity on the field, using the above-described model. A single, circular heterogeneity with sound speed and density half of their values in the surrounding tissue was included as shown in Fig. 4. All other parameters in the example were left unchanged. While such a great change in sound speed is rare within soft tissue, even greater contrasts can be found at air or vapor pockets. The main reason for choosing a large contrast here was in order to produce a significant reflection and distortion of the wavefront to best show the capabilities of the model. The density and sound speed distributions were smoothed to remove wavenumber components higher than about $0.8\pi/\Delta x$. The time increment Δt was set to 2.78 ns, well inside the Nyquist requirement (Sec. VI). This model took about 2 s per time step on a 2 GHz PC with 768 Mbytes RAM.

Figure 5, like Fig. 2, shows the evolution of the acoustic wave with time. The acoustic pressure is shown at times $t=0$, 0.33, 0.66 and 1 μs following the laser pulse. The slower passage of the wavefront through the circular region

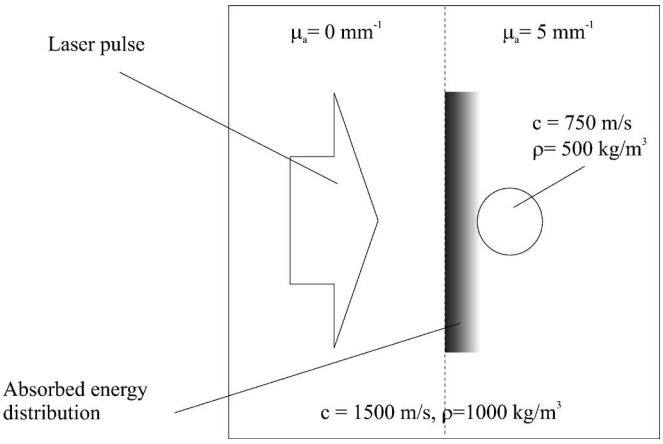

FIG. 4. An example identical to Fig. 1, except for the circular heterogeneity with sound speed and density half that of the surrounding medium.

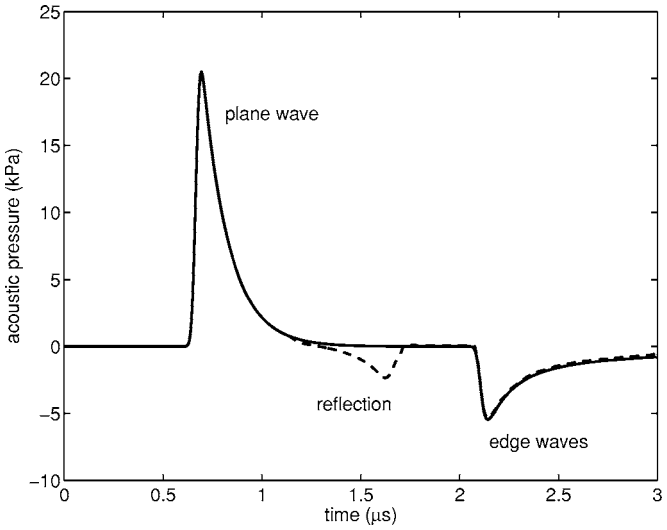

FIG. 6. Pressure time histories calculated for the point (−1,0) (see Figs. 2 and 5), for both the acoustically homogeneous (solid line) and heterogeneous (dashed line) cases. The additional wave, reflected from the acoustic inhomogeneity, is clear.

of lower sound speed, and the resulting distortion of the plane wavefront is clearly visible. The wave reflected from the heterogeneity can also be seen. Figure 6 shows time series calculated for a point 1 mm to the left of the center of the image, for both the acoustically homogeneous (solid line) and heterogeneous (dashed line) cases. The reflected wave can be seen arriving at about 1.5 μs, in between the plane and edge wave components of the initial wavefield.

The tophat example, Figs. 5 and 6, was chosen to show clearly the wavefront distortion and reflection caused by a single acoustic heterogeneity. The following example shows the acoustic radiation from three circular sources, which could, for instance, be used to represent blood vessels. Figure 7 shows the pressure field at times of 0, 0.33, 0.66,… 2.33 μs. The sound speed and density are 1500 m/s and 1000 kg/m^3, respectively, and the position of a rectangular heterogeneity (c=1000 m/s, ρ=750 kg/m^3), which distorts the circular wavefront from the right-most tube, is indicated by a dotted line. It is a result of the periodicity inherent in the FFT, that when a wavefront reaches the boundary of the image, it "wraps around" and appears on the other side. This can be seen with the wave from the leftmost source, which appears on the right-hand side of the last three frames. For calculations of transient fields, it may be possible to use a sufficiently large computational domain to avoid this wrap-around problem, or if only the pressure at a single point is required, to stop the calculations before the first arrival of a wrapped wave reaches that point. Nevertheless, for simulating measurements over an array it is not ideal to have to use a mesh considerably larger than the array in order to avoid the wrapped wave. For 3D problems, the number of elements in the mesh increases by eight times each time the linear dimensions are doubled, so the size of the computation soon becomes very large. Section V describes a first-order model for which absorbing boundary conditions can be prescribed, thus removing this problem.

V. HETEROGENEOUS MEDIUM: FIRST-ORDER *k*-SPACE MODEL

Both Eqs. (17) and (18) are discretizations of $\partial^2\hat{p}/\partial t^2 = -(c_0k)\hat{p}$. Both models use $-k^2\hat{p}$ in place of the Laplacian, ∇^2, but whereas Eq. (17) uses a k-space time propagator, Eq. (18) employs a finite-difference approximation to time derivative. By rewriting Eq. (17) as

$$\frac{\hat{p}(t+\Delta t) - 2\hat{p}(t) + \hat{p}(t-\Delta t)}{\Delta t^2\ \mathrm{sinc}^2(c_0k\Delta t/2)} = -(c_0k)^2\hat{p}(t) \tag{29}$$

it is clear that—so far as the time derivative is concerned—the k-space models described above can be thought of as FD

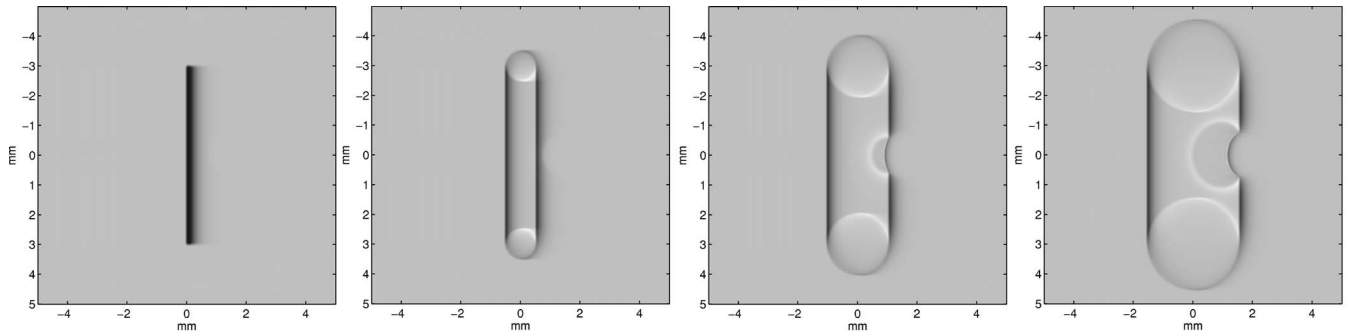

FIG. 5. The evolution of the photoacoustic pressure field for the arrangement shown in Fig. 4, including a circular heterogeneity. The acoustic pressure is shown at times t=0, 0.33, 0.66, and 1 μs following the laser pulse, calculated using the homogeneous model of Sec. III. The linear grey scale is from −10 kPa (white) to 40 kPa (black). The wave reflected from the heterogeneity, and the distorted wave front due to the reduced sound speed are clearly visible.

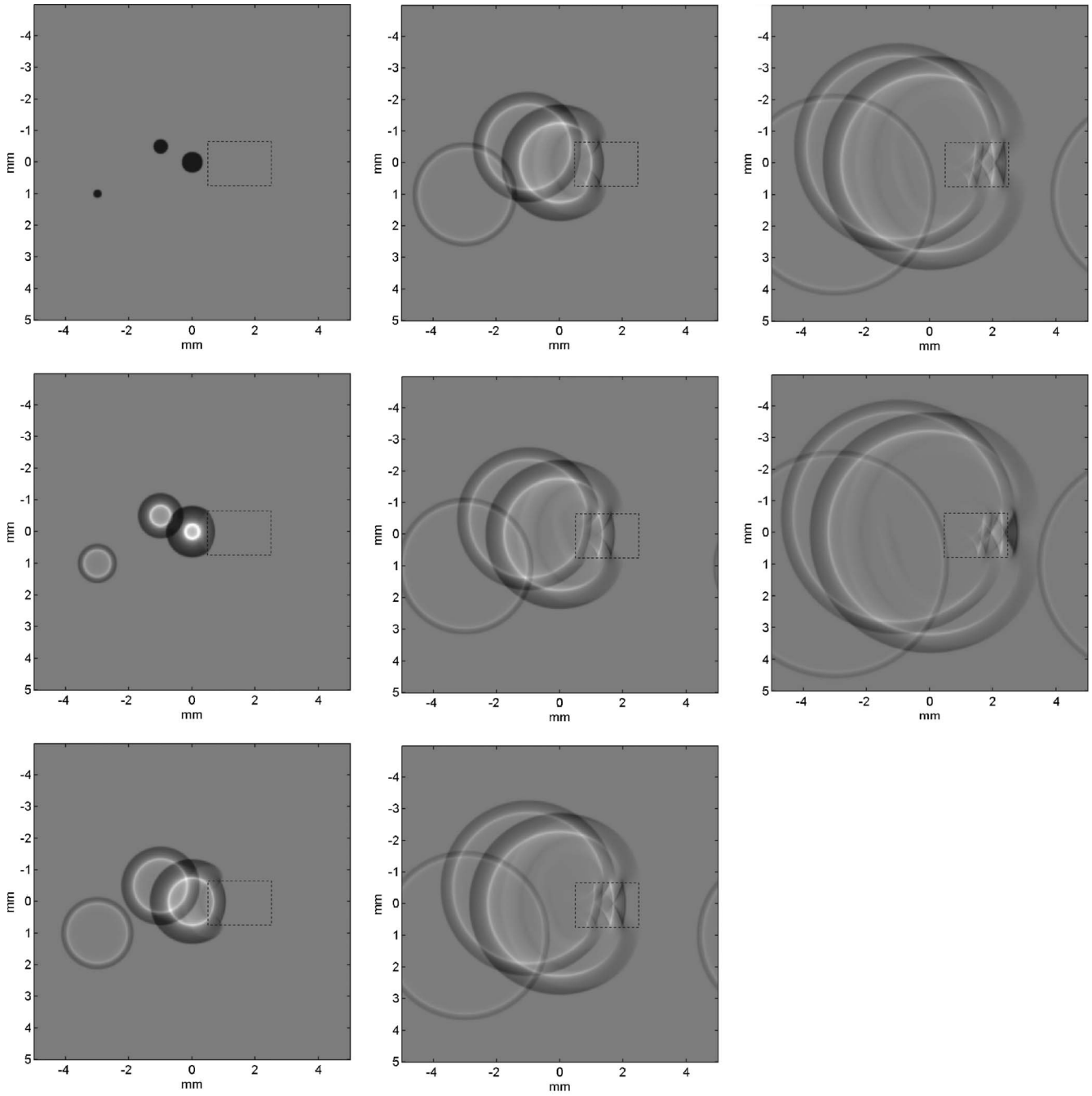

FIG. 7. The acoustic pressure field radiated from three circular photoacoustic sources is shown every 1/3 μs following an excitation light pulse. The sound speed and density are 1500 m/s and 1000 kg/m^3, respectively. The position of a rectangular acoustic heterogeneity (1000 m/s, 750 kg/m^3), which distorts the wavefront on the right of the image, is indicated by a dotted line. The periodic boundary conditions implicit in this model cause the acoustic waves to wrap around when it reaches the edge of the computational domain.

models in which Δt^2 has been replaced by $\Delta t^2 \operatorname{sinc}^2(c_0 k \Delta t/2)$ in the approximation of $\partial^2/\partial t^2$. We can also see that replacing the spatial derivative $-k^2$ with $-k^2 \operatorname{sinc}^2(c_0 k \Delta t/2)$ would give the same solution. Exact solutions for the homogeneous case can be therefore be obtained by replacing the Laplacian with $-k^2 \operatorname{sinc}^2(c_0 k \Delta t/2)$ and calculating the temporal derivative using standard finite-differences. This observation is the motivation for the model described below.

While the two models described in Secs. III and IV are based on second-order equations, this *k*-space model, first described by Tabei *et al.*,[33] is based instead on the linearized conservation of momentum and mass equations. These first-order equations, with additional terms which act as an absorbing boundary condition (ABC) to overcome the wrap-around problem, are

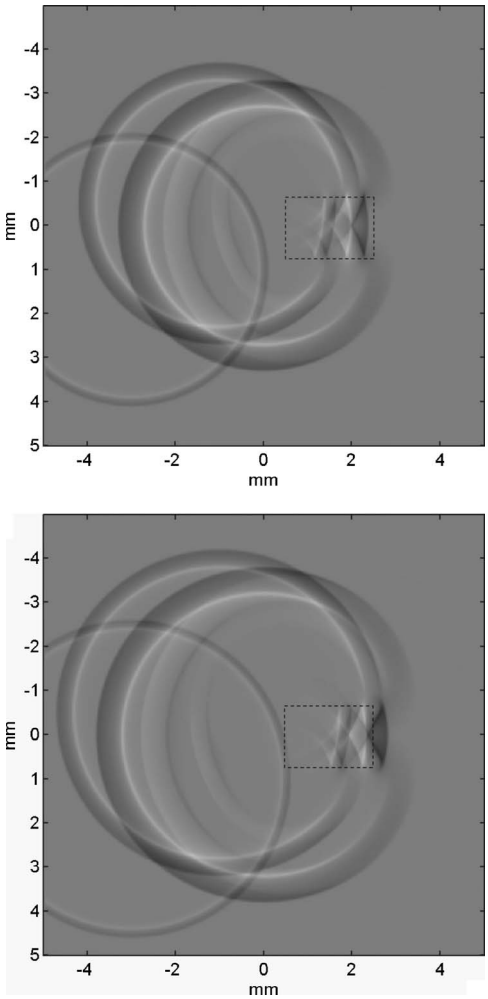

FIG. 8. The acoustic pressure field radiated from three circular photoacoustic sources, as shown in Fig. 7, at 2 and 2.33 μs following an excitation light pulse. The sound speed and density are 1500 m/s and 1000 kg/m^3, respectively. The position of a rectangular acoustic heterogeneity (1000 m/s, 750 kg/m^3), which distorts the wave front on the right of the image, is indicated by a dotted line. In contrast to the final two frames of Fig. 7, the acoustic waves do not wrap around when they reach the edge of the computational domain, but are rather attenuated to almost zero, due to the absorbing boundary condition.

$$\frac{\partial \mathbf{u}}{\partial t} = -\frac{\nabla p}{\rho} - \boldsymbol{\alpha} \cdot \mathbf{u}, \tag{30}$$

$$\frac{\partial p}{\partial t} = -\rho c^2 \nabla \cdot \mathbf{u} + \Gamma \mathcal{H} - (\alpha_x + \alpha_y) p, \tag{31}$$

where $\Gamma\mathcal{H}$ is the PA source term and the two terms containing $\boldsymbol{\alpha}=(\alpha_x(\mathbf{x}),\alpha_y(\mathbf{x}))$ represent the ABC. The principle advantage of using two first-order equations is that the vector $\mathbf{u}=(u_x,u_y)$ appears explicitly and it is therefore possible to introduce direction-dependent absorption, which cannot be done when only the scalar p is available. By defining the absorption $\boldsymbol{\alpha}$ to be zero everywhere except in a layer close to the edges of the domain, and in that layer to be zero in all directions except normal to the boundary, the amplitude of the waves leaving the domain (and only those leaving the domain) can be reduced to virtually nothing, and the wrap-around problem is eliminated. For instance, for a rectangular

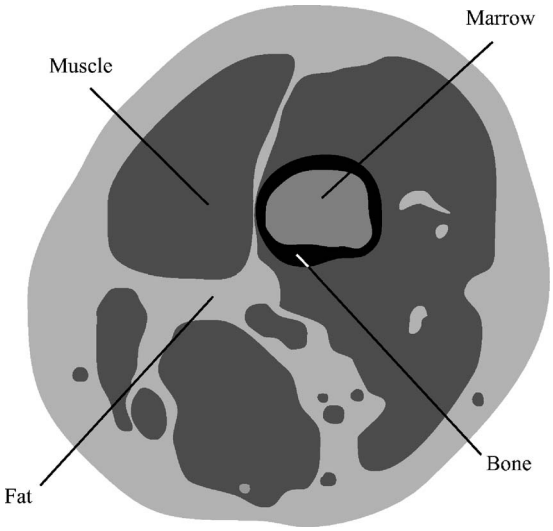

FIG. 9. The tissue properties for the example shown in Fig. 10. The sound speed and density of each region were set to: muscle, 1590 m/s and 1040 kg/m^3, fat, 1450 m/s and 900 kg/m^3, marrow, 1480 m/s and 1000 kg/m^3, and bone, 3200 m/s and 1900 kg/m^3.

domain, α_x would be chosen to be zero everywhere except within a layer close to the two boundaries perpendicular to the x axis, within which it increases nonlinearly to ensure all the outgoing energy is absorbed. α_y would be treated similarly in the y direction. This type of ABC is also called a perfectly matched layer.[41–43] Note that, as expected, Eqs. (30) and (31) can be reduced to the second-order wave equation, Eq. (1), when $\boldsymbol{\alpha}=0$.

As described earlier, instead of the usual k-space substitution for the Laplacian $\nabla^2 \rightarrow -k^2$, we use

$$\nabla^2 \rightarrow -k^2 \operatorname{sinc}^2(c_0 k \Delta t/2). \tag{32}$$

To solve Eqs. (30) and (31) numerically, however, expressions for $\partial/\partial x$ and $\partial/\partial y$ are required, not ∇^2. As $\nabla^2 \equiv \partial^2/\partial x^2 + \partial^2/\partial y^2$ and $k^2 = k_x^2 + k_y^2$, we choose $\partial/\partial x = ik_x \operatorname{sinc}(c_0 k \Delta t/2)$. In other words,

$$\frac{\partial p}{\partial x} = \mathcal{F}\{ik_x \operatorname{sinc}(c_0 k \Delta t/2)\hat{p}\} \tag{33}$$

and similarly for the gradient in the y direction. To enable the numerical calculations, the pressure is divided into two parts, $p=p_x+p_y$, and Eqs. (30) and (31) are split into four equations:

$$\dot{u}_x = -\nabla p/\rho - \alpha_x u_x, \tag{34}$$

$$\dot{u}_y = -\nabla p/\rho - \alpha_y u_y, \tag{35}$$

$$\dot{p}_x = -\rho c^2 \, \partial u_x/\partial x + \Gamma\mathcal{H}/2 - \alpha_x p_x, \tag{36}$$

$$\dot{p}_y = -\rho c^2 \, \partial u_y/\partial y + \Gamma\mathcal{H}/2 - \alpha_y p_y. \tag{37}$$

These equations are then discretized using a standard finite-difference scheme in time and Eq. (33) for the spatial derivatives. When solving for two variables, here the pressure p and particle velocity $\mathbf{u}$, it can be advantageous to use two offset (staggered) grids. This model with staggered grids (and also including bulk absorption due to relaxation pro-

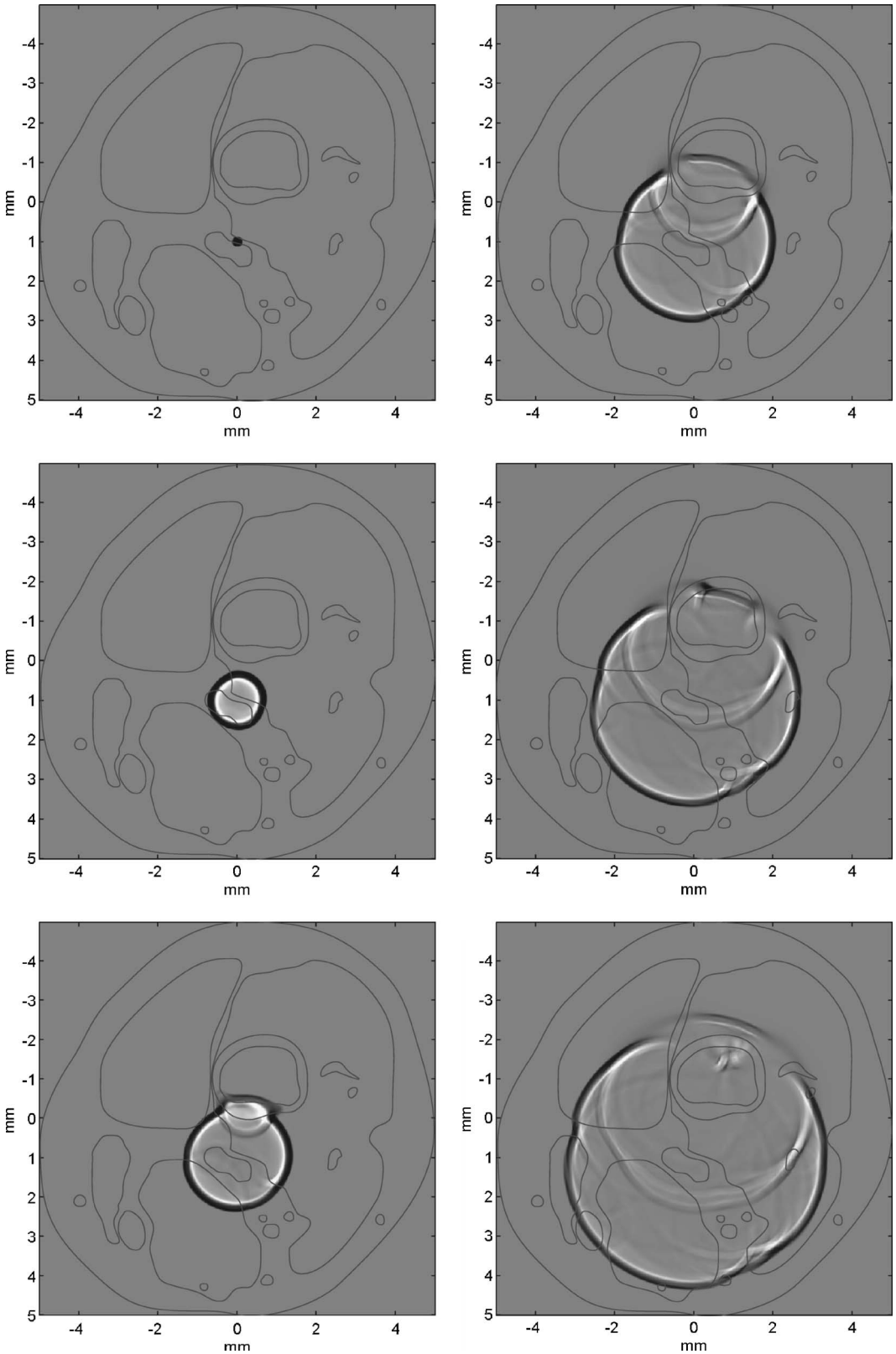

FIG. 10. Propagation of acoustic waves from a small, circular, photoacoustic source, through a heterogeneous medium with tissue-like properties (see Fig. 9). The frames are snapshots of the acoustic field at intervals of 0.21 μs following the optical pulse. The boundaries between the regions with different acoustic properties are superimposed, to show how the wave fronts are distorted by the heterogeneities.

cesses) is described in Tabei *et al.*[33] Such an implementation was used for the following examples.

Examples using the first-order model. The example shown in Fig. 7, which was calculated using the second-order model of Sec. IV, was recalculated using the first-order model described above which incorporated an absorbing boundary condition. In the last few frames in Fig. 7 the problem of the wave front wrapping around and appearing on the

far side of the image is evident. Figure 8 shows the pressure field at times corresponding to the last two frames of Fig. 7, but calculated by the first-order model. It is clear that the wrapping problem has been removed.

The final example, shown in Fig. 9, contains a degree of heterogeneity more representative of tissue. The model can account for continuously varying acoustic properties, although here the domain is divided into four types of tissue with different acoustic properties. The sound speeds and densities of the four tissue types were set to: muscle, 1590 m/s and 1040 kg/m^3, fat, 1450 m/s and 900 kg/m^3, marrow, 1480 m/s and 1000 kg/m^3, and bone, 3200 m/s and 1900 kg/m^3. A small circular PA source, that could for instance represent a blood vessel or a tumor, or a region with high chromophore concentration for another reason, is shown in the first frame of Fig. 10. This simple PA source was chosen so that the effect of the inhomogeneities on the wave fronts would be readily observable. It would be quite as straightforward to define a PA source with a complex geometry. The boundaries between the different tissue types have been superimposed on the images. The greyscale has been set the same in each image, which has led to some thresholding of the wave amplitude in the first few images. This allows the reflected and refracted waves to be seen more clearly. The frames are spaced by 0.21 μs. The most significant change to the circular wave front is, as expected, from the tissue-bone interface, where there is the greatest acoustic impedance change. The reflected wave and the reduced amplitude of the transmitted wave are visible. The distorting effect of the differences in the sound speed between the muscle and fat regions of the tissue can also be seen, for example, on the left-hand side of the wave.

VI. DISCUSSION

PA sources or distributions of acoustic properties that contain discontinuities or very large gradients at some points require high wave numbers in order to describe them accurately. In FFT-based, *k*-space methods, there is a limit to the highest permissible wave number, a requirement imposed by the need to prevent aliasing (when a wave number component is undersampled and appears at a lower wave number). There must be no components higher than the Nyquist wave number, defined as $0.5(2\pi/\Delta x)$, where Δx is the grid spacing. It is therefore important, when using *k*-space methods, to spatially smooth the acoustic properties and the spatial part of the source term in order to ensure there are no components at wave numbers above this limit. This could be considered to be a disadvantage to the *k*-space approach, because smoothed—and therefore approximate—versions of the sound speed, density, and source distributions are used when calculating the acoustic field. However, the high wave number components, which are removed by smoothing, would only have contributed to the high frequency part of the field, and as, in practice, all measurements are bandlimited by the detectors or ultrasonic absorption to some extent, only those wave numbers that contribute to the *measured* field are required for the model to simulate the acoustic pressure measurements accurately. In other words, when modeling measurements made by a pressure detector with a finite bandwidth, it is not necessary to include components of the field outside this bandwidth. Indeed, to obtain accurate simulations of data measured with a real, nonidealized, detector, a wave number model of the angle- and frequency-dependent response of a sensor[44] can be incorporated into a *k*-space model simply by multiplication, and without requiring an explicit convolution.

When calculating acoustic pressure time histories, it is important to ensure the time step, Δt, is sufficiently small to ensure the sampling rate is greater than the temporal Nyquist rate (i.e., half the maximum frequency). With *k*-space models this requirement is that Δt is less than the minimum value of $\Delta x/c$. For the above examples, Δt was $0.2-0.4\Delta x/c$.

All the models described in this paper are for photoacoustically generated waves propagating in fluids. In some circumstances it will be necessary to include the effect of shear waves on the propagation. *k*-space models for elastic wave propagation in solids have also been described,[39] and could be applied in these cases.

VII. SUMMARY

k-space models have been proposed as a straightforward and computationally efficient approach to modeling the forward problem in biomedical photoacoustics, in particular, to simulating, accurately, time series measured with a bandlimited detector. *k*-space models of photoacoustic waves can be significantly more efficient than corresponding FE and FD methods, as *k*-space methods address the particular difficulty of modeling high-frequency acoustic waves on a large scale by requiring fewer mesh points per wavelength and allowing larger time steps without reducing accuracy or introducing instability. The *k*-space method of numerical modeling of photoacoustic waves in fluids is described, and the rationale behind three particular *k*-space models (one for homogeneous media, one for heterogeneous media, and a model that can incorporate absorbing boundary conditions) has been explained. Examples of photoacoustic wave propagation in heterogenous, tissue-like, media are given.

ACKNOWLEDGMENT

This work has been supported by the Engineering and Physical Sciences Research Council, UK.

[1] A. C. Tam, "Applications of photoacoustic sensing techniques," Rev. Mod. Phys. **58**, 381–431 (1986).
[2] G. A. West, J. J. Barrett, D. R. Siebert, and K. V. Reddy, "Photoacoustic spectroscopy," Rev. Sci. Instrum. **54**, 797–817 (1983).
[3] J. G. Laufer, C. Elwell, D. Delpy, and P. Beard, "In vitro measurements of absolute blood oxygen saturation using pulsed near-infrared photoacoustic spectroscopy: Accuracy and resolution," Phys. Med. Biol. **50**, 4409–4428 (2005).
[4] A. Rosencwaig, "Photoacoustic microscopy," Am. Lab. (Shelton, Conn.) **11**, 39–49 (1979).
[5] M. Luukkala and A. Penttinen, "Photoacoustic microscope," Electron. Lett. **15**, 325–326 (1979).
[6] H. Zhang, K. Maslov, G. Stoica, and L. Wang, "Functional photoacoustic microscopy for high-resolution and noninvasive in vivo imaging," Nat. Biotechnol. **24**, 848–851 (2006).
[7] M. Xu and L. V. Wang, "Photoacoustic imaging in biomedicine," Rev. Sci. Instrum. **77**, 041101 (2006).
[8] *Photons Plus Ultrasound: Imaging and Sensing 2005*, edited by A. A.

Oraevsky and L. V. Wang (SPIE, Bellingham, WA, 2005), Vol. 5697.
[9]*Photons Plus Ultrasound: Imaging and Sensing 2006*, edited by A. A. Oraevsky and L. V. Wang (SPIE, Bellingham, WA, 2006), Vol. 6086.
[10]R. A. Kruger, K. D. Miller, H. E. Reynolds, W. L. Kiser, D. R. Reinecke, and G. A. Kruger, "Contrast enhancement of breast cancer in vivo using thermoacoustic CT at 434 MHz—feasibility study," Radiology **216**, 279–283 (2000).
[11]F. F. M. de Mul and C., G. A. Hoelen, "Three-dimensional imaging of blood vessels in tissue using photo-acoustics," J. Vasc. Res. **35**, 192–194 (1998).
[12]X. Wang, Y. Pang, G. Ku, X. Xie, G. Stoica, and L. V. Wang, "Noninvasive laser-induced photoacoustic tomography for structural and functional in vivo imaging of the brain," Nat. Biotechnol. **21**, 803–806 (2003).
[13]R. Kruger, W. Kiser, D. Reinecke, G. Kruger, and K. Miller, "Thermoacoustic molecular imaging of small animals," Mol. Imaging **2**, 113–123 (2003).
[14]S. J. Norton and M. Linzer, "Ultrasonic reflectivity imaging in 3 dimensions—Exact inverse scattering solutions for plane, cylindrical, and spherical apertures," IEEE Trans. Biomed. Eng. **28**, 202–220 (1981).
[15]R. A. Kruger, P. Liu, Y. R. Fang, and C. R. Appledorn, "Photoacoustic ultrasound (PAUS)—reconstruction tomography," Med. Phys. **22**, 1605–1609 (1995).
[16]P. Y. Liu, "The P-transform and photoacoustic image reconstruction," Phys. Med. Biol. **43**, 667–674 (1998).
[17]M. H. Xu, Y. Xu, and L. H. V. Wang, "Time-domain reconstruction-algorithms and numerical simulations for thermoacoustic tomography in various geometries," IEEE Trans. Biomed. Eng. **50**, 1086–1099 (2003).
[18]D. Finch, S. K. Patch, and Rakesh, "Determining a function from its mean values over a family of spheres," SIAM J. Math. Anal. **35**, 1213–1240 (2003).
[19]S. J. Norton and T. Vo-Dinh, "Optoacoustic diffraction tomography: Analysis of algorithms," J. Opt. Soc. Am. A **20**, 1859–1866 (2003).
[20]Y. Xu and L. V. Wang, "Time reversal and its application to tomography with diffracting sources," Phys. Rev. Lett. **92**, 033902 (2004).
[21]M. Xu and L. V. Wang, "Universal back-projection algorithm for photoacoustic computed tomography," Phys. Rev. E **71**, 016706 (2005).
[22]J. Zhang, M. A. Anastasio, X. Pan, and L. V. Wang, "Weighted expectation maximization reconstruction algorithms for thermoacoustic tomography," IEEE Trans. Med. Imaging **24**, 817–820 (2005).
[23]Y. Xu and L. Wang, "Effects of acoustic heterogeneity in breast thermoacoustic tomography," IEEE Trans. Ultrason. Ferroelectr. Freq. Control **50**, 1134–1146 (2003).
[24]J. Zhang and M. A. Anastasio, "Reconstruction of speed-of-sound and electromagnetic absorption distributions in photoacoustic tomography," Proc. SPIE **6086**, 608619 (2006).
[25]M. Frenz, G. Paltauf, and H. Schmidt Kloiber, "Laser-generated cavitation in absorbing liquid induced by acoustic diffraction," Phys. Rev. Lett. **76**, 3546–3549 (1996).
[26]G. Paltauf, H. Schmidt Kloiber, and H. Guss, "Light distribution measurements in absorbing materials by optical detection of laser-induced stress waves," Appl. Phys. Lett. **69**, 1526–1528 (1996).
[27]D.-H. Huang, C.-K. Liao, C.-W. Wei, and P.-C. Li, "Simulations of optoacoustic wave propagation in light-absorbing media using a finite-differnce time-domain method," J. Acoust. Soc. Am. **117**, 2795–2801 (2005).
[28]H. Jiang, Z. Yuan, and X. Gu, "Spatially varying optical and acoustic property reconstruction using finite-element-based photoacoustic tomography," J. Opt. Soc. Am. A **23**, 878–888 (2006).
[29]B. T. Cox and P. C. Beard, "Fast calculation of pulsed photoacoustic fields in fluids using *k*-space methods," J. Acoust. Soc. Am. **117**, 3616–3627 (2005).
[30]B. T. Cox, S. Arridge, K. Köstli, and P. Beard, "Quantitative photoacoustic imaging: Fitting a model of light transport to the initial pressure distribution," Proc. SPIE **5697**, 49–55 (2005).
[31]A. Vogel, J. Noack, G. Hüttman, and G. Paltauf, "Mechanisms of femtosecond laser nanosurgery of cells and tissues," Appl. Phys. B **81**, 1015–1047 (2005).
[32]T. D. Mast, L. P. Souriau, D.-L. D. Liu, M. Tabei, A. I. Nachman, and R. C. Waag, "A *k*-space method for large-scale models of wave propagation in tissue," IEEE Trans. Ultrason. Ferroelectr. Freq. Control **48**, 341–354 (2001).
[33]M. Tabei, T. D. Mast, and R. C. Waag, "A *k*-space method for coupled first-order acoustic propagation equations," J. Acoust. Soc. Am. **111**, 53–63 (2002).
[34]K. Köstli and P. Beard, "Two-dimensional photoacoustic imaging by use of Fourier-transform image reconstruction and a detector with an anisotropic response," Appl. Opt. **42**, 1899–1908 (2003).
[35]B. Fornberg and G. B. Whitham, "A numerical and theoretical study of certain nonlinear wave phenomena," Philos. Trans. R. Soc. London, Ser. A **289**, 373–404 (1978).
[36]N. N. Bojarski, "The *k*-space formulation of the scattering problem in the time domain," J. Acoust. Soc. Am. **72**, 570–584 (1982).
[37]N. N. Bojarski, "The *k*-space formulation of the scattering problem in the time domain: An improved single propagator formulation," J. Acoust. Soc. Am. **77**, 826–831 (1985).
[38]B. Compani-Tabrizi, "K-space scattering formulation of the absorptive full fluid elastic scalar wave equation in the time domain," J. Acoust. Soc. Am. **79**, 901–905 (1986).
[39]Q.-H. Liu, "Generalisation of the *k*-space formulation to elastodynamic scattering problems," J. Acoust. Soc. Am. **97**, 1373–1379 (1995).
[40]G. J. Diebold and T. Sun, "Properties of photoacoustic waves in one-dimension, 2-dimension, and 3-dimension," Acustica **80**, 339–351 (1994).
[41]X. Yuan, D. Borup, J. Wiskin, M. Berggren, and S. A. Johnson, "Simulation of acoustic wave propagation in dispersive media with relaxation losses by using FDTD method with PML absorbing boundary condition," IEEE Trans. Ultrason. Ferroelectr. Freq. Control **46**, 14–23 (1999).
[42]Q.-H. Liu and J. Tao, "The perfectly matched layer (PML) for acoustic waves in absorptive media," J. Acoust. Soc. Am. **102**, 2072–2082 (1997).
[43]Q.-H. Liu, "The Pseudospectral Time Domain (PSTD) algorithm for acoustic waves in absorptive media," IEEE Trans. Ultrason. Ferroelectr. Freq. Control **45**, 1044–1055 (1998).
[44]B. T. Cox and P. C. Beard, "The frequency-dependent directivity of a planar Fabry-Perot polymer film ultrasound sensor," IEEE Trans. Ultrason. Ferroelectr. Freq. Control **54**, 394–404 (2007).

Broadband multimode baffled piezoelectric cylindrical shell transducers

Tetsuro Oishi, Boris Aronov, and David A. Brown[a)]
Acoustic Research Laboratory, Advanced Technology and Manufacturing Center, and Department of Electrical and Computer Engineering, University of Massachusetts Dartmouth, 151 Martine Street, Fall River, Massachusetts 02723-1502

(Received 15 June 2006; revised 8 February 2007; accepted 8 March 2007)

Hollow piezoelectric cylindrical shell transducers may be made directional for underwater acoustic applications by the use of suitable acoustical baffles and the operational bandwidth may be extended by using multiple resonant modes. A theoretical and experimental investigation was performed for circumferentially baffled piezoelectric cylindrical shell transducers operating in the zero and one modes of extensional vibration. The frequency responses and directivity patterns were analyzed under various conditions of energizing separate halves of electrodes. It was found that the broadest frequency response with nearly constant beamwidth can be obtained when the two halves of the piezoelectric ring are electromechanically excited 90 deg out-of-phase. The experimental results obtained with a proof-of-concept transducer were in good agreement with the theoretical predictions. © *2007 Acoustical Society of America.* [DOI: 10.1121/1.2722053]

PACS number(s): 43.38.Fx, 43.38.Pf, 43.30.Yj [WMC] Pages: 3465–3471

I. INTRODUCTION

Radially polarized piezoelectric cylindrical shell transducers are commonly used for underwater acoustic applications. The fundamental extensional mode (zero mode) is employed for various applications of omni-directional projectors and hydrophones, where the uniform voltage is applied to the inner and outer electrodes of the piezoelectric ring element. The applications employing other extensional modes (predominantly the mode one) are also well known,[1–4] where the inner and outer electrodes of the piezoelectric ring are scored into two halves and the electric field is applied to each half with opposite phase and the resulting directivity pattern is a cosine, the characteristic of a dipole. In receive mode, such a configuration is common for directional sonar buoys.

The electromechanical excitation of multiple extensional modes was considered under the arbitrary distribution of the electric field in Ref. 5. Analytical calculations were described for cylindrical shell transducers under various acoustical loading conditions, which can be introduced by the application of an acoustic baffle to a part of the cylindrical surface of the transducer. The circumferentially baffled cylindrical shell transducer, illustrated in Fig. 1, has directional radiation characteristics that remain relatively constant over a broad frequency range near and between the lowest extensional resonances.

The objective of this paper is to investigate the effects of simultaneous excitation of the zero and one extensional modes on the electroacoustical performance of baffled cylindrical shell transducers. The operation of a multimode transducer is evaluated theoretically in Secs. II and III and confirmed with an experiment prototype transducer and a dual amplifier driven in quadrature-phased conditions presented in Sec. IV.

II. MODAL ANALYSIS OF A BAFFLED CYLINDRICAL SHELL TRANSDUCER

The multimode electromechanical transducer employing extensional vibrations of piezoelectric ceramic rings was theoretically analyzed in Ref. 5, where a multi-contour equivalent circuit of the transducer was introduced and the general expressions for the parameters of the equivalent circuit were presented as functions of the electric field distribution in the body of the piezoelectric rings. The fundamental resonance frequency is given as $f_0 = c_{\text{piezo}}/(\pi D)$, where c_{piezo} and D are the sound speed and mean diameter of the piezoelectric material, and the sequence of resonance frequencies corresponding to the normal modes of vibration is given as $f_i = \sqrt{1+i^2} f_0$, where $i = 0, 1, 2, 3, \ldots$. The actual modes that are excited depend on the particular electric field distribution applied to the cylinder. For example, when one half of the inner and outer electrodes is excited electromechanically [such that the electric field distribution $\Theta_E(\phi) = 1$ for $|\phi|$

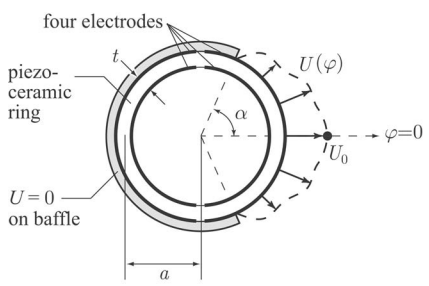

FIG. 1. Cross-section geometry of a baffled cylindrical shell transducer: a piezoelectric ring with electrodes scored into two halves and circumferential baffle.

[a)]Author to whom correspondence should be addressed. Electronic mail: dbacoustics@cox.net

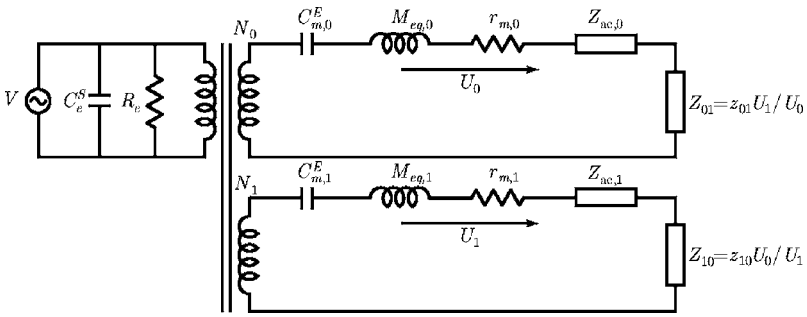

FIG. 2. Two-contour equivalent electromechanical circuit of a transducer operating in the zero and one modes.

$\leqslant \pi/2]$, the zero and one modes are dominant and strongly excited. The extensional mode number two, as well as all higher order even modes, are not excited due to symmetry, and the mode three, $f_3=\sqrt{10}f_0$, has a negligible contribution in the frequency range below approximately $2f_0$ as is shown in Ref. 2. Hence, the equivalent circuit of the baffled cylindrical shell can be reduced to the two-contour circuit as shown in Fig. 2.

The electromechanical transformation coefficient, compliances, mass, and dielectric constants for the zero and one modes are presented in Table I for several excitation conditions, where s^E_{11} is the elastic constant, a, t and h are the mean radius, thickness, and height of the piezoelectric cylinder, respectively; and k_{31} is the piezoelectric material coupling coefficient.

The parameters related to the acoustic field must be determined under consideration that a part of the transducer surface is covered with a circumferential baffle. In the present analysis, it is assumed that a half of the cylindrical surface is covered with a perfectly rigid baffle. Assuming that the height H of a transducer, which may be comprised of multiple rings of height h, is sufficiently large (i.e., H is comparable with the wavelength λ in water), the radiation impedance of the cylinder per unit height can be considered equal to the radiation impedance of the infinitely long cylinder. The calculations of the nondimensional coefficients of the self-radiation impedances $Z_{ac,ii}$ (α_{ii} and β_{ii}) and of the intermodal radiation impedance $z_{ac,01}$ (α_{01} and β_{01}) are presented in Ref. 5 and reproduced in Fig. 3. The radiation impedances in the equivalent circuit in Fig. 2 can thus be determined as $Z_{ac,00}=\pi a(\alpha_{00}+j\beta_{00})$, $Z_{ac,11}=(\pi a/2)(\alpha_{11}+j\beta_{11})$, and $z_{ac,01}=z_{ac,10}=(\pi a/2)(\alpha_{01}+j\beta_{01})$.

The modal velocities U_0 and U_1 can be found as the solution of the following set of Kirchhoff's equations that represent the two-contour equivalent circuit,

$$(Z_{m,0}+Z_{ac,00})U_0+z_{ac,01}U_1=N_0V,$$
$$z_{ac,10}U_0+(Z_{m,1}+Z_{ac,11})U_1=N_1V, \tag{1}$$

where V, N_i, and $Z_{m,i}=j\omega M_{eqv,i}+1/j\omega C^E_{m,i}+r_{m,i}$ are the input voltage, modal electromechanical transformation coefficients, and mechanical impedances, respectively. It should be noted that when used with a baffle, even if only one of the modes is electromechanically active, the other mode is also excited because the two contours of the equivalent circuit are acoustically coupled (*intermodal interaction*) by the coupled impedance $Z_{ac,i\ell}=z_{ac,i\ell}U_\ell/U_i$, where i, $\ell=0$ or 1.

The modal sound pressures can be found by substituting the modal velocities into the expression of the sound pressure generated by a baffled cylindrical shell transducer,

$$P_i(r,\varphi,\alpha)=\rho c\frac{\alpha ka}{2}\sqrt{\frac{2}{\pi kr}}e^{-j(kr-\pi/4)}U_i k_{diff,i}(\alpha)\cos i\varphi, \tag{2}$$

where r is the perpendicular distance from the cylindrical axis to the field observation point, φ is the azimuthal angle that makes with the reference plane, k is the wave number, and $k_{diff,i}$ (α) is the modal diffraction constant of the trans-

TABLE I. Illustrations of electric field distributions and electromechanical transformation coefficients for two-contour equivalent circuit of a baffled cylindrical shell transducer. $n_0=2\pi d_{31}h/s^E_{11}$ and $n_1=8d_{31}h/s^E_{11}$. In the case that only a part of electrodes is used for exciting the remaining part is assumed to be short circuited.

	N_i						
	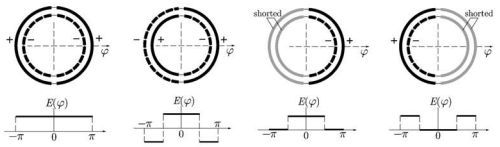				$C^E_{m,i}$	$M_{eq,i}$	ε^S_{33}
Zero mode	$N_0=n_0$	$N_0=0$	$N_0=n_0/2$	$N_0=n_0/2$	$\frac{as^E_{11}}{2\pi th}$	$2\pi ah\rho$	$\varepsilon^T_{33}(1-k^2_{31})$
One mode	$N_1=0$	$N_1=n_1$	$N_1=n_1/2$	$N_1=-n_1/2$	$\frac{as^E_{11}}{4\pi th}$		

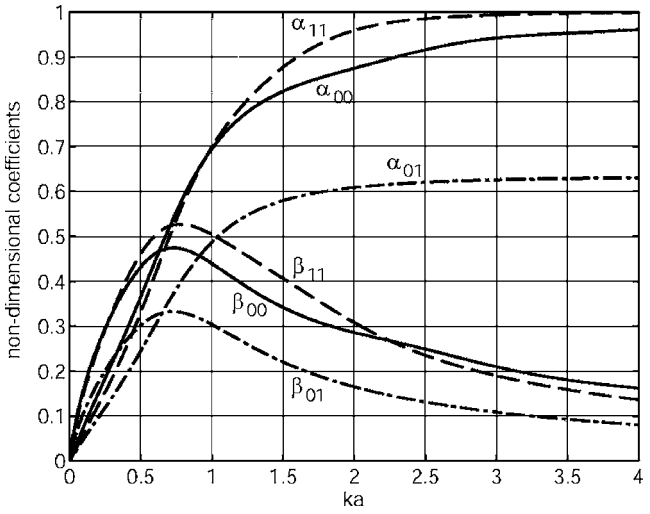

FIG. 3. Nondimensional coefficients of radiation resistance (α) and reactance (β) per unit length of infinitely long cylindrical transducer with 180-deg rigid baffle. The coefficients for the case of the compliant baffles at $ka>1$ coincides with those for the rigid baffle.

ducer as a function of baffle opening angle 2α. The diffraction coefficient per unit length of an infinitely long cylindrical radiator is

$$k_{diff,i}(\alpha) = \frac{1}{\pi\alpha ka}\sum_{n=0}^{\infty}\frac{j^{n-1}\varepsilon_n}{H_n^{(2)\prime}(ka)}a_{ni}(\alpha), \tag{3}$$

where $\varepsilon_0=1$ and $\varepsilon_n=2$ for $n\geqslant 1$, and

$$a_{ni}(\alpha) = \int_{-\alpha}^{\alpha}\cos n\varphi\cos i\varphi\, d\varphi. \tag{4}$$

Figure 4 shows the diffraction coefficients of the baffled ($\alpha=\pi/2$) cylindrical radiators for the zero and one modes, respectively.

When several modes are generated, the net sound pressure can be obtained by adding the comprising modal contributions. For the baffled cylindrical shell transducers, both

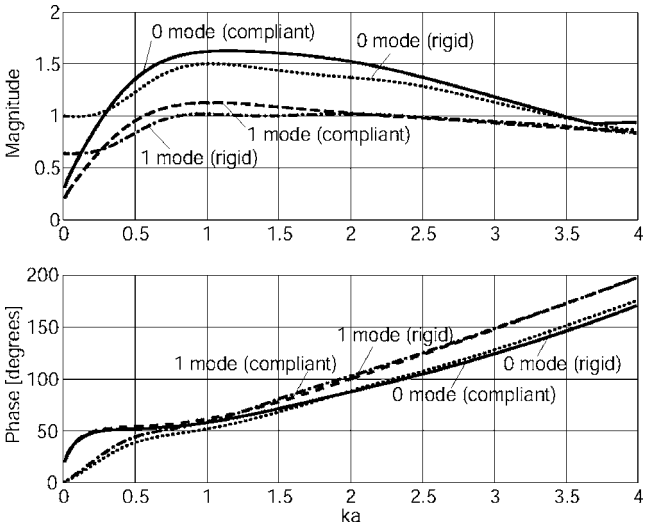

FIG. 4. Diffraction coefficients (magnitude and phase) for an infinitely long cylindrical transducer with a 180-deg baffle (for both ideally rigid and compliant cases) vibrating in the zero and one modes.

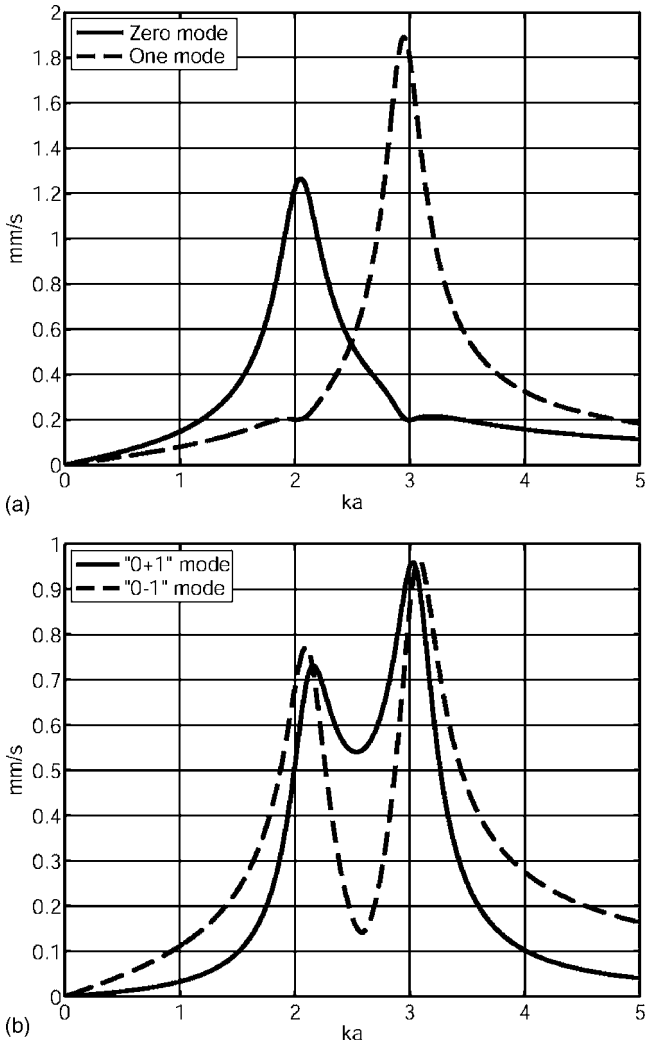

FIG. 5. Frequency responses of surface velocities of a baffled cylindrical shell transducer for various electrode configurations: (a) the zero mode (solid line) and the one mode (dashed line), (b) the "0+1" mode (solid line) and the "0−1" mode (dashed line).

the zero and one modes are generated irrespective of the condition of electrode connections due to the intermodal coupling and hence the resulting net sound pressure can be found as

$$P(\varphi,\pi/2) = P_0(\varphi,\pi/2) + P_1(\varphi,\pi/2). \tag{5}$$

The directional factor of the transducer in the horizontal plane may be calculated as

$$H(\varphi,\pi/2) = \frac{P_0(\varphi,\pi/2) + P_1(\varphi,\pi/2)}{P_0(0,\pi/2) + P_1(0,\pi/2)}. \tag{6}$$

The calculations of the frequency responses and directivity patterns were made based on Eqs. (2), (5), and (6) for the transducers comprised of radially polarized PZT-4 rings with the outer diameter $D=38.2$ mm and thickness $t=3.2$ mm. The frequency responses of the surface velocities are shown in Fig. 5 for all the electrode configurations shown in Table I. Figure 5(a) shows the frequency responses for the cases corresponding to the fully electroded elements

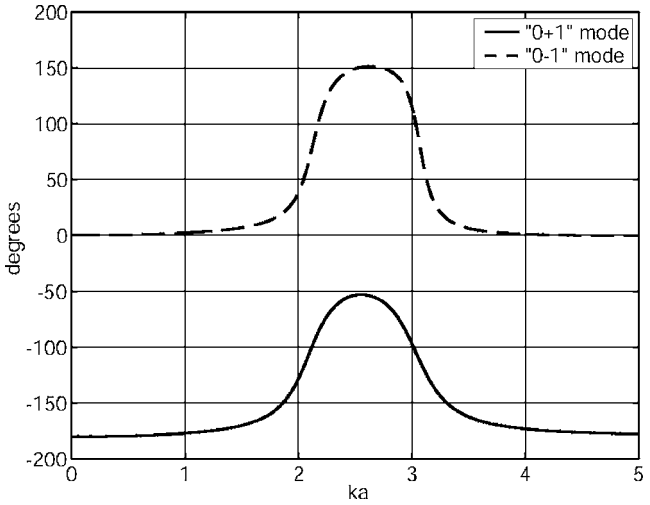

FIG. 6. Phase differences between the zero and one modal sound pressures when "0+1" and "0−1" modes are excited.

and electromechanical excitation in the zero and one modes. Figure 5(b) shows the frequency responses for the two cases that one half of the electrodes (on either baffled or unbaffled side) are used. As it follows from Table I, these two cases differ by the sign of the electromechanical transformation coefficients of the mode one. This change of the sign results in the constructive or deconstructive interference of the zero and one modal sound pressures. The phase differences of modal sound pressures between the zero and one modes are also shown in Fig. 6. We will designate the two resulting cases as the "0+1" (zero-plus-one) and "0−1" (zero-minus-one) modes, where the plus and minus signs indicate the constructive and deconstructive acoustic interference in the frequency range between the resonance frequencies f_0 and f_1. The directivity patterns corresponding to the four excitation cases are illustrated in Fig. 7 for the frequency range around and between f_0 and f_1. It is noted that the beamwidths for the zero, one, and "0+1" modes do not vary significantly in the frequency range presented. The broad characteristics of the frequency response [Fig. 5(b)] and frequency independent directional radiation pattern [Fig. 7(c)] for the "0+1" mode suggest the practical application for broadband directional projectors. However, only one half of the ceramic material is active, which results in a reduction of the sound pressure generated by the projector in comparison with the

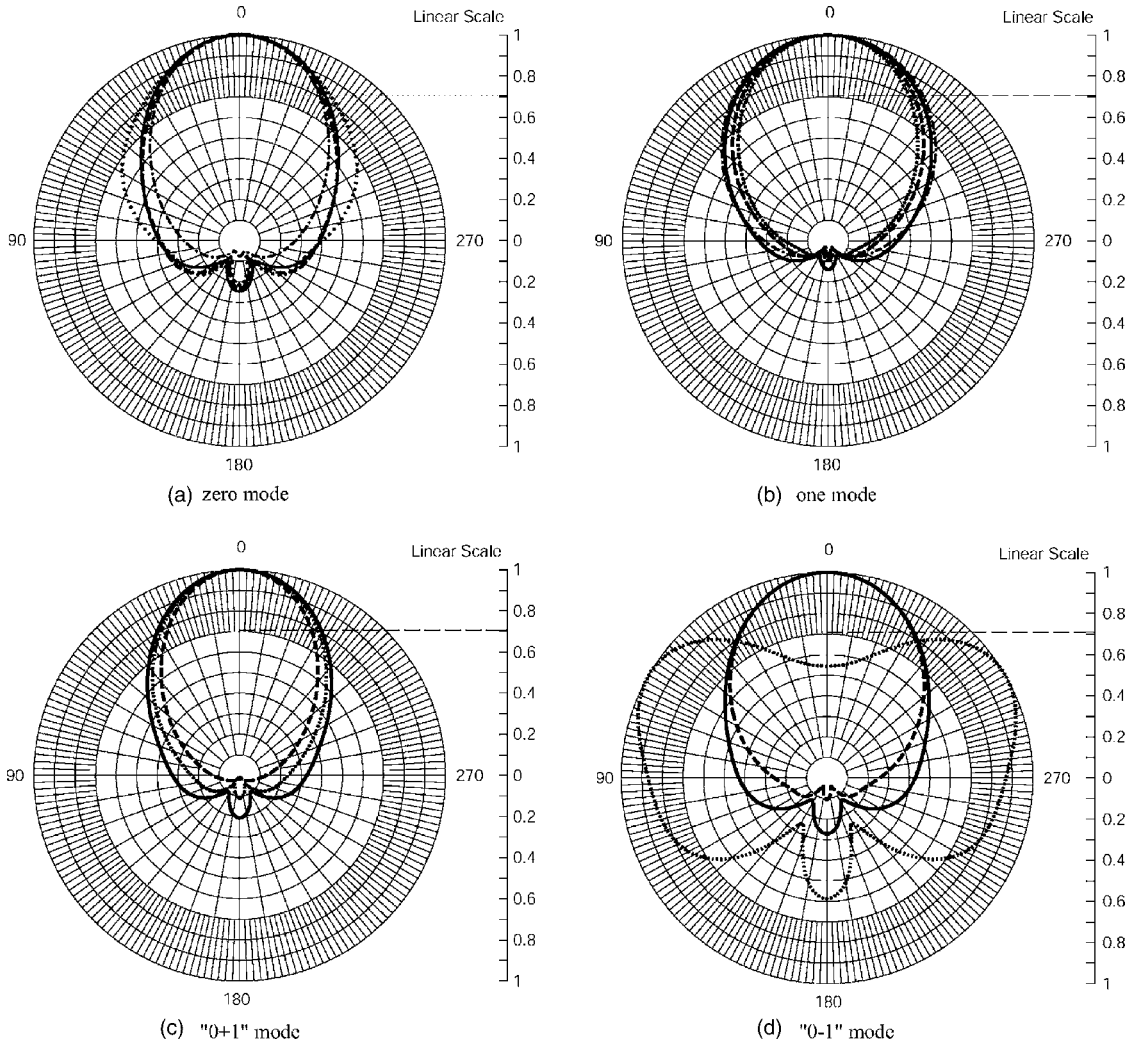

FIG. 7. Calculated directional factors (linear scale) for a rigid baffled cylindrical shell transducer at $ka=2.1$ (solid line), $ka=2.6$ (dotted line), and $ka=3.1$ (dashed line): (a) the zero mode, (b) the one mode, (c) "0+1" mode, and (d) "0−1" mode. The directional factors for a compliant baffled cylindrical transducer at $ka=2.1$ are also plotted in (a) and (b) with the dash-dotted line.

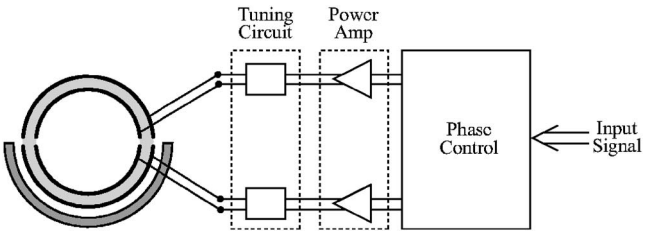

FIG. 8. Block diagram of a transmit system to operate a multimode projector.

single mode projectors utilizing all of the material for a particular frequency range. In the next section, the fully active piezoelectric dual mode is described.

While the previous analysis treated the case of an ideal rigid and thin conformal baffle, the implementation of such a boundary condition can only be approximated in practice. Also baffles that are more closely characterized as pressure release (or compliant), such as voided rubber or corprene (cork and rubber), are of practical interest. An analytical treatment of the pressure-release (compliant) boundary condition involves mixed boundary conditions and the presentation of this analysis is beyond the scope of this paper. However, results of such a treatment show that the diffraction constants and directivity patterns for the pressure-release boundary are approximately the same as for the conformal rigid boundary in the operational range for *ka* above unity. These results are included in Figs. 4 and 7. The directivity patterns (Fig. 7) are slightly narrower for the ideal pressure-release (compliant) boundary than for the rigid boundary in zero mode operation and virtually the same for mode one operation.

III. FULLY ACTIVE BROADBAND OPERATION USING PHASE BIAS

Let us consider the operation of a projector in the case that both the "0+1" and "0−1" modes are excited simultaneously by two electrical sources, whose relative phase can be controlled. Suppose that the voltage V is applied to one half of the piezoelectric rings to excite the "0+1" mode, and the voltage $Ve^{j\phi}$ is simultaneously applied to the other half to excite the "0−1" mode. This can be implemented by employing a two-channel transmit system with a controllable relative phase, ϕ, as illustrated in Fig. 8.

The simultaneous application of the voltages V and $Ve^{j\phi}$ to separate halves of the transducers results in the superposition of electromechanical forces acting in the mechanical contours. This can be expressed as

$$F_0 = n_0(1 + e^{j\phi})V/2 \quad \text{and} \quad F_1 = n_1(1 - e^{j\phi})V/2, \tag{7}$$

where F_0 and F_1 are the resulting forces of the electromechanical origin acting in the zero and one mechanical contours, respectively. Equivalently, if the voltage V is applied to the input of the equivalent circuit of the projector, the electromechanical transformation coefficients can be given in the form of

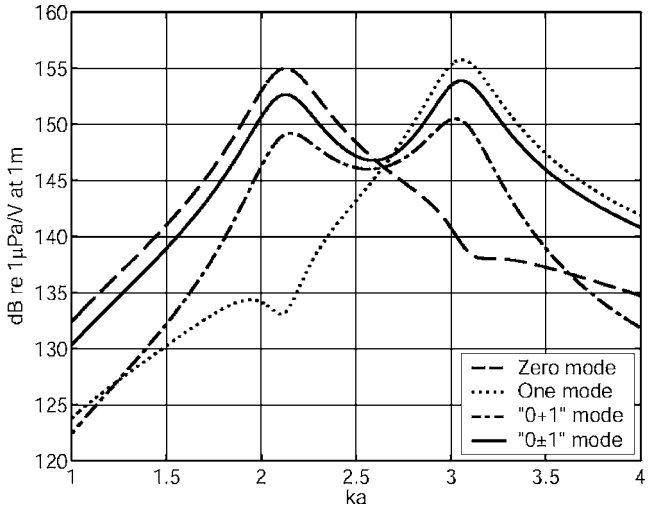

FIG. 9. Calculated transmit voltage responses (TVRs) of a baffled cylindrical shell transducer ($\alpha=\pi/2$) operating in the zero (dashed line), one (dotted line), "0+1" (dash-dotted line), and "0±1" (solid line) modes of excitation.

$$N_0 = n_0(1 + e^{j\phi})/2 \quad \text{and} \quad N_1 = n_1(1 - e^{j\phi})/2. \tag{8}$$

Thus, Eq. (1) can be used for the calculation of the modal velocities, given that the electromechanical transformation coefficients are expressed by Eq. (8). Obviously, the phase of $\phi=0$ deg results in $N_0=n_0(1+e^{j\phi})/2=n_0$ and $N_1=n_1(1-e^{j\phi})/2=0$, which is equivalent to the excitation of the zero mode, and the phase of $\phi=180$ deg results in $N_0=0$ and $N_1=n_1$, which is equivalent to the excitation of the mode one. In general, by changing the phase shift between the two channels, the frequency response of a projector can be controlled in favor of a particular frequency band in the range between the zero and one mode resonance frequencies. The analysis of the effects of various phase shifts showed that the flattest frequency response is achieved at $\phi=90$ deg. We will denote the multimode excitation of this kind as the "0±1" (zero-plus-minus-one) mode.

The transmit frequency response (TVR) was calculated for the projector operating in the 0±1 mode in water as shown in Fig. 9. TVRs of the same projector operating in the zero, one, and 0+1 modes are also presented for reference. The directional factors of the projector at selected frequencies and the −3 dB beamwidths as a function of *ka* are shown in Fig. 10. It can be seen that the beamwidth remains almost constant over the frequency range of interest.

IV. EXPERIMENTAL INVESTIGATION

An experimental study was performed on a transducer fabricated by the authors and BTech Acoustics, LLC. The transducer was built from four radially polarized PZT-4 rings with the outer diameter 38.2 mm, thickness 3.2 mm, and height 19 mm. The electrodes of the rings were scored into two halves, and the corresponding halves were connected in parallel. The overall height of the active part of the transducer is 79 mm. The transducer was encapsulated in polyurethane. The diameter of transducer after encapsulation is 48 mm. A baffle was applied to one half of the transducer surface. The baffle was made from two sheets of corprene with the total thickness of 6 mm. Two synchronized function

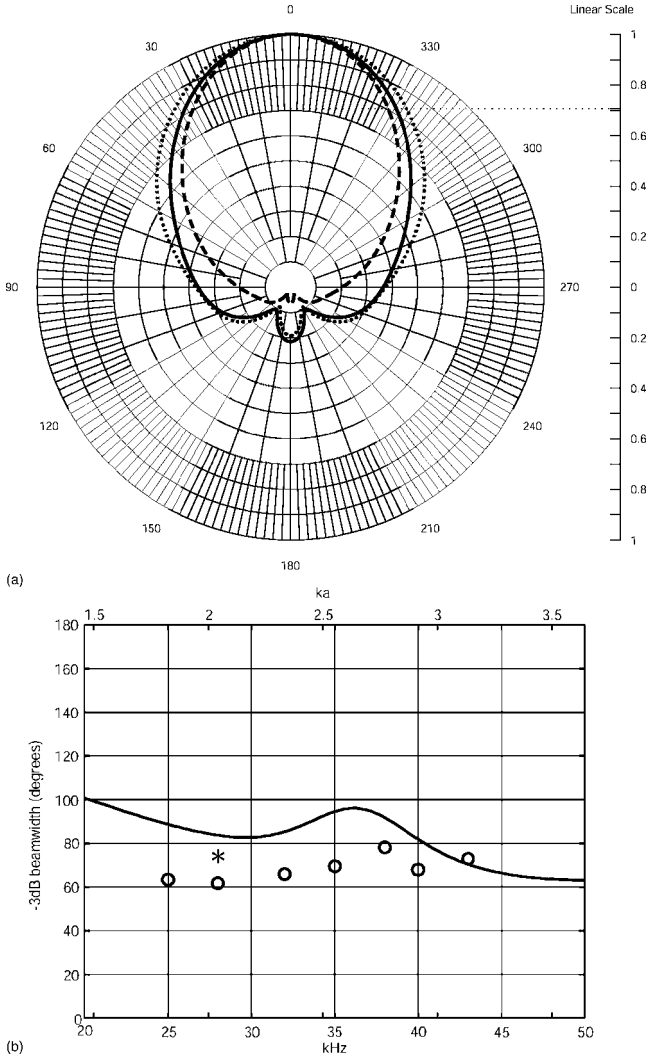

FIG. 10. Calculated directional factors with linear scale: (a) $ka=2.1$ (solid line), $ka=2.6$ (dotted line), and $ka=3.1$ (dashed line) and (b) −3 dB beamwidth for a transducer operating in the "0±1" mode (solid line), along with the experimental data (circles). The beamwidth is calculated for the case of a compliant baffle at $ka=2.1$ and is shown by an asterisk.

generators with adjustable phase shift between their outputs were employed to separately excite the halves of the transducer.

The results of the measurement of TVR of the transducer operating in the zero, one, and 0±1 modes (at the phase shifts 0, 180, and 90 deg, respectively) are presented in Fig. 11 and show good agreement with theoretical predictions. The directivity patterns were measured in the range of $ka=2.1$, 2.6, and 3.1. The −3 dB (0.707) beamwidths of directivity factors are plotted as a function of ka in Fig. 10(b). The beamwidths varied only from 60 to 80 deg in the operational frequency range of the transducer. It is of note that the beamwidths measured in the experiment are slightly smaller than the theoretical calculations of the rigid baffle as could be expected, because the corprene baffle material is closer to compliant (see the note in Sec. II about correlation between directivity patterns for the ideally rigid and ideally compliant baffles and the results presented in Fig. 7). The beamwidth

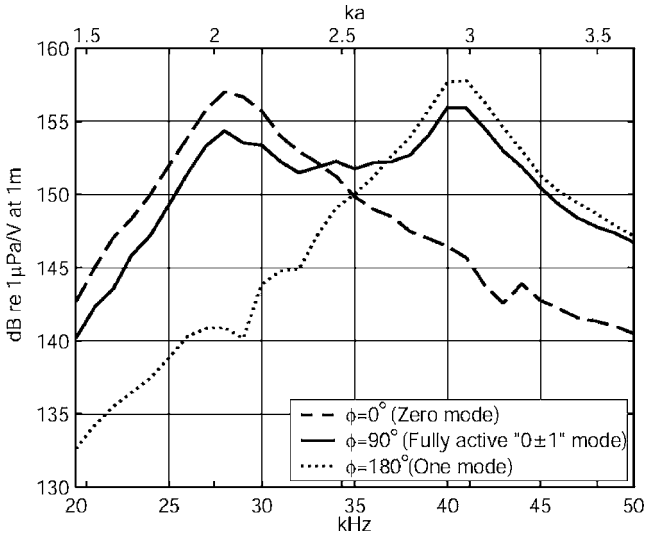

FIG. 11. Measured transmit voltage responses (TVRs) of a 180-deg corprene-baffled cylindrical shell transducer operating with various phase shifts between two electrical sources: $\phi=0$ deg for the zero mode (dashed line), $\phi=90$ deg for fully active "0±1" mode (solid line), and $\phi=180$ deg for the one mode (dotted line).

for the case of a compliant baffle is shown by an asterisk in Fig. 10(b)

V. CONCLUSION

A theoretical study employing modal analysis and multicontour equivalent electrical circuit modeling of multimode baffled cylindrical shell (or ring) transducers was presented and compared with an experimental investigation using a real electroacoustic transducer. Several variants were considered, each having distinguishing excitation conditions and corresponding frequency responses.

Broadband directional operation between resonances was obtained by exciting one half (the baffled-half) of the piezoelectric ring. This broadband mode of operation is achieved by the electromechanical excitation of the two lowest modes of extensional vibration and the corresponding acoustic radiation is made unidirectional due to the circumferential baffle. The resulting directivity patterns have nearly constant beamwidth across the frequency range encompassing these resonances. Alternatively, a broadband operation, which may be characterized as dual-band, is achieved by electromechanical excitation of the other half (unbaffled half) of the piezoelectric ring. In this variant, the contributions from the zero and one modes are constructive below the resonance of the zero mode, enhancing the low frequency response of the transducer, and destructive between resonances. In both of these half-active cases, the significant increase in usable bandwidth comes at the expense of a lower peak acoustic output compared with a fully active ring optimized for single mode operation in either the zero or one mode. Thus, a principle purpose of this study was to show that broader band operation could be achieved with an increase in acoustic output. Analytical and experimental results showed that the broadest frequency response was achieved

with simultaneous excitation of the separate halves with a 90-deg phase shift.

ACKNOWLEDGMENTS

This work was supported in part by the U.S. Office of Naval Research (ONR 321MS Lindberg) and BTech Acoustics, LLC. The author (TO) investigated the use of broadband baffled transducers in array configurations as the subject of his dissertation at the University of Massachusetts Dartmouth, and is currently employed with Bose Corporation. Calibration was performed at the Underwater Test Facility at the School for Marine Science and Technology, University of Massachusetts Dartmouth.

[1]R. S. Gordon, J. L. Butler, and L. Prasad, "Equivalent circuit of a ceramic ring transducer operated in the dipole mode," J. Acoust. Soc. Am. **58**, 1311–1314 (1975).
[2]B. S. Aronov, "Calculation of first-order cylindrical piezoceramic receivers," Sov. Phys. Acoust. **34**(5), 466–470 (1988).
[3]J. L. Butler, A. L. Butler, and J. A. Rice, "A tri-modal directional transducer," J. Acoust. Soc. Am. **115**(2), 658–665 (2004).
[4]M. E. Higgins, "DIFAR system overview," in Proc. of the Workshop on Directional Acoustic Sensors, NUWC/ONR, April 2001.
[5]B. Aronov, "The energy method for analyzing the piezoelectric electroacoustic transducers," J. Acoust. Soc. Am. **117**(1), 210–220 (2005).

High frequency vibration analysis by the complex envelope vectorization

O. Giannini, A. Carcaterra, and A. Sestieri[a)]
Dipartimento di Meccania e Aeronautica, Università di Roma "La Sapienza," Via Eudossiana 18, 00184 Rome, Italy

(Received 25 July 2006; revised 4 December 2006; accepted 27 March 2007)

The complex envelope displacement analysis (CEDA) is a procedure to solve high frequency vibration and vibro-acoustic problems, providing the envelope of the physical solution. CEDA is based on a variable transformation mapping the high frequency oscillations into signals of low frequency content and has been successfully applied to one-dimensional systems. However, the extension to plates and vibro-acoustic fields met serious difficulties so that a general revision of the theory was carried out, leading finally to a new method, the complex envelope vectorization (CEV). In this paper the CEV method is described, underlying merits and limits of the procedure, and a set of applications to vibration and vibro-acoustic problems of increasing complexity are presented. © *2007 Acoustical Society of America.* [DOI: 10.1121/1.2734402]

PACS number(s): 43.40.At, 43.55.Br, 43.20.Tb, 43.55.Ka [JGM] Pages: 3472–3483

I. INTRODUCTION

Several methods have been proposed in the last 20 years as alternatives to statistical energy analysis (SEA) to modeling high frequency vibrations and vibro-acoustic problems. The general approach of these methods involves a variable transformation: because of the large dimensions required to solve numerically high frequency problems, the physical variable, either displacement for a structure or pressure for an acoustic medium, is replaced by some kind of energy average. This transformation is generally more convenient from a numerical point of view and more significant for structures characterized by unavoidable uncertainties in the physical and geometrical parameters.

One of these methods is the complex envelope displacement analysis (CEDA).[1] Unlike most of the other energy-based high frequency techniques (SEA,[2] vibration conductivity methods,[3–6] wave intensity analysis[7]), the new used variable is not the energy but rather a complex envelope displacement defined through the Hilbert transform. This transformation maps the fast oscillating response of high frequency problems into an "envelope" response characterized by a low wave number content, and a new formulation, computationally more efficient, is obtained. Unlike SEA, but in analogy with vibration conductivity methods and others, CEDA provides a local information on the variable along the structure and presents other important advantages over the energy methods:

- the boundary conditions of the envelope problem can be easily determined from the physical boundary conditions;
- the forcing term of the envelope equation can be directly calculated from the physical load, avoiding the estimation of the input power necessary in the energy-based methods.

The complex envelope vectorization (CEV)[8,9] is an evolution of CEDA that was very successful in dealing only with one-dimensional systems. CEV uses a discrete formulation of the dynamic problem (e.g., a vibrating structure or a vibro-acoustic cavity) so that the response of the system is described by a vector. This vector can be regarded as the discrete counterpart of a one-dimensional variable to which the standard definitions and rules used in the one-dimensional CEDA are applied. In general, this procedure fulfils the features expected from the original CEDA, i.e., it is capable of describing the space response at high frequencies with a low computational effort, which is a main goal of the proposed procedure. In fact, a reduced model is obtained by the use of appropriate windows to create envelope functions of low wave number content that can be computed by a coarser mesh. Moreover, the procedure fills the medium frequency gap in between the deterministic methods, efficient at low frequencies, and the statistical methods suitable in the high frequency range.

It is interesting to point out that CEV can be also applied to other engineering fields that go beyond the analysis of vibro-acoustic problems, whenever a large number of degrees of freedom is necessary to describe the dynamics of complex linear systems (e.g., ultrasonic applications, micro/nano structures, electromagnetic waves). In this context CEV can be used to predict, at least, the characteristic trend of the solution.

In this paper a general presentation of the CEV procedure is proposed together with a critical analysis of the method and applications to systems of increasing complexity.

II. LOW FREQUENCY MAPPING OF HIGH FREQUENCY VIBRATION

The discrete equation of a conservative dynamic problem, forced by a harmonic force of radiant frequency ω_0 is

[a)]Author to whom correspondence should be addressed. Electronic mail: aldo.sestieri@uniromal.it

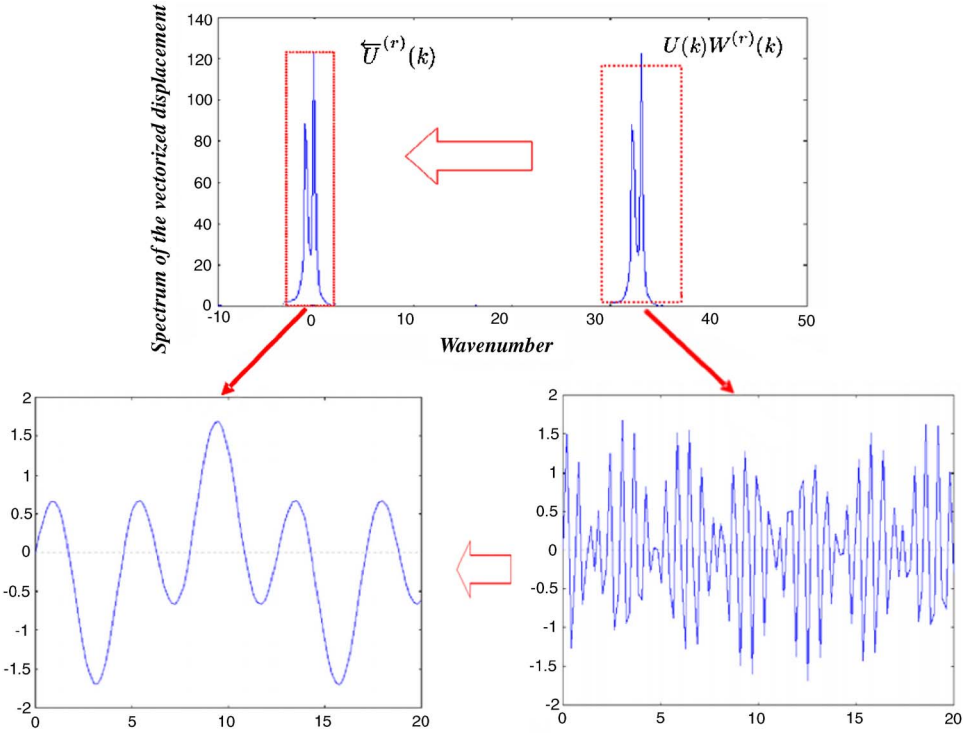

FIG. 1. (Color online) Original and shifted spectral window: wave number domain (upper figure), space domain (lower figures).

$$[-\omega_0^2\mathbf{M}+\mathbf{K}]\mathbf{u}=\mathbf{p}\Rightarrow\mathbf{A}\mathbf{u}=\mathbf{p}, \tag{1}$$

where **M** and **K** are mass and stiffness matrices, respectively. They are generally derived from a finite element discretization.

The vectors **u** and **p** can be viewed as sampled values of two continuous functions $u(s)$ and $p(s)$ of a dummy variable s:

$$\mathbf{u}=[u(s_1),u(s_2),\ldots u(s_n)]$$

$$\mathbf{p}=[p(s_1),p(s_2),\ldots p(s_n)].$$

In CEV a set of complex envelope signals $\tilde{u}^{(r)}(s)$ $(r=1,2,\ldots)$ is produced from $u(s)$, each one characterized by a narrow wave number spectrum around the origin of the wave number axis (k).

To obtain this result, the spectrum $U(k)$ of $u(s)$ is filtered by a set of narrow spectral windows $W^{(r)}(k)$:

$$W^{(r)}(k)=\begin{cases}1 & \text{for } |k-k_r|<\Delta_r/2\\ 0 & \text{elsewhere}\end{cases} \tag{2}$$

and shifted by the quantity k_r towards the wave number origin: this operation produces $\overleftarrow{U}^{(r)}$. The rth envelope signal $\tilde{\mathbf{u}}^{(r)}(s)$ is obtained by inverse Fourier transforming the total result, i.e.

$$\tilde{u}^{(r)}(s)=\mathcal{F}^{-1}\{U(k+k_r)W^r(k+k_r)\}. \tag{3}$$

Because of the hermitian symmetry of $U(k)$, it is convenient to consider the half positive spectrum $U^+(k)$ instead of $U(k)$:

$$U^+(k)=U(k)\quad \text{for } k\geqslant 0,$$

$$U^+(k)=0\quad \text{for } k<0.$$

With an appropriate choice of P adjacent filters $W^{(r)}$, each one centered around different values k_r, $U^+(k)$ is obtained as

$$U^{(+)}(k)=\sum_{r=1}^{P}\overleftarrow{U}^{(r)}(k-k_r). \tag{4}$$

The maximum wave number of $\overleftarrow{U}^{(r)}(k)$ is $\Delta_r/2$, implying that its spatial domain counterpart $\tilde{u}^{(r)}(s)$ is a slowly oscillating signal (Fig. 1). Since $\tilde{u}^{(r)}(s)$, the rth CEV solution component, does not have a symmetric wave number spectrum anymore, in general it is complex. CEV uses $\tilde{u}^{(r)}(s)$ as dynamic variables. For each of them an equation of motion is written and solved numerically with a procedure that saves computation time, because $\tilde{u}^{(r)}(s)$ has only low wave number components so that a coarse mesh is actually required.

The original real signal $u(s)$ is obtained by the complete spectrum (both negative and positive contributions) that, due to the hermitian symmetry, is

$$U(k)=U^{(+)}(k)+U^{(+)*}(-k), \tag{5}$$

where * denotes complex conjugate. Its inverse Fourier transform leads to

$$u(s)=u^+(s)+u^{+*}(s)$$

that finally produces

$$u(s)=2\,\mathrm{Re}\left\{\sum_{r=1}^{P}\tilde{u}^{(r)}(s)e^{jk_rs}\right\}. \tag{6}$$

The pair of transforms (3) and (6) are the basis of CEV method.

In summary, the operations needed to produce the complex envelopes $\tilde{\mathbf{u}}$ and $\tilde{\mathbf{p}}$ are:

- Fourier transform
- filtering
- shifting

All of them have their matrix representation. $\mathbf{F}$, $\mathbf{W}^{(r)}$ and $\mathbf{S}^{(r)}$ denote Fourier transform, filtering and shifting matrices, respectively.

Thus:

$$\tilde{\mathbf{u}}^{(r)} = (\mathbf{S}^{(\mathbf{r})}\mathbf{F}^{-1}\mathbf{W}^{(\mathbf{r})}\mathbf{F})\mathbf{u} = \mathbf{E}^{(\mathbf{r})}\mathbf{u}, \tag{7}$$

where $\mathbf{E}^{(\mathbf{r})}$ is the rth envelope matrix. Note that $\mathbf{E}^{(\mathbf{r})}$ is not invertible because $\tilde{\mathbf{u}}^{(r)}$ only contains partial information on $\mathbf{u}$: in fact, $\tilde{\mathbf{u}}^{(r)}$ is obtained from $\mathbf{u}$ by applying a suitable filter. It means that the signal information is lost except within the selected frequency band. Therefore, from $\tilde{\mathbf{u}}^{(r)}$ it is not possible to recover $\mathbf{u}$. The whole set of $\tilde{\mathbf{u}}^{(r)}$ is needed indeed to produce $\mathbf{u}$.

For damped systems, either hysteretic or viscous, the described formulation still holds. In this case $\mathbf{A}$ and $\mathbf{u}$ are complex, i.e., $\mathbf{A}=\mathbf{A}_R+j\mathbf{A}_I$ and $\mathbf{u}=\mathbf{u}_R+j\mathbf{u}_I$, where the subscripts R and I denote real and imaginary parts, respectively. To maintain the fundamental steps of the approach presented above, $\mathbf{u}_R$ and $\mathbf{u}_I$ must be rearranged into a new real vector $\bar{\mathbf{u}}$, and the same must be done for $\mathbf{A}_R$ and $\mathbf{A}_I$:

$$\bar{\mathbf{u}} = \begin{bmatrix} \mathbf{u_R} \\ \mathbf{u_I} \end{bmatrix}.$$

$$\bar{\mathbf{A}} = \begin{bmatrix} \mathbf{A_R} & -\mathbf{A_I} \\ \mathbf{A_I} & \mathbf{A_R} \end{bmatrix}.$$

Finally, let us define the new vector $\bar{\mathbf{p}}$ such that

$$\bar{\mathbf{p}} = \begin{bmatrix} \mathbf{p} \\ \mathbf{0} \end{bmatrix}.$$

Thus, instead of Eq. (1), the alternative equation must be considered:

$$\bar{\mathbf{A}}\bar{\mathbf{u}} = \bar{\mathbf{p}} \tag{8}$$

to which the mentioned approach can be identically applied.

III. CEV EQUATIONS

The explicit form of Eq. (1) is

$$\sum_k A_{hk}u_k = p_h. \tag{9}$$

This equation can be turned into a continuous form by using $u(s)$ and $p(s)$

$$\int_I a(s,\sigma)u(\sigma)d\sigma = p(s), \tag{10}$$

where the kernel of the previous integral transform, $a(s,\sigma)$, replaces the matrix $\mathbf{A}$.

Under some conditions the kernel a can assume the following form (see the Appendix):

$$a(s,\sigma) = a(s-\sigma) \tag{11}$$

so that the integral in Eq. (10) has a convolution form. This is the case considered in previous presentations of CEV, that proved to be reliable, even if it holds strictly either for infinite systems or for finite homogeneous damped systems far from the boundaries.

When the convolution-like condition holds for a, the Fourier transform of Eq. (10) with respect to s, the application of the filter $W^{(r)}$ and the shift toward the origin by the quantity k_r produce

$$A(k+k_r)W^{(r)}(k+k_r)U(k+k_r) = P(k+k_r)W^{(r)}(k+k_r). \tag{12}$$

Turning back to the space domain, one simply obtains

$$\int_I \tilde{a}^{(r)}(s-\sigma)e^{-jk_r(s-\sigma)}\tilde{u}^{(r)}(\sigma)d\sigma = \tilde{p}^{(r)}(s). \tag{13}$$

Reconsidering its discrete counterpart, one can write

$$\sum_{n=1}^{N} \tilde{a}^{(r)}_{mn}e^{-jk_r\Delta s(m-n)}\tilde{u}^{(r)}_n = \tilde{p}^{(r)}_m, \tag{14}$$

where Δs is the sampling interval of the dummy variable s.

With obvious meaning of symbols, this equation can be written in matrix form

$$\tilde{\mathbf{A}}^{(r)}\tilde{\mathbf{u}}^{(r)} = \tilde{\mathbf{p}}^{(r)}. \tag{15}$$

Equation (14) provides the rule to build up the envelope matrix $\tilde{\mathbf{A}}^{(r)}$, starting from the physical matrix $\mathbf{A}$. Its elements are

$$\tilde{a}^{(r)}_{hk} = a_{hk}e^{-jk_r\Delta s(h-k)} \tag{16}$$

and, in matrix form

$$\tilde{\mathbf{A}}^{(r)} = \mathbf{S}^{(\mathbf{r})}\mathbf{A}\mathbf{S}^{(\mathbf{r})*} \tag{17}$$

$\mathbf{S}^{(\mathbf{r})}$ is a diagonal matrix with element $s_{ii}=e^{-jk_r\Delta si}$. $\mathbf{S}^{(\mathbf{r})*}$ is the complex conjugate of $\mathbf{S}^{(\mathbf{r})}$, that is coincident with $\mathbf{S}^{(\mathbf{r})^{-1}}$.

Note that, under the hypothesis of convolution, the elements of $\tilde{\mathbf{A}}^{(r)}$ are not affected by the filtering operation.

The known term $\tilde{\mathbf{p}}^{(r)}$ is obtained from the physical load $\mathbf{p}$ by Fourier transforming, cutting off the components prescribed by the filter $W^{(r)}$, and shifting the spectrum by k_r. The inverse Fourier transform returns $\tilde{\mathbf{p}}^{(r)}$.

It must be remarked that Eq. (15) must be solved for each of the filters applied, and, repeating this operation for each filtered equation, the physical displacement is recovered by combining the set of envelope responses by using Eq. (6).

IV. UNDERSAMPLING

It is worthwhile to underline that the matrix dimensions in Eq. (15) are equal to those of Eq. (1). Since the envelope vectors $\tilde{\mathbf{u}}$ and $\tilde{\mathbf{p}}$ have components that are smooth in space, they can be described with a significant saving of points. Thus, to avoid an unnecessary over-sampling of the solution and reach the computational advantage the new variable permits, the matrix size must be suitably reduced.

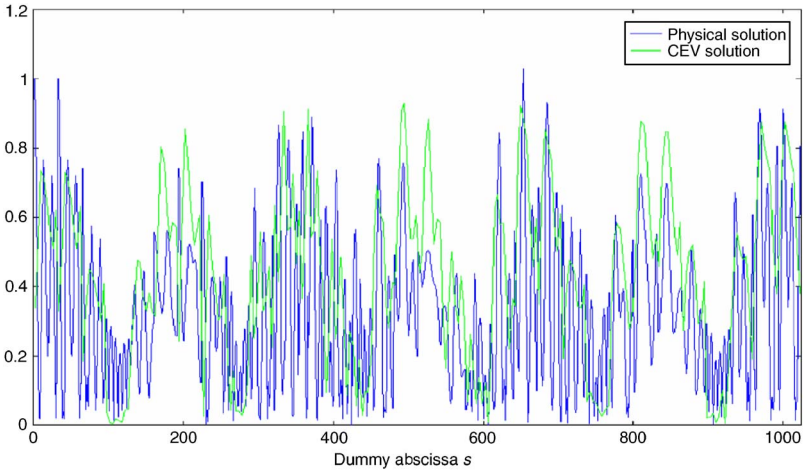

FIG. 2. (Color online) Comparison between the physical (solid line) and CEV (thin line) vectorized solutions.

Formally $\tilde{\mathbf{u}}$ can be recovered from a reduced vector $\mathbf{u}_{\text{red}}$ through an expansion matrix $\mathbf{R}$

$$\tilde{\mathbf{u}} = \mathbf{R}\tilde{\mathbf{u}}_{\text{red}} \tag{18}$$

[The superscript (r) used for the filters is here omitted for the sake of simplicity]. $\mathbf{R}$ is a suitable rectangular matrix, with less columns than rows. Such matrix can be obtained in different ways as explained later.

An equation for $\tilde{\mathbf{u}}_{\text{red}}$ is determined using Eqs. (15) and (18)

$$\tilde{\mathbf{A}}\mathbf{R}\tilde{\mathbf{u}}_{\text{red}} = \tilde{\mathbf{p}}. \tag{19}$$

By pre-multiplying by the pseudo-inverse $\mathbf{R}^+$ of $\mathbf{R}$ to obtain a square problem, one has

$$\mathbf{R}^+\tilde{\mathbf{A}}\mathbf{R}\tilde{\mathbf{u}}_{\text{red}} = \mathbf{R}^+\tilde{\mathbf{p}}, \text{ i.e., } \quad \mathbf{R}^+\tilde{\mathbf{A}}\mathbf{R}\tilde{\mathbf{u}}_{\text{red}} = \tilde{\mathbf{p}}_{\text{red}}. \tag{20}$$

Thus, letting $\mathbf{R}^+\tilde{\mathbf{A}}\mathbf{R} = \tilde{\mathbf{A}}_{\text{red}}$, one finally has

$$\tilde{\mathbf{A}}_{\text{red}}\tilde{\mathbf{u}}_{\text{red}} = \tilde{\mathbf{p}}_{\text{red}}. \tag{21}$$

Note that it is $\mathbf{R}^+\mathbf{R} = \mathbf{I}$, while $\mathbf{R}\mathbf{R}^+ \neq \mathbf{I}$.

About the choice of $\mathbf{R}$, typically the Shannon expansion matrix would be appropriate but its use is computationally heavy so that a different choice is preferable. For example, for a 6×6 matrix $\mathbf{A}$ and a reduction ratio $\tau = 2$, the expansion matrix $\mathbf{R}$ can be defined as:

$$\mathbf{R} = \begin{bmatrix} 1 & 0 & 0 \\ 1 & 0 & 0 \\ 0 & 1 & 0 \\ 0 & 1 & 0 \\ 0 & 0 & 1 \\ 0 & 0 & 1 \end{bmatrix},$$

whose pseudo-inverse is simply given by $\mathbf{R}^+ = \mathbf{R}^T/\tau$. The operation $\mathbf{R}^+\tilde{\mathbf{A}}\mathbf{R} = \tilde{\mathbf{A}}_{\text{red}}$ implies a partition of the original matrix into square submatrices, replacing each submatrix with a single value obtained by averaging its elements.

The problem (21) is the one actually solved by CEV.

As stated in the previous sections, such new problem is determined by the following steps:

- $\mathbf{A}$ ($\mathbf{M}$ and $\mathbf{K}$) is determined by a standard finite element formulation;
- $\tilde{\mathbf{A}}^{(r)}$ is built up through Eq. (17);
- $\tilde{\mathbf{p}}^{(r)}$ is produced by Fourier transforming the forcing vector $\mathbf{p}$, cutting off the wave number components as prescribed by the filter $\mathbf{W}^{(\mathbf{r})}$ and shifting the spectrum by k_r. Finally, the inverse Fourier transform returns $\tilde{\mathbf{p}}^{(r)}$;
- $\tilde{\mathbf{A}}^{(r)}_{\text{red}}$ is determined by
  $$\mathbf{R}^+\tilde{\mathbf{A}}^{(r)}\mathbf{R} = \tilde{\mathbf{A}}^{(r)}_{\text{red}},$$
- $\mathbf{p}^{(r)}_{\text{red}}$ is determined by
  $$\tilde{\mathbf{p}}^{(r)}_{\text{red}} = \mathbf{R}^+\tilde{\mathbf{p}}^{(\mathbf{r})}.$$

V. LIMITS OF THE PROPOSED PROCEDURE

CEV provides the solution for each excitation frequency at a low computational cost because the actual size of the problem is much smaller than the size of the physical problem. Generally the results are in good agreement with the numerical solution obtained by any discrete formulation (e.g., finite elements or finite differences). The solution obtained by such discrete formulation is hereafter named "physical solution." In Fig. 2 the CEV solution is compared with the physical solution presented in vector form, i.e., in the one-dimensional representation using the dummy variable s, for a particular frequency. A good match between them can be actually observed.

However, such good agreement fails sometimes, as it is shown in Fig. 3 where the same comparison is made for a different excitation frequency. Thus, it is necessary to analyze carefully the reasons that lead to these limitations before being confident with this approach. In fact, although the overall response is on average well kept, the local error is not negligible.

A. Convolution-like condition

The condition (11) can introduce important errors. In fact, the convolution-like condition is strictly valid for infinite homogeneous structures. For finite systems the assumption in not valid anymore: however, as shown in the Appen-

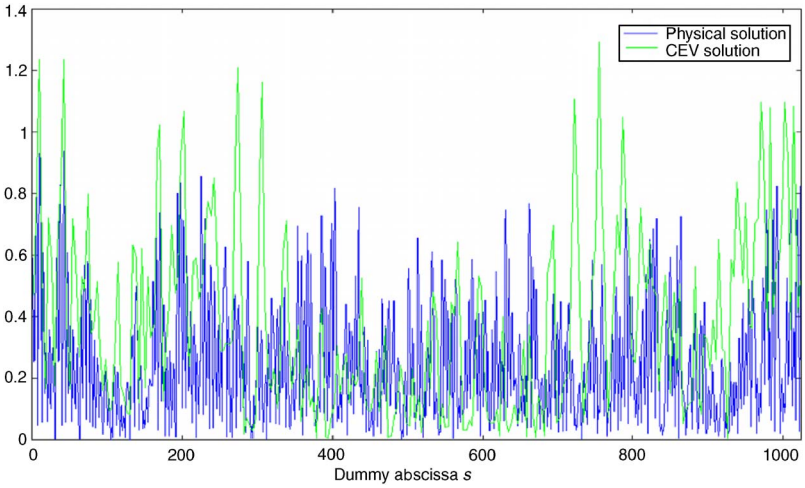

FIG. 3. (Color online) Comparison between the physical (solid line) and CEV (thin line) vectorized solutions.

dix , it is possible to perform a space average on the system response to make the convolution-like condition approximately valid even for finite systems.

B. Mistuning of CEV

The numerical results presented in Sec. VII show that, although on average the trend of the physical solution is well matched by CEV, non-negligible errors can be locally introduced. A direct inspection of the figures reveals that the determined resonance peaks are not correct. This problem is briefly indicated as CEV mistuning.

In particular, a fundamental question arises: does CEV preserve the information on the resonant behavior of the system? The question is related to the eigenfrequencies and eigen-vectors of $\overleftarrow{\mathbf{A}}^{(r)}$, replacing the physical operator $\mathbf{A}$.

Substitution for $\mathbf{u}=\Sigma_{j=1}^{N} c_j \boldsymbol{\Psi}_\mathbf{j}$ into Eq. (1) provides

$$c_j = \frac{\boldsymbol{\Psi}_j^T \mathbf{p}}{\omega_j^2 - \omega^2}, \tag{22}$$

where $\boldsymbol{\Psi}_j$ and ω_j are the eigenvectors and the associated eigenvalues of $\mathbf{A}$, respectively. Thus

$$\mathbf{u} = \sum_{j=1}^{N} \frac{\boldsymbol{\Psi}_j^T \mathbf{p}}{\omega_j^2 - \omega^2} \boldsymbol{\Psi}_j. \tag{23}$$

Similarly, for the rth component of the CEV problem

$$\overleftarrow{\mathbf{u}}^{(r)} = \sum_{j=1}^{N} \frac{\overleftarrow{\boldsymbol{\Psi}}_j^{(r)T} \overleftarrow{\mathbf{p}}}{\overleftarrow{\omega}_j^{(r)2} - \omega^2} \overleftarrow{\boldsymbol{\Psi}}_j^{(r)}, \tag{24}$$

where $\overleftarrow{\boldsymbol{\Psi}}_j$ and $\overleftarrow{\omega}_j$ are the eigenvectors and the eigenvalues of $\overleftarrow{A}^{(r)}$, respectively.

A comparison between the two last expressions suggests that, if the problem is not reduced, it would be $\overleftarrow{\omega}_j^{(r)} = \omega_j$ for any r. In fact, in this case $\mathbf{A}$ and $\overleftarrow{\mathbf{A}}^{(r)}$ are similar matrices [see Eq. (17)], and their eigenvalues coincide. However, this property does not hold anymore if $\overleftarrow{\mathbf{A}}^{(r)}$ is reduced, because in this case the matrix dimensions of the problem are lower than the original one, and the number of the eigenvalues of $\overleftarrow{\mathbf{A}}^{(r)}$ is also reduced. Thus, any chance of matching the physical and CEV eigenvalues is definitely lost.

However, although for each filtered CEV component the number of eigenvalues is lower than that of the physical matrix, the CEV problem is solved for many spectral windows. This introduces a sort of compensation mechanism that allows a rebalance of the total number of eigenvalues produced by the whole CEV solution that is comparable with the number of eigenvalues of the physical problem.

Figure 4 compares the eigenvalues obtained from the reduced problem (dots) for different windows with those of the not reduced problem (lines). Although there is not an exact match between the physical and reduced eigenvalues, the difference is within acceptable limits.

C. Leakage effect in the filtering process, due to the use of finite Fourier transforms

As mentioned before, the filtering process plays an important role in the CEV procedure. In fact, by CEV, a low wave number problem is solved at each step; this is made possible because, at each step, the applied filter cuts off any high wave number component from the spectrum of the solution. Although this is the main goal of the filtering opera-

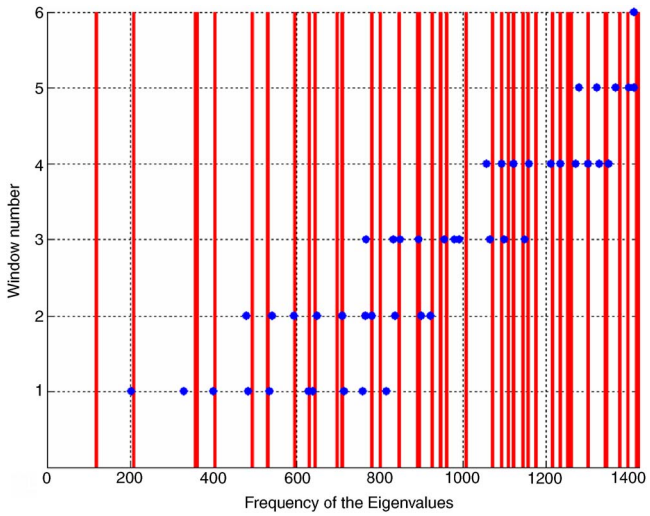

FIG. 4. (Color online) Comparison between the eigenvalues of the original problem (lines) and the eigenvalues of the reduced system for different filters.

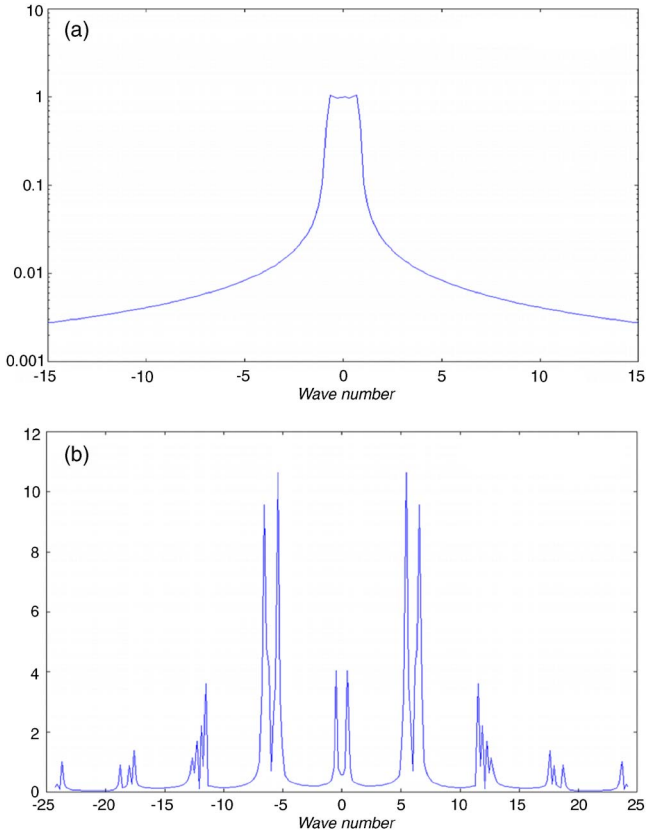

FIG. 5. (Color online) (a) Spectrum of the filtered load, (b) spectrum of the filtered response, with the filter set at $k_0=6$.

tion and although the theory explains how to handle the equation of motion to produce this effect, a direct inspection of the spectrum of the CEV solution shows that, in general, the spectrum is not confined within the desired filter bandwidth, but rather it spreads out. The presence of this spread has some important effects when considering the partial solution obtained for each filter, although it does not consistently affect the total results.

Looking at the spectrum of a point load that is flat in the wave number domain, we observe that the filtered spectrum is not sharply rectangular, presenting indeed two nonzero vanishing "tails" outside the filter bandwidth, due to the use of a finite number of points, i.e., of a truncated Fourier transform of the signal. This causes a drawback, especially in the absence of any dissipation effect. In fact, a very large response of the system outside the filter bandwidth can be excited even with a very small energy of the load spectrum.

In Fig. 5(a) the wave number spectrum of the filter is shown. The filter of bandwith 2 is applied to the central wave number $k=6$, but it is shifted to the wave numbers' origin. Even if the out-of-filter components of the load are rather small, this is not true for the correspondent solution: as it can be observed in Fig. 5(b), where the response to the same filtered load is presented, the spectrum around $k=6$ is prominent, but it spreads out to the adjacent frequencies.

The consequence of the spread is a response that is not strictly confined in the filter bandwidth. However, since the total solution is obtained by summing the contributions of adjacent filters that have different phases, in practice the global effect of the filters' spread is significantly reduced.

D. Remarks

The above arguments, especially those related to the mistuning of the natural frequencies and the out-of-filter spread, indicate that the critical weakness of CEV is mostly ascribed to the eigensolutions of the envelope operator $\tilde{\mathbf{A}}$. In practice it could be stressed that the CEV acts correctly on the forced part of the problem but is not as efficient to tackle the homogeneous part of the solution.

Before further considerations, it is worthwhile to resume the main points of the previous considerations:

- under the assumption that the CEV solution is smooth and obtained as an extension of the one-dimensional problem, i.e., by canceling the negative part of the force wave spectrum (Hilbert transform) and shifting the positive spectrum to the origin, it is not possible to determine a general invertible transformation that keeps the eigenvalues of the original problem and provides smooth eigenvectors;
- the envelope operator works appropriately on the forced part of the problem, i.e., it makes the correct job for the force, but it fails for the homogeneous part, in correspondence to the CEV eigenvalues. However, it does not mean that the method always fails, and several cases analyzed show that a good solution is obtained for complex structures and acoustic cavities;
- whenever the eigenvalues and eigenvectors of the problem do not play an important role, the CEV solution is in a good agreement with the physical solution.

VI. SUCCESSFUL APPLICATIONS OF CEV

The last point of the previous section indicates in which cases CEV can be certainly considered a successful procedure. In fact, ideally it is necessary that the modes of the system have a negligible role on the solution, and this is possible when:

- the damping of the system is relatively high;
- the direct field is preponderant with respect to the reverberant field;
- a high frequency problem (the ratio between a typical dimension of the structure with respect to the considered exciting wavelength is high) with an acceptable damping is considered;
- an external acoustic problem (no modes) is considered. It is worthwhile to stress that in this last case the convolution form of the integral Eq. (10) is strictly valid because the kernel a can be directly derived from the free space Green function that is only dependent on the distance between the source and observation points.

In the other cases CEV is not totally reliable. However, the results presented in the next section show that the general trend of the solution is always well determined and appropriate averages in frequency bands provide results at least comparable with those furnished by other methods.

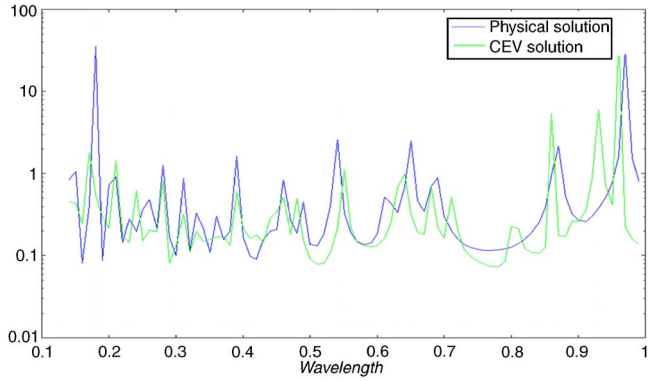

FIG. 6. (Color online) Comparison between the physical (solid line) and CEV (thin line) solution (source point).

VII. RESULTS

The previous figures (e.g., 2 and 3) show the kind of results the method can provide. However, it is preferable to present the results differently, highlighting the frequency (wave number) response of the solution. Actually this is the common output of most vibro-acoustic codes. Note that in all the graphs presented below, the frequency response is averaged on the whole set of points or on appropriate subsets.

The first system considered is a two-dimensional cavity (1×1 m) excited by a point source. In Fig. 6 the comparison between the spectrum of the physical solution and the CEV solution, when using a reduced number of points (256 instead of 1024), is shown. The number of filters used is dependent on the frequency of excitation: the code computes the exciting wave number and uses a number of adjacent filters of bandwidth 3 m^{-1}, covering the range (0–1.5) k_0, k_0 being the exciting wave number. Note that the x scale does not represent the frequency but the wavelength λ so that low values of λ imply high frequencies. The range considered is between $\lambda=0.1$ and $\lambda=1.0$, i.e., from a frequency corresponding to the first mode until a frequency close to the hundredth mode. Because the system considered is a square cavity, all the modes are double.

These graphs deserve some comments. First of all, the envelope response matches quite well the average trend of the physical response: in general the difference is within 3 dB, excluding some frequencies, particularly in the very low and very high frequency range. For high values of λ (close to 1) there is always a large peak in the envelope (independently of the source location: presumably this is the error induced by the convolution-like condition, that is naturally more important at low frequencies, but becomes negligible when decreasing λ). However, the envelope response in this region has been recently improved by simply applying an appropriate window.

Another error is met at high frequency, on the left part of the graph. Here, presumably, the error is due to an insufficient dimension of the original grid, that is in the limit of the necessary discretization.

Beyond $\lambda=0.2$ the agreement is much better and included in the abovementioned range of 3 dB.

After this first simple case that, notwithstanding the limitations involving the eigenvalues of the CEV problem and the assumption of considering the mass and stiffness matrices of the problem as convolution-like matrices, provides results whose quality is at least comparable with other proposed techniques for vibro-acoustic analysis, the attention was addressed towards more complex cases.

Several cases of increasing complexity are analyzed: a simple cavity with an internal point source, a bending plate, a foam used for automotive isolation and, finally, a set of three plates coupled together. The last one is a common benchmark used by a group of Italian University units involved in a PRIN project "Novel methods for the analysis and control of vibro-acoustic systems." In all the cases presented, the range of frequencies analyzed is much wider than in the previous case, and can be considered quite significant from a vibro-acoustic point of view.

In Fig. 7 the case of a two-dimensional square cavity (1×1 m) is presented. A source point is applied at coordinates (0.03, 0.14). It is assumed that the damping factor of the system is 0.01. The finite element (FE) code is solved using a grid 64×64. Since in the acoustic problem each node has a single degree of freedom (pressure), the number of degrees of freedom is 4096. The CEV problem was solved by reducing the grid by two, obtaining a total number of degrees of freedom equal to 1024. Although it is clearly confirmed that the eigenvalues of the CEV problem do not

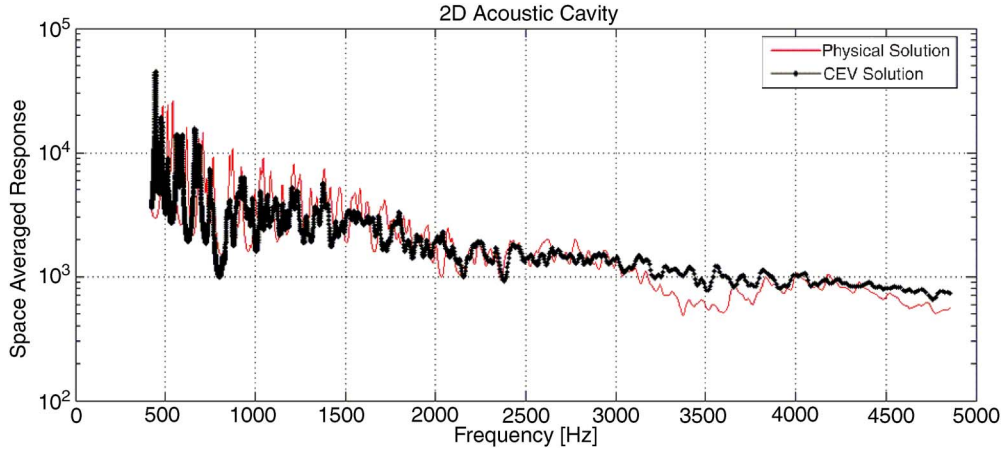

FIG. 7. (Color online) Comparison between the acoustic pressure and CEV solution (acoustic cavity).

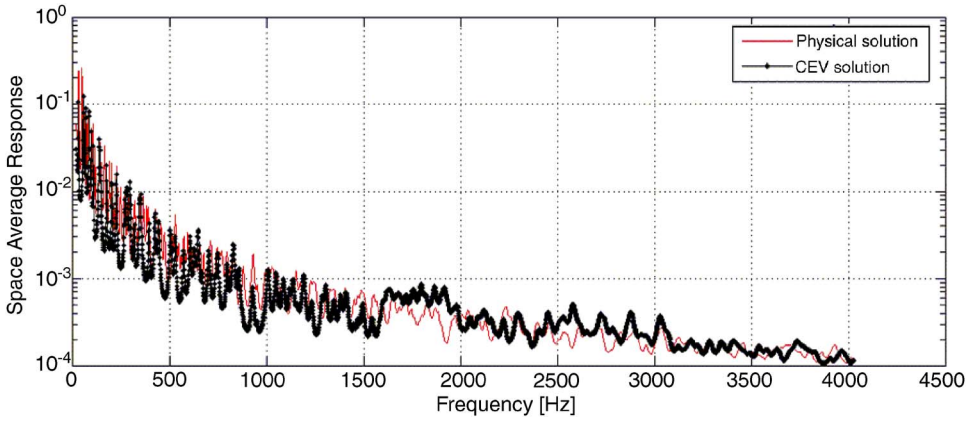

FIG. 8. (Color online) Comparison between the flexural displacements of the physical and CEV solution (bending plate).

match well those of the original problem, the trend is well described and the quality of results is acceptable.

The second case refers to a bending plate whose dimensions are $1\times1\times0.002$ m and is excited by a point force applied at coordinates (0.28,0.42). The plate is clamped at the four corners. The damping coefficient of the bending plate is assumed to be 0.01. As in the previous case, the original grid of the finite element code is 64×64: since in the present case the FE nodes have 3 degrees of freedom per node, the total number of degrees of freedom is 12,288. Unlike the previous cases, it is convenient here to order the vectors and, consequently, the matrix rows. Although not strictly necessary, this avoids too high discontinuities and irregularities in the vector response, made of translations normal to the plate (z) and rotations along the x and y axes. Therefore, the vectors are ordered to have first the translations of all the nodes, then the rotations around the x axis and finally the rotations around the y axis.

Using CEV, the number of degrees of freedom is reduced to 384, and the results of the flexural displacement are presented in Fig. 8, while in Fig. 9 the same case is presented by using a different plot that enlightens the physical solution, the maxima and minima of the CEV solution and the moving average of the CEV solution.

The second graph especially, Fig. 9, provides a clear indication of the kind of results that can be achieved by the CEV approach. The reduction rate is 32, the computer time is noticeably reduced and the agreement is outstanding for the general use of such analysis. Consider, moreover, that the damping used is quite small, and, as previously stated, this is not the ideal condition for the use of CEV. To test whether a significant damping improves the quality of CEV, a test was performed on a foam used by automotive industries for isolation purposes.

In Fig. 10 such result is presented for an unconstrained foam plate excited by a point force at coordinates (0.1,0.1). The dimensions of the foam plate are $1\times1\times0.05$ m, and the number of degrees of freedom used and the reduction performed is the same as in the case presented above. On the contrary, the damping now is much higher, i.e., 0.17. As expected, in this case the results match perfectly, confirming that the weak elements in the CEV procedure are related to the mistuning and filtering effects. In fact, in this case the damping is so high that the effect of the modes is negligible. Thus here prevails the forced solution, on which the CEV is totally efficient, while the homogeneous solution, on which the CEV is not efficient, does not play any significant role.

The final and most significant test was performed on the benchmark, made of three plates assembled together as shown in Fig. 11. The considered structure consists of three rectangular aluminum plates rigidly coupled together and freely suspended. The dimensions of the plates are: first plate (BE) 0.6×0.4 m, second plate (BB) 0.3×0.4 m, third plate (B) 0.4×0.4 m. The thickness of all the plates is 3 mm. The angle between the first and the second plate is 120°, while the angle between the first and the third plate is 60°. The

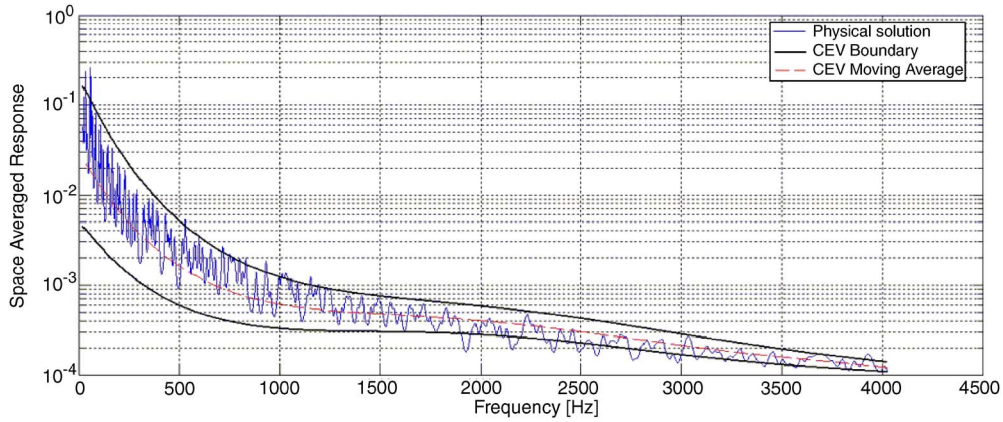

FIG. 9. (Color online) Comparison between the flexural displacements of the physical and CEV solution (bending plate).

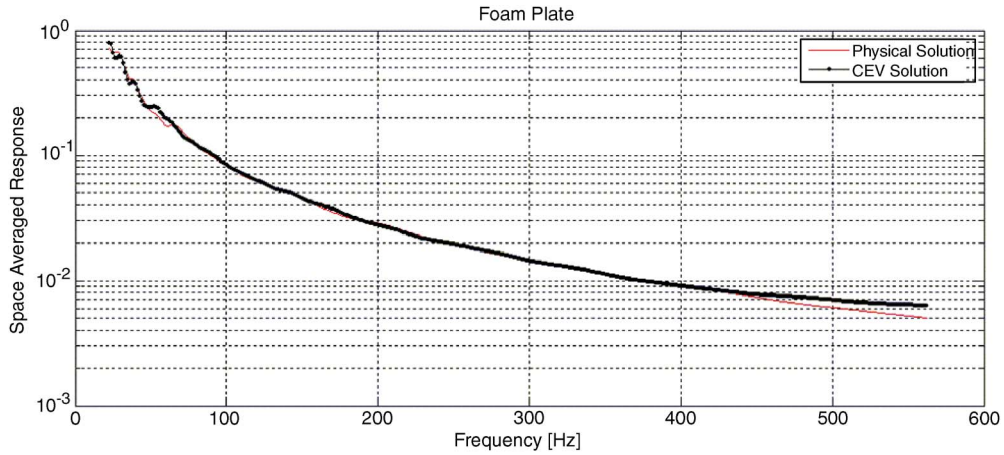

FIG. 10. (Color online) Comparison between the flexural displacements of the physical and CEV solution (foam).

assembling is obtained by bolted stirrups. The structure is assumed to be excited by a point force acting on plate BB at coordinates (0.4,0.24).

To compare the results between the CEV and the physical solution, a simple FE scheme of the benchmark was used. The joint was modeled as a line, where the three plates are clamped, without considering the stirrups and their thickness. Moreover, when considering the damped structure, the damping was spread on the plates without introducing any lumped damping in the joint.

Figures 12 and 13 present the comparison between the space average response of two of the three plates when a very low damping is present on the three plates (0.0001), while Figs. 14 and 15 show the same responses for a higher damping (0.04). The degrees of freedom used for in the finite element code were 32,226, while those used in CEV were 786, with a reduction ratio 41.

By observing these figures, one can stress again that the average trend of the response is well kept for any value of damping (low or high). However, while the CEV results for a very low damping do not match well the resonance frequencies of the physical system, those obtained for a higher damping are much better, confirming the statements made above on the positive effect of damping.

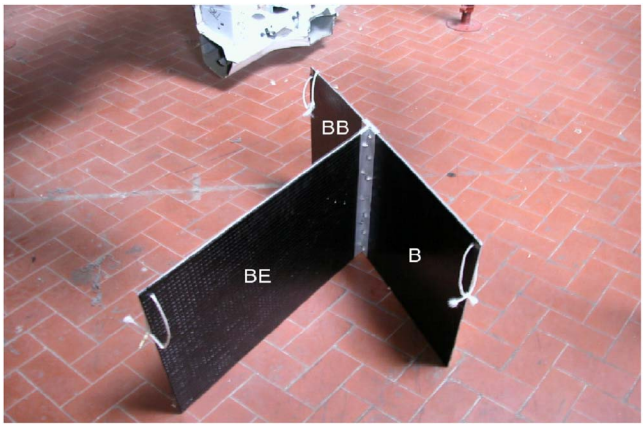

FIG. 11. (Color online) Benchmark used for the experiments.

VIII. CONCLUSIONS

Modeling high frequency vibro-acoustic problems is still a challenge since the sixties when the first basic paper on statistical energy analysis was published by Lyon and Maidanik.[10] Pushed by the increased need of comfort in the transport industry, from the nineties new efforts were devoted to this subject, with new interesting developments and advances in SEA (e.g., Refs. 11–14), with innovative methods, e.g., Wave Intensity Analysis, vibration conductivity, energy mobility[15] and, more recently, acoustic diffusion models,[16,17] ensemble energy average.[18] In such context the complex envelope displacement analysis is the only method that does not take advantage of an energy formulation, but rather it transforms the physical equation of motion into a new one, characterized by a field variable that has a low wave number content so that it can be numerically solved by a coarse mesh. Beyond this advantage, the method can account correctly for the physical boundary conditions of the problem, without the introduction of troublesome coupling coefficients and the need to estimate the input power to the system.

It is interesting to underline the good agreement obtained over the whole frequency range. In fact, while the deterministic methods (typically finite elements and boundary elements) are appropriate in the low frequency range and the statistical methods (typically SEA) work well at high frequencies, at intermediate frequencies any of these approaches fail. The first fail because the computation time is too high, while the use of SEA is generally inappropriate at low frequencies because the modal overlap factor is too small. On the contrary, CEV provides results in good agreement with the physical results, independently of the range of frequencies considered.

Notwithstanding these interesting features, the method presents theoretical limitations that are discussed in this paper. However, the method is quite successful when the modal behavior of the system is not too relevant, i.e., for structures whose damping is not too small, at high frequencies where the modal overlap is significant and for external problems. Moreover, the quality of results it provides is quite reason-

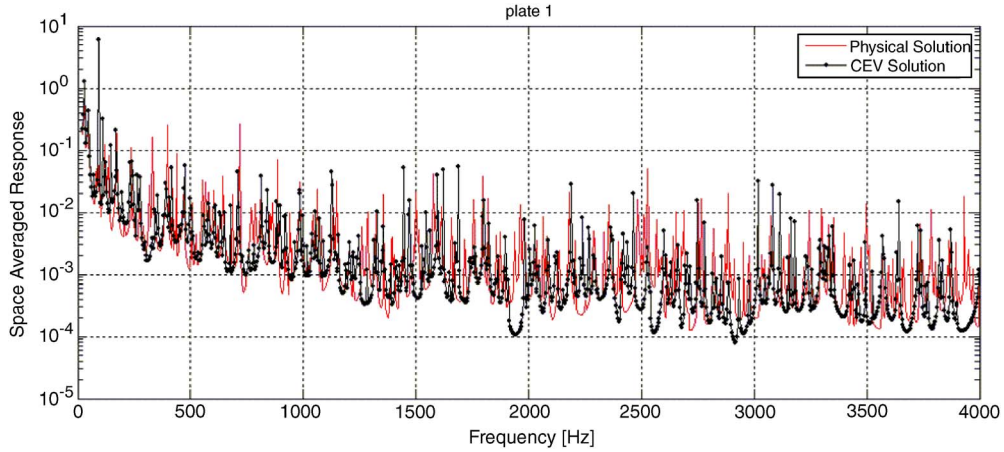

FIG. 12. (Color online) Comparison between the FEM and CEV space average response of plate 1 (damping 0.0001).

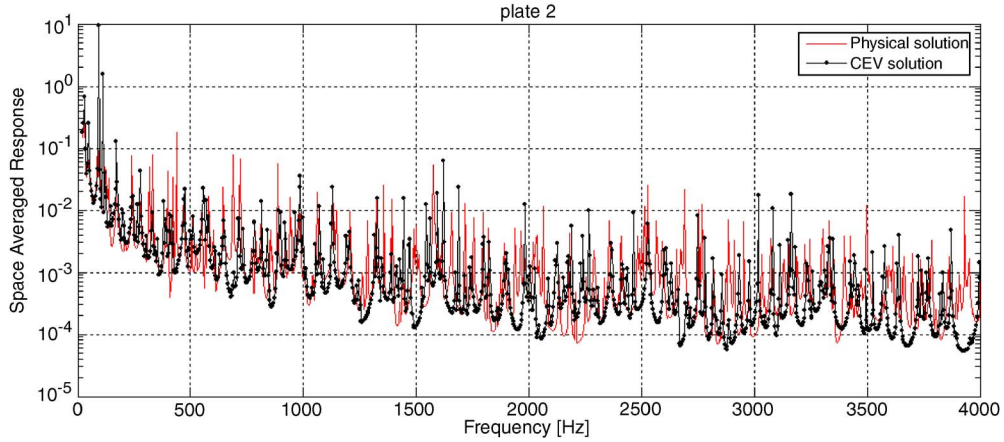

FIG. 13. (Color online) Comparison between the FEM and CEV space average response of plate 2 (damping 0.0001).

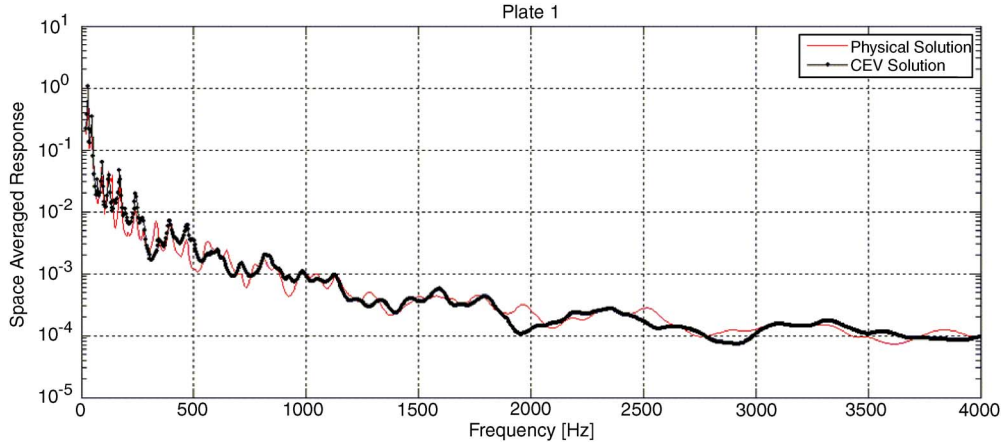

FIG. 14. (Color online) Comparison between the FEM and CEV space average response of plate 1 (damping 0.04).

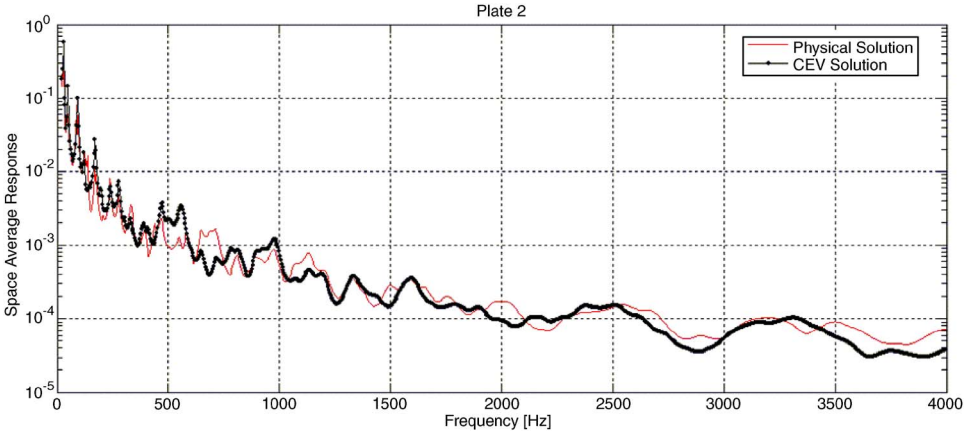

FIG. 15. (Color online) Comparison between the FEM and CEV space average response of plate 2 (damping 0.04).

able even when the above conditions are not strictly verified, so that it seems that one can look at the CEV as a convenient tool to analyze high frequency problems.

It is worthwhile to point out that this procedure could also offer appealing results if geometrical and physical uncertainties are introduced into the system, as is necessary when dealing with high frequency problems. In this case a meaningful result can be obtained only by performing frequency averages: so far none of these ingredients were considered, but it is expected that the method can conveniently manage uncertainties and random excitations, leading to more reliable results.

ACKNOWLEDGMENT

This work was developed under a PRIN project 2003, granted by MIUR (Italian Minestry of University and Research) "Novel methods for the analysis and control of vibro-acoustic system."

APPENDIX: Weak form for the kernel of Eq. (10)

For an infinite system the kernel $a(s,\sigma)$ of Eq. (10) can be directly determined from the free space Green function that is only dependent on the distance between the source and observation points. In this case it is certainly $a(s,\sigma) = a(s-\sigma)$.

For finite system this is not true anymore because the Green function is usually written in terms of the system modes. It means that a function $\tilde{a}$ does not exist such that

$$a(s,\sigma) = \tilde{a}(s-\sigma). \tag{A1}$$

However, although Equation (A1) is not strictly verified, it can hold in a weak or average form

$$\langle a(s,\sigma)\rangle = \langle \tilde{a}(s-\sigma)\rangle, \tag{A2}$$

where $\langle\cdot\rangle = \int_I \cdot\, d\sigma$.

To this aim, consider the Fourier transform of Eq. (A1) with respect to the variable s. For the first term one has:

$$\int_{\infty}^{\infty} a(s,\sigma)e^{-jk_s s} = A(k_s,\sigma)$$

and for the second

$$\int_{\infty}^{\infty} \tilde{a}(s-\sigma)e^{-jk_s s} = \tilde{A}(k_s)e^{-jk_s\sigma}.$$

Thus, it is

$$A(k_s,\sigma) = \tilde{A}(k_s)e^{-jk_s\sigma}. \tag{A3}$$

By averaging now Eq. (A3), one obtains

$$\langle A(k_s,\sigma)\rangle = \tilde{A}(k_s)\langle e^{-jk_s\sigma}\rangle$$

so that

$$\tilde{A}(k_s) = \frac{\langle A(k_s,\sigma)\rangle}{\langle e^{-jk_s\sigma}\rangle}.$$

By inverse Fourier transform it is possible to determine $\tilde{a}(s)$:

$$a(s) = \mathcal{F}^{-1}\left\{\frac{\langle A(k_s)\rangle}{\langle e^{-jk_s\sigma}\rangle}\right\}.$$

Thus, $\tilde{a}(s)$ is a function that satisfies Eq. (A2), i.e., the weak or average form of equation (A1).

This implies that in the cases where Eq. (A1) does not hold strictly, the assumption is valid in an average sense. Therefore, the CEV solution, although not strictly valid in any point of the domain, is still meaningful on average, i.e., it is valid for the prediction of the overall trend of the solution.

In the presentation of results, to fulfill with this position, the response spectra are always averaged on the whole points of the system considered.

[1] A. Carcaterra and A. Sestieri, "Complex envelope displacement analysis: A quasistatic approach to vibrations," J. Sound Vib. **201**(2), 205–233 (1997).
[2] R. H. Lyon and R. G. De Jong, *Theory and Applications of Statistical Energy Analysis* (Butterworth-Heinemann, Cambridge, 1995).
[3] D. J. Nefske and S. H. Sung, "Power flow finite element analysis of dynamic systems: Theory and application to beams," *ASME-NCA vol. 3, Statistical Energy Analysis* (1987).
[4] J. C. Wohlever and R. J. Bernhard, "Mechanical energy flow models of rods and beams," J. Sound Vib. **153**(1), 1–19 (1992).
[5] M. N. Ichchou, A. Le Bot, and L. Jezequel, "Energy models of one-dimensional multi propagative systems," J. Sound Vib. **201**, 535–554 (1997).
[6] A. Le Bot, "Geometric diffusion of vibrational energy and comparisons with the vibrational conductivity analysis," J. Sound Vib. **21**, pp. 637–647 (1998).

[7]R. S. Langley, "A wave intensity technique for the analysis of high frequency vibrations," J. Sound Vib. **159**(3), pp. 483–502 (1992).
[8]A. Carcaterra and A. Sestieri, "Complex envelope vectorization: A new approach to vibroacoustic problems," *Proceedings of Recent Advances in Structural Dynamics*, Southampton, (2003).
[9]A. Carcaterra and A. Sestieri, "Plate vibration by complex envelope vectorization," *Proc. Int. Seminar on Model Analysis 2002*, Leuven (Belgium) (2002).
[10]R. H. Lyon and G. Maidanik, "Power flow between lineary coupled oscillators," J. Acoust. Soc. Am. **34**(5), 623–639 (1962).
[11]B. Mace, "Statistical energy analysis, energy distribution models and system modes," J. Sound Vib. **264**(2), pp. 391–409 (2003).
[12]P. J. Shorter and R. S. Langley, "Vibroacoustic analysis of complex systems," J. Sound Vib. **288**, 669–699 (2005).
[13]R. S. Langley and P. G. Bremner, "A hybrid method for the vibrational analysis of complex structural-acoustic systems," J. Acoust. Soc. Am. **105**, 1657–1671 (1999).
[14]E. H. Dowell and D. Tang, *Dynamics of very high dimensional systems*, World Scientific, Singapore (2003).
[15]G. Orefice, J. L. Guyader, and C. Cacciolati, "The energetic mean mobility approach (EMMA)," *Proc. Int. Union on Theoretical and Applied Mechanics Symposium on Statistical Energy Analysis*, Southampton, (1997).
[16]N. L. Wolff and R. L. Weaver, "Towards a diffusion model of acoustic energy flow in large undamped structures," J. Sound Vib. **288**, 729–749 (2005).
[17]R. L. Weaver and O. J. Lobkis, "Anderson localization in coupled reverberation rooms," J. Sound Vib. **231**(4), 1111–1134 (2000).
[18]A. Carcaterra, "Ensemble energy average and energy flow relationships for nonstationary vibrating systems," J. Sound Vib. **288**, 751–790 (2000).

Locating air leaks in manned spacecraft using structure-borne noise

Stephen D. Holland,[a] D. E. Chimenti, Ron Roberts, and Michael Strei
Center for Nondestructive Evaluation, Iowa State Uninversity, Ames, Iowa 50011

(Received 27 July 2006; revised 4 March 2007; accepted 8 March 2007)

All manned spacecraft are vulnerable to leaks generated by micrometeorite or debris impacts. Methods for locating such leaks using leak-generated, structure-borne ultrasonic noise are discussed and demonstrated. Cross-correlations of ultrasonic noise waveforms from a leak into vacuum are used to find the location of the leak. Four methods for sensing and processing leak noise have been developed and tested and each of these can be used to reveal the leak location. The methods, based on phased-array, distributed sensor, and dual sensor approaches, utilize the propagation patterns of guided ultrasonic Lamb waves in the spacecraft skin structure to find the source or direction of the leak noise. It is shown that each method can be used to successfully locate the leak to within a few millimeters on a 0.6-m^2 aluminum plate. The relative merits of the four methods are discussed. © *2007 Acoustical Society of America.* [DOI: 10.1121/1.2722051]

PACS number(s): 43.40.Le, 43.40.Qi, 43.35.Zc, 43.35.Cg [WMC] Pages: 3484–3492

I. INTRODUCTION

Micrometeorites and space debris pose a constant danger to spacecraft in low-earth orbit. While the probability of a serious hit is quite low and large debris (>10 cm) can be avoided, small impacts routinely cause minor damage to the Space Shuttle and International Space Station.[1] The most dangerous debris, 0.5–100 mm in diameter, is too large to be stopped with certainty by shielding, but too small to be tracked and avoided.[2] An impact that penetrates the outer shielding and pressure vessel of a manned spacecraft will cause a leak that rapidly drains the limited air supply from the spacecraft. If the leak can be found rapidly and stopped, then the module can be salvaged. Otherwise, the crew will have no choice but to seal and abandon the module. In this paper, we demonstrate methods and algorithms for locating a single leak by monitoring leak-generated ultrasonic noise propagating within the skin of the spacecraft.

Our model for a leaking spacecraft is a 4.76-mm (3/16 in.) thick aluminum plate with a small hole and a vacuum behind the hole. This model is similar to the aluminum construction of the International Space Station. If a leak is present, turbulence in the leaking air will generate noise in the plate and in the air. Industrial off-the-shelf leak detectors for locating leaks in pressure vessels monitor airborne ultrasound near 40 kHz.[3] In the case of a leak into vacuum, the leak noise is generated by downstream turbulence at the exit and cannot travel up the Mach 1 free jet back into the spacecraft, where it might be detected. Instead, we exploit that portion of the leak noise that couples into the platelike skin of the spacecraft and is carried away from the leak site as guided ultrasonic Lamb waves. Our approach is to locate the leak by detecting and analyzing these guided waves. The theory and behavior of Lamb waves is well established, e.g., Ref. 4, and Lamb wave analysis is widely used as a tool for source location of acoustic emission signals.[5,6]

II. STATISTICAL SIGNAL ANALYSIS

The noise from the leak is inherently random. Moreover, it is so faint that it is often buried 20 dB or more under other noise sources. Therefore, instead of analyzing recorded noise waveforms directly, it makes sense to consider the statistics of the noise. In particular, we want to measure how sound waves detected by one sensor relate to sound waves detected by a second sensor, because this approach yields information about how the wave propagated to those sensors and hence the location of the noise source (the leak itself). The statistical tool that does this is cross-correlation,

$$\mathrm{XCORR}(x(t),y(t)) = \int_{-\infty}^{\infty} x(\tau)y(\tau - t)\,d\tau. \tag{1}$$

The cross-correlation at time t of two functions $x(t)$ and $y(t)$ is the inner product of x with y delayed by t, as given in Eq. (1). Cross-correlation is widely used industrially on leak-noise-generated guided mode waveforms to locate leaks in underground pipelines.[7–9] Cross-correlation transforms a pair of arbitrarily long noise waveforms captured simultaneously at different sensors into a composite waveform that represents the difference in propagation between the leak and each of the two sensors. Moreover, the cross-correlation is repeatable and predictable (ignoring variations from transducer coupling effects), and recording a full set of all possible cross-correlations (including autocorrelations) between sensors captures all possible useful information from those sensors about the leak. Cross-correlation also compresses extremely long measured noise waveforms into much shorter waveforms for processing and storage, and transforms very long measured noise waveforms with low signal-to-noise ratio (SNR) into shorter high-SNR correlations without loss of useful information.

[a]Address for correspondence: Iowa State University, ASC II, 1915 Scholl Road, Ames, IA 50011. Electronic mail: sdh4@iastate.edu

Let us consider a single frequency of leak-generated noise in an infinite plate. Assume the measurable amplitude of the noise in guided mode i is $|\tilde{A}_i|$ and its random phase is represented by the complex phase of $\tilde{A}_i$, which will generally be the same for the different modes. The noise in mode i at the location of the leak is

$$\tilde{A}_i \exp(j2\pi ft). \tag{2}$$

The waveform that would be measured at a distance d_1 from the leak is

$$\sum_i \tilde{A}_i \alpha_i \exp(j2\pi ft - jk_i d_1), \tag{3}$$

where k_i represents the frequency-dependent wave number of mode i and α_i represents combined the distance- and frequency-dependent attenuative effect of geometric diffraction, material absorbtion, and radiative loss (into the air). The cross-correlation between waveforms at distances d_1 and d_2 is

$$\sum_{i,l} |\tilde{A}_i||\tilde{A}_l| \alpha_i(d_1)\alpha_l(d_2) \exp(jk_i d_1 - jk_l d_2 + j2\pi ft), \tag{4}$$

or, ignoring the $i \neq l$ cross terms (thereby neglecting correlations between different modes),

$$\sum_i |\tilde{A}_i|^2 \alpha_i(d_1)\alpha_i(d_2) \exp[jk_i(d_1 - d_2) + j2\pi ft]. \tag{5}$$

The correlated noise is no longer random; the cross-correlation does not depend on the random phase of $\tilde{A}_i$, but only on its magnitude. From the point of view of waveform analysis the loss factors $\alpha_i(d_1)$ and $\alpha_i(d_2)$ are irrelevant because they vary slowly with frequency and hence affect only the broad spectrum of the waveform, but not its shape. When we ignore the loss terms and cross terms (or assume single mode propagation) the cross-correlation becomes a spatial function only of the difference in path lengths $d_1 - d_2$,

$$\sum_i |\tilde{A}_i|^2 \exp[jk_i(d_1 - d_2) + j2\pi ft]. \tag{6}$$

A propagating wave packet that arrives at both sensors simultaneously correlates at $t=0$, whereas a wave packet that arrives at one sensor 10 μs before the other correlates at either $t=10$ μs or $t=-10$ μs, depending upon which sensor the wave packet passed first. This dependence on the difference in distances can be counterintuitive. Because only the difference of distances is significant, sound need not come from the same location to correlate at the same time. A particular time in the cross-correlation maps through the modal wavespeed to a particular difference of distances. Geometrically, that difference of distances occurs along a hyperbola that has its foci at the sensor locations, so an observed arrival at that time could have come from any location on the hyperbola.

Successful source location is entirely dependent upon the leak noise being localized to a particular region of the plate by attenuation, edge absorption, and other losses. In a low-loss environment, reflected waves will interfere with direct waves, complicating the process of source location. In the extreme case of very low attenuation, resonance or a diffuse sound field can occur, and source location will become impossible because the cross-correlations will measure nothing but the resonance pattern and the Green's function between the sensors.[10] Since loss is in general a strong function of frequency, only a limited frequency range will contain useful information about the location of the leak. For our tests, we used frequencies between 200 and 600 kHz. Source location in small objects requires higher frequency measurement and analysis to assure sound field localization than source location in large objects, so lower frequencies may be more useful for actual spacecraft than in our small test configuration.

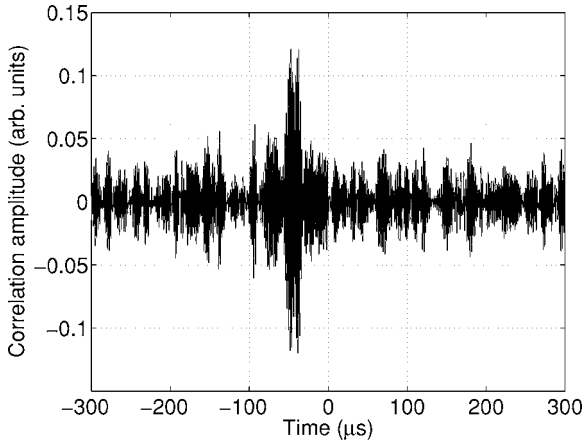

FIG. 1. A cross-correlation, filtered to eliminate low-frequency resonance.

Between 200 and 600 kHz and for our 4.76-mm plate thickness there are two detectible Lamb modes: the lowest order symmetric S_0 compressional mode and the lowest order asymmetric A_0 flexural mode. These two modes are both dispersive, in that their phase velocity depends on frequency. Their dispersion is reflected in the implicit frequency dependence of the wave number k in Eqs. (4)–(6). The dispersion relations $k_{A0}(f)$ and $k_{S0}(f)$ of the A_0 and S_0 Lamb modes can be readily calculated from the known material properties, thickness, and Lamb wave theory.[4] The two modes give rise to a total of four terms in Eq. (4), two single-mode terms plus two cross-terms. Therefore, the measured correlations will contain dispersed signals from the single-mode terms with interference from the cross-terms. Measured correlations tend to have distinct arrivals near $t=0$ or less distinct dispersed wavetrains at $t>0$ or $t<0$ depending on the magnitude and sign of the difference of distances $d_1 - d_2$. Figure 1 shows a (filtered) correlation waveform from measured data. A dispersed arrival can be seen near $t=-50$ μs. Assuming a wave speed of approximately 3 mm/μs, this translates to a difference of distances of approximately 150 mm.

Cross-correlation greatly reduces the amount of information that must be stored. Neglecting noise, the cross-correlation is only nonzero within a limited time window that comes from the total distances involved and the speed of propagation, so the cross-correlation is inherently compact, yet can represent data from arbitrarily long measured waveforms, since the integral in Eq. (1) goes out to infinity. Moreover, a full set of all possible autocorrelations (cross-

correlation of a waveform with itself) and cross-correlations between waveforms from a set of sensors is complete in the mathematical sense that it contains all possible useful information that could be extracted from the sensors. Therefore, storing and analyzing cross-correlations is an effective and efficient alternative to storing and analyzing the raw noise waveforms themselves.

We show by construction that noise waveforms equivalent to the originals can be calculated from the full set of auto- and cross-correlations, and therefore that there is no information loss from storing and processing only the correlations. Let $x(t)$, $y(t)$ be measured waveforms from a pair of sensors and $X(f)$, $Y(f)$ be their Fourier transforms. Since cross-correlation in the time domain is equivalent to multiplication by the complex conjugate in the frequency domain, the cross- and autocorrelations are $\mathrm{XCORR}(x,y)=X(f)Y^*(f)$, $\mathrm{XCORR}(x,x)=X(f)X^*(f)$, and $\mathrm{XCORR}(y,y)=Y(f)Y^*(f)$. These correlations can be measured to arbitrarily high signal-to-noise ratios by calculating them from sufficiently long recorded waveforms. First we reconstruct a frequency domain waveform $X_r(f)$ from the known amplitude spectrum $\sqrt{X(f)X^*(f)}$ and a single random function $\phi(f)$ giving random phase $e^{i\phi(f)}$. The inverse Fourier transform of $X_r(f)$ is the reconstructed noise waveform $x_r(t)$. The reconstructed noise waveform $Y_r(t)$ is the unique inverse Fourier transform of $Y_r(f)=[X(f)Y^*(f)/X_r(f)]$. Since the reconstruction is unique given $\phi(f)$, which is equivalent to (but different from) the random phase of the leak, the reconstructed waveforms are equivalent to the originals and there is no information loss in storing and processing only the correlations.

III. COUPLED TWO-DIMENSIONAL PHASED ARRAYS

Obviously a practical system for on-orbit spacecraft leak detection would need to have the fewest possible number of sensors because of measurement time and system complexity restraints. Nevertheless, to understand fully the problems and issues involved, we have collected an all-encompassing data set to represent what could be measured if time and complexity were irrelevant. Our data set contains all of the possible cross-correlations between elements of two two-dimensional phased arrays. Specialization of this data set was used to prototype the sparse methods to be described later.

A. Experimental measurements

An automated motion control system was used to position a pair of 1.5-mm-diam piezoelectric transducers used as sensors. Computer controlled stepping in 2-mm steps of each sensor over its own 32×32 mm^2 grid simulates two phased arrays on the 4.76-mm-thick aluminum plate. These phased arrays have been coupled by measuring correlations between signals from all possible pairs of locations in the two arrays. Figure 2 illustrates these arrays and the location of the leak. One-second long waveforms have been recorded at 5 megasamples per second (MSPS) for each pair of sensor locations. Cross-correlations are calculated from the recorded waveforms and stored. All possible cross-correlations between the 256 sensor positions in each array are recorded, leading to a total of 65 536 correlations arranged as a $(16\times16)\times(16\times16)$ phased array calculated from 655 billion samples.

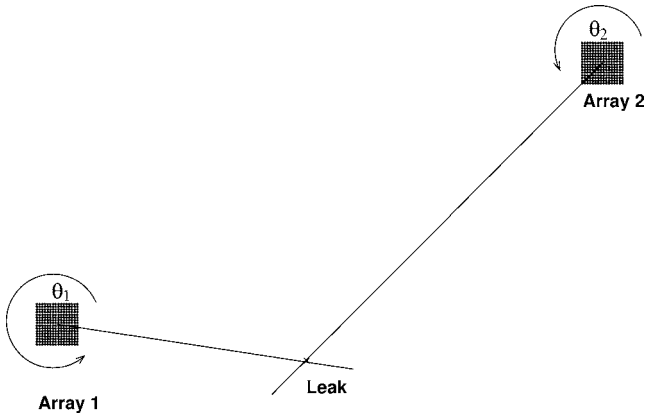

FIG. 2. Scale diagram of the four-dimensional phased array measurement. The leak is marked with an "x" and the lines indicate the measured vectors to the leak.

The processing of these data to reveal the leak location proceeds by straightforward Fourier phased-array analysis, followed by the application of *a priori* knowledge to reduce the dimensionality of the data from five dimensions to two. The raw correlation data $D(t,x_1,y_1,x_2,y_2)$ are discretely indexed along five dimensions: time, x_1, y_1, x_2, and y_2. A five-dimensional discrete Fourier transform converts the data to frequency-wavenumber space, $D(f,k_{x1},k_{y1},k_{x2},k_{y2})$. The transformed data set is then converted to polar coordinates, $D(f,|k_1|,\theta_1,|k_2|,\theta_2)$. One dimension can be eliminated from the data, along with the cross-terms of Eq. (4) by requiring the wave number magnitudes $|k_1|$ and $|k_2|$ to be equal at the two sensors and discarding all data not on the hyperplane $|k_1|=|k_2|$. The data can also be reduced in dimension by exploiting knowledge of the dispersion relations of the A_0 and S_0 modes, $k_{A0}(f)$ and $k_{S0}(f)$, to eliminate data not on the hyperplanes $|k|=k_{A0}(f)$ or $|k|=k_{S0}(f)$. The result of this reduction is a pair of three-dimensional data sets—one for A_0, one for S_0—each a function of f, θ_1, and θ_2. One more dimension can be eliminated by integrating the energy (square of the complex magnitude) of the data over frequency f, for example

$$D_{A0}(\theta_1,\theta_2)=\int_f \left|D(f,|k_1|,\theta_1,|k_2|,\theta_2)|_{|k_1|=|k_2|=k_{A0}(f)}\right|^2 df \quad (7)$$

for the A_0 mode. This leaves a pair (one for each mode) of two-dimensional functions of θ_1 and θ_2 that represent the modal energy from a common source incident on array 1 at angle θ_1 and on array 2 at angle θ_2.

B. Results

The A_0 and S_0 mode Eq. (7) energy integrals are plotted as grayscales in Fig. 3. The dark spots in Fig. 3 indicate the pairs of angles corresponding to coherent propagation past the two sensor arrays. The dark spots appear at exactly the same location for the A_0 and S_0 analyses, meaning that the

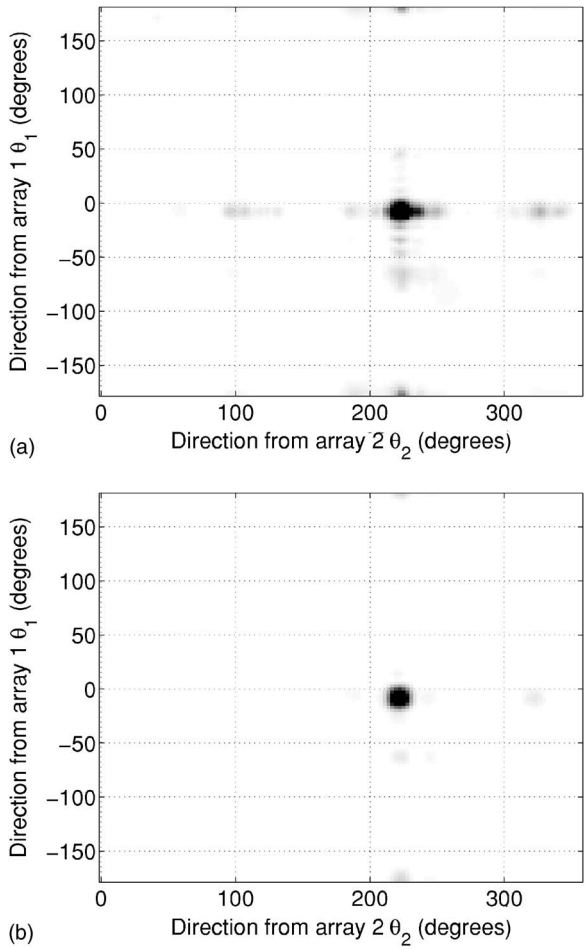

FIG. 3. Measured leak direction maps for (a) A_0 mode and (b) S_0 mode, both darkened by 100% to enhance visibility of interference.

location of the leak is independent of the mode selected for analysis. The measured propagation directions, from the location of the peaks (darkest points) in Fig. 3, are indicated as straight lines on Fig. 2, and their intersection provides an estimate of the location the source of the leak. In this case the estimated leak location is 1.8 mm from the actual location. To permit interference effects to be seen at all, the two images in Fig. 3 have been scaled in intensity by 100%. Interference is visible as faint spots on the figure away from the dark spots that indicate the primary directions. The interference comes from waves reflected by the boundary of our plate under test. Most of the interference spots are aligned vertically or horizontally with the primary spot, indicating a direct path from the leak to one sensor combined with a reflected path to the other sensor.

This measurement, while exhaustive in scope and impractical in terms of time and equipment, nonetheless demonstrates the capability to estimate the leak location accurately using random-signal guided waves. The coupled phased array method is particularly insensitive to interference and noise because only a tiny fraction of interference and noise are on the extracted hyperplanes; most interference and noise are distributed elsewhere in the five-dimensional space and are therefore suppressed. In order for interference to be visible at all in the measured data, Fig. 3 had to be scaled in intensity.

IV. TWO-DIMENSIONAL PHASED ARRAY

One strategy for reducing the quantity of data required is to reduce the coupled (x_1,y_1,x_2,y_2) array measurement described above to a pair of independent, two-dimensional array measurements: (x_1,y_1) and (x_2,y_2). For each array measurement, one sensor is fixed and the other is scanned across the 16×16 array. The number of correlations required for this measurement is $(16\times16)+(16\times16)=512$, a factor of 128 reduction in data from the 65 536 correlation full treatment. The three-dimensional (time, x, y) Fourier transform of the data from one sensor array gives a mapping of the directions of sound propagation in the vicinity of that array in terms of frequency and horizontal and vertical wave numbers. The three-dimensional transform given measured array waveforms $D(t,x,y)$ is

$$D(f,k_x,k_y)=\int_x\int_y\int_t D(t,x,y)\exp(-ik_xx-ik_yy-i2\pi ft)dt\,dy\,dx. \tag{8}$$

To display this as a two-dimensional image, we integrate the magnitude over our selected frequency range

$$D(k_x,k_y)=\int_{f_1}^{f_2}|D(f,k_x,k_y)|^2\,df \tag{9}$$

to obtain the distribution of energy in wave-number (k_x,k_y) space.

The bulk of the energy in wave-number space will be on a line emanating from the origin. The direction of this line is the direction to the leak, and the leak location can be therefore found by triangulation from two or more sensor assembly locations. The effect of decoupling the two arrays is that instead of correlating a specific mode crossing one array in one direction with the same mode crossing and the other array in the another direction, we can see only the angular energy distribution at each array. No longer is there any guarantee that the waves seen at one array match those at the other. In order to triangulate we have to assume the same waves are crossing both arrays, and, for example, in the unlikely event of multiple leaks, that assumption might be false.

A. Results

Because the required data for the two-dimensional phased array measurement are a subset of that required for the coupled measurement, instead of performing a separate experiment, we reprocess the data from the coupled experiment using only the required subset. We arbitrarily select one sensor position in sensor array 2 and extract the correlations with all possible sensor positions in sensor array 1 to obtain two-dimensional phased array data for sensor array 1 $D_1(t,x,y)$. Likewise, we select an arbitrary sensor position in array 1 and extract the correlations with array 2 to obtain phased array data for sensor array 2 $D_2(t,x,y)$. The data are processed using Eqs. (8) and (9). Figure 4 shows the pro-

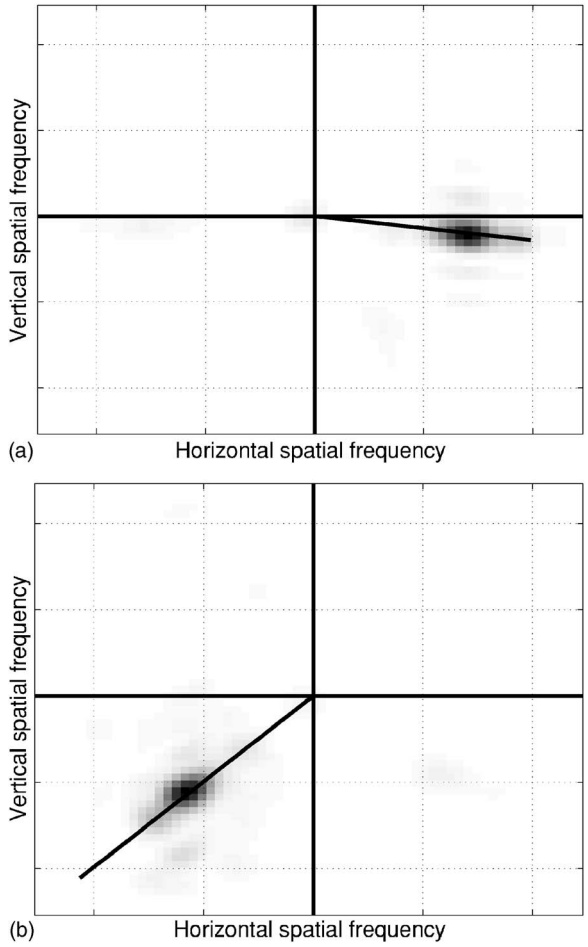

FIG. 4. Spatial frequency mapping of signal energy detected at (a) sensor array 1 and (b) sensor array 2. The black line indicates the measured direction to the source.

cessed two-dimensional phased array data from arrays 1 [Fig. 4(a)] and 2 [Fig. 4(b)]. The rays radiating from the origin in Fig. 4 indicate the measured θ_1 and θ_2 directions of −8 and 225 deg, respectively. Triangulation using these directions gives an estimated leak location 2.4 mm from the actual position of the leak on a 610×610-mm^2 plate compared with 1.8 mm when calculated from the coupled measurement. The leak location estimate of this method is nearly as accurate as the coupled measurement despite the massive reduction of data. Interference (darkened areas not on the rays) is visible in Fig. 4, even though Fig. 4 is not scaled in intensity. Interference and noise are higher than in the coupled case, in part because it has been constructed from far fewer data.

This method has the advantage that it requires far less information to find the leak location. It takes less acquisition time and less equipment than the full coupled measurement. Like the full algorithm, multimode propagation and dispersion will not create interference. Unlike the coupled method, this method treats each array independently. It finds the angular distribution of wave propagation independently under each array and triangulates from the apparently dominant direction. This two-dimensional phased array method provides a simple, robust method for locating leaks that requires far less data to be collected than the coupled phased array.

V. DISTRIBUTED DISCRETE SENSOR METHOD

While the two-dimensional phased array method requires far fewer correlations—and hence far less computation—than the four-dimensional method, it still requires two array sensors and hundreds of correlations. Using tiny subsets of the original coupled data set, we have developed an algorithm that locates the leak using only correlations between signals from a few isolated point sensors. This approach, which we have described briefly in Ref. 11, is more fully developed in Sec. V A. Our algorithm compares the measured correlations from a few arbitrarily distributed sensors with synthetic correlations calculated from all possible leak locations and identifies the closest match as the location of the leak.

A. Method and experiment

The method for locating the leak from the measured correlations has the following steps:

(1) Distribute a small number (four in our example) of sensors around a plate containing a leak, with known sensor locations $(x_1,y_1),\ldots,(x_4,y_4)$.
(2) Simultaneously record waveforms at all sensors $h_i(t)$, $i=1,\ldots,4$.
(3) Measure all (six) possible cross-correlations $R_{il}(t)=\int_\tau h_i(\tau)h_l(\tau-t)\,d\tau$ between noise waveforms from the four sensors, $R_{12}(t)$, $R_{13}(t)$, $R_{14}(t)$, $R_{23}(t)$, $R_{24}(t)$, $R_{34}(t)$.
(4) Calculate dispersion relations $k_{A0}(f)$ and $k_{S0}(f)$ for the two fundamental Lamb modes given the known thickness and material properties.
(5) Select one mode, A_0 or S_0.
(6) Select one measured correlation R.
(7) Select an arbitrary candidate leak location (x_x,y_c).
(8) Calculate a synthetic correlation R_s from Eq. (6), ignoring the loss factor α, assuming the leak is at the candidate leak location, assuming that only the selected mode is present, and assuming a flat frequency response over the selected frequency band.
(9) Calculate the inner product between the synthetic and measured correlations $\int_t R(t)R_s'(t)\,dt$.
(10) Repeat steps 7–9 for all candidate leak locations, generating a spatial mapping of the magnitude of the inner product, such as that shown in Fig. 5.
(11) Return to step 6 through step 10, multiplying the inner-product magnitudes for all the measured correlations to create a composite mapping, such as shown in Fig. 6(a) of leak intensity for the mode selected in step 5.
(12) Return to step 5, select another mode, and repeat all calculations through step 11, until all applicable modes have been accounted for. Sum the composite mappings to create an overall multi-mode map of leak intensity, as shown in Fig. 6(b).

The strongest peak in the overall multi-mode intensity map, such as Fig. 6(b), provides an estimate of the leak location.

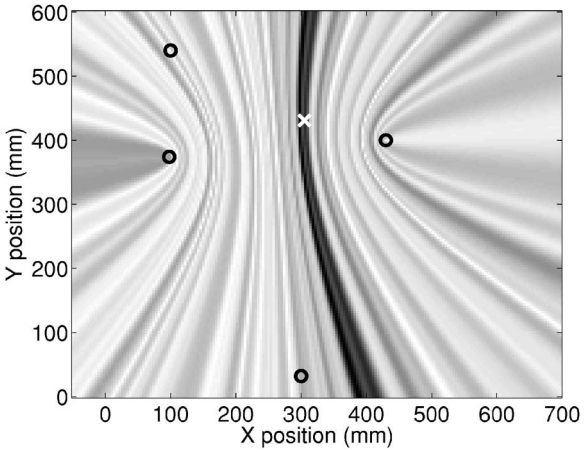

FIG. 5. Magnitude of the inner product of a measured correlation with S_0 synthetic waveforms as the assumed leak location varies spatially. The sensors are the "∘" symbols at the foci of the hyperbolas, and the actual leak location is marked with an "×".

B. Results

Because the algorithm processes the different modes independently, it is sensitive to both interference between the modes and interference from cross-terms. For example, a correlation signal from an A_0 wave mode but interpreted in the S_0 iteration could, when combined with interference in other correlations, generate a false peak in the S_0 map. To test the robustness of our procedure and to quantify the effect of this sort of interference, we have run a set of simulations with synthetic correlations assuming equal magnitudes of the A_0 and S_0 modes. These simulations are worst-case in the sense that equal A_0 and S_0 magnitudes give the highest possible relative amplitude of the cross-terms. We performed 32 simulation runs, each with a different, randomly selected, pattern of sensors. The average level of the cross-interference peak relative to the peak at the leak location is −5 dB. The largest interference peak observed is 4 dB stronger than the peak at the leak location in the overall map. Under worst-case circumstances with synthetic data, intermode interference can generate spurious peaks equal to, or larger than, the peak at the leak location. Nevertheless, in each of these cases the leak location is also predicted by means of a secondary peak. Since the interference is a function of the sensor layout pattern, careful placement can minimize interference effects. Adding sensors beyond the four probes assumed here will also tend to reduce interference. Experimental results from several sensor configurations with four probes are shown in Fig. 7. The actual location of the leak in a 610×610 mm^2 plate is found with a mean error of 10.4 mm in Figs. 7(a)–7(d). The arbitrarily distributed sensor method permits accurate, rapid leak location with a minimum of prepositioned equipment in an on-orbit spacecraft environment.

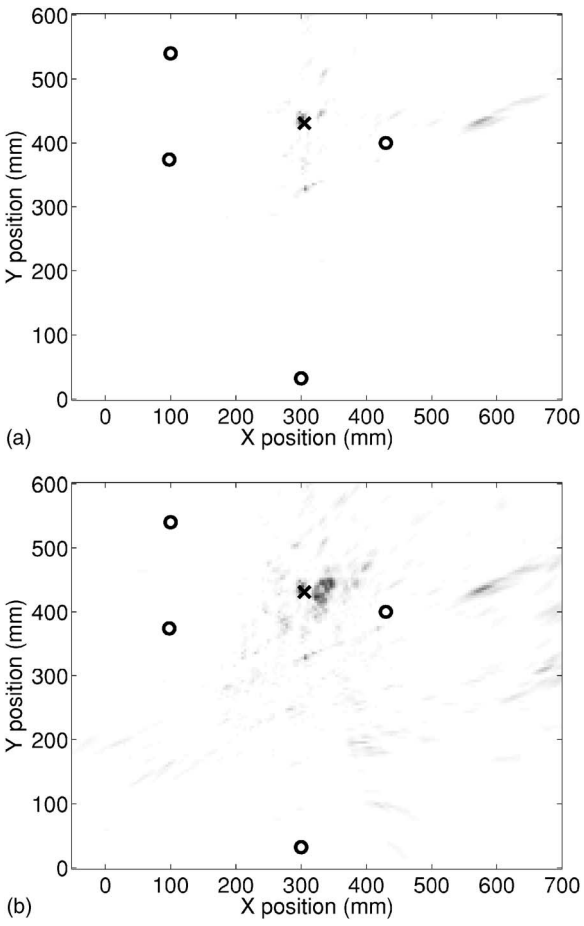

FIG. 6. (a) Product of S_0 inner product fields for all correlations (sensor pairs). (b) Sum of S_0 and A_0 products.

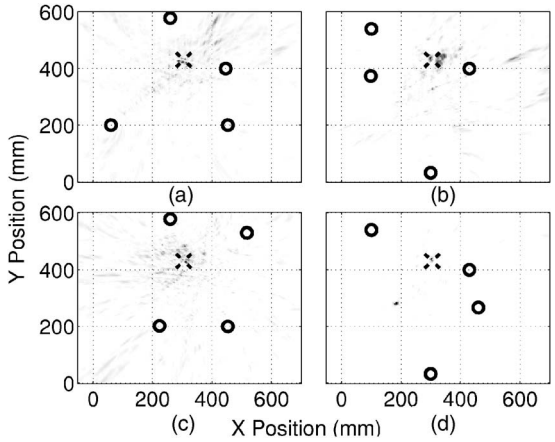

FIG. 7. Measured four-sensor source location solutions for four different sensor configurations.

VI. TWO-SENSOR METHOD

Another sparse-detector method uses two rotatable sensors. This method is appropriate for cases where a portion of the inner surface of the spacecraft pressure vessel is directly accessible to astronauts, and is suitable for smaller leaks for which the inherent delay involved in a manual measurement will not be a hazard. As we have previously discussed in a preliminary report,[12] by rotating a pair of sensors around a central point, correlation data can be collected that can be processed by a differential phase analysis or a circular synthetic aperture analysis to determine the direction of sound wave propagation. As in the phased array methods, triangulation from two or more measurement positions will locate the leak.

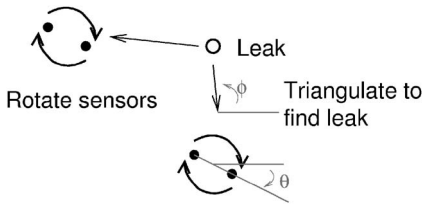

FIG. 8. Diagram showing rotation of sensors and triangulation to find leak.

A. Method and experiment

At each of two or more locations, a pair of rotatable sensors is held at a fixed separation and correlations are recorded as the sensor assembly is rotated in 15-deg increments, as illustrated in Fig. 8. The direction to the leak is found by examining the phase of the Fourier transforms of these correlations as a function of angle. Assuming a single mode incident at angle ϕ on the sensor pair rotated to angle θ, the correlation of the signals from the two sensors (separation d) will be

$$|\tilde{A}|^2 \exp\left[j2\pi ft - jkd\cos(\theta-\phi)\right]. \tag{10}$$

The phase of the Fourier transform of the correlation is $-jkd\cos(\theta-\phi)$. The phase varies sinusoidally as the sensor assembly is rotated, with the zeroes of the sinusoid occuring when the line connecting the sensors is parallel to the propagating wavefronts. The extrema of the phase occur when that line is perpendicular to the propagating wavefronts. Figure 9 shows the magnitude of the inner product

$$P(f) = \sum_{\theta} \text{angle}^{(\text{unwrapped})}(D(f,\theta))e^{j\theta} \tag{11}$$

of the unwrapped phase of a set of measured correlations with a 360 deg complex sinusoid, where $D(f,\theta)$ is the temporal Fourier transform of the measured correlation at sensor assembly angle θ. The dashed and dotted lines in Fig. 9 show expected magnitudes of the inner product assuming propagation in the flexural (A_0) and compressional (S_0) modes, respectively. In order for the phase variation to be a meaningful measure of leak direction, there must be a single dominant mode propagating at each frequency, because multiple modes propagating together will cause phase interference. Figure 9 demonstrates which mode is usable in which frequency range. In this case, the data indicate that the compressional (S_0) mode dominates from 450 to 540 kHz as marked on the plot, that the fiexural (A_0) mode dominates from 280 to 375 kHz, and that other ranges, showing large rapid fluctuations, exhibit interference between the modes. Once a frequency range has been selected the angle to the leak can be estimated by calculating the median phase over the selected frequency range of $P(f)$ from Eq. (11),

$$\underset{f}{\text{median}}[\text{angle}(P(f))]. \tag{12}$$

Angles calculated with Eq. (12) are then triangulated from two or more measurement locations to precisely locate the leak.

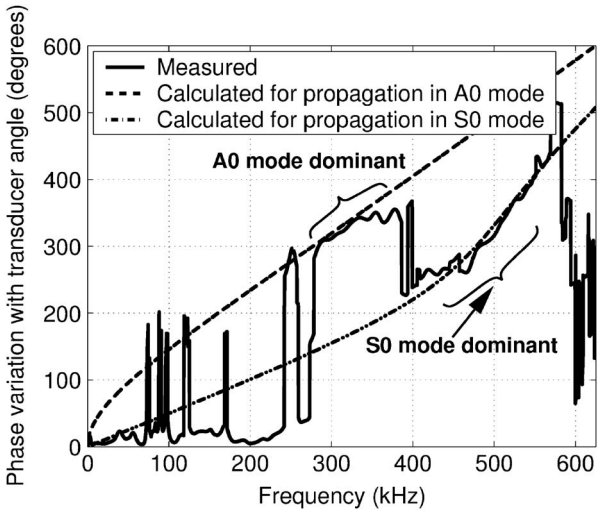

FIG. 9. Variation of phase with sensor angle, measured and calculated for A_0 and S_0 modes.

Another way to analyze these data is as a circular synthetic aperture.[13] Unlike the rectangular synthetic aperture (phased array) analysis described earlier, the basis functions of the circular synthetic aperture are nonorthogonal. Therefore, calculating the angular spectrum from the circular array data is an ill-posed inversion problem. To accomplish the inversion we use below a modified Lanczos matrix pseudoinverse, similar to that discussed by Jackson.[14]

If a sound wave is incident upon the circular synthetic aperture location at angle ϕ, and the sensor assembly, with element separation d, is rotated to direction θ, then the expected correlation [from the simplified correlation of Eq. (6)] would be

$$\sum_i |\tilde{A}_i|^2 \exp\left[j2\pi ft - jk_i d\cos(\theta-\phi)\right], \tag{13}$$

where the sum is over the mode index i. In the synthetic aperture analysis we assume incident waves in every possible direction and then solve for the amplitudes of those waves given the measured correlations. Let $\tilde{A}_{mi}$ be the amplitude and phase of the incident wave propagating in the direction ϕ_m in mode i. The measured cross-correlations with the sensor assembly at angle θ_l would be

$$\text{XCORR}_l = \sum_m \sum_i |\tilde{A}_{mi}|^2 \exp\left[j2\pi ft - jk_i d\cos(\theta_l-\phi_m)\right]. \tag{14}$$

To solve the synthetic aperture problem, we must solve for the angular and modal amplitude spectra $|\tilde{A}_{mi}|$ given the measured cross-correlations. Equation (14) can be represented as a matrix multiply. Let $D_{lmi} \equiv \exp\left[-jk_i d\cos(\theta_l-\phi_m)\right]$. At each frequency f we can construct a matrix $E_{lq} \equiv [D_{lmA_0} D_{lmS_0}]$ and a vector $C_q \equiv \begin{bmatrix} |\tilde{A}_{mA_0}|^2 \\ |\tilde{A}_{mS_0}|^2 \end{bmatrix}$ such that Eq. (14) reduced to the matrix equation

$$\text{XCORR}_l = \sum_q E_{lq} C_q \exp(j2\pi ft). \tag{15}$$

Equation (15) represents the prediction of correlations from a known angular and modal spectrum C_q as a matrix multipli-

cation. Inversion of this equation allows estimation of the angular distribution of incident waves from the measured data. In a linear synthetic aperture problem, E_{lq} is a spatial Fourier transform and is easily inverted. In the current case of a circular synthetic aperture, depending on the number of chosen values for ϕ_m and θ_l, this matrix is ill conditioned and may not be square. To construct the pseudoinverse E_{lq}^{inv}, we first calculate the singular value decomposition of E, $E = USV^t$, where U and V are unitary and S is diagonal, with its elements S_{ii} the singular values. Let the largest singular value be $S_{\max}$. The pseudoinverse is $E^{\text{inv}} = VS^{\text{inv}}U^t$, where S^{inv} is diagonal and constructed from the elements of S,

$$S_{ii}^{\text{inv}} = \frac{1}{S_{ii}} e^{-0.2(S_{\max}/S_{ii}-1)} \quad \text{(no sum)}. \tag{16}$$

Since E is ill conditioned, it likely has very small singular values. When inverted, these small singular values become very large and potentially scale any error or noise in the measured correlations. The exponential factor in Eq. (16) limits the noise gain of the inversion process by scaling down the inverses of the smallest singular values, following the concept of singular value truncation discussed in Ref. 14. The arbitrary factor of 0.2 selects the rate of scaling and corresponds to the reduction of the inverse of a singular value with half the magnitude of the largest singular value.

The estimated angular and modal distribution can be calculated from E_{ql}^{inv} according to

$$\begin{bmatrix} |\hat{\tilde{A}}_{mA_0}|^2 \\ |\hat{\tilde{A}}_{mS_0}|^2 \end{bmatrix} \equiv \hat{C}_q = \sum_l E_{ql}^{\text{inv}} \text{XCORR}_l e^{-j2\pi ft}. \tag{17}$$

Equation (17) gives the synthetic aperture calculation for estimating the incident angular and modal distribution $|\hat{\tilde{A}}_{mi}|^2$ from a single frequency component (at frequency f) of a set of measured correlations XCORR_l. By iterating this calculation over our frequency range, we obtain the estimated angular distribution as a function of frequency and mode. Integrating this distribution over frequency,

$$\int_{f_1}^{f^2} |\hat{\tilde{A}}_{mi}|^2 \, df, \tag{18}$$

will yield a peak in the integral in the dominant direction. This peak gives an estimate of the direction to the source. Figure 10 shows an example angular and modal distribution from experimental data, calculated using the circular synthetic aperture method.

Figure 11 shows an example of two-sensor leak location by triangulation from three measurement positions using both analysis methods. The solid discs indicate the measurement positions, and rays emanating from them indicate the estimated directions to the leak as determined by the two algorithms. The leak itself is located at the origin, and the estimated location is marked with an open circle is at coordinates (17 mm, 3 mm). The source location error in this case was 2.0 mm for the phase comparison method and 2.3 mm for the circular synthetic aperture method. As before, this source location was accomplished using a 610 mm^2 4.76-mm-thick aluminum plate with a l-mm-diam leak. The two-sensor method is a viable method for locating leaks. It has the disadvantages of requiring manual operation and high sensitivity to cross-mode interference, yet it requires a minimum of equipment. Unlike the other methods the equipment would not need to be manufactured as part of the spacecraft.

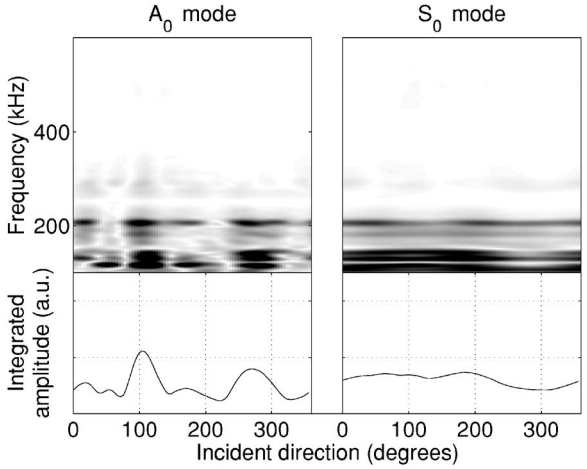

FIG. 10. Example measured angular and modal distribution from circular synthetic aperture method.

VII. CONCLUSIONS

Each of these methods developed and demonstrated here can successfully and repeatably locate air leaks into vacuum using structure-borne noise. Of the four methods, only the first—the four-dimensional phased array—is wholly impractical because of the extreme amount of data that must be collected. Each of the other methods is a viable alternative depending on the circumstances involved. We anticipate that the two-dimensional phased array could be made practical by using a miniature array transducer with high speed correlator

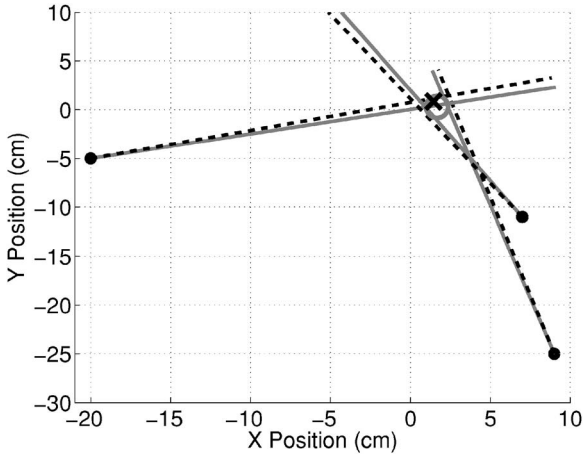

FIG. 11. Example leak location with two movable sensors. Each location of the sensor pair is marked with a disc. The measured directions to the leak with the phase comparison algorithm are shown as solid gray lines. Measured directions with the circular synthetic aperture method are shown as dashed black lines. The least-squares measured location of the leak is marked with a circle (phase comparison) and "×" (synthetic aperture). For comparison, the actual leak location was the origin (0,0).

electronics, and we are actively developing a miniature 8 $\times$ 8 array for this purpose. With a scattering of two-dimensional arrays on the inside of a spacecraft module, this method would instantly identify the location of the leak while rejecting possible interference. The distributed discrete sensor method would provide the same result, but with greater vulnerability to interference and false peaks, yet with substantially smaller hardware and computation requirements. The two-sensor method would be appropriate for the more spartan spacecraft environment in which the outer pressure walls are accessible from the inside and for which the weight of permanently embedded monitoring system would be prohibitive.

We have discussed the problem of locating air leaks in manned spacecraft. We have shown how cross-correlation can be used to transform the leak noise into a quantity that can be usefully measured, and described and demonstrated a series of algorithms for collecting and analyzing these cross-correlations to determine the location of a leak. Each of the methods works repeatably, and each is suitable for different circumstances. By applying these methods to manned spacecraft, the risk of micrometeorites and space debris to the mission and to the crew can be dramatically reduced.

ACKNOWLEDGMENT

This material is based on work supported by NASA under Award No. NAG-1-029098.

[1]L. Foster, J. Frisbee, M. Wortham, and L. Howorth, "International Space Station Debris Avoidance Operations," The Orbital Debris Quarterly News **6**(2), 4–5 (2001) http://www.orbitaldebris.jsc.nasa.gov/newsletter/newsletter.html(verified 4 March 2007).

[2]Committee on Space Shuttle Meteoroid/Debris Risk Management, NRC, *Protecting the Space Shuttle from Meteoroids and Orbital Debris* (National Academies Press, Washington, DC, 1997).

[3]G. Studor, "Ultrasonic detectors in space," http://www.ctrlsys.com/library/articles/index.php(verified 4 March 2007).

[4]A. H. Nayfeh, *Wave Propagation in Layered Anisotropic Media* (Elsevier, Amsterdam, 1995).

[5]W. H. Sachse and S. Sancar, "Acoustic emission source location on plate-like structures using a small array of transducers," US Patent #4,592,034 (1986).

[6]M. R. Gorman, "Plate wave acoustic emission," J. Acoust. Soc. Am. **90**(1), 358–364 (1991).

[7]D. S. Kupperman, "Detector relies on sound to locate underground pipe leaks," Power **134**(2), 61–62 (1990).

[8]J. Golby and T. Woodward, "Find that leak," IEE Rev. **45**(5), 219–221 (1999).

[9]L. E. Rewerts, R. A. Roberts, and M. A. Clark, "Dispersion Compensation in Acoustic Emission Pipeline Leak Location," in *Review of Progress in QNDE*, edited by D. O. Thompson and D. E. Chimenti (AIP, New York, 1997), Vol. **16**, pp. 427–434.

[10]R. L. Weaver and O. I. Lobkis, "Ultrasonics without a Source: Thermal Fluctuation Correlations at MHz Frequencies," Phys. Rev. Lett. **87**, 134301 (2001).

[11]S. D. Holland, R. Roberts, D. E. Chimenti, and M. Strei, "Leak detection in spacecraft using structure-borne noise with distributed sensors," Appl. Phys. Lett. **86**, 174105 (2005).

[12]S. D. Holland, R. Roberts, D. E. Chimenti, and M. Strei, "Two sensor ultrasonic spacecraft leak detection using structure-borne noise," ARLO **6**(2), 63–105 (2005).

[13]N. Yen, "A circular passive synthetic array: An inverse problem approach," IEEE J. Ocean. Eng. **17**(1), 40–47 (1992).

[14]D. D. Jackson, "Interpretation of inaccurate, insufficient and inconsistent data," Geophys. J. R. Astron. Soc. **28**, 97–109 (1972).

Measurement of structural intensity using boundary element method-based nearfield acoustical holography

Kenji Saijyou[a)]
Technical R & D Institute, Ministry of Defense, 3-13-1 Nagase, Yokosuka, 239-0826, Japan

(Received 1 June 2006; revised 6 March 2007; accepted 20 March 2007)

The regularization method for measurement of structural intensity (SI) using boundary element method (BEM)-based nearfield acoustical holography (NAH) is proposed. Spatial derivatives of normal displacement are necessary to obtain the structural intensity. The derivative operations amplify high-wavenumber component of measurement noise and contaminate the measurement result of SI. To overcome this difficulty, regularization method for measurement of SI using fast Fourier transform-based NAH has been introduced. In this paper, this regularization method is modified for the BEM-based NAH. The BEM-based NAH avoids the aperture replication problem; therefore, measurement aperture for BEM-based NAH can be set smaller than that for FFT-based NAH. The effectiveness of the proposed method is demonstrated by experiments.
© *2007 Acoustical Society of America.* [DOI: 10.1121/1.2724760]

PACS number(s): 43.40.Sk, 43.60.Sx, 43.40.Rj, 43.20.Ye [EGW] Pages: 3493–3500

I. INTRODUCTION

Measurement of power flow in structures, called structural intensity (SI), is very helpful for the vibration control and noise reduction. Nearfield acoustical holography (NAH)-based measurement method is suitable to analyze the interrelationship between SI and acoustic intensity (AI), because the NAH-based method can yield SI and AI simultaneously.[1–3] To obtain the SI, spatial derivatives of the normal displacement of structures are necessary. These derivatives are calculated by fast Fourier transform (FFT)-based method,[2–9] because the FFT-based method enables us to obtain spatial derivatives over the whole structure, and the amplification of high-wavenumber noise is suppressed by applying a wavenumber-space (K-space) filter. In the FFT-based method, the optimization of the K-space filter is crucial. To optimize the K-space filter, regularization method for measurement of SI using FFT-based NAH (FFT-NAH) has been introduced.[10] In this paper, this regularization method is modified for the boundary element method (BEM)-based NAH (BEM-NAH). The measurement aperture for BEM-NAH can be set smaller than that for FFT-NAH because BEM-NAH avoids the aperture replication problem.[11]

The effectiveness of the proposed method is demonstrated by experimental investigations, which SI of a thin plate is measured by the proposed BEM-NAH method and conventional FFT-NAH method, and these reconstructed results are compared.

II. SPATIAL DERIVATIVES OF BEM-NAH

A. Review of BEM-NAH

Before discussion of the measurement method of spatial derivatives by BEM-NAH, we review the basic theory of BEM-NAH. We consider two surfaces, the reconstruction surface S_v which corresponds to the structure surface, and the measurement surface S_p which represents an imaginary surface where pressure measurement is made. The geometry is shown in Fig. 1. The harmonic time dependence $e^{i\omega t}$ is suppressed throughout this paper, here $\omega=2\pi f$ and f is the frequency.

To introduce BEM-NAH, discretization of the exterior form of the Helmholtz integral equation (HIE)[1] with S_v as the integration surface with exterior point specified on S_p is necessary. The boundary element discretization of HIE and ensuing integrations converts HIE to a matrix equation. Here, the surface S_v is broken up into N small elements of area, and we set the number of measurement points on S_p as also N. As is standard practice in these problems, when $\mathbf{r} \in S_v$ one can eliminate $p(\mathbf{r}_s)$, which is the pressure on the structure surface, through matrix manipulations,[12] resulting in a final linear equation between the measured pressure vector $\mathbf{p}$ on S_p and the unknown normal velocity vector $\dot{\mathbf{w}}$ on S_v:

$$\mathbf{p} = \mathbf{H}\dot{\mathbf{w}}. \tag{1}$$

Here $\mathbf{H}$ is an $N\times N$ matrix, which is called a "vibroacoustic transfer matrix."[13] Equation (1) can be inverted by applying the inversion matrix $\mathbf{H}^{-1}$,

$$\dot{\mathbf{w}} = \mathbf{H}^{-1}\mathbf{p}, \tag{2}$$

therefore, the normal velocity $\dot{\mathbf{w}}$ can be reconstructed by Eq. (2) from the field pressure $\mathbf{p}$, which is measured on the concentric hologram surface. However, the influence of measurement noise has not been considered in this formulation.

For actual implementation of BEM-NAH, some regularization methods are applied, because the inversion matrix $\mathbf{H}^{-1}$ is very ill conditioned due to the existence of evanescent-like waves. The regularization is implemented by singular value decomposition (SVD) and regularization filter. The SVD applied to $\mathbf{H}$ in Eq. (1) is

a)Electronic mail: saijyou-kenji@com.home.ne.jp

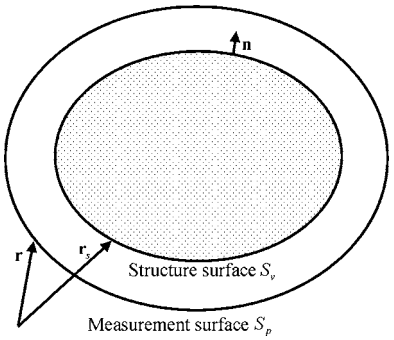

FIG. 1. Region definitions for application of HIE for arbitrary shape object.

$$\mathbf{H} = \mathbf{U}\boldsymbol{\Sigma}\mathbf{V}^H, \tag{3}$$

where $\boldsymbol{\Sigma} \equiv \mathrm{diag}(\sigma_1, \sigma_2, \ldots, \sigma_N)$ $(\sigma_1 > \sigma_2 > \ldots > \sigma_N)$ and $\mathbf{U}$ and $\mathbf{V}$ are unitary matrices defined by $\mathbf{U}^H\mathbf{U} = \mathbf{V}^H\mathbf{V} = \mathbf{I}$, respectively, and the superscript H represents the conjugate transpose of the matrix. The column vectors $\{u_j\}$ and $\{v_j\}$ mean the wave vector are the orthogonal eigenfunction or "mode," i.e., these refer to the distribution field pressure on the hologram and that of normal velocity on the structure surface at a selected frequency.[14] Thus, the inverse of the transfer matrix $\mathbf{H}^{-1}$ is

$$\mathbf{H}^{-1} = (\mathbf{U}\boldsymbol{\Sigma}\mathbf{V}^H)^{-1} = \mathbf{V}\boldsymbol{\Sigma}^{-1}\mathbf{U}^H, \tag{4}$$

where $\boldsymbol{\Sigma}^{-1} \equiv \mathrm{diag}(\sigma_1^{-1}, \sigma_2^{-1}, \ldots, \sigma_N^{-1})$.

In the reconstruction process of normal velocity, higher-order components of singular values affect the reconstructed result dominantly and they are correlated with the evanescent wave component. Usually the measured pressure is contaminated by noise. Then, the measurement noise is amplified greatly by the higher-order component; σ_j. Therefore, regularization is necessary to suppress the amplification of the noise. Some regularization procedures have been proposed,[12,15–23] and the appropriate regularization procedure of NAH has been introduced by Williams.[24] His method is based on the Tikhonov regularization procedure. The Tikhonov filter is described as

$$F^{\alpha,1} \equiv \mathrm{diag}\left(\cdots, \frac{|\sigma_j|^2}{|\sigma_j|^2 + \alpha[\alpha/(\alpha + |\sigma_j|^2)]^2}, \cdots\right), \tag{5}$$

where α is the regularization parameter. This parameter α is determined by the discrepancy principle attributed to Morozov (MDP). The MDP provides a particularly simple method of finding the parameter α when the variance of the noise σ_{noise} is known. Given Eq. (5) and knowledge of σ_{noise}, we can find the parameter α by the MDP. However, implementation of the MDP requires an estimated noise variance σ_{noise} in the data. Given that the taper of the filter matches the evanescent-like wave decay with increasing the order of singular value, then the highest order above the break point corresponds only to noise in the data. Therefore, we can expect that the noise variance σ_{noise} is estimated by averaging over the last Q basis vectors,

$$\left\| \sum_q U_q^H \mathbf{p}_{\mathrm{mea}} \right\| \Big/ \sqrt{Q} \approx \sigma_{\mathrm{noise}}, \quad N - Q + 1 \leqslant q \leqslant N, \tag{6}$$

where U_q^H is the qth row of $\mathbf{U}^H$. Then, the parameter α is determined by the MDP and the estimated noise variance σ_{noise}.

As a result, the normal velocity $\tilde{\dot{\mathbf{w}}}$ and the normal displacement $\tilde{\mathbf{w}}$ can be reconstructed from the measured pressure $\mathbf{p}_{\mathrm{mea}}$ as

$$\tilde{\dot{\mathbf{w}}} = \mathbf{V}\boldsymbol{\Sigma}^{-1}F^{\alpha}\mathbf{U}^H\mathbf{p}_{\mathrm{mea}}, \tag{7}$$

$$\tilde{\mathbf{w}} = \mathbf{V}\boldsymbol{\Sigma}^{-1}F^{\alpha}\mathbf{U}^H\mathbf{p}_{\mathrm{mea}}/(j\omega). \tag{8}$$

Here, tilde indicates the smoothed variable. This is the reconstruction equation of normal velocity by BEM-NAH.

B. Regularization method of spatial derivatives for BEM-NAH

In this section, an estimation method of a K-space filter for each order derivatives obtained by BEM-NAH is briefly described. This method is the extension of the regularization method of spatial derivatives for FFT-NAH.[10]

At first, let us review the reconstruction equation of normal velocity by FFT-NAH using Tikhonov filter. The Tikhonov filter for Cartesian coordinates is described as[23]

$$F^{\alpha,1}(k_x, k_y, \lambda_{k_x,k_y}) = \frac{|\lambda_{k_x,k_y}|^2}{|\lambda_{k_x,k_y}|^2 + \alpha[\alpha/(\alpha + |\lambda_{k_x,k_y}|^2)]^2}, \tag{9}$$

where

$$\lambda_{k_x,k_y} = \frac{\rho_0 ck}{i\sqrt{k_x^2 + k_y^2 - k^2}} \exp[-(z_m - z_s)\sqrt{k_x^2 + k_y^2 - k^2}] \tag{10}$$

is called propagator, c the sound speed, ρ_0 the fluid density, $k = \omega/c$, k_x and k_y are wavenumber in the x and y direction, and $z = z_m$ and $z = z_s$ are measurement and reconstruction planes, respectively. The regularization parameter α is determined by MDP.

Let us set $\dot{w}(\mathbf{r}_s) = \dot{w}(x, y, z_s)$, which is the normal component of the surface velocity, and $p(\mathbf{r}_m) = p(x, y, z_m)$. The following relationship exists between them:[1]

$$w(\mathbf{r}_s) = \dot{w}(\mathbf{r}_s)/(j\omega) = \mathcal{F}^{-1}[\mathcal{F}\{p(\mathbf{r}_m)\}\lambda_{k_x,k_y}^{-1}]/(j\omega). \tag{11}$$

where $\mathcal{F}$ and $\mathcal{F}^{-1}$ represent the two-dimensional forward and inverse Fourier transforms in x and y. This is the reconstruction equation. This equation is modified by applying the Tikhonov filter to suppress the amplification of noise in high-wavenumber region as

$$\tilde{w}(\mathbf{r}_s) = \tilde{\dot{w}}(\mathbf{r}_s)/(j\omega) = \mathcal{F}^{-1}[\mathcal{F}\{p(\mathbf{r}_m)\}F^{\alpha,1}(k_x, k_y, \lambda_{k_x,k_y})\lambda_{k_x,k_y}^{-1}]/(j\omega). \tag{12}$$

Next, let us introduce the measurement method of spatial derivatives using FFT-NAH.[10] The spatial derivative of normal displacement is obtained as

$$\frac{\partial^{m+n}}{\partial x^m \partial y^n} w(\mathbf{r}_s)$$
$$= \frac{\partial^{m+n}}{\partial x^m \partial y^n} \mathcal{F}^{-1}\{W(k_x,k_y)\}$$
$$= \frac{\partial^{m+n}}{\partial x^m \partial y^n} \frac{1}{2\pi} \int\int W(k_x,k_y) e^{i(k_x x+k_y y)} dk_x dk_y$$
$$= \frac{1}{2\pi} \int\int \frac{\partial^{m+n}}{\partial x^m \partial y^n} \{W(k_x,k_y) e^{i(k_x x+k_y y)}\} dk_x dk_y$$
$$= \frac{1}{2\pi} \int\int W(k_x,k_y) e^{i(k_x x+k_y y)} \frac{\dfrac{\partial^{m+n}}{\partial x^m \partial y^n} e^{i(k_x x+k_y y)}}{e^{i(k_x x+k_y y)}} dk_x dk_y$$
$$= \frac{1}{2\pi} \int\int W(k_x,k_y) e^{i(k_x x+k_y y)} (ik_x)^m (ik_y)^n dk_x dk_y, \tag{13}$$

where K-space representation of the normal displacement

$$W(k_x,k_y) = \mathcal{F}\{w(\mathbf{r}_s)\} = \frac{\mathcal{F}\{p(\mathbf{r}_m)\}\lambda^{-1}_{k_x,k_y}}{i\omega}, \tag{14}$$

indicates the complex amplitude of surface vibration mode $e^{i(k_x x+k_y y)1}$ and

$$(ik_x)^m (ik_y)^n = \frac{\dfrac{\partial^{m+n}}{\partial x^m \partial y^n} e^{i(k_x x+k_y y)}}{e^{i(k_x x+k_y y)}} \tag{15}$$

means the ratio of spatial derivative of vibration mode $\partial^{m+n} e^{i(k_x x+k_y y)} / \partial x^m \partial y^n$ and vibration mode $e^{i(k_x x+k_y y)}$. To derive the relationship between the spatial derivative of the normal displacement, and the measured pressure, Eq. (14) is substituted into Eq. (13)and two-dimensional Fourier transform is applied, then

$$\frac{\mathcal{F}\left\{\dfrac{\partial^{m+n}}{\partial x^m \partial y^n} w(\mathbf{r}_s)\right\}}{\mathcal{F}\{p(\mathbf{r}_m)\}/i\omega} = \lambda^{-1}_{k_x,k_y} \frac{\dfrac{\partial^{m+n}}{\partial x^m \partial y^n} e^{i(k_x x+k_y y)}}{e^{i(k_x x+k_y y)}}$$
$$= \lambda^{-1}_{k_x,k_y} (ik_x)^m (ik_y)^n = \lambda^{-1}_{k_x,k_y,(x,m),(y,n)} \tag{16}$$

is obtained, which can be treated as a propagator for the spatial derivative of the normal displacement. Therefore,

$$|\lambda^{-1}_{k_x,k_y,(x,m),(y,n)}| = |\lambda^{-1}_{k_x,k_y}| \left| \frac{\dfrac{\partial^{m+n}}{\partial x^m \partial y^n} e^{i(k_x x+k_y y)}}{e^{i(k_x x+k_y y)}} \right|$$
$$= |\lambda^{-1}_{k_x,k_y}| |(ik_x)^m (ik_y)^n| \tag{17}$$

can be treated as an eigenvalue of the Tikhonov filter for spatial derivative of the normal displacement reconstructed by FFT-NAH. As a result, the Tikhonov filter for the spatial derivative is obtained as

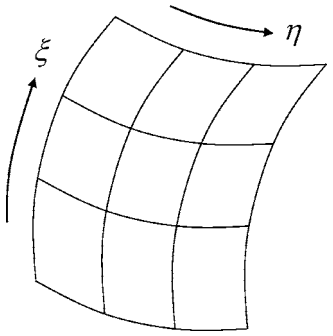

FIG. 2. The local orthogonal coordinate (ξ, η) on the surface of simple structure.

$$F^{\alpha,1}(k_x,k_y,\lambda_{k_x,k_y,(x,m),(y,n)})$$
$$= \frac{|\lambda_{k_x,k_y,(x,m),(y,n)}|^2}{|\lambda_{k_x,k_y,(x,m),(y,n)}|^2 + \alpha[\alpha/(\alpha + |\lambda_{k_x,k_y,(x,m),(y,n)}|^2)]^2}, \tag{18}$$

and the spatial derivative is obtained as

$$\frac{\partial^{m+n}}{\partial x^m \partial y^n} \tilde{w}(\mathbf{r}_s)$$
$$= \frac{\mathcal{F}^{-1}\{\mathcal{F}\{p(\mathbf{r}'_s)\} F^{\alpha,1}(k_x,k_y,\lambda_{k_x,k_y,(x,m),(y,n)}) \lambda^{-1}_{k_x,k_y,(x,m),(y,n)}\}}{i\omega}. \tag{19}$$

The regularization parameter α is determined by MDP.

Here, the spatial derivative of surface displacement reconstructed by BEM-NAH is considered to derive the Tikhonov filter. Let us set the local orthogonal coordinate (ξ, η) on the surface of simple structure with large radius of curvature (cf. Fig. 2). In this coordinate, each mode v_j spans a two-dimensional surface.[14] Therefore, we can visualize v_j spatially in matrix form by segmenting over the two coordinate dimensions (ξ axis $\times$ η axis)

$$v_j \rightarrow \mathbf{V}^{(j)}$$
$$\equiv \begin{bmatrix} v_{j,1} & v_{j,2} & \cdots & v_{j,n_2} \\ v_{j,(n_2+1)} & v_{j,(n_2+2)} & \cdots & v_{j,n_2\times 2} \\ \vdots & \vdots & & \vdots \\ v_{j,(n_2\times(n_1-1)+1)} & v_{j,(n_2\times(n_1-1)+2)} & \cdots & v_{j,N} \end{bmatrix}^{n_1\times n_2} \tag{20}$$

with rows and columns following direction along the ξ axis and η axis, respectively ($n_1 \times n_2 = N$). The reconstructed normal displacement $\mathbf{w}$ represents the same way, i.e.,

$$\mathbf{w} \equiv \begin{bmatrix} w_1 & w_2 & \cdots & w_{n_2} \\ w_{n_2+1} & w_{n_2+2} & \cdots & w_{n_2\times 2} \\ \vdots & \vdots & & \vdots \\ w_{n_2\times(n_1-1)+1} & w_{n_2\times(n_1-1)+2} & \cdots & w_N \end{bmatrix}^{n_1\times n_2}. \tag{21}$$

Here, the spatial derivatives of the normal displacement of the structure are obtained as

$$\frac{\partial^{n+m}\mathbf{w}}{\partial\xi^n\partial\eta^m}=\frac{\partial^{n+m}}{\partial\xi^n\partial\eta^m}\frac{\mathbf{V}\boldsymbol{\Sigma}^{-1}\mathbf{U}^H\mathbf{p}_{\mathrm{mea}}}{j\omega}=\frac{\partial^{n+m}\mathbf{V}}{\partial\xi^n\partial\eta^m}\frac{\boldsymbol{\Sigma}^{-1}\mathbf{U}^H\mathbf{p}_{\mathrm{mea}}}{j\omega},\tag{22}$$

where

$$\frac{\partial^{n+m}\mathbf{V}}{\partial\xi^n\partial\eta^m}=\left\{\frac{\partial^{n+m}v_1}{\partial\xi^n\partial\eta^m},\cdots,\frac{\partial^{n+m}v_N}{\partial\xi^n\partial\eta^m}\right\},\tag{23}$$

and

$$\frac{\partial^{n+m}v_j}{\partial\xi^n\partial\eta^n}\equiv\frac{\partial^{n+m}\mathbf{V}^{(j)}}{\partial\xi^n\partial\eta^n},\tag{24}$$

where $\partial^{m+n}\mathbf{V}^{(j)}/\partial\xi^m\partial\eta^n$ is the spatial derivative of surface vibration mode v_j in BEM-NAH. Equation (24) is calculated by the second-order finite difference scheme.[25] This formulation is not considered the influence of measurement noise, and Tikhonov filter is applied to modify this formulation for reduction of the influence of noise. To derive the eigenvalue of the Tikhonov filter for BEM-NAH, we consider the relationship between FFT-NAH and BEM-NAH. Comparison of Eq. (8) with Eq. (12) reveals the similarity. Thus we make the following association

$$\lambda_{k_x,k_y}\Leftrightarrow\sigma_j.\tag{25}$$

And the ratio of the spatial derivative of vibration mode $\partial^{m+n}v_j/\partial\xi^m\partial\eta^n$ and the vibration mode v_j corresponds to Eq. (15) in FFT-NAH, i.e.,

$$(ik_x)^m(ik_y)^n=\frac{\dfrac{\partial^m}{\partial x^m}\dfrac{\partial^n}{\partial y^n}e^{i(k_xx+k_yy)}}{e^{i(k_xx+k_yy)}}\Leftrightarrow\frac{\dfrac{\partial^{m+n}v_j}{\partial\xi^m\partial\eta^n}}{v_j}.\tag{26}$$

As a result, the eigenvalue of the Tikhonov filter for the spatial derivative reconstructed by FFT-NAH [cf. Eq. (17)] and that reconstructed by BEM-NAH are described as

$$\begin{aligned}\left|\lambda^{-1}_{k_x,k_y,(x,m),(y,n)}\right|&=\left|\lambda^{-1}_{k_x,k_y}\right|\left|(ik_x)^m(ik_y)^n\right|\Leftrightarrow\left|\sigma^{-1}_{j,(\xi,m),(\eta,n)}\right|\\&=\left|\sigma_j^{-1}\right|\frac{\left\|\dfrac{\partial^{m+n}v_j}{\partial\xi^m\partial\eta^n}\right\|}{\|v_j\|},\end{aligned}\tag{27}$$

and the Tikhonov filter for the spatial derivative in BEM-NAH is described as

$$F^{\alpha,1}_{(\xi,m),(\eta,n)}\equiv\mathrm{diag}\left(\cdots,\frac{\left|\sigma_{j,(\xi,m),(\eta,n)}\right|^2}{\left|\sigma_{j,(\xi,m),(\eta,n)}\right|^2+\alpha[\alpha/(\alpha+\left|\sigma_{j,(\xi,m),(\eta,n)}\right|^2)]^2},\cdots\right).\tag{28}$$

The regularization parameter α is determined by solving the following discrepancy equation:

$$\|(\mathbf{U}F^{\alpha,1}_{(\xi,m),(\eta,n)}\mathbf{U}^H-I)\mathbf{p}_{\mathrm{mea}}\|/\sqrt{N}=\sigma_{\mathrm{noise}},\tag{29}$$

where the noise variance σ_{noise} is estimated by Eq. (6). As a result, the spatial derivative of normal displacement is obtained as

$$\frac{\partial^{n+n}\tilde{\mathbf{w}}}{\partial\xi^m\partial\eta^n}=\frac{\partial^{n+n}\mathbf{V}}{\partial\xi^m\partial\eta^n}\frac{\boldsymbol{\Sigma}^{-1}F^{\alpha,1}_{(\xi,m),(\eta,n)}\mathbf{U}^H\mathbf{p}_{\mathrm{mea}}}{j\omega}.\tag{30}$$

The formulation for SI of the planar structure is as follows:[26]

$$\begin{aligned}I_\xi=D\Bigg\langle&\frac{\partial}{\partial\xi}\left(\frac{\partial^2\tilde{\mathbf{w}}(\mathbf{r}_s)}{\partial\xi^2}+\frac{\partial^2\tilde{\mathbf{w}}(\mathbf{r}_s)}{\partial\eta^2}\right)\tilde{\dot{\mathbf{w}}}(\mathbf{r}_s)-\left(\frac{\partial^2\tilde{\mathbf{w}}(\mathbf{r}_s)}{\partial\xi^2}\right.\\&\left.+v\frac{\partial^2\tilde{\mathbf{w}}(\mathbf{r}_s)}{\partial\eta^2}\right)\frac{\partial\tilde{\dot{\mathbf{w}}}(\mathbf{r}_s)}{\partial\xi}-(1-v)\frac{\partial^2\tilde{\mathbf{w}}(\mathbf{r}_s)}{\partial\xi\partial\eta}\frac{\partial\tilde{\dot{\mathbf{w}}}(\mathbf{r}_s)}{\partial\xi}\Bigg\rangle_T,\\I_\eta=D\Bigg\langle&\frac{\partial}{\partial\eta}\left(\frac{\partial^2\tilde{\mathbf{w}}(\mathbf{r}_s)}{\partial\xi^2}+\frac{\partial^2\tilde{\mathbf{w}}(\mathbf{r}_s)}{\partial\eta^2}\right)\tilde{\dot{\mathbf{w}}}(\mathbf{r}_s)-\left(\frac{\partial^2\tilde{\mathbf{w}}(\mathbf{r}_s)}{\partial\eta^2}\right.\\&\left.+v\frac{\partial^2\tilde{\mathbf{w}}(\mathbf{r}_s)}{\partial\xi^2}\right)\frac{\partial\tilde{\dot{\mathbf{w}}}(\mathbf{r}_s)}{\partial\eta}-(1-v)\frac{\partial^2\tilde{\mathbf{w}}(\mathbf{r}_s)}{\partial\xi\partial\eta}\frac{\partial\tilde{\dot{\mathbf{w}}}(\mathbf{r}_s)}{\partial\eta}\Bigg\rangle_T,\end{aligned}\tag{31}$$

where outer bracket $\langle\ \rangle_T$ indicates time average, v the Poisson's ratio, $D=Eh^3/[12(1-v^2)]$, E the Young's modulus, and h the plate thickness. This formulation of the SI is decomposed into individual contributions from bending moments, twisting moments, and shear forces.[9] Therefore, contributions of these components of the SI can be examined. The procedure of measurement of SI using BEM-NAH is shown in Fig. 3.

III. MODEL EXPERIMENT

In this section, the SI in a thin plate, which is submerged in water, is measured to demonstrate the effectiveness of the proposed method. In experiments, natural frequencies are selected. An automated scanning system was developed for measurement of pressure hologram. An experimental model is SUS 304 stainless steel (500 mm×600 mm×5 mm). A shaker (Wilcoxon F3/Z3/F9) that vibrates the sample plate is attached at the center of the plate. The shaker is driven by a (150–10 000 Hz) linear frequency modulation signal. These frequencies are sufficiently lower than coincidence frequency.[1] A Brüel & Kjaer Type 8103 hydrophone is placed at the prescribed position with scanners. Stepwise movement of the plate thus scans a two-dimensional measurement plane. Measured data of the measurement aperture are taken in 20 mm steps along x- and y-axis scanning.

In the FFT-NAH procedure, the influence of finiteness of measurement aperture, which is called "finite aperture ef-

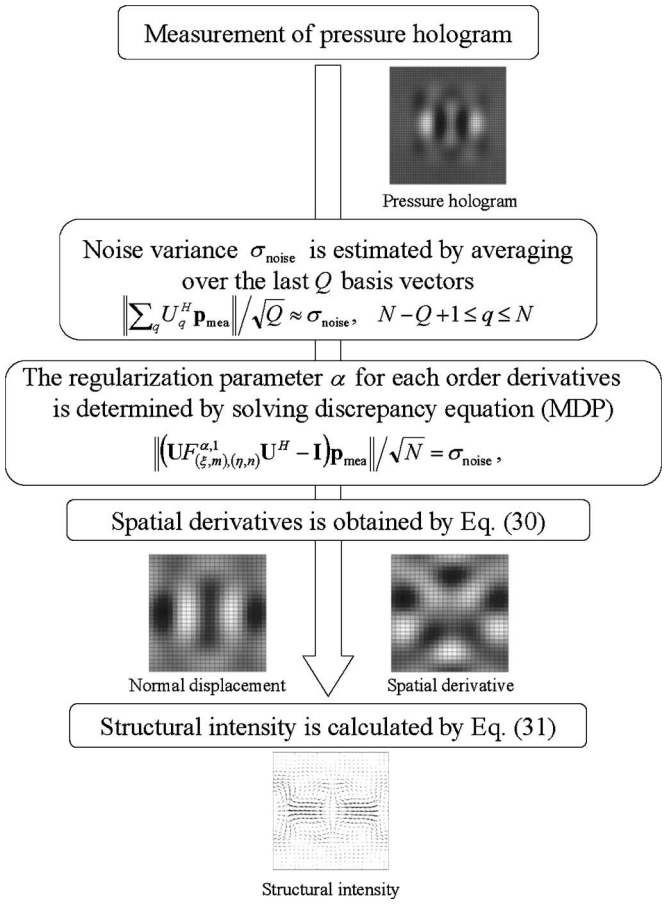

FIG. 3. The procedure of measurement of the SI using BEM-NAH.

fect," contaminates reconstructed result seriously if the size of measurement aperture is not sufficiently large. This is the aperture replication problem.[1] To mitigate the finite aperture effect, measurement aperture has to be set sufficiently large. Thus, 128×128 data points make one hologram, which is called a "full aperture hologram." Conventional FFT-based method is applied to this full aperture hologram for measurement of SI.

On the contrary, the BEM-NAH procedure avoids the aperture replication problem because it does not rely on FFT. Therefore, measurement aperture for BEM-based NAH can be set smaller than that for FFT-based NAH, and the proposed BEM-based method is applied to a "small aperture hologram," which is made of 50×50 data points. The distance between the sample plate and the measurement hologram is 50 mm. The received and amplified signal from the microphone is digitized and transferred to a personal computer. Sampling inception time is accurately controlled by the computer, which acts as the reference source for holographic interference. The ends of the plate are sealed with rubber packing to approximate the simply supported boundary condition. Here, the radius of curvature of the structure surface is infinite, therefore, coordinate systems for FFT- and BEM-NAH have the correspondency as $x \Leftrightarrow \xi$ and $y \Leftrightarrow \eta$.

Figure 4 shows the K-space filter, K-space spectrum of the third-order spatial derivative of normal displacement and reconstructed result of third-order spatial derivative $\partial^3 w / \partial \eta^3$. All variables are normalized by maximum values at the left column. The frequency is 1171.9 Hz. Figures 4(a) and 4(b) show the proposed filter [cf. Eq. (28)] and the Tikhonov filter [cf. Eq. (5)]. The cutoff singular value of the proposed filter (about 150) is smaller than that of the Tikhonov filter (about 270). Figures 4(c) and 4(d) show K-space spectrum of the third-order spatial derivatives. The amplitude of the higher-order wavenumber component smoothed by the proposed method is small [cf. Fig. 4(c)], and the amplitude vanishes in the region over 300 of singular value. On the contrary, the amplitude of the higher-order wavenumber component smoothed by the Tikhonov filter remains [cf. Fig. 4(d)]. Figures 4(e) and 4(f) show reconstructed result of third-order spatial derivative using gray-scale plots, with white and black indicating maximum positive and negative values, respectively. In Fig. 4, the horizontal and vertical axes indicate the ξ and η axis, respectively. Hereafter, the driving point is shown by a small triangle. The comparison between Figs. 4(e) and 4(f) indicates that higher-order wavenumber component (over 300 of singular value) seriously contaminates the reconstructed result. As a result, the estimation of appropriate K-space filter according to the order of spatial derivatives is necessary to measure SI.

Figure 5 shows the normal displacement, the AI, the SI and the injected power (IP), which is given by[2]

$$\Pi_C = \oint_C \mathbf{I}_{\text{SI}} \cdot \mathbf{n} dl. \tag{32}$$

Here, C is the contour surrounding each point, dl the element of a square contour C, $\mathbf{I}_{\text{SI}}$ the SI vector, and $\mathbf{n}$ the outward normal to the element of contour dl. The upper and lower rows show experimental results reconstructed by the proposed BEM-based method and the conventional FFT-based method, respectively. The frequency is 585.9 Hz. All data are normalized by the maximum value of the lower rows variables for better mutual comparison. Grey-scale plots show the normal displacement, the Al and the IP, white is positive and black is negative, respectively. In Fig. 5, the horizontal and vertical axes indicate the ξ and η axis (the x and y axis), respectively. Figures 5(a) and 5(e) represent the normal displacement reconstructed by BEM- and FFT-NAH, respectively. Reconstructed results of normal displacement [cf. Figs. 5(a) and 5(e)] show (3,3) mode (three half-wavelengths in the ξ direction and three in the η direction). These figures show that the driving point corresponds to the antinode of the vibration mode, but it is difficult to localize the vibration source from these results. SIs are reconstructed in Figs. 5(b) and 5(f), from which we know that the SI diverges from the shaker located at the plate center, and major vibration energy flow from the center is vertical direction. The length of the vector normalized by the maximum value is drawn linearly. Powers injected to the plate Π_C are indicated in Figs. 5(c) and 5(g), where the calculation is based on Eq. (32). The IP shows a large positive value at the center of the plate in both figures; therefore, we can easily localize the vibration source. AIs are shown in Figs. 5(d) and 5(h). Comparison results indicate excellent agreement between two methods. These results indicate that agreements between higher-order deriva-

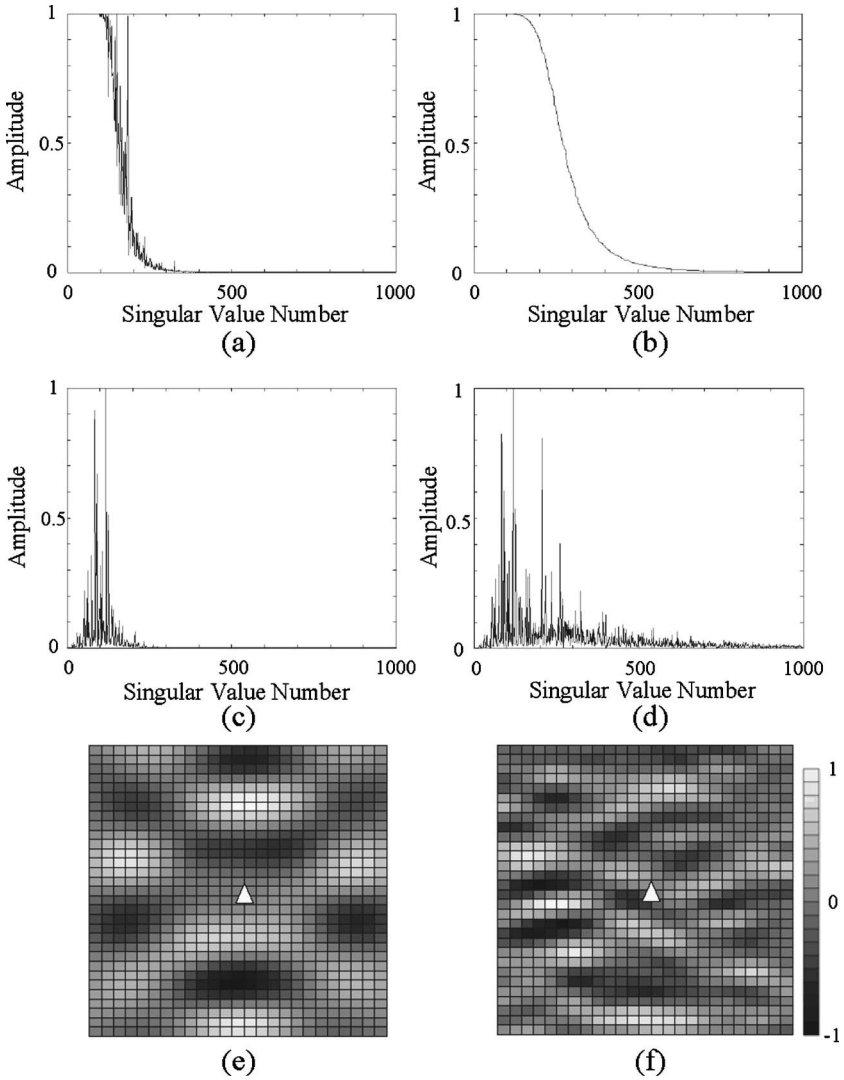

FIG. 4. *K*-space filter, *K*-space spectrum of the third-order derivative and reconstructed result of the third-order derivative of the normal displacement. The frequency is 1171.9 Hz. (a) The proposed filter for the third-order derivative $\partial^3 w/\partial \eta^3$. (b) Tikhonov filter for $\partial^3 w/\partial \eta^3$. (c) *K*-space spectrum of $\partial^3 w/\partial \eta^3$ obtained by the proposed filter. (d) *K*-space spectrum of $\partial^3 w/\partial \eta^3$ obtained by the Tikhonov filter. (e) Reconstructed result of $\partial^3 w/\partial \eta^3$ obtained by the proposed filter. (f) Reconstructed result of $\partial^3 w/\partial \eta^3$ obtained by the Tikhonov filter.

tives reconstructed by BEM-based method and those reconstructed by FFT-based method are good.

Comparisons between IPs and AIs [cf. Figs. 5(d) and 5(h)] show fairly good matching at the periphery of the plate because Π_C is equal to the negative of the normal AI away from the driver.[27] As a result, we can easily understand the mechanism of the energy flow between the structure and surrounding medium, i.e., we may infer that the vibration energy is injected to the plate at the driving point and lost from periphery of the plate. Note that the hologram size for BEM-based method is less than a quarter of that for the FFT-based method. This means that the measurement time of pressure hologram for the proposed method is shorter than a quarter of that for the conventional FFT-based method.

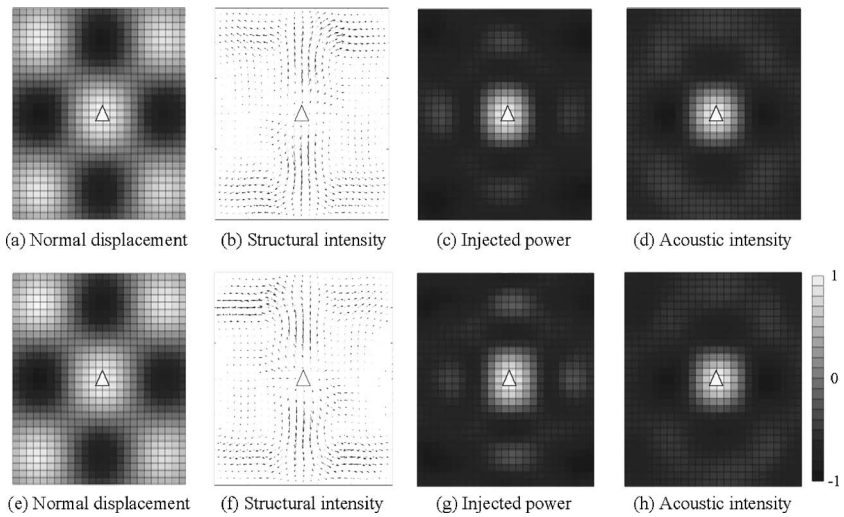

FIG. 5. Reconstructed results of BEM- and FFT-based methods. The frequency is 585.9 Hz. The triangle indicates the driving point. Upper and lower rows show the reconstructed results of the BEM-based method and the FFT-based method.

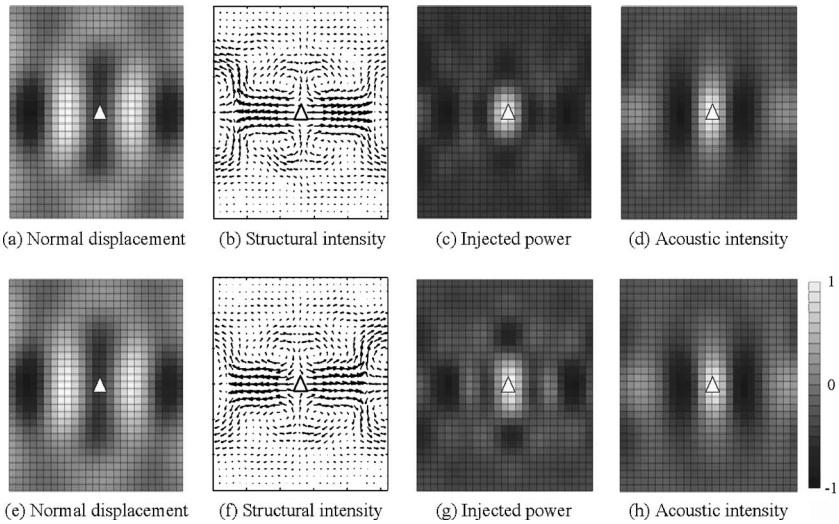

FIG. 6. Reconstructed results of BEM- and FFT-based method. The frequency is 1171.9 Hz. The triangle indicates the driving point. Upper and lower rows show the reconstructed results of the BEM-based method and the FFT-based method.

Figure 6 shows a comparison of experimental results reconstructed by the BEM-based method and that reconstructed by the FFT-based method. The frequency is 1171.9 Hz. The vibration mode appears to be (5,1) (five half-wavelengths in the ξ direction and one in the η direction). The agreement between reconstructed results by both methods is excellent.

The direction of the vibration energy flow which originates from the center of the plate is restricted to the horizontal direction as shown in Figs. 6(b) and 6(f). The peak of the IP corresponds to the center of the plate at which shaker is attached in Figs. 6(c) and 6(g), and local peaks at the periphery of the plate are matched with AIs [cf. Figs. 6(d) and 6(h)]; therefore, we can easily detect the vibration source and understand the mechanism of the energy flow between the structure and surrounding medium. These results confirm the effectiveness of the proposed method.

IV. CONCLUSIONS

In this paper, a new regularization method for measurement of SI using BEM-based NAH is presented. To measure SI, measurement of spatial derivatives of structure surface is necessary. The derivative operations amplify the high-wavenumber component of measurement noise and contaminate the measurement result. To overcome this difficulty, regularization method for measurement of SI using FFT-based NAH has been introduced previously. In this work, this regularization method is modified for the BEM-based method to measure the SI. The Tikhonov regularization filter for each order of derivatives is introduced. The regularization parameter for each order of derivatives is determined by MDP method using the measured pressure.

The effectiveness of the proposed method is demonstrated by experiments. The experimental model is a thin plate which is submerged in water. For comparison, normal displacement, SI, injected power, and AI are reconstructed by the proposed BEM-based method and the conventional FFT-based method. The experimental results are as follows;

(1) The agreement of reconstructed results by both methods is good.
(2) The hologram size for the BEM-based method is less than a quarter of that for the FFT-based method. This means that the measurement time of the pressure hologram for the proposed method is smaller than that for the conventional FFT-based method.
(3) The interrelationship between SI and AI is clearly shown.
(4) The peak of injected power corresponds to the driving point and local peaks at the periphery of the plate are matched by the AI.

As a result, the effectiveness of the proposed method is exhibited. And the formulation of SI [cf. Eq. (31)] is decomposed into individual contributions from bending moments, twisting moments, and shear forces, thus we can examine contributions of these components individually. Therefore, this method may thus be recommended to apply the measurement of SI.

[1]E. G. Williams, *Fourier Acoustics: Sound Radiation and Nearfield Acoustical Holography* (Academic, London, 1999).
[2]E. G. Williams, H. D. Dardy, and R. G. Fisk, "A technique for measurement of structure-borne intensity in plates," J. Acoust. Soc. Am. **78**, 2061–2068 (1985).
[3]J. C. Pascal, T. Loyau, and J. A. Mann III, "Structural intensity from spatial Fourier transformation and BAHIM acoustic holography method," Proceedings of the Third International Congress on Intensity Techniques, Senlis, France 1990, pp. 193–204.
[4]Y. Zhang and J. A. Mann III, "Measuring the structural intensity and force distribution in plate," J. Acoust. Soc. Am. **99**, 345–353 (1996).
[5]Y. Zhang and J. A. Mann III, "Examples of using structural intensity and force distribution to study vibrating plates," J. Acoust. Soc. Am. **99**, 354–361 (1996).
[6]J. Pascal, T. Loyau, and X. Carniel, "Complete determination of structural intensity in plate using laser vibrometers," J. Sound Vib. **161**, 527–531 (1993).
[7]A. B. Spalding and J. A. Mann III, "Placing small constrained layer damping patches on a plate to attain global or local velocity changes," J. Acoust. Soc. Am. **97**, 3617–3624 (1985).
[8]R. Morikawa, S. Ueha, and K. Nakamura, "Error evaluation of the structural intensity measured with a scanning laser Doppler vibrometer and a *k*-space signal processing," J. Acoust. Soc. Am. **99**, 2913–2921 (1996).
[9]A. Nejade and R. Singh, "Flexural intensity measurement on finite plates using modal spectrum ideal filtering," J. Sound Vib. **256**, 33–63 (2002).
[10]K. Saijyou and C. Okawara, "Regularization method for measurement of structural intensity using nearfield acoustical holography," J. Acoust. Soc. Am. **117**, 2039–2045 (2005).

[11]E. G. Williams and B. H. Houston, "Fast Fourier transform and singular value decomposition formulation for patch nearfield acoustical holography," J. Acoust. Soc. Am. **114**, 1322–1333 (2003).
[12]B.-K. Kim and J.-G. Ih, "On the reconstruction of the vibro-acoustic field over the surface enclosing an interior space using the boundary element method," J. Acoust. Soc. Am. **100**, 3003–3016 (1996).
[13]S.-C. Kang and J.-H. Ih, "Use of nonsingular boundary integral formulation for reducing errors due to near-field measurement in the boundary element method based near-field acoustic holography," J. Acoust. Soc. Am. **109**, 1320–1328 (2001).
[14]E. G. Williams, B. H. Houston, P. C. Herdic, S. T. Raveendra, and B. Gardner, "Interior nearfield acoustical holography in flight," J. Acoust. Soc. Am. **108**, 1451–1463 (2000).
[15]B.-K. Kim and J.-G. Ih, "Design of an optimal wave-vector filter for enhancing the resolution of reconstructed source field by near-field acoustical holography (NAH)," J. Acoust. Soc. Am. **107**, 3289–3297 (2000).
[16]E. G. Williams, "Continuation of acoustic near-fields," J. Acoust. Soc. Am. **113**, 1273–1281 (2003).
[17]P. C. Hansen, *Rank-Deficient and Discrete Ill-Posed Problems* (SIAM, Philadelphia, 1998).
[18]P. A. Nelson and S. H. Yoon, "Estimation of acoustic source strength by inverse method. I. Conditioning of the inverse problem," J. Sound Vib. **233**, 643–668 (2000).
[19]S. H. Yoon and P. A. Nelson, "Estimation of acoustic source strength by inverse methods. II. Experimental investigation of methods for choosing regularization parameters," J. Sound Vib. **233**, 669–705 (2000).
[20]F. Augusztionvicz, "Reconstruction of source strength distribution by inversing the boundary element method," in *Boundary Elements in Acoustics, Advances and Applications*, edited by O. von Estoff (WIT, Southampton, UK, 2000).
[21]P. A. Nelson, "Some inverse problems in acoustics," in Proceedings of the Sixth International Congress on Sound and Vibration, Copenhagen, Denmark, 1999, pp. 7–32.
[22]A. Kirsch, *An Introduction to the Mathematical Theory of Inverse Problem* (Springer, New York, 1996).
[23]A. P. Schuhmacher and P. C. Hansen, "Sound source reconstruction using inverse BEM," Proceedings of Inter-Noise 2001, pp. 2109–2114.
[24]E. G. Williams, "Regularization method for near-field acoustic holography," J. Acoust. Soc. Am. **110**, 1976–1988 (2001).
[25]S. I. Hayek, M. J. Pechersky, and B. C. Suen, "Measurement and analysis of near and far field structural intensity by scanning laser vibrometry," Proceedings of the third International Congress on Intensity Techniques, Senlis, France, 1990, pp. 281–288.
[26]G. Pavic, "Measurement of structure borne wave intensity. I. Formulation of the methods," J. Sound Vib. **49**, 221–230 (1976).
[27]E. G. Williams, "Structural intensity in thin cylindrical shells," J. Acoust. Soc. Am. **89**, 1615–1622 (1991).

Quieting Weinberg 5C: A case study in hospital noise control

Mark MacLeod, Jeffrey Dunn, Ilene J. Busch-Vishniac, and James E. West
Johns Hopkins University, 3400 North Charles Street, Baltimore, Maryland 21218

Anita Reedy
Johns Hopkins Hospital, 600 North Wolfe Street, Baltimore, Maryland 21287

(Received 28 July 2006; revised 7 February 2007; accepted 18 March 2007)

Weinberg 5C of Johns Hopkins Hospital is a very noisy hematological cancer unit in a relatively new building of a large medical campus. Because of the requirements for dealing with immuno-suppressed patients, options for introducing sound absorbing materials are limited. In this article, a case study of noise control in a hospital, the sound environment in the unit before treatment is described, the chosen noise control approach of adding custom-made sound absorbing panels is presented, and the impact of the noise control installation is discussed. The treatment of Weinberg 5C involved creating sound absorbing panels of 2-in.-thick fiberglass wrapped in an anti-bacterial fabric. Wallpaper paste was used to hold the fabric to the backing of the fiberglass. Installation of these panels on the ceiling and high on corridor walls had a dramatic effect. The noise on the unit (as measured by the equivalent sound pressure level) was immediately reduced by 5 dB(A) and the reverberation time dropped by a factor of over 2. Further, this drop in background noise and reverberation time understates the dramatic impact of the change. Surveys of staff and patients before and after the treatment indicated a change from viewing the unit as very noisy to a view of the unit as relatively quiet.
© *2007 Acoustical Society of America.* [DOI: 10.1121/1.2723655]

PACS number(s): 43.50.Jh, 43.55.Gx [BSF] Pages: 3501–3508

I. INTRODUCTION

While hospital noise is among the top complaints of patients and staff,[1,2] there is little in the literature that documents effective noise control strategies for hospitals. The challenges presented for noise control in a hospital are substantial. Sound sources abound, and many are mobile (e.g., people, carts, medical equipment). Air flow is mandated to be very high in order to enhance removal of pathogens, and fire and smoke standards are among the most stringent for buildings. Couple this with an enormous density of people and the pandemonium to which Grumet referred[3] is complete. This is particularly true in units with immuno-compromised or critically ill patients, where the density of people is enormous and the ability to use standard sound absorbing materials is low. The result as documented by Busch-Vishniac *et al.*[4] is that hospitals around the world are noisy and getting noisier at an alarming rate. Current hospital noise levels are already sufficiently high to cause concern for patient ability to sleep and for enabling clear speech communication at normal voice levels.

Only a few hospital noise control studies are reported in the literature[5–7] and these focus on administrative controls—i.e., on changing the behavior of people rather than on changing the noise environment in more permanent and people-independent ways. A recent study by Akhtar *et al.*[8] presented an example of objective noise control. In this study noise cancelling headphones were given to medical staff and the parents of children in a pediatric intensive care unit. Although subjects generally perceived the headphones to offer an improvement in the environment, they overwhelmingly said they would prefer not wearing them in spite of this improvement.

Noise in hospitals is important for a number of reasons. Noise is annoying to patients largely for its impact on sleep.[6,9–12] Further, noise might have a negative impact on healing,[13–16] although most of the work in this area either uses animal models or opportunistic surveys of hospital patients exposed to construction noise. Studies also suggest that noise contributes to stress in medical staff,[17–19] a matter for serious concern given the potentially life-threatening implications of errors and the current nursing shortage throughout the country. Most importantly, noise can negatively impact clear speech communication. This is a particularly important issue in hospitals because the vast majority of information is transmitted orally (via doctors rounding with staff, or medical staff talking with patients and their families). It has been suggested that it is the conversational challenge presented by noise in hospitals that is the underlying cause of the link between noise and stress in nursing staff that has been reported. Joseph and Ulrich[20] present a very nice review of the literature on noise impacts in hospitals and focus particularly on the conflicting needs for speech intelligibility and speech privacy.

In this article, we present a noise control case study in a particular unit of a large, urban hospital with an aim of demonstrating one method of introducing effective, long term noise reductions into hospitals while meeting the various building standards and containing costs. In the next section, we will present an objective description of the unit prior to noise control. Following that we will describe and justify our

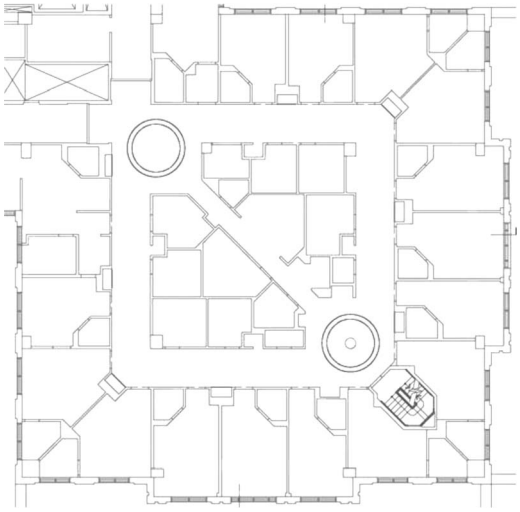

FIG. 1. The architectural floorplan for Weinberg 5C. The nursing station occupies the center of the unit and patient rooms ring the outside.

chosen sound control method. Finally, we will document the impact of the noise control strategy and discuss its applicability outside of the particular unit under study.

II. WEINBERG 5C PRIOR TO NOISE CONTROL IMPLEMENTATION

Weinberg 5C is a hematological oncology unit of Johns Hopkins Hospital in Baltimore, MD. Johns Hopkins Hospital is a large, urban medical campus that has been ranked as the top hospital in the US for 16 consecutive years by *US News and World Report*. The Weinberg Building was opened in 1999. The fifth floor is its top floor. This floor has a reflective, solid ceiling because of concern that the typical small holes in acoustical ceiling tiles might harbor bacteria and negatively impact the immuno-suppressed patients.

Figure 1 shows the architectural layout of Weinberg 5C. The center of the unit houses the nursing station and service rooms. Patient rooms are located on the outside of the unit and each houses a single patient. There are two interesting features of Weinberg 5C that directly impact its soundscape. First, as shown in Fig. 1, three of the four corners are outfitted with corner cabinets at 45 deg angles. These hard cabinets unfortunately create a waveguide with sound traveling down one hall specularly reflected into the orthogonal hall at the corner. Second, the unit has two *circular architectural features* serving a purely visual aesthetic purpose. These features extend down from the ceiling roughly one foot. The sound beneath the circular features exhibits significant echoes. Further, combined with the waveguide effect in the hallways, these features serve to channel sound into the hallways and thus throughout the unit. Nursing staff on the unit mentioned that any conversation at a nurses's station is audible throughout the entire unit.

Walls and floors in the unit are typical for hospitals. They are hard surfaces designed for durability and cleanliness. There is no obvious sound absorbing material anywhere in the unit.

The sound pressure levels on Weinberg 5C in various rooms and as a function of time of day and frequency were presented in Busch-Vishniac *et al.*[4] and will not be repeated here in detail but will be summarized. Averaging over many measurement locations in Weinberg 5C, the A-weighted equivalent sound pressure level (L_{eq}) is 55 dB(A). The spectrum is relatively flat over the 63.5 to 2000 Hz octave bands, with substantially more energy at lower frequencies and a gradual roll off at higher frequencies. Further, the noise is relatively constant, with an occasional *quiet* period corresponding to a drop of about 5 dB(A) in the L_{eq} between about 2 and 5 a.m.

We measured the reverberation time in the unit using a Bruel and Kjaer Pulse system to generate broadband noise that was amplified and played through a single speaker. Two microphones were used to monitor the sound decay from rapid turn off of the source. The reverberation time was found from the first 30 dB decay of the sound. Three trials were run of this system, each with two microphones to produce six separate results. The reliable results were averaged to produce reverberation times in third octave bands from 400 Hz to 20 kHz. The data from one microphone in one configuration were eliminated because they showed a significantly nonuniform decay rate and poor correlation with the other data sets. The reverberation time results are shown in Fig. 2 where error bars show ±two standard deviations. Generally the reverberation times range between a low of 0.24 s at 20 kHz and about 1.2 s at the low frequency end. The exception is a measured reverberation time of 1.81 s in the 800 Hz third octave band. This particular band also showed great variability in the measurements. We did a cursory search for a resonance that might explain the high reverberation time and variability but were unable to find one.

III. NOISE CONTROL STRATEGY

Given the reality of roving sound sources and a constantly changing population, we quickly decided that the best approach to noise control on Weinberg 5C would be the installation of sound absorbing materials in corridors. As this was a pilot study, we opted for sound absorbing materials in the hallways only. In a full-fledged intervention, one would likely treat patient rooms with sound absorbing materials as well. Such sound absorbing materials need to meet hospital standards for flammability, smoke generation, and cleanliness. Further, we were told to limit our options to those which would not require drilling any holes on the unit. There were three reasons for this limitation. First, there was concern that drilling in walls or ceilings would create significant particulate matter that could adversely affect patients. Second, because we were at the top floor of the building, the probability of striking a utility line was unacceptably high. Third, the nursing staff were concerned about further disruptions to the busy unit.

Because our search for appropriate sound absorbing material for a hospital unit turned up only a single vendor, we chose to make our own sound panels. We did this by wrapping fiberglass with an antibacterial fabric. The fiberglass was 2 in. thick (noncompressed) and purchased in 2 ft by 4 ft panels backed with aluminum foil. The antibacterial fabric used was Xorel purchased from Carnegie Fabrics of

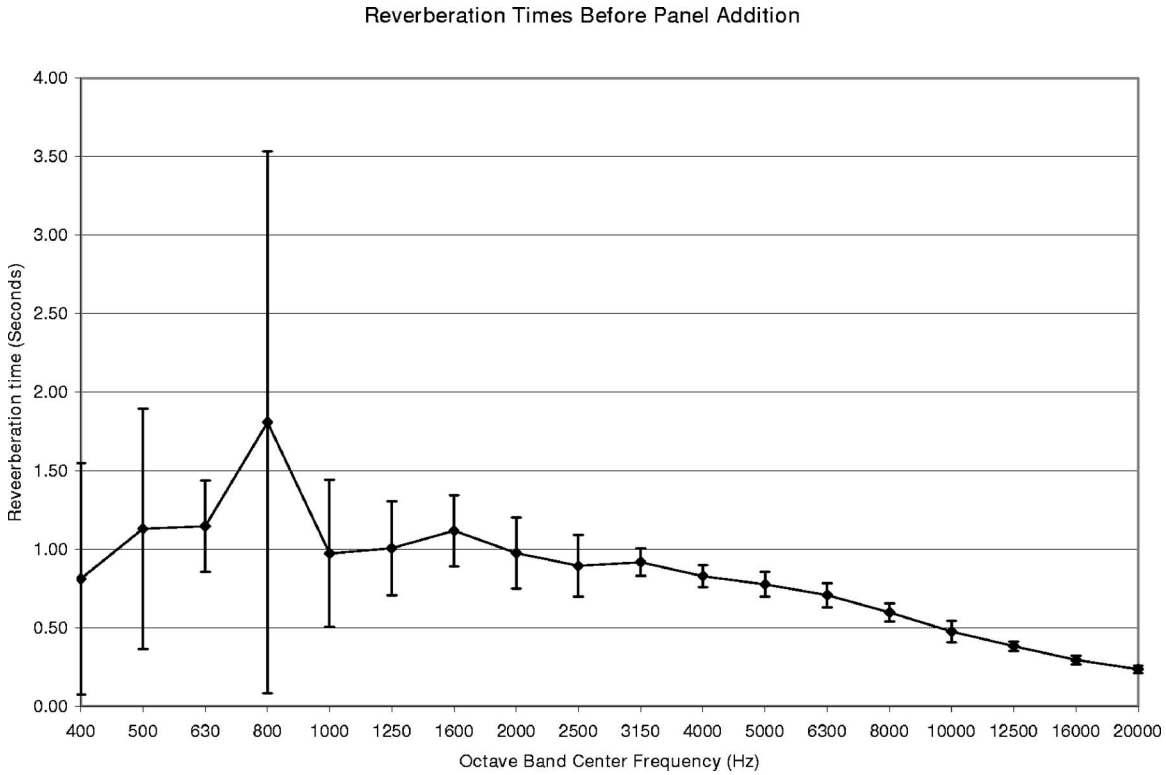

FIG. 2. Reverberation time in third octave bands. Error bars show plus and minus two standard deviations.

Rockville Centre, NY. Xorel is available in many patterns and colors and with no backing, paper backing, or a vinyl backing. We opted for the unbacked Xorel to minimize its degradation of the sound absorption by the fiberglass and asked the nursing staff to choose the pattern.

We designed the installation to cover no more than half of the ceiling and the space high on the corridor walls (top foot of height). We also concentrated on sound absorption for the corners where cabinets tended to reflect sound from one corridor to another, and for the circular architectural features at the nurses's station. These areas required that we trim the fiberglass to designed shapes and sizes. Figure 3 shows the placement of sound absorbing panels on the ceiling. The panels on the vertical walls were aligned with the ceiling panels except when they would block doors or signaling devices. The pattern was established in partnership with the hospital architects.

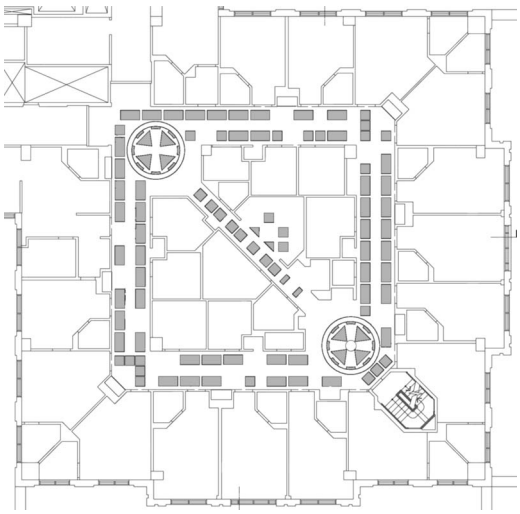

FIG. 3. The architectural floorplan for Weinberg 5C showing where sound absorbing panels were added. Large panels in the halls are 2×4 feet in size.

The Xorel was held to the back of each fiberglass part using wallpaper paste. The assembled panels were installed using industrial strength velcro. This met the need to install sound absorption without drilling a single hole in the unit and permits removal of the panels to paint the unit. While this worked well overall, the velcro we purchased was supplied with an adhesive that did not bond well with the fabric. Thus, the panels needed to be removed and reinstalled with velcro that was glued to the fabric.

We tested the sound absorbing performance of our panels in a reverberant test chamber. This test chamber is $18.7\times13.5\times9.5$ ft^3. The walls and ceilings are made of sheet rock on wood framing. The floor is linoleum tile on concrete slab. Using the Bruel and Kjaer Pulse system we found the reverberation times (T_R) in the chamber empty, with four 2×4 ft^2 fiberglass panels in the room, and with four similar panels with Xorel wrapping in the room. We then used the reverberation time results to determine the absorption coefficients from the modified Sabine reverberation time formula:

$$T_R = \frac{1.61V(1-\alpha)}{S\alpha}, \tag{1}$$

where α is the average energy absorption coefficient of the room, V is the room volume in m^3, and S is its surface area in m^2. It is common to use this particular reverberation time

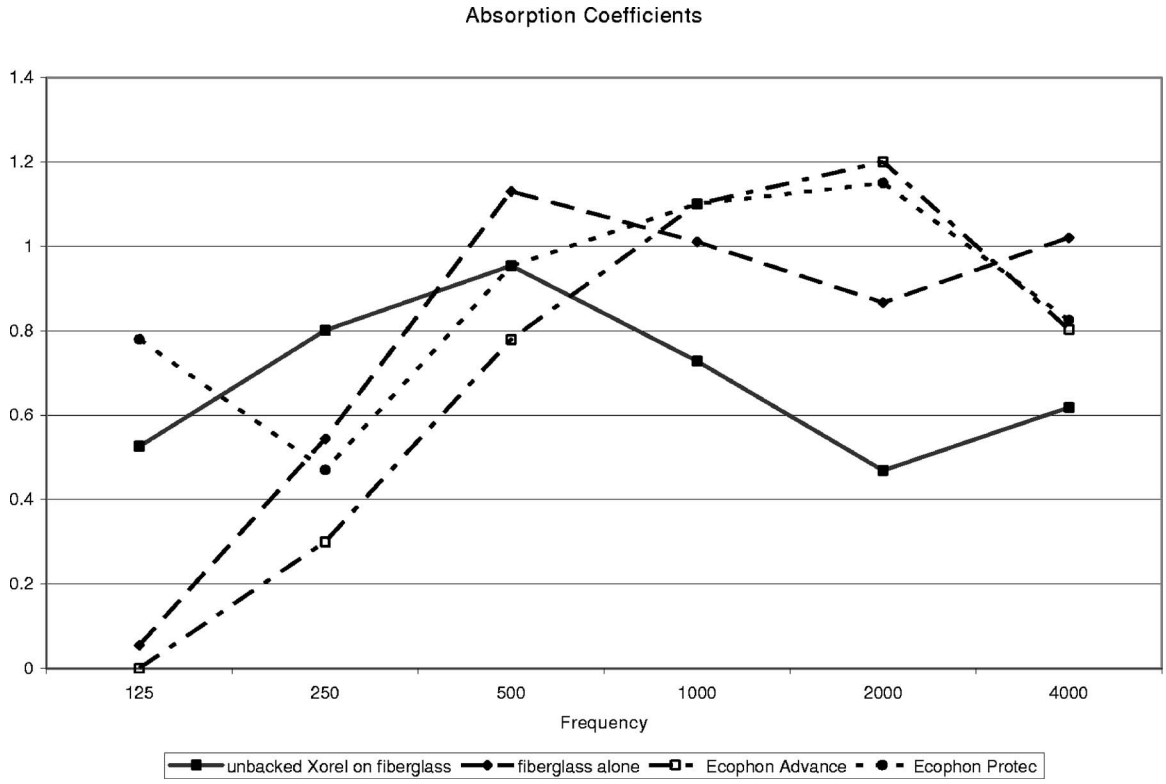

FIG. 4. Energy absorption coefficients of sound absorbing materials suitable for hospital use as a function of frequency.

formula when assessing sound decay in a room with nonuniformly distributed absorption, as is the case here. Knowing the average absorption for the empty room, one can then calculate the absorption of the covered and uncovered fiberglass by simply assuming an area weighting:

$$\frac{S\alpha}{1-\alpha} = \frac{(S_{\text{room}} - S_{\text{panels}})\alpha_{\text{room}}}{1-\alpha_{\text{room}}} + \frac{S_{\text{panels}}\alpha_{\text{panels}}}{1-\alpha_{\text{panels}}}, \tag{2}$$

where S_{room} and S_{panels} are the surface areas of the empty room and tested absorbing panels, respectively, and α_{room} and α_{panels} are the absorption coefficients of the empty room and absorbing panels.

Figure 4 shows the resulting absorption coefficients for the panels as a function of frequency. Shown in this figure are the results for bare fiberglass, the covered fiberglass used in our custom made panels, and the measured results for two commercially available products which meet hospital standards: Ecophon Hygiene Advance A and Ecophon Hygiene Protec A, made by Saint-Gobain Ecophon AB in Hyllinge, Sweden. Generally, all the materials are quite absorbent with the Ecophon products being more absorbent at high frequencies and our custom-made panels more absorbent at low frequencies. Figure 4 indicates that the Xorel wrapping has a significant negative impact on the absorption of the fiberglass at the high frequency end of the spectrum. All but one of the materials exhibit absorption coefficients exceeding 1.0, which is not unusual for this method of measurement when the edges of the panels are neglected in the area calculation. We should also note that our results differ from those obtained by Ecophon for their products under much more rigorous testing conditions. Thus, Fig. 4 permits relative comparisons but should not be viewed as a precise measurement.

IV. INSTALLATION IMPACT

The impact of the noise intervention was monitored by way of two sets of measures: objective measures of the existing sound pressure level and reverberation time on the unit, and subjective assessment of the perception of the unit by staff and patients. Both showed marked improvements and will be described below.

On the day of installation (scheduled for a Saturday morning), we started by making measurements of the sound pressure levels on the unit at a variety of locations and of the reverberation times (reported above). We then installed the panels over a period of a couple of hours. Figure 5 shows the installation in progress and also yields an indication of the extent of panel coverage of the ceilings and nail walls. Figure 6 shows a treatment at one of the 45 deg corners, and

FIG. 5. Sound absorbing panels installed on the hallway ceiling and walls.

FIG. 6. Sound absorbing panels installed around a corner cabinet.

Fig. 7 shows the panels in one of the architectural features. Immediately after installation we once again tested the unit reverberation times and monitored the sound pressure levels.

Overall, the drop in the sound pressure levels on the unit was 5 dB(A) from before installation to after. While we note that one might suspect that the level of activity simply decreased to account for some of this drop, we started our work rather early in the morning and finished when far more visitors were present. On average, we observed a drop of about 6.5 dB per octave band, although we saw a much greater drop above the 250 Hz band than at the lower frequencies. Based on anecdotal evidence, we believe that the immediate impact of the sound absorbing panels was to permit patients, staff, and visitors to lower the level of their speech while still being well understood and that it is this which accounts for most of the large sound level drop. Staff also commented on how loud the telephone ringer and overhead paging system were after installation of the panels and steps have been taken to lower the volume of these sounds. The drop in sound level also was felt to promote a safer environment with greater confidence in understanding speech.

Figure 8 shows the measured reverberation times after panel installation and can be compared directly to that shown in Fig. 2. Note that the reverberation time has dropped by a factor of more than 2. Further, the reverberation times after panel installation no longer show an anomaly in the 800 Hz third octave band.

An important measure of the effectiveness of noise control in a hospital setting is the judgment of patients and staff regarding the noisiness of the unit. To determine staff and patient perceptions, short surveys were given to staff members and patients before and after noise intervention. The same 12 nurses were surveyed before and after. Fourteen patients were surveyed before intervention and 11 patients were surveyed afterward, with an overlap of eight patients in both the before and after groups. Each were asked to evaluate a set of five statements about noise levels on a scale of one to four, one being a strong agreement and four being a strong disagreement with the statement. In general, ratings of one or two imply dissatisfaction with noise levels, while ratings of three or four imply satisfaction. Participants were also given the opportunity to write comments on their surveys.

FIG. 7. Sound absorbing panel treatment of a large circular architectural feature at the nurses's station. Note a person shown at the bottom center for scale.

The statements nurses were asked to evaluate were as follows: the noise level on this unit makes it difficult for me to safely sign off chemotherapy with another nurse, the noise level on this unit makes it difficult for me to communicate with other health care providers about a patient's condition and plan, the noise level on this unit makes it difficult for me to hear clinical conversation during morning rounds, the noise level on this unit makes it difficult for me to concentrate on the work at hand (calculating medical dose, documenting, talking to a patient or family), and the noise level on this unit is stressful for me. Figure 9 shows nurse responses to the survey before and after installation of the panels.

In general, nurses were dissatisfied with the effect noise had on communication and concentration before panel installation. As shown in Fig. 9, 83.3% and 91.7% of nurses were dissatisfied with the effect noise had on their ability to communicate with health care providers and their ability to hear clinical conversation during morning rounds, respectively. A slight majority of nurses felt noise made it difficult to concentrate on work. Staff were roughly balanced on the question of whether noise caused stress, and a slight majority of nurses said that noise did not make it difficult to sign off chemotherapy.

After panel installation, the majority of nurses were satisfied with the noise in every category. From Fig. 9, 91.7% of nurses stated that noise did not make it difficult to sign off chemotherapy, communicate with health care providers, or hear clinical conversation. Also, 91.7% of the nurses said that the noise levels were not stressful. Of those surveyed 83.3% felt that the noise did not interfere with their ability to concentrate.

The statements patients were asked to evaluate were as follows: the noise level around my room makes it difficult for me to rest during the day, the noise level around my room makes it difficult for me to sleep at night, the noise level around my room makes it difficult to concentrate on reading, watching TV, talking on the phone and other activities, the noise level around my room makes it difficult to understand people who are speaking to me, and the noise level around my room is upsetting to me. Figure 10 shows patient responses to the survey before and after installation of the panels.

Prior to installation, the majority of patients were satisfied with noise levels in every category, with 71.4% of patients saying that noise levels did not make rest during the

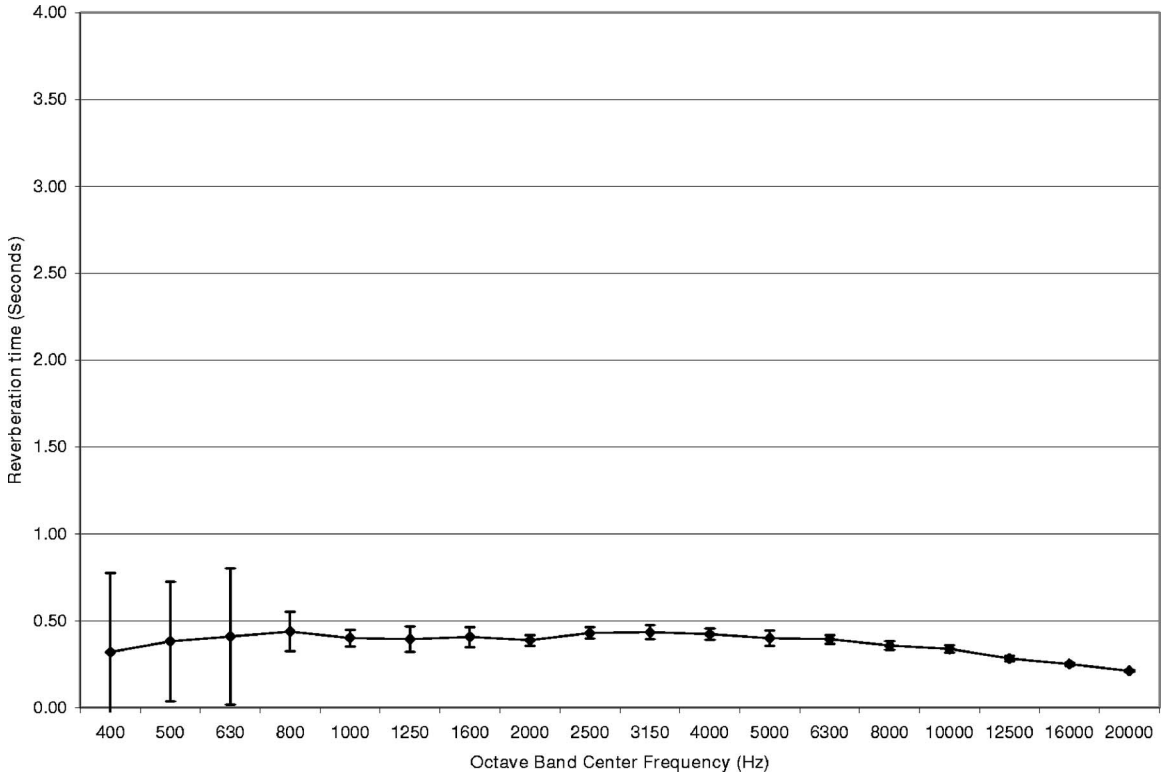

FIG. 8. Reverberation in third octave bands after installation of sound absorbing materials. Error bars show plus and minus two standard deviations.

day difficult, and 92.9% of patients saying that noise levels did not make it difficult to sleep at night, concentrate on daily activities, or understand people who are speaking, and that the noise was not upsetting to them. We note that these results are significantly different from those often reported in the literature on hospital patient satisfaction with noise, but they are not surprising. Because of the nature of the unit patient doors are always kept closed, thus affording more sound insulation than is commonly found on hospital units. After installation of the panels, all patients (100%) were sat-

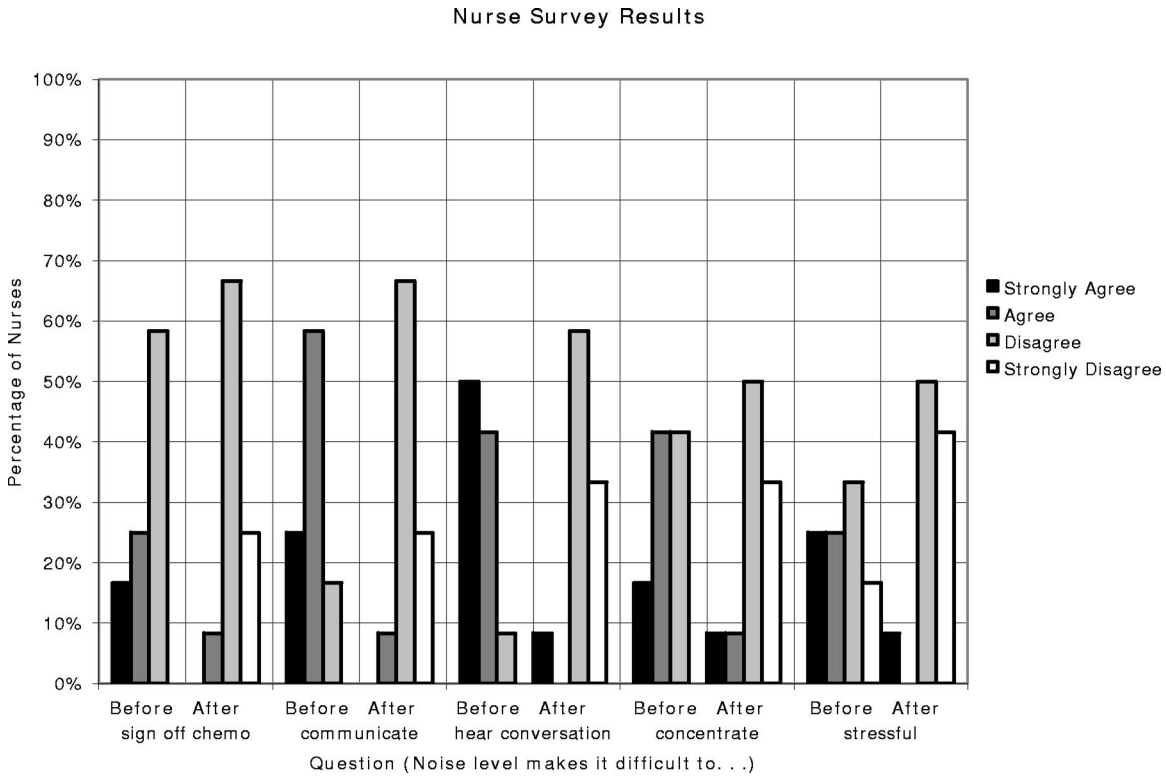

FIG. 9. Survey results for nurses on the unit before and after sound absorbing panel installation.

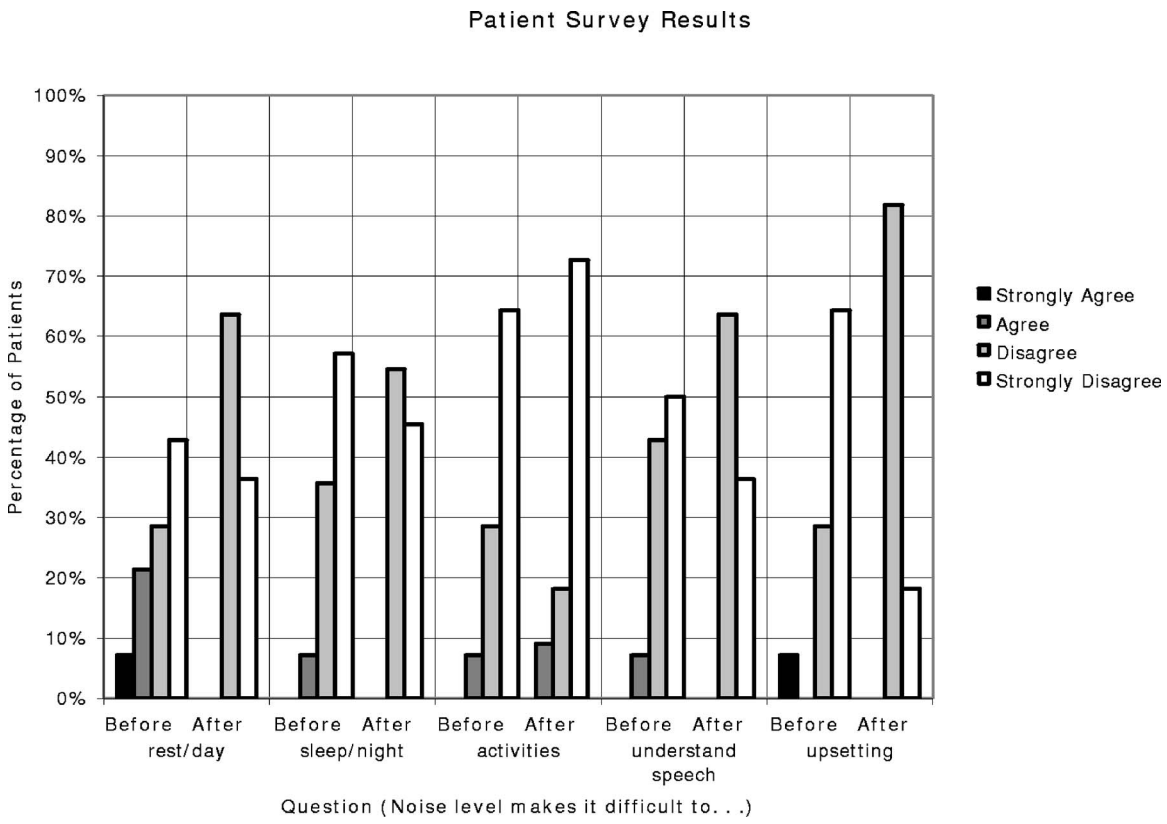

FIG. 10. Survey results for patients on the unit before and after sound absorbing panel installation.

isfied with the noise levels in every category except for one, with 9.1% saying that the noise levels made it difficult for them to concentrate on daily activities.

After the noise treatment was implemented, more than 90% of nurses and patients were satisfied with noise levels in nearly every category. This is a significant improvement for nurses, particularly in the area of communication. However, the most apparent observation is the difference between nurse and patient responses. In general the majority of patients were satisfied with noise levels before the treatment. The most common complaint among patients was the intercom, followed by machine noise. One patient commented that noise was only a problem when his door was open, and even then it only affected his daytime rest. The most notable improvement in patients was daytime rest, with nearly 30% dissatisfaction prior to installation compared with 0% afterward. These observations, combined with the fact that no treatments were applied to patient rooms and doors were generally closed, suggests that the doors and walls of the patient rooms provide adequate barriers from primary noise sources.

A possible limitation of the survey is that the patient population changed while the nurse population remained the same. Also, some survey comments did not appear to match the corresponding survey questions, suggesting that some participants may have misinterpreted the numbering system. These discrepancies, however, were not interpreted. All survey data are presented as received from participants.

V. DISCUSSION

Noise in hospitals is clearly a significant problem and little has been done to address it effectively. This study presents an approach that should provide improvement to the environment long term and regardless of the population. There is every reason to expect that the results produced on Weinberg 5C could be matched at other units in the same hospital and in other hospitals.

The approach chosen in this case study was to add sound absorbing materials in the halls and to concentrate on problem features in corners and above the nurses's stations. We were able to produce dramatic reductions in the sound levels and reverberation times, but the true measure of the success of this intervention was the transformation from a unit in which many of the staff regarded it as noisy and the vast majority felt the noise interfered with their ability to communicate to one in which over 90% of staff and patients viewed it as quiet.

It is important that we were able to produce significant improvements in the context of a remodelling rather than new construction. Hospital construction is at its highest level ever in the US[21] and our results suggest that new hospital buildings, particularly those with in-patient units, would do well to incorporate sound absorbing materials where possible in their designs. In such cases one might be able to get even greater noise reductions than achieved in this study by using suspended ceilings with air spaces above the absorbing tiles. However, if space is at a premium so that a suspended ceiling is not feasible, or if the situation calls for remodelling while a unit remains in use for patients, then this study shows that mounting sound absorbing materials directly onto surfaces still produces very significant noise reductions.

We also note that it is possible to make significant improvements in noise at relatively low costs. The noise inter-

vention reported here cost approximately $15 000, which was used to support student labor and purchased materials (a roughly 50:50 split). While costs could be minimized by incorporating sound absorbing products into initial construction, it would increase building costs, which are already high for hospitals on a per square foot basis. However, the benefits of this approach almost certainly outweigh the costs associated with remodeling at a later date or living with the noise. In particular, if the studies suggesting a link between noise and medical errors are correct,[22–25] then the added cost of sound absorbing materials in a hospital likely can be justified by prevention of a single successful law suit over a medical error.

Finally, we note that there are always considerations other than noise when introducing new materials in a space. In hospitals, safety issues require that the materials meet stringent smoke, flammability, and cleanliness standards. In addition, we found that the staff cared profoundly about the aesthetic appearance of the materials. Figures 5–7 give some indication of how the unit looks after panel installation. The choice of fabric for fiberglass covering meant that the panels blended into the ceiling and exterior walls. However, the interior walls are painted terracotta, and the cream-colored fabric panels on these walls were quite noticeable. These panels represented a small fraction of those installed, and it was ultimately decided to remove them. The effect on the soundscape from this change was negligible, but the visual impact was significant.

Although acoustical consultants working on buildings are well aware of the value of developing a good relationship with their clients, research personnel are often less cognizant of the importance of collaboration with the end users of their work. This project, in which a strong partnership was developed between the nursing staff of Weinberg 5C and the acousticians, benefitted greatly from the medical/technical collaboration. We recommend it strongly as a model for others to copy in noise reduction interventions in hospitals.

ACKNOWLEDGMENTS

Our work at Johns Hopkins Hospital would not have been possible without the support of JHH leaders. We are indebted to Ron Peterson, President of Johns Hopkins Hospital, for his support of our noise study. We are also grateful for the active collaboration of all of the Weinberg 5C nursing staff and for the assistance of Michael Iati, chief architect for JHH. Work on noise control at Johns Hopkins Hospital has been managed by the Center for Quality Improvements and Patient Safety under the direction of Chip Davis.

[1] C. Baker, "Sensory overload and noise in the ICU: Sources of environmental stress," *Critical Care Quarterly*, **6**, 66–79 (1984).
[2] A. Turner, C. King, and J. Craddock, "Measuring and reducing noise," Hospitals **49**, 85–90 (1975).
[3] G. Grumet, "Pandemonium in the modern hospital," N. Engl. J. Med. **328**, 433–437 (1993).
[4] I. Busch-Vishniac, J. West, C. Barnhill, R. Hunter, D. Orellana, and R. Chivukula, "Noise levels in Johns Hopkins Hospital," J. Acoust. Soc. Am. **118**, 3629–3645 (2005).
[5] F. Biley, "Effects of noise in hospitals," Br. J. Nurs. **3**, 110–113 (1994).
[6] C. Cmiel, D. Karr, D. Gasser, L. Oliphant, and A. Neveau, "Noise control: a nursing team's approach to sleep promotion," Am. J. Nurs. **104**, 40–48 (2004).
[7] J. Evans and M. Philbin, "The acoustic environment of hospital nurseries: Facility and operations planning for quiet hospital nurseries," J. Perinatol **20**, S105–S112 (2000).
[8] S. Akhtar, C. Weigle, E. Cheng, R. Toohill, and R. Berens, "Use of active noise cancellation devices in caregivers in the intensive care unit," Crit. Care Med. **28**, 1157–1160 (2000).
[9] J. Aaron, C. Carlisle, M. Carskadon, T. Meyer, N. Hill, and R. Millman, "Environmental noise as a cause of sleep disruption in an intermediate respiratory care unit," Sleep **19**, 707-710 (1996).
[10] N. Freedman, N. Kotzer, and R. Schwab, "Patient perception of sleep quality and etiology of sleep disruption in the intensive care unit," Am. J. Respir. Crit. Care Med. **159**, 1155–1162 (1999).
[11] S. Parathasarathy and M. Tobin, "Sleep in the intensive care unit," Intensive Care Med. **30**, 197–206 (2004).
[12] R. CuretonLane, "Sleep in the pediatric ICU: An empirical investigation," Am. J. Crit. Care **6**, 56-63 (2007).
[13] D. Fife and E. Rappaport, "Noise and hospital stay," Am. J. Public Health **66**, 680–681 (1976).
[14] A. Wysocki, "The effect of intermittent noise exposure on wound healing," Adv. Wound Care **9**, 35–39 (1996).
[15] P. Toivanen, S. Hulkko, and E. Naatanen, "Effect of psychic stress and certain hormone factors on the healing of wounds in rats," Ann. Med. Exp. Biol. Fenn **38**, 343–349 (1960).
[16] I. Cohen, "Stress and wound healing," Acta Anat. (Basel) **103**, 134–141 (1979).
[17] W. Morrison, E. Haas, D. Shaffner, E. Garrett, and J. Fackler, "Noise stress and annoyance in a pediatric intensive care unit," Crit. Care Med. **31**, 113–119 (2003).
[18] M. Topf, "Noise-induced occupational stress and health in critical care nurses," Hosp. Top. **66**, 30–34 (1988).
[19] M. Topf and E. Dillon, "Noise-induced stress as a predictor of burnout in critical care nurses," Heart Lung **17**, 567–574 (1988).
[20] A. Joseph and R. Ulrich, "Issue paper #4: Sound control for improved outcomes in healthcare settings," Technical Report, The Center for Health Design, www.healthdesign.org (2007).
[21] D. Babwin, "Building boom," Health and Hospital Networks **76**(3), 48–52, 54 (2002).
[22] C. Hawksworth, P. Sivalingam, and A. Asbury, "The effect of music on anesthetists' psychomotor performance," Fractal Rev. Nat. Appl. Sci., Proc. IFIP Work. Conf., 3rd **53**, 195–197 (1998).
[23] K. Moorthy, Y. Munz, S. Undre, and A. Darzi, "Objective evaluation of the effect of noise on the performance of a complex laparoscopic task," Surgery (St. Louis) **136**, 25–30 (2004).
[24] S. Park, H. Song, J. Han, J. Park, E. Lee, S. Park, K. Kang, J. Lee, S. Hwang, S. Rho, S. Jeong, H. Chung, and K. Shinn, "Effect of noise on the detection of rib fractures by residents," Invest. Radiol. **29**, 54–58 (1994).
[25] V. Murthy, S. Malhotra, I. Bala, and M. Raghunathan, "Detrimental effects of noise on anesthetists," Can. J. Anaesth. **42**, 608–611 (1995).

An alternative Biot's displacement formulation for porous materials

Olivier Dazel,[a] Bruno Brouard, Claude Depollier, and Stéphane Griffiths
Laboratoire d'Acoustique de l'Université du Maine - UMR CNRS 6613, Avenue Olivier Messiaen, F-72 085 Le Mans Cedex France

(Received 3 August 2006; revised 29 March 2007; accepted 29 March 2007)

This paper proposes an alternative displacement formulation of Biot's linear model for poroelastic materials. Its advantage is a simplification of the formalism without making any additional assumptions. The main difference between the method proposed in this paper and the original one is the choice of the generalized coordinates. In the present approach, the generalized coordinates are chosen in order to simplify the expression of the strain energy, which is expressed as the sum of two decoupled terms. Hence, new equations of motion are obtained whose elastic forces are decoupled. The simplification of the formalism is extended to Biot and Willis thought experiments, and simpler expressions of the parameters of the three Biot waves are also provided. A rigorous derivation of equivalent and limp models is then proposed. It is finally shown that, for the particular case of sound-absorbing materials, additional simplifications of the formalism can be obtained. © *2007 Acoustical Society of America.* [DOI: 10.1121/1.2734482]

PACS number(s): 43.55.Ev, 43.20.Bi, 43.20.Gp, 43.20.Jr [KA] Pages: 3509–3516

I. INTRODUCTION

The purpose of this paper is to propose an alternative formulation of Biot's theory[1,2] which models the deformation of a poroelastic solid saturated by a compressible fluid. Several types of materials can be modeled with this theory, including geomaterials and sound-absorbing materials. Even if Biot's theory is not able to model every type of porous materials (porous rocks…), it has been confirmed both theoretically by homogenization techniques[3,4] or volume averaging methods[5,6] and experimentally[7,8] for a wide range of materials. The application of Biot's theory to sound-absorbing materials takes its origin in the beginning of the 80's. The modeling of the viscous and thermal properties of air saturating a porous immobile solid (equivalent fluid) has been a wide research topic and many models have been proposed.[9–13] These models consist of introducing a complex density (respectively, compressibility) of air depending on frequency to take into account viscous (respectively, thermal) effects. Biot's theory has been the subject of many scientific papers and books[11,14–16] to which the reader can refer for more details.

In the paper published in 1956,[1] Biot represented the homogenized medium with six fields which are the three displacements of each homogenized phase (solid and fluid). This paper and formulation are called *original* in the following. The theory was reformulated in order to model inhomogeneous media.[2] This second formulation is referred to as the *modified* formulation. More recently, Atalla *et al.* proposed a *mixed* formulation of Biot's equations[17] whose generalized coordinates are the solid displacement and the interstitial pressure of the fluid. It exhibits four generalized coordinates instead of six for the displacement formulations. Another interest of this formulation is the introduction of an *in vacuo* stress tensor of the solid phase, which exhibits some advantages compared to the partial stress tensor of the solid phase used in the original formulation. Nevertheless, this formulation exhibits some drawbacks (valid only for harmonic problems, energy-related interpretation…) which prevents its use in the general case.

The Biot theory has nevertheless a main drawback which is not in the range of physics but lies in the scope of analytical or numerical methods to predict the response of a porous material while submitted to a given loading. The actual formulations often induce heavy analytical formulas and even discourage new analytical indicators. It is also well known that numerical models based on Biot's equations are quite huge and need tremendous calculations even for simple configurations. Given this context, it seems necessary to find alternative solutions; it is then natural to focus on Biot's equations first as they are the starting point of all analytical and numerical models.

In this paper, an alternative displacement formulation of Biot's model is proposed. Its advantage is to simplify the equations of the model without making additional assumptions. This simplification is only valid for a linear behavior of the material; in the case of nonlinearity, the present approach is not valid. Even if no new physical result is proposed in this paper, its originality is the simplification of the formalism. This simplification is available for both geomaterials and sound-absorbing materials. It is shown that for the latter, additional interesting simplifications can also be obtained.

Section II proposes an alternative choice of generalized coordinates simplifying equations of motion in the case of a nondissipative medium. Section III shows that classical Biot's results are simplified with the new formulation. Section IV focuses on the case of equivalent fluid and limp models. Section V deals with the generalization of the former results in formulations for dissipative porous material, and Sec. VI is devoted to the case of sound-absorbing materials.

[a]Electronic mail: olivier.dazel@univ-lemans.fr

II. ALTERNATIVE SET OF GENERALIZED COORDINATES IN THE ABSENCE OF DISSIPATION

A. Strain energy and stress-strain relations

The Cartesian coordinates are denoted by $\{x_1,x_2,x_3\}$. The displacement of the homogenized solid (respectively, fluid) phase is designated by the components u_i^s (respectively, u_i^f) with $i=1,2,3$ or in a vector notation by $\mathbf{u}^s$ (respectively, $\mathbf{u}^f$). For all displacement fields, the derivative with respect to space is expressed with the generic notation $u_{i,j}=\partial u_i/\partial x_j$. The deformation is $\varepsilon_{ij}=\frac{1}{2}(u_{i,j}+u_{j,i})$ and the dilatation of solid and fluid phase are, respectively, $e=u_{i,i}^s$ and $\varepsilon=u_{i,i}^f$, with convention for repeated indices. The deformation tensor is denoted by $\boldsymbol{\varepsilon}$ in tensor form.

In the original paper,[1] Biot proposed use of $\mathbf{u}^s$ and $\mathbf{u}^f$ as a set of generalized coordinates and the total stress tensor was separated into two parts. The first and second parts are the stress components acting on the solid and fluid phase, respectively. The corresponding stress tensor is denoted by σ_{ij}^s (respectively, $\sigma_{ij}^f=\sigma\delta_{ij}$), where δ_{ij} denotes the Kronecker symbol. Hence, the fluid partial stress tensor is isotropic and diagonal. The stress of the fluid part is represented by σ; it is linked to the porosity ϕ and the fluid pressure p_f by the relation $\sigma=-\phi p_f$. In tensor form, the stresses are denoted by a bold symbol (e.g., $\boldsymbol{\sigma}^s$).

In 1962 paper,[2] Biot proposed to use $\mathbf{u}^s$ and $\mathbf{w}=\phi(\mathbf{u}^f-\mathbf{u}^s)$ as generalized coordinates, where $\mathbf{w}$ is the flow of the fluid relative to the solid measured in terms of volume per unit area of the bulk medium. This new choice of generalized coordinates induces a modification of conjugate variables which are the total stress tensor (noted τ_{ij}) and the fluid pressure p_f.

The strain energy of a porous elastic solid saturated by a fluid can be defined as the isothermal free energy of the fluid-solid system. In $\{\mathbf{u}^s,\mathbf{u}^f\}$ formulation, this energy W_0 reads

$$W_0=A\frac{e^2}{2}+R\frac{\varepsilon^2}{2}+2N\varepsilon_{ij}^s\varepsilon_{i,j}^s+Qe\varepsilon. \tag{1}$$

A, R, N, and Q are the constitutive coefficients of the homogenized porous medium.[18] N is the shear modulus of the skeleton. Q is a coupling coefficient between the dilatation and stress of the two phases; R may be interpreted as the bulk modulus of the air occupying a fraction ϕ of a unit volume of aggregate. The elastic coefficients A, Q, and R can be obtained by the Biot and Willis experiments[18] from K_b, the bulk modulus of the skeleton *in vacuo*, from K_s, the bulk modulus of the elastic solid from which the skeleton is made, and from K_f, the bulk modulus of the fluid in the pores. A and N are the Lamé coefficient of the solid partial stress tensor. The expression[18] of A shows a dependence on K_f. Hence, this apparent solid parameter depends on the interstitial fluid property.

In 1962 formulation, the strain energy is then written as

$$W_1=A'\frac{e^2}{2}+2N\varepsilon_{ij}^s\varepsilon_{i,j}^s-\frac{Q+R}{\phi}e\xi+\frac{R}{\phi^2}\frac{\xi^2}{2}, \tag{2}$$

with $A'=A+2Q+R$ and $\xi=-\boldsymbol{\nabla}\cdot\mathbf{w}$. It can easily be checked that W_0 and W_1 are equivalent. The stress-strain relations of the porous media are obtained from Helmholtz relations, and for each formulation the two corresponding stress tensors depend on both generalized coordinates. Biot wrote the expressions of W_0 and W_1 by way of the virtual work of surface forces. An alternative way to obtain W_1 is to substitute in (1) the expression of ε derived from the definition of $\mathbf{w}$. The expressions of W_0 and W_1 are not formally different as both are the sum of three types of terms. The first type corresponds to quadratic terms associated with the solid deformation, the second with quadratic terms related to the dilatation of the considered second generalized coordinate, and the last with coupling terms.

B. Strain decoupled formulation

This section is central in this paper. Its purpose is to propose a strain decoupled formulation. Let $\mathbf{u}_1$ and $\mathbf{u}_2$ be an adapted set of generalized coordinates. Without loss of generality, the following linear relations can be written:

$$\mathbf{u}^s=a\mathbf{u}_1+b\mathbf{u}_2,\quad \mathbf{u}^f=c\mathbf{u}_1+d\mathbf{u}_2. \tag{3}$$

The strain energy W_2 is written as

$$W_2=\frac{e_1^2}{2}(Aa^2+Rc^2+2Qac)+\frac{e_2^2}{2}(Ab^2+Rd^2+2Qbd)+e_1e_2(Aab+Rcd+Q(ad+bc))+2N(a^2\varepsilon_{ij}^1\varepsilon_{ij}^1+b^2\varepsilon_{ij}^2\varepsilon_{ij}^2+2ab\varepsilon_{ij}^1\varepsilon_{ij}^2).$$

For the sake of simplicity it seems natural to avoid $\varepsilon_{ij}^1\varepsilon_{ij}^2$ and $\varepsilon_{ij}^2\varepsilon_{ij}^2$ terms. This implies that $b=0$ is an appropriate choice. Hence, e_1e_2 term is avoided if $c=-(Q/R)a$ and

$$W_2=a^2\hat{A}\frac{e_1^2}{2}+d^2R\frac{e_2^2}{2}+2Na^2\varepsilon_{ij}^1\varepsilon_{ij}^1, \tag{4}$$

with $\hat{A}=(A-(Q^2/R))$. All choices of a and d are mathematically equivalent. The adequate choice is $a=1$, so that $\mathbf{u}_1=\mathbf{u}^s$ and $d=\phi^{-1}$ in order to limit the influence of porosity on the model. The new generalized coordinates are now totally determined and the strain decoupled formulation is called $\{\mathbf{u}^s,\mathbf{u}^W\}$, with

$$\mathbf{u}^W=\phi\left(\mathbf{u}^f+\frac{Q}{R}\mathbf{u}^s\right), \tag{5}$$

$$W_2=\hat{A}\frac{e^2}{2}+K_{\mathrm{eq}}\frac{\zeta^2}{2}+2N\varepsilon_{ij}^s\varepsilon_{ij}^s,\quad \zeta=\boldsymbol{\nabla}\cdot\mathbf{u}^W,\quad K_{\mathrm{eq}}=\frac{R}{\phi^2}. \tag{6}$$

K_{eq} corresponds to the compressibility of the equivalent fluid model; it is now introduced in order to condensate the expression of the equations directly from now. The stress-strain relations for $\{\mathbf{u}^s,\mathbf{u}^W\}$ formulation read

$$\hat{\sigma}_{ij}^s=2N\varepsilon_{ij}^s+\hat{A}e\delta_{ij},\quad p_f=-K_{\mathrm{eq}}\zeta. \tag{7}$$

Unlike the solid partial stress tensor σ_{ij}^s, which is a function of both solid and fluid phase displacements, $\hat{\sigma}_{ij}^s$ only depends on the motion of the solid phase; this tensor $\hat{\sigma}_{ij}^s$ is called jacketed stress tensor of the solid phase by analogy to Biot and Willis' second experiment. This tensor was pro-

posed by Atalla *et al.*[17] and called *in vacuo* stress tensor. Hence, the strain energy is the sum of two terms (and not three as for W_0 and W_1). The stresses appearing in $\{\mathbf{u}^s, \mathbf{u}^W\}$ formulation are the jacketed stresses of the solid phase and the pressure. A first remark is that each stress is associated with its corresponding displacement then avoiding coupling terms. A second remark is that the pressure p_f can be expressed as the divergence of only $\mathbf{u}^W$ in (7). In the case of a motionless solid, one has $\mathbf{u}^W = \phi \mathbf{u}^f$. Hence, $\mathbf{u}^W$ corresponds to the average of the microscopic fluid displacement on the total volume of the porous medium.

It is also interesting to express the total stress tensor of the porous medium which defines an interesting coefficient,

$$\tau_{ij} = \hat{\sigma}_{ij} - \gamma' p_f, \quad \gamma' = \phi\left(1 + \frac{Q}{R}\right). \tag{8}$$

Hence, it is important to notice that $\hat{\boldsymbol{\sigma}}$ corresponds to the effective stress tensor $\boldsymbol{\tau}'$ defined by Biot in a 1962 paper if and only if $\gamma' = 1$. This coefficient plays a central role in the following and in particular for the expression of kinetic energies which is now considered.

C. Kinetic energy and equations of motion

The preceding subsection was only concerned with strain energies. In order to obtain the equations of motion, it is necessary to also express the kinetic energies. Biot's definitions of densities are

$$\rho_1 = (1-\phi)\rho_m, \quad \rho_2 = \phi\rho_f, \quad \rho_{12} = -\phi\rho_f(\alpha_\infty - 1), \tag{9a}$$

$$\rho_{11} = \rho_1 - \rho_{12}, \quad \rho_{22} = \rho_2 - \rho_{12}, \quad \rho_{\mathrm{eq}} = \frac{\rho_{22}}{\phi^2}. \tag{9b}$$

ρ_m is the density of the matter constituting the solid phase and ρ_f is the density of the fluid saturating the pores. ρ_{12} is an inertial coupling coefficient linked to the geometric tortuosity α_∞. ρ_{eq} corresponds to the density of the equivalent fluid model and, analogously to K_{eq}, is now defined in order to simplify the expressions.

The equations of motion in $\{\mathbf{u}^s, \mathbf{u}^W\}$ formulation are now obtained. The first step consists of substituting in T the expression of $\mathbf{u}^f$ as a linear combination of $\mathbf{u}^s$ and $\mathbf{u}^W$. One has

$$T_2 = \frac{\rho_s}{2}\dot{\mathbf{u}}^{s2} + \frac{\rho_{\mathrm{eq}}}{2}\dot{\mathbf{u}}^{W2} + \rho_{\mathrm{eq}}\gamma\dot{\mathbf{u}}^s\dot{\mathbf{u}}^W, \tag{10}$$

with

$$\gamma = \phi\left(\frac{\rho_{12}}{\rho_{22}} - \frac{Q}{R}\right), \quad \rho_s = \rho_1 + \rho_2\left(\frac{Q}{R}\right)^2 - \rho_{12}\frac{\gamma'^2}{\phi^2}. \tag{11}$$

The equations of motion in the $\{\mathbf{u}^s, \mathbf{u}^W\}$ formulation read

$$\boldsymbol{\nabla}\cdot\hat{\boldsymbol{\sigma}}(\mathbf{u}^s) = \rho_s\ddot{\mathbf{u}}^s + \rho_{\mathrm{eq}}\gamma\ddot{\mathbf{u}}^W, \tag{12a}$$

$$K_{\mathrm{eq}}\boldsymbol{\nabla}\zeta = \rho_{\mathrm{eq}}\gamma\ddot{\mathbf{u}}^s + \rho_{\mathrm{eq}}\ddot{\mathbf{u}}^W. \tag{12b}$$

These equations are equivalent to those proposed by Biot. Unlike the original ones, there is no stress coupling terms in them, and each stress tensor is a function of only the corresponding displacement. The symmetry is also preserved for inertial terms. It is shown in the following sections that the classical results of Biot's theory can easily be retrieved from the present formulation with the advantage of simpler expressions.

III. ADAPTATION OF CLASSICAL BIOT'S RESULTS

A. Biot and Willis experiments

Biot and Willis[18] presented three thought experiments which provide expressions for the elastic coefficient appearing in Biot's original model: A, N Q, and R. In the case of the strain decoupled formulation it is shown that the thought experiments provide the three elastic coefficients for the model $\hat{A}$, N, and K_{eq} and an expression of γ'. Biot and Willis experiments assume quasistatic deformation. In a recent contribution, Lafarge[16] shows that this assumption is not restrictive and that these experiments can be extended to harmonic excitations.

The first thought experiment is a measure of the shear modulus N of the material and consequently the shear modulus of the frame, since the fluid does not contribute to the shear force.

In the second thought experiment (called jacketed experiment), the material is surrounded by a flexible jacket that is subjected to a pressure p_{jac}. The fluid inside the jacket remains at the ambient pressure. It follows that $p_f = 0$ and $\hat{\sigma}_{ij} = -p_{\mathrm{jac}}$. The deformation of the solid phase is denoted by e_{jac}. The stress-strain relation (7) implies that

$$-p_{\mathrm{jac}} = \left(\hat{A} + \frac{2N}{3}\right)e_{\mathrm{jac}}. \tag{13}$$

This last relation must be linked to the definition of the bulk modulus K_b of the frame at constant pressure in the air $K_b = -(p_{\mathrm{jac}}/e_{\mathrm{jac}})$, and one obtains

$$\hat{A} = K_b - \frac{2N}{3}. \tag{14}$$

The last thought experiment is called an unjacketed experiment and provides two additional equations. The material is subjected to an increase of pressure p_u in the fluid inducing a total stress equal to $\tau_{ij} = -p_u\delta_{ij}$. The divergence of the $\mathbf{u}^s$ (respectively, $\mathbf{u}^f$ and $\mathbf{u}^W$) is called e_u (respectively, ε_u and ζ_u). Concerning this experiment, Biot introduced two coefficients,

$$K_f = -\frac{p_u}{\varepsilon_u}, \quad K_s = -\frac{p_u}{e_u}. \tag{15}$$

The stress-strain relations (7) and (8) are now expressed

$$-p_u = K_b e_u - \gamma' p_u, \quad K_{\mathrm{eq}} = -\frac{p_u}{\zeta_u}. \tag{16}$$

The first equation of (16) enables an expression of γ' as a function of K_s and K_b,

$$\gamma' = 1 - \frac{K_b}{K_s}. \tag{17}$$

This last result is linked to the second equation of (16) and the expression for K_{eq} is provided,

$$K_{\mathrm{eq}} = \frac{K_f}{\phi + (1-\phi)\dfrac{K_f}{K_s} - \dfrac{K_b K_f}{K_s^2}}. \tag{18}$$

Biot and Willis results for A, N, Q, and R can rigorously be obtained from the expressions of $\hat{A}$, N, γ', and K_{eq}. Nevertheless, the expressions of the latter are simpler. In particular, it is interesting to notice that $\hat{A}$ does not depend on K_f, unlike the constitutive coefficient A of Biot's original formulation.

A second and fundamental remark is that γ' is independent of the compressibility of the fluid through (17), and it is possible to express $\mathbf{u}^W$ as

$$\mathbf{u}^W = \underbrace{\phi\mathbf{u}^f + (1-\phi)\mathbf{u}^s}_{\mathbf{u}^t} - \frac{K_b}{K_s}\mathbf{u}^s. \tag{19}$$

$\mathbf{u}^t$ is called the total displacement of the porous material. It is shown here that $\mathbf{u}^W$ is independent of porosity. It is the *a posteriori* justification of the particular choice $d=\phi^{-1}$ considered in the preceding section.

B. Wave numbers of the Biot's waves

This section deals with the rewriting of the wave numbers of the three Biot's waves. The methodology is the same that the one proposed in Ref. 11. The two compressional waves are first studied. Two scalar potentials φ^s and φ^W are defined for the compressional waves. Hence, equations of motion of the strain decoupled formulation (12) are written as

$$-\omega^2[\boldsymbol{\rho}]\begin{Bmatrix}\varphi^s\\ \varphi^W\end{Bmatrix} = [\mathbf{K}]\nabla^2\begin{Bmatrix}\varphi^s\\ \varphi^W\end{Bmatrix}, \tag{20}$$

where $[\boldsymbol{\rho}]$ and $[\boldsymbol{K}]$ are, respectively,

$$[\boldsymbol{\rho}] = \begin{bmatrix}\rho_s & \rho_{\mathrm{eq}}\gamma\\ \rho_{\mathrm{eq}}\gamma & \rho_{\mathrm{eq}}\end{bmatrix}, \quad [\mathbf{K}] = \begin{bmatrix}\hat{P} & 0\\ 0 & K_{\mathrm{eq}}\end{bmatrix}, \tag{21}$$

with $\hat{P}=\hat{A}+2N$. Let δ_1^2 and δ_2^2 be the eigenvalues of the problem associated with matrices $[\boldsymbol{\rho}]$ and $[\mathbf{K}]$. An elementary algebraic calculation gives

$$\delta_i^2 = \frac{(\delta_{s2}^2 + \delta_{\mathrm{eq}}^2) \pm \sqrt{(\delta_{s2}^2 + \delta_{\mathrm{eq}}^2)^2 - 4\delta_{\mathrm{eq}}^2\delta_{s1}^2}}{2}, \tag{22}$$

with

$$\delta_{\mathrm{eq}} = \omega\sqrt{\frac{\rho_{\mathrm{eq}}}{K_{\mathrm{eq}}}}, \quad \delta_{s1} = \omega\sqrt{\frac{\rho}{\hat{P}}}, \quad \delta_{s2} = \omega\sqrt{\frac{\rho_s}{\hat{P}}},$$

$$\rho = \rho_s - \gamma^2\rho_{\mathrm{eq}}. \tag{23}$$

These expressions are equivalent to the classical expressions of these two wave numbers which can be found in Ref. 11. It is quite evident that the proposed expressions are more condensed than the classical ones. The main reason is that definitions (22) are expressed only through the three intrinsic wave numbers defined in (23). This analytical simplification was used particularly by Dazel and Pilon[19] in order to define new types of decoupling criteria between the two compressional waves.

The following symmetric relations exist between the wave numbers:

$$\delta_1^2\delta_2^2 = \delta_{s1}^2\delta_{\mathrm{eq}}^2, \quad \delta_1^2 + \delta_2^2 = \delta_{s2}^2 + \delta_{\mathrm{eq}}^2. \tag{24}$$

δ_{eq} is the wave number of the equivalent fluid model i.e., when the solid phase is immobile; more details will be found in Sec. IV. Symmetrically to the equivalent fluid model which assumes that $\mathbf{u}^s=\mathbf{0}$, an equivalent solid model can be considered, for which it is postulated that $\mathbf{u}^W=\mathbf{0}$. In this model only one compressional wave propagates whose wave number is δ_{s2}. Even if there is a perfect mathematical symmetry between these two cases, the first one is physically realistic (and has been often used in the past) while the second is not. δ_{s1} is the wave number of the wave propagating in the solid if the porous medium is in vacuum (and not saturated by air).

The eigenvectors are determined by the ratio μ_i^W of the u^W component on the u^s one. Two possible and equivalent expressions for this ratio are

$$\mu_i^W = \gamma\frac{(\delta_i^2 - \delta_{s2}^2)}{\delta_{s2}^2 - \delta_{s1}^2} = \gamma\frac{\delta_{\mathrm{eq}}^2}{\delta_i^2 - \delta_{\mathrm{eq}}^2}. \tag{25}$$

As symmetric relations (24) were obtained for the wave numbers, orthogonality relations can be obtained on μ_i^W,

$$\hat{P} + K_{\mathrm{eq}}\mu_1^W\mu_2^W = 0, \tag{26a}$$

$$\rho_s + \rho_{\mathrm{eq}}\gamma(\mu_1^W + \mu_2^W) + \rho_{\mathrm{eq}}\mu_1^W\mu_2^W = 0. \tag{26b}$$

It is also interesting to introduce the following ratios:

$$\mu_i' = \frac{\mu_i^W}{\mu_i^W - \mu_j^W} = \frac{\delta_j^2 - \delta_{\mathrm{eq}}^2}{\delta_j^2 - \delta_i^2}, \quad \text{with} \quad (i,j) \in \{1,2\}. \tag{27}$$

The shear wave is now considered by using a vector potential,

$$\mathbf{u}^s = \boldsymbol{\nabla} \wedge \Psi \quad \text{so} \quad \mathbf{u}^W = \mu_3^W\boldsymbol{\nabla} \wedge \Psi. \tag{28}$$

Substituting these expressions in the motion Eqs. (12), one obtains

$$\delta_3 = \omega\sqrt{\frac{\rho}{N}} \quad \text{and} \quad \mu_3^W = -\gamma. \tag{29}$$

IV. EQUIVALENT FLUID AND LIMP MODELS

The equivalent fluid model corresponds to a motionless solid phase ($\mathbf{u}^s=\mathbf{0}$). Equation (12b) becomes

$$K_{\mathrm{eq}}\nabla^2\mathbf{u}^W = \rho_{\mathrm{eq}}\ddot{\mathbf{u}}^W. \tag{30}$$

It is straightforward to find that the wave number of the equivalent fluid model is δ_{eq}. The characteristic impedance of the equivalent fluid in the strain decoupled formulation is defined as

$$Z_{\mathrm{eq}} = \frac{p_f}{\|\mathbf{v}^W\|} = \sqrt{\rho_{\mathrm{eq}}K_{\mathrm{eq}}}. \tag{31}$$

Let us now consider the limp model which also exhibits one compressional wave. Unlike the equivalent fluid model, the solid is not motionless and this model takes into account the inertia of the fluid phase. It is associated with materials whose rigidity is negligible (light mineral wools, cotton…). The jacketed strain energy of the solid phase is negligible compared to those of the other mechanisms of the propagation so that $\hat{A} \simeq 0 \simeq N$. Hence, the compressional term $\boldsymbol{\nabla} \cdot \hat{\boldsymbol{\sigma}}$ can be neglected in (12a), which gives a relation between $\ddot{\mathbf{u}}^s$ and $\ddot{\mathbf{u}}^W$,

$$\rho_s \ddot{\mathbf{u}}^s = -\rho_{\text{eq}} \gamma \ddot{\mathbf{u}}^W. \tag{32}$$

This relation is now inserted in (12b) and a propagation equation on $\mathbf{u}^W$ is obtained as

$$K_{\text{eq}} \boldsymbol{\nabla} \zeta = \rho_{\text{eq}} \left(1 - \frac{\rho_{\text{eq}} \gamma^2}{\rho_s} \right) \ddot{\mathbf{u}}^W. \tag{33}$$

The limp model is a one-compression wave model whose difference with the equivalent fluid is the definition of the density,

$$\rho_{\text{limp}} = \rho_{\text{eq}} \left(\frac{\delta_{s1}}{\delta_{s2}} \right)^2. \tag{34}$$

The wave number of the limp model can now be expressed as a function of the three intrinsic wave numbers (23) of the porous medium,

$$\delta_{\text{limp}} = \omega \sqrt{\frac{\rho_{\text{limp}}}{K_{\text{eq}}}} = \delta_{\text{eq}} \frac{\delta_{s1}}{\delta_{s2}}. \tag{35}$$

The characteristic impedance of the limp model is

$$Z_{\text{limp}} = \frac{p_f}{\|\mathbf{v}^W\|} = \sqrt{\rho_{\text{limp}} K_{\text{eq}}}. \tag{36}$$

Two one-compressional wave models were presented in this section. It has been shown that the $\{\mathbf{u}^s, \mathbf{u}^W\}$ formulation is well fitted to these two types of model.

V. STRAIN DECOUPLED FORMULATION WITH DISSIPATION

This section deals with the introduction of dissipative effects in the formulation. It is shown that the symmetry of Eq. (12) is preserved even if dissipation is considered. The dissipation is taken into account for harmonic excitation by modifying the constitutive and inertial coefficients of the model.

Viscous dissipation was introduced by Biot in 1956,[1] with the assumption that the flow of the fluid relative to the solid through the pores is of Poiseuille type. In order to integrate this dissipation in the Lagrangian formulation, a dissipation function D was defined as a homogeneous quadratic form with the six generalized velocities. This function is first rewritten in term of the generalized coordinates of our proposed approach,

$$D = \frac{\sigma \phi^2 G}{2} |\dot{\mathbf{u}}^f - \dot{\mathbf{u}}^s|^2 = \frac{\sigma G}{2} |\dot{\mathbf{u}}^W - \gamma' \dot{\mathbf{u}}^s|^2, \tag{37}$$

where σ is the flow resistivity of the porous sample and G is a nondimensional correction function. This function is useful to represent the variation of apparent viscosity versus frequency. This function is first assumed to be a constant, and its dependence versus frequency is considered at the end of this section. The Euler Lagrange equations read

$$\boldsymbol{\nabla} \cdot \hat{\boldsymbol{\sigma}}(\mathbf{u}^s) = \rho_s \ddot{\mathbf{u}}^s + \rho_{\text{eq}} \gamma \ddot{\mathbf{u}}^W + \sigma G (\gamma'^2 \dot{\mathbf{u}}^s - \gamma' \dot{\mathbf{u}}^W), \tag{38a}$$

$$K_{\text{eq}} \boldsymbol{\nabla} \zeta = \rho_{\text{eq}} \gamma \ddot{\mathbf{u}}^s + \rho_{\text{eq}} \ddot{\mathbf{u}}^W + \sigma G (\dot{\mathbf{u}}^W - \gamma' \dot{\mathbf{u}}^s). \tag{38b}$$

The right-hand sides of these two equations are rewritten by using (11), and one obtains

$$\boldsymbol{\nabla} \cdot \hat{\boldsymbol{\sigma}}(\mathbf{u}^s) = \left[\rho_1 + \rho_2 \left(\frac{Q}{R} \right)^2 \right] \ddot{\mathbf{u}}^s + \frac{\rho_2 (\phi - \gamma')}{\phi^2} \ddot{\mathbf{u}}^W - \frac{\gamma'^2}{\phi^2} V(\mathbf{u}^s) + \frac{\gamma'}{\phi^2} V(\mathbf{u}^W), \tag{39a}$$

$$K_{\text{eq}} \boldsymbol{\nabla} \zeta = \frac{\rho_2}{\phi^2} [\phi - \gamma'] \ddot{\mathbf{u}}^s + \frac{\rho_2}{\phi^2} \ddot{\mathbf{u}}^W + \frac{\gamma'}{\phi^2} V(\mathbf{u}^s) - \frac{1}{\phi^2} V(\mathbf{u}^W), \tag{39b}$$

with the time differential operator V defined by the functional relation,

$$V(\mathbf{u}) = \rho_{12} \ddot{\mathbf{u}} - \phi^2 \sigma G \dot{\mathbf{u}}. \tag{40}$$

The function G is actually frequency dependent.[9–13] In the case of harmonic excitation at circular frequency ω, the complex notation is used ($e^{j\omega t}$ dependence). One obtains

$$V(\mathbf{u}) = -\omega^2 \tilde{\rho}_{12} \mathbf{u}, \quad \tilde{\rho}_{12} = \rho_{12} - \frac{\phi^2 \sigma G(\omega)}{j\omega}. \tag{41}$$

It is then possible to define the complex dissipative extensions of the coefficients introduced in the preceding sections,

$$\tilde{\rho}_{22} = \rho_2 - \tilde{\rho}_{12}, \quad \tilde{\rho}_{11} = \rho_1 - \tilde{\rho}_{12}, \quad \tilde{\alpha} = \frac{\tilde{\rho}_{22}}{\rho_2}, \quad \tilde{\gamma} = \frac{\phi}{\tilde{\alpha}} - \gamma'. \tag{42}$$

The frequency equations associated with the viscous dissipating problem are

$$\boldsymbol{\nabla} \cdot \hat{\boldsymbol{\sigma}}(\mathbf{u}^s) = -\omega^2 \tilde{\rho}_s \mathbf{u}^s - \omega^2 \tilde{\rho}_{\text{eq}} \tilde{\gamma} \mathbf{u}^W, \tag{43a}$$

$$K_{\text{eq}} \boldsymbol{\nabla} \zeta = -\omega^2 \tilde{\rho}_{\text{eq}} \tilde{\gamma} \mathbf{u}^s - \omega^2 \tilde{\rho}_{\text{eq}} \mathbf{u}^W. \tag{43b}$$

Various models of viscosity of air saturating an immobile porous solid [i.e., of $G(\omega)$] have been proposed in the past[9,10] which can be used for this formulation without restriction. Even if Eqs. (43a) is expressed for harmonic motions, it can be noticed that it directly corresponds to (12) with the time-independent coefficients replaced by frequency-dependent ones.

The structural dissipation in the skeleton is taken into account by modifying the elastic coefficients of the jacketed stress tensor. As a temporal dependence is assumed, complex

frequency-dependent extensions $\widetilde{K}_s$, $\widetilde{K}_b$, and $\widetilde{N}$ can be used in the experiments instead of the constant and real parameters used in Sec. III A. Hence, frequency-dependent coefficients for $\hat{A}$ and N can be used in order to take into account the structural dissipation. This exhibits an advantage of the use of this tensor instead of the partial stress tensor of the solid phase whose parameters depends on both structural and thermal dissipation.

The thermal effects are taken in account by modifying K_f, which is now

$$\widetilde{K}_f = \frac{K_a}{\beta(\omega)}, \tag{44}$$

with K_a the adiabatic compressibility coefficient of air and $\beta(\omega)$ the thermal dynamic susceptibility. This modification acts only on K_{eq}. Like the viscous function G, various models have been proposed in order to explicit this function; the reader can refer to these models[11,13] which can be used for $\{\mathbf{u}^s, \mathbf{u}^W\}$ formulation without restriction.

VI. ADVANTAGE OF $\{\mathbf{u}^s, \mathbf{u}^W\}$ FORMULATION FOR SOUND-ABSORBING MATERIALS

This section is devoted to porous materials with a very stiff skeleton. Usual sound-absorbing materials are in this category. This assumption induces additional simplifications which are now detailed.

A. Introduction of the total displacement

The high stiffness of the solid matter means that

$$\left|\frac{\widetilde{K}_b}{\widetilde{K}_s}\right| \ll 1, \quad \left|\frac{\widetilde{K}_f}{\widetilde{K}_s}\right| \ll 1. \tag{45}$$

This assumption implies simplifications in both expressions of γ' (17) and $\mathbf{u}^W$ (19),

$$\gamma' \simeq 1, \quad \mathbf{u}^W \simeq \mathbf{u}^t. \tag{46}$$

Hence, $\mathbf{u}^W$ corresponds to the total displacement. This is an interesting result: first, it gives a direct physical interpretation of $\mathbf{u}^W$ and second, it greatly simplifies the continuity relations. In the following part of the paper, and in order to indicate that the approximation (45) is considered, all the W superscripts are replaced by t superscripts denoting the total displacement.

It is also possible to simplify $\widetilde{R}$ and $\widetilde{K}_{\text{eq}}$ in (18),

$$\widetilde{R} = \phi \widetilde{K}_f, \quad \widetilde{K}_{\text{eq}} = \frac{\widetilde{K}_f}{\phi}. \tag{47}$$

The continuity relations are now considered. The normal of the interface between the porous medium and the other media is noted $\mathbf{n}$ and any tangential vector to the connecting surface is noted $\mathbf{t}$.

The coupling with an elastic medium (superscript e) involves

$$\mathbf{u}^e \cdot \mathbf{n} = \mathbf{u}^t \cdot \mathbf{n}, \quad \mathbf{u}^e \cdot \mathbf{t} = \mathbf{u}^s \cdot \mathbf{t}, \tag{48a}$$

$$\boldsymbol{\sigma}^e \cdot \mathbf{n} = (\hat{\boldsymbol{\sigma}}^s \cdot \mathbf{n} - p_f \mathbf{n}), \quad \boldsymbol{\sigma}^e \cdot \mathbf{t} = \hat{\boldsymbol{\sigma}}^s \cdot \mathbf{t}. \tag{48b}$$

Concerning the interface with a fluid (superscript a) medium, the continuity relations are

$$\mathbf{u}^a \cdot \mathbf{n} = \mathbf{u}^t \cdot \mathbf{n}, \tag{48c}$$

$$p_a = p_f, \quad \hat{\boldsymbol{\sigma}}^s \cdot \mathbf{n} = \mathbf{0}. \tag{48d}$$

The new formulation is also interesting for the interface between two porous media,

$$\mathbf{u}_1^s = \mathbf{u}_2^s, \quad \mathbf{u}_1^t \cdot \mathbf{n} = \mathbf{u}_2^t \cdot \mathbf{n}.$$

$$p_{f,1} = p_{f,2}, \quad \hat{\boldsymbol{\sigma}}_1^s = \hat{\boldsymbol{\sigma}}_2^s. \tag{48e}$$

It can be seen from (48) that the use of $\mathbf{u}^s$ and $\mathbf{u}^t$ as general coordinates is well adapted to describe the continuity relations between two porous media. This simplification concerns both displacements and associated stresses.

B. Surface impedance of a porous material

This section is devoted to a new expression of the normal incidence surface impedance of a porous layer bonded on a rigid impervious wall. This example is inspired by an application presented in Ref. 11 (Sec. 6.6, p. 138). With the proposed formulation, the simplification of the boundary conditions allows a simplification of the final expression of the impedance.

At the surface of the porous material, three continuity conditions (48) need to be written. The first (respectively, second) one is the continuity of the pressure (respectively, total displacement). The last one is the nullity of the jacketed normal stress. The proposed set of fields is naturally adapted to these boundary conditions, while the classical $\{\mathbf{u}^s, \mathbf{u}^f\}$ implies mixture laws to obtain the total stress tensor of the porous and the total normal displacement. Hence, a determinant is obtained and the final expression of the impedance reads

$$Z = \frac{\widetilde{K}_{\text{eq}}}{j\omega} \times \frac{1}{\dfrac{\mu_2'}{\delta_2}\tan(\delta_2 l) + \dfrac{\mu_1'}{\delta_1}\tan(\delta_1 l)}, \tag{49}$$

with μ_i' defined in Eq. (27). This expression is simpler and equivalent to the classical one provided in Ref. 11. The Appendix presents alternative and simpler expressions for the reflection and transmission coefficient. A numerical example is provided in Fig. 1, where expression (49) of the normal incidence surface impedance is compared with the result provided by an industrial software MAINE 3A©,[20] developed by CTTM (based on transfer matrix method methodology for porous material.[21]) The application case is based on the example of Ref. 11. The parameters of the considered porous material are given in table 6.1 of the previous reference and the thickness of the porous layer is 5.6 cm. Figure 1 shows the perfect agreement between the original and the proposed approach.

VII. CONCLUSION

A new displacement formulation of Biot's linear equations of poroelasticity has been proposed in this paper. It

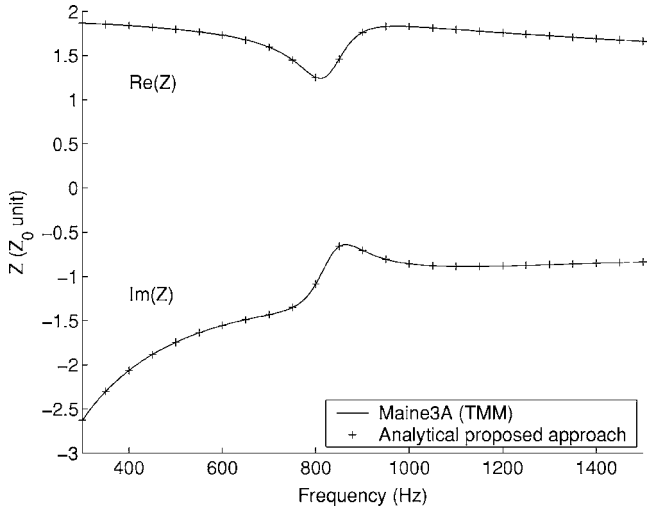

FIG. 1. Normalized surface impedance; comparison between the analytical proposed approach (+) and the numerical Maine 3A solution (continuous).

allows for a simpler expression of the different parameters of Biot's model. It is based on a choice of generalized coordinates which allows a decoupling of the strain energy of the porous medium. It is then possible to avoid the stress coupling terms in the equations of motion. The two corresponding generalized coordinates are the solid displacement and the apparent displacement for the pressure of the fluid phase taking into account the motion of the solid phase. They are associated with conjugated stresses which are the jacketed stress tensor of the solid phase and the pressure. It has also been shown that the classical Biot's results are naturally transposed to this formulation. The expressions of the constitutive coefficients, wave numbers, are equivalent and simpler in the case of the proposed approach. This formulation is also well fitted to the definition of equivalent fluid and limp model. It has been shown that the dissipation can be introduced without losing the symmetry of the problem, and the different mechanisms of dissipation can be taken into account separately. Additional simplifications were also obtained for sound-absorbing materials. Classical acoustic indicators as surface impedance, transmission, and reflection coefficients (both presented in the Appendix) have then been rewritten in a simpler form, and the expressions have been validated by a comparison to a transfer matrix method code.

The introduction of this formulation is a first step towards the simplification of numerical methods for poroelastic materials. It has been seen that for analytical results, the use of such a formulation presents great advantages compared to the classical ones. A detailed study of the discretization of these formulation is a natural perspective of this work. Another perspective of this work is the extension of the formalism to the case of inhomogeneous porous materials.

ACKNOWLEDGMENTS

The authors would like to thank Professor Jean-Francois Allard and Professor Philippe Leclaire for their useful comments on the manuscript.

APPENDIX: REFLECTION AND TRANSMISSION COEFFICIENTS

In this Appendix are presented two simplified expressions of the reflection and transmission coefficient of a porous media of thickness l. The considered porous media is laterally infinite and is exited by a normal incidence plane wave. The transmission (respectively, reflection) coefficient is defined as the ratio of the transmitted (respectively, reflected) pressure over the incident one as presented in Ref. 22.

The expressions of these coefficients read

$$T = \frac{-2i\xi\left[\mu_2'\delta_1'\vartheta_1 + \mu_1'\delta_2'\vartheta_2\right]}{\vartheta_1\vartheta_2\left[\delta_1'\delta_2'\xi^2 + \frac{\mu_1'^2\delta_2'^2 + \mu_2'^2\delta_1'^2}{\delta_1'\delta_2'}\right] + 2\mu_1'\mu_2'[1-\pi_2\pi_1] - 2i\xi\left[\mu_1'\delta_2'\pi_1\vartheta_2 + \mu_2'\delta_1'\pi_2\vartheta_1\right]}, \tag{A1}$$

$$R = \frac{\vartheta_1\vartheta_2\left[\delta_1'\delta_2'\xi^2 - \frac{\mu_1'^2\delta_2'^2 + \mu_2'^2\delta_1'^2}{\delta_1'\delta_2'}\right] - 2\mu_1'\mu_2'\left[1-\pi_1\pi_2\right]}{\vartheta_1\vartheta_2\left[\delta_1'\delta_2'\xi^2 + \frac{\mu_1'^2\delta_2'^2 + \mu_2'^2\delta_1'^2}{\delta_1'\delta_2'}\right] + 2\mu_1'\mu_2'[1-\pi_2\pi_1] - 2i\xi[\mu_1^1\delta_2'\pi_1\vartheta_2 + \mu_2'\delta_1'\pi_2\vartheta_1]}, \tag{A2}$$

with the following notations: $\xi = \widetilde{K}_{eq}/K_0$, $\delta_i' = \delta_i/\delta_0$, and $\pi_i = \cos(\delta_i l)$, $\upsilon_i = \sin(\delta_i l)$. The proposed expressions, available on the overall spectrum, of the reflection and transmission coefficients have been compared to the high-frequency expressions given by Fellah *et al.*[22] in order to point out the simplifications induced by our proposed formalism.

[1]M. Biot, "Theory of propagation of elastic waves in a fluid-filled-saturated porous solid," J. Acoust. Soc. Am. **28**, 168–191 (1956).
[2]M. Biot, "Mechanics of deformation and acoustic propagation in porous media," J. Appl. Phys. **33**, 4, 1482–1498 (1962).
[3]R. Burridge and J. Keller, "Poroelasticity equations derived from microstructure," J. Acoust. Soc. Am. **70**, 1140–1146 (1981).
[4]J. Auriault, L. Borne, and R. Chambon, "Dynamics of porous saturated media, checking of the generalized law of Darcy," J. Acoust. Soc. Am. **77**, 1641–1650 (1985).
[5]S. Pride, A. Gangi, and F. Morgan, "Deriving the equations of motion for porous isotropic media," J. Acoust. Soc. Am. **92**, 3278–3290 (1992).
[6]S. Pride and J. Berryman, "Connecting theory to experiments in poroelasticity," J. Mech. Phys. Solids **40**, 719–747 (1998).
[7]T. Plona, "Observation of a second bulk compressional wave in a porous medium at ultrasonic frequencies," Appl. Phys. Lett. **36**, 259–261 (1980).
[8]J. Berryman, "Confirmation of Biot's theory," Appl. Phys. Lett. **37**, 382–384 (1980).
[9]D. Johnson, J. Koplik, and R. Dashen, "Theory of dynamic permeability and tortuosity in fluid-saturated porous media," J. Fluid Mech. **176**, 379–402 (1987).
[10]S. Pride, F. Morgan, and A. Gangi, "Drag forces of porous media acoustics," Phys. Rev. B **47**, 4964–4975 (1993).
[11]J. Allard, *Propagation of Sound in Porous Media, Modeling Sound Absorbing Materials* (New York, 1993).
[12]Y. Champoux and J. Allard, "Dynamic tortuosity and bulk modulus in air-saturated porous media," J. Appl. Phys. **70**, 1975–1979 (1991).
[13]D. Lafarge, P. Lemarinier, J. Allard, and V. Tarnow, "Dynamic compressibility of air in porous structures at audible frequencies," J. Acoust. Soc. Am. **102**, 1995–2006 (1997).
[14]O. Coussy, *Mechanics of Porous Continua* (Wiley, New York, 1995).
[15]J. Carcione, "Wave propagation in anisotropic, saturated porous media:Plane-wave theory and numerical simulation," J. Acoust. Soc. Am. **99**, 2655–2666 (1996).
[16]D. Lafarge, *Porous Materials, Propagation Models in Acoustics and Materials* (Hermes, Paris, in French) (2006).
[17]N. Atalla, R. Panneton, and P. Debergue, "A mixed displacement-pressure formulation for poroelastic materials"J. Acoust. Soc. Am. **104**, 1444–1452 (1998).
[18]M. Biot and D. Willis, "The elastic coefficients of the theory of consolidation," J. Appl. Mech. **24**, 179–191 (1957).
[19]O. Dazel and D. Pilon, "Wave decoupling for porous media," in *French Congress of Mechanics* (in French 2005).
[20]http:// www.cttm-lemans.com/francais/acoustique/maine3a/sitemaine3a.html, *MAINE 3A*, CTTM - Le Mans. Viewed 5/7/2007.
[21]B. Brouard, D. Lafarge, and J. Allard, "A general method of modelling sound propagation in layered media," J. Sound Vib. **183**, 129–42 (1995).
[22]Z. Fellah, J. Chapelon, S. Berger, W. Lauriks, and C. Depollier, "Ultrasonic wave propagation in human cancelous bone: Application of Biot theory," J. Acoust. Soc. Am. **116**, 61–73 (2004).

Ceiling baffles and reflectors for controlling lecture-room sound for speech intelligibility

Wonyoung Yang and Murray Hodgson[a)]
Acoustics and Noise Research Group, School of Occupational and Environmental Hygiene, University of British Columbia, 2206 East Mall, Vancouver, BC, Canada V6T 1Z3

(Received 20 June 2006; revised 22 March 2007; accepted 25 March 2007)

Reinforcing speech levels and controlling noise and reverberation are the ultimate acoustical goals of lecture-room design to achieve high speech intelligibility. The effects of sound absorption on these factors have opposite consequences for speech intelligibility. Here, novel ceiling baffles and reflectors were evaluated as a sound-control measure, using computer and 1/8-scale models of a lecture room with hard surfaces and excessive reverberation. Parallel ceiling baffles running front to back were investigated. They were expected to absorb reverberation incident on the ceiling from many angles, while leaving speech signals, reflecting from the ceiling to the back of the room, unaffected. Various baffle spacings and absorptions, central and side speaker positions, and receiver positions throughout the room, were considered. Reflective baffles controlled reverberation, with a minimum decrease of sound levels. Absorptive baffles reduced reverberation, but reduced speech levels significantly. Ceiling reflectors, in the form of obstacles of semicircular cross section, suspended below the ceiling, were also tested. These were either 7 m long and in parallel, front-to-back lines, or 0.8 m long and randomly distributed, with flat side up or down, and reflective or absorptive top surfaces. The long reflectors with flat side down and no absorption were somewhat effective; the other configurations were not. © *2007 Acoustical Society of America.*
[DOI: 10.1121/1.2730623]

PACS number(s): 43.55.Fw, 43.50.Gf, 43.55.Ka [NX] Pages: 3517–3526

I. INTRODUCTION

The importance of classroom acoustics and of speech intelligibility is well recognized. The room-acoustical parameters affecting speech intelligibility are known; speech intelligibility tends to increase with increased speech-to-noise level difference (also referred to as signal-to-noise ratio) and to decrease with increased reverberation. Reverberation for speech intelligibility is best quantified by the clarity factor C_{50}, based on the early-to-late energy fraction. C_{50} is usually highly correlated with early-decay time (EDT) and reverberation time in classrooms.[1] The effect of speech-to-noise level difference on speech intelligibility dominates that of reverberation.[2] Studies[1,3,4] have confirmed that the values of these parameters are often nonoptimal. Thus, the question remains as to how to achieve the optimal values of the parameters in real classrooms in a practical, cost-effective way. Many newly designed or renovated classrooms use absorptive materials to reduce reverberation and late-arriving energy beneficially. However, these absorptive materials also cause a detrimental decrease in speech levels, and may reduce beneficial early reflections.

The purpose of the study reported here was to find an effective way to design lecture rooms — i.e., larger classrooms with an instructor at the front of the room, speaking to a group of students in front—and control sound to achieve optimum reverberation and adequate speech levels, especially at the back of the room, for speech intelligibility. The effectiveness of novel systems of ceiling baffles and reflectors for optimizing speech intelligibility is investigated, using a room-prediction model and physical scale modeling.

A room consists of a floor, walls, and ceiling. Among these three room components, the ceiling is chosen to be modified because it has a large flexibility compared to the walls and floor, and it can help reflect a teacher's voice toward the back of the room. Various ceiling-baffle and ceiling-reflector configurations were designed. Each design was incorporated into computer and physical, reduced-scale lecture-room models, and the effects of the baffles and reflectors on the sound field were determined, to evaluate the designs.

II. METHODS

A. Lecture-room configurations

A typical medium-sized university lecture room was selected as the basis for the tests. Figure 1 shows the floor plan. The lecture room has 96 seats, length = 15 m, width = 8.5 m, and height = 4 m (volume = 510 m^3, total surface area = 443 m^2, volume to surface-area ratio = 1.15 m). The room surfaces, and the seats and their writing tablets, are sound reflective. The midfrequency reverberation time measured in the unoccupied classroom was about 2 s. The corresponding reverberation radius was 1.3 m. Average octave-band surface-absorption coefficients calculated using diffuse-field theory varied from 125 to 2000 Hz as follows: 0.22, 0.12, 0.08, 0.08, 0.08. A speech source was positioned either at the front-center or at the front-side of the lecture room, and three listening positions were positioned in front (p1C—

[a)]Author to whom correspondence should be addressed; electronic mail: murray.hodgson@ubc.ca

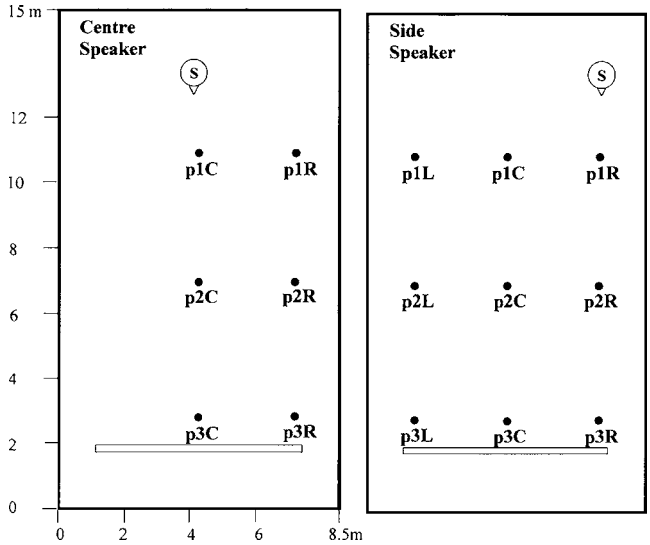

FIG. 1. Lecture-room floor plan showing the speech-source (S) and receiver (p) positions, and dimensions (in m).

source/receiver distance – 2.0 m), middle (p2C – 5.5 m), and back (p3C – 9.0 m) seats on the centerline of the lecture room. Six additional listening positions were used when predicting the acoustical conditions in side areas of the lecture room (see Fig. 1).

B. Ceiling baffle and reflector configurations

Two basic types of ceiling baffles and reflectors were studied. The first involved parallel ceiling baffles, projecting down from the ceiling and running front to back in the classroom. They were expected to absorb reverberant sound incident on the ceiling from a wide range of angles, reducing late-arriving energy, while leaving speech signals, reflecting from the (reflective) ceiling between the baffles to the back of the room, unaffected. Both sound-absorptive and sound-reflective baffles were considered. Different shapes, materials, spacings, and depths of the ceiling-baffle configurations were tested in pilot studies. Six configurations were selected for detailed study using computer prediction and scale-model measurement. These were reflective (configuration *R*) and absorptive (*A*) baffles, 0.6 m deep, separated by either 0.3 m (*R*1/*A*1), 0.6 m(*R*2/*A*2) or 1.2 m (*R*4/*A*4).

Based on the baffle results, ceiling reflectors involving lengths of obstacles of semicircular cross-sectional shape (configuration C), suspended from the ceiling with either the flat (CF) or curved (CC) side down, were evaluated in the scale model. These were expected to reflect and scatter speech sounds like "fittings" in an industrial workshop (see below). The shapes were inspired by common suspended light fixtures. The diameter of the semicircular reflectors was 0.3 m, the distance from the ceiling to the bottom of the reflectors was 0.6 m. They were 7 m long, and ran front-back in the lecture room, separated by 1.2 m, and with either the flat side down without absorption on the upper curved side (CF), with the flat side down and absorption on the upper curved side (CFA), or with the curved side down and no absorption (CC). Alternatively, either 30 (configuration

FIG. 2. (Color online) Photographs of the 1/8-scale model without ceiling baffles or reflectors: (a) showing the seats and rear partition; (b) showing the model speech source and microphone.

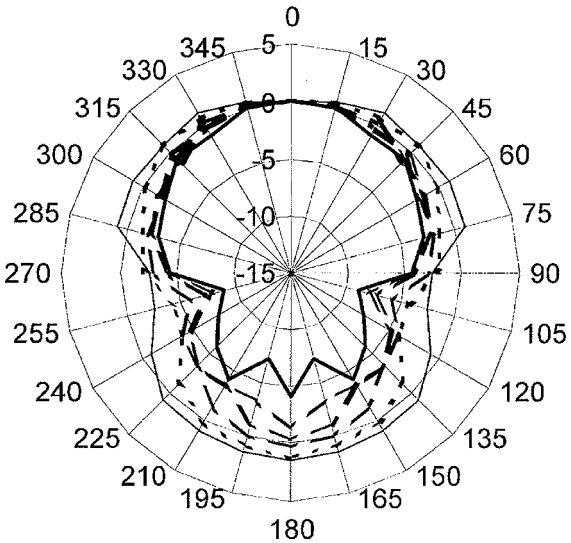

FIG. 3. Measured octave band, horizontal-plane directivity factors (in dB) of the 1:8-scale-model speech source; levels are normalized to 0 dB at 0°: (——) 63 HzFS; (·····) 125 HzFS; (–·–) 250 HzFS; (– – –) 500 HzFS; (– ·· –) 1000 HzFS; (——-) 2000 HzFS.

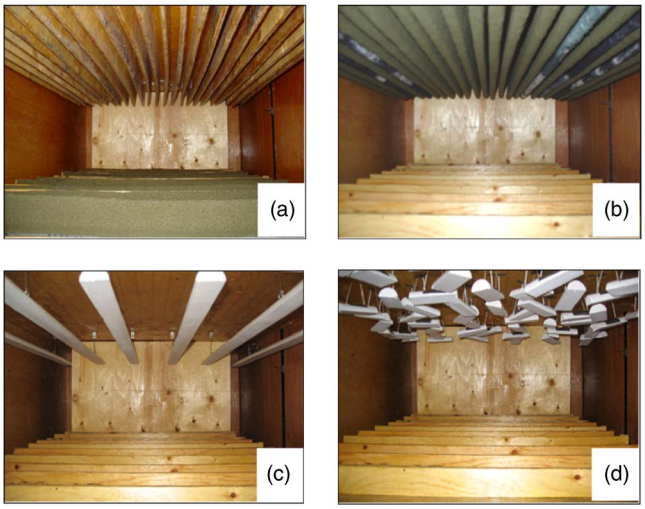

FIG. 4. (Color online) Scale-model ceiling baffle and reflector configurations in the unoccupied ("u") and occupied ('o') lecture room: (a) R1o; (b) A1u; (c) CFu; (d) CF60u.

CF30) or 60 (CF60) reflectors, 0.8 m long, were hung randomly from the ceiling with flat side down and no absorption.

C. Physical scale modeling

The lecture room was also studied without and with ceiling baffles or reflectors using a 1:8 scale model. According to the fundamental principle of the scale-modeling technique,[5] according to which all dimensions are scaled down by the scaling factor, the lecture room with length=15 m, width =8.5 m, and height=4 m, was a 1.88 m $\times$1.06 m$\times$0.50 m 1/8 scale model. The floor of the model was polished concrete. The walls, ceiling, the partition at the back of the room, and the rows of seats, were made of varnished plywood. Figure 2(a) is a photograph of the model, showing the rows of seats and the rear partition. In order to investigate how the effects of ceiling baffles and reflectors vary with

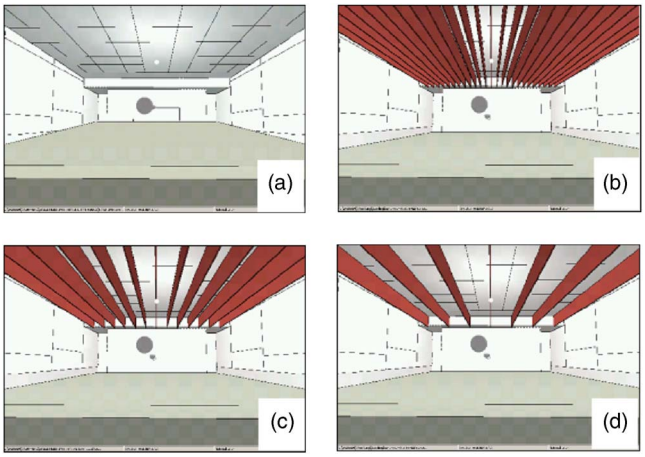

FIG. 5. (Color online) Computer models of the lecture room with: (a) no baffles; (b) *R*1/*A*1 baffles; (c) *R*2/*A*2 baffles; (d) *R*4/*A*4 baffles. Note the 1-m-deep seat block in all configurations.

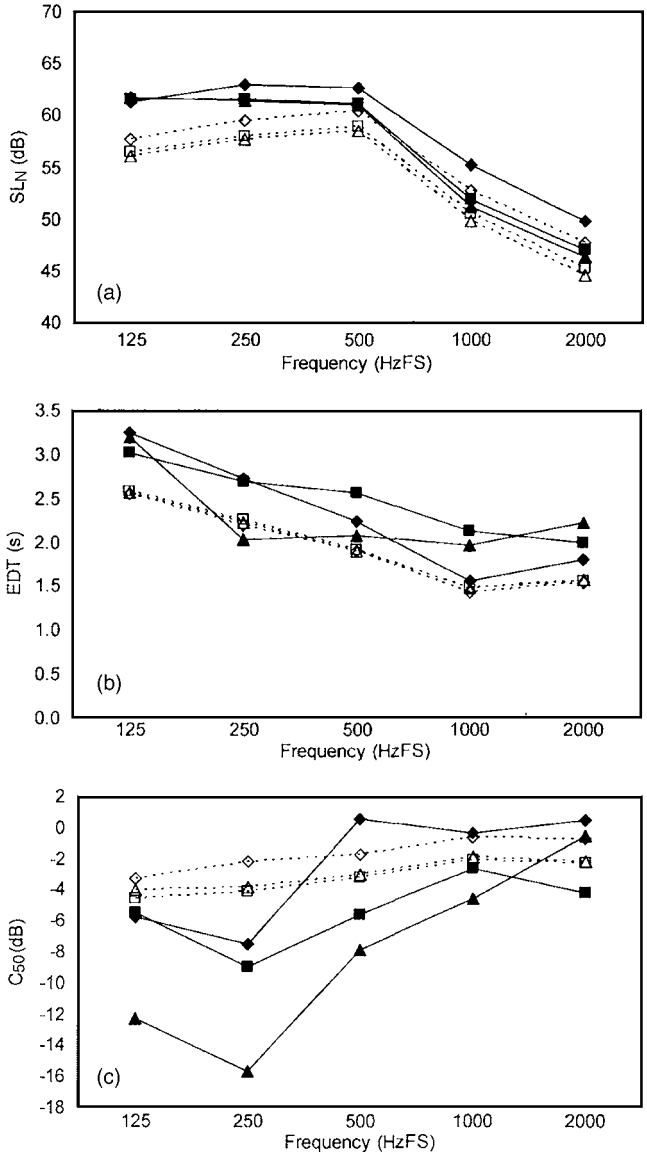

FIG. 6. Variation with frequency of (a) speech level SL_N, (b) early-decay time EDT, and (c) early-to-late energy fraction C_{50} at three central positions with the center speaker in the unoccupied lecture room without ceiling baffles or reflectors, as measured in the scale model and as predicted: (–◆–) p1C measured; (–■–) p2C measured; (–▲–) p3C measured; (···◇···) p1C predicted; (···□···) p2C predicted; (···△···) p3C predicted.

room occupancy in the lecture room, two different occupancies (unoccupied and 37% occupied/26 students) were considered in the scale model.

Air absorption is a major consideration in scale-model measurement. Air absorption increases approximately with the square of the frequency.[6] In a scale model, wavelength-to-dimension ratios are maintained, so wavelengths are scaled down by the scale factor, resulting in scaled-up model test frequencies. Since the test frequencies are high, air absorption is excessive in a scale model and cannot be neglected. For prediction, air-absorption exponents were calculated at the model test frequencies for the temperature and relative humidity measured in the scale model, as described in Ref. 6.

Speech sources in lecture rooms are mainly human talk-

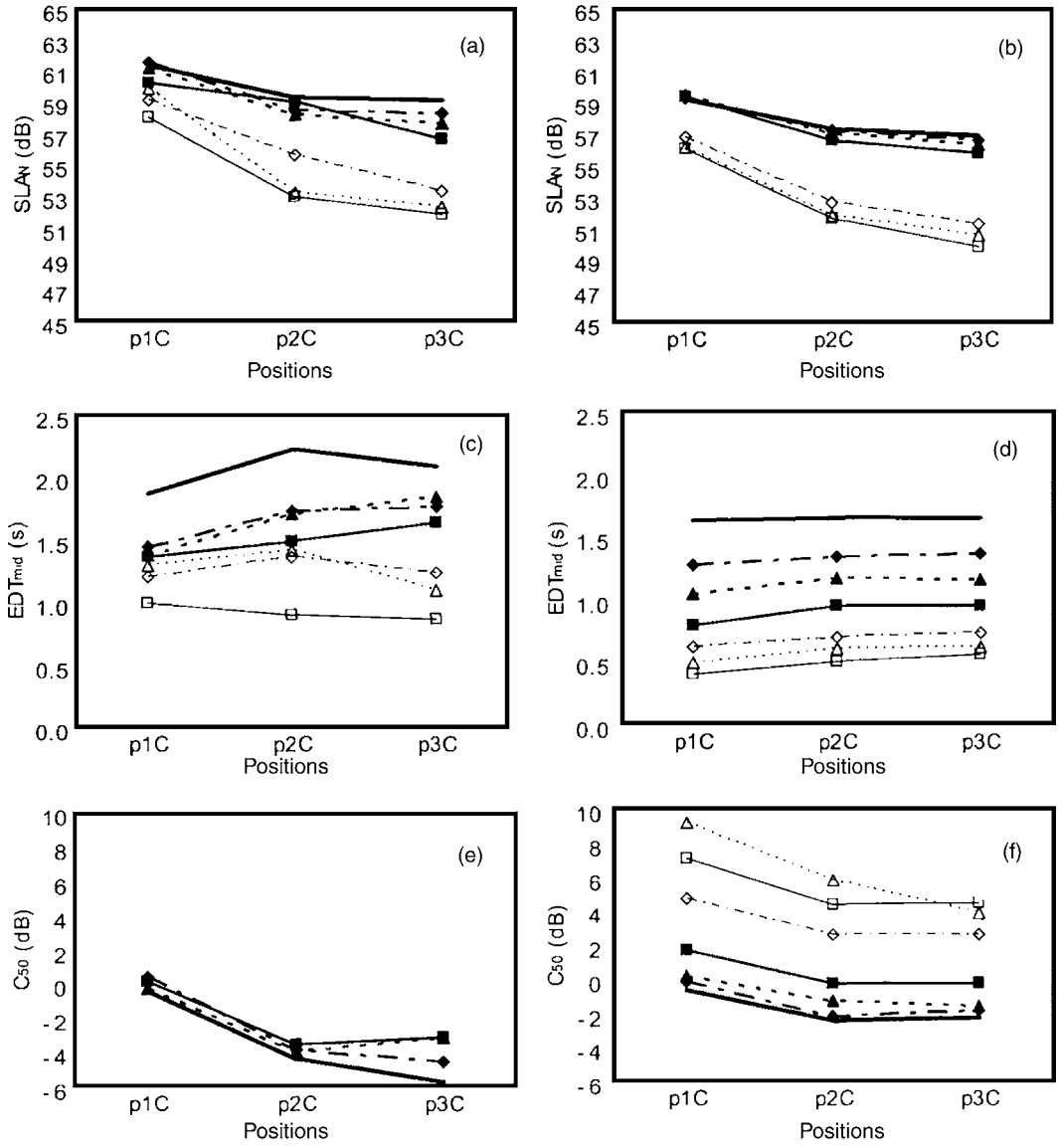

FIG. 7. Variation with position along the centerline with the center speaker of speech level SLA_N, early-decay time EDT_{mid}, and early-to-late energy fraction C_{50} in the unoccupied lecture room without and with reflective and absorptive ceiling baffles, as measured in the scale model and as predicted (C_{50} for the absorptive ceiling baffles is not available): (a) SLA_N, measured; (b) SLA_N, predicted; (c) EDT_{mid}, measured; (d) EDT_{mid}, predicted; (e) C_{50}, measured; (f) C_{50}, predicted. (———) no baffles, (–■–) *R*1, (- -▲- -) *R*2, (–·–◆–·–) *R*4, (–□–) *A*1, (- -△- -) *A*2, (–·– ◇ –·–) *A*4.

ers. Source directivity can strongly influence speech levels in lecture rooms. For accurate scale modeling of the lecture room, a model speech source is required which radiates with the directional characteristics of human speech. Such a source was created using a 1:8-scale head made of modeling clay, formed around the narrow end of a hollow cone, driven at the wide end by a "tweeter" loudspeaker, which narrowed down to a 3-mm-diameter opening as the mouth, to represent human speech directivity in the scale model (see Fig. 2(b)). Of course, the cone causes internal reflections which distort the signal spectrum; however, the effect was small in the test octave bands measured in the study. The power levels and directivities of the model speech source were measured in an anechoic chamber. Figure 3 shows the measured horizontal-plane directivity.

The ceiling baffles were made of varnished plywood, and could be covered with thin industrial carpet to make them absorbent. The absorption of the carpet was estimated from the change in reverberation time that occurred when a sample of it was introduced into the empty model, and was similar to that of 50-mm-thick glass fiber at full-scale frequencies. The semicircular ceiling reflectors were made of painted wood; the same carpet was used to make them absorbent. The carpet was also used to cover the front and top surfaces of the rows of seats, to simulate the absorption of upholstered or occupied seats approximately; the corresponding occupancy (37%) was estimated from the reduction in EDT and the typical absorption per occupant at 1 kHz.[7] Figure 4 shows photographs of some of the scale-model ceiling baffle and reflector configurations.

Acoustical measurements were made using the Maximum Length Sequence System Analyzer, which measured the impulse response between the model speech source and the Bruel & Kjaer 4135, "1/4 in." microphone used to receive the sound signals. All measurements were made after pre-calibration of the equipment. Early-decay times (EDT in

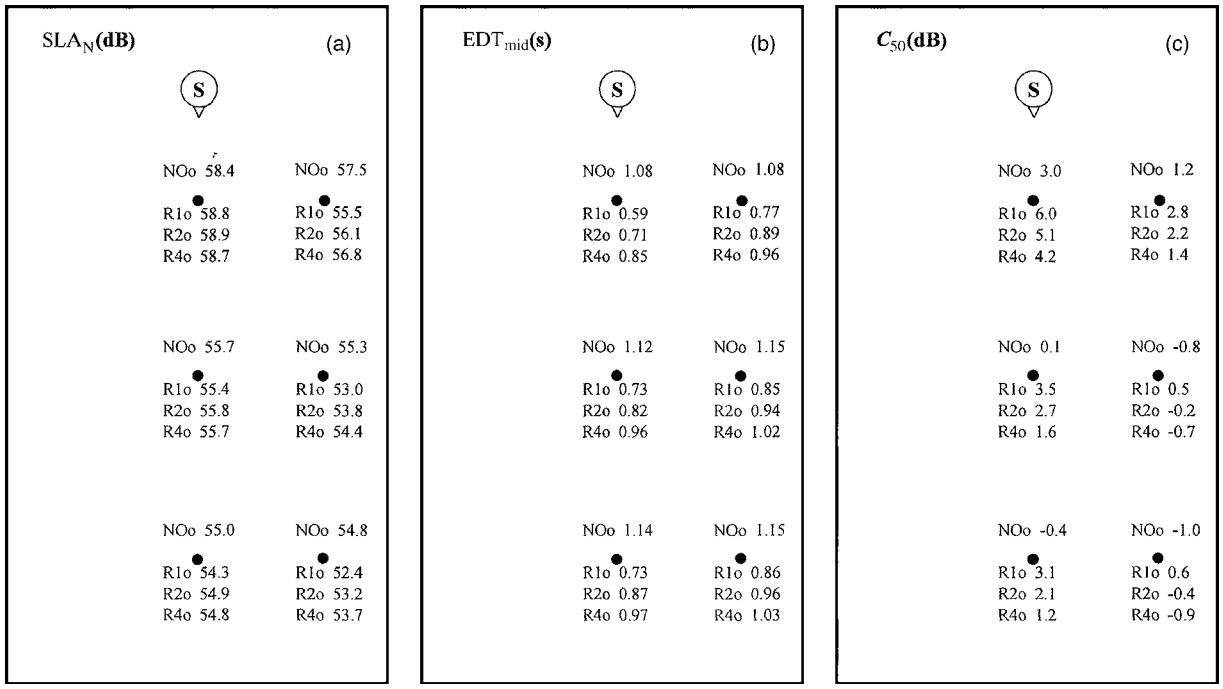

FIG. 8. Predicted variation with position of (a) SLA_N in dB, (b) EDT_{mid} in s, and (c) C_{50} in dB without and with reflective ceiling baffles, in the occupied virtual lecture room with the center speaker.

s) and steady-state levels (with the speech-source output levels kept constant) were measured. Measurements were made in octave bands from 1 to 16 kHz (125–2000 HzFS–FS=full-scale equivalent value) at all three receiver positions. The octave-band steady-state levels were converted to total, *A*-weighted "speech" levels SLA_N corresponding to a typical adult talking in a "Normal" voice level, using the relative output power levels of such a talker[8] and of the model speech source. Average midfrequency EDT_{mid} values relevant to speech intelligibility were calculated by averaging the octave-band EDTs at 500, 1000, and 2000 HzFS. In the case of the model without ceiling baffles or reflectors, average surface-absorption coefficients were calculated from the measured octave-band EDTs using diffuse-field theory; values increased with frequency from 0.06 to 0.1, close to

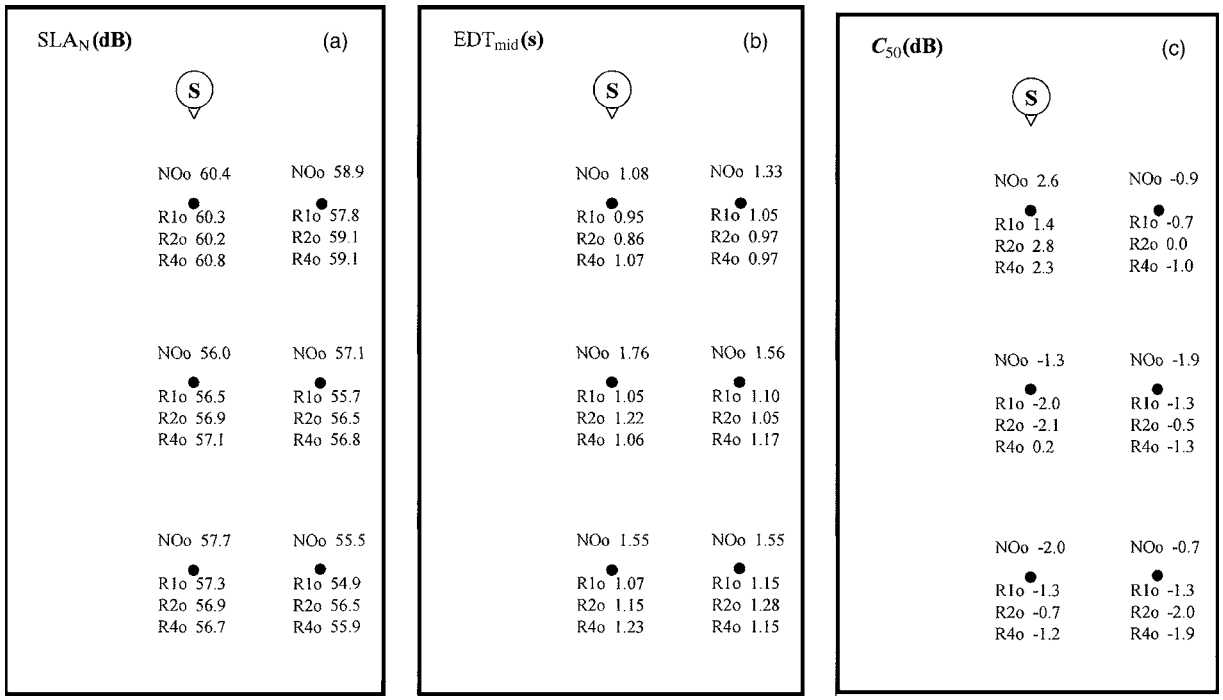

FIG. 9. Measured variation with position of (a) SLA_N in dB, (b) EDT_{mid} in s, and (c) C_{50} in dB without and with reflective ceiling baffles, in the occupied scale-model lecture room with the centre speaker.

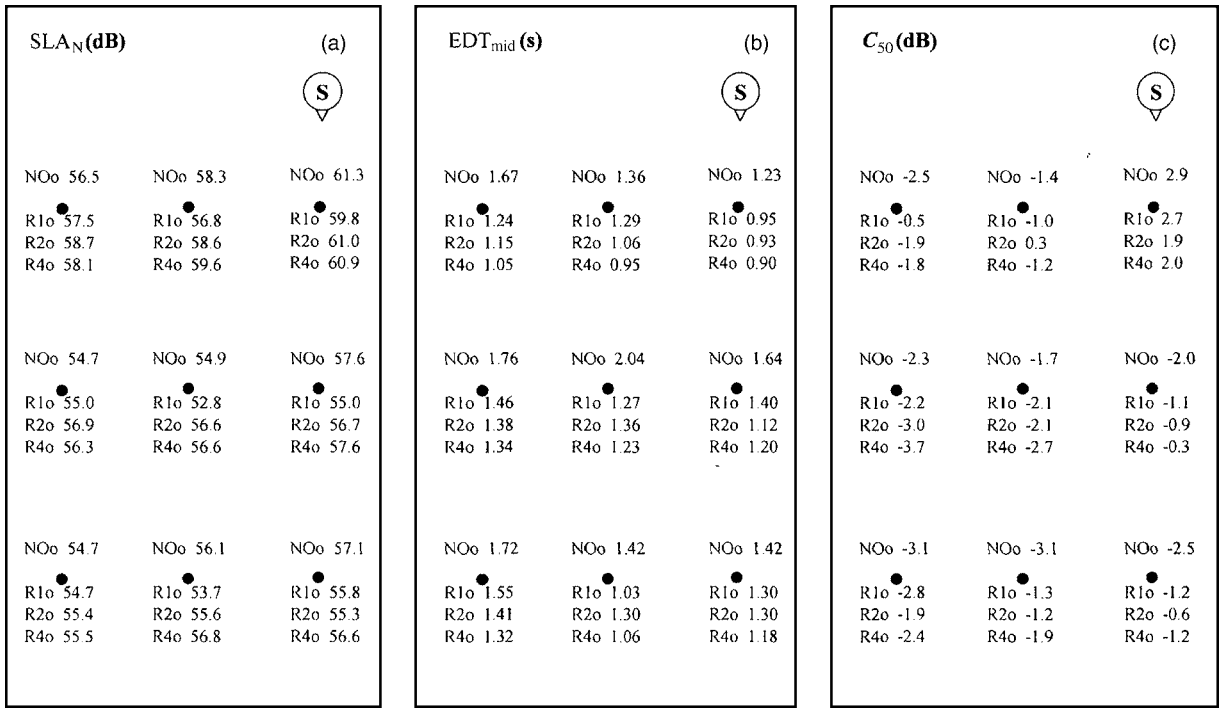

FIG. 10. Measured variation with position of (a) SLA_N in dB, (b) EDT_{mid} in s, and (c) C_{50} in dB without and with reflective ceiling baffles, in the occupied scale-model lecture room with the side speaker.

those in the full-scale room. Taking into account the model scale factor, C_{50} was calculated by calculating $C_{50/8=6.25}$ from the model impulse responses.

D. Computer simulation

The ceiling baffles were also studied using CATT-Acoustic v8.0 (Ref. 9) computer simulation. The lecture-room and ceiling-baffle configurations were modeled, octave-band EDTs and speech levels predicted, and corresponding values of SLA_N, EDT_{mid}, and C_{50} calculated. The lecture-room configuration was exactly the same as in the scale-model measurements. A sound source and nine receivers were positioned as shown in Fig. 1. The output level and directivity of the sound source were identical to the values

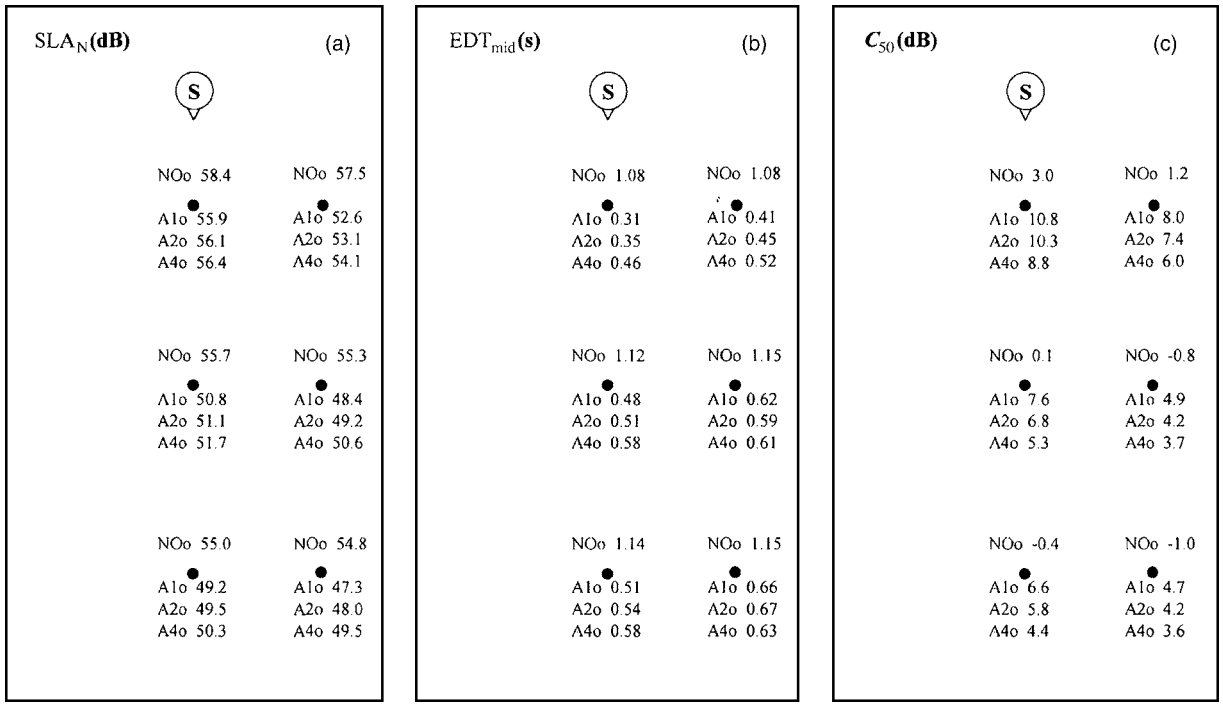

FIG. 11. Predicted variation with position of (a) SLA_N in dB, (b) EDT_{mid} in s, and (c) C_{50} in dB without and with absorptive ceiling baffles, in the occupied virtual lecture room with the center speaker.

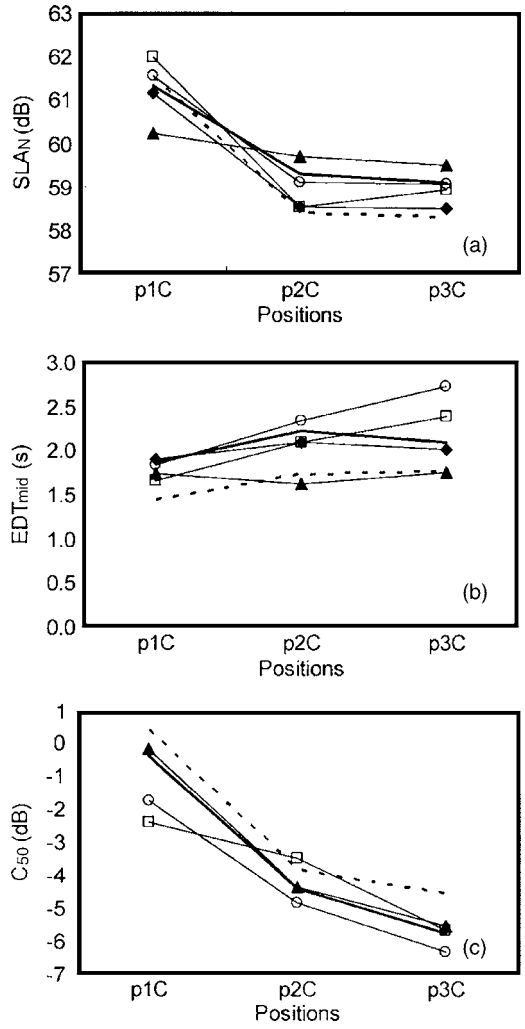

FIG. 12. Measured variation with position of (a) SLA_N in dB, (b) EDT_{mid} in s, and (c) C_{50} in dB in the unoccupied scale-model lecture room at central positions without and with ceiling baffles and reflectors: (——) no reflectors; (·····)*R*4; (– ▲ –) CF; (–◆ –) CC; (– □ –) C60; (– ○ –) C30.

used in the scale-model measurements. Unoccupied seats were modeled as one large 1 m deep seat block. Figure 5 shows computer models of the virtual lecture room without and with ceiling baffles. Ceiling reflectors were not studied by computer prediction as it was not clear how to model them accurately. The absorption coefficients of the room surfaces used in the simulation were the average values measured in the scale model without ceiling baffles or reflectors. Diffuse-reflection coefficients of the surfaces were set to increase with frequency from 0.1 to 0.3, based on previous research.[10]

III. RESULTS

Two introductory remarks must be made before discussing the results. First, it was generally found that measured and predicted EDTs and C_{50}'s were strongly inversely related, as has already been reported in the literature.[1] Even though, in principle, C_{50} is a better measure of the effect of reverberation on speech intelligibility than EDT, both parameters in fact provided similar information about the effects of the baffles and reflectors. Second, discussed below are results for two key components of speech intelligibility—speech level and C_{50}. It would clearly be useful in evaluating the ceiling baffles and reflectors to calculate values of a speech-intelligibility metric—such as speech transmission index or useful-to-detrimental energy fraction (U_{50})—from these components. However, this would require choosing values for the noise level at the receiver position under consideration, which introduces significant difficulties, as discussed in Ref. [11]. To assume a uniform noise level throughout the room is not realistic. Modeling noise as emanating from localized sources is more realistic; however, the effect of such noise sources depends on their output powers and positions relative to the speech source and receiver position. Real classrooms contain many noise sources (ventilation outlets, classroom equipment, the occupants) with different output powers and positions in the classrooms. Their characteristics cannot easily be estimated or generalized in a useful, realistic manner and, therefore, neither can the effect of noise. For this reason, no attempt was made to calculate values of speech-intelligibility metrics.

A. Comparison of measurement and prediction

In order to confirm that the scale-model and virtual lecture rooms were reasonably similar, comparisons were made between measured and predicted speech levels, early-decay times, and early-to-late energy fractions in the unoccupied lecture room without ceiling baffles or reflectors, for the center source position and the three central receiver positions. Figure 6 shows the octave-band results. Predicted SL_N values were somewhat lower than those measured by about 4 dB at low frequency, decreasing with frequency to about 1.5 dB at high frequency. Predicted EDTs varied negligibly with position; measured times showed much more variation—predicted values tended to be lower than those measured, by up to about 25%. At pC2 and pC3, as was the case for EDT, measured C_{50} values also had more variation than those predicted, and predicted values tended to be higher than those measured. The imperfect agreement between measurement and prediction is interesting, given that the average absorption coefficients involved in the virtual and scale models were very similar to one another. It can partly be explained by uncertainties in the scale-model measurements, differences in the values of important room parameters (e.g., the diffuse-reflection coefficients), possible limitations of the computer simulation (for example, the seat block), and the fact that the scale model is more realistic in, for example, including modal effects. In any case, it can be concluded that the reduced-scale and virtual lecture-room models, while not identical, are sufficiently similar that both can be used to study the effects of ceiling baffles and reflectors. The two techniques have their individual advantages and disadvantages. The scale model has the advantage of physical realism (for example, including modal effects), while prediction has the advantage that the input data defining the virtual room are more precisely known.

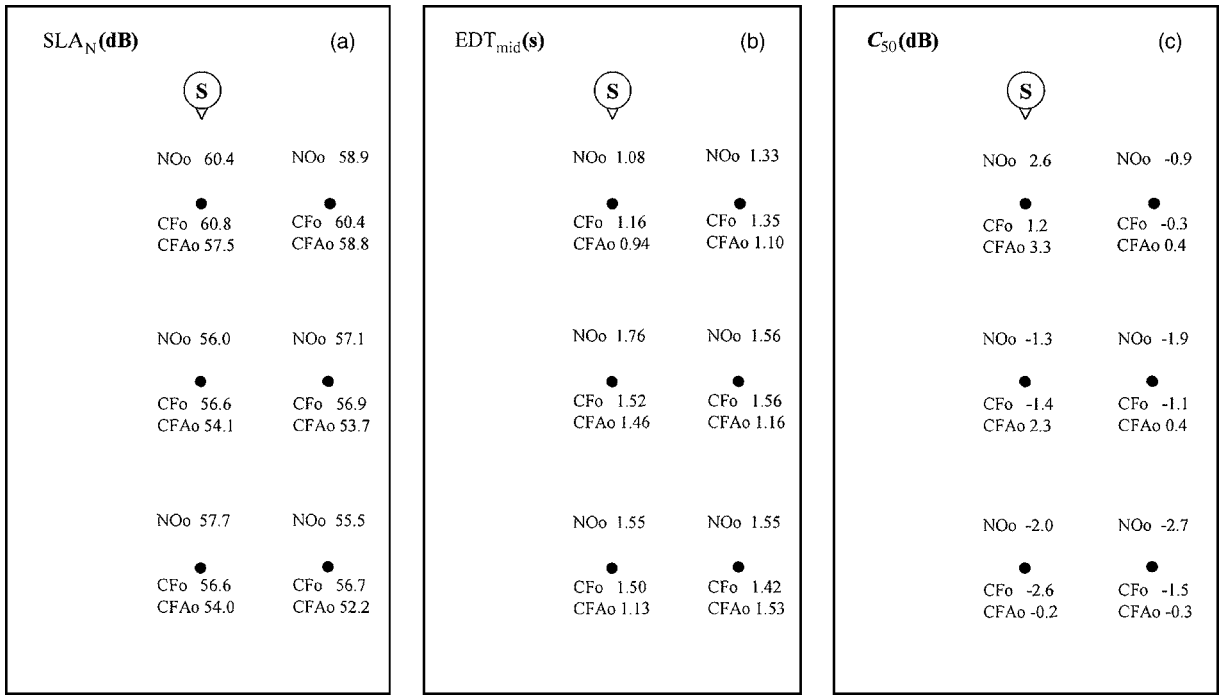

FIG. 13. Measured variation with position of (a) SLA_N in dB, (b) EDT_{mid} in s, (c) C_{50} in dB with the center speaker without and with ceiling reflectors, in the occupied scale-model lecture room.

B. Ceiling baffles

Figure 7 compares speech levels, early-decay times and early-to-late energy fractions measured and predicted in the unoccupied room with the six reflective and absorptive ceiling-baffle configurations, with the results for no baffles for the three receivers along the centerline and the center speaker. SLA_N is highest with no baffles, decreasing by about 2 dBA from the front to the back of the room. With the reflective ceiling baffles, as the number of baffles increased, predicted SLA_N remained virtually unchanged at the front of the room, but decreased by up to about 1.5 dBA at the back. Measured levels showed more variability, but similar trends, especially at p3C. With the absorptive ceiling baffles, and increasingly with the number of baffles, levels decreased more rapidly with distance relative to levels with the reflective baffles-by up to between 4 and 6 dBA at the front and back of the room, respectively. Ceiling baffles decreased the EDT_{mid} in all cases. With the reflective ceiling baffles, predicted EDT_{mid} values decreased progressively with increased number of baffles by up to about 50%—the decreases were similar at all three receiver positions. With absorptive baffles, EDT_{mid} varied little with baffle spacing and was very low. Again, measured results were similar, but showed less clear trends, and baffles resulted in smaller decreases in EDT_{mid}. C_{50} increased with an increasing number of baffles, and with baffle absorption.

Figure 8 to 11 show the SLA_N, EDT_{mid}, and C_{50} results at all receiver positions in the occupied room with ceiling baffles. Figure 8 shows that adding reflective ceiling baffles was predicted to have little effect on SLA_N along the centerline, tending to increase it slightly at the front, leave it unchanged in the middle, and decreasing it slightly at the back. At the side receiver positions, reflective baffles were predicted to decrease levels by up to 2.4 dB, the effects increasing with the number of baffles. The addition of baffles caused the decrease of SLA_N from the front to the back of the room to increase from 3.6 dB without baffles to as much as 6.4 dB. Adding reflective baffles was predicted to decrease EDT_{mid} by 10–45%. C_{50} increased by up to 3.5 dB. Both effects increased with the number of baffles, and decreased with distance from the source and, therefore, were greater at the central receivers than to the side. The effects of adding reflective ceiling baffles measured in the scale model (see Fig. 9) were more variable than as predicted, and smaller in magnitude. Figure 10 shows the SLA_N, EDT_{mid} and C_{50} values measured in the scale model with reflective ceiling baffles for the nine receiver positions and the side speaker. SLA_N tended to decrease by up to 2.6 dB at receiver positions on the same side as the speaker, but increased by about the same amount on the far side of the room. The effects were slightly greater than with the central speaker. Increasing the number of baffles resulted in lower levels. In side seats, EDT_{mid} decreased by up to 40%; C_{50} decreased slightly at the position nearest the source and at the room center, but otherwise increased by up to 1.9 dB. Figure 11 shows the predicted effects of adding absorptive ceiling baffles with the central speaker. They decreased SLA_N by 2.0–7.5 dBA, the effect increasing with the number of baffles, with source/receiver distance, and to the side of the room; front-back level differences increased to up to 8.6 dB. Adding absorbent baffles resulted in trends that were similar to those with the reflective baffles, but which were greater in magnitude; EDT_{mid} decreased by 42–71% and C_{50} increased significantly—by up to 7.8 dB.

The absorptive ceiling baffles do not achieve the desired objective since, as well as beneficially reducing early decay

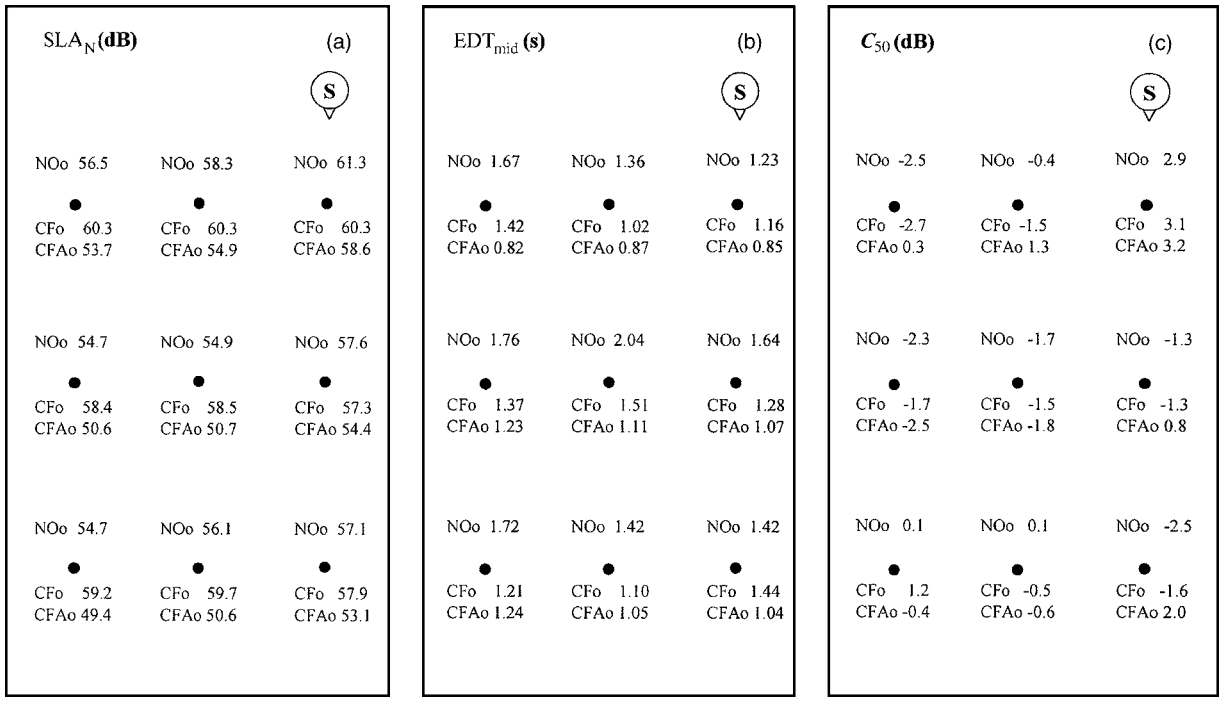

FIG. 14. Variation with position of (a) speech levels SLA_N, (b) early-decay times EDT$_{mid}$, (c) early-to-late energy fraction C_{50} with the side speaker without and with ceiling reflectors, as measured in the occupied scale-model lecture room.

times and increasing C_{50}, they detrimentally decrease speech levels significantly. Reflective baffles, on the other hand, achieve the objective better, reducing EDT$_{mid}$ and increasing C_{50} significantly, while reducing speech levels little.

C. Ceiling reflectors

The ceiling-baffle results are somewhat reminiscent of those that occur when reflective scattering obstacles (fittings) are introduced into an industrial workshop.[12] Reverberation times decrease sharply; steady-state levels from a sound source increase slightly close to the source due to back-scattering, and decrease more so far from the source. Thus, an alternative ceiling-reflector concept, based on fittings and consisting of reflective scattering obstacles suspended from the ceiling, was tested. Semicircular ceiling-reflector configurations, inspired by the shapes of common light fixtures, were evaluated. Figure 12 shows the SLA_N, EDT$_{mid}$, and C_{50} values measured in the unoccupied scale model with the four semicircular ceiling-reflector configurations (described in Sec. II B) at the three central positions with the center speaker. Also shown are the results without baffles or reflectors, and for the *R*4 ceiling-baffle configuration which had the same baffle spacing as the CF and CC reflectors. The CF reflectors decreased SLA_N by about 1 dB at p1C, and increased them insignificantly at p2C and p3C; levels were lower than with *R*4 at the front, and higher otherwise. EDT$_{mid}$ decreased by between about 10 and 30%, with the largest decreases occurring at p2C; values were very close to those for configuration *R*4. C_{50}, however, remained unchanged. The CC reflectors decreased SLA_N slightly at p2C and p3C, similar to configuration *R*4. They decreased EDT$_{mid}$ negligibly; as with configuration CF, C_{50} remained unchanged. The short, randomly distributed ceiling reflectors (configurations CF30 and CF60) showed somewhat different results from those for the longer reflectors. The CF30 reflectors had little effect on speech levels, increasing levels slightly at p1C. Both CF30 and CF60 had little effect on EDT$_{mid}$ at p1C and p2C, but increased it at p3C. Their effect on C_{50} was small, resulting in decreases of about 2 dB.

In an attempt to further improve performance, measurements were made with semi-circular ceiling reflectors with sound-absorptive materials on the upper curved surfaces (configuration CFA). Figures 13 and 14 show the measured SLA_N, EDT$_{mid}$, and C_{50} results with the center and side speaker, respectively, in the occupied scale model. When the speaker was at the center, adding the absorption decreased SLA_N by 1.6–4.5 dB; that is, adding the CFA reflectors to the untreated room decreased levels by up to 3.4 dB. When the speaker was at the side, adding absorption decreased SLA_N at receivers along the same side by between 2.4 and 4.5 dB; the decrease increased to as much as 9.8 dB at the other receiver positions, and increased towards the back of the room. Thus, introducing the CFA reflectors decreased SLA_N by up to 5.3 dB. The added absorption decreased EDT$_{mid}$ and increased C_{50}. While these effects are beneficial, the strong detrimental reduction of speech levels makes the absorbent reflectors of little interest.

IV. CONCLUSION

Reflective ceiling baffles achieved the goal of decreasing reverberation and increasing early energy with minimal speech-level reduction—the effect increased with baffle density. Reflective ceiling reflectors, in the form of long reflective obstacles of semicircular cross-section, suspended below the ceiling in parallel, front-to-back lines with flat side down, were also somewhat effective. Making the baffles or reflec-

tors sound absorptive further beneficially reduced reverberation and increased early energy, but also strongly reduced speech levels, which is highly detrimental to speech intelligibility. The shape of the semicircular ceiling reflectors was inspired by typical lighting fixtures. The results suggest that appropriately designed lighting fixtures could be effective at controlling lecture-room sound if they were made with flat, sound-reflecting (and, of course, optically transparent) bottoms, and arranged in long, parallel, front-to-back lines.

[1]M. R. Hodgson, "Experimental investigation of the acoustical characteristics of university classrooms." J. Acoust. Soc. Am. **106**(4), 1810–1819 (1999).

[2]J. S. Bradley, R. Reich, and S. G. Norcross, "On the combined effects of signal-to-noise ratio and room acoustics on speech intelligibility," J. Acoust. Soc. Am. **106**(4), 1820–1828 (1999).

[3]W. Yang and M. Hodgson, "Auralization study of optimum reverberation times for speech intelligibility for normal and hearing-impaired listeners in classrooms with diffuse sound fields," J. Acoust. Soc. Am. **120**(2), 801–807 (2006).

[4]M. Picard and J. S. Bradley, "Revisiting speech interference in classrooms," Audiology **40**(5), 221–244 (2001).

[5]M. Hodgson and R. J. Orlowski, "Acoustic scale modeling of factories, Part I: Principles, instrumentation and techniques," J. Sound Vib. **113**(1), 29–46 (1987).

[6]H. E. Bass, L. C. Sutherland, A. J. Zuckerwar, D. T. Blackstock, and D. M. Hester, "Atmospheric absorption of sound: Further developments," J. Acoust. Soc. Am. **97**(1), 680–683 (1995).

[7]M. Hodgson, "Empirical prediction of speech levels and reverberation in classrooms," Build. Acoust. **8**(1), 1–14 (2001).

[8]American National Standards Institute, ANSI S3.5-1997, "Methods for calculation of the speech intelligibility index," 1997.

[9]B.-I. Dalenback, CATT-Acoustic v8.0 (Gothenburg, Sweden, 2004).

[10]M. Hodgson, "Evidence of diffuse surface reflections in rooms," J. Acoust. Soc. Am. **89**(2), 765–771 (1991).

[11]M. R. Hodgson and E.-M. Nosal, "Effect of noise and occupancy on optimum reverberation times for speech intelligibility in classrooms," J. Acoust. Soc. Am. **111**(2) 931–939 (2002).

[12]M. Hodgson, "Measurements of the influence of fittings and roof pitch on the sound field in panel-roof factories," Appl. Acoustics **16**(5), 369–391 (1983).

On the sound field of a shallow spherical shell in an infinite baffle

Tim Mellow[a)]
Nokia UK Ltd., Farnborough, Hants GU14 0NG, United Kingdom

Leo Kärkkäinen
Nokia Research Center, Helsinki, Finland

(Received 28 August 2006; revised 31 January 2007; accepted 16 February 2007)

A method is presented for calculating the far field sound radiation from a shallow spherical shell in an acoustic medium. The shell has a concentrated ring mass boundary condition at its perimeter representing a loudspeaker voice coil and is excited by a concentrated ring force exerted by the end of the voice coil. A Green's function is developed for a shallow spherical shell, which is based upon Reissner's solution to the shell wave equation [Q. Appl. Math. **13**, 279–290 (1955)]. The shell is then coupled to the surrounding acoustic medium using an eigenfunction expansion, with unknown coefficients, for its deflection. The resulting surface pressure distribution is solved using the King integral together with the free space Green's function in cylindrical coordinates. In order to eliminate the need for numerical integration, the radiation (coupling) integrals are solved analytically to yield fast converging expansions. Hence, a set of simultaneous equations is obtained which is solved for the coefficients of the eigenfunction expansion. These coefficients are finally used in formulas for the far field sound radiation. © *2007 Acoustical Society of America.* [DOI: 10.1121/1.2715464]

PACS number(s): 43.58.Ta, 43.20.Rz, 43.20.Tb, 43.40.Ey, 43.38.Ja [LLT] Pages: 3527–3541

I. INTRODUCTION

The shallow spherical shell is a somewhat commonly used structure in acoustical transducers and methods for calculating its eigenfrequencies in a vacuum have long been established,[1–5] but little analytical work appears to have been done for calculating the radiated sound pressure when surrounded by a fluid medium. This is perhaps slightly surprising considering the extensive usage of shells in audio transducers ranging from miniature loudspeakers in mobile devices to hi-fi midrange units and high power tweeters used in PA systems. Although the use of boundary or finite element modeling is now fairly widespread in the transducer industry, analytical solutions are particularly useful in providing benchmarks for such models so that the element size and meshing geometry can be optimized. This enables more complicated geometries to be modeled with confidence.

A more general aim of this paper, though, is to provide formulas which enable very fast calculations and show the relationships between the various parameters. For example, it is useful to know how great the effect of the acoustic loading actually is and whether acoustic resistance can be used to control the modes. However, neither the ring-surround nor any other structures in a typical loudspeaker, such as the magnet and basket, are included in the model: The shell is assumed to be open to free space on both sides of the baffle which extends to infinity from the rim, although a specific acoustic impedance is included which can be used to model distributed impedances such as external damping (e.g., a mesh) or mixed mass and resistance in the form of an array of sound outlet holes. (Internal damping can be modeled using complex flexural rigidity.[6]) This specific impedance can also be used in a slightly less rigorous manner to represent lumped parameters such as the compliance of a rear cavity.

Reissner[1] provides a method for calculating the *in vacuo* eigenfrequencies based on the assumption that, if the shell is shallow, the radial and tangential components of the displacement can be ignored. Furthermore, it is suggested that this is a reasonable assumption for height/radius ratios up to around 0.25. A similar assumption is made here for the acoustic radiation whereby the shell is treated as a flat circular radiator. From a study made by Suzuki,*et al.*,[7] it can be concluded that this is a reasonable assumption up to $ka=5$ for the same range of height/radius ratios. This is somewhat fortuitous because it allows a small amount of curvature to be applied in order to increase rigidity (or reduce mass) relative to a flat plate without deviating too far from the theoretically flat far-field on-axis response of a flat piston up to the first break-up mode. Furthermore, the thin shallow shell assumptions simplify the formulation.

Jones *et al.*[4] provide an alternative approach for calculating the eigenfrequencies, which allows axial asymmetry while Thomas *et al.*[5] investigate nonlinear vibrations. Suzuki *et al.*[8] calculate the sound radiated from a fluid-loaded plate using an elastic boundary condition at the perimeter to model the suspension. However, in the current analysis it is assumed that, above the suspension resonance, the coil mass dominates, so this is included as a boundary condition too, together with the electrical/mechanical damping resistance. The Green's function in cylindrical coordinates is used, instead of the more common spherical form $e^{ikr}/(4\pi r)$, in or-

[a)]Electronic mail: tim.mellow@nokia.com

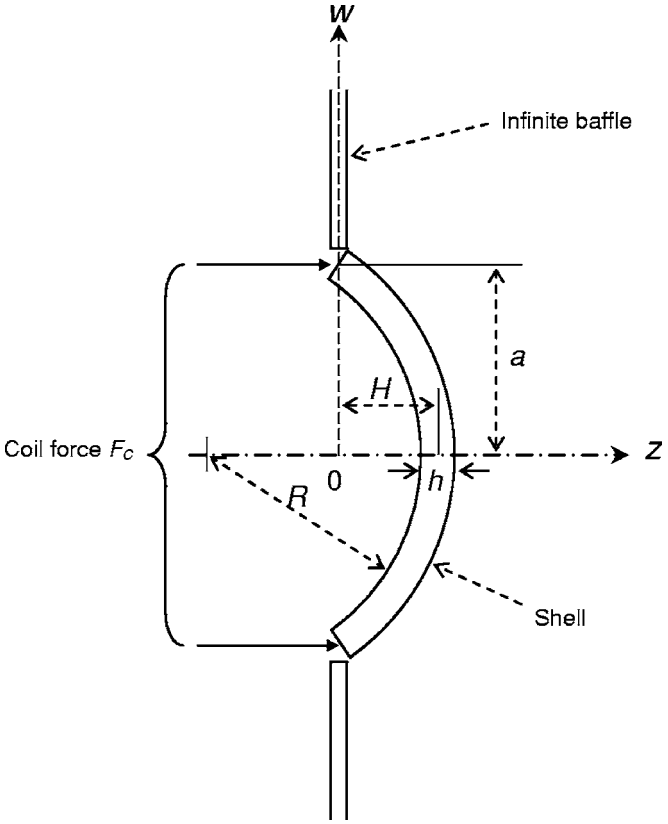

FIG. 1. Geometry of the shell.

der to facilitate the solution of the integrals and so avoid the need for numerical calculation of nested integrals.

A crucial factor in the solution of problems of sound radiation from monopole sources with arbitrary velocity distributions is the choice of trial function for the velocity or displacement at the source. In cases where the velocity is either zero or infinity at the perimeter,[9,10] a trial function based upon Bouwkamp's solution[11] to the free space wave equation in oblate spheroidal coordinates has been shown to be particularly useful, especially when calculating the near field pressure. The same applies to the trial function for the source pressure in dipole sources.[12] However, in this case, the velocity has a finite nonzero value at the shell perimeter so an eigenfunction (Bessel) expansion is used instead in order to avoid potential problems with convergence.

II. SOLUTION OF THE DYNAMIC *IN VACUO* SHELL WAVE EQUATIONS

A. Shell boundary conditions

The equations that follow are written in axisymmetric cylindrical coordinates, with w as the radial ordinate and z as the axial ordinate. An elastic spherical shell with radius a and thickness h, as shown in Fig. 1, is set in an infinite baffle of the same thickness with its center located on the z axis, which forms the axis of symmetry. Within its perimeter, the shell is homogeneous and continuous and is fabricated from an isotropic material with a Poisson's ratio of $\nu=0.3$.

For the purpose of this model, the shell and coil former are formed from the same piece of material and have the same thickness. Hence, at the rim, there is assumed to be neither bending nor radial strain. Also, the coil force $\tilde{F}_C$ is applied to the rim in the z direction. The tilde denotes a harmonically time varying quantity where the factor $e^{i\omega t}$ is suppressed. A separate suspension is assumed to be attached either to the coil or directly to the shell perimeter. It is assumed to provide pure linear stiffness K_S in the z direction with mechanical damping R_M and its mass is included with that of the voice coil, which is denoted by M_C. The coil driving force $\tilde{F}_C$ is used as the input in a wave equation for the shell, which is defined in terms of the input voltage $\tilde{e}_{\text{in}}$ by

$$\tilde{F}_C = Bl\tilde{e}_{\text{in}}/R_E, \tag{1}$$

where R_E is the electrical resistance of the coil and Bl is the magnetic flux coil length product. The total damping resistance R_S is then given by

$$R_S = R_M + (Bl)^2/R_E. \tag{2}$$

The deflection $\tilde{\eta}(w)$ of the shell is then be used as a parameter to couple it to the surrounding loss-free acoustic medium. Hence the shell and free space wave equations must be solved simultaneously.

B. Nonhomogeneous shell wave equation

Reissner's dynamic shell wave equations[1] are obtained by adding an axial inertia term to the static shell equations[13] while ignoring radial or tangential terms. Suppose that the spherical shell surface, as shown in Fig. 1, is defined by

$$z = R(\sqrt{1-w^2/R^2} - \sqrt{1-a^2/R^2}) \approx \frac{a^2-w^2}{2R}, \quad R > 2a \text{ (for surface average error} < 10\,\%). \tag{3}$$

The following simultaneous steady-state equations with an applied external harmonic load distribution $\tilde{p}(w)$ need to be solved for the displacement $\tilde{\eta}$ and an Airy stress function $\tilde{F}$,

$$D\nabla^4\tilde{\eta}(w) - \frac{1}{R}\nabla^2\tilde{F}(w) - \omega^2\rho_S h\tilde{\eta}(w) = \tilde{p}(w), \tag{4}$$

$$\nabla^4\tilde{F}(w) + \frac{hY}{R}\nabla^2\tilde{\eta}(w) = 0, \tag{5}$$

where, in the case of axisymmetric polar coordinates, the Laplace operator is given by

$$\nabla^2 = \frac{\partial^2}{\partial w^2} + \frac{1}{w}\frac{\partial}{\partial w} \tag{6}$$

and D is the flexural rigidity given by

$$D = \frac{Yh^3}{12(1-\nu^2)}, \tag{7}$$

where h is the thickness of the shell, Y is the Young's modulus of elasticity of the shell material, ν is its Poisson's ratio, and ρ_S is its density. The radius of curvature R is related to the dome height H by

$$R = \frac{a^2}{2H}. \tag{8}$$

Let a harmonic function $\tilde{\psi}$ be defined which satisfies

$$\nabla^2 \tilde{\psi} = 0 \tag{9}$$

so that

$$\nabla^2 \tilde{F}(w) = -\frac{hY}{R}(\tilde{\eta}(w) - \tilde{\psi}), \tag{10}$$

which, in turn, satisfies Eq. (5). Substituting Eq. (10) in Eq. (4) gives the following single steady-state homogeneous wave equation for the deflection:

$$\left(D\nabla^4 + \frac{hY}{R^2} - \omega^2 \rho_s h\right)\tilde{\eta}(w) = \frac{hY}{R}\tilde{\psi} + \tilde{p}(w). \tag{11}$$

C. Homogeneous shell wave equation

Suppressing the external pressure term in Eq. (11) yields the homogeneous wave equation, which can be written in the Helmholtz form as follows:

$$(\nabla^4 - k_S^4)\tilde{\eta}(w) = \frac{hY}{RD}\tilde{\psi}, \tag{12}$$

where k_S is the wave number of the shell which is given by

$$k_S = \frac{2\pi}{\lambda_S} = \frac{\omega}{c_S} = \left(\frac{\rho_S h}{D}\omega^2 - \frac{hY}{R^2 D}\right)^{1/4} \tag{13}$$

or, using Eqs. (7) and (8), it can be written

$$k_S^4 = \frac{\rho_S h}{D}\omega^2 - \frac{\xi^4}{a^4}, \tag{14}$$

where

$$\xi^4 = 48(1 - \nu^2)H^2/h^2. \tag{15}$$

The speed of sound c_S in the shell is given by

$$c_S = \omega/k_S. \tag{16}$$

As with a plate, high frequencies travel faster in the shell than low frequencies, which makes the shell a dispersive medium. It can be seen that at some transition frequency f_{INF} the speed of sound and hence also the wavelength become infinite. Below f_{INF}, the wavelength is complex with a 45° phase angle. Hence static solutions[13,14] are usually written in terms of Thomson (a.k.a. Kelvin) functions, which can be defined as Bessel functions with $e^{i\pi/4}$ in their arguments.[15] The transition frequency is given by

$$f_{\mathrm{INF}} = \frac{H}{\pi a^2}\sqrt{\frac{Y}{\rho_S}}. \tag{17}$$

Reissner[1] shows that the solutions to Eqs. (4) and (5) are eigenfunctions of the form

$$\tilde{\eta}_n(w) = \tilde{C}_{1n}J_0(k_S w) + \tilde{C}_{2n}Y_0(k_S w) + \tilde{C}_{3n}I_0(k_S w) + \tilde{C}_{4n}K_0(k_S w) + \tilde{C}_{5n}, \tag{18}$$

$$\tilde{F}_n(w) = -\frac{2HhY}{k_S^2 a^2}(\tilde{C}_{1n}J_0(k_S w) + \tilde{C}_{2n}Y_0(k_S w) - \tilde{C}_{3n}I_0(k_S w) - \tilde{C}_{4n}K_0(k_S w)) + \frac{\rho_S h a^2 \omega^2}{8H}\tilde{C}_{5n}w^2 + \tilde{C}_{6n}\log w + \tilde{C}_{7n}, \tag{19}$$

where $\tilde{C}_{5n} = \tilde{\psi}_n$ and n is the eigenindex. A useful alternative derivation to that of Reissner is provided by Gradowczyk,[14] which uses the auxiliary equation method to solve the simultaneous differential equations. In Eqs. (18) and (19), the arguments of the Bessel functions J, Y, I, and K can only have specific values, or eigenvalues, which satisfy the boundary conditions. The eigenvalues of the system are represented by setting $k_S a = \beta_n$. The eigenvalues and constants are then determined by applying boundary conditions, which are evaluated with help from the following identities:[15]

$$\frac{d}{dw}Z_0(k_S w) = \mp k_S Z_1(k_S w), \tag{20}$$

$$\frac{d^2}{dw^2}Z_0(k_S w) = k_S^2\left(\pm\frac{Z_1(k_S w)}{k_S w} \mp Z_0(k_S w)\right), \tag{21}$$

$$\frac{d^3}{dw^3}Z_0(k_S w) = k_S^3\left\{\left(1 \mp \frac{2}{k_S^2 w^2}\right)Z_1(k_S w) \pm \frac{Z_0(k_S w)}{k_S w}\right\}, \tag{22}$$

where Z can represent either J (upper sign) or I (lower sign).

D. Eigenvalues of the shell in a vacuum

1. Boundary condition of continuity at the center

In this configuration, $\tilde{\eta}_n$ and $\tilde{F}_n$ must be continuous at the apex ($w=0$). Therefore we have

$$\tilde{C}_{2n} = \tilde{C}_{4n} = \tilde{C}_{6n} = 0. \tag{23}$$

2. Boundary condition of zero bending at the perimeter

There is assumed to be zero bending at the perimeter. Therefore

$$\frac{\partial}{\partial w}\tilde{\eta}_n(w)\bigg|_{w=a} = -\frac{\beta_n}{a}\tilde{C}_{1n}J_1(\beta_n) + \frac{\beta_n}{a}\tilde{C}_{3n}I_1(\beta_n) = 0 \tag{24}$$

so that

$$\tilde{C}_{3n} = \frac{J_1(\beta_n)}{I_1(\beta_n)}\tilde{C}_{1n}. \tag{25}$$

3. Boundary condition of zero radial strain at the perimeter

At the perimeter, there is assumed to be zero radial strain.[13] Hence

$$\left(\frac{\partial^2}{\partial w^2}-\frac{\nu}{w}\frac{\partial}{\partial w}\right)\widetilde{F}_n(w)\Big|_{w=a}$$
$$=\frac{2hHY}{a^2}\left\{\widetilde{C}_{1n}\left(J_0(\beta_n)-\frac{1+\nu}{\beta_n}J_1(\beta_n)\right)+\widetilde{C}_{3n}\left(I_0(\beta_n)-\frac{1+\nu}{\beta_n}I_1(\beta_n)\right)\right\}+(1-\nu)\omega_n^2\frac{a^2\rho_S h}{4H}\widetilde{C}_{5n}=0, \quad (26)$$

where from Eq. (14)

$$\omega_n^2=\frac{D(\beta_n^4+\xi^4)}{a^4\rho_S h} \quad (27)$$

so that

$$\widetilde{C}_{5n}=-\frac{2\xi^4}{(1-\nu)(\beta_n^4+\xi^4)}\left\{\widetilde{C}_{1n}\left(J_0(\beta_n)-\frac{1+\nu}{\beta_n}J_1(\beta_n)\right)+\widetilde{C}_{3n}\left(I_0(\beta_n)-\frac{1+\nu}{\beta_n}I_1(\beta_n)\right)\right\}. \quad (28)$$

4. Coil impedance at the perimeter

The coil mass and suspension produce an axially symmetric (vertical) shear force[13] resultant Q_v at the perimeter. Hence, assuming that $a \ll R$,

$$\widetilde{Q}_{vn}(w)\big|_{w=a}=\left(\widetilde{Q}_n(w)+\widetilde{N}_n(w)\frac{w}{R}\right)_{w=a}$$
$$=(\omega_n^2 M_C-K_S-i\omega_n R_S)\frac{\widetilde{\eta}_n(a)}{2\pi a}, \quad (29)$$

where M_C is the mass of the coil and its former, K_S is the stiffness of the suspension, and R_S is the total damping resistance. Also, the shear force is defined by[13]

$$\widetilde{Q}_n(w)=-D\frac{\partial}{\partial w}\nabla^2\widetilde{\eta}_n(w)\big|_{w=a}=-\frac{\beta_n^3}{a^3}D(\widetilde{C}_{1n}J_1(\beta_n)+\widetilde{C}_{3n}I_1(\beta_n)) \quad (30)$$

and the radial membrane force is defined by

$$\widetilde{N}_n(w)=-\frac{1}{w}\frac{\partial}{\partial w}F(w)$$
$$=-\frac{2HhY}{a^2\beta_n}\left(\widetilde{C}_{1n}J_1(\beta_n)+\widetilde{C}_{3n}I_1(\beta_n)\right)-\widetilde{C}_{5n}\frac{\omega_n^2 a^2\rho_S h}{4H} \quad (30a)$$

so that

$$\widetilde{C}_{5n}=-\widetilde{C}_{1n}J_0(\beta_n)-\widetilde{C}_{3n}I_0(\beta_n)-(\beta_n^4+\xi^4)\times\frac{4\widetilde{C}_{1n}J_1(\beta_n)-\beta_n\left(\widetilde{C}_{1n}J_0(\beta_n)+\widetilde{C}_{3n}I_0(\beta_n)\right)}{\beta_n\left(\left(1+\frac{M_C}{M_S}\right)(\beta_n^4+\xi^4)-\frac{a^2K_S}{\pi D}-i\frac{R_S}{\pi}\sqrt{\frac{\beta_n^4+\xi^4}{\rho_S hD}}\right)}. \quad (31)$$

The surface area S of a shallow shell is

$$S=2\pi R(R-\sqrt{R^2-a^2})\approx\pi a^2, \quad R>2a. \quad (32)$$

The total mass M_S of the shell is therefore

$$M_S=\pi a^2\rho_S h. \quad (33)$$

Let ω_0 be a notional angular frequency, representing the suspension resonance of a perfectly rigid shell (including its coil mass). Hence, the stiffness may be defined by

$$K_S=(M_S+M_C)\omega_0^2. \quad (34)$$

From Eqs. (27), (33), and (34), the stiffness can be expressed as follows:

$$K_S=\frac{\pi D}{a^2}\left(1+\frac{M_C}{M_S}\right)(\beta_0^4+\xi^4), \quad (35)$$

where β_0 is a notional zeroth eigenvalue. Also, let the Q of this fundamental resonance be defined by

$$Q_S=\sqrt{(M_S+M_C)K_S}/R_S. \quad (36)$$

E. Calculation of the eigenvalues

Equating Eq. (28) with Eq. (31) and inserting the expressions for K_S and R_S from Eqs. (35) and (36), respectively, together with the identity for $\widetilde{C}_{3n}$ from Eq. (25) produces a characteristic equation that can be solved for the eigenvalues

$$\left(1+\frac{M_C}{M_S}\right)\left(\beta_n^4-\beta_0^4-i\frac{\sqrt{(\beta_0^4+\xi^4)(\beta_n^4+\xi^4)}}{Q_S}\right)\times\left\{((1-\nu)\beta_n^4-(1+\nu)\xi^4)W(\beta_n)+4\xi^4\frac{1+\nu}{\beta_n}J_1(\beta_n)I_1(\beta_n)\right\}-(1-\nu)(\beta_n^4+\xi^4)^2\left(W(\beta_n)-\frac{4}{\beta_n}J_1(\beta_n)I_1(\beta_n)\right)=0, \quad (37)$$

where

$$W(\beta_n)=J_0(\beta_n)I_1(\beta_n)+J_1(\beta_n)I_0(\beta_n).$$

and the notional zeroth eigenvalue β_0 is defined by

$$\beta_0^4=\frac{a^2M_S}{\pi D}\omega_0^2-\xi^4, \quad (38)$$

which is then used as a parameter in the characteristic equation (not a solution) to define the suspension stiffness.

F. Eigenvalues with zero load at the perimeter

If there is no loading at the perimeter, then $M_C=0$ and $\omega_0=0$. Eq. (37) reduces to

$$(\beta_n^4+\xi^4)\left\{W(\beta_n)-2\frac{(1-\nu)\beta_n^4+2\xi^4}{\beta_n\xi^4}J_1(\beta_n)I_1(\beta_n)\right\}. \quad (39a)$$

For zero height, setting $\xi^4=0$, yields the following eigenvalues

$$\beta_1 = 0 \quad \beta_2 = 3.8317 \quad \beta_3 = 7.0156$$

$$\beta_4 = 10.174 \quad \beta_5 = 13.324.$$

whereas setting $\xi^4 = \infty$ gives

$$\beta_1 = e^{i\pi/4}\infty \quad \beta_2 = 5.9057 \quad \beta_3 = 9.1969$$

$$\beta_4 = 12.402 \quad \beta_5 = 15.580.$$

Using the following asymptotic expressions[16] for the Bessel functions in Eq. (37),

$$J_\nu(z)\Big|_{z\to\infty} \approx \sqrt{\frac{2}{\pi z}}\cos\left(z - \frac{(2\nu+1)}{4}\pi\right), \tag{39b}$$

$$I_\nu(z)\Big|_{z\to\infty} \approx \sqrt{\frac{1}{2\pi z}}e^z, \tag{40}$$

it can be shown that

$$\beta_n|_{n\to\infty} \approx (n - 3/4)\pi, \quad H/h = 0.$$
$$\beta_n|_{n\to\infty} \approx n\pi, \quad H/h = \infty. \tag{41}$$

From Eq. (14), the eigenfrequencies are obtained as follows:

$$f_n = \frac{h}{4\pi a^2}\sqrt{\frac{Y}{3\rho_S}\left(\frac{\beta_n^4}{(1-\nu^2)} + 48\frac{H^2}{h^2}\right)}. \tag{42}$$

Not surprisingly, when $H=0$, Eq. (42) reduces to the eigenfrequency equation for a plate. However, when $H > 10h$, say, the equation for the fundamental shell eigenfrequency in asymptotic form becomes

$$f_2 \approx \frac{H}{\pi a^2}\sqrt{\frac{Y}{\rho_S}}, \quad H > 10h$$

$$= \frac{1}{2\pi R}\sqrt{\frac{Y}{\rho_S}} = f_{\mathrm{INF}}. \tag{43}$$

This slightly surprising result, due to Reissner,[1] indicates that when the height of the apex is much greater than the wall thickness, the fundamental resonant frequency (second eigenfrequency f_2) of the shell is dependent only upon its radius of curvature and material properties regardless of the wall thickness. (This does not apply to the first eigenfrequency, or piston eigenfrequency, which remains zero.) This effect is demonstrated in Fig. 2 where the eigenfrequencies are plotted against the height to thickness ratio. The eigenfrequencies f_n are normalized to the fundamental eigenfrequency f_{P2} of the corresponding flat circular plate where

$$f_{P2} = \frac{\beta_2^2 h}{4\pi a^2}\sqrt{\frac{Y}{3(1-\nu^2)\rho_S}}, \quad \beta_2 = 3.8317. \tag{44}$$

On the left-hand side of the plot, the eigenfrequencies converge to those of the flat circular plate with the same boundary conditions. On the right-hand side, the asymptotic value is $f_{\mathrm{INF}}/f_{P2} = 0.4502H/h$. However, $f_1 = 0$ for any height because the shell is free to float through space and so this is the "piston" eigenfrequency.

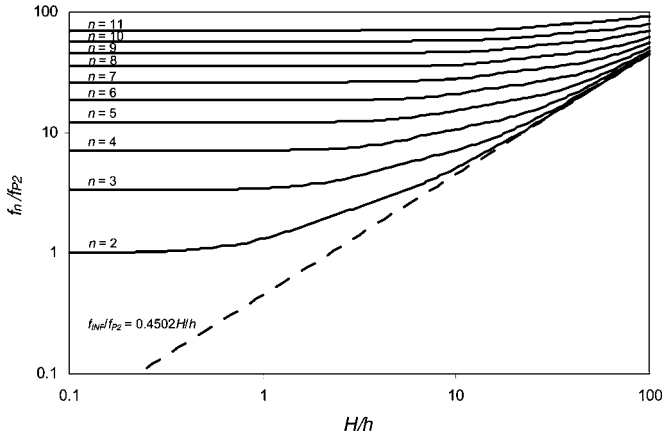

FIG. 2. Eigenfrequencies of a shallow spherical shell with zero load at the perimeter.

G. Eigenvalues with infinite load at the perimeter

If $M_C = \infty$ and $\omega_0 = 0$, then the shell's dynamic axial movement is blocked, although it can still move through space at constant velocity and hence returns a zero value for the 1st eigenfrequency, Eq. (38) reduces to:

$$(\beta_n^4 + \xi^4)\left\{W(\beta_n) + \frac{4(1+\nu)\xi^4 J_1(\beta_n)I_1(\beta_n)}{\beta_n((1-\nu)\beta_n^4 - (1+\nu)\xi^4)}\right\} = 0 \tag{45}$$

which is identical to Reissner's equation for a clamped shell, except for the factor $(\beta_n^4 + \xi^4)$ which gives the piston mode. For zero height, setting $\xi^4 = 0$, yields the following eigenvalues

$$\beta_1 = 0 \quad \beta_2 = 3.1962 \quad \beta_3 = 6.3064 \quad \beta_4 = 9.4395$$

$$\beta_5 = 12.577$$

whereas setting $\xi^4 = \infty$ gives

$$\beta_1 = e^{i\pi/4}\infty \quad \beta_2 = 5.9057 \quad \beta_3 = 9.1969$$

$$\beta_4 = 12.402 \quad \beta_5 = 15.580$$

Again, using the identities of Eqs. (39) and (40), expressions for the large eigenvalues can be obtained:

$$\beta_n|_{n\to\infty} \approx (n-1)\ \pi, \quad H/h = 0$$
$$\beta_n|_{n\to\infty} \approx n\pi, \quad H/h = \infty \tag{46}$$

In Fig. 3, the eigenfrequencies f_n of a simply supported shell are normalized to the fundamental eigenfrequency f_{P2} of the corresponding flat circular plate where

$$f_{P2} = \frac{\beta_2^2 h}{4\pi a^2}\sqrt{\frac{Y}{3(1-\nu^2)\rho_s}}, \quad \beta_2 = 3.1962. \tag{47}$$

On the left-hand side of the plot, the eigenfrequencies converge to those of a clamped flat circular plate. On the right-hand side, the asymptotic value is $f_{\mathrm{INF}}/f_{P1} = 0.6470H/h$.

H. Eigenvalues with finite load at the perimeter

With a low stiffness boundary condition, β_1 and f_1 have values fairly close to β_0 and f_0, respectively, but are not

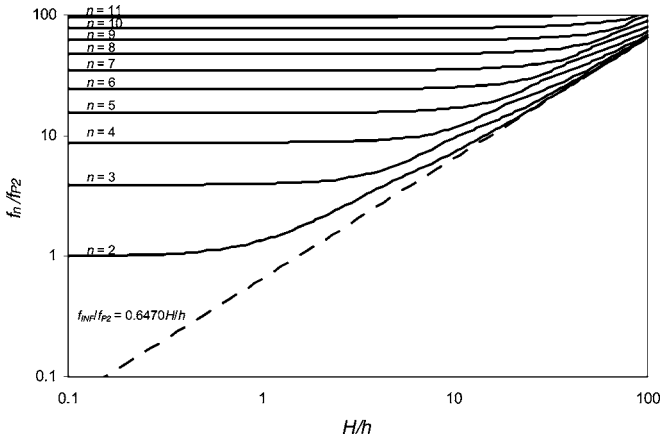

FIG. 3. Eigenfrequencies of a shallow spherical shell with infinite load at the perimeter.

coincident due to interaction between the modes. As the stiffness is increased, β_1 and f_1 approach asymptotic values representing blocked axial movement no matter how large β_0 and f_0 are.

The perimeter damping changes the angle of all the eigenvalues such that the angle of the complex eigenvalues is no longer 45° and the imaginary parts of the remainder are no longer zero.

I. Eigenfunctions

Substituting Eqs. (23), (25), and (28) in Eq. (18) yields the following eigenfunctions:

$$\eta_n(w) = J_0(\beta_n w/a) - B_n I_0(\beta_n w/a) + C_n, \tag{48}$$

which are the solutions to the following wave equation:

$$(\nabla^4 - k_S^4)(\eta_n(w) - C_n) = 0, \tag{49}$$

where

$$B_n = -\frac{\tilde{C}_3(\beta_n)}{\tilde{C}_1(\beta_n)} = -\frac{J_1(\beta_n)}{I_1(\beta_n)} \tag{50}$$

and

$$C_n = \frac{\tilde{C}_{5n}}{\tilde{C}_{1n}} = -\frac{2\xi^4(W(\beta_n) - 2(1+\nu)J_1(\beta_n)I_1(\beta_n)/\beta_n)}{(1-\nu)I_1(\beta_n)(\beta_n^4 + \xi^4)}. \tag{51}$$

III. GREEN'S FUNCTION FOR A SHALLOW SPHERICAL SHELL WITH AXIALLY SYMMETRIC EXCITATION

The Green's function for the shell that represents the particular displacement response to an axially symmetric harmonic delta excitation of unit strength may be expressed as an infinite series of modes as follows:

$$G(w|w_0) = \sum_{n=1}^{\infty} A_n \eta_n(w) \tag{52}$$

and similarly

$$C = \sum_{n=1}^{\infty} A_n C_n. \tag{53}$$

The unknown variable A_n may be solved for by substituting this Green's function in the following wave equation for a "point source" excitation at w_0, ϕ_0:

$$(\nabla^4 - k_S^4)G(w|w_0) = \frac{hY}{RD}C + \frac{1}{w}\delta(w - w_0)\delta(\phi - \phi_0). \tag{54}$$

Substituting $k_S = \beta_n/a$ in Eq. (12) yields the following identity for the Laplace operator:

$$\nabla^4 \eta_n(w) = \frac{\beta_n^4}{a^4}\eta_n + \frac{hY}{RD}C_n. \tag{55}$$

Hence

$$\nabla^4 G(w|w_0) = \sum_{n=1}^{\infty} A_n \left(\frac{\beta_n^4}{a^4}\eta_n(w) + \frac{hY}{RD}C_n \right). \tag{56}$$

Substituting Eqs. (52), (53), and (56) in the wave Eq. (54) yields

$$\sum_{n=1}^{\infty} A_n \left(\frac{\beta_n^4}{a^4} - k_S^4 \right) \eta_n(w) = \frac{1}{w}\delta(w - w_0)\delta(\phi - \phi_0), \tag{57}$$

which is then multiplied through by the eigenfunction:

$$\eta_m^*(w) = J_0(\beta_m^* w/a) - B_m^* I_0(\beta_m^* w/a) + C_m^*, \tag{58}$$

where an asterisk denotes the complex conjugate, and integrated over the surface of the shell. Due to the *orthogonality* of these functions, all terms having $m \neq n$ simply disappear. Therefore letting $m = n$ leads to

$$\frac{a^2}{2}A_n \left(\frac{\beta_n^4}{a^4} - k_S^4 \right) \int_0^{2\pi} d\phi \Delta_n = \int_0^{2\pi} \delta(\phi - \phi_0) d\phi \int_0^a \delta(w - w_0)\eta_n^*(w) dw, \tag{59}$$

where

$$\Delta_n = \frac{2}{a^2}\int_0^a \eta_n^*(w)\eta_n(w) w dw, \tag{60}$$

which is solved[18] to give

$$\begin{aligned}\Delta_n = {} & C_n C_n^* + 2\frac{\beta_n J_0(\beta_n^*)J_1(\beta_n) - \beta_n^* J_0(\beta_n)J_1(\beta_n^*)}{\beta_n^2 - \beta_n^{*2}} \\ & - 2B_n \frac{\beta_n J_0(\beta_n^*)I_1(\beta_n) + \beta_n^* I_0(\beta_n)J_1(\beta_n^*)}{\beta_n^2 + \beta_n^{*2}} \\ & - 2B_n^* \frac{\beta_n I_0(\beta_n^*)J_1(\beta_n) + \beta_n^* J_0(\beta_n)I_1(\beta_n^*)}{\beta_n^2 + \beta_n^{*2}} \\ & + 2B_n B_n^* \frac{\beta_n I_0(\beta_n^*)I_1(\beta_n) - \beta_n^* I_0(\beta_n)I_1(\beta_n^*)}{\beta_n^2 - \beta_n^{*2}} \\ & + 2C_n \frac{J_1(\beta_n^*) - B_n^* I_1(\beta_n^*)}{\beta_n^*} + 2C_n^* \frac{J_1(\beta_n) - B_n I_1(\beta_n)}{\beta_n}.\end{aligned} \tag{61}$$

If there were no damping in the system, setting $R_S = 0$ would

lead to $\beta_n^2=\beta_n^{*2}$ which would make this solution indeterminate. Hence it would be necessary to reevaluate Eq. (60) without damping in order to obtain the solution in a different form, which is not given here, since it is assumed that R_S is always nonzero. Using the property of the Dirac delta function gives the solution for A_n as follows:

$$A_n = \frac{a^2}{\pi}\frac{\eta_n^*(w_0)}{\Delta_n(\beta_n^4 - k_s^4 a^4)}. \tag{62}$$

Hence

$$G(w|w_0) = \frac{a^2}{\pi}\sum_{n=1}^{\infty}\frac{\eta_n(w)\,\eta_n^*(w_0)}{\Delta_n(\beta_n^4 - k_S^4 a^4)}. \tag{63}$$

IV. SOLUTION OF THE SHELL WAVE EQUATION WITH FLUID LOADING

The steady state wave equation for the shell can now be written adding external forces and internal resistance to the inherent shell forces given in Eq. (12),

$$(\nabla^4 - k_S'^4)\,\tilde{\eta}(w) = \frac{hY}{RD}\tilde{\psi} + \frac{\zeta}{D}\left(\frac{\delta(w-a)}{2\pi a}\tilde{F}_C - \tilde{p}_+(w) + \tilde{p}_-(w)\right), \tag{64}$$

where $\tilde{p}_+(w)$ and $\tilde{p}_-(w)=-\tilde{p}_+(w)$ are the front and rear pressure distributions, respectively, due to the surrounding acoustic medium. The modified shell wave number k_S' is related to the unmodified wave number by

$$k_S'^4 = k_S^4 - i\omega\frac{\zeta}{D}z_s, \tag{65}$$

where z_s is an arbitrary specific acoustic impedance, which, as already mentioned in Sec. I, can be used to model a mesh, sound outlet holes/mesh or a lumped cavity impedance. Combining the front and rear pressure terms, the solution for the shell deflection can be written as

$$\tilde{\eta}(w) = \frac{\zeta}{D}\int_0^{2\pi}\int_0^a\left(\frac{\delta(w_0-a)}{2\pi a}\tilde{F}_C - 2\tilde{p}_+(w_0)\right) \times G(w|w_0)w_0\,dw_0\,d\phi_0, \quad 0 \le w \le a, \tag{66}$$

where ζ is a mass loading factor given by

$$\zeta = \frac{M_S}{M_S + M_C}. \tag{67}$$

Using the modified wave number k_S', the Green's function of Eq. (63) can be written as follows:

$$G(w|w_0) = \frac{a^2}{\pi}\sum_{n=1}^{\infty}\frac{\eta_n(w)\,\eta_n^*(w_0)}{\Delta_n(\beta_n^4 - k_S'^4 a^4)}. \tag{68}$$

V. SOLUTION OF THE FREE SPACE WAVE EQUATION

As already discussed in Sec. I the shallow shell is treated here as a planar source. The monopole source elements and their images together form the shell source. Since they are coincident in the plane of the infinite baffle, they combine to form elements of double strength. Hence the shell can be modeled as a "breathing" shell in free space. Due to the symmetry of the pressure fields on either side of the plane of symmetry, there is the following Neumann boundary condition on the surface of the infinite baffle:

$$\frac{\partial}{\partial z}\tilde{p}(w,z)\big|_{z=0\pm} = -ik\rho c\tilde{u}(w) = 0, \quad a < w \le \infty. \tag{69}$$

Also, on the front and rear surfaces of the shell, there is the coupling condition

$$\frac{\partial}{\partial z}\tilde{p}(w,z)\big|_{z=0\pm}\begin{cases} = -ik\rho c\tilde{u}(w) \\ = k^2\rho c^2\tilde{\eta}(w), \quad 0 \le w \le a \end{cases} \tag{70}$$

where $\tilde{u}(w)$ is the normal particle velocity in the z direction at the surfaces and k is the wave number given by

$$k = \frac{\omega}{c} = \frac{2\pi}{\lambda}, \tag{71}$$

where ω is the angular frequency of excitation, ρ is the density of air or any other surrounding medium, c is the speed of sound in that medium, and λ is the wavelength. Values for ρ and c of 1.18 kg/m^3 and 345 m/s, respectively, are assumed. In the actual physical system (as opposed to the "breathing shell" model) the front and rear pressure distributions are related by

$$\tilde{p}(w,z) = -\tilde{p}(w,-z). \tag{72}$$

On the surface of the shell and surround, let the velocity distribution $\tilde{u}_0(w_0)$ be defined as

$$\tilde{u}_0(w_0) = \frac{\tilde{F}_C}{2\rho cS}\sum_{m=1}^{\infty}\tau_m\eta_m(w_0) = \frac{\tilde{F}_C}{2\rho cS}\sum_{m=1}^{\infty}\tau_m\left\{J_0\left(\beta_m\frac{w_0}{a}\right) - B_m I_0\left(\beta_m\frac{w_0}{a}\right) + C_m\right\}, \quad 0 \le w_0 \le a, \tag{73}$$

where S is the area defined by $S=\pi a^2$ and τ_m are the as yet unknown dimensionless eigenfunction-expansion coefficients. Using the King integral[19] and taking into account the double layer source, the pressure distribution is defined by

$$\tilde{p}(w,z) = 2\int_0^{2\pi}\int_0^a g(w,z|w_0,z_0) \times\frac{\partial}{\partial z_0}\tilde{p}(w_0,z_0)\big|_{z_0=0+}w_0\,dw_0\,d\phi_0, \tag{74}$$

where the Green's function[19] is defined in axisymmetric cylindrical coordinates by

$$g(w,z|w_0,z_0) = \frac{i}{4\pi}\int_0^{\infty}J_0(\mu w)J_0(\mu w_0)\frac{\mu}{\sigma}e^{-i\sigma|z-z_0|}d\mu \tag{75}$$

where

$$\sigma = \sqrt{k^2 - \mu^2}. \tag{76}$$

Inserting this Green's function, together with the boundary condition of Eq. (70), into the boundary integral Eq. (74) and integrating over the surface of the shell yields

$$\tilde{p}(w,z) = ka\frac{\tilde{F}_C}{2S}\int_0^\infty J_0(\mu w)\frac{a\mu}{\sigma}e^{-i\sigma z}\sum_{m=0}^{\infty}\tau_m \Xi_m(a\mu)d\mu, \tag{77}$$

where the following identity[18] has been used as follows:

$$\int_0^a J_0(\mu w_0)\,\eta_m(w_0)w_0 dw_0 = a^2\Xi_m(a\mu) \tag{78}$$

and the function Ξ_m is defined as

$$\Xi_m(a\mu) = \frac{\beta_m J_0(a\mu)J_1(\beta_m) - a\mu J_0(\beta_m)J_1(a\mu)}{\beta_m^2 - a^2\mu^2} - B_m\frac{\beta_m J_0(a\mu)I_1(\beta_m) + a\mu I_0(\beta_m)J_1(a\mu)}{\beta_m^2 + a^2\mu^2} + C_m\frac{J_1(a\mu)}{a\mu}. \tag{79}$$

Setting $z=0$, provides surface pressure as follows:

$$\tilde{p}_+(w_0) = ka\frac{\tilde{F}_C}{2S}\sum_{m=0}^{\infty}\tau_m\int_0^\infty \Xi_m(a\mu)J_0(w_0\mu)\frac{a\mu}{\sigma}d\mu. \tag{80}$$

VI. FORMULATION OF THE COUPLED PROBLEM

Substituting Eq. (80) in Eq. (66) and equating the deflection with that given by Eq. (73) [where $\tilde{\eta}(w) = -i\tilde{u}_0(w)/kc$] leads to the following coupled equation (after integrating over ϕ_0):

$$\eta_n^*(a) = -i\tau_n\frac{\Delta_{0n}(\beta_n^4 - k_S'^4a^4)D}{2ka^4\rho c^2\zeta} + 2ka\sum_{m=0}^{\infty}\tau_m\int_0^\infty \Xi_m(a\mu)\Xi_n^*(a\mu)\frac{a\mu}{\sigma}d\mu, \quad n = 1,2,\ldots, \tag{81}$$

which is obtained by equating the coefficients of $\eta_n(w)$ and again using the identity of Eq. (78).

VII. FINAL SET OF SIMULTANEOUS EQUATIONS FOR THE EIGENVALUE EXPANSION COEFFICIENTS

From Eq. (81) the following set of M simultaneous equations in τ_m can be written

$$\sum_{m=1}^{M} {}_m\Psi_n(k_S'a,ka)\tau_m = \Phi_n, \quad n = 1,\ldots,M, \tag{82}$$

where

$${}_m\Psi_n(k_S'a,ka) = -ika\frac{\Delta_n(\beta_n^4 - k_S'^4a^4)}{\zeta\alpha^2(ka)}\delta_{mn} + I(k,m,n), \tag{83}$$

$$\Phi_n = J_0(\beta_n^*) - B_n^*I_0(\beta_n^*) + C_n^*, \tag{84}$$

where

$$\alpha(ka) = a^2\omega\sqrt{\frac{2a\rho}{D}} = ka^2\sqrt{\frac{2a\gamma P_0}{D}}, \tag{85}$$

where the infinite series limit has been truncated to order M. The dimensionless parameter α is the fluid-loading factor, where P_0 is the static pressure defined by $P_0 = \rho c^2/\gamma$, and δ_{mn} is the Kronecker delta function. The integral $I(k,m,n)$ is defined by

$$I(k,m,n) = I_F(k,m,n) + iI_I(k,m,n) \tag{86}$$

where

$$I_F(k,m,n) = 2k_a\int_0^k \Xi_m(a\mu)\Xi_n^*(a\mu)\frac{a\mu}{\sqrt{k^2-\mu^2}}d\mu \tag{87}$$

and

$$I_I(k,m,n) = -2ka\int_k^\infty \Xi_m(a\mu)\Xi_n^*(a\mu)\frac{a\mu}{\sqrt{\mu^2-k^2}}d\mu. \tag{88}$$

It can be seen that the numerator and denominator of the first term of Ξ_m, given by Eq. (79), are simultaneously zero when $\beta_m = a\mu$, so these are indeterminate points. Using Taylor's series, it can be shown that the function is actually continuous. Hence, the integrals can be solved numerically so long as these indeterminate points are avoided. Also, the weak singularity at $\mu=k$ in Eqs. (87) and (88) can be removed by means of suitable substitutions, as shown in the following sections. However, the integrands are strongly oscillating and the integral I_I has an infinite limit. Therefore, it is more efficient to solve these integrals analytically to yield fast converging expansions. Although the integrand contains a total of 25 terms, when Ξ_m and Ξ_n are multiplied out there are only 6 unique integrals, each subdivided into finite and infinite parts.

VIII. SOLUTION OF THE FINITE AND INFINITE INTEGRALS

A. Expansion of the finite integral

After substituting $\mu = k\sqrt{1-t^2}$, Eq. (87) for the finite integral becomes

$$I_F(k,m,n) = 2k^2a^2\int_0^1 \Xi_m(ka\sqrt{1-t^2})\Xi_n^*(ka\sqrt{1-t^2})dt, \tag{89}$$

where Ξ_m is given by Eq. (79). The Bessel functions in Eq. (89) are then expanded using the following Lommel expansions:[17]

$$J_0(ka\sqrt{1-t^2}) = \sum_{p=0}^{\infty}\frac{J_p(ka)}{p!}\left(\frac{ka}{2}\right)^p t^{2p}, \tag{90}$$

$$J_1(ka\sqrt{1-t^2}) = \sqrt{1-t^2}\sum_{p=0}^{\infty}\frac{J_{p+1}(ka)}{p!}\left(\frac{ka}{2}\right)^p t^{2p}. \tag{91}$$

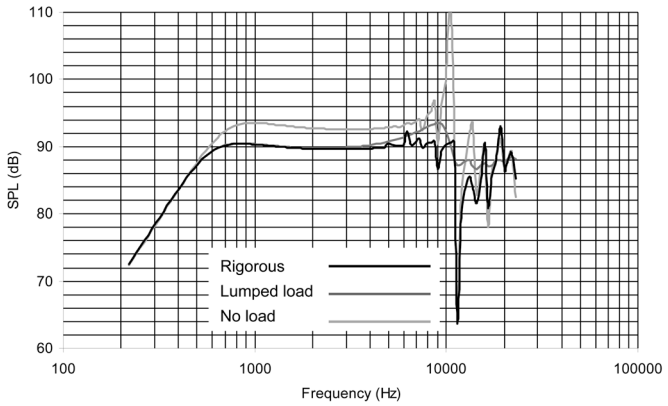

FIG. 4. On-axis far-field response with $h=10$ μm and $H=0.5$ mm ($R_M=0.06$ N s/m).

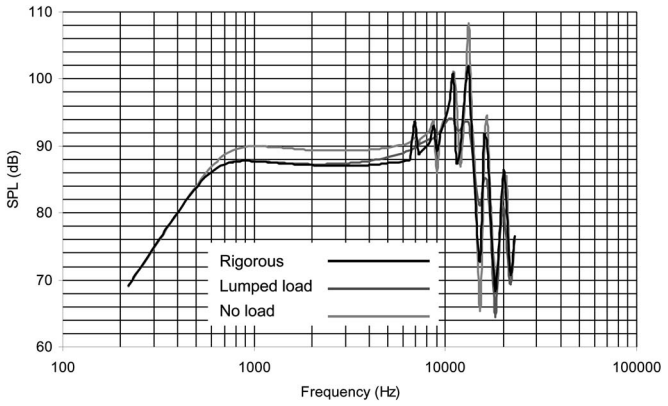

FIG. 6. On-axis far-field response with $h=20$ μm and $H=0.5$ mm ($R_M=0.13$ Ns/m).

B. Solution to the finite integral

The solution to the finite integral is given by

$$
\begin{aligned}
I_F(k,m,n) = {} & \kappa_{1a}(m,n) I_{F1}(k,\beta_m,\beta_n^*) \\
& + B_m \kappa_{1b}(m,n) I_{F1}(k,i\beta_m,\beta_n^*) \\
& + B_n^* \kappa_{1c}(m,n) I_{F1}(k,\beta_m,i\beta_n^*) \\
& + B_m B_n^* \kappa_{1d}(m,n) I_{F1}(k,i\beta_m,i\beta_n^*) \\
& + \kappa_{2a}(m,n) I_{F2}(k,\beta_m) + \kappa_{2a}(n,m) I_{F2}(k,\beta_n^*) \\
& + B_m \kappa_{2b}(m,n) I_{F2}(k,i\beta_m) \\
& + B_n^* \kappa_{2b}(n,m) I_{F2}(k,i\beta_n^*) \\
& + \kappa_{3a}(m,n) I_{F3}(k,\beta_m,\beta_n^*) \\
& + \kappa_{3a}(n,m) I_{F3}(k,\beta_n^*,\beta_m) \\
& + B_m \kappa_{3b}(m,n) I_{F3}(k,i\beta_m,\beta_n^*) \\
& + B_n^* \kappa_{3b}(n,m) I_{F3}(k,i\beta_n^*,\beta_m) \\
& + B_m B_n^* (\kappa_{3c}(m,n) I_{F3}(k,i\beta_m,i\beta_n^*) \\
& + \kappa_{3c}(n,m) I_{F3}(k,i\beta_n^*,i\beta_m)) \\
& + \kappa_{4a}(m,n) I_{F4}(k,\beta_m) + \kappa_{4a}(n,m) I_{F4}(k,\beta_n^*) \\
& - B_m \kappa_{4b}(m,n) I_{F4}(k,i\beta_m) \\
& - B_n^* \kappa_{4b}(n,m) I_{F4}(k,i\beta_n^*) \\
& + \kappa_{5a}(m,n) I_{F5}(k,\beta_m,\beta_n^*) \\
& + B_m \kappa_{5b}(m,n) I_{F5}(k,i\beta_m,\beta_n^*) \\
& + B_n^* \kappa_{5c}(m,n) I_{F5}(k,\beta_m,i\beta_n^*) \\
& + B_m B_n^* \kappa_{5d}(m,n) I_{F5}(k,i\beta_m,i\beta_n^*) \\
& + C_m C_n^* I_{F6}(k), \qquad (92)
\end{aligned}
$$

where the coefficients κ are given by Eqs. (A1)–(A22) and the solutions to the individual integral terms I_F are given by Eqs. (A23)–(A30).

C. Expansion of the infinite integral

After substituting $\mu=k\sqrt{t^2+1}$, Eq. (88) for the infinite integral becomes

$$
I_I(k,m,n) = -2k^2a^2 \int_0^\infty \Xi_m(ka\sqrt{t^2+1}) \Xi_n^*(ka\sqrt{t^2+1}) dt, \qquad (93)
$$

where Ξ_m is given by Eq. (79). The Bessel functions in Eq. (93) are then be expanded using Gegenbauer's summation theorem[15] as follows:

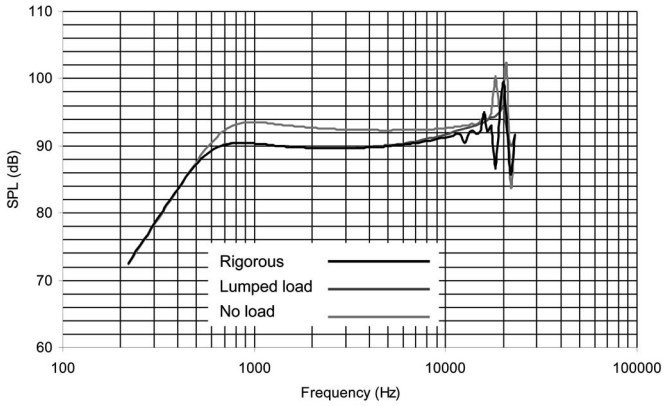

FIG. 5. On-axis far-field response with $h=10$ μm and $H=1.0$ mm ($R_M=0.06$ N s/m).

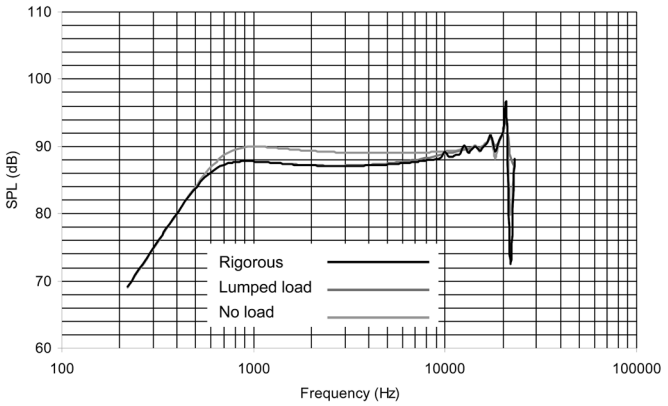

FIG. 7. (Color online) On-axis far-field response with $h=20$ μm and $H=1.0$ mm ($R_M=0.13$ Ns/m).

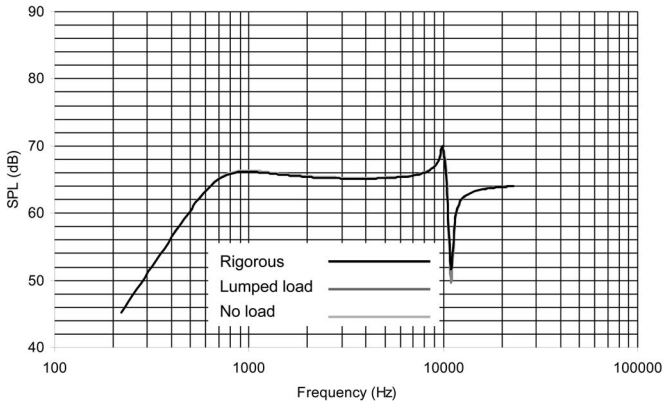

FIG. 8. On-axis far-field response with $h=475$ μm and $H=0$ mm ($R_M=3$ Ns/m).

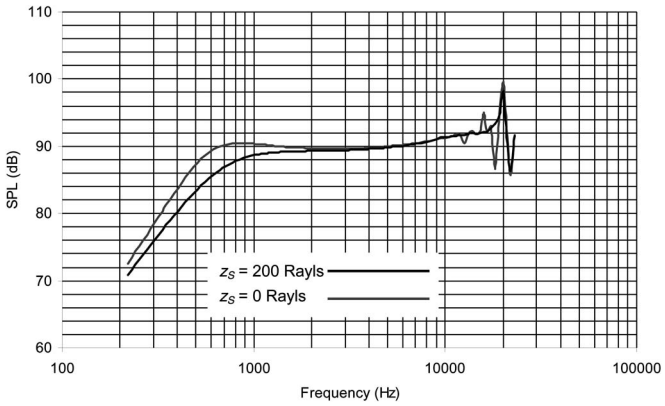

FIG. 10. On-axis far-field response with the same parameters as Fig. 5 plus an external damping resistance $z_S=200$ Ra.

$$J_0(ka\sqrt{t^2+1}) = 2\sum_{p=0}^{\infty} \frac{(-1)^p}{1+\delta_{p0}} J_{2p}(ka) J_{2p}(kat), \tag{94}$$

$$J_1(ka\sqrt{t^2+1}) = \frac{2\sqrt{t^2+1}}{kat} \sum_{p=0}^{\infty} (-1)^p (2p+1) J_{2p+1}(ka) J_{2p+1}(kat). \tag{95}$$

D. Solution to the infinite integral

The solution[18] to the infinite integral is given by

$$\begin{aligned} I_I(k,m,n) = {} & \kappa_{1a}(m,n) I_{I1}(k,\beta_m,\beta_n^*) \\ & + B_m \kappa_{1b}(m,n) I_{I1}(k,i\beta_m,\beta_n^*) \\ & + B_n^* \kappa_{1c}(m,n) I_{I1}(k,\beta_m,i\beta_n^*) \\ & + B_m B_n^* \kappa_{1d}(m,n) I_{I1}(k,i\beta_m,i\beta_n^*) \\ & + \kappa_{2a}(m,n) I_{I2}(k,\beta_m) + \kappa_{2a}(n,m) I_{I2}(k,\beta_n^*) \\ & + B_m \kappa_{2b}(m,n) I_{I2}(k,i\beta_m) \\ & + B_n^* \kappa_{2b}(n,m) I_{I2}(k,i\beta_n^*) \\ & + \kappa_{3a}(m,n) I_{I3}(k,\beta_m,\beta_n^*) \\ & + \kappa_{3a}(n,m) I_{I3}(k,\beta_n^*,\beta_m) \\ & + B_m \kappa_{3b}(m,n) I_{I3}(k,i\beta_m,\beta_n^*) \\ & + B_n^* \kappa_{3b}(n,m) I_{I3}(k,i\beta_n^*,\beta_m) \\ & + B_m B_n^* (\kappa_{3c}(m,n) I_{I3}(k,i\beta_m,i\beta_n^*) \\ & + \kappa_{3c}(n,m) I_{I3}(k,i\beta_n^*,i\beta_m)) \\ & + \kappa_{4a}(m,n) I_{I4}(k,\beta_m) + \kappa_{4a}(n,m) I_{I4}(k,\beta_n^*) \\ & - B_m \kappa_{4b}(m,n) I_{I4}(k,i\beta_m) \\ & - B_n^* \kappa_{4b}(n,m) I_{I4}(k,i\beta_n^*) \\ & + \kappa_{5a}(m,n) I_{I5}(k,\beta_m,\beta_n^*) \\ & + B_m \kappa_{5b}(m,n) I_{I5}(k,i\beta_m,\beta_n^*) \\ & + B_n^* \kappa_{5c}(m,n) I_{I5}(k,\beta_m,i\beta_n^*) \\ & + B_m B_n^* \kappa_{5d}(m,n) I_{I5}(k,i\beta_m,i\beta_n^*) + C_m C_n^* I_{I6}(k), \end{aligned} \tag{96}$$

where the coefficients κ are given by Eqs. (A1)–(A22) and the solutions to the individual integral terms I_F are given by Eqs. (A31)–(A44).

IX. FAR-FIELD PRESSURE RESPONSE: RIGOROUS CALCULATION

Starting from Eq. (73) for the surface velocity, the far-field pressure is derived using the same procedure as shown

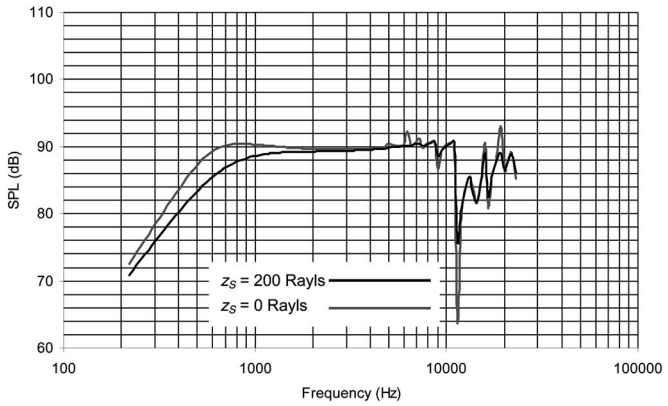

FIG. 9. On-axis far-field response with the same parameters as Fig. 4 plus an external damping resistance $z_S=200$ Ra.

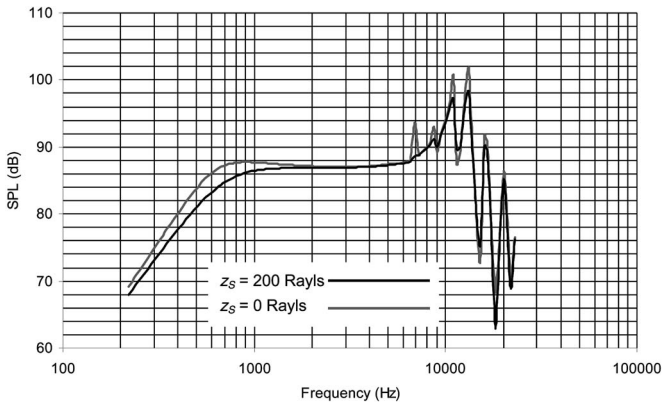

FIG. 11. On-axis far-field response with the same parameters as Fig. 6 plus an external damping resistance $z_S=200$ Ra.

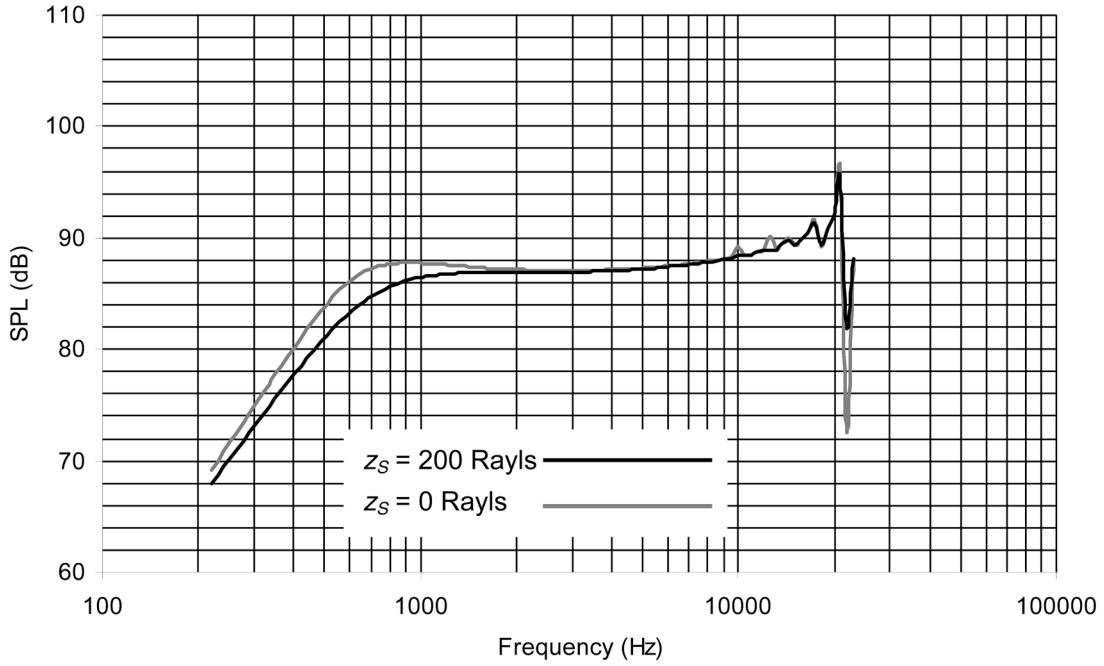

FIG. 12. (Color online) On-axis far-field response with the same parameters as Fig. 7 plus an external damping resistance z_S=200 Ra.

in Part I of Sec. II of a recent paper,[10] together with the identity of Eqs. (79) and (80) (while letting $\mu=k \sin\theta$), to give

$$\tilde{p}(r,\theta) = -i\frac{a\tilde{F}_C}{4rS}e^{-ikr}D(\theta), \tag{97}$$

where r is the distance from the center of the shell to the observation point and θ is the azimuthal angle. The directivity function $D(\theta)$ is given by

$$D(\theta) = 2ka\sum_{m=1}^{\infty}\tau_m\left(C_m\frac{J_1(ka\sin\theta)}{ka\sin\theta} - B_m \times \frac{\beta_m J_0(ka\sin\theta)I_1(\beta_m) + (ka\sin\theta)I_0(\beta_m)J_1(ka\sin\theta)}{\beta_m^2 + (ka\sin\theta)^2} + \frac{\beta_m J_0(ka\sin\theta)J_1(\beta_m) - (ka\sin\theta)J_0(\beta_m)J_1(ka\sin\theta)}{\beta_m^2 - (ka\sin\theta)^2}\right), \tag{98}$$

which, for $\theta=0$ (i.e., on-axis), simplifies to

$$D(0) = ka\sum_{m=1}^{\infty}\tau_m\left(2\frac{J_1(\beta_m)}{\beta_m} - 2B_m\frac{I_1(\beta_m)}{\beta_m} + C_m\right). \tag{99}$$

The on-axis pressure responses are shown in Figs. 4–14 using the parameters from Tables I and II where the SPL is given by

$$\mathrm{SPL} = 20\log_{10}|\tilde{p}(r,0)/20\times 10^{-6}|, \tag{100}$$

where

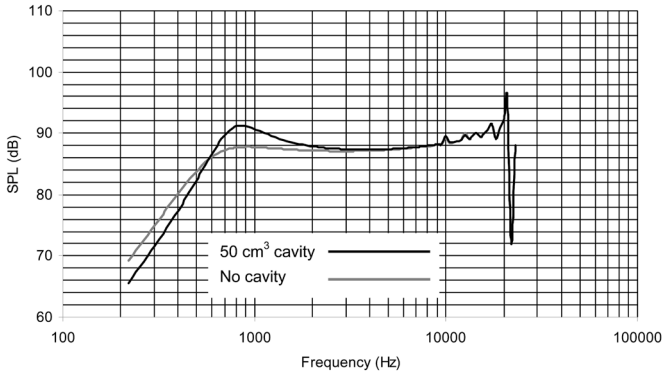

FIG. 13. (Color online) On-axis far-field response with the same parameters as Fig. 7 plus a lumped cavity with a volume of 50 cm^3.

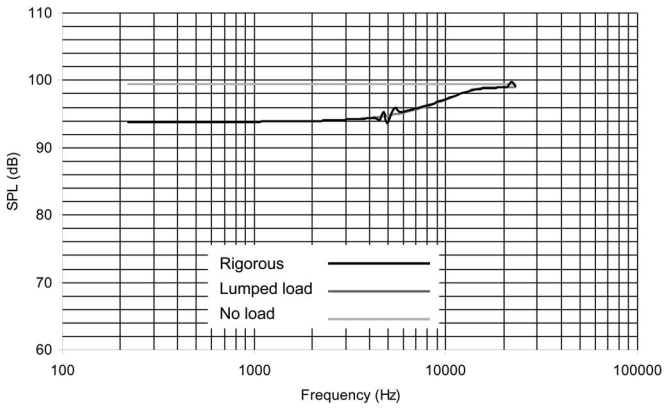

FIG. 14. On-axis far-field response with the same parameters as Fig. 4 except that the coil mass and suspension stiffness are both zero.

TABLE I. Shell parameters for the 25 mm aluminum loudspeaker.

Radius	$a=12.5$ mm
Thickness	$h=10/2/800$ μm
Apex height	$H=0/0.5/1.0$ mm
Young's modulus	$Y=69$ GN/m^2
Poisson's ratio	$\nu=0.3$
Density of shell	$\rho_S=2700$ kg/m^3
Shell mass	$M_S=\pi a^2\rho_S h=13.3/26.6/1060$ mg
Density of air	$\rho=1.18$ kg/m^3
Speed of sound in air	$c=345$ m/s
Damping/loading	$z_S=0$ kg/s unless otherwise specified
Observation distance	$r=1$ m

$$\tilde{p}(r,0)=-i\frac{ka^2\tilde{F}_C}{4rS}e^{-ikr}\sum_{m=1}^{M}\tau_m\left(2\frac{J_1(\beta_m)}{\beta_m}-2B_m\frac{I_1(\beta_m)}{\beta_m}+C_m\right). \tag{101}$$

This result can also be obtained directly by integrating the velocity $\tilde{u}_0(w_0)$ from Eq. (73) over the surface in order to derive the total volume velocity $\tilde{U}_0$ and using the standard far-field equation,[12,20]

$$\tilde{p}(r,0)=-\frac{ik\rho c\tilde{U}_0}{2\pi r}e^{-ikr}. \tag{102}$$

The calculations were performed using 80 digit precision with $M=3+2ka$ and $P=Q=2M$.

X. FAR-FIELD PRESSURE RESPONSE: WITHOUT FLUID LOADING

If the acoustic loading is ignored such that $\tilde{p}_+(w_0)=0$, Eq. (66) for the deflection can be simplified to

$$\tilde{\eta}(w)=\frac{\zeta}{D}\int_0^a\frac{\delta(w_0-a)\tilde{F}_C}{a}G(w|w_0)w_0dw_0=\frac{a^2\zeta\tilde{F}_C}{\pi D}\sum_{n=1}^{\infty}\frac{\eta_n(w)\,\eta_n^*(a)}{\Delta_n(\beta_n^4-k_S'^4a^4)}, \tag{103}$$

in which case

TABLE II. Coil and suspension parameters for the 25 mm aluminum loudspeaker.

Fundamental frequency	$f_0=700$ Hz
Coil electrical resistance	$R_E=7.6$ Ω
Coil wire diameter	$t=50$ μm
Coil wire density	$\rho_C=8900$ kg/m^3
Coil wire resistivity	$\sigma_C=15.9$ nΩm
Coil wire total length	$l=\pi t^2R_E/(4\sigma_C)=0.94$ m
Coil wire length per turn	$l_T=2\pi a=78.5$ mm
Coil number of turns	$n=l/l_T=12$
Coil mass	$M_C=2\pi ntp_Sh+\pi t^2l\rho_C/4=17.7/22.8/118$ mg
Magnetic flux density	$B=0.8$ T
Flux coil length product	$Bl=B\times l=0.75$ T m
Input voltage for 1 W	$\tilde{e}_{in}=\sqrt{R_E\tilde{W}}\vert_{\tilde{W}=1\text{Wrms}}=2.76$ V

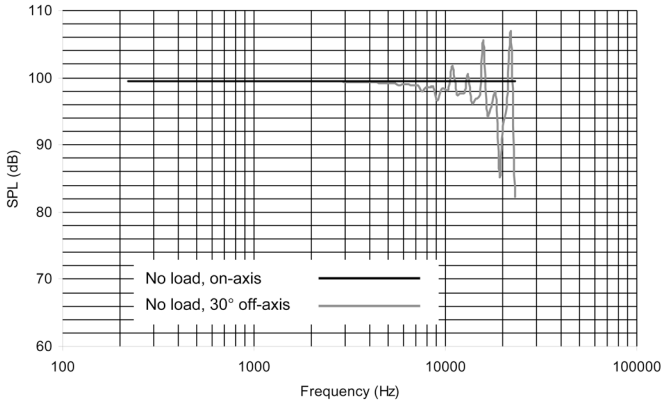

FIG. 15. 30° off-axis far-field response with the same parameters as Fig. 4 except that the coil mass and suspension stiffness are both zero.

$$\tau_m=\frac{\zeta\alpha^2(ka)(J_0(\beta_m^*)-B_m^*I_0(\beta_m^*)+C_m^*)}{ika\Delta_m(\beta_m^4-k_S'^4a^4)}, \tag{104}$$

which can be used in Eqs. (97)–(101) in order to calculate the far-field pressure response without fluid loading.

XI. DISCUSSION OF THE RESULTS

An example loudspeaker is simulated using the parameters given in Tables I and II, and the results are plotted in Figs. 4–15. Also, the eigenfrequencies in a vacuum are shown in Table III. In Figs. 4–7, results are shown for two different heights and two different thicknesses using the rigorous solution and the solution without acoustic loading. A third solution is shown which is obtained by adding the following lumped radiation impedance to the solution without loading:

$$z_S=z_{\text{Rad}}=2\rho c\left(1-\frac{J_1(2ka)}{ka}+i\frac{\mathbf{H}_1(2ka)}{ka}\right), \tag{105}$$

where z_{Rad} is the radiation impedance of a rigid disk in an infinite baffle.[12,20] It can be seen that the thin shallow shell of Fig. 4 shows significant influence from acoustic radiation load and the lumped radiation impedance is a fairly poor approximation to the rigorous solution, whereas the thicker deeper shell of Fig. 7 shows less influence and all three solutions are effectively converging. Figure 8 is for a flat plate which has been made thick enough to have its first "break-

TABLE III. Eigenfrequencies for the 25 mm aluminum loudspeaker.

Frequency No.	$h=10$ μm $H=0.5$ mm	$h=10$ μm $H=1.0$ mm	$h=20$ μm $H=0.5$ mm	$h=20$ μm $H=1.0$ mm
$n=1$	699.98	699.99	700.05	700.01
$n=2$	5149.2	10313.0	5261.9	10356.0
$n=3$	5177.8	10382.0	5775.7	10629.0
$n=4$	5314.6	10573.0	6988.3	11353.0
$n=5$	5676.3	10969.0	8963.5	12756.0
$n=6$	6376.5	11659.0	11254.0	14968.0
$n=7$	7477.3	12714.0	13177.0	17981.0
$n=8$	8952.9	14178.0	16342.0	21578.0
$n=9$	10467.0	16060.0	20626.0	27911.0
$n=10$	13658.0	18324.0	25669.0	32904.0

up" mode at the same frequency as the shell in Fig. 7. However, the penalty is drastically reduced sensitivity.

Figures 9–12 show the effect of applying acoustic resistance. Again, the thin shallow shell of Fig. 9 shows much greater influence, with a moderately damped response, than the thicker deeper shell of Fig. 12.

Figure 13 holds no surprises and simply serves to show how an approximation for a rear cavity can be included in the model using

$$z_S = z_{\mathrm{Cav}} = \frac{\rho c^2 S}{i\omega V}, \tag{106}$$

where V is the volume of the cavity and the same fully coupled acoustic loading is used as in Fig. 5. It is a lumped parameter approximation, which assumes that the cavity is anechoic at high frequencies and just provides pure compliance at low frequencies. As expected, it raises the fundamental resonant frequency and increases the associated Q_S value.

Interestingly, the on-axis response without acoustic loading or coil mass, shown in Fig. 14, is perfectly flat.[21] However, the off-axis response of Fig. 15 shows significant modal behavior, so it can be concluded that the flat on-axis response is due to the average surface velocity of the shell with a free edge (apart from a zero bending constraint) being constant at all frequencies. In Fig. 15 it can be seen that the acoustic loading disrupts this trend to a certain extent, but not as much as the coil mass in all the previous figures. Hence the effect of the mass loading from the voice coil is highly significant.

XII. CONCLUSIONS

A method for calculating the response of a loudspeaker with a diaphragm in the form of a shallow spherical shell has been derived. An example has been calculated which compares the rigorous solution with an approximation using a lumped radiation load and no load. The approximation diverges from the rigorous solution in the case of a very thin and shallow shell. Also, the effect of the mass loading from the voice coil has been explored and found to be highly significant.

ACKNOWLEDGMENT

The authors would like to express their gratitude to N. Lobo for his invaluable advice in numerical matters.

APPENDIX: SOLUTION OF THE INDIVIDUAL FINITE AND INFINITE INTEGRAL TERMS

The coefficients κ in Eqs. (92) and (96) are given by

$$\kappa_{1a}(m,n) = \beta_m \beta_n^* J_1(\beta_m) J_1(\beta_n^*), \tag{A1}$$

$$\kappa_{1b}(m,n) = \beta_m \beta_n^* I_1(\beta_m) J_1(\beta_n^*), \tag{A2}$$

$$\kappa_{1c}(m,n) = \beta_m \beta_n^* J_1(\beta_m) I_1(\beta_n^*), \tag{A3}$$

$$\kappa_{1d}(m,n) = \beta_m \beta_n^* I_1(\beta_m) I_1(\beta_n^*), \tag{A4}$$

$$\kappa_{2a}(m,n) = -C_n^* \beta_m J_1(\beta_m), \tag{A5}$$

$$\kappa_{2b}(m,n) = -C_n^* \beta_m I_1(\beta_m), \tag{A6}$$

$$\kappa_{2a}(n,m) = -C_m \beta_n^* J_1(\beta_n^*), \tag{A7}$$

$$\kappa_{2b}(n,m) = -C_m \beta_n^* I_1(\beta_n^*), \tag{A8}$$

$$\kappa_{3a}(m,n) = -\beta_m J_0(\beta_n^*) J_1(\beta_m), \tag{A9}$$

$$\kappa_{3a}(n,m) = -\beta_n^* J_0(\beta_m) J_1(\beta_n^*), \tag{A10}$$

$$\kappa_{3b}(m,n) = \beta_n^* I_0(\beta_m) J_1(\beta_n^*) - \beta_m J_0(\beta_n^*) I_1(\beta_m), \tag{A11}$$

$$\kappa_{3b}(n,m) = \beta_m I_0(\beta_n^*) J_1(\beta_m) - \beta_n^* J_0(\beta_m) I_1(\beta_n^*), \tag{A12}$$

$$\kappa_{3c}(m,n) = \beta_n^* I_0(\beta_m) I_1(\beta_n^*), \tag{A13}$$

$$\kappa_{3c}(n,m) = \beta_m I_0(\beta_n^*) I_1(\beta_m), \tag{A14}$$

$$\kappa_{4a}(m,n) = C_n^* J_0(\beta_m), \tag{A15}$$

$$\kappa_{4b}(m,n) = C_n^* I_0(\beta_m), \tag{A16}$$

$$\kappa_{4a}(n,m) = C_m J_0(\beta_n^*), \tag{A17}$$

$$\kappa_{4b}(n,m) = C_m I_0(\beta_n^*), \tag{A18}$$

$$\kappa_{5a}(m,n) = J_0(\beta_m) J_0(\beta_n^*), \tag{A19}$$

$$\kappa_{5b}(m,n) = -I_0(\beta_m) J_0(\beta_n^*), \tag{A20}$$

$$\kappa_{5c}(m,n) = -J_0(\beta_m) I_0(\beta_n^*), \tag{A21}$$

$$\kappa_{5d}(m,n) = I_0(\beta_m) I_0(\beta_n^*) \tag{A22}$$

and the solutions[18] to the individual integral terms I_F in Eq. (92) are given by

$$I_{F1}(k,\beta_m,\beta_n^*) = \int_0^1 \frac{2k^2a^2 J_0^2(ka\sqrt{1-t^2})}{(k^2a^2(1-t^2)-\beta_m^2)(k^2a^2(1-t^2)-\beta_n^{*2})} dt$$
$$= 2k^2a^2 \sum_{p=0}^{P} \sum_{q=0}^{Q} \frac{(ka/2)^{p+q} J_p(ka) J_q(ka)}{p\,!\,q\,!\,(2p+2q+1)(\beta_m^2-\beta_n^{*2})}$$
$$\times (F_{F1}(k,\beta_m,p,q) - F_{F1}(k,\beta_n^*,p,q)), \tag{A23}$$

$$I_{F2}(k,\beta_m) = \int_0^1 \frac{2ka J_0(ka\sqrt{1-t^2}) J_1(ka\sqrt{1-t^2})}{\sqrt{1-t^2}(k^2a^2(1-t^2)-\beta_m^2)} dt$$
$$= 2ka \sum_{p=0}^{P} \sum_{q=0}^{Q} \frac{(ka/2)^{p+q} J_p(ka) J_{q+1}(ka)}{p\,!\,q\,!\,(2p+2q+1)}$$
$$\times F_{F1}(k,\beta_m,p,q), \tag{A24}$$

$$I_{F3}(k,\beta_m,\beta_n^*)=\int_0^1 \frac{2k^3a^3\sqrt{1-t^2}J_0(ka\sqrt{1-t^2})J_1(ka\sqrt{1-t^2})}{(k^2a^2(1-t^2)-\beta_m^2)(k^2a^2(1-t^2)-\beta_n^{*2})}dt$$
$$=2ka\sum_{p=0}^{P}\sum_{q=0}^{Q}\frac{(ka/2)^{p+q}J_p(ka)J_{q+1}(ka)}{p\,!\,q\,!\,(2p+2q+1)(\beta_m^2-\beta_n^{*2})}$$
$$\times(\beta_m^2F_{F1}(k,\beta_m,p,q)-\beta_n^{*2}F_{F1}(k,\beta_n^*,p,q)), \tag{A25}$$

$$I_{F4}(k,\beta_m)=\int_0^1 \frac{2k^2a^2J_1^2(ka\sqrt{1-t^2})}{k^2a^2(1-t^2)-\beta_m^2}dt$$
$$=2k^2a^2\sum_{p=0}^{P}\sum_{q=0}^{Q}\frac{(ka/2)^{p+q}J_{p+1}(ka)J_{q+1}(ka)}{p\,!\,q!}$$
$$\times\left(\frac{F_{F1}(k,\beta_m,p,q)}{2p+2q+1}-\frac{F_{F4}(k,\beta_m,p,q)}{2p+2q+3}\right), \tag{A26}$$

$$I_{F5}(k,\beta_m,\beta_n^*)=\int_0^1 \frac{2k^4a^4(1-t^2)J_1^2(ka\sqrt{1-t^2})}{(k^2a^2(1-t^2)-\beta_m^2)(k^2a^2(1-t^2)-\beta_n^{*2})}dt$$
$$=2\sum_{p=0}^{P}\sum_{q=0}^{Q}\frac{(ka/2)^{p+q}J_{p+1}(ka)J_{q+1}(ka)}{p\,!\,q\,!\,(2p+2q+1)}$$
$$\times\left(1-\beta_m^4\frac{F_{F1}(k,\beta_m,p,q)}{\beta_n^{*2}-\beta_m^2}+\beta_n^{*4}\frac{F_{F1}(k,\beta_n^*,p,q)}{\beta_n^*-\beta_m^2}\right), \tag{A27}$$

$$I_{F6}(k)=\int_0^1 \frac{2J_1^2(ka\sqrt{1-t^2})}{1-t^2}dt$$
$$=1-\frac{J_1(2ka)}{ka} \tag{A28}$$

in which the subfunctions F_F are defined by the following hypergeometric functions:

$$F_{F1}(k,\beta_m,p,q)=\frac{{}_2F_1\left(1,p+q+\frac{1}{2};p+q+\frac{3}{2};\frac{k^2a^2}{k^2a^2-\beta_m^2}\right)}{k^2a^2-\beta_m^2} \tag{A29}$$

$$F_{F4}(k,\beta_m,p,q)=\frac{{}_2F_1\left(1,p+q+\frac{3}{2};p+q+\frac{5}{2};\frac{k^2a^2}{k^2a^2-\beta_m^2}\right)}{k^2a^2-\beta_m^2}. \tag{A30}$$

The solutions[18] to the individual integral terms I_I in Eq. (96) are given by

$$I_{I1}(k,\beta_m,\beta_n^*)=\int_0^\infty \frac{2k^2a^2J_0^2(ka\sqrt{t^2+1})}{(k^2a^2(t^2+1)-\beta_m^2)(k^2a^2(t^2+1)-\beta_n^{*2})}dt$$
$$=2ka\sum_{p=0}^{P}\sum_{q=0}^{Q}\frac{J_{2p}(ka)J_{2q}(ka)}{(1+\delta_{p0})(1+\delta_{q0})(\beta_n^{*2}-\beta_m^2)}$$
$$\times(F_{I1a}(k,\beta_m,p,q)-F_{I1a}(k,\beta_n^*,p,q)-F_{I1b}(k,\beta_m,p,q)+F_{I1b}(k,\beta_n^*,p,q)), \tag{A31}$$

$$I_{I2}(k,\beta_m)=\int_0^\infty \frac{2kaJ_0(ka\sqrt{t^2+1})J_1(ka\sqrt{t^2+1})}{\sqrt{t^2+1}(k^2a^2(t^2+1)-\beta_m^2)}dt$$
$$=2\sum_{p=0}^{P}\sum_{q=0}^{Q}\frac{(2q+1)J_{2p}(ka)J_{2q+1}(ka)}{(1+\delta_{p0})}(F_{I2a}(k,\beta_m,p,q)+F_{I2b}(k,\beta_m,p,q)), \tag{A32}$$

$$I_{I3}(k,\beta_m,\beta_n^*)$$
$$=\int_0^\infty \frac{2k^3a^3\sqrt{t^2+1}J_0(ka\sqrt{t^2+1})J_1(ka\sqrt{t^2+1})}{(k^2a^2(t^2+1)-\beta_m^2)(k^2a^2(t^2+1)-\beta_n^{*2})}dt$$
$$=2\sum_{p=0}^{P}\sum_{q=0}^{Q}\frac{(2q+1)J_{2p}(ka)J_{2q+1}(ka)}{(1+\delta_{p0})(\beta_m^2-\beta_n^{*2})}\{F_{I3}(k,\beta_n^*,p,q)$$
$$-F_{I3}(k,\beta_m,p,q)+k^2a^2(F_{I2a}(k,\beta_m,p,q)$$
$$-F_{I2a}(k,\beta_n^*,p,q))+\beta_m^2F_{I2b}(k,\beta_m,p,q)$$
$$-\beta_n^{*2}F_{I2b}(k,\beta_n^*,p,q)\}, \tag{A33}$$

$$I_{I4}(k,\beta_m)=\int_0^\infty \frac{2k^2a^2J_1^2(ka\sqrt{t^2+1})}{k^2a^2(t^2+1)-\beta_m^2}dt$$
$$=2\sum_{p=0}^{P}\sum_{q=0}^{Q}\frac{(2p+1)(2q+1)J_{2p+1}(ka)J_{2q+1}(ka)}{ka}$$
$$\times(k^2a^2F_{I4a}(k,\beta_m,p,q)-F_{I4b}(k,\beta_m,p,q)+\beta_m^2F_{I4c}(k,\beta_m,p,q)), \tag{A34}$$

$$I_{I5}(k,\beta_m,\beta_n^*)=\int_0^\infty \frac{2k^4a^4(t^2+1)J_1^2(ka\sqrt{t^2+1})}{(k^2a^2(t^2+1)-\beta_m^2)(k^2a^2(t^2+1)-\beta_n^{*2})}dt$$
$$=2\sum_{p=0}^{P}\sum_{q=0}^{Q}\frac{(2p+1)(2q+1)J_{2p+1}(ka)J_{2q+1}(ka)}{ka(\beta_m^2-\beta_n^{*2})}$$
$$\times\{k^4a^4(F_{I4a}(k,\beta_m,p,q)-F_{I4a}(k,\beta_n,p,q))-(k^2a^2+\beta_m^2)F_{I4b}(k,\beta_m,p,q)+(k^2a^2+\beta_n^{*2})F_{I4b}(k,\beta_n^*,p,q)+\beta_m^4F_{I4c}(k,\beta_m,p,q)-\beta_n^{*4}F_{I4c}(k,\beta_n^*,p,q)\}, \tag{A35}$$

$$I_{I6}(k)=\int_0^\infty \frac{2J_1^2(ka\sqrt{t^2+1})}{t^2+1}dt=\frac{\mathbf{H}_1(2ka)}{ka}, \tag{A36}$$

in which $\mathbf{H}$ is the Struve function and the subfunctions F_I are defined by the following hypergeometric and hyperbolic Bessel functions:

$$F_{I1a}(k,\beta_m,p,q)=\frac{{}_3F_4\left(1,1,\frac{3}{2};\frac{3}{2}-p-q,\frac{3}{2}+p-q,\frac{3}{2}-p+q,\frac{3}{2}+p+q;k^2a^2-\beta_m^2\right)}{\pi(p-q-1/2)_2(p+q-1/2)_2}, \tag{A37}$$

$$F_{I1b}(k,\beta_m,p,q)=\frac{2\pi I_{2p}(\sqrt{k^2a^2-\beta_m^2})I_{2q}(\sqrt{k^2a^2-\beta_m^2})}{\sqrt{k^2a^2-\beta_m^2}}, \tag{A38}$$

$$F_{I2a}(k,\beta_m,p,q)=\frac{{}_3F_4\left(1,\frac{3}{2},2;\frac{3}{2}-p-q,\frac{3}{2}+p-q,\frac{5}{2}-p+q,\frac{5}{2}+p+q;k^2a^2-\beta_m^2\right)}{\pi(p-q-3/2)_3(p+q-1/2)_3}, \tag{A39}$$

$$F_{I2b}(k,\beta_m,p,q)=\frac{2\pi I_{2p}(\sqrt{k^2a^2-\beta_m^2})I_{2q+1}(\sqrt{k^2a^2-\beta_m^2})}{k^2a^2-\beta_m^2}, \tag{A40}$$

$$F_{I3}(k,\beta_m,p,q)=2\frac{{}_3F_4\left(\frac{1}{2},1,1;\frac{1}{2}-p-q,\frac{1}{2}+p-q,\frac{3}{2}-p+q,\frac{3}{2}+p+q;k^2a^2-\beta_m^2\right)}{\pi(p-q-1/2)(p+q+1/2)}, \tag{A41}$$

$$F_{I4a}(k,\beta_m,p,q)=3\frac{{}_3F_4\left(1,2,\frac{5}{2};\frac{3}{2}-p-q,\frac{5}{2}+p-q,\frac{5}{2}-p+q,\frac{7}{2}+p+q;k^2a^2-\beta_m^2\right)}{2\pi(p-q-3/2)_4(p+q-1/2)_4}, \tag{A42}$$

$$F_{I4b}(k,\beta_m,p,q)=\frac{{}_3F_4\left(1,1,\frac{3}{2};\frac{1}{2}-p-q,\frac{3}{2}+p-q,\frac{3}{2}-p+q,\frac{5}{2}+p+q;k^2a^2-\beta_m^2\right)}{\pi(p-q-1/2)_2(p+q+1/2)_2}, \tag{A43}$$

$$F_{I4c}(k,\beta_m,p,q)=\frac{2\pi I_{2p+1}(\sqrt{k^2a^2-\beta_m^2})I_{2q+1}(\sqrt{k^2a^2-\beta_m^2})}{(k^2a^2-\beta_m^2)^{3/2}}. \tag{A44}$$

[1]E. Reissner, On axi-symmetrical vibrations of shallow spherical shells, Q. Appl. Math. **13**, 279–290 (1955).
[2]M. W. Johnson and E. Reissner, On transverse vibrations of shallow spherical shells, Q. Appl. Math. **15**, 367–380 (1956).
[3]A. W. Leissa, *Vibrations of Shells* (Acoustical Society of America, New York, 1993).
[4]R. Jones and J. Mazumdar, Transverse vibrations of shallow shells by the method of constant-deflection contours, J. Acoust. Soc. Am. **56**, 1487–1492 (1974).
[5]O. Thomas, C. Touzé, and A. Chaigne, Non-linear vibrations of free-edge thin spherical shells: Modal interaction rules and 1:1:2 internal resonance, Int. J. Solids Struct. **42**, 3339–3373 (2005).
[6]J. C. Snowdon, Forced vibration of internally damped circular plates with supported and free boundaries, J. Acoust. Soc. Am. **47**, 882–891 (1970).
[7]H. Suzuki and J. Tichy, Sound radiation from convex and concave domes in an infinite baffle, J. Acoust. Soc. Am. **69**, 41–49 (1981).
[8]H. Suzuki and J. Tichy, Sound radiation from an elastically supported circular plate, J. Acoust. Soc. Am. **65**, 106–111 (1979).
[9]T. J. Mellow and L. M. Kärkkäinen, On the sound field of a membrane in free space and an infinite baffle, J. Acoust. Soc. Am. **120**, 2460–2477 (2006).
[10]T. J. Mellow, On the sound field of a resilient disk in an infinite baffle, J. Acoust. Soc. Am. **120**, 90–101 (2006)
[11]C. J. Bouwkamp, Theoretical and numerical treatment of diffraction through a circular aperture, IEEE Trans. Antennas Propag. **AP18-2**, 152–176 (1970).
[12]T. J. Mellow and L. M. Kärkkäinen, On the sound field of an oscillating disk in a finite open and closed circular baffle, J. Acoust. Soc. Am. **118**, 1311–1325 (2005).
[13]S. Timoshenko and S. Woinowsky-Kreiger, *Theory of Plates and Shells* (McGraw-Hill, New York, 1959), pp. 36–42, 79–88, 429–435, 533–559.
[14]M. H. Gradowczyk, "Some remarks on the theory of shallow spherical shells," Ing.-Arch. **32**, 297–303 (1963).
[15]I. S. Gradshteyn and I. M. Ryzhik, *Table of Integrals, Series, and Products*, 6th ed., edited by A. Jeffrey (Academic, New York, 2000), p. 934, Eqs. (8.561.1) and (8.561.2), p. 935, Eqs. (8.567.1) and (8.567.2), p. 916, Eqs. (8.471.1) and (8.471.2), p. 918, Eqs. (8.486.1) and (8.486.2), p. 930, Eq. (8.532.1), p. 980, Eqs. (8.930.1)–(8.930.7).
[16]G. B. Arfken and H. J. Weber, *Mathematical Methods for Physicists*, 6th ed. (Academic, 2005), p. 723, Eq. (11.137), p. 722, Eq. (11.136).
[17]G. N. Watson, *A Treatise on the Theory of Bessel Functions*, 2nd ed., (Cambridge University Press, London, 1944), 141 pp., Sec. 5.22, Eq. (5).
[18]S. Wolfram, *The Mathematica Book*, 5th ed. (Wolfram Media, Champaign, IL, 2003). Symbolic computation by Mathematica.
[19]P. M. Morse and K. U. Ingard, *Theoretical Acoustics* (McGraw-Hill, New York, 1968), pp. 320, 321, 365.
[20]L. L. Beranek, *Acoustics* (Acoustical Society of America. New York, 1993), p. 188, Eq. (7.7), p. 118, Eq. (5.1).
[21]N. Harris and G. Bank, "A balanced modal radiator," on the CD ROM: Audio Engineering Society Convention Papers, 119th Convention Paper 6595, New York, 7–10 October 2005, available from Audio Engineering Society Inc., 60 East 42nd Street, Rm. 2520, New York, NY 10165–2520.

Properties of an entropy-based signal receiver with an application to ultrasonic molecular imaging

M. S. Hughes[a)]
School of Medicine, Washington University, St. Louis, Missouri 63108

J. E. McCarthy
Department of Mathematics, Washington University, St. Louis, Missouri 63108

J. N. Marsh, J. M. Arbeit, R. G. Neumann, R. W. Fuhrhop, K. D. Wallace, and D. R. Znidersic
School of Medicine, Washington University, St. Louis, Missouri 63108

B. N. Maurizi
Department of Mathematics, Washington University, St. Louis, Missouri 63108

S. L. Baldwin, G. M. Lanza, and S. A. Wickline
School of Medicine, Washington University, St. Louis, Missouri 63108

(Received 27 September 2006; revised 6 March 2007; accepted 6 March 2007)

Qualitative and quantitative properties of the finite part, H_f, of the Shannon entropy of a continuous waveform $f(t)$ in the continuum limit are derived in order to illuminate its use for waveform characterization. Simple upper and lower bounds on H_f, based on features of $f(t)$, are defined. Quantitative criteria for *a priori* estimation of the average-case variation of H_f and $\log E_f$, where E_f is the signal energy of $f(t)$ are also derived. These provide relative sensitivity estimates that could be used to prospectively choose optimal imaging strategies in real-time ultrasonic imaging machines, where system bandwidth is often pushed to its limits. To demonstrate the utility of these sensitivity relations for this application, a study designed to assess the feasibility of identification of angiogenic neovasculature targeted with perfluorocarbon nanoparticles that specifically bind to $\alpha_v\beta_3$-integrin expression in tumors was performed. The outcome of this study agrees with the prospective sensitivity estimates that were used for the two receivers. Moreover, these data demonstrate the ability of entropy-based signal receivers when used in conjunction with targeted nanoparticles to elucidate the presence of $\alpha_v\beta_3$ integrins in primordial neovasculature, particularly in acoustically unfavorable environments. © *2007 Acoustical Society of America.*
[DOI: 10.1121/1.2722050]

PACS number(s): 43.60.Bf, 43.60.Lq, 43.80.Jz, 43.80.Qf, 43.80.Vj [EJS] Pages: 3542–3557

I. INTRODUCTION

Detection of molecular epitopes associated with neovasculature in a growing tumor presents a unique challenge for ultrasonic clinical imaging systems. The tumor vasculature is often below the instrument's resolution, which necessitates the use of an enhancing contrast agent. We have demonstrated that a specially modified nanoparticle contrast agent can be successfully targeted toward the expression of $\alpha_v\beta_3$ integrins that are expressed in abundance on tumor neovasculature.[1]

The successful detection of cancer *in vivo* depends on various factors when using molecularly targeted contrast agents. The number of epitopes to which the ligand can bind must be sufficient to allow enough of the contrast agent to accumulate for detection, and ligand specificity must be maintained to ensure that nonspecific binding remains negligible. In addition, the pharmacokinetics of the contrast agent must be such that the agent remains in circulation long enough to bind in sufficient quantity to the desired target. Ideally, the background signal from unbound, circulating contrast agent is low enough or absent so as to not interfere with the assessment of bound, targeted agent. The imaging technology itself also must be highly sensitive and capable of detecting and/or quantifying the level of contrast agent bound to the pathological tissue. In clinical ultrasonic imaging, the sensitivity of detection depends on a physical difference in the way sound interacts with a surface covered by targeted contrast agent versus one that is not. The data presented in the following show that in many cases, the sensitivity of this determination can be improved by applying novel and specific signal processing techniques based on thermodynamic or information-theoretic analogs.

Previous work already has demonstrated for high frequency ultrasound in epitope-rich pathologies, such as fibrin in thrombus, that targeted perfluorocarbon nanoparticles act as a suitable molecular imaging agent by modifying the acoustic impedance on the surface to which they bind.[2] How-

[a)]Electronic mail: msh@cvu.wustl.edu

 0001-4966/2007/121(6)/3542/16/$23.00 © 2007 Acoustical Society of America

ever, at lower frequencies and for sparse molecular epitopes, clear delineation between nontargeted normal tissue and angiogenic vessels remains a challenge.

Site-targeted nanoparticle contrast agents, when bound to the appropriate receptor, must be detected in the presence of bright echoes returned from the surrounding tissue. In this study, we attempt to solve the problem of detection of site-specific contrast through the use of signal receivers (i.e., mathematical operations that reduce an entire radio frequency (rf) waveform or a portion of it to a single number) based on information-theoretic quantities, such as Shannon entropy (H), or its counterpart for continuous signal (H_f). These receivers appear to be sensitive to diffuse, low amplitude features of the signal that often are obscured by noise, or else lost in large specular echoes and, hence, not usually perceivable by a human observer.[3–7]

Although entropy-based techniques have a long history in image processing for image enhancement and postprocessing of reconstructed images, the approach we take is different in that entropy is used directly as the quantity defining the pixel values in the image. Specifically, images are reconstructed by computing the entropy (or a limiting form of it: H_f) of segments of the individual rf A lines that comprise a typical medical image by applying a "moving window," or "box-car," analysis. The computation of an entropy value for each location within an image is therefore possible, and the results can be superimposed over the conventional grayscale image as a parametric map.

For comparison, we also used more conventional signal processing techniques on the same beam formed rf: specifically, the signal energy and its logarithm. This was done after a preliminary B-mode grayscale analysis of backscattered data acquired for this study was unable to detect changes in backscattered rf arising from the accumulation of targeted nanoparticles in the tumor neovasculature. This result implied that acoustic characterization of sparse collections of targeted perfluorocarbon nanoparticles presented challenges that might require the application of novel types of signal processing.

II. APPROACH

All rf data are obtained by sampling a continuous function $y=f(t)$, which has associated with it two functions: its density function, $w_f(y)$, and its increasing rearrangement, $f_\uparrow(t)$. Either may be used to compute H_f and to provide bounds for the relative magnitudes of changes of H_f with respect to familiar measures such as energy, E_f, and log energy, $\log(E_f)$.

A. The function $w_f(y)$

The density function $w_f(y)$ may be used to compute the entropy H_f and the signal energy E_f (and hence also $\log[E_f]$). It corresponds to the density functions that are the primary mathematical object in much of statistical signal processing and from which other mathematical quantities are subsequently derived (e.g., mean values, variances, covariances).[8–10] In that setting, it constitutes the most fundamental unit of information that the experimentalist has about a random variable, which is often implicitly assumed to have a form that is too complicated to be worth analyzing (hence the density function is analyzed instead). Moreover, this function is usually assumed to be very well-behaved mathematically, that is, to be continuous, infinitely differentiable, and to approach zero at infinity. On the other hand, in our analysis $f(t)$ is the fundamental unit of information and $w_f(y)$ is a derived quantity obtained from it. As we shall see, $w_f(y)$ is not particularly well-behaved mathematically. In spite of the difficulties this adds to the mathematical analysis, several experimental studies indicate that signal processing using the derived $w_f(y)$ permits definition of signal receivers that are more sensitive than energy-based receivers. We will also show that signal energy can be computed using $w_f(y)$, and thus all of conventional energy-based signal processing may be placed within the mathematical framework described in the following.

Without loss of generality, we may adopt the convention that the domain of $f(t)$ is $[0, 1]$. Then, $w_f(y)$, the density function of $f(t)$, can be defined by the basic integral relation

$$\int_0^1 \phi(f(t))dt = \int_{f_{\min}}^{f_{\max}} \phi(y) w_f(y) dy, \tag{1}$$

for any continuous function $\phi(y)$. This should be compared with the expression for the expectation value of a function ϕ of a random variable X with density $p_X(x)$, which is given by

$$\int \phi(x) p_X(x) dx,$$

which explains why $w_f(y)$ is referred to as the density function for $f(t)$.[11] Most applications of either probability or information theory to signal processing proceed, usually very early in the discussion, by assuming a specific density function.[12–14] In contrast, the analysis described in this study begins with a digitized time-domain function and derives its density function.

We will see that different functions may have the same density function; these are referred to as "equidistributed" functions.

If $\phi(y)=1$, Eq. (1) implies

$$\int_{f_{\min}}^{f_{\max}} w_f(y) dy = 1, \tag{2}$$

a relation that will be used in the following. If we set $\phi(y) = \delta(y-\xi)$ then

$$\int_0^1 \delta(f(t)-\xi)dt = \int_{f_{\min}}^{f_{\max}} \delta(y-\xi) w_f(y) dy = w_f(\xi). \tag{3}$$

Thus, using the well-known expression

$$\int_0^1 \delta(f(t)-\xi)dt = \sum_{\{t_k | f(t_k)=\xi\}} \frac{1}{|f'(t_k)|}, \tag{4}$$

and Eqs. (3) and (4) we obtain

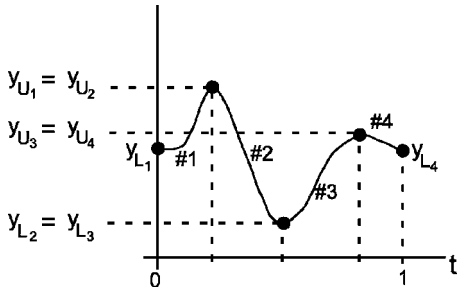

FIG. 1. An illustration of the y_{L_i} and y_{U_i} in Eq. (7) for a four lap function. $y_{L_1}=f(0)$, $y_{L_1}=y_{L_2}$, $y_{U_2}=y_{U_3}$, $y_{L_3}=y_{L_4}$, and $y_{U_4}=f(1)$.

$$w_f(\xi) = \sum_{\{t_k | f(t_k)=\xi\}} \frac{1}{|f'(t_k)|}, \tag{5}$$

an expression for w_f that reveals some of its qualitative features in terms of $f(t)$. For instance, $w_f(y) \geqslant 0$ for all y; it becomes $w_f(y-c)$ if we add a constant, c, to $f(t)$; $w_{-f}(-y) = w_f(y)$; and perhaps most importantly $w_f(y)$ has singularities at values of $y=f(t)$ where $f'(t)=0$. We will assume that all digitizable waveforms $f(t)$ are comprised of at least one section, or "lap," where it is monotonic. The lap boundaries are just the points t where $f'(t)=0$. On each lap, $f(t)$ has a well-defined inverse function. These may be used to rewrite Eq. (5)

$$w_f(y) = \sum_{k=1}^{N} |g_k'(y)|, \tag{6}$$

where N is the number of laps, $g_k(y)$ is the inverse of $f(t)$ in the kth lap and if y is not in the range of $f(t)$ in the kth lap, $g_k'(y)$ is taken to be 0. This equation may also be rewritten in a more explicit form as

$$w_f(y) = \sum_{k=1}^{N} |g_k'(y)| \Pi(y_{L_i}, y_{U_i}, y), \tag{7}$$

where y_{L_i}, y_{U_i} denote the values of $f(t)$ at the lower and upper bounds of the ith lap, respectively, and $\Pi(y_{L_i}, y_{U_i}, y)$ denotes a Heaviside-like step-function that is one for $y \in [y_{L_i}, y_{U_i}]$ and zero otherwise. These conventions are illustrated in Fig. 1. This form will prove useful in the following.

Application of Eq. (6) to the computation of the density functions of $\sin(n\pi t)$, where n is an integer, reveals that they are all equal. Figure 2 shows two such functions and approximations to their increasing rearrangements, $f_\uparrow(t)$, obtained by sorting sampled (at 100 points) versions of both functions. As shown in Fig. 2, waveforms with drastically different frequency content may be equidistributed and have equal entropy, H_f. Thus, frequency plays little, if any, direct role in our analysis.

For experimentally measured data, we may also assume that all digitizable waveforms $f(t)$ have a Taylor series expansion at all points in $[0, 1]$. Then near a time t_k such that $f'(t_k)=0$,

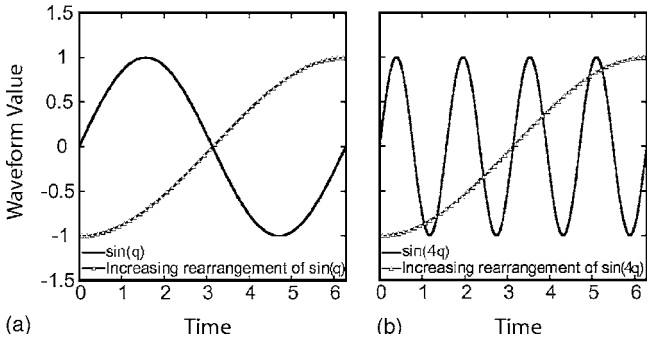

FIG. 2. Rearrangements of $\sin(2\pi t)$ and $\sin(8\pi t)$. Note that the increasing rearrangements are the same as we would expect since $\sin(2\pi t)$ and $\sin(8\pi t)$ are equimeasurable.

$$y = f(t) = f(t_k) + \frac{1}{2!} f''(t_k)(t-t_k)^2 + \cdots, \tag{8}$$

t_k is a lap boundary and on the left side of this point Eq. (8) may be truncated to second order and inverted to obtain

$$g_k(y) = \pm \sqrt{2(y - f(t_k))/f''(t_k)}, \tag{9}$$

with

$$|g_k'(y)| = 1/\sqrt{2f''(t_k)(y - f(t_k))}. \tag{10}$$

The contribution to $w_f(y)$ from the right side of the lap boundary, from $g_{k+1}(y)$, is the same, so that the overall contribution to $w_f(y)$ coming from the time interval around t_k is

$$|g'(y)| = \sqrt{2/(f''(t_k)(y - f(t_k)))}, \tag{11}$$

and so $w_f(y)$ has only a square root singularity (we have assumed that t_k is interior to the interval $[0, 1]$, if not, then the contributions to w_f come from only the left or the right). If additionally, $f''(t_k)=0$ then the square root singularity in Eq. (10) will become a cube-root singularity, and so on, so that the density functions we consider will have only integrable algebraic singularities.

Equations (6), (7), (10), and (11) determine the qualitative features of a typical density function, $w_f(y)$. From Eqs. (6) and (7) we see that the the density function may exhibit finite jump discontinuities. Equations (10) and (11) imply further that algebraic singularities may also be present.

Figure 3 illustrates, schematically, several possibile types of behaviors possible in $w_f(y)$: both discontinuities and algebraic singularities [indicated by arrows on the plots of $w_f(y)$]. Progressing from left to right in any given row also illustrates how to estimate qualitative features of $w_f(y)$ from $f(t)$. For instance, in the top row the maxima in $f(t)$ correspond to an algebraic singularity in $w_f(y)$, plotted sideways in the middle column to more clearly indicate the relationship between its features and those of $f(t)$. The third column shows $w_f(y)$ in a conventional layout (a rotated and flipped version of the plot in the middle column). These plots show that the density functions possess significantly different attributes from those usually considered in statistical signal processing.

The mathematical characteristics of the singularities are important in order to guarantee the existence of the following integral on which we base our analysis of signals:

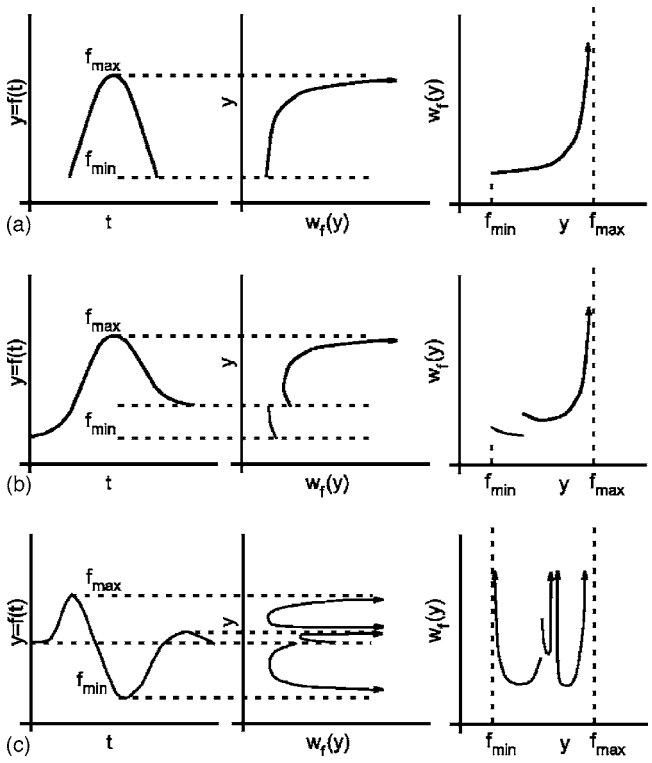

FIG. 3. Plots of three different time-domain waveforms, $f(t)$ (left column), and their associated density functions $w_f(y)$ (middle column and right columns).

$$H_f = \int_{f_{\min}}^{f_{\max}} w_f(y) \log w_f(y) dy. \tag{12}$$

In previous studies, this quantity was referred to as H_C, since it is obtained from the Shannon entropy, H, in the limit where a waveform, $f(t)$, is acquired with infinite sampling rate and dynamic range (i.e., in a limit approaching the continuum).[3–7] However, in the current study, which emphasizes the changes in entropy as the underlying waveform $f(t)$ changes, it seems more appropriate to use the notation H_f to emphasize its dependence on $f(t)$.

Typically, ultrasonic signal analysis has been based on analysis of backscattered energy or its logarithm.[3,5,7] For instance, the gray-scale images used in medical ultrasound B-mode displays of the logarithm of the envelope (i.e., analytic signal magnitude) of the backscattered signal, which is well known to represent the energy contained in the waveform over the sampling interval.[15] Energy contained in longer intervals may be estimated using the sum of the squares of digitized values contained in a "moving window." The physical motivation is based on analogy with the kinetic energy of a spring, which is proportional to amplitude of spring extension squared. This quantity, E_f, may also be expressed using $w_f(y)$ via Eq. (1)

$$E_f = \int_0^1 f(t)^2 dt = \int_{f_{\min}}^{f_{\max}} w_f(y) y^2 dy. \tag{13}$$

B. The function $f_\uparrow(t)$

Like signal energy, E_f, the entropy may also be computed directly from a time domain function, $f_\uparrow(t)$ (f "increasing"). In addition, approximations of this function may be found quickly by sorting discretely sampled data from $f(t)$. This function may also be used to rapidly estimate the relative sensitivities of entropy and energy-based receivers [which we will derive in Eqs. (56) and (57)] and is thus useful for qualitative evaluation of entropy receiver performance.

Precise definition of $f_\uparrow(t)$ begins with the observation that since $w_f(y) \geqslant 0$, the function defined by the integral

$$W_f(y) = \int_{f_{\min}}^{y} w_f(s) ds \tag{14}$$

is nondecreasing. Its inverse, a function of time denoted $f_\uparrow(t)$, is equimeasurable with $f(t)$ by Eq. (5) and the inverse function theorem. Thus, by Eq. (5), $1/f'_\uparrow(t) = w_f(f_\uparrow(t))$, so that

$$H_f = -\int_0^1 \log[f'_\uparrow(t)] dt. \tag{15}$$

The function $f_\uparrow(t)$ is referred to as the increasing rearrangement of $f(t)$. It may be approximated quickly, and with reasonable accuracy, by sorting the digitized values of $f(t)$.

Since the function $f_\uparrow(t)$ is equimeasurable with $f(t)$ it follows that $f_{\uparrow\max} = f_{\max}$ and $f_{\uparrow\min} = f_{\min}$. The increasing rearrangement has been useful for rapid computation of H_f. The calculation uses the Green's function for the second-order differential operator to simultaneously smooth and differentiate twice the approximation to $f_\uparrow(t)$ obtained by sorting the sampled values of $f(t)$.[7]

C. Physical interpretation of $w_f(y)$ and its numerical calculation

One challenge of this analysis is to achieve an intuitive appreciation for the physical meaning of entropy that relates to imaging applications and the detection of subtle pathologies. There are at least two different paths to obtaining a physical meaning for the quantity H_f appearing in Eq. (12) [or Eq. (15)]. One is based on the fact that H_f is derived from the Shannon entropy, which has been extensively investigated in communication theory. While this connects H_f to the capacity of a communications channel, which is a quasi-physical quantity, it also implies a relation with Kolmogorov complexity, an uncomputable quantity that is often approximated by the Shannon entropy. The physical significance of Kolmogorov complexity and its use in deriving Lagrangians for both classical mechanics and special relativity has been described in a recent article by Soklakov.[16]

The second approach is to understand the physical meaning of the density function $w_f(y)$ which we now discuss. Figure 4 is a diagram of a very idealized ultrasonic backscatter measurement using a single point-source transducer, which we assume to have infinite bandwidth so that it emits δ-function pulses. We suppose that the medium is composed of particulate scatterers that backscatter like perfect reflectors with either no phase inversion (e.g., fixed bound-

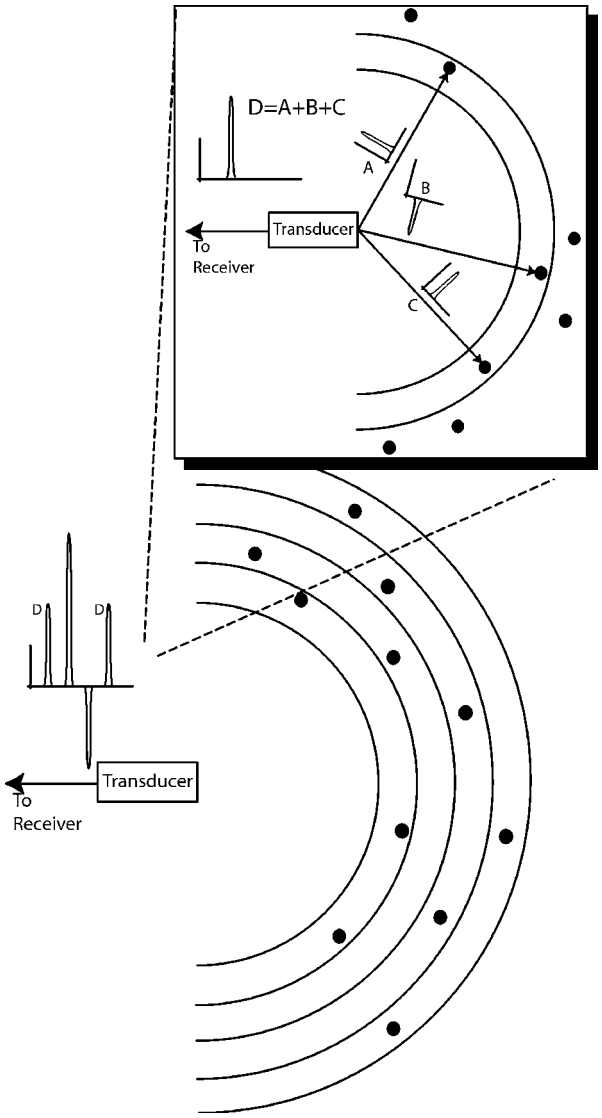

FIG. 4. An idealized scattering experiment using a transducer emitting perfect δ-function pulses. This model illuminates the physical interpretation of the function $w_f(y)$ used to compute H_f.

ary) or 180° phase inversion (e.g., free boundary). The result is that the backscattered ultrasound will be comprised of a train of sums of positive and negative delta functions. The inset of Fig. 4 shows the output at one instant that is the sum of two positive (A and C) and one negative (B) δ function. These are the reflections of the original transmit pulse from the scatterers on the spherical shell of constant time centered on the transducer face. The backscattered signal will, in the idealized case considered here, be a train of these pulses, with the height of each pulse representing the sign-weighted sum of particle scatterers on each constant-time spherical shell. The received signal from the transducer is a train of such pulses, with the received amplitude at two instants being the same when the sign-weighted sum in the corresponding shells is equal. The number of times that the output amplitude is the same is the density $w_f(y)$ for this idealized δ-function pulse train waveform. In reality, the transducer has finite bandwidth, the reflectors are neither perfect nor discrete, and the measured waveform is a convolution of transducer and scatterer transfer functions. Nevertheless, the idealized function approach sheds light on the physical interpretation of $w_f(y)$, as an approximate representation of the spatial distribution of scatterers in the acoustic field.

D. Intrinsic versus extrinsic statistics

While our approach may have certain similarities to conventional statistical signal processing, it also differs significantly in several ways as will be illustrated in the next few sections. These differences fall into two categories: mathematical and physical.

Unlike most statistical signal processing, where the underlying density is the starting point of the analysis, our analysis begins in the time domain, with a function like $\sin(t)$, $\sin(kt)$, or a weighted sum of these functions and derives their density function. Second, this is done for each waveform and not, as is typically the case (e.g., in derivation of the Rayleigh or Rician distributions), for an ensemble of waveforms. Moreover, the density functions we consider contain algebraic singularities and hence cannot typically be convolved. This eliminates the possibility of applying the central limit theorem in our analysis, which contrasts sharply with traditional statistical signal analysis, where density functions are bounded and the central limit theorem often plays a significant role. Third, the waveforms we consider are not typically independent functions, for instance $\sin(t)$ and e^{-t^2} are not independent.[17–19] Thus, we may not compute the density of a sum of waveforms from the convolution of their density functions. There are three reasons for adopting the approach described in this study. First, the assumption of statistical independence can lead to conclusions that are in some ways at "odds" with the usual assumptions of eigenfunction-based signal processing. Second, independent functions are "rare" in the sense discussed in Appendix A 2. Third, as shown in the results section and in several other studies, this approach can lead to significant improvements in detection of subtle changes in backscattered ultrasonic waveforms.[3–7,20–24]

Most applications of statistics to signal processing follow one of two paths. The simplest is to assume that a canonical noise term, e.g., Gaussian or Poisson, has been added to the signal.[8–10,25–39] The more physical analysis derives a functional form for the statistical density of the waveform (e.g., Rician, Rayleigh, K-distribution) based on an idealized "thought" experiment consisting of many different random scattering configurations.[40] As the number of these virtual experiments grows to infinity a well-defined density is obtained. waveforms are then characterized externally, by reference to this density. In the approach described here, the density of values of individual waveforms assumes central importance. Each waveform is characterized intrinsically, using its internal statistics as captured by the density function $w_f(y)$. Our motivation is the observation that a shift from extrinsic to intrinsic viewpoint has proven useful in the past: algorithmic information theory (i.e., intrinsic viewpoint) was developed in the 1960s, following statistical information theory (i.e., extrinsic viewpoint).

To pursue this approach a large number of the simplifying assumptions typically applied in statistical signal pro-

cessing must be abandoned: independence, normality, continuity of density functions. This increases the mathematical complexity of our analysis. However, much of traditional signal processing, in fact all of it that is based on integrals of the digitized waveforms, may be placed in the context of this formalism, as shown by Eq. (13). Moreover, as we will show in the following, significant gains in experimental sensitivity may be gained that make the extra effort worthwhile.

E. Scaling invariance of ΔH_f and $\Delta \log E_f$

The scaling properties of a signal receiver are also important since in a typical ultrasound experiment gain settings on imager or apparatus amplifiers are often adjusted to optimize data set dynamic range. As we will see, both ΔH_f and $\Delta \log E_f$ are invariant under scale changes. This makes their interpretation in experimental studies straightforward. To obtain this result we will first obtain the scaling behavior of $w_f(y)$. From Eq. (5) we see that if we scale $f(t)$ by a factor of σ,

$$w_{\sigma f}(\xi) = \sum_{\{t_k|\sigma f(t_k)=\xi\}} \frac{1}{|\sigma||f'(t_k)|} = \frac{1}{|\sigma|} w_f\left(\frac{\xi}{\sigma}\right), \tag{16}$$

or

$$|\sigma| w_{\sigma f}(\sigma y) = w_f(y), \tag{17}$$

which we may apply in

$$\begin{aligned} H_f &= \int_{f_{\min}}^{f_{\max}} w_f(y)\log[w_f(y)]dy \\ &= \int_{f_{\min}}^{f_{\max}} |\sigma| w_{\sigma f}(y)\log[|\sigma| w_{\sigma f}(y)]dy \\ &= \int_{\sigma f_{\min}}^{\sigma f_{\max}} w_{\sigma f}(\xi)\log[|\sigma| w_{\sigma f}(\xi)]d\xi \\ &= \int_{\sigma f_{\min}}^{\sigma f_{\max}} w_{\sigma f}(\xi)\log[w_{\sigma f}(\xi)]d\xi + \log[|\sigma|] = H_{\sigma f} + \log[|\sigma|], \end{aligned} \tag{18}$$

which tells us that if we perform a measurement where $f(t) \rightarrow \tilde{f}(t)$ to obtain ΔH_f, and then repeat the measurement at a different gain setting to measure $\sigma f(t) \rightarrow \sigma\tilde{f}(t)$ we will obtain the same change in entropy, i.e.,

$$\Delta H_{\sigma f} = \Delta H_f. \tag{19}$$

The same is true for $\log[E_f]$ since

$$\log E_{\sigma f} = \int_0^1 \log[\sigma f(t)]^2 dt = 2\log|\sigma| + \log E_f \tag{20}$$

so that

$$\Delta \log[E_{\sigma f}] = \Delta \log[E_f], \tag{21}$$

which states that signal energy is the second moment of $w_f(y)$.

F. Qualitative features of H_f

1. Inequalities bounding H_f from below

There are two inequalities useful for qualitative estimation of H_f from $f(t)$. The first of these is based on Gibbs' inequality,

$$\int_0^1 w_f(y)\log h(y)dy \leqslant \int_0^1 w_f(y)\log w_f(y)dy = H_f, \tag{22}$$

where the functions $w_f(y)$ and $h(y)$ satisfy

$$\int_0^1 h(y)dy = \int_0^1 w_f(y)dy = 1. \tag{23}$$

If we let $h(y) = e^{g(y)}/\int_0^1 e^{g(s)}ds$, then

$$\int_0^1 w_f(y)g(y)dy - \int_0^1 w_f(y)dy \int_0^1 e^{g(s)}ds \leqslant H_f, \tag{24}$$

which for the particular choice $g(y) = y^2$ becomes

$$\begin{aligned} &\int_0^1 f^2(t)dt - 0.38025 \leqslant H_f, \\ &E - 0.38025 \leqslant H_f, \end{aligned} \tag{25}$$

where E is the signal energy.

We also have

$$\begin{aligned} V[f] &= \int_0^1 |f'_{\uparrow}(t)|dt = \int_0^1 \sqrt{f'_{\uparrow}(t)}dt \leqslant \int_0^1 \log[f'_{\uparrow}(t)]dt \\ &= -H_f \end{aligned} \tag{26}$$

implying that

$$H_f \geqslant -V[f], \tag{27}$$

where $V[f]$ is the variation of $f(t)$. Somewhat more interesting is a bound based on the length of $f(t)$ obtained by considering the lengths of all functions $g(t)$ that are equidistributed with $f(t)$, which may be written as [using the notation $f(t) \sim g(t)$ to indicate that f and g are equidistributed]:

$$\begin{aligned} \min_{\{g(t)|g(t)\sim f(t)\}} \int_0^1 \sqrt{g(t)^2 + 1}dt &= \int_0^1 \sqrt{f'_{\uparrow}(t)^2 + 1}dt \\ &\geqslant \int_0^1 \log f'_{\uparrow}(t)dt \geqslant -H_f \end{aligned} \tag{28}$$

implying that

$$H_f \geqslant -L[f(t)], \tag{29}$$

where $L[f(t)]$ is the length of the graph of $f(t)$ over the interval [0,1].

2. Inequality bounding H_f from above

We also have

$$-H_f = \int_0^1 \log[f_\uparrow'(t)]dt \geq \log \int_0^1 f_\uparrow'(t)dt = \log[f_\uparrow(1)] \tag{30}$$

or

$$H_f \leq \log\left[\frac{1}{f_\uparrow(1)}\right]. \tag{31}$$

3. An inequality between ΔH_f and $\Delta \log E_f$

In this section we will derive conditions for the variation of the entropy, ΔH_f, to be greater than that of the log energy, $\Delta \log E_f$. The estimate derived in this section rests on the assumption that $H_f < 0$. While H_f can take on both positive and negative values for the data considered in this study, its value tends to be smallest for subsegments of backscattered rf corresponding to anatomical regions where accumulation of targeted nanoparticles is expected (as verified by histological staining, e.g., Fig. 8). For this reason the inequality is useful for *a priori* estimation of the sensitivities of the two receivers. These can be useful in real-time imaging applications where system bandwidth is often pushed to its limits.

If the waveform, $f(t)$, is perturbed slightly (e.g., by the slow accumulation of nanoparticles in the insonified region), then its density function $w_f(y)$ will also change to $w_f(y) + \varepsilon h(y)$, where we know that

$$\int_{f_{\min}}^{f_{\max}} w_f(y)dy = \int_{f_{\min}}^{f_{\max}} w_f(y) + \varepsilon h(y)dy = 1 \tag{32}$$

so that

$$\int_{f_{\min}}^{f_{\max}} h(y)dy = 0. \tag{33}$$

The signal energy E and the entropy H_f will therefore also change,

$$H_f = \int_{f_{\min}}^{f_{\max}} w_f(y)\log w_f(y)dy$$

becomes

$$\tilde{H}_f = \int_{f_{\min}}^{f_{\max}} [w_f(y) + \varepsilon h(y)]\log[w_f(y) + \varepsilon h(y)]dy \tag{34}$$

and

$$E_f = \int_{f_{\min}}^{f_{\max}} y^2 w_f(y)dy$$

becomes

$$\tilde{E}_f = \int_{f_{\min}}^{f_{\max}} y^2[w_f(y) + \varepsilon h(y)]dy. \tag{35}$$

The derivatives of these expressions with respect to $\varepsilon \to 0$:

$$\frac{dH_f}{d\varepsilon} = \int_{f_{\min}}^{f_{\max}} h(y)dy + \int_{f_{\min}}^{f_{\max}} h(y)\log[w_f(y)]dy = \int_{f_{\min}}^{f_{\max}} h(y)\log[w_f(y)]dy, \tag{36}$$

$$\frac{dE_f}{d\varepsilon} = \int_{f_{\min}}^{f_{\max}} y^2 h(y)dy, \tag{37}$$

may be used to estimate the change in magnitude of the entropy and energy

$$|\Delta H_f| = \varepsilon\left|\frac{dH_f}{d\varepsilon}\right| = \left|\int_{f_{\min}}^{f_{\max}} h(y)\log[w_f(y)]dy\right|, \tag{38}$$

$$\left|\Delta E_f\right| = \varepsilon\left|\frac{dE}{d\varepsilon}\right| = \left|\int_{f_{\min}}^{f_{\max}} y^2 h(y)dy\right|, \tag{39}$$

in the limit where $\varepsilon \to 0$. Given the perturbation $h(y)$, we wish to obtain an estimate of the relative magnitudes of the integrals appearing in Eqs. (38) and (39) and to establish conditions on $w_f(y)$ under which $|\Delta H_f| \geq |\Delta E_f|$ and under which $|\Delta H_f| \geq |\Delta \log[E_f]|$. *A priori*, we know that the inequality cannot hold in general since for $f(t) = t$ we have $w_f(y) = 1$ in which case $|\Delta H_f| = 0$. However, we may still obtain an estimate of average behavior by exploiting the geometric nature of Eqs. (38) and (39) to rewrite them as

$$|\Delta H_f| = \langle \log^2[w_f(y)], h(y)\rangle \tag{40}$$

$$= \|\log^2[w_f(y)]\|_2 \|h(y)\|_2 |\cos(\theta)|, \tag{41}$$

$$|\Delta E_f| = \langle y^2, h(y)\rangle = \|y^2\|_2 \|h(y)\|_2 |\cos(\phi)|. \tag{42}$$

where $\langle \cdot, \cdot \rangle$, and $\|\cdot\|_2$ denote the inner product and L_2 norm, respectively, in the infinite dimensional vector space (i.e., Hilbert space) containing the vectors $h(y)$, $\log^2[w_f(y)]$, and y^2 having magnitudes $\|\log^2[w_f(y)]\|_2$, $\|h(y)\|_2$, $\|y^2\|_2$, and subtending angles θ and ϕ. We suppose that $\log^2[w_f(y)]$ is fixed and that $h(y)$ may vary arbitrarily over the phase space and ask what the average values of the inner product appearing in Eqs. (41) and (42) will be. Geometrically, each average is obtained by sweeping the "random" $h(y)$ vector over all angles subtending the infinite dimensional unit sphere. The averages appearing in Eqs. (41) and (42) then become

$$|\Delta H_f|_{\text{avg}} = \|\log^2[w_f(y)]\|_2 \|h(y)\|_2 |\cos(\theta)|_{\text{avg}}, \tag{43}$$

$$|\Delta E_f|_{\text{avg}} = \|y^2\|_2 \|h(y)\|_2 |\cos(\phi)|_{\text{avg}}. \tag{44}$$

If we assume that the perturbation $\|h(y)\|_2$ is fixed, then since the average values: $|\cos(\theta)|_{\text{avg}}$, $|\cos(\phi)|_{\text{avg}}$ over the hypersphere are equal, we see that the relationship between $|\Delta H_f|_{\text{avg}}$ and $|\Delta E_f|_{\text{avg}}$ is governed by the relation between the quantities,

$$\|\log^2[w_f(y)]\|_2 = \left[\int_{f_{\min}}^{f_{\max}} [\log(w_f(y))]^2 dy\right]^{1/2}, \tag{45}$$

(46)

and

$$\|y^2\|_2 = \left[\int_{f_{\min}}^{f_{\max}} (y^2)^2 dy\right]^{1/2} = \left[\frac{f_{\max}^5 - f_{\min}^5}{5}\right]^{1/2}. \quad (47)$$

Suppose that $H_f < 0$ then

$$\begin{aligned}
|H_f| &\leq \left| \int_{w_f(y)\leq 1} w_f(y)\log(w_f(y))dy \right| \\
&\leq \left(\int_{w_f(y)\leq 1} (w_f(y))^2 dy \right)^{1/2} \\
&\quad \times \left(\int_{w_f(y)\leq 1} (\log(w_f(y)))^2 dy \right)^{1/2} \\
&\leq \left(\int_{w_f(y)\leq 1} w_f(y) dy \right)^{1/2} \\
&\quad \times \left(\int_{w_f(y)\leq 1} (\log(w_f(y)))^2 dy \right)^{1/2} \\
&\leq 1 \left(\int_{w_f(y)\leq 1} (\log(w_f(y)))^2 dy \right)^{1/2} \\
&\leq \left(\int_{f_{\min}}^{f_{\max}} (\log(w_f(y)))^2 dy \right)^{1/2} = \|\log[w_f(y)]^2\|_2 \quad (48)
\end{aligned}$$

thus, if $H_f < 0$ and $|H_f|^2 > (f_{\max}^5 - f_{\min}^5)/5$, i.e., $H_f < -(f_{\max}^5 - f_{\min}^5)/\sqrt{5}$, then on average $|\Delta H_f| > |\Delta E_f|$. If moreover, $E_f > 1$, so that $\log(E_f) > 0$, then

$$|\Delta H_f| > |\Delta E_f| > |\Delta E_f|/E_f = |\Delta \log E_f|. \quad (49)$$

This average-case relationship is useful for estimation of relative sensitivities of entropy and energy-based receivers as we will show in Fig. 13.

4. Rapid estimation of relative sensitivity from $f_\uparrow(t)$ and $w_f(y)$

There are several ways to rapidly estimate the relative sensitivities of H_f and $\log E$ without executing the complete calculation of entropy. These are based on estimation of the minimum of $|\Delta H_f|$ (which is relatively expensive to compute directly), which is then compared to the maximum of $|\Delta \log[E_f]|$ (which is easy to compute and will not be discussed further) to obtain a "worst-case" comparison of receiver performances. If $|\Delta \log[E_f]| > |\Delta H_f|$, these estimates may be used to avoid the relatively expensive computation of H_f.

a. Relative sensitivity from the minimum of $w_f(y)$. An obvious estimate of $|\Delta H_f|$ from the integral appearing in Eq. (45) may be found by computing

$$|\Delta H_f| \approx \sqrt{\min\{\log^2[w_f(y)]\} \times (f_{\max} - f_{\min})}. \quad (50)$$

Some care must be taken in application of this approximation, since the minimum may occur near a discontinuity. In this case, the Fourier series for w_f will "ring," which can further reduce the accuracy of Eq. (50), causing it to either over- or underestimate $|\Delta H_f|$. This effect can be reduced in the obvious way by increasing the length of Fourier series used to approximate $w_f(y)$, although at the expense of greater computational cost. A further, cruder estimate of $|\Delta H_f|$ may be based upon Eq. (50) by replacing $\min\{\log^2[w_f(y)]\}$ by $\min\{\log^2[f'(t)]\}$ permitting estimation of H_f sensitivity from

$$|\Delta H_f| \approx \min\{\log^2[f'(t)]\} \times (f_{\max} - f_{\min}). \quad (51)$$

This estimate has the advantages that it is not subject to "ringing" effects and that it may be calculated directly from $f(t)$.

b. Relative sensitivity from the maximum of $f'_\uparrow(t)$. A more sophisticated estimate may be calculated directly from the increasing rearrangement of $f(t)$, $f_\uparrow(t)$ and its derivatives, which we write as

$$g(t) = \frac{d}{dt}[f_\uparrow(t)], \quad (52)$$

and from which we obtain the following expression for the magnitude of H_f variation appearing in Eq. (48),

$$\int_0^1 g(t)\log^2[g(t)]dt = \int_{f_{\min}}^{f_{\max}} \log^2[w_f(y)]dy. \quad (53)$$

c. Relative Sensitivity from the $f(t)$: K_0, K_1. As shown in Appendix B, smoothing of $g(t)$ reduces the magnitude of the integral in Eq. (48). We apply this fact by "smoothing" $g(t)$ to two different constant levels. This may be done by using the maximum distance, K_0 of $g(t)$ below the line $y=t$ [or by using the maximum distance, K_1 of $g(t)$ above the line $y=t$], as defined in Fig. 5. The time at which this maximum

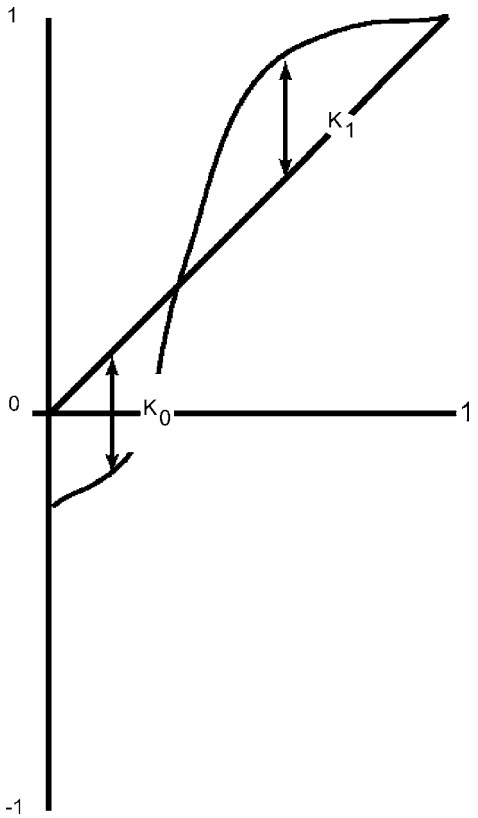

FIG. 5. Definitions of K_0, K_1 and t_0, t_1 used to derive the lower bounds on $\|\log[w_f(y)]^2\|_2$ appearing in Eqs. (56) and (57).

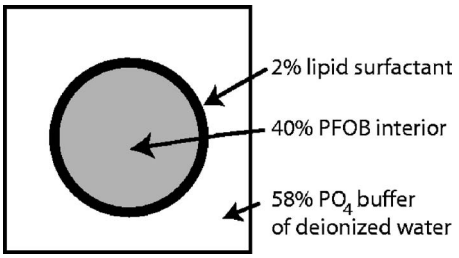

FIG. 6. A cross-sectional diagram of the nanoparticles used in our study.

occurs, t_0 (or t_1) is used to break the interval into two pieces. We replace $g(t)$ by its average value over these two intervals to obtain a "smoothed" function

$$g_1(t) = \begin{cases} \dfrac{1}{t_0}\displaystyle\int_0^{t_0} g(t)dt = \dfrac{[t_0 - K_0 - f_{\min}]}{T_0}, & t < t_0 \\ \dfrac{1}{1-t_0}\displaystyle\int_{t_0}^{1} g(t)dt = \dfrac{[f_{\max} + K_0 - t_0]}{1-t_0}, & t \geqslant t_0. \end{cases} \tag{54}$$

Then, by the smoothing lemma shown in Appendix B, we have

$$\int_0^1 g(t)\log^2[g(t)]dt \geqslant \int_0^1 g_1(t)\log^2[g_1(t)]dt \equiv I. \tag{55}$$

The integral evaluates to the following lower bound for the integral appearing in Eq. (53):

$$I = [t_0 - K_0 - f_{\min}]\log^2\left[\frac{t_0 - K_0 - f_{\min}}{t_0}\right] + [f_{\max} + K_0 - t_0]\log^2\left[\frac{f_{\max} + K_0 - t_0}{1-t_0}\right]. \tag{56}$$

A similar argument using t_1 and K_1 gives the alternate lower bound,

$$I = [K_1 - t_1 - f_{\min}]\log\left[\frac{K_1 - t_1 - f_{\min}}{t_1}\right] + [f_{\max} + t_1 - K_1]\log\left[\frac{f_{\max} + t_1 - K_1}{1-t_1}\right]. \tag{57}$$

In Sec. IV we discuss the relative trade-offs between accuracy and numerical stability of these metrics as applied to backscattered waveforms acquired from molecularly targeted neovasculature.

III. MATERIALS AND METHODS

A. Nanoparticles for molecular imaging

A cross section of the spherical liquid nanoparticles used in our study is diagrammed in Fig. 6. For *in vivo* imaging we formulated nanoparticles targeted to $\alpha_v\beta_3$ integrins of neovascularity in cancer by incorporating an "Arg-Gly-Asp" mimetic binding ligand into the lipid layer. Methods developed in our laboratories were used to prepare perfluorocarbon (perfluorooctylbromide, PFOB, which remains in a liquid state at body temperature and at the acoustic pressures used in this study[20]) emulsions encapsulated by a lipid-surfactant monolayer.[41,42] The Arg-Gly-Asp mimetic was coupled at a 1:1 molar ratio to malyimidophenyl-butyramide-polyethylene glycol2000-phosphatidylethanolamine resuspended from a dry lipid film in 3 mL of N_2-purged, 6 mmol/L ethylenediaminetetraacetic acid (EDTA) by water-bath sonication for 30 min at 37–40 °C. This ligand premix was added to the remaining surfactant components, perfluorooctylbromide, and water for emulsification.[43] Nontargeted particles were prepared by excluding the targeting ligand. The nominal sizes for each formulation were measured with a submicron particle analyzer (Malvern Zetasizer, Malvern Instruments). Particle diameter was measured at 200±30 nm.

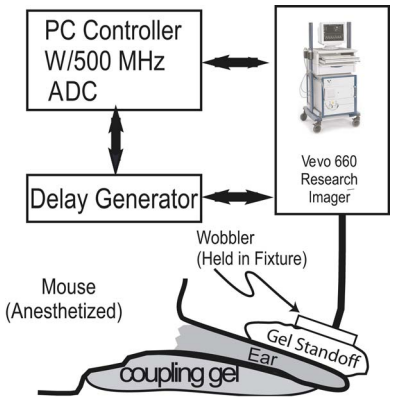

FIG. 7. (Color online) A diagram of the apparatus used to acquire rf data backscattered from HPV mouse ears *in vivo*.

B. Animal model

The study was performed according to an approved animal protocol and in compliance with guidelines of the Washington University institutional animal care and use committee.

The model used is the transgenic K14-HPV16 mouse that contains human papilloma virus-16 oncoproteins driven by a keratin promoter so that lesions develop in the skin. Typically the ears exhibit squamous metaplasia, a precancerous condition, associated with abundant neovasculature that expresses the $\alpha_v\beta_3$ integrin. Eight of these transgenic mice[44,45] were treated with 1.0 mg/kg i.v. of either $\alpha_v\beta_3$-targeted nanoparticles (n=4) or untargeted nanoparticles (n=4) and imaged dynamically for 1 h using a research ultrasound imager (Vevo 660 40 MHz probe) modified to store digitized rf waveforms acquired at 0, 15, 30, and 60 min time points. All rf data were processed off-line to reconstruct images using information theoretic and conventional receivers. Image segmentation was performed using the threshold which excluded 93% of the area under the composite histogram for all data sets (as described in the following in connection with Fig. 9). The mean value of segmented pixels was computed at each time postinjection. In both control and targeted cases, the mouse was placed on a heated platform maintained at 37 °C, and anesthesia was administered continuously with isoflurane gas (0.5%).

C. Ultrasonic data acquisition

A diagram of our apparatus is shown in Fig. 7. Radio

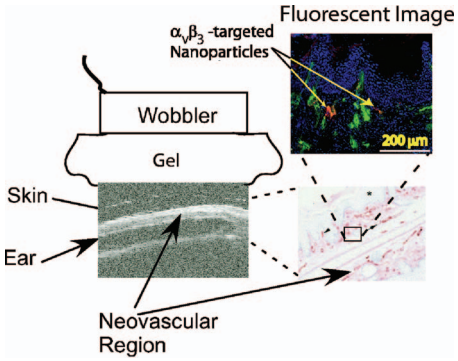

FIG. 8. Close-up of transducer, standoff, and ear, with enlarged histological image showing location of binding sites, and a fluorescent image from the same anatomical region showing that $\alpha_v\beta_3$-targeted nanoparticles indeed accumulate in this portion of the mouse ear.

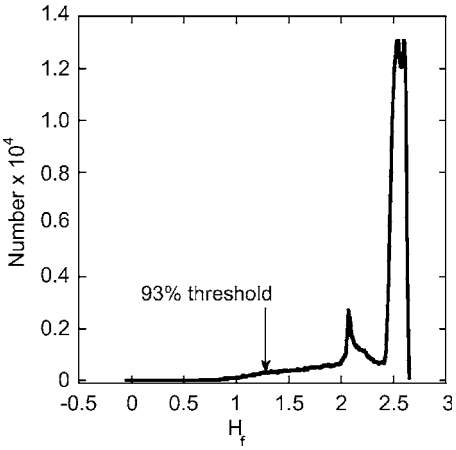

FIG. 9. A histogram from the composite H_f images acquired at 0, 15, 30, 45, and 60 min postinjection. The histogram has two peaks, a characteristic observed in several studies using different equipment and animal models (Refs. 21–23). The threshold level used in this study is indicated by the arrow.

frequency data were acquired with a research ultrasound system (Vevo 660, Visualsonics, Toronto, Canada), with an analog port and a sync port to permit digitization. The tumor was imaged with a 40 MHz single element "wobbler" probe and the rf data corresponding to single frames were stored on a hard disk for later off-line analysis. The frames (acquired at a rate of 30 Hz) consisted of 384 lines of 4096 eight-bit words acquired at a sampling rate of 500 MHz using a Gage CS82G digitizer card (connected to the analog-out and sync ports of the Vevo) in a controller PC. Each frame corresponds spatially to a region 0.8 cm wide and 0.3 cm deep.

The wobbler transducer used in this study is highly focused (3 mm in diameter) with a focal length of 6 mm and a theoretical spot size of 80×1100 μm (lateral beam width $\times$ depth of field at -6 dB), so that the imager is most sensitive to changes occurring in the region swept out by the focal zone as the transducer is "wobbled." Accordingly, a gel standoff was used, as shown in Fig. 7, so that this region would contain the mouse ear.

A close-up view showing the placement of transducer, gel standoff, and mouse ear is shown on the left side of Fig. 8. Below this is a *B*-mode gray scale image (i.e., logarithm of the analytic signal magnitude). Labels indicate the location of skin (top of image insert), the structural cartilage in the middle of the ear, and a short distance below this, the echo from the skin at the bottom of the ear. To the left of this is an image of a histological specimen extracted from a HPV mouse model that has been magnified 20 times to permit better assessment of the thickness and architecture of the sites where $\alpha_v\beta_3$ targeted nanoparticle might attach (red by β_3 staining). Skin and tumor are both visible in the image. On either side of the cartilage (center band in image), extending to the dermal-epidermal junction, is the stroma. It is filled with neoangiogenic microvessels. These microvessels are also decorated with $\alpha_v\beta_3$ nanoparticles as indicated by the fluorescent image (labeled, in the upper right of the figure) of a bisected ear from an $\alpha_v\beta_3$-injected K14-HPV16 transgenic mouse (Neumann *et al.*).[46] It is in this region that the $\alpha_v\beta_3$-targeted nanoparticles are expected to accumulate, as indicated by the presence of red β_3 stain in the magnified image of an immunohistological specimen also shown in the image.

D. Ultrasonic data processing

The analysis of rf frames corresponding to data in *B*-scan format proceeds as follows. Each of the 384 rf lines in the data was first upsampled from 4096 to 8192 points, using a cubic spline fit to the original data set in order to improve the stability of the thermodynamic receiver algorithms. Previous work has shown benefit from increased input waveform length.[5,7] Next, a moving window analysis was performed on the upsampled data set using a rectangular window that was advanced in 0.064 μs steps (64 points), resulting in 121 window positions within the original data set. The entropy, H_f ($\log[E_f]$) within each window is used to produce the H_f ($\log[E_f]$) image.

E. Image analysis

For this study, in which the same portion of the anatomy was imaged at successive intervals, the objective was to quantify changes in image features as a function of time. The first step in this process was the creation of a composite image from the images obtained at 0 through 60 min. Next, an estimate of the probability density function (PDF) of this composite image was computed by normalizing the pixel value histogram to have unit area. We emphasize that this function is not related to the density functions $w_f(y)$, that we defined in Eq. (1). Instead, it is a calculational device used to objectively segment H_f and $\log[E_f]$ images into "enhanced" and "unenhanced" regions. A typical histogram is shown in Fig. 9. Its most notable feature is the presence of two local maxima; a feature that has been observed in several different experiments involving different animal models and different imaging equipment.[20–23] The first, larger maxima, corresponds to the relatively homogeneous gray background visible in most H_f images, the smaller peak corresponds to tissue interfaces, which appear also as bright features in gray-scale B-mode images such as that shown in the inset of Fig. 8.[22]

Several different methods of image segmentation based on PDF were investigated. In all of these a specific value, or

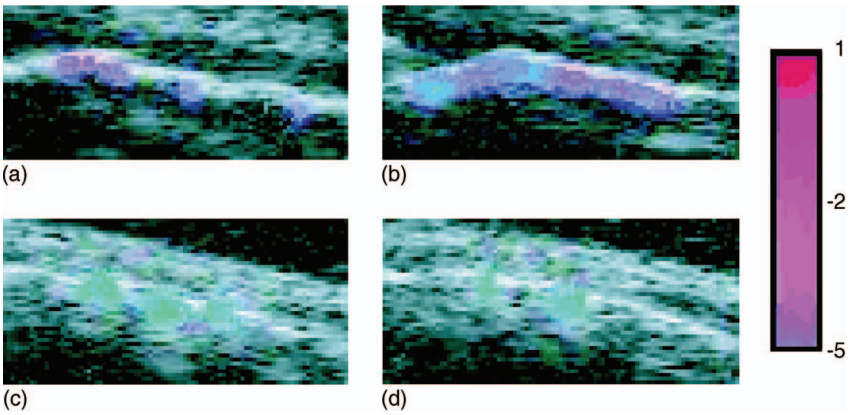

FIG. 10. Cropped images showing a comparison of H_f enhanced conventional images showing the effects of targeting (top row) vs control (bottom row).

threshold, in the histogram was chosen and the images divided into two regions: those having pixel values above the threshold (considered to be unenhanced) and those having pixel values below (referred to subsequently as enhanced pixels). The PDF of all composite images exhibited a two peak structure with a large and small peak. Thresholds were set at the second minimum, and at the halfway point between the large and small peaks. The full width at half maximum (FWHM) was also computed, and thresholds set at: 4.5, 3.5, 3.25, 3, 2.75, and 2.5 FWHM below the large peak. Thresholds were also set at points such that 97%, 95%, 93%, 90%, 87%, and 80% of the pixel values were above the threshold. After selection of a threshold value, regions of interest (ROI) were selected using NIH ImageJ (http://rsb.info.nih.gov/ij/), and the mean value of the pixels lying below the threshold were computed for each of the images acquired at 0, 15, 30, 45, and 60 min postinjection. The mean value at zero minutes was subtracted from the values obtained for all subsequent times, to obtain a sequence of changes in receiver output as a function of time postinjection. This was done for all four animals injected with targeted nanaoparticles and for the four control animals. These sequences of relative changes were then averaged over targeted and control groups to obtain a sequence of time points for change in receiver output for both groups of animals. The threshold of 93% was finally chosen since it produced the smallest p value (0.00043) for a t-test comparing the mean values of the ROI at 15 min as compared to 60 min. The corresponding p value for the control group was 0.27.

IV. RESULTS

In order to present the data in a format that combines the superior spatial resolution of conventional medical imaging with the superior detection capability of the entropy receiver we have employed a scheme similar to Doppler-enhanced imaging. Namely, we color-code pixels of the conventional gray-scale composite image using the corresponding pixel in the entropy image, to produce a composite image like that shown in Fig. 10. This figure was made by colorizing the entropy image and then superposing the colorized pixels lying below the 93% threshold onto the conventional image to indicate regions of "enhancement."

The top panel of Fig. 11 compares the growth, with time postinjection, of the mean value of the enhanced regions of H_f images obtained from all eight of the animals used in our study. Standard error bars are shown with each point. These data were obtained by computing the mean value of pixels lying below the 93% threshold at each time point (0, 15, 30, 45, and 60 min) for each animal (four injected with targeted nanoparticles, four injected with nontargeted nanoparticles) as discussed earlier. As the data show, the mean value, or enhancements, obtained in the targeted group increase linearly with time. After 30 min the mean value of enhancement is measurable. Moreover, the values at 15 and 60 min are statistically different ($p < 0.00043$). The bottom panel of Fig. 11 shows the corresponding result obtained from the control group of animals that were injected with nontargeted nanoparticles. There is no discernible trend in the group and

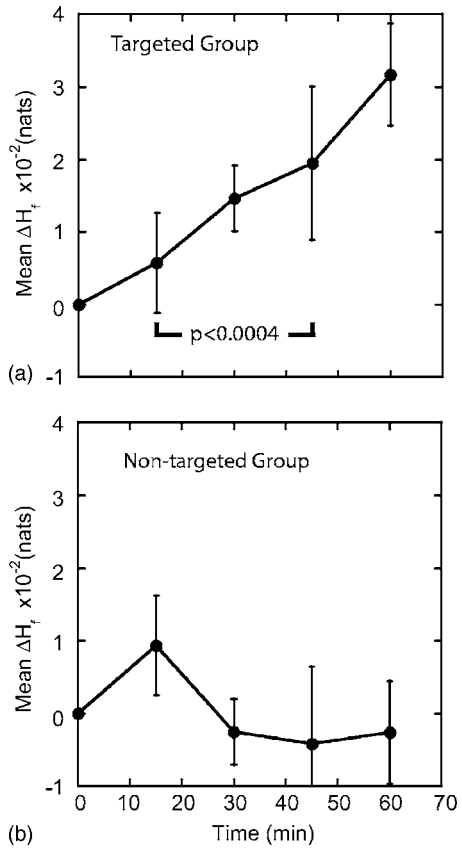

FIG. 11. A plot of average enhancement obtained by analysis of H_f images from nine HPV mice injected with $\alpha_v\beta_3$ targeted nanoparticles and five control HPV mice given no injection.

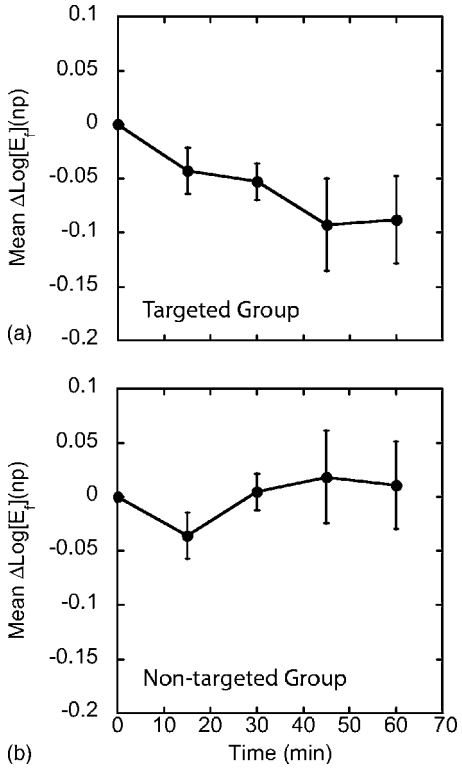

FIG. 12. A plot of average enhancement obtained by analysis of $\log[E_f]$ images from nine HPV mice injected with $\alpha_v\beta_3$ targeted nanoparticles and five control HPV mice given no injection.

the last three time points are not statistically different from zero. Comparison of the enhancement measured at 15 and 60 min yields a p value ≈ 0.27.

The corresponding results obtained using the $\log[E_f]$ receiver are shown in Fig. 12, whose top panel compares the growth, with time, of the mean value of the enhanced regions of $\log[E_f]$ images obtained from all eight of the animals used in our study. Standard error bars are shown with each point. These data were obtained by computing the mean value of pixels lying below the 93% threshold at each time point (0, 15, 30, 45, and 60 min) for each animal (four injected with targeted nanoparticles, four injected with nontargeted nanoparticles) as discussed earlier. Unlike the entropy case, the values at 15 and 60 min are not statistically different ($p = 0.10$). The bottom panel of Fig. 12 shows the corresponding result obtained from the control group of animals that were injected with nontargeted nanoparticles. There is no discernible trend in the group and the last three time points are not statistically different from zero.

The results summarized in Figs. 11 and 12 are consistent with Eqs. (47), (50), (51), (56), and (57). This is demonstrated in Fig. 13, which uses these equations to estimate the relative sensitivities, defined as the percentage change of receiver output. To obtain this fraction, the following images were made using the same 15 min data sets that were used to make Fig. 11: maximum average relative receiver sensitivity magnitude for $\log E_f$ [Eq. (47)], minimum average relative receiver sensitivity magnitude, $\|\log[w_f(y)]^2\|_2$, for H_f [Eq. (45)] with $\|y^2\|_2$, the "minimum $w_f(y)$ estimate" [Eq. (50)], the "maximum $f'_{\uparrow}(t)$ estimate" [Eq. (51)], K_0 [Eq. (56)], and

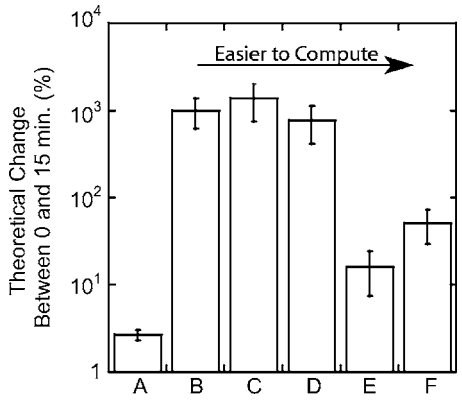

FIG. 13. Comparisons of receiver sensitivities, as defined in the text, for 15 min data sets shown in Fig. 10.

K_1 [Eq. (57)], respectively. To these were applied the ROI defined by the H_f images thresholded at the 93% level. Subsequently, the mean pixel value within the ROI was computed. Having the numerator of the sensitivity, the same ROI was applied to the $\log[E_f]$ image, and the H_f image, respectively, to compute a reference value (i.e., denominator) for either the sensitivity of $\log[E_f]$ or H_f images. These values are plotted as a percentage change relative to the 15 min value in Fig. 13, so that lower values indicate lower relative sensitivity. As Fig. 13 shows (column A) $\log[E_f]$ has the lowest sensitivity, while the sensitivity for H_f, column B, is high, consistent with the results of Fig. 11. Column C shows the estimate of $|\Delta H_f|$ based on the "minimum $w_f(y)$ estimate" [Eq. (50)]. The mean value provided by this estimate is apparently a little greater than the "exact" value although the error bar for this estimate is also greater. These result from use of a single point from $w_f(y)$, which is susceptible to Fourier "ringing," to obtain column C versus the integration of a function of $w_f(y)$, to obtain column B. However, the error bars of columns B and C overlap, so the estimates agree to within experimental error. Column D shows the estimate of entropy sensitivity obtained using the "maximum $f'_{\uparrow}(t)$ estimate" [Eq. (51)]. This estimate, which has the advantage of being rapidly computable in the time domain but the disadvantage of requiring the potentially noise enhancing operation of numerically differentiating an experimental waveform, also agrees, to within experimental error, with columns B and C. Estimates that do not require numerical differentiation of experimental data are shown in columns E and F. These were obtained using K_0 and K_1 [Eqs. (56) and (57)] to compute the numerator of the sensitivity fraction and are not susceptible to either Fourier ringing or noise enhancement by numerical differentiation. They are thus more stable than the estimates in columns C and D. All of these estimates successfully predict the greater relative sensitivity of H_f vs $\log[E_f]$ imaging shown in Fig. 11. The label on the plot indicates that they appear, from left to right, approximately in order of decreasing computational cost and increasing numerical stability, with the two columns, E, F, being computed in the time domain after the relatively inexpensive step of sorting the data. As these bars indicate, it is possible to assess, *a priori*, the sensitivity of entropy imaging without having to compute it. This information could be very useful in

imaging applications, which must balance computing requirements and frame-rate constraints.

V. DISCUSSION

The fact that the results displayed in Fig. 13 could have been used to predict the outcome of our experimental study (as summarized in Figs. 11 and 12) indicates the utility of the qualitative benchmarks derived in Sec. II (Approach). This suggests the existence of a collection of performance benchmarks, useful as an intuitive guide for experimental application of entropy receivers, similar to that which already exists for more conventional signal analysis. Traditional *B*-mode grayscale imaging (which is $\log[E_f]$ imaging in the limit where the moving window or box-car is the same size as the digitization interval[47]) is a specific example where intuitive ideas about the effects of changing gain settings, attenuation from intervening tissue, noise, or introduction of bubble-based contrast agents are routinely applied in both the laboratory and clinic.

We have described the impact of some of these factors on the entropy-based receiver, H_f. In Sec. II E, we showed that H_f is invariant with respect to rescaling of $f(t)$. In Secs. II G 3 and II G 5, we derived an average-case relationship between the sensitivities of H_f and energy-based receivers. The utility of this relation is demonstrated by our experimental results.

We have provided, in Sec. II C, a preliminary, although indirect, step toward a physical interpretation for H_f in the case of scattering problems. In that section, we described a simplified scattering model and indicated its relation to $w_f(y)$. We observed that different scattering model configurations could lead to the same density for the backscattered waves, which implies they would have the same entropies and same energies. However, from an experimental point of view the most important characteristic of any receiver is its sensitivity to subtle changes in scatterer configuration. For the study described here the entropy is more sensitive.

Ultimately, we desire a physical interpretation of H_f similar to that for energy. In acoustics, perhaps the simplest interpretation of energy arises from spring models employed to describe the interaction of sound with the supporting medium. Deeper insight is obtained by application of Hamiltonian or Lagrangian mechanics to modeling of wave propagation and scattering in a supporting medium. This setting provides immediate access to a thoroughly developed concept of energy that has proven predictive power. At this time there is no corresponding body of knowledge for H_f, and although initial experiments[3–7,20–24] have been promising and we have taken initial steps toward understanding its physical basis, the ultimate scope of applicability for this quantity remains to be determined.

ACKNOWLEDGMENTS

This study was funded by NIH EB002168, HL042950, and CO-27031 and NSF DMS 0501079. The research was carried out at the Washington University Department of Mathematics and the School of Medicine.

APPENDIX A: TWO IMPLICATIONS OF STATISTICAL INDEPENDENCE

Even though the concept of independence is widely used, it can have surprising implications when considered from the frame of mind usually adopted in deterministic signal processing. We provide two examples in the following. In the first we show that there do not exist a complete orthonormal set of functions that are statistically independent. In the second we show that there is no measurable function (i.e., random variable) that is statistically independent of the waveform $f(t)=t$.

1. Statistical independence versus linear independence of functions

Here we discuss statistical independence and its relation to eigenfunction-based signal processing. The definition of a density function $w_f(y)$ corresponds to P_X where X is a random variable. In the physics literature the term random variable is associated with functions that are unpredictable, and thus infinitely rough (i.e., everywhere continuous but nowhere differentiable), such as the Brownian motion. However, the mathematical definition of a "random" variable consists solely of the requirement that a function be measurable.[48,49] Hence, familiar functions such as $\sin(t)$ and e^t are also random variables (once a domain, e.g., $[0, 1]$ is chosen), with well-defined density functions. In probabilistic notation the density function $w_f(y)$ of $f(t)$ would be written as P_f. Just as two random functions X and Y have a joint density function $P_{X,Y}$ so do functions like $\sin(t)$ and e^t. In our notation, which is borrowed from measure theory,[11] the joint density function of two waveforms, $y=f(t)$ and $x=g(t)$, would be written $w_{f,g}(y,x)$. The fundamental integral relationship, Eq. (1), becomes

$$\int_0^1 \phi(f(t),g(t))dt = \int_0^1 \int_0^1 \phi(y,x)w_{f,g}(y,x)dydx. \qquad \text{(A1)}$$

The notion that two functions $f(t)$, $g(t)$ are independent is expressed in the measure-theoretic notation by the equation $w_f(y)w_g(x)=w_{f,g}(y,x)$. To see that this is a very strong property, possessed by few of the functions of ordinary calculus, let $\phi(y,x)=yx$ in Eq. (A1), then

$$\begin{aligned}\int_0^1 \phi(f(t),g(t))dt &= \int_0^1 \int_0^1 \phi(y,x)w_{f,g}(y,x)dydx \\ &= \int_0^1 \int_0^1 yxw_f(y)w_g(x)dydx \\ &= \int_0^1 yw_f(y)dy \int_0^1 xw_g(x)dx \\ &= \int_0^1 f(t)dt \int_0^1 g(t)dt,\end{aligned}$$

that is,

$$\int_0^1 f(t)g(t)dt = \int_0^1 f(t)dt \int_0^1 g(t)dt, \tag{A2}$$

which is certainly not true in general. To see how remarkable the notion of independence really is, assume that $f(t)$ has zero mean, then for all $g(t)$ independent of $f(t)$,

$$\int_0^1 f(t)g(t)dt = 0. \tag{A3}$$

Moreover, since Eq. (A2) generalizes immediately to

$$\int_0^1 f(t)\phi(g(t))dt = \int_0^1 f(t)dt \int_0^1 \phi(g(t))dt, \tag{A4}$$

we see that $f(t)$ and any continuous function, ϕ, of $g(t)$ are orthogonal.

Among other things, this implies that there are no complete orthonormal sets of statistically independent functions.

To see this, suppose, on the contrary, that there exist a complete set of orthonormal functions, $\{\psi_k(t)|k=1,\ldots\}$, which are pairwise statistically independent. For mathematical simplicity we will also assume that these functions are real, bounded, and that any three of the $\psi_k(t)$ are idependent.

Since the set is complete we must be able to represent a constant using this basis so that for some k,

$$\int_0^1 \psi_k(t)dt \neq 0. \tag{A5}$$

Without loss of generality, we may reorder the indexing of the $\psi_k(t)$ so that this happens for $k=1$.

If $j \neq 1$, then by orthogonality and independence,

$$0 = \int_0^1 \psi_1(t)\psi_j(t)dt = \int_0^1 \psi_1(t)dt \int_0^1 \psi_j(t)dt. \tag{A6}$$

So that

$$\int_0^1 \psi_j(t)dt = 0, \tag{A7}$$

for all $k>1$.

Since the $\psi_k(t)$ are bounded, any power of $\psi_k(t)$ is integrable. Thus, we observe that for every $k \neq j$, 1,

$$\int_0^1 \psi_j(t)^2\psi_k(t)dt = \int_0^1 \psi_j(t)^2dt \int_0^1 \psi_k(t)dt = 0. \tag{A8}$$

For $j=1$, this implies that all coefficients except the first are zero, and so $\psi_1^2(t)=\alpha\psi_1(t)$ for some constant α, i.e., $\psi_1(t)=\alpha$. Moreover, $|\alpha|=1$, since the $\psi_k(t)$ have norm 1.

For $j>1$, Eq. (A8) tells us that all coefficients except the 1st and jth are zero Thus, the expansion for $\psi_j^2(t)$ is

$$\psi_j^2(t) = a_j + b_j\psi_j(t), \tag{A9}$$

i.e., every value of $\psi_j(t)$ satisfies the same quadratic equation. Hence, $\psi_j(t)$ can have only two distinct values, which we will denote by a_j and a_j'.

Letting $\mathbb{I}_{A_j}(t)$ and $\mathbb{I}_{A_j'}$ denote the characteristic functions of the sets A_j and A_j', where $\psi_j(t)$ takes on the values a_j and a_j', respectively, we write

$$\psi_j(t) = a_j\mathbb{I}_{A_j}(t) + a_j'\mathbb{I}_{A_j'}(t). \tag{A10}$$

Specifically, for $j=2$, we have

$$\psi_2(t) = a_2\mathbb{I}_{A_2}(t) + a_2'\mathbb{I}_{A_2'}(t). \tag{A11}$$

We will now construct a nonzero function that cannot be represented in terms of the $\psi_j(t)$, contradicting the assumption of their completeness. Consider

$$f(t) = \psi_3(t)\mathbb{I}_{A_2}(t). \tag{A12}$$

We observe that any bounded measurable function $\phi(t)$ satisfying $\phi(a_2)=1$ and $\phi(a_2')=0$ also satisfies

$$\mathbb{I}_{A_j}(t) = \phi(\psi_2(t)). \tag{A13}$$

So, by pairwise independence,

$$\begin{aligned}\int_0^1 f(t)\psi_1(t)dt &= \int_0^1 \psi_3(t)\mathbb{I}_{A_2}(t)dt = \int_0^1 \psi_3(t)\phi(\psi_2(t))dt \\ &= \int_0^1 \psi_3(t)dt \int_0^1 \phi(\psi_2(t))dt = 0,\end{aligned} \tag{A14}$$

and

$$\begin{aligned}\int_0^1 f(t)\psi_2(t)dt &= \int_0^1 \psi_3(t)\mathbb{I}_{A_2}(t)\psi_2(t)dt \\ &= \int_0^1 \psi_3(t)\phi(\psi_2(t))dt\psi_2(t) \\ &= \int_0^1 \psi_3(t)dt \int_0^1 \phi(\psi_2(t))\psi_2(t)dt = 0,\end{aligned} \tag{A15}$$

since $\int_0^1\psi_3(t)dt=0$. For $k>3$, we have, using, triple-wise independence,

$$\begin{aligned}\int_0^1 f(t)\psi_2(t)dt &= \int_0^1 \psi_3(t)\mathbb{I}_{A_2}(t)\psi_k(t)dt \\ &= \int_0^1 \psi_3(t)\phi(\psi_2(t))dt\psi_k(t) \\ &= \int_0^1 \psi_3(t)dt \int_0^1 \phi(\psi_2(t)) \int_0^1 \psi_k(t)dt = 0.\end{aligned} \tag{A16}$$

Thus

$$f(t) = \alpha\psi_3(t), \tag{A17}$$

or

$$\psi_3(t)\mathbb{I}_{A_2}(t) = \alpha\psi_3(t). \tag{A18}$$

This implies that $\psi_3(t)=0$ for any t in $[0, 1]$ that is not in A_2, i.e., it takes on 0 as one of its (two possible) values contradicting $\int_0^1\psi_3(t)dt=0$. Thus, it is not possible to expand $f(t)$ in terms of the $\psi_k(t)$, which contradicts the assumption that they comprise a complete set of functions. Specific examples of independent functions may be found in the articles by Agnew and Kac, Karlin, and Kuipers.[17–19]

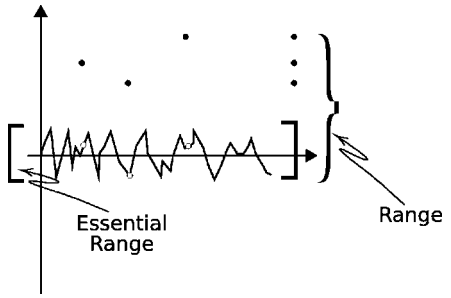

FIG. 14. A diagram of a noisy time-domain signal. The full range of the signal includes the transients. However, the essential range, indicated by the bracket beside the vertical axis excludes these.

2. Statistical independence and the function $f(t)=t$

Here we prove the somewhat surprising result that there does not exist a nonconstant function that is statistically independent of the function $y=f(t)=t$. This result may generalized to other monotonic functions, as discussed at the end of this section. The linear case is presented since it is the simplest case and illustrates the basic ideas in the most straightforward way.

We begin with the definition of the essential range, R_f, of a function $f(t)$, which is the set of all real numbers, z such that $\{x:|f(x)-z|<\epsilon\}$ has positive measure for all $\epsilon>0$. Expressed in terms of probability, this can be thought of as the set of all points, z, such that for any neighborhood of z, $f(t)$ takes on values in that neighborhood with nonzero probability, or if $z\in I$, where I is an open interval then, $f^{-1}(I)$ has positive measure, i.e., $|f^{-1}(I)|>0$ where we have used the symbol $|S|$ to denote the measure of a set S as we will do for the remainder of this section. In terms of digital waveforms, which may have sharp transients, R_f can be thought of as the range of $f(t)$ without the transients as shown in Fig. 14.

A function whose essential range is only one point is said to be essentially constant. We claim that there does not exist a measurable function $g(t)$ defined on [0, 1] that is statistically independent of $f(t)$, unless $g(t)$ is essentially constant.

To prove this assume that $g(t)$ is not essentially constant, i.e., that the essential range of $g(t)$ has at least two points. Let α, β, $\alpha\neq\beta$, be in the essential range of $g(t)$. Let $\alpha\in I_\alpha$, $\beta\in I_\beta$, I_α, I_β open intervals with $I_\alpha\cap I_\beta=\emptyset$ (p. 98 of Munkres[50]).

Now, since $f(t)$ and $g(t)$ are independent, for any measurable sets, A, B,

$$|f^{-1}(A)\cap g^{-1}(B)|=|f^{-1}(A)|\times|g^{-1}(B)| \tag{A19}$$

i.e., using probabilistic notation

$$\mathbb{P}[f\in A \text{ and } g\in B]=\mathbb{P}[f\in A]\times\mathbb{P}[g\in B]. \tag{A20}$$

Let $A=g^{-1}(I_\alpha)$, $B=I_\beta$. Then the assumption of independence leads to

$$|f^{-1}(g^{-1}(I_\alpha))\cap g^{-1}(I_\beta)|=|f^{-1}(g^{-1}(I_\alpha))|\times|g^{-1}(I_\beta)|. \tag{A21}$$

Now $f^{-1}(g^{-1}(I_\alpha))=g^{-1}(I_\alpha)$, since $f(t)=t$, so

$$\begin{aligned}|f^{-1}(g^{-1}(I_\alpha))\cap g^{-1}(I_\beta)|&=|g^{-1}(I_\alpha)\cap g^{-1}(I_\beta)|\\&=|g^{-1}(I_\alpha\cap I_\beta)|=0\end{aligned} \tag{A22}$$

On the other hand

$$\begin{aligned}|f^{-1}(g^{-1}(I_\alpha))\cap g^{-1}(I_\beta)|&=|f^{-1}(g^{-1}(I_\alpha))|\times|g^{-1}(I_\beta)|\\&=|g^{-1}(I_\alpha)|\times|g^{-1}(I_\beta)|\neq 0\end{aligned} \tag{A23}$$

since $|g^{-1}(I_\alpha)|\neq 0$ and $|g^{-1}(I_\beta)|\neq 0$ by the definition of the essential range. If we let $A=f(g^{-1}(I_\alpha))$, $B=I_\beta$ where $f(t)$ is any monotonic function, then the above-presented discussion is essentially unchanged and we see that result may be generalized to the case of monotonic functions.

APPENDIX B: SMOOTHING DECREASES ENTROPY

The following lemma states that smoothing a density function decreases its entropy. Let

$$g(t)=\frac{d}{dt}[f_\uparrow(t)]. \tag{B1}$$

If $g>0$ on any interval $I\subset[0,1]$ and we define

$$g_1(t)=\begin{cases}g(t), & t\notin I\\ \dfrac{1}{|I|}\displaystyle\int_0^1 g(t)dt, & t\in I,\end{cases} \tag{B2}$$

where $|I|$ denotes the measure of the set I, then

$$\int_0^1 g_1(t)\log_2[g_1(t)]dt<\int_0^1 g(t)\log_2[g(t)]dt \tag{B3}$$

unless $g_1\equiv g(t)$.

Proof: If g is not constant on I, choose two sets E_1, $E_2\subset I$ such that $|E_1=|E_2|>0$, and

$$g|_{E_1}<\frac{1}{|I|}\int_0^1 g(t)dt-2\varepsilon, \tag{B4}$$

$$g|_{E_2}>\frac{1}{|I|}\int_0^1 g(t)dt+2\varepsilon \tag{B5}$$

for some $\varepsilon>0$. Let $g_2=g+\varepsilon\chi_{E_1}-\varepsilon\chi_{E_2}$, where χ_{E_i} is the characteristic function of the set E_i. Then

$$\begin{aligned}&\int_0^1 g_2(t)\log_2[g_2(t)]dt-\int_0^1 g(t)\log_2[g(t)]dt\\&=\varepsilon\int_{E_1}(\log_2[g_2(t)]+2\log[g(t)])dt\\&\quad-\varepsilon\int_{E_2}(\log_2[g_2(t)]+2\log[g(t)])dt+O[\varepsilon^2].\end{aligned} \tag{B6}$$

As $g(t)$ on E_1 is everywhere less than $g(t)$ on E_2, this is negative to first order. So we can reduce the entropy integral by smoothing $g(t)$.

[1]A. H. Schmieder, P. M. Winter, S. D. Caruthers, T. D. Harris, T. A. Williams, J. S. Allen, E. K. Lacy, H. Zhang, M. J. Scott, G. Hu, J. D. Robertson, S. A. Wickline, and G. M. Lanza, "Molecular mr imaging of melanoma angiogenesis with $\alpha_v\beta_3$-targeted paramagnetic nanoparticles,"

Magn. Reson. Med. **53**, 621–627 (2005).
[2]C. S. Hall, J. N. Marsh, M. J. Scott, P. J. Gaffney, S. A. Wickline, and G. M. Lanza, "Time evolution of enhanced ultrasonic reflection using a fibrin-targeted nanoparticulate contrast agent," J. Acoust. Soc. Am. **108**, 3049–3057 (2000).
[3]M. Hughes, "A comparison of Shannon entropy versus signal energy for acoustic detection of artificially induced defects in plexiglass," J. Acoust. Soc. Am. **91**, 2272–2275 (1992).
[4]M. Hughes, "Analysis of ultrasonic waveforms using Shannon entropy," Proceedings of the 1992 IEEE Ultrasonics Symposium, Vol. **2**, pp. 1205–1209.
[5]M. Hughes, "Analysis of digitized waveforms using Shannon entropy," J. Acoust. Soc. Am. **93**, 892–906 (1993).
[6]M. Hughes, "NDE imaging of flaws using rapid computation of Shannon entropy," Proceedings of the 1993 IEEE Ultrasonics Symposium, Vol. **2**, pp. 697–700.
[7]M. Hughes, "Analysis of digitized waveforms using Shannon entropy. II. High-speed algorithms based on Green's functions," J. Acoust. Soc. Am. **95**, 2582–2588 (1994).
[8]R. S. Bucy and P. D. Joseph, *Filtering for Stochastic Processes with Applications to Guidance* (Chelsea, New York, 1987).
[9]N. Weiner, *Extrapolation, Interpolation, and Smoothing of Stationary Time Series: With Engineering Applications* (MIT, Cambridge, MA, 1949).
[10]U. Grenander and M. Rosenblatt, *Stastical Analysis of Stationary Time Series* (Chelsea, New York, 1984).
[11]R. L. Wheeden and A. Zygmund, *Measure and Integral: An Introduction to Real Analysis* (Marcel-Dekker, New York, 1977).
[12]T. M. Cover and J. A. Thomas, *Elements of Information Theory* (Wiley-Interscience, New York, 1991).
[13]S. Kullback, *Information Theory and Statistics* (Dover, New York, 1997).
[14]F. M. Reza, *An Introduction to Information Theory* (Dover, New York, 1994).
[15]L. J. Ziomek, *Fundamentals of Acoustic Field Theory and Space-Time Signal Processing* (CRC Press, Boca Raton, FL, 1995).
[16]A. Soklakov, "Occam's razor as a formal basis for a physical theory," Found. Phys. Lett. **15**, 107–135 (2002).
[17]K. Agnew and M. Kac, "Translated functions and statistical independence," Bull. Am. Math. Soc. **7**, 148–154 (1941).
[18]S. Karlin, "Orthogonal properties of independent functions," Trans. Am. Math. Soc. **66**, 44–64 (1949).
[19]L. Kuipers, "Continuous distribution mod 1 and independence of functions," Nieuw Arch. Wiskd. **XI**, 1–3 (1963).
[20]M. S. Hughes, J. N. Marsh, J. Arbeit, R. Neumann, R. W. Fuhrhop, G. M. Lanza, and S. A. Wickline, "Ultrasonic molecular imaging of primordial angiogenic vessels in rabbit and mouse models with $\alpha_v\beta_3$-integrin targeted nanoparticles using information-theoretic signal detection: Results at high frequency and in the clinical diagnostic frequency range," Proceedings of the 2005 IEEE Ultrasonics Symposium.
[21]M. S. Hughes, J. N. Marsh, C. S. Hall, D. Savy, M. J. Scott, J. S. Allen, E. K. Lacy, C. Carradine, G. M. Lanza, and S. A. Wickline, "*In vivo* ultrasonic detection of angiogenesis with site-targeted nanoparticle contrast agents using measure-theoretic signal receivers," Proceedings of the 2004 IEEE Ultrasonics Symposium, Vol. **2**, pp. 1106–1109.
[22]M. S. Hughes, J. N. Marsh, C. S. Hall, D. Savy, M. J. Scott, J. S. Allen, E. K. Lacy, C. Carradine, G. M. Lanza, and S. A. Wickline, "Characterization of digital waveforms using thermodynamic analogs: Applications to detection of materials defects," IEEE Trans. Ultrason. Ferroelectr. Freq. Control **52**, 1555–1564 (2005).
[23]M. Hughes, J. Marsh, A. Woodson, E. Lacey, C. Carradine, G. M. Lanza, and S. A. Wickline, "Characterization of digital waveforms using thermodynamic analogs: Detection of contrast targeted tissue in mda 435 tumors implanted in athymic nude mice," Proceedings of the 2005 IEEE Ultrasonics Symposium.
[24]M. S. Hughes, J. N. Marsh, H. Zhang, A. K. Woodson, J. S. Allen, E. K. Lacy, C. Carradine, G. M. Lanza, and S. A. Wickline, "Characterization of digital waveforms using thermodynamic analogs: Detection of contrast-targeted tissue in vivo," IEEE Trans. Ultrason. Ferroelectr. Freq. Control **53**, 1609–1616 (2006).
[25]A. S. Weigend and N. A. Gershenfeld, *Time Series Prediction* (Addison-Wesley, Reading, MA, 1994).
[26]E. E. Merzbacher, J. Feagin, and T. Wu, "Superposition of the radiation from n independent sources and the problem of random flights," Am. J. Phys. **45**, 964 (1977).
[27]C. Burckhardt, "Speckle in ultrasound *b*-mode scans."
[28]R. F. Wagner, S. W. Smith, J. M. Sandrik, and H. Lopez, "Statistics of speckle in ultrasound *b*-scans," IEEE Trans. Ultrason. Ferroelectr. Freq. Control **30**, 156–163 (1983).
[29]T. A. Tuthill, R. H. Sperry, and K. J. Parker, "Deviations from Rayleigh statistics in ultrasonic speckle," Ultrason. Imaging **10**, 81–89 (1988).
[30]L. Weng, J. M. Reid, P. M. Shankar, and K. Soetanto, "Ultrasound speckle analysis based on the k distribution."
[31]R. C. Molthen, P. M. Shankar, and J. M. Reid, "Characterization of ultrasonic *b*-scans using non-Rayleigh statistics," Ultrasound Med. Biol. **21**, 161–170 (1995).
[32]V. Dutt and J. F. Greenleaf, "Statistics of the log-compressed echo envelope," J. Acoust. Soc. Am. **99**, 3817–3825 (1996).
[33]P. M. Shankar, R. Molthen, V. M. Narayanan, J. M. Reid, V. Genis, F. Forsberg, C. W. Piccoli, A. E. Lindenmayer, and B. B. Goldberg, "Studies on the use of non-Rayleigh statistics for ultrasonic tissue characterization," Ultrasound Med. Biol. **22**, 873–882 (1996).
[34]P. M. Shankar, "A compound scattering pdf for the ultrasonic echo envelope and its relationship to k and Nakagami distributions," IEEE Trans. Ultrason. Ferroelectr. Freq. Control **50**, 339–343 (2003).
[35]P. Tsui and S. Wang, "The effect of transducer characteristics on the estimation of Nakagami paramater as a function of scatterer concentration," Ultrasound Med. Biol. **30**, 1345–1353 (2004).
[36]E. Ashton and K. Parker, "Multiple resolution Bayesian segmentation of ultrasound images."
[37]G. Cloutier, M. Daronatand, D. Savery, D. Garcia, L. G. Durand, and F. Foster, "Non-Gaussian statistics and temporal variations of the ultrasound signal backscattered by blood at frequencies between 10 and 58 mHz," J. Acoust. Soc. Am. **116**, 566–577 (2004).
[38]R. C. Molthen, P. M. Shankar, J. M. Reid, F. Forsberg, E. J. Halpern, C. W. Piccoli, and B. B. Goldberg, "Comparisons of the Rayleigh and *k*-distribution models using *in vivo* breast and liver tissue," Ultrasound Med. Biol. **24**, 93–100 (1998).
[39]P. Shankar, "A general statistical model for ultrasonic backscattering from tissues," IEEE Trans. Ultrason. Ferroelectr. Freq. Control **47**, 727–736 (2000).
[40]P. Beckman and A. Spizzichino, *The Scattering of Electromagnetic Waves from Rough Surfaces* (Macmillan, New York, 1963).
[41]S. Flacke, S. Fischer, M. J. Scott, R. J. Fuhrhop, J. S. Allen, M. McLean, P. Winter, G. A. Sicard, P. J. Gaffney, S. A. Wickline, and G. M. Lanza, "Novel MRI contrast agent for molecular imaging of fibrin implications for detecting vulnerable plaques," Circulation **104**, 1280–1285 (2001).
[42]G. M. Lanza, K. D. Wallace, M. J. Scott, W. P. Cacheris, D. R. Abendschein, D. H. Christy, A. M. Sharkey, J. G. Miller, P. J. Gaffney, and S. A. Wickline, "A novel site-targeted ultrasonic contrast agent with broad biomedical application," Circulation **94**, 3334–3340 (1996).
[43]P. M. Winter, S. D. Caruthers, X. Yu, S. K. Song, J. J. Chen, B. Miller, J. W. M. Bulte, J. D. Robertson, P. J. Gaffney, S. A. Wickline, and G. M. Lanza, "Improved molecular imaging contrast agent for detection of human thrombus," Magn. Reson. Med. **50**, 411–416 (2003).
[44]J. M. Arbeit, R. R. Riley, B. Huey, C. Porter, G. Kelloff, R. Lubet, J. M. Ward, and D. Pinkel, "Chemoprevention of epidermal carcinogenesis in k14-hpv16 transgenic mice," Cancer Res. **59**, 3610–3620 (1999).
[45]J. M. Arbeit, K. Mnger, P. M. Howley, and D. Hanahan, "Progressive squamous epithelial neoplasia in k14-human papillomavirus type 16 transgenic mice," J. Virol. **68**, 4358–4368 (1994).
[46]R. G. Neumann, K. Olson, G. M. Lanza, S. A. Wickline, and J. M. Arbeit, "Targeted nanoparticle imaging of angiogenic endothelial activation in premalignant neoplasia and established epithelial cancers," J. Am. Coll. Surg. **203**(3S) S83 (2006).
[47]L. Ziomek, *Fundamentals of Acoustic Field Theory and Space-Time Signal Processing* (CRC Press, Boca Raton, FL, 1995).
[48]A. Kolmogorov, *Foundations of the Theory of Probability* (Chelsea, New York, 1950).
[49]G. B. Folland, *Real Analysis Modern Techniques and Their Applications* (Wiley, New York).
[50]J. R. Munkres, *Topology* (Prentice Hall, Upper Saddle River, NJ, 2000).

Statistical modeling of intrinsic structures in impacts sounds

Sofia Cavaco[a)]
Computer Science Department, Carnegie Mellon University, 5000 Forbes Avenue, Pittsburgh, Pennsylvania 15213

Michael S. Lewicki[b)]
Computer Science Department and Center for the Neural Basis of Cognition, Carnegie Mellon University, 4400 Fifth Avenue, Pittsburgh, Pennsylvania 15213

(Received 4 May 2006; revised 20 March 2007; accepted 20 March 2007)

This paper presents a statistical data-driven method for learning intrinsic structures of impact sounds. The method applies principal and independent component analysis to learn low-dimensional representations that model the distribution of both the time-varying spectral and amplitude structure. As a result, the method is able to decompose sounds into a small number of underlying features that characterize acoustic properties such as ringing, resonance, sustain, decay, and onsets. The method is highly flexible and makes no *a priori* assumptions about the physics, acoustics, or dynamics of the objects. In addition, by modeling the underlying distribution, the method can capture the natural variability of ensembles of related impact sounds. © *2007 Acoustical Society of America.*
[DOI: 10.1121/1.2729368]

PACS number(s): 43.60.Cg, 43.60.Wy [RAL] Pages: 3558–3568

I. INTRODUCTION

When an object is struck, the sound that it produces is determined by the physical properties of the object, such as its size, geometry, and material, and also by the characteristics of the event, like the force and location of impact. It is possible to derive physical models of impact sounds given the relationship between the physical and dynamic properties of the object, and the acoustics of the resulting sound. Models of sounds have proven useful in many fields, such as sound recognition, identification of events or properties (like material or length) of the objects involved, sound synthesis, virtual reality, and computer graphics. However, physical models are limited because of the *a priori* knowledge they require and because they do not successfully model all the complexities of real sounds.

One model of impact sounds is the resonance model proposed by Gaver (1994, 1988). This model consists of a sum of amplitude-decaying sine waves:

$$y(t) = \sum_{n=1}^{N} \alpha_n e^{-\delta_n t} \sin(\omega_n t), \tag{1}$$

where ω_n is the frequency of partial n, α_n is the initial amplitude of this partial, and $e^{-\delta_n t}$ is decay function of the same partial. The values of parameters ω, α, and δ can be set from mathematical expressions derived from physics for a limited set of very simple geometries for which the functions of frequency, amplitude, and decay are known. It is also possible to deal with more complex geometries by fitting the parameters to recorded sounds (Pai *et al.* 2001). A limitation of this simplified, knowledge-based model is that it fails to account for the rich structure and variability of real impact sounds. For instance, it fails to model the complex structure of the attack and the variability of sounds resulting from roughness in the surfaces. A solution to overcome this problem was proposed by van den Doel *et al.* (2001); however, some knowledge about the surfaces of the objects and their contact dynamics is still required. Other physical models have been proposed (e.g., Avanzini and Rocchesso, 2001a, b; Lambourg *et al.*, 2001), but as with the above-noted models, they require knowledge of the acoustics, as well as the physics, dynamics of contact, and the surface texture of the objects.

In order to obtain a detailed description of the modes of vibration and parameters of objects with complex geometries, some knowledge-based techniques use rigid body simulators developed for computer graphics (James *et al.*, 2006; O'Brien *et al.*, 2001, 2002). These approaches permit the synthesis of very realistic sounds; however, they are computationally intensive and they require a detailed description of the objects.

A more fundamental limitation of all these approaches, however, is that it is difficult to derive from natural impact sounds intrinsic acoustic properties beyond those that are explicitly modeled by the equations. For instance, how can a ringing property or a nonexponential decay be modeled by Eq. (1)?

This leads to another motivation for this work, which is the extraction of intrinsic features from sounds. Algorithms have been developed to extract basic features of impact sounds, such as the decay rates or the average spectra, but these approaches fail to capture the acoustic richness and variability that is characteristic of natural impact sounds.

In this paper, we propose a statistical data-driven method for learning the intrinsic features that govern the acoustic structure of impact sounds. The method aims to characterize the structures that are common to sounds of the same type (for instance, if the impacts on the same rod have

[a)]Electronic mail: scavaco@cs.cmu.edu
[b)]Electronic mail: lewicki@cnbc.cmu.edu

 0001-4966/2007/121(6)/3558/11/$23.00 © 2007 Acoustical Society of America

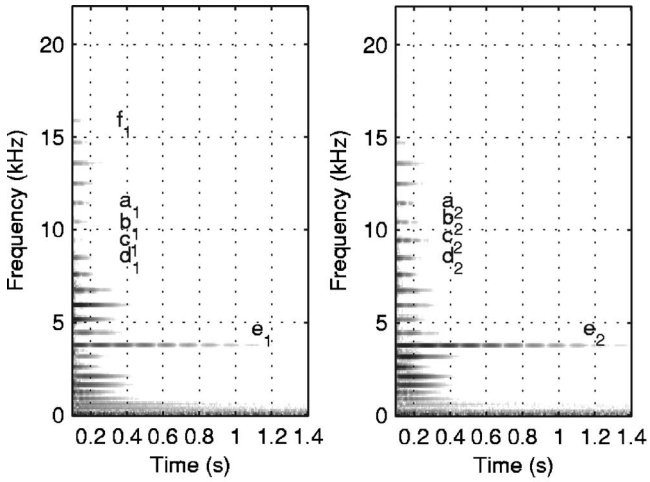

FIG. 1. Two spectrograms **S** (in decibels) of sounds (Al1 on the left and Al3 on the right) from impacts on an aluminum rod at approximately the same location and with approximately the same force (these spectrograms have been normalized). The relative power and temporal behavior of the partials varies from one instance to the other. For instance, in the left spectrogram, partial b_1 starts with a lower amplitude than partial a_1, while in the right spectrogram partial b_2 starts with a higher amplitude than a_2. The same happens with partials c and d: c_1 is weaker than d_1, while c_2 is stronger than d_2. Another example is the partial above 15 kHz. In the left spectrogram, this partial, f_1, is stronger than partial c_1, while in the right spectrogram c_2 is the strongest of the two. In fact, in the second spectrogram the partial above 15 kHz does not even appear.

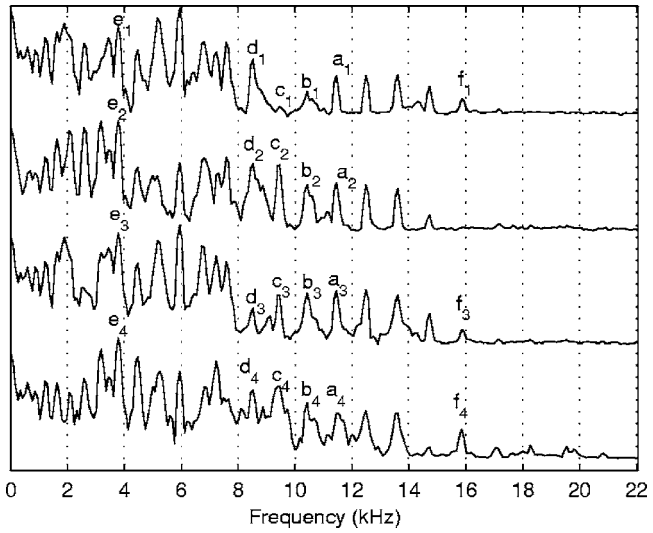

FIG. 2. Power spectra of four different impacts on aluminum (Al1, Al3, Al10, and Al19 from top to bottom) at approximately the same location and with approximately the same force. The relative power of the partials varies from one impact to another. (The partials are marked with the same labels as in Fig. 1.) Again, it can be seen that the relative powers of partials a, b, c, and d vary in the four power spectra. Also note that partial f appears in the first, third, and fourth lines (f_1, f_3, and f_4) but it is absent from the second line. Another interesting feature that can be observed is how the shape of the power spectrum changes from one sound to the next. For instance, note how partial a_1 is better defined than a_4.

a ringing property, the method should be able to learn a characterization of this intrinsic structure), as well as their variability (using the same example, the method should also capture the subtle variability of the ringing property in different impacts). At the same time, it aims for low dimensional representations of the sounds. This method requires no *a priori* knowledge and is used to create models of impact sounds that represent a rich variety of structure and variability in the sounds. The method is not restricted to learn an explicit set of properties of the sounds, and it has shown to be able to learn properties such as ringing, resonance, sustain, decay, and sharp onsets. To the best of our knowledge, this is the first statistical approach for modeling impact sounds.

II. MODELING INTRINSIC STRUCTURES

Our goal is to learn the intrinsic structure of sounds: We aim to decompose sounds in terms of the set of component signals that best describes them. For convenience, we assume the sounds are initially represented by a spectrogram, **S**. (Here we will refer to the rows of **S**, which are the power of frequencies over time, as *frequency bins* or *bins*, and we will refer to the columns of **S**, each of which is the power spectrum at a given time, as *frames*). Even though our method can be applied to a broader variety of sounds, here we will focus on impact sounds. To illustrate the data, Fig. 1 shows the spectrograms of two impact sounds on an aluminum rod (more details on how these sounds were produced and digitized are given in Sec. III).

Natural sounds of the same type have a rich variability in their acoustic structure. For example, different impacts on the same rod can generate very different acoustic waveforms. In natural environments there is variability due to reverberation and background noise, but even when the sounds are recorded in anechoic conditions, there is variability that is due to factors such as the slight variations in the impact force and location (see Sec. III for details on the recording conditions). Figures 1–3 show that, even though different impacts on the same rod have very similar spectra, the relative power

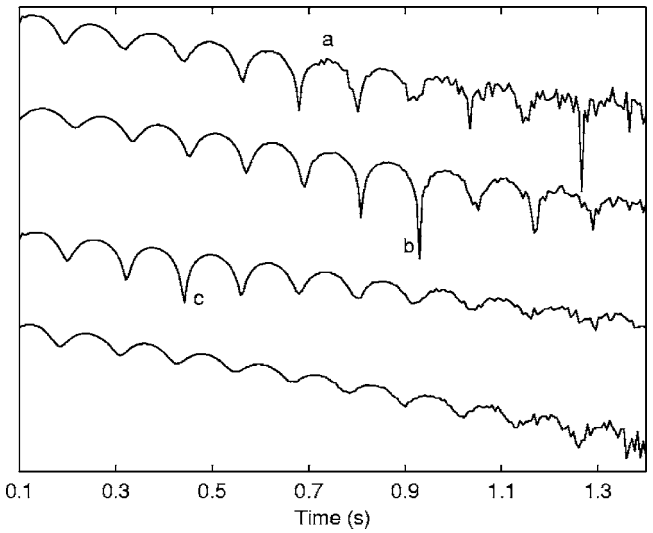

FIG. 3. The decay shape of the partial at 3.95 kHz in decibels (which is partial e in Figs. 1 and 2) for four different impacts on an aluminum rod (Al1, Al3, Al10, and Al19 from top to bottom) at approximately the same location and with approximately the same force. The temporal behavior of the partials varies from one impact to another; there is variability in the decay rate and beat pattern of this frequency bin. Note, for instance, the irregularities marked with an a in the first line, and notches b and c in the second and third lines. Also of interest is the consistency of the beating, which suggests that this rod has two close modes of vibration.

and temporal behavior of the partials varies from one instance to the other. These differences cannot be explained by a simple variation in amplitude of the whole spectrogram.

In spite of these variations, when these sounds are heard they are often perceptually very similar, that is, impacts from similar objects or materials have some common intrinsic structures that listeners can identify. Our goal is not to develop a perceptual model but rather to construct a model that learns the common intrinsic structures of similar sounds as well as their variability.

The model discussed here represents the sounds in terms of a set of component signals, in other words, it represents them in a new coordinate system. The form of the basis functions in the new coordinate system depends on the initial representation of the data, which here is the spectrogram. The frames are initially represented in an F-dimensional space with one dimension for each frequency bin f; let us call this space the *frequency space*. The bins are initially represented in a T-dimensional space, which we will call *time space*, with one dimension for each time frame t. A *spectral basis function* consists of a vector in the frequency space (that is, a spectra), while a *temporal basis function* consists of a vector in the time space (which can be thought of as a spectra's amplitude envelope). Using spectrograms as the initial representation allows us to model the sounds in spaces defined by spectral and temporal basis functions. (Section IV contains graphical examples of these basis functions.)

Given that the spectrogram $\mathbf{S}$, of size $(F \times T)$, is defined over a discrete set of frequencies, $f \in \{f_1, \ldots, f_F\}$, and a discrete set of time instants, $t \in \{t_1, \ldots, t_T\}$, we can define $\mathbf{S}$ as an ordered set of bins or as a sequence of frames. (Here we use only the power spectrum, and we ignore the phase component.) The model, which we call the bin model, or M_b, expresses the spectrogram $\mathbf{S}$ as an ordered set of bins. These are modeled as linear combinations of temporal basis functions $\boldsymbol{\phi}_i$:

$$\mathbf{b}_f = \sum_{i=1}^{I} \boldsymbol{\phi}_i c_{i,f}, \tag{2}$$

where $\mathbf{b}_f$ is the transpose of the fth bin of $\mathbf{S}$. $\boldsymbol{\phi}_i$ is scaled at this bin by coefficient $c_{i,f}$.[1] The value of I depends on the technique used to lear the basis functions $\boldsymbol{\phi}_i$. Here $I \leqslant T$ (see Sec. III and Appendix C in the supplementary material for further details). The basis functions $\boldsymbol{\phi}_i$ describe the temporal regularities in the bins in the data set, that is, in $\mathbf{S}$. These basis functions can describe a single sound, or the temporal regularities of a set of related sounds simply by including the appropriate spectrogram bins in the data set. (Section IV A shows how to learn $\boldsymbol{\phi}_i$.) The vectors of coefficients are commonly called *source signals*. Since the vector that consists of the coefficients that are associated with basis function $\boldsymbol{\phi}_i$, that is $\mathbf{c}_i = (c_{i,f_1}, \ldots, c_{i,f_F})^T$, ranges over the frequency space, here we call it a *spectral source signal*. (For graphical examples of spectral source signals see Sec. IV A.) Spectral source signal $\mathbf{c}_i$ scales basis function $\boldsymbol{\phi}_i$ across frequencies.

In order to represent the spectrograms of different sounds with a fixed basis $\boldsymbol{\Phi}$ (where $\boldsymbol{\Phi}$ represents the set of temporal basis functions $\boldsymbol{\phi}_i$), the model requires different spectral source signals to scale each basis function $\boldsymbol{\phi}_i$, i.e., there will be one set of spectral source signals for each sound. We distinguish these variables with an upper index k, that is, the set of spectral source signals associated with sound k, which is the set containing $\mathbf{c}_1^k, \ldots, \mathbf{c}_I^k$, is represented by $\mathbf{C}^k$.[2] We can thus rename some of the above-used variables to take into account the sound they refer to. Equation (2) can thus be rewritten as

$$\mathbf{b}_f^k = \sum_{i=1}^{I} \boldsymbol{\phi}_i c_{i,f}^k, \tag{3}$$

where $\mathbf{b}_f^k$ is the transpose of the fth bin of $\mathbf{S}^k$, i.e., the spectrogram of sound k, and the scalar $c_{i,f}^k$ is the fth element of $\mathbf{c}_i^k$.

If we consider all F bins in $\mathbf{S}^k$, Eq. (3) can be rewritten as

$$(\mathbf{S}^k)^T = \boldsymbol{\Phi}\ \mathbf{C}^k, \tag{4}$$

where the ith column of matrix $\boldsymbol{\Phi}$ contains $\boldsymbol{\phi}_i$, and the ith row of $\mathbf{C}^k$ contains $(\mathbf{c}_i^k)^T$. (See Appendix A in the supplementary material for figures of the matrices.)

Thus far, M_b describes the temporal structure, but not the spectral structure inherent in the spectral source signals $\mathbf{c}_i^k$. We can extend M_b to consider the regularities in the spectral source signals for an ensemble of related sounds. Instead of describing the temporal shape of a given bin, this part of the model describes the spectral source signals $\mathbf{c}_i^k$. These signals are modeled as a linear combination of spectral basis functions $\boldsymbol{\psi}_j^i$:

$$\mathbf{c}_i^k = \sum_{j=1}^{J} \boldsymbol{\psi}_j^i\, v_{i,j}^k, \tag{5}$$

where the scalar $v_{i,j}^k$ is a scaling coefficient. The spectral basis functions $\boldsymbol{\psi}_j^i$ describe the spectral regularities in the spectral signals. Again, the value of J depends on the technique used to learn the basis functions $\boldsymbol{\psi}_j^i$. Here, $J \leqslant F$ (see Appendix C in the supplementary material for further details). (Section IV B shows how to learn $\boldsymbol{\psi}_j^i$.)

We can now consider the previous equation at a given frequency bin f and express $c_{i,f}^k$ as follows:

$$c_{i,f}^k = \sum_{j=1}^{J} \psi_{j,f}^i\, v_{i,j}^k, \tag{6}$$

where $c_{i,f}^k$, and $\psi_{j,f}^i$ are the values of $\mathbf{c}_i^k$, and $\boldsymbol{\psi}_j^i$ at frequency bin f, respectively. (In other words, they are the fth values of vectors $\mathbf{c}_i^k$ and $\boldsymbol{\psi}_j^i$, respectively.)

Finally, combining Eqs. (3) and (6) it follows that the bins of $\mathbf{S}^k$ can be expressed as

$$\mathbf{b}_f^k = \sum_{i=1}^{I} \sum_{j=1}^{J} \boldsymbol{\phi}_i \psi_{j,f}^i\, v_{i,j}^k. \tag{7}$$

This shows that $\mathbf{S}^k$ can be modeled by temporal bases $\boldsymbol{\Phi}$, spectral bases $\boldsymbol{\Psi}$ (where $\boldsymbol{\Psi}$ contains all spectral basis functions $\boldsymbol{\psi}_j^i$), and a set of coefficients $\mathbf{V}^k$ (where $\mathbf{V}^k$ contains coefficients $v_{i,j}^k$), that is, $\mathbf{S}^k = M_b(\boldsymbol{\Phi}, \boldsymbol{\Psi}, \mathbf{V}^k)$. (For more details

and figures of the matrices used in this model, see Appendix A in the supplementary material.)

The model is thus defined by two sets of basis functions, and the objective is to find the sets of basis functions with which the data can be better described: ideally only a few basis functions would be needed to accurately describe the data with less redundancy. In Sec. IV, we show that the basis functions can be learned effectively by redundancy reduction techniques.

As mentioned before, we can define $\mathbf{S}^k$ as an ordered set of bins or as a sequence of frames. Model M_b describes the data as an ordered set of bins, and it is possible to build an alternative model that describes the data as a sequence of frames. Yet depending on the techniques used to learn the basis functions, model M_b is more appropriate than the alternative model, in the sense that it may give a better description of the statistics of the data used in this study (see Sec. III for a description of the data and Appendix B in the supplementary material for further details). Therefore, here we focus only on model M_b, and we do not describe the alternative model.

III. METHODS AND TECHNIQUES

We used a set of impact sounds that were produced using four rods with the same length and diameter, but made of different materials. A wooden rod, with a much shorter length but the same diameter, was used as a mallet. Several impacts on each rod were recorded in an anechoic chamber. The location of the impacts and the impact force varied slightly from one instance to the next, since the rods were hit by hand. The sounds were digitized using a sampling frequency of 44 100 Hz.

The spectrograms of the sounds were computed using a 11.6 ms sliding Hanning window. Successive frames overlapped by 5.8 ms. Like with any other system that uses spectrograms, there is a trade off between spectral and temporal resolution. Even though the type of structures obtained for different resolutions is the same, the choice of spectral versus temporal resolution affects the representation: the shapes of the structures obtained differ slightly; for instance a structure that includes a sharp onset can look more or less sharp depending on the resolution. Here, we only report the results obtained using an intermediate resolution of 512–point fast Fourier transform.

We use principal component analysis (PCA) and independent component analysis (ICA) to learn the sets of basis functions from Sec. II. PCA and ICA are redundancy reduction techniques that look for the axes that best describe the distribution of the data. These techniques are used to represent high dimensional data in a (usually lower dimensional) space with less redundancy. The data are expressed as a linear transformation of the basis functions (i.e., the axes that define the new space). Given a set of M *source signals* of size N [represented by an $(M \times N)$ matrix $\mathbf{Y}$ with one signal per row] mixed into a set of M *signal mixtures* [represented by an $(M \times N)$ matrix $\mathbf{X}$ with one signal mixture per row] PCA and ICA learn a $(M \times M)$ matrix $\mathbf{W}$ that allows extracting the source signals from matrix $\mathbf{X}$:

$$\mathbf{Y} = \mathbf{W}\mathbf{X}. \tag{8}$$

If $\mathbf{A} = \mathbf{W}^{-1}$ this equation can be rewritten as

$$\mathbf{X} = \mathbf{A}\mathbf{Y}. \tag{9}$$

The two techniques differ importantly in the way they model the distribution of the data, and in their constraints. PCA is a second-order statistical method that assumes a Gaussian distribution and is restricted to orthogonal basis functions (that are the eigenvectors of the data covariance matrix). This technique decomposes a set of signal mixtures into a set of decorrelated signals and can be used to reduce the dimensionality of the data by considering I basis functions, where $I < M$ (in which case only I source signals are obtained). ICA is a generative model that decomposes a set of signal mixtures into a set of maximally independent source signals. This higher-order statistical method models multivariate data with non-Gaussian distributions and is not restricted to orthogonal basis functions. ICA contains PCA as a special case when the marginal distributions of signals are assumed to be Gaussian and the bases are restricted to be orthogonal. [For more details on ICA and PCA, see Hyvärinen *et al.* (2001) or Stone (2004).]

For instance, in the case of the first part of M_b and when we consider K impact sounds, matrix $\mathbf{X}$ consists of the horizontal concatenation of transposed spectrograms $((\mathbf{S}^1)^T, (\mathbf{S}^2)^T, \ldots, (\mathbf{S}^K)^T)$, $\mathbf{A}$ is the spectral basis $\mathbf{\Phi}$, and $\mathbf{Y}$ is the horizontal concatenation of the matrices of spectral source signals $(\mathbf{C}^1, \mathbf{C}^2, \ldots, \mathbf{C}^K)$. A signal mixture is the concatenation of one transposed frame from each of the K spectrograms, and there are T signal mixtures. Therefore, $I \leqslant T$ in Eqs. (2)–(7).

We used a built-in function from MATLAB to do PCA and the Fast ICA software package by Hyvärinen *et al.* (2001) to do ICA (for more details see Appendix C in the supplementary material). Because both PCA and ICA model the variation around the data mean, we used both the data matrix and its negative, i.e., we used the *extended matrix* $(-\mathbf{S}^T, \mathbf{S}^T)$, so that the mean would be zero. This was done so that the model described the signal rising and falling from zero, rather than the spectrogram mean.

IV. RESULTS

In this section, we show how to learn representations of the intrinsic structures of impact sounds. We show that the method developed in Sec. II can be used to characterize the structures of a single sound or the structures of sets of related sounds. In the latter case, the method learns representations of the structures that are common to the set of sounds and models their natural variability.

Section IV A explores the first part of the model, which is characterized by the temporal basis functions $\mathbf{\Phi}$, while Sec. IV B explores the second part of the model, which is characterized by the spectral basis functions $\mathbf{\Psi}$. Finally, Sec. IV C illustrates how the natural variability of related sounds is represented by the model.

A. Temporal basis functions Φ

There are two ways of applying ICA and PCA to spectrograms: these techniques can be used to do a *spectral analysis* of $\mathbf{S}^k$, in which the signal mixtures and source signals are considered to be spectra, or a *temporal analysis* of $\mathbf{S}^k$, in which the signal mixtures and source signals are considered to be temporal signals. *Spectral analysis* considers the frames (or power spectra) of $\mathbf{S}^k$ as a linear combination of independent or uncorrelated spectral source signals (for ICA and PCA, respectively). Here the goal is to decompose $\mathbf{S}^k$ into this set of spectral source signals. (For more details see Appendix B in the supplementary material.)

In order to learn the set of temporal basis functions $\mathbf{\Phi}$ and decompose the spectrograms into sets of spectral source signals, we apply spectral PCA and ICA to the spectrogram of a single impact or to the spectrograms of different impacts on the same rod. For instance, in order to learn the temporal basis functions $\mathbf{\Phi}$ and find the sets of spectral source signals $\mathbf{C}^1, \mathbf{C}^2, \ldots, \mathbf{C}^K$ for K sounds, model M_b does a spectral analysis on matrix $((\mathbf{S}^1)^T, (\mathbf{S}^2)^T, \ldots, (\mathbf{S}^K)^T)$, where $(\mathbf{S}^1)^T$ to $(\mathbf{S}^K)^T$ are time aligned, so that the matrix has one row (or transposed frame) that corresponds to the start of all K impacts. The temporal basis functions $\mathbf{\Phi}$ are time varying functions that represent temporal properties of different subspectra of the sounds. Each spectral source signal ($\mathbf{c}_i^k$) is associated with a particular temporal basis function ($\boldsymbol{\phi}_i$) that represents a component of the signal's temporal behavior.

1. One impact sound

We start with the spectrogram $\mathbf{S}$ of a single sound. Figures 4(a) and 4(b) show six out of the ten most dominant basis functions (i.e., $\boldsymbol{\phi}_1 - \boldsymbol{\phi}_{10}$) learned by ICA.[3] As can be seen, ICA is able to isolate temporal properties of the sound: see for instance $\boldsymbol{\phi}_b$ in Fig. 4(a), which represents a ringing property of the sound, $\boldsymbol{\phi}_d$ in the same figure, which represent a decay property of the sound, $\boldsymbol{\phi}_a$ in Fig. 4(a) and $\boldsymbol{\phi}_e$ in Fig. 4(b), which represent sustain properties, and the sharp basis functions like $\boldsymbol{\phi}_a$ and $\boldsymbol{\phi}_d$ in Fig. 4(b), and $\boldsymbol{\phi}_c$ in Fig. 4(a) which are related to impact (i.e., attack) properties of the sounds.

While ICA can model the data using nonorthogonal basis functions, PCA models the data with orthogonal bases. Consequently, the temporal basis functions learned by PCA can differ from those learned by ICA. Figure 5 illustrates the results obtained by PCA of the spectrogram of the sound of an impact on an aluminum rod. This figure shows that the dominant basis function, $\boldsymbol{\phi}_1$, has a much smoother shape than the other basis functions. This basis function shapes the overall decay of all partials. In fact, the results show that PCA extracts a dominant basis function $\boldsymbol{\phi}_1$ that represents most of the temporal structure of the sound (Fig. 6). On average, this basis function accounts for more than 68% of the temporal variation in $\mathbf{S}$. This property of the dominant basis function is due to the lack of variation in the spectral structure of the sound over time. (As an example of this regularity, Fig. 1 shows that there is not much variation in which partials are active over time.) $\boldsymbol{\phi}_1$ has the ability to account for the temporal behavior of this spectral structure.

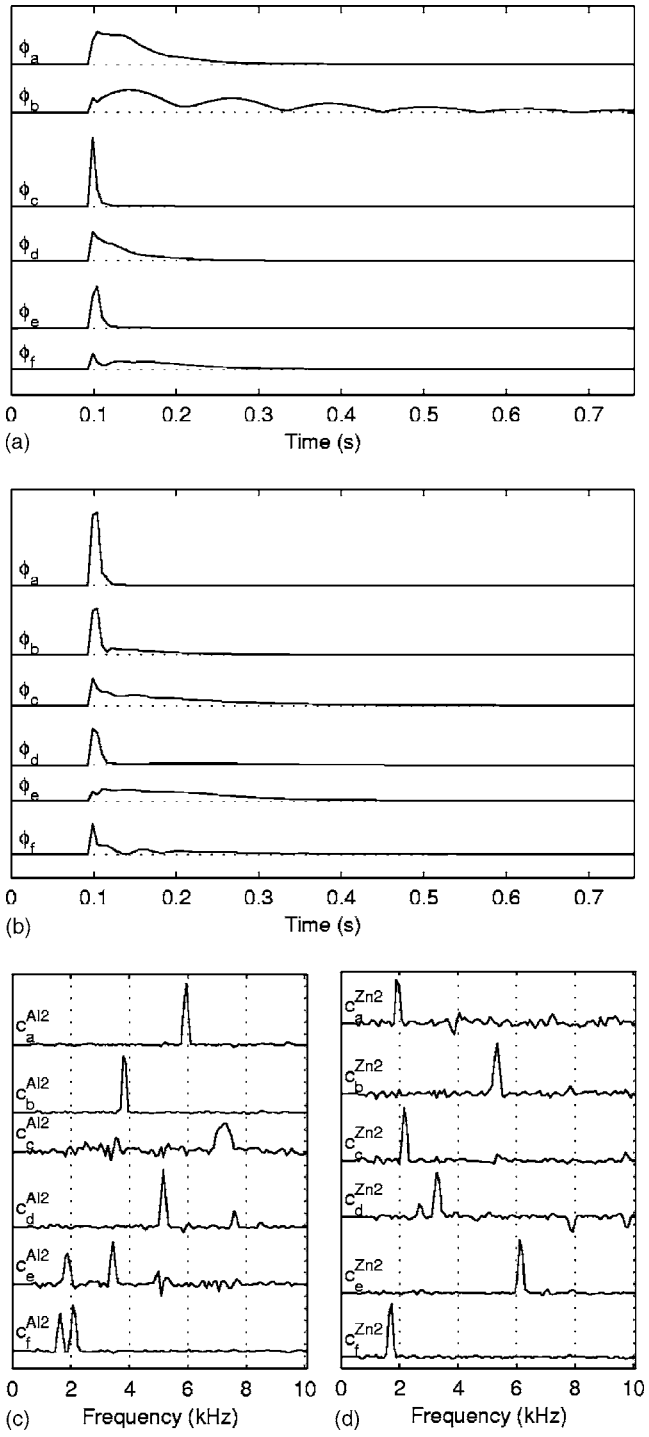

FIG. 4. Temporal basis functions $\mathbf{\Phi}$ learned by ICA of the spectrogram of: (a) a sound (Al2) from an impact on an aluminum rod; (b) a sound (Zn2) from an impact on a zinc plated steel rod. In each case, six out of the ten most dominant basis functions are shown in decreasing order of dominance from top to bottom. The corresponding spectral source signals for Al2 (c) and Zn2 (d) are shown also from top to bottom.

To illustrate this point, Fig. 7 shows the average power spectrum of a sound from an impact on an aluminum rod and spectral source signal $\mathbf{c}_1^{\mathrm{Al2}}$ obtained by PCA of the spectrogram of this sound. $\boldsymbol{\phi}_1$ describes the temporal behavior of spectra $\mathbf{c}_1^{\mathrm{Al2}}$, which, as can be seen in Fig. 7, is very similar to the sound's power spectrum, which represents the spectral structure of the sound over time.

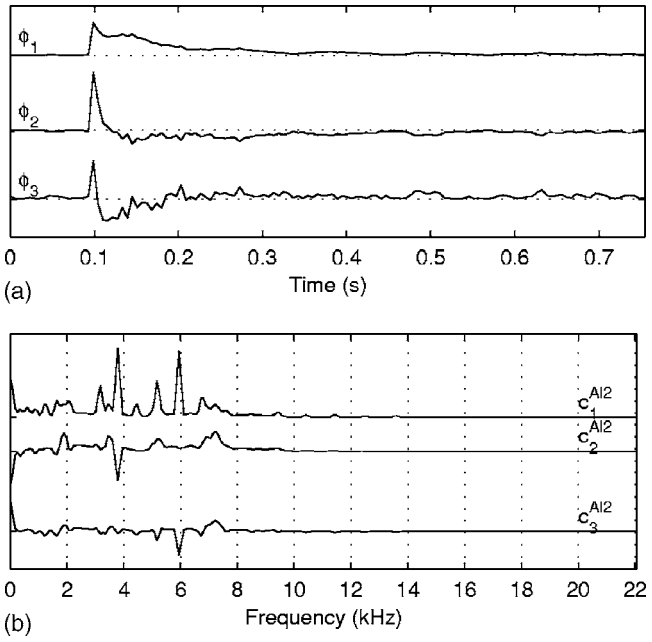

FIG. 5. Temporal basis functions $\mathbf{\Phi}$ and spectral source signals ($\mathbf{C}^{Al2}$) obtained by PCA of the spectrogram of a single sound (Al2) from an impact on an aluminum rod. (a) The first three basis functions are shown from top to bottom. (b) The first three spectral source signals are shown from top to bottom.

Other less significant basis functions account for temporal behaviors that differ from the overall decay shape described by $\boldsymbol{\phi}_1$. For example, the temporal shapes of $\boldsymbol{\phi}_2$ and $\boldsymbol{\phi}_3$ account for variations in the temporal behavior of subspectra $\mathbf{c}_2^{Al2}$ and $\mathbf{c}_3^{Al2}$ (Fig. 5). (Note also that these subspectra contain common partials with the spectral structure of the sound, but, as can be easily seen in this figure, they account for much less of the spectral structure of $\mathbf{S}$ than $\mathbf{c}_1^{Al2}$ does. The same is true for other sounds. The less variance a basis function accounts for, the fewer partials its spectral source signal shares with $\mathbf{S}$.) In contrast to what was seen with ICA, these basis functions are not as directly related to temporal properties of the sounds. (Note that since the same sound, Al2, was used in both Figs. 4(a) and 5, these are directly comparable.)

As seen earlier, ICA obtains a greater variety of basis

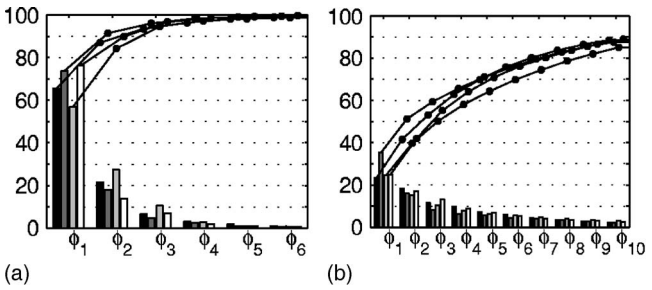

FIG. 6. Percentage of variance explained by the basis functions in $\mathbf{\Phi}$. The spectrograms from ten impact sounds from each rod (aluminum in black, zinc plated steel in dark grey, steel in light grey, and wood in white) were used. $\mathbf{\Phi}$ was learned by spectral analysis on one spectrogram at a time. The ten results obtained for each rod were averaged. Only the values for the first six or ten temporal basis functions are shown. The dots on the curves show the cumulative sums of the percentages. In (a) $\mathbf{\Phi}$ was learned by PCA. In (b) $\mathbf{\Phi}$ was learned by ICA.

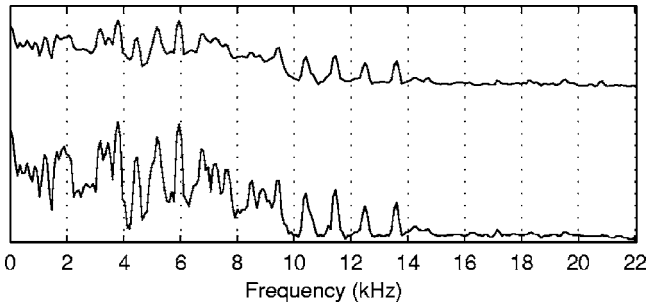

FIG. 7. Power spectrum of a sound (Al2) from an impact on an aluminum rod. The bottom line shows the power spectrum. The line on the top shows spectral source signal $\mathbf{c}_1^{Al2}$ found by PCA of the spectrogram of this sound. Note how both lines show high energy on the same partials. (Here, the source signal $\mathbf{c}_1^{Al2}$ looks different than in Fig. 5 because it is plotted in a logarithmic scale.)

function shapes: some are similar to the most significant PCA basis functions, but ICA is also able to learn basis functions that capture structures besides decay. In fact, there seems to be a more direct relation between the shape of the basis functions learned by ICA and temporal properties like ringing, resonance, decay, impact (or attack), etc. As a consequence, ICA needs more basis functions to explain the variance of $\mathbf{S}$ (Fig. 6). On average, the most significant basis function ($\boldsymbol{\phi}_1$) accounts only for about 27% of the temporal variation in $\mathbf{S}$ compared to 68% for PCA.

Up to this point, we have considered the basis functions; now we will consider the spectral source signals. Because here we consider the spectrogram $\mathbf{S}$ of a single sound, there is only one spectral source signal $\mathbf{c}_i^k$ associated with each basis function $\boldsymbol{\phi}_i$. This source signal consists of the partials that have the time varying shape described by $\boldsymbol{\phi}_i$. In other words, the source signals consist of partials that have similar time varying shape. Unlike the source signal of the dominant basis function obtained by PCA, with ICA there is no source signal that accounts for most of the spectral structure in $\mathbf{S}$. ICA separates partials with different time varying shapes into different spectral source signals, which is better suited to represent the variability in the sounds. This point is illustrated by Figs. 4(c) and 4(d), which show the spectral source signals for six out of the ten most dominant basis functions obtained by spectral ICA. As can be seen, when ICA is used, the partials in one spectral source signal are typically not present in the remaining source signals. From another perspective, ICA learns basis functions that more directly relate to the underlying acoustic properties. This desirable effect allows ICA to extract more interesting temporal structures of the sounds than those seen with PCA.

2. Ensemble of impact sounds

We will now consider the more general case of an ensemble of impacts on the same rod. In this case, the data matrix is defined over a set of K sounds aligned at time zero. The result of applying spectral ICA or PCA to this data is a set of temporal basis functions $\mathbf{\Phi}$ and K sets of spectral source signals $\mathbf{C}^k$. The temporal basis functions $\mathbf{\Phi}$ model the common temporal properties of the sounds, and each set of spectral source signals $\mathbf{C}^k$ represents the spectra of sound k

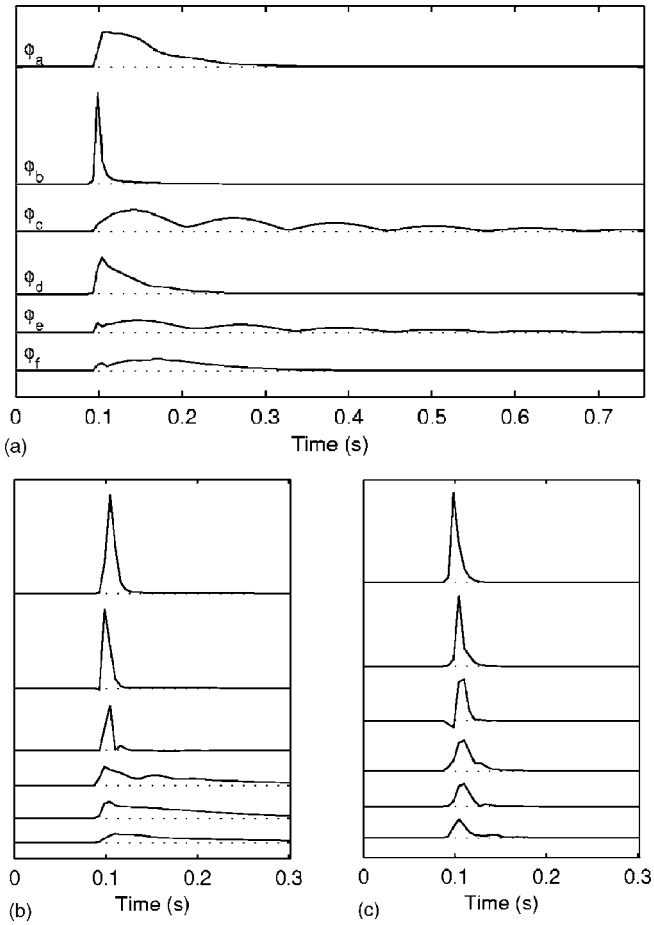

FIG. 8. Temporal basis functions $\mathbf{\Phi}$ learned by ICA of the set of: (a) ten sounds from impacts on an aluminum rod; (b) ten sounds from impacts on a zinc plated steel rod; and (c) ten sounds from impacts on a wooden rod. In each figure, six out of the ten most dominant basis functions are shown in decreasing order of dominance from top to bottom.

that have the temporal properties described by $\mathbf{\Phi}$. The spectral source signals (say $\mathbf{c}_i^{k_1}$ and $\mathbf{c}_i^{k_2}$) associated with the same basis function $\boldsymbol{\phi}_i$ are the subspectra (of sounds k_1 and k_2, respectively) that share the temporal property described by $\boldsymbol{\phi}_i$.

The results for multiple impacts resemble those for a single impact due to the similarity in the underlying acoustic structure across impacts. This is clear with the basis functions learned by ICA, for instance, compare $\boldsymbol{\phi}_a$ in Figs. 4(a) and 8(a), and is particularly obvious with the most dominant basis function learned by PCA, for instance, compare the first line from Figs. 5(a) and 9(a). Even though the temporal basis functions in these figures are not exactly the same, they have very similar shapes.

Because more impacts on the same rod imply more variability, some acoustic structures that were represented by a single basis function in Section IV A 1, are now represented by multiple basis functions. For example, the ringing structure represented by $\boldsymbol{\phi}_b$ in Fig. 4(a) is now represented by both $\boldsymbol{\phi}_c$ and $\boldsymbol{\phi}_e$ in Fig. 8(a). In order to illustrate how the temporal variability is represented, we will examine these two basis functions more carefully. By inspecting the spectral source signals associated with $\boldsymbol{\phi}_c$ and $\boldsymbol{\phi}_e$ (see second and third plots in the middle column of Fig. 10) we can

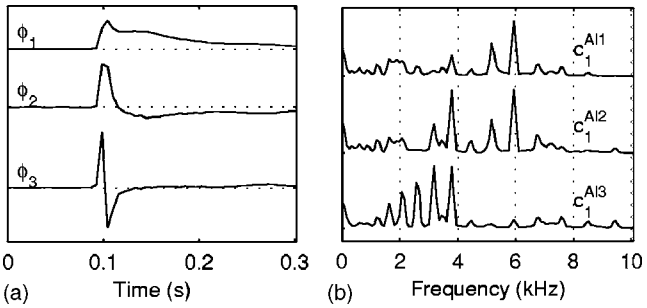

FIG. 9. Temporal basis functions $\mathbf{\Phi}$ and spectral source signals $\mathbf{C}^k$ obtained by PCA of the set of ten impacts on an aluminum rod. (a) The first three basis functions are shown from top to bottom. (b) The first spectral source signal for sounds Al1, Al2, and Al3.

conclude that these two basis functions represent the temporal behavior of the partial at 3.95 kHz. In some impacts this partial has a temporal shape that is more closely described by $\boldsymbol{\phi}_c$ (observe that for Al1 there is a peak in $\mathbf{c}_c^{\mathrm{Al1}}$ but not in $\mathbf{c}_e^{\mathrm{Al1}}$), while in other impacts the partial's temporal shape is more closely described by $\boldsymbol{\phi}_e$ (for Al3 there is a peak in $\mathbf{c}_e^{\mathrm{Al3}}$ but not in $\mathbf{c}_c^{\mathrm{Al3}}$). Still in other impacts a mixture of both $\boldsymbol{\phi}_c$ and $\boldsymbol{\phi}_e$ is required to describe the partial's temporal shape (Al2 has a peak in both $\mathbf{c}_c^{\mathrm{Al2}}$ and $\mathbf{c}_c^{\mathrm{Al2}}$).

Even though on average the basis functions account for a smaller percentage of variance than in Sec. IV A 1 and more basis functions are needed to explain the same percentage of variance, the difference is not significant. For instance, the ten most dominant basis functions learned by spectral ICA of a single sound account for at most 88% of the variance, while when a set of ten sounds is used, the same number of basis functions explains at most 84% of the variance of the data.[4] Spectral PCA shows similar results: six basis functions suffice to explain around 99% of the variance on a single sound, while for a set of ten sounds, six basis functions can explain around 96% of the variance (Figs. 6 and 11).

The results shown here were obtained from sounds recorded in an anechoic chamber; however, we also tested the model with sounds recorded in a normal room (with background noise and reverberation). In this case, $\mathbf{S}$ represented not only the structure of the sound, but also the structure of the background noise. Consequently, apart from the temporal basis functions that accounted for the temporal structure of the sound, spectral PCA and ICA also learned some basis functions that described the temporal structure of the background noise (data not shown).

The results are dependent on the sounds analyzed. Figure 8 shows that impacts on different rods are characterized by different basis functions. For instance, some of the basis functions that characterize impacts on aluminum have a longer duration than the basis functions that characterize impacts on wood. If sounds with different characteristics are used, the basis functions will reflect those characteristics.

B. Spectral basis functions Ψ

The sets of spectral source signals $\mathbf{C}^1,\ldots,\mathbf{C}^K$ represent the subspectra associated with the temporal basis functions in $\mathbf{\Phi}$. Even though each $\mathbf{C}^k$ is specific to an individual sound

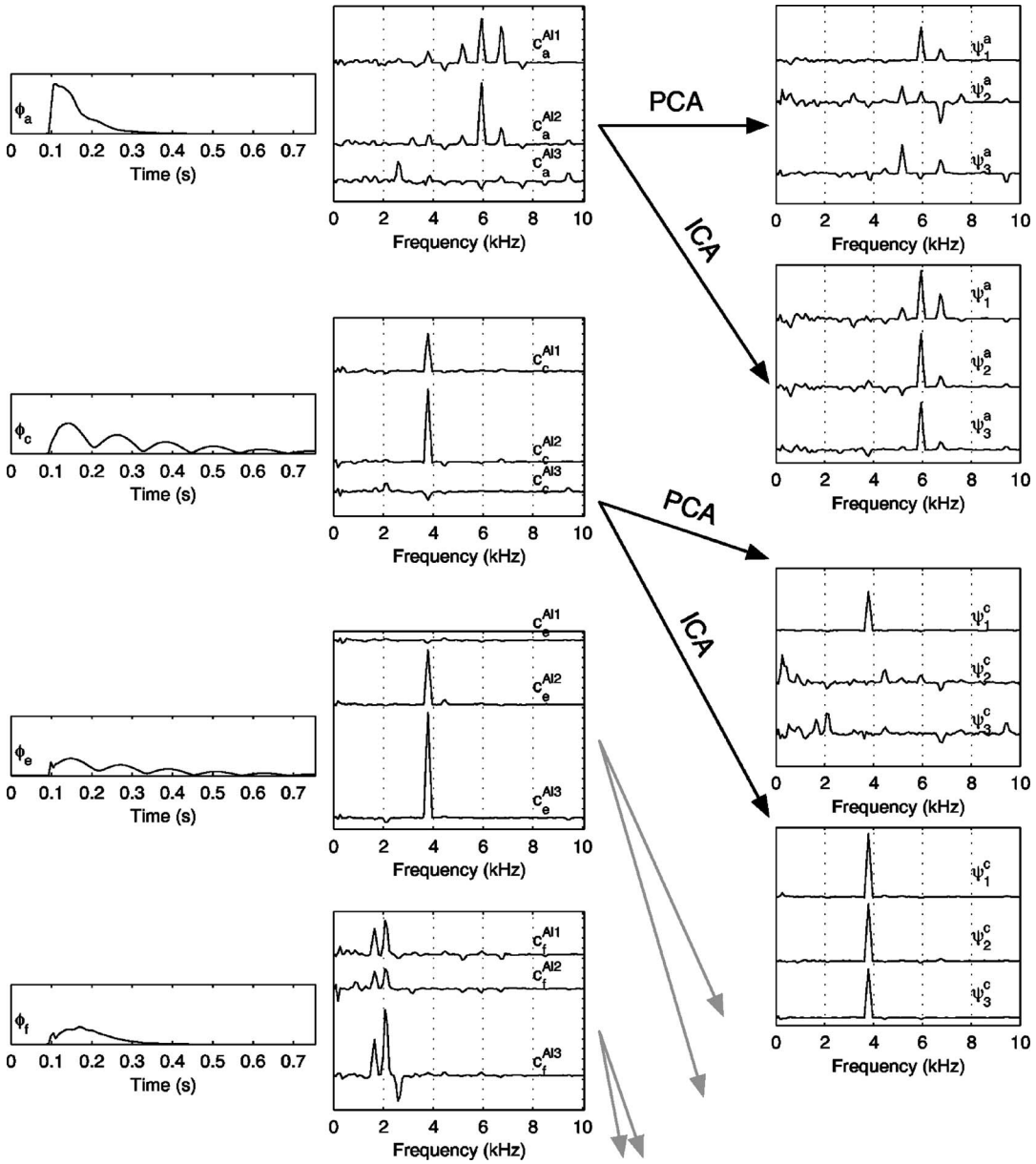

FIG. 10. Left column: Temporal basis functions $\boldsymbol{\phi}_a$, $\boldsymbol{\phi}_c$, $\boldsymbol{\phi}_e$, and $\boldsymbol{\phi}_f$ from Fig. 8(a). These are learned by ICA of the set of ten sounds from impacts on an aluminum rod. Middle column: The corresponding spectral source signals for sounds Al1, Al2, and Al3. Right column: Spectral basis functions $\boldsymbol{\Psi}$ obtained by analysis of the spectral source signals. The first and third figures in this column show the first three spectral basis functions from $\boldsymbol{\Psi}^a$ and $\boldsymbol{\Psi}^c$ learned by PCA. The second and fourth figures in this column show the first three spectral basis functions from $\boldsymbol{\Psi}^a$ and $\boldsymbol{\Psi}^c$ learned by ICA.

k, the sets of source signals do share common structures. This can be seen in Fig. 10. The middle column shows the spectral source signals obtained by spectral ICA of the set of ten sounds from an aluminum rod. Although the source signals show considerable variability, there is still much common structure. The same observations can be made on the results from spectral PCA [see Figs. 9(b) and 12(b)].

As explained in Sec. II, we can extend the approach to model the regularities in the spectral source signals. In the extended model, these regularities are represented by the set of spectral basis functions $\boldsymbol{\Psi}$, which is learned by applying PCA or ICA to matrices of spectral source signals, such that $\boldsymbol{\Psi}^i$ consists of the spectral basis functions that represent the regularities of the source signals associated with the tempo-

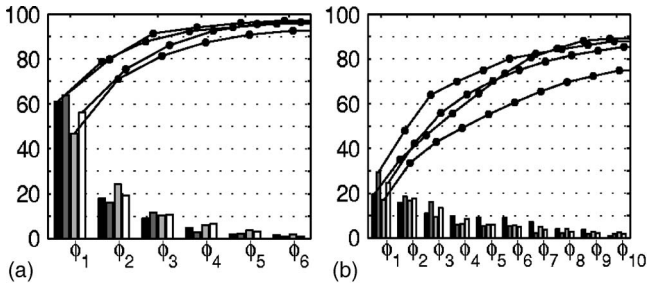

FIG. 11. Percentage of variance explained by the basis functions in $\boldsymbol{\Phi}$ learned by spectral analysis on the set of ten impacts on an aluminum rod (black), the set of ten impacts on a zinc plated steel rod (dark grey), the set of ten impacts on a steel rod (light grey), and the set of ten impacts on a wooden rod (white). Only the values for the first six or ten temporal basis functions are shown. The dots on the curves show the cumulative sums of the percentages. In (a) $\boldsymbol{\Phi}$ was learned by PCA. In (b) $\boldsymbol{\Phi}$ was learned by ICA.

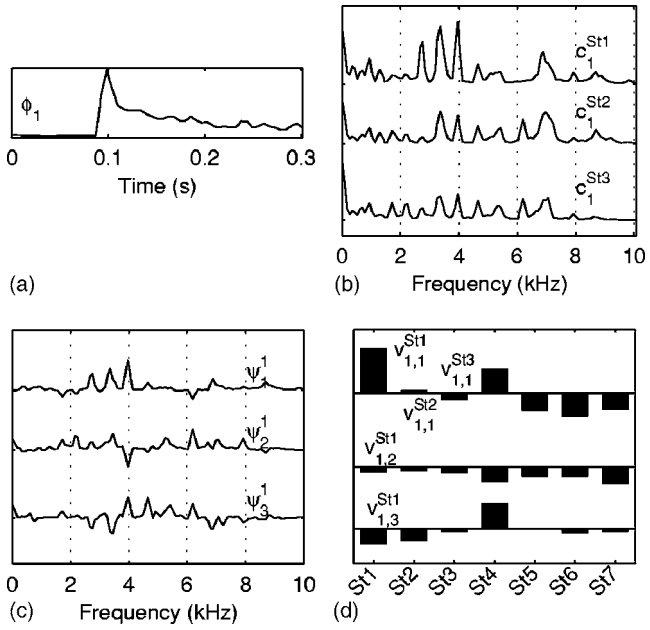

FIG. 12. Top row: Temporal basis functions $\mathbf{\Phi}$ and spectral source signals $\mathbf{C}^k$ obtained by spectral PCA of the set of ten impacts on a steel rod. (a) First (most dominant) basis function. (b) First spectral source signal for sounds St1, St2, and St3. Bottom row: Spectral basis functions $\mathbf{\Psi}$ and coefficients $\mathbf{V}^k$ (for $k \in \{\text{St1}, \text{St2}, \ldots, \text{St7}\}$) obtained by PCA of the source signals. (c) First three spectral basis functions from $\mathbf{\Psi}^1$. (d) Coefficients for spectral basis functions $\boldsymbol{\psi}_1^1$ to $\boldsymbol{\psi}_3^1$. The jth line, kth column shows $v_{1,j}^k$, that is, the coefficient for sound k and basis function $\boldsymbol{\psi}_j^1$.

ral basis function $\boldsymbol{\phi}_i$, that is, the regularities of source signals $\mathbf{c}_i^1, \ldots, \mathbf{c}_i^K$. ($\mathbf{\Psi}^i$ contains basis functions $\boldsymbol{\psi}_1^i, \ldots, \boldsymbol{\psi}_J^i$, and $\mathbf{\Psi}$ contains sets $\mathbf{\Psi}^1, \ldots, \mathbf{\Psi}^I$.)

Figure 12 shows the results obtained by PCA of the spectral source signals from PCA of the set of ten impacts on a steel rod.[5] Since PCA models the data with orthogonal bases, all basis functions within each set $\mathbf{\Psi}^i$ are orthogonal. Comparing $\boldsymbol{\psi}_1^1$ with $\mathbf{c}_1^{\text{St1}}$, it can be seen that the energy found in spectrum $\mathbf{c}_1^{\text{St1}}$ is being represented by this spectral basis function. For instance, note the three peaks between 2 and 4 kHz in both lines. Even though $\mathbf{c}_1^{\text{St2}}$ and $\mathbf{c}_1^{\text{St3}}$ have peaks in the same region, they show less energy in these partials. This variability is accounted for in part by other spectral basis functions in $\mathbf{\Psi}^1$ and in part by $\mathbf{V}^k$. Note how $v_{1,1}^{\text{St1}}$ has a much higher value than $v_{1,1}^{\text{St2}}$ and $v_{1,1}^{\text{St3}}$.

PCA can also be applied to the spectral source signals that have been obtained by spectral ICA. The first and third graphs in the right column of Fig. 10 show the results obtained by PCA of the spectral source signals from ICA of the set of ten impacts on the same aluminum rod. The set of spectral basis functions $\mathbf{\Psi}^a$ represents the regularities of the spectral source signals associated with $\boldsymbol{\phi}_a$. For instance, note how $\boldsymbol{\psi}_1^a$ represents the peaks close to 6 and 7 kHz, which can be seen in $\mathbf{c}_a^{\text{Al1}}$ and $\mathbf{c}_a^{\text{Al2}}$. Since these peaks are much lower (or negative) in $\mathbf{c}_a^{\text{Al3}}$, $v_{a,1}^{\text{Al3}}$ has a much lower value than $v_{a,1}^{\text{Al1}}$ and $v_{a,1}^{\text{Al2}}$ (these coefficients are not shown here).

The number of basis functions considered is arbitrary and depends on the application. It depends on how much of the structure of the sounds one needs to model. To completely represent the structure of the sounds, we need to be able to model all variability in all spectral source signals $\mathbf{c}_i^k$, and, therefore, we must consider all basis functions in $\mathbf{\Psi}$. However, the results show that when PCA is used there is a dominant component in each set $\mathbf{\Psi}^i$ that represents most of the structure in the spectral source signals $\mathbf{c}_i^k$. Thus, often a very good approximation of source signals $\mathbf{c}_i^k$ can be obtained by using a small subset of $\mathbf{\Psi}^i$.

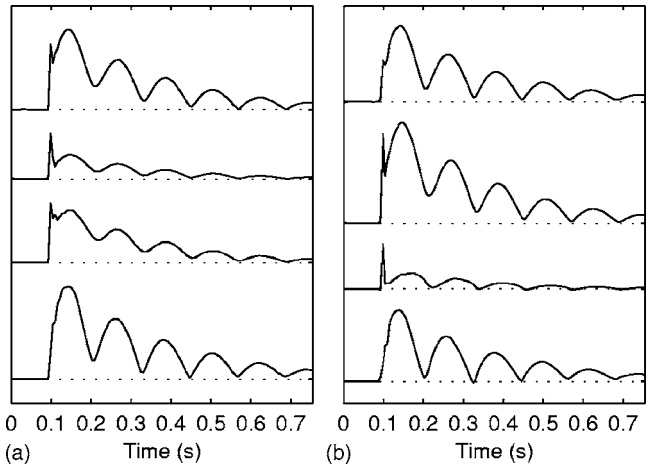

FIG. 13. The decay shape of the partial at 3.95 kHz (which is partial *e* in Figs. 1 and 2) from different spectrograms of impacts on an aluminum rod. (a) The original partials show considerable variability. The partials (from top to bottom) were extracted from the spectrograms of sounds Al2, Al4, Al9, and Al10. (The partial from Al10 looks different in Fig. 3 because there it was plotted in a logarithmic scale.) (b) The synthesized partials have a similar range of variability. The partials were extracted from four synthesized spectrograms. See the text for details.

Finally, we show some results from ICA of the spectral source signals that have been obtained by spectral ICA. Since the spectral basis functions learned by ICA are not restricted to be orthogonal, and not many sounds (and consequently not many spectral source signals)were used in this study, the basis functions $\mathbf{\Psi}$ learned by ICA are more tuned to specific spectral source signals, that is, they resemble more closely the shape of specific spectral source signals. As a consequence, the representations obtained by ICA are less compact than the representations obtained by PCA. The second and fourth graphs in the right column of Fig. 10 show the results obtained by ICA of the spectral source signals from spectral ICA of the set of ten impacts on an aluminum rod. It is interesting to note the similarities between individual spectral basis functions and spectral source signals. For instance, compare $\boldsymbol{\psi}_1^a$ to $\mathbf{c}_a^{\text{Al1}}$, and $\boldsymbol{\psi}_2^a$ to $\mathbf{c}_a^{\text{Al2}}$. See also how similar $\boldsymbol{\psi}_1^c$, $\boldsymbol{\psi}_2^c$, and $\boldsymbol{\psi}_3^c$ are.

C. Variability

Natural sounds have significant variability as was illustrated in Figs. 1–3. Because model M_b is adapted to represent the distribution of the ensemble of impact sounds, it also captures this variability. The variability is represented by different basis functions (like $\boldsymbol{\phi}_c$ and $\boldsymbol{\phi}_e$ in Fig. 10) and by the distribution of the coefficients $v_{i,j}^k$. To illustrate this, Fig. 13 shows that by giving different values to the coefficients $v_{i,j}^k$, one can use different combinations of the temporal and spectral structures represented by the basis functions in $\mathbf{\Phi}$ and $\mathbf{\Psi}$ to simulate the variability present in the sounds. By randomly sampling the coefficients $v_{i,j}^k$, we can generate differ-

ent instances from the model distribution. Figure 13(a) shows the variation in the partial at 3.95 kHz, and Fig. 13(b) shows four different synthesis instances of the same partial (3.95 kHz), each extracted from a different synthesized spectrogram. To synthesize the spectrograms, we used the temporal basis functions ($\mathbf{\Phi}$) learned by spectral ICA of the spectrograms of ten aluminum rod impacts, the spectral basis functions ($\mathbf{\Psi}$) learned by PCA of the corresponding spectral source signals, and the coefficients obtained for one of the sounds ($\mathbf{V}^{\mathrm{Al4}}$). To simulate the variability caused by $\boldsymbol{\phi}_c$ and $\boldsymbol{\phi}_e$ (from Fig. 10) we varied the weightings of these two basis functions. That was done by varying the values of $\mathbf{v}_c^{\mathrm{Al4}}$ and $\mathbf{v}_e^{\mathrm{Al4}}$ for each synthesized spectrogram. The values were randomly sampled from the coefficient's distribution. (Note that in this way we are also varying the weightings of $\mathbf{\Psi}^c$ and $\mathbf{\Psi}^e$.) Figure 13 confirms that model M_b is suited to represent the natural variability of the sounds. The variations obtained by the model are similar to those in the ensemble of impact sounds [compare the variations in Fig. 13(a) to those in Fig. 13(b)].

V. DISCUSSION AND CONCLUSIONS

Our main goal here was to develop a data-driven method for learning a representation of the intrinsic structures of impact sounds. We showed that, by using PCA and ICA, it is possible to build a model that uses temporal and spectral basis functions that represent the intrinsic temporal and spectral structures of the sounds. The method can be used to characterize the structures of a single sound or the structures common to a set of impact sounds, in which case it also captures the natural variability in the structures. Obviously, if the method receives different inputs, it produces different outputs, but if the sounds are of the same type, the structures that the method learns are comparable. For instance, the results of analyzing one sound versus several sounds of the same type are very similar. The model does not require any *a priori* knowledge of the physics, acoustics, or dynamics of the objects and events and is able to represent the underlying acoustical structures in the sounds, which could offer advantages over previous knowledge-based models.

The temporal structures of the sounds are represented by the temporal basis functions $\mathbf{\Phi}$, which are learned by spectral analysis of the spectrograms. The spectral structures of the sounds are represented by the spectral basis functions $\mathbf{\Psi}$, which are obtained in a second step by PCA or ICA of the spectral source signals associated with the temporal basis functions $\mathbf{\Phi}$.

Spectral ICA is able to decompose spectrograms into a small number of underlying features (represented in the temporal basis functions $\mathbf{\Phi}$) that characterize acoustic properties such as ringing, resonance, sustain, decay, and onsets. Since the method is not restricted to learn explicit features (or structures) of the sounds, the representations obtained include new information that was not represented by previous (physical) models. For instance, features that are more abstract than simple decay rate or average spectra, like features that characterize ringing, or decay shapes that are not exponential, can now be modeled and easily extracted from the sounds. Spectral PCA gives compact representations of the temporal structures in the spectrograms. For instance, six basis functions can explain 96% or more of the variance of the data (see Sec. IV A 2). Such low dimensional characterizations of the data can present advantages over previous physical models. For example, since impact sounds can have hundreds of partials (van den Doel *et al.*, 2002), modeling them with Eq. (1) would mean using a very big N. When the objective is to model only the perceptually relevant portions of the sound, many less partials can be used (that is, N can be substantially smaller), yet determining which partials should be used is also a difficult question (van den Doel *et al.*, 2002).

Brown and Smaragdis (2004) have used ICA to separate different notes from two-note musical trills. In another study the same authors have used non-negative matrix factorization (NMF), which is another redundancy reduction technique, to analyze polyphonic musical passages (Smaragdis and Brown, 2003). Although these approaches are related to those presented here, their goal was to separate notes from musical segments with more than two notes. Even though the analyses used in both these studies resemble our analysis method, there are some fundamental differences. The main difference is that we are partitioning individual sounds according to the temporal behavior of the partials, whereas in their studies the sounds are being segmented according to events; we are interested in representing the structure of sounds of the same type efficiently, whereas they are interested in segmenting sound events. Also, while their analyses are appropriate for highly harmonic sounds, transient sounds with high structure variability are better described by our method, given that here individual sounds are represented by more than one temporal and spectral basis functions.

Most work with redundancy reduction techniques (like ICA, PCA, NMF, singular value decomposition, and sparse coding) and spectrograms or other time-frequency structures (like constant Q-transforms and wavelets), focus on the source separation problem, and, as with the above-mentioned two studies, it segments sounds according to events (e.g., Barros *et al.*, 2002; Casey and Westner, 2000; Smaragdis, 2004; Virtanen, 2004). Some MPEG-7 audio features are obtained using similar techniques, and there has been work on sound classification, recognition, and event detection using these features (e.g., Kim *et al.*, 2004; Xiong *et al.*, 2003). All these studies use techniques similar to those used in the method presented here, but their goals are very different and, to the best of our knowledge, the method presented is the first to partition individual sounds according to the temporal behavior of the partials. Even though this paper does not discuss sound classification and recognition, the basis functions learned by the method presented here, may be particularly useful to such applications.

Although here we have only considered impact sounds, namely impacts on rods, we predict that this model can be used to represent other types of transient acoustic events. The work presented considers only the spectral content of the signals. Nonetheless, there is also complex structure in the phase of the signals, which is important for synthesizing sound waveforms from the model.

ACKNOWLEDGMENTS

This work was supported in part by fellowships from Fundação Calouste Gulbenkian (Portugal) and Fundação para a Ciência e a Tecnologia (Portugal) to S.C. and a grant from the National Science Foundation to M.S.L.

APPENDIX

See EPAPS Document No. E-JASMAN-121–046706 for Appendices A, B, and C. This document can be reached via a direct link in the online article's HTML reference section or via the EPAPS homepage (http://www.aip.org/pubservs/epaps.html).

[1]Here matrices are represented in bold upper case, vectors, which are column vectors unless the transpose is used, are represented in bold lower case, and scalars are represented in lower case. The horizontal concatenation of matrices **A** and **B** is $(\mathbf{A},\mathbf{B})$.

[2]We use upper indexes to distinguish different variables of the same type, so for instance $\mathbf{X}^1$ and $\mathbf{X}^2$ are two different matrices of the same type. Lower indices are used to index values within a matrix or vector.

[3]In order to make the graphs more readable, some of the basis functions $\boldsymbol{\phi}_i$ and corresponding spectral source signals $\mathbf{c}_i^k$ have been multiplied by -1.

[4]Since the basis functions given by PCA are orthogonal, the sum of the variances that they explain gives the total variance explained. However, the same is not true for the basis functions given by ICA, which are not restricted to being orthogonal. In this case, the sum of the variances may correspond to a quantity that is bigger than the actual variance explained by the basis functions.

[5]In order to make the graphs more readable, some of the basis functions $\boldsymbol{\psi}_j^i$ and corresponding coefficients $v_{i,j}^k$ have been multiplied by -1.

Avanzini, F., and Rocchesso, D. (**2001a**). "Controlling material properties in physical models of sounding objects," Proceedings of the International Computer Music Conference 2001, La Habana, Cuba, pp. 91–94.

Avanzini, F., and Rocchesso, D. (**2001b**). "Modeling collision sounds: Nonlinear contact force," in Proceedings of the COST G-6 Conference on Digital Audio Effects, 2001, Limerick, Ireland.

Barros, A. K., Rutkowski, T., Itakura, F., and Ohnishi, N. (**2002**). "Estimation of speech embedded in a reverberant and noisy environment by independent component analysis and wavelets," IEEE Trans. Neural Netw. **13**, 888–893.

Brown, J., and Smaragdis, P. (**2004**). "Independent component analysis for automatic note extraction from musical trills," J. Acoust. Soc. Am. **115**, 2295–2306.

Casey, M. A., and Westner, A. (**2000**). "Separation of mixed audio sources by independent subspace analysis," Proceedings of the International Computer Music Conference, Berlin, Germany.

Gaver, W. W. (**1994**). *Using and Creating Auditory Icons*, Auditory Display: Sonification, Audification and Auditory Interfaces, editied by G. Kramer (Addison-Wesley, Reading, MA), pp. 417–446.

Gaver, W. W. (**1988**). "Everyday listening and auditory icons," Ph.D. thesis, University of California at San Diego, San Diego, CA.

Hyvärinen, A., Karhunen, J., and Oja, E. (**2001**). *Independent Component Analysis* (Wiley, New York).

James, D. L., Barbič, J., and Pai, D. K. (**2006**). "Precomputed acoustic transfer: Output-sensitive, accurate sound generation for geometrically complex vibration sources," ACM Trans. Graphics **25**, 987–995.

Kim, H. G., Berdahl, E., and Sikora, T. (**2004**). "Study of MPEG-7 sound classification and retrieval," Fifth International ITG Conference on Source and Channel Coding, Erlangen, Germany.

Lambourg, C., Chaigne, A., and Matignon, D. (**2001**). "Time-domain simulation of damped impacted plates. II. Numerical model and results," J. Acoust. Soc. Am. **109**, 1433–1447.

O'Brien, J. F., Cook, P. R., and Ess, G. (**2001**). "Synthesizing sounds from physically based motion," Proceedings of ACM SIGGRAPH (Los Angeles, California) pp. 529–536.

O'Brien, J. F., Shen, S., and Gatchalian, C. M. (**2002**). "Synthesizing sounds from rigid-body simulations," in Proceedings of ACM SIGGRAPH Symposium on Computer Animation (San Antonio, Texas) pp. 175–181.

Pai, D. K., van den Doel, K., James, D. L., Lang, J., Lloyd, J. E., Richmond, J. L., and Yau, S. H. (**2001**). "Scanning physical interaction behavior of 3d objects," Proceedings of ACM SIGGRAPH (Los Angeles, California) pp. 87–96.

Smaragdis, P. (**2004**). "Non-negative matrix factor deconvolution; Extraction of multiple sound sources from monophonic inputs," Proceedings of the Fifth International Conference on Independent Component Analysis and Blind Signal Separation, Lecture Notes in Computer Science, edited by C. G. Puntonet and A. Prieto (Granada, Spain) pp. 494–499.

Smaragdis, P., and Brown, J. (**2003**). "Non-negative matrix factorization for polyphonic music transcription," IEEE Workshop on Applications of Signal Processing to Audio and Acoustics, pp. 177–180.

Stone, J. V. (**2004**). *Independent Component Analysis, A Tutorial Introduction* (MIT, Cambridge, MA).

van den Doel, K., Kry, P. G., and Pai, D. K. (**2001**). "Foleyautomatic: Physically-based sound effects for interactive simulation and animation," Proceedings of ACM SIGGRAPH, Los Angeles, California.

van den Doel, K., Pai, D. K., Adam, T., Kortchmar, L., and Pichora-Fuller, K. (**2002**). "Measurements of perceptual quality of contact sound models," Proceedings of the International Conference on Auditory Display (Kyoto, Japan) pp. 345–349.

Virtanen, T. (**2004**). "Separation of sound sources by convolutive sparse coding," Proceedings of the ISCA Tutorial and Research Workshop on Statistical and Perceptual Audio Processing, 3 Oct., Jeju, Korea.

Xiong, Z., Radhakrishnan, R., Divakaran, A., and Huang, T. (**2003**). "Audio events detection based highlights extraction from baseball, golf and soccer games in a unified framework," Proceedings of IEEE International Conference on Acoustics, Speech, and Signal Processing (ICASSP).

Directionality of generalized acoustic sensors of arbitrary order

Dean J. Schmidlin[a)]
Department of Electrical and Computer Engineering, University of Massachusetts Dartmouth, 285 Old Westport Road, North Dartmouth, Massachusetts 02747-2300

(Received 2 September 2006; revised 17 March 2007; accepted 19 March 2007)

For several decades there has been a great deal of interest in acoustic sensors that can make multiple measurements at a single point in the ocean. The order of such sensors has been defined by linking it to the order of the Taylor series approximation of the pressure field at that point. Following this definition, the pressure, vector, and dyadic sensor is of order zero, one, and two, respectively. For this theoretical study, a multichannel three-dimensional spatial filter is derived for a directional acoustic sensor of arbitrary order. Explicit formulas are found for the filter coefficients that maximize the array gain (directivity index) of the filter as well as an explicit expression for the maximum array gain (directivity index). This process is repeated for the case of a first-order null placed in the direction opposite to the look direction of the multichannel filter. Finally, an example is presented which tracks the array gain and beamwidth of a third-order acoustic sensor as the order of the null is assigned values 0, 1, 2, and 3. © *2007 Acoustical Society of America.*
[DOI: 10.1121/1.2724239]

PACS number(s): 43.60.Fg, 43.30.Wi [EJS] Pages: 3569–3578

I. INTRODUCTION

D'Spain (1994) was the first to point out a qualitative relationship between the Taylor series expansion of a pressure field and a vector sensor. Cray and Nuttall (1997) utilized the four physical quantities measured by a vector sensor as inputs to a multichannel filter and demonstrated that a single vector sensor can perform spatial filtering or beamforming. A detailed vector-sensor beam pattern analysis was presented by Wong and Chi (2002). Hawkes and Nehorai (1998) investigated and quantified the factors that lead to the improved direction-of-arrival estimation performance of a vector-sensor array as compared to a pressure-sensor array. A collection of direction-finding algorithms were developed by Wong and Zoltowski (1997), (1999), (2000) and Tichavsky, Wong, and Zoltowski (2001).

The Taylor series relationship and the multichannel filtering concept led Silvia (2001) and Silvia, Franklin, and Schmidlin (2001) to introduce and investigate the acoustic dyadic sensor. This sensor arises from the second-order approximation of the Taylor series expansion of the pressure field. It was shown that a dyadic sensor can produce a beamwidth and a maximum array gain (against isotropic noise) of 65° and 9.5 dB as compared to 105° and 6 dB for a vector sensor.

Cray (2002) and Cray *et al.* (2003) presented theory for acoustic receivers of order greater than two. It was pointed out that, although further improvement in directionality is achieved by high-order directional sensors, these sensors can be significantly more sensitive to nonacoustic noise sources. In spite of practical limitations, Hines *et al.* (2000) demonstrated that a superdirective array can provide substantial improvement over a conventional array in particular instances.

This paper extends the multichannel filtering approach of Silvia (2001) to directional acoustic sensors of arbitrary order. The resulting beam pattern function is a polynomial in a single variable. This variable represents the inner product of two unit vectors, a steering vector and a unit vector denoting the direction of a plane-wave source. The coefficients of the polynomial are not functions of any steering parameters, making it easier to maximize the directivity index (array gain) subject to linear constraints. Section II derives the multichannel filter structure and the beam pattern function. In Sec. III, explicit formulas are given for the maximum array gain (directivity index) and for the associated filter coefficients. Finally, Sec. IV considers the problem of maximizing the directivity index (array gain) subject to linear constraints imposed by the placement of nulls in the beam pattern.

II. GENERALIZED ACOUSTIC SENSORS

A. Acoustic sensor of order *v*

It is natural to define an idyllic acoustic sensor located at a point (x_0,y_0,z_0) in three-dimensional space as one that can determine the pressure field at any other point (x,y,z) solely from measurements at (x_0,y_0,z_0). What measurements are required is clearly brought out by the Taylor series expansion of the pressure field about the point (x_0,y_0,z_0). Assuming that the sensor is located at the origin $(0,0,0)$, the infinite series expansion may be written as

$$p(t,x,y,z)=\sum_{\ell=0}^{\infty}\sum_{m=0}^{\infty}\sum_{n=0}^{\infty}p_{\ell,m,n}(t)\frac{x^{\ell}y^{m}z^{n}}{\ell\,!\,m\,!\,n!}, \tag{1}$$

where

a)Electronic mail: dschmidlin@umassd.edu

$$p_{\ell,m,n}(t) = \left. \frac{\partial^{\ell+m+n} p(t,x,y,z)}{\partial x^{\ell}\, \partial y^{m}\, \partial z^{n}} \right|_{x=0,y=0,z=0} \tag{2}$$

are the various spatial partial derivatives of the pressure evaluated at the point $(0,0,0)$. The above equations show that the idyllic sensor must measure at the origin the pressure and all of its spatial partial derivatives. Clearly, this is not possible in practice. More practical sensors can be defined by truncating the three-dimensional Taylor series. In order to do this, it is useful to express the sum (1) in the equivalent form

$$p(t,x,y,z) = \sum_{d=0}^{\infty} \frac{p_d(t,x,y,z)}{d!}, \tag{3}$$

where

$$p_d(t,x,y,z) = \sum_{\ell+m+n=d} p_{\ell,m,n}(t) \binom{d}{\ell,m,n} x^{\ell} y^{m} z^{n} \tag{4}$$

is a homogeneous polynomial of degree d in the variables x,y,z and $\binom{d}{\ell,m,n} = \frac{d!}{\ell!m!n!}$ is the *multinomial coefficient*. The triple sum in Eq. (4) is taken over all non-negative integers ℓ,m,n for which $\ell+m+n=d$. A *generalized acoustic sensor of order* v is defined as one that extrapolates the pressure field by means of the formula

$$\hat{p}(t,x,y,z) = \sum_{d=0}^{v} \frac{p_d(t,x,y,z)}{d!}. \tag{5}$$

The approximation to the pressure field given by Eq. (5) is a multivariable polynomial in x,y,z of degree v. Hence, the generalized acoustic sensor of order v measures the pressure $p(t,0,0,0)$ and the spatial partial derivatives $p_{\ell,m,n}(t)$ for all ℓ,m,n such that $\ell+m+n=1,2,\ldots,v$. When $v=0$, Eq. (5) defines a generalized acoustic sensor of order 0, which is the ordinary acoustic pressure sensor. When $v=1$, Eq. (5) defines a generalized acoustic sensor of order one. This sensor is the pressure gradient or vector sensor. The vector sensor measures the pressure and the gradient of the pressure (three spatial first-order partial derivatives). When $v=2$, Eq. (5) defines a generalized acoustic sensor of order two. This sensor is the acoustic dyadic sensor. The dyadic sensor measures the pressure, the pressure gradient, and the Hessian of the pressure (six spatial second-order partial derivatives). For a given v, Eq. (5) allows for the extrapolation of the acoustic pressure in a spherical volume about the measurement point. As v increases, the accuracy of the extrapolation increases as well as the volume. For a particular set of v values, a mean-square analysis can be carried out that determines the percent error in Taylor series approximation of the pressure field as a function of the sensor radius of coverage (as a percentage of wavelength). Such an analysis was performed by Silvia (2001) for $v=0,1,2$.

B. Multichannel filtering

Of primary interest in this paper is the directionality achievable by generalized acoustic sensors. To this end, it is instructive to look at Eq. (5) in the temporal frequency domain for the case of an acoustic plane wave. Figure 1 illustrates a plane wave propagating towards the origin of a rectangular coordinate system. Located at the origin is an acoustic sensor of order v. The pressure of the planar wave front can be written in the form

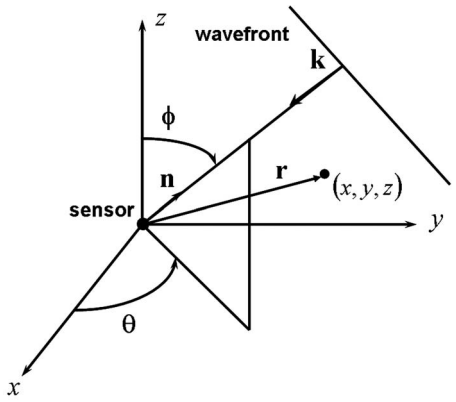

FIG. 1. Plane wave propagating towards the origin of a rectangular coordinate system.

$$p(t,x,y,x) = p\left(t + \frac{\mathbf{n}\cdot\mathbf{r}}{c}\right) = p\left(t + \frac{n_x x + n_y y + n_z z}{c}\right), \tag{6}$$

where

$$n_x = \sin\phi\cos\theta \quad n_y = \sin\phi\sin\theta \quad n_z = \cos\phi. \tag{7}$$

The form of Eq. (2) becomes

$$p_{\ell,m,n}(t) = \frac{n_x^{\ell} n_y^{m} n_z^{n}}{c^{\ell+m+n}} \frac{\partial^{\ell+m+n} p(t)}{\partial t^{\ell+m+n}}. \tag{8}$$

The temporal Fourier transform of Eq. (8) is given by

$$P_{\ell,m,n}(\omega) = \frac{n_x^{\ell} n_y^{m} n_z^{n}}{c^{\ell+m+n}} (j\omega)^{\ell+m+n} P(\omega). \tag{9}$$

Taking the temporal Fourier transform of Eq. (4) results in

$$P_d(\omega,x,y,z) = \sum_{\ell+m+n=d} P_{\ell,m,n}(\omega) \binom{d}{\ell,m,n} x^{\ell} y^{m} z^{n}. \tag{10}$$

The substitution of Eq. (9) into Eq. (10) yields

$$P_d(\omega,x,y,z) = \left(\frac{j\omega}{c}\right)^{d} P(\omega) \sum_{\ell+m+n=d} \binom{d}{\ell,m,n} \times (n_x x)^{\ell} (n_y y)^{m} (n_z z)^{n}. \tag{11}$$

Applying the multinomial formula to the summation in Eq. (11) leads to

$$P_d(\omega,x,y,z) = \left(\frac{j\omega}{c}\right)^{d} (n_x x + n_y y + n_z z)^{d} P(\omega). \tag{12}$$

Equation (12) can be expressed in the alternate form

$$P_d(\omega,\mathbf{r}) = \left(\frac{j\omega}{c}\right)^{d} (\mathbf{n}\cdot\mathbf{r})^{d} P(\omega). \tag{13}$$

The temporal Fourier transform of Eq. (5) is

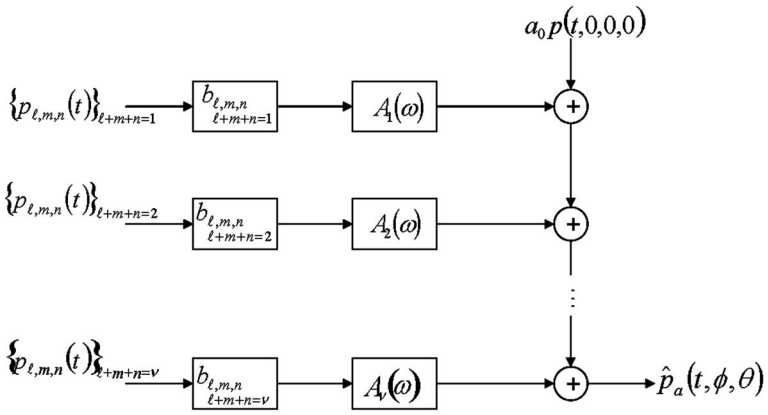

FIG. 2. Multichannel filter that arises from an acoustic sensor of order v.

$$\hat{P}(\omega,\mathbf{r}) = \sum_{d=0}^{v} \frac{P_d(\omega,\mathbf{r})}{d!}, \tag{14}$$

where the alternate notation introduced in Eq. (13) is utilized. Equation (14) represents the pressure-field extrapolation in the frequency domain made by a generalized acoustic sensor of order v. As the value of v increases, the accuracy of the extrapolation increases. Consider now a slightly more general form of Eq. (14), namely,

$$\hat{P}_a(\omega,\mathbf{r}) = \sum_{d=0}^{v} A_d(\omega) P_d(\omega,\mathbf{r}), \tag{15}$$

where the various $A_d(\omega)$ are to be interpreted as weights. Equation (15) may be interpreted as the temporal Fourier transform of the output of a multichannel filter when the inputs are the derivatives $p_{\ell,m,n}(t)$ defined by Eq. (2). When each $A_d(\omega)$ is equal to $1/d!$, the multichannel filter is an extrapolator. The vector $\mathbf{r}$ specifies the point at which the extrapolation is made. Consider now the following values for the weights:

$$A_d(\omega) = a_d\left(\frac{c}{j\omega}\right)^d, \quad d = 0,1,2,\ldots . \tag{16}$$

The substitution of Eqs. (13) and (16) into Eq. (15) gives

$$\hat{P}_a(\omega,\mathbf{r}) = P(\omega) g(\mathbf{n}\cdot\mathbf{r}), \tag{17}$$

where

$$g(\mathbf{n}\cdot\mathbf{r}) = \sum_{d=0}^{v} a_d (\mathbf{n}\cdot\mathbf{r})^d. \tag{18}$$

Equation (17) no longer represents a pressure field extrapolation. Hence, the vector $\mathbf{r}$ can no longer be interpreted as referring to the extrapolation point in space. Since Eq. (17) now corresponds to a multichannel spatial filter, the vector $\mathbf{r}$ will be replaced by

$$\mathbf{n_s} = \sin\phi_s \cos\theta_s \hat{x} + \sin\phi_s \sin\theta_s \hat{y} + \cos\phi_s \hat{z}. \tag{19}$$

Equation (18) becomes

$$g(\mathbf{n}\cdot\mathbf{n_s}) = g(\phi,\theta) = \sum_{d=0}^{v} a_d (\mathbf{n}\cdot\mathbf{n_s})^d, \tag{20}$$

where

$$\mathbf{n}\cdot\mathbf{n_s} = \sin\phi \sin\phi_s \cos(\theta-\theta_s) + \cos\phi\cos\phi_s. \tag{21}$$

The function given by Eq. (20) is the beam pattern of the multichannel filter, or equivalently, the beam pattern of the associated directional acoustic sensor of order v. The basic structural equations for the multichannel filter are

$$\hat{P}_a(\omega,\phi,\theta) = \sum_{d=0}^{v} A_d(\omega) P_d(\omega,\phi,\theta), \tag{22}$$

$$P_d(\omega,\phi,\theta) = \sum_{\ell+m+n=d} b_{\ell,m,n} P_{\ell,m,n}(\omega), \tag{23}$$

$$b_{\ell,m,n} = \binom{d}{\ell,m,n} \sin^{\ell+m}(\phi_s)\cos^n(\phi_s)\cos^\ell(\theta_s)\sin^m(\theta_s). \tag{24}$$

Equation (22) is the same as Eq. (15) with the exception that the dependence on the angles ϕ and θ is made explicit. Equations (23) and (24) follow from Eqs. (10) and (19), where x,y,z in Eq. (10) is replaced by the components of Eq. (19). Figure 2 shows the multichannel filter that arises from a generalized acoustic sensor of order v. There are v clusters of derivatives that are input to the multichannel filter. The jth cluster consists of all of the pressure derivatives of order j. The number of such derivatives is $(j+2)(j+1)/2$. These derivatives are each multiplied by a constant and added. The sum is then input to a filter whose frequency transfer function is $A_j(\omega)$ resulting in an output that corresponds to the jth cluster. Finally, these outputs are summed to obtain the output of the multichannel filter. There are two sets of coefficients associated with the multichannel filter, namely, $b_{\ell,m,n}$ and a_d. The $b_{\ell,m,n}$ coefficients, which are computed from Eq. (24), determine the angles ϕ_s and θ_s at which the magnitude of the beam pattern $g(\phi,\theta)$ attains its maximum value. The coefficients $\{a_d\}_{d=0}^{v}$ are to be chosen so as to achieve some optimality condition such as maximum array gain or optimum null placement.

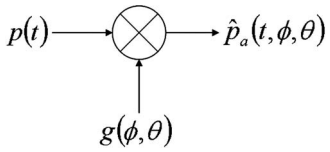

FIG. 3. Effective processing of the multichannel filter.

III. DIRECTIVITY OF GENERALIZED ACOUSTIC SENSORS

A. Beam power pattern

The directionality of the acoustic sensor of order v is achieved by the signal processing diagrammed in Fig. 2. The multichannel filter of Fig. 2 has $(v+1)(v+2)(v+3)/6$ inputs and one output. It is difficult to see from Fig. 2 the dependence of the output on the angles ϕ and θ of the input plane wave to the acoustic sensor. Equation (17) suggests the simpler diagram of Fig. 3. The input $p(t)$ is the temporal variation of the pressure at the acoustic sensor. The dependence of the output on ϕ and θ is explicitly determined by the beam pattern function $g(\phi,\theta)$. The beam pattern for the acoustic sensor of order v is given by Eq. (20). It is advantageous to express the beam pattern in the alternate forms

$$g_u(u) = \sum_{d=0}^{v} a_d u^d, \tag{25}$$

$$g_\psi(\psi) = \sum_{d=0}^{v} a_d \cos^d\psi, \tag{26}$$

where

$$u = \mathbf{n}\cdot\mathbf{n_s} = \cos\psi. \tag{27}$$

Equations (25) and (26) represent the beam pattern in u space and ψ space, respectively. The variable ψ, which is illustrated in Fig. 4, is the angle between the unit vectors $\mathbf{n}$ and $\mathbf{n_s}$. The directional acoustic sensor is "looking" in the direction indicated by the steering vector $\mathbf{n_s}$. The unit vector $\mathbf{n}$ is collinear with the wave number vector $\mathbf{k}$ of the planar wave front shown in Fig. 1. The ranges of the variables u and ψ are $-1\le u\le 1$ and $0\le\psi\le\pi$. Both of these variables are functions of the angles ϕ and θ. Generally, there are an infinite number of pairs (ϕ,θ) that result in the same value of u (or ψ).The two exceptions are $u=1$ $(\psi=0)$ and $u=-1$ $(\psi=\pi)$. In the first exception, $\phi=\phi_s$, $\theta=\theta_s$ whereas in the second, $\phi=\pi-\phi_s$ and $\theta=\theta_s+\pi$ when $0\le\theta_s\le\pi$ and $\theta=\theta_s-\pi$ when $\pi<\theta_s<2\pi$. The case $u=\pm1$ corresponds to $\mathbf{n}=\pm\mathbf{n_s}$. When $u=1$ the directional acoustic sensor is looking at the planar wave front, and when $u=-1$ it is looking in the opposite direction.

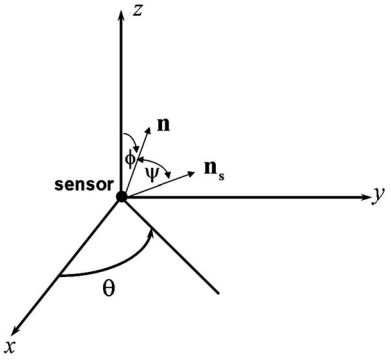

FIG. 4. The angle ψ between the steering vector $\mathbf{n_s}$ and the unit vector $\mathbf{n}$.

The beam pattern of the directional acoustic sensor has been expressed in the three forms defined by Eqs. (20), (25), and (26). Correspondingly, the beam power pattern, which is the square of the beam pattern, has the three forms

$$B(\phi,\theta) = g^2(\phi,\theta) = \sum_{n=0}^{2v} c_n(\mathbf{n}\cdot\mathbf{n_s})^n, \tag{28}$$

$$B_u(u) = g_u^2(u) = \sum_{n=0}^{2v} c_n u^n, \tag{29}$$

$$B_\psi(\psi) = g_\psi^2(\psi) = \sum_{n=0}^{2v} c_n \cos^n\psi, \tag{30}$$

where

$$c_n = \sum_{\ell=0}^{n} a_{n-\ell}a_\ell, \quad n = 0,1,\ldots,2v. \tag{31}$$

It follows from Eq. (25) that if $u=1$and

$$\sum_{d=1}^{v} a_d = 1 \tag{32}$$

then the value of the beam power pattern at $u=1$ is unity, i.e., $B_u(1)=1$. In the design of the multichannel filter, which gives the acoustic sensor its directionality, it will be assumed that the filter coefficients a_d satisfy the constraint specified by Eq. (32). In addition, the filter coefficients must be selected such that the beam power pattern $B_u(u)$ have values generally significantly less than unity when $u\neq1$. One design criterion that achieves this objective is the maximization of the array gain (directivity index).

B. Array gain and directivity index

For the purpose of detecting a plane wave signal, the array gain of a spatial filter (directional sensor) is defined as the ratio of the noise power out of an omnidirectional device to the noise power out of the spatial filter (directional sensor). Burdic (1991) defines the array gain (expressed in decibel notation) as

$$\mathrm{AG} = 10\log\left[\frac{\int_0^{2\pi}\int_0^{\pi}|N(\phi,\theta)|^2\sin\phi d\phi d\theta}{\int_0^{2\pi}\int_0^{\pi}|N(\phi,\theta)|^2 B(\phi,\theta)\sin\phi d\phi d\theta}\right]. \tag{33}$$

$|N(\phi,\theta)|^2$ is the noise field angular intensity distribution. If the noise field is isotropic, this distribution has a constant value for all ϕ and θ. The array gain simplifies to

$$\mathrm{AG} = -\log J, \tag{34}$$

where

$$J = \frac{1}{4\pi}\int_0^{2\pi}\int_0^{\pi} B(\phi,\theta)\sin\phi d\phi d\theta. \tag{35}$$

The quantity J represents the normalized noise power out of the spatial filter of Fig. 2. The power is normalized with respect to the noise power out of an omnidirectional sensor.

Another fundamental measure of the performance of a directional acoustic sensor is the directivity index. Following the definition of Nuttall and Cray (2001) for apertures and arrays, the directivity index of a directional sensor is defined as a decibel measure of the improvement in the signal-to-noise ratio that a directional sensor provides in an ideal isotropic noise field with a perfectly correlated signal, relative to an omnidirectional sensor in the free field. Using this definition for the case of a normalized beam power pattern $[B(\phi_s,\theta_s)=1]$ and isotropic noise, the value of the directivity index is the same as that of the array gain specified by Eq. (34). Appendix A evaluates the integral (35). The value of the noise power J is given by (A21). If (A22) is substituted into (A21), then

$$J = \boldsymbol{a}'\boldsymbol{H}\boldsymbol{a}, \tag{36}$$

where

$$h_{ij} = \begin{cases} \dfrac{1}{i+j+1} & \text{for } i+j \text{ even} \\ 0 & \text{for } i+j \text{ odd} \end{cases} \qquad i,j = 0,1,\ldots,v. \tag{37}$$

$$\boldsymbol{a}' = \begin{bmatrix} a_0 & a_1 & \cdots & a_v \end{bmatrix}. \tag{38}$$

The directivity index (array gain) becomes

$$\mathrm{DI} = \mathrm{AG} = -10\log(\boldsymbol{a}'\boldsymbol{H}\boldsymbol{a}). \tag{39}$$

The matrix defined by Eq. (37) is a Hankel matrix, that is, all of the elements along each skew diagonal are equal. This matrix is identical to the one found by Cray *et al.* (2003) for the case of a limited combined receiver that measures pressure derivatives, to any order, only along the z axis. The matrix $\boldsymbol{H}$ is positive definite and the noise power specified by Eq. (36) is a positive definite quadratic form in the filter coefficients a_j. Equation (36) suggests a criterion for determining the filter coefficient values, namely, the minimization of the noise power J. Mathematically, the problem is the minimization of $\boldsymbol{a}'\boldsymbol{H}\boldsymbol{a}$ subject to the constraint imposed by Eq. (32). Applying the method of Lagrange multipliers (see Appendix B), the solution is

$$\boldsymbol{a} = \frac{\boldsymbol{H}^{-1}\boldsymbol{u}}{\boldsymbol{u}'\boldsymbol{H}^{-1}\boldsymbol{u}}. \tag{40}$$

Each element of the column vector $\boldsymbol{u}$ is equal to 1. The substitution of Eq. (40) into Eq. (39) results in

$$\mathrm{DI}_{\max} = \mathrm{AG}_{\max} = -10\log(\boldsymbol{u}'\boldsymbol{H}^{-1}\boldsymbol{u}). \tag{41}$$

Equations (40) and (41) allow for the computation of the maximum array gain (directivity index) and the associated values of the filter coefficients for an arbitrary sensor order v. However, it will be shown in the next subsection that the form of matrix $\boldsymbol{H}$ is such that it is possible to derive explicit formulas for the maximum array gain and associated filter coefficients.

C. Explicit formulas for maximum array gain and associated filter coefficients

The rows and columns of the matrix $\boldsymbol{H}$ defined by Eq. (37) can be rearranged so that the new $\boldsymbol{H}$ matrix is a block Hankel matrix having the form

$$\boldsymbol{H} = \begin{bmatrix} \boldsymbol{H}_1 & 0 \\ 0 & \boldsymbol{H}_2 \end{bmatrix}, \tag{42}$$

where

$$h_{ij}^{(1)} = \frac{1}{2(i+j)+1}, \quad i,j = 0,1,\ldots,m_1, \tag{43}$$

$$h_{ij}^{(2)} = \frac{1}{2(i+j)+3}, \quad i,j = 0,1,\ldots,m_2. \tag{44}$$

The values of m_1 and m_2 depend on whether the sensor order v is even or odd, that is,

$$m_1 = \begin{cases} v/2 & \text{for } v \text{ even} \\ (v-1)/2 & \text{for } v \text{ odd}, \end{cases} \tag{45}$$

$$m_2 = \begin{cases} v/2-1 & \text{for } v \text{ even} \\ (v-1)/2 & \text{for } v \text{ odd}. \end{cases} \tag{46}$$

The noise power is now a sum of two quadratic forms, namely,

$$\mathrm{J} = \boldsymbol{a}_1'\boldsymbol{H}_1\boldsymbol{a}_1 + \boldsymbol{a}_2'\boldsymbol{H}_2\boldsymbol{a}_2, \tag{47}$$

where

$$\boldsymbol{a}_1' = \begin{bmatrix} a_0 & a_2 & a_4 & \cdots \end{bmatrix}, \tag{48}$$

$$\boldsymbol{a}_2' = \begin{bmatrix} a_1 & a_3 & a_5 & \cdots \end{bmatrix}. \tag{49}$$

The matrices $\boldsymbol{H}_1$ and $\boldsymbol{H}_2$ are positive definite Hankel matrices. The column vector $\boldsymbol{a}_1$ and $\boldsymbol{a}_2$ contains the even-indexed and odd-indexed filter coefficients, respectively. The optimization problem now becomes one of minimizing Eq. (47) subject to Eq. (32). The solution is given by Eq. (B5) in Appendix B. For this problem, $N=1$, $\sigma_1=1$, $\boldsymbol{b}_1=\boldsymbol{u}_1$, and $\boldsymbol{c}_1=\boldsymbol{u}_2$. The latter two quantities are column vectors of all one's and having lengths $\ell_1=1+m_1$ and $\ell_2=1+m_2$. The solution for λ_1 is given from (B6) as

$$\lambda_1 = \frac{2}{\boldsymbol{u}_1'\boldsymbol{H}_1^{-1}\boldsymbol{u}_1 + \boldsymbol{u}_2'\boldsymbol{H}_2^{-1}\boldsymbol{u}_2}. \tag{50}$$

In light of Eq. (B5), the solutions for $\boldsymbol{a}_1$ and $\boldsymbol{a}_2$ are

$$\boldsymbol{a}_1 = \frac{\boldsymbol{H}_1^{-1}\boldsymbol{u}_1}{\boldsymbol{u}_1'\boldsymbol{H}_1^{-1}\boldsymbol{u}_1 + \boldsymbol{u}_2'\boldsymbol{H}_2^{-1}\boldsymbol{u}_2}, \tag{51}$$

$$\boldsymbol{a}_2 = \frac{\boldsymbol{H}_2^{-1}\boldsymbol{u}_2}{\boldsymbol{u}_1'\boldsymbol{H}_1^{-1}\boldsymbol{u}_1 + \boldsymbol{u}_2'\boldsymbol{H}_2^{-1}\boldsymbol{u}_2}. \tag{52}$$

The Hankel matrices $\boldsymbol{H}_1$ and $\boldsymbol{H}_2$ are also Cauchy matrices. Let $\{\alpha_i\}|_{i=1}^{1+m}$ and $\{\beta_i\}|_{i=1}^{1+m}$ be $2+2m$ numbers such that α_i

$+\beta_j \neq 0$ for all i and j. Then a matrix $\boldsymbol{C}$ for which $\boldsymbol{c}_{ij} = 1/(\alpha_i + \beta_j)$ is called a Cauchy matrix. An explicit formula for the elements of the inverse of a Cauchy matrix is given in the appendix of Gerber and Shiru (2005). The $i-j$ entry of $\boldsymbol{C}^{-1}$ is

$$\left(\prod_{\substack{h=0 \\ h\neq i}}^{m} \frac{\beta_h + \alpha_j}{\beta_h - \beta_i}\right)(\alpha_j + \beta_i)\left(\prod_{\substack{k=0 \\ k\neq j}}^{m} \frac{\alpha_k + \beta_i}{\alpha_k - \alpha_j}\right). \tag{53}$$

Applying Eq. (53) to the matrices $\boldsymbol{H}_1$ and $\boldsymbol{H}_2$ results in

$$\begin{aligned} \boldsymbol{H}_1^{-1} &= \boldsymbol{D}_1 \boldsymbol{H}_1 \boldsymbol{D}_1 \\ \boldsymbol{H}_2^{-1} &= \boldsymbol{D}_2 \boldsymbol{H}_2 \boldsymbol{D}_2 \end{aligned}. \tag{54}$$

The matrices $\boldsymbol{D}_1$ and $\boldsymbol{D}_2$ are diagonal matrices whose elements along the main diagonal are given by

$$d_i^{(1)} = 2(-1)^i \frac{\left(i + \frac{1}{2}\right)_{m_1+1}}{i!\,(m_1 - i)!} \quad i = 0, 1, \ldots, m_1. \tag{55}$$

$$d_i^{(2)} = 2(-1)^i \frac{\left(i + \frac{3}{2}\right)_{m_2+1}}{i!\,(m_2 - i)!} \quad i = 0, 1, \ldots, m_2. \tag{56}$$

The symbol $(a)_n$ appearing in Eqs. (55) and (56) is the *Pochhammer symbol* and is defined as

$$(a)_0 = 1, \quad (a)_n = a(a+1)\ldots(a+n-1) \quad n = 1, 2, 3, \ldots . \tag{57}$$

The direct application of Eqs. (A10) and (A12) in the appendix of Gerber and Shiu (2005) leads to the relationships

$$\begin{aligned} &\boldsymbol{H}_1^{-1}\boldsymbol{u}_1 = (-1)^{m_1}\boldsymbol{d}_1 \quad \boldsymbol{H}_2^{-1}\boldsymbol{u}_2 = (-1)^{m_2}\boldsymbol{d}_2 \\ &\boldsymbol{u}_1'\boldsymbol{H}_1^{-1}\boldsymbol{u}_1 = (m_1+1)(2m_1+1) \\ &\boldsymbol{u}_2'\boldsymbol{H}_2^{-1}\boldsymbol{u}_2 = (m_2+1)(2m_2+3). \end{aligned} \tag{58}$$

The elements of the column vectors $\boldsymbol{d}_1$ and $\boldsymbol{d}_2$ are given by Eqs. (55) and (56), respectively. The substitution of Eq. (58) into Eq. (50) through Eq. (52) results in $\lambda_1 = 2/(1+v)^2$ and

$$\boldsymbol{a}_1 = \frac{(-1)^{m_1}}{(1+v)^2}\boldsymbol{d}_1 \quad \boldsymbol{a}_2 = \frac{(-1)^{m_2}}{(1+v)^2}\boldsymbol{d}_2. \tag{59}$$

From Eq. (B8), the minimum value of J is equal to $\lambda_1/2$. The maximum directivity index (array gain) is

$$\mathbf{DI}_{\max} = \mathbf{AG}_{\max} = -10\log J_{\min} = 20\log(1+v). \tag{60}$$

Equation (59) gives explicit formulas for the filter coefficients that maximize the directivity index (array gain) of a directional acoustic sensor of order v. The value of this maximum directivity index (array gain) is specified by Eq. (60). As an example consider a sensor of order 5. The Hankel Matrices $\boldsymbol{H}_1$ and $\boldsymbol{H}_2$ have the values

$$\boldsymbol{H}_1 = \begin{bmatrix} 1 & 1/3 & 1/5 \\ 1/3 & 1/5 & 1/7 \\ 1/5 & 1/7 & 1/9 \end{bmatrix} \quad \boldsymbol{H}_2 = \begin{bmatrix} 1/3 & 1/5 & 1/7 \\ 1/5 & 1/7 & 1/9 \\ 1/7 & 1/9 & 1/11 \end{bmatrix}. \tag{61}$$

Equations (45) and (46) indicate that $m_1 = m_2 = 2$. By means of Eqs. (55), (56), and (59) one finds that

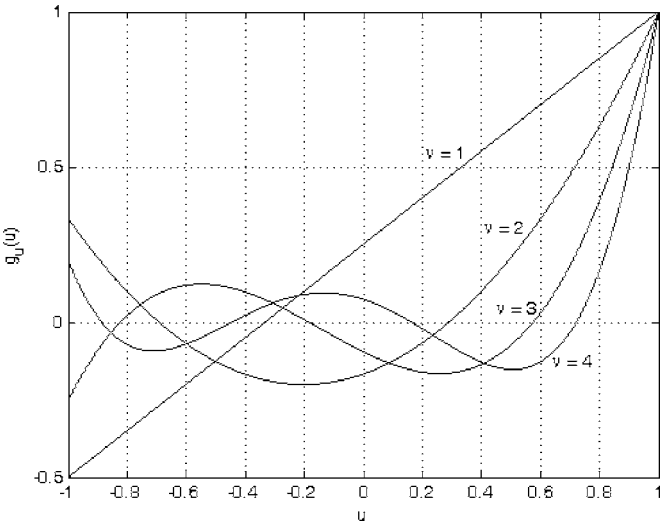

FIG. 5. The beam pattern $g_u(u)$ for several values of v.

$$\boldsymbol{a}_1 = \frac{1}{96}\begin{bmatrix} 5 \\ -70 \\ 105 \end{bmatrix} \quad \boldsymbol{a}_2 = \frac{1}{96}\begin{bmatrix} 35 \\ -210 \\ 231 \end{bmatrix}. \tag{62}$$

The filter coefficient vector $\boldsymbol{a}$ is

$$\boldsymbol{a} = \begin{bmatrix} 5 & 35 & -70 & -210 & 105 & 231 \end{bmatrix}/96. \tag{63}$$

If Eq. (63) is scaled so that the coefficient a_0 is normalized to 1, the resulting filter coefficient vector is equal to that obtained by Hines *et al.* (2000). The value of the array gain is obtained from Eq. (60) as 15.6 dB.

Illustrated in Fig. 5 is the beam pattern $g_u(u)$ for several values of v. For a particular value of v, the beam pattern is 1 when $u = 1$ and it passes through zero v times with the peak values of the oscillations decreasing as v increases. One can define the beamwidth in u space as the difference between $u = 1$ and the value of u for which $g_u(u) = \sqrt{2}/2$. Using this definition, the beamwidth is 0.395, 0.1567, 0.0852, and 0.0537 for values of v equal to 1, 2, 3, and 4, respectively. Figure 6 shows a plot of the beamwidth in θ space as a

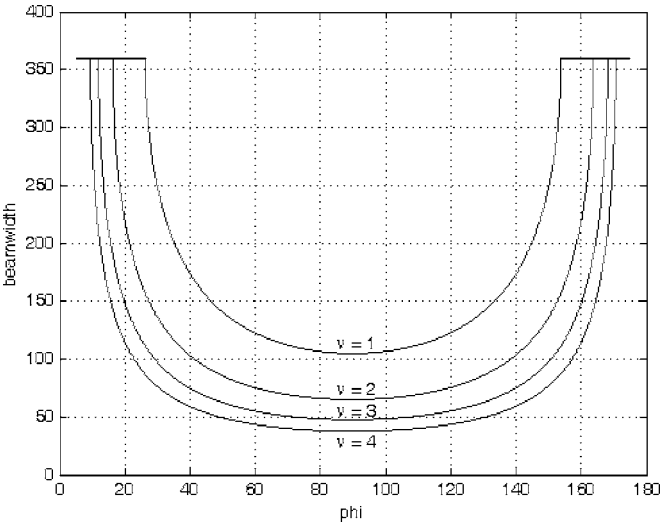

FIG. 6. The beamwidth in θ space as a function of the angle ϕ.

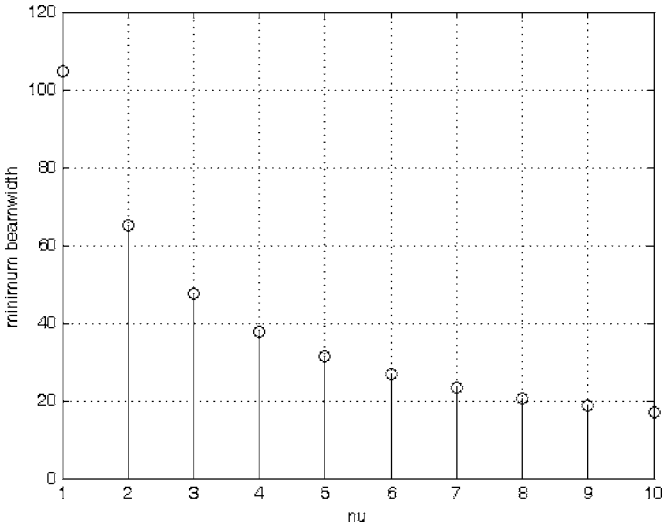

FIG. 7. The variation of minimum beamwidth with the sensor order v.

function of the angle ϕ for the same values of v. In the generation of the plot, it has been assumed that acoustic sensor's steering angle ϕ_S has been set to ϕ. For all values of v, the minimum value of the beamwidth occurs at $\phi=\pi/2$. Note that as the sensor order increases, the value of the minimum beamwidth decreases, and the beamwidth curve becomes flatter making the beamwidth less sensitive to the angle ϕ. Figure 7 gives the variation of the minimum beamwidth with the order of the directional acoustic sensor. Note that as the order increases, the amount of improvement in minimum beamwidth decreases.

IV. DIRECTIONAL ACOUSTIC SENSORS WITH NULL PLACEMENTS

A. First-order null in direction opposite to the look direction

In the design of beam patterns, it is often desirable to place one or more nulls in prescribed directions. This section is concerned with the problem of maximizing the array gain subject to a first-order null placed in the direction opposite to the look direction (ϕ_S, θ_S). This opposite direction corresponds to $u=-1$ in u space and $\psi=\pi$ in ψ space. Setting $u=\pm 1$ in Eq. (25) results in two equations

$$g_u(1) = \sum_{\substack{d=0 \\ d=\text{even}}}^{v} a_d + \sum_{\substack{d=0 \\ d=\text{odd}}}^{v} a_d = 1. \tag{64}$$

$$g_u(-1) = \sum_{\substack{d=0 \\ d=\text{even}}}^{v} a_d - \sum_{\substack{d=0 \\ d=\text{odd}}}^{v} a_d = 0. \tag{65}$$

Adding and subtracting Eqs. (64) and (65) leads to the relationships

$$\sum_{\substack{d=0 \\ d=\text{even}}}^{v} a_d = \sum_{\substack{d=0 \\ d=\text{odd}}}^{v} a_d = 1/2. \tag{66}$$

As in Sec. III of this paper, the objective is to minimize the noise power (47) subject to linear constraints. This time there are two linear constraints ($N=2$). Referring again to Appendix B, the constraints are represented by

$$\sigma_1 = \sigma_2 = \tfrac{1}{2}, \quad \boldsymbol{b}_1 = \boldsymbol{u}_1, \quad \boldsymbol{b}_2 = 0, \quad \boldsymbol{c}_1 = 0, \quad \boldsymbol{c}_2 = \boldsymbol{u}_2. \tag{67}$$

Column vectors $\boldsymbol{b}_2$ and $\boldsymbol{c}_1$ contain all zero entries. The Lagrange multipliers are determined from Eq. (B6) as

$$\lambda_1 = \frac{1}{\boldsymbol{u}_1' \boldsymbol{H}_1^{-1} \boldsymbol{u}_1}, \quad \lambda_2 = \frac{1}{\boldsymbol{u}_2' \boldsymbol{H}_2^{-1} \boldsymbol{u}_2}. \tag{68}$$

The solutions for $\boldsymbol{a}_1$ and $\boldsymbol{a}_2$ are found from Eq. (B5) as

$$\boldsymbol{a}_1 = \tfrac{1}{2} \frac{\boldsymbol{H}_1^{-1} \boldsymbol{u}_1}{\boldsymbol{u}_1' \boldsymbol{H}_1^{-1} \boldsymbol{u}_1}, \quad \boldsymbol{a}_2 = \tfrac{1}{2} \frac{\boldsymbol{H}_2^{-1} \boldsymbol{u}_2}{\boldsymbol{u}_2' \boldsymbol{H}_2^{-1} \boldsymbol{u}_2}, \tag{69}$$

which because of Eq. (58) can be expressed as

$$\boldsymbol{a}_1 = \frac{\frac{1}{2}(-1)^{m_1}}{(m_1+1)(2m_1+1)} \boldsymbol{d}_1, \quad \boldsymbol{a}_2 = \frac{\frac{1}{2}(-1)^{m_2}}{(m_2+1)(2m_2+3)} \boldsymbol{d}_2. \tag{70}$$

The value of $J_{\min}$ is gotten from Eq. (B8) as $J_{\min}=\frac{1}{4}(\lambda_1+\lambda_2)$. The utilization of Eq. (68) together with Eq. (58) leads to $J_{\min}=1/(v^2+2v)$. The maximum array gain is

$$\text{AG}_{\max} = 10 \log(v^2 + 2v). \tag{71}$$

Equation (60) gives the maximum array gain when no null constraint is placed at $u=-1$. This gain may be written in the form

$$\text{AG}_{\max} = 10 \log(v^2 + 2v + 1). \tag{72}$$

Equations (71) and (72) show that the reduction in array gain caused by the null quickly becomes insignificant as the value of v increases. For the case of a vector sensor ($v=1$), the array gain with and without the null is 4.8 and 6.0 dB, respectively, a difference of 1.2 dB. But for the dyadic sensor ($v=2$), the array gain with and without the null is 9.0 and 9.5 dB, respectively, a difference of 0.5 dB. The difference further decreases to 0.28 and 0.17 dB for $v=3$ and $v=4$, respectively.

B. Example: Third-order directional acoustic sensor

This section considers the third-order directional acoustic sensor. Multichannel filters are designed which maximize the array gain subject to first-, second- and third-order nulls at $u=-1$. The array gain and beamwidth of these spatial filters are compared with each other and with the case of no null at $u=-1$. For the special case of $v=3$, the matrices H_1 and H_2 have the values

$$H_1 = \begin{bmatrix} 1 & 1/3 \\ 1/3 & 1/5 \end{bmatrix}, \quad H_2 = \begin{bmatrix} 1/3 & 1/5 \\ 1/5 & 1/7 \end{bmatrix}. \tag{73}$$

For the third-order sensor, $m_1=m_2=1$, $\boldsymbol{d}_1'=[3/2 \quad -15/2]$, and $\boldsymbol{d}_2'=[15/2 \quad -35/2]$. The filter coefficients are deter-

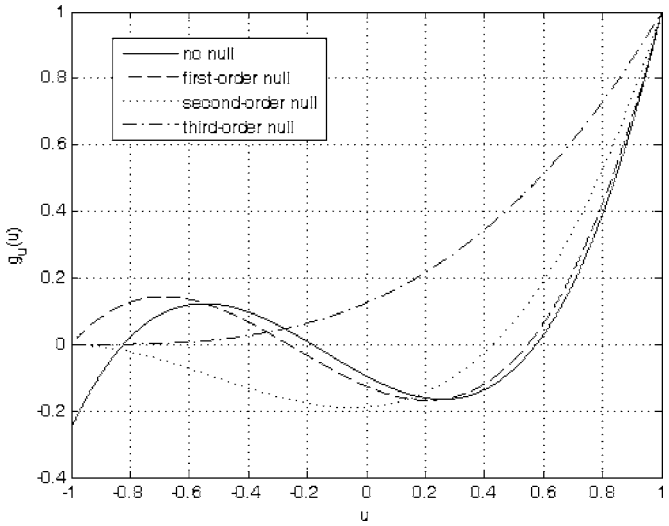

FIG. 8. Beam pattern $g_u(u)$ for various order nulls at $u=-1$.

mined from Eqs. (59) and (69) for the case of maximizing the array gain with no null and one null at $u=-1$, respectively. The solutions are

$$\boldsymbol{a}' = \begin{bmatrix} -3/32 & -15/32 & 15/32 & 35/32 \end{bmatrix}, \tag{74}$$

$$\boldsymbol{a}' = \begin{bmatrix} -1/8 & -3/8 & 5/8 & 7/8 \end{bmatrix}. \tag{75}$$

The array gains are computed from Eqs. (71) and (72) as 11.8 and 12.0 dB. With a third-order directional acoustic sensor, it is also possible to generate a second-order and a third-order null at $u=-1$. For a third-order null, the beam pattern function would have the form

$$g_u(u) = (1+u)^3/8 = (1+3u+3u^2+u^3)/8. \tag{76}$$

Computing the array gain from Eqs. (39) and (42) results in 8.5 dB. Finally, in order to design the multichannel filter so as to generate a second-order null at $u=-1$, one other linear constraint must be satisfied besides the two stated in Eq. (66), namely,

$$g_u'(-1) = a_1 - 2a_2 + 3a_3 = 0. \tag{77}$$

The constraint (77) corresponds to $\sigma_3=0, \boldsymbol{b}_3=[0 \quad -2]', \boldsymbol{c}_3=[1 \quad 3]'$. The matrix equation for the Lagrange multipliers is formed from Eq. (B6) as

$$\begin{bmatrix} 6 & 0 & -15 \\ 0 & 10 & 45 \\ -15 & 45 & 300 \end{bmatrix} \begin{bmatrix} \lambda_1 \\ \lambda_2 \\ \lambda_3 \end{bmatrix} = \begin{bmatrix} 1 \\ 1 \\ 0 \end{bmatrix}. \tag{78}$$

The solution of Eq. (78) is $\lambda_1=1/12, \lambda_2=1/4, \lambda_3=-1/30$. The value of $J_{\min}$ is $1/12$ and the array gain is $10\log(12)=10.8$ dB. The filter coefficient vectors $\boldsymbol{a}_1$ and $\boldsymbol{a}_2$ are computed from Eq. (B5) as

$$\boldsymbol{a}_1 = \frac{1}{16}\begin{bmatrix} -3 \\ 11 \end{bmatrix}, \quad \boldsymbol{a}_2 = \frac{1}{16}\begin{bmatrix} 1 \\ 7 \end{bmatrix}. \tag{79}$$

Figure 8 shows the beam pattern function $g_u(u)$ for the three cases considered in this section plus the case of maximum array gain with no null. As expected, as the order of the null at $u=-1$ increases, the beam pattern curve is more maximally flat at $u=-1$. For positive values of u, the no-null and first-order null case follow each other fairly closely. Table I gives for each case the maximum array gain and the minimum beamwidth. For the case of no null and a first-order null, the values of the maximum array gain and the minimum beamwidth are close. As the order of the null increases, the maximum array gain decreases and the minimum beamwidth increases. The most pronounced difference is between the second-order and third-order nulls (2.3 dB and 21.3°).

TABLE I. Tabulates the maximum array gain and minimum beamwidth of a third-order sensor for nulls of various orders at $u=-1$

Order of null	Maximum array gain (dB)	Minimum beamwidth (degrees)
0	12.0	47.6
1	11.8	49.3
2	10.8	55.8
3	8.5	77.1

APPENDIX A: DETERMINATION OF THE OUTPUT NOISE POWER

The normalized noise power at the output of the multichannel filter (directional sensor) is

$$J = \frac{1}{4\pi}\int_0^{2\pi}\int_0^{\pi} B(\phi,\theta)\sin\phi d\phi d\theta. \tag{A1}$$

Substituting Eq. (28) into Eq. (A1) gives

$$J = \sum_{n=0}^{2v} c_n I_n. \tag{A2}$$

$$I_n = \frac{1}{4\pi}\int_0^{2\pi}\int_0^{\pi} (\mathbf{n}\cdot\mathbf{n_s})^n \sin\phi d\phi d\theta. \tag{A3}$$

The components of the unit vectors $\mathbf{n}$ and $\mathbf{n_s}$ are given in Eqs. (7) and (19), respectively. To simplify notation, let the components of $\mathbf{n_s}$ be represented by α, β, γ. Then

$$(\mathbf{n}\cdot\mathbf{n_s})^n = (\alpha\sin\phi\cos\theta + \beta\sin\phi\sin\theta + \gamma\cos\phi)^n. \tag{A4}$$

In order to expand Eq. (A4) consider the multinomial formula

$$(x_1+x_2+x_3)^n = \sum_{i+j+k=n} \binom{n}{i,j,k} x_1^i x_2^j x_3^k. \tag{A5}$$

$$\binom{n}{i,j,k} = \frac{n!}{i!\,j!\,k!}. \tag{A6}$$

Applying the multinomial formula (A5) to Eq. (A4) results in

$$(\mathbf{n}\cdot\mathbf{n_s})^n = \sum_{i+j+k=n} \binom{n}{i,j,k} \alpha^i \beta^j \gamma^k f(\phi,\theta)$$

$$f(\phi,\theta)=\sin^{i+j}\phi\cos^{k}\phi\cos^{i}\theta\sin^{j}\theta. \tag{A7}$$

If Eq. (A7) is placed into Eq. (A3), the terms in the resulting equation can be rearranged so that

$$I_n=\frac{1}{4\pi}\sum_{i+j+k=n}\binom{n}{i,j,k}\alpha^i\beta^j\gamma^k I_A(k)I_B(i,j). \tag{A8}$$

$$I_A(k)=\int_0^{\pi}\sin^{n-k+1}\phi\cos^{k}\phi d\phi. \tag{A9}$$

$$I_B(i,j)=\int_0^{2\pi}\cos^{i}\theta\sin^{j}\theta d\theta. \tag{A10}$$

The integrals $I_A(k)$ and $I_B(i,j)$ can be evaluated with the help of the following integral which can be found on p. 389 of Gradshteyn and Ryzhik (2000):

$$\int_0^{\pi/2}\sin^{p-1}x\cos^{q-1}x dx=\frac{1}{2}B\left(\frac{p}{2},\frac{q}{2}\right)$$
$$\text{Re}\,p>0,\quad \text{Re}\,q>0. \tag{A11}$$

The function $B(\cdot)$ is the beta function. Note that the integrands of Eqs. (A9)–(A11) are identical in form. However, the limits of each are different. The values of $I_A(k)$ and $I_B(i,j)$ can be determined by expressing each integral as a sum of integrals whose form and limits of integration are the same as in Eq. (A11). When this is done, the result is

$$I_A(k)=\frac{1+(-1)^k}{2}B\left(\frac{n-k+2}{2},\frac{k+1}{2}\right). \tag{A12}$$

$$I_B(i,j)=(1+(-1)^{i+j})\frac{1+(-1)^i}{2}B\left(\frac{j+1}{2},\frac{i+1}{2}\right). \tag{A13}$$

For a particular (i,j,k), there will be a contribution to Eq. (A8) if and only if both Eqs. (A12) and (A13) are nonzero. From Eq. (A12) it is clear that k must be an even integer, and (A13) reveals that both i and j must be an even integer. Since $n=i+j+k$, n must also be an even integer. The utilization of Eqs. (A12) and (A13) in Eq. (A8) with the above mentioned restrictions on the various summation indices results in

$$I_n=\frac{1}{2\pi}\sum_{\substack{i+j+k=n\\ i,j,k\ \text{even}}}\binom{n}{i,j,k}\alpha^i\beta^j\gamma^k g(i,j,k)$$
$$g(i,j,k)=B\left(\frac{n-k+2}{2},\frac{k+1}{2}\right)B\left(\frac{j+1}{2},\frac{i+1}{2}\right). \tag{A14}$$

It will prove useful to let $i=2p, j=2q, k=2r, n=2\ell$. If this is done, Eq. (A14) becomes

$$I_{2\ell}=\frac{1}{2\pi}\sum_{p+q+r=\ell}\binom{2\ell}{2p,2q,2r}\alpha^{2p}\beta^{2q}\gamma^{2r}g(p,q,r)$$
$$g(p,q,r)=B\left(\ell-r+1,r+\tfrac{1}{2}\right)B\left(q+\tfrac{1}{2},p+\tfrac{1}{2}\right). \tag{A15}$$

Consider the following identities:

$$B(x,y)=\frac{\Gamma(x)\Gamma(y)}{\Gamma(x+y)}\quad x,y>0. \tag{A16}$$

$$\Gamma\left(m+\tfrac{1}{2}\right)=\frac{(2m)!}{2^{2m}m!}\sqrt{\pi}\quad m=0,1,2,\ldots\ . \tag{A17}$$

The identities (A16) and (A17) can be found on pp. 71 and 83 of Andrews (1992). The utilization of Eqs. (A16) and (A17) in (A15) leads to the simplification

$$I_{2\ell}=\frac{1}{2\ell+1}\sum_{p+q+r=\ell}\binom{\ell}{p,q,r}(\alpha^2)^p(\beta^2)^q(\gamma^2)^r. \tag{A18}$$

Applying the multinomial formula to Eq. (A18) gives

$$I_{2\ell}=\frac{1}{2\ell+1}(\alpha^2+\beta^2+\gamma^2)^{\ell}. \tag{A19}$$

Since $\mathbf{n_s}$ is a unit vector, Eq. (A19) simplifies to

$$I_{2\ell}=\frac{1}{2\ell+1}. \tag{A20}$$

The value of the noise power is

$$J=\sum_{\ell=0}^{v}\frac{c_{2\ell}}{2\ell+1}, \tag{A21}$$

where

$$c_{2\ell}=\sum_{k=0}^{2\ell}a_{2\ell-k}a_k. \tag{A22}$$

APPENDIX B: MINIMIZATION OF NOISE POWER SUBJECT TO LINEAR CONSTRAINTS

The objective of this appendix is to minimize the sum of two positive definite quadratic forms, namely,

$$J=\boldsymbol{a}_1'\boldsymbol{H}_1\boldsymbol{a}_1+\boldsymbol{a}_2'\boldsymbol{H}_2\boldsymbol{a}_2 \tag{B1}$$

subject to the set of N linear constraints

$$\boldsymbol{b}_i'\boldsymbol{a}_1+\boldsymbol{c}_i'\boldsymbol{a}_2=\sigma_i\quad i=1,2,\ldots,N. \tag{B2}$$

This constrained optimization problem can be transformed into an unconstrained problem by the Method of Lagrange Multipliers. The new problem involves the minimization of

$$J=\boldsymbol{a}_1'\boldsymbol{H}_1\boldsymbol{a}_1+\boldsymbol{a}_2'\boldsymbol{H}_2\boldsymbol{a}_2+\sum_{j=1}^{N}\lambda_j(\sigma_j-\boldsymbol{b}_j'\boldsymbol{a}_1-\boldsymbol{c}_j'\boldsymbol{a}_2). \tag{B3}$$

The quantities λ_j are the Lagrange multipliers. Taking the gradients of J with respect to the column vectors $\boldsymbol{a}_1$ and $\boldsymbol{a}_2$, and setting both gradients to zero, results in

$$\nabla_{\boldsymbol{a}_1} J = 2\boldsymbol{H}_1 \boldsymbol{a}_1 - \sum_{j=1}^{N} \lambda_j \boldsymbol{b}_j = 0,$$

$$\nabla_{\boldsymbol{a}_2} J = 2\boldsymbol{H}_2 \boldsymbol{a}_2 - \sum_{j=1}^{N} \lambda_j \boldsymbol{c}_j = 0. \tag{B4}$$

Solving (B4) for $\boldsymbol{a}_1$ and $\boldsymbol{a}_2$ gives

$$\boldsymbol{a}_1 = \frac{1}{2}\sum_{j=1}^{N} \lambda_j \boldsymbol{H}_1^{-1} \boldsymbol{b}_j,$$

$$\boldsymbol{a}_2 = \frac{1}{2}\sum_{j=1}^{N} \lambda_j \boldsymbol{H}_2^{-1} \boldsymbol{c}_j. \tag{B5}$$

If the derivative of J is taken with respect to each of the Lagrange multipliers λ_j and set to 0, then the result is simply the N constraints defined by Eq. (B2). With the aid of Eq. (B5) these constraints may be written in the alternate form

$$\frac{1}{2}\sum_{j=1}^{N} (\boldsymbol{b}_i' \boldsymbol{H}_1^{-1} \boldsymbol{b}_j + \boldsymbol{c}_i' \boldsymbol{H}_2^{-1} \boldsymbol{c}_j)\lambda_j = \sigma_i, \quad i = 1,2, \ldots, N. \tag{B6}$$

The constraints (B6) form a set of N linear equations in N unknowns, which can be solved for the Lagrange multipliers λ_j. This determines the values of $\boldsymbol{a}_1$ and $\boldsymbol{a}_2$ via Eq. (B5). The substitution of Eqs. (B5) into (B3) leads to

$$J = \frac{1}{4}\sum_{i=1}^{N} \lambda_i \sum_{j=1}^{N} (\boldsymbol{b}_i' \boldsymbol{H}_1^{-1} \boldsymbol{b}_j + \boldsymbol{c}_i' \boldsymbol{H}_2^{-1} \boldsymbol{c}_j)\lambda_j. \tag{B7}$$

For the value of J to be the minimum value, the second sum in Eq. (B7) must satisfy Eq. (B6). Equation (B7) then simplifies to

$$J_{\min} = \frac{1}{2}\sum_{i=1}^{N} \lambda_i \sigma_i. \tag{B8}$$

Andrews, L. C., (**1992**). *Special Functions of Mathematics for Engineers*, 2nd ed. (McGraw–Hill, New York).

Burdic, W. S. (**1991**). *Underwater Acoustic System Analysis* (Prentice-Hall, Englewood Cliffs, NJ), Chap. 11, pp. 306–307.

Cray, B. A., Evora, V. M., and Nuttall, A. H. (**2003**). "Highly directional acoustic receivers," J. Acoust. Soc. Am. **113**(3), 1526–1532.

Cray, B. A. (**2002**). "Directional point receivers: the sound and the theory," *Oceans '02*, 1903–1905.

Cray, B. A., and Nuttall, A. H. (**1997**). "A comparison of vector-sensing and scalar-sensing linear arrays," NUWC-NPT Technical Report No. 10,632.

D'Spain, G. L. (**1994**). "Relationship of underwater acoustic intensity measurements to beamforming," Can. Acoust. **22**(3), 157–158.

Gerber, H. U., and Shiu, E. S. W. (**2005**). "The time value of ruin in a Sparre Anderson model," North American Actuarial J. **9**(2), 49–84.

Gradshteyn, I. S., and Ryzhik, I. M., (**2000**). *Table of Integrals, Series, and Products*, 6th ed. (Academic, San Diego).

Hawkes, M., and Nehorai, A. (**1998**). "Acoustic vector-sensor beamforming and capon direction estimation," IEEE Trans. Signal Process. **46**(9), 2291–2304.

Hines, P. C., Rosenfeld, A. L., Maranda, B. H., and Hutt, D. L. (**2000**). "Evaluation of the endfire response of a superdirective line array in simulated ambient noise environments," *Proc. Oceans 2000*, 1489–1494.

Nuttall, A. H., and Cray, B. A. (**2001**). "Approximations to directivity for linear, planar, and volumetric apertures and arrays," IEEE J. Ocean. Eng. **26**(3), 383–398.

Silvia, M. T. (**2001**). "A theoretical and experimental investigation of acoustic dyadic sensors," SITTEL Technical Report No. TP-4, SITTEL Corporation, Ojai, California.

Silvia, M. T., Franklin, R. E., and Schmidlin, D. J. (**2001**). "Signal processing considerations for a general class of directional acoustic sensors," *Proceedings of the Workshop on Directional Acoustic Sensors*, Newport, RI.

Wong, K. T., and Chi, H. (**2002**). "Beam patterns of an underwater acoustic vector hydrophone located away from any reflecting boundary," IEEE J. Ocean. Eng. **27**(3), 628–637.

Wong, K. T., and Zoltowski, M. D., (**2000**). "Self-initiating MUSIC-based direction finding in underwater acoustic particle velocity-field beamspace," IEEE J. Ocean. Eng. **25**(2), 262–273.

Wong, K. T., and Zoltowski, M. D., (**1999**). "Root-MUSIC-based azimuth-elevation angle-of-arrival estimation with uniformly spaced but arbitrarily oriented velocity hydrophones," IEEE Trans. Signal Process. **47**(12), 3250–3260.

Wong, K. T., and Zoltowski, M. D., (**1997**). "Extended-aperture underwater acoustic multisource azimuth/elevation direction finding using uniformly but sparsely spaced vector hydrophones," IEEE J. Ocean. Eng. **22**(4), 659–672.

Wong, K. T., and Zoltowski, M. D., (**1997**). "Closed-form underwater acoustic direction finding with arbitrarily spaced vector hydrophones at unknown locations," IEEE J. Ocean. Eng. **22**(3), 566–575.

The two-dimensional source location problem for time differences of arrival at minimal element monitoring arrays

Steven J. Spencer[a)]
Lucas Heights Research Laboratory, CSIRO Minerals, Private Mail Bag 5, Menai, New South Wales, Australia

(Received 31 May 2006; revised 27 March 2007; accepted 29 March 2007)

The time difference of arrival (TDOA) source localization inverse problem is analyzed for two-dimensional signal propagation detected by a small number of sensor elements in a monitoring array. Nonlinear least-squares solutions are found based on the assumptions of geodesic rays propagating at constant speed. The two-dimensional (2D) TDOA source location problem is shown in the case of three sensors to have dual possible solutions for some combinations of arrival time differences. In the case of four non-collinear sensors, there are unique solutions for all physically possible combinations of time differences. Dual solutions to the three-sensor problem are associated with a small range of arrival time differences but large regions in physical space. The locations of the dual solutions are separated by a wide variety of distances, which in some cases prevent the use of alternative reasoning to remove the ambiguity. Three-sensor TDOA cannot be reliably used for 2D source location unless the source is *a priori* known to be within either the spatial region spanned by the sensor array or the external zones of unique solution. Determining the minimum number of sensors necessary to unambiguously solve the source location problem assists in cost-effective design of sensor arrays. © *2007 Acoustical Society of America.* [DOI: 10.1121/1.2734404]

PACS number(s): 43.60.Jn, 43.60.Fg, 43.20.Dk [EJS] Pages: 3579–3594

I. INTRODUCTION

The inverse problem of source location based on multiple sensor signals remains an active area of research in acoustics, sonar and radar (Delosme *et al.*, 1980; Schmidt, 1986; Schau and Robinson, 1987; Smith and Abel, 1987; Chan and Ho, 1994; Brandstein *et al.*, 1995; Duraiswami *et al.*, 1999; Fink *et al.*, 2000; DiBiase *et al.*, 2001; Zotkin and Duraiswami, 2004; Liu and Milios, 2005; Devaney *et al.*, 2005). There are three broad classes of source localization methods commonly utilized in passive and active radar, sonar, and microphone acoustics applications (DiBiase *et al.*, 2001; Zotkin and Duraiswami, 2004):

- *Time difference of arrival (TDOA)*—any method that relies on time delay estimates for a signal as measured across combinations of sensors in an array.
- *Steered-beamformer*—maximizing the steered response power of a beamformer, such that the signals sensed by an array are focused on a variety of locations in search of peak steered response power.
- *High-resolution spectral estimation*—analysis of the spatiospectral signal correlation matrix of the signals received at the sensors under the assumption of a statistically stationary signal. These approaches include the signal subspace methods such as multiple signal classification (MUSIC).

A detailed summary of classical techniques for source location from the viewpoint of array beamforming and spectral estimation can be found in Johnson and Dudgeon (1993).

In the case of active source localization, another area of vigorous research has been in *time-reversal* (TR) imaging. This approach is historically based on the reciprocity principle for waves in nondissipative media, with measurement of the interelement response of a reversible array of transducers to a transmitted impulse used to calculate the transfer or multistatic data matrix, which contains information on the number, location, and strength of scatterers (Fink *et al.*, 2000; Devaney *et al.*, 2005). Methods in this class include the decomposition of the time-reversal operator (DORT) (Prada *et al.*, 1996; Fink *et al.*, 2000) and time reversal multiple signal classification (TR-MUSIC) (Lehman and Devaney, 2003; Devaney *et al.*, 2005). These methods allow detection and selective focusing on multiple scattering targets. The TR-MUSIC method has also been extended to the case of non-coincident transmitter and receiver arrays (Lehman and Devaney, 2003). The DORT and TR-MUSIC methods can both be interpreted in terms of the singular value decomposition of the transfer data matrix at a particular frequency (Lehman and Devaney, 2003; Prada and Thomas, 2003; Devaney *et al.*, 2005). The location of the scatterers is found from the singular vectors, which are linear combinations of the medium Green's functions associated with the positions of the transmitter/receiver array(s) and scatterers (Lehman and Devaney, 2003; Prada and Thomas, 2003; Devaney *et al.*, 2005). Imaging of the physical location of scatterers requires an accurate Green's function model of the properties of the medium, which may be dispersive or heterogeneous (Lehman and Devaney, 2003; Prada and Thomas, 2003; Devaney *et al.*, 2005).

[a)]Electronic mail: steven.spencer@csiro.au

Source localization methods in many application areas are commonly based on TDOA of correlated signals received from a point source by a spatially distributed sensor array (Pao, 1978; Scruby, 1985; Pollock, 1986; DiBiase *et al.*, 2001). This is because they have relatively low computational complexity, depending on the time delay estimation method can work in moderately reverberative environments, and are conceptually simple (Klee *et al.*, 2006). For instance, location of source events leading to stress waves in elastic media has been undertaken with a variety of TDOA-based methods, usually utilizing times of first-arrival of a particular wave mode and assuming a geodesic wave propagation path (Scruby, 1985; Pollock, 1986; Barat *et al.*, 1993; Spencer *et al.*, 2005). This approach has been used in a wide variety of application areas, including location of anomalous sources of microseismic activity in mines (Kat and Hassani, 1989), materials characterization and structural health monitoring (Pao, 1978; Scruby, 1985; Pollock, 1986; Collins and Belchamber, 1990; Landis *et al.*, 1991), and location of large impact events inside mineral processing comminution equipment (Spencer *et al.*, 2005). Another application is in global positioning systems (GPS), where receiver location is determined by TDOA applied to time coded radio signals from multiple satellites (Kaplan, 1996; Hofmann-Wellenhof *et al.*, 2001). A related source location technique based on arrival time differences between multiple wave types with different propagation speeds (method of triangulation) has long been used in seismology for earthquake focus location (Pao, 1978; Aki and Richards, 1980).

An important practical issue in the use of TDOA is the number of arrival times associated with sensors (monitoring array elements) necessary to guarantee a unique source location estimate. It is often assumed that arrival time data for a particular wave mode at three non-collinear sensors is minimally sufficient to estimate the location of the source event in a plane, for a known propagation speed and straight-line (geodesic) ray path (Schau and Robinson, 1987; Yoon *et al.*, 1990; Barat *et al.*, 1993; Spencer *et al.*, 2005). Correspondingly, time of arrival data for a particular wave mode at four non-coplanar sensors are often assumed to be minimally sufficient to estimate the volumetric location of a source event (or receiver for GPS), for a known propagation speed and straight-line (geodesic) ray path (Pao, 1978; Scruby 1985; Schau and Robinson, 1987; Collins and Belchamber, 1990; Landis *et al.*, 1991; Kaplan, 1996; Hofmann-Wellenhof *et al.*, 2001). A far-field assumption (source distance large in comparison to the sensor array baseline length) can in some instances be used to decrease the minimum number of sensors necessary for source location and simplify the solution algorithm (Schau and Robinson, 1987; Brandstein *et al.*, 1995; Liu and Milios, 2005). However, it has also in some cases been recognized that for an unknown distance between source and sensor array in a plane (possibly outside the sensor array areal bounds), TDOA based on arrival times at three sensors can result in two equivalent solution points, with the resolution of the actual location requiring additional information (Schmidt, 1972; Keen and Rogers, 1987; Yoon *et al.*, 1990; Spiesberger, 2001). Similarly, Schau and Robinson (1987) report that for four sensors estimating volumetric location, there are two possible source locations consistent with the arrival time data. In this case the two source location estimates based on four sensor arrival times are stated as usually wide enough apart (in acoustics and radar applications) such that the correct solution can be determined by other reasoning such as one option being outside the domain of interest.

A geometric interpretation of the TDOA equations is useful in understanding uniqueness considerations associated with the source location problem. The curves of constant time difference between correlated signals detected at two sensors are known to be a branch of a hyperbola in two spatial dimensions (Schmidt, 1972; Schau and Robinson, 1987; Yoon *et al.*, 1990; Chan and Ho, 1994) and one of two sheets of a hyperboloid of revolution in three dimensions (Schau and Robinson, 1987). The location of a source detected by three sensors is defined in the case of a two-dimensional (2D) plate by the intersection of two hyperbolae associated with specific values for two independent arrival time differences (Schmidt, 1972; Delosme *et al.*, 1980; Yoon *et al.*, 1990). An alternative geometrical interpretation of the three sensor TDOA 2D source location problem places possible source locations at the foci of a conic defined by the sensor locations and arrival time differences, recognizing the possibility of dual solutions in some instances (Schmidt, 1972). For a three-dimensional (3D) problem (using event arrival times at four sensors), the intersection of three hyperboloid surfaces representative of three independent arrival time differences defines the source location (Schau and Robinson, 1987). The nonuniqueness results associated with source location estimation based on arrival time differences between a small number of sensors can be intuitively understood in terms of the geometric interpretation of the intersection of solutions of the TDOA equations for constant (independent) arrival time differences associated with a single source event—in a plane, two hyperbolae (derived from arrival time differences for three non-collinear sensors) may intersect at *two* points and, similarly, in a volume, three hyperboloid surfaces (derived from arrival time differences for four non-coplanar sensors) may intersect at *two* points in physical space. For three-sensor planar and four-sensor volumetric TDOA data, dual solutions for source location are possible, of which only one is physically valid.

A variety of solution methods have been proposed for estimation of source location from multiple sensor TDOA equations (Schmidt, 1972; Delosme *et al.*, 1980; Schau and Robinson, 1987; Smith and Abel, 1987; Kat and Hassani, 1989; Collins and Belchamber, 1990; Chan and Ho, 1994; Brandstein *et al.*, 1995; Duraiswami *et al.*, 1999; DiBiase *et al.*, 2001; Spiesberger, 2001; Huang *et al.*, 2001; Spencer *et al.*, 2005; Liu and Milios, 2005). These techniques are often iterative, in recognition that the TDOA equations for time delays between correlated signals detected at pairs of sensors are nonlinear with respect to unknown source location. In terms of the geometrical interpretation of the TDOA equations, the solutions of equations of intersection for hyperbolae are usually iteratively found by a maximum likelihood/nonlinear least-squares (NLS) estimation method (Delosme *et al.*, 1980; Kat and Hassani, 1989; Collins and Belchamber,

1990; Brandstein *et al.*, 1995; Spencer *et al.*, 2005). Limitations on the accuracy of source location by this approach can be understood in terms of small errors in time differences translating into large differences in the point(s) of intersection of two or more hyperbolae/hyperboloids in physical space (Schau and Robinson, 1987). High sensitivity of the source location to small changes in the observed time differences is a classic feature of an ill-posed inverse problem.

In practical applications, there are often significant measurement errors associated with arrival time data and limitations in the accuracy of assumptions concerning wave propagation path and speed. For instance, practical considerations in the acquisition and processing of acoustic emission (AE) signals for TDOA source location have been addressed in a number of studies (Scruby, 1985; Collins and Belchamber, 1990; Yoon *et al.*, 1990; Landis *et al.*, 1991; DiBiase *et al.*, 2001; Spencer *et al.*, 2005). The practical limitations of TDOA source location mean that typically more than three sensors are utilized for source location in a plane (Yoon *et al.*, 1990) and, correspondingly, more than four sensors for volumetric source location (Pao, 1978; Collins and Belchamber, 1990; Landis *et al.*, 1991). Solution of overdetermined systems of TDOA equations for source location based on time differences associated with a large number of sensors promotes the use of least-squares or minimum error estimators (Kat and Hassani, 1989; Collins and Belchamber, 1990; Landis *et al.*, 1991; Brandstein *et al.*, 1995; Torney and Nemzek, 2005). Such solutions may be computationally expensive and subject to convergence problems (Huang *et al.*, 2001). Recently Kalman filtering iterative techniques based on multiple (time separated) observations of time differences have been used to solve the microphone source location TDOA problem (Gannot and Dvorkind, 2006; Klee *et al.*, 2006).

A number of noniterative methods also exist for solution of the TDOA source location problem. The use of a far-field approximation leads to simplified linear problems for the intersection of two lines in 2D and three cones in 3D (Schau and Robinson, 1987; Brandstein *et al.*, 1995; Liu and Milios, 2005) but is clearly limited in application to location of sources relatively distant from a sensor array. The linear interpolation (LI) method based on the closest intersection of source bearing lines calculated from four-sensor-element subarrays under a far-field approximation is an example of this approach (Brandstein *et al.*, 2005). The 3D TDOA problem can also be re-formulated in spherical coordinates such that solutions are found in terms of intersecting spheres of distance from sensor to source (spherical intersection—SX method), leading to a noniterative two-step, closed-form analytical solution to the source location problem for an arbitrary distance to a four-sensor array (Schau and Robinson, 1987; Spiesberger, 2001). A noniterative spherical interpolation (SI) method for arrays of five or more sensors, based on minimizing equation error associated with 3D radial source location has also been found and is claimed to have localization performance superior to the SX method in the presence of noise (Smith and Abel, 1987). Closed-form solutions for TDOA source location on a plane with an arbitrary number of sensors that are optimum in a least-squares sense for low levels of noise have also been reported (Chan and Ho, 1994). Duraiswami *et al.* (1999) also report finding a family of exact solutions for 2D TDOA based on arrival times at four sensors located in a plane that can be evaluated with a small number of arithmetic operations. Single-step source location estimators simultaneously solving for source coordinates and radial distance / arrival time are also known (Spiesberger, 2001) and attempts have been made to appropriately constrain the solutions (Huang *et al.* 2001; Gannot and Dvorkind, 2006). The use of noniterative solution methods is motivated by a desire for solutions that are computationally inexpensive but may be considerably more inaccurate than the least-squares estimator, particularly in the presence of significant errors in the arrival times or other assumptions in the wave propagation model (Smith and Abel, 1987; Chan and Ho, 1994).

In this paper the TDOA 2D source location problem based on arrival time information for the minimal number of monitoring array elements needed to derive a solution (three to four sensors) is analyzed in Cartesian and polar coordinate systems and NLS solutions are derived. The source location solutions do not rely on any assumptions concerning the distance between the source and the monitoring array. The existence of dual source location solutions based on three-sensor TDOA for some combinations of arrival time differences associated with 2D signal propagation is demonstrated. Unique solutions for 2D source location based on four-sensor TDOA are presented. For the first time it is shown that small regions in arrival time difference space associated with dual solutions to the three-sensor TDOA 2D source location problem correspond to large regions in physical space. It is also shown that dual solutions to the three-sensor TDOA 2D source location problem are separated by a wide variety of linear distances, in some cases preventing the use of other information such as *a priori* restrictions on the physical location of the source to guarantee unique solutions. It should be noted that this paper does not deal with data acquisition or processing of signals for any specific type of monitoring system. Neither does it deal with methods for time delay estimation. Similarly, possible constraints on source location associated with sensor received signal amplitude are not considered in any detail.

The paper is structured as follows. In Sec. II the 2D TDOA equations are formulated in a Cartesian coordinate system and numerically solved for source locations associated with a grid of all physically possible arrival time differences. The existence of dual solutions to the three-sensor TDOA source location problem for 2D signal propagation is demonstrated and identified with small regions of arrival time difference space associated with large regions of physical source location space. In Sec. III the problem is reformulated in a polar coordinate system and analyzed for properties of time differences associated with large source distances from the monitoring array and large radial distance resolution limits for arrival times containing errors. Unique solutions for the four-sensor TDOA source location problem for 2D signal propagation are demonstrated. The linear distances between dual solutions to a three-sensor TDOA test problem are then derived and shown to vary over such a large range

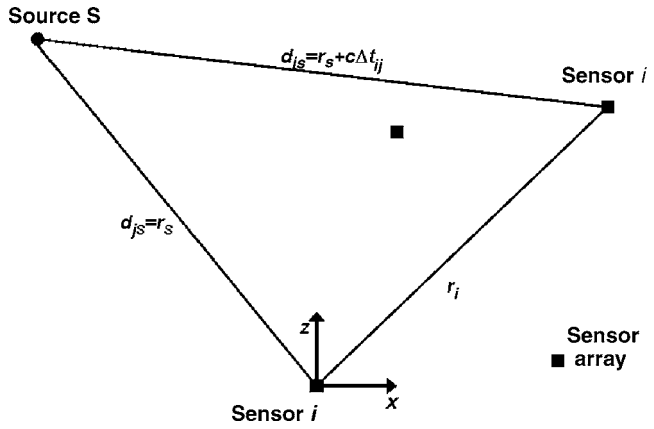

FIG. 1. Schematic diagram illustrating geometric relationships between source location and position of array sensors i and j for 2D signal propagation. Sensor j is taken as the spatial origin of the (x,z) Cartesian coordinate system. Four sensors are depicted in the monitoring array.

as to preclude the reliable removal of the ambiguity by alternative reasoning. The conclusion in Sec. IV discusses the ramifications of possible dual solutions for the three-sensor 2D source location problem and the implications for four-sensor 3D source location.

II. THE TDOA 2D SOURCE LOCATION PROBLEM IN A CARTESIAN COORDINATE SYSTEM

The difference in time of arrival Δt_{ij} of a signal generated by a point source S and detected at sensors i and j (assuming geodesic ray paths, constant speed of signal propagation, and no errors in arrival time information) can be written as

$$c\Delta t_{ij} = d_{iS} - d_{jS}, \quad i,j = 1,N. \tag{1}$$

Here c is the speed of signal propagation in the medium, d_{iS} and d_{jS} are the geodesic distances from the source to sensors i and j, respectively, and N is the number of sensors. The quantity $c\Delta t_{ij}$ is sometimes referred to as the range difference (Smith and Abel, 1987). The geodesic distance between source and sensor is often expressed in Cartesian coordinates (Pao, 1978; Schau and Robinson, 1987; Chan and Ho, 1994; Spencer *et al.*, 2005) such that

$$d_{iS}^2 = \sum_{k=1}^{K} (x_{ki} - x_{kS})^2. \tag{2}$$

Here K is the number of spatial dimensions associated with signal propagation and x_{ki} and x_{kS} are the Cartesian directional distances from the origin of the coordinate system to sensor i and source S, respectively (geodesic distances r_i and r_S, respectively). The source localization problem is to determine x_{kS} given Δt_{ij}, the speed of signal propagation, and sensor locations. For N sensors in a noiseless situation (self-consistent arrival time differences) there are $N-1$ independent equations (Smith and Abel, 1987). Figure 1 is an illustrative diagram for 2D source location in a Cartesian coordinate system. In this case, the origin of the Cartesian coordinate system is mapped to an arbitrary sensor j, without loss of generality.

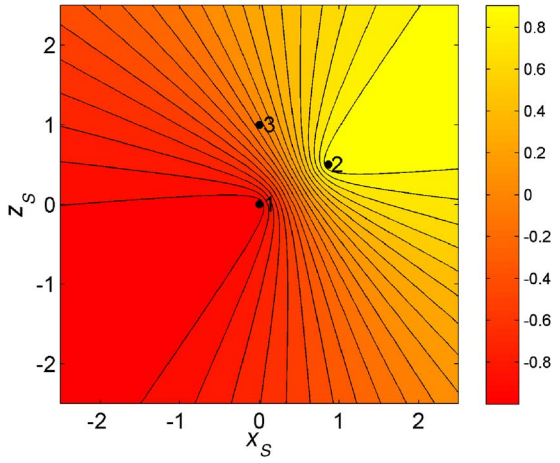

FIG. 2. (Color online) Filled contour plot with 20 equally spaced levels between maximum and minimum possible values of arrival time difference Δt_{12} between signals at sensors 1 and 2 as a function of source location Cartesian coordinates x_S and z_S in dimensionless units. Spatial positions of sensors 1, 2, and 3 are shown.

A. Numerical solution of the TDOA 2D source location problem

For a TDOA 2D source location problem with arrival time information from three sensors (1, 2, 3) in a plane, Eqs. (1) and (2) can be combined and explicitly written in an (x,z) Cartesian coordinate system as coupled nonlinear equations for the source location coordinates (Spencer *et al.*, 2005):

$$c\Delta t_{12} = \sqrt{(x_1 - x_S)^2 + (z_1 - z_S)^2} - \sqrt{(x_2 - x_S)^2 + (z_2 - z_S)^2} \tag{3}$$

and

$$c\Delta t_{13} = \sqrt{(x_1 - x_S)^2 + (z_1 - z_S)^2} - \sqrt{(x_3 - x_S)^2 + (z_3 - z_S)^2}. \tag{4}$$

The arrival time differences are here defined by

$$\Delta t_{12} = t_1 - t_2; \quad \Delta t_{13} = t_1 - t_3. \tag{5}$$

The self-consistency condition for the arrival time differences (in the absence of errors) is

$$\Delta t_{23} = \Delta t_{13} - \Delta t_{12}. \tag{6}$$

Here t_1, t_2, and t_3 are the previously estimated known event arrival times at sensors 1, 2, and 3, respectively. The pairs (x_1,z_1), (x_2,z_2), (x_3,z_3), and (x_S,z_S) are the Cartesian coordinates of sensors 1, 2, and 3, and the source S, respectively.

Solutions of the forward problem for arrival time differences as a function of two-dimensional source location were found for a test problem based on an equilateral triangle of sensors. Equations (3) and (4) were solved for time differences Δt_{12} and Δt_{13}, respectively, with a 101×101 equispaced grid of source locations in the spatial domain. Figures 2 and 3 are contour plots of these solutions for Δt_{12} and Δt_{13}, respectively. The spatial coordinates in the plots are scaled by the baseline distance between sensors 1 and 2, while the difference in arrival time is scaled by the time taken for a signal to propagate the same distance. Sensor 1 is located at

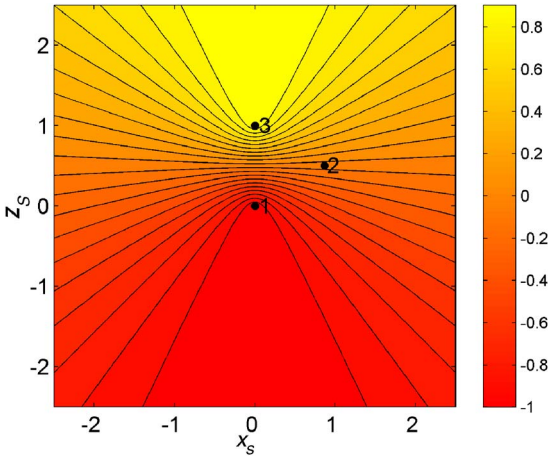

FIG. 3. (Color online) Filled contour plot with 20 equally spaced levels between maximum and minimum possible values of arrival time difference Δt_{13} between signals at sensors 1 and 3 as a function of source location Cartesian coordinates x_S and z_S in dimensionless units. Spatial positions of sensors 1, 2, and 3 are shown.

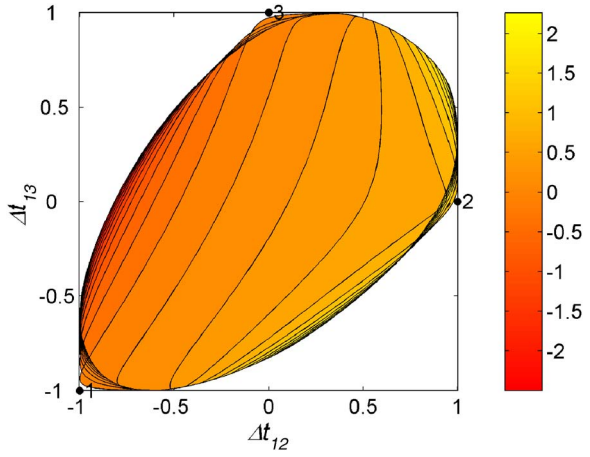

FIG. 4. (Color online) Filled contour plot with 20 equally spaced levels between maximum and minimum possible values of source location coordinate x_S as a function of possible arrival time differences Δt_{12} and Δt_{13} in dimensionless units. Positions of sensors 1, 2, and 3 in arrival time difference space $(\Delta t_{12}, \Delta t_{13})$ are shown.

the origin and arrival time differences are plotted over a 5 $\times$5 spatial domain (dimensionless units). These plots are appropriate for Rayleigh surface waves propagating at a speed of 3000 ms^{-1} on a steel plate, with 1 m sensor baseline spacing corresponding to an arrival time difference of $\sim 3.3 \times 10^{-4}$ s. Other equivalently scaled situations include sound propagating in air and water, longitudinal P-waves and transverse S-waves propagating in rock, and electromagnetic waves, with baseline spacings of $\sim$0.1, 0.5, 2.0, 1.2 and 1 $\times 10^5$ m, respectively.

Figures 2 and 3 demonstrate that, as expected, any contour of constant Δt_{12} or Δt_{13} is a branch of a hyperbola in two dimensions (Schau and Robinson, 1987; Yoon *et al.*, 1990; Chan and Ho, 1994). This can also be verified by manipulation of Eqs. (3) and (4) into a standard form for a hyperbola. Each hyperbola branch is centred about the midpoint of the relevant sensor locations and has its axis of symmetry along the directed line segment between the same locations. For instance, in Fig. 2 the hyperbola branch associated with any line of constant Δt_{12} is centred about the midpoint between sensors 1 and 2 and is symmetric about an axis defined by a line running between the same. In accordance with the scaling of arrival time differences by the time-of-flight between sensors 1 and 2, $|\Delta t_{12}, \Delta t_{13}| \leqslant 1$ over all of physical space. The location of the source is defined in the case of a two-dimensional plate by the intersection of the two hyperbolae associated with specific values for Δt_{12} and Δt_{13} (Delosme *et al.*, 1980; Yoon *et al.*, 1990).

The inverse problem for 2D source location [as defined by Eqs. (3) and (4)] was solved for arrival time differences associated with a spatially uniform grid of possible source locations. NLS solutions were found, based on an iterative solution procedure for constrained (bounded) nonlinear optimization problems, using the "lsqnonlin" routine in the MATLAB Optimization Toolbox. A practical application of this iterative solution scheme for TDOA location of large impacts in mineral processing tumbling mills from Rayleigh surface waves detected by surface vibration monitoring can be found in Spencer *et al.* (2005).

B. The possibility of dual solutions to the TDOA 2D source location problem

Contour diagrams of estimated source location coordinates (found by solution of the TDOA source location inverse problem for three sensors) as a function of arrival time differences are shown in Figs. 4 and 5. The source locations were estimated on a nonuniform grid of arrival time differences, themselves calculated by solution of the forward problem for a uniform grid on a 5$\times$5 spatial domain in dimensionless units (see Figs. 2 and 3). The source location may be within or external to the triangular area bounded by the elements of the sensor array but is restricted to within the physical domain boundaries associated with the forward problem. It should be noted that the representation of specific sources in TDOA "Δt-space" has previously been used in location of defects in structures from AE measurements (Rogers, 1994;

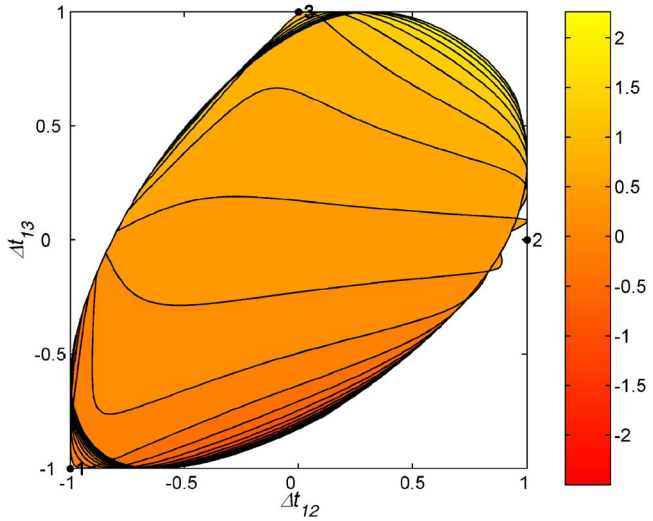

FIG. 5. (Color online) Filled contour plot with 20 equally spaced contours between maximum and minimum possible values of source location coordinate z_S as a function of possible arrival time differences Δt_{12} and Δt_{13} in dimensionless units. Positions of sensors 1, 2, and 3 in arrival time difference space $(\Delta t_{12}, \Delta t_{13})$ are shown.

Rogers and Murphy, 1996). Solutions to the inverse problem for source location were iterated to within a termination tolerance of order 10^{-8} dimensionless spatial units for 2D location. The time difference coordinates in Figs. 4 and 5 are scaled by the time taken for a signal to propagate between sensors 1 and 2, while the solution for each particular spatial coordinate is scaled by the same baseline distance.

Figures 4 and 5 demonstrate features that are characteristic of an ill-posed inverse problem in terms of existence, stability, and uniqueness of solutions. Both figures show that only certain combinations of Δt_{12} and Δt_{13} (arrival time differences in dimensionless units) can exist, i.e., are associated with physical spatial positions where source events can occur. The restricted arrival time difference domain is apparently simply connected with a smooth outer boundary. Extending the outer boundaries of the source spatial domain towards infinity only marginally extends the area of the arrival time difference domain. The stability of solutions for source location to small changes in arrival time differences is also highly variable. Figures 4 and 5 show regions in $(\Delta t_{12}, \Delta t_{13})$ space (near the outer boundaries of arrival time difference space between the positions of the sensors) where the contours of location coordinates are obviously closely spaced. In these regions the three-sensor TDOA 2D source location inverse problem is ill-posed in that a small change in arrival time difference may lead to a large change in estimated source location. In other regions of arrival time difference space, for instance near the centroid of the triangular sensor array such that $(\Delta t_{12}, \Delta t_{13}) \sim (0,0)$, the inverse problem is well-posed in that a small change in either of the time differences only results in a small change in the estimated source location. Another obvious feature in Figs. 4 and 5 is that in some regions of $(\Delta t_{12}, \Delta t_{13})$ space (adjacent to the locations in arrival time difference space of the sensors), there are intersecting contours of location coordinates. This is not an artefact of the iterative solution method, or of the contouring algorithm associated with the nonuniform mesh, but, rather, an indication that there are *nonunique* solutions to the three-sensor TDOA 2D source location inverse problem. In these circumstances at least two different source locations within the bounded spatial domain can have the same time differences associated with arrival of correlated information at three sensors.

A series of numerical experiments were conducted in order to investigate the possibility of nonunique solutions to the TDOA 2D source location problem based on three-sensor data. It was found that for some locations in $(\Delta t_{12}, \Delta t_{13})$ space there are two equally valid solutions for 2D source location based on three-sensor time of arrival information. Figure 6 shows the location of points in $(\Delta t_{12}, \Delta t_{13})$ space associated with a 51×51 uniform grid of possible source locations over a 5×5 spatial domain (dimensionless units). The obviously nonuniform spacing of the arrival time difference grid illustrates the nonlinear relationship between source location coordinates and arrival time differences. Positions of unique solution for physical source location are denoted by dots [the preponderance of $(\Delta t_{12}, \Delta t_{13})$ space], while crosses mark positions of dual solutions. Clearly, there are three relatively small regions in $(\Delta t_{12}, \Delta t_{13})$ space that

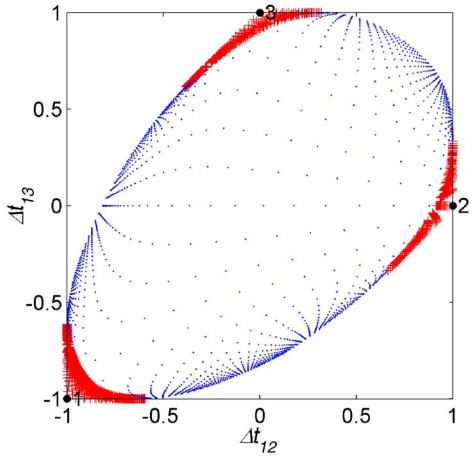

FIG. 6. (Color online) Solution mesh points in $(\Delta t_{12}, \Delta t_{13})$ space, based on a 51×51 equi-spaced (x_S, z_S) grid of possible source locations on a 5×5 physical domain (dimensionless units) associated with three-sensor TDOA source location. All grid points are associated with unique (dots) or dual (crosses) solutions to the TDOA source location inverse problem. Positions of sensors 1, 2, and 3 in arrival time difference space $(\Delta t_{12}, \Delta t_{13})$ are shown.

exhibit dual solutions for source location and they are adjacent to the sensor locations in the same space (corresponding to the three regions of intersecting contours of estimated source position coordinates—see Figs. 4 and 5). Unique and dual solutions were distinguished from one another at any point in $(\Delta t_{12}, \Delta t_{13})$ space by iteratively solving Eqs. (3) and (4) several times, each with a different initial guess of source location. The uniqueness results shown in Fig. 6 include possible source location solutions over all of physical space. However, restriction of possible solutions to those inside the 5×5 spatial domain (dimensionless units) does not substantially alter the results in terms of the extent of the region of dual solutions in arrival time difference space.

Figure 7 is a map depicting spatial regions around a sensor array that are associated with unique and dual numerical solutions to the TDOA 2D source location inverse problem based on three-sensor arrival time information [a similar

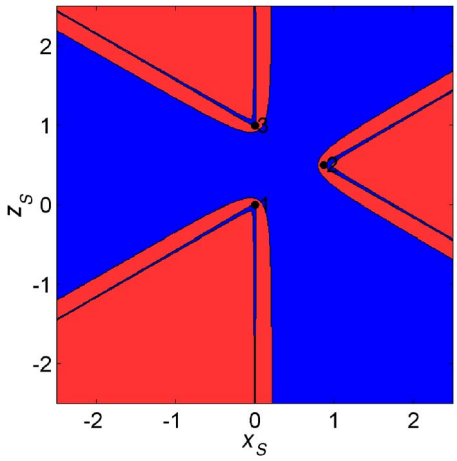

FIG. 7. (Color online) Shaded map depicting spatial regions that are associated with unique (dark gray) and dual (light gray) iterative numerical solutions to the source location inverse problem in a plane for three sensors, as a function of source location Cartesian coordinates x_S and z_S in dimensionless units. Possible solutions allowed over all of 2D physical space. Positions of sensors 1, 2, and 3 in physical space are shown.

map can be found in Schmidt, (1972)]. Regions of unique solutions are shaded in dark gray while regions of dual solutions are shaded in light gray. The map was derived from solutions for source location based on $(\Delta t_{12}, \Delta t_{13})$ coordinates associated with a 501×501 uniformly spaced grid of possible source locations over a 5×5 spatial domain (dimensionless units). Locations of unique solutions of the TDOA 2D source location problem are numerically identified as having dimensionless distances between two possible source locations less than a user-defined fractional bound (here equal to 0.1 dimensionless spatial units). In this case, alternative possible source location solutions associated with a given location in $(\Delta t_{12}, \Delta t_{13})$ space are permitted to be outside the bounded physical spatial domain. Inside the triangular region spanned by the sensor array, the source positions are in most cases unique. There are small zones inside the array boundaries (adjacent to the sensor positions) that are associated with dual solutions of the three-sensor TDOA problem. Outside of the sensor array there are three large spatial regions of apparently unique solutions. These zones are simply connected to each other via the region of unique solutions within the bounds of the sensor array. However, outside of the sensor array there are also three large spatial regions where the TDOA coordinates $(\Delta t_{12}, \Delta t_{13})$ are also valid for another physically distinct source location. The outer boundaries of the three major dual solution regions appear to be branches of hyperbolae, with foci at the sensor locations, and asymptotes parallel to the extensions beyond the sensor array of the baselines between sensors 1, 2, and 3. The sensor locations themselves are uniquely identified by the three-sensor time difference coordinates, with thin regions of apparently unique solutions extending from each of the sensor locations. These regions are parallel to the boundaries of the large regions of unique and dual solutions and directed along the extensions of baselines between the sensors of the monitoring array. In contrast to the small area of arrival time difference space associated with dual solutions to the TDOA three-sensor 2D source location problem (Fig. 6), approximately *half* of the physical space exterior to the sensor array is associated with dual solutions. This result highlights a potential major problem in the use of a three-sensor monitoring array for TDOA 2D source location.

Closer examination of the solutions to the three-sensor TDOA 2D source location problem reveals that the thin regions of apparently unique solutions show in Fig. 7 are actually lines where the dual solutions approach one another in physical separation. The location of each pair of solutions is always in the same major region of dual solution space. Near the extensions of the baselines of the sensor array it would be impossible to remove the ambiguity in source location by use of alternative reasoning such as contrast in received signal amplitudes or a restriction on the possible domain of source locations.

Figure 8 is a corresponding map of locations of unique and dual solutions to the TDOA 2D source location problem based on three-sensor arrival time information, with possible source location solutions now restricted to within a 5×5 spatial domain (dimensionless units). Comparison with Fig. 7 shows that the size of the spatial region associated with

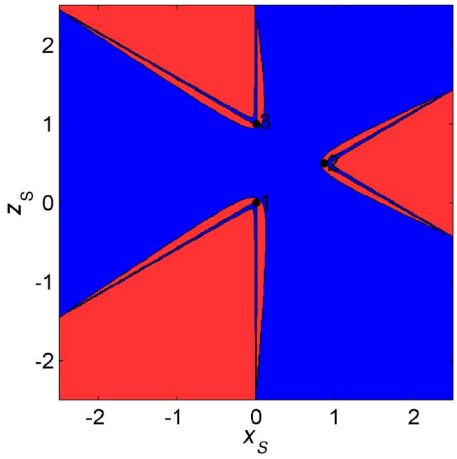

FIG. 8. (Color online) Shaded map depicting spatial regions that are associated with unique (dark gray) and dual (light gray) iterative numerical solutions to the source location inverse problem in a plane for three sensors, as a function of source location Cartesian coordinates x_S and z_S in dimensionless units. Possible solutions restricted to 5×5 spatial domain. Positions of sensors 1, 2, and 3 in physical space are shown.

dual solutions has slightly decreased. However, the imposition of boundaries on permissible source location does not remove the possibility of dual solutions in most regions outside of the area bounded by the sensor array.

An understanding of the relationship between the uniqueness of solutions to the 2D source location problem and three-sensor TDOA information can be gained by examining intersections of specific contours of Δt_{12} and Δt_{13} in the spatial domain. Figure 9 shows two sets of specific contours of Δt_{12} and Δt_{13} (in accordance with Figs. 2 and 3), one pair of contours associated with a unique solution (solid lines) and the other with a dual solution (dotted lines) for source location. In each case, the solution for source location is located by the intersection of the two hyperbolae (contour

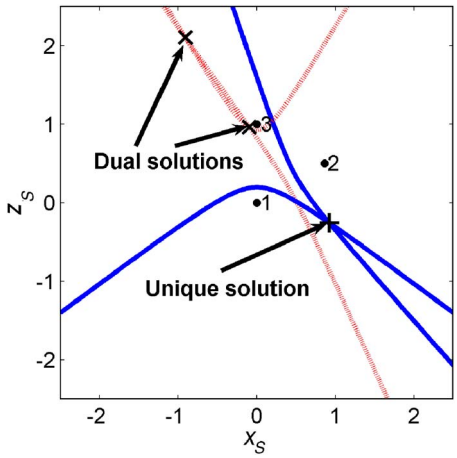

FIG. 9. (Color online) Graphical representation of examples of unique and dual solutions to the 2D source location inverse problem based on three sensor TDOA, with the points of intersection of contours (hyperbolae) in 2D space for specific values of Δt_{12} and Δt_{13} denoting source location. Physical locations of a representative unique (+) and a dual (×) solution are shown as a function of source location Cartesian coordinates x_S and z_S in dimensionless units. Associated intersecting specific contours of Δt_{12} and Δt_{13} are shown. Contour line type is according to unique (solid) or dual (dotted) source location solutions at the intersection points of the Δt_{12} and Δt_{13} contour hyperbolae.

lines) for those specific values of Δt_{12} and Δt_{13}. The characteristics of the intersection of arrival time difference curves associated with unique and dual source location solutions are as follows.

- For a unique solution in a 2D domain (bounded or unbounded), there is only one intersection within the spatial boundaries of the domain of the hyperbolae representing those respective particular values of Δt_{12} and Δt_{13}. In this particular case the solution for the source location is outside the sensor array and, as expected, within the computed region of unique solutions (see Figs. 7 and 8).
- For a dual solution, there are *two* intersections within the spatial domain of the two hyperbolae representing those respective particular values of Δt_{12} and Δt_{13}. In this particular case, one of the possible solutions is very close to sensor 3, just outside of the sensor array. The other possible solution is much more distant from the sensor array. Both possibilities are within the same computed region of dual solutions (see Figs. 7 and 8).

In general, hyperbolae in physical space representing specific values of Δt_{12} and Δt_{13} associated with a three-sensor monitoring array can intersect in only one of the following manners:

(1) No intersection—no possible source location (these specific values of Δt_{12} and Δt_{13} do not exist in association with a single physical source). Such hyperbolae can easily be found by examining Figs. 2 and 3 for nonintersecting contours of specific values of Δt_{12} and Δt_{13} arrival time differences. In Fig. 5, nonintersecting hyperbolae for specific values of independent time differences are associated with the unfilled region of $(\Delta t_{12}, \Delta t_{13})$ space that is not associated with a physical solution for source location.
(2) One intersection—unique source location, inside or outside the sensor array.
(3) Two intersections—dual possible source locations, in this case mostly (but not necessarily exclusively) outside of the sensor array. At least one of the two possible source locations is external to the area spanned by the sensor array.

Hence the geometrical interpretation of the TDOA equations can be used to investigate the existence and uniqueness of solutions to the source location inverse problem. The number of points of intersection of hyperbolae in physical space representing constant values for two independent time differences of arrival denotes the existence of unique or dual solutions to the inverse problem for source location in a plane for three sensors. It should be noted that unique source location solutions associated with a single point of intersection of hyperbolae representing independent time differences can only occur if the array elements are non-collinear.

It is interesting at this point to discuss the uniqueness properties of the solutions of the three-sensor TDOA 2D source location problem from the perspective of beamforming and TR methods.

- In the case of 2D beamforming with a three-sensor array, dual source locations should be manifested by two corresponding energy maxima in the steered response at the appropriate spatial positions. This is because both of the possible source locations are associated with the same signal intersensor time delays and hence the beamformer steered response will be maximized at both locations.
- In the case of TR for multiple scatterers, it has been shown that, provided the number of targets is less than the number of transmitter/receiver sensors, there should be unique location predictions except for certain unusual scatterer configurations that result in a linear dependence of Green's function vectors for the medium at those positions (Lehman and Devaney, 2003; Devaney *et al.*, 2005). This result implies that, for two scatterers in a 2D medium, three transmitter/receiver sensors should be sufficient for unique TR estimates of both target locations. The same result should apply to two simultaneous sources located by a three-sensor passive array.

The solution uniqueness findings of the current study initially seem at odds with those predicted by the TR methods. However, it should be remembered that the TR methods utilize information concerning the wave field spatial profile, contained in the *a priori* known Green's function of the medium, in order to image source locations. This is in contrast to the TDOA approach, which uses arrival time difference information only, incorporated into a source location model under assumptions of ray propagation at a known speed. Hence although time of arrival differences associated with signals generated by two sources as detected by three sensors in a 2D medium can in some instances be the same, the relative spatial profiles of the received signals may still be significantly different.

For some source location applications it may be possible to incorporate the measured strength of the received signal at each sensor as additional constraints on TDOA source location. In this manner possible dual solutions to the TDOA problem may be resolved where there is a substantial contrast in the received signal strength for the two candidate positions, as in the case of only one solution being in a near-field location. A quantitative implementation of such a method would effectively require a Green's function model of the medium. However, this approach would still be ineffective for TDOA dual solutions that are physically near one another (see Figs. 7 and 8).

III. ANALYSIS OF THE TDOA 2D SOURCE LOCATION PROBLEM IN A POLAR COORDINATE SYSTEM

The formulation of the three-sensor TDOA source location problem in a plane in Cartesian coordinates [see Eqs. (3) and (4)] leads to accurate and robust numerical solutions that can be easily interpreted. However, this approach is not conducive to analytical methods that may assist in further understanding the problem. A useful alternative that provides considerable scope for further analysis of the problem is to reformulate the TDOA equations for location of a source in a polar coordinate system. For a polar coordinate system (r, θ) with origin $(r=0)$ at sensor 1, it can readily be shown by a complex number representation of the distances between the

sensors and the source [or by substitution of polar representations of the Cartesian coordinates for the sensors and source in Eqs. (3) and (4)] that the TDOA equations associated with arrival times of a signal at three sensors may be written as follows:

$$c\Delta t_{12} = r_S - \sqrt{r_S^2 + r_2^2 - 2r_S r_2 \cos(\theta_S - \theta_2)} \tag{7}$$

and

$$c\Delta t_{13} = r_S - \sqrt{r_S^2 + r_3^2 - 2r_S r_3 \cos(\theta_S - \theta_3)}. \tag{8}$$

The arrival time differences are defined as in Eq. (5), while r_2 and r_3 are, respectively, the radial distance of sensors 2 and 3 from sensor 1. The coordinates θ_2 and θ_3 are, respectively, the polar (bearing) angles of sensors 2 and 3, with respect to a zero angle parallel to the x axis of the corresponding Cartesian coordinate system ($x = r\cos\theta, z = r\sin\theta$). The pair (r_S, θ_S) is the unknown polar coordinates of the source S.

A. TDOA limits for sources at large radial distances

Taylor series expansion of Eqs. (7) and (8) for large r_S compared to r_2 and r_3 leads to the following limiting expressions for arrival time differences at large radial distances from sensor 1 in comparison to the dimensions of the sensor array itself:

$$\lim_{r_S \to \infty} \Delta t_{12} = \frac{r_2}{c}\cos(\theta_S - \theta_2) \tag{9}$$

and

$$\lim_{r_S \to \infty} \Delta t_{13} = \frac{r_3}{c}\cos(\theta_S - \theta_3). \tag{10}$$

Equations (9) and (10) are parametric equations that link the limiting (large radial distance of source from sensor 1) values of Δt_{12} and Δt_{13} via the geometry of the sensor array and the wave velocity, as a function of the angular location of the source. The limiting values of the arrival time differences increase linearly with the size of the sensor array and are inversely proportional to the speed of signal propagation in the medium. The extremum values of the time differences ($\pm r_2/c$, $\pm r_3/c$) are along the extensions of baselines between sensors 1 and 2 and sensors 1 and 3 of the monitoring array. Figure 10 shows a contour plot of radial source position as a function of arrival time differences. Superimposed on the plot (dashed line) is the locus of the limiting (large radial distance) values of Δt_{12} and Δt_{13}. The time difference Δt_{13} (large radial distance of source) was actually calculated as a function of the corresponding Δt_{12} by manipulating and combining Eqs. (9) and (10) via a trigonometrical identity in order to eliminate the source angular location parameter. The contours of source radial distance from sensor 1 tend towards the theoretical limit described by Eqs. (9) and (10), which is actually an ellipse (see Fig. 10). The time differences do not reach the theoretical limiting relationship values because of the finite size of the spatial domain. However, the accuracy of the elliptical curve in representing the limiting values in $(\Delta t_{12}, \Delta t_{13})$ space at large distances from the sensor array has been confirmed by computations with larger spatial domains.

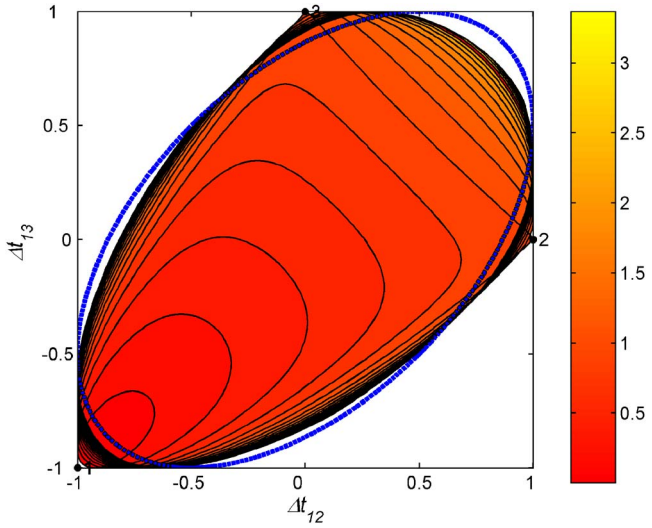

FIG. 10. (Color online) Filled contour plot with 20 equally spaced contours between maximum and minimum possible values of radial distance r_S from sensor 1 as a function of possible arrival time differences Δt_{12} and Δt_{13} in dimensionless units. Superimposed locus of limiting values of Δt_{12} and Δt_{13} at large radial distances relative to sensor 1 (dashed line). Positions of sensors 1, 2, and 3 in arrival time difference space $(\Delta t_{12}, \Delta t_{13})$ are shown.

Figures 4–6 also demonstrate the elliptical shape of contours in $(\Delta t_{12}, \Delta t_{13})$ space of source location Cartesian spatial coordinates at large distances from a sensor array. Regions of intersecting contours of source radial location indicative of dual solutions to the source location problem are readily apparent in Fig. 10.

B. Outer resolution limits for TDOA source location

A crucial consideration in the design of practical sensor arrays for TDOA source location is the far-field resolution limit of the system. This represents the outer radial distance of a source from the sensor array such that more distant sources cannot be distinguished (in terms of radial distance from the sensor array) by the TDOA method for time differences with finite resolution. For a given time difference resolution limit λ associated with the detection of differences in the arrival time of signals by sensors in an array (a function of the characteristics of the signals, sensors, and signal receiving system—including wavelength, signal to noise ratio, band pass upper frequency limit, sampling rate, and accuracy of algorithms for detection of signal arrival time), the outer radial resolution limit can be found by solving the following nonlinear equation:

$$\lambda = |\Delta t_\infty(\theta_S) - \Delta t(r_S^*, \theta_S)|. \tag{11}$$

Here $\Delta t_\infty(\theta_S)$ is the limiting value for the time difference at large radial distances (a function of source location bearing angle in 2D). The time difference $\Delta t(r_S^*, \theta_S)$ is associated with the limiting radial distance r_S^* (outer radial resolution limit) beyond which differences in source location radial distance cannot be resolved by TDOA for monitoring systems with finite time difference resolution. In 2D, $\Delta t(r_S^*, \theta_S)$ is also a function of source location bearing angle. Equation (11) states that the minimum discernible difference between a time difference associated with infinite radial source position

and a time difference associated with finite radial source position is equal to the time difference resolution limit.

For TDOA 2D source location based on three-sensor information, there are two separate expressions for radial distance resolution limit associated with the two independent time differences. An estimate of radial distance resolution limit based on Δt_{12} was derived by introducing Eqs. (7) and (9) into Eq. (11), with a Taylor series expansion of the expression for Δt_{12} truncated at first order in r_1/r_S^* (a source at a relatively large but finite radial distance from the sensor array). The same procedure was followed to obtain a radial distance resolution limit based on the Δt_{13} time difference. The resulting estimates of r_S^* are as follows:

$$r_S^*(\Delta t_{12}) \approx \frac{r_2^2 \sin^2(\theta_S - \theta_2)}{2\lambda c} \tag{12}$$

and

$$r_S^*(\Delta t_{13}) \approx \frac{r_3^2 \sin^2(\theta_S - \theta_3)}{2\lambda c}. \tag{13}$$

Both estimates of the radial resolution limit are inversely proportional to the speed of signal propagation and time difference resolution limit and proportional to the square of the relevant side length of the triangular monitoring array. For large monitoring arrays detecting signals of low propagation speed and small time difference resolution limit, the radial resolution limit is very large. Conversely, if the square of the characteristic length scale of the monitoring array is small in comparison to the signal propagation speed times the time difference resolution limit, the radial resolution limit is small. Estimates of $r_S^*(\Delta t_{12})$ and $r_S^*(\Delta t_{13})$ are strongly dependent on the bearing angle of the source relative to the bearing angles of sensors 2 and 3, respectively (for a polar coordinate system with origin coincident with sensor 1). Depending on the bearing angle of the source, the larger of the two estimates is appropriate as the actual radial resolution limit. This can be understood by considering a source along the extended baseline 12, outside of the monitoring array. In this case, Δt_{12} is a constant and the source radial distance from sensor 1 is actually determined from Δt_{13}, with associated radial resolution limit. The same argument applies to a source along the extended baseline 13, outside of the monitoring array, except in this case the source radial distance and resolution limit are determined by Δt_{13}.

Figures 11 and 12 contain plots of outer radial resolution limits [based on Eqs. (12) and (13)] for two values of dimensionless time difference resolution limit. Figure 11 shows the case $\lambda = 0.10$, corresponding to a time difference resolution limit of one tenth of the time difference of arrival associated with the sensor baseline length. Each of the two estimates of outer radial resolution limits (dashed lines) is a double-sided lobe extending outwards for sensor 1 at the coordinate system origin. The maximum of the two estimates for radial resolution limit (solid line) extends over a large proportion of the 5×5 spatial domain (dimensionless units). However, in some regions outside the monitoring array, the radial resolution limit comes within a characteristic length scale of the sensor array boundaries (e.g., outside of the array between sensors 2 and 3). In these regions, sources at larger radial distances from the sensor array cannot be accurately distinguished from one another in terms of observed time differences. This may be translated into large errors associated with estimation of radial location of these sources from TDOA calculations. Figure 12 shows the case $\lambda = 0.02$, corresponding to a five times decrease in the time difference resolution limit. In this case the radial resolution limit is well outside the 5×5 spatial domain (dimensionless units), implying that TDOA can potentially accurately locate source locations at large distances (many baseline lengths) beyond the sensor array boundaries. It should be noted that potentially more accurate expressions for outer radial resolution limits [than Eqs. (12) and (13)] can be found that are based on higher order Taylor series expansions of the TDOA equations. However, calculations of radial outer seeing limits based on Taylor series truncated at second order in r_1/r_S^* (and

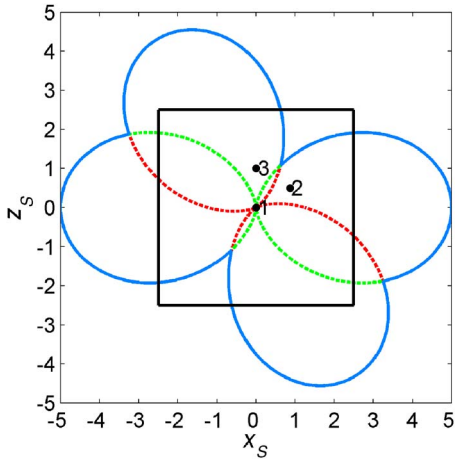

FIG. 11. (Color online) Radial outer resolution limits for time difference resolution limit $\lambda = 0.10$ as a function of source location Cartesian coordinates x_S and z_S in dimensionless units. Dashed dark gray line: Δt_{12} outer radial resolution limit. Dashed light gray line: Δt_{13} outer radial resolution limit. Solid dark gray line: maximum of Δt_{12} and Δt_{13} outer resolution limits. Solid black line: outer boundary of the 5×5 spatial domain.

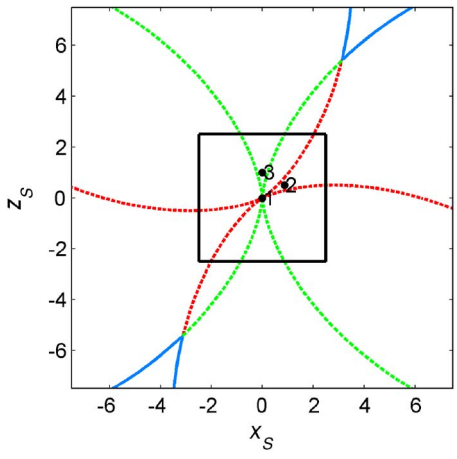

FIG. 12. (Color online) Radial outer resolution limit for time difference resolution limit $\lambda = 0.02$ as a function of source location Cartesian coordinates x_S and z_S in dimensionless units. Dashed dark gray line: Δt_{12} outer radial resolution limit. Dashed light gray green line: Δt_{13} outer radial resolution limit. Solid dark gray line: maximum of Δt_{12} and Δt_{13} outer resolution limits. Solid black line: outer boundary of the 5×5 spatial domain.

r_2/r_S^*) are not significantly different except at very high time difference resolution limits that are not useful for practical monitoring systems.

The calculation of a radial resolution limit for TDOA source location highlights the importance of ensuring the arrival time difference resolution limit of the monitoring system is appropriate to the speed of propagation of the signal. In order to accurately locate sources at radial distances several baseline lengths outside a monitoring array, the arrival time difference resolution limit multiplied by the speed of signal propagation in the medium should be a small fraction of the square of the sensor array baseline length. Another approach to increasing the radial resolution limit is to increase the size (baseline characteristic length scale) of the monitoring array. However, depending on the characteristics of signal propagation in the specific medium involved and the amount of noise in the receiving system, increasing the spread of the sensors too much may eventually result in a decrease in the accuracy of arrival time determination. In the worst case this could lead to a loss of correlation between the signals sensed at each individual sensor, due to damping, geometric attenuation, dispersion, and boundary refraction and reflection effects. Hence the arrival times of signals from individual sources may not be accurately estimated or detected at all by some sensors, implying TDOA source location is inaccurate or not possible. Increasing the sensor array baseline length may also exacerbate spurious source location due to false coincidences between signals detected by sensors from multiple spatially distributed sources. In practice, a balance between increasing the TDOA radial resolution limit by larger sensor spacing and keeping the spacing sufficiently small to ensure that correlated signal arrival times are accurately detected by all sensors may be used to estimate a suitable characteristic length scale for sensor separation.

Radial resolution limit calculations may assist in optimal placement and orientation of sensors with respect to one another and as an array. Figures 11 and 12 indicate that the optimal location for a monitoring array on a bounded 2D surface (in circumstances where the radial resolution limit does not cover the entire 2D surface) is, as intuitively expected, with the array in the middle of the spatial domain. Numerical experiments have shown that the optimal orientation of the sensors with respect to one another (in terms of maximal spatial domain inside the radial resolution limits for a given maximum baseline length based on sensor separation) is as an equilateral triangle. The orientation of the sensor array with respect to the spatial domain is not important unless there is a preferred direction in which maximal radial resolution limit is desired for a given sensor separation baseline length. In this case, a face of the triangle formed by the sensor locations (corresponding to one of the arrival time differences used in the TDOA calculations) should be at right angles to the direction of desired source location.

C. The TDOA method for four sensors

Given that the TDOA method based on arrival times for a three-sensor array in a plane sometimes results in dual solutions for source location, it is logical to investigate the effect on the problem of the addition of an arrival time associated with a fourth sensor. For an arrival time difference associated with a signal detected by sensor 1 and a fourth sensor, 4, an additional (independent) TDOA equation may be written in polar coordinates as follows:

$$c\Delta t_{14} = r_S - \sqrt{r_S^2 + r_4^2 - 2r_S r_4 \cos(\theta_S - \theta_4)}. \tag{14}$$

Here

$$\Delta t_{14} = t_1 - t_4. \tag{15}$$

The extra self-consistency conditions for the arrival time differences are

$$\Delta t_{24} = \Delta t_{14} - \Delta t_{12} \tag{16}$$

and

$$\Delta t_{34} = \Delta t_{14} - \Delta t_{13}. \tag{17}$$

In Eq. (14), the coordinate r_4 is the radial distance of sensor 4 from the origin (sensor 1), while θ_4 is the polar angle of sensor 4 with respect to the same zero angle as taken for the other sensors. It should be noted that additional TDOA equations based on time differences between other pairs of sensors can be found, but it can be shown that they are all linear combinations of those expressed in Eqs. (7), (8), and (14) [in accordance with the self-consistency conditions (6), (16), and (17)] and do not provide additional information.

Solutions of the forward problem for arrival time differences as a function of two-dimensional source location were found for a four sensor array. Equations (7), (8), and (14) (based on a polar coordinate system) were solved for time differences Δt_{12}, Δt_{13}, and Δt_{14} respectively, based on a 101×101 equi-spaced grid of source locations in the spatial domain. The hypothetical additional sensor, 4, was positioned at the same distance from the line between sensors 1 and 3 as sensor 2, but in the opposite direction, in order to create a symmetrical array. Figure 13 is a contour plot of the solution for Δt_{14}, including the position of sensor 4. Contours of constant Δt_{14} are again hyperbolae, in this case centered about the mid-point between sensors 1 and 4, and symmetric about an axis defined by a line running between the same.

The inverse problem of 2D source location for a four-sensor monitoring array [as defined by equations (7), (8), and (14)] was numerically solved for a grid of arrival time differences $(\Delta t_{12}, \Delta t_{13}, \Delta t_{14})$ associated with a uniformly spaced mesh of possible source locations in 2D physical space. Least-squares solutions were again found by use of the MATLAB "lsqnonlin" iterative solution routine. Figures 14 and 15 are two-dimensional plots of the location of points in $(\Delta t_{12}, \Delta t_{13})$ and $(\Delta t_{12}, \Delta t_{14})$ space, respectively, for a 51×51 uniform grid of possible source locations over a 5×5 spatial domain (dimensionless units). These plots are orthogonal two-dimensional perspectives of the locations in three-dimensional $(\Delta t_{12}, \Delta t_{13}, \Delta t_{14})$ space of the mesh of solution points associated with the four-sensor TDOA problem. As for the three-sensor inverse problem (see Fig. 6), the obviously non-uniform spacing of the arrival time difference grid in Figs. 14 and 15 illustrates the nonlinear relationship between source location coordinates and arrival time differences. However, in contrast to a substantial number of loca-

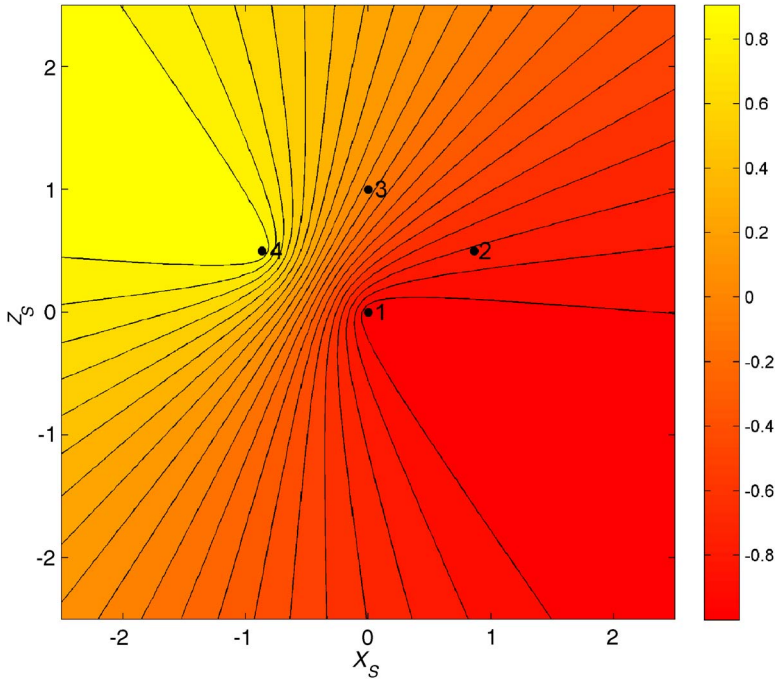

FIG. 13. (Color online) Filled contour plot with 20 equally spaced contours between maximum and minimum possible values of arrival time difference Δt_{14} between signals at sensors 1 and 4 as a function of source location Cartesian coordinates x_S and z_S in dimensionless units. Spatial positions of sensors 1, 2, 3, and 4 are shown.

tions in $(\Delta t_{12}, \Delta t_{13})$ space associated with dual solutions to the three-sensor TDOA problem (see Fig. 6), Figs. 14 and 15 show that all of the locations in $(\Delta t_{12}, \Delta t_{13}, \Delta t_{14})$ space are associated with unique solutions to the four sensor TDOA source location problem. This again confirms that source location in a plane is not a unique function of $(\Delta t_{12}, \Delta t_{13})$ time differences but is a unique function in $(\Delta t_{12}, \Delta t_{13}, \Delta t_{14})$ space. The extra information provided by the time difference associated with the fourth sensor [Eq. (14)] is necessary in order to eliminate one of the possible dual solutions in some regions of $(\Delta t_{12}, \Delta t_{13})$ space (see Figs. 7 and 8).

An understanding of the effect on the uniqueness of the 2D source location inverse problem of the addition of an independent TDOA relationship associated with a fourth sensor can be gained by examining intersections of specific contours of Δt_{12}, Δt_{13}, and Δt_{14} on an (x_S, z_S) grid. Figure 16 shows two sets of contours (hyperbolae) for specific values of Δt_{12}, Δt_{13}, and Δt_{14} time differences. One of these sets of intersecting contours is associated with a previously unique solution (solid lines) and the other with a dual solution (dotted lines) for source location, as determined from three-sensor TDOA Δt_{12} and Δt_{13} specific contour crossings (see Fig. 9). Solutions for four-sensor TDOA source location

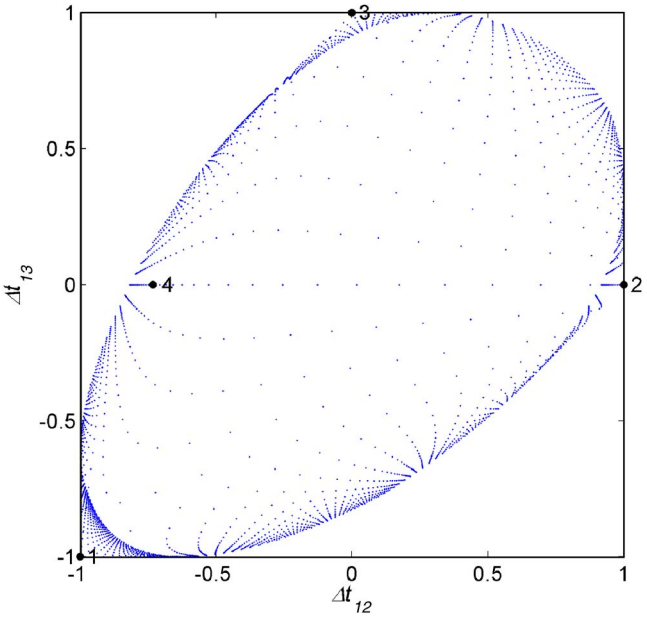

FIG. 14. (Color online) Solution mesh points in $(\Delta t_{12}, \Delta t_{13})$ space, based on a 51×51 equi-spaced (x_S, z_S) grid of possible source locations on a 5×5 physical domain (dimensionless units) associated with four-sensor TDOA source location. All grid points are associated with unique (dots) solutions to the TDOA source location inverse problem. Positions of sensors 1, 2, 3, and 4 in $(\Delta t_{12}, \Delta t_{13})$ space are shown.

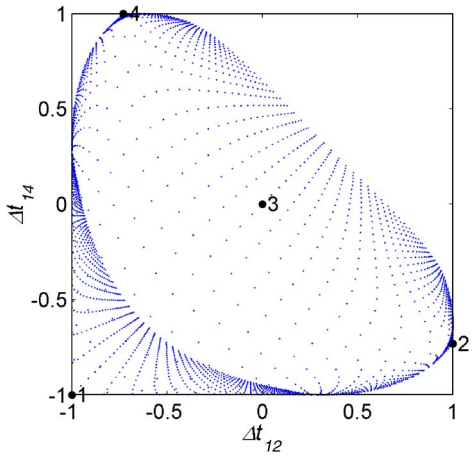

FIG. 15. (Color online) Solution mesh points in $(\Delta t_{12}, \Delta t_{14})$ space, based on a 51×51 equi-spaced (x_S, z_S) grid of possible source locations on a 5×5 physical domain (dimensionless units) associated with four-sensor TDOA source location. All grid points are associated with unique (dots) solutions to the TDOA source location inverse problem. Positions of sensors 1, 2, 3, and 4 in $(\Delta t_{12}, \Delta t_{14})$ space are shown.

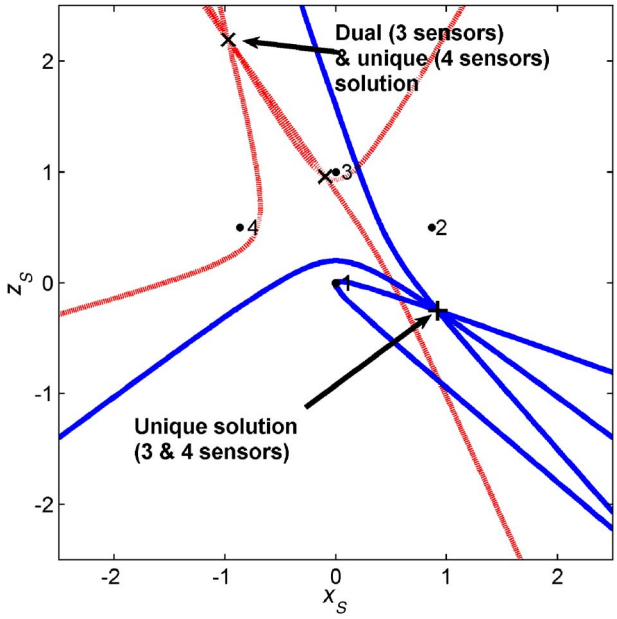

FIG. 16. (Color online) Graphical representation of the effect on the uniqueness of the 2D source location inverse problem of the addition of an independent TDOA relationship associated with a fourth sensor. Two examples are shown of exclusively unique solutions to the 2D source location inverse problem based on four-sensor TDOA, with the points of intersection of contours (hyperbolae) in 2D space for specific values of Δt_{12}, Δt_{13}, and Δt_{14} denoting source location. Physical locations of a specific unique (+) and a previously dual (×) solution based on three-sensor TDOA are shown as a function of source location Cartesian coordinates x_S and z_S in dimensionless units. Both three-sensor dual solutions are shown. Associated intersecting specific contours of Δt_{12}, Δt_{13}, and Δt_{14} are shown. Contour line type is according to three-sensor TDOA unique (solid) or dual (dotted) source location solutions at the intersection points of the Δt_{12} and Δt_{13} contour hyperbolae.

based on contours of specific values of Δt_{12}, Δt_{13}, and Δt_{14} are identified by the point of intersection (in the absence of arrival time errors) of these *three* hyperbolae in 2D space. Such solutions are unique because there is at most only *one* intersection in all of 2D physical space of hyperbolae representing particular values of three independent time differences associated with TDOA based on four spatially distributed sensors. For the particular case of a dual solution using three-sensor TDOA (dotted contour lines in Fig. 16), the hyperbola associated with the particular value of Δt_{14} intersects the other two hyperbolae at only one of the possible solution points, excluding the solution very close to sensor 3. For real data based on arrival times estimated from cross-correlated signals, the solution for source location in physical space is uniquely determined based on the estimated physical location that best satisfies the specific $(\Delta t_{12}, \Delta t_{13}, \Delta t_{14})$ time difference coordinates. For the particular case of a unique solution using three-sensor TDOA (solid contour lines), the hyperbola associated with the particular value of Δt_{14} intersects the other two hyperbolae at the same location in physical space as the Δt_{12} and Δt_{13} contour crossings. The solution at this latter location is in fact overdetermined and, for real data based on arrival times estimated from cross-correlated signals, is numerically determined in a least-squares sense.

The effect of the addition of a fourth sensor to a monitoring array can be investigated in terms of modifications to

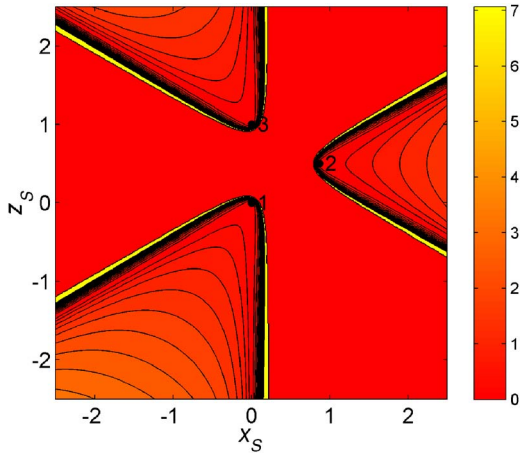

FIG. 17. (Color online) Filled contour plot with 20 equally spaced contours between nil and maximum possible values in a 5×5 spatial domain of distance between possible dual source locations as a function of source location Cartesian coordinates x_S and z_S in dimensionless units. Possible solutions allowed over all of 2D physical space. Positions of sensors 1, 2, and 3 in physical space are shown.

TDOA limits for sources at large radial distances and also outer resolution limits. The limiting expression for Δt_{14} at large radial distances can be written as

$$\lim_{r_S \to \infty} \Delta t_{14} = \frac{r_4}{c} \cos(\theta_S - \theta_4). \tag{18}$$

Equation (18) can be combined with Eqs. (9) and (10) to determine the locus of the limiting (large radial distance) values of Δt_{12}, Δt_{13}, and Δt_{14}. A plot of radial source position as a function of arrival time differences shows that an ellipsoid is the limiting shape of the $(\Delta t_{12}, \Delta t_{13}, \Delta t_{14})$ domain at large distances from the sensor array. The radial distance resolution limit associated with Δt_{14} may be written as

$$r_S^*(\Delta t_{14}) \approx \frac{r_4^2 \sin^2(\theta_S - \theta_4)}{2\lambda c}. \tag{19}$$

A plot of outer radial resolution limits [based on Eqs. (12), (13), and (19)] shows that the addition of a fourth sensor does not increase the ability of a monitoring array to resolve source locations at large radial distances but decreases the directional (bearing) dependence of the maximum outer radial resolution limit (see Figs. 11 and 12).

D. The distance between dual solutions

The straight-line distance between dual analytical solutions was calculated for the three-sensor TDOA 2D source location test problem. This was done in order to test the assertion that dual solutions are usually far enough apart such that one can be excluded by other physical reasoning such as being outside the spatial domain of interest. The solutions for source location are based on time difference coordinates associated with a 501×501 uniformly spaced grid of possible source locations over the 5×5 spatial domain (dimensionless units).

Figure 17 is a contour plot showing the distance between possible dual solutions to the TDOA 2D source location problem based on three-sensor arrival time information, as a

function of spatial location [a similar plot can be found in Spiesberger (2001)]. In this case, solutions are permitted beyond the 5×5 spatial domain (dimensionless units). The contour plot is scaled to a maximum distance of 7 dimensionless spatial units, but dual source locations were actually found at distances of up to order 10^3 dimensionless spatial units from the monitoring array. Comparison of Figs. 7 and 17 shows that, as expected, in the large, simply connected physical region where a unique iterative solution was found to the TDOA 2D source location problem for three sensors, there is nil distance between analytical solutions. Figure 17 also shows thin regions of low separation distance extending from each of the sensor locations as branches of hyperbolae, tending to straight lines along the extensions of the intersensor baselines outside the monitoring array. Again, this result is in accordance with the Fig. 7 uniqueness results. The largest distances between dual solutions are where one of the possible source locations is within one of the three thin regions between the hyperbolae of low separation distance and the large, simply connected region of nil separation distance (unique solutions). Just inside the sensor array (adjacent to the sensor locations), there are small regions where a dual solution exists at a large distance from the current location. These three thin regions of large dual solution separation distance extend outside of the sensor array to the outer boundaries of the spatial domain. Outside of the sensor array there are also three large spatial regions where dual solutions to the TDOA source location problem exist with a *wide variety of linear separations*, increasing with radial distance from the monitoring array (corresponding to the three large regions of dual source solutions in Fig. 7). Hence for three-sensor arrival time differences consistent with a source location that is within one of the three spatial regions of dual solutions bounded by the extensions of the intersensor baselines outside the monitoring array, it may be impossible to distinguish the correct solution in terms of being within an arbitrarily sized physical domain of interest (or by received signal strength). Under these circumstances, additional information, in the form of at least one more independent arrival time difference associated with an additional sensor, is needed to uniquely define the source location.

Figure 18 is a contour plot showing the distance between possible dual solutions to the TDOA 2D source location problem based on three-sensor arrival time information, with possible source location solutions now restricted to within the 5×5 spatial domain (dimensionless units). Comparison with Fig. 17 shows that the size of the spatial region associated with nonzero solution distances (dual solutions) has slightly decreased (consistent with the change in the size of regions of dual and unique solutions shown in Figs. 7 and 8). However, just inside the sensor array (adjacent to the sensor locations), there remain small regions where a dual possible source location solution exists outside of the monitoring array. Outside of the sensor array there are again three large spatial regions where the three-sensor TDOA values are also valid for another physically distinct source location at a wide variety of distances from the current source location. The size of these regions has not substantially decreased with the imposition of a boundary on the region of interest. A comparison of Figs. 17 and 18 shows that the size of the spatial region around the monitoring array associated with possible dual solutions of the three-sensor TDOA source location problem at large distances from the sensors is relatively small, with most dual solutions being within a distance of a few sensor baseline lengths. These results confirm that in many instances it is impossible to distinguish the correct solution for TDOA source location based on three-sensor arrival time information if locations external to the area spanned by the sensor array are admitted, in terms of only one solution being inside an arbitrarily sized domain of interest.

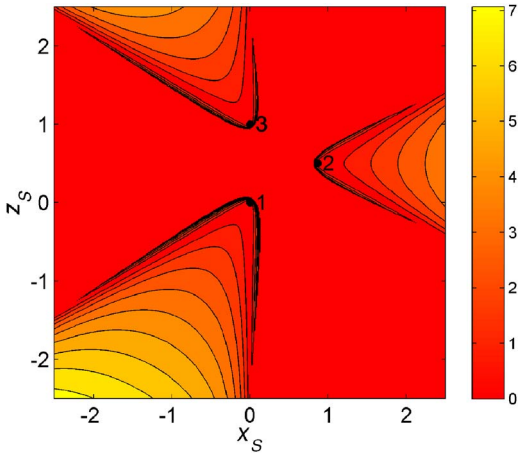

FIG. 18. (Color online) Filled contour plot with 20 equally spaced contours between nil and maximum possible values of distance between possible dual source locations as a function of source location Cartesian coordinates x_S and z_S in dimensionless units. Possible solutions restricted to 5×5 spatial domain. Positions of sensors 1, 2, and 3 in physical space are shown.

IV. CONCLUSIONS

The problem of 2D source location by time difference of arrival (TDOA) for a minimal number of sensor elements in a monitoring array has been investigated. A NLS estimator has been used to obtain accurate iterative numerical solutions over the range of possible arrival time differences, based on the assumptions of geodesic ray propagation paths and constant speed. In the case of three-sensor arrival time data, the inverse problem of source location is ill-posed, with the existence of dual possible solutions demonstrated for some combinations of arrival time differences. This does not represent an unusual situation, as small regions of arrival time difference space associated with these dual solutions have been shown to be associated with large regions of physical source location space. These dual solutions have been shown to occur for sources both inside and outside the sensor array, although the problem occurs more commonly for arrival time differences associated with sources external to the area spanned by the monitoring array. In cases where one of the dual possible solutions is within the area spanned by the sensor array, the other is always external to the same. Unique two-dimensional source location solutions are in all cases obtained with the use of arrival time difference data associated with a non-collinear four-sensor monitoring array.

The linear distance between dual solutions associated with three-sensor TDOA data varies greatly, making it impossible in some cases to determine a unique two-dimensional source location from three-sensor arrival time data by physical reasoning such as restricting the size of the domain of interest or using signal amplitude information, unless the source is *a priori* known to be within the spatial area spanned by the sensor array. In practical terms, this means that arrival time data associated with at least *four* stationary sensors should be used for estimation of two-dimensional TDOA source location in the absence of additional prior information. Alternatively, source location estimates external to the array can be utilized when they are known to be within regions of unique solutions to the problem. In cases of persistent signals from regions where the time differences correspond to dual solutions, the monitoring array could be rotated an appropriate angle in order to gain a unique estimate of source location. It can be expected that in the case of three-dimensional TDOA problems, arrival time data associated with at least *five* sensors (rather than four-sensor arrival time data as traditionally used in many applications) will also be needed in some cases in order to avoid the problem of dual possible solutions to the source location problem unless it is *a priori* known that the source is contained within the volume spanned by the sensor array.

Formulation of the two-dimensional source location problem in a polar coordinate system allows useful analytical expressions to be found for limiting values of arrival time differences due to sources at relatively large distances from the monitoring array. Further analysis of the two- and three-dimensional TDOA problems in coordinate systems matching the geodesic path of signal propagation, including investigation of the behavior of noniterative closed-form estimators in the presence of noise, will be addressed in a future paper.

ACKNOWLEDGMENTS

This research was partly supported by the Australian Minerals Industry Research Association (AMIRA), under Project Nos. P667 and P667A. CSIRO and AMIRA are thanked for permission to publish this paper. The helpful comments of the referees are gratefully acknowledged.

Aki, K., and Richards, P. G. (**1980**). *Quantitative Seismology—Theory and Methods* (Freeman, San Francisco).

Barat, P., Kalyanasundaram, P., and Raj, B. (**1993**). "Acoustic emission source location on a cylindrical surface," NDT & E Int. **26**(6), 295–297.

Brandstein, M. S., Adcock, J. E., and Silverman, H. F. (**1995**). "A closed-form method for finding source locations from microphone-array time-delay estimates," in *Proc. IEEE Int. Conf. Acoust. Speech Signal Process., ICASSP95*, pp. 3019–3022.

Chan, Y. T., and Ho, K. C. (**1994**). "An efficient closed-form localization solution from time difference of arrival measurements," in *Proc. IEEE Int. Conf. Acoust. Speech Signal Process., ICASSP94*, pp. II-393–II-396.

Collins, M. P., and Belchamber, R. M. (**1990**). "Acoustic emission source location using simplex optimization," J. Acoust. Emiss. **9**(4), 271–276.

Delosme, J. M., Morf, M., and Friedlander, B. (**1980**). "Source location from time differences of arrival: Identifiability and estimation," in *Proc. IEEE Int. Conf. Acoust. Speech Signal Process., ICASSP80*, pp. 818–824.

Devaney, A. J., Marengo, E. A., and Gruber, F. K. (**2005**). "Time-reversal-based imaging and inverse scattering of multiply scattering point targets," J. Acoust. Soc. Am. **118**(5), 3129–3138.

DiBiase, J. H., Silverman, H. F., and Brandstein, M. S. (**2001**). "Robust localization in reverberant rooms," in *Microphone Arrays Signal Processing Techniques and Applications*, edited by M. Brandstein and D. Ward (Springer-Verlag, Berlin), Chap. 8, pp. 157–180.

Duraiswami, R., Zotkin, D., and Davis, L. (**1999**). "Exact solutions for the problem of source location from measured time differences of arrival," J. Acoust. Soc. Am. **106**(4), 2277.

Fink, M., Cassereau, D., Derode, A., Prada, C., Roux, P., Tanter, M., Thomas, J.-L., and Wu, F. (**2000**). "Time-reversed acoustics," Rep. Prog. Phys. **63**, 1933–1995.

Gannot, S., and Dvorkind, T. G. (**2006**). "Microphone array speaker localizers using spatial-temporal information," EURASIP J. Appl. Signal Process. **2006**, 1–17.

Hofmann-Wellenhof, B., Lichtenegger, H., and Collins, J. (**2001**). *Global Positioning System: Theory and Practice*, 5th ed. (Springer-Verlag, Wein).

Huang, Y., Benesty, J., Elko, G. W., and Mersereau, R. M. (**2001**). "Real-time passive source localization: A practical linear-correction least-squares approach," IEEE Trans. Speech Audio Process. **9**(8), 943–956.

Johnson, D. H., and Dudgeon, D. E. (**1993**). *Array Signal Processing: Concepts and Techniques* (PTR Prentice Hall, New Jersey).

Kaplan, E. D. (**1996**). *Understanding GPS: Principles and Applications* (Artech House, Boston).

Kat, M., and Hassani, F. P. (**1989**). "Application of acoustic emission for the evaluation of microseismic source location techniques," J. Acoust. Emiss. **8**(4), 99–106.

Keen, E. J., and Rogers, L. M. (**1987**). "Location of discrete source of acoustic emission in complex tubular joints," in *Proc. 4th European Conf. NDT*, pp. 2984–3000.

Klee, U., Gehrig, T., and McDonough, J. (**2006**). "Kalman filters for time delay of arrival-based source localization," EURASIP J. Appl. Signal Process. **2006**, 1–15.

Landis, E., Ouyang, C., and Shah, S. P. (**1991**). "Automated determination of first P-wave arrival and acoustic emission source location," J. Acoust. Emiss. **10**(1), 97–103.

Lehman, S. K., and Devaney, A. J. (**2003**). "Transmission mode time-reversal super-resolution imaging," J. Acoust. Soc. Am. **113**(5), 2742–2753.

Liu, H., and Milios, E. (**2005**). "Acoustic positioning using multiple microphone arrays," J. Acoust. Soc. Am. **177**(5), 2772–2782.

Pao, Y. H. (**1978**). "Theory of acoustic emission," in *Elastic Waves and Non-Destructive Testing of Materials* (American Society of Mechanical Engineers, New York), Vol. **AMD-20**, pp. 107–128.

Pollock, A. A. (**1986**). "Classical wave theory in practical AE testing," in *Progress in Acoustic Emission III* (Japanese Society of NDI, Tokyo), pp. 708–721.

Prada, C., Manneville, S., Spoliansky, D., and Fink, M. (**1996**). "Decomposition of the time reversal operator: Detection and selective focusing on two scatterers," J. Acoust. Soc. Am. **99**(4), 2067–2076.

Prada, C., and Thomas, J.-L. (**2003**). "Experimental subwavelength localization of scatterers by decomposition of the time reversal operator interpreted as a covariance matrix," J. Acoust. Soc. Am. **114**(1), 235–243.

Rogers, L. M. (**1994**). "Sizing fatigue cracks in offshore structures by the acoustic emission method," Insight **36**(9), 661-665.

Rogers, L. M., and Murphy, F. (**1996**). "Crack life prediction based on AE measurement," in *Proc. 22nd European Conf. Acoust. Emiss. Testing*, Robert Gordon University, Aberdeen, pp. 39–50.

Schau, H. C., and Robinson, A. Z. (**1987**). "Passive source localization employing intersecting spherical surfaces from time-of-arrival differences," IEEE Trans. Acoust., Speech, Signal Process. **35**(8), 1223–1225.

Schmidt, R. O. (**1972**). "A new approach to range difference geometry of range difference location," IEEE Trans. Aerosp. Electron. Syst. **AES-8**(6), 821–835.

Schmidt, R. O. (**1986**). "Multiple emitter location and signal parameter estimation," IEEE Trans. Antennas Propag. **AP-34**(3), 276–280.

Scruby, C. B. (**1985**). "Quantitative acoustic emission techniques," *Non-Destructive Testing* (Academic, London), Vol. **8**, Chap. 4.

Smith, J. O., and Abel, J. S. (**1987**). "Closed-form Least-Squares Source Location Estimation from Range-Difference Measurements," IEEE Trans. Acoust., Speech, Signal Process. **35**(12), 1661–1669.

Spencer, S. J., Campbell, J. J., Sharp, V., Davey, K. J., Phillips, P. L., Barker, D. G., and Holmes, R. J. (**2005**). "Multiple sensor surface vibrations analysis for monitoring tumbling mill performance," in *Intelligence in a Small World—Nanomaterials for the 21st Century. Selected Papers from IPMM-2003, Sendai, Japan*, edited by J. A. Meech, Y. Kawazoe, V. Kumar, and J. F. Maguire (DEStech, Lancaster, PA), pp. 359–376.

Spiesberger, J. L. (**2001**). "Hyperbolic location errors due to insufficient numbers of receivers," J. Acoust. Soc. Am. **109**, 3076–3079 (**2001**).
Torney, D. C., and Nemzek, R. J. (**2005**). "Least-error localization of discrete acoustic sources," Appl. Acoust. **66**, 1262–1277.
Yoon, D. J., Kim, Y. H., and Kwon, O. Y. (**1990**). "New algorithm for acoustic emission source location in cylindrical structures," J. Acoust. Emiss. **9**(4), 237–242.
Zotkin, D. N., and Duraiswami, R. (**2004**). "Accelerated speech source localization via a hierarchical search of steered response power," IEEE Trans. Speech Audio Process. **12**(5), 499–508.

An exact noniterative linear method for locating sources based on measuring receiver arrival times

C. Militello and S. R. Buenafuente[a)]
Department of Fundamental and Experimental Physics, La Laguna University, Canary Islands, Spain

(Received 29 May 2006; revised 15 March 2007; accepted 19 March 2007)

In this paper an exact, linear solution to the source localization problem based on the time of arrival at the receivers is presented. The method is unique in that the source's position can be obtained by solving a system of linear equations, three for a plane and four for a volume. This simplification means adding an additional receiver to the minimum mathematically required (3+1 in two dimensions and 4+1 in three dimensions). The equations are easily worked out for any receiver configuration and their geometrical interpretation is straightforward. Unlike other methods, the system of reference used to describe the receivers' positions is completely arbitrary. The relationship between this method and previously published ones is discussed, showing how the present, more general, method overcomes nonlinearity and unknown dependency issues. © *2007 Acoustical Society of America.* [DOI: 10.1121/1.2724241]

PACS number(s): 43.60.Jn, 43.60.Fg, 43.28.Tc [EJS] Pages: 3595–3601

I. INTRODUCTION

Over the last 25 years various methods have been developed for solving the problem of localizing a source's spatial position based on the arrival times of its emission at different receivers. The solutions are based on the hyperbolic trajectory described by a source on the plane which is emitting with a constant delay to two receivers. Three receivers allow us to construct two hyperbolas, the intersection of which localizes the source. When working in three dimensions, the curves must be replaced by hyperboloid surfaces. The resulting system of equations is not linear and it generally does not have a direct analytical solution. Different approaches have been proposed: linearization of the basic equations, least squares, iterative solutions to the nonlinear problem, and even an exact solution.

For an arbitrary sensor distribution and a consistent system of equations (equal number of sensors as unknowns), Fang gives an exact solution to the system of nonlinear hyperboloid equations.[1] For an arbitrary sensor distribution and a redundant set of estimated delays, the following methods can be used: spherical intersection (SX);[2] spherical interpolation (SI);[3–5] divide and conquer;[6] Chan's method;[7] and Taylor series.[8,9] Of these methods, the Taylor series, Fang's, and Chan's methods are considered the best and are the most widely used. Unlike the Taylor series method, not only are the last two less computationally demanding, they also yield an exact solution. The Taylor series needs an initial value which, if not adequately chosen, can result in a local minimum. On the other hand, Chan's and the Taylor series method allow for the use of redundant information from any number of sensors. Fang's method requires a fixed number of sensors because they are used to set the reference frame. Adding one more receiver requires establishing a new minimum set that includes the new one. Since both the Fang and Chan methods solve a quadratic equation, they yield two answers. The resulting ambiguity must be resolved by utilizing either *a priori* information or symmetrical properties.

In any method, we must distinguish between having the minimum number of receivers or having redundant measurements and, of course, establish whether we are solving a linear or a nonlinear problem. If we have redundant measurements or uncertainty, least squares emerge as one possible way to overcome the difficulty. But a nonlinear problem is quite a different story. Schau[2] described the problem as the intersection of spherical surfaces propagating from the source, the so-called SX method. Placing the coordinate center in one of the receivers and using the distance between the source and that receiver, the range R, he greatly simplified the starting equations. At the end, a four-equation system for the unknowns x_s, y_s, z_s and R has to be solved. All the system coefficients can be computed from the time delay of arrival (TDOA) measurements but he considered R a parameter and not an unknown. In this way, it is assumed that the four equation system is not able to provide the right solution for the four unknowns. It is implicitly understood that the unknowns so obtained will not satisfy the relationship between range and source position. In the SI method, Smith *et al.*,[3] started from the same set of equations. The authors, for a redundant set of receivers, obtained the least-squares solution by two partial minimizations, one with respect to the source coordinates and the other with respect to the range. Again the independence between the unknowns is not recognized. Huang *et al.*,[10] directly solving the initial redundant system proposed in the SI method without partial minimization, surprisingly found that the same results of the SI can be obtained in one step least square method (OSLS). Section III discusses the relationship between the present method and the SX, SI, and OSLS, as well as the linear nature of the system of equations and the independency between the unknowns.

In this paper a property is presented that has not been explicitly acknowledged or exploited previously. This prop-

a)Electronic mail: srbuenaf@ull.es

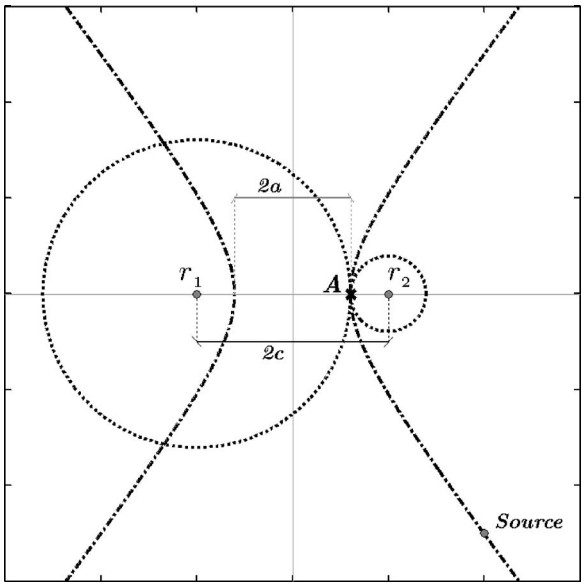

FIG. 1. Point A represents the intersection of the two wave fronts emitted from r_1 and r_2. Said intersection takes place at time $t_s=(a+c)/v$.

erty simplifies the problem statement and solution. The problem in two dimensions is first analyzed. Its generalization to three dimensions follows directly and is shown at the end. The development assumes an isotropic medium with homogeneous properties, free of noise, with a known set of delays for the arrival time.

II. METHOD

A. The basic property

First an inverse approach to solving the TDOA problem is proposed. That is, as a problem in which the receivers act as the sources, emitting circular wave fronts with their corresponding delays. At a given time all the wave fronts will intersect at the source's exact position.

Assume there is one source in each of the receivers r_1 and r_2, Fig. 1. The distance between them is $2c$. Source r_1 emits first, and source r_2 starts doing so after time t_a has elapsed

$$t_a = \frac{2a}{v}, \tag{1}$$

where v is the wave front's velocity in the medium. The spatial delay is defined as $2a$.

Doing this, the wave fronts will intersect first at point A. The circular intersections for times Δt, $2\Delta t$, and $3\Delta t$ after the first impact are shown in Fig. 2. Connecting the consecutive intersection points yields the hyperbola

$$\frac{x^2}{a^2} - \frac{y^2}{b^2} = 1 \tag{2}$$

where

$$b^2 = c^2 - a^2. \tag{3}$$

In Fig. 2, vertical lines connect the points where the two wave fronts intersect at each interval. This straight line, a kind of straight front, propagates with time in a direction

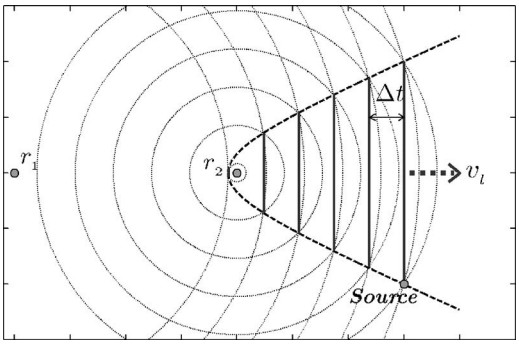

FIG. 2. Connecting the intersection points of the wave fronts at each instant in time yields the branch of the hyperbola containing the source. The solid vertical lines propagates with time at speed v_l. It constitutes a straight front.

perpendicular to the line connecting r_1 and r_2. It will do so with velocity v_l. For $t_a=0$ said velocity will be zero, and for $t_a=2c/v$ it will be the same as the wave's propagation velocity in the medium, $v_l=v$.

The x coordinate of this vertical line can be obtained from the intersection of the hyperbola and the wave front propagating from r_1 (Fig. 2).

The equation for a wave front propagating from r_1 with coordinates $(x,y)=(-c,0)$ is

$$(x+c)^2 + y^2 = R^2 \tag{4}$$

where the radius R is a linear function of time, $R=vt$. From Eq. (2);

$$y^2 = b^2\left(\frac{x^2}{a^2} - 1\right) \tag{5}$$

Substituting Eq. (5) in Eq. (4):

$$(x+c)^2 + x^2\frac{b^2}{a^2} - b^2 - R^2 = 0. \tag{6}$$

Rearranging terms gives the more familiar form

$$\left(1 + \frac{b^2}{a^2}\right)x^2 + 2cx + (c^2 - b^2 - R^2) = 0. \tag{7}$$

In Eq. (7), the general form

$$\alpha x^2 + \beta x + \gamma = 0 \tag{8}$$

can be recognized. The solution is

$$x = -\frac{\beta}{2\alpha} \pm \frac{\sqrt{\beta^2 - 4\alpha\gamma}}{2\alpha}. \tag{9}$$

Since R only appears in the discriminant, it is analyzed in more detail:

$$\beta^2 - 4\alpha\gamma = 4c^2 - 4\left(1 + \frac{b^2}{a^2}\right)(c^2 - b^2 - R^2). \tag{10}$$

Recalling from Eq. (3) that

$$\left(1 + \frac{b^2}{a^2}\right) = \frac{c^2}{a^2} \tag{11}$$

substituting it in Eq. (10) and expanding terms gives

$$4c^2 - 4\frac{c^2}{a^2}(c^2 - b^2 - R^2) = 4R^2\frac{c^2}{a^2} + 4c^2\left(1 - \frac{c^2}{a^2} - \frac{b^2}{a^2}\right)$$
$$= 4R^2\frac{c^2}{a^2} + 4c^2\left(1 - \frac{c^2 - b^2}{a^2}\right)$$
$$= 4R^2\frac{c^2}{a^2}. \tag{12}$$

Surprisingly, the discriminant becomes a monomial squared. The x coordinate of the vertical line can be obtained from

$$x = -\frac{a^2}{c} \pm R\frac{a}{c}, \tag{13}$$

and so, the straight front propagation velocity is

$$v_l = \frac{\partial x}{\partial t} = \pm v\frac{a}{c}. \tag{14}$$

In Eq. (14), the positive sign indicates that the line propagates from the source in the receiver that emits first toward the source that emits later, that is, from r_1 to r_2. Equation (14) is this paper's most important contribution. Surprisingly, the line propagation velocity is constant and depends on the spatial delay between the two receivers and their distance. Now the TDOA problem statement can be simplified.

B. Time synchronization

For an arrival time method, the time at which the perturbation emitted from the source arrives at each receiver must first be determined. These times are called t_{ri}, where r indicates that the measurement is made at the receiver and i is the receiver number. This time is set to zero for the source nearest the receiver, while the most distant receiver is assigned a maximum value, $t_r^{\max}$. For the inverse problem, the times at which the sources in the receivers begin emitting must be synchronized.

The reciprocal emission times are defined as

$$t_{ri}^{\text{inv}} = t_r^{\max} - t_{ri}. \tag{15}$$

These are always positive quantities. It will be zero for the most distant receiver and $t_r^{\max}$ for the one closest to the source. Their magnitudes are computed from the original delays recorded in the sensors.

C. The planar problem

To solve the planar problem, we first consider two receivers, r_i and r_j. Note that we need not take into account which has the smaller reciprocal time. Let us consider a wave front that starts to propagate from r_i at time t_{ri}^{inv}. This wave front will propagate to point A (Fig. 3) at velocity v. The time it will take to reach point A is given by

$$t_{rA}^{ij} = \frac{c_{ij} + a_{ij}}{v}. \tag{16}$$

In Eq. (16), the quantity c_{ij} represents the halfway point between the two receivers and is always positive. The spatial delay, which is a signed quantity, is solved for each pair of receivers as follows:

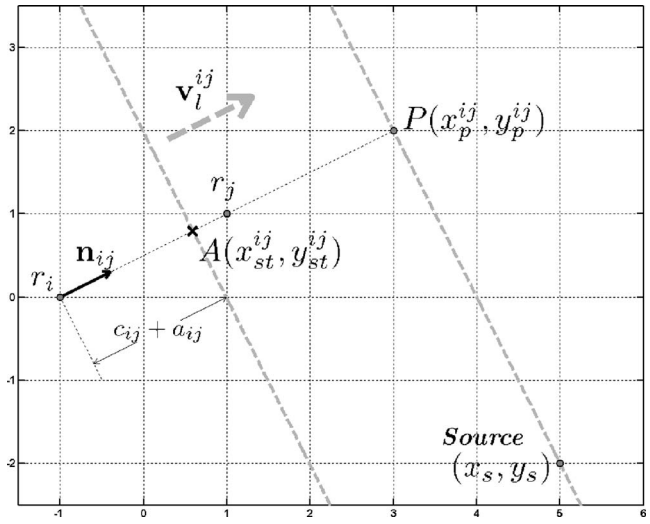

FIG. 3. The thick dashed lines represent the initial and final positions of the straight front. It advances, in the direction of vector n_{ij}, from point $A(x_{st}^{ij}, y_{st}^{ij})$, with velocity v_l^{ij} until it reaches position $P(x_p^{ij}, y_p^{ij})$ at the same time the straight front reaches the source.

$$2a_{ij} = v(t_{rj}^{\text{inv}} - t_{ri}^{\text{inv}}). \tag{17}$$

Once point A at coordinates $(x_{st}^{ij}, y_{st}^{ij})$ is reached, the wave front becomes a straight line traveling at velocity

$$v_l^{ij} = v\frac{a_{ij}}{c_{ij}}. \tag{18}$$

After a certain time, the straight front reaches the source at coordinates (x_s, y_s). At this time the straight front intersects the line going from receiver i to receiver j at P with coordinates (x_p^{ij}, y_p^{ij}), then

$$(x_p^{ij} - x_s)n_x^{ij} + (y_p^{ij} - y_s)n_y^{ij} = 0. \tag{19}$$

Based on the synchronization established in the previous section, the coordinates of point P are given by

$$\begin{aligned} x_p^{ij} &= x_{st}^{ij} + v_l^{ij}n_x^{ij}(t - t_{tA}^{ij}), \\ y_p^{ij} &= y_{st}^{ij} + v_l^{ij}n_y^{ij}(t - t_{tA}^{ij}), \end{aligned} \tag{20}$$

where t is the absolute time measured from the instant the most distant receiver starts emitting, and t_{tA}^{ij} is the absolute time at which the wave front from receiver r_i reaches point A:

$$t_{tA}^{ij} = t_{rA}^{ij} + t_{ri}^{\text{inv}}. \tag{21}$$

Substituting Eq. (20) in Eq. (19) and rearranging terms yields

$$n_x^{ij}x_s + n_y^{ij}y_s - v_l^{ij}t = n_x^{ij}x_{st}^{ij} + n_y^{ij}y_{st}^{ij} - v_l^{ij}t_{tA}^{ij}. \tag{22}$$

Equation (22) is linear in the unknowns x_s, y_s, and t. All the other quantities, as we have already shown, follow from the differences in the receiver times of arrival and from the distance between the two receivers. In order to solve the problem, three independent equations must be setup. This requires the use of three pairs of receivers for a total of four receivers.

D. The spatial problem

The spatial problem requires a modification of Eq. (22) so as to account for the third dimension:

$$n_x^{ij}x_s + n_y^{ij}y_s + n_z^{ij}z_s - v_l^{ij}t = n_x^{ij}x_{st}^{ij} + n_y^{ij}y_{st}^{ij} + n_z^{ij}z_{st}^{ij} - v_l^{ij}t_{tA}^{ij}. \tag{23}$$

Since the number of unknowns is four, a five-receiver layout is necessary to provide the four independent equations. In matrix form we have

$$\mathbf{M}\cdot\mathbf{X} = \mathbf{B}, \tag{24}$$

where

$$\mathbf{M} = \begin{bmatrix} n_x^{12} & n_y^{12} & n_z^{12} & -v_l^{12} \\ n_x^{23} & n_y^{23} & n_z^{23} & -v_l^{23} \\ n_x^{34} & n_y^{34} & n_z^{34} & -v_l^{34} \\ n_x^{45} & n_y^{45} & n_z^{45} & -v_l^{45} \end{bmatrix},$$

$$\mathbf{X} = \begin{bmatrix} x_s \\ y_s \\ z_s \\ t \end{bmatrix}, \tag{25}$$

$$\mathbf{B} = \begin{bmatrix} n_x^{12}x_{st}^{12} + n_y^{12}y_{st}^{12} + n_z^{12}z_{st}^{12} - v_l^{12}t_{tA}^{12} \\ n_x^{23}x_{st}^{23} + n_y^{23}y_{st}^{23} + n_z^{23}z_{st}^{23} - v_l^{23}t_{tA}^{23} \\ n_x^{34}x_{st}^{34} + n_y^{34}y_{st}^{34} + n_z^{34}z_{st}^{34} - v_l^{34}t_{tA}^{34} \\ n_x^{45}x_{st}^{45} + n_y^{45}y_{st}^{45} + n_z^{45}z_{st}^{45} - v_l^{45}t_{tA}^{45} \end{bmatrix}.$$

The notation for the superscripts is arbitrary, with the caveat that two rows cannot have the same superscripts. Matrix M must be nonsingular and well-conditioned.

III. ON SYSTEM LINEARITY AND VARIABLE INDEPENDENCY

In the previous sections, the unknowns are x_s, y_s, z_s, and t. They are independent variables. The coordinate center can be chosen at any spatial point and the time origin can be changed arbitrarily with no effect on the source localization. There is no *a priori* relationship among the unknowns. Moreover, because of the property presented in Eq. (14), the problem can be recast as the old problem of four cars with known constant speed, departure time, position, and direction. The problem of source localization becomes one of finding the straight trajectory intersection and the arrival time. The speed of the cars being constant, the system equations are linear without any further relationship among the unknowns.

If time starts when the receiver over which the coordinate center is placed starts emitting, the system in Eq. (24) is completely equivalent to the one developed for the SX method. Moreover, a few simple linear transformations allow replacing the time by the distance between the origin receiver and the source (the range R). In doing so, the unknowns for this particular setting become x_s, y_s, z_s, and R. There is no demonstrated reason why the values obtained from this equation system will not satisfy

$$R = \sqrt{x_s^2 + y_s^2 + z_s^2} \tag{26}$$

and so, there is no reason to enforce it. Taking as the origin of the coordinates a close neighbor to the receiver and the same time origin as before, the relationship in Eq. (26) is no longer valid, and thus irrelevant.

Schau *et al.*[2] considered Eq. (26) of capital importance, not recognizing the independence of the unknowns and the fact that their proposal exactly solved the TDOA with a simple, elegant, linear system at the expense of adding one receiver. Smith *et al.*[3–5] did not recognize the linearity and independence and proposed an unnecessary two-step least-squares procedure. That the two steps are unnecessary was demonstrated by Huang *et al.*[10] because in one step he was able to obtain the same results as Smith. This will not be possible unless the unknowns involved were independent.

The method developed in this paper is a more general statement of the problem, one that is easy to understand and program. But with our procedure the issues of linearity and independency become clear.

IV. DISCUSSION

This solution strategy depends on the ability to position the receivers. In the planar problem, four microphones aligned in a row with different distances between them cannot yield a solution since the system determinant is singular. In interpreting this layout, it is preferable that the receivers not be at right angles to each other and that the distances between them not have a common multiple.

The numerical results allow us to differentiate between the following cases:

(1) A source-receiver configuration in which the source placement within the boundary delineated by the receivers yields a null determinant. These configurations are said to exhibit an "internal singularity."
(2) A source-receiver configuration in which the source placement outside the boundary delineated by the receivers yields a null determinant. These configurations are said to exhibit an "external singularity."
(3) Receiver configurations which exhibit "internal and external singularities" simultaneously.
(4) Receiver configurations which do not exhibit any singularities and which are "robust."

An analysis of optimum receiver configurations will be the subject of a future paper.

A. System invertibility

As mentioned previously, microphone configurations exist for which the layout is stable and invertible, independently of the emitter's position with respect to the receivers. A stable configuration for a planar problem is an equilateral triangle with microphones at the vertices and another at the triangle's geometrical center. This receiver geometry is defined by the radius of the circle, r_r, delineated by the three vertices.

To demonstrate its stability, a circumference of emitters surrounding the network of microphones is simulated. Its

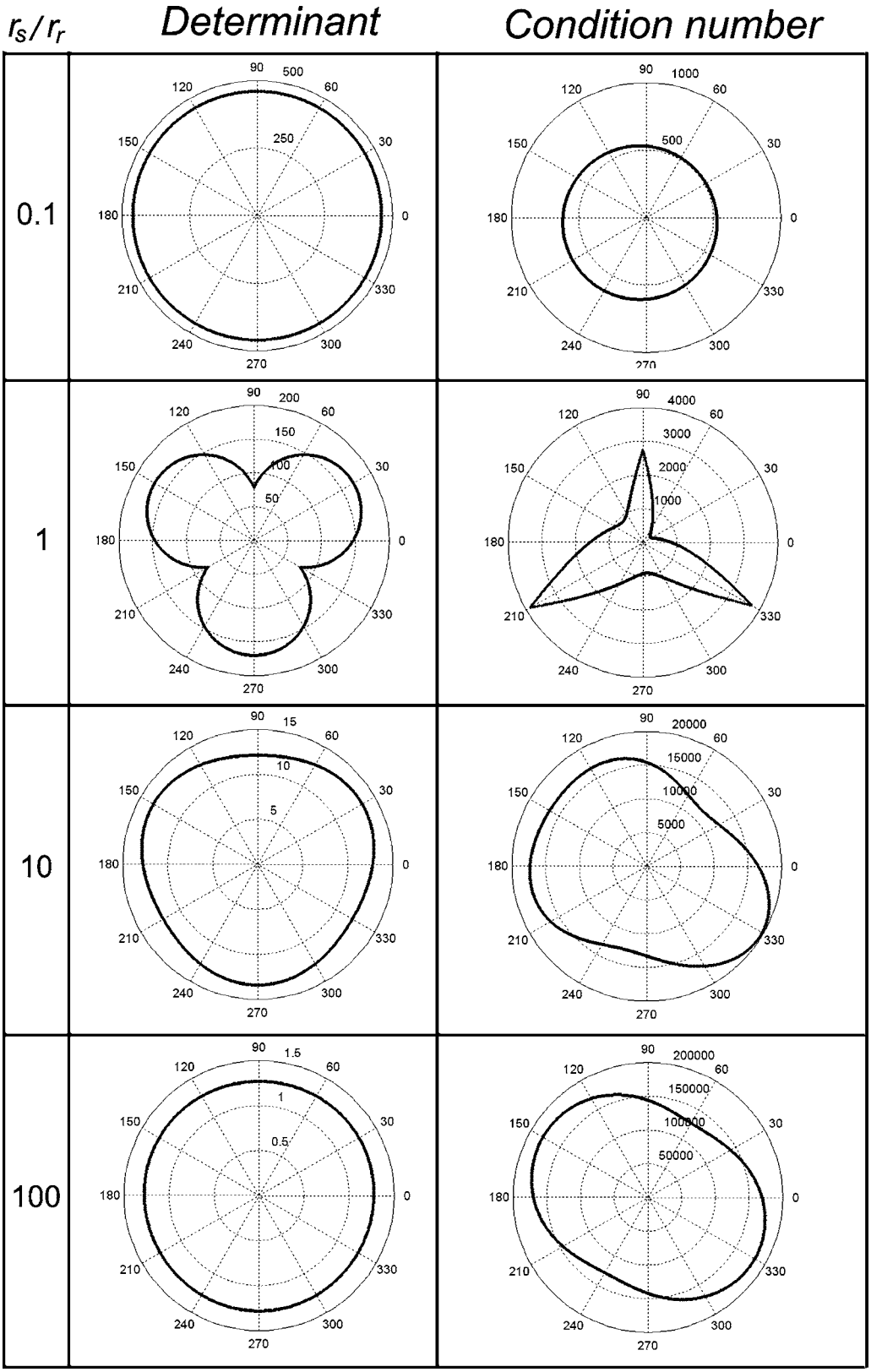

FIG. 4. Determinant and condition number for different r_s/r_r ratios. One thousand sources uniformly distributed over a circle of radius r_s are considered. Notice that while the determinant values follow the receiver pattern, the condition number does not.

radius is r_s. Consider one thousand equally spaced emitters placed along the circumference. For the r_s/r_r ratios of 0.1, 1, 10, and 100, Fig. 4 shows, in polar coordinates, the determinant of the matrix M and its condition number. The value of r_r is 1 m and the propagation speed of sound through the air is used (340 m/s). Machine precision calculated TDOAs are assumed. The figures show that the determinant's value decreases and the condition deteriorates as the source is moved further away. This is to be expected since as the source is moved away, it becomes more difficult for the set of receiv-

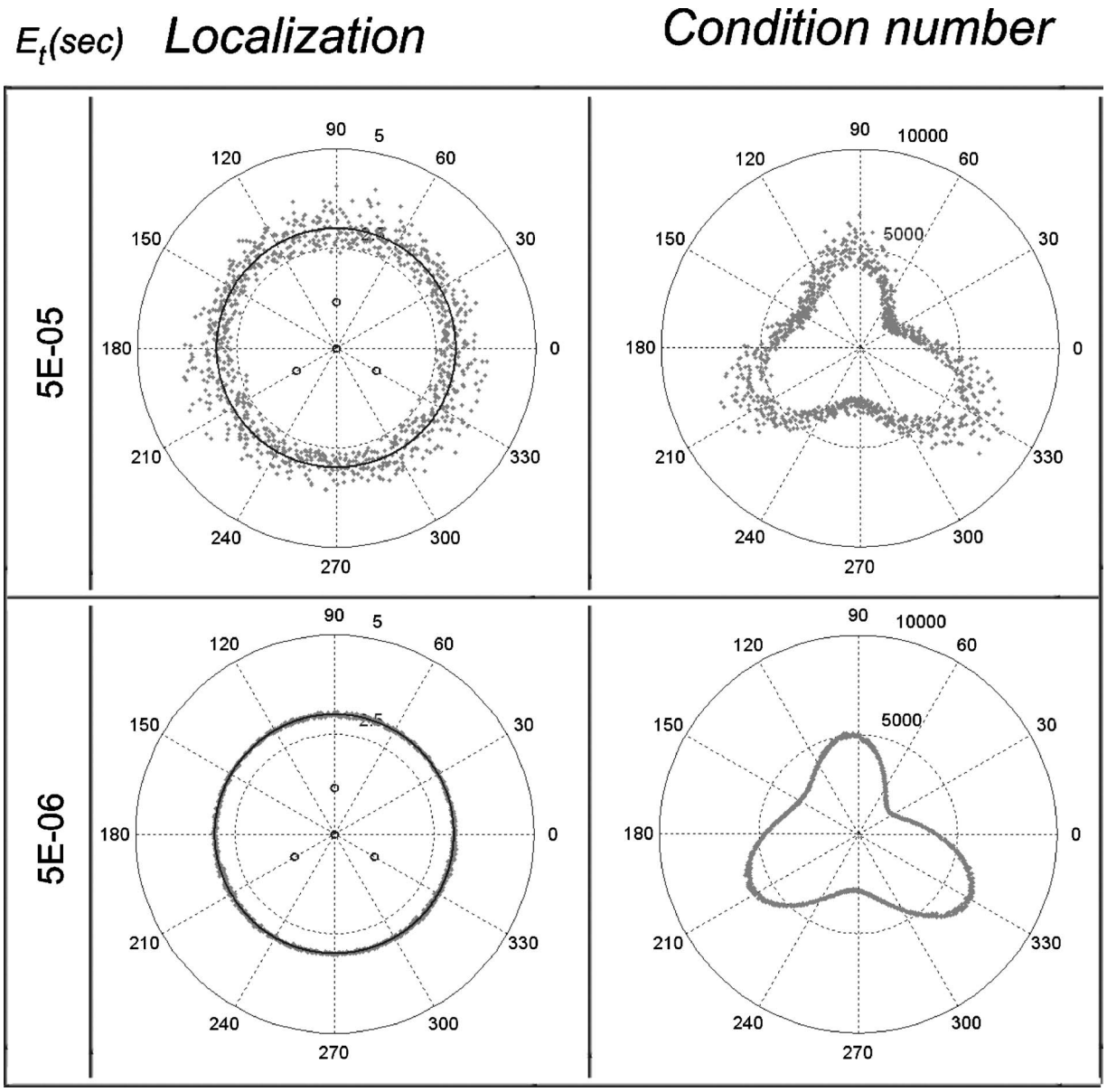

FIG. 5. Effect of TDOA error in target localization. The condition number presents maximum dispersion for the highest condition values. The localization error follows this behavior. Reducing TDOA error, E_t, one order of magnitude produces the same order reduction in the localization error.

ers to determine the wave front's curvature. The determinant's shape follows the symmetry of the microphone's layout. The condition number does not exhibit this symmetry.

B. Error amplification

Closely related to the stability issue is the question of how accurately the proposed method can detect the source's position, considering the inevitable errors in the arrival time estimation. For the previous configuration, the case of r_s equal to 3 m and r_r equal to 1 m is analyzed to see how an error in the TDOAs affects the proposed algorithm's ability to localize the emitter's position.

The receivers' error in identifying the event and the TDOAs is simulated by introducing both a fixed amplitude, as well as a random sign, into the exact calculations. Let E_t denote the maximum error magnitude. Figure 5 shows the influence of this temporal error. For E_t values of $5E-05$ s, the error in the radial position can reach 1 m. Note the dispersion of the condition. The dispersion range for the condition number values narrows where the condition is at a minimum. The source localization error is also at a minimum at these points. Reducing E_t by an order of magnitude reduces the localization uncertainty by an equal factor, going from 1 to 0.1 m, approximately.

V. CONCLUSIONS

A simple and precise linear formulation for the hyperbolic localization problem based on arrival times has been introduced. The simplification is derived from the property expressed in Eq. (14), unpublished until now. The simplification's drawback is the need to account for the unknown time variable, which requires an additional independent equation, and therefore one more receiver in addition to the theoretical minimum.

The simplicity of the matrix M allows for a direct interpretation of the conditions necessary for a robust detection in a given direction in space. The matrix condition can be analyzed directly, allowing for an *a priori* resolution of the precision necessary to determine the delay times (TOA) and their effect on the localization error.

An omnidirectional planar problem has been analyzed. The properties outlined can be extrapolated to the tridimensional problem, which will be examined in a future paper.

[1]B. T. Fang, "Simple solutions for hyperbolic and related position fixes," IEEE Trans. Aerosp. Electron. Syst. **26**, 748–753 (1990).

[2]H. C. Schau and A. Z. Robinson, "Passive source localization employing intersecting spherical surfaces from time-of-arrival differences," IEEE Trans. Acoust., Speech, Signal Process. **29**, 984–995 (1989).

[3]J. O. Smith and J. S. Abel, "The spherical interpolation method for source localization," IEEE J. Ocean. Eng. **12**, 246–252 (1987).

[4]J. O. Smith and J. S. Abel, "Closed-form least-squares source location estimation from range-difference measurements," IEEE Trans. Acoust., Speech, Signal Process. **35**, 1661–1669 (1987).

[5]J. S. Abel and J. O. Smith, "The spherical interpolation method for closed-form passive localization using range difference measurements," in ICASSP-87, Dallas, TX, pp. 471–474.

[6]J. S. Abel, "A divide and conquer approach to least-squares estimation," IEEE Trans. Aerosp. Electron. Syst. **26**, 423–427 (1990).

[7]Y. T. Chan and K. C. Ho, "A simple and efficient estimator for hyperbolic location," IEEE Trans. Signal Process. **42**, 1905–1915 (1994).

[8]W. H. Foy, "Position-location solutions by Taylor-series estimation," IEEE Trans. Aerosp. Electron. Syst. **12**, 187–194 (1976).

[9]D. J. Torrieri, "Statistical theory of passive location systems," IEEE Trans. Aerosp. Electron. Syst. **20**, 183–198 (1984).

[10]Y. Huang, J. Benesty, and G. W. Elko, "Passive acoustic source localization for video camera steering," Proceedings of the IEEE International Conference on Acoustics, Speech, Signal Processing, 2000, Istambul, Turkey, Vol. **II**, pp. 909–912.

Near-field time-reversal amplification

Stephane G. Conti,[a] Philippe Roux, and William A. Kuperman
Marine Physical Laboratory, SIO-UCSD, 9500 Gilman Drive, La Jolla, California 92093-0238

(Received 13 December 2006; revised 14 March 2007; accepted 19 March 2007)

The spatial resolution of the focused field of a classical time-reversal mirror has a wavelength-order λ diffraction limit. Previously reported results for subwavelength focus require either the full knowledge of the original source or the evanescent waves in the near field. Here it is shown that subwavelength focusing can be achieved without *a priori* knowledge of the original probe source. If the field is recorded at a few wavelengths away from the probe source, where the amplitude of the near field is too low for subwavelength focusing, it is shown that the low amplitude near field can be amplified and the spatial resolution improved, using the near-field time reversal (NTR) procedure introduced here. The NTR is performed from the phase of the spatial spectrum of the field recorded on an array around the original probe source using an analytical continuation for the amplitude of the spatial spectrum. Following theory, λ/20 resolution is experimentally demonstrated with audible acoustic wavefields in the air. © *2007 Acoustical Society of America.* [DOI: 10.1121/1.2724238]

PACS number(s): 43.60.Tj, 43.20.Gp, 43.28.Hr, 43.60.Sx [EJS] Pages: 3602–3606

I. INTRODUCTION

The implementation of a time-reversal mirror (TRM) in acoustics[1] and electromagnetics[2–4] is now well established. Using the far field of a probe source, a TRM focuses back to the probe to the wavelength (λ) diffraction resolution[5,6] as determined by the TRM aperture.[6–8] Previous studies[5,9] showed that the field resulting from the time reversal process near the focus consists of two waves: the incoming wave from the TRM and the outgoing wave after the collapse of the time-reversed field at the source. Using Lamb waves on a chaotic glass plate cavity, de Rosny and Fink[9] showed that subwavelength spatial resolution could be achieved experimentally by active cancellation of the outgoing wave at the source location at precisely the right time and amplitude as specified by the time-reversal process. This acoustic sink is implemented by adding a wave emitted from a time-reversed source, ϕ_S, to the field traveling from the TRM, ϕ_{TR}. In other words, the acoustic sink combines the *a priori* knowledge of the original source position with the far-field time-reversal data. On the other hand, near-field acoustic holography (NAH)[10,11] utilizes the evanescent wave-number structure of the nearfield for the high resolution characterization without *a priori* knowledge of the source. In this paper, we introduce a near-field time-reversal (NTR) procedure that combines the acoustic sink and NAH approaches. We show that a focus with subwavelength resolution can be obtained from a TRM at a distance of a few wavelengths of the probe source, between the near- and far-field regions. Importantly, the subwavelength focusing is achieved without *a priori* knowledge of the original source position and timing. This result is obtained in the wave-number domain from the spatial spectrum of the field ϕ_{TR} recorded with an array around the probe source. If the range is of the order of a few wavelength, the amplitude of the evanescent field is too low for subwavelength resolution focusing like in the nearfield. Nevertheless, part of the evanescent field can be amplified in the wave-number domain to significantly improve the resolution of the focus. Here, we demonstrate this principle using simulation and experiments for a range of 4 wavelengths. The NTR procedure we propose consists in extracting the phase of the time-reversed field in the wave-number domain and applying a generic amplitude to the spectrum while retaining the recorded phase.

II. THEORY

Time reversal is always implemented directly in the spatial domain whereas NAH uses the wave-number domain to reconstruct the field at the source. Near-field Time Reversal (NTR) takes advantages of the fact that in the wave-number domain, the near field of a point source ϕ_S is decomposed into an amplitude that controls the spatial resolution of the focus independent of its position and a phase that contains the spatial position information of the focus. In our case, the latter can also be extracted from the time-reversed signals ϕ_{TR} recorded around the source. The amplitude and the phase can be combined because the near-field spatial resolution is independent of the probe source position. The resulting constructed near-field time-reversal (NTR) focus occurs at the position in space and time defined by the TRM but with the spatial resolution one expects from the nearfield. The temporal resolution of the focus remains unchanged.

In other words, Near-field time reversal at the source position $\boldsymbol{R}_1=(x_1,y_1,z_1)$ is based on the combination of two fields on a near-field array $\boldsymbol{R}$ around the source. First, as usual in a time-reversal process, after the field from the source is recorded away from the nearfield on a multiple-element array that makes up a TRM, the transmitted time-reversed field $\phi_{TR}(\boldsymbol{R},\boldsymbol{R}_1,t)$ focusing to the probe source position with a wavelength-order spatial resolution is recorded on the near-field array. Second, we define the generic analytic field $\phi_S(\boldsymbol{R},\boldsymbol{R}_0,t)$ for an isotropic point source in free space at position $\boldsymbol{R}_0$ as the target field for the time-reversed imaging. This field $\phi_S(\boldsymbol{R},\boldsymbol{R}_0,t)$ defines the subwavelength

[a]Electronic mail: sconti@ucsd.edu

 0001-4966/2007/121(6)/3602/5/$23.00 © 2007 Acoustical Society of America

spatial resolution to achieve. As it will be shown later, the same generic field $\phi_S(\boldsymbol{R},\boldsymbol{R}_0,t)$ is applied to a time-reversed field from one source or two simultaneous ones separated by less than a wavelength. In both cases, this generic field will provide resolvable foci at the original positions. Note that $\boldsymbol{R}_0$ and $\boldsymbol{R}_1$ do not need to be the same point for ϕ_S and ϕ_{TR}, meaning that the NTR procedure is applied without *a priori* knowledge on the position of the focus from the TRM. For $|\boldsymbol{R}_0-\boldsymbol{R}|<\lambda$, $\phi_S(\boldsymbol{R},\boldsymbol{R}_0,t)$ is given[9]

$$\phi_S(\boldsymbol{R},\boldsymbol{R}_0,t)=A_S\frac{\exp(ik_0|\boldsymbol{R}-\boldsymbol{R}_0|)}{4\pi|\boldsymbol{R}-\boldsymbol{R}_0|}\exp(-i\omega t), \tag{1}$$

where $k_0=\omega/c=2\pi f_0/c$ for the central frequency f_0, c is the speed of sound, and A_S is the relative amplitude of the field ϕ_S. The spatial resolution for $\phi_S(\boldsymbol{R},\boldsymbol{R}_0,t)$ corresponds to a point source. For a position $\boldsymbol{R}_1$ in the nearfield of the probe source such that $|\boldsymbol{R}_1-\boldsymbol{R}|<\lambda$, and a TRM in the farfield of the probe source, the time-reversed field from the farfield $\phi_{TR\ ff}(\boldsymbol{R},\boldsymbol{R}_1,t)$ is given by[9]

$$\phi_{TR\ ff}(\boldsymbol{R},\boldsymbol{R}_1,t)=A_{TR}\frac{\exp(-ik_0|\boldsymbol{R}-\boldsymbol{R}_1|)}{4\pi|\boldsymbol{R}-\boldsymbol{R}_1|}\exp(-i\omega t) - A_{TR}\frac{\exp(ik_0|\boldsymbol{R}-\boldsymbol{R}_1|)}{4\pi|\boldsymbol{R}-\boldsymbol{R}_1|}\exp(-i\omega t), \tag{2}$$

where A_{TR} the relative amplitude of the field $\phi_{TR\ ff}$. If the TRM is in a range between the farfield and the nearfield of the probe source, the time-reversed field recorded on the near-field array is the sum of the fields from Eqs. (1) and (2), with relative amplitudes A_S and A_{TR} varying with the range:

$$\phi_{TR}(\boldsymbol{R},\boldsymbol{R}_1,t)=\phi_{TR\ ff}(\boldsymbol{R},\boldsymbol{R}_1,t)+\phi_S(\boldsymbol{R},\boldsymbol{R}_1,t). \tag{3}$$

As in Eq. (3), for a TRM in the nearfield, the relative amplitudes A_S and A_{TR} are equal, and $\phi_{TR}(\boldsymbol{R},\boldsymbol{R}_1,t)$ describes the focus whose spatial resolution corresponds to a point source. For a TRM in the farfield, A_S is equal to zero, and the spatial resolution is of the order λ corresponding to the sinc function for an ideal TRM in the farfield. Note that Eqs. (1)–(3) only require the medium to be locally homogeneous around the source. In this case, the time-reversed field obtained on the near-field array does not depend on the presence of scatterers or heterogeneities at distances greater than a few wavelengths between the TRM and the source. However, when an ideal TRM is not available, scatterers or heterogeneities can increase the effective aperture of the TRM,[6–8] making the time-reversed field behave as $\phi_{TR}(\boldsymbol{R},\boldsymbol{R}_1,t)$ around the source. Following Eqs. (1) and (2), ϕ_S and ϕ_{TR} are written as the product of space $g_S(\boldsymbol{R},\boldsymbol{R}_0)$ and $g_{TR}(\boldsymbol{R},\boldsymbol{R}_1)$, respectively, and a time dependent function $\exp(-i\omega t)$:

$$\phi_S(\boldsymbol{R},\boldsymbol{R}_0,t)=A_S g_S(\boldsymbol{R},\boldsymbol{R}_0)\exp(-i\omega t), \tag{4}$$

$$\phi_{TR}(\boldsymbol{R},\boldsymbol{R}_1,t)=A_{TR}g_{TR}(\boldsymbol{R},\boldsymbol{R}_1)\exp(-i\omega t). \tag{5}$$

The localization of the time-reversed wave at the original source position is embedded in $g_{TR}(\boldsymbol{R},\boldsymbol{R}_1)$. In the wavenumber domain, the localization of the original source only appears in the phase term, by definition of the Fourier transform. In the near field, the spatial Fourier transform $\tilde{\phi}$ of either Eq. (1) or (3) is written as

$$\tilde{\phi}_S(\boldsymbol{k},\boldsymbol{R}_1,t)=A_S\exp(-i\boldsymbol{k}\cdot\boldsymbol{R}_0)\tilde{g}_S(\boldsymbol{k})\exp(-i\omega t), \tag{6}$$

$$\tilde{\phi}_{TR}(\boldsymbol{k},\boldsymbol{R}_1,t)=A_{TR}\exp(-i\boldsymbol{k}\cdot\boldsymbol{R}_1)\tilde{g}_{TR}(\boldsymbol{k})\exp(-i\omega t). \tag{7}$$

The space dependent functions $\tilde{g}_S(\boldsymbol{k})$ and $\tilde{g}_{TR}(\boldsymbol{k})$ of the spatial Fourier transforms of ϕ_S and ϕ_{TR} act as the shaping filter of the focus. They are independent of the source localization $\boldsymbol{R}_0$ and $\boldsymbol{R}_1$, respectively. Equation (7) confirms that the focal position in $\tilde{\phi}_{TR}(\boldsymbol{k},\boldsymbol{R}_1,t)$ is only present in the phase term $\exp(-i\boldsymbol{k}\cdot\boldsymbol{R}_1)$, while Eqs. (6) and (7) confirm that $\tilde{g}_S(\boldsymbol{k})$ and $\tilde{g}_{TR}(\boldsymbol{k})$ contain the near-field spatial information of $\tilde{\phi}_S(\boldsymbol{k},\boldsymbol{R}_0,t)$ and $\tilde{\phi}_{TR}(\boldsymbol{k},\boldsymbol{R}_1,t)$, respectively. With a TRM in the farfield, the localization phase $\exp(-i\boldsymbol{k}\cdot\boldsymbol{R}_1)$ is present in the spectrum for $k\leq k_0$, and also for $k>k_0$ when the TRM is in the nearfield. For a TRM at a distance in between these two regimes, the localization phase is present for all values of the wave number k, even if the corresponding amplitude of the spectrum is lower than what is obtained with the TRM in the nearfield of the probe source.

In essence, the idea of the NTR focus, based on analytic continuation, is to combine the phase component $\exp(-i\boldsymbol{k}\cdot\boldsymbol{R}_1)$ of the spatial Fourier transform of the time-reversed field $\phi_{TR}(\boldsymbol{R},\boldsymbol{R}_1,t)$ with the near-field shaping filter $\tilde{g}_S(\boldsymbol{k})$ of the generic analytic field $\phi_S(\boldsymbol{R},\boldsymbol{R}_0,t)$, to construct $\tilde{\phi}_{NTR}(\boldsymbol{k},\boldsymbol{R}_1,t)$, the spatial Fourier transform of the NTR field:

$$\tilde{\phi}_{NTR}(\boldsymbol{k},\boldsymbol{R}_1,t)=A_S\exp(-i\boldsymbol{k}\cdot\boldsymbol{R}_1)\tilde{g}_S(\boldsymbol{k})\exp(-i\omega t). \tag{8}$$

In physical space, the focus $\phi_{NTR}(\boldsymbol{R},\boldsymbol{R}_1,t)$ is then

$$\phi_{NTR}(\boldsymbol{R},\boldsymbol{R}_1,t)=A_S g_S(\boldsymbol{R},\boldsymbol{R}_1)\exp(-i\omega t). \tag{9}$$

The NTR field $\phi_{NTR}(\boldsymbol{R},\boldsymbol{R}_1,t)$ is constructed as follows when the localization phase is present for all k:

The phase for the position $\boldsymbol{R}_1$ of the focus from the TRM is obtained from $\tilde{\phi}_{TR}(\boldsymbol{k},\boldsymbol{R}_1,t)$:

$$\exp(-i\boldsymbol{k}\cdot\boldsymbol{R}_1)=\frac{\tilde{\phi}_{TR}(\boldsymbol{k},\boldsymbol{R}_1,t)}{|\tilde{\phi}_{TR}(\boldsymbol{k},\boldsymbol{R}_1,t)|}\exp(i\omega t). \tag{10}$$

The spatial resolution $\tilde{g}_S(\boldsymbol{k})$ of the point source in the nearfield is obtained from $\tilde{\phi}_S(\boldsymbol{k},\boldsymbol{R}_0,t)$, independently of the TRM and for *any* position $\boldsymbol{R}_0$:

$$\tilde{g}_S(\boldsymbol{k})=\frac{|\tilde{\phi}_S(\boldsymbol{k},\boldsymbol{R}_0,t)|}{A_s}. \tag{11}$$

In practice, by substituting Eqs. (10) and (11) in (8), the spatial Fourier transform of the NTR field $\tilde{\phi}_{NTR}(\boldsymbol{k},\boldsymbol{R}_1,t)$ is derived from $\tilde{\phi}_{TR}(\boldsymbol{k},\boldsymbol{R}_1,t)$ and $\tilde{\phi}_S(\boldsymbol{k},\boldsymbol{R}_0,t)$:

$$\tilde{\phi}_{NTR}(\boldsymbol{k},\boldsymbol{R}_1,t)=\frac{\tilde{\phi}_{TR}(\boldsymbol{k},\boldsymbol{R}_1,t)}{|\tilde{\phi}_{TR}(\boldsymbol{k},\boldsymbol{R}_1,t)|}|\tilde{\phi}_s(\boldsymbol{k},\boldsymbol{R}_0,t)|. \tag{12}$$

Hence, a high resolution focus is constructed from time reversal combined with components in the nearfield, with the latter actually representing any generic point source independent of the position of the original probe source. From a

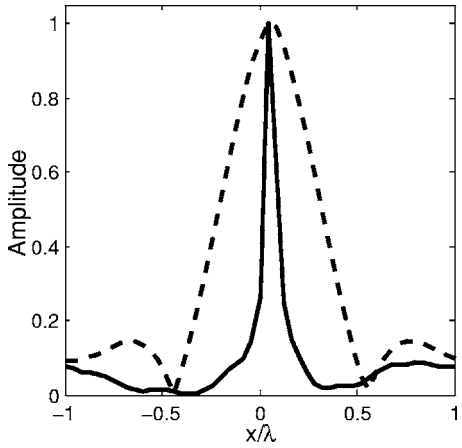

FIG. 1. Theoretical predictions for the normalized amplitude of the time-reversed field ϕ_{TR} from a TRM focusing at the center of the array (dark dashed line) and the resulting NTR ϕ_{NTR} (dark continuous line) obtained by combining ϕ_S with ϕ_{TR} following Eq. (12). The distance between the TRM and the probe source is $D=4\lambda$. The shaping filter $|g_s(\boldsymbol{R})| \approx \exp(-20k|\boldsymbol{R}|)$ was applied in this case. The different fields are generated within one wavelength and a $\lambda/25$ spatial sampling, for a 60-dB white noise relative to the maximum amplitude of ϕ_{TR}.

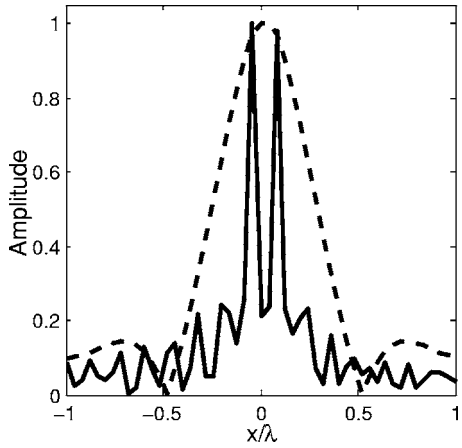

FIG. 2. Theoretical predictions for the normalized amplitude of the time-reversed field ϕ_{TR} from a TRM focusing simultaneously on two points separated by $\lambda/10$ (dark dashed line) and the resulting NTR ϕ_{NTR} (dark continuous line) obtained by combining ϕ_S with ϕ_{TR} following Eq. (12). The distance between the TRM and the probe source is $D=4\lambda$. The shaping filter $|g_s(\boldsymbol{R})| \approx \exp(-20k|\boldsymbol{R}|)$ was applied in this case. The different fields are generated within one wavelength and a $\lambda/25$ spatial sampling, with a 60-dB white noise relative to the maximum amplitude of ϕ_{TR}.

practical point of view, $|\tilde{\phi}_s(\boldsymbol{k},\boldsymbol{R}_0,t)|$ is obtained from $\tilde{\phi}_S(\boldsymbol{R},\boldsymbol{R}_0,t)$ with $|\boldsymbol{R}_0-\boldsymbol{R}|<\lambda$. Increasing the number of elements of the near-field array within one wavelength will increase the focal resolution. It also has to be noted that, due to noise and other experimental limitations, in practice the shaping filter may not be obtained from $\phi_S(\boldsymbol{R},\boldsymbol{R}_0,t)$, but generated numerically instead.

III. NUMERICAL SIMULATION

We first validate the NTR procedure using numerical computation, with added noise in anticipation of the experimental demonstration. The time-reversed field ϕ_{TR} is created on the near-field array using Eqs. (1)–(3), for either one source (Fig. 1) or two simultaneous sources separated by $\lambda/10$ (Fig. 2), with a TRM $D=4\lambda$ away from the probe source. The fields are generated within one wavelength with a $\lambda/25$ spatial sampling. A 60-dB white noise relative to the maximum amplitude is added for ϕ_{TR}. The NTR field ϕ_{NTR} is then obtained using Eq. (12) and a shaping filter defined with

$$|g_s(\boldsymbol{R})| \approx \exp(-20k|\boldsymbol{R}|). \tag{13}$$

Figure 1 shows the subwavelength focus for a single source. The spatial resolution of the focus corresponds to the one from the nearfield, with the position from the TRM. Figure 2 shows that each source is well separated from the other in ϕ_{NTR}, whereas that is not the case for the time-reversed field ϕ_{TR}. It has to be noted here that this result is not trivial since the operator in Eq. (12) is nonlinear with regard to the relative amplitudes; however, it is linear with regard to the phase of the superposition of the simultaneous sources.

IV. EXPERIMENTAL RESULTS

To confirm these results, an air acoustics experiment was conducted using loudspeakers and microphones between 100 and 200 Hz, as described in Figs. 3 and 4. For practical reasons, the experiment was done in a homogeneous free space medium. The TRM is composed of 24 speakers with a $\lambda/16$ spacing, corresponding to an aperture of $3\lambda/2$. The near-field array is composed of eight microphones with a $\lambda/47$ spacing. The arrays are linear and parallel to each other. The distance between the two arrays is $D=9$ m, corresponding to 4λ. The signal transmission and recording were done using a multichannel soundcard with a 40-dB signal-to-noise ratio. The impulse responses were recorded between each element of the TRM and each element of the near-field array. The time-reversed field ϕ_{TR} was generated from a digital time-reversal experiment by correlating the recorded im-

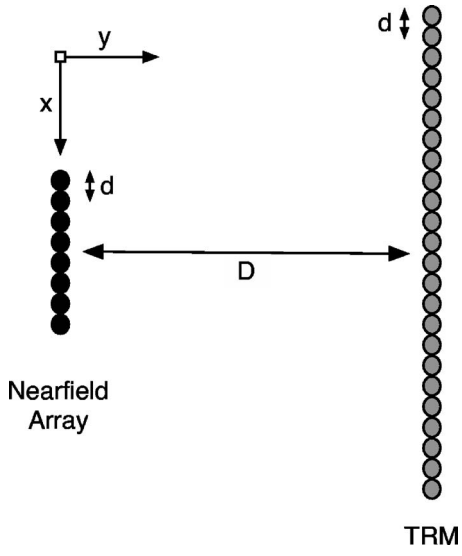

FIG. 3. Experimental setup used in the audible range from 100 to 200 Hz ($\lambda=2.3$ m, not to scale). The TRM (gray) consists in a linear array composed of 24 speakers with a $\lambda/16$ spacing. The near-field array (black) is a linear array composed of eight microphones with a $\lambda/47$ spacing. The distance between the two arrays is $D=9$ m, $D\approx 4\lambda$. The signal transmission and recording was done using a multichannel soundcard with a 40-dB signal-to-noise ratio.

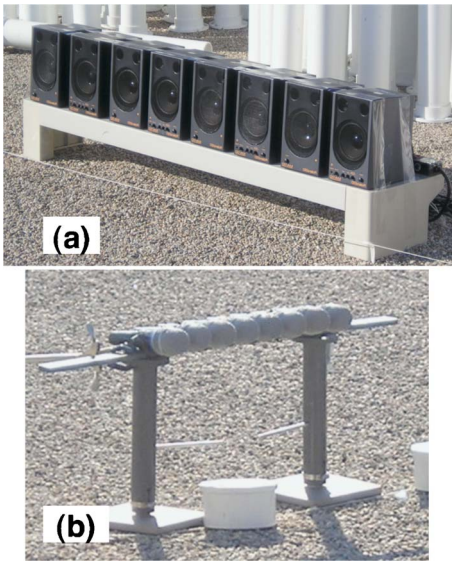

FIG. 4. (Color online) (a) Time-reversal mirror (TRM) composed of eight loudspeakers (Roland MA110). The 24-element TRM was obtained by moving the eight elements three times. (b) Near-field array composed of eight microphones (Shure PG57). Both arrays are connected to a Aardvark Direct Pro Q10 10 channels sound card and controlled by a PC computer.

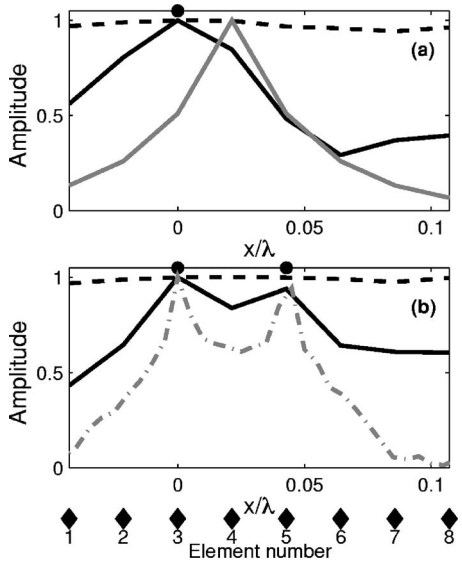

FIG. 5. (a) Experimental results in the audible range from 100 to 200 Hz ($f=150$ Hz, $c=350$ ms^{-1}, $\lambda=2.3$ m, $D\approx 4\lambda$) for the time-reversed field ϕ_{TR} (dark dashed line), the theoretically derived point source field $\phi_s(\boldsymbol{R},\boldsymbol{R}_4,t)$ (light continuous line), and the NTR field ϕ_{NTR} (dark continuous line) in the case of focusing on one element (dark point) of the near-field array. Subwavelength resolution of $\lambda/20$ to 50% down in amplitude is obtained. (b) Experimental results from 100 to 200 Hz ($\lambda=2.3$ m) for the time-reversed field ϕ_{TR} (dark dashed line) and NTR ϕ_{NTR} (dark continuous line) fields when two foci occur simultaneously on the elements 3 and 5 (dark points, $\lambda/23$ apart) of the eight-element near-field array. Also shown, the theoretical predictions for the NTR with two sources $\lambda/23$ distant for a 40-dB white noise and $\lambda/200$ spatial resolution of the array (light dash-dotted line).

pulse responses between all the elements of the TRM and the near-field array with the ones from the TRM to the desired focus.

To account for the experimental conditions, g_S was defined for this experiment with an exponential relative to the element 4 on the array instead of the theoretical target field from Eq. (1), using

$$|g_s(\boldsymbol{R},\boldsymbol{R}_4)| \approx \exp(-5k|\boldsymbol{R}-\boldsymbol{R}_4|), \tag{14}$$

where $k=2\pi f/c$, with $c=350$ m s^{-1} and $f=150$ Hz. The coefficient 5 in the exponential was chosen empirically for this experiment as a compromise between the main and side lobes of the resulting NTR focus. The time-reversed field ϕ_{TR} from the far-field TRM is recorded on the near-field array elements. The focus associated with ϕ_{TR} for a single focus under the experimental conditions corresponded to about $8\lambda/3$ at the 50% downpoints [Fig. 5(a)], corresponding to the size of the focus one might expect with a distance $D=4\lambda$ between the focus and a TRM with a $3\lambda/2$ aperture. Using the same 50% downpoints criterion, NTR achieves a $\lambda/20$ focus for a single focusing position [Fig. 5(a)]. This subwavelength focusing is of the same order as the ones reported for NAH[10,11] and smaller than that by de Rosny and Fink.[9] They obtained a $\lambda/14$ spatial resolution experimentally in a cavity, which was most likely limited by the timing and amplitude adjustments of the time-reversed source field they applied at the source to compensate the outgoing field.[9] Experimental results with a larger spacing for the near-field array showed that the NTR focus was broader. In the case of two foci occurring simultaneously on two elements (3 and 5) of the near-field array separated by one element (4) only, i.e., separated by $\lambda/23$, the improvement observed on each focus compares well to theoretical predictions [Fig. 5(b)]. This result is obtained without loss on the temporal resolution of each focus. A focus can be transmitted to different positions of the near-field array independently of the others, within the limitations of the experimental conditions.

V. CONCLUSION

In this paper, we demonstrated using theory and experiments that subwavelength focusing with time reversal is achieved without *a priori* knowledge on the original source and away from the nearfield of the probe source, as opposed to the acoustic sink procedure or NAH. This result is obtained by combining near-field and TRM components in the wave-number space following the NTR principles, within the limitation in range presented. Interestingly, the subwavelength focusing is obtained without loss of the temporal resolution. This technique is applied to an array with elements within a fraction of the wavelength from each other, using the knowledge of their relative positions only. Potentially, this technique can be used to enhance NAH imaging and increase the range between the NAH array and the sample to image. NTR also allows focusing different signals simultaneously on different elements within a fraction of a wavelength of each other, a goal very basic to construct multichannel communications techniques.

ACKNOWLEDGMENTS

The authors would like to acknowledge the valuable discussions with Mathias Fink.

[1]M. Fink, "Time reversed acoustics," Phys. Today **50**(3), 34–40 (1997).
[2]B. Y. Zel'dovitch, N. F. Pilipetsky, and V. V. Shkunov, in *Principles of Phase Conjugation* (Springer Verlag, Berlin, 1985).

[3]G. Lerosey, J. de Rosny, A. Tourin, A. Derode, G. Montaldo, and M. Fink, "Time reversal of electromagnetic waves," Phys. Rev. Lett. **92**, 193904 (2004).
[4]G. Lerosey, J. de Rosny, A. Tourin, A. Derode, G. Montaldo, and M. Fink, "Time reversal of electromagnetic waves and telecommunication," Radio Sci. **40**, RS6S12 (2005).
[5]D. Cassereau and M. Fink, "Time reversal of ultrasonic fields—Part I: Basic principles," IEEE Trans. Ultrason. Ferroelectr. Freq. Control **39**, 579 (1992).
[6]P. Blomgren, G. Papanicolaou, and H. Zhao, "Super-resolution in time-reversal," J. Acoust. Soc. Am. **111**, 230–248 (2002).
[7]D. R. Jackson and D. R. Dowling, "Phase conjugation in underwater acoustics," J. Acoust. Soc. Am. **89**, 171–181 (1991).
[8]A. Derode, P. Roux, and M. Fink, "Robust acoustic time reversal with high-order multiple scattering," Phys. Rev. Lett. **75**(23), 4206–4209 (1995).
[9]J. de Rosny and M. Fink, "Overcoming the diffraction limit in wave physics using a time-reversal mirror and a novel acoustic sink," Phys. Rev. Lett. **89**, 124301 (2002).
[10]E. G. Williams and J. D. Maynard, "Holographic imaging without the wavelength resolution limit," Phys. Rev. Lett. **45**(7), 554–557 (1980).
[11]J. D. Maynard, E. G. Williams, and Y. Lee, "Nearfield acoustic holography: I. Theory of generalized holography and the development of NAH,"J. Acoust. Soc. Am. **78**, 1395–1413 (1985).

Wideband ipsilateral measurements of middle-ear muscle reflex thresholds in children and adults[a)]

Kim S. Schairer,[b)] John C. Ellison, and Denis Fitzpatrick
Center for Hearing Research, Boys Town National Research Hospital, 555 N. 30th Street Omaha, Nebraska 68131

Douglas H. Keefe
Sonicom, Inc., 8105 Cedar St. Omaha, Nebraska 68124

(Received 22 September 2006; revised 11 March 2007; accepted 13 March 2007)

The goals of the current study were to: 1) evaluate the feasibility of a new wideband approach to measuring middle-ear muscle reflex (MEMR) status, and 2) to test the hypothesis that ipsilateral thresholds elicited with 1 or 2 kHz tones and broadband noise activators on a wideband acoustic transfer function (WATF) system are lower than thresholds elicited on a clinical system. Clinical MEMR tests have limitations, including the need for high activator levels to elicit a shift in a narrowband probe (e.g., a 0.226 or 1 kHz tone). Wideband MEMR tests using WATFs may elicit the reflex at lower levels because a wideband probe (click) is used and the threshold detection criterion can be wideband. Mean wideband MEMR thresholds across 40 normal-hearing adult ears were 2.2–4.0 dB lower than clinical MEMR thresholds, depending on the activator and specific WATF test used (admittance magnitude or energy reflectance). Wideband MEMR has potential clinical utility beyond the adult population, including use in newborn and preschool hearing screenings. In a newborn hearing screening, for example, wideband MEMR could be completed with the same system as otoacoustic emissions. However, further investigations in infants and young children are needed. © *2007 Acoustical Society of America.* [DOI: 10.1121/1.2722213]

PACS number(s): 43.64.Ha, 43.64.Yp, 43.64.Ri [BLM] Pages: 3607–3616

I. INTRODUCTION

The main goal of the current study was to compare standard clinical and wideband acoustic transfer function (WATF) measurements of the middle-ear muscle reflex (MEMR) to test the hypothesis that MEMR thresholds are lower in a prototype WATF procedure than the clinical procedure. The standard clinical MEMR test is described in this Introduction, followed by a description of a wideband MEMR test.

A. Clinical middle-ear muscle reflex test

When an intense sound is presented to the ear, and if the middle ear, cochlea, and neural afferent and efferent systems are functioning normally, the MEMR arc is stimulated (for a review, see Wiley and Fowler, 1997). The MEMR induces a contraction in the stapedius muscle in the middle ear, which then stiffens the middle-ear ossicular chain. This reduces the amount of energy that is absorbed or transferred into the cochlea. Because the ossicular chain is stiffened, the acoustic admittance measured in the ear canal at the tympanic membrane (TM) is also changed. At low frequencies such as 0.226 kHz, admittance is typically reduced by a MEMR, and the amount of energy that is reflected from the TM back through the ear canal is increased.

1. CMEMR test construction

A clinical middle-ear muscle reflex (CMEMR) test is performed after a tympanometry test (Wiley and Fowler, 1997). In a typical tympanometry test, a probe is placed in the ear canal to produce a hermetic (air-tight) seal, and a 0.226 kHz probe tone is continuously presented while pressure in the ear canal is varied. The pressure at which the acoustic admittance magnitude at the TM has its maximum is the tympanometric peak pressure (TPP). The probe stimulus of the CMEMR is usually the same probe tone used in the tympanometry test, namely, a 0.226 kHz tone. CMEMR measurements are typically made with the ear-canal pressure adjusted to the TPP in the ear receiving the probe stimulus, so that admittance is at its maximum at the probe frequency in the absence of the activator. A second stimulus, the activator, is used in the CMEMR test to elicit the MEMR, and the probe response is compared in the presence and absence of the activator.

Common activators are 0.5, 1, 2 and 4 kHz tones and broadband noise (BBN). In an ipsilateral MEMR test, the probe assembly is placed in the ear canal in which the reflex is to be measured and the activator is presented to the same ear. In a contralateral MEMR test, the probe assembly is placed in the ear canal in which the reflex is to be measured, and a sound source presents the activator in the contralateral

[a)]Portions of this work were presented in: Schairer, K. S., Ellison, J. C., Fitzpatrick, D., and Keefe, D. H., "Narrowband versus wideband measurements of middle ear muscle reflex thresholds." Presented at the American Auditory Society 2006 Scientific and Technology Meeting Program, Scottsdale, AZ.

[b)]Author to whom correspondence should be addressed. Electronic mail: kschairer@wisc.edu

ear. The MEMR threshold is defined as the lowest activator level that produces a criterion difference in the acoustic responses to the probe in the presence and absence of the activator. Another criterion is the growth of the MEMR shift in the admittance magnitude (at 0.226 kHz). That is, as the activator level increases the decrement in admittance should become larger. If not, the decrement may not be a true reflex, but perhaps a swallow or some other biological noise.

A CMEMR threshold test may be used to assist in the identification of sensorineural hearing loss, conductive hearing loss, 8th nerve tumors, or 7th nerve pathologies. In a CMEMR decay test, the activator is presented at a suprathreshold level, i.e., a level that is approximately 10 dB higher than the CMEMR threshold, and the change in the admittance magnitude at the probe frequency is assessed over activator durations of approximately 10 s. A CMEMR decay test may be used to detect acoustic neuromas. CMEMR tests may also be used as part of a screening protocol for preschool- and school-aged children (Silman *et al.*, 1992) and at-risk infants (Hirsch *et al.*, 1992). Silman *et al.* compared the sensitivity and specificity of TPP, static admittance, tympanometric width, and ipsilateral CMEMR at 1 kHz at 110 dB HL with a 0.226 kHz probe, alone and in different combinations for detecting middle-ear effusion. They found that the individual measure with the highest sensitivity and specificity was the CMEMR. Overall, they recommended a protocol in which a child is referred if the tympanometric width is greater than the 95th percentile of a normal group, the static admittance is lower than the 90% range, and the CMEMR is absent, OR if TPP is negative and CMEMR is absent. They further recommended that CMEMR should be tested first at 100 dB HL, and if absent, then test at 110 dB HL. Hirsch *et al.* used CMEMR and auditory brainstem response (ABR) to screen infants who were being discharged from an intensive care nursery. Ipsilateral CMEMR thresholds were obtained with a 0.8 kHz probe, and 2 kHz and narrowband noise activators. The authors selected a screening level (for pass/fail) of 90 dB sound pressure level (SPL) for the 2 kHz activator and 80 dB SPL for the narrowband noise. They found that the CMEMR screen identified the same ears that failed the ABR screen, and suggested that the CMEMR test could be used as a faster, cheaper first screen for a CMEMR/ABR protocol. Those who fail the CMEMR screen would then receive an ABR screen.

2. Limitations of CMEMR tests

These CMEMR tests are standard practice complete with associated normative data and a large body of literature regarding test sensitivity across a diverse body of disorders. However, several limitations still exist.

First, the measurement is restricted to a single probe frequency so that only the admittance changes at the probe frequency are evaluated. Because pathologies may not be uniformly evident at the same frequency in every ear, the 0.226 kHz probe tone used in clinical measurements may not be ideal across a diverse clinical population. Multifrequency tympanometry has been shown to provide improved sensitivity to some middle-ear pathologies (Hunter and Margolis, 1992; Li *et al.*, 1999; Margolis *et al.*, 1999). Normative data in comparison to the Vanhuyse *et al.* (1975) model are available for adults and children (e.g., Calandruccio *et al.*, 2006; Hunter and Margolis, 1992; Margolis and Goycoolea, 1993) and for infants and toddlers (e.g., Calandruccio *et al.*, 2006). Although these methods may increase the probability of detecting middle ear dysfunction, they require extra time to either sweep pressure at multiple probe frequencies or sweep probe frequency at multiple fixed pressures. Higher probe tone frequencies (such as 0.660, 0.8, or 1 kHz) have also been used for CMEMR measurements in infants (e.g., Hirsch *et al.*, 1992; Kankkunen and Liden, 1984; Sprague *et al.*, 1985; Weatherby and Bennett, 1980).

A method using a wideband probe stimulus may reduce test time and increase the probability of detecting dysfunction. This is because a response shift could be detected in a wide range of frequencies that are present simultaneously in the stimulus. For example, Feeney and Sanford (2005) measured thresholds in six-week-old infants and adults of the MEMR elicited by a contralateral BBN activator using wideband energy reflectance and admittance responses. They found that different frequency ranges in infants and adults improved detection of the MEMR. These results suggest that a single probe tone is insufficient to measure MEMR across all ages, and the authors suggested that this wideband technique could be used to track the best frequency for MEMR measurements during postnatal middle-ear development. However, an ipsilateral MEMR test appears preferable in young infants to a contralateral test, because it is simpler: the ipsilateral test is a single-ear test while the contralateral test requires simultaneous sound stimulation in both ears.

A second potential limitation is that CMEMR testing requires a hermetic seal and pressurization of the ear canal. Pressurization can displace the extremely compliant ear-canal walls of normal infants up to approximately two months of age (Holte *et al.*, 1990). Normal tympanograms can be obtained in ears diagnosed with otitis media with effusion (OME) in infants less than five months of age, with procedural limitations at younger ages possibly due in part to ear-canal wall movement (e.g., Schwartz and Schwartz, 1980). Hirsch *et al.* (1992) were able to elicit reflexes in most of their infants (who also passed the ABR screen). However, an ambient-pressure, i.e., nonpressurized, test of middle-ear status could potentially improve newborn hearing screening (NHS) outcomes (Feeney and Sanford, 2005; Keefe *et al.*, 2003b; Keefe *et al.*, 2003a; Keefe *et al.*, 2000) by avoiding the difficulties associated with pressurization. Such a MEMR test may also provide a means to identify newborns at risk for auditory neuropathy. Individuals with auditory neuropathy have present otoacoustic emissions (OAEs) and absent ABR and MEMR (Berlin *et al.*, 2005; Hood, 1999). A valid MEMR test might be used to screen for auditory neuropathy, inasmuch as it can provide evidence of retrocochlear dysfunction in a test that is faster and less costly than an ABR test.

A third limitation with current clinical immittance systems, especially in terms of application to NHS programs, is that the operator must determine whether a MEMR response is present. This may not be practical for NHS and other screening programs in which personnel without audiological

training perform the screenings. An objective method for determining the presence of a MEMR response would be of potential benefit to these programs.

A final, safety-related, limitation relates to the level of the activators required to elicit the MEMR for threshold, and especially, decay tests. Hunter *et al.* (1999) reported a case in which an acoustic reflex decay test at 1 kHz at 120 dB HL produced a temporary threshold shift above 1 kHz, and a permanent threshold shift at 1 kHz in both ears. They recommended a maximum activator level of 115 dB SPL, for this activator type, and expressed similar concerns for other activator types. With that criterion, MEMR decay tests would have been contraindicated in over half of their patients with acoustic neuromas because test levels would likely have had to exceed 115 dB SPL. Arriaga and Luxford (1993) reported a similar case in which a 120 dB HL, 2 kHz activator caused a permanent hearing loss in one ear of an older patient with preexisting sensorineural hearing loss. Arriaga and Luxford recommended limiting stimulus level to 105 dB HL in reflex decay measurements. Miller *et al.* (1984) reported another case in which an 84-year-old patient suffered from increased hearing impairment and temporary decrease in speech discrimination after acoustic reflex testing. The precise amount of pure-tone threshold and speech discrimination shift could not be determined because these tests were not performed prior to the reflex tests. The change in hearing was identified by patient report of sudden decrease in hearing during the reflex test and no measurable speech discrimination directly after the reflex tests. Serial testing over the next few months demonstrated a gradual improvement in speech discrimination. Even when the MEMR activator levels are within safe limits, they may be considered uncomfortable to many patients. Measuring MEMR thresholds at lower activator levels using a wideband rather than a single-frequency probe would also reduce the activator levels used in the MEMR decay test, and might make MEMR testing possible in those patients whose thresholds exceed clinical equipment (Feeney *et al.*, 2003; Feeney and Keefe, 1999).

B. Wideband middle-ear muscle reflex test

WATF tests include such measures as acoustic impedance, acoustic admittance, which is the inverse of acoustic impedance, and acoustic reflectance. In contrast to single-frequency tympanometry, these WATFs assess ear-canal and middle-ear functioning over a wider bandwidth, typically 0.25–8 kHz. The main rationale to construct a wideband test to measure the MEMR threshold (WMEMR) is that the threshold may be detected more easily using a wideband probe response than a single-frequency probe response. Moreover, the best frequency range to use for measuring MEMR thresholds in children may differ from that in adults and the wideband probe would allow for identification of the most sensitive frequency range in each ear, regardless of age. Finally, the WMEMR test may provide a better signal-to-noise ratio in comparison to the CMEMR test. In the version of the WMEMR test used in the current study, the response is averaged across three repetitions of the activator at each level. In contrast, the stimulus may be presented only once at each level in the CMEMR test, and it is not averaged even if presented more than once at a particular level.

A number of studies, which have discussed the above potential advantages of wideband MEMR measurements, have reported measurements of contralateral MEMR shifts in WATFs, with emphasis on shifts in energy reflectance and admittance magnitude in adults (Feeney *et al.*, 2003; Feeney and Keefe, 1999; Feeney and Keefe, 2001). MEMR-induced shifts in the acoustic power absorbed by the middle ear have also been used in these studies. Power measures are grouped with WATF measures inasmuch as acoustic power can be expressed as the product of the squared pressure and the wideband acoustic conductance, which is the real part of the admittance.

Objective rules have been developed to decide whether a particular MEMR shift differs significantly from zero or whether it is dominated by noise alone. Feeney and Keefe (2001) and Feeney *et al.* (2003) proposed the joint use of two objective tests, one based on the magnitude of the shift across the selected frequency range using an analysis of variance (ANOVA), and another based on the correlation of the MEMR shift across frequency to a suprathreshold MEMR shift measured at the highest activator level. A magnitude test is well suited to a threshold determination and is used in the present study. The correlation test is well suited to excluding a large shift due to an intermittent noise source with a spectrum different from that of a MEMR shift. However, a correlation test is not necessarily well suited to a WMEMR threshold measurement, because: (1) the MEMR shift measured at the highest activator level is assumed to be suprathreshold, but this may not be the case, and (2) the correlation test requires at least two activator levels to classify a WMEMR shift at a given level as present or absent, whereas the ANOVA test requires only one activator level. No correlation test was used in the present study.

An alternative approach to the measurement of the MEMR has been based on techniques used to measure OAE responses in combination with the known latency range of MEMR effects. Neumann *et al.* (1996) compared responses to two identical brief tone bursts that were separated in time by 110 ms. The ipsilateral MEMR, if elicited by the first tone burst, would affect the response to the second tone burst but not the first, so the difference in responses served as a measure of MEMR threshold. Müller-Wehlau *et al.* (2005) used an ipsilateral MEMR that was similar to that of Neumann *et al.* in comparing responses to two identical brief signals, but each of the signals used by Müller-Wehlau *et al.* was wideband (0.1–8 kHz) while the detection rule for the MEMR used the phase coherence between the first and second responses at a single frequency (near 1 kHz). Goodman and Keefe (2006) described a technique that combined a MEMR elicited with a BBN activator and a low frequency probe tone near 0.25 kHz, with a higher frequency tone (1.5–3.5 kHz) to elicit a stimulus frequency OAE (SFOAE). These studies have in common the measurement of an ipsilateral MEMR through the use of some change in the acoustic pressure response at a single frequency.

A system to measure ipsilateral MEMR shifts in WATFs was used to compare contralateral and ipsilateral MEMR

thresholds in 27 young adults (Feeney *et al.*, 2004). The ipsilateral test relied on the spectral separation between a probe signal, which was a bandpass filtered click (0.2–2 kHz), and a 4 kHz activator signal. The probe and activator signals were delivered simultaneously to the same ear, and the MEMR-induced shift in the WATFs (admittance magnitude and energy reflectance) was compared across the probe bandwidth by also measuring the WATFs in a probe-alone condition. A WMEMR shift was judged as present based on the joint use of a magnitude and correlation decision rule. They compared these ipsilateral WMEMR thresholds with contralateral WMEMR and CMEMR thresholds in the same subjects using a 4 kHz activator and a click probe. The WMEMR thresholds were measured using either an admittance or a reflectance wideband response. Of the 27 subjects tested, five subjects had no MEMR shift on any test and were excluded. Of the remaining 22 subjects, contralateral CMEMR thresholds were measured in 14 subjects, contralateral WMEMR thresholds were measured in 16–17 subjects (depending on WATF response type), and ipsilateral WMEMR thresholds were measured in 18–20 subjects (depending on WATF response type). The average contralateral WMEMR thresholds were 3 dB lower than the average contralateral CMEMR thresholds, but no comparison of ipsilateral WMEMR and CMEMR thresholds was reported. The requirement for spectral separation between probe and activator signals may constrain the accuracy of the measurement, and it certainly limits the choice of ipsilateral activators that can be used. It might be desirable to use a wideband activator signal such as BBN to elicit a MEMR shift in a wideband probe signal or it might be desirable to use a tonal activator whose frequency was within the bandwidth of the probe signal.

C. Goals of current study

The initial goal was to evaluate the feasibility of measuring the presence of ipsilateral MEMR using a wideband response and procedure that does not require separation of the probe and activator spectra. Second, ipsilateral WMEMR thresholds were measured and compared in groups of normal-hearing adults and children to ipsilateral CMEMR thresholds measured with a clinical system. These data were used to test the hypothesis that WMEMR thresholds are lower than CMEMR thresholds.

II. METHODS

A. Subjects

Two groups of subjects were consented to the study and tested at Boys Town National Research Hospital. The first group of 22 adults received an otoscopic evaluation and the following tests. Air and bone conduction thresholds were obtained on clinical Grason-Stadler audiometers calibrated to ANSI S3.6-2004 and using ER-3A insert earphones. Tympanometric tests were obtained on a Grason-Stadler GSI-33 or Tympstar calibrated to ANSI S3.39-1987, with a nominal 85 dB SPL, 0.226 kHz probe tone and a pressure range of +200 to −400 daPa. Ears with impacted cerumen or cerumen that precluded visualization of the TM upon otoscopy were excluded. Other inclusion criteria included: (1) air-conduction thresholds $<=15$ dB HL at octave frequencies from 0.5 to 8 kHz, bilaterally, (2) air-bone gaps $<=15$ dB, and (3) 0.226 kHz tympanometry tests in the range 0.2–1.8 mmho for peak-compensated static admittance and −150 to 100 daPa for TPP. These tympanometry ranges were slightly wider than the Margolis and Heller (1987) normative data because subjects who were otherwise otologically normal would have been excluded. Forty ears of 21 participants were included in analysis in the adult group. These participants ranged in age from 18 to 36 years (mean=27.2, standard deviation (SD)=5.9; 15 females, six males).

Sixteen children were recruited for the second group. The inclusion criteria were the same, except that audiometric thresholds were obtained using conventional audiometry (i.e., hand raises) for six children and conditioned play audiometry for eight children. For all subjects meeting the inclusion criteria, data were obtained from one ear of six children and both ears of eight children. They ranged in age from 30 to 82 months of age (mean=57 months, SD=15 months; eight females, six males), or 2.5 to 6.8 years. Twenty-one ears were included in analyses of the child group.

Each session lasted approximately 1–1.5 h for the adults and older children, with longer session devoted to younger children. All audiometric and experimental tests were completed within one session.

B. CMEMR procedures

CMEMR thresholds were obtained at the same time the tympanogram was obtained. The probe tone was the same as for the tympanometry tests, and it was on continuously throughout testing. Activators were 1 and 2 kHz tones, and BBN (0.125–4 kHz, Grason-Stadler, 2005, p. A-4), and the duration of each activator was 1.5 s (Grason-Stadler, 2005, pp. 4–31). The initial activator level was at a moderate level, for example, typically 95 dB HL for tonal activators. A CMEMR response was defined as a decrease in admittance magnitude of at least 0.02 mmho that was time locked to the stimulus (to avoid identifying swallows, movements, etc., as related to a MEMR). Although in clinical practice audiologists may use an admittance change of 0.02 mmho as the criterion for presence of an acoustic reflex (e.g., Gelfand, 2001; Silman and Silverman, 1991), that value is essentially arbitrary. The 0.02 mmho criterion was used in the current study to avoid defining threshold with questionable responses of 0.01 mmho, and to avoid higher thresholds that would have resulted if a larger magnitude criterion was used. The activator level was decreased in 5 or 10 dB steps until the response was <0.02 mmho. If a response was not produced with the initial activator level, the activator level was increased until a response of 0.02 mmho was obtained. An additional criteria for threshold was the observation of response growth, that is, the response using activator levels below the maximum level had to increase at a higher level (e.g., from 0.02 mmho at 85 dB to 0.04 mmho at 90 dB). The CMEMR threshold was the lowest activator level at which a MEMR response was observed.

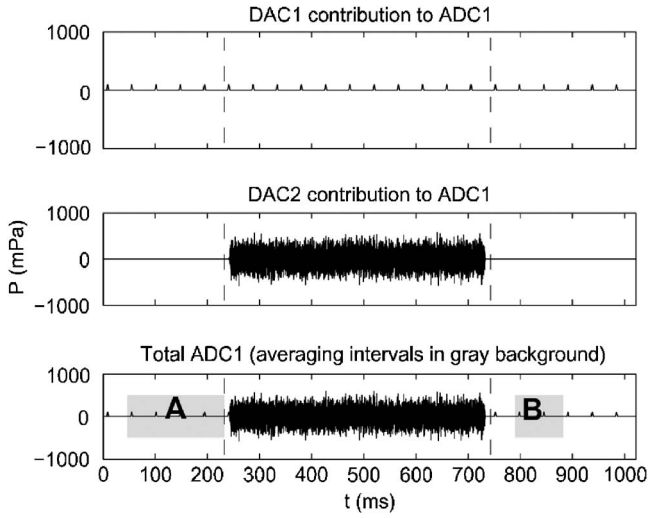

FIG. 1. An example of the stimulus input to each receiver and the response recorded by the microphone for the WMEMR procedure. The probe clicks are presented to Receiver 1 from digital-to-analog converter (DAC) 1 (top row), the activator (broadband noise is shown) is simultaneously presented to Receiver 2 through DAC 2 (middle row), and the entire buffer is recorded by the microphone (bottom row). To extract the WMEMR response, the energy in the ear canal that is present during the four probe clicks that precede the activator (shaded area A) is averaged and compared to the energy in the ear canal during the presentation of the probe clicks after the offset of the activator (shaded area B).

C. Wideband testing

1. WATF procedures

The WATF measurement system was calibrated daily according to procedures described elsewhere (Keefe and Abdala, 2007; Keefe and Simmons, 2003). The system software ran on a computer within the Windows operating system, and the computer included a high quality sound card (CardDeluxe), which delivered and recorded signals using a sample rate of 22.05 kHz. The probe assembly was an Etymotic model ER10C, which was modified by Etymotic to allow 20 dB higher output levels from the receivers. This modification was required in order to output the activator at a level sufficient to elicit a MEMR in most normal-functioning ears (as described below). The level of the click probe was 61 dB sound pressure level based on the peak-to-peak amplitude.

2. WMEMR procedures

Each WMEMR buffer was chosen to have an approximately 1 s duration, such that the activator was on for half of this duration and off for the remainder. The activator duration of approximately 0.5 s was sufficient to elicit a MEMR response, and the silent (i.e., activator-absent) duration of approximately 0.5 s was assumed to be sufficient for the MEMR response, if present, to decay back to the base line condition. The WMEMR test was based on the difference in the WATF responses measured in a base line condition, prior to the presentation of the MEMR activator, and in a postactivator condition, just after the presentation of the MEMR activator.

The response buffer of the WMEMR test is illustrated in Fig. 1, which shows the base line, activator, and postactivator sections of the mean response buffer. This response buffer consisted of the responses to 22 clicks, with each click interval containing 1024 samples and comprising a WATF response buffer. The probe stimulus (22 clicks over the 1.02 second buffer) was presented to Receiver 1 through the digital-to-analog converter (DAC) 1 of the sound card as shown in the top row. The activator stimulus, either a pure tone or a BBN (BBN is shown), was presented to Receiver 2 through DAC 2 over the same time period as DAC 1, as shown in the middle row. This set was repeated three times and averaged.

The microphone response to one presentation of the WMEMR buffer at a fixed attenuation level was recorded using the analog-to-digital converter (ADC) of the sound card, and is illustrated in the bottom row of Fig. 1. To extract the WMEMR response, the four probe clicks preceding the activator (shaded area A) were averaged to form a base line click response. Two probe clicks presented after the end of the activator (shaded area B) were averaged to form a postactivator click response. The probe click that occurred directly after the offset of the activator was not included in the postactivator response because its 46.4 ms duration includes effects of any OAEs generated in response to the activator. Because the cochlear delay times associated with OAEs are short compared to 46.4 ms, it was assumed that all OAE energy was attenuated by the time of the postactivator buffers shown in shaded area B. Nevertheless, any OAE generated in response to the click stimulus in the mean base line and postactivator responses would be cancelled in the subtraction process. Any such OAE amplitudes were also much smaller than the amplitude of the middle-ear response. The 92.9 ms duration of the pair of postactivator responses was relatively short compared to the offset latency of the MEMR so that both click responses could be averaged in the postactivator response in order to improve the signal to noise of any MEMR shift.

All measurements were completed at ambient pressure, i.e., without pressurization in the ear canal. Activators were the same as for the CMEMR tests, and were gated on and off with 5 ms ramps. The activators were presented at five levels from 16 dB down from the maximum output of the system, and in 4 dB increments up to the maximum output.

Because the GSI middle ear analyzer reports reflex thresholds in dB HL, which is defined in terms of reference equivalent threshold SPLs according to ANSI S3.39 (1987), it was necessary to calibrate the activators used in the WMEMR measurement in dB HL. This required determining the sound card attenuation on the DAC for each tonal and BBN activator signal that produced the same SPL in a reference 2 cm^3 coupler (i.e., the HA-1 coupler in ANSI S3.6-2004). This was calibrated to the activator level produced in the coupler when output by the GSI-33 at a particular dB HL. These SPLs in the 2 cm^3 coupler were measured using a sound level meter (Bruel and Kjaer Type 2231) with an octave filter set (Bruel and Kjaer Type 1625) for tonal activators.

One difference between the CMEMR and WMEMR systems was that the maximum HL available on the WMEMR system was less than that of the CMEMR system. This was due to the fact that the Etymotic ER10C probe, which was

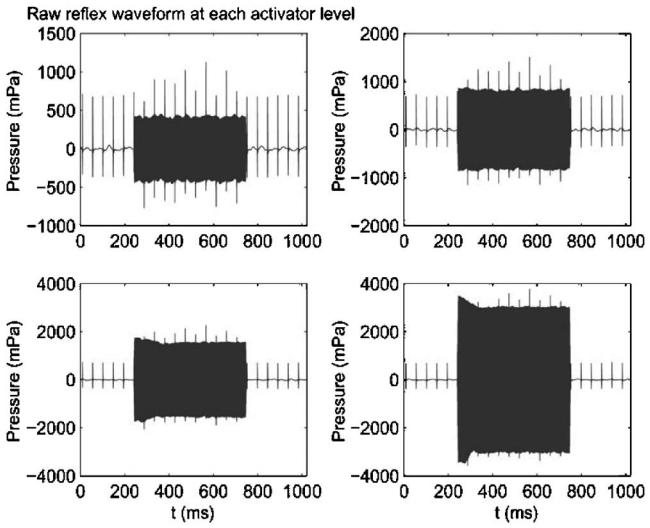

FIG. 2. Wave form responses in a normal-hearing human ear in response to a 1 kHz activator at four different activator levels. The vertical axis scale differs across panels to accommodate the level of the activator. The probe clicks are fixed in level as the activator level increases from left to right, top to bottom.

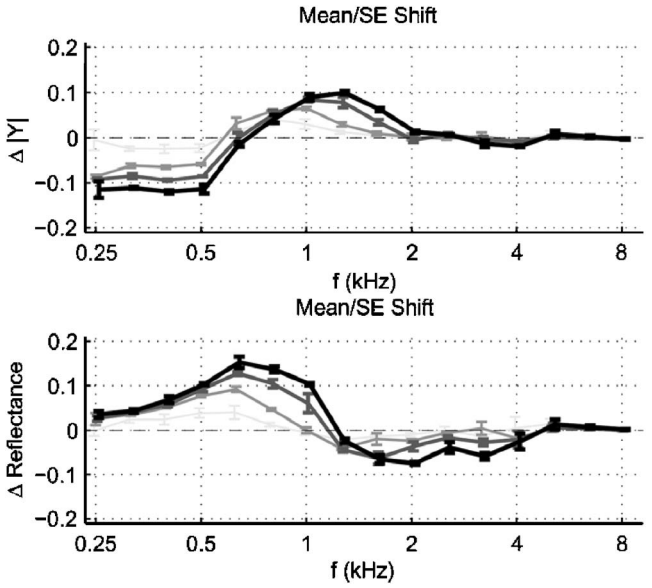

FIG. 3. Example of WMEMR shift spectra (1/3 octave averages) for admittance (top row) and reflectance (bottom row) in a normal-hearing human ear in response to a 1 kHz activator at different levels (from a maximum of 90 dB in 4 dB descending steps represented by lighter and thinner lines). Error bars represent the standard error of the mean WMEMR shift across three repetitions of the activator.

used in the WMEMR system, was not designed to produce the high activator levels typical of CMEMR instruments conforming to ANSI S3.39 (1987).

Adults were tested in the laboratory. The children were tested either in the laboratory or in the audiology clinic where their hearing was tested. All subjects were awake and sitting quietly during the testing. For each subject, there were three activators, five levels for each activator in the adult group and seven activator levels in the child group, and three repetitions at each level. The test duration was typically 1 min per ear, occasionally 2 min, and 4 min for one child.

III. RESULTS

Wave form responses of a WMEMR test in a normal-hearing human ear, which were recorded using a 1 kHz activator at four different activator levels, are shown in Fig. 2. The vertical range of pressures was increased in panels with increased activator levels. The clicks were presented at the same level in each panel. The activation of the MEMR in this ear is evident with the two highest activator levels (see bottom two panels) as a rapid decline in the activator response after its onset. This large of a shift was not always observed, but when it was observed, it was most often seen with the 1 kHz activator.

WMEMR effects were assessed in the frequency domain using the shift in a WATF in the postactivator condition relative to the base line condition. Based on the acoustic admittance magnitude $|Y_b|$ at the probe tip in the base line condition and $|Y_p|$ in the postactivator condition, the relative admittance magnitude shift ΔY was defined as

$$\Delta Y = \frac{(|Y_p| - |Y_b|)}{|Y_b|}. \quad (1)$$

Based on the acoustic energy reflectance R_b in the base line condition and R_p in the postactivator condition, the relative energy reflectance shift ΔR was defined as

$$\Delta R = \frac{(R_p - R_b)}{R_b}. \quad (2)$$

Each of ΔY and ΔR is a dimensionless relative shift.

Figure 3 shows WMEMR shifts in a normal-hearing human ear in response to a 1 kHz activator from the current data set. The mean shifts and the standard error (SE) of the mean shifts, which were based on the three repetitions of the WMEMR stimulus set, are plotted as third-octave averaged spectra. The ΔY shown in the top row is the wideband analog to a CMEMR measurement, which typically shows the difference in admittance magnitude between a postactivator relative to a base line condition. The difference is in spectral content, inasmuch as the CMEMR difference is measured at a single probe frequency, whereas the WMEMR shift is measured over a range of 0.25–8 kHz. The ΔY in Fig. 3 was negative at low frequencies, consistent with an increased middle-ear stiffness due to the MEMR, and increased in magnitude with increasing activator level to approximately −0.12, i.e., the MEMR reduced the admittance magnitude by as much as 12%. The ΔY was close to zero in this ear near the third octave at 0.63 kHz, and the zero-crossing frequency increased slightly with increasing activator level. The ΔY was positive at higher frequencies, with a maximum shift that occurred at a higher frequency at higher activator levels (this third-octave frequency ranged from approximately 0.79 to 1.26 kHz). The ΔY above the positive peak frequency decreased with increasing frequency towards zero values, and was close to zero by 2 kHz (except that the ΔY at the highest activator level differed slightly from zero at 2.5 and 4 kHz).

The ΔR for this ear, which is plotted in the bottom panel of Fig. 3, was positive at low frequencies and increased with increasing frequency up to a peak near 0.63 kHz that did not vary with activator level. This means that the energy reflec-

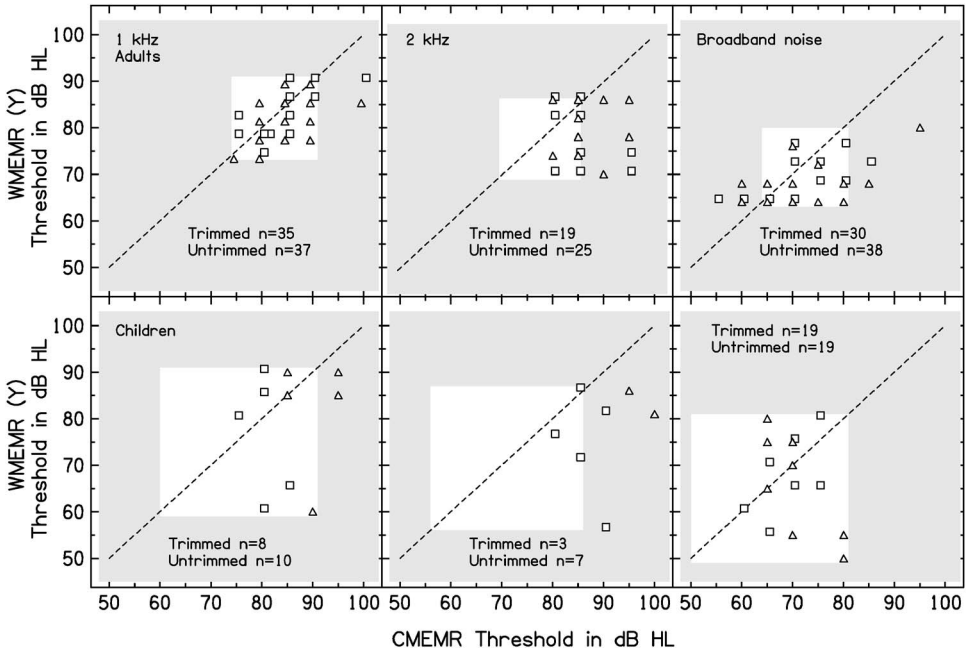

FIG. 4. Ipsilateral MEMR thresholds estimated using CMEMR and WMEMR tests in normal-hearing adult ears on the top row and children on the bottom row, with a 1 kHz activator (left panel), 2 kHz activator (middle panel), and BBN activator (right panel). Thresholds plotted within the boundary of the white square were part of the "trimmed" data set. The number of test ears *n* with thresholds in this trimmed range and the total *n* are shown for each activator type. Left-ear thresholds are plotted using squares, and right-ear thresholds using triangles, with symbols slightly offset to make right and left symbols visible (but some same-ear symbols overlap).

tance was increased by the MEMR at low frequencies relative to the base line condition. A zero-crossing frequency for ΔR increased from 1.0 to 1.26 kHz with increasing activator level. At higher frequencies the ΔR was negative and of reduced magnitude compared to lower frequencies, and ΔR approached zero with increasing frequency. The ΔR did not converge to zero until 5 kHz.

A WMEMR shift, whether ΔY or ΔR, was classified as significantly different from zero based on an one-way analysis of variance (ANOVA) performed over a range of eight third-octave frequencies from 0.32 to 2 kHz. These were selected because the WMEMR shifts were small in magnitude above 2 kHz (as shown in Fig. 3), and the lowest frequency bin at 0.25 kHz was sometimes contaminated by noise (not shown in Fig. 3). With three repetitions of the WMEMR response buffer and eight frequencies, the number of degrees of freedom was 16. The shift was classified as significant if the ANOVA output had a $p < 0.05$. In Fig. 3, the WMEMR shift spectra were plotted only for activator levels for which the shift was significant.

Thresholds were defined as the lowest level producing a significant ANOVA test. If this threshold was less than the maximum activator level, an additional stipulation was that the WMEMR shift had to be significant at a higher activator level. The purpose of that rule was to exclude a case, for example, in which only the lowest level produced a significant ANOVA result, so that the apparent significant result was likely due to artifact or noise rather than a MEMR effect. For each activator type, it was verified that the highest activator level did not produce a significant shift in an IEC 711 ear simulator (i.e., the highest activator level did not produce a "response" in a coupler). A preliminary analysis showed that the mean WMEMR thresholds estimated using ΔY were slightly lower in the adult group than those estimated using ΔR. For this reason, the focus is on WMEMR thresholds in adults and children that were estimated based on shifts in ΔY.

To compare WMEMR and CMEMR thresholds across the same range, the data sets were trimmed to adjust for differences in test procedures and hardware limitations. The WMEMR system had a limited range of activator levels and thus a limited range of WMEMR thresholds. Its upper limit was imposed by the maximum output of the ER10C receiver and the lower limit by the lowest activator level selected in the protocol prior to data collection. Clinical reflex thresholds were limited to the same range of thresholds as that on the WMEMR system. For adults, in the 1 kHz activator condition, the range was 74–90 dB HL in 35 ears trimmed from 37 ears (i.e., two of the 37 ears did not have a threshold in the range 74–90 dB HL), for the 2 kHz activator it was 70–86 dB HL in 19 ears trimmed from 25 ears, and for the BBN activator it was 64–80 dB HL in 30 ears trimmed from 38 ears. Thus, thresholds were measured in fewer ears using the 2 kHz activator compared to the other activators.

The WMEMR and CMEMR thresholds for adults (see top row of Fig. 4) were similar for right and left ears (triangles and squares, respectively). For the 1 kHz activator, the WMEMR mean (81.3 dB, standard error of the mean SE=0.81 dB) was 2.2 dB lower than the CMEMR mean (83.6 dB, SE=0.78 dB). For the 2 kHz activator, the WMEMR mean (79.6 dB, SE=1.37 dB) was 3.8 dB lower than the CMEMR mean (83.4 dB, SE=0.55 dB). For the BBN activator, the WMEMR mean (67.3 dB, SE=0.77 dB) was 4.0 dB lower than the CMEMR mean (71.3 dB, SE =0.96 dB). Each of these differences in mean thresholds was significant according to a dependent sample *t* test (see Table I). Across the three activator types, the WMEMR thresholds were 3.4 dB lower than CMEMR thresholds. The trimming action eliminated CMEMR thresholds higher than the maximum output of the WMEMR device. Larger differences up to 9.4 dB between CMEMR and WMEMR were observed in the untrimmed data set. Based on the full untrimmed set of measured thresholds and across all three activator types, the WMEMR thresholds were significantly lower by 5.5 dB than

TABLE I. Comparison between CMEMR and WMEMR thresholds for each activator.

	t	Df	Sig (2-tailed)
Adults, 1 kHz	2.82	34	0.01
Adults, 2 kHz	2.45	18	0.03
Adults, BBN	4.23	29	0.00
Children, 1 kHz	1.05	7	0.33
Children, 2 kHz	1.29	2	0.33
Children, BBN	0.97	18	0.35
Comparison of thresholds between children and adults			
CMEMR, 1 kHz	0.76	10	0.47
WMEMR, 1 kHz	0.99	7	0.35
CMEMR 2 kHz	0.05	2	0.96
WMEMR, 2 kHz	0.39	2	0.73
CMEMR, BBN	1.18	37	0.25
WMEMR, BBN	0.21	22	0.84

the CMEMR thresholds. The WMEMR thresholds based on ΔR were also lower than CMEMR thresholds for all activator types in the trimmed data sets, and for tonal activators, but not the BBN activator, in the untrimmed data set.

Some subjects had significant WMEMR shifts present at the lowest activator level in the protocol, particularly in the broadband noise activator condition in adults (see the bottom horizontal boundary of the white background region in Fig. 4). It is likely that some of these ears had WMEMR thresholds lower than the minimum activator level in the protocol.

Threshold estimates were repeated in five adults. The absolute value of the difference between runs 1 and 2 was calculated, averaged across ear, and then across subject. This value was 5.6, 3.3, and 4.8 dB for the WMEMR thresholds elicited with 1 kHz, 2 kHz, and BBN activators, respectively. For the CMEMR thresholds, the average difference was 3.0, 2.5, and 5.0 dB. Data were collapsed across ear and subject, and the correlation between CMEMR thresholds from the first and second runs were 0.56, 0.35, and 0.54 for 1 kHz, 2 kHz, and BBN activators. Correlations for WMEMR thresholds were 0.16, 0.78, and −0.08 for the same activators. The poor correlations could be the result of comparing data points within in a limited range, particularly in the WMEMR case in which a lower limit was artificially imposed. Thus, a comparison between the measures of reliability based on correlations should be interpreted with caution.

The group of children was tested after the adults. Because the range of activator levels was inadequate in the adult WMEMR protocol, the range of levels in the child WMEMR protocol was broadened to include lower levels. The step size was 5 dB. The data sets of the groups of children were trimmed to a common range of thresholds as for adults. For children, in the 1 kHz activator condition, the resulting range of WMEMR thresholds was 60–90 dB HL in eight ears trimmed from ten ears, for the 2 kHz activator it was 56 to 86 dB HL in three ears trimmed from seven ears, and for the BBN activator it was 50–80 dB HL in 19 ears with no ears trimmed.

The WMEMR and CMEMR thresholds for the child groups of ears (see the bottom row of Fig. 4) were similar for right and left ears, so results were averaged across ears. For the 1 kHz activator, the WMEMR mean (76.9 dB, SE =4.6 dB) was 5.6 dB lower than the CMEMR mean (82.5 dB, SE=1.6 dB). For the 2 kHz activator, the WMEMR mean (77.7 dB, SE=4.4 dB) was 5.6 dB lower than the CMEMR mean (83.3 dB, SE=1.7 dB). For the BBN activator, the WMEMR mean (66.8 dB, SE=2.2 dB) was 2.7 dB lower than the CMEMR mean (69.5 dB, SE =1.3 dB). Based on the small number of ears and large SE for the tonal activators, none of these threshold differences were significant in children for any activator (see Table I). The results in Table I for children were interpretable only for the BBN case, as the degrees of freedom (df) were too few for the tonal activator cases. Across all activator types, the WMEMR thresholds were 4.6 dB lower than CMEMR thresholds. Based on the full untrimmed set of measured thresholds and across all three activator types, the WMEMR thresholds were 7.6 dB lower than CMEMR thresholds. However, the restricted number of ears and larger variability in testing children than adults limits the practical assessment of whether these differences in thresholds across activator type were significant.

The WMEMR thresholds of adult and child groups were compared across activator type and trimmed and untrimmed groups using a *t* test. The CMEMR thresholds were also compared across activator type and groups using *t* tests. Adult and child thresholds were not significantly different for any condition (see Table I). Again, the results were judged to be interpretable only for df of 10 or more. Nevertheless, the trend in each condition was that WMEMR thresholds were lower than CMEMR thresholds. For the trimmed groups including the WMEMR ΔY test, the mean thresholds in children were lower than those in adults by 1.0 dB for the CMEMR test and 2.3 dB for the WMEMR test. The relatively large 4 dB step size used in the activator levels in the WMEMR test for adults and 5 dB step size in the WMEMR for children and the CMEMR test for all subjects would have constrained the ability to detect any age-related differences on the order of a couple dB in MEMR thresholds.

IV. DISCUSSION

The general patterns in the ΔY and ΔR spectra of ipsilateral WMEMR shifts are similar to previous reports of contralateral WMEMR reflex shifts (Feeney *et al.*, 2003; Feeney and Keefe, 1999; Feeney and Keefe, 2001) and ipsilateral WMEMR (Feeney *et al.*, 2004). In particular, the finding that the zero-crossing frequency in ΔR is higher than that in ΔY (see Fig. 3) was explained by Feeney and Keefe (1999) as an effect in which the zero-crossing frequency of ΔY is reduced by the compliance of the ear-canal volume between the probe and the TM. Because energy reflectance is insensitive to probe location in the ear canal, the zero-crossing frequency in ΔR is independent of the probe location in the ear canal. The zero-crossing frequency in ΔR relates solely to a MEMR change in middle-ear functioning, but the zero-crossing frequency in ΔY depends also on probe location.

The ipsilateral WMEMR shifts in children had a generally similar spectral shape to shifts in adults. In the untrimmed child groups, the BBN activator elicited a WMEMR shift (ΔY) in 19 of 22 ears, the 1 kHz activator in ten of 22 ears, and the 2 kHz activator in seven of 22 ears. Thus, the BBN activator was more successful in eliciting a WMEMR than the tonal activators. In the untrimmed adult groups, the BBN activator was able to elicit a WMEMR (ΔY) shift in 38 of 40 ears, the 1 kHz activator in 37 of 40 ears, and the 2 kHz activator in 25 of 40 ears. The 2 kHz activator was the weakest activator in both CMEMR and WMEMR testing. The 1 kHz activator was much more likely to elicit a WMEMR response in adults than children, while the BBN activator was approximately equally likely to elicit a WMEMR shift in adults and children (the same pattern was evident in the untrimmed data sets). It is unclear why this is the case, but possibly due to increased noise levels in children for measurements with the 1 kHz activator. The finding that the BBN activator was more successful in eliciting a WMEMR than either of the tonal activators in children suggests a potential advantage to using the BBN activator in reflex screening of even younger children, such as in a NHS program.

The mean ipsilateral WMEMR thresholds in children were not significantly different from the mean CMEMR thresholds for any activator type. However, only the trimmed ΔY data obtained with the BBN activator had a sufficient number of responses (19 ears). As stated previously, the BBN activator may be more appropriate for a preschool screen because it is more likely to elicit a response than the pure-tone activators, and because the response has a larger dynamic range (the size of which cannot be completely estimated here due to the lower level limit imposed). A much larger sample of children would be needed to further investigate that hypothesis, however. The lack of a significant difference in the child group contrasts with the lower WMEMR thresholds in the adult group, which, in any case, contained more responses (30 ears). It is possible that this test outcome relates to some combination of a difference in MEMR functioning in children and adults, a limitation in the WMEMR procedures, increased noise in the child responses, and an insufficient number of ears tested. The threshold determination technique was imprecise. A fixed step size of 4 or 5 dB was used, and there was insufficient control of false positives and false negatives, as the terms are used in signal detection theory.

The mean ipsilateral WMEMR thresholds in adults were 2.3–4 dB lower than the mean ipsilateral CMEMR thresholds depending on activator type. The WMEMR threshold averaged across all activator types was 3.4 dB lower than the average CMEMR threshold. There appear to be no other reports of ipsilateral WMEMR and CMEMR thresholds with which to compare these measurements. The ipsilateral threshold differences in the present study are smaller than the contralateral threshold differences reported by Feeney *et al.* (2003) and Feeney and Keefe (1999), and similar to contralateral threshold differences reported by Feeney *et al.* (2004). Feeney *et al.* (2003) reported that, compared to clinical thresholds, the contralateral WMEMR reflectance thresholds were 13.7 dB lower when using a 1 kHz activator and 12 dB lower when using a 2 kHz activator. Feeney and Keefe (1999) elicited contralateral WMEMRs with the 40-ms chirp probe in the right ear and activators of 1 and 2 kHz in the left ears of three normal-hearing adults. They found that WMEMR thresholds were at least 8 dB lower than CMEMR thresholds, and that WMEMRs were produced at the lowest activator levels for all subjects except for one subject test using a 2 kHz activator. Feeney *et al.* (2004) reported that contralateral WMEMR thresholds were approximately 3 dB lower than CMEMR thresholds, which is within the range of differences observed in the present study of ipsilateral thresholds.

The differences across studies may relate to differences in contralateral and ipsilateral MEMR functioning as detected in the WMEMR and CMEMR test procedures, and may also be due to the differences in analysis bandwidth, and the decision rule used to determine the presence of the reflex. The possibility of erroneously defining artifact as a MEMR threshold should be examined. For example, in the current study, responses that occurred at low levels, but not at any higher levels, were counted as no response. However, instances in which a WMEMR effect was observed at both a lower activator level and at least one higher level were assigned the threshold at the lower activator level. In some instances, responses to mid-level stimuli were nonsignificant, but responses to higher and lower stimuli were significant. The probability of triggering a stapedius muscle contraction increases with increasing activator level, so that the same activator level may trigger a MEMR on one trial but not another. It may be useful in future studies to incorporate an adaptive rule to increase or decrease the activator level based on the previous set of WMEMR responses. An automated MEMR test that incorporates signal averaging and adaptive procedures could improve reliability in a clinical setting.

V. CONCLUSIONS

The results demonstrated the feasibility of measuring ipsilateral WMEMR thresholds and suprathreshold shifts using a procedure that compares WATF responses before and after the presentation of an activator signal to elicit the MEMR,

based on tonal activators at 1 and 2 kHz and a broadband noise activator. The MEMR thresholds measured ipsilaterally with the wideband system were lower than those measured clinically in adults for all activator types. The ipsilateral MEMR thresholds measured in children's ears using the wideband and clinical tests did not differ when using the broadband noise activator; no valid statistical comparisons were possible with tonal activators due to an insufficient number of test ears. A WMEMR test may avoid temporary or permanent threshold shift and discomfort that may be associated with the high stimulus levels that are often necessary for clinical MEMR threshold and decay tests. Further studies with larger samples of children with normal hearing and middle ear function are necessary to fully characterize the response and its predictive ability. Potential uses for the WMEMR include a combined OAE/WMEMR newborn and preschool screen for cochlear and retrocochlear function. In particular, the broadband noise activator may have a larger dynamic range that includes much lower levels than the pure-tone activators.

ACKNOWLEDGMENTS

Research was supported by NIH Grants Nos. DC006607 and DC04662.

American National Standards Institute (**1987**). "Specifications for instruments to measure aural acoustic impedance and admittance," S3.39 (ANSI, New York).

American National Standards Institute (**2004**). "Specifications for audiometers," S3.6-2004 (ANSI, New York).

Arriaga, M. A., and Luxford, W. M. (**1993**). "Impedance audiometry and iatrogenic hearing loss," Otolaryngol.-Head Neck Surg. **108**, 70–72.

Berlin, C. I., Hood, L. J., Morlet, T., Wilensky, D., St, J. P., Montgomery, E., and Thibodaux, M. (**2005**). "Absent or elevated middle ear muscle reflexes in the presence of normal otoacoustic emissions: A universal finding in 136 cases of auditory neuropathy/dys-synchrony," J. Am. Acad. Audiol **16**, 546–553.

Calandruccio, L., Fitzgerald, T. S., and Prieve, B. A. (**2006**). "Normative multifrequency tympanometry in infants and toddlers," J. Am. Acad. Audiol **17**, 470–480.

Feeney, M. P., and Keefe, D. H. (**1999**). "Acoustic reflex detection using wide-band acoustic reflectance, admittance, and power measurements," J. Speech Lang. Hear. Res. **42**, 1029–1041.

Feeney, M. P., and Keefe, D. H. (**2001**). "Estimating the acoustic reflex threshold from wideband measures of reflectance, admittance, and power," Ear Hear. **22**, 316–332.

Feeney, M. P., Keefe, D. H., and Marryott, L. P. (**2003**). "Contralateral acoustic reflex thresholds for tonal activators using wideband energy reflectance and admittance," J. Speech Lang. Hear. Res. **46**, 128–136.

Feeney, M. P., Keefe, D. H., and Sanford, C. A. (**2004**). "Wideband reflectance measures of the ipsilateral acoustic stapedius reflex threshold," Ear Hear. **25**, 421–430.

Feeney, M. P., and Sanford, C. A. (**2005**). "Detection of the acoustic stapedius reflex in infants using wideband energy reflectance and admittance," J. Am. Acad. Audiol **16**, 278–290.

Gelfand, S. A. (**2001**). "The acoustic reflex," in *Handbook of Clinical Audiology*, 4th ed., edited by J. Katz (Lippincott, Williams and Wilkins, Philadelphia), pp. 205–232.

Goodman, S. S., and Keefe, D. H. (**2006**). "Simultaneous measurement of noise-activated middle-ear muscle reflex and stimulus frequency otoacoustic emissions," J. Assoc. Res. Otolaryngol. **7**, 125–139.

Grason-Stadler (**2005**). "GSI TympStar Version 2: Reference Instruction Manual" (Viasys Healthcare, Conshohocken, PA).

Hirsch, J. E., Margolis, R. H., and Rykken, J. R. (**1992**). "A comparison of acoustic reflex and auditory brain stem response screening of high-risk infants," Ear Hear. **13**, 181–186.

Holte, L., Cavanaugh, R. M., Jr., and Margolis, R. H. (**1990**). "Ear canal wall mobility and tympanometric shape in young infants," J. Pediatr. (St. Louis) **117**, 77–80.

Hood, L. J. (**1999**). "A review of objective methods of evaluating auditory neural pathways," Laryngoscope **109**, 1745–1748.

Hunter, L. L., and Margolis, R. H. (**1992**). "Multifrequency tympanometry: Current clinical application," Am. J. Audiol. **1**, 33–43.

Hunter, L. L., Ries, D. T., Schlauch, R. S., Levine, S. C., and Ward, W. D. (**1999**). "Safety and clinical performance of acoustic reflex tests," Ear Hear. **20**, 506–514.

Kankkunen, A., and Liden, G. (**1984**). "Ipsilateral acoustic reflex thresholds in neonates and in normal-hearing and hearing-impaired pre-school children," Scand. Audiol. **13**, 139–144.

Keefe, D. H., and Abdala, C. (**2007**). "Theory of forward and reverse middle-ear transmission applied to otoacoustic emissions in infant and adult ears," J. Acoust. Soc. Am. **121**, 978–993.

Keefe, D. H., Folsom, R. C., Gorga, M. P., Vohr, B. R., Bulen, J. C., and Norton, S. J. (**2000**). "Identification of neonatal hearing impairment: Ear-canal measurements of acoustic admittance and reflectance in neonates," Ear Hear. **21**, 443–461.

Keefe, D. H., Gorga, M. P., Neely, S. T., Zhao, F., and Vohr, B. R. (**2003a**). "Ear-canal acoustic admittance and reflectance measurements in human neonates. II. Predictions of middle-ear dysfunction and sensorineural hearing loss," J. Acoust. Soc. Am. **113**, 407–422.

Keefe, D. H., and Simmons, J. L. (**2003**). "Energy transmittance predicts conductive hearing loss in older children and adults," J. Acoust. Soc. Am. **114**, 3217–3238.

Keefe, D. H., Zhao, F., Neely, S. T., Gorga, M. P., and Vohr, B. R. (**2003b**). "Ear-canal acoustic admittance and reflectance effects in human neonates. I. Predictions of otoacoustic emission and auditory brainstem responses," J. Acoust. Soc. Am. **113**, 389–406.

Li, Y., Hunter, L. L., Margolis, R. H., Levine, S. C., Lindgren, B., Daly, K., and Giebink, G. S. (**1999**). "Prospective study of tympanic membrane retraction, hearing loss, and multifrequency tympanometry," Otolaryngol.-Head Neck Surg. **121**, 514–522.

Margolis, R. H., and Goycoolea, H. G. (**1993**). "Multifrequency tympanometry in normal adults," Ear Hear. **14**, 408–413.

Margolis, R. H., and Heller, J. W. (**1987**). "Screening tympanometry: Criteria for medical referral," Audiology **26**, 197–208.

Margolis, R. H., Saly, G. L., and Keefe, D. H. (**1999**). "Wideband reflectance tympanometry in normal adults," J. Acoust. Soc. Am. **106**, 265–280.

Miller, M. H., Hoffman, R. A., and Smallberg, G. J. (**1984**). "Stapedial reflex testing and partially reversible acoustic trauma," Hearing Instrum. **35**, 15, 49.

Müller-Wehlau, M., Mauermann, M., Dau, T., and Kollmeier, B. (**2005**). "The effects of neural synchronization and peripheral compression on the acoustic-reflex threshold," J. Acoust. Soc. Am. **117**, 3016–3027.

Neumann, J., Uppenkamp, S., and Kollmeier, B. (**1996**). "Detection of the acoustic reflex below 80 dB HL," Audiol. Neuro-Otol. **1**, 359–369.

Schwartz, D. M., and Schwartz, R. H. (**1980**). "Tympanometric findings in young infants with middle ear effusion: Some further observations," Int. J. Pediatr. Otorhinolaryngol. **2**, 67–72.

Silman, S., and Silverman, C. A. (**1991**). *Auditory Diagnosis: Principles and Applications* (Academic, San Diego).

Silman, S., Silverman, C. A., and Arick, D. S. (**1992**). "Acoustic-immittance screening for detection of middle-ear effusion in children," J. Am. Acad. Audiol **3**, 262–268.

Sprague, B. H., Wiley, T. L., and Goldstein, R. (**1985**). "Tympanometric and acoustic-reflex studies in neonates," J. Speech Hear. Res. **28**, 265–272.

Vanhuyse, V. J., Creten, W. L., and Van Camp, K. J. (**1975**). "On the w-notching of tympanograms," Scand. Audiol. **4**, 45–50.

Weatherby, L. A., and Bennett, M. J. (**1980**). "The neonatal acoustic reflex," Scand. Audiol. **9**, 103–110.

Wiley, T. L., and Fowler, C. G. (**1997**). *Acoustic Immittance Measures in Clinical Audiology: A Primer* (Singular, San Diego).

Distortion product otoacoustic emission suppression tuning and acoustic admittance in human infants: Birth through 6 months

Carolina Abdala[a)]
House Ear Institute, 2100 West Third Street, Children's Auditory Research and Evaluation Center, Los Angeles, California 90057

Douglas H. Keefe
Boys Town National Research Hospital, Omaha, Nebraska 68131

Sandra I. Oba
House Ear Institute, 2100 West Third Street, Children's Auditory Research and Evaluation Center, Los Angeles, California 90057

(Received 19 December 2006; revised 28 March 2007; accepted 29 March 2007)

Previous work has reported non-adultlike distortion product otoacoustic emission (DPOAE) suppression in human newborns at f_2=6000 Hz, indicating an immaturity in peripheral auditory function. In this study, DPOAE suppression tuning curves (STCs) were recorded as a measure of cochlear function and acoustic admittance/reflectance (YR) in the ear canal recorded as a measure of middle-ear function, in the same 20 infants at birth and through 6 months of age. DPOAE STCs changed little from birth through 6 months, showing excessively narrow and sharp tuning throughout the test period. In contrast, several middle-ear indices at corresponding frequencies shifted systematically with increasing age, although they also remained non-adultlike at 6 months. Linear correlations were conducted between YR and DPOAE suppression features. Only two correlations out of 76 were significant, and all but three YR variables accounted for $<10\%$ of the variance in DPOAE suppression tuning. The strongest correlation was noted between admittance phase at 5700 Hz and STC tip-to-tail (R=0.49). The association between middle-ear variables and DPOAE suppression may be stronger during other developmental time periods. Study of older infants and children is needed to fully define postnatal immaturity of human peripheral auditory function. © *2007 Acoustical Society of America.* [DOI: 10.1121/1.2734481]

PACS number(s): 43.64.Jb, 43.64.Kc, 43.64.Ha [BLM] Pages: 3617–3627

I. INTRODUCTION

For over a decade, studies into the maturation of distortion product otoacoustic emissions (DPOAE) suppression characteristics in human infants have reported age differences (Abdala *et al.*, 1996; Abdala, 1998). Iso-suppression tuning curves (STCs) from infants are non-adultlike in width and steepness on the low-frequency side when recorded at f_2=6000 Hz. The growth of suppression for low-frequency suppressor tones is shallow in infants relative to adults as well. These results clearly suggest immaturity in the peripheral auditory system of human newborns. More recently, DPOAE-based immaturities have been documented through at least 3 months of age (Abdala, 2004). It is not clear when these aspects of auditory function become adultlike in human infants because the timeline for maturation of DPOAE suppression tuning has not been completely defined. Additionally, the source of this immaturity is not clear.

Non-adultlike DPOAE suppression in infants was initially thought to arise from a purely cochlear immaturity. Several cochlear sources have been hypothesized and some have been systematically investigated, such as outer hair cell (OHC) function. The OHCs are morphologically developed early in gestation (Lavigne-Rebillard and Pujol, 1987, 1988) although their functional status in humans just before and after birth is not known. When aspirin is used to reversibly impair OHC motility in normal-hearing adults, DPOAE STCs become abnormal in morphology; however, they do not become like neonatal tuning curves. Rather, they become broad, bowl-shaped, and lose their tip region (Abdala, 2005). This finding does not support the hypothesis that OHC motility is the source of non-adultlike DPOAE suppression in human infants.

It is also possible that functional immaturities exist in the descending efferent system known to modulate OHC function. When the medial olivocochlear (MOC) reflex is evoked by contralateral noise, DPOAE amplitude is altered in the opposite ear (Puel and Rebillard, 1990). There are few published reports of the MOC reflex in human infants, but the existing studies suggest that MOC function remains immature just before and around the time of birth (Abdala *et al.*, 1999; Morlet *et al.*, 1993; Ryan and Piron, 1994). It is possible that an MOC immaturity contributes to non-adultlike DPOAE suppression tuning during maturation.

Noncochlear factors must also be considered as potential explanations for DPOAE-based immaturities. Although

[a)]Electronic mail: cabdala@hei.org

OAEs measure *cochlear* function, stimuli presented to evoke OAEs, as well as the emission itself, must travel the conductive pathway, and therefore are subject to immaturities in this pathway. The outer and middle ear can filter both the stimulus and the DPOAE emerging from the cochlea and measured in the car canal (Keefe, 2007). Recent work from our lab has shown that the infant middle ear attenuates the stimulus level during forward transmission to the cochlea more than does the adult middle ear, while the reduced ear canal area in infants boosts the DPOAE during reverse transmission from cochlear origin to microphone (Abdala and Keefe, 2006; Keefe and Abdala, 2007). The attenuation in forward transmission is particularly relevant because DPOAE STCs evoked with lower levels of stimuli are sharper and narrower than STCs evoked with high-level stimulation (Abdala, 2001), most likely due to initiation of low-level active processes that enhance frequency resolution.

Other acoustic ear-canal measures such as admittance and reflectance may encode aspects of middle-ear functioning that could influence DPOAEs as well. These measures indicate how the outer and middle ear absorbs and/or reflects sound. Maturation of reflectance and admittance characteristics in human infants shows a broad pattern of postnatal variation with age through 24 months (Keefe *et al.*, 1993). These variations are relevant to the present study at measurement frequencies near the primary tones (5000–6000) and DPOAE frequency (4000 Hz). Keefe found that admittance levels in infants (1–24 months of age) were significantly different from adult levels at these measurement frequencies. Additionally, admittance levels at 1 month of age differed from infant admittance at 3–24 months of age, and level at 3 months differed from level measured at ages between 12 and 24 months. These differences may be due to age-dependent growth of the cross-sectional area of the ear canal. Admittance is not yet mature at age 11 years (Okabe *et al.*, 1988). Energy reflectance shows mixed age effects. At ages 1, 6, and 12 months it differs from that of adults at 5040 Hz but no differences are observed at 4000 Hz for any age. Only 1-month-olds differ from adults at 6000 Hz. The energy reflectance at age 1 month is significantly different at 6350 Hz for ages 12 and 24 months, but, otherwise, no reflectance differences between infant age groups were observed.

When combined, independent research on maturation of DPOAE suppression tuning and maturation of middle-ear reflectance/admittance properties indicates that both are developing into the postnatal period. The purpose of the present study was to investigate: (1) the time period during which DPOAE suppression tuning becomes adultlike by testing infants from birth through 6 months of age using a longitudinal design and (2) the relationship between the maturation of DPOAE suppression tuning and maturation of middle-ear reflectance/admittance properties in the same group of infants during the first 6 postnatal months of life. By addressing these objectives, the present study sought to define when the cochlea becomes functionally mature in humans and examine the extent to which middle-ear functioning can account for DPOAE suppression immaturities and their changes over time.

II. METHODS

A. Subjects

Ten normal-hearing adults and 20 healthy infants participated as subjects in this study. Different auditory measures from this same group of infants have been previously analyzed to address related questions (Abdala and Keefe, 2006; Keefe and Abdala, 2007). The 10 adults had a mean age of 27.5 years (range=19–35 years) and audiometric thresholds $<$15 dB HL for frequencies from 250–8000 Hz. Four right and six left ears were tested. Six subjects were female and four were male. All adult subjects had negative histories of hearing loss and otologic pathology.

Of the 20 infant subjects, 11 were term born and nine were infants born prematurely but tested once they reached termlike status, i.e., 37–41 postconceptional weeks. Prematurely born infants were included in this study to address the question of whether they develop along a normal maturational time line once their age is corrected for premature birth. Infants had a mean birth weight of 2853 grams (range=1470–3960 grams) and mean 1- and 5-min Apgar scores of 7.7 and 8.7. There were 9 females and 11 male infants, 8 right and 12 left ears. Other than a stay in the Neonatal Intensive Care Unit of $>$48 h for observation (premature infants only), none of the infants had high-risk factors for hearing loss as defined by the Joint Committee on Infant Hearing (JCIH, 2000). All infant subjects passed a hearing screening at 35 dB HL with a click-evoked auditory brainstem response (ABR) and a DP-gram (f_2 frequencies ranging from 1500 to 8000 Hz).

B. Instrumentation and signal processing

A custom-designed DPOAE acquisition system (SuppDP) was used to generate stimuli and acquire data under the control of custom software using a 48 000-Hz sampling rate. The data acquisition hardware was based on an audio processor developed by House Ear Institute Engineering Department. The hardware includes 2-channel D/A, 2-channel A/D, and a DSP processor (all 24-bit), as well as an analog high-pass filter (12-dB/oct.; 700-Hz high-pass cutoff). The A/D converter received the electrical output signal from an Etymotic Research ER-10C probe microphone. The ER-10C probe contains two output transducers and a low-noise microphone. The two primary tones and suppressor tone were generated by the DSP processor. The primary tone at f_1 was generated by one D/A converter and delivered via one transducer. The primary tone at f_2 and the suppressor tone were produced by the second D/A converter and output through the second transducer. The microphone signal was high-pass filtered before being sampled by the A/D converter.

C. Data acceptance criteria

Twenty sweeps of the microphone signal were averaged by the DSP processor and comprised one block of data. A block of data was only accepted into the grand average if the noise measurements for three frequency bins (11.7 Hz wide) on either side of the $2f_1$-f_2 frequency were $<$5 dB SPL. This ensured adequate subject state.

The grand DPOAE average had to meet the following criteria: (1) the measured DPOAE level was at least 5 dB above the average noise in these six bins around $2f_1$-f_2 and (2) averaged noise measurements for the six frequency bins were not greater than 0 dB SPL. A minimum of 6 and a maximum of 12 acceptable blocks of data comprised the final DPOAE grand average. If the maximum number of blocks was collected (12 blocks or 240 sweeps) without meeting these criteria, no DPOAE response was accepted and the program moved on to the next test condition.

D. Calibration

Intermodulation distortion produced by the recording system at $2f_1$-f_2 was measured with the probe in a Zwislocki coupler for all test conditions. The mean level of distortion was −25 dB SPL. The recording system noise floor was determined using a similar method with no tones present. The level of system noise floor ranged between −23 and −30 dB SPL. An *in situ* calibration procedure was conducted on both output transducers before each subject was tested. A chirp tone (swept-frequency signal from 10 to 10 000 Hz) with fixed voltage was presented to the transducer and the resulting SPL of the tone recorded in the ear canal. Based on this information, an equalization of output levels was performed for each subject to achieve target stimulus levels across test frequencies.

E. Procedure

The most marked age effects for DPOAE suppression have been previously observed at f_2=6000 Hz (Abdala, 1998, 2001), and for this reason, it was selected as the primary test frequency to enhance the probability of detecting maturational shifts. At the beginning of this study, attempts were also made to collect low-frequency data. Thirty-eight newborns were tested at f_2=1500 Hz, but noise in this frequency range was excessive at the older ages (3–6 months) and precluded successful completion of the protocol. Three infants were successfully tested at f_2=2000 Hz and, although the group data were too few to analyze, they are described in the Results section.

Infant subjects were tested once informed parental consent had been obtained. The first test occurred within 72 h of birth if subjects were term-born and once their corrected age reached term at 37–40 weeks postconceptional age (PCA) if they were born prematurely. All infants were then tested again at 3 months (mean=85.4 days), 4 months (mean =117.4 days), 5 months (mean=148.7 days), and 6 months (mean=182.9 days) of age ± 1 week.

Following the initial test, families received phone calls from the research audiologist within 2 weeks of the target age to schedule a test session. Once the session had been scheduled, the families were mailed reminder postcards 1 week prior to the appointment date. By using this method, success rate for appointment participation was 96%. All infant testing took place at the Infant Auditory Research Laboratory on the University of Southern California + Los Angeles County (USC+LAC) campus, Women's and Children's Hospital, in a quiet room away from the normal nursery and neonatal intensive care unit. Infants were tested in their hospital isolettes whenever possible, or occasionally tested while held in the parent's arms or, at older ages, while sleeping in a car seat. All infants were tested during natural sleep and an infant test session was typically 2 to 2.5 h in duration. Adult subjects were tested within an IAC sound-attenuated booth at the House Ear Institute while sitting comfortably in a padded easy chair, reading or resting. One 1.5–2 h session was required for each adult.

All DPOAE STCs were generated with fixed stimulus tones of 65–55-dB SPL and an f_2/f_1 ratio of 1.2. In order to record a 6000-Hz STC, 15 different suppressor tones were presented at frequencies around f_2 ranging from 3047 to 7239 Hz. Suppressor tones were presented at intervals of 25–150 cents (1 octave=1200 cents) with smaller intervals in the tip region. To record a 2000-Hz STC in three infant subjects and five adults, 12 different suppressor tones were presented at frequencies around f_2, ranging from 1125 to 2520 Hz. The suppressor tones were presented ipsilaterally with the primary tones and increased in 5-dB intervals from 30 to 85 dB SPL. Unsuppressed DPOAE amplitude was measured at the start of data collection and prior to the presentation of each new suppressor frequency. STCs were generated with 2- and 6-dB suppression criteria. The suppressor levels producing criterion suppression were calculated for each suppressor tone by linear interpolation and plotted as a function of suppressor frequency

Acoustic admittance/reflectance (YR) measurement procedures are briefly summarized here and explained in more detail elsewhere (Keefe and Simmons, 2003; Keefe and Abdala, 2007). For this study, YR responses were analyzed at octave frequencies from 250 to 8000 Hz and two interoctave frequencies: 2800 and 5700 Hz. An Etymotic ER10C probe was used with a microphone and +20-dB additional gain to each of two receivers in the probe. This probe was the same probe used by Abdala and Keefe (2006). DPOAE and YR responses were acquired, whenever possible, based on the same ear-canal insertion. Receiver 1 delivered a brief "click" approximating a bandlimited impulse from 0.25 to 8 kHz. Receiver 1 was driven by the output of a D/A converter of a computer sound card (CardDeluxe) using custom-written software. The microphone output was synchronously recorded using an A/D converter on the sound card. The sample rate was 22.05 kHz using a D/A and A/D buffer length of 1024 samples.

Admittance/reflectance data were eliminated if the DPOAE in the same subject dropped by 10 dB or greater from one test session to another and parent reported the infant to be sick or congested, which indicated a possible upper respiratory infection (5% of the data). Data were also eliminated if the energy reflectance was close to zero and/or if the equivalent volume was extremely negative at low frequencies ($\leq$1 kHz). The presence of either or both conditions indicated a likely leak of the probe in the ear canal (Keefe *et al.*, 2000). Data were dropped if the energy reflectance at high frequencies (6–8 kHz) exceeded 1.2. Excessively high reflectance values (and corresponding abnormal admittance values) may have been due to a partially blocked probe tip by cerumen or resulting from placement near the ear-canal

wall, or reflectance calibration errors at high frequencies. In total 30.9% of reflectance/admittance records were eliminated to ensure data quality, using the guidelines above.

F. Data analysis

1. DPOAE

DPOAE STCs generated with 2- and 6-dB suppression criteria were analyzed in the following manner: (1) the STC width was measured 10 dB above the tip, and the tip frequency was divided by this width to obtain a Q_{10} measure; if the STC was too broad to calculate a Q_{10}, a value 2 standard deviations below the mean Q_{10} was assigned; (2) the slope of the low- and high-frequency flank of the STC was quantified by fitting regression lines from the tip of the STC to the lowest and highest frequencies on the flanks of the tuning curve; (3) the tip-to-tail value was measured by subtracting the suppressor level at the tip of the STC from the level at the lowest suppressor frequency which was approximately one octave below f_2 (3047 Hz); (4) the STC tip frequency and tip level were measured; (5) DPOAE suppression growth was calculated by measuring slope of the DPOAE amplitude x suppressor level function using a linear regression equation. Any initial amplitude plateau was eliminated in this calculation and only the linear portion of this function was included. The measured segment began 1–2 dB down from the unsuppressed value and included all points with sufficient SNR.

Three statistical analyses were conducted on DPOAE data: First, one-way analyses of variance (ANOVAs) were conducted between infants born prematurely (but tested at term-equivalent corrected age) and those born after term birth on each DPOAE feature measured. These established whether a premature birth influenced DPOAE suppression measurements. Second, unpaired *t*-tests were conducted between adults and infants at two ages: (1) Newborn vs adult (to confirm previous research published on immaturities in DPOAE suppression at birth), and (2) Six-month-old vs adult (to assess whether infant suppression responses had become more adultlike over time). A significant age difference at birth and the absence of age differences at 6 months would be indicative of some maturational shift. Conversely, significant age differences at both birth and 6 months of age would indicate continued immaturity of the response throughout the test period. Third, repeated-measures one-way ANOVAs (repeated variable=age) were also conducted on infant data for each DPOAE suppression variable that was non-adultlike at birth, to more directly test for change as a function of age. A Bonferroni factor was applied to adjust the alpha level when multiple comparisons were conducted. The alpha level was $p=0.05$.

2. Relationships between middle ear and DPOAE suppression variables

Half-octave averaged admittance and reflectance responses assessed middle-ear functioning at three frequencies (approximately 2800, 4000, and 5700 Hz). The three frequencies were chosen for analysis because 2800 Hz is in the region of the STC "tail" and closest to the suppressor frequency used in making tip to tail measurements (3047 Hz), 4000 Hz is at the DPOAE frequency, and 5700 Hz is nearest the f_2 frequency of 6000 Hz. Reflectance and admittance variables have significant correlations with one another across frequency. Therefore, either a subset of variables at particular frequencies is selected for detailed analysis, as in the present study, or new factor variables are defined as linear combinations of the original admittance and reflectance variables.

Admittance can be represented in terms of magnitude (YM) and phase (YP) or, alternatively, in terms of real and imaginary parts. The real part of admittance is the conductance (G), which can be expressed as a conductance level ($\mathrm{LG}=10\log_{10}\mathrm{G}$, with 0 dB for $G=1$ mmho). For a DPOAE experiment with fixed SPLs at the primary frequencies, the power level absorbed by the middle ear is proportional to LG. The imaginary part of admittance is susceptance (S). The correlation analyses included admittance variables in both level/phase and real/imaginary component representations. In addition, the acoustic estimate of ear-canal area was calculated for each ear and its level (in dB, normalized to the adult ear-canal area) was included in correlations. Keefe and Abdala (2007) reported that reverse DPOAE transmission is sensitive to ear-canal area, and Keefe and colleagues (1993) showed that ear-canal area was an important contributor to maturational differences in ear-canal impedance, and thus, admittance.

To assess the relationship between DPOAE suppression and YR responses measured at the ear-canal probe microphone during repeated test sessions from birth through 6 months of age, Pearson linear correlations were calculated between four DPOAE STC variables that are non-adultlike in newborns and seven middle-ear variables. The DPOAE suppression variables were (1) STC $Q10$; (2) slope of the STC low-frequency flank; (3) tip-to-tail level; and (4) tip level. The YR variables were (1) energy reflectance (ER); (2) reflectance phase (RP); (3) admittance magnitude (YM); (4) admittance phase (YP); (5) conductance (LG); (6) susceptance (S); and (7) an acoustic estimate of ear-canal area level calculated for each ear (in dB).

Correlations are shown in terms of their Pearson correlation (R) (Table I) and discussed in terms of their squared correlation (R^2) values. Correlations were tested for significance; however, it is important to distinguish between statistical significance, which only indicates whether a nonrandom association is present between two variables, and the *strength* of association, which is assessed by R^2. The R^2 assessed how much variance in any given DPOAE suppression feature could be accounted for by variance in a particular YR variable. This index best addressed our research question, i.e., to evaluate the predictive power of YR variables on DPOAE suppression. A multiple regression was also conducted to investigate whether some of the variance in DPOAE suppression features could be explained using two or more YR variables producing the strongest correlations with that feature. Given that many correlations were conducted, a more rigorous $p=0.01$ alpha level was applied.

TABLE I. Correlation coefficients (R) between DPOAE STC features ($f2$ =6000 Hz) and middle-ear admittance and reflectance features at three frequencies. Ear canal area was calculated as described in the text and although listed under 2800 Hz, estimates of ear canal area are independent of frequency. Significant correlations are in bold.

		Frequency (Hz)		
ME feature	STC feature	2800	4000	5700
Admittance magnitude (YM)	Tip-to-tail	−0.25	−0.27	−0.08
	LF slope	0.22	0.10	0.11
	Q	−0.19	−0.26	−0.13
	Tip level	0.12	0.26	0.24
Admittance phase (YP)	Tip-to-tail	0.02	0.14	**0.49**[a]
	LF slope	0.17	0.10	0.24
	Q	−0.20	−0.02	0.20
	Tip level	0.10	0.09	−0.20
Susceptance (S)	Tip-to-tail	0.04	0.16	**0.42**[a]
	LF slope	0.18	0.07	0.23
	Q	−0.21	−0.10	0.26
	Tip level	0.05	−0.02	−0.23
Conductance level (LG)	Tip-to-tail	−0.31	−0.26	0.08
	LF slope	0.19	0.10	0.19
	Q	−0.13	−0.25	−0.07
	Tip level	0.16	0.25	0.13
Energy reflectance (ER)	Tip-to-tail	0.34	0.28	−0.22
	LF slope	−0.06	−0.08	−0.31
	Q	0.02	0.14	−0.21
	Tip level	−0.23	−0.24	0.10
Reflectance phase (RP)	Tip-to-tail	0.06	−0.02	0.12
	LF slope	−0.17	−0.24	−0.21
	Q	0.09	−0.01	0.12
	Tip level	−0.04	−0.04	−0.04
Ear canal area (EC)	Tip-to-tail	0.22	⋯	⋯
	LF slope	−0.14	⋯	⋯
	Q	0.25	⋯	⋯
	Tip level	−0.25	⋯	⋯

[a] $p<0.01$.

III. RESULTS

A. DPOAE suppression

1. Newborn period

Figure 1 shows the mean DPOAE STCs recorded with both 6- and 2-dB suppression criteria from adults and infants at birth and through 6 months of age. Because STCs generated with 6- and 2-dB suppression criteria generally showed the same age-related trends, only the data from the 6-dB STCs are presented unless diverging results were observed. There was no discernible, consistent pattern that was unique to infants that were born prematurely (but tested at a corrected age equivalent to term birth) vs infants that were born following full gestation. A one-way ANOVA (collapsed across session) showed no significant difference between the two infant groups for any DPOAE variable measured; therefore, their data were combined into one infant group for all analyses. This result indicates that there is no obvious delay or difference in the maturation of DPOAE suppression for babies born prematurely, once their age is corrected for premature birth.

Four DPOAE STC variables showed infant-adult differences at birth: $Q10$, tip-to-tail level, slope on the low-frequency flank, and tip level. These four variables are shown in Fig. 2 as a function of age. Mean adult values are included at the far right of each graph (the asterisk represents a mean of values from a group of normal hearing children to be considered in the Discussion section). As is evident, at birth, STC width was significantly narrower in the combined group of infants ($p=0.0001$), the tip-to-tail value was larger ($p=0.0001$), the low-frequency flank was steeper ($p=0.0001$), and the tip level was lower in infants ($p=0.0002$). The slope on the high-frequency flank of the STC and the tuning-curve tip frequency (not shown) were similar in adults and infants at birth. These trends are consistent with previously reported DPOAE suppression data in newborns.

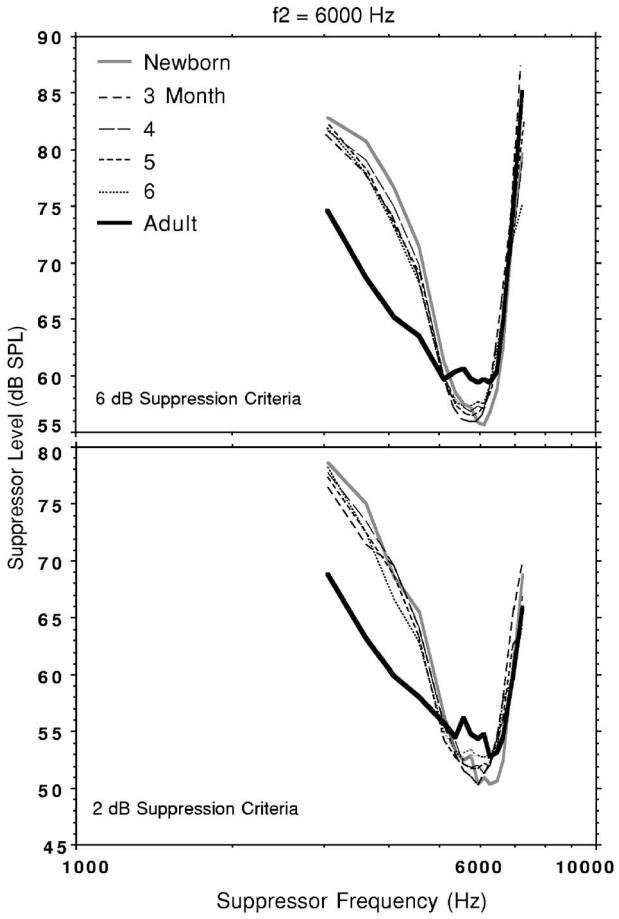

FIG. 1. Mean infant DPOAE suppression tuning curves ($f2=6000$ Hz) around birth and at four additional ages (birth: $n=20$, 3, and 4 months: $n=17$, 5, and 6 months: $n=18$). The mean adult STC is included for comparison ($n=10$). Tuning curves are presented for two suppression criteria.

The slope or "rate" of suppression growth was analyzed only for the four lowest suppressor tones because age differences were not present on the high-frequency flank of the STC (Abdala, 1998, 2001). As previously reported, suppression growth was shallower in newborns than adults for suppressor tones at 3047, 3621, and 4090 Hz ($p=0.04$, $p=0.01$, and $p=0.02$, respectively) (Fig. 3). The suppressor frequency of 4559 Hz did not show any infant-adult differences in the growth of suppression at birth.

2. Birth through 6 months

Age comparisons between adult data and infant data at 6 months showed persistent age differences for the four

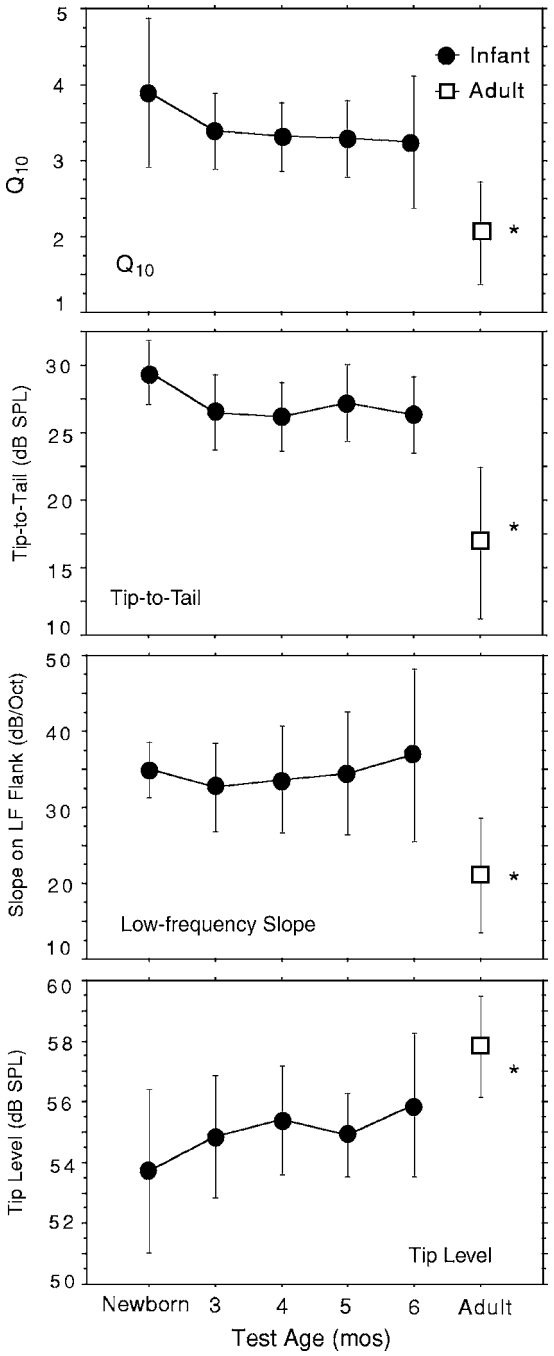

FIG. 2. The four DPOAE STC features showing newborn-adult age differences ($Q10$, tip-to-tail level, slope on the low-frequency flank, and tip level) as a function of age. Each mean represents between 17–20 infant subjects and 10 adult subjects. Error bars = +/− 1 s.d. The asterisk represents mean values from a group of 15 normal-hearing children with an average age of 10.5 years.

DPOAE STC variables that were immature during the newborn period: Q10, tip-to-tail level, slope on low-frequency STC flank, and tip level (6 month vs adult: $p=0.0001$ for all four variables). It is clear from Figs. 1 and 2 that these four features of the DPOAE STC remained immature at 6 months of age. The only exception to this result was observed for STCs recorded with 2-dB suppression criteria, in which the infant tip level was lower than adults at birth ($p=0.02$), but by 6 months of age the tip level had increased to within adult values. Additionally, slope of suppression growth for suppressor tone 3047 Hz was adultlike by 6 months of age, although it had been excessively shallow at birth. The two other low-frequency suppressor tones showing non-adultlike suppression growth at birth (3621 and 4090 Hz) remained immature at 6 months as well ($p=0.008$ and $p=0.01$, respectively).

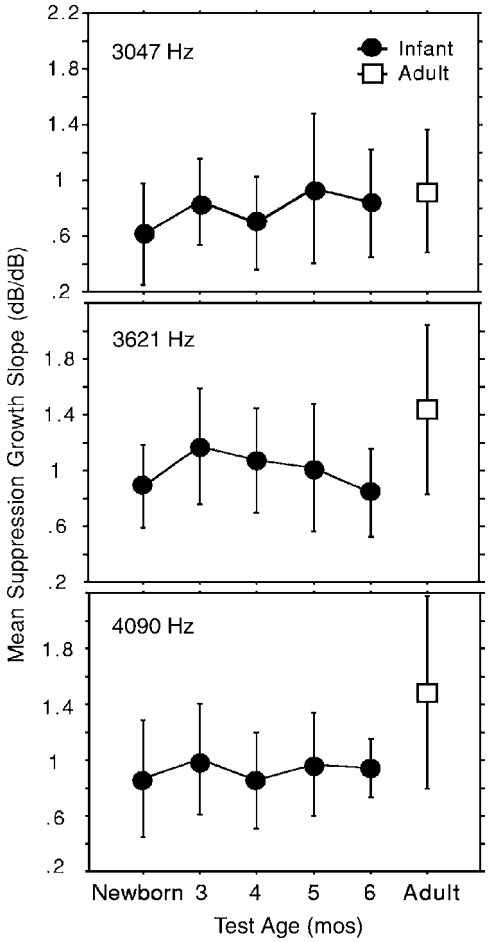

FIG. 3. Slope of suppression growth for the three lowest frequency suppressor tones (3047, 3621, and 4090 Hz) as a function of age. Each mean represents between 16–20 infants and 10 adult subjects. Error bars = +/− 1 s.d.

The repeated measures ANOVAs, conducted to directly assess change across session/infant age, included a somewhat reduced data set because each infant subject did not have measurements at each of the five test sessions. Because five ANOVAs were conducted on the same data set, the alpha level was adjusted using the Bonferonni correction factor ($0.05/5=0.01$). The five variables tested were $Q10$ ($n=12$), slope on the low-frequency flank ($n=13$), tip-to-tail ($n=7$), slope of suppression growth for the lowest suppressor tone ($n=9$), and tip level ($n=13$). There was no significant effect of age on any of these five DPOAE suppression features.

3. DPOAE suppression at f_2=2000 Hz

Three infants were tested successfully at this frequency and followed from birth through 5 months of age. In past work, low-frequency DPOAE STCs were reported to be generally adultlike or nearly adultlike by term birth and did not show robust newborn-adult age differences. As seen in Fig.

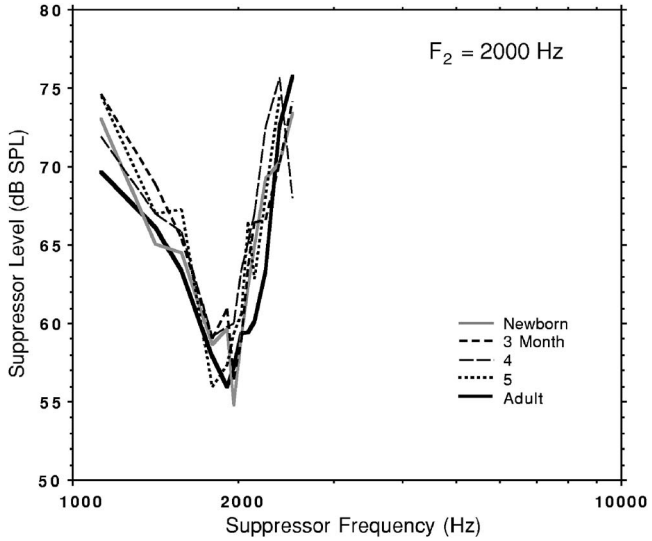

FIG. 4. Mean infant DPOAE suppression tuning curves ($f2=2000$ Hz) for three infants tested around birth and at three additional ages. The mean adult STC is included for comparison ($n=7$). The suppression criterion was 6 dB.

4, infant DPOAEs for $f_2=2000$ Hz were also generally adultlike in morphology and width and did not show systematic changes in STC width with age.

B. Acoustic admittance and reflectance

It was not the objective of the present study to provide an overall description of YR response maturation in humans. Several publications are available in the literature to describe this maturational time course in human infants, and the reader is referred to these for an overview (Keefe *et al.*, 1993, 1994; Keefe and Levi, 1996; Keefe *et al.*, 2000; Keefe and Abdala, 2007). In the present study, our interest was limited to how these middle-ear variables relate to and possibly account for changes in DPOAE suppression tuning. Although YR responses were measured in the ear canal over a wide frequency range from 250 to 8000 Hz, the DPOAE, stimuli used to evoke the DPOAE, and the suppressor tones were centered within a more narrow frequency range from 3000–6000 Hz. Thus, our analysis of YR responses was limited to this same frequency range (see Data Analysis section). The admittance is plotted as a function of age in Fig. 5 for 2800, 4000, and 5700 Hz. The entire wideband response for energy reflectance was plotted as a function of age in a companion report (Keefe and Abdala, 2007) and is not repeated here, because admittance was the more salient feature and the strongest predictor of DPOAE suppression.

Generally, the maturation of reflectance and admittance observed here was consistent with what has been reported previously for corresponding frequencies (Keefe *et al.*, 1993). The admittance magnitude (YM) increased with increasing age at each frequency (2800, 4000, 5700) but was not yet adultlike at age 6 months. The typical pattern was that YM was largest in infant ears at 5700 Hz, next largest at 4000 Hz, and smallest at 2800 Hz, although the newborn response deviated slightly from this pattern. The YM in adult

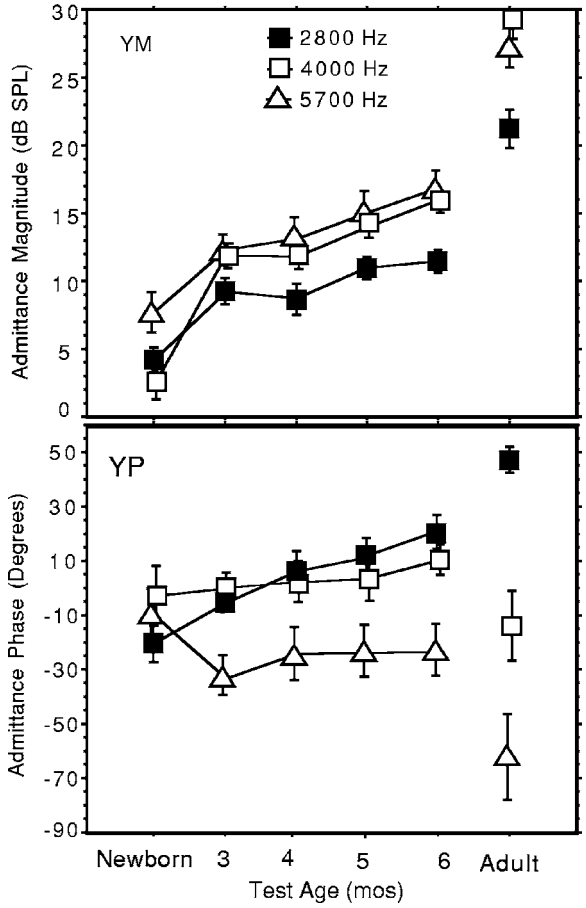

FIG. 5. The admittance magnitude (YM) at 2800, 4000, and 5700 Hz plotted as a function of age in the upper panel. YM is expressed as a level (in dB) defined by $20\log_{10} YM$, with YM measured in mmhos (i.e., YM level is 0 dB when YM=1 mmho). The admittance phase (YP), in degrees plotted as a function of age in the lower panel. Each symbol shows the mean YM or YP at each age. Error bars=+/−1 s.e.

ears did not conform to this pattern either, which was likely due to the effects of standing waves in the longer adult ear canals at higher frequencies.

The mean admittance phase (YP) increased systematically with increasing age at 2800 Hz. The admittance phase was approximately independent of infant age at 4000 Hz with a slight decrease in the adult ear. Admittance phase at 5700 is described later as having the strongest correlation with one DPOAE STC parameter (for an $f_2=6000$ Hz), and so is of particular interest. It shows a marked change between birth and 3 months and little change beyond this age. The mean YP at 5700 Hz was close to −10 deg in newborns, approximately constant at −26 deg for ages 3–6 months, and −63 deg in adults.

C. Relationship between DPOAE suppression and acoustic admittance

We calculated 76 individual correlations (4 DPOAE variables × 6 YR variables × 3 frequencies, plus 4 DPOAE variables × ear-canal area), each including approximately 55 observations. Individual correlation coefficients generated between YR variables measured at the three relevant input frequencies and DPOAE STC features are shown in Table I.

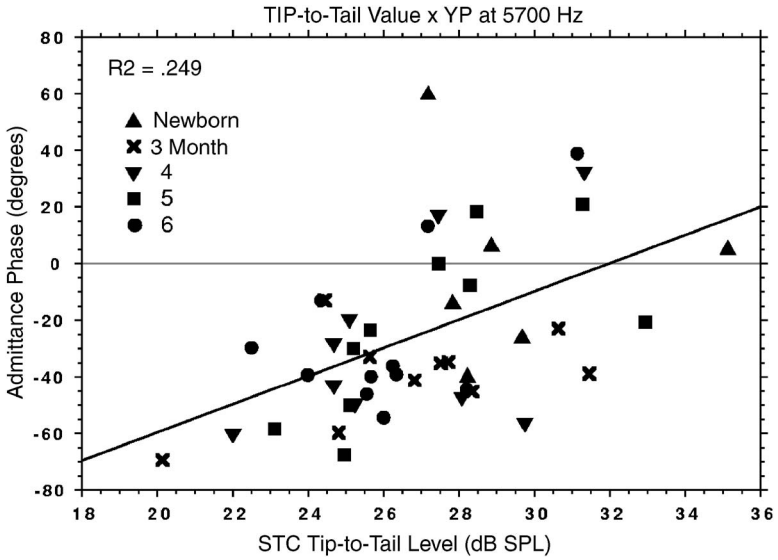

FIG. 6. The strongest correlation was observed between admittance phase (YP) at 5700 Hz and DPOAE STC tip-to-tail value. $R=0.49$.

Only two correlations were significant at the 0.01 level and those produced R^2 values of 0.18 and 0.25 (Table I).

As seen in Table I, the strongest relationship was noted between STC tip-to-tail and admittance and one significant correlation, YP at 5700 Hz, accounted for as much as 25% of the variance in STC tip-to-tail (Fig. 6). The other significant correlation, susceptance at 5700 Hz, accounted for 18%. Because STC tip-to-tail ratio showed the highest correlations with YR variables, a multiple regression was conducted with significant YR variables and ear-canal area to see whether the variance of the tip-to-tail value could be better explained using two or more features combined. Ear-canal area was included as an input because of its importance in describing DPOAE reverse transmission (Keefe and Abdala, 2007). A forward stepwise procedure was performed to calculate the multiple linear regression. Results showed that only YP at 5700 Hz was included in the final model. Thus, the regression model was not significantly better with the addition of any other variables. Cumulatively, these analyses indicate that acoustic admittance variables are not strong predictors of DPOAE suppression tuning during the first 6 months of life; that is, the most variance accounted for by any particular admittance variable was 25%.

IV. DISCUSSION

A. Maturational time course for DPOAE suppression

Because the DPOAE is a cochlear assay, we originally hypothesized that DPOAE suppression would be adultlike by 6 months of age, when the cochlea is expected to be functionally mature in humans based on anatomical, electrophysiological, and psychoacoustic data (Abdala and Folsom, 1995; Lavigne-Rebillard and Pujol, 1987, 1988; Spetner and Olsho, 1990). However, results from the present experiment did not support this hypothesis. DPOAE STCs at $f_2=6000$ Hz were not adultlike at 6 months of age and probably remain immature well beyond this age because there was no significant shift toward adult values in these data (see Figs. 1 and 2).

Although our primary research objective was to define the maturational time course for DPOAE suppression at $f_2=6000$ Hz, we were unable to do so based on the age range selected for study. Clearly, maturation of DPOAE suppression tuning occurs some time between 6 months of age and adulthood. By considering DPOAE STC results collected from school-aged children in a previous experiment (Abdala and Fitzgerald, 2003), it is possible to further narrow the time frame. Abdala and Fitzgerald reported that normal-hearing children with a mean age of 10.5 years (range=6.5 to 13 years) had generally adultlike DPOAE STC features at $f_2=6000$ Hz. In Fig. 2, the asterisk to the right of the adult data represents the mean value from this group of 15 normal-hearing children for the four DPOAE suppression features studied here. Clearly, DPOAE suppression is adultlike in these children. Therefore, we can assume that DPOAE suppression tuning at $f_2=6000$ Hz becomes mature sometime between 6 months and approximately 10 years of age. Limited data from the present experiment at $f_2=2000$ Hz, and data from previously published experiments at $f_2=1500$ Hz, suggest that low-mid-frequency DPOAE suppression is adultlike at birth or soon thereafter. Thus, we are observing an immaturity in auditory peripheral function that is present only in the high-frequency range.

B. Relationship between DPOAE suppression and acoustic admittance/reflectance

The second objective of this study was to assess whether changes in DPOAE suppression during maturation could be explained by changes in YR responses. To answer this question, the maturation of both relevant components, DPOAE suppression and admittance/reflectance, was examined for significant associations. A strong association would support the hypothesis that changes in admittance over time might account for changes in DPOAE suppression over time. It would then be reasonable to speculate that the oft-reported immaturities in DPOAE suppression are explained by changes of admittance, indicative of middle-ear rather than cochlear immaturity.

None of the DPOAE variables measured showed significant change across session, and any change that is evident from data presented in Fig. 2 clearly occurred from birth to 3 months of age, with little movement beyond this age. At the completion of this test protocol, 6 months of age, DPOAE suppression features remained non-adultlike; thus, we measured suppression during a fairly static period in development that was too short to capture the transition to adultlike functioning.

Data presented in Fig. 2 showing DPOAE suppression features, and in Fig. 5 showing admittance features as a function of age, suggest a complex relationship between these two sets of variables. Admittance data measured in the same frequency range, for the same infants, shows systematic, incremental growth from birth through 6 months of age for YM at all three frequencies shown and for YP, at 2800 Hz. This steady shift with age is in contrast to the lack of change in DPOAE suppression with age and appears to imply a dissociation between the maturational time course of these two indices over the first 6 months of life. At the same time, YP at 5700 Hz shows a pattern of change similar to what is evident for some DPOAE suppression features as seen in Fig. 2. The greatest shift is noted from birth through 3 months of age, and values remain static values beyond this age. Neither DPOAE suppression nor admittance features are mature by 6 months. Clearly, whatever underlying maturational processes ultimately produce adultlike DPOAE suppression tuning and adultlike admittance in infants occur some time after the first half-year of postnatal life.

The linear correlations conducted between suppression and admittance data from birth through 6 months of age were not strong. Only 2 of 76 correlations were significant and their YR features accounted for 18% and 25% of the variance in DPOAE suppression. The stronger correlation between YP at 5700 Hz and tip-to-tail value was intriguing. It suggests that YP may encode information on forward middle-ear transmission near the f_2 frequency (5700 Hz), and that the variance in this transmission across subjects explains some of the variance observed in the STC tip-to-tail ratio. This DPOAE STC feature has been hypothesized to reflect cochlear amplifier gain (Mills, 1998; Gorga *et al.*, 2002; Pienkowski and Kunov, 2001). If DPOAE STC tip-to-tail values are related to cochlear amplifier gain, *and* correlated with middle-ear admittance, it follows that middle-ear function must be related to cochlear amplifier gain as well. This is logical given that the cochlear amplifier functions in a level-dependent manner and the middle ear greatly influences input level (forward transmission) to the cochlea (Abdala and Keefe, 2006).

Mills (1998) suggests a strong link between DPOAE STC tip-to-tail in gerbils and estimates of cochlear amplifier gain. Through a series of model calculations and subsequent application to actual measurements in gerbils, Mills showed that this STC index can provide a fairly accurate estimate of amplifier gain. In humans, results have not been as definitive (Gorga *et al.*, 2002; Pienkowski and Kunov, 2001). Pienkowski and Kunov (2001) tested this hypothesis in humans by correlating the DPOAE STC tip-to tail values with audiometric hearing thresholds in normal-hearing individuals. They found low-to-moderate negative correlations, suggesting that the tip-to-tail index reflects cochlear amplifier gain to a limited extent in humans. Further study is needed to unravel the functional relationships underlying the link found in the present study between admittance phase around f_2 and STC tip-to-tail values.

The generally modest correlations observed here suggest that YR variables did not explain most of the variance observed in DPOAE suppression during the first 6 months of life. One factor that has not been well defined, and may have contributed to the modest correlations, is repeatability of infant DPOAE suppression and YR measurements. Additionally, although YR responses as a whole were not greatly successful in predicting changes in DPOAE suppression tuning, they may explain maturation of DPOAE suppression later in life, once suppression begins to shift toward adultlike values. This is a possibility, although the final stage of maturation for DPOAE suppression and admittance does not appear to coincide closely. DPOAE suppression tuning is adultlike by at least 10 years of age as shown by the children's mean data included in Fig. 2 (asterisk), whereas acoustic admittance is reported to remain immature beyond 11 years of age (Okabe *et al.*, 1988). One later contributor to this immaturity is ear-canal growth, which likely continues through adolescence.

C. Source of immaturity

How can we explain immature DPOAE suppression tuning so late in development? Morphological and anatomical data from humans suggest that the cochlea is mature early in gestation (21–23-weeks gestational age) and the OHC completes its final maturation sometime late in the third trimester or possibly around the time of birth. This late maturation appears to involve OHC synaptic specializations and innervation by medial efferent fibers (Lavigne-Rebillard and Pujol, 1987, 1988). The early peripheral maturation that these studies describe does not provide support for the hypothesis that cochlear function remains immature into the sixth postnatal month.

It is perhaps more parsimonious to consider segments of the auditory system that show documented postnatal maturation, such as the middle ear or the medial olivocochlear (MOC) reflex. There is compelling evidence that middle-ear transmission properties remain immature at age 6 months and can partially account for the non-adultlike morphology of newborn STCs at f_2=6000 Hz (Abdala and Keefe, 2006; Keefe and Abdala, 2007). We have shown that once these transmission properties are compensated for, adult and infant STCs become very similar in morphology. Thus, it is clear that middle-ear transmission properties are contributing to STC morphology in infants up to age 6 months. More research is needed to better understand the influences of functional immaturity in older infants.

The MOC reflex exerts its influence on cochlear function via the OHCs (Kujawa *et al.*, 1993; Kujawa and Liberman, 2001) and remains immature into the early postnatal period (Abdala *et al.*, 1999; Morlet *et al.*, 1993; Ryan and Piron, 1994). It is possible that immaturities in this feedback

loop might produce immaturities in DPOAE suppression tuning. One possible argument against this, is the observation that the most robust MOC reflex is seen at low-to-mid frequencies and not in the frequency range where DPOAE suppression immaturities are strongest. Studies with laboratory animals have not reported this frequency effect (Puel and Rebillard, 1990), and some have observed the opposite trend, finding that high-frequency stimuli evoked the strongest MOC reflex (Varghese *et al.*, 2005). At present, it is not certain whether the MOC reflex in humans shows a true frequency-dependent nature, or whether results are related to the stimulus used to elicit medial efferent activity. Contralateral broadband noise may not evoke equal firing in all efferent fibers (Moulin *et al.*, 1993). There have been no studies examining maturation of the MOC reflex in human infants beyond the newborn period, so it is not known if its maturational course is similar to that of DPOAE suppression tuning. Because of its strong potential influence on cochlear mechanics and the possibility that it shows a postnatal maturational time course, the relationship between development of the MOC reflex and DPOAE suppression tuning should be further explored.

Finally, relatively recent research has confirmed that the DPOAE recorded in the ear canal is a vector sum of at least two components arising at the overlap region between traveling waves evoked by f_1 and f_2 and the DP-site (Dhar *et al.*, 2002; Kim, 1980; Talmadge *et al.*, 1999). The results of the constructive and destructive interference between these components can be observed in DPOAE fine structure measured with high-resolution recordings of DPOAE level. There have been no published studies of DPOAE fine structure in infants. It is possible that DPOAEs measured in the infant ear canal are comprised of an immature distribution of sources relative to the adult DPOAE. An immaturity in the relative contribution of sources to the ear canal DPOAE could account for or be associated with immaturities of DPOAE suppression tuning. Middle-ear functioning can also affect DPOAE fine structure if multiple internal reflections are present (Puria, 2003; Talmadge *et al.*, 1998).

V. CONCLUSIONS

DPOAE suppression tuning at $f_2=6000$ Hz remains immature until at least 6 months of age, indicating a postnatal immaturity in peripheral auditory function. The source of this immaturity is not clear, although several indices of auditory function, such as DPOAE fine structure, middle-ear transmission, acoustic reflectance/admittance responses, and the MOC reflex, are also developing into the postnatal period and should be further explored. The present study also examined the relationship between maturation of DPOAE suppression and middle-ear function in a group of infants followed longitudinally from birth through 6 months of age. DPOAE suppression at $f_2=6000$ Hz showed little maturation during the test period studied, although admittance at corresponding frequencies changed systematically over time. Both sets of variables showed the greatest shift toward adult values from birth through 3 months. Linear correlations between suppression and admittance variables were not strong in infants: 74 of 76 YR variables were not correlated with DPOAE suppression features and could explain none of their variance over the first 6 months of life. Admittance phase near the f_2 frequency, a frequency at which middle-ear forward transmission would be expected to be important, explained 25% of the variance in STC tip-to-tail value. It is not known from these data whether a stronger association exists between maturation of DPOAE suppression and middle-ear function later in life during a time period in development when either or both responses are shifting toward adult values.

ACKNOWLEDGMENTS

This research was supported by the NIH (NIDCD Grants DC003552 and DC003784) and the House Ear Institute. The authors would like to thank Dr. Ellen Ma for collection and management of infant data, and Dr. Rangasamy Ramanathan, Chief of Neonatology at the University of Southern California, for continued support of infant research. The lead programmer in implementing the reflectance software at BT-NRH was Dr. Denis F. Fitzpatrick.

Abdala, C. (**1998**). "A developmental study of DPOAE ($2f1$-$f2$) suppression in humans," Hear. Res. **121**, 125–138.

Abdala, C. (**2001**). "Maturation of human cochlear amplifier function: DPOAE ($2f_1$-f_2) ipsilateral suppression at low- and high-levels in human adults and neonates," J. Acoust. Soc. Am. **110**, 1465–1476.

Abdala, C. (**2004**). "Distortion product otoacoustic emission (2f1-f2) suppression in 3-month-old infants: Evidence for postnatal maturation of human cochlear function?," J. Acoust. Soc. Am. **116**(6), 3572–3580.

Abdala, C. (**2005**). "Effects of aspirin on distortion product otoacoustic emissions suppression in adults: A comparison with neonatal data," J. Acoust. Soc. Am. **118**, 1566–1575.

Abdala, C., and Fitzgerald, T. (**2003**). "Ipsilateral distortion product otoacoustic emission ($2f1$-$f2$) suppression in children with sensorineural hearing loss," J. Acoust. Soc. Am. **114**, 919–931.

Abdala, C., and Folsom, R. (**1995**). "Frequency contribution to the click-evoked auditory brainstem response in human adults and infants," J. Acoust. Soc. Am. **97**, 2394–2404.

Abdala, C., and Keefe, D. H. (**2006**). "Effects of middle-ear immaturity on distortion-product otoacoustic emission suppression tuning in infant ears," J. Acoust. Soc. Am. **120**, 3832–3842.

Abdala, C., Ma, E., and Sininger, Y. (**1999**). "Maturation of medial efferent system function in human," J. Acoust. Soc. Am. **105**, 2392–2402.

Abdala, C., Sininger, Y., Eyelid, M., and Zeng, F-G. (**1996**). "Distortion product otoacoustic emission suppression tuning curves in human adults and neonates," Hear. Res. **98**, 38–53.

Dhar, S., Talmadge, C., Long, G., and Tubis, A. (**2002**). "Multiple internal reflections in the cochlea and their effect on DPOAE fine structure," J. Acoust. Soc. Am. **112**, 2882–2897.

Gorga, M. P., Neely, S. T., Dorn, P. A., and Konrad-Martin, D. (**2002**). "The use of distortion product otoacoustic emission suppression as an estimate of response growth," J. Acoust. Soc. Am. **111**, 271–284.

Joint Committee on Infant Hearing. (**2000**). "Joint Committee on Infant Hearing Year 2000 Position Statement. Principles and guidelines for early hearing detection and intervention programs," Audiology Today **12**, 6–27.

Keefe, D. H. (**2007**). "Influence of Middle-Ear Function and Pathology on Otoacoustic Emissions," in *Otoacoustic Emissions: Clinical Applications*, 3rd ed., edited by M. R. Robinette and T. J. Glattke (Thieme, New York), Chap. 7.

Keefe, D. H., and Abdala, C. (**2007**). "Theory of forward and reverse middle-ear transmission applied to otoacoustic emissions in infant and adult ears," J. Acoust. Soc. Am. **121**(2), 978–993.

Keefe, D. H., and Levi, E. (**1996**). "Maturation of the middle and external ears: Acoustic power-based responses and reflectance tympanometry," Ear Hear. **17**, 361–373.

Keefe, D. H., Bulen, J. C., Hoberg Arehart, K., and Burns, E. M. (**1993**). "Ear-canal impedance and reflection coefficient of human infants and

adults," J. Acoust. Soc. Am. **94**, 2617–2638.
Keefe, D. H., Bulen J. C., Campbell, S., and Burns, E. M. (**1994**). "Pressure transfer function and absorption cross-section from the diffuse field to the human infant ear canal," J. Acoust. Soc. Am. **95**, 355–371.
Keefe, D. H., Folsom, R. C., Gorga, M. P., Vohr, B. R., Bulen, J. C., and Norton, S. J. (**2000**). "Identification of neonatal hearing impairment: Ear-canal measurements of acoustic admittance and reflectance in neonates," Ear Hear. **21**, 443–461.
Keefe, D. H., and Simmons, J. L. (**2003**). "Energy transmittance predicts conductive hearing loss in older children and adults," J. Acoust. Soc. Am. **114**(6), 3217–3238.
Kim, D. (**1980**). "Cochlear mechanics: Implications of electrophysiological and acoustical observations," Hear. Res. **22**, 95–104.
Kujawa, S. G., Glattke, T. J., Fallon, M., and Bobbin, R. P. (**1993**). "Contralateral sound suppresses distortion product otoacoustic emissions through cholinergic mechanisms," Hear. Res. **68**, 97–106.
Kujawa, S. G., and Liberman, M. C. (**2001**). "Effects of olivocochlear feedback on distortion product otoacoustic emissions in guinea pig," J. Assoc. Res. Otolaryngol. **2**, 268–278.
Lavigne-Rebillard, M., and Pujol, R. (**1987**). "Surface aspects of the developing human organ of Corti," Acta Oto-Laryngol., Suppl. **436**, 43–50.
Lavigne-Rebillard, M., and Pujol, R. (**1988**). "Hair cell innervation in the fetal human cochlea," Acta Oto-Laryngol. **105**, 398–402.
Mills, D. (**1998**). "Interpretation of distortion product otoacoustic emission measurements. II. Estimating tuning characteristics using three stimulus tones," J. Acoust. Soc. Am. **103**, 507–523.
Morlet, T., Collet, L., Salle, B., and Morgon, A. (**1993**). "Functional maturation of cochlear active mechanisms and of the medial olivocochlear system in humans," Acta Oto-Laryngol. **113**, 271–277.
Moulin, A., Collet, L., and Duclaux, R. (**1993**). "Contralateral auditory stimulation alters acoustic distortion products in humans," Hear. Res. **65**, 193–210.
Okabe, K., Tanaka, S., Hamada, H., Miura, T., and Funai, H. (**1988**). "Acoustic impedance measurement on normal ears of children," J. Acoust. Soc. Jpn. **9**, 287–294.
Pienkowski, M., and Kunov, H. (**2001**). "Suppression of distortion product otoacoustic emissions and hearing threshold," J. Acoust. Soc. Am. **109**, 1496–1502.
Puel, J. L., and Rebillard, G. (**1990**). "Effect of contralateral sound stimulation on the distortion product $2F1$-$F2$: Evidence that the medial efferent system is involved," J. Acoust. Soc. Am. **87**, 1630–1635.
Puria, S. (**2003**). "Measurements of human middle ear forward and reverse acoustics: Implications for otoacoustic emission," J. Acoust. Soc. Am. **113**, 2773–2789.
Ryan, S., and Piron, J. (**1994**). "Functional maturation of the medial efferent olivocochlear system in human neonates," Acta Oto-Laryngol. **114**, 485–489.
Spetner, N., and Olsho, L. (**1990**). "Auditory frequency resolution in human infancy," Child Dev. **63**, 632–652.
Talmadge, C., Tubis, A., Long, G., and Piskorski, P. (**1998**). "Modeling otoacoustic emission and hearing threshold fine structures," J. Acoust. Soc. Am. **104**, 1517–1543.
Talmadge, C., Tubis, A., Long, G., and Piskorski, P. (**1999**). "Experimental confirmation of the two-source interference model for the fine structure of distortion product otoacoustic emissions," J. Acoust. Soc. Am. **105**, 275–292.
Varghese, G. I., Zhu, X., and Frisina, R. D. (**2005**). "Age-related declines in distort product otoacoustic emissions utilizing pure tone contralateral stimulation in CBA/CaJ mice," Hear. Res. **209**, 60–67.

Low-frequency characteristics of human and guinea pig cochleae

Torsten Marquardt[a)]
UCL Ear Institute, University College London, 332 Gray's Inn Road, London WC1X8EE, United Kingdom

Johannes Hensel, Dieter Mrowinski, and Gűnther Scholz
Charité, Medical Faculty of Berlin Universities, ENT Department, Charitéplatz 1, D-10117 Berlin, Germany

(Received 10 January 2007; revised 12 March 2007; accepted 14 March 2007)

Previous physiological studies investigating the transfer of low-frequency sound into the cochlea have been invasive. Predictions about the human cochlea are based on anatomical similarities with animal cochleae but no direct comparison has been possible. This paper presents a noninvasive method of observing low frequency cochlear vibration using distortion product otoacoustic emissions (DPOAE) modulated by low-frequency tones. For various frequencies (15–480 Hz), the level was adjusted to maintain an equal DPOAE-modulation depth, interpreted as a constant basilar membrane displacement amplitude. The resulting modulator level curves from four human ears match equal-loudness contours (ISO226:2003) except for an irregularity consisting of a notch and a peak at 45 Hz and 60 Hz, respectively, suggesting a cochlear resonance. This resonator interacts with the middle ear stiffness. The irregularity separates two regions of the middle ear transfer function in humans: A slope of 12 dB/octave below the irregularity suggests mass-controlled impedance resulting from perilymph movement through the helicotrema; a 6-dB/octave slope above the irregularity suggests resistive cochlear impedance and the existence of a traveling wave. The results from four guinea pig ears showed a 6-dB/octave slope on either side of an irregularity around 120 Hz, and agree with published data. © *2007 Acoustical Society of America.*
[DOI: 10.1121/1.2722506]

PACS number(s): 43.64.Kc, 43.64.Jb, 43.64.Yp [BLM] Pages: 3628–3638

I. INTRODUCTION

The sensitivity of the auditory system decreases dramatically towards the low-frequency (LF) end of auditory perception. Nevertheless, environmental sounds often contain large sound pressures in this frequency range. Questions arising from this about the annoyance and possible physiological effects of LF noise have led to much research into LF hearing. During the past decades, many physiological experiments and modeling studies have contributed to our understanding of how the apical termination of the cochlea acoustically influences the ear's sensitivity to LF sound. However, all physiological methods used so far are too invasive to be applicable to humans, and predictions about the human cochlea are based on anatomical similarities with animal cochleae. The present report introduces a technique that can noninvasively reveal individual differences in the acoustic properties of the apical cochlea that might be linked with individual differences in LF sensitivity.

The cochlear sensitivity to very low frequencies is strongly affected by the helicotrema, an apical connection between the cochlear ducts above and below the basilar membrane. Local pressure difference between the cochlear ducts causes a displacement of the basilar membrane, and leads consequently to the excitation of sensory cells that are mechanically connected to it. Stimulus energy travels along the basilar membrane in the form of a traveling wave which terminates after reaching maximum amplitude at a place characteristic for the stimulation frequency (the characteristic place). The mechanical properties of the basilar membrane are such that, for higher frequencies, the traveling wave terminates basally, and for lower frequencies further apically. For frequencies low enough that the characteristic place is close or virtually beyond the apical end of the basilar membrane, the helicotrema shunts the pressure difference across the basilar membrane, and thus determines the cochlear input impedance and sensitivity to LF sounds. This shunting constitutes a high-pass filter, and contributes to the observed rise in detection threshold towards lowest frequencies (Cheatham and Dallos, 2001).

With the aim of characterizing the cochlear input impedance at low frequencies for several animal species, Dallos (1970) monitored cochlear microphonic (CM) potentials in response to LF tones with a pair of intracochlear electrodes in the basal turn of the cochlea. Under the assumption that a given CM amplitude indicates a certain basilar membrane displacement, the intensity of the LF tone required to maintain equal CM amplitude at various frequencies, ranging from 20 Hz to 2 kHz, reveals the transfer function from pressure at the tympanum to the differential pressure across the basilar membrane at the recording site [i.e., the inverse of the forward middle ear transfer function[1] (fMETF)]. Dallos dis-

[a)]Electronic mail: t.marquardt@ucl.ac.uk

 0001-4966/2007/121(6)/3628/11/$23.00 © 2007 Acoustical Society of America

cussed his results with regard to the influence of the helicotrema on the cochlear input impedance. Since his CM measurements were invasive, he could only speculate about human cochlear impedance characteristics based on the similarities of human cochlear anatomy to that of cat and chinchilla (see Discussion). Later, Zwicker (1977) confirmed some aspects of Dallos' hypothesis by studying the effect of basilar membrane biasing by LF sounds on tone-burst detection threshold. Further physiological studies regarding the transfer of LF sound into the cochlea have been performed in animals (Weiss *et al.*, 1971; Nedzelnitsky, 1980; Dancer and Franke, 1980; Lynch *et al.*, 1982; Franke and Dancer, 1982; Franke *et al.*, 1985; Ruggero *et al.*, 1986; Magnan *et al.*, 1999) and in temporal bone preparations from human cadavers (Kurokawa and Goode, 1995; Merchant *et al.*, 1996; Puria *et al.*, 1997;Aibara *et al.*, 2001; Puria, 2003). With the exception of Zwicker's indications, which stem from psychoacoustical experiments, data have been obtained invasively. Therefore, objective physiological data from living human subjects are not available.

Zwicker measured so-called masking period patterns (MaPP) which show the detection threshold of a short tone burst as a function of its relative position to the phase of a very LF masker. With this psychophysical method, he was able to investigate the transmission of LF sounds into the cochlea noninvasively. Similar to his idea, the authors of this paper measure modulation period patterns (MoPP) of the 2f1-f2 distortion product otoacoustic emission (DPOAE) to study the transmission of LF sound into the cochlea.

DPOAEs are recorded noninvasively with a probe microphone in the ear canal (for a review, see Probst, 1991). The 2f1-f2 DPOAE is the strongest of the intermodulation products generated by nonlinear cochlear processes in response to sound stimulation with two primary tones at frequencies f1 and f2. It serves in the present study as the high-frequency carrier of information about the basilar membrane displacement caused by LF sound.

Like Zwicker's MaPP, the MoPP caused by a modulator tone show two pronounced dips. The larger dip is linked to the moment of basilar membrane displacement towards scala tympani, and the smaller dip to displacement towards scala vestibuli. MoPP of transiently evoked otoacoustic emissions (TEOAE) were measured before by Zwicker (1981), and Nubel *et al.* (1995). However, the limited time resolution of MoPP obtained by TEOAE measurements restricts the maximum modulation frequency to approximately 50 Hz. The use of DPOAE can circumvent this problem and, in addition, reduces the recording time considerably. With the aim of understanding the generation process of DPOAE, MoPPs of DPOAE were investigated earlier (Frank and Koessl, 1996, 1997; Scholz *et al.*, 1999; Bian *et al.*, 2002, 2004; Bian, 2004; Lukashkin and Russell, 2005). In order to extract the DPOAE magnitude as a function of the modulator's phase, the Fourier transform was applied to a sliding short-time window. This method, however, limits the highest modulation frequency even more. In the present report, the time course of the DPOAE modulation is retrieved from the spectral components of a long-time Fourier transform over several modulation periods. This kind of analysis allows the measurement of MoPP over a significantly wider range of modulation frequencies, so that they become useful to study the fMETF up to frequencies of several hundred Hz. Similar to Dallos' (1970) approach, the intensity of the LF tone was adjusted to maintain equal DPOAE-modulation depth at various modulation frequencies. Like his results, the resulting curves [distortion product isomodulation curve (DPIMC)] reveal the inverse of the fMETF, the frequency-dependent ratio between differential pressure across the basilar membrane and pressure at the tympanum.[1]

II. METHODS

A. Stimulus presentation and recording

The signals of the LF modulator tone and the two primary tones were converted at a sampling rate of 48 kHz using a multichannel sound card (GINA, Echo) connected to a Pentium computer. All output and input channels of this 20-bit sound card run on the same clock signal, and their conversion starts and stops synchronously. The two miniature loudspeakers of a DPOAE ear probe (ER-10C, Etymotic Research) produced the primary tones. The LF modulator signal was power amplified, then low-pass filtered (f_c=30 Hz, −6 dB/octave, passive) to prevent accidental sound delivery of more than 105 phon, before finally being converted by an acoustically closed DT-48 earphone (Beyerdynamic) and delivered into the ear canal via a polythene tube (1 mm inner diameter, 150 mm length). The details of this differed between the setups for human and guinea pig, and are described below separately. The sound pressure in the ear canal was measured with the microphone of the ER-10C probe. The high intensity LF tone in the microphone signal was attenuated (passive high-pass filter, f_c=1 kHz, 12 dB/octave) prior to signal amplification (Bruel and Kjaer 2636, A-filter on) in order to use the dynamic range of the amplifier and the A/D converter soundcard effectively for the DPOAE signal. The soundcard contained an on-board preamplifier with programmable gain. This gain was adjusted automatically prior to recording using a 400 ms test presentation of the stimulus.

To achieve a sound pressure level in the ear canal of up to 120 dB SPL at very low frequencies, the ER-10C probe had to be fitted without a leak. The frequency responses of all loudspeakers were measured in the ear canal after each probe placement using the precalibrated probe microphone (see below). This allowed checking for leaks and the assessment of acoustical differences determined by individual ear canal volume and probe placements. The stimulus amplitudes were adjusted to achieve the defined sound pressure levels and phases at the tip of the probe. At the beginning of each recording session, a software routine varied the primary parameters within a roughly defined range in order to maximize the 2f1-f2 DPOAE level for the individual ear. During this procedure, there was no presentation of the LF modulator tone. All signal generation, processing, and analysis were done with customized software.

B. Human subjects

The subjects were two females (M.B., aged 19; J.W., aged 30) and one male (T.M., aged 30). These subjects were selected for their high level of DPOAE known from earlier experiments. All subjects had normal hearing, as verified by pure-tone audiometry between 125 Hz and 8 kHz. No history of chronic ear diseases was reported. The ethics committee of the Humboldt University, Berlin, in agreement with the Declaration of Helsinki, approved the procedure, and all subjects gave their informed consent.

The recordings were made in a soundproof booth (IAC). The silicone tube for the LF tone was put through the foam plug of the ER-10C probe. In order to produce a reliable seal of the probe to the ear canal, it was in some cases necessary to apply Vaseline around the foam plug as a sealant. This affected only the entrance of the ear canal and was easily removed afterwards with cotton wool tips. The subjects were asked not to swallow and to breathe quietly during the recording sweeps (20.4 seconds). In case of an apparent noise artifact, the recording was repeated immediately. In between the recording sweeps the subjects were given time to get comfortable (e.g., to swallow). When ready for the next sweep, they gave a sign through the window of the booth. An acoustic warning signal indicated the start of the next measurement. Recordings for the estimation of a complete DPIMC were made within one session (approximately 1 hour) without removal of the ear probe.

C. Guinea pigs

Recordings were made from both ears of two pigmented guinea pigs, of 390 g (GP1) and 1200 g (GP2) weight. The animals were premedicated with atropine sulfate (0.06 mg, s.c.) and anesthetized with urethane (1.3 g/kg in 20% solution, i.p.). Further analgesia was obtained with phenoperidine (1 mg/kg, i.m.). Supplementary doses of phenoperidine (0.5–1 mg/kg, i.m.) were given on indication provided by the pedal withdrawal reflex. All animals were tracheotomized, and core temperature was maintained at 37 °C with a heating blanket. The animal was placed inside a soundproof booth (IAC). The head was fixed with hollow plastic speculum used like ear bars. After removal of its foam sealing, the three-canal tube of the ER-10C probe was placed with a tight fit into the inner canal of the speculum, which led into the ear canal. The silicone tube for the LF tone was connected to a steel tube (1 mm outer diameter), which had its own entrance into the inner canal of the speculum close to its opening into the ear canal (2 mm inner diameter). All joints were sealed with Vaseline. Early pilot measurements revealed that in order to maintain the DPOAE level constant over several hours, it was essential to equilibrate static air pressure on both sides of the tympanic membrane (Zengh *et al.*, 1997). This was done by inserting the tip of a narrow polythene tube (250 mm long, 0.3 mm inner diameter) into the bulla via a small hole sealed with Vaseline. All experiments with guinea pigs were carried out in accordance with the Animal (Scientific Procedures) Act of 1986 of Great Britain and Northern Ireland.

D. Calibration of the probe microphone

In order to interpret the recorded probe microphone signal correctly, the overall transfer function of the entire recording pathway (ER-10C probe, 1-kHz high-pass filter, B&K 2636, and soundcard) was measured in an 1.5 cm^3 cavity containing a 1/2 in. calibration microphone (B&K 4134). Its signal, amplified with an additional measurement amplifier (B&K 2636), was recorded via the second input of the soundcard. Since both signals are converted by the same soundcard, the transfer function of the soundcard could not be assessed in this way, and although the specifications of the soundcard and also the Bruel & Kjaer equipment show a linear magnitude transfer function down to at least 10 Hz, their phase transfer function at lowest frequencies might depart from linearity.

In order to assess the phase transfer function of the calibration path at low frequencies, the calibration hardware was driven outside its linear range by delivering LF tones at 115 dB SPL via the LF stimulus path. The hardware nonlinearity, most likely caused by the large LF displacements of the calibration microphone's membrane, produces minute modulation of a 2 kHz tone, generated by one of the probe's loudspeakers (94 dB SPL). This technique transposes the LF tone to the 2 kHz region where the transfer functions of equipment are known to be linear. This instantaneous modulation of the 2 kHz tone is in-phase with the LF displacement of the microphone membrane, which itself is proportional to the LF sound pressure in the cavity. This assumption was confirmed by analyzing the phase relationship between the modulation and the modulator in the calibration microphone's signal. The spectrum showed zero phase difference for modulation frequencies down to 100 Hz ($<2°$). The phase differences between modulation and modulator increased progressively towards 15 Hz modulation (25°). This departure from zero phase associated with the calibration equipment was incorporated in the calibration procedure of the probe microphone path.

E. Reconstruction of the modulation period pattern

The ear canal pressure during sound stimulation was continuously recorded for 20.4 seconds in human ears and for 4.4 seconds in guinea pig ears. The first and last 200 ms were discarded. The remaining waveform was averaged into a 200 ms buffer. This gave 100 averages for the human and 20 averages for the guinea pig recording (the signal-to-noise ratio in the recording of the anesthetized guinea pigs was considerably larger). The primary and modulator tone frequencies were chosen to be multiples of 5 Hz and, therefore, their periods fitted an integer number of times into the 200 ms buffer. Consequently, the digital Fourier transform of the buffer produced precise spectral lines for all signals used and generated [Figs. 1(A) and 2(A)]. The part of the spectrum representing the DPOAE signal was regarded as a modulated tone, consisting of the DPOAE frequency (2f1-f2) as the carrier and the spectral components spaced at modulation frequency either side of this carrier (bold gray lines). The latter were regarded as the modulation sidelines. Throughout this report, only the carrier, 2f1-f2, and the two

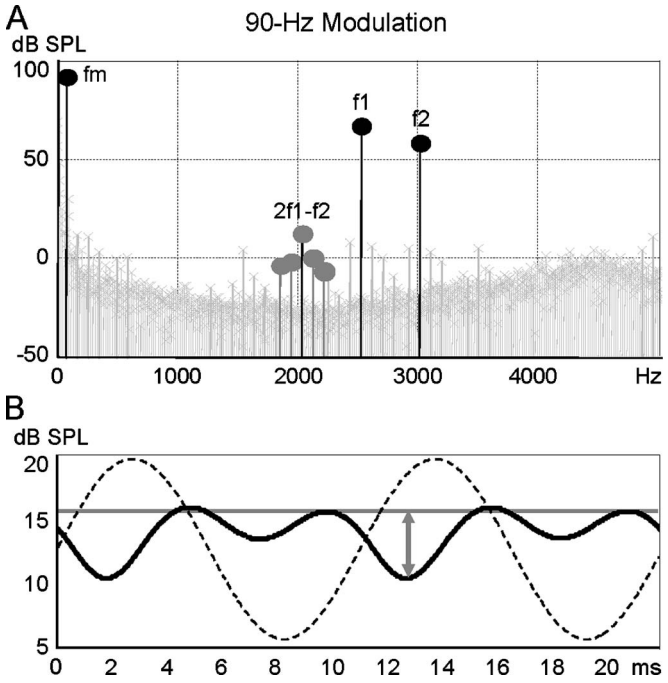

FIG. 1. Reconstruction of the modulation period pattern (MoPP) with 90-Hz modulation. (A) The spectrum of the recorded signal shows the stimulus tones with black circular markers (modulator tone, fm; primary tones, f1 and f2), and modulated DPOAE, 2f1-f2 with gray circular markers. The DPOAE consists of the 2f1-f2 carrier and modulation sidelines. Due to the appropriate rectangular buffer length of exactly 1/5 second, they show no spectral splatter and first and second order modulation sidelines stick clearly out from the noise floor. (Further singular spectral lines representing other distortion products can be identified.) (B) The time course of the 2f1-f2 DPOAE is reconstructed from the 2f1-f2 carrier and its first and second order pair of modulation sidelines. The black modulation period pattern (MoPP) represents the sound pressure level of the 2f1-f2 DPOAE in decibel as a function of time. The horizontal gray line indicates the DPOAE level without modulation. For phase reference, the sinusoidal sound pressure of the 90 Hz modulator tone in the ear canal is indicated as a dashed line (arbitrary linear scale). The difference between the DPOAE minimum and the unmodulated DPOAE level defines maximum DPOAE suppression (gray double arrow), called "modulation depth."

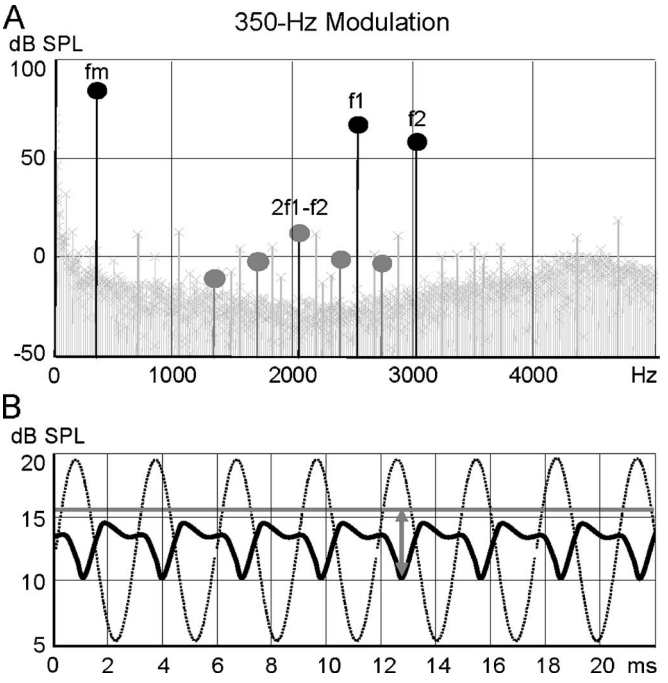

FIG. 2. Same as Fig. 1 but with 350-Hz modulation. (A) At higher modulation frequencies the modulation sidelines of the distortion product 2f1-f2 overlap with those of the primaries. Careful choice of stimulus frequencies avoids coincidence of the $2f1\text{-}f2 \pm n \cdot f_m$ ($n = 0, 1, 2$) modulation sidelines and other spectral lines representing stimuli or other distortion products. The interleaving of the spectral components enables the reconstruction of the time course of the 2f1-f2 DPOAE for modulation frequencies close to or even greater than f2-f1 (B).

sideline pairs closest to it were used to compute the time course of the DPOAE by application of the inverse Fourier transform to just these spectral components. Further distant modulation sidelines were weak and contributed little reliable information (i.e., just increased the noise). Figures 1(B) and 2(B) show examples of DPOAE modulation period patterns (MoPP), i.e., the envelope of the DPOAE magnitude. For comparison, the time course of the LF modulator tone in the ear canal is given as a dotted line (sound pressure on linear arbitrary scale).

The spectra in Figs. 1(A) and 2(A) also show modulation sidelines around the primary tones. In recordings from the ear canal, these sidelines are much stronger than those caused by hardware nonlinearities when recording in a 1.5 cm^3 cavity. They are likely to be sidelines of modulated stimulus frequency otoacoustic emissions. A coincidence in frequency of a DPOAE modulation sideline with such a primary modulation sideline would make the retrieval of the DPOAE time course impossible. Fortunately, the primary frequencies can be chosen so that their spectral modulation components do not coincide but interleave with those of the modulated DPOAE. This is illustrated in Fig. 2 for a modulation frequency of 350 Hz. In theory, the interleaving allows the retrieval of MoPP with modulation frequencies up to half of the DPOAE carrier frequency (2f1-f2). However, above approximately 250 Hz, the MoPP start to divert from the classic shape of the MoPP obtained with modulation at very low frequencies. This hinders estimation of the location of the MoPP's minimum at higher modulation frequencies [Fig. 2(B)]. Possible reasons for this distortion are the following. First, the upper frequency at which DPOAE can be modulated might be limited by a large recovery time of the DPOAE generation process from suppression. Thus the DPOAE might not be able to follow higher rates of modulation. The finding that most MoPP above 250 Hz show an increasingly sustained DPOAE suppression (i.e., the MoPP maximum does not reach the unmodulated DPOAE level) supports this possibility. Second, the reverse middle ear transfer function distorts the modulated DPOAE spectrum during retrograde travel especially at high modulation rates when the modulation sidelines are widely spaced. In most cases, however, it was possible to measure the MoPP for modulation frequencies from 15 Hz to 480 Hz.

F. Distortion product isomodulation curve

There is general agreement in the literature that the DPOAE component 2f1-f2 is generated predominantly near the characteristic place of f2 (e.g., Martin *et al.*, 1987). At this place, the basilar membrane's response to a much lower frequency tone is that of a pure compliance. The basilar

membrane displacement due to the LF tone (bias) is therefore proportional to and in phase with the slowly varying pressure difference across the basilar membrane. As shown in Figs. 1 and 2, the periodic displacement causes a modulation in the generation of the DPOAE. The depth of DPOAE modulation is unlikely to be linearly related to the amplitude of the LF basilar membrane displacement. However, a constant DPOAE modulation depth is an indicator of a constant amplitude of basilar membrane displacement, independent of the frequency of the modulator tone, given that it is well below the frequencies of the primary tones, f1 and f2, and the DPOAE, 2f1-f2. With this assumption, the authors claim that the frequency-dependent levels of the modulator tone that cause equal DPOAE modulation depth (i.e., DPIMC), constitute the equivalent to the functions originally obtained by Dallos (1970) using CM. The DPOAE modulation depth is here defined as the difference (in dB) between the unmodulated DPOAE level and DPOAE level at maximum DPOAE suppression in the MoPP [gray arrows in Figs. 1(B) and 2(B)].

The DPIMC resembles the inverse of the fMETF, and, after multiplication by the modulator's frequencies (i.e., a 6 dB/octave slope change), reveals the magnitude of the impedance across the basilar membrane, Z'_C (see Discussion). The phase of this impedance can be inferred from the phase relationship between the MoPP and the modulator tone. When obtaining this phase, the reverse traveling time of the DPOAE must be taken into account. The traveling times are estimated by matching roughly the slope of the obtained phase transfer functions with those of Dallos' CM measurements (Dallos, 1970), where no delay between basilar membrane displacement and CM recording occurs.

III. RESULTS

A. Humans

Figure 3(A) shows DPIMC of subject T.M. with several primary frequency and primary level combinations. In all curves, the LF modulator level was adjusted to yield a 6 dB DPOAE modulation depth. The dependencies on the primary parameters agree with the findings of Scholz *et al.* (1999). Higher primary frequencies require larger LF modulator levels than lower primary frequencies to yield equal DPOAE modulation depth. Higher primary levels require larger LF modulator levels than lower primary levels. Regarding the dependency on the modulation frequency, it can be generally said that lower modulation frequencies require greater LF modulator levels; except for an irregularity, showing a minimum at 40 Hz and a maximum at 60 Hz. This prominent feature, seen in all DPIMC obtained, are an indication of a cochlear resonance, and will be discussed in Sec. IV C. The frequency of its inflection point (f_{PR}) is approximately 50 Hz. For frequencies below the irregularity the slope of the DPIMC is steeper (more than −12 dB/octave) than for frequencies above the irregularity (approximately −6 dB/octave). For comparison, two straight lines with slopes of −12 dB/octave and −6 dB/octave are shown in Fig. 3(A).

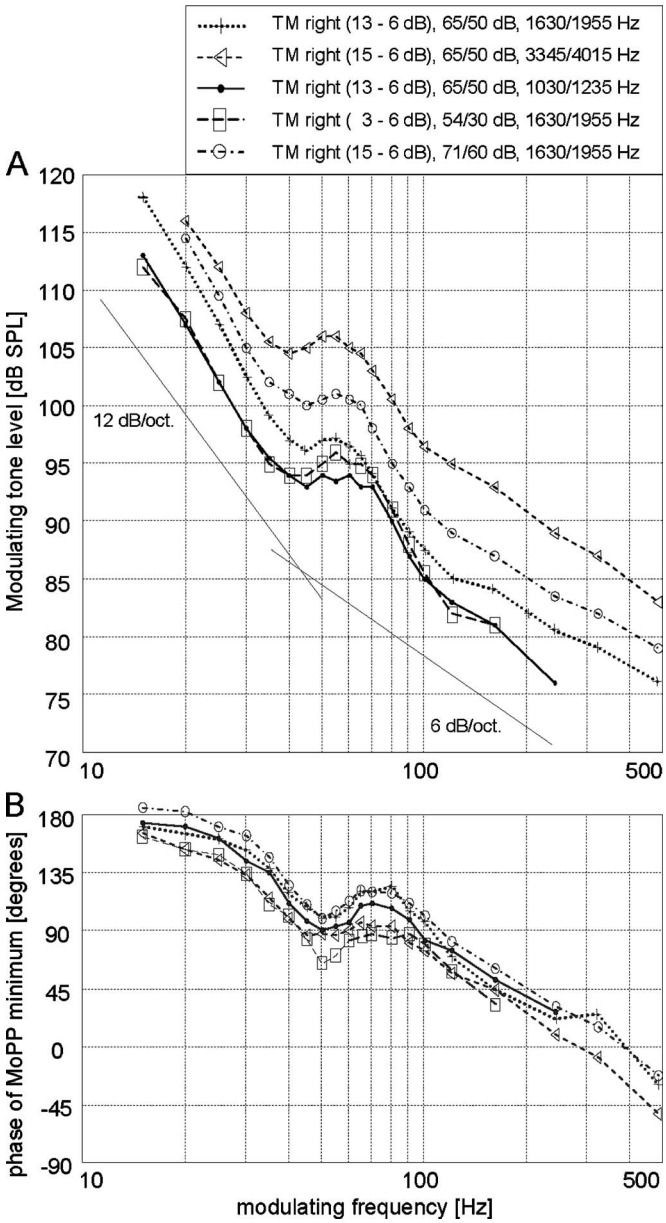

FIG. 3. Distortion product isomodulation curves (DPIMC) from the right ear of subject TM. DPIMC for various primary parameters are shown. Interpretation of the legend is "subject ear (unmodulated DPOAE level–modulation depth), L_1/L_2, f_1/f_2." For example, "TM right (13–6 dB), 65/50 dB, 1630/1955 Hz" means that subject TM's right ear was exposed to two primary tones of 1630 Hz at 65 dB SPL and 1955 Hz at 50 dB SPL and produced a 2f1-f2 DPOAE level of 13 dB SPL. In this example, LF tones at levels indicated on the ordinate in (A) for the frequencies shown on the abscissa resulted in a DPOAE modulation depth of 6 dB (in this figure, all curves stem from 6 dB isomodulation). For comparison, slopes of 6 and 12 dB/octave are indicated by straight lines with arbitrary offsets. (B) Phases of maximum DPOAE suppression with reference to the pressure maximum of the modulator tone in the ear canal are shown as a function of modulation frequency. Phase values are compensated for DPOAE reverse travel times. See text for details.

Figure 3(B) shows the respective phases of the maximum suppression within the MoPP referenced to the pressure maximum of the LF modulator tone in the ear canal. In accordance with the DPIMC, the phase curves also show an irregularity. At lowest modulation frequencies, the maximum suppression leads the ear canal pressure by approximately 180°. This phase lead generally declines towards higher

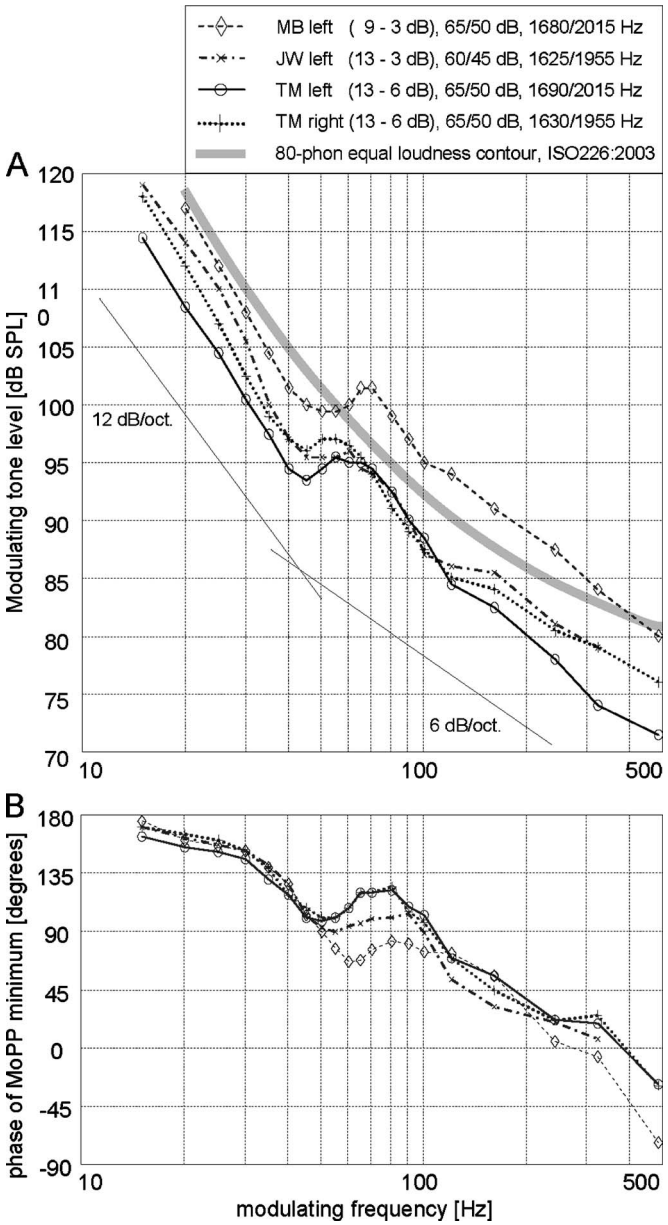

FIG. 4. Distortion product isomodulation curves (DPIMC) for four ears of three subjects with almost constant primary parameters. See legend and caption of Fig. 3. For comparison, the 80-phon equal-loudness contour (ISO226:2003) is shown in gray.

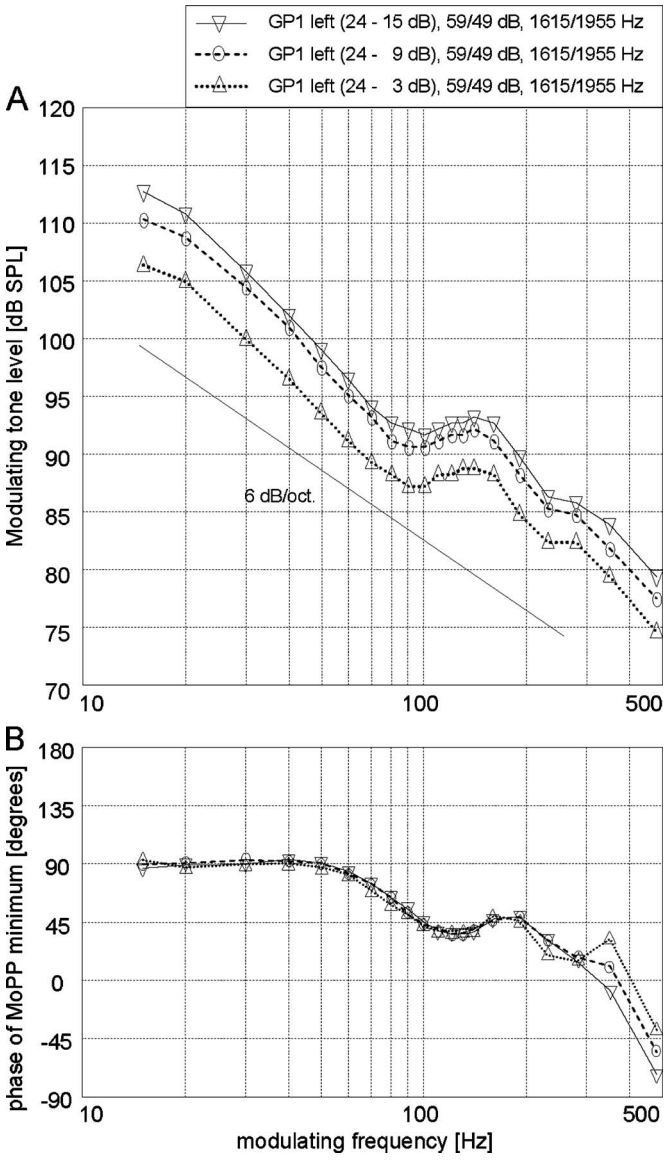

FIG. 5. Distortion product isomodulation curves (DPIMC) from one guinea pig ear for DPOAE modulation depths of 3 dB, 9 dB, and 15 dB. The primary parameters are constant. See legend and caption of Fig. 3.

modulation frequencies. Note, however, that errors in estimated reverse traveling time have increasing impact on the phase values at higher modulation frequencies; therefore these phase values should be interpreted with caution. With the aim to match the phase slopes with the slopes in Dallos' publication (1970), the DPOAE reverse traveling times were set to 2.5 ms for f2=1235 Hz, 2 ms for f2=1955 Hz, and 1 ms for f2=4015 Hz.

The results in Fig. 3 show the robustness of the DPIMC shape against changes of the primary parameters. Each curve was measured with a new placement of the probe into the ear canal. The similarity in the shapes of the curves indicates high reproducibility.

Figure 4(A) shows DPIMCs for four ears of three subjects with almost identical primary parameters. Note that the isomodulation depth for subject T.M. is 6 dB in contrast to the chosen 3 dB for the two other subjects. T.M.'s left ear data are taken from Fig. 3. The respective phases of the maximum suppression, compensated for 2 ms DPOAE reverse traveling time, are given in Fig. 4(B). The course is broadly similar in all subjects, though f_{PR} varies slightly, e.g., approximately 10 Hz higher in subject MB. There is generally a good correlation between magnitude and phase curves with respect to strength and frequency of the irregularity.

B. Guinea pigs

The DPMCs from guinea pigs, shown in Figs. 5 and 6, also show the irregularity. Its minimum and maximum in the guinea pig DPIMC are at 100 Hz and 140 Hz, respectively. The frequency of its inflection point (f_{PR}) is approximately 120 Hz and more than an octave higher than in humans. Another difference to the human data is the slope of the

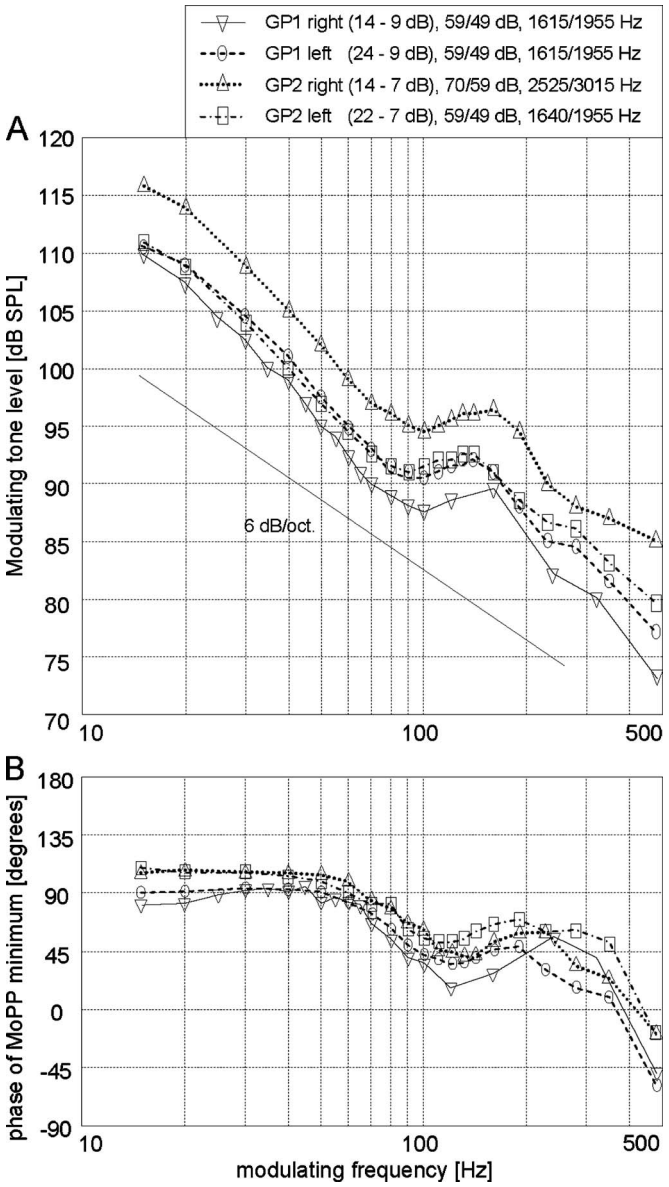

FIG. 6. Distortion product isomodulation curves (DPIMC) for four ears of two guinea pigs obtained with various primary parameters and DPOAE modulation depths. See legend and caption of Fig. 3.

DPIMC at modulation frequencies lower than the irregularity, which is close to 6 dB/octave (shown by the straight solid line). This is almost equal to the curve's slopes above the irregularity and approximately 6 dB/octave shallower than is seen in the human DPIMC. Towards the lowest of the applied modulation frequencies (15 Hz), the slopes appear to flatten even further. In accordance with the slope of −6 dB/octave, the maximum suppression in the MoPP leads the ear canal pressure below the irregularity by only 90°. However, no equivalent to the obvious flattening of the DPIMC at 15-Hz modulation frequency is apparent in the phase data.

Figure 5 shows curves of one guinea pig ear for DPOAE modulation depths of 3 dB, 9 dB, and 15 dB. The DPOAE primary parameters remained constant. The vertical relation of the three DPIMC in Fig. 5(A) show that the level of the LF biasing tone had to be increased in order to achieve deeper DPOAE modulation. However, this relationship between LF tone level and modulation depth appears to be strongly nonlinear. Note that the chosen modulation depth does not influence the shape of the curve. Figure 5(B) shows the respective phases of maximum suppression in the MoPPs relative to ear canal pressure maximum. Reverse traveling time compensation was 2 ms.

Figure 6(A) shows DPIMCs for four ears of two guinea pigs. The data from the left ear of GP1 are taken from Fig. 5. The curves are broadly similar, except for a slight variation in f_{PR}. The phases of maximum suppression in Fig. 6(B) have been compensated for DPOAE reverse traveling times of 2 ms for f2=1955 Hz and 0.25 ms for f2=3015 Hz.

IV. DISCUSSION

A. Distortion product isomodulation curve and the forward middle ear transfer function

In this study the fMETF is defined as the frequency-dependent ratio between the differential pressure across the basilar membrane and pressure at the tympanum[1]:

$$\text{fMETF} = (p_{SV} - p_{ST})/p_T, \tag{1}$$

where p_{SV} denotes the scala vestibule pressure, p_{ST} the scala tympani pressure, and p_T the pressure at the tympanum. Since the relationship between DPOAE modulation depth and the amplitude of the LF basilar membrane displacement is probably nonlinear, the fMETF was measured in the form of an iso-output function, i.e., the input parameter is adjusted to maintain constant output. This method is often used in order to remain within the optimum range of the measurement equipment (e.g., Dallos, 1970; Ruggero *et al.*, 1990). Given the investigated system is linear, the iso-output function is the inverse of the desired transfer function (iso-input function). In this study, linearity is assumed between pressure at the tympanum and basilar membrane displacement as has been shown by Dallos (1970) in a control experiment, measuring CM for one animal as both iso-input and iso-output function. The identical results confirmed linearity and that Dallos' measurements of iso-output functions indeed revealed the fMETF. The authors presume also that the DPOAE measured in this study originate from basilar membrane locations basal to sites of known nonlinear responses to the applied modulator tones. It is however possible that the characteristic place 2f1-f2, where the apically traveling part of the DPOAE is assumed to be reflected (Talmadge *et al.*, 1999), is nonlinearly affected by modulator tones of higher frequencies. It is possible that this causes the observed distortion of the MoPPs at modulation rates >150 Hz. Nevertheless, the agreement of the fMETF, obtained by inverting guinea pig DPIMC, with other published guinea pig data (Fig. 7), leads analogously to the conclusion that the inverse of the human DPIMC is equivalent in shape to the human fMETF:

$$\text{fMETF} \propto 1/\text{DPIMC}. \tag{2}$$

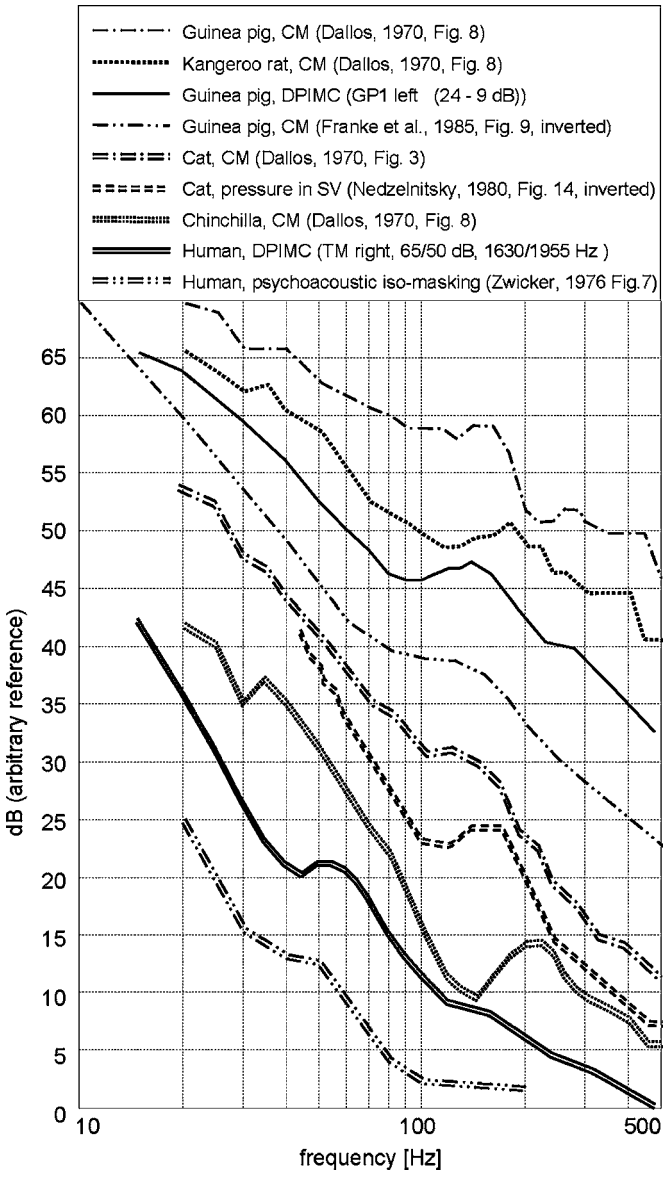

FIG. 7. Comparison with other published results measured with a variety of techniques that reveal cochlear impedance features. Curves are selected for containing a similar irregularity as seen in DPIMC. Data by Franke *et al.* (1985) and Nedzelnitski (1980), obtained as iso-output function, have been inverted. Following Dallos' (1970) species classification, single-lined graphs represent data from viscosity-dominated cochleae; double lined graphs represent data from inertia-dominated cochleae (at lowest frequencies).

B. Forward middle ear transfer function and the cochlear impedance

The fMETF gives insight into the cochlear impedance. Depending on the measurement methods, researchers discuss their data relating to two different definitions of the cochlear input impedance. Researchers measuring cochlear pressure directly often relate pressure in the basal scala vestibuli (p_{SV}) to stapes volume velocity (U_S) to calculate the cochlear input impedance:

$$Z_C = p_{SV}/U_S. \tag{3}$$

Researchers, who estimate basilar membrane displacement (x_{BM}), e.g., by measuring CM or DPOAE suppression, tend to relate ($p_{SV}-p_{ST}$) to U_s. Lynch *et al.* (1982) called this "the impedance across the basilar membrane":

$$Z'_C = (p_{SV} - p_{ST})/U_S. \tag{4}$$

Nedzelnitsky (1980) showed in cat that from frequencies above 40 Hz p_{sv} increasingly exceeds p_{ST}, which is dominated by the compliance of the round window and almost constant up to 300 Hz. Above approximately 100 Hz, p_{SV} becomes so dominant in ($p_{SV}-p_{ST}$) that Z_C and Z'_C become almost identical. Below 40 Hz, however, Z_C and Z'_C differ considerably. The flow of perilymph through the helicotrema tends to equalize the pressure between the scalae, and the round window compliance also controls p_{SV}, and consequently Z_C. In contrast, Z'_C is controlled by the small remaining difference between p_{SV} and p_{ST} resulting from perilymph movement through the helicotrema. At these low frequencies, Z'_C is species-dependent, and will be discussed in detail in Sec. IV C.

With a closed bulla, middle ear stiffness governs the displacement of the stapes (x_S) up to at least 480 Hz. Thus x_S is proportional and in-phase with p_T. Since displacement and velocity are generally related via the factor $j \bullet \omega$, the relationship between U_S and p_T has a 6 dB/octave slope and a 90° phase lead:

$$p_T \propto x_S \propto U_S/(j \bullet \omega), \tag{5}$$

where j denotes the imaginary unit, ω the angular frequency, and $\propto$ proportionality. From Eqs. (1), (4), and (5), it becomes clear that Z'_C determines the fMETF:

$$\text{fMETF} \propto j \bullet \omega \bullet Z'_C. \tag{6}$$

Equations (2) and (6) yield the relationship between Z'_C and DPIMC directly:

$$Z'_C \propto 1/(j \bullet \omega \bullet \text{DPIMC}). \tag{7}$$

C. The irregularity

All DPIMC obtained, whether from guinea pig or human ears, show a pronounced irregularity. Its shape features the characteristics of a resonance that is interacting with a dominating stiffness (Salter, 1969). The stiffness reflects unarguably the middle ear. The resonance originates most likely from within the cochlea. In fact, Ruggero *et al.* (1990) see a plateau in their malleus velocity versus frequency functions, which is strongly enhanced to a pronounced resonance when the middle ear stiffness is reduced by opening the bulla (their Fig. 5).

Although inconsistently, this resonance effect can be found in many other physiological data, obtained with a variety of techniques. Figure 7 gives a selection of previously published data showing similar irregularities. Because averaging over different ears might dampen the irregularity, data from individual ears are chosen where available. For example, in the cochlear pressure measurements of Nedzelnitzky *et al.* (1980) in cats, many transfer functions, relating p_{SV} to p_T, show the irregularity between 80 Hz and 200 Hz. Neither the appearance nor the frequency of the irregularity is consistent, so that the average curve only shows

a damped irregularity, better described as a plateau (shown by Lynch *et al.*, 1982, Fig. 20). Thus, only one of his curves with an extraordinarily strong irregularity (Nedzelnitzky *et al.* (1980), Fig. 14) is reproduced in Fig. 7, showing the irregularity is present in p_{SV} alone. Similarly, an imagined mean curve over the DPIMC of the four human individuals in Fig. 4 would show a reduced irregularity. A reduction of the irregularity also can be expected in the mean curve published by Franke *et al.* (1985) which averages CM recordings from 26 guinea pig ears. A slight increase in standard error around 100 Hz supports this assumption (their Fig. 9). Interestingly, there is no evidence of the irregularity in p_{ST} (Nedzelnitsky, 1980, Figs. 13 and 14; Franke and Dancer, 1982, Fig. 1). Thus the irregularity, seen in the data estimating Z'_C, stems only from p_{SV}, and is presumably equally present in Z_C (Ruggero *et al.*, 1990).

All of Dallos' CM data (1970) show the irregularity consistently across cat, guinea pig, chinchilla, and kangaroo rat at a similar frequency region around 150 Hz. This is also the frequency region of the irregularities seen in the other data of the same species. In contrast, the DPIMC obtained from human ears show the irregularity centered around 50 Hz. Also Zwicker's (1976) results from psychoacoustic isomasking experiments on human listeners show a slight step close to this frequency. If the assumption holds that the helicotrema is involved in the occurrence of this cochlear resonance then the frequency tuning of the most apical characteristic place on the human basilar membrane is approximately one octave lower than in the other species discussed.

The human DPIMCs follow roughly the equal-loudness-level contours (Fig. 4, bold gray line) published in ISO226:2003. Surprisingly however, neither the standardized curve nor individually published equal-loudness-level contours reflect the irregularity seen in the physiological data. Also published hearing thresholds at low frequencies show no indication of an irregularity at the expected frequency. See Møller and Pedersen (2004) for a review of published LF equal-loudness and threshold data.

In summary, the dip within the irregularity in the DPIMC reflects what would be increased pressure in scala vestibuli (Z_C peak) for constant LF tone level. A pressure loss in scala vestibuli (Z_C dip) is assumed at the frequency where the irregularity peaks. The reason why these frequency-specific pressure irregularities do not affect hearing sensation is unclear. An explanation might be found in the fact that the location of the physiological measurements is different from the location where LF sound sensation takes place. Sensory cells at the apical end of the cochlea, where the compliance and therefore the displacement of the basilar membrane is greatest, have the lowest threshold to LF stimulation. The sites of the physiological recordings are generally in the basal turns of the cochlea. In agreement with modeling studies by Puria and Allen (1991), the authors believe that the physiologically observed irregularity is caused by an apical reflection. The inertia connected with the movement of perilymph through the helicotrema causes a sharp impedance change from the resistive impedance of traveling wave along the basilar membrane. Thus, for frequencies low enough that the traveling wave reaches the apical end of the basilar membrane, a reflection at this discontinuity seems likely. In the most LF-sensitive apical turn, the reflected wave might have a phase relationship with the forward-propagating wave that alters primarily the phase, and causes only little change in the resulting amplitude of the basilar membrane response. Since the auditory system is insensitive to phase changes in tones, sensation would be unaffected by the reflection. At more basal locations, however, where the physiological data originate from, the propagation delays of forward and backward wave may result in a phase relationship such that their superposition affects the basilar membrane response amplitude, and gives rise to the observed irregularity.

D. Impedance characteristics below the irregularity

For stimulus frequencies too low to have a characteristic place on the basilar membrane, the differential pressure is partially shunted by the helicotrema. Viscosity and inertia of the perilymph moving inside the cochlear ducts and helicotrema dominate Z'_C. The slope of the guinea pig DPIMC close to −6 dB/octave and a 90° phase lead are indications that viscosity rather than inertia impedes the perilymph movement, and Z'_C is resistive. Dallos (1970) concluded that the higher number of turns and the larger tapering of the cochlear ducts of the guinea pig must be the reasons for dominance of viscous friction. He obtained further support for this hypothesis from the kangaroo rat, which has a cochlea of similar anatomy to that of the guinea pig. Selected data from viscosity-dominated cochleae are shown by single lines in Fig. 7. The cochleae of cat and chinchilla, on the other hand, have fewer turns with wider ducts and a larger helicotrema, where the effect of viscosity must be negligible and the inertia of the perilymph controls Z'_C at lowest frequencies. Indeed, Dallos' and others' data from cat and chinchilla show a slope close to −12 dB/octave and a phase lead of 180° below the irregularity (Fig. 7, double lines for inertia-dominated cochleae).

Based on anatomical similarities, Dallos (1970) predicted Z_C of the human cochlea also to be inertia-dominated at lowest frequencies, though he could not prove it by measurement at the time. Later, psychoacoustical experiments by Zwicker (1977) supported his hypothesis. The shapes of Zwicker's MaPP indicate that below a masker frequency of approximately 40 Hz, the LF masking effect on a short tone burst is linked to the masker's second derivative, which is equivalent to a 12 dB/octave slope. Above 40 Hz, the masking effect is linked to the first derivative, equivalent to a 6 dB/octave slope. The similarity of the human DPIMC of this study with the fMETF of chinchilla and cat finally confirms Dallos' conjecture.

E. Cochlear impedance and low-frequency noise hypersensitivity

Investigations into environmental LF noise problems reveal large individual differences in sensitivity to LF noise (review by Leventhall *et al.*, 2003). Being sensitive to LF sound can cause extreme distress to some people permanently exposed in their daily environment to LF noise even at intensities which others can barely detect. LF modulated

DPOAE measurements show that very-LF sound energy, even infrasound, does in fact reach the inner ear. This noninvasive technique might provide the basis for an objective diagnostic tool to identify a physiological cause of LF hypersensitivity in the acoustics of the cochlea.

The DPIMCs show an offset between the parts above and below the resonant region, that constitutes an upward step in human sensitivity to LF sounds below 40 Hz. Small deviations in individual DPIMCs might reflect differences in the conversion of LF sound energy into basilar membrane motion. The following three features in the DPIMC curve might be indicators for increased sensitivity to LF sound.

(1) The frequency of the cochlear resonance. A lower-than-normal f_{PR} means that the shallower 6 dB portion of the curve extends to lower frequencies, and would result in higher-than-normal sensitivity for frequencies below normal f_{PR} (50 Hz).

(2) The slope for frequencies below the cochlear resonance. A 6 dB slope of the curve below the transition region, as in guinea pig and kangaroo rat, would give rise to increasing sensitivity as the frequency decreases below f_{PR}.

(3) The cochlear resonance itself. Whatever the interpretation of the irregularity, an abnormality in its frequency or reduced damping might be reflected in auditory threshold or loudness perception. Taking the reflection hypothesis, the phase relationship between the superimposing forward and backward wave can potentially determine the range of hair cells along the basilar membrane responding to the LF sound. A possible widening of the BM tuning might come into effect well above sensation threshold levels and is comparable to the recruitment effect in which hearing impaired listeners report abnormally sharp loudness increase above hearing threshold.

V. CONCLUSIONS

We have shown an objective and efficient technique for making noninvasive measurements of the shape of the human forward middle ear transfer function at low frequencies. Despite the theoretical possibility that the modulation frequency could have been increased to half the DPOAE frequency, the shape of the modulation pattern became increasingly distorted above 250 Hz, and so the method appears to be limited to frequencies below 500 Hz. However, studies with even lower modulation frequencies (i.e., infrasound) seem possible and interesting. The results presented are consistent with data obtained by other researchers using different techniques in animal experiments. Further work is required towards an interpretation of the irregularity as seen in all DPIMC data, and why it is not observed consistently in studies of cochlear input impedance. In addition, the reason why the irregularity is not reflected in hearing threshold and equal-loudness contours has only been addressed speculatively. Nevertheless, the technique presented can potentially reveal abnormal LF acoustical properties of human ears, and might facilitate investigations into the cause of LF hypersensitivity that is observed in some human individuals.

ACKNOWLEDGMENTS

The authors wish to thank David McAlpine for his help during the preparation of the guinea pigs. The authors are also grateful to Ray Meddis, David Kemp, and Isabel Dean for their helpful comments on earlier versions of the manuscript.

[1]It is worth emphasizing that the fMETF is not solely determined by the middle ear, as the term implies. It is also strongly influenced by the cochlear impedance. Note that sometimes, especially when cochlear pressure is measured directly, the fMETF is defined as the ratio between pressures in the scala vestibuli and at the tympanum.

Aibara, R., Welsh, J. T., Puria, S., and Goode, R. L. (**2001**). "Human middle-ear sound transfer function and cochlear input impedance," Hear. Res. **152**, 100–109.

Bian, L. (**2004**). "Cochlear compression: effects of low-frequency biasing on quadratic distortion product otoacoustic emissions," J. Acoust. Soc. Am. **116**, 3559–3571.

Bian, L., Chertoff, M. E., and Miller, E. (**2002**). "Deriving a cochlear transfer function from low-frequency modulation of distortion product otoacoustic emissions," J. Acoust. Soc. Am. **112**, 198–210.

Bian, L., Linhardt, E. E., and Chertoff, M. E. (**2004**). "Cochlear hysteresis: Observation with low-frequency modulated distortion product otoacoustic emissions," J. Acoust. Soc. Am. **115**, 2159–2172.

Cheatham, M. A., and Dallos, P. (**2001**). "Inner hair cell response patterns: Implications for low-frequency hearing," J. Acoust. Soc. Am. **110**, 2035–2044.

Dallos, P. (**1970**). "Low-frequency auditory characteristics: Species dependence," J. Acoust. Soc. Am. **48**, 489–499.

Dancer, A., and Franke, R. (**1980**). "Intracochlear sound pressure measurements in guinea pigs," Hear. Res. **2**, 191–205.

Frank, G., and Kössl, M. (**1996**). "The acoustic two-tone distortions 2f1-f2 and f2-f1 and their possible relation to changes in the operating point of the cochlear amplifier," Hear. Res. **98**, 104–115.

Frank, G., and Kössl, M. (**1997**). "Acoustical and electrical biasing of the cochlea partition: Effects on the acoustic two tone distortions f2-f1 and 2f1-f2," Hear. Res. **113**, 57–68.

Franke, R., and Dancer, A. (**1982**). "Cochlear mechanisms at low frequencies in the guinea pig," Arch. Oto-Rhino-Laryngol. **234**, 213–218.

Franke, R., Dancer, A., Buck, K., Evrard, G., and Lenoir, M. (**1985**). "Phénomènes hydromechaniques cochléaires aux basses frequences chez le cobaye" ("Hydromecanincal cochlear phenomena at low frequencies in guinea pig"), Acustica **59**, 30–41.

Kurokawa, H., and Goode, R. L. (**1995**). "Sound pressure gain produced by the human middle ear," Otolaryngol.-Head Neck Surg. **113**, 349–355.

Leventhall, G., Pelmear, P., and Benton, S. (**2003**). "A review of published research on low frequency noise and its effects," Department for Environment Food and Rural Affairs, London, UK, ⟨http://www.defra.gov.uk/environment/noise/research/lowfrequency⟩, viewed 4/22/2007.

Lukashkin, A. N., and Russell, I. J. (**2005**). "Dependence of the DPOAE amplitude pattern on acoustical biasing of the cochlear partition," Hear. Res. **203**, 45–53.

Lynch, T. J., Nedzelnitsky, V., and Peake, W. T. (**1982**). "Input impedance of the cochlea in cat," J. Acoust. Soc. Am. **72**, 108–130.

Magnan, P., Dancer, A., Probst, R., Smurzynski, J., and Avan, P. (**1999**). "Intracochlear acoustic pressure measurements: transfer functions of the middle ear and cochlear mechanics," Audiol. Neuro-Otol. **4**, 123–128.

Martin, G. K., Lonsbury-Martin, B. L., Probst, R., and Scheinin, S. A. (**1987**). "Acoustic distortion product in the rabbit ear canal. II. Site of origin revealed by suppression contours and pure-tone exposure," Hear. Res. **28**, 191–208.

Merchant, S. N., Ravicz, M. E., and Rosowski, J. J. (**1996**). "Acoustic input impedance of stapes and cohlea in human temporal bones," Hear. Res. **97**, 30–45.

Møller, H., and Pedersen, C. S. (**2004**). "Hearing at low and infrasonic frequencies," Noise & Health **6**(23), 37–57.

Nedzelnitsky, V. (**1980**). "Sound pressures in the basal turn of the cat cochlea," J. Acoust. Soc. Am. **68**, 1676–1689.

Nubel, K., Kabudwand, A., Scholz, G., and Mrowinski, D. (**1995**). "Diag-

nostik des endolymphatischen Hydrops mit tieftonmaskierten otoakustischen Emissionen" ("Diagnosis of endolymphatic hydrops with low tone masked otoacoustic emissions"), Laryngorhinootologie **74**, 651–656.
Probst, R., Lonsbury-Martin, B. L., and Martin, G. K. (**1991**). "A review of otoacoustic emissions," J. Acoust. Soc. Am. **89**, 2027–2067.
Puria, S. (**2003**). "Measurements of human middle ear forward and reverse acoustics: Implications for otoacoustic emissions," J. Acoust. Soc. Am. **113**, 2773–2789.
Puria, S., and Allen, J. B. (**1991**). "A parametric study of cochlear input impedance," J. Acoust. Soc. Am. **89**, 287–309.
Puria, S., Peake, W. T., and Rosowski, J. J. (**1997**). "Sound-pressure measurements in the cochlear vestibule of human-cadaver ears," J. Acoust. Soc. Am. **101**, 2754–2770.
Ruggero, M. A., Rich, N. C., Robles, L., and Shivapuja, B. G. (**1990**). "Middle-ear response in the chinchilla and its relationship to mechanics at the base of the cochlea," J. Acoust. Soc. Am. **87**, 1612–1629.
Ruggero, M. A., Robles, L., and Rich, N. C. (**1986**). "Basilar membrane mechanics at the base of the chinchilla cochlea. II. Responses to low-frequency tones in relationship to microphonics and spike initiation in the VIII Nerve," J. Acoust. Soc. Am. **80**, 1375–1383.
Salter, J. P. (**1969**). *Steady State Vibrations* (Kenneth Mason, Havant), Chap. 9, Fig. 9.5, p. 109.
Scholz, G., Hirschfelder, A., Marquardt, T., Hensel, J., and Mrowinski, D. (**1999**). "Low-frequency modulation of the 2f1-f2 distortion product otoacoustic emissions in the human ear," Hear. Res. **130**, 189–196.
Talmadge, C. L., Long, G. R., Tubis, A., and Dhar, S. (**1999**). "Experimental confirmation of the two-source interference model for the fine structure of distortion product otoacoustic emissions," J. Acoust. Soc. Am. **105**, 275–292.
Weiss, T. F., Peake, W. T., and Sohmer, H. S. (**1971**). "Intracochlear potential recorded with micropipets. III. Relation of cochlear microphonic potential to stapes Velocity," J. Acoust. Soc. Am. **50**, 602–615.
Zengh, Y. L., Ohyama, K., Hozawa, H., Wada, H., and Takasaka, T. (**1997**). "Effect of anaesthetic agents and middle ear pressure application on distortion product otoacoustic emissions in the gerbil," Hear. Res. **112**, 167–174.
Zwicker, E. (**1976**). "A model for predicting masking-period patterns," Biol. Cybern. **23**, 49–60.
Zwicker, E. (**1977**). "Masking-period patterns produced by very-low-frequency maskers and their possible relation to basilar membrane displacement," J. Acoust. Soc. Am. **61**, 1031–1040.
Zwicker, E. (**1981**). "Masking period patterns and cochlear acoustical responses," Hear. Res. **4**, 195–202.

Estimating the transition bandwidth between two auditory processes: Evidence for broadband auditory filters

Bruce G. Berg[a)]
Department of Cognitive Sciences, University of California, Irvine, California 92697

(Received 7 October 2005; revised 9 March 2007; accepted 13 March 2007)

A spectral discrimination task was used to estimate the frequency range over which information about the temporal envelope is consolidated. The standard consisted of n equal intensity, random phase sinusoids, symmetrically placed around a signal component. The signal was an intensity increment of the central sinusoid, which on average was 1000 Hz. Pitch cues were degraded by randomly selecting the center frequency of the complex and single channel energy cues were degraded with a roving-level procedure. Stimulus bandwidth was controlled by varying the number of tones and the frequency separation between tones. For a fixed frequency separation, thresholds increased as n increased until a certain bandwidth was reached, beyond which thresholds decreased. This discontinuity in threshold functions suggests that different auditory processes predominate at different bandwidths, presumably an envelope analysis at bandwidths less than the breakpoint and across channel level comparisons for wider stimulus bandwidths. Estimates of the "transition bandwidth" for 46 listeners ranged from 100 to 1250 Hz. The results are consistent with a peripheral filtering system having multiple filterbanks. © *2007 Acoustical Society of America.*
[DOI: 10.1121/1.2722212]

PACS number(s): 43.66.Ba [RAL] Pages: 3639–3645

I. INTRODUCTION

The initial intent of this study was to investigate listeners' abilities to discriminate narrowband spectral profiles with the relevant acoustic information presumably isolated in the envelope of the temporal waveform. The listener's task was to detect an increase in the intensity of the central component of a densely spaced complex of equal-intensity tones. Absolute intensity information was degraded with a roving-level procedure (Spiegel and Green, 1982), pitch cues were degraded with a roving-frequency procedure (Richards, Onsan, and Green, 1989), and the spectra were often too narrow to support across channel level comparisons.

The theoretical motivation was to estimate the frequency range over which information about the temporal envelope is consolidated. The primary experimental variable was stimulus bandwidth, controlled by the number (n) and frequency separation (Δf) of tones comprising the complex. A typical experimental run might begin with $n=3$ and $\Delta f=10$ Hz, followed by conditions in which tones are progressively added to each end of the complex. The general expectation was that thresholds would increase until reaching an asymptote at some "critical bandwidth," much the same as observed in Fletcher's (1940) bandwidening, tone-in-noise detection experiment. Instead, thresholds decreased once a certain stimulus bandwidth was reached, sometimes dramatically. Individual differences presented another unexpected finding, with breakpoints ranging from less than 100 Hz to greater than 1000 Hz.

Discontinuous threshold functions imply that different auditory processes are evoked by the discrimination task, each predominating over different stimulus bandwidths. This idea is not without precedent. Feth and O'Malley (1977) had listeners discriminate two-tone stimuli with identical envelopes and equal energy, but different pitch as calculated from the envelope weighted average of the instantaneous frequency. They varied the frequency separation between the two tones and found that performance was best when the stimulus spanned several hundred Hertz and decreased for narrower and wider bandwidths. Berg, Nguyen, and Green (1992) proposed three different operating ranges in the context of a three-component, spectral discrimination task (i.e., profile analysis). Pitch cues appeared to be used over a frequency range similar to that reported by Feth and O'Malley, envelope cues appeared to dominate at the narrowest bandwidths, and across channel level comparisons were presumably used at wider bandwidths. Hall, Haggard, and Fernandes (1984) discovered comodulation masking release using a band-widening, tone-in-noise detection task in which the masking noise was amplitude modulated by a second band of low pass noise (50 Hz cutoff). Rather than reaching an asymptote, as in Fletcher's (1940) original version of the task using unmodulated maskers, thresholds decreased dramatically when the bandwidth of the noise exceeded a critical band. Presumably, single channel cues were used at narrow bandwidths and multiple channel cues predominated when the stimulus bandwidth became wide enough to support across channel comparisons.

Interpretation of the data presented here will be based on the assumption that envelope cues dominate at narrow bandwidths and across channel level comparisons dominate at wide bandwidths. In order to stress the idea of a change in the underlying process, the term *transition bandwidth* will be used rather than *critical bandwidth*, the latter having long been conceptualized as a constraining boundary of a solitary

[a)]Electronic mail: bgberg@uci.edu

process (e.g., energy integration). Another distinction is that critical bandwidth is associated with the periphery, whereas a change in the dominant auditory process implies a central mechanism.

II. METHOD

An extreme range of transition bandwidth estimates became apparent early in the study, and this motivated the use of an exceptionally large sample of listeners. Data were collected from 46 listeners in two stages spanning a five-year period. Berg, Southworth, and Turner (1993) reported some initial findings. The discrimination task was then included as one component of a test battery designed to investigate individual differences. During this later stage, minor procedural modifications were made with the aim of estimating transition bandwidths with greater efficiency. Because this is an exploratory study with no formal hypothesis testing, procedural differences across listeners should be of little concern. What is emphasized is the replicability of transition bandwidth estimates for individual listeners and the range of differences across listeners.

A. Subjects

All 46 listeners were affiliates of the University of California, Irvine. Except for several laboratory personnel, they received monetary compensation for their participation. All had puretone thresholds better than 20 dB HL within the range of stimulus frequencies.

B. Stimuli

The standard consisted of equal-intensity tones, nominally centered at 1000 Hz. The signal was an increment in the relative intensity of the central component, expressed as $20\log(\Delta a/a)$, where a is the amplitude of each component of the standard and Δa is the amplitude of the signal which is added in phase to the central component. Overall intensity and center frequency were random variables, independently sampled on each stimulus presentation. For most listeners, intensity was uniformly distributed with a range of 55–75 dB sound pressure level in 0.1/dB steps. During the initial stage of the experiment, the center frequency was randomized over a range of 948–1052 Hz by sampling the digital-to-analog conversion rate from a uniform distribution with a range of 38–42 μs and a discrete step size of 1 μs. Varying the sampling rate alters Δf by a small amount, as well as the stimulus duration. None of this variation, however, provided information about the signal. During the later stage of the experiment, stimuli were specified in the spectral domain, transformed by 1FFT to the temporal domain, and presented at a constant conversion rate of 40 μs/sample. The center frequency ranged between 950 (0.074 octaves) and 1050 (0.07 octaves) with a 10 Hz step size. Each sound interval was 300 ms in duration and was shaped with 5 ms cosine-squared onset and offset ramps. Intervals were separated by 500 ms.

Digitized waveforms were played through a two-channel, digital-to-analog converter and passed through an anti-aliasing filter with a 10 kHz cutoff. The level of the signal was controlled with a programmable attenuator. The signal and standard were added just prior to a second programmable attenuator that controlled the overall level. All electronic equipment were components of TDT System I. Sounds were delivered over Sennheisser HD414SL headphones to the listener seated in a single-walled, sound-attenuating chamber. Responses were made with a keyboard and feedback was presented on a computer monitor.

C. Procedures

The frequency separation between tones was constant within each block of trials, $\Delta f = 10$, 20, 40, 60, 80, 100, or 160 Hz. Thresholds were estimated with a two-interval, forced-choice, adaptive level procedure (Levitt, 1971). Each block consisted of 50 trials, with an initial step size of 4 dB that was reduced to 2 dB following the third reversal. A threshold estimate was obtained by averaging the levels at the last even number of reversals in the adaptive track, excluding the first three. The reported threshold for a condition is the mean from ten estimates, all obtained during the same session. Listeners completed 3–4 conditions per 2 h session, with rest periods taken at the listener's discretion. The minimal amount of training prior to the initial run consisted of ten blocks with $n = 3$ and $\Delta f = 10$ Hz.

A run is defined as a sequence of conditions with Δf held constant and n progressively increased from three to some arbitrary number until the threshold function either decreased or reached an asymptote. Additional data were sometimes collected to help clarify the breakpoint. During the first stage of the study, as many as four runs with different Δf were completed. Listeners participating in the battery generally completed one or two runs. The order and number of runs constituted the only procedural differences across listeners.

III. RESULTS

Threshold functions for individuals are shown in Figs. 1–3. In each panel, connected symbols represent a threshold function with a fixed Δf. The value in each panel is the geometric mean frequency of the stimulus bandwidth at the breakpoint of each threshold function. Breakpoints are sometimes obvious (e.g., L11, L13, and L40), but many estimates have a degree of arbitrariness. For functions displaying a plateau, the first asymptotic point rather than the point of decline was chosen as the breakpoint (e.g., L17, L20, and L31). The vertical lines in each panel demarcate the narrowest and widest breakpoints. Despite inevitable nuances in assigning breakpoints, the variability of estimates for most individuals was slight compared to the variability across listeners.

In order to avoid an excessively loud stimulus, some runs were terminated before reaching a breakpoint (e.g., L14, L21, and L22). Several functions decreased monotonically with a maximum threshold at $n = 3$ (e.g., L1 and L3). Although "monotonic" runs were not included in estimates of the transition bandwidth, they are nonetheless consistent

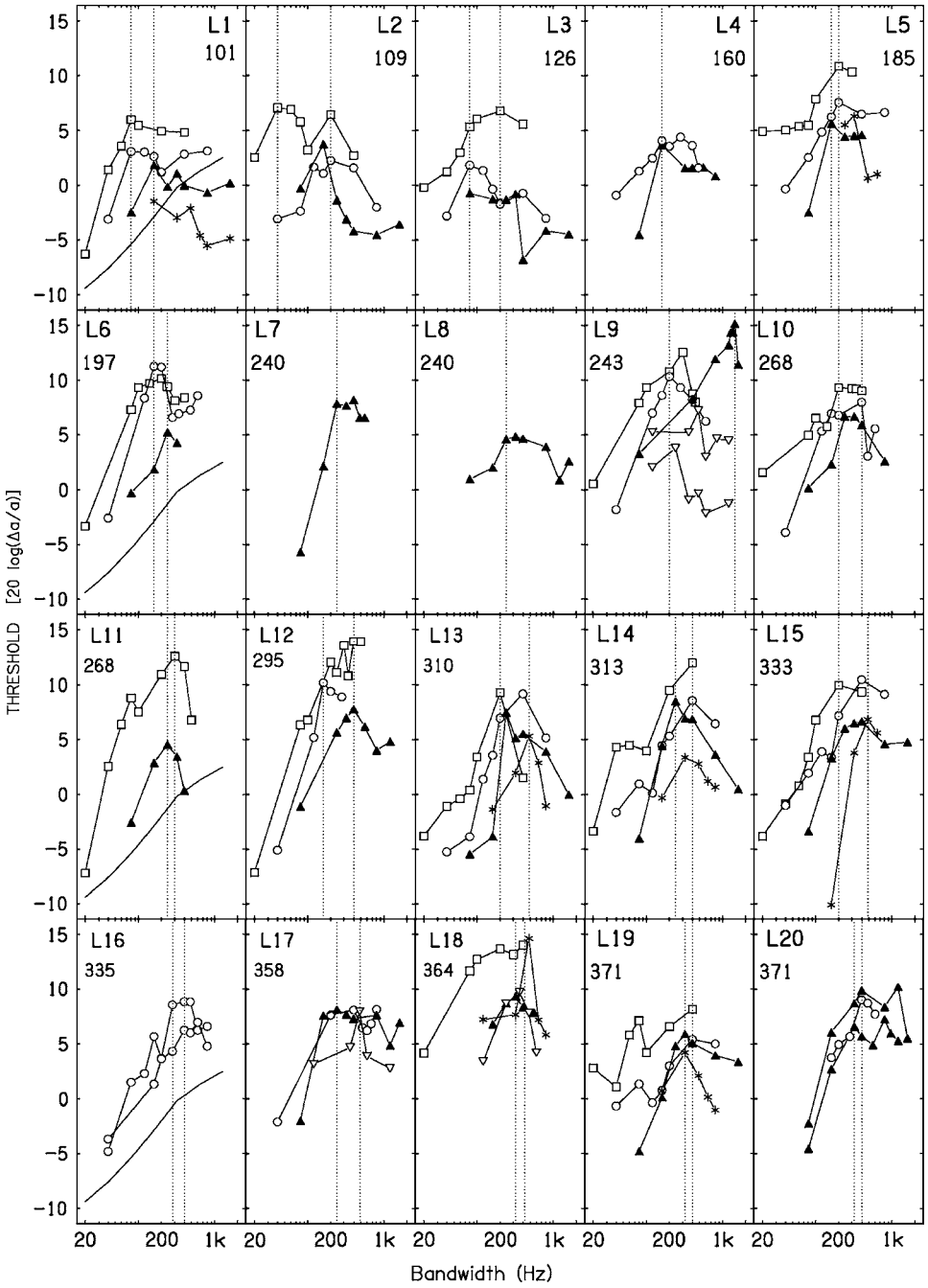

FIG. 1. Thresholds for an intensity increment in the central component of an n-tone complex plotted as a function of stimulus bandwidth. Symbols represent the frequency separation between tones for different runs; □10 Hz; ○20 Hz; ▲40 Hz; ▽60 Hz; *80 Hz; ⧗100 Hz; ☆160 Hz. The geometric mean of the breakpoints for each individual is listed in each panel and the vertical lines represent the minimum and maximum breakpoint. Lines without symbols in the left-side panels represent the performance of a leaky-integrator model.

with the general pattern of results because increasing functions are to the left of the breakpoint and decreasing functions are to the right.

Only a few runs with $\Delta f = 100$ and 160 Hz were completed. For L34, $\Delta f = 100$ Hz yielded a breakpoint and $\Delta f = 160$ Hz yielded a threshold function that declined sharply near the estimated transition bandwidth. For L40, the threshold function for $\Delta f = 160$ Hz shows both increasing and decreasing segments. When considered separately, there are an inadequate number of points for a conclusive judgment about the shape of these threshold functions. Nonetheless, they are coincident enough with the threshold functions obtained with small values of Δf that it is difficult to foster a convincing argument for a different underlying auditory process. This is of interest because for large values of Δf, each sinusoid presumably activates a separate auditory filter (Moore and Glasberg, 1983). This issue is considered in some detail below.

Estimates of transition bandwidths appear to be unaffected by practice. Some listeners show little change in performance for multiple runs with the same Δf (e.g., L31 and L41), whereas others obtained lower thresholds for repeated conditions (e.g., L36 and L39). Improvements in performance generally consist of a downward shift of the threshold function with little change in the frequency of the breakpoint. Another general observation demonstrating the stability of breakpoints is that listeners who completed four or more runs received several thousand trials between the first and last runs, with no apparent order effects. Given the important theoretical implications of experimentally altering transition bandwidths, however, a procedure more demand-

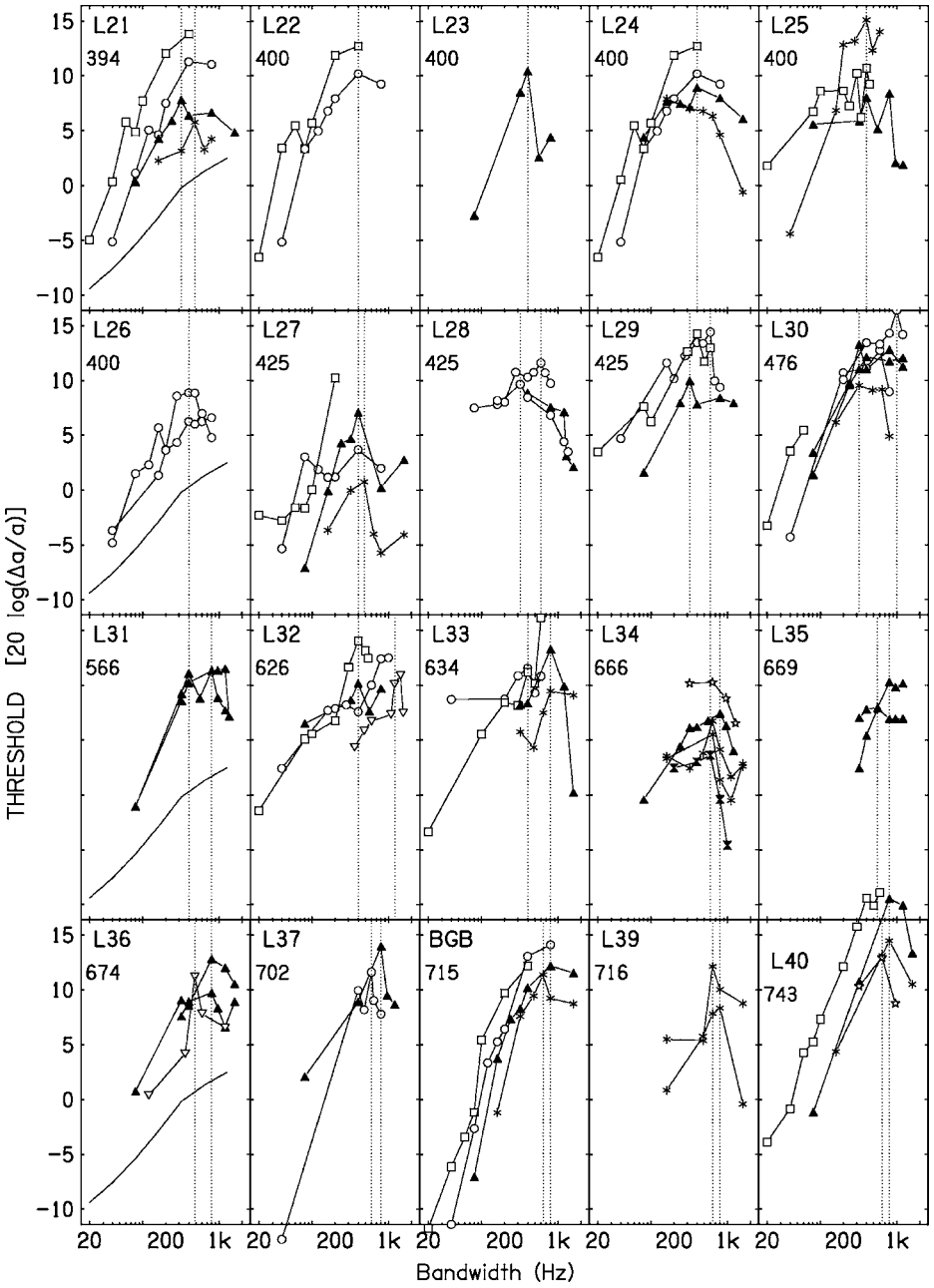

FIG. 2. See caption to Fig. 1.

ing than the incidental training of the current design should be employed before accepting any final conclusions (e.g. Leek and Watson, 1984).

To a first approximation, the slope of the increasing segment of threshold functions is similar across listeners. Functions for L1 and L46, the listeners exhibiting the narrowest and widest transition bandwidths, have comparable increasing slopes. In comparison, there is considerable diversity in the shape of threshold functions beyond the breakpoint. Some show a gradual decrease (e.g., L1, L20), whereas others decline sharply (e.g., L13 and L34). In a few cases, thresholds decreased by more than 10 dB (e.g., L44 and L41). Many runs, however, were terminated shortly after establishing the breakpoint, so the decreasing segment of threshold functions is often incomplete.

For two listeners, the frequency of the breakpoint increased systematically with Δf, so that threshold functions exhibited similar breakpoints when plotted as a function of n, as shown in Fig. 4. These functions have about the same range as those in Fig. 3, but lack the sharp decrement in thresholds beyond the breakpoint, displaying instead a relatively flat asymptote. It is plausible that these two listeners used an absolute intensity cue at wide bandwidths that was dependent on the total number of sinusoids comprising the stimulus. At high signal levels, an absolute intensity cue becomes salient as signal strength surpasses the uncertainty introduced by the roving level procedure (see Green *et al.*, 1984). The data suggest that the two listeners did not use across channel comparisons.

IV. DISCUSSION

This attempt to estimate the consolidation range for envelope information was partially successful. A number of

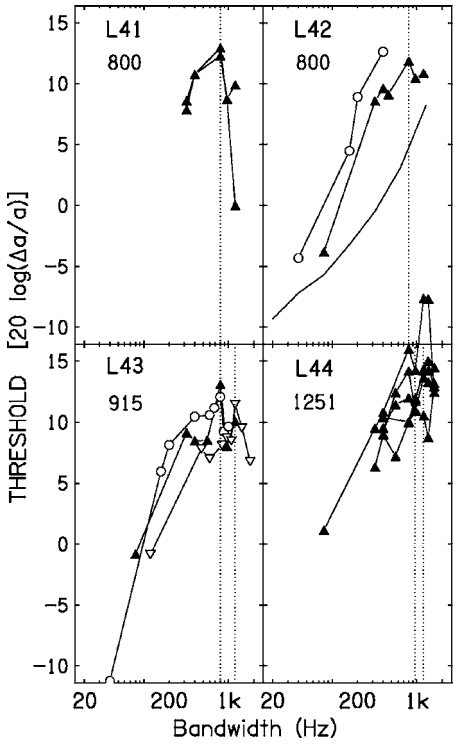

FIG. 3. See caption to Fig. 1.

listeners displayed a plateau between increasing and decreasing segments of their threshold functions. The plateau might represent that bandwidth which exceeds the limiting bandwidth of an envelope processor, but less than the bandwidth needed to engage across channel level comparisons. That is. the left corner of a plateau might manifest the maximum temporal bandwidth. Sharp, well-defined peaks, on the other hand, may simply represent the emergence of profile analysis as the dominant process and say little about a maximum temporal bandwidth. That is, a narrow breakpoint does not imply a narrow filter as much as it provides evidence of an overriding process.

It can be argued that transition bandwidths are determined primarily by listeners' abilities to resolve the sound into signal and nonsignal elements in order to engage the mechanisms of across channel level comparisons. This ability will be referred to as profile resolution, a term whose introduction will be justified shortly. According to this idea, high profile resolution is expected to yield narrow transition bandwidths with relatively low thresholds at the breakpoint. Listeners with data displayed in the top row of Fig. 1 appear to have the ability to make across-channel comparisons when the stimulus spans about two critical bands, the theoretical limit. Thresholds remain low because listeners are able to switch from envelope cues to the more efficient strategy of across channel comparisons relatively early in the course of a run. Low profile resolution, on the other hand, is expected to yield wide transition bandwidths and high thresholds. This type of listener apparently cannot partition the stimulus into signal and nonsignal elements until the stimulus is relatively broad in frequency. High thresholds result from an extended reliance on increasingly ineffectual envelope cue as tones are added during the course of a run. When across channel comparisons finally come into play, thresholds are high, as are the potential gains in efficiency, often reflected by a sharp decrement in thresholds beyond the transition bandwidth.

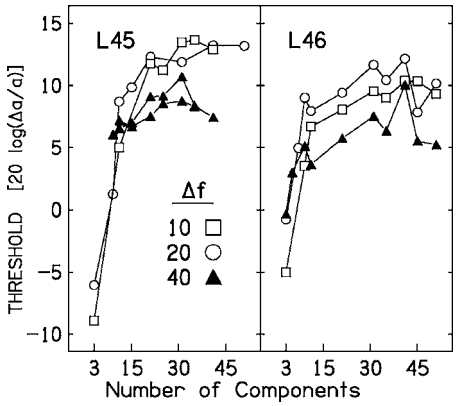

FIG. 4. Thresholds plotted as a function of n for two listeners.

This *post hoc* explanation advances a unique view of across channel comparisons and the central consolidation of information. A transition bandwidth wider than several critical bands implies that outputs from auditory filters are not the elements of comparison, and so it is useful to consider peripheral auditory filters and central auditory channels as distinct. Spiegel (1979) considered this issue under the rubric of "spectral integration." Listeners with wide transition bandwidths may base their decisions on the output of central channels that accumulate information from an indeterminate number of peripheral filters. The term profile resolution refers to this hypothetical process. A good illustration is the classification of the author (B.G.B.) as a listener with low profile resolution, having an estimated transition bandwidth of 715 Hz (bottom row of Fig. 2). Evidence for B.G.B.'s low profile resolution is found in Berg and Green (1990). Figure 5 of that paper shows spectral weight estimates from an 11-tone spectral profile discrimination task. Although the tones were distributed across different critical bands, the two surrounding the 1000 Hz signal had positive weights, as if B.G.B. had difficulty isolating the signal component.

Short of obtaining weight estimates for all listeners, there is a suggestion of a relationship between transition bandwidths and thresholds in a spectral profile discrimination task. An 11-tone spectral profile discrimination task (see Berg and Green, 1990) was a component of the battery mentioned above. The correlation between thresholds in the profile task and transition bandwidths was 0.46 ($p<0.01; n=40$). Poor profile listeners have wider transition bandwidths. In comparison, when the spectral profile was a three-tone complex narrower than a critical band, the correlation between thresholds and transition bandwidths was insignificant.

The increasing segment of threshold functions provides evidence that information about the temporal envelope of the waveform is consolidated over frequency ranges greater than current estimates of the bandwidths of auditory filters. Smoothly increasing functions imply a solitary auditory process, and an analysis of the temporal envelope is the most likely candidate.

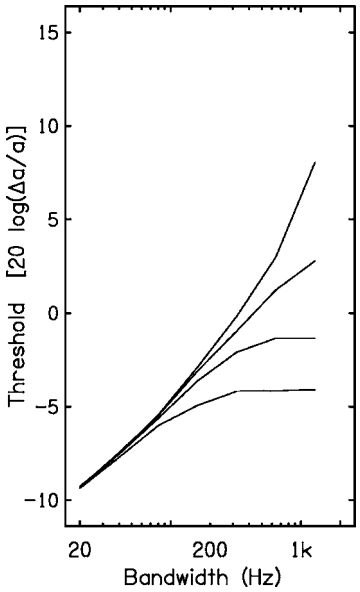

FIG. 5. Simulated thresholds for a leaky-integrator model plotted as a function of stimulus bandwidth ($\Delta f = 10$ Hz). The four simulated threshold functions, from highest to lowest, were done with bandpass filters having respective ERBs of 1729, 573, 267, and 133 Hz.

Simulations of a three-stage leaky integrator (i.e., bandpass filter, half-wave rectification, and low-pass filter; see Viemeister, 1979) were done in order to gain some understanding about the width of the bandpass filter needed to produce continuously increasing threshold functions of the same extent exhibited by listeners. A version of the model was employed that uses the amplitude spectrum of the leaky integrator output to formulate a multivariate decision variable (Berg, 1996, 2004). The effect of changing the bandwidth of a symmetric ROEX filter (Patterson and Moore, 1986) by varying the parameter p, while holding all other parameters of the model constant,[1] is illustrated in Fig. 5. The simulated threshold functions, from the lowest to highest, were obtained with bandpass filters having ERBs of 133, 267, 573, and 1729 Hz, respectively. The only parameter that significantly affects the slope of the function is the bandwidth of the initial filter. Increasing either the magnitude of simulated internal noise or the time constant of the lowpass filter generally produces parallel shifts of the simulated threshold functions.

A filter with an ERB of 133 Hz might conceivably account for some of the data, particularly those displayed in the top row of Fig. 1, but it is clear that a leaky integrator requires an exceptionally wide filter in order to mimic many of the empirical threshold functions. Simulated thresholds obtained with an ERB of 573 Hz are shown by the continuous line in the left-side panels of Figs. 1 and 2, and the results obtained with an ERB of 1729 Hz are shown in Fig. 3.

If an analysis of envelope information by listeners is indeed producing the increasing segment of threshold functions, then conventional psychophysical descriptions of the peripheral auditory system would appear inadequate, not only with respect to the bandwidth of auditory filters, but perhaps at a more fundamental level. Parsimonious explanations may require a radical restructuring of basic theories about the auditory periphery. Berg (2004) proposed parallel and independent filterbanks for spectral and temporal processes. The fundamental premise is that the information transmitted by a single primary auditory fiber is ambiguous in terms of both a temporal code and a place-rate code. Convergence at higher-order neurons is a necessary condition for the transmission of meaningful information. Following Eggermont's (2001) idea that parallel pathways originate at the cochlear nucleus, for instance, it is entirely plausible that a temporal process accumulates information across a broad swath of primary fibers and a spectral process accumulates information from a narrower swath of fibers. Arbitrarily broad filters could be constructed by combining the input of many primary fibers, even those emanating from resolved locations on the basilar membrane.

Although peripheral filtering is indisputably a basic property of the auditory system, the assumption of a solitary filterbank has neither been derived from the empirical record nor subjected to rigorous tests. Accounting for the current results with a solitary filterbank that also maintains adequate frequency resolution will likely require considerable nuance. A theory of distinct filterbanks may prove productive and will circumvent a number of conceptual limitations (see Berg, 2004). Investigations of peripheral filtering have been limited mostly to a single paradigm—tone-in-noise detection—with the assumption that the underlying process is some form of energy integration. Far from being a radical proposal, investigating auditory filtering with different paradigms and sets of assumptions is a scientifically conservative tactic that should be undertaken. If bandwidth estimates are similar across disparate paradigms, the idea of a single filterbank would gain empirical credence. Hartmann (1998) has already noted some differences across paradigms, but much additional data are needed for a comprehensive view.

A number of paradigms show how the addition of components to a masker can decrease its masking effectiveness. Comodulation masking release (CMR) is one case. A thread to the current findings is suggested by the fact that a leaky integrator can account for the basic CMR effect (Berg, 1996), but the picture is unfortunately not so clear. Berg and Kong (2004) applied a spectral weight estimation technique in a CMR task and found that simulations of different models yield distinct patterns of spectral weights. Unpublished data show decisive support for across channel envelope comparisons, as originally proposed by Hall *et al.* (1984).

In an informational masking experiment, Oh and Lutfi (1998) varied the number of components comprising the masker from 2 to 906. Plotting detection thresholds for a 1000 Hz signal against the number of masking components yielded nonmonotonic threshold functions with peaks around 10–50 components. Lutfi's (1993) component relative entropy model provided precise fits to the data, exhibiting the exceptional feature of describing a nonmonotonic threshold function while assuming a solitary auditory process. The number of components and the bandwidth of the stimulus determine the breakpoint. A key aspect of the model is that statistical uncertainty is reduced as the number of components within the frequency range of a given auditory filter increases. With respect to the current data, breakpoints are

often observed with a small number of components, particularly when Δf is large. In these cases, the distribution of components across filters may be too sparse to reduce the variability of filter outputs.

The current explanation for the decreasing segment of threshold functions comes directly from the theory of profile analysis. Thresholds in a spectral discrimination task decrease as the number of stimulus components increases (Green, 1992; Green, Mason, and Kidd, 1984) and as the stimulus bandwidth increases (Green, Kidd, and Picardi, 1983), results that are consistent with those reported here. Even so, the correspondence is not complete. The high density of components in the current task requires a more detailed explanation because the partitioning of components into different frequency channels is an unknown factor. Spiegel's (1979) ideas about spectral integration may play a role in developing a more precise theory.

Early in the development of the theory of profile analysis, Green *et al.* (1983) described the phenomenon as peculiar. This seems like an odd choice of terms in retrospect, following the discovery of CMR and informational masking, but one perfectly reasonable at a time when critical band theory offered explanations for much of the basic phenomena in psychoacoustic research. The commonality of the studies cited in the preceding paragraphs is that they violate a fundamental assumption of critical band theory, namely that detection is based on information acquired from a single auditory filter. These studies have led to a greater appreciation of the complexity of the auditory system, but there is no well defined, unifying principle. There is little consensus in the underlying mechanisms that have been proposed to account for the data from these paradigms. Perhaps a greater degree of coherence will emerge with a reconsideration of the architecture of the auditory system.

ACKNOWLEDGMENTS

I would like to thank Diedre McCarney, Curt Southworth, Matthew Turner, Lisa Khuu, Brian Branstetter, and Olegario Perales for their assistance in data collection. This work was supported by the Office of Naval Research.

[1]The peripheral stage of the model was a three-stage leaky integrator, with an initial one-parameter ROEX filter (see Patterson and Moore, 1986), followed by half-wave rectification and a low-pass, one-pole filter with a 3 -ms time constant. The decision variable was a multivariate statistic, $D=-(\mathbf{X}-\mathbf{S})\mathbf{C}_s(\mathbf{X}-\mathbf{S})'+(\mathbf{X}-\mathbf{N})\mathbf{C}_n(\mathbf{X}-\mathbf{N})'$, where $\mathbf{X}$ a vector representing the amplitude spectrum of the leaky integrator output, $\mathbf{S}=\mathrm{E}[\mathbf{X}|\text{signal}]$ and $\mathbf{N}=\mathrm{E}[\mathbf{X}|\text{no signal}]$ are the expected values of $\mathbf{X}$ given signal and no signal, respectively, and $\mathbf{C_s}$ and $\mathbf{C_n}$ are the corresponding inverse covariance matrices. Additional details are found in Berg (2004).

Berg, B. G. (**1996**). "On the relation between comodulation masking release (CMR) and temporal modulation transfer functions," J. Acoust. Soc. Am. **100**, 1013–1023.
Berg, B. G. (**2004**). "A temporal model of level-invariant tone-in-noise detection," Psychol. Rev. **111**, 914–930.
Berg, B. G., and Green, D. M. (**1990**). "Spectral weights in profile listening," J. Acoust. Soc. Am. **88**, 758–766.
Berg, B. G., and Kong, Y.-Y. (**2004**). "Models of comodulation masking release," J. Acoust. Soc. Am. **116**, 2624.
Berg, B. G., Southworth, C., and Turner, M. (**1993**). "Critical bands for envelope cues," J. Acoust. Soc. Am. **93**, 2387.
Berg, G. G., Nguyen, Q., and Green, D. M., (**1992**). "Discrimination of narrow band spectra: I. Spectral weights and pitch cues," J. Acoust. Soc. Am. **92**, 1911–1918.
Eggermont, J. J. (**2001**). "Between sound and perception: Reviewing the search for a neural code," Hear. Res. **157**, 1–42.
Feth, L. L., and O'Malley, H. (**1977**). "Two-tone auditory spectral resolution," J. Acoust. Soc. Am. **62**, 940–947.
Fletcher, H. (**1940**). "Auditory patterns," Rev. Mod. Phys. **12**, 47–65.
Green, D. M. (**1988**). *Profile Analysis: Auditory Intensity Discrimination* (Oxford University Press, New York).
Green, D. M. (**1992**). "The number of components in profile analysis tasks," J. Acoust. Soc. Am. **91**, 1616–1623.
Green, D. M., Kidd, G., Jr., and Picardi, M. C. (**1983**). "Successive versus simultaneous comparison in auditory intensity discrimination," J. Acoust. Soc. Am. **73**, 639–643.
Green, D. M., Mason, C. R., and Kidd, G. K., Jr. (**1984**). "Profile analysis: Critical bands and duration," J. Acoust. Soc. Am. **75**, 1163–1167.
Hall, J. W., III, Haggard, M. P., and Fernandes, M. A. (**1984**). "Detection in noise by spectro-temporal pattern analysis," J. Acoust. Soc. Am. **76**, 50–56.
Hartmann, W. M. (**1998**). *Signals, Sounds, and Sensation* (Springer-Verlag, New York).
Leek, M. R., and Watson, C. S. (**1984**). "Learning to detect auditory pattern components," J. Acoust. Soc. Am. **76**, 1037–1044.
Levitt, H. (**1971**). "Transformed up-down methods in psychoacoustics," J. Acoust. Soc. Am. **49**, 467–477.
Lutfi, R. A. (**1993**). "A model of auditory pattern analysis on component relative entropy," J. Acoust. Soc. Am. **94**, 1333–1334.
Moore, B. C. J., and Glasberg, B. R. (**1983**). "Suggested formulae for calculating auditory-filter bandwidths and excitation patterns," J. Acoust. Soc. Am. **74**, 750–752.
Oh, E. L., and Lutfi, R. A. (**1998**). "Nonmonotonicity of informational masking," J. Acoust. Soc. Am. **104**, 3489–3499.
Patterson, R. D., and Moore, B. C. J. (**1986**). "Auditory filters and excitation patterns as representations of frequency resolution," in *Frequency Selectivity in Hearing*, edited by B. C. J. Moore (Academic, London), pp. 123–177.
Richards, V. M., Onsan, Z. A., and Green, D. M. (**1989**). "Auditory profile analysis: Potential pitch cues," Hear. Res. **39**, 27–36.
Spiegel, M. F. (**1979**). "The range of spectral integration," J. Acoust. Soc. Am. **66**, 1356–1363.
Spiegel, M. F., and Green, D. M. (**1982**). "Signal and masker uncertainty with noise maskers of varying duration, bandwidth, and center frequency," J. Acoust. Soc. Am. **71**, 1204–1210.
Viemeister, N. F. (**1979**). "Temporal modulation transfer functions based upon modulation thresholds," J. Acoust. Soc. Am. **66**, 1364–1380.

Psychophysical estimates of level-dependent best-frequency shifts in the apical region of the human basilar membrane[a)]

Enrique A. Lopez-Poveda,[b)] Luis F. Barrios, and Ana Alves-Pinto
Unidad de Audición Computacional y Psicoacústica, Instituto de Neurociencias de Castilla y León, Universidad de Salamanca, Av. Alfonso X "El Sabio" s/n, 37007 Salamanca, Spain

(Received 24 July 2006; revised 5 March 2007; accepted 5 March 2007)

It is now undisputed that the best frequency (BF) of basal basilar-membrane (BM) sites shifts downwards as the stimulus level increases. The direction of the shift for apical sites is, by contrast, less well established. Auditory nerve studies suggest that the BF shifts in opposite directions for apical and basal BM sites with increasing stimulus level. This study attempts to determine if this is the case in humans. Psychophysical tuning curves (PTCs) were measured using forward masking for probe frequencies of 125, 250, 500, and 6000 Hz. The level of a masker tone required to just mask a fixed low-level probe tone was measured for different masker-probe time intervals. The duration of the intervals was adjusted as necessary to obtain PTCs for the widest possible range of masker levels. The BF was identified from function fits to the measured PTCs and it almost always decreased with increasing level. This result is inconsistent with most auditory-nerve observations obtained from other mammals. Several explanations are discussed, including that it may be erroneous to assume that low-frequency PTCs reflect the tuning of apical BM sites exclusively and that the inherent frequency response of the inner hair cell may account for the discrepancy. © *2007 Acoustical Society of America.* [DOI: 10.1121/1.2722046]

PACS number(s): 43.66.Ba, 43.66.Dc, 43.66.Mk [AJO] Pages: 3646–3654

I. INTRODUCTION

The basilar membrane (BM) extends from the base to the apex of the cochlea supporting the organ of Corti. Its function is crucial to hearing because it operates as a nonlinear frequency analyzer, at least to a good first approximation (Von Békésy, 1960; Rhode, 1971). Different regions of the BM respond to different frequency components of the acoustic stimulus. Basal regions respond best to high frequencies while apical regions respond best to low frequencies. Actually, any given site on the BM responds to a wide range of frequencies in a filterlike manner, but its response is greatest for one particular frequency, which we will, refer to as the best frequency (BF) (reviewed by Robles and Ruggero, 2001). This report describes a psychophysical approach to investigating how the BF of apical cochlear sites varies with sound level. McFadden (1986) provides a comprehensive review of the topic.

The BF of any given BM site depends on sound level. We will refer to the BF for low-level sounds, near the absolute hearing threshold, as the characteristic frequency (CF). It is now undisputed that the BFs of *basal* sites shift to values lower than the CF as the sound level increases (evidence reviewed by Robles and Ruggero, 2001). By contrast, the direction of the shift for *apical* sites is uncertain, mainly because of the difficulty in recording apical BM responses *in vivo* while maintaining healthy physiological conditions. Indeed, very few studies report *in vivo* recordings of the vibration of apical structures [reviewed by Robles and Ruggero (2001) and Cooper (2004)]. Of them, only one Cooper and Rhode (1995) reports some BM responses, but they are insufficient to infer the direction of the BF shift. Furthermore, the reliability of all these apical recordings is openly questioned even by their own authors (cf. p. 29 of Cooper, 2004; Robles and Ruggero, 2001). Nevertheless, even if it were possible to make these measurements reliably, the issue remains open as to whether the shift occurs in the same direction for different species.

The direction of the BF shift in lower mammals has been inferred from inner hair cell and auditory nerve responses (Rose *et al.*, 1971; Carney *et al.*, 1999; Carney, 1999; Cheatham and Dallos, 2001). These suggest that the direction of the BF shift depends on the cochlear region: for basal sites (CF $>\sim$1.5 kHz), the BF decreases as the sound level increases; for apical sites (CF $<\sim$0.75 kHz) the BF increases as the sound level increases; and for intermediate sites (0.75 kHz $<$ CF $<$ 1.5 kHz) no shift occurs. This trend is also supported by furosemide-induced changes in auditory nerve tuning curves (Sewell, 1984). A downward shift in CF was observed when recordings were made from auditory nerve fibers innervating the basal half of the cochlea. However, in fibers with CFs below approximately 800 Hz, an upward shift was recorded.

Psychoacoustic masking methods are widely used to *estimate* some response properties of the human BM (reviewed in Moore, 1998). Specifically, they have been used to investigate the direction of the BF shift in the human cochlea for basal (CFs of 4 and 6 kHz; Moore *et al.*, 2002), intermediate (CFs of 1 and 2 kHz; Moore and Glasberg, 2003; Vogten, 1978), or basal and intermediate sites (CFs $\sim$750 and 2000 Hz; McFadden and Yama, 1983). Overall, the conclu-

[a)]Portions of this work were presented at the 149th Meeting of the Acoustical Society of America, Vancouver, Canada, May 2005.
[b)]Electronic mail: ealopezpoveda@usal.es

 © 2007 Acoustical Society of America

sions of these studies match those of BM, inner hair cell, and auditory nerve studies for corresponding cochlear regions. A review of early studies is provided by McFadden (1986).

The direction of the level-dependent BF shift for apical sites of the human cochlea (CFs $\leqslant$ 0.5 kHz) has not been explicitly investigated. Yet, knowing the direction of this shift is important to fully understand the level-dependent representation of complex stimuli (including speech) in the human peripheral auditory system as well as to develop more realistic nonlinear models of the human auditory system than those already available (e.g., Lopez-Poveda and Meddis, 2001; Lopez-Poveda, 2005).

The present report describes an attempt to determine the direction of the level-dependent BF shift for apical sites of the human BM. Evidence will be shown that the BF of *both* low- and high-frequency psychophysical tuning curves (PTCs) almost always *decreases* with increasing level. Based on the (conventional) assumption that PTCs reflect BM tuning exclusively, this result would seem inconsistent with the results from most physiological studies in other mammals. It will be discussed that either human cochlear apical responses differ from those of other species or such an assumption may be erroneous for low-frequency PTCs. It will be conjectured that, if the assumption were erroneous, the inherent frequency response of the inner hair cell may account for the apparent discrepancy between psychophysical and physiological results.

II. METHODS

A. Rationale and assumptions

The direction of the level-dependent BF shift was inferred from PTCs for different response criteria (e.g., Chistovich, 1957; Moore, 1978; Moore *et al.*, 1984; reviewed by Moore, 1998). PTCs were measured using tone-on-tone forward masking to avoid potential interactions between the masker and the probe that may complicate the interpretation of the results (Munson and Gardner, 1950; Vogten, 1978; Moore and Glasberg, 1981; Moore, 1998). A pure-tone masker was presented to the listener followed by a fixed-frequency, fixed-level pure-tone probe. The task was to measure the threshold level for maskers of different frequencies that made the probe just detectable. The probe level was *fixed* a few decibels above the listener's absolute threshold for the probe. In these conditions, the threshold masker level is *assumed* to depend on the relative excitation produced by the masker and the probe at the BM place activated by the probe. Because the probe is fixed both in level and frequency, all maskers in any given PTC produce the same excitation on that BM place. For this reason, the resulting PTCs are thought of as iso-response curves and are *assumed* to correspond to BM tuning (or iso-response) curves (cf. Moore, 1998; Yasin and Plack, 2003; Stainsby and Moore, 2006). Consequently, it is assumed that the tip frequency of any given PTC matches approximately that of a corresponding BM tuning curve, and thus both of them will be hereinafter referred to as the BF.

The threshold masker level also depends on the time interval between the masker and the probe. As this interval increases, the amount of masking decreases and it becomes necessary to increase the masker level to achieve the masking threshold (Zwislocki *et al.*, 1959). Therefore, by *assuming* that the decay of forward masking is independent of masker frequency, it is possible to determine the most effective masker frequency, the BF, at different masker levels by measuring PTCs for increasing masker-probe silent periods.

This approach has important advantages for the purpose of the present study over those in which PTCs are measured for a fixed masker-probe interval and various probe levels (e.g., Vogten, 1978; Kidd and Feth, 1981). Fixing the probe level almost guarantees that the BM region under study is constant for all masker-probe intervals, and thus for all masker levels. Furthermore, the use of a very-low-level probe (just above threshold) minimizes the spread of BM excitation caused by the probe and thus off-frequency listening (Nelson *et al.*, 2001), although off-frequency listening may not be fully eliminated (O'Loughlin and Moore, 1981; see also the following text). Therefore, any change in the behaviorally estimated BF as a result of increasing the masker-probe interval can be reasonably attributed to a level-dependent change in the BF of the BM site whose CF is approximately equal to the probe frequency. Similar assumptions have been made in many other studies that estimated human BM responses behaviorally (e.g., Nelson *et al.*, 2001; Lopez-Poveda *et al.*, 2003; Yasin and Plack, 2003; Plack, 2004; Rosengard *et al.*, 2005; Stainsby and Moore, 2006).

B. Stimuli

PTCs were measured for probe frequencies, f_P, of 125, 250, 500, and 6000 Hz. For each probe frequency, masker frequencies, f_M, ranged from 0.5 to 3 times the probe frequency. Typically 16 masker frequencies were used for each probe frequency although the actual number varied across listeners and masker-probe intervals. Maskers had a fixed duration of 110 ms, including 5-ms raised-cosine onset and offset ramps. The 500- and 6000-Hz probes had 5-ms raised-cosine onset/offset ramps and no steady state portion, hence a total duration of 10 ms. The 125- and 250-Hz probes also had 5-ms onset/offset ramps but a 10-ms steady state, hence a total duration of 20 ms. Longer durations were used for these low-frequency probes in an attempt to decrease the salience of spectral splatter and thus a potential increase in probe detectability by off-frequency listening (Lopez-Poveda *et al.*, 2003; see also the following text). The masker-probe silent intervals, measured from masker offset to probe onset, ranged from 2 to 70 ms. Their actual values differed across listeners and probe frequencies with the aim of measuring PTCs over the widest possible range of masker levels for each listener. These were chosen by trial and error to guarantee that the levels for two masker frequencies, one at the probe frequency and one approximately an octave below it, were still lower than the set maximum level of the system (see the following text). The probe level was fixed at 9 dB above each listener's absolute threshold for the probe.

Stimuli were generated with a Tucker Davis Technologies™ psychoacoustics workstation (System III) at a sampling rate of 24.4 kHz and 24-bit resolution. All stimuli

TABLE I. Listeners' absolute thresholds for the probes (dB SPL).

	Probe frequency and duration			
Listener	125 Hz (20 ms)	250 Hz (20 ms)	500 Hz (10 ms)	6000 Hz (10 ms)
S1	56.0	48.6	36.9	26.1
S2	51.4	52.3	43.9	40.9
S3	59.7	36.0	36.9	30.7

were played monaurally via the system's headphone connections through the same pair of Etymotic ER2 earphones. Listeners sat in a double-walled sound-attenuating room. The sound pressure levels (SPLs) reported below are nominal electrical levels.

C. Procedure

Masker levels at threshold were measured using a two-interval, two-alternative forced-choice paradigm. A two-up, one-down adaptive rule was used to estimate the 71% correct point on the psychometric function (Levitt, 1971). The masker level was increased and decreased by 6 dB for the first two reversals and by 2 dB thereafter. For each measurement, the adaptive procedure continued (typically for 50 to 70 trials) until 12 reversals were recorded. The threshold estimate was taken as the mean of the masker levels for the final ten reversals. The estimate was discarded when the standard deviation (SD) of these ten levels exceeded 6 dB. At least three thresholds were obtained in this way for each condition and their mean was taken as the actual threshold. When the SD of the first three thresholds exceeded 6 dB, a fourth threshold was measured and included in the mean.

The maximum allowed masker level was set to 106 dB SPL. If the adaptive procedure called for a higher level on two consecutive pairs of trials, then the level was set to 106 dB SPL. If the same happened for three consecutive times, the run was aborted.

D. Listeners

PTCs were measured for three listeners, all of whom had normal hearing at the audiometric frequencies according to ANSI (1996). Prior to measuring the PTCs, the listeners' absolute thresholds for the probes were measured with an adaptive two-down one-up adaptive procedure (Levitt, 1971). Each threshold was measured at least three times and the values were averaged. Results are shown in Table I.

E. Determination of the BF and the level at which it occurs

The BF of each PTC was *not* identified directly as the masker frequency with the lowest masker level. Such a procedure might have yielded biased results in a few instances where several masker frequencies had similar levels (±2 dB). Instead, the BFs and the levels at which they occurred (L_{BF}) were obtained by fitting each side of each PTC with a double-rounded exponential (*roex*) function (Patterson *et al.*, 1982). The details of the fitting method can be found in Yasin and Plack (2003).

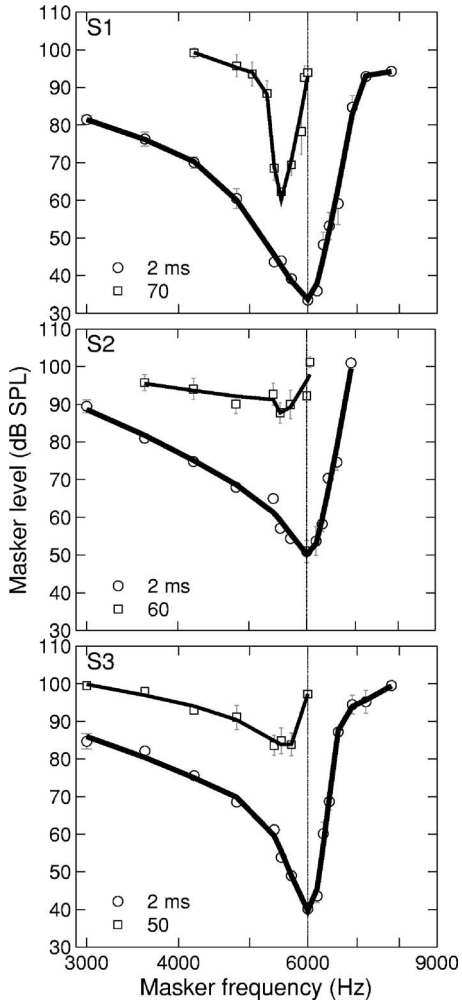

FIG. 1. Psychophysical tuning curves (PTCs) for a probe frequency of 6000 Hz. Each panel illustrates the results for a different listener, as identified by the number in the top-left corner. Symbols illustrate experimental data. Lines illustrate roex fits. PTCs are illustrated for two different masker-probe time intervals (in ms), as indicated by the legend inset on each panel. Error bars illustrate one standard error of the mean. The vertical dashed-dotted line denotes the position of the probe frequency.

III. RESULTS

A. Psychophysical tuning curves

Figures 1–4 depict the PTCs for probe frequencies of 6000, 500, 250, and 125 Hz, respectively. In every figure, each panel illustrates the results for a different listener. Symbols illustrate the experimental PTCs and lines illustrate corresponding *roex* fits.

Let us first examine the results for a probe frequency of 6000 Hz (Fig. 1). The PTCs for the shortest masker-probe interval (2 ms) always had their tips near the probe frequency (i.e., BF ~ 6 kHz) and were asymmetric when plotted on a log scale. That is, they were steeper for frequencies higher than the BF than for lower frequencies. For the longer masker-probe interval, the PTCs became broader for listeners S2 and S3, but narrower for S1. One would expect that the PTCs for the longer masker-probe interval would always be broader than those for the shorter interval. There exist, however, examples where physiological tuning curves get narrower with increasing response criterion, at least over a cer-

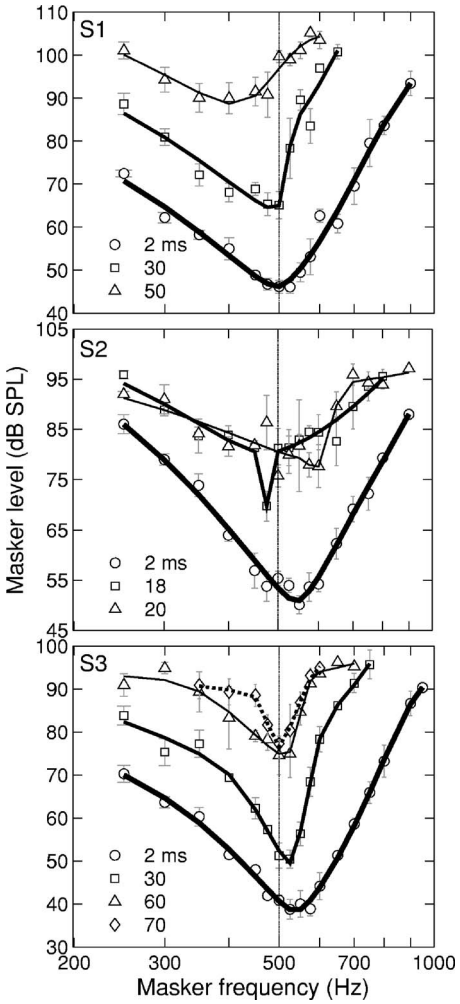

FIG. 2. As for Fig. 1 but for probe frequency of 500 Hz.

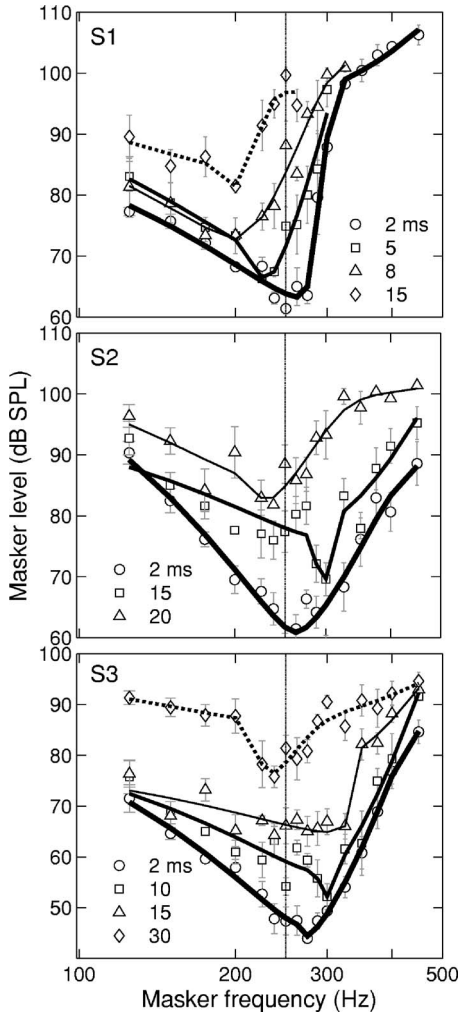

FIG. 3. As for Fig. 1 but for probe frequency of 250 Hz.

tain range of criteria [for the BM: Fig. 11 of Ruggero *et al.* (1997); for the auditory nerve: Fig. 13 of Evans (1975)]. Therefore, the result for S1 is not unphysiological.

More interesting for the purpose of the present study is that, for all three listeners, the tip frequency of the PTCs decreased as the probe delay increased. That is, the BF decreased as L_{BF} increased. The direction of this shift was consistent with level-dependent BF shifts reported in other species for basal sites of the BM (Ruggero *et al.*, 1997; Rhode and Recio, 2000) and for auditory nerve fibers with CFs above approximately 1.5 kHz (Carney *et al.*, 1999; Carney, 1999). It is also consistent with the direction of the shifts described psychophysically in humans using different methods (Moore *et al.*, 2002).

The PTCs for a probe frequency of 500 Hz (Fig. 2) looked, overall, more symmetric in all conditions than those for f_P=6000 Hz. For the shortest masker-probe interval, the tip frequency was somewhat higher than the probe frequency. It shifted to a slightly different value with increasing L_{BF}. The direction of the shift was different for different listeners. For S1, the BF decreased with increases in the masker-probe interval. For S3, the BF hardly decreased with increasing masker level. For S2, the BF first decreased and then increased as the masker-probe interval increased. BF shifts that reverse in direction with increasing sound level have been reported (in other species) for the apical region of the cochlear partition (CF~500 Hz) when the velocity of vibration rather than displacement is considered (cf. Fig. 2.3B of Cooper, 2004).

The PTCs for probe frequencies of 250 and 125 Hz (Figs. 3 and 4, respectively) were alike, but they differed qualitatively from those at 500 Hz. These PTCs appeared more asymmetric than those at 500 Hz, with their high-frequency slopes being steeper than the low-frequency ones (e.g., S1 for a probe frequency of 250 Hz). At 250 Hz (Fig. 3), the BF for the shortest masker-probe interval was slightly higher than the probe frequency for all three listeners. The BF decreased monotonically with increasing masker level for listener S1 only. For listeners S2 and S3, the BF first increased and then decreased with increasing masker level. At 125 Hz (Fig. 4), the BF for the shortest masker-probe interval was slightly higher than the probe frequency for S3 and S1, respectively. Remarkably, for S2 the BF (231.3 Hz) was almost twice the probe frequency (125 Hz). Also, the high-frequency tails of these PTCs became unusually shallower as the masker-probe interval increased. Possible reasons for these results are discussed in the following text. At 125 Hz, the BF decreased monotonically with increasing masker level for all three listeners (Fig. 4).

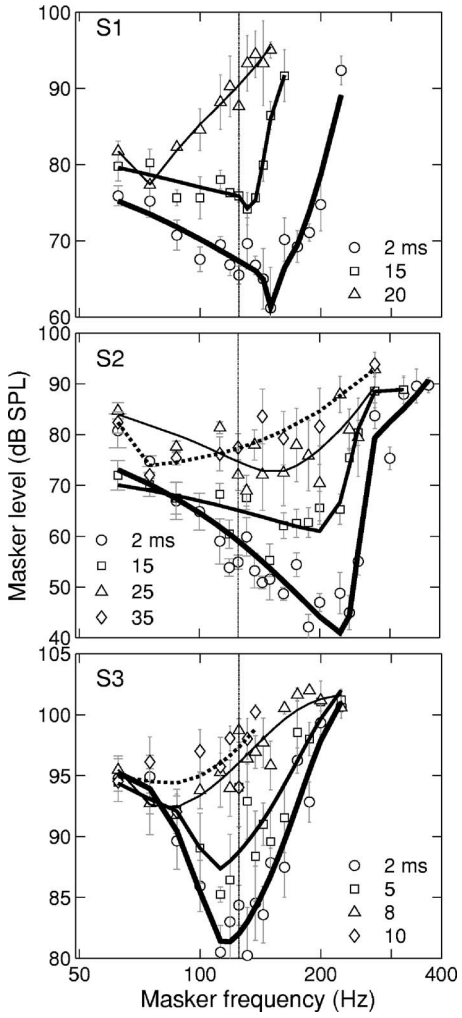

FIG. 4. As for Fig. 1 but for probe frequency of 125 Hz.

B. The direction and magnitude of level-dependent BF shifts

Figure 5 summarizes the main results pertaining to the relationship between the BFs and their corresponding levels, L_{BF}, as determined by the roex fits. Each panel illustrates the results for a different probe frequency. Each symbol illustrates the results for a different listener [as indicated by inset in Fig. 5(d)]. The figure plots deviations of the BF with respect to the probe frequency (in octaves) against L_{BF} relative to the probe level. This form of representation serves two purposes: (a) to identify the direction of any level-dependent BF shift, and (b) to quantify the extent of the shift and compare it across probe frequencies.

Figure 5 shows three striking results. First, the BF is always lower at the highest than at the lowest masker levels, except for S2 at 500 Hz, although in some cases (S2 at 500 Hz; S2 and S3 at 250 Hz) the BF varies nonmonotonically with increasing masker level. These results are inconsistent with most physiological observations in other mammalian species that monotonic level-dependent BF shifts occur in opposite directions for apical and basal cochlear sites (Rose *et al.*, 1971; Carney *et al.*, 1999; Carney, 1999; Cheatham and Dallos, 2001). Second, the magnitude of the behaviorally estimated relative BF shift is considerably greater for the lowest probe frequency tested. Third, in several instances the probe frequency is lower than the BF at the lowest masker levels and sometimes even when the masker level equals the probe level [i.e., the plots do not go across the (0, 0) point]. The latter is somewhat surprising because one would expect that the BF be equal to the probe fre-

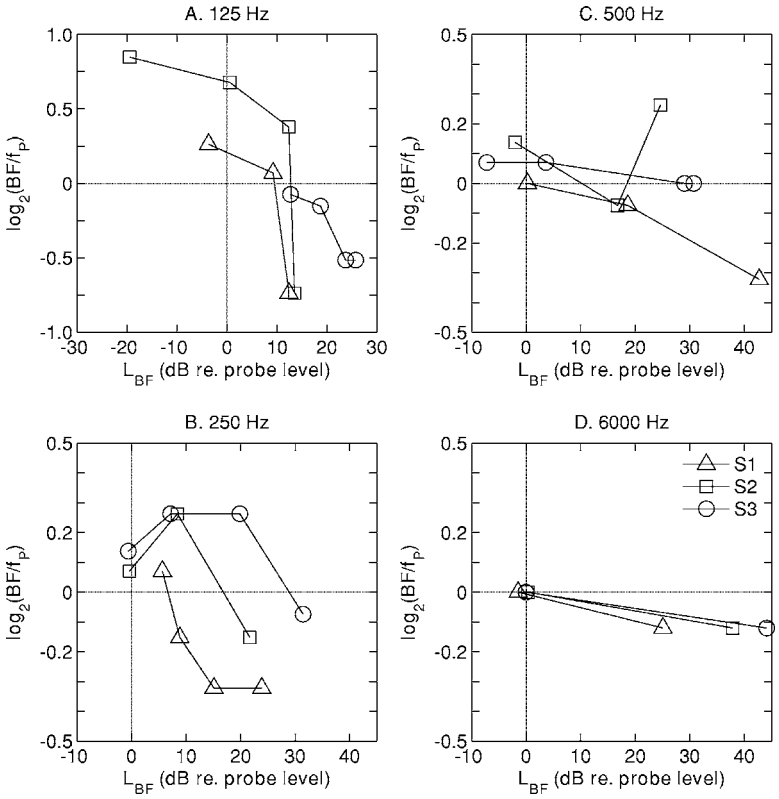

FIG. 5. The estimated BF as a function of the estimated L_{BF}. The BF is plotted relative to the probe frequency (f_P) in octaves. Positive/negative values indicate that the BF is higher/lower than the probe frequency, respectively. Different symbols illustrate the results for different listeners as indicated by the inset in the bottom, right panel. Each panel illustrates the results for a different probe frequency. Note that different probe durations were used for probe frequencies below and above 500 Hz (Sec. II B), and that different masker-probe intervals were used for different listeners (see Figs. 1–4).

quency when the relative level between the masker and the probe is 0 dB. Interpretations of these results and their implications are discussed below.

One last remark: an alternative way of estimating the BF and L_{BF} would have been to equate them to the frequency of the most effective masker (i.e., the masker requiring the lowest level instead of L_{BF} estimated from *roex* fits) and the level at which it occurs, respectively. This was done and the results (not shown) confirmed the main conclusions drawn from Fig. 5.

IV. DISCUSSION

The goal of this study was to characterize the direction of level-dependent BF shifts in the *apical* region of the *human* BM. Specifically we sought to assess whether the direction of the shift conforms to that inferred from auditory nerve studies in other mammals (Rose *et al.*, 1971; Carney *et al.*, 1999; Carney, 1999). Those physiological studies suggest that, with increases in the stimulus level, the BF decreases for basal sites but increases for apical sites. The present results (summarized in Fig. 5) appear inconsistent with this conclusion as the BF of PTCs decreased with increasing level for low ($<$500 Hz) and high (6 kHz) probe frequencies and the BF shift was sometimes nonmonotonic.

A. Comparisons with other psychoacoustical and physiological results

To our knowledge, no other study has been carried out to date with identical motivations or methods. Allowing for the differences in motivations and methods, however, the present findings agree in part with those from other masking studies. Kidd and Feth (1981), for instance, reported PTCs for several probe frequencies and levels. Their PTCs were measured using a similar method to the one employed here except that they fixed the masker-probe interval (at 10 ms) and considered two probe levels: 10 and 20 dB SL. The tip frequency of their 250-Hz PTCs decreased when the masker level increased by ~25 dB as a result of increasing the probe level (see Fig. 1 in Kidd and Feth, 1981). The present 250-Hz PTCs have BFs that either decrease monotonically (S1) or vary nonmonotonically (S2 and S3) with increasing masker level [Fig. 5(b)]. Nevertheless, their BFs decrease when the masker level increases over a range comparable to that of Kidd and Feth and therefore the two studies are mostly consistent in this respect. No BF shift occurred in the 500-Hz PTCs of Kidd and Feth.

The present results are consistent with previously reported masking patterns for low- and high-frequency tonal maskers. It has long been known that the peak of the masking pattern shifts to higher frequencies with increasing the level of a *high*-frequency ($\geq$1 kHz) masker (e.g., Munson and Gardner, 1950; Ehmer and Ehmer, 1969; Kidd and Feth, 1981). This shift is consistent with the idea that the peak of the BM traveling wave caused by the masker moves towards the base of the cochlea with increasing the masker level. Hence, it is consistent with the observation that the BF for a given cochlear site decreases with increasing level. Less well appreciated, however, is that a similar shift in the peak of the masking pattern occurs for masker frequencies $\leq$500 Hz (Table I in Ehmer and Ehmer, 1969; Tobias, 1977; Fig. 2 in Kidd and Feth, 1981; reviewed by McFadden, 1986). This is consistent with the idea that the BF of *apical* cochlear sites decreases with increasing level as occurs for basal sites.

That said, this earlier behavioral evidence must be taken with caution, as the results of Tobias (1977) were almost certainly affected by masker-probe interactions (e.g., beats, suppression) (Munson and Gardner, 1950; Vogten, 1978; Moore and Glasberg, 1981) and those of Kidd and Feth (1981) and Ehmer and Ehmer (1969) by off-frequency listening [the effects of off-frequency listening in estimates of level-dependent BF shifts are amply discussed on p. 73 of Moore and Glasberg (2003)]. Note that masker-probe interactions are minimized in the present results thanks to using nonsimultaneous masking. The use of a fixed, low-level probe also minimized off-frequency listening (Nelson *et al.*, 2001), although the fact that the BF shift was not zero when the masker and the probe had identical levels at low probe frequencies [Figs. 5(a) and 5(b)] indicates that off-frequency listening may have still occurred here for some listeners (see the following text).

The present human results appear inconsistent with those from earlier auditory nerve studies in other species (Carney *et al.*, 1999; Carney, 1999; Rose *et al.*, 1971), but are consistent with the *mechanical* data of Cooper and Rhode (1997) for a cochlear site with a CF~500 Hz. These data show that the BF of cochlear partition motion decreases with increases in the stimulus level, at least when the amplitude of vibration is expressed in units of displacement (see Fig. 2.4B in Cooper, 2004). As for inner hair cells, the ac receptor potential of apical units (CF$<$1000 Hz) peaks at a frequency that decreases with increasing sound level (Figs. 3 and 4 in Dallos, 1986; Fig. 10A in Dallos, 1985). Interestingly, dc (Fig. 10C in Dallos, 1985) and average (Fig. 3 in Cheatham and Dallos, 2001) inner hair cell receptor potential responses indicate upward BF shifts with increasing level.

B. Conjectures on the discrepancy between psychoacoustical and physiological results

1. Distortion, energy splatter, and off-frequency effects

Earphone harmonic distortion might have contributed to the observed downward BF shifts. The first harmonic of low-frequency, high-level maskers might have contributed, together with the masker, to masking the probe and, given that distortion is greater at high levels, its contribution would have increased with increasing masker level. This effect, however, would be small (if at all existent) because the SPL of the first harmonic was always 46 dB lower than the fundamental (as measured at the output of the earphones with a sound level meter placed on a Zwislocki coupler), even for the maximum output SPL of the system.

The 5-ms ramps on the probes might have been too short to prevent off-frequency probe detection by energy splatter. This might explain why the BFs differed from the probe frequency when they should have been equal (Fig. 5), particularly for PTCs below 500 Hz. If the significance of

this effect varied across listeners, it might also explain the remarkable large difference observed for S2 at 125 Hz. Possibly this effect could have been further reduced by increasing the ramps on the probes. However, off-frequency listening is an inherent difficulty with tonal forward masking and must always be considered in interpreting the results (Kidd and Feth, 1981; O'Loughlin and Moore, 1981).

Similarly, the 5-ms ramps on the masker might have been too short to prevent off-frequency masking by masker-energy splatter. This might account, at least in part, for the downward BF shifts observed at 125 Hz because energy splatter would be greater for high-level, low-frequency maskers. This, however, could have happened *only* if the splatter of masker energy were toward the base of the cochlea with increasing masker level, which is still in conflict with the apicalward shift of the peak of BM traveling wave with increasing level suggested by most physiological studies in other mammals. One possible explanation is that the response characteristics of the apical region of the *human* BM differ from those of the mammalian species for which auditory nerve and inner hair cell responses exist. This, however, seems unlikely given that at least one of the relevant auditory nerve studies (Rose *et al.*, 1971) was carried out in a primate species. Alternatively, our current interpretation of PTCs (or of auditory nerve responses) may be incorrect, at least for apical sites.

2. Influence by the acoustic reflexes

Low-frequency PTCs may have been influenced by the middle-ear acoustic reflex (Møller, 2000). The reflex starts to operate for levels around 75–78 dB *hearing level* (Neumann *et al.*, 1996) and attenuates incoming sounds to the cochlea. If it had been activated by the masker, its effect would not have decayed entirely by the time that the probe was presented. This may have made the probe inaudible at masker levels at which it would have been audible without the reflex. The reflex would be more likely (and strongly) activated by masker frequencies in the tails of the PTCs because their levels are higher. In the present task, where the probe *had* to be detected, this might have led to masker levels lower than they would have been without the reflex and hence might have "broadened" the PTCs. It is possible that this contributed to reducing the slope of the high-frequency tails of some PTCs for the longer masker-probe intervals (e.g., S2 and S3 in Fig. 4). On the other hand, the reflex might have been activated also during the later portion of the masker, thus reducing its ability to mask the probe. Therefore, the reflex might have *shaped* the PTCs through a complex combination of its effects, on the masker and on the probe.

It is doubtful, however, that activation of the acoustic reflex accounts for the downward BF shifts with increasing level observed at 125 and 250 Hz (Fig. 5). First, the BFs for all listeners and conditions occurred at SPLs below the threshold level of reflex activation [75–78 dB HL according to Neumann *et al.* (1996)]. Also, the threshold SPL of reflex activation decreases with increasing frequency from 100 to 500 Hz (cf. Fig. 12.9 of Møller, 2000). Therefore, the above-mentioned "broadening" effect of the reflex would be stronger on the high- than on the low-frequency tails of low-frequency PTCs. If anything, this would shift the BF upward relative to what would be measured without the reflex.

It is also unlikely that the activation of the olivocochlear efferent system (Guinan, 1996) accounts for the observed BF shifts because the activation of medial olivocochlear efferents reduces the sensitivity of low-CF auditory nerve without affecting their BFs (cf. Fig. 1 of Guinan and Gifford, 1988).

3. Influence by the inherent inner-hair-cell frequency response

As explained above, the ac component of the receptor potential of apical inner hair cells (CF $<$ 1000 Hz) peaks at a frequency that *decreases* with increasing sound level (Figs. 3 and 4 in Dallos, 1986; Fig. 10A in Dallos, 1985). This occurs even when the BF of the associated BM response is level independent (Shamma *et al.*, 1986). If the amount of (forward) masking at low frequencies were proportional to the amplitude of the ac receptor potential, this might explain the downward BF shift observed in the present PTCs and in earlier data, at least qualitatively. It might also explain, at least in part, why the present human results indicate a downward BF shift with increases in sound level while primate auditory-nerve iso-intensity responses indicate an upward BF shift (Rose *et al.*, 1971). The reason would be that auditory nerve iso-intensity functions plot the *average* discharge rate of the fibers, which is thought to be proportional to the dc (or average) receptor potential (Robles and Ruggero, 2001) and this peaks at frequencies that *increase* with increasing level (Fig. 10C in Dallos, 1985; Shamma *et al.*, 1986; Fig. 3 in Cheatham and Dallos, 2001). In summary, human low-frequency PTCs may reflect the tuning of the ac component of the inner hair cell receptor potential, which differs from that of the associated BM (Shamma *et al.*, 1986) and auditory nerve *average* responses.

It is uncertain how this might happen but a possible mechanism relates to the contribution of auditory-nerve post-stimulus recovery to forward masking (e.g., Harris and Dallos, 1979; Meddis and O'Mard, 2006). The magnitude of this effect is commonly thought to depend on the *average* discharge rate evoked by the masker. While this is almost certainly true for high-frequency maskers (Harris and Dallos, 1979, p. 1090), it is conceivable that for very low frequency maskers, the amount of masking depends on the (*peak*) discharge rate over, say, the last cycle of the masker, which would depend on the peak receptor potential. This needs experimental confirmation but appears plausible because in response to very low frequency masker and probes, fibers would discharge on every semicycle of the stimulus and would have time to recover partly from firing during the other semicycle. This would occur even when the stimulus greatly exceeds the SPL that elicits saturation (average) discharge rates (Rose *et al.*, 1971). Therefore, the fibers' response to the probe might be particularly conditioned by their peak discharge over the preceding masker cycle.

The same would not apply to high-frequency stimuli. For high-frequency stimuli the ac component of the receptor potential is highly attenuated relative to the dc component (Sellick and Russell, 1980). Thus, both behavioral and physiological frequency responses would "necessarily" follow the

dc component of the receptor potential. The dc response of the isolated inner hair cell (i.e., without the influence of BM tuning) is approximately frequency independent (e.g., Fig. 12A in Lopez-Poveda and Eustaquio-Martin, 2006). Consequently, PTCs and auditory nerve responses would reflect the tuning of BM responses more or less directly, as is commonly assumed.

Even if this conjecture were true, however, an important issue would remain puzzling. Evidence for a BF increase with increasing level comes not only from average-rate frequency response functions of auditory nerve fibers (Rose *et al.*, 1971). It also comes from the analysis of the instantaneous frequency of the fibers' impulse responses (Carney *et al.*, 1999; Carney, 1999) and this is likely independent of the magnitude of the ac or the dc components of the receptor potential of inner hair cells.

V. SUMMARY AND CONCLUSIONS

It has been shown that the tip frequency of low-frequency PTCs (<500 Hz) decreases with increases in the level at which the tip occurs, albeit sometimes nonmonotonically. Based on the conventional interpretation of PTCs, this would imply that the BF of BM apical sites decreases with increasing level, an interpretation that appears inconsistent with well-established evidence drawn from the analysis of the responses of low-CF auditory nerve fibers in other mammals. The reason for the inconsistency is uncertain. Activation of the middle-ear acoustic reflex probably contributed to shaping the PTCs, but it is doubtful that this accounts for the observed downward BF shifts with increasing level. It is possible that human apical cochlear responses differ from those of other mammals (including some primates). If this were the case, the observed apical downward BF shifts with increasing level might be partly due to off-frequency masking by masker-energy splatter. An alternative explanation would be that for low-frequency stimuli the amount of masking depends on the amplitude of the ac component of the inner hair cell receptor potential. This peaks at a frequency that decreases with increasing level even when the BF of the associated BM response is level independent and when the average isointensity response of auditory fibers indicates an upward BF shift with increasing level (Shamma *et al.*, 1986). This conjecture needs proof.

In any case, the evidence shown indicates that it may be erroneous to make inferences about the level-dependent frequency response properties of the *apical* region of the BM from low-frequency PTCs (or masking patterns). Further, it also may be erroneous to make such inferences from the average frequency response characteristics of low-CF inner hair cells or auditory nerve fibers (Shamma *et al.*, 1986).

ACKNOWLEDGMENTS

LFB carried out and submitted this work in partial fulfillment of the requirements for the "Grado de Salamanca" (University of Salamanca, July 2005). We thank Almudena Eustaquio-Martin for technical support. We are indebted to Magdalena Wojtczak, Ray Meddis, Wendy Lecluyse, and most especially to Brian C. J. Moore and two anonymous reviewers for their inspiring suggestions on earlier versions of this paper. Work supported by the Spanish FIS (PI020343 and G03/203), MEC (CIT-390000-2005-4 and BFU2006-07536/BFI), and IMSERSO (131/06).

ANSI. (**1996**). S3.6 Specifications for audiometers (American National Standards Inst., New York).

Carney, L. H. (**1999**). "Temporal response properties of neurons in the auditory pathway," Curr. Opin. Neurobiol. **9**, 442–446.

Carney, L. H., McDuffy, M. J., and Shekhter, I. (**1999**). "Frequency glides in the impulse response of auditory-nerve fibers," J. Acoust. Soc. Am. **105**, 2384–2391.

Cheatham, M. A., and Dallos, P. (**2001**). "Inner hair cell responses: Implications for low-frequency hearing," J. Acoust. Soc. Am. **110**, 2034–2044.

Chistovich, L. A. (**1957**). "Frequency characteristics of masking effect," Biophysics (Engl. Transl.) **2**, 743–755.

Cooper, N. P. (**2004**). "Auditory compression in the peripheral auditory system," in *Compression: From Cochlea to Cochlear Implants*, edited by S. P. Bacon, R. R. Fay, and A. N. Popper, Vol. 17 of *Springer Handbook of Auditory Research* (Springer-Verlag, New York), pp. 18–61.

Cooper, N. P., and Rhode, W. S. (**1997**). "Mechanical responses to two-tone distortion products in the apical and basal turns of the mammalian cochlea," J. Neurophysiol. **78**, 261–270.

Dallos, P. (**1985**). "Response characteristics of mammalian cochlear hair cells," J. Neurosci. **5**, 1591–1608.

Dallos, P. (**1986**). "Neurobiology of cochlear inner and outer hair cells: intracellular recordings," Hear. Res. **22**, 185–198.

Ehmer, R. H., and Ehmer, B. J. (**1969**). "Frequency pattern of residual masking by pure tone measured on the Bekesy audiometer," J. Acoust. Soc. Am. **46**, 1445–1448.

Evans, E. (**1975**). "Cochlear nerve and cochlear nucleus." In *Handbook of Sensory Physiology* edited by W. D. Keidel, and W. D. Neff **5**(2) (Springer, Berlin), pp. 1–18.

Guinan, J. J. Jr. (**1996**). "Physiology of olivocochlear efferents," in *The Cochlea* edited by P. Dallos, R. R. Fay, and A. N. Popper, Vol. 8 of *Springer Handbook of Auditory Research* (Springer-Verlag, New York), pp. 435–502.

Guinan, J. J. Jr., and Gifford, M. L. (**1988**). "Effects of electrical stimulation of efferent olivocochlear neurons on cat auditory-nerve fibers. III. Tuning curves and thresholds at CF," Hear. Res. **37**, 29–46.

Harris, D. M., and Dallos, P. (**1979**). "Forward masking of auditory nerve responses," J. Neurophysiol. **42**, 1083–1107.

Kidd, G., and Feth, L. L. (**1981**). "Patterns of residual masking," Hear. Res. **5**, 49–67.

Levitt, H. (**1971**). "Transformed up-down methods in psychoacoustics," J. Acoust. Soc. Am. **49**, 467–477.

Lopez-Poveda, E. A. (**2005**). "Spectral processing by the peripheral auditory system: Facts and models," Int. Rev. Neurobiol. **70**, 7–48.

Lopez-Poveda, E. A., and Eustaquio-Martin, A. (**2006**). "A biophysical model of the inner hair cell: The contribution of potassium currents to peripheral auditory compression," J. Assoc. Res. Otolaryngol. **7**, 218–235.

Lopez-Poveda, E. A., and Meddis, R. (**2001**). "A human nonlinear cochlear filterbank," J. Acoust. Soc. Am. **110**, 3107–3118.

Lopez-Poveda, E. A., Plack, C. J., and Meddis, R. (**2003**). "Cochlear nonlinearity between 500 and 8000 Hz in normal-hearing listeners," J. Acoust. Soc. Am. **113**, 951–960.

McFadden, D. (**1986**). "The curious half-octave shift: Evidence for a basalward migration of the traveling-wave envelope with increasing intensity," in *Basic and Applied Aspects of Noise-Induced Hearing Loss*, edited by R. J. Salvi, D. Henderson, R. P. Hamernik, and V. Colletti (Plenum, New York), pp. 295–312.

McFadden, D., and Yama, M. F. (**1983**). "Upward shifts in the masking pattern with increasing masker intensity," J. Acoust. Soc. Am. **74**, 1185–1189.

Meddis, R., and O'Mard, L. P. (**2006**). "A computer model of the auditory-nerve response to forward-masking stimuli," J. Acoust. Soc. Am. **117**, 3787–3798.

Møller, A. R. (**2000**). *Hearing, Its Physiology and Pathophysiology* (Academic, San Diego).

Moore, B. C. J. (**1978**). "Psychophysical tuning curves measured in simultaneous and forward masking," J. Acoust. Soc. Am. **63**, 524–532.

Moore, B. C. J. (**1998**). *Cochlear Hearing Loss* (Whurr, London).

Moore, B. C. J., Alcántara, J. I., and Glasberg, B. R. (**2002**). "Behavioral measurement of level-dependent shifts in the vibration pattern on the basilar membrane," Hear. Res. **163**, 101–110.
Moore, B. C. J., and Glasberg, B. R. (**1981**). "Auditory filter shapes derived in simultaneous and forward masking," J. Acoust. Soc. Am. **70**, 1003–1014.
Moore, B. C. J., and Glasberg, B. R. (**2003**). "Behavioral measurement of level-dependent shifts in the vibration pattern on the basilar membrane at 1 and 2 kHz," Hear. Res. **175**, 66–74.
Moore, B. C. J., Glasberg, B. R., and Roberts, B. (**1984**). "Refining the measurement of psychophysical tuning curves," J. Acoust. Soc. Am. **76**, 1057–1066.
Munson, W. A., and Gardner, M. B. (**1950**). "Loudness patterns – a new approach," J. Acoust. Soc. Am. **22**, 177–190.
Nelson, D. A., Schroder, A. C., and Wojtczak, M. (**2001**). "A new procedure for measuring peripheral compression in normal-hearing and hearing-impaired listeners," J. Acoust. Soc. Am. **110**, 2045–2064.
Neumann, J., Uppenkamp, S., and Kollmeier, B. (**1996**). "Detection of the acoustic reflex below 80 dB HL," Can. Respir. J. **1**, 359–369.
O'Loughlin, B. J., and Moore, B. C. J. (**1981**). "Off-frequency listening: Effects on psychoacoustical tuning curves obtained in simultaneous and forward masking," J. Acoust. Soc. Am. **69**, 1119–1125.
Patterson, R. D., Nimmo-Smith, I., Weber, D. L., and Milroy, R. (**1982**). "The deterioration of hearing with age: Frequency selectivity, the critical ratio, the audiogram, and speech threshold," J. Acoust. Soc. Am. **72**, 1788–1803.
Plack, C. J., Drga, V., and Lopez-Poveda, E. A. (**2004**). "Inferred basilar-membrane response functions for listeners with mild to moderate sensorineural hearing loss," J. Acoust. Soc. Am. **115**, 1684–1695.
Rhode, W. S. (**1971**). "Observations of the vibration of the basilar membrane in squirrel monkeys using the Mössbauer technique," J. Acoust. Soc. Am. **49**, 1218–1231.
Rhode, W. S., and Recio, A. (**2000**). "Study of mechanical motions in the basal region of the chinchilla cochlea," J. Acoust. Soc. Am. **107**, 3317–3332.
Robles, L., and Ruggero, M. A. (**2001**). "Mechanics of the mammalian cochlea," Physiol. Rev. **81**, 1305–1352.
Rose, J. E., Hind, J. E., Anderson, D. J., and Brugge, J. F. (**1971**). "Some effects of stimulus intensity on response of auditory nerve fibers in the squirrel monkey," J. Neurophysiol. **34**, 685–699.
Rosengard, P. S., Oxenham, A. J., and Braida, L. D. (**2005**). "Comparing different estimates of cochlear compression in listeners with normal and impaired hearing," J. Acoust. Soc. Am. **117**, 3028–3041.
Ruggero, M. A., Rich, N. C., Recio, A., Narayan, S. S., and Robles, L. (**1997**). "Basilar-membrane responses to tones at the base of the chinchilla cochlea," J. Acoust. Soc. Am. **101**, 2151–2163.
Sellick, P. M., and Russell, I. J. (**1980**). "The responses of inner hair cells to basilar membrane velocity during low frequency auditory stimulation in the guinea pig cochlea," Hear. Res. **2**, 439–445.
Sewell, W. F. (**1984**). "The effects of furosemide on the endocochlear potential and auditory-nerve fiber tuning curves in cats," Hear. Res. **14**, 305–314.
Shamma, S. A., Chadwick, R. S., Wilbur, W. J., Morrish, K. A., and Rinzel, J. (**1986**). "A biophysical model of cochlear processing: Intensity dependence of pure tone responses," J. Acoust. Soc. Am. **80**, 133–145.
Stainsby, T. H., and Moore, B. C. J. (**2006**). "Temporal masking curves for hearing-impaired listeners," Hear. Res. **218**, 98–111.
Tobias, J. V. (**1977**). "Low-frequency masking patterns," J. Acoust. Soc. Am. **61**, 571–575.
Vogten, L. L. M. (**1978**). "Simultaneous pure-tone masking: The dependence of masking asymmetries on intensity," J. Acoust. Soc. Am. **63**, 1509–1519.
Von Békésy, G. (**1960**). *Experiments in Hearing* (McGraw-Hill, New York).
Yasin, I., and Plack, C. J. (**2003**). "The effects of a high-frequency suppressor on tuning curves and derived basilar-membrane response functions," J. Acoust. Soc. Am. **114**, 322–332.
Zwislocki, J., Pirodda, E., and Rubin, H. (**1959**). "On some poststimulatory effects at threshold of audibility," J. Acoust. Soc. Am. **31**, 9–14.

Contralateral influences of wideband inhibition on the effect of onset asynchrony as a cue for auditory grouping

Brian Roberts[a] and Stephen D. Holmes
Psychology, School of Life and Health Sciences, Aston University, Birmingham B4 7ET, United Kingdom

(Received 6 November 2006; revised 2 March 2007; accepted 2 March 2007)

Onset asynchrony is an important cue for segregating sound mixtures. A harmonic of a vowel that begins before the other components contributes less to vowel quality. This asynchrony effect can be partly reversed by accompanying the leading portion of the harmonic with an octave-higher captor tone. The original interpretation was that the captor and leading portion formed a perceptual group, but it has recently been shown that the captor effect depends on neither a common onset time nor harmonic relations with the leading portion. Instead, it has been proposed that the captor effect depends on wideband inhibition in the central auditory system. Physiological evidence suggests that such inhibition occurs both within and across ears. Experiment 1 compared the efficacy of a pure-tone captor presented in the same or opposite ear to the vowel and leading harmonic. Contralateral presentation was at least as effective as ipsilateral presentation. Experiment 2 used multicomponent captors in a more comprehensive evaluation of harmonic influences on captor efficacy. Three captors with different fundamental frequencies were used, one of which formed a consecutive harmonic series with the leading harmonic. All captors were equally effective, irrespective of the harmonic relationship. These findings support and refine the inhibitory account. © *2007 Acoustical Society of America.* [DOI: 10.1121/1.2721874]

PACS number(s): 43.66.Ba, 43.66.Jh, 43.66.Rq, 43.71.Es [AJO] Pages: 3655–3665

I. INTRODUCTION

Differences in onset time provide an important grouping cue for the perceptual segregation of temporally overlapping sounds (e.g., Rasch, 1978; Bregman and Pinker, 1978; Dannenbring and Bregman, 1978). For example, a lead time of only 30–50 ms is sufficient largely to abolish the contribution of a single component to the timbre of a complex tone, such as the phonetic quality of a vowel (e.g., Darwin, 1984a, 1984b). This effect may be attributable primarily to peripheral adaptation, because the neural response to the leading component will have adapted substantially by the time the vowel begins (Kiang *et al.*, 1965; Westerman and Smith, 1984). However, there are two lines of evidence suggesting that peripheral adaptation cannot provide a complete account of the effect of onset asynchrony. First, a component of a short-duration vowel that ends after the others also makes a reduced contribution to vowel quality (Darwin, 1984b; Darwin and Sutherland, 1984; Roberts and Moore, 1991). This effect of offset asynchrony can be as large as about half the effect of an onset asynchrony. Second, accompanying the leading portion of a component with a pure-tone *captor* can partly reverse the effect of the onset asynchrony on judgments of vowel quality (Darwin and Sutherland, 1984).

The captor tone used by Darwin and Sutherland (1984) was an octave higher than the leading component, and hence too remote to cause any significant peripheral adaptation or lateral suppression (Houtgast, 1974) in the auditory channel centered on the leading component. They attributed the captor effect to the formation of a perceptual group consisting of the captor and the leading portion, which allowed the concurrent portion to integrate better into the vowel percept. However, Roberts and Holmes (2006a) have shown that captor efficacy does not depend on either a common onset time or harmonic relations between the captor and the leading portion, cues that should affect their perceptual grouping. They also demonstrated that captor efficacy is influenced by frequency separation, extending to about 1.5 octaves above the leading portion, and that the presence of the captor has an equivalent effect on judgments of vowel quality to that of reducing the physical level of the leading portion. They proposed that the captor effect arises from broadband inhibitory interactions within the cochlear nucleus (CN).

Figure 1 shows the inhibitory scheme proposed by Roberts and Holmes (2006a) and illustrates how the response to a 500 Hz tone (corresponding to the leading portion of the asynchronous vowel component) may be modulated by the presence of a spectrally remote captor tone. The essence of the scheme is that the presence of the captor tone increases the inhibition applied by wideband onset chopper (OC) cells tuned to 500 Hz to narrowband transient chopper (CT) cells tuned to the same frequency. This increase in inhibition reduces the ongoing excitatory response of the CT cells to the leading portion while the captor is present, and may also lead to a rebound excitation following the release from inhibition at captor offset (see Holmes and Roberts, 2006, for a full discussion). Bleeck *et al.* (2005) have recently presented physiological evidence that both kinds of inhibitory effect occur in the ventral CN of the guinea pig.

Holmes and Roberts (2006) have since provided further support for the inhibitory account of the captor effect, notably that a noise-band captor can be as effective as a pure-tone captor of equal power and matched to its center fre-

[a]Author to whom correspondence should be addressed. Electronic mail: b.roberts@aston.ac.uk

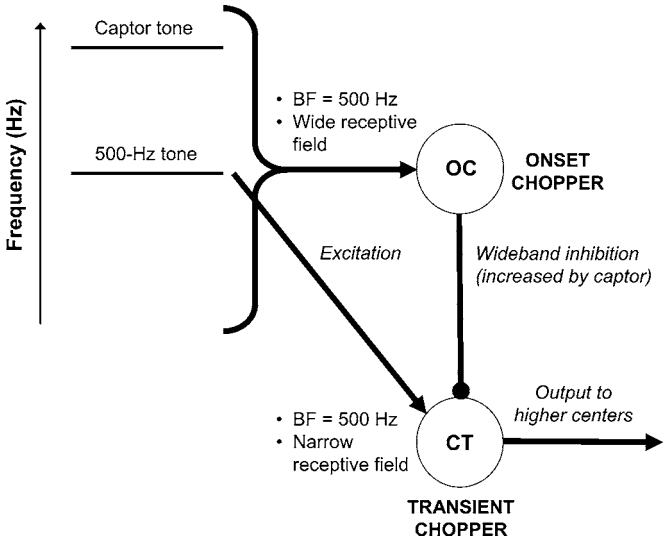

FIG. 1. Schematic of a hypothetical neural circuit in the ventral cochlear nucleus to account for the captor effect, as proposed by Roberts and Holmes (2006a). BF refers to the best frequency of a cell. The captor tone is assumed to reduce the excitatory response of transient chopper (CT) cells, tuned to the leading portion of the 500 Hz tone, by increasing the wideband inhibitory input to these cells from onset chopper (OC) cells with the same BF. Adapted with permission from "Asynchrony and the grouping of vowel components: Captor tones revisited," by B. Roberts and S. D. Holmes, 2006, J. Acoust. Soc. Am., **119**, p. 2916. Copyright 2006 by the Acoustical Society of America.

quency. Also, captor efficacy declines only gradually as captor level is reduced (Roberts *et al.*, in press), which is consistent with the wide dynamic range observed physiologically for inhibitory OC cells (Winter and Palmer, 1995). However, some properties of the captor effect are not consistent with predictions arising from the proposed CN circuit, indicating that this scheme cannot provide a complete account of the psychophysical findings. In particular, the decay time for the captor effect after captor offset (80 ms or more) is long compared to the values typically observed in physiological studies of cells in the CN (e.g., Needham and Paolini, 2003). However, wideband inhibitory cells have been identified by physiologists at several different levels in the central auditory system, and longer time constants are associated with neurons further along the auditory pathway than the CN (e.g., Bartlett and Wang, 2005). Therefore, Holmes and Roberts (2006) broadened the original proposal, noting that inhibitory interactions of the kind illustrated by the CN circuit may occur at one (or more) of several levels in the central auditory system.

If one accepts this kind of scheme, then what other properties might one expect it to display? One clear prediction arises from physiological evidence that across-ear inhibitory interactions occur throughout the central auditory system—e.g., most neurons in dorsal CN are inhibited by contralateral sounds (Young and Brownell, 1976; Joris and Smith, 1998). These across-ear interactions can be as strong as those occurring within ear. In the context of the proposed inhibitory scheme (Roberts and Holmes, 2006a), it has recently been shown that wideband inhibition from OC cells acts strongly on contralateral as well as ipsilateral CT cells (Shore *et al.*, 2003). The inhibition acts across ears via direct commissural connections between the two cochlear nuclei. These physiological findings suggest that a contralateral captor may be as effective at influencing vowel judgments as one presented in the same ear as the vowel and leading component. Even if this is not the case, the approach can offer a useful experimental tool so long as contralateral captors have an appreciable influence on the effect of onset asynchrony. This is because dichotic presentation allows the captor effect to be quantified in the guaranteed absence of unwanted peripheral effects, such as adaptation, lateral suppression, or combination tones.

To date, all studies that have used captors to explore the effects of onset asynchrony on vowel-quality judgments have employed either pure-tone or narrowband-noise captors (Darwin and Sutherland, 1984; Roberts and Holmes, 2006a; Holmes and Roberts, 2006). This is primarily because there is only a limited scope for varying the spectral properties of the captor when it is present in the same ear as the vowel and leading component. In particular: (i) the effects of lateral suppression are asymmetric—there is greater upward spread of suppression (Houtgast, 1974) and so more than an octave separation would be needed to avoid suppression effects when using a captor with a frequency below that of the leading component; (ii) the captor must be spectrally distant from each of the first three formant peaks of the vowel, because adaptation in the region of any one of them is likely to change the phonetic quality of the vowel (Roberts and Holmes, 2006a); (iii) although the captor effect is wideband, it is still band limited (Roberts and Holmes, 2006a), which leaves little room for maneuver once the other constraints have been taken into account. Satisfying all three constraints becomes especially restrictive in the context of multicomponent captors, but dichotic presentation avoids these constraints and so offers a practical way of exploring the perceptual effects of this kind of captor. This approach allows a more rigorous test of the role of harmonic relations in captor efficacy to be conducted than hitherto.

Dichotic presentation also provides an effective means of exploring whether the captor effect is influenced by another grouping principle—grouping by perceived location—because dichotic presentation produces the most extreme lateralization possible for the captor and the leading portion of the asynchronous vowel component. There are several findings demonstrating that presenting a single component in one ear and the rest of a complex tone in the other ear reduces significantly—but does not abolish—the reciprocal effects of these sounds on each other's perceptual properties. For example, Darwin and Ciocca (1992) found that the effect of a slightly mistuned harmonic (±3%) on the global pitch of a complex tone was reduced by about a third when it was presented in the contralateral ear to the rest of the complex. Similarly, Brunstrom and Roberts (2001) found that the characteristic shift in component pitch associated with mistuning a harmonic was reduced by about a half when that component and the rest of the complex were presented to opposite ears. The substantial effects that remain under dichotic presentation are consistent with the notion that auditory lateralization is sometimes a weak cue for simultaneous grouping (see Bregman, 1990; Darwin, 1997). This encourages the

belief that the efficacy of a captor under dichotic presentation will be sufficient for the approach to be a useful one, even if grouping by location proves to have some influence on the magnitude of the captor effect.

We began by comparing, for ipsilateral and contralateral presentation, the capacity of a pure-tone captor partly to reverse the effect of onset asynchrony on judgments of vowel quality (experiment 1). Contralateral presentation of the captor was found to be at least as effective as ipsilateral presentation. We then used dichotic presentation to explore whether the magnitude of the captor effect generated by a multicomponent captor is influenced by the formation of a harmonic relationship with the leading component of the vowel (experiment 2). The efficacy of multicomponent captors was found to be independent of this harmonic relationship. These findings are consistent with the inhibitory account of the captor effect (Roberts and Holmes, 2006a; Holmes and Roberts, 2006).

II. GENERAL METHOD

A. Overview

Both experiments used a paradigm designed to assess the perceptual integration of additional energy in the first-formant (F1) region of a vowel through its effect on phonetic quality (Darwin, 1984a, 1984b; Darwin and Sutherland, 1984). The English vowels /ɪ/ and /ɛ/ differ mainly in their F1 frequency; /ɪ/ has a lower F1 value than /ɛ/. Therefore, a continuum of vowel tokens can be synthesized that varies only in F1 frequency but which spans the /ɪ/–/ɛ/ phoneme boundary. These tokens can be presented to listeners in a forced-choice classification task, and the pattern of responses can be used to estimate where the phoneme boundary lies along this continuum.

Following Darwin and Sutherland (1984), extra energy was added to the 4th harmonic of vowels synthesized on a fundamental (F0) frequency of 125 Hz (i.e., to 500 Hz). When this added energy is integrated into the vowel percept, the perceived F1 frequency increases and the vowels sound more like /ɛ/. If each sound in this new continuum is specified as having the same *nominal* F1 frequency as its counterpart in the original continuum, then this perceptual change will result in a *lower* nominal F1 value at the phoneme boundary. When the size of the energy increment is kept constant across a set of conditions, differences in the size of the boundary shift can be used to estimate how much the extra energy integrates into the vowel percept in the different stimulus contexts tested.

B. Stimuli and conditions

Amplitude and phase values for the vowel harmonics were obtained from the vocal-tract transfer function using cascade formant synthesis (Klatt, 1980). Vowel stimuli in the basic F1 continuum were synthesized with an F0 frequency of 125 Hz and an F1 bandwidth of 90 Hz. All harmonics were present up to the 40th (5 kHz). Formants 2–5 were set to frequencies of 2300, 2900, 3800, and 4600 Hz, with bandwidths of 120, 170, 1000, and 1000 Hz, respectively. These parameters are identical to those used in our earlier studies

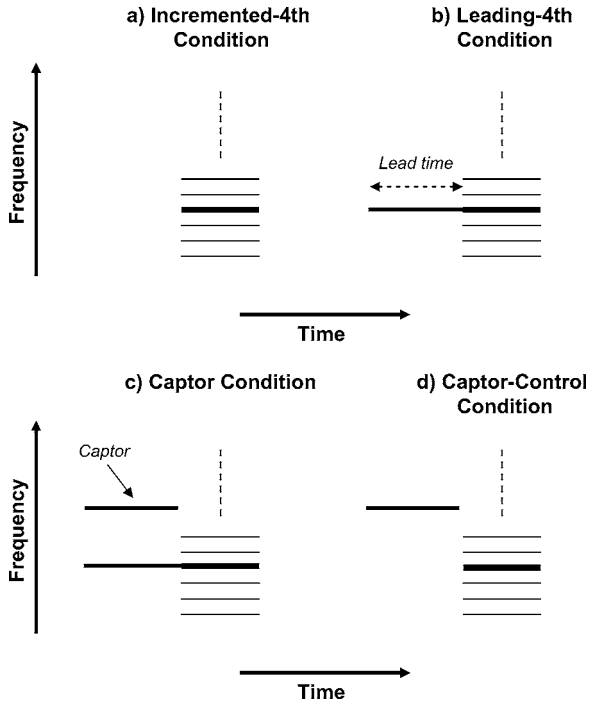

FIG. 2. Stimulus configurations used in this study for: (a) the incremented-4th condition; (b) the leading-4th condition; (c) an example captor condition, for which the captor was a pure tone; (d) the corresponding captor-control condition. Each part displays harmonics in the F1 region of a vowel (the continuation of the spectrum is shown by a vertical dashed line). In each case, a tone has been added to the vowel to increase the level of its 4th harmonic. The vowel and the additional 500 Hz tone were always presented in the left ear. The captor was presented either in the left ear (ipsilateral presentation) or in the right ear (contralateral presentation). Adapted with permission from "Asynchrony and the grouping of vowel components: Captor tones revisited," by B. Roberts and S. D. Holmes, 2006, J. Acoust. Soc. Am., **119**, p. 2907. Copyright 2006 by the Acoustical Society of America.

(Roberts and Holmes, 2006a; Holmes and Roberts, 2006). There were 20 vowels per continuum, with F1 values that varied in 10 Hz steps from 360 to 550 Hz. Vowel stimuli were 56 ms in duration (seven pitch periods), including linear onset and offset ramps of 16 ms each. To ensure roughly constant loudness across the basic continuum, all vowels were normalized to give the same root-mean-square amplitude. This continuum constituted the *vowel-alone* condition.

The continuum for the *incremented-4th* condition was created by adding in phase a pure tone at the frequency of the 4th harmonic (500 Hz) to each vowel in the normalized basic continuum. The additional tone had the same rise, steady-state, and fall times as the corresponding vowel. Its level was set to be 6 dB higher than the 4th harmonic, and so during each vowel the 500 Hz component was boosted by 9.5 dB relative to the value specified by the normalized transfer function. The continuum for the *leading-4th* condition was generated by extending the additional tone so that it began 240 ms before the vowel. Figure 2, parts (a) and (b), shows schematic spectrograms representing stimuli from the incremented-4th and leading-4th conditions, respectively.

Each *captor* condition was created by accompanying every vowel of the leading-4th condition with the appropriate captor tone. The captor always began in synchrony with the leading-4th harmonic and had 16-ms-long onset and offset

ramps. Captor offset always began at vowel onset, and so its amplitude envelope reached zero at the same moment as the envelope of the vowel reached steady state. The captors used in the various captor conditions were set, for each member of the continuum, to the same level as the corresponding added 500 Hz tone. For each captor condition, there was a corresponding *captor-control* condition created using vowels from the incremented-4th condition. These conditions differed from their counterparts only in that the leading portion of the 4th harmonic was absent. The controls were included to measure the extent to which vowel quality is influenced by the captor tones in the absence of leading energy at 500 Hz. Phoneme boundaries for these control conditions should not differ from the incremented-4th condition if the captor produces no perceptual change in the vowel. Figure 2, parts (c) and (d), shows schematic spectrograms of exemplar stimuli from the captor and captor-control conditions, respectively. In these examples, the captor is a pure tone.

All stimuli were synthesized at a sampling rate of 20 kHz using MITSYN (Henke, 1997) and stored on disk. They were played back at 16 bit resolution via a sound card (Turtle Beach, Santa Cruz) over Sennheiser HD480-II earphones. Stimuli were checked using a spectrum analyzer (Stanford Research Systems SR780). The overall output level of the sound card was set using the on-board analog attenuator (coarse adjustment) and digital multiplication (fine adjustment), and it was calibrated using a sound-level meter (Brüel and Kjaer, type 2209) coupled to the earphones by an artificial ear (type 4153). The presentation level for stimuli from the vowel-alone condition was about 69 dB sound pressure level (SPL). The level of the most intense token from the incremented-4th condition was about 76 dB SPL.

C. Listeners

Twelve listeners took part in each experiment. All volunteers were native speakers of British English who reported normal hearing. They were paid for their assistance and had earlier successfully completed a screening procedure. Screening used diotic presentation and was undertaken to ensure that each listener (i) clearly distinguished between the two vowel categories and produced monotonic identification functions with clear phoneme boundaries; (ii) produced a downward boundary shift when extra energy was added in synchrony with the 4th harmonic, and that much of this shift was lost when an onset asynchrony was introduced (e.g., Darwin 1984a, 1984b); and (iii) showed a partial return of the boundary when the leading portion of the 4th harmonic was accompanied by a synchronous 1 kHz captor tone (Darwin and Sutherland, 1984). For full details of the screening, see Holmes and Roberts (2006). About a third of the listeners screened were excluded from the study, most often because a boundary estimate fell outside the experimental range of F1 values in one or more conditions.

D. Procedure

Stimuli were played to the listeners in a double-walled sound-attenuating chamber (Industrial Acoustics 1201A). On each trial, listeners responded using a keyboard to indicate whether the vowel token was perceived as /ɪ/ or /ɛ/. Except for the practice blocks, described below, listeners were not allowed to repeat a stimulus before making their identification. The next trial began 0.5 s after the return key was pressed to confirm the choice. Listeners were asked to note the displayed trial number for any accidental key presses; these were corrected manually before data analysis. Listeners were asked to focus on the vowel and to try to ignore any additional sounds that might be present. No feedback was provided.

A block of stimuli consisted of all 20 tokens for each condition in the experiment and the stimulus order was randomized anew for each repetition of a block. This ensured that comparisons of the boundary position across conditions were not influenced by systematic contrast or range effects (e.g., Brady and Darwin, 1978). Each experiment was run as a single session that lasted about 40–70 min. The session began with a practice block consisting of every second F1 step from the full set of stimuli for the main experiment. Ten repetitions were presented to listeners during the main experiment, and listeners typically took a short break after every few hundred trials.

E. Data analysis

The data for each listener comprised the number of /ɪ/ responses out of ten repetitions for each nominal F1 value in each condition. These data were analyzed following the procedures used in our earlier studies (see Roberts and Holmes, 2006a, for a full description). An estimate of the phoneme boundary was obtained by fitting a probit function (Finney, 1971) to a listener's identification data for each condition; the nominal F1 frequency at the phoneme boundary was defined as the mean of the probit function. Changes in the F1 value at the phoneme boundary provide a measure of the extent to which the contribution of the additional energy at 500 Hz to vowel quality varies across conditions. For each experiment, a within-subjects analysis of variance (ANOVA) was performed on the boundary estimates. Only a small number of pairwise comparisons (two tailed) were required from the large set of possible comparisons, and so they were computed using the restricted least-significant-difference test (Snedecor and Cochran, 1967).

To obtain a controlled estimate of the efficacy of the captor, a measure called the *restoration effect* was calculated. The value of the restoration effect (in Hz) is defined as the boundary difference between the leading-4th and incremented-4th conditions, minus the boundary difference between the captor condition and its control. Any unintended effect that the captor may have on perceived vowel quality (i.e., other than through modulating the influence of the leading-4th harmonic) should be partialled out by comparing each captor condition with its own control rather than with the incremented-4th condition. To establish whether captor efficacy varied across conditions, a within-subjects ANOVA was performed on the calculated restoration values. It was also important to show that the restoration effects obtained were significantly greater than zero. Therefore, the one-

sample t test (two tailed) was used to compare these restoration values with zero.

III. EXPERIMENT 1

The classic study of Darwin and Sutherland (1984), and the recent follow-up studies (Roberts and Holmes, 2006a; Holmes and Roberts, 2006; Roberts *et al.*, in press), all used diotic presentation. In experiment 1, we used stimulus arrangements very similar to those used by Darwin and Sutherland (1984), but modified the design for ipsilateral and contralateral presentation of the vowel (plus leading-4th harmonic) and the pure-tone captor. According to the inhibitory account, the effect of the captor under contralateral presentation should be substantial and may even be comparable in size with the effect of an otherwise identical captor under ipsilateral presentation. Although a contralateral captor effect of moderate size would not distinguish between the inhibitory account and an account based on grouping by location, a contralateral effect comparable in size with the effect for the ipsilateral case would favor the inhibitory account.

A. Method

There were seven conditions: the three standard ones (vowel alone, incremented 4th, and leading 4th), plus two captor conditions and their controls. The captors used were 1 kHz pure tones, 240 ms long, and synchronous with the leading portion of the added 500 Hz tone (cf., Darwin and Sutherland, 1984). The vowel and the added tone were always presented in the left ear. The two captor conditions, and their corresponding controls, differed from one another only in the ear of presentation for the captor tones; either the left ear (ipsilateral presentation) or the right ear (contralateral presentation). The number of trials in the main experiment was 1400 (seven conditions $\times$ 20 F1 values $\times$ ten repetitions).

B. Results

Figure 3 shows the mean phoneme boundaries (and inter-subject standard errors) for all conditions and the restoration effect produced by each captor type. The restoration effects are shown above the histogram bars as a boundary shift in Hz, and also as a percentage of the boundary difference between the leading-4th and incremented-4th conditions. The effect of condition on the position of the phoneme boundary was highly significant [$F(6,66)=69.20$, $p<0.001$]. Incrementing the level of the 4th harmonic lowered the phoneme boundary by 60.1 Hz relative to the vowel-alone condition [$t(11)=14.05$, $p<0.001$], which indicates that most or all of the extra energy was integrated into the vowel percept. The leading-4th condition led to a phoneme boundary that was higher than that for the incremented-4th condition [$t(11)=14.59$, $p<0.001$], indicating that the extra energy at 500 Hz was excluded from the perceptual estimation of F1 frequency when it began 240 ms before the vowel. However, the boundary for the leading-4th condition was also significantly higher (by 30.1 Hz) than the boundary for the vowel-alone condition [$t(11)=5.85$, $p<0.001$]. The phoneme boundaries for the captor-control conditions did not differ significantly from that for the incremented-4th condition.

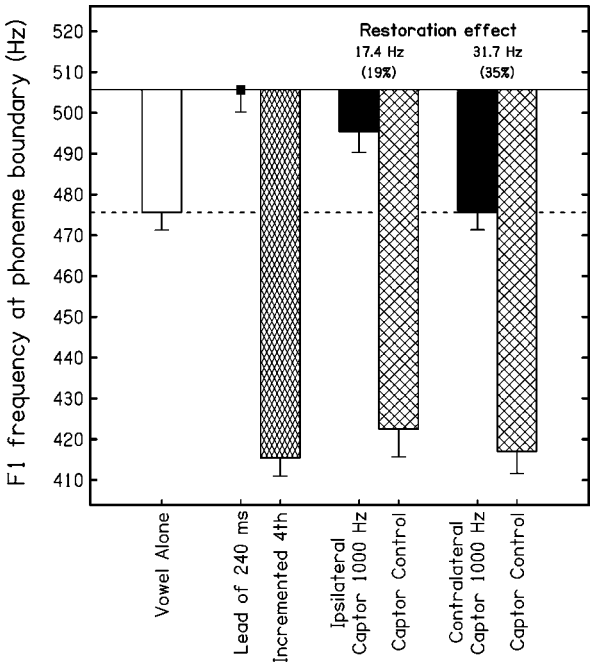

FIG. 3. Results for experiment 1—effect of pure-tone captors under ipsilateral and contralateral presentation. Mean phoneme boundaries are expressed as nominal first-formant frequencies for 12 listeners (with inter-subject standard errors). The boundary for the vowel-alone condition is indicated by the open bar and dotted horizontal line. The boundary for the leading-4th condition is shown by the square symbol and solid horizontal line, and the boundary for the incremented-4th condition is shown by the narrow-hashed bar. The boundaries for the captor conditions and for their controls are shown by the solid bars and wide-hashed bars, respectively. The extent to which each captor condition restores the effect of the leading-4th component on vowel quality, relative to its own control, is shown above each pair of bars. Each restoration effect is quoted as an F1 boundary shift in Hz and as a percentage of the boundary difference between the leading-4th and incremented-4th conditions. Note that the captor is at least as effective under contralateral as under ipsilateral presentation.

The efficacy of the captor at reducing the effect of the onset asynchrony on the added 500 Hz tone was compared for ipsilateral and contralateral presentation, using the computed restoration values. Analysis of the restoration effects revealed that there was no significant difference between these modes of presentation [$F(1,11)=3.40$, $p=0.092$], and that the overall size of the restoration effect (about 24.5 Hz, or 27%) was significantly above zero [$t(11)=5.38$, $p<0.001$]. The results suggest that the 1 kHz captor was similarly effective in both modes of presentation at reducing the effect of applying an onset asynchrony to the added 500 Hz tone. Note that the failure to find a significant reduction in captor efficacy for contralateral presentation is unlikely to reflect a lack of statistical power, because the observed size of the restoration effect was actually smaller for ipsilateral presentation. The size of the observed restoration effects is similar, in percentage terms, to that reported for 1 kHz captors under diotic presentation for otherwise comparable contexts (Darwin and Sutherland, 1984; Roberts and Holmes, 2006a).

C. Discussion

Roberts and Holmes (2006a) found that captor efficacy was not influenced by two grouping factors (common onset time and harmonic relations) that would be expected to promote the perceptual integration of a pure-tone captor with the leading portion of the 4th harmonic. The current experiment shows that captor efficacy does not depend on a major grouping cue for lateralization either, because it is not reduced when the captor and the leading portion are presented to opposite ears rather than to the same ear. Instead, this experiment supports an explanation for the captor effect in terms of comparable degrees of within- and across-ear wideband inhibition operating within the central auditory system.

One aspect of the data that merits consideration is the overshoot in the return of the boundary associated with the leading-4th condition. This refers to the finding that the rise in the phoneme boundary from the incremented-4th to the leading-4th condition was greater than that required to reach the boundary for the vowel-alone condition. This overshoot effect has not been observed in earlier research using diotic presentation. Furthermore, it does not seem to be an artifact of participant sampling, because the screening data were obtained using diotic presentation and indicated a much smaller (8.6 Hz) and nonsignificant overshoot. The size and scale of the overshoot observed in the main experiment is consistent with the notion that *all* of the energy at 500 Hz (i.e., including the original 4th harmonic of the unmodified vowel) has been excluded from the vowel percept (cf., Darwin, 1984b, 1995). However, such a total exclusion would constitute a violation of the old-plus-new heuristic[1] (Bregman, 1990) and it is unclear why this should occur. Whatever the precise cause of the overshoot, the apparent difference in the effect of asynchrony for ipsilateral and diotic presentation implies that contralateral processing can influence perception even when both ears receive identical stimuli.

IV. EXPERIMENT 2

Roberts and Holmes (2006a, experiment 3) used pure-tone captors to evaluate whether or not the captor effect first demonstrated by Darwin and Sutherland (1984) depends on harmonic relations between the captor and the leading portion of the 4th harmonic (500 Hz). Captor frequency was varied over the range 900–2250 Hz, and included three values that matched the 2nd to 4th harmonics of 500 Hz (i.e., 1000, 1500, and 2000 Hz). Roberts and Holmes found that captor efficacy depended on frequency proximity with the leading portion rather than on harmonic relations. However, there were some limitations of their experiment that prevented a definitive conclusion that captor efficacy is entirely independent of harmonic relations. First, the frequency range over which a pure-tone captor was effective was limited such that the 1.5 kHz captor fell on the upper skirt of the passband and the 2 kHz captor fell outside it altogether. In addition, neither of these captors formed a consecutive harmonic series with the leading 500 Hz component. Therefore, in practice, a frequency of 1 kHz was the only optimum value for testing the harmonicity hypothesis using pure-tone captors. Second, Roberts and Holmes noted that some researchers (e.g., Bregman, 1990) have argued that at least three components must be present before their simultaneous grouping can be influenced by harmonic relations. For example, Bregman and Doehring (1984) found that the middle component of a three-tone complex could be captured into a sequential stream more easily when it was mistuned relative to the other components, but Bregman and Pinker (1978) did not find an equivalent effect for two-tone complexes.

For diotic presentation, Roberts and Holmes (2006a) noted that a two-component captor with frequencies of 1000 and 1500 Hz is the only captor complex that would form a consecutive harmonic series with the leading 500 Hz component (starting with this partial as the F0 component), while also avoiding significant adaptation in the region of F1 or F2. Now that the efficacy of contralateral captors has been established using dichotic presentation, we can avoid these constraints and use multicomponent captors to explore the effects of harmonic relations more thoroughly in the context of judgments of vowel quality.

A. Method

There were nine conditions: the three standard ones (vowel alone, incremented 4th, and leading 4th), plus three captor conditions and their controls. The captor configurations used are illustrated in Fig. 4. The vowel and the added 500 Hz tone were always presented in the left ear, and the captors were always presented in the right ear (contralateral presentation). This was to ensure that the captors did not cause any adaptation or other peripheral effects in channels responding to the F1 region of the vowel. Each captor was a complex tone comprising harmonics 1–2 and 4–5 of F0, 240 ms long, and synchronous with the leading portion of the added tone.[2] The pure-tone captors used in experiment 1 were equal in level to the added 500 Hz tone. To ensure that the overall level of each multicomponent captor was equal to that of the corresponding added 500 Hz tone, each component was set to 6 dB below the level of that tone. The three captor conditions, and their corresponding controls, differed from one another only in the F0 frequency of the captor tones. The F0 frequency in one captor condition was set to 166.7 Hz, for which the added 500 Hz tone corresponds exactly to the frequency of the captor's missing 3rd harmonic (*shared-F0* captor). The F0 frequency was set to 153.3 and 180.0 Hz in the other two captor conditions, for which the added 500 Hz tone is mistuned from the frequency of the missing 3rd harmonic by +8% and −8%, respectively (*different-F0* captors). In the shared-F0 case, but not the different-F0 cases, the grouping together of the captor and the leading portion of the added 500 Hz tone would complete a consecutive series of harmonics 1–5. These kinds of stimulus arrangement were used by Ciocca and Darwin (1993) to explore the effects of harmonic relations between a multicomponent captor and the leading portion of a harmonic in the context of global-pitch perception. The number of trials in the main experiment was 1800 (nine conditions × 20 F1 values × ten repetitions). Six of the 12 listeners also took part in experiment 1.

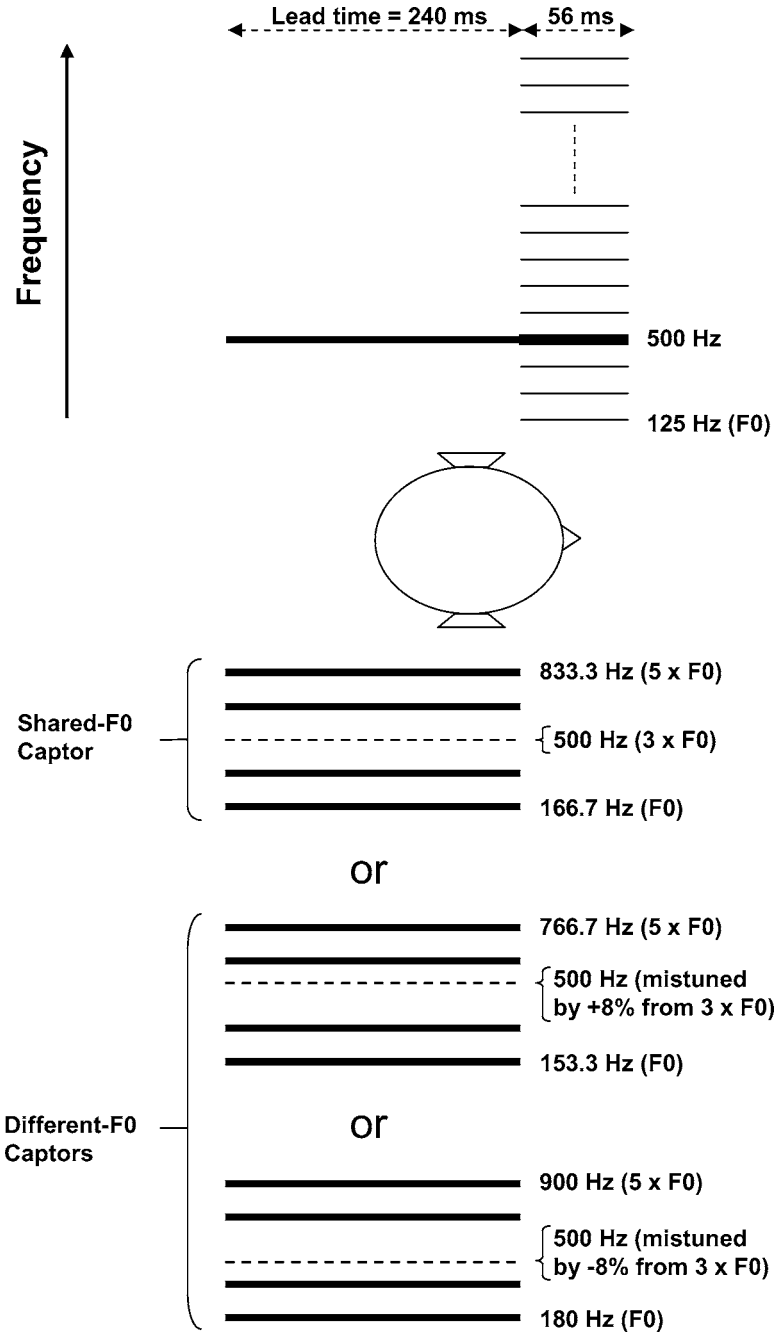

FIG. 4. Captor configurations used in experiment 2. Three different multi-component captors were used, each comprising harmonics 1–2 and 4–5 of F0. For the shared-F0 captor (F0=166.7 Hz), the leading-4th component of the vowel in the opposite ear corresponds to the missing 3rd harmonic of the captor. For the different-F0 captors (F0=153.3 Hz, 180 Hz), the leading-4th component is mistuned from the frequency of the missing 3rd harmonic by +8% and −8%, respectively. These frequency relationships are illustrated by the dotted line in the spectral center of each captor.

B. Results

Figure 5 shows the mean phoneme boundaries (and inter-subject standard errors) for all conditions, and the restoration effect for each captor F0. The effect of condition on the position of the phoneme boundary was highly significant [$F(8,88) = 33.14$, $p < 0.001$]. Incrementing the level of the 4th harmonic lowered the phoneme boundary by 57.1 Hz relative to the vowel-alone condition [$t(11) = 9.09$, $p < 0.001$], which indicates that most or all of the extra energy was integrated into the vowel percept. As before, the leading-4th condition led to a phoneme boundary that was significantly higher than for the incremented-4th condition [$t(11) = 6.97$, $p < 0.001$]. However, the overshoot in boundary return of 22.3 Hz is somewhat smaller than that observed in experiment 1, and did not quite reach statistical significance [leading-4th versus vowel-alone: $t(11) = 2.05$, $p = 0.066$]. Once again, the screening data indicated a much smaller (6.6 Hz) overshoot for these listeners under diotic presentation. Given this, and the significant overshoot observed in experiment 1, it seems reasonable to interpret these results as consistent with the suggestion that applying a 240 ms asynchrony to the added 500 Hz tone also led to an exclusion of part (or all) of the original 500 Hz component from the vowel percept. The boundaries for the captor-control conditions did not differ significantly from that for the incremented-4th condition.

Analysis of the restoration effects revealed that there was no significant difference between the three captor F0s [$F(2,22) = 0.03$, $p = 0.974$], and that the overall size of the restoration effect (about 31.8 Hz, or 40%) was significantly

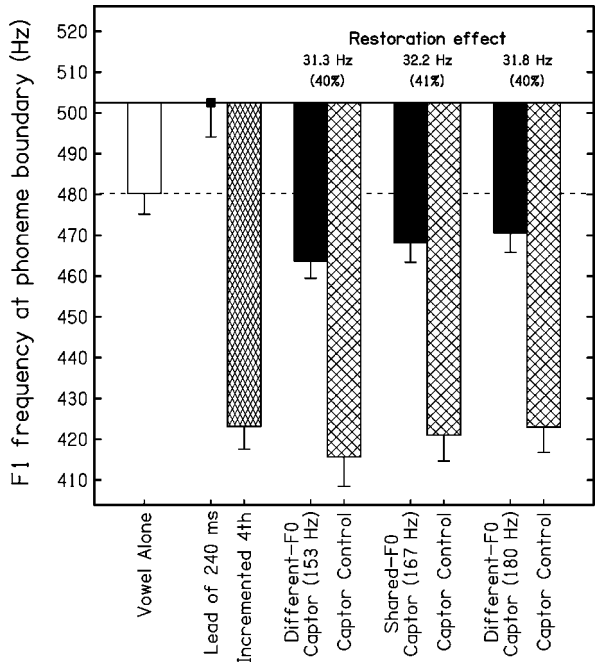

FIG. 5. Results for experiment 2—the influence of harmonic relations on the effect of multi-component captors under contralateral presentation. Phoneme boundaries and restoration effects are displayed as for Fig. 3. Note that all three captors are similarly effective, irrespective of whether they are harmonically related to the leading-4th component.

above zero [$t(11)=3.33$, $p=0.007$]. Note that the restoration effects observed here for multicomponent captors under contralateral presentation are similar in size to that observed for the contralateral pure-tone captor used in experiment 1. The key finding is that the shared-F0 and the different-F0 captors produced a similar and substantial reduction in the effect of applying an onset asynchrony to the added 500 Hz tone. Differences between captors in F0 and frequency range were small, and the shared-F0 captor was bracketed by the different-F0 captors on these dimensions. Therefore, it is reasonable to conclude that captor efficacy is not influenced by whether or not the captor and the leading portion of the added 500 Hz tone are harmonically related.

C. Discussion

The absence of an effect of harmonic relations on the efficacy of multicomponent captors observed here contrasts with the findings of Ciocca and Darwin (1993). These authors followed on from one of their earlier studies (Darwin and Ciocca, 1992), which had shown that the shift in global pitch resulting from slightly mistuning a resolved harmonic of a complex tone (Moore *et al.*, 1985) can be reduced or abolished by starting the mistuned harmonic before the other partials. Ciocca and Darwin mistuned the 4th harmonic (620 Hz) of a complex tone (F0=155 Hz, components 1–12, flat spectrum) by about ±3% (exact values = 600 and 640 Hz) and explored the effect of accompanying the leading portion of the mistuned component with a multicomponent captor (components 1–2 and 4–5 of either F0=200 Hz or 213.3 Hz), for which either the 600 or the 640 Hz leading component, respectively, constituted the in-tune 3rd harmonic of captor F0. Mismatching the captor F0 and the direction of mistuning for the leading component led to a mistuning with respect to the vacant 3rd harmonic position in the captor of about 6%. All stimuli were presented diotically. The duration of the leading portion was set to 0, 80, 160, or 320 ms (we used 240 ms), and the captor was either present (same duration as leading portion) or absent. For the longer asynchronies used (160 and 320 ms), the pitch shift was reliably larger when the captor was present than absent, but only if it was harmonically related to the leading component.

The most likely reason for the discrepancy in findings between the two studies is that captor efficacy was measured in the context of vowel-quality (timbre) judgments in our study but in the context of global-pitch judgments in the study of Ciocca and Darwin (1993). There are a number of observations illustrating substantial differences in the ways that the grouping cues of onset asynchrony and harmonic relations are used for the perceptual estimation of global pitch and timbre. For example, a harmonic must be mistuned by more than ±3% before it begins to be excluded from the global-pitch percept (Moore *et al.*, 1985), but can become audible as a separate entity—with its own pure-tone-like timbre—at much smaller mistunings (Moore *et al.*, 1986; Hartmann *et al.*, 1990; Roberts and Brunstrom, 1998). Moreover, much greater onset asynchronies are required largely to abolish the contribution of a component to global pitch (typically 160 ms or more; e.g., Darwin and Ciocca, 1992) than to vowel quality (typically 30–50 ms; e.g., Darwin, 1984a, 1984b; Roberts and Moore, 1991). This difference is maintained even when the contributions to pitch and vowel quality are compared for the same component in the same spectral context (Hukin and Darwin, 1995).

Before accepting that the discrepancy in findings between our study and that of Ciocca and Darwin (1993) reflects differences in the use of harmonicity information in the context of different perceptual judgments, we must consider an alternative explanation based on differences in ear of presentation. The leading component and the captor were presented diotically in their study, but dichotically in ours, and this difference may have affected the ability of harmonic relations to influence captor efficacy. Although this account cannot be ruled out completely, it seems very unlikely for the following reasons:

(1) As noted in the Introduction, there are examples of clear effects of harmonic relations on perception under dichotic presentation (Darwin and Ciocca, 1992; Brunstrom and Roberts, 2001). Indeed, Darwin *et al.* (1992) presented two concurrent harmonic complexes (each with a missing harmonic) to opposite ears plus a single component to one ear only, and found that the added component could affect the pitch of the complex in the opposite ear (from which it was slightly mistuned) even when it was exactly in tune with the complex in the same ear. Of course, in our study the leading portion of the 500 Hz component in the opposite ear to the captor was the only component that could potentially fill the vacant harmonic position in the middle of the captor complex. One might counter that these cross-ear effects all concern pitch perception, but there are also examples of di-

chotic fusion influencing the perception of timbre—notably the duplex perception of speech (e.g., Rand, 1974; Mann and Liberman, 1983).

(2) The captors that we used were exactly synchronous with the leading portion of the 4th harmonic of the vowel. This should encourage their grouping, and so reveal any *additional* effect of harmonic relations that may be present, even if the basic inhibitory effect of the captor does not depend on a common onset time between the captor and the leading portion (Roberts and Holmes, 2006a). Furthermore, the captor components were chosen such that the leading component would complete the set of consecutive harmonics 1–5 in the shared-F0 condition. All of these harmonics are resolved (Plomp, 1964), and the set encompasses the dominance region for pitch for the captor F0 used (Ritsma, 1967). The duration of the captors and the leading portion (240 ms) was easily long enough to maximize the opportunity for harmonic fusion to take place—only for short-duration stimuli does this grouping effect become weak or absent (e.g., Turgeon *et al.*, 2005). That there is no hint in our results of an effect of harmonic relations between the captor and the leading component suggests that there is no such effect to find in the context of judgments of vowel quality.

(3) Finally, it is not necessarily the case that presenting a pure-tone captor in the same ear as the leading component provides an inadequate test of the effect of captor harmonicity. Although Bregman (1990) has argued that at least three components must be present before harmonic relations can influence their perceptual grouping, there is evidence indicating effects of harmonic relations when only two components are present. For example, Demany and Semal (1988, 1992) have shown that listeners can detect mistuning between two pure tones from the intervals of octave and perfect fifth—even though the tones were presented to opposite ears. Furthermore, Roberts and Holmes (2006b) have shown for stimuli comprising only two components, one an octave higher than the other, that mistuning the lower component generates a pitch shift on that component in the same direction as the mistuning. This kind of pitch shift is typical of that seen when a single harmonic is mistuned in a multicomponent complex tone (e.g., Lin and Hartmann, 1998), and is often regarded as an indicator of the perceptual organization of components in a complex tone (e.g., Roberts, 2005; Roberts and Brunstrom, 2003). Therefore, we suggest that the absence of an effect of harmonic relations on captor efficacy when a pure-tone captor is presented in the same ear as the vowel and leading component (Roberts and Holmes, 2006a) is not merely an artifact of using two concurrent components. Rather, we believe that there is no appreciable influence of harmonic relations on captor efficacy in the context of vowel-quality judgments.

V. CONCLUDING DISCUSSION

The capacity of a so-called captor partly to reverse the reduction in the contribution of a component to vowel quality brought about by onset asynchrony (Darwin and Sutherland, 1984) is at least as effective under contralateral as under ipsilateral presentation. This finding is consistent with physiological evidence that wideband inhibition in the central auditory system can act strongly across as well as within ear (e.g., Shore *et al.*, 2003). Furthermore, there is no evidence of any effect of harmonic relations on captor efficacy, either for pure-tone or complex-tone captors. If such an effect exists at all, it is clearly swamped by a more general effect—presumably wideband inhibition—that is insensitive to harmonic relations. Combined with the findings of previous studies (Roberts and Holmes, 2006a; Holmes and Roberts, 2006), it is now clear that the captor effect does not depend on any of the major cues for simultaneous grouping—common onset time, harmonic relations, or lateralization. This suggests that the inhibitory interactions occur at a relatively early stage of central auditory processing, before the influence of more cognitive mechanisms of auditory grouping.

Roberts and Holmes (2006a) proposed that the psychophysical captor effect reflects the widespread operation of a network of lateral inhibition that has evolved to enhance spectral features in acoustic stimuli. One might speculate that a similar level of within- and across-ear inhibition is a requirement for such a mechanism, to avoid distortions in the perceived lateralization of sounds. Consider, for example, a stimulus arrangement in which both ears receive a 500 Hz tone (of equal level and in phase), but only the left ear receives a 1 kHz tone (matched in level to the 500 Hz tone). Roberts and Holmes (2006a) estimated that a 1 kHz captor equal in level to a 500 Hz leading component reduced the effective level of that component by about 6 dB. If this effective reduction occurred only in the (left) ear receiving the captor, then the perceived lateralization of the 500 Hz tone might be expected to shift rightwards from its originally central position. This problem is avoided if the inhibition also acts across ears.

It is interesting to consider further the differences between the mechanisms that underpin pitch and timbre perception. The findings of Ciocca and Darwin (1993) indicate not only that harmonic relations between the captor and the leading component influence captor efficacy, but also that captors that do not have this relationship are ineffective. However, this need not imply that the inhibitory interactions occurring in the context of timbre judgments do not apply to pitch. Rather, it may be that a moderate reduction in the effective level of the leading portion of a mistuned component has little influence on the effect of the asynchrony on pitch judgments, as might be expected if the pitch of a sound is less affected than its timbre by changes in the relative level of the components. We are aware of only one study germane to this suggestion. Darwin *et al.* (1995) measured the effect on the pitch of a complex tone of varying the level of a slightly mistuned 4th harmonic (±3%), relative to the level of the other partials (flat spectrum). In the contralateral case, for which the mistuned harmonic cannot be masked by the other partials, varying its relative level over the range tested (+9 to −9 dB) had no appreciable effect on its contribution to the pitch of the complex tone.[3] This finding is consistent with

our conjecture that wideband inhibition occurs in the contexts of pitch and timbre judgments, but that its effects are apparent only in the latter case.

At this point, it is unclear whether the relevance of our proposed inhibitory account is restricted primarily to timbre perception, or whether it has broader implications for auditory processing. For example, the persistence of wideband inhibition that is implied by the slow decay of captor efficacy after captor termination (80 ms or more; Holmes and Roberts, 2006) may mean that accompanying a forward masker with a concurrent suppressor acts not only to suppress the masker (e.g., Shannon, 1976; O'Loughlin and Moore, 1981; Yasin and Plack, 2003), but also to inhibit the masker *and* the following signal. Further research is required to elucidate more generally the role of wideband inhibition in auditory perception.

ACKNOWLEDGMENTS

This research was supported by Research Grant No. 6/S17805 from the Biotechnology and Biological Sciences Research Council (UK) to B.R. and by Aston University. We are grateful to Ian Winter for discussions on the neural mechanisms that may mediate the perceptual effects reported here. Our thanks go to Neal Viemeister and Chris Plack, whose observations stimulated us to consider the implications of the inhibitory account for sound lateralization and forward masking, respectively. We are also grateful to a nearly anonymous reviewer (Chris Darwin) for drawing our attention to an article from his laboratory in support of our suggestion about differences in the level dependence of a component's contribution to the pitch and timbre of a complex tone.

[1]The old-plus-new heuristic states that part of a current sound that can be interpreted as the continuation of a previous sound should be excluded perceptually. This serves to enhance the representation of new sounds in temporally overlapping mixtures.

[2]In the context of the inhibitory account, the bandwidth of each captor was set such that all the components should fall comfortably within the frequency range over which the proposed inhibitory interactions take place. The psychophysical captor effect is known to extend up to about 1.5 octaves above the frequency of the leading component (Roberts and Holmes, 2006a). Although there is no psychophysical data for captors placed below the frequency of the leading component, physiological evidence from the guinea pig indicates that the average bandwidth of inhibitory OC cells extends from about two octaves below to about one octave above best frequency (Palmer *et al.*, 1996).

[3]This result also suggests an explanation for why the time constant observed for the effect of onset asynchrony on the perceptual contribution of a component to a complex tone is much longer for global pitch than for timbre (e.g., Hukin and Darwin, 1995). If the effect of starting one component before the others is to reduce its *effective* level, then the consequence of increasing the onset asynchrony will become apparent (and approach asymptote) much later for pitch than for timbre judgments. One might counter that Darwin *et al.* (1995) did not find a similar level independence for pitch judgments when the mistuned harmonic was presented ipsilaterally. However, this was the case only when its level was reduced below that of the other components, and so most probably arose from peripheral masking effects. A reduction in the effective level of a component arising from an onset asynchrony would not be subject to such masking effects, and hence is analogous to the contralateral case.

Bartlett, E. L., and Wang, X. (**2005**). "Lost-lasting modulation by stimulus context in primate auditory cortex," J. Neurophysiol. **94**, 83–104.

Bleeck, S., Ingham, N., Verhey, J., and Winter, I. M. (**2005**). "Wideband suppression in cochlear nucleus: A role in grouping by common onset?" in ARO Abstracts, Vol. **28**, No. 671, p. 236.

Brady, S. A., and Darwin, C. J. (**1978**). "Range effect in the perception of voicing," J. Acoust. Soc. Am. **63**, 1556–1558.

Bregman, A. S. (**1990**). *Auditory Scene Analysis: The Perceptual Organization of Sound* (MIT Press, Cambridge, MA).

Bregman, A. S., and Doehring, P. (**1984**). "Fusion of simultaneous tonal glides: The role of parallelness and simple frequency relations," Percept. Psychophys. **36**, 251–256.

Bregman, A. S., and Pinker, S. (**1978**). "Auditory streaming and the building of timbre," Can. J. Psychol. **32**, 19–31.

Brunstrom, J. M., and Roberts, B. (**2001**). "Effects of asynchrony and ear of presentation on the pitch of mistuned partials in harmonic and frequency-shifted complex tones," J. Acoust. Soc. Am. **110**, 391–401.

Ciocca, V., and Darwin, C. J. (**1993**). "Effects of onset asynchrony on pitch perception: Adaptation or grouping?" J. Acoust. Soc. Am. **93**, 2870–2878.

Dannenbring, G. L., and Bregman, A. S. (**1978**). "Streaming vs. fusion of sinusoidal components of complex tones," Percept. Psychophys. **24**, 369–376.

Darwin, C. J. (**1984a**). "Auditory processing and speech perception," in *Attention and Performance X: Control of Language Processes*, edited by H. Bouma and D. G. Bouwhuis (Erlbaum, Hillsdale, NJ), pp. 197–210.

Darwin, C. J. (**1984b**). "Perceiving vowels in the presence of another sound: Constraints on formant perception," J. Acoust. Soc. Am. **76**, 1636–1647.

Darwin, C. J. (**1995**). "Perceiving vowels in the presence of another sound: A quantitative test of the 'old-plus-new' heuristic," in *Levels in Speech Communication: Relations and Interactions*, edited by C. Sorin, J. Mariani, H. Meloni, and J. Schoentgen (Elsevier, Amsterdam), pp. 1–12.

Darwin, C. J. (**1997**). "Auditory grouping," Trends Cogn. Sci. **1**, 327–333.

Darwin, C. J., Buffa, A., Williams, D., and Ciocca, V. (**1992**). "Pitch of dichotic complex tones with a mistuned frequency component," in *Auditory Physiology and Perception*, edited by Y. Cazals, L. Demany, and K. Horner (Pergamon, Oxford), pp. 223–229.

Darwin, C. J., and Ciocca, V. (**1992**). "Grouping in pitch perception: Effects of onset asynchrony and ear of presentation of a mistuned component," J. Acoust. Soc. Am. **91**, 3381–3390.

Darwin, C. J., Hukin, R. W., and Al-Khatib, B. Y. (**1995**). "Grouping in pitch perception: Evidence for sequential constraints," J. Acoust. Soc. Am. **98**, 880–885.

Darwin, C. J., and Sutherland, N. S. (**1984**). "Grouping frequency components of vowels: When is a harmonic not a harmonic?" Q. J. Exp. Psychol. **36A**, 193–208.

Demany, L., and Semal, C. (**1988**). "Dichotic fusion of two tones one octave apart: Evidence for internal octave templates," J. Acoust. Soc. Am. **83**, 687–695.

Demany, L., and Semal, C. (**1992**). "Detection of inharmonicity in dichotic pure-tone dyads," Hear. Res. **61**, 161–166.

Finney, D. J. (**1971**). *Probit Analysis*, 3rd ed. (Cambridge U.P., Cambridge, UK).

Hartmann, W. M., McAdams, S., and Smith, B. K. (**1990**). "Hearing a mistuned harmonic in an otherwise periodic complex tone," J. Acoust. Soc. Am. **88**, 1712–1724.

Henke, W. L. (**1997**). *MITSYN: A Coherent Family of High-Level Languages for Time Signal Processing*, software package (Belmont, MA); e-mail: mitsyn@earthlink.net; http://home.earthlink.net/~mitsyn

Holmes, S. D., and Roberts, B. (**2006**). "Inhibitory influences on asynchrony as a cue for auditory segregation," J. Exp. Psychol. Hum. Percept. Perform. **32**, 1231–1242.

Houtgast, T. (**1974**). "Lateral suppression in hearing," Doctoral thesis, Free University, Amsterdam.

Hukin, R. W., and Darwin, C. J. (**1995**). "Comparison of the effect of onset asynchrony on auditory grouping in pitch matching and vowel identification," Percept. Psychophys. **57**, 191–196.

Joris, P. X., and Smith, P. H. (**1998**). "Temporal and binaural properties in dorsal cochlear nucleus and its output tract," J. Neurosci. **18**, 10157–10170.

Kiang, N. Y.-S., Watanabe, T., Thomas, E. C., and Clark, L. F. (**1965**). *Discharge Patterns of Single Fibers in the Cat's Auditory Nerve* (MIT Press, Cambridge, MA).

Klatt, D. H. (**1980**). "Software for a cascade/parallel formant synthesizer," J. Acoust. Soc. Am. **67**, 971–995.

Lin, J.-Y., and Hartmann, W. M. (**1998**). "The pitch of a mistuned harmonic: Evidence for a template model," J. Acoust. Soc. Am. **103**, 2608–2617.

Mann, V. A., and Liberman, A. M. (**1983**). "Some differences between pho-

netic and auditory modes of perception," Cognition **14**, 211–235.
Moore, B. C. J., Glasberg, B. R., and Peters, R. W. (**1985**). "Relative dominance of individual partials in determining the pitch of complex tones," J. Acoust. Soc. Am. **77**, 1853–1860.
Moore, B. C. J., Glasberg, B. R., and Peters, R. W. (**1981**). "Thresholds for hearing mistuned partials as separate tones in harmonic complexes," J. Acoust. Soc. Am. **80**, 479–483.
Needham, K., and Paolini, A. G. (**2003**). "Fast inhibition underlies the transmission of auditory information between cochlear nuclei," J. Neurosci. **23**, 6257–6361.
O'Loughlin, B. J., and Moore, B. C. J. (**1981**). "Off-frequency listening: Effects on psychoacoustic tuning curves obtained in simultaneous and forward masking," J. Acoust. Soc. Am. **69**, 1119–1125.
Palmer, A. R., Jiang, D., and Marshall, D. H. (**1996**). "Response of ventral cochlear nucleus onset and chopper units as a function of signal bandwidth," J. Neurophysiol. **75**, 780–794.
Plomp, R. (**1964**). "The ear as a frequency analyzer," J. Acoust. Soc. Am. **36**, 1628–1636.
Rand, T. C. (**1974**). "Dichotic release from masking for speech," J. Acoust. Soc. Am. **55**, 678–680.
Rasch, R. A. (**1978**). "The perception of simultaneous notes such as in polyphonic music," Acustica **40**, 21–33.
Ritsma, R. J. (**1967**). "Frequencies dominant in the perception of the pitch of complex sounds," J. Acoust. Soc. Am. **42**, 191–198.
Roberts, B. (**2005**). "Spectral pattern, grouping, and the pitches of complex tones and their components," Acta. Acust. Acust. **91**, 945–957.
Roberts, B., and Brunstrom, J. M. (**1998**). "Perceptual segregation and pitch shifts of mistuned components in harmonic complexes and in regular inharmonic complexes," J. Acoust. Soc. Am. **104**, 2326–2338.
Roberts, B., and Brunstrom, J. M. (**2003**). "Spectral pattern, harmonic relations, and the perceptual grouping of low-numbered components," J. Acoust. Soc. Am. **114**, 2118–2134.
Roberts, B., and Holmes, S. D. (**2006a**). "Asynchrony and the grouping of vowel components: Captor tones revisited," J. Acoust. Soc. Am. **119**, 2905–2918.
Roberts, B., and Holmes, S. D. (**2006b**). "Grouping and the pitch of a mistuned fundamental component: Effects of applying simultaneous multiple mistunings to the other harmonics," Hear. Res. **222**, 79–88.
Roberts, B., Holmes, S. D., Bleeck, S., and Winter, I. M. (**in press**). "Wideband inhibition modulates the effect of onset asynchrony as a grouping cue," *Proc. XIVth Int. Symp. Hear.*, Cloppenburg, Germany. [To appear in: *Hearing—From Basic Research to Applications,* edited by B. Kollmeier, G. Klump, V. Hohmann, U. Langemann, M. Mauermann, S. Uppenkamp, and J. Verhey (Springer-Verlag, Berlin, 2007)].
Roberts, B., and Moore, B. C. J. (**1991**). "The influence of extraneous sounds on the perceptual estimation of first-formant frequency in vowels under conditions of asynchrony," J. Acoust. Soc. Am. **89**, 2922–2932.
Shannon, R. V. (**1976**). "Two-tone unmasking and suppression in a forward-masking situation," J. Acoust. Soc. Am. **59**, 1460–1470.
Shore, S. E., Sumner, C. J., Bledsoe, S. C., and Lu, J. (**2003**). "Effects of contralateral sound stimulation on unit activity of ventral cochlear nucleus neurons," Exp. Brain Res. **153**, 427–435.
Snedecor, G. W., and Cochran, W. G. (**1967**). *Statistical Methods*, 6th ed. (Iowa U.P., Ames, Iowa).
Turgeon, M., Bregman, A. S., and Roberts, B. (**2005**). "Rhythmic masking release: Effects of asynchrony, temporal overlap, harmonic relations, and source separation on cross-spectral grouping," J. Exp. Psychol. Hum. Percept. Perform. **31**, 939–953.
Westerman, L. A., and Smith, R. A. (**1984**). "Rapid and short-term adaptation in auditory nerve responses," Hear. Res. **15**, 249–260.
Winter, I. M., and Palmer, A. R. (**1995**). "Level dependence of cochlear nucleus onset unit responses and facilitation by second tones or broadband noise," J. Neurophysiol. **73**, 141–159.
Yasin, I., and Plack, C. J. (**2003**). "The effects of a high-frequency suppressor on tuning curves and derived basilar-membrane response functions," J. Acoust. Soc. Am. **114**, 322–332.
Young, E. D., and Brownell, W. E. (**1976**). "Responses to tones and noise of single cells in dorsal cochlear nucleus of unanesthetized cats," J. Neurophysiol. **39**, 282–300.

Effects of masker-spectral variability and masker fringes in children and adults[a)]

Lori J. Leibold[b)] and Donna L. Neff
Boys Town National Research Hospital, Omaha, Nebraska, 68131

(Received 8 September 2006; revised 14 March 2007; accepted 19 March 2007)

This study examined the degree to which masker-spectral variability contributes to children's susceptibility to informational masking. Listeners were younger children (5–7 years), older children (8–10 years), and adults (19–34 years). Masked thresholds were measured using a 2IFC, adaptive procedure for a 300-ms, 1000-Hz signal presented simultaneously with (1) broadband noise, (2) a random-frequency ten-tone complex, or (3) a fixed-frequency ten-tone complex. Maskers were presented at an overall level of 60 dB SPL. Thresholds were similar across age for the noise condition. Thresholds for most children were higher than for most adults, however, for both ten-tone conditions. The average difference in threshold between random and fixed ten-tone conditions was comparable across age, suggesting a similar effect of reducing masker-spectral variability in children and adults. Children appear more likely to be susceptible to informational masking than adults, however, both with and in the absence of masker-spectral variability. The addition of a masker fringe (delayed onset of signal relative to masker) provided a release from masking for fixed and random ten-tone conditions in all age groups, suggesting at least part of the masking observed for both ten-tone maskers was informational. © *2007 Acoustical Society of America.*
[DOI: 10.1121/1.2723664]

PACS number(s): 43.66.Dc, 43.66.Lj [RAL] Pages: 3666–3676

I. INTRODUCTION

Everyday listening environments are complex, dynamic, and often unpredictable. Listeners must separate relevant from irrelevant acoustic information even though the spectral, level, and temporal characteristics of the waveforms change over time. Understanding how infants and children select and attend to the most informative components of a complex sound under these conditions is a question of particular importance to the study of auditory development, because children must learn the characteristics of speech in this uncertain environment.

To study how well adults attend to the relevant components of complex sounds, performance has been examined under conditions of stimulus uncertainty (e.g., Watson *et al.*, 1975; Neff and Green, 1987; Kidd *et al.*, 2002; Alexander and Lutfi, 2004), created by random variations in either the target signal or the irrelevant masker. Many studies of simultaneous masking with adults have shown large detrimental effects produced by masker-spectral variability, created by varying the frequency content of the masker each time it is presented (e.g., Neff and Green, 1987). Hallmark characteristics of performance in these conditions include large individual differences and elevated thresholds, despite little overlap in peripheral excitation expected between the fixed-frequency target tone and the random-frequency multi-tonal masker. Thus, this masking is typically referred to as "informational" masking to contrast with "energetic" masking predicted by peripheral power spectrum models of masking.

Informational masking is consistently observed under conditions of maximal masker-spectral variability (i.e., random-frequency multi-tonal maskers), but there is mounting evidence that informational masking can also be produced by multi-tonal maskers with little or no variability. First, thresholds for some listeners for maskers fixed across trials or blocks of trials remain elevated above that predicted from energy detection (e.g., Alexander and Lutfi, 2004; Durlach *et al.*, 2005; Leibold and Werner, 2006). Second, temporal cues that provide a release from masking with random-frequency multi-tonal maskers (e.g., Neff, 1995) can also reduce adults' thresholds with fixed-frequency multi-tonal maskers (Leibold *et al.*, 2005). Third, both infant and adult listeners show large intra- and intersubject differences in performance with fixed-frequency, multi-tonal maskers (Wright and Saberi, 1999; Alexander and Lutfi, 2004; Durlach *et al.*, 2005; Leibold and Werner, 2006). These findings suggest the detrimental effects of random-frequency multi-tonal maskers are not due solely to spectral variability in the external stimulus. Instead, informational masking appears to reflect multiple mechanisms, including those contributing to the separation of relevant and irrelevant acoustic waveforms into independent auditory objects (e.g., Kidd *et al.*, 1994, 2002; Neff and Callaghan, 1988; Neff, 1995; Durlach *et al.*, 2003b). Consistent with this viewpoint, Durlach *et al.* (2003a) have argued that stimulus variability is not required to produce informational masking, but that informational masking may also be determined by the degree of similarity between the signal and the masker.

[a)]Portions of these results were presented to the American Auditory Society Annual Meeting in Scottsdale, AZ in March 2006.
[b)]Current affiliation: Department of Allied Health Sciences, University of North Carolina School of Medicine, Chapel Hill, NC 27599. Electronic mail: leibold@med.unc.edu

 0001-4966/2007/121(6)/3666/11/$23.00 © 2007 Acoustical Society of America

There are several indications of perceptual development in performance on informational masking tasks. Detrimental effects of varying masker spectra appear larger in children than adults (e.g., Allen and Wightman, 1995; Oh *et al.*, 2001; Wightman *et al.*, 2003). For example, studies by Oh *et al.* (2001) and Wightman *et al.* (2003) examined the ability of adults and children aged 4–16 years to detect a 1000-Hz pure tone presented simultaneously with a random-frequency multi-tonal complex. Adults and children were both susceptible to informational masking in the presence of masker-spectral variability, but children typically exhibited more masking than adults. These increased effects of masker-spectral variability in children relative to adults have been hypothesized to reflect immaturities in the ability to selectively attend to the auditory filter that contains the signal in the presence of the random-frequency multi-tonal masker (e.g., Lutfi *et al.*, 2003).

Children's poor performance in random-frequency multi-tonal masker conditions relative to adults has largely been attributed to the effect of variability in the masker spectra. Recent data, however, indicate effects of masker-spectral variability are similar for infants and adults (Leibold and Werner, 2006). The discrepancy between the infant and child findings, in part, depends on the reference condition used to estimate informational masking. Masking in random-frequency conditions can be compared to masking with broadband-noise (peripheral) maskers or fixed-frequency multi-tonal (minimal variability) maskers. In Leibold and Werner, infants' thresholds were higher than those of adults with fixed-frequency maskers, but the increase in infants' thresholds for random-compared to fixed-frequency maskers was similar to adults'. Thus, infants appear more susceptible to informational masking than adults in the presence of multi-tonal maskers, even when the masker spectra do not vary. To our knowledge, whether children are also susceptible to informational masking in the presence of a remote-frequency multi-tonal masker with fixed spectral components has not been systematically examined.

The purpose of the current study was to compare the susceptibility of both children and adults to masking produced by multi-tonal maskers with maximal masker-spectral variability (random-frequency ten-tone maskers) and with no masker-spectral variability (fixed-frequency ten-tone maskers). In particular, we were interested in the extent to which informational masking contributed to children's masking in conditions without masker-spectral variability. To address this question, we examined whether the addition of a temporal masker "fringe" (delayed onset of the signal relative to the masker) improved children's performance in fixed- and random-frequency multi-tonal masker conditions. This temporal cue provides trained adult listeners with a masking release for both random- and fixed-frequency multi-tonal maskers, but not for broadband noise maskers (Leibold *et al.*, 2005). Presumably, the temporal asynchrony provides listeners with a cue for sound source determination in conditions that produce informational masking. Hall *et al.* (2005) demonstrated that children can use temporal differences in the onset of the signal and masker to improve performance in an informational masking task related to the present study. Following the multi-burst paradigm of Kidd *et al.* (1994), Hall *et al.* reported a similar average masking release for children and adults when the masker started two bursts before the signal relative to a reference condition in which the masker and signal bursts began simultaneously. Thus, if informational masking underlies elevated thresholds for children in the presence of a simultaneous, fixed-frequency multi-tonal masker, we would expect to observe a release from masking with the temporal cue, as has been observed for adults with similar stimuli (Leibold *et al.*, 2005), and for children using a sequential multi-tonal masker (Hall *et al.*, 2005).

II. EXPERIMENT 1: EFFECTS OF MASKER-SPECTRAL VARIABILITY

In experiment 1, effects of masker-spectral variability were examined in children and adults by comparing thresholds for multi-tonal maskers with masker-spectral content randomized with each presentation versus fixed throughout a block of trials. In previous studies of children, the metric of informational masking was the difference in performance between conditions using random-frequency multi-tonal maskers and either quiet thresholds or conditions using equal power, broadband-noise maskers (e.g., Allen and Wightman, 1995; Oh *et al.*, 2001; Wightman *et al.*, 2003). Alternatively, a multi-tonal masker sample can be used as a reference condition to estimate the effect of masker-frequency variability contributing to the total amount of informational masking (Leibold and Werner, 2006). The fixed-frequency multi-tonal masker sample is matched to the random-frequency multi-tonal masker in as many aspects as possible except spectral variability, consistent with the minimal-uncertainty conditions first described by Watson *et al.* (1976). The difference in performance across random- and fixed-frequency multi-tonal conditions aids greater separation of effects of masker-frequency variability from other factors believed to contribute to information masking, such as signal-masker similarity.

A. Method

1. Listeners

Twenty-two children (5–10 years) and 11 adults (19–34 years) participated in all conditions. Eleven children were aged 5 to 7 years (younger children) and 11 children were aged 8 to 10 years (older children). The rationale for including both younger and older children is that attentional processes appear to mature rapidly around 5–7 years (reviewed by Ruff and Rothbart, 1996, Chap. 3). Moreover, younger children appear more susceptible than older children to the effects of varying the spectral content of a multi-tonal masker (e.g., Wightman *et al.*, 2003). Thus, differences in performance might well be expected across these two age groups of children as well as across children and adults. Younger children had a mean age (years:months) of 6:7 (range: 5:4 to 7:6), older children had a mean age of 9:0 (range: 8:0 to 10:5), and adults had a mean age of 27:3 (range: 19:1 to 34:10). All listeners had normal hearing (*re*: ANSI, 1996) and reported no risk factors for hearing loss. Listeners were tested individually in a single-walled, sound-

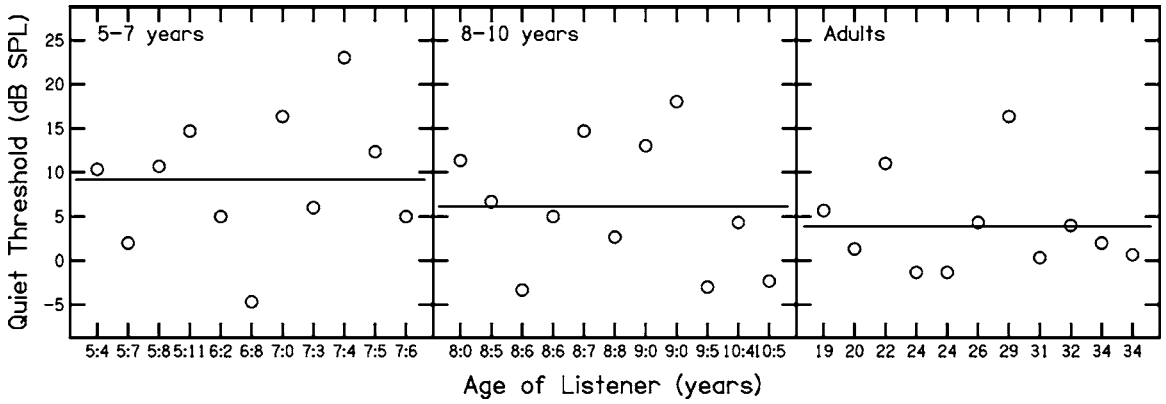

FIG. 1. Quiet thresholds for the 1000-Hz signal are plotted for individual listeners, with listeners ordered by their age in years:months. Data across panels are for younger children (5–7 years), older children (8–10 years), and adults. Solid horizontal lines indicate the mean group threshold.

treated room in a 2-h session, with the exception of three younger children tested in two, 1-h sessions. Regular breaks were provided, typically after completion of every two conditions for children and after every four conditions for adults. An additional four children (ages 5, 5, 5, and 7 years) were tested, but were excluded from data analysis because they did not meet the training criteria, outlined below.

2. Stimuli and conditions

In all conditions, the signal was a 300-ms, 1000-Hz tone. There were three types of maskers: broadband noise (300–3000 Hz); random-frequency ten-tone complex (*random*); and fixed-frequency ten-tone complex (*fixed*). Components for the ten-tone maskers were drawn randomly from a range of 300–3000 Hz, excluding a 160-Hz protected region around the signal. Component amplitudes were equal. The signal and maskers included 5-ms, cosine-squared, rise/fall ramps. Maskers were presented simultaneously with the signal (when present) for 300 ms at an overall level of 60 dB SPL, regardless of the masker type. Thus, individual components for random and fixed maskers were presented at 50 dB SPL.

Stimuli were played through a 24-bit digital-to-analog converter (Digital Audio Labs) at a sampling rate of 25 kHz. All stimuli were presented to the listener's left ear through Sennheiser HD-25 earphones. The experiment was controlled by a computer using custom software. In the random condition, 50 masker samples were generated and stored. A different masker sample was drawn from this file on each presentation. In the fixed condition, a single sample was generated and used on every presentation within and across blocks of trials. No attempt was made to select the masker properties of the fixed ten-tone masker sample. The first sample drawn randomly was used for all listeners, resulting in sinusoidal components at 407, 434, 1085, 1093, 1122, 1192, 1534, 1827, 1968, and 2160 Hz. Given that considerable variability in threshold across different masker samples has been observed in previous studies of trained adults (Wright and Saberi, 1999; Durlach *et al.*, 2005), the same masker sample was used across listeners for the fixed condition.

3. Procedure

For testing, the child sat in front of a video monitor with a touch-screen display and listened to sounds presented via headphones. An experimenter sat inside the booth with the child, initiated test trials, and entered the child's responses. Adults were tested using the same procedure, except they were alone in the booth and initiated trials and entered responses directly using the touch-screen display. For all listeners, correct responses were rewarded by an engaging image presented on the monitor in a video game format.

Signal thresholds were measured using a two-interval, forced-choice (2IFC) adaptive procedure that estimated 70.7% on the psychometric function (Levitt, 1971). The signal occurred in either interval with equal *a priori* probability. The signal was presented alone in a 300-ms warning interval prior to each trial. The level of this pretrial signal cue was matched to the level of the signal for each trial. Sessions consisted of one training phase and one testing phase. In the training phase, the signal was presented at a clearly audible level, based on previous studies and pilot data. The training phase ended when the listener responded correctly to a minimum of five consecutive training trials. As noted earlier, four children were unable to meet the training criteria.[1] In the testing phase, the starting level for the signal was approximately 10 dB above the expected threshold for each age group and condition. An initial step size of 4 dB was decreased to 2 dB after the second reversal. Testing continued until eight reversals were obtained and threshold was computed as the mean of the last six reversals. Threshold was initially measured for the signal presented in quiet. Testing order for masker conditions described in experiments 1 and 2 (discussed below) was randomized across listeners.

B. Results and discussion

1. Quiet thresholds

Figure 1 presents thresholds for the 1000-Hz signal in quiet for younger children (left panel), older children (middle panel), and adults (right panel). Data for individual listeners are rank ordered from youngest to oldest. The solid horizontal line represents the average threshold in quiet across listeners for each age group. Quiet thresholds ranged from −4.7 to 23.0 dB SPL (mean=9.2 dB SPL) for younger children

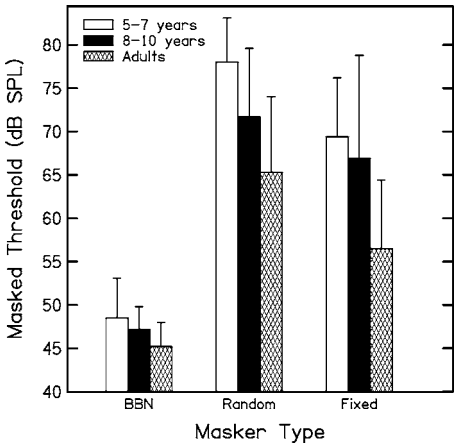

FIG. 2. Average masked thresholds across listeners (with SDs) for each of the three age groups (open bars for younger children, solid bars for older children, and hatched bars for adults) are presented for the three types of maskers: broadband noise (BBN), ten-tone random frequency (Random), and ten-tone fixed frequency (Fixed).

(5–7 years), from −3.3 to 18.0 dB SPL (mean=6.1 dB SPL) for older children (8–10 years), and from −1.3 to 16.3 dB SPL (mean=3.9 dB SPL) for adults. A one-way analysis of variance (ANOVA) indicated no significant difference in quiet threshold across the three age groups [$F(2,32)=1.6$; $p=0.2$].

2. Group differences

The data were examined in terms of both amount of masking (masked threshold minus quiet threshold) and masked threshold. The pattern of results was similar for the two measures. Given no significant group differences in quiet thresholds and the increased potential measurement error for amount of masking (i.e., using both quiet thresholds and masked thresholds), masked thresholds were selected.

Figure 2 presents average masked thresholds across listeners with standard deviations (SDs) for broadband noise, random-frequency, and fixed-frequency masker conditions. Open bars indicate performance for younger children, filled bars indicate performance for older children, and hatched bars indicate performance for adults. For the broadband noise condition, only small differences in average performance were observed across age, with thresholds of 48.5 dB SPL (SD=4.6) for younger children, 47.2 dB SPL (SD =2.6) for older children, and 45.2 dB SPL (SD=2.8) for adults. In contrast, a clear developmental effect in average threshold was evident for both the random and fixed conditions. Average thresholds for the random condition were 78.0 dB SPL (SD=5.1) for younger children, 71.7 dB SPL (SD=7.9) for older children, and 65.3 dB SPL (SD=8.7) for adults. Corresponding average thresholds for the fixed condition were 69.4 dB SPL (SD=6.7), 66.9 dB SPL (SD =11.9), and 56.5 dB SPL (SD=7.9).

Age differences were analyzed with a repeated-measures ANOVA with Masker Type (broadband noise versus random versus fixed) as a within-subjects factor and Age (younger children versus older children versus adults) as a between-subjects factor. All effects were significant: Masker Type [$F(2,60)=155.3$; $p<0.001$], Age [$F(2,30)=9.7$; $p=0.001$], and Masker Type × Age [$F(4,60)=2.9$; $p=0.03$]. *Post-hoc* comparisons were performed to examine the interaction of masker type and age group.[2] For the broadband noise condition, as expected, no differences in threshold across age were found. These findings are consistent with previous studies that have reported similar masking across preschoolers, school-aged children, and adults with a broadband noise masker (e.g., Wightman *et al.*, 2003) and provide evidence that children are adultlike in their ability to detect a tonal signal in the presence of a broadband noise. Thus, average performance for younger children, older children, and adults is similar in a condition thought to involve little informational masking.

As in previous studies (e.g., Allen and Wightman, 1995; Oh *et al.*, 2001; Wightman *et al.*, 2003), children's thresholds were substantially higher than adults when presentation-by-presentation variability in the spectra of a multi-tonal masker was present. The average child-adult difference in threshold for the random condition was 12.7 dB for younger children and 6.4 dB for older children. Note also that the average threshold for older children was 6.3 dB lower than the average threshold for younger children. These results are in agreement with the hypothesis that children are more susceptible to informational masking associated with masker-spectral uncertainty than adults and that younger children are more susceptible than older children.

This study tested adults with little training in the masking tasks. Consistent with previous studies of "trained" adults using similar stimuli (i.e., adults who completed hundreds of trials of simultaneous multi-tonal masker conditions), the current study with untrained adults found that the adults' average threshold was lower in the fixed multi-tonal masker condition than in the random condition (Wright and Saberi, 1999; Alexander and Lutfi, 2004; Durlach *et al.*, 2005). Thus, reducing masker-spectral variability produced a substantial decrease in informational masking for untrained as well as trained adult listeners. As in the random-masker condition, however, children's thresholds remained higher than adults for the fixed condition. The average child-adult difference in threshold for fixed maskers was 12.9 dB for younger children and 10.4 dB for older children. In contrast to the random condition, however, thresholds for younger children were elevated by only a small amount (2.5 dB) relative to older children in the fixed condition. These results suggest that younger and older children are, on average, more susceptible to masking than adults in *both* random and fixed masker conditions. That is, neither younger nor older children appear to take full advantage of the cues available in fixing the masker spectra.

3. Individual differences

Consistent with previous studies of informational masking for adults (e.g., Neff and Dethlefs, 1995) and for children (e.g., Oh *et al.*, 2001), individual differences in performance were considerable. Given the large between-subjects variability, the trends observed in the group data may not accurately reflect performance for individual listeners. Figure 3 presents thresholds for individual listeners for each age group (across panels). Open triangles indicate the broadband

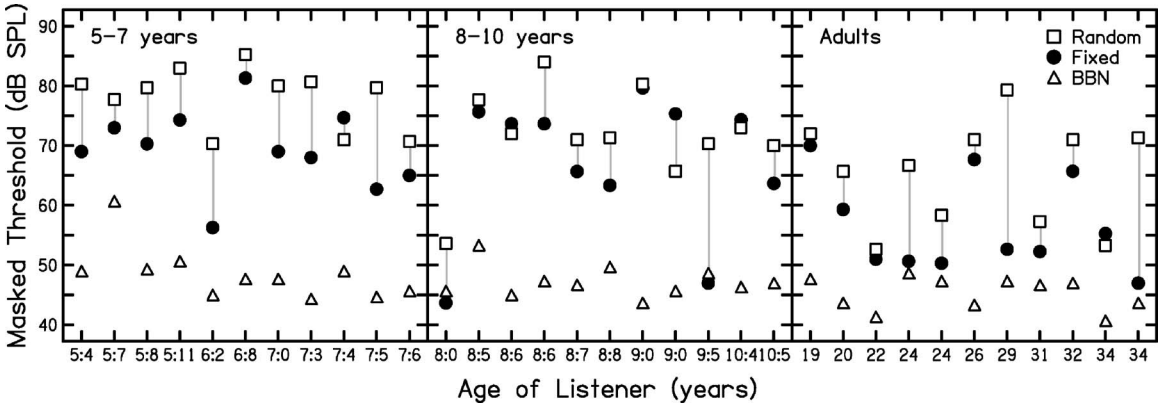

FIG. 3. Masked thresholds are plotted for individual listeners, with listeners ordered by their age in years:months. Data across panels are for younger children (5–7 years), older children (8–10 years), and adults. Symbols indicate the broadband-noise (open triangles), random-frequency (open squares), and fixed-frequency (filled circles) masker conditions. Vertical lines indicate the release from masking (random minus fixed ten-tone threshold) for each listener.

noise condition, open squares indicate the random condition, and filled circles indicate the fixed condition. The effect of masker-spectral variability, defined as the difference in threshold between the random and fixed conditions, is shown by the gray vertical lines connecting symbols for each listener.

For the broadband noise condition, the same pattern of results summarized by the average data in Fig. 2 was observed for individual listeners. Thresholds for the broadband noise masker condition were lower than for either multi-tonal masker condition, with the exception of one older child (age 8:0) with a slightly higher threshold for the broadband noise (46 dB SPL) compared to the fixed (44 dB) condition. Performance for most listeners was similar, with thresholds at or below 50 dB SPL. Several children, however, had considerable difficulty detecting the 1000-Hz tone in the presence of the broadband noise. Most notably, one of the youngest listeners (age 5:7) had a threshold of 61 dB SPL, an elevation of 11 dB relative to the average threshold for younger children. In addition, one older child (age 8:5) had a threshold of 53 dB SPL. Previous studies have noted an increased susceptibility to masking by a broadband noise masker in some preschoolers and have suggested this increased masking reflects informational masking. Wightman *et al.* (2003) provided strong evidence for this hypothesis, demonstrating that several preschoolers in their study were susceptible to masking by a *contralateral* broadband noise masker.

Thresholds for most listeners were highest for the random condition. The exceptions were one younger child (age 7:4), two older children (age 8:6 and age 10:4), and one adult (34), for whom performance was similar across random and fixed conditions. For the children, that occurred because both thresholds were high, that is, there was no reduction in threshold with reduced variability. For the adults, the opposite was true in that both thresholds were low, that is, performance was not degraded with high variability. Among adults, thresholds for the random condition varied widely, ranging from 52.7 to 79.3 dB SPL. Less variability in threshold was observed for the two groups of children, although individual differences remained substantial. For 10 of 11 older children, thresholds ranged from 65.7 to 84.0 dB SPL. Note, however, the atypically low threshold (53.7 dB) for one older child (age 8:0). Thresholds were consistently high for the younger children, ranging from 70.7 to 85.3 dB SPL.

A large range of performance was also observed across listeners for the fixed condition. Although thresholds for the fixed condition were elevated relative to adults by an average of 13 dB for younger children and 10 dB for older children, overlap in the distribution of performance across the three age groups was evident. Thresholds for 5 of 11 adults fell within 6 dB of their thresholds for the noise condition. In contrast, the remaining six adults had elevations in threshold of 10–24 dB for the fixed condition relative to performance in the presence of the noise. Similar threshold elevations and large individual differences in performance have been reported in previous studies of trained adult listeners for detection of a tonal signal in the presence of a multi-tonal masker with fixed spectra (e.g., Wright and Saberi, 1999; Alexander and Lutfi, 2004; Durlach *et al.*, 2005). Thresholds for both groups of children in the fixed condition were generally higher than observed for most adults, and children's thresholds rarely fell within the lower range of thresholds observed for the broadband noise condition. Thresholds for 9 of 11 older children in the fixed condition were elevated by 14 dB or more (range=14–36 dB) relative to thresholds in the broadband noise condition. Thresholds for all of the younger children in the fixed condition were elevated by 11 dB or more (range=11–34 dB). Two older children (ages 8:0 and 9:5), however, showed considerably lower thresholds in the fixed conditions (43.7 and 47.0 dB SPL) relative to their peers, with similar thresholds for the fixed and broadband noise masker conditions. Note, however, that the child with the lowest threshold in the random condition (8:0) still had lower thresholds when the masker spectra were fixed compared to when the masker spectra were varied. Thus, some children can develop effective strategies to improve detection for the tonal signal in the presence of the multi-tonal masker with fixed or random spectra.

In summary, thresholds for most children were higher than thresholds for most adults for both random and fixed conditions. These findings suggest that younger and older children are more likely to be susceptible to informational

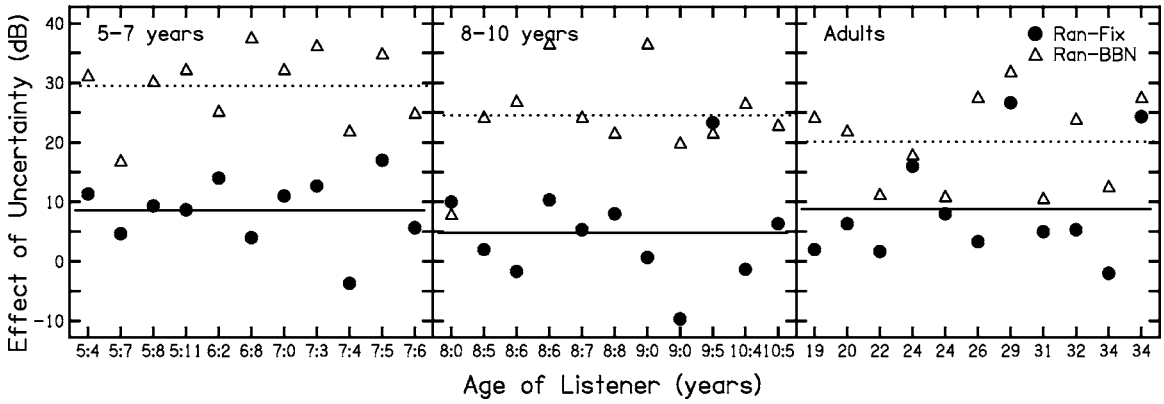

FIG. 4. The release from masking produced by reducing spectral uncertainty is plotted for each listener and for the average across listeners (Av) using the same format as Fig. 3. Masking release using the broadband noise condition as the reference (random minus broadband noise thresholds) is shown by open triangles and masking release using the fixed condition as the reference (random minus fixed thresholds) is shown by filled circles. The dotted and solid horizontal lines in each panel indicate the mean group threshold for the broadband noise and fixed-frequency reference conditions, respectively.

masking than adults in the presence of a multi-tonal masker whether the spectra are randomized or fixed. Several children, however, had performance similar to most of the adults, in that their thresholds were considerably lower than the other children and also more similar to their thresholds for broadband noise. As noted, one older child (age 8:0) performed as well as "low threshold" adults in both random and fixed conditions. Previous studies of informational masking in children have also reported large individual differences in performance. For example, Allen and Wightman (1995) measured detection thresholds in 17 children aged 3 to 4 years for a 1000-Hz tone in the presence of a broadband noise plus a remote-frequency random tonal masker. Thresholds could not be measured at or below 90 dB SPL for ten children. For the remaining seven children, however, the average increase in threshold with the distractors was 13 dB, compared with an average increase in threshold of 11 dB with the distractors for adults.

4. Effects of masker-spectral variability

The major question addressed by experiment 1 was whether the effect of masker-spectral variability is larger for children than for adults. If the effect of masker-spectral variability is defined as the difference in threshold between the fixed and random conditions, the conclusion is that children do *not* appear more susceptible to the external variability than adults. The filled circles in Fig. 4 show the effect of masker-spectral variability (random minus fixed threshold) for individual listeners and for the average across listeners (solid horizontal lines), with data for the three age groups across panels. Listeners are ordered as in Fig. 3.

The average increase in masking with masker-spectral variability was 8.6 dB (SD=5.7) for younger children, 4.8 dB (SD=8.5) for older children, and 8.8 dB (SD=9.4) for adults. A one-way ANOVA on the difference in threshold across the random and fixed conditions indicated no significant effect of Age [$F(2,32)=0.8$; $p=0.4$].

Individual differences in the effect of masker-spectral variability were striking. For younger children, 10 of 11 listeners showed elevations in threshold of 3 dB or greater when masker-spectral variability was present, with effects ranging from 4 to 17 dB. The remaining listener (age 7:4) was the one who showed similar, relatively high thresholds for both fixed and random conditions (see corresponding data in Fig. 3). For older children, 6 of 11 listeners showed an increase in thresholds of 3 dB or greater when masker-spectral variability was present, with effects ranging from 5 to 23 dB. Four listeners (ages 8:5, 8:6, 9:0, and 10:4), however, showed only small threshold changes (less than 3 dB) and one listener (age 9:0) actually showed a 10 dB *decrease* in masking when masker-spectral variability was present. For adults, 8 of 11 listeners showed increases in threshold of 3 dB or greater when masker-spectral uncertainty was introduced, with effects ranging from 3 to 27 dB. The remaining 3 adults (ages 19, 22, and 34) showed little or no change in performance. Thresholds in the fixed condition were a significant predictor of the increase in threshold with masker-spectral variability for younger children ($r=-0.67$; $p=0.03$) and for older children ($r=-0.75$; $p=0.008$). That is, children with the lowest thresholds in the fixed condition were more susceptible to further masking with the introduction of masker-spectral variability than were children with the highest thresholds. Thresholds in the fixed condition were not a significant predictor of the further masking with masker-spectral variability for adults ($r=-0.51$; $p=0.11$).

The rationale for including the fixed masker condition was to provide a reference condition that was matched to the random condition in as many aspects as possible except for masker-spectral variability.[3] When the effect of masker-spectral variability is defined as the difference in threshold between the random and fixed conditions, children do not appear to be more susceptible to masker-spectral variability than adults. These findings seem inconsistent with earlier studies that reported children were more susceptible to the effects of masker-spectral variability than adults (e.g., Allen and Wightman, 1995; Oh *et al.*, 2001; Wightman *et al.*, 2003). This apparent discrepancy appears to reflect differences in the reference condition used to estimate the effects of the external spectral variability and emphasizes the importance of separating informational masking produced by masker-spectral variability from informational masking produced by other factors. Most previous studies of informa-

tional masking have estimated the effect of masker-spectral variability relative to performance in quiet or performance in broadband noise. The open triangles in Fig. 4 show the release from masking (random minus noise threshold) for individual listeners and the average across listeners (dotted horizontal lines) when the broadband noise condition was used as the reference. A one-way ANOVA on these difference scores indicated a significant effect of Age [$F(2,32)=4.5$; $p=0.02$]. Thus, the current data indicate child-adult differences when the effect of spectral variability is defined relative to the noise condition, consistent with previous studies. The fact that most children's thresholds are elevated relative to adults for fixed-frequency multi-tonal maskers suggests, however, that masker-spectral variability is not the primary factor responsible for the child-adult differences in informational masking observed in the current study.

Although the data are limited, the results of two recent studies support the idea that detrimental effects of external spectral stimulus variability are not greater for children compared to adults when minimal-uncertainty conditions are used as the reference. First, Leibold and Werner (2006) measured detection thresholds for a 1000-Hz tone in the presence of remote-frequency two-tone maskers for 6–9-month-old infants and untrained adults. As in the current study, the frequency content of the two-tone maskers was either randomized or fixed. The difference in threshold between the random and fixed two-tone maskers was similar across infants and adults. As with children, infants' thresholds were higher than adults in both the random- and fixed-frequency conditions. Second, Buss *et al.* (2006) recently reported that children aged 5 to 10 years were *less* susceptible to external stimulus variability in an intensity discrimination task. Thresholds for both children and adults increased with the introduction of a level rove, but the increase in threshold was smaller for children compared to adults. The authors suggested that children's performance was limited by an increased level of internal noise relative to adults.

The mechanisms responsible for children's increased susceptibility to masking in the fixed condition relative to adults are unknown, as are the factors that elevate adults' thresholds in this condition. Given that cochlear function appears to be mature by 6 months of age (reviewed by Werner, 1996), however, it is difficult to attribute the child-adult age differences in threshold for the fixed condition to developmental changes in energetic masking. Instead, the elevated thresholds and large variability both within and across age groups are consistent with age differences in informational masking. This conclusion is further supported by the consistent and similar performance in noise across all age groups.

III. EXPERIMENT 2: EFFECT OF MASKER FRINGE

In experiment 1, thresholds for most listeners were higher for the random- relative to the fixed-frequency condition. Thresholds for the 1000-Hz signal remained considerably elevated, however, in the presence of the fixed masker, with most children exhibiting poorer performance than most adults. The purpose of experiment 2 was to determine whether a temporal cue in the form of a masker "fringe" would provide a release from masking for fixed and random conditions for listeners in each age group. Based on Neff (1995), a temporal offset between masker and signal should reduce informational masking, but have little effect on energetic masking (e.g., thresholds with broadband noise maskers). In a recent study testing trained adults, as much as 21 dB of masking release was observed with a 100-ms masker fringe for random-frequency ten-tone maskers and 9 dB of masking release for fixed-frequency ten-tone maskers (Leibold *et al.*, 2005). In contrast, no masking release was observed with the masker fringe when the masker was broadband noise. Children have also been shown to benefit from a similar temporal cue when both the signal and masker consist of multi-tonal sequences (Hall *et al.*, 2005). Thus, if the elevated thresholds for children for the fixed condition observed in experiment 1 reflect informational masking, adding the masker fringe should produce a further reduction in threshold.

A. Method

1. Listeners, stimuli, conditions, and procedure

All aspects of experiment 2 were the same as experiment 1, except that masker duration was increased to 500 ms. The 300-ms signal, when present, was temporally centered in the masker, with a 100-ms masker fringe preceding and following each signal. The frequency components of the fixed masker sample were identical across no-fringe and fringe conditions. The data were collected at the same time as experiment 1, with testing order randomized across conditions.

B. Results

1. Group differences

Figure 5 shows average masked thresholds for younger children, older children, and adults for conditions without (open bars) and with (filled bars) the masker fringe. Thresholds for broadband noise, random, and fixed maskers are plotted across panels. Data for no-fringe conditions are replotted from Fig. 2. The difference in threshold between no-fringe and fringe conditions defines the release from masking produced by the temporal fringe for each masker type. For the broadband noise masker, little or no differences in performance were observed across no-fringe and fringe conditions for any age group. The average threshold reduction in the broadband noise condition was −0.8 dB (SD=2.9) for younger children, −1.2 dB (SD=4.2) for older children, and 0.1 dB (SD=3.0) for adults. In contrast, reductions in average threshold were evident for both random and fixed conditions with the masker fringe, with average reductions in the random condition of 9.0 dB (SD=9.5) for younger children, 11.8 dB (SD=6.2) for older children, and 15.3 dB (SD=6.2) for adults. The average masking release in the fixed condition was 9.3 dB (SD=10.3) for younger children, 15.0 dB (SD=8.7) for older children, and 8.5 dB (SD=7.1) for adults. These findings are consistent with previous studies that have reported informational masking release with a masker fringe for trained adults for similar stimuli (Leibold *et al.*, 2005) and for children with multi-tonal sequences (Hall *et al.*, 2005), and provide further evidence that at least

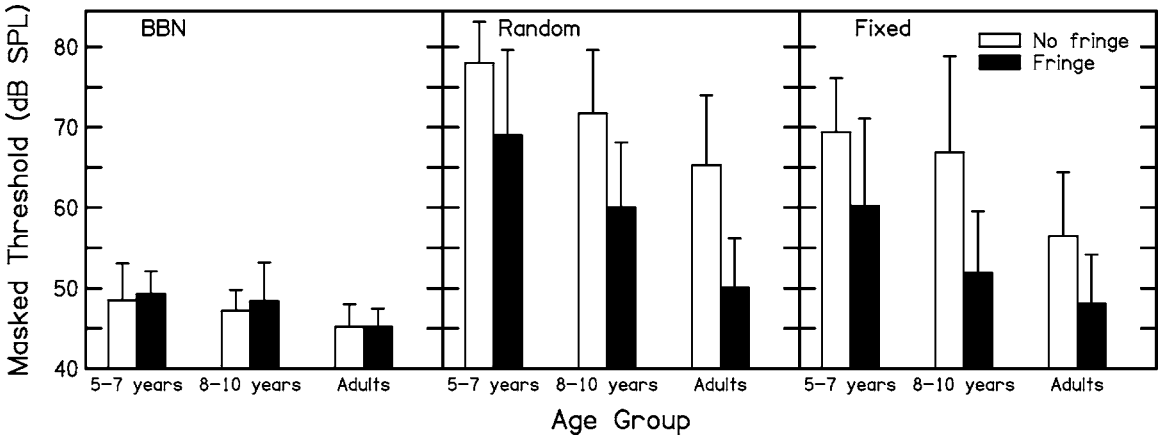

FIG. 5. Average masked thresholds (with SDs) across listeners in each age group are presented for no-fringe (open bars) and fringe (filled bars) conditions. Data for broadband noise (BBN), random-frequency (Random), and fixed-frequency (Fixed) masker conditions are plotted across panels.

part of the masking observed in both random and fixed no-fringe conditions for children and adults is informational.

To examine whether these effects of the masker fringe were significant, a repeated measures ANOVA with Masker Type as a within-subjects factor and Age as a between-subjects factor was performed on the difference in threshold between no-fringe and fringe conditions. The analysis confirmed a significant main effect of Masker Type [$F(2,60)=35.3$; $p<0.001$], indicating differences in effectiveness of the masker fringe across the three masker types. The main effect of Age was not significant ($p>0.3$), indicating the release from masking was similar for children and adults. The Masker Type × Age interaction was also not significant ($p>0.1$). A one-way ANOVA on the difference in threshold across the no-fringe and fringe conditions indicated a significant release from masking for both the fixed [$F(1,30)=51.0$; $p<0.001$] and random [$F(1,30)=85.9$; $p<0.001$] conditions, but not for the broadband noise condition [$F(1,30)=1.2$; $p=0.3$].

2. Individual differences

Considerable individual differences in masking release were evident both within and across age groups for the multi-tonal maskers. Figure 6 shows the release from masking associated with the masker fringe (no-fringe minus fringe threshold) for individual listeners, using the same format as Fig. 3. Data at or below the dotted horizontal line indicate no release from masking with the temporal cue. The temporal cue had little effect in the broadband noise condition, with the exception of one 5-year-old (5:7) who had the atypically elevated threshold of 61 dB SPL in the no-fringe condition (5.7 dB of masking release), and an 8-year-old (8:6) with 6.7 dB of release. These results confirm little influence of informational masking for most listeners for the broadband noise condition.

The majority of listeners in all age groups benefitted from the temporal cue in the random condition. For younger children, 8 of 11 children showed a masking release of 3 dB or greater with the masker fringe, with reductions in threshold ranging from 5 to 28 dB. Exceptions include a 5-year-old (5:11) and a 7-year-old (7:4) with little or no masking release and a 5-year-old (5:7) with a 3-dB threshold *increase* in the fringe relative to the no-fringe random condition. For older children, 10 of 11 listeners showed a masking release of 3 dB or greater with the fringe, with reductions ranging from 6 to 22 dB. The remaining listener, an 8-year-old (8:8), did

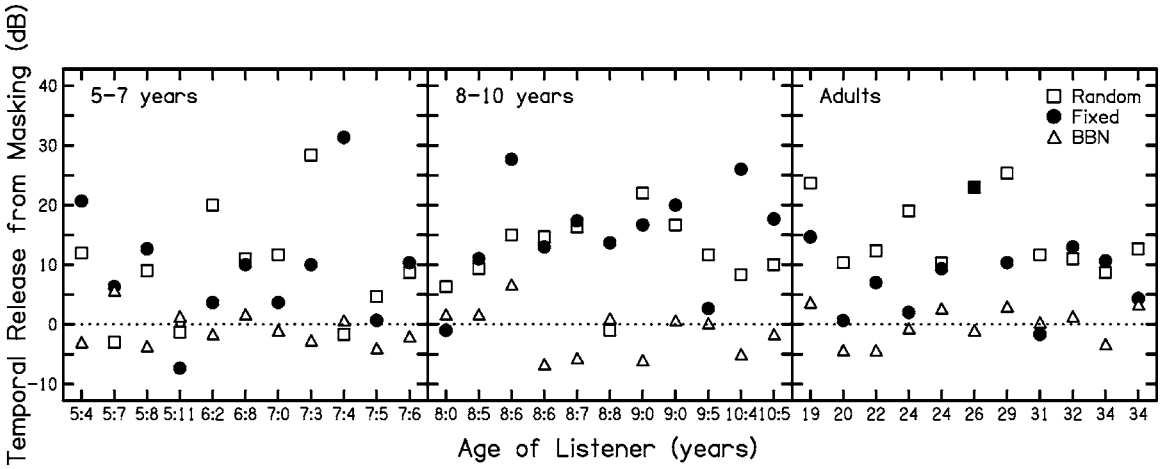

FIG. 6. Release from masking associated with the temporal masker fringe (no-fringe minus fringe threshold) is plotted for individual listeners for younger children, older children, and adults (across panels). Open triangles, open squares, and filled circles are for the broadband noise, random, and fixed conditions, respectively. Data at or below the dotted horizontal line indicate an absence of masking release.

not benefit from the temporal fringe. All adults showed a masking release of 3 dB or more with the masker fringe in the random condition, with reductions ranging from 9 to 25 dB. These data indicate that children as young as age 5 can use temporal cues to reduce informational masking in the presence of a random-frequency multi-tonal masker.

Of particular interest to the current study, Fig. 6 shows that thresholds for most listeners also improved with the masker fringe for the fixed-frequency condition. For younger children, 9 of 11 listeners showed a masking release of 3 dB or greater, with effects ranging from 4 to 31 dB. One listener (age 7:5) showed similar performance across the no-fringe and fringe fixed conditions. The remaining listener (age 5:11) showed a 7-dB *increase* in masking with the masker fringe. For older children, 10 of 11 listeners showed a masking release of 3 dB or greater with the masker fringe, with reductions ranging from 3 to 28 dB. The remaining listener (age 8:0) showed no masking release. Note that this was also the listener with the atypically low threshold in the no-fringe fixed condition, thus limiting the potential for further reductions in threshold. For adults, 8 of 11 listeners showed a masking release of 3 dB or greater with the masker fringe, with reductions ranging from 4 to 23 dB. Little or no masking release was observed for the remaining three listeners (ages 20, 24, and 31).

In summary, both adults and children appear susceptible to some degree of informational masking under conditions *without* masker-spectral uncertainty. No evidence of systematic differences in amount of masking release associated with the temporal fringe was observed across the three age groups for the fixed condition. However, the combination of reducing masker-spectral variability and adding a temporal cue (i.e., the fixed-fringe condition) yielded more thresholds that were similar to thresholds observed in broadband noise for adults than for children. In particular, thresholds for younger children remain notably elevated above adults even when both cues are available.

3. Developmental changes in benefit from reduced spectral uncertainty and temporal cues

Reports of sizeable reductions in informational masking for adults in the presence of cues thought to promote sound source determination indicate that informational masking may reflect, in whole or in part, an inability to perform sound source determination (e.g., Kidd *et al.*, 1994; Neff, 1995; Richards and Neff, 2004).The current data suggest that most children can effectively use spectral and temporal cues to distinguish between relevant and irrelevant complex sounds. This result is in partial agreement with results from Hall *et al.* (2005), who found no significant differences in release from informational masking between children and adults associated with a temporal asynchrony cue between the signal and the masker. Inconsistent with the current findings, however, Hall *et al.* observed less masking release for children relative to adults associated with a spectral cue, that is, when masker spectral variability was manipulated to aid performance. Differences in methodology across the two studies make it difficult to determine the basis for this discrepancy or may be the reason for different results. In the current study, masking release was examined using a simultaneous-masking detection paradigm (e.g., Neff and Green, 1987). In this paradigm, reductions in informational masking are typically observed when masker-spectral variability is *decreased.* Presumably, the reduced masker variability aids in sound source determination by increasing the saliency of the signal. In contrast, Hall *et al.* examined children's masking release using the multiburst pattern recognition paradigm similar to that of Kidd *et al.* (1994). In this paradigm, reductions in informational masking are typically observed when masker-spectral variability is *increased*. Presumably, the fixed-frequency signal bursts contrast with the random-frequency masker bursts to aid in perceptual segregation.

Although children benefited from the masker fringe in both fixed and random conditions in the present study, thresholds for children remained elevated relative to thresholds for adults in the presence of a spectral cue (fixed no-fringe threshold), a temporal cue (random fringe threshold), and combined spectral and temporal cues (fixed fringe threshold). The mechanisms responsible for the persistence of masking in children despite the availability of both spectral and temporal cues are unknown. Durlach *et al.* (2003a) have suggested that informational masking is largely determined by signal-masker similarity. One possible explanation for children's apparent susceptibility to informational masking for the fixed fringe condition is that the effect of similarity might be larger for children than for adults. However, thresholds for 3–4 year-old children are elevated relative to adults when the signal is a pure tone and the masker is a broadband noise with a spectral notch surrounding the signal frequency (Allen *et al.*, 1989; Hall and Grose, 1991). The degree of stimulus similarity between a notched-noise masker and tonal signal seems much smaller than the present case of a tonal signal and multi-tonal masker, yet younger children perform more poorly than adults in both cases. It is interesting to note that differences in threshold between 4-year-old children and adults are larger for noise conditions with a spectral notch surrounding the signal frequency than for noise conditions without a notch (Hall and Grose, 1991), an effect that can be accounted for by age differences in detection efficiency and different growths of loudness in noise maskers with and without a spectral notch. It is possible that a similar mechanism is responsible for the larger child-adult differences in threshold observed in the current study for multi-tonal maskers with a spectral gap around the signal frequency than for the overlapping noise masker.

Providing children with the opportunity to improve performance by reducing masker-spectral variability or adding a fringe does not mean they will or can take maximum advantage from these cues. The consistent amount of masking release observed across age groups with the introductions of these cues, however, argues that children can make effective use of the information provided by either the spectral or temporal cue. Buss *et al.* (2006) have recently argued that a higher level of internal noise in children relative to adults limits performance in an intensity discrimination task. Higher internal noise levels might likewise influence the current data in the fixed fringe condition. Alternatively, the children's increased susceptibility to masking in the fixed fringe

condition might reflect immaturities in the ability to perform sound source determination. The parameters associated with sound source determination have not been studied extensively during development and are not well understood even for trained adult listeners. Children might use other cues in these conditions or perform sound source determination in a different way than adults. Finally, there are little data on effects of training on children's performance in informational masking tasks. In particular, the effect of reducing spectral uncertainty or introducing a temporal fringe on the rate or degree of improvement is unknown. Understanding both the degree and rate of training in these conditions might provide an additional approach to assess the ability or ease with which children (or adults) can use various cues to reduce informational masking.

IV. SUMMARY AND CONCLUSIONS

The results of the present study indicate that both children and adults show informational masking in the absence of masker-spectral variability when the masker is a fixed-frequency ten-tone complex. More children than adults, however, show informational masking with fixed-frequency maskers. When the effects of masker-spectral variability are estimated as the difference in threshold between the random- and fixed-frequency conditions, children do not show larger effects of masker-spectral variability than adults. Instead, thresholds for most children were elevated relative to thresholds for most adults in *both* random and fixed conditions. Release from masking observed for all age groups in the fixed condition with the addition of a temporal cue (masker fringe) suggests contributions of informational masking despite the absence of masker-spectral variability. The masker fringe is presumed to aid perceptual segregation of the signal from the masker tones for the ten-tone masker. The mechanisms responsible for children's increased thresholds to masking relative to adults for conditions with both reduced masker-spectral variability and a masker fringe require further investigation.

ACKNOWLEDGMENTS

This research was supported by NIH Grant No. T32 DC00013. Subject recruitment supported by P30 DC04662. The authors would like to thank Walt Jesteadt for helpful discussions and comments, and Tom Creutz and Chad Rotolo for help with software development.

[1]Three of the four children excluded from the present study were able to meet the training criteria when the pretrial signal cue was removed. The use of a pretrial signal cue was intended to aid performance, as has been demonstrated in previous studies of trained adults for a fixed-frequency signal and a random-frequency multi-tonal masker (e.g., Richards and Neff, 2004). The current results suggest that young children and adults use this cue differently, however, which should be investigated in future studies.

[2]In this mixed-model design, *post-hoc* statistical tests are not recommended unless sphericity is nonsignificant, because of an inflated type I error rate if this assumption is violated. In the present experiment, sphericity was found to be nonsignificant ($p=0.3$) and Bonferroni corrections were used for the *post-hoc* tests as a conservative approach. The criterion for significance was set at $p<0.05$.

[3]The current study used a single, randomly selected masker sample for the fixed masker. Multi-tonal masker samples can differ widely in masking effectiveness (e.g., Neff and Callaghan, 1987; Wright and Saberi, 1999). This threshold variability is thought to reflect, at least in part, differences in peripheral excitation across masker samples. Thus, it is important to consider whether the specific masker sample used for the fixed-frequency masker here is representative of the average energetic masking produced by the random-frequency maskers. To examine this issue, threshold for the 1000-Hz tone in the presence of the fixed-frequency sample was predicted using the Moore *et al.* (1997) excitation-based model of loudness. The predicted threshold, obtained by finding the level at which the partial loudness of the 1000-Hz signal was equal to 2 phons was 39.6 dB SPL. To examine whether the specific masker sample used for the fixed-frequency masker is representative of the average excitation-based masking produced by the random-frequency maskers, threshold for the 1000-Hz tone was also predicted for each of ten additional, randomly selected ten-component masker samples. The predicted thresholds for these ten samples ranged from 9.3 to 45.9 dB SPL (mean=30.1 dB SPL). Thus, the predicted peripheral masking for the specific masker sample used for fixed conditions in the current study falls within this range, although it is higher than the average predicted threshold. Note also that the predicted threshold *underestimates* observed thresholds by an average of 29.8 dB for younger children, 27.3 dB for older children, and 16.9 dB for adults for the fixed, no-fringe condition, providing additional evidence that at least part of the masking observed in the fixed condition is informational.

Alexander, J. M., and Lutfi, R. A. (**2004**). "Informational masking in hearing-impaired and normal-hearing listeners: Sensation level and decision weights," J. Acoust. Soc. Am. **116**, 2234–2247.

Allen, P. A., and Wightman, F. (**1995**). "Effects of signal and masker uncertainty on children's detection," J. Speech Hear. Res. **38**, 503–511.

Allen, P. A., Wightman, F., Kistler, D., and Dolan, T. (**1989**). "Frequency resolution in children," J. Speech Hear. Res. **32**, 317–322.

ANSI (**1996**). ANSI S3.6-1996, "Specification for Audiometers," (American National Standards Institute, New York).

Buss, E., Hall, J. W., III, and Grose, J. H. (**2006**). "Development and the role of internal noise in detection and discrimination thresholds with narrow-band stimuli," J. Acoust. Soc. Am. **120**, 2777–2788.

Durlach, N. I., Mason, C. R., Kidd, G., Jr., Arbogast, T. L., Colburn, H. S., and Shinn-Cunningham, B. G. (**2003a**). "Note on informational masking," J. Acoust. Soc. Am. **113**, 2984–2987.

Durlach, N. I., Mason, C. R., Shinn-Cunningham, B. G., Arbogast, T. L., Colburn, H. S., and Kidd, G., Jr. (**2003b**). "Informational masking: counteracting the effects of stimulus uncertainty by decreasing target-masker similarity," J. Acoust. Soc. Am. **114**, 368–379.

Durlach, N. I., Mason, C. R., Gallun, F. J., Shinn-Cunningham, B., Colburn, H. S., and Kidd, G., Jr. (**2005**). "Informational masking for simultaneous nonspeech stimuli: Psychometric functions for fixed and randomly mixed maskers," J. Acoust. Soc. Am. **118**, 2482–2497.

Hall, J. W., III, Buss, E., and Grose, J. H. (**2005**). "Informational masking release in children and adults," J. Acoust. Soc. Am. **118**, 1605–1613.

Hall, J. W., III, and Grose, J. H. (**1991**). "Notched-noise measures of frequency selectivity in adults and children using fixed-masker-level and fixed-signal-level presentation," J. Speech Hear. Res. **34**, 651–660.

Kidd, G., Jr., Mason, C. R., Deliwala, P. S., Woods, W. S., and Colburn, H. S. (**1994**). "Reducing informational masking by sound segregation," J. Acoust. Soc. Am. **95**, 3475–3480.

Kidd, G., Jr., Mason, C. R., and Arbogast, T. L. (**2002**). "Similarity, uncertainty, and masking in the identification of nonspeech auditory patterns," J. Acoust. Soc. Am. **111**, 1367–1376.

Leibold, L. J., Neff, D. L., and Jesteadt, W. (**2005**). "Effects of reduced spectral uncertainty and masker fringes with multitonal maskers," J. Acoust. Soc. Am. **118**, 1893–1894.

Leibold, L. J., and Werner, L. A. (**2006**). "Effect of masker-frequency variability on the detection performance of infants and adults," J. Acoust. Soc. Am. **119**, 3960–3970.

Levitt, H. (**1971**). "Transformed up-down methods in psychoacoustics," J. Acoust. Soc. Am. **49**, 467–477.

Lutfi, R. A., Kistler, D. J., Oh, E. L., Wightman, F. L., and Callahan, M. R. (**2003**). "One factor underlies individual differences in auditory informational masking within and across age groups," Percept. Psychophys. **65**, 396–406.

Moore, B. C. J., Glasberg, B. R., and Baer, T. (**1997**). "A model for the prediction of thresholds, loudness, and partial loudness," J. Audio Eng. Soc. **45**, 224–237.

Neff, D. L. (**1995**). "Signal properties that reduce masking by simultaneous,

random-frequency maskers," J. Acoust. Soc. Am. **98**, 1909–1920.
Neff, D. L., and Callaghan, B. P. (**1988**). "Effective properties of multicomponent simultaneous maskers under conditions of uncertainty," J. Acoust. Soc. Am. **83**, 1833–1838.
Neff, D. L., and Callaghan, B. P. (**1987**). "Psychometric functions for multicomponent maskers with spectral uncertainty," J. Acoust. Soc. Am. Suppl. 1, **81**, S53.
Neff, D. L., and Dethlefs, T. M. (**1995**). "Individual differences in simultaneous masking with random-frequency, multicomponent maskers," J. Acoust. Soc. Am. **98**, 125–134.
Neff, D. L., and Green, D. M. (**1987**). "Masking produced by spectral uncertainty with multicomponent maskers," Percept. Psychophys. **41**, 409–415.
Oh, E. L., Wightman, F., and Lutfi, R. A. (**2001**). "Children's detection of pure-tone signals with random multitone maskers," J. Acoust. Soc. Am. **109**, 2888–2895.
Richards, V. M., and Neff, D. L. (**2004**). "Cuing effects for informational masking," J. Acoust. Soc. Am. **115**, 289–300.
Ruff, H. A., and Rothbart, M. K. (**1996**). *Attention in Early Development* (Oxford U.P., New York).
Watson, C. S., Wroton, H. W., Kelly, W. J., and Benbassat, C. A. (**1975**). "Factors in the discrimination of tonal patterns. I. Component frequency, temporal position, and silent intervals," J. Acoust. Soc. Am. **57**, 1175–1185.
Watson, C. S., Kelly, W. J., and Wroton, H. W. (**1976**). "Factors in the discrimination of tonal patterns. II. Selective attention and learning under various levels of stimulus uncertainty," J. Acoust. Soc. Am. **60**, 1176–1186.
Werner, L. A. (**1996**). "The development of auditory behavior (or what the anatomist and physiologists have to explain)," Ear Hear. **17**, 438–446.
Wightman, F. L., Callahan, M. R., Lutfi, R. A., Kistler, D. J., and Oh, E. (**2003**). "Children's detection of pure-tone signals: informational masking with contralateral maskers," J. Acoust. Soc. Am. **113**, 3297–3305.
Wright, B. A., and Saberi, K. (**1999**). "Strategies used to detect auditory signals in small sets of random maskers," J. Acoust. Soc. Am. **105**, 1765–1775.

Binaural weighting of monaural spectral cues for sound localization

Ewan A. Macpherson
Kresge Hearing Research Institute, University of Michigan, 1301 East Ann Street, Ann Arbor, Michigan, 48109-0506

Andrew T. Sabin
Department of Communication Sciences and Disorders, Northwestern University, 2240 North Campus Drive, Evanston, Illinois 60208-3350

(Received 17 May 2006; revised 2 March 2007; accepted 6 March 2007)

For human listeners, cues for vertical-plane localization are provided by direction-dependent pinna filtering. This study quantified listeners' weighting of the spectral cues from each ear as a function of stimulus lateral angle, interaural time difference (ITD), and interaural level difference (ILD). Subjects indicated the apparent position of headphone-presented noise bursts synthesized in virtual auditory space. The synthesis filters for the two ears either corresponded to the same location or to two different locations separated vertically by 20 deg. Weighting of each ear's spectral information was determined by a multiple regression between the elevations to which each ear's spectrum corresponded and the vertical component of listeners' responses. The apparent horizontal source location was controlled either by choosing synthesis filters corresponding to locations on or 30 deg left or right of the median plane or by attenuating or delaying the signal at one ear. For broadband stimuli, spectral weighting and apparent lateral angle were determined primarily by ITD. Only for high-pass stimuli were weighting and lateral angle determined primarily by ILD. The results suggest that the weighting of monaural spectral cues and the perceived lateral angle of a sound source depend similarly on ITD, ILD, and stimulus spectral range. © *2007 Acoustical Society of America.* [DOI: 10.1121/1.2722048]

PACS number(s): 43.66.Qp, 43.66.Ba [RAL] Pages: 3677–3688

I. INTRODUCTION

For human listeners, the primary cues for sound localization in the vertical dimension are provided by the direction-dependent acoustical filtering of the pinnae, head, and upper body. The resulting spectral cues complement the binaural cues of interaural time difference (ITD) and interaural level difference (ILD), which are the primary determinants of apparent location in the horizontal dimension. The spectral cues are often referred to as monaural cues, because, in principle, information from a single ear is sufficient to specify the location of a sound source. Although some unilaterally deaf listeners can localize well in both the horizontal and vertical dimensions (Slattery and Middlebrooks, 1994), normal-hearing listeners require access to both the binaural difference cues and the spectral cues in order to localize accurately (Wightman and Kistler, 1997b; Martin *et al.*, 2004).

Under normal circumstances, a listener receives information about a sound source's location in space simultaneously from the left- and right-ear monaural spectra. The manner in which these two sources of information are combined by the auditory system has been addressed in a number of previous studies (Musicant and Butler, 1984; Humanski and Butler, 1988; Wightman and Kistler, 1999; Morimoto, 2001; Hofman and Van Opstal, 2003; Jin *et al.*, 2004), in each of which localization accuracy was compared between normal listening conditions and conditions in which the spectral cues at one ear were distorted or degraded (a *good-ear/bad-ear* paradigm). The spectral distortion was achieved either by filling or occluding the hollows of the pinna or, as in Wightman and Kistler (1999) and Jin *et al.* (2004), by presenting the stimuli in a virtual acoustic space while altering the synthesis of the spectral cues for one ear. In all of those studies, listeners exhibited impaired vertical-plane localization performance for targets on the bad-ear side. That impairment lessened as the target location was moved across the midline to the good-ear side, and localization performance was normal for locations more than ~40 deg from the midline on the good-ear side. Those studies therefore demonstrated that the spectral cues from each ear have decreased influence when that ear is contralateral to the target and that the influence of a contralateral "bad" ear is negligible for targets sufficiently displaced from the midline.

Quantification of the weighting of the information from each ear is difficult using the good-ear/bad-ear method, because the location (if any) corresponding to the unnatural spectrum at the "bad" ear is unknown. Hofman and Van Opstal (2003) have proposed a measure of the influence of the "good" ear using that method, but in the present study, an alternative approach was used in which there was a mismatch between the locations specified by the left-ear and right-ear monaural spectra, but in which those monaural spectra were not themselves degraded (a *good-ear/good-ear* paradigm). This was achieved using virtual auditory space methods (e.g., Wightman and Kistler, 1989a) and individual measurement of each listener's directional transfer functions

(DTFs—the directional component of the head-related transfer functions, HRTFs). A direct computation of the weight given to the information from each ear was made possible by manipulating only the interaural relationship between the monaural spectral cues while preserving the natural spectrum-to-space mapping at each ear.

The present study focused on the proximal stimulus parameters (those directly available to the auditory system: ILD, ITD, and spectral range) influencing the binaural weighting of information from each ear, whereas previous studies examined primarily the effect of the physical location of the source. One obvious hypothesis is that the influence of the spectrum at each ear is determined by the relative intensity of the signal at that ear, and therefore that the binaural weighting of the spectral cues depends only upon ILD. Alternatively, the weighting might depend upon ITD, which has been shown to be the primary determinant of apparent lateral angle for sounds containing low frequencies (Wightman and Kistler, 1992; Macpherson and Middlebrooks, 2002), or upon some combination of all the stimulus properties that vary with source lateral angle.

To conceptualize the role of ILD or ITD in the binaural combination of monaural spectral information, it is helpful to refer to two alternative mechanisms proposed by Hofman and Van Opstal (2003). These are *spatial averaging* [Fig. 1(a)], in which each of the monaural spectra is mapped independently to a particular location in space and then the spatial estimates are combined in a weighted average, and *spectral averaging* [Fig. 1(b)], in which the left- and right-ear spectra are combined and the resulting single spectrum mapped to space. In both models, the weighting (w_R or w_L) applied to the information in each channel depends, via an unspecified mechanism, monotonically on the lateral location of the sound source. The auditory system, of course, does not have direct access to the source's true lateral location, which must be derived from the proximal binaural difference cues. The influence of those cues as the focus of the present study is illustrated in Fig. 1(c).

The present study was not designed to distinguish between the spatial averaging and spectral averaging models, and in fact the relatively small mismatch introduced between left- and right-ear spectra should have produced similar results from either mechanism. The method used to compute the weighting factors—a multiple linear regression between the elevations to which each ear's spectrum corresponded and the listeners' resulting elevation judgments—directly represents the spatial averaging model. That model was best suited to predicting responses to our manipulated stimuli because each monaural spectrum-to-location mapping stage received as input only normal DTF spectra (from each "good" ear), and it was therefore reasonable to assume that the output monaural location estimates corresponded accurately to the input DTF measurement locations without making any assumptions about how the mapping itself was accomplished. In the spectral averaging model, even a good-ear/good-ear stimulus could result in an unnatural (or "bad") combined binaural spectrum. If the magnitude of the mismatch were small, however, that spectrum should be close to the natural combined spectrum for a location intermediate between those presented to each ear, and thus the model should also behave approximately linearly. The regression computation should therefore yield accurate values for the weights for either model.

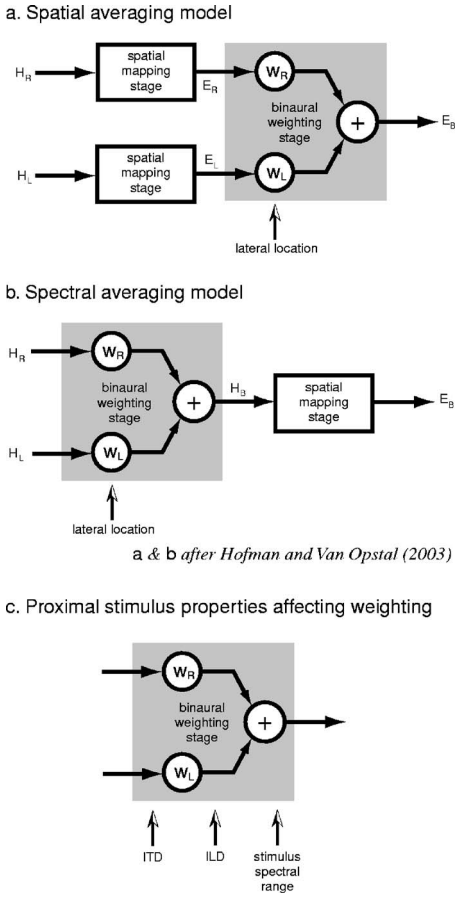

FIG. 1. Two conceptual models of the binaural weighting of monaural spectral cues proposed by Hofman and Van Opstal (2003). (a) Spatial averaging model. (b) Spectral averaging model. H_R and H_L are the spectra at the ears including the right- and left-ear head-related transfer functions. H_B is the combined binaural spectrum. E_R and E_L are the independent monaural estimates of source elevation. E_B is the final elevation estimate from the combined binaural information. (c) Proximal cues influencing the weighting coefficients.

The results of the present study demonstrate that the binaural weighting of monaural cues can be determined either by ILD or by ITD, depending upon the spectral range of the stimulus. In particular, the results demonstrate that weights are determined primarily by ILD only for high-pass stimuli, and that, in stimuli containing low frequencies, it is possible both to change the weighting without altering the stimulus ILD (by altering the ITD) and to maintain equal binaural weighting in stimuli with substantial ILDs (by maintaining near-zero ITD). The relationship between stimulus spectral range, ILD, and ITD in determining the binaural weighting parallels the relationship between those stimulus properties in the determination of perceived lateral angle (Macpherson and Middlebrooks, 2002).

II. METHODS

A. Subjects

Thirteen paid listeners (eight female and five male) aged 19–26 years (mean 21 years) were recruited from the Uni-

versity of Michigan community. All listeners had hearing loss $\leqslant$10 dB at octave frequencies from 0.25 to 8 kHz as determined by standard clinical audiometry. None had previous experience in sound localization or other psychoacoustic experiments. Before data collection began, all were given instruction and several hours of practice in free-field and virtual auditory space localization tasks using flat-spectrum, broadband noise targets. Listeners practised localization of those virtual-space targets until informal inspection of their data indicated that their performance had stabilized. No trial-by-trial feedback was provided during this training nor during the experiments.

B. Directional transfer function measurement

In order to permit the synthesis of individualized virtual auditory space stimuli, each listener's DTFs were measured using the procedure described by Middlebrooks (1999a). Briefly, 512-point, 50-kHz Golay code pairs (Golay, 1961; Zhou *et al.*, 1992) were presented from a loudspeaker (Infinity 32.3 CF) positioned 1.2 m from the listener's head. The loudspeaker was mounted on a movable hoop covered with sound-absorbing foam and was located in a sound-attenuating, double-walled anechoic chamber ($2.6\times3.7\times3.2$ m^3 of usable space), the walls and ceiling of which were lined with glass-fiber wedges $\sim$1 m deep and the floor with sound-absorbing Sonex foam wedges $\sim$15 cm deep. Measurements were made at 400 locations approximately evenly distributed in space ($\sim$10-deg separation) around the listener's head, which was held in a level and forward-facing orientation for the duration of the procedure (8–10 min). The responses to these excitation signals were recorded simultaneously by two miniature electret microphones (Knowles, model 1934) inserted approximately 5 mm into the listeners' ear canals. This was deep enough to capture all spatial information independent of any ear canal resonances (Middlebrooks *et al.*, 1989; Hammershøi and Møller, 1996).

HRTFs were computed by cross correlation of excitation and response, Fourier transformation, and the removal of the measured loudspeaker transfer function. The loudspeaker transfer function used for that correction was obtained similarly, in the absence of the listener, by recording the on-axis response to the Golay code excitation with a $\frac{1}{2}$-in. reference microphone (Larson Davis, model 2540) positioned at the location of the listener's head. DTFs for each ear were computed from the HRTFs by dividing each HRTF by the root-mean-square average magnitude spectrum (i.e., the nondirectional component) of the set of HRTFs for that ear. The nondirectional components also contained the transfer functions of the microphones and any fixed-geometry reflections from the foam-covered hoop that supported the loudspeaker, which were thus removed by this procedure. Directional impulse responses were computed from the DTFs via inverse Fourier transform, were windowed to 5.12 ms (256 samples) in duration, and contained no obvious reflections from chamber surfaces.

C. Stimulus synthesis and presentation

The target stimuli consisted of 100-ms bursts of flat-spectrum, random-phase noise with 1-ms squared-cosine onset and offset ramps. Stimulus waveforms were synthesized digitally using the inverse Fourier transform method, and the pass-band spectra of the stimuli ranged either from 0.5 to 16 kHz (*broadband* conditions) or from 4 to 16 kHz (*high-pass* conditions) with no energy beyond those frequencies. For convenience, the spectral range stimulus parameter will be referred to as *bandwidth*. Each waveform was then convolved with the time-domain counterparts of the right- and left-ear DTFs corresponding to the desired locations for presentation via headphones in virtual auditory space. The DTF filters for the two ears either corresponded to the same location (the natural situation) or to two different locations displaced horizontally from the vertical median plane by the same angle, but separated vertically by 20 deg (an artificial situation). That is, the left and right monaural spectra could "point" to the same location or to two different locations.

In some conditions (described fully in Sec. II D), such interaurally mismatched stimuli were presented without other manipulation using DTF filters corresponding to locations on or 30 deg to the left or right of the vertical median plane (lateral angles of 0, −30, or +30 deg, respectively). In other conditions, DTF filters only from midline locations were used, and the interaural time difference (ITD) and interaural level difference (ILD) cues present in the stimulus after DTF filtering were manipulated by imposing a whole-waveform delay (300 μs) or attenuation (10 dB) on the signal at one ear or the other. The imposition of delay or attenuation will be referred to as adding ITD or ILD *bias* to the stimulus, and the DTF filter lateral angle, the ILD bias, or the ILD bias will be referred to as the *lateralizing parameter*.

Stimuli were presented at a sampling rate of 50 kHz. The signal chain consisted of digital-to-analog converters and analog attenuators [Tucker-Davis Technologies (TDT) models DD1 and PA4], custom built low-pass reconstruction filters (eighth-order elliptical, 20-kHz cutoff), a headphone amplifier (TDT model HB6), and circumaural headphones (Sennheiser model HD 265). We did not attempt a rigorous equalization of the headphone response. Rather, the "diffuse-field equalized" headphone response itself restored an approximation of the diffuse-field component removed in the computation of the DTFs, and the listener's own ear canal restored the ear canal resonance. Listeners can localize accurately in the virtual auditory space generated by this method (Middlebrooks, 1999b). Stimuli were presented at sound pressure levels equivalent to free-field presentation at 50–60 dB (relative to 20 μPa rms). The stimulus level was roved randomly trial-by-trial within that range.

D. Stimulus locations and conditions

Target and response locations were described in the two-pole, *lateral-angle*, and *elevation* coordinate system shown in Fig. 2(a). Lateral angle is defined as the angle between a location and the vertical median plane, with positive values to the listener's right. Elevation is defined as the angle between a location and the horizontal plane, with positive val-

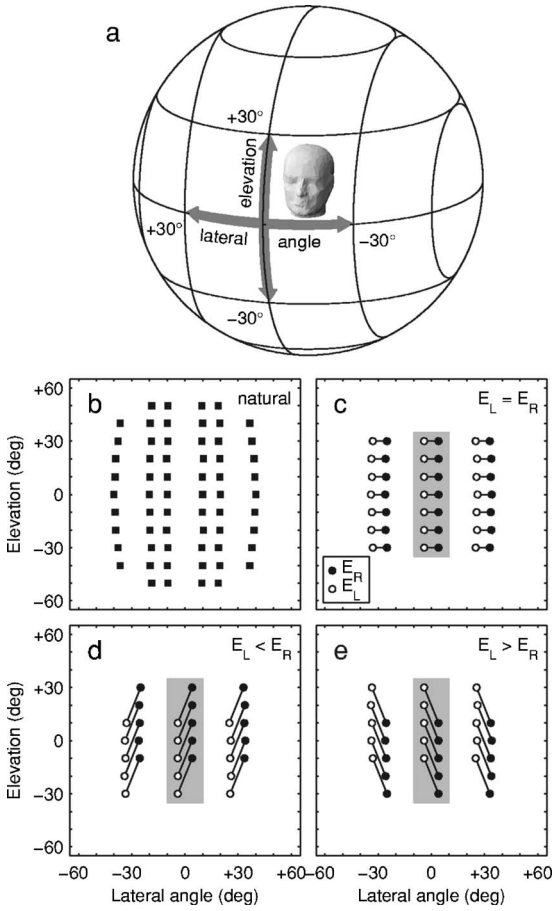

FIG. 2. Coordinate system, target locations, and stimulus conditions. (a) The two-pole, lateral-angle, and elevation coordinate system. (b) Locations of the natural (unmanipulated) stimuli that were interleaved with the experimental stimuli in each condition. (c)–(e) Locations of the right- (●) and left-ear (○) DTF filters used in lateral-angle conditions. Right- and left-ear locations are horizontally offset for clarity. ILD- and ITD-bias conditions used the set of midline locations and elevation deviations indicated by the shading in panels (c)–(e) each presented with ILD biases of −10, 0, or +10 dB, or ITD biases of −300, 0, or, +300 μs.

ues above the horizontal plane. The front- or rear-hemisphere position of each response location was also recorded. All target locations lay in the front hemisphere.

In order to promote a uniform response strategy for manipulated and unmanipulated stimuli, in each block of 118–142 trials, approximately 50% of the trials were faithfully synthesized, *natural* targets with no interaural mismatch of spectral cues. These were drawn from the locations shown in Fig. 2(b), which lay at lateral angles of ±10, ±20, or ±40 deg and at elevations between −50 and +50 deg. Equal numbers of broadband and high-pass natural stimuli were interleaved with the experimental stimuli in each trial block.

In order to evaluate the binaural weighting of the monaural spectral cues as a function both of a target's physical lateral angle and, independently, of ILD and ITD, six stimulus conditions were devised. These consisted of *lateral-angle*, *ILD-bias*, and *ITD-bias* conditions, each with a *broadband* and *high-pass* variant.

For the lateral-angle condition, the chosen DTF locations are shown in Figs. 2(c)–2(e), in which filled and open circles indicate the elevations (E_R and E_L) of the right- and left-ear DTF filters, respectively. The *elevation deviation* ($E_R - E_L$) was 0, +20, or −20 deg (Figs. 2(c)–2(e), respectively), and elevations were distributed in 10-deg increments between −30 and +30 deg. The lateral angles of the filters were −30, 0, or +30 deg, and for each stimulus, the right- and left-ear filters had the same lateral angle (although for clarity, the symbols have been offset horizontally in Fig. 2).

In the ILD- and ITD-bias conditions, only the midline DTF-filter locations [indicated by the shaded regions in Figs. 2(c)–2(e)] were used, with elevation deviations identical to those in the lateral-angle condition. For such midline locations, the natural ILD is close to 0 dB and the natural ITD is close to 0 μs. These natural binaural difference cues were altered by applying ILD bias of −10, 0, or +10 dB or ITD bias of −300, 0, or +300 μs. Those delay and attenuation values were chosen because they approximate the values of ITD and overall ILD corresponding to a broadband source 30 deg from the midline, and thus provide some equivalence between the lateralizing parameters in each condition. The ILD bias manipulation did not replicate the natural variation of ILD across frequency, but we have shown previously that application of 10 dB ILD bias to a high-pass stimulus (or 300 μs ITD bias to a broadband stimulus) produces shifts in apparent lateral angle of ~30 deg and that the details of the interaural level spectrum are relatively unimportant (Macpherson and Middlebrooks, 2002).

Broadband and high-pass stimuli were intermixed within trial blocks in all lateral-angle, ILD-bias, and ITD-bias conditions. Stimuli for the ILD-bias and ITD-bias conditions were intermixed within blocks, but stimuli for the lateral-angle condition were presented in separate blocks. Listeners typically completed four to six trial blocks in each experimental session. Over the course of multiple experimental sessions (extending over 2–3 months), each individual experimental stimulus (with a particular target elevation, elevation deviation, bandwidth, and bias or lateral angle) was presented four times to each listener. In total, each listener responded to 4200 trials distributed over 22 blocks each consisting of 118–142 trials.

E. Response procedures

The virtual auditory space stimuli were presented over headphones while the listener stood at the center of the darkened anechoic chamber. Listeners indicated the apparent location of a target either by *head-pointing* (turning the body and tilting the head to orient the face in the appropriate direction) or by using an *acoustic pointer* (a joystick-controlled virtual auditory space pointer sound alternated with the target and its position adjusted until they were aligned). Six listeners used the head-pointing method, and seven used the acoustic pointer. Each subject used only one of these methods throughout the experiment, but all were initially trained in head-pointing to free-field targets before proceeding to practice with virtual-space targets and the assigned response method. Using the head-pointing response method, each block of 118–142 trials took 8–15 min to complete, whereas each acoustic-pointer block took 15–30 min. On average, the listeners using the acoustic-pointer method

exhibited greater absolute localization accuracy for unmanipulated targets (see Sec. III A), but no systematic differences were observed between the final results for the two groups of listeners.

1. Head-pointing response method

In order to constrain the listener's head orientation at the time of stimulus presentation, the following procedure was used in the head-pointing task. At the beginning of each trial, the listener oriented toward a light-emitting diode (LED) positioned at eye-level 60 cm away. This LED indicated the same head orientation as that used in the DTF measurement procedure. The listener initiated each trial by pressing a hand-held button, and this also triggered an initial measurement of the listener's head orientation by a head-mounted electromagnetic tracking device (Polhemus FASTRAK). If the head orientation deviated from the LED fixation direction by >5 deg either horizontally or vertically, the LED began to blink, indicating that the listener should adjust his or her head position to achieve fixation. Once this was achieved, the LED was extinguished and, after 500 ms, head position measured again. If fixation had been not been maintained, the LED again began to blink and the head-adjustment phase was repeated, otherwise the stimulus was presented. After hearing the stimulus, the listener oriented toward its apparent location, then pressed the button again, which triggered a final measurement of head orientation. This head-orientation measurement constituted the listener's response.

2. Acoustic pointer response method

In the acoustic pointer response method, a trial was initiated when the listener pressed a hand-held button. The target stimulus was then presented repeatedly with an interstimulus interval of 300 ms. A second button press turned on the pointer stimulus (a DTF-filtered, 200-Hz train of single-sample impulses), which then alternated with the target with an interstimulus interval of 200 ms. The listener manipulated the location of the pointer by adjusting the orientation of a 20-cm wooden rod, fixed at one end, that could rotate freely about vertical and horizontal axes. The orientation of the rod was measured with the same electromagnetic tracking device used in the head-pointing response method. Listeners were instructed to press the button a third time when the apparent locations of the alternating target and pointer stimuli were aligned. The final location of the pointer stimulus constituted the listener's response. Listeners were instructed to hold their heads level and oriented in the forward direction during this procedure. Compliance with this instruction was monitored periodically via an infrared video camera.

The DTF filters used to generate the spatialized pointer stimulus were those corresponding to the DTF measurement location closest to the rod's orientation. No spatial interpolation was used, and therefore the resolution of the pointer location was $\sim$10 deg. A pulse train was chosen for the pointer in order to provide a timbre distinct from that of the noise-burst targets, and thus to discourage listeners from matching its location to those of the noise-burst targets on the basis of nonspatial stimulus characteristics. For each listener using the acoustic pointer method, performance in localizing the pulse-train pointer stimulus itself was evaluated in separate trial blocks using virtual auditory space presentation and the head-pointing response method. All listeners were able to localize the pulse-train pointer stimulus with accuracy similar to that for a broadband noise target.

All stimulus generation, stimulus presentation, and data collection tasks were controlled by custom software written in MATLAB (The Mathworks, Inc.) running on an Intel-based personal computer.

III. RESULTS

A. Comparison of head-pointing and acoustic-pointer performance

The head-pointing and acoustic-pointer procedures both provided listeners with a means of indicating the apparent location of the virtual space targets, but differed in several fundamental respects. As implemented in this study, head-pointing was an absolute localization task based on a single presentation of the stimulus, whereas the acoustic-pointer task was not an absolute localization task (it required the comparison of two apparent locations) and involved multiple stimulus presentations as the target and pointer alternated. Both tasks included a motor component related to the final response (orientation of the head or of the pointer stick), but, in head-pointing, undershoots in response elevation might be more expected because of the effort required to tilt the head away from the horizontal plane. Finally, head-pointing provides a continuous measure of reported location, whereas acoustic-pointer responses were quantized to $\sim$10 deg, similarly to the 10-deg resolution volunteered by many listeners using a verbal response method (e.g., Wightman and Kistler, 1989b).

To compare the localization performance of listeners using the head-pointing or acoustic-pointer methods, we computed the *rate of front-hemisphere responses*, the *elevation gain* and *scatter*, and the *lateral-angle gain* and *scatter* for those stimuli (of either broadband or high-pass bandwidth) in the lateral-angle condition with $E_R=E_L$ (i.e., unmanipulated virtual-space targets). Elevation gain, g_E, was defined as the regression coefficient between the target and response elevations following the linear model given in Eq. (1) (Hofman and Van Opstal, 1998). Systematic offset in responses was represented by the coefficient g_{oE}. Lateral-angle gain and offset, g_λ and $g_{o\lambda}$, were defined similarly for the horizontal component of the responses as in Eq. (2). Scatter values were defined as the standard deviation of the regression line residuals. Gains and scatters were computed using front-hemisphere (i.e., nonreversed) responses only. Gain values of 1 indicate veridical localization of the stimuli, and values less than or greater than 1 indicate systematic undershoots or overshoots, respectively:

$$\hat{E}_{RESP} = g_E \cdot E_{TARG} + g_{oE}, \tag{1}$$

$$\hat{\lambda}_{RESP} = g_\lambda \cdot \lambda_{TARG} + g_{o\lambda}. \tag{2}$$

As a group, listeners using the acoustic pointer exhibited more accurate localization performance than those using

head-pointing, although group differences for most measures were not statistically significant. For both groups, across listeners and cases (here, combinations of bandwidth and lateral angle), the median (and therefore modal) front-hemisphere response rates were 1, but there were fewer instances of large numbers of front-to-back reversals for the acoustic-pointer group (2/24 cases <0.9) than for the head-pointing group (11/36 cases <0.9). The Wilcoxon rank-sum statistic for the two distributions was significantly different from 0 [$z(T_W)=3.34$, $p<0.001$]. Across listeners and cases, the acoustic-pointer group had elevation gain closer to 1 (mean 0.85; s.d. 0.38) than the head-pointing group (mean 0.73; s.d. 0.34), but the difference was not statistically significant [$t(76)=1.41$, $p>0.10$]. Elevation scatter was higher in the acoustic pointer group (mean 10.48 deg; s.d. 3.80 deg) than in the head-pointing group (mean 8.75 deg; s.d. 4.01 deg), but the difference was not statistically significant [$t(76)=-1.96$, $p>0.05$]. Across listeners and bandwidths, lateral-angle gain was close to 1 for the acoustic-pointer listeners (mean 1.03; s.d. 0.14), and indicated overshooting for the head-pointing group (mean1.22; s.d. 0.32), but the difference was not statistically significant [$t(24)=2.03$, $p>0.05$]. Lateral-angle scatter was lower for acoustic-pointer listeners (mean 6.51 deg; s.d. 2.42 deg) than for head-pointing listeners (mean 9.83 deg; s.d. 2.22 deg), and this difference was statistically significant [$t(24)=3.63$, $p<0.01$].

We considered the possibility that the somewhat more accurate performance of the listeners using the acoustic pointer was an artifact of the ~10-deg quantization of their responses. To assess the effect of that quantization, we recomputed the elevation and lateral-angle gain and scatter statistics for the *head-pointing* listeners after replacing each response location with the closest DTF measurement location. The elevation and lateral-angle gain values were unaffected (after rounding to two decimal places), but the elevation and lateral-angle scatter values *increased* slightly to 9.34 and 10.14 deg, respectively. Thus, quantization seems unlikely to have resulted in overestimation of the acoustic-pointer listeners' localization accuracy.

We consider the differences between the localization performance of the groups using the acoustic-pointer and head-pointing methods to be largely quantitative, rather than qualitative. When combining data from different listeners, we employed normalization procedures to account for individual differences in elevation and lateral-angle gain, and intermixed the data from the two groups in the analyses below. We show in Sec. III E that the end results of the binaural weighting analysis are similar for the two groups.

B. Treatment of front-back confusions

Any localization responses that fell in the rear hemisphere were necessarily front-to-back confusions because all target stimuli were presented from the front hemisphere. We computed the rate of front-hemisphere responses separately for stimuli with natural ($E_R=E_L$) and manipulated ($E_R \neq E_L$) pairs of spectral cues across listeners and cases in each condition. For each condition, we used a paired-sample t test to test the significance of differences between the rates for natural and manipulated stimuli. That test controlled for intersubject differences in reversal rates. The rate of reversals varied as a function of the stimulus condition, but *not* as a function of the match or mismatch between the spectral cues presented to each ear, as shown in Table I. Only in the high-pass ILD-bias condition was the rate of front-hemisphere responses significantly different between matched and mismatched stimuli, and the magnitude of this difference was rather small. Front-hemisphere response rates were substantially reduced only in the broadband ITD-bias and ILD-bias conditions. The more numerous reversals in those conditions are presumably related to the conflict necessarily introduced between ITD and ILD cues; increases in the rate of front-back confusions for similar stimuli have been reported in previous studies from this laboratory and others (e.g., Wightman and Kistler, 1992, 1997a; Macpherson and Middlebrooks, 2002).

TABLE I. Proportion of front-hemisphere responses for unmanipulated ($E_R=E_L$) and manipulated ($E_R \neq E_L$) stimuli in each condition. The right-hand column lists the p value yielded by a paired-sample t test of the frontal response rate across listeners and values of the lateralizing parameter.

		Proportion front responses		
Lateralizing parameter	Spectral range	$E_R=E_L$	$E_R \neq E_L$	$p\{t(38)\}$
LAT	BB	0.912	0.896	0.095
LAT	HP	0.975	0.973	0.696
ILD	BB	0.554	0.532	0.088
ILD	HP	0.962	0.943	0.043*
ITD	BB	0.664	0.652	0.271
ITD	HP	0.960	0.964	0.676

The occurrence of a front-back reversal is evidence for a misinterpretation of, or ambiguity in, the spectral cues indicating the front-back location of the source. If such responses were accurate in the elevation and lateral-angle dimensions, it would be reasonable to analyze those components of reversed responses along with those from nonreversed responses. We computed the elevation and lateral-angle gain and scatter for cases yielding both front- and rear-hemisphere responses to decide whether that course of action was advisable. Across listeners, conditions, and cases, reversed responses exhibited significantly lower elevation gain [front: mean 0.73, s.d. 0.34; rear: mean 0.42, s.d. 0.32; $t(279)=6.52$, $p<0.001$] and significantly higher elevation scatter [front: mean 9.40 deg, s.d; 3.445 deg; rear: mean 11.11 deg, s.d. 4.57 deg; $t(279)=3.22$, $p<0.01$]. Across listeners and cases in the broadband and high-pass lateral-angle conditions (the only conditions for which lateral-angle gain could be computed), lateral-angle gain was similar for nonreversed and reversed responses [front: mean 1.12, s.d. 0.25; rear: mean 1.07, s.d. 0.73; $t(30)=0.33$, $p>0.50$], but lateral-angle scatter was significantly higher for reversed responses [front: mean 8.04 deg, s.d. 2.84 deg; rear: mean 15.77 deg, s.d. 1.28 deg; $t(30)=6.46$, $p<0.001$].

We concluded from these results that reversed responses were substantially less accurate than nonreversed responses, and we therefore excluded reversed responses from most of our analyses. In the broadband ITD-bias and ILD-bias con-

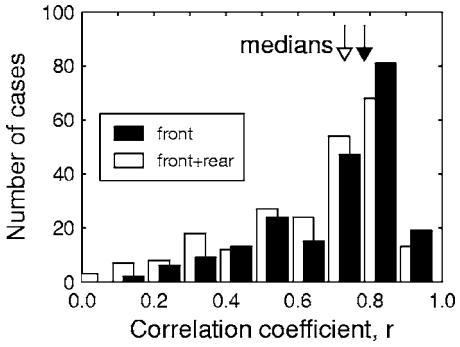

FIG. 3. Distribution of the coefficient of multiple correlation, r, for the linear model fit to data from all listeners, conditions, and cases. Regressions were computed using front-hemisphere (nonreversed) responses only (filled bars) or both front- and rear-hemisphere responses (open bars).

ditions, that strategy resulted in the exclusion of a sizable fraction of the data, and therefore in each of the following Results sections we discuss the consequences of relaxing the exclusion of reversals.

C. Computation of binaural weighting coefficients

The binaural weighting of spectral information was determined for each listener, and for targets of each bandwidth at each lateral angle, ILD bias, or ITD bias, by a multiple linear regression between the elevations to which each ear's spectrum "pointed" (E_R and E_L) and the vertical component of listeners' judgments (E_{RESP}), following the linear model given in Eq. (3). That model is an elaboration of the elevation-gain model of Eq. (1) for the situation in which spectral cues possibly corresponding to mismatched elevations are presented to each ear:

$$\hat{E}_{RESP} = w_R \cdot E_R + w_L \cdot E_L + w_o. \tag{3}$$

In each case, the weights were the resulting regression coefficients, w_R and w_L, computed for trials with nonzero elevation deviation ($E_R \neq E_L$) and for front-hemisphere responses only. Any mean offset in the responses was represented by the regression coefficient w_o.

The quality of the linear model fit was quantified by the coefficient of multiple correlation, r, between the observed (E_{RESP}) and predicted ($\hat{E}_{RESP}$) response elevations. In the majority of cases, the linear model provided a good fit to the elevation component of the listeners' localization judgments. The distribution of r values is shown in Fig. 3; the median value of r across all cases was 0.78. If reversed responses were also included in the analysis, the median value of r was significantly reduced to 0.73 [Wilcoxon rank-sum test; $z(T_W)=2.84$, $p<0.001$].

We assessed the reliability of the regression weights in each case by testing the null hypothesis that $w_R=w_L=0$ using the F test for multiple regression with $\alpha=0.05$ (Hayes, 1988, Eq. 15.19.3). The weights from cases in which the F statistic did not reach significance were treated as missing data and were not used in subsequent analyses. Possible reasons for this outcome in a particular case include inconsistency in listeners' responses and high reversal rates, which would reduce the number of front-hemisphere data on which to compute the regression. In cases for which the F statistic was significant, we refer to w_R and w_L as a *significant weight pair*. If a listener's data generated significant weight pairs at each of the three values of the lateralizing parameter in a particular condition, the result was considered to be a *significant weighting pattern*.

To illustrate the effects of elevation deviation and the computation of w_R and w_L, the elevation components of the localization judgments of one listener (S154) in the high-pass, lateral-angle condition are shown in Fig. 4. From left-to-right, the panels show the data for targets at −30, 0, and +30 deg lateral angle, respectively. The right-ear elevation, E_R, is plotted on the horizontal axis, and the response elevation on the vertical axis. Filled and open symbols indicate trials in which the left-ear elevation, E_L, was 20 deg higher or lower, respectively, than the right-ear elevation. In such plots, if the right ear spectrum alone controlled the perceived elevation, the responses should fall close to E_R, and therefore all points (both open and closed symbols) should fall close to the diagonal, as is seen in the rightmost panel. If the left ear spectrum did influence the percept, responses should be systematically displaced above or below E_R, and therefore the closed symbols should be displaced above the diagonal and the open symbols displaced below it, as is seen in the leftmost panel.

In the condition represented in the leftmost panel of Fig. 4, targets were 30 deg to the left of the midline, and the change in the elevation deviation parameter from −20 to +20 degrees is reflected in the vertical separation of the responses in the two cases. In the center panel, targets lay on the midline, and it is apparent that the effect of elevation deviation was less strong in this case. In the rightmost panel, targets

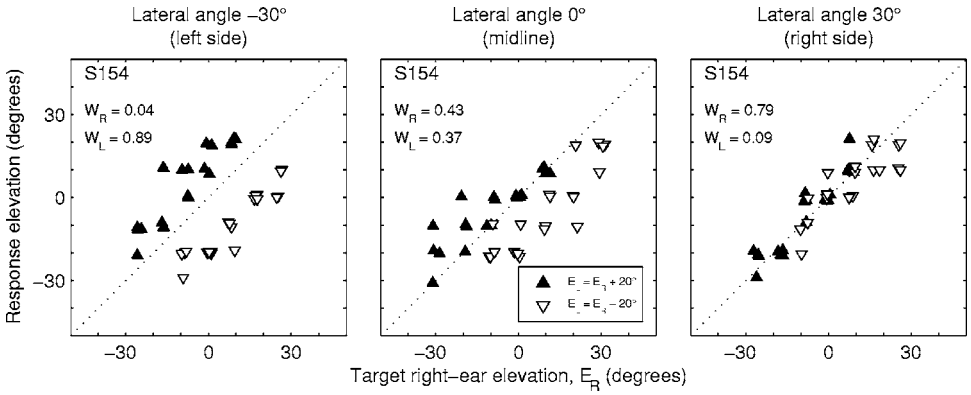

FIG. 4. Elevation components of listener Sl54's responses in the high-pass, lateral-angle condition. Horizontal axes: right-ear target elevation; vertical axes: elevation component of responses. Symbols show the responses for trials in which the left-ear DTF filter location was 20 deg higher (▲) or lower (▽) than the right. Symbol positions have been jittered horizontally and vertically for clarity. Left, center, and right panels: targets presented at lateral angles of −30, 0, and +30 deg, respectively.

lay 30 deg to the right of the midline, and the vertical displacement of responses related to changes in elevation deviation for the left ear can be seen to be negligible. Thus, these data show that the spectrum at the ear contralateral to the target had little influence in determining the apparent elevation of the stimulus, and this is borne out in the computed weights, which, for a particular ear, decrease from close to 1 for 30-deg ipsilateral targets to ~0 for 30-deg contralateral targets.

D. Weighting coefficients as a function of stimulus parameters

A full set of weighting coefficients, w_R and w_L, is plotted as an example in Fig. 5 for listener S154, for whose data the linear model provided a consistently good fit in each of the six conditions ($r > 0.73$ in all cases). Weights for broadband conditions are plotted in the left-column panels, high-pass conditions in the right-column panels, and lateral-angle, ILD bias, and ITD-bias conditions in the first, second, and third rows of panels, respectively. Open symbols represent the left-ear weighting coefficients, and closed symbols the right-ear coefficients. The weights are plotted as a function of the lateralizing parameter (lateral angle, ILD or ITD) in each condition, and error bars indicate the standard errors of the coefficients (Hayes, 1988, Eq. 15.21.3). Inset panels show the lateral-angle component of the corresponding localization responses at each value of the lateralizing parameter along with a regression line fit to those data.

In most conditions, the weights for a particular ear for listener S154 showed a monotonic decrease as the lateralizing parameter changed from favoring that ear to favoring the other. Cases in which the lateralizing parameter was 0, for which the perceived location was close to the midline, yielded approximately equal values for w_R and w_L, indicating a balance of influence for the spectral cues from the two ears. In the lateral-angle conditions (Fig. 5, top row), the change in weights from left to right was large, with weights for the ear ipsilateral to the target close to 1 and weights for the contralateral ear close to 0. In most of the ILD- and ITD-bias conditions, a similar pattern was observed for this listener, but the range of weight values was smaller than in the lateral-angle conditions. In the broadband ILD-bias condition (second row, left panel), however, the weights changed very little, and remained close to a value of 0.5 as ILD bias was varied. In the ITD-bias conditions (bottom row), the weights changed somewhat less for high-pass stimuli than for broadband stimuli.

The binaural weighting of the monaural spectral cues varied from condition-to-condition in a manner related to the apparent lateral angle of targets presented with each value of the lateralizing parameters. For example, in the broadband and high-pass lateral-angle conditions (Fig. 5, upper left and right panels, respectively), targets were localized quite accurately in lateral angle, and the regression lines indicated a mean apparent lateral angle of ~28 deg for targets presented from 30 deg lateral angle. In contrast, the mean apparent lateral angle for targets presented with a 10-dB ILD bias in the broadband ILD-bias condition (second row, left panel) was ~12 deg and therefore much closer to the midline. As

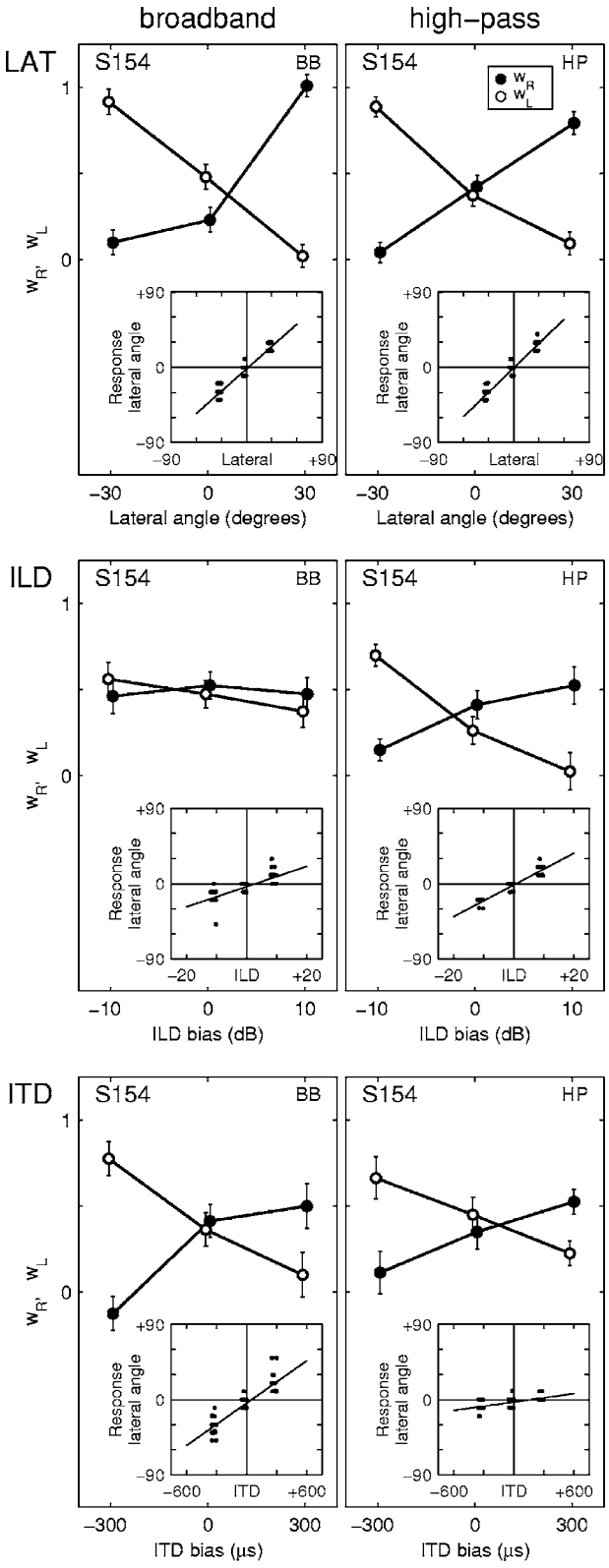

FIG. 5. Computed weighting coefficients and corresponding lateral-angle response components for listener S154 in each condition. Left column: broadband conditions; right column: high-pass conditions. First row: lateral-angle conditions; middle row: ILD-bias conditions; bottom row: ITD-bias conditions. Symbols indicate the computed right- (●) and left-ear (○) regression coefficients. Error bars indicate the standard errors of the coefficients. Inset panels show the lateral-angle components of the responses at each value of the lateralizing parameter (lateral angle, ITD bias or ILD bias) with fitted regression lines.

noted above, the monaural spectral weights, w_R and w_L, in that condition changed little when ILD bias was applied, but a robust change was observed in the lateral-angle conditions when the targets were displaced from the midline. These data suggest that the binaural weighting of the monaural spectral cues is not determined by a single binaural difference cue, but by a combination of those cues similar to that generating the *perceived* lateral location of the source. The relation between the response lateral-angle data and the weighting coefficients is analyzed in detail in Sec. III E.

To compute a mean weighting pattern across all listeners, weights for each listener in each condition were first normalized by dividing by a mean elevation gain, $\overline{g_E}$. That was the mean of the elevation gains [Eq. (1)] computed individually at each of the three values (negative, 0, and positive) of the lateralizing parameter, and using only the 0-elevation-deviation trials ($E_R=E_L$). The normalization was intended to correct for systematic listener- and response-method-dependent differences in response strategy (Sec. II E 2). We expected zero-elevation-deviation ($E_R=E_L$) stimuli to be localized accurately in the vertical dimension because they possessed a full and natural complement of high-frequency spectral cues, and we assumed therefore that nonunity elevation gains indicated a nonoptimal response strategy. When $E_R=E_L$, the bivariate weighting model [Eq. (3)] simplifies to the elevation gain model for unmanipulated stimuli [Eq. (1)] with $g_E=(w_R+w_L)=\Sigma w$. To test the assumption that $g_E=\Sigma w$, we computed a linear regression between those two variables across all 159 cases yielding significant weight pairs. This produced the result $\widehat{\Sigma w}=0.84g_E+0.14$ and a correlation coefficient of 0.80. The near-unity slope and high correlation of that fit suggest that g_E and Σw were related as expected. Dividing the weights by $\overline{g_E}$ therefore yielded values approximating those that would have been derived from a listener exhibiting unity elevation gain. Normalized weights for a particular listener were included in the mean only if their data yielded a full significant weighting pattern in a particular condition.

To represent the mean lateral-angle responses in each condition, we first calculated for each listener a linear regression between those responses and the corresponding values of the lateralizing parameter. For the lateral-angle conditions, the *lateral-angle-response slope* of the resulting linear fit was a dimensionless lateral-angle gain, whereas for the ILD- and ITD-bias conditions, it was a value with units of deg/dB or deg/μs, respectively. We then normalized those values by dividing each by the listener's lateral-angle gain computed using all front-hemisphere responses to the broadband natural targets that were interleaved with the experimental stimuli [Fig. 2(b)]. Those were the only naturally lateralized targets presented in the blocks of trials for ILD- and ITD-bias conditions. Finally, we computed the across-listener mean and standard errors of the normalized lateral-angle-response slope values.

The mean weighting pattern and lateral-angle-response slope in each condition are shown in Fig. 6, which follows the same panel layout as Fig. 5. The patterns of mean weights were in general similar to those for individual listener S154 (Fig. 5); the mean weight for a particular ear

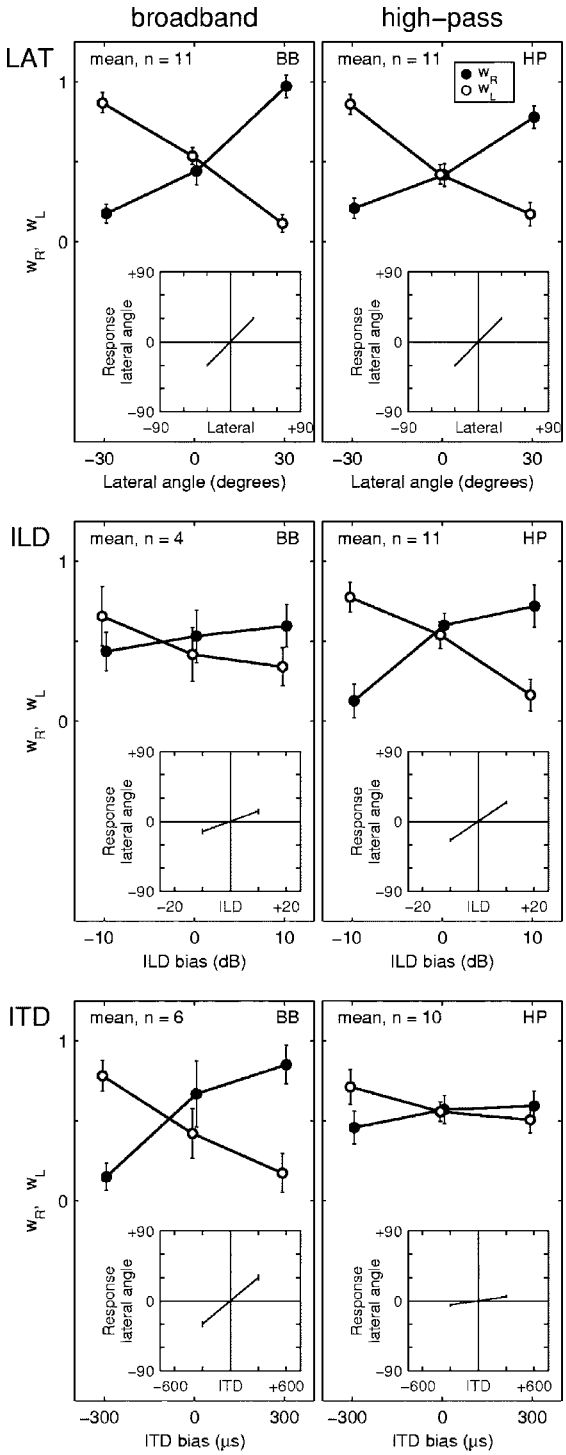

FIG. 6. Mean patterns of weighting coefficients and mean lateral-angle slopes in each condition. Left column: broadband conditions; right column: high-pass conditions. First row: lateral-angle conditions; middle row: ILD-bias conditions; bottom row: ITD-bias conditions. Symbols indicate the mean right- (●) and left-ear (○) weights. The number of listeners whose data contributed to each weighting pattern is indicated in each panel. Error bars indicate the standard errors of the means. Inset panels show the mean value of the lateral-angle-response slope.

decreased monotonically as the lateralizing parameter changed from favoring that ear to favoring the other ear, and left- and right-ear weights were approximately equal for midline or 0-bias cases. In the lateral-angle conditions, the mean weight for the ear contralateral to targets displaced 30 deg from the midline was small (<0.2), and the weight for the

ipsilateral ear was close to 1. Similar, although slightly attenuated, monotonic changes in weight from side-to-side were observed in the high-pass ILD-bias condition (right column, second row) and the broadband ITD-bias condition (left column, third row). In contrast, in the broadband ILD-bias (left column, second row) and high-pass ITD-bias (right column, third row) conditions, only small changes from the approximately equal weights in the 0-bias cases were observed when bias was applied.

In some conditions, some individual listeners' weighting patterns did deviate markedly from the means shown in Fig. 6. In the high-pass ITD-bias condition, three listeners (including S154, Fig. 5) exhibited side-to-side changes in w_R and w_L much larger than those for the mean weights. Conversely, weight changes much smaller than those of the means were sometimes seen in the high-pass ILD-bias condition (two listeners), the broadband lateral-angle condition (two listeners), and the high-pass lateral-angle condition (one listener). Most listeners' data yielded weighting patterns that were approximately symmetrical for the left and right ears, as suggested by the mean weighting patterns. For 5 of the 13 listeners, however, the mean value of w_R, across conditions and values of the lateralizing parameter, $\overline{w_R}$, was statistically different from $\overline{w_L}$ (t test, $p<0.05$). Two listeners' weights favored the left ear, and three listeners' weights favored the right ear. The magnitude of $\overline{w_R}-\overline{w_L}$ ranged from 0.20 to 0.52 for these listeners.

There were only two instances of marked deviations from the mean lateral-angle-response slopes. One listener's slope in the broadband ILD-bias condition was approximately one-half that of the mean. One other listener's slope in the broadband ITD-bias condition was also approximately one-half that of that mean.

The numbers of listeners whose data met the criteria for inclusion in each mean weighting pattern are given in the panels of Fig. 6. Listeners using head-pointing and the acoustic pointer contributed approximately equally to the means, with five or six from each group in the lateral-angle and high-pass ITD-bias and ILD-bias conditions, two from the head-pointing group and two from the acoustic-pointer group in the broadband ILD-bias condition, and four from the head-pointing group and two from the acoustic-pointer group in the broadband ITD-bias condition. The low numbers of listeners yielding significant weighting patterns in the broadband ILD- and ITD-bias conditions are presumably due to the increased rate of front-to-back confusions in those conditions and the subsequent exclusion of those trials from the weight computation (Sec. III B). To explore the effect of including rear-hemisphere responses, we recomputed the weights and mean weighting patterns using all responses. The inclusion of reversals increased the number of listeners contributing significant weighting patterns only in the broadband ILD- and ITD-bias conditions (from four to six and six to eight, respectively), and produced no qualitative changes in the mean patterns except the introduction of a slight nonmonotonicity in w_R in the broadband ILD-bias condition.

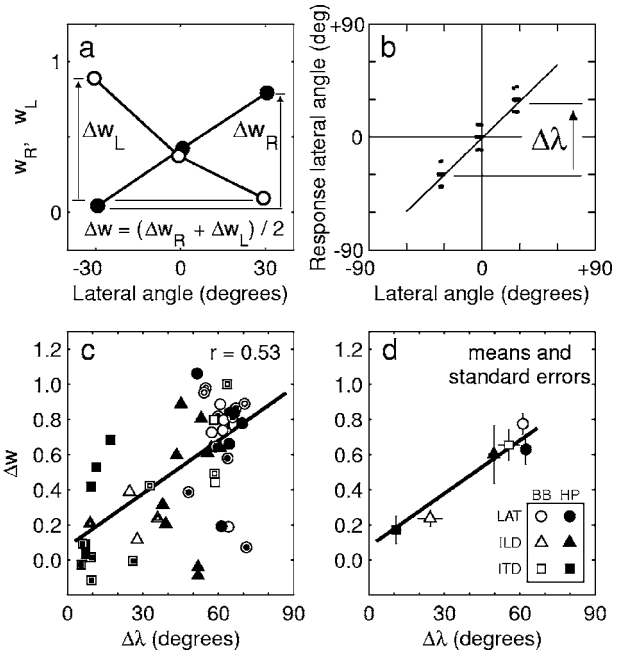

FIG. 7. Mean change in weighting coefficients as a function of mean change in apparent lateral angle. (a) Definition of Δw as the mean side-to-side weight-change. (b) Definition of $\Delta\lambda$ as the mean side-to-side change in response lateral angle. (c) Mean weight change (Δw, vertical axis) plotted against mean lateral-angle change ($\Delta\lambda$, horizontal axis) for each listener and condition (significant weighting patterns only). Symbols indicate lateral-angle (●, ○), ILD-bias (▲, △), and ITD-bias (■, □) conditions. Open symbols: broadband conditions; closed symbols: high-pass conditions. Doubled-bordered symbols (e.g., ◎): head-pointing listeners; plain symbols: acoustic-pointer listeners. (d) Means and standard errors of Δw and $\Delta\lambda$ in each condition.

E. Weighting coefficients as a function of apparent lateral angle

The relation between changes in apparent lateral angle and changes in monaural weighting coefficients was quantified through the definition of Δw and $\Delta\lambda$, the mean side-to-side changes in weighting coefficient and apparent lateral angle in a particular condition, as given in Eqs. (4)–(7):

$$\Delta w_R = w_R^+ - w_R^-, \tag{4}$$

$$\Delta w_L = w_L^- - w_L^+, \tag{5}$$

$$\Delta w = \tfrac{1}{2}(\Delta w_R + \Delta w_L), \tag{6}$$

$$\Delta\lambda = \overline{\lambda^+} - \overline{\lambda^-}. \tag{7}$$

In these equations, w_R^+ and w_L^+ are the right- and left-ear weights found for the positive value of the lateralizing parameter, w_R^- and w_L^- are the weights found for the negative value of the lateralizing parameter, and $\overline{\lambda^+}$ and $\overline{\lambda^-}$ are the mean response lateral angles for the positive and negative values of the lateralizing parameter. The interpretations of Δw_R and Δw_L as the overall side-to-side change in each ear's weighting and of $\Delta\lambda$ as the mean side-to-side change in the response lateral angle are illustrated in Figs. 7(a) and 7(b). To account for differences in response strategies between listeners and pointing methods, the values of Δw and $\Delta\lambda$

were normalized by dividing by elevation gain and lateral-angle gain as detailed in Sec. III D.

Δw and $\Delta\lambda$ were computed for each listener and each condition yielding a significant weighting pattern, and these variables are plotted against each other in Fig. 7(c). Circles, triangles, and squares represent lateral-angle, ILD-bias, and ITD-bias conditions, respectively; open and closed symbols represent broadband and high-pass conditions, respectively; and doubled-bordered and plain symbols represent head-pointing and acoustic-pointer listeners, respectively. Data points for listeners using the head-pointing and acoustic-pointer response methods were intermixed, indicating that there was no systematic difference between the results for the two groups.

The mean values (symbols) and standard errors (error bars) of Δw and $\Delta\lambda$ are plotted in Fig. 7(d), which represents the correspondence between mean weighting patterns and mean lateral-angle responses visible in Fig. 6. The lateral-angle conditions produced large mean changes in the apparent lateral angle and in the weighting coefficients, the broadband ITD-bias and high-pass ILD-bias conditions produced slightly smaller, although similar, changes, but the high-pass ITD-bias and broadband ILD-bias conditions produced very small changes in both apparent lateral angles and weights.

It is apparent that Δw and $\Delta\lambda$ are positively correlated, and a linear regression yielded a significant correlation coefficient of 0.53 ($p<0.001$). Including reversed responses in the analysis reduced the correlation to 0.49. We recomputed the correlation for front-hemisphere responses excluding cases in which responses were particularly inaccurate in the vertical dimension. Such cases were defined as those in which listeners' elevation gain fell in the lowest quartile, $g_E<0.55$. The resulting correlation between Δw and $\Delta\lambda$ increased to 0.64, suggesting that the relationship between the weights and apparent lateral angle is stronger among the listeners with more accurate localization performance. Further excluding the five outlying points in the lower right of Fig. 7(c) yielded a correlation of 0.84.

IV. DISCUSSION AND CONCLUSIONS

The computed weighting patterns obtained in the lateral-angle conditions of the present experiment are consistent with the finding from previous studies that the spectrum at the ear contralateral to a sound source more than ~40 deg from the midline contributes negligibly to vertical-plane localization (Musicant and Butler, 1984; Humanski and Butler, 1988; Wightman and Kistler, 1999; Morimoto, 2001; Hofman and Van Opstal, 2003). In both the broadband and high-pass lateral-angle conditions, weighting coefficients were close to 1 for the ear ipsilateral to a target 30 deg off the midline and <0.2 for the ear contralateral to such a target. For sources on the midline, ipsilateral- and contralateral-ear weights were approximately equal for a majority of listeners, suggesting that the spectrum at each ear had similar influence on the apparent elevation of the source.

In the lateral-angle conditions of the present study and in previous free-field studies, varying the lateral angle of the source was necessarily accompanied by the natural covariation of the proximal cues (ILD and ITD) that determine the apparent lateral angle. The ILD-bias and ITD-bias conditions of the present study were intended to dissociate the effects of these two cues. The results demonstrate that both ILD and ITD can independently, and with similar effectiveness, drive the left- and right-ear weighting coefficients away from the equal-valued state observed for midline sources. Although that finding does not discriminate between the two conceptual models proposed by Hofman and Van Opstal (2003), some specific variants of those models can be ruled out.

Based on the hypothesis that binaural weighting is determined by ILD alone, one plausible and simple mechanism for the combination of monaural spectral cues might be termed *passive spectral averaging*, in which the reduction in the influence of the contralateral ear results not from an explicit weighting applied by the auditory system, but from the acoustical attenuation provided by the head. Spectral localization cues exist primarily at frequencies above ~6 kHz (Hebrank and Wright, 1974), and at these high frequencies, head-shadowing and pinna filtering can produce ILDs in excess of 20 dB. Simply summing the energy spectra from each ear with fixed and equal weights could account for the diminished influence of the contralateral ear that has been observed experimentally.

In the spatial averaging model (and the spectral averaging model controlled by ITD), a passive mechanism is not possible, and the weighting must be based on an explicit representation of the binaural difference cue. The computational model of sound localization proposed by Middlebrooks (1992) employed spatial averaging controlled by ILD in weighting the two channels of monaural spectra information, whereas the model proposed by Macpherson (1998) employed spatial averaging controlled by ITD but not by ILD. Those models used only the shape of the spectrum at each ear, and not the absolute sound level. It can be assumed that the spectrum-to-location mapping stage of the spatial or spectral averaging model is level independent because for stimuli presented at sensation levels above ~30 dB and of duration greater than a few tens of ms, vertical plane localization is relatively unaffected by stimulus level (Vliegen and Van Opstal, 2004; Sabin *et al.*, 2005).

Although the passive spectral averaging model and the computational model implemented by Middlebrooks (1992) are consistent with the finding that changes in ILD can alter the weighting coefficients in the absence of changes in ITD, they are both inconsistent with the converse finding that ITD can drive weight changes with equal sound level at each ear. In the broadband ITD-bias condition, robust weight changes were produced by the application of ITD bias, but this manipulation had no effect on the energy of the signals at each ear nor on the interaural energy ratio. The computational model of Macpherson (1998), in which the binaural weighting was based solely on ITD, is inconsistent with the observed ILD-driven changes in weighting coefficients.

The effects of the ILD- and ITD-bias manipulations on the binaural weighting coefficients were mediated by the spectral ranges of the stimuli. In the broadband ILD-bias condition, the mean weighting pattern exhibited a small side-

to-side change in weights, whereas the same ILD-bias values resulted in much larger weight changes in the high-pass condition. Conversely, only in the broadband condition did ITD bias produce large changes in weights. Those results directly parallel the effects of spectral range on the weighting of ILD and ITD themselves in the determination of apparent lateral angle. For stimuli containing low-frequency (<1.5 kHz) components, such as the broadband noise bursts in the present study, ITD is the dominant lateral-angle cue, and ILD alone is relatively ineffective in displacing an auditory image from the midline (Wightman and Kistler, 1992, 1997b; Macpherson and Middlebrooks, 2002). For high-pass stimuli, which lack low-frequency components, ITD is a weak lateral-angle cue and ILD is the dominant determinant of apparent lateral angle.

The results of this study therefore show that stimulus spectral range interacts similarly with ITD- and ILD-driven changes in apparent lateral angle and with ITD- and ILD-driven changes in binaural spectral-cue weighting coefficients. That similarity suggests a connection between the process combining the binaural difference cues, which determine apparent horizontal position, and that combining the monaural spectral cues, which determine apparent vertical-plane location. Whether the weighting coefficients are causally derived from the apparent lateral angle, or whether both weights and perceived location are derived from a common or similar spectrum-dependent weighted average of ILD and ITD, cannot be determined from the present results. If the apparent lateral angle and the binaural difference cues could be controlled independently, the effect of each on the weighting coefficients could be independently established, but it is not obvious how this might be accomplished because ITD and ILD appear to be the *only* variables with a significant effect on apparent lateral angle (Macpherson and Middlebrooks, 2002). The present study does, however, indicate an intriguing correlation between perceived lateral location and the weighting of monaural spectral cues.

ACKNOWLEDGMENTS

The authors are very grateful to Robert Lutfi and two anonymous reviewers for comments on a previous version of this manuscript, to John Middlebrooks for advice and assistance, to Zekiye Onsan, Chris Ellinger, and Dwayne Vaillencourt for technical and administrative assistance, and to G. Christopher Stecker and Ian Harrington for helpful discussions. This work was supported by NIH Grants No. R01 DC00420, R03 DC006809, and P30 DC05188.

Golay, M. J. E. (**1961**). "Complementary series," IRE Trans. Inf. Theory **7**, 82–87.

Hammershøi, D., and Møller, H. (**1996**). "Sound transmission to and within the human ear canal," J. Acoust. Soc. Am. **100**, 408–427.

Hayes, W. L. (**1988**). *Statistics*, 4th ed. (Harcourt Brace Jovanovich, New York).

Hebrank, J. H., and Wright, D. (**1974**). "Spectral cues used in the localization of sound sources on the median plane," J. Acoust. Soc. Am. **56**, 1829–1834.

Hofman, P. M., and Van Opstal, A. J. (**1998**). "Spectro-temporal factors in two-dimensional human sound localization," J. Acoust. Soc. Am. **103**, 2634–2648.

Hofman, P. M., and Van Opstal, A. J. (**2003**). "Binaural weighting of pinna cues in human sound localization," Exp. Brain Res. **148**, 458–470.

Humanski, R. A., and Butler, R. A. (**1988**). "The contribution of the near and far ear towards localization of sound in the median plane," J. Acoust. Soc. Am. **83**, 2300–2310.

Jin, C., Corderoy, A., Carlile, S., and van Schaik, A. (**2004**). "Contrasting monaural and interaural spectral cues for human sound localization," J. Acoust. Soc. Am. **115**, 3124–3141.

Macpherson, E. A. (**1998**). "Spectral cue processing in the auditory localization of sounds with wideband non-flat spectra," Ph.D. thesis, University of Wisconsin—Madison.

Macpherson, E. A., and Middlebrooks, J. C. (**2002**). "Listener weighting of cues for lateral angle: the duplex theory of sound localization revisited," J. Acoust. Soc. Am. **111**, 2219–2236.

Martin, R. L., Patterson, M., and McAnally, K. I. (**2004**). "Utility of monaural spectral cues is enhanced in the presence of cues to sound-source lateral angle," J. Assoc. Res. Otolaryngol. **5**, 80–89.

Middlebrooks, J. C. (**1992**). "Narrow-band sound localization related to external ear acoustics," J. Acoust. Soc. Am. **92**, 2607–2624.

Middlebrooks, J. C. (**1999a**). "Individual differences in external-ear transfer functions reduced by scaling in frequency," J. Acoust. Soc. Am. **106**, 1480–1492.

Middlebrooks, J. C. (**1999b**). "Virtual localization improved by scaling nonindividualized external-ear transfer functions in frequency," J. Acoust. Soc. Am. **106**, 1493–1510.

Middlebrooks, J. C., Makous, J. C., and Green, D. M. (**1989**). "Directional sensitivity of sound-pressure levels in the human ear canal," J. Acoust. Soc. Am. **86**, 89–108.

Morimoto, M. (**2001**). "The contribution of two ears to the perception of vertical angle in sagittal planes," J. Acoust. Soc. Am. **109**, 1596–l603.

Musicant, A. D., and Butler, R. A. (**1984**). "The influence of pinnae-based spectral cues on sound localization," J. Acoust. Soc. Am. **75**, 1195–1200.

Sabin, A. T., Macpherson, E. A., and Middlebrooks, J. C. (**2005**). "Human sound localization at near-threshold levels," Hear. Res. **199**, 124–134.

Slattery, W. H. I., and Middlebrooks, J. C. (**1994**). "Monaural sound localization: Acute versus chronic impairment," Hear. Res. **75**, 38–46.

Vliegen, J., and Van Opstal, A. J. (**2004**). "The influence of duration and level on human sound localization," J. Acoust. Soc. Am. **115**, 1705–1713.

Wightman, F. L., and Kistler, D. J. (**1989a**). "Headphone simulation of free-field listening I: Stimulus synthesis," J. Acoust. Soc. Am. **85**, 858–867.

Wightman, F. L., and Kistler, D. J. (**1989b**). "Headphone simulation of free-field listening II: Psychophysical validation," J. Acoust. Soc. Am. **85**, 868–878.

Wightman, F. L., and Kistler, D. J. (**1992**). "The dominant role of low-frequency interaural time differences in sound localizations," J. Acoust. Soc. Am. **91**, 1648–1661.

Wightman, F. L., and Kistler, D. J. (**1997a**). "Factors affecting the relative salience of sound localization cues," in *Binaural and Spatial Hearing in Real and Virtual Environments*, edited by R. H. Gilkey and T. R. Anderson, (L. Erlbaum, Mahwah, NJ), pp. 1–23.

Wightman, F. L., and Kistler, D. J. (**1997b**). "Monaural localization revisited," J. Acoust. Soc. Am. **101**, 1050–1063.

Wightman, F. L., and Kistler, D. J. (**1999**). "Sound localization with unilaterally degraded spectral cues," J. Acoust. Soc. Am. **105**, 1162.

Zhou, B., Green, D. M., and Middlebrooks, J. C. (**1992**). "Characterization of external ear impulse responses using Golay codes," J. Acoust. Soc. Am. **92**, 1169–1171.

Transverse pressure distributions in a simple model ear canal occluded by a hearing aid test fixture

M. R. Stinson[a] and G. A. Daigle
Institute for Microstructural Sciences, National Research Council, Ottawa, Ontario K1A 0R6, Canada

(Received 9 November 2006; revised 12 March 2007; accepted 13 March 2007)

The sound field in a model ear canal with a hearing aid test fixture has been investigated experimentally and theoretically. Large transverse variations of sound pressure level, as much as 20 dB at 8 kHz, were found across the inner face of the hearing aid. Variations are greatest near the outlet port of the receiver and the vent port. Deeper into the canal, the transverse variations are less significant and, at depths greater than 4 mm, only a longitudinal variation remains. The model canal was cylindrical, 7.5 mm diameter, and terminated with a Zwislocki coupler to represent absorption by the human middle ear. The outer end of the canal was driven by the receiver in the hearing aid test fixture, with the acoustic output entering the canal through a 1 mm port. The hearing aid was provided with a 20-mm-long vent, either 1 or 2 mm in diameter. The sound field inside the canal was measured using a specially designed 0.2-mm-diam probe microphone [Daigle and Stinson, J. Acoust. Soc. Am. **116**, 2618 (2004)]. In parallel, calculations of the interior sound field were performed using a boundary element technique and found to agree well with measurements. © *2007 Acoustical Society of America.* [DOI: 10.1121/1.2722214]

PACS number(s): 43.66.Ts, 43.64.Ha, 43.20.Mv, 43.20.Rz [BLM] Pages: 3689–3702

I. INTRODUCTION

The sound field inside an ear canal occluded by a hearing aid can be spatially complex, with significant implications for the design of a sound delivery system. Often, the ear canal and its terminating eardrum impedance are treated as a simple compliant cavity (i.e., the 2 cc coupler). At frequencies above 2 kHz or so, longitudinal sound pressure variations arise, as standing wave patterns become apparent.[1,2] At frequencies above the canal resonance (4–6 kHz, for the occluded canal), the curvature and area function of the ear canal need to be taken into account but the sound field through most of the canal can still be described using a pseudo-one-dimensional approach.[3,4] Such an approach, though, will not be applicable in the immediate vicinity of the inner face of a hearing aid. There, with acoustical energy entering by way of a small port connected to the receiver, we have a situation similar to that described by Burkhard and Sachs,[5] in which sound entered a coupler cavity by way of a small port: Large variations of sound pressure, longitudinal and transverse, were measured using a probe microphone, signifying the presence of higher-order evanescent acoustic modes. Their Fig. 2 reveals a difference of 20 dB between two transverse positions a few millimeters apart, at 3.5 kHz. Given these results, large variations of sound pressure in the vicinity of the inner face of a hearing aid must be anticipated.

With sound pressure variations of this magnitude, the estimation of the eardrum sound pressure in the fitting of an aid could be compromised, whether using a calculated electroacoustic output of the receiver or probe measurements where the probe is located too near the inner face of the hearing aid. This suggests that some of the reported ineffectiveness of hearing aids[6,7] might be explained by uncertainties introduced by variations in sound pressure near the hearing aid. Recently, Ryan *et al.*[8] suggested the use of a second hearing aid microphone to sense the sound pressure inside canal, for reduction of the occlusion effect using active noise control. For such a scheme to be effective, the relationship between sound pressures at receiver and microphone positions, as part of the control loop, must be established.

In this paper, the spatial variations in sound pressure will be determined in a model ear canal occluded by a hearing aid test fixture, both experimentally and numerically. For this initial phase of investigation, a simple cylindrical canal was utilized, terminated with a Zwislocki coupler. The hearing aid test fixture contains receiver, vent, and an inner microphone. Measurements were made with a specially designed microprobe,[9] 0.2 mm in diameter. The results will confirm that there are, indeed, significant variations in sound pressure in the vicinity of the inner face of a hearing aid.

II. MODEL EAR CANAL

A. Experimental approach

Consider the representative hearing aid in a human ear canal as sketched in Fig. 1(a). Sound picked up by an outer microphone, located either in the mold of the aid or in a unit behind the ear, is processed and an electrical signal sent to the receiver, generating sound in the ear canal. To deal with the occlusion effect, a vent will generally be present, allowing some sound to radiate back outside the hearing aid. Following the suggestion of Ryan *et al.*,[8] we anticipate that a second, inner microphone could be useful and include such a microphone in our consideration. We are interested in the acoustical interactions among receiver, vent, and inner mi-

[a]Electronic mail: mike.stinson@nrc-cnrc.gc.ca

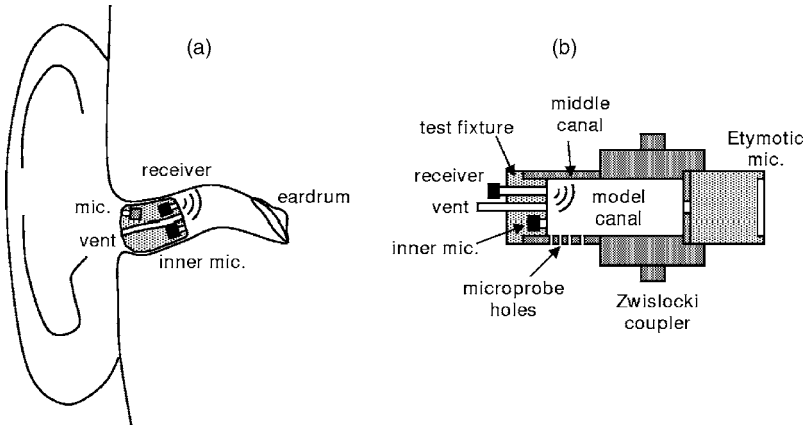

FIG. 1. (a) Sketch of a stylized hearing aid mounted in a human ear canal. A receiver produces sound and a port directs it into the ear canal; a vent is present, to reduce the occlusion effect; potentially, an inner microphone is also present to sense the interior sound field. (b) Sketch of the model ear canal used for this study. A hearing aid test fixture contains receiver, vent, and inner microphone.

crophone, so the ear canal sound field, particularly across the inner face of the hearing aid, is of primary interest.

An accurate measurement of this sound field inside real ear canals would be difficult. Instead, we will investigate the local sound field inside a model ear canal. The apparatus used is sketched in Fig. 1(b). A stainless steel test fixture represents the hearing aid: built into it are a receiver, a vent, and an inner microphone. The test fixture mates with the middle canal section, a straight tube with a circular hole of 7.5 mm diameter and length of 4 mm. The test fixture has been carefully machined to achieve a snug acoustically sealed fit in the middle canal section yet permit the fixture to rotate smoothly within the section. Forming the inner portion of the ear canal and providing an acoustical termination similar to that in human ear canals is a Zwislocki coupler.[10] The cylindrical cavity is 12.75 mm long and has a diameter of 7.44 mm. An Etymotic ER-11 microphone terminates the model canal, and provides a measurement of the sound pressure at this position. The total canal length in the model ear canal is 16.75 mm.

The interior sound field is measured with a microprobe system, making use of a probe having a 200 μm outside diameter. It is essential that microprobes of this size be used. Larger probes (such as that of the Bruel & Kjaer 4170 probe microphone) would affect the sound field they are measuring in this small volume and would not have, as will be seen later, the spatial resolution that is necessary. There are four holes in the middle canal section giving access to the microprobe. They permit measurements at four longitudinal positions, 0.15, 0.70, 1.07, and 2.07 mm, measured from the inner face of the hearing aid test fixture. At the first of these, the microprobe is as close to the face of the hearing aid as was practical. During measurements, the three holes not being used were sealed with clear tape.

The use of a simple cylindrical model canal permits the investigation of effect of vent and receiver without the added complexity of ear canal geometry.[3,4]

Two different test fixtures were used, one with a vent tube of 1 mm inner diameter (i.d.) and the other with a vent tube of 2.2 mm i.d. In both cases, the vent tube was 20 mm long and its opening into the canal located 2.01 mm from the center axis of the canal. The receiver was a Knowles EH-9833. It communicated with the interior of the canal by way of a 10 mm sound delivery tube of 1 mm i.d.; the center of this tube was located 2.49 mm from the canal axis. The inner microphone was a Knowles FG-3329, coupled to the canal volume through a port 0.5 mm long and 1 mm i.d.; the port center was 1.75 mm from the canal axis. The receiver, vent, and microphone ports are located in the test fixture in an approximately triangular arrangement.

The model ear canal and hearing aid test fixture are shown in the photograph of Fig. 2. The system is oriented so that the test fixture is upwards; vent and receiver are seen coming out of the top. The test fixture plugs into the middle canal section which, in turns, connects on to the Zwislocki coupler. The Etymotic microphone is below the coupler and not evident in this view. The microprobe can be seen as it approaches an access hole in the middle canal section. The whole assembly is mounted on a turntable. The microprobe system is rigidly mounted on a motorized translation stage; positioning along the direction of the probe is controlled to better than 0.01 mm. Two other translation stages, oriented perpendicularly, give complete three-dimensional (3D) control of the position of the microprobe.

Output from the microprobe and the Etymotic microphone were measured using a Stanford Research SR785 signal analyzer. Results were obtained at 1024 frequencies spaced logarithmically between 200 Hz and 10 kHz, for an input level to the receiver of 200 mV peak.

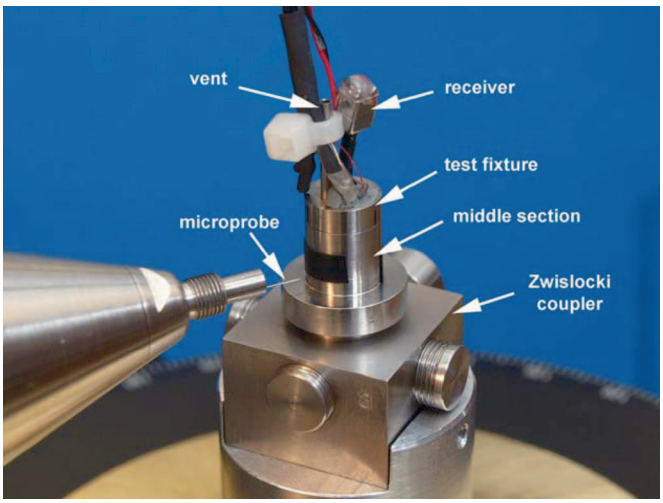

FIG. 2. Photograph of the model ear canal and hearing aid test fixture, with microprobe approaching an access hole.

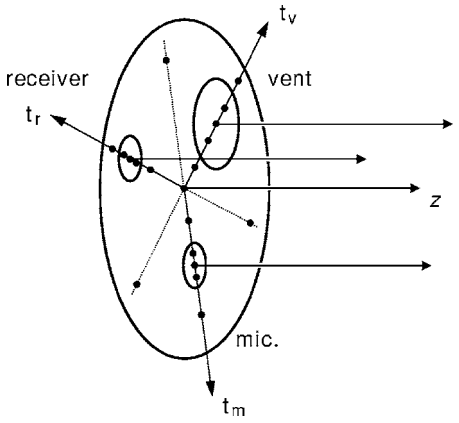

FIG. 3. Definition of the longitudinal and transverse measurement axes. The central z axis measures longitudinal position from the inner face of the hearing aid test fixture. Parallel axes, centered at receiver, vent, and inner microphone, were also used. The microprobe was translated along three transverse axes, one passing across the position of the receiver, one across the vent position, and one across the inner microphone position. For each transverse slice through the model ear canal, 19 measurement positions (indicated by the solid dots) were used.

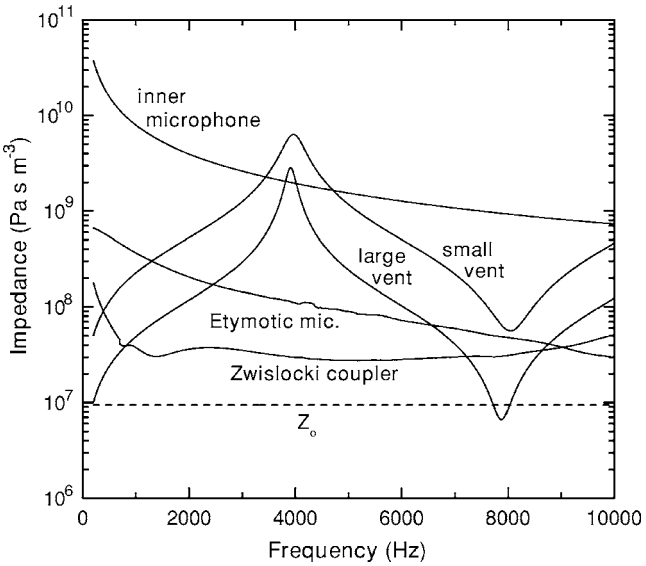

FIG. 4. Acoustic impedances of the Zwislocki coupler, the large and small vents, and the Etymotic and inner microphones. The impedances may be converted to cgs units noting that 1 cgs acoustic Ω is 10^5 Pa s m^{-3}. The characteristic impedance (94 cgs acoustic Ω) of the model ear canal is indicated by the dashed line.

B. Measurement locations

We wish to map out pressure variations within the model canal, particularly near the hearing aid test fixture. The longitudinal variations are determined along the horizontal lines shown in Fig. 3. The z axis shown follows the center of the canal, with position z being measured from the inner face of the hearing aid. Three other parallel axes are aligned with the centers of the receiver, inner microphone, and vent. Longitudinal measurements are obtained at the four z permitted by the microprobe access holes and at the innermost end of the canal (i.e., at the Etymotic microphone).

Transverse variations of sound pressure are obtained through cross sections at each longitudinal position. Translation of the microprobe into and out of an access hole gives us the sound pressure along one radial line in a cross section. By rotating the test fixture within the middle canal section, the variations along different radial lines relative to the test fixture can be obtained. In Fig. 3, the three transverse axes used, across receiver (t_r), vent (t_v), and the inner microphone (t_m), are shown. The solid dots show the 19 measurement positions used for each ear canal cross section. It should be noted that the microprobe can extend only 4 mm or so into the canal. To reach the final measurement points on each transverse axis, a rotation of the test fixture by 180° is required.

C. Load impedances

The interior sound field will be affected by the acoustical loads presented by the various elements in the model canal. Figure 4 compares the impedances of vents, Zwislocki coupler, Etymotic microphone, and inner microphone. Shown as the dashed line for comparison is the characteristic impedance Z_0 of the model canal.

The impedance of the Zwislocki coupler and the Etymotic microphone, at the terminating end of the canal, were determined experimentally. Acoustical signals were generated by the hearing aid receiver to produce a standing wave in the model canal. A Bruel & Kjaer 4170 probe microphone was inserted through the vent to measure the sound pressure along the length, and the pressure distribution analyzed to determine the terminating impedance due to both Zwislocki coupler and Etymotic microphone. Repeating the measurement with the Etymotic microphone replaced by a solid plug, the terminating impedance due solely to the coupler was obtained, and comparison of the results then gave the load impedance due to the Etymotic microphone. In the analysis, the effective position of the Zwislocki coupler impedance was assumed to be 3.6 mm from the inner end of the canal, based on inspection of the location of the four inner branches of the coupler.

The vent impedance was calculated, treating the vent as an acoustical transmission line (with viscous and thermal boundary layer effects included) with appropriate end corrections. The details of the calculation may be found in the Appendix. For both large and small vents, there is a minimum at about 8 kHz, due to a length resonance in the tube. The impedance at the minimum is still relatively high for the small diameter vent, but for the large vent it is lower than the other impedances and would be expected to have a significant effect on the canal sound field.

The acoustic input impedance for the inner microphone in the test fixture was not measured. Instead, a calculation using a PSPICE representation[11] gave the impedance shown in Fig. 4. Its magnitude is relatively large and would not be expected to be a factor.

III. THEORY

A. One-dimensional approximation

The diameter of the ear canal is small compared to the wavelength, for the frequencies (up to 10 kHz) being considered. A one-dimensional treatment can be effective in de-

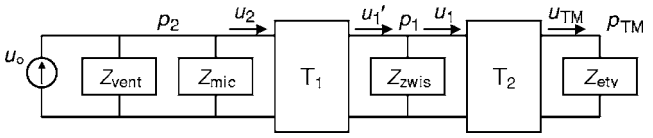

FIG. 5. Analogous circuit for the one-dimensional model of the ear canal. The acoustic excitation is provided by the volume velocity output of the receiver u_o.

scribing the interior sound fields over much of the ear canal length.[3,4] Near the inner face of the hearing aid, though, "spreading inertance" effects are expected,[5] leading to breakdown of the one-dimensional approximation. It will be useful to see how this approximation compares to the full 3D solution.

It is assumed, in this approximation, that there are no transverse variations so the pressure field can be described using a single spatial variable z shown in Fig. 1(b). The ear canal cross-sectional area is constant—plane wave solutions $\exp\pm ikz$ describe the propagation into and out of the canal. This leads to the analogous circuit representation shown in Fig. 5. The acoustical load at the innermost end of the model canal is Z_{Ety} due to the Etymotic microphone. A transfer matrix $\mathbf{T}_2$ relates sound pressure p_{TM} and volume velocity u_{TM} at this location to the sound pressure p_1 and volume velocity u_1 at the position of the four branches in the Zwislocki coupler, as

$$\begin{pmatrix} p_1 \\ u_1 \end{pmatrix} = \begin{pmatrix} \cos kL_1 & Z_0 \sin kL_1 \\ \sin kL_1/Z_0 & \cos kL_1 \end{pmatrix} \begin{pmatrix} p_{\mathrm{TM}} \\ u_{\mathrm{TM}} \end{pmatrix}, \tag{1}$$

where L_1 is the distance between innermost end and the four branch location, k is the wave number, and Z_0 is the characteristic impedance of the canal. Some of the volume velocity is tapped off by the Zwislocki impedance at the four branch location. The sound pressure p_2 at the hearing aid end of the canal and the volume velocity u_2 entering the canal are obtained from p_1 and u_1' through the transfer matrix $\mathbf{T}_1$,

$$\begin{pmatrix} p_2 \\ u_2 \end{pmatrix} = \begin{pmatrix} \cos kL_2 & Z_0 \sin kL_2 \\ \sin kL_2/Z_0 & \cos kL_2 \end{pmatrix} \begin{pmatrix} p_1 \\ u_1' \end{pmatrix}, \tag{2}$$

with L_2 being the distance from hearing aid to four branch location. The volume velocity output u_o from the hearing aid receiver is split between the acoustical loads presented by the vent (Z_{vent}), the inner microphone (Z_{mic}), and the canal. Standard circuit analysis yields all the quantities, given a specification for receiver output. Because u_o could not be measured easily and could not be calculated directly with any confidence, we rely on the calibration obtained from the 3D boundary element analysis. The assumed one-dimensional nature of the sound field prohibits any transverse sound field variations.

B. Three-dimensional solution

The full 3D calculation of sound field in the model ear canal is performed using the LMS SYSNOISE computational bundle. A boundary element method (BEM) is utilized, with direct, interior, and element options selected. A mesh of 2832 elements (12 triangular and 2820 quadrilateral) bounding the enclosed volume was generated using Altair HyperMesh and is shown in Fig. 6. The requirement that all elements have dimensions less than 1/8 wavelength for a BEM calculation is easily met, for the frequencies up to 10 kHz that will be used. The size of mesh elements at the hearing aid end of the canal is considerable smaller (0.15 mm or so) than elsewhere, for two reasons. First, smaller elements were needed to capture the geometrical details of the hearing aid components. Second, smaller elements are necessary to enable evaluation of interior sound pressures at points very close to the face of the hearing aid: After running the BEM code and establishing sound pressures and normal velocities on the bounding surface elements, interior sound fields are evaluated at selected locations, i.e., the field points. Field points must be no closer to the bounding surface than the local size of the surface mesh elements, else numerical artifacts arise.

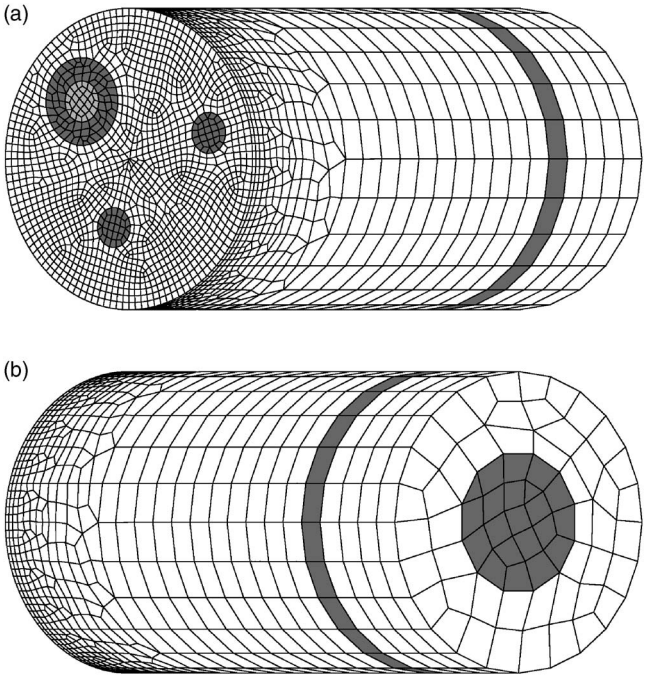

FIG. 6. The boundary element mesh used for the numerical calculations. In (a), the canal has been rotated to show the test fixture end of the canal. The elements representing the vent, receiver, and inner microphone are indicated by shading (upper left, upper right, and lower middle, respectively). For the vents, the inner light gray elements correspond to the small vent and the surrounding darker elements are added to form the large vent. The mesh elements are smaller at this hearing aid end of the canal to permit resolution of changes in sound pressure over small distances near the hearing aid. In (b), the terminating end of the model canal is shown. The shaded circular area corresponds to the Etymotic microphone. The band of elements around the circumference of the canal corresponds to the four-branch impedance of the Zwislocki coupler.

In Fig. 6(a), the model ear canal has been rotated to show the elements used in representing the inner microphone, the receiver, and the vents. The 28 elements representing the inner microphone have a total area of 0.765 mm^2 and the 28 elements representing the receiver outlet port, 0.812 mm^2. An inner circle of 28 elements, 0.812 mm^2 area, models the small vent, and an outer annulus of 76 elements, 2.872 mm^2 area, is added to form the large vent representation. In Fig. 6(b), the canal is rotated the other way to show the 21 elements, area 9.24 mm^2, that represent the terminat-

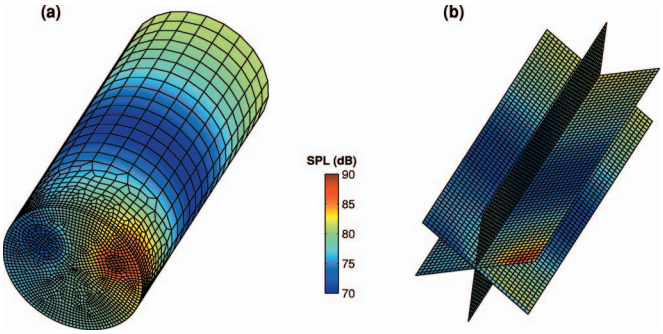

FIG. 7. Color plots showing the sound pressure level calculated using the boundary element method. The calculation is for the model canal with a large vent, at 8 kHz. In (a), the sound pressure level on the bounding surface of the model canal is shown. The longitudinal standing wave pattern along z is evident. In (b), the interior sound pressure level, on longitudinal slices, is shown. Higher SPL (red) are evident in the vicinity of the receiver, lower SPL (blue), near the vent.

ing Etymotic microphone. A band of 24 elements between $z=12.75$ mm and $z=13.55$ mm represents the impedance presented by the four branches of the Zwislocki coupler; these elements have a total area of 18.67 mm^2.

In SYSNOISE, impedance boundary conditions are handled by assigning specific admittance values to appropriate mesh elements. For each impedance component, given a target acoustical impedance Z_x and a total area A_x of representative mesh elements, a specific admittance $1/(A_xZ_x)$ is assigned to each element.

The elements representing the outlet port of the receiver are assigned a velocity: This is the acoustical excitation driving the system. A generic PSPICE model[11] gave an estimate u_o' for the driving volume velocity of the receiver, assuming an electrical input of 200 mV peak. A velocity u_o'/A_r, where A_r is the area of the outlet port of the receiver, was used in the BEM calculations. However, this estimate does not account for individual variations between receivers. Therefore, all calculations were normalized using a comparison of experiment to theory at one reference location, $z=0.15$ mm on the center axis. This effectively determines the actual receiver volume velocity u_o. The difference between u_o' and u_o was not insignificant, being as much as 10 dB and varying with frequency. This calibration was performed separately for the small and large vent cases—the two u_o obtained were the same, within 1 to 2 dB, except at 8 kHz where a 4 dB difference was observed.

A sample BEM calculation is shown in Fig. 7. For this example, the model canal with the large vent was used with a sound frequency of 8 kHz. Figure 7(a) shows the sound pressure on the bounding surface of the model ear canal. The different colors correspond to different sound pressure levels, as given by the color bar scale. A region of high SPL is noted at the position of the receiver port. At the vent, a region of low SPL is evident in this case. At other frequencies and for the small vent model canal, such regions of pronounced low vent SPL were not noted. In Fig. 7(b), the sound pressures at interior points on longitudinal slices are shown. There are clearly transverse variations in sound pressure near the face of the hearing aid. Deeper into the canal, these transverse variations die off, leaving only a longitudinal standing wave.

IV. RESULTS

The results of the measurements and numerical calculations are brought together here. It is noted that for the experiments, we have a large number of frequencies at a relatively small number of positions. For the calculations, we have a relatively small number of frequencies but results are generated at a large number of positions.

A. Frequency responses

At each measurement position, the sound pressure was determined as a function of frequency. In Fig. 8, the frequency response curves using the model canal with the large vent are collected together. The four panels Figs. 8(a)–8(d), show the results at the four transverse measurement planes, for z equal to 0.15, 0.70, 1.07, and 2.07 mm, respectively. Both magnitude and phase are shown. The different curves correspond to different transverse positions: For the solid curve, the probe tip was at the center axis of the model canal; for the dashed curve, the probe was over the inner microphone [see Fig. 3(a)]; for the dash-dotted curve, the probe was over the vent; and for the dotted curve, the probe was over the receiver. The numerical BEM calculations are plotted on these same graphs. Shown as open circles, triangles, inverted triangles, and squares are the calculated values for positions over the center axis, inner microphone, vent, and receiver. Note that all phases, calculation and experiment, are reported relative to the phase obtained at the $z=0.15$ mm center axis position.

Large transverse variations of SPL are evident: There is more than a 15 dB difference from the receiver position to the opposite side of the canal. There is a 10 dB difference between the vent position and the center axis near 8 kHz—this corresponds to the length resonance of the vent tube. The variations are most evident near the plane of the hearing aid, i.e., the $z=0.15$ mm position. As the probe moves away from the hearing aid surface, the curves come closer together, so by $z=2.07$ mm, variations are less than about 4 dB.

The agreement between experiment and numerical calculations is generally good, with differences typically less than 1 to 2 dB and 10° phase. Near 8 kHz, though, theory and experiment do differ by more. The sound field calculation is quite sensitive to the assumed vent impedance function near the 8 kHz resonance of the vent tube: Small differences (in the end corrections applied, for example) lead to a shift in the frequency response dip, yielding uncertainties of 5 dB or so at this frequency.

In Fig. 9, frequency response curves for the small vent model canal have been collected together. The definition of curves and symbols is the same as in Fig. 8. Significant transverse variations in SPL are noted for this model ear canal also. Agreement between numerical calculations and experiment is also good. The impedance for the small vent is larger and does not affect the ear canal sound field to the same extent as for the large vent case.

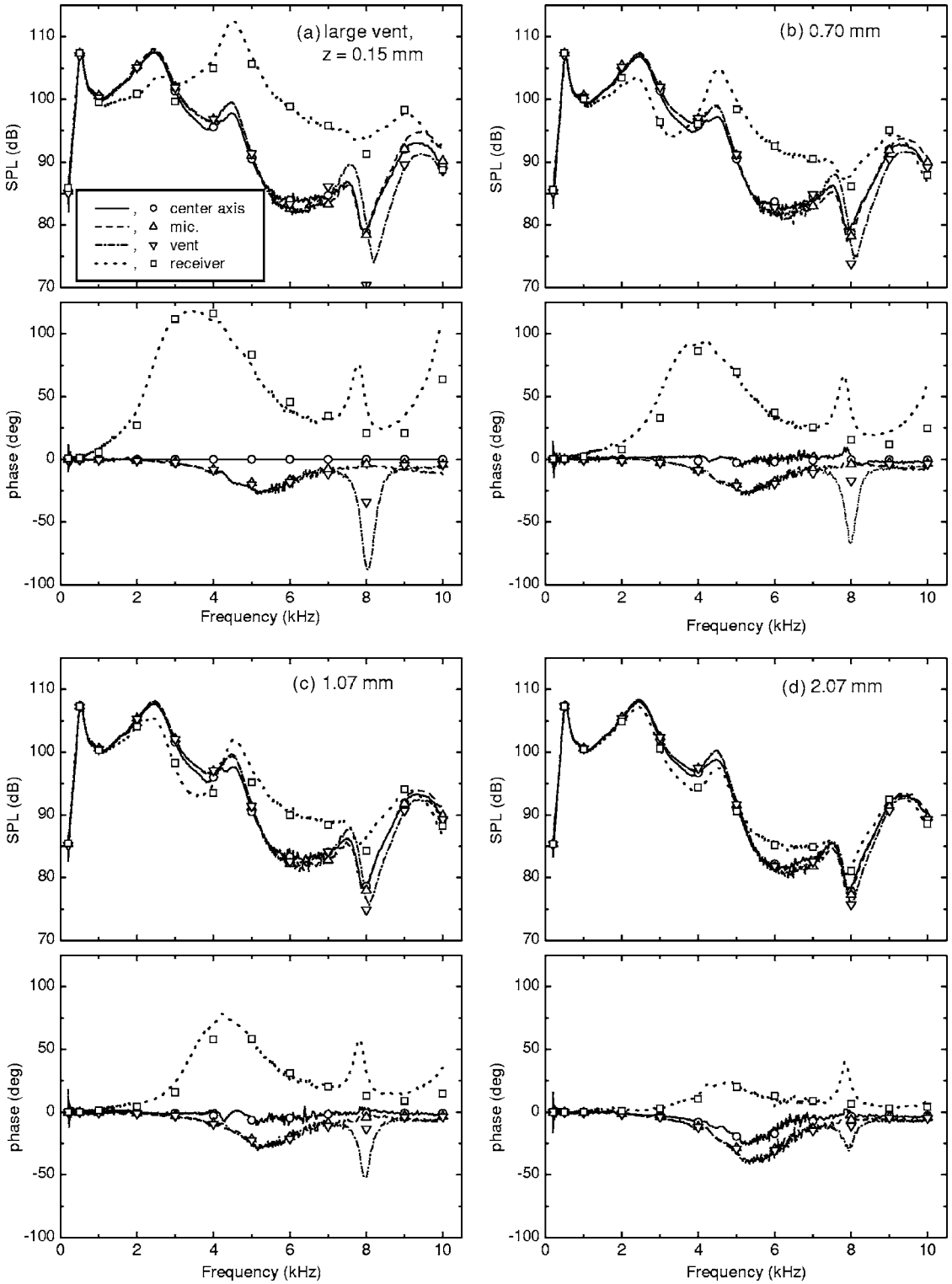

FIG. 8. Sound pressure, magnitude, and phase, as a function of frequency at various locations in the model canal having the large diameter vent. Measurements are shown with the curves, the numerical BEM results are shown with the symbols. The different panels (a)–(d) correspond to different longitudinal positions, z being the distance from the face of the hearing aid. On each panel, the difference curves correspond to different transverse locations, either at the center of the canal, over the inner microphone, over the vent, or over the receiver.

B. Longitudinal variations

The variation of sound pressure along the length of the model canals is displayed in Figs. 10 and 11, for the large vent and small vent cases, respectively. In each figure, the three panels (a), (b) and (c) show the results for 2, 4, and 8 kHz. The longitudinal variations are tracked along four different parallel lines, as indicated in Fig. 3. Note that for Figs. 10 and 11 (and the figures that follow these), symbols are used to represent the experimental data and continuous curves are used to represent the numerical calculations, a reversal of what was used for Figs. 8 and 9. The solid curve corresponds to the numerical prediction along the center axis

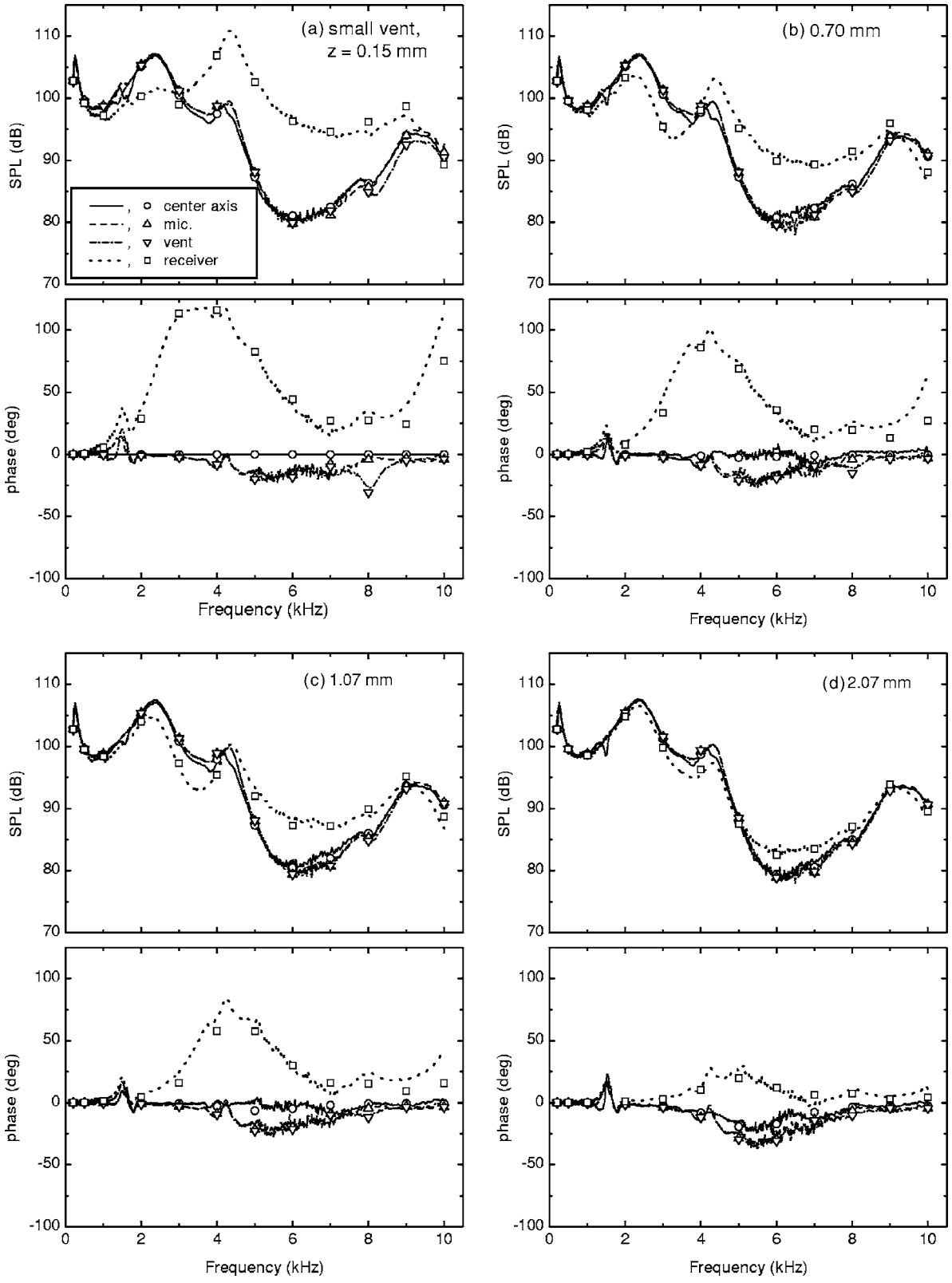

FIG. 9. Sound pressure, magnitude, and phase, as a function of frequency at various locations in the model canal having the small diameter vent. The definition of symbols and curves is the same as in Fig. 8.

of the canal; the corresponding experimental results are shown with the open circles. Along the line passing through the center of the inner microphone, we have the dashed curve for numerical predictions and open triangles for experiment. Similarly, for the line through the vent we have dash-dotted line and inverted triangles, and for the line through the receiver, dotted line and open squares. At the innermost end of the canal, $z=16.75$ mm, there is an additional experimental point obtained from the Etymotic microphone at this location.

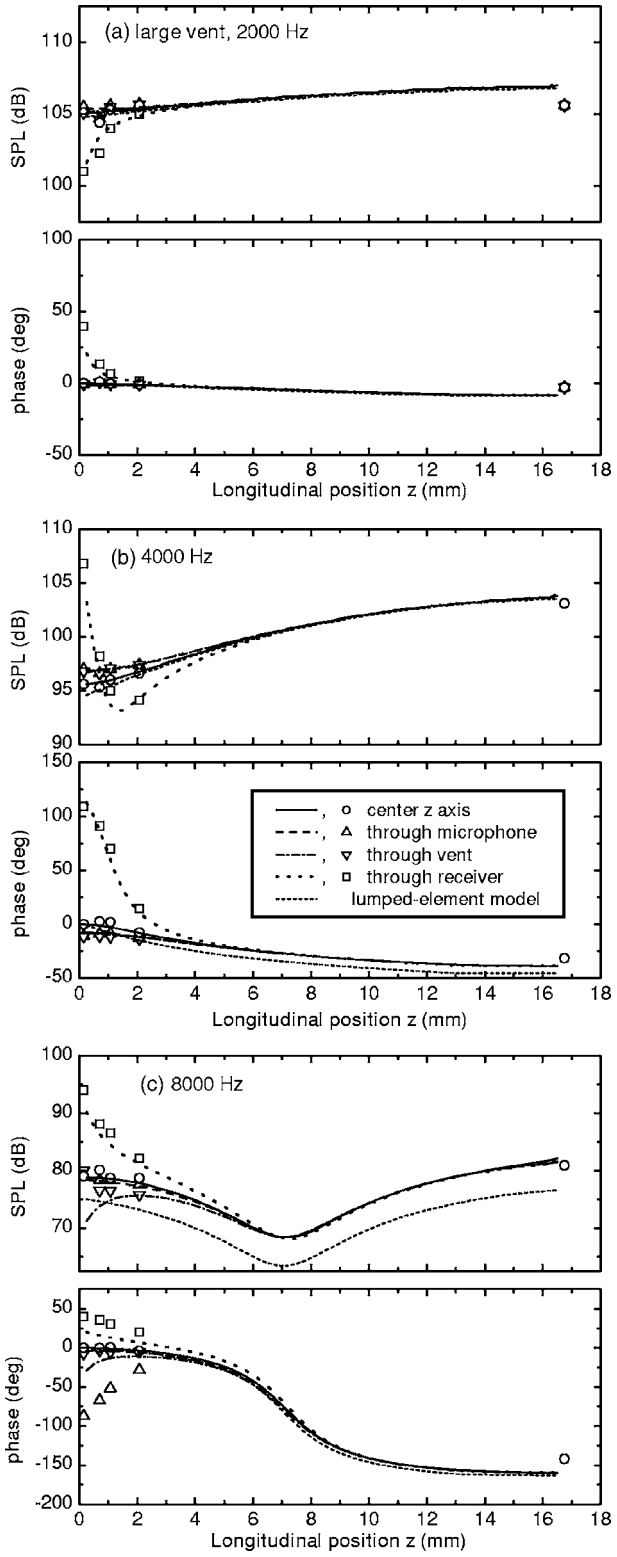

FIG. 10. Longitudinal variation in sound pressure, magnitude, and phase, in the large vent model ear canal. Panels (a), (b), and (c) correspond to frequencies of 2, 4, and 8 kHz. The different curves and symbols correspond to longitudinal lines located at different transverse positions, passing along the center z axis and through the inner microphone, vent, and receiver. The symbols indicate the measured results; the curves are the BEM calculations. The differences in sound pressure near the hearing aid for different transverse positions are evident. For longitudinal positions greater than 4 or 5 mm, all results converge. The dotted curve gives the prediction from a simple one-dimensional model.

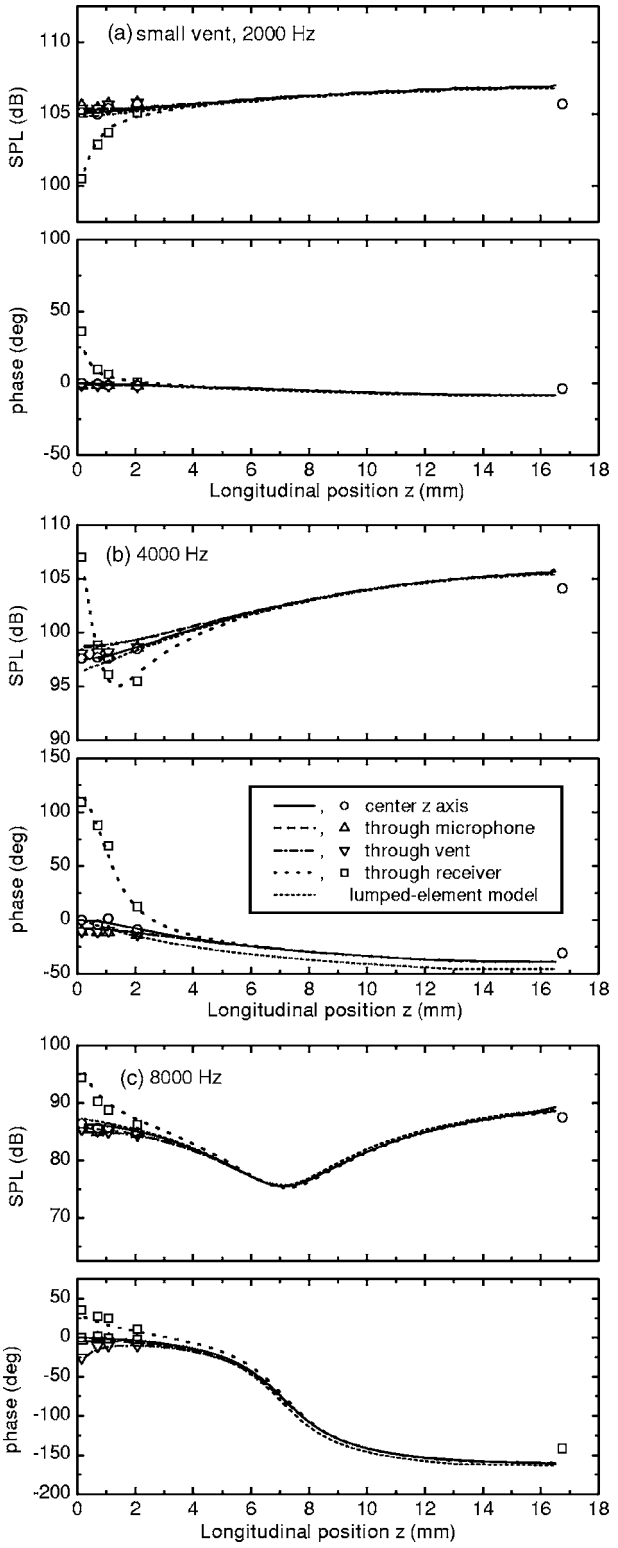

FIG. 11. Longitudinal variation in sound pressure, magnitude, and phase, in the small vent model ear canal. The definition of symbols and curves is the same as in Fig. 10.

The variation with transverse position is evident at the hearing aid end of each model canal. However, the variation decreases as longitudinal position increases, so that 3 or 4 mm away from the face of the hearing aid the four curves have converged and there is essentially plane wave propagation.

Also shown in Figs. 10 and 11 as dotted curves are the standing wave patterns predicted from the one-dimensional model described in Sec. III A. By its nature, it cannot predict the observed transverse variations near the hearing aid. In most cases, though, this model follows the center line results fairly well. The shape of the standing wave pattern at larger z is correctly obtained, not surprising since this shape is controlled by the impedances at the innermost end (Zwislocki coupler and Etymotic microphone). For the large vent case at 8 kHz, the one-dimensional model shows a constant shift in magnitude from the other results. This is a result of using the BEM-derived receiver output u_o coupled with the sensitivity of the sound field pressure distribution to the assumed vent impedance.

C. Transverse variations

The detailed transverse variations are examined more closely in the next series of figures. Referring to Fig. 3, the sound pressure along the three transverse axes will be reported, for the four transverse cross sections considered.

In Fig. 12, we show the variation of sound pressure along a transverse line that passes through the receiver, for the large vent case. Results for three frequencies, 2, 4, and 8 kHz, magnitude and phase, are presented in Figs. 12(a)–12(c). On each panel, there are numerical calculations shown by solid, dotted, dash-dotted, and dashed lines and experimental results shown by circle, triangle, inverted triangle, and square corresponding to the four positions z used for the transverse slices. The transverse variations of sound pressure become increasingly large as frequency increases. At 8 kHz, along the line closest to the face of the hearing aid (z=0.15 mm), there is a variation of nearly 20 dB. The 4 kHz results demonstrate that large variations in the phase component can also arise.

In Figs. 13 and 14, results are presented for transverse lines passing through the inner microphone and through the vent positions, for the large vent case. The definitions of the curves and the symbols are the same as for Fig. 12. Variations of sound pressure are not as great as observed in Fig. 12, but 5 dB effects at 8 kHz across the vent are observed. Across the inner microphone, variations are less than about 2 dB.

In Figs. 15–17, results are presented for the small vent case, examining transverse variations along lines passing through receiver, inner microphone, and vent positions, respectively. Curves, symbols, and panels are the same as for Fig. 12. Significant variations of sound pressure are observed for this model canal also. The biggest variations, up to 12 dB, are observed in the vicinity of the receiver. The variations across the vent are comparable to those across the inner microphone position, both being less than 2 or 3 dB. The acoustic input impedance of the small vent is relatively large compared to the other impedances involved (Fig. 4) so it is not expected to contribute significant absorption

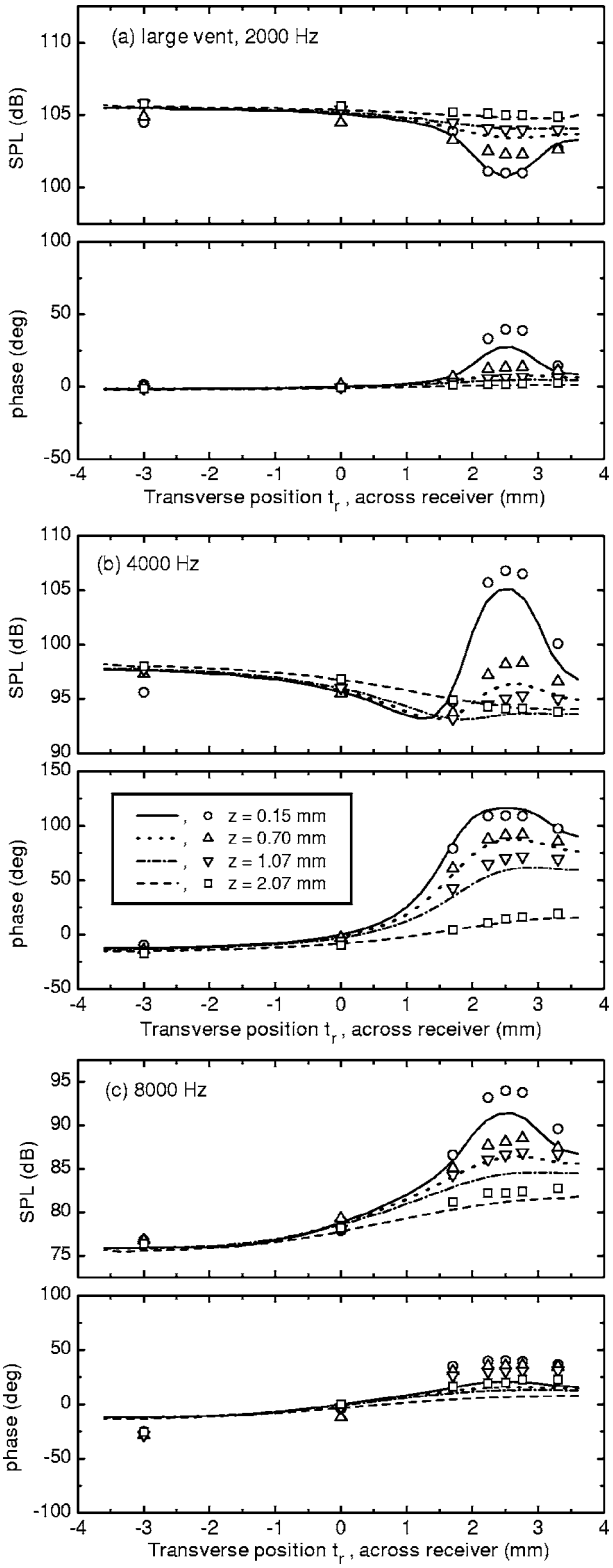

FIG. 12. Transverse variation in sound pressure, magnitude, and phase, along a line that passes across the receiver position (as shown in Fig. 3), for the large vent model ear canal. For the abscissa, the canal center axis is at 0 mm and the receiver is centered about 2.49 mm. Panels (a), (b), and (c) correspond to frequencies of 2, 4, and 8 kHz. The different curves and symbols correspond to data at different longitudinal positions, z=0.15, 0.70, 1.07, and 2.07 mm. The symbols indicate the measured results, the curves are the BEM calculations.

V. DISCUSSION

The largest transverse variations in sound pressure occur in the vicinity of the receiver. Sound radiating from the port of the receiver into the canal spreads roughly hemispherically and dominates the local sound field. There are also

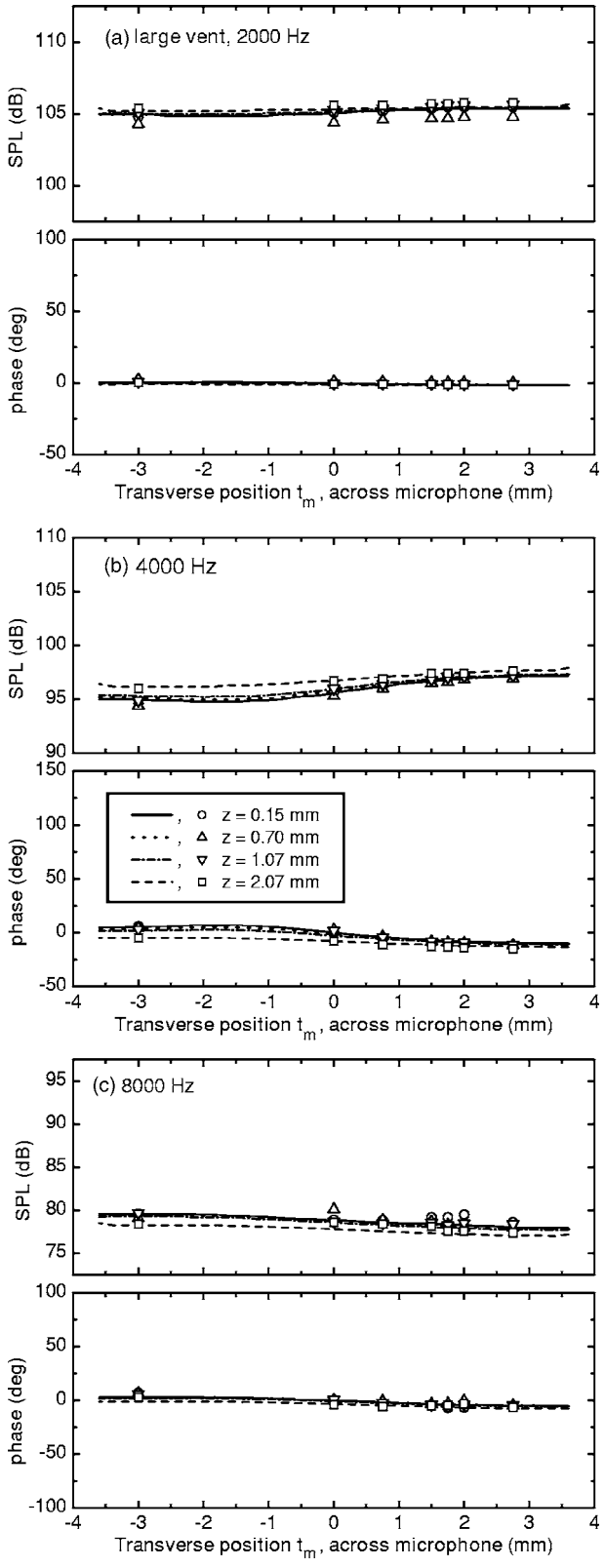

FIG. 13. Transverse variation in sound pressure, magnitude, and phase, along a line that passes across the inner microphone position, for the large vent model ear canal. The microphone is centered about −1.75 mm. (??) The definition of symbols and curves is the same as in Fig. 12.

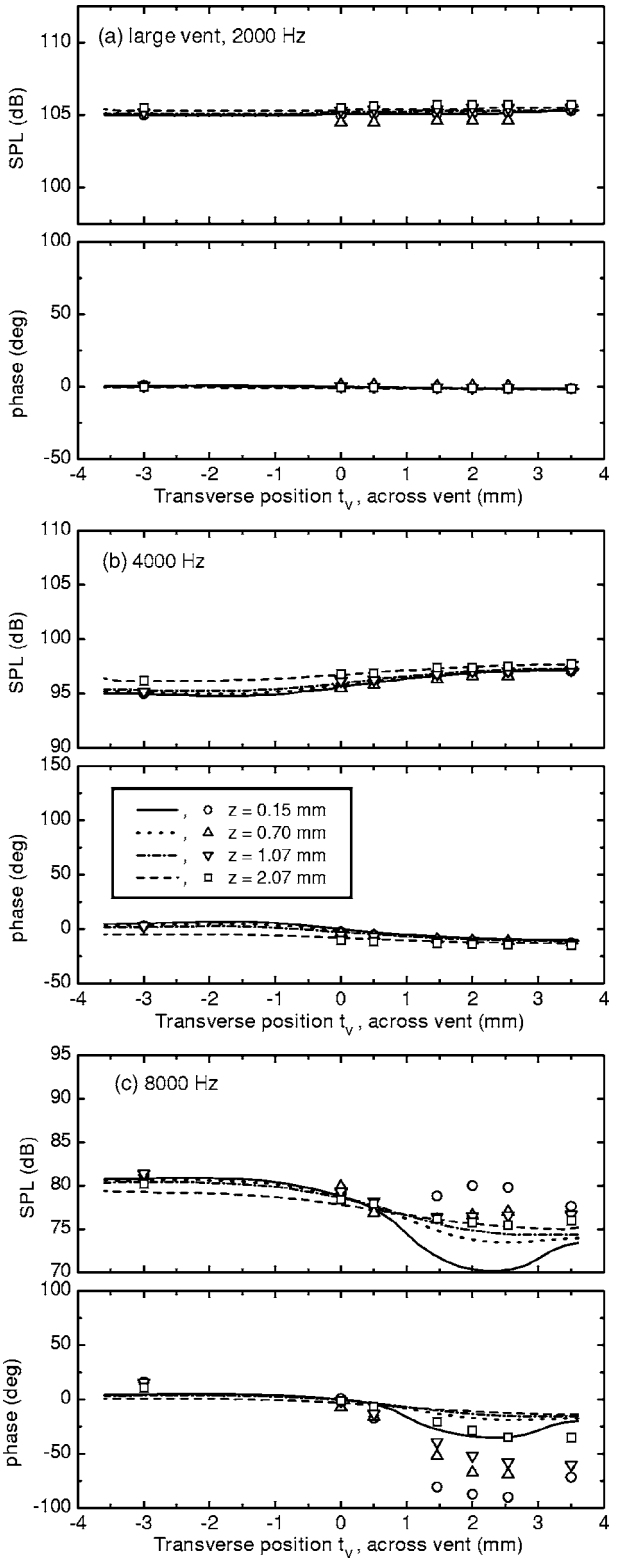

FIG. 14. Transverse variation in sound pressure, magnitude, and phase, along a line that passes across the vent position, for the large vent model ear canal. The vent is centered about 2.01 mm. The definition of symbols and curves is the same as in Fig. 12.

significant variations in sound pressure near the vent at 8 kHz. For this frequency, in our model experiments, the vent impedance is low (see Fig. 4) and there will be significant acoustic energy lost from the canal interior and radiated out through the vent. Real hearing aids will present a different vent impedance, and variations proximal to the vent would arise at different frequencies. The inner microphone presents a relatively high impedance that does not affect the canal sound field to any obvious extent.

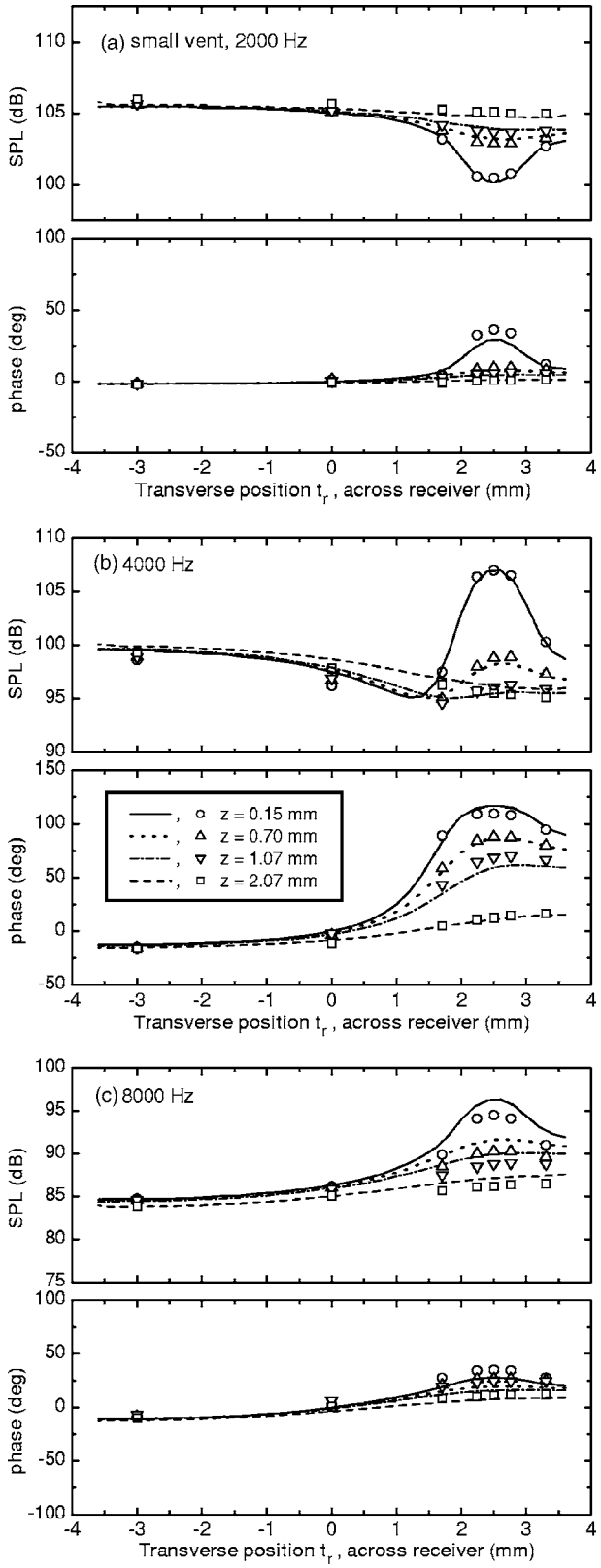

FIG. 15. Transverse variation in sound pressure, magnitude, and phase, along a line that passes across the receiver position, for the small vent model ear canal. The receiver is centered about 2.49 mm. The definition of symbols and curves is the same as in Fig. 12.

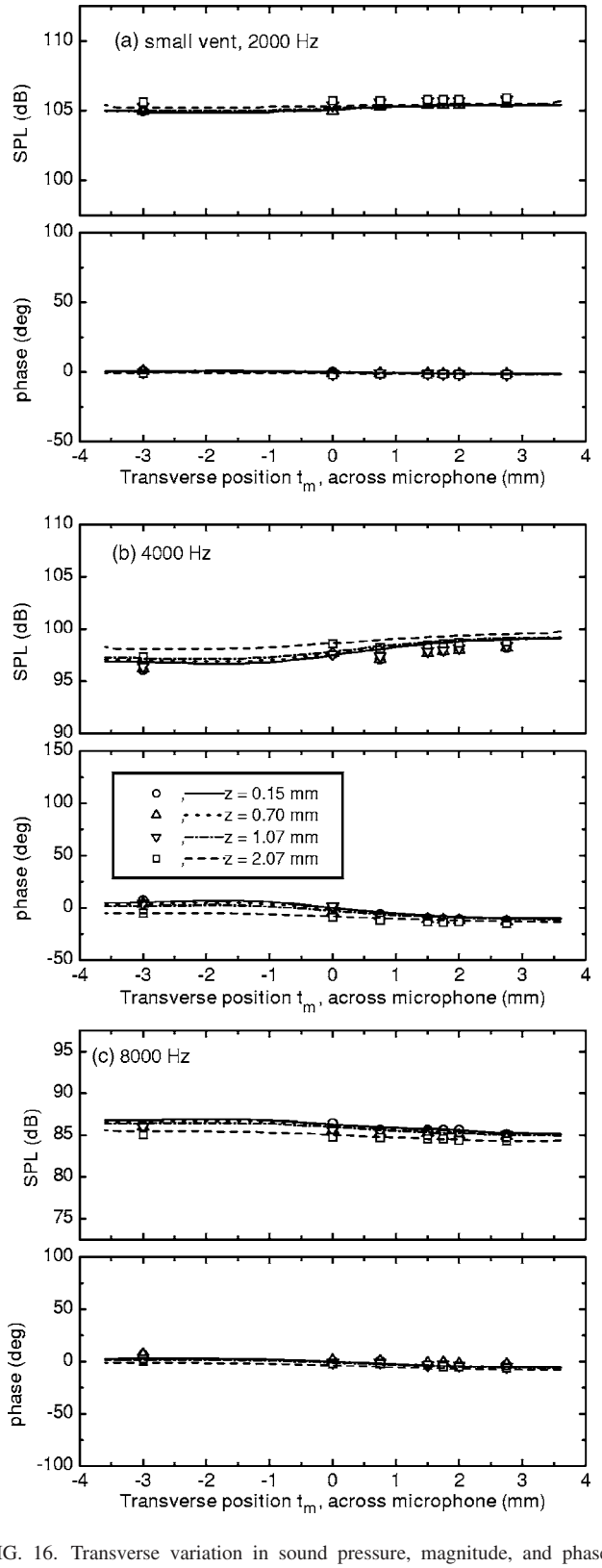

FIG. 16. Transverse variation in sound pressure, magnitude, and phase, along a line that passes across the inner microphone position, for the small vent model ear canal. The microphone is centered about −1.75 mm. (??) The definition of symbols and curves is the same as in Fig. 12.

The numerical results are in reasonable agreement with the experimental results, both showing the same qualitative features overall. There are some differences, though. They can be attributed to two main factors. First, the sound pressure shows very large spatial variations in the vicinity of the hearing aid, where the microprobe is located. An uncertainty of 0.1 mm in the positioning of the microprobe can lead to

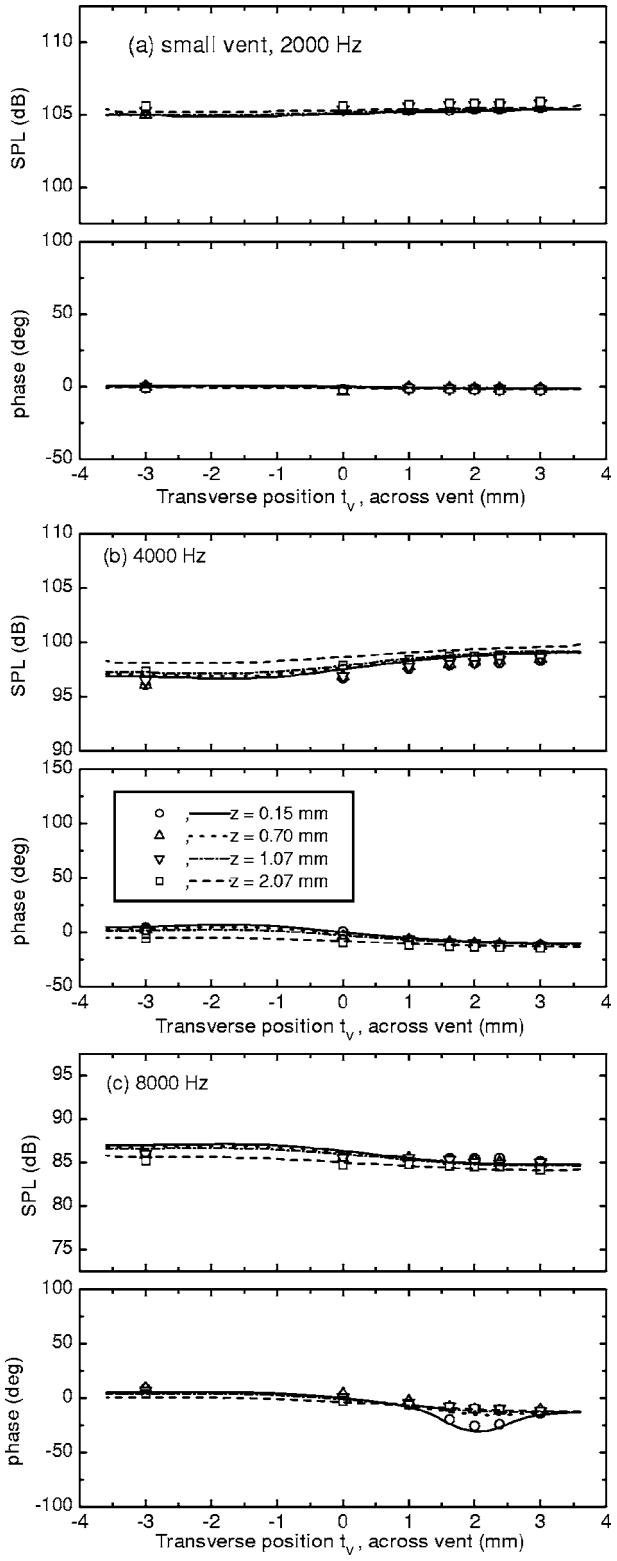

FIG. 17. Transverse variation in sound pressure, magnitude, and phase, along a line that passes across the vent position, for the small vent model ear canal. The vent is centered about 2.01 mm. The definition of symbols and curves is the same as in Fig. 12.

an uncertainty of 1 to 2 dB in the regions of large sound pressure gradients. The other factor is the uncertainty in the vent impedance assumed for the numerical calculations, near the 8 kHz resonance, for the large vent model. Subsidiary calculations show that slight modifications of the vent impedance (e.g., adjusting the length of the vent tube or the end corrections used) can lead to quite different sound pressure distributions near the vent.

The simple one-dimensional model cannot predict the transverse variations of sound pressure. But away from the face of the hearing aid, more than 3 to 4 mm into the canal, the sound field is essentially one dimensional and the simple model does a reasonable job. In all the longitudinal results of Figs. 10 and 11, this model gives the correct *shape* of the standing wave pattern, i.e., the location of the standing wave minima and their depth relative to the maxima. This is not surprising because the shape of the standing wave patterns, for both simple model and the BEM calculations, is controlled by the terminating impedance (Zwislocki coupler and Etymotic microphone). In most of the cases shown, the one-dimensional and BEM models are also in agreement about the overall SPL. However, for the large vent model at 8 kHz, the one-dimensional model prediction is 4 dB lower than the BEM result. This is the situation for which the vent impedance is smaller than the characteristic impedance of the canal. Since the one-dimensional model effectively places this impedance at the same position as the receiver, the shunting effect on the receiver output will be overestimated, as compared to the true 3D case for which the vent and receiver are separated by several millimeters.

VI. CONCLUDING REMARKS

Large transverse variations of sound pressure level, up to 20 dB, are found in the vicinity of the inner face of a hearing aid, both through measurements on a model canal and through numerical calculations using a boundary element method. The most dramatic variations are immediately adjacent to the face of the hearing aid, particularly near the receiver outlet port. About 3 or 4 mm away from the hearing aid, into the canal, the transverse variations are negligible and only the longitudinal standing wave is present. These results are consistent with the work by Burkhard and Sachs[5] on the sound field in couplers.

The use of a 0.2-mm-diam probe microphone[9] was critical in these experiments. A larger probe would not have been able to resolve the large variations of sound pressure levels occurring over distances of less than 1 mm.

Ryan *et al.*[8] have suggested the use of a second microphone in a hearing aid to sense the canal sound field for use in adaptive feedback control of noise and occlusion effect. Clearly, the large transverse variations of SPL observed here are part of the feedback loop and will need to be accommodated.

The introduction of a second microphone could also be useful ultimately in predicting the sound pressure generated at the eardrum. Such a prediction, though, would need to accommodate the variations of sound pressure over the inner face of the hearing aid that have been described in this paper. The prediction would depend on the relative positions of vent, receiver, and inner microphone and would require some knowledge of the ear canal geometry. The model ear canal

used in this current study was a simple uniform cylinder. An extension to investigate spatial variations of sound pressure for real ear canal geometries is under way.

ACKNOWLEDGMENTS

Discussions with James Ryan and Steve Armstrong of Gennum Corp. are acknowledged. The authors thank René St. Denis for performing the sound pressure measurements, in appreciation of his painstaking efforts maneuvering 0.2 mm probes into position, and Randy Hartwig for making the subsidiary impedance measurements.

APPENDIX

This vent impedance calculation accounts for viscous and thermal boundary layer effects in the vent tube and end effects at either end of the tube. From Egolf[12] or Iberall,[13] we relate the sound pressure and volume velocity (p_2 and u_2) at the outer end of the tube to the sound pressure and volume velocity (p_1 and u_1) at the end inside the canal, through a transfer matrix

$$\begin{pmatrix} p_2 \\ u_2 \end{pmatrix} = \begin{pmatrix} \cosh \Gamma L' & Z \sinh \Gamma L' \\ \sinh \Gamma L'/Z & \cosh \Gamma L' \end{pmatrix} \begin{pmatrix} p_1 \\ u_1 \end{pmatrix}, \tag{A1}$$

where L' is the effective length of the tube, and propagation constant Γ and characteristic impedance Z are given by

$$\Gamma = \frac{i\omega}{c} \left(\frac{T_\alpha}{T_\beta} \right)^{1/2}, \tag{A2}$$

$$Z = \frac{\rho c}{\pi a^2 (T_\alpha T_\beta)^{1/2}}, \tag{A3}$$

where ρ is the density of air, c is the sound speed, a is the inner radius of the tube, and ω is angular frequency. The T_α and T_β terms describe the thermal and viscous boundary layer effects, respectively,

$$T_\alpha = 1 + 2(\gamma - 1) \frac{J_1(\alpha a)}{\alpha a J_0(\alpha a)} \tag{A4}$$

and

$$T_\beta = 1 - \frac{2J_1(\beta a)}{\beta a J_0(\beta a)}, \tag{A5}$$

where

$$\alpha = \left(-i \frac{\rho \omega N_{\mathrm{Pr}}}{\mu} \right)^{1/2} \tag{A6}$$

and

$$\beta = \left(-i \frac{\rho \omega}{\mu} \right)^{1/2}. \tag{A7}$$

In these equations, μ is the viscosity of air (1.82×10^{-5} N s m^{-2}), N_{Pr} is the Prandtl number (0.702), and γ is the specific heat ratio (1.4). We have used 346 m/s for the sound speed and 1.185 kg/m^3 for the air density, appropriate for the experimental conditions.

The effective length of the tube L' is greater than the physical length L due to end effects.[14] On the canal side, a flanged end condition is assumed, contributing an end correction $\delta_2 = 8a/3\pi$. The outer end of the vent tube was unflanged, contributing a correction[15] $\delta_1 = 0.613a$. This gives

$$L' = L + (0.613 + 8/3\pi)a. \tag{A8}$$

Since there are viscous and thermal losses within the tube, this treatment effectively applies the lengthening to these as well, consistent with a previous treatment of orifice impedance.[16,17]

The outer end of the tube is unflanged and the radiation of sound can be described by the inviscid theory of Levine and Schwinger.[15] For a tube diameter that is small relative to the wavelength, the radiation impedance is computed assuming a piston source having the same diameter, giving[18,19]

$$Z_{\mathrm{rad}} = R_{\mathrm{rad}} + iX_{\mathrm{rad}} = \frac{\rho c}{\pi a^2} [0.25(ka)^2 + 0.613ika]. \tag{A9}$$

The reactive component X_{rad} acts to increase the effective length of the tube and has already been included in the calculation of L'. The resistive component corresponds to acoustic energy radiated into free space and is handled by setting $p_1 = R_{\mathrm{rad}} u_1$.

The vent impedance is then calculated as

$$Z_{\mathrm{vent}} = \frac{p_2}{u_2} = Z \frac{R_{\mathrm{rad}} \cosh \Gamma L' + Z \sinh \Gamma L'}{R_{\mathrm{rad}} \sinh \Gamma L' + Z \cosh \Gamma L'}. \tag{A10}$$

[1] B. W. Lawton, "A survey of the sound field within the occluded ear canal," Proc. Inst. Acoust., (1979).

[2] M. R. Stinson, E. A. G. Shaw, and B. W. Lawton, "Estimation of acoustical energy reflectance at the eardrum from measurements of pressure distribution in the human ear canal," J. Acoust. Soc. Am. **72**, 766–773 (1982).

[3] M. R. Stinson, "The spatial distribution of sound pressure within scaled replicas of the human ear canal," J. Acoust. Soc. Am. **78**, 1596–1602 (1985).

[4] M. R. Stinson and G. A. Daigle, "Comparison of an analytic horn equation approach and a boundary element method for the calculation of sound fields in the human ear canal," J. Acoust. Soc. Am. **118**, 2405–2411 (2005).

[5] M. D. Burkhard and R. M. Sachs, "Sound pressure in insert earphone couplers and real ears," J. Speech Hear. Res. **20**, 799–807 (1977).

[6] H. G. Mueller and R. A. Bentler, "Fitting hearing aids using clinical measures of loudness discomfort levels: An evidence-based review of effectiveness," J. Am. Acad. Audiol **16**, 461–472 (2005).

[7] R. A. Bentler, "Effectiveness of directional microphones and noise reduction schemes in hearing aids: A systematic review of the evidence," J. Am. Acad. Audiol **16**, 473–484 (2005).

[8] J. G. Ryan, B. Rule, and S. W. Armstrong, "Reducing the occlusion effect with active noise control," J. Acoust. Soc. Am. **119**, 3385 (2006).

[9] G. A. Daigle and M. R. Stinson, "Design and performance of a microprobe attachment for a $\frac{1}{2}$-in. microphone," J. Acoust. Soc. Am. **120**, 186–191 (2006).

[10] M. D. Burkhard and R. M. Sachs, "Anthropometric manikin for acoustic research," J. Acoust. Soc. Am. **58**, 214–222 (1975).

[11] PSPICE model for hearing aid receiver, at Knowles Electronics website, http://www.knowleselectronics.com/engineering/reports.asp./Analogsr8.zip, viewed November 9, 2006.

[12] D. P. Egolf, "Techniques for modeling the hearing aid receiver and associated tubing," in *Acoustical Factors Affecting Hearing Aid Performance*, edited by G. A. Studebaker and I. Hochberg (University Park, Baltimore, 1980), pp. 297–319.

[13] A. S. Iberall, "Attenuation of oscillatory pressures in instruments," J. Res. Natl. Bur. Stand. **45**, 85–108 (1950).

[14] J. W. Strutt (Lord Rayleigh), *Theory of Sound*, 2nd ed. (Dover, New York, 1945), Vol. **II**, Sec. 487.

[15] H. Levine and J. Schwinger, "On the radiation of sound from an unflanged

circular pipe," Phys. Rev. **73**, 383–406 (1948).
[16]G. B. Thurston, "Periodic fluid flow through circular tubes," J. Acoust. Soc. Am. **24**, 653–656 (1952).
[17]M. R. Stinson and E. A. G. Shaw, "Acoustic impedance of small, circular orifices in thin plates," J. Acoust. Soc. Am. **77**, 2039–2042 (1985).
[18]C. T. Molloy, "Response peaks in finite horns," J. Acoust. Soc. Am. **22**, 551–557 (1950).
[19]A. D. Pierce, *Acoustics, An Introduction to Its Physical Principles and Applications* (Acoustical Society of America, New York, 1989), pp. 358–359.

Focused intracochlear electric stimulation with phased array channels[a)]

Chris van den Honert[b)]
Cochlear Americas, 400 Inverness Parkway, Englewood, Colorado 80112

David C. Kelsall
Colorado Neurological Institute–Rocky Mountain Cochlear Implant Center, 601 East Hampden Avenue, Suite 530, Englewood, Colorado 80110

(Received 1 August 2006; revised 17 January 2007; accepted 6 March 2007)

A method is described for producing focused intracochlear electric stimulation using an array of N electrodes. For each electrode site, N weights are computed that define the ratios of positive and negative electrode currents required to produce cancellation of the voltage within scala tympani at all of the $N-1$ other sites. Multiple sites can be stimulated simultaneously by superposition of their respective current vectors. The method allows N independent stimulus waveforms to be delivered to each of the N electrode sites without spatial overlap. Channel interaction from current spread associated with monopolar stimulation is substantially eliminated. The method operates by inverting the spread functions of individual monopoles as measured with the other electrodes. The method was implemented and validated with data from three human subjects implanted with 22-electrode perimodiolar arrays. Results indicate that (1) focusing is realizable with realistic precision; (2) focusing comes at the cost of increased total stimulation current; (3) uncanceled voltages that arise beyond the ends of the array are weak except when stimulating the two end channels; and (4) close perimodiolar positioning of the electrodes may be important for minimizing stimulation current and sensitivity to measurement errors. © *2007 Acoustical Society of America.*
[DOI: 10.1121/1.2722047]

PACS number(s): 43.66.Ts, 43.64.Me [RYL] Pages: 3703–3716

I. INTRODUCTION

Multichannel cochlear implants exploit the tonotopic organization of the cochlea by mapping audio energy in specific frequency bands to stimulation at corresponding "places" along the spiral array of auditory nerve fibers. In this context the term "channel" is often used interchangeably in referring to either (1) the frequency band with its associated signal processing path or (2) a set of electrodes among which currents are passed with specified ratios, in order to excite nerve fibers at a single spatially restricted "place" within the cochlea (e.g., monopolar, bipolar, or tripolar). For clarity we have adopted the term "processing channel" where the first sense is intended, but use the generic term "channel" only in the second sense.

Although stimulation through one channel is intended to excite at a single place, the actual locus of neural excitation can be broad and complex due to spread of current throughout the conducting fluids and tissues of the cochlea. Nevertheless, a modest degree of spatial specificity is possible even with a simple monopolar channel, although the extent of excitation is generally broad (van den Honert and Stypulkowski, 1987; Bierer and Middlebrooks, 2002; Snyder *et al.*, 2004; Cohen *et al.*, 2003). Despite this breadth many listeners are able to discriminate spatial shifts in the place of stimulation of a fraction of a millimeter when a single channel is activated in isolation (Busby *et al.*, 1994; Busby and Plant, 2005; Collins *et al.*, 1997; Donaldson *et al.*, 2005), probably by detecting movement of either the centroid or the skirts of the excited region.

However, when two or more channels are activated concurrently, the locus of excitation is not the simple union of their individual loci because of the nonlinearity of the neural excitation process. Instead, neurons that fall outside of the individual loci (i.e., those that would not respond to any one channel) may nevertheless be excited by the summed current fields. This results in the well-known phenomenon of "channel interaction." Channel interaction can lead to unpredictable loudness fluctuations, and smearing of the spatial representation of spectrum (Shannon, 1983b; Fu and Nogaki, 2005; Boex *et al.*, 2003; Stickney *et al.*, 2006).

Almost all successful stimulation strategies in clinical use today circumvent channel interaction by using sequential pulsatile stimulation (Skinner, 1994; Wilson *et al.*, 1991; Skinner *et al.*, 2002; Bosco *et al.*, 2005). Such strategies deliver stimulation through only one (usually monopolar) channel at any given instant. Stimulation is time-multiplexed across channels at rates high enough to produce a fused percept for the listener. Although monopoles excite broad spatial extents of the nerve array, spatial/spectral information is nevertheless adequately conveyed, presumably by the trajectory of the centroids of those ranges. In this way a reasonable

[a)]Portions of this work were presented at the 2005 Conference on Implantable Auditory Prostheses, Pacific Grove, CA, August 2005.
[b)]Electronic mail: cvdhonert@cochlear.com

representation of a sound's time-varying magnitude spectrum can be appreciated by the listener, such that formant peaks can be perceived.

Prior to the widespread adoption of sequential-monopolar stimulation for clinical use, several more complex channel configurations were explored with the objective of producing more focused electrical fields and hence narrower stimulation regions (Clark *et al.*, 1979; Walsh *et al.*, 1980; Van Compernolle, 1985a, b; Busby *et al.*, 1994; Miyoshi *et al.*, 1996; Kral *et al.*, 1998; Jolly *et al.*, 1996). Except for strategies where simultaneous stimulation of multiple channels was obligatory, the complex channel configurations that have been tested clinically have not resulted in speech understanding gains (Loizou *et al.*, 2003; Stickney *et al.*, 2006; Xu *et al.*, 2005; Zwolan *et al.*, 1996; Pfingst *et al.*, 1997; von Wallenberg *et al.*, 1995; Mens and Berenstein, 2005).

A renewed interest in stimulus focusing has developed in recent years, motivated in part by the demands of strategies that seek to preserve within-channel fine temporal patterns of stimulation (van Hoesel and Tyler, 2003; Clopton *et al.*, 2002; Nie *et al.*, 2005; Grayden *et al.*, 2004; van den Honert, 1990). These strategies deliver stimuli at instants in time determined from features of a processing channel's audio filter output (e.g., peaks or zero crossings). In general, those instants in time are asynchronous across channels, and so cannot satisfy the nonsimultaneity constraint of sequential stimulation. This means that stimulus pulses inevitably will overlap in time. An arbitration scheme can be adopted to discard stimuli that would overlap with others, but there is a more fundamental problem. The temporal patterns themselves are corrupted by overlap between regions of excitation. That is, due to the overlapping stimulus regions, any given neuron will generally be driven by pulses from multiple channels, receiving the composite of multiple temporal patterns rather than one. To prevent this, the stimulation regions must be narrowed.

A second motivation for revisiting the topic of stimulus focusing stems from the need for improved representation of periodicity (musical) pitch by cochlear implants. Besides its importance for music, pitch recognition is important for segregating one voice from multiple competitors (Brokx and Nooteboom, 1982; Scheffers, 1983; Chalika and Bregman, 1989; Summerfield and Assmann, 1990; Drullman and Bronkhorst, 2004) and for transmission of semantic information in tonal languages (Chao, 1968; Wang, 1973; Xu, 2003). Perhaps ironically, periodicity pitch is only weakly conveyed by the repetition rate of an electrical stimulus, and then only for an isolated fundamental (as opposed to a chord) and over a limited frequency range (Shannon, 1983a; Tong and Clark, 1985; Pijl and Schwartz, 1995; Laneau and Wouters, 2006; Carlyon *et al.*, 2002). There is evidence that fine spatial resolution may be necessary (if not sufficient) for recognition of periodicity pitch, at least for resolved harmonics (Oxenham *et al.*, 2004; Shackleton and Carlyon, 1994; Carlyon and Shackleton, 1994; Shamma and Klein, 2000). Significantly improved focusing of the stimulation will be needed if these detailed spatial patterns are to be recreated with a cochlear implant.

The work reported here builds upon the "current deconvolution" approach described by Van Compernolle (1985a, b) and subsequently elaborated by Townshend and White (1987). Van Compernolle's method inverted the current-spread functions of a set of monopoles in order to calculate a combination of currents that would maximize stimulation at selected places and minimize it elsewhere. This method was impractical at the time because (1) the inversion was over-specified (thus inexact) in that it determined stimulus strength at more places than the number of electrodes; (2) spread was measured imprecisely using a psychophysical estimate; and (3) contemporary electrodes had broad spread functions, resulting in impractically high compensating currents. Rodenhiser and Spelman (1995) extended Van Compernolle's work, determining spread functions from a lumped-constant model of the cochlea in place of psychophysical measures. Although less time consuming, their approach does not incorporate specific spread functions of an individual subject.

The 22-electrode Nucleus® Contour Softip™ perimodiolar array (Roland, 2005) overcomes limitations (1) and (3) above. To address limitation (2) we measured subject-specific spread functions in the form of a matrix of transimpedance values between stimulated and idle electrodes. These values were then used to compute an inverse matrix of transadmittance values. Each column of the inverse matrix constitutes a vector of numerical weights defining the current contribution from each electrode that is required to produce a nonzero intrascalar voltage at one, and only one, place. So, each such vector of weights defines a channel in the second sense of the opening paragraph above. This focusing process is loosely analogous to that of a phased array radar system in that both exploit constructive and destructive interference from multiple sources in order to modulate the spatial properties of the resulting field. Thus we have adopted the term "phased array" channels to describe the weight vectors. The purpose of this paper is to describe the stimulus focusing method, analyze its limitations, and validate its application with physical data.

II. METHODS

A. Subjects and electrodes

Subjects were three adult users of an experimental cochlear prosthesis that contained no implanted electronic components (Fig. 1). It consisted of a 22-contact intracochlear Nucleus® Contour Softip™ perimodiolar electrode array and two extracochlear electrodes located below the temporalis muscle. Wires from all electrodes were terminated directly to a connector housed in a percutaneous titanium pedestal mounted to the skull behind the ear. For take-home use, each subject was equipped with an externally worn receiver-stimulator that was electrically equivalent to a Nucleus® Contour Advance™ implant. The receiver-stimulator plugged into the external surface of the pedestal and was driven by cable connection from an ESPrit 3G™ behind-the-ear processor.

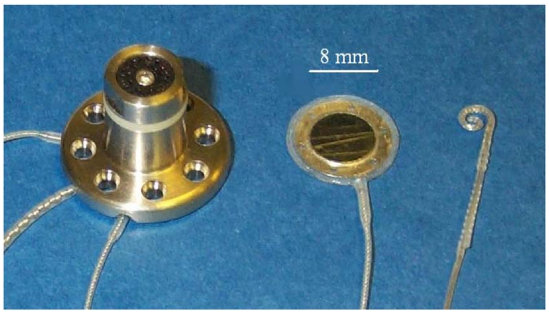

FIG. 1. (Color online) Experimental implant. The titanium percutaneous pedestal houses a 24-pin connector. Extracochlear electrodes include a platinum disc and a ball electrode (not shown). The spiral intracochlear array of 22 electrodes is shown on the right.

B. Stimulation equipment

During experimental sessions in the laboratory the processor and receiver/stimulator were disconnected, and each of the 22 intracochlear and 2 extracochlear electrodes was connected to a dedicated current source [Fig. 2(a)]. Input signals to the 24 current sources were provided from an array of high-speed 16-bit D/A converters under control of an embedded DSP board within a host PC. This configuration provided simultaneous independent control of the current through every intracochlear and extracochlear electrode.

A surface electrode on the wrist was connected to a current-limited driven ground lead that was maintained equipotential with the current source isolated circuit ground [Fig. 2(b)]. This electrode kept the subject referenced to the stimulation circuitry. It also provided a return path for any net error current that might flow if a hardware or software fault were to cause the instantaneous algebraic sum of implanted

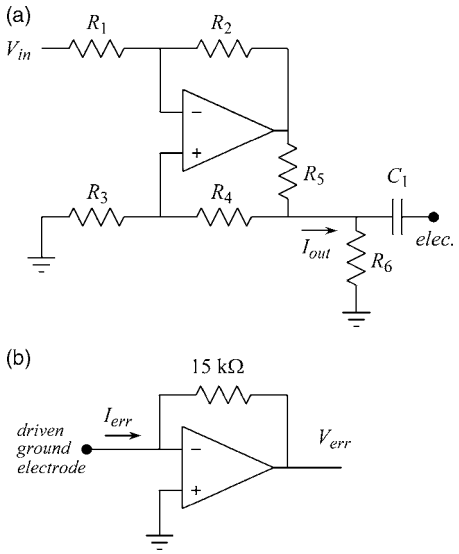

FIG. 2. (a) Schematic diagram of the enhanced Howland current source [see Ross *et al.* (2003) for circuit analysis]. To maximize output impedance, resistor R_2 is trimmed such that $R_1/R_2=R_3/R_4$. Series capacitor C_1 (100 nF) blocks direct current to the electrode. Shunt resistor R_6 (5 MΩ) provides dc stability. (b) Schematic diagram of the driven ground circuit. Current flowing through the driven ground electrode is limited by the 15 kΩ resistor in conjunction with the ±15 V maximum output of the operational amplifier. Output voltage is proportional to the error current flowing through the driven ground electrode.

electrode currents to become nonzero. Small transient error currents were expected due to finite precision of gain and speed matching across current sources. However, if current through the driven ground exceeded ±50 μA for more than 5 μs, an error condition was flagged, causing immediate interruption of all subject connections.

C. Transimpedance measures

When a monopolar current is passed through an intracochlear electrode a corresponding voltage can be measured at any other intracochlear electrode. The transimpedance between the two electrodes is defined as the ratio of the voltage to the current. For frequencies of interest here (≤20 kHz) the cochlear fluids and tissue are essentially resistive (Spelman *et al.*, 1982; Clopton and Spelman, 1982; Vanpoucke *et al.*, 2004a; van den Honert, unpublished data) such that the voltage is instantaneously proportional to the current to a close approximation, and the reactive component of the transimpedance can be ignored. Nevertheless, we retain the term transimpedance in preference to transresistance as a reminder that the analysis below could be carried out with complex arithmetic if reactive components were significant.

For each intracochlear electrode, a 3-second 50-Hz train of monopolar biphasic pulses (40 μs/phase) was delivered at the maximum comfortable current level. Because the transimpedance values are constants of proportionality, each can be measured with a current of any convenient intensity. The use of the maximum comfortable level allowed us to maximize the signal-to-noise ratio in the voltage measurements. Return current was divided equally between the two extracochlear electrodes via their corresponding current sources. Using an isolated oscilloscope with 10 MΩ input impedance, the voltage pulse at each of the 21 remaining electrodes was measured with respect to the current source ground (which was equipotential with the wrist electrode). The 40-μs phase width was selected to be long enough for the voltage pulse waveform to plateau, but short enough to permit relatively high currents while remaining comfortable. Current pulse amplitudes ranged from 192 to 469 μA, with a mean value of 383 μA. The amplitude of the voltage pulse was measured from an average of 32 traces, yielding a residual noise level that was approximately 5 mV peak-to-peak.

For stimulating electrode j and measuring electrode i, transimpedance z_{ij} has units of V/mA (kΩ) and is given by

$$z_{ij} = v_i/i_j, \tag{1}$$

where v_i is the measured plateau voltage and i_j is the amplitude of the current pulse. In this way a 22×22 matrix $\mathbf{Z}_m$ of transimpedance values was determined for each subject:

$$Z_m = \begin{bmatrix} z_{1,1} & z_{1,2} & \cdots & z_{1,22} \\ z_{2,1} & z_{2,2} & \cdots & z_{2,22} \\ \vdots & \vdots & \ddots & \vdots \\ z_{22,1} & z_{22,2} & \cdots & z_{22,22} \end{bmatrix}. \tag{2}$$

Each column j of the matrix represents the spread function for stimulation through electrode j, with a peak at the diagonal value z_{jj}.

TABLE I. Transimpedance values for subject S1 (V/mA). Stimuli were 3-s 50-Hz trains of monopolar biphasic (40 μs/phase) pulses at maximum comfortable intensity. Transimpedance was computed from the ratio of averaged peak voltage at the measuring electrode (re: neutral wrist electrode) to peak current through the stimulating electrode. Values on the diagonal were extrapolated from surrounding values (see text for details).

Stimulating electrode	Voltage measurement electrode																					
	1	2	3	4	5	6	7	8	9	10	11	12	13	14	15	16	17	18	19	20	21	22
1	**1.66**	1.19	0.76	0.63	0.56	0.53	0.50	0.47	0.45	0.44	0.42	0.41	0.41	0.39	0.38	0.37	0.37	0.36	0.35	0.36	0.36	0.35
2	1.21	**1.99**	1.41	0.83	0.64	0.58	0.55	0.52	0.50	0.47	0.46	0.45	0.44	0.47	0.40	0.40	0.39	0.39	0.38	0.38	0.37	0.38
3	0.76	1.38	**2.25**	1.51	0.81	0.67	0.61	0.55	0.53	0.51	0.49	0.47	0.45	0.45	0.43	0.42	0.41	0.40	0.40	0.40	0.39	0.39
4	0.63	0.82	1.53	**2.25**	1.34	0.85	0.71	0.62	0.58	0.55	0.53	0.51	0.49	0.48	0.46	0.45	0.45	0.43	0.42	0.42	0.42	0.42
5	0.54	0.61	0.81	1.34	**2.30**	1.67	1.04	0.72	0.65	0.60	0.57	0.55	0.52	0.52	0.48	0.47	0.47	0.45	0.45	0.44	0.43	0.44
6	0.51	0.56	0.67	0.84	1.66	**3.35**	2.14	0.92	0.75	0.65	0.62	0.58	0.56	0.55	0.52	0.50	0.50	0.48	0.47	0.47	0.47	0.51
7	0.50	0.53	0.60	0.71	1.05	2.11	**3.23**	1.40	0.91	0.71	0.66	0.62	0.59	0.56	0.54	0.52	0.51	0.50	0.48	0.49	0.47	0.48
8	0.45	0.49	0.54	0.61	0.72	0.92	1.41	**2.31**	1.56	0.85	0.73	0.67	0.63	0.60	0.56	0.54	0.53	0.51	0.49	0.49	0.48	0.48
9	0.45	0.48	0.53	0.57	0.66	0.76	0.91	1.57	**2.24**	1.21	0.84	0.73	0.67	0.64	0.61	0.57	0.56	0.54	0.53	0.53	0.51	0.51
10	0.41	0.44	0.49	0.52	0.58	0.64	0.69	0.84	1.19	**1.57**	1.19	0.82	0.71	0.65	0.62	0.59	0.57	0.54	0.52	0.52	0.51	0.51
11	0.41	0.43	0.47	0.50	0.55	0.61	0.65	0.72	0.82	1.19	**1.56**	1.06	0.78	0.71	0.66	0.62	0.60	0.58	0.55	0.55	0.54	0.53
12	0.41	0.43	0.46	0.49	0.54	0.58	0.61	0.67	0.72	0.84	1.08	**1.33**	0.97	0.78	0.72	0.67	0.64	0.61	0.58	0.57	0.57	0.56
13	0.39	0.44	0.44	0.47	0.51	0.55	0.57	0.62	0.67	0.72	0.78	0.96	**1.19**	0.96	0.78	0.71	0.67	0.64	0.61	0.60	0.58	0.58
14	0.40	0.50	0.45	0.48	0.52	0.55	0.58	0.61	0.65	0.69	0.72	0.79	0.98	**1.17**	0.93	0.79	0.74	0.69	0.66	0.64	0.62	0.61
15	0.36	0.39	0.41	0.43	0.47	0.49	0.52	0.55	0.58	0.61	0.65	0.70	0.77	0.90	**1.08**	0.89	0.76	0.69	0.64	0.62	0.61	0.60
16	0.37	0.39	0.41	0.43	0.47	0.49	0.51	0.55	0.57	0.60	0.63	0.67	0.73	0.78	0.91	**1.19**	0.99	0.78	0.70	0.68	0.65	0.64
17	0.35	0.38	0.41	0.43	0.46	0.49	0.50	0.53	0.55	0.58	0.61	0.64	0.68	0.72	0.78	0.99	**1.33**	1.04	0.75	0.72	0.68	0.66
18	0.36	0.38	0.41	0.43	0.46	0.48	0.50	0.52	0.55	0.57	0.59	0.62	0.66	0.69	0.72	0.80	1.05	**1.30**	0.92	0.78	0.73	0.71
19	0.35	0.37	0.39	0.41	0.44	0.46	0.47	0.49	0.52	0.53	0.56	0.58	0.61	0.64	0.66	0.70	0.76	0.90	**1.30**	1.04	0.81	0.74
20	0.36	0.38	0.39	0.42	0.45	0.46	0.48	0.50	0.52	0.54	0.56	0.58	0.60	0.63	0.65	0.69	0.73	0.78	1.06	**1.33**	1.03	0.83
21	0.35	0.37	0.39	0.42	0.43	0.46	0.47	0.48	0.51	0.53	0.54	0.56	0.60	0.61	0.63	0.65	0.68	0.72	0.82	1.01	**1.25**	1.03
22	0.35	0.37	0.40	0.42	0.45	0.52	0.48	0.49	0.52	0.53	0.55	0.56	0.58	0.60	0.62	0.64	0.66	0.70	0.76	0.83	1.03	**1.24**

The peak values on the diagonal of $\mathbf{Z}_m$ could not be measured directly due to polarization of the electrode carrying the current pulse. The electrochemical potential required to force a current pulse across the series impedance of the metal-electrolyte interface increases the measured voltage.[1] This precludes using the same electrode both to deliver current and to measure potential in the cochlear fluid. It is possible to estimate the diagonal values using a lumped-constant model, but published data (Vanpoucke *et al.*, 2004b) suggest that the complexity of this approach can lead to substantial errors.[2] Instead we estimated values on the diagonal of $\mathbf{Z}_m$ by simple linear extrapolation from surrounding values in the matrix. We used the maximum among the four values extrapolated from adjacent pairs in the matrix as follows:

$$z_{jj} = \max(2z_{j+1,j} - z_{j+2,j}, \quad 2z_{j-1,j} - z_{j-2,j}, \quad 2z_{j,j+1} - z_{j,j+2}, \quad 2z_{j,j-1} - z_{j,j-2}). \tag{3}$$

For $j \leq 2$ and $j \geq 21$ only two adjacent pairs were available for extrapolation. In those cases the two arguments of the max function that referenced elements outside of the matrix boundaries were omitted.

The maximum extrapolated value was used for a practical reason. We felt that it was preferable not to underestimate the sharpness of the spread function, as this would result in unnecessarily high peak currents in the focused stimuli. The effect of errors introduced by the extrapolation is considered below in Sec. II F.

Table I shows the matrix $\mathbf{Z}_m$ for one subject. Close inspection reveals that it is very nearly diagonally symmetric. Indeed, for a three-port network where a single node serves as both the return current path and the voltage measurement reference, the reciprocity theorem holds that diagonal symmetry obtains exactly—i.e., $z_{ij}=z_{ji}$ for all i and j (Van Valkenburg, 1960). In practice, due to the same polarization issue discussed above, the extracochlear electrodes could not serve as both return current path and voltage reference. Instead, the surface electrode on the wrist served as the reference. The observed deviations from diagonal symmetry were small and comparable to the noise in the measurements. This implies that the tissue surrounding the return electrodes was essentially neutral, or equipotential with the wrist, and that the voltage gradients of consequence occur within and about the cochlea. We therefore assumed the true matrix was in fact diagonally symmetric, and that deviations from diagonal symmetry were attributable to noise in the measurements. In order to reduce this noise we averaged diagonally opposite elements to compute a new transimpedance matrix,

$$\mathbf{Z} = \frac{1}{2}(\mathbf{Z}_m + \mathbf{Z}_m^T) \tag{4}$$

where $\mathbf{Z}_m^T$ denotes the transpose of $\mathbf{Z}_m$. Matrix $\mathbf{Z}$ is diagonally symmetric by definition.

D. Computation of channel weights

Superposition of fields in a linear medium allows calculation of the voltages $\mathbf{v}=(v_1, v_2, \ldots, v_{22})$ that arise at the

electrode sites when an arbitrary vector of 22 simultaneous currents $\mathbf{i}_e=(i_{e_1},i_{e_2},\ldots,i_{e_{22}})$ is delivered through the electrodes:

$$\mathbf{v}=\mathbf{Z}\mathbf{i}_e. \tag{5}$$

The matrix notation of Eq. (5) is equivalent to a set of 22 simultaneous equations expressing voltage at each place as a linear combination of 22 currents. We refer to this as solving the forward problem.

In order to focus the stimulating field we seek to solve the inverse problem—viz. given a desired vector of stimulating voltages[3] $\mathbf{v}_d=(v_{d_1},\ldots,v_{d_{22}})$, we seek to determine the required vector of electrode currents that will produce them. Provided that it is nonsingular, the square matrix $\mathbf{Z}$ can be inverted. Then solving Eq. (5) for $\mathbf{i}_e$ yields

$$\mathbf{i}_e=\mathbf{Z}^{-1}\mathbf{v}_d=\mathbf{Y}\mathbf{v}_d, \tag{6}$$

which represents the solution of the inverse problem. The elements of the inverse matrix $\mathbf{Y}$ are transadmittance values with units of mA/V (mS).

Consider the special case $\mathbf{v}_d=(0,\ldots,0,v_{d_p},0,\ldots,0)$, where we seek to produce the specified voltage v_{d_p} at a single place p, and exactly zero volts at every other place. This represents optimally focused single-place stimulation. The required vector of currents is the product of scalar v_{d_p} and column p of $\mathbf{Y}$:

$$\mathbf{i}_e=v_{d_p}\begin{bmatrix} y_{1p} \\ \vdots \\ y_{22p} \end{bmatrix}. \tag{7}$$

The transadmittance elements $(y_{1_p}\cdots y_{22_p})$ of column p constitute a set of 22 signed weights that define the current ratios needed to produce a stimulating voltage only at place p. Thus each column of $\mathbf{Y}$ defines a multipolar channel.

We refer to these weight sets as "phased array" (PA) channels in contrast to monopolar, bipolar, or tripolar channels. It is apparent that each of the 22 PA channels employs all 22 of the intracochlear electrodes. Multiple PA channels can be stimulated simultaneously. The general solution of Eq. (6) provides for concurrent stimulation at all 22 places with 22 independent voltages by summing the corresponding single-channel current vectors.

Matrix $\mathbf{Y}$ defines channel weights for the 22 intracochlear electrodes, but each channel also employs extracochlear current as well. The total current flowing into the tissue must equal the total current flowing out. Therefore, the extracochlear current must be equal and opposite to the algebraic sum of the intracochlear currents. Its weight y_{x_p} for channel p is given by

$$y_{x_p}=-\sum_i y_{ip}. \tag{8}$$

In practice the desired stimulus intensity for each place is specified not in absolute volts, but as a relative intensity with respect to some place-specific criterion level such as perceptual threshold. We therefore normalized the weights for each channel with respect to its "on-center" value y_{pp} to produce a dimensionless set of weights $\mathbf{w}_p=(w_{1p}\ldots w_{22p})$ as follows:

$$\begin{bmatrix} w_{1p} \\ \vdots \\ w_{22p} \end{bmatrix}=\frac{1}{y_{pp}}\begin{bmatrix} y_{1p} \\ \vdots \\ y_{22p} \end{bmatrix}. \tag{9}$$

The extracochlear current weight was similarly normalized as $w_{x_p}=y_{x_p}/y_{pp}$. Normalization of the weights preserves the ratios of currents used for stimulation through a single channel p [Eq. (7)], so that it still produces exactly 0 V at all other places $k\neq p$.

The normalized channel weights formed the columns of a new matrix $\mathbf{W}$ that was used to compute current vectors for experimental stimulation. The input was no longer a vector of desired voltages. Instead the currents were computed from

$$\mathbf{i}_e=\mathbf{W}\mathbf{i}_c, \tag{10}$$

where input $\mathbf{i}_c$ was a vector of channel stimulus intensities expressed as "on-center" currents (in mA). The on-center current for a channel is its contribution to the current carried by the electrode located at its stimulation place, while it contributes smaller currents of equal or opposite polarity to the other "off-center" electrodes. Specifying a channel's stimulus intensity in mA this way has the advantage that it allows intuitive comparison with monopolar channels that deliver on-center current only.

E. Electrode current waveforms

Equation (10) provides an instantaneous solution to the inverse problem. In practice each of the stimulus intensities $[i_{c_1}(t),\ldots,i_{c_{22}}(t)]$ is a function of time. For example, those functions might be a set of biphasic pulse trains with varying rates, intensities, and pulse widths, or sinusoids of varying frequency and amplitude. Consequently, the electrode currents $[i_{e_1}(t),\ldots,i_{e_{22}}(t)]$ are also functions of time. A new current vector $\mathbf{i}_e$ must be computed each time that any signal $i_{c_p}(t)$ changes value. In general, for sampled signals, a new matrix multiplication is required for every sample interval. Thus by applying electrode current waveforms $\mathbf{i}_e(t)$ derived from repeated solution of Eq. (10) it is possible to deliver 22 completely independent stimulus waveforms to each of the 22 intracochlear places.

F. Effect of extrapolation errors

As noted above under Sec. II C, the diagonal elements of matrix $\mathbf{Z}$ were necessarily estimated by extrapolation from surrounding values. It is important to understand the extent to which estimation errors compromise the resulting stimulation voltages. If $\mathbf{Z}$ is the true transimpedance matrix, we define the imperfect matrix $\mathbf{Z}'$ as

$$\mathbf{Z}'=\mathbf{Z}+\mathbf{\Delta}, \tag{11}$$

where $\mathbf{\Delta}$ is the diagonal matrix of estimation errors $\delta_{pp}=z'_{pp}-z_{pp}$. Using imperfect transimpedances $\mathbf{Z}'$ and given a desired vector of stimulating voltages $\mathbf{v}_d$, the solution of Eq. (6) yields an imperfect vector of stimulating currents:

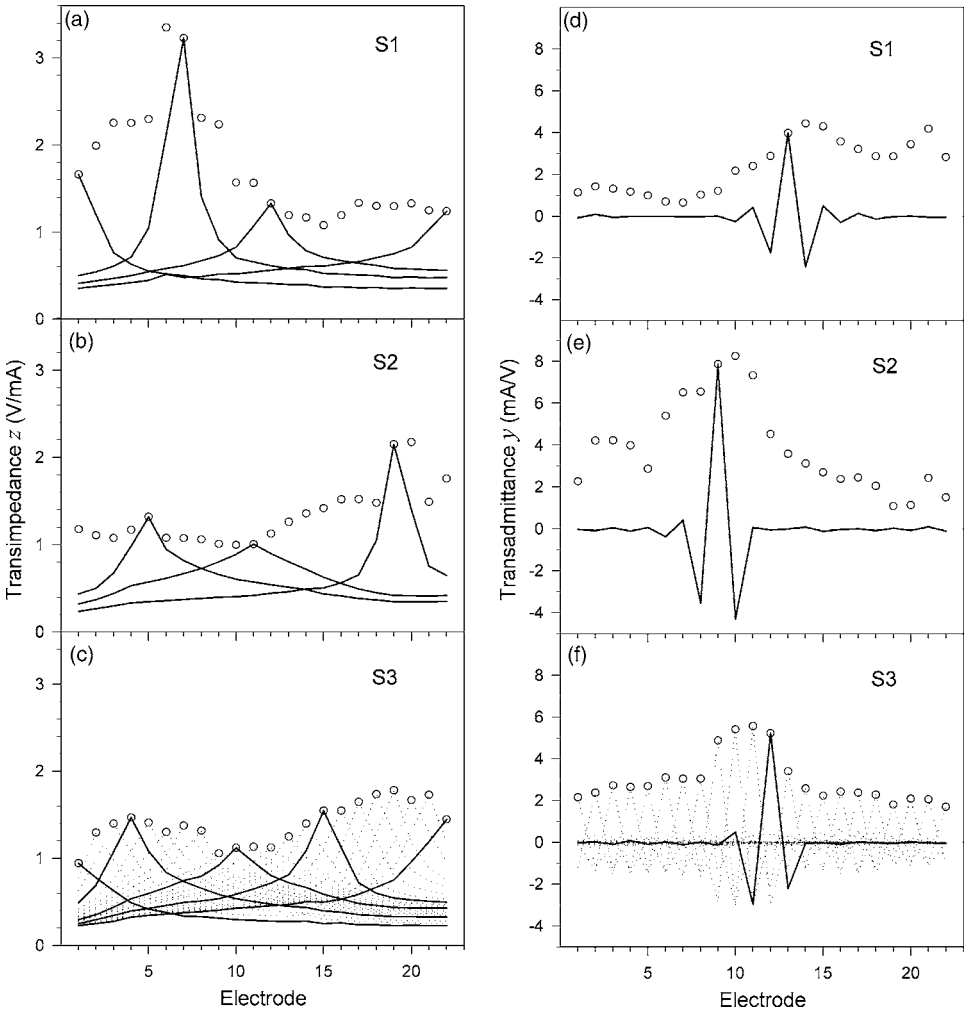

FIG. 3. Transimpedance and transadmittance data from three subjects plotted against electrode place. Electrode 1 is most basal. Left panels (a–c) show spread functions of transimpedance. Solid lines are exemplary functions, each of which represents one column of matrix **Z** (see text for details). Open circles represent peaks of all 22 spread functions for each subject. Dotted lines of panel (c) show all 22 spread functions for subject S3. Right panels (d–f) show corresponding transadmittance data. Solid lines are exemplary individual PA channels, each of which represents one column of matrix **Y**. Open circles represent peaks of all 22 channels. Dotted lines of panel (f) show all 22 PA channels for subject S3.

$$\mathbf{i}'_e = \mathbf{Z}'^{-1}\mathbf{v}_d. \tag{12}$$

When the imperfect currents $\mathbf{i}'_e$ are passed through the electrodes the actual voltages $\mathbf{v}'$ will differ from the desired voltages $\mathbf{v}_d$. From Eq. (5) the actual voltages are given by

$$\mathbf{v}' = \mathbf{Z}\mathbf{i}'_e. \tag{13}$$

Actual voltages $\mathbf{v}'$ can be compared with the correct voltages $\mathbf{v}_d$ that would have arisen if the transimpedances really were given by $\mathbf{Z}'$. Solving Eq. (12) for $\mathbf{v}_d$ gives

$$\mathbf{v}_d = \mathbf{Z}'\mathbf{i}'_e. \tag{14}$$

Subtracting Eq. (14) from Eq. (13) yields the vector of error voltages $\boldsymbol{\varepsilon}$:

$$\boldsymbol{\epsilon} = \mathbf{v}' - \mathbf{v}_d = \mathbf{Z}\mathbf{i}'_e - \mathbf{Z}'\mathbf{i}'_e = (\mathbf{Z} - \mathbf{Z}')\mathbf{i}'_e = -1\boldsymbol{\Delta}\mathbf{i}'_e. \tag{15}$$

Two observations from Eq. (15) are noteworthy. First, since $\boldsymbol{\Delta}$ is diagonal, the error voltage ε_p at place p is determined entirely by the corresponding estimation error δ_{pp} and the current through electrode p:

$$\varepsilon_p = -\delta_{pp} i'_{e_p}. \tag{16}$$

Second, the negative multiplier of Eq. (15) indicates that overestimating the transimpedance z_{pp} results in a weaker than intended voltage and vice versa.

III. RESULTS

For purposes of describing the data, each PA channel is identified by the number of its center electrode. We distinguish between "end channels" centered at electrodes 1 and 22 (basal and apical ends of the array, respectively) and the remaining "internal channels." We further define a "flanker" as an electrode adjacent to the center of a channel. Each end channel has a single flanker, whereas each internal channel has two.

A. Transimpedances

Exemplary spread functions are plotted for each of the three subjects in Figs. 3(a)–3(c). Each curve represents one column of transimpedance matrix **Z**. Spread functions generally declined monotonically toward the base (electrode 1), but approached a nonzero asymptote apically. The open circles represent the peaks of all spread functions, including those not plotted. The ratio of largest to smallest peak ranged from 3.1 for S1 to 1.9 for S3.

Sharpness and symmetry of the spread functions varied within each subject. The curves do not have true space constants because most are not well characterized by simple exponentials. In lieu of a space constant we initially quantified sharpness by normalizing each curve to a peak value of 1.0 and then averaging slopes on each side of the peak. Peak z

and normalized slope were positively correlated for all three subjects, indicating that sharp spread functions have high peak z. However, that correlation may have been an artifact of the extrapolation that related the two variables. To eliminate the possibility of a spurious correlation, two proxy variables were defined to represent magnitude and sharpness of the spread function. For electrode p, magnitude M was represented by the average of the flanker values in V/mA,

$$M = \frac{z_{p+1,p} + z_{p-1,p}}{2}, \tag{17}$$

and sharpness S was represented by the average decrement in dB/electrode from each flanker to the next adjacent point on the spread function:

$$S = \frac{20 \log (z_{p+1,p}/z_{p+2,p}) + 20 \log (z_{p-1,p}/z_{p-2,p})}{2}. \tag{18}$$

As shown in Fig. 4, magnitude and sharpness of the spread functions traced similar subject-specific trajectories across the electrode array. Variables S and M were positively correlated ($p < 0.001$ for all subjects), confirming that sharper spread functions tend to have higher magnitude.

B. Transadmittances and channel weights

Figures 3(d)–3(f) show transadmittance values for each subject. Each curve represents one column of matrix **Y**. Channel weights **W** (not shown) were derived by normalizing each curve to a peak value of 1.0 according to Eq. (9). The channel weights exhibit a characteristic pattern of decreasing absolute magnitude and alternating polarity with distance from the center electrode. There are exceptions to both patterns at larger distances.

Weights for flanker electrodes were invariably negative. Magnitude and symmetry of the flankers of internal channels were quantified by the average $\bar{w}_f$ and ratio α_f, respectively, of the smaller and larger weights. The average fell in the range $-0.626 \leq \bar{w}_f \leq -0.433$ with mean −0.523. The ratio fell in the range $0.472 \leq \alpha_f \leq 0.999$ with mean 0.819. Neither was correlated with place of the channel center ($p > 0.50$ for each subject). The mean flanker weight for end channels was −0.736. Extracochlear weights w_x were generally small and negative, indicating that most PA channels include a weak "monopolar" return current of polarity opposite to that of the on-center current. The extracochlear weight was stronger for end channels, markedly so at the basal end. The mean value of w_x was −0.224 for basal end channel 1, −0.088 for apical end channel 22, and −0.023 for internal channels.

Figure 5 shows an exemplary solution of Eq. (6) for subject S1 with the arbitrary set of desired voltages all equal to zero except $v_{d_5}=0.3$, $v_{d_{10}}=0.2$, $v_{d_{15}}=0.1$. The vertical bars represent the required currents $\mathbf{i}_e$, and the dotted lines represent voltages that would result from each individual current. The sum of the individual voltages curves, shown by the solid line and circles, is the desired voltage profile. Extensive cancellation of contributions from various electrodes is evident in comparing the magnitudes of the dotted curves to that of their sum.

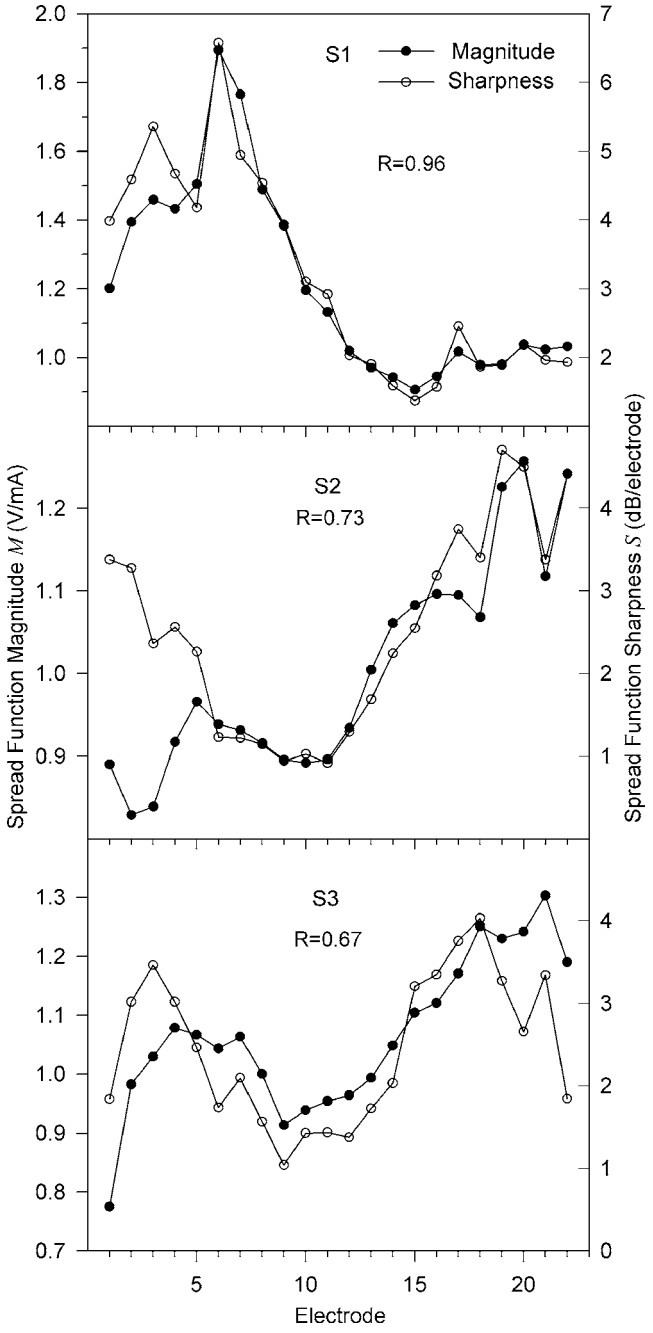

FIG. 4. Spread function magnitude M and sharpness S as functions of electrode place. Magnitude M is the average of the two flanker values surrounding the extrapolated spread function peak. Sharpness S is the average decrement (in dB/electrode) from each flanker to the next adjacent point on the spread function. For electrodes 1, 2, 21, and 22 M and R were computed from the single internal flanker. Vertical scales vary among panels to illustrate similarity of the trajectories. Inset R values indicate Pearson product moment correlation coefficients between M and S. See text for details.

C. Focusing current penalty

Comparison of the open circle peak trajectories of Figs. 3(a)–3(c) with those of Figs. 3(d)–3(f) suggests an inverse relationship between the two. PA channels centered on electrodes with high peak z have low peak y and vice versa. This relationship is illustrated in the scatter plot of Fig. 6. Peak z on the abscissa is the voltage that develops adjacent to a

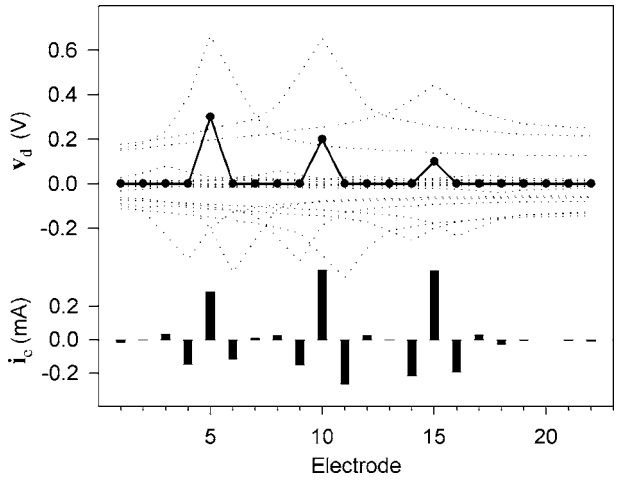

FIG. 5. Exemplary solution of Eq. (6) for subject S1, illustrating currents required to generate the desired voltage vector $\mathbf{v}_d$ defined by $v_{d_p}=0$ for all p except $v_{d_5}=0.3$, $v_{d_{10}}=0.2$, and $v_{d_{15}}=0.1$. Vertical bars represent the current on each electrode (vector $\mathbf{i}_e$). Dotted lines indicate the voltages that would arise from each of the individual currents applied separately. The solid line and filled circles show the net voltage at each electrode, which is identically equal to the desired voltage vector $\mathbf{v}_d$.

monopole carrying 1 mA. Peak y on the ordinate is the on-center current of the PA stimulus that produces 1 V at the same place.

The data of Fig. 6 are compared with the hyperbola $zy=1$. The hyperbola represents the equivalent relationship for a simple monopolar channel where the two values are simply reciprocals. The elevation of the plotted points above the hyperbola indicates the extent to which the on-center current of the PA channel exceeds the monopolar current that would produce an equivalent on-center voltage. It is evident that use of the PA channel imposes a penalty in the form of elevated on-center current, and that the penalty rises steeply with decreasing peak z below about 1.5 V/mA.

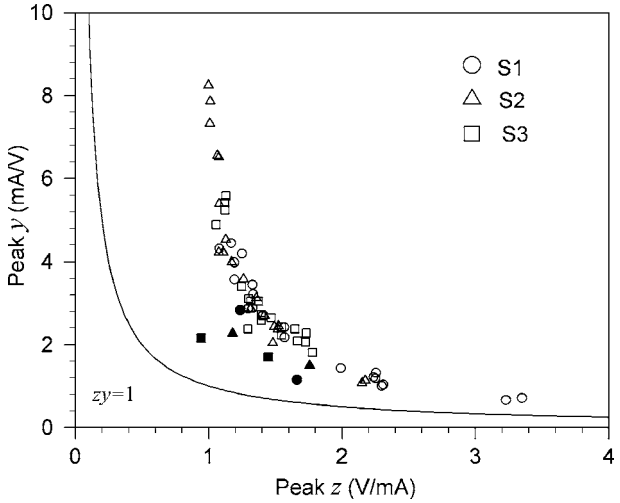

FIG. 6. Comparison of spread function peak z with transadmittance peak y of a PA channel centered at the same electrode. The abscissa represents the local voltage that arises from passing 1 mA through the electrode. The ordinate represents the on-center PA current required to generate the same local voltage. Hyperbola $zy=1$ represents the same comparison for monopolar channels where $z=1/y$. Filled symbols represent end channels 1 and 22. Open symbols represent internal channels.

In fact the data of Fig. 6 underestimate the total current penalty because they do not include compensating currents delivered to the off-center electrodes of the PA channel. To determine the full penalty we compared total current flowing into (and thus out of) the tissue in the PA and monopolar cases. For monopolar stimulation the positive current required to produce +1.0 V at place p flows entirely through electrode p and is given by

$$I_{\mathrm{MP}_p}=\frac{1}{z_{pp}}. \tag{19}$$

For PA stimulation the total positive current needed to achieve the same +1.0 V at place p is computed from Eqs. (7) and (8) as

$$I_{\mathrm{PA}_p}=\sum_i \begin{Bmatrix} y_{ip}, & y_{ip}>0 \\ 0, & \text{otherwise} \end{Bmatrix} + \begin{Bmatrix} y_{x_p}, & y_{x_p}>0 \\ 0, & \text{otherwise} \end{Bmatrix}. \tag{20}$$

Total focusing penalty β_p for PA channel p is then defined as the ratio of positive currents:

$$\beta_p=\frac{I_{\mathrm{PA}_p}}{I_{\mathrm{MP}_p}}. \tag{21}$$

Focusing penalty β is plotted as a function of channel center in Fig. 7(a). The penalty across all 66 channels fell in the range $2.18\leq\beta\leq 9.56$ with mean 5.11. The penalty for each end channel was consistently lower than for the adjacent internal channel.

The scatter plot of Fig. 7(b) shows that the penalty was lower for channels centered on electrodes with sharp spread functions (high S). This is intuitively sensible. In the limit of an infinitely sharp spread function, off-center compensatory currents are unnecessary and the PA channel converges toward the monopolar case as off-center weights all approach zero.

D. Effects of transimpedance measurement errors

The two-norm condition numbers of the $\mathbf{Z}$ matrices for subjects S1, S2, and S3 were 136, 192, and 141, respectively. These values indicate a potential for sensitivity to measurement errors in the original data when computing the inverse matrix $\mathbf{Y}$ (Watkins, 2002). If the true matrix $\mathbf{Z}$ is in fact diagonally symmetric as argued above, then the measurement errors can be characterized from the difference values above or below the diagonal in the matrix:

$$\mathbf{\Theta}=\mathbf{Z}_m-\mathbf{Z}_m^T. \tag{22}$$

Assuming that each transimpedance value $z_{m_{ij}}$ includes an error component e that is normally distributed with mean 0 and variance σ_e^2, then the difference values

$$\theta_{ij}=(z_{ij}+e_x)-(z_{ji}+e_y)=e_x-e_y \tag{23}$$

are also normally distributed with variance $2\sigma_e^2$. The 231 differences above the diagonal of matrix Θ satisfied ($p>0.05$) a Kolmogorov-Smirnov test for normality (Blum and Rosenblatt, 1972) for subjects S1 and S3, and for S2 with one outlier excluded. For each subject the variance of the underlying error distribution was estimated from

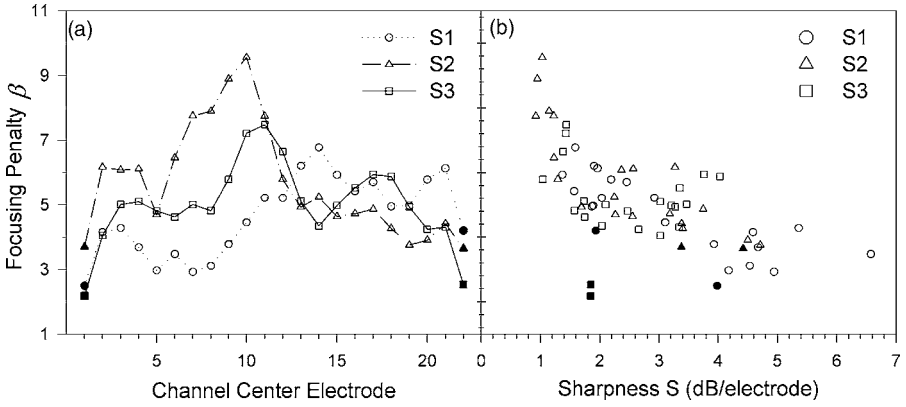

FIG. 7. Panel (a) shows focusing penalty plotted as a function of cochlear place for each subject. Focusing penalty β is the ratio of total positive PA current required to generate +1 V at a given place to the positive monopolar current required to do the same. Thus a value of 1.0 indicates no penalty. Panel (b) shows focusing penalty plotted against sharpness S of the spread function for the center electrode of the PA channel. Focusing penalty is lower for PA channels whose center electrodes have sharp spread functions (i.e., high S). Filled symbols in both panels represent end electrodes 1 and 22.

$$\sigma_e^2 \cong \frac{s_\theta^2}{2}, \tag{24}$$

where s_θ^2 is the unbiased variance of the difference values θ_{ij} above the diagonal.

The effect of measurement errors was examined with simulations. For purposes of simulation, the original matrix $\mathbf{Z}$ was assumed to be exact. A simulated $\mathbf{Z}_m$ was generated by adding normally distributed random errors with mean 0 and variance σ_e^2 to the elements of $\mathbf{Z}$. Perturbed PA channel weights $\mathbf{W}$ were then computed. Ten simulations were conducted per subject, each yielding 462 weight errors (normalized diagonal weights $w_{pp} \equiv 1.0$ have no error). Table II shows statistics of the simulated weight errors. The influence of a high condition number is evident in that weight errors for S2 were larger than for S3 and S1, despite S2's smaller measurement errors.

E. Validation with reduced solutions

Due to the polarization phenomenon discussed above (see Sec. II C), it was not possible to measure actual voltages for comparison with expected values when stimulating through a PA channel. In order to validate the procedure we computed reduced PA_{even} channel sets employing only the 11 even-numbered electrodes. This left the odd-numbered electrodes idle and available for voltage measurements. Voltages measured on the odd electrodes were then compared with values predicted by the full 22-electrode solution of Eq. (5). In order to evaluate the success in canceling off-center stimulation, we used single-channel PA_{even} stimuli for the comparisons.

TABLE II. Results of simulated measurement errors in transimpedance data. PA weights were computed from transimpedance matrices perturbed by adding normally distributed errors to each element of matrix $\mathbf{Z}$. The standard deviation σ_e of simulated z errors was derived from an estimate of actual measurement errors in the original data (see text for details). Ten simulations, resulting in 4620 weight errors, were conducted for each subject. Statistics of the errors in the weights are shown.

			Weight errors (N=4620 per subject)			
Subject	Condition no. of matrix $\mathbf{Z}$	S.D. of z errors σ_e (V/mA)	Mean	Standard deviation	Max	Min
S1	136	0.0093	0.000 040	0.031	0.14	−0.15
S2	192	0.0088	0.000 068	0.045	0.24	−0.26
S3	141	0.0097	0.000 046	0.035	0.20	−0.19

Figure 8 shows predicted and measured voltages for stimulation through PA_{even} channels 8 and 16 at maximum comfortable intensity. There is generally good agreement between measured and predicted voltages, with some discrepancies at the immediately adjacent off-center electrodes (S3 center-16, S1 center-8). However, all cases showed effective focusing with small off-center voltages predicted and measured between the ideal zeros at the even electrodes. Note that the panels of Fig. 8 have different vertical scales to illustrate focusing profiles relative to peak on-center voltage.

The validation measures for S1, S2, and S3 were conducted 185, 302, and 210 days, respectively, after measurement of the spread functions of matrix $\mathbf{Z}$. The discrepancies noted might have arisen from drift in the spread functions between the original measurements and the subsequent validation. To assess the stability of the transimpedances we replicated selected measurements over time as shown in Fig. 9. Only measured (not extrapolated) values are plotted.

Measurement dates ranged between 133 and 680 days postoperatively across the three subjects. The spread functions exhibit generally good stability over time, with a slight tendency toward gradual sharpening in several cases (S1: centers 1, 6, 11; S2: center 1; S3: centers 1, 11, 22). Because the earliest measurements were made more than 4 months postoperatively, we do not know how rapidly this stability was achieved.

F. Voltage spread beyond the array ends

PA stimulation regulates voltages within the bounds of the electrode array precisely, but substantial uncanceled voltages might exist beyond the ends of the array. Since voltages beyond the physical array could not be measured, we explored this possibility using a subset of the electrodes to represent a shortened array. Current vectors were computed for a reduced PA_{short} channel set using only basal electrodes

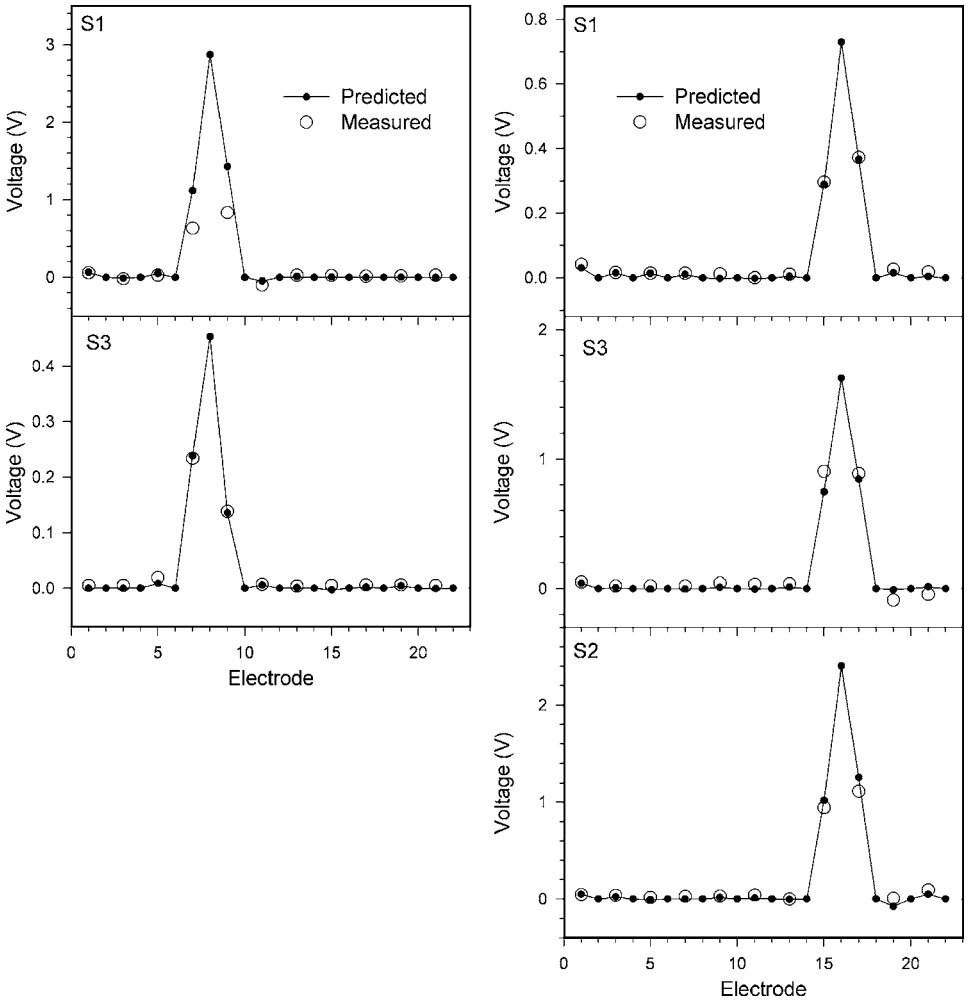

FIG. 8. Comparison of predicted (filled circles) and measured (open circles) voltages with single-channel PA_{even} stimuli centered at electrodes 8 and 16. Voltages were measurable only at idle odd electrodes. Predicted values at even electrodes are 0 by definition. Measures for S1, S2, and S3 were made 185, 302, and 210 days, respectively, after measurement of the spread functions of matrix **Z**.

1–11. Those current vectors then served as inputs to the full 22-electrode solution of Eq. (5), with zero current on idle electrodes 12–22. Voltages computed for idle electrodes 12–22 reflect stimulus spread beyond the apical end of the short array. Exemplary results from subject S2 are shown in Fig. 10 for the most apical six PA_{short} channels. For end channel 11 (circles) the apical spread was substantial—only slightly less than that of a monopole at the same place (dotted line). For internal channels 6–10, however, voltages beyond the array were relatively weak. In general, the uncanceled voltages grew smaller as the channel center shifted away from the end.

IV. DISCUSSION

The primary purpose of this paper is to describe the phased array stimulus focusing method, analyze its limitations, and validate its application with physical data. The results presented confirm that (1) the method is effective in canceling off-center voltages within the scala tympani; (2) extrapolation errors in estimating on-center transimpedances affect only the potential at the corresponding site; (3) with 22-contact perimodiolar electrodes **Z** matrices can be measured with sufficient accuracy, and are sufficiently well conditioned, that their inversion yields acceptable weight errors; and (4) transimpedances are stable over time.

The pattern of alternating polarities in the PA channel weights [Figs. 3(d)–3(f)] is consistent with an intuitive approach to focusing. Negative currents are needed on the flanker electrodes to cancel the skirts of the spread function around a positive monopole. The flankers' skirts themselves require cancellation by positive currents on adjacent electrodes, and so on.

The validation measures of Fig. 8 show good agreement in most cases between predicted and measured voltages. In particular, substantial off-center cancellation was confirmed between the active electrodes (i.e. at the odd electrodes) where complete cancellation was not predicted. The discrepancies that were observed cannot be attributed to extrapolation errors in diagonal elements of **Z**, because the odd electrodes carried no current, and thus had no extrapolation error [$\varepsilon=0$ in Eq. (16)]. Some of the discrepancy may be due to weight perturbations resulting from z measurement errors. Another possibility is that spread functions changed during the 185 to 302 days that elapsed between transimpedance and validation measurements. The gradual sharpening that was observed over time for some spread functions (Fig. 9) may reflect encapsulation of the electrode array and subsequent reduction in longitudinal shunting. Such sharpening could account for the lower-than-expected voltages measured between center and flanker electrodes in some panels of Fig. 8 (S1 channel 8, S2 channel 16). Low voltages suggest that

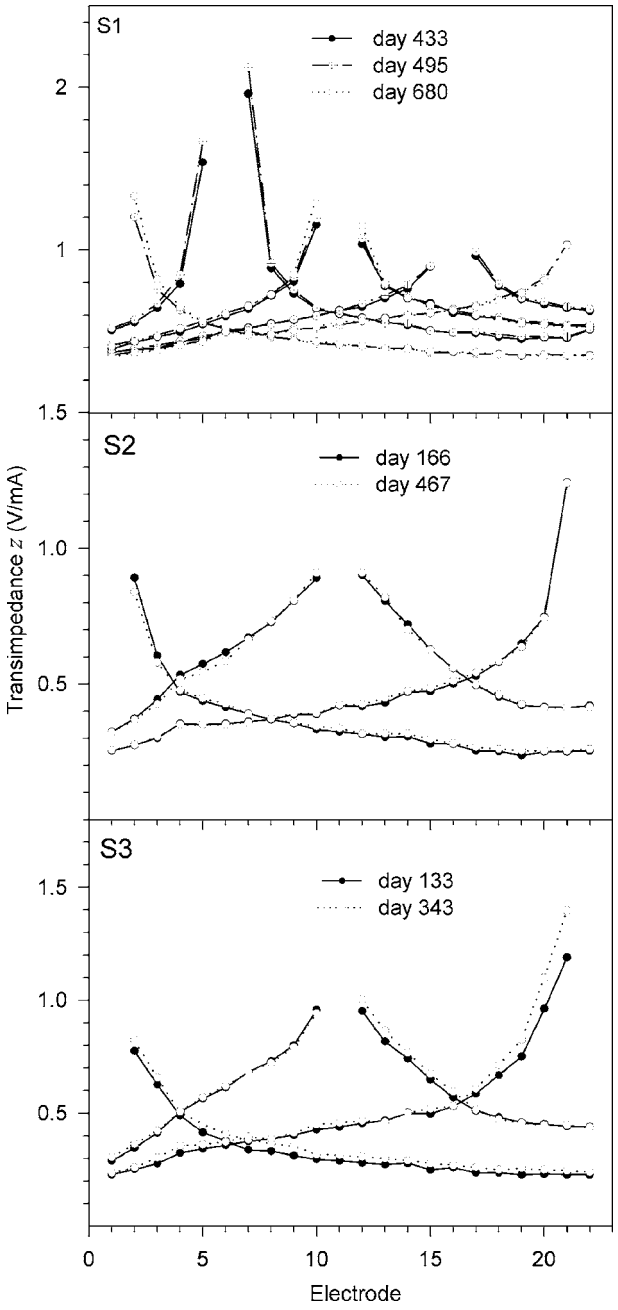

FIG. 9. Stability of transimpedances (spread functions). Days indicated are days after implantation surgery. Some functions exhibit a slight tendency to become sharper over time (S1: centers 1, 6, and 11; S2: center 1; S3: centers 1, 11, and 22).

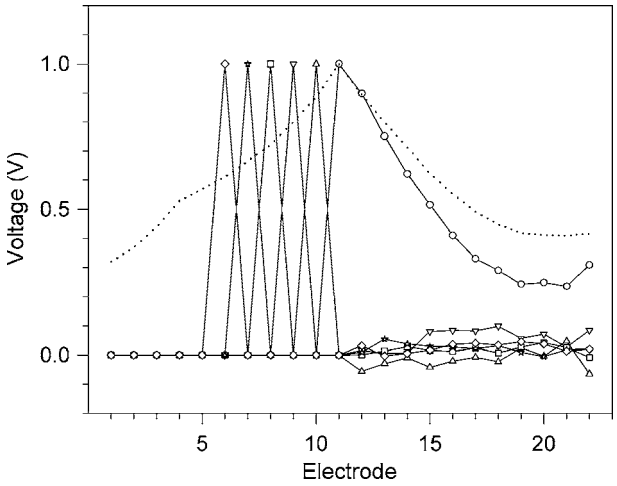

FIG. 10. Exemplary plots of voltage spread apical to the electrode array with stimulation through PA_{short} channels 6–11 (see text for details). PA_{short} channels use only electrodes 1–11. Each curve represents voltages computed for stimulation through a single PA_{short} channel. Off-center voltages at active electrodes (≤ 11) are zero by definition. Voltages at idle electrodes (>11) indicated uncanceled spread apical to the array. End-channel 11 (circles) exhibits substantial apical spread that is only slightly less than that of a monopole at the same place (dotted line). In contrast, internal channels 6–10 exhibit relatively weak apical spread beyond electrode 11.

the flanker currents were stronger than necessary, which would have been the case if the spread functions had become sharper. In a practical implementation such slow drift could be accommodated by occasionally updating the **Z** matrix.

Zierhoffer (2003) has described "sign-correlated" stimulation as a method for determining currents through multiple electrodes to reduce summation of voltage fields. While this method appears to have some mathematical similarity to the derivation of PA channels described here, in fact the two are quite different. Zierhoffer's method constrains all intracochlear currents to have equal polarity. With this constraint a flanker electrode cannot deliver an inverted current to cancel the skirt from an adjacent center electrode. Therefore, no stimulus voltage profile can ever be made narrower than the original monopolar spread function, and no focusing can be achieved. Zierhoffer's method may help to ameliorate the loudness fluctuations associated with monopolar channel overlap, but it does not correct the associated spatial smearing.

Some investigators have proposed the use of tripolar (Miyoshi *et al.*, 1996; Kral *et al.*, 1998; Bierer and Middlebrooks, 2002) or quadrupolar channels (Jolly *et al.*, 1996; Clopton and Spelman, 1982, 1995; Mens and Berenstein, 2005) to achieve focal stimulation. A tripolar channel has symmetrical negative flankers that return some of the current sourced by the center electrode ($-0.5 \leq w_f < 0$). The balance of the current, if any, returns through an extracochlear electrode. A quadrupole is the limiting case where all of the current returns through the flankers ($w_f = -0.5$). Tripolar approximations are compared with the flanker weights of internal PA channels from our data set in the scatter plot of Fig. 11. The solid line represents a range of tripolar alternatives, with the quadrupolar limit indicated by the square symbol. The paucity of data points surrounding the line suggests that most tripoles do not closely approximate a PA channel. The quadrupole may represent a reasonable first-order approximation to those PA channels that fall near the square, provided that the other PA weights (not shown) are small. But many PA channels demonstrate significant asymmetry between the flankers, which implies that a symmetrical quadrupolar substitute would not achieve good off-center cancellation in those cases. In order to assess the adequacy of the tripolar approximations, their residual uncanceled off-center voltages must be compared with corresponding voltages at perceptual threshold for specific subjects. Similarly, the effects of measurement errors and extrapolation errors in the **Z**

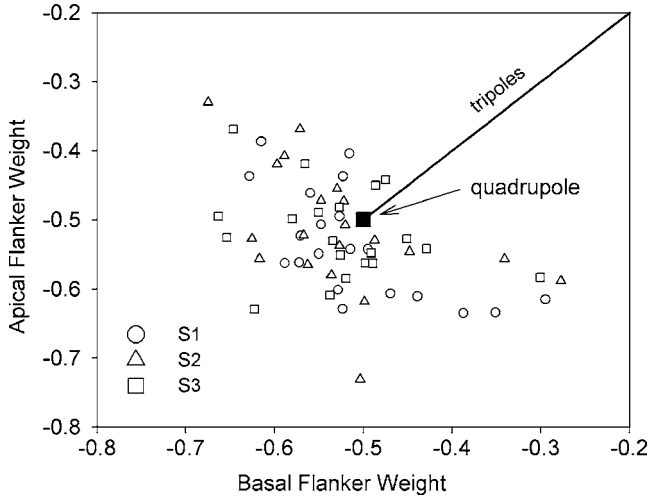

FIG. 11. Scatter plot of PA flanker weights for all internal channels. The solid line represents the locus of weights that implement symmetrical tripolar channels, including the limiting quadrupolar case where both flankers have weight −0.5 (filled square).

matrix must also be assessed in the context of behavioral thresholds. These issues will be addressed in a subsequent paper.

The common trajectories across cochlear place that are traced by magnitude M and sharpness S of the spread functions (Fig. 4) suggest that the two parameters reflect a common property of the electrical environment surrounding an electrode. A simple interpretation of these data is that electrodes in closer proximity to the modiolar wall suffer less longitudinal shunting of current by surrounding fluid. Less shunting would produce both higher voltage and steeper longitudinal attenuation. The idiosyncrasies of the trajectories in Fig. 4 varied across subjects, probably reflecting individual differences in electrode position within the cross section of scala tympani.

This interpretation leads to the implication that perimodiolar placement of the electrode array is important in order to maximize sharpness of the spread functions. Two significant benefits accrue from sharp spread functions: (1) the total stimulation current is lower because of the reduced focusing penalty (Fig. 7) and (2) sensitivity to measurement errors is reduced because the condition number of the **Z** matrix is lowered (Table II). Conversely electrodes lying at the center of scala tympani or along its lateral wall would likely have broad spread functions leading to impractically severe focusing penalties and high error sensitivity.

Focusing at the end channels is compromised by uncanceled spread beyond the ends of the array (Fig. 10). This phenomenon was characterized at the center of the array where spread functions were relatively broad for all subjects. Actual uncanceled spread at the ends of scala tympani may be different due to details of the local electroanatomy. For example, it may be worse at the apical end than the basal end because apical spread functions level off instead of declining monotonically. However, if the electrode array subtends most or all of the extent of spiral ganglion, there may be few neurons to be stimulated in the regions beyond the ends. In that case the spread from the end channels might not be problematic. In any case, if lack of focus precludes their use, only two channels are lost for stimulation purposes.

V. CONCLUSIONS

The results presented here demonstrate that phased array stimulation is realizable with modern perimodiolar electrodes. Significant focusing of the stimulating field is possible in comparison to monopolar stimulation. Before PA channels can be implemented in a practical prosthesis, two issues remain to be addressed. First, due to the focusing penalty, impractically high currents may be required to achieve audibility. Second, future implanted electronics will have to provide sufficient precision in both transimpedance measurement and current regulation so as to limit off-center cancellation errors to acceptable levels. An "acceptable" error voltage is presumably one that falls below the perceptual threshold voltage for the same cochlear place. Both the audibility and precision issues have been examined with perceptual measures from the three subjects above, to be reported in a subsequent paper. Future improvements in electrode technology may relax the demand for both high current and high precision. More intimate proximity of electrodes to the target neural population would be expected to reduce both focusing penalty and sensitivity to measurement errors.

ACKNOWLEDGMENTS

We would like to thank Wendy Parkinson for assistance in collecting the transimpedance data. We would also like to thank the three experimental subjects who invested many tireless hours into these and related experiments. Brett Swanson, Jim Patrick, Bomjun Kwon, Bas van Dijk, Peter Busby, Peter Seligman, and Bob Carlyon provided valuable comments on an initial draft of the manuscript. This research was funded by Cochlear Americas and Rocky Mountain Cochlear Implant Center.

[1]The additional voltage drop from polarization can be substantial even with a small current flow. In the absence of any interface impedance, each diagonal transimpedance value would be approximately equal to the impedance measured between the intracochlear electrode and a large extracochlear electrode. But actual impedances, measured with a 22 nA peak 1 kHz sinusoidal test current, generally exceeded the extrapolated transimpedance values by a factor of 4 to 10. It is clear that measured electrode impedances are dominated by the series interface impedances rather than the bulk resistance of the electrolyte between the contacts.

[2]Vanpoucke *et al.* (2004b) estimated the diagonal transimpedances using a lumped-constant model of electrode interface impedances and cochlear tissue. They used numerical methods to determine a best fit of model parameters to their $\mathbf{Z}_m$ data, and then computed estimates of the diagonal transimpedances (which they termed normalized potentials) from the fitted model parameters. The estimated values of their example solution (their Fig. 12) appear to be substantially in error. This is most easily appreciated when the 16 estimated values (Fig. 12, rTissue plot) are replotted on a common set of axes with the surrounding measured values (Fig. 12, zOff plots). Each of the 16 estimated rTissue values represents the "missing peak" of the corresponding zOff spread function curve. But most of those estimated missing peaks actually fall below one or both of the adjacent measured values. This is not possible in a passive volume conductor with a single point of current injection, where the highest tissue potential (and hence the highest transimpedance) must exist at the site of the stimulating

electrode. It should be noted that Vanpoucke *et al.* did not develop their model for purposes of estimating transimpedances, but rather for examining current flow pathways.

[3]The effective stimulus for an axon is determined by the axial gradient of the potential in the fluid that surrounds it (Altman and Plonsey, 1990). We assume that the central ends of all auditory nerve axons share a common extracellular potential within the internal auditory meatus that is approximately neutral (0 V). In that case, axons originating near points of high voltage within scala tympani experience strong potential gradients along their lengths. In contrast, axons originating near points at 0 V within scala tympani experience little or no gradient. Hence the term "stimulating voltages" in referring to the potentials $(v_{d_1},\ldots,v_{d_{22}})$ at the electrode sites within scala tympani.

Altman, K. W., and Plonsey, R. (**1990**). "Analysis of excitable cell activation: Relative effects of external electrical stimuli," Med. Biol. Eng. Comput. **28**, 574–580.

Bierer, J. A., and Middlebrooks, J. C. (**2002**). "Auditory cortical images of cochlear-implant stimuli: Dependence on electrode configuration," J. Neurophysiol. **87**, 478–492.

Blum, R. J., and Rosenblatt, J. I. (**1972**). *Probability and Statistics* (Saunders, Philadelphia), pp. 413–414.

Boex, C., de Balthasar, C., Kos, M. I., and Pelizzone, M. (**2003**). "Electrical field interactions in different cochlear implant systems," J. Acoust. Soc. Am. **114**, 2049–2057.

Bosco, E., D'Agosta, L., Mancini, P., Traisci, G., D'Elia, C., and Filip, R. (**2005**). "Speech perception results in children implanted with Clarion devices: Hi-Resolution and standard resolution modes," Acta Oto-Laryngol. **125**, 148–158.

Brokx, J. P. L., and Nooteboom, S. G. (**1982**). "Intonation and perception of simultaneous voices," J. Phonetics **10**, 23–26.

Busby, P. A., and Plant, K. L. (**2005**). "Dual electrode stimulation using the nucleus CI24RE cochlear implant: Electrode impedance and pitch ranking studies," Ear Hear. **26**, 504–511.

Busby, P. A., Whitford, L. A., Blamey, P. J., Richardson, L. M., and Clark, G. M. (**1994**). "Pitch perception for different modes of stimulation using the cochlear multiple-electrode prosthesis," J. Acoust. Soc. Am. **95**, 2658–2669.

Carlyon, R. P., and Shackleton, T. M. (**1994**). "Comparing the fundamental frequencies of resolved and unresolved harmonics: Evidence for two pitch mechanisms?" J. Acoust. Soc. Am. **95**, 3541–3554.

Carlyon, R. P., van Wieringen, A., Long, C. J., Deeks, J. M., and Wouters, J. (**2002**). "Temporal pitch mechanisms in acoustic and electric hearing," J. Acoust. Soc. Am. **112**, 621–633.

Chalika, M. H., and Bregman, A. S. (**1989**). "The perceptual segregation of simultaneous auditory signals: Pulse train segregation and vowel segregation," Percept. Psychophys. **46**, 487–496.

Chao, Y. R. (**1968**). *A Grammar of Spoken Chinese* (Univ. of California, Berkely, CA), pp. 25–32.

Clark, G. M., Patrick, J. F., and Bailey, Q. (**1979**). "A cochlear implant round window electrode array," J. Laryngol. Otol. **93**, 107–109.

Clopton, B. M., Lineaweaver, S. K. R., Corbett, S. S., and Spelman, F. A. (**2002**). "Method of processing auditory data," U.S. Patent No. 6,480,820.

Clopton, B. M., and Spelman, F. A. (**1982**). "Neural mechanisms relevant to the design of an auditory prosthesis: Location and electrical characteristics," Ann. Otol. Rhinol. Laryngol. **89**(Suppl. 98), 9–14.

Clopton, B. M., and Spelman, F. A. (**1995**). "Electrode configuration and spread of neural excitation: Compartmental models of spiral ganglion cells," Ann. Otol. Rhinol. Laryngol. **105**(Suppl. 166), 115–118.

Cohen, L. T., Richardson, L. M., Saunders, E., and Cowan, R. S. (**2003**). "Spatial spread of neural excitation in cochlear implant recipients: Comparison of improved ECAP method and psychophysical forward masking," Hear. Res. **179**, 72–87.

Collins, L. M., Zwolan, T. A., and Wakefield, G. H. (**1997**). "Comparison of electrode discrimination, pitch ranking, and pitch scaling data in postlingually deafened adult cochlear implant subjects," J. Acoust. Soc. Am. **101**, 440–455.

Donaldson, G. S., Kreft, H. A., and Litvak, L. (**2005**). "Place-pitch discrimination of single- versus dual-electrode stimuli by cochlear implant users," J. Acoust. Soc. Am. **118**, 623–626.

Drullman, R., and Bronkhorst, A. W. (**2004**). "Speech perception and talker segregation: Effects of level, pitch, and tactile support with multiple simultaneous talkers," J. Acoust. Soc. Am. **116**, 3090–3098.

Fu, Q. J., and Nogaki, G. (**2005**). "Noise susceptibility of cochlear implant users: The role of spectral resolution and smearing," J. Assoc. Res. Otolaryngol. **6**, 19–27.

Grayden, D. B., Burkitt, A., Kenny, O., Clarey, J., Paolini, A., and Clark, G. (**2004**). "A cochlear implant speech processing strategy based on an auditory model," ISSNIP Workshop on Biologically Inspired Models, Melbourne.

Jolly, C. N., Spelman, F. A., and Clopton, B. M. (**1996**). "Quadrupolar stimulation for cochlear prostheses: Modeling and experimental data," IEEE Trans. Biomed. Eng. **43**, 857–865.

Kral, A., Hartmann, R., Mortazavi, D., and Klinke, R. (**1998**). "Spatial resolution of cochlear implants: The electrical field and excitation of auditory afferents," Hear. Res. **121**, 11–28.

Laneau, J., and Wouters, J. (**2006**). "Improved music perception with explicit pitch coding in cochlear implants," Audiol. Neuro-Otol. **11**, 38–52.

Loizou, P. C., Stickney, G., Mishra, L., and Assmann, P. (**2003**). "Comparison of speech processing strategies used in the Clarion implant processor," Ear Hear. **24**, 12–19.

Mens, L. H., and Berenstein, C. K. (**2005**). "Speech perception with mono- and quadrupolar electrode configurations: A crossover study," Otol. Neurotol. **26**, 957–964.

Miyoshi, S., Iida, Y., Shimizu, S., Matsushima, J., and Ifukube, T. (**1996**). "Proposal of a new auditory nerve stimulation method for cochlear prosthesis," Artif. Organs **20**, 941–946.

Nie, K., Stickney, G., and Zeng, F. G. (**2005**). "Encoding frequency modulation to improve cochlear implant performance in noise," IEEE Trans. Biomed. Eng. **52**, 64–73.

Oxenham, A. J., Bernstein, J. G. W., and Penagos, H. (**2004**). "Correct tonotopic representation is necessary for complex pitch perception," Proc. Natl. Acad. Sci. U.S.A. **101**, 1421–1425.

Pfingst, B. E., Zwolan, T. A., and Holloway, L. A. (**1997**). "Effects of stimulus configuration on psychophysical operating levels and on speech recognition with cochlear implants," Hear. Res. **112**, 247–260.

Pijl, S., and Schwartz, D. W. F. (**1995**). "Melody recognition and musical interval perception by deaf subjects stimulated with electrical pulse trains through single cochlear implant electrodes," J. Acoust. Soc. Am. **98**, 886–895.

Rodenhiser, K. L., and Spelman, F. A. (**1995**). "A method for determining the driving currents for focused stimulation in the cochlea," IEEE Trans. Biomed. Eng. **42**, 337–342.

Roland, J. T., Jr. (**2005**). "A model for cochlear implant electrode insertion and force evaluation: Results with a new electrode design and insertion technique," Laryngoscope **115**, 1325–1339.

Ross, A., Saulnier, G., Newell, J., and Isaacson, D. (**2003**). "Current source design for electrical impedance tomography," Physiol. Meas **24**, 509–516.

Scheffers, M. T. M. (**1983**). "Sifting Vowels: Auditory Pitch Analysis and Sound Segregation," Ph.D. thesis, Rijksuniversiteit te Groningen, The Netherlands.

Shackleton, T. M., and Carlyon, R. P. (**1994**). "The role of resolved and unresolved harmonics in pitch perception and frequency modulation discrimination," J. Acoust. Soc. Am. **95**, 3529–3540.

Shamma, S., and Klein, D. (**2000**). "The case of the missing pitch templates: How harmonic templates emerge in the early auditory system," J. Acoust. Soc. Am. **107**, 2631–2644.

Shannon, R. V. (**1983a**). "Multichannel electrical stimulation of the auditory nerve in man: I. Basic Psychophysics," Hear. Res. **11**, 157–189.

Shannon, R. V. (**1983b**). "Multichannel electrical stimulation of the auditory nerve in man: II. Channel interaction," Hear. Res. **12**, 1–16.

Skinner, M. W., Arndt, P. L., and Staller, S. J. (**2002**). "Nucleus 24 advanced encoder conversion study: Performance versus preference," Ear Hear. **23**(Suppl. 1), 2S–17S.

Skinner, M. W., Clark, G. M., Whitford, L. A., Seligman, P. M., Staller, S. J., Shipp, D. B., Shallop, J. K., Everingham, C., Menapace, C. M., Arndt, P. L., Antogenelli, T., Brimacombe, J., Pijl, S., Daniels, P., George, C., McDermott, H., and Beiter, A. (**1994**). "Evaluation of a new spectral peak coding strategy for the Nucleus 22 channel cochlear implant system," Am. J. Otol. **15**(Suppl. 2), 15–27.

Snyder, R. L., Bierer, J. A., and Middlebrooks, J. C. (**2004**). "Topographic spread of inferior colliculus activation in response to acoustic and intracochlear electric stimulation," J. Assoc. Res. Otolaryngol. **3**, 305–322.

Spelman, F. A., Clopton, B. M., and Pfingst, B. E. (**1982**). "Tissue impedance and current flow in the implanted ear. Implications for the cochlear prosthesis," Ann. Otol. Rhinol. Laryngol. **89**(Suppl. 98), 3–8.

Stickney, G. S., Loizou, P. C., Mishra, L. N., Assmann, P. F., Shannon, R. V., and Opie, J. M. (**2006**). "Effects of electrode design and configuration

on channel interactions," Hear. Res. **211**, 33–45.
Summerfield, A. Q., and Assmann, P. F. (**1990**). "Perception of concurrent vowels: Effects of pitch-period asynchrony and harmonic misalignment," J. Acoust. Soc. Am. **89**, 1364–1377.
Tong, Y. C., and Clark, G. M. (**1985**). "Absolute identification of electric pulse rates and electrode positions by cochlear implant patients," J. Acoust. Soc. Am. **77**, 1881–1888.
Townshend, B., and White, R. L. (**1987**). "Reduction of electrical interaction in auditory prostheses," IEEE Trans. Biomed. Eng. **BME-34**, 891–897.
Van Compernolle, D. (**1985a**). "Speech processing strategies for a multichannel cochlear prosthesis," Ph.D. thesis, Stanford University.
Van Compernolle, D. (**1985b**). "A computational model of the Cochlea used with Cochlear prosthesis patients," title *Proceedings of IEEE International Conference on ICASSP*, Tampa, Florida, pp. 427–429.
van den Honert, C. (**1990**). "Reproduction of auditory nerve temporal patterns with sharply resonant filters," in *Cochlear Implants Models of the Electrically Stimulated Ear*, edited by J. M. Miller and F. A. Spelman (Springer Verlag, New York), pp. 115–131.
van den Honert, C., and Stypulkowski, P. H. (**1987**). "Single fiber mapping of spatial excitation patterns in the electrically stimulated auditory nerve," Hear. Res. **29**, 195–206.
van Hoesel, R. J., and Tyler, R. S. (**2003**). "Speech perception, localization, and lateralization with bilateral cochlear implants," J. Acoust. Soc. Am. **113**, 1617–1630.
Van Valkenburg, M. E. (**1960**). *Modern Network Synthesis* (Wiley, New York), p. 37.
Vanpoucke, F., Zarowski, A., Casselman, J., Frijns, J., and Peeters, S. (**2004a**). "The facial nerve canal: An important cochlear conduction path revealed by Clarion electrical field imaging," Otol. Neurotol. **25**, 282–289.
Vanpoucke, F. J., Zarowski, A. J., and Peeters, S. A. (**2004b**). "Identification of the impedance model of an implanted cochlear prosthesis from intracochlear potential measurements," IEEE Trans. Biomed. Eng. **51**, 2174–2183.
von Wallenberg, E. L., Battmer, R. D., Doden, I., Gnadeberg, D., Hautle, K., and Lenarz, T. (**1995**). "Place-pitch and speech perception measures with bipolar and monopolar electrical stimulation of the cochlea," Ann. Otol. Rhinol. Laryngol. **105** (Suppl. 166), 372–375.
Walsh, S. M., Merzenich, M. M., Schindler, R. A., and Leake-Jones, P. A. (**1980**). "Some practical considerations in development of multichannel scala tympani prostheses," Audiology **19**, 164–175.
Wang, W.S.-Y. (**1973**). "The Chinese language," Sci. Am. **228**, 50–63.
Watkins, D. S. (**2002**). *Fundamentals of Matrix Computations* (Wiley, New York), pp. 133–136.
Wilson, B. S., Finley, C. C., Lawson, D. T., Wolford, R. D., Eddington, D. K., and Rabinowitz, W. M. (**1991**). "Better speech recognition with cochlear implants," Nature (London) **352**, 236–238.
Xu, L. (**2003**). "Relative importance of temporal envelope and fine structure in lexical-tone perception," J. Acoust. Soc. Am. **114**, 3024–3027.
Xu, L., Zwolan, T. A., Thompson, C. S., and Pfingst, B. E. (**2005**). "Efficacy of a cochlear implant simultaneous analog stimulation strategy coupled with a monopolar electrode configuration," Ann. Otol. Rhinol. Laryngol. **114**, 886–893.
Zierhoffer, C. M. (**2003**). "Electrical nerve stimulation based on channel specific sampling sequences," U.S. Patent No. 6,594,525 B1.
Zwolan, T. A., Kileny, P. R., Ashbaugh, C., and Telian, S. A. (**1996**). "Patient performance with the Cochlear Corporation "20+2" implant: bipolar versus monopolar activation," Am. J. Otol. **17**, 717–723.

Improved speech recognition in noise in simulated binaurally combined acoustic and electric stimulation[a)]

Ying-Yee Kong[b)] and Robert P. Carlyon
MRC—Cognition & Brain Sciences Unit, 15 Chaucer Road, Cambridge CB2 2EF, United Kingdom

(Received 16 May 2006; revised 16 February 2007; accepted 22 February 2007)

Speech recognition in noise improves with combined acoustic and electric stimulation compared to electric stimulation alone [Kong *et al.*, J. Acoust. Soc. Am. **117**, 1351–1361 (2005)]. Here the contribution of fundamental frequency (F0) and low-frequency phonetic cues to speech recognition in combined hearing was investigated. Normal-hearing listeners heard vocoded speech in one ear and low-pass (LP) filtered speech in the other. Three listening conditions (vocode-alone, LP-alone, combined) were investigated. Target speech (average F0=120 Hz) was mixed with a time-reversed masker (average F0=172 Hz) at three signal-to-noise ratios (SNRs). LP speech aided performance at all SNRs. Low-frequency phonetic cues were then removed by replacing the LP speech with a LP equal-amplitude harmonic complex, frequency and amplitude modulated by the F0 and temporal envelope of voiced segments of the target. The combined hearing advantage disappeared at 10 and 15 dB SNR, but persisted at 5 dB SNR. A similar finding occurred when, additionally, F0 contour cues were removed. These results are consistent with a role for low-frequency phonetic cues, but not with a combination of F0 information between the two ears. The enhanced performance at 5 dB SNR with F0 contour cues absent suggests that voicing or glimpsing cues may be responsible for the combined hearing benefit. © *2007 Acoustical Society of America.* [DOI: 10.1121/1.2717408]

PACS number(s): 43.66.Ts, 43.71.Ky [RAL] Pages: 3717–3727

I. INTRODUCTION

Fundamental frequency (F0) information has been shown to be one of the most powerful cues for sound-source segregation in competing backgrounds (e.g., Brokx and Nooteboom, 1982; Assmann and Summerfield, 1990). The difficulties of speech understanding in noisy environments in cochlear-implant (CI) listeners (Friesen *et al.*, 2001; Stickney *et al.*, 2004) have been attributed, at least partly, to an inability to encode voice pitch (e.g., Qin and Oxenham, 2005; Vongphoe and Zeng, 2005).

Much research has been dedicated to improving pitch coding in cochlear implants, with the long-term goal of enhancing music perception and speech recognition in noise. Such efforts include high-rate stimulation (Litvak *et al.*, 2003), changing filter properties in the speech processor (Geurts and Wouters, 2004), delivering temporal fine structure (Nie *et al.*, 2005), and enhancing the F0-related modulations in each channel (Vandali *et al.*, 2005; Laneau *et al.*, 2006). Recently, the increased availability of a clinical population with low-frequency residual hearing has provided an alternative way of improving implant users' speech perception in noise. Given that pitch is best encoded with the fine timing information carried in the peripherally resolved lower-order harmonics (e.g., Plomp, 1967; Houtsma and Smurzynski, 1990), the low-frequency acoustic hearing in these patients may allow them to better perceive pitch, thereby improving speech recognition in noise.

Several studies, using real cochlear-implant listeners (e.g., Ching *et al.*, 2004; Turner *et al.*, 2004; Kong *et al.*, 2005) and normal-hearing listeners listening to simulations of cochlear implants (Qin and Oxenham, 2006), have shown that speech recognition improved with additional low-frequency information, compared to cochlear implant or vocoded speech alone. Turner *et al.* (2004) tested a group of implant users who were implanted with short-electrode arrays and had substantial low-frequency residual hearing in the implanted ear. Compared to performance in the traditional long-electrode users, they reported that short-electrode users showed greater improvement in speech recognition in a competing talker background than in a steady-state noise background. They attributed the enhanced speech recognition performance to listeners' ability to exploit the voice differences between the target and the masker speech. A similar conclusion was reached by Qin and Oxenham (2006), who found that adding low-pass filtered speech to a "vocoder" simulation of implant hearing improved speech recognition in the presence of a competing masker, and also aided identification of pairs of concurrent vowels. A recent study by Kong *et al.* (2005), which prompted the present study, also showed that low-frequency information could aid speech recognition in noise in cochlear-implant users. They tested a group of implant listeners with substantial low-frequency residual hearing in the contralateral ear. First they reported that while the low-frequency acoustic stimulation alone did not allow any words to be recognized in a speech-recognition test, it enhanced speech understanding when combined with electric stimulation. Second, they showed that the improve-

[a)]Portions of this work were presented at the 150th Meeting of Acoustical Society of America, Providence, RI 2006.

[b)]Author to whom correspondence should be addressed. Present address: Department of Speech-Language Pathology and Audiology, 106A Forsyth Building, Northeastern University, Boston, MA 02115. Electronic mail: yykong@neu.edu

ment in performance produced by contralateral low-frequency hearing was greater when the masker voice was of the opposite sex to the (male) target voice. Third, they showed that melody recognition with low-frequency acoustic hearing was better than with a CI—the opposite pattern of results to that obtained in the speech recognition task. Based on these three findings, Kong and colleagues proposed that the segregation of target speech from the masker is based on the temporal periodicity cues in both the acoustic and electric signals. Specifically, they suggested that CI listeners may extract the pitch of the target speech from the nonimplanted ear, and correlate the resulting pitch values with the degraded F0 information presented via their implant.

Although it has yet to be directly tested, implant researchers generally accept that the enhanced speech recognition in competing noise, provided by adding acoustic information to electric stimulation, is largely due to the addition of F0 information (e.g., Turner *et al.*, 2004; Kong *et al.*, 2005; Qin and Oxenham, 2006). There are two main reasons for this. First, it is known that residual low-frequency hearing does, in fact, produce better pitch perception than is available via an implant (Kong *et al.*, 2005). Because it also improves speech understanding in noise, it is tempting to posit a causal link—particularly given that pitch cues are indeed important for sound segregation (e.g., Brokx and Nooteboom, 1982; Assmann and Summerfield, 1990). However, it should be noted that this causality remains unproven, and it has not been demonstrated whether or how acoustic pitch information can be combined with the highly degraded representation of F0 provided by an implant. Second, the effects of combining low-frequency acoustic hearing with an implant are sometimes "super-additive" (Brill *et al.*, 2001; Wilson *et al.*, 2002; Dunn *et al.*, 2005; Kong *et al.*, 2005). As noted earlier, Kong *et al.* (2005) found that aiding the ear with hearing helped speech understanding when combined with an implant, but led to zero words being correctly reported using the aided ear alone. However, it should be noted that, even though very low-frequency hearing (or unintelligible auditory signals) may not be sufficient to correctly identify any whole words, this does not mean that it conveys no phonetic information at all. An example of this comes from the well-documented observation that, even though a single-channel implant alone may provide little open-set word recognition, it can aid lipreading substantially (e.g., Rosen and Ball, 1986).

The main purpose of this study was to examine which cues are responsible for the improved speech recognition in noise in binaurally combined acoustic and electric stimulation. To do so, we used simulations of a cochlear implant and profound high-frequency (>500 Hz) hearing loss, presented to normal-hearing listeners. Two types of cues, potentially provided by low-frequency acoustic hearing, were manipulated in this study. The first cue, concerning the variation in F0 over time, has already been described. We distinguished it from the voicing cue, which referred to information on the timing of the voiced segments of speech, independent of the F0 of that voicing. The second type of cue arose from the fact that information on the segmental phonetic features of speech, such as first formant (F1), formant transition cues, manner and place of articulation of consonants, may be available acoustically at the low-frequency region, and could be combined with speech information presented to the (simulated) implant ear. We referred to this general class of cues as "low-frequency phonetic" cues.

Four experiments were conducted. The first consisted of a baseline condition to replicate the results of Kong *et al.* (2005) in normal-hearing listeners, with simulations of cochlear implant processing and low-frequency hearing. The second experiment was designed to examine the hypothesis proposed by Kong *et al.* (2005) by eliminating the periodicity cues in the vocoded simulation. Kong and colleagues proposed that CI listeners extract the pitch of the target speech from the nonimplanted ear, and correlate the resulting pitch with degraded F0 information, which is carried in the temporal envelope, in the implanted ear. If listeners still show improvement when envelope periodicity cues are removed in the vocoded ear, it suggests that the combined benefits are not due to the enhanced temporal pitch. The third experiment examined the role of low-frequency phonetic cues, while the fourth experiment examined the role of the F0 cue.

II. GENERAL METHODS

A. Participants

All participants were normal-hearing listeners with ages ranging from 17 to 35 years, and with normal audiometric thresholds (<20 dB HL) between 125 and 8000 Hz. Six listeners took part in experiment 1, and separate sets of twelve listeners took part in all other experiments.

B. Stimuli

1. Left ear

Target sentences, each of which contained three keywords, were taken from the Adaptive Sentence Lists ("ASL," MacLeod and Summerfield, 1990). They were produced by a male speaker of Southern British English. There were 18 lists in the corpus and each list contained 15 sentences and therefore, each experimental condition was tested in blocks of 15 sentences. The target sentences were first equated to have the same root-mean-squared (rms) amplitude. They were then processed using the PRAAT speech synthesis program (Boersma and Weenink, 2005) to change the mean F0 of the original sentences to 120 Hz (by a simple linear shift) while preserving their natural F0 contours. After processing, the average F0 of the different sentences ranged from 100 to 140 Hz. The within-sentence variation of F0 (i.e., the difference between the lowest F0 and the highest F0 measured within a sentence) ranged from 52 Hz (101–153 Hz) to 122 Hz (77–199 Hz), and the typical within-sentence variation of F0 was 90 Hz (80–170 Hz). Each of the target sentences was then mixed with one of 15 different masker stimuli. Similar to the method used by Deeks and Carlyon (2004), each masker was constructed from three concatenated Bench-Kowal-Bamford (BKB) sentences (Bench and Bamford, 1979), which were time-reversed and truncated to

TABLE I. Cutoff frequencies of the analysis and resynthesis bands used in a six-band noise-vocoder cochlear implant simulation.

Frequency band	Analysis band center and cutoff frequencies (Hz)			Resynthesis band center and cutoff frequencies (Hz)		
	Lower	Center	Upper	Lower	Center	Upper
1	70	140	229	140	278	457
2	229	344	494	457	688	987
3	494	687	937	987	1374	1875
4	937	1261	1680	1875	2522	3359
5	1680	2221	2921	3359	4442	5844
6	2921	3828	5000	5844	7656	10000

a duration of 3.5 s, with 20 ms raised-cosine ramps. The BKB sentences were first processed to change the mean F0 of the original sentences to 172 Hz (range from 150 to 200 Hz). The average F0 of the final 15 different masker stimuli (constructed from three concatenated BKB sentences) ranged from 161 to 180 Hz. The within-masker variation of F0 ranged from 119 Hz (101–229 Hz) to 154 Hz (121–257 Hz), and the typical within-masker variation of F0 was 130 Hz (110–240 Hz). The target ASL sentence was added to one of the 15 masker stimuli with an offset of 1.0 s before undergoing further signal processing. The level of the target speech was fixed at 65 dB A, with the level of masker varied to produce different signal-to-noise ratios (SNRs): 0, 5, 10, 15, and 20 dB.

The target+masker mixture was then bandpass filtered into six contiguous frequency bands between 70 and 5000 Hz, spaced according to Greenwood's (1990) map, using sixth-order Butterworth filters. The envelope of the output of each of these analysis filters was then extracted by half-wave rectification and low-pass filtering at 300 Hz (fourth-order Butterworths). Each envelope then modulated a wideband noise, which was subsequently filtered by a bandpass filter whose center frequency was twice that of the corresponding analysis filter. The center frequencies and cutoffs of each analysis and synthesis filter are shown in Table I. The upward-frequency shift of the synthesis filters simulates the frequency-to-electrode mismatch of approximately 5 mm in electric stimulation, in a situation where implant listeners have a deep electrode insertion of about 30 mm from the basal end of the cochlea (Hochmair *et al.*, 2003), according to the Greenwood (1990) equation. Finally, the modulated narrowband noises were summed to resynthesize the input stimuli.

2. Right ear

In experiments 1 and 2 the right ear received the target+masker mixture, low-pass (LP) filtered at 125 Hz (fourth-order Butterworth). The target stimuli were presented at about 85 dB A, a comfortable listening level for normal-hearing subjects, as determined from our preliminary study. To restrict the upward spread of excitation beyond 500 Hz, a narrowband noise (500–1500 Hz) with an overall level of 55 dB SPL was added to the same ear. The right-ear stimuli used in experiments 3 and 4 will be described later.

C. Procedure

All experiments were created using a within-subject design. In other words, each subject was tested on both the baseline condition and the experimental conditions, and the subsequent analyses were performed using a repeated-measures ANOVA or a paired-t test.

All subjects listened through headphones in a double-walled sound-treated booth. Stimuli were first processed as described earlier and then played out via a sound card (Turtle Beach Sonic Fury) with 24 bit resolution at a sampling frequency of 22.05 kHz. Stimuli for the left and right ears were passed through separate programmable attenuators (TDT PA4) and to different channels of a headphone buffer (TDT HB6), before being presented to the Sennheiser HD580 headphones.

For each experiment, subjects were evaluated under three listening conditions [vocoded speech alone (left ear), LP stimuli alone (right ear), and combined vocoded and LP stimuli], and different SNRs. All three listening conditions were first tested at the highest SNR, then at the next-highest, and so on. Within each SNR, the order of the three listening conditions was counterbalanced among subjects to minimize the learning effect in the group data. Also, to minimize the effect of sentence list, the presentation of the sentences was also counterbalanced for the three listening conditions. This meant that, when combined across subjects, each sentence was presented an equal number of times in each listening condition.

Each subject received one training session prior to the experiment. In this session, subjects listened to 15 IEEE (1969) sentences in quiet, processed the same way as described earlier for each listening condition. After the training, subjects were further instructed that the target sentences would be presented in a nonsensical background, which they should ignore. Subjects responded by typing in the words they heard at the keyboard in the sound booth and they were encouraged to guess if unsure. Responses were hand-scored for the number of keywords correctly recognized.

III. EXPERIMENT 1: BASELINE CONDITION

A. Rationale

This experiment attempted to replicate the pattern of results reported by Kong *et al.* (2005), using normal-hearing

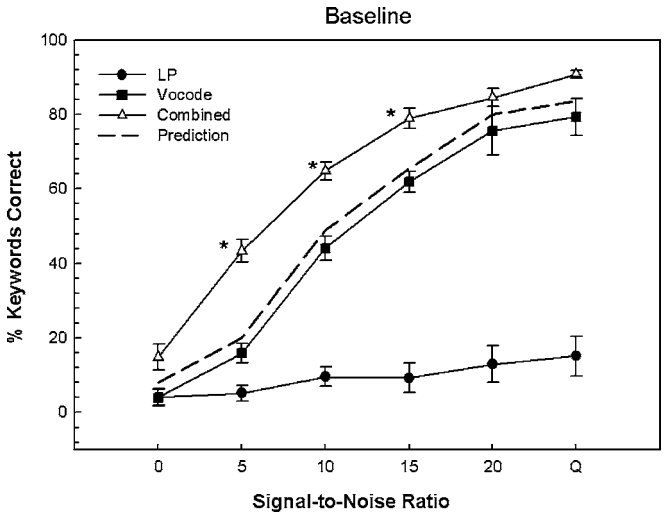

FIG. 1. Percent correct word recognition from six listeners. The closed symbols represent the monaural listening condition (circles: LP-alone; squares: vocode-alone) and the open triangles represent the combined hearing condition. The dashed lines indicate the probability of correct recognition for either the LP-alone, or vocode-alone condition or both. The asterisks (*) indicate significant difference between the vocode-alone and the combined hearing conditions after corrections for the multiple comparisons. The vertical lines indicate the standard errors adjusted using the Loftus and Masson (1994) method.

listeners listening to simulations of a Cl in one ear and a profound high-frequency (>500 Hz) hearing loss in the other. Results from this experiment also helped determine the SNRs that would be tested in the subsequent experiments.

B. Methods

Six subjects took part. All subjects were evaluated on all three listening conditions and five different SNRs and in quiet. Stimuli were the same as described in Sec. II. In sum, the same speech+masker mixtures were presented to both ears via headphones, but the left ear received the vocoded version of the stimuli and the right ear received the LP version.

C. Results

Average speech recognition performance (% keywords correct) in quiet and at five different SNRs is summarized in Fig. 1. Several aspects of the results are very similar to those reported in Kong *et al.* (2005).

(1) With only limited low-frequency hearing, subjects' performance was generally very poor, ranging from 15% correct in quiet to near zero at 0 dB SNR. This level of performance is slightly higher than that reported for the nonimplanted ear in the cochlear implant listeners of Kong *et al.*, probably because we used ASL sentences here, which contain more contextual information than the IEEE sentences employed by Kong *et al.*

(2) Performance improved monotonically with increasing SNR in both the vocode-alone and combined hearing condition. With vocoded speech alone, the average performance increased from 4% to 79% correct as SNR increased from 0 dB to the quiet condition. This level of performance was similar to that of the best subjects in the study of Kong *et al.*, and somewhat higher than the average performance in that study.

(3) Performance was superior with combined hearing compared to the vocode-alone condition. A two-way (listening condition × SNR) repeated-measures ANOVA, performed with the LP-alone condition excluded, revealed significant main effects of listening condition [$F(1,5)=24.0$, $p<0.005$] and SNR [$F(5,25)=174.8$, $p<0.001$], and a nonsignificant interaction between the two factors [$F(5,25)=2.0$, $p>0.1$]. Pairwise comparisons using a paired t-test with the Bonferroni correction revealed significantly higher scores in the combined hearing condition than in the vocode-alone condition with average differences of 27, 21, and 17 percentage points at 5, 10, and 15 dB SNR ($p<0.01$), respectively. The amount of improvement obtained in the present study was comparable to that observed in Kong *et al.* at the same SNRs with a male target and a female masker.

(4) Consistent with the results of Kong *et al.*, a "super-additive" effect was observed at 5 and 10 dB SNR ($p<0.01$), in which the combined hearing performance exceeded the performance of the probability of correct recognition for either the LP-alone, or vocode-alone condition, or both (see the dashed line in Fig. 1). The estimated scores were calculated as

$$\mathrm{Pc} = 1 - [(1 - \mathrm{Pc(LP)}) \times (1 - \mathrm{Pc(vocode)}], \quad (1)$$

where Pc(LP) represented the percent correct score with LP stimuli alone and Pc(vocode) was the percent correct score with vocoded stimuli alone (Boothroyd and Nittrouer, 1988).

IV. EXPERIMENT 2: REMOVING ENVELOPE-PERIODICITY CUES IN THE VOCODED SPEECH

A. Rationale

Given the significant sex of masker effects in the combined acoustic and electric stimulation, Kong and colleagues hypothesized that patients correlate the temporal fine structure in the nonimplanted ear and the temporal envelope-periodicity cues in the implanted ear to enhance voice pitch perception, which in turn improves speech recognition in a competing background. To test this hypothesis, experiment 2 manipulated the usefulness of the temporal envelope-periodicity cues by removing the F0 information in the vocoded speech, keeping all other cues constant across conditions. We hypothesize that if listeners improve speech recognition by correlating the F0 cues from the LP speech with the envelope-periodicity cues in the vocoded stimulus, then the LP speech should not improve performance when the envelope cutoff for the vocoded speech is reduced to 35 Hz to eliminate any envelope-periodicity information.

B. Methods

A new group of 12 subjects took part. In addition to the 35 Hz envelope experimental condition, all subjects were also tested on the baseline condition (300 Hz envelope) to

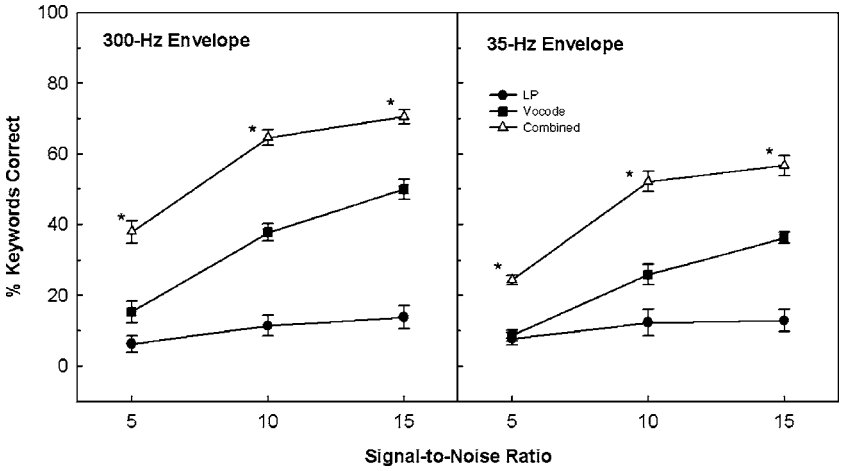

FIG. 2. Average speech recognition performance from 12 listeners. Both the baseline (left panel: 300 Hz envelope) and experimental condition (right panel: 35 Hz envelope) are presented. Different symbols represent different listening conditions (circles: LP-alone; squares: vocode-alone; triangles: combined hearing). The asterisks (*) indicate significant difference between the vocode-alone and the combined hearing conditions and the vertical lines indicate the adjusted standard errors.

facilitate comparisons. Half of the subjects were tested with the 300 Hz envelope condition first followed by the 35 Hz envelope condition, and the other half had the reversed sequence. The stimuli and the test procedures used in this experiment were otherwise the same as those described in Sec. II.

C. Results

Subjects showed improvement in the combined hearing compared to vocode-alone in the 300 Hz envelope condition at the three SNRs tested (5, 10, and 15 dB), consistent with results in experiment 1 (Fig. 2, left panel). Importantly, they showed a similar, significant improvement when the F0 cue was removed in the vocoded speech, by low-pass filtering the envelope in each channel at 35 Hz (Fig. 2, right panel). This pattern of results persisted at all SNRs [at 5 dB SNR: $t(1,11)=6.8$, $p<0.001$; 10 dB SNR: $t(1,11)=6.0$, $p<0.001$; 15 dB SNR: $t(1,11)=6.3$, $p<0.001$]. Performance in the vocode-alone condition was worse with the lower envelope cutoff frequency [$F(1,11)=12.1$, $p=0.005$]. These results are consistent with the improved vowel, consonant, and sentence recognition in quiet with increasing envelope cutoff for the vocoder processing up to 500 Hz in Mandarin Chinese (e.g., Fu *et al.*, 1998; Xu *et al.*, 2002). Shannon and colleagues (1995) also reported that, in English, sentence recognition in quiet decreased by about 10–20 percentage points when envelope-periodicity cues were removed (envelope cutoff frequency=16 Hz). Although performance in the vocode and combined conditions was lower overall when the envelope was low-pass filtered at 35 Hz, the improvement from the vocode-alone to the combined conditions was similar to that when the envelope was filtered at 300 Hz. The average improvement was 18, 26, and 20 percentage points at 5, 10, and 15 dB SNR in the 35 Hz envelope condition, compared to an average of 23, 27, and 21 percentage points when the envelope was filtered at 300 Hz. The interaction between envelope cutoff (300 vs 35 Hz) and listening condition (vocode versus combined) was not statistically significant [$F(1,11)=0.48$, $p>0.05$]. These findings suggest that the improved speech recognition in the combined hearing is not attributable to the enhanced F0 information based on the temporal periodicity cues in the vocoded ear. However, we cannot rule out the possibility that F0 cues from the LP ear aided performance in some other way, without allowing listeners to better use degraded pitch information in the vocoded ear. Experiments 3 and 4 further investigated the role of F0 cues in the LP ear for speech recognition in noise in combined hearing.

V. EXPERIMENT 3: REMOVING PHONETIC CUES IN THE LP EAR

A. Rationale

Experiment 3 examined the extent to which improved speech recognition can be accounted for when F0 cues are available, but when other phonetic cues were removed in the LP stimuli. Speech recognition performance was compared between the vocode-alone and combined conditions at different SNRs. The idea was to reveal the extent to which low-frequency phonetic cues are necessary for an advantage from combined hearing by measuring the improvement in performance, if any, conferred by a new LP stimulus in which phonetic cues (except for voicing) are absent.

B. Methods

Another 12 subjects were tested in this experiment. Half of the subjects were tested with the baseline condition first followed by the new experimental condition with phonetic cues removed from the LP stimuli, and the other half had the reversed sequence. The stimuli and the test procedures were the same as those described in Sec. II, except that the LP filtered stimuli in the right ear were manipulated to remove low-frequency phonetic cues while preserving the F0, voicing, and temporal envelope cues of the target speech. The manipulation is described as follows.

We used the PRAAT (Boersma and Weenink, 2005) speech analysis and synthesis program to first extract the F0 of the original target speech. Using the PRAAT program, we then created a harmonic complex with the same F0 variation over those time segments when voicing occurred. Voiceless portions of the original target speech were represented by silence. This frequency-modulated (FM) complex was then modulated with the envelope of the voiced portions of the original (unfiltered) speech extracted by the PRAAT program. Crucially, the shape of the spectral envelope of the new

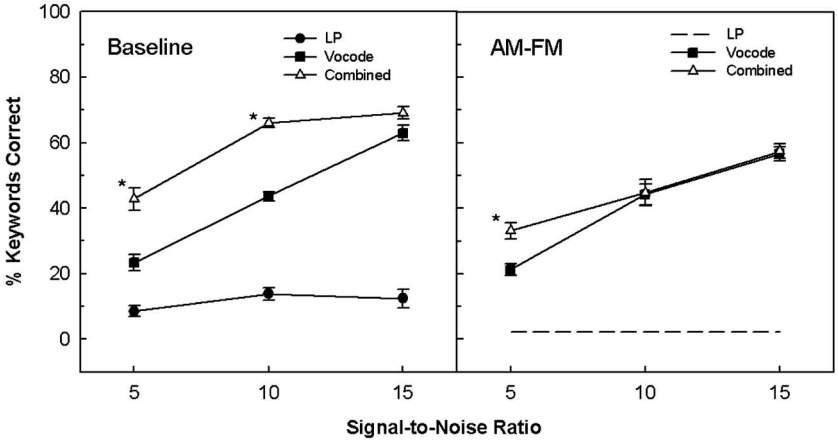

FIG. 3. Average speech recognition for the baseline (left panel) and the AM-FM condition (right panel). Since the LP stimuli alone were presented without a masker, the average data are indicated with a dashed line. Again, the asterisks (*) indicate significant difference between the vocode-alone and the combined hearing conditions and the vertical lines indicate the adjusted standard errors.

stimulus remained constant throughout, thereby eliminating low-frequency phonetic information but preserving the F0, voicing, and temporal envelope cues of the voiced portions of the target speech. The temporal envelopes provide temporal cuing, known as temporal glimpsing cues (Assmann and Summerfield, 2004), to indicate the time segments where target speech was present. We carried out a careful examination on the AM-FM stimuli for 1/3 of the test speech materials. In general, the voiced portions of the natural speech were accurately represented in the AM-FM stimuli. We did find occasionally that part of the voicing information in the original speech was missing in the AM-FM stimuli, but this happened mostly when voicing continued from a voiced segment to a supposedly unvoiced segment due to coarticulation.[1]

The AM-FM harmonic complex was later LP filtered with the same LP settings as in the baseline experiment, but without mixing with the masker. We omitted the masker in order to maximize the chances that listeners could exploit the F0 contour of the target sentence in the LP ear. Also, in the Kong *et al.* study, the masker may have been inaudible at some of the SNRs tested due to the limited dynamic range of impaired hearing. Our simulation more accurately reflected this situation than if we had mixed targets and maskers at a moderate SNR in normal-hearing subjects, for whom both the target and masker would have been within their dynamic range. The vocoded stimuli used for the opposite ear were based on the target+masker mixture, as in the baseline experiment, for SNRs of 5, 10, and 15 dB.

C. Results

Figure 3 shows speech recognition performance for both the baseline (left panel) and AM-FM conditions (right panel). The improved speech recognition in noise in the baseline was evidenced at 5 [$t(1,11)=3.4$, $p<0.01$] and 10 dB SNR [$t(1,11)=10.5$, $p<0.001$] in this group of subjects. At 15 dB SNR, two subjects did not show the combined hearing benefit and therefore the statistical analysis revealed a nonsignificant difference [$t(1,11)=1.8$, $p>0.05$]. Otherwise, results were consistent with those reported in the previous two experiments.

The pattern of results in the AM-FM condition was different from the baseline. The vocode-alone performance was essentially the same as the vocode-alone performance in the baseline condition [$F(1,11)=2.0$, $p>0.1$], which is as expected as the stimuli were identical in the two studies. However, the LP-alone performance with the AM-FM harmonic complex was at 0%, indicating that information about the F0 contour and the voiced segments of the speech envelope were not sufficient for subjects to identify any words correctly. More important, the AM-FM complex, which preserved the F0, voicing, and glimpsing cues, did not enhance performance when combined with the vocoded stimuli at SNRs of 10 [$t(1,11)=0.1$, $p<0.1$] and 15 dB [$t(1,11)=0.2$, $p<0.1$]. However, the advantages of combined hearing of 12 percentage points did persist at the lowest SNR of 5 dB [$t(1,11)=3.0$, $p=0.012$]. These findings suggest that the improvement of speech recognition at the higher SNRs in the baseline condition was due to the phonetic information preserved in the LP stimuli. A three-way (LP stimulus $\times$ listening condition $\times$ SNR) repeated-measures ANOVA revealed a significant two-way interaction between the LP stimulus (baseline versus AM-FM) and the listening conditions (vocode-alone versus combined) [$F(1,11)=9.7$, $p=0.01$], reflecting the fact that speech information plays an important role in the enhanced speech recognition compared to vocode-alone. The persistence of improvement at the lowest SNR, however, suggests that, to some extent, either F0, voicing, or glimpsing cues, or a combination of these cues, can contribute to speech recognition in combined hearing.

The exact mechanism underlying the improvement in the combined hearing condition at the lowest SNR in experiment 3 is unclear. It is possible that the onset of the LP stimuli signaled the onset of the target speech in the vocoded ear, which was presented 1 s after the start of the masker. This cue may be especially important at the less favorable SNRs, where, without it, the small increase in loudness accompanying the onset of the target speech in the vocoded stimulus may be insufficient to tell the subject "when to start listening." To investigate the possibility of this speech onset cue we tested an additional condition, in which we presented the target speech starting at the same time as the masker in the vocoded ear. The AM-FM complex in the LP ear was in synchrony with the onset of the target speech in the vocoded ear.

The pattern of results from 12 subjects in this new con-

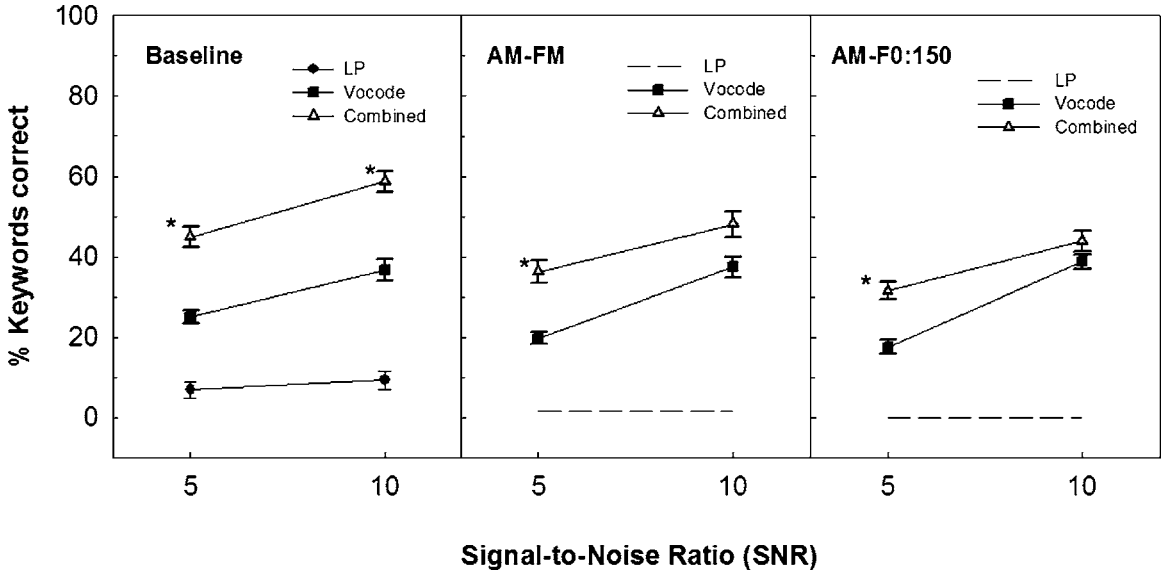

FIG. 4. Speech recognition performance for three conditions: baseline (left panel), AM-FM (middle panel), and AM-F0:150 (right panel). Only 5 and 10 dB SNRs were tested.

dition was essentially identical to that obtained in the previous condition when the target sentence started 1 s after the onset of the masker. This finding eliminated the possible explanation that listeners merely used the gross timing information (onset of the target speech) provided by the LP stimuli to enhance speech recognition in noise.

VI. EXPERIMENT 4: REMOVING BOTH F0 CONTOUR AND PHONETIC INFORMATION IN THE LP EAR

A. Rationale

The cue(s) used to aid speech recognition in combined hearing in the AM-FM LP stimuli at the lowest SNR is/are still undetermined. A number of cues, including F0, voicing, and glimpsing were present in the AM-FM harmonic complex, and any of these cues alone or a combination of them could contribute to better speech recognition in a more challenging listening situation. Experiment 4 was designed to evaluate the contribution of F0 cues by eliminating the F0 contour of the target speech information in the LP stimuli. If this manipulation eliminates the advantage seen in experiment 3 at the lowest SNR, then we can conclude that F0 cues do indeed provide useful information.

B. Methods

Another group of 12 subjects took part. The F0 contours of the target speech in the LP stimuli in experiment 3 were replaced by a harmonic complex with an F0 fixed at 150 Hz, which fell between the average F0s of the target speech and of the masker. The fixed F0 harmonic complex was then amplitude modulated by the envelope of the voiced portions of the target speech. Because this complex was present only when the target speech was voiced, and because it was modulated by the target speech envelope, both the voicing and glimpsing cues were still present as before. It should be noted that the target was presented at the onset of the masker.

To facilitate comparison, each subject was tested on three LP stimulus conditions: baseline (i.e., LP speech), AM-FM, and this new manipulation with fixed F0 (AM-F0:150). The baseline and the AM-FM conditions were identical to experiment 3 with the target sentence presented at the onset of the masker. Because we wanted to present each sentence only once to each listener, and because the number of ASL sentences is limited, we tested only two SNRs: 5 and 10 dB for each condition.

C. Results

Figure 4 shows the average performance for the baseline, AM-FM, and AM-F0:150 conditions. First, note that the pattern of results in this group of subjects in the baseline and AM-FM conditions resembled those found in experiment 3, in which the advantage of combined hearing was evidenced in both SNRs in the baseline condition [5 dB SNR: $t(1,11)=5.3$, $p<0.001$; 10 dB SNR: $t(1,11)=4.6$, $p=0.001$], but only at the lowest SNR at 5 dB in the AM-FM condition [$t(1,11)=4.0$, $p<0.005$]. The difference between the combined and vocode-alone condition was not significant at 10 dB SNR [$t(1,11)=1.96$, $p=0.076$]. The most interesting finding is that the pattern of results was essentially the same in the AM-FM condition and in the AM-F0:150 condition, even though in the latter case there was no F0 contour information in the LP stimuli. While the combined hearing benefit disappeared at a higher SNR of 10 dB [$t(1,11)=1.4$, $p>0.1$], it persisted at the more challenging SNR of 5 dB [$t(1,11)=4.0$, $p<0.005$]. The persistence of combined hearing advantage in the 5 dB SNR condition suggests that voicing and/or glimpsing cues play a role in the enhanced speech performance in the combined hearing condition. The average performance for the vocode-alone condition was similar across the three conditions. A three-way (LP stimulus condition × listening condition × SNR) repeated-measures ANOVA revealed a significant two-way interaction between the LP stimulus condition and the listening condition

([$F(2,22)=4.1$, $p<0.05$]), suggesting that the improvement in performance at the 5 dB SNR is smaller in the AM-FM and AM-F0:150 conditions compared to the baseline condition, further indicating the contribution of speech information in combined hearing. When the data from the baseline condition were removed, leaving only the AM-FM and AM-F0:150 conditions, the interaction disappeared ([$F(1,11)=1.38$, $p>0.05$]), indicating that F0 information was not important.

VII. DISCUSSION

A. Mechanisms underlying enhanced speech recognition in noise

Kong *et al.* (2005) reported that low-frequency acoustic hearing could enhance speech recognition in noise, when combined with a cochlear implant. Two findings led them to suggest that this improvement was due to a combination of F0 information between the acoustic and electric stimuli presented to opposite ears. First, pitch perception, as assessed by melody recognition, was superior with LF acoustic hearing than with electric stimulation. Second, performance in combined hearing was better when the target and masker speech were produced by speakers of opposite sex, and the same was true for the improvement in performance *re* electric stimulation alone. In contrast, the experiments reported here suggest that low-frequency acoustic hearing improves speech understanding in noise not via the use of F0 cues, but rather by providing low-frequency phonetic information on the variation in the low-frequency spectrum over time. Other cues, such as voicing and/or glimpsing cues may also be responsible for the observed improvement in the combined hearing, especially at the lower SNRs.

One way of resolving the different conclusions of the two studies arises from the fact that the present study did not employ real CI users, but instead used simulations of acoustic and electric stimulation presented to normal-hearing listeners. One obvious reason for not observing an effect of F0 would be if the simulations of low-frequency hearing we used did not in fact preserve adequate F0 information. To test this, we applied the LP AM-FM processing used in experiment 3 to the low-frequency melody stimuli used by Kong *et al.* (2005). The F0s of the notes comprising the melodies ranged from 104 to 262 Hz. Two normal-hearing listeners were able to recognize the melodies with scores greater than 80% correct, suggesting that our LP stimuli did indeed preserve pitch cues. In contrast, when the same stimuli were subjected to the vocoder processing described here, performance was at chance level, consistent with the findings reported in Kong *et al.* (2004). Hence our results show, at the very least, that it is possible to simulate several key aspects of the results presented by Kong *et al.* including (1) superior melody recognition with acoustic compared to electric stimulation, (2) greatly superior speech perception with electric than with acoustic stimulation, and (3) *apparently* "super-additive" benefits when combined with electric stimulation. Our results show that F0 variations are neither necessary nor sufficient for an advantage from adding LP acoustic stimuli to be observed. Specifically, (1) the combined hearing advantages persisted at the lowest SNR when the F0 cue was removed from the LP stimulus; and (2) the combined hearing advantages disappeared at the higher SNRs when we preserved the F0 cue but eliminated low-frequency phonetic cues.

How, then, can we explain the results of Kong *et al.*? As our results show, the fact that acoustic stimuli may provide superior pitch information and improve speech recognition in noise does not mean that these two facts are causally linked. In fact, results from our study showed that improved speech recognition in combined acoustic and electric stimulation was not attributed to the better encoding of voice pitch information with additional low-frequency cues. However, the greater improvement *re* CI hearing alone, observed by Kong *et al.* with male target speech, when the masking speech came from a female compared to another male talker could be explained with the following possibilities:

(1) *Better represented target F1 in the nonimplanted ear*. Not only the F0 but also the F1 will be higher with the female masker. Due to the nature of the high-frequency hearing loss in the nonimplanted ear, the masker F1 will be attenuated more, with respect to that of the target, in the nonimplanted ear.
(2) *Nonadditivity of percent-correct scores*. Although the effect of masker sex was smaller for the CI-only condition than for combined hearing, some of the subjects of Kong *et al.* did perform better with CI hearing alone when the masker was a female, compared to a male voice. It is likely that the difference in the percentage of words correct produced by adding an additional source of information will depend on the baseline level of performance. For instance, the amount of improvement (if any), may be less if the baseline performance is approaching a ceiling (e.g., 80%–100%) or a floor (e.g., 0%–20%), compared to the performance of 50%.
(3) *Source segregation in the nonimplanted ear*. The greatest advantage of combined hearing reported by Kong *et al.* (2005) was at high SNRs, where, due to the reduced dynamic range in sensory hearing loss, only the target may have been audible in the nonimplanted ear. At lower SNRs, subjects may have been able to segregate the masker and target speech in the nonimplanted ear, particularly when they had different F0s. This would require patients' residual frequency selectivity to be good enough to resolve at least some of the harmonics or the formant frequencies in the masker/target mixture. If this were the case then having a representation of two distinct sources in the nonimplanted ear might allow the listener to select one of these sources and combine it with the information presented via the CI.

The possible use of source segregation in the nonimplanted ear may help explain some recent results reported by Qin and Oxenham (2006). They required subjects to identify pairs of simultaneous vowels processed by an eight-channel vocoder, in which the lowest three or four bands could be replaced by versions of the stimuli that were unprocessed except for low-pass filtering at 300 and 600 Hz, respectively. They found that identification of these "combined" stimuli

was better than for completely vocoded stimuli, and, interestingly, improved as the F0 difference between the vowels increased. We agree with their conclusion that this latter finding was probably due to improved segregation of the low-frequency portions of the two vowels. Qin and Oxenham also proposed an explanation similar to that of Kong *et al.*, whereby F0 information in the low-frequency stimuli allowed listeners to exploit F0 cues in the envelopes of the vocoded stimuli, that by themselves were too weak to promote segregation. However, we think it is more likely that F0 differences simply allowed listeners to extract the F1s of the two vowels, and that this information was combined with upper formants based on top-down mechanisms that make use of prior knowledge of vowel structures. First, it is worth noting that the effect of F0 differences in Qin and Oxenham's findings occurred primarily over the range 0–2 semitones, where the effect is largely due to beating between adjacent harmonics of the two vowels, which causes the composite spectrum to become alternately dominated by one vowel then the other (Culling and Darwin, 1994). Second, we believe that some F1 information survived even the 300 Hz low-pass filtering implemented by Qin and Oxenham. We resynthesized Qin and Oxenham's vowel stimuli (F0=100 Hz) and LP filtered them with the same parameters used in their study. We found that the relative amplitudes of the harmonics in Qin and Oxenham's stimuli are preserved across vowels following low-pass filtering at 300 Hz, and this information is available at frequencies as low as 300 Hz, which falls in the frequency region where Qin and Oxenham replaced the vocoded stimulus with LP but otherwise unprocessed speech.[2] Of course, the explanation of combining formant information across ears remains untested, and it is theoretically possible that the combination of low-frequency and vocoded information may be different when presented to the same ears as by Qin and Oxenham, rather than to opposite ears, as done here. However, we believe that the results and analyses presented here demonstrate that speech perception can be improved even by severely low-pass filtered stimuli, and that this improvement does not depend on there being any usable F0 information in the vocoded speech. In this regard it is worth noting that, in our experiment 2, low-pass speech improved speech perception with a competing masker having a different F0, even when F0 periodicity cues were removed from the vocoded stimuli. We believe that the relative role of integration of speech information and F0 grouping cues in Qin and Oxenham's paradigm could be usefully explored using the manipulations employed in our experiments 2–4.

B. Presence of phonetic cues in the LP ear

The results of experiment 3 clearly demonstrated that the low-frequency hearing contained information other than F0 contour cues that could be integrated with the speech information in the vocoded speech to enhance speech recognition in noise. The average 10% correct word recognition in the LP ear at high SNRs also indicated the presence of some phonetic cues after severe LP filtering. This filtering simulated the hearing profiles in the nonimplanted ear of the subjects tested in Kong *et al.* (2005). The types of phonetic information that were potentially preserved by our low-pass filtering include:

(1) F1 cues below 500 Hz, such as in high and mid vowels;
(2) Coarticulation cues, such as formant transition (Strange *et al.*, 1983); and
(3) Low-frequency consonant cues, such as nasal formant (Fujimura, 1962) and voicing cues.

While we obtained an average of 10% correct word recognition with our LP speech material, we do not know the relative importance of these cues in combined acoustic and electric stimulation, or the level of representation at which the information is combined between the ears. For example, at least for normal-hearing listeners, it is possible to identify vowels even when F1 and F2 are presented to opposite ears (Cutting, 1976; Darwin, 1981; Remez, 2001). Hence if listeners can overcome the marked quality differences between acoustic and electric stimuli, it may be possible for them to combine F1 and F2 information across ears.

C. Application to cochlear implants

The experiments described here have examined the relative contribution of a number of cues to the improved speech recognition in simulated combined acoustic and electric stimulation in normal-hearing listeners. The results have several potential implications for the intervention and treatment of CI candidates having residual hearing. Before discussing these, we should note that the results were obtained only from simulations of Cl hearing, rather than from real patients. However, given our success in replicating several key features of the results obtained with CI patients (Kong *et al.*, 2005), the potential implications warrant some cautious discussion.

First, we have argued that estimates of F0 derived from the nonimplanted ear are neither necessary nor sufficient for improved speech understanding in noise. This finding suggests that optimizing hearing aids to maximize pitch perception in the nonimplanted ear may not be an appropriate way of improving speech recognition in noise when combined with a cochlear implant. Second, we showed that information on the time-varying spectral shape is important, even when subjected to quite severe low-pass filtering. These two facts combined lead us to disagree with Qin and Oxenham's (2006) suggestion that explicitly encoding F0 and presenting it to an ear with residual low-frequency hearing is likely to improve speech understanding in noise, at least when the acoustic and electric information is presented to opposite ears. Rather, we would argue that retaining information on F1 and other low-frequency phonetic cues is likely to be more important. Our results also suggest that improvements in combined hearing will be greatest when sound is presented to an ear that can derive this information. This may guide the choice of intervention for a candidate with, for example, some residual hearing in both ears. Presently, the choice of ear of implantation is based mostly on audiometry, in which most clinicians and surgeons recommend implanting the ear with better hearing thresholds. If both ears have

similar duration of hearing impairment and amount of substantial residual hearing, it could be more beneficial to spare the ear that supports better spectrotemporal processing. It may be possible to derive a psycho-acoustic test that taps into this residual auditory ability. This will, of course, require further investigations into the exact nature of the low-frequency information that is effectively combined with electric stimulation, as well as tests using real Cl patients. Both of these approaches are under way in our laboratory.

VIII. SUMMARY

Benefits of combined acoustic and electric stimulation for speech recognition in noise were evaluated in normal-hearing listeners using noise-vocoder simulation in one ear and a low-pass filtering in the contralateral ear. Four experiments were conducted. Three listening conditions: vocode-alone, LP-alone, and combined hearing were tested in each experiment. Differences in performance between the vocode-alone and the combined hearing conditions were the main focus of comparison. Results are summarized as follows:

(1) Listeners showed advantages of combined hearing in our baseline experiment, when speech stimuli were presented to the vocoded ear and the LP ear. These results replicated the findings reported in Kong *et al.* (2005).
(2) Experiment 2 removed the F0 information in the vocoded stimulus. The improvement in speech recognition in combined hearing compared to vocode-alone was similar to that obtained when F0 cues were present in both ears, suggesting that the improved speech recognition performance was not due to the enhanced voice pitch perception in the vocoded ear when provided with the additional low-frequency fine structure information in the opposite ear.
(3) Advantages of combined hearing disappeared at the higher SNRs when low-frequency phonetic cues were eliminated by replacing the speech stimuli with a harmonic complex which followed the F0 contour and the temporal envelope of the voiced portions of the original target speech. This suggests that, at high SNRs, F0 is not the contributing factor for the improvement of speech recognition in combined hearing. Low-frequency phonetic cues, on the other hand, provide information that is crucial for improved speech recognition. However, at the lowest SNR of 5 dB, listeners still showed a slight improvement.
(4) When the F0 cue was eliminated by fixing the F0 at 150 Hz in the harmonic complex, an advantage from combined hearing was still obtained at low SNRs. This suggests that, in addition to the low-frequency phonetic cues, voicing or glimpsing cues also aid speech recognition in noise in combined hearing.

ACKNOWLEDGMENTS

This work would not have been possible without the assistance of Patrick Axon FRCS, and was supported by the Otology Research Fund and a grant from the National Organization for Hearing Research Foundation. We thank Dr. Hedwig Gockel and Dr. Peter Assmann for useful discussions, and Dr. Wesley Grantham and two anonymous reviewers for their helpful comments on the earlier version of this manuscript.

[1]Assimilation is a phonological process that occurs when the articulation of one sound is influenced by adjacent sounds. For example, in the original speech, the /s/ of the first syllable in the word "raspberries" became voiced due to the influence of the preceding vowel. The voicing weakened in the later part of the segment and eventually became voiceless. The AM-FM stimuli, however, only preserved the voicing information of the first part of the segment while voicing was very strong. Out of the 90 sentences examined, there were only three occasions that voicing corresponding to a vowel was missing in the AM-FM stimuli. These were short vowels and were positioned in-between two highly aspirated consonants, such as the schwa /ə/ in the second syllable of the word "pockets." The aspiration in the adjacent consonants may weaken the periodicity detection on the basis of the autocorrelation method employed in the PRAAT program.

[2]We should note that the 300 Hz low-pass-filtered speech used by Qin and Oxenham was not sufficient to support above-chance performance when presented alone. However, very poor performance has been reported by Culling and Darwin (1993) for intact F1s presented alone, who reported scores of between 10% and 15% correct for pairs of vowels selected from a set of five. Culling and Darwin also showed that the performance for complete double vowels exceeded that predicted by performance obtained in separate conditions where information from either F1 or F2 was presented separately, even when the F0s of the upper and lower formants were swapped. Hence, just because information in one spectral region is insufficient to support identification of any one vowel pair, it still can convey formant information that can be combined with that on other formants, even in the face of conflicting grouping cues.

Assmann, P. F., and Summerfield, Q. (**1990**). "Modeling the perception of concurrent vowels: Vowels with different fundamental frequencies," J. Acoust. Soc. Am. **88**, 680–696.

Assmann, P. F., and Summerfield, Q. (**2004**). "The perception of speech under adverse conditions," in *Speech Processing in Auditory System*, Springer Handbook of Auditory Research, edited by W. Ainsworth, S. Greenberg, and A. N. Popper (Springer, New York), pp. 231–308.

Bench, J., and Bamford, J. (**1979**). *Speech-hearing Tests and the Spoken Language of Hearing Impaired Children* (Academic, London).

Boothroyd, A., and Nittrouer, S. (**1988**). "Mathematical treatment of context effects in phoneme and word recognition," J. Acoust. Soc. Am. **84**, 101–114.

Boersma, P., and Weenink, D. (**2005**). "Praat: doing phonetics by computer (Version 4.3.14)" (Computer program). Retrieved 26 May 2005, from http://www.praat.org/.

Brill, S., Lawson, D., Wolford, R., Wilson, B., and Schatzer, R. (**2001**). "Speech processors for auditory prostheses," 11th Quarterly Progress Report, NIH Project N01-DC-8-2105, 1 April to 30 June.

Brokx, J. P. L., and Nooteboom, S. G. (**1982**). "Intonation and the perception separation of simultaneous voices," J. Phonetics **10**, 23–26.

Ching, T. Y., Incerti, P., and Hill, M. (**2004**). "Binaural benefits for adults who use hearing aids and cochlear implants in opposite ears," Ear Hear. **25**, 9–21.

Culling, J. F., and Darwin, C. J. (**1993**). "Perceptual separation of simultaneous vowels: Within and across formant grouping by F0," J. Acoust. Soc. Am. **93**, 3454–3467.

Culling, J. F., and Darwin, C. J. (**1994**). "Perceptual and computational separation of simultaneous vowels: Cues arising from low-frequency beating," J. Acoust. Soc. Am. **95**, 1559–1569.

Cutting, J. E. (**1976**). "Auditory and linguistic process in speech perception: Inferences from six fusions in dichotic listening," Psychol. Rev. **83**, 114–140.

Darwin, C. J. (**1981**). "Perceptual grouping of speech components differing in fundamental frequency and onset-time," Q. J. Exp. Psychol. **33A**, 185–207.

Deeks, J. M., and Carlyon, R. P. (**2004**). "Simulations of cochlear implant hearing using filtered harmonic complexes: Implications for concurrent sound segregation," J. Acoust. Soc. Am. **115**, 1736–1746.

Dunn, C. C., Tyler, R. S., and Witt, S. A. (**2005**). "Benefit of wearing a hearing aid on the unimplanted ear in adult users of a cochlear implant," J. Speech Lang. Hear. Res. **48**, 668–680.

Friesen, L. M., Shannon, R. V., Baskent, D., and Wang, X. (**2001**). "Speech

recognition in noise as a function of number of spectral channels: Comparisons of acoustic hearing and cochlear implants," J. Acoust. Soc. Am. **110**, 1150–1163.
Fu, Q. J., Zeng, F. G., Shannon, R. V., and Soli, S. D. (**1998**). "Importance of tonal envelope cues in Chinese speech recognition," J. Acoust. Soc. Am. **104**, 505–510.
Fujimura, O. (**1962**). "Analysis of nasal consonants," J. Acoust. Soc. Am. **34**, 1865–1875.
Geurts, L., and Wouters, J. (**2004**). "Better place-coding of the fundamental frequency in cochlear implants," J. Acoust. Soc. Am. **115**, 844–852.
Greenwood, D. D. (**1990**). "A cochlear frequency-position function for several species—29 years later," J. Acoust. Soc. Am. **87**, 2592–2605.
Hochmair, I., Arnold, W., Nopp, P., Jolly, C., Muller, J., and Roland, P. (**2003**). "Deep electrode insertion in cochlear implants: Apical morphology, electrodes and speech perception results," Acta Oto-Laryngol. **123**, 612–617.
Houtsma, A. J. M., and Smurzynski, J. (**1990**). "Pitch identification and discrimination for complex tones with many harmonics," J. Acoust. Soc. Am. **87**, 304–310.
IEEE (**1969**). "IEEE recommended practice for speech quality measurement," IEEE Trans. Audio Electroacoust. **17**, 225–246.
Kong, Y. Y., Cruz, R., Jones, A. J., and Zeng, F. G. (**2004**). "Music perception with temporal cues in acoustic and electric hearing," Ear Hear. **25**, 173–185.
Kong, Y. Y., Stickney, G., and Zeng, F.-G. (**2005**). "Speech and melody recognition in binaurally combined acoustic and electric hearing," J. Acoust. Soc. Am. **117**, 1351–1361.
Laneau, J., Moonen, M., and Wouters, J. (**2006**). "Factors affecting the use of noise-band vocoders as acoustic models for pitch perception in cochlear implants," J. Acoust. Soc. Am. **119**, 491–506.
Litvak, L. M., Delgutte, B., and Eddington, D. K. (**2003**). "Improved temporal coding of sinusoids in electric stimulation of the auditory nerve using desynchronizing pulse trains," J. Acoust. Soc. Am. **114**, 2079–2098.
Loftus, G. R., and Masson, M. E. (**1994**). "Using confidence intervals in within-subject designs," Psychon. Bull. Rev. **1**, 476–490.
MacLeod, A., and Summerfield, Q. (**1990**). "A procedure for measuring auditory and audio-visual speech-reception thresholds for sentences in noise: Rationale, evaluation, and recommendations for use," Br. J. Audiol. **24**, 29–43.
Nie, K., Stickney, G., and Zeng, F.-G. (**2005**). "Encoding frequency modulation to improve cochlear implant performance in noise," IEEE Trans. Biomed. Eng. **52**, 64–73.
Plomp, R. (**1967**). "Pitch of complex tones," J. Acoust. Soc. Am. **41**, 1526–1533.
Qin, M. K., and Oxenham, A. J. (**2005**). "Effects of envelope-vocoder processing on F0 discrimination and concurrent-vowel identification," Ear Hear. **26**, 451–460.
Qin, M. K., and Oxenham, A. J. (**2006**). "Effects of introducing unprocessed low-frequency information on the reception of envelope-vocoder processed speech," J. Acoust. Soc. Am. **119**, 2417–2426.
Remez, R. E. (**2001**). "The interplay of phonology and perception considered from the perspective of organization," in *The Role of Speech Perception Phenomena in Phonology*, edited by E. V. Hume and K. A. Johnson (Academic, New York), pp. 27–52.
Rosen, S., and Ball, V. (**1986**). "Speech perception with the Vienna extracochlear single-channel implant: A comparison of two approaches to speech coding," Br. J. Audiol. **20**, 61–83.
Shannon, R. V., Zeng, F. G., Kamath, V., Wygonski, J., and Ekelid, M. (**1995**). "Speech recognition with primarily temporal cues," Science **270**, 303–304.
Stickney, G., Zeng, F. G., Litovsky, R. Y., and Assmann, P. (**2004**). "Cochlear implant speech recognition with speech masker," J. Acoust. Soc. Am. **116**, 1081–1091.
Strange, W., Jenkins, J. J., and Johnson, T. (**1983**). "Dynamic specification of coarticulated vowels," J. Acoust. Soc. Am. **74**, 695–705.
Turner, C. W., Gantz, B. J., Vidal, C., Behrens, A., and Henry, B. A. (**2004**). "Speech recognition in noise for cochlear implant listeners: Benefits of residual acoustic hearing," J. Acoust. Soc. Am. **115**, 1729–1735.
Vandali, A. E., Sucher, C., Tsang, D. J., McKay, C. M., Chew, J. W., and McDermott, H. J. (**2005**). "Pitch ranking ability of cochlear implant recipients: A comparison of sound-processing strategies," J. Acoust. Soc. Am. **117**, 3126–3138.
Vongphoe, M., and Zeng, F. G. (**2005**). "Speaker recognition with temporal cues in acoustic and electric hearing," J. Acoust. Soc. Am. **118**, 1055–1061.
Wilson, B., Wolford, R., Lawson, D., and Schatzer, R. (**2002**). "Speech processors for auditory prostheses," Third Quarterly Progress Report, NIH Project N01-DC-2-1002. 1 October–30 December.
Xu, L., Tsai, Y., and Pfingst, B. E. (**2002**). "Features of stimulation affecting tonal-speech perception: Implications for cochlear prostheses," J. Acoust. Soc. Am. **112**, 247–258.

Numerical simulation of turbulence transition and sound radiation for flow through a rigid glottal model

Jungsoo Suh[a] and Steven H. Frankel[b]
Maurice J. Zucrow Laboratories, School of Mechanical Engineering, Purdue University, West Lafayette, Indiana 47907-2014

(Received 2 June 2006; revised 6 March 2007; accepted 15 March 2007)

Large eddy simulation (LES)-based computational aeroacoustics techniques were applied to a static model of the human glottis, idealized here as a planar channel with an orifice, to study flow-acoustic interactions related to speech. Rigid models of both converging and diverging glottal passages, each featuring a 20 deg included angle and a minimal glottal diameter of 0.04 cm, with an imposed transglottal pressure of 15 cm H_2O, were studied. The Favre-filtered compressible Navier-Stokes equations were integrated for this low-Mach-number flow using an additive semi-implicit Runge-Kutta method and a high-order compact finite-difference scheme with characteristic-based nonreflecting boundary conditions and a multiblock approach. Flow asymmetries related to the Coanda effect and transition to turbulence, as well as the far-field sound, were captured. Acoustic-analogy-based far-field sound predictions were compared with direct simulations and showed that dipole sources, arising from unsteady flow forces exerted on the glottal walls, are primarily responsible for the tonal sound observed in the divergent glottis case. © *2007 Acoustical Society of America.* [DOI: 10.1121/1.2723646]

PACS number(s): 43.70.Aj, 43.70.Bk, 43.28.Ra [AL] Pages: 3728–3739

I. INTRODUCTION

Improvements in fundamental understanding and predictive accuracy of voice production are vital for speech synthesis and clinical applications. In voice production, sound waves are generated by air flow through the various flow passages and restrictions along the vocal tract.[1] In most flow transport systems, geometric constrictions offer the greatest resistance to flow. In the human airway system, the main constriction is the time-varying glottis, i.e., the orifice between the vocal folds. The glottal flow resistance may be characterized by the *glottal impedance*, defined as the ratio of the transglottal pressure drop and the volume flow rate through the glottis. It is a time-varying quantity, with both steady (DC) and periodic (AC) components, and is determined by the size and shape of the glottis, the inflow (subglottal) and outflow (supraglottal) conditions, among other factors. Glottal impedance calculations require detailed knowledge of the glottal flow field. Due to the complexity of the glottal geometry and the intra- and supra-glottal flow physics, which may involve unsteady flow separation and turbulence, the calculation of the glottal impedance using analytical or computational methods is a challenging problem. The quasi-steady assumption, often made to simplify fluid flow analysis in glottal impedance investigations, states that temporal flow variations can be substituted by a sequence of steady flows, thereby neglecting unsteady effects related to flow acceleration or hysteresis. The quasi-steady assumption allows the instantaneous glottal impedance to be approximated by the steady (DC) glottal impedance of a geometrically similar system at rest.

Based on the quasi-steady assumption, empirical studies[2–6] using rigid glottal models and computational studies[7–10] on a static glottal flow with two-dimensional, steady laminar flow equations have been performed previously. The flow separation and pressure-flow relationship for both steady and unsteady flows through rigid glottal models was investigated and theoretical models using the Pohlhausen or Thwaite's method were also developed.[11–15] These models can make reasonably accurate predictions of the pressure and flow velocity but have more difficulty when unsteady or viscous effects become predominant.

While the quasi-steady assumption does greatly simplify the problem, complex flow features still abound. Alipour *et al.*[16] and Alipour and Scherer[17] observed in their static physical glottal models that the jet flow downstream of the glottis transitioned to turbulence even for laminar upstream conditions. Flow asymmetries due to the Coanda effect in steady flows through the static glottal model have been observed experimentally[16,18–20] and numerically.[8] By estimating the time needed for establishment of the Coanda effect and transition to turbulence in their models, Hofmans *et al.*[14] suggested that both effects are unlikely to occur during normal voiced speech production, since they require a relatively long time to establish themselves and the glottis completely closes during one oscillation cycle. Recently, the unsteady Coanda effect was found to be present in pulsatile flows through static diverging glottal models,[21] driven vocal fold models,[22] and self-oscillating vocal fold models.[23] Neubauer *et al.*[23] suggested the Coanda effect might be induced by antisymmetric flow structures downstream beyond the potential core of the glottal jet.

McGowan[24] proposed an aeroacoustic approach to study the sound sources during phonation, concentrating on two distinct features of the vocal tract during phonation: abrupt

[a]Electronic mail: suhj@ecn.purdue.edu
[b]Electronic mail: frankel@ecn.purdue.edu

 0001-4966/2007/121(6)/3728/12/$23.00 © 2007 Acoustical Society of America

area change and the finite length of the vocal tract. McGowan identified a sound source distinct from the monopole source arising from the unsteady volume velocity of the pulsating jet. This is a dipole source arising from an oscillating force between solid surfaces and the air and related to interactions of vortical structures shed from the glottis and the velocity field itself. Barney *et al.*[25] and Shadle *et al.*[26] made aerodynamic and acoustic measurements in a dynamic mechanical model of the larynx and obtained results in support of the aforementioned study by McGowan. Zhao *et al.*[27] performed the numerical simulations of pulsating axisymmetric low-Mach-number jets through converging and diverging static glottal models. Lighthill's acoustic analogy was used for sound source identification. The dominant sound sources were found to be associated with the monopole source at the inlet and the dipole source related to unsteady forces on the wall boundary. The quadrupole sources were insignificant, contributing only about 4% of the total acoustic pressure, at high-frequency, due to the presence of vortex pairing. Zhang *et al.*[20] conducted an experimental study to characterize the broadband sound emissions of confined steady jets through a static rubber model of the vocal folds. For the straight and convergent orifices, the quadrupole source contributions dominated. For divergent orifices, whistling tonal sounds were emitted at low flow rates. At high flow rates within the same configuration, dipole source contributions dominated. Zhao *et al.*[28] also performed numerical simulations within a simplified dynamic vocal tract model resembling the converging-diverging shapes of the actual vocal folds during phonation. The model geometry and the flow field were assumed to be axisymmetric. Applying an acoustic analogy based on the Ffowcs Williams–Hawkings (FW-H) equation,[29] the far-field sound was decomposed into contributions from monopole, dipole, and quadrupole sources. At lower vocal fold oscillation frequencies, a dipole source due to the unsteady force dominated the radiated sound. At higher vocal fold frequencies (above approximately 400 Hz) the monopole component related to the displacement flow was found to be significant. In a related parametric study, Zhang *et al.*[30] studied the effects of subglottal pressure, glottal oscillation frequency, and the presence of the ventricular folds. It was found that glottal oscillation frequency influenced monopole and quadrupole sources, and subglottal pressure (in other words, Reynolds number) influenced the dipole source. The presence of the ventricular folds introduced an additional dipole source related to glottal jet impingement on the ventricular folds and also a potential shear layer mode due to cavity noise. Using the same glottal motion as Zhao *et al.*,[28] Bae *et al.*[31] numerically investigated unsteady airflow and acoustic fields around the vocal folds using a new hydrodynamic/acoustic splitting method. The converging/diverging variation of the orifice geometry is found to have significant influences on the glottal impedance and improves the efficiency of vocal fold motion during phonation.

In the present study, two static glottal models were considered, each representing a typical glottal geometry during the phonation cycle. Although rigid glottal models were used, the *three-dimensional flow physics* through the glottal model are still challenging to simulate, especially if one is interested in capturing both the flow and acoustics. One of the many important goals of the present study is to predict whether, when, and where the air flow separates from the vocal folds, since this is important in determining the volume flow through the glottis, as well as the hydrodynamic forces on the vocal folds.[14] The location of the separation point changes according to the flow regime, which is determined by the Reynolds number. In the present study (to be described below), the Reynolds number, based on the minimum glottal diameter and the reference velocity $\sqrt{2\Delta p/\rho}$, was set to 1315. In the subglottal passageway, this Reynolds number implies laminar flow. However, in the supraglottal region where a glottal jet exits, the flow may be turbulent. This implies a transition from laminar subglottal flow to turbulent intraglottal or supraglottal flow downstream of the glottis. Another interesting glottal flow phenomenon that may affect separation is the Coanda effect. For flow through divergent glottal passages, the flow may attach to one wall, causing the jet centerline to skew with respect to the glottal centerline, and thus have a considerable effect on flow separation. Hence, an appropriate numerical model able to accurately capture transition to turbulence and the Coanda effect is very essential for the accurate prediction of flow separation. Previous simulations have been steady, two-dimensional, planar or axisymmetric, and laminar. Therefore, they were insufficient to explain many complicated flow features found in experimental studies. This limitation has been noted by McGowan,[32] Kaiser,[33] and Teager and Teager.[34]

In this study, complex unsteady flow features including separation, instability, and transition to turbulence, as well as confinement effects on the supraglottal jet and aeroacoustics in a model glottis, were fully considered by using three-dimensional unsteady compressible large eddy simulation (LES). In LES, the large, energy carrying flow structures are accurately resolved on the computational mesh, while the effects of the small, unresolved scales on the large, resolved scales are modeled. Since the dynamics of the small scales tend to be homogeneous and insensitive to boundary conditions, the models for the small scales can be relatively simple and somewhat universal. The use of LES for aeroacoustic studies is gaining in popularity as evidenced by the recent book edited by Wagner *et al.*[35] In what follows, LES of flow through a static model of the human vocal tract will be presented to study both the near-field flow features and the far-field sound signal. Far-field sound predictions were compared to directly simulated sound signals. Near-field acoustic sources were identified using the FW-H acoustic analogy.

II. NUMERICAL METHODS

A. Spatial and temporal discretization

The governing equations under consideration here are the unsteady, three-dimensional, compressible, Favre-filtered, Navier-Stokes equations (NSEs), written in nondimensionalized conservative form for a generalized curvilinear coordinate system. Ideal gas behavior with constant thermodynamic and transport properties was assumed. A third-order accurate, additive, semi-implicit, Rosenbrock

Runge-Kutta (ASIRK-3C) scheme[36] and a sixth-order accurate, compact finite-difference scheme[37] were used for time advancement and spatial discretization, respectively. A multiblock approach featuring newly designed characteristic interface conditions is used to facilitate complex geometries more efficiently.[38] At the nodes on the block interfaces and the nodes adjacent to these interfaces, third-order, one-sided compact finite-difference and fourth-order, central compact schemes are used, respectively. The convective terms in the wall-normal direction are treated implicitly to remove the time-step limitation associated with the use of fine meshes in the near-wall region for high Reynolds number confined viscous flows. LES with the dynamic Smagorinsky subgrid-scale (SGS) model, first proposed by Germano *et al.*[39] for incompressible flows and later extended by Moin *et al.*[40] for compressible flows, is used for turbulence closure. Padé-type filters, as derived by Lele,[37] are used here for both grid- and test-filter operations associated with the dynamic Smagorinsky SGS turbulence model. For the boundary nodes and the interfaces of the computational blocks, fourth-order explicit, near-boundary formulas[37] are used. The full implementation details associated with the ASIRK-3C and compact schemes, as well as the SGS model, can be found in Ref. 41.

B. Characteristic boundary conditions

Periodic boundary conditions are used for all flow variables in the spanwise direction. A transglottal pressure of 15 H_2O is imposed as part of the inflow and outflow boundary conditions. In the present computational aeroacoustics approach to glottal flow, both the nonreflecting condition and the mean flow condition should be satisfied simultaneously. Hixon *et al.*[42] and Hixon *et al.*[43] suggested a way to set the mean flow, while avoiding reflections at the boundaries. In the present study, a simpler approach using linear relaxation[44] is employed to maintain the mean flow while avoiding reflections at the boundaries. However, although this linear relaxation method (LRM)[44–46] is frequently referred to as being "nonreflecting," Selle *et al.*[47] showed these boundary conditions are indeed partially reflecting. Therefore, the present study also uses the modification proposed by Polifke *et al.*[48] to allow nonreflecting conditions—at least for plane waves with normal incidence on the boundary. For the inlet conditions of the present study, the amplitudes of four incoming waves L_1, L_2, L_3, and L_4 are specified by

$$L_1 = 0, \tag{1}$$

$$L_2 = K[\tilde{\xi}_x(w-\bar{w}) - \tilde{\xi}_z(u-\bar{u})]/2, \tag{2}$$

$$L_3 = K[-\tilde{\xi}_x(v-\bar{v}) + \tilde{\xi}_y(u-\bar{u})]/2, \tag{3}$$

$$L_4 = K[\bar{\rho}\bar{c}(\tilde{\xi}_x(u-\bar{u}) + \tilde{\xi}_y(v-\bar{v}) + \tilde{\xi}_z(w-\bar{w}) + g) + (p-\bar{p})], \tag{4}$$

with

$$(\tilde{\xi}_x, \tilde{\xi}_y, \tilde{\xi}_z) = (1/\sqrt{\xi_x^2 + \xi_y^2 + \xi_z^2})(\xi_x, \xi_y, \xi_z),$$

where u, v, w are the Cartesian velocity components representing here streamwise, spanwise, and normal velocity components, respectively, ρ is the density, p is the pressure, c is the sound speed, and ξ is the streamwise coordinate of the uniformly spaced computational domain. Note that the tilde denoting the filtering operation for LES will be dropped for clarity here; it will be clear from the context whether the discussion refers to the total or the filtered variable. Here the overbar denotes mean value at the boundary and K is a constant suggested by Rudy and Strikerda[45] as

$$K = \sigma(1 - \mathrm{M}_\infty^2)(\bar{c}/l), \tag{5}$$

where $\sigma = 0.25$ is used as proposed by Kim and Lee,[44] M_∞ is the reference Mach number, and l is the characteristic length. For the outlet condition, the amplitude of one incoming wave L_5 is specified by

$$L_5 = K[-\bar{\rho}\bar{c}f + (p-\bar{p})]. \tag{6}$$

Also, the acoustic signal components f and g are defined as follows:

$$f = \frac{1}{2}\left(\frac{\delta p}{\rho c} + \delta u\right) \text{ for a plane wave propagating downstream,} \tag{7}$$

$$g = \frac{1}{2}\left(\frac{\delta p}{\rho c} - \delta u\right) \text{ for a plane wave propagating upstream} \tag{8}$$

with deviations

$$\delta u = \langle u - \bar{u} \rangle, \quad \delta p = \langle p - \bar{p} \rangle \tag{9}$$

from the mean value. Here $\langle\rangle$ means an instantaneous area average over sampling planes perpendicular to the duct axis.[48] An approach similar to Giles[49] is used for the wall boundaries. The implementation details of this no-slip reflective wall boundary condition are available in Ref. 41.

In addition to the above boundary conditions, an exit-zone approach is used involving application of artificial damping of the solution for grid points near the outlet in order to minimize acoustic reflections at the boundaries of the computational domain and maintain the mean flow rate.[50,51]

C. Acoustic analogy for a planar uniform duct

Lighthill's acoustic analogy[52] is used to predict the radiated acoustic field from a finite region of a turbulent flow. It is based on a rearrangement of the continuity and NSE into an inhomogeneous wave equation for an acoustic variable. The acoustic analogy is exact in the sense that no approximations have been made during the derivation. However, its practical use requires that the source distribution be known and that it be zero in the region where the sound is calculated (homogeneous and quiescent).[53] For application of the acoustic analogy to the noise generated in a confined turbulent flow, the presence of solid walls must be considered and an acoustic analogy including the effect of solid surfaces can be developed by applying the FW-H equation.[29] The deriva-

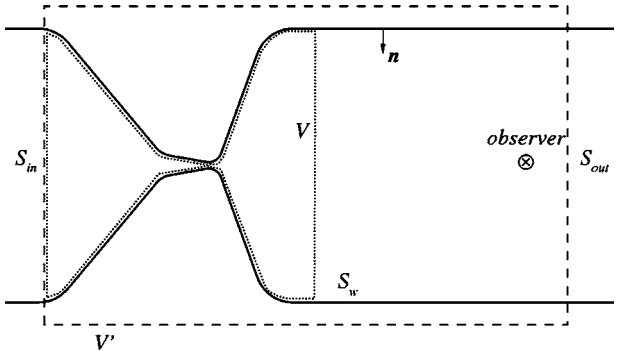

FIG. 1. Sketch of the integral domains associated with applying Lighthill's acoustic analogy to a confined region.

tion for the solution of the FW-H equation for the planar domain with low-frequency Green's function depicted in Fig. 1 is available in Suh and Frankel[38] and takes the form

$$\langle Hp' \rangle(x_1,t) = \frac{1}{2A_0 c_\infty} \frac{\partial}{\partial t} \int_{S'} [\langle T_{11} \rangle]_{t^*} \, dS'(\mathbf{y}) \tag{I}$$

$$- \frac{1}{2A_0} \int_{C_w} [\langle p' \delta_{ij} - \sigma_{1j} \rangle]_{t^*} n_j sign(x_1 - y_1) \, dC(\mathbf{y}) \tag{II}$$

$$+ \frac{1}{2A_0} \int_{C_{in}} [\langle c_\infty^2 \rho' + \rho c_\infty u_1 + T_{11} \rangle]_{t^*} \, dC(\mathbf{y}) \tag{III}$$

$$+ \frac{1}{2A_0} \int_{C_{out}} [\langle c_\infty^2 \rho' - \rho c_\infty u_1 + T_{11} \rangle]_{t^*} \, dC(\mathbf{y}), \tag{IV}$$

where C_w, C_{in}, and C_{out} are boundary curves for the duct wall, inlet, and outlet, respectively. Also, $t^* = t - |x_1 - y_1| / c_\infty$ is the retarded time, and T_{ij} is the Lighthill source tensor defined as

$$T_{ij} = \rho u_i u_j + \delta_{ij}(p' - c_\infty^2 \rho') - \sigma_{ij}, \tag{10}$$

where σ_{ij} is the viscous stress tensor and δ_{ij} is the Dirac delta function, $p' = p - p_\infty$ is the pressure perturbation, and $\rho' = \rho - \rho_\infty$ is the density perturbation with p, ρ_∞, and c_∞ representing the far-field pressure, density, and sound speed, respectively. Here, (I), (II), (III), and (IV) represent the quadrupole sources from the kinetic energy along the streamwise direction inside of the duct, the dipole sources from the unsteady streamwise forces acting on wall, and the sources from the inlet and outlet related to acoustic waves incoming to the boundary and the Lighthill stress tensor at the boundary, respectively. Hofmans[54] obtained a similar solution by using Curle's equation.[55] Aeroacoustic accuracy of the present method was assessed by comparing direct simulations of far-field sound to FW-H acoustic analogy predictions for the case of pulsatile flow through a duct with either a convergent or divergent orifice.[38]

III. PROBLEM DESCRIPTION

The geometry and mesh for the human vocal tract model considered here are shown in Fig. 2 for the convergent and divergent glottal cases, respectively. The included glottal

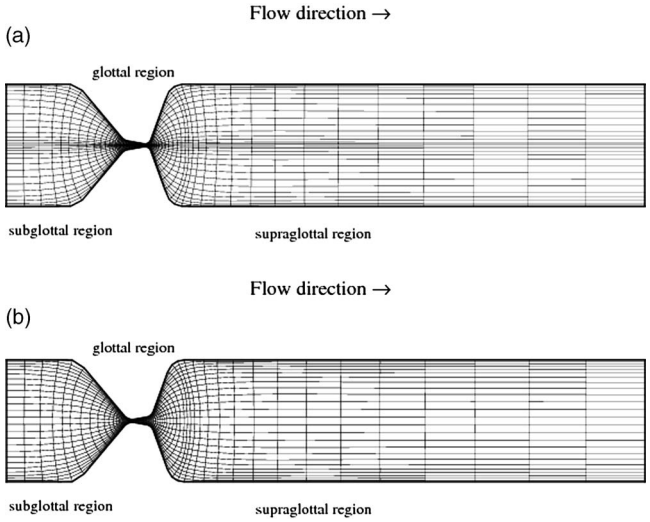

FIG. 2. Computational grid of human vocal tract model with included glottal angle of 20 deg (every fourth node is shown). (a) Convergent glottis, (b) Divergent glottis.

angle is ±20 deg. These glottal shapes are typical of the opening and closing phases in human phonation. The rigid vocal tract is modeled here as a planar channel with an orifice consisting of an upper and lower vocal fold. The glottis region is the slit between the two vocal folds and the minimal glottal diameter (δ) was set at 0.04 cm. Both upstream and downstream corners, formed by the channel and vocal fold, are rounded with a radius of 6δ. The length of the planar channels upstream and downstream of vocal fold models are 25δ and 166δ, respectively. The ventricular vocal folds are not included in this initial study but will be considered in future work. The vocal fold models employed in this research are based on the canonical M5 geometries studied by Scherer *et al.*[18] The shape of the vocal folds at the glottal entrance and exit is rounded by radii that depend on the glottal angle, and a straight section connects the entrance and exit. The superior vocal fold surface angle of the original M5 model is 0 deg, but, in the present study, a negative angle of −20 deg was used, which allowed easier mesh generation. Here a negative angle means that the lateral portion of the surface is higher, more superior, than the medial portion. Li *et al.*[56] found, for constant entrance and exit glottal radii, the intraglottal pressures were unchanged for superior vocal fold surface angles up to approximately −70 deg, at least for laminar flow cases. In spanwise direction, domain width of 5δ was used.

The meshes were produced by using the orthogonal grid generation technique of Eça.[57] A structured grid consisting of $241 \times 50 \times 121$ points in the streamwise, spanwise, and wall-normal directions, respectively, was used for the convergent glottis, whereas for the divergent glottis a mesh of $241 \times 50 \times 101$ points was used. The accurate prediction of the separation point is important for the present study as it determines the forces between the air and the vocal folds.[32] The intraglottal grid was refined to capture possible flow separation and complex jet flow phenomena. For the convergent glottis, the region near the centerline was also refined to resolve possible jet transition to turbulence, Uniform grid

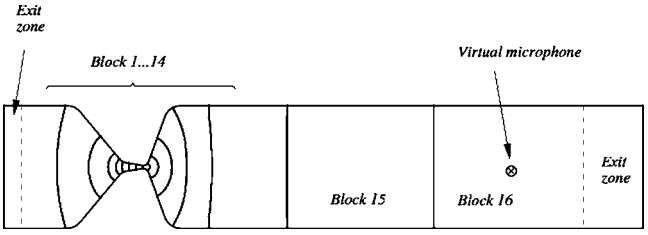

FIG. 3. Computational domain decomposition into 16 blocks for the convergent glottis case.

spacing in the spanwise direction was used. Figure 3 shows the computational domain decompositions and schematics for the convergent glottis (the divergent case used a similar decomposition). A total of 12 or 16 computational blocks were used for the divergent or convergent glottis, respectively. In each block, a mesh of $(21\times50\times101)$ or $(16\times50\times121)$ was used for the divergent or convergent model. The Reynolds number based on the minimum glottal diameter and reference velocity $\sqrt{2\Delta p/\rho}$ was 1315 and the Mach number was 0.1.

IV. RESULTS AND DISCUSSION

A. Near-field flow analysis

Figures 4 and 5 show instantaneous vorticity magnitude and streamwise velocity for the convergent and divergent glottis cases, respectively. For the convergent case, relatively large-scale vortical structures are observed downstream of the glottal exit, indicating that transition to turbulence occurred downstream of the glottis. In contrast, the divergent case shows the presence of small-scale vortical structures within the glottis and immediately downstream of the glottal exit, demonstrating that the flow begins to transition to turbulence within the glottis. However, unlike in the convergent case, impingement of the glottal jet on the supraglottal tract wall limits further development of these flow structures. The glottal jet is skewed and attached to one wall for the divergent case. This indicates the occurrence of flow separation from the upper wall (nonflow wall) upstream of the lower wall (flow wall) separation point. On the flow wall, many small vortical structures exist, including vortices separated from the nonflow wall, and the flow is unstable. Fox and Kline[58] presented a systematic flow regime map for flow through two-dimensional, straight-walled diffusers. According to their work (see Fig. 3 of Ref. 58), the flow through the present divergent glottis is in the region of large transitory stall. Hence, large scale vortices separate from the wall and continue to move along the wall. As a result of this disturbance, the flow becomes unstable and transitions to turbulence inside the orifice. In addition, it is observed that the jet from the divergent orifice is skewed. There are many studies supporting the existence of asymmetric flow through symmetric static divergent glottal shapes.[14,16,18–20] Since the symmetric jet is meta-stable, a small flow field difference

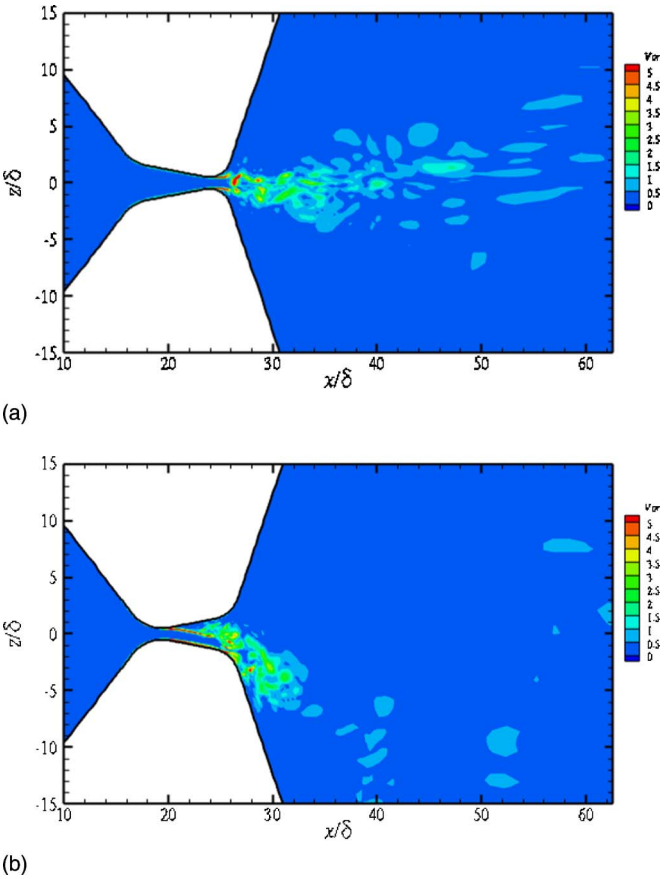

FIG. 4. (Color online) Instantaneous vorticity magnitude. (a) Convergent glottis. (b) Divergent glottis. Contour levels: Min=0, Max=5. Number of levels is 11.

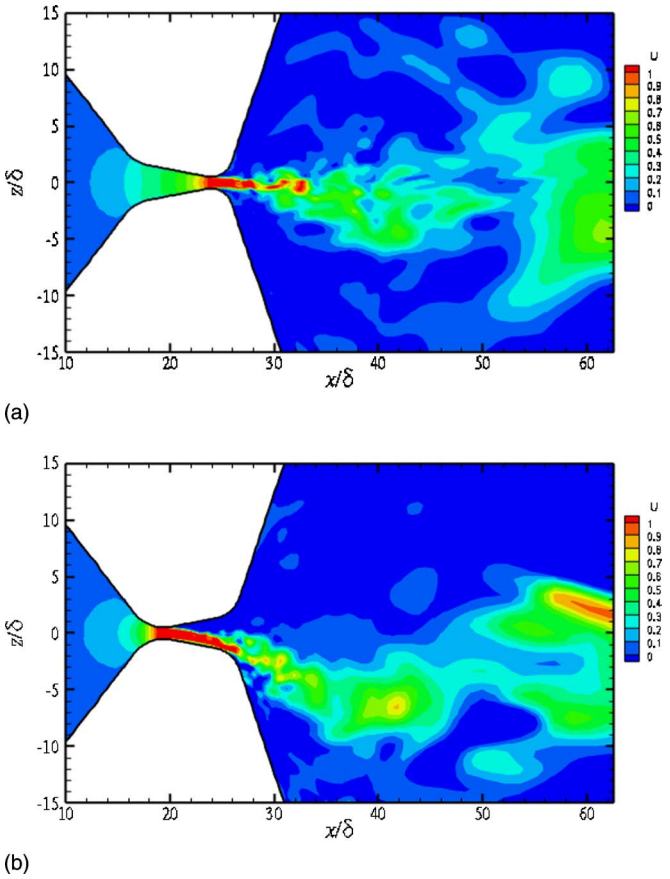

FIG. 5. (Color online) Instantaneous streamwise velocity. (a) Convergent glottis. (b) Divergent glottis.

TABLE I. Time-averaged overall flow characteristics.

	Agarwal and Scherer[62]		Present simulation	
Orifice configuration	Convergent	Divergent	Convergent	Divergent
Flow rate (cm^3/s)	219.77	235.12	236.12	244.08
Transglottal pressure (cm H_2O)	14.97	15.00	15.80	16.06
Included angle (deg)	20	−20	20	−20
Vocal fold superior surface angle (deg)	0	0	−20	−20
Side wall	Yes	Yes	No	No

between the upper and lower walls may be enough for the jet to attach to one of the walls. Neubauer *et al.*[23] suggested the flow structures downstream from the vocal folds may induce such an asymmetric disturbance. Sato[59] observed two kinds of sinusoidal velocity fluctuations when a two-dimensional planar jet becomes unstable. One is symmetrical (varicose) and the other is antisymmetrical (sinuous) with respect to the centerline of the jet. The symmetrical jet fluctuates at high frequencies when the velocity profile is nearly (undeveloped) flat. The antisymmetrical jet is low frequency and generated when the velocity distribution is (well-developed) parabolic. Accordingly, antisymmetric flow structures may be generated far downstream from the exit of the glottis (here the velocity profile develops a parabolic shape) and affect the flow inside of the glottis skewed via a feedback mechanism. Once the jet is skewed, then it can be attached to the wall due to the Coanda effect. The Coanda effect occurs when the jet is so close to the wall that entrainment from the neighboring fluid is insufficient. Hence, accurate prediction of separation and vortex dynamics are important to capture the Coanda effect. Extension of the computational domain sufficiently far downstream of the glottis is needed because the antisymmetric flow structures, which can affect the glottal jet skewness, are generated far downstream of the glottis. The Coanda effect occurs much more frequently and strongly when the flow is turbulent because turbulent flow requires higher entrainment rates than laminar flow. It should also be noted that two-dimensional planar geometries, as studied here, would tend to exhibit the Coanda effect more strongly than flows associated with three-dimensional geometries.[60] Scherer *et al.*[18] and Kucinschi *et al.*[61] reported that the Coanda effect became stronger as the Reynolds number increased. Hofmans *et al.*[14] insisted the Coanda effect might not occur at all during the production of normal voiced speech because of the need for a relatively long time to develop, but recent works have shown the existence of the unsteady Coanda effect. Erath and Plesniak[21] showed that the unsteady Coanda effect occurred in pulsatile flows through static diverging glottal models. Recently, Triep *et al.*[22] and Neubauer *et al.*[23] reported the existence of the unsteady Coanda effect in the case of a dynamically driven glottal model. In contrast, the flow is stable inside the glottis and maintains a laminar state for the convergent case, and turbulence transition only occurs after the flow has emanated from the glottis. In this case, flow transition is associated with the Kelvin-Helmholtz instability downstream of the jet, whereas in the divergent case flow transition was due to unsteady separation within the glottis.

Table I shows the flow rate for the experimental data[62] and the present numerical results in dimensional values. Both experiments and numerical simulations show 5%–7% higher flow rate for the divergent glottis. However, the absolute values show 3% to 7% difference because of vocal fold superior surface angle modifications in our simulation and other reasons including additional resistance from the side-wall boundary layer at the experiments.

Computed intraglottal pressure distributions are compared to available experimental data[62,63] in Fig. 6. The present computed wall pressure is in good agreement with the experimental data up to the separation point, but the present simulations yield a higher pressure drop than experiments. Unfortunately, the transglottal pressure used here could not be set at the exact same locations as in the experiment. The present simulations set the transglottal pressure at the inlet and outlet of the computational domain, whereas the experiments used the pressure measured immediately upstream and downstream of the vocal folds. As a result of this difference, the actual transglottal pressure of the present simulation was about 1 cm H_2O greater than the experiments. Also, differences in the superior vocal fold surface angle and the existence of radii between vocal folds and vocal tract may also contribute to this discrepancy, although Li *et al.*[56] showed the superior vocal fold surface angles had a negligible influence on the intraglottal pressure distribution. It should also be noted that their work was limited to laminar flow (up to 8 cm H_2O) and the influence of turbulent flow was not investigated. Hence, the geometry differences under the present turbulent flow condition may also be one further explanation for the differences in the intraglottal pressure distribution between the present simulations and the experiments (especially for the convergent glottis case because the flow transitioned to turbulence downstream of the glottis in that case).

Figure 7 shows the profiles of flow statistics within the glottis and immediately downstream for the convergent case. As shown in Fig. 5, the mean streamwise velocity is slightly skewed downward downstream of the exit of the glottis. Separation from both walls was observed at the exit. In contrast, flow inside the glottis was relatively stable and remains laminar and symmetric. The mean skin friction coefficient $C_f = \tau_w / \rho U_0^2 / 2$, based on the estimated maximum velocity $U_0 = \sqrt{2\Delta P / \rho}$, shows that the wall shear stresses τ_w on both the upper and lower walls are almost same until the glottal exit, which implies symmetric intraglottal flow. The highest skin friction values are observed near the minimum glottal

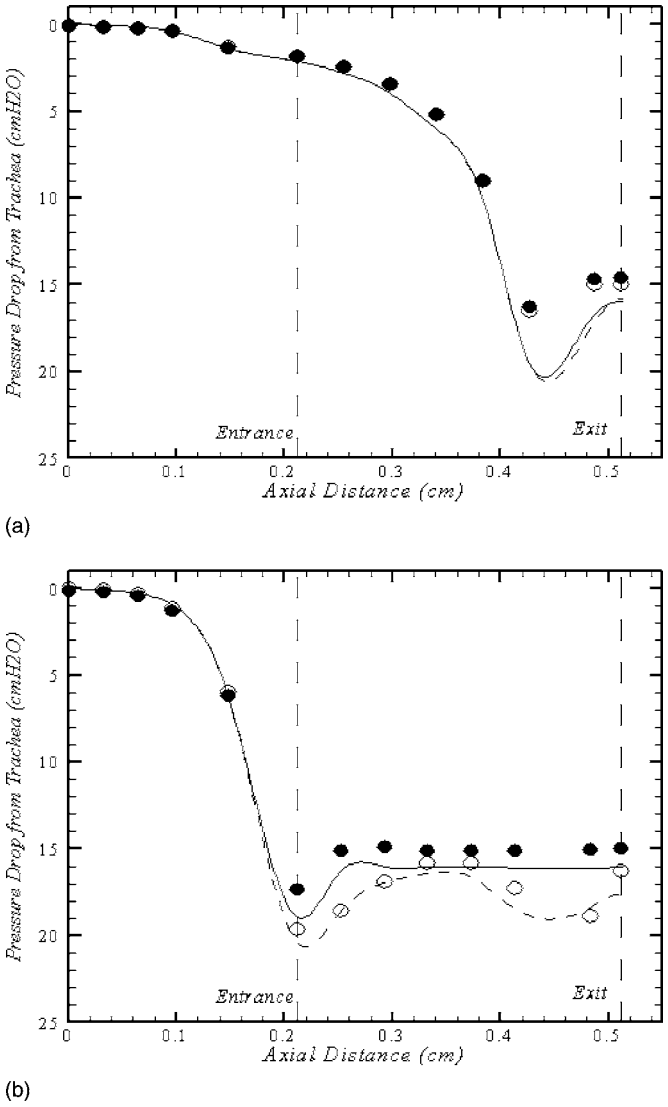

FIG. 6. Intraglottal pressure distribution: nonflow wall/experiment (●), flow wall/experiment (○), Nonflow wall/present LES (—), flow wall/present LES (- - -). (a) Convergent glottis. (b) Divergent glottis.

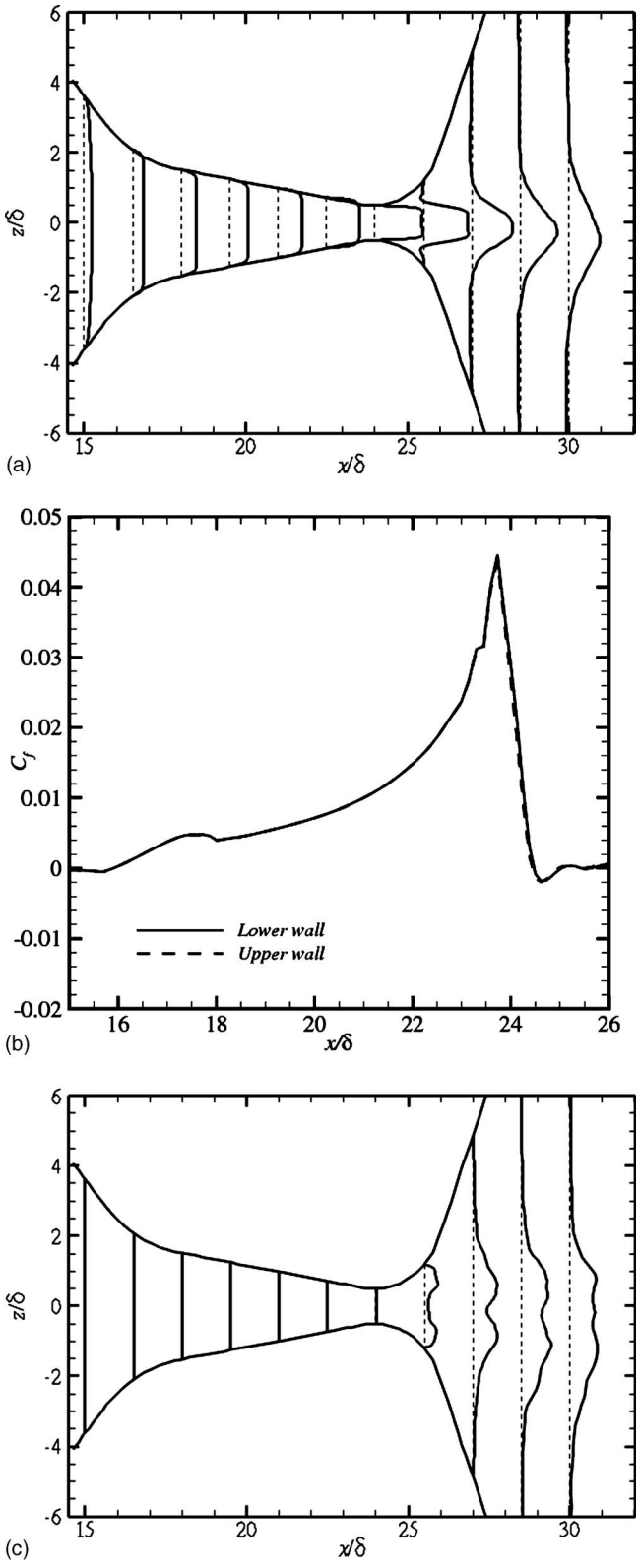

FIG. 7. Flow statistics for a convergent glottis. (a) Mean streamwise velocity $x/\delta+1.5\times U/U_{\max}$. (b) Mean skin friction coefficient C_f based on the estimated maximum velocity $\sqrt{2\Delta P/\rho}$. (c) Spanwise velocity fluctuation $x/\delta+5.0\times v_{\mathrm{rms}}/U_{\max}$.

diameter. From there, the flow separates from both walls at the glottal exit. The profile of spanwise velocity fluctuations demonstrates the absence of turbulent fluctuations within the glottis. Immediately downstream of the glottal exit, turbulent fluctuation profiles feature a double peak showing the laminar glottal jet undergoes shear layer instability or flapping.

Figure 8 shows similar flow statistics within the glottis and immediately downstream of the glottis for the divergent glottis case. It is observed from the mean streamwise velocity profiles that the flow has separated from the upper wall and is skewed to the lower wall due to the Coanda effect. Streamwise velocities near the upper wall are almost zero. The difference between flow separation locations on the two walls imparts the mean skin friction coefficient C_f, which is based on the estimated maximum velocity. Negative values of C_f indicate flow separation from the wall. Around $x=19.94\delta$, the flow is separated from the upper wall. However, the flow is not separated from the lower wall and remains attached until the glottal exit. At the minimum glottal diameter, the highest skin friction was predicted for both walls. This maximum wall shear stress is almost the same as the maximum value in the convergent case. Note the skin friction on the lower wall is higher than on the upper wall due to jet skewness. Also, an additional wall stress peak is

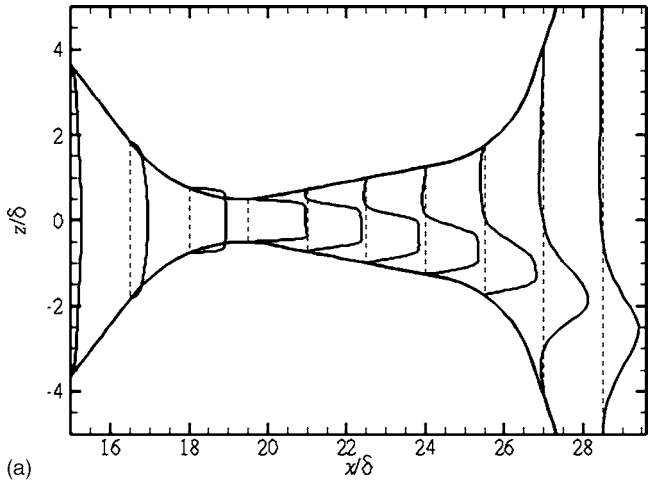

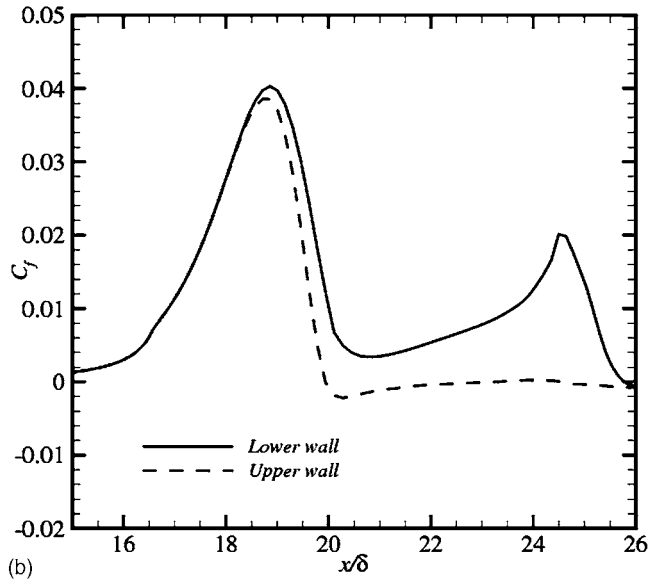

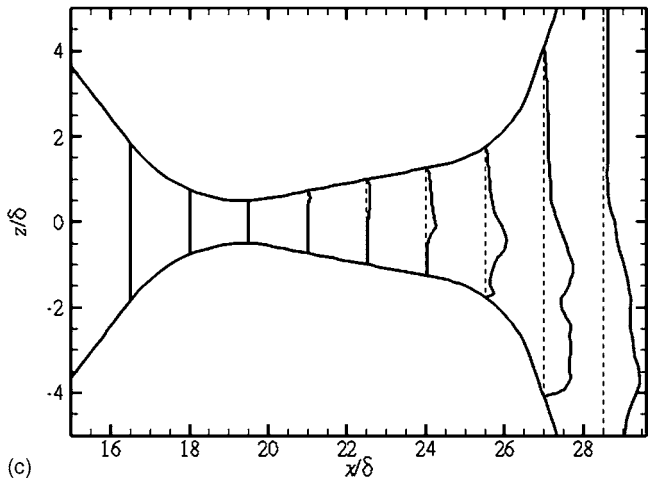

FIG. 8. Flow statistics for a divergent glottis. (a) Mean streamwise velocity $x/\delta+1.5\times U/U_{\max}$. (b) Mean skin friction coefficient C_f based on the estimated maximum velocity $\sqrt{2\Delta P/\rho}$. (c) Spanwise velocity fluctuation $x/\delta+5.0\times v_{\rm rms}/U_{\max}$.

observed near the glottal exit at the lower wall. The root mean square (rms) value of spanwise velocity fluctuations is shown in Fig. 8(c). At $x=22\delta$, turbulent fluctuations near the upper wall are observed to be higher than the lower wall

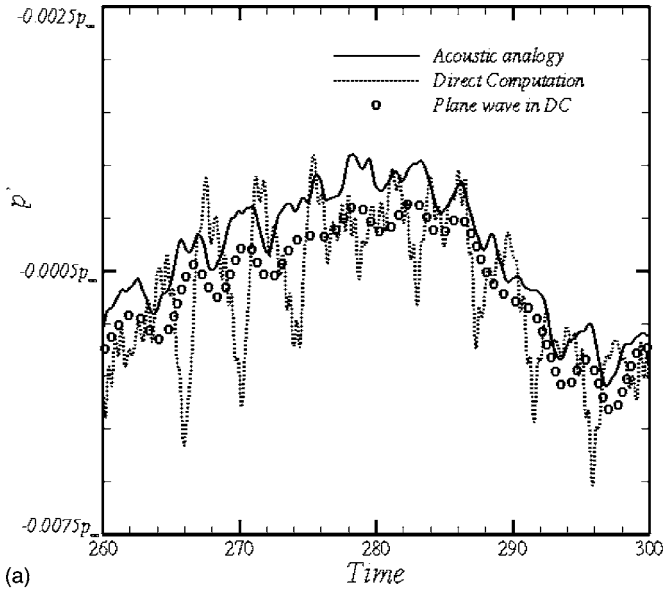

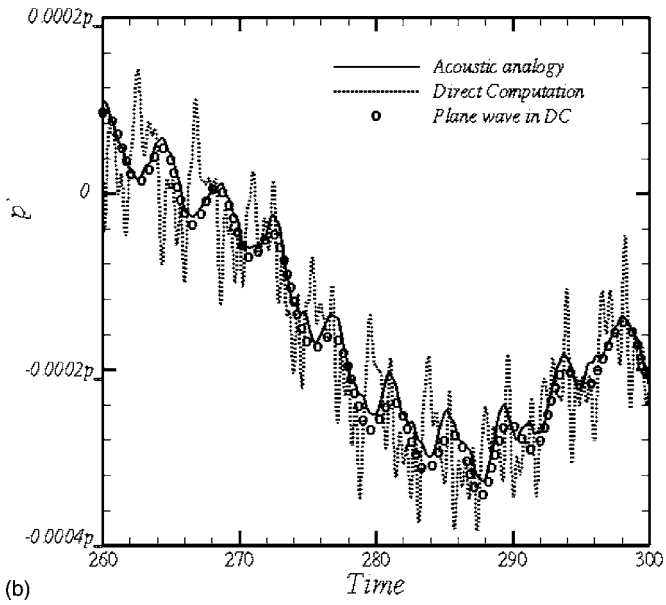

FIG. 9. Comparison between directly computed acoustic pressure and FW-H prediction. (a) Convergent glottis. (b) Divergent glottis.

because the flow was attached to the lower wall, producing less viscous drag at the upper wall. However, the vertical location of peak turbulent fluctuations migrates to the lower wall due to jet skewness. At the entrance of the glottis, velocity fluctuations are almost zero and so clearly the flow entered the glottis as laminar and transitioned to turbulence within the glottis.

B. Far-field sound radiation

In order to record the directly computed far-field acoustic signal, a *virtual microphone* was located at a distance of about 144δ from the leading edge of the vocal fold, near the centerline of the supraglottal duct, for both the divergent and convergent glottis cases (see Fig. 3). Comparisons between the directly computed pseudo-sound $p'=p-p_\infty$ and the FW-H prediction are shown in Fig. 9 for the convergent and divergent glottal cases. For both cases, discrepancies in mag-

nitude and frequency between the directly computed sound and the acoustic analogy prediction are observed. In particular, note the presence of high frequencies in the directly computed sound, which are not captured by the acoustic analogy. This suggests that the plane wave assumption associated with the use of the one-dimensional, low-frequency Green's function in the present acoustic analogy solution is not perfectly correct for both cases. Hence, the acoustic signal is not uniform in the wall-normal direction and there exist higher modes possibly excited by the glottal jet. Thus, the plane wave component of the far-field sound was extracted by averaging over the cross-sectional area where the *virtual microphone* was located. The plane wave component of the directly computed sound and the acoustic analogy prediction show reasonable agreement for the convergent glottis [Fig. 9(a)], but the acoustic analogy still underpredicts the magnitude of the far-field sound. This may be attributed to the fact that the flow through the convergent glottis transitioned to turbulence after it emerged from the glottis, so the downstream domain may not be sufficient in length for acoustic waves to develop into far-field planar waves and the region near the outlet is still influenced by near-field convection effects. The divergent glottis shows better agreement between the plane wave component of the directly computed sound and the acoustic analogy prediction [Fig. 9(b)] because flow through the divergent glottis has already transitioned to turbulence within the glottis so the computational domain is sufficiently long compared to the convergent case.

The FW-H acoustic analogy was next used to decompose the contributions to the far-field sound from the different near-field sound source terms in Eq. (10) for both cases. The results are shown in Fig. 10. Here the inlet and outlet contributions are not shown for clarity because they remain almost positive and negative constants, respectively. Recall that the perfectly nonreflecting boundary condition was not used for both cases so there were incoming waves at the inlet and outlet. The values of the Lighthill source tensor at the inlet and outlet were also nonzero because both boundaries should maintain the mean flow rate as set by the pressure difference between the inlet and outlet of the domain. Notice that the quadrupole sources are negligibly small and the dipole sources are dominant. This is consistent with the previous studies on axisymmetric flows.[28] However, this does not mean turbulence transition and vortical structures are not important for sound generation. They can and do contribute to the dipole sources responsible for the far-field sound through modifying near-field flow. Turbulence transition can alter the flow by changing the flow separation location and the strength of the Coanda effect. Both vortices generated inside the glottis and far downstream are also important for the flow asymmetry found in the divergent glottis case. The appearance of the Coanda effect is dependent on the presence of antisymmetric vortical structures downstream of the glottis. The dipole sound source contribution is greatly affected by changes in the vocal fold shape. Dipole sources arise due to the reaction of the vocal folds to the air flow. Hence, while the dipole from the forward part of the vocal folds (facing the inlet) is always out of phase with the inlet contribution, the dipole from the rearward part of the vocal folds (facing the outlet) is always in phase with the inlet contribution. For the convergent case, the main contribution of the dipole is from the forward part of the vocal folds, so it has a negative value. However, for the divergent case, the rearward part of the vocal folds also contributes to the dipole sources (positive value) significantly, so the absolute value of the dipole contribution decreases. As a result, the pseudo-sound pressure is always negative for the convergent case, but sometimes positive for the divergent case. Dipoles 1 and 2 characterize the unsteady forces on the upper and lower walls of the glottis, respectively. Their difference is due to the unsteady flow features. In addition, flow asymmetries associated with the Coanda effect also affect these differences for the divergent case. However, the difference is larger for the convergent case due to the order difference of the absolute value of the magnitudes.

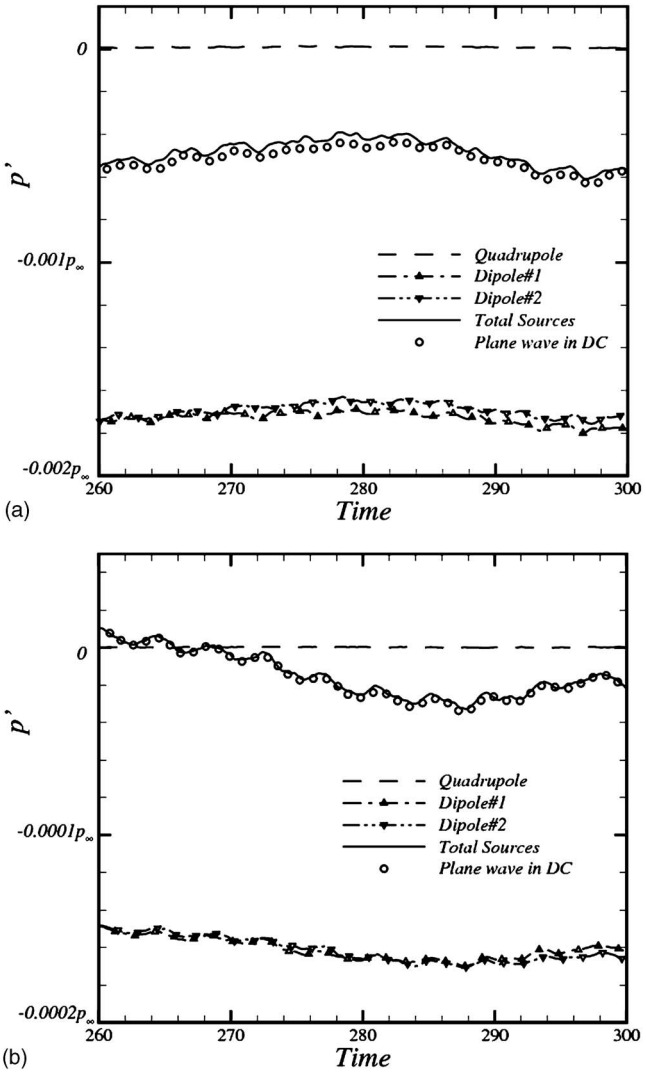

FIG. 10. Contribution to far-field sound radiation from different sources. (a) Convergent glottis. (b) Divergent glottis.

Figures 11 and 12 show the acoustic pressure spectra of sound sources and directly computed sound for the convergent and divergent glottis case, respectively. For the convergent case, directly computed sound and its plane wave component approximately follow the St^{-2} trend, where Strouhal number $St = f\delta/U_0$ and f is the frequency of the far-field

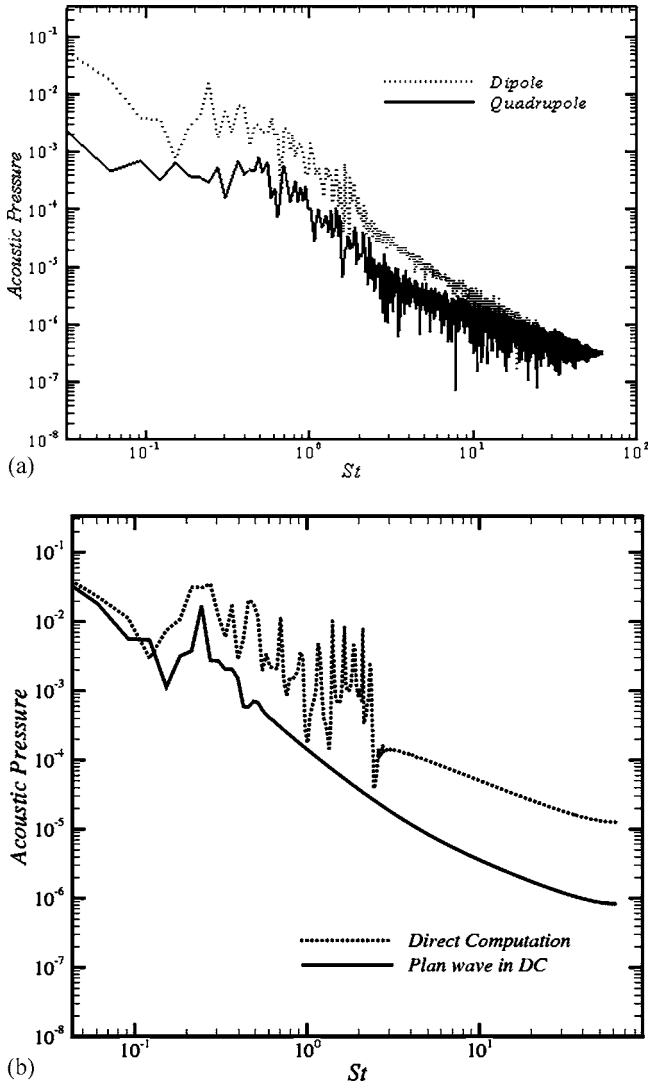

FIG. 11. Acoustic pressure spectra for the convergent glottis. (a) Acoustic sources. (b) Directly computed far-field sound.

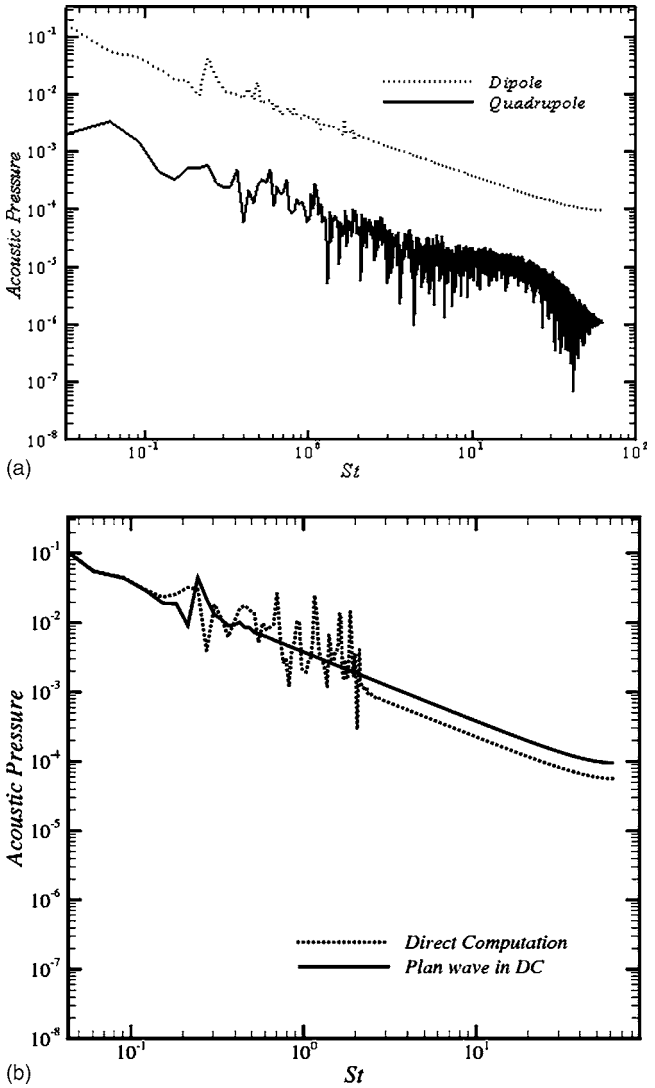

FIG. 12. Acoustic pressure spectra for the divergent glottis. (a) Acoustic sources. (b) Directly computed far-field sound.

sound. The dipole and quadrupole sources follow the St^{-2} trend in the high-frequency range, but display a different trend in the low-frequency range. The dipole source follows the St^{-1} trend, but the quadrupole source follows the previous St^{-2} trend. Hence, the dipole sources are one order higher than the quadrupole sources in the low-frequency range, but differences between the two sources decrease in the high-frequency range. The relatively high magnitude of the quadrupole source is not surprising because large vortical structures are distributed over a wider range after the jet emerges from the glottis. Conversely, all spectra from the divergent case approximately follow the St^{-1} trend. For the divergent glottis, dipole sources are much stronger than the quadrupole sources over most of the Strouhal number range and contribute almost exclusively to the plane wave component of the directly computed far-field sound. This confirms that the dipole is the dominant sound production mechanism for this case. The results are consistent with the trends obtained using the spectral decomposition method by Zhang *et al.*[20]

One strong peak is observed at Strouhal number St $=0.245$ and a weaker peak near $St=0.49$ for the plane wave component of the directly computed sound for the divergent case. The locations of these peaks are consistent with the fundamental ($St\approx0.23$) and its first harmonic frequencies ($St\approx0.46$) of tonal sound observed in steady flow sound measurement by Zhang *et al.*[20] Note that these Strouhal numbers correspond to the values reported for vortex shedding in shear layers.[20] In Ref. 20, tonal sounds were produced for low flow rate and the broadband component became dominant when the transglottal pressure was increased above 9 cm H_2O, although tones were still present in the spectra. Since the transglottal pressure of the present case was about 15 cm H_2O, the tonal sound may not be very significant as in the experimental work. However, the present work does provide a clue about the acoustic source responsible for the tonal sound via the FW-H acoustic analogy. Dipole sources predicted peaks at the same Strouhal numbers with the plane wave component of far-field sound, which suggests that the tonal sounds are generated by the dipole sources due to the unsteady forces between the air flow and the vocal folds, affected by the vortex shedding downstream. This finding

supports Zhang *et al.*[20] with regard to their point that the jet tones are caused by aerodynamic phenomenon and not by the resonance due to the confinement. Note the dipole source and the plane wave component of the directly computed sound for the convergent glottis also predicted peaks at the same Strouhal number where there also exists vortex shedding downstream. However, it is not strong enough to generate tonal sound. In addition to these peaks, the directly computed sound shows more peaks that do not exist in the plane wave component for the range St=0.6 to 2.1, indicating that there exist higher modes of acoustic waves in the downstream far field.

V. CONCLUSIONS

Numerical simulations of the flow and acoustics through a static model of the human vocal tract were conducted using large eddy simulation. Rigid models with both convergent and divergent glottis shapes, each with a 20-deg included angle and a minimum glottal diameter of 0.04 cm, were studied. The compressible Navier-Stokes equations were integrated in a generalized curvilinear coordinate using an additive semi-implicit Runge-Kutta method and high-order compact schemes enabling accurate and efficient simulations of the flow and acoustics for this complicated low-Mach flow. A transglottal pressure of 15 cm H_2O was enforced across the inlet and outlet through the linear relaxation method. The simulated flow fields feature complex phenomena including the unsteady separation, Coanda effect, and transition to turbulence. Accurate flow simulation using a sufficiently long computational domain in the streamwise direction was found necessary to capture the Coanda effect previously observed in experiment studies. A Ffowcs Williams–Hawkings acoustic analogy was applied to identify acoustic sources and the results showed that dipole sources due to the unsteady forces exerted on the glottal walls were dominant. Turbulence and vortical structures affect the far-field sound indirectly through the dipole source by modifying the flow field rather than through direct contributions as quadruple sources. The spectral analysis showed the dipole sources from vortex shedding are responsible for the tonal sound observed in the divergent glottis.

ACKNOWLEDGMENTS

This work was supported by research grants No. R01 DC 03577 and No. R01 DC 05788 from the National Institute on Deafness and other Communication Disorders, National Institutes of Health. The simulations presented in this paper were performed using the AVIDD-O Opteron parallel cluster at Indiana University and the Macbeth Opteron parallel cluster at Purdue University. The authors would like to especially thank the journal reviewers and editors, as well as Professor Luc G. Mongeau, McGill University, and Professor Ronald C. Scherer, Bowling Green State University, for their valuable comments and suggestions on this work.

[1]I. R. Titze, *Principles of Voice Production*, 2nd ed. (National Center for Voice and Speech, Iowa City, IA, 2000).
[2]R. L. Wegel, "Theory of vibration of the larynx," Bell Syst. Tech. J. **9**, 207–227 (1930).
[3]K. Ishizaka and M. Matsudaira, "*Fluid mechanical considerations of vocal cord vibration*," SCRL (Speech Communications Research Laboratory) Monograph No. 8 (1972), pp. 207–227.
[4]R. C. Scherer, I. R. Titze, and J. F. Curtis, "Pressure-flow relationships in two models of the larynx having rectangular glottal shapes," J. Acoust. Soc. Am. **73**, 668–676 (1983).
[5]R. C. Scherer and I. R. Titze, "Pressure-flow relationships in a model of the laryngeal airway with a diverging glottis," in *Vocal Fold Physiology: Contemporary Research and Clinical Issues*, edited by D. M. Bless and J. H. Abbs (College-Hill, San Diego, CA, 1983), pp. 179–193.
[6]R. C. Scherer and C. G. Guo, "Laryngeal modeling: Translaryngeal pressure for a model with many glottal shapes," in *ICSLP Proceedings, 1990 International Conference on Spoken Language Processing* (Acoustical Society of Japan, Tokyo, 1990), Vol. **1**, pp. 3.1.1–3.1.4.
[7]F. Alipour and V. C. Patel, "Numerical simulation of laryngeal flow," in *Advances in Bioengineering* (ASME Bioengineering Division, New York, 1991), Vol. **20**, pp. 111–114.
[8]J. Liljencrants, "Numerical simulations of glottal flow," in *Vocal Fold Physiology: Acoustic, Perceptual, and Physiological Aspects of Voice Mechanisms*, edited by J. Gauffin and B. Hammarberg (Singular, San Diego, CA) (1991), pp. 99–104.
[9]C. Guo and R. C. Scherer, "Finite element simulation of glottal flow and pressure," J. Acoust. Soc. Am. **94**, 688–700 (1993).
[10]S. Slimon, D. Davis, S. Levinson, M. Krane, G. Richard, D. Sinder, H. Duncan, Q. Lin, and J. Flanagan, "Low Mach number flow through a constricted, stylized vocal tract," AIAA Paper No. 96–1734 (1996).
[11]X. Pelorson, A. Hirschberg, R. R. van Hassel, A. P. J. Wijnands, and Y. Auregan, "Theoretical and experimental study of quasi-steady flow separation within the glottis during phonation. Application to a modified two-mass model," J. Acoust. Soc. Am. **96**, 3416–3431 (1994).
[12]A. Hirschberg, X. Pelorson, G. C. J. Hofmans, R. R. van Hassel, and A. P. J. Wijnands, "Starting transient of the flow through an *in-vitro* model of the vocal folds," in *Vocal Fold Physiology: Controlling Complexity and Chaos*, edited by P. J. Davis and N. H. Fletcher (Singular, San Diego, CA, 1996), pp. 31–46.
[13]X. Pelorson, "On the meaning and accuracy of the pressure-flow technique to determine constrictions within the vocal tract," J. Acoust. Soc. Am. **35**, 179–190 (2001).
[14]G. C. J. Hofmans, G. Groot, M. Ranucci, G. Graziani, and A. Hirschberg, "Unsteady flow through in-vitro models of the glottis," J. Acoust. Soc. Am. **113**, 1658–1675 (2003).
[15]C. E. Vilain, X. Pelorson, C. Fraysse, M. Deverge, A. Hirschberg, and J. Willems, "Experimental validation of a quasi-steady theory for the flow through the glottis," J. Sound Vib. **276**, 475–490 (2004).
[16]F. Alipour, R. C. Scherer, and J. Knowles, "Velocity distributions in glottal models," J. Voice **10**, 50–58 (1996).
[17]F. Alipour and R. C. Scherer, "Pressure and velocity profiles in a static mechanical hemilarynx model," J. Acoust. Soc. Am. **112**, 2996–3003 (2002).
[18]R. C. Scherer, D. Shinwari, K. J. De Witt, C. Zhang, B. R. Kucinschi, and A. A. Afjeh, "Intraglottal pressure profiles for a symmetric and oblique glottis with a divergence angle of 10 degrees," J. Acoust. Soc. Am. **109**, 1616–1630 (2001).
[19]D. Shinwari, R. C. Scherer, K. J. De Witt, and A. A. Afjeh, "Flow visualization and pressure distributions in a model of the glottis with asymmetric and oblique glottis with a divergence angle of 10 degrees," J. Acoust. Soc. Am. **113**, 487–496 (2003).
[20]Z. Zhang, L. Mongeau, S. H. Frankel, S. Thomson, and J. B. Park, "Sound generation by steady flow through glottis-shaped orifices," J. Acoust. Soc. Am. **116**, 1720–1728 (2004).
[21]B. D. Erath and M., W. Plesniak, "The occurrence of the coanda effect in pulsating flow through static models of the human vocal folds," J. Acoust. Soc. Am. **120**, 1000–1011 (2006).
[22]M. Triep, C. Brücker, and W. Schröder, "High-speed PIV measurements of the flow downstream of a dynamic mechanical model of the human vocal folds," Exp. Fluids **39**, 232–245 (2005).
[23]J. Neubauer, Z. Zhang, R. Miraghaie, and D. A. Berry, "Coherent structures of the nearfield flow in a self-oscillating physical model of the vocal folds," J. Acoust. Soc. Am. **121**, 1102–1118 (2007).
[24]R. S. McGowan, "An aeroacoustic approach to phonation," J. Acoust. Soc. Am. **83**, 696–704 (1988).
[25]A. Barney, C. H. Shadle, and P. O. A. L. Davies, "Fluid flow in a dynamic mechanical model of the vocal folds and tract. I. Measurements and theory," J. Acoust. Soc. Am. **105**, 444–455 (1999).

[26]C. H. Shadle, A. Barney, and P. O. A. L. Davies, "Fluid flow in a dynamic mechanical model of the vocal folds and tract. II. Implications for speech production studies," J. Acoust. Soc. Am. **105**, 456–466 (1999).
[27]W. Zhao, S. H. Frankel, and L. Mongeau, "Numerical simulation of sound from confined pulsating axisymmetric jets," AIAA J. **39**, 1869–1874 (2001).
[28]W. Zhao, C. Zhang, S. H. Frankel, and L. Mongeau, "Computational aeroacoustics of phonation, Part I: Numerical methods, acoustic analogy validation and effects of glottal geometry," J. Acoust. Soc. Am. **112**, 2134–2146 (2002).
[29]J. E. Ffowcs Williams and D. L. Hawkings, "Sound generation by turbulence and surfaces in arbitrary motion," Philos. Trans. R. Soc. London, Ser. A **264**, 321–342 (1969).
[30]C. Zhang, W. Zhao, S. H. Frankel, and L. Mongeau, "Computational aeroacoustics of phonation, Part II: Effects of subglottal pressure, glottal oscillation frequency and ventricular folds," J. Acoust. Soc. Am. **112**, 2147–2154 (2002).
[31]Y. M. Bae, Y. J. Moon, and Y. I. Son, "Numerical simulation of aeroacoustic fields in human larynx," in *Proceeding of the 6th KSME-JSME Thermal & Fluids Engineering Conference*, Jeju, Korea (2005).
[32]R. S. McGowan, "The quasisteady approximation in speech production," J. Acoust. Soc. Am. **94**, 3011–3013 (1993).
[33]J. F. Kaiser, "Some observations on vocal tract operation from a fluid point of view," in *Vocal Fold Physiology: Biomechanics, Acoustics, and Phonatory Control*, edited by I. R. Titze and R. C. Scherer (Denver Center for the Performing Arts, Denver, CO, 1983), pp. 358–386.
[34]H. M. Teager and S. M. Teager, "Active fluid dynamic voice production models, or there is a unicorn in the garden," in *Vocal Fold Physiology: Biomechanics, Acoustics, and Phonatory Control*, edited by I. R. Titze and R. C. Scherer (Denver Center for the Performing Arts, Denver, CO, 1983), pp. 387–401.
[35]C. Wagner, T. Hüttl, and P. Sagaut, eds., *Large-Eddy Simulation for Acoustics*, 1st ed. (Cambridge U. P., New York, 2007).
[36]X. Zhong, "Additive semi-implicit Runge-Kutta methods for computing high-speed nonequilibrium reactive flows," J. Comput. Phys. **128**, 19–31 (1996).
[37]S. K. Lele, "Compact finite difference schemes with spectral-like resolution," J. Comput. Phys. **103**, 16–42 (1992).
[38]J. Suh and S. H. Frankel, "Large eddy simulations of low-Mach number aeroacoustics for complex wall-bounded turbulent flows via a multiblock/characteristic interface approach," AIAA Paper No. 2006–2633 (2006).
[39]M. Germano, U. Piomelli, P. Moin, and W. H. Cabot, "A dynamic subgrid-scale eddy viscosity model," Phys. Fluids A **3**, 1760–1765 (1991).
[40]P. Moin, P. Squires, W. H. Cabot, and S. Lee, "A dynamic subgrid-scale model for compressible turbulence and scalar transport," Phys. Fluids A **3**, 2746–2757 (1991).
[41]J. Suh, S. H. Frankel, L. Mongeau, and M. W. Plesniak, "Compressible large eddy simulations of wall-bounded turbulent flows using a semi-implicit numerical scheme for low Mach number aeroacoustics," J. Comput. Phys. **215**, 526–551 (2006).
[42]R. Hixon, M. Nallasamy, S. Sawyer, and R. Dyson, "Mean flow boundary conditions for computational aeroacoustics," AIAA Paper No. 2003-3299 (2003).
[43]R. Hixon, M. Nallasamy, S. Sawyer, and R. Dyson, "Unsteady validation of a mean flow boundary condition for computational aeroacoustics," AIAA Paper No. 2004-521 (2004).
[44]J. W. Kim and D. J. Lee, "Generalized characteristic boundary conditions for computational aeroacoustics," AIAA J. **38**, 2040–2049 (2000).
[45]D. H. Rudy and J. C. Strikwerda, "A nonreflecting outflow boundary condition for subsonic Navier-Stokes calculations," J. Comput. Phys. **36**, 55–70 (1980).
[46]T. J. Poinsot and S. K. Lele, "Boundary conditions for direct simulations of compressible viscous flows," J. Comput. Phys. **101**, 104–129 (1992).
[47]L. Selle, F. Nicoud, and T. Poinsot, "Actual impedance of nonreflecting boundary conditions: Implications for computation of resonators," AIAA J. **42**, 958–964 (2004).
[48]W. Polifke, C. Wall, and P. Moin, "Partially reflecting and non-reflecting boundary conditions for simulation of compressible viscous flow," J. Comput. Phys. **213**, 437–449 (2006).
[49]M. B. Giles, "Nonreflecting boundary conditions for Euler equation calculations," AIAA J. **28**, 2050–2058 (1990).
[50]J. B. Freund, "Proposed inflow/outflow boundary condition for direct computation of aerodynamic sound," AIAA J. **35**, 740–742 (1997).
[51]A. Uzun, "3-D large eddy simulation for jet aeroacoustics," Ph.D. thesis, School of Aeronautics and Astronautics, Purdue University, West Lafayette, IN, 2003.
[52]M. J. Lighthill, "On sound generated aerodynamically, I. General theory," Proc. R. Soc. London, Ser. A **211**, 546–587 (1952).
[53]U. Piomelli, C. L. Street, and S. Sarkar, "On the computation of sound by large-eddy simulation," J. Eng. Math. **32**, 217–236 (1997).
[54]G. C. J. Hofmans, "Vortex sound in confined flows," Ph.D. thesis, Technische Universiteit Eindhoven, Eindhoven, the Netherlands, 1998.
[55]N. Curle, "The influence of solid boundaries upon aerodynamic sound," Proc. R. Soc. London, Ser. A **231**, 505–514 (1955).
[56]S. Li, R. C. Scherer, M. Wan, S. Wang, and H. Wu, "Numerical study of the effects of inferior and superior vocal fold surface angles on vocal fold pressure distributions," J. Acoust. Soc. Am. **119**, 3003–3010 (2006).
[57]L. Eça, "2D orthogonal grid generation with boundary point distribution control," J. Comput. Phys. **125**, 440–453 (1996).
[58]R. W. Fox and S. J. Kline, "Flow regimes in curved subsonic diffusers," J. Fluids Eng. **84**, 303–316 (1962).
[59]H. Sato, "The stability and transition of a two-dimensional jet," J. Fluid Mech. **7**, 53–80 (1960).
[60]D. J. Tritton, *Physical Fluid Dynamics*, 1st ed. (Van Nostrand Reinhold, Berkshire, UK, 1977).
[61]B. R. Kucinschi, R. C. Scherer, K. J. DeWitt, and T. T. M. Ng, "Flow visualization and acoustic consequences of the air moving through a static model of the human larynx," J. Biomech. **128**, 380–390 (2006).
[62]M. Agarwal, "The false vocal folds and their effect on translaryngeal airflow resistance," Ph.D. thesis, Bowling Green State Univ., Bowling Green, OH (2004).
[63]B. Erath, "An experimental investigation of velocity fields in diverging glottal models of the human vocal tract," Master's thesis, School of Mechanical Engineering, Purdue University, West Lafayette, IN 2005.

An articulatory basis for the labial-to-coronal effect: /pata/ seems a more stable articulatory pattern than /tapa/

Amélie Rochet-Capellan[a] and Jean-Luc Schwartz[b]
Institut de la Communication Parlée, UMR5009 CNRS/INPG/Université Stendhal, 46 Avenue Félix Viallet, 38031 Grenoble Cedex 01, France

(Received 15 June 2006; revised 29 March 2007; accepted 30 March 2007)

This paper investigates the coordination between the jaw, the tongue tip, and the lower lip during repetition with rate increase of labial-to-coronal (L_aC_o) consonant-vowel-consonant-vowel disyllables (e.g., /pata/) and coronal-to-labial (C_oL_a) ones (e.g., /tapa/) by French speakers. For the two types of disyllables: (1) the speeding process induces a shift from two jaw cycles per disyllable to a single cycle; (2) this shift modifies the coordination between the jaw and the constrictors, and (3) comes with a progression toward either a L_aC_o attractor [e.g., (/pata/ or /tapa/) → /patá/ → /ptá/] or a C_oL_a one (e.g., /pata/ or /tapa/ → /tapá/ → /tpá/). Yet, (4) the L_aC_o attractor is clearly favored regardless of the initial sequencing. These results are interpreted as evidence that a L_aC_o CVCV disyllable could be a more stable coordinative pattern for the lip-tongue-jaw motor system than a C_oL_a one. They are discussed in relation with the so-called LC effect that is the preference for L_aC_o associations rather than C_oL_a ones in CV.CV disyllables in both world languages and infants' first words. © *2007 Acoustical Society of America.* [DOI: 10.1121/1.2734497]

PACS number(s): 43.70.Aj, 43.70.Fq [AL] Pages: 3740–3754

I. INTRODUCTION

The analysis of CV.CV disyllables in world languages lexicons reveals that labial-to-coronal (L_aC_o) sequences (e.g., /pata/) are about 2.5 times more used than coronal-to-labial (C_oL_a) ones (e.g., /tapa/) (Locke, 1983; MacNeilage and Davis, 2000; Rousset, 2003). This asymmetry, also displayed in infants' first words in the course of ontogeny (Ingram, 1974; Locke, 2000; MacNeilage and Davis, 2000), is known as the "LC effect." The existence of the same trend in infant and adult speech led MacNeilage and Davis (2000) to propose a "substance-based" explanation of the LC effect in the framework of the "frame-content theory" of speech development (MacNeilage, 1998). Yet, there are some problems with their explanation, leaving space for further hypotheses. The present investigation is an attempt to test an original explanation of the LC effect, based on motor principles likely to intervene both in speech development and in on-line adult speech production.

A. The "simple first" hypothesis

MacNeilage and Davis, 2000 proposed that the LC effect might result from the conjunction of two principles in the course of speech development: (1) labial protoconsonants (or closants in the frame-content terminology) would be easier to produce by infants than coronal ones, and (2) in order to deal with the complexity of the mental lexicon access required in the production of their first words, infants would focus on easier forms. Thus, they would select sequences of actions beginning by the simpler gesture, supposed to be the labial one. The preference for L_aC_o disyllables in development would then have been preserved in adults' languages.

The assumed greater simplicity of labial gestures is one component of the frame-content theory of speech motor control development (MacNeilage, 1998; MacNeilage and Davis, 2000). This theory claims that speech production begins in babbling with phonation associated with repeated vertical oscillations of the jaw. Apart from vocal tract presettings, the other articulators would stay stable all along the jaw cycles. Thus, besides their alimentary function, jaw cycles would induce alternation of closing and opening patterns (*closants* and *vocants*) and constitute the *frame* of speech. Then, the speech segmental *content* (independent control of consonants and vowels inside the frame) would progressively emerge from the development of the central and peripheral motor control of the other articulators. According to MacNeilage and Davis, for neutral vocal tract presetting, that is purely passive tongue and lips, jaw raising gestures would induce a labial closure of the vocal tract and so the production of labial closants ("pure frames"). On the contrary, coronal closants would require an active motion of the tongue in presetting ("fronted frames"). Therefore, labial closures would be easier to realize than coronal ones. However, the "simple first" explanation suffers in our view from several weaknesses. First, it is a bit ad hoc. Second, the "simpler" nature of labial closants in babbling has been questioned by Vilain *et al.* (1999) in a study exploiting articulatory models of the vocal tract. They compared three models with different morphologies—coming from the statistical analysis of cineradiographic data recorded from three different adult speakers. They simulated pure frames on the three models, by applying jaw upward commands, all other articulators being kept passive, and they obtained different kinds of closures. In one model the jaw raise resulted in closing the

[a]Electronic mail: amelie.rochet-capellan@icp.inpg.fr
[b]Electronic mail: jean-luc.schwartz@icp.inpg.fr

 0001-4966/2007/121(6)/3740/15/$23.00 © 2007 Acoustical Society of America

lips first, producing a labial contact, while in another one it first resulted in a closure inside the vocal tract, producing a coronal contact. In the last model, a labial and a coronal contact were obtained almost in synchrony. Therefore, both /ba/, /da/ and /bda/ could be pure frames according to the vocal tract morphology. This could explain why analyses of babbling inventories do not display a preference for labial patterns over coronal ones (Locke, 1983).

Another problem concerns the extrapolation from infants to adults. Indeed, there is no reason to believe that labial plosives would stay simpler than coronal ones in adult speech, both involving a specific articulatory control superimposed on the jaw, respectively, for the lips in labials and for the tongue in coronals (Munhall and Jones, 1998). Finally, the "simple first" hypothesis tends to consider the articulatory control of L_aC_o and C_oL_a utterances as a sequence of independent phonetic segments while it might be better characterized as coordinative structures (Kelso *et al.*, 1986; Nittrouer, 1991).

B. An alternative hypothesis based on jaw-tongue-lips coordination

It is widely assumed that some coordinative patterns are more stable and economic than others and that the repetition of a multieffectors gesture with rate increase would attract the system toward its most stable coordinative mode. This has been first established for interlimb coordination (Hoyt and Taylor, 1981; Haken *et al.*, 1985) and then extended to articulators' coordination in speech production (Kelso *et al.*, 1986; Lindblom, 1990a; Kelso, 1995). Such criteria of stability and economy have been introduced in substance-based criteria shaping the sound systems of human languages (e.g., Stevens, 1989; Lindblom, 1990b). In this vein, it has been shown that rate increase induced repeated VC syllables to switch toward cycled CV ones (Stetson, 1951; Tuller and Kelso, 1991; de Jong, 2001). This led the authors to conclude that CV sequences are more stable than VC ones, which could explain the preference for CV syllables over VC ones in language inventories (Redford and Diehl, 1999; Rousset, 2003).

These studies provide an interesting framework for attempting to anchor the LC effect in the properties of the articulatory motor system rather than in a pure developmental framework. More precisely, we assume that a labial constriction followed by a coronal one could be a better coordinative pattern for the lip-tongue-jaw system than the coronal-then-labial one. This assumption is inspired from Sato *et al.* (2006). The authors supposed that in CCV or CVC sequences involving a labial and a coronal consonant, there was a trend to anticipate the coronal constriction during the labial one, rather than the inverse. Hence, lips and tongue were more in-phase in /psə/ than in /spə/. The reason is that in /psə/, the tongue tip may be prepared for /s/ during the labial closure, so that the /p/ release is almost synchronous with the tongue-driven onset of the next /s/. On the contrary, in /spə/, the lips must stay open during the production of the /s/, before labial closure followed by the /p/ release, so that the tongue-lip synchrony is difficult to achieve (see also Byrd, 1996; Zsiga, 1996; Surprenant and Goldstein, 1998, for compatible data in English; and Chitoran *et al.*, 2002 for Georgian). This articulatory asymmetry between the two sequences of consonantal gestures could be a part of the LC effect explanation in both language development and world languages lexicons.

C. An experimental scenario

The presumed greater stability of the coordination in L_aC_o compared with C_oL_a could be investigated through the speeding paradigm. The slow regular repetition of C_1VC_2V disyllables should be characterized by a regular alternation of C_1 and C_2 gestures over time. On the contrary, rate increase could lead to asymmetries, the C_2 constriction being either closer to the previous or to the next C_1 one. This would induce the reduction of either the vowel after C_1 or after C_2. The French language, under study here, displays a stress on the word's last syllable. Therefore, in the repetition with rate increase of a CVCV disyllable, French speakers should rather reduce the first vowel, and a CCV resyllabification could be expected. Hence, two hypotheses may be contrasted. In a first one, there would be no asymmetry between L_aC_o and C_oL_a coordination, and the French speakers would preserve the original disyllable prosody through speeding. In this first hypothesis, L_aC_o CVCV sequences would evolve toward a L_aC_o attractor (e.g., /pata/ →/patá/ → /ptá/) while C_oL_a CVCV sequences would evolve toward a C_oL_a CCV attractor (e.g. /tapa/ → /tapá/ → /tpá/). Yet, if, as we expect, the L_aC_o coordination is more stable than the C_oL_a one, this would attract the system toward a L_aC_o attractor regardless of the initial CVCV sequence [e.g., (/pata/ or /tapa/) → /patá/ → /ptá/]. Hence, in this second hypothesis, the repetition with rate increase of both L_aC_o and C_oL_a CVCV disyllables would evolve toward a L_aC_o attractor. The first experiment, based on acoustic measurements, aimed at selecting which of these two assumptions is true.

In a second experiment based on articulatory measurements, we studied how the articulatory coordination between jaw, tongue, and lips would be reorganized in order to subtend the progression from one constriction per jaw cycle (e.g., /pata/) toward two constrictions per jaw cycle (e.g., /ptá/). A prediction was that the two constrictions would be realized on a single jaw cycle before the fading of the vowel was completed (e.g., /patá/). In other words, the variation of the articulation place between the first and the second constriction would allow the production of two syllables on a single jaw cycle, while most studies of jaw movements associate the jaw cycle with the CV syllable (Nelson *et al.*, 1984; Ostry and Flanagan, 1989; Perkell and Zandipour, 2002; Perkell *et al.*, 2002).

II. AN ACOUSTIC STUDY OF LC AND CL STABILITY

The aim of this first study is to test if L_aC_o sequences are more stable than C_oL_a ones in a speeding paradigm, using an acoustic measure of vowel reduction.

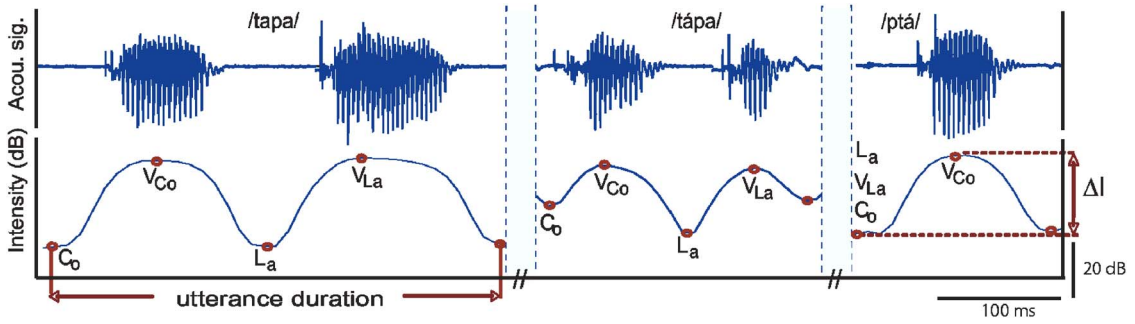

FIG. 1. (Color online) Labeling of intensity curves and measurements: Intensity curves (bottom) of the acoustic signal (top) against time for three samples of a /tapa/ trial. The repetition progressively evolves from /tapa/ (left) toward /tápa/ (middle) until /ptá/ (right). L_a and C_o are the labial and coronal consonants; V_{La} and V_{Co} are the vowels respectively following L_a and C_o. This labeling allows computing the duration of an utterance and the intensity variation of intensity between V_{La} and V_{Co}(ΔI).

A. Method

1. Speakers and phonetic material

Twenty-eight native French speakers with no speech or hearing problem and naive as to the purpose of the study participated in the experiment. The phonetic material consisted in six CVCV disyllables: three L_aC_o (/pata/, /pasa/, and /fata/) and their three C_oL_a counterparts (/tapa/, /sapa/, and /tafa/). This choice aimed at contrasting L_aC_o and C_oL_a sequences while controlling for a possible "plosive-to-fricative" effect. Indeed, in the framework of "sonority" principles (Selkirk, 1984; Clements, 1990) it could be supposed that utterances containing a fricative and a plosive would switch toward plosive-fricative attractors (e.g., /tfa/, /psa/), rather than the L_aC_o attractors /pta/, /psa/, and /fta/ expected in the framework of our basic assumptions. The /a/ vowel was selected to provide an open configuration, mainly involving the jaw, with basically no strong requirements on the lips and the tongue. The six disyllables were randomly arranged inside three lists. The three lists were presented to each speaker in different orders. Hence each disyllable was presented three times to each speaker. The test began with three items provided as training stimuli (/vada/, /daba/, and /dava/).

2. Procedure

In order to simplify post-treatments the experiment was assisted by a computer program that allowed one to record utterances and to display a kind of visual metronome. The participants were sitting in front of a computer connected to a microphone. The instruction was to repeat the disyllable displayed on the screen at an increased and then decreased rate following as much as possible the rhythm of a visual flash. The aim of this flash was not to precisely control the speakers' rate but rather to give global timing marks in order to homogenize acceleration and deceleration phases between speakers and to attempt to drive the speakers to their limit rate. It was mentioned that the flash would reach rates impossible to follow and the instruction was to maintain a rate as high as possible during this period until the decelerating phase. Moreover, speakers were encouraged to go on without interruption even if they perceived any kind of transformation of the uttered sequence.

The experiment began by the three practice trials. Then, the three lists were successively displayed. Each trial started with the presentation of the CVCV sequence to repeat, displayed in the middle of the screen. Speakers initiated the flash pressing the "space" key. A blue square took the place of the disyllable on the screen for 1 s, followed by the flash. The flash was an alternation of a black and a white square. The instruction was to produce one syllable on the black flash and the other on the white one. Duration of each square presentation started at 300 ms and progressively decreased to reach 125 ms at the middle of the acceleration phase and 50 ms at the end of the acceleration phase (8 s). The progression was shaped in order to obtain a large amount of rapid productions. The timing of the deceleration phase was the symmetric of the acceleration one. Thus, each trial record lasted 16 s. Speakers sometimes took a breath inside the whole acceleration-deceleration process, but this occurred seldom and at random positions inside the 16 s utterance. Then the speaker spontaneously resumed the process at about the same tempo he/she had reached before the breath.

3. Hypotheses and measurements

The working hypothesis is that both L_aC_o and C_oL_a repetitions would evolve toward a L_aC_o CVCV sequencing until eventually reaching a L_aC_o CCV consonantal cluster. For example, if /pata/ is indeed more stable than /tapa/, the speeding process should be: (/pata/ or /tapa/) → /patá/ → /ptá/. The contrasted prediction is that, if there were no asymmetry between L_aC_o and C_oL_a utterances in terms of coordinative structure, the French prosodic pattern with a stress on the final syllable of a word should drive the behavior with e.g., /pata/ → /patá/ → /ptá/ and /tapa/ → /tapá/ → /tpá/. Finally, both trends could be observed, with a L_aC_o vs C_oL_a asymmetry, superimposed on an effect of the initial uttered sequence. These predictions were tested by prosodic measurements based on vowel intensity. Acoustic energy was continuously estimated, within the PRAAT software[1] using a 42.6 ms Kaiser-20 window (sidelobes below −190 dB). Maxima and minima of energy curves were automatically detected and then hand-selected as vowels and consonants (Fig. 1). When a speaker's production evolved toward a single consonantal cluster (e.g., /ptá/), the labeling rule was to mark the "vanished" vowel and the two consonants around

as a same event (e.g., Fig. 1, right). Speakers' errors such as repetition of a single syllable or pauses were removed. From these data, two parameters were computed for each CVCV or CCV sequence correctly produced (now referred as "utterances"): (1) the utterance duration and (2) the variation of intensity between the two vowels, that is the difference between the intensity of the vowel after the coronal consonant (V_{Co}) and the intensity of the vowel after the labial consonant (V_{La}):

$$\Delta I = I(V_{Co}) - I(V_{La}).$$

The operational hypothesis was that ΔI would be positive for both the L_aC_o and the C_oL_a utterances for fast productions, with very high positive values indicating a shift toward a single L_aC_o CCV syllable (e.g., from /pata/ or /tapa/ to /ptá/, as in Fig. 1).

B. Results

The analyses excluded two speakers, one because he did not manage to alternate the labial and the coronal constrictions at a fast rate and the other for recording problems. Apart from local errors, all the 26 remaining speakers' utterances respected a "…$L_aVC_oVL_aVC_oV$…" sequencing, L_a and C_o respectively being the labial and the coronal consonants of the target CVCV sequence, and "V" the vowel /a/ or nothing.

1. Evolution of ΔI across rate: Global tendencies

The plot of ΔI values against utterance durations for all the speakers' L_aC_o and C_oL_a utterances shows very similar patterns for the three L_aC_o and C_oL_a pairs. Hence, only the graphs for /pasa/ and /sapa/ are displayed in Fig. 2 (top), as a representative example. Globally and for both the L_aC_o (left) and C_oL_a (right) groups, utterance durations range from 100 to 700 ms. Furthermore, ΔI values are close to 0 for durations longer than about 300 ms whereas they vary from −40 to 40 dB for shorter durations. Actually, standard deviations of ΔI values (Fig. 2, bottom) are small above 300 ms, and larger under 300 ms. The shift from small to large ΔI values is stable around 300 ms for all CVCV sequences, leading us to select this value as a limit for further analyses. Thus, for slow rates, the speakers keep a regular alternation of labial and coronal syllables without any strong reduction effect. Then, rate increase induces the reduction of either V_{La} (positive ΔI values) or V_{Co} (negative ΔI values). Hence, both the L_aC_o (/psá/) and the C_oL_a (/spá/) CCV clusters seem to constitute possible attractors for the repetition of either L_aC_o or C_oL_a CVCV logatoms. Yet, the graphs display more positive than negative ΔI values for the two types of disyllables. Therefore, the L_aC_o attractor seems to prevail over the C_oL_a one, particularly for the L_aC_o trials (Fig. 2, top left).

2. Detailed analysis according to the disyllables and to the speakers

In order to investigate more precisely possible reorganizations of productions in the speeding process, the analysis of ΔI was restricted to utterances with durations shorter than

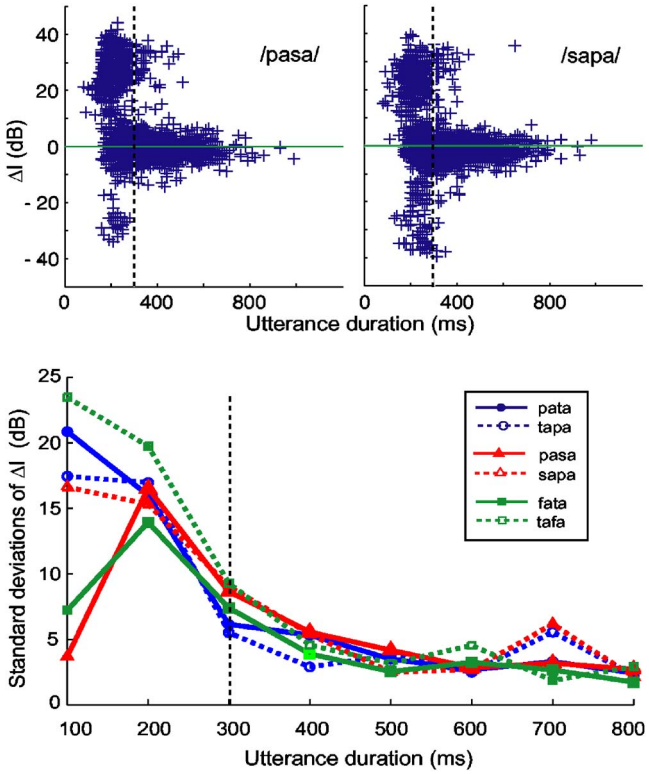

FIG. 2. (Color online) Intensity variation between the vowel after the labial constriction and the vowel after the coronal constriction (ΔI) plotted against duration for /pasa/ (left) and /sapa/ (right) CVCV and CCV correctly produced utterances for all subjects (top). Results for /pasa/ and /sapa/ are representative of the two other L_aC_o (/pata/, /fata/) and C_oL_a (/tapa/, /tafa/) pairs. Bottom: Standard deviations of ΔI against utterances durations (100 ms meantime) for the six CVCV sequences. Dispersion increases when duration becomes shorter than 300 ms.

300 ms. In spite of the flash, the utterance durations varied a lot according to the speaker and to the trial. Therefore, for the analysis, we kept only speakers achieving a sufficient amount of quick data with the following criterion: For each of the six CVCV logatoms, the speaker should have produced at least five quick utterances (durations shorter than 300 ms) for at least two of his/her three trials. Then, only the two trials with the largest number of quick utterances were analyzed. This criterion excluded five speakers. In the following, only the utterances with durations less than 300 ms are analyzed, for the two selected trials of the 21 remaining subjects.

Global means of the 42 trials are positive for all disyllables, and all significantly different from 0 except for /sapa/ (Table I, first row). Moreover, the distribution of the 42 means according to their sign (last four rows in Table I) shows that the ratio of positive means related to negative ones (rows 3 and 5) is 2.5 for /pata/ and /tapa/, 7.4 for /fata/, 3.6 for /tafa/, and 1.8 for /pasa/ whereas it is 1 for /sapa/. A Chi-square test shows significant difference between the frequencies of positive versus negative means [$\chi^2(1)=6.6, p<0.001$]. Restricted to means that significantly differ from 0 (rows 4 and 6) the prevalence of positive means over negative ones is even greater with a ratio of 4.75 for /pata/, 2.5 for /tapa/, 3 for /pasa/, 1.4 for /sapa/, 13 for /fata/, and 5.3 for /tafa/ [frequency of significant positive means significantly

TABLE I. Analysis of intensity variations between the vowel after the labial and the vowel after the coronal consonant for utterances shorter than 300 ms for the 42 analyzed trials (see the text for details about data selection). For each disyllable: means (dB) and are compared with 0 according to a two-tails t-test ($df=41$) with Bonferroni correction; standard errors; repartition of the 42 means according to their sign: for all the means and for the means that significantly differ from 0 according to a two-tails t-test with Bonferroni correction ($p \leqslant 0.05/42$).

		pata	tapa	pasa	sapa	fata	tafa
Means		6.6[a]	7.0[a]	7.5[a]	3.8	8.9[a]	8.6[a]
Standard errors		1.9	1.9	1.7	1.7	1.7	2.1
Number of positive means	All signif.	30	30	27	21	37	33
		19	15	18	13	26	21
Number of negative means	All signif.	12	12	15	21	5	9
		4	6	6	9	2	4

[a] $p \leqslant 0.01/6$.

different from significant negative ones, $\chi^2(1)=6.8$, $p<0.001$]. Hence, the speeded repetition of L_aC_o and C_oL_a CVCV disyllables more often evolves toward the corresponding L_aC_o attractor (e.g., /pasá/ or /psá/) than the C_oL_a one (e.g., /sapá/ or /spá/). However, C_oL_a forms appear in some cases for both L_aC_o and C_oL_a trials. Furthermore, two additional factors tend to emerge. Indeed, there is some trend that ΔI values are larger, and more systematically positive, for L_aC_o than for C_oL_a trials on one hand, and for /pata/-/tapa/ and /fata/-/tafa/ than for /pasa/-/sapa/ trials on the other hand.

Considering that two attractors seem to coexist, though with a preference for the L_aC_o one, we wondered whether they might coexist for a given speaker. For this aim, Fig. 3 (left) displays the relation between mean ΔI values for the first and the second selected trial, for each speaker and for each CVCV sequence, provided that the two means significantly differed from 0. It appears that mean ΔI values are both significantly positive for 41 cases, both significantly negative for seven cases and have different signs in five cases. Therefore, the dominant behavior is to evolve toward the same attractor for the two trials with a large preference for the L_aC_o compared to the C_oL_a one. Yet, in some cases, the attractor differs from one trial to the other. Then, grouping all logatoms, it appears that some speakers tend to be "L_aC_o stable" (e.g., S12, right part of Fig. 3) whereas others are, to a lower extent, rather "C_oL_a stable" (e.g., S23). Finally, some speakers are "bistable:" the category of attractor they evolved toward changes according to the trial (S20) or to the logatom (S6).

In summary, the speeded repetition of L_aC_o and C_oL_a logatoms could evolve both toward the L_aC_o or the C_oL_a attractor. Yet, and despite variability between disyllables and between speakers, the L_aC_o attractors are largely favored compared to the C_oL_a ones. Thus, /patá/-/ptá/ is the favorite attractor for /pata/ and /tapa/; /pasá/-/psá/ for /pasa/ and to a lower extent for /sapa/ and /fatá/-/ftá/ for both /fata/ and /tafa/.

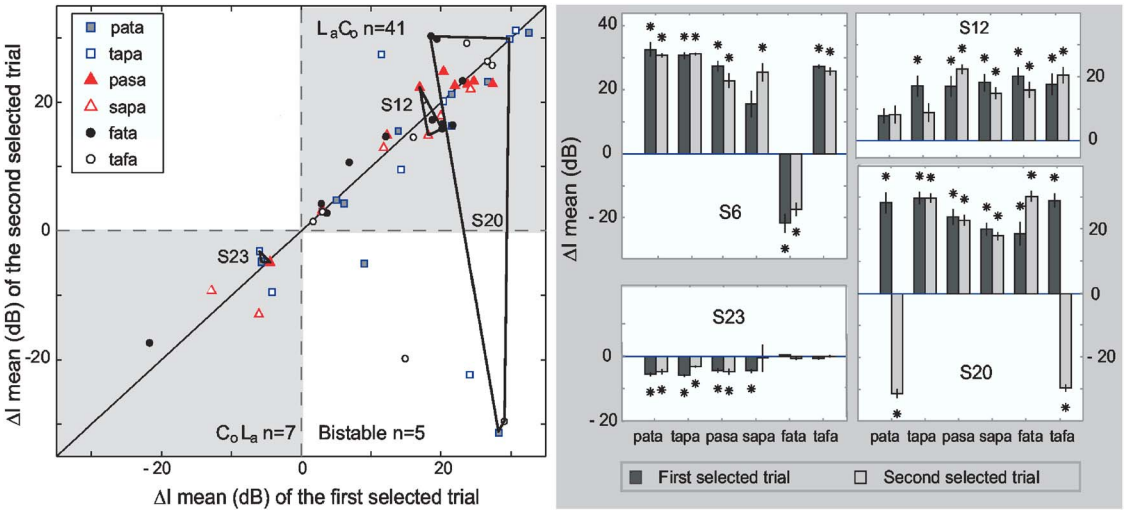

FIG. 3. (Color online) Attractor stability and speakers' profiles. On the left: ΔI mean (variation of intensity between the vowel after the labial consonant and the vowel after the coronal consonant) of the second trial against ΔI mean of the first trial for each CVCV and each speaker when the two means significantly differ from zero (two-tails Student test with Bonferroni correction $p \leqslant 0.05/42$). Points inside the top left and the bottom right squares correspond to cases with attractor shift from one trial to the other. Points inside the top right and bottom left squares respectively represent L_aC_o and C_oL_a stability for the two trials. On the right: ΔI means for the two selected trials for each CVCV of four typical speakers with S20 and S6 as bistable profiles; S12 as L_aC_o stable and S23 as C_oL_a stable. The convex hulls of S23, S20, and S12 are displayed on the left-hand side. An asterisk means significantly different from zero, $p \leqslant 0.05/42$.

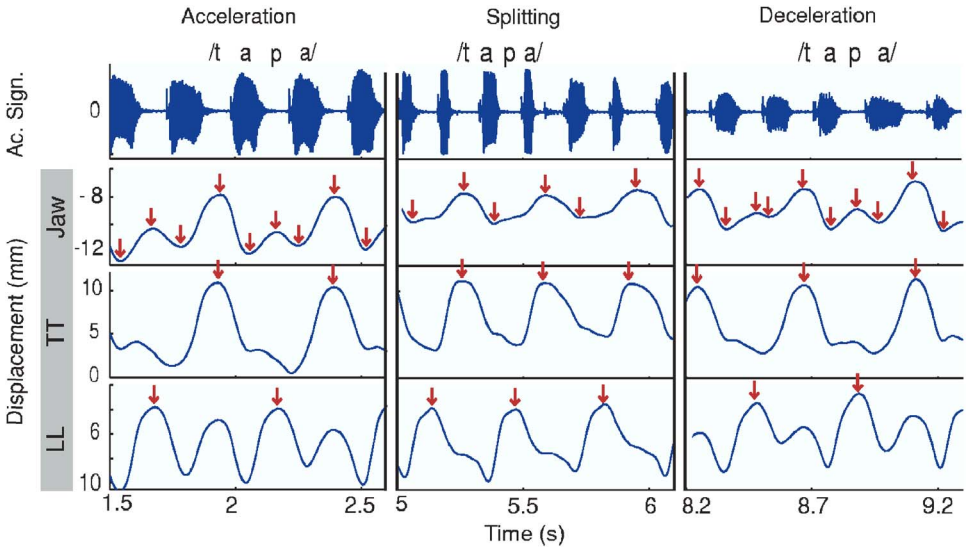

FIG. 4. (Color online) Acoustic signal, jaw tongue tip (TT), and lower lip (LL) displacements against time for samples of a /tapa/ trial (S3). From left to right: sample of the acceleration phase; sample of the period with one jaw cycle for two syllables (splitting); and sample of the deceleration phase. The arrows on trajectory curves represent the labeled minima and maxima for the jaw and the maxima for the constrictors. Notice the secondary maxima for TT and LL due to passive motion induced by the jaw gesture that comes with the other constriction (these secondary maxima are not incorporated in further analyses in Experiment 2).

III. AN ARTICULATORY STUDY OF L_aC_o AND C_oL_a STABILITY

The main purpose of the second study is to understand from EMMA recordings how the articulatory system could evolve with rate increase from a L_aC_o or a C_oL_a CVCV disyllable toward either a L_aC_o or a C_oL_a attractor, with a preference for the first one.

A. Method

1. Speakers and phonetic material

The participants were five college-aged French speakers (three females—S1, S3, and S4—and two males—S2 and S5), without any speech or hearing deficits. They did not participate in Experiment 1. The L_aC_o and C_oL_a disyllables were the same as in the acoustic study. Two duplicated CVCV logatoms (/papa/ and /tata/) were added as control items.

2. Procedure, data recording, and processing

The instruction was to continuously repeat the disyllable enounced by the experimenter starting at a slow rate and then at an increasingly rapid rate up to the highest possible one. The speakers then had to progressively decrease the rate to return to the initial slow one. Contrary to the first experiment, no external tempo driver was used because of the already difficult conditions of EMMA recording. Speakers were encouraged not to stop their productions even if they seemed different from the initial sequence. The eight disyllables were repeated three times with orders that varied from one subject to another. The articulator motions were tracked over time at 500 Hz using a Cartens electromagnetic articulograph. Two reference transducers, one at the bridge of the nose and the other on the gums above the upper teeth, allowed one to correct the data for head movements. The three measurement points were: the jaw (transducer placed beneath the lower teeth); the tongue tip (TT, transducer placed at about 1 cm from the tip of the tongue), and the lower lip (LL, transducer just beneath the vermilion border of the lower lip). These raw measurements were then processed according to classical procedures [see Hoole (1996) for more details]. These involved translation and rotation correcting for head movement, resulting in setting the origin at the reference coil located on the upper incisors, the vertical axis as the line joining the reference coils on upper incisors and nose bridge, and the x axis aligned with the occlusal plane. The acoustic signal was simultaneously recorded by the way of a microphone fixed on the articulograph helmet and then digitized at 20 kHz.

3. Hypotheses

The first hypothesis is that the mandible would evolve from a one-cycle-per-syllable relationship to a one-cycle-per-disyllable relationship when speeding L_aC_o or C_oL_a CVCV logatoms. However, duplicated L_aL_a (/papa/) or C_oC_o (/tata/) CVCV logatoms were expected not to display this behavior. The second hypothesis concerns the lips-tongue coordination inside a single jaw cycle at high rates. Two attractors were expected, either L_aC_o or C_oL_a. In the first case, the labial constriction and the next coronal constriction (respectively, maximum values of LL and TT trajectories) should be close together. In the second case, the coronal constriction should be close to the next labial one. Considering the small number of speakers, and the variability observed in the first experiment, no strong claim was made about a preference for L_aC_o attractors. Instead, the hope was that interspeaker variability would enable one to observe both kinds of attractors, in order to be able to characterize them articulatorily.

4. Measurements

Processing of acoustical data was the same as in Experiment 1. It led to computation of the duration and intensity variation between the two vowels (ΔI) for each utterance (CVCV or CCV items correctly produced). Articulatory analysis used articulator trajectories preprocessed by a low-pass Chebychev filter (cutting frequency at 15 Hz). Jaw maxima and minima (Fig. 4, row 2) were automatically detected on the jaw trajectory as the zero crossings in velocity signal, allowing trajectory segmentation into closing and opening phases (up and down strokes). Postprocessing dis-

TABLE II. Number of CVCV or CCV utterances correctly produced (Tot) and number of utterances produced with sufficient jaw motion (see the text) and kept for further articulatory analysis (Ar) for each speaker and each sequence.

	papa		tata		pata		tapa		pasa		sapa		fata		tafa	
Speaker	Tot	Ar	Tot	Ar	Tot	Ar	Tot	Ar	Tot	Ar	Tot	Ar	Tot	Ar	Tot	Ar
S1	63	63	63	60	61	59	59	54	60	59	54	54	53	51	51	47
S2	51	49	53	52	58	47	52	48	62	43	59	43	65	59	58	49
S3	53	51	56	54	60	59	63	61	59	59	64	64	57	57	65	65
S4	66	63	68	60	76	52	73	55	74	73	62	60	69	64	71	53
S5	94	85	100	76	109	93	102	80	99	73	95	82	98	79	100	74

carded movements realized during pauses or errors (detected from the acoustical labeling). For the correct utterances, two criteria were used in order to discard productions subtended by too small jaw movements. First, we checked for the regular alternation of opening and closing strokes; second, we removed strokes with an amplitude lower than 0.1 mm, which is the claimed precision of the EMMA system (Hoole, 1993), and did provide a floor above which jaw trajectories appeared consistent all along this study. Table II summarizes the total number of correct utterances and the number of correct utterances kept for further articulatory analysis. Then, TT and LL events were labeled in the articulatory signals, with the help of acoustic events. TT constrictions were defined as the highest TT positions between the vowel after the labial consonant (V_{La}) and the vowel after the coronal consonant (V_{Co}) (Fig. 4, row 3). Similarly, LL constrictions were defined as the highest LL positions between V_{Co} and V_{La} (Fig. 4, row 4). This method [similar to Hertrich and Ackermann's one (2000)] discards secondary maxima due to passive motion induced by the jaw gesture that comes with the other constriction.

Then, jaw cycles were separated into an up stroke and its adjacent down stroke. The jaw cycle duration was the sum of its up and down stroke durations and the jaw cycle amplitude was the mean of its up and down stroke amplitudes [Fig. 5(A)]. Each constriction event was assigned to the jaw cycle that temporally included it and positioned relatively to this jaw cycle [Fig. 5(B)]. This measure, expressed in percent of jaw cycle, constitutes an indicator of the phasing relationship between the jaw and constrictors. Finally, the coordination between TT and LL was characterized by the duration of the labial-to-coronal phase (time from LL constriction to TT constriction D_{LaCo}). normalized by the whole disyllable duration (time from a LL constriction to the next LL one D_{LaLa}):

$$\Delta_{(LaCo/LaLa)} = D_{LaCo}/D_{LaLa}.$$

B. Results

1. Acoustic analysis

The global pattern of ΔI against utterance duration for L_aC_o or C_oL_a sequences is very close to the pattern observed in the first experiment (compare Fig. 6, right, with Fig. 2). That is, ΔI values are close to 0 for durations longer than 300 ms whereas ΔI values far from 0 appear for shorter durations, with more positive than negative values. On the contrary, ΔI values are always close to 0 for duplicated L_aL_a or C_oC_o logatoms (Fig. 6, left).

Moreover, the mean ΔI values for utterances with durations shorter than 300 ms (Table III) represent the panel of behaviors observed in the first experiment. Indeed, as a subset of speakers of the acoustic study, S3 fails to produce enough rapid productions. This may indicate that this speaker rarely shifts toward a CCV structure. Then, S1 and S4 tend to favor the C_oL_a attractor (more negative than positive means) especially for /pasa/ and /sapa/ for S1 and for the three C_oL_a disyllables for S4. On the contrary S2 and S5 tend to favor the L_aC_o attractor for all disyllables except for S5's

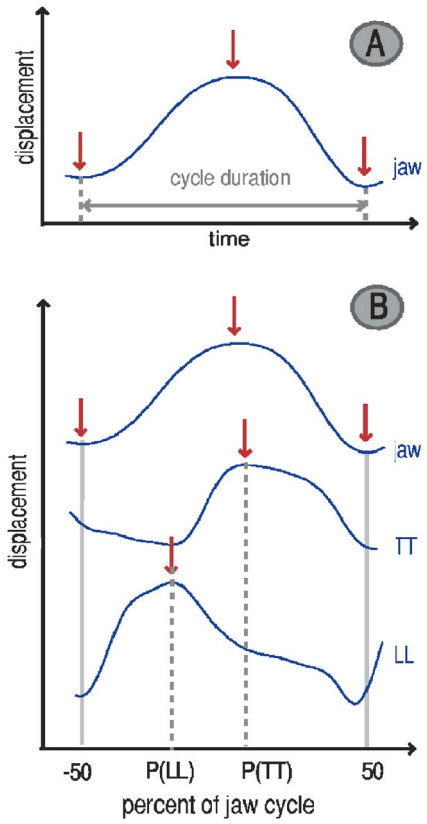

FIG. 5. (Color online) Articulatory measurements. (A) Duration and amplitude of the jaw cycle are, respectively, the sum of its up and down stroke durations and the mean of its up and down stroke amplitudes.(B) Position of the tongue tip [P(TT)] and of the lower lip [P(LL)]; constriction events were displayed on the jaw cycle normalized between −50% and 50% with −50% at the beginning of the up stroke, 0% at the jaw maxima, and 50% at the end of the down stroke.

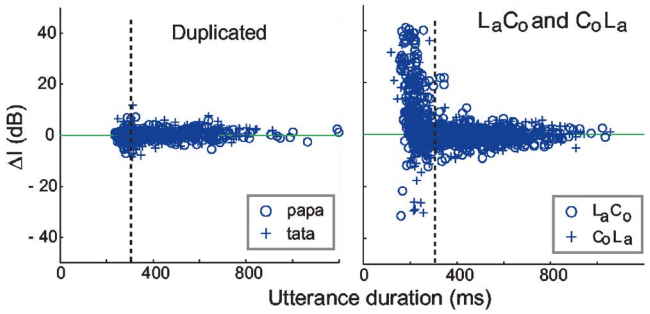

FIG. 6. (Color online) Intensity variation between the vowel after the labial constriction and the vowel after the coronal constriction (ΔI) against utterance duration for all subjects' duplicated (left) and $L_aC_o-C_oL_a$ (right) productions. ΔI does not vary much with duration for duplicated logatoms whereas duration around 300 ms (vertical dotted line) appears as a boundary for the range of possible ΔI values for L_aC_o and C_oL_a logatoms (see the text).

/sapa/ productions. Interestingly, these behaviors correspond to both the speakers' profiles and the variability between sequences observed in the first experiment.

2. Global analysis of jaw cycles

The /tapa/ utterance samples displayed in Fig. 4 illustrate the speeding process generally observed for a L_aC_o or a C_oL_a trial. First, during the acceleration phase (left), each constriction comes with its own jaw gesture. Yet, the amplitude and the duration of the jaw cycle for the labial constrictions tend to be smaller than for the coronal constrictions. Then, rate increase induces the progressive fading of the jaw cycle that supports the labial constriction, resulting in a single jaw cycle for the two constrictions. For this example, the plot of the acoustic signal (top) shows that the speaker does not evolve toward a CCV syllable but produces two syllables on a single jaw cycle (splitting phase, middle). Finally, the deceleration progressively brings the system back to its initial state with one jaw cycle per syllable (right).

Plots of jaw cycle durations (y) against CVCV durations (x) for all speakers' productions (Fig. 7, first row) and separately for the duplicated (left) and variegated (right) CVCV sequences show that duplicated productions are grouped around the ($y=x/2$) line (i.e., two jaw cycles for one disyllable) whereas both L_aC_o and C_oL_a ones are distributed around the ($y=x/2$) and ($y=x$) lines (i.e., two versus one jaw cycle per disyllable). This distribution splitting occurs for utterance durations less than about 400–450 ms. Analyses of ΔI in the acoustic study showed that the shift toward a CCV cluster, characterized by high ΔI values, occurs for durations shorter than 300 ms. Therefore, the shift toward a single cycle for two syllables occurs before the total suppression of one of the two vowels (that is, for longer utterance durations).

The utterance duration histograms (Fig. 7, second row) display similar values for the duplicated and the L_aC_o/C_oL_a group. Yet, the durations of duplicated utterances are never shorter than 225 ms and are mostly around 300 ms whereas around 15% of L_aC_o/C_oL_a productions reach durations from 175 to 225 ms with a peak of distribution around 250–275 ms. On the contrary, the jaw cycle durations (Fig. 7, third row) are clearly shorter for the duplicated productions (peak of distribution around 150 ms) than for L_aC_o/C_oL_a ones (peak of distribution around 225 ms). Finally, the jaw cycle duration is never shorter than 100 ms for all logatoms. Altogether, this portrait is coherent with the fact that at a fast rate L_aC_o/C_oL_a sequences can be produced on one single jaw cycle. The progression toward a single cycle limits jaw motion and keeps it at a more comfortable duration for the fastest production rates. Thus, it probably limits the energy consumption.

In order to analyze the shift from two jaw cycles to a single one, the speaker's productions were classified into three periods (e.g., Fig. 4). The "splitting" phase includes the utterances realized on a single jaw cycle. The "acceleration" and the "deceleration" phases include the utterances realized on two jaw cycles, respectively before and after the splitting phase.

3. Patterns of jaw motion in the acceleration phase

The amplitude and duration of jaw opening and closing strokes in the acceleration phase are plotted in Fig. 8, for each speaker, respectively, for duplicated (left) and L_aC_o/C_oL_a (right) sequences. Strokes are seldom shorter than 50 ms, which agrees with the 100 ms threshold observed for the jaw cycle durations (Fig. 7). Separate regression lines are superimposed for labial and coronal cycles. In their study of jaw motion for duplicated sequences (/sa/), Nelson *et al.* (1984) used the same kind of display. A theo-

TABLE III. Means (m) of intensity variation between the vowel after the coronal and the vowel after the labial consonant for utterances shorter than 300 ms for the three trials taken together, for each speaker and each disyllable (n is the number of observations for m computation). Thirty t-tests ($df=n-1$) with Bonferroni correction compare each mean to 0.

	pata		tapa		pasa		sapa		fata		tafa	
Speaker	n	m	n	m	n	m	n	m	n	m	n	m
S1	31	0.8	29	−0.1	29	−1.4[b]	27	−2.9[c]	23	−0.2	24	−0.7
S2	25	23.2[c]	11	9.2	25	11.7[b]	20	5.5	30	20.3[c]	20	13.9[c]
S3	5	−0.8	9	−0.7	0	⋯	0	⋯	0	⋯	10	1.5
S4	43	−0.7	37	−4.7[a]	37	−0.1	30	−2.4[c]	28	0.3	29	−1.6[a]
S5	67	6.9[c]	59	4.7[c]	56	1.7[a]	45	−2.5[c]	54	7.6[c]	53	1.1

[a] $p \leq 0.005$.
[b] $p \leq 0.05/30$.
[c] $p \leq 0.01/30$.

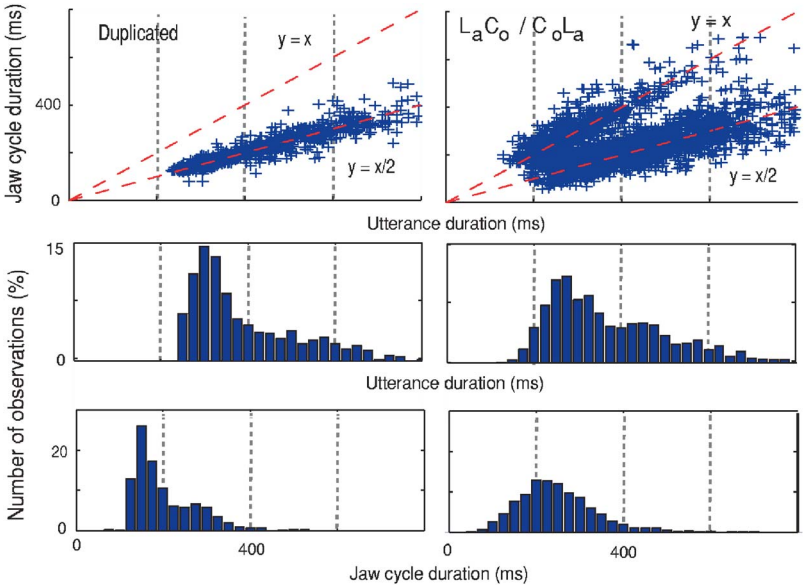

FIG. 7. (Color online) First row: Jaw cycle durations against utterance durations for all speakers' productions and separately for duplicated (left) and L_aC_o/C_oL_a sequences (right). Distribution splitting observed for the L_aC_o and C_oL_a groups shows that these disyllables could be produced on a single jaw cycle whereas duplicated disyllables are always realized on two jaw cycles. Second and third rows: Distribution of utterance and jaw cycle durations for all speakers' productions. The utterance durations tend to be shorter for the L_aC_o/C_oL_a group as compared to the duplicated one whereas the contrary tends to appear for the jaw cycle durations.

retical analysis allowed the authors to define a limit parabolic curve, such that for a given value of the maximum acceleration during a jaw stroke, the corresponding amplitude versus duration points were always on the right of the limit parabolic curve. Without entering their explanation in too many details, the principle is basically that to achieve a given trajectory extent in a given duration, the acceleration along the trajectory must achieve a sufficient maximum value. Reciprocally, for a given maximum acceleration value and a given trajectory extent, duration cannot be lower than a limit, specified by the parabolic curve. In Fig. 8, we have superimposed three such limit curves, respectively corresponding to maximum acceleration values of 0.25, 0.50, and 1.5 g [see also Nelson (1983)].

It appears that for duplicated utterances (Fig. 8, left), Speakers S3 and S4 follow a different pattern from Speakers S1, S2, and S5. For S3 and S4, stroke amplitude decreases with duration for both the labials (in /papa/) and the coronals

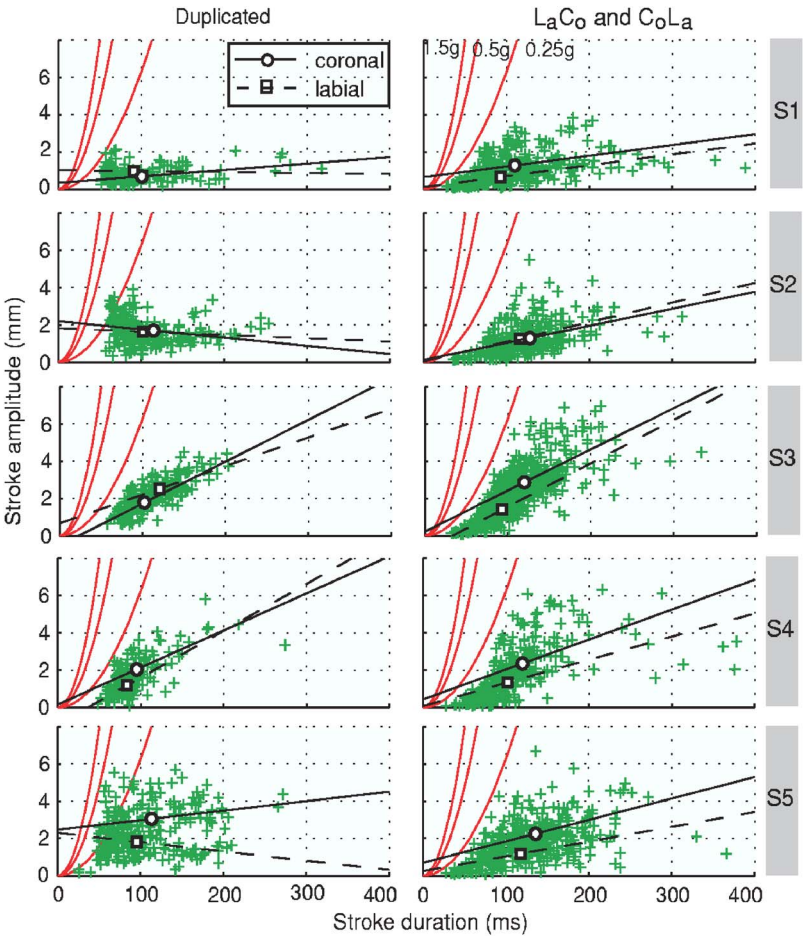

FIG. 8. (Color online) Jaw strokes amplitude (up and down) against duration during the acceleration phase (when the disyllables are realized with two jaw cycles) for each speaker and separately for duplicated (left column) and L_aC_o/C_oL_a (right column) disyllables. The parabolic curves are the theoretical minimum-time boundaries for mandible movements for three control acceleration limits [from left to right: 1.5, 0.5, and 0.25 g, see Nelson (1983)]. Regression lines and distribution means (squares and circles) are displayed separately for jaw strokes that come with labials and with coronals (see the text for details).

TABLE IV. Means of amplitudes and durations for the jaw cycles that come with the labial and the coronal constrictions in the acceleration phase, for each speaker and each L_aC_o/C_oL_a pair (n is the number of observations for means computations). The significance of the difference between means was tested using t-tests ($df=n-1$) with Bonferrorri corrections.

			Amplitudes (mm)			Durations (ms)		
Speaker	Sequence	n	Labial	Coronal	P	Labial	Coronal	P
S1	pata/tapa	47	0.58	0.91	[a]	163.6	198.6	[a]
	pasa/sapa	38	0.59	2.06	[a]	162.7	247.2	[a]
	fata/tafa	23	0.98	0.77	[b]	272.6	222.1	[b]
S2	pata/tapa	21	1.83	1.57	[b]	231.9	244.0	[b]
	pasa/sapa	28	1.07	1.48	[a]	209.1	285.2	[a]
	fata/tafa	23	1.00	0.83	[b]	263.7	235.7	[b]
S3	pata/tapa	59	1.17	2.75	[a]	178.3	229.7	[a]
	pasa/sapa	55	1.01	3.46	[a]	169.9	269.5	[a]
	fata/tafa	54	2.02	2.36	[a]	211.2	219.5	[b]
S4	pata/tapa	23	1.16	2.67	[a]	174.7	247.0	[a]
	pasa/sapa	18	1.20	3.89	[a]	206.1	279.2	[b]
	fata/tafa	33	1.57	1.34	[b]	223.3	214.6	[b]
S5	pata/tapa	35	0.85	2.53	[a]	204.7	268.0	[a]
	pasa/sapa	14	1.08	3.78	[a]	196.0	370.7	[a]
	fata/tafa	52	1.43	1.66	[b]	267.8	247.0	[b]

[a] $p \leq 0.01/15$.
[b] Not significant.

(in /tata/) cycles. Moreover, the distribution of amplitude versus duration tends to follow the theoretical curve corresponding to an acceleration of 0.25 g. On the contrary, amplitude does not decrease with duration for S1, S2, and S5. Moreover, while S1 keeps a small amplitude for all durations, rate increase leads S2 and S5 beyond the 0.25 g limit curve, toward an acceleration up to 0.5 g. Therefore, to support rate increase, speakers either decrease the jaw stroke amplitude without increasing acceleration (S3 and S4) or increase acceleration without changing amplitude (S1, S2, and S5). These results agree with the study by Sonoda and Nakakido (1986). These authors observed that jaw motion speeding induced either an increase in velocity and little change in amplitude or little velocity change and a decrease in amplitude [see also Lindblom (1990a) for a link with phonetic variations; and Perkell *et al.* (2002) for a more detailed discussion of intersubject differences].

The jaw behavior is more homogeneous for the L_aC_o/C_oL_a group. For all speakers, there is a global decrease of amplitude with duration (Fig. 8, right) and the distributions more or less follow the 0.25 g curve. Furthermore, the means of amplitude and duration tend to be smaller for the strokes for the labial constrictions as compared to the strokes for the coronal constrictions.

These smaller values for the labials are significantly different from the values for the coronal in a number of cases while the opposite pattern is not statistically significant in any case (see Table IV). This pattern is modulated by two factors. First, there are individual differences, with, for example, larger differences between the labial and coronal jaw strokes for Speaker S3, and smaller for Speaker S2. Second, the labial to coronal difference is increased for /pasa/ and /sapa/ logatoms (for which the labial jaw cycle is of a significantly lower amplitude and duration for all speakers) and decreased for /fata/ and /tafa/ logatoms (for which the difference is significant only for Speaker 3). This portrait suggests that in the acceleration phase, the passage from two jaw cycles to a single one rather corresponds to a progressive removal of the "labial cycle," as displayed in Fig. 4. We shall now explore how the reorganization among jaw, tongue, and lips occurs in the "splitting" phase.

4. Coordination between jaw and constrictors in the acceleration, splitting, and deceleration phases

For most of the productions realized on two jaw cycles (during the acceleration and the deceleration phases), the TT and LL constrictions are around 0% of the jaw trajectory (Fig. 9, top and bottom). This indicates that each constriction occurs when the mandible is at its highest position. So, TT and LL successively move in phase with the jaw. Yet, the distributions look less peaked at 0% for TT (Fig. 9, right top and bottom) than for LL (Fig. 9, left top and bottom) for both duplicated and L_aC_o/C_oL_a groups. Moreover, for L_aC_o and C_oL_a logatoms, there was some trend for more variations during the deceleration phase than during the acceleration phase. This could be interpreted as a sign of hysteresis: The system progressively evolves from the much more complex portrait in the splitting phase that sustains the production of two constrictions on a single cycle, back toward its initial state of each constriction on its own cycle. The complexity of the splitting phase would expand toward the deceleration phase.

In the splitting phase, the labial and coronal constrictions must reorganize within one jaw cycle. The basic trend for reorganization is clearly displayed in Fig. 9: The tongue constriction is around the highest jaw position (phase 0%), while the labial constriction is around the lowest position (phase 50% or −50%). On this basic pattern, a global shift toward the right of the jaw cycle can appear, with a coronal

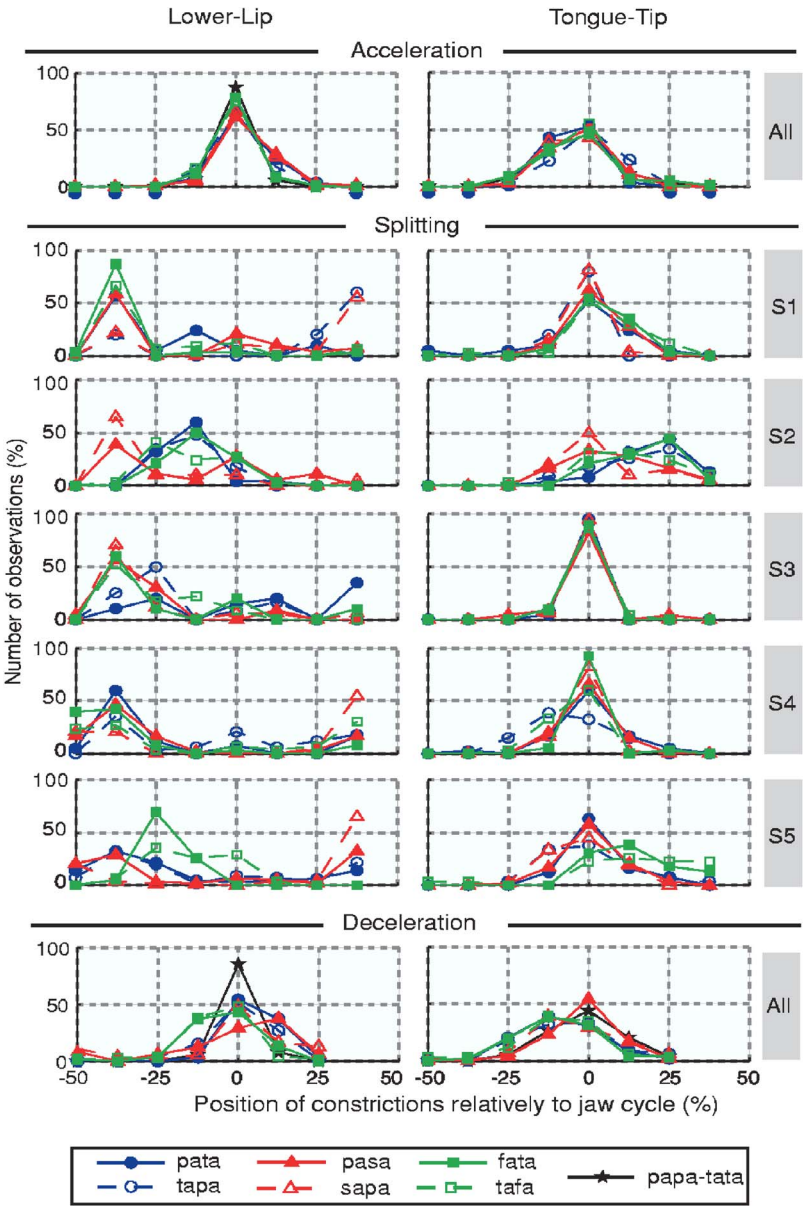

FIG. 9. (Color online) Distribution of speakers' productions according to the position of the lower-lip (left) and the tongue-tip (right) constrictions relative to the jaw cycle. The three phases (acceleration, splitting, and deceleration) are plotted separately. For the acceleration and the deceleration phases, histograms include all speakers taken together and both duplicated and L_aC_o/C_oL_a sequences. For the splitting phase (when utterances are realized on a single jaw cycle), distributions are given for each L_aC_o and C_oL_a sequence and for each speaker.

constriction in the beginning of the opening phase (around 25%) and a labial constriction in the beginning of the closing phase (around −25%). Two factors seem to intervene in this possible shift. The first factor is speaker variability, with S2 showing more of a right shift than all other speakers. The second factor is the nature of the labial and coronal consonants. Thus, for /pasa/ and /sapa/, the coronal constriction is strictly located around the jaw highest position (0% phase) while for /fata/ and /tafa/ it is often shifted toward positive values. The correspondence with the predominance of the coronal jaw cycle upon the labial one in terms of amplitude and duration, displayed in the previous section, is obvious. It is rather straightforward. Indeed, the coronal fricative /s/ induces a specifically high jaw position, generally higher than all other phonemes, including the coronal plosive /t/ or /d/ (Keating, 1983; Keating *et al.*, 1994; Lindblad and Lundqvist, 1999, see also data for French in Rhardisse and Abry, 1994). Hence the coronal jaw cycle is increased, and the coronal constriction is more strictly stuck on the highest jaw value. On the contrary, the labiodental /f/, also inducing a high jaw position, increases the labial jaw cycle, which induces the shift toward the right, with higher values of the labial constriction in the jaw trajectory. This global pattern is also modulated by the difference between L_aC_o and C_oL_a attractors.

5. Articulatory characterization of L_aC_o and C_oL_a attractors

L_aC_o utterances should be characterized by both a higher intensity of the second vowel over the first one (positive value of ΔI, Table III) and a proximity of the labial and next coronal constrictions ($\Delta_{(L_aC_o/L_aL_a)}$ smaller than 50%, Table V). Notice however that data selection for these two analyses satisfy different criteria, that is utterance duration less than 300 ms for the acoustic analysis and utterances produced on a single jaw cycle for the articulatory analysis. Despite these differences, the two analyses are relatively coherent.

Indeed, means of $\Delta_{(LaCo/LaLa)}$ tend to be higher than 50% for S1, which agrees with the C_oL_a profile that characterizes

TABLE V. Labial-to-coronal duration means (m) normalized by the whole utterance duration $\Delta(L_aC_o/L_aL_a)$, expressed in percent, for each speaker and each disyllable (n is the number of utterances involved in computing m). Values smaller than 50% indicate that the duration from the labial constriction to the following coronal one is smaller than the duration from the coronal constriction to the following labial one, which signals an evolution toward the L_aC_o attractor. On the contrary, values higher than 50% signal an evolution toward the C_oL_a attractor. Thirty two-tails t-tests ($df=n-1$) with Bonferroni correction compare each mean to 50.

	pata		tapa		pasa		sapa		fata		tafa	
	n	*m*	*n*	*m*	*n*	*m*	*n*	*m*	*n*	*m*	*n*	*m*
S1	20	49.3	5	53.0	27	50.8	26	51.0	31	53.7[a]	32	52.0
S2	25	36.3[a]	21	40.3[b]	20	41.1	22	43.9	40	30.5[a]	36	36.1[a]
S3	19	44.3[b]	11	38.6[a]	22	41.5[a]	17	42.5[a]	10	44.8	23	43.7[a]
S4	56	45.4[b]	48	49.5	60	46.3[a]	44	52.0	38	42.8[a]	30	51.4
S5	67	42.1[a]	58	40.8[a]	67	51.8	71	53.5[b]	35	37.9[a]	41	44.9[b]

[a] $p \leq 0.01/30$.
[b] $p \leq 0.05/30$.

this speaker in the acoustic space. On the contrary, all $\Delta_{(LaCo/LaLa)}$ means for S2 are smaller than 50%, which confirms the speaker's tendency to be L_aC_o-stable. For S4, means of $\Delta_{(LaCo/LaLa)}$ are smaller than 50% for all L_aC_o sequences whereas they are greater than 50% for /sapa/ and /tafa/, which agrees with acoustic data showing that this speaker tends to be L_aC_o-stable for the L_aC_o logatoms and C_oL_a-stable for the C_oL_a ones. For S5, $\Delta_{(LaCo/LaLa)}$ means are smaller than 50% for all the sequences except /pasa/ and /sapa/, which confirms his acoustic profile: L_aC_o for /pata/, /tapa/, /fata/, and /tafa/ but rather C_oL_a for /sapa/. Finally, results for S3 show that though this speaker does not often reach utterance durations shorter than 300 ms (Table III), she evolves toward a single jaw cycle for all sequences. Moreover, she tends to be L_aC_o-stable with $\Delta_{(LaCo/LaLa)}$ values always significantly smaller than 50% except for /fata/.

Therefore, quite logically the L_aC_o attractor corresponds to a decrease of the temporal distance between the labial and the next coronal constriction, while the C_oL_a attractor corresponds to a decrease of the temporal distance between the coronal and the next labial constriction. However, there is a clear predominance of switches toward the L_aC_o attractor (e.g., /patá/ or /ptá/) over the 21 speakers of the acoustic study (Experiment 1). This agrees with the hypothesis according to which the anticipation of the tongue gesture during the labial constriction, typical of L_aC_o CVCV' (e.g. /patá) or CCV' (e.g. /ptá/) sequences, is much more likely than the anticipation of the labial gesture during the tongue constriction.

IV. DISCUSSION

The present work aimed at testing the hypothesis that the L_aC_o sequencing is a more stable articulatory pattern than the C_oL_a one. The results of Experiment 1 provide arguments for this hypothesis for native speakers of French. Furthermore, the results of Experiment 2 allow one to better describe the articulatory phenomena that subtend this asymmetry.

A. The L_aC_o/C_oL_a coordinative system "on line"

The results of the articulatory study confirm that rate increase could induce the repetition of L_aC_o and C_oL_a CVCV sequences to evolve from one jaw cycle per syllable toward a single jaw cycle for two syllables until a single CCV syllable is eventually achieved. This progression seems more economic regarding jaw motion. In this process, the determination of the attractor (L_aC_o vs C_oL_a) may result from the interaction of several factors.

1. The motor program shift

At the beginning of the repetition process, the speakers produce one jaw cycle per syllable. During this period, each constriction occurs at the highest jaw position. Then, with rate increase, the amplitude and the duration of the jaw strokes decrease together until reaching a threshold value (near 50 ms for an opening or a closing gesture). Coupled with the anticipation of one constriction during the previous one, this induces the shift on a single cycle. This shift rests on the reorganization of the tongue-lip-jaw coordination. Globally, two coordinative patterns are displayed to achieve the two constrictions on a single jaw cycle (Fig. 10, right), depending on the initial profile of jaw motions (Fig. 10, left). First, and in most of the cases, the jaw cycle that carries the labial constriction becomes shorter and smaller than the jaw cycle that carries the coronal constriction (Fig. 10, top left). Hence, when rate increases, the labial cycle reaches the

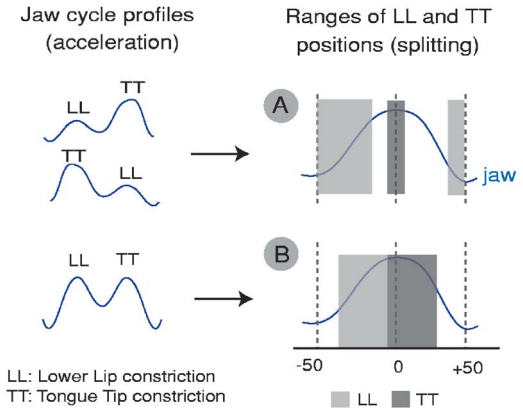

FIG. 10. (Color online) Coordination between the jaw and the constrictors from two jaw cycles for a disyllable to a single one. Two patterns [(A) and (B)] of lower-lip (LL) and tongue-tip (TT) constriction positions relative to the jaw cycle are observed when the two plosives are realized on a single jaw cycle (splitting, right). They tend to correspond to specific jaw motion profiles during the acceleration phase (left, see the text for detail).

threshold duration of 50 ms per stroke earlier than the coronal one. This induces the preservation of the phasing between the jaw and the tongue tip highest positions, whereas the lower lip constriction occurs during the jaw closing gesture or at the end of the opening gesture (Fig. 10, top right). This is typically the case for Speaker 3, and for /pasa/ and /sapa/ utterances. Second, when no asymmetry appears between the two cycles during the acceleration phase (Fig. 10, bottom left), the tendency is to observe a dephasing of both TT and LL in reference to the jaw cycle. Thus, the LL and TT constrictions respectively occur during the closing gesture and during the opening gesture (Fig. 10, bottom right). This is the trend for Speaker S2 and for /fata/ and /tafa/ utterances.

These results are interesting in the context of previous articulatory studies (Nelson *et al.*, 1984; Kelso *et al.*, 1985; Hertrich and Ackermann, 2000), modeling works (Redford and Diehl, 1999; Redford *et al.*, 2001; Oudeyer, 2001) or theories (MacNeilage, 1998) that always associated the jaw cycle to the CV syllable. Moreover, patterns of mandible motions are close to data published in the literature and tend to confirm the general principle of economy of effort.

2. Economy of effort

Various possible indicators of economy of effort have been proposed in the literature, e.g., maximum speed or jerk that is acceleration derivative (Nelson, 1983). In their already mentioned study, Nelson *et al.* (1984) characterized jaw strokes by the maximum acceleration compatible with the observed movement, which is the indicator we used in Sec. III. Furthermore, they showed that during the repetition of /sa/ with rate increase, the jaw motion progressed in a way that tended to minimize energy consumption. In their data, the durations of jaw opening and closing strokes were never shorter than 50 ms. Similar values appear in the present articulatory study. Then, for one of their three analyzed speakers, Nelson *et al.* observed "a maximum in the movement distance as the movement times decreased into the region of 125 ms." According to the authors, this "resonance" effect shows that 125 ms could be the most economic duration for up and down jaw strokes. It would correspond to the "natural" rate of 3 to 4 cycles and so, 3 to 4 syllables per second. In our study (Experiment 2), durations of jaw cycles for L_aC_o and C_oL_a utterances are mainly around 225 ms (Fig. 7), which corresponds to jaw stroke durations around 112.5 ms, close to the 125 ms value observed by Nelson *et al.* On the other hand, the production of duplicated CVCV sequences at very fast rates requires a decrease of the jaw cycle down to 150 ms and so, to stroke durations around 75 ms, close to the saturation value. Furthermore, estimation of the maximal acceleration value in Fig. 8 indicates that it is generally smaller for the L_aC_o and C_oL_a sequences compared to the duplicated ones. Taken together, these results suggest that when rate increases, the coordination of the two constrictions on a single jaw cycle might be more economic for the jaw than the alternation of two jaw cycles.

3. Multideterminism of a bistable system

The results show that with rate increase, the lips-tongue-jaw system could evolve either toward a L_aC_o attractor (e.g., /pata/→/patá/→/ptá/) or a C_oL_a one (e.g., /pata/→/tapá/→/tpá/). Thus, the coordinative system is bistable. Yet, according to the first study, the L_aC_o attractor prevails. On this basic pattern, a number of other additional factors are observed or could be assumed to play a role. First, the initial coordination provides a bootstrap toward the corresponding attractor: The preference for the L_aC_o attractor is less marked for the repetition of C_oL_a CVCV sequences as compared to L_aC_o ones. This is particularly the case for /pasa/ and /sapa/, with /pasa/ more frequently evolving toward the L_aC_o attractor whereas /sapa/ often evolved toward the C_oL_a one. This is likely to be due to the fact that, in spite of the instruction to continue even if transformations occurred, some speakers tried to respect the initial structure and even tended to reduce the speed when they perceived a shift to the reverse sequencing. Second, the C_oL_a attractor was more often observed for /sapa/ as compared to /tapa/ and /tafa/. The difference between /sapa/ and the other C_oL_a disyllables could rest on articulatory factors. Indeed, analysis of the jaw cycles in the second experiment showed that in the acceleration phase, the asymmetry between the jaw cycles that come with the labial constriction and the jaw cycles that come with the coronal one are more systematic for /pasa/-/sapa/ than for the other sequences, which was interpreted in terms of the need for a specific high jaw position for achieving /s/. This could favor the progression toward the C_oL_a attractor for /pasa/ and /sapa/. Third, interspeaker differences, which could come from specific individual patterns of coordination, lead to differences in the selection of one or the other attractor, as displayed in Sec. II B 2.

But a number of other factors, not studied in the present work, could also intervene in the selection of one or the other attractor. An obvious one is the selected language. Indeed, it is likely that the CCV resyllabification process observed here results from the fact that these forms are possible in French and that the language stresses the last syllable of a word. Therefore, future experiments should be done to assess the L_aC_o greater stability in languages with other prosodic behaviors or phonological constraints. Other additional experiments should also be done on the role of the vowel context, the consonantal mode (e.g., voiced or nasal consonants), etc. Nevertheless, in spite of all these established or potential additional factors, the L_aC_o attractor is globally the dominant one over all speakers and disyllables in the present study, which suggests that it could indeed be the most stable and economic, at least in French.

B. Substance-based selection of phonological sequences

The underlying assumption of this work is that world languages inventories might be shaped by substance-based constraints such as properties of the motor control system. Thus, some sequencing of syllables might be preferred because they are easier to produce in the sense that they are more economic (less energy consuming) or more stable

(easier to control). In this framework (Liljencrants and Lindblom, 1972; Lindblom *et al.*, 1984; Kelso, 1995; Davis *et al.*, 2002), the present study brings at least two interesting contributions: (1) the production of duplicated CVCV sequences may be more costly than the production of CVCV sequences that vary the constrictor from the first to the second consonant, and (2) the L_aC_o sequencing seems more stable than the reverse C_oL_a one.

1. Variegated rather than duplicated

Statistical analyses of world languages lexical inventories show that in C_1VC_2V sequences, lexicons favor associations that vary the articulation places in C_1 and C_2, rather than those that repeat the same constriction (MacNeilage and Davis, 2000; Rousset, 2003). This means that languages prefer, e.g., "pata" to "papa." Yet, duplication could, *a priori*, be considered as simpler in terms of control, which could explain that it is the core behavior in canonical babbling (MacNeilage and Davis, 2000). However, the articulatory data obtained here lead us to propose that the preference for variegated sequencing in the world's languages could result in part from the fact that the repetition of the same constriction is more costly for the jaw than the alternation of two constrictions made by different articulators. Indeed, the comparison of the production of L_aC_o/C_oL_a and duplicated CVCV sequences shows that quicker production rates could be achieved for L_aC_o/C_oL_a sequences with less energy consumption for the jaw, since anticipation allows producing L_aC_o and C_oL_a CVCV utterances on a single jaw cycle whereas it is impossible for duplicated ones. Thus, without involving the extreme speeds obtained here at the end of the acceleration phase, it appears that the alternation of the movement of two constrictors is probably easier and more economic than the repetition of the movement of a single constrictor for the mature speech production system. Similar principles govern other synergies such as fingers in typing or piano playing. This results from the fact that when two different organs are involved, the motion of one organ could be anticipated during the realization of the other one, which is not possible when a single organ realizes the two successive gestures. The possibility to produce two syllables on a single jaw cycle might be generalized to other kinds of sequencing than L_aC_o and C_oL_a ones in further investigations. Moreover, the preference for the L_aC_o attractor in the two experiments shows that inside the preference for variegated forms, some associations might be more appropriate than others.

2. L_aC_o rather than C_oL_a

The results of Experiment 1 are in favor of the idea that L_aC_o sequences appear as a natural and coherent production unit, more stable and better "in-phase" than their C_oL_a inverse counterpart. This could explain the preference for L_aC_o utterances in infant production, rather than the "simple first" explanation previously proposed. There is actually no reason to believe that the greater stability of L_aC_o sequences in the present experiments on adults could be due to any "simple first" mechanism. Rather, articulatory coherence could provide a common basis to both infant data and our results. Of course, the fact that the C_oL_a structure may also be locally stable, though less often selected in the speeding process, is not incompatible with this reasoning.

It just suggests that C_oL_a sequences are also viable, though suboptimal in comparison with L_aC_o ones, which agrees well with typological and developmental data.

V. CONCLUSION

The experimental data analyzed here point out a major difference between L_aC_o and C_oL_a sequences at the production level: L_aC_o sequences can be considered as a more stable coordinative pattern for the motor system than C_oL_a ones. Then, a causal relationship between this asymmetry and the universal "LC effect" has been advanced. Of course, such a claim has to be improved testing L_aC_o and C_oL_a sequences' stability in both other languages and more directly in infants' first words. To this aim, the paradigm and the acoustic analysis method proposed here could allow comparing L_aC_o and C_oL_a stability for speaker samples of different languages, which is necessary for generalization. Specific methodologies should be developed for studying stability in infant speech. Moreover, further articulatory investigations of jaw-tongue-lip coordination in the production of C_1VC_2V disyllables would be necessary to better understand the anticipation processes, and their link with the asymmetry in jaw cycles for different constriction places in C_1 and C_2. It remains that the present study adds some new material to the already significant set of perceptuo-motor constraints likely to play a role in the shaping of phonological systems, hopefully taking substance-based approaches to language universals one step further.

ACKNOWLEDGMENTS

This work is part of the "Patipapa" project funded by the French Ministry of Research (Action Concertée Incitative "Systèmes Complexes en Sciences Humaines et Sociales"). We also thank C. Savariaux and C. Vilain for their technical support and all the speakers for their essential participation.

[1]The PRAAT software is developed by P. Boersma and D. Weenink, at the Institute of Phonetic Sciences. It is available (29 March 2007) to free download on their web page (http:/www.fon.hum.uva.nl/praat/).

Byrd, D. (**1996**). "Influences on articulatory timing in consonant sequences," J. Phonetics **24**, 209–244.

Chitoran, I., Goldstein, L., and Byrd, D. (**2002**). *Gestural Overlap and Recoverability: Articulatory Evidence from Georgian*, in Laboratary Phonology Vol. **7**, edited by C. Gussenhoven and N. Warner (Mouton de Gruyter, Berlin) pp. 419–448.

Clements, G. N. (**1990**). "The role of the sonority cycle in core syllabication," in *Papers in Laboratory Phonology 1: Between the Grammar and the Physics of Speech*, edited by J. Kingston and M. Beckman (Cambridge University Press, New York), pp. 283–333.

Davis, B. L., MacNeilage, P. F., and Matyear, C. (**2002**). "Acquisition of serial complexity in speech production: A comparison of phonetic and phonological approaches to first word production," Phonetica **59**, 75–107.

de Jong, K. J. (**2001**). "Effects of syllable affiliation and consonant voicing on temporal adjustment in a repetitive speech-production task," J. Speech Lang. Hear. Res. **44**, 826–840.

Haken, H., Kelso, J. A. S., and Bunz, H. (**1985**). "A theoretical model of phase transitions in human hand movements," Biol. Cybern. **51**, 347–356.

Hertrich, I., and Ackermann, H. (**2000**). "Lip-jaw and tongue-jaw coordina-

tion during rate-controlled syllable repetitions," J. Acoust. Soc. Am. **107**, 2236–2247.
Hoole, P. (**1993**). "Methodological considerations in the use of electromagnetic articulography in phonetic research," FIPKM **31**, 43–64.
Hoole, P. (**1996**). "Issues in the acquisition, processing, reduction and parameterization of articulographic data," FIPKM **34**, 158–173.
Hoyt, D., and Taylor, C. R. (**1981**). "Gait and the energetic of locomotion in horses," Nature (London) **292**, 239–240.
Ingram, D. (**1974**). "Fronting in child phonology," J. Child Lang **1**, 233–242.
Keating, P. (**1983**). "Comments on the jaw and syllable structure," J. Phonetics **11**, 401–406.
Keating, P., Lindblom, B., Lubker, J., and Kreiman, J. (**1994**). "Variabihty in jaw height for segments in english and Swedish VCVs," J. Phonetics **22**, 407–422.
Kelso., J. A. S. (**1995**). *Dynamic Patterns: The Self-Organization of Brain and Behavior* (MIT, Cambridge, MA).
Kelso, J. A. S., Saltzman, E. L., and Tuller, B. (**1986**). "The dynamical perspective on speech production: Data and theory," J. Phonetics **14**, 29–59.
Kelso, J. A. S., Vatikiotis-Bateson, E., Saltzman, E. L., and Kay, B. (**1985**). "A qualitative dynamic analysis of reiterant speech production: Phase portraits, kinematics, and dynamic modeling," J. Acoust. Soc. Am. **77**, 266–280.
Liljencrants, J., and Lindblom, B. (**1972**). "Numerical simulations of vowel quality systems: The role of perceptual contrast," Iowa Dent. Bull. **48**, 839–862.
Lindblad, P., and Lundqvist, S. (**1999**). "How and why do the tongue gestures of [t], [d], [1], [n], [s], and [r] differ?," in *Proceedings of the 14th International Congress of Phonetic Sciences*, San Francisco, CA, pp. 417–420.
Lindblom, B. (**1990a**). "Explaining phonetic variation, a sketch of the H&H theory," in *Speech Production and Speech Modeling*, edited by W. J. Hardcastle and A. Marchal (Academic, New York), pp. 403–439.
Lindblom, B. (**1990b**). "On the notion of 'possible speech sound', J. Phonetics **18**, 135–152.
Lindblom, B., MacNeilage, P. F., and Studdert-Kennedy, M. (**1984**). "Self-organizing processes and the explanation of languages universals," in *Explanations of Linguistic Universals*, edited by B. Butterworth, B. Comrie, and O. Dahl (Mouton), pp. 181–203.
Locke, J. L. (**1983**). *Phonological Acquisition and Change* (Academic, New York).
Locke, J. L. (**2000**). "Movement patterns in spoken language," Science **288**, 449–451.
MacNeilage, P. F. (**1998**). "The frame/content theory of evolution of speech production," Behav. Brain Sci. **21**, 499–511.
MacNeilage, P. F., and Davis, B. L. (**2000**). "On the origins of internal structure of word forms," Science **288**, 527–531.
Munhall, K. G., and Jones, J. A. (**1998**). "Articulatory evidence for syllabic structure," Commun. Math. Sci. **21**, 524–525.
Nelson, W. L. (**1983**). "Physical principles for economies of skilled movements," Biol. Cybern. **46**, 135–147.
Nelson, W. L., Perkell, J. L., and Westbury, J. R. (**1984**). "Mandibule movements during increasingly rapid articulations of single syllables: Preliminary observations," J. Acoust. Soc. Am. **75**, 945–951.
Nittrouer, S. (**1991**). "Phase relations of jaw and tongue tip movements in the production of VCV utterances," J. Acoust. Soc. Am. **90**, 1806–1815.
Ostry, D. J., and Flanagan, J. R. (**1989**). "Human jaw movement in mastication and speech," Arch. Oral Biol. **34**, 685–693.
Oudeyer, P. Y. (**2001**). "The origins of syllable systems: An operational model," in *Proceedings of the 23rd Annual Conference of the Cognitive Science Society*, edited by J. D. Moore and K. Stenning (Erlbaum) pp. 744–749.
Perkell, J. S., and Zandipour, M. (**2002**). "Economy of effort in different speaking conditions. II. Kinematic performance spaces for cyclical and speech movements," J. Acoust. Soc. Am. **112**, 1642–1651.
Perkell, J. S., Zandipour, M., Matthies, M. L., and Lane, H. (**2002**). "Economy of effort in different speaking conditions. I. A preliminary study of intersubject differences and modeling issues," J. Acoust. Soc. Am. **112**, 1627–1641.
Redford, M. A., Chen, C. C., and Miikkulainen, R. (**2001**). "Constrained emergence of universals and variation in syllable systems," Lang Speech **44**, 27–56.
Redford, M. A., and Diehl, R. L. (**1999**). "The relative perceptual distinctiveness of initial and final consonants in cvc syllables," J. Acoust. Soc. Am. **103**, 1555–1565.
Rhardisse, N., and Abry, C. (**1994**). "La coarticulation mandibulaire comme principe d'organisation syllabique – Mandibular coarticulation as a principle for syllabique organization," in *Proceedings of the XXèmes Journées d'Etudes sur la Parole* (JEP – Days on speech studies), Trégastel, France, pp. 421–426.
Rousset, I. (**2003**). "From lexical to syllabic organization: Favored and disfavored co-occurrences." *Proceedings of the 14th International Congress of Phonetic Sciences*, Barcelona, Spain, pp. 715–718.
Sato, M., Schwartz, J. L., Cathiard, M. A., Abry, C., and Loevenbruck, H. (**2006**). "Multistable syllables as enacted percepts: A source of an asymmetric bias in the verbal transformation effect," Percept. Psychophys. **68**, 458–474.
Selkirk, E. (**1984**). *On the Major Class Features and Syllable Theory* (MIT, Cambridge, MA).
Sonoda, Y., and Nakakido, K. (**1986**). "Effect of speaking rate on jaw movements in vowel sequence," J. Acoust. Soc. Jpn. (E) **7**, 5–12.
Stetson, R. H. (**1951**). *Motor Phonetics*, 2nd ed. (North-Holland, Amsterdam).
Stevens, K. N. (**1989**). "On the quantal nature of speech," J. Phonetics **17**, 3–45.
Surprenant, A. M., and Goldstein, L. (**1998**). "The perception of speech gestures," J. Acoust. Soc. Am. **104**, 518–529.
Tuller, B., and Kelso, J. A. S. (**1991**). "The production and perception of syllable structure," J. Speech Hear. Res. **34**, 501–508.
Vilain, A., Abry, C., Badin, P., and Brosda, S. (**1999**). "From idiosyncratic pure frame to variegated babbling: Evidence from articulatory modelling," in *Proceedings of the 14th International Congress of Phonetic Sciences*, San Fransisco, pp. 2497–2500.
Zsiga, E. C. (**1996**). "Acoustic evidence for gestural overlap in consonant sequence," J. Phonetics **22**, 121–140.

The effects of prosodic boundaries on nasality in Taiwan Min

Ho-hsien Pan
Department of Foreign Languages and Literatures, National Chiao Tung University, 1001 Ta Hsueh Road, Hsinchu, 300, Taiwan

(Received 22 June 2006; revised 9 March 2007; accepted 12 March 2007)

This study explores the effects of prosodic boundaries on nasality at intonational phrase, word, and syllable boundaries. The subjects were recorded saying phrases that contained a syllable-final nasal consonant followed by a syllable-initial stop. The timing, duration, and magnitude of the nasal airflows measured were used to determine the extent of nasality across boundaries. Nasal amplitudes were found to vary in a speaker-dependent manner among boundary types. However, the patterns of nasal contours and temporal aspects of the airflow parameters consistently varied with boundary type across all the speakers. In general, the duration of nasal airflow and nasal plateau were the longest at the intonational phrase boundary, followed by word boundary and then syllable boundary. In addition to the hierarchical influence of boundary strength, there were unique phonetic markings associated with individual boundaries. In particular, two nasal rises interrupted by nasal inhalation occurred only across an intonation phrase boundary. Also, unexpectedly, a word boundary was marked by the longest postboundary vowel, whereas a syllable boundary was marked with the shortest nasal duration. The results here support the hierarchical effect of boundary on both domain-edge strengthening and cross-boundary coarticulation.
© *2007 Acoustical Society of America.* [DOI: 10.1121/1.2722208]

PACS number(s): 43.70.Aj, 43.70.Fq, 43.70.Bk [BHS] Pages: 3755–3769

I. INTRODUCTION

Cross-linguistically, articulatory movements vary according to focus condition and boundary strength. Though focus and prominence are signaled by hyperarticulation, the effect of boundary can be implemented by either the weakening or strengthening of articulatory movements (Edwards, Beckman, and Fletcher, 1991; de Jong, 1995; Fougeron and Keating, 1996; Tabain, 2003b). These articulatory weakening and strengthening effects show gradient variations according to the strengths of adjacent boundaries.

Like traffic signs that control deceleration and acceleration of vehicular movements, boundary strength controls the duration and magnitude of articulatory movements in pre- and postboundary position. Though some languages prefer final strengthening in the preboundary position, such as phrase-final lengthening before an English IP boundary, other languages prefer initial strengthening in the postboundary position, such as phrase-initial lexical tonal strengthening in Taiwanese (Pan, in press). Thus, it is more difficult to generalize the prosodic effect of boundary on surface articulation across languages. To fully explore the effect of boundary, diversified data need to be collected from languages with different rhythmic structures.

This study expands the scope of prosodic articulatory studies from intonation-based languages, such as English (Cho, 2002, 2004, 2005, 2006) and French (Fougeron and Keating, 1996; Fougeron, 2001; Tabain, 2003a b) to a tone-based language by investigating how nasal consonants in Taiwan Min (Taiwanese) are influenced by prosodic boundaries.

A. Taiwanese nasal consonants and vowels

Min, a Chinese dialect, spoken in Fujian and Southeast Asia among Overseas Chinese who trace their roots back to Fujian, is spoken by 70% of the population in Taiwan. Taiwan Min has around 16 oral vowels and 11 nasal vowels, depending on the dialect. Taiwanese phonotactic constraints require that nasal vowels occur after initial nasal consonants /m, n, ŋ/, such as /mĩ/ "thing," and that oral vowels occur after initial oral stops /b, g, l/, such as /bi/ "rice." These phonotactic constraints have led researchers to devise various phonological rules stating the alternation between homorganic initial nasal and voiced stops. Based on auditory impressions with little empirical phonetic data, these rules change voiced stops into a homorganic nasal when followed by a nasal vowel, or vice versa, e.g., /b, l, g/ -> [m, n, ŋ]/_ [nasal vowel] or /m, n, ŋ / -> [b, l, g] /_ [oral vowel] (Ting, 1985; Zhang, 1989; Cheng, 1968, 1973). It should be noted that there is no /d/ in Taiwanese and /l/ is considered to be a voiced stop due to its stoplike quality (Zhang, 1989). Preliminary EPG data concerning /l/ collected by the author showed that speakers produced /l/ with an alveolar closure and with either a lateral or central release. Therefore, /l/ was included as an alveolar stop along with /b, g/.

Pan (2004) in an earlier airflow study found that Taiwanese initial voiced stops changed into homorganic nasals when preceded by a final nasal consonant. For example /b/ becomes [m] in /saŋ bi/ [saŋ mi] "send rice." This finding challenges the accepted phonological rules that govern the distribution of nasal vs oral vowels. Since oral vowels can occur after both initial nasals, as in /saŋ bi/ [saŋ mi] "send rice," and after initial voiced stop /be bi/ [be bi] "purchase rice," this contradicts the traditional description of a phonotactic constraint in which oral vowels occur after initial

voiced stops and nasal vowels occur after initial nasals. Relevant to the current study is the fact that initial stops and vowels are not always nasalized to the same extent after a nasal consonant. The current investigation explores the extent of nasalization from a nasal consonant across a boundary. If a boundary is strong, then less nasalization is expected to occur on the upcoming segment; if the boundary is weak, then more nasalization across the boundary is expected. As airflow is an effective means of capturing nasality patterns in Taiwanese, data relating to it will be used in this study.

B. Nasality and prosodic boundary

Studies on articulation and boundary encompass three major issues: (1) domain-edge strengthening; (2) variation of articulation in relation to the strength of the adjacent boundary; and (3) variation of cross-boundary coarticulation in relation to the strength of the intervening boundary.

Turning to the first issue of domain-edge strengthening, previous studies have discovered hyperarticulation to be greater in domain-initial segments or domain-final segments than in domain-medial segments (Fougeron and Keating, 1997; Krakow, 1999; Cho, 2002, 2004, 2006).

To capture domain-edge-strengthening effects on velic movement, Krakow (1989, 1993) in a velocontour study investigated the coordination pattern between velic and lip movements, by placing a syllable initial nasal /m/ in either word-initial [V#mV] or -medial [V.mV] positions, and a syllable-final nasal /m/ in either word-final [Vm#] or medial [Vm.V] positions. She measured the duration and amplitude of velic and lip raising/lowering, and found that, regardless of the position within a word, the offset of velic lowering was closely timed to the end of lip raising for initial nasals but to the onset of lip raising for final nasals. In other words, velic lowering began earlier for final /m/ than for initial /m/. The velic and lip coordination patterns are influenced by the boundary positions. In addition to coordination patterns, she also discovered that a syllable's position within a word influenced the magnitude and duration of the velic and lip movements. For instance, nasals in word-final positions were lower in velic displacements, higher in velic raising, and longer in duration for both lip lowering and raising than nasals in syllable-final (and word-medial) positions. That is to say, syllable-final nasals are more hyperarticulated in word-final than in word-medial positions.

In Taiwanese, Hsu and Jun (1996a, 1996b) in a study on voice onset time (VOT) at the edge of Taiwanese tone groups discovered that VOT was longer in segments produced in the tone-group-initial position than in the tone-group-final position. So, one can surmise that evidence exists indicating that speakers of Taiwanese use articulatory strategies to indicate the existence of a boundary. However, little is known about the effect of boundary type on nasality in Taiwanese.

Turning to the second issue on boundary strengthening and articulation variations, it has been found that jaw, lingual, and lip movements vary from the most canonical to the least canonical form as boundaries vary from strong to weak in languages such as English, French, Tamil, and Korean (Fougeron and Keating, 1997; Byrd *et al.*, 2000; Fougeron, 2001; Cho and Keating, 2001; Tabain, 2003a, 2003b; Cho, 2005, 2006). Moreover, in French, velic lowering varies in a hierarchical manner at intonational phrase, accentual phrase, word, and syllable junctures. By calculating the amount of nasal airflow as an indicator of velic lowering, differences were found in a nasal airflow study on French initial /n/ (Fougeron and Keating, 1996). In this study, one of two subjects differentiated three out of four levels of boundaries based on the extent of nasality during the production of the nasal consonant. However, the other male speaker failed to produce any difference between any of the boundaries (Fougeron and Keating, 1996). Keating *et al.* (2004) extended this study by adding more speakers, and found that three out of four speakers produced differences in the amount of nasality in relation to boundary type in a speaker-dependent manner (Keating *et al.*, 2004). Both studies discovered that the stronger the preceding prosodic boundary, the lesser the amount of nasal airflow recorded from the initial /n/. Following Fougeron and Keating's study (1996), which found nasal airflow to be an effective means to study the influence of boundary on postboundary nasality, the present study also uses nasal airflow to investigate the effect of boundary on nasality patterns in Taiwanese.

Turning to the third issue, the effect of boundary type on cross-boundary coarticulation, it has been found that anticipatory nasal coarticulation is affected by boundary type in English. MacClean (1973) used frame-by-frame tracing of velic movements recorded on lateral high-speed cinefluorographic film to observe the effects of syntactic boundaries on velic movements. McClean found that the presence of major syntactic boundaries (including marked phrase, clause, or sentence boundaries) between two vowels in a CV#VN context delayed the onset of velic movements relative to the offset of the preceding initial vowels more than less-marked syntactic boundaries (including word boundary). Since English vowels are unspecified in terms of phonemic nasal features, the velum started to decline during the articulation of the preboundary vowel in CV#VN. The commencement of velic lowering in anticipation of the upcoming nasal consonant was found to be earlier in productions by English speakers after weak boundaries and later after strong boundaries (MacClean, 1973).

Generally speaking, cross-boundary coarticulation weakens as the intervening prosodic boundary varies from weaker to stronger levels in the prosodic hierarchy. As articulatory movement becomes more canonical next to a strong boundary, it is less likely to coarticulate with neighboring segments. For example, Cho (2004) reported greater V-to-V coarticulation resistance across stronger prosodic boundaries. So far there has been no study on the effect of boundary on cross-boundary carry-over nasalization. Hence, this study uses nasal airflow to investigate how cross-boundary carry-over nasalization from a final nasal to an initial voiced stop in Taiwanese varies according to the hierarchical strength of the intervening boundaries.

C. Speaker-dependent articulatory patterns

Before moving on to investigate the relationship between boundary and nasality in Taiwanese, it should be noted

that, as previously mentioned in the airflow study on French nasality (Fougeron and Keating, 1996; Keating *et al.*, 2004), speaker-dependent nasality patterns have already been widely observed. Furthermore, the effect of boundary type on jaw, lip, and acoustical parameters also varies from speaker to speaker (Tabain, 2003a, 2003b; Cho, 2005). For example, among the acoustical and articulatory data of five speakers producing English /#bi/ and /#ba/, it was found that all the speakers produced /a/ with the greatest jaw movement and /i/ with the least jaw movement at strong boundaries; however, the duration of lip opening during the articulation of a vowel varied among the same speakers. Only two speakers produced vowels with a longer lip opening after a strong boundary (Cho, 2005). Tabain (2003a) studied the acoustic patterns of French word-final /a#C/ sequences produced at an utterance, intonational phrase, accentual phrase, or word boundary and found that there was much variation among speakers. Speakers used different cues to indicate different prosodic strengths. For example, some speakers used vowel duration to distinguish four types of boundaries, i.e., utterance $>$ intonational phrase $>$ accentual phrase $>$ word, whereas others classified the vowel duration before different boundaries into two groups, i.e., utterance $=$ intonational phrase $=$ accentual phrase $>$ word. Moreover, when looking at the spectral tilt for consonants, /#f, s, ʃ/, all subjects grouped the boundaries at two levels; however, two subjects also made a distinction between word and higher level boundaries (utterance $=$ intonational phrase $=$ accentual phrase $>$ word), whereas another subject made a distinction between utterance and lower level boundaries (utterance $<$ intonational phrase $=$ accentual phrase $=$ word).

Keating *et al.* (2004), in an EPG study on VOT and lingual contacts during the production of Taiwanese initial /t/ and /n/ after utterance, intonational phrase, accentual phrase, word, and syllable boundaries by two speakers, discovered that although there was a general trend for lingual peak contact to vary with boundary type, speaker-dependent patterns were nonetheless still observed. It was found that one speaker failed to vary the production of /t/ at all, whereas another speaker varied the production of /t/ in relation to the prosodic boundary strength.

Nearly all previous studies on articulation and boundary have discovered speaker-dependent articulatory patterns (Fougeron and Keating, 1996; Keating *et al.*, 2004). It is, therefore, likely that there are a certain number of patterns that a speaker can choose from, as well as some other factors which influence articulatory pattern in addition to boundary. The following is a discussion on the influence of focus, declination, and speaking rate on velic movements.

D. Other factors influencing velic movements

Stress, declination, and speaking rate have been found to influence velic movements (Krakow, 1993; Bell-Berti *et al.*, 1995). For example, stress affects velic height by enhancing the position of the velum. That is, the high velic position for an oral stop is higher, whereas the low velic position for a nasal stop is lower in stressed syllables (Vaissiere, 1988). In addition to stress, declination also affects velic movements. It was discovered that velic displacement of nasals produced in words in serial position gradually decreased from the beginning to the end of a sentence. In other words, the earlier the nasal is in a sentence, the lower the position of the velum (Bell-Berti and Krakow, 1991; Krakow, Bell-Berti, and Wang, 1995).

In addition to stress and declination, speaking rate also influences velic height. Bell-Berti and Krakow (1991) in a study on velic height for /s/ and /n/ found that the faster the speaking rate is, the lesser the difference in velic height between the oral and nasal consonants. Conversely, the slower the speaking rate, the larger the difference between the velic positions for /s/ and /n/. Kuehn (1976) noticed that these effects are speaker dependent. Though both speakers in Kuehn's (1976) study reduced the distance of velic movement in fast speech, one speaker reduced the extent of velic lowering by raising the lowest velic position, whereas the other speaker reduced the distance of velic movement by lowering the highest velic position. Kent, Carney, and Severeid (1974) reported that as speaking rate increased from a conversational to a rapid rate, speakers increased the velocity of velic movements, or reduced the extent of the velic movement, or used both strategies to produce the same sentence.

In addition to a control on the effects of focus and declination, as previous studies have done, this study also adopts a control on global speaking rate in an attempt to minimize speaker-dependent variations, and to reveal the effect of boundary on nasality.

E. Objectives

After controlling the confounding factors, this study followed the line of study of the variations of velic movements within multiple prosodic domains. By using nasal airflow, a successful method used to record the effect of boundary on French initial nasals and on cross-boundary nasalization in Taiwanese, the present study explores the effects of different prosodic boundaries on (1) domain-final nasality and (2) cross-boundary nasalization.

II. METHOD

A. Speakers

Three male native Taiwanese speakers participated in the experiments. They were students at National Chiao Tung University at the time of recording. The three speakers were also fluent in Mandarin and had received more than 10 years of ESL education.

B. Materials

Three types of contexts were used in the current study. The first was a baseline context which elicited utterances not ending with a nasal and, thus, no cross-boundary nasalization. The baseline data set consisted of syllable-final vowels followed by initial voiceless stops, abbreviated as Vptk (vowel # /p/, /t/, /k/) or voiced stops, abbreviated as Vblg (vowel # /b/, /l/, /g/). The syllable-final vowels and following stops were produced across intonational phrase, word, and syllable boundaries. As previously mentioned, /l/ was in-

cluded together with /b, g/ due to its stoplike quality. (2) The second context elicited comparison data with a final nasal followed by an initial voiceless stop that prohibits cross-boundary nasalization, abbreviated as Nptk (nasal # /p/, /t/, /k/) across intonational phrase, word, and syllable boundaries. (3) The third and final context elicited experimental data with a final nasal that allows for cross-boundary nasalization. The experimental data consisted of final nasals placed before voiced stops across intonational phrase, word, and syllable boundaries, abbreviated as Nblg (nasal # /b/, /l/, /g/). The comparison data in the Nptk context address the first research question involving the effect of boundary on final nasals, whereas the data in the Nblg context address the second research question concerning the strength of the intervening boundary on cross-boundary nasalization.

To minimize speaker-dependent articulatory variation, focus and declination were controlled in the corpus design. Although lexical stress does not exist in Taiwanese, words are produced with a longer duration and an expanded *f*0 range for lexical tones when under narrow focus (Pan, 2006). Therefore, the effect of focus condition is controlled by asking the subjects to produce the utterances with a broad focus.

To control declination effects, intonational phrase, word, and syllable boundaries were placed between the second and third syllables of sentences containing six syllables [$\sigma\sigma$ # $\sigma\sigma\sigma\sigma$]. The final oral vowels and three final nasals, /m, n, ŋ/ at the end of second syllable were followed by either one of the three initial voiced stops, /b, l, g/, or one of the three initial voiceless unaspirated stops, /p, t, k/, at the beginning of the third syllable, [Vmnŋ] # [blg], [Vmnŋ] # [ptk], [V] # [blg], or [V] # [ptk]. Declination effect was minimized by having target syllables far from the end of the sentence.

Sentence (1) is an example of a sentence used to elicit utterances with an intonational phrase boundary between the target syllables. In sentence (1), the first and second syllables formed a surname. A comma was placed after the second syllable in the sentence to elicit the production of the surname as a vocative. The right edge of the intonational phrase (IP) boundary was defined by an *f*0 final lowering and a long pause and a postboundary pitch reset.

Tonal grouping:

$((\sigma_s\ \sigma_j)^{\text{tone group}})^{\text{IP}}((\sigma_s\ \sigma_s\ \sigma_s\ \sigma_j)^{\text{tone group}})^{\text{IP}}$

Syntactic grouping:

[$_{\text{np}}$ a **pa**], PRO [lai k$^{\text{h}}$i təŋ la]

dad come go home exclamation

"Daddy, let's go home."

s: syllable with sandhi tone; j: syllable with juncture tone; PRO: pronoun (1)

In Taiwanese every lexical item has two tones, namely a juncture and a sandhi tone. A juncture tone surfaces on the last syllable within a tone group, whereas a sandhi tone surfaces on syllables located at the nonfinal position of a tone group. The domains of tone group are syntactically and prosodically determined; however, no complete account on Taiwanese tone group delineation has been offered yet. In order to elicit productions with a word boundary but not with a tone-group boundary between the target syllables, sentences composed of an NP followed by an adjective phrase were used, as in (2).

Tonal grouping:

$((\sigma_s\ \sigma_s\ \sigma_s\ \sigma_j)^{\text{tone group}}(\sigma_s\ \sigma_j)^{\text{tone group}})^{\text{IP}}$

Syntactic grouping:

[$_{\text{np}}$[$_{\text{n}}$si k**in**]][$_{\text{n}}$**l**ai a]][$_{\text{ap}}$ sĩũ dzɛ]

four kilogram pear too much

"Four kilograms of pears are too much."

AP: adjective phrase (2)

In sentence (2), the first and second syllables, /si kin/ "four kilograms," is a quantifier, whereas the third and fourth syllables /lai a/ "pear," is the noun modifed by "four kilograms." There is a word boundary between the second and third syllables, that is, between the quantifier and the noun. The tone-group boundary is located after the NP, e.g. "four kilograms of pears."

To elicit utterances with a syllabic boundary between the target syllables, sentences such as (3) containing a word spanning from the preboundary (second) syllable to the postboundary (third) syllable were used. The word containing target final nasal /oral vowel and initial stops was either a noun, or a verb, or an adjective. In the following case, the word was an adjective.

Tonal grouping:

$((\sigma_s\ \sigma_s\ \sigma_s\ \sigma_j)^{\text{tone group}}\ (\sigma_s\ \sigma_j)^{\text{tone group}})^{\text{IP}}$

Syntactic grouping:

[$_{\text{vp}}$ [v ts$^{\text{h}}$i ŋ] [$_{\text{np}}$[$_{\text{Adj}}$ **k**an tan e] [$_{\text{n}}$ hɔk tsɔŋ]] (3)

wear simple clothing

"Wear simple clothing."

After designing the corpus, three reading lists were composed, with each reading list containing only sentences with only one type of boundary between target syllables. In other words, there was one reading list with sentences designed to elicit an intonational phrase boundary between second and third syllables, another to elicit a word boundary, and a third one to elicit a syllable boundary. The order of sentences within each list was randomized.

C. Instrumentation

Nasal airflow was recorded from a transducer mounted on a nasal airflow mask, a Hans Rudolph model P0789 adult nasal mask, which covered only the nose of the speaker. The transducer was connected to an MS100-A2 airflow system manufactured by Glottal Enterprises. Nasal airflow was low-

pass filtered at 36.5 Hz and then dc recordings were made by using a DT-2801 card installed in a PC. The signals were digitized at 11 kHz using CSPEECHSP software.

Acoustic signals picked up by a TEV microphone connected to a TEAC cassette deck were sent to a PC to be digitized simultaneously with nasal airflow at 11 kHz using CSPEECHSP software.

A Seiko quartz metronome with blinking lights and ticking sounds to signal beats was used to regulate the global speaking rate. The ticking sounds were sent through a Beyerdynamic headphone to pace speaking rates for the first and second syllables of each sentence. See below for further discussion of how the global speaking rate was controlled.

D. Recording procedure

Airflow system calibration was carried out first by warming up the system for 1 h before recording and then adjusting the voltage displayed on the front panel of the system to zero "0" while no signals were being received. Then, the software was also calibrated by adjusting the volts of empty signals recorded to 0 volts as well. The flow was not actually calibrated; thus, the amplitudes reported in this study were volts rather than units of actual flow (e.g., cc/s).

After hardware and software calibrations, the recordings were made in a sound-proofed room in the phonetics laboratory of National Chiao Tung University, Taiwan. During the recordings, both the speaker and the experimenter were present in the sound-proofed room. The experimenter controlled the CSPEECHSP software, signaled the speaker to put on the nasal airflow mask, and to read one sentence from the reading list. Speakers paused after each sentence to allow the experimenter time to save the nasal airflow and acoustic data at 11 kHz.

To control for global speaking rate, which previously had been found to influence nasal patterns, speakers wore a headphone emitting the ticking sounds from the metronome at a speed of 144 beats per minute. Based on native speakers' judgments, this speed is compatible with the speaking rate during a normal conversation. None of the speakers reported that the speed deviated from what they normally used during conversation. There was also a blinking light on the metronome which was synchronized with the beats. Before the recordings were made, speakers were instructed to read the first and second syllables of the sentence at a speed with one ticking sound corresponding to the first syllable, and the second ticking sound corresponding to the second syllable. After pacing the speed at the beginning of the sentence, speakers were then free to slow down or speed up while producing the rest of the sentences to preserve the natural prosodic cadence of their utterances.

Altogether there were 162 target sentences recorded in the Nblg and Nptk contexts (3 final nasals ×6 initial consonants ×3 prosodic boundaries ×3 repetitions) and 54 baseline sentences in the Vblg and Vptk contexts (1 final vowel ×6 initial consonants ×3 prosodic boundaries ×3 repetitions). Due to typing errors on the reading lists, three repetitions of one sentence that should have had a final /m/ followed by an /l/ across a syllable boundary and three repetitions for each of the two sentences containing a final vowel followed by an /l/ across an intonational phrase boundary were discarded from the Nblg context.

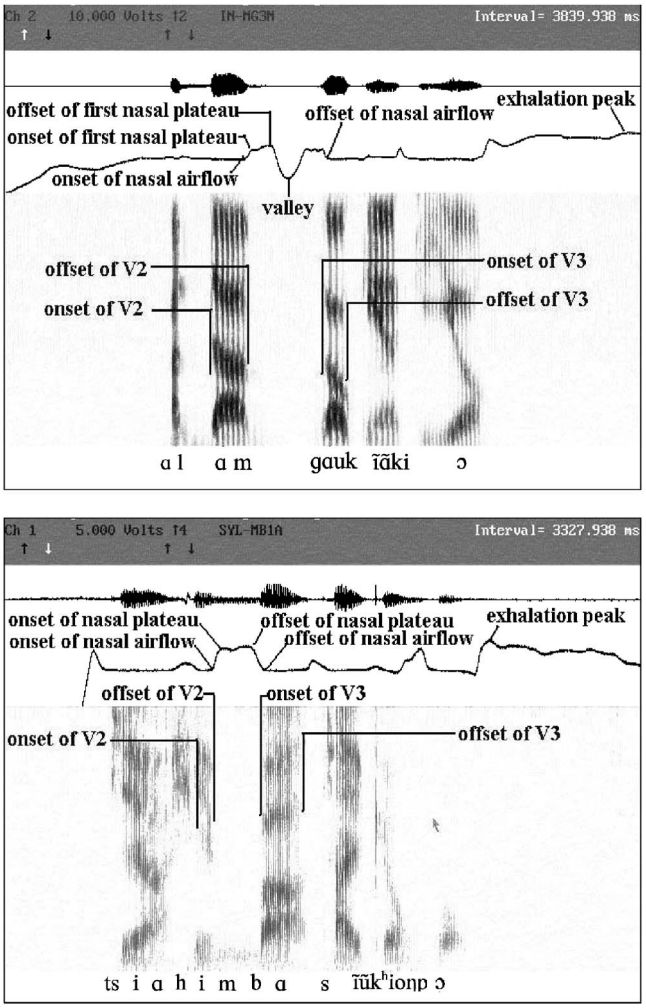

FIG. 1. Measurement points taken from nasal airflow with (a) two rises and (b) one rise between the second and third vowels.

E. Data analysis

As shown in Fig. 1, spectrograms generated by CSPEECHSP were used to locate the time at the second vowel onsets (V2On), and the offsets (V2Off) as well as the third vowel onsets (V3On), and the offsets (V3Off).

The time and amplitude of nasal airflow during production of the first nasal rise were taken to determine the timing and amplitude of nasality. These values were extracted at the following locations: (1) the onset of the initial nasal rise (On); (2) the start of the first nasal plateau (1On); (3) the end of the first nasal plateau (1Off); (4) the offset (Off) of the falling slope for the last nasal rise; and (5) the magnitude of the maximal nasal peak at the end of each utterance during normal exhalation was extracted (max) (Fig. 1). The start of a nasal plateau was the point in time when the rising slope of first nasal rise stopped and turned into a level contour, whereas the end of a nasal plateau was the point where the level nasal plateau started to change into a falling slope. If there was only a nasal peak without a plateau, then ampli-

tudes and times of two points at the peak were taken. For nasal contours with two rises, the lowest point between the two rises (*V*) was also taken.

For the following discussion, refer to (4a)–(4e). After taking these measurements, further calculations were applied to these values to derive the temporal aspects of the nasal airflow, including the duration of the nasal plateau during the first nasal rise [R1PlDur (4a)], and the duration of the nasal airflow [NasDur (4b)]. In utterances with two nasal rises, the duration of the nasal airflow did not truly represent the duration of the continuous nasal airflow because it included the duration of the nasal inhalation between the two nasal rises. According to Pan (2004), in the Nblg, Vblg, and Vptk contexts, postboundary vowel nasalization occurs only during the initial 25% of vowel duration. In order to reveal the actual duration of nasalization during postboundary initial stops and vowels, the current study calculated the offset latency of nasal airflow relative to the onset of the third vowel, by subtracting the time at the offset of the nasal airflow from the time of the onset of the third vowel, as shown in [CVNasDur (4c)]. The positive values of the duration of postboundary initial consonant and vowel nasalization (CVNasDur) indicate the duration of the third vowel nasalization, whereas the negative values revealed the duration of nasalization in the initial voiced and voiceless stops. In addition to the magnitude and temporal aspect of nasal airflow, the duration of the second and third vowel /a/ was also calculated in [V3Dur (4d); V2Dur (4e)].

Duration of first nasal plateau (R1PlDur)
= time at end of first nasal plateau (1Off)
- time at start of first nasal plateau (1On); (4a)

Duration of nasal airflow (NasDur)
= time at offset of nasal airflow (Off)
- time at onset of first nasal airflow rise (On); (4b)

Duration of postboundary stop and vowel nasalization (CVNasDur)
= time at offset of nasal airflow (Off)
- time at onset of third vowel (V3On); (4c)

Duration of postboundary vowel /a/(V3Dur)
= offset of postboundary vowel (V3Off)
- onset of postboundary vowel (V3On); (4d)

Duration of preboundary vowel /a/(V2Dur)
= offset of preboundary vowel (V2Off)
- onset of pre-boundary vowel (V2On). (4e)

The overall nasal amplitude contour, the nasal amplitudes at the start and end of the first nasal plateau, and the derived parameters were analyzed statistically. The purpose of the statistical analysis was to determine interactions using three-way repeated analysis, to isolate the interactions by dividing the data into subsets according to interactions, to reveal the effect of boundary on each data set, and to identify the ranking and distinction for levels of boundary. The α level was set at 0.05. The following is the rationale behind each statistical analysis.

Due to the widely reported speaker-dependent variations in previous literature, even though speaker and context were not of interest in the present study, their effects must be determined before data can be pooled across different factors for further statistical analyses. Thus, a three-way repeated MANOVA (speaker $\times$ context $\times$ boundary) was used to analyze the effect of speaker (speaker 1, 2, and 3) and contexts (Vblg, Vptk, Nblg, and Nptk) and boundaries (intonational phrase, word, and syllable) on six dependent variables, including nasal amplitudes at the offset of the second vowel, the onset of nasal airflow, the start of the first nasal plateau, the end of first nasal plateau, the offset of nasal airflow, and the onset of the third vowel. For utterances that showed a flat contour of nasal airflow, the average nasal amplitude at the offset of the second vowel and the onset of the third vowel were used to replace the values at the onset of the first nasal rise, the start of the nasal plateau during the first nasal rise, the end of the first nasal plateau, and the offset of nasal airflow. It should be noted that the repeated measurements were actually the six data points from each of the three repetitions of the nine sentences in the Nblg or Nptk contexts, and the three sentences in the Vblg or Vptk contexts.

After determining the interactions with the three-way MANOVAs, the data were further divided according to contexts, Nblg, Nptk, Vblg, and Vptk, if there was a two-way interaction between context and boundary, but no three-way interactions between speaker, context, and boundary. For parameters with significant three-way interactions between speaker, context, and boundary, the data were further divided into 12 different subsets according to the three speakers and four contexts, speaker 1 Nblg, speaker 1 Nptk, speaker 1 Vblg, speaker 1 Vptk, speaker 2 Nblg, speaker 2 Nptk, speaker 2 Vblg, speaker 2 Vptk, speaker 3 Nblg, speaker 3 Nptk, speaker 3 Vblg, and speaker 3 Vptk. After dividing the data into subsets according to interactions, one-way MANOVAs (boundary) on each of the six previously discussed subdata sets were used to explore the effect of boundary on overall nasal contours.

In addition to the overall nasal contour, the nasal amplitudes at specific points, including the start and end of the first nasal plateau (1On, 1Off), were divided into subsets according to the interactions on nasal contours, and then analyzed with one-way repeated ANOVAs (boundary) and *posthoc* Duncan tests to access the possibility of boundary distinction at particular time points.

The four parameters derived from further calculations, i.e. (4a) to (4d), were each analyzed with a three-way repeated ANOVA (speaker $\times$ context $\times$ boundary) to determine the nature of the interactions. Data for each of the four parameters showing interactions between context and boundary, but no three-way interactions between speaker, context, and boundary, were further divided into four data sets ac-

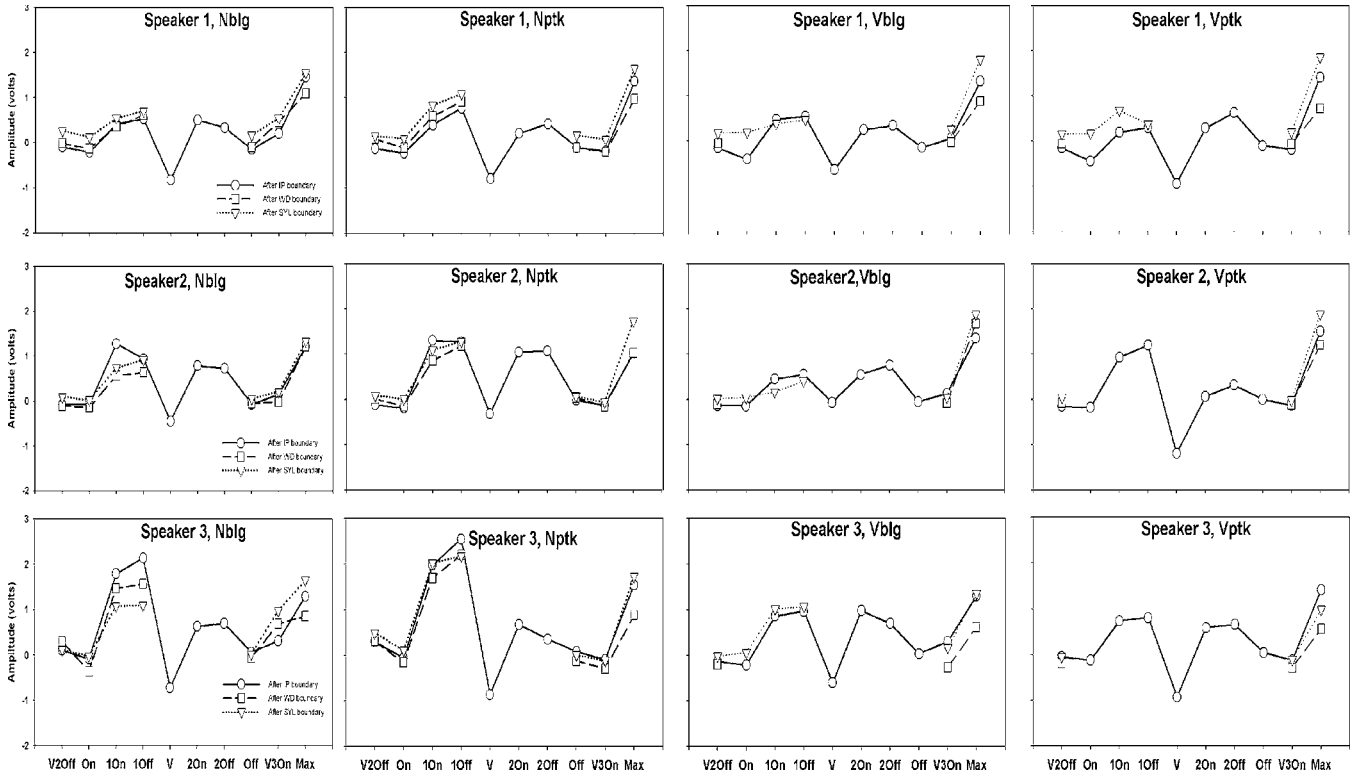

FIG. 2. Amplitudes of nasal airflow taken at ten time points through the production of target segments by three speakers at three boundaries types (intonational phrase, word, and syllable) in four segmental contexts (Nblg: final nasal followed by initial voiced stop, Nptk: final nasal followed by initial voiceless stop, Vblg: final oral vowel followed by initial voiced stop, Nptk: final nasal followed by initial voiceless stop). The points include: offset of second vowel (V2Off), onset of nasal airflow (On), start of the first nasal plateau (1On), end of the first nasal plateau (1Off), nasal inhalation (V), start of the second nasal plateau (2On), end of the second nasal plateau (2Off), offset of nasal airflow (Off), onset of the third vowel (V3On), and maximal nasal exhalation at the end of utterance (Max).

cording to contexts. The data of a parameter showing three-way interactions between speaker, context, and boundary were further divided into 12 data sets according to three speakers and four contexts. Each of these data sets was analyzed with a one-way repeated ANOVA (boundary) to access the effect of boundary. It should be noted that the repeated measurements were theoretically the 216 repetitions (3 speakers $\times 3$ boundaries $\times 3$ final nasals $\times 3$ stops $\times 3$ repetitions) in the Nblg and Nptk contexts, and the 81 repetitions (3 speakers $\times 3$ boundaries $\times 1$ final vowel $\times 3$ stops $\times 3$ repetitions) in the Vblg and Vptk contexts. However, since the first nasal rise did not appear in some repetitions in the Nblg and Nptk contexts or in most of the repetitions in the Vblg and Vptk contexts, the actual number of observations varied among the parameters. After analyzing the main effect of boundary, *posthoc* Duncan tests were performed to reveal the ranking and differences in the levels of boundary for each derived parameter.

III. RESULTS

A. Global speaking rate

This study controlled the global speaking rate by pacing the speakers' production of the first and second syllables at a speed of 144 beats per minute. To access the effectiveness of this speed-controlling method, the duration of the second vowel /a/ was compared between three speakers. The means and standard deviations of /a/ produced by speaker 1 were longer than those by speakers 2 and 3 (speaker 1: mean $=159$ ms, S.D. $=47$ ms; speaker 2: mean $=148$ ms, S.D. $=42$ ms; speaker 3: mean $=146$ ms, S.D. $=50$ ms). The results of 2-tailed t-tests showed that /a/ was significantly longer in productions by speaker 1 than by speaker 2 ($p < 0.01$) or by speaker 3 ($p < 0.01$). However, the duration of /a/ produced by speakers 2 and 3 were not significantly different from each other ($p = 0.67$). Not all speakers responded to the metronome method in a similar pattern; speaker 1 exhibited a slower rate and produced longer vowels than were exhibited by speakers 2 or 3. Perceptually, speaker 1 indeed sounded slower and softer than speakers 2 and 3.

B. Nasal contour patterns and boundary types

As illustrated in Fig. 2, excluding the data from speakers 2 and 3 in the Nblg and Nptk contexts, the amplitudes of nasal airflow during the utterances were lower than the maximal nasal exhalation peak at the end of utterances (max). Therefore, speakers only used a portion of the nasal amplitude range that was available to them in most productions.

The average nasal contours across the intonational phrase boundary exhibited a first nasal rise followed by a nasal valley (inhalation) and then a second nasal rise. Across the word boundary in the Nblg and Nptk contexts, the only pattern of nasal contours observed was one nasal rise, but in the Vblg and Vptk contexts, only flat nasal contours could be

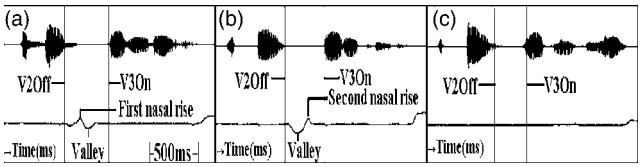

FIG. 3. Examples for nasal contours with (a) a nasal rise followed by a valley (RV); (b) a valley followed by a nasal rise (VR); and (c) no nasal rise or valley (flat). Nasal airflow is aligned with the speech signal.

observed. Nasal contours across a syllable boundary exhibited either one nasal rise or a flat nasal contour in all four contexts.

Detailed observation of the nasal contours revealed five patterns: (1) a first nasal rise followed by nasal inhalation, seen as a nasal valley with a negative nasal amplitude, and then a second nasal rise (RVR), as shown in Fig. 1(a); (2) a nasal rise (R), as shown in Fig. 1(b); (3) a nasal rise followed by a nasal inhalation (RV), as shown in Fig. 3(a); (4) a nasal inhalation followed by a nasal rise (VR), as shown in Fig. 3(b); and (5) no nasal rise or inhalation (flat), as shown in Fig. 3(c). The distribution of the five nasal patterns across speakers and boundary types is shown in Table I.

As shown in Table I, nasal inhalation could only be observed across an intonational phrase boundary when there was a pause between intonational phrase boundaries; moreover, second nasal rises were observed only across intonational phrase boundaries. Although nasal inhalation and a second nasal rise occurred only across intonational phrase boundaries, not all IPs were marked in this manner. Generally speaking, nasal inhalation occurred more often in the Nblg and Nptk contexts than in the Vblg and Vptk contexts. The frequency of nasal inhalation across intonational phrase boundaries varied from speaker to speaker. The presence of a nasal rise and nasal inhalation across an intonational phrase boundary in the Vblg and Vptk contexts where no nasal segments were present suggested that the intonational phrase boundary was a strong factor in inducing velic movements.

TABLE I. Nasal patterns categorized according to boundaries and contexts. "I," intonational phrase boundary; "W," word boundary; "S," syllable boundary; RVR, first nasal rise followed by a nasal valley (inhalation), and then a second nasal rise; RV, first nasal rise followed by a nasal valley (inhalation); VR, a nasal valley (inhalation) followed by a nasal rise; R, one nasal rise; Flat, no nasal rise or valley.

Speaker 1	Nblg			Nptk			Vblg			Vptk		
	I	**W**	**S**	**I**	**W**	**S**	**I**	**W**	**S**	**I**	**W**	**S**
RVR	17			7								
RV	1			1								
VR		1					3			3		
R	7	26	23	19	27	24	5		2	6		2
Flat			1					9	7		9	7
Speaker 2		Nblg			Nptk			Vblg			Vptk	
	I	**W**	**S**	**I**	**W**	**S**	**I**	**W**	**S**	**I**	**W**	**S**
RVR	4			3			2					
RV												
VR										1		
R	21	27	24	24	27	24	7		1	7		
Flat								9	8		9	9
Speaker 3		Nblg			Nptk			Vblg			Vptk	
	I	**W**	**S**	**I**	**W**	**S**	**I**	**W**	**S**	**I**	**W**	**S**
RVR	10			8			3			4		
RV	1			4			2			2		
VR												
R	14	25	24	15	24	24	4		2	3		
Flat		2			3			9	6		9	9

Across a word boundary in the Nblg and Nptk contexts, the pattern of nasal contours was predominantly a single nasal rise (Fig. 2). The exceptions were one utterance produced by speaker 1 with VR pattern and five utterances produced by speaker 3 with flat nasal contours. In the Vblg and Vptk contexts, the nasal contours were flat across all speakers (Table I).

Across the syllable boundary in the Nblg and Nptk contexts, the nasal patterns were one nasal rise for all, except for one production by speaker 1 in the Nblg context. In the Vblg and Vptk contexts, a flat nasal contour was the most commonly observed pattern.

In short, the existence of a strong prosodic boundary stopped nasalization from extending into the neighboring segment and so speakers produced two separate nasal contours. In contrast, when there was a weaker syllable or word boundary, nasalization extended over the boundary and so speakers were likely to produce only one nasal rise.

C. Nasal amplitude and boundary type

Nasal amplitudes taken at six points during nasal contours, including the offset of the second vowel, the onset of the nasal rise, the start of the first nasal plateau, the end of the first nasal plateau, the offset of the nasal airflow, and the onset of the third vowels, were analyzed with a three-way MANOVA (speaker $\times$ context $\times$ boundary). The results of a three-way MANOVA revealed a significant three-way interaction between speaker, context, and boundary $[F(72, 3096.1) = 3.53,\ p < 0.0001]$. In other words, the effect of boundary on nasal amplitudes produced by the three speakers varied according to context. Thus, it was not possible to pool the data either across speakers or contexts. As a result, the data were further divided into 12 data sets according to the three speakers and four contexts.

To further determine the effect of boundary on overall nasal contours, 12 one-way repeated MANOVAs (boundary) were used to analyze the nasal contours in the Nblg, Nptk, Vblg, and Vptk contexts that were produced by all the speakers. The results of the 12 one-way repeated MANOVAs (boundary) are shown in Table II. The significant effects of boundary can be observed in the nasal contours produced by the three speakers in the four contexts. In other words, the nasal contours were influenced by the boundary types, regardless of the contexts and speakers.

In addition to the nasal contours, the nasal amplitude at specific points, including the start and the end of the first nasal plateau (1On, 1Off), were also analyzed. As the results of previous three-way repeated MANOVAs have shown three-way interactions between speakers, contexts, and boundaries, the nasal amplitudes at the start of the first nasal plateaus were divided into 12 sets according to the three

TABLE II. Results of one-way repeated MANOVAs (boundary) on nasal contours produced by three speakers in four contexts. "**" $p<0.01$.

		Nblg	Nptk	Vblg	Vptk
Speaker	1	$F(12,132)=19.35^{**}$	$F(12,140)=48.81^{**}$	$F(12,32)=8.12^{**}$	$F(12,32)=24.62^{**}$
	2	$F(12,136)=15.94^{**}$	$F(12,140)=16.03^{**}$	$F(12,38)=22.45^{**}$	$F(12,36)=11.53^{**}$
	3	$F(12,132)=16.06^{**}$	$F(12,134)=13.18^{**}$	$F(12,36)=18.93^{**}$	$F(12,38)=20.13^{**}$

speakers and four contexts, as were the nasal amplitudes at the end of the first nasal plateau. Each of the data sets was then analyzed with a one-way repeated ANOVA (boundary). The results of the one-way ANOVAs (boundary) revealed a significant effect of boundary in almost all data sets, excluding the production of speakers 2 and 3 in the Nptk context (Table III). Furthermore, the *posthoc* Duncan tests revealed no consistent cross-speaker ranking of boundary type in the Nblg and Nptk contexts (Table III). In other words, in the Nblg and Nptk contexts, the nasal amplitudes at the start and the end of the first nasal plateaus were not used to mark boundary types. However, in the Vblg and Vptk contexts there was a consistent ranking of boundary types, intonational phrase > syllable > word, on nasal amplitudes at the

TABLE III. One-way ANOVA (boundary) and *posthoc* Duncan tests on amplitudes of nasal airflow at onset (1On) and offset (1Off) of the first nasal plateau. The intonational phrase boundary is represented by "I," the word boundary by "W," the syllable boundary by "S." "=" the levels of boundary were not significantly different from each other. ">" the levels of boundary were significantly different from each other. "*" $p<0.05$; "**" $p<0.01$.

			1On		1Off	
Context	Speaker	Boundary	Mean	ANOVA *posthoc* Duncan	Mean	ANOVA *posthoc* Duncan
Nblg	1	**I**	0.412	$(2,71)=4.12^{*}$	0.532	$(2,71)=3.15^{*}$
		W	0.359	S>I=W	0.616	S=W, W=I
		S	0.544		0.708	S>I
	2	**I**	1.277	$(2,73)=31.57^{**}$	0.939	$(2,73)=5.51^{**}$
		W	0.564	I>S=W	0.640	I>S=W
		S	0.737		0.919	
	3	**I**	1.790	$(2,71)=5.95^{**}$	2.142	$(2,71)=8.21^{**}$
		W	1.467	I=W, W=S	1.571	I>W=S
		S	1.081	I>S	1.094	
Nptk	1	**I**	0.393	$(2,75)=25.94^{**}$	0.771	$(2,75)=8.04^{**}$
		W	0.578	S>W>I	0.903	S>W=I
		S	0.830		1.083	
	2	**I**	1.303	$(2,75)=7.72^{**}$	1.271	$(2,75)=0.74$,
		W	0.852	I=S>W	1.178	$p=0.48$
		S	1.088		1.273	
	3	**I**	1.976	$(2,72)=1.44$	2.548	$(2,72)=2.03$
		W	1.695	$p=0.24$	2.201	$p=0.14$
		S	2.023		2.171	
Vblg	1	**I**	0.478	$(2,21)=11.02^{**}$	0.541	$(2,21)=11.20^{**}$
		W	−0.039	I=S>W	−0.039	I=S>W
		S	0.380		0.465	
	2	**I**	0.444	$(2,24)=28.47^{**}$	0.550	$(2,24)=28.11^{**}$
		W	−0.090	I>S=W	−0.090	I>S=W
		S	0.043		0.044	
	3	**I**	0.855	$(2,23)=13.37^{**}$	0.967	$(2,23)=18.79^{**}$
		W	−0.238	I>S>W	−0.238	I>S>W
		S	0.229		0.251	
Vptk	1	**I**	1.517	$(2,21)=121.88^{**}$	0.294	$(2,21)=12.48^{**}$
		W	−0.063	I>S>W	-0.063	I=S>W
		S	0.260		0.193	
	2	**I**	0.795	$(2,23)=21.35^{**}$	1.033	$(2,23)=31.46^{**}$
		W	−0.096	I>S=W	−0.096	I>S=W
		S	0.009		0.004	
	3	**I**	0.740	$(2,24)=19.93^{**}$	0.803	$(2,24)=34.67^{**}$
		W	−0.256	I>S=W	−0.256	I>S=W
		S	−0.082		−0.082	

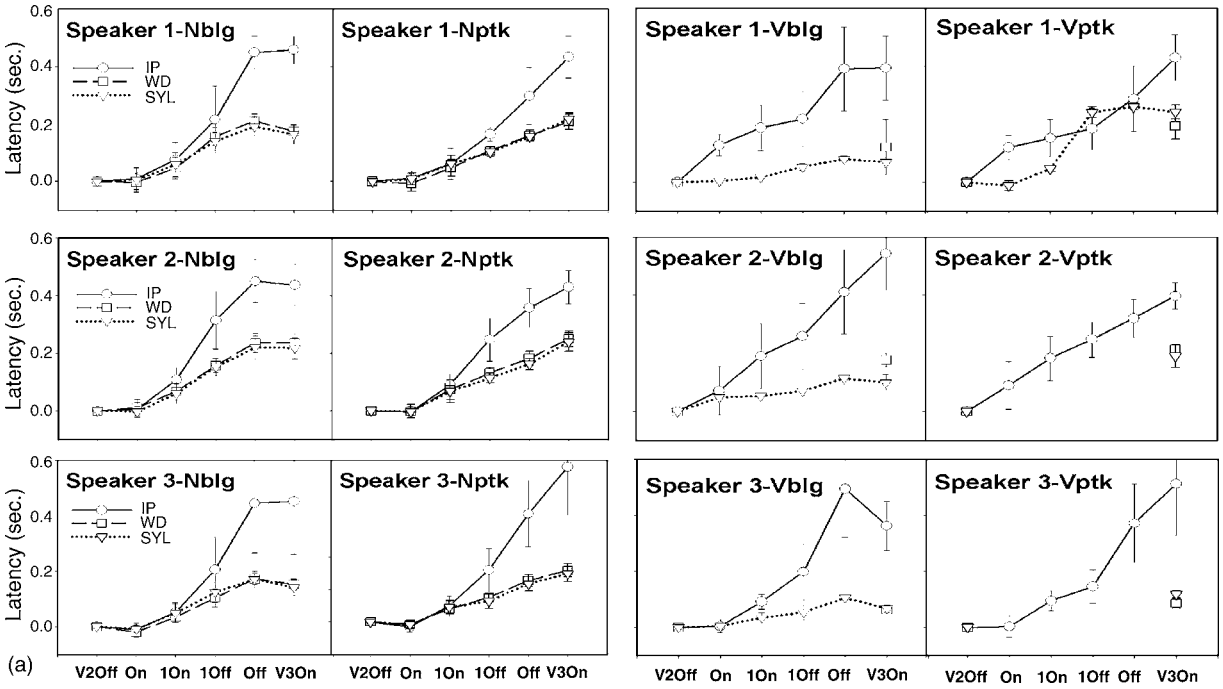

FIG. 4. Six latency measures (in seconds) of nasality taken during the production target sounds. Measures include: the end of the second vowel (V2Off), the onset of the nasal airlfow (On), start of the first nasal plateau (1On), end of the first nasal plateau (1Off), the offset of nasal airflow (Off), and the onset of the third vowel (V3On) relative to offset of the second vowel (V2Off).

start and the end of the first nasal plateau. By comparing the distribution of nasal contour patterns in Table I and the mean nasal amplitudes in Table III, it was found that this consistent ranking in the Vblg and Vptk contexts was due to the constant surface of the first nasal rise around an intonational phrase boundary which contributed to the high mean nasal amplitudes, the occasional surface of the first nasal rise at syllable boundary which led to the second highest mean nasal amplitude, and the lack of a first nasal rise at a word boundary which led to negative nasal amplitudes. In other words, speakers rarely produce a nasal rise in the Vblg and Vptk contexts. Even if they produced nasal rises, as in the Nptk and Nblg contexts, the nasal amplitudes at the start and the end of the first nasal plateau did not consistently vary with hierarchical boundary influences.

D. Temporal domain of nasal airflow and boundary type

Turning to the temporal domain of nasal airflow, as shown in Fig. 4, after the start of the first nasal plateau, as the nasal rises and valleys began to emerge, the duration of nasal airflow increased at a faster rate at the intonational phrase boundary than at other boundaries. Moreover, the duration of the nasal airflow was found to be longer at an intonational phrase boundary than at word and syllable boundaries. The temporal domain of a nasal airflow remained relatively the same at word and syllable boundaries.

As shown in Fig. 4, the duration of the first nasal plateau [R1PlDur, (4a)], between the start (1On) and end (1Off) of the first nasal rise, was shorter at word or syllable boundaries than at intonational phrase boundary. In response to the significant two-way interaction between context and boundary on the duration of the first nasal plateau revealed by a three-way repeated ANOVAs (speaker × context × boundary) (Table IV), the data were further divided into four sets according to contexts to isolate the interactions. After dividing the data, the effect of boundary on each subdata set was further analyzed through one-way ANOVAs (boundary). As shown in Table V, the results of four one-way repeated

TABLE IV. Significant interactions according to results of five three-way repeated ANOVAs (subject × context × boundary) on duration of first nasal plateau (R1PlDur), duration of nasal airflow (NasDur), duration of postboundary stop and vowel nasalization (CVNasDur), and duration of the third vowel (V3Dur). $\alpha=0.05$.

Parameters	N	Interactions	F value	p value
R1PlDur	504	Context × boundary	$F(4,476)=3.59$	$p<0.01$
		subject × context × boundary	$F(6,476)=0.38$	$p=0.89$
NasDur	514	Context × boundary	$F(4,486)=11.03$	$p<0.01$
		subject × context × boundary	$F(6,486)=1.32$	$p=0.25$
CVNasDur	515	Context × boundary	$F(4,487)=2.99$	$p<0.05$
		subject × context × boundary	$F(6,487)=1.28$	$p=0.26$
V3Dur	570	Context × boundary	$F(6,534)=5.95$	$p<0.01$
		subject × context × boundary	$F(12,534)=1.21$	$p=0.28$

TABLE V. Results of one-way repeated ANOVA (boundary) and *posthoc* Duncan tests on the duration of the first nasal plateau (R1PlDur), the nasal airflow (NasDur), the postboundary stop and vowel nasalization (CV-NasDur), and the postboundary vowel (V3Dur). "I" intonational phrase boundary, "W" word boundary, "S" syllable boundary. "=" the levels of boundary were not significantly different from each other. ">" the levels of boundary were significantly different from each other "**" $p<0.001$, "*" $p<0.05$.

		R1PlDur		NasDur	
Context	Boundary	Means	ANOVA *posthoc* Duncan	Means	ANOVA *posthoc* Duncan
Nblg	**I**	0.167	$(2,221)=29.89^{**}$	0.447	$(2,222)=247.13^{**}$
	W	0.089	I>W=S	0.211	I>W=S
	S	0.084		0.196	
Nptk	**I**	0.124	$(2,228)=70.56^{**}$	0.333	$(2,228)=201.84^{**}$
	W	0.052	I>W>S	0.163	I>W=S
	S	0.035		0.147	
Vblg	**I**	0.075	$(1,26)=1.6$	0.368	$(1,29)=13.57^{**}$
	W		$p=0.217$		I>S
	S	0.026		0.084	
Vptk	**I**	0.055	$(1,19)=13.36^{**}$	0.262	$(1,25)=0.01$
	W		S>I		$p=0.917$
	S	0.195		0.272	
		CVNasDur		V3Dur	
Context	Boundary	Means	ANOVA *posthoc* Duncan	Means	ANOVA *posthoc* Duncan
Nblg	**I**	−0.001	$(2,221)=9.26^{**}$	0.144	$(2,208)=43.10^{**}$
	W	0.018	S=W>I	0.202	W>S>I
	S	0.019		0.163	
Nptk	**I**	−0.118	$(2,228)=52.03^{**}$	0.171	$(2,231)=46.68^{**}$
	W	−0.049	W=S>I	0.218	W>I>S
	S	−0.056		0.155	
Vblg	**I**	−0.084	$(1,30)=0.48$	0.160	$(2,41)=8.19^{**}$
	W		$p=0.494$	0.243	W>S=I
	S	0.021		0.175	
Vptk	**I**	−0.119	$(1,26)=7.42^{*}$	0.164	$(2,78)=20.37^{**}$
	W		S>I	0.244	W>S>I
	S	0.018		0.206	

ANOVAs (boundary) revealed a significant effect of boundary type on the duration of the first nasal plateau (R1PlDur) in the Nblg and Nptk contexts. A *posthoc* Duncan test showed the ranking for the mean duration of the first nasal plateau in the Nblg and Nptk contexts: intonational phrase >word>syllable. However, the durations of the first nasal plateau at word and syllable boundaries in the Nblg contexts were grouped together.

In the Vblg and Vptk contexts, due to the lack of a first nasal rise at the word boundary and a smaller number of tokens with a first nasal rise at the syllable boundary (Table I), there were no consistent rankings of boundary types on the duration of nasal plateau in the Vblg and Vptk contexts. In other words, only in the Nblg and Nptk contexts was the duration of the first nasal rise significantly longer at the IP than at the word and syllable boundaries.

As shown in Fig. 4, the duration of nasal airflow [NasDur (4b)], between the onset of nasal airflow (On) and the offset of nasal airflow (Off), was longer at an intonational phrase than at word and syllable boundaries. Results of three-way repeated ANOVAs (speaker×context ×boundary) revealed significant two-way interactions between context and boundary affecting the duration of nasal airflow (NasDur) (Table IV). In response to this observation, the data were further divided into four sets according to contexts.

Results of the four one-way repeated ANOVAs (boundary) and the *posthoc* Duncan tests revealed significant effects of boundary on nasal airflow duration (NasDur) in the Nblg, Nptk, and Vblg contexts. There were consistent cross-boundary rankings on the mean duration of nasal airflow (NasDur), intonational phrase>word≥syllable (Table V). However, the *posthoc* Duncan tests tended to group nasal duration at the word and syllable boundaries together in the Nblg and Nptk contexts. In other words, the duration of nasal airflow was longer at an intonational phrase boundary than at word and syllable boundaries.

In sum, the intonational phrase boundary was marked by the longest duration of the first nasal plateau and nasal airflow. Although the duration of the first nasal plateau and nasal airflow at a word boundary was the second longest, they were not significantly longer than the duration of the first nasal plateau and nasal airflow at a syllable boundary.

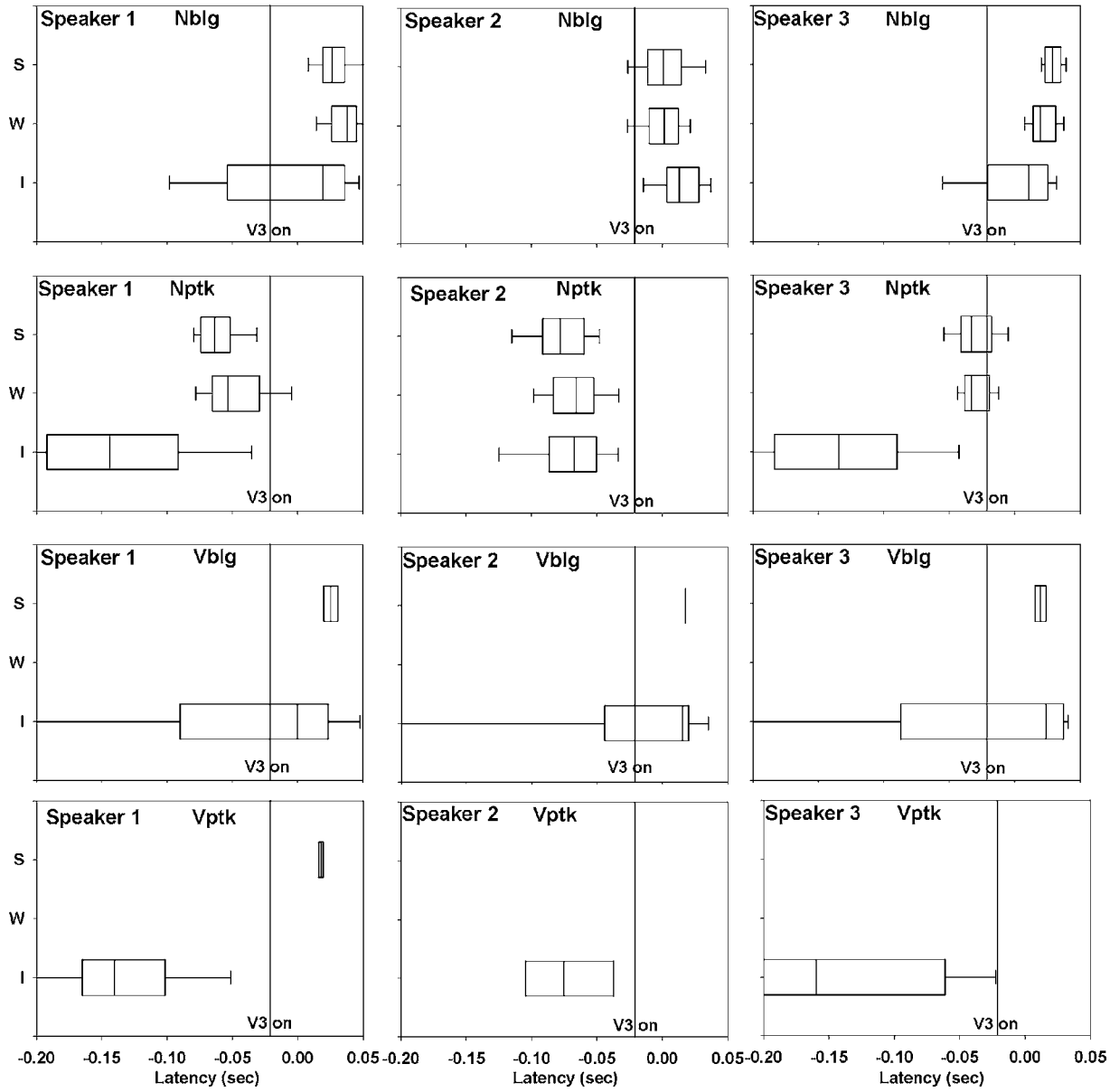

FIG. 5. Box plots for latency between the offset of nasal airflow (Off) and the onset of the third vowel (V3On) produced by three speakers, in four contexts (Nblg: the final nasal followed by the initial voiced stop, Nptk: the final nasal followed by the initial voiceless stop, Vblg: the final vowel followed by the initial voiced stop, and Vptk: the final vowel followed by the initial voiceless stop) across three boundaries (IP: intonation phrase, WD: word, and SYL: syllable boundaries). The means are indicated by the lines in the middle of the boxes, standard deviations are indicated by the frame of boxes, and the 10% and 90% data ranges are indicated by the whiskers.

E. Postboundary initial stop and vowel nasalization

Turning to the duration of the postboundary stop and vowel nasalization (CVNasDur), which was determined by the offset of nasal airflow relative to the onset of the postboundary vowel, it can be seen in Fig. 5 that there was a trend for nasal airflow to cease before the onset of the postboundary vowel in the Nptk and Vptk contexts, but after the onset of the postboundary vowel in the Nblg and Vblg contexts. In addition, boundary type also played a role in the extent of nasalization. Cross-boundary nasalization in these former two contexts was blocked earlier relative to the onset of the third vowel when there was an intonational phrase boundary. In other words, nasalization carried over from one word to the next in the Nblg and Vblg contexts as long as there was no intervening intonational phrase boundary. There were no data at word and syllable boundaries in the Vblg and Vptk contexts, as shown in Fig. 5. This was because the nasal contour remained flat in these conditions, as shown in Table I; therefore no nasalization was observed.

Due to a significant two-way interaction between context and boundary on duration of nasalization for initial stops and the vowel in the postboundary position (Table IV), the data were further divided into four sets according to contexts. The results of the one-way repeated ANOVAs (boundary) show a significant effect of boundary in the Nblg, Nptk, and Vptk contexts. The only consistent ranking observed was that the nasalization was shortest when an intonational phrase boundary separated words (Table V).

To sum up, as shown in Fig. 5, in the Vptk context there

was no nasalization. In the Vblg context, the nasality terminated after the IP boundary. In the Nptk context, the nasality was terminated before or during postboundary initial voiceless stops. In the Nblg context, the nasalization process spread from the final nasal across the boundary into the postboundary initial voiced stop and vowel. Moreover, the nasal airflow was terminated earlier across an IP boundary than across other boundaries.

F. Vowel length

The results of a three-way repeated ANOVAs (speaker $\times$context$\times$boundary) found that there was a significant two-way interaction between context and boundary on the length of the postboundary vowel /a/ [V3Dur (4d)] (Table IV). Therefore, the durations of the third vowel /a/ were divided according to context: Nblg, Nptk, Vblg, and Vptk. The results of the four one-way repeated ANOVAs (boundary) and the Duncan tests revealed that the duration of the postboundary vowel was consistently the longest after a word boundary in all contexts (Table V). In other words, the longest postboundary vowel duration was observed after word boundary.

IV. DISCUSSION

A. Nasality and boundary type

This study addresses two research questions, namely (1) the effect of boundary on nasality, and (2) the effect of boundary on cross-boundary nasalization. The effect of boundary on nasality was revealed through patterns of nasal contours, the duration of the first nasal plateau, the duration of nasal airflow, and the measurement of nasal temporal latency and nasal amplitudes at the onset of nasal airflow, the start and the end of the first nasal plateau, and the offset of nasal airflow. The effect of boundary on nasalization was revealed by the duration of nasalization on initial stop and following vowel combinations in postboundary syllables.

It was found that boundary influences the pattern of nasal contour. For example, nasal patterns with a first nasal rise followed by a nasal inhalation and a second nasal rise can only be observed at an intonational phrase boundary, whereas nasal contours with one nasal rise were observed at word and syllable boundaries in the Nblg and Nptk contexts. Flat nasal contours were found at word and syllable boundaries in the Vblg and Vptk contexts.

In order to capture the differences in patterns of nasal contour, various measures, including (1) magnitude differences and (2) temporal aspects of nasal airflow, were investigated. Although there were significant effects of boundary on overall nasal contours, neither the nasal amplitudes at the start (1On) or the nasal amplitudes at the end (1Off) of the first nasal rise varied consistently according to boundary type in the Nblg and Nptk contexts. Regardless of the lack of a consistent pattern in the magnitude of nasal airflow, the duration of the first nasal plateau (NasPlDur) and nasal duration (NasDur) varied consistently according to boundary type in the Nblg and Nptk contexts: intonational phrase$>$word $\geqslant$syllable. It was observed that the stronger the prosodic boundary, the longer was the nasal duration and the duration of the first nasal plateau in both the Nptk and Nblg contexts. It should be noted that the durations of the first nasal plateau and nasal airflow at word and syllable boundary tend to be grouped together in the current study. It is actually a common finding in articulatory prosody studies that word and syllable boundaries are not distinguished. Future studies are necessary to further explore this issue.

With reference to the first research question identified earlier regarding the influence of prosodic boundary on nasality, it can be said that although there were no consistent patterns in the magnitude of nasalization at the onset and offset of the first nasal plateau, due to the different amplitude ranges used by different speakers, each speaker realized boundary strength differences in the same direction (Fig. 2). In addition, there was an effect of boundary strength on the overall nasal trace for individual speakers (Table II). Moreover, there were consistent patterns in the temporal domain that varied in relation to boundary type. These included the duration of nasal airflow and duration of the first nasal plateau.

Taiwanese is not the only language where prosodic influences on articulation are more prominent on temporal patterns than on spatial magnitude patterns. For example, Byrd *et al.* (2000) in a study of the jaw, lip, and lingual movements of [n#m] and [m#n] across the word and phrasal boundaries in Tamil, discovered little effect of phrasal position on the spatial domain, but did find a significant effect of phrasal position on timing and duration. In the current study boundaries influence the pattern of nasal contour and nasal temporal, but not nasal magnitude, parameters in Taiwanese.

The lack of consistent variations in nasal magnitudes at the onset and offset of the nasal plateau across speakers may be random variability, due to the fact that once the velopharyngeal port is open, it is difficult to control airflow magnitude in a sufficiently variable manner, especially if respiratory effort remains fairly constant. Thus, nasal magnitudes do not vary according to boundary type. Alternatively, it is suggested that there may be several patterns of boundary effects on nasal magnitudes that speakers can choose from; thus, no consistent rankings of boundary type can be observed. To fully reveal the patterns of nasal magnitudes that speakers can use, in further prosodic articulatory studies, more subjects are needed in order to find out how many patterns of variations actually exist.

Although the results of this study indicate that nasal magnitude does not vary according to boundary type in the Nblg and Nptk contexts, the variation in the duration of nasal airflow in relation to hierarchical boundary strength suggests that speakers may use temporal cues to signal boundary types. In fact, a study which did not use speech signals as stimuli found that for two tones played with the same frequency but with differing lengths, the thresholds for longer signals were lower in dB than for short signals (Watson and Gengel, 1969; Yost, 2000). In other words, the longer signals required less intensity to be perceived, whereas the shorter signals required higher intensity. Thus, the duration of a sound can influence its perceptibility. Furthermore, Ha *et al.* (2004) found that the mildly hypernasal speech of children with a cleft palate showed longer temporal characteristics of

a nasal onset interval, nasal offset interval, and total nasalization duration, than did children of the same age without cleft palates. In other words, the longer nasal temporal characteristics may contribute to the perception of hypernasality. This evidence suggests that nasal duration affects the degree of perceived nasality. Further perceptual studies are necessary to explore the relationship between nasal duration and nasality as perceived at different boundary types.

B. Cross-boundary nasalization and boundary type

With reference to the second research question regarding the effect of boundary on cross-boundary nasalization, this study has found that cross-boundary nasalization terminates earlier when it occurs across an intonational phrase boundary. This pattern supports Cho's hypothesis (2004) which states that the stronger the prosodic boundary, the more resistance there is to cross-boundary coarticulation. Furthermore, as articulatory gestures become more canonical, as when around a stronger boundary, the gesture is less likely to coarticulate with the neighboring segments. Both the hierarchical influence of boundary on domain-edge strengthening and the effect of intervening boundary on cross-boundary coarticulation find support in this paper.

When considering context, it was found that nasal airflow ceases before the end of words closed with a voiceless stop (Nptk context), but continues after a word boundary in words closed with a voiced stop (Nblg context). In other words, nasalization can cross over voiced consonants. It is proposed that there are speech aerodynamic reasons behind the different nasalization patterns observed in Nptk and Nblg contexts. First, from the point of building up intraoral air pressure, complete vocal-tract closure involving the oral cavity and the velopharyngeal port is necessary for voiceless stops to develop and maintain the required intraoral air pressure between the oral cavity and the atmosphere. Second, in reference to the maintenance of voicing, the opening of the velopharyngeal port during the production of voiced stops helps to release the supralaryngeal pressure, which must be lower than the sublaryngeal pressure, in order for pulmonic air to flow through the glottis and to cause the vocal folds to vibrate (Ohala and Riodan 1979). Thus, for aerodynamic reasons, the closure of the velopharyngeal port leads to the cessation of nasality during voiceless stops, and the opening of the velopharyngeal port leads to nasalization during voiced stops.

C. Idiosyncratic and gradient hierarchical boundary markers

In addition to the prosodic and hierarchical influence of boundaries on patterns of nasal contours and nasal temporal parameters [i.e., duration of the first nasal plateau (R1PlDur) and duration of the nasal airflow (NasDur)], there are acoustic markers uniquely associated with each boundary type that facilitate boundary identification. For example, an intonational phrase boundary can be marked by nasal inhalation and a second nasal rise, the longest duration of a first nasal plateau and duration of nasal airflow, or the shortest duration of postboundary stops and vowel nasalization (CVNasDur), whereas a syllable boundary is marked by the shortest duration of nasal temporal parameters, such as duration of the first nasal plateau and duration of nasal airflow. As for a word boundary, it is marked by the longest duration of the postboundary vowel (V3Dur). In fact, this same effect was also discovered in Pan's (in press) study on the initial lexical tone after a word boundary. As there are two types of word boundaries in Taiwanese, it is proposed that the longest postboundary vowel duration marks a word boundary that does not coincide with a tone group boundary, whereas the surface of juncture tone in a preboundary vowel marks a word boundary that coincides with a tone group boundary. Future studies are necessary to further explore this issue.

Not all articulatory or acoustical cues contribute equally to perception. Wightman *et al.* (1992) in a perceptual study of the boundary effect on final lengthening found that the lengthening of the rhyme of the syllables preceding boundaries can be used perceptually to distinguish at least four types of boundaries. They asked subjects to assign seven levels of break indices to a read speech corpus. The results showed that different boundaries were distinguished by different sets of durational cues including the coda consonants, the vowel nucleus, all segments between the final stressed vowel and the final vowel, and the final stressed vowel of preboundary syllables. Moreover, the perception of certain boundaries relied more on the duration of coda consonants and vowel nuclei, whereas the perception of other boundary types relied more on the duration of the final stressed vowels. In the present study, different types of boundaries have been distinguished hierarchically not only by nasal temporal cues, but also by unique phonetic markers, such as patterns of the nasal contour and the duration of the postboundary vowel.

From a perceptual point of view, further perceptual experiments which analyze the perceptual salience of patterns of nasal contour, hierarchical nasal temporal cues, and idiosyncratic boundary markers can shed light on cues that listeners use to distinguish boundary types. As the influence of language-specific phonemic categorization has been demonstrated to influence the perception of nasality and cross-boundary nasalization (Beddor and Strange, 1982; Beddor and Krakow, 1999), it is necessary to conduct cross-linguistic perceptual studies to enhance our understanding of domain-edge nasality strengthening and cross-boundary nasalization.

V. CONCLUSIONS

The present study reveals how boundary type influences the pattern of nasal contours and the temporal aspects of both acoustic and nasal airflow data in Taiwanese. In addition to the hierarchical ranking of boundary type on nasal temporal parameters, each boundary type is associated with specific phonetic markings that facilitate the identification of boundary. Finally, with a view to future work in this area, it would be interesting to expand the scope of prosodic articulatory studies on nasality into the area of speech pathology and to explore the effect of boundary on nasality and nasalization produced by subjects who exhibit hypernasal speech.

ACKNOWLEDGMENTS

This study was supported by the National Science Council in Taiwan (NSC 90-2411-H-009-011). Parts of this article were presented at *Laboratory Phonology VIII* at Yale University. I would like to express my gratitude to Professor Anne Chao, Professor Pi-Chiang Li, Dr. Yi-Huei Jiang, and Dr. Chih-Wei Lin for their assistance with statistical analysis and to Jane Liao, Daphne Liao, and Yi-hsin Tai for their assistance with data analysis.

Beddor, P. S., and Krakow, R. A. (**1999**). "Perception of coarticulatory nasalization by speakers of English and Thai: Evidence for partial compensation," J. Acoust. Soc. Am. **106**(5), 2868–2887.

Beddor, P. S., and Strange, W. (**1982**). "Cross-language study of perception of the oral-nasal distinction," J. Acoust. Soc. Am. **71**, 1551–1561.

Bell-Berti, F., and Krakow, R. A. (**1991**). "Anticipatory velar lowering: A co-production account," J. Acoust. Soc. Am. **90**, 112–123.

Bell-Berti, F., Krakow, R. A., Gelfer, C. E., and Boyce, S. E. (**1995**). "Anticipatory and carryover effects: Implication for models of speech production," in *Producing Speech: Contemporary Issues*, edited by F. Bell-Berti and L. J. Raphael (AIP, New York).

Byrd, D., Kaun, S., Narayanan, S., and Saltzman, E. (**2000**). "Phrasal signatures in articulation," in *Papers in Laboratory Phonology V: Language Acquisition and the Lexicon*, edited by M. B. Broe and J. B. Pierrehumbert (Cambridge University Press, Cambridge).

Cheng, R. (**1968**). "Tone sandhi in Taiwanese," Linguistics **41**, 19–42.

Cheng, R. (**1973**). "Some notes on tone sandhi in Taiwanese," Linguistics **100**, 5–25.

Cho, T. (**2002**). *The Effects of Prosody on Articulation in English* (Routledge, New York).

Cho, T. (**2004**). "Prosodically conditioned strengthening and vowel-to-vowel coarticulation in English," J. Phonetics **32**, 141–176.

Cho, T. (**2005**). "Prosodic strengthening and featural enhancement: Evidence from acoustic and articulatory realizations of /a, i/ in English," J. Acoust. Soc. Am. **117**(6), 3867–3878.

Cho, T. (**2006**). "Manifestation of prosodic structure in articulatory variation: Evidence from lip movement kinematics in English," in *Laboratory Phonology VIII*, edited by L. Goldstein, D. H. Whalen, and C. T. Best (de Gruyter, Berlin), pp. 519–543.

Cho, T., and Keating, P. A. (**2001**). "Articulatory and acoustical studies of domain-initial strengthening in Korea," J. Phonetics **29**, 155–190.

de Jong, K. (**1995**). "The supraglottal articulation of prominence in English," J. Acoust. Soc. Am. **97**, 491–504.

Edwards, J., Beckman, M., and Fletcher, J. (**1991**). "The articulatory kinematics of final lengthening," J. Acoust. Soc. Am. **89**, 369–382.

Fougeron, C., and Keating, P. A. (**1996**). "Variations in velic and lingual articulation depending on prosodic position: Results for two French speakers," in The European Student Journal of Language and Speech, http://www.essex.ac.uk/web-sls/ viewed 27 Feb. 07.

Fougeron, C., and Keating, P. A. (**1997**). "Articulatory strengthening at edges of prosodic domains," J. Acoust. Soc. Am. **101**(6), 3728–3740.

Fougeron, C. (**2001**). "Articulatory properties of initial segments in several prosodic constituents in French," J. Phonetics **29**, 109–135.

Ha, S., Sim, H., Zhi, M., and Kuehn, D. P. (**2004**). "An acoustic study of the temporal characteristics of nasalization in children with and without cleft palate," Cleft Palate J. **41**(5), 535–543.

Hsu, C.-S., and Jun, S.-A. (**1996a**). "Is tone sandhi group part of the prosodic hierarchy in Taiwanese?" J. Acoust. Soc. Am. **100**(4, Pt. 2), 2824.

Hsu, C.-S., and Jun, S.-A. (**1996b**). "Prosodic strengthening in Taiwanese: Syntagmatic or paradigmatic?" UCLA Working Papers in Phonetics **92**, 69–89.

Keating, P. A., Cho, T., Fougeron, C., and Hsu, C.-S. (**2004**). "Domain-initial articulatory strengthening in four languages," in *Phonetic Interpretation: Papers in Laboratory Phonology VI*, edited by J. Local (Cambridge University Press, Cambridge).

Kent, R. D., Carney, P. J., and Severeid, L. R. (**1974**). "Velar movement and timing: Evaluation of a model of binary control," J. Speech Hear. Res. **17**, 470–488.

Krakow, R. A. (**1989**). "The articulatory organization of syllables: A kinematic analysis of labial and velar gestures," PhD. dissertation, Yale University.

Krakow, R. A. (**1993**). "Nonsegmental influences on velum movement patterns: Syllables, sentences, stress and speaking rate," in *Nasal, Nasalization and the Velum*, edited by M. A. Huffman and R. A. Krakow (Academic, New York), pp. 87–116.

Krakow, R. A. (**1999**). "Physiological organization of syllables: A review," J. Phonetics **27**, 23–54.

Krakow, R. A., Bell-Berti, F., and Wang, Q. E. (**1995**). "Supralaryngeal declination: Evidence from the velum," in *Producing Speech: Contemporary Issues (for Katherine Safford Harris)*, edited by F. Bell-Berti and L. J. Raphael (AIP, Woodbury, NY), pp. 333–354.

Kuehn, D. P. (**1976**). "A cineradiographic investigation of velar movement in two normals," Cleft Palate J. **13**, 88–103.

MacClean, M. (**1973**). "Forward coarticulation of velar movement at marked junctural boundaries," J. Speech Hear. Res. **16**, 286–296.

Ohala, J. J., and Riodan, C. J. (**1979**). "Passive Vocal Tract Enlargement During Voiced Stops," in *Speech Communication Papers*, edited by J. J. Wolf and D. H. Klatt (Acoust. Soc. of Am., New York), pp. 89–92. [Abstract: J. Acoust. Soc. Am. **65**, S23 (1978).]

Pan, H.-H. (**2007**). "Nasality in Taiwanese," Lang Speech **47**(3), 267–297.

Pan, H.-H. (**2007**). "Focus and Taiwanese unchecked tones," in *Topic and Focus: Intonational and Meaning from a Cross-linguistic Perspective*, edited by C. Lee, M. Gordon, and D. Buring, in *Studies in Linguistics and Philosophy*, edited by G. Chierchia, K. von Fintel, and F. J. Pelletier (Springer, The Netherlands), Vol. 82, pp. 195–214.

Pan, H.-H. (**in press**). "Initial Strengthening of Lexical Tones in Taiwanese Min," in *Tones and Tunes: Phonetic and Behavioural Studies in Word and Sentence Prosody*, edited by C. Gussenhoven and Tomas Riad, in *Phonology and Phonetics*, edited by A. Lahiri (Mouton de Gruyter, Berlin).

Tabain, M. (**2003a**). "Effects of prosodic boundary on /aC/ sequences: Acoustic results," J. Acoust. Soc. Am. **113**(1), 516–531.

Tabain, M. (**2003b**). "Effects of prosodic boundary on /aC/ sequences: Articulatory results," J. Acoust. Soc. Am. **113**(5), 2834–2849.

Ting, P. H. (**1985**). *Taiwan Yuyan Yuanliou (Sources of Languages in Taiwan)* (Student, Taipei).

Vaissiere, J. (**1988**). "Prediction of velum movement from phonological specifications," Phonetica **45**, 122–139.

Watson, C. S., and Gengel, R. W. (**1969**). "Signal duration and signal frequency in relation to auditory sensitivity," J. Acoust. Soc. Am. **46**, 989–997.

Wightman, C. W., Shattuck-Hufnagel, S., Ostendorf, M., and Price, P. J. (**1992**). "Segmental durations in the vicinity of prosodic phrase boundaries," J. Acoust. Soc. Am. **91**(3), 1707–1717.

Yost, W. A. (**2000**). *Fundamentals of Hearing: An Introduction* (Elsevier Academic, San Diego), pp. 152–153.

Zhang, Z.-X. (**1989**). *Notes on Southern Min Dialects of Taiwan* (Language of publication: Chinese) (The Liberal Arts Press, Taipei).

Time dependence of vocal tract modes during production of vowels and vowel sequences

Brad H. Story[a)]
Speech Acoustics Laboratory, Department of Speech, Language, and Hearing Sciences, University of Arizona, Tucson, Arizona 85721

(Received 6 June 2006; revised 22 March 2007; accepted 23 March 2007)

Vocal tract shaping patterns based on articulatory fleshpoint data from four speakers in the University of Wisconsin x-ray microbeam (XRMB) database [J. Westbury, UW-Madison, (1994)] were determined with a principal component analysis (PCA). Midsagittal cross-distance functions representative of approximately the front 6 cm of the oral cavity for each of 11 vowels and vowel–vowel (VV) sequences were obtained from the pellet positions and the hard palate profile for the four speakers. A PCA was independently performed on each speaker's set of cross-distance functions representing static vowels only, and again with time-dependent cross-distance functions representing vowels and VV sequences. In all cases, results indicated that the first two orthogonal components (referred to as modes) accounted for more than 97% of the variance in each speaker's set of cross-distance functions. In addition, the shape of each mode was shown to be similar across the speakers suggesting that the modes represent common patterns of vocal tract deformation. Plots of the resulting time-dependent coefficient records showed that the four speakers activated each mode similarly during production of the vowel sequences. Finally, a procedure was described for using the time-dependent mode coefficients obtained from the XRMB data as input for an area function model of the vocal tract. © *2007 Acoustical Society of America.*
[DOI: 10.1121/1.2730621]

PACS number(s): 43.70.Bk, 43.70.Aj [AL] Pages: 3770–3789

I. INTRODUCTION

The structure of the vocal tract and the acoustic characteristics produced by it are well known to be speaker-dependent. There seem to exist, however, vocal tract shaping patterns for vowel production that are common across speakers. The purpose of this study was to determine whether these common shapes could be revealed from spatially sparse articulatory fleshpoint data of the oral portion of the vocal tract and, if so, to exploit this commonality in order to develop a means by which time-dependent changes of the vocal tract shape can be realistically simulated with an area function model.

The use of factor analysis for determining displacement patterns of the midsagittal tongue shape was established by Harshman *et al.* (1977). They found that only two factors (patterns) accounted for a large amount of the variance in the tongue shape during vowel production. When appropriately weighted and superimposed on the mean shape, these two factors could be used to reconstruct the configuration of the tongue for ten English vowels. At nearly the same time Shirai and Honda (1977) demonstrated that the tongue configuration could be described by two empirically determined displacement patterns. Subsequent studies of tongue shape using either factor or principal component analyses have similarly concluded that two shaping patterns can generally describe the midsagittal tongue shape during vowel production in various languages (Johnson *et al.*, 1993; Nix *et al.*, 1996; Hoole, 1999; Zheng *et al.*, 2003; Iskarous, 2005). In each study, the shaping patterns more or less conform to the view that one pattern captures the forward and upward movement of the tongue, while a second pattern describes upward and backward motion.

Similar analyses of vocal tract area functions have indicated that the shape of the airspace, extending from glottis to lips, can also be efficiently described by only a few canonical patterns. Story (2005b) showed that sets of 11 vowel area functions from six speakers could each be represented by two principal components, referred to as *modes*,[1] and a mean area function. The shape of each mode was highly correlated across the six speakers, whereas the mean area functions tended to be more speaker-specific. These results were similar to the earlier findings of Story and Titze (1998) for ten vowel area functions of one speaker. As an example, two modes, based on the ten vowel area functions of Story *et al.* (1996), are shown in Fig. 1 (note that the origin is assumed to be at the lips, hence, the negative numbers on the x axis indicate a leftward direction). When superimposed on the mean area function with a positive weighting coefficient, the first mode ϕ_1 would have the effect of expanding the oral cavity portion of the vocal tract while constricting the pharynx; a negative coefficient would have the opposite effect. The region near lips, however, would be left nearly unchanged by either a positive or negative coefficient. This suggests that a large negative weighting on ϕ_1 may produce a vocal tract shape representative of an [i], whereas a positive weighting would produce a shape similar to an [ɔ] (i.e., an expanded oral cavity but relatively small opening at the lips). A positively weighted second mode ϕ_2 would impose expansions in the lip and midtract regions, and constrictions

a)Electronic mail: bstory@u.arizona.edu

 0001-4966/2007/121(6)/3770/20/$23.00 © 2007 Acoustical Society of America

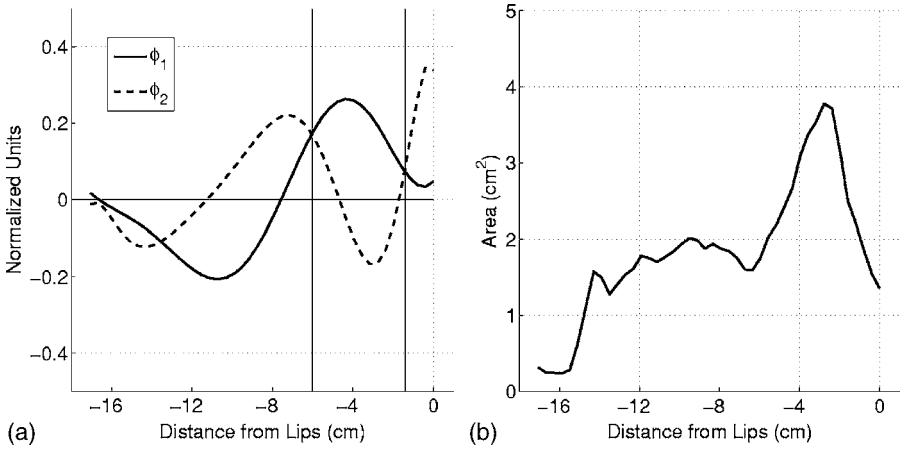

FIG. 1. Modes and mean area function determined from a ten-vowel set of area functions for an adult male [from Story *et al.* (1996)] shown as a function of the distance from the lips; A negative sign is used because of the leftward orientation of the glottis to the lips. (a) Modes ϕ_1 (solid line) and ϕ_2; the vertical lines denote points at which the modes intersect in the front half of the vocal tract; and (b) mean area function.

from 1 to 5 cm posterior to the lips and just above the glottis. This roughly produces an [æ]-like vowel, whereas a negative weighting would approximate more of an [o]-like vowel.

Recently, Mokhtari *et al.* (2007) have performed a principal component analysis on area functions of the Japanese vowels [i,e,ɑ,o,ɯ] obtained with MRI from one male speaker. They found that the first two components accounted for over 97% of the variance in the five-vowel set, and their spatial variation along the vocal tract length was remarkably similar to those shown in Fig. 1 (and in Story, 2005b) that were derived from American English vowels. A second principal component analysis was performed on the original five "still" vowels, but augmented with a set of 35 area functions obtained with a three-dimensional (3D) cine-MRI technique over the time course of the vowel transition utterance [ɑiɯeo]. Although the variance accounted for by each component was slightly different, their shapes were essentially the same as in the PCA of the five-vowel set, indicating a robust existence of the component shapes over time.

The modes (or factors, components, etc.) are, in a strict sense, statistical constructs that explain certain levels of variance in collections of articulatory postures and reduce the dimensionality of the original data set. Whereas a significant compression of data may be reason enough to utilize a technique such as PCA, there is no *a priori* reason to expect that the resulting basis functions would reveal information that could be interpreted specifically as articulatory or phonetic in nature. Nonetheless, the particular shapes of the modes, components, and factors reported in a succession of studies all seem to describe essentially the same type of basic tongue and vocal tract shaping patterns for vowels, as described previously. Although such common patterns could potentially be interpreted as an artifact of the particular statistical methods applied to similar types of data (i.e., articulatory data for vowel production), such cross-speaker and cross-linguistic commonalities have led to the suggestion that these patterns may capture some surface aspects of underlying muscle synergies and biomechanical constraints utilized during speech production (e.g., Kelso *et al.*, 1986; Fowler and Saltzman, 1993; Maeda, 1991; Hoole, 1999; Perrier *et al.*, 2000; Story 2005a). Limited physiological evidence supporting this view has been reported by Maeda and Honda (1994), but certainly further studies are needed to establish whether a relation between the planning and execution of speech production movements and the kinematic patterns described by the mode shapes actually exists. In the least, however, it is well established that a mode-based model of the area function allows for an efficient representation of a wide variety of realistic vocal tract shapes and provides a means by which to investigate the relation between the area function and resulting acoustic characteristics.

The shaping patterns provided by a set of modes are ultimately of most use if they can parsimoniously explain the time-dependent changes that occur in the vocal tract during continuous (connected) speech. Their time dependence may then be interpreted as a type of "activation signal" of a particular synergy of various portions of vocal tract. There is some evidence that this may be the case. Maeda (1991) demonstrated that the time-dependent weighting of statistically derived articulatory parameters (similar to factors but guided *a priori* with respect to individual articulators), could produce realistic vocal tract shapes. Later, Bouabana and Maeda (1998) used a novel multipulse Linear Prediction Coding (LPC) technique for determining the temporal variation of their statistical patterns. Iskarous (2005) has also recently shown that a weighted combination of two tongue shaping patterns provides a reasonable description of tongue configuration over the time course of articulatory transitions.

From the perspective of the area function representation of the vocal tract, the mode shapes shown previously in Fig. 1, as well as those for the six speakers in Story (2005b), have been used as the basis for generating one-to-one (or nearly so) mappings between the first two formant frequencies and the weighting coefficients of the modes. Shown in Fig. 2(a) is an 80×80 grid of weighting coefficients for the modes in Fig. 1. Any point within this grid can be used to generate an area function according to,

$$V(x) = \frac{\pi}{4}[\Omega(x) + q_1\phi_1(x) + q_2\phi_2(x)]^2, \quad (1)$$

where x is, in this case, the distance from the lips, $\Omega(x)$ is the mean diameter function, $\phi_1(x)$ and $\phi_2(x)$ are the modes, and q_1 and q_2 are the weighting coefficients. Since the principal component analysis was performed on the equivalent diameters of each cross-sectional area within the area function sets, the squaring operation and scaling by $\pi/4$ are needed to

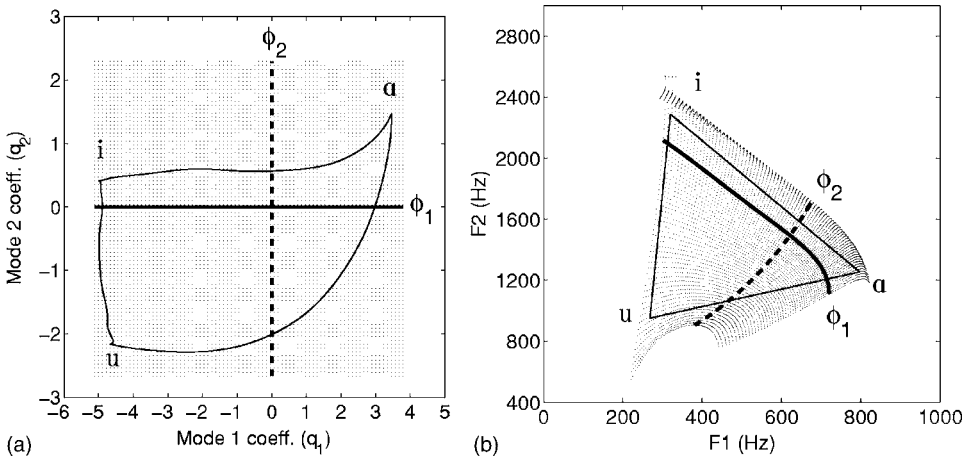

FIG. 2. Mapping between the mode coefficients (q_1 and q_2) in (a) and formant frequencies (the $F1$ and $F2$) in (b). The dark solid line and the dashed line in (a) indicate the range of coefficient values for each of the two modes, respectively; the [F1,F2] pairs produced by the coefficients (via an area function) along each line are shown in (b) by the same line styles. The curved light lines in the left plot are the coefficient variations that correspond to the triangular, hypothetical $[F1, F2]$ trajectory for [iɑui] shown on the right.

convert diameter to area. F1 and F2 formant frequencies calculated for each area function defined by the 6400 points in Fig. 2(a) are plotted as a grid in Fig. 2(b). With the exception of the upper left corner, there is only one formant pair in Fig. 2(b) associated with each coefficient pair in Fig. 2(a). The acoustic effect of each mode in isolation (i.e., when q_1 or q_2 is equal to zero) is indicated by the solid dark line (ϕ_1) and dashed line (ϕ_2). Both these individual mode lines and the grids show that the coefficient space is warped as it is transformed into the formant space by the nonlinear relation between the area function and acoustic resonances, but a nearly one-to-one relation between them is maintained.

It is noted that this approach to parametrizing the vocal tract area function shares some similarities with the methods reported by Schroeder (1967). Based on purely acoustic considerations of perturbing the shape of a uniform tube (closed at one end), both authors showed that the area function could be represented as the sum of a Fourier series, which serves as the basis function set, and a constant area from glottis to lips. In both studies, the many-to-one nature of the mapping between formant frequencies and the area function was apparent when both even and odd terms of the Fourier series were used, i.e., since the even terms are related to the zeros in the spectrum, they do not change the formant frequencies (poles) but do alter the shape of the area function. In comparison, the mode-based representation given by Eq. (1) also generates an area function as the sum of a constant tract shape, $\Omega(x)$, with the sum of a set of scaled basis functions, $q_1\phi_1(x)+q_2\phi_2(x)$. The difference is that the constant tract shape is nonuniform along the length of the vocal tract and the basis functions are the empirically based modes. The relation between the two mode coefficients (or more precisely, the area functions generated by them) and the first two formant frequencies is limited to being essentially one-to-one because of the natural constraints that are imposed when extracting the modes from an empirically based set of area functions. Thus, a Fourier series representation of the area function can be considered to be based on the *theoretically derived acoustical* possibilities of deforming a uniform tube, whereas Eq. (1) is based on the *empirically derived kinematic* possibilities of deforming the neutral vocal tract shape. Theoretical acoustic studies of a nonuniform, but neutral, vocal tract shape may eventually be able to bridge these two representations, perhaps by determining an acoustic origin for the mode shapes.

The mapping shown in Fig. 2 has served as a means by which time-dependent weighting coefficients for each mode may be obtained from time-varying formant frequencies (Story and Titze, 1998, 2002). As an example, the triangle superimposed on the formant space in Fig. 2(b) is a hypothetical trajectory for the vowel transition [iɑui]. The corresponding coefficient trajectory is shown as the solid line superimposed on the coefficient space in Fig. 2(a). Note that some curvature is imposed on each leg of the triangle as it is transformed from the formant to coefficient space. The coefficient trajectory is shown alternatively in Fig. 3(a) as two functions of time, $q_1(t)$ and $q_2(t)$; the vertical lines indicate

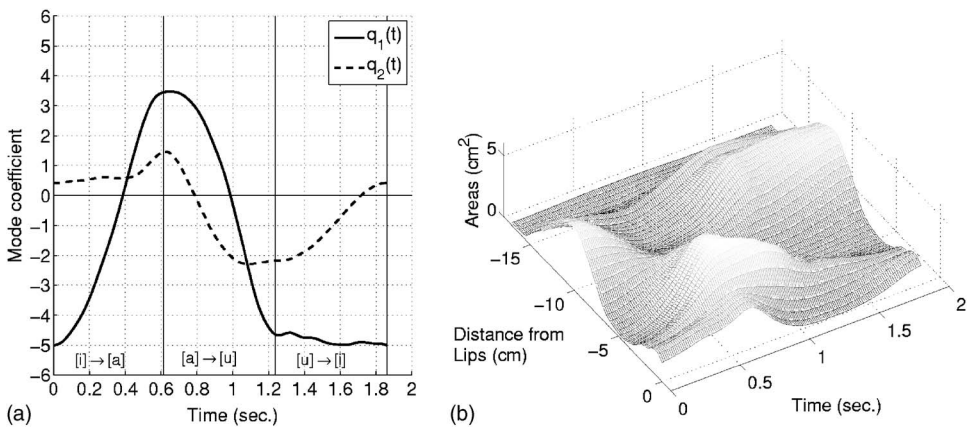

FIG. 3. (a) Time-dependent mode coefficients for [iɑui]. (b) Time-dependent area function generated by the coefficients in (a) and a time-dependent version of Eq. (1).

the points in time that correspond to the corners of the triangle. The $q_1(t)$ and $q_2(t)$ can then be used as input "signals" in a time-dependent version of Eq. (1) (Story, 2005a), which will produce an area function that varies continuously over the time course of the utterance. The resulting time-varying area function is shown in Fig. 3(b).

The representation of the area function by linear combinations of modes has been shown to be a useful approach for modeling and studying the change in vocal tract shape over the time course of speech utterances (Story, 2005a). The coefficient-to-formant mapping has also proved to be an effective technique for transforming formant frequency data to time-varying area functions. There still remains a question, however, as to whether the area function perturbations derived via the mapping are representative of *actual* vocal tract shape changes produced by a real speaker. The answer to this question would ideally be explored by comparing the time-varying area function determined with the mapping (e.g., Fig. 2) to that obtained with 3D time-dependent MRI, similar to that used by Mokhtari *et al.* (2007). There are, however, much larger amounts of articulatory flesh-point data in existence that can potentially be a source of information about the time dependence of articulatory modes.

In the present study, a principal component analysis (PCA) was applied to data from the University of Wisconsin's x-ray microbeam (XRMB) database (Westbury, 1994). Coordinates of the XRMB fleshpoint pellets, along with the outline of the hard palate, were used to approximate the shape of the vocal tract in terms of a midsagittal *cross-distance* function, extending posteriorly from the lips to approximately the soft palate. Although cross-sectional *area* is the acoustically relevant quantity for defining the vocal tract shape, a transformation from cross distance to area tends to be speaker dependent (Sundberg *et al.*, 1987; Baer *et al.*, 1991). Without information concerning such a transformation for each speaker in the XRMB database, and having only fleshpoint data (as opposed to a midsagittal x-ray projection), conversion from distance to area would likely impose a high degree of error. Furthermore, in previous studies (e.g., Story and Titze, 1998; Story, 2005b; Mokhtari *et al.*2007), the PCA was performed on the square root of the area (or equivalent diameter), a quantity that is dimensionally similar to the cross distance. Another potential limitation is that since the placement of the pellets was limited to the oral cavity, the cross-distance functions, as well as the subsequent "modes" determined with the PCA, strictly describe only the oral portion of the vocal tract. If, however, the shapes of the modes within the oral cavity exhibit features similar to those derived from whole-tract area functions (e.g., Fig. 1), it may be speculated that the pharyngeal (missing) part of the XRMB-based modes would be similar to the pharyngeal portion of the whole-tract modes.

The specific aims were (1) to determine and compare mode shapes for four speakers based on 11 vowels each, and again when vowel-to-vowel sequences were included; (2) to compare the mode coefficients determined over the time course of vowel–vowel sequences across speakers; and (3) to demonstrate the use of time-varying coefficients extracted from XRMB data as input signals for an area function model of the vocal tract. The method, results, and some discussion for each aim are presented in separate, consecutive sections.

TABLE I. Speakers from the XRMB database chosen for this study. All were native speakers of American English.

Speaker	Sex	Age (years)	Dialect base
JW26	F	24	Verona, WI
JW56	F	22.3	Edina, MN
JW12	M	21.1	Marinette, WI
JW61	M	20.4	Middleton, WI

II. MODES FOR FOUR SPEAKERS

The initial goal of this part of the study was to develop a method for extracting a midsagittal representation of the oral portion of the vocal tract airspace from XRMB data. This method was applied to data of isolated vowels and vowel–vowel sequences produced by four speakers. The collections of midsagittal cross-distance functions were then individually subjected to a principal component analysis in order to derive mode shapes and corresponding mode coefficients for each speaker.

A. Speakers and speaking tasks

The four speakers chosen from the XRMB database are listed in Table I. Although chosen somewhat arbitrarily, these speakers were included because (1) their data contained no mistracked pellets and (2) three of the speakers (JW56, JW12, JW61) produced vowel-to-vowel sequences that were not specified in the original protocol, and thus, inadvertently generated additional information concerning the vocal tract shape that was not available in other speakers' data.

For each speaker, the XRMB data chosen for analysis consisted of 11 vowels spoken in isolation. These were targeted to be / i ɪ e ɛ æ ʌ ɑ ɔ o ʊ u /. A series of vowel–vowel (VV) sequences was also analyzed. The XRMB protocol specified these to be /iu/, /iɑ/, /uɑ/, /ɑu/, /ɑi/, and /ui/, but JW56 mistakenly produced [oɑ] in addition to the other six VVs, JW12 substituted [ue] in place of /uɑ/, and JW61 produced [iui] instead of the target /ui/. Although many other instances of vowels and VVs embedded within connected speech (i.e., words, sentences, etc.) could also be included in the present analysis, it was decided that the influence of a consonant environment should be avoided at this point to facilitate the most direct comparison to previous vowel-based analyses of area function data.

B. Cross-distance functions from XRMB data

The XRMB data consist of time-dependent displacements of pellets attached to the tongue, jaw, and lips, where the sampling interval is 6.866 ms. As an example, the positions of the pellets on the tongue (T1–T4), incisor (MNi), lower lip (LL), and upper lip (UL) are shown in Fig. 4(a) for a specific time frame representative of JW26's [ɪ] vowel. Also shown is the palatal outline and an approximation of the posterior pharyngeal wall for this speaker.[2] To extract a representation of the vocal tract shape, a method was devel-

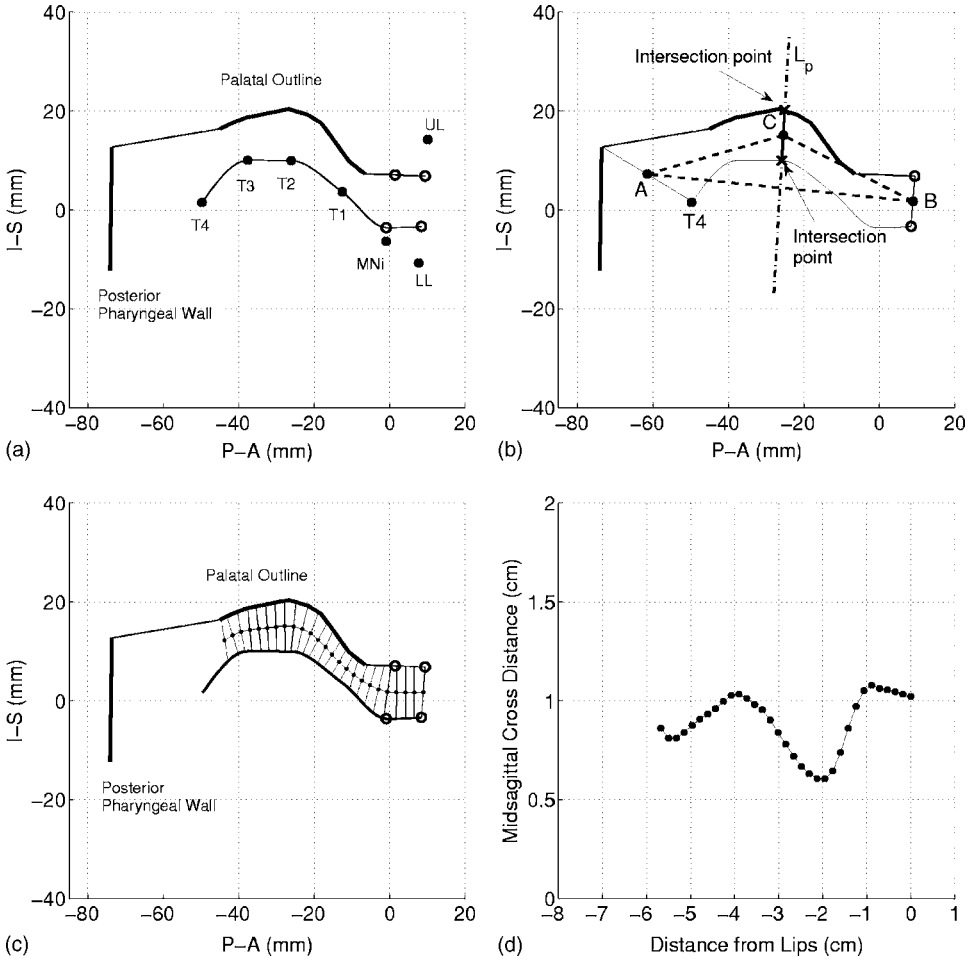

FIG. 4. Demonstration of determining a *cross-distance function* from XRMB data. (a) Sagittal view of a time frame representative of JW26's [ɪ] vowel. A superior and inferior vocal tract boundary are generated based on the tongue points (T1–T4), palatal outline, pharyngeal wall, and four "phantom" points (open circles) related to the mandible and lips. (b)Bisection method of determining initial centerline points and cross distances. (c) Result of multiple iterations of the bisection technique. The lines extending across the vocal tract are perpendicular to the centerline and comprise the *cross-distance* measurements. (d) Cross-distance function.

oped by which a midsagittal cross-distance function can be determined from a two-dimensional vocal tract profile for any time frame of data produced by a given speaker.

Although the tongue pellets (T1–T4) provide a reasonable approximation of the inferior air–tissue boundary, the placement of the mandibular (MNi) pellet at the buccal surface of the central incisor and the lip pellets on the vermillion border do not. Hence, the first step in the process was to generate four *phantom* pellet locations, from the actual pellet and palatal outline data, that reasonably approximated the airspace boundaries. These phantom points are shown as the open circles in Fig. 4(a). The two most anterior points are determined by a correction function applied to the upper and lower lip pellet positions such that they would be brought into contact during production of a bilabial consonant. The Euclidean distance between points UL and LL during the [m] of [əmɑ] (from a VCV speaking task) was used to define a correction factor. Using the slope and y intercept calculated from the UL and LL coordinates, the lip phantom points were found by moving downward and upward, respectively, by one-half the correction factor along a line between UL and LL. The mean of the coordinate values of the upper lip phantom point and the most anterior point on the palatal outline were used to generate the upper, posterior phantom pellet. The lower, posterior phantom point was determined by adding one-half the distance measured between pellet MNi and the tip of the lower incisor to the y component of MNi. Defining this last point was the most problematic because so little information exists in the XRMB data to describe the shape of the vocal tract between the T1 pellet and the lips. Other possibilities that were considered included using MNi without any correction factor, correcting MNi with the full distance to the tip of the lower incisor, or eliminating the influence of MNi completely. Based on visual inspection, each method appeared to capture a reasonable tract shape for some, but not all, vowels. Thus, the particular choice is a compromise that could be used for a wide range of vocal tract shapes.

The next step was to estimate the superior and inferior boundaries of the vocal tract. The inferior boundary was generated by a piecewise cubic interpolation [Fritsch and Carlson (1980), specifically the "pchip" algorithm available in MATLAB (Mathworks, 2006)] fit through the four points on the tongue (T1–T4) and the two lower phantom points. In contrast to a cubic spline, this type of interpolation reduces the possibility of overshoot and oscillation; hence, the curve is prevented from assuming unnatural or impossible shapes such as passing through the hard palate. The superior vocal tract boundary was similarly generated by interpolating through all of the points comprising the palatal outline and the two superior phantom points; this boundary was also extended linearly from the most posterior palatal outline point to the superior point of the pharyngeal wall approximation. Both boundaries are shown as thin solid lines in Fig. 4(a).

The final step consisted of measuring the distance from

the inferior to superior boundaries at consecutive points along the centerline of vocal tract. The centerline was determined with an iterative bisection technique (e.g., Hoffman *et al.*, 1992) that is initiated with two seed points as shown in Fig. 4(b). The midpoint, *B*, between the two lip phantom points served as the anterior seed, while the midpoint, *A*, between T4 and the most superior pharyngeal wall coordinate was set to be the posterior seed. A line, *AB*, was then fit between the two seed points and bisected with another line, L_p, perpendicular to it. An approximate location of the intersection of L_p with the superior boundary was found by detecting the zero-crossing point of a curve formed by their difference. A more precise location of the intersection point was calculated analytically by finding the roots of a first-order polynomial where L_p and a linearized portion of the superior boundary around the *approximated* intersection were set equal to each other. The intersection point of L_p with the inferior boundary was determined by the same process. Next, the midpoint, *C*, of a line connecting the inferior and superior intersection points was determined and the Euclidean distance between these two points was calculated. This produces a new point along the vocal tract centerline and the midsagittal *cross distance* at that point. The entire process is continued iteratively between each two known consecutive points within the centerline until a desired number of iterations are completed as is shown in Fig. 4(c). Typically for each frame, 33 centerline points[3] are calculated; however, any points located posterior to the palatal outline (including the initial posterior seed point) are eliminated because a cross-distance measurement in this region is inaccurate (i.e., there is no measured superior boundary in this region). Hence, the actual number of measured cross distances will generally be fewer than 33; for example, in Fig. 4(c), there are 25 cross distances shown. The cross-distance measurements corresponding to the midsagittal view shown in Fig. 4(c) are plotted as a function of the distance from the lips[4] in Fig. 4(d). For purposes of applying the principal component analysis described in the Section II D, each "cross-distance function" was resampled with a cubic spline so that it contained 33 elements separated by equal length intervals.

This process can be performed over a sequence of consecutive XRMB time frames which results in a time-dependent cross-distance function. Although the present study is concerned primarily with vowels, an example is shown in Fig. 5 for the sequence of cross-distance functions measured for JW26's production of [əmɑ] (the VCV utterance from which the lip correction was derived). The lips are located at 0 cm on the *x* axis and the variation of the cross distance extends posteriorly about 5.5 cm. The bilabial closure for the [m] can be seen at 0.14 s at which point the cross distance becomes zero at the lips.

C. Formant frequency analysis and frame identification

Each XRMB pellet coordinate file has an accompanying audio signal. For the files containing both the isolated vowels and VV sequences, this audio signal was read into the PRAAT (Boersma and Weenink, 2006) software system and used to identify sequences of time frames that specifically corresponded to voiced vowel production (i.e., periods of time for which formant frequencies could be measured). Formant frequencies were then estimated over the course of each time-frame sequence with the formant analysis module of PRAAT, which utilizes Burg's method (as described by Anderson, 1978). Depending on the particular speaker and vowel or VV transition, formant analysis parameters were manually adjusted so that the formant contours of F1, F2, and F3 were aligned with the centers of their respective formant bands in a simultaneously displayed wide-band spectrogram. The window size was set so that the time interval between consecutive formant values was identical to the sampling interval of the pellet coordinates (6.866 ms). All time-dependent formant values were transferred to MATLAB matrix form in order to be used in conjunction with the midsagittal cross-distance algorithm described in Sec. II B.

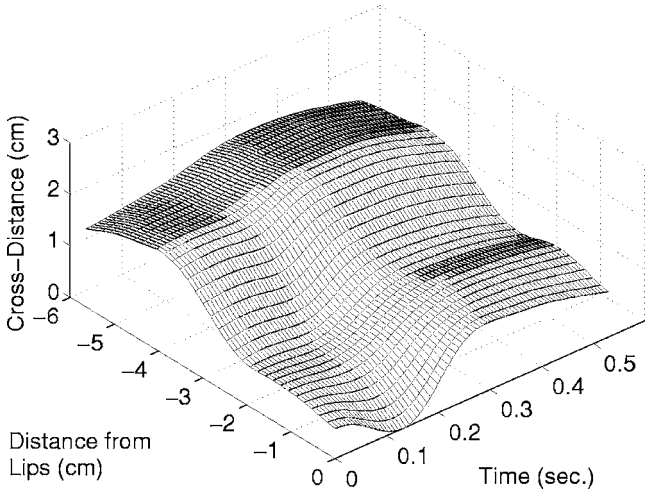

FIG. 5. Temporal variation of the cross-distance function measured over the course of [əmɑ] spoken by JW26. Note the bilabial closure for [m] occurs at 0.14 s.

D. Modes from cross-distance functions

Modes were calculated by subjecting a given set of cross-distance functions, determined by the method described in Sec. II B, to a principal component analysis similar to that described in Sec. I for vocal tract area functions. For each of the four speakers' XRMB data, modes were calculated twice. In the first case, modes were calculated for single time frames corresponding to the midpoint of the duration of each of the 11 isolated vowels. These modes were considered to be most comparable to those reported for MRI-based area functions since they too were based on isolated vowel productions. In the second case, modes were calculated for sets of cross-distance functions corresponding to time-dependent portions (i.e., many time frames) of both isolated vowels and VV sequences. Although all of the time frames identified as "voiced" (i.e., Sec. II C) could potentially be used in a PCA, consecutive frames over which there was little acoustic change (e.g., 10–30 ms of sustained /i/ prior to a transition to an /ɑ/) would include redundant information that may bias the results. To avoid this possibility, beginning and ending portions of the formant contours for

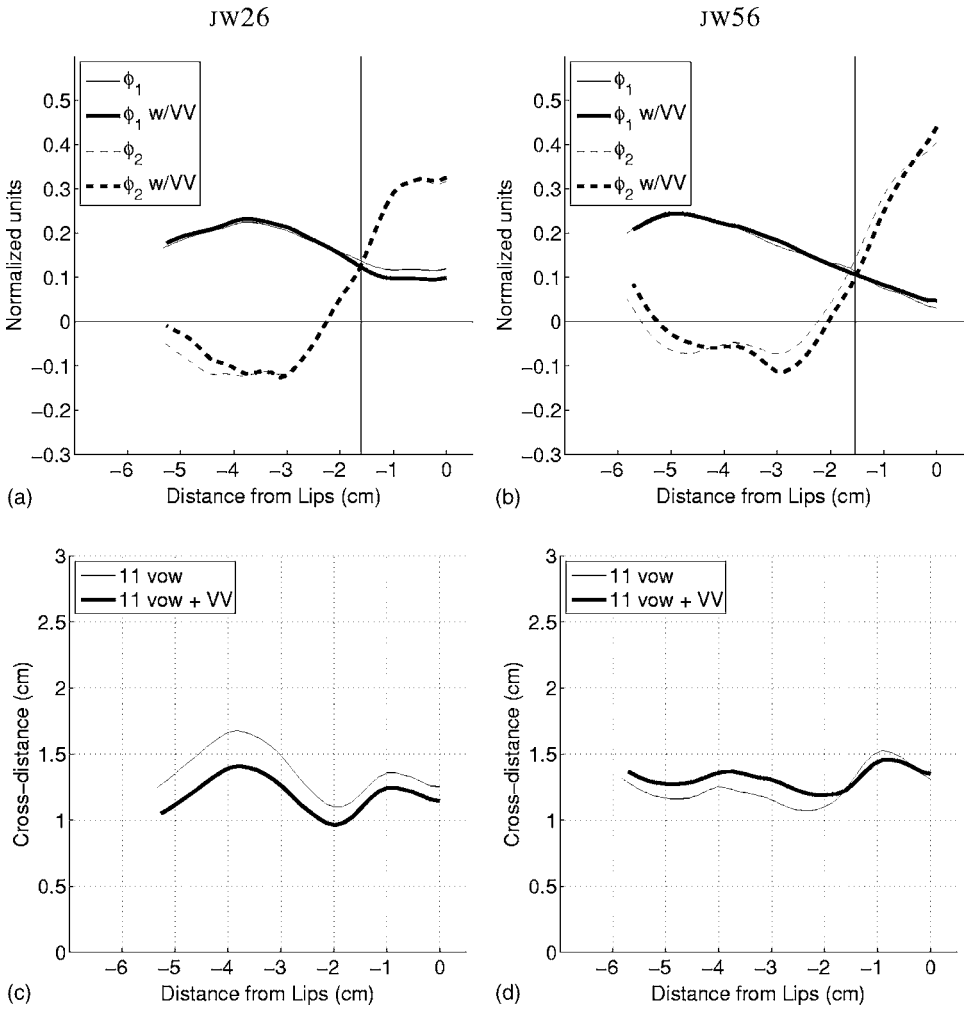

FIG. 6. Modes, ϕ_1 and ϕ_2, and mean cross-distance functions, Ω, for female speakers JW26 and JW56. The vertical lines indicate points at which ϕ_1 and ϕ_2 intersect; these are comparable to vertical lines shown in Fig. 1(a). (a) ϕ_1 and ϕ_2 for JW26, (b) ϕ_1 and ϕ_2 for JW56, (c) Ω for JW26, and (d) Ω for JW56.

each vowel and VV transition were trimmed so that what remained were formant frequencies that varied from one frame to the next by approximately 1 Hz/ms or more. Cross-distance functions associated with these remaining time frames were included in the subsequent analysis. It is noted that, even though the vowels were produced in isolation, there were changes in the formant frequencies over time. Hence, they are considered to be time dependent as well as the VV sequences.

In either case, modes were calculated for a particular speaker by setting a collection of cross-distance vectors in matrix form as $D(i,n)$, where i is an index that indicates a distance from the lips and n denotes a specific data frame. A speaker's $D(i,n)$ can be represented by a mean and variable part,

$$D(i,n) = \Omega(i) + \alpha(i,n), \tag{2}$$

where $\Omega(i)$ is the mean cross-distance vector over $D(i,n)$ and $\alpha(i,n)$ is the variation superimposed on $\Omega(i)$ to produce a specific cross-distance vector. The PCA was carried out by calculating the eigenvectors of a covariance matrix formed with $\alpha(i,n)$. This results in the following representation of the original *cross-distance* matrix:

$$D(i,n) = \left[\Omega(i) + \sum_{k=1}^{M} q_k(n)\phi_k(i) \right], \quad i,k = [1,M], \quad n = [1,N], \tag{3}$$

where $\phi_k(i)$ are M-element ($M=33$) eigenvectors (modes), and $q_k(n)$ are weighting coefficients for each mode at a particular data frame n. N is the number of data frames considered in the analysis. For the vowel-only cases, $N=11$, but for the time-dependent cases $N=256,417,311,225$ for JW26, JW56, JW12, and JW61, respectively. It is also noted that when vowels and VV sequences are both included in the PCA, $q_k(n)$ represents time-dependent mode coefficients and could be alternatively written as $q_k(t)$ where $t=(n) \times(0.006866)$ s.

E. Mode shapes

The two most significant modes calculated for each female speaker are shown in Figs. 6(a) and 6(b), and the mean cross-distance functions Ω are plotted in Figs. 6(c) and 6(d). In each plot, the thin lines (solid or dashed) are based on the 11 vowel set, whereas the thick lines are based on the time-dependent vowels and VV sequences. The modes and mean cross-distance functions for the male speakers, JW12 and JW61, are similarly shown Fig. 7. For all four speakers, there

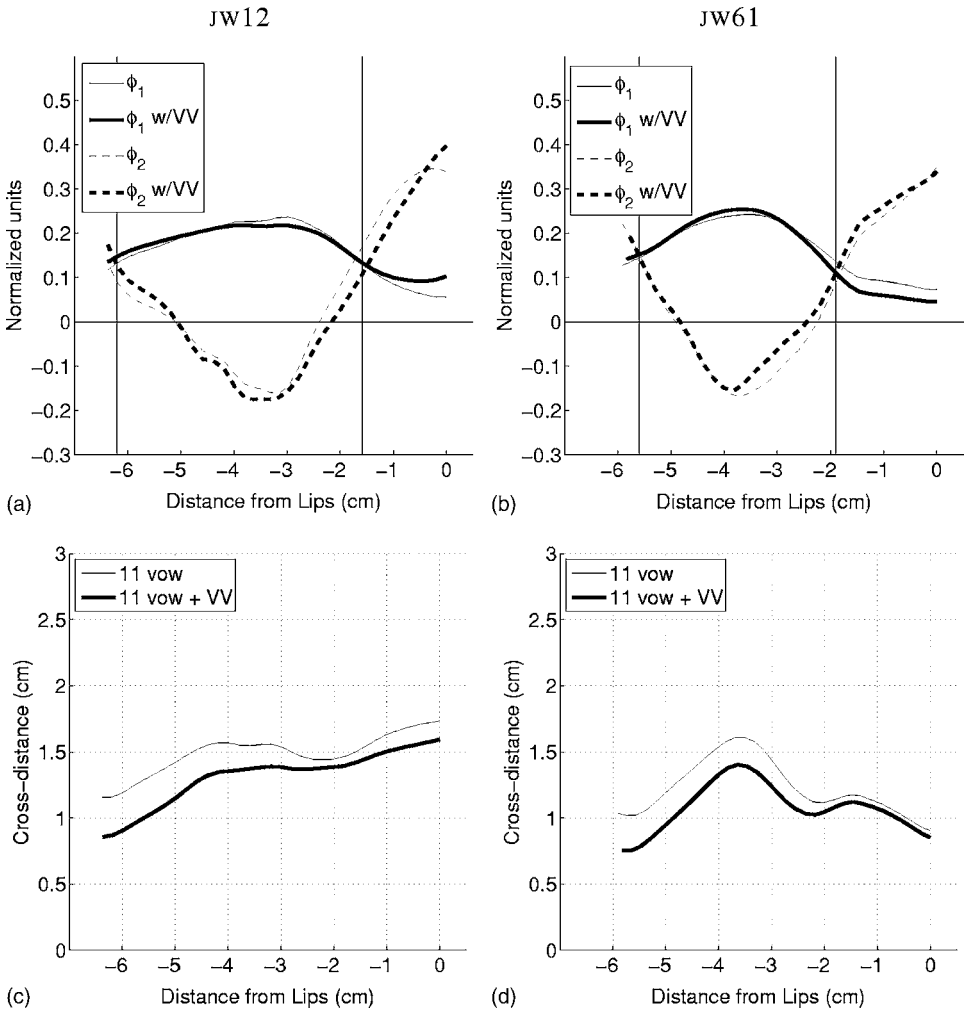

FIG. 7. Modes, ϕ_1 and ϕ_2, and mean cross-distance functions, Ω, for male speakers JW12 and JW61. The vertical lines indicate points at which ϕ_1 and ϕ_2 intersect; these are comparable to vertical lines shown in Fig. 1(a). (a) ϕ_1 and ϕ_2 for JW12, (b) ϕ_1 and ϕ_2 for JW61, (c) Ω for JW12, and (d) Ω for JW61.

are only minor differences in the mode shapes calculated for the 11 vowel set relative to those determined from the time-dependent vowel and VV sets. For the mean cross-distance functions, the shapes are nearly the same regardless of whether they were based on the 11 vowel or time-dependent set. For three of the four speakers, the 11 vowel mean maintains a slightly larger cross distance along the length of oral cavity. This suggests that using a large number of data frames tends to reduce the magnitude of the mean cross-distance function perhaps because more centralized vocal tract shapes are included in the PCA.

Although there are speaker-specific differences between the modes of the four speakers, their effect on the vocal tract shape in the oral cavity is similar. When superimposed on their respective mean cross-distance functions, all speakers' ϕ_1 would create an expansive effect with a positive weighting coefficient and a constrictive effect when the coefficient is negative. Also for all speakers, a positively weighted second mode ϕ_2 would produce an expansion near the lips, followed posteriorly by a constriction; opposite effects would be produced by a negative weighting. For all but JW26, ϕ_2 extends far enough in the posterior direction that an additional zero crossing is revealed which would allow for an expansive effect at distances −5 cm or more from the lips.

In Table II are the percentages of variance accounted for by each speaker's modes. In all cases, the first mode ϕ_1 accounted for nearly 87% or more of the total variance, whereas the second mode ϕ_2 accounted for as much as 15.9% in JW56's 11-vowel set and as little as 6.9% for the

TABLE II. Percentage of variance accounted for by each mode for four speakers. The "vowel" and "w/VV" labels indicate the PCA based on 11 vowels only and the time-dependent case including VV sequences, respectively. JW26 and JW56 are the female speakers and JW12 and JW61 are the males.

	JW26		JW56		JW12		JW61	
Mode	11 vowel	w/VV	11 vowel	w/VV	11 vowel	w/VV	11 vowel	w/VV
ϕ1	86.9	89.8	83.1	87.7	90.2	90.6	88.7	88.0
ϕ2	11.9	8.7	15.9	10.4	6.9	7.1	9.4	9.3
Total	98.8	98.5	99.0	98.1	97.1	97.7	98.1	97.3

TABLE III. Mean correlation coefficients ($\bar{R}$) and rms error ($\bar{E}$) of the original cross-distance functions relative to those reconstructed with only two modes. The "vowel" and "w/VV" labels again indicate the PCA based on 11 vowels only and the time-dependent case including VV sequences, respectively.

	J26		J56		J12		Jw61	
	11 vowel	w/VV	11 vowel	w/VV	11 vowel	w/VV	11 vowel	w/VV
$\bar{R}$	0.96	0.92	0.97	0.95	0.92	0.96	0.92	0.94
$\bar{E}$ (cm)	0.059	0.066	0.056	0.079	0.101	0.070	0.067	0.065

11-vowel set of JW12. The first and second modes combined to account for 97% or more of the variance in the vocal tract cross-distance function for vowel production in all cases. In comparison to the modes calculated for area function sets in Story and Titze (1998) and Story (2005b), the variance accounted for by ϕ_1 is about 20% higher in the present study, whereas ϕ_2 accounts for approximately 10% less variance than in those studies. Mokhtari *et al.* (2007), however, reported that the first two modes in their study accounted for about 88% and 8.5% of the variance, respectively, which is quite similar to those in Table II.

When the cross-distance functions in either the 11-vowel static sets or the time-dependent sets are reconstructed by using only two modes in Eq. (3) (i.e., $k=[1,2]$), there are some differences relative to the original cross-distance functions. To assess the magnitude of these differences, a correlation coefficient and rms error value were calculated for each frame of data in both the 11-vowel and time-dependent VV sets. The mean values of these two measures over all data frames are listed in Table III for each speaker. The mean correlation coefficients range from 0.92 to 0.97, whereas the rms error values range from 0.056 to 0.101 cm. Both measures indicate a reasonably good match regardless of speaker and type of data set used.

With regard to their effect on vocal tract shape in the oral cavity, the modes calculated for the four speakers are similar to those obtained from the MRI-based area functions previously shown in Fig. 1(a) (see also Story, 2005b; Mokhtari *et al.*, 2007). For comparison purposes; the vertical lines in Figs. 1(a), 6(a), 6(b), 7(a), and 7(b) mark the points at which ϕ_1 and ϕ_2 intersect each other in the oral cavity. The exact locations of the intersection points will depend on the vocal tract structure and speaking habits of a speaker. But for these four cases the most anterior intersection point occurs between 1 and 2 cm behind the lips. The second intersection point occurs 5–6.2 cm posterior to the lips in Figs. 1(a), 7(a), and 7(b), whereas for JW26 and JW56 ϕ_1 and ϕ_2 are suggestive that, if data were available at more posterior locations, they would also intersect each other like those of JW12 and JW61, perhaps between about 6 and 7 cm behind the lips.

In Fig. 1(a) it can be observed that the most anterior positive peak in ϕ_1 occurs about 1 cm farther from the lips than the most anterior negative peak (or valley) in ϕ_2. A similar difference is also apparent for the modes of JW56 [Fig. 6(b)], but is much smaller for the other three speakers. This is consistent with Story (2005b) and Mokhtari *et al.* (2007) where this portion of the ϕ_1 and ϕ_2 modes were typically offset by less than a centimeter. It would seem that such an offset, or phase difference, would be desirable to prevent positive weightings of each mode from canceling each other in the oral cavity. Although the mode coefficients will be discussed in more detail in subsequent sections, an example is shown in Fig. 8 of reconstructions of three of JW26's

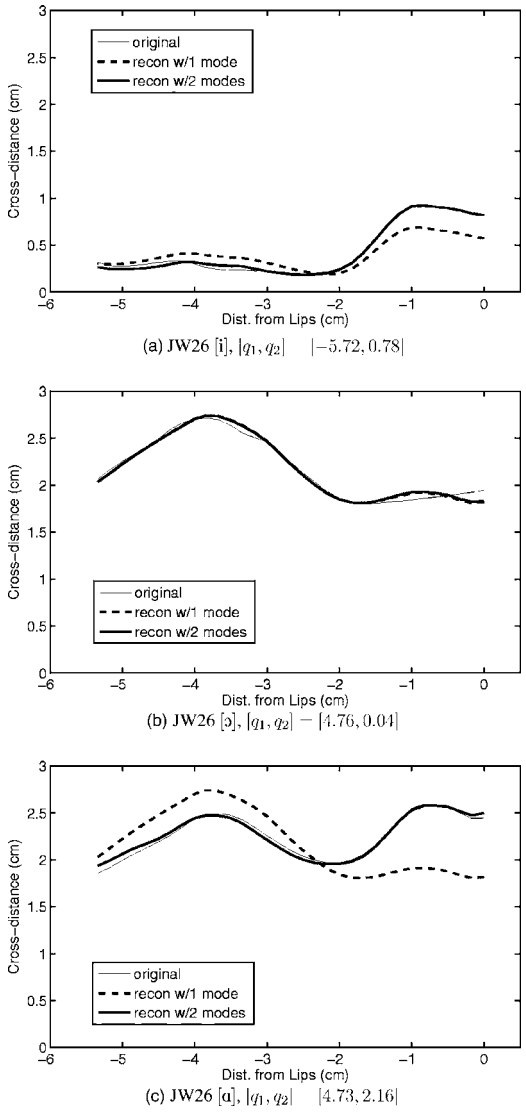

FIG. 8. Reconstructions of three vowels from JW26. The q_1 and q_2 coefficients used to reconstruct each cross-distance function are shown below the plots. In each plot the thin solid line denotes the original cross-distance function, the dashed thick line is the reconstruction with only one mode, and the thick solid line is the reconstruction with two modes. (a) Vowel [i], (b) vowel [ɔ], and (c) vowel [ɑ].

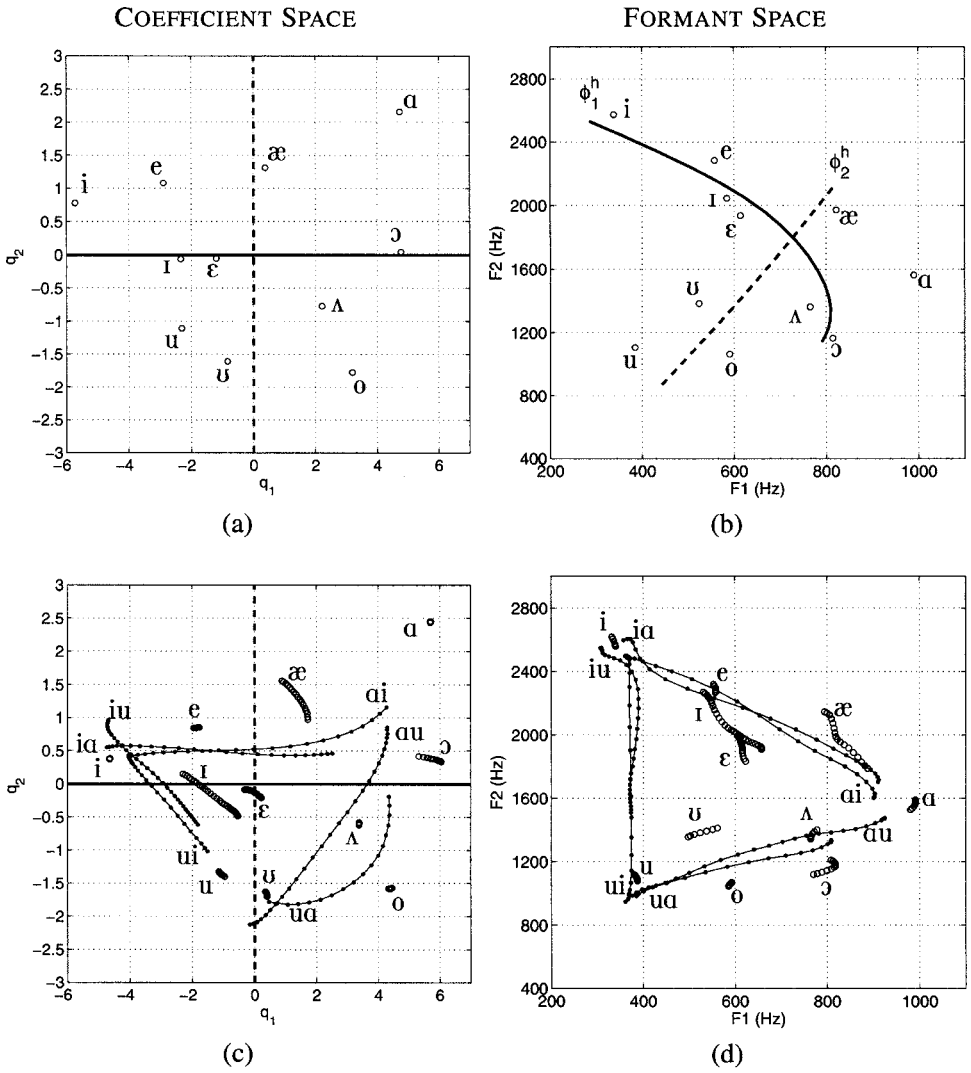

FIG. 9. Coefficient and formant spaces for JW26 based on principal component analysis and formant frequency measurements. (a) $[q_1, q_2]$ space based on single data frames of the isolated vowels, (b) $[F1, F2]$ space for isolated vowels, (c) $[q_1, q_2]$ space based on time-dependent vowels and VV sequences, and (d) $[F1, F2]$ space corresponding to the vowels and VVs in (c). In (c) and (d) the time-dependent vowels are represented as a series of open circles whereas the VV sequences are shown with solid dots connected by lines. The IPA labels for each VV are located, when practical, near the beginning of the transition.

vowels based on one and two modes, respectively [using Eq. (3)]. The [i] vowel [Fig. 8(a)] was reconstructed with mostly the contribution of a large negative coefficient for ϕ_1, but the small, positively valued ϕ_2 coefficient was needed to slightly reduce the cross distance along a portion of tract length from −2 to −5 cm and increase it near the lips. The cross-distance function for [ɔ] [Fig. 8(b)] is almost completely reconstructed by a contribution from only the ϕ_1 coefficient; the difference between the one mode and two mode reconstruction is hardly visible in the plot. The [ɑ] vowel [Fig. 8(c)] required nearly the same value of the ϕ_1 coefficient as for [ɔ], but additionally needed a fairly large positive value of the ϕ_2 coefficient to reduce the cross distance along the length from −2.5 to −5.5 cm, and increase it at the lips. These reconstructions show that, even though the ϕ_1 and ϕ_2 would appear to cancel each other in the palatal region (when both q_1 and q_2 are positive), the magnitude of the coefficients are scaled so that they efficiently contribute to producing the original shape.

F. Mode weighting coefficients

1. Isolated vowels

The ϕ_1 and ϕ_2 weighting coefficients (q_1 and q_2) for the static (single frame) 11 vowels of each of the four speakers are plotted against each other in Figs. 9(a), 10(a), 11(a), and 12(a). In each plot, the solid horizontal line and the dashed vertical line indicate the range of q_1 and q_2 values, respectively. The coefficients determined for each target vowel are plotted and labeled with IPA symbols. Although the location of the coefficient pairs for each vowel is speaker dependent, there is a general structure to the coefficient space that is similar across speakers. For instance, the $[q_1, q_2]$ coefficient pairs for the vowels [i] and [e] are always in the upper left quadrant (with the exception of JW26, [ɛ] also resides in this quadrant), [æ] and [ɑ] are in the upper right, [o] is in the lower right, and [u] is in the lower left. Other vowels such as [ɪ ʌ ɔ u] do shift quadrant affiliations depending on the speaker.

The first and second formant frequencies that were measured for each vowel (one time frame/vowel) are plotted in Figs. 9(b), 10(b), 11(b), and 12(b). To be comparable to Fig. 2, the solid and dashed lines shown in each plot are hypothetical formant characteristics that may be produced by each mode in isolation (labeled ϕ_1^h and ϕ_2^h), and would correspond to the solid and dashed lines shown in each speaker's coefficient space [see Figs. 9(a), 10(a), 11(a), and 12(a)]. These were created manually by estimating a path through the formant space whose proximity to the vowels was similar to

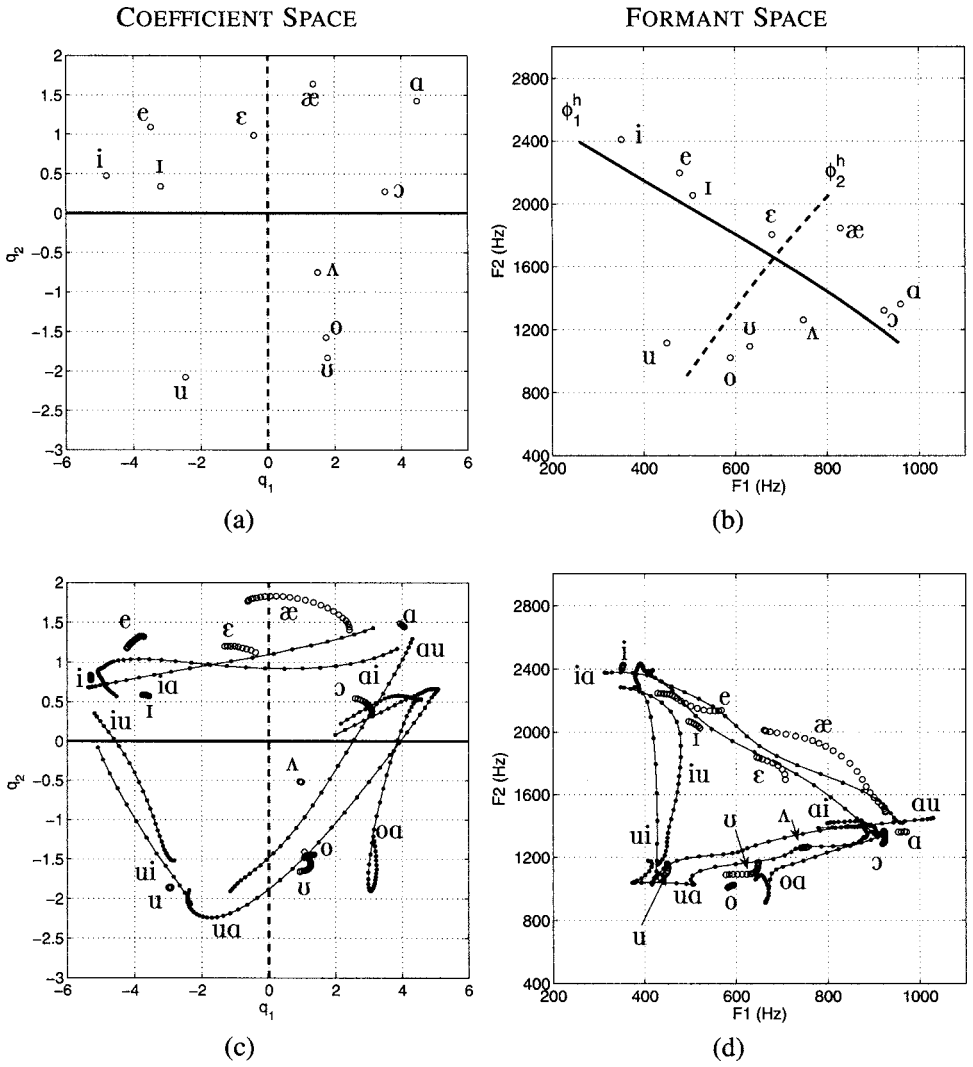

FIG. 10. Coefficient and formant spaces for JW56 based on principal component analysis and formant frequency measurements. (a)–(d) The same as in Fig. 9.

that in the coefficient space. For example, in Fig. 9(b) the ϕ_1^h line (solid) passes below [i] and [e], above [ɪ] and [ɛ], and then curves downward where it terminates slightly to the left of [ɔ]. The path of this line is similar to the ϕ_1 line shown in Fig. 2(b) which also begins slightly below the typical location of an [i] vowel in the upper left corner, and then curves downward and away from the [ɑ] as it approaches the right side of the [F1,F2] space. The hypothetical ϕ_1^h lines for the other speakers in Figs. 10(b), 11(b), and 12(b) similarly pass through the formant space of the vowels, although their shape and the location of each formant pair is speaker dependent, as were the coefficient pairs. In general, as the ϕ_1 weighting coefficient is varied from its most negative to positive values, vocal tract shapes are generated along a continuum roughly from a high front vowel like [i] to a low-mid back vowel such as [ɔ]. As Figs. 9(a), 10(a), 11(a), and 12(a) indicate, this means that an [ɑ] vowel would be generated with contributions from both modes as discussed in Sec. II E, and that a coefficient trajectory extending from [i] to [ɑ] would necessarily have an upward tilt or curvature. This result is consistent with the mapping shown in Fig. 2, as well as with the results reported by Story (2005b) where the largest positive and negative coefficients for ϕ_1 were always affiliated with [ɔ] and [i], respectively. Accounting for a difference in the polarity of the modes, Mokhtari *et al.* (2007) also reported that the coefficients for [ɑ] were both large.

For each speaker, the ϕ_2 lines in the coefficient space and the hypothetical ϕ_2^h lines in the formant space suggest that the second mode influences the vocal tract shape along a continuum from a low front vowel such as [æ] on the positive weighting side, to a mid or high back vowel, e.g., [o ʊ u] on the negative side. It is the negative coefficients for ϕ_2, however, that are the most variable with regard to a specific vowel affiliation. This again is consistent with the results in Story (2005b) where the largest negative coefficient for ϕ_2 was, depending on the speaker, associated with [u], [ʊ], and [ʌ].

2. Time-dependent vowels and VV sequences

Shown in part (c) of Figs. 9–12 are the mode coefficients based on the sets of cross-distance functions containing time-varying portions of the 11 isolated vowels and the VV sequences. In each case, the axes have been set to be identical to the coefficient space in part (a) of each figure. For many of the isolated vowels, the coefficients form a short trajectory indicating a continuous change in the vocal tract shape during production of the vowel[5] as determined during the for-

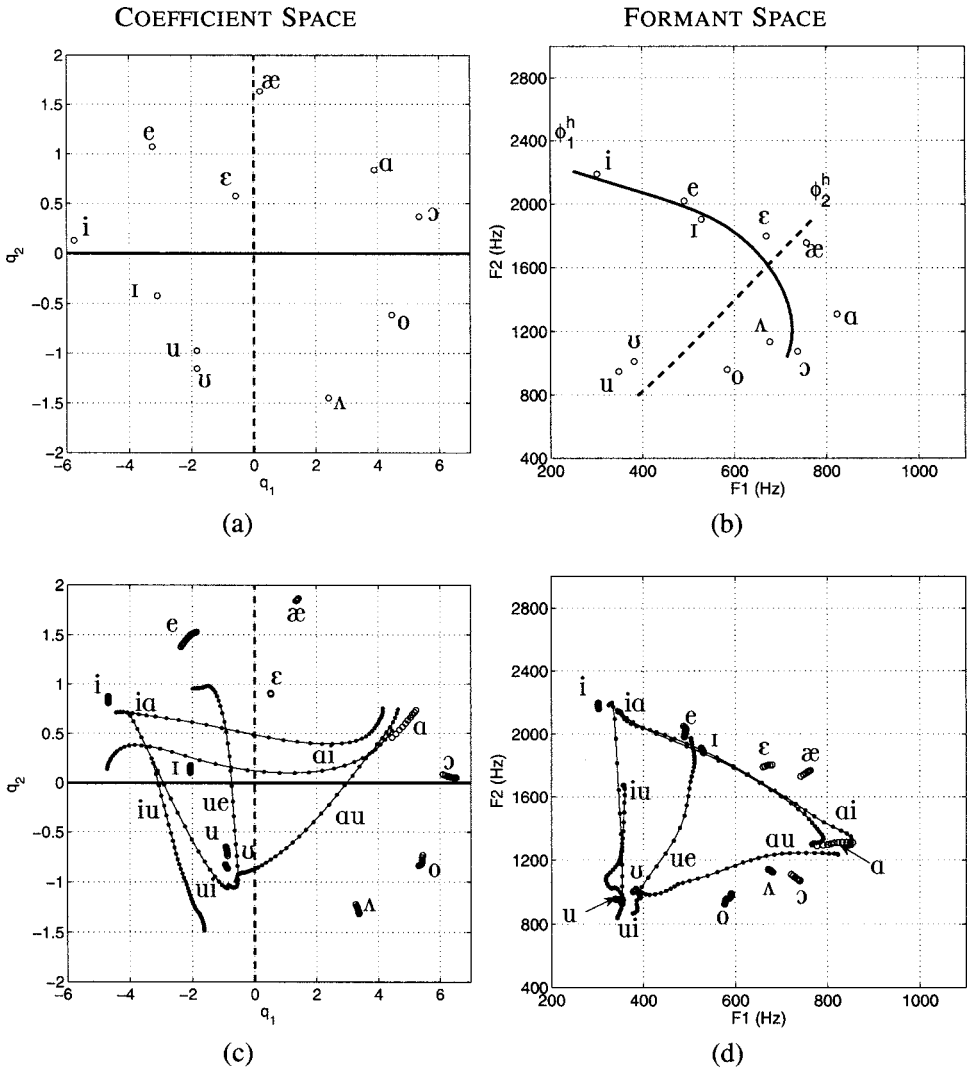

FIG. 11. Coefficient and formant spaces for JW12 based on principal component analysis and formant frequency measurements. (a)–(d). The same as in Fig. 9.

mant analysis. Each of these trajectories is shown as a series of open circles and is labeled with the IPA symbol appropriate for the particular vowel target. Each VV trajectory is indicated by a series of solid dots connected by a line, and IPA symbols have been placed, when practical, near the beginning of the trajectory. For example, in Fig. 9(c), [ɑu] is the label for the trajectory that begins at $[q_1, q_2]$=[4, 0.8] and then extends downward and to the left. In comparison to part (a) of Figs. 9–12, the coefficient trajectories for the isolated vowels are located at slightly different absolute positions within the $[q_1, q_2]$ space, but their locations relative to each other are nearly the same as for the PCA of the isolated vowels based on single data frames. This result is not unexpected considering that the shape of the modes in both cases was nearly the same for all four speakers.

In part (d) of Figs. 9–12 are the formant frequency trajectories that correspond to each coefficient trajectory in part (c), and are labeled in the same manner. For example, the [F1,F2] trajectory for [ɑu] in Fig. 9(d), which begins at about [930, 1470] Hz and then slopes downward and to the left before terminating at [360, 950] Hz, corresponds to the [ɑu] coefficient trajectory that was described in the previous paragraph. Comparison of the (c) and (d) parts of Figs. 9–12 for each speaker gives some indication of the relation that may exist between the acoustic domain and the mode coefficient domain. For all four speakers, the [iɑ], [ɑu], and [ui] formant trajectories, as well as their reverse-order counterparts [ɑi], [iu], and [uɑ], form a triangle in the [F1, F2] space. The coefficient trajectories that correspond to each leg of the formant triangles also form somewhat of triangular shape, albeit rotated and distorted. This is similar to the relation of the [F1,F2] triangle shown previously in Fig. 2(b), to the curved coefficient trajectories in Fig. 2(a), indicating that a similar mapping may also exist for the four speakers in the present study.

For JW26 (Fig. 9), it can be observed that both the [iɑ] and [ɑi] coefficient trajectories traverse much of the q_1 range, while q_2 is nearly constant at a value of around 0.5 except near the "a" end of [ɑi] where q_2 rises to about 1.1; note that a similar rise in q_2 for an [a] is also present in Fig. 2(a). Above each of these trajectories are those for the [e] and [æ] vowels, and below them are [ɪ] and [ɛ]. Similarly, in the [F1,F2] plot [Fig. 9(d)], both [e] and [æ] are above [iɑ] and [ɑi] for at least part of their trajectories, whereas [ɪ] and [ɛ] are again below. Although these vowel trajectories appear much closer to the VVs than in the coefficient space, the

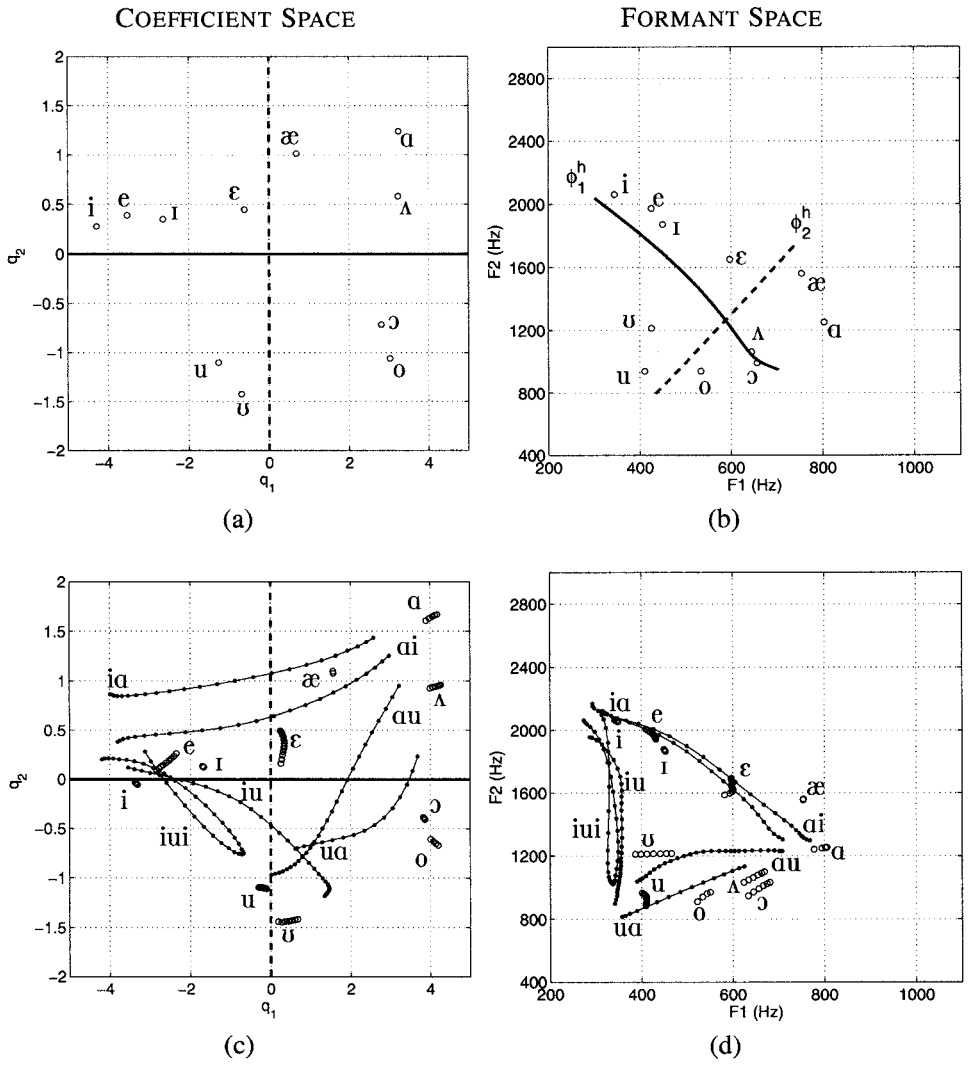

FIG. 12. Coefficient and formant spaces for JW61 based on principal component analysis and formant frequency measurements. (a)–(d). The same as in Fig. 9.

mapping shown in Fig. 2 suggests that [F1,F2] pairs in this portion of the formant space would be highly compressed relative to their corresponding $[q_1, q_2]$ pairs. It is also observed that the isolated [ɑ] vowel occupies a location in the upper right part of the coefficient space [Fig. 9(c)] that appears quite distant from the "a" end points of the [ɑi], [iɑ], [ɑu], and [uɑ] trajectories. The location of [ɑ] in the formant space [Fig. 9(d)], however, is also distant from the end points of the VV trajectories, primarily because of a higher F1. Again referring to Fig. 2, it is noted that increasing F1 in this region of the formant space would require an increase of both the q_1 and q_2 coefficients, much like that observed for this speaker. The other VV sequences and vowels also, more or less, conform to the general structure of the mapping in Fig. 2. For example, [ɔ] and [o] are located to the right of the [uɑ] and [ɑu] trajectories in the coefficient space and are apparently mapped to a location below these same trajectories in the formant space due to the downward curvature of the q_1 continuum when transformed to formant frequencies. In addition, the "u" end points of the [ɑu], [uɑ], [ui], and [iu] trajectories, as well as the [u] and [ʊ] vowels, are relatively distant in the coefficient space but are brought together by the upward curvature of [F1,F2] pairs in the lower part of the formant space (i.e., vocal tract shapes defined by distant q_1 coefficients and a large negative q_2 would produce formant pairs that are much closer to each other than if q_2 were large and positive.)

The coefficient plot for JW56 [Fig. 10(c)] indicates trajectories with characteristics similar to the previous speaker. That is, [iɑ] and [ɑi] primarily traverse the q_1 range, [ɑu] and [uɑ] are represented along diagonals of decreasing q_1 and q_2 or vice versa, and [ui] and [iu] are produced along diagonals of decreasing q_1 and increasing q_2 or vice versa. Each of these trajectories corresponds to an [F1,F2] trajectory in Fig. 10(d) that is a "leg" of a triangle in the vowel space. The $[q_1, q_2]$ coefficients for the [ɑ] vowel are somewhat separated from the end points of the nearest VV sequences, but this distance is again maintained in the formant space. The [æ] exhibits a fairly long trajectory above the [iɑ] and [ɑi] sequences which is also maintained and similarly located in the formant space. The [ɛ] trajectory, however, is located just above these same VV sequences in the coefficient space but appears just below them in the formant space. A unique feature of this speaker's coefficient and formant plots is the presence of the extra [oɑ] transition. In the coefficient space, this trajectory begins at $[q_1, q_2]=[3.1, -1.2]$, moves almost directly downward before changing course and moving up-

ward to $[q_1, q_2]=[4.5, 0.5]$. The trajectory then makes a sharp turn toward the center of the plot and terminates at $[q_1, q_2]=[2.1, 0.2]$. The corresponding [F1,F2] trajectory also exhibits similar behavior when considered relative to the presumed nonlinear mapping between the coefficients and formant pairs.

For JW12 (Fig. 11), the $[q_1, q_2]$ and [F1,F2] trajectories are similar to those of the other speakers, however, because this speaker is male the formant space is shifted downward and to the left. The compression of the [F1,F2] pairs corresponding to the upper part of the coefficient space is readily apparent for the [iɑ, ɑi, e, i, ɛ, æ] trajectories. In particular, the distance between the [iɑ] and [ɑi] trajectories in the coefficient space [Fig. 11(c)] is almost completely eliminated in the formant space [Fig. 11(d)]. It can also be noted that, unlike the previous two speakers, the coefficient trajectory for [ɑ] is located in close proximity to the nearest VV end points, and this proximity is maintained in the formant space. Unique to this speaker is the [ue] transition that begins near $[q_1, q_2]=[-0.5, -1]$ and traverses upward before terminating at about $[q_1, q_2]=[-2, 1]$ which is directly below the isolated vowel [e]. With the exception of the end portion, this transition consists almost entirely of an increase in q_2 while q_1 is nearly constant at about −1.0. The corresponding [F1,F2] trajectory moves from the "u" region of the formant space, across the middle portion, and terminates just below, and to the right of the trajectory for [e]. This is the only VV transition across all four speakers to possess these characteristics and indicates that the q_2 range, extending from negative to positive values, does indeed represent a traversal across the formant space in which both F1 and F2 tend to increase (although more for F1). A seemingly anomolous result is the location of the coefficient pair representing [ʌ]. For the previous two speakers, the [ʌ] coefficients were in a more central position (i.e., small values of both q_1 and q_2) as would be expected for this vowel, but here they are located in a region more likely to be an [o]. In fact, based on the locations of the [F1,F2] pairs for [ʌ] and [o] [Fig. 11(d)], it would appear that the IPA labels for the [ʌ] and [o] coefficients were interchanged. These were, however, subsequently verified to be correct. Thus, it must be concluded that either the speaker produced the [ʌ] in an unusual manner, or the two modes were not able to adequately represent the tract shape for this vowel.

The coefficient and formant spaces for the final speaker, JW61 (Fig. 12), demonstrate similar overall characteristics to those of the previous three speakers, but with idiosyncratic variations. For example, this speaker produced an [iui] transition in place of the prescribed [ui] spoken by the others. This trajectory begins in the coefficient space near the [i] vowel at $[q_1, q_2]=[-4.2, 0.2]$, moves downward and to the right before reversing direction at $[q_1, q_2]=[-0.7, -0.8]$, and then ends at $[q_1, q_2]=[-3.1, 0.3]$. It is noted that the turnaround point in the middle of this trajectory does not extend as far into the negative q_2 and positive q_1 regions as the [u] and [ʊ] vowels or the [iu], [uɑ], and [ɑu] VVs. This is also demonstrated by the [F1,F2] trajectory for [iui] [Fig. 12(d)] whose extent in the decreasing F1 direction is well short of the other u's. There are some aspects of this speaker's results that are difficult to reconcile in terms of a possible mapping as in Fig. 2. For instance, the coefficients for [æ] are located between the [iɑ] and [ɑi] trajectories, but positioned above them (upward and to the right) in the formant space. Furthermore, the [e] and [ɛ] trajectories are located below these same VV sequences in the coefficient space, but between them in the formant space. In contrast, the proximity of the [e] coefficient trajectory to that of the [i] is well preserved in the formant space.

In summary, the PCA based on time-dependent vowel and VV sequences produced coefficient trajectories that, with some noted exceptions, appear to be related to their corresponding formant trajectories in much the same way as the coefficient-to-formant mapping shown in Fig. 2, and those reported in Story and Titze (1998), Story (2005b), and Mokhtari *et al.* (2007). Without access to the area function for the entire vocal tract it is not possible to know exactly the characteristics of this mapping for the four speakers. But the results do suggest that coordination of changes to the vocal tract shape across speakers can be described by similar time-dependent, linear combinations of modes that are superimposed on a mean, or neutral, tract configuration.

III. TRANSFORMATION FROM XRMB MODE COEFFICIENTS TO A TIME-VARYING AREA FUNCTION

Each of the VV trajectories plotted previously in Figs. 9(c), 10(c), 11(c), and 12(c) represented mode weighting coefficients for a sequence of XRMB data frames over the time course of a spoken utterance. Shown in the lower panels of Figs. 13–16 are these same trajectories for each of the four speakers, but plotted against time as coefficient *contours* [i.e., $q_1(t)$ and $q_2(t)$], much like those shown in Fig. 3(a) for the area function-based modes. The duration of each vowel sequence is shown along the x axis, however, the time scale is different for each speaker. In addition, the time-aligned F1 and F2 contours are plotted in the upper panels of each figure. The gray vertical bars represent periods of time where there was either silence or no change in the formant frequencies (as defined in Sec. II C) and, to conserve space for plotting, have been made to be the same length regardless of their duration.

It is perhaps easier in these figures to observe the similarities of the coefficient contours across speakers than in the trajectories discussed in Sec. II. For example, the [iu] vowel sequence is defined by a gradually decreasing $q_2(t)$ and an increasing $q_1(t)$ for all four speakers, whereas [ui] is produced by just the opposite (for JW61 in Fig. 16, this refers to the "ui" part of the [iui]). Also, in all four cases, $q_1(t)$ increases over the time course of [iɑ] and similarly decreases during [ɑi], while $q_2(t)$ remains nearly constant or exhibits only a slight change. In Figs. 13, 14, and 16, the [uɑ] transition is characterized by a gradual increase of both the $q_1(t)$ and $q_2(t)$ coefficients, whereas they both decrease over the course of the [ɑu] sequences. Figure 15 would have presumably indicated the same time-dependent behavior for [uɑ] but the speaker produced [ue] instead, which is characterized by a rapid increase in $q_2(t)$ and a small, gradual decrease of $q_1(t)$.

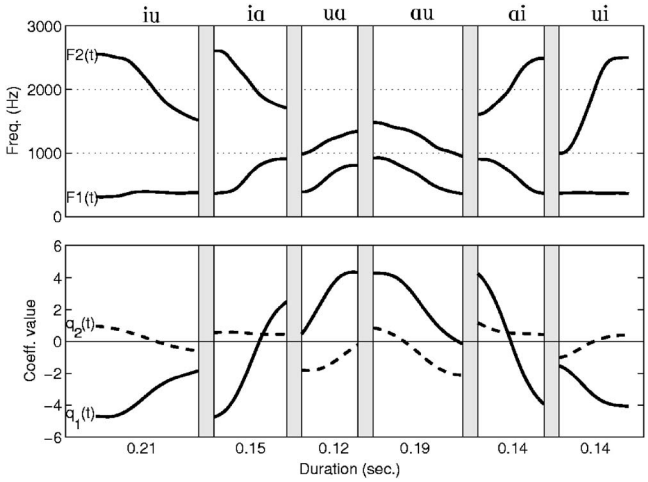

FIG. 13. F1 and F2 formant frequencies (top), and mode coefficients (bottom) shown over the time course of six vowel sequences for JW26. The areas with white back-ground indicate time periods where formant frequencies could be estimated from the audio signal, whereas gray areas denote periods of silence between the production of the vowel sequences.

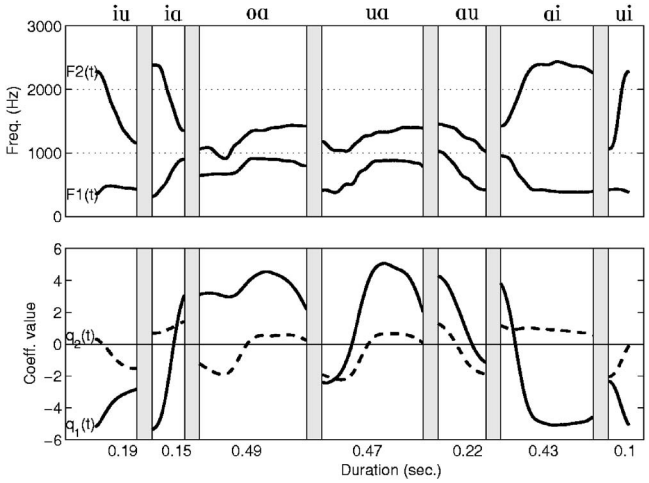

FIG. 14. F1 and F2 formant frequencies (top), and mode coefficients (bottom) shown over the time course of six vowel sequences for JW56.

Because the spatial patterns represented by the XRMB-based modes have been shown to be essentially the same as those derived from area function data of the entire vocal tract, the temporal variation of the mode coefficients determined for an utterance in the XRMB database, such as the vowel sequences shown in Figs. 13–16, may be expected to be the same as if they were, in fact, based on data of the entire vocal tract. This means that the pharyngeal portion of each speaker's vocal tract would be assumed to vary in the manner as that prescribed by the whole-tract modes. Because of the similarity of the mode shapes across speakers, it can be further hypothesized that $q_1(t)$ and $q_2(t)$ describe a series of articulatory events that could be superimposed on *any* speaker's vocal tract. Hence, they should be applicable as input "signals" for a mode-based, area-function model of the vocal tract, as described by Eq. (1) (Story 2005a, b), regardless of the speaker on which it is based. Since each speaker's coefficient ranges are somewhat different [e.g., Figs. 2(a), 9(c), 10(c), 11(c), and 12(c); Story 2005a], however, a transformation must be applied to any particular set of time-varying coefficients to convert them from one speaker's range to another.

A. Speaker-to-speaker coefficient transformation

The first step in the transformation consists of normalizing an XRMB speaker's time-dependent coefficients, $q_1(t)$ and $q_2(t)$, by their possible range of coefficient values. The range of the coefficients can be computed for each of the two modes as

$$r_{q_k} = q_k^{\max} - q_k^{\min}, \quad k = [1,2], \tag{4}$$

where $q_k^{\max}$ and $q_k^{\min}$ are the maximum and minimum coefficient values for each of the two modes obtained for a particular speaker's mode analysis (i.e., PCA of time-dependent vowels and VVs). The range can then be used to normalize the time-varying model coefficients by

$$N_k(t) = \frac{q_k(t) - q_k^{\min}}{r_{q_k}}, \quad k = [1,2] \tag{5}$$

for which the $N_k(t)$ are constrained to vary from 0 to 1.0.

The next step is to convert the $N_k(t)$ into a range of values appropriate for the speaker on which the area function model is based. To avoid confusion, the variable p will be used to denote the new (second) speaker's coefficients values. The range of the second speaker's mode coefficients are calculated as

$$r_{p_k} = p_k^{\max} - p_k^{\min}, \quad k = [1,2]. \tag{6}$$

The transformation of the normalized time-varying coefficients to those appropriate for the area function model is carried out with the following operation:

$$p_k(t) = N_k(t) r_{p_k} + p_k^{\min}, \quad k = [1,2]. \tag{7}$$

The new coefficients $p_k(t)$ can now be used to generate a continuously changing area function with a time-dependent version of Eq. (1),

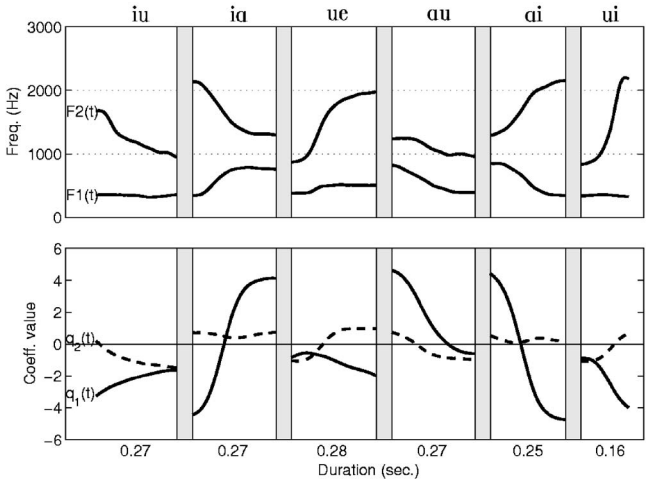

FIG. 15. F1 and F2 formant frequencies (top), and mode coefficients (bottom) shown over the time course of six vowel sequences for JW12.

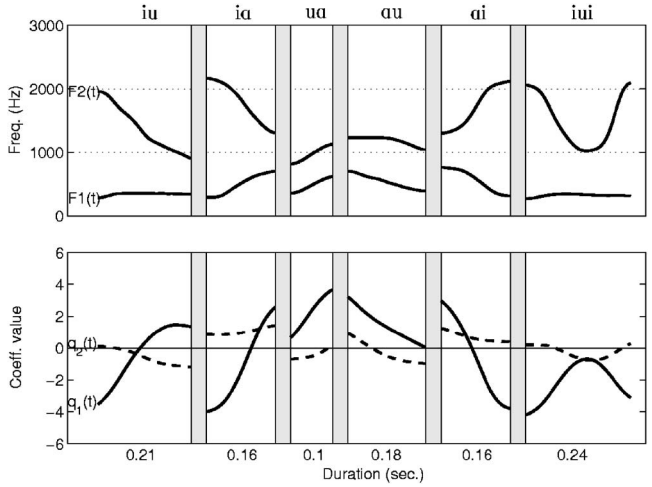

FIG. 16. F1 and F2 formant frequencies (top), and mode coefficients (bottom) shown over the time course of six vowel sequences for JW61.

$$V_p(x,t) = \frac{\pi}{4}[\Omega_p(x) + p_1(t)\phi_{1p}(x) + p_2(t)\phi_{2p}(x)]^2, \qquad (8)$$

where x is the distance from the lips,[6] $\Omega_p(x)$, $\phi_{1p}(x)$, and $\phi_{2p}(x)$ are mean diameter function, first mode, and second mode, respectively, for the area function model. The squaring operation and multiplication by $\pi/4$ are necessary to convert from equivalent diameters to areas.

B. Coefficient and formant trajectories produced by an area function model

Using Eqs. (4)–(7), the coefficient contours for the latter three vowel sequences from each of the four XRMB speakers (Figs. 13–16), and [oɑ] and [ue] from JW56 and JW12, respectively, were transformed to be appropriate for an area function model based on the modes, neutral vocal tract shape, and coefficient ranges shown previously in Figs. 1 and 2.[7] The transformed coefficient trajectories are shown in Figs. 17(a), 17(c), 18(a), and 18(c). Although they appear nearly identical to the original trajectories in Figs. 9(c), 10(c), 11(c), and 12(c), the actual coefficient values and the ranges of the coefficients now conform to the coefficient space depicted by the grid, and the ϕ_1 and ϕ_2 lines shown in the background [i.e., same grid as in Fig. 2(a)]. Thus, the trajectory shapes produced by the four speakers are preserved, but they now "fit" into a different speaker's coefficient space.

Time-varying area functions $V_p(x,t)$ were generated for each of the vowel sequences with Eq. (8). The implementation of this equation in the present study produced a 44-element area function at each point in time, where each element had a length of approximately 0.4 cm, and is representative of an adult male vocal tract. An example is shown in Fig. 19 for the [ɑi] of JW12 where the x axis is shown as the distance from the *lips to the glottis*, the y axis

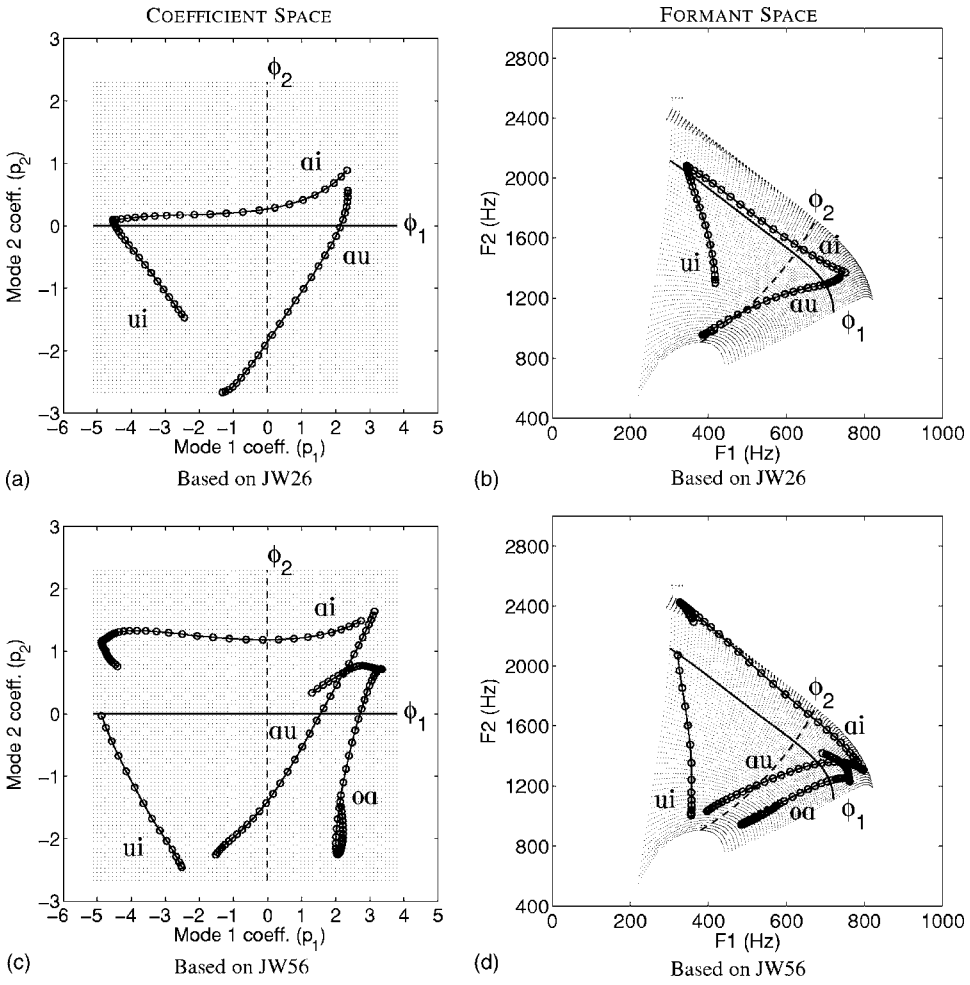

FIG. 17. Coefficient and formant trajectories of vowel sequences for female speakers JW26 and JW56 relative to an area function model. The coefficient trajectories are transformed versions of those in Figs. 9(c) and 10(c) [via Eqs. (4)–(7)]. The formant trajectories were calculated from area functions generated by Eq. (9). The background grids in (a) and (c) represent the possible coefficient space based on the area function model, whereas the grids in (b) and (d) result from the coefficient-to-formant mapping. The solid and dashed lines represent the effects of each mode in isolation.

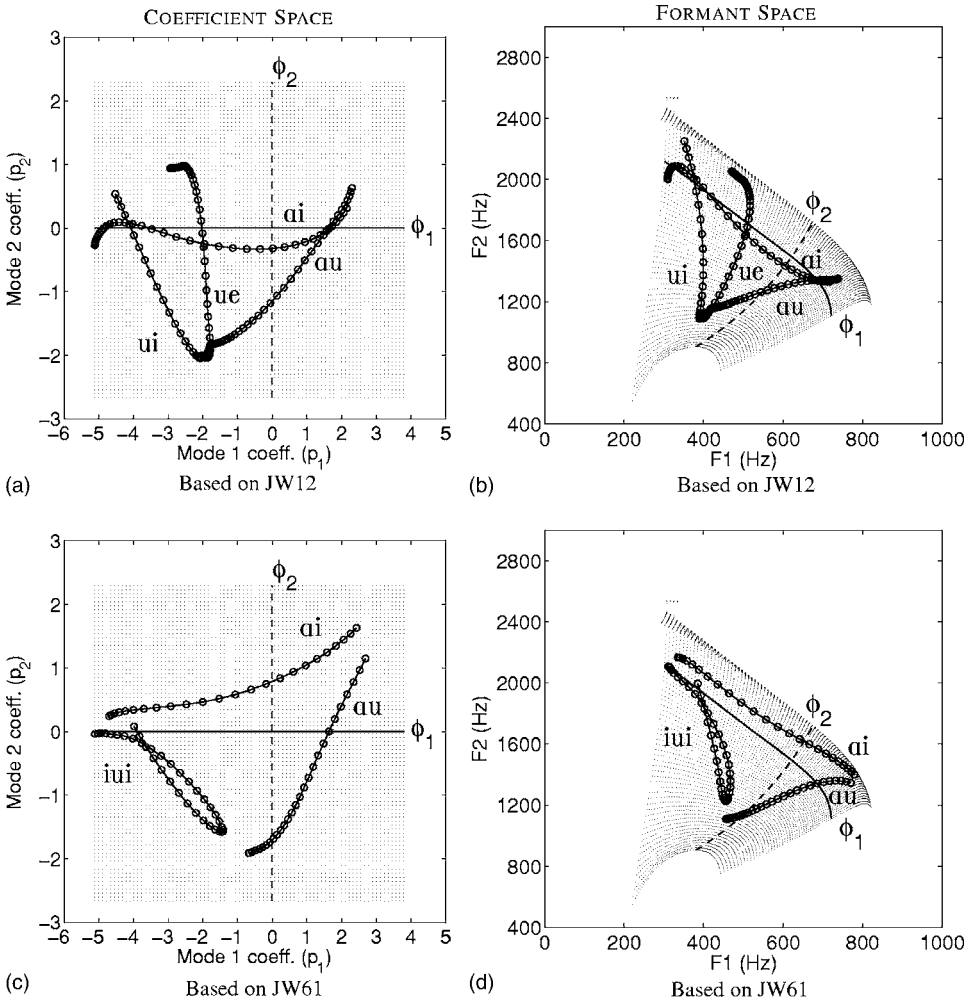

FIG. 18. Transformed coefficient and formant trajectories of vowel sequences for male speakers JW12 and JW61 relative to an area function model. The coefficient trajectories are transformed versions of those in Figs. 11(c) and 12(c) [via Eqs. (4)–(7)]. The formant trajectories were calculated from area functions generated by Eq. (9). Further description of the figure is the same as Fig. 17.

corresponds to the temporal duration for this vowel sequence in Fig. 15, and the z axis indicates the cross-sectional area.

Frequency response functions were calculated at every time sample within a vowel sequence [i.e., for $V_p(x,t_1)$, $V_p(x,t_2),\ldots$] with a frequency-domain algorithm based on cascaded "ABCD" matrices (Sondhi and Schroeter, 1987; Story *et al.* 2000). This calculation included energy losses due to yielding walls, viscosity, heat conduction, and radiation. Formant frequencies were determined by finding the peaks in the frequency response functions. The resulting [F1, F2] trajectories for each vowel sequence are plotted in Figs. 17(b), 17(d), 18(b), and 18(d). Also shown in the background of each subplot is an [F1,F2] grid and ϕ_1 and ϕ_2 lines. Together these represent the mapping of the coefficient space, and the trajectories therein, into the acoustic ([F1,F2]) domain of the area function model.

As expected, in all cases the formant trajectories for [ɑu], [ɑi], and [ui] (or [iui]) trace out a triangle representative of the three target vowels contained in the sequences. It is noted that the variation in the p_2 dimension during [ɑi] production is largely reduced in the formant space because this region is compressed relative to the coefficient space. Also for each speaker, the diagonal nature of the [ɑu] coefficient trajectory is preserved in the formant space, however, the curvature near the two ends of each trajectory is altered by the transformation to the acoustic domain. In contrast, the shapes of the [ui] and [iui] coefficient trajectories are fairly well preserved throughout their duration because there is less compression of the [F1, F2] pairs in this part of the formant space. The production of these vowel sequences suggests that the time-dependent coefficients extracted from XRMB data can serve as activation "signals" for an area function model of the entire vocal tract based on an arbitrary speaker.

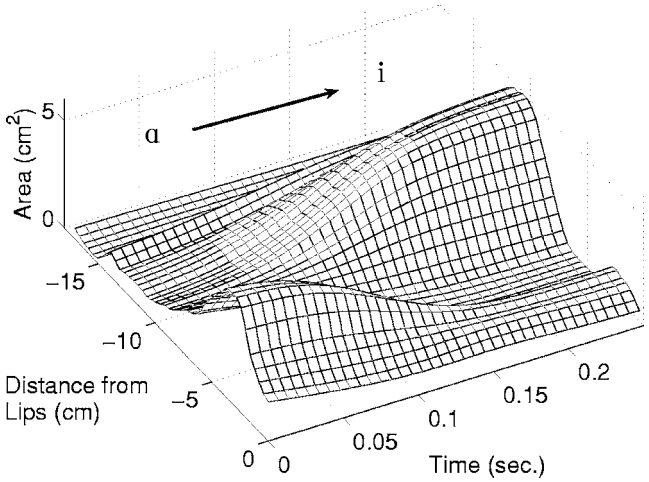

FIG. 19. Time-varying area function for JW12's [ɑi] generated with Eq. (11).

IV. SUMMARY AND DISCUSSION

A method was described in Sec. II for obtaining cross-distance functions from XRMB data and deriving vocal tract modes from them. For each of the four speakers, modes were determined twice. In the first case, only 11 cross-distance functions representing the shape of target vowels were subjected to a PCA. This was done to replicate, as closely as possible, the type of analyses previously reported for MRI-based area functions. A second PCA was performed on a much larger set of cross-distance functions that represented time-dependent vocal tract shapes produced during vowels and vowel sequences. Although only the oral part of the vocal tract was represented, the mode shapes obtained for the four speakers, in both the static and time-dependent cases, exhibit similar spatial characteristics (in the oral portion) to those previously reported for area functions of the entire vocal tract. Specifically, it was found that the mode which accounts for the most variance (ϕ_1) describes an expansion or constriction within the midportion of the oral cavity, depending on whether the weighting coefficient is positive or negative, respectively, but has a smaller effect on the region near the lips. The second most significant mode (ϕ_2) is positively valued near the lips, then becomes negative in the midportion of the oral cavity. When multiplied by a positive weighting coefficient, this mode would simultaneously create an expansion at the lips and a constriction within the oral cavity, whereas a negative weighting would produce opposite spatial effects. Based on the coefficient and formant spaces shown in Figs. 9–12, the isolated effect of each mode roughly corresponds to continua from [i] to [ɔ] for ϕ_1 and from [ʊ, o, u] to [æ] for ϕ_2. Other analyses of sets of area functions have produced similar results. In Story (2005b), the largest negative coefficient for ϕ_1 was associated with the vowel [i] for each of six speakers, whereas the largest positive coefficient was associated with [ɔ]. This presumably occurs because the shape of ϕ_1 creates an expansion or constriction within the oral cavity, but not at the lips. In contrast, production of an [ɑ] vowel may need a wider opening at the lips and, hence, would require at least some contribution of a positively weighted ϕ_2. The analysis of Mokhtari *et al.* (2007) of Japanese vowels also indicated that an [ɑ] vowel would require contributions of both components.

Although factor analysis and principal components analysis of tongue shape only (e.g., Harshman *et al.*, 1977; Nix *et al.*, 1996; Hoole, 1999) have produced shaping patterns that are somewhat similar to those of the present study, as well as to those based on area function sets, they cannot be directly compared because they only account for configuration of the tongue, rather than the shape of the airspace extending from the lips to some posterior location (i.e., soft palate for the present study and to the glottis for area functions). In Harshman *et al.* (1977) the first factor was associated with an [i] to [o] continuum, whereas the second factor indicated a change from [ɑ] to [u]. This is different from the effect of the modes shapes derived in the present study and from PCA of area functions. A careful examination of Fig. 7 in Harshman *et al.* (1977), however, suggests that the coefficient space they derived is rotated by about 45° with respect those shown in Figs. 9–12 of this study. Perhaps the use of a representation of the vocal tract shape, rather than tongue configuration, has the effect of shifting the mode coefficients in a systematic way. In any case, the mode shapes presented in the present study can be considered vocal tract shaping patterns that have a systematic relation to the [F1, F2] space.

A natural consequence of performing the PCA on a data set containing time-dependent cross-distance functions is that the mode weighting coefficients are also time dependent, and effectively parametrize the variation of the tract shape over consecutive time frames throughout a series of spoken vowels and vowel sequences. Plots of the resulting coefficient trajectories and contours (Figs. 9–16) revealed that they continuously vary over the time course of an utterance, suggesting that the vocal tract shape can be represented by time-dependent linear combinations of two modes. Comparison of the coefficient and formant trajectories for each speaker's time-dependent vowels and vowel sequences indicated a possible relation similar to that demonstrated in Fig. 2. That is, the trajectories in the coefficient space appear to be nonlinearly warped as they are transformed into the formant space, while a one-to-one relation between formant pairs and coefficient pairs is more or less preserved. There were some noted exceptions (e.g., [e] for JW56) that violate the notion of a one-to-one mapping but these are not unexpected considering the sparse spatial data on which the cross-distance functions are based. It also possible that a speaker could modify some aspect of the pharyngeal cavity to affect formant frequencies that does not conform to the hypothesized shape of the modes throughout the entire vocal tract. With only oral cavity data, the methods used in this study are insensitive to the structure of the pharynx and, hence, would not indicate any such change. Nonetheless, taken as a whole, the coefficient and formant trajectories across the four speakers do suggest a relation between them of the type shown in Fig. 2 for an area-function based mapping. Although there were idiosyncratic differences, it can be further noted that the time-dependent shape of the coefficient contours for each mode were similar across speakers during production of the vowel sequences. This suggests that, like the mode shapes themselves, the time-dependent mode coefficients are, to a degree, common across speakers. The same analysis, however, would need to be carried out for additional speakers in order to more formally assess their interspeaker commonality.

In Sec. III a normalization procedure was described for transforming the coefficient trajectories of one speaker into the coefficient space of another. This transformation was used to convert the time-dependent coefficients of three vowel sequences spoken by each of the four XRMB speakers (as well as two additional sequences for JW56 and JW12), into the coefficient space appropriate for an area function model. Time-varying formant frequencies were calculated for the continuously changing area function generated with these coefficients, along the time course of the vowel sequences. The resulting formant trajectories were shown to be reasonable representations of the vowel sequences, however, the vowel space in which they now existed was representa-

tive of the male speaker on which the area function model was based. Thus, even though XRMB data strictly capture information only about the oral cavity, time-dependent mode coefficients extracted by the methods described in this study can be used to drive a model of the entire vocal tract shape. Furthermore, the common nature of the modes essentially has a speaker-normalization effect such that coefficient contours from one speaker can be used to move the vocal tract shape of another speaker. This is effectively a speaker-to-speaker transformation; that is, the temporal patterns of articulatory movement of one speaker can be superimposed on the vocal tract structure of another.

The results of this study are intended to provide a new tool for studying the articulatory-acoustic relation in speech and to augment the previously developed formant-to-coefficient or cepstral-to-coefficient techniques discussed in Sec. I (i.e., Story and Titze, 1998; Mokhtari *et al.* 2007). The advantage is that the time-dependent coefficients are obtained directly from articulatory data rather than via a transformation from an acoustic domain to an articulatory domain. Thus, the temporal patterns of the mode coefficients are known to be representative of actual articulation.

There are, however, some limitations of the study. First it is noted that the time dependence of the modes has been demonstrated only for portions of utterances where there is both continuous change in the vocal tract shape and vocal fold vibration (i.e., voicing). This was done so that the PCA would be balanced with respect to a range of vocal tract shapes corresponding to [F1, F2] pairs distributed widely over the formant space. But methods could also be developed to extract the time dependence of the mode coefficients during periods of silence, providing a view of a speaker's actions in preparation for an utterance, as well as those that occur during its execution. This may potentially be carried out by performing a PCA on thousands of cross-distance functions from data frames over the time course of a long utterance without regard to whether voiced speech sounds are produced (i.e., silent pauses and unvoiced portions would be included). The result would provide time-dependent mode coefficients over all portions of an utterance and not just those identified with voiced segments. Whether the collection of cross-distance functions used in such a technique would be sufficiently balanced so as to not bias the PCA would need to be investigated. Alternatively, a database lookup approach could also be devised in which the results of a PCA, such as those demonstrated in the present study, are used to create a database of thousands of cross-distance functions based on incremental combinations of the mode coefficients extending throughout their respective ranges. Then a cross-distance function extracted from any time frame could be matched to the best fit in the database and the associated coefficients would be assigned to this particular frame.

Another limitation is that all of the methods and results were based on vowels and vowel-like utterances. Including consonants will require deriving additional modes that represent a wide range of vocal tract occlusions (or near occlusions), or developing a technique similar to that proposed by Story (2005a) where consonants are considered to be constrictions superimposed on an underlying vowel substrate. Also limiting is that there does not yet exist a set of MRI-based area functions and XRMB data from the same speaker. Such information could be used to further verify the results of this study.

V. CONCLUSION

In conclusion, the results show that statistically derived modes are commonly shaped across speakers, as are their weighting coefficients for vowels and time-dependent vowel sequences. Because these results were based on articulatory data, this means that linear combinations of the modes can provide a reasonably accurate description of the vocal tract shape over time. As with any statistical method that reduces the dimensionality of a data set, the interpretation of the resulting dimensions must be based on their observed function. In the present study, it is clear that, in isolation, the first vocal tract mode ϕ_1 is related to moving F1 and F2 in opposite directions, whereas the second mode ϕ_2 moves F1 and F2 in the same direction. When combined, the two modes can apparently position the two formants over a wide range of the possible [F1, F2] vowel space. Whether the concept of modes is directly related to the planning and control of speech production cannot be answered by these results. But, they do describe an efficient system for deforming the vocal tract shape that directly affects the first two formant frequencies in a systematic manner, and allows for time-varying mode coefficients to be extracted from the data of one speaker and applied to an area function model of another.

ACKNOWLEDGMENTS

This research was supported by NIH Grant No. R01-DC04789. A preliminary version of this work was presented at the 2006 Conference on Motor Speech in Austin, TX. The author would like to thank two anonymous reviewers for their thorough critiques of earlier versions of this paper. Anubhav Swami is acknowledged for assistance on an early version of the iterative bisection algorithm.

[1]By analogy to the natural orthogonal modes of a dynamical system, Story and Titze (1998) referred to the principal components as "orthogonal modes."

[2]According to Westbury (1994), the outline of the hard palate for a given speaker was determined from measurement of a dental cast of the oral cavity, or by recording the $x-y$ coordinates of a tongue pellet as the speaker drew it slowly along the palatal midline. The pharyngeal wall outline was determined from the initialization scan taken prior to the acquiring $x-y$ pellet data. It consists of only two points; the line connecting them is intended to represent the "dorsal-most surface bounding the pharynx."

[3]Because of the successive bisections needed for this method, the choices for the "desired" number of iterations are limited to 2^n+1 where $n=[1,2,3,4,5,6,\ldots]$. This translates to [3, 5, 9, 17, 33, 65,…] possible iterations. For this study the choice was always 33 iterations ($n=5$).

[4]Vocal tract area functions are often plotted as a function of the distance from the glottis. For the XRMB data, however, the lips are the only terminating end of the vocal tract that is available. Hence, the cross distances for a given tract shape are plotted as a function of the distance from the lips. The negative x axis is used so that the orientation of a cross-distance function is the same as that of an area function plotted relative to the distance from the glottis.

[5]In the XRMB protocol, the speakers produced "citation vowels" for which they were instructed to speak slowly and clearly. Had they been produced as long, sustained vowels they may have been less likely to exhibit trajectory-like behavior.

[6]x could also be the distance from the glottis, depending on how the area function is structured. Distance from the lips is maintained here to coincide with the midsagittal cross-distance functions. In Story (2005a) and other studies, x is assumed to be the distance from the glottis.

[7]Modes, neutral tract shape, and coefficient ranges for any of the six speakers reported in Story (2005b) or from other studies (e.g., Mokhtari *et al.*, 2007) could also be used to define the structure of the area function model prescribed by Eq. (1).

Anderson, N. (**1978**). "On the calculation of filter coefficients for maximum entropy spectral analysis," in Childers, *Modern Spectrum Analysis* (IEEE Press, New York), pp. 252–255.

Baer, T., Gore, J. C., Gracco, L. C., and Nye, P. W. (**1991**). "Analysis of vocal tract shape and dimensions using magnetic resonance imaging: Vowels," J. Acoust. Soc. Am. **90**, 799–828.

Boersma, P., and Weenink, D. (**2006**). PRAAT. Version 4.4.07, www.praat.org. Viewed 4/22/2007.

Bouabana, S., and Maeda, S. (**1998**). "Multi-pulse LPC modeling of articulatory movements," Speech Commun. **24**, 227–248.

Fowler, C. A., and Saltzman, E. L. (**1993**). "Coordination and coarticulation in speech production," Lang Speech **36**, 171–195.

Fritsch, F. N., and Carlson, R. E. (**1980**). "Monotone piecewise cubic interpolation," SIAM (Soc. Ind. Appl. Math.) J. Numer. Anal. **17**, 238–246.

Harshman, R., Ladefoged, P., and Goldstein, L. (**1977**). "Factor analysis of tongue shapes," J. Acoust. Soc. Am. **62**(3), 693–707.

Hoffman, E. A., Gnanaprakasam, D., Gupta, K. B., Hoford, J. D., Kugelmass, S. D., and Kulawiec, R. S. (**1992**). "VIDA: An environment for multidimensional image display and analysis," SPIE Proceedings of Biomedical Image Processing and 3-D Microscopy, San Jose, CA, **10–13**, February 1992, p. 1660.

Hoole, P. (**1999**). "On the lingual organization of the German vowel system," J. Acoust. Soc. Am. **106**, 1020–1032.

Iskarous, K. (**2005**). "Patterns of tongue movement," J. Phonetics **33**, 363–381.

Johnson, K., Ladefoged, P., and Lindau, M. (**1993**). "Individual differences in vowel production," J. Acoust. Soc. Am. **94**, 701–714.

Kelso, J. A. S., Saltzman, E. L., and Tuller, B. (**1986**). "The dynamical perspective on speech production: Data and theory," J. Phonetics **14**, 29–59.

Maeda, S. (**1991**). "On articulatory and acoustic variabilities," J. Phonetics **19**, 321–331.

Maeda, S., and Honda, K. (**1994**). "From EMG to formant patterns of vowels: The implication of vowel spaces," Phonetica **51**, 17–29.

The Mathworks (**2006**). MATLAB, Version 7.2.0.232.

Mokhtari, P., Kitamura, T., Takemoto, H., and Honda, K. (**2007**). "Principal components of vocal tract area functions and inversion of vowels by linear regression of cepstrum coefficients," J. Phonetics **35**, 20–39.

Nix, D. A., Papcun, G., Hogden, J., and Zlokarnik, I. (**1996**). "Two cross-linguistic factors underlying tongue shapes for vowels," J. Acoust. Soc. Am. **99**, 3707–3717.

Perrier, P., Perkell, J., Payan, Y., Zandipour, M., Guenther, F., and Khalighi, A. (**2000**). "Degrees of freedom of tongue movements in speech may be constrained by biomechanics," in Proceedings of the Sixth International Conference on Spoken Language Professes, ICSLP-2000, Vol. **2**, pp. 162–165.

Schroeder, M. R. (**1967**). "Determination of the geometry of the human vocal tract by acoustic measurements," J. Acoust. Soc. Am. **41**, 1002–1010.

Shirai, K., and Honda, M. (**1977**). "Estimation of articulatory motion," in *Dynamic Aspects of Speech Production*, edited by M. Sawashima and F. Cooper (University of Tokyo Press, Tokyo), pp. 279–302.

Sondhi, M. M., and Schroeter, J. (**1987**). "A hybrid time-frequency domain articulatory speech synthesizer," IEEE Trans. Acoust., Speech, Signal Process. **35**, 955–967.

Story, B. H. (**2005a**). "A parametric model of the vocal tract area function for vowel and consonant simulation," J. Acoust. Soc. Am. **117**, 3231–3254.

Story, B. H. (**2005b**). "Synergistic modes of vocal tract articulation for American English vowels," J. Acoust. Soc. Am. **118**, 3834–3859.

Story, B. H., Laukkanen, A. M., and Titze, I. R. (**2000**). "Acoustic impedance of an artificially lengthened and constricted vocal tract," J. Voice **14**, 455–469.

Story, B. H., and Titze, I. R. (**1998**). "Parameterization of vocal tract area functions by empirical orthogonal modes," J. Phonetics **26**, 223–260.

Story, B. H., and Titze, I. R. (**2002**). "A preliminary study of voice quality transformation based on modifications to the neutral vocal tract area function," J. Phonetics **30**, 485–509.

Story, B. H., Titze, I. R., and Hoffman, E. A. (**1996**). "Vocal tract area functions from magnetic resonance imaging," J. Acoust. Soc. Am. **100**, 537–554.

Sundberg, J., Johansson, C., Wilbrand, H., and Ytterbergh, C. (**1987**). "From sagittal distance to area," Phonetica **44**, 76–90.

Westbury, J. R. (**1994**). *X-ray Microbeam Speech Production Database User's Handbook* (version 1.0)(UW-Madison, Madison, WI).

Zheng, Y., Hasegawa-Johnson, M., and Pizza, S. (**2003**). "Analysis of the three-dimensional tongue shape using a three-factor analysis model," J. Acoust. Soc. Am. **113**, 478–486.

Interactions of speaking condition and auditory feedback on vowel production in postlingually deaf adults with cochlear implants[a)]

Lucie Ménard[b)]
Département de Linguistique, Université du Québec à Montréal, Montréal (Québec), H3C 3P8 Canada and Speech Communication Group, Research Laboratory of Electronics, Massachusetts Institute of Technology, Cambridge, Massachusetts 02139

Marek Polak
Department of Otolaryngology, University of Miami Medical School, Miami, Florida 33149

Margaret Denny
Speech Communication Group, Research Laboratory of Electronics, Massachusetts Institute of Technology, Cambridge, Massachusetts 02139

Ellen Burton
Applied Public Health, Johns Hopkins Bloomberg School of Public Health, Baltimore, Maryland 21205 and Maryland Association of County Health Officers, Baltimore, Maryland 21205

Harlan Lane
Department of Psychology, Northeastern University, Boston, Massachusetts and Speech Communication Group, Research Laboratory of Electronics, Massachusetts Institute of Technology, Cambridge, Massachusetts 02139

Melanie L. Matthies and Nicole Marrone
Department of Speech, Language and Hearing Sciences, Boston University, Boston, Massachusetts, and Speech Communication Group, Research Laboratory of Electronics, Massachusetts Institute of Technology, Cambridge, Massachusetts 02139

Joseph S. Perkell
Speech Communication Group, Research Laboratory of Electronics, and Department of Brain and Cognitive Sciences, Massachusetts Institute of Technology, Cambridge, Massachusetts 02139 and Department of Cognitive and Neural Systems, Boston University, Boston, Massachusetts 02115

Mark Tiede
Speech Communication Group Research Laboratory of Electronics, Massachusetts Institute of Technology, Cambridge, Massachusetts 02139 and Haskins Laboratories, New Haven, Connecticut 06511

Jennell Vick
Department of Speech and Hearing Sciences, University of Washington, Seattle, Washington 98015

(Received 13 April 2006; revised 30 January 2007; accepted 31 January 2007)

This study investigates the effects of speaking condition and auditory feedback on vowel production by postlingually deafened adults. Thirteen cochlear implant users produced repetitions of nine American English vowels prior to implantation, and at one month and one year after implantation. There were three speaking conditions (clear, normal, and fast), and two feedback conditions after implantation (implant processor turned on and off). Ten normal-hearing controls were also recorded once. Vowel contrasts in the formant space (expressed in mels) were larger in the clear than in the fast condition, both for controls and for implant users at all three time samples. Implant users also produced differences in duration between clear and fast conditions that were in the range of those obtained from the controls. In agreement with prior work, the implant users had contrast values lower than did the controls. The implant users' contrasts were larger with hearing on than off and improved from one month to one year postimplant. Because the controls and implant users responded similarly to a change in speaking condition, it is inferred that auditory feedback, although demonstrably important for maintaining normative values of vowel contrasts, is not needed to maintain the distinctiveness of those contrasts in different speaking conditions. © *2007 Acoustical Society of America.*
[DOI: 10.1121/1.2710963]

PACS number(s): 43.70.Dn, 43.70.Bk, 43.66.Ts, 43.70.Fq [BHS] Pages: 3790–3801

[a)]This study was conducted in collaboration with the Dept. of Otolaryngology, University of Miami Medical School, Miami, Florida.
[b)]Author to whom correspondence should be addressed. Electronic mail: menard@speech.mit.edu

 © 2007 Acoustical Society of America

I. INTRODUCTION

The production of speech can be thought of in terms of a trade-off between two competing constraints, namely the need to ensure intelligibility and the tendency to minimize effort (Lindblom, 1990; Guenther *et al.*, 1998; Perkell *et al.*, 2000). When asked to speak clearly, speakers put more weight on intelligibility requirements (cf. Picheny *et al.*, 1985, 1986; Liu *et al.*, 2004; Chen, 1980; Krause and Braida, 2004; Payton *et al.*, 1994; Ferguson and Kewley-Port, 2002). On the other hand, instructions to speak rapidly tend to induce a speaker to rely on a strategy dominated by minimizing effort (Perkell *et al.*, 2000). Previous studies have shown that varying speaking condition greatly influences the acoustic properties of vowels and consonants (e.g., Krause and Braida, 2004). For normal-hearing speakers, clear speech—in comparison to conversational speech—is characterized, among other respects, by longer sound segments, tighter acoustic clustering within vowel categories, expanded vowel spaces and greater voice onset time (VOT) contrasts (Picheny *et al.*, 1986; Moon and Lindblom, 1994; Moon, 1991). However, the extent to which these contrasts are affected by speaking condition varies considerably across speakers (cf. Perkell *et al.*, 2000).

Previous research on the speech of cochlear implant users conducted by our group and others has provided a large body of evidence that those phonetic parameters affected by variations in speaking condition (acoustic distance between vowels, acoustic clustering within vowel categories, and vowel duration) are also affected by degradation of auditory feedback (Vick *et al.*, 2001; Perkell *et al.*, 2001; Svirsky and Tobey, 1991; Lane *et al.*, 2005; Lane *et al.*, 1995; Perkell *et al.*, 2007). Speakers who become profoundly deaf postlingually usually continue to produce intelligible speech for years or even decades following hearing loss, hypothetically due to the robustness of feedforward commands (commands that are executed without regard for sensory feedback) and somatosensory phonemic goals they acquired while they could hear (cf. Guenther *et al.*, 2006). Nevertheless, such speakers do experience some gradual degradation of their speech, presumably as a result of some deterioration of acquired auditory phonemic goals and feedforward commands. Compared to normal hearing speakers, postlingually deafened speakers produce decreased spectral contrast distances among vowels (Vick *et al.*, 2001; Perkell *et al.*, 2001; Svirsky and Tobey, 1991), increased vowel dispersion in the formant space (Lane *et al.*, 2005), and increased vowel duration (Lane *et al.*, 1995). In this paper, *contrast distance* for two vowels is defined as the Euclidean distance between them in the formant space. When more than one vowel pair is studied, *average vowel spacing* is the mean of all possible inter-vowel Euclidean distances in the formant space. For multiple repetitions of a given vowel, *vowel dispersion* is defined as the mean of the Euclidean distances, in the formant space, between each repetition and the target mean of all repetitions.

When deaf speakers have some hearing restored with cochlear implants, their vowel and consonant recognition scores increase significantly as early as 1 month postimplant.

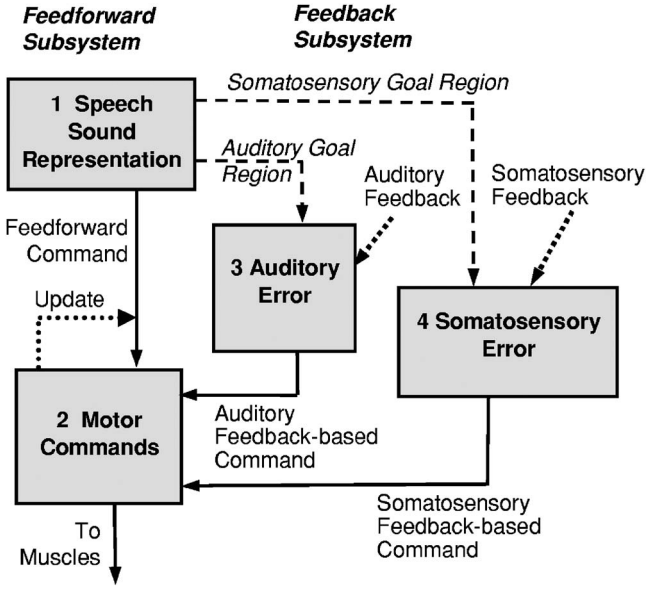

FIG. 1. Schematic diagram of the functionality of the DIVA model.

However, those speakers may show little improvement—or even some diminution—in produced contrast distances compared to the pre-implant stage (Lane *et al.*, 2006). Presumably these deaf speakers have not had enough experience with the new auditory feedback to update their feedforward commands adequately. After an extended period of implant use, however (1 year, for instance), speakers apparently have retuned their auditory feedback and have begun to use the new auditory feedback to retune their feedforward commands. By one year postimplant, contrast distances have increased, while vowel token dispersions in the formant space have decreased, and vowel durations have decreased in the direction of normative values (Schenk *et al.*, 2003; Langereis *et al.*, 1998; Vick *et al.*, 2001; Economou *et al.*, 1992; Smyth *et al.*, 1991; Lane *et al.*, 2005, 2006). Even when auditory feedback is interrupted by switching the implant processor off, vowel contrasts remains greater and vowel dispersions lower than at the pre-implant stage (Lane *et al.*, 2005, 2006). Taken together, these studies show that contrast distances, token dispersions around the vowel type mean, and vowel durations are altered by variation in speaking condition and by deprivation of auditory feedback. This study explores further the interaction between those independent and dependent variables.

A. Theoretical background

The present study was guided by the Directions into Velocities of Articulators (DIVA) model (Guenther, 1995; Guenther *et al.*, 1998, 2006), a neuro-computational model of speech motor planning (see Fig. 1). In this model, phonemes are encoded in terms of goals in a multidimensional sensory space (auditory and somatosensory). Speech sounds are produced through the use of feedback and feedforward control systems. In the feedback system, sensory goals are compared to the current sensory state, and error signals arise if there is a mismatch (dotted arrows in Fig. 1). In this model, removal of auditory feedback (by switching the im-

TABLE I. Predicted differences in the dependent variables as a function of the independent variables.

Independent variables / Dependent variables	Speaking condition (controls)	Hearing status	Time post-implant	Hearing state
	Clear compared to conversational speech	Postlingually deaf compared to normal hearing	Implant users at one year post-implant compared to pre-implant	Implant users with processor on compared to processor off
Vowel contrast distance	Higher	Lower	Higher	Higher
Vowel dispersion	Lower	Higher	Lower	Lower
Vowel duration	Higher	Higher	Lower	Lower

plant processor off, for instance) leads the model to rely on feedforward commands, in combination with somatosensory feedback control. In the short term, this degrades speech only slightly since the feedforward subsystem is still well tuned. However, if hearing loss continues for a long period (years, for instance), the feedforward commands degrade slowly. This degradation would be accelerated if changes in vocal tract morphology invalidate the speaker's existing feedforward commands.

Deterioration of speech motor control can be observed as reduced acoustic contrast distances between speech sounds, and/or increased token dispersions around the mean. When feedback is restored, the speaker's task is first to retune the auditory feedback control subsystem, by re-defining auditory targets and relearning corrective mechanisms. As reported in previous studies, new implant users characteristically have low scores on word recognition tests (see Tyler *et al.*, 1997). As their acuity for discriminating those sounds improves with prosthesis use, they can relearn auditory goals for their speech as well as new mappings between auditory errors and the changes in speech movements that will correct them. As auditory feedback becomes more accurate, the speaker is able to use corrective motor commands based on that auditory feedback to recalibrate the feedforward commands. The DIVA model's account of feedback and feedforward interactions in speech production is used here as a framework for making predictions and interpreting results.

B. Objective

To our knowledge, no study has focused on the combined effects of speaking condition and auditory feedback on contrast distance, vowel dispersion, and vowel duration. Our objective is thus to determine whether the strategies used by speakers to differentiate between various speaking conditions are regulated by auditory feedback. Implant users provide a unique opportunity to assess both the effects of long-term absence or degradation of auditory feedback and the consequences of restoring some form of hearing.

There are three dependent variables in the current study:(1) average vowel spacing (AVS), (2) dispersion of vowel tokens around their vowel type mean (in the M1 *vs.* M2 space), and (3) vowel duration. The primary independent variable is speaking condition (clear, normal, or fast). We ask whether there is an influence of auditory feedback on changes in the dependent variables as a function of speaking condition. To address this question, we introduce three additional independent variables: hearing *status* (normal-hearing subjects and postlingually deaf subjects); for implant users, time relative to implantation (pre-implant, one-month postimplant, or one-year postimplant); and for implant users, hearing *state* (presence or absence of auditory feedback, manipulated by switching the implant processor on or off). Table I summarizes the predicted changes in the three dependent variables for each of the four independent variables.

If the phonetic differences associated with changes in speaking condition are influenced by auditory feedback, there will be a significant interaction between speaking condition and one or more of the secondary independent variables related to auditory feedback (hearing status, time relative to implantation, hearing state). This interaction may be observed in any or all of the three dependent variables (AVS, dispersion of vowel tokens, and vowel duration). For example, if AVS is greater for clear speech than for fast speech in normal-hearing subjects but not in implant users, we infer that the poorer audition of implant users prevents them from implementing speaking condition changes in the same way as normal-hearing speakers.

II. METHODS

A. Participants

Thirteen postlingually deafened speakers (five female, eight male) who received cochlear implants (hereafter, cochlear implant users - CI) and ten normal-hearing controls (hereafter, controls - NH) (five female, five male) participated in the study. Table II presents pertinent characteristics of the implant users. The implant was either the Clarion (Advanced Bionics - Buechner *et al.*, 2005), the Combi 40+ (Med-El - Muller *et al.*, 2002) or the Nucleus 24 device, (Cochlear Corp.—Vandali *et al.*, 2000). The implant users were implanted at the Department of Otolaryngology, University of Miami Medical School. As shown in Table II, the group was heterogeneous in several respects. Age at onset of change in hearing varied from 1 to 80 years; age at onset of profound hearing loss ranged from 16 to 80 years. Age at

TABLE II. Characteristics of participants with cochlear implants.

Speaker gender-number	Etiology	PTA unaided thresholds (L-R)	Hearing aid used pre- CI: L, R, both	Implant	Speech strategy	Age at onset of change in hearing	Age at onset of profound loss	Age at cochlear implantation	Years between profound loss and implantation
F_1	Genetic	Aided 55	Right	N24 Contour	ACE	35	59	59	0
M_2	Unknown	109-110	Left	CII Hifocus I	CIS	1	16	33	17
M_3	Unknown	112-110	Right	N24 Contour	ACE	29	56	57	1
F_4	Unknown	100-98	Right	N24 Contour	ACE	7	38	39	1
M_5	Idiopathic	100-102	Left	CII	ACE	1	16	22	6
F_6	Unknown	115-113	Right	N24 Contour	ACE	26	56	57	1
F_7	Genetic	113-106	Left	N24 Contour	ACE	1	24	41	17
M_8	Unknown	110-110	None	N24 Contour	ACE	80	80	81	1
M_9	Noise exposure	Aided bin. 40	Left	N24 Contour	ACE	25	74	75	1
F_10	Unknown	107-110	Right	Combi 40+	CIS	1	26	65	39
M_11	Unknown	85-110	Right	N24 Contour	ACE	50	76	77	1
M_12	Unknown	115-120	Right	Combi 40+	CIS	1	21	46	25
M_13	Surgery	110-110	Right	N24 Contour	ACE	37	37	38	1

cochlear implantation also varied from 22 to 81 years. Normal-hearing controls did not report any speech or hearing anomalies.

B. Procedure

1. Production

The procedure was similar to an earlier study, which was carried out with English and Spanish speakers (Perkell *et al.*, 2001). For the production part of this study, repetitions of the nine American English vowels /*i* ɪ e ɛ a ɑ ʌ o u/ were elicited in random order in a /pVp/ context: "peep, pip, paip, pep, pap, pop, pup, pope, poop." This bilabial consonant context yields minimal lingual coarticulation with the vowel, thus reducing spectral and durational effects of context. Each word was embedded in the following carrier sentence: "Repeat a /pVp/ aboard a bus."[1] (Perkell *et al.*, 2001).

Speakers were asked to produce ten repetitions of the carrier sentence in three speaking conditions: clear, normal, and fast. Normal speech was elicited by asking the subjects to read the utterances aloud at a conversational rate. Fast speech was elicited by asking the subjects to speak as rapidly as possible without eliminating any sounds. Clear speech was elicited by asking the subjects to read the words carefully without increasing loudness (since speaking loudly can introduce spectral changes—Pickett, 1956).

The implant users were first recorded prior to implantation (wearing their hearing aid, if any), one month following implantation, and 1 year postimplant. At the pre-implant stage, subjects read ten repetitions of each utterance, in each of the speaking conditions: normal, fast, clear. At each of the two postimplant time samples (1 month and 1 year), the implant users were recorded in a two-session protocol. Each session contained four blocks of 15 repetitions of each utterance (five in each of the three speaking conditions) in random order for a total of 120 determinations per vowel. Within each block, the order of the three speaking conditions was always the following: normal, fast, clear. During the first session postimplant, the subject read the first and second blocks with the speech processor of the cochlear implant on, the third and fourth blocks with the processor off (hence listening conditions on, on, off, off). The subject kept the processor off for at least 24 h before the second postimplant recording session. During that session, the same protocol was followed, except that the sequence of listening conditions was processor off, off, on, on. To follow up on a previous study conducted in our laboratory (Perkell *et al.*, 2001), this protocol was used in the current study to determine if the magnitude of any observed changes is larger after 24 h of hearing deprivation (by keeping the implant speech processor off) than the magnitude of the changes observed when turning the processor off within a single recording session (Svirsky *et al.*, 1992). Table III shows the arrangement of the utterance materials and processor state in the two time samples postimplantation.

Elicitation utterances were presented to the subjects on a computer monitor. Implant users employed the normal settings of their speech processors for the feedback-on conditions. Participants were seated comfortably in a sound-attenuating room. A head-mounted omnidirectional electret microphone (Audio-Technica, model AT803B) was placed at

TABLE III. Arrangement of recording materials and processor state at 1 month and 1 year following implantation for the implant users.

Time sample	Session	Block 1	Block 2	Block 3	Block 4
One-month	1	On	On	Off	Off
postimplant	2	Off	Off	On	On
One-year	1	On	On	Off	Off
postimpiant	2	Off	Off	On	On

a fixed distance of 20 cm from the speaker's lips. The audio signal was digitized in real time on a computer with a 16 kHz sampling rate.

2. Perception

In order to assess the participants' perceptual abilities, each subject also took a vowel recognition test. Implant users were tested at each of the three time samples (prior to implantation, 1 month and 1 year after implantation), and hearing controls were tested once. The stimuli were /pVp/ syllables, where V was one of the nine American English vowels /*i* ɪ e ɛ a ɑ ʌ o u/. Syllables were recorded by a normal-hearing male speaker and a normal-hearing female speaker at 16 kHz sampling frequency and the signals were amplitude normalized. Female subjects listened to the test with the female speaker and male subjects listened to the test with the male speaker. Stimuli were presented through computer speakers at a comfortable listening level. The task consisted of making a choice among the set of nine American vowels which were also elicited in the production experiment. All nine possible answers appeared as a grid on a touch screen. The participants were instructed to touch the word on the screen that most closely matched what they heard. The sound level was set at a comfortable level for the participants and they were free to adjust the gains on their processors. Stimuli were presented in three blocks and randomized with replacement within each block. Each word was presented at least ten times per block.[2]

C. Data extraction and analysis

The start and end points of each speaker's vowel utterances were labeled automatically based on smoothed rms thresholding exceeding 20% of the peak value for the utterance. For "paip" and "pope," the end point was labeled at the end of the steady state portion of the vowel, before the F1 lowering associated with the offglide. Formant values (F1, F2, and F3) and fundamental frequency values (F0) were extracted algorithmically from an Linear Predictive Coding (LPC) spectrum approximately at mid-vowel using a 40 ms analysis window for F0 and a 25 ms window for the formants. An interactive program developed in MATLAB was used for this analysis.

Formant values were then transformed into mel units (M), a perceptually motivated scale, yielding an M1 by M2 formant plane. Euclidean distances were then calculated between the mean formant frequencies (for each of the 10 repetitions) for all possible pairs of vowels, within each subject. These mean distances were then averaged across subjects to produce a measure of average vowel spacing (AVS—Lane *et al.*, 2001). In order to calculate dispersion values for each vowel type, the Euclidean distance of each token from the mean position of all tokens of that phoneme was determined in the M1 *vs*. M2 space. Those distances were then averaged across repetitions and subjects to obtain the dispersion measure for that vowel. These calculations were completed for each subject, time sample, hearing state, and speaking condition.

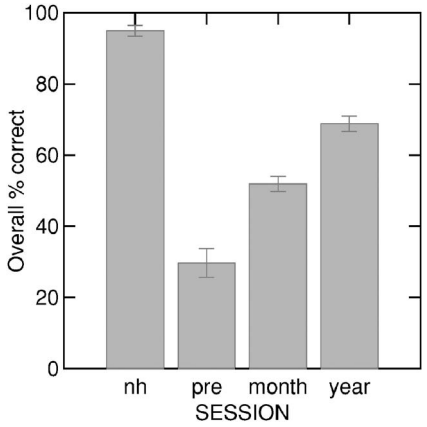

FIG. 2. Percent correct vowel identification, by 13 cochlear implant users in three time samples: prior to activation of their implant speech processors; 1 month postactivation; and 1 year postactivation. Normative data from a group of control subjects with normal hearing are also shown (NH).

III. RESULTS

A. Perception

Results of the vowel recognition test are shown in Fig. 2 for the controls and for the implant users in three time samples (pre-implant;, 1 month, and 1 year postimplantation). For the implant users, a one-way repeated measures analysis of variance (ANOVA) with time sample as a within-subject variable revealed that time sample had a significant effect on the overall percentage correct ($F(2,24)=6.78; p<0.05$). Planned comparisons showed that results increased significantly from the pre-implant stage to 1 month after implantation ($F(1,12)=6.34; p<0.05$) and further improved from this stage to 1 year after implantation ($F(1,12)=5.21; p<0.05$). The use of a cochlear implant thus improved speech perception. However, as shown by a one-way ANOVA contrasting hearing controls and implant users 1 year postimplantation, the implant users' performance at the 1 year postimplant did not reach the nearly perfect score of the controls ($F(1,21)=4.39; p<0.05$).

B. Production

Results are presented separately for the three dependent variables (AVS in the M1 *vs*. M2 space, dispersion around the mean for each type vowel type in that space, and duration). Recall that for each postimplant time sample and hearing state there were two data sets gathered in separate recordings several days apart. There were no significant differences between the two processor-on data sets with respect to each of the three dependent variables (contrast distance: $t=-1.79$, $p>0.05$; dispersion: $t=1.04$, $p>0.05$; duration: $t=-1.80$, $p>0.05$). *T* tests did not reveal any difference between the two processor-off data sets (contrast distance: $t=-1.73$, $p>0.05$; dispersion: $t=2.11$, $p>0.05$; duration: $t=-1.25$; $p>0.05$). Thus, for each time sample and each hearing state, data from the two recording sessions were pooled to provide 60 determinations per vowel, 20 for each of the three speaking conditions.

For each dependent variable (contrast distance, dispersion, and vowel duration) five mixed repeated-measures

TABLE IV. Analysis of variances for ten controls (NH) and 13 implant users (CI) (*=$p<0.05$). Since there were no significant main effects or interactions of the gender variable for any of the dependent variables, this variable is not presented.

(a) Dataset: NH and CI pre-implant			
Source	AVS	Dispersion	Duration
Hearing status (NH, CI)	$F(1,19)=9.91^*$	$F(1,19)=0.01$	$F(1,19)=11.14^*$
Speaking condition (clear, normal, fast)	$F(2,38)=33.00^*$	$F(2,38)=0.48$	$F(2,38)=15.40^*$
Hearing status*speaking condition	$F(2,38)=2.15$	$F(2,38)=1.59$	$F(2,38)=1.48$
(b) Dataset: NH and CI 1 year postimplant (with processor on)			
Source	AVS	Dispersion	Duration
Hearing status (NH, CI)	$F(1,19)=0.55$	$F(1,19)=9.77^*$	$F(1,19)=11.33^*$
Speaking condition (clear, normal, fast)	$F(2,38)=37.28^*$	$F(2,38)=0.10$	$F(2,38)=13.03^*$
Hearing status*speaking condition	$F(2,38)=1.74$	$F(2,38)=2.07$	$F(2,38)=0.64$
(c) Dataset: CI pre, month, year (processor off)			
Source	AVS	Dispersion	Duration
Time sample (pre, 1 month, 1 year)	$F(2,22)=1.51$	$F(2,22)=3.86^*$	$F(2,22)=1.39$
Speaking condition (clear, normal, fast)	$F(2,22)=17.61^*$	$F(2,22)=0.91$	$F(2,22)=11.73^*$
Time sample*speaking condition	$F(4,44)=1.73$	$F(4,44)=1.13$	$F(4,44)=0.40$
(d) Dataset: CI pre, month, year (processor on)			
Source	AVS	Dispersion	Duration
Time sample (pre, 1 month 1 year)	$F(2,22)=6.07^*$	$F(2,22)=11.40^*$	$F(2,22)=1.50$
Speaking condition (clear, normal, fast)	$F(2,22)=16.77^*$	$F(2,22)=3.18$	$F(2,22)-11.83^*$
Time sample*speaking condition	$F(4,44)=0.69$	$F(4,44)=0.40$	$F(4,44)=0.71$
(e) Dataset: Cl month and year			
Source	AVS	Dispersion	Duration
Time sample (1 month, 1 year)	$F(1,11)=3.11$	$F(1,11)=0.88$	$F(1,11)=1.71$
Speaking condition (clear, normal, fast)	$F(2,22)=19.39^*$	$F(2,22)=1.04$	$F(2,22)=9.77^*$
Hearing state (processor on, off)	$F(1,11)=16.07^*$	$F(1,11)=0.01$	$F(1,11)=0.01$
Time sample*speaking condition	$F(2,22)=1.74$	$F(2,22)=0.05$	$F(2,22)=0.25$
Time sample*hearing state	$F(1,11)=2.50$	$F(1,11)=0.22$	$F(1,11)=0.71$
Speaking condition*hearing state	$F(2,22)=1.73$	$F(2,22)=1.28$	$F(2,22)=1.49$
Time sample*speaking condition*hearing state	$F(2,22)=0.24$	$F(2,22)=1.89$	$F(2,22)=1.00$

ANOVAs were carried out using the following within-subject variables: (1) speaking condition (clear, normal, or fast), (2) for implant users, time sample relative to implantation (pre-implant, 1 month postimplant, or 1 year postimplant), and (3) hearing state (processor on or off). Hearing status (implant users, controls) and speaker gender (female or male) were the between-subject variables. Those ANOVAs correspond to Tables IVa through IVe. There were no significant main effects or interactions of the gender variable for any of the dependent variables. For the sake of clarity, this variable is not presented in the tables.

1. Average vowel spacing (AVS)

Mean AVS values in mels are plotted in Fig. 3, for implant users at each time sample and for each speaking condition (circles=clear; triangles=normal; squares=fast). Filled symbols represent utterances produced by the controls or by implant users with the implant processor on (connected by solid lines). Utterances produced with the processor off (or pre-implant) are shown by unfilled symbols connected by dashed lines. Results of repeated measure ANOVAs are reported in Tables IVa to IVe.

a. Hearing status and speaking condition. As Fig. 3 shows at the left, for controls (NH), the mean AVS value increased by 29 mels from the fast (squares) to the normal condition (triangle) and 26 mels from normal to clear (circle). A similar effect of speaking condition was observed for implant users at the pre-implant stage (pre). Table IVa reports the outcome of an ANOVA based on production measures for the controls and those for the implant users pre-implant. The table shows there was a significant effect of speaking condition on AVS. Planned comparisons of that effect showed that AVS was significantly greater in clear than in normal speech ($F(1,19)=17.36; p<0.05$), and was significantly greater in normal than in fast speech ($F(1,19)=41.81; p<0.05$). Figure 3 also shows that implant users at the pre-implant stage and hearing controls varied AVS similarly in response to changes in speaking conditions, confirmed by the lack of a significant interaction between hear-

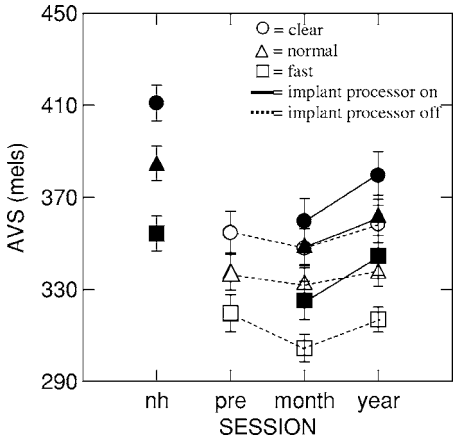

FIG. 3. Mean values of average vowel space (AVS) for control subjects (NH) and implant users in three speaking conditions (clear, normal, fast). For the latter group, data are shown at three time samples: prior to implantation (pre), 1 month (month) and 1 year (year) after implantation. Solid line: implant processor on; dotted line: implant processor off. Error bars are 0.5 standard error of the mean.

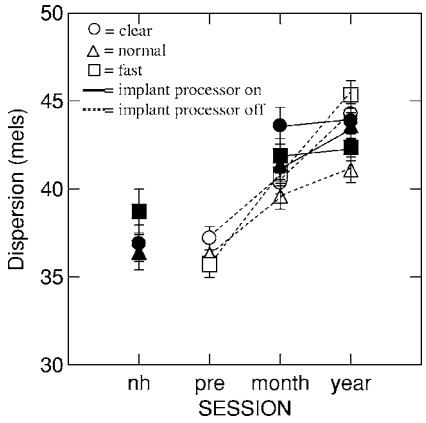

FIG. 4. Mean values of token dispersion in the M1 *vs.* M2 plane for the nine vowels elicited for controls (NH) and implant users in three speaking conditions (clear, normal, fast). Data for the implant users are presented at three time samples: prior to implantation (pre), 1 month (month) and 1 year (year) after implantation. Solid line: implant processor on; dotted line: implant processor off. Error bars are 0.5 standard error of the mean.

ing status and speaking condition (Table IVa).

When comparing hearing controls and implant users after 1 year of implant use in the processor on condition, it can be observed in Fig. 3 that both groups varied average vowel spacing with speaking condition to approximately the same extent. Table IVb shows that this effect was significant, and that there was no significant interaction between speaking condition and hearing status.

Pooling across speaking conditions, average vowel spacing produced by implant users at the pre-implant stage was significantly smaller than produced by hearing controls (significant effect of hearing status in Table IVa). Even though it appears in Fig. 3 that the controls' AVS values are higher than the implant users' with processor on at 1 year postimplant, this difference was not significant (Table IVb).

b. Time sample and speaking condition. Inspection of Fig. 3 suggests that among the implant users, the differences between AVS in clear, normal, and fast speaking conditions did not change with implant use from the pre-implant stage to 1 month and 1 year postimplantation for the processor off condition. This finding is confirmed in Table IVc by the presence of a significant effect of speaking condition on AVS with processor off, but the lack of a significant interaction between speaking condition and time sample.

Figure 3 and Table IVd show that no significant interaction was found between speaking condition and time sample in the processor on condition. Thus, in the three time samples with their evolving enhancement of perceptual accuracy and contrast distance, the effects of speaking condition remained comparable. When averaging across speaking conditions, AVS values increased with implant use: planned comparisons tests revealed that implant users' mean AVS did not change from pre-implant (no processor) to 1 month postimplant with processor on; however, values at 1 year postimplant with processor on were significantly higher than values at pre-implant ($F(1,11)=13.36; p<0.05$) and values at 1 month postimplant ($F(1,11)=10.38; p<0.05$). Hence, the use of an implant increased contrast distance, but only from 1 month to 1 year after implantation.

c. Hearing state and speaking condition. Figure 3 shows that AVS values were larger in the processor on condition (solid line) than in the processor off condition (dotted line), also demonstrated by a significant effect of hearing state in Table IVe. This difference in AVS between the two hearing-state conditions is observed both at 1 month and 1 year postimplant, as confirmed by the lack of a significant interaction between hearing state and time sample (Table IVe).

Temporarily depriving the speaker of auditory feedback by turning the implant processor off did not change the extent to which implant users increased contrast distances when changing from fast to normal to clear speaking conditions. As can be seen in Table IVe, speaking condition had a significant effect on AVS values for implant users (pooling across hearing state) but the interaction between hearing state and speaking condition was not significant.

To summarize, averaging across speaking conditions, implant users pre-implant had smaller values of average vowel spacing than controls. After 1 year of implant use, in the processor on condition, implant users' AVS values overlapped with those found for controls. Temporarily depriving the implant user of auditory feedback after implantation yielded a significant decrease of values of AVS, compared to the condition where auditory feedback was provided by the implant. However, this manipulation of auditory feedback did not affect the differences in AVS between speaking conditions. Thus the effects of speaking condition are similar for both groups, at all time samples and for both hearing states.

2. Dispersion

The effects of speaking condition, time sample, and hearing state on dispersion values are shown in Fig. 4. All values are in mels. Results of repeated measures ANOVAs are reported in Tables IVa–IVe in the Dispersion column.

a. Hearing status and speaking condition. As Fig. 4 indicates, dispersion values did not differ significantly with changes in speaking condition, pooled over hearing status with pre-implant measures for the implant users (Table IVa). The same was true if the 1 year postimplant measures were

used instead (Table IVb). There were no significant interactions between hearing status and speaking condition.

When averaging across speaking conditions, it can be observed from Fig. 4 that the dispersion values for the implant users at the pre-implant stage did not differ reliably from those of controls (no significant effect of hearing status in Table IVa). However, values at 1 year postimplant with processor on were significantly higher than those of normal-hearing speakers (significant effect of hearing status in Table IVb).

b. Time sample and speaking condition. Inspection of Fig. 4 suggests that the use of the implant did not induce implant users to vary dispersion values according to speaking condition. No significant interaction of time sample and speaking condition was found in the processor off condition (Table IVc) or the processor-on condition (Table IVd). There was, however, a significant effect of time sample on dispersion for each processor state (pooling over speaking condition). With processor off, planned comparisons showed that dispersion values at 1 month postimplant were significantly higher than at the pre-implant stage ($F(1,11)=5.33; p<0.05$), but were not significantly different at 1 year from dispersion values measured at 1 month after implantation. Planned comparisons also revealed that dispersion values increased significantly (by about 5 mels) from pre-implant to 1 month postimplant in the processor on condition ($F(1,11)=4.32; p<0.05$). However, dispersion values at 1 year postimplantation did not significantly differ from those measured at 1 month postimplantation (mean value of 41 mels).

c. Hearing state and speaking condition. Among implant users, dispersion values did not vary from fast to normal to clear speech condition, regardless of whether feedback was supplied or not in the 1 month and 1 year recording sessions. As observed in Table IVe, the interaction between time sample, hearing state, and speaking condition was not significant.

To summarize, when pooling across speaking conditions, dispersion values for implant users at the pre-implant stage were similar to those of controls but values 1 year postimplant with processor on were higher than those of controls. Implant users' overall mean dispersion values increased significantly from pre-implant to 1 month postimplant, but didn't change significantly thereafter. No difference in dispersion values according to speaking condition was found for either of the speaker groups. Thus, at all three time samples, when changing from fast to normal to clear speech conditions, implant users did not produce vowels that were more tightly clustered within vowel categories.

3. Duration

Figure 5 gives the variation of vowel duration according to speaking condition, hearing state, and time sample for implant users. Mean values for controls are also shown. Results of repeated measures ANOVAs are reported-in Tables IVa–IVe in the right-most column.

a. Hearing status and speaking condition. An examination of Fig. 5 reveals that controls and implant users at the pre-implant stage increased vowel duration when changing from fast to normal to clear speech conditions. Indeed, a

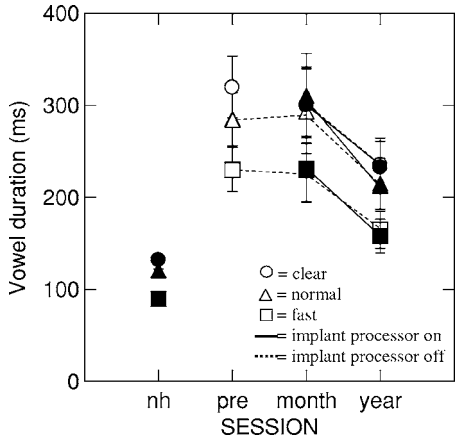

FIG. 5. Mean values of vowel duration for controls (NH) and implant users in three speaking conditions (clear, normal, fast). For the latter group, data are shown at three time samples: prior to implantation (pre), 1 month (month) and 1 year (year) after implantation. Solid line: implant processor on; dotted line: implant processor off. Error bars are 0.5 standard error of the mean.

significant effect of speaking condition was found (Table IVa). Planned comparisons showed that vowels were significantly shorter (by about 50 ms) in fast speech than in normal speech ($F(1,19)=20.29; p<0.05$), and vowels were significantly longer (by about 18 ms) in clear speech than in normal speech ($F(1,19)=5.35; p<0.05$). When comparing controls and implant users at 1 year postimplant (processor on condition), a similar pattern was found (significant effect of speaking condition in Table IVb). It is worth noting that both speaker groups varied duration values to the same extent (no significant effect of interaction between speaking condition and hearing status in Tables IVa and IVb).

When averaging across speaking conditions, it can be observed that implant users produced longer vowels (mean duration ~280 ms) than controls (mean duration of 114 ms) (significant effect of hearing status, Table IVa). Even after 1 year of implant use, in the processor on condition, implant users' vowels remained longer (mean duration of 205 ms) than those found for controls (significant effect of hearing status, Table IVb).

b. Time sample and speaking condition. As can be seen in Fig. 5, no interaction of time sample and speaking condition was found among the implant users in the processor off condition (Table IVc). The same was true for a comparison of duration measures at the pre-implant stage and at the postimplant stages in the processor on condition (Table IVd). Thus, duration of implant use did not change the extent to which postlingually deaf speakers changed vowel duration across speaking conditions.

Figure 5 shows that duration tends to be reduced in the direction of normative values from 1 month to 1 year postimplant; however, this effect of time sample was not significant. Furthermore, duration did not significantly decrease from the pre-implant stage to 1 year after implantation, neither in the processor off condition (Table IVc) nor in the processor on condition (Table IVd).

c. Hearing state and speaking condition. The interaction of hearing state (processor on or off) and speaking condition

in determining vowel duration was not significant (Table IVe), leading to the inference that the maintenance of durational differences between clear, normal, and fast speech did not depend on whether or not auditory feedback was supplied by the implant processor.

To summarize, long-term deprivation of auditory feedback induced implant users to produce longer vowels than controls, but there were no differences in vowel duration related to the interaction of speaking condition and hearing state in either group.

IV. DISCUSSION

A. Evaluating the role of auditory feedback

The results of this study show that postlingually deafened adults, instructed to speak under three different speaking conditions, varied contrast distances and vowel duration, but not dispersion. The section on objectives stated that if the phonetic differences associated with changes in speaking condition were influenced by auditory feedback, there would be a significant interaction between speaking condition and one or more of the independent variables related to auditory feedback (hearing status, time relative to implantation, hearing state) in determining changes in average vowel spacing, dispersion of vowel tokens, and vowel duration. As discussed below, no such interactions were found.

1. Average vowel spacing (overall vowel contrast)

There was a significant effect of speaking condition on overall vowel contrast. Figure 3 shows that for both groups based on hearing status (implant users and controls), AVS in clear speech was larger than in normal speech, which was larger than in fast speech. However, no significant interaction was found between speaking condition and hearing status or hearing state or time relative to implantation. These results lead to the inference that the maintenance of spectral distinctions between speaking conditions was not altered by profound hearing loss, which had lasted at least a year for all but one of the implant users. Consistent with the conclusion that auditory feedback did not influence changes in contrast due to speaking condition, the differences in contrast distances between clear, normal, and fast speech did not change from pre-implant to 1 month postimplant, nor from 1 month postimplant to 1 year postimplant, whether or not auditory feedback was supplied by the implant processor (Fig. 3). The absence of a significant interaction between speaking condition and the other independent variables does not by itself confirm that there were no such interactions but it is worth noting significant main effects were found for hearing status, speaking condition, and time sample (with processor on). The corresponding caveat applies to the other dependent variables, discussed below.

2. Dispersion

Regarding the dispersion of vowel tokens around their mean positions in the formant plane, an interaction between speaking condition and auditory feedback would have suggested that the differences in dispersion among speaking conditions are regulated by auditory feedback. As shown in Fig. 4, implant users at the pre-implant stage did not vary dispersion values significantly when changing from fast to normal to clear speech condition. No interaction effect of time sample and speaking condition was found in the processor on condition or the processor off condition. Since there was no change in the effect of speaking condition on dispersion despite a year's use of the implant, there was no evidence that auditory feedback plays a role in regulating the differences in dispersion values among speaking conditions.

For hearing controls, token dispersion around the mean did not differ significantly according to speaking condition. This pattern contrasts with previously published studies on the effects of speaking conditions on dispersion values, where it was found that when instructed to speak clearly, speakers produced tighter clustering of vowel tokens around the mean (cf., Picheny *et al.*, 1986). This disparity in results may be attributable to differences between experimental paradigms. For example, in the study of Picheny *et al.*, speakers read nonsense sentences with embedded real words. Phonemic and prosodic contexts varied from one sentence to the next. In the present study, target vowels were elicited in the same phonemic environment and prosodic context across repetitions (/pVp/). There were also differences between the methods for eliciting clear speech. In Picheny *et al.* (1986), feedback was provided to the speaker during the recording to reinforce the clear speech instruction; in the current study, the speaking conditions were elicited only by instructions to the subjects.

3. Duration

If duration measures had yielded a significant interaction effect between any of the independent variables related to auditory feedback (hearing status, time sample, hearing state) and speaking condition, that would lead to the inference that auditory feedback regulates the durational contrasts between speaking conditions. It was found that the differences in vowel duration between clear, normal, and fast conditions for implant users were in the range of those found for controls, at all time samples and in both hearing states. No interaction of speaking condition with hearing status or time sample was found. Thus, the maintenance of durational contrasts among speaking conditions was not influenced by sustained auditory deprivation or the subsequent provision of auditory feedback.

Recall that vowels produced in the clear speech condition were longer than those produced in the normal condition. When averaging across speaking conditions, it was found that implant users at the pre-implant stage produced significantly longer vowels than controls (280 ms compared to 114 ms). Even after 1 year of implant use, vowels remained longer than normative values found for controls.

B. Interpreting the results in the light of the DIVA model

Our results can be interpreted in the light of the DIVA model, described earlier and represented in Fig. 1.

1. Contrast distances

In the present study, the observation that vowel contrast distances (measured by AVS) in deaf speakers prior to implantation were lower than hearing controls, is compatible with the idea that feedforward commands had been degraded by auditory deprivation. Average vowel spacing remained unchanged from the pre-implant stage to 1 month postimplantation. AVS increased from 1 month to 1 year postimplant in the processor-on condition, but remained unchanged in the processor-off condition. This pattern is in line with the behavior of the DIVA model. DIVA predicts that speakers with cochlear implants will first use the new auditory feedback provided by the implant to recalibrate their feedback control subsystem. Until the feedback control system has been recalibrated, feedforward commands cannot be recalibrated since their tuning relies on a well-tuned feedback control system. The use of the newly acquired auditory feedback may even be detrimental to the speech of implant users shortly after implantation because the auditory feedback provided by the implant is very different from the feedback provided by the auditory system before the onset of deafness. As a result, the implant recipient's feedback control system will be improperly tuned initially, leading to somewhat degraded speech when auditory feedback is available, which in turn may degrade feedforward commands. This pattern has been reported earlier (Lane *et al.*, 2005). After implantation, according to the model, the newly acquired auditory feedback is recalibrated increasingly with time, and only after it is properly tuned will it start improving the feedforward commands. These processes may require some time, and the 1 year postimplantation stage has been chosen here to represent a reasonable extended period of implant use after which implant users may have recalibrated their feedforward commands. Our results, as others (Lane *et al.*, 2006) suggest that, although this retuning of the feedforward command has typically begun before 1 year after implantation, it is not complete by 1 year.

The strategies for changing contrast distance with speaking condition were not mediated by auditory feedback in this experiment. We reach this conclusion because implant users as well as controls increased contrast distance from normal to clear speaking condition by similar amounts and there was no evidence of an effect of processor state nor of the length of time the speaker had been using the implant. Taken together, those results suggest that long-term deprivation of auditory feedback (as in postlingually deaf speakers) results in a deterioration of contrast distances for among vowel categories of a language, but the ability to enhance contrast distance when given instructions to vary speaking condition is not affected. Since the implant users in the present study are *postlingually* deafened, they had long-term auditory experience during which their feedback system was used to calibrate their feedforward commands. During the sustained auditory deprivation of profound deafness, their feedforward command systems could not have been maintained by the auditory feedback system. However, these speakers still have residual feedforward commands that were acquired when they could hear and they have intact somatosensory feedback. In this condition, deaf speakers may rely on their own knowledge of speech motor control encoded in the feedforward commands to implement variations required for different speaking conditions (for example, greater or lesser separation between contrasting vowels).

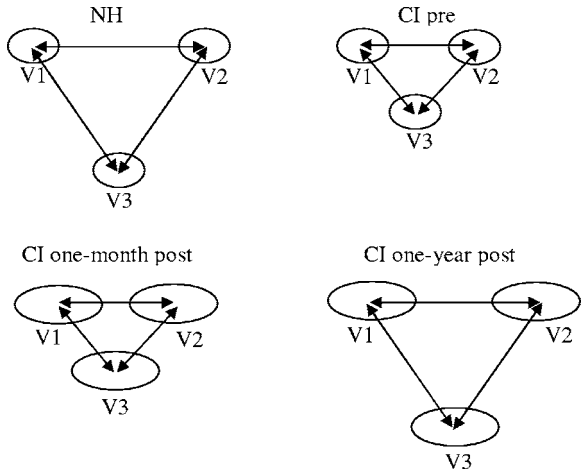

FIG. 6. Schematic representations of the results for contrast distance and vowel dispersion in the present study for controls (upper left panel) and implant users at three time samples: pre-implant (upper right panel), 1 month postimplant with processor on (lower left panel) and 1 year postimplant with processor on (lower right panel). For the sake of clarity, only three vowels (V1, V2, V3) are represented. The size of the ellipses associated with the vowels represents dispersion, and the size of the double-headed arrows corresponds to the magnitude of contrast distance.

2. Dispersion

With respect to the dispersion of vowel tokens around their mean in the formant plane, our results show a somewhat different pattern from that obtained with contrast distance. Figure 6 schematizes the results obtained for contrast distance and vowel dispersion, for controls and implant users at the three time samples, in the processor on condition for the postimplant stages. For the sake of clarity, only three vowels are represented (V1, V2, V3). Vowel dispersion, related to the size of the goal region for each vowel category, is denoted by the size of the ellipses associated with the vowels. The length of the double-headed arrows represents the magnitude of contrast distance between pairs of vowels. Data from the present study reveal that even after long-term auditory deprivation, implant users at the pre-implant stage produced dispersion values that were still in the range of those found for controls, whereas contrast distance had significantly decreased (compare the left and right upper panels with one another in Fig. 6). Thus, the lack of auditory feedback affected the control of contrast distance but goal region size, measured by the value of vowel dispersion, remained unaffected.

One month after implantation, the use of auditory feedback provided by the implant resulted in an increase in dispersion, and no significant change in contrast distance (compare the upper right panel and the lower left panel in Fig. 6). The increase in dispersion with the use of an implant is consistent with the DIVA model since it reflects the fact that the auditory feedback system is poorly tuned, thus leading to an additional degradation of speech production shortly after implantation (i.e., the speaker's poorly tuned auditory feedback

control system actually degrades, rather than improves, speech). This may be attributable to the very different nature of the auditory feedback provided by the prosthetic device, compared to the feedback available when the speaker was still hearing. It is also predicted by DIVA that the low resolution of the implant will lead to a larger target region (dispersion): the implant recipients cannot hear some subtle differences that distinguish poor from good exemplars of a phoneme category, thus they include some relatively poor exemplars in their production target regions, yielding greater dispersion. Consistent with this account, prior research has shown a relation between contrast distance and acuity, leading to the inference that speakers with greater acuity have smaller target regions for vowel production (Villacorta *et al.*, 2005; Perkell *et al.*, 2004a, b). Contrast distance values and dispersion values can thus follow different time courses from pre-implant to 1 year postimplantation.

It is, however, worth noting that in the present study, implant users increased dispersion values (pooling across feedback conditions and speaking conditions) from the pre-implant stage to 1 month postimplant, whereas a different pattern was observed in a bite-block study conducted in our laboratory on a different group of implant users (Lane *et al.*, 2005). In the latter study, mean token dispersion measured without bite blocks dropped significantly from the pre-implant stage (around 55 Hz) to the 1 month postimplant stage (around 45 Hz). In another difference between the two studies, the current one found implant users' dispersion values were not higher at the pre-implant stage than the normal controls' (mean value of 37 mels), whereas in Lane *et al.* (2005) dispersion values at the pre-implant stage were higher than those of hearing control subjects. The differences between these two sets of results may be due in part to differences in subject populations, dialect regions, and elicitation procedures. Subjects recorded in the present study were from the Miami area, a different dialectal region compared to the study of Lane *et al.*, in which subjects were recruited in the Boston area. Furthermore, in the present study, values were averaged over nine vowels in /pVp/ contexts embedded in a carrier phrase whereas in Lane *et al.* (2005), dispersion values were calculated over five vowels in carefully pronounced isolated words ("heed," "hid," "head," "had," and "hot"). We do not have an explanation at this time that links those methodological differences to the disparity between the two sets of results.

In the current study, we infer that the implant users, after 1 year of implant use, had time to successfully retune their auditory feedback systems, following which the system was used to recalibrate the feedforward control commands effectively. As a result, contrast distances increased at 1 year postimplant compared to 1 month postimplant (compare lower panels in Fig. 6), but dispersion values remained unchanged. The low resolution of the implant no doubt contributed to the larger target region (dispersion) at 1 year postimplant relative to controls. It is unlikely that further improvements in the feedforward commands will be able to reduce this resolution-related portion of the overall variability seen at 1 year postimplant unless there is some improvement in implant users' perceptual acuity that might result from improved signal processing.

ACKNOWLEDGMENTS

This research was supported by Grant No. R01-DC003007 from the National Institute on Deafness and Other Communication Disorders, National Institutes of Health. We are grateful to Dr. Robert Balkany of the Department of Otolaryngology, University of Miami Medical School, for providing the facilities and subject referrals for this study. We are grateful to Frank Guenther for fruitful discussions about the DIVA model.

[1]This carrier phrase was chosen to make it prosodically as compatible as possible with a phrase spoken by Spanish-speaking participants (data not reported here), "Repita/pVp ə/ por favor."

[2]Due to a technical problem with the stimulus presentation software, the exact number of repetitions of each syllable varied from 27 to 34 depending on the speaker.

Buechner, A., Frohne-Buechner, C., Stoever, T., Gaertner, L., Battmer, R. D., and Lenarz, T. (**2005**). "Comparison of a paired or sequential stimulation paradigm with Advanced Bionics' high-resolution mode," Otol. Neurotol. **26**, 941–947.

Chen, F. R. (**1980**). "Acoustic characteristics and intelligibility of clear and conversational speech," Master's project, MIT, Cambridge, MA.

Economou, A., Tartter, V., Chute, P., and Hellman, S. (**1992**). "Speech changes following reimplantation from a single-channel to a multichannel cochlear implant," J. Acoust. Soc. Am. **92**, 1310–1323.

Ferguson, S. H., and Kewley-Port, D. (**2002**). "Vowel intelligibility in clear and conversational speech for normal-hearing and hearing-impaired listeners," J. Acoust. Soc. Am. **112**, 259–271.

Guenther, F. H. (**1995**). "Speech sound acquisition, coarticulation, and rate effects in a neural network model of speech production," Psychoanal. Rev. **102**, 594–621.

Guenther, F. H., Hampson, M., and Johnson, D. (**1998**). "A theoretical investigation of reference frames for the planning of speech movements," Psychoanal. Rev. **105**, 611–633.

Guenther, F. H., Ghosh, S. S., and Tourville, J. A. (**2006**). "Neural modeling and imaging of the cortical interactions underlying syllable production," Brain Lang **96**, 280–301.

Krause, J. C., and Braida, L. D. (**2004**). "Acoustic properties of naturally produced clear speech at normal speaking rates," J. Acoust. Soc. Am. **115**, 362–378.

Lane, H., Matthies, M., Denny, M., Guenther, F., Perkell, J., Stockmann, E., Tiede, M., Vick, J., and Zandipour, M. (**2007**). "Effects of short- and long-term changes in auditory feedback on vowel and sibilant contrasts," J. Speech, Lang. and Hear. Res. (in press).

Lane, H., Denny, M., Guenther, F., Matthies, M., Menard, L., Perkell, J., Stockman, E., Tiede, M., Vick, J., and Zandipour, M. (**2005**). "Effects of bite blocks and hearing status on vowel production," J. Acoust. Soc. Am. **118**, 1636–1646.

Lane, H., Matthies, M., Perkell, J., Vick, J., and Zandipour, M. (**2001**). "The effects of changes in hearing status in cochlear implant users on the acoustic vowel space and CV coarticulation," J. Speech Lang. Hear. Res. **44**, 552–563.

Lane, H., Wozniak, J., Matthies, M., Svirsky, M., and Perkell, J. (**1995**). "Phonemic resetting *vs.* postural adjustments in the speech of cochlear implant users: An exploration of voice-onset time," J. Acoust. Soc. Am. **98**, 3096–3106.

Langereis, M. C., Bosman, A. J., Van Olphen, A. F., and Smoorenburg, G. F. (**1998**). "Changes in speech production in post-linguistically deafened adults after cochlear implantation," Clin. Otolaryngol. **23**, 383.

Lindblom, B. (**1990**). "Explaining phonetic variation: A sketch of the H and H is theory," in *Speech Production and Speech Modeling*, edited by W. J. Hardcastle and A. Marchal (Kluwer, Dordrecht), pp. 403–439.

Liu, S., Rio, E. D., Bradlow, A. R., and Zeng, F.-G. (**2004**). "Clear speech perception in acoustic and electric hearing," J. Acoust. Soc. Am. **116**, 2374–2383.

Moon, S.-J. (**1991**). "An acoustic and perceptual study of undershoot in clear and citation-form speech," Phonetic Experimental Research at the Institute of Linguistics University of Stockholm XIV, University of Stockholm, Institute of Linguistics, 153–156.

Moon, S.-J., and Lindblom, B. (**1994**). "Interaction between duration, context, and speaking style in English stressed vowels," J. Acoust. Soc. Am. **96**, 40–55.

Muller, J., Schon, F., and Helms, J. (**2002**). "Speech understanding in quiet and noise in bilateral users of the MED-EL COMBI 40/40+ cochlear implant system," Ear Hear. **23**, 198–206.

Payton, K. L., Uchanski, R. M., and Braida, L. D. (**1994**). "Intelligibility of conversational and clear speech in noise and reverberation for listeners with normal and impaired hearing," J. Acoust. Soc. Am. **95**, 1581–1592.

Perkell, J. S., Denny, M., Lane, H., Guenther, F. H., Matthies, M. L., Tiede, M., Vick, J., Zandipour, M., and Burton, E. (**2007**). "Effects of masking noise on vowel and sibilant contrasts in normal-hearing speakers and postlingually deafened cochlear implant users," J. Acoust. Soc. Am. **121**, 505–518.

Perkell, J. S., Guenther, F. H., Lane, H., Matthies, M. L., Stockmann, E., Tiede, M., and Zandipour, M. (**2004a**). "The distinctness of speakers' productions of vowel contrasts is related to their discrimination of the contrasts," J. Acoust. Soc. Am. **116**, 2338–2344.

Perkell, J. S., Matthies, M. L., Tiede, M., Lane, H., Zandipour, M., Marrone, N., Stockmann, E., and Guenther, F. H. (**2004b**). The distinctness of speakers' /s/-/ʃ/ contrast is related to their auditory discrimination and use of an articulatory saturation effect, J. Speech Lang. Hear. Res. **47**, 1259–1269.

Perkell, J., Numa, W., Vick, J., Lane, H., Balkany, T., and Gould, J. (**2001**). "Language-specific, hearing-related changes in vowel spaces: A preliminary study of English- and Spanish-speaking cochlear implant users," Ear Hear. **22**, 461–470.

Perkell, J. S., Guenther, F. H., Lane, H., Matthies, M., Perrier, P., Vick, J., Wilhelms-Tricarico, R., and Zandipour, M. (**2000**). "A theory of speech motor control and supporting data from speakers with normal hearing and with profound hearing loss," J. Phonetics **28**, 233–272.

Picheny, M. A., Durlach, N. I., and Braida, L. D. (**1986**). "Speaking clearly for the hard of hearing II: Acoustic characteristics of clear and conversational speech," J. Speech Hear. Res. **29**, 434–436.

Picheny, M. A., Durlach, N. I., and Braida, L. D. (**1985**). "Speaking clearly for the hard of hearing I: Intelligibility differences between clear and conversational speech," J. Speech Hear. Res. **28**, 96–103.

Pickett, J. (**1956**). "Effects of vocal force on the intelligibility of speech sounds," J. Acoust. Soc. Am. **28**, 902–905.

Schenk, B. S., Baumgartner, W. D., and Hamzavi, J. S. (**2003**). "Changes in vowel quality after cochlear implantation," ORL **65**, 184–188.

Smyth, V., Murdoch, B., McCormack, P., and Marshall, I. (**1991**). "Objective and subjective evaluation of subjects fitted with the cochlear multichannel prostheses: 3 studies," Austral. J. Hum. Comm. Dis. **9**, 31–52.

Svirsky, M., Lane, H., Perkell, J., and Webster, J. (**1992**). "Speech of cochlear implant patients: Results of a short-term auditory deprivation study," J. Acoust. Soc. Am. **92**, 1284–1300.

Svirsky, M. A., and Tobey, E. A. (**1991**). "Effect of different types of auditory stimulation on vowel formant frequencies in multichannel cochlear implant users," J. Acoust. Soc. Am. **89**, 2895–2904.

Tyler, R. S., Parkinson, A. J., Woodworth, G. G., Lowder, M. W., and Gantz, B. J. (**1997**). "Performance over time of adult patients using the Ineraid or Nucleus cochlear implant," J. Acoust. Soc. Am. **102**, 508–522.

Vandali, A. E., Whitford, L. A., Plant, K. L., and Clark, G. M. (**2000**). "Speech perception as a function of electrical stimulation rate: Using the Nucleus 24 cochlear implant system," Ear Hear. **21** 608–624.

Vick, J., Lane, H., Perkell, J., Gould, J., and Zandipour, M. (**2001**). "Covariation of cochlear implant users' perception and production of vowel contrasts and their identification by listeners with normal hearing," J. Speech Lang. Hear. Res. **44**, 1257–1267.

Villacorta, V., Perkell, J. S., and Guenther, F. H. (**2005**). "Relations between speech sensorimotor adaptation and perceptual acuity," J. Acoust. Soc. Am. **117**, 2618–2619.

The effect of emphatic stress on consonant vowel coarticulation

Björn Lindblom
Department of Linguistics, The University of Texas at Austin, Austin, Texas 78712 and Phonetics Department, Stockholm University, Stockholm, Sweden S10691

Augustine Agwuele
Department of Anthropology, Texas State University, San Marcos, Texas 78666

Harvey M. Sussman[a)]
Departments of Linguistics and Communication Sciences & Disorders, The University of Texas at Austin, Austin, Texas 78712

Elisabet Eir Cortes
Phonetics Department, Stockholm University, Stockholm, Sweden

(Received 11 September 2006; revised 23 March 2007; accepted 23 March 2007)

This study assessed the acoustic coarticulatory effects of phrasal accent on [V1.CV2] sequences, when separately applied to V1 or V2, surrounding the voiced stops [b], [d], and [g]. Three adult speakers each produced 360 tokens (six V1 contexts × ten V2 contexts × three stops × two emphasis conditions). Realizing that anticipatory coarticulation of V2 onto the intervocalic C can be influenced by prosodic effects, as well as by vowel context effects, a modified locus equation regression metric was used to isolate the effect of phrasal accent on consonantal F2 onsets, independently of prosodically induced vowel expansion effects. The analyses revealed two main emphasis-dependent effects: systematic differences in F2 onset values and the expected expansion of vowel space. By accounting for the confounding variable of stress-induced vowel space expansion, a small but consistent coarticulatory effect of emphatic stress on the consonant was uncovered in lingually produced stops, but absent in labial stops. Formant calculations based on tube models indicated similarly increased F2 onsets when stressed /d/ and /g/ were simulated with deeper occlusions resulting from more forceful closure movements during phrasal accented speech. © *2007 Acoustical Society of America.* [DOI: 10.1121/1.2730622]

PACS number(s): 43.70.Fq, 43.70.Bk [BHS] Pages: 3802–3813

I. INTRODUCTION

A. Locus equations

The locus equation metric (Lindblom, 1963) is a useful phonetic tool to acoustically analyze the coarticulatory relationship between a given stop consonant preceding a variety of vowels. The F2 onset of a CV transition plotted against the F2 of the vowel midpoint typically yields a tight cluster of linearly distributed $\langle x,y\rangle$ coordinates when the vowel is varied and the stop consonant is held constant. The straight lines fit to such data have been called locus equations (LEs). Sussman *et al.* (1991), using a speaker population of 10 males and 10 females, demonstrated how slope *X y*-intercept LE plots captured bV, dV, and gV stop place productions, displayed as nonoverlapping data clusters, despite the inherent variability of vowel-context effects on the F2 transition onsets. LE slope and *y* intercepts were shown to be extremely effective predictors of stop place of articulation, with classification accuracy scores of 100%.

B. Quantifying degree of coarticulation

Krull (1988), influenced by Lindblom's earlier locus equation work, was the first investigator to formally state that the slope of the LE regression line indexes the degree of consonant-vowel anticipatory coarticulation. Slopes closer to a value of 0 indicated that the consonantal locus (or F2 onset of a CV) is minimally affected by the vowel, whereas slopes nearer to 1.0 indicated the opposite, viz. the consonantal locus is strongly influenced by the following vowel contexts. An important addendum, however, is missing from Krull's (1988) characterization of LE slopes as an index of degree of coarticulation. An amendment is needed stating that this is the case *only when F2mid values remain stable* across speaking conditions. Many prosodic sources of phonetic variation, such as stress, have well-documented effects on the vowel's spectral make-up and consequent location in phonetic space. Prosodically induced changes are independent from, but interactive with, the vowel *context-induced* anticipatory coarticulation considered to be encoded by the value of the LE slope.

C. Stress dependence of phonetic space

In the F1/F2 plane, vowel space reduces under unstressed conditions (Tiffany, 1959), and expands under stressed conditions (Koopmans-van Beinum, 1980). Under stress, vowel nuclei move toward higher F2 formant values for front vowels and lower F2 formant values for low back vowels. Thus, the V midpoint is further away from anticipa-

[a)]Electronic mail: sussman@mail.utexas.edu

 0001-4966/2007/121(6)/3802/12/$23.00 © 2007 Acoustical Society of America

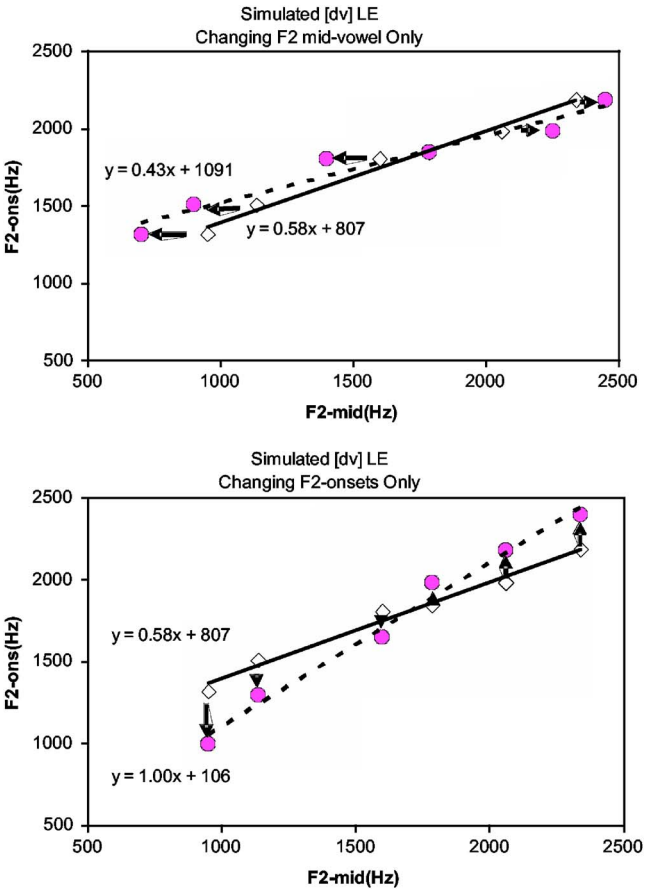

FIG. 1. (Color online) Top graph: The flattening effect on LE slope when F2 midvowels change (back vowels decrease and front vowels increase), while F2 onsets remain stable. Dashed line shows the lowered slope (0.43) that results. Bottom graph: The elevating effect on LE slope when only F2 onsets are changed in the same way, with F2 vowel midpoints remaining stable.

tory contextual influences on C onsets. The vowel and consonant have more freedom to move in independent directions during stressed speech.

D. Simulated changes to F2 onsets and F2 midvowels

The following hypothetical simulations demonstrate how LE slopes are altered if vowel F2 midpoints and consonantal F2 onsets are independently changed. Figure 1 (top) shows the case for changing F2 midvowel frequencies, while keeping F2 onsets constant. The reference LE, shown as the solid line ($y=0.58x+807$) was derived from an adult male speaker producing [dVt] tokens with five vowel contexts (i ɛ e ʌ ɔ). Emphatic stress was simulated by expanding the vowel space such that low vowels decreased and high vowels increased in F2 frequency, as shown by the arrows. The new LE is shown by the dashed line, $y=0.43x+1091$. Expanding F2 vowel space, while keeping F2 onsets constant, clearly decreases the LE slope. Lower LE slopes indicate reduced vowel influence on the onset frequency of the F2 transition. Obviously, vowel context effects are unrelated to the lowered LE slopes demonstrated in Fig. 1.

Figure 1 (bottom) shows changes to the LE slope when F2 onsets similarly expand due to emphatic stress. The reference slope (0.58) now becomes considerably steeper (1.0). Parallel changes to F2 onsets bring about a disproportionally greater slope change, and on the surface, indicate enhanced "anticipatory coarticulation" (in the sense of Krull's 1988 definition). Phonetic reality is presumably somewhere between these two hypothetical situations.

E. Goals of present study

When contextually induced variation interacts with prosodically induced variation, coarticulatory interactions between the C and V undergo complex, and often subtle, "pulls" and "pushes." The focus of this study was to empirically document the separate effects of emphatic stress on C onset and V midpoint F2 frequencies. More specifically, we explored novel analysis techniques to dissociate the effects of emphatic stress on the vowel F2 midpoints relative to the F2 onsets at the CV interface. F2 onset changes were observed and interpreted in two ways—those that were directly due to prosodically induced expansion of the vowel space, and those due to prominence-dependent changes on coarticulation per se. Of additional interest was to document how emphatic stress differentially affects lingual (/d/ and /g/) relative to labial (/b/) intervocalic stops. Since the formation and release of labial stops are independent of accentually altered vowel influences, we would expect different coarticulatory effects relative to lingual stops, /d/ and /g/, where vowel emphasis can more directly influence the contact pattern and/or spatial position of consonantal occlusions and their subsequent release.

F. Phonetic effects of lexical and emphatic stress

An array of descriptive terms have been used to capture the articulatory and acoustic changes owing to lexical and emphatic stress—e.g., "extra force" (Jones, 1932), "enhanced phonetic distinctiveness" (Öhman, 1967), "local hyperarticulation" (De Jong, 1995). Sound segments produced in prosodically strong positions have speech gestures with increased velocity, amplitude, and duration of movement (Beckman and Edwards, 1994; Beckman and Cohen, 2000). An important consequence of such hyperarticulated movement trajectories is a reduction in coarticulation, as the articulatory gestures for adjacent sounds are further apart, producing a diminished influence on their neighbors (de Jong, 1995; de Jong *et al.*, 1993).

Strengthening effects due to accentual prominence and lexical stress have also been documented with acoustic measures. Vowels and consonants have longer durations (lexical stress: Crystal and House, 1988; Klatt, 1974; Umeda, 1977; accent: Beckman and Edwards, 1994; Turk and White, 1999). The articulatory strengthening that accompanies stressed/accented syllables is also seen in spectral changes in the vowel as it more strongly resists coarticulatory undershoot and becomes less like surrounding segments (Fowler and Saltzman, 1993). Wouters and Macon (2002) documented accentual strengthening via increases in the spectral rate of change in the transitions between vowels and adjacent liquids and glides.

Only a few studies have employed locus equation metrics to assess the extent of CV coarticulation under prosodic/stylistic variations. Duez (1992) reported that LE slopes for

accented syllables were greater than those of unaccented syllables in Swedish and French. Van Son and Pols (1996) measured F2 spectral differences in V.CV sequences to assess intervocalic consonant reduction in informal spontaneous speech relative to more formal read speech. Using locus equations to capture F2 attributes of reduced speech, they reported that strong correlations between F2 onsets, measured at the C-V boundary, and V2 target frequencies were preserved across speaking conditions. They interpreted the stability of the locus equation slope to indicate, in principle, that "*consonant reduction is strongly linked to vowel reduction* (p. 18)." As the F2 "target" values increased or decreased with changing speaking-style conditions, they reasoned that it was to be expected that the F2 onset frequencies would also show commensurate changes.

Sarraf *et al.* (2000) reported minimal changes to LE slopes when emphatic stress was differentially applied to V1 and V2 in V1.CV2 utterances surrounding voiced stops. Most recently, Cole *et al.* (2004) examined the effect of accent on CV coarticulation with voiced and voiceless stops. Collapsing across voicing conditions, they reported increased LE slopes for labial, alveolar, and front/back velars in accented relative to unaccented tokens. They tempered their contradictory findings, however, as lengthened voice onset time (VOT) values during accented speech moved F2 onsets closer to the vowel's target F2 value, and hence LE slopes were spuriously inflated for accented words.

II. METHODS

A. Participants

The subjects of this study were three male speakers of American English between the ages of 25 and 35. All subjects were graduate students in the Department of Linguistics at the University of Texas at Austin. They all had extensive phonetic training. Two were from Texas (MB and MM) and one from Minnesota (BR). None of the subjects were judged to have strong regional or dialectal accents, and all had the test vowels as part of their vowel inventory.

B. Speech sample and elicitation of emphatic stress

The test tokens consisted of vowel-stop-vowel (V.CV) sequences placed in a carrier phrase. Prosodically contrastive vowels were separated by a word boundary pause. All test words in the V2 position were monosyllabic and meaningful English words with V2 always in medial position. The vowel-to-vowel sequences were structured in prosodically strong/weak positions as follows:

	Emphatic	Nonemphatic
1.	(C) (V) (C) V1	CV_2CC
	Nonemphatic	Emphatic
2.	(C) (V) (C) V1.	CV_2CC

The phrasal accent pattern was either emphatic stress falling on the first word, or on the second word. There were six V1 contexts ([i, u, ɔ, o, aɪ, a]) in the words: [i], *three*; [u] *two*; [ɔ] *draw*; [o] *low*; [al] *high*; [a] *viva*. The three intervocalic consonants were the voiced stops /b/, /d/, /g/. There were ten V2 contexts ([i, ɛ, e, æ, ɔ, o, u, ʌ, aɪ, au) contained within the following words:

[bV]: *beads, bells, bays, bags, balls, bowls, boots, bums, buys, bouts*,

[dV]: *deeds, debts, days, dads, dogs, doles, dunes, duds, dyes, doubts*,

[gV]: *geeks, guests, gates, gaps, galls, goals, goons, gums, guys, gouts*,

In order to elicit emphatic stress, the investigator engaged in a dialogue with each subject that simulated a natural conversation. First, the subject (S) read the first sentence (S(a)) and the investigator (I), pretending as if he did not understand the subject's utterance, replies with a question [1(a)]. The subject then replies, stressing the test word [S(b)]. The investigator, still feigning ignorance, follows up with another question [1(b)] that targets the test word and the subject is forced to answer, placing the strongest emphasis on the test word [S(c)].

	V1 emphatic stress	V_2 emphatic stress
S(a):	*I found two beads today.*	*I found two beads today*
I(a)	One bead?	Two deeds?
S(b):	*No,* ***TWO*** *beads*	*No, two* ***BEADS***
I(b):	What? Three beads?	What? two weeds?
S(c)	*No!* ***TWO*** *beads!*	*No! two* ***BEADS!***

Each speaker produced a total of 1080 tokens (3 levels of stress $\times$ 6 V1 $\times$ 10 V2 $\times$ 3 consonants $\times$ 2 vowel stress positions). Only productions from the third stage (c), producing maximally prominent tokens, were acoustically analyzed. LE analyses were performed only on the CV2 sequences (N=360 tokens)—1 stress level $\times$ 6 V1 $\times$ 10 V2 $\times$ 3 consonants $\times$ 2 vowel stress positions). The comparison of nonemphatic relative to emphatic productions was done only on the matched words containing the 10 V2 vowels (e.g., beads versus BEADS, boots versus BOOTS, etc.).

C. Recording and digitizing

All subjects were recorded in a sound attenuated room using a high-quality microphone (SHURE BG 3.1) and a digital master recorder (Fostex D-5). The utterances were recorded on DAT tape. The recorded signal was digitized using a Power Macintosh 7100/80 at 16 bits with a 20 kHz sampling rate. All playbacks, displays, and acoustic measurements were carried out using PRAAT-4.2 software for speech analysis (http://www.praat.org). Spectrograms were generated using a view range of 0.0–5000 Hz, at a window length of 0.005 s and with a 50.0 dB dynamic range. The time and frequency resolutions were 1000 and 250 steps, respectively. The method of analysis was Fourier transform and the window shape was Gaussian. The spectrogram was drawn with autoscaling and 6.0 (dB/ octive) preemphasis.

Measurement points. F1 and F2 midvowel: For all vowels, the first and second formant of V1 and V2 were measured at the same visually determined midpoints by placing the cursor on the spectrogram. Decisions on the time point of measurement of F2 were made based on the following crite-

ria (from Sussman *et al.*, 1991)—When the second formant was steady throughout the vowel, the cursor was placed at the visually determined midpoint of the vowel; where the second formant was either rising or falling a visually determined midpoint was selected. Finally, where the second formant trajectory was either concave or convex, the lowest and highest peaks of the F2 trajectories were measured. F2 midvowel measurement loci of diphthongs were taken in the visually determined midpoint of the onset portion of the vowel. F1 midpoints were taken at same time point selected for F2 midpoints. F2 frequencies were averaged across values taken from the (1) wide-band spectrographic display, (2) narrow-band fast Fourier transform (FFT), and (3) linear predictive coding (LPC) spectra. FFT and LPC readouts were taken from spectral windows corresponding to the same F2 vowel midpoints determined by positioning the marker on the spectrographic display.

F_2 onset: F2 onsets were taken at the first glottal pulse following the release of the consonant occlusion, i.e., at the CV2 boundary. This was done by placing the cursor on an expanded wide-band spectrogram view showing only the first few glottal cycles and reading off the indicated value.

D. Multiple regression analyses

The departure point of this study was deriving analysis procedures to dissociate emphasis-induced acoustic effects on F2 onsets from those affecting F2 vowel midpoints. A simple baseline model to account for F2 onset variations was first developed from three basic assumptions:

(i) Coarticulation does not change as phrasal accent is increased or decreased; coarticulation in this sense is defined as "context-dependent."
(ii) Vowel formant patterns do depend on phrasal accent: The vowel space expands with emphatic stress.
The assumption to be evaluated is:
(iii) "Degree of coarticulation" can be specified in terms of LE slope.

With the aid of these assumptions "expected" (or "predicted") values of F2 onsets were derived to compare with "observed" data. The aim of this strategy was to use the match, or mismatch, between expected and observed F2 onset values to tease apart the vowel expansion effect per se from possible coarticulation changes independently impacting F2 onsets. The underlying rationale is that, if there is agreement between observed and expected values, the model can be considered successful in capturing F2 onset variability. Such a result would imply that the observed F2 onset variations are solely associated with the emphatic stress-induced vowel space expansion and not to coarticulatory changes occurring in consonantal adjustments to emphatic stress. If, on the other hand, systematic discrepancies are found, we may have evidence for emphatic stress-dependent changes that directly affect the stop consonantal onsets.

In order to isolate the effect of emphatic stress on F2 onsets, we used a modified locus equation with two independent variables. Regression analyses were carried out with F2 onset as the dependent variable and the F2 midpoints of V2 and V1 serving as predictor variables. Equation (1) shows the baseline expression:

$$\underset{}{\text{F2onset(V2)}} = a + \underset{\text{nonemphatic}\uparrow}{b^*\ \text{F2mid(V2)}} + \underset{\uparrow\text{emphatic}}{c^*\ \text{F2mid(V1)}} \qquad \textit{[baseline]} \tag{1}$$

Using the Y-intercept (a) and the two slope coefficients (b,c), expected F2 onsets were generated by substituting V2 F2mid (emphatic) and V1 F2mid (nonemphatic) frequency values into Eq. (1), originally established for the complimentary baseline condition. The substituted emphasis condition that generated the array of expected F2 onset values is shown in the following:

$$\underset{}{\text{F2onset(V2)}} = a + \underset{\text{emphatic}\uparrow}{b^*\text{F2mid(V2)}} + \underset{\uparrow \textit{nonemphatic}}{c^*\text{F2mid(V1)}} \qquad \textit{[expected]} \tag{2}$$

The rationale underlying this substitution is that, by inserting F2mid(V2) (emphatic) and F2mid(V1) (nonemphatic) into the equation originally derived for nonemphatic CV2's, we apply assumption (i) of the model—coarticulation, as traditionally defined by LE slopes, does not change due to emphasis. The baseline slope coefficients (b,c) should not, "theoretically speaking," be inappropriate to use with the substituted *emphatically stressed* values for V2. This substitution implements assumption (ii). It allowed the use of emphatically stressed, and hence, expanded V2 formant values, as predictor variables in an equation originally derived for the nonemphatic CV2 condition. The substituted F2mid(V2) emphatic values should not affect *contextually induced coarticulation* to modify the dependent variable, as the same LE slope (b) is still in the equation. However, the substituted V2 midvowel frequencies do add *phrasal accent-dependent*

TABLE I. Locus equation slopes and y-intercepts for /b/, /d/, and /g/ for the three speakers across conditions.

	Non-Emphatic		Emphatic	
Subjects	Slope	Intercept	Slope	Intercept
BR /b/	0.75	281	0.74	281
BR /d/	0.57	795	0.38	1180
BR /g/	0.95	219	0.85	4667
MB /b/	0.77	225	0.80	218
MB /d/	0.48	968	0.43	1121
MB /g/	0.91	304	0.86	401
MM /b/	0.67	377	0.71	297
MM /d/	0.51	917	0.47	1000
MM /g/	1.01	138	0.88	335

coarticulation into the mix. Therefore, any mismatch between expected and observed F2 onsets can now be cautiously attributed to the phrasal emphatic stress factor operating on F2 onsets independently of the vowel.

This procedure of extrapolating from nonemphatic to emphatic F2 onsets was applied to the three stops from all three speakers. Once the expected values were calculated for all relevant tokens, corresponding observed and expected F2 onset frequencies were compared for each speaker, as well as averaged across the three speakers. Before presenting these results, a set of preliminary findings will first be described.

III. RESULTS

A. Locus equation analysis

Table I shows LE slopes for non-emphatic and emphatic productions. The same basic pattern was evident across all speakers—viz. labial slopes remained more or less constant across emphatic stress conditions, while alveolar and velar slopes decreased under emphatic stress. The grand mean LE slope, averaged across the three stops and speakers, was 0.74 for the nonemphatic CVs, relative to a slope of 0.68 for emphatically stressed CVs. The slope values were statistically compared as a function of stress in a paired *t*-test and the difference was significant [$t(8)=2.611$; $p=0.03$].

The standard error of estimate (SE), which measures the average root mean square distance of data points from the regression line, consistently reflected the effect of emphatic stress. SE values of emphatic segments (mean=89 Hz) were lower than their nonemphatic counterparts (mean=102 Hz) in all stop contexts and for all speakers. A paired *t*-test showed the SE values to be significantly different as a function of emphasis, [$t(8)=5.94$, $p=0.0003$]. Thus, prosodically strong segments were produced with less acoustic variability.

B. Emphatic stress effects on F2 onsets

A preliminary assessment of how emphatic stress affected F2 onsets was performed by a series of *t*-tests on overall means contrasted across the two speaking conditions. For labials, the emphatic mean F2 onset (1414 Hz) was significantly higher than the nonemphatic mean (1383) [$t(178)=-3.78$; $p<0.01$]; for alveolars, mean emphatic F2 onset (1833 Hz) was significantly higher than the nonemphatic counterpart (1781 Hz) [$t(178)=-7.93$; $p<0.001$]; and for velars, means were identical (emphatic mean=1833 Hz; nonemphatic mean=1831 Hz).

Figure 2 indicates that emphatic stress had small, but systematic effects on the F2 onsets that depend on the place of articulation of the stop. For [b] the data form a fairly regular linear rising cluster as vowel place goes from back to front. A different pattern is seen for [d] where data points generally lie above the line of equality. The mean differential is 50 Hz. The vowels of the [g] syllables behave in an intermediate fashion—back vowels producing a somewhat rising pattern similar to that for [b], but front vowels show negligible differences.

For [b] we note that nonemphatic F2 onsets that are high (as in "*beads*") become higher and that low F2 onsets (e.g., "*bowls*") become lower. Similarly, for [g] before "back" vowels, the low nonemphatic F2 onsets give rise to somewhat lower values than the higher F2 onsets. Despite the small effects, the patterns are nonetheless consistent, calling for an interpretation. It would be tempting to suggest that for [b] and [g] before "back" vowels the data show that articulators anticipate the upcoming V2 to a greater extent under emphasis. In labial stops the tongue is free to anticipate the articulatory position intended for V2. For the velar [g]'s, emphatic stress appears to make the V2 dependence of the stop's place of articulation greater.

However, do these effects really reflect coarticulatory processes? Could they simply be due to phrasal accent-dependent vowel changes? Until we have examined how V2 vowels behave under emphasis, such conclusions are premature.

C. Emphatic stress effects on F1×F2 vowel space

To investigate the effect of emphatic stress on the vowels, we examined changes in F1/F2 vowel space, measured at V2 vowel midpoints, in normal relative to emphatically stressed conditions. Figure 3 shows the expansion of vowel space under accentual conditions for each speaker. Nonemphatic vowels are shown as open circles, with lines connecting them to their emphatic counterparts, shown as closed diamonds. While each speaker revealed an idiosyncratic alteration of vowel space, all three revealed an expansion similar to those reported by Koopmans-Van Beinum (1980).

D. Dissociation of emphatic stress on the vowel relative to the consonant

Table II presents the results of the multiple regression analyses to initially establish the baseline slope coefficients to predict F2 onsets from the independent variables of V1 and V2 midpoints [see Eq. (1)]. The numerical accuracy of using two independent variables, and a split of the [g] data into front and back categories, improved the standard error of estimate (SE) from a mean of 89 to 56 Hz for emphatic segments and from 102 to 81 Hz for their nonemphatic counterparts.

For [b] and [d] the degree of V2 anticipation as reflected by the *b* coefficient (the traditional LE slope) shows numeri-

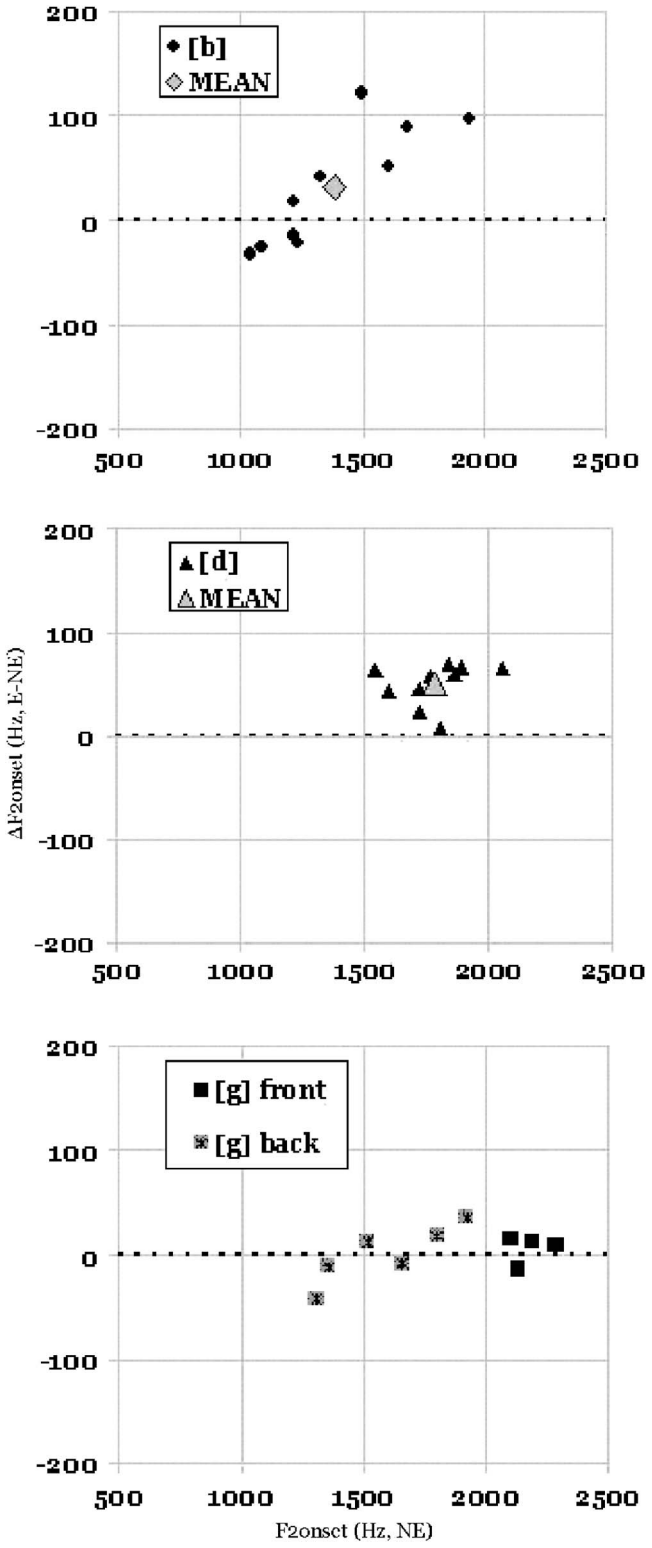

FIG. 2. Mean F2 onset differences across emphatic (E) and nonemphatic (NE) conditions plotted against corresponding F2 onsets in nonemphatic condition. The data were averaged across the three speakers. The [g] measurements were split into front and back groups. Mean labial F2 onset difference is shown by large shaded diamond; mean alveolar difference is shown by large shaded triangle.

cal values similar to the results based on a single independent variable [V2 F2 midpoint (Hz)]. As can be expected, the split of the [g] data yields steep slopes for back vowel environments and flat slopes for front vowel contexts (Sussman *et al.*, 1991). In keeping with our earlier observations, there was a tendency for emphatic stress to bring about negligible changes in V2 slopes in [b] contexts, lower V2 slopes in [d] contexts, and a decrease in V2 slopes in [g] contexts, but only for front vowels. Back vowel [g] contexts had mixed results, with slopes increasing for two speakers and decreasing in one. The *c* coefficient—which reflects the perseveratory effect of V1 on F2 onsets—shows a relatively consistent pattern of reducing in emphatic conditions.

To dissociate prosodic effects on the vowel midpoints from those affecting F2 onsets, we then performed the final set of multiple regression analyses that maintained V1 (*c*) and V2 (*b*) slope coefficients, but substituted phasal accented F2mid V2 values for nonemphasis F2mid V2 values as previously described in Sec. II D [see Eq. (2)]. Table III presents the mean values of *observed* F2 onsets during stressed CVs versus *expected* F2 onsets derived from the multiple regression analyses using F2mid V2's from emphatic productions with slope coefficients derived from the benchmark equation (1.0). A series of *t*-tests were initially performed to test for statistical differences between these two values of F2 onsets for each speaker and stop consonant context. The *t*-tests were each performed on 60 measures—six V1 contexts $\times$ 10 V2 contexts per stop. Seven of the nine comparisons showed significant differences (at $p<0.01$) as observed F2 onsets exceeded expected F2 onsets. Only labials for speaker BR and velars for speaker MM failed to show statistically significant differences.

A graphic view of the regression analysis is presented for each speaker in Fig. 4 which compares [observed-expected] F2 onsets for [b], [d], and [g]. The *y* axis shows by how much the observed F2 onsets differ from expected values. Observed values for the corresponding F2 midpoints of emphatically stressed V2's are plotted along the abscissa. Recall these data are averages across all six V1 contexts. There are ten data points per panel for each V2 context in alveolar and velar stop contexts, and nine vowel contexts for labial productions. Labial tokens with the vowel /ɛ/, as contained in word "*bells*," were outliers and removed from the analysis. A possible explanation for this deviant behavior could be that the vowel became strongly velarized by the following dark /l/. Accordingly, this item may be exceptional in showing a more marked influence from the syllable final cluster than any of the other test words. All vowels have been divided up into front and back groups.

In examining labial data across the three speakers, the data points more or less cluster near the line of equality, with only MB showing differences between observed and expected values of F2 onset for three vowel contexts (two front and one back). Alveolars exhibited a different pattern across the speakers with all back vowels consistently above the equality line and front vowels slightly above the zero line. Velars showed a similar pattern to alveolars with primarily back vowels showing larger deviations between observed and expected F2 onsets, with front vowels basically showing equality between observed and expected.

To gain a more generalized perspective and smooth out individual speaker variations, a mean [observed-expected] F2 onset plot was derived by averaging across the three

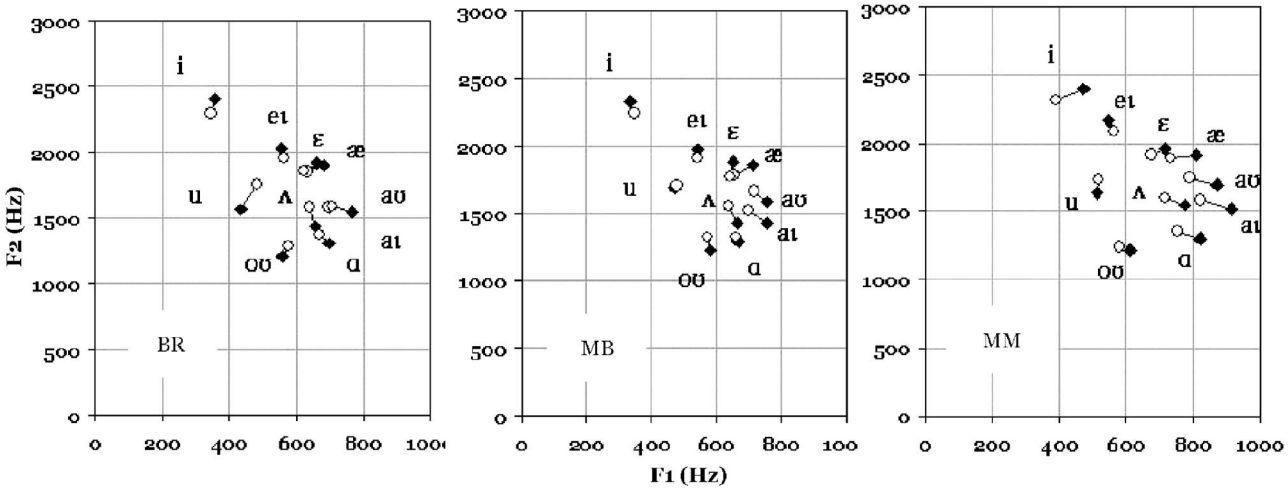

FIG. 3. Expansion of V2 vowel space under emphatic stress. Open circles represent nonemphatic vowels, connected to the corresponding emphatically stressed variant (closed diamonds) by straight lines.

speakers and is shown in the left side column of Fig. 5. The [b] points in Fig. 5 are all located near the zero line. The meaning of this outcome is as follows. The differences are compatible with the changes that would be expected from the observed phrasal accent induced vowel changes.

Now turn to the right column of Fig. 5, whose format is that of a locus equation plot. At the top the observed emphatically produced F2 onsets for [b] are plotted as closed circles. The linear line represents the expected LE estimate generated by means of Eq. (1) and is based on the [b] regression data shown in Table II. Note that the data points all fall along the expected line—a result in keeping with the fact that LE slopes for [b] showed minimal or no slope changes due to emphatic stress.

The analogous comparison for [d] invites a different conclusion. The left column panel for [d] in Fig. 5 shows a pattern of F2 onsets that falls as a function of F2mid(V2). In other words, before back vowels, [d]'s are shifted up further in frequency than before front vowels. The LE diagram to the right makes clear that these shifts have the effect of flattening the slope of the cluster of data points (triangles) for emphatically stressed [d]'s relative to the expected LE line. This can be visualized by imagining another straight line fit to the dark triangles (observed F2 onsets under emphatic stress)—the regression line would be shifted upwards to better fit the back vowel points, and hence the new LE line would tilt to a flatter position. This was exactly what was seen in the original LE analysis as slopes decreased under emphatic speech. The interpretation of these findings is also relatively straightforward. The flatter than expected slope implies that, as the range of F2 onsets becomes more restricted under emphatic stress, [d] F2 onsets show less V2 dependence. Consequently, increased emphasis seems to be producing less coarticulation.

In the bottom left panel of Fig. 5 the F2 onsets for [g]'s before front vowels show no or minimal accent-dependent differences, whereas the corresponding points for back vowels show a small rising trend as F2 midpoints increase. Looking at the right panel for velars, a linear fit to the "deviant" (observed) F2 onsets, relative to the expected LE line, would steepen the back vowel cluster and slightly flatten the front vowel cluster. A new single regression line through all these points (dark squares) would result in an overall decrease in LE slope, as previously documented.

For [b] we concluded that this pattern could be entirely accounted for in terms of the accent-related vowel expansion effect. Is this also the case for [g]? The left and right diagrams at the bottom of Fig. 5 suggest that this can only be

TABLE II. Results of multiple regression analysis. N=nonemphatic CV; E=emphatic CV. Anticipatory coefficient (*b*) refers to independent variable vowel 2; perseveratory coefficient (*c*) refers to independent variable vowel 1 in $V1.CV_2$ sequence.

			[b]		[d]		[g] front		[g] back	
Subject	Coefficient		N	E	N	E	N	E	N	E
BR	Intercept	*a*	153	214	635	1128	909	1383	−312	−167
BR	Anticipatory	*b*	0.74	0.74	0.54	0.37	0.54	0.38	0.94	1.11
BR	Perseveratory	*c*	0.09	0.05	0.14	0.05	0.11	0.04	0.38	0.2
MB	Intercept	*a*	181	216	918	1100	992	1305	−378	−345
MB	Anticipatory	*b*	0.76	0.8	0.46	0.43	0.46	0.42	1.19	1.38
MB	Perseveratory	*c*	0.04	0	0.06	0.02	0.13	−0.02	0.22	0.04
MM	Intercept	*a*	250	208	761	941	1379	1409	−580	−334
MM	Anticipatory	*b*	0.7	0.71	0.5	0.45	0.41	0.37	1.38	1.28
MM	Perseveratory	*c*	0.06	0.06	0.1	0.07	0.00	0.00	0.13	0.08

TABLE III. Results of t-tests between F2 onsets observed vs F2 onsets expected for each speaker and stop consonant. T-values significant at $p < 0.01$ indicated by an asterisk (*); $df = 59$ in all cases.

	Labial			Alveolar			Velar		
	Obs	Exp	*t*	Obs	Exp	*t*	Obs	Exp	*t*
BR	1465	1414	0.82	1825	1760	4.79*	1872	1791	5.47*
MB	1415	1373	5.02*	1841	1772	9.41*	1859	1818	3.37*
MM	1586	1429	8.41*	1825	1802	2.44*	1820	1824	−0.27
Mean	1489	1405		1830	1778		1850	1811	

part of the explanation. For some of the back vowel contexts F2 onset shifts can be seen that are considerably higher than expected onsets, suggesting significant differences between emphatic and nonemphatic [g] productions. However, lacking the articulatory data on these samples we can only speculate on what these differences might be.

IV. DISCUSSION

The goal of this study was to develop new analysis metrics to investigate coarticulation during prosodically induced changes to vowels flanking voiced stop consonants. Our strategy was to isolate the acoustic effects of emphatic stress on F2 transition onsets, independently of the stress effect on vowel midpoint frequencies. The observed F2 onset (Hz) variations during emphatic CV2 productions had two possible causes: (i) a passive effect of being linked to a vowel undergoing expansion in F2 phonetic space (picture a rubber band-like proportional scaling), or (ii) independent adjustments of the consonants to emphasis. If we simply claimed, based on our LE slope values, that emphatic stress reduces

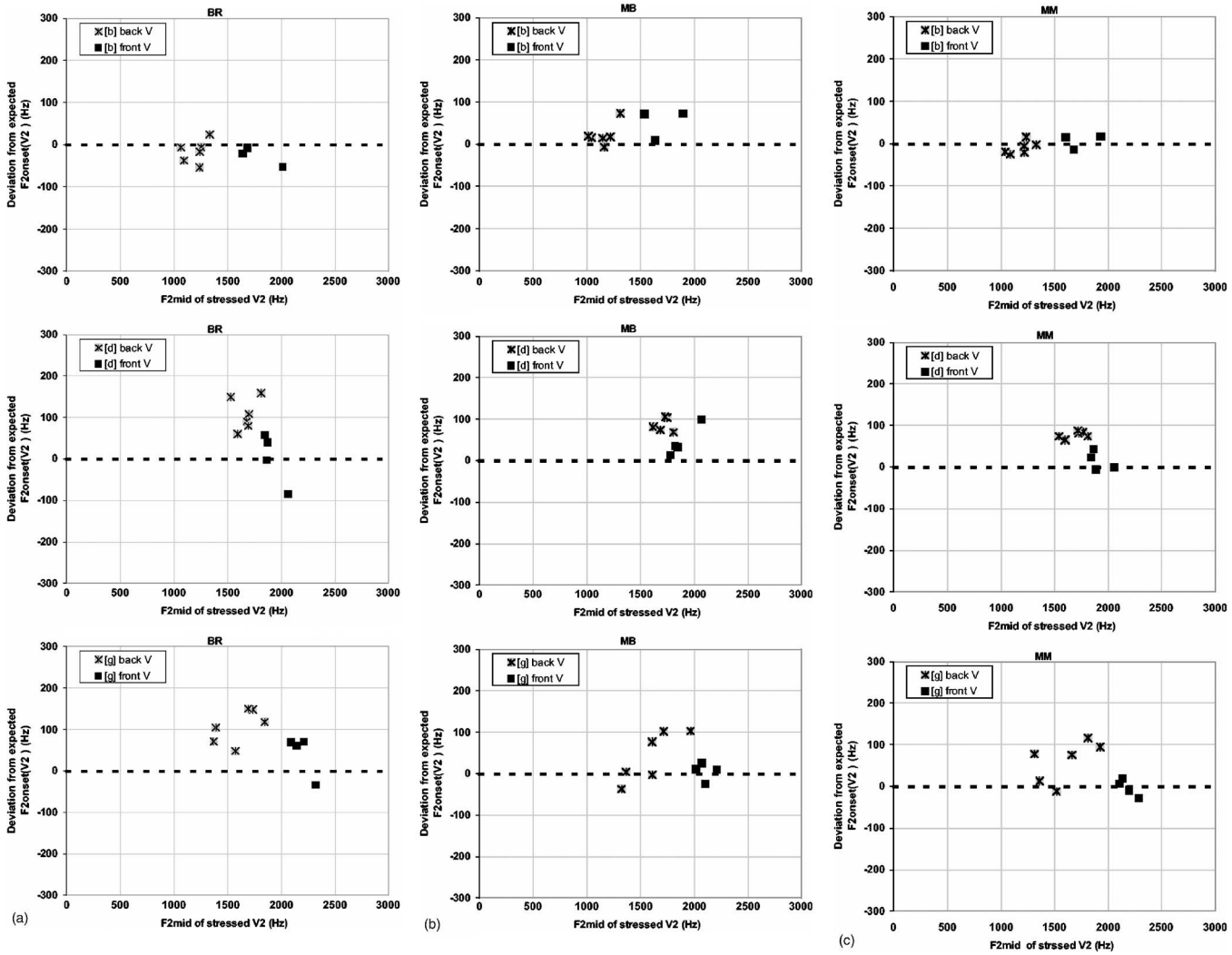

FIG. 4. Deviation of observed F2 onsets from expected F2 onsets plotted against observed F2mid (Hz) of stressed V2. The V2 contexts were divided into front and back groups. Values above the line of equality (0) indicate that observed F2 onsets exceed expected/predicted values (A=speaker BR; B=speaker MB; C=speaker MM).

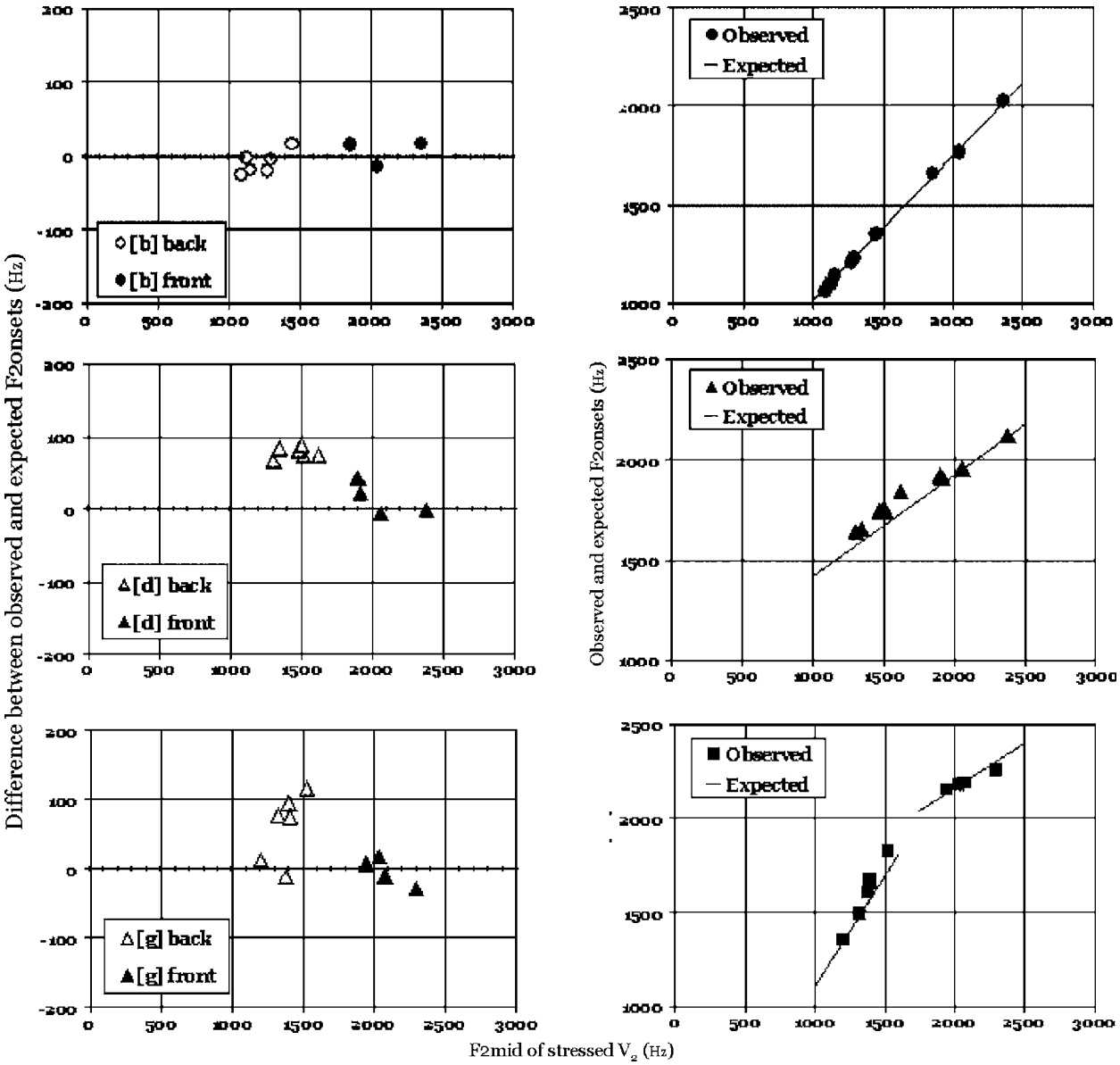

FIG. 5. Left column: Mean deviations of observed vs expected F2 onsets, averaged across the three speakers, plotted against F2mid (Hz) of stressed V2. From top to bottom are scatterplots for labials, alveolars, and velars. The V2 contexts are shown as front and back groups. Right column: Expected F2 onsets are indicated by the straight lines which were derived by means of the LE metric with two independent variables. The closed symbols alongside each regression line represent observed F2 onset means for [bV]-circles, [dV]-triangles, and [gV]-squares tokens. F2 onset variations, relative to straight lines, indicate stress-induced changes to F2onsets.

coarticulation by virtue of vowel nuclei moving further away from their C-onset linkages, then a reasonable corollary to that would be stability in consonantal onsets. A straightforward comparison of F2 onsets between nonemphatic relative to emphatic conditions clearly showed departures from equality, negating a stability notion for F2 onsets. The analysis metrics of this study showed both proportional, as well as disproportional scaling, as expanding vowel nuclei sometimes dragged along the F2 onsets (as with labial stops), and other times did not (as with alveolar and velar stops).

A take home message for the above-noted set of exercises can be summarized as follows: The existence of disproportionate scaling between changes to F2 onsets relative to vowel expansion effects implies explicit changes to CV coarticulation under emphatic stress; proportionate scaling implies overall maintenance of CV coarticulation, as changes to F2 onsets are simply correlated adjustments to expanded vowel positions. In the next section we will attempt to provide an articulatory interpretation for the patterned acoustic data obtained.

A. Articulatory interpretation of acoustic prominence results

This study used formant measurements as a window on articulation, a poor man's x-ray in a sense. While the absolute frequency changes were small, they did reveal a consistent and interesting pattern between phrasal accent effects on labially formed relative to lingually formed stop consonants. De Jong (1995), in an x-ray microbeam study investigating the kinematics underlying linguistic prominence, clearly showed that "the jaw, lip, and tongue interact in the articu-

lation of stress in subject dependent ways" (p. 491). His intersubject differences highlighted the fact that "stress effects are more profitably described in terms of abstract articulatory goals than in terms of actual articulators" (p. 501). In the following discussion we will also strive for a goal-oriented interpretation. We will first show that the acoustic data are in accord with the emphatic stops being produced with a "deeper contact" for the lingual occlusion.

1. "Deeper contact" hypothesis

The deeper contact hypothesis suggests that there is a greater degree of tongue tissue compression and hence larger contact areas on the alveolar ridge/hard palate during the longer occlusion interval of emphatically stressed relative to nonemphatic lingual consonants. Greater tissue compression at the lips for emphatically produced labial + vowel sequences is also hypothesized, but unconstrained tongue movements during the occlusion precludes the same acoustic results as seen with lingual stops.

Closure duration values, where consonant occlusion duration was defined as the interval between the last glottal pulse of V1 and the first glottal pulse of V2, showed a mean increase due to CV_2 emphasis of 82 ms for [bV_2], 79 ms for [dV_2], and 76 ms for [gV_2] tokens. Thus, emphatic stop closures were significantly longer (oral average 79 ms) than their nonemphatic variants.

Evidence that deeper stop closures are associated with increased stress comes primarily from work on electropalatography (Farnetani, 1990). Farnetani's study is particularly relevant to the present work in that it contains observations on how tongue-palate contact patterns for apical stops (/t/ and /d/) vary as a function of stress. Activation of a larger number of front electrodes on the tongue-palate contact area was shown to be strongly dependent on closure duration.

Before discussing the simulation of acoustic consequences of "deeper closures," another closely related and compatible kinematic effect often observed during the production of intervocalic stops is relevant. Houde (1968) was the first to report a forward movement of the tongue mass during the closure gesture into velar stops. Since that early cineradiographic study, several more recent kinematic studies of both lip and tongue movements in V-stop-V contexts have shown that the articulators move, at high velocities, toward a virtual stop closure target, and continue to move during closure through a curved trajectory, with concomitant tissue compression that maintains an airtight seal (Mooshammer *et al.*, 1995; Löfqvist and Gracco, 1999; Fuchs *et al.*, 2001; Löfqvist & Gracco, 2002).

2. Acoustic simulations

To ascertain possible acoustic effects of more extensive tongue-palate contact during stop closure we modeled alveolar stops as a constriction imposed on a uniform tube. A 17.5 cm tube with a cross-sectional area of 8 cm^2 and a 1.5 cm constriction at 14 cm from the glottis was chosen. The constriction area was set at 0.16 cm^2 to approximate the articulatory opening occurring near the first postrelease glottal pulse of a [dV] sequence (an approximate value corresponding to F2 onsets).

For such a radically constricted configuration, F1 would be expected to show a low value (Fant, 1960). Since the ratio between wide and narrow areas is large, the coupling between the cavities can be considered negligible. We would expect F2 to depend primarily on the length of the back cavity which approximates a tube closed at both ends and whose resonance frequencies would therefore occur at multiples of $c/2l$. For the speed of sound $-c=35\,000$ cm/s at body temperature-the estimate for F2 becomes $35000/(2\times14)=1250$ Hz.

A deeper alveolar closure could be simulated by making the constriction more extensive at the expense of the back cavity. As the constriction of the tube model is thus broadened and the back (and front) cavity correspondingly shortened, we find that its resonance—here equated with F2—would rise by approximately 10 Hz per mm increase in constriction extent.

Recall that we observed an average stress-dependent difference for F2 onsets for [d] of the order of 50 Hz. In terms of the tube model such a value implies a stop occlusion length difference of about 5 mm, a value in good agreement with Farnetani's EPG observation (1990).

A similar exercise is useful in the interpretation of the results for [g]. As a point of departure we selected a modified version of the velar consonant model explored by Stevens (1998, p. 366). The velar constriction is located at two-thirds of the distance between the glottis and the lips (a total tube length of 16 cm). Figure 6 (left side) illustrates the constriction length modifications of the model. The most constricted region of the articulation has a length of 2 cm. Behind this constriction, and in front of it, a 2 cm linear interpolation between the narrow and wide areas is applied. To simulate more extensive contacts we incremented the constriction length in five steps of 1 mm, both at its front and back ends, while keeping the anterior and posterior location of the start and end of the linear tapering unchanged. The left half of Fig. 6 compares two constriction lengths 2 and 3 cm and associated interpolating lines.

Area functions were then derived for the five incremented constriction lengths and formant frequencies were calculated using the FORMF.C program based on Liljencrants and Fant (1975). The result of this exercise is shown in the right panel of Fig. 6, which shows the frequencies of F2 and F3 as a function of increasing the length of the constriction. Recall that an increment of 0 mm implies a constriction length of 2 cm. Figure 6 shows that F2 rises by approximately 11 Hz

In Fig. 4 we observed that the stress-dependent effect for the F2 onsets of [g] was minimal suggesting limited, if any, increase in tongue-palate contact areas. However, in Fig. 5, the plots that compare expected with observed F2 onsets in emphatic velar stops indicate that, for several back vowel contexts, F2 onsets greatly exceeded the expected values. This could possibly indicate that the higher than expected F2 onsets were produced with more fronted [g] articulations.

Interestingly, the results estimated from the above-

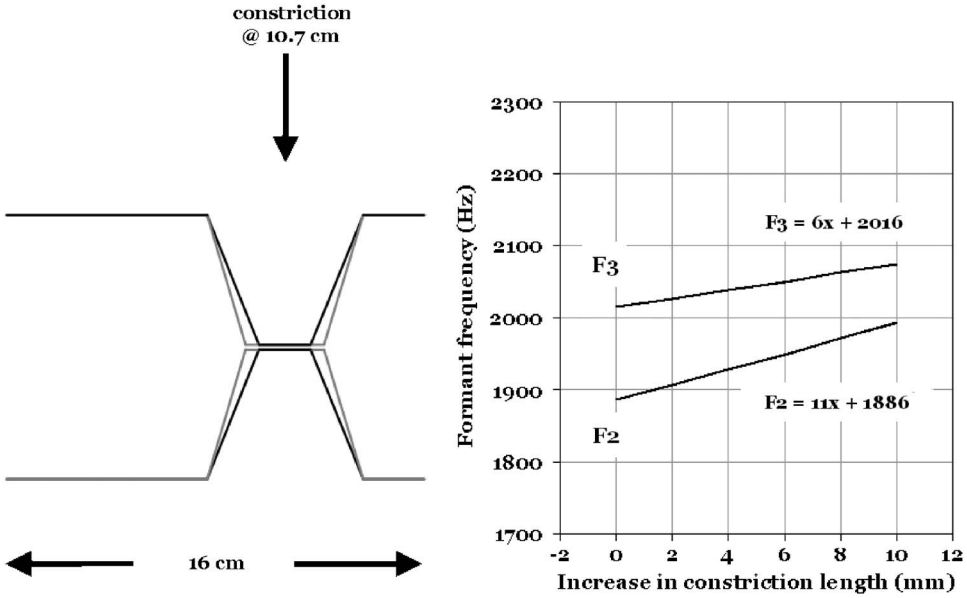

FIG. 6. Simulation of "deep closure" in the production of a velar stop. Regression lines on the right indicate the rise in F2 and F3 frequency as a function of increasing constriction length (mm).

mentioned velar modeling exercise are compatible with kinematic lingual displacements of tongue-body movement recently documented during closure for velar stops (Löfqvist and Gracco, 2002; Mooshammer *et al.* (1995). Löfqvist and Gracco (2002) concluded that "…*at the instant of the acoustically defined oral closure for a velar stop the tongue body is moving forward in the majority of cases* (p. 2826). Mooshammer *et al.* (1995) reported approximately 1 mm of tongue (fronting) movements in V1=/i/ contexts and from 4 to 10 mm when the preceding vowel was either /u/ or /a/. Our data were based on averages across ten vowel contexts, but back vowels illustrated the most extensive changes under emphatic stress, in agreement with the above-mentioned results.

B. Differences between labial and lingual stops

The mechanical uncoupling between the C-articulator relative to the V-articulator is often cited as a reason for greater anticipatory coarticulation in [bV] sequences than, for example, [dV] sequences. Using a magnetometer system for recording tongue and lip movements, Löfqvist and Gracco (1999) determined that in vowel-bilabial stop-vowel sequences, "more than 50% of the tongue movement trajectory from the first to the second vowel tends to occur during the stop closure for the consonant" (p. 2812). Thus, in phrasally accented labial productions, the unconstrained tongue can easily maintain constancy in anticipatory coarticulation extents despite the expanded V2 vowel space. When alveolar and velar stops are flanked by vowels, however, the tongue is actively involved in forming the stop closure and must maintain the airtight seal, foregoing the degree of anticipatory movement seen in the vowel-to-vowel gestures surrounding labial stops. As vowel midpoints expand during emphatic stress, with F2 of low vowels moving lower and F2 in high vowels moving higher, the tongue dorsum contact points for closure "dig in" and resist, to a greater extent, the following vowel's front-back position.

C. On the use of LEs in the analysis of coarticulation

Several studies have attempted to establish a direct (rather than an inferred) link between specific articulatory gestures and the degree of anticipatory coarticulation as indexed by the LE slope (e.g., Löfqvist, 1999; Tabain, 2000, 2002). The Löfqvist study used magnetometers to record tongue and lip movements from four receivers, and the Tabain study utilized EPG recordings. In general, both studies reported negative results, with Löfqvist concluding "*it appears that caution is necessary in making claims that locus equation slope can be used to assess differences in coarticulation*… (p. 2029). In defense of the LE slope, and as similarly stated by Löfqvist (see p. 2028), it is very difficult to equate the phonetic playing fields of specific kinematic recordings to the acoustically based, and higher-order category-level analysis of the LE. Since LE slopes are derived across many and varied vowel contexts (Löfqvist used only three vowels in his analyses), and since the F2 transitions reflect area functions of the entire vocal tract, the well-intentioned affirmation strategy falls well short of a valid test. Perhaps the single most informative technique that can speak to this issue is the use of articulatory models, such as APEX (Lindblom, 1998; Stark *et al.* 1998). For example, Lindblom's simulation (1998) clearly showed how two different tongue body configurations for the vowel, one already in vowel position during the oral closure for [dV], relative to a more neutral tongue body position at closure, yielded two vastly different LE slopes—0.94 in the "anticipatory" position and 0.07 in the vowel-neutral position.

In conclusion, caution is needed in strictly interpreting LE slopes as numerical markers of degree of coarticulation. While basically valid, there are sources of phonetic variation, such as emphatic stress and tempo, that can introduce a confound into the linkage between the LE slope and degree of coarticulation. The methodology described in this study can help account for this interaction.

Beckman, M., and Edwards, J. (**1994**). "Articulatory evidence for differentiating stress categories," in *Phonological Structure and Phonetic Form: Papers in Laboratory Phonology III*, edited by P. A. Keating (Cambridge University Press, Cambridge), Chap. 2, pp. 7–33.
Beckman, M. E., and Cohen, K. B. (**2000**). "Modeling the articulatory dynamics of two levels of stress contrast," in *Prosody: Theory and Experiment*, edited by M. Horne (Kluwer, Dordrecht), pp. 169–200.
Cole, J., Choi, H., and Kim, H. (**2004**). "Acoustic evidence for the effect of accent on CV coarticulation in Radio News speech," Proceedings of the 2003 Texas Linguistics Society Conference, edited by A. Agwuele, W. Warren, and S.-H. Park, Cascadilla Proceedings Project, Somerville, MA, pp. 62–72.
Crystal, T. H., and House, A. S. (**1988**). "Segmental durations in connected-speech signals: Syllabic stress," J. Acoust. Soc. Am. **83**, 1574–1585.
De Jong, K. (**1995**). "The supraglottal articulation of prominence in English: Linguistic stress as localized hyperarticulation," J. Acoust. Soc. Am. **97**, 491–504.
De Jong, K., Beckman, M. E., and Edwards, J. (**1993**). "The interplay between prosodic structure and coarticulation," Lang Speech **36**, 197–212.
Duez, D. (**1992**). "Second formant locus nucleus patterns: An investigation of spontaneous French speech," Speech Commun. **11**, 417–427.
Fant, G. (**1960**). *Acoustic Theory of Speech Production* (Mouton, The Hague).
Farnetani, E. (**1990**). "V-C-V lingual coarticulation and its spatiotemporal domain," in *Speech Production and Speech Modelling*, edited by W. Hardcastle and A. Marchal (Kluwer, Dordrecht), pp. 93–130.
Fowler, C. A., and Saltzman, E. (**1993**). "Coordination and coarticulation in speech production," Lang Speech **36**, 171–195.
Fuchs, S., Perrier, P., and Mooshammer, C. (**2001**). "The role of the palate in tongue kinematics; An experimental assessment in VC sequences," Eurospeech 2001, Aalborg, Denmark, 3–7 September.
Houde, R. (**1968**). "A study of tongue body motion during selected consonant sounds," Speech Communications Research Laboratory, Santa Barbara, SCRL Monograph 2.
Jones, D. (**1932**). *An Outline of English Phonetics*, 3rd ed. (Teubner, Leipzig).
Klatt, D. H. (**1974**). "Duration of [s] in English words," J. Speech Hear. Res. **17**, 51–63.
Koopmans-Van Beinum, F. J. (**1980**). "Vowel contrast reduction: An acoustic and perceptual study of Dutch vowels in various speech conditions," Ph.D. dissertation, Institute of Phonetic Sciences, University of Amsterdam.
Krull, D. (**1988**). "Acoustic properties as predictors of perceptual responses: A study of Swedish voiced stops," Phonetic Experimental Research at Institute of Linguistics, University of Stockholm (PERILUS), Vol. **VII**, pp. 66–70.
Liljencrants, J., and Fant, G. (**1975**). "Computer program for VT-resonance frequency calculations," Speech Trans, Lab. Quart. Prog. Rep. **4**, 15–20.
Lindblom, B. (**1963**). "On vowel reduction," Report No. 29, Speech Transmission Laboratory, The Royal Institute of Technology, Stockholm, Sweden.
Lindblom, B. (**1998**). "An articulatory perspective on the locus equation," Behav. Brain Sci. **21**, 274–275.
Löfqvist, A. (**1999**). "Interarticulator phasing, locus equations, and degree of coarticulation," J. Acoust. Soc. Am. **106**, 2022–2030.
Löfqvist, A., and Gracco, V. L. (**1999**). "Interarticulator programming in VCV sequences: Lip and tongue movements," J. Acoust. Soc. Am. **105**, 1864–1876.
Löfqvist, A., and Gracco, V. L. (**2002**). "Control of oral closure in linugual stop consonant production," J. Acoust. Soc. Am. **111**, 2811–2827.
Mooshammer, C., Hoole, P., and Kühnert, B. (**1995**). "On loops," J. Phonetics **23**, 3–21.
Öhman, S. E. G. (**1967**). "Word and sentence intonation: A quantitative model," STL Q. Progr. Status Rep. (Stockholm) **2–3**, 20–54.
Sarraf, R., Sussman, H. M., and Lindblom, B. (**2000**). "The effect of stress on F2 onsets in VCV utterances," J. Acoust. Soc. Am. **108**, 2465(A).
Stark, J., Ericsdotter, C., Lindblom, B., and Sundberg, J. (**1998**). "The APEX model; From articulatory positions to sound," J. Acoust. Soc. Am. **104**, 1820(A).
Stevens, K. N. (**1998**). *Acoustic Phonetics* (MIT, Cambridge).
Sussman, H. M., McCaffrey, H. A., and Matthews, S. A. (**1991**). "An investigation of locus equations as a source of relational invariance for stop place categorization," J. Acoust. Soc. Am. **90**, 1309–1325.
Tabain, M. (**2000**). "Coarticulation in CV syllables: A comparison of EPG and locus equation data," J. Phonetics **28**, 137–159.
Tabain, M. (**2002**). "Voiceless consonants and locus equations: A comparison with EPG data on coarticulation," Phonetica **59**, 20–37.
Tiffany, W. R. (**1959**). "Nonrandom sources of variation in vowel quality," J. Speech Hear. Res. **2**, 305–317.
Turk, A. E., and White, L. (**1999**). "Structural influences on accentual lengthening in English," J. Phonetics **27**, 171–206.
Umeda, N. (**1977**). "Consonant duration in American English," J. Acoust. Soc. Am. **61**, 846–858.
Van Son, R. J. J. H., and Pols, L. C. W. (**1996**). "A comparison between the acoustics of vowel and consonant reduction," Proceedings of the Institute of Phonetic Sciences, University of Amsterdam, Vol. **20**, 13–25, The Netherlands.
Wouters, J., and Macon, M. W. (**2002**). "Effects of prosodic factors on spectral dynamics. I. Analysis," J. Acoust. Soc. Am. **111**, 417–427.

Plasticity in vowel perception and production: A study of accent change in young adults

Bronwen G. Evans and Paul Iverson
Department of Phonetics and Linguistics, University College London, 4 Stephenson Way, London NW1 2HE, United Kingdom

(Received 30 December 2005; revised 12 March 2007; accepted 12 March 2007)

This study investigated changes in vowel production and perception among university students from the north of England, as individuals adapt their accent from regional to educated norms. Subjects were tested in their production and perception at regular intervals over a period of 2 years: before beginning university, 3 months later, and at the end of their first and second years at university. At each testing session, subjects were recorded reading a set of experimental words and a short passage. Subjects also completed two perceptual tasks; they chose best exemplar locations for vowels embedded in either northern or southern English accented carrier sentences and identified words in noise spoken with either a northern or southern English accent. The results demonstrated that subjects at a late stage in their language development, early adulthood, changed their spoken accent after attending university. There were no reliable changes in perception over time, but there was evidence for a between-subjects link between production and perception; subjects chose similar vowels to the ones they produced, and subjects who had a more southern English accent were better at identifying southern English speech in noise. © *2007 Acoustical Society of America.*
[DOI: 10.1121/1.2722209]

PACS number(s): 43.71.Es, 43.71.Ft [ARB] Pages: 3814–3826

I. INTRODUCTION

Native speakers of regional accents typically modify their speech when living in a community where that accent is not commonly spoken (e.g., Munro *et al.*, 1999; Sankoff, 2004). Speakers often avoid variants that are markedly regional or unusual to facilitate communication (Trudgill, 1986) and to fit in with their new community (Foulkes and Docherty, 1999). However, they also retain some regional variants in order to show their allegiance to particular social or geographical groups (e.g., Foulkes and Docherty, 1999; Trudgill, 1986). For example, in British English, the focus of the present study, speakers of northern English who live in southern England typically modify their production of the vowel in words such as *luck* from a high back vowel [ʊ] to a centralized vowel, [ə], so that it is closer to how southerners produce this vowel (Evans and Iverson, 2004; Trudgill, 1986; Wells, 1982). However, they also retain [a] when producing words like *bath* just like in their native northern English accent, rather than producing it with the southern vowel [ɑː] (Evans and Iverson, 2004; Trudgill, 1986; Wells, 1982).

The present study focused on accent change in a group of university students from a small town in the Midlands, U.K., where the local accent is a variety of northern English, a nonstandard accent. In Britain, it is usual for students to attend university in a different area from the one in which they have been raised, and so students come into contact with speakers of a wide variety of accents. In particular, they come into contact with speakers of Standard Southern British English (SSBE), the prestige accent of English and the accent of education.[1] As a result, students from the north of England typically change their accent from regional to educated (i.e., SSBE) norms in order to better fit in with their new university community. The aim of this study was to quantify these changes in accent among university students from the north of England, and to investigate whether the adjustments in production were accompanied by changes in perceptual processing.

One could imagine that perception and production might be based on the same underlying phonetic categories, and that any changes in production would be accompanied by changes in perception (e.g., Liberman *et al.*, 1967; Liberman and Mattingly, 1985; Fowler, 1981, 1986). However, the evidence for such a strong relationship between perception and production is mixed. Bell-Berti *et al.* (1979) demonstrated that differences in production strategies for the vowel /i/ were significantly correlated with differences in perception for /i/. They took this as evidence for a common mechanism or process that mediates the production and perception of vowels. Newman (2003) also found significant, though small, correlations between listeners' perceptual prototypes and their average voice onset time (VOT) for stop consonants, as well as between their perceptual prototypes and spectral peaks for voiceless fricatives. Other studies have failed to find such correlations. For example, Bailey and Haggard (1973, 1980) found no correlation between average VOTs produced in voiced and voiceless consonants and listeners' perceptual category boundaries for a /g/-/k/ continuum. Similarly, Ainsworth and Paliwal (1984) found no correlation between performance on production and perception tasks for glides, and Frieda *et al.* (2000) for the vowel /i/.

Results from studies of production and perception in second language (L2) learning are also not clear-cut. Flege *et al.* (1997) found evidence for correlations between the perception and production of the four English vowels, /i/, /ɪ/, /ɛ/

 0001-4966/2007/121(6)/3814/13/$23.00 © 2007 Acoustical Society of America

and /a/ by non-native learners of English, but the magnitude of these correlations was small (see also Flege *et al.*, 1999). Other studies of L2 acquisition have found no evidence for the existence of these perception-production correlations. For example, Bradlow *et al.* (1997) demonstrated that Japanese learners improved in both their production and perception of the phonemes /r/ and /l/ after perceptual training, but found no significant correlations between individual learners' improvement in perception and production. That is, even though subjects changed their production and perception, the subjects who showed the most change in production did not always show the most change in perception.

Even if there is no direct link between changes in production and perception, subjects may still adjust their perceptual processes when listening to a non-native accent. For example, studies of talker-specific learning (e.g., Nygaard and Pisoni, 1998) have shown that after only a short amount of experience with an unfamiliar talker, word recognition for that talker improves. Moreover, listeners are able to adapt rapidly to foreign-accented speech (Clarke and Garrett, 2004; Nygaard *et al.*, 2005); adaptation to foreign-accented speech has been shown to require exposure to only two to four sentence-length utterances (Clarke and Garrett, 2004), and listeners appear to be able to shift their VOT categorization boundary for stop consonants to better match a speaker's productions after less than 2-min experience with that speaker (Clarke and Luce, 2005). Based on this evidence, one might expect that in a multidialectal situation, where subjects are regularly exposed to a non-native accent, subjects would be able to easily adapt perceptually to that accent. In the present study, northern listeners who are regularly exposed to SSBE might thus be able to easily adjust their perceptual processes to better adapt to SSBE.

However, our evidence (Evans and Iverson, 2004) suggests that adaptation to a non-native accent may be slower. In this previous work, we investigated whether listeners from the north of England changed their best exemplar locations when listening to speech produced in their native accent and SSBE. Subjects with different backgrounds were tested; northerners who had been living in London (south of England) for a minimum of 1 year, and northerners aged 16–17 years who had been born and raised in the north of England. The results demonstrated that northerners living in the south of England adjusted their best exemplar locations when listening to SSBE speech; listeners chose best exemplar locations for vowels in SSBE sentences that more closely matched how southerners produce these vowels. However, northerners still living in the north of England did not adjust their best exemplar locations; these subjects used their native (i.e., northern) vowel categories when listening to both SSBE and northern English. This was surprising as these northerners had extensive experience of listening to southern English speech through the media. This suggests that, although subjects are able to adjust their perceptual categorizations, these changes take place over a long period of time and are not just determined by short-term exposure to a particular speaker or accent (see also Eisner and McQueen, 2005).

The present study used a longitudinal design to investigate whether subjects changed their production as a result of attending university, and whether these changes were accompanied by changes in perception. Students were tested before beginning university, 3 months later, and on completion of their first and second years at university. At each testing session they completed three experiments. Experiment 1 investigated whether subjects changed their speech production. Experiment 2 created perceptual vowel space maps (i.e., best exemplar locations) in a three-dimensional space that varied $F1$, $F2$, and duration for vowels embedded in SSBE and northern English carrier sentences. The aim was to investigate if subjects changed the acoustic qualities of the vowels according to whether the sentence was spoken with an SSBE or northern English accent. Further analysis addressed whether any changes in the perceptual vowel space maps were linked to changes in production. Experiment 3 investigated whether any changes in production and the best exemplar locations had an effect on sentence recognition in noise.

II. EXPERIMENT 1: MEASUREMENT OF PRODUCTION

A. Method

1. Participants

Twenty-seven subjects were tested and paid for their participation. All were native monolingual English speakers and reported no speech, hearing, or language difficulties.

Subjects were recruited from Ashby de la Zouch, Leicestershire, UK, a small market town in the Midlands where the local accent can be classified as a variety of northern English (Evans, 2005; Wells, 1982). At the time of recruitment, subjects were aged 17–18 years, and were completing their school education at Ashby Grammar School, the local comprehensive school. All subjects had lived in Ashby since at least age 5 years,[2] and had been educated at local schools. This period of development, characterized by the influence of the peer group, is thought to be particularly important for the development of regional accent (Kerswill and Williams, 2000). All had parents and immediate family local to the area, minimizing the risk that subjects had regular contact with speakers of southern English accents.

Subjects attended different universities in England,[3] and so all testing was carried out in Ashby. Students in Britain typically attend university in a different area from the one in which they have been raised, so the location of the university has little influence on the accent background of the student body as a whole. Thus, subjects attending university in the north of England and those attending university in the south of England were both likely to interact with SSBE speakers. All students lived in university accommodation and reported that they spent the majority of their time interacting with fellow students.

Two subjects did not complete the experiment because they dropped out of university during their first term. Of the remaining 25 subjects, two subjects were dropped from the experiment because their best exemplar locations for the vowels found in experiment 2 were not reliable (i.e., their

best exemplar locations for words that are produced the same in SSBE and Sheffield English accents, such as in the words *bird* and *bead*, differed by more than 2 ERB in the two carrier sentences). This gave a test sample of 23 subjects, 7 male and 16 female. Due to problems in contacting all of the subjects, only 19 of these subjects were tested at the last testing time.

2. Stimuli and apparatus

The stimuli consisted of 11 test words in the carrier sentence *I'm asking you to say the word [ ] please*, and a phonetically balanced passage, "Arthur the Rat." The test words were *bad, bard, bawd, bed, bird, booed, bud, bead, cud, could*, and *bath*. This allowed potential changes in subjects' best exemplar locations (experiment 2) to be compared with changes in production. Of particular interest were the vowels in the words *bud, cud*, and *bath* that are produced differently in northern and southern English accents (e.g., Wells, 1982). Speakers of SSBE produce words like *bud* and *cud* using the vowel [ʌ]. However, speakers of northern English do not have this vowel in their phoneme inventory; they say words like *bud* and *cud* using the high back vowel [ʊ], such that *bud* is produced with the same vowel as *book*, and *cud* becomes a homophone or near homophone of *could*. Northerners and southerners both have the vowels [a] and [ɑː] but with somewhat different lexical distributions; words like *bath* are produced with [ɑː] by southerners, but with [a] by northerners.

All recordings were made in a quiet room and recorded onto DAT with a sampling rate of 44.1 kHz, 16-bit resolution.

3. Procedure

a. Recording. Subjects recorded two repetitions of each target word in a randomized order and one reading of the passage. Subjects were instructed to read the passage as if they were reading it to a friend. The researcher was the first author, who lived in Ashby from age 2–18 years when she moved away to attend university. Although she still uses some local features in her accent (e.g., short "a," [a], in *bath*), she has changed her accent so that it is more similar to that of the SSBE speakers in the community where she now lives. She conducted all testing and was known to the subjects as the sister of a friend. It was thought that the relationship of the researcher to the subjects and the researcher's own linguistic background would encourage subjects to speak in the way that they would when interacting with friends at university (Milroy, 1987a, 1987b).

b. Accent ratings. Six phonetically trained listeners rated for accent samples of subjects' speech from each testing session [i.e., before beginning university (Time 1;T1), 3 months later (Time 2; T2), after 1 year (Time 3; T3), and after 2 years (Time 4; T4)]. All listeners were native British English speakers. They gave ratings on a short sample of the reading passage: *Just then the old captain saw Arthur. "Stop," he ordered the others coarsely. "You are coming, of course?" "I'm not certain," said Arthur, undaunted. "The roof may not come down yet."* This passage was selected because it was thought to be revealing of accent. That is, it contains examples of the vowels that were expected to change after living in a multidialectal environment (e.g., the vowels in the words *just, coming*, and *come*).

The rating sessions were self-paced and listeners could listen to each sample as many times as they wished. Listeners gave their ratings by indicating on a response sheet, on a scale of 1 to 10, how northern or southern they thought the speaker sounded. A rating of "10" corresponded to "very northern" and a response of "1" to "very southern." Stimuli were presented in a random order (i.e., all recording times presented together). Listeners were not made aware of the design of the study. That is, they were not told that they would hear the same speaker more than once, and were unaware that speakers were expected to have changed their accent. All listeners were native British English speakers.

c. Acoustic analysis. $F1$, $F2$, and duration were measured for the vowels in each target word spoken in the carrier sentence, giving two sets of measurements for each word. $F1$, $F2$, and duration were averaged across repetitions of each word and these measurements were used in the subsequent analyses. The test words rather than the passage were used because this enabled any effects of consonantal context to be controlled. In contrast, the accent ratings were made on the passage to give a more global measure of each subject's accent.

The acoustic measurements were made in PRAAT (Boersma and Weenink, 2004). The stimuli were located manually, and then $F1$ and $F2$ were extracted using hand-corrected LPC analyses. Formant frequencies were measured from the midpoint of the steady-state portion of the vowel. The steady-state portion of the vowel was defined as the part of the vowel that was closest to the midpoint and where the formant frequencies were most stable. All duration measurements were taken from the beginning of the $F2$ transitions to the end of the $F2$ transitions.

So that the data from male and female speakers could be compared, a version of Nearey's (1978) individual log mean procedure was used to normalize the acoustic measurements. The procedure expresses each log-transformed formant frequency as a distance to a reference point, the log mean, which is calculated by averaging the log-transformed $F1$ and $F2$ values for all vowels for a given speaker. This procedure was chosen because it has been shown to be one of the most effective methods for reducing the effects of anatomical and physiological variation, while retaining the phonemic variation that is important for accent variation (Adank, 2003; Adank *et al.*, 2004). The average formant frequencies for each test word were normalized following the equation:

$$F_{ijk\ \mathrm{norm}} = G_{ijk} - \underline{G}, \tag{1}$$

where i is the formant, j is the vowel being transformed, k is the speaker, G is the log-transformed frequency of formant i, and $\underline{G}$ is the log mean for a speaker k. In this study the log mean was calculated using the vowels that are produced similarly in northern and southern English accents (i.e., *bad, bard, bawd, bead, bed, bird*, and *booed*) for that talker, averaged over all testing sessions. The vowels in *bud, cud,*

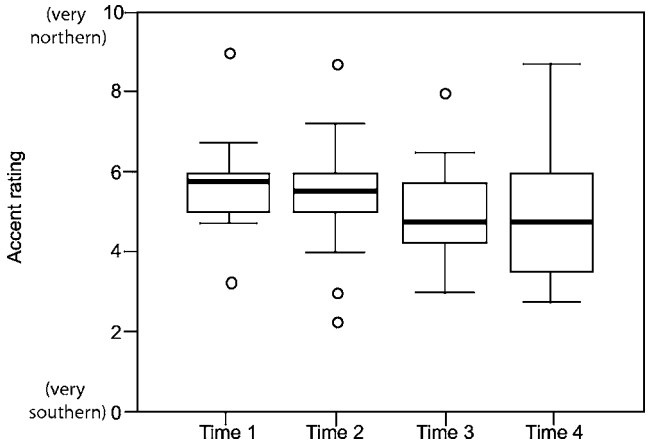

FIG. 1. Boxplot of the accent ratings for subjects at T1, T2, T3, and T4 ($N=23$ at T1, T2, and T3; $N=19$ at T4). Boxplots display the interquartile range of scores. The box shows the 25th to 75th percentiles, with a line at the median value. The lower and upper "whiskers," respectively, show the minimum and maximum values of the data range, with outliers represented by the unshaded circles. Subjects changed their spoken accent over time; subjects were given a more southern (i.e., lower) rating at T4 than at T1.

could, and *bath* were omitted from the log mean calculation because these vowels were expected to change over time.

B. Results

1. Perceived accent rating

As displayed in Fig. 1, subjects changed their accent over time. Subjects were judged to sound more southern at T4 than at T1, though there appeared to be little change between the testing sessions at T3 and T4, and there was more variability in the ratings at T4 than at T1, T2, or T3 (see Table I). The potential differences between the ratings at T1, T2, T3, and T4 were tested in a repeated-measures ANOVA, with time (T1, T2, T3, and T4) coded as a within-subject variable. There was a main effect of time, $F(1,20)=22.94$, $p<0.001$, confirming that subjects changed their accent to sound more southern after attending university.

However, as displayed in Table I, there were differences in the amount and direction of accent change between subjects. Although the majority of subjects (18 out of 23) was rated as sounding more southern at the final testing time than at T1, the change in accent rating[4] from T1 to the final testing session was often small; for nine subjects, the change in accent rating was less than 1 point on the 10-point rating scale. Also, three subjects were judged not to have changed their accent at all and one was judged to have a more northern accent at the final testing session than T1.

There were also large individual differences in the accents of the talkers. For example, as can be seen from the data in Table I, one subject had an accent rating greater than 8 at T1, T2, T3, and T4 (i.e., very northern), but another subject had an accent rating between 2.67 and 2.83 at T1, T2, T3, and T4 (i.e., very southern). These differences can be seen clearly when the overall accent rating (i.e., the average of each subject's rating at T1, T2, T3, and T4 or T1, T2, and T3 when the subject could not be contacted at T4), is calculated (Table I).

A Pearson correlation investigated whether the change in accent rating was related to the overall accent rating, that is,

TABLE I. Individual accent ratings for subjects at T1, T2, T3, and T4, the overall accent rating and change in accent rating.

Sex	Accent rating				Overall accent rating	Change in accent rating (final–first testing time)
	T1	T2	T3	T4		
F	6.50	5.67	6.33	⋯	6.21	−0.17
F	6.83	7.33	5.67	6.33	6.54	−0.50
F	6.83	5.83	5.50	⋯	5.92	−1.33
M	6.50	6.67	4.17	4.17	5.38	−2.33
F	5.33	4.50	4.83	3.67	4.58	−1.67
F	6.33	5.83	5.33	4.17	5.42	−2.17
F	6.50	6.33	6.67	6.00	6.38	−0.50
F	5.17	5.50	5.50	6.17	5.58	+1.00
F	5.83	5.83	4.83	5.00	5.38	−0.83
F	2.83	2.83	2.67	⋯	2.72	−0.17
M	8.00	6.83	5.83	5.83	6.63	−2.17
F	6.67	6.33	5.67	5.50	6.04	−1.17
F	6.50	6.17	5.83	6.33	6.21	−0.17
M	6.67	6.33	5.83	5.50	6.08	−1.17
M	5.83	6.33	5.83	5.00	5.75	−0.83
M	⋯	8.00	7.50	6.33	7.28	−1.67
F	3.33	5.33	3.67	3.33	3.92	0.00
F	6.17	5.83	4.83	6.17	5.75	0.00
F	6.17	3.67	5.50	⋯	5.21	−0.67
F	5.33	5.83	4.83	4.67	5.17	−0.67
F	5.83	4.00	5.33	2.83	4.50	−3.00
M	8.67	8.33	8.17	8.67	8.46	0.00
M	5.00	3.33	3.83	3.83	4.00	−1.17

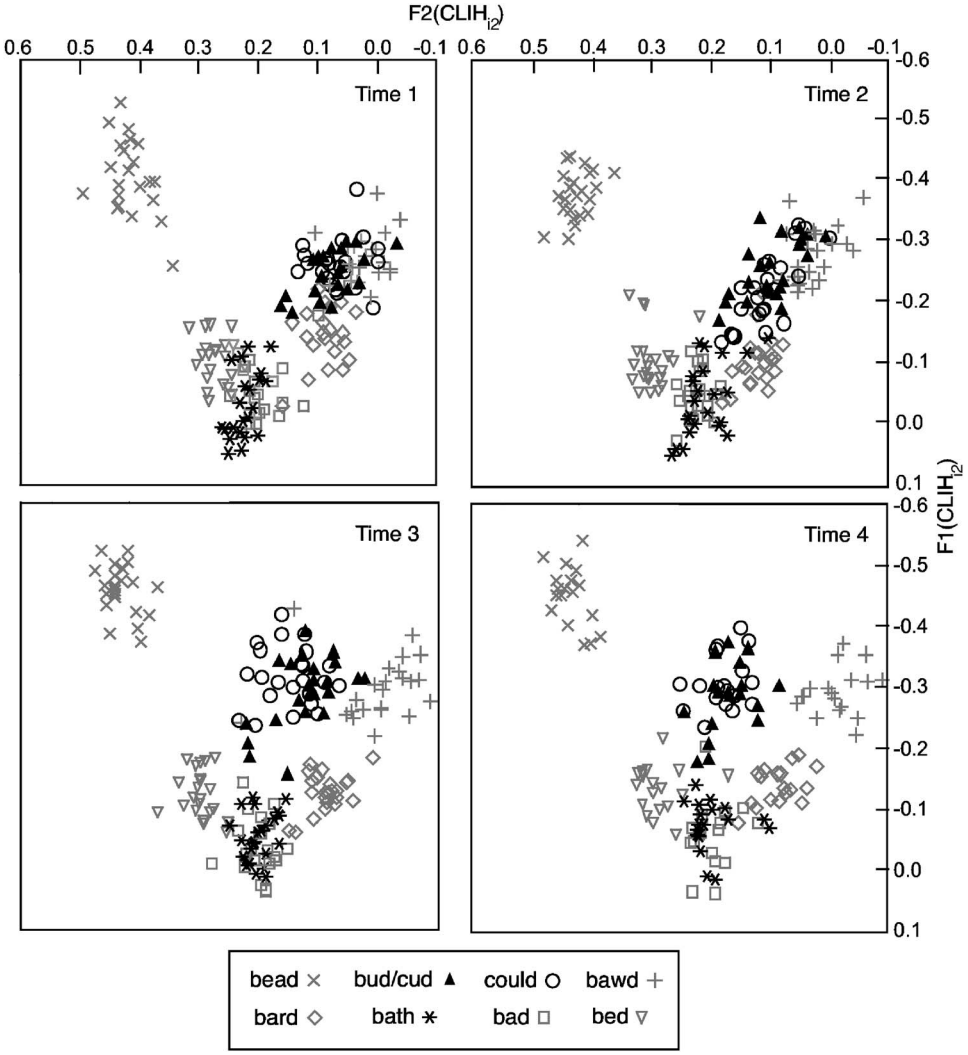

FIG. 2. *F*1 and *F*2 formant frequency plots of subjects' productions of target words at T1, T2, T3, and T4. *Bud* and *cud* (averaged), *could* and *bath* (i.e., the vowels that were expected to change with accent), are shown in black symbols. All other vowels (i.e., those that are produced similarly in both northern and southern English accents) are shown in gray. Measurements are given in Nearey's log mean units ($CLIH_{I2}$). This measure was used to normalize the data so that male and female speech could be compared. Subjects changed their production of *bud, cud*, and *could* so that it was more centralized at T4. This changed occurred in both the *F*1 and *F*2 dimensions. No changes occurred in any other vowels.

whether subjects who were judged to sound more northern at T1 changed their accent more than those who were judged to sound more southern. The results demonstrated that there was no significant relationship between the overall accent rating and the change in rating, $r=0.35$, $p>0.05$.

2. Acoustic analysis

Based on our previous work (Evans and Iverson, 2004), test words were divided into groups that would be likely to change (i.e., *bud, cud, could*, and *bath*) and groups that would likely not change (i.e., all other words). This enabled us to avoid multiple statistical tests.

a. Bud and cud. As displayed in Fig. 2, subjects changed the way in which they produced the vowels in *bud* and *cud*. At T1, subjects produced these words with a high-back vowel, as is typical for speakers of northern English accents. At T2, some, but not all, subjects had begun to centralize these vowels. This centralization process continued over time, so that at T3 and T4 almost all subjects produced these words with a more central vowel that is acoustically similar to the vowel in *bird*. The shift appeared to occur in both the *F*1 and *F*2 dimensions, though the amount of change appeared to differ amongst subjects.

The potential changes in *F*1 and *F*2 were tested in separate repeated-measures ANOVA analyses, with word (*bud* or *cud*) and time (T1, T2, T3, and T4) coded as within-subject variables. For *F*1, there was a main effect of time, $F(3,48)=6.80$, $p<0.01$, demonstrating that subjects produced this vowel with a higher *F*1 at T4. There was also a main effect of time for *F*2, $F(3,48)=29.33$, $p<0.001$, demonstrating that subjects produced this vowel with a higher *F*2 at T4. There was a significant interaction of word and time for both *F*1, $F(3,48)=8.22$, $p<0.01$, and *F*2, $F(3,48)=10.08$, $p<0.001$. Inspection of the data revealed that this was because changes in *F*1 and *F*2 for *cud* occurred faster than those for *bud*; at T1 *bud* was produced with a higher *F*1 and *F*2 (i.e., more central) than *cud*, but at T2 *cud* was produced with a higher *F*1 and *F*2 than *bud*. There was also a main effect of word for *F*2, $F(1,16)=13.42$, $p<0.01$; overall *F*2 was lower (i.e., further back in the vowel space) for *cud* than for *bud*.

As displayed in Table II, there was little change over time in duration for *bud* and *cud*, although subjects appeared to be producing a shorter vowel at T1, T2, T3, and T4 for *cud*. A repeated-measures ANOVA for duration revealed that there was a main effect of word, $F(1,16)=38.24$, $p<0.001$, indicating that subjects were producing a shorter vowel for

TABLE II. Average durations (ms) of vowels in test words at T1, T2, T3, and T4.

Word	T1	T2	T3	T4
bud	135.67	133.65	136.67	120.11
cud	119.24	117.62	117.38	93.67
could	124.48	123.62	123.10	95.06
bath	121.38	122.43	121.71	115.78
bad	160.85	170.62	159.42	139.21
bard	268.53	297.02	266.00	272.10
bawd	262.72	320.99	262.74	247.86
bead	239.13	292.84	238.38	283.40
bed	140.55	184.62	140.07	121.31
bird	269.51	332.52	268.02	248.87
booed	252.64	304.81	251.03	234.32

cud, but there was no significant main effect of time, and no significant interaction of word and time, $p>0.05$.

b. Could. As displayed in Fig. 2, subjects changed the way in which they produced the vowel in *could*. At T1, subjects produced this word with a high-back vowel, as is typical for speakers of northern and southern English accents. At T2, some, but not all, subjects had begun to centralize this vowel, and by T3 and T4 almost all subjects produced this word with a more central vowel. This is surprising as both northerners and southerners produce this word with the same vowel, [ʊ]. As for *bud* and *cud*, the shift appeared to occur in both the $F1$ and the $F2$ dimension, though the degree of change appeared to differ among subjects. The differences in $F1$ and $F2$ were tested in separate repeated-measures ANOVA analyses, with time coded as a within-subject variable. There was a significant effect of time for $F1$, $F(1,16)=30.48$, $p<0.001$, and $F2$, $F(1,16)=39.00$, $p<0.001$. As displayed in Table II, there did not appear to be any change in duration. A repeated-measures ANOVA confirmed that there was no significant effect of time, $p>0.05$.

c. Bath. As displayed in Fig. 2, there appeared to be some changes in the production of *bath* in the $F1$ and the $F2$ dimensions; some subjects seemed to be producing this word with a lower $F1$ and lower $F2$ at T3 and T4, so that it was closer to how they produced the vowel in *bard*. The differences in $F1$, $F2$, and duration were tested in separate repeated-measures ANOVA analyses, with time coded as a within-subject variable. There was a significant effect of time for $F1$, $F(1,16)=7.11$, $p<0.05$, and $F2$, $F(1,16)=9.39$, $p<0.01$, confirming that subjects changed their production of this vowel in these dimensions. For duration, there was no significant effect of time, $p>0.05$, indicating that subjects produced this vowel with a similar duration at each testing session.

d. Other vowels. As displayed in Fig. 2, subjects did not appear to change their production of any other vowels, although there was a possible shift in *bawd* in the $F2$ dimension. The potential differences in $F1$ and $F2$ were tested in separate repeated-measures ANOVA analyses, with word (i.e., all words other than *bud, cud, could*, and *bath*) and time coded as within-subject variables. There was a main effect of word for $F1$, $F(1,16)=20.50$, $p<0.001$, and $F2$, $F(1,16)=7.26$, $p<0.05$, demonstrating that subjects produced these words with different formant frequency values, but there was no main effect of time and no significant interaction of word and time, $p>0.05$. The shift in *bawd* was thus not reliable.

As displayed in Table II, subjects chose different durations for different words, but there did not appear to be any change in duration from T1 to T4. A repeated-measures ANOVA analysis confirmed that there was a main effect of word, $F(1,16)=20.04$, $p<0.001$, demonstrating that subjects produced these words with different durations, but there was no main effect of time and no significant interaction of word and time, $p>0.05$.

e. Comparison with accent ratings. To verify that the changes observed in the $F1$ and $F2$ frequency measurements for *bud, cud, could*, and *bath* were related to the change in accent ratings, individual accent ratings from each testing session were correlated with $F1$ and $F2$ values for *bud, cud, could*, and *bath*. Significant correlations were found between the accent ratings and $F1$ for *bud*, $r=-0.44$, $p<0.05$, $F2$ for *bud*, $r=-0.61$, $p<0.05$, $F2$ for *cud*, $r=-0.55$, $p<0.05$, and $F2$ for *could*, $r=-0.5$, $p<0.05$. This indicates that the observed changes in formant frequencies corresponded to the changes in perceived accent.

3. Discussion

The results demonstrated that subjects changed their accent after attending university. Although the change in accent rating was relatively small, the acoustic analysis demonstrated that there were substantial changes in how these speakers produced *bud, cud, could*, and *bath*. For *bud, cud*, and *could* this shift occurred in both the $F1$ and $F2$ dimensions; subjects produced a more fronted and lower vowel in these words at T4 than at T1, which is closer to how southerners produce the vowel in words like *bud* and *cud*. For *could* this was particularly surprising because northerners and southerners produce this word using the same vowel, [ʊ]. It is possible that subjects produced *could* with a more centralized vowel, just like the vowel they used to produce *bud* and *cud*, because they were unable to split a category that is merged in their native accent. In SSBE, words such as *cud* and *could* are produced with two different vowels, [ʌ] and [ʊ]. However, northern English speakers do not have the vowel [ʌ]; they produce these words with the same vowel [ʊ], such that *cud* and *could* are homophones. One could imagine that these subjects had changed their underlying [ʊ] category so that it was closer to how SSBE speakers produce words like *bud* and *cud*, and that they used this new vowel category in all words containing [ʊ] in their native accent, even when this did not match how those words are produced in SSBE (see also Sankoff, 2004; Evans and Iverson, 2004). Equally, subjects may have acquired a new category alongside their native [ʊ] category, but were hypercorrecting (Evans, 2005; Sankoff, 2004; Wells, 1982). That is, subjects may have used a more central vowel in words where they would use the lower back vowel [ʊ] in their native accent in order to "posh-up" their accent (Wells, 1982, p. 353).

Subjects also modified their production of *bath*; they changed their $F1$ and $F2$ formant frequency locations over time. This was surprising as northerners typically retain their native pronunciation of this vowel when adjusting to SSBE

speech (Trudgill, 1986; Wells, 1982). However, the amount of change in the *F*1 and *F*2 dimension was much smaller than that in *bud, cud*, and *could*, and there was no change in duration. If subjects had been adjusting their pronunciation to match SSBE speakers, then there should have been a significant change in duration; southerners produce words like *bath* with the long vowel [ɑː] but northerners use the short vowel [a]. This indicates that although subjects were making small changes to their production of this vowel, they were still using a vowel that would be categorized as [a]. It is perhaps more likely that subjects were retaining [a] in words like *bath*, but were making small changes to this category in order to "soften" their native accent (i.e., to sound less northern).

III. EXPERIMENT 2: AN INVESTIGATION OF PERCEPTUAL VOWEL SPACES

In experiment 2, subjects created perceptual vowel space maps (i.e., best exemplar locations) in a three-dimensional space that varied *F*1, *F*2, and duration for vowels embedded in SSBE and northern English carrier sentences. The aim was to investigate if subjects changed the acoustic qualities of the vowels according to whether the sentence was spoken with an SSBE or northern English accent. Subjects heard synthesized vowels embedded in natural carrier sentences that were produced in either a northern English (i.e., native) or SSBE (i.e., non-native) accent. They gave goodness ratings on the vowels and a computer program iteratively adjusted the *F*1, *F*2 and duration values on successive trials until a best exemplar was found. Of particular interest were the vowels in *bud, cud, could*, and *bath*, as subjects had changed their production of these words to better fit in with southerners.

A. Method

1. Participants

Same as experiment 1.

2. Stimuli and apparatus

The stimuli were the same as those used in Evans and Iverson (2004). They consisted of synthesized vowels in the phonetic environments /b/-V-/d/, /b/-V-/θ/, and /k/-V-/d/, embedded in natural recordings of the carrier sentence *I'm asking you to say the word [ ] please*. This carrier sentence was chosen because it contained an overt cue to accent; the word *asking* is produced with a long, back vowel [ɑː] in SSBE, but in Sheffield English with a short vowel, [a]. There were 11 test words; *bad, bard, bawd, bed, bird, booed, bud, bead, cud, could*, and *bath*.

The carrier sentence was produced in both Sheffield English and SSBE accents by the same male speaker ([əmaskɪnjəʔseɪʔwʔːd---pliːz̥] in Sheffield English and [aɪmɑːskɪŋjuːtəseɪðəwɜːd---pliːz̥] in SSBE). The speaker had lived in Sheffield until the age of 19 years when he moved to the south of England to attend university, where he had lived for 7 years at the time of recording. This speaker was selected because he was able to switch between accents at will, and was able to produce versions of both accents that were judged by trained phoneticians to sound like those of native speakers. In addition to the carrier sentences, the speaker was recorded reading a 2-min passage from a novel in both accents. This was used for familiarization.

CVCs were embedded in the carrier sentences. The bursts, fricatives, and aspiration were spliced from the sentence recording, and the voiced portions were synthesized in advance using the cascade branch of a Klatt synthesizer (Huckvale, 2003; Klatt and Klatt, 1990). Each stimulus had a middle portion in which the formant frequencies were static, and had formant transitions appropriate for the consonants. All transitions were linear. The stimuli varied in terms of *F*1 and *F*2 frequencies and duration of the middle portion. *F*1 frequency was restricted so that it had a lower limit of 150 Hz and an upper limit of 950 Hz. *F*2 was restricted to have a lower limit of *F*1+50 Hz, and had an upper limit defined by the equation

$$F2_{\text{upper-limit}} = 3000\ \text{Hz} - 1.7 * F1. \quad (2)$$

The duration of the middle portion was restricted to be greater than 20 ms and less than 403 ms. *F*3 frequency was fixed at 2500 Hz. All other synthesis parameters were chosen to mimic the natural speech. After synthesis, the CVC stimuli were processed using a multiband filter to fine-tune the match between the long-term average spectra of the synthetic and natural speech (see Evans and Iverson, 2004; Evans, 2005, for a fuller description of this process).

The entire range of possible vowels was synthesized with a resolution of 0.5 ERB in *F*1 and *F*2. Duration was quantized in 16 steps on a log scale. There were a total of 7616 stimuli synthesized for each of the CVC contexts.

The stimuli were played at a sampling rate of 11 kHz using a computer sound card, over headphones (Sennheiser HD 414) in a quiet room.

3. Procedure

The procedure was the same as that described in Evans and Iverson (2004). There were two testing sessions, one for each accent. The order of sessions was counterbalanced across subjects. Sessions were conducted on separate days (i.e., at least 1 day apart) to minimize the risk that subjects would be influenced by the fact that the speaker was the same in both conditions.

At the start of each session, subjects listened to a short passage read by the speaker in order to familiarize them with the accent. They then found the best exemplar for one practice word (*kid*), and best exemplars for 11 test words in succession: *bad, bard, bawd, bed, bird, booed, bud, bead, cud, could*, and *bath*. The order of presentation was randomized across subjects. To find the best exemplars, the Goodness Optimization procedure was used (Evans and Iverson, 2004; Iverson and Evans, 2003; Iverson *et al.*, 2005). Subjects heard a synthesized word embedded in a carrier sentence on each trial, and rated whether it was close to being a good exemplar of the target word that was displayed orthographically on a computer screen. They were instructed to make their rating based on what sounded like a good version of the word to them in the sentence context. They gave their response by positioning and clicking a computer mouse on a continuous scale from *close* to *far away*. Based on their judg-

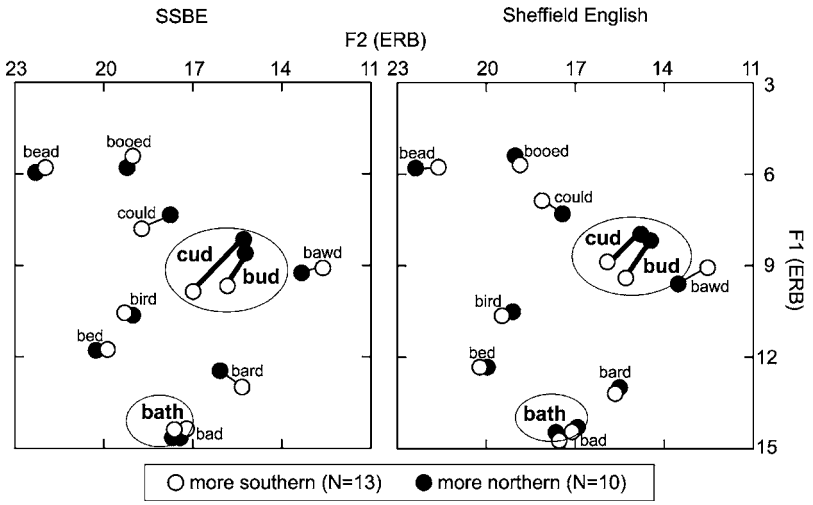

FIG. 3. Average $F1$ and $F2$ formant frequency (ERB) locations for best exemplars in SSBE and Sheffield English carrier sentences. The open circles represent the average formant frequency locations at T1, T2, T3, and T4 for subjects who had an overall accent rating lower than or equal to the median overall accent rating (i.e., had a more southern accent overall; $N=13$). The filled circles represent the average formant frequency locations for subjects who had an overall accent rating greater than the median overall accent rating (i.e., had a more northern accent overall; $N=10$). Subjects who had a more southern accent overall chose more southern vowels, and subjects who had a more northern accent overall chose more northern vowels.

ments, the computer program iteratively adjusted the acoustic parameters ($F1$, $F2$, and duration) to converge on a best exemplar. The acoustic parameters were adjusted over 24 trials with a total of 6 trials per stage, with subjects having the opportunity to repeat stages if needed. Briefly, the procedure adjusted $F1$ and $F2$ in stage 1, starting along a path that passed through the average $F1$ and $F2$ frequencies that the speaker of the carrier sentence had used for that word, averaged over the two accents. This meant that the procedure would be likely to approximate a best exemplar quickly. Stage 2 adjusted $F1$ and $F2$ along a straight-line path that was orthogonal in the $F1/F2$ plane to the stage 1 path and included the best exemplar found in stage 1. The procedure then adjusted the more secondary dimension of duration in stage 3 and fine-tuned the best exemplar location in stage 4 by covarying $F1$, $F2$, and duration along a single vector.

4. Results

a. Bud and cud. Separate repeated-measures ANOVA analyses for $F1$, $F2$, and duration tested whether subjects changed their best exemplar locations for *bud* and *cud*. Word (*bud* or *cud*), time (T1, T2, T3, and T4) and sentence context (SSBE or Sheffield English) were coded as within-subject variables. To investigate whether any changes in production were accompanied by changes in perception, the change in accent rating (experiment 1) was entered as a continuous factor. The overall accent rating (experiment 1) was also entered as a continuous factor in order to investigate if the overall differences in spoken accent were accompanied by individual differences in perception.

For $F1$, an inspection of the data indicated that some subjects were choosing a more southern vowel (i.e., higher $F1$) for *bud* and *cud* after attending university. However, there was no significant main effect of time or word for $F1$, $p>0.05$. This indicates that subjects were not changing their preferred $F1$ frequencies over time, and were choosing similar $F1$ frequencies in both words. There was also no main effect of sentence context, $p=0.05$, indicating that subjects were choosing similar $F1$ formant frequencies for SSBE and Sheffield English carrier sentences.

However, there was a between-subjects effect of overall accent rating for $F1$, $F(1,14)=6.65$, $p<0.05$. This can be seen in Fig. 3;[5] subjects who were judged to have a more southern accent overall chose more southern best exemplar locations for *bud* and *cud* in both SSBE and Sheffield English sentence contexts. These subjects chose a lower vowel (i.e., higher $F1$), which does not exactly match what native speakers of SSBE or Sheffield English would produce, but which matches what northerners produce when interacting with southerners (Evans and Iverson, 2004; Trudgill, 1986). Subjects who were judged to have a more northern accent overall chose more northern best exemplar locations for *bud* and *cud*. This demonstrates that individual differences in production were accompanied by individual differences in best exemplar locations.

There were no significant main effects or interactions for $F2$, $p>0.05$. This indicates that subjects were not changing their best exemplar locations for *bud* and *cud* in this dimension, and that they were choosing similar $F2$ locations in both northern English and SSBE carrier sentences.

There were also no significant main effects or interactions for duration, $p>0.05$. This can be seen in Table III: There are few changes in duration over time, and all subjects chose similar durations in both SSBE and Sheffield English carrier sentences.

b. Could. Separate repeated measures analyses for $F1$, $F2$, and duration tested whether subjects changed their best exemplar locations for *could*, and whether any changes were linked to the change in accent rating or overall accent rating. Time (T1, T2, T3, and T4) and sentence context (SSBE or Sheffield English) were coded as within-subject variables; change in accent rating and overall accent rating were coded as continuous factors.

There was some evidence in the raw data to suggest that subjects chose a different best exemplar in SSBE and Sheffield English sentences; some subjects changed their best exemplar location in SSBE carrier sentences after attending university so that it was similar to the vowel they chose for *bud* and *cud*. However, the analysis demonstrated that there were no significant main effects or interactions of sentence context, time, change in accent rating or overall accent rating for $F1$, $F2$, or duration, $p>0.05$. This suggests that there were no reliable differences or changes in subjects' best exemplar locations for *could*.

TABLE III. Average duration (ms) of the vowels in best exemplars for listeners in SSBE and Sheffield English sentences at T1, T2, T3, and T4.

	SSBE				Sheffield English			
Word	T1	T2	T3	T4	T1	T2	T3	T4
bud	72.4	70.6	75.4	76.1	74.0	64.4	72.3	71.9
cud	59.0	70.2	71.8	68.8	59.1	68.3	62.9	65.2
could	73.0	88.0	81.3	64.8	76.2	71.7	78.9	70.2
bath	80.8	95.7	79.6	97.3	70.7	79.3	79.6	80.4
bad	87.0	103.1	95.0	83.3	67.5	86.5	89.2	85.3
bard	157.7	164.3	166.6	157.3	148.8	148.5	157.2	164.1
bawd	155.6	145.7	145.0	155.0	140.8	144.3	145.9	152.8
bead	125.9	135.8	128.1	150.1	118.7	136.3	130.4	154.8
bed	70.3	84.7	74.6	61.8	60.3	67.1	62.7	65.2
bird	125.7	131.4	151.4	145.8	116.2	144.0	134.7	129.8
booed	152.4	132.7	146.9	142.8	123.9	146.9	135.3	144.2

c. Bath. Separate repeated-measures analyses for $F1$, $F2$, and duration investigated whether subjects changed their best exemplar location for *bath*. Time (T1, T2, T3, and T4) and sentence context (SSBE and Sheffield English) were coded as within-subject variables, and change in accent rating and overall accent rating were coded as continuous factors.

The analysis demonstrated that there were no significant main effects or interactions for $F1$ and $F2$, $p > 0.05$, indicating that subjects did not change their best exemplar location for *bath* over time and that they did not normalize this vowel for accent (i.e., they chose similar best exemplars for *bath* in both sentence contexts). There were also no significant between-subject effects of overall accent rating or change in accent rating, $p > 0.05$, demonstrating that the changes in production in *bath* in experiment 1 were not accompanied by changes in best exemplar locations. There were also no significant main effects or interactions for duration, $p > 0.05$.

d. Other vowels. Separate repeated-measures analyses for $F1$, $F2$, and duration tested whether there were any changes for all other words. Word (i.e., all words other than *bud, cud, could*, and *bath*), sentence context, and time were coded as within-subject variables, and change in accent rating and overall accent rating as continuous factors. There was a main effect of word for $F1$, $F(1,14)=51.91$, $p < 0.001$, and $F2$, $F(1,14)=13.69$, $p < 0.001$, demonstrating that different words had different formant frequency values. However, there were no main effects of sentence context or time, and no between-subject effects of change in accent rating or overall accent rating, $p > 0.05$, indicating that subjects did not change their best exemplar locations over time for any other words.

For duration there were no significant main effects or interactions, $p > 0.05$; subjects chose similar vowel durations for each target word in both SSBE and Sheffield English carrier sentences at T1, T2, T3, and T4. This was a result of a lack of power in the test; when the change in accent rating and overall accent rating continuous factors were omitted, there was a highly significant main effect of word, $F(1,16)=37.33$, $p < 0.001$, indicating that subjects chose different durations for different words. This can be seen in Table III; subjects chose vowels with a longer duration for words like *bard* and *bird*, but vowels with a shorter duration for words like *bad* and *bed*.

5. Discussion

Experiment 1 demonstrated that subjects changed their spoken accent, and the aim of experiment 2 was to investigate whether the changes in production were accompanied by changes in perception. The results demonstrated that there were no reliable changes in subjects' best exemplar locations; subjects chose similar vowels at T1, T2, T3, and T4 for *bud, cud, could, bath*, and all other vowels. However, there was a between-subjects link between production and perception. That is, subjects chose similar best exemplar locations for *bud* and *cud* to those that they produced; subjects who produced more southern vowels overall chose more southern best exemplars, and subjects who produced more northern vowels overall chose more northern best exemplars.

Our previous work (Evans and Iverson, 2004) demonstrated that northerners who had been living in London for a minimum of 1 year chose different best exemplar locations for *bud* and *cud* in SSBE and northern English carrier sentences; northerners chose best exemplar locations in their native accent that matched what native speakers of that accent produce (i.e., a high-back vowel), but chose more centralized best exemplars in SSBE sentences that are closer to what SSBE speakers produce. In contrast, northerners living in the north of England, and who were less experienced with SSBE speakers, chose best exemplars for *bud* and *cud* that would be appropriate for northern English speakers in both northern English and SSBE carrier sentences. Based on this evidence, we had expected that after experience of living in a multidialectal environment and interacting with SSBE speakers, subjects in this study would choose different best exemplars in SSBE and northern English sentences. However, there was no evidence that, even after experience of living in a multidialectal environment, subjects, as a group, were learning to normalize. This suggests that rather than being a process that is rapidly learned (e.g., Clarke and Garrett, 2004), the ability to normalize for a non-native accent may require a great deal of experience with a particular accent, perhaps being immersed in that accent for a long period of

time. Alternatively, it is possible that the subjects in this study had not had the same experience with a non-native accent as those in our previous study. Subjects in our previous study were living in London, a multidialectal community where they regularly came into contact with speakers of a wide variety of different accents. Although a university environment is multidialectal, it is possible that the range of accents that subjects encountered was not as wide as that encountered by our subjects in London, and that this affected their ability to normalize. Another possibility is that subjects had learned to normalize but that the testing location affected their responses. Subjects in the present study were tested in Ashby. It is possible that if they had been tested at university, a multidialectal environment where SSBE is regularly used, normalization effects may have been found.

IV. EXPERIMENT 3: SENTENCE RECOGNITION IN NOISE

Experiment 3 further investigated whether the changes in production found in experiment 1 were accompanied by changes in perception. The aim of the experiment was to investigate whether changes in production had an effect on a more basic measure of speech perception, the ability to recognize speech in noise.

A. Method

1. Subjects

Same as in experiment 1.

2. Stimuli and apparatus

The stimuli were recordings of the BKB sentences (Bench *et al.*, 1979). The BKB sentences are a standardized sentence list that is widely used as an assessment tool in clinical and nonclinical tests of speech perception. There are 21 lists of 16 sentences, and each sentence contains 3, 4, or 5 highly familiar keywords that are identified by the listener, e.g., "The *house* had *nine rooms*," "They are *buying some bread*" (keywords are in italics). Only the sentences with 3 keywords were used in this experiment. The sentence lists were recorded by two female speakers of different accents, a northern English speaker and a SSBE speaker. The northern English speaker had been born and raised in Ashby-de-la-Zouch. The stimuli for the SSBE speaker were taken from existing recordings made at University College London. All recordings were made in a sound-isolated booth. Stimuli were recorded at a sampling rate of 44.1 kHz and then downsampled to 16 kHz. The speech was mixed with white noise; the noise level was fixed to 71 dBA, and the level of the speech was varied adaptively.

Stimuli were played using a computer sound card. Subjects listened over headphones (Sennheiser HD 414) in a quiet room.

3. Procedure

There were six blocks of testing, three blocks for each speaker. Three blocks were completed on the first day of testing, and three on the second day. In each three-block testing session, the speakers were presented in alternate blocks (i.e., subjects did not hear the same speaker in consecutive blocks), with the order of presentation counterbalanced across subjects. The maximum number of trials per block is 20 and so, at each testing session, subjects were randomly assigned a set of 60 sentences for each speaker (120 sentences in total). List 1 was used for familiarization. Subjects were assigned a different set of sentences for each speaker at T1, T2, T3, and T4, so that for each speaker, each sentence was only identified once.

A modified Levitt procedure (Baker and Rosen, 2001) was used to find subjects' noise thresholds. The procedure started with an easy stimulus with an SNR of +10 dB (i.e., above threshold) in order to enable subjects to tune in to the talker. The SNR then decreased in 8 dB steps after each correct response (i.e., becomes more difficult), until the first reversal (i.e., an incorrect response). After the first reversal the SNR changed in steps of 2 dB for a further eight reversals.

A one-up/one-down procedure was used, with sentences scored as correct when they repeated all three keywords aloud to the researcher. If subjects only repeated one or none of the keywords, then the sentence was scored as incorrect. If subjects repeated two keywords then the SNR remained the same and this was not counted as a reversal. The procedure thus converged on a 66.6% identification level. The test terminated when subjects completed eight reversals or after 20 stimuli had been presented.

4. Results

A repeated-measures analysis tested whether the observed differences in performance were linked to the change in accent rating and the overall accent rating. Speaker (northern or SSBE) and time (T1, T2, T3, and T4) were coded as within-subject variables, and change in accent rating and overall accent rating were coded as continuous factors.

There was a main effect of speaker $F(1,15)=136.61$, $p<0.001$; all subjects performed better with the SSBE speaker (see Fig. 4[5]). The northern speaker was from Ashby-de-la-Zouch, Leicestershire, and one of the features of the local accent is that it has a flat intonation contour. This difference, combined with the fact that subjects were highly familiar with SSBE through the media (Foulkes and Docherty, 1999), may have resulted in the SSBE speaker being more intelligible in noise than the northern speaker. There was no main effect of time and no interaction of time and speaker, $p>0.05$, indicating that subjects did not perform better with SSBE after the experience of living in a multidialectal community.

There was a significant interaction between speaker and overall accent rating, $F(1,18)=10.78$, $p<0.01$. As displayed in Fig. 4, subjects who were judged to have a more southern accent performed better with SSBE speech than those who had a more northern accent; all subjects performed similarly with northern speech. However, there were no interactions between the change in accent rating and speaker, $p>0.05$, demonstrating that subjects who were judged to have changed their accent to sound more southern had no advantage over subjects who had not changed their accent.

5. Discussion

As in experiment 2, there was a between-subjects link between individuals' production and perception. Subjects who produced more southern vowels overall were better able to identify SSBE speech in noise than those who produced more northern vowels overall. This indicates that individual differences in speech production were accompanied by differences in perceptual processing. However, there was no evidence to suggest that subjects' ability to recognize SSBE speech in noise changed over time.

V. GENERAL DISCUSSION

The results of this study demonstrated that subjects changed their accent as a result of attending university. For example, subjects changed their production of *bud, cud*, and *could* so that they produced them with a more fronted (higher $F2$) and lower (higher $F1$) vowel at T4, which is closer to how southerners produce the vowel in words like *bud* and *cud*. Although subjects changed their production, there were no reliable changes in perception; there were no changes in subjects' best exemplar locations in experiment 2, and no change in subjects' ability to recognize SSBE speech in noise in experiment 3. However, there was a between-subjects link between individuals' overall production and perception. That is, subjects who produced more southern vowels chose more southern best exemplar locations for *bud* and *cud*, and subjects who produced more northern vowels chose more northern best exemplars for *bud* and *cud*. Likewise, subjects who produced more southern vowels performed better with SSBE speech in noise than did those who produced more northern vowels.

Even though subjects were selected so that they were from a homogeneous background (i.e., they had all been exposed to the same regional accent until leaving for university and had attended local schools since age 5 years), it is not surprising that we found overall differences in production. Previous research has shown that within a homogeneous community, structured differences in production emerge as a result of sociolinguistic influences. For example, Eckert (1989, 2000) found that high-school students in Detroit used phonetic variation to define their social groups (e.g., "jocks" and "burnouts") and construct their own identity. The idiolectal variation in the present study may have likewise emerged as markers of how each individual fitted within their community. The production differences may thus have reflected how these individuals chose to present themselves to the world, rather than being reflective of underlying differences in perceptual experience (i.e., the phonetic content of the speech that they had heard during their lifetime).

Given that these individual differences in production are likely due to sociolinguistic influences, it was surprising that they were directly linked to differences in perception. That is, even though spoken accent is a marker of social identity, perception is essentially private and it would be adaptive for individuals to be able to understand as wide a range of speakers as possible. Our subjects likely had very similar perceptual experiences when growing up, but the idiolectal variation in production had influences on both subjective ratings (i.e., best exemplar locations in experiment 2) and speech-in-noise recognition. It thus appears that the sociophonetically driven differences found in production had an impact on perceptual processing, suggesting that there is a strong perception-production link.

Given this link between perception and production in terms of overall individual differences (i.e., averaged across time), it is unclear why perception and production were not linked in terms of changes over time. For example, individuals who changed their spoken accent to sound more southern did not improve in their ability to recognize SSBE speech in noise. It is notable, however, that the changes in accents were relatively small (e.g., the changes in accent ratings were smaller than the overall individual differences). In order to understand speech from a range of talkers (e.g., different accents and idiolects), listeners' category representations presumably need to be tolerant to a range of acoustic variation. It is possible that the changes in production fell within this range of tolerance. That is, listeners may have had some degree of freedom to change their spoken accent without making corresponding changes to their underlying category representations or their perceptual processing.

Although we found no changes in perception over time, previous studies of L1 perception have found that subjects are able to rapidly adapt to foreign accented speech (e.g., Clarke and Garrett, 2004). One difference between the present study and previous work on perceptual adaptation (e.g., Clarke and Garrett, 2004; Nygaard *et al.*, 2005) is that our study investigated adaptation to a regional accent, not to a particular talker or group of talkers. For example, Nygaard *et al.* (2005) found that American English listeners were most accurate at transcribing items spoken by Spanish-accented talkers after a short amount of training with the same speakers; listeners who were exposed to Spanish-accented speech produced by different talkers were less accurate. In our study, subjects heard a range of accents while attending university, but were not regularly exposed to the specific talkers that they heard in our experiments. It is possible that we did not see the same perceptual adaptation effects that have been found previously (e.g., Clarke and Garrett, 2004; Nygaard *et al.*, 2005) because such changes may be talker-specific and not easily generalizable to other speakers of that accent. Adaptation to accent-general patterns of variation may thus require more long-term experience with speakers of that accent.

In summary, the present study demonstrated that subjects were able to change their spoken accent at a late stage in their language development, young adulthood, although the changes in production were not accompanied by changes in perception. There was evidence for a between-subjects link between production and perception; subjects who produced more southern vowels chose more southern best exemplar locations and were better at identifying SSBE speech in noise. Such individual differences in production and perception were particularly remarkable because subjects were selected so that they had a relatively homogeneous background. These findings suggest that individual differences in production are accompanied by fine-grained differences in

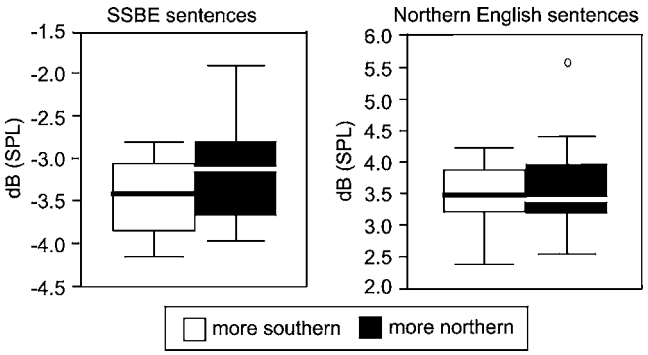

FIG. 4. Boxplots of subjects' average SNR threshold for SSBE and northern English sentences. Subjects are grouped according to their overall accent rating; the open boxes represent subjects who were judged to sound more southern overall ($N=13$) and the filled boxes represent subjects who were judged to sound more northern overall ($N=10$). Subjects who had a more southern accent overall performed better with SSBE speech than subjects who had a more northern accent overall.

perceptual representations, and that these small individual differences have an impact on speech processing.

ACKNOWLEDGMENTS

This research was supported by an EPSRC Doctoral Training Award to the first author. We are grateful to Richard Dewire, Natasha Fish, Graham Fisher, and Graham Hobbs for help with recordings, and to Jackie and Alexandra Evans for help with subject recruitment.

[1]The term SSBE instead of Received Pronunciation (RP) is used here to denote the standard, prestige British English accent. This is to avoid confusion with a more narrow definition of RP (see Wells, 1982 for a full discussion of the definition and scope of RP, as well as other varieties of RP).

[2]Of the 27 subjects tested, 26 were born and raised in the East Midlands. One subject was born in Ireland but his mother, his primary caregiver, was originally from Ashby and they returned to Ashby when he was 5 years old.

[3]All subjects attended university in England. Consequently, they did not come into regular contact with speakers with Scottish, Welsh, and Irish accents.

[4]As a result of the fact that not all subjects could be contacted at T4, the change in accent rating was calculated by subtracting each subject's accent rating at the final testing session (T3 or T4) from the accent rating at T1.

[5]For the purposes of Figs. 3 and 4, subjects were divided into two groups based on the accent ratings (experiment 1). Those who had an overall accent rating lower than or equal to the median overall accent rating of 5.75 were assigned to the "more southern" group ($N=13$). Those who had an accent rating greater than the median overall accent rating were assigned to the ″more northern″ group ($N=10$)

Adank, P. (**2003**). "Vowel normalization: A perceptual-acoustic study of Dutch vowels," Unpublished Ph.D. dissertation, University of Nijmegen, The Netherlands.

Adank, P., Smits, R., and van Hout, R. (**2004**). "A comparison of vowel normalization procedures for language variation research," J. Acoust. Soc. Am. **116**, 3099–3107.

Ainsworth, W. A., and Paliwal, K. K. (**1984**). "Correlation between the production and perception of the English glides /w, r, l, j/," J. Phonetics **12**, 237–243.

Bailey, P. J., and Haggard, M. P. (**1973**). "Perception and production: Some correlations on voicing of an initial stop," Lang Speech **16**, 189–195.

Bailey, P. J., and Haggard, M. P. (**1980**). "Perception-production relations in the voicing contrast for initial stops in 3-year-olds," Phonetica **37**, 377–396.

Baker, R. J., and Rosen, S. (**2001**). "Evaluation of maximum-likelihood threshold estimation with tone-in-noise masking," Br. J. Audiol. **35**, 43–52.

Bell-Berti, F., Raphael, L. J., Pisoni, D. B., and Sawusch, J. R. (**1979**). "Some relationships between speech production and perception," Phonetica **36**, 373–383.

Bench, J., Kowal, A., and Bamford, J. (**1979**). "The BKB (Bamford-Kowal-Bench) sentence lists for partially-hearing children," Br. J. Audiol. **13**, 108–112.

Boersma, P., and Weenink, D. (**2004**). PRAAT: Doing phonetics by computer (Computer software) (University of Amsterdam, The Netherlands).

Bradlow, A. R., Pisoni, D. B., Akahane-Yamada, R., and Tohkura, Y. (**1997**). "Training Japanese listeners to identify English /r/ and /l/: IV. Some effects of perceptual learning on speech production," J. Acoust. Soc. Am. **101**, 2299–2310.

Clarke, C. M., and Garrett, M. F. (**2004**). "Rapid adaptation to foreign-accented English," J. Acoust. Soc. Am. **116**, 3647–3658.

Clarke, C. M., and Luce, P. A. (**2005**). "Perceptual adaptation to speaker characteristics: VOT boundaries in stop voicing categorization," in Proceedings of the ISCA Workshop on Plasticity in Speech Perception, London, U.K.

Eckert, P. (**1989**). *Jocks and Burnouts: Social Categories and Identity in the High School* (Teachers College Press, New York).

Eckert, P. (**2000**). *Linguistic Variation as Social Practice* (Blackwell, Oxford).

Eisner, F., and McQueen, J. M. (**2005**). "The specificity of perceptual learning in speech processing." Percept. Psychophys. **67**, 224–238.

Evans, B. G. (**2005**). "Plasticity in Speech Perception and Production: A study of accent change in young adults," Unpublished Ph.D. thesis, University College London: University of London, U.K.

Evans, B. G., and Iverson, P. (**2004**). "Vowel normalization for accent: An investigation of best exemplar locations in northern and southern British English sentences," J. Acoust. Soc. Am. **115**, 352–361.

Flege, J. E., Bohn, O.-S., and Jang, S. (**1997**). "The production and perception of English vowels by native speakers of German, Korean, Mandarin, and Spanish," J. Phonetics **25**, 437–470.

Flege, J. E., Mackay, I. R. A., and Meador, D. (**1999**). "Native Italian speakers' perception and production of English vowels," J. Acoust. Soc. Am. **106**, 2973–2987.

Foulkes, P., and Docherty, G. J. (**1999**). "Urban Voices—Overview," in *Urban Voices: Accent Studies in the British Isles*, edited by P. Foulkes and G. J. Docherty (Arnold, London).

Fowler, C. A. (**1981**). "Production and perception of coarticulation among stressed and unstressed vowels," J. Speech Hear. Res. **24**, 127–139.

Fowler, C. A. (**1986**). "An event approach to the study of speech perception from a direct-realist perspective," J. Phonetics **14**, 3–28.

Frieda, E. M., Walley, A. C., Flege, J. E., and Sloane, M. E. (**2000**). "Adults perception and production of the English vowel /i/," J. Speech Lang. Hear. Res. **43**, 129–143.

Huckvale M. (**2003**). Speech Filing System (computer software) (University College, London, UK).

Iverson, P., and Evans, B. G. (**2003**). "A goodness optimization method for investigating phonetic categorization," Paper presented at the International Congress of Phonetic Sciences (ICPhS), Barcelona, Spain.

Iverson, P., Smith, C. A., and Evans, B. G. (**2005**). "Vowel recognition via cochlear implants and noise vocoders: The effects of formant movement and duration," J. Acoust. Soc. Am. **120**, 3998–4006.

Kerswill, P., and Williams, A. (**2000**). "Creating a new town koine: Children and language change in Milton Keynes," Language in Society **29**, 65–115.

Klatt D. H., and Klatt L. C. (**1990**). "Analysis, synthesis, and perception of voice quality variations among female and male talkers." J. Acoust. Soc. Am. **87**, 820–857.

Liberman, A. M., and Mattingly, I. G. (**1985**). "The motor theory of speech perception revised," Cognition **21**, 1–36.

Liberman, A. M., Cooper, F. S., Shankweiler, D. P., and Studdert-Kennedy, M. (**1967**). "Perception of the speech code," Psychol. Rev. **74**, 431–461.

Milroy, L. (**1987a**). *Observing and Analysing Natural Language* (Blackwell, Oxford).

Milroy, L. (**1987b**). *Language and Social Networks*, 2nd ed. (Blackwell, Oxford).

Munro, M. J., Derwing, T. M., and Flege, J. E. (**1999**). "Canadians in Alabama: A perceptual study of dialect acquisition in adults." J. Phonetics **27**, 385–403.
Nearey, T. M. (**1978**). "Phonetic Feature Systems for Vowels" (Indiana University Linguistics Club, Bloomington, IN).
Newman, R. S. (**2003**). "Using links between speech perception and speech production to evaluate different acoustic metrics: A preliminary report," J. Acoust. Soc. Am. **113**, 2850–2860.
Nygaard, L. C., and Pisoni, D. B. (**1998**). "Talker-specific learning in speech perception," Percept. Psychophys. **60**, 355–376.
Nygaard, L. C., Sidaras, S., and Duke, J. (**2005**). "Perceptual learning of accented speech," in Proceedings of the ISCA Workshop on Plasticity in Speech Perception, London, U.K.
Sankoff, G. (**2004**). "Adolescents, young adults and the critical period: Two case studies from 'Seven Up,'" in *Sociolinguistic Variation*, edited by C. Fought (Oxford University Press, Oxford).
Trudgill, P. (**1986**). *Dialects in Contact* (Blackwell, Oxford).
Wells, J. C. (**1982**). *Accents of English: The British Isles* (Cambridge University Press, Cambridge), Vol. 2.

Spectral weighting strategies for sentences measured by a correlational method

Lauren Calandruccio[a] and Karen A. Doherty
Department of Communication Sciences and Disorders, Institute for Sensory Research, Syracuse University, Syracuse, New York

(Received 29 September 2006; revised 8 March 2007; accepted 12 March 2007)

Listeners' ability to understand speech in adverse listening conditions is partially due to the redundant nature of speech. Natural redundancies are often lost or altered when speech is filtered, such as done in AI/SII experiments. It is important to study how listeners recognize speech when the speech signal is unfiltered and the entire broadband spectrum is present. A correlational method [R. A. Lutfi, J. Acoust. Soc. Am. **97**, 1333–1334 (1995); V. M. Richards and S. Zhu, J. Acoust. Soc. Am. **95**, 423–424 (1994)] has been used to determine how listeners use spectral cues to perceive nonsense syllables when the full speech spectrum is present [K. A. Doherty and C. W. Turner, J. Acoust. Soc. Am. **100**, 3769–3773 (1996); C. W. Turner *et al.*, J. Acoust. Soc. Am. **104**, 1580–1585 (1998)]. The experiments in this study measured spectral-weighting strategies for more naturally occurring speech stimuli, specifically sentences, using a correlational method for normal-hearing listeners. Results indicate that listeners placed the greatest weight on spectral information within bands 2 and 5 (562–1113 and 2807–11000 Hz), respectively. Spectral-weighting strategies for sentences were also compared to weighting strategies for nonsense syllables measured in a previous study (C. W. Turner *et al.*, 1998). Spectral-weighting strategies for sentences were different from those reported for nonsense syllables. © *2007 Acoustical Society of America.*
[DOI: 10.1121/1.2722211]

PACS number(s): 43.71.Es, 43.71.Gv, 43.72.Ar [JHG] Pages: 3827–3836

I. INTRODUCTION

Many of the spectral and temporal cues in speech provide redundant linguistic information (Rosen and Fourcin, 1986). This redundant nature allows for speech to remain robust even in adverse listening conditions, such as when speech signals are manipulated in the laboratory temporally (Calandruccio *et al.*, 2005; Jenstad and Souza, 2005) and spectrally (Baer and Moore, 1997; Greenberg *et al.*, 1998; Shannon *et al.*, 1998; Warren *et al.*, 1995; Warren *et al.*, 2004). Filtering a signal is one of the more common experimental methods used to estimate a listener's use of spectral information in speech. However, one limitation in using this method is that it can also reduce or alter the natural redundancies in speech.

The Articulation Index (AI; ANSI, 1969), later revised and renamed the Speech Intelligibility Index (SII; ANSI, 1997), is one method that has been used to predict speech intelligibility of filtered speech. Originally developed for and tested on listeners with normal hearing, the AI assumes that speech intelligibility increases with increases in audibility (Fletcher and Galt, 1950; French and Steinberg, 1947). This method has been used for a wide variety of applications, from predicting speech intelligibility over communication systems (Steinberg and Gardner, 1937) to predicting hearing-aid candidacy (Humes, 1991; Mueller and Killion, 1990; Pavlovic, 1991). The AI/SII is calculated based on the system transfer function, noise, and speech level of specific speech material. System transfer functions, or frequency-importance functions, are determined by testing speech recognition for speech materials using a series of low- and high-pass filter conditions. However, in natural-listening environments listeners typically do not listen to filtered speech, rather they have access to the entire (broadband) speech spectrum.

The correlational method (Lutfi, 1995; Richards and Zhu, 1994) has been shown to be a viable method in determining how listeners weight spectral information. Doherty and Turner (1996) were the first to use a correlational method with speech stimuli while listening in a broadband listening condition. Application of a correlational method requires the signal to be degraded in some manner. The degradation of the stimulus is essential when applying a correlational method so that the level of degradation can be correlated with the listener's performance. For example, to degrade the spectral information in speech a noise can be added to the signal at various signal-to-noise ratios (SNRs). If performance decreases with increases in SNR it suggests that the spectral information was important for speech recognition. However, if performance remains unchanged as the SNR increases then the spectral information contributed little to the listener's recognition. A point-biserial correlation is used to assess the relationship between a listener's response on a task (either incorrect or correct) and the degradation in the stimulus (SNR). The higher the correlation between these two values (the listener's performance and the SNR in an individual frequency band), the stronger that specific component in the signal is assumed to contribute to the listener's performance on the listening task. The relative contribution,

[a]Author to whom correspondence should be addressed. Electronic mail: lcalandr@syr.edu

or weight of each frequency band in the signal, is referred to as the listener's weighting strategy. Doherty and Turner (1996) reported that weighting strategies for nonsense syllables were similar across a group of normal-hearing listeners.

Turner *et al.* (1998) later compared the correlational method and AI method by contrasting frequency-importance functions and listeners' weighting strategies for nonsense syllables from the Nonsense Syllable Test (NST; Levitt and Resnick, 1978). Specifically, they filtered stimuli from the NST into four adjacent frequency bands of equal intelligibility based on previously reported AI frequency-importance functions (Dirks *et al.*, 1990). Thus, each of the four bands contained approximately equal importance (i.e., 0.25 of the total intelligibility was provided by each band) and in isolation should produce the same relative "weight," or contribute equal information on the NST recognition task. However, listeners did not weight each band equally, but consistently weighted the first (1120 Hz and below) and third (2250–3500 Hz) frequency bands the greatest. Therefore, estimates of the effect of spectral information on nonsense syllable recognition differ depending on whether the AI (filtered) method or the correlational (broadband) method is used.

The correlational method has also been used to measure spectral shape discrimination (Lentz and Leek, 2002), temporal envelope cue discrimination (Apoux and Bacon, 2004) and cochlear implant channel weighting strategies (Mehr *et al.*, 2001). Of the studies that have examined speech, all have used NST stimuli. To date, spectral weights have not been obtained using the correlational method for word or sentence materials, which would more closely represent everyday listening conditions. Therefore, the present study was designed to obtain listeners' spectral-weighting strategies for sentence stimuli.

The two main goals of this study were 1), to determine how listeners use information in sentences while having the entire speech spectrum available (i.e., in a broadband listening condition) (Experiment I), and 2), to compare weighting strategies for sentence stimuli to those obtained for the NST stimuli reported in Turner *et al.* (1998) (Experiment II). Listeners' weighting strategies for sentences, measured using a correlational method, will provide insight into how listeners use spectral information in more naturally occurring listening conditions.

II. EXPERIMENT I

A. Methods

1. Subjects

Spectral-weighting strategies for sentences using a correlational method were measured on 15 listeners with normal hearing, age 18–28 (mean age 23; eight females and seven males), with normal audiometric thresholds $\leq$15 dB HL at 250–8000 Hz (ANSI, 2000) bilaterally. Pure-tone audiometric thresholds were recorded via a GSI-16 audiometer (Grason-Stadler; Madison, WI) using standard audiometric procedures (ANSI, 2004). All participants were native speakers of American English.

2. Speech material

Harvard/IEEE (IEEE, 1969) sentences spoken by a female speaker (recorded by Galvin and Fu, 2003) were used for all speech testing. There are 720 Harvard/IEEE sentences (72 lists $\times$ 10 sentences) that portray everyday conversational low-contextual speech. Each sentence has five keywords used for scoring.

3. Experimental conditions

Spectral-weighting strategies were obtained for Harvard/IEEE sentence stimuli filtered into five adjacent equally intelligible bands based on previously reported importance functions for sentences. That is, the bandwidth of the five bands was chosen so that each band would provide an importance value of approximately 0.20. Five bands, rather than the four bands used by Turner *et al.* (1998), were chosen in order to increase the frequency resolution of the weighting strategy measurement. Frequency-importance functions are not available for Harvard/IEEE sentence stimuli. To the best of our knowledge, frequency-importance functions for sentence materials only exist for two sentence recognition tests, the Connected Speech Test (CST; Cox, Alexander, and Gilmore, 1987; Sherbecoe and Studebaker, 2002) and the Speech Perception in Noise (SPIN) Test (ANSI, 1997; Bell, Dirks, and Trine, 1992). Both the CST and the SPIN tests have a limited number of sentences ($<$500 sentences/test), and therefore were not appropriate for the number of trials required in the present study. Because the CST and the SPIN have slightly different frequency-importance functions, pilot testing was conducted on four listeners using two sets of bandwidths, one based on the CST and the other based on the SPIN frequency-importance functions. Two of the piloted listeners were tested using the CST bandwidths, and the other two piloted listeners were tested using the SPIN bandwidths. The relative shape, based on qualitative judgments, of the listeners' weighting strategies for the Harvard/IEEE sentences did not change regardless of which set of cutoff frequencies were used. Specifically, listeners placed the greatest weight on the spectral information in bands 2 and 5 in comparison to the other three spectral bands. Thus, generating upper and lower cutoff frequencies for the five spectral bands based on the frequency-importance data for either of these two speech materials did not affect the relative shape of our listeners' weighting strategies for the Harvard/IEEE sentences. Therefore, either set of cutoff frequencies could have been used for Experiment I. For this study the cutoff frequencies for the spectral bands were selected based on a combination of the CST and SPIN frequency importance functions (see Table I).

Rectangular finite impulse response (FIR) filter algorithms with less than 0.5 dB of passband ripple, over 60 dB of stopband attenuation and a 20 Hz transition region were created in MATLAB (MathWorks; Natick, MA) to filter the sentences and a spectrally shaped noise (16 bit, 22 kHz sampling rate), which was matched to the long-term average speech spectrum (LTASS) of the Harvard/IEEE sentences. The spectrally shaped noise was generated in MATLAB by passing a Gaussian white noise through an FIR filter with a

TABLE I. Cutoff frequencies and bandwidths of filters used in Experiment I.

Band No.	Low Hz cutoff	High Hz cutoff	Bandwidth
1	111	561	596
2	562	1113	405
3	1114	1788	1113
4	1789	2806	1332
5	2807	11,000	7439

magnitude response equal to the LTASS of the 720 sentences.

On each trial a specific SNR from a predetermined range was assigned to each of the bands relative to the level of the speech signal within that band. Throughout testing, five different SNRs were used for each listener. The range of these SNRs was 13 dB wide with a 3 dB step size. For example, the SNRs used for one listener ranged from −14 to −2 dB, which included SNRs of $[-14,-11,-8,-5,-2]$. On each trial, one of these SNR values was randomly assigned to each band independently of the other bands. Therefore, on a given trial, the same SNR could be assigned to more than one band. However, within each specific band the SNRs were sampled without replacement. As a result, all five possible SNRs were presented 120 times in each band. In this paper the SNR range will be identified by the SNR midpoint, or the middle value within the SNR range. Thus, in the previous example the SNR range would be defined as −8 dB. The midpoint of the SNR range varied across listeners to generate overall performance scores between 60 and 80% correct. A PC and Tucker-Davis Technologies (TDT; Alachua, FL) digital signal processor (DSP) board were used to generate the stimuli. A schematic diagram is shown in Fig. 1 to illustrate how 1) the speech and noise were filtered into five frequency bands, 2) in each respective band the noise and speech were combined at randomly assigned SNRs from a specific SNR range and 3) the five speech and noise bands were recombined to result in a noisy sentence.

4. Procedure

Listeners were seated in a sound-treated booth 1 m in front of the custom-made loudspeaker with a flat frequency response through 11,000 Hz. Signal level was controlled by a Crown D-75 amplifier and the long-term average rms of the speech level of the Harvard/IEEE sentences was fixed at 75 dB sound pressure level (SPL). Listeners were asked to repeat the sentence they had just heard and an examiner outside of the booth scored the listeners' responses online. Listeners' responses were also digitally recorded using an Olympus WS100 Digital Voice Recorder and were later rescored for reliability offline. Subsets of 30 sentences [150 keywords (30 sentences × 5 keywords)] were used to adjust the SNR midpoint to force listeners' performance scores between 60 and 80% correct on the task. All further testing was performed using the SNR range corresponding to this midpoint. Listeners' spectral weighting strategies were based on scores from 600 sentences [3000 keywords (600 sentences × 5 keywords)]. Testing took approximately 3 h and was collected in one or two sessions, dependent on the listener's ability to attend to the task.

B. Analysis

For each trial the following data were recorded: the SNR for each band, the sentence played, the listener's verbal response, and a score for all five keywords of 0 or 1 for each incorrect or correct response, respectively. Weights were derived using a point-biserial correlation between the SNR for a given spectral band and the listener's correct and incorrect responses. Listeners' responses to the words were either correct (score=1) or incorrect (score=0). A point-biserial correlation estimates the strength of the relationship between a dichotomous nominal scale and an interval (or ratio) scale (Brown, 1998). For example, if a listener's response was always correct (score=1) with high SNRs in band 1 and incorrect (score=0) with low SNRs in band 1 then the correlation, and therefore the weight, would be high for band 1. To perform the point-biserial correlation, 3000 responses

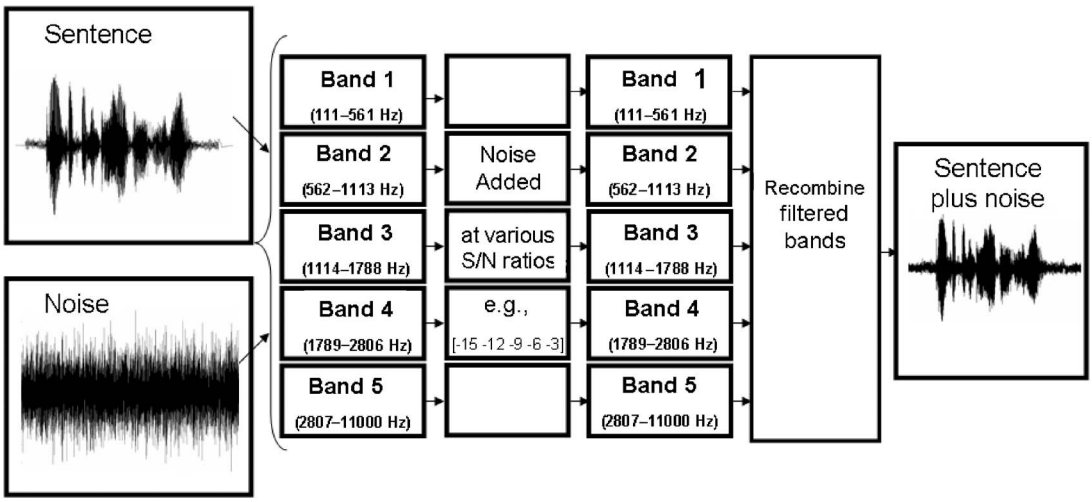

FIG. 1. A schematic diagram of stimulus generation for Exp. I. A single Harvard/IEEE sentence and a spectrally shaped noise matched to the Harvard/IEEE sentences were filtered into five frequency bands. Within a given band the filtered noise was added to the filtered sentence at different SNRs. The five bands were then recombined to generate a noisy sentence.

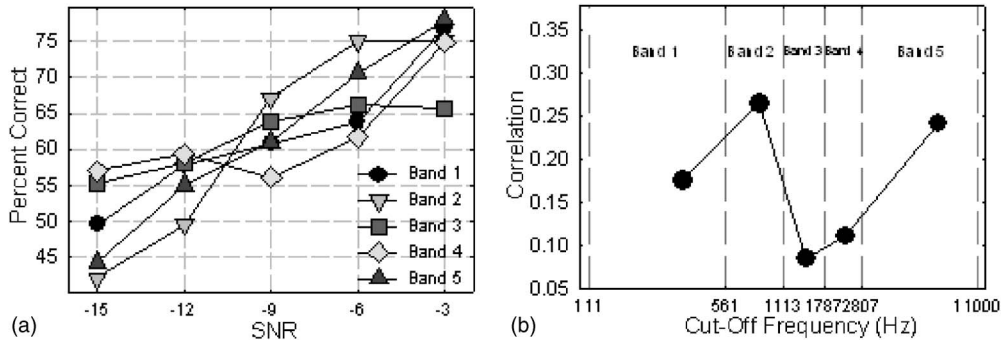

FIG. 2. a) Speech intelligibility performance for one subject (NH1) as a function of SNR for each band. The stronger the correlation between the listener's percent correct scores and the SNR, the greater the weight. b) Listener NH1's weighting strategy, which corresponds to the correlations shown in Panel A. Vertical lines represent the filter cutoff frequencies of each band. Band numbers are labeled at the top of each band.

(600 sentences × 5 keywords/sentence) were correlated with 3000 SNRs (600 keywords × 5 SNRs) for each of the five bands. Doherty and Turner (1996) and Turner *et al.* (1998) used the point-biserial correlation the same way except they scored listener's recognition of nonsense syllables as correct/incorrect.

Figure 2 is an example of NH1's individual data. The same analysis was calculated for all 15 listeners. NH1's data is shown for illustrative purposes only; note that the same technique was used for all 15 listeners. Figure 2(A) illustrates NH1's performance as a function of SNR. NH1's performance on the sentence recognition task was correlated with SNR for each of the five spectral bands. The stronger the correlation, the greater that band contributed to the listener's performance on the task [see Fig. 2(B)]. Each listener's correlations were normalized to sum to one to allow for comparisons to be made across listeners and are thus referred to as their "relative" weighting strategy. As in Doherty and Turner (1996) and Turner *et al.* (1998) a graph of the normalized correlations for each frequency band will be referred to as the listener's weighting strategy.

C. Results

The point-biserial correlation coefficients for the five bands for all 15 listeners who participated in Experiment I are shown in Table II. The SNR midpoint value ranged from −9 to −6 dB across listeners. Listeners' overall performance scores ranged from 61 to 81% correct. All listeners had a similar weighting strategy in that they placed the greatest weight on bands 2 (562–1113 Hz) and 5 (2807–11,000 Hz). Simple linear regression analyses indicated a significant relationship between SNR and performance for all five bands (p values ranging from 0.0052 to <0.0001). Throughout this paper, statistical significance was determined using an alpha level <0.05. Post-hoc testing of the equality of regression coefficients (Chiswick and Chiswick, 1975) indicated that the weighting for bands 2 and 5 was significantly greater from those of bands 1, 3, and 4; however, the weights on these three bands were not significantly different from each other. Also, there was no significant difference between the weights for bands 2 and 5. Individual listener data all fol-

TABLE II. Raw point-biserial correlational data for 15 listeners with normal hearing who participated in Experiment I. Bold numbers indicate point-biserial correlations that are significantly different from zero (α=0.05) in a one-tailed test. SNR midpoints used for testing and overall percent correct scores are also shown.

Subject	Midpoint	Overall PC	Band 1	Band 2	Band 3	Band 4	Band 5
NH1	−9	61.8	**0.175**	**0.265**	**0.084**	**0.111**	**0.242**
NH2	−9	79.4	**0.125**	**0.187**	**0.066**	**0.097**	**0.168**
NH3	−8	67.5	**0.061**	**0.143**	**0.088**	**0.084**	**0.204**
NH4	−8	74.0	**0.097**	**0.155**	0.014	**0.098**	**0.181**
NH5	−7	77.0	**0.072**	**0.155**	**0.055**	**0.063**	**0.213**
NH6	−9	79.4	0.020	**0.154**	**0.084**	**0.132**	**0.158**
NH7	−7	64.3	**0.060**	**0.110**	−0.002	**0.066**	**0.103**
NH8	−7	80.3	**0.070**	**0.116**	**0.071**	**0.054**	**0.206**
NH9	−8	73.9	**0.071**	**0.195**	**0.094**	**0.086**	**0.226**
NH10	−7	67.4	**0.054**	**0.175**	**0.098**	**0.102**	**0.228**
NH11	−8	70.8	**0.101**	**0.239**	0.018	**0.101**	**0.268**
NH12	−8	81.4	**0.111**	**0.232**	0.033	**0.093**	**0.223**
NH13	−8	75.9	**0.153**	**0.203**	**0.044**	**0.100**	**0.213**
NH14	−7	80.9	0.034	**0.184**	**0.038**	**0.092**	**0.162**
NH15	−6	73.5	**0.074**	**0.113**	**0.078**	**0.060**	**0.248**

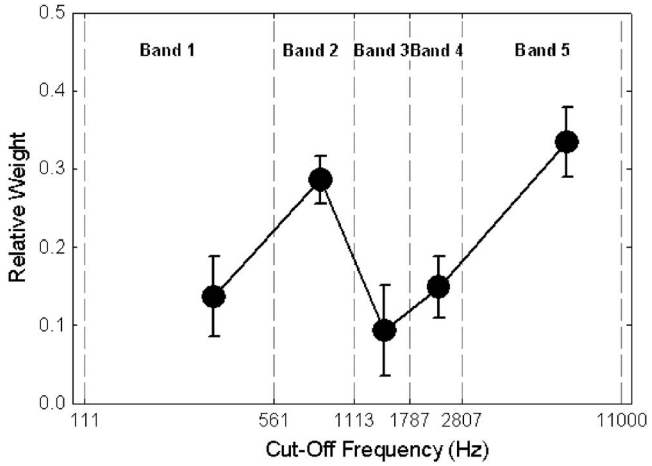

FIG. 3. Mean relative weighting strategies for 15 listeners who participated in Exp. I. Error bars are indicative of one standard deviation of the normalized mean. Vertical lines represent filter cutoff frequencies. Band numbers are labeled at the top of each band.

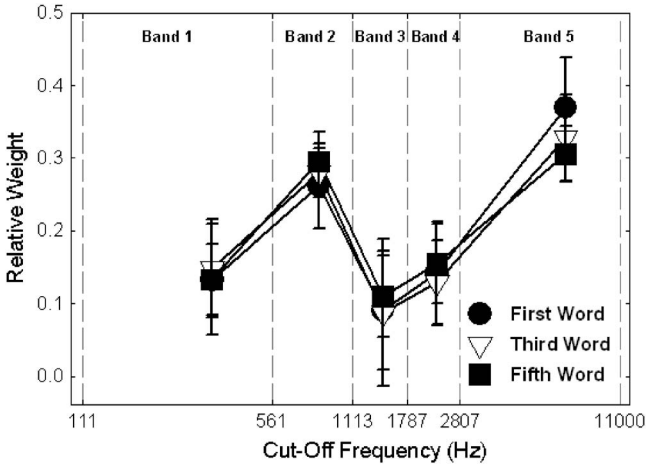

FIG. 5. Mean relative weighting strategies calculated using only the first (filled circles), third (open triangles), and fifth (filled squares) word of each sentence for 15 listeners. Error bars are indicative of one standard deviation of the normalized mean.

lowed the same trend, thus the normalized correlation coefficients were averaged across listeners and are shown in Fig. 3.

Regression analyses were performed on weighting strategy data to determine the minimum number of trials needed for listeners' weighting strategies to become *stable*. A stable weighting strategy was defined as the number of trials needed for the weighting strategy to remain approximately unchanged with the addition of more trials, e.g., a stable weighting strategy by 200 trials meant that the relative weighting strategy shape was the same for trials No. 1–200 as for No. 201–400 and so forth. All 15 listeners who participated in Experiment I demonstrated stable weighting strategies after approximately 200 trials [1000 keywords (200 sentences×5 keywords)] (p values ranging from 0.1348 to 0.9679 across the five bands). To assess the reliability of the weighting strategy for a given listener, two separate weighting strategies were derived using the first 300 and last 300 trials for all 15 listeners (see Fig. 4). Weighting strategies were consistent across the first and last half of the trials for all listeners.

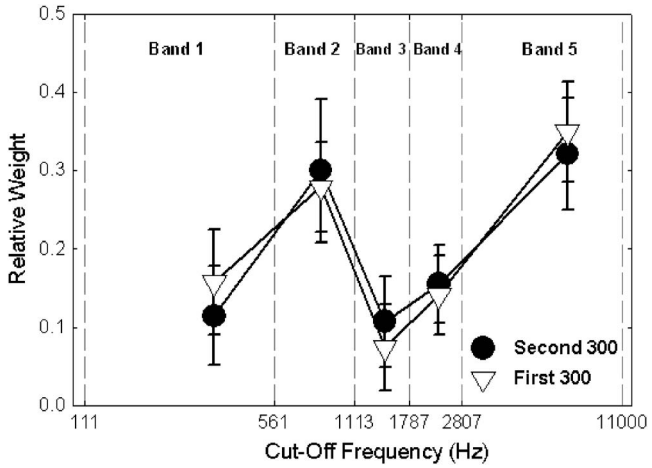

FIG. 4. Mean relative weighting strategies for the first 300 trials (open triangles) and the last 300 trials (filled circles) for the 15 listeners who participated in Exp. I. Error bars are indicative of one standard deviation of the normalized mean.

To insure that the position of the keyword and the number of keywords scored in each sentence did not change the relative shape of the weighting strategy, three separate weighting strategies were computed for keywords positioned in the first (initial), third (middle) and fifth (final) position for all 15 listeners. These weighting strategies were based on 600 keywords (600 sentences×1 keyword position). The position of the keyword had minimal affect on the relative shape of the listener's weighting strategies (see Fig. 5). Testing of the equality of coefficients in a regression analysis indicated no significant differences between the first and third keyword position (p values ranging from 0.092 to 0.921) and the third and fifth keyword position (p values ranging from 0.227 to 0.500). There was also no significant difference seen in bands 1–4 between the first and the fifth keyword position (p values ranging from 0.174 to 0.985), however, there was a significant difference in band 5 between the first and fifth keyword position ($p=0.004$).

To determine whether correct responses were independent across keywords an additional analysis was conducted in which scores were based on a sentence-by-sentence basis and not on each individual word. That is, a correct score (1) would require the listener to get all five keywords in each sentence correct; otherwise their score would be incorrect (0) for that particular sentence. This analysis was completed for six listeners (see Fig. 6). Regression analyses indicated no statistical differences between the two types of scoring methods across all five bands (p values ranging from 0.423 to 0.907).

One listener (NH17) was tested using two different SNR midpoints (−13 and −8 dB) to insure that overall performance did not impact the relative shape of the weighting strategy. Overall percent correct scores were 59% and 75% for the −13 and −8 dB SNR midpoints, respectively (see Fig. 7). Although overall performance differed by 16%, the shapes of the weighting strategies were similar.

To assess whether weighting strategies remained stable

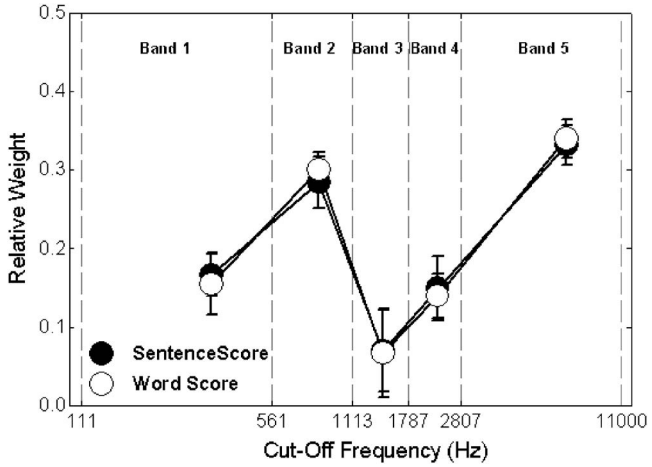

FIG. 6. Mean relative weighting strategies for six listeners based on two different scoring methods. The five-keyword scoring method allowed the examiner to score each keyword with either a 1 (correct) or a 0 (incorrect). The sentence-scoring method scored the entire sentence, i.e., a correct score entailed all five keywords within the sentence repeated correctly (score =1), otherwise that sentence was incorrect (score=0). Error bars are indicative of one standard deviation of the normalized mean.

over time, one listener, NH2, was tested two times three months apart. Collecting data at these two different intervals had minimal effect on the shape of the weighting strategy (see Fig. 8). This testing also provided information regarding the feasibility of testing a listener using the same set of sentence stimuli twice. Using the same set of sentences, the listener's overall percent correct scores only differed by 3%.

III. EXPERIMENT II

A. Methods

The purpose of Experiment II was to make a comparison between the spectral-weighting results reported for nonsense syllables in Turner *et al.* (1998) and those for sentences. Sentence stimuli were filtered into the same four spectral bands as those used by Turner *et al.* (1998). These bandwidths were generated based on frequency-importance functions reported for the UCLA version of the Nonsense Syllable Test (NST) (Dirks *et al.*, 1990) and were used to divide the NST into four approximately equal intelligible bands. The bands used for Experiment II are shown in Table III.

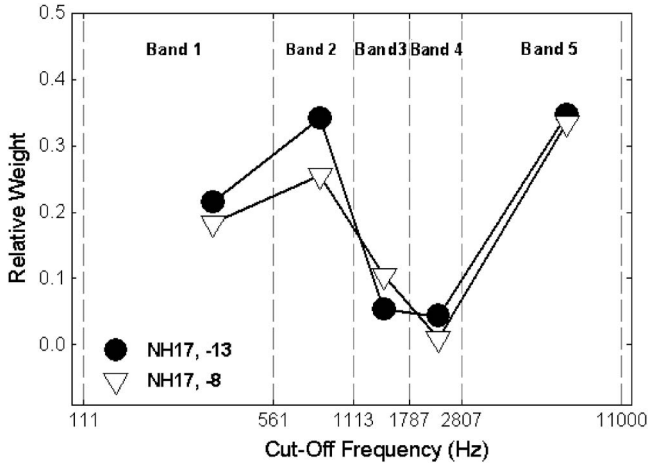

FIG. 7. Relative weighting strategies for listener NH17, who was tested with two different SNR midpoint values, −13 and −8 dB. Overall percent correct scores differed by 16% using these different midpoint values (scores were 59% and 75%, respectively).

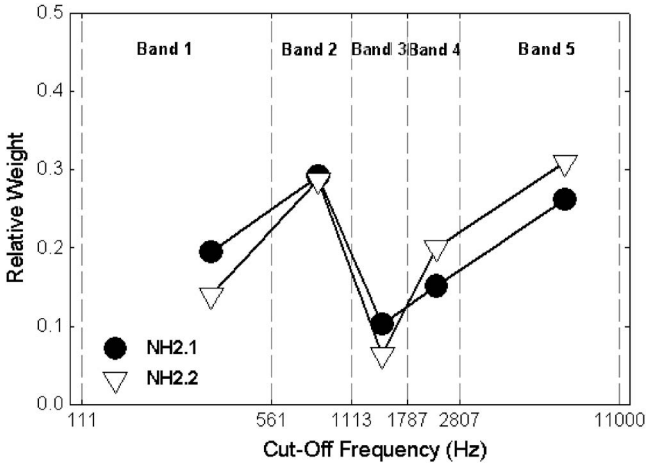

FIG. 8. Relative weighting strategies for listener NH2. Two separate weighting strategies were measured for NH2 three months apart.

1. Subjects

Five listeners (mean age of 22, ranging from 19 to 26 years) with normal hearing [≤15 dB HL between 250–8000 Hz (ANSI, 2000)] participated in Experiment II. Four of the five listeners also participated in Experiment I.

2. Experimental conditions

Stimulus generation, procedures and analyses were identical to those used in Experiment I with two exceptions. First, the Harvard/IEEE sentences and the noise were filtered in MATLAB using the *four* frequency bands listed in Table III. Second, only 400 sentences [2000 keywords (400 sentences × 5 keywords)] were used to derive the spectral weighting strategies. Experiment II was completed in 1 2-h session.

B. Results

Point-biserial correlations obtained from the five listeners who participated in Experiment II are shown in Table IV. A comparison of point-biserial correlation coefficients indicated that weighting strategies across listeners were very similar. In this experimental condition the greatest amount of weight was placed on band 1. Regression analyses indicated all five of the listeners tested in Experiment II demonstrated stable weighting strategies by approximately 200 trials [1000

TABLE III. Cutoff frequencies and bandwidths of filters used in Experiment II [based on filters used in Turner *et al.* (1998)].

Band No.	Low Hz cutoff	High Hz cutoff	Bandwidth
1	100	1120	1020
2	1121	2250	1129
3	2251	3500	1249
4	3501	10,000	6499

TABLE IV. Raw point-biserial correlational data across four bands for five listeners with normal hearing who participated in Experiment II. Bold numbers indicate point-biserial correlations that are significantly different from zero (α=0.05) in a one-tailed test. Also included are the SNR midpoints used for testing and overall percent correct scores.

Subject	Midpoint	Overall PC	Band 1	Band 2	Band 3	Band 4
NH3	−3	8.3	**0.259**	**0.166**	**0.159**	**0.147**
NH4	−2	83.0	**0.170**	**0.107**	0.037	**0.086**
NH12	−6	70.2	**0.336**	**0.174**	**0.086**	**0.051**
NH14	−4	70.0	**0.388**	**0.199**	**0.174**	0.021
NH16	−3	78.8	**0.334**	**0.145**	**0.150**	**0.128**

keywords (200 sentences×5 keywords)] (p values ranging from 0.5345 to 0.7649 across the four bands).

Simple linear regression analyses indicated p values of $<$0.0001 for all four bands. Post-hoc testing of the equality of regression coefficients (Chiswick and Chiswick, 1975) indicated that band 1 was weighted significantly greater compared to bands 2, 3, and 4; however, these three bands were not weighted significantly differently from each other. Listeners' overall percent correct scores (ranging from 70.0 to 83.0% correct) and the SNR midpoints (ranging from −6 to −2 dB) used to generate these scores are shown in Table IV. The averaged normalized weighting strategy for all five listeners is shown in Fig. 9 and is compared to the average normalized weighting strategy reported in Turner *et al.* (1998). Similar to Turner *et al.* (1998), our listeners placed the most weight on the information in band 1, however, for sentence stimuli band 3 was not weighted as highly as it was for NST stimuli. When interpreting the results of Experiment II it should be noted that the cutoff frequencies of the bandwidths were based on the frequency-importance functions for nonsense syllables (*not* sentences) to produce equal AI values in each of the four bands.

IV. DISCUSSION

Spectral-weighting strategies for sentences were measured for listeners with normal hearing. Two experiments were designed to determine how listeners use spectral information to identify sentences (Experiment I) and evaluate how listeners weight spectral information in sentences in comparison to nonsense syllables (Experiment II). The frequency ranges of the five bands in Experiment I were computed based on previously reported AI/SII frequency-importance functions for sentences, which is consistent with the approach other studies have used to apply the correlational method to speech (Apoux and Bacon, 2004; Doherty and Turner, 1996; Turner *et al.*, 1998). In the present study the bands were divided so that each would theoretically contribute approximately 20% intelligibility. However, listeners did not place equal weight on each band, rather they consistently weighted bands 2 (562–1113 Hz) and 5 (2807–11,000 Hz) the greatest.

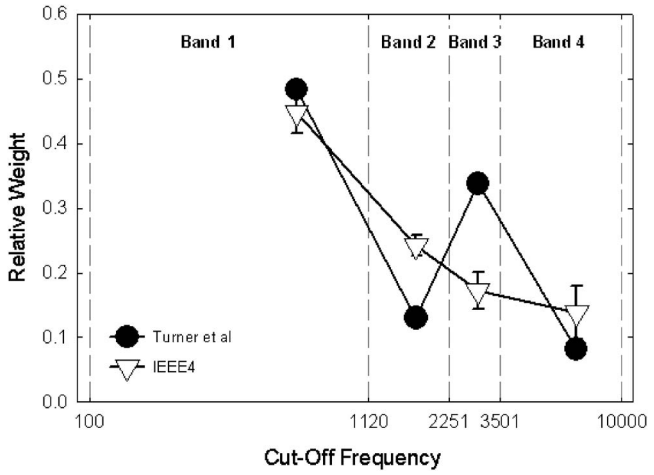

FIG. 9. Mean relative weighting strategies for five listeners who participated in Exp. II (gray triangles). For comparison purposes, NST data reported in Turner *et al.* (1998) are also shown (filled circles). Error bars are indicative of one standard deviation of the normalized mean.

Listeners' weights were consistent across trials and test sessions. All 15 listeners in Experiment I established a consistent weighting strategy by as few as 200 trials. One listener, NH2, was tested three months apart during Experiment I with the same set of sentences and the same SNR midpoint. NH2's weighting strategy was the same and her overall percent correct scores differed by only 3% (see Fig. 6 in Results section) across the two sessions. Learning effects were likely reduced because a large number of low-context sentences, degraded with noise, were used throughout testing. Based on the lack of learning effects demonstrated by NH2, four listeners from Experiment I were chosen to participate in Experiment II. Similar to NH2, an interval of at least three months elapsed between experimental test sessions for each listener that participated in both experiments.

Since learning could also take place within a test session (even though different sentences were presented on each trial) a comparison was made between the performance across the first 100 trials to that of all of the trials. On average, intelligibility scores for all listeners in Experiments I and II improved by 2.0% and 0.5%, respectively. The relative shape of the listener's weighting strategy was not greatly affected by the overall percent correct score as long as there was not a ceiling or floor effect.

The similarity and stability of weighting strategies for sentences across listeners, time, and performance level is consistent with previous studies. Doherty and Turner (1996) and Turner *et al.* (1998) reported that listeners with normal hearing used similar weighting strategies to identify NST stimuli. In fact, Turner *et al.* (1998) suggested that the consistency across listeners could imply that a "normal" listening strategy exists. All listeners used a similar weighting

strategy to perform the sentence recognition task in Experiments I and II. Based on the consistency of listeners' weighting strategies demonstrated in these experiments, a normal listening strategy may also exist for sentences.

The purpose of Experiment II was to compare spectral weights for sentences with those previously reported for NST stimuli (Turner *et al.*, 1998). The comparison was made because the two studies generated their stimuli in the same way, used the correlational method to obtain weights and used the same four spectral bands (i.e., four spectral bands of equal intelligibility based on previously reported AI-weighting functions for the NST). However, there were some small differences between the two studies. For example, in Turner *et al.* (1998) listeners were tested monaurally under headphones, the level of the NST was fixed at 70 dB SPL, NST stimuli were spoken by both a male and female speaker, and the SNRs were chosen from a range of 24 dB with a 2 dB step size. In the present study, listeners were tested in the sound field, the level of the sentences was fixed at 75 dB SPL, Harvard/IEEE stimuli were spoken by a female speaker, and SNRs were chosen from a 13 dB SNR range with a 3 dB step size.

Results from Turner *et al.* (1998) indicated that listeners placed significantly greater weight on bands 1 and 3 in comparison to bands 2 and 4 when recognizing NST stimuli. In the present study, listeners in Experiment II weighted the spectral information in band 1 (100–1120 Hz) the greatest. Bands 2, 3, and 4 were not weighted significantly different from each other. Differences observed between the weighting strategies obtained in Experiment II and those reported in Turner *et al.* (1998) could have been due to the difference in the speakers used in the two studies. In Experiment II, sentences were spoken by a female speaker, whereas in Turner *et al.* (1998) the NST was spoken by both a male and female speaker. The addition of the male speaker may have reduced the weight in the higher frequencies. However, the spectral resolution provided by only four bands was probably not sensitive enough to measure such a small effect. Interestingly, listeners did not place equal weight across the spectral bands in either study. Turner *et al.* (1998) suggested that the main reason their results differed from the results of AI-importance functions (i.e., equal weight placed across the spectral bands) was that when using the correlational method listeners had the entire speech spectrum available, whereas in experiments using filtering techniques only the high- or low-pass filtered speech spectrum was available. Results from the present study also suggest that listeners use spectral information differently depending on the condition in which the spectral information is presented to them (e.g., broadband vs. filtered).

A comparison between the spectral weights obtained in Experiments I and II in the current study was made in an attempt to better understand the effect spectral divisions of the bands and the number of bands may have on weighting strategies. However, first recall that, although sentences were used in both Experiments I and II, the cutoff frequencies used to generate the spectral bands for Experiment I were based on previously reported importance functions for sentences, whereas the cutoff frequencies for Experiment II were based on the AI importance functions for NST. In Experiment I the highest frequency band was band 5, which included frequencies between 2807and 11,000 Hz. However, band 4 was the highest frequency band in Experiment II [bandwidths based on the Turner *et al.* (1998) paper] and included frequencies between 3501 and 10,000 Hz. Thus, all of the frequency information in band 4 of Experiment II was included in band 5 of Experiment I. In addition, band 5 of Experiment I also included frequencies between 2807 and 3501 Hz. Listeners in Experiment I placed relatively greater weight on the highest frequency band (band 5), but in Experiment II they did not place relatively greater weight on the highest frequency band (band 4). Instead listeners placed their greatest weight on the lower frequency information (band 1). It is unclear why the listeners did not weight the highest frequency information consistently. Again, information between 2807 and 3501 Hz was included in band 5 of Experiment I, but not in band 4 of Experiment II. Perhaps listeners were able to use the higher frequency information present in both bands with the information within the 2807–3501 Hz range to make it more useful in Experiment I. Another possibility is that band 5 in Experiment I simply included more spectral information regarding fricatives, plosives and voicing, as well as information from the third formant (and possibly some second-formant information) that allowed it to be more useful when presented in the same band.

It is easier to interpret the differences in weights observed in Experiments I and II at the lower frequencies due to the spectral overlap within the lower frequency bands. In Experiment I, band 2 was weighted the highest, whereas band 1 was weighted the highest in Experiment II. All of the spectral information in band 2 of Experiment I was also present in band 1 of Experiment II. Thus, it is probable that the low frequency information in band 1 that listeners found so useful in Experiment II was the same spectral information that listeners placed a relatively high weight on in band 2 of Experiment I (~562–1120 Hz). This spectral region most likely contained F1 and F2 information. Bands 3 and 4, in Experiment I, were spectrally comparable to band 2 in Experiment II, and similarly were not weighted significantly greater than any of the other bands.

Due to the different results of Experiments I and II it is apparent that large disparities in spectral divisions will affect the shape of a weighting strategy. Interestingly, pilot testing conducted prior to experimental testing indicated that small differences in cutoff frequencies do not have a significant effect on the shape of the relative weighting strategy of normal-hearing listeners. In fact, varying the cutoff frequencies by as much as 750 Hz (in bands 3, 4 and 5 of Experiment I) had no effect on the shape of the weighting strategies. Thus, the actual number of bands may play a more critical role than the specific cutoff frequencies of the bands. To determine if this is a plausible explanation, one would need to experiment with a larger number of bands and vary the bandwidth of the filters.

The above discussion and the results from Experiments I and II suggest that listeners use spectral information in different ways depending on how it is presented to them. War-

ren *et al.* (2005) also reported that listeners use spectral information differently depending upon what other spectral information is presented in tandem. They found that the relationship between intelligibility and audibility differed when information was presented in octave bands in isolation versus in nonadjacent and adjacent octave band pairs. Specifically, they showed that spectral information within octave bands was not purely additive but instead synergistic. In other words, when listeners were allowed to combine information that they previously heard separately (within one isolated octave band), their intelligibility scores did not simply add together from the isolated conditions, rather their scores were higher than a simple additive effect.

Thus, it appears that when listening in a broadband condition, listeners are able to combine spectral information to make it more useful than if the information had been presented in isolation or in narrower bands, such as in the AI/SII method.

Weighting strategies indicate how spectral information within a given band contributed to a listener's performance on a task. However, one limitation of using the correlational method is that the testing must be done in the presence of background noise or some other method of degrading the signal. The presence of background noise likely influences the importance of spectral information in speech (e.g., Hogan and Turner, 1998; Turner and Henry, 2002). For example, high frequency speech cues, such as those used for place, are generally less intense, aperiodic, and more vulnerable to noise than low frequency cues. Thus, these cues would be masked in the lower SNR conditions more than other cues, such as voicing and nasality, which occur over a wider frequency range of the speech spectrum and are more intense [see Rosen and Fourcin (1986) for a detailed review]. Nevertheless, the main advantage of using the correlational method is that the entire speech spectrum, though partially degraded, is always available to the listener, and thus listeners are able to take advantage of redundant speech cues while performing the task. It should also be noted that listening in a noisy condition is not only more realistic to real-life listening environments, but is also the condition in which listeners with hearing impairment (Alacantara *et al.*, 2003; Kochkin, 2005; Ricketts and Dhar, 1999; Schum, 2000) and hearing aid users (Dhar *et al.*, 2004; Gordon-Salant and Fitzgibbons, 1997; Nordrum *et al.*, 2006; Plyler and Fleck, 2006) have the most difficulty. Thus, a listener's spectral weighting strategy may provide useful information when fitting hearing aids and cochlear implants. However, further research in this area is needed before such clinical applications could be seriously considered.

V. SUMMARY AND CONCLUSIONS

The results from Experiments I and II indicate that reliable weighting strategies can be obtained for sentences using the correlational method. While listening to sentences in a broadband listening condition, listeners weight spectral information differently than they do in a filtered-listening condition (such as the AI/SII). The consistency across listeners' weighting strategies suggests there is a "normal" listening strategy that listeners with normal hearing tend to use to process spectral information in sentences. Further research is needed to determine how listeners with hearing loss weight spectral information in broadband-listening conditions in comparison to normal-hearing listeners. With further research there is potential for this information to be helpful in identifying the frequency response of a hearing aid and the spectral information that should be mapped to specific cochlear implant channels.

ACKNOWLEDGMENTS

This work was supported by the ASHFoundation Student Audiology Research Grant and the Jerome R. and Arlene L. Gerber Fund. The authors are thankful to Dr. Michael Anzalone who assisted with all computer programming for this project and Kristi Lalor who helped with data collection. Many thanks to Dr. Laurel Carney, Dr. Kathy Vander Werff, Dr. Andy Faulkner and Dr. Stuart Rosen, for helpful comments while writing this manuscript. We are appreciative to Dr. John Grose and two anonymous reviewers for their time spent editing and attention paid to detail.

Alacantara, J., Moore, B., Kuhnel, V., and Launer, S. (**2003**). "Evaluation of the noise reduction system in a commercial digital hearing aid," Int. J. Audiol. **42**, 32–42.

American National Standards Institute (ANSI). (**1969**). "American national standards methods for the calculation of the articulation index," (ANSI, New York).

American National Standards Institute (ANSI). (**2004**). "American national standard specifications for audiometers (ANSI S3.6-2004)," (ANSI, New York).

American National Standards Institute (ANSI). (**2000**). "International Organization for Standardization – Acoustics – Statistical distribution of hearing thresholds as a function of age (ISO 7029:2000)," (ANSI, New York).

American National Standards Institute (ANSI). (**1997**). "American national standard methods for the calculation of the speech intelligibility index (ANSI S3.5-1997)," (ANSI, New York).

Apoux, F., and Bacon, S. P. (**2004**). "Relative importance of temporal information in various frequency regions for consonant identification in quiet and in noise," J. Acoust. Soc. Am. **116**, 1671–1680.

Baer, T., and Moore, B. C. J. (**1997**). "Evaluation of a scheme to compensate for reduced frequency selectivity in hearing-impaired subjects," in *Modeling Sensorineural Hearing loss*, edited by W. Jesteadt (Lawrence Erlbaum Associates, London), pp. 329–341.

Bell, T. S., Dirks, D. D., and Trine, T. D. (**1992**). "Frequency-importance functions for words in high- and low-context sentences," J. Speech Hear. Res. **35**, 950–959.

Brown, J. D. (**1998**). "Understanding research in second language learning," *A Teacher's Guide to Statistics and Research Design* (Cambridge University Press, Cambridge).

Calandruccio, L., Kikkeri, H. N., Doherty, K. A., and Carney, L. H. (**2005**). "Perception of temporally processed speech by hearing-impaired listeners," *American Auditory Society 2005 Annual Meeting*, Scottsdale, AZ.

Chiswick, B. R., and Chiswick, S. J. (**1975**). *Statistics and Econometrics – A Problem Solving Text* (University Park Press, London).

Cox, R. M., Alexander, G. C., and Gilmore, C. (**1987**). "Development of the connected speech test (CST)," Ear Hear. **8** (5 Suppl.), 119S–126S.

Dirks, D. D., Dubno, J. R., Ahlstrom, J. B., and Schaefer, A. B. (**1990**). "Articulation index importance and transfer functions for several speech materials," ASHA **32**, 91.

Dhar, S., Humes, L., Calandruccio, L., Barlow, N., and Hispkind, N. (**2004**). "Predictability of speech-in-noise performance from real ear measures of directional hearing aids," Ear Hear. **25**, 147–158.

Doherty, K. A., and Turner, C. W. (**1996**). "Use of a correlational method to estimate a listener's weighting function for speech," J. Acoust. Soc. Am. **100**, 3769–3773.

Fletcher, H., and Galt, R. H. (**1950**). "The perception of speech and its relation to telephony," J. Acoust. Soc. Am. **22**, 89–150.

French, N. R., and Steinberg, J. C. (**1947**). "Factors governing the intelligibility of speech sounds," J. Acoust. Soc. Am. **19**, 90–119.
Galvin, J. J. III, and Fu, Q.-J. (**2003**). "IEEE subcommittee on subjective measurements (1969)," Recorded at House Ear Institute, Los Angeles, CA.
Gordon-Salant, S., and Fitzgibbons, P. (**1997**). "Selected cognitive factors and speech recognition performance among young and elderly listeners," J. Speech Lang. Hear. Res. **40**, 423–431.
Greenberg, S., Arai, T., and Silipo, R. (**1998**). "Speech intelligibility derived from exceedingly sparse spectral information," *Proceedings of the International Conference of Spoken Language Processing*, Sydney, Australia, Dec. 1–4.
Hogan, C. A., and Turner, C. W. (**1998**). "High-frequency audibility: Benefits for hearing-impaired listeners," J. Acoust. Soc. Am. **104**, 432–441.
Humes, L. E. (**1991**). "Understanding the speech-understanding problems of the hearing impaired," J. Am. Acad. Audiol **2**, 59–69.
IEEE Subcommittee on Subjective Measurements IEEE Recommended Practices for Speech Quality Measurements. (**1969**). IEEE Trans. Audio Electroacoust. **AU–17**, 227–246.
Jenstad, L. M., and Souza, P. E. (**2005**). "Quantifying the effect of compression hearing aid release time on speech acoustics and intelligibility," J. Speech Lang. Hear. Res. **48**, 651–667.
Kochkin, S. (**2005**). "Marke Trak VII: Hearing loss population tops 31 million people," Hear. Rev. **127**, 16–29.
Lentz, J. J., and Leek, M. R. (**2002**). "Decision strategies of hearing-impaired listeners in spectral shape discrimination," J. Acoust. Soc. Am. **111**, 1389–1398.
Levitt, H., and Resnick, S. B. (**1978**). "Speech reception by the hearing-impaired: Methods of testing and the development of new tests," Scand. Audiol. Suppl. **6**, 107–133.
Lutfi, R. A. (**1995**). "Correlation coefficients and correlation ratios as estimates of observer weights in multiple-observation tasks," J. Acoust. Soc. Am. **97**, 1333–1334.
Mehr, M. A., Turner, C. W., and Parkinson, A. (**2001**). "Channel weights for speech recognition in cochlear implant users," J. Acoust. Soc. Am. **109**, 359–366.
Mueller, H. G., and Killion, M. C. (**1990**). "An easy method for calculating the articulation index," Hear. J. **43**, 14–17.
Nordrum, S., Erler, S., Garstecki, D., and Dhar, S. (**2006**). "Comparison of performance on the Hearing in Noise Test using directional microphones and digital noise reduction algorithms," Am. J. Aud. **15**, 81–91.
Pavlovic, C. (**1991**). "Speech recognition and five articulation indexes," Hear. Instr. **42**, 20–24.
Plyler, P. N., and Fleck, E. L. (**2006**). "The effects of high-frequency amplification on the objective and subjective performance of hearing instrument users with varying degrees of high-frequency hearing loss," J. Speech Lang. Hear. Res. **49**, 616–627.
Richards, V. M., and Zhu, S. (**1994**). "Relative estimates of combination weights, decision criteria, and internal noise based on correlational coefficients," J. Acoust. Soc. Am. **95**, 423–424.
Ricketts, T., and Dhar, S. (**1999**). "Comparison of performance across three directional hearing aids," J. Am. Acad. Audiol **10**, 180–189.
Rosen, S., and Fourcin, A. (**1986**). "Frequency selectivity and the perception of speech," in *Frequency Selectivity in Hearing*, edited by B. C. J. Moore (Academic, London), pp. 373–487.
Schum, D. J. (**2000**). "Combining advanced technology noise control solutions," Semin. Hear. **21**, 169–177.
Shannon, R. V., Zeng, F., and Wygonski, J. (**1998**). "Speech recognition with altered spectral distribution of envelope cues," J. Acoust. Soc. Am. **104**, 2467–2476.
Sherbecoe, G. A., and Studebaker, R. L. (**2002**). "Audibility-Index functions for the connected speech test," Ear Hear. **23**, 385–398.
Steinberg, J. C., and Gardner, M. B. (**1937**). "The dependency of hearing impairment on sound intensity," J. Acoust. Soc. Am. **9**, 11–23.
Turner, C. W., and Henry, B. A. (**2002**). "Benefits of amplification for speech recognition in background noise," J. Acoust. Soc. Am. **112**, 1675–1680.
Turner, C. W., Kwon, B. J., Tanaka, C., Knapp, J., and Doherty, K. A. (**1998**). "Frequency-weighting functions for broadband speech as estimated by a correlational method," J. Acoust. Soc. Am. **104**, 1580–1585.
Warren, R. M., Reiner, K. R., Bashford, J. A., and Brubaker, B. S. (**1995**). "Spectral redundancy: Intelligibility of sentences heard through narrow spectral slits," Percept. Psychophys. **57**(2), 175–182.
Warren, R. M., Bashford, J. A., and Lenz, P. W. (**2004**). "Intelligibility of bandpass filtered speech: Steepness of slopes required to eliminate transition band contributions," J. Acoust. Soc. Am. **115**, 1292–1295.
Warren, R. M., Bashford, J. A., and Lenz, P. W. (**2005**). "Intelligibilities of 1-octave rectangular bands spanning the speech spectrum when heard separately and paired," J. Acoust. Soc. Am. **118**, 3261–3266.

Training native English speakers to identify Japanese vowel length contrast with sentences at varied speaking rates[a)]

Yukari Hirata,[b)] Elizabeth Whitehurst, and Emily Cullings
Colgate University, Department of East Asian Languages and Literatures, Hamilton, New York 13346

(Received 18 August 2006; revised 26 March 2007; accepted 26 March 2007)

Native English speakers were trained to identify Japanese vowel length in three types of training differing in sentential speaking rate: slow-only, fast-only, and slow-fast. Following Pisoni and Lively's high phonetic variability hypothesis [Pisoni, D. B., and Lively, S. E., *Speech Perception and Linguistic Experience*, 433–459 (1995)], higher stimulus variability by means of training with two rates was hypothesized to aid learners in adapting to speech rate variation more effectively than training with only one rate. Trained participants identified the length of the second vowel of disyllables, short or long, embedded in a sentence of the respective rate, and received immediate feedback. The three trained groups' abilities before and after training were examined with tests containing sentences of slow, normal, and fast rates, and were compared with those of a control that was not trained. A robust effect of slow-fast training, a marginal effect of slow-only training, but no significant effect of fast-only training were found in the overall test scores. Slow-fast and slow-only training showed small advantages over fast-only training on the fast-rate test scores, while effects for all three training types were found on the slow- and normal-rate test scores. The degree to which the results support the high phonetic variability hypothesis is discussed. © *2007 Acoustical Society of America.* [DOI: 10.1121/1.2734401]

PACS number(s): 43.71.Hw, 43.71.Es [ARB] Pages: 3837–3845

I. INTRODUCTION

This study examined the way non-native speakers perceive Japanese vowel length contrast in sentences produced at various speaking rates. The vowel length distinction (short versus long) is phonemic in Japanese, e.g., /kuɾo/ "black" versus /kuɾoː/ "hardships," and all five short vowels /i e a o u/ contrast with the corresponding long vowels (/iː eː aː oː uː/) (Vance, 1987). Long vowels are 2.2–3.2 times longer in duration than short vowels, whereas only small differences have been observed between the formant frequencies of short and long vowels (Kondo, 1995; Tsukada, 1999; Ueyama, 2000; Hirata, 2004a; Hirata and Tsukada, 2004). This vowel length distinction, as well as a consonant length distinction (e.g., /kata/ "shoulder" versus /katːa/ "won") has been found difficult for native English (NE) speakers to acquire (e.g., Landahl *et al.*, 1992; Han, 1992; Landahl and Ziolkowski, 1995; Yamada *et al.*, 1995; Toda, 1997; Oguma, 2000; Tajima *et al.*, 2002; Hirata, 2004b). Native Japanese speakers' primary perceptual cue to the Japanese vowel length distinction is vowel duration (Fujisaki *et al.*, 1997), but a long vowel spoken quickly can be shorter than a short vowel spoken slowly (Hirata, 2004a). Speaking rate variation is thought to contribute to the difficulty of acquiring the length distinctions.

Research over the past 50 years has shown how a native speaker's perception of a phonetic segment is affected by the rates of the segment and of the surrounding context (Denes, 1955; Port, 1977; Verbrugge and Shankweiler, 1977; Miller and Liberman, 1979; Port and Dalby, 1982; Johnson and Strange, 1982; Gottfried *et al.*, 1990; Newman and Sawusch, 1996; Sawusch and Newman, 2000). For example, Pickett *et al.* (1999) found that native Italian speakers' perception of Italian single and geminate stops was based on the stop closure duration *relative* to the preceding vowel. Listeners also use the speaking rate of a sentence to perceive native language (L1) contrasts of which the primary acoustic correlate is duration (e.g., Miller, 1987, and Wayland *et al.*, 1994, for English /p/-/b/ contrast; Magen and Blumstein, 1993, for Korean short and long vowels). These studies in L1 perception show *rate normalization*: native listeners do not identify a phonetic segment based on the absolute duration of the segment. Rather, their perception takes into account both the duration of neighboring segments and the segments that are contrastive in the language.

Consistent with the findings above, native Japanese (NJ) speakers use the rate of a sentence as a perceptual cue for distinguishing Japanese consonant and vowel length (Hirata, 1990a; Hirata and Lambacher, 2004). NJ listeners in Hirata (1990a) identified the pair of words /ita/ "stayed" versus /itːa/ "went" based on the durational ratio of the stop closure to the preceding vowel /i/ when the words were presented in isolation. In a second experiment, an edited word [it(ː)ta] in which the durational ratio was identified as ambiguous by NJ listeners was embedded in a carrier sentence produced at different speaking rates. NJ listeners identified this ambiguous word as /ita/ or /itːa/ based on the rate of the sentence. When the sentence was spoken slowly, the word was clearly identified as /ita/, and when the sentence was spoken faster,

[a)]Portions of this work were presented at the International Conference on Spoken Language Processing, Pittsburgh, September 2006, and at the fourth Joint Meeting of the Acoustical Society of America and the Acoustical Society of Japan, Honolulu, Hawaii, December 2006.

[b)]Author to whom correspondence should be addressed. Electronic mail: yhirata@mail.colgate.edu

the word was clearly identified as /itːa/. The perceptual cue present in the sentence rate superseded the ambiguous cue present in the isolated word.

Compared to rate normalization by native listeners, less is known as to how second language (L2) learners normalize speech rate and learn to make duration-based distinctions in sentences. In Hirata (1990b), when the Japanese words /ita/ and /itːa/ were presented in isolation, NE speakers distinguished the words, similarly to NJ speakers, using the durational ratio of the stop closure to the preceding vowel as a perceptual cue. However, when the words were embedded in a sentence spoken at different rates, NE speakers were unable to use the rate of the sentences as a perceptual cue as NJ listeners did. Thus, NE learners of Japanese have difficulty in normalizing rate over a sentence in Japanese, even though they can use the localized perceptual cue when isolated words are presented.

What method would most effectively enable NE speakers to normalize the rate of sentences and identify vowel length in an embedded word accurately? Given the results of Hirata (1990b), training L2 learners on isolated syllable or word contexts might not be the best method. The development of training methods for difficult L2 contrasts has been one of the most fruitful areas of L2 research (English /ɹ/-/l/: Strange and Dittmann, 1984; Logan *et al.*, 1991; Bradlow *et al.*, 1997; English /ð/-/θ/: Jamieson and Morosan, 1986; Mandarin tones: Wang *et al.*, 1999; Korean stops: Francis and Nusbaum, 2002; Japanese length contrasts: Yamada *et al.*, 1995; Kawai and Hirose, 2000; Tajima *et al.*, 2002). However, these studies provided L2 contrasts in isolated syllables or words. Investigation of effects of training using sentence stimuli has only recently begun (Hirata, 2004b; Hirata, 2004c; Kato *et al.*, 2005). Studying the L2 vowel length distinction in a sentence context is particularly important, as research has shown that native listeners use the rate of sentences for making duration-based distinctions (Hirata, 1990a; Hirata and Lambacher, 2004). A recent study (Kato *et al.*, 2004) showed that, after perceptual training with isolated words, NE speakers learned to perceive short and long vowels in sentences, indicating that their ability gained for the isolated word context generalized to the sentence context (see also Hirata, 2004b). However, Tajima *et al.*'s (2005) results showed that the accuracy of NE speakers' perception of Japanese length contrast was affected by the speaking rate of test stimuli, and that this effect did not decrease after training with isolated words.

Pisoni and Lively's (1995) high phonetic variability hypothesis provides a useful guide in the search for a method which would enable NE speakers to successfully identify Japanese vowel length. This hypothesis claims that the diversity of acoustic cues present in materials produced by multiple speakers helps rather than hinders non-native listeners in forming new perceptual categories. Traditionally, stimulus variability in voices and speaking rates was viewed as troublesome noise, extraneous to the encoding of linguistic units, and was deliberately excluded from experiments by the use of carefully controlled materials (Pisoni, 1997). However, evidence has accumulated that high stimulus variability in voices and phonetic contexts is informative, rather than distracting, and actually assists perceptual learning (Pisoni and Lively, 1995; Bradlow *et al.*, 1997). In the present study, we tested this high variability hypothesis with regard to speaking rate variation. We hypothesized that providing variation in speaking rate helps non-native listeners to normalize rate and to learn to distinguish vowel length accurately.

The present study compared the relative effectiveness of three types of perceptual training: one with only a slow rate, one with only a fast rate, and one with both slow and fast rates. Training materials were sentences naturally produced by four NJ speakers at these rates. We chose this method rather than creating various speaking rates with a synthesizer because faster natural speech is not simply compressed slower speech, but involves changes in the size and velocity of various muscle contractions (Gay and Hirose, 1973; Gay *et al.*, 1974; Gay, 1981). According to the hypothesis tested in the present research, the variations that exist in natural speech spoken at slow and fast rates are informative for non-native listeners. The prediction was that speech materials spoken at two rates (slow and fast), contain more diverse and rich acoustic cues than those spoken only at one rate (slow-only or fast-only), and that this diversity aids non-native listeners in adjusting to different rates of speech and identifying short/long vowels accurately.

Effects of the three types of training were examined by a pretest and a post-test consisting of sentences produced by two additional NJ speakers at three speaking rates: slow, normal, and fast. These three rates were included in order to examine whether the ability gained through training with a given rate or rates would generalize to rate(s) to which participants had not been exposed. The present study compared each type of training with a control group that did not participate in training. Comparison with a control was important because our pilot results indicated effects of repetition and exposure, i.e., improvement of test scores simply by taking the tests twice without training. Thus, training is said to be "effective" if the amount of improvement from the pretest and the post-test was significantly greater for the trained than the control group. The study addressed the following questions:

(1) How do NE speakers perform in identifying Japanese vowel length in carrier sentences spoken at three speaking rates (slow, normal, and fast)? Previous studies have shown that rate effects interacted with word type (Hirata, 2005a), vowel length (i.e., short or long; Hirata, 2005b), and context (i.e., in isolation or in sentences; Tajima *et al.*, 2002 and Tajima *et al.*, 2005). In these studies, identification accuracy in the sentence context is generally lower for faster rates. The present study will examine if this result is replicable.
(2) Does perceptual training with sentences, as opposed to isolated words or syllables as in most previous studies, aid NE speakers in identifying Japanese vowel length accurately? This study will determine whether the present three types of training with sentences enable effective L2 contrast learning.
(3) Does training with sentences spoken at two rates (slow

TABLE I. Training stimuli.

	Block and speaker	Carrier sentence	Rate
Show-only training			
Session 1	(a)–(h) Male 1		sssssssss[a]
Session 2	(a)–(h) Female 1		sssssssss
Session 3	(a)–(h) Male 2		sssssssss
Session 4	(a)–(h) Female 2		sssssssss
Fast-only training			
Session 1	(a)–(h) Male 1	soko wa___to kaite arimasu	fffffffff
Session 2	(a)–(h) Female 1	('___ is written there.')	fffffiff
Session 3	(a)–(h) Male 2		fffffffff
Session 4	(a)–(h) Female 2		fffffffff
Slow-fast training			
Session 1	(a)–(h) Male 1		sfsfsfsf
Session 2	(a)–(h) Female 1		sfsfsfsf
Session 3	(a)–(h) Male 2		sfsfsfsf
Session 4	(a)–(h) Female 2		sfsfsfsf

[a]Indicates rate of stimuli that was presented within each of the eight blocks.
"s"=slow rate. "f"=fast rate. (a)–(h) indicate blocks.

and fast) improve overall perceptual accuracy more than training with only one rate (slow-only or fast-only)? According to Pisoni and Lively's (1995) hypothesis, the overall improvement should be higher for two-rate than one-rate training.

(4) How does the perceptual ability of NE speakers generalize from trained rate(s) to tested rates? For example, does slow-only training improve accuracy only for the slow rate, or improve it for other rates as well? Does slow-fast training improve accuracy only for these two rates, but not for the untrained (normal) rate?

II. METHODS

A. Participants

Sixty-two monolingual native speakers of American English, whose ages ranged from 18 to 22, were randomly assigned to one of the following four groups: slow-only training group (n=16; mean age=19.2), fast-only training group (n=16; mean age=19.2), slow-fast training group (n=14; mean age=19.7), and a control group (n=16; mean age =19.3). None of the participants had previously studied Japanese or had extensive exposure to spoken Japanese. All but one participant had studied one or two foreign languages, usually Spanish and/or French, and one participant had studied five languages. None of the participants, however, had native-level fluency in any foreign language. No participant reported having any hearing problems. Participants were paid for their participation.

B. Training procedure

Participants assigned to one of the three training groups (slow-only, fast-only, and slow-fast) completed four training sessions in addition to a pretest and a post-test. Participants completed the experiment over a minimum period of 11 days and a maximum of 17 days. Participants had any two consecutive training sessions at least 24 hours apart, and no more than four days apart.

Training materials were a subset of materials used in Hirata (2004a). The target words were nonsense Japanese words in the form of /mVmV/ and /mVmVV/ (V=/i, e, a, o, u/; e.g., /mimi/ vs /mimi:/), with the pitch accent always on the first vowel. These words were embedded in a single carrier sentence spoken by four native Japanese speakers (Male 1, Female 1, Male 2, and Female 2; Table I). For slow-rate and fast-rate training materials, the speakers were instructed to speak as slowly and as fast as possible, respectively. The four speakers' mean speaking rate was 263 ms/mora for the slow rate and 105 ms/mora for the fast rate.[1]

Each type of training consisted of four sessions. Each session contained 160 stimuli by one speaker. As described in Table I, only slow-rate materials were used for slow-only training, and only fast-rate materials of the same speakers were used for fast-only training [5 vowels×2 lengths×2 repetitions×8 blocks]. For slow-fast training, both of those slow- and fast-rate materials were used, but the total number of trials was the same as that in other training [2 rates×5 vowels×2 lengths×2 repetitions×4 blocks]. For slow-fast training, the rate of stimuli stayed constant within each block, either slow or fast. Slow-rate and fast-rate blocks were presented alternately (see Table I for the block structure).

Each session was broken into 8 blocks of 20 trials, and the first and the fifth blocks were preceded by three examples. When participants heard audio stimuli through headphones attached to a PC, the carrier sentence, *soko wa___ to kaite arimasu* ("___ is written there") was displayed on the screen. Participants were asked to identify whether the second vowel of the disyllables inserted in the underlined part of the sentence was short or long. The participants received feedback on each response during training. The feedback consisted of a screen with the correct answer written out as either "short" or "long" and the target word spelled out in Romanized letters. Words with short vowels (containing two moras) had two dots over them, and words with a long vowel (containing three moras) had three dots. When participants answered correctly, the sign "Correct" appeared on the screen, and it enabled the participants to go on to the next

TABLE II. Test stimuli.

	Block and speaker	Carrier sentence	Rate
Pretest			
	(a) Male 3	sore ga ___ da to omoimasu ('I think *that* is ___.')	snf[a]
	(b) Female 3	asoko ni ___ to arimasu ('It says ___ over there.')	snf
	(c) Male 3	koko wa ___ dʒa arimasen ('This is not ___.')	snf
	(d) Female 3	honto: ni ___ wa kaitenai ('It's true that ___ is not written.')	snf
	(e) Male 3	soko de ___ to wa iwanakat:a ('I didn't say ___ there.')	snf
	(f) Female 3	kit:o ___ de wa nai deʃo: ('It certainly won't be ___.')	snf
Post-test			
	(a) Male 3	kore ga ___ da to kikimaʃita ('I heard that *this* is ___.')	snf
	(b) Female 3	koko ni ___ to arimasu ne ('It says ___ here, right?')	snf
	(c) Male 3	are wa ___ dʒa nai desu jo ('I tell you, that's not ___.')	snf
	(d) Female 3	zet:ai ni ___ wa kakareteta ('___ was definitely written.')	snf
	(e) Male 3	soʃite ___ to it:e kudasai ('And then, please say ___.')	snf
	(f) Female 3	tabun ___ de wa arimasen ('It's probably not ___.')	snf

[a]"snf" indicates that stimuli of slow, normal, and fast rates were presented randomly within the block. (a)–(f) indicate blocks.

trial. When participants answered incorrectly, the sign "Sorry…" appeared, and they were made to click "Play again" to hear the stimulus repeated three additional times. In each session, participants were asked to take a three-minute break after the fourth block.

C. Testing procedure

All of the four groups (slow-only, fast-only, slow-fast, and control) took a pretest and a post-test approximately two weeks apart. Each test consisted of 180 stimuli. Each stimulus used one of ten words drawn from five pairs of real Japanese words: /ɾubi/-/ɾubi:/, /ise/-/ise:/, /ɾika/-/ɾika:/, /kato/-/kato:/, and /saju/-/saju:/ (meaning "agate"-"ruby," "(name of a place)"-"opposite gender," "science"-"liquor," "transition"-"(surname)," and "hot water"-"left and right"), all accented on the first vowel. The stimuli were recorded by two NJ speakers who did not appear in the training sessions (Male 3 and Female 3; Table II). The NJ speakers recorded the words in three different carrier sentences, and each test had different carrier sentences (see Table II). Each sentence was spoken at three rates: slow, normal, and fast. Following Hirata (2004a) and Port (1977), speakers were given the following definition of the speaking rates: "tempo that is relaxed and comfortable" for the normal rate, "slowest tempo possible while keeping the sentence flowing together without obviously inserting breaks between words" for the slow rate, and "fastest tempo possible without making errors" for the fast rate.

Analyses on duration of sentences and target vowels confirmed (1) that speakers spoke with three distinct speaking rates, and (2) that they made a clear distinction between short and long vowels within each rate. The sentence speaking rates across speakers were 239 (SD=24.8), 136 (SD =15.2), and 105 (SD=6.4) ms/mora for slow, normal, and fast rates, respectively, and the effect of rate was significant [$F(2,66)=435.62$, $p<0.001$]. Comparisons of any two rates showed significant differences [$p<0.001$]. The effect of speaker was not significant [$F(1,66)=0.17$, $p=0.686$], although there was a significant interaction of rate and speaker [$F(2,66)=4.29$, $p=0.018$]. The two speakers' rates did not significantly differ for slow (244 vs 235 ms/mora) and fast rates (106 vs 103 ms/mora), but their normal rates were different (128 vs 145 ms/mora). The important point here, however, is that there were three distinct speaking rates across speakers. Analysis on target vowel duration also confirmed that the three speaking rates were distinct for both speakers and for both short and long vowels. Each speaker's short vowels were significantly different among the three rates (Male 3: 152 vs 75 vs 64 ms; Female 3: 148 vs 83 vs 59 ms for slow, normal, and fast rates, respectively), and so were the long vowels (Male 3: 405 vs 165 vs 141 ms; Fe-

TABLE III. Summary of significant main effects and interactions in 4×2×3 ANOVA.

Effect	*F*	*df*	*p*
Test	104.83	(1,58)	0.000
Rate	67.95	(2,116)	0.000
Test×rate	11.24	(2,116)	0.000
Group×test	2.51	(3,58)	0.068
Group×rate	2.23	(6,116)	0.045
Group×test×rate	3.37	(6,116)	0.004

male 3: 341 vs 165 vs 109 ms)[$p<0.01$]. These results were very similar to those of the materials in Hirata (2004a), a subset of which was used for the present training stimuli. An NJ speaker identified vowel length of these test stimuli with 98.9% accuracy.

The pretest and post-test each included 5 vowels×2 lengths×3 rates×3 carrier sentences×2 speakers for a total of 180 trials. Each test consisted of six blocks of 30 trials. Within a given block, every trial used the same carrier sentence, spoken by the same speaker (Table II). The stimuli were presented in a random order across rates. No words, sentences, or speakers from training were used in the tests. The pretest and the post-test used identical words but different carrier sentences. Each block was preceded by two examples using the same nonsense words used in training (e.g., /meme/ and /meme:/). Immediately after each example, the answer, either "short" or "long," was displayed on the screen. Participants were asked to take a three-minute break after the first three blocks.

The testing procedure was the same as the training procedure, except that participants did not receive any feedback on their responses.

D. Analysis

Raw percent correct test scores were transformed into rationalized arcsine units (RAU; Studebaker, 1985) to correct nonlinearity of the test score scale. A mixed-design Analysis of Variance (ANOVA) was conducted with these RAU scores. Group (slow-only, fast-only, slow-fast, control) was a between-subjects factor, and test (pretest, post-test) and rate (slow, normal, fast) were repeated-measures factors. If there is an overall effect of training, a significant group×test interaction should be found. Furthermore, if an effect of training is found only for specific rates, a significant group ×test×rate should be found. Figures were made with the raw percent correct scale for ease of interpretation.

III. RESULTS

The results of ANOVA are summarized in Table III. With regard to the participants' performance on the three speaking rates (question 1), a significant effect of rate was found. The mean test scores were significantly higher for the slow (75.6%) than normal rate (68.8%), and for the normal than fast rate (64.8%). It is important to note that the tests for the three rates included identical sets of words and sentences, and the only difference was that of the speaking rates. Thus, we can say that participants were less able to identify length of vowels in the same words spoken at faster rates than at slower rates.

A significant main effect was found for test (pretest: 65.8%; post-test: 73.6%), and a significant test×rate interaction was found in ANOVA (Table III), indicating that participants showed significant improvement from the pretest to the post-test, but that the amount of improvement differed across rates. The mean improvement, averaged over groups, was highest for the slow rate (from 69.9 to 81.1%) (11.2 percentage points improvement; below expressed as % improvement) [$p<0.001$], less for the normal rate (7.8% improvement from 64.9 to 72.7%) [$p<0.001$], and lowest for the fast rate (4.1 % improvement from 62.7 to 66.8%) [$p=0.001$].

A group×test interaction, which would indicate the overall effectiveness of training, was only marginally significant (Table III). The post-test scores were significantly higher than the pretest scores for all four groups (slow-fast training group: 65.5 vs 74.6% [$t=6.52, p<0.001$]; slow-only training group: 66.7 vs 75.3% [$t=6.86, p<0.001$]; fast-only training group: 65.5 vs 73.3% [$t=4.95, p<0.001$]; control group: 65.6 vs 69.9% [$t=2.43, p=0.028$]). Differences among the four groups in the overall amount of improvement between the pretest and post-test scores were small, as shown in Fig. 1.

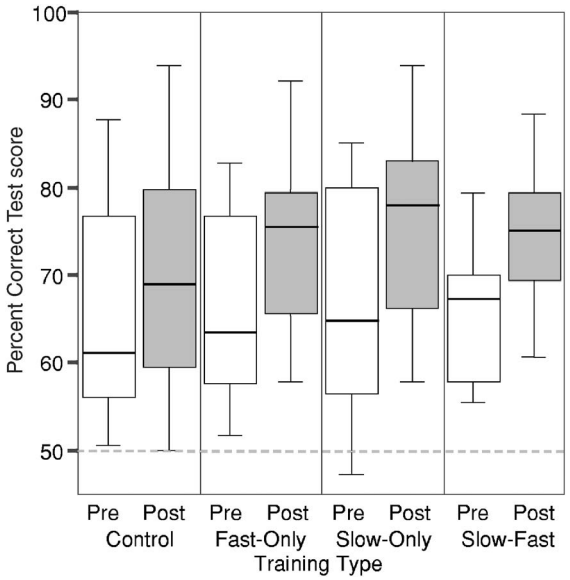

FIG. 1. Overall pretest (white boxes) and post-test (dark boxes) scores of the four groups. All test rates combined. The horizontal dashed line indicates the chance level performance.

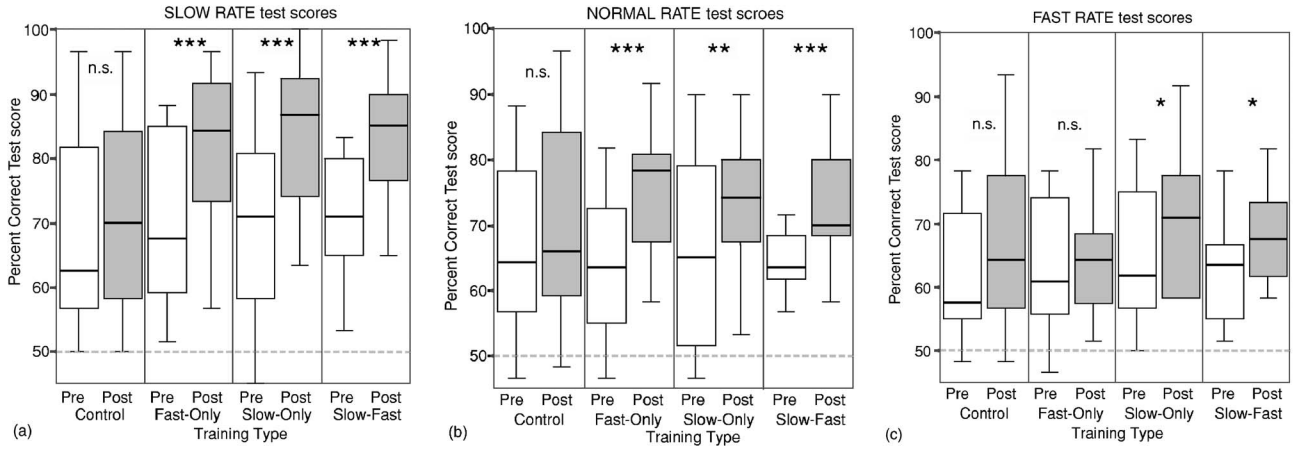

FIG. 2. Percent correct test scores of the four groups by rate (a: slow; b: normal; c: fast). Significant difference between pretest (white boxes) and post-test (dark boxes) [$^{***}p=<0.001$; $^{**}p=<0.01$; $^{*}p=<0.05$], nonsignificant difference between pretest and post-test [n.s. $p>0.05$]. The horizontal dashed lines indicate the chance level performance.

The overall improvement made by the control group was due to effects of repetition and exposure, since they took two tests. As mentioned in the introduction, training was said to be "effective" if the amount of improvement made by the individual trained groups was significantly greater than that made by the control group. Dunnett's pairwise multiple comparison *t*-tests (which contrasted the three training groups against the control group) indicated that the amount of improvement made by the slow-fast training group (9.1% improvement) was significantly greater than that by the control (4.3%) [$p=0.040$], indicating a genuine effect of training. However, the slow-only training group's improvement (8.6%) was only marginally greater than the control group's improvement [$p=0.059$]. The fast-only training group's improvement (7.8%) was not significantly greater than the control group's improvement [$p=0.116$]. Thus, with regard to question (2), we found that training with sentences, particularly slow-fast training, was indeed effective in enabling participants to improve their perceptual ability to identify Japanese vowel length contrast. With regard to question (3), we found that, as far as the overall test scores were concerned, two-rate training was advantageous to one-rate training: slow-fast training was most effective, while only a marginal effect was found for slow-only training and no effect was found for fast-only training.

A significant group × test × rate interaction was found in ANOVA (Table III), indicating that the four groups' differing amount of improvement from the pretest to the post-test depended on the speaking rate. Below, the four groups' test scores were examined separately for each rate.

Robust effects of training were found for the slow rate, as shown in Fig. 2(a). All of the three training groups' scores improved significantly from the pretest to the post-test: 12.3% improvement (means=from 70.4 to 82.7%) for the fast-only training group [$p<0.001$]; 15.5% improvement (69.7 to 85.2%) for the slow-only training group [$p<0.001$]; and 15.2% improvement (70.2 to 85.4%) for the slow-fast training group [$p<0.001$]. In contrast, the control group did not significantly improve their slow rate scores (2.4% improvement from 69.4 to 71.8%) [$p=0.230$]. Thus, significant effects of training were found for all three trained groups. It is interesting to note that the trained groups improved on the slow rate test scores regardless of the type of training they had received.

The results of the normal rate test scores [Fig. 2(b)] were similar to those of the slow rate scores. All of the three training groups improved their scores significantly from the pretest to the post-test. A 10.9% improvement (means =from 63.4 to 74.3%) was made by the fast-only training group [$p<0.001$], 7.4% improvement (65.5 to 72.9%) by the slow-only training group [$p=0.007$], and 8.0% improvement (64.4 to 72.4%) by the slow-fast training group [$p=0.001$]. In contrast, the control group's 4.9% improvement (66.2 to 71.1%) was not significant [$p=0.072$]. Thus, effects of training on the normal rate test scores were found for all three trained groups. Compared to the slow rate test scores, however, the amount of improvement was less for the normal rate. It is noteworthy that the trained groups improved on the normal rate scores even though none of them had received normal rate materials in training.

The results of the fast rate test scores [Fig. 2(c)] differed from those of the other rates. The fast-only training group, rather unexpectedly, did not significantly improve on the fast rate test scores (1.6% improvement from 62.6 to 64.2%) [$p=0.524$], as was the case for the control group (5.6% improvement from 61.5 to 67.1%) [$p=0.061$]. In contrast, the slow-only training group made a significant 4.0% improvement (64.7 to 68.7%) [$p=0.046$], and finally, the 5.5% improvement made by the slow-fast training group (61.9 to 67.4%) was statistically robust [$p=0.013$].

In summary, regarding question (4) from the introduction, we found that the perceptual ability of NE speakers generalized from trained rate(s) to tested rates. For example, slow-fast training showed the strongest effects not only on the participants' overall scores, but also on all of the three rate test scores separately, including the normal rate which was not used in training. Slow-only training improved participants' performance most prominently on the slow and normal rate test stimuli, and much less but still significantly

on the fast rate stimuli, even though their overall, cross-rate scores did not show a clear effect of training as a whole. Least effective was fast-only training where an overall effect of training was not found. Examining each rate separately, effects of fast-only training were found in the slow and normal rate test scores, but not in the fast rate scores.

IV. DISCUSSION AND CONCLUSIONS

This study examined the extent to which training with sentences of different rates helped native English speakers to learn to perceive Japanese vowel length contrast in the sentence context. One major finding, related to our first question, was that the speaking rate of sentences was a crucial factor in participants' perceptual abilities. The participants' test scores were lower for faster rates, and the amount of improvement shown by trained participants was also smaller for faster rates. These results are consistent with previous findings by Tajima *et al.* (2005) and Hirata (2005a and 2005b), and suggest that even if non-native speakers are able to perceive L2 contrasts at a slow rate, this does not guarantee the same ability at faster rates.

The second major finding, related to our second question, was that non-native speakers can learn to perceive L2 contrasts given only sentence input, supporting Hirata (2004b). The present slow-fast training, in particular, which provided only sentences but no words in isolation, was found to improve the identification of Japanese vowel length contrast in the sentence context. The overall improvement of the slow-fast training group was significantly greater than that of the control group, which did not participate in training. Slow-only and fast-only training also showed some limited effects (discussed further, below). This study provides additional evidence that adults are capable of learning difficult L2 contrasts with laboratory training, and not only with syllables or words in isolation (Jamieson and Morosan, 1986; Logan *et al.*, 1991; Bradlow *et al.*, 1997; Tajima *et al.*, 2002; Wang *et al.*, 1999), but also with sentences (Hirata, 2004b and 2004c).

It should be noted, however, that the overall effect of training in the present study was fairly small, as indicated by the improvement of 9.1 percentage points for slow-fast training. This is less improvement than that shown in some previous studies of L2 contrast training that used a two-alternative forced choice identification method. For example, Bradlow *et al.*'s (1997) subjects showed a significant improvement of 16 percentage points in distinguishing English /ɹ/ and /l/. (The mean pretest score in Bradlow *et al.* (1997) was 65%, comparable to the pretest score of 65.8% in the present study.) On the lower end, Logan *et al.*'s (1991) subjects showed a significant improvement of 7.8 percentage points (though their mean pretest score was higher: 78.1%). The present study's low level of improvement might partially be due to the fact that the test stimuli were embedded in sentences. This makes sense given that trained participants consistently showed less improvement in the sentence than word context in Hirata (2004b). However, the crucial role of sentence training cannot be overlooked. Hirata (2004b) found that participants who were trained with sentences made robust perceptual improvement in both the isolated-word and sentence contexts, but those who were trained only with isolated words made less improvement in the sentence context. Thus, even though training with sentences is more time consuming, there is a practical advantage to using sentences in training, if our ultimate goal includes enabling non-native speakers to perceive difficult L2 contrasts in fluent speech. Following Hirata (2004b), it would be interesting to examine whether the present sentence training would improve participants' ability to perceive isolated words as well as words in sentences, as in the present experiment.

The third major finding of the present study relates to the differential effects of the three types of training, as addressed in our third question. The participants who received fast-only training improved least on their overall, cross-rate test scores. Their overall improvement (7.8 percentage points) was not significantly greater than that of the control group (4.3 percentage points). Slow-fast training was slightly more beneficial than slow-only training. The overall, cross-rate improvement made by the slow-fast training group (9.1 percentage points) was significantly greater than that made by the control group, but the slow-only training group's improvement (8.6 percentage points) was only marginally greater than the control group's. In summary, only the slow-fast training group improved significantly on the total test scores, as well as on the scores for each of the three rates. This result, that training with two rates was more effective than training with one rate (slow-only or fast-only), supports Pisoni and Lively's (1995) high phonetic variability hypothesis. Their original hypothesis concerned the effectiveness of training with variability in talker and phonetic context. The present study provides support for the effectiveness of training with variability in speaking rate: the more variability in the rates of training stimuli, the more effective for non-native speakers' perceptual learning. That slow-only training was slightly advantageous over fast-only training might also be consistent with the high variability hypothesis: variability of vowel as well as sentence duration in the present training was higher for the slow than fast rate (see Hirata, 2004a). This claim, however, should be examined in the future by comparing effects of high-variability fast rate training versus low-variability slow rate training.

The above conclusions in support of Pisoni and Lively's (1995) high variability hypothesis merit further discussion. First, the difference among the three types of training was quite small (Fig. 1). Second, regardless of the type of training, participants showed a similar amount of improvement for the slow and normal rates (Fig. 2). Note that no participant heard normal-rate sentences in training, but that all trained participants improved their test scores for the normal rate. These results, relevant to our fourth question, imply that even beginning L2 learners are able to normalize different speaking rates fairly easily within the range of slow to normal speaking rates. The ability to normalize speaking rate in native languages has been examined extensively, as reviewed in the introduction, and this ability seems to be utilized for L2 speech within a limited range of speaking rates even at an early stage of L2 learning. This result is in line with Kato *et al.*'s (2004) finding that, with perceptual training, NE speak-

ers were able to learn to adapt their categorical boundary positions of Japanese vowel length contrast according to different contexts.

Also worthy of discussion are the results of fast-only training, which perhaps are counterintuitive. Previous studies suggested that abilities acquired during L2 training are largely to deal with the kinds of stimuli that had been presented in training (e.g., synthetic versus natural speech, word versus sentence stimuli) (Strange and Dittmann, 1984; Morosan and Jamieson, 1989; Hirata, 2004c). This would predict that fast-only training should improve scores for the fast rate, but not the other rates. However, the opposite results were found: the fast-only training participants improved on slow and normal stimuli, but not on fast stimuli. In addition, this training was found to be least effective. Jamieson and Morosan's (1986) perceptual fading technique, which successfully enabled Canadian francophones to identify the English /ð/-/θ/ contrast, is useful in understanding these results. Their method initially reduces stimulus uncertainty by providing the longest consonant frication in the /ðʌ/-/θʌ/ syllable continuum, and as training progresses, increases stimulus uncertainty by including syllables with progressively shorter frication. This method helps learners to initially focus their attention on critically relevant cues, and then to gradually learn to handle within-category acoustic variation. It is possible, then, that participants in the present fast-only training suffered from not having first been provided with critically relevant cues with little uncertainty. The durational difference between short and long vowels is about 50 ms for the fast rate, compared to about 150 ms for the slow rate (Hirata, 2004a) and, thus, fast-only training participants might have been unable to grasp the most critical cue, which is vowel duration, solely from the fast stimuli.[2]

Another possible interpretation of the ineffectiveness of fast-only training as compared to slow-only training might concern short-term memory effects. It is possible that attentional resources available in short-term memory are limited when learning to perceive unfamiliar non-native contrasts, and that there is a higher demand in processing fast than slow rate sentences. If so, then because of this higher demand, the fast rate speech signals might have degraded more quickly than the slow rate speech signals in short-term memory, and this might be why participants with fast-only training were unable to learn the critical acoustic cue of vowel duration as effectively. We expected from Pisoni and Lively's (1995) high phonetic variability hypothesis that single rate training, whether fast-only or slow-only, would have the same effect on overall perceptual learning. However, the differential results of fast-only and slow-only training cannot be explained so simply by this hypothesis in regards to the issue of speaking rate variability. The present results may suggest that different processing and memory demands for slow versus fast rate stimuli are at play, and the amount and quality of information transmitted from short-term memory to long-term memory do matter. This factor may augment Pisoni and Lively's (1995) high phonetic variability hypothesis in understanding how temporal characteristics of stimuli play a role in the ultimate formation of an L2 perceptual category.

On a final note, in order to achieve more robust perceptual learning, we might wish to train subjects on sentences spoken at a greater number of speaking rates. Introducing several more speakers would also create additional, possibly useful, speaking rate variation. A related issue is the distribution of stimuli among slow, normal, and fast rates. The speaking rates of the present test materials were 239, 136, and 105 ms/mora for slow, normal, and fast rates, respectively, showing a greater difference between the slow and normal rates than the difference between the normal and fast rates. It is possible that differential effects of training might appear more strongly if fast rate materials are even faster or if three speaking rates are distributed more equally. A future study should also examine whether non-native listeners benefit from randomizing rates at every trial instead of by block, as the former has been found to provide more difficulty than the latter (Tajima *et al.*, 2005). Finally, the carrier sentence in the present training was held constant for the purpose of examining the precise effect of speaking rate, but a future study should also examine whether providing different carrier sentences would benefit learners. Although additional research is thus necessary, the present study reveals that sentential speaking rate is an important factor in L2 learners' acquisition of duration-based distinctions.

ACKNOWLEDGMENTS

This study was supported by National Science Foundation Grant No. BCS0418246, given to Y.H. We thank Jon Bernard for his assistance in creating the training program and editing the manuscript, and Jacob Whiton, Connor Forbes, Lucia Livak, Jess Worby, Carol Glenn, Stephen Lambacher, and Spencer Kelly for their help in various stages of this project. We also thank reviewers for their insightful comments on the earlier version of this manuscript.

[1]See Hirata (2004a) for more details of duration measurements of these training materials. A subset of the materials was also used for NJ speakers' perception in Hirata and Lambacher (2004). In that study, NJ speakers identified short and long vowels of these materials with 98.1% accuracy.

[2]Here, we used differences in absolute vowel duration as an example of speaking rate differences, but what the precise measure of variability should ideally be is an empirical question. One could argue that relational measures, such as ratios of short and long vowels, might be more appropriate than the measure of absolute duration. The present experiment showed generalizability of learning from one rate to another, which might suggest that relational measures are more suitable as a measure of variability. However, other evidence suggests that absolute duration plays an important role for non-native listeners (Hirata, 2005a; Tajima, 2006), as well as for native listeners when stimuli are impoverished (Hirata and Lambacher, 2004).

Bradlow, A. R., Pisoni, D. B., Yamada, R. A., and Tohkura, Y. (**1997**). "Training Japanese listeners to identify English /r/-/l/: IV. Some effects of perceptual learning on speech production," J. Acoust. Soc. Am. **101**, 2299–2310.

Denes, P. (**1955**). "Effect of duration on the perception of voicing," J. Acoust. Soc. Am. **27**, 761–764.

Francis, A. L., and Nusbaum, H. C. (**2002**). "Selective attention and the acquisition of new phonetic categories," J. Exp. Psychol. Hum. Percept. Perform. **28**, 349–366.

Fujisaki, H., Nakamura, K., and Imoto, T. (**1975**). "Auditory perception of duration of speech and non-speech stimuli," in *Auditory analysis and perception of speech*, edited by G. Fant and M. A. A. Tatham (Academic Press, London), pp. 197–219.

Gay, T. (**1981**). "Mechanisms in the control of speech rate," Phonetica **38**, 148–158.
Gay, T., and Hirose, H. (**1973**). "Effect of speaking rate on labial consonant production," Phonetica **27**, 44–56.
Gay, T., Ushijima, T., Hirose, H., and Cooper, F. S. (**1974**). "Effect of speaking rate on labial consonant-vowel articulation," J. Phonetics **2**, 47–63.
Gottfried, T. L., Miller, J. L., and Payton, P. E. (**1990**). "Effect of speaking rate on the perception of vowels," Phonetica **47**, 155–172.
Han, M. (**1992**). "The timing control of geminate and single stop consonants in Japanese: A challenge for nonnative speakers," Phonetica **49**, 102–127.
Hirata, Y. (**1990a**). "Perception of geminated stops in Japanese word and sentence levels," The Bulletin of the Phonetic Society of Japan **194**, 23–28.
Hirata, Y. (**1990b**). "Perception of geminated stops in Japanese word and sentence levels by English-speaking learners of Japanese language," The Bulletin of the Phonetic Society of Japan **195**, 4–10.
Hirata, Y. (**2004a**). "Effects of speaking rate on the vowel length distinction in Japanese," J. Phonetics **32**, 565–589.
Hirata, Y. (**2004b**). "Training native English speakers to perceive Japanese length contrasts in word versus sentence contexts," J. Acoust. Soc. Am. **116**, 2384–2394.
Hirata, Y. (**2004c**). "Computer assisted pronunciation training for native English speakers learning Japanese pitch and durational contrasts," Comp. Assist. Lang. Learning **17**, 357–376.
Hirata, Y. (**2005a**). "Effects of speaking rate on native English speakers' identification of Japanese vowel length," ISCA Workshop on Plasticity in Speech Perception, A36.
Hirata, Y. (**2005b**). "Factors affecting native English speakers' identification of Japanese vowel length," First ASA Workshop on Second Language Speech Learning, 13.
Hirata, Y., and Lambacher, S. G. (**2004**). "Role of word-external contexts in native speakers' identification of vowel length in Japanese," Phonetica **61**, 177–200.
Hirata, Y., and Tsukada, K. (**2004**). "The effects of speaking rates and vowel length on formant movements in Japanese," in *Proceedings of the 2003 Texas Linguistics Society Conference: Coarticulation in Speech Production and Perception*, edited by A. Agwuele, W. Warren, and S. H. Park (Cascadilla Proceedings Project, Somerville, MA), pp. 73–85.
Jamieson, D. G., and Morosan, D. E. (**1986**). "Training non-native speech contrasts in adults: Acquisition of the English /ð/-/θ/ contrast by francophones," Percept. Psychophys. **40**, 205–215.
Johnson, T. L., and Strange, W. (**1982**). "Perceptual constancy of vowels in rapid speech," J. Acoust. Soc. Am. **72**, 1761–1770.
Kato, H., Tajima, K., Rothwell, A., Akahane-Yamada, R., and Munhall, K. (**2004**). "Perception of phonemic length contrasts in Japanese with or without a carrier sentence by native and non-native listeners," *Proceedings of the 18th International Congress on Acoustics*, I-609-612.
Kato, H., Wilson, A., Tajima, K., and Akahane-Yamada, R. (**2005**). "Effects of training conditions on the learning of phonemic length contrasts in Japanese: Speaking rate and presentation context," Nihon Onkyoo Gakkai Kooen Ronbunshuu, 851–852.
Kawai, G., and Hirose, K. (**2000**). "Teaching the pronunciation of Japanese double-mora phonemes using speech recognition technology," Speech Commun. **30**, 131–143.
Kondo, Y. (**1995**). "Production of schwa by Japanese speakers of English: A crosslinguistic study of coarticulatory strategies," doctoral dissertation (University of Edinburgh, UK).
Landahl, K., and Ziolkowski, M. (**1995**). "Discovering phonetic units: Is a picture worth a thousand words?" Papers from the 31st Regional Meeting of the Chicago Linguistic Society **1**, 294–316.
Landahl, K., Ziolkowski, M., Usami, M., and Tunnock, B. (**1992**). "Interactive articulation: Improving accent through visual feedback," in *The Proceedings of the Second International Conference on Foreign Language Education and Technology*, edited by I. Shinjo *et al.* (The Language Laboratory Association of Japan, Kasugai, Aichi, Japan), pp. 283–292.
Logan, J. S., Lively, S. E., and Pisoni, D. B. (**1991**). "Training Japanese listeners to identify English /r/ and /l/: A first report," J. Acoust. Soc. Am. **89**, 874–886.
Magen, H. S., and Blumstein, S. E. (**1993**). "Effects of speaking rate on the vowel length distinction in Korean," J. Phonetics **21**, 387–409.
Miller, J. L. (**1987**). "Rate-dependent processing in speech perception," in *Progress in the Psychology of Language*, Vol. 3, edited by A. Ellis (Erlbaum Associates, Hillsdale), pp. 119–157.
Miller, J. L., and Liberman, A. M. (**1979**). "Some effects of later-occurring information on the perception of stop consonant and semivowel," Percept. Psychophys. **25**, 457–465.
Morosan, D., and Jamieson, D. G. (**1989**). "Evaluation of a technique for training new speech contrasts: Generalization across voices, but not word-position or task," J. Speech Hear. Res. **32**, 501–511.
Newman, R. S., and Sawusch, J. R. (**1996**). "Perceptual normalization for speaking rate: Effects of temporal distance," Percept. Psychophys. **58**, 540–560.
Oguma, R. (**2000**). "Perception of Japanese long vowels and short vowels by English speaking learners," Japanese-Language Education Around the Globe **10**, 43–55.
Pickett, E. R., Blumstein, S. E., and Burton, M. W. (**1999**). "Effects of speaking rate on the singleton/geminate consonant contrast in Italian," Phonetica **56**, 135–157.
Pisoni, D. B. (**1997**). "Some thoughts on "normalization" in speech perception," in *Talker Variability in Speech Processing*, edited by K. Johnson and J. W. Mullennix (Academic Press, New York), pp. 9–32.
Pisoni, D. B., and Lively, S. E. (**1995**). "Variability and invariance in speech perception: A new look at some old problems in perceptual learning," in *Speech Perception and Linguistic Experience: Issues in Cross-Language Speech Research*, edited by W. Strange (York, Timonium, MD), pp. 433–459.
Port, R. F. (**1977**). *The Influence of Speaking Tempo on the Duration of Stressed Vowel and Medial Stop in English Trochee Words* (Indiana University Linguistics Club, Bloomington, IN), pp. 1-77.
Port, R. F., and Dalby, J. (**1982**). "Consonant/vowel ratio as a cue for voicing in English," Percept. Psychophys. **32**, 141–152.
Sawusch, J. R., and Newman, R. S. (**2000**). "Perceptual normalization for speaking rate II: Effects of signal discontinuities," Percept. Psychophys. **62**, 285–300.
Strange, W., and Dittmann, S. (**1984**). "Effects of discrimination training on the perception of /r-l/ by Japanese adults learning English," Percept. Psychophys. **36**, 131–145.
Studebaker, G. A. (**1985**). "A "rationalized" arcsine transform," J. Speech Hear. Res. **28**, 455–462.
Tajima, K. (**2006**). "Perceiving prosodic units in a second language: A cross-language comparison," International Workshop on the Auditory Processing of Prosodic Features and its Applications: Acquisition of Linguistic Organization and Human Audition, 40.
Tajima, K., Rothwell, A., and Munhall, K. G. (**2002**). "Native and non-native perception of phonemic length contrasts in Japanese: Effect of identification training and exposure," J. Acoust. Soc. Am. **112**, 2387.
Tajima, K., Kato, H., Yamada, R., Rothwell, A., and Munhall, K. G. (**2005**). "Native and non-native perception of phonemic length contrasts in Japanese: Effect of speaking rate," Nihon Ninchi-Shinri Gakkai Dai 3-kai Taikai Happyoo Ronbunshuu, 69.
Toda, T. (**1997**). "Strategies for producing mora timing by non-native speakers of Japanese," in *Acquisition of Japanese as a Second Language*, edited by Daini Gengo Shuutoku Kenkyuukai (Bonjinsha, Tokyo), pp. 157–197.
Tsukada, K. (**1999**). "An acoustic phonetic analysis of Japanese-accented English," doctoral dissertation (Macquarie University).
Ueyama, M. (**2000**). "Prosodic transfer: An acoustic study of L2 English vs L2 Japanese," doctoral dissertation (University of California at Los Angeles).
Vance, T. J. (**1987**). *An Introduction to Japanese Phonology* (State University of New York Press, Albany, NY).
Verbrugge, R. R., and Shankweiler, D. (**1977**). "Prosodic information for vowel identity," Haskins Laboratories Status Report on Speech Research SR-51/52, 27–35.
Wang, Y., Spence, M. M., Jongman, A., and Sereno, J. A. (**1999**). "Training American listeners to perceive Mandarin tones," J. Acoust. Soc. Am. **106**, 3649–3658.
Wayland, S. C., Miller, J. L., and Volaitis, L. E. (**1994**). "The influence of sentential speaking rate on the internal structure of phonetic categories," J. Acoust. Soc. Am. **95**, 2694–2701.
Yamada, T., Yamada, R. A., and Strange, W. (**1995**). "Perceptual learning of Japanese mora syllables by native speakers of American English: Effects of training stimulus sets and initial states," *Proceedings of the 14th International Congress of Phonetic Sciences* **1**, 322–325.

Training humans in non-native phoneme perception using a monkey psychoacoustic procedure

Joan M. Sinnott,[a] Christopher L. Gonzales, Ambrin F. Masood, and Toshimasa Ishihara
Comparative Hearing Laboratory, Psychology Department, University of South Alabama, Mobile, Alabama 36688

(Received 4 July 2006; revised 31 January 2007; accepted 13 March 2007)

Humans were trained to categorize problem non-native phonemes using an animal psychoacoustic procedure that trains monkeys to greater than 90% correct in phoneme identification [Sinnott and Gilmore, Percept. Psychophys. **66**, 1341–1350 (2004)]. This procedure uses a manual left versus right response on a lever, a continuously repeated stimulus on each trial, extensive feedback for errors in the form of a repeated correction procedure, and training until asymptotic levels of performance. Here, Japanese listeners categorized the English liquid contrast /r-l/, and English listeners categorized the Middle Eastern dental-retroflex contrast /d-D/. Consonant-vowel stimuli were constructed using four talkers and four vowels. Native listeners and phoneme contrasts familiar to all listeners were included as controls. Responses were analyzed using percent correct, response time, and vowel context effects as measures. All measures indicated nativelike Japanese perception of /r-l/ after 32 daily training sessions, but this was not the case for English perception of /d-D/. Results are related to the concept of "robust" (more easily recovered) versus "fragile" (more easily lost) phonetic contrasts [Burnham, Appl. Psycholing. **7**, 207–240 (1986)]. © *2007 Acoustical Society of America.* [DOI: 10.1121/1.2722236]

PACS number(s): 43.71.Hw, 43.71.Es, 43.71.An [MSS] Pages: 3846–3857

I. INTRODUCTION

The purpose of this study is twofold. First, on a technical level, we explore the use of a monkey psychoacoustic procedure (Sinnott and Gillmore, 2004) to train humans to categorize problem non-native phoneme contrasts. Second, on a theoretical level, we relate our training results to the concept of "robust" (more easily recovered) versus "fragile" (more easily lost) phonetic contrasts (Burnham, 1986).

There is now is an extensive literature documenting the perceptual problems experienced by adult listeners in differentiating certain non-native speech contrasts (e.g., Burnham, 1986; Best, 1994; Pisoni *et al.*, 1994; Werker, 1994; Kuhl and Iverson, 1995). Important questions have emerged "as to whether it is possible to train adults to discriminate all non-native distinctions, whether some training methods are more effective than others, and whether some non-native contrasts are untrainable" (Werker, 1994, p. 101). While most researchers agree that non-native perception can be *improved* with laboratory training, there is little evidence that it can become *nativelike*. The present study reexamines this issue using two phoneme contrasts that have consistently caused problems in non-native listeners: (1) The English liquid contrast /r-l/, as perceived by Japanese listeners, and (2) the Middle Eastern dental-retroflex stop contrasts /t-T/ or /d-D/, as perceived by English listeners.

A. Japanese perception of English liquids

Goto (1971) first documented the problems experienced by Japanese listeners for the /r-l/ contrast. He presented natural speech word pairs (e.g., correct/collect) for identification and discrimination. While the English listeners attained scores of ⩾98% correct, the Japanese listeners achieved 75% at best. Later studies using Goto-type paradigms found similar results: Identification scores, even for Japanese listeners experienced in English conversation, typically remained well below 90% correct. (e.g., Sheldon and Strange, 1982; Yamada and Tohkura, 1992; Takagi, 1994; Flege *et al.*, 1996; Ingram and Park, 1998; Gordon *et al.*, 2001). However, none of these studies made any attempt to train their listeners by using feedback for errors.

Strange and Dittman (1984) were the first to actively train Japanese listeners to distinguish /r-l/ by giving them explicit feedback. They used a pretest/train/posttest design, in which the training stimuli were tokens from a synthetic continuum presented for same-different discrimination (with feedback), and the test stimuli were natural word pairs presented for identification (no feedback). Training resulted in improvement on the training stimuli themselves, but did not significantly improve identification of the test stimuli, which hovered at 69% correct.

Logan *et al.* (1991) also used a pretest/train/posttest design to train Japanese listeners to identify /r-l/ word pairs. Their high-stimulus-variability training procedure presented words from five different talkers, thus making the training routine (with feedback) more similar to the actual testing routine (no feedback). During training, the Japanese listeners reached 83% correct. Testing showed an increase from the pretest (78%) to the posttest (86%) and generalization test (84%). Further studies by this group (Lively *et al.*, 1993; Lively *et al.*, 1994; Bradlow *et al.*, 1997; Bradlow *et al.*, 1999) report similar levels of identification. Thus, even though the Japanese listeners clearly *improved* their perfor-

[a]Corresponding author.

 0001-4966/2007/121(6)/3846/12/$23.00 © 2007 Acoustical Society of America

mance, they were far from *nativelike* during either training or testing. Takagi (2002) conducted the most recent /r-l/ training study, using an elaborate 5-level pretest-train1-midtest-train2-posttest design. Final training scores reached a high of 85% correct, while final testing scores reached a high of 81%. Takagi concluded that "*truly nativelike identification of /r/ and /l/ may never be achieved by adult Japanese learners of English*" (p. 2887).

While the above studies all used highly variable /r-l/ stimuli varying in talker, vowel context, and word position, other studies have examined /r-l/ perception using synthetic speech and a simple CV context. Miyawaki *et al.* (1975) presented a 3-formant /ra-la/ continuum varying in *F*3 onset for oddity discrimination. In a now classic result, the English listeners showed categorical functions with enhanced discrimination at the phoneme boundary, while the Japanese listeners discriminated all pairs at chance levels. But when the *F*3 cue was presented in isolation, the Japanese listeners performed as well as the English listeners. In addition, MacKain *et al.* (1981) found nativelike identification functions along a synthetic /ra-la/ continuum in "experienced" Japanese listeners. Both of these studies indicate that, under certain experimental conditions using synthetic stimuli, Japanese listeners can perceive the *F*3 cue underlying /r-l/ in a seemingly nativelike manner. Since there is evidence for a correlation between synthetic and natural speech /r-l/ perception (Yamada and Tohkura, 1992; Gordon *et al.*, 2001), it might also be possible to train Japanese listeners to nativelike levels of accuracy for natural speech tokens of /r-l/.

B. English perception of dental versus retroflex stops

Another infamous example of problematic non-native phonemes involves English perception of the Middle Eastern dental-retroflex stop contrasts /t-T/ or /d-D/. Werker *et al.* (1981) first studied this contrast developmentally, comparing native Hindi listeners, non-native English listeners, and preverbal infant English listeners (6–8 months). Their stimuli were multiple CV tokens from a single male talker articulating a single /a/ vowel, and their procedure was the infant headturn (or adult button-press) technique, which gives feedback for hits, but not for misses. Results showed that the adult English listeners, even after a certain amount of familiarization training, performed worse than the infants. Specifically, while the infants learned to discriminate the contrast in about 25 trials, the adults did not. Infants were thus shown to be more similar to native Hindi than non-native English listeners. Later studies pinned this infant ability down to a very young age (6–8 months), after which it deteriorated in older infants and children (Werker and Tees, 1983; Werker and Tees, 1984a; Werker and Lalonde, 1988).

Other studies with adult English listeners used various discrimination procedures (all with no feedback) to recover the apparently "lost" dental-retroflex contrast (Werker and Logan, 1985; Werker and Tees, 1984b: Polka, 1991). While results suggested that the contrast was to some extent recoverable under low-uncertainty procedures requiring minimal memory load (e.g., simple same-different procedures combined with short interstimulus intervals), they did not demonstrate nativelike accuracy.

Pruitt *et al.* (2006) conducted the most elaborate study of dental-retroflex identification training, using a pretest/train/posttest design with simple CV syllables. Their stimulus variability approach used different talkers and vowel contexts during training and testing, and their trainees were both English and Japanese listeners. For the pretest, English, Japanese, and native Hindi listeners reached 59%, 71%, and 96% correct, respectively. At the end of training, English and Japanese trainees reached 74% and 84% correct, respectively, far from native performance on the pretest. Final posttest scores for the English and Japanese trainees were 72% and 83% correct, respectively, still far from nativelike performance.

C. Purpose of the present study

To summarize, while both /r-l/ and /t-T/ or /d-D/ are considered to be problem non-native contrasts, there is some evidence that the /r-l/ contrast is more recoverable (Miyawaki *et al.*, 1975; MacKain *et al.*, 1981). Burnham (1986) has proposed that phonetic contrasts may differ in basic psychoacoustic salience, and that this factor may interact with perceptual learning. Thus more salient robust contrasts may be recovered in adulthood, while less salient fragile contrasts may be lost at a much earlier age.

The acoustic cues differentiating /r-l/ are certainly very robust. Synthetic /ra-la/ continua use basically similar parameters (Miyawaki *et al.*, 1975; Polka and Strange, 1985). The primary acoustic cue is the initial spectral pattern in *F*3. An endpoint /ra/ token has an *F*3 onset at approximately 1500 Hz, which remains more or less steady for 60 ms, and then transits upwards in frequency over approximately 60 ms towards the steady-state vowel *F*3. An endpoint /la/ token has a much higher *F*3 onset of approximately 3000 Hz, which is typically *twice as high* as that for /ra/, and then decreases slightly toward the vowel *F*3.

In contrast, the acoustic cues differentiating /t-T/ or /d-D/ appear much more fragile. These sounds are stops consisting of brief 30–40 ms frequency transitions. Analysis and synthesis studies report a lower *F*2 onset for /da/ (about 1500 Hz) compared to /Da/ (about 2000 Hz, or a mere 33% *change* from /da/), as well as a minor change in *F*3 onset (Werker and Logan, 1985; Werker and Lalonde, 1988; Polka, 1991).

Thus there is evidence from both perceptual studies and acoustic analysis that /r-l/ is a more robust contrast that theoretically could be more easily recovered by Japanese listeners, while /d-D/ is a more fragile contrast that could be more easily lost by English listeners. The aim of the present study is to compare these two contrasts under similar conditions, and to determine if differences will emerge in the extent to which non-native perception can approach nativelike performance. Since previous training studies using natural speech have not been able to show nativelike perception in non-

natives, we propose to reconsider what has been tried previously, and start with some new approaches, as outlined below.

1. Focus on training, not testing

We propose to focus exclusively on the training (feedback) as opposed to the testing (no feedback) aspects of perception. For the most part, previous studies deemphasized their training data and focused primarily on pretests, posttests, and generalization tests. Yet the most recent and intensive Japanese training study (Takagi, 2002) did not show nativelike performance emerging during training, let alone testing. Thus we ask the following: Can nativelike perception be attained during the actual training process, when the listeners receive constant feedback for a limited set of relatively simple stimuli?

2. Monkey psychoacoustic procedure

We propose to use a two-alternative forced-choice procedure that has successfully trained monkeys to categorize natural speech /b-d/ CVs (Sinnott and Gilmore, 2004). Monkeys are in essence "non-native" listeners, and this procedure brings them to levels of 90–95% correct, which is higher than most human training studies have so far attained. The important features of this procedure are the following: (1) A go-left/go-right manual response on a lever is used to label the phonemes; (2) the stimulus is repeated indefinitely on each trial until a response is made, allowing unlimited time for listening; (3) a correction procedure repeats each missed stimulus on successive trials until a correct response is made, allowing undivided attention on a missed stimulus without the distraction of intervening stimuli; (4) finally, training is continued until asymptotic levels of performance are reached. To the best of our knowledge, these features taken together have never been incorporated into any human training procedure. For /r-l/ training, Logan *et al.* (1991) presented each stimulus only twice per trial, and repeated it only once on the next trial after each error. Also, they did not train their listeners to asymptotic levels. In fact, Logan *et al.* remarked that "an additional direction for future research is to train subjects until they reach asymptotic levels of performance" (p. 883).

3. Moderate level of stimulus variability

We propose to use a moderate level of stimulus variability identical to that used in our previous study of monkey /b-d/ categorization (Sinnott and Gilmore, 2004). The stimuli are natural CV tokens from four talkers and four vowel contexts. Limiting the stimuli to CVs eliminates the distraction of categorizing phonemes in different word positions, since Japanese perception of /r-l/ varies drastically with word position (Logan *et al.*, 1991). It also reduces the chance that confounding semantic variables in word stimuli may differentially influence the performance of natives and non-natives (Flege *et al.*, 1996).

4. Vowel context effects

In our previous study of monkey /b-d/ categorization (Sinnott and Gilmore, 2004), we found different vowel context effects for the "non-native" monkeys versus the "native" humans. The monkeys performed best with the back vowels /u,a/, where formant transition differences distinguishing /b-d/ are most prominent. In contrast, the humans (from five different native languages) all performed best with the front vowel /i/, where formant transition differences are almost nonexistent. This result indicated different processing mechanisms in humans and monkeys, even after the monkeys had been trained to asymptotic levels. Thus vowel context effects might also be useful to compare native versus non-native perception of problem phoneme contrasts in humans. There are currently no reports of using vowel context effects as a measure for either /r-l/ or dental-retroflex perception.

5. Response time measure

In addition to the percent correct measure, we propose also to use response time to assess perception. In the event that non-native listeners attain nativelike percent correct data, the response time data can indicate if they have attained a nativelike, more automatic categorization process with regard to processing speed. While Logan *et al.* (1991) used response time as a training measure, they did not use it to compare native and non-native performance. Additionally, there are no reports of using response time in dental-retroflex training.

6. All possible controls

Finally, to more precisely determine the degree of nativelike perception attained by non-native listeners, we include native listeners as control listeners, and phoneme contrasts familiar to all listeners as control stimuli. Thus, if our monkey training procedure is successful in producing nativelike perception in non-natives, there should be, at the end of training, no significant differences in percent correct, vowel context effects, or response time, for the problem versus familiar phoneme contrasts. On the other hand, if our results show similar performance in natives and non-natives for the familiar, but not for the problem phonemes, then this would indicate that our procedure was unsuccessful in producing nativelike perception in non-natives.

II. METHOD

A. Participants

Adult listeners were recruited from the student and staff populations of the University of South Alabama, and were paid $10 per daily 30 min testing session. Several English listeners had participated in previous speech experiments unrelated to the present one, and were familiar with the *go-left/go-right* procedure (see below). No Japanese or Middle Eastern listeners had participated in any previous speech experiments. No participant reported any speech or hearing disabilities.

For */r-l/ training*, eight Japanese listeners (5 females; 3

males) were recruited from the University's English Language Institute. They ranged in age from 18 to 52 years (mean=25.5; SD=10.2) and had lived in the U.S. for periods ranging from 3 months to one year. None considered themselves fluent in English. Six control female English listeners ranged in age from 20 to 43 years (mean=31.3; SD=9.5).

For */d-D/ training*, ten English listeners (5 females; 5 males) ranged in age from 21 to 44 years (mean=31.7; SD =9.0). Eight were monolingual English and two were bilingual (Spanish-English and Greek-English), but none had experience with any Middle Eastern language. Ten control Middle Eastern listeners (3 females; 7 males) ranged in age from 22 to 34 years (mean=25.7; SD=4.5) and their native languages were Telegu, a Hindi dialect ($n=6$), Urdu ($n=2$), and Punjabi ($n=2$). Author and native Urdu talker A.F.M. verified that all these languages use the dental-retroflex contrast.

B. Stimuli

CV stimuli were recorded in a room with low noise (<30 dB SPLA) using an AKG B18 microphone, and then digitized (10 kHz) and edited using CSRE (Canadian Speech Research Environment, AVAAZ Innovations, Ontario, Canada).

For */r-l/ training*, four English talkers (females: J.M.S. and L.A.M.; males: C.L.G. and K.W.M.) each recorded several tokens of eight CVs /ru, ra, re, ri; lu, la, le, li/. Two clear tokens of each CV from each talker were chosen, for a total of 64 stimuli (4 talkers × 8 CVs × 2 tokens), and then organized into eight /r-l/ stimulus sets as follows: CLG1, CLG2, JMS1, JMS2, KWM1, KWM2, LAM1, and LAM2. Japanese author T.I. reported that none of these stimuli were (phonetically) legal CVs in the Japanese language.

In addition, 64 control stimuli consisting of /b-d/ CVs /bu, ba, be, bi; du, da, de, di/ were constructed in a similar manner and organized into eight /b-d/ stimulus sets as follows: CLG3, CLG4, JMS3, JMS4, KWM3, KWM4, LAM3, and LAM4. Japanese author T.I. reported that all these stimuli were legal CVs in Japanese. The /b-d/ contrast was chosen here as a control contrast because humans from a wide variety of language backgrounds (English, Hindi, Japanese, Spanish, and Urdu) all perceive this contrast in a similar manner with regard to measures of percent correct, response time, and vowel context effects (Sinnott and Gilmore, 2004).

For */d-D/ training*, four Middle Eastern talkers (two Urdu [female: A.F.M.; male: F.A.R.] and two Telegu [female: S.M.I.; male: L.A.K.]) each recorded several tokens of eight CVs /du, da, de, di; Du, Da, De, Di/. Two clear tokens of each CV from each talker were chosen, for a total of 64 stimuli (4 talkers × 8 CVs × 2 tokens), and then organized into eight /d-D/ stimulus sets as follows: AFM1, AFM2, FAR1, FAR2, LAK1, LAK2, SMI1, and SMI2. All these stimuli are legal CVs in English, because the initial coronal (dental and retroflex) phonemes are all basically indistinguishable from the English alveolar /d/ phoneme.

In addition, 64 control stimuli consisting of /b-g/ CVs /bu, ba, be, bi; gu, ga, ge, gi/ were constructed in a similar manner and organized into eight /b-g/ stimulus sets as follows: AFM3, AFM4, FAR3, FAR4, LAK3, LAK4, SMI3, and SMI4. All these stimuli are legal CVs in English. We chose to use a labial-velar /b-g/, rather than a labial-coronal /b-d/ contrast here in order to avoid possible interactions with the problem /d-D/ contrast (see above), where all the CVs contained coronal consonants.

C. Apparatus

The test situation and response apparatus have been previously described in greater detail (Sinnott and Gilmore, 2004). Testing took place in a free field inside a large double-walled IAC booth lined with sound-insulating material. Stimuli were presented using Tucker-Davis-Technology equipment, an NAD amplifier, and a Genesis speaker. A Dell computer controlled stimulus delivery, experimental contingencies, and response recording. During testing, each listener sat in a chair inside the booth, approximately 84 cm from the loudspeaker. Stimuli were presented at 65 dB SPLA during testing, calibrated by a B&K SPL meter placed in position of the listener's head. The response apparatus consisted of a 3 in. long, contact-sensitive metal lever that moved left or right to trigger a switch. A cue light located above the lever signaled the listener to begin a trial (see below).

D. Procedure

The basic *go-left/go-right* procedure was designed to obtain phoneme identification data from monkeys (Sinnott and Gilmore, 2004). At the start of a trial, the listener grasped the metal lever positioned below the flashing cue light. Upon contact, the cue light illuminated and a CV started to repeat indefinitely (1 per s) until a response was made. For */r-l/ training*, a correct response was to move the lever left to /r/ (or /b/) CVs and right to /l/ (or /d/) CVs. For */d-D/ training*, a correct response was to move the lever left to /d/ (or /b/) CVs and right to /D/ (or /g/) CVs. Left and right side stimuli were randomly presented. A correct response was immediately followed by a 2 kHz 100 ms tone pip as feedback and a 1 s intertrial interval. An incorrect response was followed by a 5 s timeout during which the light extinguished and a 300 Hz tone was presented. After each incorrect response, a correction procedure repeated the missed stimulus on successive trials until a correct response was made. Correction procedure trials were not analyzed nor counted in the data analysis. Response times were measured from the onset of the first CV to the time that the lever moved 1 cm to a left or right position to trigger the switch.

All listeners were informed that the purpose of the experiment was to compare aspects of speech perception in native and non-native listeners. For */r-l/ training*, instructions were first given in English by author C.L.G., and then in Japanese by author T.I. For */d-D/ training*, instructions were given in English by author A.F.M., who is fluent in both English and Urdu. Non-natives were informed that the experiment would test their ability to differentiate non-native sounds that would sound very similar to them. For Japanese listeners, C.L.G. articulated the contrast "right" versus "light." For English listeners, A.F.M. articulated the contrast

"daal" (to put) versus "Daal" (lentils). Non-natives were also told that they would hear sounds used in their native language, which would be very easy to differentiate, and that training would start with the native sounds. Natives were told that they were a control group for the experiment, and that all the stimuli would be easy for them to differentiate.

Test sessions were conducted as follows. The first day was a practice session to introduce the *go-left/go-right* procedure. For */r-l/ training*, eight /b-d/ control stimuli from CLG3 were presented. For */d-D/ training*, eight /b-g/ control stimuli from AFM3 were presented. The session consisted of 120 trials, resulting in about 15 trials per CV, and lasted about 10 min. All participants performed at >98% correct in the practice session. Actual testing started on the second day. From this time on, two test sessions occurred on each day, with random order of talker presentation. For */r-l/ training*, one session consisted of one /r-l/ (e.g., CLG1), and one control /b-d/ (e.g., JMS3) stimulus set. For */d-D/ training*, one session consisted of one /d-D/ (e.g., AFM1), and one control /b-g/ (e.g., FAR3) stimulus set.

A block was defined as one run through all the 16 different stimulus sets and required 8 days. Non-native listeners were tested for 4 blocks (32 test days). Native listeners were only tested for three blocks because of their high initial accuracy scores. Thus in the final analysis block 3 data from the natives was compared with block 4 data from the non-natives. Listeners were normally tested for about 4–5 days per week, so it typically took about 8 weeks to complete four testing blocks.

TABLE I. Mean percent correct identification as a function of training block (B1–B4). ×=was not tested. p=significance level comparing group performance.

(A) Comparison of native English and non-native Japanese listeners for the control /b-d/ and problem /r-l/ contrasts.

	English	Japanese	
CONTROL	/b-d/	/b-d/	p
B1	99.2	99.1	0.172
B2	99.3	99.3	0.836
B3	99.3	99.2	0.578
B4	×	99.2	0.939
PROBLEM	/r-l/	/r-l/	p
B1	99.4	88.1	0.009*
B2	99.5	93.4	0.028*
B3	99.4	95.5	0.049*
B4	×	96.2	0.079

(B) Comparison of native Middle Eastern and non-native English listeners for the control /b-g/ and problem /d-D/ contrasts.

	Middle Eastern	English	
CONTROL	/b-g/	/b-g/	p
B1	99.2	98.8	0.766
B2	99.2	99.0	0.999
B3	99.1	98.4	0.417
B4	×	98.7	0.543
PROBLEM	/d-D/	/d-D/	p
B1	91.3	67.0	0.000*
B2	94.0	74.7	0.000*
B3	96.2	81.0	0.000*
B4	×	83.8	0.002*

III. RESULTS

Our basic question is as follows: At the end of training, are there statistically significant differences in percent correct, response time, or vowel context, between natives and non-natives in categorizing the problem contrasts /r-l/ and /d-D/? No differences are predicted for the familiar control contrasts /b-d/ and /b-g/. Preliminary analyses showed no effects of talker so all data were collapsed across this variable. For each contrast, data from the final training block (block 3 for natives, block 4 for non-natives) were submitted to a 2×4 repeated measures ANOVA to assess the effects of GROUP (native versus non-native), VOWEL context (u, a, e, i), and GROUP×VOWEL interactions. In addition, percent correct data were analyzed for earlier blocks in order to determine at which block, if any, perception became nativelike for the problem contrasts. All percent correct data were arcsine transformed to compensate for non-normal distributions at high accuracy levels. All response time data were log-transformed to equate for proportional changes across the possible range of response times. For example, an increase of 100 ms relative to 400 ms (25%) would be considered equal to an increase of 150 ms relative to 600 ms (25%).

A. Percent correct data

1. Percent correct data as a function of block

Japanese /r-l/ training. Table I(A) shows mean percent correct identification as a function of training block. For /b-d/, both the English and Japanese listeners performed at ⩾98% correct in all blocks. In the final block, there was no effect of GROUP (F=0.006 [1,2] p=0.939), an effect of VOWEL (F=4.988 [3,36] p=0.005; see below), and no interaction (F=0.412 [3,36] p=0.746). For /r-l/, the English listeners performed at ⩾98% correct in all blocks, while the Japanese listeners improved steadily throughout training, reaching 96% in block 4. In the final block, there was no effect of GROUP (F=3.682 [1,12] p=0.079), no effect of VOWEL (F=2.794 [df=3,36] p=0.054), and no interaction (F=0.284 [3,36] p=0.836). *These results indicate similar processing in English and Japanese listeners for both /b-d/ and /r-l/ at the end of training*.

English /d-D/ training. Table I(B) shows mean percent correct identification as a function of training block. For /b-g/, both the Middle Eastern and English listeners performed at ⩾98% correct in all blocks. In the final block, there was no effect of GROUP (F=0.385 [1,18] p=0.543), an effect of VOWEL (F=7.140 [3,54] p=0.000; see below), and no interaction (F=0.442 [3,54] p=0.724). For /d-D/, the Middle Eastern listeners reached 96% correct in block 3, while the English listeners reached only 84% correct in block 4. For /d-D/, there was an effect of GROUP (F=13.346 [1,18] p=0.002), no effect of VOWEL (F=1.007 [3,54] p=0.397), and an interaction (F=5.792 [3,54] p=0.002). *These results indicate similar processing for Middle Eastern and English listeners for /b-g/, but different processing for /d-D/ at the end of training*.

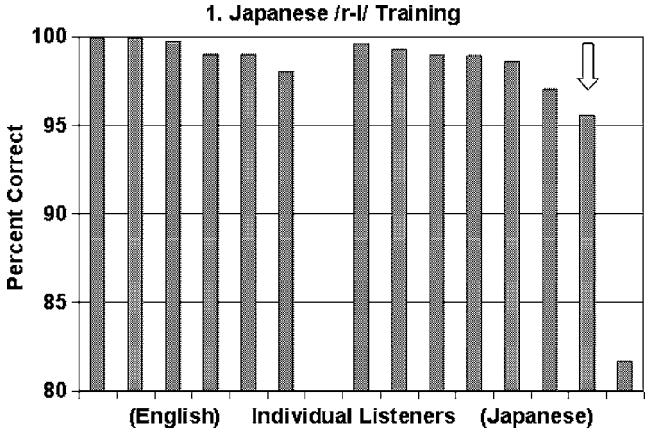

FIG. 1. Individual percent correct scores in the final /r-l/ training block comparing six native English listeners (left side) and eight non-native Japanese listeners (right side). The arrow denotes the 52-year-old Japanese listener.

2. Individual percent correct data

Japanese /r-l/ training. Figure 1 shows individual percent correct data for the final /r-l/ training block. Note that five of the eight Japanese listeners attained scores in the range of the English listeners at ⩾98% correct.

English /d-D/ training. Figure 2 shows individual percent correct data for the last /d-D/ training block. Note that only two of the ten English listeners attained scores in the range of the Middle Eastern listeners at ⩾93% correct.

3. Vowel context effects

Japanese /r-l/ training. Table II(A) shows the vowel context effects in the final /b-d/ and /r-l/ training blocks. As discussed above, for /b-d/, there was an effect of VOWEL ($p=0.005$; due to lower percent correct identification for /e/), but no GROUP × VOWEL interaction ($p=0.746$). For /r-l/, there was no effect of VOWEL ($p=0.054$), and no interaction ($p=0.836$). *These results indicate similar vowel context effects in English and Japanese listeners for both /b-d/ and /r-l/ at the end of training*.

English /d-D/ training. Table II(B) shows the vowel context effects in the final /b-g/ and /d-D/ training blocks. As discussed above, for /b-g/, there was an effect of VOWEL ($p=0.000$; due to lower percent correct identification for /u/), but no GROUP × VOWEL interaction ($p=0.724$). In contrast, for /d-D/, there was no effect of VOWEL ($p=0.397$), but there was a significant GROUP × VOWEL interaction ($p=0.002$). Middle Eastern accuracy was higher for the back vowels /u,a/ than for the front vowels /e,i/, while English listeners showed the opposite pattern. *These results indicate similar vowel context effects for Middle Eastern and English listeners for /b-g/, but different vowel context effects for /d-D/ at the end of training*.

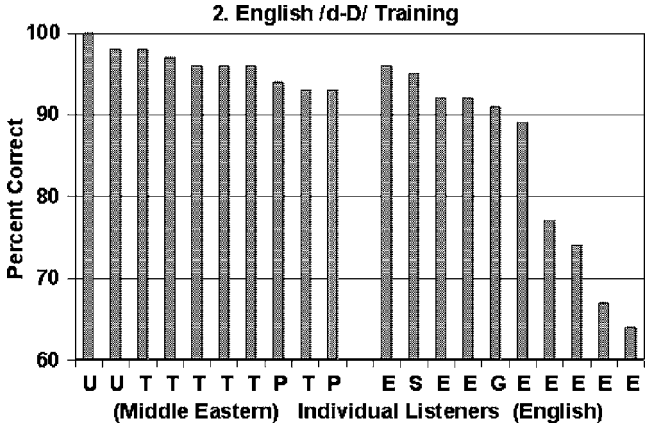

FIG. 2. Individual percent correct scores in the final /d-D/ training block comparing ten native Middle Eastern listeners (left side) and ten non-native English listeners (right side). Native languages of the various listeners are U=Urdu, T=Telegu, P=Punjabi, E=English, S=Spanish, and G=Greek.

TABLE II. Vowel context effects in percent correct identification in the final training block.

(A) Comparison of native English and non-native Japanese listeners for the control /b-d/ and problem /r-l/ constants.

CONTROL	/u/	/a/	/e/	/i/
English /b-d/	99.8	99.3	98.9	99.2
Japanese /b-d/	99.7	99.2	98.8	99.3
PROBLEM	/u/	/a/	/e/	/i/
English /r-l/	99.7	99.3	99.4	99.1
Japanese /r-l/	98.2	94.5	96.7	95.4

(B) Comparison of native Middle Eastern and non-native English listeners for the control /b-g/ and problem /d-D/ contrasts.

CONTROL	/u/	/a/	/e/	/i/
Middle Eastern /b-g/	98.5	99.3	99.4	99.5
English /b-g/	97.9	99.2	98.6	99.1
PROBLEM	/u/	/a/	/e/	/i/
Middle Eastern /d-D/	98.1	96.6	95.6	93.9
English /d-D/	82.5	81.0	85.5	86.1

B. Response time data

Response time data were analyzed for all listeners who attained ⩾85% correct in the final training block, averaged over all talkers and vowels. This arbitrary cutoff served to eliminate data with potentially high guessing rates. This criterion eliminated one Japanese listener in /r-l/ training and four English listeners in /d-D/ training.

1. Vowel context effects in response time

Japanese /r-l/ training. Table III(A) shows mean raw response times for /b-d/ and /r-l/ as a function of vowel context. For /b-d/, there was an effect of GROUP ($F=7.185$ [1,12] $p=0.020$), an effect of VOWEL ($F=39.650$ [3,36] $p=0.000$; due to decreased response times for /i/), and no interaction ($F=0.941$ [3,36] $p=0.431$). For /r-l/, there was also an effect of GROUP ($F=11.148$ [1,11] $p=0.007$), an effect of VOWEL ($F=3.961$ [3,33] $p=0.016$; due to decreased response times for /u,i/), and no interaction ($F=0.989$ [3,33] $p=0.410$). These results indicate overall decreased response times for English than Japanese listeners for both /b-d/ and /r-l/. But more importantly, *these results indicate similar vowel context effects for English and Japanese listeners for both /b-d/ and /r-l/*.

English /d-D/ training. Table III(B) shows mean raw response times for /b-g/ and /d-D/ as a function of vowel

TABLE III. Vowel context effects in mean response time for the final training block.

(A) Comparison of native English and non-native Japanese listeners for the control /b-d/ and problem /r-l/ contrasts.

CONTROL	/u/	/a/	/e/	/i/
English /b-d/	652	651	666	593
Japanese /b-d/	815	804	807	745
PROBLEM	/u/	/a/	/e/	/i/
English /r-l/	655	662	657	644
Japanese /r-l/	823	853	848	828

(B) Comparison of native Middle Eastern and non-native English listeners for the control /b-g/ and problem /d-D/ contrasts.

CONTROL	/u/	/a/	/e/	/i/
Middle Eastern /b-g/	581	578	587	596
English /b-g/	625	605	605	604
PROBLEM	/u/	/a/	/e/	/i/
Middle Eastern /d-D/	691	695	726	712
English /d-D/	1096	1059	1031	920

context. For /b-g/, there was no effect of GROUP ($F=0.152$ [1,18], $p=0.702$), an effect of VOWEL ($F=3.515$ [3,54], $p=0.021$), and an interaction ($F=6.656$ [3,54], $p=0.001$). For /d-D/, there was an effect of GROUP ($F=14.916$ [1,18], $p=0.002$), an effect of VOWEL ($F=4.186$ [3,54], $p=0.011$), and an interaction ($F=8.399$ [3,54], $p=0.000$). These results indicate similar response times for Middle Eastern and English listeners for /b-g/, but faster response times for Middle Eastern than English listeners for /d-D/. In addition, the interactions indicate different vowel context effects for both /b-g/ and /d-D/. For /b-g/, Middle Eastern response times are faster to /u,a/ than to /e,i/, while the opposite effect occurs in English listeners. Note that this interaction with /b-g/ was not apparent in the percent correct analysis, shown in Table II(B). For /d-D/, the interaction mirrors the effect in the percent correct data [see Table II(B)]. Middle Eastern response times are again faster to /u,a/ than to /e,i/, while the opposite effect occurs in English listeners. *These interactions indicate different vowel context effects for Middle Eastern and English listeners for both /b-g/ and /d-D/.*

2. Analysis of response time difference scores

Japanese /r-l/ training. Since the Japanese listeners were overall slower motor responders than the English listeners in responding to both /b-d/ and /r-l/, the raw response time data were also analyzed using difference scores (Burnham, 1986). For each listener, an overall response time for both /r-l/ and /b-d/ was calculated in the final training block by averaging over all talkers and vowel contexts. Next, response times to /b-d/ were subtracted from those to /r-l/. A score near zero would indicate that the /r-l/ contrast had been processed as quickly as the /b-d/ contrast, which might be expected for native English listeners. In contrast, a positive score would indicate that the /r-l/ contrast was taking longer to process than the /b-d/ contrast, which might be expected for non-native Japanese listeners. Difference scores were computed from the log-transformed response time data and analyzed by

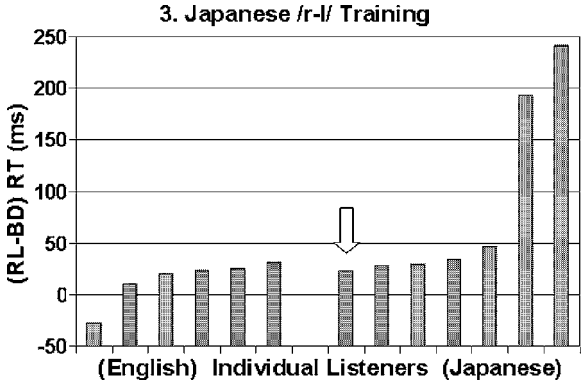

FIG. 3. Individual RT difference scores in the final training block comparing (/r-l/-/b-d/) scores for six native English listeners (left side) and seven non-native Japanese listeners (right side). The arrow denotes the 52-year-old Japanese listener.

t test. Analysis showed that the scores for the English and Japanese listeners did not differ ($t=1.888$; $p=0.101$). Thus this additional analysis that uses control /b-d/ response times as baseline data indicates that by block 4, *the seven Japanese listeners with identification scores of >85% correct had attained the same relative speed as the English listeners in responding to /r-l/.* Individual response time difference scores are shown in Figure 3. Note that four of these seven Japanese listeners had scores in the range of the English listeners (≥34 ms).

English /d-D/ training. Difference scores for (/d-D/-/b-g/) were also computed from the log-transformed data in the final block and analyzed by *t* test. The scores for Middle Eastern listeners were significantly lower compared to English listeners ($t=2.822$; $p=0.036$). Thus, in contrast to the Japanese listeners responding to /r-l/ (see above), *the six English listeners with identification scores of ≥85% correct did not attain the relative speed of the Middle Eastern listeners in responding to /d-D/.* Individual difference scores are shown in Fig. 4. Note that none of the English listeners had scores in the range of the Middle Eastern listeners (≥168 ms).

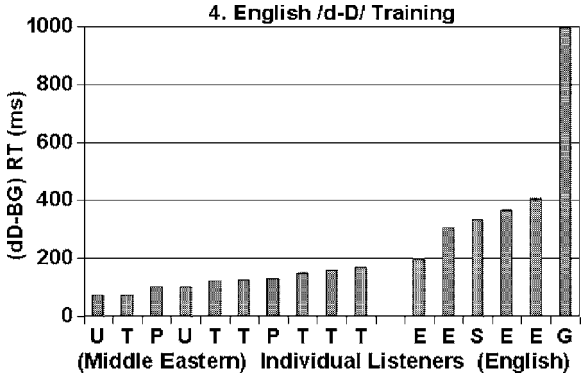

FIG. 4. Individual RT difference scores in the final training block comparing (/d-D/-/b-g/) scores for ten native Middle Eastern listeners (left side) and six non-native English listeners (right side). Native languages of the various listeners are U=Urdu, T=Telegu, P=Punjabi, E=English, S=Spanish, and G=Greek.

IV. DISCUSSION

The specific question posed in this study was as follows: Given a moderate level of stimulus variability, can a monkey psychoacoustic procedure train human listeners to nativelike perception of problem non-native contrasts? For Japanese listeners categorizing /r-l/, the answer appears to be affirmative, since none of our measures showed any statistical differences from native listeners at the end of training. On the other hand, for English listeners categorizing /d-D/, the answer appears to be negative, since all our measures still showed significant statistical differences from native listeners at the end of training.

A. Comparison with previous Japanese /r-l/ training data

Previous /r-l/ training studies have used different talkers, vowels, and syllable positions in their stimuli (e.g., Logan *et al.*, 1991; Lively *et al.*, 1993; Lively *et al.*, 1994; Takagi, 2002). None reported final training scores of 90% correct, except for Lively *et al.* (1993), Experiment 2, where 93% correct was attained by using only one talker. Since we trained Japanese listeners to 96% correct using four talkers and four vowels, our procedure appears more effective than any used previously. Our result is likely due to a combination of factors associated with our monkey procedure: (1) A stimulus set limited to CVs, (2) repeating the stimulus indefinitely on a given trial, (3) a repeated correction procedure after errors, and (4) training to asymptotic levels of performance.

The present results are the first to indicate statistically verified nativelike Japanese performance in a training study using a moderate level of stimulus variability. Our /r-l/ stimulus sets, each of which consisted of 64 different tokens, probably elicited some sort of /r-l/ prototyping (Iverson and Kuhl, 1996), because all the tokens could not possibly have been individually memorized. Future research could explore making the stimulus sets more variable by adding new talkers, vowels, or syllable positions, to investigate the conditions under which nativelike Japanese perception might deteriorate. An additional manipulation would be to simply eliminate the response feedback, to investigate whether listeners would revert back to a non-native mode of perception.

B. Comparison with previous English /d-D/ training data

Our /d-D/ training results are best compared with those of Pruitt *et al.* (2006), since we both used feedback combined with a moderate level of stimulus variability. Our English trainees reached 84% correct at the end of training, while those of Pruitt *et al.* reached only 74% correct. Thus, while our trainees outperformed those of Pruitt *et al.*, neither study resulted in nativelike performance. One possibility for future research might be to maintain the present conditions of using repeated stimulus presentations, complete feedback, and a repeated correction procedure, but to use a much more limited stimulus set consisting of multiple tokens by a single talker articulating a single vowel (e.g., Werker *et al.*, 1981).

With regard to the present study, it is of interest to consider if further training might have resulted in more nativelike performance. While we cannot rule out this possibility, our tentative answer is negative. For the first three training blocks (24 days), performance clearly improved (68% to 75% to 82% correct). But by block 4 (32 days), performance appeared to asymptote at 84% correct. Thus our data resemble those from other training studies that report most improvement initially, followed by decelerated improvements (e.g., Logan *et al.*, 1991; Takagi, 2002). Statements from our English listeners also indicated that further training would not be effective, since all claimed to be very fatigued at the end of training, and none wished to continue.

Another reason to suspect that further training would not aid our English listeners to become nativelike /d-D/ perceivers arises from the analysis of vowel context effects. Recall that the natives performed best with the back vowels /u,a/, while the non-natives performed best with the front vowels /i,e/. While we cannot suggest specific reasons for this interaction, it appears that the natives and non-natives were focusing on different acoustic cues in /d-D/ perception, and thus that the English listeners were not using a nativelike strategy in their efforts to master the /d-D/ contrast.

C. Comparison of Japanese and English training for problem contrasts

Clearly the present Japanese listeners were more successful than the English listeners in attaining nativelike perception of their respective problem phoneme contrast. Assuming that the two listener groups were similarly motivated, there are both phonological and psychoacoustic factors to consider to account for training differences.

1. Phonological factors

Best (1994, p. 191) theorizes that the native phonological system may assist or interfere in varying degrees with learning a new non-native phoneme contrast. The most powerful case of facilitation is when the two new phonemes to be contrasted are very familiar sounding and resemble two different native phonemes, such that they become assimilated to two categories (type TC). The most difficult case is when the two new phonemes are assimilated equally well, or poorly, to a single native category (type SC). A case of midlevel difficulty is when the two new phonemes are assimilated to a single native category, but one may be more similar than the other to a native prototype phoneme, such that the new phonemes show differences in category goodness (type CG).

Japanese perception of problem /r-l/. This case is most likely an example of type CG perception, because goodness-of-fit ratings show that Japanese listeners do not perceive either English retroflex /r/ or lateral /l/ as identical to their /r/ flap (Takagi, 1994; Guion *et al.*, 2000). For example, Takagi reported that some Japanese listeners actually perceive their /r/ flap as more similar to English /l/ than to English /r/. Thus it is possible that differences in category goodness allowed the present trainees to master the /r-l/ contrast in terms of the measures used here.

Japanese perception of control /b-d/. Regarding our con-

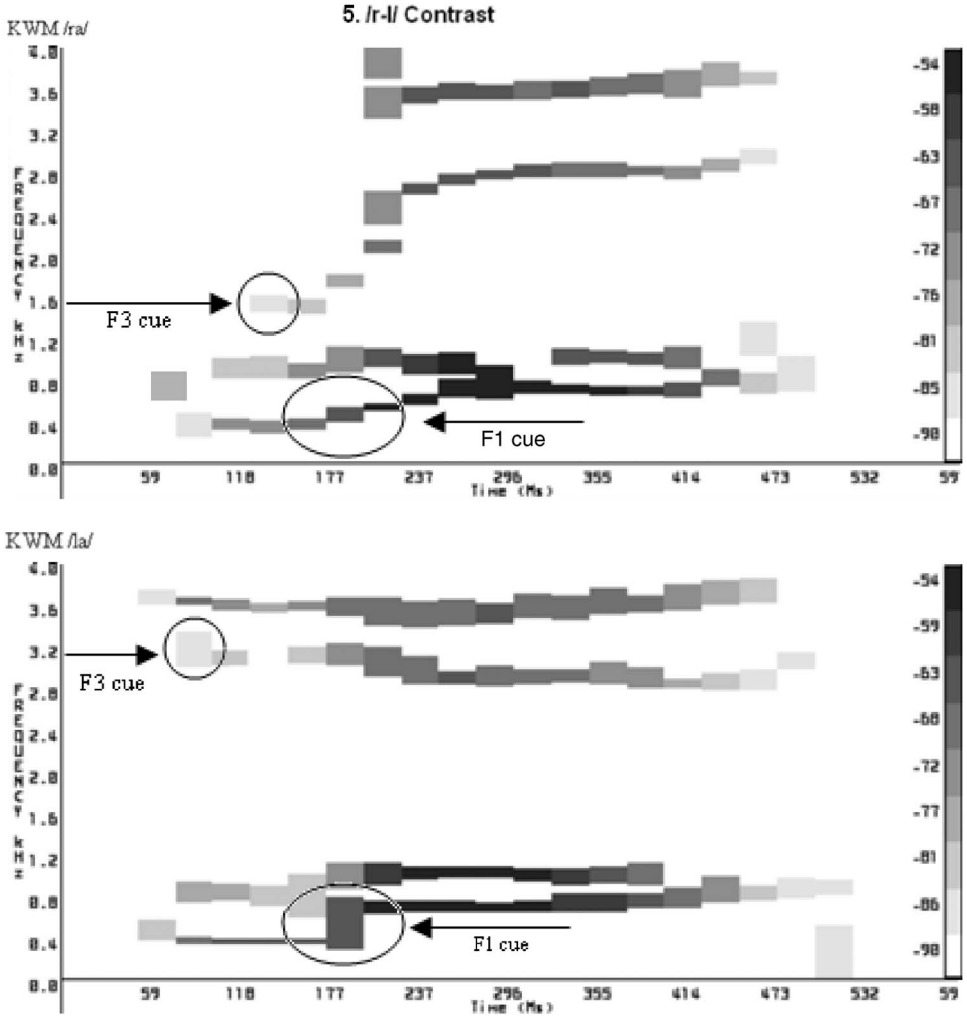

FIG. 5. Formant tracking analysis of a /ra/ versus /la/ token from native male English talker K.W.M. Arrows point to the spectral cues in *F*3 and the temporal cues in *F*1 differentiating /ra/ from /la/.

trol contrast /b-d/, it is of interest to note that Guion *et al.* (2000) obtained Japanese ratings for English /b/ and /d/ and reported excellent goodness-of-fit data for these stops to their Japanese counterparts. Thus we believe that /b/ and (presumably) /d/ were legitimate familiar control stimuli for the Japanese listeners in the present experiment, and that they were being perceived as very similar, if not identical, to their Japanese counterparts. Even though the Japanese listeners were overall slower responders than the English listeners for this contrast, we believe that this effect was simply due to the lack of previous (motor) experience with the *go-left/go-right* procedure.

English perception of problem /d-D/. This case is obviously an example of type SC perception, since English listeners perceive dental /d/ and retroflex /D/ as highly similar, if not identical, to English alveolar /d/. This observation was made by every one of our English listeners, and was also obvious to author J.M.S., who spent many hours trying to master the present /d-D/ stimuli to no avail. Polka (1991) reached a similar conclusion in her extensive study of dental-retroflex perception. Nevertheless, to verify this hypothesis, goodness-of-fit data from English listeners would show conclusively if both Middle Eastern /d/ and /D/ are indistinguishable from English /d/.

English perception of control /b-g/. We assumed that /b-g/ would elicit exactly the same percept for all listeners. However, indications are that it might actually be an example of type TC perception for the English listeners. Recall that we found unanticipated differences in vowel context effects in the response time measure for Middle Eastern and English listeners, suggesting that the /b-g/ contrast is not phonetically or acoustically identical in the two language groups. Despite this, the English listeners apparently totally assimilated Middle Eastern /b-g/ into their respective native /b-g/ categories, such that no measurable deficits in percent correct or response times (averaged over all vowels) emerged.

2. Psychoacoustic factors

As discussed above, Burnham (1986) proposes that phonetic contrasts may differ in basic psychoacoustic salience, and that this factor interacts with perceptual learning in non-native adults. It is proposed that robust contrasts are psychoacoustically very salient, and thus are recovered more easily in adulthood. In contrast, fragile contrasts are less salient, and thus are more easily lost in infancy. So /r-l/ could be a very robust contrast, more easily recovered by adult Japanese listeners, while /d-D/ could be a very fragile contrast, more easily lost by adult English listeners. There are several ways in which the degree of robust versus fragile salience might be determined for any given problem contrast, as discussed below.

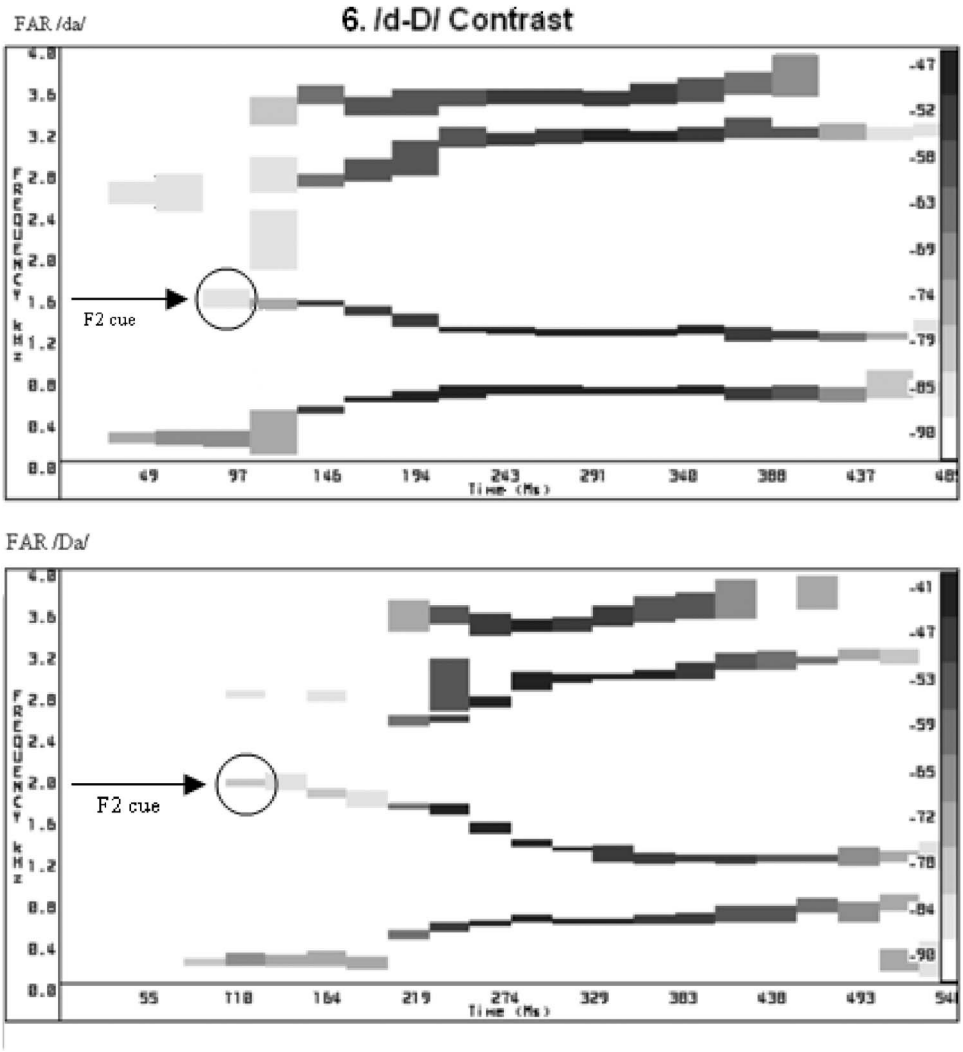

FIG. 6. Formant tracking analysis of a dental /da/ versus retroflex /Da/ token from native male Middle Eastern Urdu talker F.A.R. Arrows point to the differing *F*2 onset frequencies for /da/ versus /Da/.

Objective acoustic measurements. As discussed earlier, the primary acoustic cue differentiating the /r-l/ liquid contrast is a change in *F*3 onset, which is much higher for /l/ compared to /r/ (Miyawaki *et al.*, 1975; Polka and Strange, 1985). Our stimuli show a similar pattern. Figure 5 shows a /ra/ and a /la/ token from male English talker K.W.M., plotted using the formant tracking option of CSRE. The /ra/ token has an *F*3 onset at approximately 1500 Hz, remaining more or less steady for 50 ms, and then transiting upwards in frequency over approximately 60 ms towards the steady-state vowel *F*3. The /la/ token has a much higher *F*3 onset of approximately 3200 Hz, and then decreases slightly toward the vowel *F*3. These stimuli also show a secondary temporal cue in *F*1 (Polka and Strange, 1985). For /ra/, *F*1 starts at 400 Hz and then exhibits a gradual upward 150 ms frequency transition into the *F*1 of the vowel, while for /la/, *F*1 remains steady for 100 ms, and then exhibits a steep 10 ms transition into the *F*1 of the vowel.

As discussed earlier, the primary acoustic cue differentiating the /d-D/ stop contrast is a change in *F*2 onset, which is lower for /d/ compared to /D/, as well as a change in *F*3 onset (Werker and Logan, 1985; Werker and Lalonde, 1988; Polka, 1991). Our stimuli show a similar pattern in *F*2 onset. Figure 6 shows a dental /da/ and a retroflex /Da/ token from male Urdu talker F.A.R. The *F*2 transition is lower for /da/ (1600 Hz) compared to /Da/ (2000 Hz). But our stimuli do not show a change in *F*3 onset, which serves to underscore the more elusive nature of the acoustic cues differentiating this fragile dental-retroflex stop contrast. No temporal cues have been reported for this contrast.

Human difference limens. Human difference limens (DLs) could also be used to predict the relative salience of phoneme contrasts. Human DLs have been measured for both synthetic stop place-of-articulation and liquid continua, using a very low-uncertainty, repeating-standard AX discrimination procedure (Sinnott, 1994). For an *F*2 change along a /ba-da/ continuum (*F*2=1000 to 1600 Hz), the DL at 1000 Hz is 160 Hz, so the 600 Hz change from /ba/ to /da/ is about 3.7 times the 160 Hz DL. For an *F*3 change along a /ra-la/ continuum (*F*3=1500 to 3000 Hz), the DL is 180 Hz at 1500 Hz, so the 1500 Hz change from /ra/ to /la/ is about 8.3 times the 180 Hz DL. Therefore, assuming that DLs could be used in this way to predict sensitivity to natural speech sound contrasts, the change from /ra/ to /la/ should be much more discriminable than a change from /ba/ to /da/.

Perceptual evidence from natives. Finally, evidence from the native Middle Eastern listeners themselves indicates that /d-D/ was a more fragile contrast, compared, for example, to control /b-g/. During training, native percent correct scores

for /d-D/ always remained below those for /b-g/ [see Table I(B)], and native response times were up to 200 ms slower in responding to /d-D/ than /b-g/ [see Table II(B)]. Note that this was not the case for English perception of /r-l/ and /b-d/, which appeared more equally salient in all our measures [see Tables I(A) and II(A)].

V. CONCLUSION

The present experiment used a monkey psychoacoustic procedure with extensive feedback to train human listeners to categorize non-native problem phonetic contrasts. While Japanese perception became nativelike for /r-l/, according to measures of percent correct, vowel context effects, and RT difference scores, this was not the case for English perception of /d-D/. Acoustic analyses and difference limen predictions indicate that the /r-l/ contrast is much more robust in both its spectral and temporal characteristics compared to the /d-D/ contrast, which could be considered more fragile (Burnham, 1986). Future research could explore using a nonhuman animal model to provide a more objective criterion for the robust versus fragile salience of any human phonetic contrast, an idea put forth by Best *et al.* (1988, p. 347). We propose the Japanese monkey as a good candidate for this purpose, since it provides a good match to human psychoacoustics for complex sounds (Sinnott, 1994). At the same time, it appears to remain a "clean slate" uncontaminated by human phonological systems (e.g., Sinnott and Saporita, 2000; Sinnott and Gilmore, 2004; Sinnott *et al.*, 2006). The present human data would lead us to predict that a monkey, if put to a comparison, would find /r-l/ easier to differentiate than /d-D/. Of course the monkey model would be even more useful if we make the added assumption that the monkey auditory system is qualitatively similar to that of the preverbal human infant at birth. In any case, the combined efforts of cross-language, developmental, and comparative researchers should have great potential for untangling the various factors involved in speech perception and its development.

ACKNOWLEDGMENTS

This research was supported by NIH NIDCD PHS R01 DC00541-16 to J.M.S., and was based on two separate Masters theses by authors C.L.G. and A.F.M. in the Department of Psychology at the University of South Alabama. Portions of these data were presented at the 143rd ASA Meeting in Atlanta, GA, May 2002, and at the First ASA Workshop on Second Language Speech Learning, Simon Fraser University, Vancouver, British Columbia, Canada, May, 2005.

Best, C. (**1994**), in *The Development of Speech Perception: The Transition from Speech Sounds to Spoken Words*, edited by J. Goodman and H. Nusbaum (MIT Press, Cambridge, MA), pp. 167–223.

Best, C., McRoberts, G., and Sithole, N. (**1988**). "Examination of perceptual reorganization for nonnative speech contrasts: Zulu click discrimination by English-speaking adults and infants," J. Exp. Psychol. Hum. Percept. Perform. **14**, 345–360.

Bradlow, A., Akahane-Yamada, R., Pisoni, D., and Tohkura, Y. (**1999**). "Training Japanese listeners to identify English /r/ and /l/: Long-term retention of learning in perception and production," Percept. Psychophys. **61**, 977–985.

Bradlow, A., Pisoni, D., Akahane-Yamada, R., and Tohkura, Y. (**1997**). "Training Japanese listeners to identify English /r/ and /l/. IV. Some effects of perceptual learning and speech production," J. Acoust. Soc. Am. **101**, 2299–2310.

Burnham, D. (**1986**). "Developmental loss of speech perception: Exposure to and experience with a first language," Appl. Psycholinguist. **7**, 207–240.

Flege, J., Takagi, N., and Mann, V. (**1996**). "Lexical familiarity and English-language experience affect Japanese adults' perception of /r/ and /l/," J. Acoust. Soc. Am. **99**, 1161–1173.

Gordon, P., Keyes, L., and Yung, Y. (**2001**). "Ability in perceiving non-native contrasts: Performance on natural and synthetic speech stimuli," Percept. Psychophys. **63**, 746–758.

Goto, H. (**1971**). "Auditory perception by normal Japanese adults of the sounds 'L' and 'R'," Neuropsychobiology **9**, 317–323.

Guion, S., Flege, J., Akahane-Yamada, R., and Pruitt, J. (**2000**). "An investigation of current models of second language speech perception: The case of Japanese adults' perception of English consonants," J. Acoust. Soc. Am. **107**, 2711–2724.

Ingram, J., and Park, S. (**1998**). "Language, context and speaker effects in the identification and discrimination of English /r/ and /l/ by Japanese and Korean listeners," J. Acoust. Soc. Am. **103**, 1161–1174.

Iverson, P., and Kuhl, P. (**1996**). "Influence of phonetic identification and category goodness on American listeners' perception of /r/ and /l/," J. Acoust. Soc. Am. **99**, 1130–1140.

Kuhl, P., and Iverson, P. (**1995**), in *Speech Perception and Linguistic Experience: Issues in Cross Language Research*, edited by W. Strange (York Press, Timonium, MD), pp. 121–154.

Lively, S., Logan, J., and Pisoni, D. (**1993**). "Training Japanese listeners to identify English /r/ and /l/. II. The role of phonetic environment and talker variability in learning new perceptual categories," J. Acoust. Soc. Am. **94**, 1242–1255.

Lively, S., Pisoni, D., Yamada, R., Tohkura, Y., and Yamada, T. (**1994**). "Training Japanese listeners to identify English /r/ and /l/. III. Long term retention of new phonetic categories," J. Acoust. Soc. Am. **96**, 2076–2087.

Logan, J., Lively, S., and Pisoni, D. (**1991**). "Training Japanese listeners to identify English /r/ and /l/: A first report," J. Acoust. Soc. Am. **89**, 874–886.

MacKain, K., Best, C., and Strange, W. (**1981**). "Categorical perception of English /r/ and /l/ by Japanese bilinguals," Appl. Psycholinguist. **2**, 369–390.

Miyawaki, K., Strange, W., Verbrugge, R., Liberman, A., and Jenkins, J. (**1975**). "An effect of linguistic experience: The discrimination of [r] and [l] by native speakers of Japanese and English," Percept. Psychophys. **18**, 331–340.

Pisoni, D., Lively, S., and Logan, S. (**1994**), in *The Development of Speech Perception: The Transition from Speech Sounds to Spoken Words*, edited by J. Goodman and H. Nusbaum (MIT Press, Cambridge, MA), pp. 121–165.

Polka, L. (**1991**). "Cross-language speech perception in adults: Phonemic, phonetic, and acoustic contributions," J. Acoust. Soc. Am. **89**, 2961–2977.

Polka, L., and Strange, W. (**1985**). "Perceptual equivalence of acoustic cues that differentiate /r/ and /l/," J. Acoust. Soc. Am. **78**, 1187–1197.

Pruitt, J., Jenkins, J., and Strange, W. (**2006**). "Training the perception of Hindi dental and retroflex stops by native speakers of American English and Japanese," J. Acoust. Soc. Am. **119**, 1684–1696.

Sheldon, A., and Strange, W. (**1982**). "The acquisition of /r/ and /l/ by Japanese learners of English: Evidence that speech production can precede speech perception," Appl. Psycholinguist. **3**, 243–261.

Sinnott, J. (**1994**). "Comparisons of human and monkey differential sensitivity to speech, non-speech and monkey speech sounds," Current Topics in Acoust. Res. **1**, 355–364.

Sinnott, J., and Gilmore, C. (**2004**). "Perception of place-of-articulation information in natural speech by monkeys vs. humans," Percept. Psychophys. **66**, 1341–1350.

Sinnott, J., Powell, L., and Camchong, J. (**2006**). "Using monkeys to explore perceptual "loss" versus "learning" models in English and Spanish voice-onset-time perception," J. Acoust. Soc. Am. **119**, 1585–1596.

Sinnott, J., and Saporita, T. (**2000**). "Differences in American-English, Spanish and monkey perception of the *say-stay* trading relationship," Percept. Psychophys. **62**, 1312–1319.

Strange, W., and Dittman, S. (**1984**). "Effects of discrimination training on the perception of /r-l/ by Japanese adults learning English," Percept. Psychophys. **36**, 131–145.

Takagi, N. (**1994**). "Signal detection modeling of Japanese listeners' /r-l/ labeling behavior in a one-interval identification task," J. Acoust. Soc. Am.

97, 563–574.
Takagi, N. (**2002**). "The limits of training Japanese listeners to identify English /r/ and /l/: Eight case studies," J. Acoust. Soc. Am. **111**, 2887–2896.
Werker, J. (**1994**), in *The Development of Speech Perception: The Transition from Speech Sounds to Spoken Words*, edited by J. Goodman and H. Nusbaum (MIT Press, Cambridge, MA), pp. 93–120.
Werker, J., Gilbert, J., Humphrey, K., and Tees, R. (**1981**). "Developmental aspects of cross-language speech perception," Child Dev. **52**, 349–355.
Werker, J., and Lalonde, C. (**1988**). "Cross-language speech perception: Initial capabilities and developmental change," Dev. Psychol. **24**, 672–683.
Werker, J., and Logan, J. (**1985**). "Cross-language evidence for three factors in speech perception," Percept. Psychophys. **37**, 35–44.
Werker, J., and Tees, R. (**1983**). "Developmental changes across childhood in the perception on non-native speech sounds," Can. J. Psychol. **37**, 278–286.
Werker, J., and Tees, R. (**1984a**). "Cross-language speech perception: Evidence for perceptual reorganization during the first year of life," Infant Behav. Dev. **7**, 49–63.
Werker, J., and Tees, R. (**1984b**). "Phonemic and phonetic factors in adult cross-language speech perception," J. Acoust. Soc. Am. **75**, 1866–1878.
Yamada, R., and Tohkura, Y. (**1992**). "The effects of experimental variables on the perception of American English /r/ and /l/ by Japanese listeners," Percept. Psychophys. **52**, 376–392.

Simulation and analysis of nasalized vowels based on magnetic resonance imaging data[a)]

Tarun Pruthi[b)] and Carol Y. Espy-Wilson
Speech Communication Laboratory, Institute of Systems Research and Department of Electrical and Computer Engineering, University of Maryland, College Park, Maryland 20742

Brad H. Story
Speech Acoustics Laboratory, Department of Speech, Language and Hearing Sciences, University of Arizona, Tucson, Arizona 85721

(Received 29 July 2005; revised 10 January 2007; accepted 13 March 2007)

In this study, vocal tract area functions for one American English speaker, recorded using magnetic resonance imaging, were used to simulate and analyze the acoustics of vowel nasalization. Computer vocal tract models and susceptance plots were used to study the three most important sources of acoustic variability involved in the production of nasalized vowels: velar coupling area, asymmetry of nasal passages, and the sinus cavities. Analysis of the susceptance plots of the pharyngeal and oral cavities, $-(B_p+B_o)$, and the nasal cavity, B_n, helped in understanding the movement of poles and zeros with varying coupling areas. Simulations using two nasal passages clearly showed the introduction of extra pole-zero pairs due to the asymmetry between the passages. Simulations with the inclusion of maxillary and sphenoidal sinuses showed that each sinus can potentially introduce one pole-zero pair in the spectrum. Further, the right maxillary sinus introduced a pole-zero pair at the lowest frequency. The effective frequencies of these poles and zeros due to the sinuses in the sum of the oral and nasal cavity outputs changes with a change in the configuration of the oral cavity, which may happen due to a change in the coupling area, or in the vowel being articulated. © *2007 Acoustical Society of America.* [DOI: 10.1121/1.2722220]

PACS number(s): 43.72.Ar, 43.70.Bk, 43.70.Fq [DOS] Pages: 3858–3873

I. INTRODUCTION

Vowel nasalization has been studied extensively over the last several decades. Although researchers have been successful in finding several acoustical (Bognar and Fujisaki, 1986; Dickson, 1962; Fant, 1960; Fujimura and Lindqvist, 1971; Hattori *et al.*, 1958; Hawkins and Stevens, 1985; House and Stevens, 1956; Maeda, 1982b, c; Stevens *et al.*, 1987) and perceptual (Beddor, 1993; Bognar and Fujisaki, 1986; Hattori *et al.*, 1958; Hawkins and Stevens, 1985; House and Stevens, 1956; Maeda, 1982c) correlates of nasality, automatically extractable acoustic parameters (APs) that work well in a speaker-independent manner still remain elusive. A study to understand the salient features of nasalization, and the sources of acoustic variability in nasalized vowels is, therefore, not just desirable, but in fact needed to find knowledge-based APs to detect vowel nasalization.

Vowel nasalization is not an easy feature to study because the exact acoustic characteristics of nasalization vary not only with the speaker (i.e., with changes in the exact anatomical structure of the nasal cavity), but also with the particular sound upon which it is superimposed (i.e., vowel identity), and with the degree of nasal coupling (Fant, 1960, page 149). Further, even though the articulatory maneuver required to introduce nasalization, a falling velum, is simple, the acoustic consequences of this coupling are very complex because of the complicated structure of the nasal cavity. The human nasal cavity consists of a movable fold called the velum which controls the coupling between the vocal tract and the nasal tract, two asymmetrical nasal passages which end at the two nostrils, and several paranasal cavities (also called sinuses). This combination of degree of velum lowering, asymmetry in the left and right nasal passages, and side branches due to sinuses is the major source of acoustic variability observed in the spectra of nasalized vowels. Several researchers in the past have tried to understand the spectral effects of each of these components in isolation.

Fujimura and Lindqvist (1971) obtained continuous frequency functions of the transfer characteristics of several vowels, stops, nasal consonants and nasalized vowels by exciting the vocal tract by an external sweep-tone signal. They observed the appearance of an extra nasal pole-zero pair around 400 Hz and damping of F2 in the spectra of the nasalized vowels /u/, /o/ and /ɑ/. They also proposed several rules to predict the movement of the poles and zeros with changes in velar coupling area for a lossless system based on the plots of susceptance (imaginary part of the admittance) of the pharyngeal, oral and nasal cavities looking into the respective cavities from the coupling location. Maeda (1993) simulated the spectra for French nasal vowels, and reiterated

[a)]Portions of this work have been presented in Pruthi, T., and Espy-Wilson, C.Y. (2005), "Simulating and understanding the effects of velar coupling area on nasalized vowel spectra," J. Acoust. Soc. Am. **118**(3), p. 2024 (ASA Meeting abstract), and Pruthi, T., and Espy-Wilson, C.Y. (2006), "An MRI based study of the acoustic effects of sinus cavities and its application to speaker recognition," in Proceedings of Interspeech, pp. 2110–2113.

[b)]Author to whom correspondence should be addressed. Electronic address: tpruthi@umd.edu

the rules for pole-zero movements suggested by Fujimura and Lindqvist (1971) for varying coupling areas. He proposed four different kinds of spectral modifications corresponding to the vowels /i/, /u/, /ɛ/, and /ɔ/. Feng and Castelli (1996) viewed nasalized vowels as a dynamic trend from an oral configuration towards an /ŋ/-like configuration. The latter configuration corresponds to the case of just the pharyngonasal tract when the velum falls to such an extent that it blocks off the oral cavity completely. The first two resonance frequencies were used to characterize this pharyngonasal configuration. Simulations of the 11 French nasal vowels with configurations varying between oral and pharyngonasal were presented to illustrate pole-zero evolutions with varying coupling areas. Feng and Castelli (1996) also suggested that the main effect of maxillary sinus was to add complexity to the low-frequency nasal spectrum. However, they did not deal with the effects of the sinuses in detail.

Dang *et al.* (1994) recorded the nasal cavities of six male speakers and one female speaker using magnetic resonance imaging (MRI). They observed a large asymmetry between the left and right nasal passages of the speakers and suggested that this asymmetry leads to the introduction of a pole-zero pair in the spectrum because of the side branch effect. Acoustic modeling of the nasal cavity as two passages confirmed the appearance of the extra pole-zero pair between 2 and 2.5 KHz. Further, simulation of nasal consonant spectra with the inclusion of the maxillary and sphenoidal sinuses suggested that it was necessary to include the paranasal cavities to model the acoustic characteristics of the nasal cavity adequately.

Lindqvist-Gauffin and Sundberg (1976) indicated that a simple two-tract model for the nasal cavity is insufficient to explain the complications seen in the low frequency spectrum of nasals and nasalized vowels obtained by the sweep tone experiments of Fujimura and Lindqvist (1971). They suggested that the observed acoustic effects could, however, be explained if additional shunting cavities (i.e., sinuses) were included in the modeling of the nasal cavity. They also suggested that asymmetries in the two nasal passages, or the sinuses, would introduce additional pole-zero pairs in the spectrum. Maeda (1982b) has shown that the low resonance characteristic of nasalized vowels is due to the sinus cavities. He also found that the low resonance was important to make the nasalized vowels sound more natural. However, he suggested that further corroborations based on acoustic and anatomical data were required to confirm the effects. Dang and Honda (1996) estimated the zero frequencies and the locations of the sinus openings by directly measuring the transmission characteristics of the nasal tract of three subjects. Their results indicated that each of the sphenoidal, maxillary and frontal sinuses introduce their own zeros into the transmission characteristics of the nasal tract. In two out of the three cases considered, the maxillary sinuses accounted for the lowest zeros in the spectrum.

These studies, however, still leave several questions unanswered. While the study by Fujimura and Lindqvist (1971) gave a theoretical basis for predicting the movement of poles and zeros as a function of the coupling area using susceptance plots, they assumed a very simplistic but nonrealistic model for changes in the coupling area. Therefore, this model might be slightly inaccurate in predicting pole/zero movements in a real setting and a more realistic model should be pursued. Further, even though past literature has clearly illustrated that each sinus can introduce its own zero in the spectrum, it still does not tell us how these poles/zeros would move with changes in coupling area or vowel. Moreover, only the studies by Dang *et al.* (1994) and Dang and Honda (1996) were based on real anatomical data collected by MRI.

MRI has become a standard for volumetric imaging of the vocal tract during sustained production of speech sounds (Alwan *et al.*, 1997; Baer *et al.*, 1991; Dang *et al.*, 1994; Matsumura, 1992; Moore, 1992; Narayanan *et al.*, 1995, 1997). Story *et al.* (1996) used MRI to create an inventory of speaker-specific, three-dimensional (3D), vocal tract air space shapes for 12 vowels, three nasals and three plosives. They also imaged the speaker's nasal tract along with his left and right maxillary sinuses and sphenoidal sinuses. The area functions for the nasal cavity were not included in Story *et al.* (1996), but were made available in Story (1995). Hardly any attempts have ever been made to analyze nasalized vowels using MRI data. In this work, therefore, we will use the MRI based area functions recorded by Story (1995) and Story *et al.* (1996) to simulate the spectral effects of vowel nasalization and analyze them in detail.

II. AREA FUNCTIONS

A. Vocal tract

Vocal tract area functions measured with MRI were reported by Story *et al.* (1996) for one adult male speaker (the first author of that study). The area function collection included 12 vowels, three nasal consonants, and three stop consonants. For the present study, area functions for the /i/ and /ɑ/ vowels reported in Story *et al.* (1996) served as the two vocal tract shapes for simulation of vowels. They are shown in the middle (/i/) and bottom (/ɑ/) panels of Fig. 1. Also indicated on these plots are the approximate locations of the coupling of the main vocal tract to the nasal tract under the condition of nasalization. These locations are specified to be 8 cm from the glottis in both cases, as was reported for the nasal consonants of Story *et al.* (1996). The coupling location serves to divide the vocal tract into pharyngeal cavity and oral cavity. The region from glottis to the coupling location is called the pharyngeal cavity, and the region from the coupling location to the lips is called the oral cavity. It is acknowledged that these coupling points may be fairly rough approximations of their actual locations during nasalized vowel production. Furthermore, it is also possible, and perhaps likely, that the vocal tract shape for each of these vowels would be somewhat modified from those shown in Fig. 1 under nasalized conditions.

B. Nasal tract

MRI-based area functions of the nasal system were obtained at the same time as the vowels and consonants. The availability of area functions of the vocal and nasal tracts,

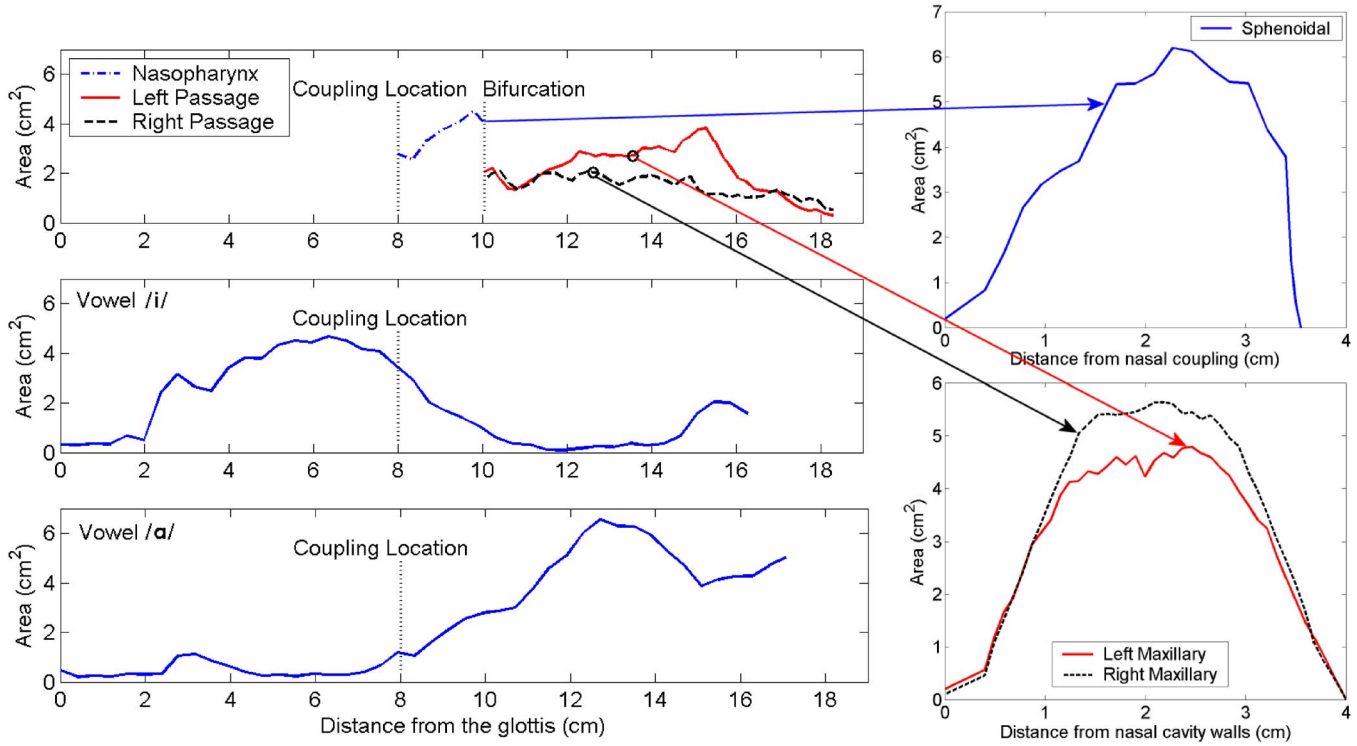

FIG. 1. (Color online) Areas for the vocal tract (oral cavity and pharyngeal cavity), nasal tract, maxillary sinuses and sphenoidal sinus.

both from the same speaker, made this data set particularly attractive for simulating nasalized and nonnasalized vowels.

The MR images of the nasal system used in the present study were acquired in June 1994 at the University of Iowa Hospitals and Clinics. A General Electric Signa 1.5 T scanner was used with the data acquisition mode set to Fast Spin Echo and the scanning parameters set to TE=13 ms, TR =4000 ms, ETL=16 ms, and NEX=2. During normal respiration (no specific speech task), an image set was acquired as a contiguous series of 3-mm-thick coronal image slices extending from the nares (nostrils) to approximately the posterior pharyngeal wall. The field of view for each slice was 26 cm×26 cm which, with a pixel matrix of 256×256, provided a pixel dimension of 1.016 mm/pixel. Two image sets of the speaker's nasal system were obtained. The first captured the *natural* state of the speaker's nasal tract at the specific point in time at which the images were collected. The second image set was obtained after the speaker's nasal system had been treated with oxymetazoline nasal spray (e.g., *Afrin*) to reduce any nasal tissue swelling that may have caused slight congestion. Although the first image set may represent a more natural speaking condition, the second set presumably represented the most open condition of the nasal system and would also be considered the most repeatable for making subsequent audio recordings of the speaker (i.e., because the nasal spray can be reapplied at any time to bring the speaker's nasal system to its most open state). Thus, all subsequent analysis and modeling will be concerned only with the image set based on this *decongested* condition.

The analysis of the image sets was performed with VIDA (Volumetric Image Display and Analysis) which is a general image display and analysis package (Hoffman *et al.*, 1992). Each image set was first subjected to a cubic voxel interpolation so that the spatial resolution was the same in all dimensions (1.015 mm). The airspace within each consecutive coronal slice was then determined with a seeded-region growing algorithm. Two views of a 3D reconstruction of the nasal airspace in the *decongested* condition are shown in Fig. 2. These indicate the natural separation of the nasal system into several distinct passages and cavities. In Fig. 2(a), the inferior portion of the nasopharynx (labeled A) can be seen as a tubular structure that acoustically and aerodynamically couples the main vocal tract to the nasal system when the velum is in a lowered position (as it was during the image collection). As the nasopharynx tube extends superiorly it bifurcates into the left and right nasal passages, the inferior portion of which can be seen in Fig. 2(b) (E_L and E_R). The openings of these passages into the nasopharynx are called the posterior nares. These passages extend anteriorly to their termination at the anterior nares/nostrils (D in Fig. 2(a) and D_L and D_R in Fig. 2(b)). Located at nearly the same point as the bifurcation of the nasopharynx is the connection of the ostia leading into the Sphenoid Sinus (SS) cavity; the cavity can be seen in the upper left part of Fig. 2(a) (labeled B) but the ostia are not visible. Connected to the left and right nasal passages are the Maxillary Sinus (MS) cavities. These can be seen in Fig. 2(b) (C_L and C_R) as the wing-like structures extending laterally from both sides of the nasal system. No visible connection from any part of the nasal system to either the Frontal Sinus (FS) or the Ethmoid Sinus (ES) cavities could be determined. Hence, they were excluded from the image analysis.

Cross-sectional areas of the nasopharynx tube were measured with the same iterative bisection algorithm used for measurement of the vocal tract area functions (Story *et al.*,

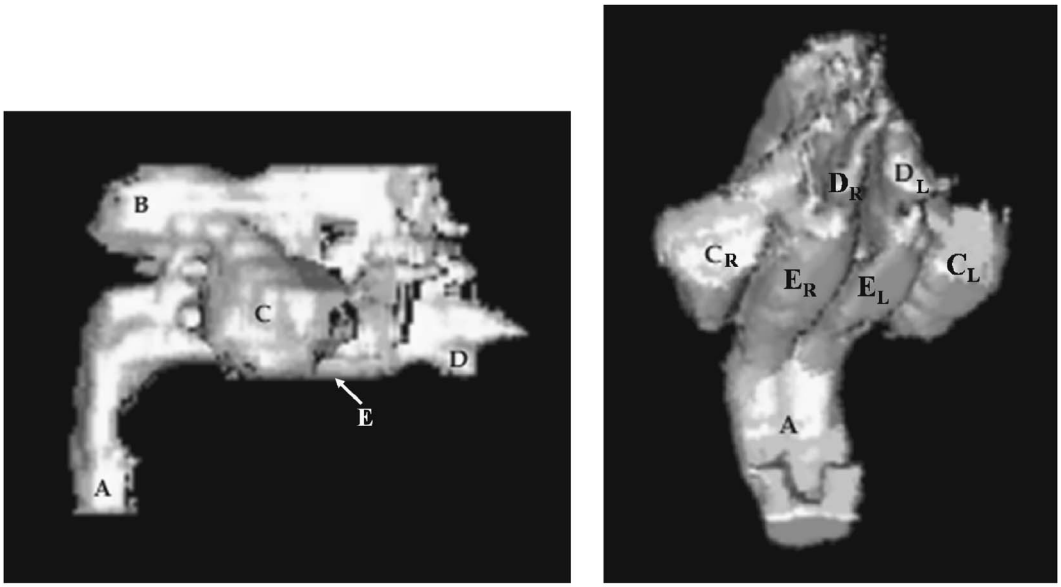

FIG. 2. Two views of the 3D reconstruction of the nasal cavity from the MRI data used in this study. The labels refer to specific regions within the nasal tract. (a) Sagittal projection showing the speaker's right side where *A* is the inferior portion of the nasopharynx, *B* is the sphenoid sinus cavity, *C* is the maxillary sinus, and *D* is the nostril. (b) Nasal tract rotated to show the left and right sides from an inferior view where *A* is again the inferior portion of the nasopharynx, C_L and C_R are the left and right maxillary sinuses, D_L and D_R are the left and right nostrils, and E_L and E_R are the left and right nasal passages, respectively.

1996, page 542). The measured area variation can be seen in the upper panel of Fig. 1 as the section that extends from 8–10 cm from the glottis. Although this is a short (2 cm) section, the iterative bisection technique was needed to traverse the curved portion of the nasopharynx. The 10 cm point in this plot signifies the location at which the nasopharynx bifurcates into the left and right nasal passages. The cross-sectional areas along the length of these passages were measured slice by slice with a region-of-interest (ROI) algorithm, and the resulting area functions are again shown in the upper panel of Fig. 1. Both begin at 10 cm from the glottis, and, due to the bifurcation, it is noted that the cross-sectional areas of the left and right passages at this point sum to nearly the final cross-sectional area of the nasapharynx; their sum is not exactly the same because the measurements of the left and right nasal passages were made at a slightly more anterior location than the final section of the nasopharynx. Both the left and right passages extend to a location shown as 18.25 cm from the glottis. Between approximately 12–17 cm from the glottis, the right nasal passage maintains cross-sectional areas that are about 1–1.5 cm^2 less than those of the left passage, thus producing a left versus right asymmetry. Because these were measured from the *decongested* condition, it is unlikely that the asymmetry is due to congestion. A more likely cause is the speaker's deviated nasal septum that was revealed, in the raw images, to constrict the right passage.

The cross-sectional areas of the SS and the right and left MS were also measured with the ROI algorithm. Anatomically, the sphenoid bone contains two sinus cavities separated by an irregular midline septum (Zemlin, 1998, pages 220, 224). Ostia provide the coupling of these two cavities to the left and right nasal passages. Based on the images collected, however, the separation of the sphenoid into two separate cavities was not visible. Hence, the airspace within the SS was analyzed as if it were one cavity. Consequently, the measurements of the two ostia were summed to provide one coupling port. The variation in cross-sectional area of the sphenoid cavity is shown in the upper right plot of Fig. 1. The *x* axis represents the distance from the point of coupling to the left and right nasal passages. The cross-sectional areas of both maxillary cavities were measured along the extent from their respective anterior to posterior walls, and are shown in the lower right plot of Fig. 1. They are nearly identical in shape, though the left cavity is slightly smaller than the right. The coupling of these cavities to the left and right passages occurs at the locations indicated with open circles in the upper panel of Fig. 1.

III. METHOD

In this study, VTAR (Zhang and Espy-Wilson, 2004), a computer vocal tract model, was used to simulate the spectra for nasalized vowels with successive addition of complexity to the nasal cavity to highlight the effects of each addition. Given the description of area functions in Sec. II, the complete structure of the model of the vocal tract and the nasal tract used in this study is shown schematically in Fig. 3(c). Section IV A analyzes the acoustic changes due to the introduction of coupling between the vocal tract and the nasal tract, and due to changes in the coupling area. Hence, in this section a simplified model of the vocal tract and nasal tract (shown schematically in Fig. 3(a)) is considered. Section IV B analyzes the effects of asymmetry between the left and right nasal passages, and therefore, the model shown in Fig. 3(b) adds the complexity due to nasal bifurcation in the model considered in this section. Section IV C examines the effects of MS and SS on the acoustic spectrum. Hence, the

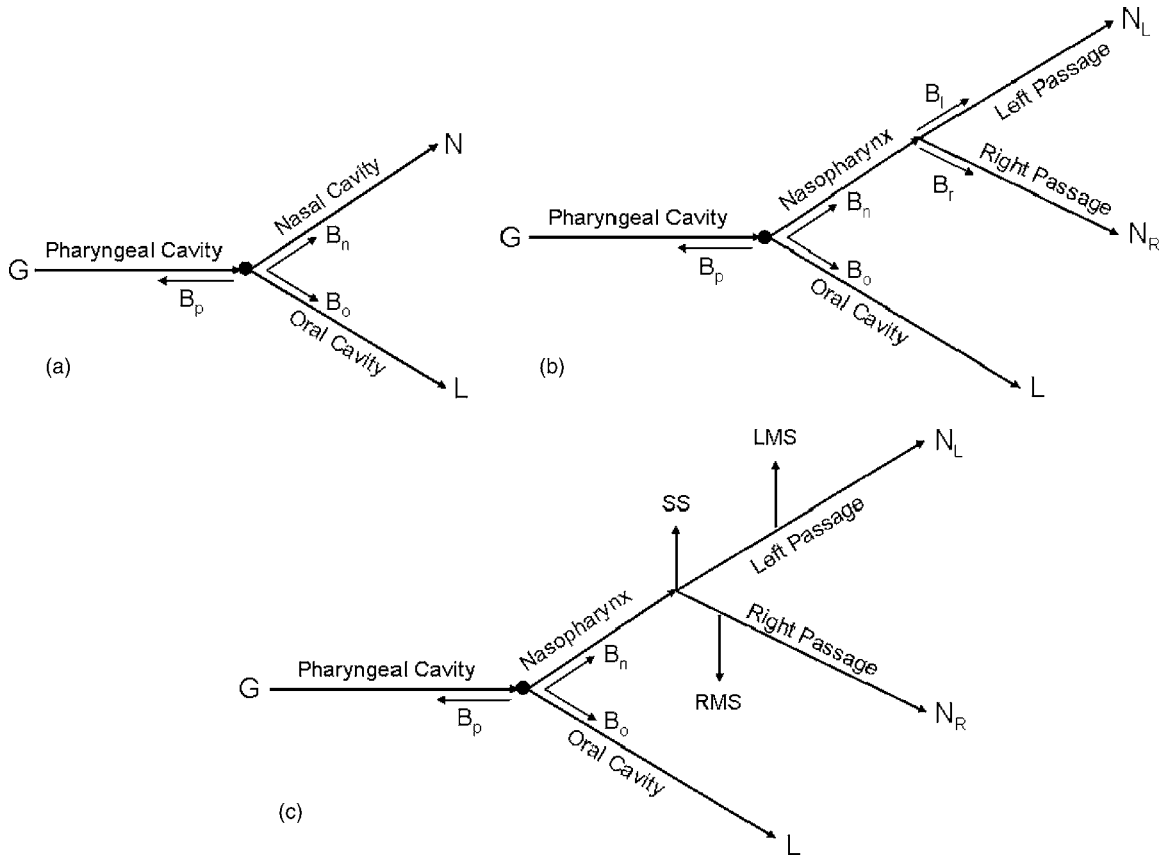

FIG. 3. Structure of the vocal tract model used in this study. (a) Simplified structure used in Sec. IV A, (b) simplified structure used in Sec. IV B, (c) complete structure. G= glottis, L= lips, N= nostrils, N_L= left nostril, N_R= right nostril, RMS= right maxillary sinus, LMS= left maxillary sinus, SS= sphenoidal sinus, B_p= susceptance of the pharyngeal cavity, B_o= susceptance of the oral cavity, B_n= susceptance of the nasal cavity, B_l= susceptance of the left nasal passage, and B_r= susceptance of the right nasal passage. The black dot marks the coupling location.

model shown in Fig. 3(c) is used for simulations in this section.

The nasal cavity data shown in Fig. 1 were combined with the oral cavity data for vowels /i/ and /ɑ/ to obtain the area functions for the nasalized vowels /i/ and /ɑ/. It is assumed that this combination gives an approximate model for nasalized vowels. Two different methods to couple the vocal tract with the nasal tract were considered in this study:

- **Trapdoor coupling method:** The area of the first section of the nasopharynx (of length 0.34 cm) was set to the desired coupling area and no other changes were made to either the areas of the nasopharynx or the areas of the oral cavity. This method of coupling approximates the model used by Fujimura and Lindqvist (1971) where the coupling port is essentially treated as a trap door with variable opening and no effect on the shape of the vocal tract and nasal tract.
- **Distributed coupling method:** The area for the first section of the nasopharynx was set to the desired coupling area and the areas of the rest of the sections of the nasopharynx were linearly interpolated to get a smooth variation in areas (i.e., the coupling was distributed across several sections). The difference between the areas of the sections of the nasopharynx with the given coupling area and the areas of the sections of the nasopharynx with no coupling (0.0 cm^2) was subtracted from the corresponding sections of the oral cavity to model the effect of reduction in the areas of the oral cavity because of the falling velum. This procedure is also illustrated in the flow chart in Fig. 4(a). Figure 4(b) shows an example of the adjusted/new areas of the nasopharynx and the corresponding sections of the oral cavity calculated by this procedure when the coupling area is increased from 0.0 to 1.0 cm^2. Maeda (1982b) and Feng and Castelli (1996) used a similar procedure to model the reduction in oral cavity areas. According to Maeda (1982b), this reduction in the oral cavity area is very important to produce natural sounding nasalized vowels.

In Sec. IV A, both the methods are used for introducing coupling. The coupling areas are varied between 0.0 cm^2 and a maximum value which is limited by the vocal tract area at the coupling location. In the case where the coupling area is equal to the maximum value, the oral cavity is completely blocked off by the velum and sound is output only from the nasal cavity. This maximum value of the coupling area will, henceforth, be referred to as the **maximum coupling area**. Even though this pharyngonasal configuration is interesting in an asymptotic sense (Feng and Castelli, 1996), it should be noted that it is unnatural or nonphysiological in the sense that it would never really happen. A close look at Fig. 1 reveals that although /i/ is more closed than /ɑ/ in the oral

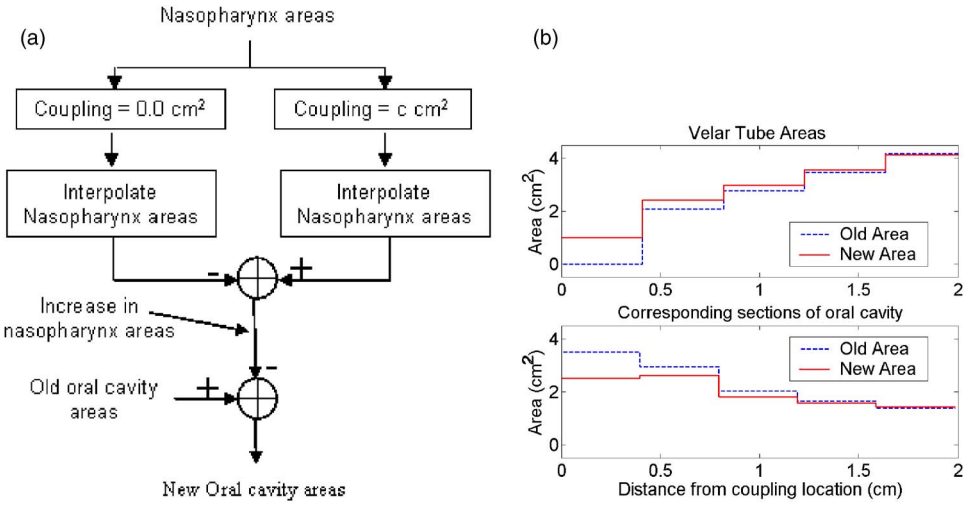

FIG. 4. (Color online) (a) Flow chart of the procedure to get the area functions for the oral and nasal cavity for increase in coupling area, (b) An example to illustrate the changes in nasopharynx areas and areas of corresponding sections of the oral cavity when the coupling area is changed from 0.0 to 1.0 cm^2.

cavity, it is much more open than /ɑ/ at the coupling location. Hence, the possible range of coupling areas is much larger for /i/ than for /ɑ/. Simulations discussed in all other sections of this paper use only the distributed coupling method.

Losses in the vocal tract and nasal tract were not included in the simulations in this work in order to clearly show the effects of each change in terms of poles and zeros. The actual effects of additional poles and zeros introduced into the spectrum due to nasalization might be small because of these losses.

The following convention has been followed throughout the paper: All peaks and dips due to the vocal tract are always referred to as formants and antiformants. All peaks and dips due to the nasal cavity, asymmetrical passages, or the sinuses are referred to as poles and zeros and pole-zero pairs. A set of peaks or dips, some of which are due to the vocal tract and some due to the nasal tract, is also referred to as poles and zeros. This convention has been used partly because in many of the cases, extra peaks and dips due to sinuses and asymmetry may only appear as small ripples in the spectrum because of losses, and because of their proximity to each other. Therefore, it might not be fair to refer to each small ripple as a formant. It must be noted, however, that a peak (dip) in the spectrum is due to a pair of complex conjugate poles (zeros), even though in this paper the pair of complex conjugate poles (zeros) is simply referred to as "pole (zero)." Further, note that the method used to decide whether a peak or a dip is due to either the vocal tract or the nasal tract is described below in Sec. IV A.

IV. VOCAL TRACT MODELING SIMULATIONS

In the simulations below, the effects of the following will be analyzed in detail: (1) Degree of coupling between the nasal cavity and the rest of the vocal tract, (2) asymmetry between the two parallel passages in the nasal cavity, and (3) the Maxillary and Sphenoidal sinuses.

A. Effect of coupling between oral and nasal cavities

Figures 5(a), 5(b), 6(a) and 6(b) show the transfer functions, as calculated by VTAR (see Appendix A for a description of the procedure used to calculate the transfer functions), for the simulated vowels /i/ and /ɑ/ for several different coupling areas. Figure 5 corresponds to the trapdoor coupling method, and Fig. 6 corresponds to the distributed coupling method. The curve for the coupling area of 0.0 cm^2 corresponds to the transfer function of the pharyngeal and oral cavities (from the glottis to the lips) in the absence of any nasal coupling. The curve for the maximum coupling area, as defined in Sec. III, corresponds to the transfer function from the glottis to the nostrils when the oral cavity is completely blocked off by the velum. Note that for the trapdoor coupling method, only the output from the nose is considered for the case of maximum coupling area, even though the oral cavity does not get blocked in this case. Further, note that the transfer functions for the maximum coupling area for the vowels /i/ and /ɑ/ do not match because of differences in the area function of the pharyngeal cavity even though the nasal cavity is approximately the same. The curves for the other coupling areas correspond to the combined output from the lips and the nostrils.

Figures 5(c) and 5(d) show the susceptance plots, as calculated by VTAR (see Appendix A for a description of the procedure used to calculate the susceptance plots), for the combined pharyngeal and oral cavities, $-(B_p+B_o)$, along with the nasal cavity, B_n, for different coupling areas. These, susceptances are calculated by looking into the particular cavity from the coupling location (as illustrated in Fig. 3(a)). As seen in the figures, the susceptance curves have singularities at the frequencies where the corresponding impedance is equal to zero. In Figs. 5(c) and 5(d), B_n and $-(B_p+B_o)$ are plotted for all the coupling areas for which the transfer functions are plotted in Figs. 5(a) and 5(b). With an increase in coupling area, plots for B_n move to the right, while the plot for $-(B_p+B_o)$ does not change since there is no change in the oral and pharyngeal cavity areas. Plots of B_n correspond to areas which vary between the least nonzero coupling area and the maximum coupling area (for, e.g., 0.1–3.51 cm^2 for /i/), since the nasal cavity is completely cut off for 0.0 cm^2 coupling area. Figure 6 gives the same information as Fig. 5 except that Fig. 6 corresponds to the distributed coupling method as described in Sec. III. Thus, in Figs. 6(c) and 6(d), in addition to the movement of the plots of $B_n$to the right, the plots for $-(B_p+B_o)$ move to the left with an increase in the

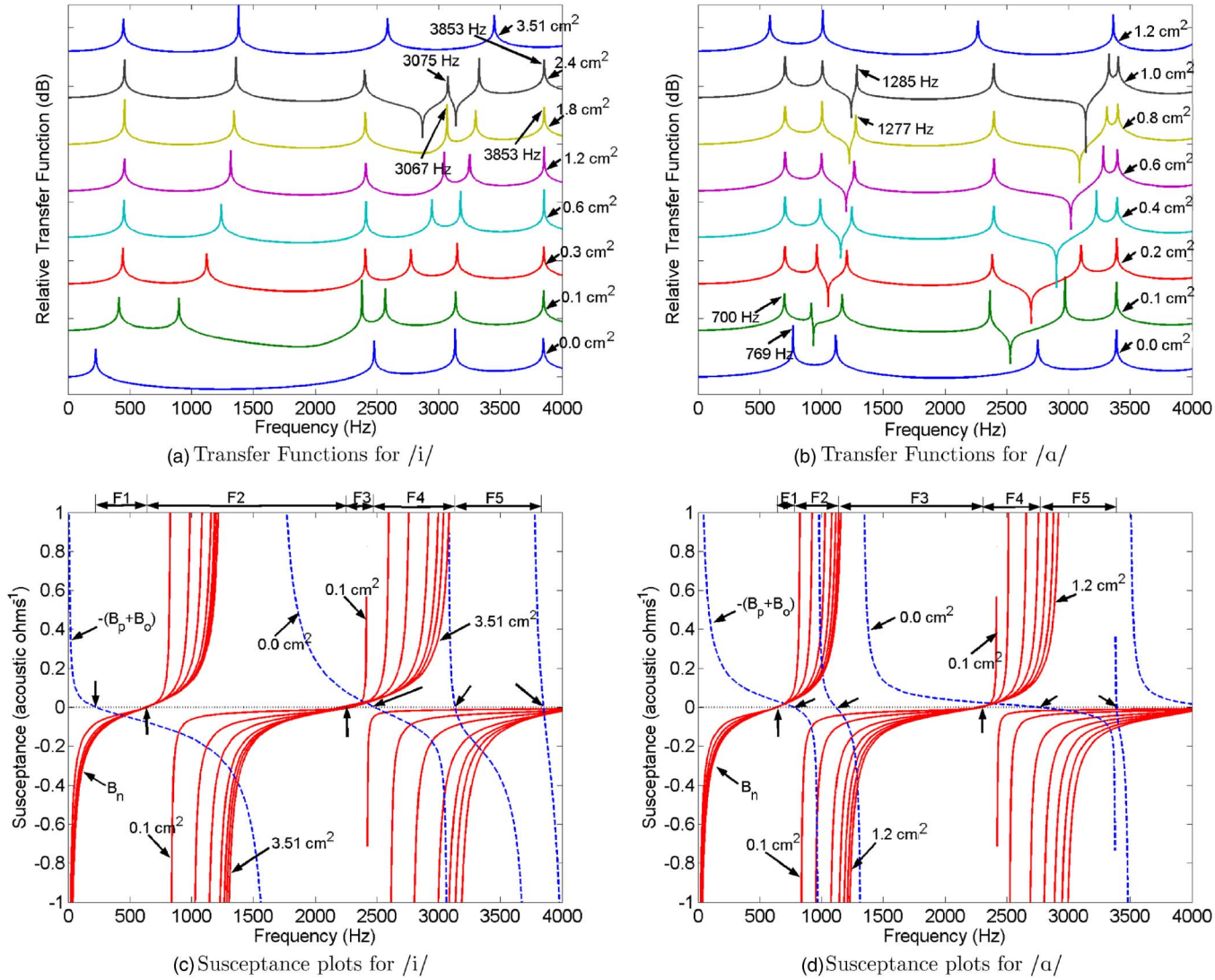

FIG. 5. (Color online) Plots of the transfer functions and susceptances for /i/ and /ɑ/ for the trapdoor coupling method as discussed in Sec. III. (a,b) Transfer functions for different coupling areas, (c,d) plots of susceptances $-(B_p+B_o)$ (dashed) and B_n (solid) for different coupling areas. The arrows above the zero susceptance line mark the frequencies where $B_p+B_o=0$, and the arrows below the zero susceptance line mark the frequencies where $B_n=0$. The markers above the (c) and (d) figures highlight the frequencies between which the different poles can move.

coupling area. The plots for $-(B_p+B_o)$ correspond to areas which vary between 0.0 cm^2 and the second highest coupling area (for, e.g., 0.0–2.4 cm^2 for /i/), since the oral cavity is completely cut off for the maximum coupling area. In Figs. 5(c), 5(d), 6(c) and 6(d) the arrows above the zero susceptance line mark the frequencies where $B_p+B_o=0$. These frequencies are the formant frequencies for the non-nasalized vowels. The arrows below the zero susceptance line mark the frequencies where $B_n=0$. These frequencies are the pole frequencies of the uncoupled nasal cavity. The poles of the combined output from the lips and the nostrils appear at frequencies where the curves for B_n and $-(B_p+B_o)$ intersect (i.e., frequencies where $B_p+B_o+B_n=0$). Note that the frequencies of the poles in Figs. 5(a), 5(b), 6(a) and 6(b) correspond exactly to the frequencies at which the curves for $-(B_p+B_o)$ and B_n for the corresponding coupling areas in 5(c), 5(c), 6(c) and 6(d) respectively intersect.

Let us first consider the trapdoor coupling method. Stevens (1998, page 306), modeled this system as an acoustic mass, $M=\rho\ell_f/A_f$ (where ρ= density of air, l_f= length of the first section, and A_f= area of the first section), in series with the impedance of the fixed part of the nasal cavity, Z_{nf} (see Fig. 7(a)). This lumped approximation is valid until a frequency of 4000 Hz (the maximum frequency in consideration here), because $f=4000\ \text{Hz} \ll (c/\ell_f)=(35{,}000/0.34)=102{,}941$ Hz. Since losses have been removed, the circuit shown in Fig. 7(a) can be solved to obtain

$$B_n = \frac{B_{nf}}{1-\omega B_{nf} M}, \tag{1}$$

where $\omega=2\pi f$ and $B_{nf}=-1/Z_{nf}$. Thus, when $M=\infty$ (that is, the velar port is closed). $B_n=0$, and when $\omega M \ll 1/B_{nf}$, $B_n=B_{nf}$. Further, the zero crossings of B_n do not change with a change in the coupling area, but the singularities of B_n occur at frequencies where $1/B_{nf}=\omega M$. The static nature of the zero crossings can be confirmed in Figs. 5(c) and 5(d). Thus the frequencies of intersections of the susceptance plots

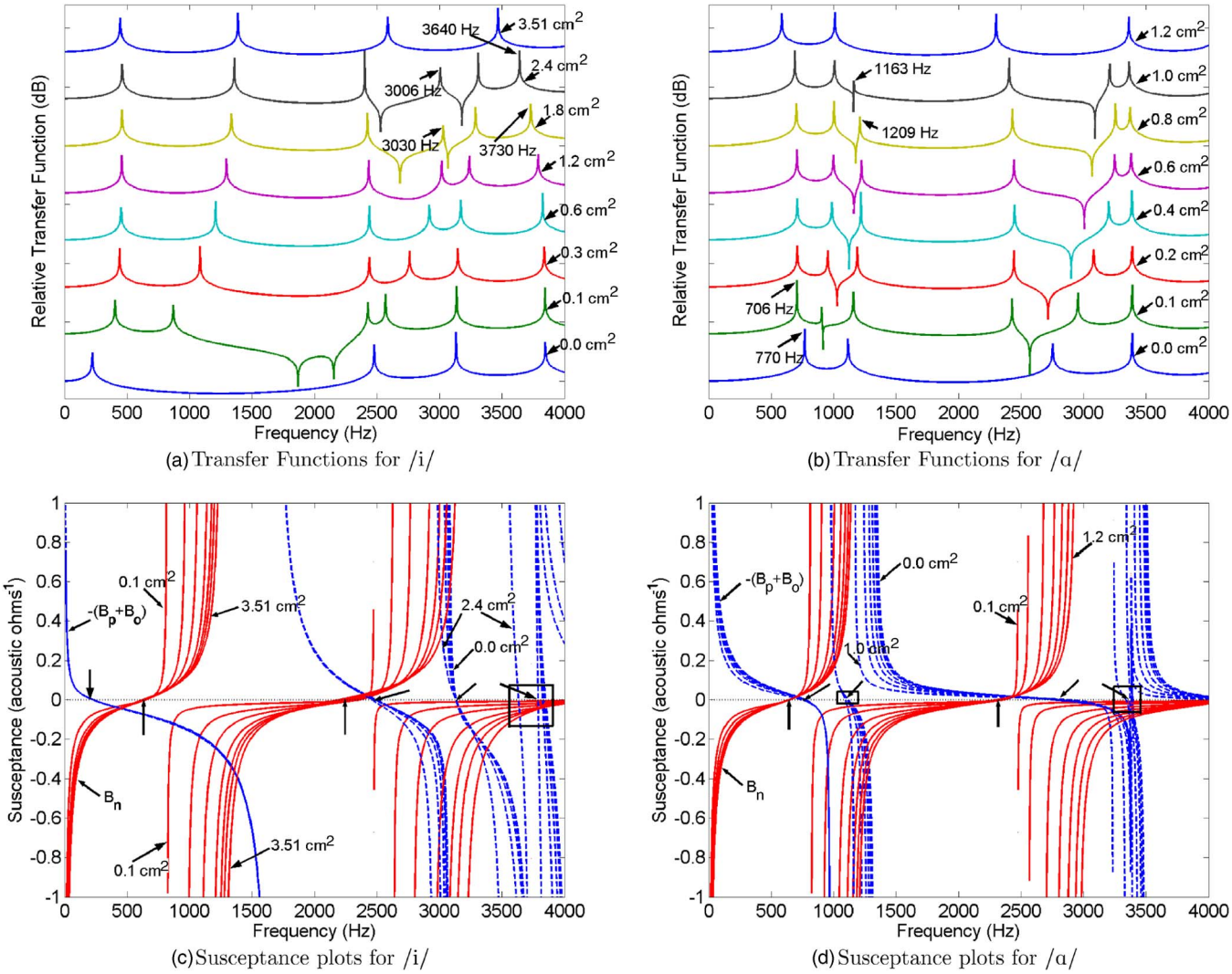

FIG. 6. (Color online) Plots of the transfer functions and susceptances for /i/ and /ɑ/ for the distributed coupling method as discussed in Sec. III. (a,b) Transfer functions for different coupling areas, (c,d) plots of susceptances $-(B_p+B_o)$ (dashed) and B_n (solid) for different coupling areas. The boxed regions highlight the regions where the zero crossings change. The arrows above the zero susceptance line mark the frequencies where $B_p+B_o=0$, and the arrows below the zero susceptance line mark the frequencies where $B_n=0$.

change with the coupling area while the zero crossings remain anchored. A pole in the uncoupled system (decided by the zero crossing of either $-(B_p+B_o)$ or B_n) will move to the frequency of the next intersection of $-(B_p+B_o)$ and B_n in the coupled system. This pole in the coupled system will be referred to as affiliated to the nasal cavity if the pole due to a zero crossing of B_n moved to this frequency, and as affiliated to the vocal tract if a formant due to the zero crossing of $-(B_p+B_o)$ moved to this frequency. For example, in Fig. 5(d), the first pole due to the zero crossing of B_n around 640 Hz moves to approximately 700 Hz in the coupled system, and the pole due to the zero crossing of $-(B_p+B_o)$ around 770 Hz moves to approximately 920 Hz in the coupled system. Thus the zero crossings of the plots for $-(B_p+B_o)$ and B_n determine the order of principle cavity affiliations of the poles in the coupled system. Further, the static nature of the zero crossings, along with the fact that susceptance plots are monotonically increasing functions of frequency, leads to the conclusion that the order of principle cavity affiliations of the poles of the system cannot change with a change in the coupling area (Fujimura and Lindqvist, 1971; Maeda, 1993) because, if for example, the zero crossing of B_n is before the zero crossing of $-(B_p+B_o)$, then the curves for B_n and $-(B_p+B_o)$ would intersect before the zero crossing of $-(B_p+B_o)$.Thus, according to this convention, the order of principle cavity affiliations of the six poles for nasalized /ɑ/ is N, O, O, N, O, and O, where N= nasal cavity, and O= vocal tract (i.e. either oral or pharyngeal cavities). Further

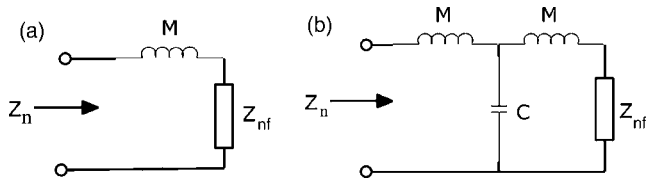

FIG. 7. (a) Equivalent circuit diagram of the lumped model of the nasal cavity. (b) Equivalent circuit diagram of a simplified distributed model of the nasal tract.

$$\frac{dB_n}{dM} = \frac{\omega B_{nf}^2}{(1-\omega B_{nf} M)^2} \geqslant 0, \tag{2}$$

which shows that B_n decreases as M decreases (or coupling area increases) except at frequencies where $B_{nf}=0$ (recall that B_{nf} is a function of f). Since B_n is a monotonically increasing function of frequency except at singularities, Eq. (2) explains the rightward shift of B_n curves with increasing coupling area along with the fact that this shift is not uniform across all frequencies, and it saturates as the coupling area increases (i.e., M approaches zero). Hence, increase in coupling area has the effect of increasing all the pole frequencies (see Figs. 5(a) and 5(b)). Because susceptance plots are monotonically increasing functions of frequency, and the zero crossings are always at the same location, limits can be placed on the movement of each pole. Thus, coupling between two cavities can only cause a pole to move between the frequency location of the zero crossing corresponding to the pole, and the frequency location of the next zero crossing. These limits on pole movements are illustrated by the markers above Figs. 5(c) and 5(d).

The behavior of the susceptance curves described above essentially outlined the rules proposed by Fujimura and Lindqvist (1971) and Maeda (1993, page 150). The rules, however, change for the more realistic case corresponding to the distributed coupling method. This case is shown in Figs. 6(c) and 6(d). The following changes occur for such a case:

- A simplified distributed system model for this case is shown in Fig. 7(b). This model corresponds directly to the lossless transmission line model used for the calculation of susceptance plots by VTAR. Note, however, that this is a simplified model because, in the simulations, several such T sections were concatenated to model the change in velar coupling area since the areas of the whole nasopharynx were changed with a change in the coupling area. In this case, the circuit shown in Fig. 7(b) can be solved to obtain

$$B_n = \frac{B_{nf}(1-\omega^2 MC) + \omega C}{B_{nf}(\omega^3 M^2 C - 2\omega M) - \omega^2 MC + 1}, \tag{3}$$

where $C=(A_f \ell_f)/(\rho c^2)$. This equation shows that the frequencies of both the zero crossings and the singularities of B_n will change with a change in M and C corresponding to a change in coupling area. A similar analysis for B_o leads to the conclusion that a change in the coupling area will lead to a change in the frequencies of the zero crossings and singularities of $-(B_p+B_o)$. The change will be even more prominent when the areas of not just the first section, but the first few sections change with a change in the coupling area. This is clearly evident in the plots for $-(B_p+B_o)$ for both /i/ and /ɑ/ (see the boxed regions in Figs. 6(c) and 6(d)). Further. Eq. (3) also suggests that the change in the zero crossing frequency should be more prominent at higher frequencies which is again evident in the boxed regions in Figs. 6(c) and 6(d). The zero crossing frequency changes by about 200 Hz for /i/ around 3700 Hz, by about 30 Hz for /ɑ/ around 1100 Hz, and by 50 Hz for /ɑ/ around 3400 Hz. This change in the zero crossing frequency also happens for B_n although the change is much less evident in this case.
- In Figs. 6(c) and 6(d), plots of B_n move to the right, and plots of $-(B_p+B_o)$ move to the left with an increase in the degree of coupling. The zero crossings of B_n and $-(B_p+B_o)$ usually fall in frequency with an increase in the degree of coupling, although no consistent pattern was observed across all instances. Nothing, however, seems to suggest that there cannot be a case where the zero crossings of the two susceptance plots might cross over each other. That is, it is possible that while one of the zero crossings of $-(B_p+B_o)$ was below B_n for a particular coupling area, the zero crossing of B_n might be below the zero crossing of $-(B_p+B_o)$ for another coupling area. Therefore, we speculate that there might be cases where the order of principle cavity affiliations (as defined by the convention above) of the poles of the coupled system does change with a change in the coupling area, This change in the order of principle cavity affiliations is especially possible if the zero crossings of B_n and $-(B_p+B_o)$ are close to each other at a high frequency. Hence, the principle cavity affiliations can only be determined from the susceptance plot for that particular coupling area.
- Pole frequencies need not increase monotonically with an increase in coupling area. Pole frequencies may decrease with an increase in the coupling area when the increase in the nasal cavity area is more than compensated by a reduction in the oral cavity area. For example, the fourth formant for the nasalized /i/ in Fig. 6(a) falls from 3030 Hz at a coupling area 1.8 cm^2 to 3006 Hz at a coupling area of 2.4 cm^2 and the sixth formant falls from 3730 Hz at a coupling area of 1.8 cm^2 to 3640 Hz at a coupling area of 2.4 cm^2. Similarly, the third formant for the nasalized /ɑ/ in Fig. 6(b) falls from 1209 Hz at a coupling area of 0.8 cm^2 to 1163 Hz at a coupling area of 1.0 cm^2. This is an example of reduction in the formant frequency because of a change in the cavity configuration. This reduction was also observed by Maeda (1982b). Contrast this with Figs. 5(a) and 5(b) where formant frequencies never decrease.

It must be noted, however, that the very act of introducing coupling to a side cavity (i.e., changing the coupling area from 0.0 cm^2 to a finite value) cannot cause a pole frequency to decrease. That is so because the susceptance plots are monotonically increasing functions of frequency. Hence, introduction of any kind of coupling can only lead to an increase in the pole frequency. If the pole frequency decreases after the introduction of coupling, then it means that the pole at the lower frequency belongs to the side cavity (owing to a lower frequency of zero crossing for the susceptance plot for the side cavity). One such example is the first pole of the nasalized vowel /ɑ/ in Fig. 6(b). Introduction of coupling to the nasal cavity causes a reduction in the frequency of the first pole from 770 Hz at a coupling area of 0.0 cm^2 coupling to 706 Hz at a coupling area of 0.1 cm^2 coupling, because of a switch in the principle cavity affiliation of the first pole from the oral cavity to the nasal cavity. This switch is evident from the susceptance plot for /ɑ/ in Fig. 6(d) which shows the lower frequency of the zero crossing for B_n.

It is clear from Figs. 6(a) and 6(b) that coupling with the nasal cavity introduces significant changes in the spectrum. In the case of /i/, nasal coupling of 0.1 cm^2 introduces two pole-zero pairs between F1 and F2 of the non-nasalized vowel /i/. In the case of /ɑ/, nasal coupling of 0.1 cm^2 introduces a pole below F1, a zero between F1 and F2, and another pole-zero pair between F2 and F3 of the non-nasalized /ɑ/. With an increase in the coupling area, the distance between the nasal pole and zero increases and the nasal poles become more and more distinct. The nasal zero can get closer to an oral formant and reduce it in prominence. The reduction in the prominence of an oral formant is clearly visible for /ɑ/ in Fig. 6(b) at a coupling area of 0.1 cm^2. In this case, the lowest peak in the spectrum is due to a nasal pole. F1 is now around 900 Hz, however it is reduced in amplitude due to the close proximity of the nasal zero (note that in this case, according to the convention proposed above, the lowest pole of the transfer function is interpreted to be a nasal pole, and the weak second pole due to the presence of the zero nearby as the shifted oral F1), and again around 1200 Hz at a coupling area of 1.0 cm^2, when the nasal zero is close to oral F2. The advantage of using the susceptance plots to study the evolution of poles and zeros with changing coupling area is evident here. These plots provide a systematic method to affiliate the poles to the oral/nasal cavities and follow their evolution with changing coupling areas. Without following this convention there would be no way of judging whether the first pole in /ɑ/ is affiliated with the oral cavity or the nasal cavity.

Figure 6(a) shows that, as the coupling area for /i/ is increased from 0.1 to 0.3 cm^2, the two zeros around 2000 Hz seem to disappear, and then reappear at a coupling of 1.8 cm^2. This can be explained by the fact that the nasalized vowel configuration is equivalent to a parallel combination of two linear time variant systems which, in the case of nasalized vowels, have the same denominator. Therefore, at the output, the transfer function of the system from the glottis to the lips, AR_{lip}, will get added to the transfer function of the system from the glottis to the nostrils, AR_{nose}. The net effect of this addition is that the zeros of the resulting combined transfer function may become obscured. Figure 8 shows the plots for AR_{lip} (top plot), AR_{nose} (middle plot), and $AR_{\text{lip}}+AR_{\text{nose}}$ (bottom plot) for a coupling area of 0.3 cm^2 for /i/. This figure shows that even though the top and middle plots have zeros, the bottom plot does not. Thus, no zeros are seen in the log-magnitude transfer function plots for /i/ at a coupling area of 0.3 cm^2.

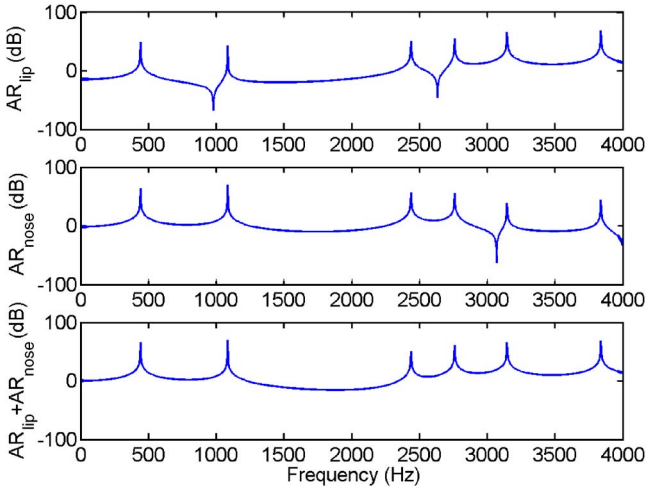

FIG. 8. (Color online) Plots of AR_{lip} (transfer function from the glottis to the lips) (top plot), AR_{nose} (transfer function from the glottis to the nostrils) (middle plot) and $AR_{\text{lip}}+AR_{\text{nose}}$ (bottom plot) at a coupling area of 0.3 cm^2 for vowel /i/.

B. Effect of asymmetry of the left and right nasal passages

When the acoustic wave propagates through two parallel passages, zeros can be introduced in the transfer function because of the following reasons:

- A branching effect, where one of the passages acts as a zero impedance shunt at a particular frequency, thus short circuiting the other passage and introducing a zero in the transfer function of the other passage. A single zero is observed in the combined transfer function of the two passages. The location of this combined zero is in between the frequencies of the zeros of the two passages (Stevens, 1998, page 307).
- A lateral channel effect, which is analogous to the case for /l/. Two kinds of zeros are observed in the transfer function in this case. The first type of zero occurs because of a reversal of phase with comparable magnitudes in the outputs of the two passages due to a difference in the lengths. A difference in the area functions of the two passages because of asymmetry can be treated as being equivalent to a difference in the length. The other type of zero occurs at a frequency corresponding to a wavelength equal to the total length of the two lateral channels (Prahler, 1998; Zhang and Espy-Wilson, 2004).

When the two passages are symmetrical, they can be treated as a single cavity by summing the areas of the two passages since none of the above phenomena would occur for such a case (Prahler, 1998). However, when the two passages are asymmetrical, as will be true generally, the reasons outlined above can lead to the introduction of zeros in the transfer function. It is not reasonable to treat this case as an analogue to the case for /l/ because the two nostrils have different opening areas (as can be seen from Fig. 1), leading to different radiation impedances, and hence, different pressure at the openings. In the case of /l/, the two parallel paths have the same output pressure since the parallel paths combine at the opening (Zhang and Espy-Wilson, 2004). Another important factor is that both the nostrils open into free space, and therefore, there is no more reason to treat them as "lateral channels" than it is to treat the oral and nasal tracts as lateral channels. Thus, it is more reasonable to treat the zero introduced by the asymmetrical nasal passages as being because of the branching effect.

So, the two nasal passages introduce their own zeros at frequencies f_l (frequency at which the susceptance of the right nasal passage $B_r=\infty$), and f_r (frequency at which the susceptance of the left nasal passage $B_l=\infty$). The susceptan-

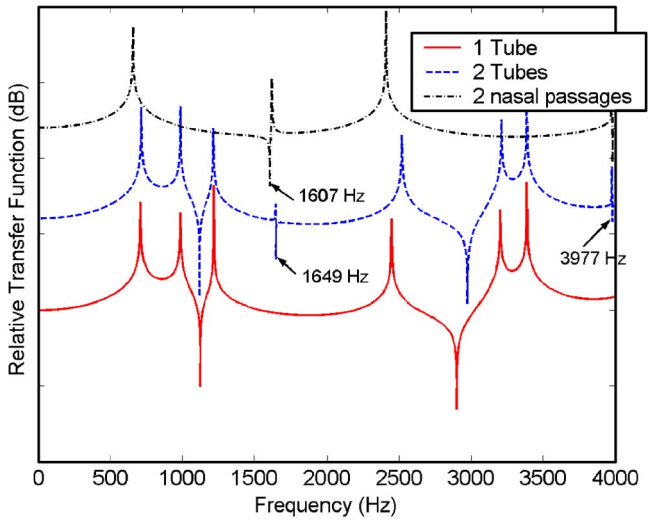

FIG. 9. (Color online) Simulation spectra obtained by treating the two nasal passages as a single tube, and by treating them as two separate passages, for vowel /ɑ/ at a coupling area of 0.4 cm^2. It also shows the transfer function from posterior nares to anterior nares.

ces B_r and B_l are marked in Fig. 3(b). A combined zero (as explained in Stevens (1998, page 307)) will be observed in the combined output of the two nasal passages at frequency f_z given by

$$f_z = f_l \sqrt{\frac{1+\frac{M_l}{M_r}}{1+\left(\frac{f_l}{f_r}\right)^2 \frac{M_l}{M_r}}}, \tag{4}$$

where

$M_{r/l}$ = acoustic mass of the right/left passage

$$= \sum_{\substack{\text{i=all sections of} \\ \text{right/left passage}}} \frac{\rho l_i}{A_i} \tag{5}$$

ρ is the density of air, l_i is the length of the ith section and A_i is the area of the ith section.

Figure 9 shows the transfer functions of the combined vocal tract and nasal tract for the vowel /ɑ/ at a coupling area of 0.4 cm^2, obtained by combining the left and right nasal passages into a single tube of area equal to the sum of the areas of the two tubes, and by treating the left and right passages as two different tubes. The transfer function plots show that the use of two tubes instead of one for the two asymmetrical nasal passages leads to the introduction of additional pole-zero pairs around 1649 Hz and around 3977 Hz. This figure also shows the combined transfer function of just the two nasal passages from the posterior nares to the anterior nares. The location of the first zero in this transfer function is 1607 Hz. Values of f_r and f_l were determined to be 1429 and 1851 Hz, respectively, from the susceptance plots of B_l and B_r. Further, from our calculations $M_l = 0.005\,653$ and $M_r = 0.006\,588$. Using these values in the formula above gives $f_z = 1615$ Hz which is close to the value (i.e., 1607 Hz) obtained from the simulated transfer function. Dang *et al.* (1994) observed the introduction of zeros around 2–2.5 KHz due to two asymmetrical nasal passages.

C. Effect of paranasal sinuses

Figures 10(a) and 10(b) show the transfer functions of the vocal tract with successive addition of the two asymmetrical nasal passages and the right maxillary sinus (RMS), left maxillary sinus (LMS) and SS to highlight the changes in the transfer functions of the nasalized vowels /i/ and /ɑ/ with every addition of complexity to the nasal cavity. The topmost curves in Figs. 10(a) and 10(b) show the transfer functions with all the complexity due to the sinuses and the asymmetrical passages added in. These curves correspond to the model shown in Fig. 3(c). Figures 10(c) and 10(d) show the susceptance plots corresponding to the topmost curves in Figs. 10(a) and 10(b), respectively. A comparison of the B_n curves in Figs. 10(c) and 10(d) with the B_n curves in 6(c) and 6(d) reveals the presence of four extra zero crossings in the B_n curves in Figs. 10(c) and 10(d), thus leading to four extra poles in the transfer function of the uncoupled nasal cavity, one each due to RMS, LMS, SS and the asymmetrical nasal passages. It must be noted that, in reality, the curves of B_n would be even more complicated since the human nasal cavity has eight paranasal sinuses (four pairs) whereas only three have been accounted for here. However, the effects of most of these extra, pole-zero pairs may be small in real acoustic spectra because of the proximity of poles and zeros, and because of losses.

Figures 10(a) and 10(b) clearly show that one extra pole-zero pair appears in the transfer functions of the nasalized vowels /i/ and /ɑ/ with the addition of every sinus. For /i/ the poles are at 580, 664, and 1538 Hz, and for /ɑ/ the poles are at 451, 662, and 1537 Hz for RMS, LMS and SS, respectively. The corresponding zeros are at 647, 717, and 1662 Hz for /i/ and 540, 665, and 1531 Hz for /ɑ/. Note that the pole frequencies due to the sinuses are different for the two vowels because the pole frequencies are decided by the locations where $B_n = -(B_p + B_o)$, and both B_p and B_o are different for the two vowels (see Figs. 10(c) and 10(d)). The pole frequencies due to the sinuses will also change with a change in the coupling area, since, a change in the coupling area corresponds to a change in both B_n and B_o. This observation is in contrast to Stevens (1998, page 306) where it was suggested that sinuses introduce fixed-frequency prominences in the nasalized vowel spectrum. The surprising observation, however, is that even the frequencies of the zeros due to the sinuses in the combined output of the oral and nasal cavities change. The change in the frequencies of the zeros is surprising because sinuses have always been thought of as Helmholtz resonators, branching off from the nasal cavity, which would introduce fixed pole-zero pairs in the nasal vowel spectrum (Dang and Honda, 1996; Dang *et al.*, 1994; Maeda, 1982b; Stevens, 1998). A plausible explanation is as follows:

Consider Fig. 11 which shows a simplified model of the vocal tract and nasal tract. In this figure, the nasal cavity is modeled as a single tube with only one side branch due to a sinus cavity. In this system both U_o/U_s and U_n/U_s will have the same poles (given by frequencies where $B_n = -(B_p + B_o)$),

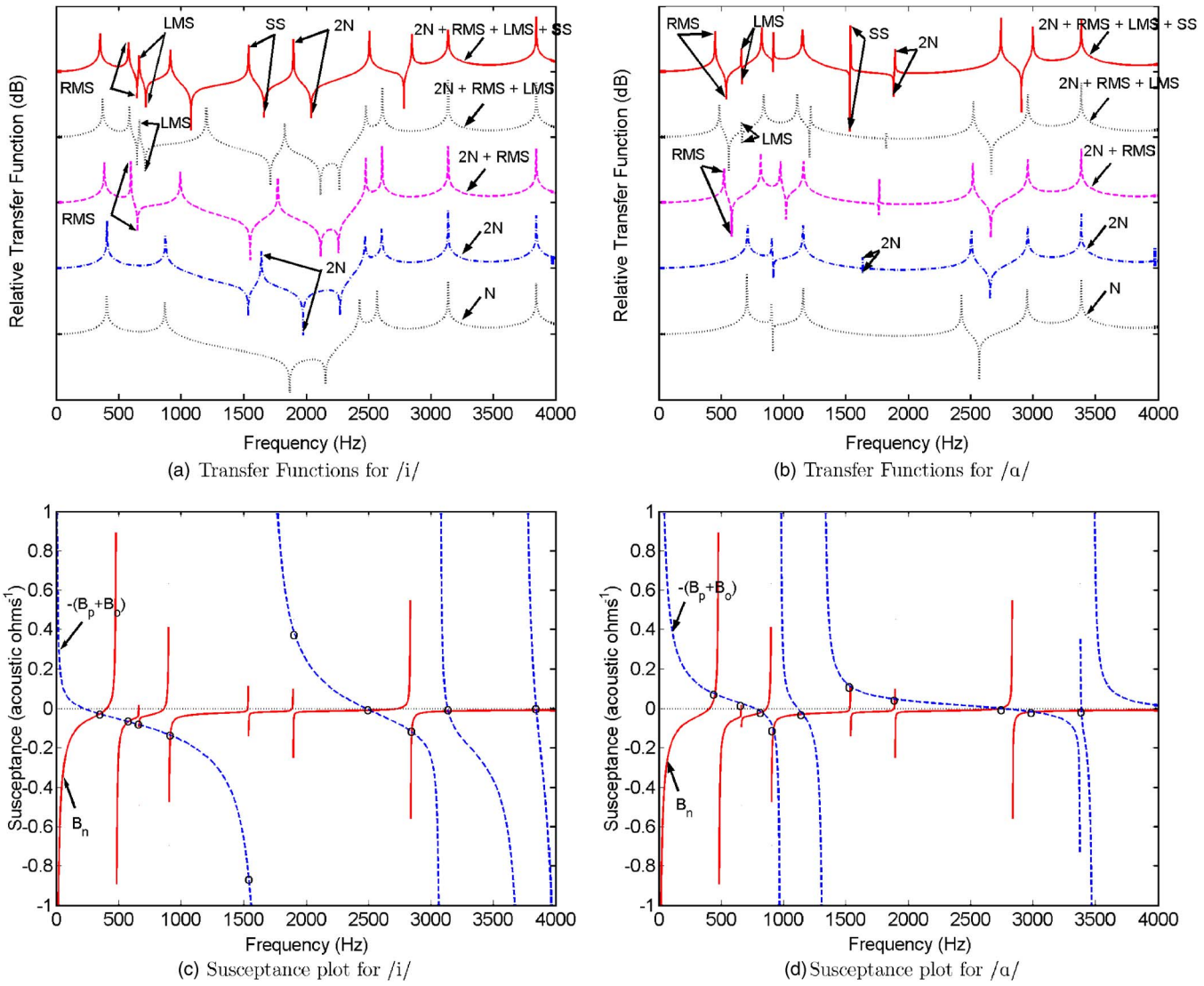

FIG. 10. (Color online) Plots for /i/ and /ɑ/ at a coupling of 0.1 cm^2. (a,b) Transfer functions with successive addition of the asymmetrical nasal passages and the sinuses (N= Nasal Cavity where the areas of the two asymmetrical nasal passages are added and they are treated as a single combined tube, 2N=2 Nasal passages, RMS= right maxillary sinus, LMS= left maxillary sinus, SS= sphenoidal sinus), (c,d) plots of $-(B_p+B_o)$ (dashed) with B_n (solid) for /i/ and /ɑ/ when all the sinuses are included. o's mark the locations of the poles for the coupled system.

but different zeros. Zeros in the transfer function U_o/U_s occur at frequency f_n at which $B_n=\infty$, and zeros in the transfer function U_n/U_s occur at frequency f_o at which $B_o=\infty$, and at frequency f_s at which the susceptance of the side cavity $B_s=\infty$. Then the overall transfer function $T(s)=(U_o+U_n)/U_s$ is given by

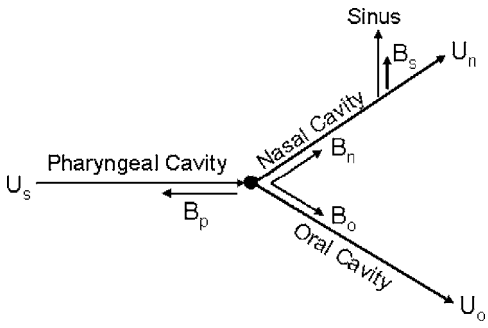

FIG. 11. An illustration to explain the reason for the movement of zeros in the combined transfer function $(U_o+U_n)/U_s$. The black dot marks the coupling location.

$$T(s)=a\frac{(s-s_n)(s-s_n^*)}{s_n s_n^*}P(s)+(1-a)\times\frac{(s-s_o)(s-s_o^*)(s-s_s)(s-s_s^*)}{s_o s_o^* s_s s_s^*}P(s), \quad (6)$$

where $s_n=j2\pi f_n$, $s_o=j2\pi f_o$, $s_s=j2\pi f_s$ and $P(s)$ is an all-pole component that is normalized so that $P(s)=1$ for $s=0$. Further, $a=M_n/(M_o+M_n)$, where M_n is the acoustic mass of the nasal cavity and M_o is the acoustic mass of the oral cavity as marked in Fig. 11 (note that other than the addition of a zero due to the sinus, this analysis is similar to that presented in Stevens (1998, page 307)). Equation (6) shows that the frequencies of the zeros in $T(s)$ will change with a change in either s_n, s_o, or s_s. Note that, s_o and s_n will change with a change in the oral cavity and nasal cavity area functions, respectively. A change in the oral cavity area function can either be due to a change in the vowel being articulated, or due to a change in the velar coupling area. A change in the nasal cavity area function can be due to a change in the velar

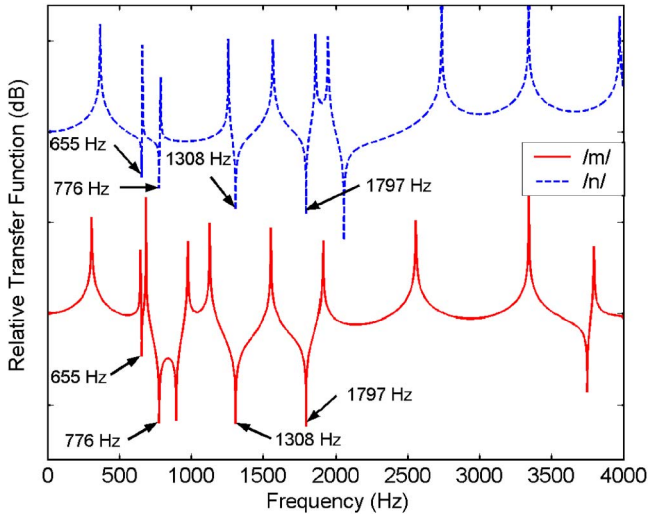

FIG. 12. (Color online) Transfer functions for nasal consonants /m/ (solid, at a coupling area of 1.04 cm^2) and /n/ (dashed, at a coupling area of 1.2 cm^2) showing the invariance of zeros due to the sinuses and the asymmetrical nasal passages. The zero frequencies are 665 Hz (RMS), 776 Hz (LMS), 1308 Hz (SS) and 1797 Hz (asymmetrical passages).

coupling area. The important point here is that even though the sinuses themselves are static structures, what we observe at the microphone is the combined output of the oral and nasal cavities, and the effective frequencies of the zeros due to the sinuses in this combined output can change with a change in the configuration of the oral and nasal cavities. Given this, it would not be correct to say that the effect of the sinus cavities is constant for a particular speaker. Therefore, although the configuration and area functions of the sinuses may be unique for every speaker, the acoustic effects of the sinus cavities on nasalized vowels may not be a very good cue for speaker recognition.

Equation (6), however, also implies that if the output from only one of the cavities, say the nasal cavity, was observed, then the frequencies of the zeros due to the sinuses in the nasal cavity output will be static as long as there is no change in the area function of the sinuses themselves. Therefore, it can be concluded that the frequencies of the zeros due to the sinuses in the nasal consonant spectra will not change regardless of the area functions of the nasal cavity and the oral side branch. The invariance in the frequencies of the zeros due to the sinuses for the nasal consonants is confirmed in Fig. 12 which plots the calculated transfer functions for the nasal consonants /m/ and /n/. The pole locations will still be different depending on the configuration of the vocal tract, and the antiformant due to the oral cavity will also change depending on which nasal consonant is being articulated (see Fig. 12). Thus, for the case of nasal consonants, the acoustic effects of the sinus cavities may be a much more robust cue for speaker recognition. A more detailed study of the implications of this result for speaker recognition was presented in Pruthi and Espy-Wilson (2006). The power spectrum during the nasal consonants was, in fact, used by Glenn and Kleiner (1968) for the purposes of speaker recognition. Using a simple procedure, they were able to obtain an accuracy of 93% for 30 speakers.

Note that Eq. (6) would become much more complicated if terms due to all the other sinuses are added to it. However, the argument presented above is still applicable. Further, this analysis is also directly applicable to the zero due to the asymmetrical nasal passages in the combined output of the oral and nasal cavities. The frequency of this zero in the combined output of the oral and nasal cavities would change with a change in the oral cavity configuration for nasalized vowels, and would not change for nasal consonants (see Figs. 10(a), 10(b), and 12). The analysis presented in Sec. IV B would still remain valid if the sinuses are added in to the model. The only change would be that the frequency location of the zero due to the asymmetrical nasal passages would now be governed by a much more complicated equation of the form of Eq. (6). Further, the analysis for changes in velar coupling areas presented in Sec. IV A would also remain valid, except that B_n would now be a lot more complicated than the B_n shown in Figs. 6(c) and 6(d).

As discussed in Sec. IV A, the principle cavity affiliation of each pole for a particular coupling area can only be determined from the susceptance plot for that particular coupling area. Thus, for the case shown in Fig. 10, the principle cavity affiliations for /i/ are O, N, N, N, N, N, O, N, O, O and the principle cavity affiliations for /ɑ/ are N, N, O, N, O, N, N, N, O, O. Note that, in Fig. 10(c) around 2500 Hz, the zero crossing of $-(B_p+B_o)$ occurs at a lower frequency than the zero crossing of B_n, and in Fig. 10(d) around 2700 Hz, the zero crossing of B_n occurs at a lower frequency than the zero crossing of $-(B_p+B_o)$. This means that in the case of nasalized /i/, the oral F2 always stays around 2500 Hz, and the extra nasal pole moves to 3000 Hz, whereas in the case of nasalized /ɑ/, the oral F3 moves to a frequency around 3000 Hz.

As observed by Chen (1995, 1997), we also find an extra pole due to nasal coupling in the 1000 Hz region. However, this does not mean that that this pole will always be in the vicinity of 1000 Hz since its location can change significantly with a change in the coupling at-area. In the simulations here, this pole was found to go as high as 1300 Hz in frequency for large coupling areas (see Fig. 6(a)). Thus using the amplitude of the highest peak harmonic around 950 Hz as an acoustic cue to capture the extra pole, as proposed by Chen (1995, 1997), might not be appropriate.

In the simulations here, the zeros due to MS were found to be in the range of 620–749 Hz, and the zeros due to SS were found to be in the range of 1527–1745 Hz. These values correspond well with the zero frequencies found by Dang and Honda (1996) which were in the range of 400–1100 Hz for MS, and 750–1900 Hz for SS.

V. GENERAL DISCUSSION

The above analysis has provided critical insight into the changes brought about by nasalization. Listed below are the acoustic changes that have been shown to accompany nasalization, and the reasons behind those changes from the point of view of knowledge gained in this study.

- **Extra poles and zeros in the spectrum**: Several researchers in the past have reported the introduction of extra poles and zeros in the spectrum as the most important and con-

sistent acoustic correlate of nasality (Fant, 1960; Fujimura and Lindqvist, 1971; Hattori *et al.*, 1958; Hawkins and Stevens, 1985; House and Stevens, 1956). Simulations in this study have shown that extra pole-zero pairs are introduced in the spectrum of a nasalized vowel because of (1) coupling between the vocal tract and the nasal tract, (2) asymmetry between the left and right passages of the nasal tract, and (3) the sinuses branching off from the nasal cavity walls. These pole-zero pairs move with a change in the coupling area, and the prominence of an extra pole for a particular coupling area depends on the frequency difference between the pole and an adjacent zero. Previous research has shown that the most prominent effects of these poles are in the first formant region. Hawkins and Stevens (1985) suggested that a measure of the degree of prominence of the spectral peak in the vicinity of the first formant was the basic acoustic property of nasality. It has also been suggested that the low frequency prominence characteristic of nasalized vowels is due to the sinuses (Chen, 1997; Dang and Honda, 1995; Lindqvist-Gauffin and Sundberg, 1976; Maeda, 1982b). Simulations presented above support these views by confirming that the most important change for /i/ is the appearance of the extra nasal pole around 1000 Hz, and for /ɑ/ it is the extra pole below 500 Hz due to MS.

- **F1 amplitude reduction**: Reduction in the amplitude of F1 with the introduction of nasalization has been reported in the past by Fant (1960) and House and Stevens (1956). The above analysis has shown that this effect should be expected more for the case of low vowels than for high vowels; the reason being that for low vowels, the sinus pole can occur below the first formant. With an increase in coupling, the pole-zero pair due to the sinus begins to separate, and as the zero gets closer to F1, the amplitude of F1 falls. For high vowels, however, if the pole-zero pair due to the MS is above F1, then an increase in coupling would only move the zero due to the sinus to a higher frequency, and thus, further awav from F1. This observation supports the view offered by Stevens *et al.* (1987) where it was suggested that the main reason behind the reduction of F1 amplitude was the presence of the nasal zero, not the increase in the bandwidth of poles.
- **Increase in bandwidths**: An increase in F1 and F2 bandwidths has also been cited as a cue for nasalization (Fant, 1960; House and Stevens, 1956). It has been confirmed by simulations that an increase in losses in the nasal cavity has little effect on the bandwidth of formants affiliated with the oral/pharyngeal cavities. Therefore, the bandwidths of all poles need not increase with the introduction of nasalization. However, the poles belonging to the nasal cavity would have higher bandwidths due to higher losses in the nasal cavity because of soft walls and a larger surface area. The bandwidths of other formants might appear to be higher because of an unresolved extra pole lying close by.
- **Spectral flatness at low frequencies**: Maeda (1982c) suggested that a flattening of the nasalized vowel spectra in the range of 300–2500 Hz was the principal cue for nasalization. We now know that the introduction of a large number of extra poles leads to the filling up of valleys between regular oral formants, and the larger prominence of extra poles in the first formant region leads to the spectral flatness effect being more prominent at low frequencies.
- **Movement of the low frequency center of gravity towards a neutral vowel configuration**: Arai (2004), Beddor and Hawkins (1990), Hawkins and Stevens (1985), and Wright (1986) noted a movement in the low frequency center of gravity towards a neutral vowel configuration with nasalization. The analysis above has shown that this effect should be expected both for low and high vowels, since, for low vowels extra poles are introduced below F1, and for high vowels the extra poles above F1 increase in prominence with nasalization. The extra poles would cause the low frequency center of gravity for low vowels to decrease and for high vowels to increase.
- **Reduction in the overall intensity of the vowel**: House and Stevens (1956) observed an overall reduction in the amplitude of the vowel. This reduction is most likely due to the presence of several zeros in the nasalized vowel spectrum as shown in the simulations above.
- **Shifts in pole frequencies**: It must be remembered that the nasal cavity is a large and complicated cavity, and also gives a volume velocity output. Therefore, even a tiny amount of coupling between the oral and nasal cavities can introduce large changes in the spectrum. Poles can suddenly switch their affiliation from the oral cavity to the nasal cavity. Thus, some of the prominent poles might now be affiliated with the nasal cavity instead of the oral cavity. It might as well be these nasal poles which seem to be moving in frequency as the degree of coupling is changed. Further, this effect need not be limited only to the low frequency poles. As seen in the simulations in this study, even F2 and F3 might also change significantly. Such shifts in formant frequencies have been observed in the past by Bognar and Fujisaki (1986), Dickson (1962) and Hawkins and Stevens (1985).

VI. SUMMARY AND CONCLUSIONS

This paper analyzed in detail the three most important sources of acoustic variability in the production of nasalized vowels: velar coupling area, asymmetry of nasal passages, and the sinuses. This analysis was based on real anatomical data, obtained by imaging the vocal tract of one American English speaker using MRI. Area functions obtained from the MRI data clearly show significant asymmetry between the left and right nasal passages, and the left and right maxillary sinuses of this speaker. A computer vocal tract model called VTAR (Zhang and Espy-Wilson, 2004) was used to simulate the spectra for nasalized vowels based on these area functions. A simple extension to VTAR to calculate susceptance plots was proposed and implemented for this study. These susceptance plots have been used extensively in this study to understand the introduction and the movement of poles with changes in the velar coupling area.

The susceptance plots were also used to propose a systematic method to affiliate the poles to either the nasal tract or the vocal tract (similar to Fujimura and Lindqvist (1971))

to follow their evolution with changing velar coupling areas. Analysis of pole movements with changing coupling area showed that the rules concerning the behavior of the poles of the transfer function (as proposed by Fujimura and Lindqvist (1971) and Maeda (1993)) change when a realistic model is assumed for velar coupling. Specifically, it was shown that: (1) the frequency of zero crossings of the susceptance plots changes with a change in the coupling area, and (2) pole frequencies need not shift monotonically upwards with an increase in coupling area. Further, as a consequence of (1), there could be cases where the order of principle cavity affiliations (as defined in this study) of the poles of the coupled system change.

Analysis using two asymmetric nasal passages showed that asymmetry between the left and right nasal passages introduces extra pole-zero pairs in the spectrum due to the branching effect where one of the passages acts as a zero impedance shunt, thus short circuiting the other passage and introducing a zero in the transfer function of the other passage. This result is in agreement with Dang *et al.* (1994). The exact location of the zero in the combined output of the two passages obtained through simulations was found to be a good match with the theoretical frequency calculated by assuming the distribution of the volume velocity into the two passages in a ratio of the acoustic mass of the two passages (as proposed in Stevens (1998, page 307)).

Simulations with the inclusion of maxillary and sphenoidal sinuses showed that each sinus can potentially introduce one pole-zero pair in the spectrum (maxillary sinuses produced the poles lowest in frequency), thus confirming the results of Dang and Honda (1996). The effective frequencies of these poles and zeros due to the sinuses in the combined output of the oral and nasal cavities change with a change in the oral cavity configuration for nasalized vowels. This change in the oral cavity configuration may be due to a change in the coupling area, or due to a change in the vowel being articulated. Thus, it was predicted that even if there was a way to find the frequencies of zeros due to sinuses, it would not be correct to use the effects of sinuses in the nasalized vowel regions as a cue for speaker recognition, although the anatomical structure of the sinuses might be different for every speaker. At the same time, it was also shown that the locations of zeros due to the sinuses will not change in the spectra of nasal consonants regardless of the area functions of the nasal cavity and the oral side branch. Hence, the effects of sinuses can be used as a cue for speaker recognition in the nasal consonant regions. A more detailed study of the application of the acoustic effects of sinus cavities to speaker recognition has been presented in Pruthi and Espy-Wilson (2006).

ACKNOWLEDGMENTS

We wish to thank the anonymous reviewers and Thomas Baer for their helpful comments on an earlier version of this manuscript. We would also like to thank Osamu Fujimura for valuable discussions on some of the issues presented in the paper. This work was supported by NSF Grant No. BCS0236707.

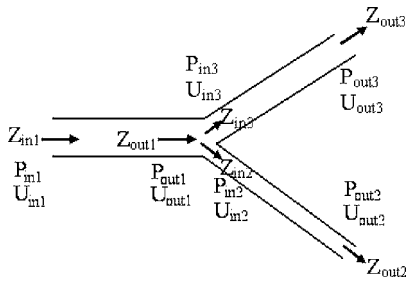

FIG. 13. An illustration to show the procedure to calculate the transfer functions and susceptance plots.

APPENDIX A: PROCEDURE TO CALCULATE THE SUSCEPTANCE PLOTS AND THE TRANSFER FUNCTIONS

The susceptance plots and the transfer functions shown in this work have been obtained using a model of the vocal tract called VTAR (Zhang and Espy-Wilson, 2004). A brief description is as follows:

The input and output pressures (p_{in} and p_{out}) and volume velocities (U_{in} and U_{out}) of a section of the vocal tract are related by the transfer matrix

$$\begin{bmatrix} p_{in} \\ U_{in} \end{bmatrix} = \begin{bmatrix} A & B \\ C & D \end{bmatrix} \begin{bmatrix} p_{out} \\ U_{out} \end{bmatrix}, \tag{A1}$$

where A, B, C, and D depend on the properties of the air and the vocal tract walls and can be calculated by using the transmission-line model (as shown in Zhang and Espy-Wilson (2004)). The transfer function can then be calculated as

$$\frac{U_{out}}{U_{in}} = \frac{1}{CZ_{out} + D}, \tag{A2}$$

where $Z_{out} = p_{out}/U_{out}$. The impedance at a point in the vocal tract can be obtained as a by-product of the transfer function calculation. Hence,

$$Z_{in} = \frac{p_{in}}{U_{in}} = \frac{AZ_{out} + B}{CZ_{out} + D}. \tag{A3}$$

Every branch constitutes a parallel path. Therefore, $Z_{out1} = 1/(1/Z_{in2} + 1/Z_{in3})$ (see Fig. 13). Further, a branch coupling matrix can be used to relate the state variables cross the branching point. Therefore, for Fig. 13

$$\begin{bmatrix} p_{out1} \\ U_{out1} \end{bmatrix} = \begin{bmatrix} 1 & 0 \\ 1/Z_{in3} & 1 \end{bmatrix} \begin{bmatrix} p_{in2} \\ U_{in2} \end{bmatrix} \tag{A4}$$

and

$$\begin{bmatrix} p_{out1} \\ U_{out1} \end{bmatrix} = \begin{bmatrix} 1 & 0 \\ 1/Z_{in2} & 1 \end{bmatrix} \begin{bmatrix} p_{in3} \\ U_{in3} \end{bmatrix}, \tag{A5}$$

where Z_{in2} and Z_{in3} are obtained as shown in Eq. (A3). Thus, the impedance and transfer function at any point in the vocal tract can be found by starting at the output and successively considering each section of the vocal tract without any branches, finding Z_{in}, U_{in} and p_{in} for that section, adding the parallel contribution of any branches, and proceeding in that manner to obtain the required input impedance and the trans-

fer function from the input to that particular output. This procedure can, therefore, be used to obtain Z_{in1}, Z_{in2}, Z_{in3}, U_{out2}/U_{in1} and U_{out3}/U_{in1}. The susceptance B is equal to the imaginary part of the inverse of impedance Z (i.e., the admittance). Thus, plotting the values of impedance/susceptance and the transfer function with respect to frequency generates the impedance/susceptance and the transfer function plots.

To generate good impedance/susceptance plots, losses in the model need to be removed. Losses in the model can be removed by removing the resistive elements from the circuit, which can be achieved by assuming zero resistance due to flow viscosity, zero heat conduction, and infinite wall resistance to remove the loss due to wall vibrations. It should also be noted that for this lossless case,

$$B_{in} = \frac{1}{Z_{in}} = \frac{U_{in}}{p_{in}} = \frac{CZ_{out} + D}{AZ_{out} + B}, \tag{A6}$$

where the susceptance $B_{in}=\infty$ if either $CZ_{out}+D=\infty$ or $AZ_{out}+B=0$. Thus, Eqs. (A2) and (A6) also show that the transfer function does not necessarily have zeros when $B_{in}=\infty$. The transfer function will, however, have zeros when $CZ_{out}+D=\infty$.

Alwan, A., Narayanan, S., and Haker, K. (**1997**). "Toward articulatory-acoustic models for liquid approximants based on MRI and EPG data. Part II. The rhotics," J. Acoust. Soc. Am. **101**(2), 1078–1089.

Arai, T. (**2004**). "Formant shifts in nasalization of vowels," J. Acoust. Soc. Am. **115**(5), 2541.

Baer, T., Gore, J. C., Gracco, L. C., and Nye, P. W. (**1991**). "Analysis of vocal tract shape and dimensions using magnetic resonance imaging: Vowels," J. Acoust. Soc. Am. **90**(2), 799–828.

Beddor, P. S. (**1993**). *Phonetics and Phonology: Nasals, Nasalization and the Velum*, (Academic, New York), Chapter on The perception of nasal vowels, pp. 171–196.

Beddor, P. S., and Hawkins, S. (**1990**). "The influence of spectral prominence on perceived vowel quality," J. Acoust. Soc. Am. **87**(6), 2684–2704.

Bognar, E., and Fujisaki, H. (**1986**). "Analysis, synthesis and perception of French nasal vowels," *Proceedings of ICASSP*, Tokyo, pp. 1601–1604.

Chen, M. Y. (**1995**). "Acoustic parameters of nasalized vowels in hearing-impaired and normal-hearing speakers," J. Acoust. Soc. Am. **98**(5), 2443–2453.

Chen, M. Y. (**1997**). "Acoustic correlates of English and French nasalized vowels," J. Acoust. Soc. Am. **102**(4), 2360–2370.

Dang, J., and Honda, K. (**1995**). "An investigation of the acoustic characteristics of the paranasal cavities," in *Proceedings of the XIIIth International Congress of Phonetic Sciences*, Stockholm, pp. 342–345.

Dang, J., and Honda, K. (**1996**). "Acoustic characteristics of the human paranasal sinuses derived from transmission characteristic measurement and morphological observation," J. Acoust. Soc. Am. **100**(5), 3374–3383.

Dang, J., Honda, K., and Suzuki, H. (**1994**). "Morphological and acoustical analysis of the nasal and the paranasal cavities," J. Acoust. Soc. Am. **96**(4), 2088–2100.

Dickson, D. R. (**1962**). "Acoustic study of nasality," J. Speech Hear. Res. **5**(2), 103–111.

Fant, G. (**1960**). *Acoustic Theory of Speech Production* (Mouton, The Hague, Netherlands).

Feng, G., and Castelli, E. (**1996**). "Some acoustic features of nasal and nasalized vowels: A target for vowel nasalization," J. Acoust. Soc. Am. **99**(6), 3694–3706.

Fujimura, O., and Lindqvist, J. (**1971**). "Sweep tone measurements of vocal-tract characteristics," J. Acoust. Soc. Am. **49**(2), 541–558.

Glenn, J. W., and Kleiner, N. (**1968**). "Speaker identification based on Nasal phonation," J. Acoust. Soc. Am. **43**(2), 368–372.

Hattori, S., Yamamoto, K., and Fujimura, O. (**1958**). "Nasalization of vowels in relation to nasals," J. Acoust. Soc. Am. **30**(4), 267–274.

Hawkins, S., and Stevens, K. N. (**1985**). "Acoustic and perceptual correlates of the non-nasal-nasal distinction for vowels," J. Acoust. Soc. Am. **77**(4), 1560–1575.

Hoffman, E. A., Gnanaprakasam, D., Gupta, K. B., Hoford, J. D., Kugelmass, S. D., and Kulawiec, R. S. (**1992**). "VIDA: An environment for multidimensional image display and analysis," Proc. SPIE **1660**, 694–711.

House, A. S., and Stevens, K. N. (**1956**). "Analog studies of the nasalization of vowels," J. Speech Hear Disord. **21**(2), 218–232.

Lindqvist-Gauffin, J., and Sundberg, J. (**1976**). "Acoustic properties of the nasal tract," Phonetica **33**(3), 161–168.

Maeda, S. (**1982b**). "The role of the sinus cavities in the production of nasal vowels," in *Proceedings of ICASSP*, Paris, Vol. **2**, pp. 911–914.

Maeda, S. (**1982c**). "Acoustic cues for vowel nasalization: A simulation study," J. Acoust. Soc. Am. **72**(S1), S102.

Maeda, S. (**1993**). *Phonetics and Phonology: Nasals, Nasalization and the Velum* (Academic, New York), Chapter on Acoustics of vowel nasalization and articulatory shifts in French Nasal Vowels, pp. 147–167.

Matsumura, M. (**1992**). "Measurement of three-dimensional shapes of vocal tract and nasal cavity using magnetic resonance imaging technique," in *Proceedings of ICSLP*, Banff, pp. 779–782.

Moore, C. A. (**1992**). "The correspondence of vocal tract resonance with volumes obtained from magnetic resonance imaging," J. Speech Hear. Res. **35**, 1009–1023.

Narayanan, S., Alwan, A., and Haker, K. (**1995**). "An articulatory study of fricative consonants using magnetic resonance imaging," J. Acoust. Soc. Am. **98**(3), 1325–1347.

Narayanan, S., Alwan, A., and Haker, K. (**1997**). "Toward articulatory-acoustic models for liquid approximants based on MRI and EPG data, Part I. The laterals," J. Acoust. Soc. Am. **101**(2), 1064–1077.

Prahler, A. (**1998**). "Analysis and synthesis of American English lateral consonant," Master's thesis, MIT, Cambridge, MA.

Pruthi, T., and Espy-Wilson, C. (**2006**). "An MRI based study of the acoustic effects of sinus cavities and its application to speaker recognition," in *Proceedings of Interspeech* (Pittsburgh), pp. 2110–2113.

Stevens, K. N. (**1998**). *Acoustic Phonetics* (MIT Press, Cambridge, MA).

Stevens, K. N., Fant, G., and Hawkins, S. (**1987**). *In Honor of Ilse Lehiste* (Foris Publications), Chapter on Some acoustical and perceptual correlates of nasal vowels, pp. 241–254.

Story, B. H. (**1995**). "Physiologically-based speech simulation using an enhanced wave-reflection model of the vocal tract," Ph.D. thesis. University of Iowa.

Story, B. H., Titze, I. R., and Hoffman, E. A. (**1996**). "Vocal tract area functions from magnetic resonance imaging," J. Acoust. Soc. Am. **100**(1), 537–554.

Wright, J. T. (**1986**). *Experimental Phonology* (Academic, New York) Chapter on The bahavior of nasalized vowels in the perceptual vowel space, pp. 45–67.

Zemlin, W. R. (**1998**). *Speech and Hearing Science: Anatomy and Physiology*, 4th ed. (Allyn and Bacon, Boston).

Zhang, Z., and Espy-Wilson, C. Y. (**2004**). "A vocal-tract model of American English /l/," J. Acoust. Soc. Am. **115**(3), 1274–1280.

Vocal tract length perturbation and its application to male-female vocal tract shape conversion

Seiji Adachi,[a] Hironori Takemoto, Tatsuya Kitamura, Parham Mokhtari, and Kiyoshi Honda
ATR Human Information Science Laboratories, 2-2-2 Hikaridai, Keihanna Science City, Kyoto 619-0288, Japan

(Received 31 March 2006; revised 26 March 2007; accepted 26 March 2007)

An alternative and complete derivation of the vocal tract length sensitivity function, which is an equation for finding a change in formant frequency due to perturbation of the vocal tract length [Fant, Quarterly Progress and Status Rep. No. 4, Speech Transmission Laboratory, Kungliga Teknisha Högskolan, Stockholm, 1975, pp. 1–14] is presented. It is based on the adiabatic invariance of the vocal tract as an acoustic resonator and on the radiation pressure on the wall and at the exit of the vocal tract. An algorithm for tuning the vocal tract shape to match the formant frequencies to target values, such as those of a recorded speech signal, which was proposed in Story [J. Acoust. Soc. Am. **119**, 715–718 (2006)], is extended so that the vocal tract length can also be changed. Numerical simulation of this extended algorithm shows that it can successfully convert between the vocal tract shapes of a male and a female for each of five Japanese vowels. © *2007 Acoustical Society of America.* [DOI: 10.1121/1.2730743]

PACS number(s): 43.72.Ct, 43.20.Ks, 43.20.Mv, 43.25.Qp [BHS] Pages: 3874–3885

I. INTRODUCTION

Perturbation analysis is often used in vocal tract acoustics to calculate the change in formant frequency when the shape of the vocal tract is slightly modified. The general rules in this analysis are as follows. If a constriction is made in the vicinity of a pressure antinode (i.e., pressure maximum) or a velocity node (i.e., velocity minimum), the formant frequency is increased, while if a constriction is made near a pressure node or a velocity antinode, the frequency is decreased. In the pioneering works,[1,2] the relationship between the vocal tract shape and the formant frequencies was discussed under these rules. Schroeder[3] later derived a very useful perturbation formula by using Ehrenfest's theorem[4] for the adiabatic invariance. In this formula, the increase in the formant frequency is proportional to the acoustic radiation pressure on the vocal tract wall where a constriction is made. Because the radiation pressure is equal to the difference between the potential and kinetic energy densities on the vocal tract wall, this formula supplies a quantitative representation of the general rules.

Fant and Pauli[5] and Fant[6] obtained the same formula by using a circuit analog of the vocal tract system. They first defined the sensitivity function as the relative frequency change caused by local perturbations of the cross-sectional area. This is hereafter referred to as the "area sensitivity function." Mrayati and Carré[7] investigated the relationship between the area perturbation and the acoustic characteristics of the vocal tract in detail by using this function. Fant[6] also considered another type of perturbation—local expansion or contraction along the vocal tract length. It derived a sensitivity function for this type of perturbation, which is referred to here as the "length sensitivity function."

The area sensitivity function was extensively used in Story *et al.*;[8] the area functions measured by magnetic resonance imaging were manually corrected in order to match their computed formant frequencies with those extracted from recorded speech. Carré[9] proposed an algorithm to alter the area function iteratively by calculating the area sensitivity functions at each step. Story[10] developed a similar algorithm for automatically modifying the area function using the area sensitivity functions as a guide so that the formant frequencies are matched with the desired values. With this algorithm, one can easily find, for example, how an area function is altered so that the frequency of one formant is changed while those of the others remain fixed. Although these attempts have been successful, only the area has been modified so far. Since the vocal tract area and length differ between children and adults and between males and females, it is of interest to extend this algorithm so that length deformation is also allowed.

In extending the algorithm, we find only scarce literature on length perturbation. As far as we know, Fant[6] is virtually the only study addressing this topic. Although the length sensitivity function was clearly defined and validated experimentally there, the derivation was not as complete as that for area perturbation. In particular, Eq. (32) in Fant[6] holds only under the assumptions that the potential and kinetic energy densities do not change to the first order of the length perturbation and that the increases of the energies in a section of the vocal tract are proportional to the local expansion or contraction ratio. No explanations were, however, provided for these assumptions. Moreover, the relationship between the length sensitivity function and the radiation pressure was

[a]Current address: Fraunhofer Institute for Building Physics, Nobelstrasse 12, 70569 Stuttgart, Germany. Electronic mail: seiji.adachi@ibp.fraunhofer.de

not clarified. This may explain why the length sensitivity function has not yet been used as extensively as that for area perturbation.

To complete the length perturbation analysis, this paper first presents a thorough derivation of the length sensitivity function, which has been done in a manner similar to that of Schroeder[3] for the area perturbation. The algorithm for vocal tract deformation[10] is then extended so that both area and length perturbations are allowed. Numerical simulation of this extended algorithm showed that it can successfully convert between the vocal tract shapes of a male and a female.

II. REVIEW OF PERTURBATION ANALYSIS

A. Radiation force

The lossless sound field in three-dimensional space is considered first. Let $\bar{p}(\mathbf{x},t)$ and $v_i(\mathbf{x},t)$ be pressure and velocity along the ith coordinate, respectively, at time t and at a position specified by vector $\mathbf{x}=(x_1,x_2,x_3)$. Sound pressure $p(\mathbf{x},t)$ is written as $p(\mathbf{x},t)=\bar{p}(\mathbf{x},t)-p_0$, where p_0 is the ambient pressure when no sound field is excited. Similarly, air density $\bar{\rho}(\mathbf{x},t)$ is written as $\bar{\rho}(\mathbf{x},t)=\rho(\mathbf{x},t)+\rho_0$, where ρ_0 is the equilibrium density.

Radiation force P_i is the temporal average of a force (minus ambient pressure p_0) acting on a unit surface.[11,12] Because the momentum flux tensor[13] can be represented by

$$M_{ij}(\mathbf{x},t)=\bar{p}(\mathbf{x}',t)\delta_{ij}+\bar{\rho}v_i(\mathbf{x},t)v_j(\mathbf{x},t), \tag{1}$$

the radiation force on a unit surface normal to the jth coordinate can be written as

$$P_i(\mathbf{x})=\langle p(\mathbf{x},t)\rangle\delta_{ij}+\langle\bar{\rho}v_i(\mathbf{x},t)v_j(\mathbf{x},t)\rangle, \tag{2}$$

where $\langle *\rangle$ means the time average of $*$. The jth component $P_j(\mathbf{x})$, which is the force normal to this unit surface, is referred to as the radiation pressure and denoted as $P(\mathbf{x})$.

We assume that the sound field is stationary, so $\langle v_i(\mathbf{x},t)\rangle$ should be zero. Otherwise, air, which is the sound propagation medium, would be displaced against the assumption over time. As far as we consider the linear wave equations, $\langle p(\mathbf{x},t)\rangle$ would also vanish in the case of $\langle v_i(\mathbf{x},t)\rangle=0$. This is, however, not the case if the nonlinearity in sound is considered. To evaluate this nonlinear effect, we must deal with the Euler equations for a perfect fluid, from which the ordinary wave equations are derived. The flow governed by the Euler equations is assumed to be irrotational. As shown in Appendix A, P_i is given by

$$P_i(\mathbf{x})=\{\langle \mathrm{PE}(\mathbf{x},t)\rangle-\langle \mathrm{KE}(\mathbf{x},t)\rangle\}\delta_{ij}+\rho_0\langle v_i(\mathbf{x},t)v_j(\mathbf{x},t)\rangle, \tag{3}$$

up to the second order, where the $\mathrm{PE}(\mathbf{x},t)$ and $\mathrm{KE}(\mathbf{x},t)$ are the potential and kinetic energy densities,

$$\mathrm{PE}(\mathbf{x},t)=\frac{1}{2}\frac{1}{\rho_0c^2}p^2(\mathbf{x},t), \tag{4}$$

$$\mathrm{KE}(\mathbf{x},t)=\frac{1}{2}\rho_0\mathbf{v}\cdot\mathbf{v}(\mathbf{x},t). \tag{5}$$

Here, we assume that the vocal tract is well characterized by area function $A(x)$, where x is the distance from the entrance along the central axis. This is equivalent to assuming that the vocal tract is a tube with a cross section of area $A(x)$, in which a planar wave propagates along the central axis. This one-dimensional wave is characterized by sound pressure $p(x,t)$ and volume flow rate $U(x,t)$. Because the flow does not pass through the vocal tract wall, the radiation pressure on the vocal tract wall is

$$P(x)=\mathrm{PE}(x)-\mathrm{KE}(x), \tag{6}$$

where $\mathrm{PE}(x)$ and $\mathrm{KE}(x)$ are the time averages of

$$\mathrm{PE}(x,t)=\frac{1}{2}\frac{1}{\rho_0c^2}p^2(x,t), \tag{7}$$

$$\mathrm{KE}(x,t)=\frac{1}{2}\rho_0\left(\frac{U(x,t)}{A(x)}\right)^2. \tag{8}$$

At the exit of the vocal tract, the velocity is not zero. The radiation pressure on the cross-sectional area at the exit is

$$\begin{aligned}P_{\mathrm{exit}}&=\mathrm{PE}(L)-\mathrm{KE}(L)+\rho_0\left\langle\left(\frac{U(L,t)}{A(L)}\right)^2\right\rangle\\&=\mathrm{PE}(L)+\mathrm{KE}(L),\end{aligned} \tag{9}$$

where L is the length of the vocal tract. Note that this equation holds regardless of the boundary condition imposed at the exit. Later, P_{exit} will be calculated under a boundary condition implying the actual radiation from the mouth.

B. Adiabatic invariance

Consider the resonance of the nth eigenmode excited in an oscillation system. Let the frequency and the energy be f_n and E_n, respectively. As described in Schroeder,[3] Ehrenfest's theorem dictates that the ratio of E_n/f_n remains unchanged as the system is perturbed "adiabatically." For the vocal tract, this means that the perturbation is so slow that a large number of oscillation cycles are repeated during the perturbation. With this principle, we can estimate the change in formant frequency δf_n from the increase in energy δE_n during a perturbation:

$$\frac{\delta f_n}{f_n}=\frac{\delta E_n}{E_n}. \tag{10}$$

C. Area sensitivity function

Suppose that we already know the nth formant frequency f_n of a vocal tract shape whose area function and length are $A(x)$ and L, respectively. In this section, the deformation of the vocal tract is limited to that in the area—the length does not change. As shown in Fig. 1, the area function is perturbed by $\delta A(x)$.

The work needed for this deformation, which is equal to the increase in energy δE_n, is

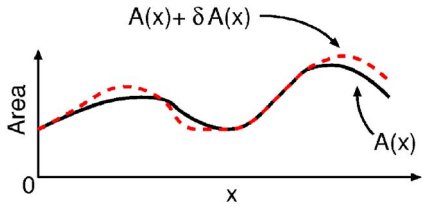

FIG. 1. (Color online) Vocal tract area function $A(x)$ (solid line) and area perturbation $\delta A(x)$ (dashed line).

$$W = -\int_0^L P^{(n)}(x)\,\delta A(x)dx = \delta E_n, \tag{11}$$

where $P^{(n)}(x)$ is the radiation pressure on the vocal tract wall when the nth resonance mode is generated. The total energy E_n can be calculated from the potential and kinetic energy densities of the nth mode:

$$E_n = \int_0^L \{\mathrm{PE}^{(n)}(x) + \mathrm{KE}^{(n)}(x)\}A(x)dx. \tag{12}$$

From Eq. (10), the change in the formant frequency δf_n due to deformation becomes

$$\frac{\delta f_n}{f_n} = -\frac{\int_0^L \{\mathrm{PE}^{(n)}(x) - \mathrm{KE}^{(n)}(x)\}\delta A(x)dx}{\int_0^L \{\mathrm{PE}^{(n)}(x) + \mathrm{KE}^{(n)}(x)\}A(x)dx}. \tag{13}$$

It is reasonable to refer to

$$S^{(n)}(x) = -\frac{P^{(n)}(x)A(x)}{E_n} \tag{14}$$

as the sensitivity function[5,8] and to rewrite Eq. (13) as

$$\frac{\delta f_n}{f_n} = \int_0^L S^{(n)}(x)\frac{\delta A(x)}{A(x)}dx. \tag{15}$$

Let us consider the case where the vocal tract is represented by a series of N_s concatenated cones, or where the area function is represented by a piecewise linear function having nodes (x_s, A_s) for $s=0,\ldots,N_s$. Using the trapezoidal rule, we can numerically integrate Eq. (15):

$$\frac{\delta f_n}{f_n} = \sum_{s=0}^{N_s} S_s^{(n)}\frac{\delta A_s}{A_s} \tag{16}$$

with

$$S_s^{(n)} = -\frac{1}{2E_n}\begin{cases} (\mathrm{PE}_0^{(n)} - \mathrm{KE}_0^{(n)})A_0\Delta x_1 \\ \qquad \text{for } s = 0 \\ (\mathrm{PE}_s^{(n)} - \mathrm{KE}_s^{(n)})A_s(\Delta x_s + \Delta x_{s+1}) \\ \qquad \text{for } s = 1, \ldots, N_s - 1 \\ (\mathrm{PE}_{N_s}^{(n)} - \mathrm{KE}_{N_s}^{(n)})A_{N_s}\Delta x_{N_s} \\ \qquad \text{for } s = N_s, \end{cases} \tag{17}$$

where $\mathrm{PE}^{(n)}(x_s) = \mathrm{PE}_s^{(n)}$, $\mathrm{KE}^{(n)}(x_s) = \mathrm{KE}_s^{(n)}$, and $x_s - x_{s-1} = \Delta x_s$.

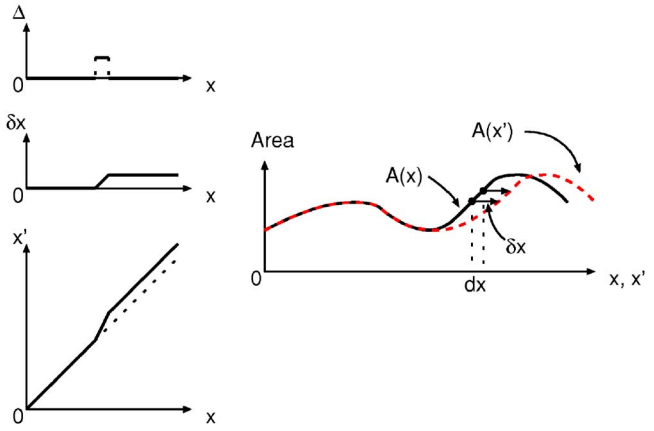

FIG. 2. (Color online) Local stretch or contraction ratio $\Delta(x) \equiv d\delta x(x)/dx$ (upper left), perturbation in vocal tract length $\delta x(x)$ (middle left), new distance x' (lower left), and new area function after length perturbation $A(x')$ (right: dashed line) with original area function $A(x)$ (right: solid line).

III. PERTURBATION OF VOCAL TRACT LENGTH

In this section, only deformation in the vocal tract length is considered. We express this deformation by letting the cross-sectional area at distance x be displaced along the length axis by $\delta x(x)$. To suppress unnecessary translational movement of the vocal tract, $\delta x(0)$ is set to zero. The local expansion or contraction ratio at x is denoted as $\Delta(x) \equiv d\delta x(x)/dx$. A new distance is defined as $x' = x + \delta x(x)$. The area function after the deformation is $A(x') \equiv A(x)$. Figure 2 illustrates $\Delta(x)$, $\delta x(x)$, x', and $A(x')$.

Suppose the nth resonance mode is excited in the vocal tract. Let us calculate the increase in energy in the vocal tract due to the length deformation. Because this is equal to the work needed for the deformation, it can be calculated by multiplying the radiation pressure by the displacement normal to the surface element and by integrating this quantity over the entire surface of the vocal tract including the exit:

$$\delta E_n = \int_0^L P^{(n)}(x)\,\delta x(x)\frac{dA}{dx}(x)dx - P_{\mathrm{exit}}^{(n)}\delta x(L)A(L). \tag{18}$$

Substituting Eqs. (6) and (9) into Eq. (18), and integrating the first term by parts, we get

$$\begin{aligned}\delta E_n = &-\int_0^L \{\mathrm{PE}'^{(n)}(x) - \mathrm{KE}'^{(n)}(x)\}\delta x(x)A(x)dx \\ &-\int_0^L \{\mathrm{PE}^{(n)}(x) - \mathrm{KE}^{(n)}(x)\}\Delta(x)A(x)dx \\ &-2\mathrm{KE}^{(n)}(L)\,\delta x(L)A(L);\end{aligned} \tag{19}$$

where PE′ and KE′ are the derivatives of PE and KE with respect to distance x, respectively. By substituting Eqs. (B11) and (B12) derived in Appendix B, we can write the increase in energy more concisely:

$$\delta E_n = -\int_0^L \{\mathrm{PE}^{(n)}(x) + \mathrm{KE}^{(n)}(x)\}\Delta(x)A(x)dx. \tag{20}$$

Similar to that for area perturbation, a change in the formant frequency due to length perturbation can be represented as

$$\frac{\delta f_n}{f_n} = -\frac{\int_0^L \{\mathrm{PE}^{(n)}(x) + \mathrm{KE}^{(n)}(x)\}\Delta(x)A(x)dx}{\int_0^L \{\mathrm{PE}^{(n)}(x) + \mathrm{KE}^{(n)}(x)\}A(x)dx}. \tag{21}$$

This formula is equivalent to Eq. (33) in Fant.[6] The length sensitivity function can be defined as

$$\hat{S}^{(n)}(x) = -\frac{\{\mathrm{PE}^{(n)}(x) + \mathrm{KE}^{(n)}(x)\}A(x)}{E_n}. \tag{22}$$

Equation (21) can now be written as

$$\frac{\delta f_n}{f_n} = \int_0^L \hat{S}^{(n)}(x)\Delta(x)dx. \tag{23}$$

If the area function is represented by a piecewise linear function, we have a useful expression for Eq. (23) amenable to numerical calculation as follows:

$$\frac{\delta f_n}{f_n} = \sum_{s=1}^{N_s} \hat{S}_s^{(n)}\Delta_s, \tag{24}$$

where $\Delta_s = (\delta x_s - \delta x_{s-1})/\Delta x_s$ implies the expansion or contraction rate of the sth section, and where the length sensitivity function in discrete form is

$$\hat{S}_s^{(n)} = -\frac{\Delta x_s}{2E_n}\{(\mathrm{PE}_s^{(n)} + \mathrm{KE}_s^{(n)})A_s + (\mathrm{PE}_{s-1}^{(n)} + \mathrm{KE}_{s-1}^{(n)})A_{s-1}\} \quad \text{for } s = 1, \ldots, N_s. \tag{25}$$

Although this paper considers only the case where the vocal tract is represented as concatenated cones, for the sake of readers, we also present a formulation for the case where the tract is represented as concatenated cylinders. In this case, Eq. (18) does not stand because the area function $A(x)$ is no longer continuous. Nevertheless, the increase of energy can be calculated with the same principle as applied to the derivation of Eq. (18). Suppose that the vocal tract is composed of N_s concatenated cylindrical sections each of which has area A_s and length $\Delta x_s = x_s - x_{s-1}$. The increase of energy due to the length perturbation becomes

$$\delta E_n = \sum_{s=1}^{N_s-1} \delta x_s F_s^{(n)} - P_{\mathrm{exit}}^{(n)}\delta x_{N_s}A_{N_s}, \tag{26}$$

where δx_s is the perturbation at node s, and where $F_s^{(n)}$ is the force acting on the annulus formed at the junction between sections s and $s+1$. As shown in Appendix C, Eq. (26) can be transformed into

$$\delta E_n = -\sum_{s=1}^{N_s} (\mathrm{PE}_s^{(n)} + \mathrm{KE}_s^{(n)})\Delta_s A_s \Delta x_s, \tag{27}$$

where $\mathrm{PE}_s^{(n)}$ and $\mathrm{KE}_s^{(n)}$ are potential and kinetic energy densities in section s. The length sensitivity function therefore becomes

$$\hat{S}_s^{(n)} = -\frac{\Delta x_s}{E_n}(\mathrm{PE}_s^{(n)} + \mathrm{KE}_s^{(n)})A_s. \tag{28}$$

IV. APPLICATION TO VOCAL TRACT DEFORMATION

A. Method

Story[10] proposed an automated process for modifying the area function that uses the sensitivity functions as a guide to match the formant frequencies with the target frequencies. Our extension of this algorithm enables it to handle not only area perturbation but also length perturbation in the deformation process.

Suppose that the vocal tract is represented by a series of N_s concatenated cones and the area function has nodes (x_s, A_s) for $s = 0, \ldots, N_s$, where x_s and A_s are the distance from the vocal tract entrance and the cross-sectional area at this point, respectively. Given a set of (x_s, A_s), we compute formant mode frequencies f_n as well as the pressure $p_s^{(n)}$ and volume flow $U_s^{(n)}$ patterns for each formant. Using Eqs. (7) and (8), we calculate the potential and kinetic energy densities, $\mathrm{PE}_s^{(n)}$ and $\mathrm{KE}_s^{(n)}$. The total energy is computed using Eq. (12). These immediately yield the sensitivity function $S_s^{(n)}$ for the area perturbation through Eq. (17). Likewise, the length sensitivity function $\hat{S}_s^{(n)}$ is calculated using Eq. (25).

Let the target frequency of the nth formant be F_n. The difference between F_n and f_n normalized by f_n is given by

$$z_n = \frac{F_n - f_n}{f_n}. \tag{29}$$

The deformation process is done iteratively using the following update rules:

$$A_s^{\mathrm{new}} = A_s\left(1 + \alpha\sum_{n=1}^{N_f} z_n S_s^{(n)}\right) \quad \text{for } s = 0, \ldots, N_s, \tag{30}$$

$$x_s^{\mathrm{new}} = x_{s-1}^{\mathrm{new}} + \Delta x_s\left(1 + \beta\sum_{n=1}^{N_f} z_n \hat{S}_s^{(n)}\right) \quad \text{for } s = 1, \ldots, N_s \text{ with } x_0^{\mathrm{new}} = x_0, \tag{31}$$

where N_f is the number of formants to tune and α and β are coefficients used to control the perturbation amplitudes for the area and length, respectively. These parameters may be set to constant values prior to iteration, but for convergence, they should be small for the second terms in the parentheses in Eqs. (30) and (31) to be sufficiently smaller than 1. Although the original rules of Story[10] are mainly additive; they are multiplicative only for a small area, only the multiplicative update rules are used here. This prevents introducing an additional parameter (specifying at which area the update rules are changed from additive to multiplicative) and thus leads to a simpler algorithm.

Three additional rules are applied at each iteration step after the main process given by Eqs. (30) and (31). The first two prevent the laryngeal tube from being overly narrowed and elongated. Introducing minimum area $A_{\min}$ and maximum section length $\Delta x_{\max}$, we apply

TABLE I. Lowest six formant frequencies $f_1, \ldots, f_6$ (in Hz) for vowels /i/, /e/, /a/, /o/, and /u/ calculated from area functions for KH (male) and YN (female) and male-female scale factors of formant frequencies for each vowel (defined as $k_n = f_n^{\text{female}}/f_n^{\text{male}} - 1$).

	KH (male)						YN (female)						Scale factors					
Vowel	f_1	f_2	f_3	f_4	f_5	f_6	f_1	f_2	f_3	f_4	f_5	f_6	k_1	k_2	k_3	k_4	k_5	k_6
/i/	272	2082	3131	3517	4341	5040	316	3497	3665	4962	5730	7017	0.16	0.68	0.17	0.41	0.32	0.39
/e/	485	1756	2614	3476	4366	4871	607	2663	3553	4613	5482	6721	0.25	0.52	0.36	0.33	0.26	0.38
/a/	610	1304	2563	3568	4231	4596	868	1486	3456	4846	5559	6602	0.42	0.14	0.35	0.36	0.31	0.44
/o/	461	949	2498	3447	3918	4652	707	1308	3531	4734	5456	6695	0.53	0.38	0.41	0.37	0.39	0.44
/u/	323	1360	2293	3573	4060	4739	412	2616	3436	4582	5413	6871	0.28	0.92	0.50	0.28	0.33	0.45

$$A_s^{\text{new}} = \max\{A_{\min}, A_s^{\text{new}}\}, \tag{32}$$

$$x_s^{\text{new}} = \min\{x_{s-1}^{\text{new}} + \Delta x_{\max}, x_s^{\text{new}}\}, \tag{33}$$

where s is less than N_l, which is the number of sections representing the larynx. The third rule prevents the area function from becoming unnaturally discontinuous—A_s is smoothed out so that

$$\left| \frac{A_{s+1}^{\text{new}} - 2A_s^{\text{new}} + A_{s-1}^{\text{new}}}{2} \right| < A_{2\text{d}}, \tag{34}$$

where $A_{2\text{d}}$ is a parameter for specifying smoothness. These iteration rules given in Eqs. (30)–(34) are applied until the norm of z_n becomes smaller than threshold value z_{th}.

B. Male-female vocal tract shape conversion

1. Area functions and preliminary experiments

We used the extended algorithm presented in Sec. IV A to convert between male and female vocal tract shapes. The area functions of the main vocal tract measured with three-dimensional cine-MRI in Takemoto *et al.*[14] were resliced with 30 sections and used as those of a male (KH) for the five Japanese vowels. Corresponding area functions of a Japanese female (YN) were also prepared in the same manner. For each vowel, conversions were done reciprocally, i.e., for both male-to-female and female-to-male directions.

For the calculations of the resonance frequencies f_n, the pressure $p^{(n)}(x)$, and the volume flow $U^{(n)}(x)$ mode patterns, the same acoustic model used in Adachi and Yamada[15] was employed. This model considers the viscothermal loss on the vocal tract wall and the effect of yielding vocal tract wall. The radiation impedance from the mouth was assumed to be the same as that from a round piston surrounded by an infinite baffle. The glottal impedance was set to infinite, assuming a complete closure at the glottis. This model provides more realistic transfer functions with accurate formant frequencies and bandwidths than an acoustic model that does not consider the losses. Justification of the use of these losses is, however, needed because the theory of perturbation analysis has been developed for the lossless sound field with the notion of the radiation pressure. One supportive evidence is that in an actual acoustic tube such as an organ pipe, the measured radiation pressure is in fairly good agreement with the theoretical value.[16] From this, it can be assumed that the sensitivity functions calculated here can reasonably serve as those in the lossless case. The justification is also confirmed *posteriori* by the convergence of the extended algorithm.

The lowest six formant frequencies $f_1, \ldots, f_6$ calculated for each vocal tract shape are listed in Table I. Male-female scale factors of the formant frequencies for each vowel $k_n = f_n^{\text{female}}/f_n^{\text{male}} - 1$ are also listed. In connection with vowel normalization, it is of interest to briefly review the scale factors calculated. For vowel /i/, a large k_2 of 0.68 is obtained while k_3 is as small as 0.17. The second and third formant frequencies of YN (female) are thus very close to each other. For vowel /e/, the scale factors are more uniform, except for a large k_2 of 0.52. For open vowel /a/, k_1 is relatively large and k_2 is small. These findings are in accord with observations in other languages.[17–19] Discrepancies are found for the rounded vowels /o/ and /u/. A large k_1 for vowel /o/ is obtained in our case while a small one is obtained for a six language study.[17] The first formant frequency of YN is thus as high as 707 Hz, but is still in the range where the vowel would likely be perceived as /o/. For vowel /u/, a k_2 of 0.98 is extraordinarily large, while k_1 is relatively small, as obtained in Fant.[17] Because the second formant frequency of 2616 Hz is actually too high to be that of vowel /u/, the sound may not be perceived as /u/. One possible cause is that the lip rounding for the phonation of /u/ became insufficient due to growing fatigue during the scanning of the vocal tract shape.

The parameters for the vocal tract shape conversions were set as follows: $z_{\text{th}}=0.01$, $N_s=30$, $N_l=4$, $A_{\min}=0.25$ cm^2, $\Delta x_{\max}=0.65$ cm, and $A_{2\text{d}}=2.0$ cm^2. Because the values of α and β could not been determined *a priori*, they were fixed on the basis of preliminary experiments, which were done using five pairs of values, (5.0, 1.0), (4.5, 1.5), (4.0, 2.0), (3.5, 2.5), and (3.0, 3.0), while N_f was set to 6. As shown in Table II, the root mean square of the errors in the vocal tract length over the bidirection conversions for the five vowels had a minimum of 4.4 mm when (α, β) was equal to (4.0, 2.0). It was also found that any set of the values multiplied or divided by a common factor affects only the iteration time for convergence and hardly affects the re-

TABLE II. Root mean squares of errors in vocal tract length (in mm) over all conversions for five vowels and different values of parameters α and β of vocal tract deformation algorithm, which are coefficients to control perturbation amplitude for area and length, respectively.

(α, β)	(5.0, 1.0)	(4.5, 1.5)	(4.0, 2.0)	(3.5, 2.5)	(3.0, 3.0)
rms of ΔL (mm)	11.6	6.7	4.4	5.7	7.8

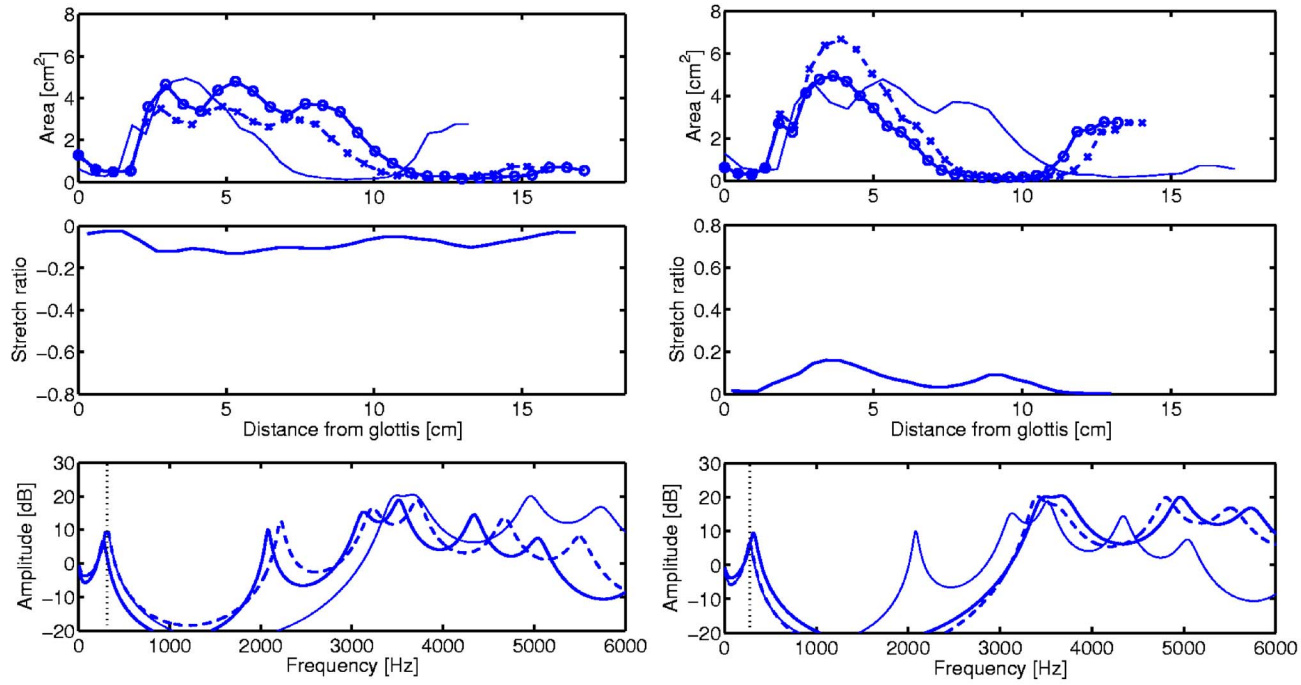

(a) N_f= 1; Left: male-to-female; Right: female-to-male

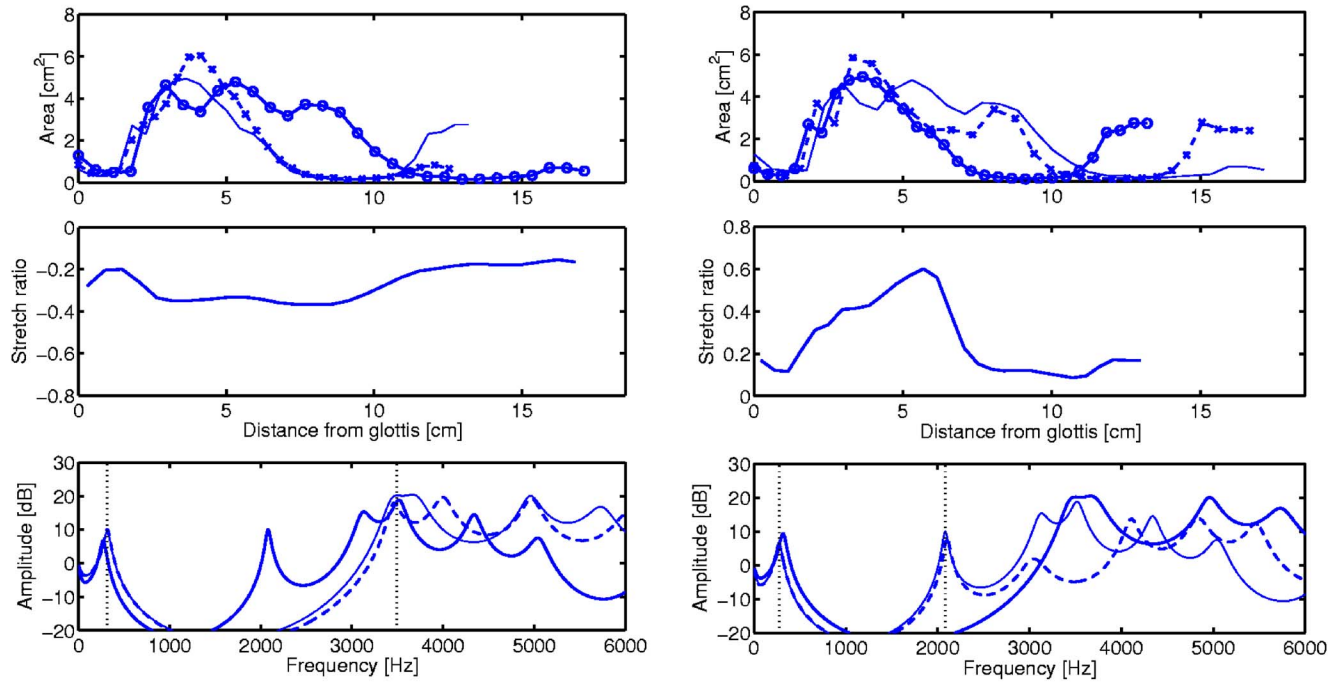

(b) $N_f = 2$; Left: male-to-female; Right: female-to-male

FIG. 3. (Color online) Results of conversions of male and female vocal tract shapes for vowel /i/ for different numbers of formants N_f matched. (a), (b), (c), and (d) show results for N_f=1, 2, 4, and 6, respectively. Graphs on the left show results of male-to-female conversions, and those on the right show them for female-to-male conversion. Upper panels show area function of initial vocal tract shape (thick solid line with open circle representing nodes), that of converted shape (thick dashed line with cross), and that of target shape (thin solid line). Middle panels represent local expansion or contraction ratio as a function of distance x from glottis. Lower panels shown transfer functions of initial, converted, and target vocal tract shapes as thick solid, thick dashed, and thin solid lines, respectively.

sults. The parameters α and β were thus set to 4.0 and 2.0, respectively.

2. Effects of number of target formants

To show how the number of formants N_f affects the results, we next performed the conversions by changing N_f from 1 to 6. Figures 3(a)–3(d) show the results for the conversions for vowel /i/ in N_f=1, 2, 4, and 6, respectively. In each figure, the left column shows the result of the conversion from male to female, and the right column shows that from female to male. In each column, the upper panel depicts the area function of the initial vocal tract shape (thick solid

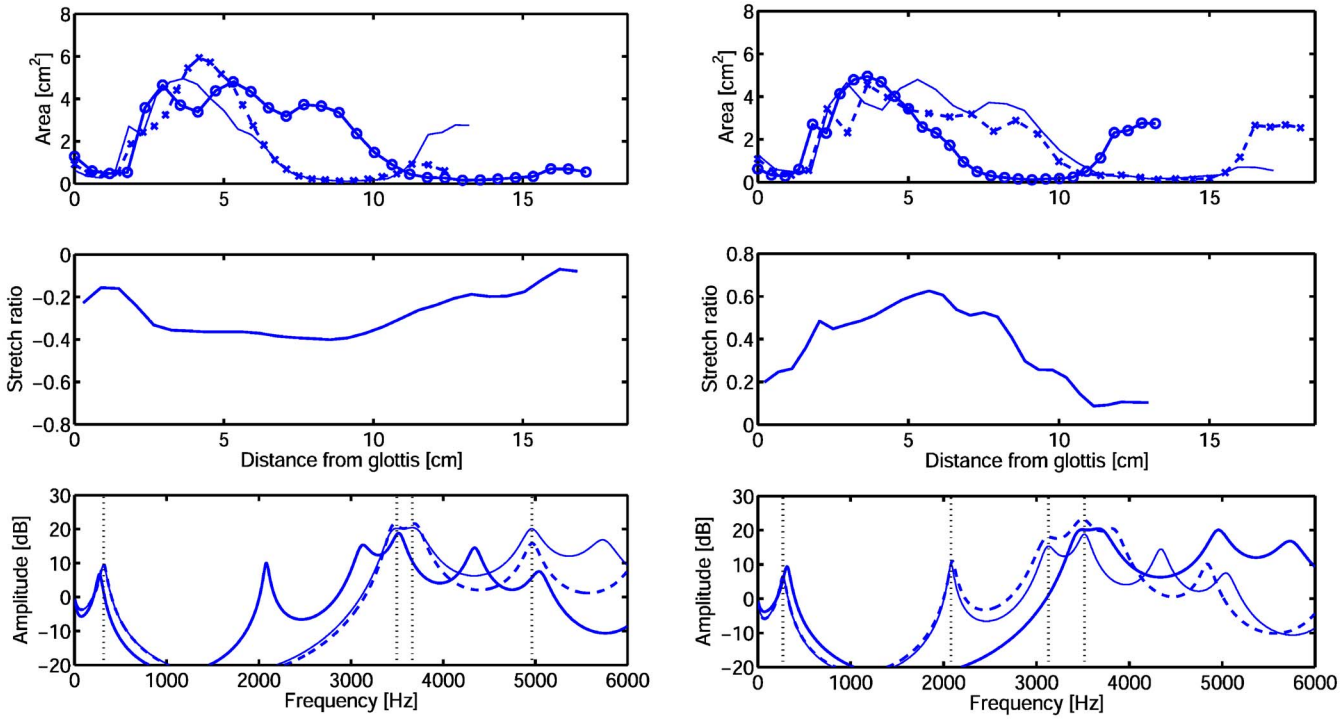

(c) $N_f = 4$; Left: male-to-female; Right: female-to-male

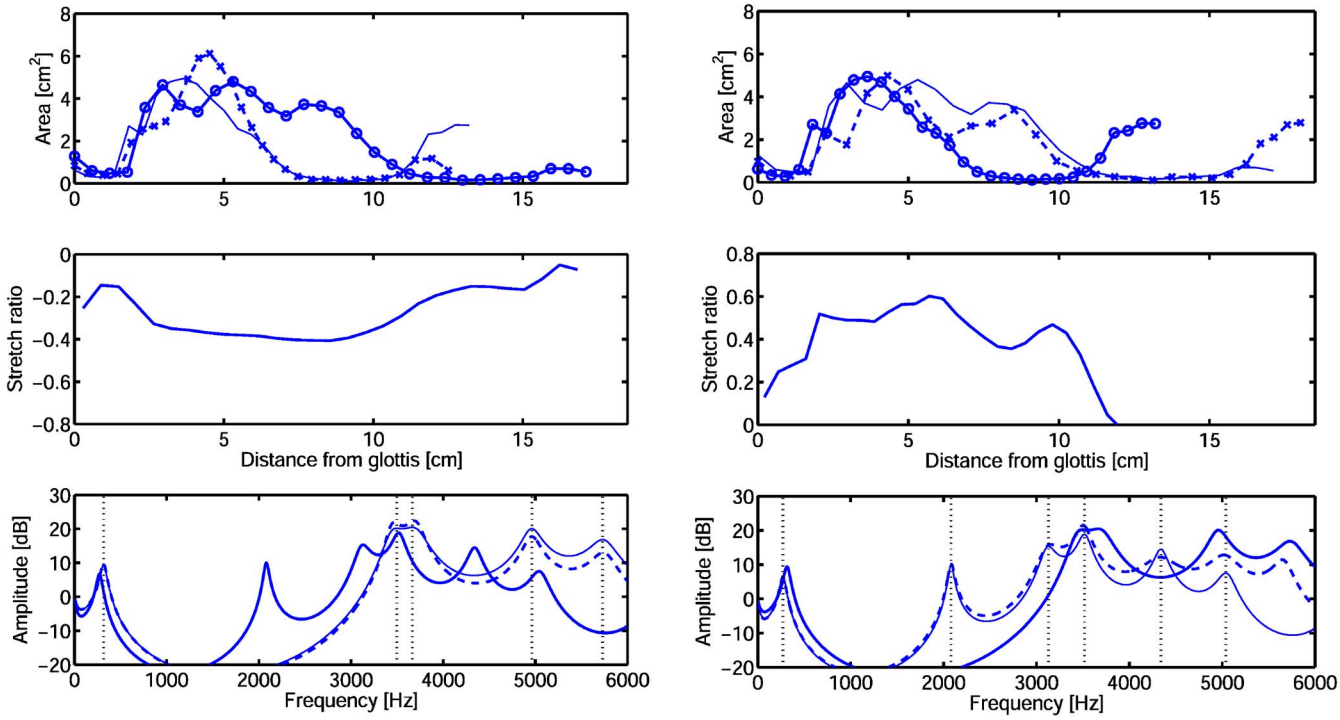

(d) $N_f = 6$; Left: male-to-female; Right: female-to-male

FIG. 3. (*Continued*).

line with open circles representing nodes), that of the converted shape (thick dashed line with cross), and that of the target shape (thin solid line). The middle panel represents the local expansion or contraction ratio as a function of the distance x from the glottis. The lower panel depicts the transfer functions of the initial, converted, and target vocal tract shapes in thick solid, thick dashed, and thin solid lines, respectively.

For N_f=1, male-to-female conversion was made by contracting both the pharynx and the mouth the same degree.

This is a reflection of the length sensitivity function for the first formant taking large negative values both in the pharynx and the mouth. It is in accord with the observation that the first formant mode of vowel /i/ has an equal amount of potential energy in the pharynx and kinetic energy in the mouth.[5] The amount of the contraction, however, was not enough to reproduce the female vocal tract shape. The area was not changed very much from that of the male vocal tract shape, except for it becoming smaller in the pharynx, which contributed to the increment of the first formant frequency. The larynx was rarely modified. This is because both the kinetic and potential energies of the first formant mode almost vanish in the larynx so both the area and length sensitivities become zero.[20] A similar observation can be made for the female-to-male conversion in the right column of Fig. 3(a). While there was expansion of both the pharynx and the mouth, it was not sufficient. Only the area in the pharynx became larger. The shape of the larynx did not change.

For $N_f=2$, conversions in both directions were made with large deformations and to a nearly complete degree. In the male-to-female conversion, a large increase in the second formant frequency of about 68% was achieved. The reproduction of the female vocal tract shape was, nevertheless, fairly good. In particular, the length of the vocal tract was simulated within 6.7 mm. It is noteworthy that the contraction of the pharynx was larger than that of the mouth. This is because the length sensitivity function for the second formant took a large negative value in the upper part ($x=6-7$ cm) of the pharynx. This is again in accord with the observation that the second formant of /i/ is affiliated with the back cavity.[5] The larynx shape was also simulated well. This is probably because the second formant frequency of the female subject was very high (3497 Hz) and the resonance in the larynx made some contribution to this formant. It is a coincidence that the simulated fourth formant frequency was very close to that of the target (female) vocal tract. The female-to-male conversion was also made very well. The second formant frequency was reduced about 40% due to the expansion of the pharynx and significant enlargement of the upper part of the pharynx. The total length of the vocal tract was converted within 4.7 mm. The larynx was not, however, converted very well. It remained very close to that of the initial female vocal tract.

The male-to-female conversions for $N_f=4$ and 6 did not differ essentially from those for $N_f=2$. In the female-to-male conversions, the larynx was well converted to that of the male vocal tract, as were the pharynx and mouth. This results from the condition for the fourth formant frequency to match that of the male vocal tract. This is in accord with the fact that the resonance of the fourth formant is affiliated to the larynx.[20]

3. Vocal tract conversions for /e/, /a/, /o/, and /u/

By fixing the number of formants N_f matched to the target ones to six, the vocal tract conversions were performed for the other vowels. Figures 4(a)–4(d) show the results for vowels /e/, /a/, /o/, and /u/, respectively. In the male-to-female conversion for /e/, the vocal tract contracted uniformly both in the pharynx and the mouth. This is mainly because the length sensitivity functions $\hat{S}^{(n)}(x)$, especially that for the second formant, were roughly constant in the pharynx and the mouth. The converted vocal tract was only 1.1 mm shorter than that of the target. The converted and target vocal tract shapes were also very similar. In the female-to-male conversion, the expansion was uniform in the pharynx but it was larger in the mouth toward the lips. The area in the mouth was larger in the converted vocal tract than in the target. Except for this difference, the conversion was made fairly well. The difference in length between the converted and target vocal tracts was only 0.1 mm.

The male-to-female conversion for /a/ was made with a larger contraction in the lower part of the pharynx. Similarly, in the female-to-male conversion, a larger expansion occurred in the lower part of the pharynx. This is because the sensitivity function for the first formant $\hat{S}^{(1)}(x)$ has a large negative value in this part. Although area, especially in the mouth, was not very well converted in either direction, the conversion of the vocal tract length was good: the tract was 2.8 mm longer in the male-to-female direction and 1.2 mm shorter in the female-to-male direction. The conversions for /o/ were very good in both directions. The converted and target area functions almost overlapped. As in the conversions for /a/, the lower part of the pharynx contracted more in the male-to-female conversion and expands more in the female-to-male conversion. The male-to-female conversion for /u/ was also very good. The contraction was roughly uniform in the pharynx and the mouth, but larger contraction was found near the lips. This is because $\hat{S}^{(2)}$ has a large negative value near the lips. In the female-to-male conversion, area was converted with some differences both in the pharynx and the mouth. For the same reason as in the male-to-female conversion, the length near the lips expanded more completely.

V. CONCLUSION

To complete the length perturbation analysis of the vocal tract,[6] a thorough derivation of the length sensitivity function has been presented. The derivation, which is similar to that of Schroeder[3] for area perturbation, is based on two physical quantities: the adiabatic invariance of the vocal tract as an acoustic resonator and the radiation pressure at the wall and at the exit of the vocal tract. Special care was taken in calculating the radiation pressure at the exit because the velocity does not vanish there. An algorithm for tuning the vocal tract shape[10] to match the resonance frequencies to the target values was extended to include a length sensitivity function so that both the area and the length of the vocal tract can be changed locally. The extended algorithm was applied to the conversion of the vocal tract shape between a male and a female. For each of five Japanese vowels, the vocal tract shape of the male was converted to that of the female by giving the female formant frequencies as targets. The conversions in the opposite direction were also examined. The root mean square of the differences in total length between the converted and target vocal tract shapes was 4.4 mm on average over the conversions in both directions for the five

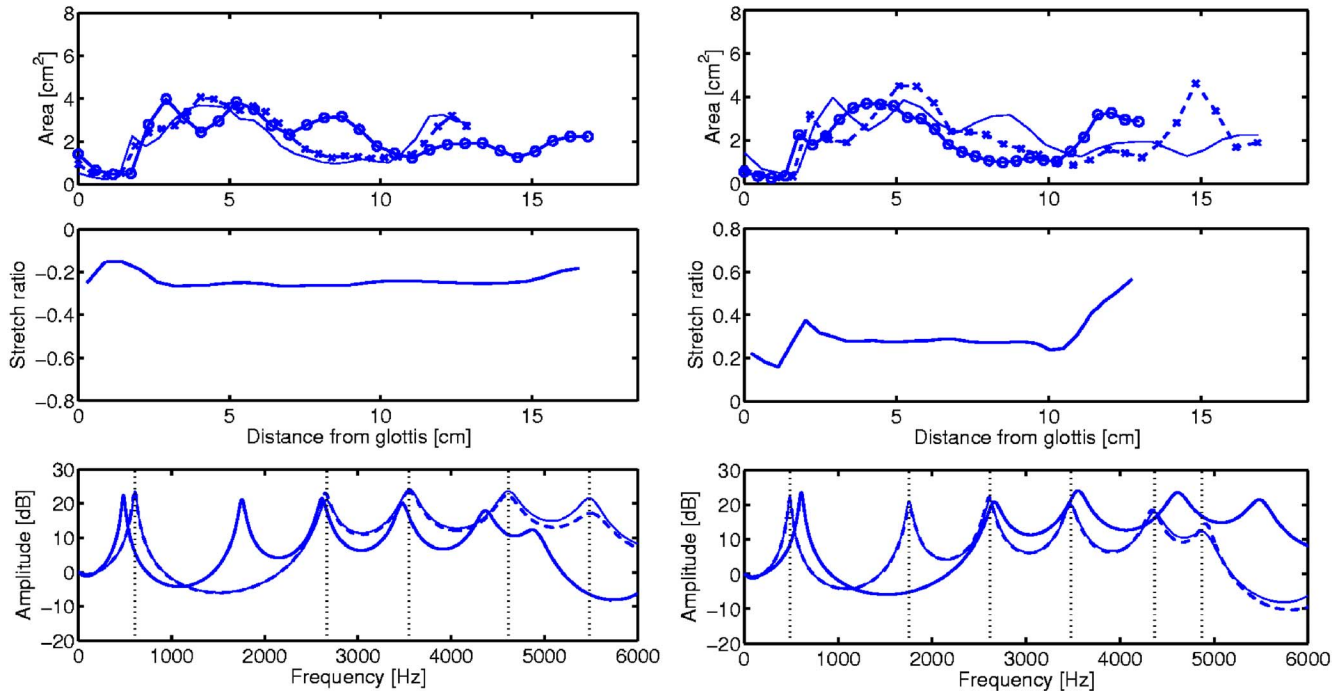

(a) Vowel /e/; Left: male-to-female; Right: female-to-male

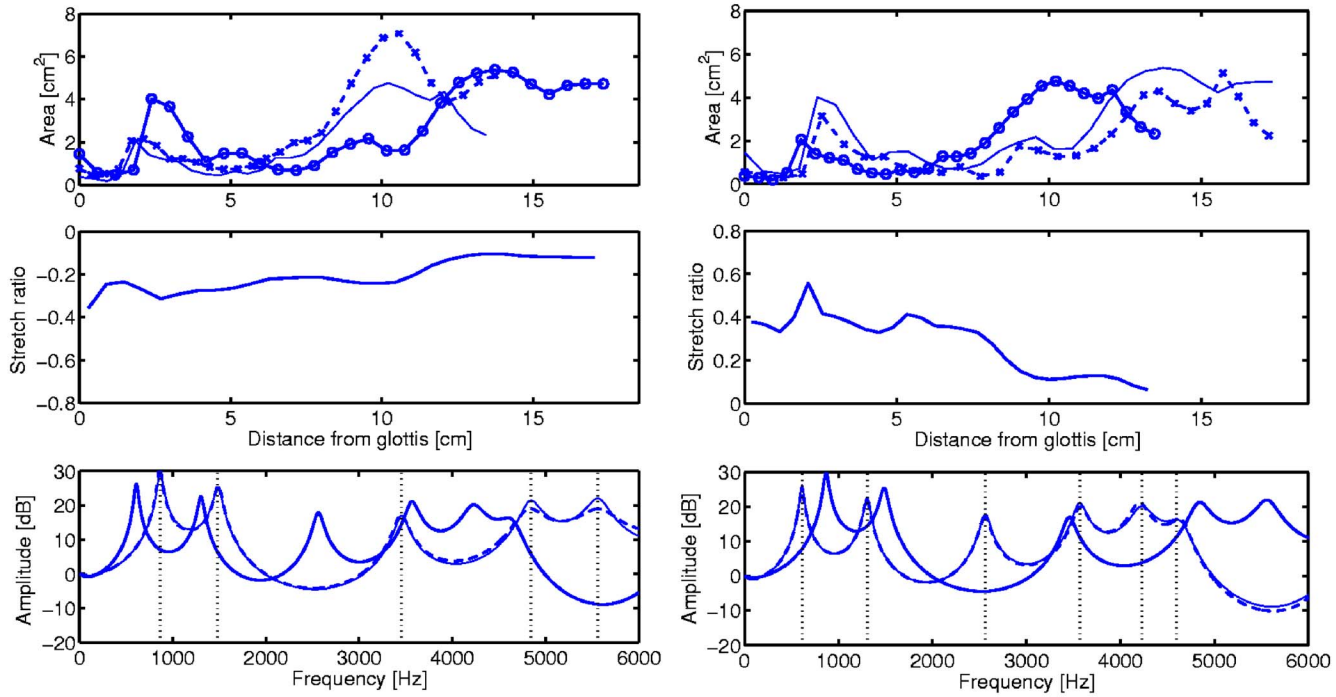

(b) Vowel /a/; Left: male-to-female; Right: female-to-male

FIG. 4. (Color online) Results of conversions of male and female vocal tract shapes for vowels (a) /e/, (b) /a/, (c) /o/, and (d) /u/ when the number of formant N_f matched to the target ones is set to six. Graphs on the left show the results of male-to-female conversion, and those on the right show them for female-to-male conversion. Lines have the same meaning as in Fig. 3.

vowels. The area was also well converted. In the male-to-female conversions for vowels /e/, /o/, and /u/ and the female-to-male conversion for vowel /o/, the converted area function was very similar to the target one. In the other conversions, the area function was generally well reproduced except for a few local discrepancies.

A few points were not addressed in this work. Determination of the vocal tract shape for different phonations from measured spectra of the speech signal has been a central problem in speech science. Investigation of acoustic-to-articulatory inversion has shown that significant information about vocal tract shape is provided additionally by the for-

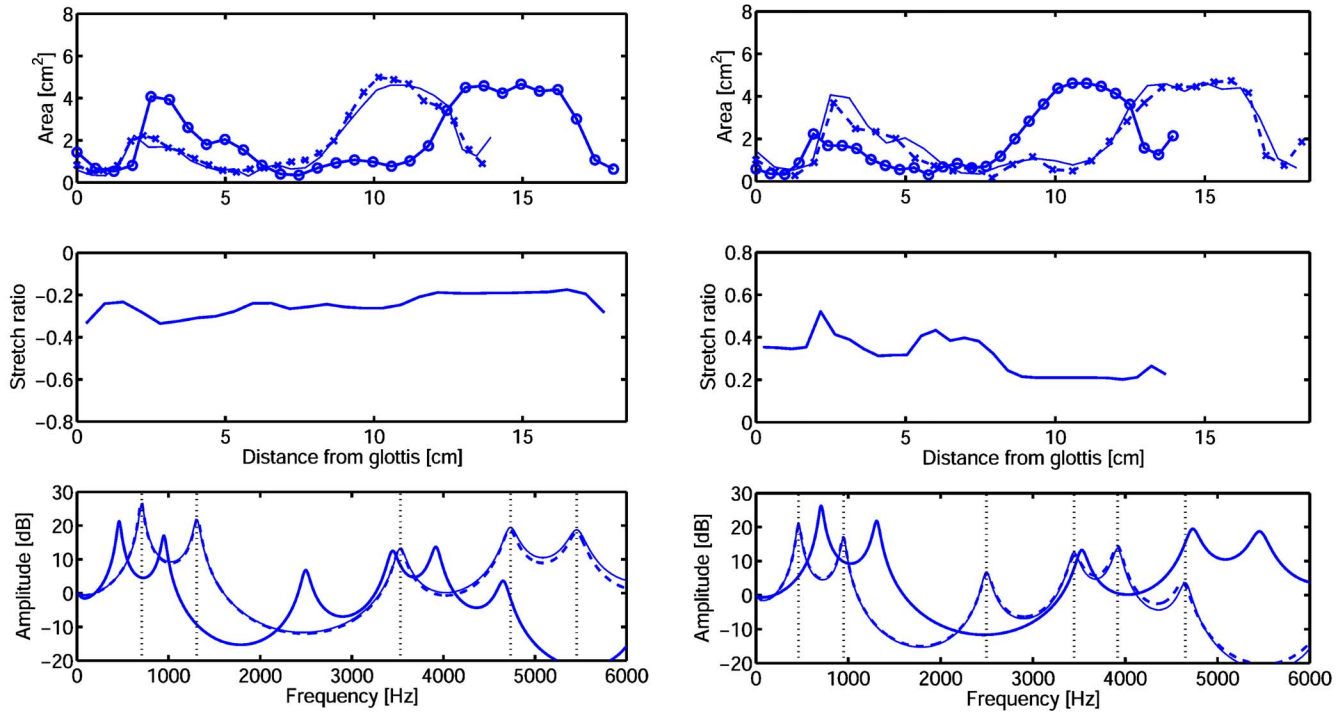

(c) Vowel /o/; Left: male-to-female; Right: female-to-male

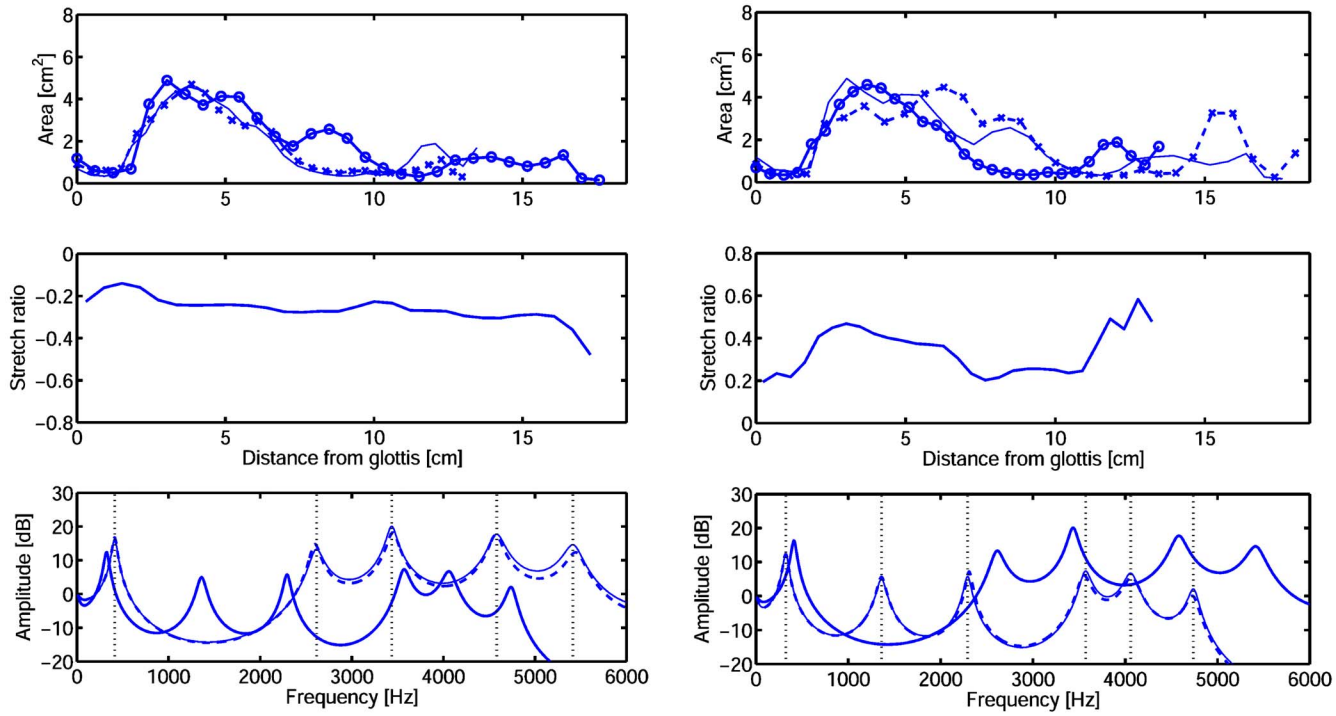

(d) Vowel /u/; Left: male-to-female; Right: female-to-male

FIG. 4. (*Continued*).

mant bandwidths.[21–23] It would therefore be worthwhile to incorporate this kind of information into the vocal tract deformation algorithm. Since different vocal tract shapes can have an identical transfer function, it would be difficult to solve this problem with an algorithm using only spectral information. To obtain better conversion results, an algorithm that also considers physiological and articulatory constraints on the vocal tract deformation may be needed.

ACKNOWLEDGMENTS

The authors are indebted to Dr. B. Story for advice concerning demonstration of the vocal tract deformation algorithm presented in this paper. This research was conducted as part of "Research on Human Communication" with funding from the National Institute of Information and Communications Technology (NICT).

APPENDIX A

Using the same notations as in the paper, we can write the momentum component of the Euler equations as

$$\bar{\rho}\left(\frac{\partial}{\partial t}+\mathbf{v}\cdot\boldsymbol{\nabla}\right)\mathbf{v}+\boldsymbol{\nabla}\bar{p}=0. \tag{A1}$$

Assuming the disturbances are all small, that is, $\rho \ll \rho_0$, $p \ll p_0$, and $|\mathbf{v}| \ll c$, we consider Eq. (A1) up to the second order of these disturbances and calculate the time average of p here.

By disregarding the third and higher order terms in Eq. (A1),

$$\rho_0\frac{\partial \mathbf{v}}{\partial t}+\rho\frac{\partial \mathbf{v}}{\partial t}+\rho_0\mathbf{v}\cdot\boldsymbol{\nabla}\mathbf{v}+\boldsymbol{\nabla}p=0 \tag{A2}$$

holds. To eliminate ρ from Eq. (A2), we use the equation of state

$$\frac{\bar{p}}{\bar{\rho}^{\gamma}}=\text{const}, \tag{A3}$$

where $\gamma=C_p/C_v=1.4$ is the ratio of the specific heats of air at constant pressure and at constant volume, respectively. Because the second term of Eq. (A2) is of the second order, we can use the linearized Eq. (A3), that is, $p/\rho=\gamma p_0/\rho_0 \equiv c^2$, instead. Substituting this into Eq. (A2), we get

$$\rho_0\frac{\partial \mathbf{v}}{\partial t}+\frac{1}{c^2}p\frac{\partial \mathbf{v}}{\partial t}+\rho_0\mathbf{v}\cdot\boldsymbol{\nabla}\mathbf{v}+\boldsymbol{\nabla}p=0. \tag{A4}$$

Following the same reasoning, we can rewrite the second term using the linearized Eq. (A2), that is, $\rho_0\partial\mathbf{v}/\partial t+\nabla p=0$. Equation (A4) then becomes

$$\rho_0\frac{\partial \mathbf{v}}{\partial t}-\frac{1}{\rho_0 c^2}p\,\boldsymbol{\nabla}p+\rho_0\mathbf{v}\cdot\boldsymbol{\nabla}\mathbf{v}+\boldsymbol{\nabla}p=0. \tag{A5}$$

Using the identity

$$\mathbf{v}\cdot\boldsymbol{\nabla}\mathbf{v}=\frac{1}{2}\boldsymbol{\nabla}(\mathbf{v}^2)-\mathbf{v}\times(\boldsymbol{\nabla}\times\mathbf{v}) \tag{A6}$$

and the assumption of an irrotational flow $\boldsymbol{\nabla}\times\mathbf{v}=0$, we obtain

$$\rho_0\frac{\partial \mathbf{v}}{\partial t}+\boldsymbol{\nabla}\left(-\frac{1}{2}\frac{1}{\rho_0 c^2}p^2+\frac{1}{2}\rho_0\mathbf{v}^2\right)+\boldsymbol{\nabla}p=0. \tag{A7}$$

We now take the time average of Eq. (A7). Assuming $\langle\mathbf{v}\rangle=0$, we have

$$\langle p\rangle=\text{PE}-\text{KE}+\text{const}, \tag{A8}$$

where const is a constant independent of space. $\langle p\rangle$ should be regarded as zero when no sound is excited and both PE and KE are zero. This constant can thus be set to zero.

APPENDIX B

We consider a lossless one-dimensional wave in a vocal tract characterized by sound pressure $p(x,t)$ and acoustic velocity $v(x,t)$ where x is the distance from the vocal tract entrance along the length and t is time. As shown in Morse,[24] $p(x,t)$ and $v(x,t)$ satisfy the following wave equations:

$$\rho_0\frac{\partial v}{\partial t}=-\frac{\partial p}{\partial x}, \tag{B1}$$

$$A\frac{\partial p}{\partial t}=-\rho_0 c^2\frac{\partial Av}{\partial x}, \tag{B2}$$

where $A(x)$ is the area function of the vocal tract. When one of the resonance modes is excited, each of the pressure and velocity mode patterns oscillates in phase along the vocal tract length. The phase of the pressure oscillation is 90° different from that of the velocity oscillation. With real functions $p(x)$ and $v(x)$ representing the pressure and velocity mode patterns, respectively, the mode oscillation can be written as

$$p(x,t)=p(x)e^{i\omega t}, \tag{B3}$$

$$v(x,t)=iv(x)e^{i\omega t}, \tag{B4}$$

where ω is the angular resonance frequency. By substituting Eqs. (B3) and (B4) into Eqs. (B1) and (B2), we get

$$p'(x)=-\omega\rho_0 v(x), \tag{B5}$$

$$v'(x)=\frac{\omega}{\rho_0 c^2}p(x)-\frac{A'(x)}{A(x)}v(x), \tag{B6}$$

where $(\,)'$ means to take the space derivative. Because time averages of the potential and kinetic energy densities can be expressed as

$$\text{PE}(x)=\frac{1}{4}\frac{1}{\rho_0 c^2}p^2(x), \tag{B7}$$

$$\text{KE}(x)=\frac{1}{4}\rho_0 v^2(x), \tag{B8}$$

their space derivatives are

$$\text{PE}'(x)=-\frac{1}{2}\frac{\omega}{c^2}p(x)v(x), \tag{B9}$$

$$\text{KE}'(x)=\frac{1}{2}\frac{\omega}{c^2}p(x)v(x)-\frac{1}{2}\rho_0\frac{A'(x)}{A(x)}v^2(x). \tag{B10}$$

Using Eqs. (B9) and (B10), we obtain the following integral formulas:

$$\int_0^L \text{PE}'(x)\,\delta x(x)A(x)dx=-\frac{1}{2}\frac{\omega}{c^2}\int_0^L p(x)v(x)\,\delta x(x)A(x)dx, \tag{B11}$$

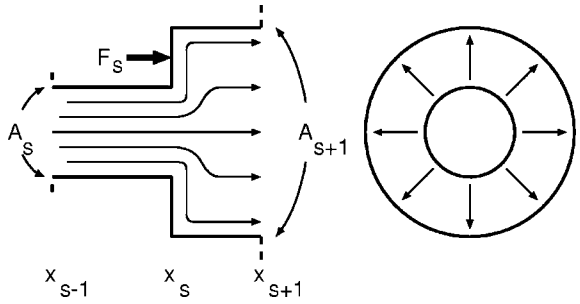

FIG. 5. A part of the vocal tract modeled with concatenated cylindrical sections. Radiation force F_s acts on the annulus formed at the junction between sections s and $s+1$.

$$\int_0^L \mathrm{KE}'(x)\,\delta x(x)A(x)dx = -\frac{1}{2}\frac{\omega}{c^2}\int_0^L p(x)v(x)\,\delta x(x)A(x)dx - 2\int_0^L \mathrm{KE}(x)\Delta(x)A(x)dx + 2\mathrm{KE}(L)\,\delta x(L)A(L), \quad \text{(B12)}$$

where L is the length of the vocal tract, $\delta x(x)$ is perturbation imposed at x, and $\Delta(x) \equiv d\delta x(x)/dx$ is the local expansion or contraction ratio. In the derivation, integration by parts was performed several times.

APPENDIX C

The derivation of Eq. (27) from Eq. (26) is presented here. As it is found from Eqs. (B9) and (B10), the sum of potential and kinetic energy densities has a constant value independent of a position within a cylindrical section, although each of them is not a constant. The sum of the energy densities in section s can therefore be written as

$$\mathrm{PE}_s + \mathrm{KE}_s = \mathrm{PE}_s^{\mathrm{L}} + \mathrm{KE}_s^{\mathrm{L}} = \mathrm{PE}_s^{\mathrm{R}} + \mathrm{KE}_s^{\mathrm{R}}, \quad \text{(C1)}$$

where $\mathrm{PE}_s^{\mathrm{L/R}}$ and $\mathrm{KE}_s^{\mathrm{L/R}}$ are potential and kinetic energy densities at the left/right ends of this section, respectively. At the junction between sections s and $s+1$, continuity of the acoustic pressure and volume flow is satisfied. This yields the boundary conditions for the potential and kinetic energy densities as follows:

$$\mathrm{PE}_s^{\mathrm{R}} = \mathrm{PE}_{s+1}^{\mathrm{L}}, \quad \text{(C2)}$$

$$\mathrm{KE}_s^{\mathrm{R}} A_s^2 = \mathrm{KE}_{s+1}^{\mathrm{L}} A_{s+1}^2. \quad \text{(C3)}$$

At the junction, the acoustic velocity along the tract axis cannot be defined due to the discontinuity. As shown in Fig. 5, the acoustic flow at the junction can be assumed to be in the radial direction of the annulus formed between the sections. The radiation pressure on the annulus then becomes a function of radius r that is

$$P(r) = \mathrm{PE}_s^{\mathrm{R}} - \mathrm{KE}_s^{\mathrm{R}}\frac{A_s^2}{\pi^2 r^4}. \quad \text{(C4)}$$

Integrating $P(r)$ over the annulus, we find the force acting on it:

$$F_s = \int_{r_s}^{r_{s+1}} P(r)2\pi r dr = (A_{s+1} - A_s)\left(\mathrm{PE}_s^{\mathrm{R}} - \mathrm{KE}_s^{\mathrm{R}}\frac{A_s}{A_{s+1}}\right), \quad \text{(C5)}$$

where r_s is the radius of section s, or $A_s = \pi r_s^2$. Substituting Eq. (C5) into Eq. (26) and using Eqs. (C1)–(C3), we obtain Eq. (27).

[1] T. Chiba and M. Kajiyama, *The Vowel: Its Nature and Structure* (Kaiseikan, Tokyo, 1941).
[2] G. Fant, *Acoustic Theory of Speech Production* (Mouton and Co., The Hague, 1960).
[3] M. R. Schroeder, "Determination of the geometry of the human vocal tract by acoustic measurements," J. Acoust. Soc. Am. **41**, 1002–1010 (1967).
[4] P. Ehrenfest, "Adiabatic invariants and the theory of quanta," Philos. Mag. **33**, 500–513 (1917).
[5] G. Fant and S. Pauli, "Spatial characteristics of vocal tract resonance modes," Proc. Speech Comm. Sem. **74**, 121–132 (1974).
[6] G. Fant, "Vocal-tract area and length perturbations," Quarterly Progress and Status Report No. 4, Speech Transmission Laboratory, Kungliga Tekniska Högskolan, Stockholm, 1975, pp. 1–14.
[7] M. Mrayati and R. Carré, "Relations entre la forme du conduit vocal et les caractéristiques acoustiques des voyelles françaises," Phonetica **33**, 285–306 (1976).
[8] B. H. Story, I. R. Titze, and E. A. Hoffman, "The relationship of vocal tract shape to three voice qualities," J. Acoust. Soc. Am. **109**, 1651–1667 (2001).
[9] R. Carré, "From an acoustic tube to speech production," Speech Commun. **42**, 227–240 (2004).
[10] B. H. Story, "Technique for 'tuning' vocal tract area functions based on acoustic sensitivity functions," J. Acoust. Soc. Am. **119**, 715–718 (2006).
[11] L. Brillouin, *Tensors in Mechanics and Elasticity* (Academic, New York, 1964).
[12] K. Beissner, "The acoustic radiation force in lossless fluids in Eulerian and Lagrangian coordinates," J. Acoust. Soc. Am. **103**, 2321–2332 (1998).
[13] L. D. Landau and E. M. Lifshitz, *Fluid Mechanics* 2nd ed. (Butterworth-Heinemann, Oxford, 1987), Chap. 1.
[14] H. Takemoto, K. Honda, S. Masaki, Y. Shimada, and I. Fujimoto, "Measurement of temporal changes in vocal tract area function from 3D cine-MRI data," J. Acoust. Soc. Am. **119**, 1037–1049 (2006).
[15] S. Adachi and M. Yamada, "An acoustical study of sound production in biphonic singing, Xöömij," J. Acoust. Soc. Am. **105**, 2920–2932 (1999).
[16] D. Stanzial, D. Bonsi, and G. Schiffer, "Four-dimensional treatment of linear acoustic fields and radiation pressure," Acta. Acust. Acust. **89**, 213–224 (2003).
[17] G. Fant, "Non-uniform vowel normalization," Quarterly Progress and Status Rep. No. 2-3, Speech Transmission Laboratory, Kungliga Tekniska Högskolan, Stockholm, 1975, pp. 1–19.
[18] G. Fant, "Vocal tract energy functions and non-uniform scaling," J. Acoust. Soc. Jpn. **S76-24**, 1–18 (1976).
[19] G. Fant, *Speech Acoustics and Phonetics* (Kluwer Academic, Dordrecht, 2004), Chap. 2.2.
[20] H. Takemoto, S. Adachi, T. Kitamura, P. Mokhtari, and K. Honda, "Acoustic roles of the laryngeal cavity in vocal tract resonance," J. Acoust. Soc. Am. **120**, 2228–2238 (2006).
[21] G. Fant, "The relations between area functions and the acoustic signal," Phonetica **37**, 55–86 (1980).
[22] P. Mokhtari, "An acoustic-phonetic and articulatory study of speech-speaker dichotomy," Ph.D. dissertation, University of New South Wales, Canberra, Australia, 1998, Chap. 5.
[23] P. Mokhtari and F. Clermont, "New perspectives on linear-prediction modelling of the vocal-tract: Uniqueness, formant-dependence and shape parameterisation," in Proceedings of the Eighth Australian International Conference on Speech Science and Technology (SST'00), Canberra, Australia, 2000, pp. 478–483.
[24] P. M. Morse, *Vibration and Sound*, 2nd ed. (McGraw-Hill Book Co., New York, 1948), Chap. 24.

Speech enhancement using the modified phase-opponency model

Om D. Deshmukh[a] and Carol Y. Espy-Wilson
Department of Electrical and Computer Engineering and Institute for Systems Research, University of Maryland, College Park, Maryland 20742

Laurel H. Carney
Department of Biomedical and Chemical Engineering and Institute for Sensory Research, Syracuse University, Syracuse, New York 13244

(Received 1 February 2006; revised 11 February 2007; accepted 13 February 2007)

In this paper we present a model called the Modified Phase-Opponency (MPO) model for single-channel speech enhancement when the speech is corrupted by additive noise. The MPO model is based on the auditory PO model, proposed for detection of tones in noise. The PO model includes a physiologically realistic mechanism for processing the information in neural discharge times and exploits the frequency-dependent phase properties of the tuned filters in the auditory periphery by using a cross-auditory-nerve-fiber coincidence detection for extracting temporal cues. The MPO model alters the components of the PO model such that the basic functionality of the PO model is maintained but the properties of the model can be analyzed and modified independently. The MPO-based speech enhancement scheme does not need to estimate the noise characteristics nor does it assume that the noise satisfies any statistical model. The MPO technique leads to the lowest value of the LPC-based objective measures and the highest value of the perceptual evaluation of speech quality measure compared to other methods when the speech signals are corrupted by fluctuating noise. Combining the MPO speech enhancement technique with our aperiodicity, periodicity, and pitch detector further improves its performance. © *2007 Acoustical Society of America.* [DOI: 10.1121/1.2714913]

PACS number(s): 43.72.Ne [DOS] Pages: 3886–3898

I. INTRODUCTION

Speech signals in real-world scenarios are often corrupted by various additive noise types (e.g., computer fan noise, subway noise, car noise, and babble), convolutive noise types (e.g., change in microphone or telephone-band-limited speech), and nonlinear disturbances. Speech enhancement techniques that can attenuate the interfering noise with minimal distortions to the speech signal can be used in various speech communication applications like automatic speech recognition, hearing aids, car and mobile phones, cockpits, and multiparty conferencing devices.

The problem of speech enhancement has received a tremendous amount of research attention over the past several decades. A thorough discussion of the different speech enhancement techniques can be found in Benesty *et al.* (2005). A bulk of the speech enhancement techniques are based on modifying the short time spectral amplitude (STSA) of the noisy speech signals. The techniques based on subtractive-type algorithms assume that the background noise is locally stationary to the degree that noise characteristics computed during the speech pauses are a good approximation to the noise characteristics during the speech activity. In addition to the basic spectral subtraction algorithm (Boll, 1979), several extensions and improvements have been proposed (Beh and Ko, 2003; Berouti *et al.*, 1979; Compernolle, 1992; Gustafsson *et al.*, 2001). Virag (1999) presents a detailed analysis of the effect of variations in the subtraction parameters like the over-subtraction factor, the spectral flooring factor, and the exponent on the residual noise as well as the intelligibility of the enhanced speech. It also presents a spectral subtraction algorithm that adapts the subtraction parameters in time and frequency based on the masking properties of the human auditory system.

McAulay and Malpass (1980) have shown that, under certain assumptions about the spectral characteristics of the speech signal and the noise, the spectral subtraction method is the maximum likelihood estimator of the variance of the speech spectral components. Ephraim and Malah (1984) have proposed a system that utilizes the minimum mean square-error short-time spectral amplitude (MMSE-STSA) estimator to enhance speech signals. This method assumes that each of the Fourier expansion coefficients of the speech and of the noise process can be modeled as Gaussian random variables with zero mean. Moreover, it is also assumed that these coefficients are independent of each other. The MMSE-STSA estimator which takes into account the uncertainty of speech presence (McAulay and Malpass, 1980) is also presented. The quality of the enhanced speech is better using the MMSE estimator that takes into account the speech presence uncertainty than the one that does not. The residual noise is perceived more as white noise than as musical noise and is attributed to the smooth variation of *a priori* signal-to-noise ratio (SNR) estimates (Cappe, 1994). The MMSE-STSA al-

[a]Electronic mail: omdesh@glue.umd.edu

 0001-4966/2007/121(6)/3886/13/$23.00 © 2007 Acoustical Society of America

gorithm is extended by Ephraim and Malah (1985) to compute the STSA estimator that minimizes the mean-square error of the log-spectral amplitude, which is a more relevant criterion for perceivable distortions in speech. Loizou (2005) replaced the squared-error cost function used in the MMSE estimator by perceptually more relevant cost functions that take into account the auditory masking effects.

All of these speech enhancement methods make various restricting assumptions about the temporal and spectral characteristics of the speech signals and the corrupting noise. It will be shown in Sec. VI D that the performance of some of these methods deteriorates when the speech signals are corrupted by fluctuating noise. In this paper we present a speech enhancement technique, called the Modified Phase Opponency (MPO) speech enhancement technique, that makes minimal assumptions about the noise characteristics. The MPO speech enhancement scheme does not assume that the noise satisfies any statistical model or any degree of stationarity, nor does it need to estimate/update the noise characteristics but takes advantage of the known nature of speech signals. The MPO speech enhancement technique is thus potentially robust to fluctuating background noise. The performance of the MPO technique on fluctuating noise is presented in Sec. VI D. The MPO speech enhancement scheme is based on the auditory Phase Opponency (PO) model (Carney *et al.*, 2002) for tone-in-noise detection that includes a physiologically realistic mechanism for processing the information in neural discharge times. Some of the other speech enhancement techniques based on models of human auditory systems include Cheng and O'Shaughnessy (1991), Hansen and Nandkumar (1995), Mesgarani and Shamma (2005), and Tsoukalas *et al.* (1997).

In the present work, the MPO enhancement scheme is also combined with our Aperiodicity, Periodicity and Pitch (APP) detector (Deshmukh *et al.*, 2005b) to develop the MPO-APP speech enhancement scheme. The APP detector was developed to estimate the proportion of periodic and aperiodic energy in a speech signal. The MPO scheme is combined with the APP detector to remove the narrowband noise that might be seen as speech-like by the MPO processing and to retain some of the wideband speech signal that might be seen as noise-like by the MPO processing. The MPO-APP speech enhancement scheme produces a binary spectrotemporal mask called the *MPO profile* that distinguishes spectrotemporal regions where the speech signal is more dominant than the regions where the noise is more dominant. The use of binary masks is fairly common in the auditory scene analysis based speech enhancement and robust speech recognition techniques (Wang, 2005) and is motivated by the phenomenon of masking in the human auditory system. Hu and Wang (2004) proposed a computational auditory scene analysis method for segregating speech signals corrupted by various additive interferences. This method segregates the low-frequency resolved harmonics of the speech signals based on temporal continuity and cross-channel correlation and the high-frequency unresolved harmonics based on amplitude modulation and temporal continuity. The segments from the resolved harmonics are grouped according to common periodicity estimates and the segments from the unresolved harmonics are grouped according to common amplitude modulation rates. The proposed MPO-APP technique also contains an algorithm that reliably estimates the proportion of periodicity in speech signals but combines it with an algorithm that detects the presence of narrowband signals in noise to separate speech signals from the background noise.

The proposed speech enhancement scheme leads to the lowest value of the linear-predictive coefficients based objective measures and the highest value of the perceptual evaluation of speech quality (PESQ) measure compared to some of the other methods when the speech signals are corrupted by fluctuating noise. The performance of the proposed speech enhancement scheme is comparable to some of the other enhancement techniques when the global SNR and the noise type of the corrupting noise are not fluctuating.

II. THE PHASE OPPONENCY MODEL

A model for detection of tone-in-noise based on processing the information in neural discharge times is presented in Carney *et al.* (2002). This model exploits the frequency-dependent phase properties of the tuned filters in the auditory periphery and uses cross-auditory-nerve-fiber coincidence detection to extract temporal cues. It is shown that the responses of some of the cross-channel coincidence detectors are reduced when a tone is present in the background noise. This reduction in response to the presence of the target is referred to as Phase Opponency (PO). The performance of the PO model in the detection of low-frequency tones embedded in fixed-level or roving-level masking noise is consistent with that of humans (Carney *et al.*, 2002), making it a suitable model to detect narrowband signals corrupted by additive noise. In the present work, the PO model is extended to develop a speech enhancement scheme by utilizing the facts that (a) much of the speech signal is voiced and can be thought of as a combination of narrowband signals (i.e., harmonics) with varying amplitudes and (b) retaining the high-amplitude harmonics near the formant frequencies is perceptually more significant than the harmonics in the valley regions. The MPO processing scheme will thus not be able to retain the obstruents in a given speech signal although it does detect the frequency onset of strident friction in high SNR situations.

Figure 1 shows the PO model with center frequency (CF) equal to 900 Hz. The two nerve fibers are modeled as two gammatone filters with slightly different CFs. The magnitude and the phase response of the two gammatone filters are also shown in Fig. 1.

When the input is a tone at 900 Hz, the outputs of the two filters will be out of phase and the cross correlation will lead to a negative output. The output will remain negative as long as the input is a bandlimited signal centered at the CF (900 Hz in this case) and with bandwidth (BW) within the out-of-phase frequency region ($F_a - F_b$ in Fig. 1). We refer to the frequency region $F_a - F_b$ as the *out-of-phase* region and the rest of the frequency region as the *in-phase* region. When the input is a wideband signal, the output of the two filters will exhibit some degree of correlation and the cross-

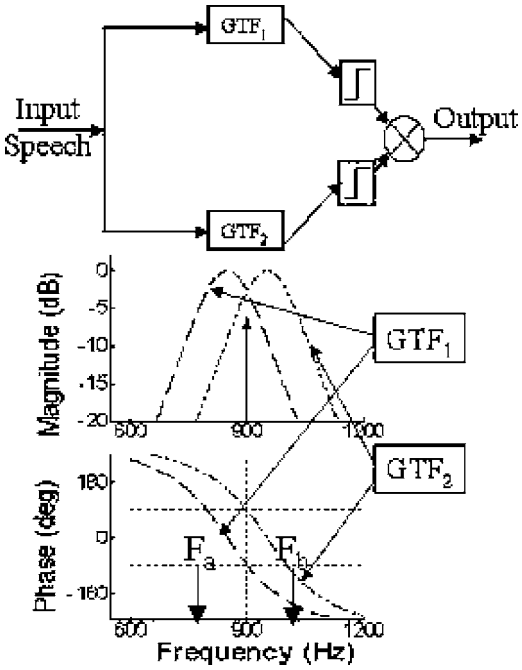

FIG. 1. PO filter pair to detect a tone at 900 Hz. GTF: Gammatone filter. The relative phase response of the two GTFs is out-of-phase in the frequency range $[F_a - F_b]$. The CFs for the two filters are 848.5 and 951.5 Hz. Adapted from Carney *et al.* (2002).

correlation output will be positive or very slightly negative. Thus the model is able to distinguish between narrowband signals and wideband noise. A saturating nonlinearity is applied to the output of each of the filters to minimize the effect of amplitude fluctuations on the overall output of the PO model.

Some of the issues with the PO model shown in Fig. 1 are that the relative magnitude response and the relative phase response of the two paths depend on the same set of parameters, making it difficult to manipulate either of the two independent of the other. It is difficult to predict the relationship between the parameters controlling the characteristics of the PO model and the width and the location of the *out-of-phase* region.

III. MODIFIED PHASE OPPONENCY MODEL

To address the concerns raised in Sec. II about the PO model, the MPO model was developed in such a way that the basic functionality of the PO model is maintained, but the various properties of the model can be analyzed and modified independent of each other. Figure 2 shows the schematic of the MPO model used in the present work. In the MPO

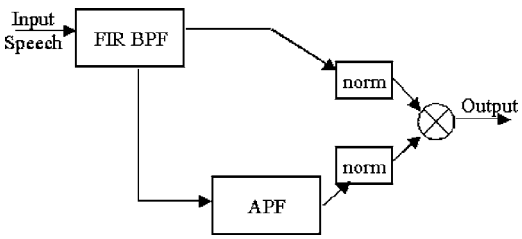

FIG. 2. Modified PO filter pair. "Norm" indicates amplitude normalization.

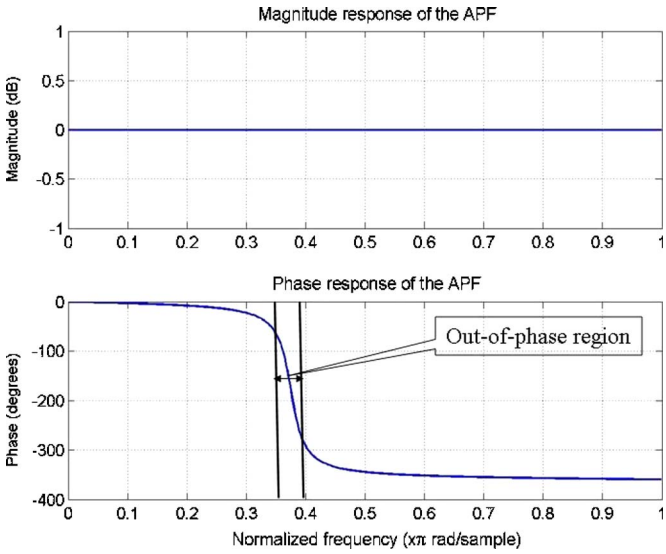

FIG. 3. (Color online) Magnitude and phase response of a typical all pass filter with one pair of complex conjugate poles. The *out-of-phase* frequency region is also shown.

model, one of the paths is modeled as a linear-phase finite impulse response (FIR) bandpass filter (BPF). The other channel is modeled as a concatenation of the same FIR BPF followed by an all pass filter (APF). The relative phase response of the two paths can be manipulated by changing the parameters of the APF which does not introduce any changes in the relative magnitude response. The magnitude response of the two paths can be manipulated by changing the parameters of the BPF which does not introduce any changes in the relative phase response. Thus the MPO model shown in Fig. 2 allows for manipulation of the relative magnitude response and the relative phase response independently of the other. The filters are followed by an amplitude normalizing scheme to minimize the effect of magnitude information in the cross-frequency coincidence. The characteristics of the BPF are mainly decided by the range of the target frequency that is to be detected. The characteristics of the APF are mainly decided by the expected frequency range and BWs of the target signals. The relation between the parameters of the APF and its phase response is explored below.

A. Mathematical formulation of the MPO model

Consider a second-order APF, $H(z)$, with one pair of complex conjugate poles,

$$H(z) = \frac{(z^{-1} - a^*)(z^{-1} - a)}{(1 - a^* z^{-1})(1 - a z^{-1})},$$

where $a = re^{j\theta}$ is the complex pole and a^* is its complex conjugate. Figure 3 shows the magnitude and the phase response of the APF for $r = 0.93$ and $\theta = 0.375\pi$. The magnitude response is uniformly 0 dB for all values of the frequency ω. The phase response, $\Phi(\omega)$, is given by

$$\Phi(\omega) = -2\omega - 2\tan^{-1}\left[\frac{2r\sin(\omega)\cos(\theta) - r^2\sin(2\omega)}{1 - 2r\cos(\omega)\cos(\theta) + r^2\cos(2\omega)}\right]. \quad (1)$$

We are interested in deriving the relationship between r and θ and the location and the width of the *out-of-phase* region. Notice from Fig. 3 that locating the *out-of-phase* region is equivalent to locating the frequency region where the phase response is the steepest. The frequency region where the phase response, $\Phi(\omega)$, is the steepest can be located by finding the frequency where the slope of the phase response has an inflection point, i.e., by finding the ω for which $d^2(\Phi(\omega))/d\omega^2 = 0$. Equating the numerator of the second-order derivative to zero and simplifying leads to

$$D(r,\omega,\theta)\cos\theta = \cos\omega,$$

where

$$D(r,\omega,\theta) = \left[\frac{1 + 2r^2 + 4r^2(\cos^2\omega + \sin^2\theta) + r^4}{4r(1+r^2)}\right]. \quad (2)$$

If we assume $\omega = \theta$, then the $\cos\theta$ term on the left-hand side of Eq. (2) is balanced by the $\cos\omega$ term on the right-hand side. Further, if we assume $r = 1$, then the sum of the coefficients in the numerator of $D(r,\omega,\theta)$ $[1+2+4+1=8]$ is exactly equal to that of the coefficients in the denominator $[4 \times (1+1) = 8]$. Thus, the equality in Eq. (2) holds for $\theta = \omega$ and $r = 1$. However, stability of the APF dictates that the magnitude of r be less than 1. It can easily be verified (Deshmukh, 2006) that $D(r,\omega,\theta)$ remains close to 1 even for various values of r less than 1. Thus, it is reasonably accurate to assume that:

The slope of the phase response, $\Phi(\omega)$, of a stable APF with a pair of complex conjugate poles at $re^{\pm j\theta}$ is the steepest at frequency $\omega = \theta$. Moreover, this frequency location is independent of r, the magnitude of the pole.

The phase response, $\Phi(\omega)$, of the APF at $\theta = \omega$, under the assumption of $r \approx 1$ simplifies to:

$$\Phi(\omega) \approx \begin{cases} \pi & \text{if } \cot\theta < 0 \\ -\pi & \text{if } \cot\theta > 0. \end{cases} \quad (3)$$

The phase response at $\omega = \theta$ can thus be approximated as $\pm\pi$.

The closer the value of r to 1, the more accurate the approximation is. The next step is to express the dependence of the width of the *out-of-phase* region on the values of r and θ. This is equivalent to expressing the slope of $\Phi(\omega)$ at $\omega = \theta$ in terms of r and θ. Evaluating the derivative of $\Phi(\omega)$ with respect to ω at $\omega = \theta$ for various values of θ and ω shows that for a given value of r, the value of $d(\Phi(\omega))/d\omega$ is not very sensitive to the value of θ. On the other hand, it is very sensitive to the choice of r. It can thus be assumed that:

$d(\Phi(\omega))/d\omega$ evaluated at $\omega = \theta$ (i.e., at the frequency where the phase response of the APF is the steepest) is independent of θ and is dependent only on the value of r.

In summary, for an APF with poles at $a = re^{j\theta}$ and a^*, the *out-of-phase* region is centered around $\omega = \theta$ irrespective of the value of r (the phase response at $\omega = \theta$ is approximately equal to $\pm\pi$) and the width of the *out-of-phase* region is controlled only by the value of r, irrespective of the value of θ.

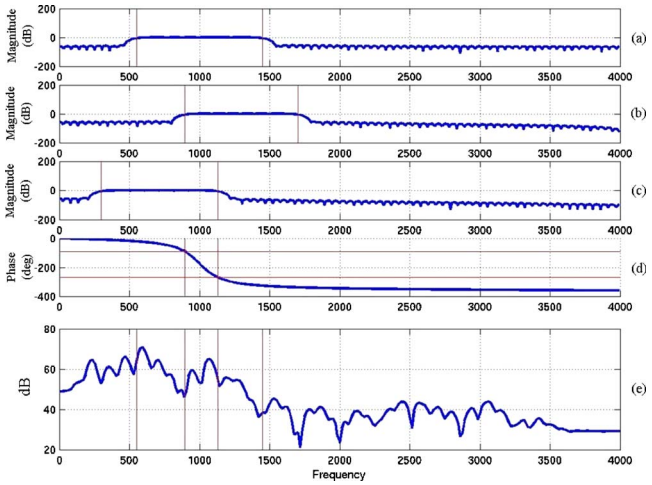

FIG. 4. (Color online) Magnitude response of the (a) symmetric BPF; (b) upward-skewed BFP; and (c) downward-skewed BPF that will be used in the MPO structure with CF = 1000 Hz. (d) Phase response of the APF that will be used in the MPO structure with CF = 1000 Hz. (e) Spectral slice of a sonorant region in speech signal.

B. MPO design

Our aim is to design a MPO structure to detect signals centered at ω_c and of bandwidths less than or equal to $\Delta\omega$. The first requirement is to choose the APF such that the phase response is about $-\pi$ at ω_c. Analysis in Sec. III A shows that this requirement is satisfied by choosing the phase of the pole of the APF as $\theta = \omega_c$ [see Eq. (3)], irrespective of what the value of r, the magnitude of the pole of the APF, is. The expected bandwidth of the target signal, $\Delta\omega$, dictates the value of r. The value of r should be such that the phase response, $\Phi(\omega)$, of the APF spans $-\pi/2$ to $-3\pi/2$ in $\Delta\omega$ rad centered around ω_c (i.e., the *out-of-phase* region corresponds to the expected bandwidth of the input signal). Unfortunately, there is no closed form relation between r and the BW of the *out-of-phase* region. For a given expected bandwidth, $\Delta\omega$, the value of r has to be computed using multiple trials. But, as is shown in Sec. III A, for a given bandwidth, the value of r is dependent only on the bandwidth and is independent of the center frequency of the signal. Assume that the optimal value of r for the expected bandwidth of $\Delta\omega$ is $r = r_c$. The APF is completely defined by specifying the parameters r and θ.

The next step is to choose the FIR BPF. The BPF has to satisfy two constraints:

(1) The passband of the BPF should include the *out-of-phase* region.
(2) The passband should be such that the MPO output is negative for narrowband signals (with bandwidth less than or equal to $\Delta\omega$ and centered at the CF) and positive for wideband signals.

Several BPFs can be designed that satisfy the two above-mentioned constraints. Figure 4 shows three such BPFs for a

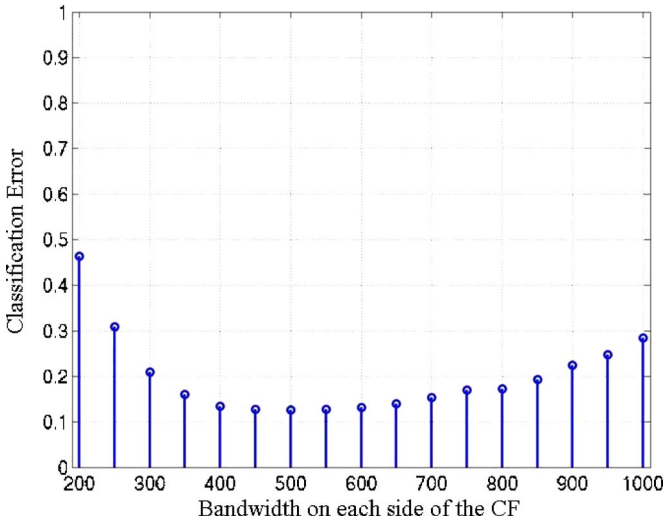

FIG. 5. (Color online) Variation in the binary classification error as the bandwidth of the BPF is varied. The two classes are: (a) presence of narrowband signal in broadband noise at 0 dB SNR and (b) broadband noise.

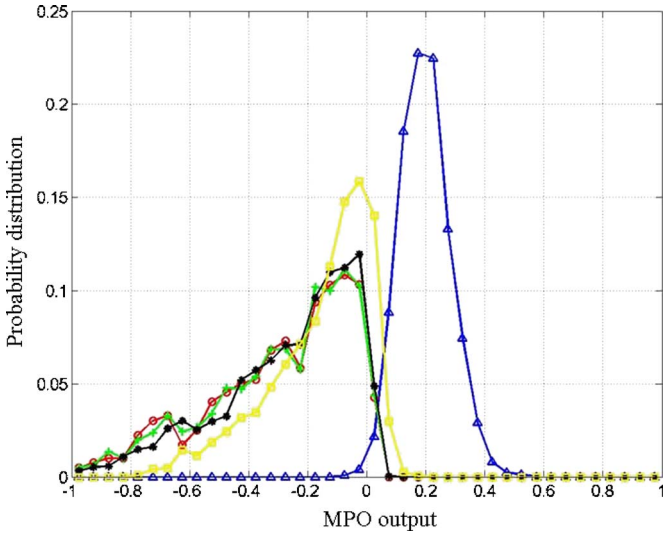

FIG. 6. (Color online) Distribution of the output of MPO model when the input is white noise (△); band-limited signal at ∞ dB SNR (○); at 20 dB SNR (+); at 10 dB SNR (black curve: *); and at 0 dB-SNR (□).

MPO structure that can be used to distinguish narrowband signals centered at 1000 Hz with bandwidth less than 250 Hz from wideband noise signals. Initial versions of the MPO-based speech enhancement scheme (Deshmukh and Espy-Wilson, 2005; Deshmukh *et al.*, 2005a) used BPFs with passband symmetry across the CF of the MPO structure. Figure 4(a) shows the magnitude response of such a symmetric BPF. Figure 4(d) shows the phase response of the APF used in the corresponding MPO structure. The optimal bandwidth of the BPF is computed by calculating the two-class (narrowband-signal-in-noise versus noise-only) classification error for different choices of bandwidths and choosing the one that gives the least error. For low values of bandwidth the output for the presence-of-signal situations as well as for the absence-of-signal situations will be negative leading to many false-positive errors whereas for high values of bandwidth the output for the absence-of-signal situations as well as for the presence-of-signal situations will be positive leading to many correct-miss errors. Figure 5 plots the total classification error for a MPO structure that uses the APF shown in Fig. 4(d) and for different bandwidths of the corresponding symmetric BPF. The optimal BPF is $450\times2=900$ Hz. Note that the classification error is close to the minimum value over a wide range of the BPF bandwidths (800–1200 Hz) and is thus not very sensitive to the exact choice of the BPF bandwidth. In all the simulations, the BPF length was kept constant at 76 samples, and was constructed using the standard MATLAB routine *fir1*.

Figure 6 shows the distribution of the output of the MPO model shown in Figs. 4(a) and 4(d) for 5000 frames (a frame is 30 ms long with a frame rate of 5 ms) each of white noise and a bandlimited signal centered at 1000 Hz and of bandwidth 250 Hz corrupted with white noise at ∞, 20, 10, and 0 dB SNR. Notice that the distribution of the output for white noise is well separated from that for the bandlimited signal at ∞ dB SNR. Moreover, the distribution of the bandlimited signal corrupted by white noise remains quite similar over a wide range of SNRs (∞ to 0 dB). The threshold to discriminate the presence of the signal from the absence of signal is computed using the maximum likelihood (ML)-based likelihood ratio test (LRT). The optimal threshold value is −0.0215. Figure 7 shows the receiver operating characteristic (ROC) curve for MPO detectors at three different CFs: 950 Hz (dash curve), 1000 Hz (dotted curve), and 1050 Hz (solid curve). The optimal threshold values are: −0.0183, −0.0215, and −0.0197, respectively. The ROC curves in Fig. 7 were obtained by varying the threshold over the range: [opt_thresh −0.05 : −0.005] where opt_thresh is the optimal threshold for the corresponding MPO detector. In general, it is observed that the probability of false alarm is below 3% for threshold values below 0 (the theoretical threshold) and the probability of detection remains above 96% for threshold values as low as opt_thresh −0.05 indicating that the exact value of the threshold is not critical for the overall operation of the MPO detectors. It is worth pointing out that the thresholds for the MPO detectors at different CFs are computed using the two extremes of (a) narrowband sig-

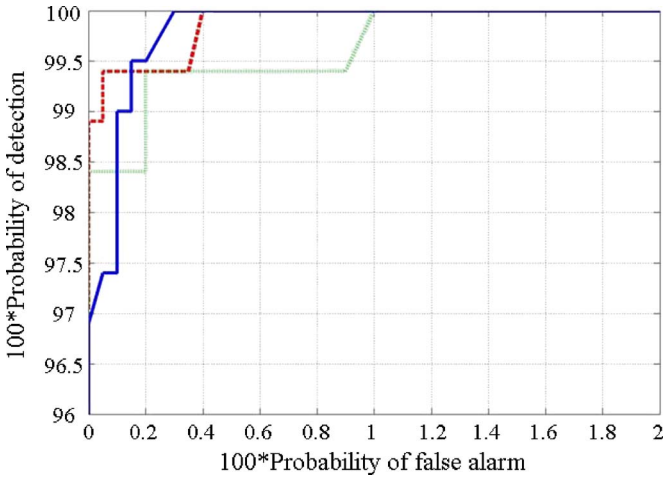

FIG. 7. (Color online) ROC curves for MPO detectors at three different CFs: 950 Hz (dash curve); 1000 Hz (dotted curve); and 1050 Hz (solid curve).

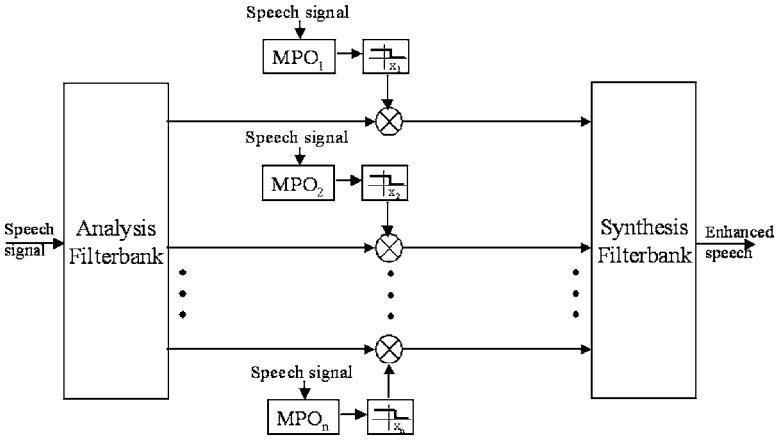

FIG. 8. Schematic of the MPO-based speech enhancement scheme. The threshold, x_i, is trained using the ML-LRT technique and all the regions with output above this threshold are suppressed.

nals centered at the CF and (b) white noise. These thresholds are not retrained when the background conditions change. It is shown in Sec. VI that the MPO speech enhancement scheme is robust to various noise types at different levels with no additional noise-specific training.

The other two BPFs shown in Fig. 4 have passbands skewed upward or downward in frequency with respect to the CF of the MPO structure [Figs. 4(b) and 4(c), respectively]. Both of these BPFs offer some advantages over the symmetric BPF and will be discussed in Sec. IV A.

IV. MPO-BASED SPEECH ENHANCEMENT

Speech signals, for the most part, are composed of narrowband signals (i.e., harmonics) with varying amplitudes. The MPO-based speech enhancement scheme attempts to detect and maintain these time-varying narrowband signals while attenuating the other spectro-temporal regions. Figure 8 shows the schematic of the MPO-based speech enhancement scheme. The analysis-synthesis filterbank can be any near-perfect reconstruction (PR) filterbank. The overall performance of the MPO enhancement scheme is insensitive to the choice of the analysis-synthesis filterbank. In the present work, a DFT-based PR filterbank is used. In a related work (Anzalone *et al.*, submitted), a near-PR analysis-synthesis gammatone filterbank proposed by Hohmann (2002) was used. The input speech signal is split into overlapping frames of length 30 ms at a frame rate of 5 ms. Each MPO_i in the figure is a MPO structure (Fig. 2) with a different CF. The CFs are spaced every 50 Hz from 100 Hz to just below the maximum frequency. The threshold, x_i, to discriminate the presence of signal from the absence of signal is trained separately for each MPO structure as described in Sec. III B. The MPO structures act as switches allowing the speech frame to either pass as it is for reconstruction if the corresponding MPO output is less than the threshold (indicating presence of signal) or be attenuated by 10 dB if the output is greater than or equal to the threshold (indicating absence of signal). Attenuating the signal-absent regions by 10 dB, instead of zeroing them out completely, reduces the perceptual effect of the residual noise. Higher attenuation of the speech-absent regions leads to an overall increase in the objective distortion measures as well as a lower PESQ measure.

In the initial version of the MPO-based speech enhancement scheme (Deshmukh and Espy-Wilson, 2005; Deshmukh *et al.*, 2005a), each of the MPO_i in Fig. 8 consisted of a symmetric BPF and the APF was configured so that signals with bandwidths less than or equal to 150 Hz would lead to negative outputs. Such a scheme performs well when the input speech signal is corrupted by additive white noise which has a relatively flat spectrum with minimal level fluctuations over time. But it passes a lot more noise when the corrupting signal is colored noise with fluctuating levels. To overcome this problem, the present version of the speech enhancement scheme uses two sets of MPO structures at each CF. Each set has five different MPO structures such that each one of them has a different *out-of-phase* region ranging from 120 to 250 Hz. Noise can be wrongly seen as speech by one or more of the five different structures in either set, but it is rarely seen as a narrowband speech signal by all five structures. Similarly, narrowband speech signals are almost always seen as speech signals by *all* five MPO structures. Using five structures in each set strikes a better balance between computational cost and the amount of residual noise as compared to a higher or lower number of structures per set.

A. Choosing the BPF for speech signals

Consider the spectral slice shown in Fig. 4(e). The harmonics close to F2 (around 1050 Hz) fall in the out-of-phase frequency region of the MPO structure whereas the harmonics close to F1 (around 550 Hz) fall in the in-phase frequency region of the MPO structure with symmetric BPF. The amplitude of F1 (and hence that of the harmonics close to F1) is greater than that of F2 due to the known spectral tilt in sonorant regions of speech signals. As a result, although there is a narrowband signal at the CF of the MPO, the output of this MPO structure will be positive and therefore the speech information present in that frequency region will be missed. The upward skewed BPF shown in Fig. 4(b) will attenuate the F1 region and thus the output of the upward-skewed MPO structure will be driven mainly by the frequency content near the CF and in the frequency region above the CF. Most of the time, such upward skewed MPO structures are able to correctly detect the speech information as they inherently take advantage of the spectral tilt present in sonorant speech regions. The F2 information in Fig. 4(e)

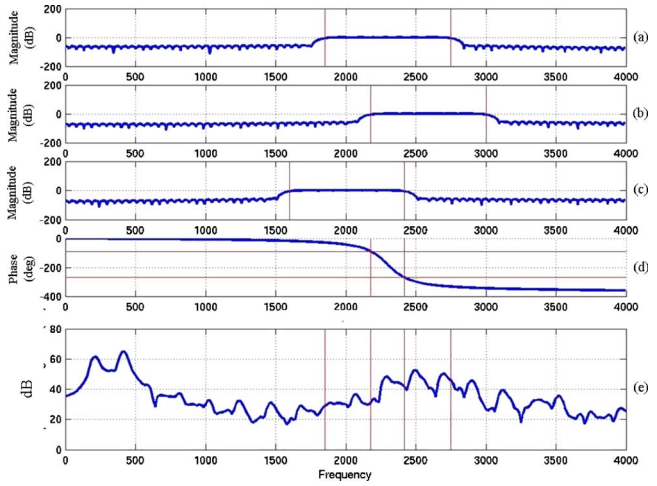

FIG. 9. (Color online) Magnitude response of the (a) symmetric BPF; (b) upward-skewed BFP; and (c) downward-skewed BPF that will be used in the MPO structure with CF=2300 Hz. (d) Phase response of the APF that will be used in the MPO structure with CF=2300 Hz. (e) Spectral slice of a sonorant region in speech signal.

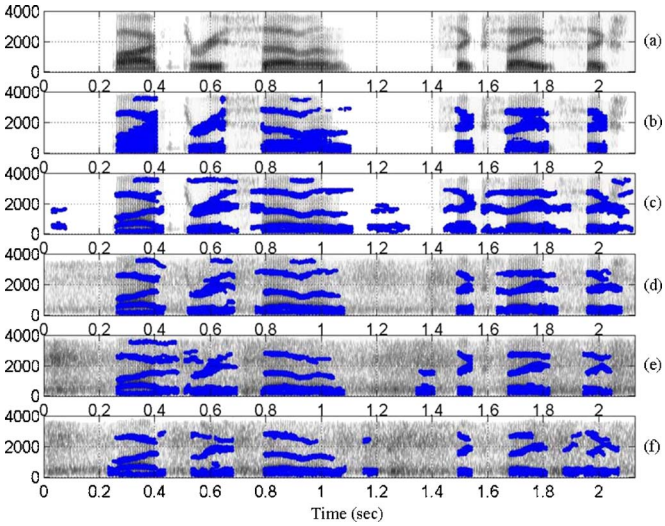

FIG. 10. (Color online) (a) Spectrogram of the utterance "five three seven six eight six;" (b) the energy-based *maximal mask*; and (c), (d), (e), and (f) MPO profile at ∞, 20, 10, and 5 dB SNR, respectively.

that was missed by the symmetric MPO structure will be detected by the upward-skewed MPO structure.

The downward-skewed filter shown in Fig. 4(c) is the exact opposite of the upward-skewed filter. The passband of the downward-skewed filter extends downward in frequency with respect to the CF of the MPO structure. Consider the case shown in Fig. 9(e) when two formants are of comparable amplitudes and are in close proximity in frequency (hence, the harmonics near these formant frequencies have comparable amplitudes). In such cases, the upward skewed MPO structures will detect the higher frequency harmonics, but will fail to detect the lower frequency harmonics. The downward skewed MPO structures centered on the lower frequency harmonics will be able to successfully detect such instances because their *in-phase* region extends on the lower frequency side. Each CF is thus analyzed using an upward MPO structure as well as a downward MPO structure.

B. Speech enhancement scheme

As explained in Sec. IV A each MPO_i in Fig. 8 consists of five upward-skewed MPO structures (one set) and five downward-skewed MPO structures (second set) all tuned to the same CF, but with the width of the *out-of-phase region* ranging from 120 to 250 Hz. The speech enhancement scheme can now be described as a two-step process. In the first step, the temporal regions where speech is present are computed. For a temporal region to be voted as *speech present*, it has to satisfy two conditions: (a) The MPO output of at least one frequency channel from all five different upward-skewed or all five different downward-skewed MPO structures should be at least four times more negative than the threshold for that particular channel and (b) the temporal region should be at least 50 ms long.

In the second step, the frequency channels within the *speech-present* temporal regions where speech information is present are computed by finding the channels where the MPO output from all five upward skewed or all five downward skewed MPO structures is below the corresponding threshold. The noisy speech signal from only these channels is used for reconstruction.

The first step is to ensure that wrongful insertions in the decision of temporal *speech-present* regions are kept to a minimum and the second step is to ensure that all of the valid *speech-present* spectral channels in a given *speech-present* temporal region are detected.

The MPO speech enhancement scheme can thus be thought of as applying a time-frequency two-dimensional binary mask to the input speech signal. The binary mask has a value of one in *speech-present* spectrotemporal regions where the speech signal is dominant and has a value of zero in the *speech-absent* spectrotemporal regions where the noise signal is more dominant. The binary mask is referred to as the "MPO profile." Figure 10(a) shows the spectrogram of the utterance "five three seven six eight six" in clean. Figures 10(c)–10(f) shows the corresponding MPO profile when the utterance is corrupted by subway noise at ∞, 20, 10, and 5 dB SNR, respectively. The dark (blue) regions are the spectrotemporal channels where the MPO profile is one. The speech signal from these channels is used "as-is" to construct the enhanced speech signal. The MPO processing retains almost all of the perceptually significant speech information when the input signal is clean. Some of the formant transitions through the fricative regions as well as the frequency onset of strident frication are also tracked (e.g., around 1.6 and around 2.2 s). As the SNR is reduced, most of the strong sonorant information is detected by the MPO processing while very little noise is mistaken as speech signal [e.g., around 1.4 s in Fig. 10(e) and around 1.2 and 1.9 s in Fig. 10(f)].

Figures 11(a) and 11(c) compare the MPO profiles of two utterances "four three six four six three" (left) and "one five" (right) in clean and when they are corrupted by car noise and subway noise, respectively, at 10 dB SNR. The MPO processing retains almost all of the perceptually significant speech information when the input signal is clean.

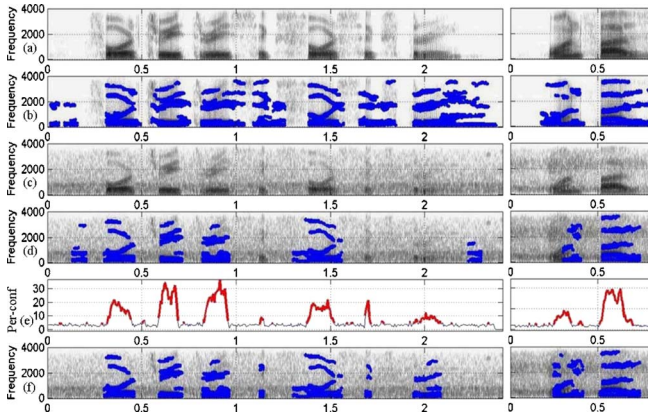

FIG. 11. (Color online) (a) Spectrograms of clean signals "four three three six four six three" (left) and "one five" (right). (b) The MPO profiles of the corresponding signals. (c) Spectrograms of the signals corrupted by car noise (left) and subway noise (right) at 10 dB SNR. (d) The MPO profiles of the corresponding noisy signals. (e) Periodicity confidence. Frames with periodicity confidence greater than per_thresh are shown with a thicker line. (f) The combined MPO-APP profiles of the noisy signals.

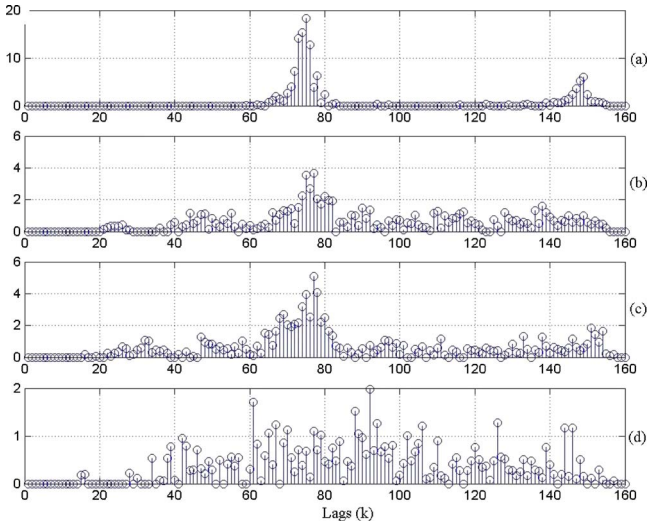

FIG. 12. AMDF clusters for a periodic frame at different SNRs and for an aperiodic frame.

When the input signal is noisy, the MPO processing, while detecting most of the strong harmonics, fails to detect the short vowel /I/ in both the instances of "six" [1.12–1.16 and 1.68–1.73 s in Fig. 11(d)] as well as completely misses the last "three" (1.9–2.3 s). Also notice that the /w/ in the noisy "one" [0.22–0.3 s Fig. 11(d) on the right] is not detected by the MPO processing. F1 and F2 for /w/ are very close and thus look like a wideband signal which is not detected by the MPO processing. Also note that in all of these regions the temporal signal has strong periodicity which distinguishes it from the temporal signal in the noise-only regions. On the other hand, some of the noise is wrongly seen as narrowband signal by the MPO processing and is passed for reconstruction [e.g., 0.12–0.2 and 2.23–2.3 s in Fig. 11(d)]. But these noise regions are not as periodic as the speech-present regions.

The number of noise-insertions and the number of speech-deletions can be reduced by combining the MPO processing with an algorithm that reliably estimates the periodicity information in speech signals. In the present work, the MPO processing is combined with our APP detector (Deshmukh *et al.*, 2005b). The APP detector estimates the proportion of periodic and aperiodic energy in each spectrotemporal channel as well as the confidence of periodicity in each time frame. Such a time-frequency analysis by the APP detector makes it convenient to combine the APP detector with the MPO processing. The narrowband noise that is inserted in the reconstructed speech signal by the MPO processing does not have a harmonic structure across the frequency channels similar to that of the periodic regions in a speech signal. On the other hand, the locally wide-band regions of speech signals formed due to the proximity of two or more formants retain a coherent harmonic structure across the frequency channels. The APP detector captures this coherence of across-frequency-channel periodicity and can reduce such speech-deletions in the MPO speech enhancement scheme.

Section V presents a brief overview of the APP detector, the use of the APP detector as a separate speech enhancement technique, and the way in which the MPO processing is combined with the APP detector.

V. APERIODICITY, PERIODICITY, AND PITCH DETECTOR

The processing in the APP detector begins by splitting the speech signal into 60 frequency channels that are equispaced on the ERB scale. The average magnitude difference function (AMDF) is computed on the envelope of each of the frequency channels at a frame rate of 2.5 ms and a frame length of 20 ms. The AMDF is given by

$$\gamma_n(k) = \sum_{m=-\infty}^{m=\infty} |x(n+m)w(m) - x(n+m-k)w(m-k)|,$$

where $x(n)$ is the envelope signal, k is the lag value in samples, and $w(m)$ is a 20-ms-long rectangular window.

For a periodic signal, the AMDF attains minima (referred to as dips) values close to one at lags equivalent to the pitch period and its integer multiples. Moreover, for a frame in a periodic speech region, the pitch period is quite similar across the different frequency channels. Thus, lag-wise addition of the AMDF dips across the frequency channels leads to clustering at integer multiples of the pitch period as shown in Fig. 12(a) for a frame during the /w/ centered at 0.27 s in clean condition (Fig. 11, right-hand side). Figures 12(b) and 12(c) show that the clusters are retained even as the SNR is reduced to 10 and 5 dB, respectively. For an aperiodic frame, the lag-wise addition of the AMDF dips across the frequency channels results in dips that are randomly scattered over the range of the possible lag values. For example, Fig. 12(d) shows the lag-wise addition of the AMDF dips for an aperiodic frame centered at 0.46 s in the utterance shown on the right-hand side in Fig. 11 and corresponds to the phoneme /f/ in "five."

The periodicity confidence of a given temporal frame is computed as the strength of the dips close to the cluster peaks relative to the strength of the rest of the dips. The

locations of the cluster peaks is the estimate of the pitch frequency. For aperiodic frames, where no strong clusters exist, a cluster is formed around the lag with the maximum strength. The periodicity confidence values for the plots in Figs. 12(a)–12(d) are: 50.8, 9.7, 9.3, and 0.4, respectively. The periodicity confidence can thus distinguish a periodic frame from an aperiodic frame even when the speech signal is corrupted by noise. The optimal threshold of the periodicity confidence, per_thresh, to distinguish periodic frames from aperiodic frames is computed using periodic and aperiodic frames from clean speech signals and is not altered as the background conditions change.

Frequency channels where the AMDF dips close to the cluster peaks are stronger than the AMDF dips away from the cluster peaks are classified as periodic channels. The rest of the channels are classified as aperiodic channels. This leads to a spectrotemporal binary mask, called the "APP profile," which has a value of 1 in frequency channels which are estimated to be periodic and a value of 0 in channels which are estimated to be aperiodic. Also, note that if any of the frequency channels has periodic noise then the periodic noise will be classified as periodic speech signal only if the corresponding period of the noise is very close to the estimated pitch period of the speech signal. [Please refer to Deshmukh *et al.* (2005b) for more details on the various stages of the APP detector.]

A. APP-based speech enhancement technique

The APP speech enhancement technique consists of the APP detector sandwiched between a near-PR analysis-synthesis gammatone filterbank proposed by Hohmann (2002). (The setup is similar to the one shown in Fig. 8 for the MPO speech enhancement scheme.) The filters of the near-PR filterbank are equi-spaced on the ERB scale and the CFs and the bandwidths are chosen such that they match the filters used in the analysis of the APP detector. The spectrotemporal channels where the APP profile is one (indicating presence of periodic signal) are passed as-is to the synthesis filterbank and the rest of the spectrotemporal channels are attenuated by 10 dB before being passed to the synthesis filterbank.

B. Combining MPO processing with the APP detector

As mentioned earlier, some of the main shortcomings of the MPO processing are: (1) Noise insertions: Where some of the narrowband noise is detected as speech-like although it lacks the harmonicity typical of the sonorant speech regions and (2) speech deletions: Where locally wideband regions of speech signals are not retained although they have a coherent harmonic structure across the frequency channels.

For each of the frequency channels analyzed by the MPO processing, the AMDF dips are computed on the envelope of the channel signal. The periodicity confidence of each temporal frame is computed by the lag-wise addition of the AMDF dips across the frequency channels as mentioned in Sec. V. A given *speech-present* region in the MPO-processing is classified as *speech-absent* (and thus not used for reconstruction) if the maximum value of the periodicity confidence in the corresponding region is below per_thresh. For example, consider the MPO-estimated speech-present region between 0.13 and 0.20 s [Fig. 11(d), left-hand side]. The maximum value of the periodicity confidence in this region is below per_thresh [frames with periodicity confidence greater than per_thresh are shown with a thicker line in Fig. 11(e)]. Thus, this region will not be used for reconstruction. Such a strategy leads to a reduction in noise insertions.

All the frames that are classified as *speech absent* by the MPO processing but have the corresponding periodicity confidence greater than $2 \times$ per_thresh (indicating strong periodicity) are classified as *speech present* and reintroduced for synthesis. Figure 11(f) shows the combined MPO-APP profile for the noisy utterances shown in Fig. 11(c). Notice that the noise insertions are removed and most of the speech deletions are reintroduced.

VI. EVALUATION

A. Database

The Aurora database (Hirsch and Pearce, 2000) was used to evaluate the MPO-based speech enhancement scheme. This database is a derivative of the TIdigits database resampled at 8 kHz. The database has three different subsets for testing. In the present study, only the test subset A was used for evaluation. Subset A consists of utterances corrupted by four different noise types at seven different SNRs from ∞ to -5 dB. Each utterance in the Aurora database is corrupted by one of the noise types at a given SNR. The four different noise types are: Subway noise, babble, car noise, and exhibition hall noise. These are referred to as N1, N2, N3, and N4, respectively.

A database of speech signals corrupted by fluctuating noise (F-DB) was formed from this subset of the Aurora database. Each utterance in F-DB database consists of seven digits. Each of the seven digits is corrupted by a different noise type at a different SNR. The F-DB database consists of 1120 such utterances.

The overall MPO speech enhancement strategy (i.e., number of MPO structures at each CF, combining the output of these MPO structures) was developed using a subset of the TIMIT database corrupted by white noise and a subset of the Aurora database.

The performance of the MPO and the combined MPO-APP speech enhancement technique was compared with some of the speech enhancement techniques presented in the literature: (a) MMSE-STSA (Ephraim and Malah, 1984); (b) MMSE-STSA with noncausal SNR estimation (NC-MMSE) (Cohen, 2004); (c) logMMSE-STSA (Ephraim and Malah, 1985); (d) Generalized Spectral Subtraction (GSS) (Compernolle, 1992); (e) Hu-Wang method (2004); and (f) APP-based speech enhancement technique. The code for the Hu-Wang method was downloaded from their lab website. The code was used as-is except the sampling rate was changed from 16 to 8 kHz.

The evaluations presented here only compare the quality of the enhanced speech signals and not their intelligibility.

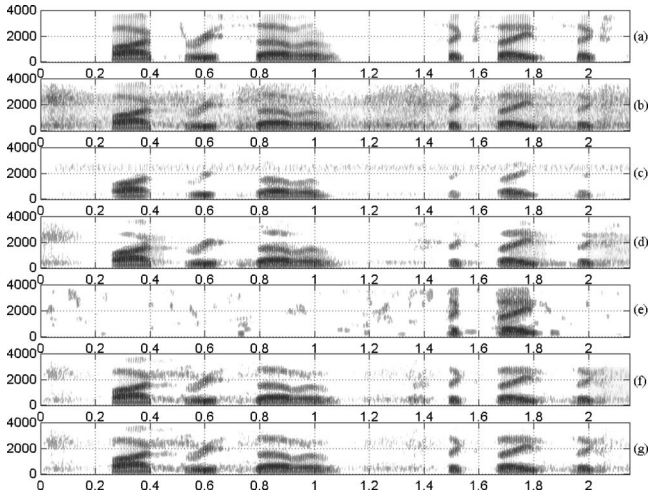

FIG. 13. Spectrogram of (a) the clean speech signal "five three seven six eight six." (b) The speech signal corrupted by subway noise at 10 dB SNR. The speech signal enhanced using the (c) GSS technique, (d) MMSE technique, (e) Hu-Wang technique, (f) MPO technique, and (g) MPO-APP technique.

Detailed evaluations comparing the intelligibility of the speech signals enhanced using the different techniques will be reported in the future.

B. Spectrograms displays

We begin the evaluations by comparing the spectrograms of the speech signals enhanced using different techniques. Figure 13 shows the spectrograms of a clean speech signal, the speech signal corrupted by subway noise at 10 dB SNR, and the speech signals enhanced by the GSS method, the MMSE-STSA method, the Hu-Wang method, the proposed MPO method, and the combined MPO-APP method. The GSS method has a relatively less amount of residual noise but suppresses alot of high-frequency low-energy speech information. The MMSE-STSA method is able to retain most of the speech information but passes alot more noise compared to the other methods. The MPO method, on the other hand, attenuates most of the residual noise while retaining much of the speech signal including the high frequency low energy speech information. For example, the MPO method is able to retain the weak F3 information around 2500 Hz near 0.65 s and again around 2700 Hz near 1.5 and 1.95 s while passing very little noise. Also notice that the combined MPO-APP method removes the noise around 1.4 s which was passed by the MPO method.

C. Evaluation using objective measures

The performance of the MPO speech enhancement scheme was evaluated using three objective quality assessment measures that have a high degree of correlation with subjective quality. These three measures are based on the dissimilarity of the linear predictive (LP) coefficients between the original and the enhanced speech signals (Hansen and Pellom, 1998).

(1) *Itakura-Saito (IS) distortion measure*: The IS distortion measure between a frame of clean speech signal and the corresponding frame of the enhanced speech signal is computed by

$$d_{\mathrm{IS}} = \left[\frac{\sigma_c^2}{\sigma_p^2}\right]\left[\frac{L_p R_c L_p^T}{L_c R_c L_c^T}\right] + \log\left[\frac{\sigma_p^2}{\sigma_c^2}\right] - 1,$$

where L_c and L_p are the LPC vectors for the clean frame and the processed frame, respectively, σ_c^2 and σ_p^2 are the all-pole gains for the clean frame and the processed frame, respectively, and R_c is the autocorrelation matrix of the clean frame.

(2) *Log-likelihood ratio (LLR) measure*: The LLR measure, unlike the IS measure, does not compare the all-pole gains of the clean frame and the processed frame and thus lays more emphasis on the difference in the overall spectral envelopes of the two frames. The LLR measure is computed using

$$d_{\mathrm{LLR}} = \log\left[\frac{L_p R_c L_p^T}{L_c R_c L_c^T}\right].$$

(3) *Log-area-ratio (LAR) measure*: The LAR measure is computed using the Pth order LP reflection coefficients of the clean frame and the processed frame in the following way:

$$d_{\mathrm{LAR}} = \left[\frac{1}{P}\sum_{j=1}^{P}\left[\log\frac{1+r_c(j)}{1-r_c(j)} - \log\frac{1+r_p(j)}{1-r_p(j)}\right]^2\right]^{1/2},$$

where r_c and r_p are the reflection coefficients of the clean frame and the processed frame, respectively.

All three measures return frame-level scores for a given processed speech signal. An overall score is computed by calculating the mean of the frame-level scores of the frames with the lowest 95% scores. Such a scheme removes a fixed number of frames which may have unrealistically high scores (Hansen and Pellom, 1998). An overall score of zero implies the processed speech signal is exactly identical to the original clean speech signal. Higher values indicate a greater degree of distortion in the processed speech signal.

The performance was also evaluated using the objective perceptual quality measure called the PESQ measure (Rix *et al.*, 2001). The PESQ measure is the ITU-T standard to evaluate the perceptual quality of processed speech signal. The PESQ evaluation includes aligning the clean (reference) signal and the enhanced signal in time and processing them through an auditory transform. The auditory transform includes models of various stages of the human auditory appa-

TABLE I. IS distortion measure at different SNRs. The results are averaged across the four different noise types used in this study.

Type	Clean	20 dB	10 dB	5 dB
GSS	1.407	3.839	3.774	3.427
MMSE	0.526	1.448	2.571	3.453
logMMSE	1.642	3.584	5.230	7.468
NC-MMSE	0.623	2.221	3.712	8.765
Hu-Wang	NaN	NaN	NaN	NaN
APP	15.084	4.771	3.183	3.257
MPO	1.034	1.425	2.018	2.511
MPO-APP	1.083	1.399	1.981	2.469

TABLE II. LAR measure at different SNRs. The results are averaged across the four different noise types used in this study.

Type	Clean	20 dB	10 dB	5 dB
GSS	1.712	3.987	5.372	5.758
MMSE	0.994	3.215	4.871	5.496
logMMSE	1.160	3.218	5.211	5.867
NC-MMSE	0.779	2.867	4.881	6.013
Hu-Wang	7.761	17.841	32.533	40.827
APP	2.590	4.538	5.433	5.923
MPO	1.939	4.070	5.003	5.577
MPO-APP	1.919	4.022	4.941	5.507

ratus. The outcome of the PESQ measure is an estimate of the subjective mean opinion score (MOS), which has values between 0 (poor quality) and 4.5 (no perceptual distortion).

Table I compares the IS distortion measure at different SNRs for the output of different enhancement techniques. The MPO processing leads to the lowest IS measure when the input speech signal is noisy. Combining the MPO processing with the APP detector (MPO-APP) leads to a further drop in the IS distortion measure in noisy conditions. The IS distortion measure computed on MPO-processed clean speech signals is higher than that computed on clean speech signals processed by other enhancement techniques. One of the reasons for this higher value could be that the spectral valleys in clean speech signal are further attenuated by the MPO processing. The IS distortion values for the Hu-Wang method were quite high and are hence replaced by NaNs (not-a-number). One of the reasons for the drop in the performance of the Hu-Wang method could be the change in the sampling rate. (Some of the parameters in the algorithm could be optimized for the default sampling rate of 16 kHz.).

Tables II and III compare the LAR and LLR measures, respectively, at different SNRs for the output of different enhancement techniques. The LAR and LLR measures obtained for the proposed MPO enhancement scheme are comparable with those obtained for some of the other enhancement schemes although the values are consistently higher (indicating more distortion) than those obtained for the MMSE-STSA enhancement scheme. Combining the MPO enhancement scheme with the APP detector (MPO-APP) consistently leads to a drop in the distortion values. Table IV compares the PESQ measure at different SNRs for the output of different enhancement techniques. The results are similar to those obtained for the LAR and LLR measures. The combined MPO-APP enhancement technique is an improvement over the MPO enhancement technique and its performance is comparable to that of some of the other enhancement techniques.

TABLE III. LLR measure at different SNRs. The results are averaged across the four different noise types used in this study.

Type	Clean	20 dB	10 dB	5 dB
GSS	0.103	0.453	0.782	0.958
MMSE	0.081	0.397	0.748	0.942
logMMSE	0.111	0.392	0.784	0.998
NC-MMSE	0.064	0.366	0.765	1.032
Hu-Wang	2.746	11.362	26.807	35.710
APP	0.241	0.556	0.775	0.923
MPO	0.159	0.519	0.761	0.943
MPO-APP	0.158	0.510	0.750	0.929

TABLE IV. PESQ measure at different SNRs. The results are averaged across the four different noise types used in this study.

Type	Clean	20 dB	10 dB	5 dB
GSS	3.718	3.042	2.361	1.928
MMSE	4.086	3.060	2.464	2.072
logMMSE	4.054	3.133	2.502	2.075
NC-MMSE	4.136	3.045	2.440	2.020
Hu-Wang	1.402	1.012	0.780	0.625
APP	3.002	2.768	2.377	2.059
MPO	4.116	2.955	2.331	1.958
MPO-APP	3.815	2.994	2.420	2.051

D. Robustness to fluctuating noise types and noise levels

The salient features of the MPO-based speech enhancement scheme are as follows: (a) It makes minimal assumptions about the noise characteristics (the only assumption is that noise is broader than the harmonics of the speech signal), (b) it does not need to estimate the noise characteristics nor does it assume the noise satisfies any particular statistical model, and (c) the noise removal performance on a given frame is independent of the performance on the adjoining frames. This scheme can thus be potentially robust when the level and the type of the background noise are fluctuating. The performance of the proposed MPO enhancement scheme was evaluated on the F-DB database of speech signals corrupted by fluctuating noise. Figure 14(a) shows the spectrogram of one of the clean signals "oh three zero six zero two four" from the F-DB database. The noisy signal is shown in Fig. 14(b). Figures 14(c)–14(f) compare the spectrograms of

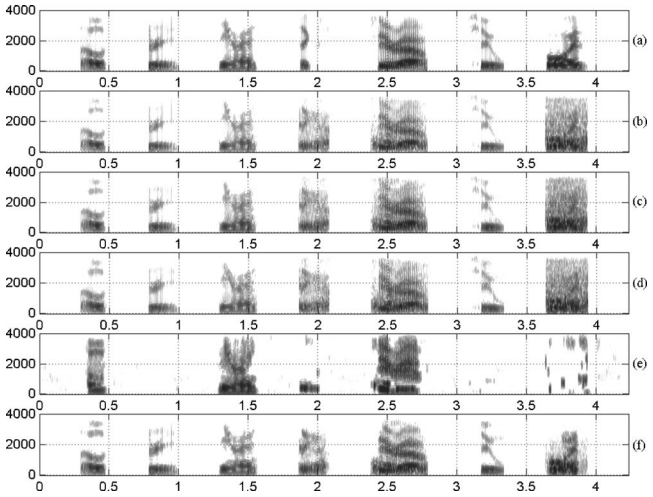

FIG. 14. The efficiency of the MPO method in enhancing the speech signal when the background noise is fluctuating is demonstrated. The digit sequence is "oh three zero six zero two four." Spectrogram of (a) the clean signal, (b) the noisy signal, the speech signal enhanced using the (c) GSS technique, (d) logMMSE technique, (e) Hu-Wang technique, and (f) MPO technique.

TABLE V. Performance of different speech enhancement techniques using various objective measures when the speech signals are corrupted by fluctuating noise.

Type	IS	LAR	LLR	PESQ
GSS	41.301	2.972	0.377	2.030
MMSE	23.473	2.542	0.351	1.974
NC-MMSE	29.975	3.061	0.474	2.024
logMMSE	34.946	2.646	0.370	1.911
Hu-Wang	NaN	16.997	8.250	0.800
APP	43.148	2.952	0.344	2.271
MPO	5.241	2.167	0.276	2.282
MPO-APP	4.971	2.175	0.277	2.320

the speech signals obtained using the GSS enhancement scheme, the logMMSE method, the Hu-Wang method, and the proposed MPO enhancement method, respectively. Notice that the MPO method is able to retain most of the speech information while passing very little noise. The MPO method attenuates the noise in between the spectral peaks of "four" (3.6–3.9 s, local SNR −5 dB) and "zero" (2.5–2.8 s, local SNR 5 dB) while retaining most the spectral peaks. The performance of the different enhancement techniques in terms of the various objective measures on the F-DB database is tabulated in Table V. The IS, LAR, and LLR measures show lower distortion values on MPO-processed speech signals compared to the output of the other enhancement techniques and the PESQ measure shows that the speech signals enhanced using the MPO enhancement scheme have a better perceptual quality than those obtained using the other enhancement schemes. Also, the combined MPO-APP enhancement scheme introduces further improvements in the MPO-enhanced speech signals.

VII. CONCLUSIONS AND FUTURE WORK

We have presented an algorithm for enhancing speech signals corrupted by additive noise. The proposed MPO enhancement scheme alters the components of the PO model in such a way that the basic functionality of the PO model is maintained but the various properties of the model can be analyzed and modified independently of each other. The MPO speech enhancement scheme is based on the fact that speech signals, for the most part, are composed of narrowband signals (i.e., harmonics) with varying amplitudes and that the harmonics that are higher in amplitude are perceptually more significant. Combining the MPO speech enhancement technique with the APP detector further improves its performance by reducing the number of speech deletions and noise insertions. The speech enhancement scheme presented here does not need to estimate the noise characteristics, nor does it assume that the noise satisfies any particular statistical model. The performance of the proposed enhancement scheme, evaluated using different objective measures, is comparable to that of some of the other speech enhancement schemes when the characteristics of the background noise are not fluctuating. The proposed MPO-APP enhancement scheme outperforms other speech enhancement schemes when the speech signals are corrupted by fluctuating noise.

The proposed enhancement scheme is implemented in MATLAB and is about 30 times real time on a typical PC with 2.99 GHz CPU and 2.0 Gbytes of RAM. One of the main factors contributing to the computational cost is the frequency spacing of the MPO structures. In the present work, the MPO structures are spaced every 50 Hz. Preliminary evaluations show that increasing the spacing to 100 Hz drastically reduces the computational cost while degrading the performance only slightly. Several other modules in the implementation of the MPO method can be optimized to reduce the computational cost and will be addressed in the near future. The residual noise passed by the proposed enhancement scheme is usually narrowband in nature and is perceived as musical noise. Work is in progress to propose algorithms to reduce the insertions of the musical noise. The main limitations of the proposed MPO enhancement scheme are its inability to retain turbulent speech sounds and its inability to separate target speech signals from competing speech signals. Evaluations of the MPO enhancement scheme on the task of recognizing speech from a target speaker in the presence of speech from competing speakers show only a slight improvement in the recognition rate especially at low SNRs (Deshmukh and Espy-Wilson, 2006). The MPO-APP processing has to be combined with other speech separation methods to improve the overall performance in such cases. Work is in progress to evaluate the subjective quality of the speech signals enhanced using the proposed MPO-APP scheme. Work is also in progress to evaluate the effectiveness of MPO processing as a preprocessing block for robust speech recognition systems using large databases like the Aurora database and to compare its performance with that of some of the other enhancement schemes.

ACKNOWLEDGMENTS

This work was supported by NSF BCS0236707. The authors would like to thank Dr. Michael Anzalone for helpful discussions on the PO model; Ayanah George for her help in coding the spectral subtraction speech enhancement method proposed in Boll (1979); E. Zavarehei for making the source code for the MMSE, logMMSE, and NC-MMSE publicly available; and J. Hansen and B. Pellom for making the source code for the objective quality evaluations publicly available.

Anzalone, M. C. (**2006**). "Time-frequency gain manipulation for noise-reduction in hearing aids: Ideal and phase-opponency detectors," Ph.D. thesis, Syracuse University.

Beh, J., and Ko, H. (**2003**). "A novel spectral subtraction scheme for robust speech recognition: Spectral subtraction using spectral harmonics of speech," in Proceedings of the IEEE International Conference on Acoustics, Speech, and Signal Processing, Hongkong, pp. 648–651.

Benesty, J., Makino, S., and Chen, J. (**2005**). *Speech Enhancement* (Springer, The Netherlands).

Berouti, M., Schwartz, R., and Makhoul, J. (**1979**). "Enhancement of speech corrupted by additive noise," in Proceedings of the IEEE International Conference on Acoustics, Speech, and Signal Processing, Washington, DC, pp. 208–211.

Boll, S. F. (**1979**). "Suppression of acoustic noise in speech using spectral subtraction," IEEE Trans. Acoust., Speech, Signal Process. **ASSP-27**, 113–120.

Cappe, O. (**1994**). "Elimination of the musical noise phenomenon with the Ephraim and Malah noise suppressor," IEEE Trans. Speech Audio Pro-

cess. **2**, 345–349.
Carney, L., Heinz, M. G., Evilsizer, M. E., Gilkey, R. H., and Colburn, H. S. (**2002**). "Auditory phase opponency: A temporal model for masked detection at low frequencies," Acta Acust. **88**, 334–347.
Cheng, Y. M., and O'Shaughnessy, D. (**1991**). "Speech enhancement based conceptually on auditory evidence," IEEE Trans. Signal Process. **39**, 1943–1954.
Cohen, I. (**2004**). "Speech enhancement using a noncausal a-priori SNR estimator," IEEE Signal Process. Lett. **11**, 725–728.
Compernolle, D. V. (**1992**). "DSP techniques for speech enhancement," ESCA tutorial and research workshop on speech processing in adverse conditions, Cannes, France, pp. 21–30.
Deshmukh, O., and Espy-Wilson, C. (**2005**). "Speech enhancement using auditory phase opponency model," in Proceedings of the Eurospeech, pp. 2117–2120, Lisbon, Portugal.
Deshmukh, O., Espy-Wilson, C., Azalone, M., and Carney, L. (**2005a**). "A noise reduction strategy for speech based on phase-opponency detectors," in 149th Meeting of the Acoustical Society of America, Vancouver, Canada.
Deshmukh, O. D. (**2006**). "Synergy of acoustic phonetics and auditory modeling towards robust speech recognition," Ph.D. thesis, University of Maryland, College Park, MD.
Deshmukh, O. D., and Espy-Wilson, C. Y. (**2006**). "Modified phase opponency based solution to the speech separation challenge," in International Conference on Spoken Language Processing, Pittsburgh, PA, pp. 101–104.
Deshmukh, O. D., Espy-Wilson, C. Y., Salomon, A., and Singh, J. (**2005b**). "Use of temporal information: Detection of periodicity, aperiodicity, and pitch in speech," IEEE Trans. Speech Audio Process. **13**, 776–786.
Ephraim, Y., and Malah, D. (**1984**). "Speech enhancement using a minimum mean-square error short-time spectral amplitude estimator," IEEE Trans. Acoust., Speech, Signal Process. **32**, 1109–1121.
Ephraim, Y., and Malah, D. (**1985**). "Speech enhancement using a minimum mean-square log-spectral amplitude estimator," IEEE Trans. Acoust., Speech, Signal Process. **33**, 443–445.
Gustafsson, H., Nordholm, S. E., and Claesson, I. (**2001**). "Spectral subtraction using reduced delay convolution and adaptive averaging," IEEE Trans. Speech Audio Process. **9**, 799–807.
Hansen, J., and Pellom, B. (**1998**). "An effective quality evaluation protocol for speech enhancements algorithms," in Proceedings of the IEEE International Conference on Acoustics, Speech, and Signal Processing, pp. 2819–2822.
Hansen, J. H., and Nandkumar, S. (**1995**). "Robust estimation of speech in noisy backgrounds based on aspects of the auditory process," J. Acoust. Soc. Am. **97**, 3833–3849.
Hirsch, H. G., and Pearce, D. (**2000**). "The AURORA experimental framework for the performance evaluations of speech recognition systems under noisy conditions," in ISCA ITRW ASR2000 Automatic Speech Recognition: Challenges for the Next Millennium, Paris, France, pp. 18–20.
Hohmann, V. (**2002**). "Frequency analysis and synthesis using a gammatone filterbank," Acta Acust. **88**, 334–347.
Hu, G., and Wang, D. L. (**2004**). "Monaural speech separation based on pitch tracking and amplitude modulation," IEEE Trans. Neural Netw. **15**, 1135–1150.
Loizou, P. C. (**2005**). "Speech enhancement based on perceptually motivated Bayesian estimators of the magnitude spectrum," IEEE Trans. Speech Audio Process. **13**, 857–869.
McAulay, R. J., and Malpass, M. L. (**1980**). "Speech enhancement using a soft-decision noise suppression filter," IEEE Trans. Acoust., Speech, Signal Process. **ASSP-28**, 137–145.
Mesgarani, N., and Shamma, S. A. (**2005**). "Speech enhancement based on filtering the spectrotemporal modulations," in Proceedings of the IEEE International Conference on Acoustics, Speech, and Signal Processing, Philadelphia, PA, pp. 1105–1108.
Rix, A. W., Beerends, J. G., Hollier, M. P., and Hekstra, A. P. (**2001**). "Perceptual evaluation of Speech Quality (PESQ), an objective method for end-to-end speech quality assessment of narrowband telephone networks and speech codecs," Technical Rep., ITU-T recommendation, P. 862.
Tsoukalas, D. E., Mourjopoulos, J. N., and Kokkinakis, G. (**1997**). "Speech enhancement based on audible noise suppression," IEEE Trans. Speech Audio Process. **5**, 497–514.
Virag, N. (**1999**). "Single channel speech enhancement based on masking properties of the human auditory system," IEEE Trans. Speech Audio Process. **7**, 126–137.
Wang, D. L. (**2005**). *Speech Separation by Humans and Machines*, Chap. 12 (Kluwer Academic, Norwell, MA).

Violin *f*-hole contribution to far-field radiation via patch near-field acoustical holography

George Bissinger
Physics Department, East Carolina University, Greenville, North Carolina 27858

Earl G. Williams and Nicolas Valdivia
Naval Research Laboratory, Washington, DC 20375

(Received 25 July 2006; revised 9 January 2007; accepted 1 March 2007)

The violin radiates either from dual ports (*f*-holes) or via surface motion of the corpus (top+ribs +back), with no clear delineation between these sources. Combining "patch" near-field acoustical holography over just the *f*-hole region of a violin with far-field radiativity measurements over a sphere, it was possible to separate *f*-hole from surface motion contributions to the total radiation of the corpus below 2.6 kHz. *A*0, the Helmholtz-like lowest cavity resonance, radiated essentially entirely through the *f*-holes as expected while *A*1, the first longitudinal cavity mode with a node at the *f*-holes, had no significant *f*-hole radiation. The observed *A*1 radiation comes from an indirect radiation mechanism, induced corpus motion approximately mirroring the cavity pressure profile seen for violinlike bowed string instruments across a wide range of sizes. The first estimates of the fraction of radiation from the *f*-holes F_f indicate that some low frequency corpus modes thought to radiate only via surface motion (notably the first corpus bending modes) had significant radiation through the *f*-holes, in agreement with net volume changes estimated from experimental modal analysis. F_f generally trended lower with increasing frequency, following corpus mobility decreases. The *f*-hole directivity (top/back radiativity ratio) was generally higher than whole-violin directivity. © *2007 Acoustical Society of America.* [DOI: 10.1121/1.2722238]

PACS number(s): 43.75.De, 43.40.At [JGM] Pages: 3899–3906

I. INTRODUCTION

General radiation properties of the violin have been measured since at least 1937 when Meinel[1] compared the radiation from a violin with and without a soundpost. In 1972 Meyer looked at the directivity patterns of violins, violas, cellos, and contrabasses, observing in the violin, for example, an evolution from nearly omnidirectional at low frequencies ($\lambda \geq$ size), few-lobed up to about 2 kHz and many-lobed above that.[2] All of these measurements, however, looked at the total radiation of the violin because there was no way to separate the dual port contribution (*f*-holes) from the surface motion radiation, the only two radiation sources for a violinlike instrument. Recently Wang and Burroughs,[3] using four measurement planes and planar near-field acoustical holography[4] (NAH), determined magnitudes and phases of volume flows from surface and port regions to give a more detailed view of radiation sources in the violin. (Driving force frequencies however were limited to open strings and harmonics up to 3 kHz only.) They observed that the area across the top plate in the C-bout (central) region around the bridge and soundpost (cf. their Fig. 3) was consistently a prominent region for radiation. However their spatial resolution at 294 Hz was not sufficiently good to demonstrate that radiation from *A*0, a Helmholtz-like cavity resonance near this frequency believed to radiate only through the *f*-holes, was indeed only from the *f*-holes and not partly from the corpus (top+ribs+back).

While various small substructures such as tailpiece, neck-fingerboard, bridge, and strings, were not important radiators, in agreement with general acoustic expectations,[5] much of acoustic importance about the compliant-wall violin corpus enclosing a dual-port cavity is still to be discovered. For example, corpus wall motions are capable of exciting various cavity modes, most prominently *A*0 (air modes all labeled with the prefix *A*), the lowest frequency strongly radiating mode in the violin or any other current bowed string instrument. Once any cavity mode is excited, and there are more than 40 cavity modes in the violin below 4 kHz,[6,7] the question of how strongly they in turn back-couple to the compliant corpus walls becomes important since pressure oscillations for modes below 1.3 kHz have already been observed to excite significant surface vibrations.

One such mode, *A*1, the first longitudinal cavity mode near 450 Hz coupled to *A*0,[8] has a nodal line crossing the *f*-hole region, suggesting an acoustic short; hence it should not radiate effectively through the *f*-holes, yet some violins have significant *A*1 radiation. Indeed for the violin octet a general trend of *A*1 radiation increasing with size relative to the nearby first corpus bending modes—the dominant low frequency corpus mode radiators in smaller instruments—actually led to it far outstripping radiation from these modes for the large bass.[9] If no radiation issued from the *f*-holes, but the violin overall still radiated, only an indirect radiation mechanism of cavity-mode-induced surface motion could be the cause.

Another interesting indirect radiation mechanism possibility is compliant wall motion associated with individual violin corpus modes resulting in substantial net cavity volume changes, which in turn are capable of forcing acoustically significant volume flows through the *f*-holes. At low

frequencies where $\lambda >$ violin size, and the air can be treated as approximately incompressible, experimental evidence can validate this mechanism.

These matters can only be resolved using advanced techniques with spatial resolution capable of unambiguously determining where the radiation originates. Such an experiment could ideally use NAH techniques since it is capable of determining surface and *f*-hole radiation equally well, but experimental difficulties in getting close to every part of the surface of the entire violin combined with the computational effort and measurement surface constraints for such an unusual shape make it impracticable at present. However a recent important variant of NAH, "patch" NAH (pNAH), where only a small part of a vibrating object is closely scanned and radiation from only the measured area, or some circumscribed portion thereof, is computed,[10,11] offers a practical alternative when combined with standard acoustical and vibrational measurements.[12]

Radiativity profiles, volume flows, relative phases, and radiation directivity for each *f*-hole, with special attention to the low frequency "signature" modes—*A*0 (Helmholtz-like cavity mode), *A*1 (first longitudinal cavity mode), CBR (‡ top and back plate nodal patterns), and $B1^-$ and $B1^+$ (first corpus bending modes)—were created from pNAH measurements. Computed volume flows through the *f*-holes were compared to estimated net volume flows from experimental modal analysis for selected normal modes below 0.8 kHz. Finally averaged-over-sphere far-field total radiativity combined with these pNAH computations for *f*-hole far-field radiation was used to provide the first estimates of the fraction of the violin's total far-field radiation emitted from the *f*-holes.

II. EXPERIMENTAL

A. Experimental modal and acoustic analysis

The experimental modal analysis and acoustic measurements as well as various analysis techniques have been extensively covered,[12] and so will not be covered here. A playable student violin (but without chinrest) chosen for its significant far-field averaged radiativity $\langle R \rangle$ (pressure/force, transfer function) for *A*1 near 450 Hz was employed to determine whether this cavity mode radiated directly through the *f*-holes or indirectly via induced wall motion. Excitation of the violin was always via an automated miniature force hammer striking the G-string corner of the violin bridge in the plane of the bridge parallel to the top plate surface similar to configuration shown in Fig. 1(a); pressure measurements were made over an $r=1.2$ m sphere in an anechoic chamber, with the violin supported "free-free" by two thin elastics, to compute top and back hemisphere $\langle R_{\text{top}} \rangle$ and $\langle R_{\text{back}} \rangle$ (the ratio $\langle R_{\text{top}} \rangle / \langle R_{\text{back}} \rangle$ defines the directivity $\langle D \rangle$) and, averaged-over-sphere $\langle R_{\text{total}} \rangle$ radiativities. These averaged radiativities are all comprised of *f*-hole and surface radiation contributions. The Fourier analysis was over 0–4 kHz, with $\Delta f=1.25$ Hz resolution, for the modal and acoustic measurements. A mobility profile of the violin top plate obtained with a scanning laser verified that mode frequencies, shapes, and mobility amplitudes had not changed significantly from an earlier complete scan over the entire violin.[13] Mobility data from the earlier scan were then used for the corpus. Another total radiativity $\langle R_{\text{total}} \rangle$ scan was performed to average with the earlier data. Radiativity errors incorporated ~5% support fixture losses that were neglected, ~5% microphone calibration errors, and ~3% excitation force angle/plane variations (all somewhat frequency dependent), for a combined nominal ±10% value.

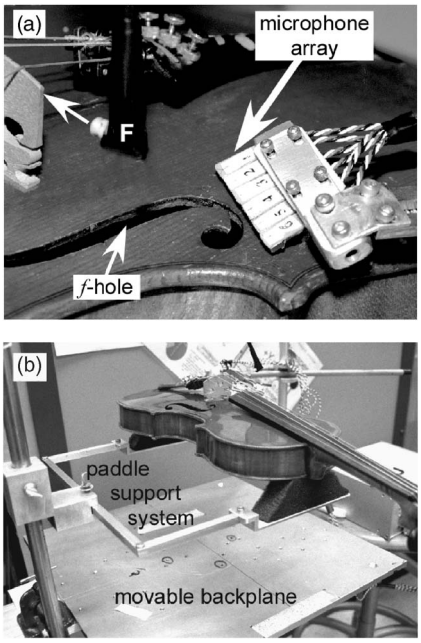

FIG. 1. (a) Translating-shifting microphone array over *f*-hole region with excitation force hammer at bridge corner driving point; (b) support paddle-variable backplane positioning setup with lab jack (not shown) under backplane.

B. "Patch" near-field acoustical holography

The pNAH measurements of *f*-hole radiation required very close, very accurate positioning of the scanning microphone array, a practical impossibility with the anechoic chamber support fixture and violin suspension where force hammer excitation created 2–3 mm low frequency residual rigid body motion. To eliminate the possibility of the microphone array striking and possibly scratching the surface an alternative suspension was necessary, placing the violin on two cut out foam pieces attached with double-sided tape to a rigid aluminum plate to support the end blocks. This arrangement had been used previously[14] and its effect on the violin's vibrational behavior was well understood: Raising rigid body mode frequencies to roughly 20 Hz, significantly higher than the thin elastic support system but still much lower than any corpus mode vibrational frequency (lowest ~400 Hz) so that any effect on mode frequencies and shapes would be small, and adding ~20% support fixture damping to the total, although all corpus mode dampings were still ≤1.2% of critical. Again these acoustic scans have nominal ±10% errors, after correction for the additional support fixture losses.

The pNAH microphone data were acquired over the same frequency range and Δf as the modal and acoustic data, using 6 Knowles EA-OKPL omnidirectional microphone

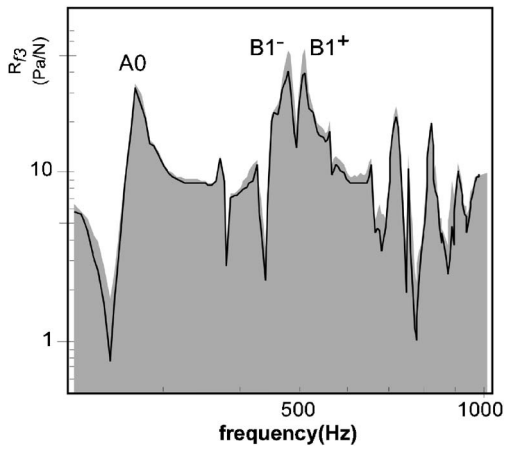

FIG. 2. Maximum (shaded) and minimum (thin line) radiativity R_{f3} for microphone 3 at mid-f-hole versus frequency over all backplane distances and absorber configurations. (Narrow structures are string resonances.) Especially note curve separation in $B1$ region.

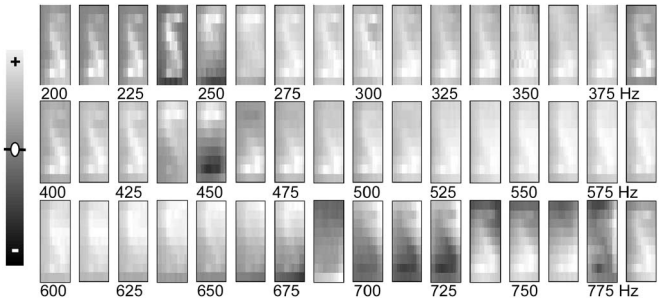

FIG. 3. A 12×9 array of raw radiativity data from bass bar side f-hole with scale denoting positive-negative values. Individual blocks correspond to 12.5 Hz interval stepped-frequency results (every tenth frequency step). Blurred f-hole outline clearly apparent.

modules mounted in a linear array oriented at ~45° to the scan plane as pictured in Fig. 1(a). The microphone spacing was 5.8 mm, but a calibrated shift of the array created an effective spacing of 2.9 mm. The array was translated using a specially constructed positioning support fixture to cover 9 steps with 1.05 cm spacing between each, starting just below, stepping along the length, and ending just above each f-hole, resulting in a 12×9 array of points for each f-hole. At each position of the array the excitation force on the violin was recorded simultaneously to create pNAH radiativity transfer functions so that relative acoustic phase information could be determined at each of the 108 points. The overall area covered by each plane was 26.8 cm^2, about 20% of which was taken up by the f-hole itself. The microphone array calibration was made using a white noise source in the anechoic chamber and an adjacent calibrated microphone.

Near-surface reflection/interference effects (herein labeled backplane loading) on measured pressures over the f-hole region were checked independently in another support fixture that placed the violin on the same foam supports now attached to a pair of thin support paddles that floated above the original $A1$ plate [Fig. 1(b)], which was placed on a lab jack to vary the violin-plate distance. Although this support fixture introduced some additional relative microphone-violin motion, pressure response variations could easily be observed as the backplane distance was varied. The microphone array was placed close to the bridge, with the innermost microphone at the bridge foot and the outermost microphone overlapping the edge of the violin.

A sequence of measurements, starting as close as possible to the original position ($1\times$) during actual measurements and then stepping to $2\times$, $4\times$, and $8\times$ the original distance (plus $8\times$ with Sonex© absorber foam), was used to observe systematic variations in microphone output. The output of microphone 3, directly over the middle of the f-hole, was used as a measure of backplane loading on radiation from the f-hole. Maximum and minimum radiativity values were extracted from this family of curves and plotted versus frequency in Fig. 2. Overall little significant backplane loading was observed across the 4 kHz range examined, with $8\times$ (with or without Sonex© foam) typically being the greatest, a few percent larger than $1\times$ results except in the minima. There was however one important exception: The first corpus bending modes near 500 Hz had a minimum radiativity at $1\times$ and maximum at $8\times$ for microphone 3, which corresponded to 19% and 29% changes, respectively. These values were used to correct for $B1^-$ and $B1^+$ backplane loading when computing the fraction of radiation from f-holes F_f.

With the foam support system on the rigid aluminum plate, it was possible to scan the array <1 mm from the irregular surface at the closest points without danger of violin motion creating accidental strikes on the microphone array. Over the entire scan the microphone-surface distance ranged from ~1 to ~4 mm. A 12×9 array of raw radiativity data from a complete scan over one f-hole is shown in Fig. 3.

C. "Patch" near-field acoustical holography

The raw radiativity data represent phased nearfield holograms that were processed to reconstruct the radiativity, normal velocity, and normal intensity in the plane of the f-hole.[10,11] Patch NAH provides accurate reconstructions and removes the need for holograms extending past the ends of the violin body, as was done by Wang and Burroughs.[3] The determination of the normal velocity in the f-hole plane provided by pNAH is difficult to measure by any other means and provides a direct measure of the volume flow from the f-holes. Furthermore, the determination of the normal acoustic intensity in the f-hole plane provides a means of computing the total power radiated from the f-hole alone.

NAH processing sharpens the raw microphone data (Fig. 3, showing blocks at every tenth frequency step, 12.5 Hz intervals) to give a much clearer outline of the f-hole in the final normal volume velocity display as shown in Fig. 4. The real part of the volume velocity is shown in Fig. 4, with positive and negative phase information provided by gray scale coding.

The NAH processing also provides detailed information on surface motion immediately adjacent to each f-hole that is directly comparable to mobility data gathered in a laser scan. Once the data have been NAH-processed, the final step is to demarcate the region from which radiation to the far field will be computed.

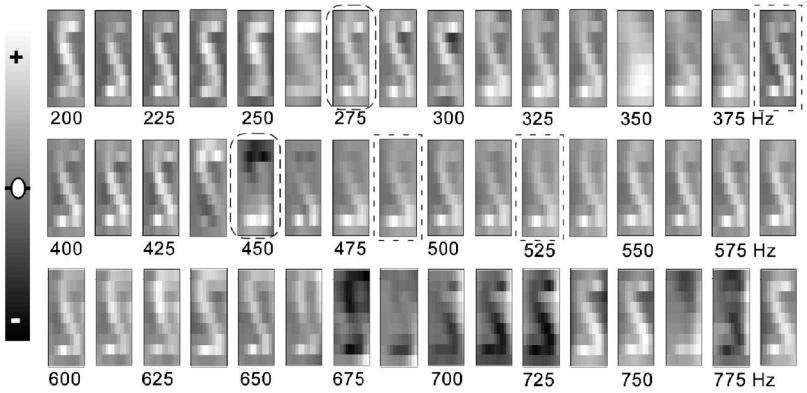

FIG. 4. Volume velocity derived from patch NAH using raw radiativity holograms (Fig. 3). The *f*-hole outlines are sharpened due to difference between motion of wood surrounding *f*-holes and the enclosed air. [Signature cavity $A0$ (~275 Hz) and $A1$ (~450 Hz), and corpus CBR (~387 Hz) and $B1^-$, $B1^+$ (~487 and ~525 Hz, respectively) modes are shown boxed.)

D. Boundary element model computations

To compute the radiation on an $r=1.2$ m sphere from the measured volume flow in the *f*-holes, a boundary element model employing a rigid violin-shaped corpus with *f*-holes was generated. BEM discretization decomposed the violin surface into 1326 linear triangular elements with 665 node points. Close to each *f*-hole, a special distribution of points corresponding to the NAH reconstructed velocity from the 12 by 9 array of microphone points was inserted. Figure 5 shows the element distribution of the violin surface with the increased density of elements near and in the *f*-hole regions. This boundary element decomposition of the violin surface was used to create a matrix transfer function via the direct-explicit approach[15] to take velocity into acoustical pressure over the surface of the sphere. In the Results section the measured radiativity from the *f*-holes alone as determined from pNAH and the BEM projection is compared with the direct measurement of the violin total radiativity in an anechoic chamber.

III. RESULTS

The pNAH radiativity data from the *f*-hole scans were used to extract: (1) surface and volume velocities over the scanned area, (2) comparisons of $A0$ radiation with Cremer model monopole predictions in the top hemisphere,[16] (3) radiation patterns for far-field pressures from the *f*-holes only (using the BEM model), at selected frequencies for a few important individual modes, (4) an averaged-over-sphere far-field radiativity $\langle R_f \rangle$ at 1.2 m from measured *f*-hole volume velocities (and the BEM model) for comparison with $\langle R_{\text{total}} \rangle$ measured in the anechoic chamber to compute fraction of acoustic energy radiated from both *f*-holes F_f, and (5) the directivity $\langle D_f \rangle$ of radiation from the *f*-holes (computed from the ratio of averaged top to back plate hemisphere radiativities) for comparison with equivalent directivity $\langle D \rangle$ computed from the anechoic chamber total radiativity measurements. All of these are new results for the violin.

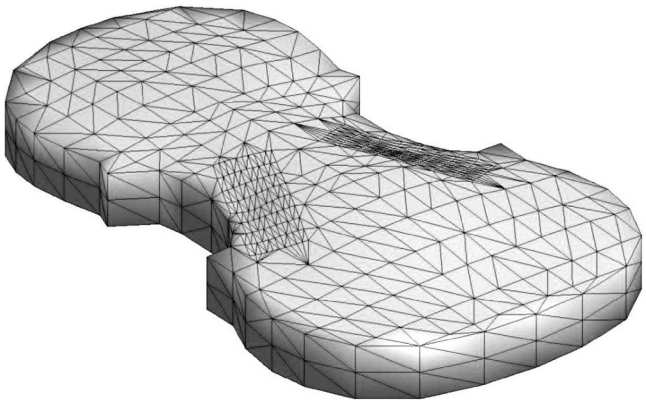

FIG. 5. BEM geometry model to compute far-field radiativity using pNAH *f*-hole volume velocity profiles. Note insertion of *f*-hole measurement grids over violin corpus grid.

A. Surface and volume velocities

All of the low frequency cavity and corpus modes of the violin up to about 600 Hz (sometimes called signature modes) are readily identifiable from violin to violin, and will be discussed individually due to their importance for the sound in the open-string pitch region. Above this range variations in individual materials and construction methods modify mode shapes and so interviolin mode comparisons become unreliable and statistical measures become necessary. Fortunately above 1 kHz the violin also enters a frequency region where (a) the radiation efficiency has increased so that all modes radiate well and (b) significant mode overlap is common. Hence the importance of individual modes decreases, justifying the statistical approach.

Referring to the results shown in Fig. 4 for $A0$ near 275 Hz and $A1$ near 453 Hz, there is essentially zero surface motion for both modes (midgray outside *f*-holes) compared with the volume velocity in the *f*-holes. $A1$ however induces significant cavity wall motions in the upper and lower bout regions of the violin that reflect the pressure polarity reversal of this first longitudinal cavity mode, leading to a surface motion nodal area in the central *C*-bout region. $A0$ has all positive volume velocities over the *f*-holes as expected, while $A1$ shows a polarity reversal corresponding to its expected node at the *f*-hole, producing an intra-*f*-hole acoustic short that signifies weak far-field radiation from the *f*-holes.

A further demonstration of the detail available from these NAH scans comes from expanding the display to include both *f*-holes for two signature modes in Fig. 6. The CBR mode looks like a rhomboid in the *C*-bout region cross-section, with ‡ top and back plate nodal patterns that indicate weak radiation from the corpus of the violin. Note that the CBR mode *f*-hole air motion on both sides of the violin is out of phase with the top plate motion immediately adjacent

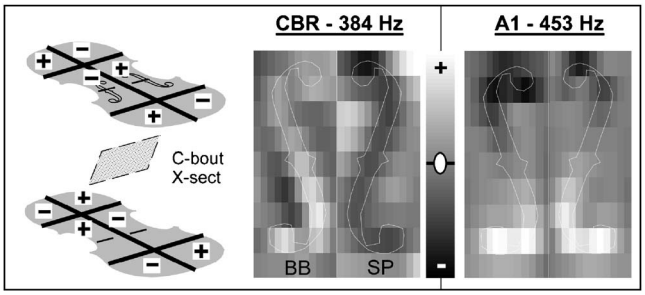

FIG. 6. Acoustic shorts (*f*-hole outlines superimposed): *inter*-*f*-hole for the CBR mode (plate nodal lines and *C*-bout cross section shown); *intra*-*f*-hole for *A*1. (Bass bar–soundpost sides notated in CBR.)

to it, indicating an inter-*f*-hole acoustic short for the *f*-hole radiation. The CBR mode is a good example of a mode with approximately zero radiation damping, hence its total damping consists of just internal damping.

Finally, no example of negligible air motion in the *f*-holes was observed below 2.5 kHz in the pNAH results, irrespective of the motion or lack of motion of the surface immediately adjacent to the *f*-holes, or its in- or out-of-phase behavior relative to the *f*-holes. This observation underscores the highly vibroacoustic character of the violin's dynamic response where the mechanical motions of the corpus affect the enclosed air motions, while enclosed air oscillations affect corpus motions.

B. *A*0 monopole radiativity

The *f*-hole monopole radiation of *A*0 was computed directly from Cremer's lumped element mode,[16] which assumes that the excitation force on the bridge drives a plate stiffness (spring) in series with a parallel branch consisting of the air cavity stiffness in parallel with the air-slug mass in the *f*-holes (Cremer's equations 10.11a and 10.14). In addition a resistance due to air viscosity was assumed in series with the air-slug mass to limit the *f*-hole resonance to a finite radiated pressure. Once the volume flow q_0 in the *f*-hole is determined, the radiated pressure p_f at $r=1.2$ m is determined using the simple monopole formula, $p_f = -i\omega\rho q_0(e^{ikr}/4\pi r)$. In this model it was assumed that the total Q (viscous+radiation damping) was 20 (from anechoic chamber measurement results), and that the vibrating plate area (S_1 in Cremer's model) was 500 cm^2. It is remarkable how closely Cremer's model prediction compares with the direct measurement of radiativity $\langle R_{\text{top}}\rangle$ (see Fig. 7).

To compute the radiated pressure (always normalized to 1 N force) on a sphere of radius 1.2 m from the pNAH measurements the normal velocity reconstructed in each *f*-hole (Fig. 4 shows bass-bar side *f*-hole results) was inserted into the BEM model. The normal velocities at all BEM nodes except the nodes in each *f*-hole were set to zero. Thus the violin body acts as a rigid baffle, with radiation only from the *f*-holes. The pressure was spatially averaged over the violin top and back hemispheres individually or combined, to produce pNAH averages analogous to those computed for the experimental radiativities (Sec. II A). A measure of *f*-hole radiation directivity $\langle D_f\rangle$ was computed from ratio of pNAH top-to-back pressures, again analogous to the experimental estimates. (Radiativity units are always Pa/N indicating normalization to driving force on bridge.) The pNAH predictions of *A*0 radiation from the *f*-holes into the top hemisphere are compared in Fig. 7 with the Cremer monopole and $\langle R_{\text{top}}\rangle$ results. The agreement within experimental error with the direct measurement at the *f*-hole resonance frequency of ~275 Hz indicates that the *A*0 radiation is due solely to the volume flow out of the *f*-hole, confirming prior assumptions about this mode.

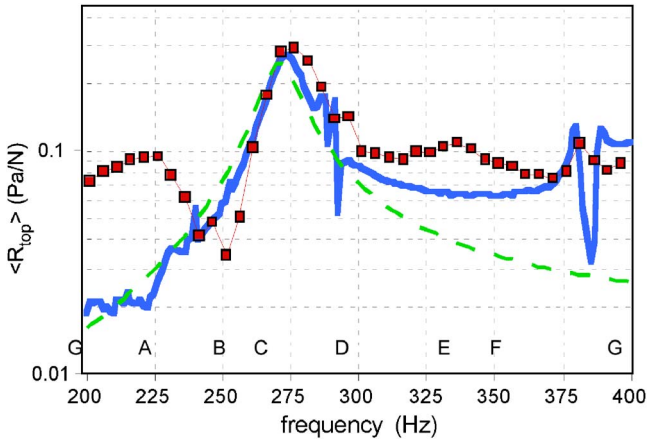

FIG. 7. (Color online) Comparison among monopole model for Helmholtz resonance *A*0 ($Q=20$, $S_1=500$ cm^2; dashed line), pNAH prediction (-■-), and measured (solid line) top hemisphere total radiativities. (Approximate violin fingered pitches starting at open *G* shown for reference.)

Note that below this resonance from 200–230 Hz the averaged top hemisphere *f*-hole radiativity was considerably larger than the violin $\langle R_{\text{top}}\rangle$. The explanation is simple (as hinted in Fig. 4) the corpus near the *f*-hole vibrates 180° out of phase with the air velocity in the *f*-hole. This 180° phase change results in a volume flow cancellation dramatically reducing the radiation from the complete violin. Mathematically, resorting again to Cremer's model (ignoring losses for simplicity) we can rewrite it as $q_0 = -[1/1-(\omega/\omega_H)^2]q_b$, where q_b is the total outward volume flow of the corpus and ω_H is the *f*-hole resonance frequency. This equation demonstrates the fact that as $\omega \to 0$, $q_0 \to -q_b$ and the volume flow from the *f*-holes is equal, and opposite, to the volume flow from the corpus. Above the *f*-hole resonance the volume flows from the corpus and *f*-holes would tend to be in phase, according to the above equation. However, Cremer's model fails to incorporate the presence of higher corpus modes and relative phase with these, a point addressed by Schelleng,[17] or to incorporate the coupling between *A*0 and the next higher (first longitudinal) cavity mode *A*1.[8] Clearly the various phase cancellations and couplings must be incorporated properly before such matters can be discussed appropriately.

C. *f*-hole radiation patterns for low frequency modes

The far-field *f*-hole radiation pattern for *A*0 is approximately isotropic at 1.2 m as can be seen from Fig. 8, with $\langle D_f\rangle = 1.08$. This is quite similar to the value of 1.15 for the overall violin directivity $\langle D\rangle$, computed from the anechoic chamber measurement ratio $\langle R_{\text{top}}\rangle/\langle R_{\text{back}}\rangle$. The radiation pat-

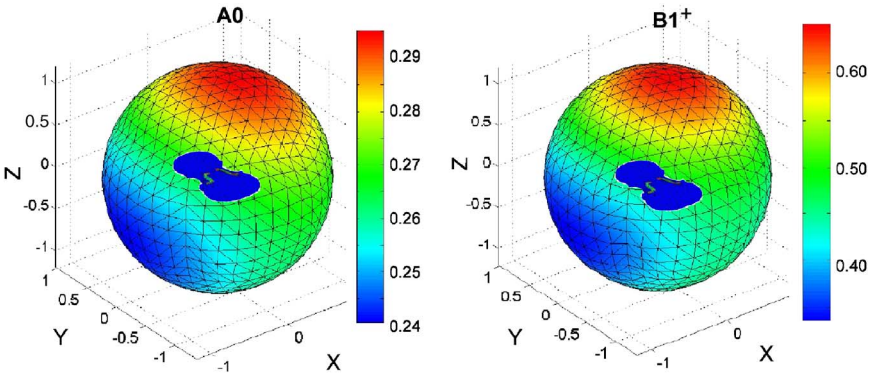

FIG. 8. (Color online) Computed pNAH *f*-hole radiation patterns (Pa/N) shown as color plots on a sphere with $r=1.2$ m for (1) *A*0 at 270 Hz and (r) $B1^+$ at 521 Hz. $B1^-$, the lower first corpus bending mode, has a shape very similar to $B1^+$. (Violin top plate in overlay for orientation.)

tern was computed using BEM for a motionless corpus (baffle) as described above and the pNAH results for the *f*-hole volume flow. This result is unsurprising since *A*0 has a wavelength ($\lambda \approx 1.25$ m) much greater than any *f*-hole or plate dimension. The *f*-hole radiation pattern for the $B1^-$ and $B1^+$ modes is also close to isotropic with $\langle D_f \rangle = 1.23$ and 1.27, close to the overall violin $\langle D \rangle = 1.01$ and 1.31, respectively. Neither *A*1 nor CBR modes radiated significantly through the *f*-holes (see Fig. 6).

D. Total versus *f*-hole radiativity

With the *f*-hole volume velocity it is straightforward to compute a pNAH radiativity into the top hemisphere for comparison to the analogous averaged farfield top radiativity $\langle R_{\text{top}} \rangle$ measured in the anechoic chamber.[13] The comparison is presented in Fig. 9. As expected, within our total and pNAH radiativity errors, *A*0 radiates entirely from the *f*-holes. On the other hand, the dip at *A*1 indicates no significant radiation through the *f*-holes, confirming the long-held belief that since these fall near a node for *A*1 (created of course by the *f*-holes themselves) there would be an acoustic

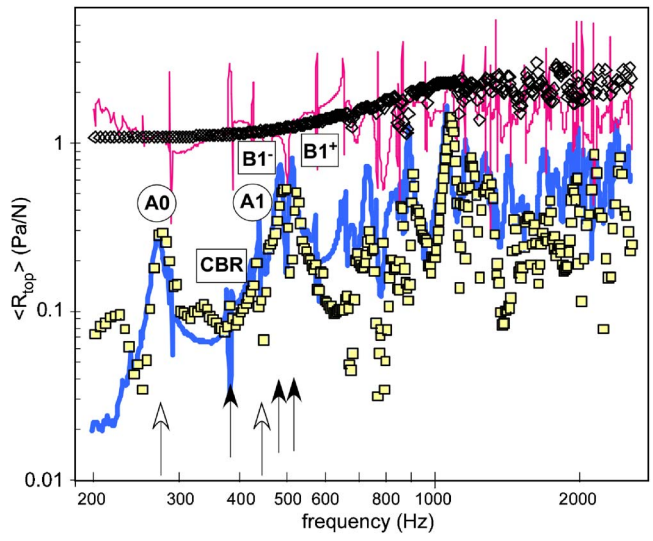

FIG. 9. (Color online) Lower curves: Top hemisphere pNAH radiativity from *f*-holes (□) versus $\langle R_{\text{top}} \rangle$ (thick line) up to 2.6 kHz. (Narrow structures due to undamped string resonances.) Upper curves: *f*-hole directivity $\langle D_f \rangle$ (◇) versus violin directivity $\langle D \rangle$ (thin line). (Signature cavity modes noted with open arrows and corpus modes with filled arrows.)

short in the *f*-holes. Consequently the sole source of the measured total radiativity must be the *A*1-induced surface vibrations.

As can be seen from Fig. 9 *A*1 is not a major radiating mode for this violin. Even though Schelleng completely dismissed *A*1 and higher cavity modes as significant radiators in his original violin octet scaling, *A*1 has been observed to evolve in strength to finally become *the* major radiator in the "main wood" region for the large bass member of the violin octet.[18] The source of the large bass' radiation in this region, assuming insignificant *A*1 radiation through the *f*-holes as observed in this violin experiment, must therefore come primarily from induced surface motion.

Another new result from Fig. 9 is that some corpus modes radiate strongly through the *f*-holes. For example, a major part of this violin's first corpus bending modes' overall radiation is *indirect* through the *f*-holes, not direct from surface motion. For certain "corpus" modes the fraction of the radiation from the *f*-holes approaches 1, e.g., the corpus mode near 1.1 kHz. This surprising result further complicates our understanding of violin sound because it concerns a hitherto unexamined source of radiation.

A brief summary of the significant direct and indirect violin radiation mechanisms discovered to date seems in order here: *Cavity* modes radiating (1) directly through the *f*-holes such as *A*0, or (2) indirectly through induced cavity wall vibrations such as *A*1 (and *A*2 and possibly higher cavity modes in larger instruments[18]); corpus modes radiating (3) directly from the surface (most modes) and/or (4) indirectly through the *f*-holes.

E. Mechanical estimate of volume flow

The experimental modal analysis (EMA) results provide an independent albeit crude check on this indirect corpus mode radiation path since the mobility scans covered almost the complete violin corpus. By scaling the normal mode mobility results in the modal analysis program to compliance (displacement/force) and using surface areas for each corpus substructure in the violin it was straightforward to make a rough mechanical estimate of volume changes over a cycle for individual normal modes. Approximate estimates of the volume flow out of the *f*-holes are possible if the air inside can be considered incompressible, restricting computations to modes that have $\lambda >$ violin length ($f < 800$ Hz). An additional caution—the pNAH computations were done at a par-

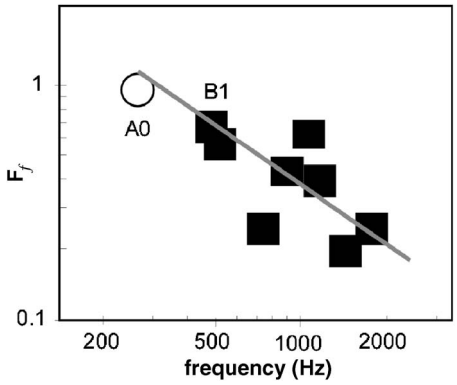

FIG. 10. Fraction of total radiation from *f*-holes F_f for normal modes below 2 kHz [symbol: (○) A_0, (■) corpus modes, and nominal errors ≈ symbol size]. Trendline (corpus modes only) to guide eye.

ticular frequency and thus incorporate whatever normal modes were participating at whatever level and relative phase in the overall vibration at this frequency (some indication of overlap can be seen in Fig. 9), whereas our normal mode volume changes were computed for one particular mode only, with no participation from other modes. Hence some variation between EMA and pNAH results must be expected, especially for overlapping modes, although at the peak of an isolated strong mode it is a good assumption that this mode dominates the measured overall mobility.

The EMA *f*-hole volume flow calculations were performed for *A*0, the first corpus bending modes $B1^-$ and $B1^+$ and a strong mode near 730 Hz (Fig. 9). Because *A*0 is not a corpus mode—although some corpus motion obviously is required to excite *A*0—its corpus volume change should be much less than its volume flow would imply; the estimated EMA volume flows for *A*0 were 323 $cm^3/s/N$, much less than the 2290 $cm^3/s/N$ pNAH estimates. The corpus mode EMA versus pNAH *f*-hole volume flow comparisons for $B1^-$ were 1571 versus 2343 $cm^3/s/N$, for $B1^+$ 2689 versus 2088 $cm^3/s/N$, and 1695 vs 755 $cm^3/s/N$ for the mode at 735 Hz. *A*0 corpus motion-induced volume flow estimates were only 14% of the pNAH value, the lowest ratio by far and too weak to result in the observed average radiativity at 1.2 m. The corpus modes had much larger EMA/pNAH volume flow ratios, ranging from 0.67 to 2.24, considered nominally equivalent for these crude estimates. It is worth noting that Saunders, using a bowing machine for excitation and a silk fiber observed through a microscope, saw some indication of *f*-hole air motion for the violin "main body" resonance (now $B1^- - B1^+$) but no higher body modes.[19]

F. Fraction of radiation from *f*-holes

Using separate averaged-over-a-sphere *f*-hole $\langle R_f \rangle$ and total radiativity $\langle R_{\text{total}} \rangle$ results, estimates of the fraction of violin radiation from the *f*-holes $F_f = \langle R_f \rangle / \langle R_{\text{total}} \rangle$ were computed for strongly excited modes up to 2.6 kHz (first corpus bending modes corrected for backplane air loading); above this frequency pNAH calculations were not carried out. These results are shown in Fig. 10 along with a superimposed trendline. The overall falloff in F_f results from the fusion of two dynamic trends: Less corpus motion (typically corpus mobility falls off at frequencies $> \sim 1$ kHz) and increased radiation efficiency (up to critical frequency ~4 kHz for violins,[20] where the radiation efficiency plateaus) as frequency increases. Thus steadily decreasing surface motion, which implies smaller volume flows, combined with steadily increasing ability to turn surface motion into radiation leads to the general conclusion that the fraction of acoustic energy radiated through the violin *f*-holes will diminish steadily with increasing frequency, even above the critical frequency; extrapolating from the trendline F_f drops to ~0.1 at 4 kHz. Interestingly, much of the radiation from a guitar in the lower octaves—in addition to the cavity resonance radiation—was also observed to issue from the sound hole in the earliest application of NAH to a musical instrument,[21] and back plate motions were often the major reason for the volume flow, rather than the top plate (confirmed by later modal analysis of another acoustic guitar[22]).

An interesting general argument to support "breathing" behavior of a violin based on conservation of momentum principles was provided by Cremer based on a simplistic 4-mass model of the violin,[23] where the center of mass of the violin must remain fixed, hence the top and back plates, which comprise most of the violin's mass, must vibrate in opposite phases, creating an overall breathing behavior to provide most of the radiation at low and possibly midfrequencies. Cremer also noted that the nonzero mass and kinetic energy of the ribs in this 4-mass model led to two "chief body resonances," not one, possibly analogs to the two first corpus bending modes, $B1^-$ and $B1^+$. However an earlier experiment examining removal of the violin soundpost on a violin's mode frequencies and shapes indicates that one of the first corpus bending modes disappeared.[24]

G. Directivity

The anechoic chamber measurements were used to compute a simple measure of radiation directivity $\langle D \rangle$ from a ratio of top to back averaged-hemisphere radiativities as presented in Fig. 9. Although $\langle D \rangle$, which includes the corpus and *f*-hole contributions, showed structure as different violin modes were traversed a gradual general rise from ~1 at the lowest frequencies, where $\lambda >$ violin size and hence nominally isotropic radiation is expected, to ~2 at 4 kHz was observed for all violins.[13] The *f*-hole directivity $\langle D_f \rangle$ showed little structure below 1 kHz, but considerably more above. $\langle D_f \rangle$ rises more rapidly than $\langle D \rangle$, but appears to roughly plateau above 1.2 kHz. This behavior appears to be of some value to violinists at low frequencies, always the least efficient region, when the violin is held as usual, canted at an angle toward the audience. Since radiation from the top would be more effective in reaching the audience, the *f*-hole contribution—raising the overall directivity at lower frequencies—somewhat enhances the effective ability to radiate toward the audience.

IV. CONCLUSIONS

Details inherently accessible in a fine mesh patch NAH experiment have greatly increased our ability to understand

some of the complexities of violin *f*-hole radiation. These first pNAH measurements on a musical instrument have given us important insights into *intra-* and *inter-f*-hole phase relationships, volume flow phase relationships with immediately adjacent surface motions, radiation from only the *f*-holes of the violin, and the basic direct and indirect radiation mechanisms of the violin. When used in combination with standard acoustic far-field measurements we find that the *f*-holes participate in the overall radiation from the violin far more than previously supposed, with many low frequency "corpus" modes radiating strongly, even predominantly, through the *f*-holes.

To some extent the already complex problem of understanding how the violin radiates has been complicated further, even though evidence for vibroacoustic coupling has been around a long time. The two traditional violin direct radiation mechanisms—*A*0 cavity mode radiation from the *f*-holes and corpus modes radiating from the surface—have now been joined by two indirect mechanisms—cavity-mode-induced wall vibrations and corpus-motion-induced air flow through the *f*-holes. Because *A*0 and *A*1 have been observed to dominate radiation in the open string region for some very large bowed string instruments, while indirect radiation through the *f*-holes modes can dominate the total radiation for some low frequency major corpus radiators in smaller instruments, it has become clear that all four of these radiation mechanisms must be accounted for in any complete analysis of the radiation from violins and other members of the bowed string instrument family.

ACKNOWLEDGMENTS

We would like to acknowledge the assistance of Janice Debro in acquisition of the pNAH data, and Knowles Acoustics for providing the miniature microphones. This research, performed as part of the VIOCADEAS Project, was supported by the National Science Foundation (DMR-9802656; GB) and by the Office of Naval Research (EGW and NV).

[1]H. Meinel, "On the frequency curves of violins," Akust. Z. **2**, 22–33 (1937).
[2]J. Meyer, "Directivity of string instruments," J. Acoust. Soc. Am. **51**, 1994–2009 (1972).
[3]L. M. Wang and C. B. Burroughs, "Acoustic radiation from bowed violins," J. Acoust. Soc. Am. **110**, 543–555 (2001).
[4]E. G. Williams, *Fourier Acoustics: Sound Radiation and Nearfield Acoustical Holography* (Academic, London, UK, 1999).
[5]G. Bissinger and A. Gregorian, "Relating normal mode properties of violins to overall quality: part I: signature modes," Catgut Acoust. Soc. J. **4**, 37–45 (2003).
[6]E. Jansson, "On higher air modes in the violin," Catgut Acoust. Soc. Newsletter **19**, 13–15 (1973); "Acoustical properties of complex cavities. Prediction and measurements of resonance properties of violin-shaped and guitar-shaped cavities," Acustica **37**, 211–221 (1977).
[7]G. Bissinger, "Acoustic normal modes below 4 kHz for a rigid, closed violin-shaped cavity," J. Acoust. Soc. Am. **100**, 1835–1840 (1996).
[8]G. Bissinger, "A0 and A1 coupling, arching, rib height, and *f*-hole geometry dependence in the 2-degree-of-freedom network model of violin cavity modes," J. Acoust. Soc. Am. **104**, 3608–3615 (1998).
[9]G. Bissinger, "Modal analysis of a violin octet," J. Acoust. Soc. Am. **113**, 2105–2113 (2003).
[10]E. G. Williams, "Continuation of acoustic near-fields," J. Acoust. Soc. Am. **113**, 1273–1281 (2003).
[11]E. G. Williams, B. H. Houston, and P. C. Herdic, "Fast Fourier transform and singular value decomposition formulations for patch nearfield acoustical holography," J. Acoust. Soc. Am. **114**, 1322–1333 (2003).
[12]G. Bissinger, "A unified materials-normal mode approach to violin acoustics," Acustica **91**, 214–228 (2005), and references therein.
[13]G. Bissinger and J. C. Keiffer, "Radiation damping, efficiency, and directivity for violin normal modes below 4 kHz," Acoust. Res. Lett. Online **4**, 7–12 (2003). http://scitation.aip.org/ARLO.
[14]K. Ye and G. Bissinger, "Attaining 'free-free' normal mode frequency *and* damping conditions for the violin," *Proc. 18th Intern. Modal Analysis Conf.- Soc. Exp. Mechanics*, Bethel, CT, 2000, pp. 398–403.
[15]N. Valdivia and E. G. Williams, "Implicit methods for NAH," J. Acoust. Soc. Am. **116**, 1559–1572 (2004).
[16]L. Cremer, *The Physics of the Violin, translated by J. Allen* (MIT Press, Cambridge, MA, 1983), Chap. 10.
[17]J. Schelleng, "On polarity of resonance," Catgut Acoust. Soc. Newslett. **10**, 14–21 (1968).
[18]G. Bissinger, "Modal analysis of a violin octet," J. Acoust. Soc. Am. **113**, 2105–2113 (2003).
[19]F. A. Saunders, "Recent work on violins," J. Acoust. Soc. Am. **25**, 491–498 (1953).
[20]G. Bissinger, "The role of radiation damping in violin sound," Acoust. Res. Lett. Online **5**, 82–87 (2004). http://scitation.aip.org/ARLO.
[21]W. Strong, T. B. Beyer, D. J. Bowen, E. G. Williams, and J. D. Maynard, "Studying a guitar's radiation properties with nearfield holography," J. Guitar Acoust. **6**, 50–59 (1982).
[22]C. D. Van Karsen and R. Sun, "Experimental modal analysis and operating deflection shapes of an acoustic guitar," *Proc. 15th Intern. Modal Analysis Conf.– Soc. Exp. Mechanics*, Bethel, CT, 1997, pp. 686–691.
[23]L. Cremer, "Remarks on the predictions of eigenmodes of violins," Catgut Acoust. Soc. J. **1**, 1–5 (1990).
[24]G. Bissinger, "Some mechanical and acoustical consequences of the violin soundpost," J. Acoust. Soc. Am. **97**, 3154–3164 (1995).

Three-dimensional finite element modeling of guided ultrasound wave propagation in intact and healing long bones

Vasilios C. Protopappas
Department of Medical Physics, Medical School, University of Ioannina, GR 451 10 Ioannina, Greece, and Unit of Medical Technology and Intelligent Information Systems, Department of Computer Science, University of Ioannina, GR 451 10 Ioannina, Greece

Iraklis C. Kourtis
Unit of Medical Technology and Intelligent Information Systems, Department of Computer Science, University of Ioannina, GR 451 10 Ioannina, Greece

Lampros C. Kourtis
Biomechanical Engineering Division, Mechanical Engineering, Stanford University, Stanford, California 94305

Konstantinos N. Malizos
Department of Orthopaedics, Medical School, University of Thessaly, GR 412 22 Larissa, Greece

Christos V. Massalas
Department of Material Science and Engineering, University of Ioannina, GR 451 10 Ioannina, Greece

Dimitrios I. Fotiadis[a)]
Unit of Medical Technology and Intelligent Information Systems, Department of Computer Science, University of Ioannina, GR 451 10 Ioannina, Greece

(Received 19 May 2006; revised 19 August 2006; accepted 21 August 2006)

The use of guided waves has recently drawn significant interest in the ultrasonic characterization of bone aiming at supplementing the information provided by traditional velocity measurements. This work presents a three-dimensional finite element study of guided wave propagation in intact and healing bones. A model of the fracture callus was constructed and the healing course was simulated as a three-stage process. The dispersion of guided modes generated by a broadband 1-MHz excitation was represented in the time-frequency domain. Wave propagation in the intact bone model was first investigated and comparisons were then made with a simplified geometry using analytical dispersion curves of the tube modes. Then, the effect of callus consolidation on the propagation characteristics was examined. It was shown that the dispersion of guided waves was significantly influenced by the irregularity and anisotropy of the bone. Also, guided waves were sensitive to material and geometrical changes that take place during healing. Conversely, when the first-arriving signal at the receiver corresponded to a nondispersive lateral wave, its propagation velocity was almost unaffected by the elastic symmetry and geometry of the bone and also could not characterize the callus tissue throughout its thickness. In conclusion, guided waves can enhance the capabilities of ultrasonic evaluation. © *2007 Acoustical Society of America.*
[DOI: 10.1121/1.2354067]

PACS number(s): 43.80.Ev, 43.80.Qf, 43.80.Jz [CCC] Pages: 3907–3921

I. INTRODUCTION

Quantitative ultrasound has gained significant interest in the assessment of osteoporosis and the evaluation of fracture healing. The so-called axial transmission technique has been used to examine the properties of long bones, such as the tibia and radius. Typically, a transmitter and a receiver are placed in contact with the skin (percutaneous application) along the long axis of the bone. The emitted ultrasonic pulse (typically in the 0.2–2-MHz frequency range) propagates along the bone and the first arriving signal (FAS) at the receiver is used to determine the ultrasound propagation velocity. To compensate for the effect of the overlying soft tissues, methods using either multiple percutaneous transducers (Bossy *et al.*, 2004a; Saulgozis *et al.*, 1996) or transducers implanted directly into the fracture region (Protopappas *et al.* 2005; Malizos *et al.*, 2006) have been proposed.

In the assessment of osteoporosis, experimental (Moilanen *et al.*, 2003; Njeh *et al.*, 1999b; Tatarinov *et al.*, 2005; Raum *et al.*, 2005) and simulation studies (Bossy *et al.*, 2002, 2004b; Camus *et al.*, 2000; Nicholson *et al.*, 2002) have demonstrated that the propagation velocity of the FAS is related to the bone mineral density, the thickness of the cortex, and the elastic properties of the bone, and is also a significant discriminator of osteoporotic fracture risk. In the

[a)]Author to whom correspondence should be addressed. Electronic mail: fotiadis@cs.uoi.gr

context of bone healing, the aim of the ultrasonic evaluation is to monitor the course of healing, detect any complications (e.g., delayed unions or nonunions) and early assess functional bony union. Animal (Abendschein and Hayatt, 1972; Gill *et al.*, 1989; Malizos *et al.*, 2006; Protopappas *et al.*, 2005) and clinical studies (Cunningham *et al.*, 1990; Gerlanc *et al.*, 1975; Maylia and Nokes, 1999) have shown that the FAS propagation velocity in fractured bones gradually increases over the healing period as a result of the fracture callus consolidation process. Experiments on acrylic plates immersed in water have also been performed to investigate the dependence of the FAS velocity on the soft tissue thickness, cortical thickness, and fracture gap width and depth (Lowet and Van der Perre, 1996; Njeh *et al.*, 1999a).

However, when the wavelength of the transmitted wave is comparable to or smaller than the thickness of the cortex, the type of wave that contributes to the FAS corresponds to a lateral (also known as P-head) wave (Rose, 1999). Lateral waves propagate only along the bone's subsurface at the bulk longitudinal velocity and therefore FAS velocity measurements reflect mainly the periosteal region (outer layer) of the bone. Conversely, when the wavelength is larger than the cortical thickness, the bone acts as a waveguide and the received signal waveform is a superposition of multiple guided wave modes. The use of guided waves has recently drawn increased attention in the ultrasonic evaluation of bone because guided waves propagate throughout the cortical thickness and are thus sensitive to both mechanical and geometrical properties.

Studies focusing on osteoporosis have investigated guided wave propagation by making use of acrylic plates and tubes of varying thickness (Lee and Yoon, 2004; Nicholson *et al.*, 2002; Tatarinov *et al.*, 2005) and of two-dimensional (2D) finite difference simulations on isotropic bone-mimicking plates (Bossy *et al.*, 2002; Nicholson *et al.*, 2002). It has been shown that by incorporating the theory that describes guided modes in plates (Lamb theory) generally two dominant modes could be detected in signals; the fastest one corresponds to the lowest-order symmetric Lamb mode (denoted as S0 mode), whereas the slowest one to the lowest-order antisymmetric Lamb mode (denoted as A0 mode). Assuming that guided waves in a plate agree closely to the type of waves propagating in the cortical shell, *ex vivo* and *in vivo* studies (Lee and Yoon, 2004; Lefebvre *et al.*, 2002; Moilanen *et al.*, 2003; Nicholson *et al.*, 2002; Tatarinov *et al.*, 2005) demonstrated that the velocity of the S0 and A0 modes was able to reflect structural changes in the cortex and thus provide an enhanced approach for characterizing healthy and osteoporotic bones.

In a recent study, we investigated guided ultrasound propagation in a 2D model of a healing bone (Protopappas *et al.*, 2006). Using time-frequency (t-f) signal analysis techniques, it was made possible to represent the dispersion of the velocity of the fundamental as well as of higher-order Lamb modes. We demonstrated that the propagation of Lamb modes was sensitive to both the material and geometrical properties of the fracture callus tissue during a simulated healing process. However, analysis of ex vivo measurements from an intact bone showed that the Lamb wave theory could not sufficiently describe the dispersion of the propagating guided modes (Protopappas *et al.*, 2006). This was further supported by a recent three-dimensional (3D) finite difference study (Bossy *et al.* 2004b) reporting on the effect of the tubular geometry and anisotropy of the bone on wave propagation.

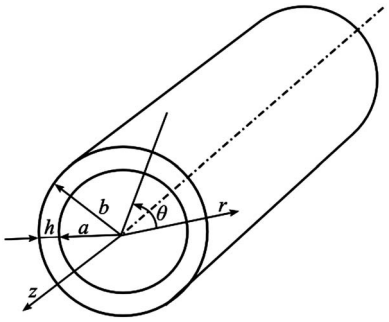

FIG. 1. Reference coordinates and dimensions of the hollow circular cylinder.

In this work, we extend our previous computational study by addressing more realistic conditions. The 3D geometry and anisotropy of the bone and the fracture callus tissue are taken into account. The objectives of this work are (a) to elucidate the parameters (irregular geometry and anisotropy) that affect wave propagation in intact bones and (b) to investigate the influence of callus formation and consolidation on the characteristics of propagation. In this respect, we first examine a simplified geometry of the bone (hollow circular cylinder) for two cases of material symmetry: isotropy and transverse isotropy. Next, the curvature of the cortical bone is considered and the callus tissue is modeled as an inhomogeneous material consisting of several ossification regions. The velocity of the FAS wave is determined using traditional time-domain techniques. The propagating guided modes are characterized in the t-f representation of the signal by incorporating theoretical velocity dispersion curves. The present study is the first to address guided wave propagation in 3D healing bones.

II. GUIDED WAVES IN AN ELASTIC HOLLOW CIRCULAR CYLINDER

The theory of elastic wave propagation in a hollow circular cylinder satisfying traction-free boundary conditions on the inner and outer surfaces will be briefly described in this section. Dispersion curves of the velocity of guided modes in a transversely isotropic medium and their degeneration to the case of isotropy will be presented and compared to those derived by the Lamb wave theory.

Let there an infinitely be long linear elastic hollow circular cylinder (Fig. 1). The three-dimensional stress equations of motion in cylindrical coordinates are (Rose, 1999)

$$\frac{\partial \sigma_{rr}}{\partial r} + \frac{1}{r}\frac{\partial \sigma_{r\theta}}{\partial \theta} + \frac{\partial \sigma_{rz}}{\partial z} + \frac{1}{r}(\sigma_{rr} - \sigma_{\theta\theta}) = \rho \frac{\partial^2 u_r}{\partial t^2},$$

$$\frac{\partial \sigma_{r\theta}}{\partial z} + \frac{1}{r}\frac{\partial \sigma_{\theta\theta}}{\partial \theta} + \frac{2}{r}\sigma_{r\theta} + \frac{\partial \sigma_{r\theta}}{\partial r} = \rho \frac{\partial^2 u_\theta}{\partial t^2},$$

$$\frac{\partial \sigma_{zz}}{\partial z} + \frac{1}{r}\frac{\partial \sigma_{\theta z}}{\partial \theta} + \frac{1}{r}\sigma_{rz} + \frac{\partial \sigma_{rz}}{\partial r} = \rho \frac{\partial^2 u_z}{\partial t^2}, \tag{1}$$

where r, θ, and z are the cylindrical coordinates; σ_{rr}, $\sigma_{\theta\theta}$, σ_{zz}, $\sigma_{\theta z}$, σ_{zr}, and $\sigma_{r\theta}$ are the stress components; u_r, u_θ, u_z are the particle displacement components; t is the time; and ρ is the density.

The strain-displacement relations are given by (Fotiadis *et al.*, 2006)

$$\varepsilon_{rr} = \frac{\partial u_r}{\partial r}, \quad \varepsilon_{\theta\theta} = \frac{1}{r}\frac{\partial u_\theta}{\partial \theta} + \frac{u_r}{r}, \quad \varepsilon_{zz} = \frac{\partial u_z}{\partial z},$$

$$\varepsilon_{rz} = \frac{1}{2}\left(\frac{\partial u_r}{\partial z} + \frac{\partial u_z}{\partial r}\right), \quad \varepsilon_{r\theta} = \frac{1}{2}\left[r\frac{\partial}{\partial r}\left(\frac{u_\theta}{r}\right) + \frac{1}{r}\frac{\partial u_r}{\partial \theta}\right],$$

$$\varepsilon_{\theta z} = \frac{1}{2}\left(\frac{\partial u_\theta}{\partial z} + \frac{1}{r}\frac{\partial u_z}{\partial \theta}\right), \tag{2}$$

where ε_{rr}, $\varepsilon_{\theta\theta}$, ε_{zz}, $\varepsilon_{\theta z}$, ε_{zr}, and $\varepsilon_{r\theta}$ are the strain components. The stress-strain relations for a transversely isotropic medium, when the symmetry axis is in the z direction, are given by (Fotiadis *et al.*, 2006)

$$\sigma_{rr} = C_{11}\varepsilon_{rr} + C_{12}\varepsilon_{\theta\theta} + C_{13}\varepsilon_{zz},$$

$$\sigma_{\theta\theta} = C_{12}\varepsilon_{rr} + C_{11}\varepsilon_{\theta\theta} + C_{13}\varepsilon_{zz},$$

$$\sigma_{zz} = C_{13}\varepsilon_{rr} + C_{13}\varepsilon_{\theta\theta} + C_{33}\varepsilon_{zz},$$

$$\sigma_{\vartheta z} = 2C_{44}\varepsilon_{\theta z}, \quad \sigma_{rz} = 2C_{44}\varepsilon_{rz}, \quad \sigma_{r\vartheta} = 2C_{66}\varepsilon_{r\theta}, \tag{3}$$

where C_{11}, C_{12}, C_{13}, C_{33}, and C_{44} are the five independent elastic constants required to characterize the transverse isotropy of the material, whereas the constant C_{66} is given as $C_{66}=(C_{11}-C_{12})/2$ (Fotiadis *et al.*, 2006).

For the propagation of free harmonic waves, substituting Eqs. (2) and (3) into Eq. (1), the assumed displacement components are (Mirsky, 1965)

$$u_r = U_r(r)\cos n\theta \cos(\omega t + \xi z),$$

$$u_\theta = U_\theta(r)\sin n\theta \cos(\omega t + \xi z),$$

$$u_z = U_z(r)\cos n\theta \cos(\omega t + \xi z), \tag{4}$$

where ξ is the wave number and ω is the circular frequency. The functions U_r, U_θ, and U_z are the corresponding components of the radial distribution of the displacement amplitudes. These functions are composed of Bessel functions (or modified Bessel, depending on the arguments) and contain six (unknown) amplitude coefficients (Mirsky, 1965). The index $n=0,1,2,3,\ldots$ is called the circumferential order (Rose, 1999) and specifies the order of symmetry around the axis of the cylinder.

For traction-free boundary conditions (free motion), the stresses must vanish on the inner and outer surfaces of the hollow-cylinder, i.e.,

$$\sigma_{rr} = \sigma_{rz} = \sigma_{r\theta} = 0 \quad \text{at } r = a \text{ and } r = b, \tag{5}$$

where a and b is the inner and outer radii of the hollow-cylinder, respectively. The stress components in Eq. (5) can be represented in terms of the six amplitude coefficients by applying Eqs. (2) and (3) to the displacements in Eq. (4) (Mirsky, 1965). Satisfaction of the boundary conditions results in a system of six linear equations with respect to the amplitude coefficients. For nontrivial solutions, the determinant, D, of the system must vanish (Mirsky, 1965):

$$|D_{ij}| = 0 \quad (i,j = 1 \text{ to } 6). \tag{6}$$

Equation (6) is called the characteristic frequency equation. The element D_{ij} is analytically expressed in terms of the elastic constants of the material, the dimensions of the hollow cylinder (i.e., the inner and outer radius), the frequency, and the wave number (Mirsky, 1965). For given material and geometry, Eq. (6) is a transcendental equation of the frequency and wave number. The roots of Eq. (6) provide the dispersion curves of the guided modes, i.e., the wave number as a function of frequency. In the context of this work, we are practically interested in the dispersion of the group velocity (c_{gr}) of the guided modes, which is defined in terms of the derivative of the dispersion curves:

$$c_{gr} = \frac{\partial \omega}{\partial \xi}. \tag{7}$$

The group velocity dispersion curves express the velocity at which the energy of a guided mode propagates as a function of frequency.

The characteristic frequency equation [Eq. (6)] can be degenerated to the case of an isotropic material (Gazis, 1959) by reducing the number of elastic constants from five to two using the following relationships:

$$C_{33} = C_{11}, \quad C_{13} = C_{12}, \quad C_{44} = C_{66} = \frac{(C_{11} - C_{12})}{2}. \tag{8}$$

The different guided modes that propagate in the z direction of a hollow circular cylinder are commonly notated by their type, circumferential order, and consecutive order (Rose, 1999). For $n=0$ [from Eq. (4)], the particle displacement of the modes is axisymmetric. In this case, there exist two types of modes: longitudinal modes, denoted as $L(0,m)$, consisting of axial and radial displacement components, and torsional modes, denoted as $T(0,m)$, containing only displacement in the circumferential direction. A third type of mode called flexural modes, $F(n,m)$, $n=1,2,3,\ldots$, corresponds to modes with non-axisymmetric displacements and contains all three possible displacements. The index $m=1,2,3,\ldots$ denotes the order (numbering) of the mode.

Group velocity dispersion curves of the $L(0,m)$ and $F(1,m)$ modes for a bone-mimicking hollow circular cylinder with wall thickness 4.08 mm and outer radius 8.61 mm are shown in Fig. 2. Two cases are presented: the first for isotropic material (dashed lines) and the second for transversely isotropic material (solid lines) whose properties are provided in Table I. It can be seen that the symmetry of the material has a significant effect on the dispersion of the higher-order modes and almost no effect on the fundamental $L(0,1)$ and $F(1,1)$ modes. When the wall thickness is thinner than half the outer radius, the dispersion of the $F(1,1)$ and the higher-order modes is almost identical to the corre-

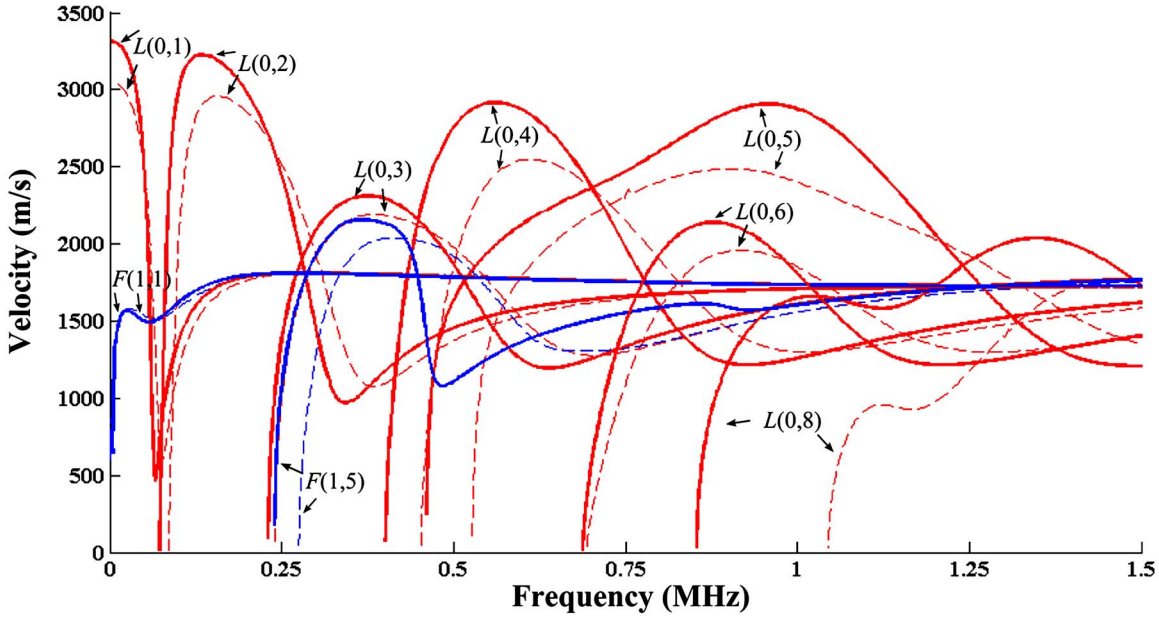

FIG. 2. (Color online) Group velocity dispersion curves of the longitudinal and flexural modes for a free hollow circular cylinder (wall thickness 4.08 mm and outer radius 8.61 mm) for the case of material isotropy (dashed lines) and transverse isotropy (solid lines).

sponding Lamb modes in a plate of equal thickness, whereas the $L(0,1)$ mode is different than the S0 mode only for very low frequencies (Lefebvre *et al.*, 2002; Protopappas *et al.*, 2006).

III. MATERIALS AND METHODS

A. Finite element model

1. Geometry of cortical bone

The cross section of the cortical bone was determined by Computer Tomography transverse scans (Phillips Secura, acquisition parameters: 140 kV, 220 mA, slice thickness 2 mm, slice distance 1 mm) obtained from the middle diaphysis region of a sheep tibia. The periosteal (external) and endosteal (internal) contours of the cortex were determined using a threshold-based region-growing segmentation technique (Protopappas *et al.*, 2005). The endosteal contour of the cortex, however, was simplified to the circle (with radius 4.53 mm) that fits to the extracted endosteal contour in a least-squares sense (Fig. 3). The average thickness of the cortex was 4.08 mm (min: 3.36 mm, max: 4.74 mm), which is within the range found in some types of human long bones, such as tibia and radius (Njeh *et al.*, 1999b).

The 3D model describes a diaphyseal segment of the bone with length $L=50$ mm. As opposed to the convex curvature of the cortex in the transverse plane, the curvature along the bone axis at the level of diaphysis may reasonably be neglected (Bossy *et al.*, 2004b). Therefore, the 3D bone model was considered uniform in the long axis direction with constant cross section.

TABLE I. Elastic constants for isotropic and transversely isotropic cortical bone.

Material properties	Isotropy	Transverse isotropy
Elastic constants (GPa)		
$C_{11}=C_{22}$	24.76	17.50
C_{33}	24.76	24.76
C_{12}	14.54	10.15
$C_{23}=C_{31}$	14.54	10.69
$C_{44}=C_{55}$	5.11	5.11
C_{66}	5.11	3.67
Density (Kg/m^3)	1500	1500
Bulk longitudinal velocity (m/s)	4063	4063

2. Equivalent hollow circular cylinder

We also modeled a hollow circular cylinder with inner and outer radii 4.53 and 8.61 mm, respectively, and length $L=50$ mm. The outer diameter corresponds to the circle that best fits to the periosteal contour of the cortex, in a least-squares sense. This model corresponds to a simplified geom-

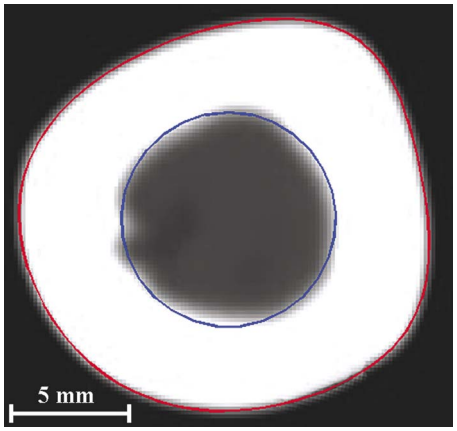

FIG. 3. (Color online) Cross section of a sheep tibia obtained from computer tomography scans along with the extracted periosteal and endosteal contours of the cortex.

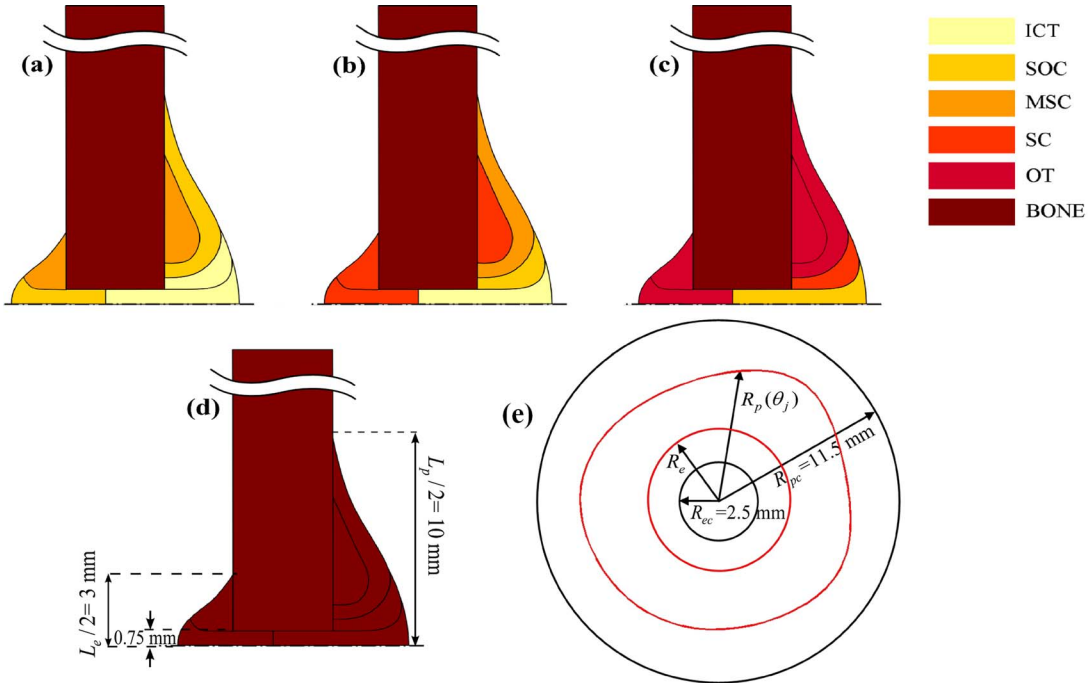

FIG. 4. (Color online) One quarter of the callus model (left side corresponds to endosteal regions) and the types of tissues involved in (a) Stage1, (b) Stage2, (c) Stage3, and (d) the "hypothetical" Stage0. The geometry of the healing bone in a transverse plane at the middle of the model's length is shown in (e).

etry of the bone and was used to investigate the effects of the convex curvature of the cortex on the propagation of guided waves.

3. Model of fracture callus

The secondary (indirect) type of fracture healing involves the formation and gradual consolidation of a soft tissue called fracture callus. Secondary healing takes place when small axial motion is allowed between the bone fragments, e.g., in the case of external fixation device treatment. Spatial and temporal sequences of tissue differentiation and ossification are fundamental processes in this type of healing.

The geometry of the callus tissue was described by a periosteal region bulging out of the cortex and an endosteal region bulging into the cortex. Following a previous computational study of fracture healing (Claes and Heigele, 1999), we modeled the callus tissue as an inhomogeneous material segmented into six different ossification regions. The healing course was simulated as a three-stage process. At each stage, the properties of the callus regions evolved corresponding to various types of soft tissues involved in the healing process. We assumed five soft tissue types, namely, initial connective tissue (ICT) describing nonmineralized connective tissue, soft callus (SOC), intermediate stiffness callus (MSC), and stiff callus (SC) representing the phases of new bone formation; and finally ossified tissue (OT). More specifically, at the first stage (Stage1), the callus consisted of regions of MSC along the endosteal and periosteal surfaces of the cortex at some distance from the fracture gap, of SOC adjacent to them, while the remainder consisted of ICT [Fig. 4(a)]. At the second stage (Stage2), ossification has progressed in the direction of fracture gap and the callus tissue contained ICT, SOC, MSC, and SC [Fig. 4(b)]. At the third stage (Stage3), bone formation has taken place and only a small region of SOC separates the bone margins [Fig. 4(c)]. According to Claes and Heigele (1999), Stage1 and Stage2 correspond to the fourth and eighth week after fracture, respectively, whereas Stage3 reflects the phase before bone remodeling. We also incorporated a "hypothetical" zero stage (Stage0), in which the callus region consisted only of cortical bone [Fig. 4(d)]. Although there is no physical meaning of this stage, it allows for the investigation of the effect of the callus geometry itself on wave propagation. The geometry of the callus remained the same for all the stages.

4. Mesh generation

The geometrical model of the intact bone was constructed using a 3D structured volume meshing routine implemented in MATLAB (The Mathworks, Inc., MA). The nodes of the mesh have been seeded in three dimensions according to analytical expressions. More specifically, the cylindrical coordinates, $r_{ijk},\theta_{ijk},z_{ijk}$, of the ijk node were defined as

$$r_{ijk} = R_e(\theta_j) + [R_p(\theta_j) - R_e(\theta_j)]r_i, \quad \theta_{ijk} = \theta_j, \quad z_{ijk} = z_k, \tag{9}$$

with

$$\begin{aligned} &r_i \in [0,1], \quad r_{i+1} > r_i, \quad i = 1, \ldots, M, \\ &\theta_j \in [0,2\pi], \quad \theta_{j+1} > \theta_j, \quad j = 1, \ldots, N, \\ &z_k \in [0,L], \quad z_{k+1} > z_k, \quad k = 1, \ldots, K, \end{aligned} \tag{10}$$

where M, N, and K are the number of nodes in the radial, circumferential, and axial directions, respectively, and $R_e(\theta_j)$

TABLE II. Material properties of the types of soft tissues involved in the healing process.

Tissue type	Density (kg/m^3)	Young's modulus (MPa)	Poisson's ratio	Bulk longitudinal velocity (m/s)
Initial connective tissue (ICT)	1050	3	0.4998	1543
Soft Callus (SOC)	1100	1000	0.47	2337
Intermediate stiffness callus (MSC)	1200	3000	0.45	3079
Stiff callus (SC)	1250	6000	0.43	3697
Ossified tissue (OT)	1400	10 000	0.40	3912

and $R_p(\theta_j)$ are the endosteal and periosteal radii of the cortex at angle θ_j, respectively. Note that since the endosteal contour was assumed circular, $R_e(\theta_j)=R_e$. A number of Q points (usually peaks and values) were selected along the periosteal contour extracted from the CT scan, with R_{p_q} and θ_{p_q}, where $q=1,\ldots,Q$, representing their polar coordinates. The $R_p(\theta_j)$ was determined from the selected points according to

$$R_p(\theta_j) = F(\theta_j, \theta_{p_q}, R_{p_q}), \tag{11}$$

where F is a piecewise cubic interpolation continuous function.

The mesh of the hollow circular cylinder model was constructed in a similar manner by defining $R_p(\theta_j)=R_p$.

The model of the healing bone incorporated the callus at the middle of the model's length, i.e., at $L/2$. The cross sections of the endosteal and periosteal callus regions were assumed circular with their radii varying along the length of the callus according to a Hanning function. By denoting with R_{ec} and R_{pc} the radii of the endosteal and periosteal callus regions at $L/2$, respectively [Fig. 4(e)], and with L_e and L_p the lengths of the endosteal and periosteal callus regions, respectively [Fig. 4(d)], the radial position of the nodes given in Eq. (9) was modified at the callus area as follows:

$$R'_e(\theta_j) = \begin{cases} R_e, & |z_k - L/2| > L_e/2, \\ R_e - (R_e - R_{ec}) \cdot 0.5\left[1 + \cos\left(2\pi \dfrac{z_k - L/2}{L_e}\right)\right], & |z_k - L/2| \leq L_e/2, \end{cases} \tag{12}$$

$$R'_p(\theta_j) = \begin{cases} R_p(\theta_j), & |z_k - L/2| > L_p/2, \\ R_p(\theta_j) + [R_{pc} - R_p(\theta_j)] \cdot 0.5\left[1 + \cos\left(2\pi \dfrac{z_k - L/2}{L_p}\right)\right], & |z_k - L/2| \leq L_p/2. \end{cases} \tag{13}$$

5. Material properties

The cortical bone was modeled as a linear elastic homogeneous material. In a first series of experiments, cortical bone was considered isotropic, whereas in a second series it was considered transversely isotropic with properties shown in Table I. Although the cortical bone is generally anisotropic, transverse isotropy is a realistic approximations observed experimentally (Reilly and Burstein, 1975; Rho, 1996) and used in models (Bossy *et al.*, 2004b). The elastic constants were derived from longitudinal and shear bulk velocity values typically used for bone (Bossy *et al.*, 2004b; Protopappas *et al.*, 2006; Rho, 1996). The cortical density, $\rho=1500\ kg/m^3$, represents the average value that has been measured in a previous animal study (Protopappas *et al.*, 2005) from quantitative CT-based densitometry performed on the midshaft cortical region of sheep tibiae. Table I also contains the resulting bulk longitudinal (compressional) velocity, c_3, for propagation in the z direction, given by (Fotiadis *et al.*, 2006)

$$c_3 = \sqrt{\frac{C_{33}}{\rho}}. \tag{14}$$

All soft tissues types incorporated in the callus model were assumed isotropic. Their elastic properties have been assessed by indentation tests on tissue sections obtained from different callus regions (Augat *et al.*, 1998; Claes and Heigele, 1999). Table II contains their material properties in the form of Young's modulus, E, and Poisson's ratio, ν, and also their resulting bulk longitudinal velocity (c_L), given by (Fotiadis *et al.*, 2006)

$$c_L = \sqrt{\frac{E(1-v)}{\rho(1+v)(1-2v)}}. \tag{15}$$

We have modified the values of the Poisson's ratio from those given in Claes and Heigele (1999) so the bulk longitudinal velocities will correspond to realistic values. For instance, in Claes and Heigele (1999), the Poisson's ratio for the ICT was 0.4, which would result in $c_L=78$ m/s [Eq.

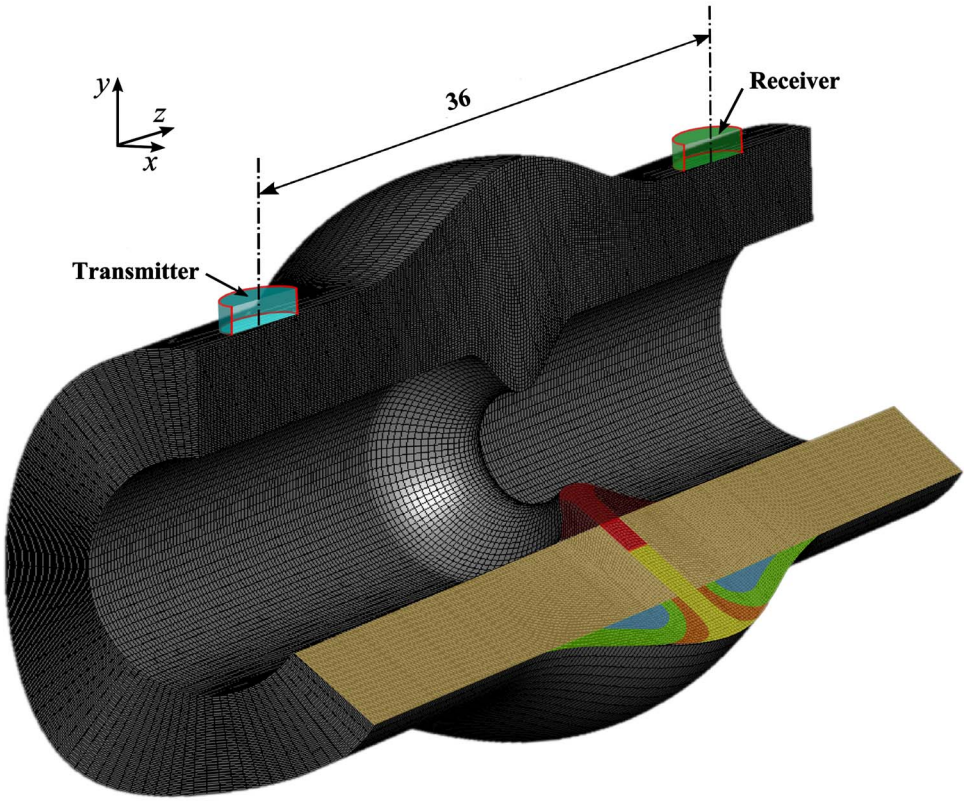

FIG. 5. (Color online) The model of the diaphyseal segment of cortical bone incorporating the fracture callus (sagittal section). The transmitter-receiver configuration is also illustrated.

(15)], whereas the value commonly used in the literature for soft tissues is close to 1500 m/s (Bossy *et al.*, 2004b). Similarly, by experimenting with the Poisson's ratio for the SOC, MSC, SC, and OT, we achieved a smooth transition of their bulk velocities to the cortical bone bulk longitudinal velocity.

6. Element properties

We used eight-node linear hexahedral continuum elements (element type C3D8R in ABAQUS version 6.4) with reduced integration and hourglass control (hourglassing is a numerical phenomenon by which zero-energy modes propagate) (ABAQUS, 2003).

The spatial discretization of the model is a critical issue when simulating wave propagation. The internodal distance in the i direction, d_{elem_i}, must be smaller than the smallest wavelength in that direction, λ_i, such that the propagating waves are spatially resolved (Moser *et al.*, 1999; Zerwer *et al.*, 2003). This can be expressed as

$$d_{elem_i} \leqslant \frac{\min(\lambda_i)}{g}, \tag{16}$$

where g is a factor indicating the minimum number of nodes per smallest wavelength and must be larger than 6 (ABAQUS, 2003). The average internodal distances in our model were approximately $d_{elem_1}=0.10$ mm in the radial direction, $d_{elem_2}=0.44$ mm in the circumferential direction, and $d_{elem_3}=0.18$ mm in the z direction. The resulting total number of degrees of freedom was 4 022 040.

7. Simulation of axial transmission

The 3D configuration and location of the transmitter and receiver relative to the bone and callus are shown in Fig. 5. The excitation signal consisted of a transient loading in the y direction applied to the bone surface over a circular area of 5-mm diameter. The amplitude of the excitation was a three-cycle Gaussian-modulated 1-MHz sine (0.55-MHz bandwidth at −6 dB). The time histories of the y displacements of the nodes located at the bone surface over a circular area of 5-mm diameter were recorded. The receiver's signal waveform was the average time history of the nodal y displacements. The transmitter and receiver were equidistant from the fracture gap and their center-to-center distance was 36 mm, which is in the range typically used in ultrasonic studies of bone (Bossy *et al.*, 2002; Protopappas *et al.*, 2005).

Two sites of transmitter-receiver positioning were investigated. The first (Site1) corresponded to a region where the cortical shell has average local thickness 3.4 mm and exhibits an irregular curvature (Fig. 6). Conversely, Site2 corresponded to a region where the cortical shell has local average thickness 3.97 mm and its curvature resembles a circular cylindrical shell (Fig. 6). In this respect, the influence of the anatomical site of measurement on guided wave propagation can be evaluated.

8. Boundary conditions

The bone was considered free and thus the influence of the surrounding soft tissues and the bone marrow was not taken into account. Also, infinite elements (element type CIN3D8 in ABAQUS version 6.4) were attached at the ends

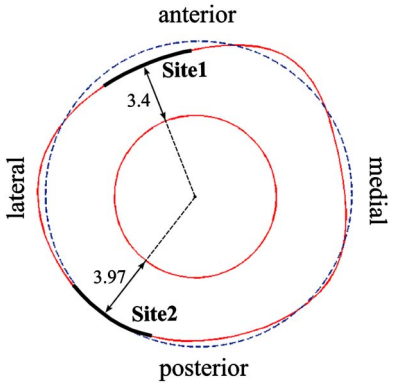

FIG. 6. (Color online) The anatomical sites of measurement, Site1 and Site2, and the corresponding average local thicknesses of the cortex (in mm). The circle that fits to the external contour of the cortex is also illustrated (dashed line).

of the model to absorb the energy of the incoming waves and thus simulate an infinitely long model. The infinite elements introduce additional normal and shear stress components, called boundary damping stresses, which eliminate all the reflections from the longitudinal and shear waves that impinge normally on the boundary between the finite and infinite elements (Lysmer and Kuhlemeyer, 1969). However, this formulation does not provide perfect transmission of energy out of the ends of the model for waves arriving from other directions (i.e., other than the z direction).

9. Numerical solution

Solution to the elastic wave propagation problem was performed using the explicit elastodynamics finite element analysis (ABAQUS/Explicit, version 6.4). Explicit analysis requires the integration time increment (Δt) to be smaller than the stability limit (ABAQUS, 2003; Hughes, 2000):

$$\Delta t \leqslant \min\left(\frac{\sqrt{(d_{elem_1}^2 + d_{elem_2}^2 + d_{elem_3}^2)/3}}{c_i}\right), \tag{17}$$

where c_i denotes the bulk longitudinal velocity of the material in the i direction. The integration time increment was automatically set by ABAQUS. We obtained nodal displacements at 0.05-μs time points corresponding to a 20-MHz sampling frequency. The time history of the nodal displacements was recorded for 50 μs and thus the length of the signal was 1001 points. The problem was solved using a 64-CPU, Origin 2000 supercomputer (SGI, Mountain View, CA) with 32 Gbytes shared memory. Typical computational time was 40 min.

B. Ultrasound signal analysis in the time domain

Detection of the FAS in the signal waveform was performed using a threshold equal to 10% of the amplitude of the first signal extremum. Such a detection criterion minimizes erroneous estimation of the transition time as opposed to other criteria based on constant thresholds, zero-crossings, signal extrema, etc., which are affected by frequency-dependent attenuation, mode interference, etc. (Bossy *et al.*, 2002; Nicholson *et al.*, 2002; Protopappas *et al.*, 2005).

C. Ultrasound signal analysis in the time-frequency domain

Time-frequency analysis has previously been employed in studying velocity dispersion of Lamb waves in nondestructive applications of flaw detection and localization in aluminum and composite plates (Niethammer *et al.*, 2001; Proseer *et al.*, 1999). As opposed to traditional time domain (Lee and Yoon, 2004; Moilanen *et al.*, 2003; Nicholson *et al.*, 2002) and 2D fast Fourier transform techniques (Lefebvre *et al.*, 2002; Moser *et al.*, 1999), which require the collection of multiple signals recorded at equally spaced distances, t-f analysis can represent the dispersion of multiple wave modes using only a broadband signal.

In our previous 2D study, three different t-f distribution functions were investigated. It was shown that the reassigned smoothed-pseudo Wigner-Ville (RSPWV) energy distribution provided sufficient t-f resolution and signal localization ability (Protopappas *et al.*, 2006), and therefore in this study we used this distribution function. The RSPWV function belongs to the Cohen's class of energy distributions, in which the distributions are covariant by translation in time and frequency. A function in the Cohen's class, $C(t,f)$, is given as (Auger *et al.*, 1995)

$$C(t,f) = \int\int\int e^{i2\pi v(u-t)} g(v,\tau) x^*\left(u - \frac{\tau}{2}\right) \times x\left(u + \frac{\tau}{2}\right) e^{-i2\pi f\tau}\, dv\, du\, d\tau, \tag{18}$$

where $x^*(t)$ is the complex conjugate of the signal and $g(v,\tau)$ is an arbitrary function called the kernel. The kernel for the smoothed-pseudo Wigner-Ville distribution $SPWV(t,f)$ is (Auger *et al.*, 1995)

$$g(v,\tau) = G(v)h(\tau), \tag{19}$$

where $G(v)$ is a frequency-smoothing window and $h(\tau)$ is a time-smoothing window. In order to improve the time-frequency resolution of the $SPWV(t,f)$, the reassignment version $SPWV^{(r)}(t,f)$ can be used (Auger *et al.*, 1995):

$$SPWV^{(r)}(t',f') = \int_{-\infty}^{+\infty}\int_{-\infty}^{+\infty} SPWV(t,f)\,\delta(t' - \hat{t}(t,f)) \times \delta(f' - \hat{f}(t,f))dt\, df, \tag{20}$$

where $\delta(t)$ is the Dirac function. The reassigned coordinates $(\hat{t},\hat{f})$ for each (t,f) in the original SPWV are

$$\hat{t}(t,f) = t - \frac{SPWV_{T_h}(t,f)}{2\pi SPWV_h(t,f)},$$

$$\hat{f}(t,f) = f + i\frac{SPWV_{D_h}(t,f)}{2\pi SPWV_h(t,f)}, \tag{21}$$

where $SPWV_h$, $SPWV_{T_h}$, and $SPWV_{D_h}$ are the $SPWV$ with window functions $h(t)$, $th(t)$, and $dh(t)/dt$, respectively. In this study, the frequency- and time-smoothing windows were $W/10$ point Hamming windows, where W denotes the number of points of the signal.

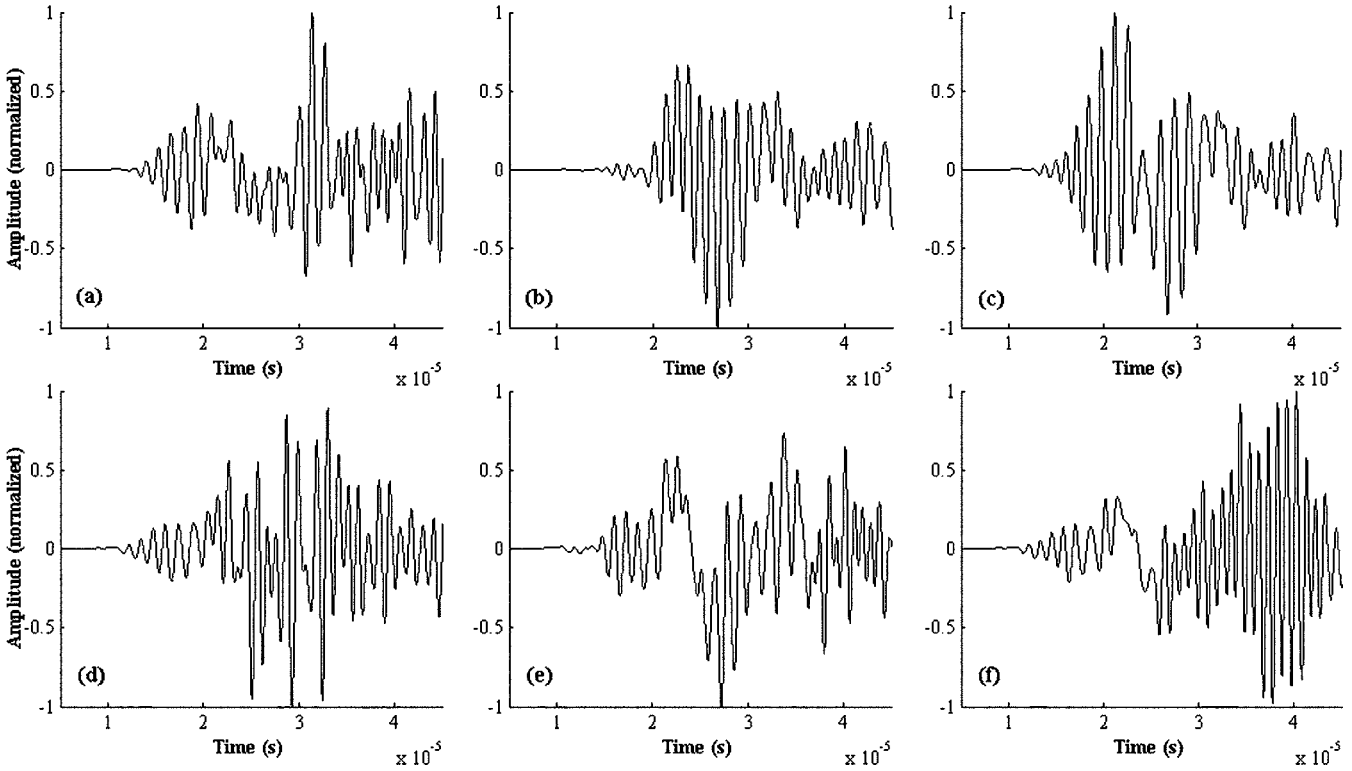

FIG. 7. Signal waveforms obtained from the intact isotropic models of (a) hollow circular cylinder, (b) bone at Site1, (c) bone at Site2, and intact anisotropic models of (d) hollow circular cylinder, (e) bone at Site1, and (f) bone at Site2.

IV. RESULTS

A. Analysis in the time signal domain

The signal waveforms obtained from the intact hollow cylinder and from the bone at Site1 and Site2 in the case of isotropy and anisotropy are illustrated in Fig. 7. It can be seen that the waveforms were significantly influenced by the model geometry, anatomical site, and material symmetry. On the other hand, the arrival time of the FAS was slightly affected only by the material symmetry. By dividing the in-between distance of the transducers (i.e., 31 mm) by the FAS time, the calculated propagation velocity of the FAS was 3954 m/s for the isotropic and 4042 m/s for the anisotropic models. Since the FAS wave propagated at a velocity close to the bulk longitudinal velocity of the bone (4063 m/s), it did not correspond to a guided wave but rather to a lateral wave.

Typical snapshots of wave propagation in the anisotropic healing bone at Stage2 are presented in Fig. 8. The propagation of the lateral wave along the surface of the cortex just before the end of the excitation is illustrated in Fig. 8(a). Wave reflections at the inner and outer boundaries cause the formation of guided modes that propagate in the axial and circumferential directions [Fig. 8(b)]. When the waves propagate in the callus region, the wavelengths are smaller depending on the properties of the soft tissues [Figs. 8(c)–8(f)]. Besides the axially propagating waves, additional waves arrive at the receiver due to reflections from the callus geometry [Fig. 8(d)] and propagation along circumferential paths.

The variation of the FAS velocity over the simulated healing stages of the bone model is presented in Fig. 9. The FAS velocity decreased at Stage1, remained the same up to Stage2, and then increased at Stage3. The velocity values at each stage were again higher for the anisotropic case, but no difference was observed between the measurements from Site1 and Site2. The fact that the velocity did not change from Stage1 to Stage2 possibly indicates that the propagation of the FAS wave was only affected by the ICT material that filled the fracture gap during these stages [Figs. 4(a) and 4(b)].

B. Analysis in the time-frequency domain

The t-f representations of the signals obtained from the intact hollow-cylinder, in the case of isotropy and anisotropy, are shown in Figs. 10(b) and 10(d), respectively. The t-f representations are shown in the form of pseudo-color images, where the color of a point represents the amplitude (in dB) of the energy distribution. In order to identify the propagating guided modes in the t-f representation, we used the theoretical frequency-group velocity (f, c_g) dispersion curves of the free hollow circular cylinder. Using the center-to-center distance between the transmitter and receiver, the corresponding (f, c_g) dispersion curves were converted to (t, f) curves in which the theoretically anticipated arrival time of each mode is plotted as a function of frequency. The (t, f) curves were then superimposed on the t-f representations. For the isotropic case, it can be seen that the dispersion of the $L(0,5)$ was clearly characterized in the 0.55–0.8-MHz range and of the $L(0,4)$ mode in the 0.7–0.85-MHz range. Furthermore, the $L(0,8)$ mode was identified at its cutoff frequency

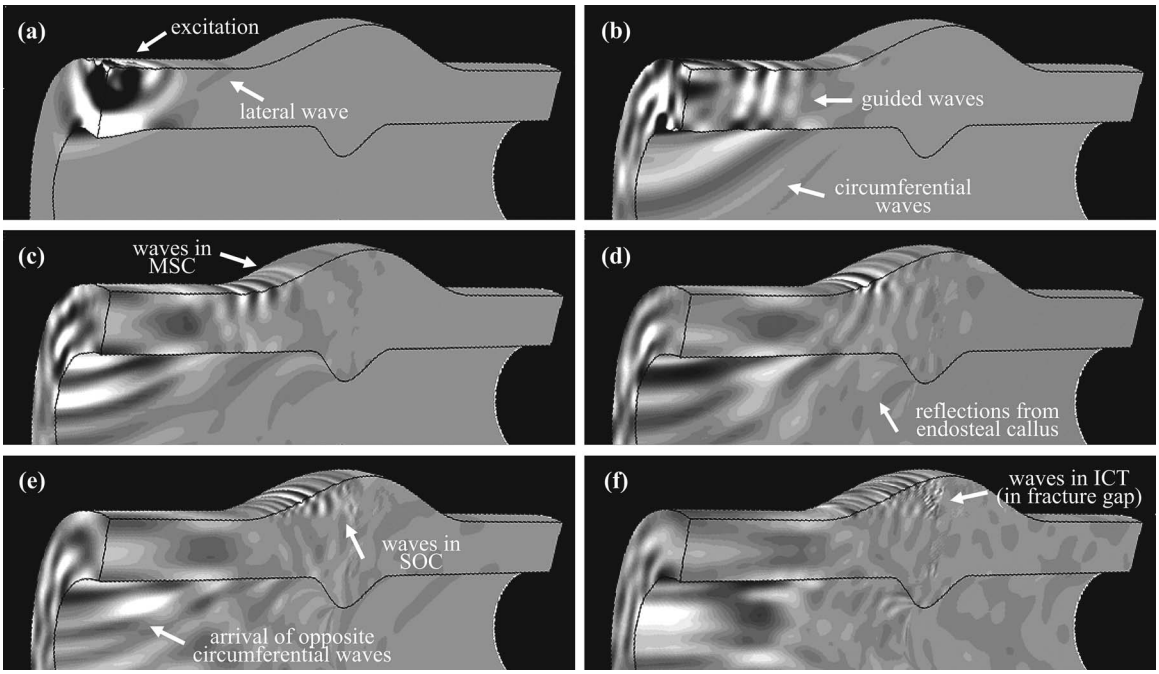

FIG. 8. Snapshots of wave propagation in the anisotropic healing bone at Stage2 for excitation applied to Site2. Time instances at (a) 2.5 μs, (b) 5.0 μs, (c) 8.0 μs, (d) 10 μs, (e) 14 μs, and (f) 20 μs. We display the amplitude of the y displacements (amplified by a 10^4 scale factor), in which the black color corresponds to maximum positive value and white to minimum negative value.

(1.05 MHz) and the fundamental $L(0,1)$ and $F(1,1)$ modes in the 0.05–0.15-MHz range. When the material was assumed anisotropic, the $L(0,5)$ mode was again described by the new dispersion curves (in the 0.5–0.85-MHz range), whereas the $L(0,4)$ mode did not propagate. The $L(0,8)$ mode was identified from its cutoff frequency (0.92 MHz) up to 1.05 MHz and appeared to carry most of the signal energy. The fundamental modes remained similar to those in the isotropic hollow cylinder. In both cases, the t-f representations contained additional waves that did not correspond to any theoretical modes and can be possibly attributed to circumferential waves that arrived later at the receiver.

The t-f signal representations obtained from the intact anisotropic bone at Site1 and Site2 are shown in Figs. 11(a) and 11(b), respectively. Poor agreement exists between the higher-order modes propagating in the hollow cylinder and those in the bone. However, the t-f signal representation from Site2 contained two modes with dispersion close to that of $L(0,5)$ and $L(0,8)$. On the other hand, the irregularity of the bone either at Site1 or Site2 had almost no effect on the dispersion of the fundamentals modes. Similar conclusions can be drawn for the isotropic case.

Figures 12(a)–12(d) illustrate the t-f signal representations from the simulated healing stages measured at Site2 of the anisotropic healing bone. At the hypothetical Stage0, where only the geometry of callus was taken into account, the $L(0,5)$ and $L(0,8)$ modes were different from those in the intact bone. On the other hand, the fundamental modes were less sensitive to this geometrical change. From Stage1 to Stage3, the properties of the callus tissue significantly affected the propagating guided modes. However, at Stage3, the fundamental modes and the $L(0,5)$ mode started to approach the behavior observed at Stage0.

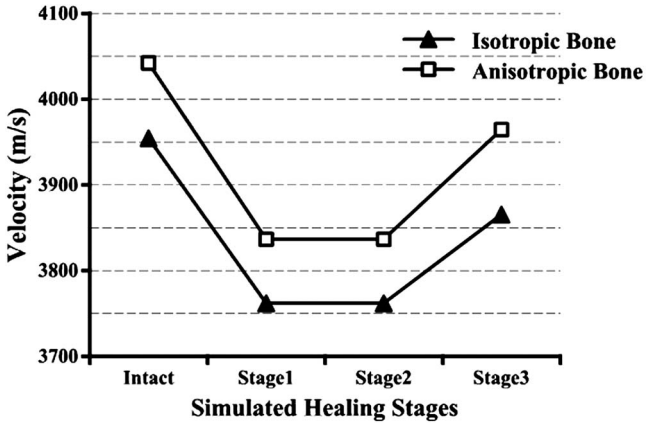

FIG. 9. Evolution of the FAS propagation velocity over the healing stages for the isotropic (▲) and anisotropic (■) bone models.

V. DISCUSSION

In this work, a finite element study of guided ultrasound wave propagation in intact and healing long bones was presented. We first examined wave propagation in a structure with idealized geometry and made comparisons with analytical solutions and then we proceeded to investigate the parameters that affect the characteristics of propagation under more realistic conditions.

The bone was modeled as a tubular solid with constant cross section describing the diaphysis of a sheep tibia. We neglected the small variations in the dimensions and shape of the cortex along the long axis. Our primary interest was to examine whether the irregularity of the cortical shell has an effect on wave propagation rather than provide an accurate model of a long bone. It should be noted that the shape of a human tibial cortex is different from that of the sheep; nev-

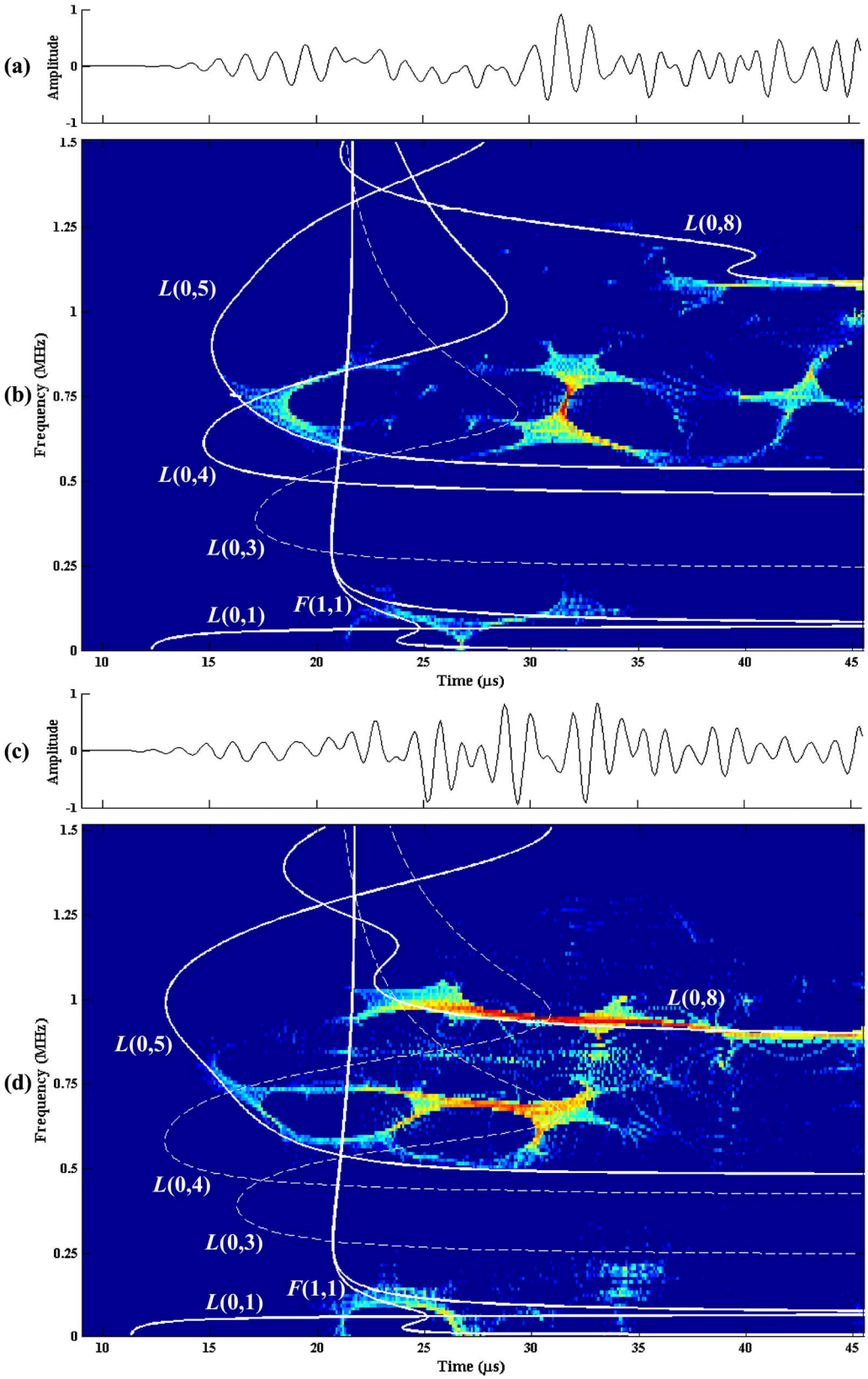

FIG. 10. (Color online) The t-f signal representations obtained from the hollow circular cylinder with (b) isotropic and (d) anisotropic properties along with the corresponding signal waveforms (a) and (c), respectively. The analytical dispersion curves of the longitudinal and flexural modes are also superimposed.

ertheless, the mesh of the model is parametric and can be easily used to construct any arbitrary tubular geometry.

We extended to the context of fracture healing by incorporating a model for callus. The callus tissue consisted of several regions, each holding different material properties through time according to Claes and Heigele (1999). The simulated stages represent critical phases of the healing course. However, the early stage of haematoma development

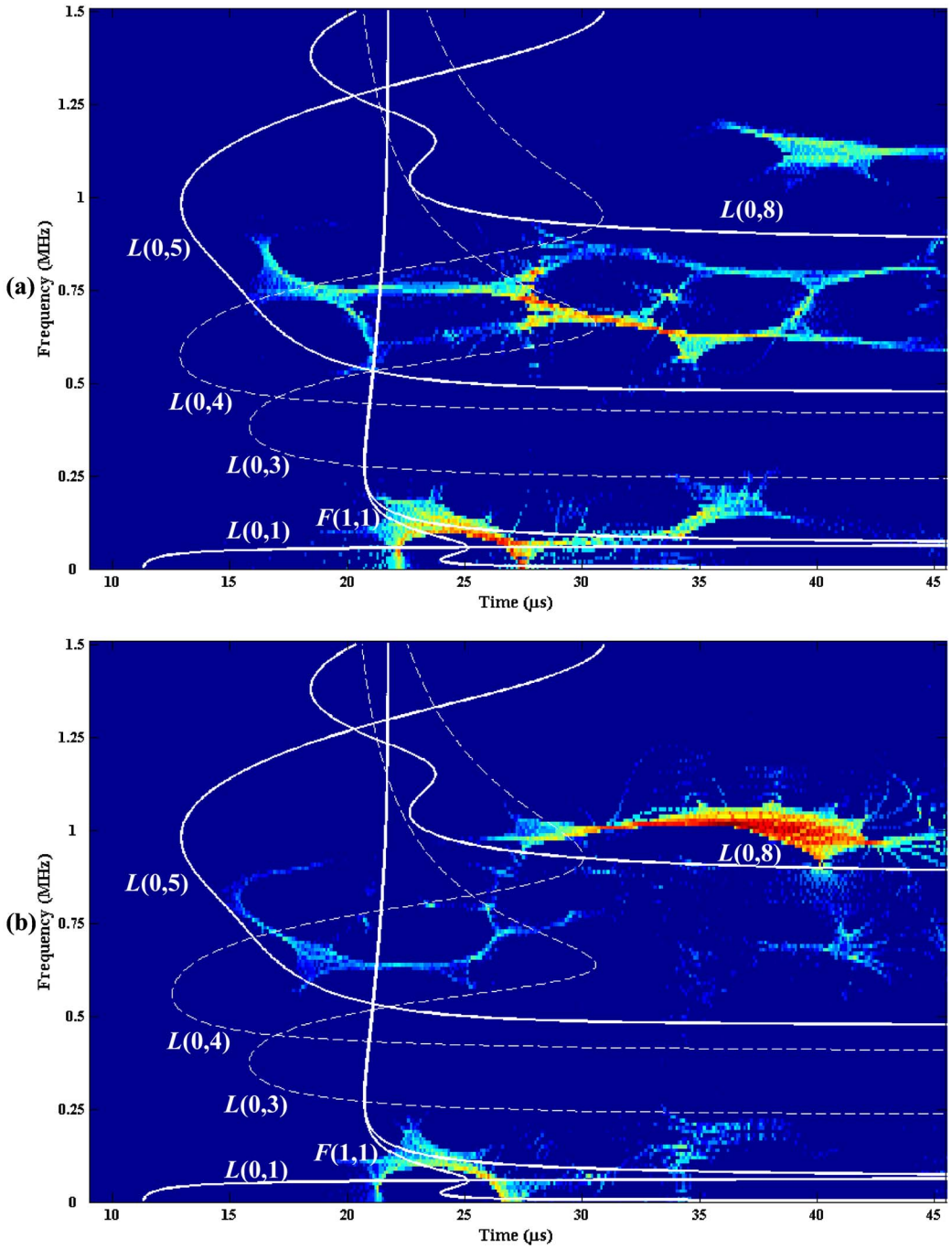

FIG. 11. (Color online) The t-f signal representations obtained from the intact anisotropic bone at (a) Site1 and (b) Site2.

and the gradual reduction in the dimensions of callus as a result of the bone remodeling process were not taken into account.

We examined two cases of material symmetry. In both cases, the elastic constant in the axial direction (C_{33}) was identical and thus the bulk longitudinal velocity was the same, allowing for direct comparisons between the FAS velocity measurements. The anisotropic constants represent effective elastic constants at the macroscopic level and they do not only reflect the elastic properties at the material level, but also the cortical microporosity (Bossy *et al.*, 2004b; Raum *et al.*, 2005). However, the porosity network in the cortical bone (consisting mainly of Haversian longitudinal canals with average pores diameter of 50–100 μm) as well as the biphasic nature of the callus tissue (i.e., a solid and a viscous component) introduce wave attenuation, which was neglected in our study. Attenuation, may have a significant influence on the characteristics of guided waves and can affect the measurements.

Efficient modeling of elastic wave propagation necessitates a detailed discretization of the spatial and temporal domains. For 1-MHz excitation, the smallest wavelengths were 1.54 and 2.34 mm in the ICT and the SOC materials, respectively. Thus, the internodal distance in the circumferential direction (d_{elem_2}) was not sufficient, according to Eq. (16),

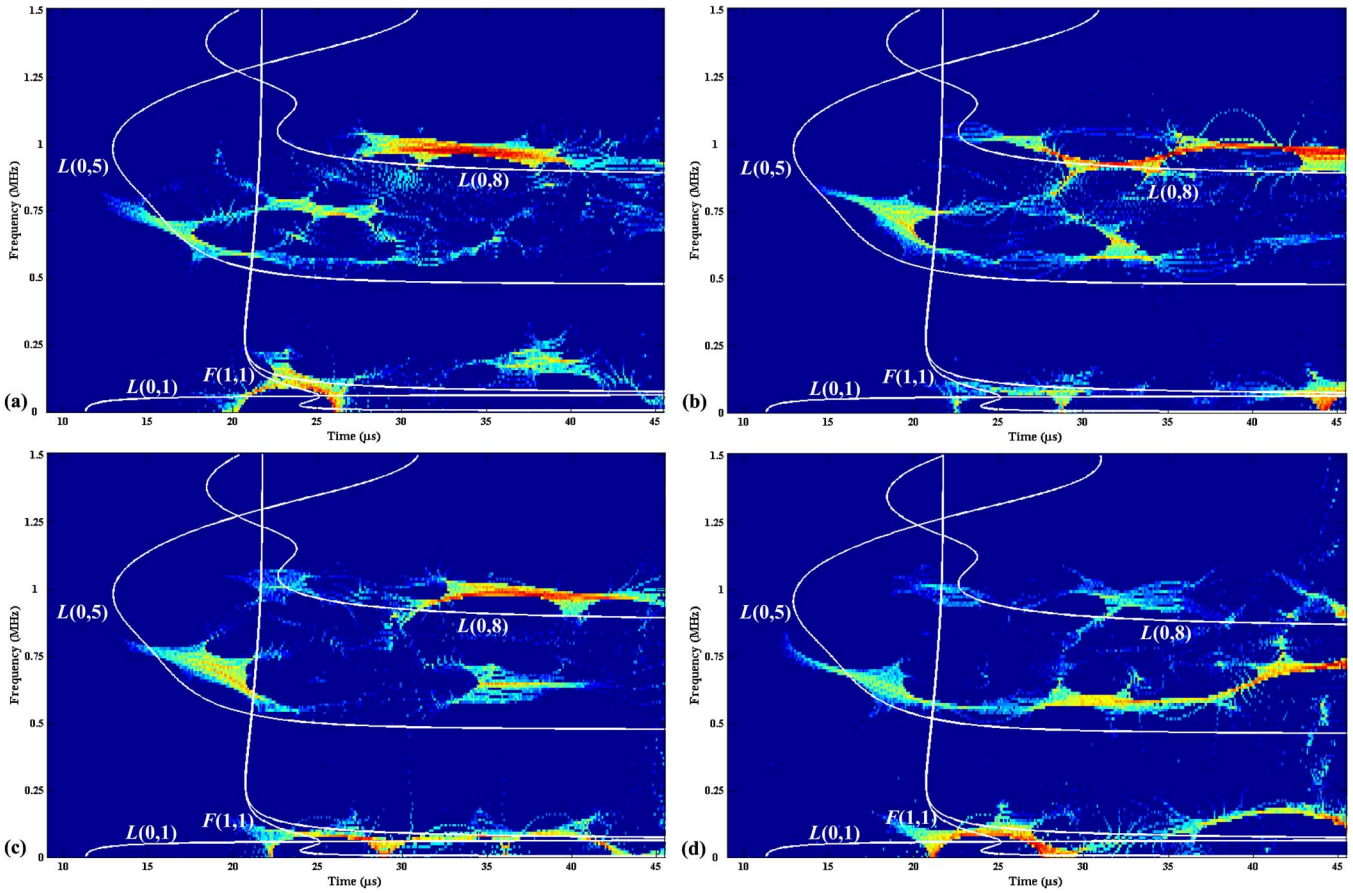

FIG. 12. (Color online) The t-f signal representations obtained from Site2 of the healing bone at (a) Stage0, (b) Stage1, (c) Stage2, and (d) Stage3.

for the stages that involved regions filled with those two soft tissue types. This was a compromise in our study in order to keep low the memory requirements and computational time. However, those materials occupy relatively small regions and mainly are away from the recording region.

For 1-MHz excitation, the wavelength in the bone (approximately 4 mm) was comparable to the cortical thickness. Using traditional velocity measurements, we showed that the FAS wave propagated in the intact models as a nondispersive lateral wave, which is in agreement with previous studies (Bossy *et al.* 2002, 2004b; Nicholson *et al.* 2002; Njeh *et al.*, 1999b). Therefore, the propagation velocity of the FAS was not affected by the geometry of the model or the site of measurement and changed only by 2.2% between isotropy and anisotropy. When we investigated the variation of the FAS velocity over the simulated healing stages, we found that the propagation of the FAS wave was sensitive only to the tissue that filled the fracture gap and thus its velocity remained constant between Stage1 and Stage2. This is due to the fact that lateral waves propagate only along a 1.4-mm-deep layer at 1 MHz (Bossy *et al.* 2004b; Raum *et al.*, 2005) and thus cannot characterize the medium throughout its thickness.

However, our broadband excitation supports the generation of multiple wave modes that are sensitive to the geometrical properties of the bone. These modes could not be identified in the waveform of the signal due to their temporal superposition and thus we used t-f signal analysis techniques. We first examined the hollow circular cylinder for which there exist analytical dispersion curves. The simulated dispersion of the fundamental modes and of some higher-order longitudinal modes was in agreement with the theoretical dispersion, in both the isotropic and anisotropic cases. The simulated dispersion of each mode was identified within specific frequency ranges. In our previous study on an isotropic 2D plate with the same isotropic properties (Protopappas *et al.*, 2006), the dispersion of the S2 and A3 Lamb modes was similar to that of the $L(0,5)$ and $L(0,8)$ modes, although the solution methods were different and the excitation applied to the plate was more broadband. This is justified by the theory for the specific wall thickness and the outer radius values (Lefebvre *et al.*, 2002; Protopappas *et al.*, 2006). Direct comparisons with other 2D bone studies cannot be made since they used low-frequency transducers (250 kHz) that excite only the fundamental modes.

In the intact bone model, the high-order guided waves were significantly different from the modes described by the simplified geometry. However, when the geometrical characteristics of the site of measurement were similar to those of the circular cylinder, we identified two modes with dispersion close to that of the $L(0,5)$ and $L(0,8)$. This geometry-dependent behavior of the higher-order modes may also be observed in real bones where the cross section is not uniform in the direction of the long axis. On the other hand, we found that the fundamental tube modes were almost unaffected by

the irregularity of the bone. Similar behavior is expected in real bone geometries. Furthermore, our results demonstrate that anisotropy has an impact on higher-order mode propagation even if, in the case of isotropy, the properties along the propagation axis are kept constant. However, our finding that the dispersion of the fundamental modes remained practically unchanged between the two elastic symmetries possibly explains why previous ex vivo and in vivo studies reported on the detection of the isotropic A0 and S0 Lamb modes.

For the model of the healing bone, we found that the propagating guided modes were influenced by both the geometry and the properties of the callus. The effect of the geometrical disturbance induced by the formation of callus on mode propagation was evaluated separately at Stage0. It was also shown that mode dispersion was sensitive to the transition from Stage1 to Stage2 and, as the callus properties increased to the bone values, the dispersion of the modes gradually returned to that observed at Stage0. Nevertheless, we were not able to quantify our observations and select significant ultrasonic features that can provide monitoring capabilities.

We made use of the theory that describes elastic wave propagation in circular cylinders since there are no analytical solutions for complex geometries. Recently, FE and boundary element methods have been developed to numerically obtain the dispersion relations for bars of arbitrary cross section (Gunawan and Hirose, 2005; Hayashi *et al.*, 2003). Thus, the computation of the dispersion curves for the bone under examination could make feasible the interpretation of the signals obtained from real experiments. A parameter not provided by the dispersion relations is the amplitude with which a mode is excited at a specific frequency. The excitation of each mode depends on source loading conditions, such as the size of transducers, their pressure distribution, angle of incidence, etc. This justifies why the detected modes exhibited dispersion within narrow frequency ranges, whereas most of the modes were not excited despite that the spectral content of the excitation was sufficiently broad. The amplitudes of each mode in such transient partial loading problems can be determined using integral transform techniques or the Normal Mode Expansion technique (Ditri and Rose, 1992).

One major simplification made in our study was the application of unrealistic boundary conditions. The soft tissues provide leakage paths for the ultrasonic energy resulting in the so-called leaky guided waves and in this case the dispersion curves are modified (Berliner and Solecki, 1996). The soft tissues can be considered as a layer on top of the bone and thus a bilayer model (Rose, 1999) can be used for the analysis of the signals measured in practice. The soft tissues also play an important role in coupling to the percutaneous transducers and in the excitation of specific modes. Free boundary conditions are only met in *ex vivo* experiments on excised bone specimens. A further consideration regarding the boundary conditions is that, despite the attachment of infinite elements at the ends of the model, some energy may not be transmitted out of the model. However, the boundary between the finite and infinite elements is normal to the dominant direction of wave propagation, which optimizes the transmission of energy out of the finite element mesh (ABAQUS, 2003). Since the use of infinite elements is the suggested solution by ABAQUS for simulating infinitely long domains, we extended the mesh to some reasonable distance (7 mm) from the recording region.

VI. CONCLUSIONS

In this work, we presented a 3D computational study of guided wave propagation in intact and healing long bones. We observed that the velocity of propagation determined by the FAS wave was not affected by the convex curvature of the cortex and remained almost the same between different material symmetry assumptions, provided that the cortical thickness is comparable to the wavelength. On the other hand, the irregular bone geometry, as a whole, as well as the anatomical characteristics of the site of measurement had a significant impact on the propagation of the higher-order modes. The effect of the complex geometry and anisotropy of the bone was less pronounced on the dispersion of the fundamental tube modes. Therefore, 2D and 3D simulations on idealized geometries have limited efficiency in interpreting wave-guidance phenomena in real bones; however, they can be reliably used to assess the dependence of the FAS velocity on the cortical thickness. We also demonstrated that traditional velocity measurements cannot reflect the material and mechanical changes that take place during a simulated healing process. Although guided waves were sensitive to both the geometry and the properties of callus, it was not made feasible to provide quantitative results. This study can be proved useful for the interpretation of clinical measurements. We suggest that monitoring of bone fracture healing can be enhanced by analyzing the characteristics of the higher-order guided modes, such as $L(0,5)$ and $L(0,8)$.

ABAQUS, version 6.4, (**2003**). *ABAQUS Analysis User's Manual, and ABAQUS Theory Manual* (Hibbitt, Karlsson and Sorensen, Inc., Pawtucket).

Abendschein, W., and Hayatt, G. W. (**1972**). "Ultrasonics and physical properties of healing bone," J. Trauma **12**, 297–301.

Augat, P., Margevicius, K., Simon, J., Wolf, S., Suger, G., and Claes, L. (**1998**). "Local tissue properties in bone healing: influence of size and stability of the osteotomy gap," J. Orthop. Res. **16**(4), 475–481.

Auger, F., Flandrin, P., Goncalves, P., and Lemoine, O. (**1995–1996**). *Time-Frequency Toolbox Tutorial* (CNRS-RICE University).

Berliner, M. J., and Solecki, R. (**1996**). "Wave propagation in fluid-loaded, transversely isotropic cylinders. Part I. Analytical formulation," J. Acoust. Soc. Am. **99**(4), 1841–1847.

Bossy, E., Talmant, M., and Laugier, P. (**2002**). "Effect of cortical thickness on velocity measurements using ultrasonic axial transmission: a 2D simulation study," J. Acoust. Soc. Am. **112**(1), 297–307.

Bossy, E., Talmant, M., Defontaine, M., Patat, F., and Laugier, P. (**2004a**). "Bidirectional axial transmission can improve accuracy and precision of ultrasonic velocity measurement in cortical bone: A validation on test materials," IEEE Trans. Ultrason. Ferroelectr. Freq. Control **51**(1), 71–79.

Bossy, E., Talmant, M., and Laugier, P. (**2004b**). "Three-dimensional simulations of ultrasonic axial transmission velocity measurement on cortical bone models," J. Acoust. Soc. Am. **115**(5), 2314–2324.

Camus, E., Talmant, M., Berger, G., and Laugier, P. (**2000**). "Analysis of the axial transmission technique for the assessment of skeletal status," J. Acoust. Soc. Am. **108**(6), 3058–3065.

Claes, L. E., and Heigele, C. A. (**1999**). "Magnitudes of local stress and strain along bony surfaces predict the course and type of fracture healing," J. Biomech. **32**(3), 255–266.

Cunningham, J. L., Kenwright, J., and Kershaw, C. J. (**1990**). "Biomechani-

cal measurement of fracture healing," J. Med. Eng. Technol. **13**(3), 92–101.
Ditri, J. J., and Rose, J. L. (**1992**). "Excitation of guided elastic wave modes in hollow cylinders by applied surface tractions," J. Appl. Phys. **72**(7), 2589–2597.
Fotiadis, D. I., Protopappas, V. C., and Massalas, C. V. (**2006**). "Elasticity," in *Wiley Encyclopedia of Biomedical Engineering*, edited by M. Akay (Wiley-Interscience, New York).
Gazis, D. (**1959**). "Three-dimensional investigation of the propagation of waves in hollow circular cylinders. I. Analytical foundation," J. Acoust. Soc. Am. **31**(5), 568–573.
Gerlanc, M., Haddad, D., Hyatt, G. W., Langloh, J. T., and Hillaire, P. S. (**1975**). "Ultrasonic study of normal and fractured bone," Clin. Orthop. Relat. Res. **111**, 175–180.
Gill, P. J., Kernohan, G., Mawhinney, I. N., Mollan, R. A., and McIlhagger, R. (**1989**). "Investigation of the mechanical properties of bone using ultrasound," Proc. Inst. Mech. Eng., Part H: J. Eng. Med. **203**(1), 61–63.
Gunawan, A., and Hirose, S. (**2005**). "Boundary element analysis of guided waves in a bar with an arbitrary cross-section," Eng. Anal. Boundary Elem. **29**, 913–924.
Hayashi, T., Song, W. J., and Rose, J. L. (**2003**). "Guided wave disperson curves for a bar with an arbitrary cross-section, a rod and rail example," Ultrasonics **41**, 175–183.
Hughes, T. J. R. (**2000**). *The Finite Element Method: Linear Static and Dynamic Finite Element Analysis* (Dover, New York).
Lee, K. I., and Yoon, S. W. (**2004**). "Feasibility of bone assessment with leaky Lamb waves in bone phantoms and a bovine tibia," J. Acoust. Soc. Am. **115**(6), 3210–3217.
Lefebvre, F., Deblock, Y., Campistron, P., Ahite, D., and Fabre, J. J. (**2002**). "Development of a new ultrasonic technique for bone and biomaterials in vitro characterization," J. Biomed. Mater. Res. **63**(4), 441–446.
Lowet, G., and Van Der Perre, G. (**1996**). "Ultrasound velocity measurements in long bones: measurement method and simulation of ultrasound wave propagation," J. Biomech. **29**(10), 1255–1262.
Lysmer, J., and Kuhlemeyer, R. L. (**1969**). "Finite Dynamic Model for Infinite Media," J. Engrg. Mech. Div. **95**, 859–877.
Malizos, K. N., Papachristos, A. A., Protopappas, V. C., and Fotiadis, D. I. (**2006**). "Transosseous Application of Low-Intensity Ultrasound for the Enhancement and Monitoring of Fracture Healing Process in a Sheep Osteotomy Model," Bone (Osaka) **38**(4), 530–539.
Maylia, E., and Nokes, L. D. (**1999**). "The use of ultrasonics in orthpaedics—a review," Technol. Health Care **7**, 1–28.
Mirsky, I. (**1965**). "Wave propagation in transversely isotropic circular cylinders. Part I. Theory," J. Acoust. Soc. Am. **37**(6), 1016–1021.
Moilanen, P., Nicholson, P. H. F., Kärkkäinen, T., Wang, Q., Timonen, J., and Cheng, S. (**2003**). "Assessment of the tibia using ultrasonic guided waves in pubertal girls," Osteoporosis Int. **14**, 1020–1027.
Moser, F., Jacobs, L. J., and Qu, J. (**1999**). "Modeling elastic wave propagation in waveguides with the finite element method," NDT & E Int. **32**, 225–234.
Nicholson, P. H. F., Moilanen, P., Karkkainen, T., Timonen, J., and Cheng, S. (**2002**). "Guided ultrasonic waves in long bones: modeling, experiment and in vivo application," Physiol. Meas **23**, 755–768.
Niethammer, M., Jacobs, L. J., Qu, J., and Jarzynski, J. (**2001**). "Time-frequency representations of Lamb waves," J. Acoust. Soc. Am. **109**(5), 1841–1847.
Njeh, C. F., Kearton, J. R., Hans, D., and Boivin, C. M. (**1999a**). "The use of quantitative ultrasound to monitor fracture healing: a feasibility study using phantoms," Med. Eng. Phys. **20**(10), 781–786.
Njeh, C., Hans, D., Wu, C., Kantorovich, E., Sister, M., Fuerst, T., and Genant, H. (**1999b**). "An in vitro investigation of the dependence on sample thickness of the speed of sound along the specimen," Med. Eng. Phys. **21**, 651–659.
Proseer, W. H., Seale, M. D., and Smith, B. T. (**1999**). "Time-frequency analysis of the dispersion of lamb modes," J. Acoust. Soc. Am. **105**(5), 2669–2676.
Protopappas, V. C., Baga, D., Fotiadis, D. I., Likas, A., Papachristos, A. A., and Malizos, K. N. (**2005**). "An ultrasound wearable system for the monitoring and acceleration of fracture healing in long bones," IEEE Trans. Biomed. Eng. **52**(9), 1597–1608.
Protopappas, V. C., Fotiadis, D. I., and Malizos, K. N. (**2006**). "Guided ultrasound wave propagation in intact and healing long bones," Ultrasound Med. Biol. **32**(5), 693–708.
Raum, K., Leguerney, I., Chandelier, F., Bossy, E., Talmant, M., Saïed, A., Peyrin, F., and Laugier, P. (**2005**). "Bone microstructure and elastic tissue properties are reflected in QUS axial transmission measurements," Ultrasound Med. Biol. **31**(9), 1225–1235.
Reilly, D. T., and Burstein, A. H. (**1975**). "The elastic and ultimate properties of compact bone tissue," J. Biomech. **8**(6), 393–396.
Rho, J. Y. (**1996**). "An ultrasonic method for measuring the elastic properties of human tibia1 cortical and cancellous bone," Ultrasonics **34**, 777–783.
Rose, J. L. (**1999**). *Ultrasonic Waves in Solid Media* (Cambridge U. P., Cambridge).
Saulgozis, J., Pontaga, L., and Van Der Perre, G. (**1996**). "The effect of fracture and fracture fixation on ultrasonic velocity and attenuation," Physiol. Meas **17**(3), 201–211.
Tatarinov, A., Sarvazyan, N., and Sarvazyan, A. (**2005**). "Use of multiple acoustic wave modes for assessment of long bones: Model study," Ultrasonics **43**, 672–680.
Zerwer, A., Polak, M. A., and Santamarina, J. C. (**2003**). "Rayleigh wave propagation for the detection of near surface discontinuities: Finite element modeling," J. Nondestruct. Eval. **22**(2), 39–52.

Call repertoire of infant African elephants: First insights into the early vocal ontogeny

Angela S. Stoeger-Horwath,[a] Simon Stoeger, and Harald. M. Schwammer
Vienna Zoo, Maxingstrasse 13b, 1130 Vienna, Austria

Helmut Kratochvil
Department for Evolutionary Biology, University of Vienna, Althanstrasse 14, 1090 Vienna, Austria

(Received 21 September 2006; revised 13 March 2007; accepted 13 March 2007)

African savannah elephants (*Loxodonta africana*) have a complex acoustic communication system, but very little is known about their vocal ontogeny. A first approach in ontogenetic studies is to define the call repertoire of specific age groups. Twelve hundred calls of 11 infant elephants from neonatal to 18 months of age recorded at the Vienna Zoo in Austria and at the Daphne Sheldrick's orphanage at the Nairobi National Park, Kenya were analyzed. Six call types were structurally distinguished: the rumble, the bark, the grunt, the roar (subdivided into a noisy-, tonal-, and mixed-roar), the snort, and the trumpet. Generally, within-call-type variation was high in all individuals. In contrast to adult elephants, the infants showed no gender-dependent variation in the structure or in the number of call types produced. Male infants, however, were more vocally adamant in their suckle behavior than females. These results give a first insight to the early vocal ontogeny and should promote further ontogenetic studies on elephants. Due to their vocal learning ability in combination with the complex fission-fusion society, elephants could be an interesting model to study the role of imitation in the vocal ontogeny of a nonprimate terrestrial mammal.
© *2007 Acoustical Society of America.* [DOI: 10.1121/1.2722216]

PACS number(s): 43.80.Ka [JAS] Pages: 3922–3931

I. INTRODUCTION

African savannah elephants exhibit extraordinary vocal abilities and even proved to be capable of vocal learning (Poole *et al.*, 2005). Recent studies of elephant vocalizations indicate that their vocal repertoire is extensive and highly variable (Langbauer, 2000). However, all major repertoire papers have focused on adult individuals (Berg, 1983; Poole *et al.*, 1988; Leong *et al.*, 2003). For the first time, we provide data on the vocal repertoire of infant elephants from neonatal to 18 months of age. Our study aimed at (1) defining the structural and functional characteristics of infant calls, (2) standardizing call terminology, and (3) determining early sex- and age-dependent variations of call types.

Elephants produce structurally different sounds like low-frequency rumbles, trumpets, snorts, and a variety of higher frequency calls (Langbauer, 2000). In a review on elephant communication, Langbauer (2000) reports a classification into 31 call types, based on functional context. Berg (1983) and Leong *et al.* (2003) analyzed calls from captive groups of African elephants, whereas Berg (1983) distinguished ten, and Leong *et al.* (2003) eight, call types based on visual examination of spectrograms. The most commonly heard structural type of call is the rumble. Poole *et al.* (1988) characterized seven rumble subtypes by behavioral context, but there is no consensus about the number of rumble subtypes from a structural standpoint. Soltis *et al.* (2005) examined the acoustic structure of rumbles of a captive group and found a graded structure across this call type. Wood *et al.* (2006), in contrast, analyzed calls from one family group recorded at the Kruger National Park and documented three rumble subtypes based on acoustic parameters.

Elephants exhibit a pronounced sexual dimorphism in calling patterns, with males producing significantly fewer vocalizations and types of calls than females (Poole, 1994). Ontogenetically, the sexes do not only differ in growth (Lee and Moss, 1995), but also in early social development (Lee, 1986; Lee and Moss, 1986) and social interactions (Lee and Moss, 1999). This reflects the differences of associations between the sexes, pointing to an early sexual differentiation in vocal ontogeny.

To date, only few studies have dealt with the vocal behavior of calves or juveniles. In her thesis about the development of social behavior in translocated juvenile African elephants, Gerai (1997) presented some behavioral and acoustic aspects of vocalizations by 2- to 7-year-old individuals. We documented certain aspects of calls by a newborn African elephant in captivity (Horwath *et al.*, 2001; Horwath, 2002), but next to nothing is known about the call repertoire of different age classes and when elephants acquire the full adult vocal repertoire.

In this paper we provide acoustic details of infant elephant calls. Our recordings focused on two calves born in a zoo, which provided us with an opportunity to follow their vocal development over a longer period of time. Additionally, we observed a semi-captive group of orphaned elephants in Kenya to improve sample size and to compare calls at two distinct locations and environments.

[a]Electronic mail: astoeger-horwath@zoovienna.at

TABLE I. Acoustic features and parameters measured.

Main acoustic feature	Parameter measured
Manner features: [modified from Fant (1960)]: Via visual examination of the spectrogram	Feature 1: Tonal (frequency contours of the harmonics in tonal signals: straight, bent, left skewed, right skewed, bimodal, increasing, decreasing, multimodal)
	Feature 2: Noisy
	Feature 3: Transient
Duration	Signal duration
	Duration from signal onset to maximum frequency
Fundamental frequency: Automatically measured via Stx using simple inverse filter tracking method (one measurement/frame)	Minimum, maximum, mean, starting-, mid-, and ending frequency
First harmonic: Measured by cursor placement	Minimum, maximum, mean (calculated) starting-, mid-, and ending frequency
Amplitude difference	Difference in dB from the fundamental frequency to the second harmonic
Dominant frequency: The frequency of highest intensity	Mid-point of the dominant frequency
Bandwidth: Only high-quality calls that had been recorded in less than 10 m distance	Bandwidth at the mid-point of the call
First formant: Only low-frequency calls using LPC coef 60, for calls of up to 5-month-old elephants, 80 for those aged between 6 and 12 months, and 100 for calls of elephants older than 12 months	Minimum, maximum, mean, and mid point
Second formant	Minimum, maximum, mean, and mid point

II. MATERIAL AND METHODS

A. Study animals and housing

The studied animals were 11 infant elephants from neonatal to 18 months of age. We recorded a male (Abu) and a female (Mongu) calf at the Vienna Zoo in Austria from neonatal to 18 months, and five males aged 3 (Ndomot and Madiba), 11 (Taita), 13 (Tomboi), and 15 (Napasha) months, as well as four females aged 6 (Sunyei), 9 (Olmalo), 10 (Selengai), and 14 (Wendy) months at the Daphne Sheldrick orphanage in Nairobi National Park, Kenya. At the Vienna Zoo, the whole elephant group consisted of four adult females, the two calves, and an adult male, who was kept separately. Both calves are not related and had been raised by their mothers within the elephant group. The keepers have direct contact with the female group for approximately 1.5 h per day. The elephants spend the night unchained in the indoor stall (2100 m^2) within the family and are released into their outdoor enclosure (4700 m^2) for the day. At the Daphne Sheldrick orphanage, the elephants spend the night in small separated stables, accompanied by a keeper. At 6:00 a.m., the keepers and the elephants leave to the bush, return at midday for 1 h of public presentation, leave again to the bush and come back to the stables at 6:00 p.m. Approximately every 3 h, the orphans are fed a special milk formula compiled by Daphne Sheldrick, but otherwise move freely in the bush. Due to visitor- or shower-related noise, no recordings were made during public presentations.

B. Data collection

We recorded 1400 h at the Vienna Zoo from 2001 to 2004 and 300 h in January and February 2004 at the orphanage in Kenya. Recordings were made at 48 kHz sampling rate on a DA-P1 DAT recorder (frequency response: 100 Hz:−0.2 dB, 20 Hz:−0.26 dB, 15 Hz:−0.26 dB, 12 Hz:−0.3 dB, 8 Hz:−0.32 dB, and 4 Hz:−0.45 dB), with the condenser microphone AKG C 480 B and the omni directional condenser capsule AKG CK 62—ULS (frequency response: 100 Hz:0 dB, 30 Hz:0 dB, 20 Hz:−0.16 dB, 15 Hz:−0.23 dB, 10 Hz:−0.44 dB, and 8 Hz:−2.72 dB). Data recording took place only outdoors. At the zoo, recording distances ranged from 1 to 25 m. At the Sheldrick orphanage we were able to walk with the elephants in the bush during the day, yielding recording distances of approximately 0.5 to 30 m.

The following data were recorded for each call: identity of the caller (due to the short distance to the vocalizing animals, the caller could be identified by hearing), approximate distance to the vocalizing elephant, number and identity of individuals present, position of the other elephants in relation to the vocalizing animal within the group, presence or absence of the keepers, the behavioral context, and aperture angle of the mouth during vocalization, whereas two categories were distinguished: 1=almost closed, 2=opened.

C. Data analysis

We analyzed the signals with the computer program S_TOOLS-STx from the Acoustic Research Institute of the Austrian Academy of Sciences Vienna. For the frequency analyses in low-frequency calls, the signals have been downsampled to 8000 Hz. We analyzed 1200 calls of known infant individuals, taking 26 acoustic parameters (Table I). For measurements of the first and second formant we used the linear prediction coding method (LPC). Although we were

sometimes able to define up to six formants, we considered only the first two; these were the most consistent ones.

D. Call type classification

Call types were defined from a structural point of view. Before the acoustic analyses, we developed two main call categories based on the way sound was produced: calls produced by the larynx (laryngeal calls) and sounds produced by a blast of air through the trunk (trunk calls).

We categorized putative call types and subtypes by ear and by visual inspection of the sound spectrograms based on manner features (Fant, 1960), e.g., a tonal versus a noisy production characteristic, as well as on structural differences in the frequency and time characteristics.

We tried to fit our calls into the established nomenclature where possible, based on qualitative descriptions and acoustic information. We additionally achieved an agreement on call terminology with the World's leading scientist on elephant vocal communication, Joyce Poole, from the Amboseli Elephant Research Project.

E. Statistical verification

For the statistical analyses we created balanced data sets by taking the same number of calls per individual for each putative call type/subtype. Discriminant function analysis (DFA) was used to test the validity of call type categories previously constructed by visual inspection. We performed one DFA for the laryngeal calls, and one separate DFA for the trunk calls. We used duration of the signal, start, mid, end, minimum, and maximum fundamental frequency and the dominant frequency. These were the parameters available for all call types, because especially in noisy signals, measurable acoustic features were limited to these parameters. Table IV provides acoustic details of the balanced data set of each call type. However, in the text we also give information about the total number of calls in the data set and the total number of individuals for which each call type has been recorded. We used "n_{ind}" to refer to the number of individuals and "n_{c}" to refer to the number of calls.

As the rumble dominates the acoustic repertoire of elephants, and to address the recent discussion on rumble subtypes, we analyzed this call in more detail. We used multidimensional scaling analyses (MDS) to examine the pattern of acoustic variation in rumbles without specifying prior subtypes. We randomly selected nine calls of each of the 11 individuals and entered them into MDS using 21 acoustic parameters (all acoustic parameter mentioned in Table I, excluding manner features and the second formant, because it was often absent in soft rumbles). We also performed MDS with calls from each infant individual to test whether the observed tendencies are consistent on the individual level, i.e., to exclude wrong results due to individual- or age-dependent variations. We used all available calls from each individual (at most 100). The Stress1 values were assessed after Kruskal: 0.20 poor, 0.10 fair, 0.05 good, and 0.02 excellent. We used a bivariate correlation coefficient to test for a correlation between the fundamental frequency and bandwidth in the rumbles.

F. Analyses of functional context

The functional contexts exhibited during the recording period were put into categories (Table II). We calculated the frequency of occurrence of behavioral categories for each call type. These descriptions are provisional and can serve as a basis for actual hypothesis testing later.

G. Analyses of age- and gender-dependent variations

To demonstrate age-dependent differences of the fundamental frequency in the rumble, we used rumbles recorded in reaction to abnormal suckle terminations, and took at least eight calls per individual at a specific age recorded solely in this context.

We used three male (Napasha, Taita, Tomboi) and three female (Olmalo, Selengai, Wendy) orphans between age 10 and 15 months to show a gender-dependent vocal activity in suckling situations. These six orphans were fed simultaneously each time. The keepers brought the milk bottles (two for each elephant) and each elephant was fed by one keeper. We analyzed the vocal activity of 18 such feeding situations by calculating the number of vocalizations of each individual. We used the chi-square test to show significant variations between gender and individuals.

III. RESULTS

A. Call repertoire

By visual examination of the spectrograms, we defined six putative call types: four laryngeal ones—the rumble, the bark, the grunt, and the roar, which we subdivided into the noisy roar, the tonal roar, and the mixed roar—and two trunk calls—the snort and the trumpet. We randomly selected 30 calls from each putative call type/subtype and performed DFA to test the validity of our previously constructed categorization. Laryngeal calls and trunk calls were tested separately. Table III shows the eigenvalues and variances explained by the first three functions for the laryngeal calls and the first function for the two trunk calls, and the correlation of variables. In the laryngeal calls, fundamental frequency parameters mainly separate call types in the first function, duration in the second function. Figure 1 shows the results of DFA for the laryngeal calls. In a leave-one-out classification, 100% of rumbles, 100% of barks, 96% of grunts, and 100% of roars were correctly classified. Within the roar, 100% of noisy roars, but only 73.3% of mixed roars and 60.6% of tonal roars were classified correctly. Six percent of tonal roars and 10% of mixed roars have been classified to noisy roars, otherwise tonal and mixed roars intermixed. In the trunk calls, dominant frequency is the most important factor separating snorts and trumpets. In the leave-one-out classification, 100% of trumpets and snorts were correctly classified. Table IV gives the duration, mean fundamental frequency, mean dominant frequency, and manner features for call types, and Fig. 2 spectrographically presents a typical example of each call type.

TABLE II. Description of the most important functional contexts.

Functional context	Explanation
Suckle intention	The calf repeatedly touches the mothers legs or teats (with mouth or trunk) attempting to make nipple contact. The orphans repeatedly touched the blankets (which have been fixed between two branches to facilitate feeding and to imitate the body of the mother)
Suckle start	The beginning of a suckle bout (one or more successful or unsuccessful nipple contacts separated by less than 60 s of time off the nipple (Lee and Moss, 1986)
Infant break	Calf removes its mouth from the nipple/bottle in between two nipple contacts
Abnormal suckle termination	Mother/keeper rejects, or anything that disturbed the calf during suckling, resulting in a compelled suckle break or termination, e.g., after receiving a push or "genital check" by another elephant during suckling
Trunk touch	The calf is being touched with the trunk by another elephant (e.g., at the genitals, mouth, temporal glands,…)
Begging	Repeatedly touching the keeper with the trunk begging for tidbits
Spatial separation	The calf does not see the mother or the other orphans because of bushes or other structures
Intraspecific agonistic behavior	The calf is being pushed, kicked, trunk slapped, or chased
Interspecific or object aggression	Making mock charges, chasing birds or warthogs, attacking machines, cars,…
Require care/help	E.g., the calf fell down and could not get up alone
Alerting to external stimuli	E.g., a sudden appearance of a rhino, or buffalo, or unfamiliar machine,…
Play behavior	play fights, pushing head/trunks, climbing on each other, object play,…

B. Description of call types and within-call type variation

1. Rumble

The rumble is conspicuous because of its very low fundamental frequency near the infrasonic range. In the infants, 53% of the total number of recorded calls were rumbles (n_c=795). We recorded rumbles in all 11 individuals ranging from neonatal to 18 months of age (Fig. 3). These rumbles are low-frequency tonal signals with formant formation. No infrasonic fundamental frequencies below 20 Hz were produced. Similar to adults (O'Connell-Rodwell *et al.*, 2001), the second harmonic has more energy than the fundamental one; on average, the mean difference ±SE was 15.90±5.304 dB (n_c=220, n_{ind}=11). Infant rumbles can be soft with a minimal documented bandwidth of 70 Hz, as well as very loud with extreme bandwidth values of up to 20 kHz; intermediate stages are also present. When producing rumbles with a bandwidth below 2000 Hz, the mouth was closed in 71.8% of cases. When producing rumbles with a bandwidth above 2000 Hz, the mouth was open in 68%.

TABLE III. Results of discriminant function analyses for laryngeal and trunk calls. Eigenvalues, variances explained, and structure matrix giving the correlation of variables.

Laryngeal calls				**Trunk calls**
	Function 1	Function 2	Function 3	Function 1
Eigenvalue	11.772	2.349	1.280	8.398
% Variance	75.9	15.2	8.3	100
Variables		**Correlation**		
Maximum F0	**0.916**[a]	0.170	−0.030	0.537
F0 mid	0.898	0.153	−0.037	0.493
F0 end	0.819	0.030	−0.377	0.496
Minimum F0	0.814	−0.053	−0.398	0.491
F0 start	0.790	−0.033	−0.270	0.462
Duration	−0.016	**0.966**[a]	0.040	0.211
Dominant frequency	0.231	−0.016	**0.823**[a]	**0.812**[a]

[a]The strongest factor loading of the variables on each discriminant function is shown in bold (F0=fundamental frequency).

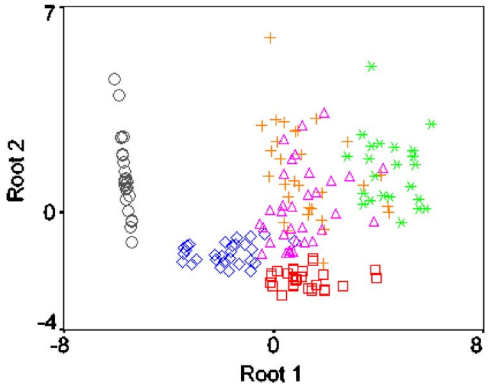

FIG. 1. (Color online) Scatter plot of laryngeal calls representing the results of function (root) 1 and function (root) 2 of discriminant analyses. Rumbles (circles), grunts (rhombus), barks (squares), and roars (triangles, stars, and crosses) separate well in these two functions. Noisy roars (stars) also separate from the other two roar subtypes, however tonal roars (triangles) and mixed roars (crosses) are intermixed.

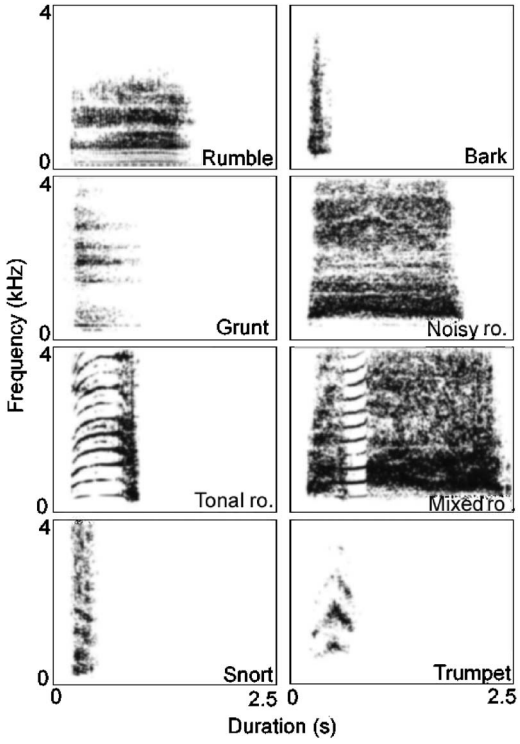

FIG. 2. Spectrograms giving a typical example of each call type (256-point fast Fourier transform, overlap 75%, Hanning window). Call types vary in manner features and structural differences in the frequency and time characteristics. (ro.=roar).

There is a weak positive correlation between the mean fundamental frequency and bandwidth ($r=0.249$, $n_c=220$, $p=0.000$). Loud rumbles with a bandwidth above 2000 Hz tended to have higher fundamental frequencies ($\bar{X}\pm SE=29.82\pm5.139$ Hz, $n_c=100$) than soft rumbles with a bandwidth below 2000 Hz ($\bar{X}\pm SE=25.27\pm2.634$ Hz, $N_c=100$). The correlation coefficient was stronger on the individual level (e.g., Madiba from the Nairobi orphanage: $r=0.695$, $p=0.000$, $n_c=80$). The rumbles had a harmonic structure in the lower frequencies but, when they were loud, often had noisy components in the upper frequency range.

a. Are there acoustically distinctive rumble subtypes? The infant rumbles showed a high degree of variation in the measured acoustic features. We applied MDS to test for distinctive subtypes in infant rumbles using 99 calls ($n_{ind}=11$) and 21 acoustic parameters. No separation into discrete subtypes was obvious within the infant rumbles [Fig. 4(a)]. These MDS results were constant on the individual level [Figs. 4(b)–4(d)]. Whether different frequency contours represent further subdivisions remains unclear and needs to be investigated in more detail. The most common frequency contour, with 26.9%, was "straight," followed by "bent" and "left skewed," both with 15.5%, "right skewed" (13.3%), and "decreasing" (8.9%).

2. Bark

The bark is a transient and mainly noisy call. It differs from the other calls due to its short duration. We recorded a total of 80 barks in all individuals from the age of 3 weeks to 18 months. It consists of a single excitation of the vocal

TABLE IV. Basic acoustic features of each call type and subtype. D=duration of the signal, Mean F0=mean fundamental frequency, Do. Freq.=mid position of dominant frequency.

Call type	n_{ind}	n_c/Individual	D (s) $\bar{X}\pm SE$	Mean F0 (Hz) $\bar{X}\pm SE$	Do. Freq. (Hz) $\bar{X}\pm SE$	Manner features
Laryngeal calls						
Rumbles	11	20	1.6±0.5	28.1±5.0	53.32±8.6	Tonal
Barks	8	7	0.3±0.2	340.2±106.8	710.0±255.2	Transient
Grunts	2	40	0.5±0.3	250.2±102.4	405.9±67.0	Noisy
Roars						
Noisy roars	7	8	1.4±0.4	561.6±53.1	730.0±109.5	Noisy
Tonal roars	7	6	1.1±0.5	341.4±66.7	1093.3±310.7	Mainly tonal end noisy
Mixed roars	6	8	1.6±0.5	409.1±95.0	986.8±364.3	Multiple switching from noisy to tonal
Trunk calls						
Snorts	6	6	0.6±0.3	185.0±79.2	413.5±164.4	Noisy
Trumpets	4	9	1.16±0.7	586.43±156.4	1306.53±219.1	Tonal

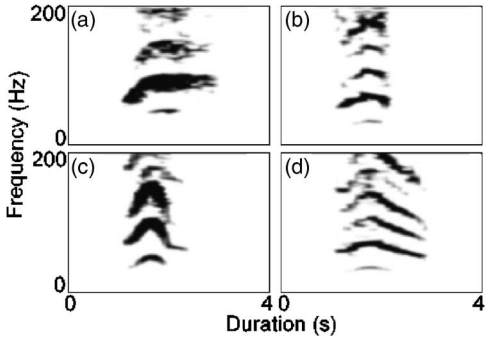

FIG. 3. Spectrograms giving the first 200 Hz of loud rumbles of one individual (Mongu, Vienna) at different ages: (a) 2 h after birth, (b) 2 months of age, (c) 5 months of age, and (d) 10 months of age (4096-point fast Fourier transform, overlap 75%, Hanning window).

cavities caused by the release of an overpressure. When uttering barks, the mouth of the elephants was wide open (posture 2). The short duration and the transient production characteristic are consistent; the call does vary to some extent in fundamental and dominant frequency (Table IV). Often, the bark is immediately followed by a rumble without an inhalation period (bark-rumble).

3. Grunt

The grunt (n_c=93) did not resemble any previously named vocalization. Such calls were sufficiently acoustically distinct and were recorded in both individuals at the zoo, necessitating the classification into a new call type. We chose the term grunt because it is a nonfunctional name and has not yet been applied to elephant calls. Grunts were stereotyped in structure, being noisy with merely first indications of harmonics. Most grunt recordings stemmed from Mongu and Abu within the first few days of their lives. They stopped producing grunts at approximately 2 months of age. Grunts were very soft and barely audible when we were more than 20 m away. The mouth seems to be almost closed during most grunting vocalizations. The grunt was never produced in combination with rumbles or any other call.

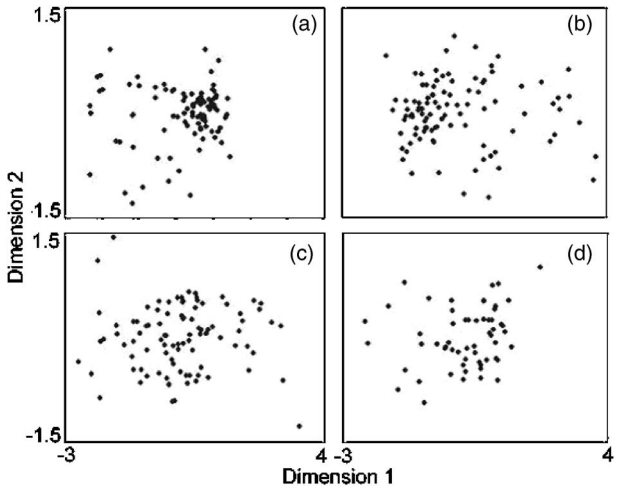

FIG. 4. Results from MDS analyses of infant rumbles using 21 acoustic parameters. (a) MDS results of 99 calls from 11 individuals (stress=0.0785, RSQ=0.989); (b) 100 randomly selected rumbles of Madiba (3 months old) recorded in January 2004 (stress=0.0843, RSQ=0.984); (c) 100 randomly selected rumbles from Mongu recorded from May to August 2003 (from neonatal to 3 months of age; stress=0.0633, RSQ=0.991); and (d) 70 rumbles from Ndomot (3 months old), recorded in January 2004 (stress =0.0718, RSQ=0.992). Results of each MDS analysis show no clustering into discrete subtypes, but point towards a graded variation of infant rumbles.

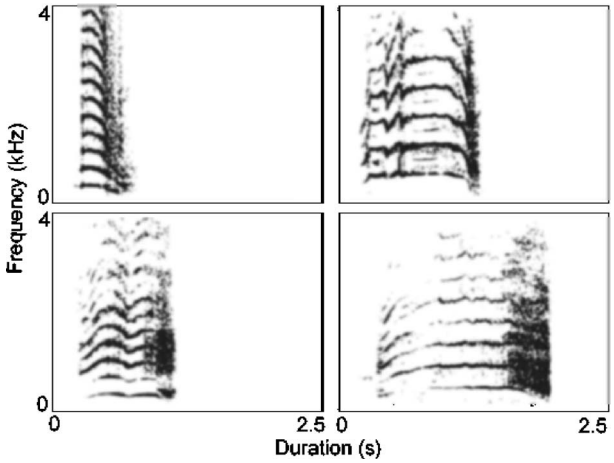

FIG. 5. Spectrograms (256-point fast Fourier transform, overlap 75%, Hanning window) presenting examples of tonal roars of four different individuals demonstrating structural variation within this roar subtype. Tonal roars vary in overall duration, and in the duration of the tonal and noisy segments. Furthermore, the tonal segments show different grades of modulation.

4. Roar

We recorded various roars (n_c=203) of all 11 individuals from neonatal to 18 months of age. When uttering roars, the mouth of the infants was usually wide open. Based on manner features, we grouped the roars into three subtypes. Eighty roars were totally noisy with no tonal segments and are termed noisy roars. We recorded the noisy roars of ten individuals (6♂, 4♀). Noisy roars varied in fundamental frequency, but were highly stereotyped in their noisy acoustic structure characteristic (Table IV).

We characterized calls as tonal roars (n_c=60; n_{ind}=6♂, 3♀, age 0–18 months) when they were tonal for the main part of the call, sometimes with an abrupt and noisy ending. This call was not highly stereotyped (Fig. 5). The main variation involves the appearance and duration of the noisy ending (86% of calls had a noisy ending). The mean duration of the tonal part ±SE was 0.72±0.67 s; the mean duration of the noisy ending (if present) ±SE was 0.21±0.19. In contrast to the noisy roar, this call sounds very clear.

We further recorded calls characterized by multiple switching from tonal to noisy segments, termed mixed roars (n_c=63). We recorded these calls in ten individuals (6♂,4♀) between the ages of 2 weeks and 18 months. Mixed roars were also not stereotyped in structure (Fig. 6); 44.4% switch from a noisy beginning to a tonal mid-part and to a noisy ending. The tonal segments varied in temporal placing, frequency contours of the harmonics, and duration. We documented a maximum of seven switches in one call. The error rates of approximately 30% (mixed roars) and 40% (tonal roars) in the leave-one-out classification show that solely duration and frequency parameters are inadequate to separate these subtypes. Manner features was the most im-

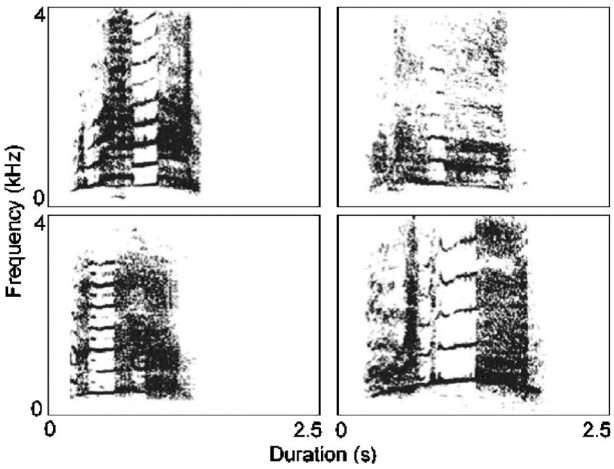

FIG. 6. Spectrograms (256-point fast Fourier transform, overlap 75%, Hanning window) presenting examples of mixed roars of four different individuals demonstrating structural variation within this subtype. Mixed roars vary in the number of tonal and noisy segments. The tonal segments vary in temporal placing, frequency contours of the harmonics, and duration.

portant factor enabling us to distinguish between tonal and mixed roars. All roar subtypes were often uttered in combination with rumbles, either before or after the rumble, without an inhalation period (rumble-roar, roar-rumble, rumble-roar-rumble, or roar-rumble-roar).

5. Snort

The snort (n_c=68) is a strong blast of air through the trunk without producing a tonal signal and a proper sound. The structure of this sound is very consistent, yet with some variations in frequency features (Table IV). It was recorded in eight individuals (5♂, 3♀), whereas 79.8% of all snorts were recorded in calves younger than 4 months.

6. Trumpet

We recorded trumpets (n=72) in seven (4♂, 3♀) individuals aged from 3 to 18 months. Infant trumpets are mainly tonal sounds, but harmonics are overlaid with noise. They appear in several forms, vary in duration, and can have a pulsated structure when the elephant is running while producing the call. The most common call structures were "increasing" (27.8%), "straight" (25%), and "multimodal" (12.5%).

C. Functional context

Although all calls were emitted in more than one context, we were able to determine predominant functions for all call types. The most common functional contexts of specific calls are given in Table V.

Rumbles in infant elephants were used in a variety of contexts. Generally, excited calves tended to produce calls with more harmonics than less excited calves. Soft rumbles were often answered by the mother or other elephants, indicating also a vocal contact function, whereas louder rumbles were mainly used as a protest or distress call. The bark was often produced after being pushed or kicked during walking or feeding, when the affected calf did not expect such an interaction. Grunts backed up suckle intention behavior; however, often they were immediately answered by a soft rumble of the mother, again indicating a vocal contact function. Most noisy roars where recorded when the animals required immediate care or were separated from the group. In contrast, the tonal and the mixed roars were most often produced as a reaction to abnormal suckle terminations. Many of our recorded snorts had no apparent communicational function; they probably represented a strong blast of air through the trunk for cleaning purposes. However, calves younger than 3 months sometimes snorted when producing

TABLE V. Functional contexts of specific call types and subtypes (%=frequency of occurrence of behavioral categories for each call type/subtype). The most common context is shown in bold.

Call type	Functional contexts
Rumble	
Soft rumbles (bw<2 kHz)	**Suckle contexts** (43%: suckle intention, suckle start, infant break); trunk touch (20%), begging (7.3%)
Loud rumbles (bw>2 kHz)	**Abnormal suckle termination** (39%); trunk touch (18%), begging (8%)
Grunt	**Suckle intention** (46%); play behavior (22%);
Bark	**Intraspecific agonistic behavior** (33.9%), begging (17.9%); trunk touch (14.3%)
Roar	
Mixed roar	**Abnormal suckle termination** (61.1%); requiring care/help (9.3%), intraspecific agonistic behavior (7.4%)
Noisy roar	**Requiring care/help** (28.5%); abnormal suckle termination (18%); intraspecific agonistic behavior (14%); spatial separation (10%);
Tonal roar	**Abnormal suckle termination** (54.9%); begging (11.8%); intraspecific agonistic behavior (7.8%)
Snort	**No communicative function** (59.9%); interspecific or object aggression (mock charges, 13.9%)
Trumpet	**Interspecific or object aggression** (mock charges, 57.9%), external stimuli (13.6%)

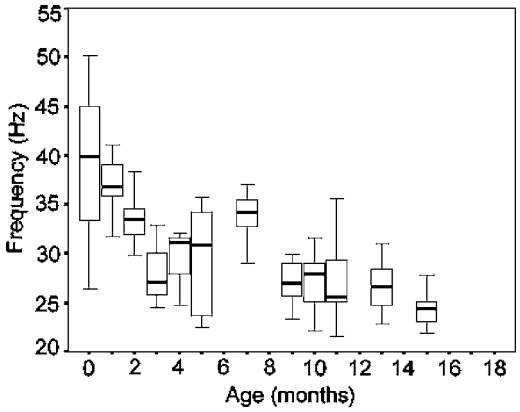

FIG. 7. Box plot presentation of the age-dependent fundamental frequency development in rumbles uttered after abnormal termination of suckling. Mongu 0–5 months (Vienna); 7, 9, and 10 months (females, Nairobi); and 11, 13, and 15 months (males, Nairobi).

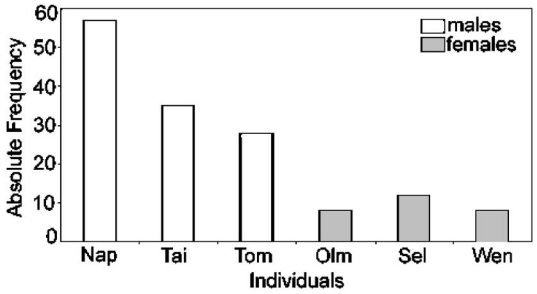

FIG. 8. Histogram demonstrating the frequency of vocalization of each individual (males: Napasha, Taita, Tomboi; females: Olmalo, Selengai, Wendy) in 18 suckle situations. Although there are individual differences, each male vocalized significantly more than each female (chi-square test, all $P<0.05$).

mock charges. Most trumpets involved interspecific or object aggression. In infants, however, it is difficult to determine whether there is some aggressive intention when mock charging birds or warthogs, or if mere play is involved.

D. Age- and gender-dependent variations

We clearly documented age-dependent variation in the appearance of two call types, the grunt and the trumpet. We never recorded grunts in an individual older than 2 months. In contrast, although we intensively recorded the two zoo elephants from birth on, neither produced trumpets until they were 3 months old.

We documented age-dependent variation, particularly in the low-frequency rumble. As expected, older individuals tended to have lower fundamental frequencies in the rumble than younger individuals (Fig. 7), and there was a tendency for rumble duration to slightly increase with age.

We observed no gender-dependent variation in the acoustic structure of any call type. Furthermore, there was no difference in the number of call types produced by male and females calves at this ontogenetic level. We documented each call type in both genders.

In the feeding situations at the orphanage, male infants vocalized more frequently than females. Usually, when one bottle of milk was finished, the keepers had to remove the bottle from the mouth, creating abnormal breaks or terminations of suckling for the infants. We also observed a lot of pushing and barging between the infants, again resulting in abnormal suckle breaks. In 18 such feeding situations, the three male infants vocalized significantly more than the females (chi-square test: $1=54.6$, $p<0.001$). Although there are individual differences, each male vocalized significantly more than each single female (chi-square test: all $p<0.05$; Fig. 8). The calls were mainly loud rumbles and roars as well as combinations of both call types.

IV. DISCUSSION

This study is the first to describe the acoustic structure and the basic functional contexts of infant elephant calls. Due to the considerable gradation of the acoustic parameters, we did not distinguish more than six call types. Based on our acoustic analyses, the rumble in infants seems to be graded with no distinctive subtypes. A similar result was reported by Soltis *et al.* (2005), who analyzed rumbles produced by six adult females. Gerai (1997) distinguished a "low-rumble" and a "growl" in juvenile African elephants. She defines the "low-rumble" as a soft, low, monotone rolling sound, with the mouth appearing closed. The "growl" is a more guttural, rolling, periodic, and slightly louder sound than the "low-rumble," whereby the mouth is generally open. In the parameter described, however, her "low-rumble" and her "growl" differ in mean duration and frequency, but the ranges overlap and it is unclear weather they are discrete call types. Her general descriptions agree with our observations of soft and loud rumbles, but, in contrast to Gerai (1997), we did not separate them as discrete call types or subtypes. Gerai (1997) further reported higher-frequency calls she termed "cries," "bellows," and "squeals," but because of too small sample size, she was unable to adequately differentiate and structurally define the various loud sounds. Based on her general description and the given spectrograms, those high-frequency calls seem to fit into our roar categories. Note, however, that Gerai (1997) recorded 2- to 7-year-old juvenile African elephants, whose vocal behavior might differ from that of infants.

Elephants typically exhibit a very flexible and open communication system (Poole *et al.*, 2005), and gradation of acoustic features seems to be characteristic for elephants, complicating the classification of calls. Even a few calls in our data could not be clearly classified to a specific call category. We, for example, recorded few trunk sounds that differ from trumpets and snorts. The infants forced air out of the trunk pressing the trunk tips together, producing a squelching sound. Each call had a unique structure, and these sounds are probably idiosyncratic sounds with no communicative function. Our observed within-call type variation might also reflect individual characteristics of sound production and the different origins of the elephants. We recorded two unrelated infants in Vienna, whose parents originally come from different parts of Africa, and nine randomly joined infants, who originated from South Africa and different parts of Kenya. Considering that elephants are able to recognize one another based on their calls (McComb *et al.*, 2003), it is supposable that elephants—similar to other species capable of vocal

learning and living in complex societies (e.g., Tyack, 2003)—use family-, bond group-, or population-specific dialects. Although elephant calves probably have to learn these dialect-specific call features by imitating calls of their mothers and other family members, genetically preprogrammed call type variation between distinct elephant populations may play a role.

The infants used their vocalizations to announce their needs and emotions to their mother, keeper, or closest individuals. Because of their milk dependency, we recorded many calls in the suckle context. Talking about the functional use of calls, we have to consider that there are situations in the wild that do not exist in captivity or at the orphanage. However, infants living in the wild, in the zoo, or in the orphanage share the same needs and similar "problems," go out on a limb, and require help and reassurance. Infant vocalizations are mainly associated with the satisfaction of needs and are therefore not strongly influenced by external conditions.

The fundamental frequency in the rumble decreased with age as the elephants grew and the mass of their vocal cords increased. In mammals, this growth is negatively correlated to voice pitch (Fitch, 1997). The louder rumble of very young infants (up to approximately 3–4 months old) sounded very harsh and subjectively differed from the rumbles of the older ones. Based on acoustic parameters and call structure, however, we did not to distinguish it as a discrete call type from rumbles produced by older infants. In the two zoo elephants observed for a longer period of time, they gradually sounded more like a rumble of older individuals as fundamental frequency decreased with age.

Grunts seem to be characteristic for new-born elephants. The calves stopped producing grunts at around 2 months of age. Nothing similar has yet been documented in a juvenile or adult African elephant. This call was very soft, which might explain why it has not been previously recorded, even in infants. In contrast, no trumpets were recorded in individuals younger than 3 months. Instead of the trumpet, they produced snorts during play behavior and when exhibiting mock charges. These are situations in which older elephants produce trumpets. More control of the trunk muscles and more power of the respiratory muscles may be needed to produce a proper sound when pressing air through the trunk. The complex coordination of the trunk must be practiced by infants (Moss, 1988). Therefore it would have been surprising if an elephant was able to trumpet from birth on.

We did not observe gender-dependent variations in the number of call types, in call structure, or in their general usage. Future studies targeting different ontogenetic levels will be necessary to determine the onset of the vocal sexual dimorphism. Male elephants require a second distinct phase of socialization (Bradshaw *et al.*, 2005) in which they leave their natal family to join the floating community of adult, reproductive males (Poole, 1994). This might be the ontogenetic level at which the pronounced sexual dimorphism in vocal behavior of elephants develops. In both genders, however, infancy starts with similar communicating, i.e., with the mother and closely allied individuals. We even observed that males were more vocally adamant in their suckle behavior than the females. Lee and Moss (1986) found that more suckle attempts are initiated by male infants, and that females appear to be less demanding as well as less persistent. Our observations confirm this.

Our results should promote further studies on the vocal ontogeny of elephants. Besides studying the call repertoire of different age groups, it would be important to examine the extent to which learning influences vocal development. Determining the role of learning in vocal ontogeny and the alignment of group-specific call characteristics in calves will be one of our main future research interests. Due to their vocal learning ability (Poole *et al.*, 2005) in combination with the complex fission-fusion society (Moss and Poole, 1983; Wittemayer *et al.*, 2005), elephants could be an interesting model to study the role of imitation in the vocal ontogeny and the social system of a nonprimate terrestrial mammal.

ACKNOWLEDGMENTS

We wish to express special thanks to elephant keeper Gerd Kohl, who died in February 2005, for supporting our scientific research in numerous ways. It was a honor to meet someone who knew and loved his elephants the way Gerd Kohl did. We are grateful to Dr. Daphne Sheldrick and her team, in particular the elephant keeper Edwin Luitschi, for providing us the opportunity to walk with the orphans in the bush for several weeks. We acknowledge Dr. Joyce Poole for the discussion upon call terminology. We are further grateful to Claudia Kandler, Elke Schmelzer, and Dr. Michael Stachowitsch for their numerous and instructive comments on the manuscript. We acknowledge AKG Acoustics for supporting the project with the AKG 480 B microphone and the condenser capsule CK 62. The research was financially supported by the Vienna Zoo and the FWF Austrian Science Fund.

Berg, J. K. (**1983**). "Vocalizations and associated behaviors of the African elephant (*Loxodonta africana*) in captivity," Z. Tierpsychol **63**, 63–79.

Bradshaw, G. A., Schore, A. N., Brown, J. L., Poole, J. H., and Moss, C. J. (**2005**). "Elephant breakdown," Nature (London) **433**, 807.

Fant, G. (**1960**). *Acoustic Theory of Speech Production*, 2nd ed. (Mouton, The Hague).

Fitch, T. W. (**1997**). "Vocal tract length and formant frequency dispersion correlate with body size in rhesus macaques," J. Acoust. Soc. Am. **102**, 1213–1222.

Gerai, M. E. (**1997**). "The development of social behaviour in translocated juvenile African elephants *Loxodonta africana*," Ph.D. thesis, University of Zurich.

Horwath, A. (**2002**). "Schallsignale Afrikanischer Steppenelefanten (*Loxodonta africana*) in zoologischer Haltung (Acoustic communication of African elephants in captivity)," M. Sc. thesis, University of Vienna.

Horwath, A., Kratochvil, H., and Schwammer, H. M. (**2001**). "Sounds of a new borne African Elephant (*Loxodontat africana*) in Captivity," in *A Research Update on Elephants and Rhinos, Proceedings of the International Elephant and Rhino Research Symposium*, Vienna, 7–11 June, pp. 265–267.

Langbauer, R. W., Jr. (**2000**). "Elephant communication," Zoo Biol. **19**, 425–445.

Lee, P. C. (**1986**). "Early social development among African elephant calves," Nat. Geogr. Res. **2**, 388–401.

Lee, P. C., and Moss, C. J. (**1986**). "Early maternal investment in male and female African elephant calves," Behav. Ecol. Sociobiol. **18**, 353–361.

Lee, P. C., and Moss, C. J. (**1995**). "Statural growth in known-age African elephants (*Loxodonta africana*)," J. Zool., Lond. **236**, 29–41.

Lee, P. C., and Moss, C. J. (**1999**). "The social context for learning and behavioural development among wild African elephants," in *Mammalian Social Learning*, edited by H. O. Box and K. J. Gibson (Cambridge U. P., Cambridge), pp. 102–125.

Leong, K., Ortolani, A., Burks, K. D., Mellen, J. D., and Savage, A. (**2003**). "Quantifying acoustic and temporal characteristics of vocalizations for a group of captive African elephants *Loxodonta africana*," Bioacoustics **13**, 213–231.

McComb, K., Reby, D., Baker, L., Moss, C., and Sayiales, S. (**2003**). "Long-Distance communication of acoustic cues to social identity in African elephants," Anim. Behav. **65**, 317–329.

Moss, C. J. (**1988**). *Elephant Memories* (Elm Tree, London).

Moss, C. J., and Poole, J. H. (**1983**). "Relationship and social structure in African Elephants," in *Primate Social Relationships: An Integrated Approach*, edited by R. A. Hinde (Blackwell Scientific, Oxford), pp. 315–325.

O'Connell-Rodwell, C. E., Hart, L. A., and Arnason, B. T. (**2001**). "Exploring the potential use of seismic waves as a communication channel by elephants and other large mammals," Am. Zool. **41**, 1157–1170.

Poole, J. H. (**1994**). "Sex differences in the behaviour of African Elephants," in *The Differences between the Sexes*, edited by R. V. Short and E. Balabab (Cambridge U. P., Cambridge), pp. 331–346.

Poole, J. H., Payne, K., Langbauer, W. R., Jr., and Moss, C. (**1988**). "The social contexts of some very low frequency calls of African elephants," Behav. Ecol. Sociobiol. **22**, 385–392.

Poole, J. H., Tyack, P., Stoeger-Horwath, A. S., and Watwood, S. (**2005**). "Elephants capable of vocal learning," Nature (London) **434**, 455–456.

Soltis, P., Leong, K., and Sanage, A. (**2005**). "African elephant vocal communication II: rumble variation reflects the individual identity and emotional state of callers," Anim. Behav. **70**, 589–599.

Tyack, P. L. (**2003**). "Dolphins communicate about individual-specific social relationships," in *Animal Social Complexity: Intelligence, Culture, and Individualized Societies*, edited by F. de Waal and P. L. Tyack (Harvard U. P., Cambridge), pp. 432–362.

Wittemayer, G., Douglas-Hamilton, I., and Getz, W. M. (**2005**). "The socioecology of elephants: analyses of the processes creating multitiered social structures," Anim. Behav. **69**, 1357–1371.

Wood, J. D., McCowan, B., Langbauer, W. R., Viljoen, J. J., and Hart, L. A. (**2006**). "Classification of African elephant *Loxodonta africana* rumbles using acoustic parameters and cluster analyses," Bioacoustics **15**, 143–161.

Caller sex and orientation influence spectral characteristics of "two-voice" stereotyped calls produced by free-ranging killer whales

Patrick J. O. Miller[a)]
School of Biology, University of Saint Andrews, St. Andrews, Fife, KY16 9LB, United Kingdom; Laboratory for Computer Science, Massachusetts Institute of Technology, Cambridge, Massachusetts 02139 and Biology Department, Woods Hole Oceanographic Institution, Woods Hole, Massachusetts 02543

Filipa I. P. Samarra and Aurélie D. Perthuison
School of Biology, University of Saint Andrews, St. Andrews, Fife, KY16 9LB, United Kingdom

(Received 14 September 2006; revised 7 March 2007; accepted 12 March 2007)

This study investigates how particular received spectral characteristics of stereotyped calls of sexually dimorphic adult killer whales may be influenced by caller sex, orientation, and range. Calls were ascribed to individuals during natural behavior using a towed beamforming array. The fundamental frequency of both high-frequency and low-frequency components did not differ consistently by sex. The ratio of peak energy within the fundamental of the high-frequency component relative to summed peak energy in the first two low-frequency component harmonics, and the number of modulation bands off the high-frequency component, were significantly greater when whales were oriented towards the array, while range and adult sex had little effect. In contrast, the ratio of peak energy in the first versus second harmonics of the low-frequency component was greater in calls produced by adult females than adult males, while orientation and range had little effect. The dispersion of energy across harmonics has been shown to relate to body size or sex in terrestrial species, but pressure effects during diving are thought to make such a signal unreliable in diving animals. The observed spectral differences by signaler sex and orientation suggest that these types of information may be transmitted acoustically by freely diving killer whales. © *2007 Acoustical Society of America.* [DOI: 10.1121/1.2722056]

PACS number(s): 43.80.Ka [WWA] Pages: 3932–3937

I. INTRODUCTION

Animal sounds are shaped by the characteristics of both the source and associated resonant structures, and these are constrained by their size and shape (Bradbury and Vehrencamp, 1998). Variation in energy dispersion across signal harmonics has been attributed to body size or vocal tract length (Fitch, 1997), though sex differences may be greater than expected from the direct effect of body size in human speech (Rendall *et al.*, 2005). Voice features such as formant frequency dispersion and sometimes pitch (called F_0 in human speech) can vary substantially between calling individuals. For example, dominant frequency and pulse rate (pitch) of calls produced by cricket frogs (*Acris crepitans*) correlate strongly with body size (McClelland *et al.*, 1996). Relative maximum levels of harmonics and maximum echolocation call frequency differ between individuals and families in the big brown bat (*Eptesicus fuscus;* Masters *et al.*, 1995).

Fish-eating killer whales (*Orcinus orca*) produce calls with stereotyped time-frequency contours (Ford, 1991), and many calls contain two independently modulated contours (referred to as "two-voice calls") each with multiple harmonics (Fig. 1; Hoelzel and Osborne, 1986; Miller and Bain, 2000; Miller, 2002). Odontocete cetaceans possess a pair of nasal lips that could be used to generate two independently controlled signals (Cranford, 2000). The low-frequency component (LFC) of killer whale calls is thought to be a burst-pulse sound with the pitch, or fundamental frequency, generated by the pulse-repetition rate. Gradations in the LFC pulse rate range from slow-rate intervals in which individual pulses are apparent, often observed at the start of calls, to high-rate intervals, which sound more tonal. Though little is known about the high-frequency component (HFC), calls can contain modulation sidebands that appear above and below the HFC (Fig. 1). In all calls that we have inspected with sidebands, they are always spaced from the HFC by precise multiples of the frequency of the LFC (Fig. 1), indicating that the source mechanism driving the LFC also modulates the HFC.

Time-frequency contours of both components of killer whale calls differ primarily by social group (Ford, 1991; Deecke *et al.*, 2000; Miller and Bain, 2000), with only minor differences between individuals within the same matrilineal group (Nousek *et al.*, 2006). Extreme body-size dimorphism (adult males are $\frac{1}{3}$ longer and have twice the volume as adult females; Matkin and Leatherwood, 1986) may provide an anatomical basis for spectral differences in acoustic signals by sex. Because the time-frequency contour is primarily group specific, such differences might be useful as a cue to aid within-group recognition or to identify caller sex.

Unlike terrestrial animals that live in static ambient pressure, breath-hold divers can routinely experience severe pres-

[a)]Electronic mail: pm29@st-and.ac.uk

 0001-4966/2007/121(6)/3932/6/$23.00 © 2007 Acoustical Society of America

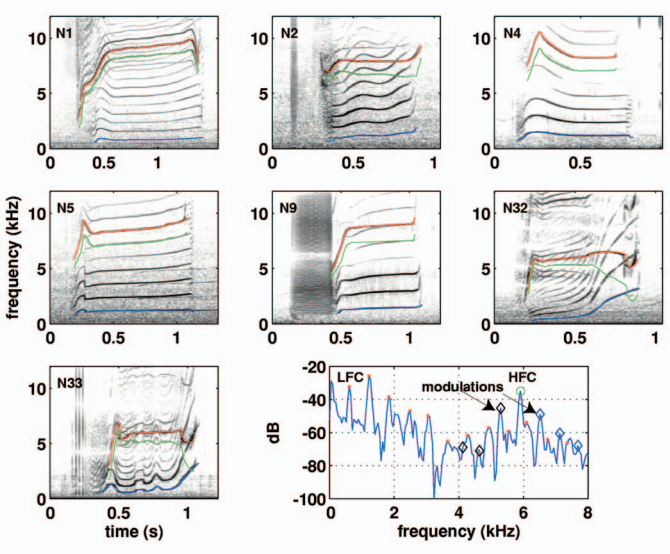

FIG. 1. Spectrograms of the seven call types analyzed. The time-frequency contour of the LFC fundamental is shown in blue, and the HFC fundamental in red. Note the presence of sidebands above and below the HFC. The frequency positions of these bands correspond precisely to the HFC ± multiples of the LFC. The HFC contour minus the LFC contour is shown in green and overlaps a modulation band in all call types except N9. Lower right: power spectral density plot of the N33 call at time point 0.6 s. Note peaks corresponding to the LFC (red dot), HFC (green circle), and HFC modulations (black and blue diamonds). We recorded the peak levels of the first two harmonics of the LFC and the fundamental of the HFC.

sure changes. The acoustic properties of air-filled structures should be affected by reduction of total air volume and by increased density of the air when under pressure (Bradbury and Vehrencamp, 1998). This fact has led to the conjecture that anatomical voice cues that rely on passive resonant effects of air cavities may not be reliable in diving animals (Tyack, 1991; Janik and Slater, 2000; Tyack and Miller, 2002). The frequency pattern of response whistles produced by diving beluga whales (*Delphinapterus leucas*) in a training task was shown to change strongly with depth though the fundamental frequency was unchanged (Ridgway *et al.*, 2001). The pitch of calls produced by diving seals did not vary with caller depth (Moors and Terhune, 2005), suggesting that the fundamental frequency of calls may be more effectively controlled than the dispersion of energy across harmonics. Diving may thereby select for active control of acoustic features used for individual or sex recognition, such as frequency modulation recently shown to be important in bottlenose dolphin signature whistle recognition (Janik *et al.*, 2006). However, it is possible that calling divers could compensate for pressure effects on air resonant cavities (Amundin, 1991) or that anatomical voice cues are generated by tissue-borne resonances that are less affected by depth (Cranford *et al.*, 1996). It is therefore valuable to explore whether acoustic features that might be shaped by resonant effects, such as the distribution of energy across frequencies, differ consistently by the signaler sex or body size of free-ranging breath-hold divers.

We consider here how the relative intensity of harmonics in both low- and high-frequency components and number of HFC modulation sidebands are influenced by adult signaler sex in calls produced by freely diving adult killer whales. Signaler range and orientation relative to the receiver must be considered in analysis of frequency spectra of sounds from free-ranging animals, and signaler range and orientation are also potentially useful to communicate in group-living mobile animals (Miller, 2002; Lammers and Au, 2003). The key question we address is whether the spectra of calls received from freely diving whales correlate with sex, orientation, and range of the signaler. Such a relationship would demonstrate that the influence of these signaler characteristics on the communication signals of killer whales can exist and be detected during natural diving behavior.

II. METHODS

Recordings were made during August and September 1998 and 1999 off Vancouver Island, Canada, using a beamforming array towed from an 11-m research vessel. This system allows calls to be ascribed to a focal animal when it is separated in azimuth from other group members by 20 deg or more (Miller and Tyack, 1998; Miller *et al.*, 2004). Each time the focal animal surfaced to breathe, we recorded its identification based on dorsal fin and saddle patch shapes (Ford *et al.*, 2000) as well as its orientation and range to the recording array. Animals were classified as juvenile (J) if they were estimated to be under 15 years old or as adult male (AM) or adult female (AF) if otherwise (Olesiuk *et al.*, 1990). The 16-bit, 48-kHz sampling rate acoustic recordings were transferred from Tascam recorders to a computer using Cool Edit Pro.

Only stereotyped calls produced by the identified focal whale were used in the analysis. The orientation of the focal animal at the time a call was received was estimated by interpolating the observed orientations during the surfacings before, and after, production of the call. To reduce errors in the orientation estimate during call production, calls were not included if these were produced between two surfacings for which the observed orientations changed by more than 120 deg. Left- and right-side off-axis orientations were combined, and then converted to radians with values ranging from zero for animals oriented directly toward the array to π for animals oriented directly away from the array. Stereotyped calls were classified to type using visual analysis of spectrograms and aural recognition (Ford, 1987; Miller *et al.*, 2004). We only considered call types with both high- and low-frequency components, which resulted in the inclusion of seven call types: N1, N2, N4, N5, N9, N32, and N33 (Fig. 1).

We used a trace of the LFC and HFC contours, obtained using a pitch tracking algorithm (Wang and Seneff, 2000), to identify peaks corresponding to the LFC harmonics and the HFC peak (Fig. 1). Each call was divided into 0.01-s time intervals for which a power density spectrum was created and the peaks identified automatically. Because the fundamental frequency, or pitch, of killer whale calls is quite high in most portions of calls, formant patterns could not be directly observed as is possible in analysis of human speech. Most of the energy in the low-frequency component (LFC) occurred in the first two harmonics (the first harmonic refers

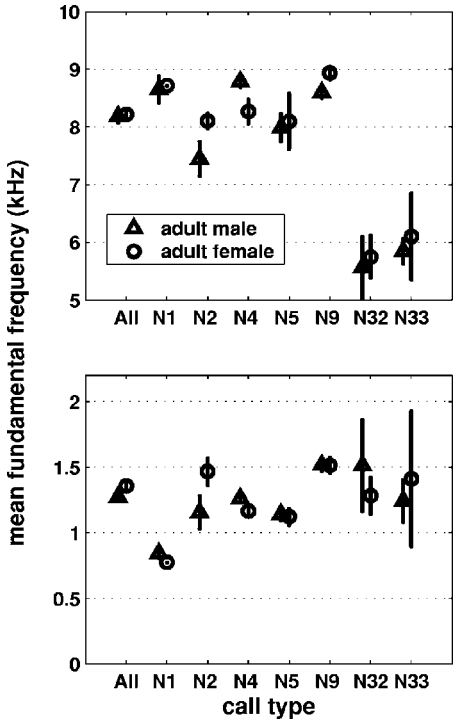

FIG. 2. Mean fundamental frequency of the HFC (top) and LFC (bottom) of calls produced by adult females and adult males. Vertical bars represent ±2 standard errors (s.e.) about the mean. Note that there is no consistent pattern by which mean fundamental frequency varies by sex across the different call types.

to the fundamental frequency contour), but harmonics up to the fifth could commonly be measured. Each peak within each interval was inspected by eye to assure that a single, clear peak emerged from the background noise, and that the peak frequency corresponded with the frequency of the contour at that point in time. Peaks within 5 dB of the noise floor were rejected. Calls were rejected if they did not include at least ten usable intervals. We calculated the average fundamental frequency for LFC and HFC contours, the ratio in intensity between the first and the second LFC harmonics across each call (LFC h2/h1), and the intensity ratio between the HFC and the first two harmonics of the LFC (HFC/LFC). For each call we also counted the maximum number of modulation bands above and below the HFC fundamental that were visible for at least half the call duration.

Statistical analyses were conducted using linear mixed effects models created in R (R Development Core Team, 2004). Linear mixed effects models differ from straightforward linear models in that these are used when the data are grouped according to one or more classification factors, allowing for the incorporation of both effects that influence the mean (fixed factors) and effects that influence the variance (random factors) of the response variable (Pinheiro and Bates, 2000). Fundamental frequency differs by call type (Fig. 2). An analysis of the variation within-calls, using each call number as a random factor, indicated that fundamental frequency of the LFC influences the relative intensity of the first two LFC harmonics ($t_{20465}=-11.88$, $p<0.001$), and that HFC fundamental frequency influences the level of the HFC relative to LFC ($t_{6152}=2.53$; $p=0.011$). This matches the predicted behavior of a resonant system excited with different input frequencies. Therefore, the different fundamental frequency contents within the various call types could be predicted to influence the relative intensities of the LFC harmonics and the LFC relative to the HFC. Different call types also differ in the number of HFC modulation bands (Fig. 1). For this reason, call type is treated as a random factor in the models that relate spectral intensity to orientation, range, and adult sex. The mixed model accounted for a significantly greater amount of the variation in the data than a simple linear model ($P<0.0001$), justifying the use of this somewhat more complex model design. An autocorrelation term was added to each model as some degree of temporal correlation was present in the data.

Two models were run to test whether LFC and HFC fundamental frequencies differed significantly by sex of the caller. In a second analysis, three models related the intensity ratio of the first two harmonics of the LFC (LFC h2/h1), the ratio of the HFC to the summed intensity of the first two harmonics of the LFC (HFC/LFC), and the number of HFC modulations to the orientation, range, and age-sex class of the signaler. Range was log transformed. The dependent variables used in the spectral analysis showed low levels of intercorrelation (HFC/LFC with LFC h2/h1: $r=0.126$; HFC/LFC with no. of HFC sidebands: $r=0.131$; LFC h2/h1 with no. of HFC sidebands: $r=-0.19$). Such low correlation levels justify the use of separate models for each dependent variable.

In the mixed models used here, the degrees of freedom equal the total sample of calls minus the number of parameters estimated in the model, and again minus the number of groups within the random variable (Pinheiro and Bates, 2000). As five separate models were run, we used the Bonferroni correction to set the level of significance within each model to 0.01, which assures an experimental probability of Type-I error of 0.05.

III. RESULTS

The process of data selection resulted in a total of 335 calls of seven types produced by 16 individual whales being usable to compare the intensities of the first two harmonics of the LFC (Table I). Due to a very small sample size (17 calls from two juveniles), we removed juveniles from all analyses. This yielded 318 calls total of which 210 were produced by nine adult males and 108 by five adult females. Of these 318 calls, 194 had sufficient peaks to be included in analysis of the HFC, the others being rejected either because the fundamental of the HFC was within 5 dB of the noise floor or overlapped a harmonic of the LFC. Of these 194, 125 were produced by the nine adult males and 69 were produced by the adult females.

Sex of the caller did not consistently influence the mean fundamental frequency of either the low- or high-frequency components of calls (Fig. 2). Testing using the mixed model concluded that for both the LFC and HFC, there was no consistent influence of caller sex on the fundamental frequency comparisons (LFC: $t_{310}=-1.212$, $p=0.23$; HFC: $t_{310}=-1.207$, $p=0.23$).

TABLE I. Total number of calls by type recorded from each focal animal: AF—adult female, AM—adult male, and J—juvenile of either sex.

	Age/Sex	N1	N2	N4	N5	N9	N32	N33	Total
A12	AF	1	6	1	1	⋯	⋯	⋯	9
A23	AF	⋯	1	⋯	⋯	3	⋯	⋯	4
A34	AF	⋯	2	3	5	1	⋯	⋯	11
A8	AF	⋯	27	26	2	22	⋯	⋯	77
W3	AF	⋯	⋯	⋯	⋯	⋯	2	5	7
A27	AM	⋯	1	⋯	⋯	⋯	⋯	⋯	1
A32	AM	4	7	10	8	19	⋯	⋯	48
A33	AM	⋯	⋯	⋯	3	⋯	⋯	⋯	3
A37	AM	9	⋯	15	13	7	⋯	⋯	44
A38	AM	⋯	2	25	⋯	17	⋯	⋯	44
A46	AM	2	6	11	9	8	⋯	⋯	36
A6	AM	1	⋯	6	⋯	5	⋯	⋯	12
W2	AM	⋯	⋯	⋯	⋯	⋯	3	17	20
W5	AM	⋯	⋯	⋯	⋯	⋯	⋯	2	2
A55	J	1	3	3	2	5	⋯	⋯	14
A62	J	⋯	⋯	3	⋯	⋯	⋯	⋯	3
Total		18	55	103	43	87	5	24	335

Orientation of the signaler, estimated from surfacing orientation, was a significant predictor of the HFC/LFC intensity ratio ($t_{184}=-2.64$, $p=0.009$), while range and adult sex were not (Table II, column 1). There was a nonsignificant trend for HFC/LFC ratio to differ by adult sex ($t_{184}=-1.70$, $p=0.091$; Fig. 3). The HFC/LFC ratio was higher when the caller was oriented more directly toward the hydrophone array (Fig. 3). Orientation was also a significant predictor ($t_{184}=-3.93$, $p=0.0001$) of the number of modulations of the HFC fundamental by the LFC, with more sidebands observed when whales were oriented toward the hydrophone array, but range and adult sex were not (Table II, column 2).

Adult sex was a significant predictor of the relative level of the first two harmonics of the LFC ($t_{308}=-2.72$, $p=0.007$), while signaler orientation and range were not (Table II, column 3). Males had consistently more energy in the second harmonic than the fundamental across all seven call types, with an overall mean difference of 3.4 dB (Fig. 4).

IV. DISCUSSION

Killer whale stereotyped calls appear to be an example of complex signals (Hebets and Papaj, 2005) with different information being encoded, and potentially transmitted, within different call components. The intensity ratio of the first two LFC harmonics is significantly influenced by signaler sex, possibly because of the substantial body size differences in adult killer whales. On the other hand, the intensity ratio of the HFC relative to the LFC (HFC/LFC), and the number of HFC modulation bands, reflects the orientation of the signaler.

Interestingly, the fundamental frequency or pitch of both the LFC and HFC did not consistently vary between adult male and adult female body sizes (Fig. 2). Though diversity in mean fundamental frequency occurred within some call types in our sample (Fig. 2), there was no consistent pattern for either HFC or LFC across call types. Absolute frequency of the two components does not appear to be strongly influenced by sex and is probably constrained as stereotyped calls are shared within stable matrilineal groups.

Signaler orientation influenced the intensity of the HFC relative to the LFC, and the number of HFC sidebands, but not the relative intensity of the first two harmonics of the LFC (Table II and Fig. 3). These results indicate that low-frequency adult sex cues may be more omnidirectional than other signal features. Miller (2002) found strong differences in the spectral structure of calls recorded from groups of whales moving toward versus away from the receiver. By

TABLE II. Mean ±95% confidence interval of spectral features of received calls by orientation, range, and adult sex. The units of the values in the table are the column unit divided by the row unit [e.g., for −2.5±1.8 dB/rad, the difference in the HFC to LFC intensity ratio of calls produced by animals oriented directly toward the array (0 rad) versus directly away (π rad) is −7.9±5.7 dB].

	HFC/LFC (dB)	HFC sidebands (n)	LFC h2/h1 (dB)
Orientation (rad)	−2.5±1.8[a]	−0.43±0.21[a]	−0.2±1.0
Range (log 10 m)	0.5±1.1	−0.07±0.14	0.1±0.6
Adult male relative to adult female	−3.2±3.7	−0.04±0.42	2.8±2.0[a]
Degrees of freedom	184	184	308

[a]Significant at $P<0.01$.

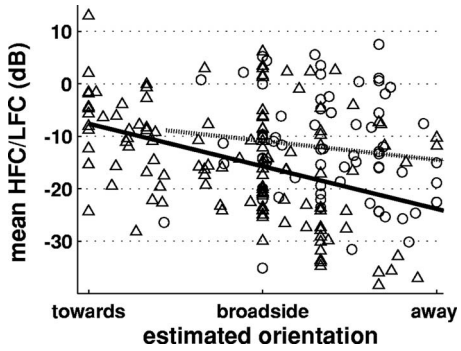

FIG. 3. The mean ratio of the peak energy of HFC to the summed energy in the first two harmonics of the LFC (HFC/LFC) versus estimated signaler orientation to the receiver based on surfacings before and after each call was produced. Calls of adult males are shown as triangles, with a solid regression line, while those of female are circles with a dashed regression line. Note the tendency for calls produced by adult males to have higher HFC/LFC ratios than calls produced by adult females.

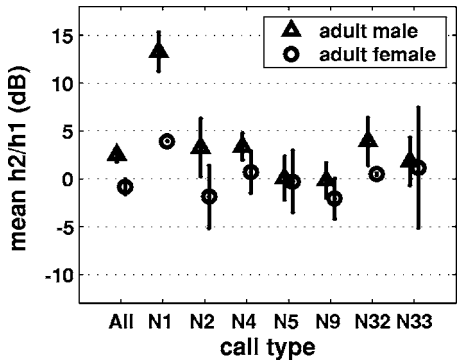

FIG. 4. The mean intensity ratio of the first two harmonics of the LFC (LFC h2/h1) by call type for calls produced by adult males and adult females. The vertical bars are ±2s.e. Note that the intensity ratio is greater in calls produced by adult males for all seven call types.

measuring the energy in the fundamental of the HFC directly, this study confirms that this call component specifically encodes information on signaler orientation. In our sample, signaler orientation was estimated based on surfacing orientation before and after each call, so it would be interesting to investigate finer scale effects of orientation on HFC energy when signaler orientation at the time of the call is known with more precision. Higher frequencies of the HFC contour and the number of HFC sidebands would be predicted to be more directional than the LFC as there is more effective absorption, reflection, and focus of smaller wavelengths by sound source resonators and tissue structures. The ranges from caller to the hydrophone (16–834 m) seem to have little effect on the relative levels of the spectral features measured in this study, although range should strongly influence the absolute received levels of both the HFC and LFC as well as call reverberation patterns (Naguib and Wiley, 2001; Miller, 2002).

Adult sex influenced the relative energy in the first two harmonics of the LFC, but did not strongly influence the number of HFC sidebands (Table II). Our results may indicate that adult sex influences the HFC/LFC intensity ratio ($p=0.091$), but more data would be necessary to confirm this trend. Despite the mixed pattern in fundamental frequency, adult males had relatively more average energy in the LFC second harmonic than females across all seven analyzed call types (Fig. 4). Across all the 318 calls used in this study, the difference by adult sex in the relative levels of the first two harmonics averaged 3.4 dB. As we also found that fundamental frequency within calls affects the relative level of the harmonics (see Sec. II), variation in the frequency content of analyzed calls probably dilutes the difference attributable to caller sex when values are averaged over the entire call, as was done in this study. Nonetheless, perception tests indicate that changes smaller than 3 dB in the relative levels of harmonics are detectable in birds and humans (Versfeld and Houtsma, 1995; Lohr and Dooling, 1998), and recent research suggests that a false killer whale (*Pseudorca crassidens*) can perceive small differences in relative harmonic intensities (Yuen *et al.*, 2007). We can predict that the sex differences reported here should at least be detectable by the killer whales themselves. Playback experiments could test the salience of harmonic intensity patterns, and any role they might have in sex recognition.

A. Implications for killer whale call production mechanism

The presence of HFC sidebands at precise multiples of the LFC (Fig. 1) is evident that the physical process which generates the LFC also modulates the intensity of the HFC in some fashion. This interaction between the LFC and HFC seems to indicate that the two independent sources are in close proximity to each other within the whale. This is consistent with the possibility that the two contours are produced by independent, simultaneous control of the left and right monkey-lip dorsal bursae complexes, which are implicated in the production of sonar clicks of odontocetes (Cranford, 2000). However, alternative explanations for how these two independent contours might be produced cannot be ruled out.

We tentatively suggest that the sex differences in the relative intensity of the first two LFC harmonics may be explained by the presence of one or more resonant structures, which alter the relative intensities of the harmonics, and that males have lower-frequency resonances than females because of their larger size. We were able to measure the intensity of the first five LFC harmonics in 243 of the 318 calls produced by adult males or adult females (169 from adult males, 74 from adult females). Inspection of the relative energy in the first five harmonics indicated that frequencies within the second harmonic are supported in calls produced by males, while frequencies within the fourth harmonic are relatively more supported in calls from females. This seems to match predictions based on anatomy as adult males have roughly twice the body volume of adult females (Matkin and Leatherwood, 1986). In odontocetes several structures have been indicated as potential resonators, such as the nasal sacs or the dorsal bursae (Cranford, 2000; Cranford *et al.*, 1996). If the size of these structures correlates with body size, then it could explain differences in resonances between adult male and female killer whales. However, more detailed knowledge of the sound production mechanism in killer whales would be necessary to identify the structures that do act as resonators and therefore to understand the influence of body size on the size of these structures.

Our interpretation that resonant effects influence the relative level of the LFC harmonics in killer whale calls is further supported by our finding that the relative intensity of the first two LFC harmonics changes with fundamental frequency within calls (6.5 dB/kHz, $P<0.001$; see Sec. II). The relative intensity of the harmonics changes as the frequencies excited by the harmonics change, which is consistent with the expected behavior of frequency-dependent resonant filters. Interestingly, time from the start of a call did not affect the relative intensity of the harmonics, suggesting that the movement of air during sound production itself does not strongly alter resonant characteristics in the sound-production apparatus (Dormer, 1979). The observed differences in the relative levels of harmonics is consistent with the presence of resonances, but other analysis methodologies such as linear predictive coding (LPC; Fitch, 1997) are better suited to detect and quantify resonances. LPC is made difficult, though, in the case of killer whale calls because the fundamental frequency of the calls is quite high.

V. CONCLUSIONS

The sounds analyzed in this study were recorded from identified individuals during natural diving behavior, though the horizontal beamforming system does not allow measurement of caller depth directly. It is possible that, at fixed calling depths, sex or orientation differences might be greater than those observed here, and that natural variation in caller depth degrades these effects on the relative intensity of the harmonics. It would be useful to assess whether diving influences the features measured in this study using a method that can track the depth of calling animals. Such data could assess whether calling occurs in preferred depth bands (Hastie

et al., 2006), which could be a simple way by which divers could reduce or enhance effects of diving on air-resonant properties, if they exist. Alternatively, it is possible that low-frequency resonances could be under active control or occur in tissues rather than air, which should result in less sensitivity to caller depth. A heliox experiment with harbor porpoises indicated that the low-frequency component of clicks was based on air resonance and influenced by breathing heliox, but that high-frequency components were based in tissues and so uninfluenced (Amundin, 1991). Research on the mechanism by which the complex "two-voice" calls are produced could help elucidate the influence of diving ecology on acoustic signal structure, and the role of different signal features in communication.

ACKNOWLEDGMENTS

Thanks to the field and vessel crews during the fieldwork, to D. Bain for suggesting this analysis, and to V. Janik and P. Slater for useful comments. Monique MacKenzie of CREEM provided advice on the statistical analysis. A. Nousek, C. Wang, A. Hodgins-Davis, and S. Seneff at MIT's Laboratory for Computer Science helped build the corpus of sounds analyzed here. Funding was provided by WHOI's Rinehart Coastal Research Center and Ocean Ventures Fund, and a Royal Society USA/Canada fellowship to PJOM. All field recordings were conducted under a Canadian permit and followed Canadian law.

Amundin, M. (**1991**). "Helium effects on the click frequency spectrum of the harbor porpoise, *Phocoena phocoena*," J. Acoust. Soc. Am. **90**, 53–59.

Bradbury, J. W., and Vehrencamp, S. L. (**1998**). *Principles of Animal Communication* (Sinauer, Massachusetts).

Cranford, T. W. (**2000**). "In search of impulse sound sources in Odontocetes," in *Hearing by Whales and Dolphins*, edited by W. W. L. Au, A. N. Popper, and R. R. Fay (Springer, New York), pp. 109–155.

Cranford, T. W., Amundin, M., and Norris, K. S. (**1996**). "Functional morphology and homology in the odontocete nasal complex: Implications for sound generation," J. Morphol. **228**, 223–285.

Deecke, V. B., Ford, J. K. B., and Spong, P. (**2000**). "Dialect change in resident killer whales: Implications for vocal learning and cultural transmission," Anim. Behav. **60**, 629–638.

Dormer, K. J. (**1979**). "Mechanisms of sound production and air recycling in delphinids: Cineradiographic evidence," J. Acoust. Soc. Am. **65**, 229–239.

Fitch, W. T. (**1997**). "Vocal tract length and formant frequency dispersion correlate with body size in rhesus macaques," J. Acoust. Soc. Am. **102**, 1213–1222.

Ford, J. K. B. (**1987**). "A catalogue of underwater calls produced by killer whales (*Orcinus orca*) in British Columbia," Can. Data Rep. Fish. Aq. Sci. No. 633.

Ford, J. K. B. (**1991**). "Vocal traditions among resident killer whales (*Orcinus orca*) in coastal waters of British Columbia," Can. J. Zool. **69**, 1454–1483.

Ford, J. K. B., Ellis, G. M., and Balcomb, K. C. (**2000**). *Killer Whales*, 2nd ed. (Univ. of British Columbia, Vancouver).

Hastie, G. D., Wilson, B., and Thompson, P. M. (**2006**). "Diving deep in a foraging hotspot: Acoustic insights into bottlenose dolphin dive depths and feeding behaviour," Mar. Biol. (Berlin) **148**, 1181–1188.

Hebets, E. A., and Papaj, D. R. (**2005**). "Complex signal function: Developing a framework of testable hypotheses," Behav. Ecol. Sociobiol. **57**, 197–214.

Hoelzel, A. R., and Osborne, R. W. (**1986**). "Killer whale call characteristics: Implications for cooperative foraging strategies," in *Behavioral Biology of Killer Whales*, edited by B. C. Kirkevold and J. S. Lockard (Liss, New York, New York), pp. 373–403.

Janik, V. M., Sayigh, L. S., and Wells, R. S. (**2006**). "Signature whistle shape conveys identity information to bottlenose dolphins, " Proc. Natl. Acad. Sci. U.S.A. **103**, 8293–8297.

Janik, V. M., and Slater, P. J. B. (**2000**). "The different roles of social learning in vocal communication," Anim. Behav. **60**, 1–11.

Lammers, M. O., and Au, W. W. L. (**2003**). "Directionality in the whistles of Hawaiian spinner dolphins (*Stenella longirostris*): A signal feature to cue direction of movement?" Marine Mammal Sci. **19**, 249–264.

Lohr, B., and Dooling, R. J. (**1998**). "Detection of changes in timbre and harmonicity in complex sounds by zebra finches (*Taeniopygia guttata*) and budgerigars (*Melospittacus undulatus*)," J. Comp. Physiol. **112**, 36–47.

Masters, W. M., Raver, K. A. S., and Kazial, K. A. (**1995**). "Sonar signals of big brown bats, *Eptesicus fuscus*, contain information about individual identity, age and family affiliation," Anim. Behav. **50**, 1243–1260.

Matkin, C., and Leatherwood, S. (**1986**). "General biology of the killer whale, *Orcinus orca*: A synopsis of knowledge," in *Behavioral Biology of Killer Whales*, edited by B. C. Kirkevold and J. S. Lockard (Liss, New York, New York), pp. 35–68.

McClelland, B. E., Wilczynski, W., and Ryan, M. J. (**1996**). "Correlations between call characteristics and morphology in male cricket frogs (*Acris crepitans*)," J. Exp. Biol. **199**, 1907–1919.

Miller, P. J. O. (**2002**). "Mixed-directionality of killer whale stereotyped calls: A direction of movement cue?" Behav. Ecol. Sociobiol. **52**, 262–270.

Miller, P. J. O., and Tyack, P. L. (**1998**). "A small towed beamforming array to identify vocalizing *resident* killer whales (*Orcinus orca*) concurrent with focal behavioural observations," Deep-Sea Res., Part II **45**, 1389–1405.

Miller, P. J. O., and Bain, D. E. (**2000**). "Within-pod variation in the sound production of a pod of killer whales, *Orcinus orca*," Anim. Behav. **60**, 617–628.

Miller, P. J. O., Shapiro, A. D., Tyack, P. L., and Solow, A. R. (**2004**). "Call-type matching in vocal exchanges of free-ranging killer whales, *Orcinus orca*," Anim. Behav. **67**, 1099–1107.

Moors, H. B., and Terhune, J. M. (**2005**). "Calling depth and time and frequency attributes of harp (*Pagophilus groenlandicus*) and Weddell (*Leptonychotes weddellii*) seal underwater vocalizations," Can. J. Zool. **83**, 1438–1452.

Naguib, M., and Wiley, H. (**2001**). "Estimating the distance to a source of sound: Mechanisms and adaptations for long-range communication," Anim. Behav. **62**, 825–837.

Nousek, A. E., Slater, P. J. B., Wang, C., and Miller, P. J. O. (**2006**). "The influence of social structure on vocal signatures in northern resident killer whales (*Orcinus orca*)," Biol. Lett. **2**, 481–484.

Olesiuk, P. F., Bigg, M. A., and Ellis, G. M. (**1990**). "Life history and population dynamics of resident killer whales (*Orcinus orca*) in the coastal waters of British Columbia and Washington state," Rep. Int. Whaling Com., Spec. Issue **12**, pp. 209–243.

Pinheiro, J. C., and Bates, D. M. (**2000**). *Mixed-Effects Models in S and S-Plus* (Springer, New York).

R Development Core Team (**2004**). R: A language and environment for statistical computing, (version 1.9.1), R Foundation for Statistical Computing, Vienna, Austria, ISBN 3-900051-00-3, URL http://www.R-project.org, viewed 4/20/2007.

Rendall, D., Kollias, S., Ney, C., and Lloyd, P. (**2005**). "Pitch (F_o) and formant profiles of human vowels and vowel-like baboon grunts: The role of vocalizer body size and voice acoustic allometry," J. Acoust. Soc. Am. **117**, 944–955.

Ridgway, S. H., Carder, D. A., Kamolnick, T., Smith, R. R., Schlundt, C. E., and Elsberry, W. R. (**2001**). "Hearing and whistling in the deep sea: Depth influences whistle spectra but does not attenuate hearing by white whales (*Delphinapterus leucas*) (Odontoceti, Cetacea)," J. Exp. Biol. **204**, 3829–3841.

Tyack, P. L. (**1991**). "If you need me, whistle," Nat. Hist. Aug, 60-61.

Tyack, P. L., and Miller, E. H. (**2002**). "Vocal anatomy, acoustic communication and echolocation," in *Marine Mammal Biology: An Evolutionary Approach*, edited by A. R. Hoelzel (Blackwell Science, Oxford, UK), pp. 142–184.

Versfeld, N. J., and Houtsma, J. M. (**1995**). "Discrimination of changes in the spectral shape of two-tone complexes," J. Acoust. Soc. Am. **98**, 807–816.

Wang, C., and Seneff, S. (**2000**). "Robust pitch tracking for prosodic modeling in telephone speech," in IEEE International Conference on Acoustics, Speech and Signal Processing, Istanbul, Turkey.

Yuen, M. M. L., Nachtigall, P. E., Breese, M., and Vlachos, S. A. (**2007**). "The perception of complex tones by a false killer whale (*Pseudorca crassidens*)," J. Acoust. Soc. Am. **121**, 1768–1774.

Echolocation click sounds from wild inshore finless porpoise (*Neophocaena phocaenoides sunameri*) with comparisons to the sonar of riverine *N. p. asiaeorientalis*

Songhai Li
Institute of Hydrobiology, The Chinese Academy of Sciences, Wuhan, 430072, People's Republic of China, and Graduate School of the Chinese Academy of Sciences, Beijing, 100039, People's Republic of China

Ding Wang[a] and Kexiong Wang
Institute of Hydrobiology, The Chinese Academy of Sciences, Wuhan, 430072, People's Republic of China

Tomonari Akamatsu
National Research Institute of Fisheries Engineering, Fisheries Research Agency, Hasaki, Kamisu, Ibaraki 314-0408, Japan

Zhiqiang Ma and Jiabo Han
Liaoning Academy of Marine Fishery Sciences, Dalian, 116023, People's Republic of China

(Received 14 June 2006; revised 9 March 2007; accepted 12 March 2007)

Acoustic signals from wild *Neophocaena phocaenoides sunameri* were recorded in the waters off Liao-dong-wan Bay located in Bohai Sea, China. Signal analysis shows that *N. p. sunameri* produced "typical" phocoenid clicks. The peak frequencies f_p of clicks ranged from 113 to 131 kHz with an average of 121 ± 3.78 kHz ($n=71$). The 3 dB bandwidths Δf ranged from 10.9 to 25.0 kHz with an average of 17.5 ± 3.30 kHz. The signal durations Δt ranged from 56 to 109 μs with an average 80 ± 11.49 μs. The number of cycles N_c ranged from 7 to 13 with an average of 9 ± 1.48. With increasing peak frequency there was a faint tendency of decrease in bandwidth, which implies a nonconstant value of $f_p/\Delta f$. On occasion there were some click trains with faint click energy presenting below 70 kHz, however, it was possibly introduced by interference effect from multiple pulses structures. The acoustic parameters of the clicks were compared between the investigated population and a riverine population of finless porpoise. © *2007 Acoustical Society of America.* [DOI: 10.1121/1.2721658]

PACS number(s): 43.80.Ka [WWA] Pages: 3938–3946

I. INTRODUCTION

The finless porpoise (*Neophocaena phocaenoides*) is one of the smallest odontocete species and has a wide distribution throughout coastal Indo-Pacific waters (Reeves *et al.*, 1997; Kasuya, 1999). Living sporadically in freshwater and inshore, the taxonomic status of the finless porpoise remains confused. Using mainly morphological and life history data, recent classifications (Wang, 1992; Gao and Zhou, 1993, 1995) recognized three subspecies of the finless porpoise: *N. p. asiaeorientalis* found mainly in the Yangtze River, *N. p. phocaenoides* found mainly in the South China Sea and Indian Ocean, and *N. p. sunameri* found mainly in the Yellow Sea, Bohai Sea, Japanese coastal waters, and the northwest Pacific Ocean.

In recent years, vocalizations produced by *N. p. asiaeorientalis* from the Yangtze River have been extensively described both in captivity (Wang, 1996; Akamatsu *et al.*, 1998) and in the wild (Akamatsu *et al.*, 1998, 2005a, 2005b; Li *et al.*, 2005a, b). Goold and Jefferson (2002) demonstrated that *N. p. phocaenoides* off the coastal waters of Hong Kong produced both "typical" narrowband, high-frequency phocoenid sounds, and "atypical" broadband pulses, with an occasional low-frequency component. Mizue *et al.* (1968), Kamminga *et al.* (1986), and Nakahara *et al.* (1997) have reported on vocalizations by captive *N. p. sunameri* originating from the Japanese coastal waters.

Comparing the vocalizations between different populations of the finless porpoise might put the taxonomic classifications in a new perspective. We expect there might be considerable differences in the acoustic aspects between different finless porpoise subspecies.

Based on vocalization studies of a number of species of inshore and riverine porpoise and dolphins, their sonar capabilities were considered in relation to their habitat (Dudok van Heel, 1981; Kamminga and Wiersma, 1981; Wiersma, 1983). The inshore populations of porpoises and dolphins were suggested to have two-component signals with a low-frequency component to detect long-distance targets and a high-frequency one for short-range, high-resolution target detection; however, for the populations of porpoises and dolphins living in a turbid, and muddy riverine habitat, a short-range, uni-modal and high-frequency sonar would suffice (Kamminga *et al.*, 1983). These expectations have been supported by findings in both inshore populations: *Delphi-*

[a]Author to whom correspondence should be addressed. Electronic mail: wangd@ihb.ac.cn

 0001-4966/2007/121(6)/3938/9/$23.00 © 2007 Acoustical Society of America

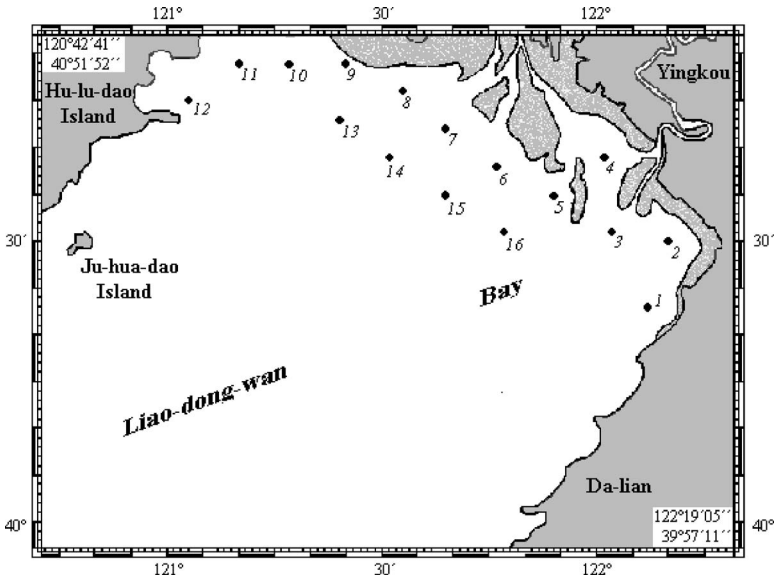

FIG. 1. The investigated waters in Liao-dong-wan Bay and locations of the finless porpoise encounters, detailed in Table I.

napterus leucas (Kamminga and Wiersma, 1981), *Phocoena phocoena* (Kamminga and Wiersma, 1981), and *Sotalia fluviatilis guianensis* (Kamminga, personal communication), and riverine populations: *Inia geoffrensis* (Kamminga, 1979; Kamminga *et al.*, 1993), *Orcaella brevirostris* (Kamminga *et al.*, 1983), and *Sotalia fluviatilis fluviatilis* (Kamminga *et al.*, 1993). In the finless porpoise, Li *et al.* (2005a) did not find any low-frequency (<70 kHz) components in the free-ranging riverine population, *N. p. asiaeorientalis*; Kamminga *et al.* (1986) rejected the two-component sonar hypothesis for the coastal *N. p. sunameri* from the Japanese waters; Goold and Jefferson (2002) claimed that there was clearly low-frequency energy in some of the Hong Kong finless porpoise (*N. p. phocaenoides*) clicks. A comparison between the sonar produced by inshore and riverine populations of the finless porpoise might shed further light on the possible correlation between habitat and sonar performance.

In this study, we recorded and analyzed the vocalizations of wild inshore finless porpoise (*N. p. sunameri*) in Liao-dong-wan Bay located in Bohai Sea, using a broadband recording system. To our knowledge it would be the first work published to date on the natural vocalizations of this subspecies. To test the Dudok van Heel hypothesis (Dudok van Heel, 1981), a comparison was made with vocalizations from the riverine population of finless porpoise, *N. p. asiaeorientalis*, recorded in the Tian-e-zhou Baiji National Natural Reserve.

II. MATERIALS AND METHODS

A. Data collection

From 28 June to 2 July 2005, underwater sound recordings were made of *N. p. sunameri* in the Liao-dong-wan Bay located in the Bohai Sea, during a series of ongoing investigations of jellyfish resource conducted by the Liao-ning Academy of Marine Fishery Sciences. The investigations were carried out from a 20 m, ligneous and diesel powered vessel, using a 2 cm mesh size trawl on 16 pre-designed sites (see Fig. 1). During trawling, finless porpoises were often seen following the vessel with a distance of 5–50 m, and foraging fish escaped from the trawl. Underwater acoustic recordings were manually activated by the operator, when finless porpoises were spotted in the vicinity of the vessel. The hydrophone was towed about 5 m behind the vessel in a cable deployed over the stern. The hydrophone (ST1020, Oki Electric Co. Ltd., Japan) consisted of a piezoelectric element with built-in preamplifier, which passed acoustic signals up the tow cable to a data recorder located on the boat. The hydrophone had a sensitivity of −180 dB $re:1\ \mathrm{V}\ \mu\mathrm{Pa}^{-1}+3/-12$ dB, up to 150 kHz. The sensitivity declined with an increase in frequency from 100 to 150 kHz, and at 125 kHz (the average peak frequency of the Yangtze finless porpoise; Li *et al.*, 2005a) the sensitivity is approximately −185 dB $re:1\ \mathrm{V}\ \mu\mathrm{Pa}^{-1}$. Recordings were made using a Sony PCHB244 digital data recorder, with a flat frequency response from dc to 147 kHz within 3 dB (Akamatsu *et al.*, 1998). An overall recording bandwidth of 147 kHz was considered sufficient to record the echolocation sounds of the finless porpoise (see Akamatsu *et al.*, 1998; Li *et al.*, 2005a).

The porpoises' surface behaviors, abundance, and visually estimated distances to the hydrophone were announced by the operator. These comments were recorded on the subtrack of the data storage tape of the digital data recorder synchronously with the broadband recordings.

B. Data analysis

Sound analysis was performed using a PC-based signal processing system, the SIGNAL/RTS™ software (Version 3.0, July 1996; American Engineering Design). The recorded signals were replayed at half speed and were digitized using a 12 bit Data Translation-2821G analog-to-digital board with a sampling frequency of 200 kHz (i.e., equivalent to a real time sample rate of 400 kHz). Raw click trains were first reviewed to assess the signal-to-noise ratio; then individual clicks with high signal-to-noise ratio were manually acquired for detailed analysis (see Li *et al.*, 2005a, b for details). The porpoise click wave form tended to be very stable over a whole click train, although it was often distorted by amplitude dips due to reverberations interfering with the primary

TABLE I. Details of finless porpoise encounters and acoustic recordings.

Encounter site No.	Date	Time	GPS position	Acoustic recordings	Group size, composition, and behavior
16	28 June	12:37	40°31′N 121°46′E	42 min recordings	10–20 individuals, including several calves, foraging behind the survey vessel with a distance of 5–50 m
15	28 June	16:03	40°35′N 121°39′E	11 min recordings	1 individual, foraging behind the survey vessel with a distance of about 30 m
14	28 June	19:07	40°39′N 121°31′E	18 min recordings	3–4 individuals, foraging behind the survey vessel with a distance of about 30 m
10	1 July	11:00	40°49′N 121°17′E	No recordings	3–4 individuals, foraging behind the survey vessel with a distance of about 15 m
13	2 July	07:00	40°43′N 121°22′E	No recordings	1 individual, foraging behind the survey vessel with a distance of about 5 m
6	2 July	18:43	40°38′N 121°45′E	40 min recordings	Over 20 individuals, including many calves, foraging behind the survey vessel with a distance of 5–30 m

signal (Kamminga *et al.*, 1986; Li *et al.*, 2005a, b). For the subsequent analysis, only clicks with a very distinct primary component, having a clear sinusoidal wave form and a smooth envelope, were selected and all reverberations were eliminated. Since the echolocation clicks are directional, and the orientation of a phonating animal could not be determined with the method used here, the recorded clicks were very likely acquired from both directly on and off the axis of its sonar transmission beam. However, off-axis echolocation signals would be distorted, with lower amplitude levels, relative to the on-axis signals (Au, 1993; Amundin, 1991; Au *et al.*, 2006). Therefore, only one click with the highest recorded amplitude (indicated by a distinct main click component) per click train was analyzed. Limiting the data in this way maximized the likelihood that the analyzed signals were acquired from as close to the beam axis as possible. The following acoustic parameters were calculated (defined as in Li *et al.*, 2005a): signal duration (Δt, time between two points at which the click oscillations rose from the background noise and descended into the background noise, or inflexion formed by reverberation), peak frequency (f_p, frequency of maximum energy), 3 dB bandwidth (Δf, width of the frequency band between the two points that are 3 dB lower than the maximum amplitude of a spectrum), number of cycles in one click (N_c), relative width of the frequency spectra ($Q=f_p/\Delta f$), time-bandwidth product ($\Delta t \times \Delta f$). Because of uncertainties of the distances of animals with respect to the hydrophone, it is impossible to accurately estimate the source level of clicks. These acoustic parameters, together with those acquired from *N. p. asiaeorientalis* in the Tian-e-zhou Baiji National Natural Reserve using the same acoustic recording system and method (Li *et al.*, 2005a), were fed into spreadsheets in SPSS 13.0 Windows and STATISTICA software for quantitative analysis.

III. RESULTS

A. General aspects

Finless porpoises were encountered at sites 16, 15, 14, 10, 13, and 6 (Table I and Fig. 1) on 28 June, 1 and 2 July. They were foraging on the fish that escaped from the trawl, and came less than 50 m from the stern of the vessel (Table I). Click signals from porpoises were successfully acquired at sites 16, 15, 14, and 6 on 28 June and 2 July (Table I). A total of 2 h of underwater signal recordings were obtained, and 71 click trains (approximately 10% of the total recorded click trains) with both high signal-to-noise ratios and very distinct main click component were used for extraction of the acoustic parameters.

Typical clicks of *N. p. sunameri* have a clear sinusoidal wave form and a smooth envelope followed by some reverberations [Figs. 2(a)–2(d)], similar to clicks recorded from *N. p. asiaeorientalis* in open riverine waters [Figs. 2(e) and 2(f)]. A closer inspection of the clicks reveals that *N. p. sunameri* clicks are nearly identical in both duration (Fig. 2) and frequency spectrum (Fig. 3) to those of *N. p. asiaeorientalis*. Figure 3(a) shows a typical example of a click frequency spectrum, computed from click wave form Fig. 2(a), together with the click frequency spectrum of *N. p. asiaeorientalis* [Fig. 3(b)] from wave form Fig. 2(e). We note that the spectral energy in both Figs. 3(a) and 3(b) is narrowly concentrated in the frequency span between 120 and 130 kHz.

A detailed inspection of *N. p. sunameri* click wave forms shows an absolute absence of low-frequency components (Fig. 2), which is confirmed by the fact that most of the click trains had no click energy presenting below 70 kHz except for the background noise. Figures 4(a) and 4(b) show an example of such click trains. However, there were also instances when click trains had faint click energy presenting below 70 kHz. Figure 5(a) shows an example of such click trains, together with its spectrogram [Fig. 5(b)]. The arrows in Fig. 5(b) denote the low-frequency energy part of several clicks. Interestingly, on a closer inspection of the click wave forms, we found that the main first click in the click trains without low-frequency energy always had a bell-shaped basic wave form, with no or neglectable reverberations [Fig. 4(c)], while the click trains with low-frequency energy had abundant reverberations following immediately after or slightly overlapping the main part [Fig. 5(c)]. The frequency

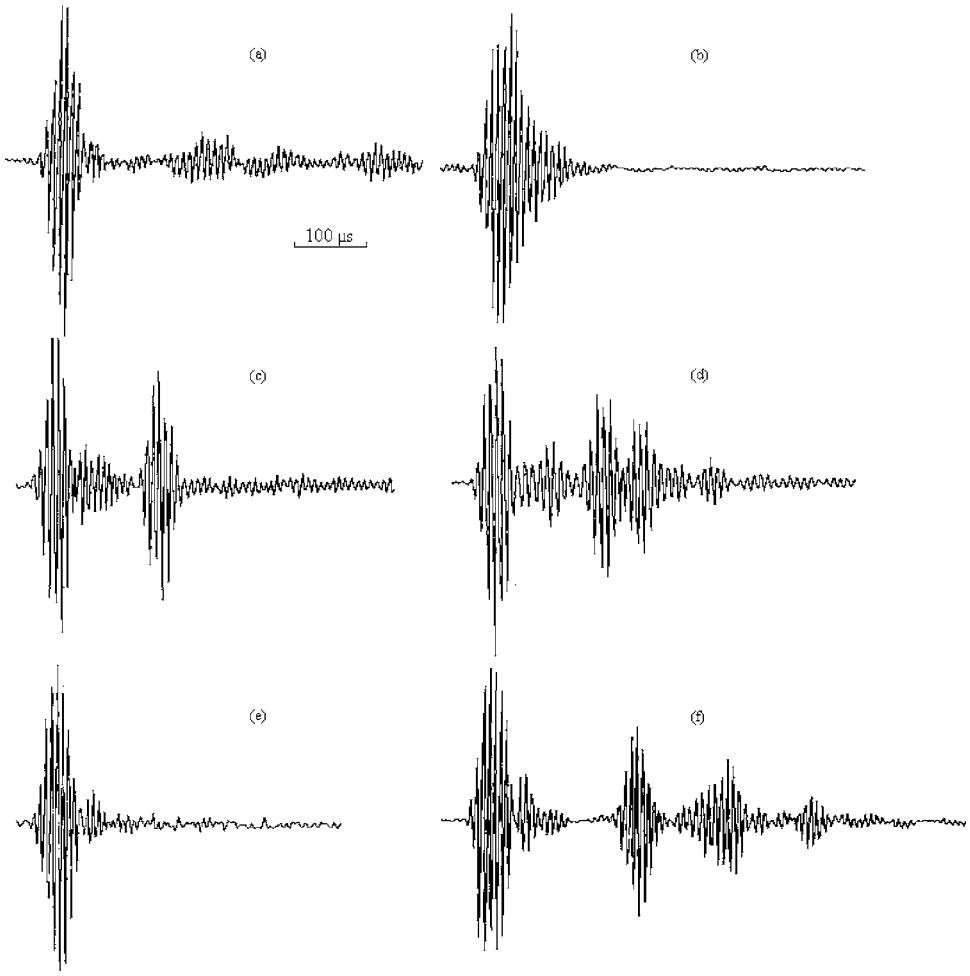

FIG. 2. Typical click wave forms, note a main part which has a smooth envelope followed by some reverberations. (a), (b), (c), and (d): Clicks from wild *N. p. sunameri* off Liao-dong-wan Bay located in the Bohai Sea, China. (e) and (f): Clicks from *N. p. asiaeorientalis* recorded in the Tian-e-zhou Baiji National Natural Reserve during October to November 2003.

spectrum of the complete click in Fig. 4(c) and Fig. 5(c) is shown in Fig. 4(d) and Fig. 5(d), respectively.

B. Time and frequency parameters of click

Relative frequency histograms of the peak frequencies, 3 dB bandwidths, signal durations, and number of cycles of the 71 measured clicks from *N. p. sunameri* are shown in Fig. 6. The peak frequency histogram clearly presents a normal distribution ($p<0.001$, Chi-Square Test) with over 95% of the clicks having peak frequencies between 115 and 130 kHz, and all of the peak frequencies in the range of 100–135 kHz [Fig. 6(a)]. The 3 dB bandwidth histogram shows that the bandwidth of the clicks is narrow, with over 90% of the clicks having bandwidths between 12.5 and 22.5 kHz [Fig. 6(b)]. Eighty percent of the clicks have duration between 60 and 90 μs, and only 1% and 6% of the clicks have duration shorter than 60 and longer than 100 μs, respectively [Fig. 6(c)]. The number of cycles is distributed between 7 and 13, with most of them in the range of 8 and 11 [Fig. 6(d)].

Means, standard deviations, and ranges of the calculated click parameters are presented in Table II. Characteristics of clicks from *N. p. asiaeorientalis* in open riverine waters (Li *et al.*, 2005a) are shown for comparison. The analyzed clicks of *N. p. sunameri* have a high peak frequency ($f_p=121\pm3.78$ kHz), narrow 3 dB bandwidth ($\Delta f=17.5\pm3.30$ kHz), short signal durations ($\Delta t=80\pm11.49$ μs), and low time-bandwidth product ($\Delta t\times\Delta f=1.36\pm0.12$). Note that the peak frequencies are significantly lower ($F=22.565$, $df=1$, $p<0.001$), the 3 dB bandwidths are significantly narrower ($F=23.572$, $df=1$, $p<0.001$), the signal durations are significantly longer ($F=41.461$, $df=1$, $p<0.001$), the numbers of cycles are significantly more ($F=17.089$, $df=1$, $p<0.001$), the Q values are significantly higher ($F=10.734$, $df=1$, $p<0.01$), and the products of $\Delta t\times\Delta f$ are significantly larger ($F=8.856$, $df=1$, $p<0.05$) in the *N. p. sunameri* clicks than in the *N. p. asiaeorientalis* clicks [one-way analysis of variance (ANOVA) test, a p value of 0.05 was considered significant, Table II].

A scatter plot of 3 dB bandwidth as a function of peak frequency for both the *N. p. sunameri* (NPS) clicks and the *N. p. asiaeorientalis* (NPA) clicks is shown in Fig. 7, along with two ellipsoid boundaries indicating a 95% variance.

IV. DISCUSSION AND CONCLUSIONS

With the present recording setup, the effect of click directionality and the uncertain position of the phonating porpoises made it impossible to determine which clicks were on axis and which were not (Li *et al.*, 2005a). However, our method of selecting clicks maximized the likelihood that the analyzed clicks were recorded close to the beam axis. It is highly unlikely that the recorded clicks were produced by other cetacean species, as our recordings were made only

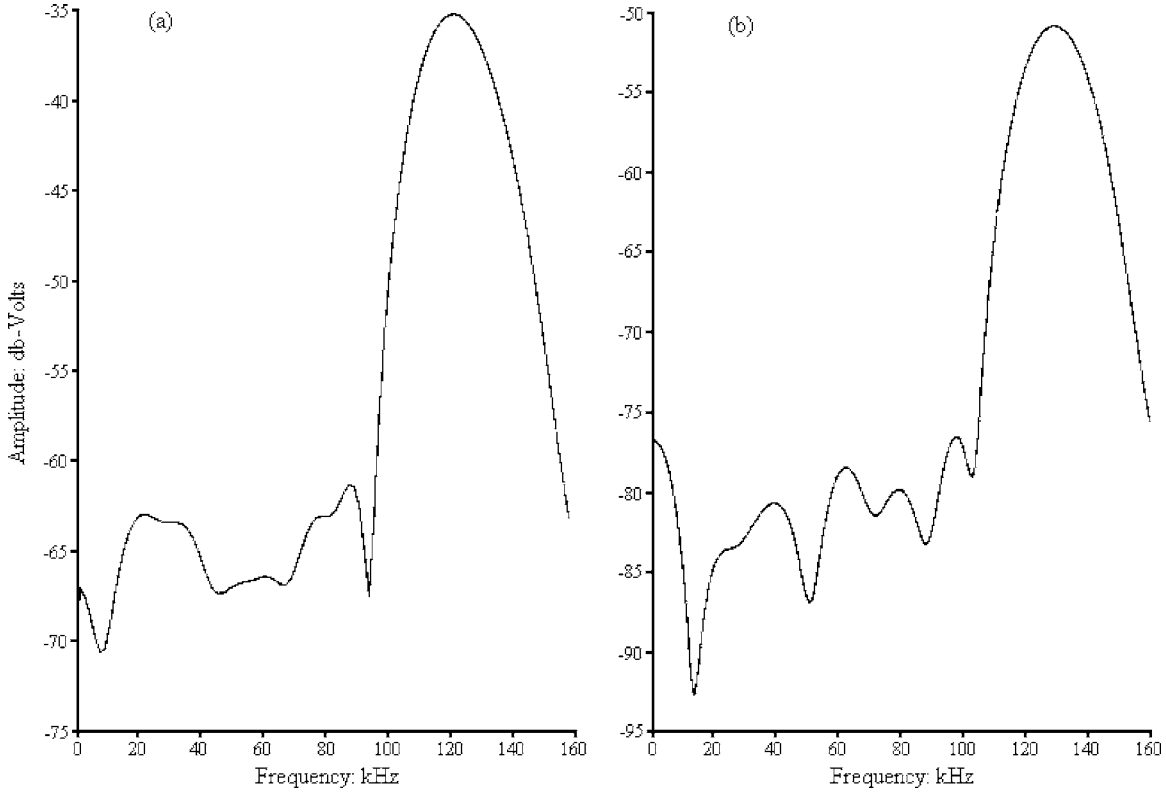

FIG. 3. Typical frequency spectrum (frequency resolution DF=781 Hz, FFT=256) of the *N. p. sunameri* clicks (a) and the *N. p. asiaeorientalis* clicks.

with groups of finless porpoises present in the vicinity of the vessel, no other species were sighted at any time.

As all the investigated species in the *Phocoenidae* family (Dubrovskii *et al.*, 1971; Møhl and Andersen, 1973; Awbrey *et al.*, 1979; Kamminga and Wiersma, 1981; Kamminga *et al.*, 1986; Evans and Awbrey, 1988; Kamminga, 1988; Silber, 1991; Goold and Jefferson, 2002) and even including the species in the distantly related delphinids, *Cephalorhynchus spp*. (Watkins and Schevill, 1980; Kamminga and Wiersma, 1982; Dziedzic and De Buffrenil, 1989) have clicks with similar wave form structures and frequency spectra, it does not then come as a surprise that the *N. p. suna-*

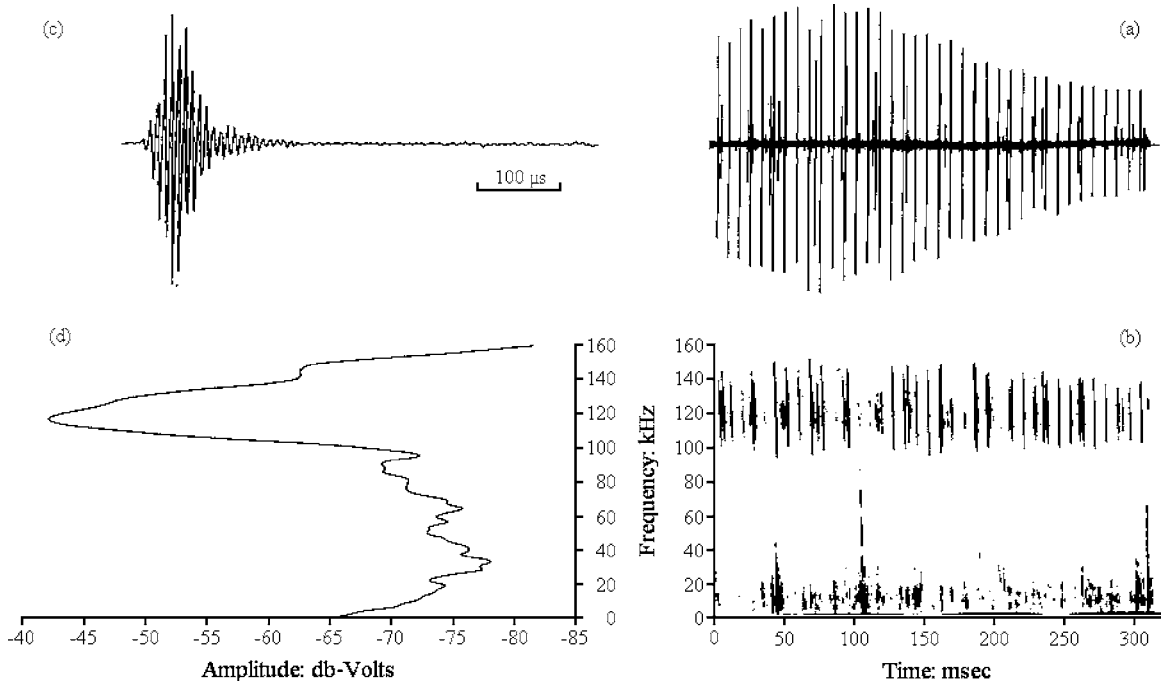

FIG. 4. (a) and (b): A click train example of *N. p. sunameri*, which has no click energy presenting below 70 kHz. (c) and (d): The wave form and spectrum (frequency resolution DF=781 Hz, FFT = 256) of a single click from (a).

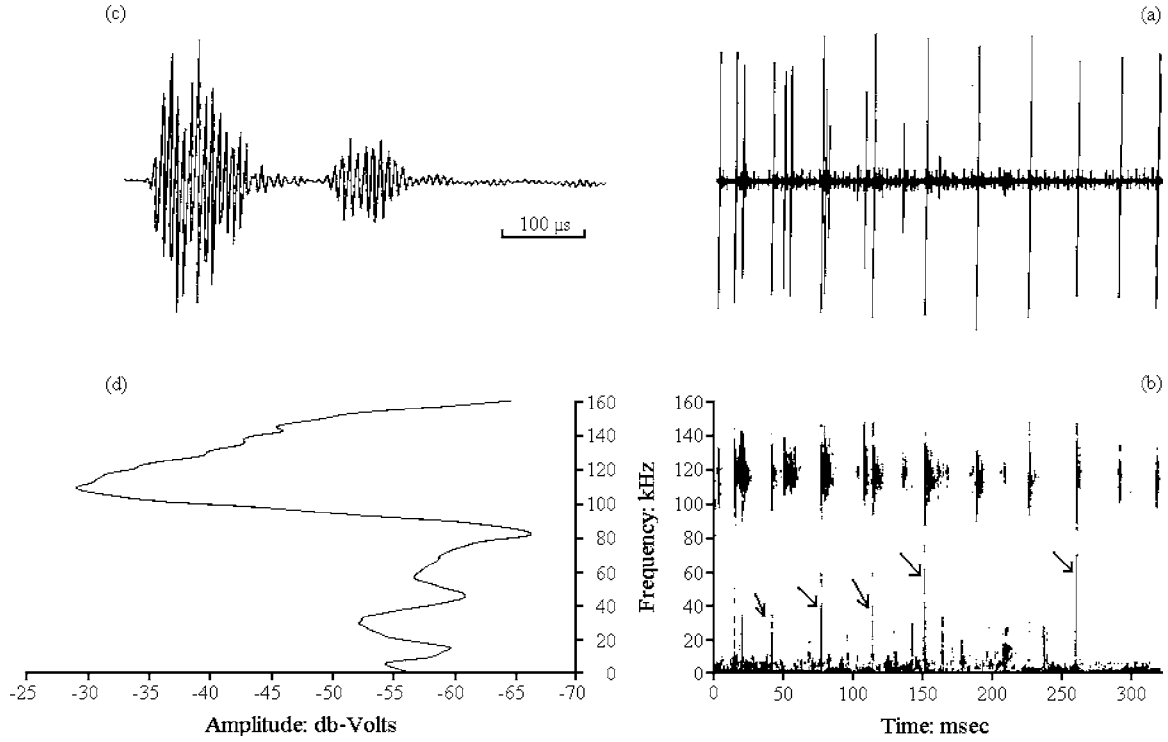

FIG. 5. (a) and (b): A click train example of *N. p. sunameri*, which has faint click energy presenting below 70 kHz, note the low-frequency parts which are denoted by arrows in (b). (c) and (d): The wave form and spectrum (frequency resolution DF=781 Hz, FFT = 256) of a single click from (a).

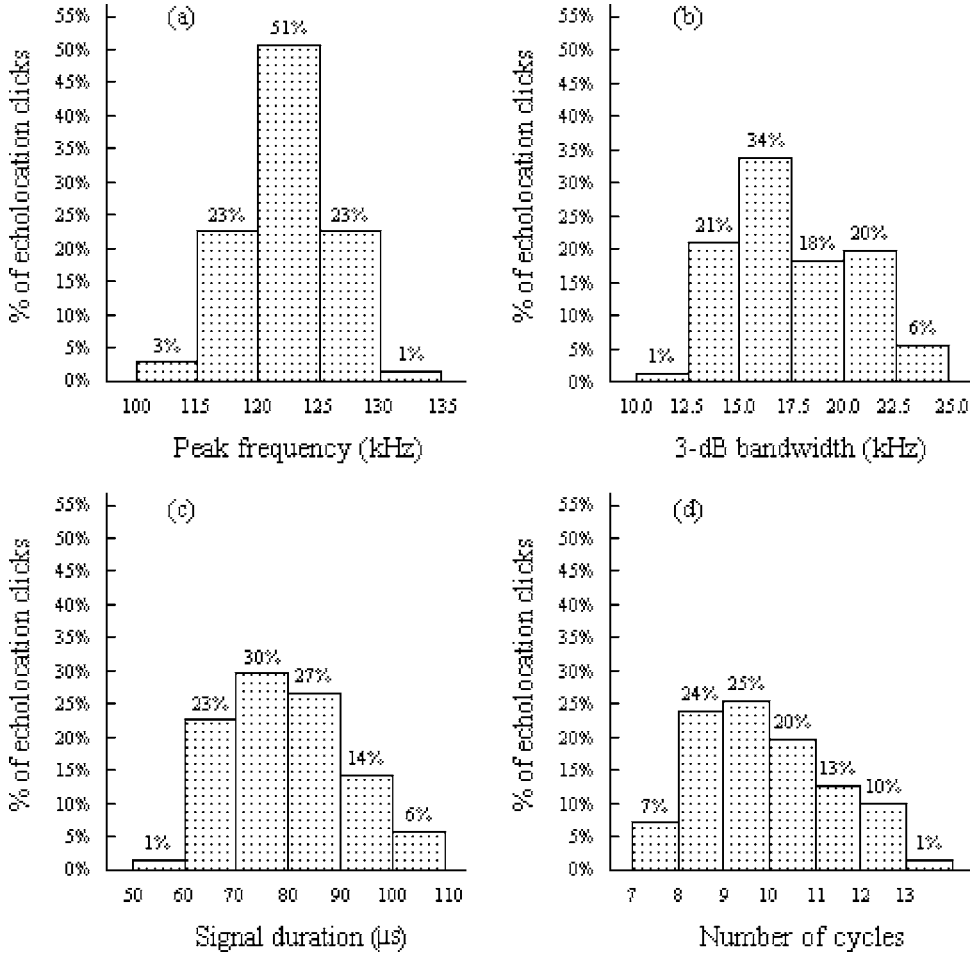

FIG. 6. Relative frequency histograms of the distribution of peak frequency f_p (a), 3 dB bandwidth Δf (b), signal duration Δt (c), and number of cycles N_c (d) of the measured clicks in *N. p. sunameri*.

TABLE II. Calculated click characteristics (Mean ± S. D.), including f_p (frequency of maximum energy), Δf (width of the frequency band between the two points that are 3 dB lower than the maximum amplitude of a spectrum), Δt (time between two points at which the click oscillations rose from the background noise and descended into the background noise, or inflexion formed by reverberation), N_c (number of cycles in one click), Q (relative width of the frequency spectra), and $\Delta t \times \Delta f$ (time-bandwidth product), for all the measured *N. p. sunameri* clicks. Characteristics of clicks from *N. p. asiaeorientalis* recorded in open riverine waters (Li *et al.*, 2005a) are shown for comparison. The p value was shown for each characteristic (one-way ANOVA, a p value of 0.05 was considered significant). NPS represents *N. p. sunameri* and NPA represents *N. p. asiaeorientalis*.

		NPS (n=71)	NPA (n=548)	p value
f_p (kHz)	Mean±S. D.	121±3.78	125±6.92	<0.001
	Range	113–131	87–145	
Δf (kHz)	Mean±S. D.	17.5±3.30	20.0±4.24	<0.001
	Range	10.9–25.0	9.3–41.9	
Δt(μs)	Mean±S. D.	80±11.49	68±14.12	<0.001
	Range	56–109	30–122	
N_c	Mean±S. D.	9±1.48	8±1.94	<0.001
	Range	7–13	4–16	
Q	Mean±S. D.	7.2±1.44	6.6±1.56	<0.01
	Range	4.8–11.3	3.0–12.5	
$\Delta t \times \Delta f$	Mean±S. D.	1.36±0.12	1.31±0.11	<0.05
	Range	1.15–1.63	1.00–1.68	

meri clicks are very similar in both wave form and frequency spectrum to those of *N. p. asiaeorientalis* (Figs. 2 and 3).

Close inspection of many *N. p. sunameri* click wave forms revealed that there is no low-frequency component in the vocalizations of this population. Sporadically, however, click trains or clicks had faint click energy presenting below 70 kHz in the spectrograms. This was most likely due to interference effect from multiple pulses structures (see the differences between Fig. 4 and Fig. 5).

The absence of low-frequency components in the click wave forms from the inshore *N. p. sunameri*, which is consistent with the sonar clicks of riverine *N. p. asiaeorientalis* (Li *et al.*, 2005a), rejects the hypothesis of two-component sonar clicks from an ecological classification of odontocete sonar (Dudok van Heel, 1981; Kamminga and Wiersma, 1981; Wiersma, 1983) considering the *N. p. sunameri* as an inshore population. Kamminga *et al.* (1986) also noted that there was no low-frequency component in the clicks of captive *N. p. sunameri* from Japanese coastal waters. Nevertheless, Goold and Jefferson (2002) stated that there was clearly low-frequency energy in some of the Hong Kong finless porpoise (*N. p. phocaenoides*) clicks. Whether this was a true case of the two-component sonar or a counterfeit due to interference effect from multiple pulses structures as shown in the present study could not be determined. Since the same recording system and analyzing method were used to describe the clicks of present investigated population *N. p. sunameri* and those of *N. p. asiaeorientalis*, the similarity in the sonar behavior with one-component high-frequency sonar clicks between these two populations is most likely real. If the two-component sonar hypothesis from an ecological point of view (i.e., inshore porpoises and dolphins were suggested to have two-component signals with a low-frequency component to detect long-distance targets and a high-frequency one for short-range, high-resolution target detection) is justified, a possible explanation is that on account of certain changes in the marine environment, the common ancestor of *N. p. sunameri* and *N. p. asiaeorientalis* entered into the riverine system such as Yangtze River, from the marine system, and was already adapted to the riverine environment in the sonar behavior, through evolutionary refinement over millions of years. Subsequently, a recent ecological reversal, i.e., reinvasion of the marine coastal habitat, resulted in the radiation of some individuals to the inshore. But the period of time is not so long to bring an adaptation in sonar behavior of this population to the inshore environment.

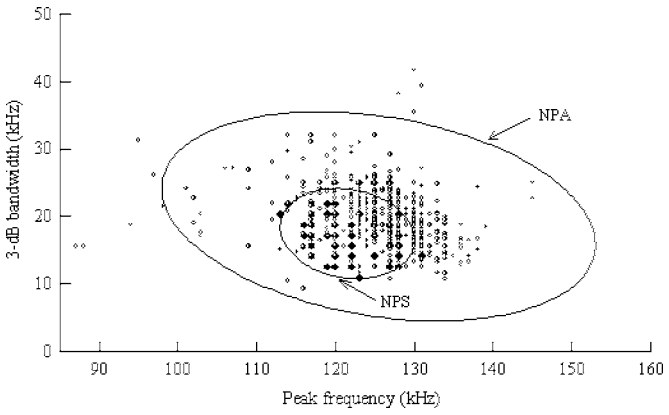

FIG. 7. Scatter plot of 3 dB bandwidth Δf versus peak frequency f_p from 71 *N. p. sunameri* clicks (NPS), and 548 *N. p. asiaeorientalis* clicks (NPA). Ellipsoid boundaries indicate a 95% variance domain.

The mean click parameters are significantly different between *N. p. sunameri* and *N. p. asiaeorientalis* (Table II). As a mass of field studies of bats have demonstrated that the structures of echolocation calls, including sound duration, bandwidth, peak frequency, and so on, are closely associated with ecological conditions (reviewed by Denzinger *et al.*, 2003), one explanation might be that the differences of mean click parameters are intrinsic, due to the different habitat types, foraging modes, and diets between the two porpoise populations. Alternatively, the differences are artifacts due to the small click sample size (n=71) and single foraging be-

havior (Table I) in the *N. p. sunameri* vocalization recordings. The latter is perhaps more likely, since the click parameters have a wider range in *N. p. asiaeorientalis* (Table II and Fig. 7).

The scatter plot in Fig. 7 shows that there is a relatively large spread in peak frequency and bandwidth. There is also a faint tendency of a decrease in bandwidth with increased peak frequency, in both the two porpoise populations. The decrease in bandwidth with increasing peak frequency implies that the value of $Q=f_p/\Delta f$ is not constant but increases with the peak frequency. This is different from *Delphinapterus leucas* (Au *et al.*, 1985), *Pseudorca crassidens* and *Tursiops truncatus* (Kamminga and van Velden, 1987; Kamminga and Beitsma, 1990), *Stenella frontalis* (Au and Herzing, 2003), *S. longirostris* and *S. attenuate* (Schotten *et al.*, 2003), where $Q=f_p/\Delta f$ is constant. The specific reason for this characteristic is still open to investigation. Popov *et al.* (2006) reported a nonconstant Q_{ERB} representation of sound frequencies in the auditory system of porpoises, *Phocoena phocoena* and *Neophocaena phocaenoides*. Hence, the nonconstant value of $Q=f_p/\Delta f$ in the vocalizations of *N. p. sunameri* and *N. p. asiaeorientalis* might match their vocalizations to their hearing.

ACKNOWLEDGMENTS

Grateful thanks are given to Professor Whitlow W. L. Au for his great effort to improve this manuscript. Special thanks to the crew and staff of the Ying-kou Fishery Team, Peijun Li, Kun Lin and Benfang Yu. The assistance of Xinqiao Zhang when this wild experiment was carried out is also appreciated. We would also like to express our thanks to two reviewers for their valuable comments and detailed revision on the manuscript. This research was supported by grants from the Chinese Academy of Sciences (CAS, The President Fund), the Institute of Hydrobiology, CAS (Nos. 220103), and the Program for Promotion of Basic Research Activities for Innovative Biosciences of Japan.

Akamatsu, T., Wang, D., Nakamura, K., and Wang, K. (**1998**). "Echolocation range of captive and free-ranging baiji (*Lipotes vexillifer*), finless porpoise (*Neophocaena phocaenoides*), and bottlenose dolphin (*Tursiops truncatus*)," J. Acoust. Soc. Am. **104**, 2511–2516.

Akamatsu, T., Wang, D., Wang, K., and Naito, Y. (**2005a**). "Biosonar behaviour of free-ranging porpoises," Proc. R. Soc. London, Ser. B **272**, 797–801.

Akamatsu, T., Wang, D., and Wang, K. (**2005b**). "Off-axis sonar beam pattern of free-ranging finless porpoises measured by a stereo pulse event data logger," J. Acoust. Soc. Am. **117**, 3325–3330.

Amundin, M. (**1991**). "Sound production in Odontocetes with emphasis on the harbor porpoise, *Phocoena phocoena*," Ph.D. dissertation, University of Stockholm, Sweden.

Au, W. W. L. (**1993**). *The Sonar of Dolphins* (Springer-Verlag, New York).

Au, W. W. L., and Herzing, D. L. (**2003**). "Echolocation signals of wild Atlantic spotted dolphin (*Stenella frontalis*)," J. Acoust. Soc. Am. **113**, 598–604.

Au, W. W. L., Carder, D. A., Penner, R. H., and Scronce, B. L. (**1985**). "Demonstration of adaptation in beluga whale echolocation signals," J. Acoust. Soc. Am. **77**, 726–730.

Au, W. W. L., Kastelein, R. A., Benoit-Bird, K. J., Cranford, T. W., and Mckenna, M. F. (**2006**). "Acoustic radiation from the head of echolocating harbor porpoises (*Phocoena phocoena*)," J. Exp. Biol. **209**, 2726–2733.

Awbrey, F. T., Norris, J. C., Hubbard, A. B., and Evans, W. E. (**1979**). "The bioacoustics of the Dall porpoise—salmon net interaction," Hubbs-Sea World Research Institute Technical Report No. 79–120.

Denzinger, A., Elisabeth, K. V. K., and Jones, G. (**2003**). "Ecological and evolutionary aspects of echolocation in bats," in *Echolocation in Bats and Dolphins*, edited by J. Thomas, C. E. Moss, and M. Vater (University of Chicago, Chicago), pp. 311–331.

Dubrovskii, N. A., Krasnov, P. S., and Titov, A. A. (**1971**). "On the emission of echolocation signals by the Azov sea harbor porpoise," Sov. Phys. Acoust. **16**, 444–448.

Dudok van Heel, W. H. (**1981**). "Investigations on cetacean sonar III: A proposal for an ecological classification of odontocetes in relation with sonar," Aquat. Mammal. **8**, 65–69.

Dziedzic, A., and De Buffrenil, V. (**1989**). "Acoustic signals of the Commerson's dolphin, *Cephalorhynchus commersonii*, in the Kerguelen Islands," J. Mammal. **70**, 449–452.

Evans, W. E., and Awbrey, F. T. (**1988**). "Natural history aspects of marine mammal echolocation: Feeding strategies and habitat," in *Animal Sonar, Process and Performance*, edited by P. E. Nachtigall and P. W. B. Moore (Plenum, New York), pp. 521–534.

Gao, A., and Zhou, K. (**1993**). "Growth and reproduction of three populations of finless porpoise, *Neophocaena phocaenoides*, in Chinese waters," Aquat. Mammal. **19**, 3–12.

Gao, A., and Zhou, K. (**1995**). "Geographical variation of external measurements and three subspecies of *Neophocaena phocaenoides* in Chinese waters," Acta Theriologica Sinica. **15**, 81–92.

Goold, J. C., and Jefferson, T. A. (**2002**). "Acoustic signals from free-ranging finless porpoises (*Neophocaena phocaenoides*) in the waters around Hong Kong," Raffles Bull. Zool., Suppl. **10**, 131–139.

Kamminga, C. (**1979**). "Remarks on dominant frequencies of cetacean sonar," Aquat. Mammal. **7**, 93–101.

Kamminga, C. (**1988**). "Echolocation signal types of odontocetes," in *Animal Sonar, Process and Performance*, edited by P. E. Nachtigall and P. W. B. Moore (Plenum, New York), pp. 9–22.

Kamminga, C., and Beitsma, G. R. (**1990**). "Investigations on cetacean sonar IX: Remarks on dominant sonar frequencies from *Tursiops truncatus*," Aquat. Mammal. **16**, 14–20.

Kamminga, C., and van Velden, J. C. (**1987**). "Investigations on cetacean sonar VIII: Sonar singals of *Pseudorca crassidens* in comparison with *Tursiops truncatus*," Aquat. Mammal. **13**, 43–49.

Kamminga, C., and Wiersma, H. (**1981**). "Investigations on cetacean sonar II: Acoustical similarities and differences in odontocete sonar signals," Aquat. Mammal. **8**, 41–62.

Kamminga, C., and Wiersma, H. (**1982**). "Investigations on cetacean sonar V: The true nature of the sonar sound of *Cephalorhynchus commersonii*," Aquat. Mammal. **9**, 95–104.

Kamminga, C., Kataoka, T., and Engelsma, F. J. (**1986**). "Investigations on cetacean sonar VII: Underwater sounds of *Neophocaena phocaenoides* of the Japanese coastal population," Aquat. Mammal. **12**, 52–60.

Kamminga, C., Wiersma, H., and Dudok van Heel, W. H. (**1983**). "Sonar sounds in *Orcaella brevirostris* of the Mahakam River, East Kalimantan, Indonesia; the first descriptions of the acoustic behaviour," Aquat. Mammal. **10**, 83–95.

Kamminga, C., van Hove, M. T., Engelsma, F. J., and Terry, R. P. (**1993**). "Investigations on cetacean sonar X: A comparative analysis of underwater echolocation clicks of *Inia* spp. And *Sotalia* spp.," Aquat. Mammal. **19**, 31–43.

Kasuya, T. (**1999**). "Finless porpoise *Neophocaena phocaenoides* (G. Cuvier, 1829)," in *Handbook of Marine Mammals, Volume 6: The Second Book of Dolphins and the Porpoises*, edited by S. H. Ridgway and R. Harrison (Academic, San Diego), pp. 411–442.

Li, S., Wang, K., Wang, D., and Akamatsu, T. (**2005a**). "Echolocation signals of the free-ranging Yangtze finless porpoise (*Neophocaena phocaenoides asiaeorientialis*)," J. Acoust. Soc. Am. **117**, 3288–3296.

Li, S., Wang, K., Wang, D., and Akamatsu, T. (**2005b**). "Origin of the double- and multi-pulse structure of echolocation signals in Yangtze finless porpoise (*Neophocaena phocaenoides asiaeorientialis*)," J. Acoust. Soc. Am. **118**, 3934–3940.

Mizue, K., Takemura, A., and Nakasai, K. (**1968**). "Studies on the little toothed whales in the west sea area of Kyusyu-XV. Underwater sound of the Chinese finless porpoise caught in the Japanese coastal sea," Bul. Faculty of Fisheries, Nagasaki University, **25**, 25–32.

Møhl, B., and Andersen, S. (**1973**). "Echolocation: high frequency component in the click of the harbour porpoise (*Phocoena phocoena* L.)," J. Acoust. Soc. Am. **54**, 1368–1373.

Nakahara, F., Takemura, A., Koido, T., and Hiruda, H. (**1997**). "Target discrimination by an echolocating finless porpoise, *Neophocaena phocae-*

noides," Marine Mammal Sci. **13**, 639–649.
Popov, V. V., Supin, A. Y., Wang, D., and Wang, K. (**2006**). "Nonconstant quality of auditory filters in the porpoises, *Phocoena phocoena* and *Neophocaena phocaenoides* (Cetacea, Phocoenidae)," J. Acoust. Soc. Am. **119**, 3171–3180.
Reeves, R. R., Wang, J. Y., and Leatherwood, S. (**1997**). "The finless porpoise, *Neophocaena phocaenoides* (G. Cuvier, 1829): A summary of current knowledge and recommendations for conservation action," Asian Mar. Biol. **14**, 111–143.
Silber, G. K. (**1991**). "Acoustic signals of the Vaquita (*Phocoena sinus*)," Aquat. Mammal. **17**, 130–133.
Schotten, M., Au, W. W. L., Lammers, M. O., and Aubauer, R. (**2003**). "Echolocation recordings and localization of wild-spinner dolphins (*Stenella longirostris*) and pantropical spotted dolphins (*Stenella attenuata*) using a four hydrophone array," in *Echolocation in Bats and Dolphins*, edited by J. Thomas, C. F. Moss, and M. Vater (University of Chicago Press, Chicago), pp. 393–400.
Wang, D. (**1996**). "A preliminary study on sound and acoustic behavior of the Yangtze River finless porpoise, *Neophocaena phocaenoides*," Acta Hydrobiol. Sin. **20**, 127–133.
Wang, P. (**1992**). "The morphological characters and the problem of subspecies identification of the finless porpoise," Fish. Sci. **11**, 4–9.
Watkins, W. A., and Schevill, W. E. (**1980**). "Characteristic features of the underwater sounds of *Cephalorhynchus commersonii*," J. Mammal. **61**, 738–740.
Wiersma, H. (**1983**). "Investigations on cetacean sonar IV: A comparison of wave shapes of odontocete sonar signals," Aquat. Mammal. **9**, 57–67.

Do acoustic features of lion, *Panthera leo*, roars reflect sex and male condition?

Dana Pfefferle[a)]
Research Group Cognitive Ethology, German Primate Center, Kellnerweg 4, 37077 Göttingen, Germany

Peyton M. West
American Association for the Advancement of Science, 1200 New York Avenue NW, Washington, DC 20005

Jon Grinnell
Department of Biology, Gustavus Adolphus College, 800 West College Avenue, St. Peter, Minnesota 56082

Craig Packer
Department of Ecology, Evolution and Behavior, University of Minnesota, 1987 Upper Buford Circle, St. Paul, Minnesota 55108

Julia Fischer
Research Group Cognitive Ethology, German Primate Center, Kellnerweg 4, 37077 Göttingen, Germany

(Received 1 November 2006; revised 14 March 2007; accepted 14 March 2007)

Long distance calls function to regulate intergroup spacing, attract mating partners, and/or repel competitors. Therefore, they may not only provide information about the sex (if both sexes are calling) but also about the condition of the caller. This paper provides a description of the acoustic features of roars recorded from 18 male and 6 female lions (*Panthera leo*) living in the Serengeti National park, Tanzania. After analyzing whether these roars differ between the sexes, tests whether male roars may function as indicators of their fighting ability or condition were conducted. Therefore, call characteristics were tested for relation to anatomical features as size, mane color, or mane length. Call characteristics included acoustic parameters that previously had been implied as indicators of size and fighting ability, e.g., call length, fundamental frequency, and peak frequency. The analysis revealed differences in relation to sex, which were entirely explained by variation in body size. No evidence that acoustic variables were related to male condition was found, indicating that sexual selection might only be a weak force modulating the lion's roar. Instead, lion roars may have mainly been selected to effectively advertise territorial boundaries. © *2007 Acoustical Society of America.* [DOI: 10.1121/1.2722507]

PACS number(s): 43.80.Ka, 43.80.Jz [JAS] Pages: 3947–3953

I. INTRODUCTION

Long distance calls provide information about the location of the caller(s) and hence are assumed to serve intergroup spacing (e.g., Mitani, 1985, 1988, 1994; Mitani and Nishida, 1993; Notman and Rendall, 2005; Wilson *et al.*, 2001). In the case of several animals calling at the same time, they may also transmit information about party size (lions: Grinnell *et al.*, 1995; Grinnell and McComb, 1996; McComb *et al.*, 1994; chimpanzee: Wilson *et al.*, 2001). Although in some species females also produce long distance calls (e.g., African elephant: Langbauer *et al.*, 1991; McComb *et al.*, 2003; Poole *et al.*, 1988; Gibbons: Dallmann and Geissmann, 2001; Zebra finches: Cynx and Gell, 2004; Bengalese finches: Kobayasi and Okanoya, 2003; Arctic foxes: Frommolt *et al.*, 2003; lions: McComb *et al.*, 1994), long distance calls are more commonly uttered by males only, presumably serving to attract mates and/or repel competitors. In a diverse range of taxa including birds, amphibians, and mammals, males have been found to produce loud, repetitive calls that apparently function as displays of size, condition, or fighting ability (e.g., Clutton-Brock and Albon, 1979; Davies and Halliday, 1978; Fischer *et al.*, 2004; Kitchen *et al.*, 2003; Reby and McComb, 2003). Such calls may provide listeners with accurate information about the signalers' relative competitive abilities. This is the case when the production of such calls is more costly or difficult for individuals in poor condition than for those in good condition, (Grafen, 1990; Zahavi, 1975, but see also Maynard Smith, 1994; Silk *et al.*, 2000; Vehrencamp, 2000). Alternatively, physiological constraints may determine the quality of the signal, as in the case of so-called "index" signals (Vehrencamp, 2000).

In this paper we examine the loud calls or "roars" of lions (*Panthera leo*). Roars are loud, low-pitched vocalizations that are delivered in bouts, which typically last 30–60 s and consist of several soft introductory moans, a series of full-throated roars, and a terminating sequence of grunts (Grinnell *et al.*, 1995; McComb *et al.*, 1994). Figure 1 shows an example of a male lion call. Male and female lions advertise their territory by roaring and they use the numbers of

[a)]Electronic mail: dpfefferle@dpz.eu

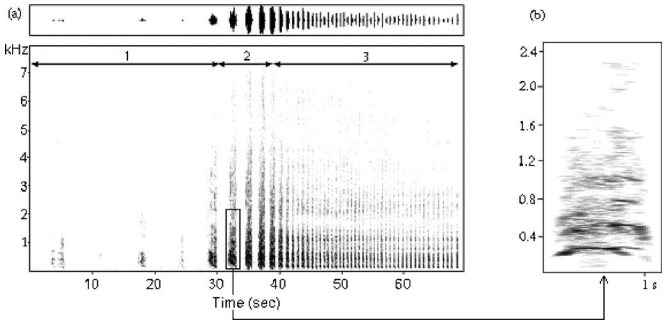

FIG. 1. (a) Spectrogram of a complete male lion call (FFT length: 1024; Frame [%]: 100; Window: Hamming; Overlap: 87.5). The call starts with a series of soft introductory moans (1), followed by a series of full-throated roars (2), and terminates with a sequence of grunts (3). (b) Example of one call unit extracted from the series of full-throated roars (2) (FFT length: 1024; Frame [%]: 100; Window: Hamming; Overlap: 87.5; Sampling frequency: 5000 Hz).

roars they hear to estimate the strength of the opposition (McComb *et al.*, 1994). Roars also function to stay in contact with other pride members, strengthening the bond within the social group, intimating rivals, and, under certain circumstances, to attract mates (Funston, 1999; Grinnell *et al.*, 1995; Grinnell and McComb, 1996; McComb *et al.*, 1994; Schaller, 1972). Because of their social system, males and females can regularly judge males, and excess females can freely choose among them (West and Packer, 2002). Thus physical properties, like body size and mane length as well as color, might have evolved to signal male genetic and/or phenotypic condition. If that is the case, those characteristics may also be encoded in acoustic call features. Indeed, shorter manes reflect poor fighting ability or short term health, whereas dark manes indicate maturity and high levels of testosterone and nutrition (West and Packer, 2002). Mane darkness influences both female choice and male-male competition. It tends to be a costly signal, because dark-maned males suffer higher surface temperature, abnormal sperm, and lower food intake during the hot months of the year. Nevertheless, because such males tend to be dominant, they enjoy longer reproductive life span and higher offspring survival. Estrous females prefer to mate with males with darker manes while males assess their opponents' mane length and darkness and thereby avoid healthier, older, and more aggressive individuals (West and Packer, 2002).

The purpose of this analysis is to describe the acoustic features of lion roars in detail, and examine (1) whether calls differ between the sexes, and (2) whether, in males, acoustic characteristics are related to anatomical features of the callers. We predicted that larger subjects should produce lower values of spectral parameters (e.g., fundamental frequency, formant dispersion, peak frequency) than smaller bodied animals. Thus, we expected males to differ significantly from females. We also predicted that males with darker and longer manes should exhibit longer calls with more and longer call units. If measures of body size correlate with mane length or color, then dark- or long-maned males should also exhibit low values in the corresponding spectral parameters. The analysis presented below is based on a relatively small number of subjects; however, we would like to highlight that these kinds of data, including measurements from anaesthetized males, estimates of male length and color, as well as recordings, are extremely difficult to collect.

II. METHODS

A. Subjects and study site

We studied 24 lions (18 males and 6 females), living in the Serengeti National Park, Tanzania. All subjects were individually identifiable from natural markings. Continuous demographic records have been maintained on lions in a 2000-km^2 study area in Serengeti National Park since 1975 (Packer *et al.*, 1988; Schaller, 1972).

B. Anatomical measurements

In the context of previous studies of Packer and colleagues, animals were anesthetized using 200–500 mg Telazol. Chest circumference was measured using a commercial measuring tape positioned immediately behind the forelegs. For each measurement the accuracy was 1 cm. IACUC (International Animal Care and Use Committee) approval was obtained for all conducted immobilizations. Mane characteristics were evaluated using photographs taken of 568 males from 1964 to 2000 (West and Packer, 2002). Most photographs taken from 1964 to 1990 were black and white; color film was used from 1991. Each photograph was graded for length and color by five undergraduate judges who had never seen the animals in the wild. Students graded both the overall color and length of the mane as well as the color and length of individual areas of the mane (chest, forehead, neck, and shoulders). Multiple images of the same male were evaluated collectively if they were taken within a 1-week period. For each male, the judges' highest and lowest scores were discarded, and the remaining three were averaged. We found no statistically significant effect of picture quality or film type on the judges' scores.

C. Sound recording and analysis

Between October 1984 and December 2000 vocalizations were recorded *ad libitum* using a Panasonic SV 250 portable digital audio tape-recorder or a Sony Professional Walkman WM-D6C as well as a Sennheiser MKH816T directional microphone. Recording distance ranged between 30 and 60 m. In two instances, calls were recorded from 80 and 100 m. While the call recorded at 80 m could only be used for temporal analysis, the "100 m call" appeared to be of sufficient quality for temporal and spectral analysis. Digital recordings were either transferred into a 1990s vintage Macintosh computer using built-in digitizer and Soundedit 16 software or to a PC using an optical wire and USB wave converter (U2A Waveterminal, EGO SYStems Inc.). Recordings were saved in mono format, 16-bit resolution, and 44.1 kHz sampling rate using CoolEdit 2000 (Syntrillium, Phoenix, AZ) software. A total of 33 recordings were available from 24 individuals, and 30 calls were of sufficient quality to permit spectral analysis, i.e., they were not disturbed by background noise such as bird song or the roars of additional lions. Nine of the 33 recordings were missing

some or all of the introductory moans, but the middle part as well as the terminating sequence were still available. Although we included these calls in the spectral analysis, they could not be included in the temporal analysis.

The temporal analysis was conducted using the program Avisoft SASLab Pro 3.92. The start and end of each unit were visually identified and marked. Using these marks, the program automatically calculates various temporal variables. In the complete recordings, we measured the total call duration, number of call units, and average unit duration. Data were stored into a log file and later transferred to a spreadsheet for further analysis.

For spectral analysis we chose the two call units with the highest amplitude from the full-throated roars. This selection was done because differences in the call structure should especially be reflected in those pronounced roar units. Since most of the energy is located in the lower frequencies, by reducing the sampling frequency to 5000 Hz (corresponding to a frequency range of 2500 Hz) we concentrated our analysis to this most interesting area. Calls were down-sampled using the program Avisoft SASLab Pro 3.92. We then extracted the source- (fundamental frequency) and filter- (formant) related acoustic features using PRAAT 4.0.41 (http://www.praat.org) and SpeechStation2 (Sensimetrics, Somerville, MA). To calculate the fundamental frequency, PRAAT uses an autocorrelation method described by Boersma (1993). Time step in this analysis was 100 ms. In order to increase the accuracy of the output results by limiting the number of "octave jumps," we specified the frequency range in which the fundamental frequency was predicted using the pitch settings command. The forecast of the fundamental frequency ranged between 100 and 350 Hz. The limits of this range were determined by visually inspecting the calls. Since fundamental frequency varies within a call unit, we calculated its minimum, maximum, and mean value. In order to determine formant frequencies we conducted a linear predictive coding (LPC) analysis using SpeechStation2 (Sensimetrics, Somerville, MA). LPC analysis is based on assumptions about the source characteristic, which was extensively studied in humans (e.g., Fant, 1960; Liebermann and Blumstein, 1988). While conducting the LPC analysis our study, and in fact all other formant determining studies on animals (e.g., nonhuman primates: Owren *et al.*, 1997; Rendall, 2003; Rendall *et al.*, 2004; dogs: Riede and Fitch, 1999; red deer: Fitch and Reby, 2001; Reby and McComb, 2003), assumed that the source characteristics of humans and the species under examination are not fundamentally different. To our knowledge, no study exists examining the source and filter characteristics and its interaction in lions. We checked the proposed formant frequencies by superimposing them on a corresponding 512-point fast Fourier transformation (FFT) of the same time slice and found that the formants identified were effectively equivalent to the fundamental frequency and the harmonics. Therefore, the LPC did not provide additional information and we refrained from a further evaluation of the formant frequencies. In addition, we carried out a fast Fourier transformation (1024-pt FFT, time step: 5 ms, frequency range: 2500 Hz, frequency resolution: 4.9 Hz) using Avisoft SASLab Pro 3.92. We submitted the resulting frequency time spectra to the custom software program LMA 8.4 that extracts several acoustic parameters from the signal (Hammerschmidt, 1990). In order to describe additional spectral features of the roar we assessed parameters describing the distribution of the amplitude in the frequency spectrum. This is done by first determining the overall amplitude for each time segment. Subsequently, we assessed the mean frequency at which the distribution of the amplitude in the frequency spectrum reaches 50% (DFA2mean) of the total distribution. Second, we calculated a parameter that describes the location of the second dominant frequency band (DFB2mean). The dominant frequency bands are characterized by amplitudes that exceed a given threshold in a consecutive number of frequency bins. Note that the number of DFBs count from the lowest frequency up; the first DFB is not necessary the DFB with the highest amplitude. Additionally, we determined the location of the mean peak frequency (PFmean), the frequency with the highest amplitude in a certain time segment. A description of the algorithms is given in Schrader and Hammerschmidt (1997). A summary of calculated acoustic features can be found in Table I. For a schematic representation of DFA, DFB, and PF, see Fig. 2.

TABLE I. Calculated acoustic variables. Variables marked with "*" were used for statistical analysis.

Acoustic variable	Unit	Description
call duration*	s	time from beginning to end of call
unit #*		number of call units
unit duration*	s	average unit duration of all units in a complete call
F0min*	Hz	minimal fundamental frequency
F0mean*		mean fundamental frequency
F0max*		maximal fundamental frequency
F1	Hz	first formant
F2	Hz	second formant
DF*	Hz	distance between the first and second formant
DFA2 mean*	Hz	frequency at which the amplitude distribution reaches the 2nd quartile, mean across time segments
DFB2mean*	Hz	Frequency of the second dominant frequency band
PF mean*	Hz	mean of the frequencies with the highest amplitude across all time segments

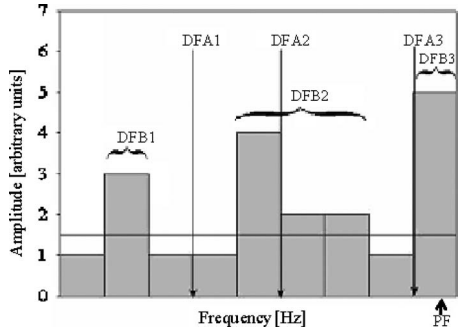

FIG. 2. Schematic representation of variables determined using LMA 8.4 (Hammerschmidt, 1990). DFA: frequency at which the amplitude distribution in the frequency spectrum reaches 25% (DFA1), 50% (DFA2), or 75% (DFA3) of the total value. DFB: frequency of the dominant frequency bands (here: DFB1, DFB2, DFB3) characterized by amplitudes exceeding a given threshold (in this example: 1.5 dB). PF: frequency of the highest amplitude.

D. Statistical analysis

Temporal and spectral parameters of each analyzed call were averaged within each subject. With the exception of the predictor variables chest circumference, mane length, and mane color, all data were normally distributed (normal distribution was determined by visually inspecting histograms and Q-Q Plots). To test whether or not acoustic features vary with sex, we conducted a univariate general linear model using sex as fixed factor. To investigate if physical properties of males (chest circumference, mane length, mane color) influence acoustic features, we carried out a univariate analysis using physiological measurements as covariates. The univariate mode was used to avoid problems with multicollinearity of highly correlating variables ($r>0.7$). Because of missing values we had to perform the univariate analysis separately for each predictor variable. Subsequently we tested for an overall statistical effect using Fisher's omnibus procedure (Quinn and Keough, 2002). Due to differential predictions, we conducted this correction separately for the influence of sex, chest circumference, mane length, and mane color. To test the statistical power of our results a *post hoc* power analysis (G-Power 2.0f, http://www.psycho.uni-duesseldorf.de/aap/projects/gpower) was conducted. Considering all available individuals, an α error of 0.05, and an effect size of 0.4 the probability of detecting a given effect was 0.46 (critical $F_{(1,22)}=4.3$, $\lambda=3.84$); in other words, our analysis had a relatively low power of detecting significant effects, the implications of which are considered in Sec. IV.

III. RESULTS

Males had a significantly larger chest circumference than females (mean±SD males: 122.12±4.8 cm, females: 103.4±5.9 cm; Mann-Whitney *U*-Test $U=0$, $N_1=13$, $N_2=5$, $P<0.001$). The age when recordings were taken did not differ significantly between the sexes (mean±SD males: 7.8±2.0 years, females: 7.7±2.8 years; $U=50$, $N_1=6$, $N_2=18$, n.s.). Male mane length averaged 1.3±0.18 (units), and the color 1.24±0.23 (units). None of the anatomical measurements correlated with one another, and neither did any of these variables correlate with age (mane length versus color, Spearman's correlation coefficient $r_S=0.259$, $P=0.394$, $N=13$; all other analyses $r_S<0.5$, all $P>0.2$). An overview of physical features of all individuals is given in Table II.

The average (mean) call duration of lion calls available for analysis was 39 s (SD=17.4), with the longest (95.7 s) and shortest (23 s) call given by a male. The maximum number of call units was 49 and was uttered by a male. On average, call units lasted 0.67 s (SD=0.21). The fundamental frequency in males was on average (mean) 194.55 Hz (SD=26.3) and in females 206.57 Hz (SD=28.67). The first formant was located at 204.9 Hz (SD=35.2) in males and 222.3 Hz (SD=32.5) in females, while the second formant was located at 444.7 (SD=51.7) in males and 500.5 Hz (SD=66.2) in females, respectively.

The Fisher's omnibus test revealed an overall effect of sex ($\chi^2=38.8$, df=18, $p=0.003$) on the acoustic structure of roars. Following this effect, the univariate analyses showed significant differences between the sexes for the mean frequency of the second amplitude quartile (DFA2mean), the mean frequency of the second dominant frequency band (DFB2mean), as well as for the minimum fundamental frequency (F0min; see Table III). Males produced lower values than females in all three acoustic features. However, the explained variance was quite low with a corrected R^2 of 0.277 (DFA2mean), 0.262 (DFB2mean), and 0.213 (F0min). All

TABLE II. Overview of physical variables: m=male, f=female.

ID	Sex	Chest circumference (Hz)	Age (year)	Mane length	Mane color
BC4	m	127	11.4	1.46	1.28
CA	m		9.6		
CK	m	121	9.4	1.37	1.58
JO	m	121	6.4	1.54	1.24
M10	m	126	5.8	1.01	1.01
M14	m	126	5.8	1.03	1.19
NO	m	120	9.8		
PL	m	123	10.6		
PN	m	117	7.4	1.46	1.18
PS	m	116	10.3		
SN	m	114	7.5	1.36	1.55
TW	m	120	8.8		
CL5	m	129	5.6	1.50	1.44
OL	m		7.9	1.50	1.16
ME	m	128	6.5	1.38	1.20
VD	m		7.2	1.25	1.26
DO	m		6.5	1.25	1.38
WN	m		4.4	1.08	0.71
G06	f		5.4		
G07	f	102	5.5		
SB	f	113	4.5		
SMC	f	104	10.9		
SY	f	98	10.1		
WO	f	100	9.8		

TABLE III. Results of univariate analyses displaying sex differences in acoustic variable minimal fundamental frequency (F0min), mean fundamental frequency (F0mean), maximal fundamental frequency (F0max), formant dispersion (DF), call duration (call dur), number of call units (unit #), average unit duration (unit dur), mean frequency of the second amplitude quartile (DFA2mean), frequency of the second dominant frequency band (DFB2mean), and peak frequency (PFmean). *F* values, degrees of freedom, and *P* values are displayed. The Fisher's omnibus test revealed an overall significant effect ($\chi^2=38.8$, df=18, $p=0.003$). The column "prediction" indicates whether the predictions are met, with males producing lower spectral and longer temporal acoustic values than females. A "+" indicates "yes" predictions are met, while a "–" indicates "no" the relationship is contrary to the predictions.

Fixed factor	Dependent variable	*F*	Hypothesis df	Error df	*P*	*N*	Prediction
Sex	F0min	6.684	1	20	0.018	22	+
	F0mean	0.869	1	20	0.362	22	+
	F0max	0.095	1	20	0.761	22	+
	call dur	1.280	1	17	0.274	19	+
	unit #	0.040	1	17	0.844	19	+
	unit dur	0.58	1	17	0.457	19	+
	DFA2mean	9.044	1	20	0.007	22	+
	DFB2mean	8.473	1	20	0.009	22	+
	PFmean	2.752	1	20	0.113	22	+

TABLE IV. Results of the univariate analyses of chest circumference, mane length, and mane color on acoustic features (legend as in Table III). The Fisher's omnibus test for chest circumference: $\chi^2=33.6$, df=18, $p=0.01$; mane length: $\chi^2=25.28$, df=18, $p=0.1$; male color: $\chi^2=26.7$, df=18, $p=0.08$. The column "direction/prediction" indicates whether the acoustic variable under examination increases (↑), decrease (↓), or does not show any trend (—) with increasing size, mane length or coloration, respectively. A '+' indicates that the predictions are met, while '–' indicates that predictions are not fulfilled.

Covariate	Dependent variable	F	Hypothesis df	Error df	P	N	Direction/prediction
Chest circumference	F0min	2.944	1	10	0.153	12	↓/+
	F0mean	2.839	1	10	0.123	12	↓/+
	F0max	0.157	1	10	0.700	12	—
	call dur	0.669	1	7	0.440	9	↓/–
	unit #	1.136	1	7	0.322	9	↓/–
	unit dur	1.151	1	7	0.319	9	↓/–
	DFA2mean	4.032	1	10	0.072	12	↓/+
	DFB2mean	11.158	1	10	0.007	12	↓/+
	PFmean	8.135	1	10	0.017	12	↓/+
Mane length	F0min	0.173	1	9	0.688	11	—
	F0mean	0.005	1	9	0.948	11	—
	F0max	4.128	1	9	0.073	11	↓/+
	call dur	6.13	1	6	0.048	8	↓/–
	unit #	2.499	1	6	0.165	8	↓/–
	unit dur	6.244	1	6	0.047	8	↓/–
	DFA2mean	0.704	1	9	0.423	11	↓/+
	DFB2mean	0.004	1	9	0.951	11	—
	PFmean	0.612	1	9	0.454	11	↓/+
Mane color	F0min	5.124	1	9	0.050	11	↑/–
	F0mean	5.951	1	9	0.037	11	↑/–
	F0max	0.732	1	9	0.414	11	↑/–
	call dur	0.094	1	6	0.769	8	—
	unit #	1.508	1	6	0.265	8	↓/–
	unit dur	1.580	1	6	0.255	8	↑/+
	DFA2mean	2.252	1	9	0.168	11	↑/–
	DFB2mean	0.529	1	9	0.485	11	↑/–
	PFmean	0.520	1	9	0.489	11	↑/–

other spectral variables showed a trend in the predicted direction (Binomial test: $p<0.05$). When we controlled for body size (chest circumference), no differences between the sexes remained ($p>0.2$).

In addition, we examined whether or not features that might be related to male status varied with certain aspects of their vocalizations. The corresponding Fisher's omnibus effect test revealed that chest circumference ($\chi^2=33.6$, df=18, $p=0.014$) but not mane color ($\chi^2=26.7$, df=18, $p=0.08$) and mane length ($\chi^2=25.28$, df=18, $p=0.12$) were related to roar structure (see Table IV). Smaller males produce roars with a higher frequency of the second dominant frequency band (DFB2mean) and a higher peak frequency ($p<0.02$), and, again, the remaining spectral variables showed a relation with size in the predicted direction. The picture was less clear for mane length and mane color, where some of the trends were in the predicted and some in the opposite direction, supporting the notion that there is a poor correlation between these measures of male status and roar structure.

IV. DISCUSSION

Our analysis revealed significant differences in the structure of male and female lion roars, which, however, could entirely be explained by differences in body size. The acoustic features of male roars neither varied with mane color nor with mane length. Both mane color and mane length are signals of male status and have been characterized as costly signals, because larger manes and darker hair increase the surface temperature and decrease the rates of heat transfer, which can harm sperm production (West and Packer, 2002). Moreover, previous analyses revealed a correlation between mane length and color with age and testosterone—another costly trait (West and Packer, 2002). Thus, male lions have apparently been subjected to intense sexual selection. Somewhat surprisingly, it seems that sexual selection has not affected the structure of their calls, as the call structure was neither related to signs of male condition nor did they exhibit pronounced differences between the sexes. Notably, the duration of the overall call did not correlate with any of the variables that have been implied in signifying male status; in addition call duration also failed to exhibit significant differences between the sexes. In contrast, high ranking male baboons produce longer bouts of calls than lower ranking baboons (Kitchen *et al.*, 2003). Note that among adult baboons, rank is not related to size. Thus, acoustic variation related to condition is not simply an indicator of subject size.

In terms of the acoustic features, we found that fundamental frequency, the frequency of the second amplitude quartile (DFA2mean) and the second dominant frequency band (DFB2mean) varied between the sexes and thus with the size of the caller. This is in line with other studies indicating that fundamental frequency can be used to assess size differences (e.g., Fischer *et al.*, 2001; Hammerschmidt *et al.*, 2000; Hauser, 1993; Pfefferle and Fischer, 2006). Variation in acoustic structure is salient to listeners: a previous study showed that female lions become agitated, retreating with their cubs (if those reached 4.5 months of age) when presented with roars of unfamiliar males. However, movement towards the loudspeaker was observed after playbacks of unfamiliar female roars. This response difference indicates that female lions are able to identify the sex of the stranger (McComb *et al.*, 1993). Furthermore, while females with cubs remained relaxed on hearing roars from resident males, they immediately become agitated on hearing unfamiliar males, i.e., females with cubs more often retreated with or showed behavior related to cub defense (McComb *et al.*, 1993). This discrimination ability could be mediated by knowledge of the individual call characteristics of pride members.

Within the category of adult males, we found significant differences between peak frequency (PF) and the frequency of the second dominant frequency band (DFB2mean), suggesting information about body size is encoded in the calls and potentially available to listeners. Analysis concerning the relationship between fundamental frequency and body size revealed no correlation. However, the P values were rather low (0.15 and 0.12, respectively). In light of the low power, it might therefore be possible that a larger data set would indeed reveal a significant correlation between fundamental frequency and body size.

The fact that female and male roars differ only slightly in terms of their spectral structure, but not fundamentally in terms of their overall structure, raises the question of the primary function of these calls. Possibly, the structure of roars has been selected to effectively advertise territorial boundaries. This hypothesis is supported by the fact that both male and female lions are territorial and use roars to advertise and defend their territory (McComb *et al.*, 1994). Thus, unlike in baboons where only males produce long distance two-syllable calls ("wahoos") that serve to advertise a male's fighting ability and stamina (Fischer *et al.*, 2004; Kitchen *et al.*, 2003), the operative selection pressure on lion roaring might have been the same for both sexes. Interestingly, Grinnell and McComb (2001) found that resident males remained silent outside of their territories even when presented with playbacks of unfamiliar males roaring, and nomadic males started roaring only when they took over a pride (Grinnell and McComb, 2001), supporting the view that the primary function of roars is the advertisement and defense of the territory.

Differences in response to male and female calls could be mediated by attending to features related to size differences. However, overall, the lack of differences between male and female lion roars is striking given the fact that, otherwise, this species exhibits signs of strong sexual selection.

ACKNOWLEDGMENTS

We would like to thank Kurt Hammerschmidt for valuable discussion and for kindly making his sound analysis program LMA available.

Boersma, P. (**1993**). "Accurate Short-Term Analysis of the fundamental Frequency and the Harmonics-To-Noise-Ratio of a Sampled Sound," Proceedings of the Institute of Phonetic Science (IFA) **17**, 97–110.

Clutton-Brock, T. H., and Albon, S. D. (**1979**). "The roaring of red deer and the evolution of honest advertisement," Behaviour **69**, 145–170.

Cynx, J., and Gell, C. (**2004**). "Social meditation of vocal amplitude in a songbird, *Taeniopygia guttata*," Anim. Behav. **67**, 451–455.

Dallmann, R., and Geissmann, T. (**2001**). "Different levels of variability in the female song of wild silvery gibbons (*Hylobates moloch*)," Behaviour **138**, 629–648.

Davies, N. B., and Halliday, T. R. (**1978**). "Deep croaks and fighting assessment in toads *Bufo bufo*," Nature (London) **274**, 683–685.

Fant, G. (**1960**). *Acoustic Theory of Speech Production* (Mouton, The Hague).

Fischer, J., Hammerschmidt, K., Cheney, D. L., and Seyfarth, R. M. (**2001**). "Acoustic features of female chacma baboon barks," Ethology **107**, 33–54.

Fischer, J., Kitchen, D. M., Seyfarth, R. M., and Cheney, D. L. (**2004**). "Baboon loud calls advertise male quality: acoustic features and their relation to rank, age, and exhaustion," Behav. Ecol. Sociobiol. **56**, 140–148.

Fitch, W. T., and Reby, D. (**2001**). "The descended larynx is not uniquely human," Proc. R. Soc. London, Ser. B **268**, 1669–1675.

Frommolt, K. H., Goltsman, M. E., and MacDonald, D. W. (**2003**). "Barking foxes, Alopex lagopus: field experiments in individual recognition in a territorial mammal," Anim. Behav. **65**, 509–518.

Funston, P. J. (**1999**). "Predator-prey relationships between lions and large ungulates in the Krüger National Park," Ph.D. thesis, University of Pretoria.

Grafen, A. (**1990**). "Biological signals as handicaps," J. Theor. Biol. **144**, 475–546.

Grinnell, J., and McComb, K. (**1996**). "Maternal grouping as a defence against potentially infanticidal males: evidence from field playback experiments on African lions," Behav. Ecol. **7**, 55–59.

Grinnell, J., and McComb, K. (**2001**). "Roaring and social communication in African lions: the limitations imposed by listeners," Anim. Behav. **62**, 93–98.

Grinnell, J., Packer, C., and Pusey, A. E. (**1995**). "Cooperation in male lions: kinship, reciprocity or mutualism?" Anim. Behav. **49**, 95–105.

Hammerschmidt, K. (**1990**). "Individuelle Lautmuster bei Berberaffen (*Macaca sylvanus*): Ein Ansatz zum Verständnis ihrer vokalen Komunikation" ("Individual vocal pattern of Barbary macaques (*Macaca sylvanus*): An approach towards the understanding of their vocal communication"), Ph.D. thesis, FU Berlin, Berlin, Germany.

Hammerschmidt, K., Newman, J. D., Champoux, M., and Suomi, S. J. (**2000**). "Changes in rhesus macaque 'coo' vocalizations during early development," Ethology **106**, 873–886.

Hauser, M. D. (**1993**). "The evolution of nonhuman primate vocalizations: Effects of phylogeny, body weight, and social context," Am. Nat. **142**, 528–542.

Kitchen, D. M., Fischer, J., Cheney, D. L., and Seyfarth, R. M. (**2003**). "Loud calls as indicators of dominance in the male baboon (*Papio cynocephalus ursinus*)," Behav. Ecol. Sociobiol. **53**, 374–384.

Kobayasi, K. I., and Okanoya, K. (**2003**). "Sex differences in amplitude regulation of distance calls in Bengalese finches, *Lunchula striata var. domestica*," Anim. Biol. **53**, 173–182.

Langbauer, W. R., Payne, K. B., Charif, R. A., Rapaport, L., and Osborn, F. (**1991**). "African elephants respond to distant playbacks of low-frequency conspecific calls," J. Exp. Biol. **157**, 35–46.

Liebermann, P., and Blumstein, S. E. (**1988**). *Speech Physiology, Speech Perception, and Acoustic Phonetics* (Cambridge U. P., Cambridge, England).

Maynard Smith, J. (**1994**). "Must reliable signals always be costly?" Anim. Behav. **47**, 1115–1120.

McComb, K., Packer, C., and Pusey, A. (**1994**). "Roaring and numerical assessment in contests between groups of female lions, *Panthera leo*," Anim. Behav. **47**, 379–387.

McComb, K., Pusey, A., and Packer, C. (**1993**). "Female lions can identify potentially infanticidal males from their roars," Proc. R. Soc. London, Ser. B **252**, 59–64.

McComb, K., Reby, D., Baker, L., Moss, C., and Sayialel, S. (**2003**). "Long-distance communication and acoustic cues to social identity in African elephants," Anim. Behav. **65**, 317–329.
Mitani, J. C., and Nishida, T. (**1993**). "Contexts and social correlates of long-distance calling by chimpanzees," Anim. Behav. **45**, 735–746.
Mitani, J. C. (**1985**). "Sexual selection and adult male orangutan loud calls," Anim. Behav. **33**, 271–283.
Mitani, J. C. (**1988**). "Male gibbon (Hylobates agilis) singing behaviour: natural history, song variations and function," Ethology **79**, 177–194.
Mitani, J. C. (**1994**). "Ethological studies of chimpanzee vocal behaviour," in *Chimpanzee cultures*, edited by R. W. Wrangham, W. C. McGrew, F. B. M. de Waal, and P. G. Heltne (Harvard U. P., Cambridge, MA), pp. 241–254.
Notman, H., and Rendall, D. (**2005**). "Contextual variation in chimpanzee pant hoots and its implications for referential communication," Anim. Behav. **70**, 177–190.
Owren, M. J., Seyfarth, R. M., and Cheney, D. L. (**1997**). "The acoustic features of vowel-like grunt calls in chacma baboons (*Papio cyncephalus ursinus*): Implications for production processes and functions," J. Acoust. Soc. Am. **101**, 2951–2963.
Packer, C., Herbst, L., Pusey, A. E., Bygott, J. D., Hanby, J. P., Cairns, S. J., and Borgerhoff-Mulder, M. (**1988**). "Reproductive success of lions," in *Reproductive Success*, edited by T. H. Clutton-Brock (Univ. of Chicago, Chicago), pp. 363–383.
Pfefferle, D., and Fischer, J. (**2006**). "Sounds and size: identification of acoustic variables that reflect body size in hamadryas baboons, *Papio hamadryas*," Anim. Behav. **72**, 43–51.
Poole, J. H., Payne, K., Langbauer, W. R., and Moss, C. (**1988**). "The social contexts of some very low frequency calls of African elephants," Behav. Ecol. Sociobiol. **22**, 385–392.
Quinn, G. P., and Keough, M. J. (**2002**). *Experimental Designs and Data Analysis for Biologists* (Cambridge U. P., Cambridge, England).
Reby, D., and McComb, K. (**2003**). "Anatomical constraints generate honesty: acoustic cues to age and weight in the roars of red deer stags," Anim. Behav. **65**, 519–530.
Rendall, D. (**2003**). "Acoustic correlates of caller identity and affect intensity in the vowel-like grunt vocalization of baboons," J. Acoust. Soc. Am. **113**, 3390–3402.
Rendall, D., Owren, M. J., Weerts, E., and Hienz, R. D. (**2004**). "Sex differences in the acoustic structure of vowel-like grunt vocalizations in baboons and their perceptual discrimination by baboon listeners," J. Acoust. Soc. Am. **115**, 411–421.
Riede, T., and Fitch, T. W. (**1999**). "Vocal Tract Length and Acoustics of Vocalization in the Domestic Dog (*Canis familiaris*)," J. Exp. Biol. **202**, 2859–2867.
Schaller, G. B. (**1972**). *The Serengeti Lion* (Univ. of Chicago, Chicago).
Schrader, L., and Hammerschmidt, K. (**1997**). "Computer-Aided Analysis of Acoustic Parameters in Animal Vocalisations: A Multi-Parametric Approach," Bioacoustics International Journal of Animal Sound and its Recording **7**, 247–265.
Silk, J. B., Kaldor, E., and Boyd, R. (**2000**). "Cheap talk when interests conflict," Anim. Behav. **59**, 423–432.
Vehrencamp, S. L. (**2000**). "Handicap, index, and conventional elements of bird song," in *Animals Signals: Signaling and Signal Design in Animal Communication*, edited by Y. Espmark, T. Amundsen, and G. Rosenquist (Trondheim, Tapir), pp. 277–300.
West, P. M., and Packer, C. (**2002**). "Sexual Selection, Temperature, and the Lion's Mane," Science **297**, 1339–1343.
Wilson, M. L., Hauser, M. D., and Wrangham, R. W. (**2001**). "Does participation in intergroup conflict depend on numerical assessment, range location, or rank for wild chimpanzees?" Anim. Behav. **61**, 1203–1216.
Zahavi, A. (**1975**). "Mate Selection - A Selection for Handicap," J. Theor. Biol. **53**, 205–214.

Modeling the detection range of fish by echolocating bottlenose dolphins and harbor porpoises

Whitlow W. L. Au[a)]
Marine Mammal Research Program, Hawaii Institute of Marine Biology, University of Hawaii, Kailua, Hawaii 96734

Kelly J. Benoit-Bird
College of Atmospheric and Oceanic Sciences, Oregon State University,

Ronald A. Kastelein
Sea Mammal Research Company, Harderwijk, The Netherlands

(Received 25 October 2006; revised 1 March 2007; accepted 29 March 2007)

The target strength as a function of aspect angle were measured for four species of fish using dolphin-like and porpoise-like echolocation signals. The polar diagram of target strength values measured from an energy flux density perspective showed considerably less fluctuation with azimuth than would a pure tone pulse. Using detection range data obtained from dolphin and porpoise echolocation experiments, the detection ranges for the Atlantic cod by echolocating dolphins and porpoises were calculated for three aspect angles of the cod. Maximum detection ranges occurred when the fish was broadside to the odontocete and minimum detection ranges occurred when the cod was in the tail aspect. Maximum and minimum detection ranges for the bottlenose dolphin in a noise-limited environment was calculated to be 93 and 70 m, respectively. In a quiet environment, maximum and minimum detection ranges for the bottlenose dolphin were calculated to be 173 and 107 m, respectively. The detection ranges for the harbor porpoise in a quiet environment were calculated to be between 15 and 27 m. The primary reason for the large differences in detection ranges between both species was attributed to the 36 dB higher source level of the bottlenose dolphin echolocation signals. © *2007 Acoustical Society of America.*
[DOI: 10.1121/1.2734487]

PACS number(s): 43.80.Ka, 43.80.Jz, 43.80.Ev, 43.80.Nd [JAS] Pages: 3954–3962

I. INTRODUCTION

Target detection experiments with echolocating dolphins and porpoises have been conducted for over three decades using various types of targets. The first set of target detection experiments was conducted in open waters of Kaneohe Bay, Oahu, HI, with bottlenose dolphins (*Tursiops truncatus*) by Murchison (1980) using a 7.62-cm-diam water-filled stainless steel sphere and a 2.54-cm solid steel sphere. The 50% correct detection threshold was found to be 74 m for the 2.54-cm sphere (target strength of −42 dB) and 79 m for the 7.62-cm sphere (target strength of −28 dB). The detection range for the 7.62-cm sphere measured by Murchison (1980) was negatively affected by the presence of an underwater shelf in the vicinity of the measured threshold range that was a source of bottom reverberation which masked the target echoes (Au and Snyder, 1980). Au and Snyder (1980) remeasured the threshold detection range with one of the bottlenose dolphins used by Murchison (1980), but in a different part of the bay and obtained a threshold range of 113 m. Thomas and Turl (1990) also used a 7.62-cm-diam water-filled stainless steel sphere and the same experimental range as Au and Snyder (1980), and measured a target detection threshold range of 119 m for a false killer whale (*Pseudorca crassidens*). All of the animals in the Kaneohe Bay experiments were masked by snapping shrimp sounds (Au and Snyder, 1980). Kastelein *et al.* (1999) measured the threshold detection range of echolocating harbor porpoise (*Phocoena phocoena*) to be approximately 26 m for the same 7.62-cm sphere used by the investigators in Kaneohe Bay, and 16 m for a 5.08-cm sphere. One of the most important differences in Kastelein *et al.* (1999) experiment and the experiments in Kaneohe Bay was the absence of masking noise at the Neeltje Jans facility in The Netherlands.

The target detection experiments with captive odontocetes have been useful in understanding the basic capabilities of the echolocation systems of these animals. However, there has not been much effort transferring the basic understanding of detection ranges to how well odontocetes can detect fish in their natural habitat. In recent years, there have been some modeling studies of echolocation detection range by three species of odontocetes, *Orcinus orca* (Au *et al.*, 2004), *Pseudorca crassidens*, and *Grampus griesus* (Madsen *et al.*, 2004). Au *et al.* (2004) measured the echolocation signals of fish-eating killer whales in the waters of Vancouver Island, British Columbia, and estimated the detection ranges for a 70-cm-long Chinook salmon by echolocating killer whales to be well over 100 m under quiet conditions. Madsen *et al.* (2004) measured the echolocation signals of false killer whales and Risso's dolphin in off-shore habitat and estimated detection ranges for a 1-m-long tuna and 20- and 80-cm-long

[a)]Electronic mail: wau@hawaii.edu

 0001-4966/2007/121(6)/3954/9/$23.00 © 2007 Acoustical Society of America

squid. Madsen *et al.* (2004) estimated detection ranges that varied from 80 to 210 m. The shortcoming of both of these studies is that realistic target strength values for the prey were not used. The target strength in the Au *et al.* (2004) study was based on theoretical calculations for a narrow band signal at 50 kHz using a Kirchoff ray model (Jech and Horne, 1995; Horne and Jech, 1999). The estimate of detection ranges of Madsen *et al.* (2004) were based on target strength measurements using tonal signals and they did not take into account the aspect dependence of acoustic backscatter from the fish or squid.

One of the obstacles in modeling echolocation detection ranges for different species of fish has to do with our poor understanding of how odontocete echolocation signals reflect off different fish species. Measurements of deep-dwelling snappers using simulated dolphin echolocation signals by Benoit-Bird *et al.* (2003) and Au and Benoit-Bird (2003) indicated that the echoes were about 4.5 times longer in duration than the incident signals, suggesting a very complicated backscatter process that is not well understood. They also found that the variation in target strength based on energy with angle did not fluctuate nearly as much as with tonal sonar signals. In this study we measured the acoustic backscatter of four different species of fish that are prey of bottlenose dolphins and harbor porpoises using simulated bottlenose dolphin and harbor porpoise echolocation signals in order to estimate target detection range for these species.

II. PROCEDURE

A. Experimental geometry

The backscatter measurements were conducted in an outdoor tank of Sea Mammal Research Company, at the field station of the Netherlands National Institute for Coastal and Marine Management (RIKZ) at Jacobahaven, Zeeland, The Netherlands, in a 7 m $\times$ 4 m rectangular tank with a water depth of 2 m. The measurement geometry is depicted in Fig. 1(a) showing a rotor with a cylindrical rod supporting a monofilament net. Fish subjects were contained in a monofilament bag that was in turn attached to the center of the monofilament net which was attached to a rotor. The fish could be placed in the bag in the two different aspects depicted in Fig. 1(b). The transducer was a custom-made circular disk with the active element being a 1-3 piezo-ceramic circular disk with a diameter of 6.4 cm and a thickness of 0.64 cm. The transducer was placed 2 m from the fish and at the same depth as the fish, which was 1 m.

A monostatic echoranging system was used in which the same transducer transmitted the signals and received the echoes. The echoes were time-gated and filtered before being digitized at a sample rate of 1 MHz. A total of 1024 points were digitized per echo and stored to disk. The waveform and frequency spectra of the incident signals are shown in Fig. 2. An acoustic mirror consisting of a flat 0.63 thick aluminum plate covered with a close cell neoprene sheet was used to obtain the signals shown in Fig. 2. The dolphin-like signal had a peak frequency of 130 kHz while the porpoise-like signal had a peak frequency of 138 kHz. The duration of the dolphin-like signal was approximately 70 μs vs 270 μs for the porpoise-like signal. The bandwidth of the porpoise signal was clearly narrower than the dolphin-like signal. Both dolphin-like and porpoise-like signals were replicates of previously recorded signals.

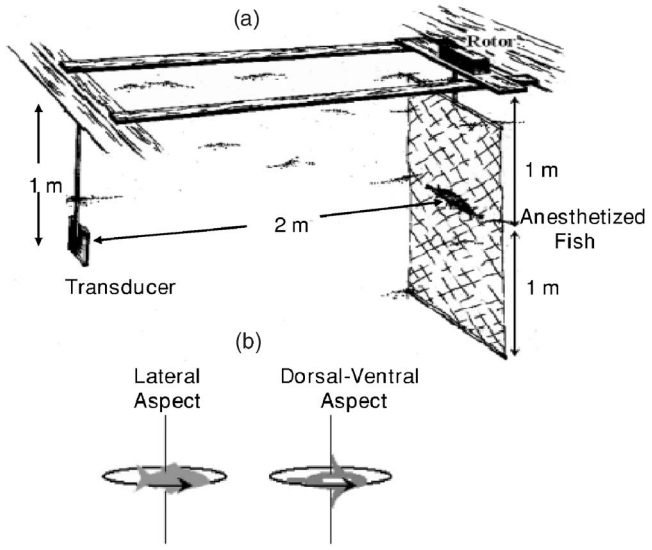

FIG. 1. (a) Fish backscatter measurement geometry showing the fish in a net bag attached to a monofilament, net supported by a rod connected to a rotor. (b) Rotational geometry of the fish.

B. Fish subjects

The species of fish used were Atlantic cod (*Gadus morhua*), grey mullet (*Chelon labrosus*), pollack (*Pollachius pollachius*), and sea bass (*Dicentrarchus labras*). Three fish of each species except for the pollack were acoustically examined. The lengths of the subjects were cod (29 to 30 cm), mullet (15–17 cm), and sea bass (14–17 cm). Only one pollack having a length of 21 cm was used. Acoustic backscatter from the Atlantic cod has been studied fairly intensely by Clay and Horne (1994) and will therefore be used as our model fish in detection range calculations. These fishes were on loan from "The Arsenaal Aquarium," Vlissingen, The Netherlands. The Animal Welfare Commission of The Netherlands stipulated that the fish must feed readily in captivity, so they had to come from aquaria though all were originally wild-caught. They were fed to satiation each day after the sessions on a diet of raw fish. Fish were returned to the aquarium following the experiment to comply with animal care regulations. Three fish per species were used to ensure that the backscatter results were consistent and repeatable. We did not expect the target strength to vary much since the lengths within a species varied very little. Each fish was anesthetized by placing it in a bath containing 1 mL of 2-phenoxy-ethanol per 10 L of seawater. Once anesthetized, the fish was enclosed in the fitted monofilament net bag to restrain its movements and the net bag was mounted to the monofilament net. Echoes from the fish were collected as a function of azimuth. The rotor incremented approximately 2.2° after each transmission and reception cycle until the fish was rotated through 360°. Most of the measurements were done with the fish in the lateral aspect having its dorsal surface aligned upwards and the ventral surface pointing down-

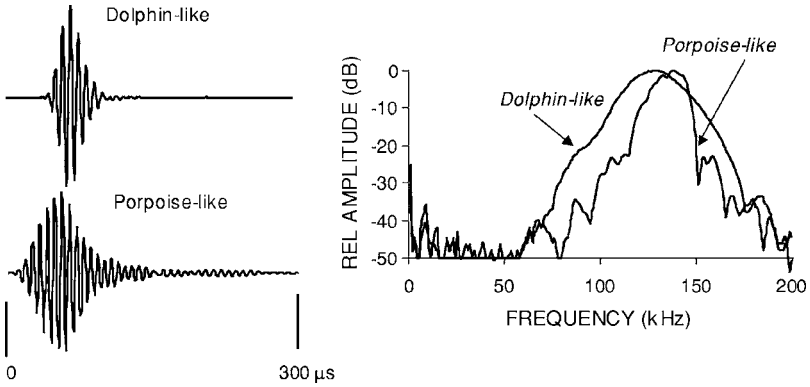

FIG. 2. Simulated bottlenose dolphin and harbor porpoise echolocation signals in the time and frequency domains.

wards although some measurements were also done in the dorsal-ventral plane [Fig. 1(b)].

III. RESULTS

A. Fish backscatter

Examples of echo waveforms obtained with both the dolphin-like and porpoise-like signals for a cod in the lateral plane are shown in Fig. 3 for three different aspect angles of the fish; broadside (90°), 135° or 45° from the broadside and tail aspects, and the tail aspects (180°). At broadside, the echo is relatively simple with a single large highlight followed by a much smaller highlight, where the major highlight is probably a reflection off the surface of the swim bladder. Highlights are local maxima within the structure of the echoes. The swimbladder of a fish is the structure having the most dominant influence on the echo intensity (Foote, 1980; Foote and Ona, 1985). As the aspect angle changes from broadside, the echo structure becomes extremely complex, with many highlights and an elongated duration much longer than that of the incident signals. The amplitude of each echo is normalized to its maximum value in Fig. 3 so that the structure of the echoes can be readily seen. Otherwise, the amplitude of the echoes at 135° and tail aspect would be at least 1/4 of what is shown. More highlights can be seen for the dolphin-like signal than the porpoise signal for the 135° and tail aspect. This is the result of the dolphin-like signal having a better range resolution capability by virtue of its broader bandwidth than the porpoise-like signal. Nevertheless, the echo structure of the porpoise-like echoes is still very complex.

Typical variations in target strength as a function of the aspect angle of a cod in the lateral plane are shown in Fig. 4. Target strengths based on both the energy in the echoes (dark line) and peak amplitude for a tonal signal (light line) are included. The target strength for a tonal signal fluctuated considerably with azimuth, having deep nulls. On the other hand, the target strength based on energy for a broadband click had considerably less fluctuation with azimuth, and did not have the deep sharp nulls that were present for the tonal signal. The tonal results were obtained by using the values of the incident and reflected signal at a frequency of 130 kHz. The difference between the maximum and minimum values

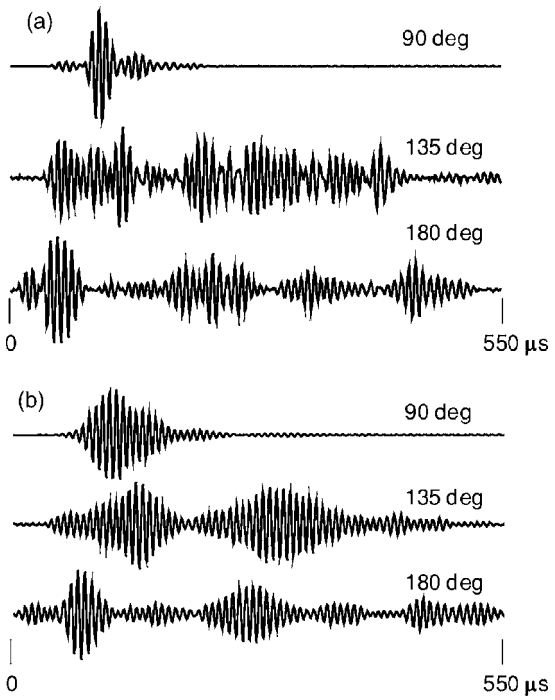

FIG. 3. Backscatter signal wave form for different aspect angles and for the two simulated echolocation signals used in this study.

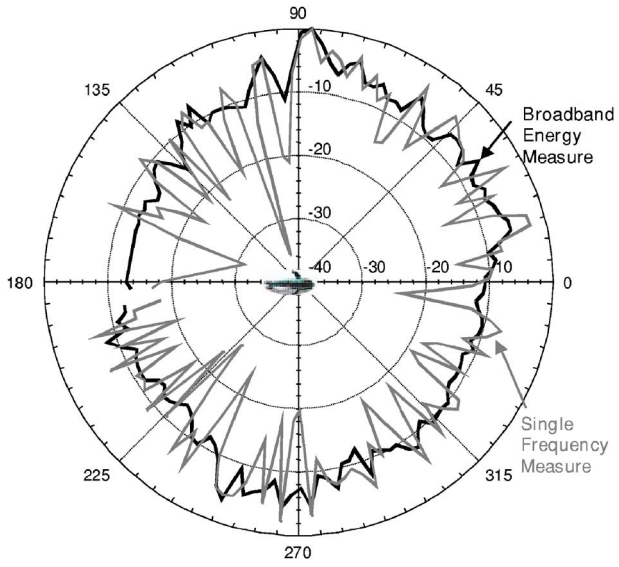

FIG. 4. (Color online) Polar diagram of the target strength determined on the basis of energy flux density of a simulated dolphin echolocation signal (black line) and the target strength based on a single frequency of 130 kHz.

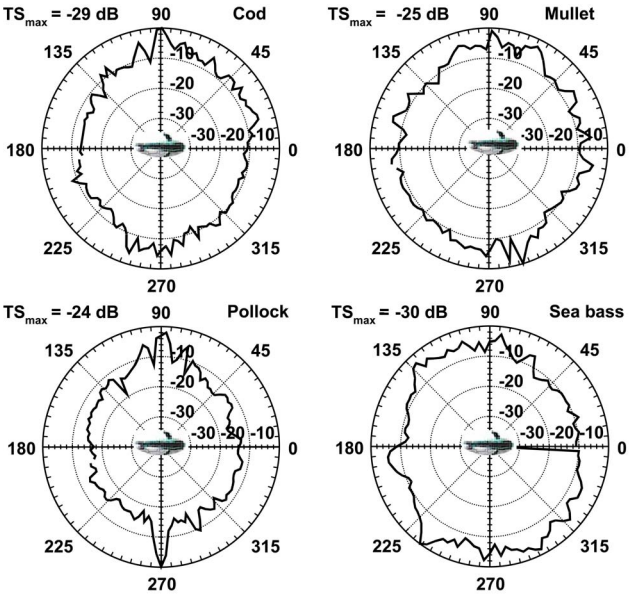

FIG. 5. (Color online) Polar diagram of the target strength in the lateral plane for the four fish species. The data were obtained with a simulated bottlenose dolphin echolocation signal.

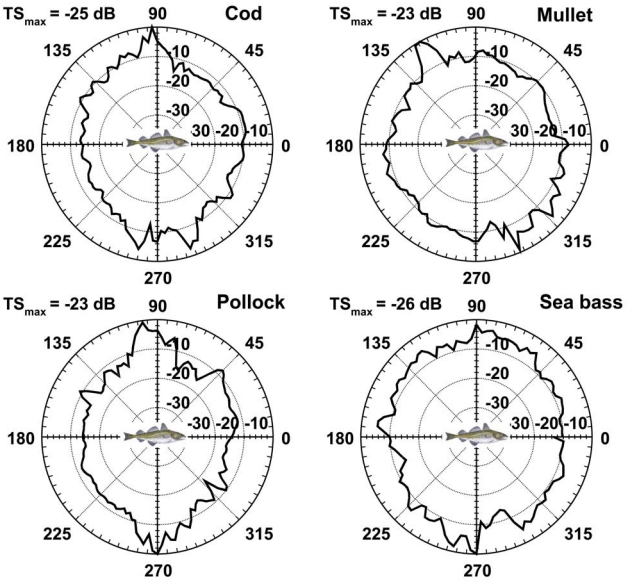

FIG. 7. (Color online) Polar diagram of the target strength in the dorsal-tilt plane for the four fish species. The data were obtained with a simulated bottlenose dolphin echolocation signal.

of the target strength based on energy was about 13 dB compared to over 30 dB for the tonal signal. These results are similar to those of Benoit-Bird *et al.* (2003), who also compared target strength versus azimuth for snappers using target strength values based on energy in broadband clicks and on the peak values of tonal signals.

The target strength of the four species of fish is shown in polar form in Fig. 5 for the dolphin-like echolocation signal and in Fig. 6 for the porpoise-like signal. The polar plots are normalized with the maximum value of the target strength indicated next to each plot. The maximum values typically occurred when the fish was at a broadside aspect (90° and 270°). The minimum values typically occurred in the tail aspect orientation. The maximum target strengths obtained with the porpoise-like signal were 1–3 dB larger in value than the values obtained using the dolphin-like signal. The polar diagrams of target strength are similar between the dolphin-like and porpoise-like echolocation signals for a given species. The pollack had the most unusual variation of target strength with azimuth, showing a major lobe at 270°. We cannot state with certainty why the pollack backscatter had this lobe, however, the probability is fairly high that the shape of the swim bladder was the major contributor to the presence of the lobe. Unfortunately, the fishes had to be returned to The Arsenaal Aquarium and were not available for x-ray measurements. There are also some minor differences in the maximum target strength values for the two types of signals and these differences were probably caused by the signals having different peak frequencies. Target strength of fish generally increases with frequency and the 9 kHz higher peak frequency of the porpoise signal may have contributed to the slightly higher target strength values for the porpoise signal.

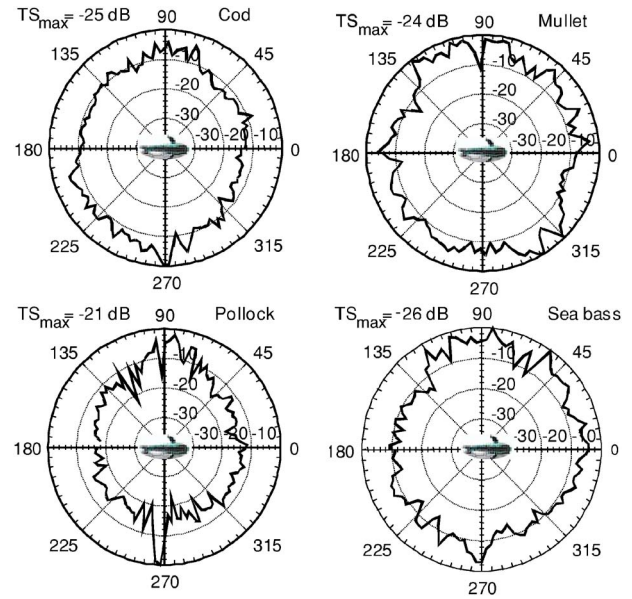

FIG. 6. (Color online) Polar diagram of the target strength in the lateral plane for the four fish species. The data were obtained with a simulated harbor porpoise echolocation signal.

The polar diagrams of the target strength in the dorsal-ventral plane for the four species of fish that were obtained with the dolphin-like echolocation signal are shown in Fig. 7. The angle of maximum reflection probably occurred when the incident signal was perpendicular to the longitudinal axis of the swimbladder (Benoit-Bird *et al.*, 2003), which in most fishes is tilted slightly. The minimum target strength occurred close to the tail and head aspects. For the tail and head aspects, the target strength with the fish rotated in the lateral plane should be the same as in the dorsal-tilt plane. Any differences were probably caused by slight misalignment of the fish when mounted to the monofilament net. The polar plots of the target strength in the dorsal-ventral plane measured with the porpoise-like signals were similar to the plots in Fig. 7 and are not shown.

B. Modeling fish detection ranges by echolocating odontocetes

1. Atlantic bottlenose dolphin

The results of Murchison (1980) using a 2.54-cm-diam solid steel sphere and the results of Au and Snyder (1980) using a 7.62-cm water-filled stainless steel sphere were used to calculate the bottlenose echolocation detection ranges searching for a cod. Kaneohe Bay has a large population of snapping shrimps which produced noise that limited the dolphins' detection capability, i.e., a noise-limited environment (Au *et al.*, 1974; Au and Snyder, 1980). In order to determine the detection ranges for a fish using the results of Murchison (1980) and Au and Snyder (1980), the noise-limited transient form of the sonar equation should be used (Urick, 1983). The transient form of the sonar equation (expressed in dB) that is applicable to a dolphin can be expressed as

$$\mathrm{DT}_E = \mathrm{SE} - 2\mathrm{TL} + \mathrm{TS}_E - (\mathrm{NL} - \mathrm{DI}), \tag{1}$$

where DT_E is the detection threshold, SE is the source energy flux density, TL is the one-way transmission loss, TS_E is the target strength based on energy, NL is the ambient noise spectral density, and DI is the receiving directivity index at the peak-frequency of the dolphin's echolocation signal. Assuming simple spherical spreading loss propagation, the one-way transmission loss can be expressed as

$$\mathrm{TL} = 20 \log R + \alpha R, \tag{2}$$

where R is range in meters and α is the sound absorption coefficient in dB/m at the peak frequency of the animal's echolocation signal. If we assume that the dolphin uses echolocation signals having similar source levels for both an artificial steel sphere and a fish, then the results obtained with the steel sphere can be used to predict the performance of a dolphin echolocating a fish. This can be done by equating Eq. (1) for a fish to the same equation, but for a sphere and using Eq. (2). Therefore, we obtain the following equation that can be used to determine the threshold detection range for a fish:

$$40 \log R + 2\alpha R = \mathrm{TS}_{E\mathrm{fish}} - \mathrm{TS}_{E\mathrm{sphere}} + 2\mathrm{TL}_{\mathrm{sphere}}. \tag{3}$$

This is a transcendental equation and does not have a closed form solution. The solution must be determined by iteration, inserting a value for R and determining if the value of the left side of the equation matches the right side. If the left side is larger then a smaller R is chosen on the next iteration until the appropriate R is determined. However, it should be noted that the 2.54-cm results of Murchison and the 7.62 cm of Au and Snyder did not agree completely when transient form of the sonar equation was applied to their results; there was approximately a 2.5-dB difference in the calculated value of the detection threshold for the range where the animal's threshold occurred. Both experiments were performed with the same animal but about 2 years apart (Au and Snyder, 1980). However, considering this time interval between both experiments, the 2.5-dB discrepancy was considered rather minor and both results were considered remarkably close for psychophysical experiments, which often have very large variations (Au, 1993).

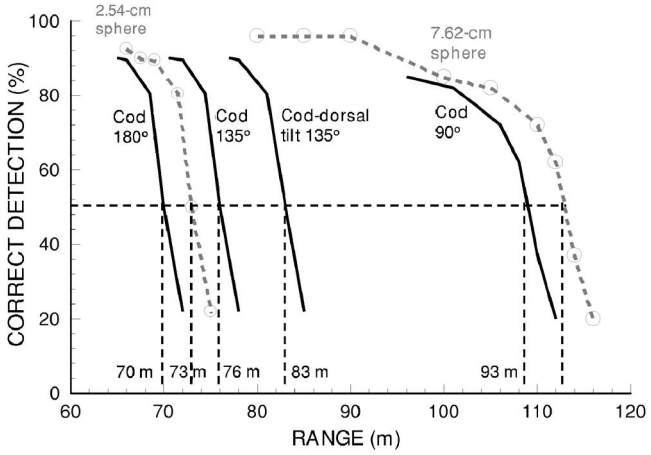

FIG. 8. Predicted correct detection performance for a bottlenose dolphin echolocating on a 30-cm-long Atlantic Cod in a noise-limited environment. The actual bottlenose dolphin performance curves with real water-filled spheres are shown by the dark gray curves. The 50% correct detection threshold ranges are shown for different aspects of the fish.

In order to estimate the detection range the backscatter results for cod at different aspect angles were used. When the fish target strength at a particular aspect angle is closer to the target strength of the 2.54-cm sphere then Murchison's results were used and when the fish target strength is closer to that of the 7.62-cm sphere then Au and Snyder's results were used. The target strength for the cod in the lateral plane at broadside (90°) was −29 dB (Fig. 5), at 135° it was approximately −41 dB, at tail aspect (180°) it was approximately −43 dB, and in the dorsal-ventral plane (Fig. 7) at 135° it was approximately −39 dB. Applying Eqs. (2) and (3) the detection performance curves for the cod were calculated and the results are shown in Fig. 8. The 50% correct detection threshold is shown for the three aspect angles of the cod in the lateral plane and for 135° in the dorsal-ventral plane. The detection threshold range is maximum at the broadside (90°) aspect with a value of 93 m and minimum at the tail aspect (180°) with a value of 70 m in a noise-limited environment.

Au *et al.* (2002) determined the nonmasked detection threshold of an Atlantic bottlenose dolphin using two broadband signals resembling the echoes from a 7.62-cm water-filled sphere. They obtained an average energy flux detection threshold of 33.1 dB re 1 $\mu\mathrm{Pa}^2$ s. In order to calculate the detection range for any target the energy flux density of the echo must be determined using

$$\mathrm{EE} = \mathrm{SE} - 2\mathrm{TL} + \mathrm{TS}_E, \tag{4}$$

where EE is the energy flux density of the echo, SE is the source energy flux density, and TL is defined by Eq. (3). Assuming an echolocating dolphin emitting a signal with an average source level of 222 dB re 1 μPa (Au *et al.* 1980) which equated to a source energy flux density of 167 dB re 1 $\mu\mathrm{Pa}^2$ s and inserting the appropriate values into Eq. (4), the threshold detection range can be expressed as

$$40 \log(R) + 2\alpha R = 133.9 + \mathrm{TS}_E. \tag{5}$$

Au *et al.* (2002) calculated the threshold range of a bottlenose dolphin searching for a 7.62-cm sphere to be approximately 178 m. We also used the shape of the performance

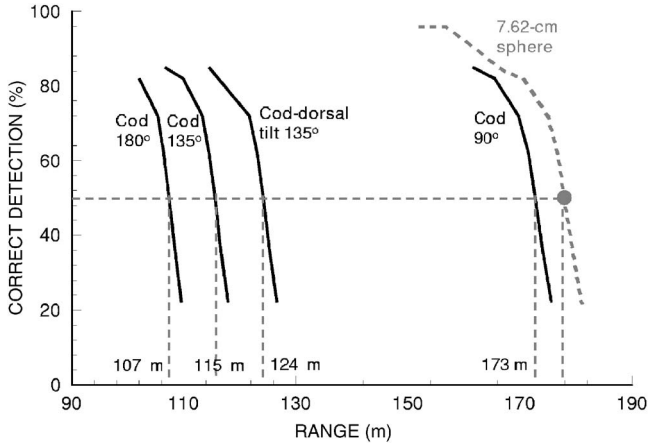

FIG. 9. Predicted correct detection performance for a harbor porpoise echolocating on a 30-cm-long Atlantic Cod. The actual harbor porpoise performance curves with real water-filled spheres are shown by the dark gray curves. The 50% correct detection threshold ranges are shown for different aspects of the fish.

curve for the 7.62-cm sphere shown in Fig. 8 (dashed gray line) to estimate a performance curve for detection of the sphere as a function of range in a nonmasking condition.

The same procedure can be used here for calculating the detection range for a single fish in a quiet environment. Using the same cod aspect angles and the corresponding target strength values, the results of this calculation are shown in Fig. 9. The largest threshold detection range of 173 m occurred when the cod is broadside to the dolphin and the lowest threshold detection range of 107 m occurred at the tail-aspect angle. These detection ranges are considerably larger in a quiet environment than in a noise-limited environment. The lowest threshold detection range in the quiet environment was larger than the highest threshold detection range in the noise-limited environment (107 m vs 93 m). The maximum threshold detection range in the quiet environment is almost double the corresponding range for the noise-limited environment (173 m vs 93 m). These results clearly demonstrate how ambient noise produced by snapping shrimp can severely limit the echolocation detection range of a dolphin.

We can generalize the threshold detection range by calculating the threshold detection range as a function of target strength. Using the threshold values and the corresponding target strength used to generate Figs. 8 and 9, the generalized threshold detection ranges that can be applied for any fish of known broadband target strength are shown in Fig. 10. A linear curve fit of the points for the quiet condition is given by

$$\text{nonmasked threshold range} = 4.75\text{TS}_E + 310.10 \text{ m}. \quad (6)$$

Similarly, for the noise-limited condition of Kaneohe Bay, the linear curve fit is given by

$$\text{noise-limited threshold range} = 1.52\text{TS}_E + 138.15 \text{ m} \quad (7)$$

with r^2 values of 1.00 for the nonmasked curve and 0.96 for the noise-masked curve.

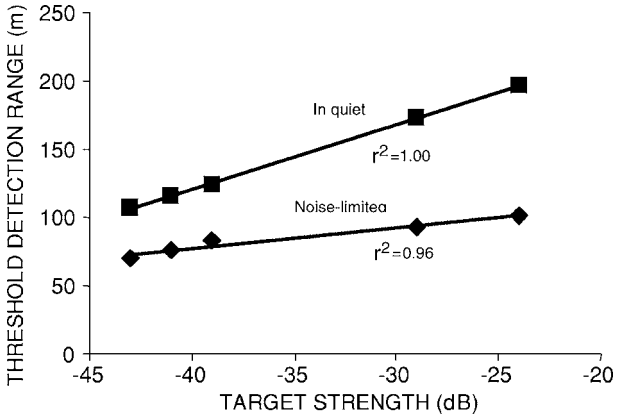

FIG. 10. Predicted echolocation detection threshold range as a function of target strength for the Atlantic bottlenose dolphin in a quiet environment and in noise masking environment where the masking noise is produced by snapping shrimps.

2. Harbor porpoise

Kastelein *et al.* (1999) used a 5.08- and a 7.62-cm-diam water-filled sphere to measure the echolocation detection capability of a harbor porpoise (*Phocoena phocoena*) in a large open pen at Neeltje Jans, The Netherlands. The 5.08-cm sphere had a target strength of −36 dB and the 7.62-cm sphere had a target strength of −26 dB. The correct detection threshold ranges were 16 and 26 m, respectively. Using Eq. (4) and assuming that the harbor porpoise used the same source level while searching for the two targets, the echo energy flux density of the echoes for both spheres at their respective threshold range agreed within 1 dB. We again used the cod as our fish of interest and the target strength values shown in Fig. 6, which are −25 dB at broadside (90°), −35 dB at 135°, and −36 dB for the tail aspect (180°). The detection performance of the harbor porpoise can be calculated with Eq. (2) and the results are shown in Fig. 11, for detection in the lateral plane. The detection threshold range is maximum at the broadside (90°) aspect with a value of 27 m and minimum at the tail-aspect (180°)

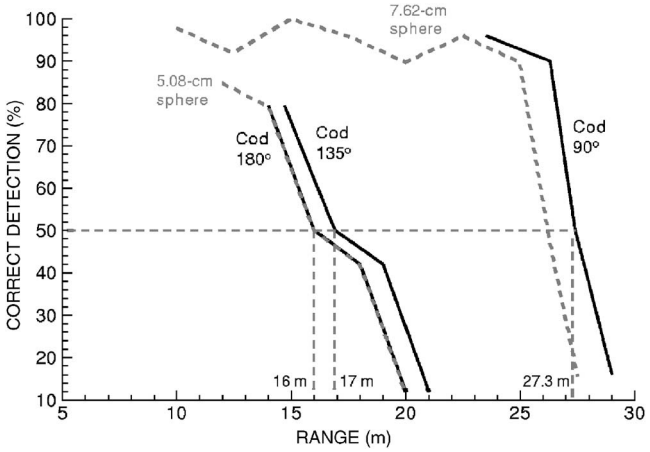

FIG. 11. Predicted correct detection performance for a harbor porpoise echolocating on a 30-cm-long Atlantic Cod. The actual harbor porpoise performance curves with real water-filled spheres are shown by the dark gray curves. The 50% correct detection threshold ranges are shown for different aspects of the fish.

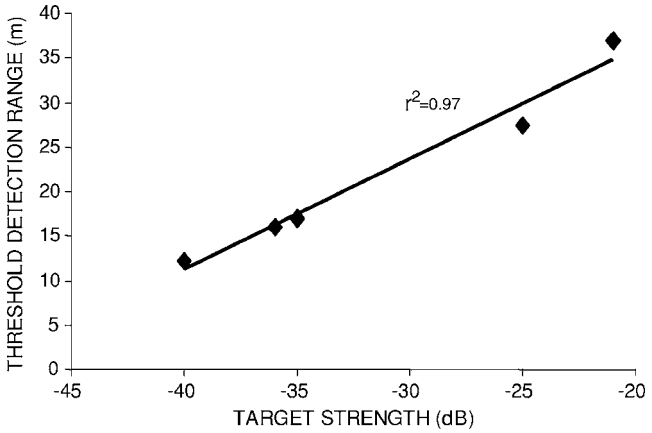

FIG. 12. Predicted echolocation detection threshold range as a function of target strength for the harbor porpoise in a quiet environment.

with a value of 16 m in a quiet environment. The target strength for the cod at tail aspect was the same as the 5.08-cm sphere so that both detection performance curves were the same.

We generalized the threshold detection range for *Phocoena phocoena* by plotting the threshold detection range as a function of the target strength. The results are shown in Fig. 12 with a linear curve fitted to the calculated values. The equation of the fitted curve is

$$\text{nonmasked threshold range} = 1.25\ \text{TS}_E + 61.10\ \text{m} \qquad (8)$$

with an r^2 value of 0.97. Equation (8) can be used in conjunction with the target strength values shown in polar form for any of the four species to determine the echolocation threshold detection range for *Phocoena phocoena* in a nonmasked environment.

IV. DISCUSSION AND CONCLUSIONS

The target strength of several species of fish was measured with simulated odontocete echolocation signals as a function of fish aspect angle, in order to estimate how far dolphins and porpoises can detect fish prey by echolocation. The results obtained in this study pertained to the detection of a single fish. This would represent the most difficult detection task a foraging odontocete would confront. If there is a cluster of fishes, the target strength of the cluster would be greater than that of the single fish. The amount of increase in target strength would depend on the orientation of the fish to one another and the spacing between them. How a greater target strength would increase the detection range of an echolocating odontocete is far from obvious. The critical issue is knowing what the integration time of the animal's auditory system that should be used in such a situation where there are echoes from more than one fish. Johnson (1968) used pure tone signals of different duration to measure the integration time of a bottlenose dolphin. The integration time varied with frequency and was greater than 5 ms for a 100-kHz signal. Au *et al.* (1988) used a phantom echo system and broadband replica of the dolphin's emitted signal and measured an integration time of 264 μs, which is considerably shorter than the integration time determined with narrow band signals. However, the results of Au *et al.* (1988) may not be applicable here since their phantom echoes had gaps in them, i.e., two replicas of the outgoing signal separated by a silent period was played back to the animal. The waveform of an echo from a cluster of fishes would not have gaps in it but would be similar to the wave forms shown in Fig. 3 for the 135° and 180° aspects, only longer.

The minimum detection range of 70 m for a single cod in the tail aspect in a noise-masked environment seems to be large enough that a bottlenose dolphin would need to expend energy to close the separation distance and not alert the fish by its swimming motion. It would seem that in most cases a dolphin would definitely be more interested in prey at closer ranges. The maximum detection range of 93 m for a cod at broadside seems to suggest that dolphins really should not have much problem detecting prey by echolocation, even in a noise-limited environment, in order to maintain their dietary requirements (Kastelein *et al.*, 2002, 2003) assuming that a sufficient amount of prey is in the area. The noise condition in Kaneohe Bay is not atypical for many shallow off-shore waters from the temperate zone to the equator. Snapping shrimps are found throughout the world in shallow coastal waters (depth less than 60 m) at latitudes between approximately ±35°. The detection problem may be more affected by bottom reverberation rather than by ambient noise or a combination of reverberation and noise. The effects of reverberation will be considered in a later study.

Snapping shrimps produce high intensity sounds by creating a bubble in the process of rapidly closing their large claw, and the bubble eventually cavitates creating an almost impulsive sound (Versluis *et al.*, 2000). However, at depths beyond about 60 m, the cavitation progress would probably not be possible. Therefore, as water depth progressively increases beyond about 60 m, snapping shrimp noise in temperate waters should also progressively decrease in intensity so that in sufficiently deep waters the environment becomes nonmasking. In such an environment, the minimum detection range for the bottlenose dolphin increases to about 107 m. The maximum detection range is at about 178 m. These are very long ranges and a foraging echolocating dolphin may not pay much attention to these long range echoes but would probably concentrate on closer prey if they are present.

Harbor porpoises are found in cool temperate and subpolar coastal waters of the northern hemisphere (Jefferson *et al.*, 1993) and are not exposed to snapping shrimp noise. Since the echolocation signals are very high in frequency, there are not many noise sources that have frequency components overlapping with harbor porpoise echolocation frequencies. Therefore, the sonar system of harbor porpoises should not be limited by natural ambient noise. Nevertheless, the minimum threshold detection range of 16 m for a cod by an echolocating harbor porpoise is much smaller than the corresponding minimum detection range for a bottlenose dolphin in a noise-limited environment, about 0.22 that of a bottlenose dolphin. The limited echolocation detection range would make it difficult, if not impossible, for harbor porpoise to inhabit a noisy environment such as Kaneohe Bay. This limited sonar range may be one of the most important reasons for harbor porpoise not being usually found in lower

latitude waters inhabited by snapping shrimp. In such a noisy environment, the harbor porpoise echolocation system would be severely limited or even nonfunctional.

It is interesting that even with its limited echolocation range, harbor porpoises are able to adequately detect and forage on different types of fish. This suggests that the coastal waters that harbor porpoise inhabit have high densities and number of fishes. The bottlenose dolphin in a noisy environment can detect a fish at distances anywhere from 3.4 to 4.4 times longer than the harbor porpoise. In a quiet environment, the bottlenose dolphin could probably detect a fish at a distances anywhere from 6.3 to 6.7 times further than the harbor porpoise. Bottlenose dolphins may need the longer range detection capability perhaps because of a possible lower density of prey or less fish biomass in their habitat compared to that of harbor porpoises.

The large difference in detection ranges between the bottlenose dolphin and the harbor porpoise can probably be attributed to the difference in source level of echolocation signals emitted by both species. In the modeling of the bottlenose dolphin detection range for a cod in a quiet environment, a source level of 222 dB re 1 μPa, which translates to a source energy flux of 167 dB re 1 μPa^2 s, was used. Unfortunately, the echolocation signals of the harbor porpoise were not measured during the range threshold experiment of Kastelein *et al.* (1999). Au *et al.* (1999) measured source levels in the same test pen and from the same porpoise used by Kastelein *et al.* (1999) and obtained an average value of 167.5 dB. However, the target used in the Au *et al.* (1999) study had about a 10 dB greater target strength than that of the 5.08-cm diameter sphere used by Kastelein *et al.* (1999) and the target range was much shorter (7–9 m) than in the target detection experiment. In a latter study to determine the capability of a harbor porpoise to detect a target in noise, we measured an average source level of 186 dB re 1 μPa (unpublished data). This is a rather surprising result and is the highest measured source levels for harbor porpoises to date. However, researchers at the Kerteminde facility in Denmark have recorded echolocation signals of a free swimming *Phocoena phocoena* having amplitudes comparable with these results. Having the porpoise echolocate in the presence of masking noise probably induced the animal to emit higher amplitude signals with peak-to-peak amplitude between 184 and 190 dB. Therefore, the bottlenose dolphin may be using an average source level that was about 36 dB higher in amplitude than that of the harbor porpoise. A 36-dB difference would explain most of the difference between the maximum detection range in a quiet environment between a bottlenose dolphin and a harbor porpoise. The porpoise minimum detection threshold range for the cod was 16 m (see Fig. 11), which corresponds to a two-way transmission loss of 49.3 dB. Add 36 dB to this two-way transmission loss and we have a new two-way transmission loss of 85.3 dB, which corresponds to a range of approximately 95 m, using an absorption coefficient at 130 kHz of 0.038 dB/m, which is appropriate for water temperatures between 15 and 21 °C. The dolphin minimum detection range for a cod in Fig. 9 is 107 m. The minimum detection ranges for the bottlenose dolphin and the harbor porpoise in a quiet environment do not match up perfectly when adjusted for differences in the source levels, so other factors must be taken into consideration. One other obvious factor is the difference in hearing sensitivities between the two species or even within a species.

The use of broadband clicks for echolocation is an important part of the echolocation process. There are other types of signals that may provide long detection ranges, but longer detection ranges would not necessarily be an advantage in foraging. The detection ranges that both the dolphin and porpoise can achieve are sufficient for their needs in their ecological niches. The low amount of variation in the reflectivity as a function of azimuth when considered from an energy flux density perspective, compared to the large variation obtained with tonal pulses has the advantage of minimizing the variations of the echo energy as the fish orientation with respect to a dolphin changes. Such changes in prey orientation are to be expected in a dynamic situation in which the both the dolphin and the prey are constantly moving.

ACKNOWLEDGMENTS

We thank Sander van der Hel for assistance conducting the experiments. Jan van der Veen, Sea aquarium "het Arsenaal," The Netherlands, lent us the study animals. Gijs Rutjes (Coppens International) provided some of the sea bass. We thank Brigitte Kastelein and the volunteers for logistical support. The facilities of the research station were made available thanks to Dick Vethaak (RIKZ), Roeland Allewijn (RIKZ), and Wanda Zevenboom (North Sea Directorate). This work was supported by the US Office of Naval Research, Mardi Hastings, program manager and the Netherlands Ministry for Agriculture, Nature, and Food Quality (DKW-program 418: North Sea and Coast. This project complied to the Dutch standards for animal experiments (Chris Pool, head of the Committee for Animal Experiments of RIKZ) and was conducted under University of Hawaii Animal Care Protocol 04-019. This is HIMB contribution No. 1270.

Au, W. W. L., Floyd, R. W., Penner, R. H., and Murchison, A. E. (**1974**). "Measurement of Echolocation Signals of the Atlantic Bottlenose Dolphin, Tursiops truncatus Montagu, in Open Waters," **56**, 1280–1290.

Au, W. W. L. (**1993**). *The Sonar of Dolphins* (Springer-Verlag, New York).

Au, W. W. L., and Snyder, K. J. (**1980**). "Long-range target detection in open waters by an echolocating Atlantic bottlenose dolphin (*Tursiops truncatus*)," J. Acoust. Soc. Am. **68**, 1077–1084.

Au, W. W. L., Moore, P. W. B., and Pawloski, D. A. (**1988**). "Detection of complex echoes in noise by an Echolocating Dolphins," J. Acoust. Soc. Am. **83**, 662–668.

Au, W. W. L., Kastelein, R. A., Rippe, T., and Schooneman, N. M. (**1999**). "Transmission beam pattern and echolocation signals of a Harbor Porpoise (Phocoena phocoena)" J. Acoust. Soc. Am. **106**, 3699–3705.

Au, W. W. L., Lemonds, D. W., Vlachos, S., Nachtigall, P. E., and Roitblat, H. L. (**2002**). "Atlantic bottlenose dolphin hearing threshold for brief broadband signals," J. Comp. Psychol. **116**, 151–157.

Au, W. W. L., and Benoit-Bird, K. (**2003**). "Acoustic backscattering by Hawaiian Lutjanid snappers. II. Broadband temporal and spectral structure," J. Acoust. Soc. Am. **114**, 2767–2774.

Au, W. W. L., Ford, J. K. B., Home, J. K., and Newman-Allman, K. A. (**2004**). "Echolocation signals of free-ranging killer whales (*Orcinus orca*) and modeling of foraging for chinook salmon (*Oncorhynchus tshawytscha*)," J. Acoust. Soc. Am. **56**, 1280–1290.

Benoit-Bird, K. J., Au, W. W. L., and Kelley, C. D. (**2003**). "Acoustic backscattering by Hawaiian Lutjanid snappers. I. Target strength and swimbladder characteristics," J. Acoust. Soc. Am. **114**, 2757–2766.
Clay, C. S., and Horne, J. K. (**1994**). "Acoustic models of fish. The Atlantic cod (*Gadus morhua*)," J. Acoust. Soc. Am. **96**, 1661–1668.
Foote, K. G. (**1980**). "Importance of swimbladder in acoustic scattering by fish. A comparison of gadoid and mackerel target strengths," J. Acoust. Soc. Am. **67**, 2084–2089.
Foote, K. G., and Ona, E. (**1985**). "Swimbladder cross sections and acoustic target strengths of 13 pollack and 2 saithe," Fiskeridir. Skr., Ser. Havunders. **18**, 1–57.
Horne, J. K., and Jech, J. M. (**1999**). "Multi-frequency estimates of fish abundance: Constraints of rather high frequencies," ICES J. Mar. Sci. **56**, 1054–1199.
Jech, J. M., and Horne, J. K. (**1995**). "Application of three sound scattering models to threadfin shad (*Dorosoma petenese*)," J. Acoust. Soc. Am. **98**, 2262–2269.
Jefferson, T. A., Leatherwood, S., and Webber, M. A. (**1993**). *FAQ Species Identification Guide. Marine Mammals of the World* (UNEP/FAO, Rome), 320 pp.
Johnson, S. C. (**1968**). "Relation between absolute threshold and duration of tone pulses in the bottlenosed porpoise," J. Acoust. Soc. Am. **43**, 757–763.
Kastelein, R. A., Au, W. W. L., Rippe, T., and Schooneman, N. M. (**1999**). "Target detection by an echolocating harbor porpoise (*Phocoena phocoena*)," J. Acoust. Soc. Am. **105**, 2493–2498.
Kastelein, R. A., Vaughan, N., Walton, S., and Wiepkema, P. R. (**2002**). "Food intake and body measurements of Atlantic bottlenose dolphins (*Tursiops truncatus*) in captivity," Mar. Environ. Res. **53**, 199–218.
Kastelein, R. A., Staal, C., and Wiepkema, P. R. (**2003**). "Food consumption, food passage time, and body measurements of captive bottlenose dolphins (*Tursiops truncatus*)," Aquat. Mamm. **29**, 53–66.
Murchison, A. E. (**1980**). "Maximum detection range and range resolution in echolocating bottlenose porpoise (*Tursiops truncates*)," in *Animal Sonar Systems*, edited by R. G. Busnel and J. F. Fish (Plenum, New York) pp. 43–70.
Madsen, P. T., Kerr, I., and Payne, R. (**2004**). "Echolocation clicks of two free-ranging delphinids with different food preferences: False killer whales (*Pseudorca crassidens*) and Risso's dolphin (*Grampus griseus*)." J. Exper. Biol. **207**, 1811–1823.
Thomas, J. A., and Turl, C. W. (**1990**). "Echolocation characteristics and range detection threshold of a false killer whale (*Pseudorca crassidens*)," in *Sensory Abilities of Cetaceans: Laboratory and Field Evidence*, edited by J. A. Thomas and R. A. Kastelein (Plenum, New York), pp. 321–334.
Urick, R. J. (**1983**). *Principles of Underwater Sounds*. 3rd ed. (McGraw Hill, New York).
Versluis, M., Schmitz, B., von der Heydt, A., and Lohse, D. (**2000**). "How snapping shrimp snap: Through cavitating bubbles," Science **269**, 2114–2117.

High-frequency ultrasound backscattering by blood: Analytical and semianalytical models of the erythrocyte cross section

David Savéry[a] and Guy Cloutier[b]
Laboratory of Biorheology and Medical Ultrasonics, University of Montreal Hospital Research Center, 2099 Alexandre de Séve, Room Y-1619-Pavillion de Séve, Notre-Dame Hospital, Montréal, Québec H2L 2W5, Canada

(Received 27 July 2006; revised 13 February 2007; accepted 15 February 2007)

This paper proposes analytical and semianalytical models of the ultrasonic backscattering cross section (BCS) of various geometrical shapes mimicking a red blood cell (RBC) for frequencies varying from 0 to 90 MHz. By assuming the first-order Born approximation and by modeling the shape of a RBC by a realistic biconcave volume, different scattering behaviors were identified for increasing frequencies. For frequencies below 18 MHz, a RBC can be considered a Rayleigh scatterer. For frequencies less than 39 MHz, the general concept of acoustic inertia tensor is introduced to describe the variation of the BCS with the frequency and the incidence direction. For frequencies below 90 MHz, ultrasound backscattering by a RBC is equivalent to backscattering by a cylinder of height 2 μm and diameter 7.8 μm. These results lay the basis of ultrasonic characterization of RBC aggregation by proposing a method that distinguishes the contribution of the individual RBC acoustical characteristics from collective effects, on the global blood backscattering coefficient. A new method of data reduction that models the frequency dependence of the ultrasonic BCS of micron-sized weak scatterers is also proposed. Applications of this method are in tissue characterization as well as in hematology. © *2007 Acoustical Society of America.* [DOI: 10.1121/1.2715452]

PACS number(s): 43.80.Qf, 43.80.Ev, 43.20.Bi, 43.20.Fn [FD] Pages: 3963–3971

I. INTRODUCTION

A. Background

Ultrasound (US) tissue characterization techniques provide means to assess the pathophysiological state of organs by measuring a number of ultrasonic tissue properties. There is however a certain need to understand how these measurable acoustical indices relate to biophysical phenomena occurring at the cellular or the subcellular scale. Tissue microstructural characteristics (such as cell size, cellular organization, fiber anisotropy, etc.) are indeed expected to provide meaningful information for diagnosis, as they are directly related to biological processes.

Previous works in ultrasonic tissue characterization have studied the relation between the microstructure and various acoustical tissue properties as the backscattering coefficient and spectral characteristics.[1,2] The typical approach considers that mammal tissue can be acoustically modeled as a continuous random distribution of mass density and bulk compressibility. The correlation length of their correlation function can be related to the size of a discrete microscopic scatterer, with replicas randomly spread in the bulk volume. The propagation of the interrogating US wave within this type of medium is conditioned by the particle acoustic properties, the properties of the embedding medium, the particle number density and size, and the level of spatial organization of the scatterers.

This paper focuses on a typical example of heterogeneous biological milieu: blood. This biofluid can be mechanically described as a colloidal suspension of flexible cells flowing within the plasma, which is itself a Newtonian liquid. Erythrocytes form the vast majority of blood cells (99% in number) and occupy a large volume fraction (hematocrit) of 35–45% under normal conditions. Because of the coexistence of erythrocytes and liquid phases, blood exhibits a shear-thinning rheological behavior. When flowing at a low shear rate, red blood cells (RBCs) adhere and form a structured network of clusters. The increase of the shear rate results in a reversible disaggregation of RBCs. The intricate packing of the so-called *rouleaux* of RBCs results in a viscosity increase. In various pathological conditions, including cardiovascular diseases and hemoglobinopathies, blood viscosity is abnormally high. Hemodynamics can be markedly affected by such hyperviscosity syndrome, especially in the microcirculation.

Several groups are investigating the possibility to detect abnormal RBC aggregation and the associated hemorheological disorders with US. Some clinical observations of blood hyperechogenicity appearing in low shear or static flow conditions have qualitatively demonstrated the potential of US to image RBC aggregation. This phenomenon is encountered in echocardiography or in vascular imaging and was given the name of spontaneous echo contrasts or smoke-like echoes.[3,4] A better quantification of this scattering enhancement would allow the extraction of valuable biophysical parameters that characterize red cell adhesion.

The measurement of RBC aggregation indices (aggregate size, anisotropy, etc.) through the quantification of blood

[a]Present address: Supersonic Imagine, Aix-en-Provence, France.
[b]Electronic mail: guy.cloutier@umontreal.ca

ultrasound backscattering however requires an acoustical model. Before understanding backscattering of US by an ensemble of interacting RBCs, a first obvious step is to properly quantify US backscattering by a single erythrocyte. This is the purpose of this paper.

B. Literature review

At a low frequency (in the range of a few megahertz) and for weak scattering particles, the relation between the backscattering cross section (BCS) and the RBC acoustical properties is simple and is conveyed by the Rayleigh formulation.[5] In this approximation, subwavelength geometric details do not affect the BCS and therefore cannot be inferred by "inverting" low frequency scattering data. In the case of red blood cells, the validity of the Rayleigh assumption can be questioned when the acoustical frequency exceeds 27 MHz. This approximation is indeed valid when $ka \ll 1$, where $k=\omega/c$ is the wave number and $a=2.82$ μm is the effective erythrocyte radius. The effective radius is defined in this paper as $4\pi a^3/3=V_s$ where V_s is the volume of the RBC, roughly 94 μm^3. When the frequency is above 27 MHz, $ka=\pi/10\approx 0.31$ considering that the speed of sound $c=1540$ m/s (Ref. 6) and therefore the Rayleigh validity is questionable. As high frequency ultrasound imaging systems (intravascular imaging, small animal scanners) currently use frequencies above 20 MHz, the need to extend Rayleigh formulation of the BCS seems obvious.

A few studies of various domains of acoustics experimentally, theoretically or numerically examined non-Rayleigh aspects of weak acoustical backscattering when ka becomes nonnegligible. In marine acoustics, Stanton *et al.*[7] proposed a number of models of the angle-averaged backscattering cross section of individual zooplankton based on the Born first-order approximation. By modeling the animals as bent cylinders for $ka \leqslant 5$, the study showed good agreements between predictions given by the backscattering models (obtained by measuring animal dimensions) and experimental acoustical data. This proved the utility of the simple first-order Born approximation to take into account the complex geometry of the scatterer.

For the problem of ultrasound backscattering by a single red blood cell, Kuo and Shung[8] and Coussios[9] also discussed the limitations of the Rayleigh formulation. Kuo and Shung[8] measured the backscattering coefficient of a diluted suspension of porcine RBCs and the experimentally determined BCS was shown to scale as $k^4V_s^2$ for frequencies below 30 MHz, as predicted by the Rayleigh approximation. In the same study, numerical results obtained by the Jakeman's T-matrix method predicted that the red cell shape affected the BCS and that the frequency dependence only slightly deviated from $k^4V_s^2$ for $ka<1$ (87 MHz). This study considered frequencies from 1 MHz to 1.7 GHz, approximately. Coussios[9] analytically derived the BCS of a thin cylinder with approximate RBC dimensions, using the Born weak scattering assumption and showed that the spherical and cylinder models gave similar values of the BCS for frequencies $\leqslant$20 MHz. The effect of the particle shape became only significant for frequencies above 20 MHz (the maximum frequency considered in this study being 60 MHz).

C. Objectives

Following these studies, this paper has two objectives. The analytical framework opened by Coussios[9] who used the Born approximation is generalized to take into account the realistic biconcave shape of the RBC. Analytical or semi-analytical results are then used to predict how microscale geometric features influence the high frequency BCS of erythrocytes above 20 MHz. It is shown that different scattering behaviors can be distinguished depending on the ultrasonic frequency.

II. THEORY AND METHODS

A. The backscattering cross section

The ability of a material particle to generate acoustical echoes is commonly quantified by the BCS that is defined as follows. Consider a monochromatic plane wave with complex amplitude $p_i(\mathbf{r})=p_0e^{i\mathbf{k}\cdot\mathbf{r}}$, where $\mathbf{r}$ is the spatial vector, p_0 is the incident pressure amplitude, and $\mathbf{k}$ represents the wave vector. This pressure wave propagates in a linear fluid characterized by a mass density ρ_0 and an adiabatic compressibility κ_0. A fluid particle of volume V_s centered in O creates a fluctuation of density and compressibility. The interaction between the incident wave and the particle results in a deviation of the incident wave that redistributes the acoustical energy in space.[10] The total pressure amplitude $p(\mathbf{r})$ can be mathematically decomposed as the sum of the unperturbated incident pressure field $p_i(\mathbf{r})$ and of the scattered pressure $p_s(\mathbf{r})$. In the far field of the particle, the scattered field has the asymptotic form[11]

$$p_s(r\mathbf{e}_r)=p_0\frac{e^{i\mathbf{k}\cdot\mathbf{r}+i\theta_0}}{r}\sigma(\mathbf{e}_r,\mathbf{k})^{1/2}. \tag{1}$$

In this expression, $\mathbf{e}_r$ is the unit vector pointing in the observation direction, θ_0 is a phase term (that will not be further discussed in this paper), and $\sigma(\mathbf{e}_r,\mathbf{k})$ is the scattering cross section of the particle. In pulse-echo US, when the target lies in the far field of the transducer, the scattering direction that mainly contributes to the transduced radio-frequency signal corresponds to the reverse direction: $\mathbf{e}_r=-\mathbf{k}/k$. For this reason, the quantity that characterizes particle backscattering is the backscattering cross-section (noted σ_b) defined as $\sigma_b(\mathbf{k})=\sigma(-\mathbf{k}/k,\mathbf{k})$.

In the rest of the paper, one will be interested only in backscattering, and therefore the term insonification angle or simply angle will be used to describe the direction of the wave vector $\mathbf{k}$ with respect to the RBC. There will be no ambiguity on the scattering vector direction which is simply $-\mathbf{k}$.

B. Rayleigh scattering

The expression of the BCS of a small fluid sphere ($ka \ll 1$) that has a constant density $\rho=\rho_0(1+\gamma_\rho)$ and compressibility $\kappa=\kappa_0(1+\gamma_\kappa)$, where γ_ρ and γ_κ are the relative con-

trasts in density and compressibility with respect to the background medium, was originally derived by Rayleigh (see Ref. 10). It can be expressed as

$$\sigma_b(\mathbf{k}) = \frac{k^4 V_s^2}{16\pi^2}\left(\gamma_\kappa - \frac{\gamma_\rho}{1-\gamma_\rho/3}\right)^2. \quad (2)$$

In the case of a weak scatterer, the contrast values γ_ρ and γ_κ are small and a second-order approximation reduces Eq. (2) to:

$$\sigma_b(\mathbf{k}) = \frac{k^4 V_s^2}{4\pi^2}\gamma_z^2, \quad (3)$$

where $\gamma_z=(\gamma_\rho-\gamma_\kappa)/2$ is the small relative contrast of acoustical impedance between the scatterer and the surrounding medium. It can be noted that the acoustic cross section of a small sphere scales as the fourth power of frequency and therefore increases rapidly with increasing frequency.

C. Form factor of a homogeneous scatterer considering the Born approximation

Equation (3) is valid for a small, homogeneous, and weak spherical scatterer. Now, for any type of scattering particle, a nondimensional corrective term $F(\mathbf{k})$, named the form factor, can be defined as

$$\sigma_b(\mathbf{k}) = \frac{k^4 V_s^2}{4\pi^2}\langle\gamma_z\rangle^2 F(\mathbf{k}), \quad (4)$$

where $\langle\gamma_z\rangle=(1/V_s)\int_{V_s}\gamma_z(r)d^3r$ represents the spatially averaged impedance contrast of the particle. The deviation of the form factor from one quantifies the influence of the particle geometry and orientation on the BCS. In the Born approximation ($p_s \ll p_i$) that applies for weak scattering conditions, the form factor has a simple expression [easily retrieved from Eq. (8.1.20) of Ref. 10] related to the spatial Fourier spectrum of the impedance contrast:

$$F(\mathbf{k}) = \frac{1}{\langle\gamma_z\rangle^2 V_s^2}\left|\int_{V_s}\gamma_z(r)e^{2i\mathbf{k}\cdot\mathbf{r}}d^3r\right|^2. \quad (5)$$

This expression is in agreement with the fact that the form factor approaches unity (and Rayleigh scattering) when the particle size is negligible with respect to the wavelength ($e^{2i\mathbf{k}\cdot\mathbf{r}}\to 1$).

D. Form factors of simple geometrical shapes

Analytical expressions of the form factor can be found for homogeneous scatterers having simple shapes. The case of three important shapes (sphere, ellipsoid, and cylinder) is given in Table I. The range of wave numbers for which Rayleigh scattering applies within 5% accuracy is also indicated. Note that these analytical forms are compatible with Ref. 12 for spheres and ellipsoids and the cylinder form agrees with the general expression obtained by Coussios [Eq. (13) of Ref. 9].

TABLE I. Form factors of several descriptive shapes. The wave vector $\mathbf{k}$ is decomposed in the ellipsoid system of axes $\mathbf{k}=k_1\mathbf{e}_1+k_2\mathbf{e}_2+k_3\mathbf{e}_3$, where (1, 2, and 3 or x, y, and z) refer to the ellipsoid principal directions of the axes (a_1, a_2, and a_3), or in a cylindrical system of axes $\mathbf{k}=k_z\mathbf{e}_z+k_r\mathbf{e}_r$. The height of the cylinder is h_0 and its radius is R. The form factor of the sphere is $F(\mathbf{k})=\Phi_s(2ka)$, where a is its radius. J_1 is the first-order Bessel function.

Particle shape	Form factor $F(\mathbf{k})$	Rayleigh limit $[F(\mathbf{k})>0.95]$
Sphere	$\Phi_s(2ka)$, $\Phi_s(u)=(3\sin u-3u\cos u)^2/u^6$	$ka<0.25$
Ellipsoid	$\Phi_s(2((k_1a_1)^2+(k_2a_2)^2+(k_3a_3)^2)^{1/2})$	$((k_1a_1)^2+(k_2a_2)^2+(k_3a_3)^2)^{1/2}<0.25$
Cylinder	$(\sin k_zh_0/k_zh_0)^2\times(J_1(2k_rR)/k_rR)^2$	$(k_z^2h_0^2+3k_r^2R^2)^{1/2}<0.38$

E. Form factor of an axisymmetrical particle mimicking a RBC

Consider now a homogeneous particle having the symmetries of a RBC (see Fig. 1), i.e., a symmetry of revolution around (O_z) and a mirror symmetry with respect to (O_{xy}). The shape of the RBC can then be described by the radial profile:[13]

$$z_0(r) = \frac{h_0}{2}\phi(2r/D), \quad (6)$$

where h_0 is the particle thickness along (O_z), $\phi(u)$ is the normalized geometric profile, and D is the diameter. This function, defined for $u\in[0,1]$, describes the particle shape and satisfies $\phi(0)=1$, $\phi(1)=0$. As detailed in Appendix A, the form factor of the RBC can be formulated by using Eq. (3) and by considering that the acoustic impedance is constant, i.e., $\gamma_z(\mathbf{r})=\langle\gamma_z\rangle$ when $\mathbf{r}$ lies within the RBC and $\gamma_z(\mathbf{r})=0$ when $\mathbf{r}$ is outside of the RBC. This yields to

$$F(k_r\mathbf{e}_r,k_z\mathbf{e}_z) = \left|\int_0^1 u\phi(u)J_0(k_rDu)\frac{\sin(k_zh_0\phi(u))}{k_zh_0\phi(u)}\times du\Big/\int_0^1 u\phi(u)du\right|^2, \quad (7)$$

where J_0 is the Bessel function of order 0.

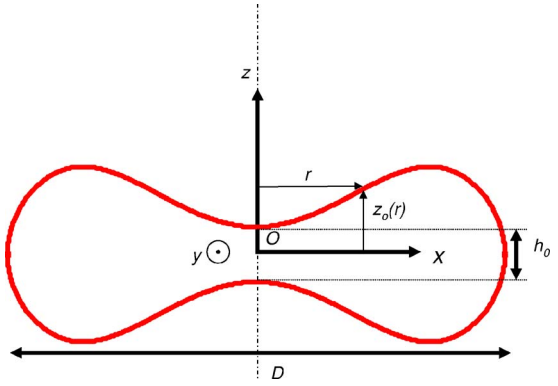

FIG. 1. (Color online) Geometric cross section of a red blood cell defined by the function $z_0(r)$, where h_0 is the thickness along O_z and D is the diameter along O_{xy}.

F. Acoustical inertia tensor

A second order expansion of $F(\mathbf{k})$ in ka is helpful to examine the deviation of the form factor of a homogeneous particle from one when the frequency is increased. As detailed in Appendix B, a second order Taylor expansion of Eq. (A1) gives:

$$F(\mathbf{k}) = 1 - 4\mathbf{k} \cdot \mathbf{\Sigma}\mathbf{k} + o(k^2a^2), \tag{8}$$

where $\mathbf{\Sigma}$ is a second order symmetrical positive tensor, a characteristic tensor of the particle shape referred here as the acoustical inertia tensor, defined by

$$\mathbf{\Sigma} = \frac{1}{V_s}\int_{V_s} \mathbf{r} \otimes \mathbf{r} d^3r. \tag{9}$$

In Eq. (9), the dyadic product of the two vectors is noted $\otimes$. The principal axes of the particle are the eigenvectors of $\mathbf{\Sigma}$ and its eigenvalues noted $\Sigma_{11} \leqslant \Sigma_{22} \leqslant \Sigma_{33}$ scale as the surface of the particle. Note that the acoustical inertia tensor $\mathbf{\Sigma}$ as defined here is directly related to the inertia tensor $\mathbf{J}$ (as defined in solid mechanics) of a solid particle of unit mass density rotating around $\mathbf{O}$ (part 5.3.1 of Ref. 14):

$$\mathbf{J} = \mathrm{tr}(\mathbf{\Sigma})\mathbf{U} - \mathbf{\Sigma}, \tag{10}$$

where $\mathbf{U}$ is the identity tensor and tr represents the trace. This analogy leads us to name this tensor *acoustical inertia tensor*, as it directly relates to the inertia moments of a rigid particle having the same shape. To give an example, an ellipsoid of semi-axes $\{a_i\mathbf{e}_i\}_{i=1,2,3}$ has an acoustical inertia tensor $\mathbf{\Sigma}$ of expression:

$$\mathbf{\Sigma} = \frac{a_1^2}{5}\mathbf{e}_1 \otimes \mathbf{e}_1 + \frac{a_2^2}{5}\mathbf{e}_2 \otimes \mathbf{e}_2 + \frac{a_3^2}{5}\mathbf{e}_3 \otimes \mathbf{e}_3. \tag{11}$$

For the case of the symmetrical particles as described earlier in Eq. (6), the inertia tensor is diagonal in the base $\{\mathbf{e}_x, \mathbf{e}_y, \mathbf{e}_z\}$ and can be expressed as:

$$\mathbf{\Sigma} = \left(D^2 \frac{\int_0^1 u^3\phi(u)du}{8\int_0^1 u\phi(u)du}(\mathbf{e}_x \otimes \mathbf{e}_x + \mathbf{e}_y \otimes \mathbf{e}_y) + h_0^2 \frac{\int_0^1 u\phi(u)^3du}{12\int_0^1 u\phi(u)du}\mathbf{e}_z \otimes \mathbf{e}_z \right). \tag{12}$$

This reduces to $\mathbf{\Sigma} = D^2/16(\mathbf{e}_x \otimes \mathbf{e}_x + \mathbf{e}_y \otimes \mathbf{e}_y) + h_0^2/12\mathbf{e}_z \otimes \mathbf{e}_z$ in the case of a cylinder of diameter D and height h_0 ($\phi(u) = 1$ for $|u| < 1$).

G. Modeling of the physical and geometrical properties of plasma and of a erythrocyte

In this study, the plasma is supposed non-viscous, characterized by a compressibility $\kappa_p = 4.09 \times 10^{-10}$ Pa^{-1} and a mass density $\rho_p = 1021$ kg m^{-3} (see Ref. 15). The hemoglobin solution encapsulated by the RBC membrane is supposed nonviscous and acoustically described by the compressibility $\kappa_{\mathrm{RBC}} = 3.41 \times 10^{-10}$ Pa^{-1} and mass density $\rho_{\mathrm{RBC}} = 1092$ kg m^{-3}. The resulting impedance contrast defined in Eq. (3) is $\gamma_z = 0.13$. The effect of the RBC membrane on acoustical scattering is neglected. This assumption is based on the fact that the membrane of an intact RBC has a small thickness of 10 nm. It could be argued that the measured backscattering by ghost cells (damaged red cells with removed hemoglobin) is far from negligible (see Ref. 16, Chap. 7) and this could be attributed to membrane backscattering effects. However, as carefully discussed in Ref. 16, this interpretation seems inappropriate. Membranes of damaged cells act like nets, which suggest that lysed cells are actually smaller but denser particles that strongly scatter US.

Red cells are very deformable and their shapes vary in response to mechanical stress (e.g., the hemodynamic shear forces) and to the osmolarity of the surrounding environment. In static equilibrium, as shown in Fig. 1, the RBC is a biconcave disk[13] with a volume $V_s = 4\pi a^3/3 = 94$ μm^3 (effective radius $a = 2.82$ μm) and an optimal exchange surface area of 135 μm^2. The mean axial and radial maximum dimensions are, respectively, $h_0 = 0.81$ μm and $D = 7.82$ μm. Evans and Fung[13] have formulated a convenient analytic formula that gives the normalized profile of a nonstressed RBC membrane:

$$\phi(u) = \sqrt{1 - u^2}(1 + \alpha_2 u^2 + \alpha_4 u^4), \tag{13}$$

where $\alpha_2 = 9.7$ and $\alpha_4 = -5.4$.

H. Backscattering cross sections of particles mimicking a RBC

According to Eq. (4) and knowing the values of V_s and γ_z, one can derive the backscattering cross-section of elementary particles from the definition of the form factor $F(\mathbf{k})$. Table I provides analytical expressions of $F(\mathbf{k})$ for a sphere, an ellipsoid and a cylinder. By considering cylindrical coordinates, the form factor of a biconcave disk that better mimic the shape of a RBC was shown in Eq. (7). Numerical integration is required to compute this form factor. Equations (8) and (12) can also be utilized if one uses Cartesian coordinates.

At the second order in ka and if the Born approximation holds, the frequency dependence of the red cell BCS is given by a Taylor expansion using Eq. (4) and the definition of the inertia axes introduced earlier in Sec. II F [Eqs. (8) and (11)]. This results in

$$\sigma_b(\mathbf{k}) = \frac{k^4V_s^2}{4\pi^2}\gamma_z^2\left(1 - \frac{4}{5}k_x^2a_x^2 - \frac{4}{5}k_y^2a_y^2 - \frac{4}{5}k_z^2a_z^2\right) + o(k^6). \tag{14}$$

Two particles with the same material properties but different shapes will have equivalent backscattering behaviors (up to the sixth order in ka and for all insonification angles) if they have the same volume and the same inertia axes.

TABLE II. Volume V and inertia characteristics of the red blood cell and other equivalent descriptive shapes. The equivalent axes a_i are computed from the eigenvalues $a_i^2/5$ of the inertia tensor $\mathbf{\Sigma}$. The geometrical descriptors h_0, D, and a are, respectively, the height, the diameter, and the effective radius of the red blood cell (a is the radius of the sphere with equivalent volume).

Particle shape	Volume (μm^3)	Inertia axes $a_x/a=a_y/a$	Inertia axis a_z/a	Geometrical descriptors (μm)
Red blood cell	94	1.54	0.50	$h_o=0.81$ $D=7.82$
Sphere	94	1	1	$a=2.82$
Ellipsoid	94	1.54	0.42	$a_z=V/(4\pi a_x^2/3)$
Cylinder	94	1.54	0.46	$h_o=V/(\pi D^2/4)=2$ $D=2\sqrt{0.8}a_x=7.76$

I. Numerical integration

The different definite integrals involved to compute the form factors were computed by a trapezoidal method. The interval $[0, 1]$ was divided in $N=10^4$ segments.

III. RESULTS

A. Dimensions of the equivalent particles

The inertia axes of the model of a red cell were computed using Eqs. (11) and (12). Adjunct to the volume, these quantities allow to derive the dimensions of the equivalent sphere (same volume), of the equivalent ellipsoid (same volume and same radial inertia axes) and of the equivalent cylinder (same volume and same radial inertia axes) as given in Table II. Cross sections of these different shapes are represented in Fig. 2 for visual comparison.

B. Form factor of the particles

The variations of the various form factors as a function of the frequency and two different angles are given in Fig. 3. The decrease of the form factor from one to zero depends on the scattering shape and on the direction of insonification. The more elongated a particle is along the incident direction, the faster the form factor decreases as a function of frequency. In other words, the backscattering as a function of the incidence angle is maximal when the propagation direction is aligned with the smallest inertia axis ($k=k_z$). The incident wave perpendicularly intersects the biggest section of the particles.

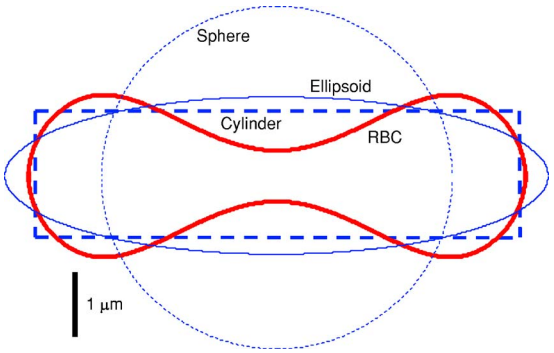

FIG. 2. (Color online) Geometric cross sections of a red blood cell and equivalent descriptive shapes.

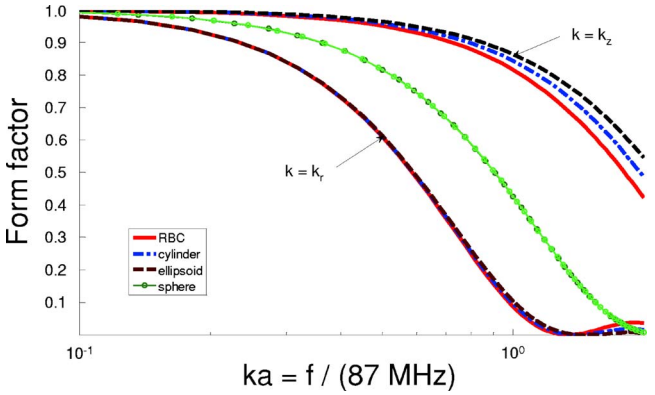

FIG. 3. (Color online) Variation of the form factor as a function of the reduced size parameter (ka) for different descriptive shapes. The insonification direction is either along O_z ($k=k_z$) or perpendicular to it ($k=k_r$).

C. Frequency dependence of the backscattering cross-section

Figure 4 shows the backscattering cross section of a RBC and of the equivalent simpler shapes along the O_z and O_x axes, as a function of ka. Along O_z, with the exception of the spherical descriptor, the backscattering behavior only slightly deviates from Rayleigh scattering below 87 MHz. Perpendicular to the long axis of each particle, non-Rayleigh behavior quickly arises for all shape descriptors as the frequency is increased.

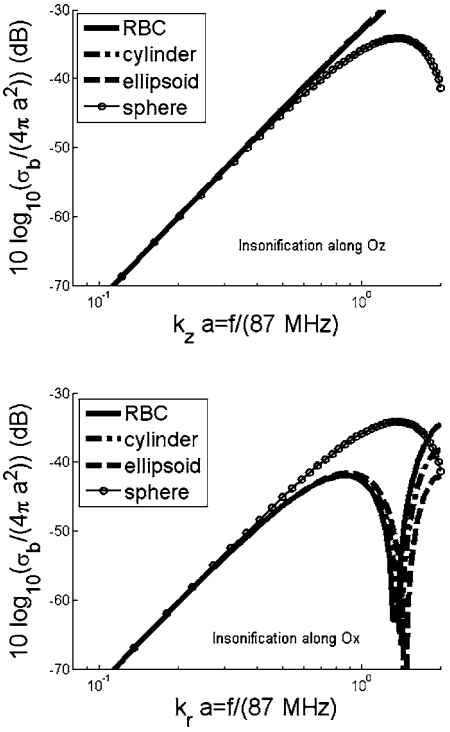

FIG. 4. Normalized backscattering cross section with respect to $4\pi a^2$ as a function of frequency (ka) for different descriptive shapes and incident wave directions along O_z ($k=k_z$) and O_x ($k=k_r$).

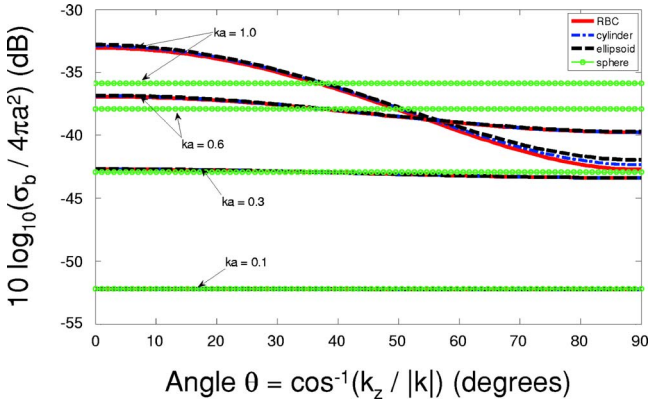

FIG. 5. (Color online) Angle dependency of the normalized backscattering cross section for different descriptive shapes at $ka=0.1$, 0.3, 0.6, and 1.0 (frequencies of 8.7, 26.1, 52.2, and 87 MHz). The angle θ is the angle between O_z and the incident wave direction.

D. Dependence of the backscattering cross section on the angle of incidence of the transmitted wave

At four frequencies corresponding to $ka=0.1$, 0.3, 0.6, and 1.0, the angular dependencies of BCS between 0° and 90° (angle between $\mathbf{e}_z$ and $\mathbf{k}$) are shown in Fig. 5 for the RBC, and the cylindrical, ellipsoidal, and spherical shapes. For the spherical particle, no angular dependencies are noted, as expected. At 8.7 MHz ($ka=0.1$), isotropic scattering is verified for all particles. Non-Rayleigh anisotropic scattering is observed at 26, 52, and 87 MHz for the RBC, cylinder, and ellipsoid. The angular variability of BCS increases for anisotropic particles as the frequency is increased. For example, variations of the order of 10 dB are noted at 87 MHz for the RBC.

IV. DISCUSSION

The backscattering cross section of weak scattering particles with arbitrary shapes can be semianalytically computed in the Born approximation. In this case, a Fourier duality exists between the geometry of the scatterer and the wave vector dependence of the backscattering cross section. A semianalytical model of the RBC profile enabled to compare the BCS of a red cell modeled by a biconcave volume with the BCS of simpler geometrical shapes. The notion of equivalence between two types of particles was defined in the low frequency scattering regime. Two particles with any given shape (sphere, ellipsoid, cylinder,…) were defined equivalent if the coefficients of the Taylor expansion of the BCS as a function of the wave number coincided up to the sixth order. Up to the sixth order, finding a shape equivalent to the RBC basically consists in matching first their volume and then their inertia axes as defined by the inertia tensor $\mathbf{\Sigma}$.

A. Weak scattering approximation

The computation of the BCS of fluid particles by Eq. (5) follows the first-order Born approximation: it is valid when the scattered wave amplitude remains negligible with respect to the incident wave. The case of scattering by a sphere that has the volume of a RBC is of interest to investigate the validity of this approximation.

TABLE III. Transition frequency (and of ka) above which biconcave RBC scattering differs by more than 5% than reference particle shapes.

	Rayleigh	Sphere	Second-order approximation of a RBC	Ellipsoid	Cylinder
ka	0.20	0.24	0.45	1.06	1.55
Frequency (MHz)	18	21	39	92	135

According to Refs. 9 and 17, Anderson's exact solution[18] of sphere backscattering and the Born approximation are in close agreement for frequencies corresponding to $0 \leqslant ka \leqslant 1$ (frequency $\leqslant$87 MHz). In the case of weak scatterers, the physical reasons for the nonvalidity of the Born approximation are the presence of multiple scattering, which is very unlikely for a single scatterer, and the arising of a resonance phenomenon. Minnaert resonance frequency for a fluid sphere predicts resonance for a wave number corresponding to $ka=3^{1/2}$ (i.e., a frequency of 150 MHz).

Even if the scatterer is not strictly spherical, multiple scattering is improbable due to the small contrasts in density and compressibility. Resonant frequencies are more difficult to predict, but one can postulate that it should occur around 150 MHz for a RBC. Therefore, for practical purpose, one can estimate that our BCS prediction must be valid up to ~87 MHz, whereas the predictions for frequencies higher than 87 MHz would have to be confronted to acoustical scattering simulations that take non-Born conditions into account.

B. Transition frequency to the non-Rayleigh scattering regime

The shape of a given particle influences the BCS through the nondimensional form factor $F(\mathbf{k})$. Under Rayleigh scattering conditions ($ka \ll 1$), the BCS is essentially independent on the particle shape, as $F(\mathbf{k}) \approx 1$. Increasing the frequency and changing the insonification angle enable to extract geometric details finer than the simple volume at the spatial scale of the wavelength. Having computed $F(\mathbf{k})$ for different descriptive shapes as a function of frequency and angle, one can assess the transition frequency to which their BCS differ by less than 5% of the Rayleigh limit $[F(\mathbf{k})=1]$. The bounds are given in Table III. For practical purpose, the biconcave RBC and the flat cylinder behave equivalently for frequencies below 90 MHz.

C. Comparison with previous studies

Using the T-matrix numerical method, Kuo and Shung[8] predicted that the shape (modeled by a sphere, a rounded cylinder and a realistic biconcave shape all having the same volumes) was of minor importance for frequencies below 30 MHz, and that the simulated BCS exhibited a k^4 dependence at those frequencies. However, their results at $ka < 0.1$ showed a dependence of the BCS with the angle of

incidence of the incident wave, and that the different types of BCS (cylinder, biconcave disk, sphere) had diverging values even when $ka \to 0$. This notably contradicts Rayleigh law that states that low frequency BCS from particles having the same volume and same acoustical properties do not differ and are moreover isotropic. One could attribute these discrepancies to the numerical T-matrix approach. For instance, low stability and approximation formulas of special functions can induce such errors. In our study, the angle and shape influences were negligible up to 21 MHz, and the RBC behaved as a sphere. We predict that angular variations from a single particle can only be observed above 21 MHz, if one considers that differences are significant when larger than 5%.

Coussios[9] also proposed an analytical approach to compute the scattering cross section of a RBC. The present study can be considered as a generalization of the previous formulation to a more realistic RBC shape, as it similarly used the Fourier integral formulation of the cross section. Our results are, however, restricted to the BCS (that considers $\mathbf{e}_r = -\mathbf{k}/k$) as the 180° scattering angle prevails in medical US. In Ref. 9, the RBC morphology was modeled by two types of isovolumic cylinders. By introducing the notion of acoustical inertia tensor, our study permits to find the dimensions of the equivalent cylinder by matching its inertia axes with the realistic RBC shape. Our conclusions concerning the bounds of the different scattering regimes are close to the predictions made by Coussios.[9] Moreover, our results readily showed that the biconcave RBC and the acoustical equivalent cylinder similarly backscatter ultrasonic waves, with a 5% accuracy for $ka < 1$ ($f < 87$ MHz).

D. A new approximation formula for the frequency dependence of backscattering from a scatterer with cellular dimensions

According to the second order approximation of the form factor of a RBC (using the acoustical inertia tensor) that predicts Rayleigh scattering up to 39 MHz ($ka = 0.44$), it seems appropriate to state that current medical US systems are not sensitive to geometric details of scatterers below the cell scale dimension of ~ 5 μm. Such details may only be detected if one considers higher frequencies. Accordingly, we can propose here a simple model of frequency dependence of the BCS of any type of weak scattering homogeneous particles with micrometric size:

$$\sigma_b(k\mathbf{e}_x) = \frac{1}{4\pi^2} k^4 V_s^2 \langle \gamma_z \rangle^2 (1 - 4\Sigma_{xx} k^2 + \cdots)$$

$$\approx \frac{1}{9} \langle \gamma_z \rangle^2 k^4 a^6 - \frac{4}{9} \Sigma_{xx} \langle \gamma_z \rangle^2 k^6 a^6. \quad (15)$$

In this expression, $\Sigma_{xx} = \mathbf{e}_x \Sigma \mathbf{e}_x$ is the component of the inertia tensor along the direction of propagation of the insonifying wave and a is the effective radius defined by $\frac{4}{3}\pi a^3 = V_s$. Notice that the resulting frequency dependence is here approximated by a sixth-order polynomial, with two nonvanishing coefficients. The coefficient in k^4 represents the Rayleigh contribution and the second coefficient in k^6 is the contribution of the inertia axis along O_x (the second order geometric correction is similar to the Guinier radius of gyration extracted from neutron/x-ray diffraction studies[19]).

E. Frequency dependence of backscattering from a collection of scatterers with cellular dimensions

Classical models of backscatter in US tissue characterization studies[5] usually model the frequency dependence by a power law:

$$\sigma_b(k\mathbf{e}_x) = \sigma_0 (k/k_0)^n, \quad (16)$$

where σ_0 is the low-frequency limit of the BCS, k_0 is a reference wave number (often selected at 1 MHz), and n is the spectral slope. This nonlinear regression is characterized by two material properties $\{\sigma_0, n\}$ in a given frequency range. According to our analytical study, an alternative set of frequency independent parameters $\{\langle \gamma_z \rangle V_s, \Sigma_{xx}\}$, derived from Eq. (15), would be more pertinent for US particle characterization. This new approach of data reduction should deserve some attention.

1. Characterization of RBC aggregation

The average number density of RBCs in blood is $m \approx 5 \times 10^6$ mm^{-3}, for a volume fraction $H = mV_s \approx 40\%$. Blood can be seen as a very dense suspension of red cells. As each RBC is surrounded by many neighboring cells, particle interactions are strong. The backscattering coefficient $\chi(\mathbf{k})$, or differential backscattering cross section from a collection of cells, defined as the BCS of the group of cells by unit volume, can be expressed as[20,21]

$$\chi(\mathbf{k}) = m\sigma_b(\mathbf{k}) S(-2\mathbf{k}), \quad (17)$$

where $S(-2\mathbf{k})$ is the structure factor and $\sigma_b(\mathbf{k})$ is the BCS of the individual RBC. The structure factor represents a corrective term taking into account the spatial correlations between scatterers. If RBCs independently scatter US, its value would simply be one. However, RBC mutual interactions induced by the strong particle number density and adhesion forces leading to cell clustering result in a strong deviation of $S(-2\mathbf{k})$ from one. The feasibility of measuring experimentally this deviation would rely on a good model of red cell BCS as:

$$S(-2\mathbf{k}) = \chi(\mathbf{k}) / m\sigma_b(\mathbf{k}). \quad (18)$$

The backscattering coefficient $\chi(\mathbf{k})$ can be measured experimentally, m can be approximated by measuring the hematocrit in a microtube following centrifugation and the mean volume of RBCs, whereas $\sigma_b(\mathbf{k})$ can be approximated by Eq. (15). It is then straightforward to obtain the structure factor and its frequency dependence to characterize cell aggregation.

2. Potential use of US in hematology

The erythrocyte BCS may also be of interest for hematological profiling, as proposed in the late seventies.[22] Diluted suspensions of RBCs (at $H < 8\%$) roughly have a unit structure factor, which yields to $\chi(\mathbf{k}) = m\sigma_b(\mathbf{k})$. The measurements of the backscatter coefficient and of the hematocrit permit a straightforward derivation of the RBC volume V_s

and inertia axes from $\boldsymbol{\Sigma}$. A number of genetic diseases alter erythrocyte morphology and deformability (hereditary anemia as β-thalassemia, sickle cell anemia, spherocytosis, etc.). It could be of interest to develop such US tools that would allow a characterization of the related phenotypes, by studying the volume and shape response of pathologic RBCs to pH, pO_2, osmotic, or mechanical stimuli. Such studies may eventually be attempted *in vitro* or *in vivo* in the microcirculation where the volume fraction of RBCs is reduced.

V. CONCLUSION

A semianalytical expression of the erythrocyte ultrasonic backscattering cross section has been proposed. It took into account the acoustical contrasts between plasma and cell hemoglobin and the peculiar biconcave shape of the RBC. Provided the Born approximation is valid, the frequency and angle dependencies of the erythrocyte BCS were evaluated up to 90 MHz. By the use of these results as a reference, the accuracy of several other simplified analytical formulas could be assessed. The Rayleigh approximation (form factor=1, angle and shape independencies) appeared satisfactory up to 18 MHz; a quadratic correction of the form factor gave good approximations up to 39 MHz (over all insonifying angles, with errors below 5%). By deriving the inertia tensor $\boldsymbol{\Sigma}$ from the Hessian of the form factor $F(\mathbf{k})$ at a frequency of 0 Hz, the notion of acoustical inertia axis of a homogeneous scattering particle was defined. The RBC was shown acoustically equivalent to a thin cylinder of height 2 μm and diameter 7.8 μm or to an oblate spheroid of semi axes 4.3 and 1.2 μm ($f \leqslant 90$ MHz) as those simple shapes and the biconcave RBC have equivalent volume and acoustical inertia tensors. These findings give new bases to the description of the scattering of US by blood. The knowledge of the backscattering by a single erythrocyte is necessary to further study US scattering by millions of packed RBCs, as required to properly characterize red cell adhesion in shear flow.

ACKNOWLEDGMENTS

This work was supported by Grant No. MOP-36467 from the Canadian Institutes of Health Research. The second author is recipient of the National Scientist Award from the "Fonds de la Recherche en Santé du Québec" (2004–2009).

APPENDIX A

This appendix details the computations required to obtain the form factor of a symmetrical scatterer that has a relative impedance contrast given by $\gamma_z(\mathbf{r}) = \gamma_z(r,\theta,z) = \langle \gamma_z \rangle \mathbf{I}_{[|z|<z_0(r)]}$, where $z_0(r)$ is the radial profile of the scatterer shape, (r,θ,z) are the cylindrical coordinates, and $\langle \gamma_z \rangle$ is the homogeneous contrast of acoustical impedance of the particle.

The backscattering cross section of a scatterer in the Born approximation can be obtained from the general formulation of Eq. (3). That is given by

$$\sigma_b(\mathbf{k}) = \frac{k^4}{4\pi^2} \left| \int_{V_s} \gamma_z(\mathbf{r}) e^{2i\mathbf{k}\cdot\mathbf{r}} d^3r \right|^2. \tag{A1}$$

This integral can be written in a cylindrical system of coordinates, i.e.,

$$\sigma_b(\mathbf{k}) = \frac{k^4}{4\pi^2} \left| \int \gamma_z(r,\theta,z) e^{2i(k_r r \cos\theta + k_z z)} r dr d\theta dz \right|^2. \tag{A2}$$

The symmetries of the acoustical impedance allow to simplify Eq. (A2) to

$$\begin{aligned}\sigma_b(\mathbf{k}) &= \frac{k^4}{4\pi^2} \langle \gamma_z \rangle^2 \left| \int r \mathbf{I}_{[|z|<z_0(r)]} e^{2i(k_r r \cos\theta + k_z z)} dr d\theta dz \right|^2 \\ &= \frac{k^4}{4\pi^2} \langle \gamma_z \rangle^2 \left| \int r dr \int dz \mathbf{I}_{[|z|<z_0(r)]} e^{2ik_z z} \right. \\ &\quad \left. \times \int_{-\pi}^{\pi} d\theta e^{2ik_r r \cos\theta} \right|^2. \end{aligned} \tag{A3}$$

Now, the equality

$$J_0(x) = \frac{1}{2\pi} \int_{-\pi}^{\pi} e^{ix\cos\theta} d\theta \tag{A4}$$

is used to compute the integral in θ:

$$\sigma_b(\mathbf{k}) = k^4 \langle \gamma_z \rangle^2 \left| \int J_0(2k_r r) r dr \int \mathbf{I}_{[|z|<z_0(r)]} e^{2ik_z z} dz \right|^2. \tag{A5}$$

As

$$\int \mathbf{I}_{[|z|<x]} e^{2iuz} dz = 2x \,\mathrm{sinc}(2ux), \tag{A6}$$

where sinc represents the sinus cardinal function, then Eq. (A5) can be simplified to:

$$\sigma_b(\mathbf{k}) = 4k^4 \langle \gamma_z \rangle^2 \left| \int r J_0(2k_r r) z_0(r) \mathrm{sinc}(2k_z z_0(r)) dr \right|^2. \tag{A7}$$

As the form factor $F(\mathbf{k})$, given in Eq. (4), is defined by the formula:

$$\sigma_b(\mathbf{k}) = \frac{k^4 V_s^2}{4\pi^2} \langle \gamma_z \rangle^2 F(\mathbf{k}), \tag{A8}$$

then the comparison of Eq. (A7) with Eq. (A8) gives

$$F(\mathbf{k}) = \frac{16\pi^2}{V_s^2} \left| \int r J_0(2k_r r) z_0(r) \mathrm{sinc}(2k_z z_0(r)) dr \right|^2. \tag{A9}$$

To further simplify, let the volume of the scatterer be written as

$$V_s = \int r \mathbf{I}_{[|z|<z_0(r)]} dr d\theta dz = 4\pi \int z_0(r) r dr. \tag{A10}$$

This results in the following expression of the form factor:

$$F(k_r\mathbf{e}_r,k_z\mathbf{e}_z)=\left|\frac{\int rJ_0(2k_r r)z_0(r)\mathrm{sinc}(2k_z z_0(r))dr}{\int rz_0(r)dr}\right|^2. \quad \text{(A11)}$$

Finally, to obtain a normalized expression of $F(\mathbf{k})$, it can be recalled from Eq. (6) that $z_0(r)=h_0\phi(u)/2$, where $u=2r/D$. By rearranging Eq. (A11), the expected formula of the form factor given in Eq. (7) is obtained:

$$F(k_r\mathbf{e}_r,k_z\mathbf{e}_z)=\left|\frac{\int_0^1 u\phi(u)J_0(k_r Du)\mathrm{sinc}(k_z h_0\phi(u))du}{\int_0^1 u\phi(u)du}\right|^2. \quad \text{(A12)}$$

APPENDIX B

The second order expansion of the form factor of an homogeneous scatterer of volume V_s centered in O takes the form $F(\mathbf{k})=1-4\mathbf{k}\cdot\boldsymbol{\Sigma}\mathbf{k}+O(k^2a^2)$. This appendix proves that:

$$\boldsymbol{\Sigma}=\frac{1}{V_s}\int_{V_s}\mathbf{r}\otimes\mathbf{r}d^3r. \quad \text{(B1)}$$

Let's consider the Born approximation of the backscattering cross section, as given by Eq. (A1):

$$\sigma_b(\mathbf{k})=\frac{k^4}{4\pi^2}\left|\int_{V_s}\gamma_z(\mathbf{r})e^{2i\mathbf{k}\cdot\mathbf{r}}d^3r\right|^2. \quad \text{(B2)}$$

As $e^x=1+x+x^2/2+\cdots$, the second order expansion in $\mathbf{k}$ of Eq. (B2) is

$$\sigma_b(\mathbf{k})=\frac{k^4}{4\pi^2}\left|\int_{V_s}\gamma_z(r)(1+2i\mathbf{k}\cdot\mathbf{r}-2(\mathbf{k}\cdot\mathbf{r})^2+\cdots)d^3r\right|^2. \quad \text{(B3)}$$

By definition of the dyadic product,

$$(\mathbf{k}\cdot\mathbf{r})^2=\mathbf{k}(\mathbf{r}\otimes\mathbf{r})\mathbf{k}. \quad \text{(B4)}$$

As the scatterer is homogeneous and centered in O:

$$\int_{V_s}\gamma_z(\mathbf{r})\mathbf{r}d^3r=\langle\gamma_z\rangle\int_{V_s}\mathbf{r}d^3r=0. \quad \text{(B5)}$$

Consequently, combining Eqs. (B3)–(B5), and using $\gamma_z(\mathbf{r})=\langle\gamma_z\rangle\mathbf{I}_{[r\in V_s]}$, one obtains:

$$\sigma_b(\mathbf{k})=\frac{k^4}{4\pi^2}\langle\gamma_z\rangle^2\left|\int_{V_s}d^3r-2\mathbf{k}\cdot\left(\int_{V_s}\mathbf{r}\otimes\mathbf{r}d^3r\right)\mathbf{k}+\cdots\right|^2, \quad \text{(B6)}$$

or

$$\sigma_b(\mathbf{k})=\frac{k^4}{4\pi^2}\langle\gamma_z\rangle^2V_s^2\left(1-4\mathbf{k}\cdot\left(\frac{1}{V_s}\int_{V_s}\mathbf{r}\otimes\mathbf{r}d^3r\right)\mathbf{k}+\cdots\right). \quad \text{(B7)}$$

The comparison of Eq. (B7) to the definition of Eq. (4) of the form factor $F(\mathbf{k})$ yields the expected result:

$$F(\mathbf{k})=1-4\mathbf{k}\cdot\left(\frac{1}{V_s}\int_{V_s}\mathbf{r}\otimes\mathbf{r}d^3r\right)\mathbf{k}+\cdots. \quad \text{(B8)}$$

[1] M. F. Insana and D. G. Brown, "Acoustic scattering theory applied to soft biological tissues," in *Ultrasonic Scattering in Biological Tissues*, 1st ed., edited by K. K. Shung and G. A. Thieme (CRC Press, Boca Raton, FL, 1993), Chap. 4, pp. 75–124.

[2] F. L. Lizzi, M. Ostromogilsky, E. J. Feleppa, M. C. Rorke, and M. M. Yaremko, "Relationship of ultrasonic spectral parameters to features of tissue microstructure," IEEE Trans. Ultrason. Ferroelectr. Freq. Control **34**, 319–329 (1987).

[3] A. A. Aiazian, M. A. Taams, F. J. Ten Cate, and J. R. T. C. Roelandt, "Spontaneous echocontrast: Etiology, technology dependence and clinical implications," in *Advances in Echo Imaging Using Contrast Enhancement*, 2nd Ed., edited by N. C. Nanda, R. Schlief, and B. B. Goldberg (Kluwer Academic, Dordrecht, Boston, 1997), Chap. 4, pp. 65–83.

[4] I. W. Black, "Spontaneous echo contrast: where there's smoke there's fire (review)," Echocardiogr. **17**, 373–382 (2000).

[5] K. K. Shung and G. A. Thieme, *Ultrasonic Scattering in Biological Tissues*, 1st ed., edited by K. K. Shung and G. A. Thieme (CRC Press, Boca Raton, FL, 1993).

[6] A. Ishimaru, "Scattering and absorption of a wave by a single particle," in *Wave Propagation and Scattering in Random Media*, 1st ed., edited by A. Ishimaru (Academic, New York, 1978), Vols. **1** and **2**, pp. 9–27.

[7] T. K. Stanton, D. Chu, P. H. Wiebe, and C. S. Clay, "Average echoes from randomly oriented random-length finite cylinders: Zooplankton models," J. Acoust. Soc. Am. **94**, 3463–3472 (1993).

[8] I. Y. Kuo and K. K. Shung, "High frequency ultrasonic backscatter from erythrocyte suspension," IEEE Trans. Biomed. Eng. **41**, 29–34 (1994).

[9] C. C. Coussios, "The significance of shape and orientation in single-particle weak-scatterer models," J. Acoust. Soc. Am. **112**, 906–915 (2002).

[10] P. M. Morse and K. U. Ingard, "The scattering of sound," in *Theoretical Acoustics*, 1st ed., edited by P. M. Morse and K. U. Ingard (Mc-Graw-Hill, New York, 1968), Vol. **8**, pp. 400–446.

[11] D. Colton, J. Coyle, and P. Monk, "Recent developments in inverse acoustic scattering theory," SIAM Rev. **42**, 369–414 (2000).

[12] J. J. Bowman, T. B. A. Senior, and P. L. E. Uslenghi, *Electromagnetic and Acoustic Scattering by Simple Shapes* (North-Holland, Amsterdam, 1969).

[13] E. Evans and Y. C. Fung, "Improved measurements of the erythrocyte geometry," Microvasc. Res. **4**, 335–347 (1972).

[14] A. Rao, *Dynamics of Particles and Rigid Bodies* (Cambridge University Press, Cambridge, U.K., 2006).

[15] K. K. Shung, R. A. Sigelmann, and J. M. Reid, "Scattering of ultrasound by blood," IEEE Trans. Biomed. Eng. **23**(6), 460–467 (1976).

[16] C. C. Coussios, "Monitoring of hemolysis by acoustic scattering," Ph.D. Thesis, University of Cambridge, Cambridge, U.K., 2001.

[17] R. A. Roy, "Quantitative particle characterization by scattered ultrasound," Ph.D. Thesis, Yale University, 1987.

[18] V. C. Anderson, "Sound scattering from a fluid sphere," J. Acoust. Soc. Am. **22**, 426–431 (1950).

[19] A. Guinier and J. Fournet, *Small Angle Scattering of X-rays* (Wiley Interscience, New York, 1955).

[20] I. Fontaine, D. Savéry, and G. Cloutier, "Simulation of ultrasound backscattering by red cell aggregates: Effect of shear rate and anisotropy," Biophys. J. **82**, 1696–1710 (2002).

[21] D. Savéry and G. Cloutier, "A point process approach to assess the frequency dependence of ultrasound backscattering by aggregating red blood cells," J. Acoust. Soc. Am. **110**, 3252–3262 (2001).

[22] K. K. Shung and J. M. Reid, "Ultrasonic instrumentation for hematology," Ultrason. Imaging **1**, 280–294 (1979).